XII ICG

Geosynthetics

Leading the Way to a Resilient Planet

Edited by

Giovanni Biondi
Daniele Cazzuffi
Nicola Moraci
Claudio Soccodato

CRC Press
Taylor & Francis Group

GEOSYNTHETICS: LEADING THE WAY TO A RESILIENT PLANET

This volume contains the proceedings of the 12th International Conference on Geosynthetics (12 ICG), held in Roma, Italy, 17–21 September 2023. About 750 Authors – Academics, Researchers, Students, Practitioners, Contractors and Manufacturers – contributed to the peer-reviewed papers of this volume, which includes the Giroud lecture, the Bathurst lecture, the Rowe lecture, four keynote lectures and 296 technical papers. The content of these proceedings illustrates the sustainable use of geosynthetics in a variety of innovative as well as consolidated applications. After the sustainability implications in the correct use of geosynthetics, the ability to overcome the natural events effects, often related to the climate change, and to adequately afford the human activities (as the increase of pollution) forced to refer to a new keyword: Resiliency.

Hence the 12 ICG intends to become the base for the next step, therefore the conference theme is "Geosynthetics, Leading the Way to a Resilient Planet".

The conference topics, through general and parallel sessions, invited presentations and keynote lectures, address the most recent developments in geosynthetic engineering, and stimulate fruitful technical and scientific interaction among academicians, professionals, manufacturers, students.

The 12 ICG proceedings contain a wealth of information that could be useful for researchers, practitioners and all those working in the broad, innovative and dynamic field of geosynthetics.

Geosynthetics: Leading the Way to a Resilient Planet

Edited by

Giovanni Biondi
University of Messina, Italy

Daniele Cazzuffi
CESI SpA Milano, Italy

Nicola Moraci
Mediterranea University of Reggio Calabria, Italy

Claudio Soccodato
Italian Geotechnical Society, AGI, Roma, Italy

Table of Contents

Geosynthetics properties and testing

Soil-geosynthetic interaction

Durability and long term performance

Reinforced walls and slopes

Seismic design with geosynthetics

Unpaved and paved roads

Railways and other transportation applications

Landfills and remediation of contaminated sites

Innovative materials and technologies

Design approaches and other applications

Case histories

IGS technical committee on 'soil reinforcement' – special session on "Design methods for basal reinforcement of embankments"

Young member contest

Preface

This volume contains the contributions to the 12th International Conference on Geosynthetics – "Geosynthetics: leading the way to a resilient planet" – held in Roma (Italy) from September 17th to 21st, 2023.

Years after the successful EuroGeo 2, which was held in Bologna (Italy) in October 2000, the geosynthetics and geotechnical engineering community has reached full awareness over the last two decades, and the whole geosynthetics industry has focused on the sustainable use of geosynthetics in a variety of innovative as well as consolidated applications. After the sustainability implications in the correct use of geosynthetics, the ability to overcome the natural events effects, often related to the climate change, and to adequately afford the human activities (as the increase of pollution) forced to refer to a new keyword: Resiliency.

Hence the 12ICG intends to become the base for the next step therefore the conference theme is

GEOSYNTHETICS, LEADING THE WAY TO A RESILIENT PLANET

The conference topics will address, through general and parallel sessions, invited presentations and keynote lectures, the most recent developments in geosynthetic engineering, stimulating fruitful technical and scientific interaction among academicians, professionals, manufacturers and students.

We believe that the 12 ICG will provide an excellent opportunity to present recent experiences and developments to an audience of engineers, geologists and consultants, public and private contractors, local, national and international authorities, and to all those involved in research and practice related to geosynthetics.

The ICG conferences have always provided a unique and fruitful forum for the exchange of new ideas and discussion on key issues within the largest gathering of world's experts, academics and non-academics, working in the broad, innovative and dynamic area of geosynthetics.

About 750 Authors, coming from academic institutions, private companies and public bodies worldwide, contributed to the peer-reviewed papers included in this volume. The Scientific Committee was especially pleased with the general high quality of the papers.

A total of 296 manuscripts were finally accepted for publication in the Conference Proceedings. The papers were sorted into 19 topic categories, according to the subject areas typically addressed in ICG events:

- Sustainability with Geosynthetics
- Geosynthetics Properties and Testing
- Soil-Geosynthetic Interaction
- Durability and Long-Term Performance
- Reinforced Walls and Slopes
- Basal reinforced Embankments, GEC, piles and shallow foundations
- Seismic design with geosynthetics
- Unpaved and paved roads
- Railways and other Transportation Applications
- Landfills and remediation of contaminated sites
- Filtration and Drainage

- Hydraulic applications: canals, reservoirs and dams
- Innovative materials and technologies
- Design approaches and other applications
- Case Histories

The proceedings also include the Giroud lecture, the Bathurst lecture, the Rowe lecture and four outstanding keynote lectures presented by renowned experts on selected key topics.

A significant effort was made to provide the Authors with a rigorous and fair review of the papers. The Editors are therefore very grateful to the numerous assessors and reviewers, for their generous and valuable work.

We gratefully acknowledge the support of the Italian Geotechnical Society (AGI) and to the Italian Chapter of IGS (AGI-IGS), which organized the Conference. We would also like to express our appreciation to all the Sponsors that helped us in making this conference a success.

Many thanks to all Keynote Lecturers, Invited Speakers and Authors for their enthusiastic and proactive response to 12 ICG, and for their contribution to this Proceedings volume.

Finally, sincere thanks to Susanna Antonielli for her long-term dedication and tireless efforts towards the correct organization of this volume of proceedings and also to the success of the overall conference aspects.

We do hope you will find its content of valuable and long lasting use.

Giovanni Biondi
Daniele Cazzuffi
Nicola Moraci
Claudio Soccodato

Conference Organizers

Italian Geotechnical Society (AGI) – Italian Chapter of IGS (AGI-IGS)

With the endorsement of

International Geosynthetics Society

International Society for Soil Mechanics and Geotechnical Engineering

Federation of International Geo-Engineering Societies

Committees

Organizing Committee

Chairs

Daniele **Cazzuffi**
Nicola **Moraci**

AGI Staff

Sebastiano **Rampello** (AGI President)
Claudio **Soccodato** (AGI Secretary General)
Susanna **Antonielli** (AGI Secretariat)

Board members

Giovanni **Biondi** (Chair of the Scientific Committee)
Giuseppe **Cardile** (Chair of the Public Relation Committee)
Pierpaolo **Fantini** (Chair of the Sponsorship & Exhibition Committee)
Francesco **Fontana** (Chair of the Special Event Organization Committee)
Stefania **Bilardi**
Marilene **Pisano**
Piergiorgio **Recalcati**
Filippo **Soccodato**

Other members

Riccardo **Berardi**
Andrea **Bodigoi**
Anna **Bortolussi**
Nicola **Brusa**
Lidia Sarah **Calvarano**
Laura **Carbone**
Paolo **Carrubba**
Francesco **Castelli**
Massimo **Cunegatti**
Sabatino **Cuomo**
Claudio **di Prisco**
Evelina **Fratalocchi**
Andrea **Galli**
Domenico **Gioffrè**
Guido **Gottardi**
Nicolò **Guarena**

Matteo **Iegre**
Giulia **Lugli**
Mario **Manassero**
Maria Clorinda **Mandaglio**
Viviana **Mangraviti**
Luca **Masini**
Lorella **Montrasio**
Quintilio **Napoleoni**
Paolo **Pavanello**
Pietro **Pezzano**
Mauro **Redemagni**
Angelo **Ricciuti**
Pietro **Rimoldi**
Ugo **Stefani**
Marco **Viganò**

Advisory Committee

Promotion Committee

Dimiter **Alexiev** (Germany)
Augusto **Alza** (Peru)
Peter **Atchison** (UK)
Fatma **Baligh** (Egypt)
Adam **Bezuijen** (The Netherlands)
Eric **Blond** (Canada)
Richard **Brachmann** (Canada)
Gerhard **Braeu** (Germany)
Laura **Carbone** (Germany)
Giuseppe **Cardile** (Italy)
Barry **Christopher** (USA)
Steve **Corbet** (UK)
Jacques **Coté** (Canada)
John **Cowland** (Hong Kong)
Sabatino **Cuomo** (Italy)
Philippe **Delmas** (France)
Claudio **di Prisco** (Italy)
Neil **Dixon** (UK)
Houssine **Ejjaaouani** (Maroc)
Pierpaolo **Fantini** (Italy)
Valentin **Feodorov** (Romania)
Francesco **Fontana** (Italy)
Patrick J. **Fox** (USA)
Ian **Fraser** (UK)
Antonio **Gomes Correia** (Portugal)
J.P. **Gourc** (France)
Jie **Han** (USA)
Véronique **Heili** (France)
Bob **Holtz** (USA)
Warren **Hornsey** (Australia)
Chiwan **Hsieh** (Taiwan)
Grace **Hsuan** (USA)
Han-Yong **Jeon** (Korea)
Takeshi **Katsumi** (Japan)
Jacek **Kawalec** (Poland)
Preston **Kendall** (Australia)
Hong Kwan **Kim** (Korea)
Anastasios **Kollios** (Greece)
Marines **Lagemaat** (Belgium)
Gali Madhavi **Latha** (India)
Chris **Lawson** (Malaysia)
Angel **Leiro** (Spain)
Dov **Leshchinsky** (USA)
Imad **Lifa** (Switzerland)
Robert **Lozano** (USA)
Radoslaw **Michalowski** (USA)
Yoshihisa **Miyata** (Japan)

Mikael **Moeller** (Denmark)
Flavio **Montez** (Brazil)
Jun **Otani** (Japan)
Elizabeth **Peggs** (USA)
Andrei **Petriaev** (Russia)
K. **Rajagopal** (India)
Boyd J. **Ramsey** (USA)
Piergiorgio **Recalcati** (Italy)
Jan **Retzlaff** (Germany)
Pietro **Rimoldi** (Italy)
Sanjay Kumar **Shukla** (Australia)
Eun-Chul **Shin** (Korea)
Derek **Smith** (UK)
Ugo **Stefani** (Italy)
Gholamhosein **Tavakoli Mehrjardi** (Iran)
Erol **Tutumluer** (USA)
Ivan **Vanicek** (Czech Republic)
M. **Venkataram** (India)
Delma **Vidal** (Brazil)
Kent **von Maubeuge** (Germany)
Wim **Voskamp** (The Netherlands)
Arnstein **Watn** (Norway)
Yang **Yaolin** (China)
Edoardo **Zannoni** (South Africa)
Helmut **Zanzinger** (Germany)
Askar **Zhussupbekov** (Kazakhstan)

Scientific Committee

EDITORS

Giovanni Biondi
Daniele Cazzuffi
Nicola Moraci
Claudio Soccodato

ASSESSORS

Riccardo Berardi
Laura Carbone
Giuseppe Cardile
Paolo Carrubba
Francesco Castelli
Sabatino Cuomo
Claudio di Prisco
Evelina Fratalocchi
Andrea Galli
Domenico Gioffrè
Guido Gottardi
Maria Clorinda Mandaglio
Luca Masini
Lorella Montrasio
Paolo Pavanello
Marilene Pisano
Sebastiano Rampello
Piergiorgio Recalcati
Pietro Rimoldi

REVIEWERS

Peter	Atchison	UK
Madalena	Barroso	Portugal
Adam	Bezuijen	Belgium
Stefania	Bilardi	Italy
Eric	Blond	Canada
Orazio	Casablanca	Italy
Barry	Christopher	USA
Steve	Corbet	UK
Matteo	Corigliano	Italy
Giampaolo	Cortellazzo	Italy
Philippe	Delmas	France
Gemmina	Di Emidio	Belgium

Giuseppe	Di Filippo	Italy
Jelke	Dijkstra	The Netherlands
Andrea	Dominijanni	Italy
Kazem	Fakharian	Iran
Marco	Favaretti	Italy
Luca	Flessati	Italy
Ian	Fraser	UK
Michele	Gatto	Italy
Domenico	Gaudio	Italy
Daniela	Giretti	Italy
Nicolò	Guarena	Italy
Jie	Han	Usa
Nader	Hataf	Iran
Ivo	Herle	Czech Republic
Chiwan	Hsieh	Taiwan
Grace	Hsuan	USA
Han-Yong	Jeon	Korea
Takeshi	Katsumi	Japan
Hong Kwan	Kim	Korea
Anastasios	Kollios	Greece
Jiro	Kuwano	Japan
Gali Madhavi	Latha	India
Valentina	Lentini	Italy
Dov	Leshchinsky	USA
Imad	Lifa	Switzerland
Bal Krishna	Maheshwari	India
Viviana	Mangraviti	Italy
Dawie	Marx	USA
Luca	Masini	Italy
Francesco	Mazzieri	Italy
Alberto	Mazzucato	Italy
Salvatore	Misiano	Italy
Mikael	Moeller	Denmark
Arash	Nayeri	Iran
Ernest	Olinic	Romania
Jun	Otani	Japan
Ivan	Puig Damians	Spain
Anand J.	Puppala	USA
Roberto	Raga	Italy
Mizanur	Rahman	Australia
Karpurapu	Rajagopal	India
Boyd	Ramsey	USA
Jonathan	Schamrock	New Zeland
Amir	Shahkolahi	Australia
Sanjay Kumar	Shukla	Australia
Derek	Smith	UK
Castorina	Vieira	Portugal
Arnstein	Watn	Norway
Hiroshi	Yokawa	Japan
Kasia	Zamara	Poland
Helmut	Zanzinger	Germany
Yewei	Zheng	China
Askar	Zhussupbekov	Kazakhstan

Invited lectures

Geotextile filters: From idealization to real behaviour (Giroud lecture)

E.M. Palmeira
University of Brasília, Brasília, Brazil

ABSTRACT: Geotextiles have been used as filters in geotechnical and geoenvironmental works for decades. Despite their broad utilization, these filters still find obstacles to the expansion of their application in larger projects and under complex soil and flow conditions. However, environmental issues are increasingly pressing for a greater use of geotextile filters in substitution to natural granular materials. Even though many important studies in the literature have improved the understanding of soil-fluid-geotextile filter interaction, some issues still require thorough investigation aiming at a better understanding of the behaviour of geotextile filters and the development of better design methodologies. This paper discusses how geotextiles filters are expected to behave in the field and some contradictions between idealized and expected behaviour. Concerns regarding the use of geotextile filters under severe and critical conditions and how filter malfunction can be avoided or minimised are also addressed.

1 INTRODUCTION

Geotextiles have been used extensively as filters in geotechnical and geoenvironmental works for over five decades. The main reasons for the increasing use of these materials are the ease of transportation and installation, reduction or non-use of natural materials, consistency and repeatability of relevant properties and cost-effectiveness. More recently, an additional increasingly important benefit of the use of geotextile filters as substitutes for granular filters is the less environmental impacts caused by the former. Frischknecht *et al.* (2012) report that a geotextile filter can reduce important environmental impact parameters (greenhouse gas emissions, consumption of renewable and non-renewable energy, consumption of water etc.) by over 80% in comparison to sand filters. However, despite the huge success of geotextile filters, some issues remain regarding their actual behaviour in a geotechnical work and on how accurate current design and specification methods are. Failures of geotextile filters have been reported (Koerner & Koerner 2015) and, although representing a very small fraction of the use of such filters, the consequences of such failures can be very important.

For a significant fraction of designers and users, the substitution of a granular filter by a geotextile counterpart looks so natural and easy that important aspects for filter performance may be commonly overlooked. The general idea of a geotextile filter application is schematically shown in Figure 1a, where the geotextile will substitute the entire granular transition zone between the base soil and the coarser drainage layer. However, in most situation the expected conditions under which the geotextile filter will function are actually those shown in Figure 1b. Depending on the application, in the field the geotextile may be subjected to compression, tension, shear and impregnation by degradable or non-degradable solids. These conditions will influence the filter performance in a very complex way.

A huge number of examples of successful applications of geotextile filters can be found in the literature. Wilson-Fahmy *et al.* (1996) conducted a comprehensive study on the performance of geotextile filters of highway edge drains and some retaining walls and erosion

control systems. The sampling of specimens from the case histories investigated was not based on a random collection of sites, but on specific sites where there was suspicion of drainage system malfunction. Hence, a number of nonacceptable performance should be expected. Despite this biased selection, 77% of the filters presented acceptable performance. In another study involving the investigation of 91 case-histories, Koerner *et al.* (1994) concluded that if construction and maintenance related problems were eliminated, only 4 (4.4%) out of the 91 case-histories investigated would be considered nonacceptable situations, which is considered an excellent performance record. Lopes *et al.* (1991) and Morilha Jr. *et al.* (1994) also report the exhumation of geotextile filters over 10 years old from 6 highway drains suspected of malfunctioning in the state of Paraná, Brazil. No clogging nor degradation was observed in the geotextile filters and the apparent poor performance of the drains was a consequence of poor construction practice, improper location of the drain, drain outlet blocking or preferential flow of water through more permeable soil layers not intercepted by the drainage trenches. Lopes *et al.* (1991) and Morilha Jr. *et al.* (1994) also report the good performance of a geotextile filter in a road edge drain where partial clogging was observed in a conventional French drain. Despite these examples of successful performance of geotextile filters, some problems have been identified. An important analysis on unsatisfactory performance of such filters is presented by Koerner & Koerner (2015), where poor behaviour or failures have been caused by inadequate design, presence of atypical soils, unusual permeants and improper installation, corroborating what was found by the authors mentioned above. In addition, Koerner & Koerner stress that most of the conditions where geotextile filters failed are also known to be troublesome for sand filters.
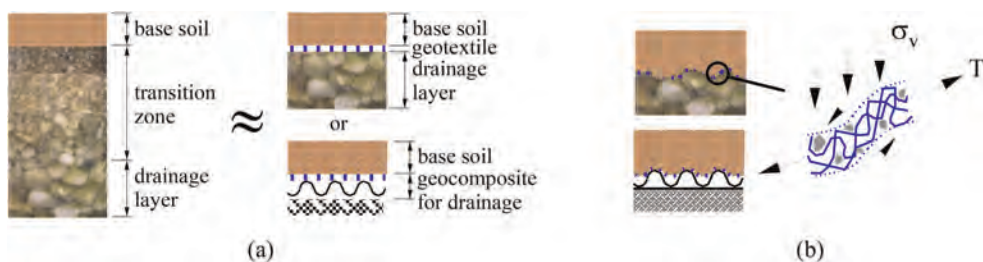
Figure 1. Granular *vs.* geotextile filter. (a) Idealization; (b) Actual working condition of a nonwoven geotextile.

Geotextile filters must attend retention, permeability and anti-clogging criteria for proper performance. In addition, they have also to present suitable mechanical properties and resistance to degradation to withstand mechanical solicitations during installation and construction, as well to guarantee a satisfactory service life. The behaviour of geotextile filters has been investigated by many researchers under laboratory conditions, not rarely under conditions significantly more severe than those expected in the field. Very simple to quite complex testing techniques and methodologies can be found for the determination of important geotextile filter properties or to predict filter performance. However, unfortunately, all of them have limitations to model real filter in-service conditions. This is particularly so in situations where the filter will be in contact with problematic soils (internally unstable soils, for instance) or permeants (leachate, for instance). In addition, nonwoven geotextiles are highly compressible materials that in the great majority of the situations will work under confined conditions but may also function under tension. Besides, they can be impregnated by base soil particles during construction, which will influence its compressibility and clogging potential (Figure 1b). Thus, when the fluid reaches the filter the conditions of the latter may be quite different from those assumed in design and in current

standard laboratory tests. Conservative approaches have been the practice in these cases, although conservatism may not necessarily result in a problem free design since some uncertainties on how the filter will actually behave may remain.

The studies described above are just very few examples of the good performance of geotextile filters in general, but also raises important questions to be addressed to avoid unsatisfactory performance. Thus, it is of special concern the behaviour of filters under severe and critical conditions that may lead to filter (granular or geotextile) failure, being of utmost importance to identify such conditions in order to avoid or minimise the detrimental consequences of filter poor performance and/or to establish in advance appropriate monitoring and maintenance practices throughout the structure service life. So, this paper presents and discusses factors affecting the behaviour of geotextile filters, particularly under severe conditions of utilization, as well as how these factors can be considered in design.

2 PHYSICAL FACTORS INFLUENCING GEOTEXTILE FILTER BEHAVIOUR

2.1 *Geotextile impregnation by base soil particles*

The behaviour of nonwoven geotextile filters can be influenced by confinement and the presence of soil particles entrapped in its matrix. This particle entrapment can occur during placement and compaction of soil on the geotextile layer or due to the retention of particles brought to the filter by the action of seepage forces. The intensity of the impregnation can be quite significant (Lawson 1990, Qureshi *et al.* 1990, Palmeira *et al.* 1996, Palmeira & Gardoni 2000, Legge 2004), depending on the base soil and geotextile characteristics. These particles in the geotextile voids can reduce geotextile compressibility, geotextile permeability and the conditions for further internal clogging since their presence changes the available openings in the filter. Large soil particles can intrude the geotextile voids during spreading and base soil compaction, as shown in Figure 2 (Gardoni 2000, Palmeira & Gardoni 2000, Palmeira *et al.* 2010). Similar large, entrapped soil particles were observed by Niec *et al.* (2019) in geotextile specimens exhumed from a small dam in Poland. Impregnation of the geotextile can also occur in the laboratory in tests such as the gradient ratio test (*GRT*), particularly when vibration is used to compact a cohesionless fine grained base soil. The level of particle entrapment can be assessed by the impregnation level (λ) of the geotextile, defined as the ratio between the mass of entrapped soil particles and the mass of fibres of the geotextile (Palmeira *et al.* 1996). Impregnation of the filter by base soil particles may be relevant for base soils consisting of cohesionless fine grained materials and dispersive clays. Table 1 presents some ranges of variation of λ values obtained in laboratory and field studies. It should be noted that the value of λ and the geotextile void occupancy by soil particles depend on the density of the fibres of the geotextile.
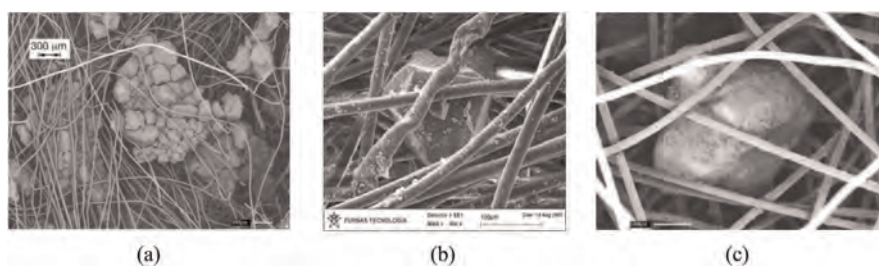
Figure 2. Example of entrapped soil particles inside geotextile voids. (a) Cluster of particles in a geotextile specimen exhumed from a road drainage trench (Palmeira & Gardoni 2000), (b) Particle in an exhumed tailings dam filter (Palmeira *et al.* 2010), (c) Large entrapped soil particle in a geotextile exhumed from a road drainage trench (Gardoni 2000).

Significant reductions in the permeability coefficient of systems consisting of internally unstable soils and nonwoven geotextiles were observed by Qureshi *et al.* (1990) and the results suggest that these permeability reductions were caused by significant impregnation of the geotextile voids by base soil particles. Similar detrimental influence of soil impregnation in the soil-geotextile system permeability coefficient was observed by Lawson (1990), where the data available suggest values of impregnation level (λ) of the order of 8. Values of up to 15 were observed under laboratory conditions (Palmeira & Gardoni 2000). Table 1 also shows significant values of λ for geotextile specimens exhumed from field tests and real works.

A maximum value of λ considering a mass of soil particles (smaller than the geotextile voids) uniformly distributed inside the geotextile can be estimated by

$$\lambda_{\max} = \frac{\rho_s}{\rho_f}(1 - n_s)\left(\frac{n}{1-n}\right) \tag{1}$$

Table 1. Typical values of λ for nonwoven needle-punched geotextiles.

Source	Geotextile property value or range tested[(*)]		Soil Type*	Impregnation mechanism**	λ value or range*,***
	M_A (g/m²)	*FOS* (mm)			
Lawson (1990)	580	0.04	Loess soil	S/L	8
Palmeira *et al.* (1996), Gardoni (2000), Palmeira & Gardoni (2000), Palmeira *et al.* (2005), Zaman *et al.* (2022)	140–600	0.06–0.14	GB, sands, silty sands	C/S/L	0.23–15
Faure *et al.* (1999)****	468–603	0.072	Sandy silt	C/S/F	1.4–9.1
Gardoni (2000)	200–600	0.06–0.13	Sands	C/F	0.30–5.46
			Clay	C/L	0.06–0.88
			Clay	C/F	0.37–0.52
Palmeira & Gardoni (2000)	200–600	0.13	Clay	C/F	0.06, 0.70
Palmeira *et al.* (2005)	150–600	0.06–0.15	Tailings	C/S/L	0.24–1.27
Palmeira *et al.* (2010)	400	0.09–0.16	Tailings	C/S/F	2–10
Moraci *et al.* (2016)	151.1	0.268	Silty clay	C/S/F	1.7–2.4
Niec *et al.* (2019)	277	0.125	Sands	C/S/F	0.7–2.5
Kim *et al.* (2020a)	420	0.125	Soil in suspension	S/L	0.1–1.5
Liu *et al.* (2021b)	200	0.099	Tailings (silt)	S/L	4.93
Khan *et al.* (2022)	120–1200	0.060–0.12	Sands, PFA	S/L*****	0.30–1.79
Du *et al.* (2022)	125–400	0.066–0.17	Silty clay, silt	C/S/L	1.02–5.66
Markiewicz *et al.* (2022)	450	NA	Silty sand	C/S/F	0.88

*M_A = geotextile mass per unit area, *FOS* = geotextile filtration opening size (O$_{95}$, O$_{90}$ or AOS, Apparent Opening Size, depending on the source), *GB* = glass beads, *NA* = not available, *PFA* = pulverised fuel ash mixture, λ = impregnation level, λ for tailings may be larger than for common soils depending on the particle density of the former, **Mechanism of impregnation: compaction (vibration etc., code C) and/or seepage (code S) under laboratory (code L) or field (code F) conditions,*** Some values were calculated based on data from tests reported by the sources, ****From Valcros Dam (Faure *et al.*, 1999) – geotextile porosity (n) assumed as 0.9 to estimate λ, *****Static and cyclic loadings.

where λ_{max} is the maximum value of λ, ρ_s is the density of the soil particles, ρ_f is the density of the geotextile fibres, n_s is the porosity of the mass of particles in the geotextile voids and n is the geotextile porosity not considering the presence of the entrapped particles.

For a mass of entrapped particles in a nonwoven polyester geotextile (ρ_f = 1380 kg/m³), with n = 0.92, n_s = 0.3 and ρ_s = 2650 kg/m³, equation 1 gives a value of λ_{max} of 15.5, which compares well with the maximum values of impregnation level for light geotextiles listed in Table 1. If all the geotextile voids are entirely occupied by a solid mass, which would be an extreme case of geotextile impregnation yielding to k_{GT} = 0, where k_{GT} is the geotextile permeability coefficient, equation 1 can still be used making n_s = 0.

With more data obtained from the sources listed in Table 1 (Palmeira 2023) it is possible to plot the variation of λ with the ratios O_{95}/d_{10} and O_{50}/d_{10} shown in Figure 3 for different soil conditions, where O_{95} is the geotextile filtration opening size (*AOS* in some cases) and d_{10} is the base soil particles for which 10% in mass is smaller. It should be acknowledged that significant deviations between values of geotextile opening sizes (O_{95}, *AOS*, O_{90} etc.) can be obtained, depending on the test method used (Bhatia & Smith 1996, Blond e al. 2015, Fatema & Bhatia 2019). However, satisfactory comparisons have been obtained by some authors regarding results from bubble point and hydrodynamic sieving tests (Vermeersch & Mlynarek 1996, Palmeira & Trejos-Galvis 2017). The results in Figure 3 show a large scatter for λ, which is certainly associated with different geotextile properties, soils, hydraulic conditions and impregnation mechanisms, and highlights the complexity of the problem. Greater scatter and no clear trend of λ variation can be observed for O_{95}/d_{10} between 0.5 and 30 and O_{50}/d_{10} between 0.6 and 20, but a trend of λ increasing with O_{95}/d_{10} and O_{50}/d_{10} can be noted in the case of internally unstable soils for values of those ratios greater than 40 and 20, respectively. Similar levels of scatter are observed if different O_{95}/d ratios are considered (using d_{15} or d_{50}, for instance). It is interesting to note values of λ of up to 15 for internally stable soils, up to 10 for internally unstable soils and up to 10 for specimens exhumed from the field. For clayey soils, a maximum value of λ equal to 4.7 was observed. Large values of λ for clayey soils are likely to be associated with dispersive clays or clusters of clay particles. A statistical evaluation of the results in Figure 3 shows that λ is greater than 2.5 in approximately 66% of the cases. As an example, for a value of λ equal to 2.4, normal permeability tests on a confined impregnated nonwoven geotextile showed reductions in the geotextile permeability coefficient between 40.2% and 50.0%, depending on the vertical stress considered (Palmeira & Gardoni 2000).
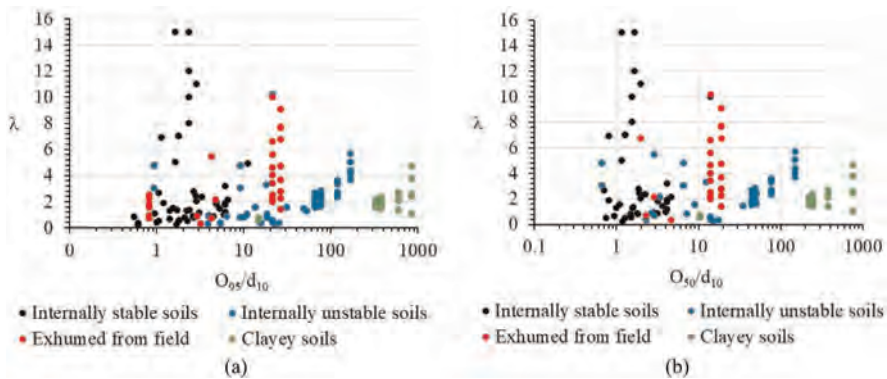
Figure 3. λ versus geotextile pore size: (a) λ vs. O_{95}/d_{10}, (b) λ vs. O_{50}/d_{10}. Data from sources listed in Table 1 (Palmeira 2023).

Giroud (1996) investigated the influence of impregnation on geotextile hydraulic properties and developed an equation to estimate the coefficient of permeability of impregnated

nonwoven geotextiles. Palmeira and Gardoni (2000) rewrote that equation as a function of the geotextile impregnation level (λ) yielding to

$$k_{G\sigma}^* = \frac{\beta \rho_w g \left[n - \lambda \cdot \frac{\rho_f}{\rho_s} \cdot (1 - n) \right]^3}{\eta_w \left(\frac{4}{d_f} + \lambda \frac{\rho_f}{\rho_s} \frac{6}{d_s} \right)^2 (1 - n)^2} \tag{2}$$

where β is a dimensionless shape factor which depends on the path followed by the fluid, ρ_w is the density of the fluid, g is the acceleration of gravity, η_w is the dynamic viscosity of the fluid, n is the porosity of the geotextile without considering the presence of the soil particles in the voids, λ is the geotextile impregnation level, ρ_f is the density of the geotextile fibres, ρ_s is the density of the soil particles, d_f is the fibre diameter and d_s is the average diameter of the soil particles inside the geotextile (see Palmeira & Gardoni 2000 for predictions of d_s).

Satisfactory comparisons between predictions by equation 2 and measurements of geotextile permeability coefficient were obtained by Palmeira and Gardoni (2000) with β equal to 0.11 and 0.14 for virgin ($\lambda = 0$) and partially clogged nonwoven geotextiles, respectively. Thus, using equation 2, a predicted reduction factor due to geotextile impregnation can be expressed as

$$RF_\lambda = \frac{k_{GT0}}{k_\lambda} \tag{3}$$

where RF_λ is the reduction factor for geotextile impregnation, k_{GTo} is the coefficient of permeability of the virgin (clean) unconfined geotextile and k_λ is the coefficient of permeability of the impregnated unconfined geotextile.

As an example of the influence of the impregnation of the geotextile by soil particles on its permeability coefficient, Figure 4 presents the predicted variation of RF_λ with λ for a nonwoven, needle-punched, geotextile with a mass per unit area of 200 g/m^2, porosity of 0.92, uniformly impregnated throughout its thickness of 1.9 mm. This figure shows that under these conditions a value of λ of 5 would result in a RF_λ of 8.6, already quite close to the usual value of 10 suggested by some permeability criteria. Geotextile compression due to confinement increases the complexity of the problem. However, if the geotextile rests on coarse drainage material (gravel, rock or a geocomposite drainage core), sagging of the geotextile in the voids of the drainage material will cause a non-uniform compression of the filter, and geotextile tension, ground vibration and seepage may remove some of the entrapped base soil particles, reducing the value λ to some extent.
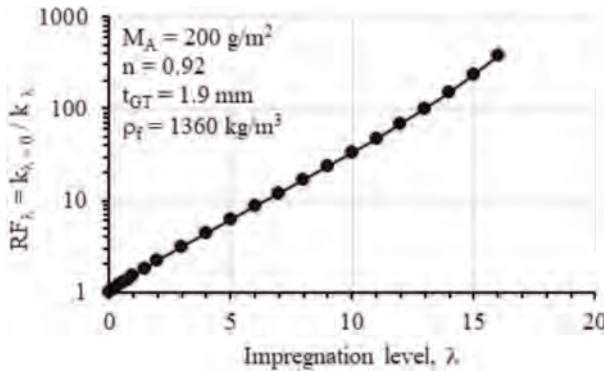
Figure 4.   Predicted reduction factor for geotextile permeability due to partial clogging.

Laboratory investigations have shown that uniform impregnation of the geotextile thickness by soil particles tends to occur for thin light nonwovens. The impregnation of thicker geotextiles tends to occur predominantly along a small fraction of the geotextile thickness at its face in contact with the base soil. In such cases, impregnation is likely to influence little geotextile compressibility. The results presented above show that some level of impregnation of a nonwoven geotextile filter soils should be considered in design.

2.2 Filters under confinement

Geotextile filters can be subjected to high compressive stresses in geotechnical works. By being compressible materials, confinement will influence filter performance, particularly in the case of nonwoven geotextiles. Figure 5 shows how significantly the pore dimensions of a nonwoven needle-punched geotextile can be affected by compressive stresses (Gardoni 2000, Gardoni & Palmeira 2002). Hence, compression will influence the retention capacity of the filter as well as conditions for potential clogging. These changes in the filter microstructure are difficult to predict and still not addressed by current filter criteria.
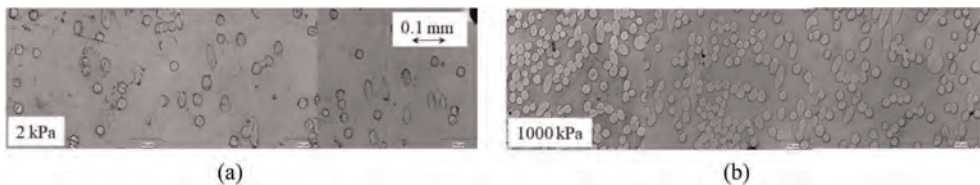
Figure 5. Effect of confining stress on a nonwoven geotextile (Gardoni 2000). (a) 2 kPa, (b) 1000 kPa.

Results from Bubble Point Tests (*BBP*) on compressed nonwoven, needle-punched, geo-textiles have shown significant reductions in the geotextile pore sizes relevant for filter design. Figure 6a depicts pore size distribution curves for a nonwoven, needle-punched, geotextile (mass per unit area, M_A, of 200 g/m^2) in tests under vertical stresses ranging from 0 to 1000 kPa (Palmeira 2020). Figure 6b presents the influence of confinement on different geotextile pore diameters. These results show that the conditions of a buried geotextile filter will be significantly different from those simulated in laboratory tests commonly carried out to determine geotextile pore size dimensions.
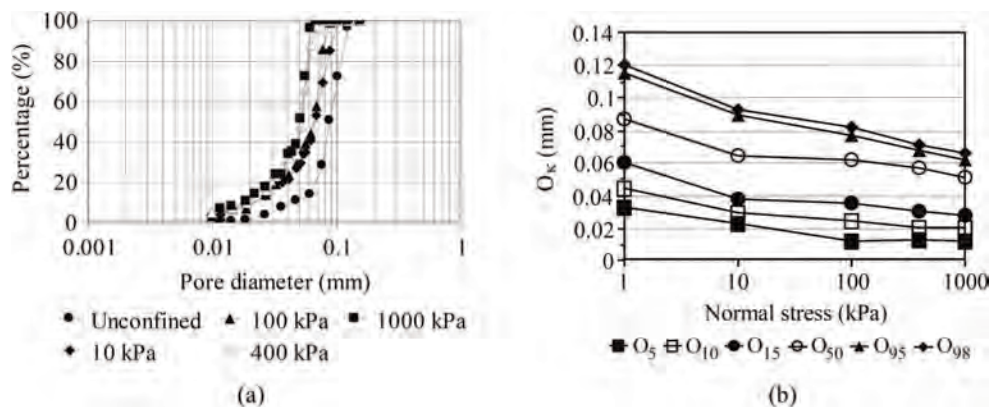
Figure 6. Influence of confinement on geotextile pore diameter (Palmeira 2020). (a) Pore size distribution curves for different confining stresses, (b) Geotextile pore diameter *vs.* confining stress.

The capability of a geotextile filter to retain a moving soil particle depends on the number of confrontations (m) the particle will have to face to cross the geotextile. Compression of the geotextile will also influence the number of confrontations, as it reduces the geotextile thickness. Palmeira & Trejos Galvis (2018) backanalysed the value of m using the equation proposed by Giroud (1996) for five nonwoven, needle-punched, geotextiles (M_A in the range 200 to 1800 g/m^2) and obtained the results shown in Figure 7. A linear relationship between m and the geotextile thickness (t_{GT}) normalised by the geotextile fibre diameter (d_f) can be observed for the products tested. Thus, thinner or compressed thicker geotextiles will present a smaller number of confrontations. For the products tested in Figure 7, the recommended minimum value of m of 30 (Giroud 1996) would be achieved for a t_{GT}/d_f ratio of approximately 110. The number of confrontations decreases with confinement. However, so do the geotextile pore sizes.
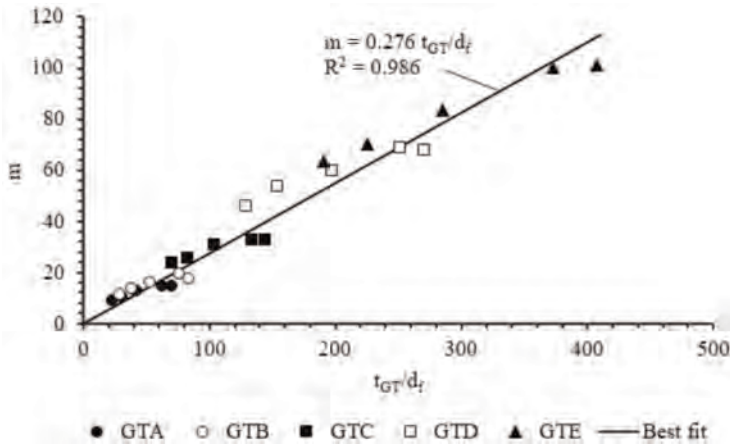
Figure 7.   Number of confrontations vs. normalised geotextile thickness (Palmeira & Trajos Galvis 2018).

The geotextile retention capacity increases when the filter is subjected to the combined action of partial clogging and confinement, as shown in Figure 8. This figure presents the variation of geotextile filtration opening size (expressed as O_{95}) of a nonwoven needle-punched geotextile, obtained in *BBP* tests, normalised by the fibre diameter (d_f) with the confining vertical stress for different values of impregnation level (λ) (Palmeira & Trejos
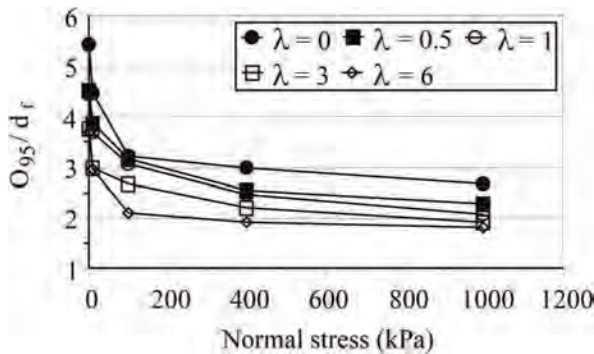
Figure 8.   Geotextile filtration opening size *vs.* confining stress for different impregnation levels (Palmeira & Trejos-Galvis, 2017).

Galvis 2017). Reductions in O_{95} of up to 36% with respect to the result for the confined virgin specimen can be noted, depending on the impregnation level and vertical stress considered. In comparison with the unconfined ($\sigma_v = 0$) virgin ($\lambda = 0$) geotextile, the same geotextile with a value of λ of 6 under 1000 kPa showed a reduction in O_{95} of 67%. Hence, filter retention capacity is enhanced by confinement and partial clogging. It should be noted that the range of O_{95}/d_f values in Figure 8 covers the dimensions of particles of very fine sands and silts. This, to some extent, explains why cohesionless silts are usually viewed as problematic materials for geotextile filter performance.

2.3 *Filters under tension*

Geotextile filters can work under tension in some geotechnical structures, such as in drainage layers at the base of embankments on soft soils, in geotextile tubes, silt fences and as separators in roads on compressible grounds, for instance. The tensile strains developed can influence geotextile pore dimensions and filtration behaviour. Several studies can be found in the literature on the behaviour of geotextile filters under tension (Fourie & Kuchena 1995, Adel *et al.* 1996, Fourie & Addis 1997 and 1999, Moo-Young & Ochola 1999, Wu *et al.* 2008, Wu & Hong 2016, Palmeira *et al.* 2012, Chen *et al.* 2019, Palmeira *et al.* 2019, Tang *et al.* 2020a, b). Conflicting results have been obtained among different researchers, particularly in tests with woven geotextiles. These differences in results are likely to be due to different geotextiles properties and fabric structures as well as different experimental techniques being used.

Fourie and Addis (1997) investigated the effect of tensile loads on the filtration opening size of geotextiles. Tests with the geotextile specimens subjected to uniaxial and biaxial loads were carried out. The authors commented that the effect of an in-plane tensile load appeared to be more pronounced for the woven than the nonwoven geotextile. They also observed erratic variations of O_{95} of a nonwoven geotextile under tension and concluded that, despite increasing the geotextile retention capacity, the reduction in O_{95} may favour blinding or clogging of the geotextile filter. In another study on the influence of tension on geotextile filter behaviour, Fourie and Kuchena (1995) observed up to 80% reduction in flow rate in highly stressed woven and nonwoven geotextile specimens. The authors attribute this reduction to closure of pore spaces impeding flow of water through the geotextile. However, the dimensions of the tensioned geotextile sample strip from where the specimens used in the tests were collected did not satisfy plane strain conditions; hence, necking of the nonwoven specimens may have influenced the results. Necking of the specimen under tension must have also influenced the results obtained by Tang *et al.* (2020a) due to the size of the specimens tested.

The influence of uniaxial strain on geotextile pore size, flow rate capacity and compatibility (*GRT*) with soil was investigated by Wu *et al.* (2008). Increases in O_{95} were observed with increasing strain, with a slight rate of increase for the heavier nonwoven geotextile tested. The authors comment that uniaxial strain causes the straps to bulge in woven geotextiles in the direction normal to that of the load, enlarging the interstitial spaces. For all geotextiles tested, the tensile strains caused an increase in pore size, decrease in the gradient ratio, *GR*, (being more pronounced in the nonwoven geotextiles) and an increase in flow rate. Fourie and Addis (1999) observed that unequal orthogonal loads may distort the shape of the openings in a woven geotextile, effectively decreasing the pore spaces and that different mechanisms of expansion and flattening of geotextile strands under tension may influence differently the pore opening sizes in thinner and thicker geotextiles. Hong and Wu (2011) also observed the influence of geotextile straining on the results of filtration tests under sustained and pulsatory loads.

Chen *et al.* (2019) investigated the variation of nonwoven heat-bonded geotextile pore size distribution with tensile strain using the Discrete Element Method (*DEM*). The authors utilized image analysis to obtain the variations of geotextile pore size distribution.

They observed compression of some fibres in uniaxial loading depending on the direction considered. Overall, the geotextile opening size linearly increased with the tensile strain in both uniaxial and biaxial tensile tests, but with less intensity and magnitude when compared with the experimental results by Wu *et al.* (2008). The authors attribute these differences to simplifications made in the model such as the bonds between fibres in the same fibre web having been considered as unbreakable.

The effects of unequal tensile strains in warp and weft directions on the per cent open area (*POA*) and filtration opening size (O_{95}) of woven geotextiles were investigated by Tang *et al.* (2020b). The authors observed that *POA* and O_{95} showed marked increases with increasing unequal biaxial strain, similarly to what was observed by Palmeira *et al.* (2019) in tests on nonwoven geotextiles, and that tensile strains had a greater impact on smaller pores. An unequal biaxial strain may decrease or increase the geotextile *FOS* depending on the initial shape of the pores. Strain values, ratio between warp and weft strains and biaxial strains had a greater impact on geotextile *POA* than uniaxial strains.

Sagging of the geotextile filter between particles of the bedding material will also cause tensile strains in the geotextile filter. Palmeira *et al.* (2012) investigated this mechanism of geotextile deformation in tests with nonwoven, needle-punched, geotextiles resting on different bedding materials (steel spheres or gravel). Large strains were observed in the geotextile, particularly for the lighter ones, depending on the type and spacing between bedding material particles and vertical stress (Figure 9a). An adaptation of the method proposed by Giroud *et al.* (1990) to estimate geotextile strains in soil-geotextile layers overlying circular voids yielded to good comparisons between predicted and observed average geotextile strains in tests with spheres as bedding materials, as shown in Figure 9b. However, for the case of gravel as bedding material, the prediction should be multiplied by a factor of the order of 3 or more to improve accuracy. Thus, tensile strains due to geotextile sagging in the voids of coarse material can influence its retention capacity.
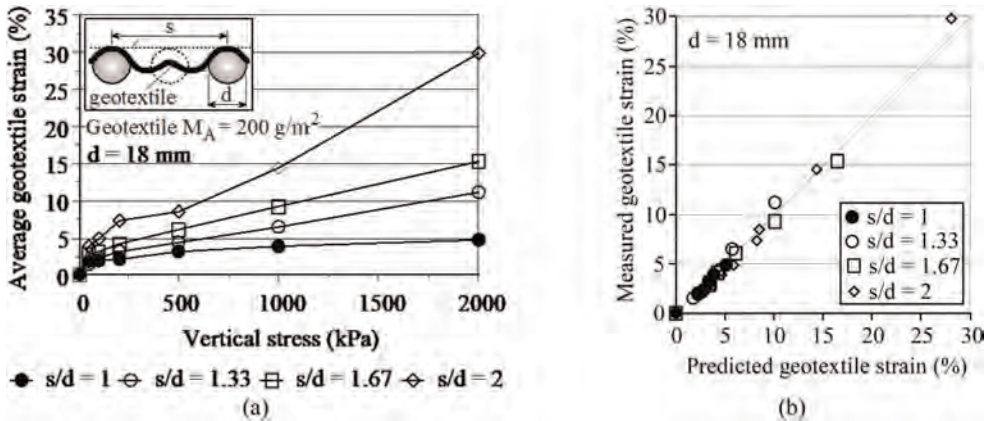
Figure 9. Tensile strains due to geotextile sagging in the bedding material voids (Palmeira *et al.* 2012). (a) Strain versus vertical stress, (b) Predicted vs. measured geotextile strain.

The variation of pore dimensions of nonwoven, needle-punched, geotextile filters due to tension and confinement was investigated by Palmeira *et al.* (2019). In their study, the authors used a bubble point test equipment capable of performing tests on previously in-plane tensioned geotextile specimens with or without the application of compressive stresses normal to the geotextile plane. It was observed that the values of O_{50}, O_{30} and O_{10} of the geotextile, particularly the latter, were less sensitive to the tensile strains than O_{95} and O_{98}. Contrary to what was observed in uniaxially tensioned geotextiles, the values of O_{98} and O_{95}

were rather insensitive to the tensile strain applied under plane strain conditions (Figure 10a), which is consistent with the observations by Fourie and Addis (1997) and Moo-Young and Ochola (1999). Confinement reduced the value of O_{98} independent on the tensile strain in the specimen, with the reduction of the influence of tensile strains due to confinement being more evident for the thicker geotextiles. The largest pore diameter increases were obtained in tests on specimens subjected to equal biaxial strains (Figure 10b). In this case, increases in O_{98} of up to 64% were noted in comparison with results from test on unstrained specimens, depending on the geotextile considered. However, again the pore dimensions of the tensioned geotextile were reduced by confinement.
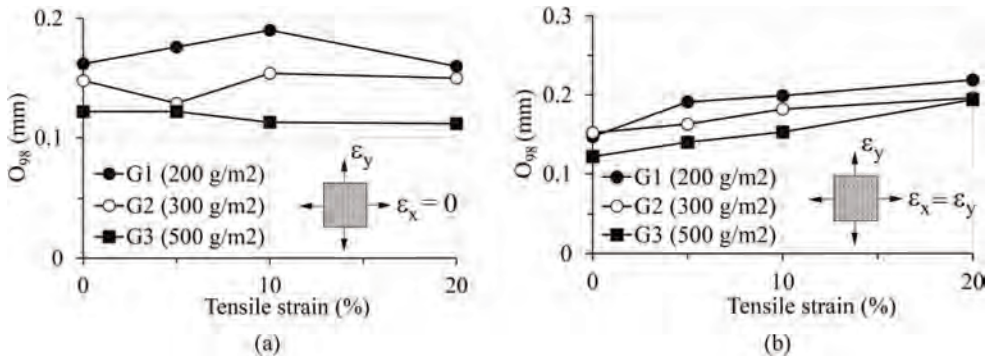
Figure 10.   Pore dimension vs. tensile strain (modified from Palmeira, 2020). (a) Plane strain condition, (b) Equal biaxial strain condition.

Palmeira *et al.* (2019) proposed a solution to estimate an upper bound value for the filtration opening size of a tensioned nonwoven geotextile under equal biaxial tensile strains. The approach is based on Kirsh (1898) elastic solution for the increase in the diameter of a circular hole in a linear elastic, homogeneous and isotropic tensioned plate. This solution was adapted to consider large tensile strains. Figure 11 shows results of the ratio between geotextile filtration opening size (O_ε) for a given tensile strain (ε) and the filtration opening size under unstrained conditions (O_o) versus tensile strain (ε) obtained in bubble point tests. It also shows the predicted upper bound curves for different values of geotextile Poisson ratio
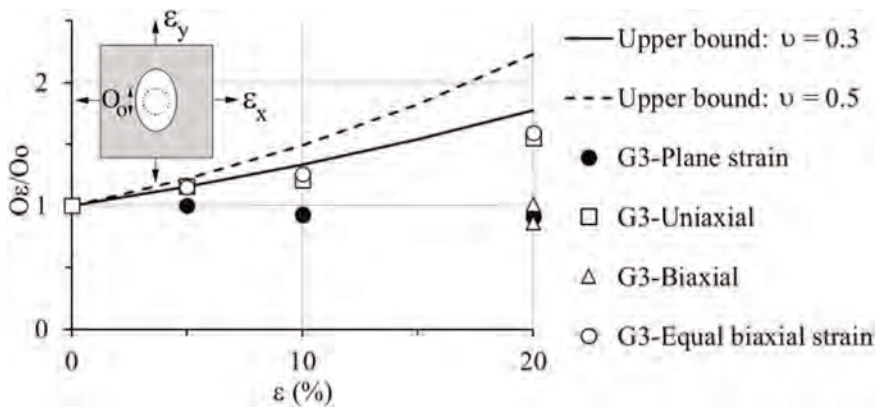
Figure 11.   Comparisons between measurements and upper bound values for filtration opening size (modifield from Palmeira 2020).

(*v*). The predicted upper bound for geotextile filtration opening size for a Poisson ratio of 0.3 was satisfactory regarding the experimental results. This approach may be useful for the prediction of a conservative upper bound for the geotextile filtration opening size under equal biaxial tensile strains, which would to some extent simulate the conditions expected for a geotextile separator in a road or for a geotextile sagging in the voids of a coarse underlying material.

The upper bound for filtration opening sizes of tensioned nonwoven, needle-punched, geotextiles described above was compared to the diameter of particles that actually piped through geotextile filters in Gradient Ratio tests under confinement performed by Palmeira *et al.* geotextile (2012). In these tests, the bedding layer consisted of 18 mm diameter steel spheres with different values of spacing to diameter ratios (*s/d*, Figure 9). Vibration and water flow were the main mechanisms causing soil particle to pass through the geotextile filter in the tests. Figure 12 shows the variation of the maximum diameter (D_{95}) of the piped particles or geotextile filtration opening size (O_{98}, from *BBP* tests on confined and tensioned geotextiles, Palmeira *et al.* 2019) versus the vertical stress acting on the voids between bedding layer particles as calculated by the method proposed by Giroud *et al.* (1990). The upper bound (Palmeira *et al.* 2019) in Figure 12 was calculated using a geotextile Poisson ratio of 0.3. The results show piped soil particles considerably larger than the upper bound for low vertical stresses. This can be attributed to large particles being pushed through the geotextile voids or passing through needle holes in the geotextile due to the needle-punching process during geotextile manufacturing, base soil compaction or due to high seepage forces. For greater vertical stresses, the diameters of the largest piped particles were below the upper bound curve. The values of D_{95} oscillated around the curve of O_{98} vs. vertical stress in Figure 12a or were a little greater (Figure 12b). Bearing in mind the limited amount of experimental data available, the results in Figure 12 are encouraging with regard to the development of more realistic predictions of the retention capacity of nonwoven, needle-punched, geotextiles overlying coarse drainage materials.
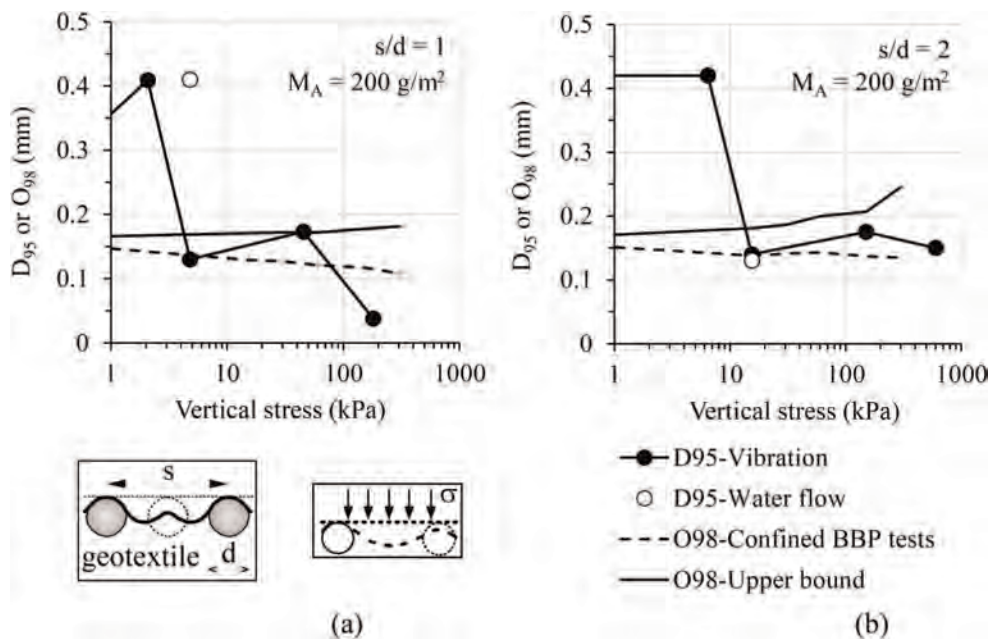
Figure 12.   Diameter of the largest soil particle piping through a nonwoven geotextile overlying a granular drainage layer (modified from Palmeira 2020). (a) *s/d* = 1, (b) *s/d* = 2.

In summary, tension can influence geotextile filter performance in different ways, depending on the geotextile type and tensioning mechanism (uniaxial, biaxial, plane strain etc.). The situation is more complex in woven geotextiles, since opening size variation will depend on the type and characteristics of the geotextile fibres and on how they will behave under tension. The filtration opening size of nonwoven, needle-punched, geotextiles seem to be little affected by tension under plane strain conditions. Equal biaxial strain condition increases filtration opening sizes of woven and nonwoven geotextiles.

3 BEHAVIOUR OF GEOTEXTILE FILTERS UNDER SEVERE WORKING CONDITIONS

Geotextile filter failure under severe conditions can be the result of the following:

- Physical clogging (blinding, blocking or particle intrusion)
- Chemical clogging (precipitation of chemicals)
- Biological clogging (action of microorganisms)
- Biochemical clogging (combined action of chemical substances and microorganisms)

Commonly, a combination of two or more of the aforementioned mechanisms takes place under field conditions. However, under laboratory conditions, most researchers have tried to isolate or enhance a specific clogging mechanism to reduce the complexity of the problem. The following points discuss the behaviour of geotextile filters under severe working conditions.

3.1 *Geotextile filters in internally unstable soils*

A major concern of filter failure is on filters, either granular or synthetic, in contact with internally unstable soils. In an internally unstable soil, its smaller particles can be carried by the water through the voids of the soil skeleton formed by its larger particles in a process called suffusion. Gap-graded soils and soils with the gradation curve concave upwards with large values of coefficient of uniformity (C_u) are potentially internally unstable soils. According to Skempton and Brogan (1994), the critical content of fines below which the fine particles in a gap graded soil do not fill the voids in the coarse component ranges from 24% (dense packing) to 29% (loose packing). If the content of fines is greater than 35% the coarse particles are dispersed in a matrix of fine particles (Moraci *et al.* 2022). If the filter retains the soil particles carried by seepage forces, it may be blinded. On the other hand, if the filter allows the passage of a substantial amount of these particles internal clogging of the filter, clogging of drainage pipes or structural instability of the base soil due to excessive piping can occur. In addition, an internally unstable soil can clog itself, causing deviation of flow from the expected directions and pore pressure increases without necessarily being caused by filter malfunctioning. This may happen in the field in the case of heterogeneous soil masses and has not been simulated under laboratory conditions due to the complexity of dealing with heterogeneous materials.

The performance of geotextile filters in internally unstable soils has been evaluated by several researchers. Haliburton and Wood (1982) suggest that a percentage of open area (*POA*) of 23% of a woven geotextile would be required to attend the limit gradient ratio, *GR*, of 3 in gap-graded soils with 70% silt content. Fischer *et al.* (1994) report reductions between 68% and 94% in the geotextile permeability coefficient of the region comprising 25 mm of soil and geotextile in gradient ratio tests. Lee *et al.* (2002) present results of in-plane and cross-plane filtration tests on nonwoven geotextiles with reductions in geotextile permeability ranging from 27% to 67%, with a gradient ratio value of 1.5. Markiewicz *et al.* (2022) observed reductions in nonwoven geotextile filters permeability coefficient between 2.7 and 5.5 times in gradient ratio tests on geotextile-unstable soil systems. Khan *et al.* (2022) report

values of *GR* between 0.38 and 1.79, depending on the internally unstable soil gradation and that the dynamic loading applied to the soil-geotextile system enhanced the instability of specimens with high percentage of fines. For dynamic conditions, these authors also recommend the use of an indicative grain size d_{30} as an upper retention limit to stop washing out of coarse fraction of internally unstable soil through geotextiles. For internally unstable soils, a critical diameter of suffusion, d_c, is suggested as a lower retention limit to avoid blinding of soil-geotextile interfaces. The value of d_{85} of the soil in retention criteria for internally unstable soils does not guarantee the retention of particles below that value. If passage of the fine soil particles through the geotextile filter is allowed, the characteristic geotextile opening size should be greater than the value of d_c to avoid geotextile blinding (Khan *et al.* 2022). Instead of the commonly used piping limit of 2500 g/m^2 (Lafleur *et al.* 1989), Khan *et al.* (2022) suggest that the piping limit should be defined based on the gradation of the particles that constitute less than 30% (for uniformly graded soils) or 20% (for broadly graded soil) of the original soil gradation.

The discrete element method was employed by Tao (2018) to assess suffusion in soils and the formation of arches of smaller particles on voids between large particles was observed (Figure 13). Similar studies were carried out by Ryoo *et al.* (2022a, b). The intensity of suffusion will depend on the soil characteristics and the hydraulic gradient. It is interesting to note that Figure 13a is a numerical evidence of the potential of internally unstable soils to self-clog, as commented above, due to the retention of significant amounts of smaller particles in specific regions of the soil. Figure 13c shows impregnation of the geotextile filter in *DEM* simulations. The higher the hydraulic gradient the higher the intensity of suffusion. Regarding expected hydraulic gradients under field conditions, Giroud (1996), Moraci and Tondello (1996), and Moraci *et al.* (2010, 2022) present typical ranges of values in different geotechnical structures under one-way and reverse flow conditions.
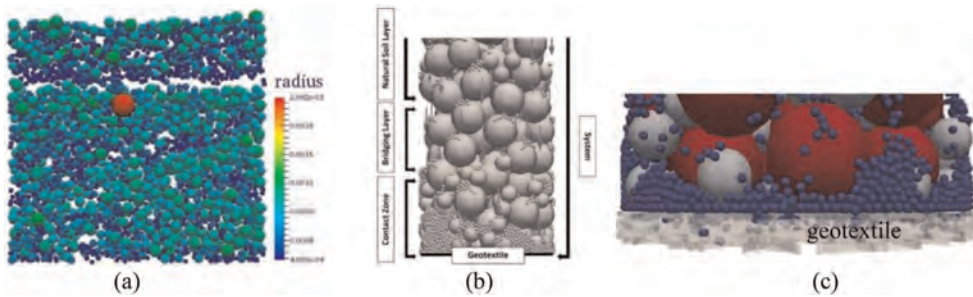
Figure 13. Arching effect in internally unstable soils in DEM simulations: (a) Tao (2018), (b) Ryoo *et al.* (2022a), (c) Ryoo *et al.* (2022b).

Several studies can be found in the literature regarding the behaviour of geotextile filters in internally unstable soils showing a wide range of results. Table 2 summarises results from a rather large number of investigations present in the literature. Most soils have large values of coefficient of uniformity (C_u), coefficient of curvature (C_c) and some of them are gap-graded materials. The main results of the tests are expressed in Table 2 in terms of the ratio between the geotextile permeability coefficient (k_{GT}) after different types of filtration tests and that under virgin conditions (k_{GTo}), ratio between geotextile (k_{GT}) and soil coefficients of permeability (k_s) and/or the ratio between final (k_{sys}) and the initial (k_{sys-o}) permeability coefficients of the system (soil and geotextile). Some tests were carried out under confinement (vertical stresses up to 2000 kPa). Two studies tested undisturbed soil-geotextile systems in filtration tests and three tested geotextile specimens exhumed from field works. Values of k_{GT}/k_{GTo} in the range 0.000126 to 0.8 can be observed. Ratios k_{sys}/k_{sys-o}, which are also equal

to the ratios between final and initial flow rates, between 0.009 and greater than 1 can be noted as well as values of k_{GT}/k_s in the range 0.11 to 450. However, low values of k_{GT}/k_{GTo} or k_{sys}/k_{sys-o} do not necessarily mean drainage problems since the permeability coefficient of the partially clogged geotextile may still be considerably higher than that of the soil and the flow rate greater than that required.

Table 2.   Examples of permeability coefficient reduction of filters in internally unstable soils.

Reference	Geotextile and soil properties*	Permeability ratio range
Williams & Abouzakhm (1989)	NW, M_A = 136–300 g/m^2, mixtures of S and St.	k_{sys}/k_s = 0.08–0.52
Lawson (1990)	NW, W, M_A = 70–580 g/m^2, loess soil, $C_u > 23$.	k_{sys}/k_{sys-o} = 0.02–0.5
Qureshi et al. (1990)	NW, M_A = 143–550 g/m^2, mixtures of S and St, C_u = 4.0–38.8.	k_{sys}/k_{sys-o} = 0.19–0.98
Williams & Luettich (1990)	NW, M_A = 136 and 142 g/m^2, StS	k_{sys}/k_s = 0.9
Wayne & Koerner (1993)	NW, NP, W, M_A = 128–249 g/m^2, StS	k_{GT}/k_s = 0.11–450
Morilha Jr. et al. (1994)	NW, M_A = 150–600 g/m^2, soil A-7-5 and A-7-6 (AASHTO).	k_{GT}/k_{GTo} = 0.37–0.80
Bhatia & Huang (1995)	NW, M_A = 136–285 g/m^2, glass beads mixtures, C_u = 11.1–30.0, σ_v = 0.	k_{sys}/k_{sys-o} = 0.21–0.85
Gardoni (1995)	NW, NP, M_A = 282 g/m^2, C_u = 2.3, C_c = 1.6, RS/USS, ES from a field drain, σ_v = 0.	k_{GT}/k_{GTo} (ES) = 0.48–0.60, PCA
	NW, M_A = 200 g/m^2, RS/USS (C_u = 16.3), C (C_u = 13.3), StS ($C_u > 482$), σ_v = 0.	k_{sys}/k_{sys-o} = 0.009–0.56
Palmeira et al. (1996)	NW, NP, M_A = 180–600 g/m^2, StS, C_u = 25 and 105, σ_v = 0–200 kPa.	k_{GT}/k_{GTo} = 0.36–0.68
		k_{sys}/k_{sys-o} = 0.47–0.84
Gardoni & Palmeira (1999)	NW, M_A = 200 g/m^2, RS, $C_u > 527$, σ_v = 0.	k_{GT}/k_{GTo} (USS) = 0.13
		k_{sys}/k_{sys-o} = 0.075
		k_{GT}/k_s = 99.3, PCA
Gardoni (2000), Palmeira et al. (2005)	NW, M_A = 300 and 600 g/m^2, RS, C_u = 21, σ_v = 0–2000 kPa.	k_{GT}/k_{GTo} = 0.00087–0.0027
		k_{GT}/k_s = 40.38–126.4
Lee et al. (2002)	NW, M_A = 300 g/m^2, RS, C_u = 90.8, σ_v = 0.	k_{GT}/k_{GTo} = 0.36–0.67, PCA
Beirigo (2005), Palmeira et al. (2010)	NW, M_A = 200–637 g/m^2, T, C_u = 3.7 and 9.2, σ_v = 0–2000 kPa.	k_{sys}/k_{sys-o} = 0.18–0.53
		k_{sys}/k_s = 0.21–0.98
Lee & Bourdeau (2006)	NW, M_A = 253 g/m^2, C, $C_u > 14$, σ_v = 0, test on geotextile specimens exhumed from a field drain.	k_{GT}/k_{GTo} (ES) = 0.000126
		$k_{GT}/k_s \sim 5.0$
		k_{sys}/k_{sys-o} = 0.022
	NW, M_A = 135 and 405 g/m^2, S and St mixtures, C_u = 10.6–78.3.	k_{sys}/k_{sys-o} = 0.022–0.24
Hong & Wu (2011)	NW, M_A = 210 and 337 g/m^2, S, C_u = 9.26, σ_v = 0–196 kPa.	k_{sys}/k_{sys-o} = 0.31–1.03

(*continued*)

Table 2.   Continued

Reference	Geotextile and soil properties[*]	Permeability ratio range
Miszkowska *et al.* (2017)	*NW*, *NP*, M_A = 200–450 g/m², *StS*, C_u = 8.3, σ_v = 10 kPa.	k_{GT}/k_{GTo} = 0.11–0.33
Du *et al.* (2022)	*NW*, *NP*, M_A = 200 and 400 g/m², *St*, C_u = 40.8, σ_v = 0 and 25 kPa.	k_{sys}/k_{sys-o} = 0.06–0.24
Markiewicz *et al.* (2022)	*NW*, M_A = 95–310 g/m², *StS*, C_u = 9.2, σ_v = 0.	k_{GT}/k_{GTo} = 0.18–0.37, *PCA*
	NW, M_A = 450 g/m², *ES* after 23 years in service, σ_v = 5 kPa.	k_{GT}/k_{GTo} (*ES*) = 0.11, *PCA*
Odabasi *et al.* (2022)	*NW*, *W*, M_A = 115–407 g/m², re-cycled materials, C_u = 2.63–72.1, σ_v = 0.	k_{sys}/k_{sys-o} = 0.06–19.2
		k_{sys}/k_s = 0.053–1
Santos & Palmeira (2023)	*NW*, *StS*, M_A = 200 g/m², C_u = 5.07–55.27, σ_v = 0 and 25 kPa.	k_{sys}/k_{sys-o} = 0.01–0.60

[*]C = clay, C_c = coefficient of curvature, C_u = soil coefficient of uniformity, ES = exhumed geotextile specimen, k_{GT} = geotextile permeability coefficient after test, k_{GTo} = permeability coefficient of the virgin geotextile, k_s = base soil permeability coefficient, k_{sys} = permeability coefficient of a soil-geotextile system, k_{sys-o} = initial k_{sys} value, M_A = mass per unit area, NW = nonwoven, PCA = permeability criterion ($k_{GT} > 10k_s$) attended, RS = residual soil, S = sands, St = silts, StS = silty sands, T = tailings, USS = undisturbed soil specimen, W = woven, σ_v = range of vertical stress on the soil-geotextile system.

The plotting of all the k_{sys}/k_{sys-o} data from the original references in Table 2 (Palmeira 2023) is shown in Figure 14 as a function of the nonwoven geotextile filtration opening size (FOS = O_{95}, O_{90} or AOS) normalised by d_{10} or d_{30} of the internally unstable cohesionless base soil. Scatter of the test results are due to different techniques employed to measure FOS, different hydraulic gradients and different equipment and experimental methodologies adopted in the tests. Figure 14a shows greater scatter in comparing k_{sys}/k_{sys-o} with FOS/d_{10}, whereas Figure 14b suggests values of k_{sys}/k_{sys-o} greater than 0.5 for values of FOS/d_{30} greater than 8. This may be because for large FOS/d_{30} values piping of the fine fraction of the base soil may prevail, whereas for smaller values of that ratio blinding and/or significant geotextile impregnation may cause greater k_{sys} reductions.
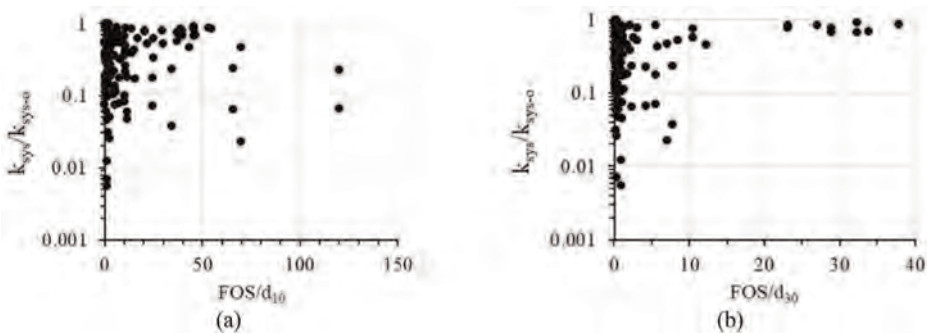
Figure 14.   *ksys/ksys-o* from filtration tests on internally unstable cohesionless soils-nonwoven geotextile systems. (a) *ksys/ksys-o vs. FOS/d₁₀*, (b) *ksys/ksys-o vs. FOS/d₃₀*.

A detailed analysis (Palmeira 2023) of the results in Table 2 also allows the calculation of what would be the appropriate flow rate reduction factor (RF_Q) for the soil-geotextile system. Figure 15 shows the frequency of RF_Q values for the tests in Table 2. It can be noted that in 42.9% of the cases the value of RF_Q should fall within the range 1 to 2, in 17.0% of the cases the appropriate reduction factor should be greater than 10 and in 2.7% of the cases between 100 and 200. So, the results in Table 2 and Figure 14 show that, in the absence of proper test results, a significantly higher RF_Q value should be adopted in preliminary analyses of problems involving internally unstable soils in comparison with values commonly used for internally stable soils.

It should be pointed out that the coefficient of permeability of an internally unstable soil is likely to vary during a filtration test. If this value is reduced during the test, a low ratio of
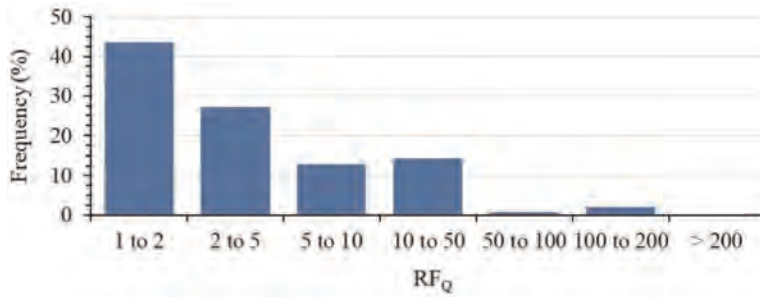
Figure 15.   Frequency distribution of required flow rate reduction factor.

k_{sys}/k_{sys-o} does not necessarily mean significant geotextile clogging or blinding. This can be exemplified considering the situation shown in Figure 16 in a filtration test, where the system is divided into two soil regions (A and B) after water flow stabilisation, where region B comprises the geotextile layer plus some thickness of soil above it where the fine soil particles dragged by the seepage forces have accumulated or from where they have been removed. From basic soil mechanics, the equivalent permeability coefficient of the system in the vertical direction is

$$\frac{k_{sys}}{k_{so}} = \frac{1 + L_s/t_c}{L_s/t_c + \frac{\alpha_s}{\alpha_c}} \alpha_s \qquad (4)$$

where k_{sys} is the equivalent permeability coefficient of the system, k_{so} is the soil permeability coefficient at the start of the test, L_s is the thickness of soil above region B, t_c is the thickness of region B (soil + geotextile), α_s is a parameter to account for the variation of soil permeability of region A during the test ($\alpha_s = k_{sL}/k_{so}$, where k_{sL} is the final soil permeability coefficient of region A) and α_c is a parameter to account for the variation of permeability of
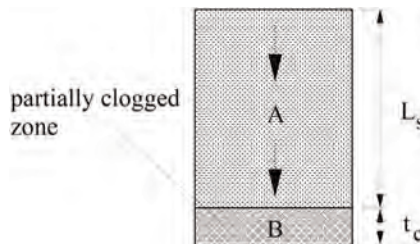
Figure 16.   Schematic simplified condition in a filtration test.

region B ($\alpha_c = k_{st}/k_{so}$, where k_{st} is the final permeability coefficient of region B). If there is no change in the permeability coefficients (stable soils) during the test, $\alpha_c = \alpha_s = 1$. In a filtration test, a value of k_{sys}/k_{so} greater than one (α_c and/or $\alpha_s > 1$) is an indication of piping, rather than clogging. It can be assumed that in most test configurations ($L_s \gg t_{GT}$) the initial permeability coefficient of the system (k_{sys-o}) should be equal to k_{so}. Then, if L_s/t_c is large, the soil coefficient of permeability has a higher influence on the final value of k_{sys}. In addition, the variation of soil permeability coefficient due to suffusion is likely to be non-uniform along the specimen height (Figure 13a).

A wide variety of scenarios for the system in Figure 16 can be considered, depending on the values of L_s/t_c, α_s and α_c adopted in equation 4. It should be noted that α_s can be greater than one if the erosion of fine particles along the thickness L_s increases the permeability coefficient of that region. In the present case, α_c will be considered smaller than one, since it is assumed that the finer soil particles are retained by the geotextile. Under such conditions, Figure 17 shows the variation of k_{sys}/k_{so} with α_s for different values of L_s/t_c and α_c, assuming that at the start of the test the soil specimen is homogeneous, with a permeability coefficient equal to k_{so}. It can be observed that for $L_s/t_c = 1$, one order of magnitude reduction ($\alpha_s = \alpha_c = 0.1$) in the average permeability coefficients of the soil in regions A and B during the test, can yield to a k_{sys}/k_{so} (or k_{sys}/k_{sys-o}) value of 0.1 (Figure 17a), which is in the range of the lower values presented in Table 2. It can be argued that if the permeability in region B is reduced, the permeability in region A should increase. This is not necessarily true since localized blockings of soil pores in region A (Figure 13a) by the moving particles may still reduce the permeability coefficient in that region.
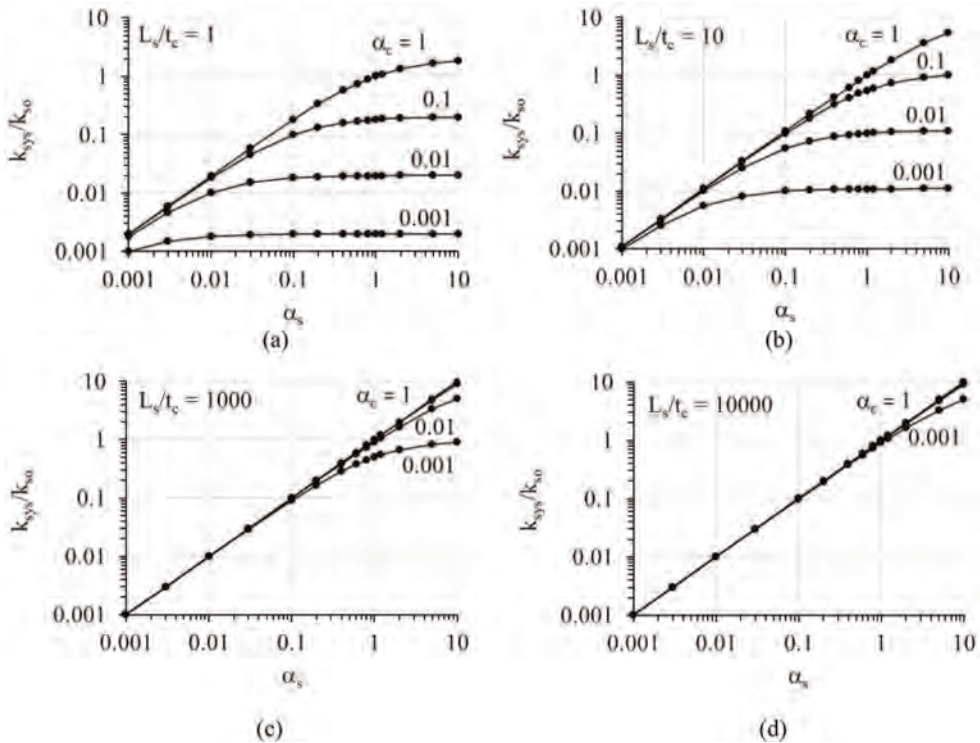
Figure 17.   Possible variations of k_{sys} during a filtration test on an internally unstable soil: (a) $L_s/t_c = 1$, (b) $L_s/t_c = 10$, (c) $L_s/t_c = 1000$, (d) $L_s/t_c = 10000$.

For larger ratios of L_s/t_c (Figure 17c and d) even large reductions in the permeability coefficient of region B ($\alpha_c = 0.001$, for instance) would result in k_{sys}/k_{so} close to 1 and the reduction in k_{sys} would be basically equal to the reduction in the soil permeability above the partially clogged zone. This type of behaviour will take place when the thickness of the soil mass affected by clogging is smaller compared to the thickness of the rest of the soil specimen. The results of filtration tests on internally unstable soils will depend on the intensity of suffusion that takes place during testing and how it influences the permeability coefficient along the soil thickness. Thus, under these conditions, thicker soil specimens should be used in this type of test (Giroud 1996) with the measurement of the permeability coefficient of the soil in different regions along the specimen height. The same comments apply to gradient ratio tests on unstable soils because the hydraulic gradient away from the geotextile specimen may also be affected by suffusion, influencing the value of GR obtained. Palmeira & Matheus (2000) recommend due care when deciding on the acceptance or not of a geotextile filter based only on the value of GR from tests on internally unstable soils. In such cases, the flow rate variation with time and the requirements from the project itself (minimum required flow rate, for instance) must also be considered for a final decision. In this sense, the advantage of working with the variation of k_{sys} with time is that it may anticipate the expected flow rate reduction. Long-term filtration tests are highly recommended under such conditions (Palmeira & Matheus 2000, Cazzuffi et al. 2015). Despite some simplifications, equation 4 shows that a very severe reduction in the permeability of the geotextile (or of a thin region adjacent to it) is necessary for a serious compromise of flow rate in typical field conditions.

Based on the comments above, it is clear that internally unstable soils are problematic soils either for granular and synthetic filters. Hence, it is of utmost importance to identify whether a soil is internally unstable or not beforehand. Different approaches for such evaluation are available (Kezdi 1979, de Graauw et al. 1984, Kenney & Lau 1985, Bhatia & Huang 1995, Indraratna et al. 2008, Moraci et al. 2012, for instance). Moraci et al. (2022) confirmed the greater reliability of the semi-empirical method proposed by Kenney and Lau (1985) in comparison with other criteria in assessing soil internal instability. Based on tests on 57 cohesionless soils (25 gap-graded and 32 broadly graded), Li & Fannin (2008) found that Kezdi (1979) criterion predicted better the internal instability or stability of the soil for values of the percentage of mass passing (F, as defined by Kenney and Lau 1985) greater than 15%, whereas Kenney and Lau (1985) predicted better for values of F smaller than 15%. Khan et al. (2022) also observed good predictions of soil internal instability by Kenney and Lau's and Kezdi's methods.

3.2 *Filters subjected to biological clogging mechanisms*

Geotextile filters can be used in environments which favour biological clogging. These are the cases of applications of such filters in landfills, for instance. Under such conditions, severe filter clogging can occur with repercussions on landfill slope stability and greater pollutant potential in case of failure of the underlying lining system. Granular filters and drainage systems can also clog due to bacteria activity (Fleming et al., 1999, Rowe et al. 2000a, McIsaac & Rowe 2007). Figure 18 shows images of landfill stone drainage layers, where in one of the cases (Figure 18a) that layer clogged after only 3 years in contact with leachate (Fleming et al., 1999). Rowe et al. (2000a) report reductions of 6 orders of magnitude in the hydraulic conductivity of 15 mm glass beads after 320 days of column tests with leachate as permeant.

The formation of bacteria films in the geotextile voids will certainly reduce its permeability. Figure 19 shows microscopic images of bacteria films in a nonwoven geotextile and the reduction in its permeability with time as the number of bacteria increases (Remigio 2006, Palmeira et al., 2008). In addition, the presence of solids in suspension in the leachate can further increase the clogging potential due to geotextile blinding or impregnation.

Mlynarek and Rollin (1995) found that for the filtration of wastewater, the intensity of the growth of biofilm depended on the geotextile opening size, with 17% reduction in the hydraulic capacity of a more open geotextile after 6 months of service under anaerobic conditions and 60% reduction under aerobic conditions.
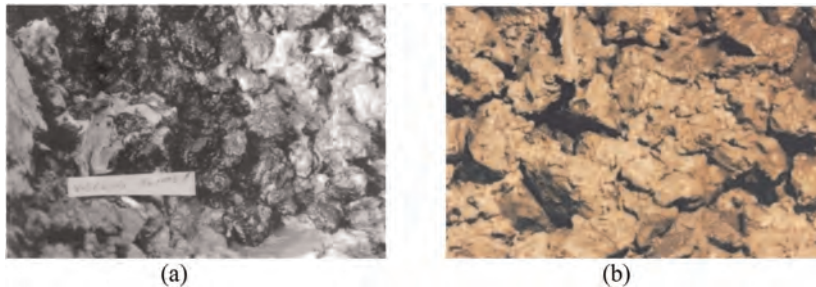
Figure 18.   Examples of clogging of stone drainage blankets. (a) After 3 years in contact with leachate (Fleming *et al.* 1999), (b) Sever clogging of a gravel drainage layer (Fleming & Rowe 2004).
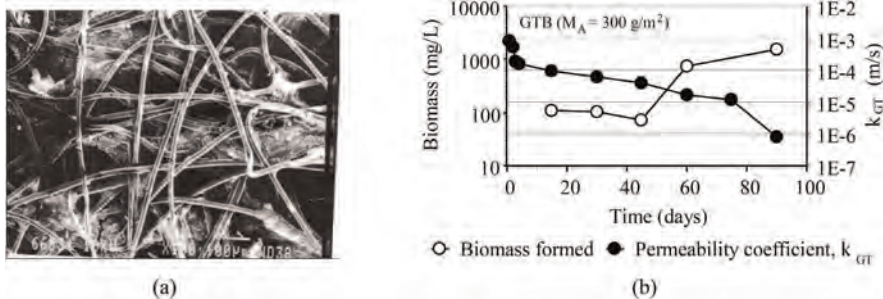
Figure 19.   Effects of bacteria film formation in a nonwoven geotextile after 90 days of leachate flow. (a) Bacteria films in the geotextile (Remigio 2006), (b) Mass of bacteria and geotextile permeability *vs.* time (Palmeira *et al.* 2008).

Laboratory column tests by different researchers have observed reductions in the geotextile coefficient of permeability to leachate between 10% and 100% (Koerner & Koerner 1991, Fourie *et al.* 1994, Kossendey *et al.* 1996, Colmanetti & Palmeira 2002, Silva *et al.* 2002, Goycoechea *et al.* 2020), being common reductions between 3 and 5 orders of magnitude (Cancelli & Cazzuffi 1987, Cazzuffi and Cossu 1993, Koerner & Koerner 1995, Palmeira *et al.* 2008, Liu & Liu 2020). Severe reductions in geotextile permeability can take place in a few hours under laboratory conditions when the leachate contains large amounts of solids in suspension (Cancelli & Cazzuffi 1987, Silva *et al.* 2002). However, large reductions in the geotextile permeability (due to its small thickness) may not necessarily compromise the drainage system performance (see section 3.1). Corcoran & Bhatia (1996) concluded that the reduction of one order of magnitude in the permittivity of a nonwoven geotextile filter of a drainage trench in Fresh Kills landfill should not affect the capacity of the filter to perform its function. Koerner & Koerner (1995) state that flow rate in leachate collection systems should not be altered until the filter coefficient of permeability becomes smaller than approximately 1×10^{-7} cm/s, which represents typically a 6 orders of magnitude reduction in typical values of permeability coefficients of nonwoven, needle-punched, geotextiles. Rowe *et al.* (2000a) assumed failure of a granular medium due to clogging when the reduction in its hydraulic conductivity was about 7–8 orders of magnitude for the

prediction of the time for clogging of a landfill leachate collection system. Based on field observations, drainage pipes wrapped (or socked) with a nonwoven geotextile showed intense clogging and should not be used in leachate collection systems (Koerner & Koerner, 1995). Better filter performance of nonwoven geotextiles than of woven geotextiles filters in drainage systems subjected to leachate flow have been reported (Fourie *et al.* 1994, Fleming and Rowe 2004, McIsaac & Rowe 2006, Goycoechea *et al.* 2020). Cancelli & Cazzuffi (1987) observed larger permeability reductions in heat bonded geotextiles than in nonwoven needle-punched geotextiles.

Biological clogging of geotextile filters is a complex mechanism and some conflicting results on its intensity and consequences can be found in the literature, where mild (Ionescu *et al.* 1982, Mlynarek and Rollin 1995) or severe (Koerner and Koerner 1991, 1995, Cazzuffi and Cossu 1993, Palmeira *et al.* 2008, Liu and Liu 2020, Silva and Lodi 2020) clogging was observed, depending on the type of filter and conditions to which the filter was subjected. Because severe clogging of the drainage systems of a landfill is very common, it has been argued whether a filter layer should actually be used between the waste mass and the drainage layer (usually coarse granular material). Giroud (1996) suggests that sand filters and geotextile filters should not be used in municipal solid waste landfills and wastewater treatment sludge landfills. However, significant intrusion of fines in the drainage layer at the waste-gravel interface has been observed when there is no filter (Figure 18) and that the presence of suitable filter between the waste and the drainage layer improves the performance of the drainage layer against clogging (Carey *et al.* 2000, Fleming & Rowe 2004, McIsaac & Rowe 2006). McIsaac & Rowe (2006) point out that the presence of the geotextile filter may prevent most of the fines from entering the underlying gravel layer. These authors also indicate that the use of a nonwoven geotextile inside the gravel can be a good approach since even if this layer is severely clogged the top gravel layer above the geotextile will allow the flow of leachate, avoiding leachate mounding. A drainage layer of a landfill where this solution was adopted was working very effectively for 11 years (McIsaac & Rowe 2006, Rowe *et al.* 2000b).

The development of encrustations can clog even an open material such as gravel, forming a block that has the consistency of a lean concrete (Brune *et al.* 1991, Turk 1995). Brune *et al.* (1991) observed very few mineral particles carried by the leachate in the incrustations, which were essentially composed of bacteria, their secretions and crusts of inorganic compounds. They also point out that there is much less biological growth in a landfill in its methane production phase (old waste, neutral pH) than in the early stages of landfill operation (fresh waste, acidic conditions). In addition, methane and sulphate-reducing bacteria increase the leachate pH, yielding to the precipitation of carbonates and sulphides from metal ions dissolved in the leachate (Brune *et al.* 1991, Rowe *et al.* 2000a). Biofilm formation and $CaCO_3$ precipitation were the primary clogging mechanisms observed by Liu & Liu (2020) in laboratory column tests on granular and geotextile filters subjected to leachate flow.

Management of the waste disposal processes and of the drainage systems in municipal solid waste landfills can inhibit or favour filter clogging. For instance, detrimental practices to the filter leachate collection system are the presence of a greater amount of organic matter, disposal of dewatered sludge and incinerated ash, which foster the generation of $CaCO_3$ (Liu and Liu 2020), and the disposal of construction debris, which favours an increase in the supply of calcium carbonate and iron, major components of encrustations in filters (Brune *et al.* 1991). Leachate recycling worsens the situation regarding filter clogging (Koerner & Koerner 1995). On the other hand, Legge (2004) reports on experiences gained in remediating biological clogging of geotextile filters by inducing sudden changes to the environment within which the organic material develops, such as the use of a "p-trap" on the drain outlet. This can suddenly change the conditions in the blanket drain from aerobic to anaerobic on a regular basis to control bacterial growth as required, with later removal of the "p-trap" from the outlet drainage pipe. Pretreatment by aeration of the waste for approximately 6 months prior to landfilling has been proposed to eliminate the acidic phase and hence the development of encrustations (Giroud 1996). Kossendey *et al.* (1996) also

recommend the pre-treatment of organic waste to keep the leachate carbon content as low as possible to reduce the potential of geotextile biological clogging.

Leachate collection systems are prone to clogging due to solid particles retention, bacteria growth, iron oxide precipitation and salt precipitation. Iron oxide precipitation may be caused by the action of bacteria such as *Gallionella*, *Sphaerotilus*, *Leptothix*, *Thiobacillus ferooxydans* and *Sphaerotilus* (Mlynarek and Rollin 1995, Rollin and Lombard 1988). Crystals of salts can adhere to the geotextile fibres as water evaporates, eventually blocking the filter voids if the drying period is long enough. Studies by Koerner and Koerner (1991), Colmanetti (2000) and Colmanetti and Palmeira (2002) have shown that there is a great potential for filter clogging due to the presence of solids in suspension in the leachate. According to Koerner & Koerner (1995), although subjective, leachates with *TSS* (Total Suspended Solids) $\geq$ 2500 mg/l and/or $BOD_5 \geq$ 2500 mg/l should be viewed as harsh and of special concern. Figure 20 shows grain size distribution curves of solids in suspension in the leachate in tests performed by Koerner and Koerner (1991) and Colmanetti (2000). Results for the material blinding a nonwoven geotextile filter in large column tests performed by Silva *et al.* (2002) are also shown in that figure. It should be pointed out that a young leachate (160 days) was used in the tests reported by Colmanetti (2000), whereas in the case of Koerner and Koerner (1991) older leachates were tested. Most of the data from Koerner and Koerner (1991) fall in the silt size range (as well as the data from Silva *et al.* 2002, to some extent), whereas coarser material was observed by Colmanetti (2000). It should be noticed that in some of the cases shown in Figure 20, the leachate specimens tested by Colmanetti (2000) were collected after the effluent had passed through a 45 mm thick uniform gravel drainage layer (d_{50} = 12.5 mm, possibly very low filtration capacity) or by a drainage system consisting of a nonwoven geotextile (M_A = 600 g/m^2) overlying a 55 mm thick layer of the same gravel. Compared to the case where the leachate only passed through the gravel layer, it can be noted that the presence of the geotextile filter significantly reduced the diameters of the particles in suspension in the effluent. This type of diameter reduction in solids in suspension was also observed in the effluent from large field experimental domestic waste cells, as reported by Junqueira *et al.* (2006). The results in Figure 20 show a wide range of possible diameters and types of solids (degradable and nondegradable) in suspension in the leachate, depending on its age. Hence, a filter will have to face different conditions regarding clogging potential due to solids in suspension throughout its service life.
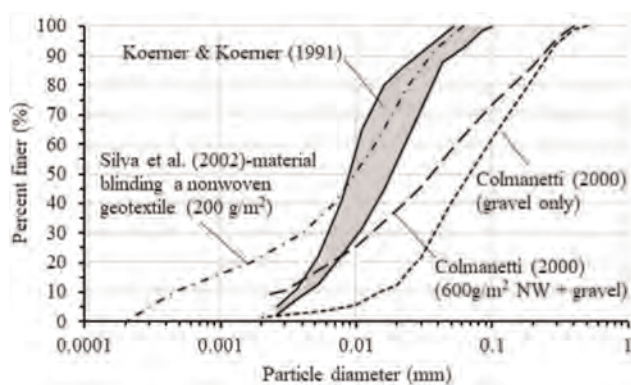
Figure 20.   Particle size distributions of solids in suspension in leachates.

The addition of antimicrobial agent during the manufacturing process of the geotextile has been suggested in order to reduce or avoid filter bioclogging (Fourie *et al.* 1994) aiming at inhibiting the attachment of bacteria to the fibre surface as well as reducing the adhesive

strength of the bioslime. However, Koerner & Koerner (1991) report that the remnants due to the use of biocide treated geotextiles in laboratory column tests were as troublesome as the viable bacteria in favouring subsequent geotextile clogging. Some studies have indicated that biological growth may be easily removed from the geotextile fibre surface (Koerner & Koerner 1991, Silva *et al.* 2002, Palmeira *et al.* 2008). However, that may not be the case for physical clogging due to the entrapment of non-degradable particles and incrustations. Colmanetti & Palmeira (2002) report physical clogging, rather than chemical or biological, as the clogging mechanism prevailing in large laboratory experiments on drainage systems for domestic wastes. The presence of fine-grained soils adjacent to leachate collection trenches can also partially clog the filter due to particles intrusion (Corcoran & Bhatia 1996).

Techniques to unclog geotextiles have also been investigated by different researchers, namely backflush or reverse flow with different substances, with conflicting results. According to Koerner & Koerner (1991), backflush in column tests on geotextiles showed best performance when using water (50% improvement) followed by leachate (32% improvement) and by nitrogen gas (29% improvement). Vacuum (254 mmHg) extraction was the least effective (6% improvement) remediation measure, and only nominally improved flow rates. Silva *et al.* (2002) report that backflushing in large field column tests under a total water head of 0.18 m partially restored geotextile drainage capacity, but severe clogging followed after a few hours of leachate flow because the main clogging mechanism in this case was geotextile blinding by suspended solids in the leachate. Goycoechea *et al.* (2020) observed that filter unclogging with reverse flow in column tests was also unsuccessful because the flow rate increased little even when the applied hydraulic gradient was 5 times the initial value. Figure 21 shows results of geotextile permittivity versus total hydraulic head in column tests on a previously biologically clogged nonwoven needle-punched geotextile ($M_A = 600$ g/m^2) (Palmeira *et al.* 2008). In this case, it can be noted that just a total head loss approximately 1 m high, equivalent to a 1 m high mounding of leachate, was sufficient to wash out the bacteria films from the geotextile and restore the same trend of permittivity variation with head loss of the virgin geotextile. However, these tests were carried out on specimens where clogging was caused basically by the presence of biofilms in the geotextile voids (Figure 19a). Had non degradable particles or incrustations been present in the geotextile voids, certainly higher total head losses would be required to increase the drainage capacity of the geotextile. Thus, the efficiency of backflushing under low water pressures depends on the intensity and type of clogging mechanism developed. Under field conditions, special engineering facilities would be required to allow the use of the backflush technique, which would also face the difficulties associated with more complex clogging mechanisms and the typical dimensions of actual landfill cells.
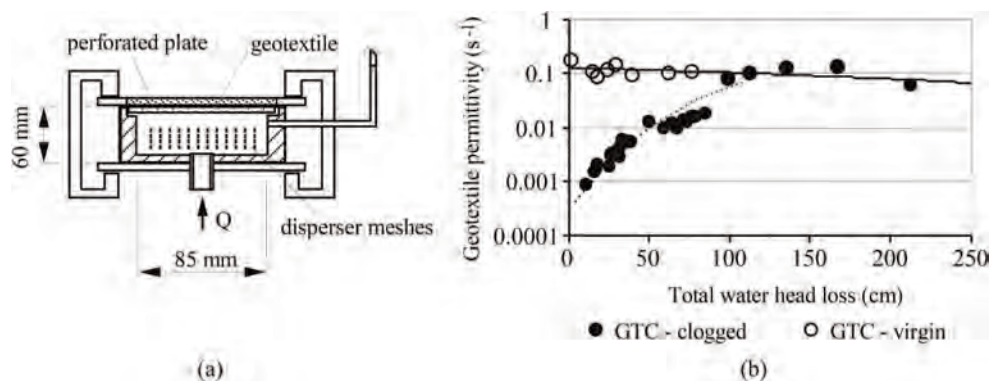
Figure 21. Geotextile permittivity vs. total water head loss in backflush tests on a clogged geotextile specimen: (a) Apparatus, (b) Geotextile permittivity *vs.* total water head loss (Palmeira *et al.*, 2008).

Another issue that may be raised is the possible influence of the contact between leachate and geotextile filter on its mechanical properties. Researchers have reported no influence of the contact with leachate on the geotextile tensile properties (Ionescu *et al.* 1982, Cazzuffi & Cossu 1993, Corcoran & Bhatia 1996, Koerner & Koerner 1991), although Koerner & Koerner (1991) observed some strength reduction in a heat bonded geotextile due to weakening of thermally fused fibre junctions after 36 months duration column tests. Koerner and Koerner (1991) observed no influence of the polymer from which the geotextile was manufactured on its biological clogging behaviour.

Field and laboratory experiences seem to suggest that a more open product should be specified when using a geotextile filter in an environment that favours biological clogging, (Koerner & Koerner 1991, Cazzuffi & Cossu 1993, Mlynarek & Rollin 1995, Giroud 1996, Rollin 1996). Geotextile and/or soil filters to be used in leachate collection systems must be sufficiently open to pass the sediments, or particulates, along with micro-organisms contained in the leachate. In the case of woven geotextiles, Koerner & Koerner (1991) observed severe clogging in woven geotextiles with *POA* equal to 4% and limited clogging in a woven geotextile with *POA* equal to 10%. Giroud (1996) recommends that, if used, monofilament woven filters should have a *FOS* of 0.5 mm and $POA > 15\%$ (preferably, $> 30\%$) and the drainage medium should consist of an open graded material (gravel, minimum particle size of 10 mm, not limestone, and possibly geonet in slopes).

3.3 *Filters subjected to chemical and biochemical clogging mechanisms*

Chemical and biochemical clogging of filters are very complex and difficult mechanisms to simulate in the laboratory. A countless number of different scenarios are possible, depending on the chemicals and geotextiles characteristics and on in-service filter conditions. Thus, the results of laboratory research are still limited and focused on specific situations. Despite the complexity of the problem, important contributions can be found in the literature regarding chemical and biochemical clogging of geotextile filters under laboratory and field conditions.

High alkalinity ground water will precipitate calcium and magnesium (Koerner & Koerner 2005) and conditions such as those found in tailings dams or in natural soils may favour the precipitation of different elements. Chemical clogging of geotextiles in iron tailings can be influenced by multiple factors, such as concentration of ferrous iron ions, pH, hydraulic conditions, temperature, microorganisms, redox potential and oxygen partial pressure, and reductions in flow rates in column tests of up to 73% have been reported (Liu *et al.* 2021a). Woo (2005) reports calcium oxide (a major component of cement), dissolved from cement grouts used for ground reinforcement during tunnel construction, as being one of the main clogging materials in tunnel drainage systems, in addition to calcium carbonate and red sediments containing iron and soil particles (Kim *et al.* 2020a). According to Carey *et al.* (2000) the precipitation of chemicals, sulphates and iron oxides which can commonly cause clogging is much less prevalent under anaerobic and reduced conditions.

Veylon *et al.* (2016) present a thorough investigation on the performance of geotextile filters in trenches after 18 years in service. The formation of a calcite crust on the downstream face of the geotextile envelopes and of the reference drainage system (gravel without filter) (Figure 22) was the primary mechanism observed underlying the reduction in filter performance. The results of field instrumentation in the trenches revealed that the reference trench and the trench with the woven geotextile showed severe reductions in flow rate (93% for the reference trench and 94% for the trench with the woven geotextile filter). The measurements of flow rate in a trench with a nonwoven geotextile were compromised due to possible leakage of fluid to neighbouring trenches. The clogging rate, defined as a function of the reduction of flow capacity with time, varied from 16 to 21% for the trenches with geotextile filter and 73% for the reference trench. It was also observed that the presence of the geotextile filters reduced clogging of the slotted drainage pipes of the trenches. The authors

concluded that after 18 years in service the geotextiles performed well in terms of mechanical resistance and filtration performance.
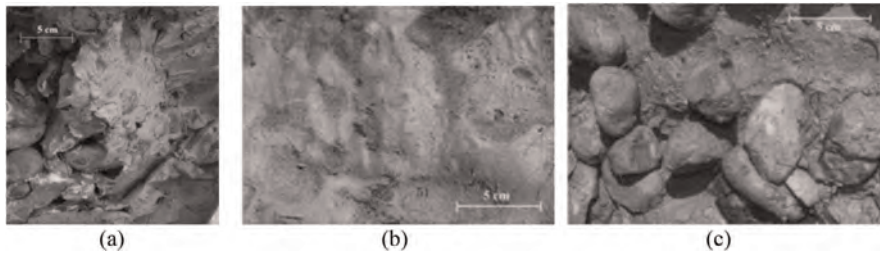
Figure 22. Calcified interfaces between gravel and downstream calcite crust: (a) Reference trench (no filter), (b) Nonwoven geotextile filter, (c) Woven geotextile filter (modified from Veylon *et al.* 2016).

The clogging mechanism of geotextile filter envelopes of perforated corrugated pipes (socked pipes), 3 to 15 years old, in an arid region, was investigated by Guo *et al.* (2020). Three major slightly soluble salts (calcium carbonate, calcium sulphate and magnesium carbonate) are present in arid and semi-arid soils. Reductions in geotextile permeability of up to 99.5% were observed, although the permeability coefficients of the partially clogged geotextiles were still close or greater than those of the neighbouring soils ($k_{GT}/k_{soil} = 0.85$, or between 8.8 and 42.7). Silicon dioxide (SiO_2) and calcium carbonate ($CaCO_3$) were identified as common clogging substances in arid and semi-arid regions.

Increase in precipitation of salt crystals with increasing temperature and flow rate was observed by Guo *et al.* (2021) in immersion and permeability tests on geotextiles (Figure 23). The authors observed that the structure of the geotextiles tested did not promote or inhibit the chemical precipitation process under static (no flow) conditions. Guo *et al.* (2022) present a coupled model of chemical clogging and permeability coefficient of a geotextile filter considering the processes of geotextile fibre diameter increase after crystal precipitation and accumulation of crystal precipitates on the surface of the geotextile fibres.
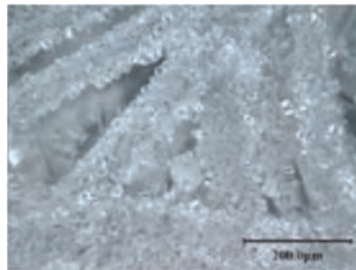
Figure 23. Salt crystals attached to the fibres of a nonwoven geotextile (Guo *et al.* 2021).

The use of construction and demolition residues in geotechnical construction works has markedly increased in the last decades in response to environmental protection requirements and better sustainable construction practices, besides the significant volume that this type less harmful or inert residues can occupy in landfills. Therefore, researchers have investigated the clogging potential of geotextile filters in contact with such materials. The deposition of tufa precipitate (Figure 24) from the effluent of recycled concrete aggregate (*RCA*) in the voids of nonwoven geotextiles was investigated by Abbaspour & Tanyu (2021). The two major minerals

were identified as calcium carbonate ($CaCO_3$, mainly calcite, more dominant at the top face of geotextile specimens subjected to column tests) and calcium sulphate ($CaSO_4.2H_2O$, mainly gypsum, more frequently encountered on the bottom surface of the specimens). The authors observed a good performance of the filter but pointed out that a loss of filtration capacity of the system of the order of 50% to 80% after 25 years should be expected, which would require a reduction factor to account for chemical clogging between 2 to 3.5. Bilgen *et al.* (2020) also investigated the performance of geotextile filters in contact with *RCA* by means of column tests. In this case woven, monofilament, geotextiles were tested and average reductions in flow rates between 19 and 81%, reductions of *POA* between 37% and 65% and reductions in O_{95} between 25% and 51% were observed. Nevertheless, the authors report post-test geotextile permeability coefficients still between 5 and 200 times that of typical clean uniform sand layers. Britto (2020) reports no significant variations in the coefficient of permeability of systems consisting of sand and rubble dust from recycled construction and demolition wastes and nonwoven geotextiles in permeability tests under confinement. No significant changes in effluent rate were observed by Lee & Bourdeau (2006) in 2 weeks duration filtration tests on systems consisting of a nonwoven geotextile filter underneath rubbleized concrete aggregate agglomerated with asphalt emulsion and polymer modified prime chemicals exhumed from an old concrete pavement. Odabasi *et al.* (2022) also found satisfactory performance of geotextile-recycled materials combinations in long-term filtration tests. In this case, woven and nonwoven geotextiles were tested in contact with *RCA*, recycled asphalt pavement, foundry sand and recycled asphalt shingle. In 82% of the tests the performance of the geotextile filter was satisfactory. The authors discuss the limitations of current filter criteria to recycled material-geotextile systems. Thus, despite the still limited amount of data, the results so far seem to indicate satisfactory performance of geotextile filters in contact with construction wastes commonly used in geotechnical works.

The formation of ochre is a biochemical clogging process and can severely compromise the performance of filters, being common in lateritic soils of tropical regions. In Brazil, the first observation of this type of clogging mechanism in granular drainage systems occurred in the Rio Grande Dam, built between 1926 and 1937, close to the city of São Paulo (Kanji *et al.* 1981). Results of variable head permeability tests, 1.5-year duration, showed the formation of ochre and a 28-fold reduction in the permeability coefficient of the granular filter material over a period of 550 days. Other cases of clogging of granular filters caused by ochre formation can be found elsewhere (Terzaghi and Leps 1958, Spencer *et al.* 1963, Petersen 1966, Grass 1969, Infanti and Kanji 1974, Xu *et al.* 1976, Ferreira 1978, Guerra 1980, Lindquist and Bosegno 1981, Nogueira Junior 1988). Obviously, ochre formation can also clog geotextile filters, as shown in Figure 25 (Palmeira & Fannin 2002) and will occur only under suitable electrochemical conditions found at nonaerated-aerated soil-filter interfaces (Mendonca and Ehrlich 2006).
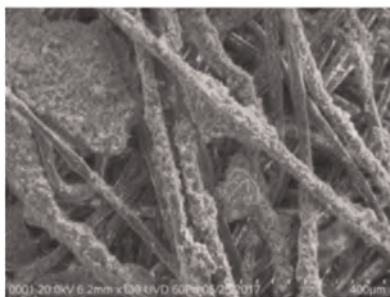
Figure 24.   Microscopic image of tufa precipitates on geotextile fibres (Abbaspour & Tanyu 2021).

The presence of a noticeable ochre-brown deposit on the geotextile as well as on the enclosed stone aggregate of the underdrainage system of two tailings dams in South Africa is reported by Scheurenberg (1982). The clogging mechanism was attributed to the precipitation of ferric hydroxides, such as goethite, and oxidation of ferrous compounds in solution at pH smaller than about 5. The author states that similar clogging mechanism would have occurred had graded sand drains, without a geotextile filter, been used.
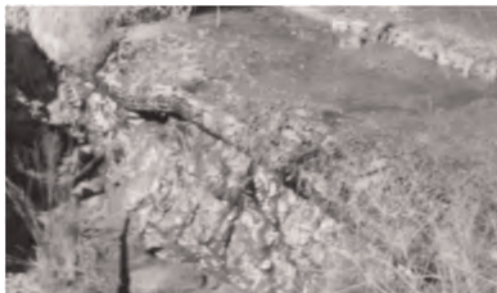
Figure 25.   Clogging of a geotextile filter caused by ochre formation.

Puig *et al.* (1986) highlight the importance of the identification of the parent rock, presence and type of vegetation, pedologic analysis and chemical analysis of the water to assess the potential of ferric clogging of geotextile filters. Based on the case-histories analysed, the authors state that ferric clogging risk is extremely low (but not eliminated, depending on the influence of organic matter) in calcareous areas where water is free from any ferrous iron. On the other hand, non-calcareous areas rich in ferrous iron and organic matter favour the development of heterotrophic bacteria *Sphaerotilus* which may cause ferric clogging.

The influence of ochre formation on the performance of a geotextile filter will depend on the clogging intensity. Ochre formation in a geotextile filter envelope of a drainage layer had no influence on the hydraulic conductivity of the drainage system of Torcy-Vieux dam, in France (Testemale *et al.* 1999). In this case, it was observed that the partial clogging was caused by clay particles associated to some level of ochre formation, particularly up to a depth of 1.2 mm in the geotextile layer.

Fibre roughness, specific surface, distance between fibres, geotextile thickness and flow rate are important factors in iron ochre biofilm formation (Mendonca 2000, Mendonca *et al.* 2003). Mendonca *et al.* (2003) comment that more severe clogging of woven geotextiles than of nonwoven geotextiles should be expected due to the discrete localised openings of the former. Metcalf *et al.* (1995) observed more severe reductions in geotextile permeability caused by iron staining in woven slit-film (up to 95% reduction) and heat-bonded nonwoven (up to 85.5%) than in needle-punched nonwoven geotextiles (up to 76% reduction) separator geotextiles in permanent highways. Iron-oxide precipitates were also observed in exhumed geotextile (nonwoven, heat bonded and slit-film geotextiles) separators after 5 years in service in highways with a long history of poor pavement performance (Black and Holtz 1999). The observations suggested that precipitation was probably higher in slit-film geotextiles (14.5% to 95% permeability coefficient reduction) and that heat-bonded nonwovens were more susceptible to clogging ($\cong$ 85% permeability reduction) than needle-punched nonwoven geotextiles (33.7% to 76% permeability reduction). Iron-oxide precipitates on the woven geotextiles seemed to be deposited on the tapes, whereas they tended to be distributed throughout the structure of the nonwoven geotextiles. According to Koerner and Koerner (2015), a woven slit-film geotextile should not be used for critical filtration applications because of poor control over its opening sizes due to nonbonding of its intersecting fibres.

Mlynarek *et al.* (1990) observed ochre formation on only 5% of the geotextile surface of the upstream side of a geotextile filter in specimens exhumed from a small dam in Poland after 8 years in service. Roots of plants crossing the full thickness of the geotextile in four points were also observed. Permeability tests on the exhumed specimens revealed reductions of geotextile permeability between 11% (drainage system downstream face) and 50% (upstream face), but still with a geotextile permeability coefficient 10 times higher than that of the base soil.

Significant clogging (7.5 to 45.3-fold reductions in geotextile permeability) due to ochre formation (Figure 26) was observed in sand and geotextile filters by Mendonca and Ehrlich (2006) in long-term (up to 1,573 hours) column tests on soil-geotextile (or sand) filter-gravel systems. The significant clogging mechanisms observed (more intense in a light nonwoven tested) did not cause relevant reductions in the hydraulic conductivity of the soil-filter system. Reductions of up to 95.5% in the coefficient of permeability of nonwoven geotextile filters due to ochre formation have also been observed in bank protection works in canals, rivers and coast structures (van Zanten and Thabet 1982, Abromeit 2002). According to van Zanten and Thabet (1982), clogging was observed in most of the sites investigated in a research study in Dutch canals, river and coast structures, but the geotextile permeability remained larger than that of the subsoil.
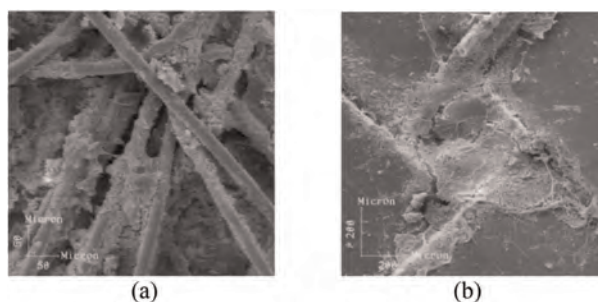
Figure 26.   Examples of ochre formation in geotextile filters in column tests (Mendonca 2000): (a) Light nonwoven geotextile (200X magnification), (b) Woven geotextile (80X magnification).

Submersion of the filter has been commonly adopted to avoid conditions favouring ochre formation, for both granular and synthetic filters. The effect of submersion on ochre formation in a woven geotextile was investigated by Correia *et al.* (2017). The authors point out that despite submersion, dissolved oxygen can cause ochre formation due to diffusion, but even a small depth of submersion can reduce significantly ochre biofilm formation. In general, ochre was found deposited on the surface of the geotextile filaments (Figure 27, Correia 2014) and that the geotextile pores were not completely blocked. Results of tests performed by Correia *et al.* (2017) suggest that there is a maximum submersion depth threshold of the geotextile beyond which the influence of submersion becomes negligible, since the results of tests with geotextile submersion depths of 20 mm and 45 mm were equivalent.
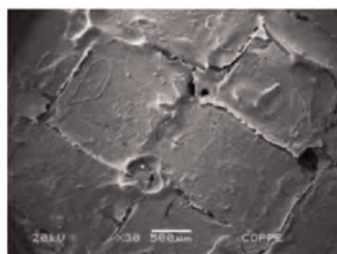
Figure 27.   Image of ochre formation on the woven geotextile surface (Correia 2014).

Correia *et al.* (2022) performed column tests on a woven geotextile under three different submersion conditions and observed a marked reduction in Fe(II) and Fe(III) retention in the geotextile after percolation with D-glucose. The flow of D-glucose stimulated a pre-existing population of iron-reducing bacteria, which reduced Fe(III) to Fe(II) in anoxic pockets within the ochre biofilm, causing some loss of the ochre structural integrity.

The use of water jet to remove ochre formation in deep horizontal drains has been commonly used in periodical maintenance works. Ehrlich *et al.* (2021) report the influence of clogging of geotextile filters of deep horizontal drains on the movement of a talus-colluvium deposit in the state of Rio de Janeiro, Brazil. Maintenance works of the drains consisted of applying water jet to the drains once a year, before the raining season (Ehrlich 2023). However, for three years in a row maintenance was not done, causing dehydration of the ochre, making it impossible to remove by water jetting. This caused the movements of the slope to increase, requiring the installation of new deep horizontal drains.

3.4 *Mining tailings-geotextile filter interaction*

Geotextile filters have been extensively used in mining applications. The good performance of the filter in such applications is of utmost importance for the stability of mining structures such as tailings dams. This section discusses some aspects of applications and performance of geotextile filters in such works.

One of the complicating factors for filter performance in tailings dams is how the tailings are disposed. If the tailings or base soil adjacent to the filter is placed hydraulically, the mobility of its fine fraction may cause impregnation or blinding of the geotextile, which may compromise its performance (Legge 2004, Palmeira *et al.* 2010). In case of tailings disposed far from the filter, only fine particles and particles in suspension will reach the filter (larger particles will sediment along the way). Microscopic images of geotextile specimens exhumed from two tailings dams support this statement, as shown in Figure 28, where values of impregnation level (λ) ranging from 2 to 10 were obtained for geotextile specimens exhumed from tailings dams, as reported by Palmeira *et al.* (2010). These authors suggest that a testing technique simulating more accurately the type of deposition of the tailings in the field, such as the use of flumes, may provide more accurate information on filter performance than conventional filtration tests.
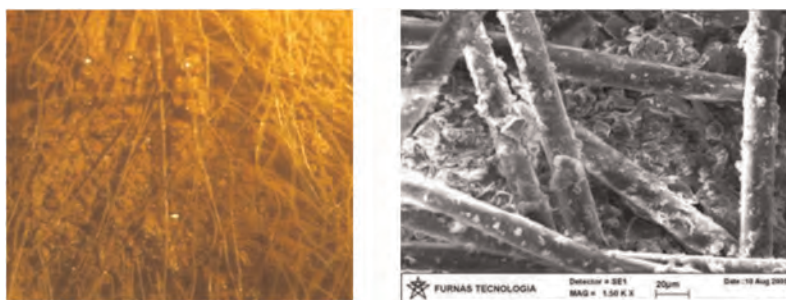
Figure 28. Intense impregnation of geotextile filters by fine tailings (Beirigo 2005).

Wind blow of the fine fraction of tailings can also cause impregnation of filters and drains. In such instances, Legge (2004) recommends the use of a sacrificial layer of geotextile (typically a light nonwoven product) as cover to the drain during construction to be removed immediately before the placement of tailings adjacent to the permanent filter. As commented earlier in this paper, the presence of the entrapped soil particles in the geotextile voids will

reduce its compressibility (Palmeira *et al.* 1996, Palmeira & Gardoni 2000). However, the partially clogged geotextile can still undergo significant compression, depending on the degree of impregnation and stress level. In addition, the presence of the particles in the geotextile voids reduces pore dimensions through which additional base soil particles may pipe (Palmeira & Trejos-Galvis, 2017), changing the conditions for filter clogging.

Despite the severe conditions of utilization, numerous examples of good performance of geotextile filters in tailings dams have been reported in the literature. The performance of different drainage systems incorporating geotextiles in some mine tailings dams in South Africa is presented by Bentel *et al.* (1982), who reported cost savings of up to 33% with solutions incorporating geotextiles and equally good performance as granular filters over 6 years of monitoring. The possibility of filter clogging due to ochre formation is considered of particular relevance by those authors. Similar good performance of geotextile (woven and nonwoven) filters in a tailings dam was observed by Haas (1982), as well as of a nonwoven geotextile in drainage blankets, chimney drain and foundation relief wells in tailings dams up to 74 m high in Brazil (Montez 1987). Similar good performance was observed by Mansen and Balbin (2008) with the use of a light geotextile filter and of a geocomposite for drainage in a 30 m high tailings dam in Peru.

Palmeira *et al.* (2010) report values of GR_{ASTM} (as per ASTM D5101) close to 1 in gradient ratio tests on a tailings-geotextile system for which clogging was observed in the filter of a vertical drainage system of a tailings dam (same tailings and geotextile as tested in the laboratory) after 6 years in service. These authors point out that the value of GR_{ASTM} alone may not be sufficient for the prediction of a good performance of the filter of vertical drainage systems similar to those employed in one of the dams studied and the values of gradient ratio obtained from ports closer to the geotextile specimen may be useful for a sounder decision on the filter to be used. This is particularly relevant in the case of internally unstable materials. Besides, tailings specimen preparation in the laboratory may not be realistic regarding the influence of tailings disposal in the field, as commented earlier. Values of *GR* between 0.7 and 1.2 were obtained in gradient ratio tests on tailings-nonwoven geotextile systems using cyclic flow by Fannin and Pishe (2001). In tests on a woven geotextile, values of *GR* between 0.1 and 2.0 were obtained, with intense piping through the more open woven geotextile tested.

Palmeira *et al.* (2005) obtained values of gradient ratios (GR_{ASTM}) varying between 1.1 and 1.3 in gradient ratio tests on tailings-nonwoven geotextile systems subjected to vertical stresses of up to 2000 kPa. Entrapped tailings particles in the geotextile reduced its compressibility. Despite partial clogging having been observed the geotextiles remained 5.5 to 420 times more permeable than the tailings. It was noted that considerably large particles (Figure 2b) were capable of intruding the geotextile voids due to vibration during specimen preparation, confinement and greater particle density in the case of ore tailings, which can facilitate the displacement of fibres and the intrusion of particles in the geotextile. Large particles in the geotextile voids were also observed by Niec *et al.* (2019) in specimens of a nonwoven geotextile filter exhumed from a small dam drainage system in Poland and by Palmeira *et al.* (2010) in a geotextile filter of a tailings dam. In similar gradient ratio tests on internally unstable tailings-geotextile systems, Palmeira *et al.* (2010) observed piping through two nonwoven geotextiles with values of *GR* close to 0.5, but rather constant with increasing vertical stress throughout the test. Even smaller *GR* values were obtained using the hydraulic heads measured at ports closer (3mm and 8 mm above the filter) to the geotextile layer. For the heavier geotextile tested (M_A = 627 g/m2), the authors argue that the presence of needle holes left after the needle-punching manufacturing process may be a reason for the low values of *GR*. Haliburton and Wood (1982) observed that for one of the needle-punched geotextiles subjected to *GR* tests flow occurred through the needle holes even when the other portions of the geotextiles were clogged with silt particles. However, under field conditions, such holes may not play an important role with respect to piping due to possible geotextile distortion during its installation and placement and compaction (when executed) of the cover material (Palmeira *et al.* 1996).

The use of nonwoven geotextiles in association with thin granular filter layers may be effective in reducing clogging of geotextile filters in mining applications, besides additional benefits (Legge 2004). The use of thin sand layers between the tailings and the geotextile filter in gradient ratio tests was investigated by Liu *et al.* (2021b). Values of *GR* between 0.38 and 0.53 were obtained even with the sand layer above the geotextile. However, much less quantities of tailings particles piped through the filters than the commonly used limit of 2500 g/m^2 proposed by Lafleur *et al.* (1989). The presence of the sand layer prevented the formation of a mass of fine particles at the soil-geotextile boundary, lowering the clogging potential of the geotextile and increasing the drainage capability of the system, especially under high hydraulic gradients. Nevertheless, it should be pointed out that too thin sand layers with uniform thicknesses are difficult to execute in the field.

4 MODELLING FILTER PERFORMANCE

Because of the complex nature of geotextile filter behaviour, different approaches for modelling geotextile filter performance have been proposed by several authors using simple or sophisticated solutions. Early proposals for the investigation of geotextile retention capacity employed geometrical models for nonwoven geotextile filters simulated as an array of cylinders (Laflaive & Puig 1974, Fayoux & Evon 1982, Giroud 1996, for instance). Methods based on probabilistic analyses have also been developed to estimate the nonwoven geotextile pore size distribution (Gourc 1982, Faure 1988, Lombardi 1989, Faure *et al.* 1990, Sória & Viviani 1993, Elsharief & Lovell 1996, Urashima & Vidal 1998, Simmonds *et al.* 2007, Rawal 2010 and 2012, for instance). More recent research has employed more sophisticated approaches such as the use of the discrete element method (*DEM*), fractal geometry theory and elementary cellular automata neural networks (Liu *et al.* 2011, Ozelim *et al.* 2016, Chen *et al.* 2019, Ibrahim & Meguid 2022, Ryoo *et al.* 2022b).

To some extent, both geometrical and probabilistic models may predict satisfactorily the geotextile pore size if appropriate parameters intrinsic to these methods are properly chosen or backanalysed. For instance, Giroud (1996) proposed the following equation to estimate geotextile filtration opening size based on a geometrical model

$$\frac{O_F}{d_f} = \frac{\delta}{\sqrt{1-n}} - 1 + \frac{\xi n}{(1-n)t_{GT}/d_f} \tag{5}$$

Where O_F is the geotextile filtration opening size, d_f is the geotextile fibre diameter, n is the geotextile porosity, t_{GT} is the geotextile thickness and δ and ξ are empirical parameters.

Palmeira & Trejos-Galvis (2018) extended the application of equation 5 to different values of the geotextile pore sizes (O_κ) corresponding to a given percentage (κ), where κ is the percentage of remaining pores that are smaller than O_κ. With appropriate values of δ and ξ, a satisfactory comparison between O_κ/d_f predicted by equation 5 and measured values using bubble point tests was obtained, as shown in Figure 29a, in tests on five nonwoven geotextiles under different vertical confining stresses (up to 1000 kPa). However, the values of δ and ξ in this case are likely to be product specific. The method proposed by Faure *et al.* (1990) was also calibrated to predict O_κ for the same geotextiles in Figure 29a. This method is based on the probability of a soil particle passing through a nonwoven geotextile assumed as a random stacking of elementary films with a given thickness. The calibration of the elementary film thickness yielded the comparison between predicted and measured O_κ/d_f values shown in Figure 29b, where a satisfactory level of agreement can also be noted. The calibrated Faure *et al.* (1990) method was also capable of predicting well the geotextile pore size distribution curve, as shown in Figure 30. However, the predictions of the pore size distribution curves using the geometrical approach (equation 5) were not as accurate as those of the probabilistic method (Palmeira & Trejos-Galvis 2018). Thus, probability seems a

powerful tool for the prediction of nonwoven geotextile pore dimensions, although some improvements are necessary for a broader application to any nonwoven product.
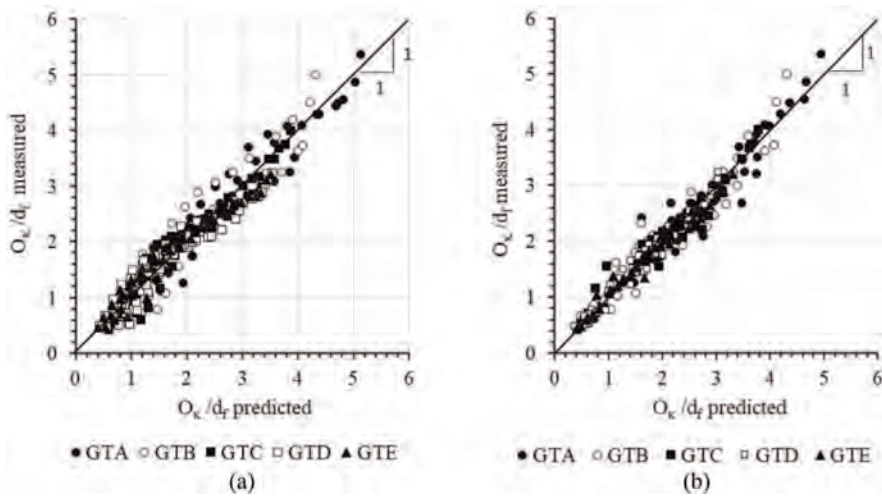
Figure 29. Comparisons between predicted and measured pore sizes: (a) Predictions by equation 5, (b) Predictions by Faure *et al.* (1990) (modified from Palmeira & Trejos-Galvis 2018).
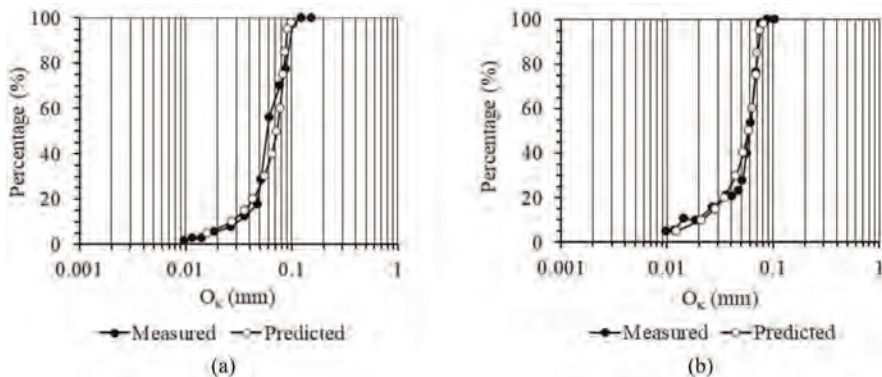
Figure 30. Measured and predicted pore sizes distribution curves by Faure *et al.* (1990): (a) For zero vertical confining stress, (b) For a vertical stress of 100 kPa. (Palmeira & Trejos-Galvis 2018).

Rawal (2010) developed a model for the prediction of nonwoven geotextile pore size distribution combining stochastic and stereological or geometrical probability approaches, which incorporates the influence of geotextile fibre orientation. The model predicted variations in O_{95} of a light (75 g/m^2) nonwoven geotextile of up to 26% for the range of values of the fibre directional parameter used in the method. An approach to model the compression induced morphological behaviour of nonwoven geotextiles was introduced by Rawall (2012). A mechanistic model of pore size distribution was proposed for geotextiles under compression also considering the out-of-plane orientation of the geotextile fibres. Predicted and measured pore diameters of a thermally bonded nonwoven product were compared, but under much lower vertical stresses (< 2.1 kPa) than those expected in geotechnical works. The trend of the predictions was satisfactory, but deviations between predicted and measured O_{95} ranging from 20% to 48% were observed. Regarding geotextile fibre orientation, using X-ray computed

34

tomography, Ishikawa (2018) observed that most of the fibres tend to be oriented parallel to the plane of a nonwoven web in the case of parallel-laid webs. The needle-punching manufacturing process can locally orient some fibres perpendicular to the web plane. Compression will further increase the percentage of fibres parallel to the plane of the geotextile.

The discrete element method was employed by Chen *et al.* (2019) to evaluate the variation of the apparent opening size of a heat bonded nonwoven geotextile with tensile strain under uniaxial and biaxial tensile loadings. The results obtained suggest that the change in the orientation angle of the fibres was smaller during biaxial tensile tests than during uniaxial tensile tests. The authors also observed that the deformation pattern of the modelled geotextile during the biaxial tensile test was almost axisymmetric. The rates of opening size increase with tensile strain under uniaxial and biaxial loading were similar to those obtained by Palmeira *et al.* (2019) in bubble point tests on nonwoven, needle-punched, geotextiles subjected to tension, but significantly smaller than those obtained by Wu *et al.* (2008) in tests on a heat bonded geotextile.

5 INNOVATION AND ADVANCES IN GEOTEXTILE FILTERS

The need for better performance of geotextile filters facing severe conditions as those described in this paper has led to the development of new geotextile products. Combinations of existing products with alternative drainage materials have also been the subject of research and applications by several authors (Palmeira 2016, Palmeira *et al.* 2021a, b, Touze 2021). For instance, Narejo *et al.* (2013) report the good performance of a hybrid layered monolithic filter consisting of a nonwoven needle-punched and a woven monofilament for the filtration of fine particles of coal combustion residuals. A better performance of a filter consisting of the combination of a thin layer of one nonwoven needle-punched geotextile and a thicker layer of a second nonwoven needle-punched geotextile in comparison with a conventional monolayer geotextile is reported by Sabiri *et al.* (2017). Ryoo *et al.* (2022b) describe and analyse the use of woven and nonwoven conical filters by means of laboratory and computational modelling (*DEM* simulations), where higher simulated system permeabilities with the new product were obtained in comparison with conventional geotextile counterparts. The use of alternative geocomposites for drainage and the potential use of biodegradable geotextiles in temporary filter applications are discussed in Junqueira *et al.* (2006), Silva & Palmeira (2013) and Prambauer *et al.* (2019). In addition, the development of new and advanced geotextile filters has also increased.

In addition to the ingenious combinations of existing geotextile products with alternative materials, materials science and advances in manufacturing processes have produced innovations in geotextiles with repercussions on their applications in geotechnical and geoenvironmental engineering. One example of such developments is the use of wicking geotextiles, which are products capable of draining water out from unsaturated soils. Wang *et al.* (2017) describe the development and application of a type of wicking woven geotextile made of special hydrophilic and hygroscopic fibres with multi-channel cross sections (Figure 31). The geotextiles contain micro-channels with diameters varying between 5.7 and 47.8 microns, high shape factor and hight wicking fibre specific surface area. In an experiment with this geotextile in a base course on a fine-grained subgrade, the authors observed that the geotextile did remove water out of the cross section of the model road, especially after a simulated rainfall of 38 mm/h intensity for 40 min. The wicking geotextile effectively wicked water out from the base soil even when this layer was prepared at a moisture content close to the optimum moisture content. Guo *et al.* (2019) observed that in average the wicking geotextile reduced the water content of the overlying soil in a region approximately 200 mm thick above the geotextile layer in column tests. Guo *et al.* (2022) tested a modified wicking geotextile with additional wicking fibre yarns artificially knitted into the geotextile. The results obtained in laboratory tests showed that the wicking geotextile drained both free

and capillary water, reducing the average gravimetric water content of the soil. The wicking geotextiles were also able to wick water from both the overlying and the underlying soils, and the results suggest that the influence range of reducing the moisture content of the underlying soil due to a siphon effect was of at least 100 mm. Other successful applications of wicking geotextiles under unsaturated conditions are reported by Azevedo & Zornberg (2013), Zhang *et al.* (2014), Guo *et al.* (2017), Lin *et al.* (2017) and Zornberg *et al.* (2017), Lin *et al.* (2021). Zaman *et al.* (2022) observed greater wettability of a wicking woven geotextile in comparison with a non-wicking one and to a nonwoven geotextile, indicating that water penetrates faster in wicking geotextiles. Wettability of nonwoven geotextiles can be increased during manufacturing with the addition of a surfactant solution to the geotextile fibres surface to make them hydrophilic. Bouazza (2014) shows significant increases in the wettability of two nonwoven geotextiles along their in-plane direction after this type of treatment.
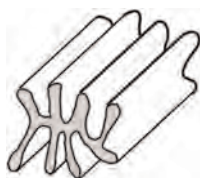
Figure 31.   Shape of a wicking geotextile fibre.

Guo *et al.* (2021) carried out an experimental study on the performance of pavement bases under three conditions: without geotextile on the subgrade, with a non-wicking geotextile on the subgrade and with a wicking geotextile on the subgrade. The pavement consisted of a granular layer (0.3 m thick) on a subgrade (0.9 m thick, *CBR* of 4% or 5%) which was constructed in a large testing box and subjected to cyclic loading by a circular rigid plate. The pavement was subjected to series of simulated rain fall and surface loading. Overall, the authors observed that the water content in the wicking geotextile section decreased at a significantly faster rate than in the control and non-wicking geotextile sections. The permanent surface deformation of the section with the wicking geotextile was considerably smaller than those of the other sections, as shown in Figure 32.
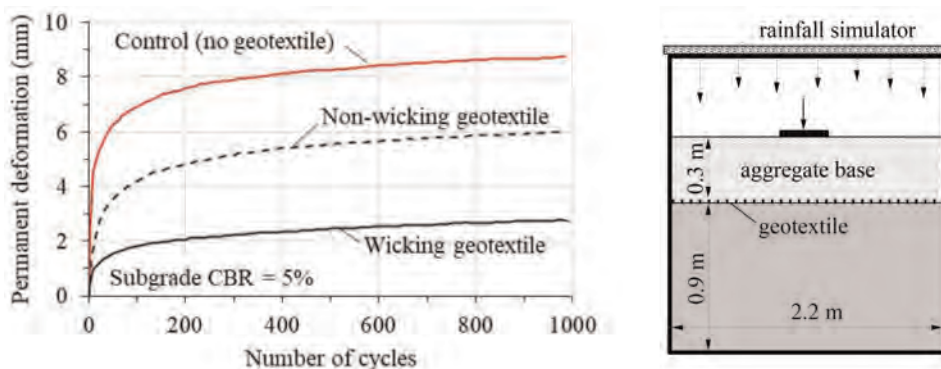
Figure 32.   Permanent deformation at the pavement surface at 7 days after the first rainfall simulation (modified from Guo *et al.* 2021).

Filtration tests on nonwoven geotextiles treated by negative ions were carried out by Lee and Jeon (2008) aiming at evaluating the influence of the treatment on the reduction of clogging. The principle was that the negatively charged fine clay particles would be repelled

by the negatively charged geotextile fibres. The level of geotextile clogging calculated based on the mass of soil particles entrapped in the geotextile was reduced by 33.8% and the discharge rate increased 16% for the geotextile with higher electric charge in comparison with the control one (no electric charge). The highest clogging level was observed in the control geotextile.

Significant improvements in the performance of geotextiles are expected in the coming years due to the promising results of recent research on the use of geotextiles with fibres coated with graphene and nanoparticles (Kelsey 2015, 2016, Kim *et al.* 2020, Senadheera *et al.* 2022), as well as due to other forms of incorporating advanced materials in the manufacture of geotextiles. Regarding the filtration function, the incorporation of graphene is expected to improve filter performance and endurance by increasing mechanical strength, antimicrobial performance (filter biological clogging prevention) and hydrophilic behaviour, for instance (Kelsey 2015). Strength increase will reduce or avoid the possibility of mechanical damages in geotextile filters. Antimicrobial action may reduce biological clogging of geotextile filters in landfills, for instance. Graphene enhanced geotextiles are already being manufactured in Australia and in the United States (Kelsey 2016). It is also likely that in the future geotextile filters may benefit from the advances in the research on smart textiles, particularly as a response to the COVID-19 pandemics. For example, the use of new antimicrobial agents to be incorporated into advanced masks used as personal protective equipment for healthcare professionals has been investigated (Ivanoska-Dacikj & Stachewicz 2020), whose application in the manufacture of geotextile filters could be considered.

6   CONCLUSIONS

This paper discussed factors that may influence the actual behaviour of geotextile filters. By being cost-effective and easy to install, some important issues are frequently overlooked in geotextile filter applications. Based on the experience gained and lessons learned over the years, the main conclusions regarding the behaviour of geotextile filters are as follows.

Most (if not all) problematic situations for geotextile filters are also problematic for natural filters. These are the cases where biological and/or chemical clogging can take place as well as for filters in contact with internally unstable soils. Under complex field conditions such as those of filters in tailings dams, filters in contact with internally unstable base soils or subjected to the flow of liquids with solids in suspension, it is very difficult, if possible, to specify a problem-free filter material, be it natural or synthetic. Despite such uncertainties, some general recommendations can reduce or avoid poor filter performance.

Partial clogging of the filter before its operation can take place due to spreading and compaction of the base soil on the geotextile layer. Impregnation of the filter will reduce its permeability, increase its retention capacity and change the condition for further clogging during filter operation. Thus, appropriate reduction factors should be used to account for nonwoven geotextile impregnation by soil particles. Investigations on the behaviour of internally unstable soil-geotextile systems have shown that significantly greater reductions factors than the usual value of 10 may be necessary to account for the flow rate reduction caused by geotextile impregnation and/or blinding. Some contributions in the literature discussed in this paper may provide useful tools to predict geotextile performance under such conditions.

In case of drainage systems of landfills, waste management and selection may reduce the risk of drainage system malfunction. Practices such as leachate recirculation, disposal of construction debris, large amounts of organic matter, dewatered sludge and incinerated ash should be avoided. In addition, drainage pipes wrapped (or socked) with nonwoven geotextiles should not be used in leachate collection systems. More open geotextile filters (say $FOS > 0.13$ mm for nonwoven geotextiles and $FOS > 0.5$ mm and $POA > 15\%$ for woven geotextiles) and coarser ($d > 15$ mm) granular drainage materials have performed best. It is

recommended that leachate collection and removal systems should be kept under anaerobic conditions or under unsaturated conditions as long as possible to extend their service lives. Under similar severe conditions, nonwoven needle punched geotextiles seem less prone to clogging than heat bonded ones and woven geotextiles.

Due care should be taken with filters in arid and semi-arid regions due to the possible clogging action of silicon dioxide and calcium carbonate. The same applies to possible salt precipitation in engineering works in marine environment. Submersion of the drainage system can avoid or reduce the risk of filter clogging due to ochre formation.

In mining applications, tailings deposition may influence filter performance, particularly for vertical drainage systems. The possibility of ochre formation in the filter should also be foreseen depending on the composition of the tailings. The combination of a thin sand layer and a geotextile filter may be an appropriate solution when geotextile blinding is a possibility.

Laboratory testing should try to simulate as accurately as possible the hydraulic and physical conditions expected in the field. This includes the use of appropriate surcharges to simulate the overburden stresses on the buried geotextile filter as well as the deposition and compaction of the base soil on the geotextile filter. The simulation of the tailings deposition process is highly recommended in tests on tailings-geotextile systems. In tests with internally unstable soils, the measurement of the variation of soil permeability coefficient at different positions along the specimen heigh may provide useful information on system behaviour. Soil specimens in these tests should be high enough (say 100 mm or more) to accurately reproduce the internal instability mechanism taking place along the specimen height during testing. Measurements of hydraulic heads close to the geotextile filter may also provide useful information on geotextile clogging mechanism in gradient ratio tests.

Besides some conventional and simpler solutions to predict geotextile filter behaviour, recent more sophisticated theoretical solutions have been employed such and the use of discrete element modelling, neural networks, complex probabilistic analyses etc. that will certainly contribute to a better understanding and prediction of the behaviour of geotextile filters.

Despite the filter performance issues raised in this paper, geotextile filters are undoubtfully a great success. Failures often receive great exposition (and they should be exposed!). However, one should bear in mind that they have represented a tiny fraction of geotextile filter applications, many of them occurring due to the lack of appropriate design considerations and construction practices. A great advantage of a synthetic filter over a natural one is that the technological developments that may be incorporated into the former and the development of new products based on material science studies can reduce the possibility of failures and improve design. The future will certainly bring new products that will be more efficient, less expensive and will provide more environmentally friendly engineering solutions.

REFERENCES

Abbaspour, A. & Tanyu, B.F. 2021. Chemical Clogging and Geotextile Serviceability in Subdrains Adjacent to Recycled Concrete. *Geosynth. Intl.* 28(4): 402–420.

Abromeit, H.-U. 2002. Revetment Damage as a Result of Geotextile Colmation by Flocculated Ochreous Products and Possible Repair Methods. *Proc. 7th Intl. Conf. on Geosynthetics*, Nice, France, vol. 3: 1085–1088.

Adel, H.D., Bruin, P.D. & Hofmans, G. 1996. Influence of Stress on the Characteristic Opening Size. In J. Lafleur & A.L. Rollin (eds.), *GeoFilters'96*, Montréal, Québec, Canada, vol. 1: 157–166.

ASTM D5101. *Standard Test Method for Measuring the Soil-geotextile Clogging Potential by the Gradient Ratio*. ASTM Intl., West Conshohocken, PA, USA.

Azevedo, M. & Zornberg, J.G. 2013. Capillary Barrier Dissipation by New Wicking Geotextile. In Caicedo et al. (Eds.), *Proc. 1st Pan. Conf. on Unsatd. Soils*, Taylor & Francis Group, London, vol. 1: 559–565.

Beirigo, E.A. 2005. *Filter Behaviour of Geotextiles in Tailings Dams*. MSc. Thesis, Graduate Programme of Geotechnics, University of Brasília, Brasília, Brazil, 192 p. (in Portuguese).

Bentel, D., Robbertze, J., Smith M., 1982. The Use and Behaviour of Geotextiles in Underdrainage Systems of Gold Mine Tailings Dam in South Africa. *Proc. 2nd Intl. Conf. on Geosynthetics*, Las Vegas, USA, Vol. 1: 183–188.

Bhatia, S.K. & Huang, Q. 1995. Geotextile Filters for Internally Stable/unstable Soils. *Geosynth. Intl.* 2(3): 537–565.

Bhatia, S.K. & Smith, J.L. 1996. Geotextile Characterization and Pore-size Distribution: Part II. A Review of Test Methods and Results. *Geosynth. Intl.* 3(2): 155–180.

Bilgen, G., Houlihan, M., Ryoo, S., Wang Y. & Aydilek, A.H. 2020. Hydraulic and Environmental Compatibility of RCA with Filters and Subgrades in Highways. *Env. Geotech.*, 1–13 (Ahead of print), doi.org/10.1680/jenge.20.00040.

Black, P.J. & Holtz, R.D. 1999. Performance of Geotextile Separators Five Years After Installation. *J. of Geotech. and Geoenv. Engng.* 125(5): 404–412.

Blond, E., Veermersch, O. & Diederich, R. 2015. A Comprehensive Analysis of the Measurement Techniques used to Determine Geotextile Opening Size: AOS, FOS, O_{90}, and Bubble Point. *Proc. Geosynthetics 2015*, Portland, Oregon, USA, IFAI, vol 1: 1–10.

Bouazza, A. 2014. A Simple Method to Assess the Wettability of Nonwoven Geotextiles. *Geotext. and Geomembr.* 42: 417–419.

Britto, A.F.S. 2020. *Permeability of Systems Consisting of Recycled Concrete and Demolition Wastes and Nonwoven Geotextiles*. MSc. Thesis, Federal University of Goiás, Brazil (in Portuguese).

Brune, M., Ramke, H.G., Collins, H.J., Hanert, H.H. 1991. Incrustation Processes in Drainage Systems of Sanitary Landfills. *Proc. 3rd Intl. Landfill Symp.*, Sardinia, Italy, vol. 1: 999–1035.

Cancelli, A. & Cazzuffi, D. 1987. Permittivity of Geotextiles in Presence of Water and Pollutant Fluids. *Proc. of Geosynthetics'87*, New Orleans, LA, USA, vol. 2: 471–481.

Carey, P., Carty, G., Donlon, B. Howley, D. & Nealon, T. 2000. *Landfill Manuals: Landfill Site Design*. Irish Environmental Protection Agency, Wexford, Ireland, ISBN 1840950269.

Cazzuffi, D. & Cossu, R. 1993. Experimental Evaluation of Filter Performance for Geotextiles in Landfills. In S. Corbet and J. King (eds.), *Proc. Geotextiles in Filtration and Drainage*, Thomas Telford, UK., 78–94.

Cazzuffi, D., Ielo, D., Mandaglio, M.C. & Moraci, N. 2015. Recent Developments in the Design of Geotextile Filters. *Proc. 2nd Int. GSI-Asia Geosynthetics Conf.*, Seoul, Korea, vol. 1: 1–12.

Chen, H.-X., Liu, X., Feng, S.-J., Chen, J.-N., Zhang, D.-M. & Zhou, A. 2019. Microscale Investigation into Mechanical Behaviors of Heat-bonded Nonwoven Geotextile using DEM. *Geotext. and Geomembr.* 47: 429–438.

Colmanetti, J.P. 2000. *Performance of Geotextile Filters in Drainage Systems of Municipal Solid Wastes*. MSc. Thesis, Graduate Programme of Geotechnics, University of Brasília, Brazil (in Portuguese).

Colmanetti, J.P. & Palmeira, E.M. 2002. A Study on Geotextile-leachate Interaction in Large Laboratory Tests. *Proc. 7th Intl. Conf. on Geosynthetics*, Nice, France, vol. 2: 749–752.

Corcoran, B.W. & Bhatia, S.K. 1996. Evaluation of Geotextile Filter in a Collection System at Fresh Kills Landfill. In S.K. Bhatia and L.D. Suits (Eds), *Proc. of Recent Developments in Geotextile Filters and Prefabricated Drainage Geocomposites*, ASTM STP 1281, ASTM, USA, vol. 1: 182–195.

Correia, L.G.C.S. 2014. *Evaluation of the Influence of Oxygen Diffusion on the Formation of Ochre in Geotextile Filters*. MSc. Thesis, Coppe/Federal University of Rio de Janeiro, RJ, Brazil (in Portuguese).

Correia, L.G.C.S., Ehrlich, M. & Mendonca, M.B. 2017. The Effect of Submersion in the Ochre Formation in Geotextile Filters. *Geotext. and Geomembr.* 45: 1–7.

Correia L.G.C.S., Ehrlich, M., Mendonca, M.B. & Keim, C.N. 2022. Laboratory Studies on Ochre formation and Removal from Geotextile Filters. *Canadian Geotech. J.* 60(1): 31–43.

de Graauw, A. F., van Der Meulen, T. & van de Does de Bye, M.R. 1984. Granular Filters: 32 Design Criteria. *J. of Waterway, Port, Coastal, and Ocean Engng.* 110(1): 80–96.

Du, C., Xu, C., Yang, Y. & Wang, J. 2022. Filtration Performance of Nonwoven Geotextile Filtering Fine-grained Soil Under Normal Compressive Stresses. *Applied Sciences* 12(12638):1–29.

Elsharief, A.M. & Lovell, C.W. 1996. A Probabilistic Retention Criterion for Nonwoven Geotextiles. *Geotext. and Geomembr.* 14: 601–617.

Ehrlich, M. 2023. *Personal Communication*.

Ehrlich, M., Costa, D.P. & Silva, R.C. 2021. Long-term Monitoring of the Behavior of a Talus-colluvium Deposit. *Landslides* 18: 2225–2245.

Fannin, R.J. & Pishe, R. 2001. Testing and Specifications for Geotextile Filters in Cyclic Flow Applications. *Proc. Geosynthetics 2001*, Portland, Oregon, USA, vol. 1: 423–435.

Fatema, N. & Bhatia, S. 2019. Correlation between Capillary Flow and Dry Sieving Test Results of Woven and Nonwoven Geotextiles. *Proc. Geosynthetics 2019*, Houston, Texas, USA, IFAI, vol. 2: 974–983.

Faure, Y.H. 1988. *Approche Structural du Comportement Filtrant-drainant des Geotextiles*. PhD. Thesis, Université Joseph Fourier, Grenoble, France (in French).

Faure, Y.H., Farkouh, B., Delmas, Ph. & Nancey, A. 1999. Analysis of Geotextile Filter Behaviour After 21 Years in Valcros dam. *Geotext. and Geomembr.* 17:353–370.

Faure, Y.H., Gourc, J.P. & Gendrin, P. 1990. Structural Study of Porometry and Filtration Opening Size of Geotextiles. In I.D. Peggs (ed.), *Proc. Geosynthetics: Microstructure and Performance*, ASTM STP 1076, West Conshohocken, Pennsylvania, USA, vol. 1: 102–119.

Fayoux, D. & Evon, E. 1982. Influence of the Fibre Size on the Filtration Characteristics of Needle-punched Geotextiles. *Proc. 2nd Intl. Conf. Geotextiles*, Las Vegas, USA, vol. 1: 102–119

Ferreira, R.C. 1978. Physicochemical Clogging of Filters: A Trial Simulation in the Laboratory. *Proc. 6th Brazilian Cong. on Soil Mech. and Found. Engng.*, Brazil, vol. 1: 81–100 (in Portuguese).

Fischer, G.R., Holtz, R.D. & Christopher, B.R. 1994. Filtration Behaviour of Broadly Graded, Cohesionless Tills. *Proc. 5th Intl. Conf. on Geosynthetics*, Singapore, vol. 2: 659–662.

Fleming, I.R. & Rowe, R.K. 2004. Laboratory Studies of Clogging of Landfill Leachate Collection and Drainage Systems. *Canadian Geotech. J.* 41: 134–153.

Fleming, I.R., Rowe, R.K. & Cullimore, D.R. 1999. Field Observations of Clogging in a Landfill Leachate Collection System. *Canadian Geotech. J.* 36: 685–707.

Fourie, A.B. & Addis, P.C. 1997. The Effect of In-plane Tensile Loads on the Retention Characteristics of Geotextiles. *Geotech. Testing J.* 20(2): 211–217.

Fourie, A.B & Addis, P.C. 1999. Changes in Filtration Opening Size of Woven Geotextiles Subjected to Tensile Loads. *Geotext. and Geomembr.* 17: 331–340

Fourie, A.B., Kuchena, S.M. & Blight, G.E. 1994. Effect of Biological Clogging on the Filtration Capacity of Geotextiles. *Proc. 5th Intl. Conf. on Geosynthetics*, Singapore, vol. 2: 721–724.

Fourie, A.B. & Kuchena, S.M. 1995. The Influence of Tensile Stresses on the Filtration Characteristics of Geotextiles. *Geosynth. Intl.* 2(2):455–471.

Frischknecht, R., Stucki, M., Büsser, S. & Itten, R. 2012. Comparative Life Cycle Assessment of Geosynthetics versus Conventional Construction Materials. *Ground Engng.* 45(10): 24–28.

Gardoni, M.G. 1995. *Evaluation on the Applicability of Laboratory Tests and Filter Criteria for the use of Geotextiles with Soils of the Federal District*. MSc. Thesis, Graduate Programme of Geotechnics, University of Brasília, Brazil (in Portuguese).

Gardoni, M.G. 2000. *Study of the Draining and Filtering Behaviour of Geosynthetics Under Compression*. PhD. Thesis, Graduate Programme of Geotechnics, University of Brasília, Brazil (in Portuguese).

Gardoni, M.G. & Palmeira, E.M. 1999. Long Term Filtration Tests on Tropical Soil-geotextile Systems. Proc. *XI Panamerican Conf. on Soil Mech. Geotech. Engng.*, Foz do Iguaçu, Brazil, vol. 1: 69–73.

Gardoni, M.G. & Palmeira, E.M. 2002. Microstructure and Pore Characteristics of Synthetic Filters Under Confinement. *Géotechnique* 52(6): 405–418.

Goycoechea, J. Montoro, M.A. & Glatstein, D.A. 2020. Effects of Bio-clogging on Leachate Exposed Geotextiles for Filter and Drainage Layer Construction. *Proc. GeoAmericas 2020*, RJ, Brazil, 11 p.

Giroud, J.P. 1996. Granular Filters and Geotextile Filters. In Lafleur, J. & Rollin, A. (eds), Proc. Geofilters'1996, Montréal, Québec, Canada, vol. 1: 565–680.

Giroud, J.P., Bonaparte, R., Beech, J.F. & Gross, B.A. 1990. Design of Soil Layer-geosynthetic Systems Overlying Voids. *Geotext. and Geomembr.* 9(1):11–50.

Gourc, J.-P. 1982. *Quelques Aspects du Comportement des Geotextiles em Mécanique des Sols*. PhD. Thesis, University of Grenoble, France (in French).

Grass, L.B. 1969. Tile Clogging by Iron and Manganese in Imperial Valley, California. *J. of Soil and Water Conserv.*, 24: 135–138.

Guerra, M.O. 1980. Ação Química e Biológica na Colmatação de Filtros e Drenos. Implicações na Barragem do Rio Grande. *Proc. 13th Nat. Large Dams Sem.*, RJ, Brazil, vol. 2: 257–289 (in Portuguese).

Guo, C., Wu, J., Zhu, Y., Lin, Z., He, S., Qian, Y., Yang, H., Li, H. & Mao, W. 2020. Influence of Clogging Substances on Pore Characteristics and Permeability of Geotextile Envelopes of Subsurface Drainage Pipes in Arid Areas. *Geotext. and Geomembr.* 48: 745–746.

Guo, C., Yang, H., Lin, Z., Wu, J., Li, H., Wu, Z. & Mao, W. 2021. Effects of Chemical Precipitation on the Permeability of Geotextile Envelopes for Subsurface Drainage Systems in Arid Areas. *Geotext. and Geomembr.* 49: 941–951.

Guo, C., Zhao, Q., Wu, J., Li, H., Yang, H. & Wu, Z. 2022. Permeability Prediction in Geotextile Envelope After Chemical Clogging: A Coupled Model. *Geotext. and Geomembr.* 50: 1172–1187.

Guo, J., Han, J. Zhang, X. & Li, Z. 2019. Evaluation of Moisture Reduction in Aggregate base by Wicking Geotextile using Soil Column Tests. *Geotext. and Geomembr.* 47: 306–314.

Guo, J., Han, J., Zhang, X. & Li, Z. 2021. Experimental Evaluation of Wicking Geotextile-stabilized Aggregate base Over Subgrade Under Rain Fall Simulation and Cyclic Loading. *Geotext. and Geomembr.* 49: 1550–1564.

Guo, J., Wang, F., Zhang, X. & Han, J., 2017. Quantifying Water Removal Rate of a Wicking Geotextile under Controlled Temperature and Relative Humidity. *J. Mater. Civ. Engng.* 29(1): 04016181.

Guo, Y., Lin, C., Leng, W. & Zhang, X. 2022. Laboratory Evaluation of Different Geosynthetics for Water Drainage. *Geosynth. Intl.* 29(3): 254–269.

Haas, W.M. 1982. Geotextiles in Tailings Dike Construction: Laboratory and Field Observations. *Proc. 2nd Intl. Conf. on Geotextiles*, Las Vegas, USA, vol. 1: 205–210.

Haliburton, T.A. & Wood, P.D. 1982. Evaluation of the U.S. Army Corps of Engineer Gradient Ratio Test for Geotextile Performance. *Proc. 2nd Int. Conf. on Geosynthetics*, Las Vegas, USA, vol. 1: 97–101.

Hong, Y.-S. & Wu, C.-S. 2011. Filtration Behaviour of Soil-nonwoven Geotextile Combinations Subjected to Various Loads. *Geotext. and Geomembr.* 29: 102–115.

Ibrahim, A. & Meguid, M.A. 2022. CFD-DEM Modeling of Geotextile Clogging in Tunnel Drainage Systems. *Geotext. and Geomembr.* 50: 932–945.

Indraratna, B., Trani, L.D.O. & Khabbaz, H. 2008. A Critical Review on Granular Dam Filter Behaviour-from Particle Sizes to Constriction-based Design Criteria. *Geomech. and Geoengng: An Intl. J.* 3(4): 279–290.

Infanti, N., Jr. & Kanji, M.A. 1974. Preliminary Considerations on Geochemical Factors Affecting the Safety of Earth Dams. *Proc. 2nd Int. Cong. of the Int. Assoc. of Engng. Geology*, SP, Brazil, 33.1–33.11.

Ionescu, A., Kiss, S., Dragan-Bularda, M. Radulescu D., Kolozsi, E. Pintea, H. & Crisan, R. 1982. Methods used for Testing the Bio-colmatation and Degradation of Geotextiles Manufactured in Romania. *Proc. 2nd Int. Conf. on Geotextiles*, Las Vegas, NV, USA, vol. 2: 547–552.

Ishikawa, T. 2018. *Structure Analysis of Nonwoven Fabric by X-ray Computed Tomography*. PhD. Thesis, Shinshu University, Matsumoto, Nagano, Japan.

Ivanoska-Dacikj, A. & Stachewicz, U. 2020. Smart Textiles and Wearable Technologies – Opportunities Offered in the Fight Against Pandemics in Relation to Current COVID-19 State. *Rev. Adv. Mater. Sci.* 59: 487–505.

Junqueira, F.F., Silva, R.L & Palmeira, E.M. 2006. Performance of Drainage Systems Incorporating Geosynthetics and their Effect on Leachate Properties. *Geotext. and Geomembr.* 24: 311–324.

Kanji, M.A., Ferreira, R.C., Guerra, M.O. & Infanti Jr. 1981. Geoquímica do ferro nas obras de Engenharia Em Solos Tropicais: Breve Histórico do Conhecimento. *Proc. Braz. Symp. on Tropical Soils in Engng.*, Rio de Janeiro, Brazil, vol. 2: 146–158 (in Portuguese).

Kelsey, C. 2015. Graphene and the Next Generation of Geosynthetics. In www.geosynthetica.net/graphene-nanogeocomposites-geosynthetics/, access on March 7th 2019.

Kelsey, C. 2016. Graphene-enhanced Geotextiles Coming to US with Haydale Agreement. In www.geo-synthetica.com/graphene-enhanced-geotextiles-imagine-haydale/, access on Sept. 16th 2021.

Kenney, T.C. & Lau, D. 1985. Internal stability of Granular Filters. *Canadian Geotech. J.* 22(2): 215–225.

Kezdi, A. 1979. *Soil Physics: Selected Topics-Developments in Geotechnical Engineering*). Elsevier Science Ltd., Amsterdam, The Netherlands.

Khan, M.W., Dawson, A.R. & Marshall, A.M. 2022. Filtration Performance of Non-woven Geotextiles with Internally-stable and –unstable Soils Under Dynamic Loading. *Geotext. and Geomembr.* 50: 293–311.

Kim, K.-H., Park, N.-H., Kim, H.-J. & Shin, J.-H. 2020a. Modelling of Hydraulic Deterioration of Geotextile Filter in Tunnel Drainage System. *Geotext.s and Geomembr.* 48: 210–219,

Kim, I., Best, C. & Seunghee, K. 2020b. Feasibility of Electromagnetic Soil Heating using Magnetic Nanoparticle-coated Geotextiles. *Géotechnique Letters* 10: 149–154.

Kirsch, G. 1898. Die Theorie Der Elastizität und Die Bedürfnisse Der Festigkeitslehre. *Zeitschrift des Vereines Deutscher Ingenieure* 42: 797–807 (in German).

Koerner, R.M. & Koerner, G.R. 1991. *Landfill Leachate Clogging of Geotextile (and Soil) Filters*. Report No. EPA/600/2-91/025, U.S. Env. Protec. Ag., Cincinnati, Ohio, USA, 164 p.

Koerner, R.M. & Koerner, G.R. 1995. *Leachate Clogging Assessment of Geotextile and Soil Landfill Filters*. Report, Cooperative Agrmt. CR-819371, Nat. Risk Mngmt. Rsrch. Lab., EPA, Cincinnati, Ohio, USA.

Koerner, R.M. & Koerner, G.R. 2005. *Reduction Factors (RFs) used in Geosynthetic Design*. GSI White Paper #4, Geosynthetics Inst., PA, USA.

Koerner, R.M. & Koerner, G.R. 2015. Lessons Learned from Geotextile Filter Failures Under Challenging Field Conditions. *Geotext. and Geomembr.* 43: 272–281.

Koerner, R.M., Koerner, G.R., Fahim, A. & Wilson-Fahmy, R.F. 1994. *Long-term Performance of Geosynthetics in Drainage Applications*. Report 367, NCHRP, Transp. Research Board, DC, USA.

Kossendey, T.H., Gartung, E. & Schmidt, St. 1996. Microbiological Influences of the Long-term Performance of Geotextile Filters. In J. Lafleur & A.L. Rollin (eds.), *GeoFilters'96*, Montréal, Québec, Canada, vol. 1: 115–124.

Laflaive, E. & Puig, J. 1974. Emploi des textiles dans les travaux de terrassement et de drainage. *Bulletin de Liaison Laboratoires des Ponts et Chaussées* 69: 61–79 (in French).

Lafleur, J., Mlynarek, J. & Rollin, A.L. 1989. Filtration of Broadly Graded Cohesionless Soils. *J. of Geotech. and Geoenv. Engng.*, 132(10): 1284–1292.

Lawson, C.R. 1990. Geotextile Filter Performance with Fine Grained Soils. *Proc. 4th Int. Conf. on Geosynthetics*, The Hague, The Netherlands, vol. 1: 301–306.

Lee, S. & Bourdeau, P.L. 2006. *Filter Performance and Design for Highway Drains*. Report FHWA/IN/JTRP-2005/1, Purdue University, Indiana, USA.

Lee, K. & Jeon, H. 2008. Evaluation of Clogging Effects on Nonwoven Geotextile Filters by Negative-ion Treatment. *Fibers and Polymers* 9: 365–373.

Lee, I.-M., Kim, J.-H & Reddy, L.N. 2002. Clogging Phenomena of the Residual Soil-geotextile Filter System. *Geotech. Testing Journal* 25(4): 1–12.

Lee, S. & Bourdeau, P.L. 2006. *Filter Performance and Design for Highway Drains*. Final Report No. FHWA/IN/JTRP-2005/1, Purdue University, IN, US.

Legge, K.R. 2004. Geotextile Selection as Filters within Embankment and Tailings Dams. *Proc. 4th Int. Conf. on Filters and Drainage in Geotech. and Environ. Engng. – GeoFilters 2004*, Stellenbosch, South Africa, vol. 1: 333–345.

Li, M. & Fannin, R.J. 2008. Comparison of Two Criteria for Internal Stability of Granular Soil. *Canadian Geotech. J.* 45: 1303–1309.

Lin, C., Galinmoghadam, J., Han, J., Liu, J. & Zhang, X. (2021). Quantifying and Incorporating the Benefits of Wicking Geotextile into Pavement Design. *ASCE J. Transp. Engng.* 147(3): 04021044-1-12.

Lin, C., Presler, W., Zhang, X., Jones, D. & Odgers, B., 2017. Long-term Performance of Wicking Fabric in Alaskan Pavements. *J. Perform. Constr. Facil.* 31(2): D4016005: 1–12.

Lindquist, L.N., and Bonsegno, M.C. 1981. Análise de Sistemas Drenantes de Nove Barragens de terra da CESP, através da instrumentação instalada. *Proc. 14th Natl. Large Dams Sem.*, PE, Brazil, vol. 1: 267–290 (in Portuguese).

Liu, L., Ji, L., Guo, F. & Yu, J. 2011. Prediction of the vertical permeability of needle-punched nonwoven geotextiles by fractal geometry theory. *Geosynth. Intl.* 18(4): 169–177.

Liu, S., Wang, Y. & Feng, D. 2021a. Chemical clogging of synthetic filters in tailings pond caused by ferrous iron ions. *Env. Geotech.*: 1–10 (Ahead of print), doi.org/10.1680/jenge.20.00063.

Liu, S., Wang, Y. & Feng, D. 2021b. Compatibility of tailings-nonwoven geotextile under stress and the effect of sand filter. *Geosynth. Intl.* 28(2): 206–213.

Liu, Y. & Liu, J. 2020. The Biochemical Clogging of Landfill Leachate Collection System based on Laboratory Studies. *Intl. J. Env. Research and Public Health* 17: 1–14.

Lombardi, G., Rollin, A. & Wolff, C. 1989. Theoretical and Experimental Opening Sizes of Heat-bonded Geotextiles. *Textile Research J.* 59: 208–217.

Lopes, J.A.U., Salgado, J.A., Fernandes, J.A.A., Morilha Junior, A., Maroni, L.G., Bosso, A.C.N. & Schimdt, L.A. 1991. O dreno experimental de Prudentópolis – Resultados preliminares. *25ª Reunião Anual de Pavimentação*, São Paulo, SP, Brazil, 1–25 (in Portuguese).

Mansen, A.J. & Balbin, M. 2008. El Limonar tailings dam case study. *Proc. 1st Pan. Conf. on Geosynthetics-GeoAmericas 2008*, Cancun, Mexico, 1483–1491.

Markiewicz, A., Kiraga, M. & Koda, E. 2022. Influence of Physical Clogging on Filtration Performance of Soil-geotextile Interaction. *Geosynth. Intl.* 29(4): 356–368.

McIsaac, R. & Rowe, R.K. 2006. Effect of Filter-separators on the Clogging of Leachate Collection Systems. *Canadian Geotech. J.* 43: 674–693.

McIsaac, R. & Rowe, R.K. 2007. Clogging of Gravel Drainage Layers Permeated with Landfill Leachate. *J. of Geotech. and Geoenv. Engng.* 133(8): 1026–1039.

Mendonca, M.B. 2000. *Evaluation of Ochre Formation on the Performance of Geotextile Filters*. PhD. Thesis, Federal University of Rio de Janeiro, Brazil, 320 p. (in Portuguese).

Mendonca, M.B. & Ehrlich, M. 2006. Column Test Studies of Ochre Biofilm Formation in Geotextile Filters. *J. of Geotech. and Geoenv. Engng.* 132: 1284–1292.

Mendonca, M.B., Ehrlich, M. & Cammarota, M.C. 2003. Conditioning Factors of Iron Ochre Biofilm Formation on Geotextile Filters. *Canadian Geotech. J.* 40: 1225–1234.

Metcalf, R.C., Holtz, R.D. & Allen, T.M. 1995. Field Investigations to Evaluate the Long-term Separation and Drainage Performance of Geotextiles Separators. *Proc. of Geosynthetics'95*, Nashville, Tennessee, USA, vol. 3: 951–962.

Miszkowska, A., Lenart, S & Koda, E. 2017. Changes of Permeability of Nonwoven Geotextiles due to Clogging and Cyclic Water Flow in Laboratory Conditions. *Water 2017* 9(9)660:1–15.

Mlynarek, J., Lafleur, J. & Lewandowski, J.B. 1990. Field Study on Long Term Geotextile Filter Performance. *Proc. 4th Int. Conf. on Geosynthetics*, The Hague, The Netherlands, vol. 1: 259–262.

Mlynarek, J. & Rollin, A.L. 1995. Bacterial Clogging of Geotextiles – Overcoming Engineering Concerns. *Proc. Geosynthetics'95*, Nashville, Tennessee, USA, vol. 1: 177–188.

Montez, F.T., 1987. Utilização de geotêxteis em barragens de rejeitos. *Proc. Simp. sobre Barragens de Rejeitos e Disposição de Resíduos Industriais e de Mineração – REGEO'87*, Rio de Janeiro, RJ, Brazil, vol. 1: 333–348 (in Portuguese).

Moo-Young, H. & Ochola, C. 1999. Strain Effects on the Filtration Properties of Geotextiles. *Proc. Geosynthetics'99*, USA, vol. 2: 757–768.

Moraci, N., Bilardi, S. & Mandaglio, M.C. 2022. Factors Affecting Geotextile Filter Long-term Behaviour and their Relevance in Design. *Geosynth. Intl.* 29(1): 19–42.

Moraci, N., Mandaglio, M.C. & Cazzuffi, D. 2010. I geotessili con funzione di filtro a contatto con terreni granulari: criteri e parametri di progetto. *Riv.Italiana di Geotecnica* 2:45–69 (in Italian).

Moraci, N., Mandaglio, M.C. & Ielo, D., 2012. A New Theoretical Method to Evaluate the Internal Stability of Granular Soils. *Canadian Geotech. J.* 49(1): 45–58.

Moraci, N., Mandaglio, M.C. & Salmi, M. 2016. Long Term Behavior of Woven and Nonwoven Geotextile Filters. *Proc. of GeoAmericas 2016*, Miami, Florida, USA, vol. 1: 740–749.

Moraci, N. & Tondello, M. 1996. The Design of Filter in Coastal Engineering. *AIOM Conf., Padova*, Italy, No. 34 (in Italian).

Morilha Jr., A., Lopez, J.A.U., Salgado, J.A., Maroni, L.G. & Montez, F.T. 1994. Geotextile and Granular filter Performance After Four Years of Real Scale Test. *Proc. 5th Int. Conf. on Geosynthetics*, Singapore, vol. 2: 667–672.

Narejo, D., Mengjia, L., Zimmel, E. & Wu, Y. 2013. A Monolithic Layered Nonwoven-woven Geotextile for Use with Drainage Geocomposites In Coal Combustion Residual Projects. *Geotext. and Geomembr.* 37: 16–22.

Niec, J. Zawadzki, P. & Nowacki, F. 2019. Small Dam Drainage with Nonwoven Geotextile After 40 Years of Exploitation. *Applied Sciences* 9(4161): 1–15.

Nogueira Junior, J. 1988. *Possibilidades de colmatação química dos filtros e drenos da barragem de Porto Primavera (SP) por compostos de ferro*. MSc. Thesis, University of São Paulo, Geosciences Institute, São Paulo, Brazil, 229 p. (in Portuguese).

Odabasi, E., Dayioglu, A.Y., Yetis, A.D. & Aydilek, A.H. 2022. Long-term Hydraulic Performance of Geotextiles Filtering Recycled Materials. *Geosynth Intl.* (Ahead of Print), doi.org/10.1680/jgein.21.00047.

Ozelim, L.C.S.M., Zubeldia, E.H., Cavalcante, A.L.B. & Palmeira, E.M. 2016. On Modeling Geotextiles by Means of Elementary Cellular Automata. *Electronic J. of Geotech. Enng.* 21(Bund 02): 1311–1323.

Palmeira, E.M. 2016. Sustainability and Innovation in Geotechnics: Contributions from Geosynthetics. *Soils and Rocks* 39(2): 113–135.

Palmeira, E.M. 2020. A Review on Some Factors Influencing the Behaviour of Nonwoven Geotextile Filters. *Soils and Rocks* 43(3): 351–368.

Palmeira, E.M. 2023. *A Study on the Use of Geosynthetics for Drainage and Filtration in Railway Tracks*. Research Report, May/2023, Project 6744-FUB/DNIT/FT, FINATEC/Brazilian National Department of Transportation Infrastructure (DNIT), Brasília, Brazil (in Portuguese).

Palmeira, E.M., Araújo, G.L.S. & Santos, E.C. 2021a. Sustainable Solutions with Geosynthetics and Alternative Construction Materials – A Review. *Sustainability* 13(12756): 1–29.

Palmeira, E.M., Gardoni, M.G. & Araújo, G.L.S. 2021b. Geosynthetics in Geotechnical and Geoenvironmental Engineering: Advances and Prospects. *Geotecnia* 152: 337–368 (in Portuguese).

Palmeira, E.M., Beirigo, E.A. & Gardoni, M.G. 2010. Tailings-nonwoven Geotextile Filter Compatibility in Mining Applications. *Geotext. and Geomembr.* 28: 136–148.

Palmeira, E.M. & Fannin, R.J. 2002. Soil-geotextile Compatibility in Filtration. *Proc. 7th Int. Conf. on Geosynthetics*, Nice, France, Balkema Publishers, vol. 3: 853–872

Palmeira, E.M., Fannin, R.J. & Vaid, Y.P. 1996. A Study on the Behaviour of Soil-geotextile Systems in Filtration Tests. *Canadian Geotech. J.* 33: 899–912.

Palmeira, E.M. & Gardoni, M.G. 2000. The Influence of Partial Clogging and Pressure on the Behaviour of Geotextiles in Drainage Systems. *Geosynth. Intl.* 7(4–6): 403–431.

Palmeira, E.M., Gardoni, M.G. & Bessa da Luz, D. 2005. Soil-geotextile Filter Interaction Under High Stress Levels in the Gradient Ratio Test. *Geosynth. Intl.* 12(4): 162–175.

Palmeira, E.M. & Matheus, E. 2000. Gradient Ratio Tests on Artificially Clogged Nonwoven Geotextiles. In Wolski & Mlynarek (eds), *Proc. of Filters and Drainage in Geotech. and Env. Engng.*, Balkema, ISBN 90 5809 1465, vol. 1: 149–156.

Palmeira, E.M., Melo, D.L.A. & Moraes-Filho, I.P. (2019). Geotextile Filtration Opening Size Under Tension and Confinement. *Geotext. and Geomembr.* 47: 566–576.

Palmeira, E.M., Remigio, A.F.N., Ramos, M.L.G. & Bernardes, R.S. 2008. A Study on Biological Clogging of Nonwoven Geotextiles Under Leachate Flow. *Geotext. and Geomembr.* 26: 205–219.

Palmeira, E.M., Tatto, J. & Araújo, G.L.S. 2012. Sagging and Filtration Behaviour of Nonwoven Geotextiles Overlying Different Bedding *Materials. Geotext. and Geomembr*. 31:1–14.

Palmeira, E.M. & Trejos Galvis, H.L. 2017. Opening Sizes and Filtration Behaviour of Nonwoven Geotextiles Under Confined and Partial Clogging Conditions. *Geosynth. Intl.* 24(2): 125–138.

Palmeira, E.M. & Trejos Galvis, H.L. 2018. Evaluation of Predictions of Nonwoven Geotextile Pore Size Distribution Under Confinement. *Geosynth. Intl.* 25(2): 230–241.

Petersen, L. 1966. Ochreous Deposits in Drain-pipes. *Acta Agriculturae Scandinavica* 16: 120–128.

Prambauer, M., Wendeler, C., Weitzenböck, J. & Burgstaller, C. 2019. Biodegradable Geotextiles – An Overview of Existing and Potential Materials. *Geotext. and Geomembr*. 47: 48–59.

Puig, J., Gouy, J.L. & Labroue, L. 1986. Ferric Clogging of Drains. *Proc. 3rd Int. Conf. on Geotextiles*, Vienna, Austria, vol. 4: 1179–1184.

Qureshi, S., Kogler, R.M. & Bhatia, S.K. 1990. Long Term Filtration Behavior of Nonwoven Geotextiles. *Proc. 4th Int. Conf. on Geosynthetics*, The Hague, The Netherlands, vol. 1: 279–283.

Rawal, A. 2010. Structural Analysis of Pore Size Distribution of Nonwovens. *The J. of the Textile Inst.* 101(4): 350–359.

Rawal, A. 2012. Modeling the Compression-induced Morphological Behavior of Nonwoven Materials. *J. of Mat. Science* 47: 2365–2374.

Remigio, A.F.N. 2006. *Study of Biologic Clogging of Synthetic Drainage Systems of Waste Disposal Areas under Anaerobic Conditions*. PhD. Thesis, University of Brasília, Brasília, DF, Brazil (in Portuguese).

Rollin, A.L. 1996. Bacterial Clogging of Geotextiles. In J. Lafleur & A.L. Rollin (eds.), *GeoFilters'96*, Montréal, Québec, Canada, vol. 1: 125–134.

Rollin, A.L. & Lombard, G. 1988. Mechanisms Affecting Long-term Filtration Behavior of Geotextiles. *Geotext. and Geomembr.* 7: 119–145.

Rowe, R.K., Armstrong, M.D. & Cullimore, D.R. 2000a. Particle Size and Clogging of Granular Media Permeated with Leachate. *J. of Geotech. and Geoenv. Engng.* 126(9): 775–785.

Rowe, R.K., Caers, C.J., Reynolds, G. & Chan, C. 2000b. Design and Construction of the Barrier System for the Halton Landfill. *Canadian Geotech. J.* 37(3): 662–675.

Ryoo, S.C., Erucar, S., Evans, T.M. & Aydilek, A.H. 2022a. CFD-DEM Modelling of Filtration through Conventional and Conical Geotextile Filter Systems. *Geosynth. Intl.* (Ahead of print), doi.org/10.1680/jgein.21.00098.

Ryoo, S., Bensi, M.T. & Aydilek, A.H. 2022b. Hydraulic Compatibility of Nonwoven Conical Filters with a Backfill Material. *Geosynth. Intl.* (Ahead of print). doi.org/10.1680/jgein.22.00281

Sabiri, N.-E., Caylet, A., Montillet, A., Le Coq, L. & Durkheim, Y. 2017. Performance of Nonwoven geotextiles on Soil Drainage and Filtration. *Eur. J. Env. Civil. Eng.* 24(5): 1–19.

Santos, D.S.C. & Palmeira, E.M. 2023. Behaviour of Geotextile Filter in Internally Unstable Soil Under Confinement. *Proc. IX Braz. Cong. on Geosynthetics*, Salvador, Bahia, Brazil, vol. 1: 1–7 (in Portuguese).

Scheurenberg, R.J. 1982. Experiences in the use of Geofabrics in Underdrainage of Residue Deposits. *Proc. 2nd Int. Conf. on Geotextiles*, Las Vegas, NV, USA, vol. 1: 199–204.

Senadheera, H., Deo, R., Azoor, R., Bouazza, A. & Kodikara, J. 2022. Electro-mechanical Behaviour of graphene-based Geotextiles for Pavement Health Monitoring. *Geotext. and Geomembr.* 51(2): 303–315.

Silva, J.L.V. & Lodi, P.C. 2020. Evaluation of Superficial and Internal Clogging of Geotextiles. *Int. J. Civil Engng.* 18: 1125–1137.

Silva, C.A. & Palmeira, E.M. 2013. Performance Comparison of Conventional Biplanar and Low-cost Alternative Geocomposites for Drainage. *Geosynth. Intl.* 20(3): 226–237.

Silva, A.R.L., Palmeira, E.M & Vieira, G.R. 2002. Large Filtration Tests on Drainage Systems using Leachate. In L.G. Mello & M.S.S. Almeida (eds), *Proc. 4th Int. Cong. on Env. Geotech.*, Rio de Janeiro, Brazil, vol. 1: 125–128.

Simmonds, G.E., Bomberger, J.D. & Bryner, M.A. 2007. Designing Nonwovens to Meet Pore Size Specifications. *J. of Engineered Fibers and Fabrics* 2(1): 1–15.

Skempton, A.W. & Brogan, J.M. 1994. Experiments on Piping in Sandy Gravels. *Géotechnique* 44(3): 449–460.

Sória, M.H.A. & Viviani, E. 1993. Determination of Pore Size Distribution through Filtration Test and Probabilistic Theory. *Proc. of Geosynthetics'93*, NAGS/IFAI/IGS, Vancouver, BC, Canada, vol. 1: 519–531.

Spencer, W.F., Pratrick, R. & Ford, H.W. 1963. The Occurrence and Cause of Iron Oxide Deposits in Tile drains. *Soil Science Soc. of America Proc.* 27: 134–137.

Tang, L., Tang, Q., Zhong, A. & Li, H. 2020a. Prediction of Pore Size Characteristics of Needle-punched Nonwoven Geotextiles Subjected to Uniaxial Tensile Strains. *Adv. in Civil Engng.*, ID 8869519, 1–12.

Tang, L., Tang, X.-W., Liu, Y. & Qu, S.-X. 2020b. Prediction of Pore Size Characteristics of Woven Slit-Film Geotextiles Subjected to Unequal Biaxial Tensile Strains. *Geotext. and Geomembr.* 48: 724–734.

Tao, H. 2018. *Numerical Modelling of Soil Internal Erosion Mechanism*. PhD Thesis, University of Akron, OH, USA.

Terzaghi, K. & Leps, T.M. 1958. Design and Performance of Vermilion Dam, California. *Journal of the Soil Mech. and Fdn. Engng. Division* 84(3): 1728.1–1728.30.

Testemale, J.P., Faure, Y.H., Parron, C., Lambert, S., Royet, P. & Fagon, Y. 1999. Filtre geotextile du barrage de Torcy-Vieux (71): Prelevements et Analyses. *Proc. of Rencontres Géosynthétics 99*, Bordeaux, France, vol. 1:311–318 (in French).

Touze, N. 2021. Healing the world: A Geosynthetic Solution. *Geosynth. Intl.* 28(1): 1–31.

Turk, M. 1995. Maintaining Proper Landfill Drainage by Aerobic Waste Pre-treatment. *Proc. 5th Int. Landfill Symp.*, Sardinia, Italy, vol. 2: 667–680.

Urashima, D.C. & Vidal, D.M. 1998. Geotextile Filter Design by Probabilistic Analysis. *Proc. 6th Int. Conf. Geosynthetics*, Atlanta, Georgia, USA, vol. 2: 1013–1016.

Van Zanten, R.V. & Thabet, R.A.H. 1982. Investigation on Long-term Behavior of Geotextiles in Bank Protection Works. *Proc. 2nd Int. Conf. on Geotextiles*, Las Vegas, NV, USA, vol. 1: 259–264.

Vermeersch, O.G. & Mlynarek, J. 1996. Determination of the Pore Size Distribution of Nonwoven Geotextiles by a Modified Capillary Flow Porometry Technique. In S.K. Bhatia & L.D. Suits (eds), *Proc. Recent Develop. in Geotextile Filters and Prefabricated Drainage Geocomposites*, ASTM STP 1281, ASTM, vol. 1: 19–34

Veylon, G., Stoltz, G., Mériaux, P., Faure, Y.-H. & Touze-Foltz, N. 2016. Performance of Geotextile Filters after 18 years' Service in Drainage Trenches. *Geotext. and Geomembr.* 44: 515–533.

Wang, F., Han, J., Zhang, X., Guo, J. 2017. Laboratory Tests to Evaluate Effectiveness of Wicking Geotextile in Soil Moisture Reduction. *Geotext. and Geomembr.* 45: 8–13.

Wayne, M.H. & Koerner, R.M. 1993. Correlation between Long-term Flow Testing and Current Geotextile Filtration Design Practice. *Proc. of Geosynthetics'93*, NAGS/IFAI/IGS, Vancouver, BC, Canada, vol. 1: 501–518.

Williams, N.D. & Abouzakhm, M.A. 1989. Evaluation of geotextile/soil filtration characteristics using the hydraulic conductivity ratio analysis. *Geotext. and Geomembr.* 8(1):1–26.

Williams, N.D. & Luettich, S.M. 1990. Laboratory Measurement of Geotextile Filtration Characteristics. *Proc. 4th Int. Conf. Geotex., Geomemb. and Reltd. Products*, The Hague, Netherlands, vol. 1: 273–278.

Wilson-Fahmy, R.F., Koerner, G.R. & Koerner, R.M. 1996. Geotextile Filter Design Critique. In S.K. Bhatia and L.D. Suits (eds), *Proc. of Recent Develop. in Geotextile Filters and Prefabricated Drainage Geocomposites*, ASTM STP 1281, ASTM, USA, 132–161.

Woo, J.T. 2005. A Study on Inflow Rate of Urban Subway Tunnels and Sediments in the Tunnel Drainage System. *Tunn. Technol.* 7(3): 219–226 (in Korean).

Wu, C.S. & Hong, Y.S. 2016. The Influence of Tensile Strain on the Pore Size and Flow Capability of Needle-punched Nonwoven Geotextiles. *Geosynth. Intl.* 23(6):422–434.

Wu, C.S., Hong, Y.S. & Wang, R.H. 2008. The Influence of Uniaxial Tensile Strain on the Pore Size and Filtration Characteristics of Geotextiles. *Geotext. and Geomembr.* 26(3): 250–262.

Xu, J.K., Guo, B.J., & Chen, D.C. 1976. Experience in using Residual Soils for Earth Dam Construction in Guandong Province, China. *Proc. 12th Congrès Int. des Grands Barrages*, Mexico, vol. 2: 821–838.

Zaman, M.W., Han, J. & Zhang, X. 2022. Evaluating Wettability of Geotextiles with Contact Angles. *Geotext. and Geomembr.* 50(4): 825–833.

Zhang, X., Presler, W., Li, L., Jones, D. & Odgers, B., 2014. Use of Wicking Fabric to Help Prevent Frost Boils in Alaskan pavements. *J. Mater. Civ. Eng.* 26(4): 728–740.

Zornberg, J.G., Azevedo, M., Sikkema, M. & Odgers, B., 2017. Geosynthetics with Enhanced Lateral Drainage Capabilities in Roadway Systems. *Transp. Geotech.* 12: 85–100.

Research and practice on geosynthetic MSE walls: Past, present and future
(Bathurst lecture)

Y. Miyata
National Defense Academy, Yokosuka, Japan

ABSTRACT: Although technology on geosynthetic mechanically stabilized earth (MSE) walls can help solve classical geotechnical earth retaining wall problems, it also contributes to achieving new required performance for these infrastructures. To further develop this technology, it is essential to analyze the history of its progress. This study summarizes the state-of-the-art on the mechanical and soil interaction properties of geosynthetics, physical modeling and in-situ measurements, analytical and numerical modeling, and reliability analyses by reviewing approximately 700 papers published in well-known international journals in this field and some notable conference paper contributions. The latest analytical methods, such as risk-based life cycle cost and CO_2 emission assessments and damage/failure predictions, are introduced to evaluate the resilience and sustainability performance of geosynthetic MSE walls. Finally, prospects of a seismic isolation technique with new types of geosynthetics and life cycle management with a long-life sensor for geosynthetic MSE walls are discussed.

1 INTRODUCTION

Traditionally, classical infrastructure design only considered basic performance aspects, such as structural safety and economic efficiency. In modern design, more advanced performance aspects such as resilience and sustainability are also considered (Lounis & Mcallister 2016). New infrastructure technologies are needed to meet these advanced performance requirements.

Geosynthetic mechanically stabilized earth (MSE) walls mainly consist of geomaterials, geosynthetics, and facing materials. The performance of these structures can be controlled by varying the reinforcement conditions. Research on geosynthetic MSE walls began in the 1970s (Holtz 2017). The good performance of these wall systems has been demonstrated in both research and practice. For example, seismic damage investigation of actual structures has reported the high performance of geosynthetic MSE walls (Koseki 2012; Kuwano *et al.* 2017; Ling *et al.* 2001; Tatsuoka *et al.* 1996; White & Holtz 1997). Nevertheless, classical geosynthetic MSE wall design methods have much room for improvement (ex. Bathurst *et al.* 2005b, 2014). If a design method able to reasonably determine the reinforcement conditions by considering the required performances can be developed, technology on geosynthetic MSE walls will be able to contribute to the success of various civil engineering projects more than ever before. The keywords considered in this study are the "past," "present," and "future" of research and practice on geosynthetic MSE walls. For the "past," research trends in geosynthetic MSE walls over the past 40 years are reported based on a review of approximately 700 technical papers. Changing research topics and approaches over time are visualized. For the "present," the latest analytical methods, such as risk-based life cycle cost and CO_2 emission assessments and damage/failure predictions, are presented to evaluate the performances of geosynthetic MSE walls. Finally, for the "future," prospects

of a seismic isolation technique with new types of geosynthetics and information and communication technology (ICT)-based life cycle management with fiber optics for geosynthetics are discussed.

2 REVIEW OF RESEARCH ON GEOSYNTHETIC MSE WALLS OVER THE LAST 40 YEARS

2.1 *Aim of the review*

Research on geosynthetic MSE walls can be divided into four categories: research on the mechanical and soil interaction properties of geosynthetics, research to clarify their mechanical behavior through physical model tests and in-situ measurements, research on analytical and numerical modeling to predict the mechanical behavior of geosynthetic MSE walls and research on reliability analyses for evaluating their performance. The relationships among these four research areas are shown in Figure 1. They can be connected by correlations, understandings, suggestions, and/or validation processes. It is important to clarify the detailed progress in these research areas and their interrelationships for the future development of technology on geosynthetic MSE walls.

The information required to identify research trends in geosynthetic MSE walls includes journal articles, technical reports, test standards, and design specifications. Journal articles can be obtained even if time has passed since their publication, and their contents can be easily verified. More importantly, they are peer-reviewed and, therefore, judged to be reliable for information. For these reasons, the author focused on journal papers in this study. Nevertheless, there are a number of valuable conference papers cited in this review.
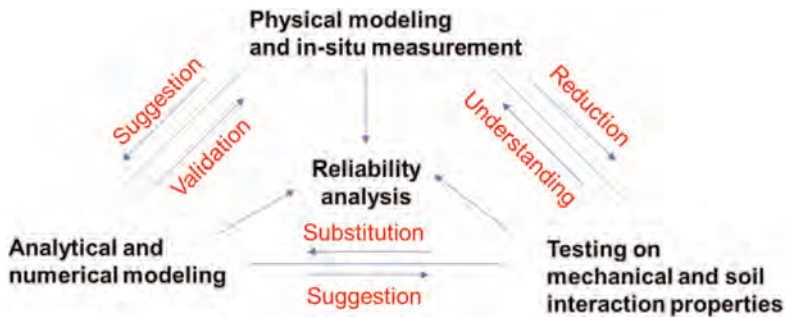
Figure 1.   Research areas in technology on geosynthetic MSE walls and relationships.

In many state-of-the-art papers on geosynthetic MSE walls, technological progress was explained by relating to important papers with significant contributions to progress in research and practice (ex. Bathurst & Alfaro 1997; Otani *et al.* 1997; Palmeira 2009; Rowe & Ho 1993; Rowe & Li 2003; Bathurst & Kaliakin 2005). Giroud (1994) published a two-volume book of article lists on geosynthetic engineering such as books, journals, conference papers, theses, and reports and publications from selected authors. Many of these studies have made significant contributions not only to solving practical problems but also to setting research directions in the early stages of research on geosynthetic MSE walls. Insofar as the present study, the author believes that the degree of progress is closely related to the number of published papers; thus, progress is demonstrated using statistical data on the number of papers on geosynthetic MSE walls. The advantage of this research method is that it allows us to visualize the research direction with objective indicators. It is a survey approach that can only be implemented once research results have been sufficiently accumulated. This section discusses the overall research trends in geosynthetic MSE walls and chronological changes in research topics and methods.

2.2 Review methodology

Technology on geosynthetic MSE walls is an interdisciplinary field, with relevant papers published in various fields. This study only considered journal papers published in the field of geotechnical engineering. Based on this policy, three categories of journals were examined: 1) journals covering all areas of geotechnical engineering, 2) journals specializing in geomaterials testing, and 3) journals specializing in geosynthetic engineering. Specifically, for Category 1, the following journals were reviewed: Geotechnique (GT, Institution of Civil Engineers (ICE)), Journal of Geotechnical and Geoenvironmental Engineering (JGE, American Society of Civil Engineers), Soils and Foundations (S&F, Japanese Geotechnical Society), and Canadian Geotechnical Journal (CGJ, Canadian Geotechnical Society). These journals were first published in the 1960s and are well-suited for examining long-term research trends in geosynthetics. Category 2 included the Geotechnical Testing Journal (GTJ, American Society for Testing and Materials (ASTM) International). This journal publishes papers that include testing and experimental methods for geosynthetics. Two journals were included in Category 3: Geotextiles and Geomembranes (G&G, Elsevier) and Geosynthetics International (GI, ICE). These are the official journals of the International Geosynthetics Society (IGS) and were first published in 1983 and 1994, respectively. They contain many papers on geosynthetic MSE walls.

The papers were collected from each journal's website. Keywords were entered into the search engine of each journal's website to generate a list of candidate papers. After downloading the papers, their contents were reviewed, and those meeting the objectives of this review were included in the database. Table 1 shows statistics of journal papers collected. A total of 701 papers were collected. The largest contributor was G&G, followed by GI.

2.3 Considerations

The number of papers on the mechanical and soil interaction properties of geosynthetics, analytical and numerical modeling, physical modeling and in-situ measurements, and relia-

Table 1. Statistics of journal papers collected on the technology of geosynthetic MSE walls.

Journal	GT	JGE	S&F	CGJ	GTJ	G&G	GI	Total
Total	24	100	56	33	20	285	183	701

GT: Geotechnique, JGE: Journal of Geotechnical and Geoenvironmental Engineering, S&F: Soils and Foundations, CGJ: Canadian Geotechnical Journal, GTJ: Geotechnical Testing Journal, G&G: Geotextiles and Geomembranes and GI: Geosynthetics International.

bility analyses of geosynthetic MSE walls are shown in Figures 2–5. The vertical axis represents the cumulative number of publications, and the slope of the curve represents the number of publications per year. Changes in the number of publications over time should be understood in the context of academic, practical, and social trends. Table 2 provides a chronological table of events that can be considered relevant to geosynthetic MSE walls. All the curves in the four research areas can be approximated by a group of straight lines whose slopes change twice from small to large, regardless of the type of research. It can be assumed that a period with a small slope represents the accumulation phase, and one with a large slope represents the development phase. In this case, it can be understood that these phases have repeated themselves twice, and MSE wall technology is now in the second development phase. Interestingly, the timing of the first accumulation and development phases is almost the same in the three research areas of mechanical and soil interaction properties, physical
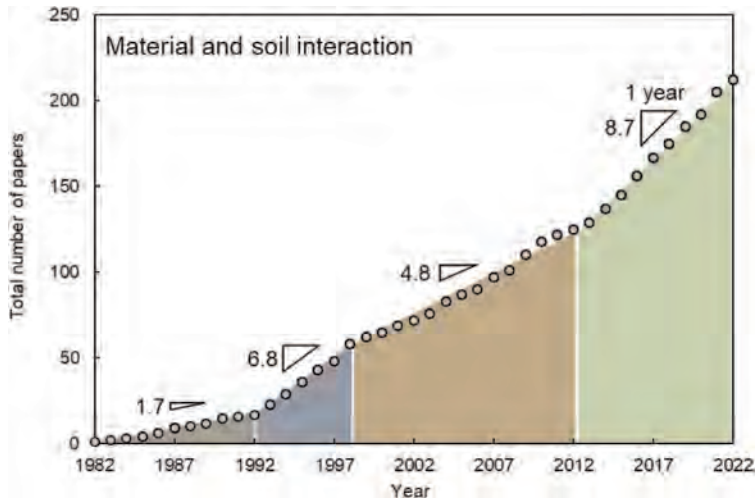
Figure 2. Total number of papers on the mechanical and soil interaction properties of geosynthetics as published in selected leading journals.
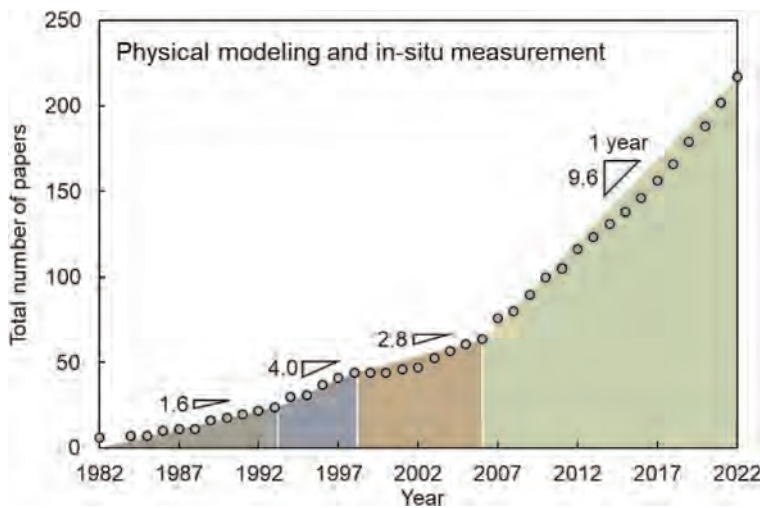
Figure 3. Total number of papers on physical modeling and in-situ measurement of geosynthetic MSE walls as published in selected leading journals.

modeling and in-situ measurements, and analytical and numerical modeling. As shown in Table 2, during the first accumulation period, the IGS was established, and technical committees on geosynthetics were formed in the ASTM and International Society for Soil Mechanics and Geotechnical Engineering (ISSMGE). In addition to establishing academic societies and technical committees, an international conference on geosynthetics and the international symposium on soil reinforcement were regularly organized (Ochiai 2007). Thus, a development phase was achieved owing to the dissemination of technical information and the exchange of research ideas.

During this first development phase, several earthquakes caused significant societal losses. The high reliability of technology on geosynthetic MSE walls was demonstrated in damage investigations of these earthquakes (Koseki 2012; Kuwano *et al*. 2014; Tatsuoka *et al*. 1996;
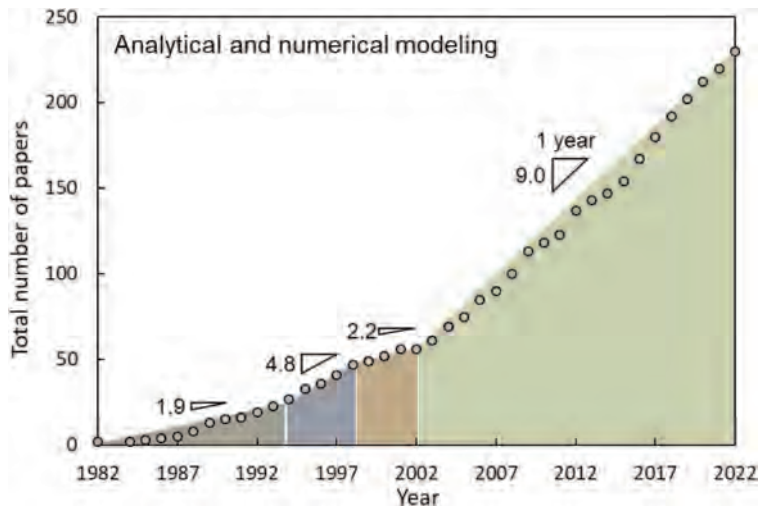
Figure 4.   Total number of papers on analytical and numerical modeling of geosynthetic MSE walls as published in selected leading journals.
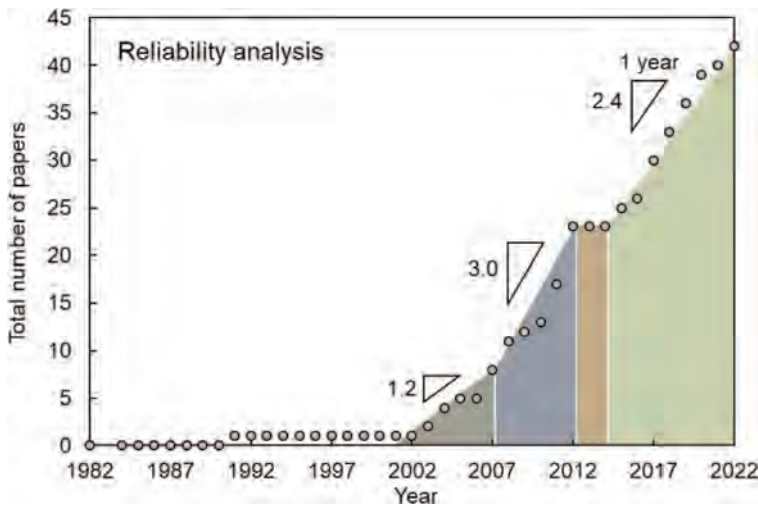
Figure 5.   Total number of papers on reliability analyses of geosynthetic MSE walls as published in selected leading journals.

White & Holtz 1997). These works have contributed to the widespread use of MSE wall technology. In research on mechanical and soil interactions, physical modeling and in-situ observations, and analytical and numerical modeling, the earliest transition from the second accumulation phase to the development phase was in research on analytical and numerical modeling. During this period, computers began to be used in all aspects of practice. This trend probably stimulated further research on analytical and numerical modeling. Research on reliability analyses began in the 2000s.

The third edition of the International Organization for Standardization (ISO) 2394 on the general principles for the reliability of structures was published in 1998. It stated that the target performance of a structure should be expressed in terms of probabilities. This trend is

Table 2. Events relevant to technology on geosynthetic MSE walls.

Year	Society and technical committee establishment	Journal launch	Int. Conf. on Geosynthetics	Int. Symposium (IS) or Workshop (WS) on soil reinforcement	Comprehensive design code	Major earthquake (Economic loss[#], year; Daniell et al. 2012)
1980	IGS (1983)		1st (1977)			Irpinia, IT ($58.0B, 1980)
	ASTM/D35 (1984)	GG (1984)	2nd (1982)			
	ISSMGE/TC9 (1986)		3rd (1986)	IS-Kyushu (1988)	ISO (1986) 2394 2nd ed.	
1990			4th (1990)	IS-Kyushu (1992)		
		GI (1994)	5th (1994)	IS-Kyushu (1996)	AASHTO (1994) LRFD 1st ed.	Northridge, US ($79.1B, 1994)
2000	ISO/TC221 (2000)		6th (1998)	IS-Kyushu (2001)	ISO (1998) 2394 3rd ed.	Kobe, JP ($187.6B, 1995)
			7th (2002)		CEN (2002) Eurocode Basis	Niigata, JP ($35.5B, 2004)
			8th (2006)	IS-Kyushu (2007)	CEN (2004, 2007) Eurocode 7	Sichuan, CN ($189.8B, 2008)
2010			9th (2010)			Tohoku, JP ($324.0B, 2011)
	IGS/TC-R (2011)		10th (2014)		ISO (2015) 2394 4th ed.	
2020			11th (2018)	IGS WS TC-R (2018)		
			12th (2023)	IGS WS TC-R (2020)	AASHTO (2020) LRFD 9th ed.	

IGS International Geosynthetics Society, ASTM: American Society for Testing and Materials, ISSMGE: International Society for Soil Mechanics and Geotechnical Engineering, ISO: International Organization for Standardization, AASHTO: American Association of State Highway and Transportation Officials.
[#]2012 HNDECI (Hybrid. Natural Disaster Economic Conversion Index) Adjusted US Dollar direct economic loss value

considered to have strongly influenced the research field of geosynthetic MSE walls, especially research on reliability analyses. To identify the area with the largest number of publications in each period, i.e., the most-active research area in geosynthetic MSE walls, the ratios of the number of papers in the four areas mentioned above to the total number of papers for each year were calculated. The chronological changes were visualized as shown in Figure 6. In the early 1980s, research on physical modeling and in-situ measurements represented the largest proportion of publications. Approximately five years later, the proportion of papers on the mechanical and soil interaction properties of geosynthetics took the lead.

After that, the proportions of papers on mechanical modeling and interactions shifted to favor papers concerning analytical and numerical modeling. Currently, the proportion of papers in these three areas is approximately 30%, and the proportion concerning reliability
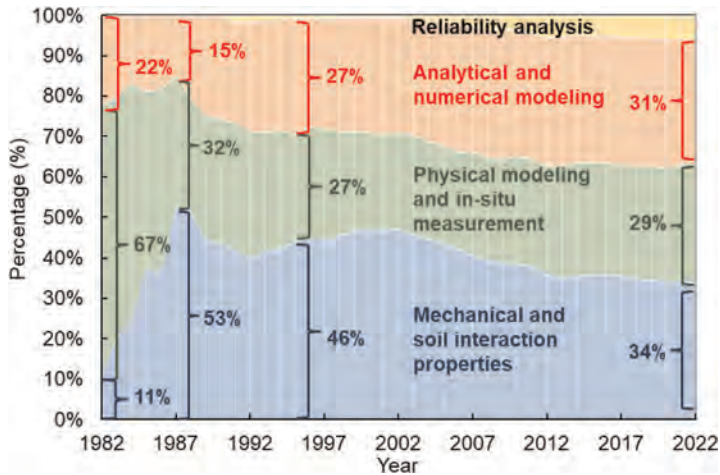
Figure 6.   Changes in four research areas on geosynthetic MSE walls over time.

analyses is 10%; this has remained constant for the last 10 years. These changes indicate that research on geosynthetic MSE walls has progressed in the following order: understanding of the macroscopic behavior of the walls, elucidation of the elemental properties, development of analysis methods, and evaluations of reliability.

Changes have also occurred in research topics related to the mechanical and soil interaction properties of geosynthetics. This area of research can be divided into four categories: tensile, creep, pullout resistance, and interface shear resistance. Figure 7 depicts the time-series changes in the proportions of papers as classified by year of publication. In the early 1980s, even if the total number of papers was small, most papers focused on pullout tests.

In the mid-1980s, the proportion of papers on mechanical properties, such as tensile and creep, increased. Subsequently, the proportion of papers on mechanical properties shifted to papers on soil interactions. Presently, the ratio of papers on mechanical properties to those on soil interactions is reversed from the ratio in the mid-1980s.
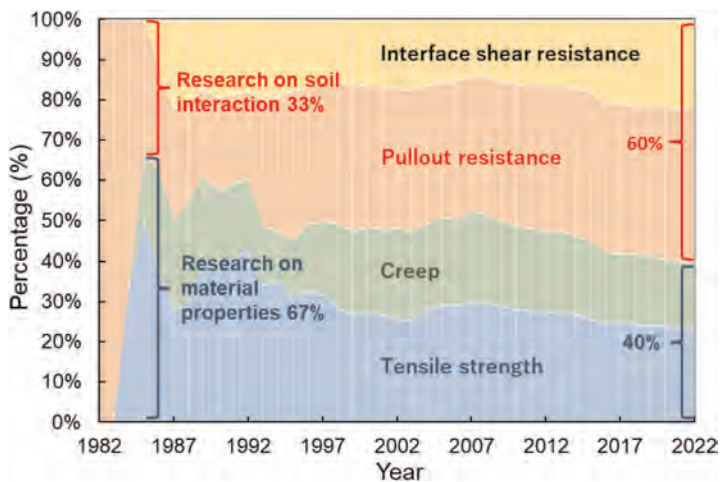
Figure 7.   Changes in research topics on mechanical and soil interactions of geosynthetics over time.

The changes in the research topics in physical modeling, in-situ measurements, and analytical and numerical modeling can also be discussed. Studies in these areas can be categorized into those on static deformation properties, static stability, and behaviors under extreme loads, such as earthquakes and rainfall, and others, which include case histories and environmental performance.

The proportions of papers are classified by year of publication, and the time-series changes are visualized in Figure 8. In the mid-1990s, the good performance of geosynthetic MSE walls was revealed through post-disaster investigations of large earthquakes occurring during this period. Since then, the proportion of studies on the dynamic behavior of geosynthetic MSE walls through physical modeling and numerical analysis has increased. More recently, the number of papers on hydraulic effects has increased in consideration of the effects of climate change. Notably, the percentage of papers on static deformation has remained almost unchanged over the past 40 years. It can be considered that the basic reinforcement mechanism, in which the soil deformation is constrained by reinforcing materials, has already been elucidated. Nevertheless, this trend indicates that unresolved issues remain, such as those concerning long-term behavior.
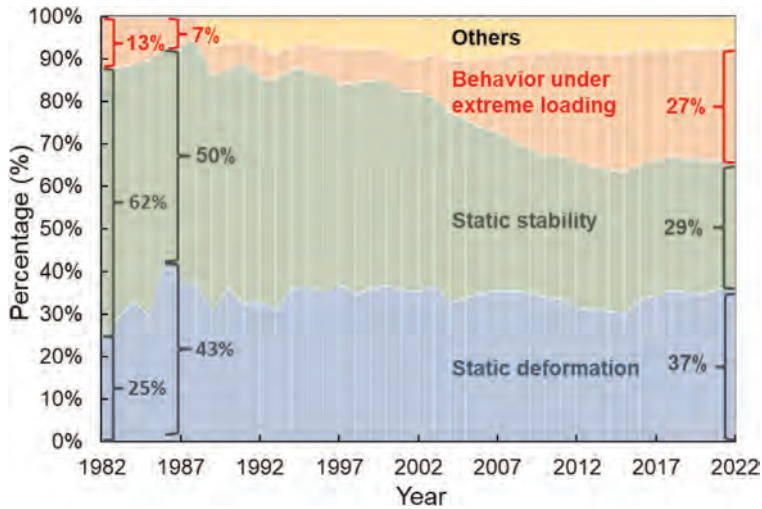
Figure 8. Changes in research topics on the mechanical behavior of geosynthetic MSE walls over time.

3 ADVANCED ANALYSIS METHODS FOR RESILIENCE AND SUSTAINABILITY OF GEOSYNTHETIC MSE WALLS

3.1 Background

In classical structural design, emphasis has traditionally been placed on indicators related to structural safety and economic efficiency. Structural safety has been evaluated based on a factor of safety, and economic efficiency has been evaluated based on the initial cost, i.e., the construction cost. In recent years, structural designs have required advanced performance with respect to resilience and sustainability (Lounis & Mcallister 2016). Resilience generally refers to the ability to respond to changes. In the design of a structure, it is often assessed as the ability of a structure to maintain a minimum level of functionality and recover quickly after damage from natural disasters or external events. In contrast, sustainability is more

holistic and generally refers to a system or process being able to continue to function without losing its functionality in environmental, social, economic, etc., terms. In the design of a structure, sustainability is often evaluated in terms of the degree of global environmental impact. It has been suggested that both performances need to be evaluated throughout the life cycle of a structure (Bocchini *et al.* 2014). Damians *et al.* (2018) demonstrated a methodology to evaluate the sustainability of earth retaining wall structures considering the three pillars that contribute to sustainability (economics, societal/functional/resilience and environmental) and showed that MSE walls were more sustainable than candidate conventional gravity and cantilever wall types performing the same function.

When evaluating the resilience and sustainability of a structure over its lifetime, it is necessary to assume potential scenarios of events occurring to the structures during their service lives. As these events include damage caused by natural disasters, the evaluation includes a high degree of uncertainty. Therefore, the assessment should be risk-based, i.e., the uncertainties in the events should be assessed probabilistically (Lounis & Mcallister 2016). As the chair of the technical committee of the IGS Japan Chapter, the author has been working on this task from the beginning and has been advocating the advantages of geosynthetic MSE walls in the Japanese social infrastructure development community (Miyata *et al.* 2010, 2013). This section presents the extended analysis results of this activity as an advanced analysis method in current practice.

Another important perspective when evaluating the life cycle resilience and sustainability of structures is the prediction of the damage or failure modes of structures. The latest Japanese design standard on geostructures requires consideration of the effects of the damage or failure of geostructures on adjacent roads and houses (MLIT 2015).

Numerical analyses are expected to be introduced to predict the damage to or failure modes of such structures. Figure 9 shows the applicable ranges of the finite element method (FEM) finite difference method (FDM) and particle method as continuum analyses, and the discrete element method (DEM) to assess the limit state of a structure. Although this classification is tentative, because research on each method is currently being conducted to expand their range of applications, it is understood that the discrete element method and particle method can be applied to reproduce structural behavior up to and after collapse. However, these analysis methods have not been sufficiently developed for geosynthetic MSE walls. To overcome this problem, the authors' group has been developing a particle method for geosynthetic MSE walls (Nonoyama *et al.* 2022). The main contents of this latest analysis method in current practice are introduced in section 3.4.

Analysis method / Performance level		Deformation	Damage	Failure
Continuum approach	FEM, FDM			
	Particle Method			
Discontinuous approach	DEM			

Figure 9. Applicability of numerical analysis to limit state estimations of structures. (FEM = finite element method, FDM = finite difference method, DEM = discrete element method).

3.2 *Risk-based life cycle cost analysis*

In ISO (2015) 2394: General principles for the reliability of structures, the risk *R* is defined as follows:

$$R = \sum P_i \, C_i \qquad (1)$$
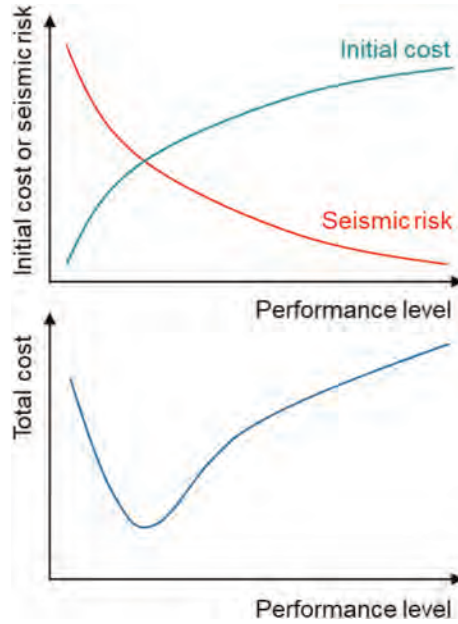
Figure 10. Relationship between the performance level of the structure, initial cost, seismic risk, and total cost.

In the above, P_i is the probability associated with event i (probability of failure) and C_i is the magnitude of the damage if the event i occurs.

In this section, the discussion is limited to earthquake risks. Figure 10 shows the relationship between the performance level of the structure, initial cost, seismic risk, and total cost. The total cost is a simple sum of the initial cost and seismic risk. The higher the performance level of the structure, the higher the initial cost. In addition, the higher the performance of the structure, the lower the seismic risk, because the probability of failure is lower. Therefore, the total cost is a downward convex curve as shown in the bottom plot of the figure. A probability-based risk analysis can help to reasonably set the target performance level for a structure while considering the balance between the initial cost and risk. This section explains a risk-based life cycle cost analysis method for geostructures. The analysis results are shown for geosynthetic MSE walls, L-shaped retaining walls, and non-reinforced embankments under simple conditions (Miyata *et al.* 2010). The life cycle cost (LCC) considers the seismic risk and maintenance costs and can generally be calculated as follows:

$$LCC = C + M + R \qquad (2)$$

Here, C is the initial construction cost, M is the maintenance cost, and R is the seismic risk. The current Japanese design method for geosynthetic MSE walls assumes multiple failure modes as shown in Figure 11 (PWRC 2013), as do popular design specifications elsewhere in the world. Based on this, the probability of occurrence of each failure mode $P(E_i)$ is calculated using the reliability analysis method. Finally, the
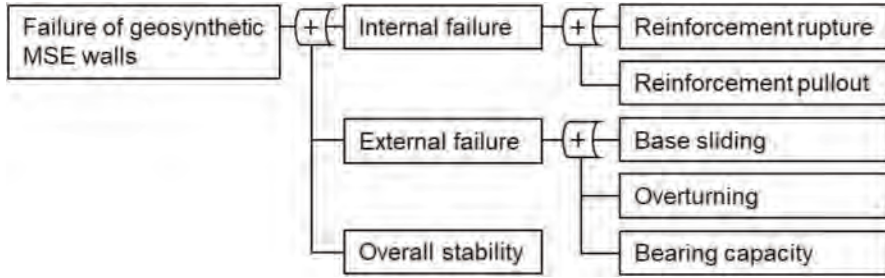
Figure 11.   Failure modes considered in the current design (PWRC 2013).

seismic failure probability P_f of the geosynthetic MSE wall is calculated as follows:

$$P_{\mathrm{f}} = 1 - \prod_{i=1}^{Life} \{1 - P(E_i)\} \tag{3}$$

In the above, Π is an operator denoting the product probability. Total cost caused by seismic failure event C_f can be calculated as follows:

$$C_{\mathrm{f}} = C_{\mathrm{s}} + C_{\mathrm{c}} + C_{\mathrm{j}} + C_{\mathrm{d}} + C_{\mathrm{p}} \tag{4}$$

Here, C_s is the cost of demolition and removal, C_c is the cost of reconstruction, C_j is the cost of lost time owing to road damage, C_d is the cost of lost travel owing to detours during reconstruction, and C_p is the cost of human losses owing to damage.

The LCC calculations were performed for geosynthetic MSE walls, L-shaped retaining walls, and non-reinforced embankments constructed for local roads. In the series of analyses, the following conditions were assumed.

(1) Geomaterial properties: Unit weight: $\gamma = 19.0$ kN/m^3, Cohesion: c = 0 kN/m^2, Angle of internal friction: $\phi = 30°$.
(2) Safety factors and seismic action: Required safety factor: $F_s = 1.2$ for permanent actions, $F_s = 1.0$ for seismic action; Design horizontal seismic intensity $k_h = 0.20$.
(3) Service condition: Service life = 50 years, average daily traffic condition = 10000 vehicles.
(4) Collapse area: 30 m in the direction of road expansion, regardless of the seismic conditions.
(5) Structure dimension: Width = 30 m, H = 4.0, 6.0, 8.0, and 10.0 m, respectively.
(6) Uncertainty of design parameters: Coefficients of variation were 10% for the geomaterials, 5% for the tensile strength of the geogrid, and 50% for the seismic intensity. Figure 12 shows the typical cross-sections that were analyzed.

Figure 13 shows the calculated LCCs of the soil structures. The geosynthetic MSE wall has the lowest LCC, followed by the non-reinforced embankment and L-shaped retaining wall. One reason for the high LCC of the L-shaped retaining wall is that it requires a greater number of days for rehabilitation after being damaged by a disaster. The non-reinforced embankment incurs the lowest initial construction cost. When compared with the risk-based LCC, the order of the embankment and geosynthetic MSE wall is reversed. When selecting the type of structure for road construction, the risk of failure should be properly considered.
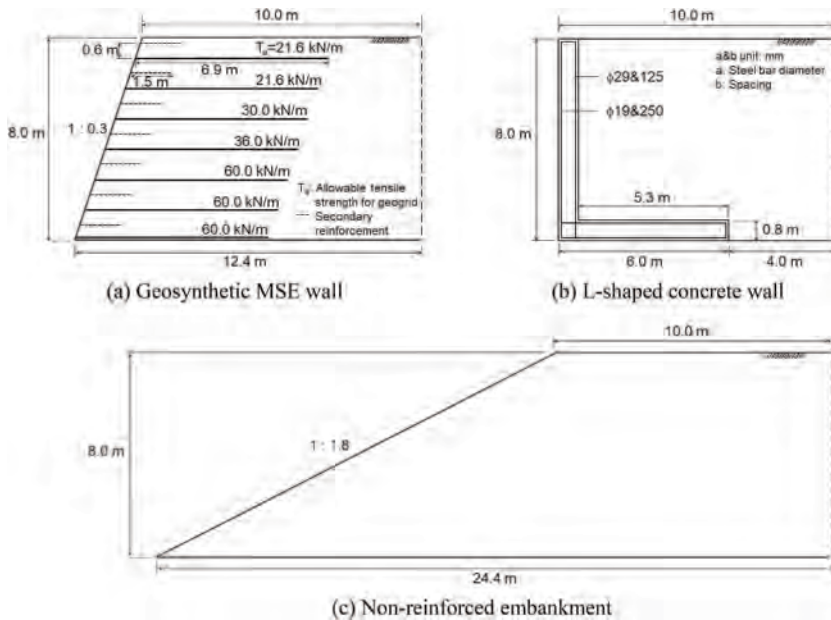
Figure 12. Typical cross-sections of geosynthetic MSE wall, L-shaped concrete wall, and non-reinforced embankment.
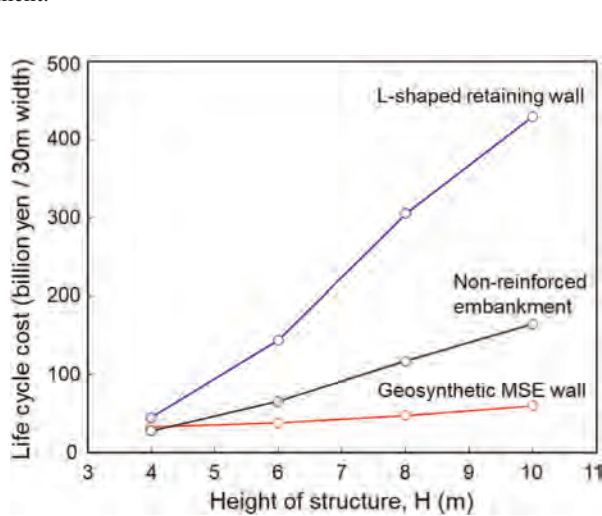
Figure 13. Life cycle cost analysis results for geosynthetic MSE wall, L-shaped concrete retaining wall, and non-reinforced embankment.

3.3 *Risk-based CO_2 emission analysis*

This section briefly explains an analysis method for CO_2 emissions and the advantages of geosynthetic MSE walls with greening. Similar analyses were performed by Heerten (2012) and Damians *et al.* (2017). They performed rigorous environmental analyses and showed the advantages of geosynthetic MSE walls. One improvement in this study is that the CO_2 emissions are considered in a risk-based analysis. This study presents the CO_2 emissions by the CO_2 equivalent weight [kg-CO_2] based on ISO (2006) 14040 and Miyata *et al.* (2013).

The life cycle CO_2 (LCCO$_2$) is assumed, as shown in Equation (5).

$$LCCO_2 = I_c + S_c + R_c \qquad (5)$$
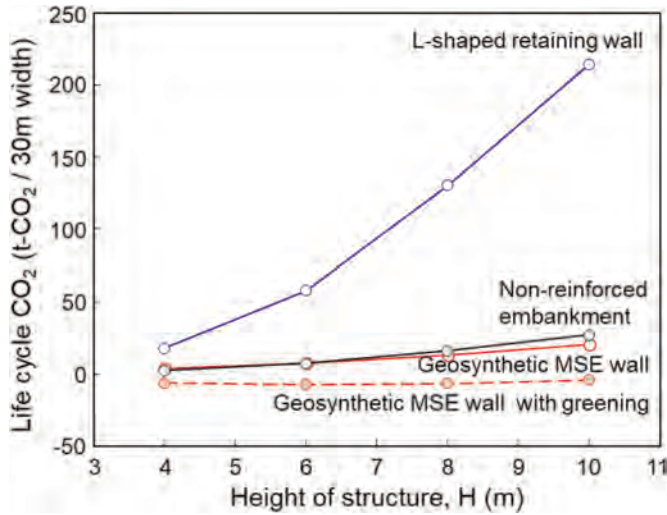
Figure 14.   Life cycle CO_2 analysis results for geosynthetic MSE wall, L-shaped concrete retaining wall, and non-reinforced embankment.

(a) During construction　　　　　　　　(b) Greened wall facing

Figure 15.   Greening technique combining geogrid and geotextile for geosynthetic MSE wall (courtesy of Dr. Hironaka).

In the above, I_c denotes the initial construction emissions, S_c is the absorption by the greening of the facing, and R_c is the risk of disaster recovery. R_c can be evaluated by multiplying the failure probability of the structures and CO_2 emissions during disaster recovery. A CO_2 emission analysis was performed for geosynthetic MSE walls with and without greening, L-shaped retaining walls, and non-reinforced embankments. Figure 14 shows the analysis results. One feature of the geosynthetic MSE walls is that the type of facing can be selected according to the construction conditions. Figure 15 depicts a greened geosynthetic MSE wall during construction and while in public service.

In the case of geosynthetic MSE walls, the greening of the facing can be accomplished using geogrids, geotextiles, steel mesh wall materials, and greening sheets, even if the construction conditions are complex. The analysis results show that the structure with the largest LCCO$_2$ emission among the four cases is the L-shaped retaining wall. In contrast, the lowest LCCO$_2$ emission is the geosynthetic MSE wall with greening. Surprisingly, assuming a service life of 50 years, the CO$_2$ emissions become negative. Thus, the geosynthetic MSE walls could be recognized as a structure type that contributes to carbon neutrality, i.e., sustainability.

3.4 *Damage/failure analysis*

This section discusses the damage/failure analysis and advantages of geosynthetic MSE walls based on the analysis results (Nonoyama *et al*. 2022). To analyze the damage and failure conditions of a geosynthetic MSE wall using the particle method, the soil is represented by an elastoplastic model, the soil-geosynthetics-soil hybrid element is represented by an elastoplastic model based on a two-mixture theory, and the facing panel is represented by an elastic model. In the mixture model for reinforced soil, the rate dependence of the geosynthetics and the constraining effect of the soil reinforcement are introduced. A strain-based yield criterion is introduced for the reinforced soil elements. In this modeling, when the calculated horizontal strain of a reinforced soil element reaches the limit value in one cal-
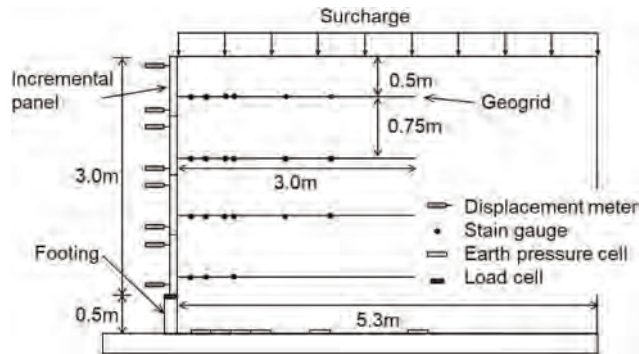
Figure 16.   Analyzed cross-section of the full-scale testing of geosynthetic MSE wall (Bathurst *et al*. 1993).

culation step, the incremental displacements are calculated in the next step by reducing the element stiffness to practically zero. In the present study, the horizontal limit strain is set at 2.0% based on Allen *et al*. (2003) and Bathurst and Allen (2023). To validate the proposed model, a full-scale loading experiment on a geosynthetic MSE wall with a height of 3.0 m as conducted by Bathurst *et al*. (1993) was analyzed. In this experiment, the geosynthetic MSE wall was damaged by airbag surcharge loading on the top surface. An overview of the full-scale model is shown in Figure 16. The fill material was sandy soil with gravel with a unit volume weight $\gamma = 18.0$ kN/m^3, water content w = 2%, cohesion c = 0 kPa, and angle of internal friction $\phi = 53°$. The reinforcement material was a biaxial geogrid with a tensile strength T$_{ult}$ = 12.0 kN/m and thickness t =1 mm.

Figure 17 compares the analytical and measured strain distributions along the geogrids at the end of construction. Good agreements are obtained for the location and magnitude of the peak strain. Figure 18 compares the measured and calculated displacements of the facing panels during surcharge loading pressures of 12, 30, 50, and 70 kPa. In both phases, the
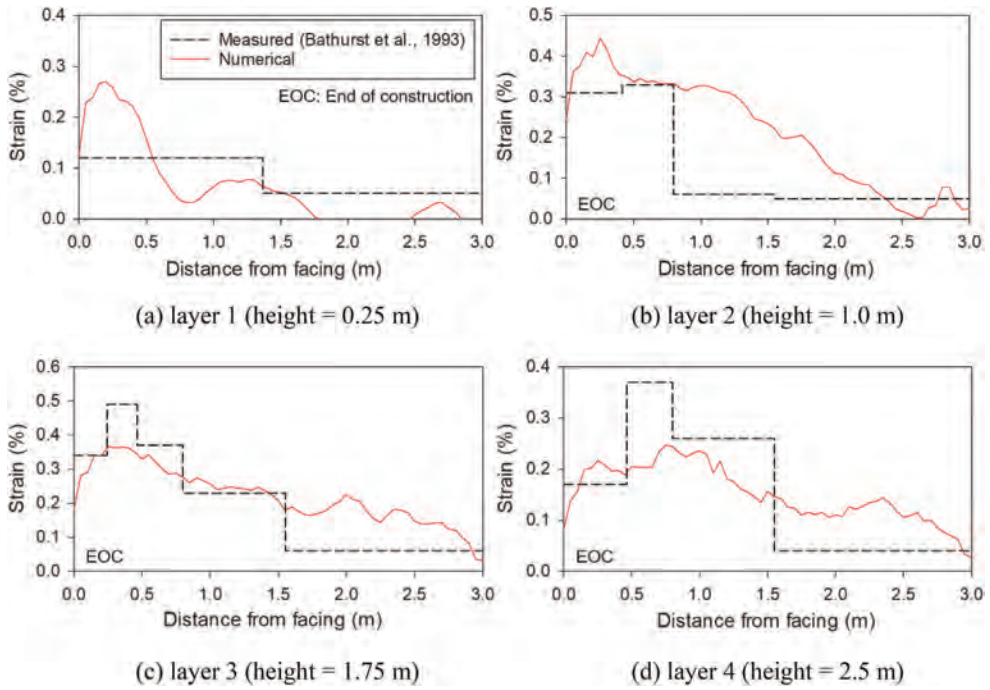
Figure 17.   Measured and numerical strain distribution along the geogrid reinforcement layers (Nonoyama *et al*. 2022).
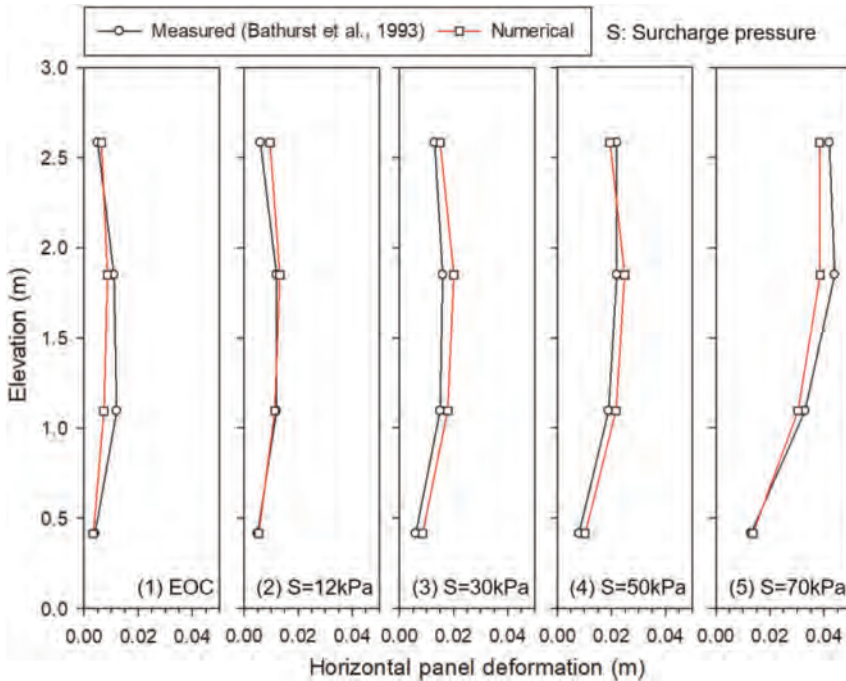
Figure 18.   Measured and numerical horizontal panel deformations (Nonoyama *et al*. 2022).

calculated values generally agree well with the measured values. Thus, the proposed particle method can be applied in damage analyses of geosynthetic MSE walls.

To validate the proposed failure analysis method, a scenario-based numerical analysis was performed. A scenario was assumed in which the foundation directly below the wall of a geosynthetic MSE wall slides horizontally, eventually resulting in the functional loss of the foundation and facing panels. This assumption was based on full-scale testing considering the foundation failure (Miyata *et al.* 2015).

In a series of analyses, a horizontal displacement rate of 1.0 cm/sec was applied to the
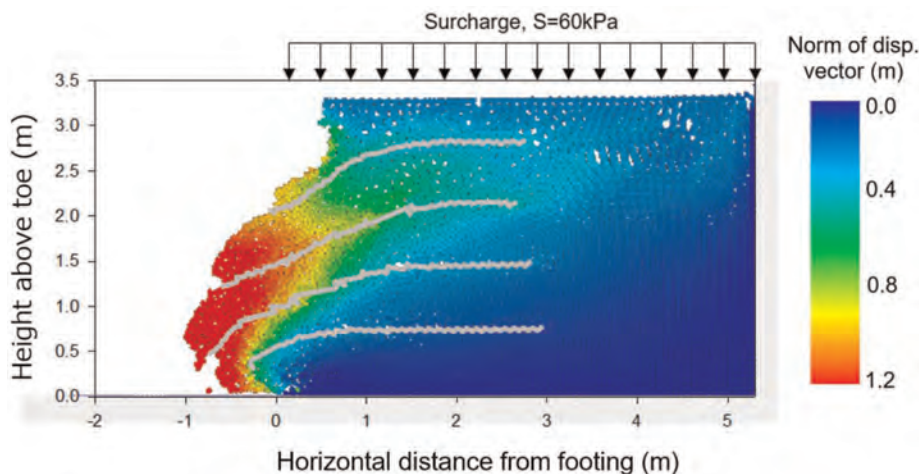
Figure 19.   Numerical analysis of failure behavior of geosynthetic MSE wall (Nonoyama *et al.* 2022).

foundation with an initial surcharge of 60 kPa applied to the top of the backfill. After the horizontal displacement of the foundation reached 4 cm, the foundation and facing elements were removed from the analysis.

Figure 19 shows the displacement field of the fill material after the foundation and wall material lose their functionality. It would be difficult to fully simulate the entire failure process of geosynthetic MSE walls using particle methods. In previous post-disaster reports on geosynthetic MSE walls (ex. Kuwano *et al.* 2014), almost no cases occur where the geosynthetic MSE wall completely collapsed. As shown in Figure 19, many geosynthetic MSE walls reach equilibrium conditions at the large-deformation stage following structural failure. Therefore, the particle method can qualitatively simulate the failure behavior of geosynthetic MSE walls.

4   ADVANCED SOLUTIONS FOR THE NEXT DECADE

4.1   *Background*

Geotechnical challenges are becoming increasingly complex, requiring the further development of geosynthetic MSE wall technology. One requiring improvement is the earthquake-resistance technique. This is because earthquake damage is becoming increasingly severe. As shown in Table 2, a severe earthquake leads to massive economic losses and human suffering, and a great deal of effort is required to recover from the damage. In the field of structural engineering, seismic isolation and vibration control technology have been actively developed to reduce seismic actions on structures and increase their resistance to earthquakes

(Ikeda *et al.* 2019; Spencer Jr & Nagarajaiah 2003). In the geosynthetic MSE wall field, new systems such as integral bridges and their combinations with soil improvement and anchoring are being considered for improved seismic performance (e.g., Tatsuoka *et al.* 2009). For vibration control, the application of expanded polystyrene (EPS) has been studied (Koseki 2022). Notably, Bathurst *et al.* (2007) and Zarnani & Bathurst (2008) conducted a pioneering study on the use of compressible EPS geofoam as seismic buffers to attenuate dynamic loads against rigid retaining wall structures. However, few studies have been conducted on seismic isolation control for geosynthetic MSE walls. This study considers the potential of seismic isolation using geosynthetics having three-dimensional structures which are beginning to be used as vibration-reducing materials on construction sites.

Life cycle management methods also require improvement. To rationally perform life cycle management, it is necessary to periodically diagnose conditions and rationally determine the necessity of measured performance. In geosynthetic MSE wall life cycle management, the first question is which data to measure? Allen *et al.* (2003) showed that the reinforcement strain is an important indicator of the integrity of a geosynthetic MSE wall. They proposed that prediction models developed based on a statistical approach using measured strain data from various geosynthetic MSE walls are useful not only for design but also for evaluating structural integrity.

Another question is how to collect the field data quickly, inexpensively, and securely. The authors' research group developed a prototype sensor system for geosynthetic MSE walls and confirmed the effectiveness of ICT-based management (Miyata *et al.* 2012). However, issues have remained regarding providing reinforcement strain monitoring applicable throughout the actual service life of a geosynthetic MSE wall. In the next section, the applicability of ICT management and an attachment-type fiber optic sensor for geosynthetic MSE wall life cycle management are discussed.

4.2 *Seismic isolation technique*

Figure 20 shows a geosynthetic MSE wall with a seismic isolation layer. This type of structural system is expected to demonstrate high seismic performance owing to the inherent reinforcement and seismic isolation effects of the geosynthetic MSE wall. The seismic isolation layer must have frictional resistance properties to provide sufficient sliding resistance to horizontal earth pressures from the retained backfill during (operational) static loading and a function to reduce the vibration transmitted to the geosynthetic MSE wall during earthquakes. The author focused on applying geosynthetics, as these are beginning to be used as construction vibration reduction materials (Ogawa *et al.* 2022). An example of
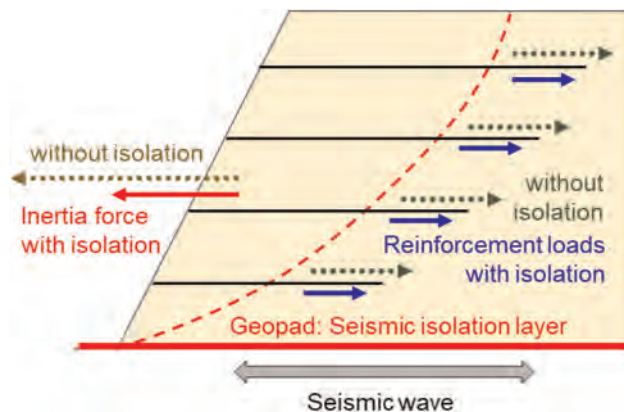
Figure 20.   Concept of geosynthetic MSE wall with seismic isolation layer.
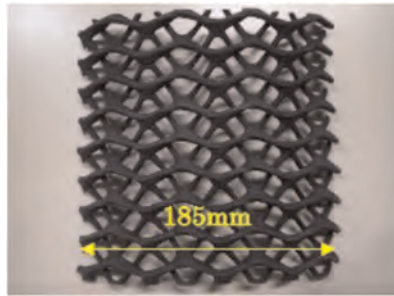
Figure 21.   Geosynthetics made from polyolefin elastomer with three-dimensional structure.
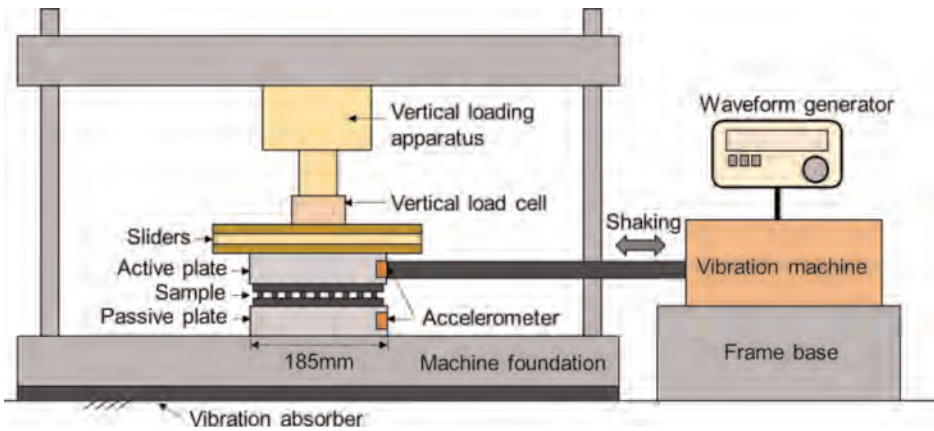
Figure 22.   Laboratory model test apparatus to investigate isolation efficiency of geopad geosynthetic samples.

geosynthetic is shown in Figure 21. This product is made of polyolefin elastomer and has a three-dimensional structure. This product is referred to as a geopad in this paper. Figure 22 shows a schematic of the laboratory tests conducted to investigate the seismic isolation characteristics of this product. The apparatus consists of a vertical stress loading apparatus, a vibration machine, and specimen mounting apparatus. In the experiment, the specimen was sandwiched between two steel plates. The upper plate was subjected to sinusoidal vibration and the acceleration transmitted to the lower plate was measured. The experimental results were summarized by calculating the isolation efficiency E from the acceleration measured on the upper steel plate a_{in} and that measured on the lower steel plate a_{out}.

$$E = a_{out}/a_{in} \tag{5}$$

Experiments were conducted using a natural rubber sheet, commonly used for construction vibration countermeasures, a single geopad layer, and double geopad layers. Vibrations were applied at five different frequencies ranging from 5 to 80 Hz.

The experimental results are shown in Figure 23. In the case of the natural rubber sheet, the vibration transmission is 185% at 5 Hz and 45% to 52% at 10 to 40 Hz. The double geopad layers improve the isolation effect, transmitting only 20% to 30% of the vibration of the natural rubber. These experimental results demonstrate the applicability of the geopad
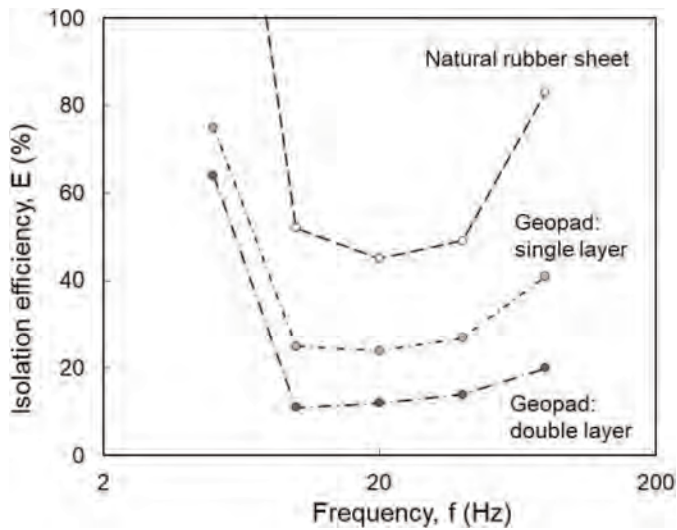
Figure 23.   Relationship between the frequency of shaking and isolation efficiency (modified from Hironaka *et al.* 2023).
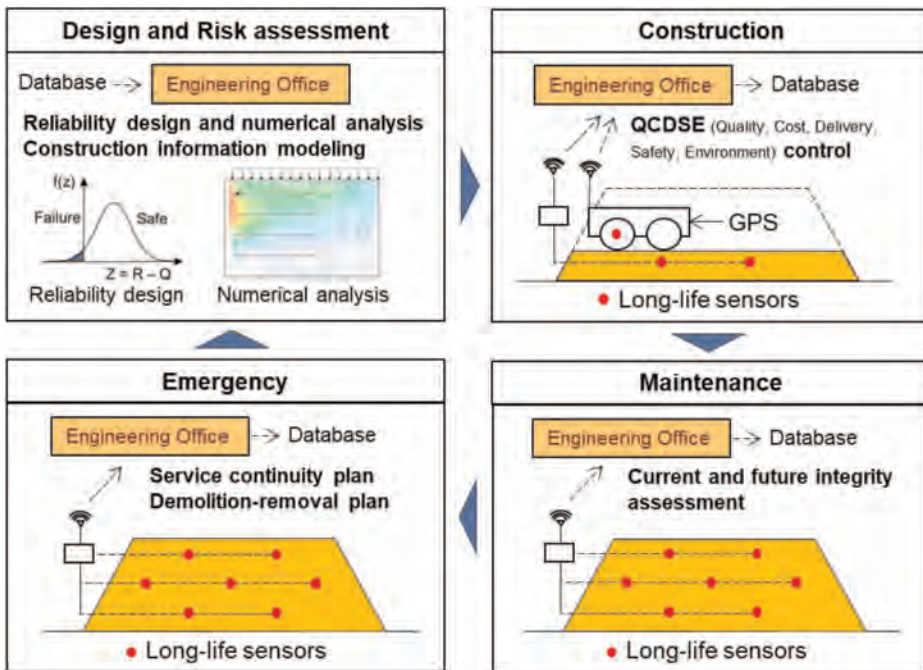
Figure 24.   Concept of information and communication technology (ICT)-based life cycle management of geosynthetic MSE wall.

used herein to improve the seismic isolation effect of geosynthetic MSE walls. As a next step, we plan to verify the seismic isolation effect of the geopad based on shaking table experiments on geosynthetic MSE walls. After that, we plan to establish a method for analyzing the seismic isolation effect and evaluating the material properties of the geopad.

4.3 *Information and Communication Technology (ICT)-based life cycle management*

Figure 24 schematically depicts the roles of the ICT-based geosynthetic MSE wall life cycle management for the stages of "Design and Risk Assessment," "Construction," "Maintenance," and "Emergency." The structural data is always sent to the engineering office so that all the data can be used to make decisions for any life cycle stage of a structure.

The technical reliability of geosynthetic MSE walls will be further enhanced once such a system is developed, and a management approach is put into practice. Two key issues must be addressed for the practical application of this management. One concern is the need for long-life sensors for monitoring the internal conditions of geosynthetic MSE walls throughout the life of the structure. Geosynthetic strain measurements have been shown to be effective in assessing the structural integrity of geosynthetic MSE walls (Allen *et al.* 2003). Corresponding long-term measurements should be developed. Hatami *et al.* (2009) proposed a strain-sensitive conductive geosynthetic based on nanotechnology. Fiber optic sensing is another candidate approach for long-term measurements. It has recently been applied in the
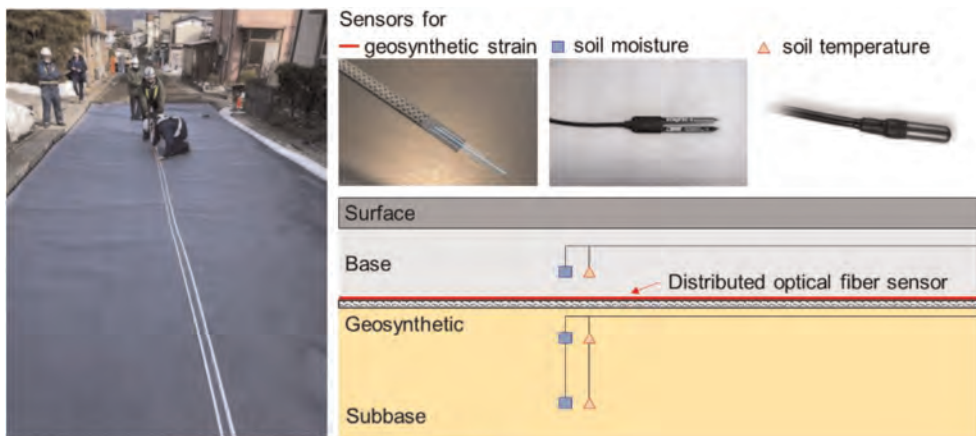
Figure 25.   Fiber optics applied to a field construction site with geosynthetic reinforced soil (courtesy of Dr. Nagatani and Dr. Hironaka).

measurement of civil engineering structures (Soga & Luo 2018). In the geosynthetic MSE wall technical field, pioneering work has been performed by Yashima *et al.* (2009). In recent years, the progress in optical fiber sensors has been remarkable. The latest sensor system makes it possible to acquire structural data with higher accuracy and speed than ever before. The author and researchers at civil and geosynthetics engineering companies have jointly initiated a study to confirm the applicability of using distributed fiber optic sensors examined by Kishida *et al.* (2022) for geosynthetic MSE walls. As a first step in the research, strain measurements were conducted at an actual site. Figure 25 shows the site situation. The measurement data will be presented at another time, but the author can report that the results show the effectiveness of the measurement system. It is expected that many engineers/researchers will study new long-life sensing for geosynthetic MSE walls.

Another issue is the need to further develop reliability analyses to utilize data from long-life sensors in practice. Allen and Bathurst (2015) developed reinforcement tensile load prediction models for MSE walls under operational conditions based on a statistical approach. Bathurst and Allen (2019, 2023) calibrated the load and resistance factors for geosynthetic MSE walls. Miyata *et al.* (2018, 2019) and Bathurst *et al.* (2020) demonstrated

how this general approach can be applied to PET strap walls. Reliability analysis is very powerful for improving design methods by using in-situ data. Reliability analysis can be used for other phases of the MSE wall life cycle. In the construction process, reliability analyses using design estimates and observed data can be used to evaluate deviations between design assumptions and actual as-built conditions. In addition, probabilistic reliability indices can be used as a basis for considering measures such as halting construction and changing the design before a serious accident occurs.

During the maintenance period, monitoring systems can assist to predict the future internal conditions of a structure using reliability analysis applied to observed data, allowing the user to consider changes to the inspection schedule and measures to be taken. Deep learning will undoubtedly be effective for future predictions. In emergency situations where damage is caused by large actions such as earthquakes and rainfall, data on the internal condition of the structure before and after such actions can be compared and checked for anomalies on a reliability basis. Even if demolition or removal is deemed necessary, a reliability analysis using the observed data can be a useful tool for safety evaluations during planning and execution. Finally, reliability theory can be used in the risk assessment phase. The massive amounts of data collected by ICT management will contribute to more realistic risk estimations.

5 SUMMARY

The paper describes the overall research trends in geosynthetic MSE walls over the past 40 years, the latest analysis methods based on the author's research, and an outlook on the future of this technology. In the research summary section, the author visualized the evolution of the number of papers and the content of the research on geosynthetic MSE walls by reviewing approximately 700 journal papers published on geosynthetic MSE walls. These changes were discussed together with events in the academic, practical, and social trends. The importance of preparing a place for the exchange of technical information and presentation of research was reaffirmed. The advanced analysis section, how to calculate life cycle costs and carbon dioxide emissions on a risk-based basis was introduced and it was shown that the benefits of geosynthetic MSE walls become clearer when considered on a life cycle basis. In addition, it was shown that the particle method could solve the entire process of a geosynthetic MSE wall from deformation to failure. New performance requirements such as resilience and sustainability can be adequately evaluated by using these advanced engineering tools for geosynthetic MSE walls. Finally, the author discussed a seismic isolation technique and more rational life cycle management as future applications for geosynthetic MSE walls. For the former, the isolation efficiency of geosynthetics with three-dimensional structures was discussed based on the results of recently conducted laboratory tests. For the latter, the new potential of management methods using the latest ICT such as fiber optic sensors was discussed. As civil engineering structures become increasingly complex, the design and maintenance of infrastructure must become more rational, economical, and environmentally friendly. Technology on geosynthetic MSE walls has great potential to meet these demands and should be further developed, taking into account developments in other technology fields.

REFERENCES

AASHTO. 1994. *LRFD Bridge Design Specifications*, 1st ed. American Association of State Highway and Transportation Officials, Washington DC/USA.

AASHTO. 2020. *LRFD Bridge Design Specifications*, 9th ed. American Association of State Highway and Transportation Officials, Washington DC/USA.

Allen, T.M., Bathurst, R.J., Walters, D.L., Holtz, R.D. & Lee, W.F. 2003. A New Working Stress Method for Prediction of Reinforcement Loads in Geosynthetic Walls. *Canadian Geotechnical J.* 40(5): 976–994.

Allen, T.M. & Bathurst, R.J. 2015. An Improved Simplified Method for Prediction of Loads in Reinforced Soil Walls. *J. Geotechnical and Geoenvironmental Engineering* 141(11): 04015049.

Bathurst, R.J., Jarrett, P.M. & Benjamin, D.J.R.S. 1993. Database of Results From an Incrementally Constructed Geogrid-reinforced Soil Wall Test. *Proc. Soil Reinforcement: Full Scale Experiments of the 80's*: 401–430.

Bathurst, R.J. & Alfaro, M.C. 1997. Review of Seismic Design, Analysis and Performance of Geosynthetic Reinforced Walls, Slopes and Embankments, Invited Keynote. Proc. 3rd International Symposium on Earth Reinforcement (IS-Kyushu '96) Vol. 2: 887–918.

Bathurst, R.J. & Kaliakin, V.N. 2005a. Review of Numerical Models for Geosynthetics in Reinforcement Applications, Invited Issue Paper. *Proc. 11th International Conference of the International Association for Computer Methods and Advances in Geomechanics* Vol. 4: 407–416.

Bathurst, R.J. Allen, T.M. & Walters, D.L. 2005b. Reinforcement Loads in Geosynthetic Walls and the Case for a New Working Stress Design Method, 2002–2004 Mercer Lecture. *Geotextiles and Geomembranes* 23: 287–322.

Bathurst, R.J., Zarnani, S. & Gaskin, A. 2007. Shaking Table Testing of Geofoam Seismic Buffers. *Soil Dynamics and Earthquake Engineering* 27(4): 324–332.

Bathurst, R.J. 2014. Challenges and Recent Progress in the Analysis, Design and Modelling of Geosynthetic Reinforced Soil Walls, 2014 Giroud Lecture. *Proc. 10th International Geosynthetics Conference*: 38 pages.

Bathurst, R.J., Allen, T.M., Lin, P. & Bozorgzadeh, N. 2019. LRFD Calibration of Internal Limit States for Geogrid MSE walls. *J. Geotechnical and Geoenvironmental Engineering* 145(11): 04019087.

Bathurst, R.J., Miyata, Y. & Allen, T.M. 2020. Deterministic and Probabilistic Assessment of Margins of Safety for Internal Stability of As-built PET Strap Reinforced Soil Walls. *Geotextile and Geomembranes.* 48 (6): 780–792.

Bathurst, R.J. & Allen, T.M. 2023. LRFD Calibration for Soil Failure Limit State using the Stiffness Method. *Canadian Geotechnical J.*: https://doi.org/10.1139/cgj-2022-0499.

Bocchini, P., Frangopol, D.M., Ummenhofer, T., & Zinke, T. 2014. Resilience and Sustainability of Civil Infrastructure: Toward a Unified Approach. *J. Infrastructure System* 20(2): 04014004.

Damians, I.P., Bathurst, R.J., Garcia, E., Josa, A. & Lloret, A. 2017. Environmental Assessment of Earth Retaining Wall Structures. *Environmental Geotechnics* 4(6): 415–431.

Damians, I.P., Bathurst, R.J., Adroguer, E.G., Josa, A. & Lloret, A. 2018. Sustainability Assessment of Earth Retaining Wall Structures. *Environmental Geotechnics* 5(4): 187–203.

Daniell, J.E., Khazai, B., Wenzel, F. & Vervaeck, A. 2012. The Worldwide Economic Impact of Historic Earthquakes. *Proc. 15th World Conference of Earthquake Engineering*, Paper No. 2038: 10 pages.

CEN. 2002. Eurocode -Basis of Structural Design, EN 1990: 2002. European Committee for Standardization (CEN), Brussels/ Belgium.

CEN. 2004. Eurocode 7: Geotechnical Design - Part 1: General rules, EN 1997-1: 2004. European Committee for Standardization (CEN), Brussels/ Belgium.

CEN. 2007. Eurocode 7: Geotechnical Design - Part 2: Ground Investigation and Testing, EN 1997-2: 2007. European Committee for Standardization, Brucellas/ Belgium.

Giroud, J.P. (with cooperation of Beech, J.F. & Khatami, A.) 1993. Geosynthetics Bibliography Vol. 1. IFAI Publishers, MN/USA.

Giroud, J.P. (with cooperation of Beech, J.F., Khatami, A., & Badu-Tweneboah, K.) 1994. *Geosynthetics Bibliography* Vol. 2. IFAI Publishers, MN/USA.

Hatami, K., Grady, B.P. & Ulmer, M.C. 2009. Sensor-enabled Geosynthetics: Use of Conducting Carbon Networks as Geosynthetic Sensors. *J. Geotechnical and Geoenvironmental Engineering*. 135: 863–874.

Heerten, G. 2012. Reduction of Climate-damaging Gases in Geotechnical Engineering Practice using Geosynthetics. *Geotextile and Geomembrane* 30: 43–49.

Holtz, R.D. 2017. Geosynthetic Reinforced soil: From the Experimental to the Familiar, 46th Terzaghi Lecture. *J. Geotechnical and Geoenvironmental Engineering* 143(9): 3117001.

Hironaka, J., Ogawa, R., Aoyama, M., Sato, I., Nagatani, H., & Miyata, Y. 2023. Laboratory Testing on Reducing Ground Vibration Effects on Polyolefin Elastomer Pad (Part 3). *Proc. Annual Japan Civil Engineers Society Conference: Two Pages Abstract* (in press).

Ikeda, Y., Yamamoto, M., Furuhashi, T. & Kurino, H. 2019. Recent Research and Development of Structural Control in Japan. *Japan Architectural Review* 2(3): 219–225.

ISO. 1986. *General Principles on Reliability for Structures*, ISO 2394: 2nd ed. International Organization for Standardization, Geneva/Switzerland.

ISO. 1998. *General Principles on Reliability for Structures*, ISO 2394: 3rd ed. International Organization for Standardization, Geneva/Switzerland.

ISO. 2006. *Environmental Management -Life Cycle Assessment- Principles and Framework*, ISO 14040. International Organization for Standardization, Geneva/Switzerland.

ISO. 2015. *General Principles on Reliability for Structures*, ISO 2394 4th ed. International Organization for Standardization, Geneva/Switzerland.

Koseki, J. 2012. Use of Geosynthetics to Improve Seismic Performance of Earth Structures, 2011 Mercer Lecture. *Geotextiles and Geomembranes* 34: 51–68.

Koseki, J. 2022. Geosynthetic-reinforcement and its Combination with Other Methods for Soil Retaining Walls to Resist Against Large Seismic Loads, 2022 Tatsuoka Lecture. Proc. 7th Asian Regional Conference on Geosynthetics (GeoAsia 7): 10 pages.

Kishida, K., Imai, M., Kawabata, J., & Guzik, A. 2022. Distributed Optical Fiber Sensors for Monitoring of civil Engineering Structures. *Sensors* 22: 4368.

Kuwano, J., Miyata, Y. & Koseki, J. 2014. Performance of Reinforced Soil Walls in the 2011 off the Pacific Coast of Tohoku Earthquake. *Geosynthetics International* 21(3): 179–196.

Ling, H.I., Leshchinsky, D. & Chou N.N.S. 2001. Post-earthquake Investigation on Several Geosynthetic-reinforced Soil Retaining Walls and Slopes during the Ji-Ji Earthquake of Taiwan. *Soil Dynamics and Earthquake Engineering* 21: 297–313.

Lounis, Z. & Mcallister, T.P. 2016. Risk-based Decision Making for Sustainable and Resilient Infrastructure Systems. *J. Structural Eng.* 142(9): F4016005.

MLIT. 2015. Technical Standard on Road Earth Work. Ministry of Land, Infrastructure, Transport and Tourism, Tokyo/Japan.

Miyata, Y., Shinoda, M., Konami, T., Ohno K., Yonezawa, T. & Hironaka, J. 2010. Lifecycle Cost Analysis of Geosynthetics Reinforced Soil Wall. *Geosynthetic Engineering J.* 25: 177–182.

Miyata, Y., Hirakawa, D., Tada, T., Konami, T. & Bathurst, R.J. 2012. Concept of ICT-based Maintenance Technique for Geo-structure and Application. *Proc. International Workshop on ICT in Geo-Engineering*: 185–191.

Miyata, Y., Ohno K., Shinoda, M., Hironaka, J. & Tatta, N. 2013. Analysis of CO_2 Emissions on Construction of Geogrid Reinforced Soil Wall and Investigation. *Geosynthetic Engineering J.* 28: 289–294.

Miyata, Y., Bathurst, R.J. & Miyatake, H. 2015. Performance of Three Geogrid Reinforced Soil Walls Before and After Foundation Failure. *Geosynthetics International* 22(4): 311–326.

Miyata, Y., Bathurst, R.J. & Allen, T.M. 2018. Evaluation of Tensile Load Model Accuracy for PET Strap MSE Walls. *Geosynthetics International* 25(6): 656–671.

Miyata, Y., Bathurst, R.J. & Allen, T.M. 2019. Calibration of PET Strap Pullout Models using a Statistical Approach. *Geosynthetics International* 26(4): 413–427.

Nonoyama, H., Miyata, Y. & Bathurst, R.J.: 2022. Deformation/damage/post Failure Analysis Method of Reinforced Soil Walls Using SPH Method. *J. Japan Society of Civil Engineers* 77(1): 35–45.

Ochiai, H. 2007. Earth Reinforcement Technique a Role of New Geotechnical Solutions - Memory of IS Kyushu, Special Lecture. *Proc. 5th International Symposium on Earth Reinforcement* (IS-Kyushu '07): 1–23.

Ogawa, R., Hironaka, J., Aoyama, M., Nagatani, H., Sato I. & Miyata, Y. 2022. Reducing Ground Vibration due to Construction Works by Polyolefin Elastomer Pad with 3D Mesh Structures. *Geosynthetic Engineering J.* 37: 9–12.

Otani J. Yamamoto, A., Yasufuku, N. Yashima, A. & Kodaka, T. 1997. Current State on Numerical Analysis of Reinforced Soil Structures. *Proc. 3rd International Symposium on Earth Reinforcement* (IS-Kyushu '96) Vol. 2: 1159–1170.

Palmeira (2009) Soil–geosynthetic Interaction: Modelling and Analysis, 2007–2008 Mercer Lecture. *Geotextiles and Geomembranes* 27: 368–390.

PWRC. 2013. *Design and Construction Manual of Geosynthetics Reinforced Soil*, 2nd Revision. Public Works Research Center, Tsukuba/Japan.

Rowe, R.K. & Ho, S.K. 1993. A Review of the Behaviour of Reinforced Soil Walls. Invited Keynote. *Proc. 2nd International Symposium on Earth Reinforcement (IS-Kyushu'92)* Vol. 2: 801–830.

Rowe, R.K. & Li, A.L. 2003. Insights from case histories: Reinforced Embankments and Retaining Walls, Invited Keynote. *Proc. 4th International Symposium on Earth Reinforcement (IS-Kyushu'01)* Vol. 2: 803–829.

Soga K. & Luo, L. 2018. Distributed Fiber Optics Sensors for Civil Engineering Infrastructure Sensing. *J. Structural Integrity Maintenance* 3(1): 1–21.

Spencer Jr, B.F. & Nagarajaiah, S. 2003. State of the Art of Structural Control. *J. Structural Engineering* 129 (7): 845–856.

Tatsuoka, F., Tateyama, M. & Koseki, J. 1996. Performance of Soil Retaining Walls for Railway Embankments. *Soils and Foundations*, Special Issue of Soils and Foundations on Geotechnical Aspects of January 17, 1995, Hyogoken-Nambu Earthquake: 311–324.

Tatsuoka, F., Tateyama, M., Uchimura, T. & Koseki, J. 1997. Geosynthetic-reinforced Soil Retaining Walls as Important Permanent Structures, 1996 - 1997 Mercer Lecture. *Geosynthetics International* 4(2): 81–136.

Tatsuoka, F., Hirakawa, D., Nojiri, M., Aizawa, H., Nishikiori, H., Soma, R., Tateyama, M. & Watanabe, K. 2009: A New Type of Integral Bridge Comprising Geosynthetic-reinforced Soil Walls. *Geosynthetics International* 16(4): 301–326.

White D.M. & Holtz, R.D. 1997. Performance of Geosynthetic-reinforced Slopes and Walls during the Northridge California Earthquake of January 17, 1994, Special Report. *Proc. 3rd International Symposium on Earth Reinforcement (IS-Kyushu '96)* Vol. 2: 965–972.

Yashima, A., Tsuji, S., Yoshida, K. & Yokota, Y. 2009. A New Optical Fibre Sensor to Assess the Stability of Geogrid-reinforced Soil Walls. *Geosynthetics International* 16(4): 238–245.

Zarnani, S. & Bathurst, R.J. 2008. Numerical Modeling of EPS Seismic Buffer Shaking Table Tests. *Geotextiles and Geomembranes* 26(5): 371–383.

Selection of long-term shear strength parameters for strain softening geosynthetic interfaces (Rowe lecture)

R. Thiel

Thiel Engineering, Oregon House, CA, USA

ABSTRACT: The behavior of strain-softening geosynthetic interfaces that can lead to progressive failures in lined containment facilities has been a source of confusion in slope stability evaluations for over 30 years. The paper presents fifteen mechanisms that can potentially induce displacements along strain-softening interfaces, along with measures that can be considered to reduce strain-softening displacement. New quantifications of shear strength variability that can be caused by manufacturing, installation, and construction practices are introduced. Guidance and recommendations are given that are applicable to numerical continuum as well as limit-equilibrium approaches to assist in selecting appropriate geosynthetic shear strength parameters for containment facilities that have strain-softening interfaces. While most of the paper focuses on deep-seated critical interfaces for high normal stress bottom liners, low normal stress veneer covers are also addressed.

1 INTRODUCTION

1.1 *General*

Slope instability of large waste or mining containment facilities presents one of the most potentially immediate and consequential impacts to the greatest spectrum of stakeholders. Often a sizable portion of the critical slip surfaces for these facilities follows a strain-softening geosynthetic interface. The present paper identifies numerous factors that can be considered when selecting appropriate long-term shear strength parameters along these interfaces.

This specific topic has been an active, and occasionally intense, subject of technical papers in the geosynthetic industry for at least 35 years. Indeed, there have been several references with nearly the same title as the present paper over the past 20 years (e.g. Eid 2011; Gilbert 2001; Sabatini et al. 2001; Stark & Choi 2004; Stark 2022; Thiel 2001). Even so, confusion still exists among design practitioners regarding the appropriate testing, interpretation, and selection of long-term shear strength parameters for geosynthetic interfaces. Undoubtedly there will be future papers with a similar title, especially as more knowledge and experience becomes available related to the effects of ageing, durability, and latent weak zones within strain-softening geosynthetic interfaces.

Due to length restrictions, the present paper is shortened from a longer companion paper version that will be published in *Geosynthetics International* under the same title. Where appropriate, the reader is directed to consult the longer version for more information. For example, definitions of several geotechnical terms as used in this paper that are in common usage by practitioners in the containment industry are provided in the *Geosynthetics International* companion paper appendices.

1.2 *Concept of strain softening and progressive failure*

Probably the greatest amount of confusion and controversy regarding the selection of appropriate shear strengths for geosynthetic interfaces occurs because many of these interfaces are characterized as 'strain-softening'. A quasi-synonymous term that is sometimes used in the literature is 'brittle.' However the connotation of brittle might imply a narrower amount of strain deformation to achieve peak and residual strength conditions than might occur, and so the term 'strain softening' is adopted in the present paper. Whatever term is preferred, the shear strength of many geosynthetic interfaces reaches their peak value with a relatively small amount of relative shear deformation, often less than 2-20 mm, and then degrades relatively rapidly with continued deformation to lower values, as illustrated in Figure 1. These lower values are variously referred to as 'post-peak' shear strength, 'large-displacement' shear strength (commonly cited as occurring at approximately 75 mm of relative displacement), ultimately reaching a constant minimum value of what is called 'residual' shear strength.

In classical geotechnical engineering, strain-softening soils have been, and continue to be some of the most difficult to evaluate for slope stability analyses. Thus, it is not surprising that confusion exists in the geosynthetics profession, considering that this complex type of shear strength interface is the norm in geosynthetics engineering.
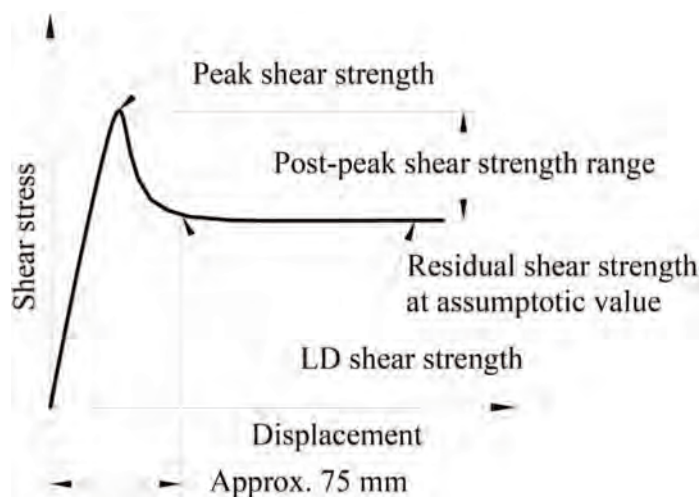
Figure 1.   Schematic of shear-stress versus displacement at geosynthetic interface illustrating strain-softening behavior.

In simplest terms, the problem with strain-softening interfaces is that even though a correctly performed limit equilibrium stability analysis based on peak strength indicates a generally accepted factor of safety (*FS*) greater than 1.5, the slope may still fail. The reason for this is a phenomenon called 'progressive failure.'

Strain-softening soils, or geosynthetic interfaces, promote the phenomenon of progressive failure, and make it impossible to count on mobilizing peak strength simultaneously at all locations along the failure surface (Duncan & Wright 2005). Perhaps the best, and first description of progressive failure was made by Skempton (1964), and it bears repeating here, as it is directly applicable to our subject. Note that the current author has substituted the words [geosynthetic interface] where the original quote used the word 'clay':

> *"Irrespective of the physical explanation of the drop in strength after passing the peak, the existence of this decrease in strength must be accepted as a fact which has been well established. Thus, if for any reason a [geosynthetic interface] is forced to*

pass the peak at some particular point, the strength at that point will decrease. This action will throw additional stress onto the [geosynthetic interface] at some other point, causing the peak to be passed at that point also. In this way progressive failure can be initiated and, in the limit, the strength along the entire length of a slip surface will fall to the residual value. Obviously, in any given case, a slip may occur before the residual strength is attained throughout the [geosynthetic interface], but once a progressive failure has started the average strength of the [geosynthetic interface] will decrease inexorably towards the limiting residual value."

The next paragraph in Skempton's 1964 paper explains that zones of weakness and zones that have already failed past peak strength can act as stress concentrators and can then cause shear deformations to take place at an average stress that is far less than the ideal strength of the material. The current author is not aware of attempts, and has not himself attempted, to quantify the magnitude of stress concentrations within the plane of a strain-softening shear interface containing abrupt boundaries with weak zones. This concept is explored in later sections of this paper as a potential contributing factor to progressive failure, and a subject that merits further research.

1.3   *Strain-softening potential of typical geosynthetic interfaces*

The magnitude of strain softening, R_{ss}, is defined by Gilbert and Byrne (1996) as the ratio of residual to peak shear strength:

$$R_{ss} = \frac{\tau_r}{\tau_p} \tag{1}$$

Given that much of the geosynthetics literature and testing results are based on LD rather than the true residual, this term can receive a modified subscript as R_{ss-LD} when it is known that the basis is LD. A value of $R_{ss} = 100\%$ would mean that the geosynthetic interface would not lose any of its shear strength after exceeding the peak strength and would not be considered strain-softening. A value of $R_{ss} = 60\%$ would mean that the geosynthetic interface would lose 40% of its shear strength after exceeding the peak strength, a significant loss of strength that would define that interface as highly strain-softening.

   Koerner and Narejo (2005) provide peak and LD shear strength data on 48 different geosynthetic interfaces that was collected from the Geosynthetic Accreditation Institute's database of proficiency test results from 3,260 large-scale direct shear tests performed by many laboratories in general accordance with ASTM D5321. A synopsis of those results is provided in the *Geosynthetics International* companion paper appendices.

   The author commonly specifies aggressive texturing which results in $R_{ss-LD} \approx 40\text{-}60\%$ for these interfaces (e.g. see Figure 2). While aggressive texturing will provide the highest available peak shear strength, is that peak strength reliable given the high magnitude of strain-softening potential? This is a significant aspect of the subject of this paper considering that an average overall $R_{ss} \leq 67\%$ could potentially cause an *FS* value of 1.5 that is based on peak strength to fall below 1.0.

1.4   *Limit equilibrium and numerical continuum analysis approaches*

For deep-seated failures that have strain-softening interfaces, limit equilibrium analyses that assume peak strengths can give non-realistic and non-conservative results, and also give no indication of the distribution or magnitude of mobilized shear stresses or displacements. However, the vast majority of the slope stability analyses performed in the geo-environmental containment industry are done by professionals using computer software programs based on limit-equilibrium models, such 'Spencer's method', or the 'Janbu method', or any of several
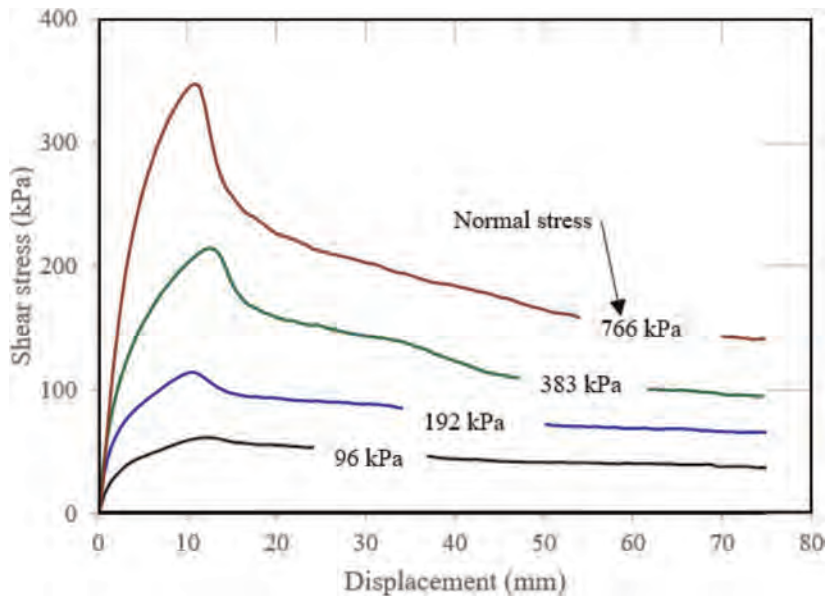
Figure 2. Shear-displacement graph for interface of aggressively textured HDPE geomembrane against geo-composite drainage layer having non-woven geotextile surfaces. Note that the magnitude of strain softening increases with normal stress, with $R_{ss\text{-}LD}$ ranging from 61% at 96 kPa to 41% at 766 kPa.

other limit-equilibrium models that have been accepted and used for slope stability for many decades. Many users of these common and popular slope stability computer programs either do not realize that all of these models employ an assumption that soil blocks function as rigid bodies, or they do not understand the implications of this assumption. Because this assumption is a distinct limitation of these models, using them can lead to the following misleading or incomplete results when the critical interface is strain-softening and when peak strengths are assumed:

- The outputs of these models present a non-realistic, non-conservative uniform variation of shear stress mobilization that is proportional to normal stress, and an equally non-realistic uniform factor of safety along the entire sliding surface.
- The real-world non-uniform mobilization of stresses and strains, which are a significant driver for the inducement of displacements that lead to progressive failure in strain-softening materials, cannot be predicted by these popular programs.
- If peak strength is preserved everywhere, with no exceedance of peak strength at any point along the sliding surface, then the average factor of safety represented by limit equilibrium methods may be correct. Likewise, if residual strength exists everywhere along the sliding surface and is used in the model, then the average factor of safety represented by limit equilibrium methods may be correct.
- The results of these popular programs are non-conservative when using peak strength for strain-softening shear interfaces that would experience a drop-off in shear strength with a small amount of displacement, unless special precautions are taken to model the appropriate locations within the cross-sections being analyzed, using degraded shear strengths that are less than the peak shear strengths (e.g. residual shear strength).

Numerical analyses that employ continuum mechanics models (e.g. finite element or finite difference computer programs) are able to approximately predict the complex patterns of

73

displacements and non-uniform mobilization of stresses along the critical interfaces. However, the greater amount of time, effort, and expense required to perform numerical analyses makes them unattractive for everyday use. Although the use of continuum analyses is generally increasing, the vast majority of slope stability analyses in engineering practice continue to be performed using limit-equilibrium programs.

The limitations of limit equilibrium methods may not be as severe in the evaluation of relatively thin soil (veneer) layers on sloped lining systems, but even in these cases the potential for degradation of geosynthetic interface shear strength is significant and should be considered.

1.5 *Goals of the present paper*

The present paper has three goals: (1) provide a contextual history of our understanding of progressive failure along strain-softening geosynthetic interfaces for lined containment, (2) describe mechanisms that could lead to progressive exceedance of peak strength along strain-softening interfaces, and (3) describe measures that can be used to allow for or mitigate strain softening mechanisms.

Due to space limitations for the present paper, the significant discussion of the history and literature related to the issue of strain softening and progressive failure along geosynthetic interfaces in lined containment facilities is provided in the *Geosynthetics International* companion paper appendices, which includes a rather lengthy list of references, and which serves as a resource for anyone interested in conducting their own research or evaluation of this topic. In conjunction with the extensive reference material, the *Geosynthetics International* companion paper appendices also present a historic review of bottom liner slope stability failures that involved geosynthetic or geosynthetic-like interfaces.

1.6 *Organization of the present paper*

The present paper is organized as follows:

1. Introduction and background.
2. Review of mechanisms that can potentially induce displacements along strain-softening geosynthetic interfaces.
3. Review of measures that can be implemented to reduce or mitigate displacements that can lead to progressive failure along critical strain-softening interfaces.
4. Discussion of risk and other considerations when considering peak strength.
5. Conclusions and recommendations.

2 MECHANISMS AFFECTING DISPLACEMENT ALONG STRAIN SOFTENING INTERFACES

This section of the paper presents a list of 15 Mechanisms that can potentially induce displacements along strain-softening interfaces, and thus contribute to a progressive failure mechanism. This is the most extensive such list that has been published to date. All 15 of the potential Mechanisms discussed in this section are relevant to bottom liner (high normal stress) situations, while 9 of these mechanisms are also deemed to be potentially relevant to veneer (low normal stress) situations. Some of the Mechanisms suggested by the author may be considered speculative, unproven, or theoretical. Several of the Mechanisms that affect displacements as discussed in this paper are interrelated and may seem redundant from a purely technical point of view. Even so, it is worthwhile discussing them separately to develop an awareness of the range of influences and their nuances that might affect the exceedance of peak strength, and hence the propagation of displacements, at the interfaces.

The Mechanisms that could lead to progressive displacements are grouped into five categories based on the nature of their causes.

- Category 1 includes five Mechanisms that are related to static stress and strain mobilization due to planned geometry, gravity, and constitutive material properties such as density, stiffnesses, compressibility, and Poisson's ratio. For a given geometry and material properties, the strain-softening effects from this set of Mechanisms are unavoidable and can best be estimated using numerical analyses.
  o Mechanism #1: Non-uniform mobilization of shear stresses.
  o Mechanism #2: Waste settlement, stiffness, compressibility, creep, and degradation.
  o Mechanism #3: Static lateral spreading of the waste.
  o Mechanism #4: Foundation settlement.
  o Mechanism #5: Strain/deformation incompatibility between overlying waste/ore material and the liner system interface.

- Category 2 includes four Mechanisms that are related to the aggravation of stresses and strains caused by construction and operational activities.
  o Mechanism #6: Waste placement activities.
  o Mechanism #7: Slope overfilling/oversteepening.
  o Mechanism #8: Toe excavation.
  o Mechanism #9: Construction-induced shear strength degradation.

- Category 3 includes three Mechanisms that are related to different types of short- or long-term transient influences that are not due to construction and operational forces, and that could affect mobilized shear stresses.
  o Mechanism #10: Pore pressures.
  o Mechanism #11: Seismic loading.
  o Mechanism #12: Increased operating temperature.

- Category 4 includes one Mechanism related to the factor of time.
  o Mechanism #13: Long-term ageing and creep of geosynthetics.

- Category 5 includes two Mechanisms related to variability.
  o Mechanism #14: Variability of material manufacturing.
  o Mechanism #15: Variability of installation practices.

2.1 *Mechanism #1. Non-uniform mobilization of shear stresses*

This Mechanism, which was previously described in Section 1.4, is reiterated here for the sake of completeness. Byrne (1994) was the first landmark paper to clearly demonstrate, using numerical analyses, that the non-uniform mobilization of shear stresses is a significant cause of the initiation and progression of failures in strain-softening materials for bottom liner systems. The reason for this is that with deformable materials some areas will be stressed much higher than the average, which could cause those areas to exceed their peak strength. Such a situation can be further exacerbated if those areas have weak spots (e.g., localized delamination) or other conditions (e.g., pore pressures, downdrag) that increase the shear demand on adjacent areas, as discussed later as contributory mechanisms. In the present paper we list this Mechanism first in our list of reasons why peak strength could be exceeded, as we highlighted more than 20 years ago in Thiel (2001). Acknowledgment of this fact established our acknowledgment that waste and soil materials do not act like rigid bodies, and that limit equilibrium analyses are only approximate tools that do not accurately represent physical reality.

We also list this as the #1 Mechanism because (a) this mechanism will co-exist with all other mechanisms that may exist, and (b) this mechanism is generally not intuitive and often needs to be explained and emphasized to practitioners. It could be true that many, perhaps

even the majority of designers who perform limit equilibrium slope analyses, have not studied the implications of the numerical analyses presented in the literature cited herein. In the evaluation of slopes that involve strain-softening interfaces, which includes most lined containment facilities, limit equilibrium analyses on bottom liners should be overseen by trained geotechnical professionals who have studied these principles and can exercise appropriate engineering judgement.

While the principle of the static non-uniform distribution of shear stresses is general to all geotechnical structures, its effect is generally less pronounced for veneer liner systems due to the quasi planar load distribution Considerations of non-uniform distribution of shear stresses in veneer systems is typically ascribed to other mechanisms such as differential settlement below the liner, localized pore pressures, construction activities, or variabilities in materials or installation as described below.

2.2 *Mechanism #2. Waste settlement, stiffness, compressibility, creep, and degradation*

Localized strength degradation of liner interfaces due to waste settlement that results in significant displacements adjacent to the lining system is probably the most commonly cited reason for the promotion of progressive failure (Gilbert & Byrne 1996; Kavazanjian et al., 2006; Long et al. 1995; Richardson & Thiel 2001; Sabatini et al. 2002; Stark 2022; Stark & Poeppel 1994; Thiel 2001).

Slope stability studies based on continuum numerical approaches described in the literature references (e.g. Byrne 1994) generally model waste settlement that is due only to the elastic compression of the waste. The development of relative displacements occurs more readily and to a greater extent on sideslopes as compared to the flatter base of a deep-seated critical surface. Reddy et al. (1996) and Gilbert et al. (1996) both mention that waste stiffness is a major factor affecting mobilized shear stresses and displacement distribution. More compressible, less stiff waste results in more accumulation of strain along the base, especially towards the toe, due to the transfer of stresses from the waste above the sideslope to the waste on the base that acts as a buttress.

Note on the concept of liner-system integrity related to downdrag. Downdrag of the waste along a liner system due to settlement also affects another aspect of liner-system performance, which is generally termed 'integrity.' This concept regards the issue of strains in the liner system that might ultimately cause a tensile failure in the liner, particularly at the crests of slopes at intermediate benches, and the top anchor trench where strains are the greatest. The issue of 'integrity' is not to be confused with the issue of slope stability, though they are related to each other by the causal mechanism of waste settlement and by the nature of the interface shear strengths. The numerical analyses that are used to evaluate both issues are quite similar. Thus, discussion of the integrity issue is relevant to the subject of the present paper. The subject of liner integrity being compromised due to waste settlement was apparently first discussed by VonPein and Lewis (1991), with the first numerical solutions being proposed by Long et al. (1995). Yazdani et al. (1995) measured smooth HDPE geomembrane strains on a 2.1 m high 3(H):1(V) slope in a California landfill to confirm design assumptions and confirmed that the maximum strains occurred near the top of the slope. Villard et al. (1999) measured strains and displacements on a slope in a full-scale field experiment and correlated their results with a numerical analysis that showed, interestingly but not surprisingly, that the maximum strains in tension and compression occurred where there was the least relative displacement (at the toe and crest of the slope), with the minimum strain (zero) occurring where there was the maximum relative displacement in the middle of the slope. Another numerical simulation of a failure of integrity was presented by Jones and Dixon (2005), a work that was carried forward by the same group in the UK as published in a series of papers related to doctoral work presented in Fowmes (2007). The subject of integrity has received much additional attention in the past decade as well, including

publications by Thiel et al. (2014), Yu and Rowe (2018), and Gao et al. (2022). The focus of these studies has been the impact of waste settlement on strains in the geomembrane, rather than relative displacements along the geomembrane. The assumptions in these cited papers from this past decade did not model the strain-softening characteristics of the interfaces but assumed the most conservative case, from the point of view of the criterion of integrity failure, namely that of peak strengths being maintained, to illustrate the worst-case strains at the top of the slope. The important lessons learned from these papers, relative to the subject matter of the present paper, are:

- The length of a sideslope, sideslope inclination, waste loading and settlement, and relative interface shear strengths above and below a geomembrane all influence the maximum geomembrane strain (Yu & Rowe 2018). Similar conclusions were drawn by Gao et al. (2022), and those same factors would also be relevant to the amount of potential displacement on strain-softening interfaces.
- Sideslope flattening provides the most significant mitigation against downdrag and sideslope displacement problems. VonPein and Lewis (1991) state that "there does not appear to be any problems where the slopes are 3(H):1(V) or flatter", based on their experience and field observations. Yu and Rowe (2018) state that numerical analyses, for the conditions they evaluated, indicate that without geosynthetic reinforcement, slopes steeper than 3(H):1(V) display long-term problematic strains, while the 3(H):1(V) slopes had acceptable strains. Similar conclusions were later expressed by Gao et al. (2022). The penalty for flatter slopes, of course, is reduced airspace for waste or mining ore.
- Increasing the number of intermediate benches on a sideslope is very beneficial in that it reduces the maximum liner strains (Breitenbach & Athanassopoulos 2013; Gao et al. 2022; Thiel et al. 2014; Yu & Rowe 2018), and is also a means of improving the overall slope stability in the case of weak and strain-softening interfaces, as will be discussed later in Section 3.5.
- Gao et al. (2022), who employed the most sophisticated constitutive model for the waste fill, were able to show that mechanical creep and biodegradation can be significant factors in the development of tensile strains in a liner system and can lead to a continuing increase in maximum tensile strains (and displacements) after capping of the landfill.
- The benefit of introducing a stiff, strong geosynthetic reinforcing layer (e.g., a geogrid or high-strength geotextile) to reduce strains in the sideslope geomembrane was emphasized as a possible solution by Long et al. (1995), Thiel et al. (2014), and Yu and Rowe (2018).

This Mechanism is not considered applicable for veneer systems. Related mechanisms that would be applicable to veneer systems would include foundation settlement and construction activities, as discussed below.

2.3   *Mechanism #3. Static lateral spreading of waste*

The issue of static out-of-slope lateral spreading of waste causing displacements along a bottom liner appears to have been raised first by VonPein and Lewis (1991), who suggested that "it is probably reasonable to assume that the toe of a large canyon landfill will move 60 cm or more during filling." Stark et al. (2000) presents inclinometer data taken at the bottom of a 16.5 m high waste fill into the underlying native clay, installed adjacent to, and immediately after, the 1996 Rumpke landfill slope failure, which showed significant out-of-slope movements of the waste that extended into the native clay. They suggest that this phenomenon could have caused excessive shear displacements in the weak base layer that contributed to the progressive failure mechanism of strain softening in the native clay that resulted in the Rumpke slope failure. The reason for static lateral spreading is described by Duplancic (1990), who presents landfill inclinometer data similar to that of Stark et al. (2000), and states that: "Fills on slopes commonly experience lateral deformation due to the

lateral force component imposed by the slope." This mechanism is generally not considered applicable for veneer systems.

2.4 *Mechanism #4. Foundation settlement*

Gilbert and Byrne (1996) refer to foundation settlement as another mechanism that could cause localized deformations that lead to the exceedance of peak strength of strain-softening geosynthetic interfaces. This factor might be especially prevalent in the case of piggyback liner systems installed atop old waste. USEPA (2004) describes potential magnitudes and effects of waste settlement on cover systems. In general, total settlement below veneer systems would be expected to have negligible impact on displacements, while differential settlements will locally increase shear stresses in a manner that would promote progressive displacements on the critical interface.

2.5 *Mechanism #5. Strain/deformation incompatibility between overlying waste/ ore material and the liner system interface*

A situation where the critical failure surface is along the base of a bottom liner system, and then daylights up through the waste, illustrates the concept of 'strain incompatibility' between a strain-softening interface and the overlying waste. This has been emphasized by Stark et al. (2000) as being a mechanism that can promote progressive failure. It is a dynamic of 'incompatibility' which occurs because as the waste/ore mobilizes shear stresses in order to resist collapse, the degree of strain needed to mobilize peak stresses on the strain-softening interface is quite low as compared to the degree of strain needed to mobilize significant shear stresses in the waste/ore material. The result is an unbalanced development of shear stresses mobilized between these two materials, which results in the exceedance of peak strength in the strain-softening geosynthetic interface, which can then lead to progressive failure. This mechanism was identified by Stark et al. (2000) as a contributing factor in the Rumpke failure. This mechanism is generally not considered significant for veneer systems.

2.6 *Mechanism #6. Waste placement activities*

Stark and Choi (2004) mentioned waste placement activities as a contributory factor in promoting progressive failure, referencing Yazdani et al. (1995) as a source. As discussed in Mechanism #2 above, the field measurements presented by Yazdani et al. (1995) represent the strain that would accumulate from waste settlement, and the data collected in that study would be more germane to the issue of downdrag as related to 'integrity' as discussed above. However, one could also imagine that the effects of waste or mine ore operational placement activities could be similar to those of construction activities, as described in Mechanism #9 (Section 2.9), where the presence of heavy equipment in proximity to the liner interface could potentially induce additional temporary dynamic forces that might cause some localized displacement, especially where there are weak spots that would act as stress concentrators that could contribute to progressive failure. In the context of veneer systems, this mechanism would be related to construction activities as described for Mechanism #9.

2.7 *Mechanism #7. Slope overfilling/oversteepening*

Normal waste filling and its concomitant settlement have already been mentioned as being the most commonly recognized mechanism causing liner displacement (Mechanism #2). Stark et al. (2000) mention *over*-filling as an exacerbating factor when the filling exceeds the approved design/operations plan. This often happens when a new cell is not ready in time and the existing capacity of the landfill is overextended. Overfilling then creates additional shear stress and deformations that are often beyond the design limitations. This mechanism

is really an extension of the mechanisms of non-uniform mobilization of shear stresses (Mechanism #1) and waste or mine ore settlement (Mechanism #2) but is listed as a separate mechanism that is a result of operational decisions that can promote progressive failure. This mechanism was identified by Stark et al. (2000) as a contributing factor in the Rumpke failure.

2.8 *Mechanism #8. Toe excavation*

Though the removal of a small amount of toe buttressing may seem innocuous, it can actually be quite devastating due to the initiation of non-uniform mobilization of shear stresses and the static lateral spreading of waste. The plots of the numerical analyses performed by Byrne (1994, Figure 10 of that paper) for mobilized friction angle, and by Filz et al. (2001, Figure 6 of that paper) of the mobilized shear stresses clearly indicate that the real-world phenomenon of non-uniform mobilization of shear stresses (Mechanism #1) concentrates shear stresses at the toe of the fill on the base. Stark et al. (2000) point to the excavation at the toe of the Rumpke landfill as being not only a contributing factor to the failure, but also a factor that allowed the runout of the translational landslide to extend further than it otherwise might have.

What is particularly pernicious about a toe excavation is that it reduces buttressing, thus inviting progressive lateral displacements, and could be the triggering mechanism for a failure. Given that real-world mobilization of shear stresses favors increased stresses at the toe, as demonstrated by Byrne (1994), a small displacement that exceeds the peak strength at the toe makes that zone weaker, which means it can carry less of the lateral load. That in turn puts more of the load on zones adjacent to the critical plane, which may in turn cause another part of that plane to become overstressed and exceed its peak strength (which is the classical description of progressive failure). This mechanism is also applicable to veneer situations. The full-scale field study by Villard et al. (1999) showed how removal of the toe at the base of a veneer fill significantly increased the geosynthetic strains. Stark et al. (2012) describes the value of a toe buttress when constructing veneer layers.

2.9 *Mechanism #9. Construction-induced shear strength degradation*

Concern over the effects of deformations and displacements on the long-term operational peak strength of interfaces that occur during construction has been previously expressed by Gilbert and Byrne (1996), Thiel (2001), Sabatini et al. (2002), and Stark and Choi (2004). None of these sources, however, specifically addressed exactly how construction activities could impact liner system interfaces. The present paper provides updates regarding this issue.

The construction of geosynthetic-lined containment facilities commonly involves a relatively thin layer of soil to be spread over one or more geosynthetic layers; this applies to both bottom liner and final veneer liner systems. A key point here is that the *localized* shear stresses caused by a soil-spreading operation using a dozer are significantly higher than the *average* shear stresses that are assumed to be distributed over the entire slope length. This is due to forces needed to overcome the friction at the base of the soil pile being spread, the weight of the dozer, and any acceleration/deceleration of the dozer.

We would note that this consideration is completely different from the usual consideration of the stability of equipment operation on slopes that is most commonly cited from sources such as Koerner and Soong (1998), Qian et al. (2001), Druschel and Underwood (1993), McKelvey (1994), and USEPA (2004). These references only consider an entire slope reach, and equipment stresses are assumed to be distributed over the entire slope length, often with the objective of calculating the anchorage strength required to secure the geosynthetics, thereby preserving slope stability during this type of construction. If the veneer stability of the entire slope length is at issue, then the references cited in this paragraph can be used, and the calculation is straightforward.

A much more pernicious situation, which is dangerous from the point of view of progressive failure, is if the peak shear strength of any of the interfaces is exceeded by the construction-induced *localized* shear stresses. In this case the shear resistance of these interfaces will be degraded little by little as they experience relative displacements during construction. Such localized relative displacements, and the resulting localized shear strength degradation, may or may not be apparent as construction proceeds. Obvious failures that the author has seen in this regard include a case history presented in Thiel and Narejo (2005), and another confidential case history used as an example in Thiel and Giroud (2023). Localized track spinning, which would cause relative displacements of a geotextile to a textured geomembrane on the order of one to twenty centimeters, would be deleterious to the integrity of the interface's peak shear strength at all locations where that occurred. These types of small but impactful slippages could occur over and over without attracting the attention of the dozer operator or the construction observer. The cumulative effect of such localized shear strength degradation events over the course of construction of an entire slope can thus be seen as detrimental to the slope's static and dynamic stability in the long term, especially in light of a progressive failure.

There are five references that suggest methods to quantify the elevated localized shear stresses below the dozer tracks could cause localized exceedance of shear strength: Paruvakat and Richardson (1999), Kerkes (1999), Jones et al. (2000), Thiel and Narejo (2005), and Thiel and Giroud (2023). Each of these references either adds to or improves upon the work presented in the other references, and taken as a whole, they provide useful approaches to quantification of the problem, as well as suggestions for construction specifications and construction quality assurance (CQA) that can mitigate the problem.

To the author's knowledge, the effect of interface deformation at low normal stresses on the subsequent shear strength at higher normal stresses has only been documented in one study, that of Esterhuizen et al. (2001). They showed that for a particular smooth geomembrane/clay interface, deformations at low normal stresses would reduce the peak strength of the interface at higher normal stresses. They present results showing that the peak shear strength at 345 kPa normal stress was reduced by approximately 13% due to pre-shearing at 35 kPa normal stress. They provided an interesting "work-softening" model to describe this behavior in a manner that can be used in a finite-element analysis. Although their model fits the data very well, it is only applicable to the specific clay and geomembrane used for their study.

Limited testing was performed for the present paper in order to provide some insight into this issue for a textured geomembrane/geocomposite interface, where the geocomposite surface was a nonwoven geotextile that was heat-bonded to a geonet. Two cases were checked: one for high normal stress (bottom liner) situations and one for long-term low-normal stress (veneer) situations. For the high-normal stress situation, this particular interface was pre-sheared at a low normal stress of 24 kPa, representative of dozer loading, and then final-sheared at a higher normal stress of 192 kPa. The results, presented in Figure 3, indicated that the peak strength at the high normal stress was reduced by approximately 13% due to pre-shearing at the dozer construction stress, as compared to shearing a virgin sample at the high normal stress. For the low-normal stress situation, this particular interface was pre-sheared at a construction normal stress of 24 kPa to represent the dozer loading, and then final-sheared at a lower normal stress of 10 kPa, representative of the typical long-term loading of a cover system. The results, presented in Figure 4, indicated that the dozer-induced pre-shearing resulted in LD shear strength under the design normal stress of 10 kPa to be approximately 42% lower than the peak strength that would typically be obtained by shearing a virgin sample.

Note related to the expansion/contraction of exposed geosynthetics. Stark and Poeppel (1994), Stark and Choi (2004), and Zamara et al. (2014) mention thermal expansion/contraction of exposed geosynthetics as being a possible cause that peak strength could be reduced at strain-softening interfaces. The present author has commissioned testing on two
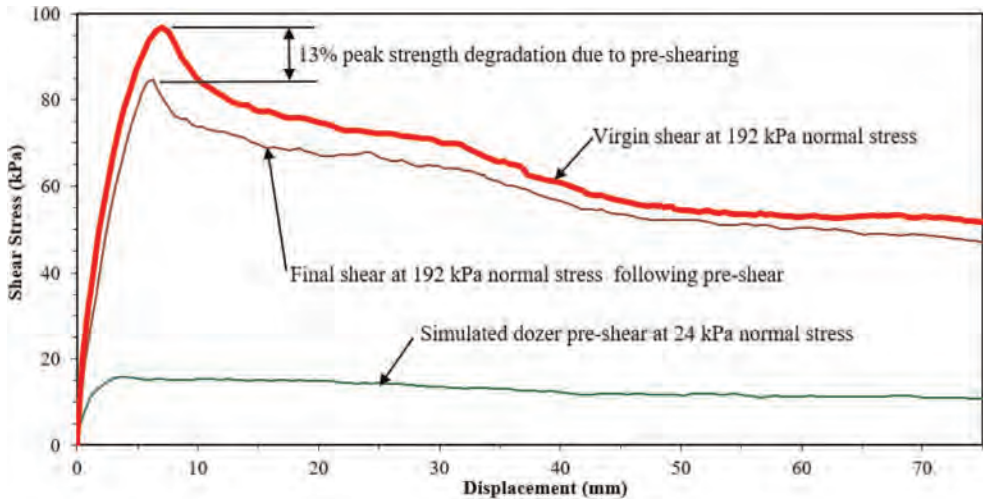
Figure 3. Test results showing effect of pre-shearing at low normal stress on peak strength at high normal stress for an interface of a textured HDPE geomembrane against the nonwoven geotextile surface of a drainage geocomposite.
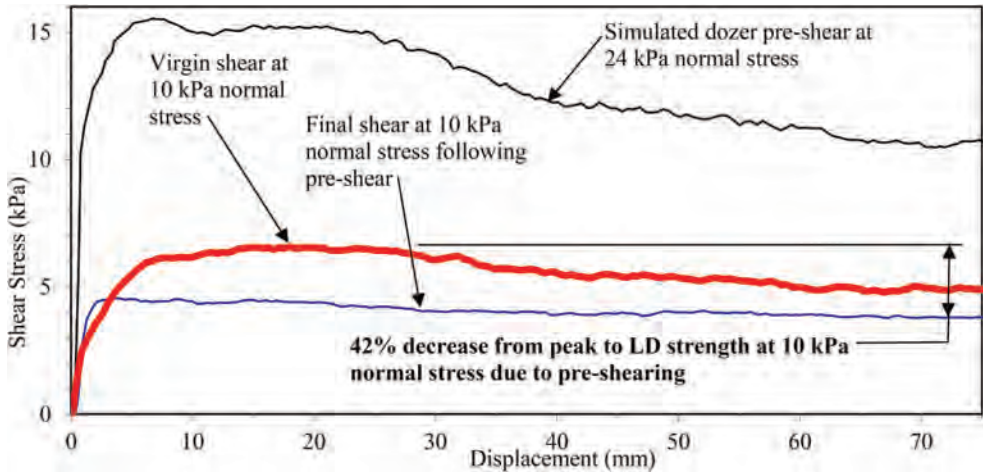
Figure 4. Test results showing effects of pre-shearing at dozer construction normal stress on peak strength at low veneer normal stress for an interface of a textured HDPE geomembrane against the non-woven geotextile surface of a drainage geocomposite.

separate projects that used different types of textured geomembranes that had been dragged over non-woven geotextile based GCLs during deployment to determine if the dragging caused any degradation of shear strength as compared to virgin materials tested at 400 kPa normal stress. The result was that no perceptible differences were noted. The author is not aware of any other such zero-normal-load shear-degradation studies that have been conducted. This cause for possible peak strength degradation is included here as a subset of potential construction-induced strength degradation, a possibility that remains to be verified by further testing.

2.10 Mechanism #10. Pore pressures

Apart from gravity, pore pressures (most pervasively those caused by liquid, but also possibly caused by gas) are the single most prevalent factor contributing to slope stability failures. The reason for this is that pore pressures reduce the effective normal stress that gives interfaces their shear strength, but the applied shear stress is often unaffected by pore pressures. Examples of significant excess pore pressure buildups in bottom liner systems that have been observed are failure or malfunction of pumps, power, or controls; leachate collection systems that experience collapsed pipes (observed by author via in-pipe cameras and exhumations); and leachate collection systems that clog due to poor design (Koerner et al. 1994) and/or long-term inorganic precipitation where biological clogging is typically a catalyst (Rowe & VanGulck 2004). Localized waste saturation can create conditions for the development of significant pore-gas pressures which have been measured in excess of 200 kPa that are suspected of causing a stability failure in a high-food-waste-content MSW landfill (Ma et al. 2019). In final cover systems the overloading of the drainage layer on top of the barrier layer is the most common cause of the many veneer-cover failures caused by inadequate transmissivity, susceptibility to being overloaded with water during construction, and inadequate or blocked outlets. Even if pore pressure buildups are just temporary, such as during a control system failure in a storm event, progressive failure can be triggered.

Pore pressures on the underside of the liner system could manifest as a result of saturated high-plasticity clays in the subgrade that do not have adequate time to dissipate relative to the rate of loading for bottom liner systems, or landfill gas pressures for final cover systems.

2.11 Mechanism #11. Seismic loading

Seismic loading increases the potential for displacements to occur along the critical failure plane which, in conjunction with the non-uniform mobilization of shear stresses, can locally (or globally) cause displacements that reduce the strength of the critical interface below its peak strength, thus leading to progressive failure. In this regard the design practitioner should assess the potential for this type of deformation.

When performing calculations to determine if seismic deformations due to the design earthquake will be within acceptable limits (as defined by standard practice or the regulations), LD or residual values for the strengths should be assumed along the entire critical interface for purposes of those calculations, even if peak strengths have been determined to be acceptable for purposes of the static stability (Kavazanjian 1999, 2023). The design should then be checked to meet other project-specific standards or regulatory requirements separately for static FS, and for the maximum estimated displacement due to the design earthquake.

2.12 Mechanism #12. Variations in operating temperature

Hanson et al. (2015) performed laboratory testing to determine the effects of temperature on the shear strength of the interface between a textured HDPE geomembrane (asperity height of 0.45 mm) and a needle-punched GCL having a woven geotextile interface with the geomembrane. Tests were performed for low-normal load (cover system) applications at an average normal stress of 15 kPa, and high-normal load (bottom liner) applications at an average normal stress of 150 kPa. The temperatures for the low-normal load load testing were 2, 20, and 40°C. The temperatures for the high-normal load testing were 20 and 40°C. Their research suggests that the design values of shear strengths for interfaces between textured geomembranes and a non-woven geotextile-based product could potentially be prorated downwards by as much as 15-20% for cover systems, and 10-15% for bottom liner systems, to account for the effects of temperature.

Karademir and Frost (2021) performed an extensive interface shear program to evaluate the effects of temperature on interface shear strength between several different types of geomembranes (smooth PVC and HDPE, as well as three different types of textured HDPE) and needle-punched nonwoven (NPNW) polypropylene (PP) geotextiles. Tests were performed at normal stresses of 10, 100, and 400 kPa, and at temperatures of 21, 26. 30. 35. 40, and 50°C. In all cases their results indicated that the interface shear strength increased with temperature. The increases in strength going from 21 to 50°C ranged from 14-23% for peak strength and from 14-18% for large displacement strength for the various interfaces tested. They concluded that for the range of normal stresses and materials tested that interface shear behavior determined at room temperature yields interface friction values that are conservative.

Given the differing conclusions between the two studies mentioned above, the present author does not recommend adjustments to interface shear strength due to temperature effects, and that the standard factor of safety of 1.5 would be appropriate to account for variations in this regard.

2.13   *Mechanism #13. Long-term ageing and creep of the geosynthetics*

Several authors have pointed to long-term ageing and creep as being potentially significant contributors to a mechanism of progressive failure along strain-softening interfaces for both high- and low-normal-load situations (e.g., Byrne 1994; Breitenbach 1997; Gilbert & Byrne 1996; Jones & Dixon 2003; Skempton 1964; Sabatini et al. 2002; Thiel 2001; Zanzinger & Alexiew 2002; Zanzinger & Saathoff 2012).

Trauger et al. (1997) performed long-term internal shear testing of soaked reinforced GCL specimens at both low (24 kPa) and high (97-389 kPa) normal stresses with applied shear stresses equivalent to 26.6° and 19.3° friction, respectively, for up to 10,000 hours without shear failure. Zanzinger & Alexiew (2002) performed long-term internal shear testing on GCL specimens at low normal stresses with applied shear stress ratios of up to 90% of the short-term internal shear strength on reinforced GCLs for up to 5,000 hours without shear failure. These studies indicate good long-term durability for GCL reinforcement exclusive of ageing of the geotextile fibers.

Marr and Christopher (2003) considered long-term ageing and creep of the internal reinforced needle-punched fibers of GCLs. This is important because if the internal shear strength of the GCL exceeds its peak then the remaining residual strength will be that of hydrated bentonite, which can be as low as 4° friction. Most designs provide another interface that is weaker than the peak internal strength of the GCL to 'ensure' that the peak internal GCL strength never fails (this is known as the 'fuse' concept, where the 'critical interface' is defined as the one that has the lowest peak strength, even if it does not have the lowest residual strength). Marr and Christopher (2003) cautioned that long-term creep could challenge this design concept, and recommended that the following reduction factors (R_f) be applied to the *difference between* the peak and residual internal shear strength of the project-specific GCL: R_{f-cr} = 3 to account for long-term creep; and R_{f-age} = 1.1 (100-year life) or 2.0 (300-year life) to account for ageing. The two values of R_f would be multiplied by each other to yield a total R_f ranging from 3.3 to 6.0. The resulting value would be *added back* to the residual value of the GCL internal shear strength to obtain the maximum allowable long-term internal design strength, $\delta_{GCL-all}$, of the project-specific GCL. Marr and Christopher (2003) further suggested that to prevent failure from occurring inside the GCL, another interface should be provided in a layer above the GCL that has a short-term peak interface strength less than $\delta_{GCL-all}$. This latter goal cannot always be achieved within the constraints of the available materials and design goals, and the present author suggests that the same design intent could also be met by verifying, through analyses, that the long-term mobilized shear stress of the design is less than $\delta_{GCL-all}$. Note that this type of calculation can only be quasi-reliable when numerical analyses are used, since limit equilibrium methods do not provide an accurate picture of the true mobilization of stresses or strains of deformable

bodies. The present author believes that this approach is conservatively biased because the high peak internal shear strength at high normal stresses for needle-punched reinforced GCLs, even under fully hydrated conditions, is much greater than the sum of the bentonite shear strength and geotextile tensile strength, due to some mechanism that is not fully understood at this time (Thiel & Maubeuge 2002). The R_f values suggested by Marr and Christopher (2003), therefore, might not need to be applied to the entire difference between the peak and residual internal shear strength of the GCL. More research is needed in this regard.

Abdelaal and Solanki (2022) performed laboratory testing to investigate, among other things, the effect of geotextile ageing on the interface shear behavior, using a 2 mm thick blown-film textured HDPE geomembrane having an average asperity height of 0.45 mm. Three different single-layer non-woven needle-punched staple fiber geotextiles with mass per unit areas of 200, 580, and 1500 g/m^2 were tested at normal stresses of 250, 700 and 1000 kPa. The results showed that for the interfaces that involved geotextiles that were aged prior to the shear box experiments for up to 2 years at 85°C, all the highly aged single-layered geotextiles showed an increase in the peak interface friction angles as their ageing increased. For these single-layered geotextiles, the results suggest that assessing the interface friction angles using unaged geotextiles for a stability analysis is a conservative practice as long as the geotextile remains intact in the field. This is a welcome finding in light of the previous ambiguity that dogged the question of long-term ageing relative to shear strength, at least for interfaces involving nonwoven geotextiles set against textured HDPE geomembranes.

2.14   Mechanism #14. Variability of material manufacturing

Consideration of material variability is endemic to geotechnical engineering in which the accurate characterization of soil properties is often a statistical endeavor. One of the often-touted benefits of geosynthetics is their relative uniformity, compared to soils, due to their being manufactured under controlled conditions. While there is merit to this perception, casual acceptance of this as a fact has led to abuse in the adoption of geosynthetics via the assumption that single tests, especially those related to shear strength, can be taken as representative for entire projects. Even worse is when published values of shear strength are blindly accepted as a design basis with no further qualification.

The idea that facilities constructed without the benefit of project-specific testing can be less reliable than those verified with testing is generally well accepted and espoused in the literature (e.g., Dixon et al. 2006; McCartney et al. 2004; Richardson et al. 1998; Sabatini et al. 2002; Thiel 2001). Construction conformance (verification) testing of shear strength is standard practice for lined containment facilities where slope stability is important.

Often it can be time consuming and costly to conduct numerous interface shear performance tests during construction. For that reason, index tests are often performed, where it is presumed that attainment of certain minimum index values will infer that the shear strengths that had been verified by performance tests will be achieved. Example index tests that might be relevant to shear strength for soils could include grain size distribution, Atterberg limits, clay fraction, moisture, and density. Example index tests that might be relevant to shear strength for geosynthetics include asperity height for geomembranes, and peel strength for GCLs and geocomposites. Although precise correlations between the results for these various index tests and shear strength might not be available, engineering judgement indicates that replication of benchmark values that have been previously demonstrated to be satisfactory should result in acceptable performance.

However, even when conformance testing of materials supplied to a job site is performed, weak locations can exist that are not representative of the average strength may become host to impactful stress concentrations. This fact, when combined with the fact of non-uniform mobilization of shear stresses (Mechanism #1 above), could result in a localized progressive exceedance of peak strength that could contribute to a stability failure. Examples of

geosynthetic manufacturing variability that have been observed to create weak zones are non-uniform texturization of HDPE geomembranes (e.g. 'tiger striping'), variation of peel strength across the roll width of GCLs, and variations of peel strength of GCLs from beginning to end of needle-board changes during the manufacturing run. Perhaps one of the most highly variable interfaces that currently exists for geosynthetic shear interfaces is the heat bonding of a geotextile to a geonet that is commonly performed to create a geocomposite drainage layer. While the relationship between peel strength and (internal) interface shear strength of the geotextile/geonet products is not well understood, an attempt to study this and demonstrate such a relationship exists was published by Thiel and Narejo (2005) as a result of an investigation of a field failure of this interface. Standard testing for geocomposite peel strength, which is an index of shear strength, is almost always performed in the USA according to ASTM D7005, Standard Test Method for Determining the Bond Strength (Ply Adhesion) of Geocomposites. This test only requires reporting of the results based on the average of five 100 mm wide specimens across the panel width. Because there is a natural laboratory bias towards cutting specimens from the sample that do not fall apart, zero-strength specimens are almost never taken, even though they commonly exist due to manufacturing limitations. Thiel and Gatrell (2019) tested the variability of the peel strength of samples in which contiguous 100 mm wide specimens were cut in a checkerboard pattern across the panel width. Figure 5 presents the results for a sample that yielded 38 specimens, which resulted in an average peel strength of 290 N/m with a standard deviation (assuming normal distribution of data) of 230 N/m, not counting the unbonded edges of the panel. It is noteworthy that even though the average value was soundly above the target specification of 175 N/m and 'passed' the conformance testing requirements, 12 of the 38 specimens (32%) were below the target specification. Of these 12, 7 of the values (18.4%) were less than one-fourth (25%) of the target specification, which is very low (< 44 N/m). The test results presented in Figure 5 may represent the lower end of quality that can be achieved for geocomposite bonding, but such results have been qualitatively reported to the author by others and experienced by Thiel and Narejo (2005).
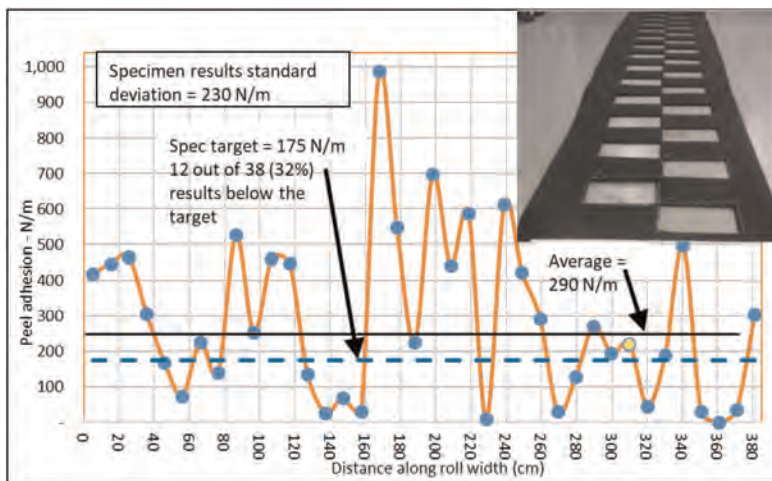
Figure 5.   Results of contiguous peel tests across geocomposite panel width (from Thiel & Gatrell 2019).

The study concluded that the current practice of taking only five specimens across the panel width is inadequate to verify the variability of bonding across geocomposite drainage products that are created by heat bonding. In addition, even with contiguous

specimen testing across the panel width the question remains as to which value would be representative for design purposes, considering the strain-softening nature of the interface.

2.15 *Mechanism # 15: Variability in the installation of geosynthetic interfaces*

The present paper introduces the idea that variability in installation practices is a potentially significant contributor to the introduction of repetitive weak zones in geosynthetic installations, as related to the seaming of geosynthetics. Examples of this apply both to high- and low-normal-load situations and include:

- Smooth edges on otherwise textured geomembranes that are intentionally manufactured to improve seam quality. The width of the smooth edges is commonly 0.15 m on both sides of a 6.86 m wide panel. Considering that seam overlaps are commonly 0.1 m, this leaves 0.2 m of smooth surface for every 6.76 m, or about 3.0% of the area.
- Geocomposite drainage layers comprised of geonets with geotextiles heat-bonded to one or both sides typically have the geotextiles unbonded along each edge to allow for seaming. The width of the unbonded edges is commonly 0.3 m on both sides of a 4.42 m wide panel. Considering that seam overlaps are commonly 0.1 m, this leaves 0.5 m of unbonded surface for every 4.32 m, or about 11.6% of the area.
- GCLs are commonly overlapped with an approximately 0.08 m wide ribbon of free bentonite applied within the overlaps. The width of the overlap is commonly 0.15 m on both sides of a 4.42 m wide panel. This leaves 0.08 m of potentially hydrated loose bentonite for every 4.27 m, or about 1.9% of the area.

The shear strengths of each of the seam zones for each of these materials will generally be substantially weaker than those of the non-seam zones, depending on which type of materials are placed against these interfaces. It is possible that some designers have taken some of these considerations of installation variability into account and have prorated the design shear strength accordingly. However, even simple proration of shear strengths may not be a completely adequate response to this issue with strain-softening materials in bottom liner situations because of the potential consequences of shear stress concentrations that would likely occur at the edges of these weak inclusions.

The relative significance of this issue depends upon not only the pervasiveness of the weak zones and the degree of their weakness, but also the configuration of the site-specific lining system. Consider the example of a liner system that was used in a design example presented by Qian and Koerner (2010), shown in Figure 6.

Primary geocomposite
(heat-bonded geotextile/
geonet/geotextile)

Primary textured
geomembrane

Needle-punched GCL
Secondary geocomposite

Secondary textured
geomembrane

Granular protective soil layer 0.45 m

Fine-grained soil subgrade
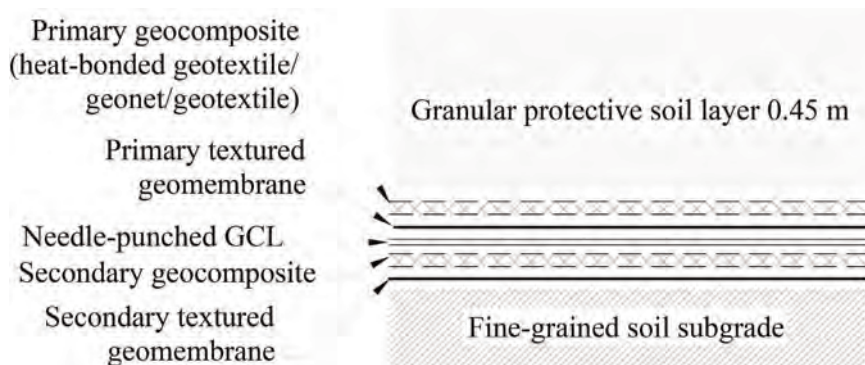
Figure 6.   Detail of liner system that was used in a design example presented by Qian and Koerner (2010).

The detail shows that there are two layers of geomembrane, two layers of geocomposite, and one layer of GCL, all in close proximity to one another (<15 mm). The shear strengths of each of the seam zones for this cross-section could be evaluated as follows:

- The smooth edges of both geomembranes would have one side against the geotextile surface of a geocomposite. Stark and Richardson (2000) report secant peak and residual smooth geomembrane/geotextile shear strengths as being 9° and 5°, respectively, with peak strength mobilization occurring at 2 mm of displacement, for a normal stress of 400 kPa. This compares to peak and residual secant strengths of 30° and 15°, respectively, for textured interfaces, with peak strength mobilization occurring at approximately 6 mm of displacement.
- Regarding the geocomposite panel edges with the unbonded geotextile, limited testing was performed for purposes of the present paper in order to provide information regarding the interface strength between a loose geotextile and a geonet with the shear taking place *parallel to the geonet rails*. Whereas testing the shear strength of this interface in either the machine- or transverse-panel-direction of the geonet will deliver apparently high friction values, the shear strength parallel to the geonet rails is very low, as can be experienced by simply walking around construction sites and stepping on the edge of an unbonded geocomposite. The test results indicated peak and large-displacement geonet/geotextile shear strengths of 12.5° and 9.7°, respectively, over a normal stress range of 50-200 kPa, with peak strength mobilization occurring at approximately 5 mm of displacement.
- Since in this case the GCL is designed to be installed in the dry secondary layer, bentonite hydration in the seam is ignored in this exercise.

Consider the installation of this liner system on a 3(H):1(V) sideslope. Typically, the geosynthetic materials would be deployed with their machine-direction going downhill in the direction of the slope. Since the unbonded geonet edge strength was measured parallel to the geonet ribs, this is the orientation that should be considered. Figure 7 is a photograph of the sample testing in the laboratory showing a 25° angle of the geonet ribs relative to the machine direction of the geonet. (This value will be specific to the product being tested.) To account for this orientation when considering the shear stresses and potential for progressive failure on a 3(H):1(V) (18.4°) slope, it can be calculated that the angle of the sideslope at a 25° skew is 16.7°. Adding up the tributary areas of the weak seam zones for the two layers of
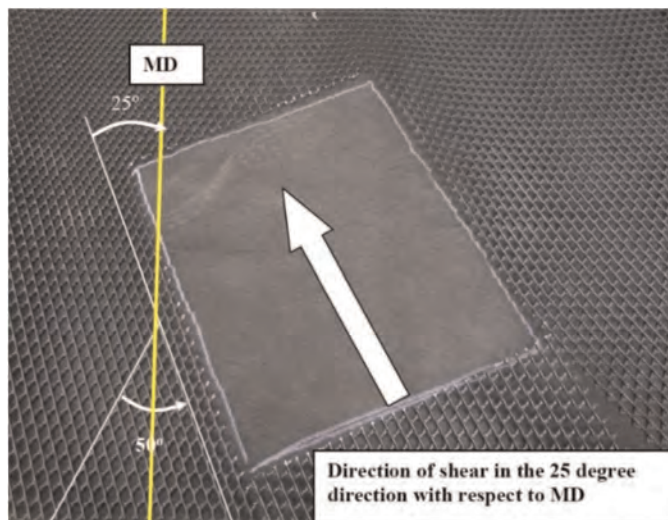
Figure 7. Photograph of test setup with geotextile on top of geonet for shear parallel to the geonet ribs. (Courtesy of SGI Testing, Atlanta, GA).

geomembranes and the two layers of geocomposites yields a result of $2 \times (3\% + 11.6\%) = 29.2\%$ of the area having a shear strength of less than $10°$ friction at the critical inclination of $16.7°$. This indicates a very significant proportion of weak areas could exist that have a shear strength substantially less than the critical slope inclination, and which would be significantly less than either the peak or residual strength of a textured geomembrane/geotextile interface.

The conclusion we reach from this discussion of Mechanism #15 is that the seaming mechanics required for each of the different types of geosynthetics can introduce regularly spaced weak areas in the liner system that provide sites for the initiation and promotion of progressive failure. The detrimental effects of these weak zones may also be exacerbated by shear stress concentrations that induced by the sudden changes in shear strength at their edges. A related weak-zone issue can also be created during installation by leaving excess geosynthetic scraps and rubsheet materials below geomembranes rather than collecting these materials and throwing them away, a practice which should be addressed by vigilant specifications and CQA.

2.16 *Note regarding the combined material and installation variability of drainage geocomposites*

This discussion of the material and installation shear strength variability that is potentially introduced by the use of drainage geocomposites should be cause for designers and owners to exercise a high level of scrutiny when using those materials where slope stability is important. Consider the large variability of material with regard to geocomposite peel strength described in Section 2.14, where test data indicated that 18.4% of the 'bonded' area was less than one-quarter of the specified valued of 175 N/m peel (i.e. < 44 kN/m). A reasonable and prudent assumption is that areas with bonding of less than 44 N/m (0.25 pounds per inch) will become fully unbonded during construction and in-service conditions. For a net installed panel width of 4.32 m this would represent 16.2% of the total installed area for that side of the geocomposite having a low shear strength (< $10°$ friction) in the direction parallel to the geonet rails. (Although the other side had similar bonding problems, the geonet rails on the other side run in a different direction and so only one side would be counted.) To this could be added the unbonded edge zones that represent 11.6% of the installed area, as described in Section 2.15, now producing a total unbonded area on the order of 27.8% of the total planimetric area that could have a low shear strength (< $10°$ friction) in the direction parallel to the geonet rails. If two layers of geocomposite are used in a liner system, such as the one depicted in Figure 6, then a value potentially greater than 50% of the lined area in service could have this low degree of shear strength in the direction of the geonet rails due to the poor bonding, depending on how much overlap of the poorly bonded zones occurred between the two geocomposite layers from a planimetric perspective. The debilitating nature of the high frequency of both known and random poorly bonded areas in a geocomposite can play an outsized role in reducing the dependable shear strength. It is highly recommended then, to give special attention to specifications for the bonding between geotextiles and geonets when using drainage geocomposites. Where slope stability is critical, specifications for these materials should be written that require minimal widths of unbonded edge zones, and higher average peel strengths to compensate for the very high standard deviations in manufacturing that seem endemic to these manufactured products. In addition, increased conformance (verification) testing frequency of peel strength would be advised, requiring that more specimens be tested across the panel width, and perhaps even contiguous specimens for CQA, as illustrated in Figure 5. The examples of materials and variability in installation presented herein are for specific products and situations that have been encountered by the author. The frequency, magnitude, and distribution of defects could therefore be quite different for other products in other regions, and for different installation practices. While the author regularly specifies these products with confidence, it is always done with these considerations.

3 THIRTEEN MEASURES THAT CAN BE ADOPTED TO REDUCE OR MITIGATE DISPLACEMENTS THAT CAN LEAD TO PROGRESSIVE FAILURE

There are measures that can be adopted to reduce the tendency for shear displacement along a critical strain-softening interface, thus improving the liner's reliability against failure. The development of relative displacements occurs more readily and to a greater extent on side-slopes as compared to at the base of deep-seated critical surfaces. The target zones for application of the measures described below would have to be evaluated on a case-by-case basis. For example, while it may be advantageous to pursue bolstering of the peak strength of a liner system along the base, to attempt to do so along a steep sideslope could prove detrimental due to the threat of high-strain integrity (i.e. ripping) failures on the sideslope.

This section presents a list of thirteen Measures that can reduce or mitigate the tendency for displacements that might lead to progressive failure in the presence of strain-softening interfaces in high normal load bottom liners, of which ten also apply to veneer situations. These Measures have been grouped into five categories depending upon the treatment mechanism, and can generally be targeted to benefit the base, sideslope, or both areas of a given design.

- Category 1 includes five Measures that are related to geometric modifications that would increase the factor of safety and reduce the magnitude of relative displacements that could occur.
  - Measure #1: Fill slope flattening and avoidance of over-filling.
  - Measure #2: Sideslope flattening.
  - Measure #3: Longer base design.
  - Measure #4: Buttressing of the toe and avoidance of excavation at the toe.
  - Measure #5: Geometric interruptions in the subgrade.

- Category 2 includes five Measures that are related to the attempt to preserve peak strength to the extent possible. Preserving peak strength can be useful for one or more phases of the project, which include construction, operations, and final build-out stability. These measures could target the base liner, or the sideslope liner, or both.
  - Measure #6: Increase peak strength.
  - Measure #7: Reduce weak spots resulting from variabilities in materials and installation practices.
  - Measure #8: Minimize any significant interface damage resulting from construction or waste filling.
  - Measure #9: Mitigate foundation settlement.
  - Measure #10: Implement high strength reinforcement along sideslopes.

- Category 3 includes one Measure that is related to avoiding the transient destabilizing influence of pore pressures.
  - Measure #11: Mitigate potential against high pore pressures.

- Category 4 includes one Measure that is related to the assumption that residual strength will develop along the geosynthetic interfaces.
  - Measure #12: Increase the residual strength of the interface with the lowest peak.

- Category 5 includes one Measure related to adaptive management:
  - Measure #13: Long-term instrumentation and monitoring.

3.1 *Measure #1: Fill slope flattening and avoidance of over-filling*

Fill slope flattening is a common geotechnical measure taken to improve slope stability and reduce the risk of failure. Since the only reason slope stability is an issue is the presence of a

slope, reducing the severity of the slope quite naturally reduces the risk of instability. The penalty for fill slope flattening, of course, is less capacity for waste or mining ore. This Measure has a significant beneficial influence on veneer stability.

3.2 Measure #2: Sideslope flattening (discussion for bottom liner situations only; see Measure #1 for veneer situations)

Although flattening of the lined sideslope at the back of the waste or mining ore mass might have a greater chance of preserving peak strength on the sideslope, this Measure does not necessarily improve slope stability, and may even worsen it for bottom liners. A relatively steep sideslope for bottom liners can be a more stable configuration than a flatter sideslope because a steeper sideslope typically allows more base area to develop forces that resist sliding. A proof of this is provided in the *Geosynthetics International* companion paper appendices.

3.3 Measure #3: Longer base

Having a greater ratio of base length to sideslope length is a proven means of improving slope stability (Reddy et al. 1996; Stark 2022). This fact is also demonstrated in the example proof described above in Measure #2, which is published in the *Geosynthetics International* companion paper appendices. Even so, a very long base is not a panacea against displacements along a liner with low-stiffness waste materials that can experience significant static lateral spreading. This measure is not applicable to veneer systems.

3.4 Measure #4: Construct toe buttress and avoid excavation at the toe

Constructing a buttress at the toe of a slope is a common geotechnical solution employed to improve the stability of slopes in general. This technique is commonly used in canyon landfills and in valley-fill mining leach pads. The size and resistance of a toe buttress can be designed to allow the containment facility to safely mobilize residual shear strength conditions along the lined interface. A toe buttress is essentially a dam that provides resistance to prevent the waste or mining ore body from sliding down the canyon or valley, or from spreading laterally. Providing a buttress at the toe greatly reduces the likelihood that the toe of the fill will displace, which is important, because numerical analyses have shown that this can be the location that triggers a progressive failure. The obverse of a toe berm is excavation at the toe, which can be especially debilitating and is suspected of having played a role in the Rumpke failure (Stark et al. 2000).

USEPA (2004) shows examples of toe buttresses for veneer situations that not only support the toe but also allow general slope flattening. A variation of a toe buttress is a tapered thickness cover soil (Koerner & Soong 1998). Designing shorter slope lengths between benches on a veneer slope is another way to increase the effect of intrinsic toe buttressing by limiting the finite slope length of any given slope reach. For practical engineering purposes, when the ratio of the slope length to veneer soil thickness exceeds 10-20, the slope will act like an 'infinite slope', and the benefits of toe resistance to slope instability then provide diminishing returns as the slope length increases.

3.5 Measure #5: Geometric interruptions in subgrade

Among the most effective and reliable methods of improving the stability of a containment facility that has strain-softening liner interfaces is to create non-planar interruptions along the critical slip interface that will force the critical failure surface to intermittently pass through stronger materials that are above and/or below the geosynthetic interfaces. This Measure generally applies to bottom liner systems rather than veneer systems. The best

overall description of this approach is provided by Breitenbach and Athanassopoulos (2013), who describe three types of geometrical subgrade interruptions that improve stability:

1. Stability Berms. Also referred to as "speed bumps", stability berms can be constructed in the subgrade before the liner is placed. They cause the critical slip plane to either pass along a non-planar surface, or to pass through higher strength materials. Depending upon the details of the geometry it is likely that both phenomena will occur, and overall stability will be improved as compared to having a planar surface lined with geosynthetics. Breitenbach and Athanassopoulos (2013) provide an example sensitivity analysis which considers the effects of the number, width, height, spacing, and subgrade shear strength of stability berms upon the slope stability factor of safety.
2. Stability Trenches. The geometrical inverse of a berm is a trench, and in this regard a stability trench can provide an effect similar to the that of a stability berm. Trenches can be excavated into the subgrade, lined, and backfilled with the waste, mining ore, or other materials in order to cause the critical slip plane to either pass along a non-planar surface, or to pass through higher strength materials. Breitenbach and Athanassopoulos (2013) note that trenches can create more complications when implemented with gravity drainage systems on the liner than would be the case with stability berms.
3. Stability Benches. The use of benches on slopes to improve stability and reduce downdrag liner strains, a practice that functions similarly to the way stability berms function on the base, has also been emphasized by Thiel et al. (2014), Yu and Rowe (2018), and Gao et al. (2022).

While the implementation of these various techniques to interrupt the subgrade geometry all involve extra earthworks, drainage, and lining complexities, they are viable means of increasing the stability factors of safety, even as some displacement does occur along the strain-softening geosynthetic interfaces.

3.6 *Measure #6: Increase peak strength*

If the design basis is to preserve peak strength along a portion of the liner system (e.g., along the base) then specifying materials that increase the peak interface strength will enhance that goal. Examples of methods to accomplish this include more aggressive texturing of geomembranes, and the incorporation of high-friction (granular) soil layers between geosynthetics. Where GCLs are used, enhanced needle punching should be employed to ensure that the internal shear strength of the GCL is not the weak link, and to ensure its strength by a confidence-inducing margin, as discussed in Section 2.13.

3.7 *Measure #7: Reduce weak spots due to variabilities in materials and installation practices*

This Measure can be considered a direct countermeasure to Mechanism Nos. 14 (material variability) and 15 (installation variability). Tools for the practical implementation of a reduction in the negative effects caused by the variability of material and installation interface strengths are: (a) an understanding of the limitations of manufacturing and installation, (b) strict specifications regarding what is required as related to material manufacturing and installation, and (c) diligent CQA to verify that what is specified is actually provided. There are limits as to what can be provided through manufacturing and installation, which is why it is important for the designer to be very familiar with those limitations.

Section 2.16 directly addressed specific issues related to the variability of geocomposites, which typically present a greater degree of variability in terms of both manufacturing and installation than do other geosynthetic materials, at least in the USA. Possible approaches to address these variabilities include:

- The geocomposite drainage layer could potentially be replaced with a granular drainage layer which has a very dependable internal and interface shear strength. The emphasis of concern would then switch to the potential for damage during construction resulting from the placement of a thin granular layer.
- Geocomposites are typically manufactured with a certain unbonded distance near the edge to allow for seaming by overlap and zip-tying of the geonet cores. The manufacturer could be requested to manufacture the material with the minimum amount of unbonded distance from the edge. If the design does not depend on the transverse-direction transmissivity, then the material could perhaps be manufactured without unbonded edges.
- To compensate for the weak spots caused by the high standard deviation of peel strength associated with geocomposite drainage materials, a higher average peel strength may need to be specified. For products created by heat-bonding, this will usually require a thicker geonet core because of the reduction in transmissivity that goes with obtaining a higher peel strength. It is also good to be aware that a high average peel strength requirement can make it very difficult to peel the geotextile back at the ends of the panels where butt seams need to be performed.

Regardless of the approach taken, a high level of project-specific preparation of the specifications, conformance testing, and CQA construction enforcement is required to reduce the incidence and degree of variability, which the author has found to be a successful approach.

3.8 Measure #8: Minimize any significant interface damage due to construction or waste filling

As discussed in Section 2.9, the main cause of construction damage to the geosynthetic interface is excessive shear stresses and displacements induced by construction equipment. The most common issue in this regard is the shear forces induced by dozer tracks when drivers attempt to push too large of a soil pile upslope, or often worse, downslope. Other conditions of excessive shear stress can occur when construction equipment applies braking forces when moving in a downslope direction. Solutions to these issues require clearly defined enforceable constraints in the specifications that require review by the responsible engineer for all proposed equipment operations on thin (veneer) soil layers being placed on lined slopes. Approaches to the required calculations are presented in Paruvakat and Richardson (1999), Kerkes (1999), Jones et al. (2000), Thiel and Giroud (2023), and Thiel and Giroud (2024).

3.9 Measure #9: Mitigate foundation settlement

To the extent that foundation settlement might introduce additional undesirable relative displacements along the liner system, foundation improvements such as dynamic compaction, preloading, or bridging weak zones to the extent feasible with geosynthetic reinforcement, can help mitigate this issue.

3.10 Measure #10: High strength reinforcement along sideslopes

Insertion of a stiff reinforcement layer within a sideslope liner system to carry a large portion of the tangential stresses, and thus reduce displacements and strains along all the other interfaces, is a well-known design approach. This concept is especially relevant for thin layer cover systems in general, especially during construction (e.g. Druschel & Underwood 1993; Koerner & Soong 1998; McKelvey 1994; USEPA 2004), but is also applicable to bottom liner systems (Long et al. 1995; Thiel et al. 2014).

3.11 Measure #11: Mitigate the potential for high pore pressures

Control of, and proper accounting for pore pressures is a fundamental geotechnical design requirement that is not unique to lined containment facilities. What can be particularly problematic for lined containment facilities, though, is the fact that excessive pore pressures generated at the lined interface can cause a localized exceedance of the peak shear strength, which in strain-softening materials can promote a progressive failure mechanism. Such situations can arise due to equipment malfunctions, power failures, failures of backup systems, leachate mounding within the waste mass above fouled or crushed leachate/liquid collection systems, long-term reductions in drainage infrastructure capacities, and the low permeability of high-organic waste leading to waste saturation and localized high gas pressures. Redundancy and robust reduction factors in drainage infrastructure can improve reliability.

Design of bottom liner leachate or solution collection systems should account for long-term clogging mechanisms appropriate for the site-specific hydraulic and chemical loading, drainage layer and pipe layout design, and filtration. A good review of these mechanisms and design approaches to address site-specific issues is presented by Rowe and Yu (2010), and an interesting design case history is presented by Yu and Rowe (2016).

Proper design of reliable lateral drainage layers above and/or below the barrier layers of veneer lining systems, and providing robust drainage outlets, cannot be over emphasized due to the sensitivity of veneer stability to relatively small increases in pore pressures. When designing a lateral drainage layer above a veneer liner system in order to control pore pressures that would be caused by meteoric water infiltration from above, it is advisable to use the unit-gradient technique as recommended by Thiel and Stewart (1993) along with conservative long-term hydraulic conductivity estimates of the cover soil to estimate the amount of water coming into the drainage layer. NRC (2011) suggests that regardless of climate, cover profile, or placement condition, the saturated hydraulic conductivity of most cover soils will increase over time until it is in the range of approximately 8×10^{-8} to 6×10^{-6} m/s. The typical lateral drainage factor of safety related to pore pressure relief should be greater than 2 after applying appropriate reduction factors (Giroud et al. 2000). When designing a lateral drainage layer below a veneer liner system in order to control gas pressures it is recommended to follow the methods outlined by Thiel (1998). A special need for caution is noted here since veneer slopes are especially vulnerable to failure during an intermediate stage of the construction process when the drainage layer may be exposed to direct precipitation before topsoil placement is completed, making it vulnerable to washout (a type of stability failure).

3.12 Measure No.12: Increase the residual strength of the interface with the lowest peak

The critical interface within a liner system is the one that has the lowest peak strength. Once the peak strength of that interface is exceeded, stability will depend upon the residual strength of that particular interface. It is common for designs to introduce a weak interface, sometimes referred to as a 'fuse layer', so that the location of slippage can be controlled above the critical containment geosynthetics in such a way as to avoid damaging the containment integrity of the liner system. This concept was mentioned in Section 2.13 with regard to protecting the internal shear strength of the GCL, as recommended by Marr and Christopher (2003). Within limits, certain geosynthetic materials can potentially be selected for the 'fuse layer' that will have higher residual shear strengths than other options. While this is an excellent goal to pursue, it may be difficult to achieve with reliability and precision, especially considering manufacturing variability. Brown et al. (1999) describes a case history for a California steep sideslope canyon landfill where selection of the geosynthetic interfaces was carefully tested and specified in an attempt to 'dial in' an optimal combination of (a) protection of the critical containment geosynthetics against an integrity failure via the

selection of a reliable 'fuse layer', and (b) maintaining as high a degree of a residual strength as possible along the 'fuse layer.'

3.13 *Measure No.13: Adaptive management; Long-term instrumentation and monitoring*

Considering that intensive use of geosynthetics has only occurred since the 1980s, we could say that we really don't have enough data on the long-term performance of geosynthetics used in liner systems to make accurate estimates of performance regarding ageing and creep of geosynthetics, considering that structures such as landfills may need to remain stable for hundreds of years (i.e., until they become inert). This situation mandates either incorporating extra conservatism in design decisions, or long-term monitoring.

A design that includes reliable methods of monitoring the system performance, and adapting fill plan operations to the results of instrumented feedback, could be a component of risk management that supports a slope stability design basis. The ideal is that real-time monitoring can aid in addressing uncertainties in the analysis by allowing for a comparison between the system's actual performance and its predicted performance, thus allowing for corrective measures if needed.

An excellent review of the approaches, value, and technology for instrumentation and monitoring of slope stability is provided by Marr (2013). Advances in communication and data management technology over the past 30 years have made real-time monitoring and data evaluation a practical reality that is within reach of projects of all sizes. Instrumentation can be used to monitor performance during all phases of a project, including construction, operations, and post-closure. Instrumentation that could be considered include various types of inclinometers and extensometers to keep track of settlement and lateral movements along a vertical profile; survey monuments to keep track of settlement and lateral movements on the surface; piezometers and pressure transducers to keep track of fluid pressures at specified point locations; pressure cells to keep track of actual normal pressures at various locations; temperature sensors installed during construction or in boreholes, pipes, wells, or sumps; different types of strain or deformation gauges to measure elongation, contraction, or relative movement (i.e. slippage) at an interface; load cells to measure total or effective normal stress; and accelerometers to measure dynamic forces from equipment, blasting, or earthquakes. See Marr (2013) for further discussion.

The measurement of strains or deformations along a liner system are possible in concept (e.g. Daniel & Scranton 1996; Fowmes 2007; Villard et al. 1999; Yazdani et al. 1995; Zamara et al. 2014), but the long-term viability of instrumentation of this type, especially at significant distances or depths, has not been fully proven along liner system interfaces. Though a handful of field-scale instrumented studies have been performed, and the results of numerical analyses have compared favorably with limited observed failures, the validation of numerical models via a comparison with the results of field measurements is needed (Fowmes 2007; Kavazanjian et al. 2018). The reporting of full-scale case studies of such monitoring would be a great contribution to the profession.

In concert with any monitoring plan there should be a response-action plan. For example, if cracks are observed near slope crests, or lateral spreading of the waste toe is observed, or tension-thinning of a geomembrane at a slope crest is observed, etc., what should be done? A typical hierarchy of responses could include, for example, immediate increased/expanded monitoring of movements with survey points and inclinometers, engagement of qualified geotechnical professionals to assess the situation, cessation of any continued slope loading or toe excavation, aggressive removal of any sources of pore pressures (liquid or gas), consideration of toe buttressing with earthworks, and consideration of crest unloading. One of the greatest lessons learned in past failures as related to the designer's limitation of liability is to provide operational plans to owners as part of their scope of work. Important elements of

such plans, as related to the subject of the current paper, would be fill sequencing plans, periodic inspections and monitoring, and basic response-action plans.

4 DISCUSSION OF RISK AND OTHER CONSIDERATIONS IN THE USE OF PEAK STRENGTH

Duncan (1996) writes that the only fully reliable design in the presence of a strain-softening interface is the use of residual strengths. Admittedly, there are situations where designers believe that the geometry, high peak shear strengths, control of pore pressures, and lack of a significant seismic threat should allow peak strengths to be used. As described by Baecher (2023) geotechnical uncertainties are generally epistemic in nature, meaning that selected parameters and approaches are often subjectively based on our experience, and invoke what is called 'engineering judgement'. Designers should be sufficiently experienced and qualified to make such judgements and should provide well documented justification for their decisions. Such determinations should also include consideration of the level of risk and the consequences of failure. A discussion of risk, reliability, and consequences as relates to this paper is provided in the *Geosynthetics International* companion paper appendices.

4.1 *Designs for bottom liners based on peak strength*

Recognizing that all designs will have higher reliability when using LD or residual shear strengths, there are possible project-specific scenarios in which the use of appropriately modified peak strengths is viable. In such cases the following considerations might be taken into account for bottom liner systems:

1. The first element that should be considered is the geometry and the presence of slopes. Industry field experience, and numerical analyses, have confirmed that slope inclinations approaching and exceeding 3(H):1(V) have a high susceptibility to experiencing displacements caused by the non-uniform mobilization of shear stresses and settlement of the overlying fill, and the resulting stress and strain distributions on the slopes can also affect the flatter areas. Influential in this regard will be the relative stiffness of the contained waste or mining ore, and its long-term compressibility and settlement. Estimations of the propensity for displacements to cause exceedance of peak strength can be approximated using examples of numerical analyses previously published in the literature. Otherwise, project-specific numerical analyses can be performed.
2. If pore pressures or seismic factors have significant potential to cause liner displacements, then residual strengths should be used.
3. In all cases where 'peak' strengths are considered they should be appropriately modified or adjusted to account for construction impacts, spatial variabilities due materials manufacturing and installation, ageing, and any other factors deemed relevant.
4. The designer should consider preparing an operational plan that illustrates safe parameters for the fill sequencing, maximum fill limits, and perimeter buttressing.
5. An adaptive approach to management can be implemented through the use of instrumentation and monitoring. Such a program is only useful in conjunction with a reliable response action plan, and when early warning signs are not ignored.
6. Designing around an appropriately adjusted peak strength for the early phases of a project life may be feasible. Settlement strain values during this period will be less than the long-term post-closure values. Thus, while the stability analysis of the final geometry of a filled facility can be based on rule-based approaches such as those recommended by Stark and Choi (2004), it may be legitimate to count on peak strength, with caution, during certain early operations of facilities when a well-engineered filling plan is provided and followed.

4.2 *Designs for veneer liner systems based on peak strength*

Stark and Choi (2004) present recommendations that landfill cover systems (which represent a major category of veneer liner systems) can be designed using the peak strength of the weakest interface with a factor of safety greater than 1.5. Stark and Choi (2004) mention three situations in which residual shear strength with a factor of safety greater than 1.0 should be considered: (1) if the slope angle of the final cover system is greater than the peak strength of the weakest interface, (2) if large construction-induced displacements are expected, and (3) if seismically induced displacements can be expected. Stark and Choi (2004) do not describe how the peak strength would be measured and evaluated. A standard design practice is to obtain manufactured samples for laboratory shear strength testing in order to determine the peak interface strengths. Those results are then commonly used in the slope stability analyses without further modification. For the reasons described previously, the present paper recommends that the measured peak strength of any veneer system interface should be modified on a project-specific basis from the test results normally obtained in the laboratory. While thoughtful specifications and a high-level of CQA can help mitigate the need for some conservatism, there are other factors that require engineering judgement related to peak shear strength adjustments from laboratory-measured values.

Based on the above discussion, the present paper recommends that, while the use of 'peak' strength can be appropriate for veneer lining systems, the peak strength be selected such that it accounts for conditions that include variabilities in materials and installation practices, construction damage, seismic displacements, foundation settlement, potential effects of long-term ageing and creep, and the potential for any of these factors to cause stress concentrations at the boundaries of a change shear strength (e.g. going from an unbonded to a bonded condition of a geotextile lamination to a geonet.) Having considered these possible adjustments, the design factor of safety is typically recommended to be greater than 1.5 to account for geotechnical variabilities, unknowns, and simplifying assumptions, as is standard in the geotechnical profession.

5 CONCLUSIONS AND RECOMMENDATIONS

The present paper has identified that:

1. Limit equilibrium stability analyses are based on the fictitious assumption that the soil or waste blocks above a liner system function as rigid bodies. This could result in an unrealistic uniform variation of shear stress mobilization and FS along the critical surface that could be highly non-conservative for strain-softening interfaces if the design is based on peak strengths.
2. Limit equilibrium stability analyses provide no feedback on the amount of displacement that may occur. Thus, the available shear strength of strain-softening materials in the field is unknown.
3. Limit equilibrium analyses are the most common type of slope stability analyses used in general.
4. Most geosynthetic interfaces are strain-softening.
5. Numerical continuum modeling can roughly predict the non-uniform distribution of mobilized shear stress and displacements along the critical surface, considering strain-softening behavior.
6. Only a handful of numerical modeling studies of geosynthetic lined containment facilities have been published. The use of numerical analyses in practice is relatively limited due to the time they require and the expense of performing them, although their use is becoming slightly more prevalent as time goes on.
7. The number of bottom liner failures that have occurred in the containment industry over the past 35 years that can be attributed to progressive failure along strain-softening

geosynthetic interfaces is relatively small. They have definitely occurred though, and when they have, they have been large, costly, and consequential. The failures that have occurred represent conditions and circumstances ranging from base liners to sideslopes, and from smooth interfaces to textured.

8. For containment facilities containing strain-softening interfaces there are potentially: 15 Mechanisms that could promote displacement that could lead to progressive failure initiation and propagation in bottom liner systems, and 9 such Mechanisms in veneer systems; and 13 Measures that can be taken to reduce or mitigate the development of displacements in bottom liner systems, and 10 such Measures in veneer systems.

9. For bottom liner systems the likelihood that significant interface displacements will be experienced is project-specific, and dependent upon the complex interaction of all of the considerations discussed in the present paper. A responsible evaluation can be made based on a combination of numerical analyses, engineering judgement that is based on a review of case histories and inductive reasoning, sensitivity studies, reliability analyses, and heedfulness of the Mechanisms and Measures described in Sections 2 and 3.

10. Bottom liner systems with sideslopes approaching and steeper than 3(H):1(V) have a high probability of experiencing significant interface displacements that will lead to strain softening. Inclusion of a sacrificial slip layer above the critical containment liner element on slopes, with the assumption of residual strength along this interface, is a common design remedy that could be considered to protect the liner's integrity.

11. It may be legitimate to count on appropriately adjusted peak strength, with caution, during early operations of bottom liner facilities as long as well-engineered construction and filling plans are prepared with good construction monitoring.

12. The state of our understanding of the specific causation and propagation of progressive failure along strain-softening geosynthetic interfaces is, overall, in a semi-quantitative and semi-empirical phase. It is simply not easy to accurately deduce the mobilized stresses and displacements, and the available shear strength, in the field at all points along a strain-softening bottom-liner interface. Detailed numerical continuum analyses can be of great help in this regard. And even with such analyses, there are numerous stress concentration possibilities (localized variabilities in materials, installation, or construction damage) that have not been captured by, or incorporated into, such models to date. Also, many of the factors that potentially affect displacement along interfaces are not fully understood. Though a handful of field-scale instrumented studies have been performed, and the results of numerical analyses have compared favorably with the limited observed failures, we still await validation of numerical models as compared with field measurements (Fowmes 2007; Kavazanjian et al. 2018).

13. Most slope stability designs are driven by rules that were formulated by a combination of inductively obtained conclusions from past failures, along with approximate engineering models for slope stability. Forensic studies have attempted to apply numerical analyses in a deductive manner with the goal of determining the root cause of slippages, but there are significant nuances to these dynamics that have yet to be completely modeled.

14. Over-reliance on a small number of laboratory shear and conformance testing results, and ignorance of variabilities in the installation process, remain a large area of concern.

15. The factor of pore pressures has been mentioned in the literature as one of the contributors to many of the documented (and undocumented) bottom liner and veneer system failures in the containment industry. Some of the cases reported pore pressures due to head buildup above the liner, and some due to saturated non-consolidated clays or gas pressures below the liner.

16. If the use of peak strength values is relevant to the slope stability design, the basis of the definition of peak strength should be documented. It may not be appropriate to adopt the peak strength results measured from a factory sample that is tested in the laboratory. Modifications to the peak strength should be considered based on the several factors described in this paper.

17. It is the responsibility of the design engineer to communicate relative degrees of risk concerning slope stability to owners so that owners can make informed decisions.
18. Simple reliability analyses are helpful because they can highlight where small variations in assumptions can have a significant impact on the probability of failure.
19. If a designer follows the rule-based analysis of Stark and Choi (2004) for bottom liner systems, the design will intrinsically be substantially safe.

Based on these findings the following recommendations are suggested:

1. Designers should be concerned about activities that may affect strain-softening interfaces after they issue a design for construction. This would include the construction, operational, and post-closure phases. They should also consider the possibility of changes in project ownership. Designers should convey their expectations clearly in the project documentation, which would include the construction specifications, construction inspection requirements, facility operations, and post-closure monitoring expectations.
2. Project-specific testing is recommended in order to determine the peak and LD (or residual) shear strengths that are representative of the actual materials being used for construction and representative of field conditions (e.g. spraying all interfaces being tested with water during the shear test assembly process to mimic the condensation that occurs in the field, in addition to being flooded during testing).
3. In the evaluation of slopes that involve strain-softening interfaces, which includes most lined containment facilities, limit equilibrium analyses of deep-seated failure surfaces (e.g., bottom liners) should be overseen by trained and experienced geotechnical professionals who have studied the principles described in the present paper and can exercise appropriate engineering judgement.
4. When peak strengths are being assumed in stability analyses of bottom liner or veneer lining systems, consideration should be given to modification of the peak strengths to account for variabilities in materials and installation processes, construction damage, seismic displacements, foundation settlement, potential effects of long-term ageing and creep, and the potential for any of these factors to cause stress concentrations at the boundaries of a change in shear strength, such as can be found in the transition from an unbonded to a bonded condition of a geotextile lamination to a geonet. Following these adjustments, the design factor of safety should be greater than 1.5 to account for geotechnical variabilities, unknowns, and simplifying assumptions, as is standard in the geotechnical profession.
5. It is recommended to give special attention to specifications for the bonding between geotextiles and geonets when using drainage geocomposites. Where slope stability is critical, specifications for these materials should be written that require minimal widths of unbonded edge zones, and higher average peel strengths to compensate for the very high standard deviations in manufacturing that seem endemic to these manufactured products. In addition, increased conformance (verification) testing frequency of these parameters would be advised, requiring that more specimens be tested across the panel width than typically suggested by ASTM D7005.
6. Sensitivity and probabilistic studies can provide insight into determining which elements of the design are the most critical so that design efforts can be focused. An evaluation of the failure risk, especially as regards potential consequences, should be considered as part of this type of evaluation.
7. A degree of uncertainty can be addressed by implementing a long-term program of instrumentation and monitoring, combined with a response action plan.
8. When considering the use of peak strengths, the consequences of failure should be weighed against the uncertainties in the design.
9. Where designers wish to minimize uncertainties and follow a safe defensible standard practice for bottom liner static stability without the use of sophisticated numerical analyses, the rule-based recommendations of Stark and Choi (2004) are probably the

most pragmatic and straightforward. This is the case because they address regulatory concerns (FS > 1.5), as well as the work of Gilbert and Byrne (1996), which seeks to achieve FS > 1.0 under residual strength conditions. The Stark and Choi (2004) rules can be summarized as follows:

- For landfill bottom liners, assign residual shear strengths to the sideslopes, peak shear strengths to the base of the liner system, and satisfy a factor of safety greater than 1.5.
- Assign residual strengths to the sideslopes and base of the liner system, and satisfy a factor of safety greater than unity.

10. When performing calculations to determine if seismic deformations due to the design earthquake will be within acceptable limits (as defined by standard practice or the regulations), LD or residual strengths should be assumed along the entire critical interface for purposes of those calculations, even if peak strengths have been determined to be acceptable all parts or all of the critical interface for purposes of the static stability. The design should then be checked to meet other project-specific standards or regulatory requirements separately for static FS, and for the maximum estimated displacement due to the design earthquake.

11. Designers should attempt to position the critical slip plane above the primary geo-membrane to the extent feasible for a given project.

12. The stability of veneer liner systems can be based on peak strength, but consideration should be given to modify the peak strength to take into account the factors described in Section 4.

13. Recommendations for future studies include: (1) the effects of regularly or irregularly spaced weak zones in the plane of geosynthetic strain-softening interfaces, such as those created by commonly found manufacturing weaknesses or installation seaming practices, and how those might initiate interface displacements that could contribute to progressive failure; (2) the potential for weak zones to act as stress concentrators within the plane of the interface, and thus enhance the tendency for progressive interface displacement initiation and propagation; and (3) the long-term ageing, durability, and creep performance of geosynthetic interface shear strength.

REFERENCES

Abdelaal, F.B. and Solanki, R. 2022. Effect of Geotextile Ageing and Geomembrane Surface Roughness on the Geomembrane-Geotextile Interfaces for Heap Leaching Applications. *Geotextiles and Geomembranes*, 50(1): 55–68.

Baecher, G.B. 2023. 2021 Terzaghi lecture: Geotechnical Systems, Uncertainty, and Risk. *J. Geotech. Geoenviron. Eng.*, 149(3): 03023001, 23 pp.

Bonaparte, R., Daniel, D.E., Koerner, R.M. 2002. *Assessment and Recommendations for Improving the Performance of Waste Containment Systems, EPA/600/R-02/099*. Cincinnati, OH: USEPA.

Breitenbach, A. 1997. Overview Study of Several Geomembrane Liner Failures Under High Fill Load Conditions. *Proceedings of Geosynthetics 1997*, March 11–13 Long Beach, CA: 1045–1061.

Breitenbach, A. and Athanassopoulos, C. 2013. Improving the Stability of High Fill Load Structures Built on Low Strength Geosynthetic Interfaces. *Proceedings of Geosynthetics 2013*, April 1–4 Long Beach, CA.

Brown, D., Thiel, R., Brummer, C., and Huvane, S. 1999. Innovative Design and Construction of Landfill Side-slope Liners in High Seismic Risk Areas, A Case Study. *Proceedings to Geosynthetics '99* held in Boston, MA in April 1999: 589–600.

Byrne, R. J. 1994. Design Issues with Strain Softening Interfaces in Landfill Liners. *Proceedings of Waste Tech'94 Conference, Charleston, SC, January 1994*. National Solid Waste Management Association.

Daniel, D.E. and Scranton, H.B. 1996. *Report of 1995 Workshop on Geosynthetic Clay Liners, EPA/600/R-96/149*. Cincinnati, OH: USEPA.

Dixon, N., Jones, D. R. V. & Fowmes, G. J. 2006. Interface Shear Strength Variability and its Use in Reliability-based Landfill Stability Analysis. *Geosynthetics International* 13(1): 1–14.

Druschel, S.J. and Underwood, E.R. 1993. Design of Lining and Cover System Side Slopes. *Proc. Of Geosynthetics '93*, March 30-April 1, 1993, Vancouver B.C.: 1341–1355

Duncan, J.M. 1996. State of the Art: Limit Equilibrium and Finite-element Analyses of Slopes. *ASCE J. of Geotechnical Engineering*, May 1996, 122(7): 577–596.

Duncan, J.M. and Wright, S.G. 2005. *Soil Strength and Slope Stability*. Wiley&Sons, Hoboken, NJ.

Duplancic, N. 1990. Landfill Deformation Monitoring and Stability Analysis. *Geotechnics of Waste Fills – Theory and Practice*. ASTM STP 1070.

Eid, H.T. 2011. Shear Strength of Geosynthetic Composite Systems for Design of Landfill Liner and Cover Slopes. *Geotextiles and Geomembranes* 29: 335–344.

Esterhuizen, J.B., Filz, G.M., and Duncan, J.M. 2001. Constitutive Behavior of Geosynthetic Interfaces. *J. of Geotechnical and Geoenvironmental Engineering*, ASCE, 127(10): 834–840.

Filz, G.M., Esterhuizen, J.B., and Duncan, J.M. 2001. Progressive Failure of Lined Waste Impoundments. *J. of Geotechnical and Geoenvironmental Engineering*, ASCE, Vol. 127, No. 10, Oct., pp. 841–848.

Fowmes, G.J. 2007. *Analysis of Steep Sided Landfill Lining Systems*. Doctoral dissertation, Department of Civil and Building Engineering, Loughborough University, Loughborough, UK.

Gao, W., Kavazanjian, E., and Wu, X. 2022. Numerical Study of Strain Development in High-density Polyethylene Geomembrane Liner System in Landfills using a New Constitutive Model for Municipal Solid Waste. *Geotextiles and Geomembranes* 50(2): 216–230.

Gilbert, R.B. 2001. Peak Versus Residual Strength for Waste Containment Systems. *Proceedings of the 15th Annual GRI Conference Hot Topics in Geosynthetics – II, Houston, TX, Dec. 13, 2001*. Folsom, PA: Geosynthetics Institute, 29–39.

Gilbert, R. B. & Byrne, R. J. 1996. Strain-softening Behavior of Waste Containment System Interfaces. *Geosynthetics International*, 3(2): 181–203.

Gilbert R.B., Long J.H., and Moses B.E. 1996. Analytical Model of Progressive Slope Failure in Waste Containment Systems. *International Journal of for Numerical and Analytical Method in Geomechanics*, 20 (1): 35–56.

Giroud, J.P., Zornberg, J.G., and Zhao, A. 2000. Hydraulic Design of Geosynthetic and Granular Liquid Collection Layers. *Geosynthetics International*, 7(4–6): 285–380.

Hanson, J. L., Chrysovergis, T. S., Yesiller, N. and Manheim, D. C. 2015. Temperature and Moisture Effects on GCL and Textured Geomembrane Interface Shear Strength. *Geosynthetics International* 22(1): 110–124.

Jones, D.R.V. and Dixon, N. 2005. Landfill Lining System Stability and Integrity: The Role of Waste Settlement. *Geotextiles and Geomembranes* 23(12): 27–53.

Jones, D.R.V., Dixon, N. and Connell, A. 2000. Effect of Landfill Construction Activities on Mobilized Interface Shear Strength, *Proc. EuroGeo 2000*, Bologna, Italy: 581–586.

Karademir, T., Frost, J.D. 2021. Elevated Temperature Effects on Geotextile-geomembrane Interface Shear Behavior. *J. Geotech. Geoenviron. Eng.*, 147(12):642–659

Kavazanjian, E. 1999. Seismic Design of Solid Waste Containment Facilities. *8th Canadian Conference on Earthquake Engineering*, Vancouver, BC, Canada, June 1999: 51–89.

Kavazanjian, E. 2023. *Personal Communication*.

Kavazanjian, E., Dixon, N., Katsumi, T., Kortegast, A., Legg, P., and Zanzinger, H. 2006. Geosynthetic Barriers for Environmental Protection at Landfills. *8th International Conference on Geosynthetics*, Yokohama, Japan, September 18–22, 2006.

Kavazanjian Jr., E., Wu, X., Arab, M., Matasovic, N. 2018. Development of a Numerical Model for Performance-based Design of Geosynthetic Liner Systems. *Geotextiles and Geomembranes* 46(2):166–182.

Kerkes, D.J. 1999. Analysis of Equipment Loads on Geocomposite Liner Systems. *Proc. Of Geosynthetics '99.* April 28-30, 1999 in Boston, MA.: 1043–1054.

Koerner, R.M. and Narejo, D. 2005. Direct Shear Database of Geosynthetic-to-geosynthetic and Geosynthetic-to-soil Interfaces. *GRI Report #30, Geosynthetics Research Institute, Folsom, PA.*

Koerner, R.M. and Soong, T.Y. 1998. Analysis and Design of Veneer Cover Soils. *Proc. Of 6th Int'l Conf. on Geosynthetics*, 25-29 March 1998, Atlanta, GA.

Koerner, G., Koerner, R., and Martin, J. 1994. Design of Landfill Leachate Collection Filters. *J. Geotech. Engrg.*, 120(10): 1792–1803.

Long, J.H., Gilbert, R.B., and Daly, J.J. 1995. Effect of Waste Settlement on Slope Lining Systems. *Proceedings of Geosynthetics '95*, Nashville, TN: 729–744.

Ma, P., Ke, H., Lan, J., Chen, Y., and He, H. 2019. Field Measurement of Pore Pressures and Liquid-gas Distribution using Drilling and ERT in a High Food Waste Content MSW Landfill in Guangzhou, China. *Engineering Geology*, 250: 21–33.

Marr, A. 2013. Instrumentation and Monitoring of Slope Stability, *State-of-the-Art Paper for ASCE GeoCongress*, ASCE GSP 231: 2224–2245.

Marr, A. and Christopher, B. 2003. Recommended Design Strength for Needlepunched Geosynthetic Clay Liner Products. *GFR Magazine* 21(8):18–23.

McCartney, J. S., Zornberg, J. G., Swan, R. H. Jr & Gilbert, R. B. 2004. Reliability-based Stability Analysis Considering GCL Shear Strength Variability. *Geosynthetics International* 11(3): 212–232.

McKelvey, J.A. 1994. Consideration of Equipment Loadings in Geosynthetic Lined Slope Designs. *Computer Methods and Advances in Geomechanics*, Siriwardane and Zaman (Eds.) Balkema, Rotterdam:1371–1377.

NRC (US Nuclear Regulatory Commission). 2011. NUREG/CR-7028: *Engineered Covers for Waste Containment: Changes in Engineering Properties and Implications for Long-term Performance Assessment.* Prepared by Craig Benson and others, December 2011.

Paruvakat, N. and Richardson, G. 1999. Landfill Cover Failure Prompts Standards Upgrade. *GFR Magazine*, 17(7).

Qian, X. and Koerner, R.M. 2010. Modification to Translational Failure Analysis of Landfills Incorporating Seismicity. *ASCE Journal of Geotechnical and Geoenvironmental Engineering* 136(5): 718–727.

Qian, X., Koerner, R.M. and Gray, D. 2001. *Geotechnical Aspects of Landfill Design and Construction*, Pearson, 1st Ed.

Reddy, K.R., Kosgi, S. and Motan, S. 1996. Interface Shear Behavior of Landfill Composite Liner Systems: A Finite Element Analysis. *Geosynthetics International*, 3(2): 247–275.

Richardson, G.N., Thiel, R.S., and Mackey, R. 1998. Designing with Needlepunched Reinforced GCLs: Stability Fundamentals. *Geotechnical Fabrics Report* Oct/Nov 1998: 22–27.

Richardson, G.N. and Thiel, R.S. 2001. Interface Shear Strength: Part 2 – Design Considerations. *Geotechnical Fabrics Report* 19(5): 16–19.

Rowe, R.K and VanGulck, J.F. 2004. Filtering and Drainage of Contaminated Water. Keynote Lecture, *4th International Conference on GeoFilters*, Stellenbosch, South Africa, October, University of Witswatersrand, A.Fourie (Ed): 1–63.

Rowe R.K. and Yu Y. 2010. Factors Affecting the Clogging of Leachate Collection Systems in MSW Landfills. *Keynote Lecture, 6th International Conference on Environmental Geotechnics*, New Delhi, India

Sabatini, P.J., Griffin, L.M., Bonaparte, R., Espinoza, R.D., and Giroud, J.P. 2002. Reliability of State of Practice for Selection of Shear Strength Parameters for Waste Containment System Stability Analyses. *Geotextiles and Geomembranes*, 20(4): 241–262.

Skempton, A.W. 1964. Long-term Stability of Clay Slopes. *Geotechnique* 14(2): 77–102.

Stark, T.D. and Poeppel. 1994. Landfill Liner Interface Strengths from Torsional-ring-shear Tests. *ASCE Journal of Geotechnical Engineering* 120(3): 597–615.

Stark, T.D. and Richardson, G. 2000. Flexible Geomembrane Interface Strengths. *Geotechnical Fabrics Report, April*: 22–26.

Stark, T.D., Eid, H.T., Evans, W.D., and Sherry, P.E. 2000. Municipal Solid Waste Slope Failure. II: Stability Analyses. *ASCE Journal of Geotechnical and Geoenvironmental Engineering* 126: 408–419.

Stark, T.D. and Choi, H. 2004. Peak Versus Residual Interface Strengths for Landfill Liner and Cover Design. *Geosyntethics International* 11(6): 491–498.

Stark, T.D., Choi, H., Lee, C., and Queen, B. 2012. Compacted Soil Liner Interface Strength Importance. *ASCE Journal of Geotechnical and Geoenvironmental Engineering* 138(4): 544–550.

Stark, T.D. 2022. *FGI Webinar: Mobilized Interface Strengths on Geosynthetic Lined Slopes*. Fabricated Geomembrane Institute, October 18, 2022.

Thiel, R. 1998. Design Methodology for a Gas Pressure Relief Layer Below a Geomembrane Landfill Cover to Improve Slope Stability. *Geosynthetics International*, 5(6): 589–616.

Thiel, R.S. 2001. Peak vs. Residual Shear Strength for Landfill Bottom Liner Stability Analyses. *Proceedings of the 15th Annual GRI Conference Hot Topics in Geosynthetics – II, Houston, TX, Dec. 13, 2001*. Geosynthetics Institute, Folsom, PA: 40–70.

Thiel, R. and Maubeuge, Kent von. 2002. Current Industry Performance and Construction Issues Related to GCLs. *Proceedings of the 16th GRI Conference on Hot Topics in Geosynthetics II*. Geosynthetic Institute, Folsom, PA, December 16–17: 227–241.

Thiel, R. and Narejo, D. 2005. Lamination Strength Requirements for Geonet Drainage Geocomposites. *Proceedings of the 18th Annual GRI Conference/ASCE Geofrontiers Conference, Austin, TX*.

Thiel, R., Kavazanjian, E., and Wu, X. 2014. Design Considerations for Slip Interfaces on Steep-wall Liner Systems. *Proceedings for Tenth International Conference on Geosynthetics (ICG 10)*, Berlin, Germany, Sep 21-25, 2014. Reprinted in *Geosynthetics Magazine*, Feb/Mar 2015,33(1): 24–33.

Thiel, R. and Gatrell, D. 2019. Geocomposite Lamination Strength Design and Testing: A New Approach. *Proceedings for Geosynthetics 2019*, February 10-13, 2019, Houston, TX.

Thiel, R. and Giroud, J.P. 2023. Localized Shear Strength Mobilization At Geosynthetic Interfaces Caused by Spreading Soil Upslope. Submitted to *GeoAfrica23, 4th African Regional Conference on Geosynthetics*, February 20th–23rd, 2023, Cairo, Egypt.

Thiel, R. and Giroud, J.P. 2024. Localized Shear Strength Mobilization at Geosynthetic Interfaces Caused by Spreading Soil Downslope. In preparation for *GeoAmericas 2024, 5th Pan-America Conference on Geosynthetics*, Apr 28–May 1, 2024, Toronto, Canada.

Thiel, R. and Stewart, M. 1993. Geosynthetic Landfill Cover Design Methodology and Construction Experience in the Pacific Northwest. *Proceedings for Geosynthetics '93*, held in Vancouver, B.C. in April 1993: 1131–1134

Trauger, R.J., Swan, R.H., and Yuan, Z. 1997. Long-term Shear Strength Behavior of a Needlepunched Geosynthetic Clay Liner. *ASTM STP 1308: Testing and Acceptance Criteria for Geosynthetic Clay Liners, Larry Well Ed.*: 103–120.

USEPA. 2004. *EPA (Draft) Technical Guidance For RCRA/CERCLA Final Covers*, Office of Solid Waste and Emergency Response, EPA 540-R-04-007, OSWER 9283.1–26.

Villard, P., Gourc, J.P. and Feki, N. 1999. Analysis of Geosynthetic Lining Systems (GLS) Undergoing Large Deformations. *Geotextiles and Geomembranes*, 17: 17–32.

VonPein, R.T. and Lewis, S.P. 1991. Composite Lining System Design Issues. *Geotextiles and Geomembranes*10: 507–513.

Yazdani, R., Campbell, J.L., and Koerner, G.R. 1995. Long-term in situ Strain Measurements of a High-Density Polyethylene Geomembrane in a Municipal Solid Waste Landfill. *Proceedings of Geosynthetics '95*. Nashville, TN: 893–906.

Yu Y. and Rowe R.K. 2016. Modelling Leachate Collection System Design Options for a Canadian Landfill. 3rd Pan-American Conference on Geosynthetics, *Geo America's 2016*, Miami Beach, Florida, April 2016.

Yu Y. and Rowe R.K. 2018. Development of Geomembrane Strains in Waste Containment Facility Liners with Waste Settlement. *Geotextiles and Geomembranes* 46: 226–242.

Zamara. K.A., Dixon, N., Fowmes, G., Jones. D.R.V. and Zhang, B. 2014. Landfill Side Slope Lining *Geotextiles and Geomembranes* 42: 224–235.

Zanzinger, H. and Alexiew, N. 2002. Long-term Internal Shear Testing on Clay Geosynthetic Barriers. *Clay Geosynthetic Barriers*. Zanzinger, H., Koerner, R.M. and Gartung, E. (Eds.), A.A. Balkema Publishers, Lisse, The Netherlands: 111–117.

Zanzinger, H. and Saathoff, F. 2012. Long-term Internal Shear Strength of a Reinforced GCL based on Shear Creep Rupture Tests. *Geotextiles and Geomembranes* 33(1):43–50.

Keynote lectures

The road to resilience: Advanced soil-geosynthetic interface characterization and its role in reinforcing soil structures for sustainability

G. Cardile
Department of Civil Engineering, Energy, Environment and Materials (DICEAM),
Mediterranea University of Reggio Calabria, Calabria, Italy

ABSTRACT: Geotechnical Engineering, as a scientific discipline, plays a crucial role in advancing sustainable development and enhancing resilience to natural hazards. The concepts of resilience and sustainability are closely linked: resilience pertains to the ability of a system to withstand and recover from disturbances (such as seismic events, landslides, and floods), while sustainability focuses on the long-term well-being of society and the environment. The augmentation of resilience cannot be limited to a single action but instead demands an ongoing process of adaptation and enhancement as conditions change and new insights emerge. The design and implementation of geotechnical projects must address immediate societal needs and consider the long-term environmental impacts and potential for future disasters. For these reasons, assessing the resilience and sustainability of geotechnical systems requires considering both technical performances and environmental-social-economic factors.

Geosynthetics within civil and environmental engineering structures can enhance safety and serviceability, minimising ecological impact. Specifically, geosynthetics used as reinforcement have gained wide recognition as an efficient approach to enhance the resilience of earthworks. Their effectiveness is particularly notable in their ability to withstand deformation and failure under various loading scenarios. However, a comprehensive understanding of the mechanical behaviour of the geosynthetic-soil interface and the mechanisms of load transfer is crucial for designing and constructing geosynthetic-reinforced structures (GRS), as they govern their performance. In this paper, the author will conduct a comprehensive analysis of experimental data to delve into the intricacies of the geosynthetic-soil interface by examining the effects of different pullout-loading conditions on design parameters and highlighting recent advancements in the field.

1 INTRODUCTION: BUILDING STRONGER, GREENER STRUCTURES

According to the World Commission on Environment and Development, "sustainable development is a development that meets the needs of the present without compromising the ability of future generations to meet their own needs" (1987). Integrating sustainability criteria into the decision-making process of Civil Engineering design is becoming a prevalent practice. Characterising sustainability involves fulfilling the demands of the interdependent "three pillars", the three domains: environmental, economic, and social/functional. Sustainable design requires striking a proper balance among these conflicting objectives (Basu et al. 2015; Basu & Puppala 2015). The interplay between these domains renders the comprehension of sustainability complex, as changes in the requirement and solutions of one domain have a ripple effect on the requirement and solutions of the other ones. The concept

of time is integral to sustainability, and addressing sustainability issues necessitates examining fluctuating resources and needs over a temporal framework. Therefore, a crucial aspect of sustainable design is an approach that considers a structure or project's entire life cycle, from "cradle to grave", "cradle to operation", or "cradle to gate" (ISO 14040, 2006a; ISO 14044, 2006b).

The construction sector and its associated industries contribute significantly to the exploitation of the Earth's natural resources, both renewable and non-renewable, resulting in a detrimental environmental impact. Specifically, this industry accounts for the depletion of two-fifths of the world's raw stone, gravel, sand, and one-fourth of virgin wood. Additionally, it consumes 40% of the total energy utilisation and 16% of the global water supply annually (Dixit et al. 2010). In Geotechnical Engineering, geostructures are frequently integral components of crucial infrastructures, and therefore sustainability considerations must encompass both the reliability and robustness of engineering design. A geostructural plan prioritising the environment or economy in Civil Engineering may result in a structurally insufficient structure and lacking reliability. Despite being cost-conscious, this design may be prone to failure under unforeseen external threats and not support sustainability goals, particularly in critical infrastructure structures. The absence of resilience to unaccounted external forces is frequently unacceptable in this field.

Incorporating innovative approaches and utilising innovative materials in civil and environmental engineering may offer a viable solution that meets the desired outcome. Geosynthetics are probably the most crucial development in Civil Engineering practice in the 20th Century (Giroud 2005). Unlike disposable plastics, geosynthetics, despite being polymeric materials, allow high sustainability due to their long service life in the engineering applications that utilise them. Geosynthetics provide technological solutions that can aid in addressing the issue of global warming and climate change by reducing emissions compared to conventional geotechnical structures. Geosynthetics have a lower environmental impact than traditional materials because they require fewer natural resources for production and entail a lower carbon footprint throughout the life cycle (Wallbaum et al. 2014). Using these materials aligns with the United Nations' 2030 Agenda for sustainable development, addressing issues such as clean water and sanitation, responsible consumption and production, and climate action. Today, geosynthetics represent a sustainable and mature technological solution in civil engineering, a flexible and adaptable solution to the specific needs of different applications. Moreover, geosynthetics can be combined with other materials to optimise the performance of geotechnical structures. Furthermore, stringent environmental regulations have imposed limitations or banned the utilisation and exploitation of certain conventional construction materials, thereby driving the development and adoption of innovative and eco-friendly materials as geosynthetics in the construction industry (Palmeira 2016).

Engineering applications, such as reinforced earth-retaining structures, bridge abutments, embankments, and steep slopes, can utilise geosynthetic materials as soil-reinforcing components. These materials can also play a role in safeguarding against landslides by constructing passive structural barriers. Moreover, they can function as basal reinforcement beneath embankments on soft foundation soils, even in the presence of piles, providing benefits to the soft soil through geosynthetic-encased columns. Furthermore, geosynthetics can be used to avoid sinkholes, build waterways and flood protection structures, reinforce landfill barriers, reduce seismic pressure on retaining walls, improve foundation soil, stabilise roadway and railway foundations, and prevent pavement cracking (Brandl 2011; Correia & Zornberg 2016; Koffler et al. 2008; Kwon et al. 2005; Palmeira et al. 2008; Perkins & Ismeik 1997a; Perkins & Ismeik 1997b; Touze-Foltz et al. 2016; Wu et al. 2015; Yang & Al-Quadi 2007; Zornberg & Kavazanjian Jr 2001).

Using geosynthetics in retaining walls and reinforced slopes reduces environmental impact as determined by various metrics. Adopting a Geosynthetic-Reinforced Soil (GRS) wall leads to a substantial decrease in environmental impact, with cuts ranging from 63% to 87%

(the values considering a functional unit of 1 m of slope retention with a 3 meters high wall), as a result of replacing traditional concrete and steel reinforcement materials (Frischknecht et al. 2011). Specifically, for the same functional unit, the climate change impact associated with using geosynthetics is approximately 1 ton CO_2-eq per meter lower than conventional methods, which represents 84% of the overall climate change impact generated by the construction and disposal of a traditional system throughout its 100-year design life.

Damians et al. (2018) utilised the Value Integrated Model for Sustainable Evaluations (MIVES) methodology to demonstrate that GRS retaining wall solutions were consistently the preferred choice for sustainability across the environmental, economic, and social/functional categories to conventional gravity and cantilever wall solutions. Furthermore, GRS wall solutions were the most commonly selected optimal option when considering the aggregate of all three pillars.

Using geosynthetics in geotechnical systems has decreased the depletion of raw materials such as stone, gravel, and sand, thereby preserving natural resources. It has been aided by the fact that the cost of materials and installation is reduced compared to utilising their natural counterparts (Christopher 2014). One illustration of the efficacy of geosynthetics pertains to road construction projects executed over soil with limited bearing capacity. Research indicates that by incorporating geosynthetics, the depletion of raw aggregate materials can be reduced by as much as 40%, thereby reducing costs.

Geosynthetics can provide a cost-effective solution for many engineering applications, reducing the overall cost of construction and maintenance. Compared to traditional reinforced concrete technologies, the short-term economic savings from geo-reinforcements in a retaining wall can range from 25% to 50% (Christopher 2014). Additionally, it is often possible to reduce construction costs significantly by utilising the granular soil available on the construction site or a portion of it, thus eliminating or reducing transportation costs from quarries. Furthermore, using geosynthetics in the road and railway embankments allows for steeper batters and consequent savings in expropriation fees. Geosynthetics solutions also ensure considerable cost savings over the structure service life, measurable through the lower maintenance required and superior performance, especially during seismic events (Fang et al. 2003; Huang & Wang 2005; Huang 2000; Koseki et al. 2006; Koseki et al. 2000; Koseki et al. 2009; Kuwano et al. 2014; Ling & Leshchinsky 2005; Ling et al. 2001; Sandri 1997; Tatsuoka et al. 1995 1997; Wartman et al. 2006; White & Holtz 1994).

2 ENHANCING RESILIENCE IN GRS WALL: AN APPROACH THROUGH ADVANCED SOIL-GEOSYNTHETIC INTERFACE CHARACTERISATION

Resilience refers to the ability of GRS walls to withstand and recover from extreme events, minimising damage and disruption to the surrounding community. These structures exhibit exemplary behaviour compared to traditional walls after a high magnitude of seismic events because they efficiently dissipate energy from the activation of internal plastic mechanisms and permit significant deformations, increasing their ductility (Masini et al. 2015). A complete collapse in seismic conditions is infrequent in reinforced retaining walls or steep slopes, except for dynamic liquefaction of the foundation soils or excessive settlements caused by seismic motion. Typically, the observed damage consists of the development of permanent deformations (with displacements affecting the entire structure or a portion of it) and, in some cases, the collapse of a part of the facing system.

Climate change has increased natural disasters, such as typhoons, landslides, and floods, significantly impacting human health, food production, and global economic and political stability. To address this, reducing greenhouse gas emissions, particularly carbon dioxide, is a pressing and imperative task. Geosynthetics can also play a role in adapting to the effects of climate change. Adaptation measures, such as GRS passive structural barriers for

landslide risk mitigation and embankments for flood protection, can increase the resilience of infrastructural and geotechnical structures to natural disasters.

In conclusion, the concepts of resilience and sustainability are closely interlinked. Resilience refers to the capacity of a system to endure and bounce back from disruptions, whereas sustainability concentrates on the long-term prosperity of society and the planet.

As is well known, a GRS wall structure is constructed by alternately layering compacted soil and polymeric reinforcements (mainly geogrids or geotextiles). These reinforcements can either be wrapped around the structure facing or securely connected to it, utilizing cast-in-place concrete or precast concrete blocks or panels. The differentiation between GRS retaining walls and GRS steep slopes is a convention stemming from differing traditional design and analysis methods. In both instances, designers must consider ultimate limit states regarding external stability, such as base sliding, overturning, bearing resistance, and overall stability. These can be assessed using standard geotechnical engineering practices for these structures. Additionally, internal stability limit states, including failure of the reinforcements due to insufficient structural tensile strength or insufficient interaction resistance at the soil-geosynthetic interface (i.e. pullout failure), as well as the failure of the facing due to inadequate strength of the facing or low strength of the reinforcement connections, must also be evaluated. Finally, compound stability limit states involving significant slip mechanisms that affect both the reinforced block and the back retained soil must also be considered. Serviceability limit states, which occur when in-service deformation exceeds prescribed limits, can be attributed to both external factors, such as foundation settlements, or internal factors, such as reinforced mass deformations due to creep strain of polymeric reinforcements, creep of fine-grained fill soil, presence of a layer of wet fill, or polymer degradation. Analysing possible internal instability mechanisms is crucial for determining the appropriate tensile strength and stiffness of reinforcements, their spacing and anchorage length, and the structural characteristics of facing and connections in GRS structures.

The continual advancement of knowledge regarding the mechanical behaviour of geosynthetic materials and the intricacies of soil-geosynthetic interaction has supported using these environmentally conscious design solutions. Through research, innovation has emerged to provide resilient solutions for developing and protecting the territory following social and environmental sustainability.

Currently, the design of reinforced soil structures is deemed sufficiently advanced and reliable. The design parameters for both the backfill soil and the mechanical properties of the reinforcement are determined using a conservative approach due to multiple factors, including the cautious choice regarding the shear strength angle of the highly compacted soil used for the reinforced block (Cardile & Pisano 2020). Additionally, specific design choices prompted by seismic recommendations, such as using the creep reduction factor on material tensile resistance in combination with seismic loads, may result in an overly conservative approach (Kongkitkul et al. 2007; Tatsuoka et al. 2004).

Conversely, advanced characterisation of the soil-geosynthetic interface parameters under pullout conditions is one aspect that requires additional attention and further investigation. Specifically, there is a need for greater understanding and implementation of more rigorous design practices, particularly regarding the serviceability performance of these structures under cyclic/seismic loading and long-term conditions. Acquiring a thorough comprehension of the mechanical behaviour of the interface and the mechanisms of load transfer is essential for designing and constructing GRS structures, as it greatly influences their performance.

Experimentation has been, and continues to be, the starting point and driving force behind technological and design advancements in this field. Recent research results about determining short- and long-term design parameters of geosynthetics and geosynthetics-soil interface will develop this Keynote Lecture. Design parameters have been investigated using a Representative Elementary Volume and large-scale (prototype) test apparatuses, which reproduce monotonic, sustained, and cyclic load conditions. The results obtained will be discussed regarding the interaction mechanisms activated along the geosynthetic specimen

under pullout conditions. The author will also examine the factors affecting the results of pullout tests and explore the theoretical approaches for analysing soil-geosynthetic interface behaviour. Finally, the potential for incorporating these research findings into engineering design practices will be regarded.

2.1 *Investigating the tensile performance of geogrids under cyclic loading and sustained loading scenarios*

Before continuing in the following paragraphs to examine the pullout behaviour of the soil-geogrid interface under various load conditions and its effects on design parameters, it is crucial to comprehend the in-air tensile behaviour of the geosynthetic reinforcing material under sustained or cyclic loads.

According to studies conducted by Hirakawa et al. (2003), Kongkitkul et al. (2004), Tatsuoka (2008), and Chantachot et al. (2018), creep effects do not result in material degradation, unlike the impact of chemical, physical, mechanical, environmental, and biological factors that can cause a degradation of the material structure. The tensile rupture strengths recorded in monotonic tensile tests with one or more pre-rupture sustained load stages (constant loading over time, e.g. sustained load for 30 days) were comparable to the tensile rupture strengths observed at the same temperature and for the same geogrid during standard constant strain rate (CSR) tensile tests. This finding suggests that creep does not result in material degradation. However, it is essential to note that the above considerations are valid in the absence of soil confinement and other deteriorating agents (such as chemical, physical, mechanical, and biological factors).These factors must be taken into account when developing constitutive models for geosynthetics.

Cardile et al. (2017b) developed a multistage (MS) test procedure for evaluating the influence of cyclic tensile load applied on geosynthetic mechanical behaviour; the test comprised three distinct phases (Figure 1):

- First phase: a pre-stress stage at CSR equal to $\varepsilon'=0.2\%$ per minute, reaching a fixed tensile monotonic load P_i chosen as T_{max} (maximum tensile strength per unit width) percentage;
- Second phase: a cyclic stage using a sinusoidal function, with a fixed, controlled tensile loading amplitude A (chosen as T_{max} percentage) and frequency f, for 1000 cycles;
- Third phase: a post-cyclic stage at CSR equal to $\varepsilon'=0.2\%$ per minute until specimen rupture occurs; it is helpful to verify the influence of the applied cyclic loading on geogrid tensile strength.
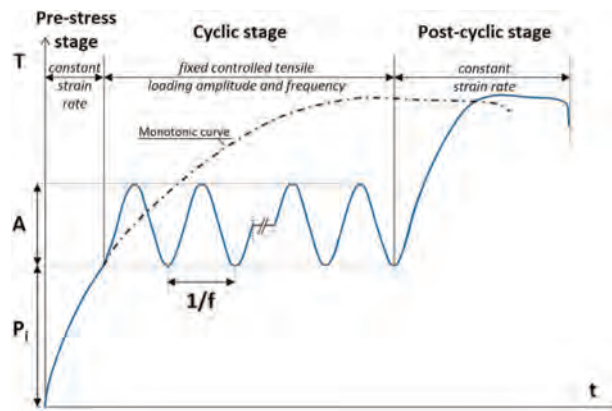
Figure 1.   Multistage test procedure (Cardile et al. 2017b).

The residual strain, denoted as ε_r, represents the strain accumulation in a specimen after each cycle of tensile cyclic loading when the load returns to the pre-stress value (P_i). The graph in Figure 2a, which pertains to a frequency of 0.1 Hz, displays the residual strain ε_r as a function of the number of cycles (N) on a logarithmic scale, grouping the results of all tests by A/T_{max} classes, where the P_i/T_{max} ratio varies. It can be seen that the ε_r increases with both the number of cycles and the normalised loading amplitude (A), and its trend deviates increasingly from linearity. Furthermore, for the lower A/T_{max} classes, the dependence of ε_r on the normalised pre-stress load P_i is negligible during early loading cycles. However, as the number of cycles increases, this dependence becomes more apparent, especially at higher loading amplitudes.

As Cardile et al. (2017b) show, for a fixed number of cycles, the residual strain ε_r increases with decreasing frequency across the various A/T_{max} classes examined (Figure 2b). The difference in strain accumulation at different frequencies can be linked to the variation in loading time, with longer loading times leading to a higher strain component due to creep. The relationship between ε_r and N at a frequency of 0.01 Hz is concave downward, and its slope decreases with the increasing number of cycles. Conversely, the relationship at a frequency of 1 Hz is concave upward until N reaches 100, after which it decreases. This trend can be attributed to the gradual disappearance of residual strain increments with increasing cycles, reaching a stable state.

The comparison between the tensile load-strain relations for the monotonic CSR test and those for the MS tests was also conducted to assess the impact of cyclic loading on maximum tensile strength. Figure 3 presents the maximum tensile strength per unit width Tmax (MS) obtained from all multistage tests, normalised to Tmax, for varying normalised loading amplitude (A) and different ranges of normalised pre-stress load P_i. A slight increase in strength with increasing loading amplitude (A) can be observed, which could be attributed to the increased strain rate during the cyclic stages at the same frequency. However, these differences are negligible and within the bounds of material production variability, always positive and less than 6%. Furthermore, the results show that pre-stress load levels do not significantly affect the outcomes. Hence, the results support the conclusion that cyclic loading histories do not reduce geosynthetic tensile strength.
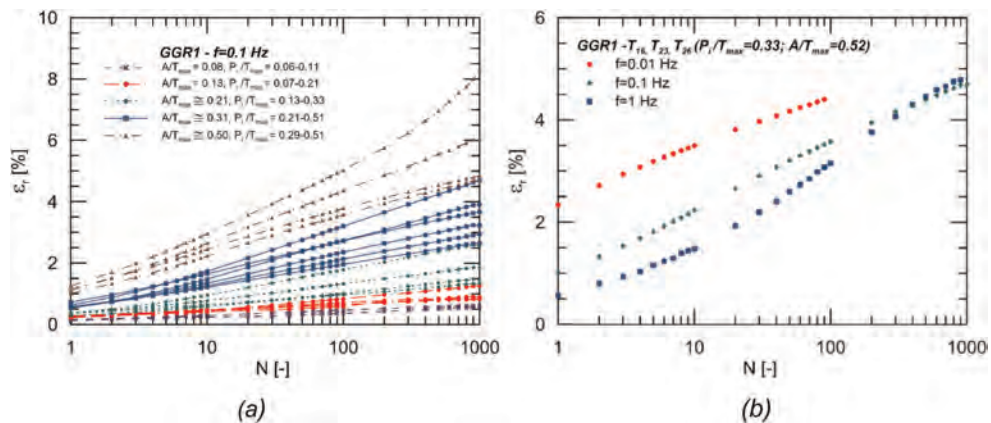
Figure 2. Trends in residual strain with the number of loading cycles for tests conducted at a frequency of 0.1 Hz (a) and tests with P_i/T_{max} equal to 0.33 and A/T_{max} equal to 0.52 at various frequencies (b) (Cardile et al. 2017b).

2.2 *Examining the soil-geosynthetics interaction*

It is crucial to understand that, within the Geosynthetic Reinforced Soil (GRS) structures, the forces mobilised along the reinforcement can be transmitted in varying directions from soil to geogrid or vice versa. The existence of distinct force transfer mechanisms arises from identifying two zones, referred to as the Pushout and Pullout zones, as described by Derksen et al. (2021). The Pushout area (within the active soil area) is characterised by the soil displacement being more significant than the geogrid displacement; in this area, the force transferred to the geogrid is induced by the lateral spreading of the soil. This results in the transfer of interaction stress into the reinforcement through its longitudinal and transverse members, which is directed towards the wall's front face. In contrast, the Pullout zone (within the resistant soil area) is defined by the geogrid displacement being more significant than the soil displacement. In this scenario, the geogrid mobilises elementary interaction mechanisms through the resistance provided by the soil (Cardile & Pisano 2020), and the transfer of shear stresses into the reinforcement occurs towards the interior of the wall.

Improving soil-reinforcement interaction enhances the load transfer from the soil to the reinforcement, from the reinforcement to the soil and its neighbouring layers (Cardile et al. 2016a; Morsy et al. 2020).

To summarise, in each reinforced layer, the tensile force acting on the geogrid starts with a value near the facing, which is contingent upon the stiffness of the facing and its connection type with the geosynthetic, and then gradually increases (in the active area) towards the interior of the wall until reaching a maximum value. This maximum tensile load works as a pullout load for the geosynthetic portion anchored to the resistant zone. At this stage, the tensile forces acting on the geosynthetic commence decreasing until they can reach zero value when relative displacement between the soil and reinforcement nullifies.

Measurements on full-scale tests of geosynthetic-reinforced retaining walls have revealed that the trend of tensile forces along the geosynthetic specimens under serviceability conditions remains unchanged as the load approaches failure conditions. In contrast, the magnitude of these forces in each longitudinal bar increases as long as it might fail. In the reinforced soil mass, failure might occur due to the formation of a critical sliding surface, which coincides with the locus of points of maximum tensile load mobilised in each layer. Therefore, it is essential to ensure that this maximum tensile load is compatible with the design pullout resistance (P_{Rd}) and the design resistance of connections (if present), in addition to not exceeding the design tensile strength (R_{td}).

Comprehending parameters associated with soil-reinforcement interaction and their variations over time concerning applied loads is indispensable for designing geosynthetic reinforced soil structures. The reinforcement length and, as a result, the size of the reinforced soil mass depend on the coefficient of friction chosen to represent the interaction between soil and geosynthetic materials.

Three distinct elementary interaction mechanisms can be mobilised at the soil-geosynthetic interface, contingent upon the failure mechanism and the reinforcement structure (continuous or open mesh-type). These mechanisms include (i) the skin friction between soil and the solid surface of the reinforcement (applicable to both geotextiles and geogrids), (ii) the passive resistance mobilised against elements placed transversely to the direction of tensile load application, and (iii) the skin friction arising due to soil shearing over soil through the apertures of the geogrid (Jewell et al. 1985). These mechanisms have been extensively studied and documented in the literature by various authors: theoretical and experimental studies have been carried out to enhance the comprehension of soil-geosynthetic interaction in geosynthetic-reinforced soil structures (Cardile et al. 2017a; Cardile & Pisano 2020; Cazzuffi 1983; Derksen et al. 2022; Derksen et al. 2021; Jacobs et al. 2014; Moraci & Gioffrè 2006; Moraci et al. 2014; Palmeira 2009; Wang et al. 2014; Zhou et al. 2012). These studies have demonstrated that various interaction mechanisms mobilise when specific failure mechanisms occur, such as sliding a reinforced soil section along a

soil-geosynthetic interface or the pullout of reinforcement from the passive zone. These mechanisms can be replicated in laboratory settings through large-scale test apparatuses.

To study the pullout failure mechanisms gathering the interaction mechanism in the anchorage zone at the soil-geosynthetic interface is possible to use a pullout test apparatus and related tests procedure (ASTM D6706-01 2013). The equipment used in this test typically includes a large and rigid steel box, a system for applying vertical loads, a device for applying horizontal forces, a clamp system, and various measurement, control, and data acquisition instruments.

The behaviour of the soil-geosynthetic interface is influenced by many factors, such as the stress state acting on the interface, the type, geometry, and stiffness of the geosynthetics, the soil grain size distribution, the soil plasticity, the soil density and water content, the specimen size, the drainage and loading conditions, the test displacement rate and magnitude, and other parameters.

Several factors have been identified to affect the outcome of pullout tests, including the impact of the vertical load application system, the boundary conditions at the front wall, the efficiency of methods used to reduce friction between the side walls and soil, the size of the box and the width of the geosynthetic specimen, the type of clamping device used, and the displacement rate during the test. Based on the results of pullout testing studies, specific measures can be implemented to minimise the impact of factors such as boundary conditions and friction on test outcomes (Moraci & Recalcati 2006; Moraci et al. 2017). Specifically, a flexible membrane should be utilised to exert vertical confining pressure on the specimen to ensure proper evaluation of soil-geosynthetic interaction. At the same time, materials with low friction characteristics (such as Teflon) should be applied to the lateral surfaces of the pullout apparatus. Additionally, sleeves of a minimum length of 200-300 mm should be employed on the front walls of the pullout apparatus. An internal clamping system should restrain the specimen throughout the test duration. The pullout apparatus should be enough size to accommodate a representative geosynthetic specimen (have a width that matches the device's width as closely as possible). They should allow for the containment of a soil sample of at least 600 mm in height.

The procedure for conducting a pullout test involves (i) preparing the internal walls of the pullout box, (ii) filling the lower half of the box with soil and compacting it, (iii) placing the geosynthetic specimen and installing test instrumentation on it, (iv) filling the upper half of the box and compacting the soil, (v) placing the vertical load application system, (vi) closing the pullout box by using a steel plate, (vii) connecting the clamp system to the horizontal force application device, (viii) connecting the test instrumentation, and (ix) starting the test.

The experimental data summarised in the following paragraphs refer to tests carried out on specimens of High-Density PolyEthylene (HDPE) uniaxial extruded geogrids embedded in granular soils compacted within the pullout box until soil dry unit weight value (γ_d) be at least 95% of the maximum value ($\gamma_{d,max}$). Compaction was carried out manually with a rammer; loose soil was spread in layers of such thickness as to reach, after compaction, a final value of 150 mm. In any case, the type of soil aggregate and geosynthetic used in the research ensure that the damage induced during test preparation is nil. The graphs and results presented herein may pertain to different interfaces as they are derived from prior research studies. Their primary purpose is to facilitate a qualitative comprehension of the load transfer mechanism at the interface and its mechanical response under shear conditions.

2.2.1 *Characterising pullout behavior in monotonic loading conditions*

The peak shear resistance, which soil-geogrid interfaces oppose to the tensile loads that reinforced earth structures may be subject to during their service life, can be mathematically expressed through the equation:

$$P_R = 2 \cdot L_R \cdot \sigma'_n \cdot f_b \cdot \tan \phi' \tag{1}$$

where P_R is the maximum shear resistance per unit width; L_R is the length of reinforcement in the anchorage zone; σ'_n is the effective stress acting orthogonally to the plane of reinforcement; ϕ' is the soil shear strength angle; f_b is the soil-geosynthetic interaction coefficient under shear conditions.

The values of the soil-geosynthetic interaction coefficient, f_b, can be determined through back-analysis using the results of pullout tests. However, the choice of the mobilised soil shear strength angle to use in the expressions (1) for f_b is a crucial but challenging task, as a variety of factors, such as 3D effects, dilatancy phenomena, and the extensibility of the reinforcement, influence it. One potential approach to address this uncertainty is to utilise an alternative parameter to describe the interface, specifically, the peak apparent coefficient of friction at the soil-geosynthetic interface, $\mu^P_{S/GSY}$, as determined by the equation provided:

$$\mu^P_{S/GSY} = f_b \cdot \tan \phi' = \frac{P_R}{2 \cdot L_R \cdot \sigma'_n} \tag{2}$$

This design parameter eliminates the need for assumptions regarding the values of the mobilised soil shear strength angle, resulting in a more accurate interface characterisation. The parameters in equation (2) can be easily obtained through large-scale pullout tests.

Ezzein & Bathurst (2014) developed a novel integration of technologies which enables the quantification of the continuous displacement field of reinforcements during pullout tests (Figure 4). The apparatus comprises a transparent bottom made of Plexiglas that allows for the visual examination of geosynthetics embedded in a synthetic soil substrate, which is constituted by a non-crystalline form of silicon dioxide quartz sand. The soil becomes translucent upon saturation with a blend of oils, namely Puretol 7 and Krystol 40.

Figure 4 clearly shows that the transfer of pullout load along an extensible geosynthetic specimen embedded in compacted soil can significantly elongate the reinforcement. Focusing on soil-geogrid interfaces, at the start of pullout loading (at time $t_i > t_0$), the head of the geogrid moves by an amount equal to δ_i and at the same time, only a tiny portion of the interface (referred to as the active length, L_A) experiences shear stresses (Figure 5), which are a function of skin friction and bearing resistance. Simultaneously, tensile strains occur in the reinforcement, with each portion between two transverse bars, S, experiencing an elongation ΔS_i, which becomes smaller for the parts farther from the geogrid's head ($\Delta S_{i1} > \Delta S_{i3} > \Delta S_{i3}$).
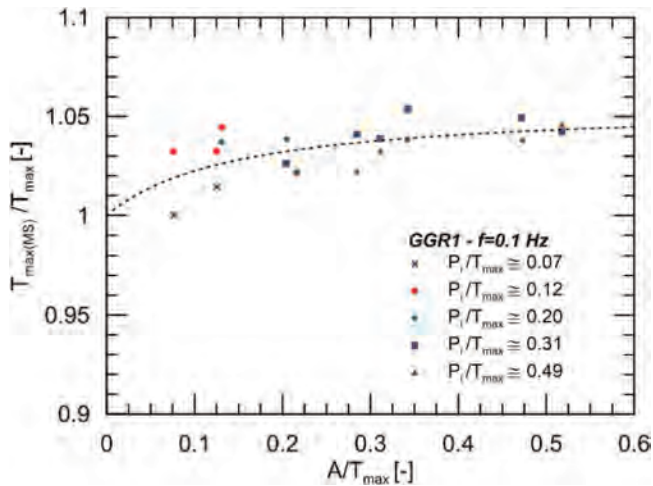
Figure 3. Normalised maximum tensile strength across varying normalised loading amplitudes for distinct ranges of normalised pre-stress loads at a frequency of 0.1 Hz (Cardile et al. 2017b).
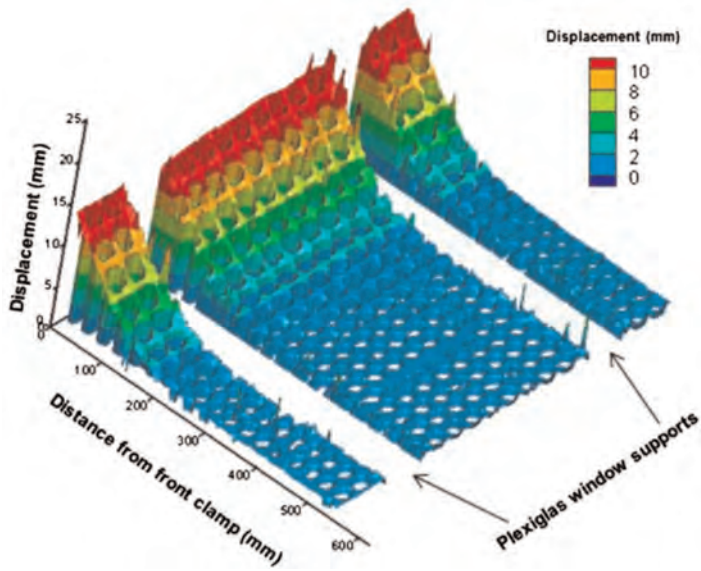
Figure 4. The longitudinal displacement field of a geogrid specimen across the width of the geogrid specimen during a pullout test, captured by Digital Image Correlation (DIC) technique and transparent granular soil (Ezzein & Bathurst 2014).
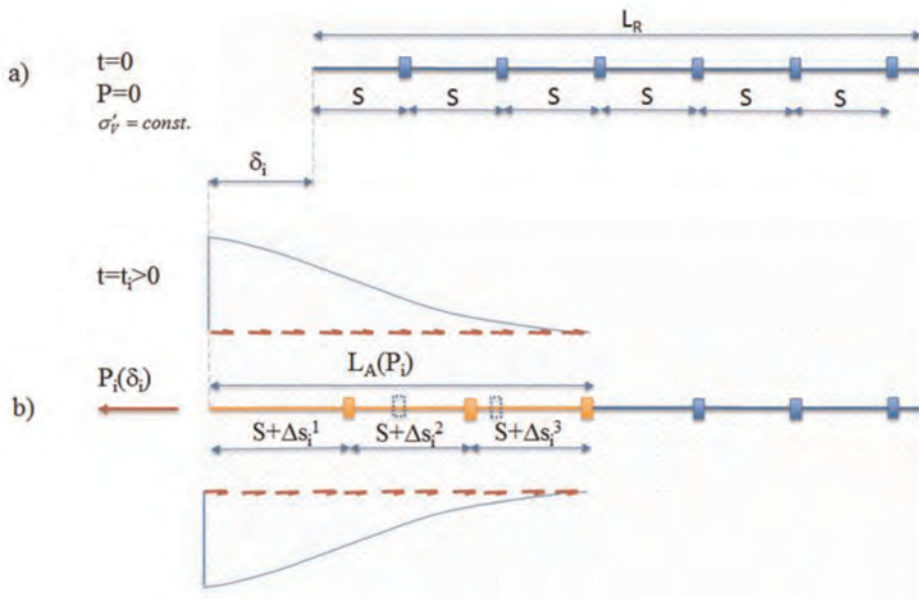
Figure 5. Pullout load transfer mechanism: (a) P=0; (b) P>0 (Cardile et al. 2016a).

The form of the distribution and the local magnitude of mobilised shear stresses at the interface are complex and depend on: (i) loading and boundary conditions; (ii) physical properties and mechanical characteristics of the soil; and (iii) structural, geometric, and mechanical characteristics of the geosynthetic. The active length (L_A) is the portion of the geogrid specimen that experiences the mobilisation of the interaction mechanisms (skin friction and bearing resistance) to withstand the applied load. The evaluation of the active length is crucial to understanding the behaviour of soil-geosynthetic interfaces during the two phases of the pullout process, which are (i) the load transfer phase and (ii) the pullout phase.

The pullout load transfer mechanism can be better understood by examining results obtained from pullout tests. Figure 6 illustrates the distribution of transverse rib displacements along a geogrid specimen for varying applied pullout forces, specifically under monotonic loading conditions. The upper and lower graphs depict long (L_R = 1.15 m) and short (L_R = 0.40 m) reinforcements. The graphs on the left show the tensile load transfer phase (Figure 6a), in which the active length increases with increasing applied pullout force until a limit value (known as the triggering force, P_{ini}) is reached, causing the movement of the last transverse rib. The pullout phase is shown in the graphs on the right (Figure 6b), which begins when the rear end of the geogrid starts to move, with the active length coinciding with the entire length of the specimen plus its elongation. In this study, the short reinforcement resulted in the pullout failure phenomenon, characterised by two adjacent curves parallel to each other when considering different pullout load levels (bottom graph of Figure 6b). The pullout failure is characterised by a reached stage in which the geogrid
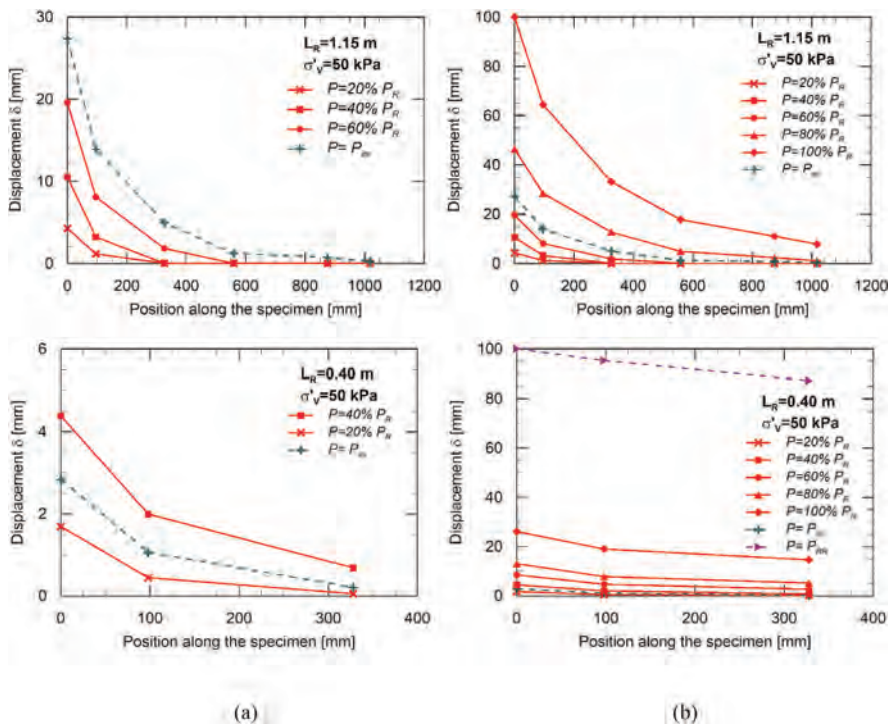
Figure 6. Distributions of the nodal displacements along the geogrid specimen for a fixed vertical effective stress (50 kPa) and different values of the applied pullout force. The upper graphs refer to long reinforcements, while the lower graphs refer to short reinforcements, showing both (a) the tensile load transfer phase and (b) the pullout phase (Cardile et al. 2016a).
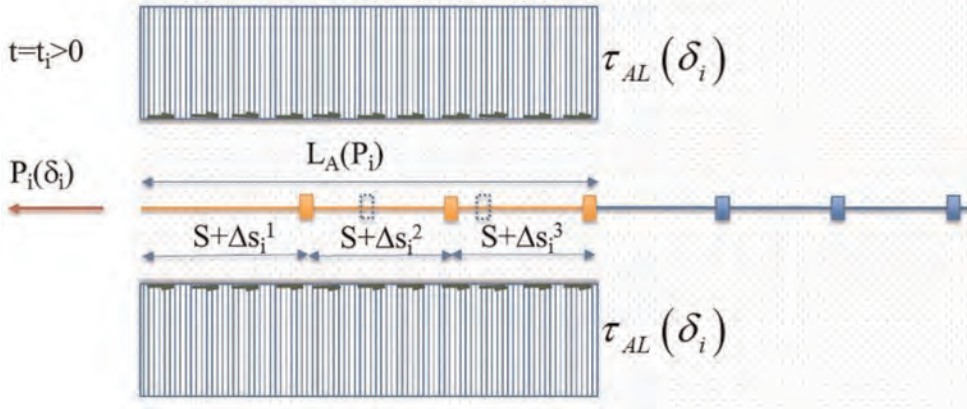
Figure 7.   Equivalent, uniform shear-stress distribution (Cardile et al. 2016a).

translates inside the soil without deforming and, therefore, cannot further increase pullout resistance.

The nonlinear shear stress distribution at the interface leads to a nonlinear transverse rib displacement distribution in extendable reinforcements. This non-linearity increases as the reinforcement tensile stiffness decreases. Conversely, for rigid reinforcements (inextensible), the shear stress at the interface could be assumed to be constant along the specimen (in the case of specimens having a uniform surface). Geogrids with the same tensile stiffness generally exhibit a marked extensibility effect in long reinforcement specimens, which leads to a progressive mobilisation of the interface interaction mechanisms that determine pullout resistance (Figure 6a). On the other hand, generally, short reinforcement specimens exhibit lower longitudinal strains (lower extensibility effects) and almost immediate development of the interface interaction mechanisms along the specimen (Figure 6b).

Analysing the discrete displacement field of different pullout tests, Cardile et al. (2016a) defined the average longitudinal strain, ε_A, which considers that load and elongation act on a varying portion of the reinforcement during pullout tests. Specifically, the ratio of the recorded total elongation of the specimen, ΔL, to the difference between the related active length, L_A, and ΔL, represents ε_A. As previously stated, the distribution of shear stress along the length of the reinforcement is not linear (Moraci & Recalcati 2006; Moraci & Cardile 2012; Perkins & Cuelho 1999; Wang et al. 2014), but it can be approximated by an equivalent, uniform, average shear-stress distribution, τ_{AL} (Figure 7). This shear-stress value can be found by taking the applied pullout load (P) ratio to twice the active length ($2L_A$).

The ratio between the average shear stress value and the effective vertical stress, σ'_v, is represented by the apparent coefficient of friction, $\mu^{AL}_{S/GSY}$, at the soil-geosynthetic interface, calculated using the active length. Figure 8 presents a comparison of the coefficient of friction calculated with the total anchorage length ($\mu_{S/GSY}$, represented by dashed lines) and with the active length (represented by lines with symbols) under a fixed effective vertical stress and varying specimen lengths embedded in compacted granular soil, subject to monotonic loading.

During the load transfer phase of a pullout test, the ratio of $\mu^{AL}_{S/GSY}$ remains independent of the reinforcement length. This fact is indicated by the three coinciding lines with different symbols. The value of this ratio depends solely on the applied confining vertical stress for a given geogrid and soil. When the geogrid's inactive segment remains immobile relative to the adjacent soil, it does not make a substantial contribution to the mechanical interaction and does not play a role in reinforcing the soil during that specific period. Derksen et al. (2021) refer to this stationary region as the "interlocking zone", which denotes a region of force
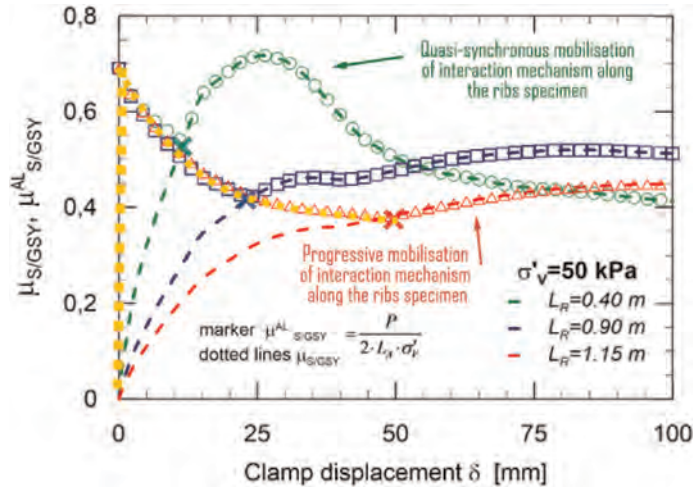
Figure 8. Apparent coefficient of friction at the soil-geosynthetic interface for a fixed vertical effective stress (50 kPa) and different specimen lengths (Cardile et al. 2016a).

balance at the interface where interlocking mechanisms dominate the interaction between soil and reinforcement. This phenomenon arises due to the absence of any appreciable relative displacement between the soil and the reinforcement.

The large x-shaped markers in Figure 8 indicate the onset of the pullout phase: as the length of the reinforced specimen increases, the displacement value at which the entire geogrid becomes activated increases. As the tensile load transfer phase progresses, the active length of the reinforcement increases rapidly, leading to a decrease in the $\mu^{AL}_{S/GSY}$ as the displacement of the first confined section increases. The trend of $\mu^{AL}_{S/GSY}$ reflects that of average longitudinal stress (τ_{AL}), as the latter is equal to the normalised value of $\mu^{AL}_{S/GSY}$ with respect to the effective vertical stress σ'_v acting upon the system. However, once the pullout phase begins, the active length becomes almost constant ($L_R+\Delta L$) while the pullout load continues to increase, resulting in a change in the trend of the average shear stress, which now increases with displacement. In this phase, the interaction mechanisms at the soil-geosynthetics interface are mobilised almost simultaneously along a short specimen. In contrast, they are mobilised progressively in a long specimen, resulting in more pronounced extensibility effects and a lower peak of average shear stress, which is mobilised at higher displacement than shorter reinforcements (progressive failure). Once the longitudinal strain stops increasing, pullout failure occurs.

Summarising the results obtained for a geosynthetic-soil interface at different vertical effective stresses and using various reinforcement specimen lengths, presented in Figure 9, it is possible to observe a clear correlation between the dilatancy of the soil and the apparent coefficient of friction at the interface. As the effective vertical stress on the interface increases, there is a significant decrease in the peak apparent coefficient of friction. Notably, the tensile strength mobilised at a given average longitudinal strain (mobilised on the active length) of the same geosynthetic material exhibits a significant variation depending on the boundary conditions.

The apparent pullout stiffness (defined as the ratio between the applied pullout load and the related average longitudinal strain) is generally higher than the tensile stiffness allowable for geosynthetic material solely stressed in air through a tensile force applied at the same test rate and for the same strain level (Figure 10a) (Cardile et al. 2016a). This phenomenon is mainly observable in specimens with high anchoring lengths (even more so for higher
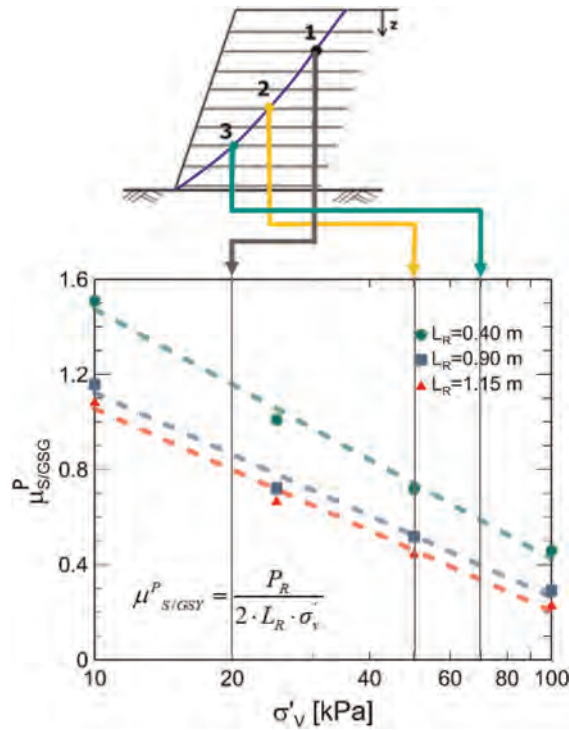
Figure 9. Peak apparent coefficient of friction for varying effective vertical stress for different specimen lengths.
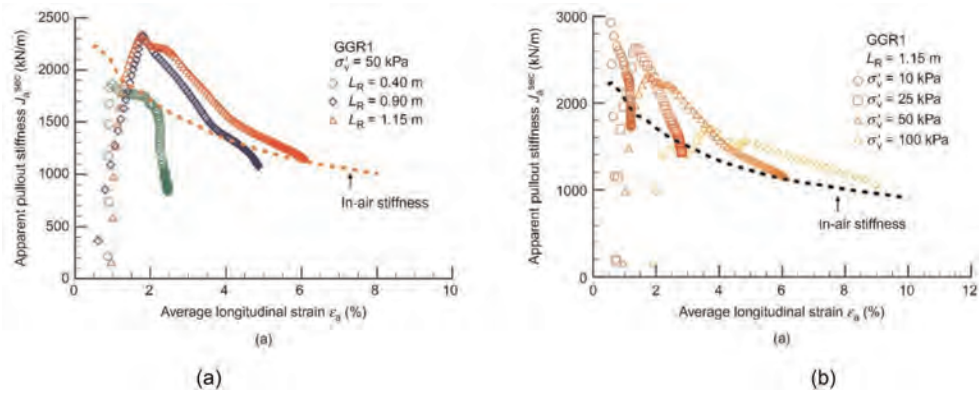
Figure 10. Apparent pullout stiffness plotted against average longitudinal strain obtained by pullout tests: (a) HDPE geogrid of different specimen lengths and under the same effective vertical pressure (50 kPa); (b) influence of effective vertical pressure on the apparent pullout stiffness for geogrid of specimens length L_R=1.15 m (Cardile et al. 2016a).

confinement stresses), where progressive failure mechanisms play a crucial role in gradually and increasingly slower load transmission along the specimen (Figure 10b). The confinement effect, the related different load transfer mechanisms, and the viscoelastic nature of the polymer thus contribute to an increase in the mobilised average stiffness in pullout

118

conditions. Furthermore, confined stiffness curves show a well-defined stiffness peak, which could be attributed to the mechanical behaviour of the compacted granular soil in contact and the related dilation effects at the interface.

2.2.2 *Characterising pullout behaviour in sustained loading conditions*

Throughout both the construction and service life of a Geosynthetic Reinforced Soil (GRS) wall, it is critical for the various reinforcements in the anchorage zone to sustain the tensile load resulting from lateral earth pressure acting within their influence area. Lateral earth pressures are primarily generated during construction, as successive layers are added, and lateral strains are induced. It is worth noting that the lateral stress state within a horizontal plane along a reinforcement layer is not uniform and undergoes changes during loading. Furthermore, the lateral earth pressure varies in tandem with changes in the strain experienced by the reinforcements (Morsy & Zornberg 2021). This tensile load initiates soil-geosynthetic interactions, which generate pullout resistance and activate a portion of the anchorage length of the geogrid. Once equilibrium is attained, a deformed configuration of the geogrid is temporarily reached. However, it is subject to change over time due to the viscoelastic properties of the reinforcement and, eventually, changes in loading and boundary conditions. Specifically, the strains in the active portion of the geosynthetic due to the tension, which remain constant during a given balance configuration, lead to a decrease in mobilised resistance (relaxation phenomenon) due to the geosynthetic's viscoelastic properties. This decrease in resistance means that to handle the tension again, previously unused portions of the geogrid must be activated, and the interaction mechanisms (skin friction and bearing resistance) must move forward, meaning the reinforcement is further deformed to regain the lowered tensile resistance, reaching a new temporary balance configuration. This process continues until the pullout limit state is reached, at which point the reinforcement can no longer deform, and further resistance cannot be mobilised.

In light of the above, the interface parameters obtained from conventional soil-geosynthetic interaction tests may not be sufficiently conservative concerning the serviceability of the structure during its design working life. As this aspect has not yet been explored in the scientific literature, to investigate how the behaviour of the soil-geosynthetic interface evolves, Cardile et al. (2021) have designed and constructed a large-scale prototype apparatus (Figure 11) that can exert a constant pullout load over a prolonged period. This research represents a significant advancement in the field as it allows for the simulation and monitoring of the temporal variation of the strain state along the specimen by reproducing the geosynthetic pullout mechanism typically observed in the anchorage zone of geosynthetic-reinforced soil (GRS) structures.

The long-term pullout apparatus utilises a fully mechanical system comprising weights, gear wheels, and pulleys, configured to yield a theoretical transmission ratio of 10:1 (with a maximum potential force of 70 kN). The apparatus comprises a large, sturdy steel box measuring 625x400x1700 mm designed to minimise scale effects. The box walls are constructed with a suitable thickness and coated with Teflon films to reduce friction. Furthermore, the apparatus features metal sleeves, 200 mm in length, which are positioned in the crack of the front wall to mitigate the effects of its stiffness on the results. It also includes an internal clamping system for the geosynthetic and a pneumatic system for applying vertical loads. Additionally, there is a reserve tank to ensure continuity of air supply in case of power interruption, a mechanical system for applying horizontal loads, and six rotary variable displacement transducers (RVDT) to measure geosynthetic displacements. A data acquisition system is also included to monitor the apparatus and testing process.

The HDPE geogrid was characterised through various tests, including wide-width tensile tests and conventional tensile creep tests following UNI EN ISO 13431 (2002) guidelines. The tests were conducted under controlled temperature and humidity conditions (T = 20 ± 2 °C at 65 ± 5% RH). The specimens were loaded smoothly, with the full tensile creep load
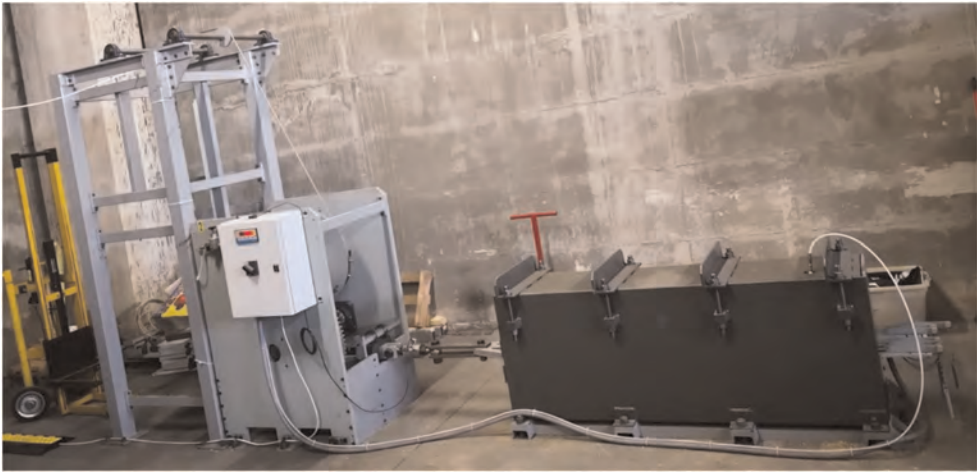
Figure 11.   Large-scale prototype apparatus for long-term pullout tests.

applied within 60 seconds, using the same two levels of load used in subsequent confined long-term tests.

Two long-term pullout tests were parallel conducted on twin apparatus under controlled temperature and humidity conditions by applying an effective vertical stress of 50 kPa to both soil-geogrid specimens (330 mm in width and 1200 mm in length, with 19 longitudinal ribs and five transverse bars in total). The used soil was classified as SW and A1-b according to the USCS (ASTM D2487 2017) and UNI EN ISO 14688-1 (2018) classification systems, respectively. The sustained pullout loads applied were set to be 50% and 70% of the peak pullout resistance obtained from the standard pullout test on the same interface at a constant displacement rate of 1 mm per minute and carried out at the same vertical effective stress. During the initial loading phase, the tensile load was applied at a controlled rate of approximately 0.7 kN/m per minute to prevent excessive stiffening of the geogrid specimen. This procedure avoided an accelerated load transfer along the reinforcement, causing displacements of the reinforcement higher than those anticipated during the construction phase of an actual GRS structure.

Figure 12 presents the results of strains values calculated along the portion of the geogrid closest to the clamp, designated as $\varepsilon_{\text{H-B1,conf}}$ (i.e. the segment subjected to the highest stress, extending from the initial confined section, H, to the first transverse bar, B_1), normalised to the cumulative strain at the first hour (coefficient b) as a function of time in a logarithmic scale (Cardile et al. 2021). The $\varepsilon_{\text{H-B1,conf}}$/b strains were compared with those obtained by tensile creep tests carried out in-air at the same load level. The objective of the comparison is to examine the distinctive slopes of the curves, which is crucial in determining the performance of soil-reinforcement interfaces over their design working life. This comparison is feasible due to the assumption that the geogrid experiences a near-constant tensile loading in the short portion from the initial confined section to the first transverse bar (H-B1). Stationary creep condition is evident throughout the test for the confined geogrid specimen subjected to a sustained pullout load.

Upon conducting data analysis, it is apparent that initially, the two curves exhibit similar gradients for the first 20 hours. However, after reaching the 20th hour, it can be seen that the strains in $\varepsilon_{\text{H-B1,conf}}$ display a lower gradient for the test duration. This change in trend reflects the progression of the pullout interaction mechanisms along the geogrid. The active
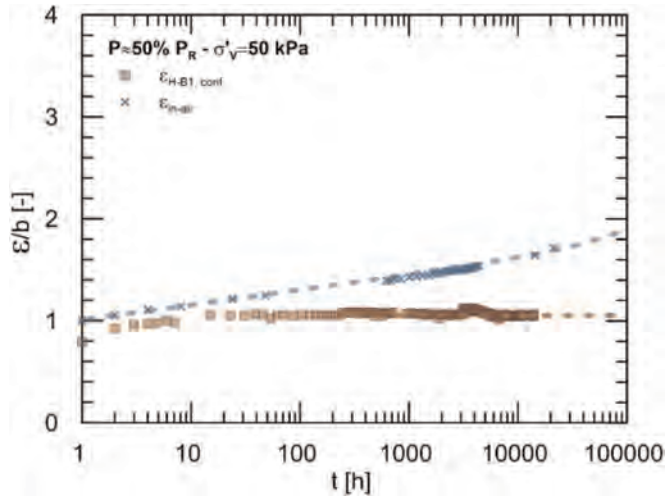
Figure 12.   Comparison between $\varepsilon_{\text{H-B1,conf}}$ strains normalised to corresponding cumulative strain at the first hour (b coefficient) (Cardile et al. 2021).

length of the geogrid segment that can resist the applied load gradually increases over time, reducing the deformation rise of the most stressed geogrid part (H-B1). If the observed trend persists, attaining a potential tensile creep rupture under pullout conditions would significantly surpass the time recorded in traditional in-air tensile creep tests. It implies that the creep reduction factor extrapolated from accelerated laboratory tests (as per ISO/TR 20432 2007) to the design working life and used to decrease the geosynthetic tensile strength in current design practices may be overly conservative.

It can be observed that the strains of the most stressed specimen portion (H-B1) resulting from the application of a sustained tensile load (i.e., the creep strains) are lower in the confined test scenario (as illustrated in Figure 12) due to the soil confinement effect and its related load transfer mechanisms. Therefore, a prediction of structure deformation under serviceability conditions based only on isochronous curves obtained from in-air creep tests may be conservative.

BS 8006 (2010) recommends considering both the ultimate limit state and the serviceability limit state when determining the design tensile strength of a polymeric reinforcement. Therefore, the geosynthetic tensile strength must be calculated considering the lesser between the short-term tensile strength (reduced by the reduction factor for creep) and the tensile strength concerning creep strain. The latter is the tensile load which induces a prescribed limiting value of post-construction strain in the reinforcement. This value can be estimated from isochronous load-strain curves for the end of construction and the end of the design life. The prescribed post-construction strain value varies based on the type of structure. To conform to the serviceability limit state, it must not exceed 0.5% for bridge abutments and retaining walls with permanent structural loading and 1% for retaining walls with only transient live loadings.

It is important to note that the aforementioned isochronous curves, obtained from in-air creep tests, do not account for the interaction with the soil. As a result, it is necessary to analyse the extent to which the peak apparent coefficient of friction mobilised at the interface should be reduced to consider the creep and relaxation phenomena that impact the deformation of the geosynthetic over time. Cardile et al. (2021) plotted the isochronous curves by
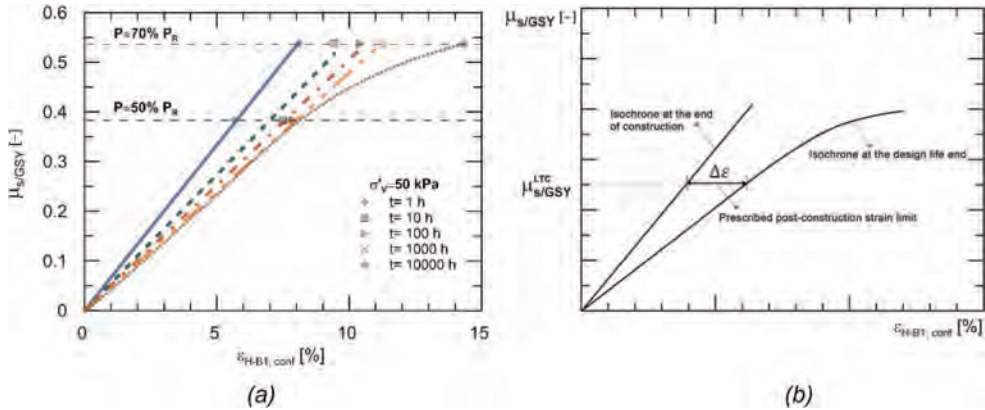
Figure 13. Isochronous interaction curves under long-term pullout conditions. (a) Test results (Cardile et al. 2021); (b) Long-term apparent coefficient of friction assessed at a prescribed limiting value of post-construction strain in reinforcement using isochronous curves.

computing the $\mu_{S/GSY}$ values by experimentally investigating two sustained load levels (P = 50% P_R and 70% P_R). For each value of the $\mu_{S/GSY}$, they calculated the $\varepsilon_{H\text{-}B1,conf}$ strains mobilised at set times (1 hour, 10 hours, 100 hours, 1000 hours, and 10000 hours). Then, curve fitting was applied to the pairs of $\mu_{S/GSY}$-$\varepsilon_{H\text{-}B1,conf}$ values to obtain the isochronous trend shown in Figure 13. It can be seen that this trend is nearly linear, assuming no local rupture phenomena or tertiary creep occurs (except for the isochrone at 10000 hours close to the higher load levels).

The study by Cardile et al. (2021) shows that for a given $\mu_{S/GSY}$ value (i.e. sustained applied load P), the cumulative strains in the anchorage zone decrease over time, moving from one time in logarithmic scale to the next (except for the isochrone at 10000 hours at higher load levels). As expected, the graph shows that with increasing sustained applied load, the increasing mobilisation of the $\mu_{S/GSY}$ value necessary to maintain the stability of the structure over time results in an increase of reinforcement strains in the anchorage zone. It is valid for each reinforcement layer, as the effective vertical stress varies. In conclusion, it is crucial to determine if the strain reached during the design working life complies with the serviceability standards of the structure.

The construction of the isochronous interaction curves under long-term pullout conditions (Figure 13a), created for various vertical effective stresses, can aid in the design to choose a peak apparent coefficient of friction that considers the long-term mechanical behaviour of the soil-geosynthetics interface. If design methods focusing on the ultimate limit state are used, the design parameter $\mu_{S/GSY}$ may be selected through the $\mu_{S/GSY}$-$\varepsilon_{H\text{-}B1,conf}$ isochronous curves to also indirectly consider the serviceability limit state. It will suffice to search for the ordinate at which the horizontal distance between the two reference isochronous curves (at the end of construction and the end of design life) corresponds to the strain limit set for the designed structure (Figure 13b).

Post-construction allowable strain limit may vary based on the type and functionality of the structure. The correlation between $\varepsilon_{H\text{-}B1,conf}$ and the actual deformation of the structure (e.g. horizontal deformation of GRS wall facing) for each reinforcement layer performed through numerical analyses and full-scale wall measurements would be permitted to calibrate this threshold strain value. To effectively transform the design proposal into a comprehensive design scheme, it is essential to determine the isochrones, which will be

calculated at the design working life of the structure for different vertical effective stress levels. Therefore, future research in this field will focus on conducting accelerated long-term pullout tests using higher temperatures to speed up the analysis of the confined creep behaviour.

2.2.3 *Characterising pullout behavior in cyclic loading conditions*

Previous experimental studies have demonstrated that geosynthetic reinforcing materials (generally geogrids) exhibit no degradation under various loading conditions. The wide-width tensile strength (obtained by using standard monotonic procedure tests) remains unchanged even after the application of cyclic loading (Cardile et al. 2016b, 2017b) or constant loading sustained over time (Chantachot et al. 2018; Hirakawa et al. 2003; Kongkitkul et al. 2004; Tatsuoka 2008).

It should be noted, however, that this may not hold for the geosynthetic-soil interface. The pullout behaviour of geogrids under cyclic tensile loads is a complex phenomenon influenced by various factors. These include the frequency, amplitude, and number of cycles of the cyclic loading history and the static tensile load level already acting on the geosynthetic at the initiation of the cyclic load. Understanding how these factors interact is essential for adequately designing and applying geosynthetic systems subjected to cyclic loads. To determine the effect of cyclic loading on interface design parameters when the reinforcement is embedded in the soil, Cardile et al. (2019) conducted pullout tests using a multistage (MS) test procedure (Moraci & Cardile 2009).

The test procedure for evaluating the geosynthetic-soil interface behaviour comprises three distinct phases:

– First phase: The pullout test is conducted under controlled displacement using a constant rate of displacement (CRD) of 1 mm per min until a specified tensile load, P_i, is reached.
– Second phase: During this phase, load-controlled cyclic loading is applied using a sinusoidal function with a specified amplitude, A, and frequency, f, for a fixed number of cycles, N.
– Third phase: The test is once again conducted under controlled displacement, specifically at the same velocity used in the first phase of the multistage test (v=1 mm per min), until either the geogrid fails in tension or the pullout conditions are reached.

The MS pullout tests involved varying the applied vertical effective stress (10, 25, 50, and 100 kPa) and the cyclic load amplitude (30% and 45% of the peak pullout resistance obtained from static pullout tests at a constant rate of displacement of 1mm per minute). A total of 1000 cycles were applied. The cyclic loading frequency was 1 Hz, and the initial tensile loading level was set at 35% of the peak pullout resistance. Specifically, $P_i \approx 35\% \ P_R$ was adopted for the first step as it could be considered an upper bound value for those representatives of GRS structures' design.

The comparison between the curves obtained from monotonic tests and those obtained from MS tests has revealed that for geogrids installed in well-compacted granular soils, the applied cyclic loading history can lead to a reduction in post-cyclic pullout resistance. For the specific test conditions, a decrease (ranging from 10% to 33%) in the post-cyclic peak apparent coefficient of friction concerning the values obtained in monotonic pullout tests has been observed (Figure 14).

Specifically, this reduction increases with decreasing effective vertical stress (becoming negligible at higher stress values) and increases with increasing cyclic load amplitude. These effects should be considered when designing GRS structures in seismic areas or subjected to cyclic vehicular loads. It is advisable to appropriately reduce the interface parameters generally obtained through constant rate of displacement pullout tests, as the reduction of interface parameters affects the shallower reinforcement levels, which are more susceptible to the pullout limit state.
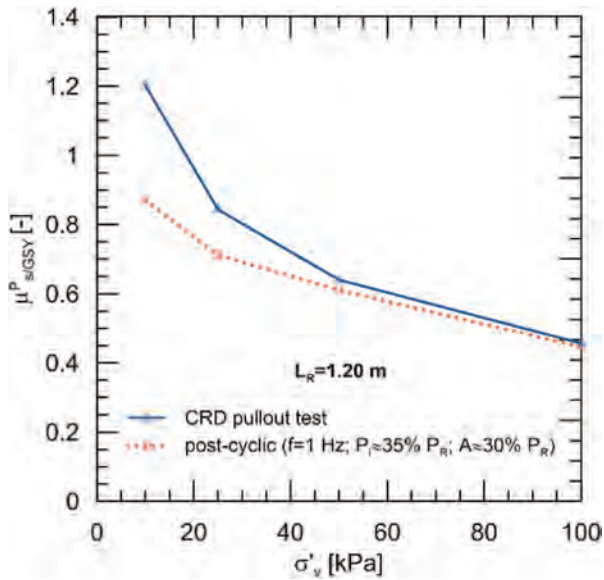
Figure 14. Comparison between apparent peak coefficients of friction evaluated under post-cyclic conditions and those obtained using CRD pullout tests for varying effective vertical stress (Cardile et al. 2019).

To more clearly explain the reduction of the interface design parameters in post-cyclic conditions, the results of two of the tests conducted (static and MS tests for σ'_v = 50 kPa, A ≈ 30% P_R and P_i=35% P_R) on the same interface are presented in a dual graph, plotting the displacement of the first confined section of the specimen, δ, against the confined average strain, ε, mobilised by a specific pullout load, P (Figure 15a).

Data points 1 and 5, which correspond to the beginning and end of the cyclic phase, reveal that compared to static result (CRD test), the application of the cyclic load results in more significant strain (ε) of the geogrid (due to viscous effects associated with the application of loading over time) as well as increased displacement of the first confined geogrid's section (δ). It implies that after the cyclic phase, the displacements of internal points along the specimen are greater than those mobilised in the corresponding reference static test at the same load level P_i (refer to the top of Figure 15b). As a result, as the pullout process progresses, the pullout load is transferred to a rapidly increasing portion of the geosynthetic, leading to a reduction in the "reserve" of pullout resistance available for the post-cyclic phase.

During the third phase of the test, the interface attempts to mobilise the same pullout resistance as it would have without the cyclic stage (the polymeric material itself does not degrade under cyclic loading, and it could still mobilise the ultimate tensile strength T_F, (Cardile et al. 2017b)), exhibiting a hardening behaviour. However, this is not possible due to the degradation of the interface. If the cyclic pullout load had not progressed the interaction mechanisms along the specimen, the post-cyclic δ-ε curve would have followed the "ideal" trend of the monotonic curve (path 5-7). In reality, the curve is more bent due to the effects of the cyclic load (path 5-8). Therefore, when the first confined section reaches the maximum displacement allowed by the pullout device (100mm, bottom of Figure 15b), the configuration of the displacements of the internal points of the geogrid (6b curve) deviates from the ideal trend (6a curve). The geogrid begins to deform less and reaches the pullout limit state sooner.

124
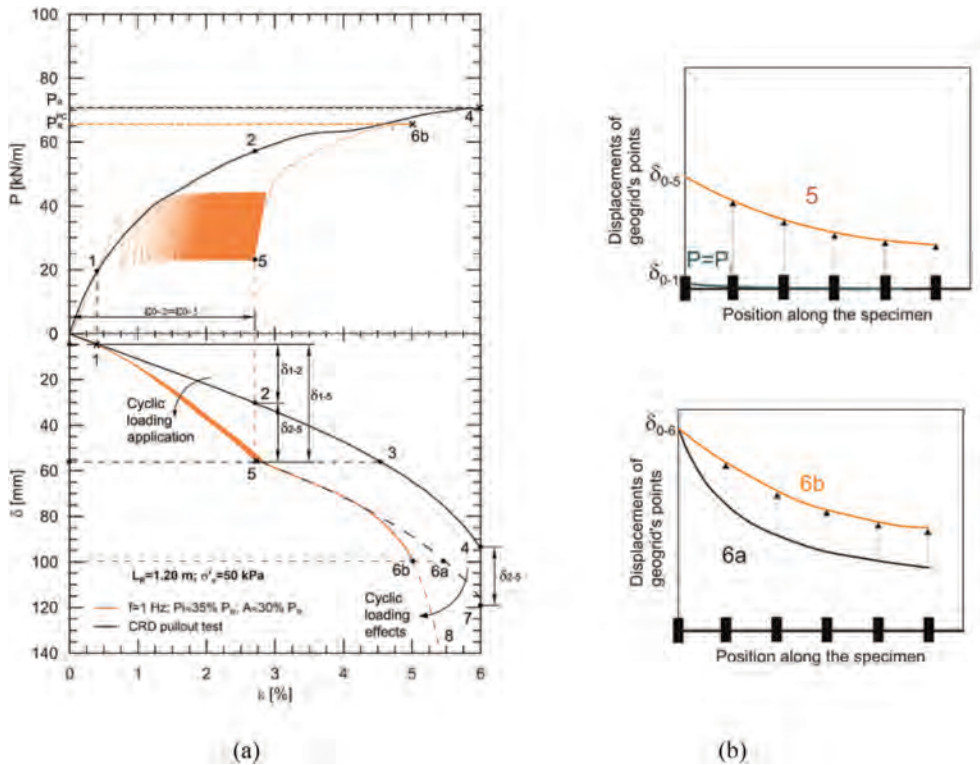
Figure 15. Comparison between P-ε and δ-ε trends obtained in CRD and multistage conditions (a) and qualitative distribution of the geogrid's points displacements in various phases of the test (b) (Cardile et al. 2019).

This outcome can affect the mobilisation of the maximum pullout resistance, namely the peak apparent coefficient of friction at the soil-geosynthetic interface. Reaching the geogrid average strain corresponding to the peak pullout resistance obtained under static conditions is still theoretically possible if the first confined section can undergo further displacement. However, this is only possible if the pullout limit state has not been reached (when the 6b-8 curve reaches a vertical asymptote, Figure 15a), as the geogrid can no longer deform and thus cannot increase the mobilised resistance.

2.3 Analytical modeling of the interface: A simplified approach

As previously discussed, the primary mechanisms influencing the pullout resistance of geogrids embedded in compacted soil are the skin friction between the soil and the solid surface of the reinforcement and the bearing resistance generated against the transverse members. Accordingly, the peak pullout resistance (P_R) of soil-geogrid interfaces is usually modelled as the sum of these two components:

$$P_R = P_{RS} + P_{RB} \tag{3}$$

where P_{RS} is the skin friction component of the peak pullout resistance, and P_{RB} is the bearing resistance component.

The pullout-loading force applied to the soil-geosynthetic system triggers the mobilisation of passive soil resistance in front of the transversal rib-bearing surface, leading to a rise in stress and a rotation of the principal stresses (Palmeira 2004). The pullout displacement of the geogrid creates a decrease in stress behind each transversal rib, producing a disturbed soil volume. If the subsequent bearing member is situated too close, perturbed soil volume may negatively impact the maximum bearing resistance developed along this geogrid member. For a fixed equivalent bearing member thickness (B_{eq}), the reduction in strength due to the interference phenomenon increases as the spacing (S) between consecutive transversal ribs decreases.

In recent years, various researchers have employed micro-image analysis systems to examine the pullout behaviour at the interface (Bathurst and Ezzein 2015a, b; Ezzein and Bathurst 2014; Zhou et al. 2012). This novel combination of technologies enables the measurement of the entire displacement field of the reinforcement and target particles seeded in the surrounding soil during pullout tests. Zhou et al. (2012) used micro-image analysis to capture the interaction mechanisms between compacted sand and the transverse ribs of the HDPE geogrid (by positioning the geogrid close to the glass side wall) and particle image velocimetry (PIV) technology for analysis, allowing it to be captured. Figure 16 displays particle motion around a transverse rib at various stages above and below the interface. Sand particles ahead of the transverse rib rotate during pullout, with particles above the longitudinal axis of the geogrid rotating clockwise and particles below the longitudinal axis rotating counterclockwise. Particles on the top right side of the transverse rib fall into the voids created by the movement of the geogrid in the softened region. The micro-image analysis confirms that the soil in front of the transverse rib is subjected to a passive state of stress, while behind it, an active state is reached, resulting in a loose soil region.

Furthermore, interference is affected by the thickness of the bearing member, referred to as Beq, and its relationship with the soil particle diameter (B_{eq}/D_{50}). The minimum ratio S/B_{eq}, beyond which interference affects pullout behaviour, decreases as the B_{eq}/D_{50} ratio increases (Sukmak et al. 2015). To provide a deeper understanding, a decrease in D_{50} generally reduces soil shear strength, impacting the softened region and shaping the failure plane that develops in front of the transverse ribs.

Cardile et al. (2017a) modified the theoretical method Moraci & Gioffrè (2006) devised to determine the maximum pullout resistance of geogrids extruded into compacted granular soil. This upgraded method is based on the results of several extensive pullout tests,
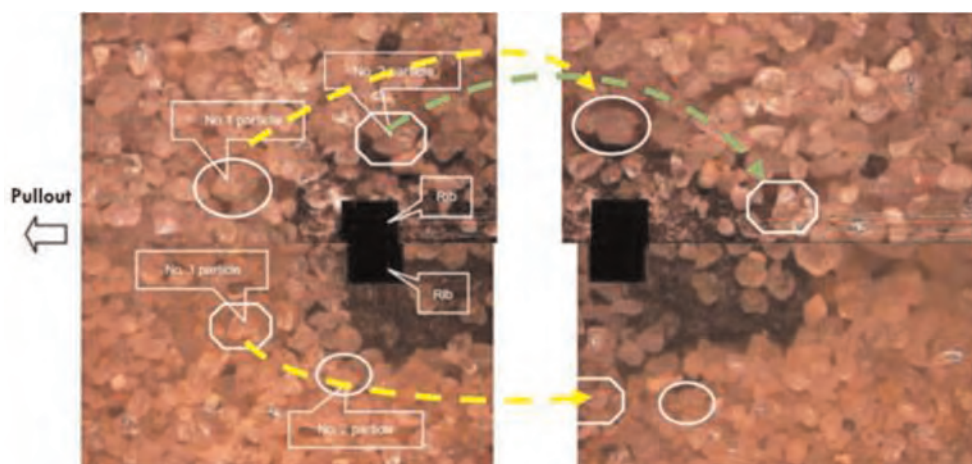
Figure 16. Particles motion around transverse rib (modified from Zhou et al. 2012).

including those performed by Calvarano et al. (2012), Cazzuffi et al. (2011) and Cazzuffi et al. (2014). The method is suitable for soil-geogrid interfaces where the scale effect is negligible and considers the nonlinear behaviour of compacted granular soils arising from dilatancy and the progressive mode of soil-geogrid interaction development resulting from the deformability of the reinforcement. The method is significant in the design and optimisation of geosynthetics, particularly in their geometry, shape, and stiffness. It also considers the interference mechanism in closely spaced bearing members, specifically when S/Beq is less than 50.

According to Cardile et al. (2017a), the pullout resistance can be evaluated using the following equation:

$$P_R = 2 \cdot C_{\alpha S} \cdot \alpha_S \cdot L_R \cdot \sigma_n^{'} \cdot \tan \delta + C_{\alpha b} \cdot n_t \cdot n_{tb} \cdot A_b \cdot \sigma_b^{'} \qquad (4)$$

where $C_{\alpha S}$ is a reduction coefficient to take into account the geogrid's area in which skin friction develops; δ is the mobilised friction angle between soil and the geogrid, which depends on soil dilatancy and reinforcement extensibility; $n_t = (L_R/S)$ is the number of geogrid's bearing members; n_{tb} is the number of nodes in a transverse element; A_b is the area of each rib element, which includes the single node and the bar portion between two nodes where the bearing resistance can be mobilised; and $C_{\alpha b}$ is a reduction coefficient taking into account the interference mechanism.

In their initial stage, Cardile et al. (2017a) conducted a study in which they sought to eliminate the impact of interfaces that had a non-negligible scale effect. They determined the value of $\sigma_b^{'EXP}$ using equation (4) to accomplish this objective by using the peak pullout resistance obtained through experimentation on those interfaces where the interference effect was negligible (i.e. $S/B_{eq} > 50$). This methodology allowed them to set $C_{\alpha b}=1$.

To facilitate a comparison between the experimental $\sigma_b^{'EXP}$ values obtained for various soil types, Figure 17 presents the results that have been normalised relative to the ($\sigma_n^{'} \tan \varphi'$) value. The data indicates that, beyond a threshold of $B_{eq}/D_{50} > 10$, the normalised bearing resistance is independent of the average grain size, regardless of the normal effective stress. Upon discovering this threshold, all the tested interfaces with a B_{eq}/D_{50} ratio greater than 10
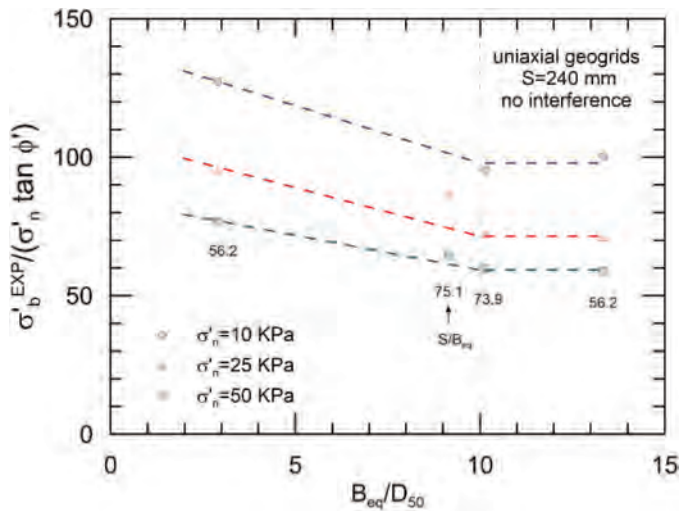
Figure 17.   Scale effect: results of pullout tests in terms of $\sigma_b^{'}/(\sigma_n^{'} \tan \varphi')$ ratio, carried out on different soils using uniaxial geogrids in which interference effect is negligible (Cardile et al. 2017a).

were analysed to determine the $C_{\alpha b}$ coefficient through the application of the following equation:

$$C_{\alpha b} = \frac{P_R^{Exp} - P_{RS}^{Theor}}{P_{RB}^{Theor}} = \frac{P_R^{Exp} - 2\alpha_S L_R \sigma_n' \tan \delta}{n_t \cdot n_{tb} \cdot A_b \cdot \sigma_b'} \tag{5}$$

where the peak pullout resistance P_R^{Exp} is obtained experimentally and σ_b' is evaluated using the equation proposed by Matsui et al. (1996).

P_{RS}^{Theor} component was evaluated using an average shear strength angle, calculated as the mean between the peak and constant volume values. This methodology facilitated the integration of both reinforcement extensibility and the nonlinear failure envelope of soil into the analysis of the mobilisation of interaction mechanisms. On the other hand, the P_{RB}^{Theor} component was evaluated by utilising the peak soil shear strength angles that corresponded to the various normal effective stresses.

Figure 18 shows the interference reduction factors $C_{\alpha b}$, which were determined through linear regression analysis for varying S/B_{eq} ratios. For S/B_{eq} values greater than 50, the interference effect can be considered negligible, leading to a $C_{\alpha b}$ factor equal to one. As a result, the $C_{\alpha b}$ interference reduction factor can be calculated using the following equation:

$$C_{\alpha b} = \begin{cases} \alpha \cdot \dfrac{S}{B_{eq}} & \dfrac{S}{B_{eq}} \leq 50 \\ 1 & \dfrac{S}{B_{eq}} > 50 \end{cases} \tag{6}$$

In equation (6), the constant coefficient α is equal to 0,02. In summary, the peak pullout resistance can be determined by combining Equations (4) and (6).
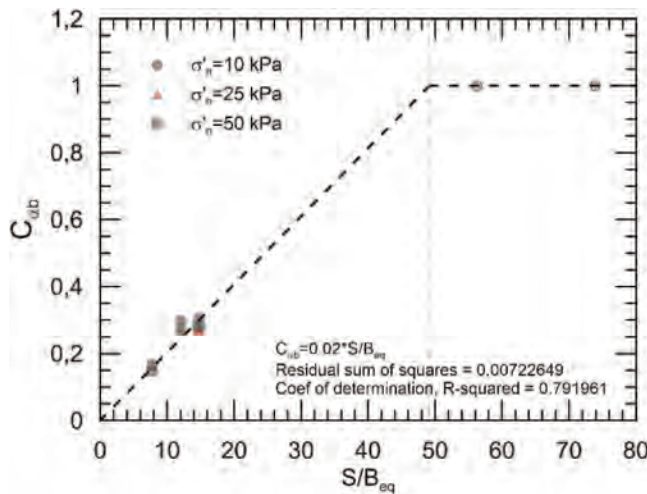
Figure 18. Variation of the reduction factor for the bearing resistance with varying the normalised spacing between transversal members (Cardile et al. 2017a).

Figure 19 compares experimental and theoretical values of the peak pullout resistance computed for selected interfaces. This comparison was conducted as part of the research undertaken by Cardile et al. (2017a) and was executed at different normal effective stress levels. The results of this comparison provide clear evidence of the efficacy and usefulness of the analytical method proposed.
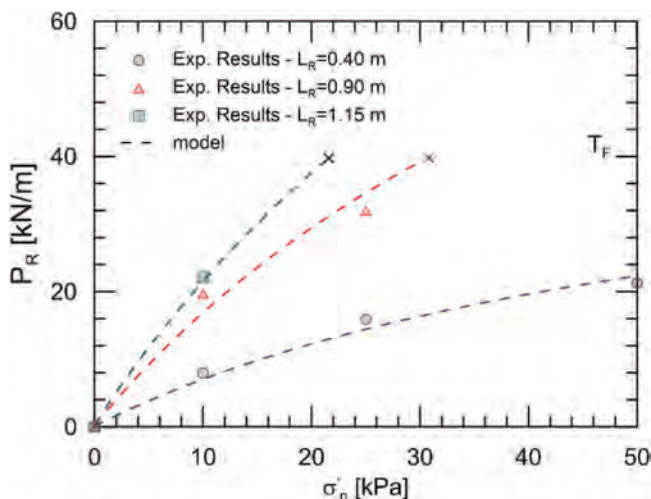
Figure 19.   Comparison between experimental and theoretical values of peak pullout resistance for a biaxial geogrid embedded in a compacted uniform medium sand (Cardile et al. 2017a).

3   CONCLUSIONS

The results summarised in the keynote, obtained through several experimental investigations conducted over the last 15 years, highlight the complexity of the interaction mechanisms that mobilise at the interface between geogrid and soil during the service life of a GRS wall. The evidence obtained under different load conditions (static, sustained, and cyclic) has allowed a detailed understanding of the complex load transfer mechanism under pullout conditions, identifying some critical aspects that are not yet fully codified in the design of such structures.

In particular, the research has highlighted the importance of viscous phenomena characterising the tensile-deformation behaviour of the polymeric geosynthetic reinforcement installed in the GRS structures. The mode and rate at which the tensile load is transferred along the reinforcement affect the mechanical behaviour of the geogrid and its interaction with the surrounding soil.

The complexity of load transfer mechanisms, dependent on the geometry, structure, and stiffness of the reinforcement and the geotechnical characteristics of the soil in contact, is amplified by the progressive failure phenomena characteristic of the pullout of long extensible reinforcements embedded in compacted soils.

It has been highlighted that the current codified design practice does not sufficiently consider the actual effects of the long-term behaviour of the geosynthetic-soil interface under pullout conditions. The first tests conducted through a prototype long-term pullout apparatus have allowed us to verify that the confinement offered by the compacted soil interferes with load transfer mechanisms, modifying the effects of tensile creep and improving the mechanical behaviour over time of the HDPE polymer material constituting the

geosynthetic. For these reasons, it could reach creep failure under confined conditions over a longer time than that modelled through current standard procedures performed in the absence of confinement. On the other hand, the effects of a constant pullout load over time cause a slow advancement of elementary interaction mechanisms along the anchored part of the reinforcement, causing deformed configurations of the structure that may not satisfy the serviceability for which it was designed. It is, therefore, necessary to consider these effects by adopting a design parameter at the interface calibrated through long-term pullout tests.

The experiments conducted through a new multistage pullout testing method, which alternates monotonic loading phases with a stage in which a sinusoidal pullout load of a given amplitude and frequency is applied, have allowed verification that contrary to current design practice, it would be advisable to reduce (especially at the lowest vertical confinement stresses) the interface parameters due to the degradation of the pullout resistance caused precisely by the cyclic loading phase. This more cautious approach should be adopted, especially in those areas most susceptible to seismic risk.

An in-depth analysis of the numerous experimental data produced on several soil-geosynthetic interfaces has also allowed the development of a simple theoretical model that predicts the pullout resistance mobilised under peak conditions, taking into account interference phenomena, soil dilation, and reinforcement extensibility.

ACKNOWLEDGEMENT

REFERENCES

ASTM D2487, 2017. *Standard Practice for Classification of Soils for Engineering Purposes (Unified Soil Classification System)*, ASTM, West Conshohocken, PA, USA.

ASTM D6706-01, 2013. *Standard Test Method for Measuring Geosynthetic Pullout Resistance in Soil*, ASTM, West Conshohocken, PA, USA.

Basu, D., Misra, A., Puppala, A.J., 2015. Sustainability and Geotechnical Engineering: Perspectives and Review. *Canadian Geotechnical Journal* 52, 96–113.

Basu, D. & Puppala, A., 2015. Principles of Sustainability and Their Applications in Geotechnical Engineering, in: IOS, A., Netherlands, (Ed.), Proceedings of 15th Pan-American Conference on Soil Mechanics and Geotechnical Engineering, Buenos Aires, Argentina, pp. 162–183.

Bathurst, R.J. & Ezzein, F.M., 2015. Geogrid and Soil Displacement Observations During Pullout Using a Transparent Granular Soil. *Geotechnical Testing Journal* 38, 1–13.

Brandl, H., 2011. Geosynthetics Applications for the Mitigation of Natural Disasters and for Environmental Protection. *Geosynthetics International* 18, 340–390.

BS 8006, 2010. *Code of Practice for Strengthened/reinforced Soils and Other Fills*. British Standards Institution, London, UK, 249 pp.

Calvarano, L.S., Cardile, G., Moraci, N. & Recalcati, P., 2012. The Influence of Reinforcement Geometry and Soil Types on the Interface Behaviour in Pullout Conditions, 5th European Conference on Geosynthetics - Eurogeo 5, Valencia, Spain, pp. 708–714.

Calvarano, L. S., Gioffrè, D., Cardile, G. & Moraci, N., 2014. A Stress Transfer Model to Predict the Pullout Resistance of Extruded Geogrids Embedded in Compacted Granular Soils. 10th International Conference on Geosynthetics, ICG 2014, 21–24 September. Berlin, Germany.

Cardile, G., Calvarano, L. S., Gioffrè, D. & Moraci, N., 2014. Experimental Evaluation of the Pullout Active Length of Different Geogrids. *10th International Conference on Geosynthetics, ICG 2014*, 21–25 September. Berlin, Germany.

Cardile, G., Gioffrè, D., Moraci, N. & Calvarano, L.S., 2017a. Modelling Interference between the Geogrid Bearing Members Under Pullout Loading Conditions. *Geotextiles and Geomembranes* 45, 169–177.

Cardile, G., Moraci, N. & Calvarano, L.S., 2016a. Geogrid Pullout Behaviour According to the Experimental Evaluation of the Active Length. *Geosynthetics International* 23, 194–205.

Cardile, G., Moraci, N. & Pisano, M., 2016b. In-air Tensile Load-strain Behaviour of HDPE Geogrids Under Cyclic Loading. *Procedia Engineering* 158, 266–271.

Cardile, G., Moraci, N. & Pisano, M., 2017b. Tensile Behaviour of an HDPE Geogrid under Cyclic Loading: Experimental Results and Empirical Modelling. *Geosynthetics International* 24, 95–112.

Cardile, G. & Pisano, M., 2020. Advances in Soil Reinforcement with Geosynthetics: From Laboratory Tests to Design Practice. *Rivista Italiana di Geotecnica*, 52–82.

Cardile, G., Pisano, M. & Moraci, N., 2019. The Influence of a Cyclic Loading History on Soil-geogrid Interaction under Pullout Condition. *Geotextiles and Geomembranes* 47, 552–565.

Cardile, G., Pisano, M. & Moraci, N. A. 2020. Predictive Model for Pullout Bearing Resistance of Geogrids Embedded in a Granular Soil. In: CALVETTI, F., COTECCHIA, F., GALLI, A. & JOMMI, C., eds. *Geotechnical Research for Land Protection and Development*, Cham. Springer International Publishing, 438–445.

Cardile, G., Pisano, M., Recalcati, P. & Moraci, N., 2021. A New Apparatus for the Study of Pullout Behaviour of Soil-geosynthetic Interfaces under Sustained Load Over Time. *Geotextiles and Geomembranes* 49, 1519–1528.

Cazzuffi, D., 1983. The Use of Geotextiles in Retaining Structures: Design Criteria and Experimental Investigations (in Italian: L'impiego Dei Geotessili Nelle Opere di Sostegno: Criteri di Progettazione e Indagini sperimentali), *Proceedings XV Italian Geotechnical Conference*, Vol. 3, pp. 311–320.

Cazzuffi, D., Calvarano, L.S., Cardile, G., Moraci, N. & Recalcati, P., 2011. European Experience in Pullout Tests: The Influence of Geogrid's Geometry and Structure on Interface Behaviour. *Geosynthetics* 29, 42–51.

Cazzuffi, D., Moraci, N., Calvarano, L.S., Cardile, G., Gioffrè, D. & Recalcati, P., 2014. The Influence of Vertical Effective Stress and of Geogrid Length on Interface Behaviour under Pullout Conditions. *Geosynthetics* 32, 40–50.

Chantachot, T., Kongkitkul, W. & Tatsuoka, F., 2018. Effects of Temperature Rise on Load-strain-time Behaviour of Geogrids and Simulations. *Geosynthetics International* 25, 287–303.

Christopher, B.R., 2014. Cost Savings by Using Geosynthetics in the Construction of Civil Works Projects, 10th International Conference on Geosynthetics, ICG 2014.

Correia, N.S. & Zornberg, J.G., 2016. Mechanical Response of Flexible Pavements Enhanced with Geogrid-reinforced Asphalt Overlays. *Geosynthetics International* 23, 183–193.

Damians, I.P., Bathurst, R.J., Adroguer, E.G., Josa, A. & Lloret, A., 2018. Sustainability Assessment of earth-retaining Wall Structures. *Environmental Geotechnics* 5, 187–203.

Derksen, J., Fuentes, R. & Ziegler, M., 2022. Geogrid-soil Interaction: Experimental Analysis of Factors Influencing Load Transfer. *Geosynthetics International*, 1–22.

Derksen, J., Ziegler, M. & Fuentes, R., 2021. Geogrid-soil Interaction: A New Conceptual Model and Testing Apparatus. *Geotextiles and Geomembranes* 49, 1393–1406.

Dixit, M.K., Fernández-Solís, J.L., Lavy, S. & Culp, C.H., 2010. Identification of Parameters for embodied Energy Measurement: A Literature Review. *Energy and Buildings* 42, 1238–1247.

Ezzein, F.M. & Bathurst, R.J., 2014. A New Approach to Evaluate Soil-geosynthetic Interaction using a Novel Pullout Test Apparatus and Transparent Granular Soil. *Geotextiles and Geomembranes* 42, 246–255.

Fang, Y.S., Yang, Y.C. & Chen, T.J., 2003. Retaining Walls Damaged in the Chi-Chi Earthquake. *Canadian Geotechnical Journal* 40, 1142–1153.

Frischknecht, R., Stucki, M., Büsser, S. & Itten, R., 2011. Comparative Life Cycle Assessment of Geosynthetics Versus Conventional Construction Materials. *Ground Engineering* 45, 24–28.

Giroud, J.P., 2005. Geosynthetics Engineering: Successes, Failures and Lessons Learned - The Vienna Terzaghi Lecture, Proceedings of 5. Osterreichische Geotechniktagung, Osterreichischer Ingenieur und Architekten Verein, Vienna, pp. 11–54.

Hirakawa, D., Kongkitkul, W., Tatsuoka, F. & Uchimura, T., 2003. Time-dependent Stress–strain Behaviour Due to Viscous Properties of Geogrid Reinforcement. *Geosynthetics International* 10, 176–199.

Huang, C.-C. & Wang, W.-C., 2005. Seismic Displacement of a Geosynthetic-reinforced Wall in the 1995 Hyogo-ken Nambu earthquake. *Soils and Foundations* 45, 1–10.

Huang, C.C., 2000. Investigations of Soil Retaining Structures Damaged During the Chi-Chi (Taiwan) Earthquake. *Journal of the Chinese Institute of Engineers* 23, 417–428.

ISO 14040, 2006a. Environmental Management – Life Cycle Assessment – Principles and Framework. *ISO, International Organization for Standardization*, Geneva, Switzerland.

ISO 14044, 2006b. Environmental Management – Life Cycle Assessment – Requirements and Guidelines. *ISO, International Organization for Standardization*, Geneva, Switzerland.

ISO/TR 20432, 2007. Guidelines to the Determination of Long-term Strength of Geosynthetics for Soil Reinforcement. *International Organization for Standardization, ISO*, Ginevra.

Jacobs, F., Ziegled, M., Vollmert, L. & Ehrenberg, H., 2014. Explicit Design of Geogrids with a Nonlinear Interface Model, X International conference on Geosynthetics, Berlin, Germany.

Jewell, R.A., Milligan, G.W.E., Sarsby, R.W. & Dubois, D., 1985. Interaction Between Soil and Geogrids, in: Telford, T. (Ed.), *Symposium on Polymer Grid Reinforcement in Civil Engineering*, pp. 18–30.

Koffler, A., Choura, M., Bendriss, A. & Zengerink, 2008. Geosynthetics in Protection Against Erosion for River and Coastal Banks and Marine and Hydraulic Construction. *Journal of Coastal Conservation* 12, 11–17.

Kongkitkul, W., Hirakawa, D., Tatsuoka, F. & Uchimura, T., 2004. Viscous Deformation of Geosynthetic Reinforcement under Cyclic Loading Conditions and its Model Simulation. *Geosynthetics International* 11, 73–99.

Kongkitkul, W., Tatsuoka, F. & Hirakawa, D., 2007. Creep Rupture Curve for Simultaneous Creep Deformation and Degradation of Geosynthetic Reinforcement. *Geosynthetics International* 14, 189–200.

Koseki, J., Bathurst, R.J., Guler, E., Kuwano, J. & Maugeri, M., 2006. Seismic Stability of Reinforced Soil Walls, *8th International Conference on Geosynthetics*, Yokohama,. Japan.

Koseki, J., Hayano, K., Watanabe, K. & Huang, C.C., 2000. Damage to Retaining Walls Caused by the 1999 Chi-Chi Earthquake and Model Tests on Seismic Behaviour of Retaining Walls, *International Workshop on Annual Commemoration of Chi-Chi Earthquake*, Taipei, pp. 251–262.

Koseki, J., Nakajima, S., Tateyama, M., Watanabe, K. & Shinoda, M., 2009. Seismic Performance of Geosynthetic-reinforced Soil Retaining Walls and their Performance-base Design in Japan, *Performance-Based Design in Earthquake Geotechnical Engineering*, Tokyo, Japan.

Kuwano, J., Miyata, Y. & Koseki, J., 2014. Performance of Reinforced Soil Walls During the 2011 Tohoku Earthquake. *Geosynthetics International* 21, 179–196.

Kwon, J., Tutumluer, E. & Kim, M., 2005. Development of a Mechanistic Model for Geosynthetic-reinforced Flexible Pavements. *Geosynthetics International* 12, 310–320.

Ling, H. & Leshchinsky, D., 2005. Failure Analysis of Modular-Block Reinforced-Soil Walls during Earthquakes. *Journal of Performance of Constructed Facilities* 19, 117–123.

Ling, H.I., Leshchinsky, D. & Chou, N.N.S., 2001. Post-earthquake Investigation on Several Geosynthetic-reinforced Soil Retaining Walls and Slopes During the Ji-Ji Earthquake of Taiwan. *Soil dynamics and earthquake engineering* 21, 297–313.

Masini, L., Callisto, L. & Rampello, S., 2015. An Interpretation of the Seismic Behaviour of Reinforced-earth Retaining Structures. *Géotechnique* 65, 349–358.

Matsui, T., San, K.C., Nabeshima, Y. & Amin, U.N., 1996. Bearing Mechanism of Steel Grid Reinforcement in Pullout Test, International Symposium on Earth Reinforcement, Fukuoka, Kyushu, Japan, pp. 101–105.

Moraci, N., (2011). Il rinforzo del terreno con geosintetici – recenti sviluppi tecnologici, progettuali e normativi. Relazione Generale. XXIV Convegno Nazionale Geotecnica. Innovazione Tecnologica nell'Ingegneria Geotecnica. Ed. AGI.

Moraci, N., Cardile, G. & Gioffrè, D., 2007. A Theoretical Method to Predict the Pullout Behaviour of Extruded Geogrids Embedded in Granular Soils, *5th International Symposium on Earth Reinforcement*, Fukuoka, Japan.

Moraci, N. & Cardile, G., 2008. Pullout Behaviour of Different Geosynthetics Embedded in Granular Soils. 4th Asian Regional Conference on Geosynthetics, 17 ÷ 20 June. Shanghai, China. 146–150.

Moraci, N. & Cardile, G., (2009). Influence of Cyclic Tensile Loading on Pullout Resistance of Geogrids Embedded in a Compacted Granular Soil. Geotextiles and Geomembranes, Vol. 27, pp. 475–487

Moraci, N. & Cardile, G., (2012). Deformative Behaviour of Different Geogrids Embedded in a Granular Soil Under Monotonic and Cyclic Pullout Loads. Geotextiles and Geomembranes, Vol. 32, pp. 104–110, (ISSN: 0266-1144), IF (2012) = 2.159. Q1. SJR (2012) = 2.637. DOI 10.1016/j.geotexmem.2011.11.001. Ed. Elsevier. Scopus Index = 2-s2.0-84976443910.

Moraci, N., Cardile, G. & Pisano, M., 2017. Soil-geosynthetic Interface Behaviour in the Anchorage Zone [Comportamento all'interfaccia terreno-geosintetico nella zona di ancoraggio]. Rivista italiana di geotecnica 51, 5–25.

Moraci N., Cazzuffi D., Calvarano L.S., Cardile G., Gioffrè D. & Recalcati P. (2014). European Experience in Pullout Tests: Part 3. The Influence of Soil Type on Interface Behaviour under Pullout Conditions. Geosynthetics, Vol. 32, 3, pp.42–50

Moraci, N. & Gioffrè, D. (2006). A Simple Method to Evaluate the Pullout Resistance of Extruded Geogrids Embedded in a Compacted Granular Soil. Geotextiles and Geomembranes, Vol. 24, pp.116–128.

Moraci N., Cardile G., Gioffre' D, Mandaglio M.C., Calvarano L.S. & Carbone L., (2014). Soil Geosynthetic Interaction: Design Parameters From Experimental and Theoretical Analysis. Transportation Infrastructure Geotechnology. Vol.1, 2, pp.165–227

Moraci, N. & Montanelli, 1997. F. Behavior of Geogrids Under Cyclic Loads. *Geosynthetics '97*, March. Long Beach, CA, USA.

Moraci, N. & Recalcati, P., 2006. Factors Affecting the Pullout Behaviour of Extruded Geogrids Embedded in Compacted Granular Soil. *Geotextiles and Geomembranes* 24, 220–242.

Morsy, A.M. & Zornberg, J.G., 2021. Soil-reinforcement Interaction: Stress Regime Evolution in Geosynthetic-reinforced Soils. Geotextiles and Geomembranes 49, 323–342.

Morsy, A.M., Zornberg, J.G., Leshchinsky, D., Christopher, B.R., Han, J. & Tanyu, B.F., 2020. Experimental Evaluation of the Interaction among Neighboring Reinforcements in Geosynthetic-Reinforced Soils. Journal of Geotechnical and Geoenvironmental Engineering 146, 04020107.

Palmeira, E., 2016. Sustainability and Innovation in Geotechnics: Contributions from Geosynthetics. Soils and Rocks 39, 113.

Palmeira, E.M., 2004. Bearing Force Mobilisation in Pull-out Tests on Geogrids. Geotextiles and Geomembranes 22, 481–509.

Palmeira, E.M., 2009. Soil–geosynthetic Interaction: Modelling and Analysis. Geotextiles and Geomembranes 27, 368–390.

Palmeira, E.M., Tatsuoka, F., Bathurst, R.B., Stevenson, P.E. & Zornberg, J.G., 2008. Advances in Geosynthetics Materials and Applications for Soil Reinforcement and Environmental Protection Works. Electronic Journal of Geotechnical Engineering 13, 1–38.

Perkins, S.W. & Cuelho, E.V., 1999. Soil-geosynthetic Interface Strength and Stiffness Relationships from Pullout Tests. Geosynthetics International 6, 321–346.

Perkins, S.W. & Ismeik, M., 1997a. A Synthesis and Evaluation of Geosynthetic-Reinforced Base Layers in Flexible Pavements- Part I. Geosynthetics International 4, 549–604.

Perkins, S.W. & Ismeik, M., 1997b. A Synthesis and Evaluation of Geosynthetic-Reinforced Base Layers in Flexible Pavements- Part II. Geosynthetics International 4, 605–621.

Pisano, M., Cardile, G. & Moraci, N., 2019. Soil-geogrid Interface Behaviour under Cyclic Pullout Conditions. *7th International Conference on Earthquake Geotechnical Engineering (VII ICEGE)*, 17–20 June. Roma (Italy).

Sandri, D., 1997. A Performance Summary of Reinforced Soil Structures in the Greater Los Angeles Area after the Northridge Earthquake. Geotextiles and Geomembranes 15, 235–253.

Sukmak, K., Sukmak, P., Horpibulsuk, S., Han, J., Shen, S.-L. & Arulrajah, A., 2015. Effect of Fine Content on the Pullout Resistance Mechanism of Bearing Reinforcement Embedded in Cohesive–Frictional Soils. Geotextiles and Geomembranes 43, 107–117.

Tatsuoka, F., 2008. Geosynthetics Engineering, Combining Two Engineering Disciplines, *4th Geosynthetics Asia - Special Lecture*, Shanghai, Cina, pp. 1–35.

Tatsuoka, F., Hirakawa, D., Shinoda, M., Kongkitkul, W. & Uchimura, T., 2004. An Old but New Issue; Viscous Proprieties of Polymeric Geosynthetic Reinforcement and Geosynthetic-reinforced Soil Structures, *3rd Asian Regional Conference on Geosynthetics*, Seoul, Korea, pp. 29–77.

Tatsuoka, F., Koseki, J. & Tateyama, M., 1995. Performance of Geogrid-reinforced Soil Retaining Walls During the Great Hanshin-Awaji Earthquake, January 17, 1995. *Earthquake Geotechnical Engineering Journal*, 55–62.

Tatsuoka, F., Koseki, J. & Tateyama, M., 1997. Performance of Reinforced Soil Structures during the 1995 Hyogo-ken Nanbu Earthquake. Special Lecture, *International Symposium on Earth Reinforcement* (IS Kyushu'96), Balkema, Vol.2, pp. 973–1008.

Teixeira, S.H.C., Bueno, B.S. & Zornberg, J.G., 2007. Pullout Resistance of Individual Longitudinal and Transverse Geogrid Ribs. Journal of Geotechnical and Geoenvironmental Engineering, 37–50.

Touze-Foltz, N., Bannour, H., Barral, C. & Stoltz, G., 2016. A Review of the Performance of Geosynthetics for Environmental Protection. Geotextiles and Geomembranes 44, 656–672.

UNI EN ISO 13431, 2002. *Geotessili e prodotti affini - Determinazione delle proprietà di viscosità a trazione (tensile creep) e comportamento a rottura (creep rupture)*. Ente Nazionale Italiano di Unificazione, Milano.

UNI EN ISO 14688-1, 2018. *Indagini e prove geotecniche - Identificazione e classificazione dei terreni - Parte 1: Identificazione e descrizione*. Ente Nazionale Italiano di Unificazione, Milano.

Wallbaum, H., Büsser, S., Itten, R., Frischknecht, R., 2014. Environmental Benefits by Using Construction Methods with Geosynthetics, *10th International Conference on Geosynthetics, ICG 2014*.

Wang, Z., Jacobs, F. & Ziegler, M., 2014. Visualisation of Load Transfer Behaviour between Geogrid and Sand using PFC2D. *Geotextiles and Geomembranes* 42, 83–90.

Wartman, J., Rondinel-Oviedo, E.A. & Rodriguez-Marek, A., 2006. Performance and Analyses of Mechanically Stabilized Earth Walls in the Tecomán, Mexico Earthquake. *Journal of Performance of Constructed Facilities* 20, 287–299.

White, D.M. & Holtz, R.D., 1994. Performance of Geosynthetic-Reinforced Slopes and Walls During the Northridge, California Earthquake of January 17, 1994*, Earth Reinforcement: Proceedings of the International Symposium on Earth Reinforcement*, IS-Kyushu '96, Fukuoka, Kyushu, Japan, pp. 965–972.

Wu, H., Huang, B., Shu, X. & Zhao, S., 2015. Evaluation of Geogrid Reinforcement Effects on Unbound Granular Pavement Base Courses Using Loaded Wheel Tester. *Geotextiles and Geomembranes* 43.

Yang, S.-H. & Al-Quadi, I.L., 2007. Cost-effectiveness of Using Geotextiles in Flexible Pavements. *Geosynthetics International* 14, 2–12.

Zhou, J., Chen, J.-F., Xue, J.-F. & Wang, J.-Q., 2012. Micro-mechanism of the Interaction between sand and Geogrid Transverse Ribs. *Geosynthetics International* 19, 426–437.

Zornberg, J.G. & Kavazanjian Jr, E., 2001. Prediction of the Performance of a Geogrid-reinforced Slope Founded on Solid Waste. *Soils and Foundations* 41, 1–16.

Sustainable development: UK perspective on the role of geosynthetics

D.R.V. Jones
WSP UK Limited

N. Dixon
Loughborough University

G. Fowmes
Warrwick University

P. Guerra Escobar
Geosynthetics Limited

G. Horgan
Huesker Limited

D. Shercliff
ABG Limited

K. Zamara
Tensar International Limited

ABSTRACT: There is a growing realization that the current model of development is unsustainable. In other words, we are living beyond our means. Climate change is the defining crisis of our time, and it is happening even more quickly than we feared. Rising temperatures are fueling environmental degradation, natural disasters, weather extremes, food and water insecurity, economic disruption, conflict, and terrorism. Sea levels are rising, the Arctic is melting, coral reefs are dying, oceans are acidifying, and forests are burning. The goal of sustainable development is to enable all people throughout the world to satisfy their basic needs and enjoy a better quality of life, without compromising the quality of life of future generations. This paper will provide a perspective from the UK on how geosynthetics are supporting the global cause of limiting climate change. Examples of sustainable geosynthetic solutions are given from a team of UK researchers and practitioners.

1   INTRODUCTION

This paper is the written version of the keynote lecture delivered to the 12th International Conference on Geosynthetics in Rome, Italy in September 2023. It presents a brief summary of the UK government policy on sustainable development in the context of the United Nations Sustainability Development Goals. It aims to show how geosynthetics can support sustainable development with focus on six of the Sustainability Development Goals. The paper considers ways of measuring the sustainability of civil engineering projects with a focus on Life Cycle Analysis and embodied carbon assessment. Examples are presented of sustainable development using geosynthetics and these include accelerated embankment consolidation, reinforced bund construction with contaminated cohesive fill, temporary working platform construction, pavement construction, instrumented and "smart" geosynthetics and

finally active geosynthetics. These examples, whilst not all from the UK, present a brief insight into sustainable development using geosynthetics from a UK perspective.

2 UNITED NATIONS SUSTAINABILITY GOALS

The United Nations has set out 17 Sustainable Development Goals (SDGs) as part of the 2030 Agenda for Sustainable Development (United Nations 2016), and these are depicted in Figure 1. These high-level goals are designed to influence national decisions, and focus the scale and priorities for funding, with each country facing specific range and combination of challenges. The SDGs are:

- Goal 1 – No Poverty: End poverty in all its forms, everywhere.
- Goal 2 – Zero Hunger: End hunger, achieve food security and improved nutrition, and promote sustainable agriculture.
- Goal 3 – Good Health and Well-being: Ensure healthy lives and promote well-being for all at all ages.
- Goal 4 – Quality Education: Ensure inclusive and equitable quality education and promote lifelong learning opportunities for all.
- Goal 5 – Gender Equality: Achieve gender equality and empower all women and girls.
- Goal 6 – Clean Water and Sanitation: Ensure availability and sustainable management of water and sanitation for all.
- Goal 7 – Affordable and Clean Energy: Ensure access to affordable, reliable, sustainable, and modern energy for all.
- Goal 8 – Decent Work and Economic Growth: Promote sustained, inclusive, and sustainable economic growth, full and productive employment, and decent work for all.
- Goal 9 – Industry, Innovation, and Infrastructure: Build resilient infrastructure, promote inclusive and sustainable industrialization, and foster innovation.
- Goal 10 – Reduced Inequalities: Reduce inequality within and among countries.
- Goal 11 – Sustainable Cities and Communities: Make cities and human settlements inclusive, safe, resilient, and sustainable.
- Goal 12 – Responsible Consumption and Production: Ensure sustainable consumption and production patterns.
- Goal 13 – Climate Action: Take urgent action to combat climate change and its impacts.
- Goal 14 – Life Below Water: Conserve and sustainably use the oceans, seas, and marine resources for sustainable development.

Figure 1. UN sustainability goals launched in January 2016 (United Nations 2016).

- Goal 15 – Life On Land: Protect, restore, and promote sustainable use of terrestrial eco-systems, sustainably manage forests, combat desertification, and halt and reverse land degradation and biodiversity loss.
- Goal 16 – Peace, Justice, and Strong Institutions: Promote peaceful and inclusive societies for sustainable development, provide access to justice for all, and build effective, accountable, and inclusive institutions at all levels.
- Goal 17 – Partnerships for the Goals: Strengthen the means of implementation and revitalize the global partnership for sustainable development.

These goals provide a comprehensive and ambitious agenda for sustainable development, addressing a wide range of economic, social, and environmental challenges facing the world today. Kraus (2022) argues that the SDGs need to be considered within the context of remaining within the "planetary boundaries concept" developed by Stockholm University (Rockström et al., (2009). The authors state that crossing the nine defined planetary boundaries increases the risk of generating large-scale abrupt irreversible environmental changes. Kraus (2022) argues that there is a fundamental tension between the minimum resources required for human development and the planetary boundaries and presents the "doughnut" model developed by Raworth (2012).

Figure 2. The "doughnut" model proposed by Raworth (2012).

The Doughnut consists of two concentric rings: an inner social foundation, to ensure that no one is left falling short on life's essentials, and an outer ecological ceiling, to ensure that humanity does not collectively overshoot the planetary boundaries that protect Earth's life-supporting systems. Between the two boundaries lies an area – shaped like a doughnut – which represents an environmentally safe and socially just space for humanity to live in. It is also the space in which inclusive and sustainable economic development takes place.

Kraus (2022) discusses the interaction of geosynthetics with the planetary boundaries and gives examples of the positive effects geosynthetics can have on the climate change boundary. It could be argued that geosynthetics can also have a positive impact on all other planetary boundaries particularly with the reduction of greenhouse gases (GHGs), air pollution and chemical pollution.

3 UK GOVERNMENT POLICY

The UK government's policy on sustainable development is guided by the SDGs and is based on a holistic approach that takes into account economic, social, and environmental considerations. The UK government has committed to achieving these goals by 2030 and has set out a plan for doing so in its 25 Year Environment Plan, published in 2018 (Defra 2018). It's approach to sustainable development involves balancing economic growth with social and environmental considerations, which aims to create a prosperous and sustainable economy that benefits everyone, while protecting and enhancing the natural environment. The 25 Year Environment Plan outlines a range of policies and initiatives aimed at achieving this goal by reducing GHG emissions, protecting and restoring natural habitats, promoting sustainable consumption and tackling equality and poverty.

The UK government has set a legally binding target of net zero greenhouse gas emissions by 2050 which was supported by all main political parties. The Climate Change Act 2008 committed the UK to an 80% reduction in carbon emissions relative to the levels in 1990, to be achieved by 2050, then in June 2019, secondary legislation was passed that extended that target reduction to "at least 100%". The UK government has introduced a range of measures to achieve the target, including investing in renewable energy, encouraging energy efficiency, and promoting low-carbon transport. There is a focus on zero carbon operation of infrastructure but no mention of savings during the construction phase. However, the UK construction industry has developed a strategy articulated in the report Construction 2025 (HM Government 2013), which identifies low carbon and sustainable construction as a strategic priority of the industry, with an ambition to reduce GHG emission by 50% by 2025. There is an expectation that GHG emission will be a criterion used to select construction solutions and all major projects will have to have GHG evaluation as part of their environmental assessment. To date, there is no independent assessment of the likelihood that the construction industry will meet the 2025 target.

In the UK, the pre-eminent professional body for construction is the Institution of Civil Engineers (ICE). This body is leading debate and knowledge transfer to help deliver a reduction in carbon emissions produced by construction and infrastructure activities (e.g. Skinner 2020). Infrastructure is responsible for more than half of the UK's carbon emissions, which justifies the significance given by the ICE to this challenge. In recent years, the ICE has produced a range of opinion pieces and information to enable the engineering community to make a meaningful contribution to meeting the UK's net zero target. For example, Skinner (2020) selected achieving net zero carbon as the focus for her prestigious and high-profile Presidential Address, and as the primary theme for her year in office. The ICE has established a Decarbonisation Community Advisory Board to facilitate collaboration, share knowledge and best practice, and hence deliver low-carbon solutions across the construction sector. Solutions incorporating geosynthetics are contributing to the achievement of this goal, but more can still be done.

4   USING GEOSYNTHETICS TO SUPPORT SUSTAINABLE DEVELOPMENT

Geosynthetics are synthetic materials used in civil engineering and construction projects to enhance the performance of soil, rock, and other materials. They can be used to support sustainable development in a number of ways including:

4.1   Goal 2 – zero hunger

Geosynthetics can be used to stabilize soil and prevent erosion, which helps to protect ecosys-tems, reduce water pollution, and maintain soil fertility. Heibaum (2010) describes how surface erosion can be reduced by the use of geosynthetics, and Touze (2021) presents example of how geosynthetics can improve crop protection by drainage of agricultural land, promoting germination and plant growth through using ground cover and control of growing conditions, pests and insects. Touze (2021) gives example of the use of geosynthetics in fish farming thus reducing the pressure on wild fish stock, and also using geosynthetics to support the management of agricultural waste through manure storage and sludge man-agement, and the production of energy from waste through anaerobic digestion. Geosynthetic solutions can also be used to create, shelter and regulate the internal envir-onment in agricultural buildings which has a positive effect on livestock yields and geosyn-thetics also contribute to the capture, storage and distribution of water, see below.

4.2   Goal 6 – clean water and sanitation

Geosynthetics can be used in the construction of dams, canals, and other water management structures, helping to conserve water resources, prevent flooding, and mitigate the effects of drought. Koerner et al. (2008) described a geosynthetics freshwater cycle for capture, transportation, storage and distribution of freshwater, and Touze (2021) presents examples of the use of geosynthetics in three main elements of this cycle, namely dams, canals and pipes. In addition, Touze (2021) gives examples of how geosynthetics can be used to preserve water quality.

4.3   Goal 7 – affordable and clean energy

Geosynthetics can be used to support the development of renewable energy sources such as wind and solar power, by providing stable foundations for infrastructure and reducing the environmental impact of construction.

4.4   Goal 9 – industry, innovation and infrastructure

Geosynthetics can be used to build roads, bridges, and other infrastructure more efficiently, reducing the use of resources and minimizing the environmental impact of construction. In paved and unpaved roadways, geotextiles and other materials are used as a separating layer or to improve soil performance and capabilities. In these cases, the geosynthetics are covered with asphalt, concrete, or on-site soils. Geogrids are used to reduce construction footprint by steepening slopes and allowing the use of site-won soils limiting the importation of virgin aggregate.

4.5   Goals 14 and 15 – life below water and life on land

Geosynthetics can provide useful support to pollution control and thus improving the quality of life on land and below water. Minimising the impact of waste on the environment is a key aspect of geosynthetics use worldwide and this comprises using barrier systems to limit contaminant migration from landfill bodies, prevent water infiltration into waste

bodies and prevention of uncontrolled gas migration to atmosphere. New geosynthetic permeable re-active filters selectively protect the underground from the contaminant while allowing the carrier medium to pass through. contaminated water percolates through the filter, the transport of the pollutants is stopped, but the water can follow its natural flow path into the underground unimpeded and thus continue to serve as a potential habitat, water reservoir, nutrient reservoir. These goals are also supported by the use of geosynthetics in mining applications where the operation of heap leach pads, tailings storage facilities and mine waste storage facilities benefit from geosynthetic containment.

In addition to these specific applications, geosynthetics can support sustainable development by improving the efficiency, safety, and durability of civil engineering and construction projects. By enabling the construction of more sustainable and resilient infrastructure, geosynthetics can help to support the long-term economic, social, and environmental well-being of communities and regions around the world.

5 ASSESSING SUSTAINABILITY OF GEOSYNTHETICS

5.1 *Carbon footprint*

Carbon footprint is a measure of the total amount of greenhouse gases (primarily carbon dioxide) caused directly and indirectly by a person, organisation, event or product. It is measured in tonnes of carbon dioxide equivalent (tCO2e). A carbon footprint can cover emissions over the whole life of a product, service or a construction solution and embodied carbon (EC) is an indicator of cumulative carbon emissions used in the solution adopted. Dixon et al. 2017 show an example subdivision of a hypothetical material and processes contributing to the EC of an end product, such as a geosynthetic, see Figure 3.

It should be noted that sometimes Embodied Energy is reported in place of Embodied Carbon. Conversion between the two measures needs knowledge of the CO2 emitted during generation of the energy used (Defra 2013). This is country specific and hence is a challenging calculation to undertake as information on mixes of energy sources is sparse and this currently makes international comparisons difficult. Comparison of calculated carbon
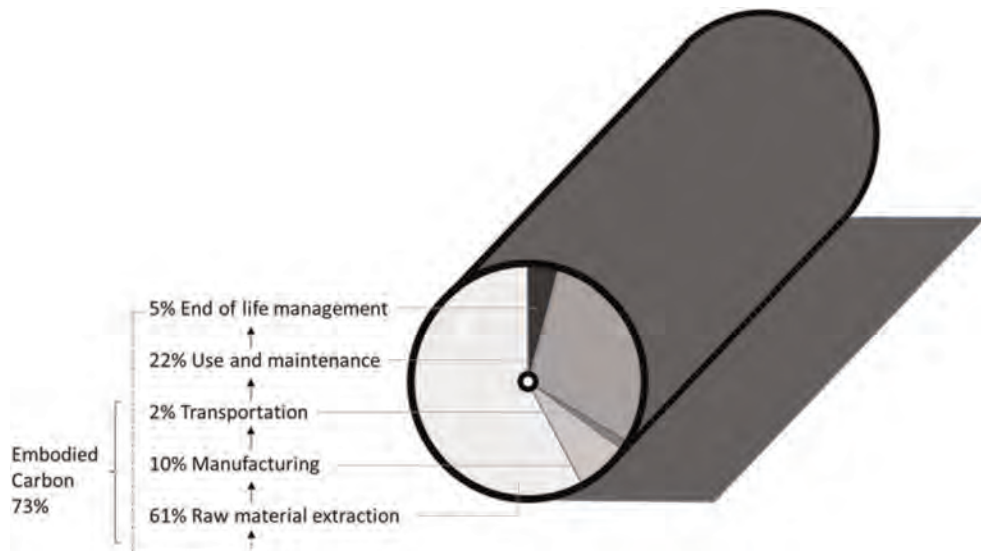
Figure 3. Example of contributions to the EC of a geosynthetic product (after Dixon et al. 2017).

footprints for alternative solutions can be used to inform selection of the most 'sustainable' option. A site-by site approach can consider project specifics such as available materials on-site and nearby, supply logistics, site layout, method of construction etc.

Assessing the carbon footprint can support sustainable development in several ways. Firstly, measuring or calculating a carbon footprint can help raise awareness of the impact of human activities on the environment and climate change. By understanding the amount of carbon emissions associated with various activities, individuals, businesses, and governments can take action to reduce their carbon footprint through selection of solutions with least emissions and hence minimize the impact of their actions on the environment. Secondly, the carbon footprint can be used as a basis for setting targets to reduce greenhouse gas emissions. By setting targets to reduce carbon footprint, businesses and governments can take action to reduce their environmental impact and work towards achieving sustainable development. Once targets have been set, ongoing measurement of the carbon footprint can be used to quantify the progress towards meeting them. Businesses and governments can assess the effectiveness of their sustainability initiatives by tracking changes in carbon emissions over time, and then adjust their strategies as needed to achieve their goals. Measuring carbon footprint can also encourage innovation by promoting the development of new technologies and practices that reduce greenhouse gas emissions.

5.2 *Life cycle analysis*

Life Cycle Assessment (LCA) is a tool for measuring the environmental impact of products or systems over their lifetime. It can consider extraction of raw materials, through production, use, recycling and disposal of waste, and provides a systematic and comprehensive approach to evaluating the environmental impacts of products and processes. LCA is often used to compare the impact of two competing products or systems, with the analysis process informed by ISO14040 (ISO 2006a) and ISO14044 (ISO 2006b) or other approved tools. LCA boundaries are clearly defined boundary conditions and are required to describe which parts of the material production, manufacture and deployment are taken into account in calculating the carbon footprint. Typically used LCA are shown in Figure 4 mapped against the stage of product manufacture and application.

There is a growing trend for product manufacturers (e.g. concrete, steel, geosynthetic) to develop in-house carbon calculators for quantifying LCA of products and designs that can be used for comparisons between alternative solutions. While this is a welcome development, in some cases these are perceived as being marketing tools and there is a danger that they will be considered unreliable, in part due to a lack of transparency of the method and material EC values employed. There is need for a geosynthetics industry standard approach endorsed
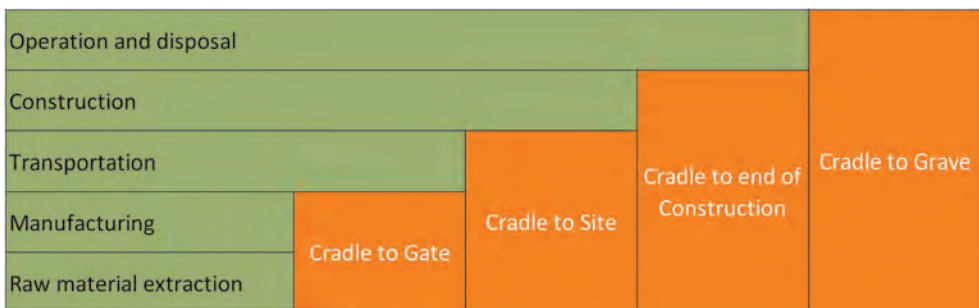
Figure 4. Life Cycle Analysis boundaries for typical stages of geosynthetic product manufacture and application.

by geosynthetic manufacturers and suppliers, recognised and trusted by construction organisations and clients.

A number of geosynthetic manufacturers have started to provide independently verified Environmental Production Declarations (EPDs). Construction products are assessed using a single set of Product Category Rules (PCR) ensuring consistent reporting for similar products. EPDs for construction products in Europe use EN 15804 (2019), as their PCR, to ensure that the information is provided using the same LCA rules and boundary conditions, with the same environmental indicators, and in a way that means the information for different products can be brought together to provide the environmental impacts for adopted solutions.

5.3 *LCA for geosynthetic solutions*

There is a growing body of literature detailing studies of the sustainability credentials for geosynthetic based solutions. While all use EC as a measure, a subset also considers a wider range of criteria for a broader evaluation of sustainability including: cumulative energy demand; photochemical ozone formation; particulate formation; acidification, eutrophication, land competition; and water use. The large majority use EC for the geosynthetic products taken either from the ICE database (Hammond & Jones 2011) and earlier versions of the EcoInvent Centre (2016) databases. Whilst the number of case studies using product specific EC values is growing, a direct comparison between case studies is not possible because the type of study varies, with some using project level information and others defining functional units of a given application/solution, and in addition different ranges of LCA boundaries are employed, however, general trends can be identified.

The UK Waste & Resources Action Programme (WRAP) published a report in 2010 (WRAP, 2010) which delivered an accessible report with a very clear unambiguous conclusion that construction solutions incorporating geosynthetics led to significant cost and CO_2 savings. The European Association of Geosynthetic Manufacturers (EAGM) commissioned a study of the environmental performance of solutions using commonly applied construction materials versus geosynthetics. The findings of the in-depth analysis are reported by Stucki et al. (2011). The study provided comprehensive qualitative and quantitative information on the environmental performance of commonly applied construction materials (i.e. concrete) versus geosynthetics. The key finding from this study is that geosynthetic based solutions are consistently assessed as more 'sustainable' using a range of environmental performance measures.

Since these two early studies, many authors have presented the results of a variety of projects such as: assessment of geosynthetic solutions in steep slope and road applications (Heerten, 2012), analysis of EC for a landfill capping project (Raja et al. 2014), environmental assessment of earth retaining wall structures (Damians et al. 2016), non-reinforcement applications of geotextiles (Dixon et al. 2016; Koerner et al. 2019; Whitty et al. 2020).

Some geosynthetics manufacturers have recently introduced a range of geosynthetics produced from 100% recycled polymers, and whilst consideration should be given to the impact of recycled polymer use has on the end product properties, material produced from recycled polyester for example, it stated to require 59% less energy in its manufacturing compared to virgin polyester (Huesker 2023).

These 'new' recycled products have already been applied in asphalt and soil reinforcement applications and are subject to the same manufacturing quality assurance and certification standards as virgin polymer counterparts. The use of recycled material within geosynthetic additionally supports the sustainability benefits of a circular economy preventing the disposal to landfill in the first instance and its reuse again at end of its current life/form as a geosynthetic.

6 EXAMPLE OF SUSTAINABLE SOLUTIONS USING GEOSYNTHETICS

Polymer based geosynthetics represent high embodied energy materials (Raja et al. 2015) and their sustainability benefits come from their careful use within wider geosystems rather than the materials themselves. The following examples present case histories which demonstrate the environmental benefits of using a range of geosynthetics and promote the United Nations' SDGs.

6.1 Example 1: Accelerated embankment consolidation

A large distribution centre needed considerable areas of earthworks and ground improvement to enable the rapid construction of a new logistics and business park to provide 770,000 m² of logistics floor space. A large proportion of this development was constructed on weak soil and it was first necessary to drain the sub-formation using prefabricated vertical drains with a horizontal geocomposite drainage blanket. The enabling works involved a 9 m change in site elevation levels and the embankment fill and sub-formation required consolidation before foundations for the new sheds could be constructed. Additional horizontal geocomposite drainage layers were placed at 3 m vertical intervals to accelerate the rate of consolidation by up to 70%.
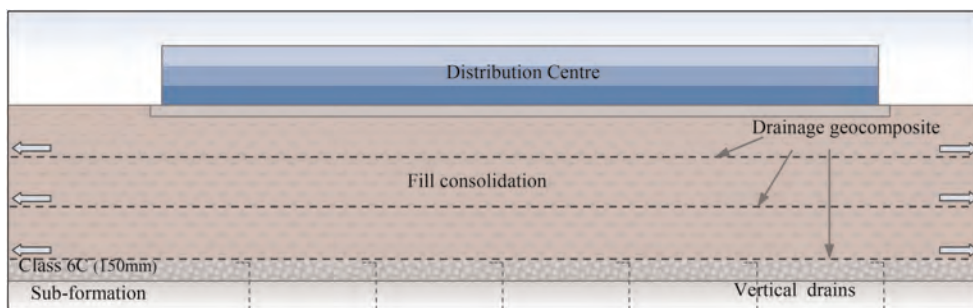
Figure 5.   9 m of ground level rise ready to receive logistic sheds showing starter and consolidation geocomposite drain layers.

Each of the geocomposite drainage layers replaced an equivalent performance 150 mm stone drainage saving on stone transportation and carbon production impact. 31 deliveries of geocomposite replaced 8,000 aggregate deliveries. Total savings using the geocomposite resulted in 2,998 tonnes of embedded carbon, cradle to end of construction savings for 400,000 m² of treated area.

6.2 Example 2: Reinforced bund with geosynthetics using contaminated cohesive fill

This example describes the construction of a visual and acoustic bund to separate a new housing development from a neighboring metal recycling facility, located in Coventry, East Midlands, UK. The bund required to be 9.5 m high and 450 m long with a 2 m fence on top. The design solution included the use of 80,000 m³ of hydrocarbon and heavy metal contaminated fill, that otherwise would have gone into landfill. The dimensions of the base footprint were reduced by designing the bund was a geogrid reinforced soil slope with a 70 deg face angle on the external face and a 26 deg slope on the internal face.

The contaminated fill was provided from local construction sector and imported under license and treated on site prior to being used in the bund construction. The imported

Figure 6. Placement of starter layer geocomposite prior to raising of formation level (ABG Geosynthetics Ltd).

material was managed in accordance with the Development Industry Code of Practice (CL: AIRE 2011) and an environmental permit that promoted the sustainable use of waste soils. Site specific hazard and environmental risk assessments ensured that reusable soils did not pose a threat to the environment of future users of the site.

The imported fill was a dry cohesive/stoney cohesive Class 2A/2C soil, in accordance with Standards for Highways (2017), and the design was carried out in accordance with BS 8006 (2010) and BS EN 1997-1 (2004).
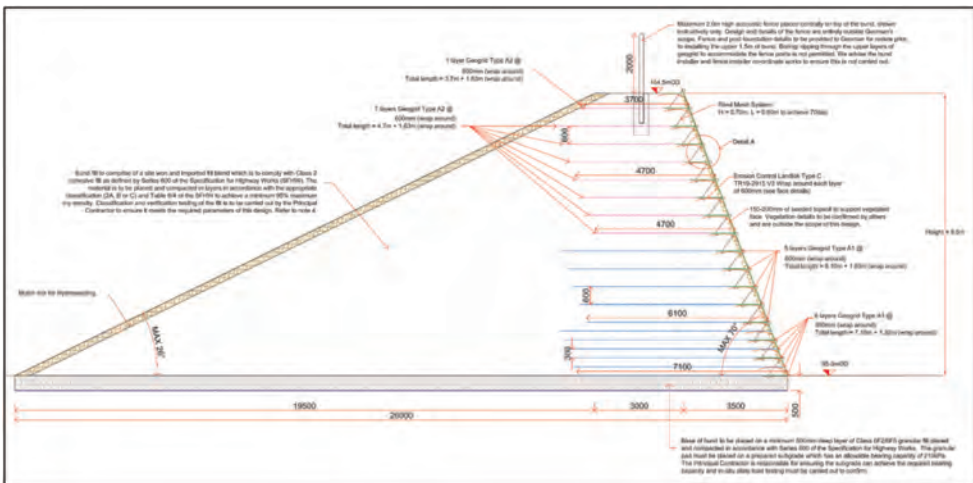
Figure 7. Cross-section Visual and Acoustic Bund – Reinforced Soil Bund (Geosynthetics Ltd).

While the sustainability benefits of re-using a fill that would otherwise go to landfill are self-evident, a calculation of the total CO_2 emissions associated with the materials used for the bund was performed using the UK National highways carbon tool, taking into consideration the principles of PAS 2080 (2016) to quantify, promote and deliver a low carbon solution for the project. The analysis was carried out for the Product and Construction process stages, to compare the CO_2 footprint of the reinforced bund using geosynthetics versus a conventional unreinforced solution using selected granular material Cass 6I/6J (Standards for Highways (2017) for the bund.

Table 1. Reinforced soil bund, carbon calculations for materials.

OPTION 1: Reinforced Soil Bund Materials	Total CO2e (Tonnes)	3,315.65								
Classification under National Highways Carbon Tool	Description	Item (National Highways)	Type (National Highways)	Unit	Quantity	Carbon Factor Value	Carbon Factor Unit	Conversion Factor	tCO2e
Bulk Materials: Civil Structures	Fill material for bund Class 2A/2C (contaminated fill from local construction sites, imported and treated on site)	Fill, Aggregate and sand	Recycled Resources, no heat treatment	Tonnes	142,299.79	0.0061	tCO2e/t	1.00	867.360
Earthworks	Mulch mix for Hydroseeding (for 1:2 slope. Note: slope 70deg protected with Landlok)	Imported soil	General soil/topsoil	Tonnes	23.00	0.024	tCO2e/t	1.00	0.552
Earthworks	Stratagrid SGU for slope reinforcement	Geosynthetics	PP/PET/PE	m2	56,050.00	2.36	tCO2e/t	0.001	132.278
Earthworks	Landlok TRM for Erosion control	Geosynthetics	PP/PET/PE	m2	11,899.40	2.42	tCO2e/t	0.001	28.797
Civil Structures	Steel mesh A252 and Hooks H10: formwork face 70deg slope	Steelwork (Rivel mesh face)	General Steel	Tonnes	41.30	1.55	tCO2e/t	1.00	64.015
	Materials CO2e (Tonnes)								**1,093.00**

Calculations were carried out for the selected reinforced soil bund solution and a traditional bund bult from granular fill and are presented in the tables below.

From the calculations in Tables 1 and 2 it can be seen that the total carbon for this option was 3,315 tCO2e. This is considerably lower than the value calculated for the second option of 7,843 tCO2e, see Tables 3 and 4. This comprises a 58% reduction in the carbon footprint of the bund.

Using geogrids for the reinforced soil bund allowed the use of contaminated cohesive fill that would otherwise be transported and disposed into a landfill. The reinforced solution provided significant benefits such as less excavation, less disposal of unsuitable material, less vehicle movements, less land required for the construction of the bund and costs reduction.

6.3 Example 3: Temporary working platforms on HS2

Temporary working platforms are increasingly becoming an important element of construction. They support heavy construction site equipment such piling rigs and cranes, where ground conditions do not carry enough bearing capacity to withstand heavy loadings.

Table 2. Reinforced soil bund, carbon calculations for transport.

Transport					
Classification under National Highways Carbon Tool	Description	Transport mode	Transport distance value (km)	Carbon Factor (tCO2e/t. km)	tCO2e
Bulk Materials: Civil Structures	Fill material for bund Class 2A/2C (contaminated fill from local construction sites, imported and treated on site)	HGV	80	0.0000975	2,219.88
Earthworks	Mulch mix for Hydroseeding (for 1:2 slope. Note: slope 70deg protected with Landlok)	Van	60	0.0004219	1.164
Earthworks	Stratagrid SGU for slope reinforcement	HGV	18	0.0000975	0.197
Earthworks	Landlok TRM for Erosion control	HGV	18	0.0000975	0.042
Civil Structures	Steel mesh A252 and Hooks H10: formwork face 70deg slope	HGV	170	0.0000975	1.369
		Transport CO2e (Tonnes)			**2,222.65**

Table 3. Conventional soil bund, carbon calculations for materials.

OPTION 2: Traditional bund with Granular imported material, without reinforcement Materials	Total CO2e (Tonnes)	7,843.57							
Classification under National Highways Carbon Tool	Description	Item (National Highways)	Type (National Highways)	Unit	Quantity	Carbon Factor Value	Carbon Factor Unit	Conversion Factor	tCO2e
Bulk Materials: Civil Structures	Granular material Class 6I/6J (Selected material from construction sites, imported and selected)	Fill, Aggregate and sand	Recycled and secondary mixture	Tonnes	220,077.00	0.0142	tCO2e/t	1.00	3,120.692
Earthworks	Mulch mix for Hydroseeding (for 1:2 slope, both sides)	Imported soil	General soil/top-soil	Tonnes	46.00	0.024	tCO2e/t	1.00	1.104
Waste	Contaminated soil from local construction sites	Aggregate and soil exported off-site	Landfill	Tonnes	142,299.80	0.0012	tCO2e/t	1.00	176.309
	Materials CO2e (Tonnes)								**3,298.11**

Table 4. Conventional soil bund, carbon calculations for transport.

Transport					
Classification under National Highways Carbon Tool	Description	Transport mode	Transport distance value (km)	Carbon Factor (tCO2e/t.km)	tCO2e
Bulk Materials: Civil Structures	Granular material Class 6I/6J (Selected material from construction sites, imported and selected)	HGV	80	0.0000975	3433.201
Earthworks	Mulch mix for Hydroseeding (for 1:2 slope, both sides)	Van	60	0.0004219	2.329
Waste	Contaminated soil from local construction sites	HGV	40	0.0000975	1109.938
		Transport CO2e (Tonnes)			**4,545.47**

Figure 8. Installation of the working platform at HS2 Stoneleigh Park (Tensar International Ltd).

Geogrids are now routinely installed in temporary working platforms, as they offer contractors cost, time and carbon savings compared to alternative non-stabilised solutions.

This case study presents a classic example where a temporary working platform utilising stabilising geogrids was constructed at the mega project High Speed Rail 2 (HS2) in the UK. A working platform was required for the Stoneleigh Park Overbridge, Warwickshire, for piling operations, which needed to address the issues of high rig track pressures over a variable subgrade. Using reinforcing geogrids in the working platform design means that significant aggregate thickness reductions can be achieved. This contributes to reduced construction time platform installation, and significant savings on carbon emissions.

Utilizing publicly available design and value calculation methodology (www.TensarPlus. com) design solution and quantification of cost and environmental benefits, compared with non-stabilised alternative, was estimated as follow:

- £250,000 (65%) estimated reduction in construction cost;
- 15 days (75%) estimated reduction in construction time; and
- 100,000 CO2e (75%) estimated saving in carbon emissions.

The above represents a typical saving on a relatively small size platform (this example was around 5,000 m^2).

6.4 *Example 4: Pavements Construction, Essex UK*

Geogrids are also often utilized in surfaced or non-surfaced (temporary or permanent) pavement designs. They allow for reduction in aggregate thicknesses required in the design solution, maintaining the same performance as the alternative non-geogrid solutions. In addition to that, pavement utilizing stabilisng geogrids allow for increased lifespan of the construction, contributing to reduction of maintenance costs for the asset owners.

To facilitate the construction of a new road at North Heybridge, a mechanically stabilised layer incorporating geogrid was used to act as a capping over low strength soils (Figure 9). This was required to achieve a Foundation Class 1 as required by the project specification from the Design Manual for Roads and Bridges CD 225 – Design for new pavement foundations (Standards for Highways 2020).

A cost-effective solution was required when low strength subgrade soils were encountered across the site. The pavement design needed to achieve a prescribed CD225 foundation class to allow the client to adopt the carriageway. Project granular fill costs were high as it was being imported from outside of the local area, and so a geogrid based solution was adopted to meet the CD225 foundation requirements as well as dealing with construction trafficking close to the low strength subgrade. The stabilised capping layer reduced granular fill quantities, as well as project excavation operations and also offered a more sustainable solution by reducing the carbon footprint of construction and transportation activities.

Figure 9.   Installation of the pavement capping layer at North Heybridge (Tensar International Ltd).

Design solution and quantification of cost and environmental benefits, compared with non-stabilised alternative, was calculated as:

- £177,000 (54%) estimated reduction in construction cost;
- 12 days (50%) estimated reduction in construction time; and
- 80,000 CO2e (57%) estimated saving in carbon emissions.

6.5   *Example 5: Instrumentation and "Smart" geosynthetics*

As previously discussed, the sustainability benefits can come from the careful use of geo-syntheyics within wider geosystems, and so over-specifying the quantity or grade of geosynthetic, through either poor design, or excessive conservatism will have a detrimental impact to the sustainability of the project. Conversely under-specification can lead to catastrophic failures and reputational damage to not only those involved, but the geosynthetics industry as a whole. It remains imperative that we fully understand the mechanisms of interaction between the geosynthetics and the surrounding environment and are able to validate our designs against measured performance. Whilst there is ever increasing complexity of numerical assessment of geosynthetic performance, validation against measured in situ performance remains scarce. Instrumentation allows us to measure performance but is inherently challenging due i) the often-aggressive environment ii) technical installation of appropriate sensors iii) selection and installation of sensors that do not, by their presence, alter the behaviour of the geosynthetics.

To date, much of the instrumentation applied to geosynthetics has focussed on physical strain measurement. Zamara et al. (2022) summarised the types of instrumentation available, in this case for geogrids, but also applicable across a wide variety of geosynthetics and they were broadly categorised as foil type strain gauges, fibre optic instrumentation, strain meters and conductive coatings or elements.

Fibre optics have attracted significant attention as a method of installing a chemically inert corrosion resistant sensor. Zamara et al. (2012) reported successful instrumentation of geomembranes across a fixed 500 mm gauge length using fibre bragg gratings which allow strain measurement as an average value between main point of attachment whilst Chen *et al.* (2015) report use of distributed optical fibre sensors that allow strain measurement independent of the node fixities. More recently, promising results were shown in the work by Xu et al. (2022) where fibre optics were integrated into geogrids for ground movement detection systems.

Sensor development is evolving with material and manufacturing techniques. Hatami et al. (2014) considers a tensoresistive PVC coating whilst Bi et al. (2023) highlight the use of Flexible conductive materials which are widely used in other forms of structural health monitoring and can be adapted to allow strain measurement in conductive geosynthetics. Whilst challenges remain of how such coatings or materials would be applied in the geosynthetic manufacture and installation processes, they offer more opportunities to the industry to adopt these techniques.

Increasing we are seeing the use of Smart Geosynthetics where sensors are incorporated into or onto geosynthetics and couple with sensing technologies and advances in data processing and visualization allowing for more efficient design, operation and maintenance of construction and infrastructure assets.

Radar detectable geosynthetics are an early example of this technology where radar detectable strips are incorporated in a geosynthetic. In 2001, Terram produced a thermally bonded non-woven polypropylene incorporating a 50 mm wide aluminium foil. The addition of the stripe of electrically conductive material, which is an extremely good reflector of radar energy, was the key to both improving the accuracy of depth prediction of GPR surveys, and providing additional diagnostic tools to assess changes in the condition of ballast over time and deterioration in formation and development of soft spots.

Figure 10. Non-woven polypropylene incorporating a 50 mm wide aluminium foil (Terram Ltd).

These early radar geotextiles did not prove to provide long term effectiveness as a measuring system principally due to the degradation of the reflective strip. More recent developments have incorporated more durable reflective strips and enhanced reflectivity.

Figure 11. Radar detectable geosynthetic.

The increased durability of the sensing strip coupled with enhancement in the Ground Penetrating Radar technology (GPR) and its visualization are allowing for better classification and condition of the penetrated ground and allow more informed decisions as to the existing condition and health of the infrastructure for planned interventions and maintenance and provide potentially an early warning system of sub-formation geohazards, depending on the frequency of GPR readings. Radar Detectable Geosynthetics are a relatively low-tech example of smart geosynthetics.

A more sophisticated form of smart geosynthetics is Optical Fibre Integrated Geosynthetics (OFIG) which combine geosynthetics with fibre optic technology. The optical fibre can take a number of forms such as Fibre Bragg gratings, Simulated Brillouin Scattering, Raman Scattering and Distributed Fibre Optic Sensing (DFOS). DFOS enables
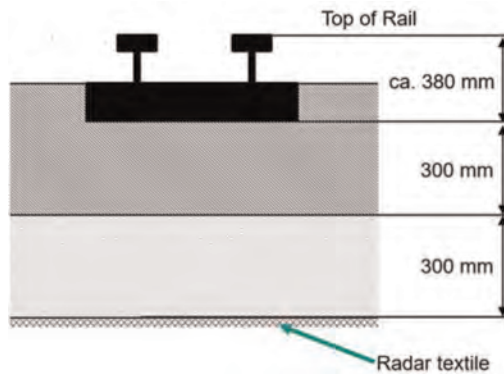
Figure 12. Section indicating RDG in track ballast renewal.
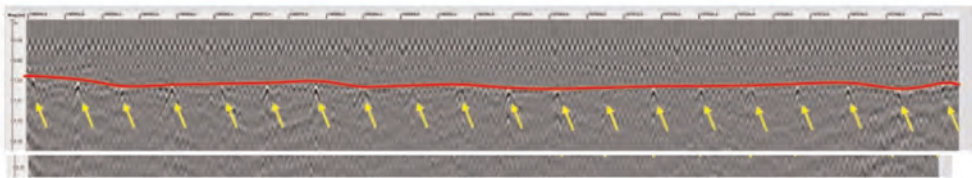
Figure 13. Ground penetrating Radar plot with clear chevron of reflective strip.

Figure 14. Improved visualization technology with GDPR.

measurement of temperature, strain, and acoustic energy distributions along the entire length of a fibre optic sensing cable (Kerchavarzi et al. 2016; Xu et al. 2022).

The incorporation of DFOS cables into the ground could provide significantly improved information on the location and magnitude of subsurface ground movement and subsidence (Möller et al. 2022) and have reported that the quality of fibre optic sensing data is highly reliant on the mechanical coupling between fibre optic cables and their surrounding soil.

A recent fibre optic-instrumented geogrid (Sensorgird) was developed in collaboration between Huesker, the Centre for Smart Infrastructure and Construction at the University of Cambridge and Epsimon Ltd. This fibre optic-instrumented geogrid was recently deployed to monitor potential ground movement beneath a 100 m long, 10 m wide stretch of the mainline alignment on the HS2 site at Tilehouse Lane Cutting, where the cutting though chalk had highlighted a number of solution features, the condition of the infill material varies, and voids are occasionally present. Engineered mitigation has been constructed for the highest risk features, but this approach is not sustainable for the whole of the affected area.

The cutting is being utilised during construction for the transportation of the Colne Valley viaduct concrete segments units. The units are to be transported through the cutting on self-propelled mobile transporters. The fibre optic-instrumented geogrid installation is centred

around a new over bridge over the cutting where the clearance envelope around the over-bridge is limited and the presence of potentially unmapped chalk solution features in the chalk cutting developing while transporting the viaduct units posed an unacceptable ground risk which could significantly impact the delivery of the project.

To mitigate the residual risk, a geogrid-reinforced mattress is constructed over the area. This will span any potential voids that migrate to the formation depicted either side of cement stablised layer indicated orange in Figure 15, with the fibre optic-instrumented geogrid being installed beneath this to enable identification of movements occurring beneath the reinforced mattress, (Xu et al. 2022).
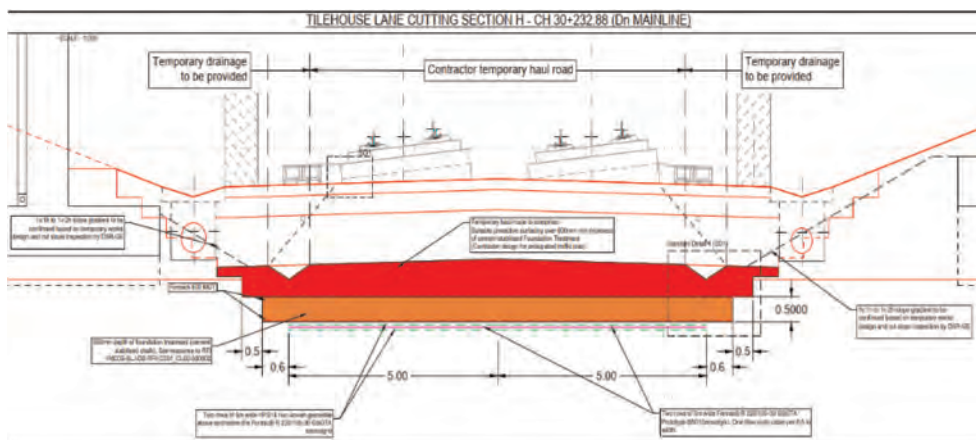
Figure 15.   Cross section though construction haul road/mainline at Tilehouse Lane Cutting.

Prior to its use in the mainline a field trail was initiated on site as 'proof of concept' of the fibre optic-instrumented geogrid with the following intended trail outcomes:

- Realistic field-scale data (scalability);
- Real-world test of fibre/grid arrangement (sensitivity);
- Assessment of fibre resilience to damage in a construction environment (durability);
- Comparison with traditionally measured deformations (usability);
- Test dataset to assess post processing requirements (near real-time?);
- Opportunity to explore temporal visualisation (early warning of surface movement);
- Explore requirements for field installation & check robustness (splicing, protection, etc); and
- Confirm any changes to fibre or general set-up in advance of Tilehouse Lane Cutting works.

Controlled field tests were first performed on two simulated sinkholes using 3x3m pits in which water-filled bags were placed and covered with stabilised chalk and granular soils. By deflating the bags in varying sequences, the captured strain signature profiles from the instrumented geogrid were compared with displacement measurements from conventional instrumentation, to assess the geogrid's sensitivity to millimetre-scale settlements.

Separate onsite durability tests were conducted adjacent to the trial pit area to simulate the construction process that it would encounter on site in Tilehouse Lane Cutting which included placement and levelling of a stabilised chalk fill over the fibre optic-instrumented
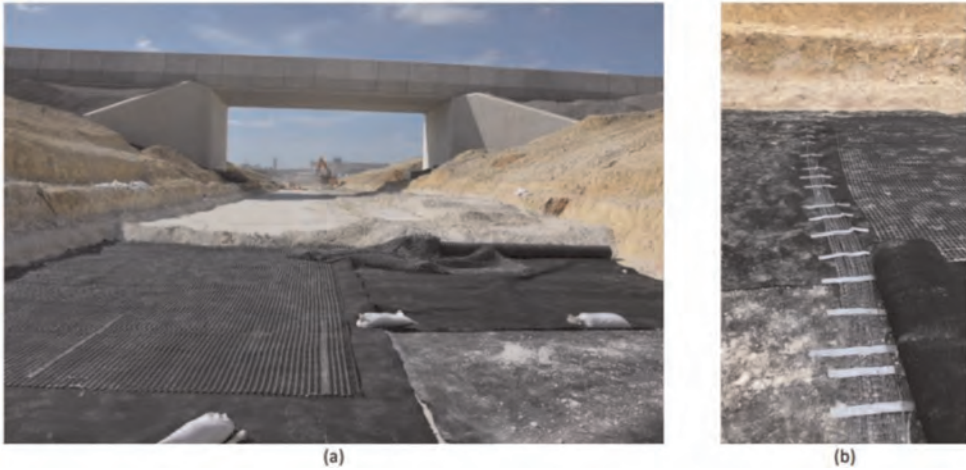
Figure 16: Installation of fibre optic-instrumented geogrid and supporting geogrid at Tilehouse Lane Cutting (Huesker Ltd.)

geogrid, and compaction of that fill with eight passes of a 20-tone vibratory roller. For all treatments, the optical power measured along the fibre optic cables integrated in the fibre optic-instrumented geogrid was measured and some unacceptable losses of signal were observed which were likely due to excessive bending in the fibres generated by sharp aggregates.

Figure 17. Visualization dashboard displaying strains in monitored section at Tilehouse lane cutting.

The fibre optic cables used in these two trials were 2.5 mm in diameter and consisted of single-mode optical fibre with a 0.9 mm Hytrel coating embedded in an elastic 2.5 mm polyurethane outer sheath. They were knitted into a geogrid by substituting it for yarns of similar size. They were subsequently substituted with a more robust cable following on from on-site installation trials.

The data acquired from the fibre optic cables is automatically processed and displayed in real-time on a web-based visualisation dashboard. This enables the project engineers to detect any incipient ground movement below the road surface in the monitored section, enabling them to take timely preventative action if necessary.

Smart geosynthetics that incorporate simple and sophisticated sensors which potentially allow for the non-intrusive, continuous, remote monitoring of critical infrastructure network can highlight their deterioration to allow for the potential for planned interventions and maintenance. This is preferable to the reactivate/emergency interventions moreover they are able to provide early warning of geohazards whether these geohazards occur naturally due to the local geology or a legacy of underground mineral extraction.

6.6 *Example 6: Active geocomposites*

Active geocomposites can be installed as large-area contaminant filters respectively barriers for soil and groundwater protection as well as for remediation of contaminated sites. These newly developed geosynthetic contaminant barriers allow protection of the clean subsoil and groundwater by filtration of pollutants from seepage or runoff (i.e., persistent organic pollutants, including per- and polyfluoroalkyl substances (PFAS), heavy metals, oil, and petrochemicals). The current standard, in which subsoil and groundwater protection is ensured by sealing, is overcome by the contaminant filters. As a result, the subsoil retains its natural function as a water reservoir, nutrient store, and habitat. Geosynthetic contaminant filters are also used for site remediation. In sediment or soil capping applications they avoid or reduce earthworks with transportation and landfilling of contaminated soil/sediments.

In many places, anthropogenic processes generate substances with negative effects on the environment and/or human health. These substances move with carrier media (water, gas) or on carrier substances (particles, dust). Volatile substances move with the air, dissolved substances disperse with water, and bound substances move with particles to which they adhere. They can enter the body through inhalation, fluid ingestion, or through our food. Medical research is increasingly revealing the effects of the uptake of these substances in our bodies. A very recent example is the persistent pollutant group of PFAS. As a result, interrupting the pathways of pollutant effects has long been a high priority in environmental engineering.

The use of geosynthetic contaminant filters (GCF) protects the subsurface by collecting only the environmentally relevant contaminant, but not the carrier medium. The concept offers innovative groundwater protection without removing the water from the natural cycle. This also has the advantage that the soil below the GCF continues to be available, for example, as a water reservoir during heavy rain events and, if necessary, as a planting area.

The term geosynthetic contaminant filter refers to a new product group in the field of geosynthetics. It includes products consisting of at least two layers of geotextiles sandwiching an amendment material (Figure 18). Due to its novelty, the term has not yet been standardized. In some cases, therefore, different terms are used, such as sorption mats or geotextile contaminant barrier. However, all terms refer to the same product group.

The geotextile components consist of woven and/or nonwoven. They are joined together by mechanical bonding techniques, such as needle-punching or stitching. GCF have a coefficient of permeability $k \geq 1 \times 10^{-5}$ m/s. This is important to ensure that the contaminated water (in other applications also suitable for contaminated gas) can flow through the filter. This free flow ensures that the natural water flow remains unaffected. The geotextile components take on various application-specific functions. For example, they not
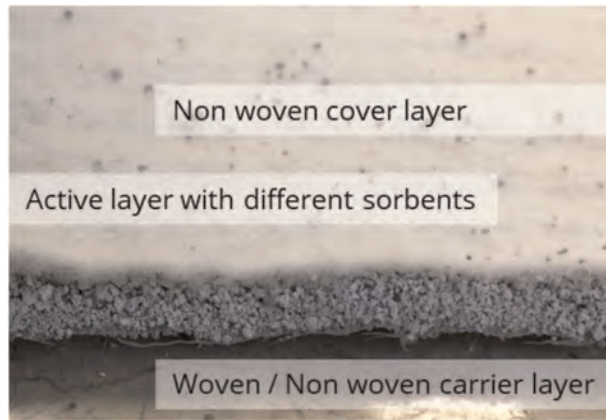
Figure 18.   Detailed view on geosynthetic contaminant filter (Huesker Ltd).

only serve as a carrier for the amendments, but also perform other important tasks in the field of pollutant filtration (acc. to ISO 10318-1):

- Reinforcement: use of the stress-strain behaviour of a geosynthetic material to improve the mechanical properties of soil or other construction materials;
- Separation: prevention from intermixing of adjacent dissimilar soils and/or fill materials by the use of a geosynthetic material; and
- Filtration: restraining of uncontrolled passage of soil or other particles subjected to hydrodynamic forces, while allowing the passage of fluids into or across a geosynthetic material.

The durability of the materials is also important. The pollutants must be chemically isolated until they decompose naturally. This process can sometimes take several decades, so the geotextiles must also have a similar life expectancy. Oxidation tests can be used to simulate the ageing of the geotextile components to make statements about their service life *in situ*. A life expectancy of 100 years can be considered normal for quality manufactured geotextiles which have been correctly installed and exposed to natural conditions with soil pH values of $4 \leq pH \leq 9$ and soil temperatures of $\leq 25 \,°C$.

Amendments are materials that remove and bind environmentally relevant substances/contaminants from a liquid or gaseous carrier medium. Since not every amendment is suitable for every pollutant, the most suitable type must be selected for the specific application. For this selection, the pollutant must be sufficiently known. Relevant pollutants can initially be divided, for example, into water-soluble and non-water-soluble substances.

An example of a non-water-soluble, i.e. non-polar, group of substances is hydrocarbons. For these pollutants, active substances can be used that absorb non-polar substances and at the same time are resistant to contamination by the oil itself. Special absorbent polymers fulfil these properties. They bind hydrocarbons in their inner structure and thus separate them from the runoff. The absorbent material can bind many times more oil than their own weight.

Water-soluble pollutants can be further divided into organic and inorganic substances. Organic pollutants include compounds such as polycyclic aromatic hydrocarbons, polychlorinated biphenyls or PFAS. A prominent active ingredient for the removal of these substances from water is activated carbon. Due to its mesoporous structure, activated carbon has a very large surface area. For example, 10 g of activated carbon, made from coconut shells, has a surface area the size of a soccer field. This surface area is important because the

Table 5. German preliminary max. permissible concentrations for corresponding recovery classes (BMUV 2022).

PFAS congeners	RC 1 Unrestricted open replacement (μg/l)	RC 2 Restricted open replacement in areas with elevated PFAS concentration (μg/l)	RC 3 Restricted emplacement in technical structures with defined safety measures (μg/l)
Perfluorobutanoic acid, PFBA	≤ 10.0	≤ 20.0	≤ 50.0
Perfluorohexanoic acid, PFHxA	≤ 6.0	≤ 12.0	≤ 30.0
Perfluorooctanoic acid, PFOA	≤ 0.1	≤ 0.2	≤ 1.0
Perfluorononanoic acid, PFNA	≤ 0.06	≤ 0.12	≤ 0.6
Perfluorobutane sulfonic acid, PFBS	≤ 6.0	≤ 12.0	≤ 30.0
Perfluorohexane sulfonic acid, PFHxS	≤ 0.1	≤ 0.2	≤ 1.0
Perfluorooctane sulfonic acid, PFOS	≤ 0.1	≤ 0.2	≤ 1.0

pollutants adhere to it due to Van der Waals forces, and so the larger the surface area, the more pollutants will find a place on the adsorber.

Inorganic pollutants are typically salt-like, molecular compounds and include metals such as copper, zinc or lead. Some of these substances pose a risk to the environment and human health even at low concentrations, as they accumulate in the tissue of living organisms. For the removal of these contaminants, which are sometimes referred to as "heavy metals", amendments with the functions of adsorption, precipitation or ion exchange are suitable. The adsorption takes place schematically in the same way as with the activated carbon. In the case of precipitation, the pH value is adjusted by the sorbent in such a way that the metals dissolve from the water and can be separated. In ion exchange, an environmentally harmless substance, such as calcium, dissolves from the amendment and gives its place to an environmentally harmful substance. In this way, a strong bond is formed between the amendment and the pollutant.

A recently developed GCF for PFAS removal was tested in both laboratory and field trials as proof of concept and are described herein (Niewerth et al. 2022). Guidelines for PFAS Assessment of the German Federal Ministry for the Environment (BMU 2022) provisional maximum permissible concentrations for PFAS are defined in the 2:1 liquid/solid-eluate. These values result in a recovery classes (RC), which in turn decides on the containment measure to be taken.

The division into the three classes results from the consideration that the concentration in the technical structure will be transported into the subsoil over time. The aim of the GCF underneath the technical structure is to filter the leachate before it percolates into the uncontaminated subsurface. The PFAS concentration must reach a concentration of RC 1 below the GCF, see Figure 19.

In addition to groundwater protection, the advantage of this approach is the successive decontamination of the soil. The infiltration of rainwater into the structure is used specifically to dissolve PFAS compounds. The leachate loads itself with the environmentally relevant components and transports them to the permeable filter. To eliminate the concern of
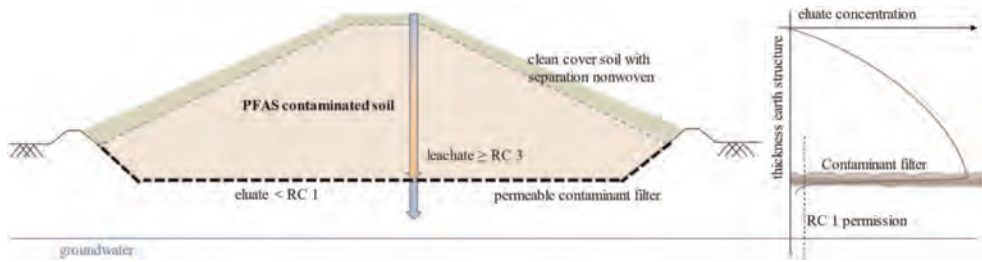
Figure 19. Schematic of technical structure with GCF at the base of the structure and leachate concentration.

pollutants entering the subsurface, the effective removal of the contaminants and a long-term binding of PFAS to the filter must be proven and ensured. Extensive testing with PFAS-contaminated soil from a former US airbase in Germany was performed to meet these requirements.

A series of tests were carried out in close cooperation between Huesker Synthetic GmbH and CDM Smith. Large-scale lysimeter tests were established, see Figure 20. Three different rain events were simulated in different 1 m³ HDPE-containers. Their effect on PFAS mobilization was investigated and the effectiveness of the GCF was tested.

As a control, all rain scenarios were also carried out in a container without the active component. In the test setup, the active geocomposite was laid out in the bottom of a container that was open at the top. A contaminated silty sand with a thickness of 0.7 m was placed on top. The leachate produced during the respective rainfall simulations was collected and analyzed at different times. The water quantities follow the definitions for moderate, heavy, and extremely heavy rain events according to the German Weather Service (Deutscher Wetterdienst, DWD):

- Rain Event 1: moderate rain with 10 L/m² in 60 minutes;
- Rain Event 2: heavy rain with 30 L/m² in 60 minutes; and
- Rain Event 3: extremely heavy rain with 50 L/m² in 60 minutes.

No PFAS were detected in the leachate after filtration by the GCF in these tests for all three simulated rain events.

Figure 20. Outdoor trials with active geocomposite for PFAS and results of Rain Event 3, (Huesker Ltd.).

7 CONCLUSIONS

The landmark Paris Agreement adopted by 196 parties at the UN Climate Change Conference (COP21) in Paris in 2015, entered into force on 4 November 2016. Its overarching goal was to limit the increase in the global average temperature to 1.5°C above pre-industrial levels. This is because the UN's Intergovernmental Panel on Climate Change warns that crossing this 1.5°C threshold risks severe impact such as more frequent and severe droughts, heatwaves and rainfall. A recent report issued by the World Meteorological Organization (WMO 2023) concluded that there is a 66% likelihood that the annual average global temperature between 2023 and 2027 will be more than the 1.5°C target for at least one year. The report states that this does not mean that the world will permanently exceed the 1.5°C level, but it is a warning that the 1.5°C level will be breached on a temporary basis with increasing frequency. It is clear, therefore, that the shift towards sustainable development needs to accelerate.

Geosynthetics can play an important role in supporting the world's goal of limiting the effect of global warming. This paper has presented example of where geosynthetics can reduce the carbon footprint of civil engineering projects in several ways. Firstly, they can reduce the need for importing virgin aggregate to be used for drainage, working platform and pavement applications. The thickness of aggregate can be reduced, and eliminated in some cases, minimising the need to use primary aggregate and the carbon emissions associates with its excavation, haulage and placement. Secondly, geosynthetics can enable the use of poor quality site-won soil, and in the example shown even use contaminated soils in the engineered solution to prevent the off-site disposal at landfill. This paper has also highlighted new developments which will provide further environmental benefits to using geosynthetics. Instrumenting geosynthetics is becoming increasingly possible with fibre optics, radar detectable materials and distributed fibre optic sensing techniques allowing continuous, non-intrusive remote monitoring of critical infrastructure. Finally, active geosynthetics are an exciting development that can provide protection to clean subsoil and groundwater by filtration of pollution from seepage or runoff.

The examples given in this paper are not an exhaustive list of how geosynthetics can support sustainable development. The International Geosynthetics Society (IGS) in its Sustainability Statement states that it believes that geosynthetics and associated technologies make a significant contribution to the achievement of sustainable development. The IGS website has an excellent section on sustainability (IGS 2023) and the authors encourage readers to seek further examples of the sustainable development benefits of geosynthetics from this source.

REFERENCES

BMU (2022). *Guidelines for PFAS Assessment, Recommendations for the Uniform Nationwide Assessment of Soil and Water Contamination and for the Disposal of Sol Material Containing PFAS*, German Federal Ministry for the Environment, 21 January 2022.

Bi, G., Yang, S., Wu, Y., Sun,Y., Xu,H., Zhu, B., Huang, C., Cao, C., (2023) A Preliminary Study of the Application of the Strain-self-sensing Smart Geogrid Rib in Expansive Soils. *Geotextiles and Geomembranes*. Vol 51, 1, 275–281.

BS 8006 (2010). Code of Practice for Strengthened/reinforced Soils and Other Fills, British Standards Institution, October 2010.

BS EN 1997-1 (2004). Eurocode 7: Geotechnical Design – Part 1: General rules, November 2004.

Chen R.P., Wang Y.W., Ye X.W., Bian X.C., Dong X.P. (2016). Tensile Force of Geogrids Embedded in Pile-supported Reinforced Embankment: A Full-scale Experimental Study. *Geotextiles and Geomembranes* 44. 157–169.

CL:AIRE (2011). The Definition of Waste: Development Industry Code of Practice, Version 2, March 2011.

Damians, I.P., Bathurst, R.J., Adroguer, E., Josa, A. & Lloret, A. (2016). Environmental Assessment of Earth Retaining Wall Structures. *ICE Environmental Geotechnics*, http://dx.doi.org/10.1680/jenge.15.00040.

Defra (2013). *Guidelines to Defra's GHG Conversion Factors for Company Reporting, Department for Environment, Food and Rural Affairs*, London, UK.

Defra (2018). *A Green Future: Our 25 Year Plan to Improve the Environment, Department for Environment, Food and Rural Affairs*, London, UK.

Dixon, N., Raja, J., Fowmes, G. & Frost, M. (2016). *Chapter 26 Sustainability aspects of using geotextiles. In Geotextiles from Design to Applications*. Editor Robert M. Koerner, Publisher Elsevier Science & Technology, pp. 642.

Dixon, N, Fowmes, G and Frost M (2017). Global Challenges, Geosynthetic Solutions and Counting Carbon, *Geosynthetics International*, Vol. 24(5), pp. 451–464.

Ecoinvent Centre (2016) *Ecoinvent Database v3.3. Ecoinvent Centre*, Swiss Centre for Life Cycle Inventories, Zurich, Switzerland. See http://www.ecoinvent.ch (accessed 05/01/2017).

EN 15804 (2019). Sustainability of Construction Works – Environmental Product Declarations – Core Rules for the Product Category of Construction Products, European Committee for Standaardization.

Hammond, G. P. & Jones, C. I. (2011). *Inventory of (Embodied) Carbon & Energy (ICE) v2.0.* Department of Mechanical Engineering, University of Bath, Bath, UK.

Hatami, K., Hassanikhah, A., Yazdani, H and Grady, B.P. (2014). Tensoresistive PVC Coating for Sensor-Enabled Geogrid, *Journal of Nanomechanics and Micromechanics*, Volume 4, Issue 4: Special Issue: Mechanics of Nanocomposites and Nanostructure, December 2014.

Heerten, G. (2012). Reduction of Climate-damaging Gases in Geotechnical Engineering Practice Using Geosynthetics. *Geotextiles and Geomembranes*, 30, 43–49.

Heibaum, M. 2010. Geosynthetics in Agricultural and Aquacultural Applications. Proceedings 9th International Conference on Geosynthetics, Guaruja, Brazil, pp. 259–271.

HM Government (2013). Construction 2025, July 2013.

Huesker (2023). HUESKER ecoLine: Geotextiles from Recycled Raw Material, https://www.huesker.us/ geosynthetics/products/ecoline/ (accessed 21/5/2023).

IGS (2023). International Geosynthetics Society, Sustainability https://www.geosyntheticsociety.org/sustain-ability/ (accessed 21/5/2023).

ISO (2006a) ISO 14040: *Environmental Management – Life Cycle Assessment – Principles and Framework*, International Organization for Standardization, Geneva, Switzerland.

ISO (2006b) ISO 14044: *Environmental Management – Life Cycle Assessment – Requirements and Guidelines*, International Organization for Standardization, Geneva, Switzerland.

Kerchavarzi, C., Soga, K., de Battista, N., Pelecanos, L., Elshafie, M.Z.E.B. and Mair, R.J. (2016). *Distributed Fibre Optic Strain Sensing for Monitoring Civil Infrastructure, a Practical Guide*, ICE Publishing, One Great George Street, London.

Koerner, R.M., Hsuan, Y.G. & Koerner, G.R (2008). Freshwater and Geosynthetics: A Perfect Marriage. the first Pan American Geosynthetics Conference and Exhibition, GeoAmericas, Cancun, 2-5 March 2008, pp. 4–28.

Koerner, R.M., Koerner, J.R. and Koerner G.R. (2019). Relative Sustainability (embodied carbon) Calculations with Respect to Applications using Traditional Materials Versus Geosynthetics, GSI White Paper #41, Geosynthetic Institute, 10 April 2019.

Kraus, J. (2022). Geosynthetics, Sustainability and Planetary Boundaries: Real Global Benefits and Potential Policy Risks in Europe, Proc. 32nd National Geosynthetics Conference, Bologna, 20 October 2022.

Möller, T., da Silva Burke, T.S., Xu, X, Ragione, G.D., Bilotta, E. and Abadie, C.N. (2022). Distributed Fibre Optic Sensing for Sinkhole Early Warning: Experimental Study, Geotechnique, February 2022.

Niewerth, S., Carbone, L. and Lassnig, H. (2022). Containment and Passive Decontamination of PFAS Soil in Technical Structures by Means of Sorption Mats (translated from German), Proceedings of Recy und DepoTech, Leoben, Austria.

PAS 2080 (2016) Carbon Management in Infrastructure, British Standards Institution, May 2016.

Raja, J., Dixon, N., Fowmes, G., Frost, M.W. & Assinder, P. (2014). Comparison of Carbon Dioxide Emissions for Two Landfill Capping. *Proc., ICE - Engineering Sustainability*, Vol. 167, 5, 197–207.

Raja, J., Dixon, N., Fowmes, G., Frost, M.W. & Assinder, P. (2015). Obtaining Reliable Embodied Carbon Values for Geosynthetics, *Geosynthetics International*, Volume 22, NO. 5, pp. 393–401.

Raworth, K. (2012). A Safe and Just Space for Humanity: Can We Live within the Doughnut? Oxfam Discussion Paper, February 2012.

Rockström , J., W. Steffen, W., Noone, K., Persson, Å., Chapin, F. S., Lambin, E., Lenton, T. M. Scheffer, M. Folke, C., Schellnhuber, H., Nykvist, B., De Wit, C. A., Hughes, T., an der Leeuw, S., Rodhe, H., Sörlin, S., Snyder, P. K. Costanza, R. , Svedin, U., Falkenmark, M. , Karlberg, L. , Corell, R. W., Fabry,

V. J. , Hansen, J., Walker, B., Liverman, D., Richardson, K., Crutzen, and P.J., Foley, (2009). Planetary Boundaries: Exploring the Safe Operating Space for Humanity. *Ecology and Society* 14(2): 32.

Skinner, R. (2020). ICE Presidential Address 2020: Net Zero Carbon. https://www.ice.org.uk/events/past-events-and-recordings/recorded-lectures/ice-presidential-address-2020 (accessed 21/5/2023)

Standards for Highways (2020) CD225 - *Design for New Pavement Foundations, Design Manual for Roads and Bridges*, April 2020.

Standards for Highways (2017) *Series 600 Earthwork, Volume 1 Specification for Highway Works, Manual of Contract Documents for Highway Works*, February 2017.

Stucki, M., Büsser, S., Itten, R., Frischknecht, R. & Wallbaum, H. (2011). *Comparative Life Cycle Assessment of Geosynthetics Versus Conventional Construction Materials, Report for the European Association of Geosynthetic Manufacturers*, ESU-services GmbH, Uster, Switzerland and ETH Zürich, Switzerland.

Touze, N. (2021). Healing the World: A Geosynthetics Solution, *Geosynthetics International*, 28, pp. 1–31.

——— (2008). *Climate Change Act*. http://www.legislation.gov.uk/ukpga/2008/27/contents (accessed 15/12/2016)

United Kingdom Government (2013). *Construction 2025*. https://www.gov.uk/government/uploads/system/uploads/attachment_data/file/210099/bis-13-955-construction-2025-industrial-strategy.pdf.

United Nations (2016). *Sustainability Goals 17 Goals to Change Our World*. http://www.un.org/sustainabledevelopment/sustainable-development-goals/.

Whitty, J.E., Koerner, J.R. and Koerner, G.R. (2020). Relative Sustainability of Road Construction/Repair: Conventional Materials versus Geosynthetic Materials, GRI White Paper #44, Geosynthetic Institute, 16 March 2020.

WMO (2023). WMO Global Annual to Decal Climate Update (Target years: 2023-2027), World Meteorological Organization, 17 May 2023.

WRAP (2010). Sustainable Geosystems in Civil Engineering Applications. Waste and Resources Action Programme, Banbury, UK, Project MRF116.

Xu, X., Kechavarzi1 , C., Wright, D., Horgan, G., Hangen, H., De Battista, N., Woods, D., Bertrand, E., Trinder, S. and Sartain, N. (2022). Fibre Optic Instrumented Geogrid for Ground Movement Detection. Proc. 11th International Symposium in Field monitoring in Geomechanics.

Zamara, K.A., Dixon, N., Jones, D.R.V., Fowmes, G., (2012). Monitoring of a Landfill Side Slope Lining System: Instrumentation Selection, Installation and Performance. *Geotextiles and Geomembranes* 35, 1–13.

Zamara, K.A., Fowmes, G.J. and Kawalec, J. (2022) Geogrid Stabilisation Application – Review of Strain Measurement Methods, Research and Implications on Design Approaches. Proceedings of EuroGeo 7.

Insight towards the stability of complex geosynthetic reinforced soil structures

B.A. Leshchinsky
Oregon State University, USA

ABSTRACT: Typical design of geosynthetic-reinforced soil structures is based on the arbitrary classification of a wall and slope, which require different checks of internal and compound stability. However, both limit state conditions may be evaluated consistently through Limit Equilibrium (LE) analyses, particularly when the solutions are used to solve for tensile loads within reinforcements, such as that proposed by Leshchinsky et al. (2017). Herein various expanded examples using the top-down LE method and associated tension maps are explored to demonstrate the nuance and complexity of internal and compound stability, even for seemingly simple geosynthetic reinforced soil structures. Further, a special limit state design condition is explored – called "hybrid" stability conditions, where specific applications such as a footing placed on reinforced soil, may encounter a variety of failure mechanisms that related to external stability, compound stability and internal stability. Nuances of these complex, but increasingly relevant case are discussed, and potential limit state analyses are proposed. Lastly, future directions are briefly described.

1 INTRODUCTION

Geosynthetics have been widely used as an economical means of soil reinforcement in earth retention and slope construction for decades. The design of geosynthetic reinforced soil structures (e.g. AASHTO 2020) treats reinforced walls and slopes (differentiated by a 20° or 30° batter, depending on the internal stability method) with different design criteria – namely earth pressure-based and slope stability-based design, respectively. Despite the different basis for evaluating reinforcement loading, at strength limit state conditions, both reinforced walls and slopes are subject to design focused on internal stability, external stability, and compound stability. Internal stability is traditionally focused on pullout and rupture strength of reinforcements. External stability often focuses on sliding, overturning and bearing failure of the reinforced mass. Compound stability is traditionally a "final" check to ensure that failure through or around the reinforced mass is unlikely. While walls are often designed based on earth pressure theory, a more consistent alternative would be evaluation through limit equilibrium methods, i.e. the methods used to design reinforced slopes. The different techniques used for design of reinforced slopes commonly apply (or adapt) concepts of the limit equilibrium method (or limit analysis method) to determine critical failure mechanisms and associated reinforcement loading (Duncan & Wright 1991; Leshchinsky & Reinschmidt 1985; Leshchinsky & Boedeker 1989). However, in many some instances, use of internal and compound stability checks may be inconsistent with one another, lead to paradoxical results, and most importantly, cannot encompass the breadth of design constraints often required for each structure (Leshchinsky et al. 2017). This is particularly true for complex, but realistic, design scenarios, such as supporting footing loads, building walls on slopes, tiered structures, etc. Further, there exists scenarios, such as reinforced walls or slopes supporting surcharge

loading, that lie outside of traditional internal, external and compound stability checks, i.e. "hybrid" stability checks. Herein, the importance of mechanics-based design procedures as a means of exploring internal, external, compound and hybrid stability of geosynthetic reinforced soil structures is explored.

1.1 *Limit state methods*

Limit state analyses, such as that proposed by Leshchinsky et al. (2017) inherently assume that the *design* strength of the soil in consideration is mobilized and consequently, the degree of mobilization signifies the margin of stability or factor of safety, *Fs*. Coupled with this assumption is the expectation that reinforcements are implicitly only installed in slopes that otherwise would be inherently unstable. Therefore, at an actual limit state, the *design* strength of the soil is fully mobilized (i.e. *Fs*=1.0) and the stability of any trial slip surface hinges upon the mobilized tensile resistance of the reinforcement. At that state, design should ensure that the long-term strength of the reinforcement (e.g. factored rupture strength) will be available throughout the reinforcement (e.g., Leshchinsky et al. 2017; Liu 2016). It is assumed that reinforcements will not rupture and that they are compatible with the soil as it deforms, mobilizing tensile strength (e.g., Liu 2016). These assumptions are reasonable as geosynthetic reinforcements are generally ductile and capable of developing substantial strains that are much larger than those needed for nonplastic backfill to mobilize its strength (i.e., to form an 'active' mass). Consequently, these limit state concepts and limit equilibrium or limit analysis methods in particular are suitable for design of geosynthetic reinforced slopes and walls. Note that while LE and LA are employed to analyze the limit state in this study, one may use alternative approaches, such numerical methods that can deal with limit state, such as finite element (FE) and finite difference (FD) analyses (Ambauen et al. 2015; Leshchinsky & Han 2004; Leshchinsky & Vulova 2001; Mohamed et al. 2014). These methods are also valuable for exploring stability problems where there are feedbacks between potential failure modes, such as bearing capacity and/or slope stability (e.g. Leshchinsky 2015; Leshchinsky & Xie 2017; Yang et al. 2019, 2021). For example, when reinforced structures are required to support a surcharge load (Xie et al. 2019), the stability of such a system is inherently external, internal, and compound, consequently termed a "hybrid" stability problem herein. While continuum mechanics-based numerical methods are insightful to all of these possible controls on reinforced structure stability, implementation of these approaches in ordinary design may add unnecessary complexity, and more simplistic but representative solutions are valuable. In this study, exploration of more holistic internal and compound stability checks based on limit equilibrium are explored. Further, the role of hybrid stability problems is described with a particular focus on surcharge loading of reinforced walls and slopes. In all cases, mechanics-based design enables consistent and explainable design.

2 INTERNAL AND COMPOUND STABILITY

For geosynthetic reinforced soil structures, internal stability design is focused on reinforcement strength, pullout and connection strength (Xie et al. 2016). Previous literature has described pullout resistance between geosynthetics to be dependent on soil particle size, apertures (if applicable), soil type, and interface friction (Jewell 1990; Lee 2000). When sufficient interlocking behavior between geogrid and soil is realized, pullout may be inhibited, where shear strains may propagate in the soil adjacent to the reinforcement instead of at the soil-geogrid interface, demonstrated experimentally and numerically (Ambauen et al. 2015; Boyle 1995; Bathurst & Ezzein 2016; Hatami & Bathurst 2005; Yoo & Kim 2008) for geosynthetic reinforced soil structures. Connection strength is an important design consideration, particularly for walls with block or panel facings. Connection loads may be

amplified when vertical spacing between reinforcements is large or there is significant differential settlement; however, with proper construction practices (i.e. compaction) and sufficiently small vertical reinforcement spacing, connection issues may be mitigated (Soong & Koerner 1997). Internal stability design for rupture strength is based on evaluation of a single (or multiple) potential slip surfaces contained within the reinforced mass. Such a limit state analysis typically assumes that a slip surface is fully formed, consequently allowing calculation of required reinforcement loads under a given set of assumptions (e.g. mobilization of soil strength, modifications for reinforcement extensibility, etc.). However, these traditional approaches largely ignore the potential influences of multiple shear surfaces, internal and compound, and potential feedbacks between reinforcement mobilization, pullout and connection loads (Leshchinsky et al. 2017). Typically, these requisite reinforcement loads must account for potential durability, installation damage, and creep reduction factors in addition to a margin of safety (Leshchinsky et al. 2020).

2.1 *Limit state design framework for geosynthetic-reinforced soil structures*

The limit state approach used here was first explored by Han and Leshchinsky (2006) using planar slip surfaces. It was further modified to deal with rigorous log spiral limit equilibrium framework for simple geotechnical problems (Leshchinsky et al. 2014). This modification showed that in many cases, curved slip surfaces are more critical. Additional work by Leshchinsky et al. 2016 generalized the framework to deal with internal/compound stability of nearly any practical geotechnical problem utilizing Bishop's method. For example, typical geotechnical problem is different properties of reinforced and retained soils, complex wall geometry or complex reinforcement layout, permeating water, and impact of facing. Such generalization made the general framework as a subset of geotechnical slope stability analysis with particular emphasize on the resulted load distribution along each layer. This 2016 report also provides experimental and numerical assessment of the framework. Finally, Leshchinsky et al. (2017) presents the method in a complete and concise fashion.

As per the prior work of Leshchinsky et al. (2017), the use of the top-down Limit Equilibrium method is used to explore the complexities and nuances of internal and compound stability of geosynthetic reinforced soil structures for a variety of cases, both simple and complex. This approach uses a spatial distribution of slip surfaces for a prescribed safety factor (typically unity) for a soil mass, and consequently attains the required reinforcement tensions needed to yield equilibrium at any location. Implemented through an iterative, top-down procedure of limit equilibrium-based slope stability analyses, the mobilized reinforcement loading can be visualized through a *Tension Map* that illustrates the required distribution of reinforcement tension to attain a prescribed limit state of equilibrium. This tension map is directly constrained by both rear- and front-end pullout capacity, providing a unified, LE-based approach towards evaluating the internal and compound stability of simple or complex geosynthetic reinforced soil structures using explainable, mechanics-based criteria. A brief overview of the method is presented, followed by several examples of internal and compound stability of geosynthetic reinforced soil structures.

As described by Leshchinsky et al. (2017), the *Tension Map* illustrates the tensile load distribution along trial reinforcement layers to ensure that a limit state defined by a prescribed safety factor – typically unity – is determined. Specifically, rather than assuming or determining the long-term strength of each reinforcement before analysis, the required reinforcement tension at the intersection of an analyzed slip surface is modified to produce a prescribed safety factor in each slip surface of concern. Consequently, the *Tension Map* yields the maximum load in the reinforcement including its connection load: T_{max} and T_o, respectively. Determination of the *Tension Map* requires application of the top-down procedure (Leshchinsky et al. 2017). This procedure is characterized by numerous trial failure geometries exiting throughout the face of the geosynthetic reinforced soil structure, which is iteratively used to develop a *Tension Map*. A detailed description of the top-down procedure

and determination of a tension map is presented in Leshchinsky et al. (2017), but a brief overview is provided below and Figure 1.
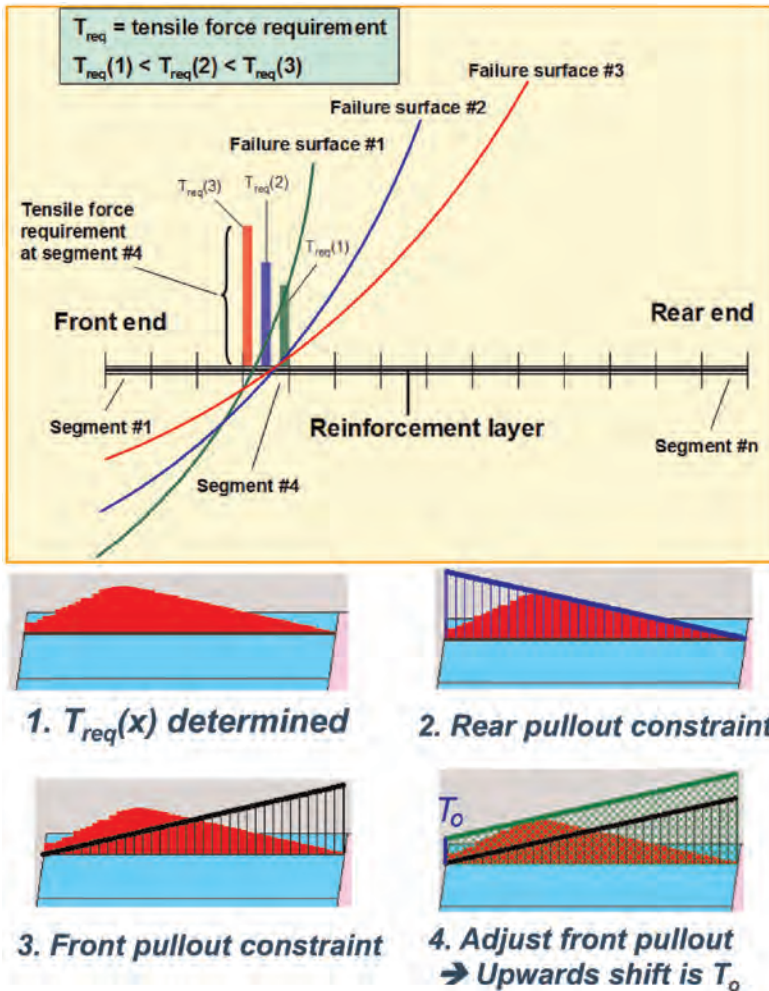
Figure 1. Overview of the top-down limit equilibrium method used to determine mobilized reinforcement loading for internal and compound stability of geosynthetic reinforced soil structures (after Leshchinsky et al. 2017).

1. Select a layout of reinforcement layers for a given set of geometric specifications and soil properties.
2. Assign a top-down arrangement for reinforcement layers whereas trial failure surfaces are analyzed starting at the slope crest and emerging at the wall face. For each layer that is intersected by a slip surface, determine the mobilized reinforcement force T that yields the predefined, specified safety factor. For each location along a reinforcement, the maximum T (defined as T_{max}) is determined and assigned spatially along its length evaluated using this procedure (Figure 1). This procedure is repeated sequentially from the crest to the toe of the trial design for each layer of reinforcement, whereas the mobilized T at the intersection of a trial surface and reinforcement layer(s) must not exceed the rear pullout

164

capacity (Figure 2). If T does exceed rear pullout capacity, the excess loading is shared with other intersection layers. If the new T determined at a given location along a reinforcement exceeds the previous T_{max}, the new T is now the maximum. This process is repeated until the toe of the structure is reached and a distribution of maximum T that satisfies rear end pullout criteria is found along each reinforcement layer, including that at the lowest elevation.

3. Thereafter, connection loads (T_o) may be determined for each reinforcement layer based on the distribution of T_{max}, where the frictional envelope of front-end pullout may be translated to determine unfactored connection loading T_o that enables sufficient pullout capacity at the front end. The magnitude of the shift from zero resistance is the minimum required connection load at each elevation (Figure 2).
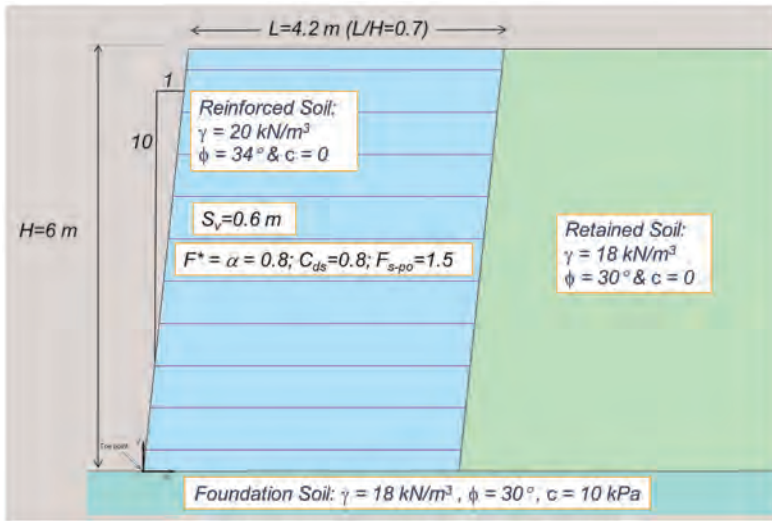
Figure 2. Benchmark case geometric conditions, the dimensions, and properties of which are shown above.

4. From both T_{max} and T_o determined at each layer, the governing long-term design strength can be determined based on reinforcement demands and other relevant design factors.
5. Check global and compound stability for the actual selected reinforcement to ensure that it meets design specifications. If necessary, repeat steps 1-4 for more economical or satisfactory design. Note that compound failures are considered when assessing T for a selected layout of reinforcement.
6. If desired, numerically integrate the reinforcement tensile distribution divided by reinforcement tensile stiffness J to determine displacement, or outwards stretching, d at each reinforcement layer, proposed as: $d = \int_0^L (T_{max}/J)dL$

2.2 Benchmark example conditions

A simple benchmark example is presented, illustrating systematic comparison of the sensitivity of internal and compound stability of simple and complex geosynthetic reinforced soil structures to common design conditions. Consider a reinforced wall, $H=6$ m tall having a batter of $\omega=8°$, reinforcement spacing (S_v) of 0.6 m with a bottom layer 0.3 above the foundation soil and the top layer is 0.3 m below the horizontal crest. The length of reinforcement, L, meets typical specifications of $L/H=0.7$; i.e., $L= 4.20$ m, as shown in Figure 3.

The reinforced, retained, and foundation soils have unit weights, γ, of 22, 20, and 18 kN/m^3 and internal angles of friction, ϕ, of 34, 30, and 28 degrees, respectively. No cohesion is considered. Stability analyses are performed using Bishop's method and circular failure geometries. The selected geosynthetic has long-term design strength and connection strength, T_{LTDS}, of 16 kN/m. The coverage ratio of the reinforcements is unity (i.e. continuous), the interface friction is 64% of that of internal friction, and the factor of safety against pullout is 1.5. The stiffness J of the reinforcements is assumed to be 500 kN/m. These conditions yield satisfactory global stability (Figure 3) and serve as a simplified set of conditions that can be compared against other cases.
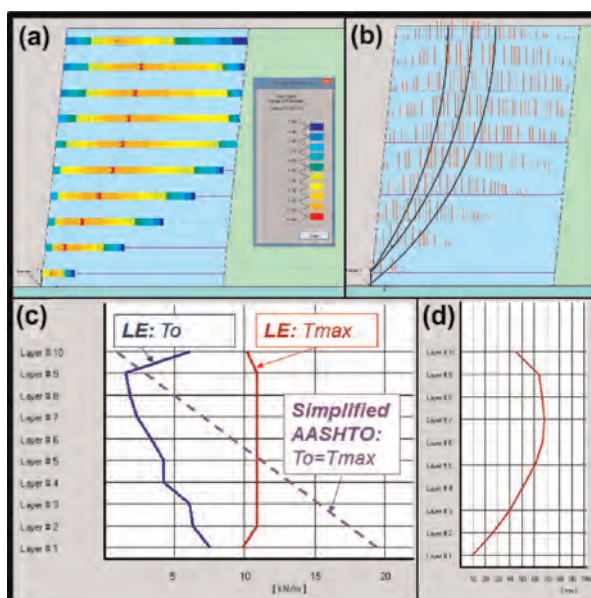
Figure 3. (a) Tension map for benchmark conditions. Note that the location of the maximum T_{max} on each layer is shown with a white, hollow marker. (b) Slip surfaces associated with maximum T_{max}. (c) Distribution of T_{max} and T_o along the profile of the given geometry. Note the comparison to earth pressure-based design estimates of reinforcement tensile loading. (d) Estimated lateral displacement profile based on a stiffness of J=500 kN/m.

The aforementioned top-down procedure and the associated tension map that satisfies rear end pullout constraints and load shedding amongst layers is shown in Figure 4a. Note that the maximum load in the reinforcement is located closer to the slope face as lower layers are considered. This reflects the convergence of slip surface geometries at the slope toe. Interestingly, the locus of T_{max} does not necessarily lie on a singular trace of slip surface, shown in Figure 4b. This owes to the top layer being controlled by rear pullout while lower layers are affected by compound failures. Closer and/or longer reinforcements may result in uniform mobilization of reinforcement occurring along a singular slip surface. Other configurations of reinforcement length and geometry may result in non-uniform mobilization of reinforcement strength, an aspect that cannot be addressed using conventional global LE design approaches. From this tension map, front-end pullout can also be determined (Figure 4c). Front-end pullout resistance increases with depth, especially in steeper slopes such as the proposed example, owing to increased overburden and associated frictional resistance. The maximum connection load is approximately half of the maximum force in the reinforcement, which enables quantitative selection of connection strength specifications. Figure 4c

166

compares T_{max} and T_o as calculated by AASHTO 2010 and the LE approach, where unlike LE, AASHTO uses a lateral earth pressure-based approach that is proportional to simple overburden pressure and reinforcement spacing. Consequently, if the maximum T_{max} is used to select a reinforcement, AASHTO requires about twice the strength than that determined by LE. Lastly, Figure 4d shows that the extensibility of the given reinforcement results in a standard deflection profile observed in many reinforced walls. (e.g. Ambauen et al. 2015). Simple integration of local displacement due local loading determined from LE and stiffness provides a means of estimating a displacement profile near failure and potentially ensuring that service-state deflections are satisfactory. It can also a useful tool in assessing the severity of deformed walls as evidenced by their exposed profile. This simple benchmark problem enables systematic comparison to a variety of relevant design criteria explored herein.
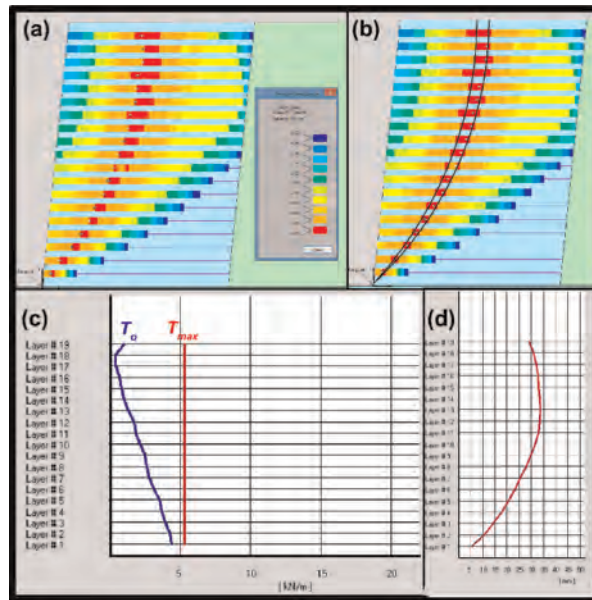
Figure 4. (a) Tension map for closely spaced reinforcement (S_v=0.3m) conditions. Note that the location of the maximum T_{max} on each layer is shown with a white, hollow marker. (b) Slip surfaces associated with maximum T_{max}. (c) Distribution of T_{max} and T_o along the profile of the given geometry. (d) Estimated lateral displacement profile based on a stiffness of J=500 kN/m.

2.3 Close reinforcement spacing

The vertical spacing between reinforcements is a primary design condition which may influence internal stability. Closely spaced reinforcements are being used more frequently for such structures as they enable better load-carrying capacity, enhanced serviceability, require weaker reinforcements, and facilitate consistent compaction quality. The same example problem is considered but evaluated with close vertical spacing (S_v=0.3m) vs. standard vertical spacing of 0.6m, shown in Figure 5. A comparison with benchmark conditions (Figure 4) demonstrates a drop in maximum loading (Figure 5a) and a relatively uniform maximum loading – which arguably reflects a more efficient design, demonstrated by a narrow band of maximum tensions and very few slip surfaces associated with maximum loading. Specifically, the value of max(T_{max}) drops from 11.28 kN/m for the baseline problem to 5.65 kN/m for 0.3 m spacing, a 50% drop that is effectively proportional to the spacing. More noteworthy however, is the dramatic drop in connection loads in the upper

layers (Figure 5c). This owes to diminished loading within each layer, reduced pullout demands, and consequently a decrease in the required translation of the front-end pullout envelope and connection load. Lastly, the deflection profile is reduced by approximately 50%, consistent with the reduction in loading compared to the benchmark case.
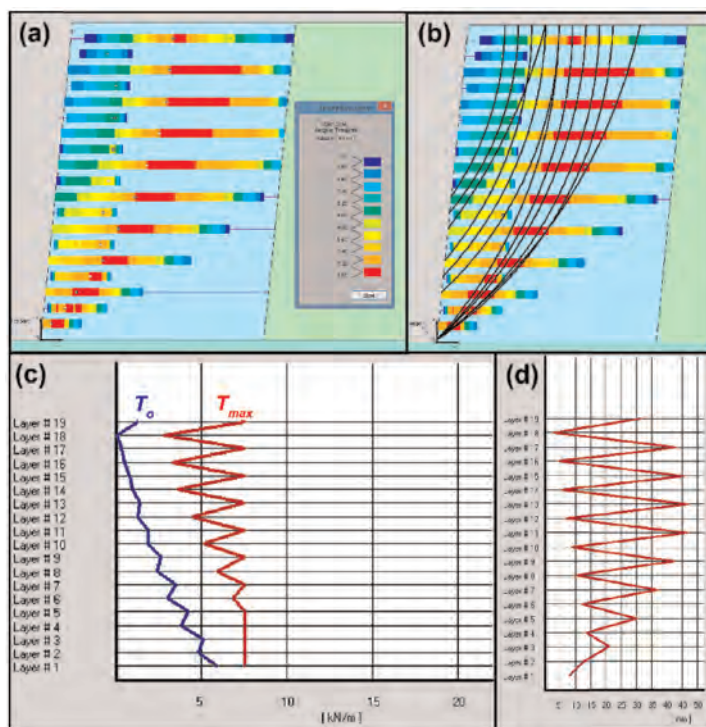
Figure 5.   (a) Tension map for primary and secondary reinforcement for closely spaced (S_v=0.3m) conditions. Note that the location of the maximum T_{max} on each layer is shown with a white, hollow marker. (b) Slip surfaces associated with maximum T_{max}. (c) Distribution of T_{max} and T_o along the profile of the given geometry. (d) Estimated lateral displacement profile based on a stiffness of J=500 kN/m.

2.4   *Secondary reinforcements*

Shorter, secondary reinforcements may be placed between primary reinforcements to enable a more efficient reinforced soil structure through reduced connection loading without using as much reinforcement as those systems with closely spaced reinforcements. It enables adequate compaction near the face. The benchmark problem is considered but evaluated with close vertical spacing (S_v=0.3m) and alternating reinforcement lengths of 4.2m for primary reinforcements and 1.2m for secondary reinforcements, shown in Figure 6. A comparison against benchmark conditions reduced maximum loading (Figure 6a, 6c) although tensile loads are mostly higher in primary reinforcement and lower in secondary reinforcements. This pattern owes to secondary reinforcement loads being controlled by rear-end pullout, and consequently shedding some load to primary reinforcements. As shown, max(T_{max}) drops from 11.28 kN/m for the baseline problem to 7.55 kN/m for this case. However, connection loading is now similar to the case of closely spaced reinforcements (Figure 5c), but the quantity of reinforcement is only ~65% of this case. This demonstrates that secondary reinforcements can indeed shed problematic

connection loads. The loci of maximum loading is associated with numerous slip surfaces, demonstrating the complexity of such a problem (Figure 5b). Lastly, the deflection profile (Figure 5d) is similar to that of closely spaced reinforcements, although significantly less reinforcement material is required.
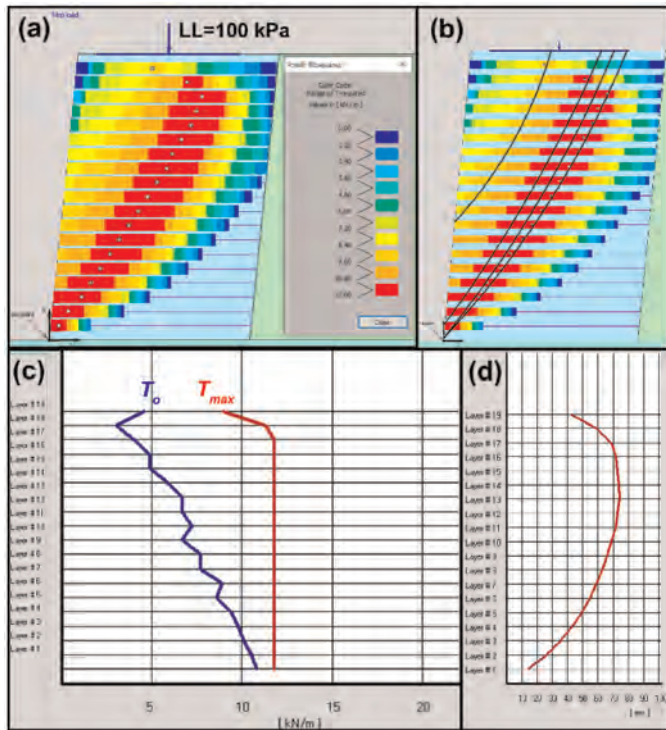
Figure 6. (a) Tension map for closely-spaced conditions with a surcharge of 100 kPa. Note that the location of the maximum T_{max} on each layer is shown with a white, hollow marker. (b) Slip surfaces associated with maximum T_{max}. (c) Distribution of T_{max} and T_o along the profile of the given geometry. (d) Estimated lateral displacement profile based on a stiffness of J=500 kN/m.

2.5 Load supporting conditions

Often, geosynthetic reinforced soil structures support surcharge loads that may be in the form of dead loads (e.g. footings, construction material, etc.) and/or live loads (e.g. traffic, temporary loads). The benchmark problem is considered but evaluated with close vertical spacing (S_v=0.3m) and a live load of 100 kPa, applied along a 3.5m area on top of the reinforced mass, shown in Figure 7. A comparison against benchmark conditions shows increased maximum loading (Figure 7a, 7c) vs. the benchmark conditions, although the max tensile loads are rather uniform when sufficient far from the surcharge. Connection loading increases monotonically with overburden, suggesting increasing loading demand with limited gain in connection strength with depth (Figure 7c). The loci of maximum loading is associated with numerous slip surfaces that either reflect local shear loading (i.e. the upper surface) or a propensity to incorporate the entire surcharge (surfaces situated near the far heel of the surcharge), again demonstrating importance to capturing reinforcement demands, both in magnitude and location (Figure 7b). The deflection profile (Figure 7d) has a more pronounced bulge owing to the increased swatch and magnitude of loading at lower reinforcement layers. Such deflection profiles are expected for such loading conditions (e.g.

Ambauen et al. 2015). The condition presented herein – internal stability conditions accounting for a flexible surcharge considering only slope failure – will be shown to be a special case later in this study, where numerous mechanisms may control the load-carry capacity upon a reinforced soil slope.
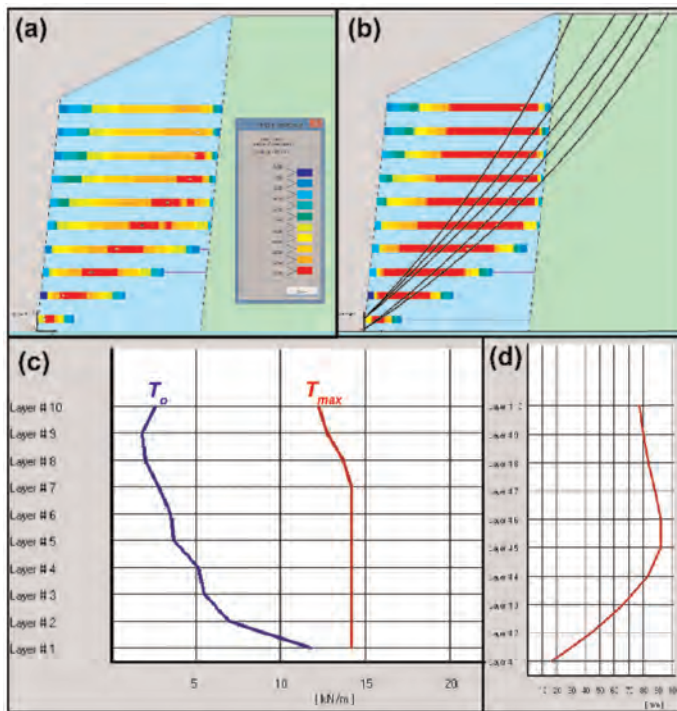
Figure 7. (a) Tension map for the benchmark case but with a2.1m tall, 2H:1V broken backslope. Note that the location of the maximum T_{max} on each layer is shown with a white, hollow marker. (b) Slip surfaces associated with maximum T_{max}. (c) Distribution of T_{max} and T_o along the profile of the given geometry. (d) Estimated lateral displacement.

2.6 Backslope and narrow walls

As reinforced soil structures are often placed in locations with limited right-of-way and/or flat ground, it is common to have backslopes adjacent to the structure itself. The benchmark problem is modified to have a broken backslope, 2.1m in height and with a 2H:1V slope. As shown in Figure 8a and 8b, the mechanisms that dictate T_{max} are largely compound, resulting in larger tensile loads than the benchmark conditions (Figure 8c). This behavior is sensible, as the unreinforced slope atop the reinforced structure has a natural propensity to drive slope failure further back from the reinforced mass owing to insufficient shear strength. The remaining shear forces are supported by the reinforced soil below. Consequently, reinforcement loads are significantly higher than the benchmark example and connection loads are particularly large, especially at lower portions of the wall (Figure 8c). Such behavior can also be reflected for narrow walls (Figure 9), where compound stability governs reinforcement loading and results in larger connection loading owing to insufficient rear-end pullout capacity and consequential enhanced loading. Similar to backslope conditions, compound failures correspond with the loci for maximum tensile loading. This behavior also demonstrates that the LE method is effective at characterizing both internal *and* compound stability

170
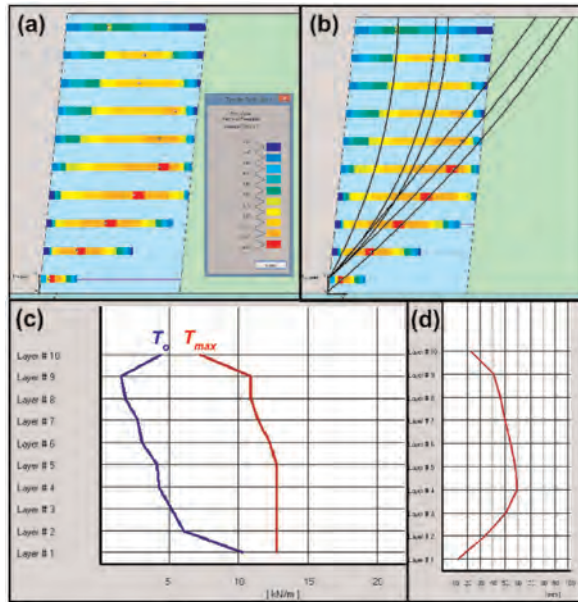
Figure 8. (a) Tension map for the benchmark case but for a narrow wall with L/H=0.5. Note that the location of the maximum T_{max} on each layer is shown with a white, hollow marker. (b) Slip surfaces associated with maximum T_{max}. (c) Distribution of T_{max} and T_o along the profile of the given geometry. (d) Estimated lateral displacement.
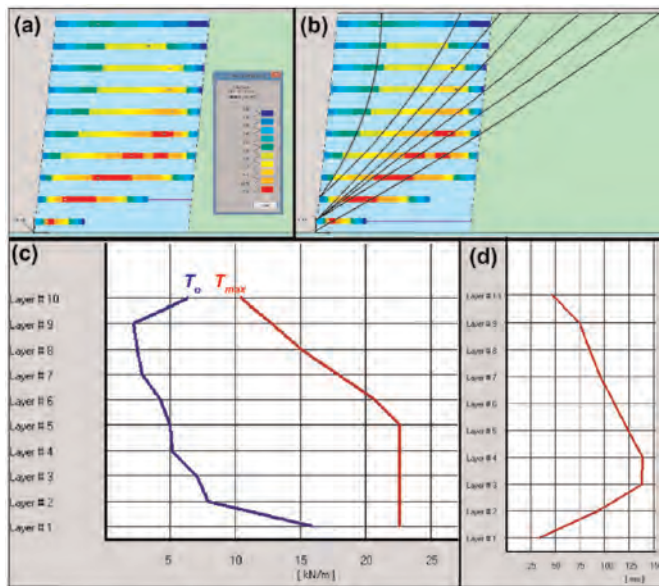
Figure 9. (a) Tension map for the benchmark case but subject to 0.2g of horizontal seismic loading. Note that the location of the maximum T_{max} on each layer is shown with a white, hollow marker. (b) Slip surfaces associated with maximum T_{max}. (c) Distribution of T_{max} and T_o along the profile of the given geometry. (d) Estimated lateral displacement.

171

simultaneously, demonstrating that T_{max} may be controlled by both internal and compound failure surfaces. This complex behavior is reflected in the deflection profile, which has amplified tilt in the upper portion of the structure in comparison to the benchmark case (Figure 8d).

2.7 Seismic loading

Earthquakes are known to yield deeper critical failure geometries; when reinforced soil structures are subject to earthquake loading, deeper, compound failure surfaces may govern stability. The benchmark case subjected to 0.2g of pseudostatic earthquake loading is presented in Figure 10. As shown, once again, compound failure surfaces dictate T_{max} in all reinforcement layers except the top two layers. This behavior owes to deepening of critical failure geometries from earthquake loading. The importance of compound stability is illustrated by the profile of T_{max} (Figure 10c), where the largest tensions occur in the lower reinforcement layer owing to very deep, partially reinforced failure surfaces. In these surfaces, pullout capacity is sufficient, but the overall size of the failure surface results in much larger loading than static conditions. These loads also create a unique bulge in the deflection profile (Figure 10c) that is shifted downwards in comparison to the static case.
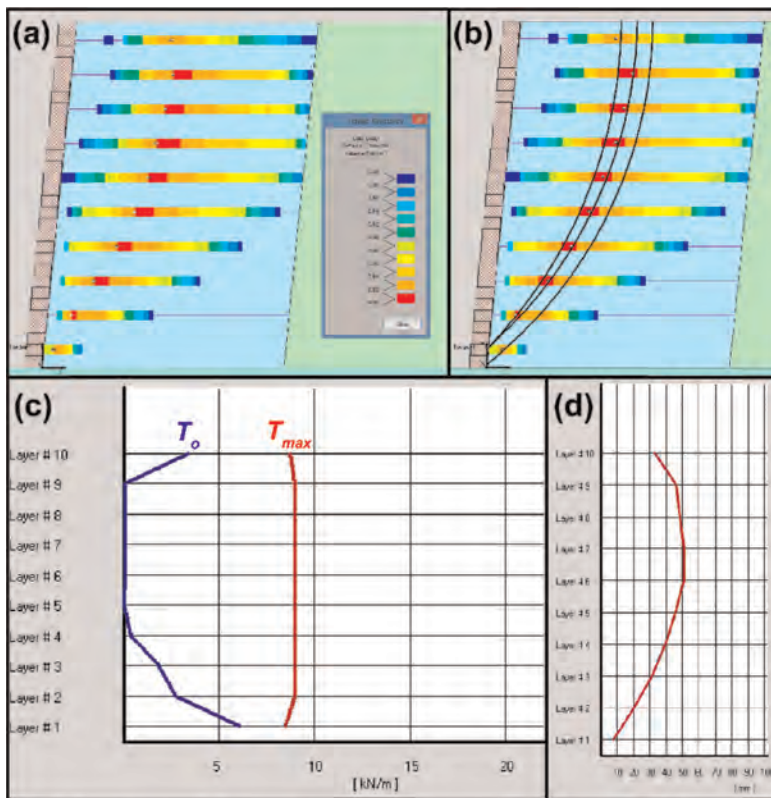
Figure 10. (a) Tension map for the benchmark case but with a modular block facing. Note that the location of the maximum T_{max} on each layer is shown with a white, hollow marker. (b) Slip surfaces associated with maximum T_{max}. (c) Distribution of T_{max} and T_o along the profile of the given geometry. (d) Estimated lateral displacement.

2.8 Influence of facing systems

Various facing elements are available for reinforced wall construction, many of which may significantly influence the observed reinforcement loading and overall internal stability. Addition of 0.2m×0.3m modular blocks with an interface friction angle of 30° and an 'adhesion' (more likely interlocking of rough interfaces between stacked blocks) of 10 kPa are added to the benchmark case, shown in Figure 10. Addition of these facing elements demonstrates a modest decrease in T_{max}, but a very significant decrease in connection loading. Such an observation is sensible as the block weight and its associated interblock shear resistance reduce T near the front due to its contribution to local stability, similar to secondary reinforcements. In fact, there is near zero connection loading throughout much of the wall owing to the localized stabilizing effects of the wall facing. Of course, the influence of facing units on overall loading should be used conservatively, based on whether this resistance is available in the long term; however, this analysis demonstrates that LE can enable the influence of such systems, which is particularly helpful for a variety of block wall systems (e.g. hybrid walls, full height panels, etc.). It is noted that that the LE analysis provides a rational assessment of connection load at a limit state; however, at working load conditions soil and interblock strengths are not fully mobilized yet meaning that the connection load might be larger.

2.9 Tiered walls

Thus far, only simple walls subject to modest complexities have been considered, demonstrating that even small complexities can greatly affect internal stability *but* may be captured using the proposed limit equilibrium approach. A tiered wall of complex structure is considered as such systems often fall outside the classification of wall or a slope (Figure 11). As
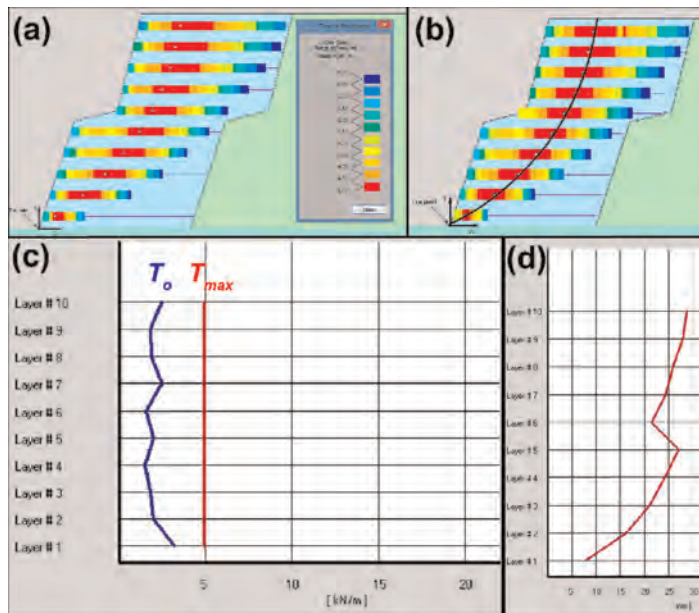
Figure 11. (a) Tension map for a complex, tiered wall system. Note that the location of the maximum T_{max} on each layer is shown with a white, hollow marker. (b) Slip surfaces associated with maximum T_{max}. (c) Distribution of T_{max} and T_o along the profile of the given geometry. (d) Estimated lateral displacement profile.

shown, increasing the batter and adding a bench between tiers reduces loading by over 50%. The locus of maximum tensile load varies, but several zones of increased loading may be observed, such as those on the lower tier, near the facing. These localized regions may be better visualized in the deflection profile, which shows a discontinuity in lateral displacement between the tiers.

The series of simple and complex examples presented demonstrate that internal and compound stability well-captured by the proposed LE approach. The LE approach demonstrates its utility for a variety of reasons, including that it (1) does not use arbitrary thresholds in geometry as a basis for design, (2) quantifies connection and maximum reinforcement loading accounting for internal design criteria such as pullout and without separate internal stability analyses, and (3) maintains the ability to holistically evaluate internal and compound stability in one framework. However, there are some instances where additional limit state tools are necessary, particularly when evaluating even more complex systems, such as geosynthetic reinforced soil structures supporting footings, which is discussed in more detail in the following section.

3   EXTERNAL, GLOBAL, AND "HYBRID" STABILITY CRITERIA

External stability is focused on ensuring that the reinforced soil mass is not predisposed to sliding, overturning, bearing capacity failure, or global failure. It may be argued that compound stability is a special case of global stability, whereas the critical failure mechanism passes through foundation soil and/or retained backfill *in addition* to the reinforced soil mass. However, as these design criteria are often evaluated after initial design of internal stability, meeting external and global stability is an iterative process that may seem to be performed independent of other design criteria. While some external design checks are rather straightforward – e.g. direct sliding – others can be complex, particularly for common but irregular design conditions and geometries. Some instances of focus discussed in this paper are the nuances of hybrid stability problems, particularly as it relates to bearing capacity on reinforced walls.

One increasingly common application of geosynthetic reinforced soil structures is use for small-span bridge supports, often relying on load-bearing resistance in addition to earth retention purposes. Typically, such structures require shallow foundations that are placed on the reinforced soil zone – for good performance, these footings must have sufficient bearing resistance as to reduce settlements and support limit state design criteria. However, the increasing prevalence of such "hybrid" structures and their demands has resulted in a significant design question: how does one do limit state design for such foundations? Is it an internal stability problem? External stability? Consequently, building upon prior limit state methods, we explore the importance of "hybrid" stability problems and where its limit state evaluation exists in context of existing methods.

The performance of reinforced soil structures supporting footing loads is more complex in terms of design than unsurcharged counterparts as localized loading that may result in complex earth pressure distributions and a variety of potential yield mechanisms that are not singularly a slope or bearing capacity failure. These complexities largely rely on several dominant design parameters, outlined herein: (1) footing location (setback, S_b), width (B) and associated dead/live loads (q), (2) wall geometry, particularly height (H), and (3) strength (T), and spacing (S_v). Herein, we synthesize prior findings surrounding the importance of these design parameters, shown schematically in Figure 12.

Intuitively, the location of a footing with respect to the wall facing (i.e. "setback") and its distributed load strongly influence deformations and potential failure within the reinforced soil mass. These design parameters are of importance for bridge-supporting GRS structures as the span of the bridge deck is a primary material expense for such structures. Consequently, the smaller the setback distance (i.e. the clearance between the footing edge
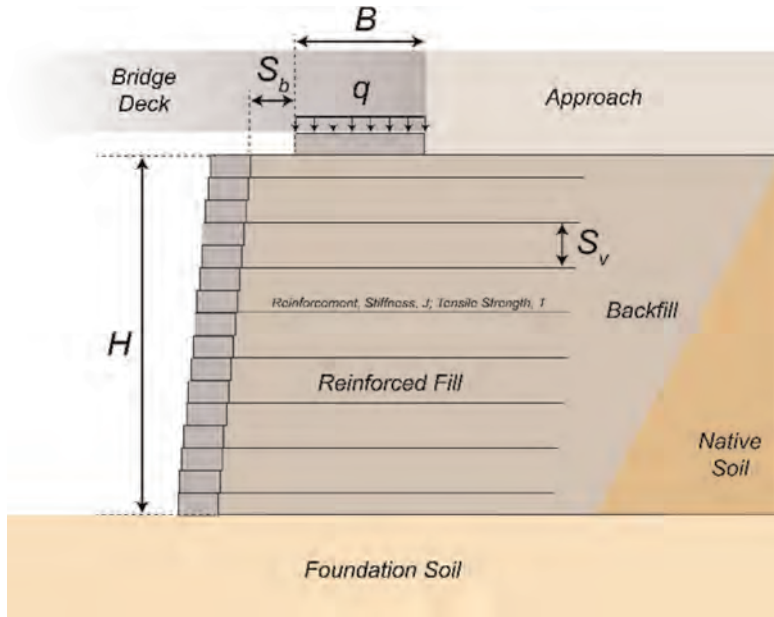
Figure 12.   Schematic of governing design variables for GRS-supported footings.

and wall facing), the more potential to decrease the bridge span length. However, short setback distances may result in excessive deformations (Ambauen et al. 2016; Doger & Hatami 2020) as well as diminished bearing capacity and ULS conditions (Xie et al. 2016, 2019; Xie & Leshchinsky 2015). Consequently, there are opportunities for improved design to shorten bridge deck length or support larger spans (i.e. larger footing loads), as well as explore the complex controls on stability.

From an ultimate limit state perspective, increased setback from the wall facing yields higher ultimate bearing capacity, which is largely dependent on reinforcement strength spacing, wall height, and to a level, batter (Xie et al. 2019). Specific combinations of these factors result in differing mechanisms and associated ultimate bearing pressures that can be supported, typically associated with a slope failure, bearing capacity, or hybrid mechanisms (Xie et al. 2019). Bearing capacity mechanisms (Figure 13a) may be one-sided (to the facing or towards unreinforced backfill), two-sided (either a Prandtl mechanism or constrained above the uppermost geosynthetic). Using the standard bearing capacity equation ignoring embedment, cohesion, eccentricity and assuming plane strain conditions, the bearing capacity equation is defined as:

$$q = 0.5\gamma B N_\gamma \qquad (1)$$

One-sided mechanisms and two-part wedge failures (red triangles) along the reinforcement interface tend yield lower bearing capacity factors (N_γ) than two-sided bearing capacity mechanisms, particularly at modest setbacks and large wall heights. Two-sided mechanisms become dominant at larger setbacks and for taller walls; however, constrained failures only occur under very high reinforcement strengths (black and white labels). For weaker reinforcements and especially taller walls, a log-spiral "wedge" is the dominant failure mechanism as the self-weight of the backfill is a large destabilizing element in addition to surcharges loading (Figure 13b). Effectively, decreased footing setback or increasing footing load will result in a predisposition towards failure above the wall toe, typically as a two-part
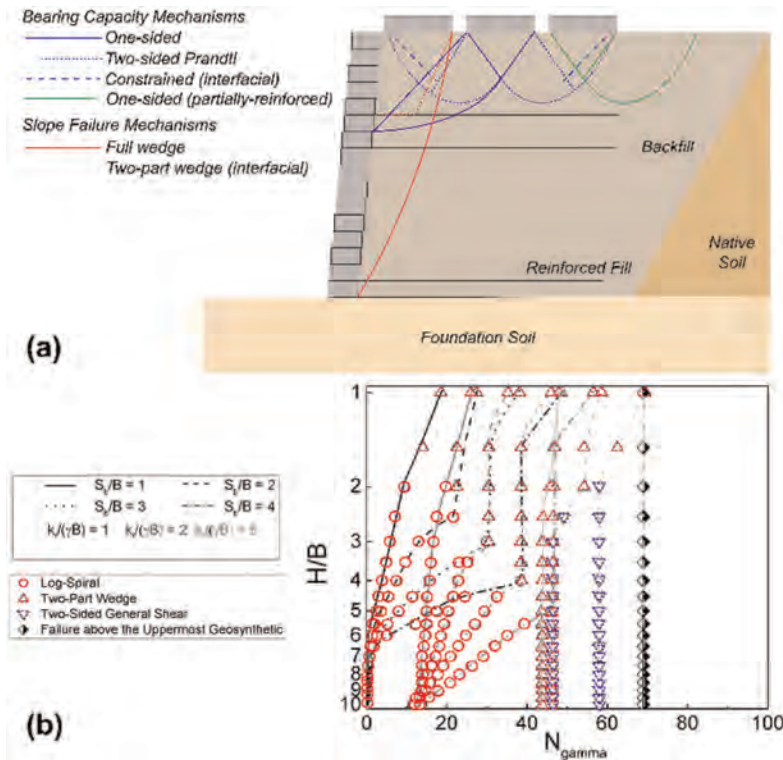
Figure 13. (a) Proposed failure mechanisms associated with ultimate bearing pressures. (b) Example design charts for different mechanisms and capacity based on Xie et al. (2019).

wedge or a one-sided bearing capacity failure. This is particularly prevalent when reinforcement strength is sufficiently large. In the presence of weaker reinforcement strengths or tall wall heights, the relative weight of the backfill results in a predisposition to an active failure, typically in the form of a wedge or log-spiral exiting the wall toe. Sufficient setback will result in bearing capacity failures becoming the dominant mechanism, either through Prandtl mechanisms through reinforcements or constrained above the uppermost reinforcement for relatively weak and strong reinforcements, respectively. With sufficient setback distance and proximity to the end of the reinforced fill, a one-side bearing capacity failure may occur through both reinforced and unreinforced fill; however, these bearing capacity conditions rarely govern as setbacks of this magnitude make the system uneconomical for supporting bridge spans. The predisposition of these failure mechanisms and their associated N_γ are shown in Figure 13b (based off of Xie et al. 2019). As shown, various governing failure mechanisms may be observed in the presence of weaker reinforcements as proportional wall height and setback change.

Other considerations for ULS conditions include the influence of facing-backfill interactions, nonuniform reinforcement spacing and loading inclination. Xie et al. (2016) showed that high levels of interface friction between block facings, backfill and between facing blocks may reduce reinforcement loads significantly (Figure 14), in agreement with field tests from Doger and Hatami (2020) and numerical modeling of Zheng et a. (2018), Zhang et al. (2022) which suggest that the structural importance of the facing cannot be ignored. Further, observed mobilized tension in the reinforcements is sensitive to backfill strength, footing
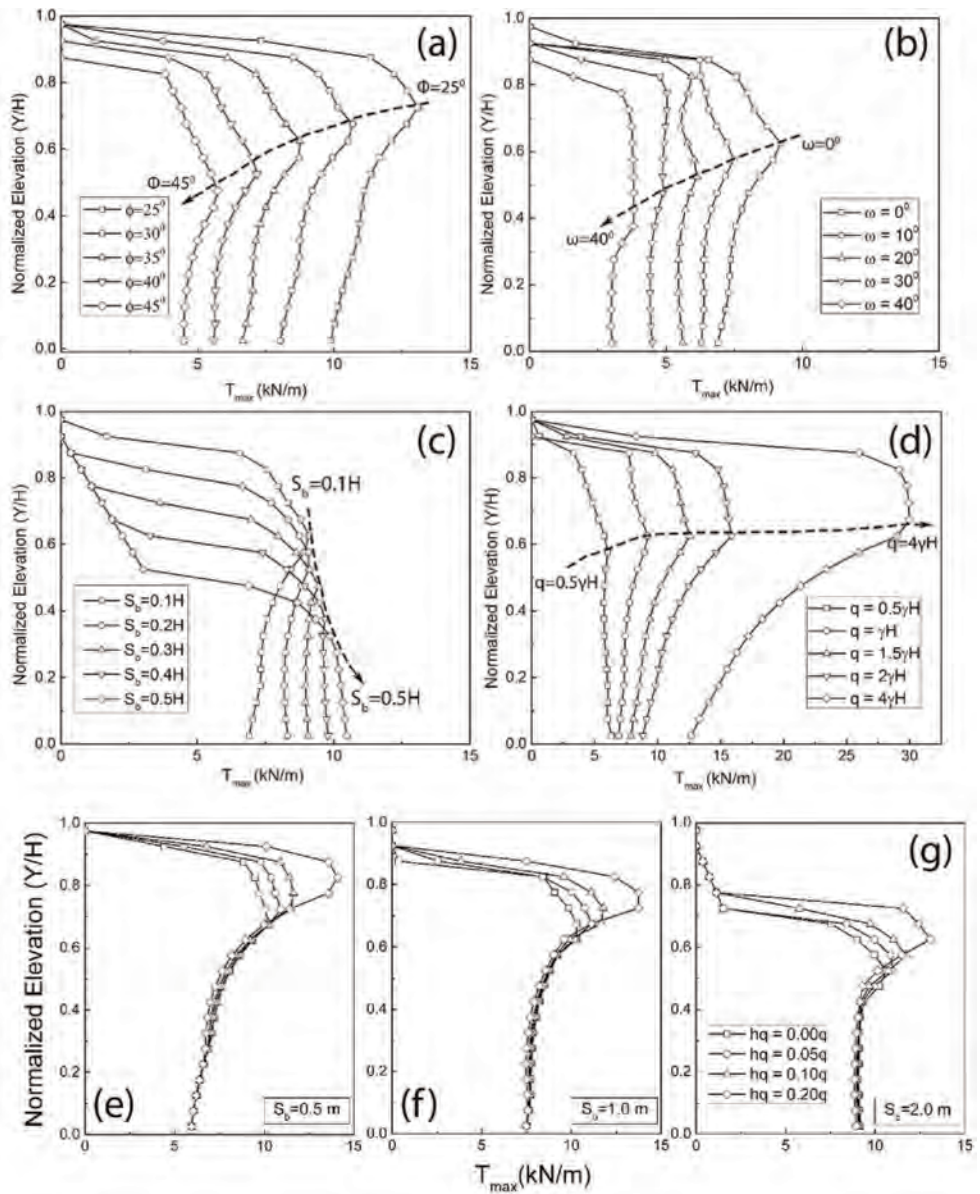
Figure 14.   Reinforcement tensile mobilization for GRS structures supporting footings modified from Xie et al. (2017). (Top left) Reinforcement load distribution considering a range of backfill friction angles. (Top right) Reinforcement load distribution considering a range of wall batters. (Middle left) Reinforcement load distribution considering a range of setbacks. (Middle right) Reinforcement load distribution considering increasing surcharge load. (Bottom) Reinforcement load distributions for S_b of 0.5m, 1m, and 2m for footings with horizontal inclinations.

setback, footing load, and to lesser levels wall batter and loading inclination of the footing (Xie et al. 2017). Further, ULS conditions for bearing capacity can be enhanced through strategic placement of small reinforcement spacing (S_v) in the region beneath the footing, but not necessarily throughout the wall. Xie and Leshchinsky (2015) demonstrated that

placement of stronger and/or denser reinforcements in the upper $1B$-$2B$ of the wall could yield near-full realization of bearing capacity as that of a wall constructed with dense reinforcements throughout. However, when wall height is sufficiently large, stronger and/or denser reinforcements within the wall toe help prevent an internal or compound failure. Effectively, reinforcement spacing, and strength can be tailored to create a more efficient GRS structure. This work also demonstrates that ULS failure mechanisms of GRS supporting footings can be exceedingly complex, often consisting of hybrid failures relating to both slope stability and bearing capacity.

4 CONCLUSIONS

The presented LE framework explored herein and proposed in Leshchinsky et al. (2017) has great utility towards unifying compound and internal stability of geosynthetic reinforced structures. It demonstrates that even relatively simple geosynthetic reinforced soil structures can have complex internal and compound stability conditions. This framework, however, enables exploration of internal and compound stability holistically, enabling evaluation of distributions of tensile and connection loading, as well as deflection. As expected, specific loading or geometric conditions can result in scenarios where compound failure governs. However, there are many more examples that could be explored – for example, hybrid walls, anchored MSE walls, less extensible reinforcements, etc. Future work could further describe the nuances of design under such scenarios. Further, future modifications of the LE framework could account for various failure kinematics, facing details and loading conditions. Evaluating the role of marginal soils, creep, long-term degradation and better connection with service limit state conditions would also enhance the utility of the proposed framework. Finally, better analysis of uncertainty would enable a more probabilistic approach to design and the range of wall or slope behavior observed in practice.

The importance of failure kinematics is further described by the latter section of this manuscript, where hybrid stability analyses with multiple potential failure mechanisms is possible – for example, such a scenario is available considering bearing capacity atop geosynthetic reinforced soil structures. Consequently, there is extensive need for further work on the ultimate limit state of GRS supporting footings, and there has been significant progress to evaluate a suite of important conditions. More full-scale tests are being performed (e.g. Doger & Hatami 2020; Zheng et al. 2019). For example, seismic performance is of paramount performance and extensive modeling at both full-scale and using numerical tools continues to advance this technology in earthquake-prone regions (Zheng et al. 2018). Other opportunities include improved understanding of the use of different backfills (Hatami & Boutin 2022), particularly marginal materials. Further investigation is needed regarding the importance of GRS foundations, including placement near slopes or banks subject to scour and erosion. Application in environments where hydraulic loading and or flooding is very much needed considered the preferential use of these systems for small span bridges across smaller streams that may flood. Other opportunities include improved optimization of these systems in terms of internal stability, reinforcement spacing, and especially length of reinforcements. Many of the design templates for these reinforced systems include relatively long L/H ratios (often much larger than 1.2), which precludes applications in areas where minimal right-of-way is available. Investigation of different facing systems, such as full-height rigid, gabion, and big blocks could also present opportunities for further enhancing the design of these systems. Lastly and most importantly, there is ample opportunity to further extend the growing body of knowledge surrounding these systems from research to practice, where current design guidelines are effective and economical, but very likely overly conservative and tailored to very specific applications.

REFERENCES

Ambauen, S., Leshchinsky, B., Xie, Y., & Rayamajhi, D. (2015). Service-state Behavior of Reinforced Soil Walls Supporting Spread Footings: A Parametric Study Using Finite-Element Analysis. *Geosynth. Int.*, *23* (3).

Boyle, S.R., 1995. *Deformation Prediction of Geosynthetic Reinforced Soil Retaining Walls.* PhD Thesis, Seattle, WA: University of Washington.

Doger, R., & Hatami, K. (2020). Influence of Facing on the Performance of GRS Bridge Abutments. *International Journal of Geosynthetics and Ground Engineering*, *6*(4), 1–14.

Flexible Reinforced Earth Structures," *ASCE, Journal of Geoenvironmental and Geotechnical Engineering*, *132* (11), 2006, 1427–1435.

Han, J., and Leshchinsky, D., *"General Analytical Framework for Design of.*

Hatami, K., & Bathurst, R. J., 2005. Development and Verification of a Numerical Model for the Analysis of Geosynthetic-reinforced Soil Segmental Walls under Working Stress Conditions. *Canadian Geotechnical Journal*, *42*(4), 1066–1085.

Jewell, R. A. "Reinforcement Bond Capacity." *Geotechnique* 40.3 1990. 513–518.

Lee, W.F., 2000. *Internal Stability Analyses of Geosynthetic Reinforced Retaining Walls.* PhD thesis, Seattle, WA: University of Washington.

Leshchinsky, B. (2015). Bearing Capacity of Footings Placed Adjacent to c′-ϕ′ slopes. *Journal of Geotechnical and Geoenvironmental Engineering*, *141*(6), 04015022.

Leshchinsky, B., & Xie, Y. (2017). Bearing Capacity for Spread Footings Placed Near c′-ϕ′ slopes. *Journal of Geotechnical and Geoenvironmental Engineering*, *143*(1), 06016020.

Leshchinsky, B., Berg, R., Liew, W., Kawakami-Selin, M., Moore, J., Brown, S., ... & Wayne, M. (2020). Characterization of Geogrid Mechanical and Chemical Properties from a Thirty-six Year Old Mechanically-stabilized Earth Wall. *Geotextiles and Geomembranes*, *48*(6), 793–801.

Leshchinsky, D. and Boedeker, R. H., (1989). "Geosynthetic Reinforced Soil Structures," *Journal of Geotechnical Engineering, ASCE*, *115*(10), 1459–1478.

Leshchinsky, D. and Han, J., 2004. "Geosynthetic Reinforced Multitiered Walls," ASCE, *Journal of Geotechnical and Geoenvironmental Engineering*, *130*(12), 1225–1235.

Leshchinsky, D. and Reinschmidt, A.J., (1985). "Stability of Membrane Reinforced Slopes," *Journal of Geotechnical Engineering, ASCE*, *111*(11), 1285–1300.

Leshchinsky, D., & Vulova, C. (2001). Numerical Investigation of the Effects of Geosynthetic Spacing on Failure Mechanisms in MSE Block Walls. *Geosynthetics International*, *8*(4), 343–365.

Leshchinsky, D., Kang, B.J., Han, J., Ling, H.I., "Framework for Limit State Design of Geosynthetic-Reinforced Walls and Slopes," *Transportation Infrastructure Geotechnology*, Springer, *1*(2), May 2014, 129–164.

Leshchinsky, D., Leshchinsky, B., & Leshchinsky, O. (2017). Limit State Design Framework for Geosynthetic-reinforced Soil Structures. *Geotextiles and Geomembranes*, *45*(6), 642–652.

Leshchinsky, D., Leshchinsky, O., Zelenko, B., and Horne, J., *Limit Equilibrium Design Framework for MSE Structures with Extensible Reinforcement*, **FHWA-HIF-17-004**, Contract DTFH6114D00047-5010, October 2016.

Liu, H. (2016). Required Reinforcement Stiffness for Vertical Geosynthetic-reinforced-soil Walls at Strength Limit State. *Géotechnique*, *66*(5), 424–434.

Mohamed, S. B., Yang, K. H., & Hung, W. Y. (2014). Finite Element Analyses of Two-tier Geosynthetic-reinforced Soil Walls: Comparison Involving Centrifuge Tests and Limit Equilibrium Results. *Computers and Geotechnics*, *61*, 67–84.

Soong, T. Y., & Koerner, R. M. 1997. On the Required Connection Strength of Geosynthetically Reinforced Walls. *Geotextiles and Geomembranes*, *15*(4), 377–393.

Wright, S. G., & Duncan, J. M. (1991). Limit Equilibrium Stability Analyses for Reinforced Slopes. *Transportation Research Record*, (1330).

Xie, Y., & Leshchinsky, B. (2015). MSE Walls as Bridge Abutments: Optimal Reinforcement Density. *Geotextiles and Geomembranes*, *43*(2), 128–138.

Xie, Y., Leshchinsky, B., & Han, J. (2019). Evaluation of Bearing Capacity on Geosynthetic-reinforced Soil Structures Considering Multiple Failure Mechanisms. *Journal of Geotechnical and Geoenvironmental Engineering*, *145*(9), 04019040.

Xie, Y., Leshchinsky, B., & Yang, S. (2016). Evaluating Reinforcement Loading within Surcharged Segmental Block Reinforced Soil Walls using a Limit State Framework. *Geotextiles and Geomembranes*, *44*(6), 832–844.

Yang, S., Leshchinsky, B., Cui, K., Zhang, F., & Gao, Y. (2019). Unified Approach Toward Evaluating Bearing Capacity of Shallow Foundations Near Slopes. *Journal of Geotechnical and Geoenvironmental Engineering*, *145*(12), 04019110.

Yang, S., Leshchinsky, B., Cui, K., Zhang, F., & Gao, Y. (2021). Influence of Failure Mechanism on Seismic Bearing Capacity Factors for Shallow Foundations Near Slopes. *Géotechnique*, *71*(7), 594–607.

Yoo, C., Kim, S., 2008. Performance of a Two-tier Geosynthetic Reinforced Segmental Retaining Wall under a Surcharge Load: Full-scale Load Test and 3D Finite Element Analysis. *Geotextiles and Geomembranes*. *26* (6), 460–472.

Zhang, J., Jia, Y., Guo, W., Zhao, J., Ling, J., & Zheng, Y. (2022). Experimental Study on the Load Bearing Behavior of Geosynthetic Reinforced Soil Bridge Abutments with Different Facing Conditions. *Geotextiles and Geomembranes*.

Zheng, Y., Fox, P. J., & McCartney, J. S. (2018). Numerical Study on Maximum Reinforcement Tensile Forces in Geosynthetic Reinforced Soil Bridge Abutments. *Geotextiles and Geomembranes*, *46*(5), 634–645.

Zheng, Y., McCartney, J. S., Shing, P. B., & Fox, P. J. (2019). Physical Model Tests of Half-scale Geosynthetic Reinforced Soil Bridge Abutments. II: dynamic loading. *Journal of Geotechnical and Geoenvironmental Engineering*, *145*(11), 04019095–04019095.

Zheng, Y., Sander, A. C., Rong, W., Fox, P. J., Shing, P. B., & McCartney, J. S. (2018). Shaking Table Test of a Half-scale Geosynthetic-reinforced Soil Bridge Abutment. *Geotechnical Testing Journal*, *41*(1), 20160268–20160268.

Geosynthethic-reinforced foundations

S.N. Moghaddas Tafreshi

K.N. Toosi University of Technology, Tehran, Iran

ABSTRACT: Construction of structures on soft foundations presents a major challenge for geotechnical engineers due to the limited bearing capacity of foundation, resulting in excessive settlement under construction loads. To address this issue, various ground improvement techniques are used, including preloading, soil replacement, grouting, piling, and geosynthetic reinforcement. Geosynthetic reinforcement, which involves incorporating geosynthetic layers into the foundation bed, is particularly effective in enhancing the shear strength of soil and creating a well-structured foundation with high bearing capacity and minimal settlement. The choice of geosynthetic reinforcement, such as geotextile, geogrid, or geocell, influences failure modes and stress distribution within the soil. Recent advancements in understanding the technical aspects of geosynthetic reinforcement have led to their widespread application in stabilizing and reinforcing footings, buried pipes, pavements, embankments, slopes, etc. This paper provides an overview of recent scientific achievements, reinforcing mechanisms, and research findings related to the protection of footings, buried pipes, and roads.

Keywords: Geosynthetic, Two and Three reinforcements, Footing, Buried pipe, Pavement

1 INTRODUCTION

In the past few decades, geosynthetic materials have become widely used in geotechnical applications, including construction projects involving footings on soft soil, road construction, stable embankments, slope stabilization, protecting buried pipes and underground utilities. Two-dimensional (2D) reinforcements like geotextiles and geogrids, as well as three-dimensional (3D) reinforcements like geocells and tire cells, have been employed for these purposes. One of the conventional uses of geosynthetic reinforcements is in supporting paved and unpaved roads and footings on weak subsoil layers. By distributing the applied loads over a larger area of the underlying soil, geosynthetic soil reinforcements improve the bearing capacity and reduce settlement of the foundation bed. In traditional unreinforced construction, a thick layer of granular soil is required to counteract the effects of weak subsoil layers. However, using such a layer can be costly, time-consuming, or impractical, especially when high-quality granular materials are scarce. The simplicity of constructing soil reinforcements, along with the economic and time-saving advantages over conventional approaches, has motivated engineers and researchers to consider geosynthetic-reinforced foundation soil in geotechnical projects. Consequently, numerous studies have been conducted in recent years (e.g., Amiri et al. 2023; Inti & Tandon 2021; Moghaddas Tafreshi & Dawson 2010; Madhavi Latha & Pokharel et al. 2010; Rajabian & Shukla 2023; Somwanshi 2009a; b; Shukla 2012; Sitharam & Hegde 2013; Tavakoli Mehrjardi et al. 2012; Thakur et al. 2012; Wehbi & Nogy 2022; Yang et al. 2012; Zhang et al. 2010) to investigate the optimal use of geosynthetic inclusions to effectively enhance the behavior of foundation beds. These studies have examined various aspects, including reinforcing mechanisms, and

have provided valuable insights into the application of geosynthetics for protecting footings, buried pipes, roads, pavements, etc.

This paper aims to provide an overview of the reinforcing mechanisms employed by 2D and 3D reinforcements in reinforced soil foundations. Additionally, it presents research findings on the application of geosynthetics for protecting footings, buried pipes, roads, and pavements, serving as a useful reference for further studies in the field.

2 SOIL REINFORCEMENT INTERACTION

2.1 Two-dimensional reinforcement

2D reinforcement systems consist of geotextile or geogrid materials that commonly contribute to the load-carrying mechanism by virtue of frictional resistance mobilized at its interface with surrounding soil (e.g., geotextile) or combination with interlocking between the ribs of reinforcement and soil particles (e.g., geogrid). These reinforcements are arranged in the horizontal planes inside the backfill to resist the outward movement of the reinforced soil mass. The interaction between soil and geogrid consists of (1) shear strength on top and bottom plane areas of the geogrid- i.e., mobilized friction strength between the soil and the geogrid's horizontal surfaces as shown in Figure 1a and (2) passive soil resistance along the transverse ribs of the geogrid as illustrated in Figure 1b. Stress transfer between the soil and the geogrid reinforcement takes place through one or a combination of both actions which mobilize due to the elongation of the geogrid. Geotextile reinforcement transfer stress to the soil through friction and then generation of a tension force in the reinforcement layer.
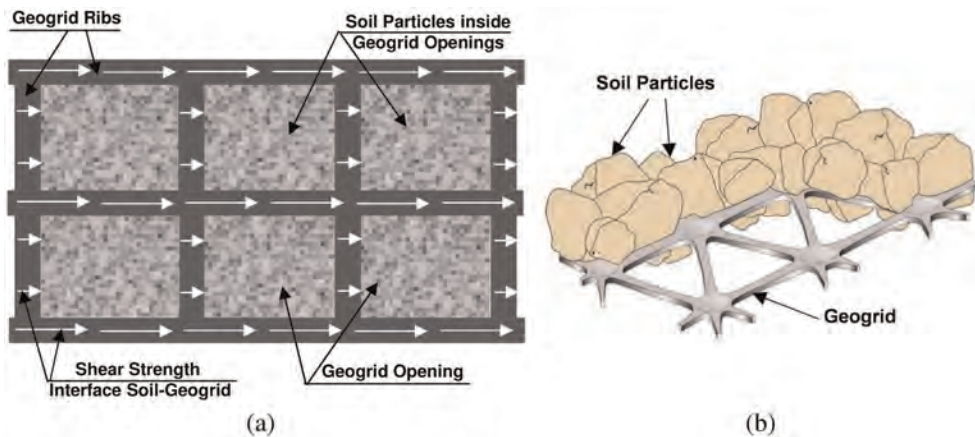
Figure 1. Soil and geogrid interaction (a) stress transfer between soil and geogrid, (b) passive soil resistance by ribs of geogrid.

2.2 Three-dimensional reinforcement

Geocell as a 3D reinforcement provides a cellular mechanical soil stabilization/reinforcement method. When a geocell layer fills with soil materials, due to the unique interaction of geometry, soil, and the cell-wall material act as a mattress (or slab) that distributes a portion of applied vertical forces (e.g., footing load and vehicle wheel load) laterally. Figure 2a-c shows the typical stresses exerted on a cell of geocell reinforcement (Schary 2019). The confinement restrains the lateral movement of soil particles via hoop stress on the geocell walls. This maximizes the distribution of lateral and vertical stresses, resulting in stabilized
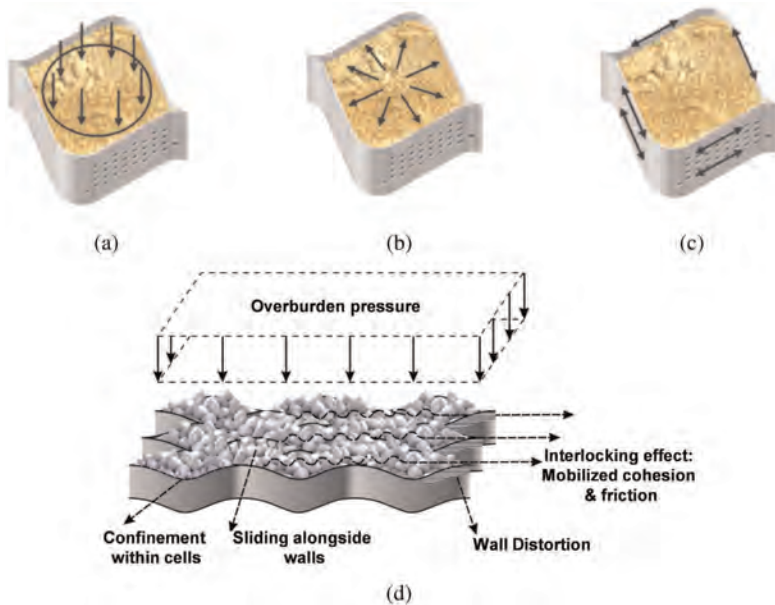
Figure 2. Geocell performance under loading (a) vertical stress on cell (b) lateral stress into cell wall, (c) hoop stresses on cell wall (Schary 2019), (d) interaction and interfacial behaviour of soil and geocell (Tavakoli Mehrjardi & Motarjemi 2018).

soil, basal layer reinforcement and reduced surface degradation, among other benefits (Kief et al. 2014).

Moreover, to capture the interaction and interfacial behaviour of soil-geocell, Figure 2d illustrates, the interlocking effect of geocell and soil particles which can mobilize apparent cohesion and friction at the interface, besides the confinement effect on grains within the geocell's cells, producing the interface's shear strength. Based on the acquired results, it was found that the shear strength of the interface encountered weakness in the aftermath of grain sliding alongside the geocell's walls and also, geocell's wall distortion (Tavakoli Mehrjardi & Motarjemi 2018).

3 EQUIVALENT CONFINING STRESS CONCEPT: REINFORCED AND UNREINFORCED TRIAXIAL TESTS

The behavior of granular soil specimens, whether unreinforced, 2D reinforced, or 3D reinforced, can be understood by examining their failure stresses in triaxial tests. These failure stresses are visualized in the σ (normal stress) and τ (shear stress) space using Mohr's circles, as depicted in Figure 3. Mohr's circle "1" represents the failure of an unreinforced specimen under a confining stress of $\sigma 3$ and a principal stress of σ_1. The Mohr's circle "1" is tangent to the Mohr-Coulomb failure envelope I_{Un}.

When a reinforcement layer, such as 2D materials (e.g., geotextile and geogrid), or 3D materials (e.g., geocell), is placed at specific locations within the soil specimens, it increases the ultimate principal stresses to $(\sigma_1)_1$ and $(\sigma_1)_2$, respectively, while subjected to a confining pressure of σ_3. These stresses are represented by Mohr's circles "4" and "5," which are tangent to the Mohr-Coulomb failure envelopes I_{2D} and I_{3D}, corresponding to the 2D and 3D reinforced specimens, respectively.

To achieve the ultimate principal stresses of $(\sigma_1)_1$ and $(\sigma_1)_2$ for the unreinforced specimens, the confining stress needs to be increased from σ_3 to $\sigma_3+(\Delta\sigma_3)_1$ and $\sigma_3+(\Delta\sigma_3)_2$. This results in the formation of Mohr's circles "2" and "3," representing principal stresses of $(\sigma_1)_1$ and $(\sigma_1)_2$ at failure. These principal stresses are defined as $(\sigma_1)_1=\sigma_1+(\Delta\sigma_1)_1$ and $(\sigma_1)_2=\sigma_1+(\Delta\sigma_1)_2$. The corresponding deviatoric stresses $(\Delta\sigma_1)_1$ and $(\Delta\sigma_1)_2$ are determined by multiplying $(\Delta\sigma_3)_1$ and $(\Delta\sigma_3)_2$ by k_p, where k_p denotes the coefficient of passive soil pressure. Figure 3 illustrates two Mohr's circles, labeled "2," and "3," are tangent to the Mohr-Coulomb failure envelope I_{Un}. like Mohr's circle "1".

The application of 2D and 3D reinforcement leads to an increase in normal stress from $\sigma1$ (in unreinforced specimen) to $(\sigma_1)_1$ and $(\sigma_1)_2$, respectively. This increase corresponds to a rise in confining pressure to $\sigma_3 + (\Delta\sigma_3)_1$ and $\sigma_3 + (\Delta\sigma_3)_2$ in unreinforced specimens (Mohr's circles "2," and "3,"). Figure 3 illustrates that $(\Delta\sigma_3)_1$ and $(\Delta\sigma_3)_2$ for 2D and 3D reinforced specimens are termed as "apparent confining pressure" or "internal confining pressure," while $(c_a)_{2D}$ and $(c_a)_{3D}$ represent the apparent cohesion resulting from the inclusion of reinforcement. The values of $(\Delta\sigma_3)_1$, $(\Delta\sigma_3)_2$, $(c_a)_{2D}$, and $(c_a)_{3D}$ can be determined by conducting a series of triaxial tests on both unreinforced and reinforced specimens, under the assumption that the internal friction angle of the soil (ϕ) remains constant until slippage occurs at the soil-reinforcement interface.

The superior effectiveness of 3D reinforcement, as opposed to 2D reinforcement, can be attributed to the interaction between the soil and reinforcement, as discussed in section 2.
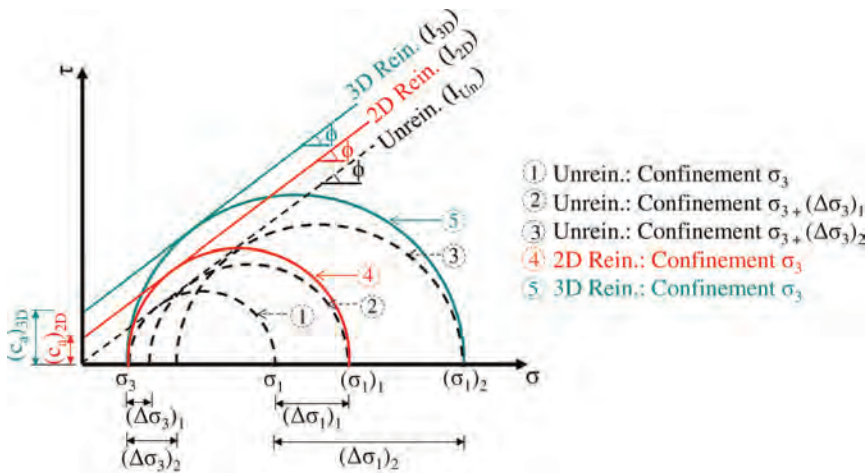
Figure 3. Mohr's circles for unreinforced, 2D and 3D reinforced specimens.

4 REINFORCING MECHANISM

4.1 *Two-dimensional reinforcement*

Based on the experiments conducted by several researchers (e.g., Chen & Abu-Farsakh 2015; Guo et al. 2020; Madhavi Latha & Somwanshi 2009a, b), four types of reinforcing mechanisms have been observed in planar reinforcement, as illustrated in Figure 4.

(1) Lateral restraint effect: The mobilization of this effect occurs when there is relative movement between the soil layer and the reinforcement layer along the surface of the reinforcement. This movement activates the friction force at the interface between the reinforcement layer and the soil particles (Figure 4a). The interaction between the reinforcement and the soil effectively constrains the horizontal displacement of the soils, thereby increasing

the lateral confining pressure and compressive strength of the soils beneath the footing (Chen & Abu-Farsakh 2015). Consequently, the foundation's ultimate bearing capacity of foundation increases. In the case of geogrid, the grid component plays a crucial role in facilitating the interaction between the soil and the reinforcement. It effectively restricts the displacement of soils, especially in the case of gravel soil or sand with larger particle sizes, further strengthening the constraint on the soils (as depicted in Figure 1b).

(2) Tensioned membrane effect: As a result of the relatively thin profile of planar geosynthetics, the reinforcement layer experiences deflection and bending when subjected to transferred loads. This deflection causes downward movement and generates a tension force, as illustrated in Figure 4b. The vertical component of this tension force within the reinforcement layer plays a beneficial role in reducing the pressure exerted on the underlying layers. Consequently, it leads to an increase in the bearing capacity of the foundation and a decrease in deformation or settlement of the foundation bed (Chen & Abu-Farsakh 2015).

(3) Vertical stress dispersion effect: The phenomenon initially described by Binquet & Lee (1975), was based on laboratory model tests conducted on reinforced earth slabs. Figure 4c demonstrates that this effect leads to reduced pressure on the underlying bed compared to an unreinforced bed. The reinforcing mechanisms depicted in Figure 4a-c are observed when the strength of the reinforcement zone slightly surpasses that of the underlying unreinforced layer. Specifically, for values of u (the distance between the footing base and the upper reinforcement layer) and h (the distance between reinforcement layers) that are smaller than 0.5 times the footing diameter/width ($u \leq 0.5B$ or $h \leq 0.5B$), failure occurs within the reinforcement zone, as shown in Figure 5a. Conversely, when there is a significant distance between the foundation base and the upper reinforcement layer (u), likely exceeding $u > 0.5B$, failure is more likely to occur above the upper reinforced layer (Binquet & Lee 1975). Similarly, when there is a considerable distance between the reinforcement layers (h), presumably $h > 0.5B$, failure between the reinforced layers is more likely to occur (Wayne et al. 1998). In both cases ($u > 0.5B$ or $h > 0.5B$), the effectiveness of soil reinforcement on the bearing capacity of the foundation bed is compromised.

(4) Deep footing effect: Based on Figure 4d, the formation of the deep footing effect occurs when the strength of the reinforced zone significantly exceeds that of the underlying unreinforced layer, the reinforcement length is very short or equal to the footing width, and the spacing between reinforcement layers is small. This effect manifests as shear punching failure within the reinforced zone, followed by total shear failure in the unreinforced zone beneath it. Essentially, the performance of a reinforced foundation resembles that of an
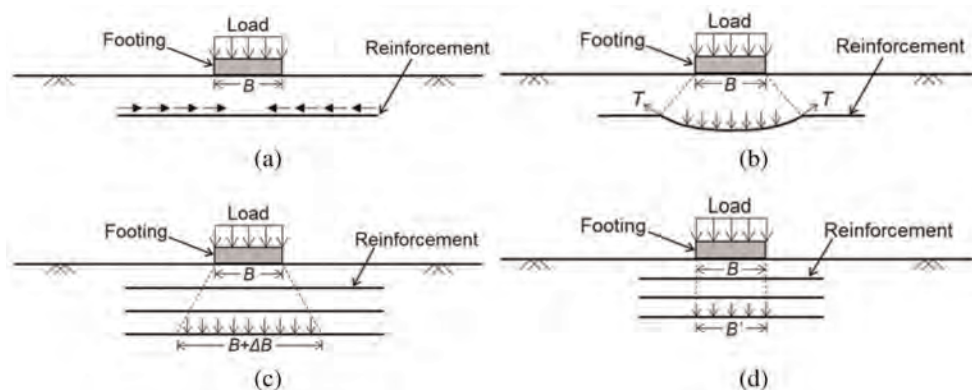
Figure 4. Schematic view of four reinforcing mechanisms of 2D reinforcement (a) lateral restraint effect, (b) tensioned membrane effect, (c) stress dispersion effect, (d) deep footing effect (Guo et al. 2020).

unreinforced foundation, but with an additional embedment depth equivalent to the depth of the reinforced zone (Sharma et al. 2009). Failure occurs within the underlying unreinforced layer beneath the reinforcement zone, as depicted in Figure 5b. By increasing the embedment depth of the "equivalent footing over the underlying unreinforced layer," the bearing capacity of the footing improves, albeit to a lesser extent compared to what is illustrated in Figure 5a. This failure mechanism was initially proposed by Meyerhof & Hanna (1978) for a strong unreinforced soil layer placed on a weak soil layer. Wayne et al. (1998) further elaborated on this effect with slight adjustments to the solution presented by Meyerhof & Hanna (1978) for calculating the bearing capacity of foundations on reinforced beds.
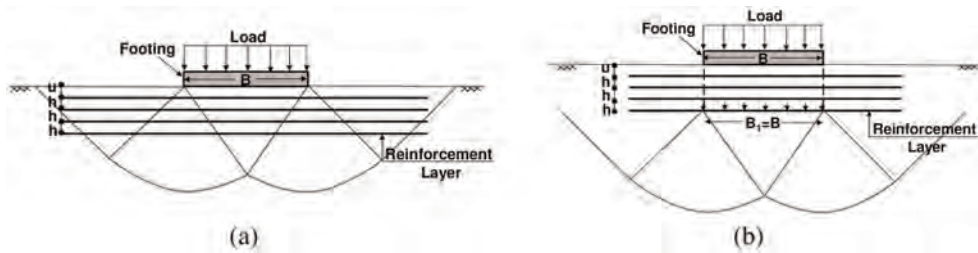
Figure 5.   Failure (a) inside the reinforced zone (Sharma et al. 2009), (b) like footings on a two layered soil (Wayne et al. 1998)

4.2   *Three-dimensional reinforcement*

The reinforcing mechanism of a geocell layer as a three-dimensional reinforcement are defined in three main aspects as shown in Figure 6 (Zhang et al. 2010).
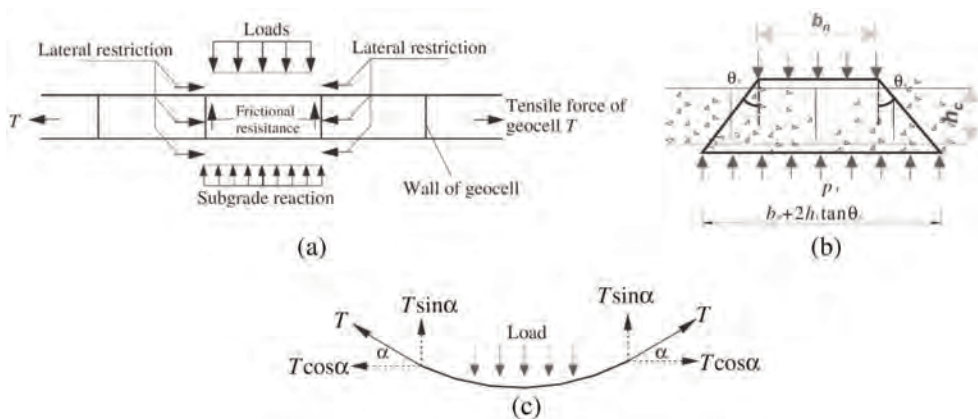
Figure 6.   Schematic view of three reinforcing mechanisms of 3D reinforcement (a) lateral resistance effect, (b) vertical stress dispersion effect, (c) tensioned membrane effect (Zhang et al. 2010).

(1) Lateral resistance effect: A geocell is a geosynthetic product that utilizes a 3D cellular network to contain and confine the materials it is filled with. This confinement effectively prevents lateral spreading, thereby enhancing the shear strength of the filled materials. Additionally, the interaction between the geocell reinforcement and the soils both below and above it, as illustrated in Figure 6a, leads to interfacial horizontal resistances. These resistances further enhance lateral confinement and reduce lateral strain, resulting in an increased

modulus of the cushion layer and improved vertical stress distribution on the subgrade. This phenomenon is known as the "vertical stress dispersion effect," which reduces the vertical pressure exerted on the top of the underlying unreinforced layer.

(2) Vertical stress dispersion effect: The horizontally reinforced geocell cushion acts as an immediate working slab, redistributing the applied load on the footing across a wider area, as depicted in Figure 6b. This phenomenon is referred to as the "vertical stress dispersion effect." Consequently, the soil pressure exerted on the underlying unreinforced layer, such as the soft subgrade soil layer, is lower compared to the absence of geocell reinforcement. The load applied on the footing surface, with a width of "b_n," can be distributed across an equivalent footing with a width of "$b_n+2h_c.tan \Theta$," where b_0, h_c, and Θ respectively represent the footing width, the thickness of the geocell layer, and the angle of load distribution.

(3) Tensioned membrane effect (Beam effect): The beam effect or tensioned membrane effect refers to the tension that develops in the curved geocell-reinforced mattress to resist vertical loads (Rajagopal et al. 1999; Zhou & Wen 2008). The loads exerted by footings, pavements, roads, and embankments cause deflection in the geocell reinforcement, resulting in additional tension forces, as depicted in Figure 6c. The vertical component of these tension forces in the reinforcement is beneficial in reducing the pressure on the underlying unreinforced layer, such as soft soil or subgrade soil. Consequently, the vertical deformation of the unreinforced layer beneath the reinforced zone decreases, leading to an overall increase in the bearing capacity of the foundation bed. Additionally, as the surface settles, the geocell layer undergoes further deformation, generating additional tension forces due to this membrane effect.

The behavior of the geocell mattress varies depending on the aspect ratio, h/d, where h represents the thickness and d denotes the pocket size of the geocell layer. According to Avesani Neto et al. (2013), when the geocell layer has a small thickness (i.e., $h/d \leq 1$, approximately), it behaves like a centrally loaded shallow beam. This results in increased deflection, higher contact pressure underneath, and the development of tension stress at the bottom and compression stress at the top, accompanied by significant shear stress mobilization. On the other hand, a geocell layer with a large thickness ($h/d > 1$, approximately) exhibits high rigidity and tends to behave similar to a raft foundation. It settles more uniformly, leading to a relatively even distribution of pressure (Dash et al. 2007; Han et al. 2008; Madhavi Latha & Somwanshi 2009b). In this case the confinement effect is only marginal, and the most important improvement effect is the stress dispersion.

5 PRESSURE AND SETTLEMENT IN DEPTH OF UNREINFORCED AND REINFORCED BED

Figure 7 depicts a schematic representation of the vertical pressure isobar and vertical settlement in depth of unreinforced, geogrid reinforced, and geocell reinforced beds under a load applied to a footing. As shown in Figure 7a, the pressure is distributed vertically to a depth of "h" and horizontally to a width of "W." In the case of 2D reinforcement (geogrid in Figure 7b), its reinforcing mechanism (Figure 4c), allows for the load to be distributed over a wider area with less depth compared to the unreinforced bed. The width and depth of load distribution range from $0.6h$-$0.8h$ and $1.2W$-$1.8W$, respectively. Additionally, Figure 7c highlights that 3D reinforcement further contributes to a wider area and reduced depth of pressure distribution, due to the geocell's reinforcing mechanism (Figure 6), when compared to the 2D reinforced bed. In the case of a geocell reinforced bed, the load distributes in a width range of $0.4h$-$0.6h$ and $1.5W$-$2.5W$ within the bed's depth. As shown in Figure 7, the vertical settlement in the foundation bed decreases progressively from "S," "$0.5S$-$0.6S$," and "$0.2S$-$0.3S$" for the unreinforced bed, geogrid reinforced bed, and geocell reinforced bed, respectively. This indicates the significant role of geosynthetic reinforcement in controlling

the settlement of the footing. Thus, incorporating 2D and 3D reinforcement enhances the stiffness of the reinforced bed, allowing for higher bearing pressure and reduced settlement with a smaller thickness of geosynthetic-reinforced bed. The inclusion of geocell and the confinement effect further increases the stiffness of the reinforced base.
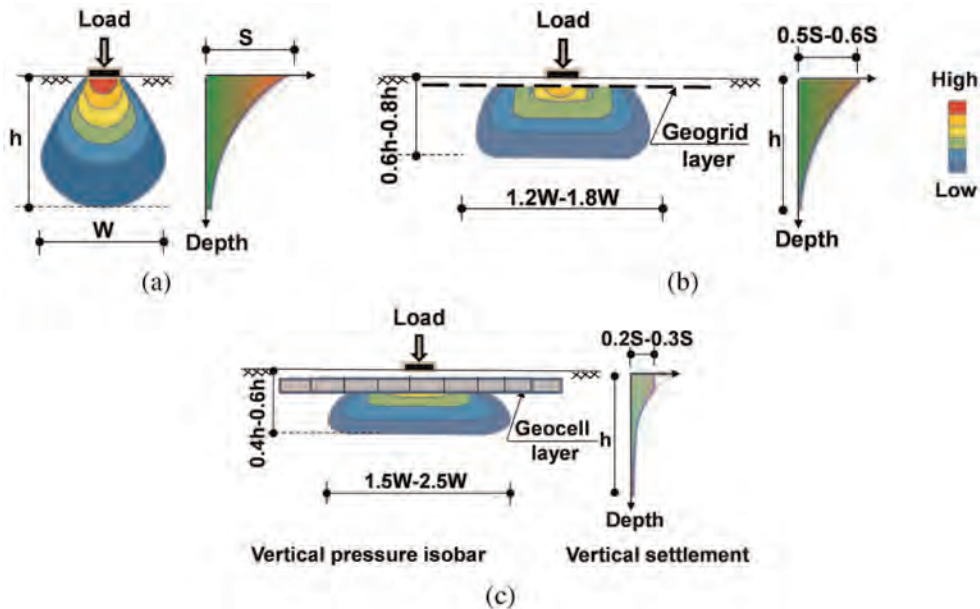
Figure 7. Vertical pressure isobar and vertical settlement in depth for (a) unreinforced bed, (b) geogrid reinforced bed, (c) geocell reinforced bed.

6 GEOSYNTHETIC-REINFORCED BED IN VARIOUS ASPECTS

Utilizing one or multiple layers of geosynthetic reinforcement, such as geotextile, geogrid, and geocell, to reinforce foundation beds offers significant potential as a cost-effective alternative for supporting shallow footings, buried pipes, roads, pavements, and retaining walls. This section aims to present the application of geosynthetics in safeguarding footings, buried pipes, roads, and pavements.

6.1 Shallow footings supported on geosynthetic-reinforced bed

Geocell reinforcement is an advantageous soil reinforcement method that can provide stiffer and stronger foundations compared to planar reinforcement (i.e., geotextile and geogrid) methods. Due to the three-dimensional honeycomb nature of geocell, it can generate several mechanisms for improving the performance of shallow footings. A higher stiffness, bearing capacity and better pressure distributing characteristic could be achieved by incorporating single and multiple layers of geocell or planar reinforcement. In this section, the advantages of geocell reinforcement compared to geotextile reinforcement are described. Then the usage of geocell and geotextile reinforcements is extended to multiple layers of geocell reinforcement. The results presented in this section are fully obtained from scaled models or full-scale experiments and thus, could provide a solid understanding for designing and constructing geocell-reinforced foundations.

6.1.1 *Comparison of single geocell layer and multiple geotextile layers*

Comprehensive results from laboratory model tests on strip footings with a width of 75 mm supported on the geocell and geotextile reinforced sand beds with the same characteristics of geotextile are reported by Moghaddas Tafreshi & Dawson (2010). The soil used is relatively uniform silica sand with grain sizes between 0.85 and 2.18 mm, a specific gravity (G_s) of 2.68 and the maximum and minimum void ratio (e_{max} and e_{min}) of the sand were 0.82 and 0.54, respectively. The soil is classified as poorly graded sand with the letter symbol SP with particle size distribution curve, as shown in Figure 8a. The angle of internal friction of sand obtained through drained triaxial compression tests on dry sand sample at a relative density of 72% was 37.5 (all tests being run on dry sand at this relative density).

The geocell layer in Figure 8b was fabricated from the same non-woven geotextile material that forms the geotextile. This geocell comprises a polymeric, honeycomb-like structure with open top and bottom manufactured from strips of geotextile that are thermo-welded into a cellular system. The area weight, tensile strength, and thickness under a tensile stress of 200 kN/m^2 are 190 g/m^2, 13.1 kN/m and 0.47 mm, respectively. The pocket size (d) of the geocell used was kept constant (at d=50 mm). It was used at heights (H) of 25, 50 and 100 mm in the testing program.
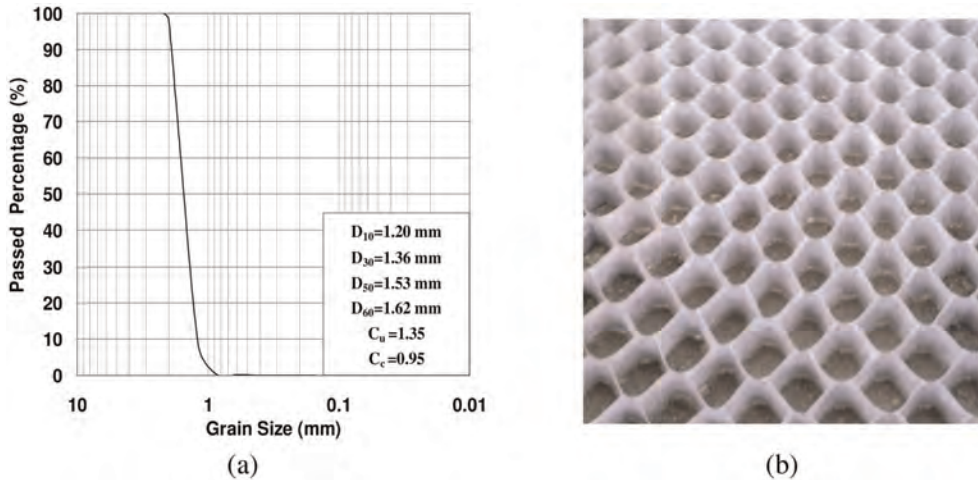
Figure 8.   (a) Particle size distribution curve (b) Isometric view of the geocell (Moghaddas Tafreshi & Dawson 2010).

In order to provide a meaningful comparative assessment between the geotextile and geocell reinforcement, the quantity of material used must be matched. The quantity of material used in each test relative to that used in the least reinforced test is termed as '*a*', which is equivalent to the mass of a single sheet of geotextile reinforcement of the smallest width used in the tests. Assessment of performance was undertaken for arrangements with geotextile sheet and geocell reinforcement of the same mass of geotextile being paired together. For example, the experiment reinforced by 2 layers of short geotextile reinforcement has exactly the same mass of geotextile as that reinforced by the short geocell reinforcement at H/B=0.66 (see Figure 9 for definition of H and B). This pair both have 2 units '*a*' of reinforcement the same as the long pair of 1 layer for geotextile or H/B=0.33 for geocell reinforcement.

Important factors for obtaining the best performance are the embedment depth (u) of the top reinforcement layer, the vertical spacing of the geotextile layers and the width of

reinforced layer (b_{gc} for geocell and b_{gt} for geotextile layer- see Figure 9). The optimum depth of the topmost layer of geotextile reinforcement and geocell layers were obtained about 0.35 and 0.1 times the footing width ($u/B=0.35$ and 0.1), respectively and the vertical spacing of the geotextile layers was obtained 0.35 times the footing width ($h/B=0.35$) which not reported here as detailed. The tests performed with different reinforcement widths (short, medium and long reinforcement) indicate that increasing the reinforcement width more than 4.2 and 5.5 (i.e., long width) times the footing width for the geocell and geotextile reinforcement, respectively, would not provide much additional improvement in bearing pressure.
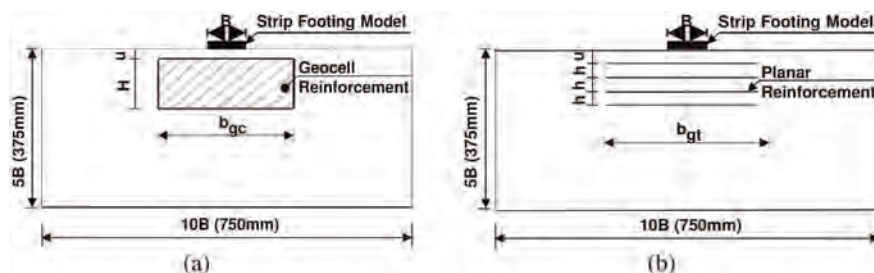
Figure 9.   Geometry of the (a) geocell reinforced foundation bed (b) geotextile reinforced foundation bed (Moghaddas Tafreshi & Dawson 2010).

The variation of bearing pressure with footing settlement (s/B) for the geocell-reinforced, geotextile-reinforced, and unreinforced beds is shown in Figure 10. From this figure, it may be clearly observed that with increasing the mass of reinforcement (increase in the height of the geocell layer, H/B or in the number of geotextile layers, N), both stiffness and bearing pressure (bearing pressure at a specified settlement) considerably increase but the efficiency of reinforcement decreases by increasing H/B or N. Provision of the geocell reinforcement in reinforcing the foundation bed is more than the geotextile reinforcement with the same characteristics and the same mass used. In the case of the unreinforced sand bed, it is apparent that the bearing capacity failure has taken place at a settlement equal to 12% of footing width while in the case of both the geocell and geotextile reinforced sand beds, no clear failure point is evident for the larger masses of reinforcement ($N \geq 2$ or $H/B \geq 0.66$).
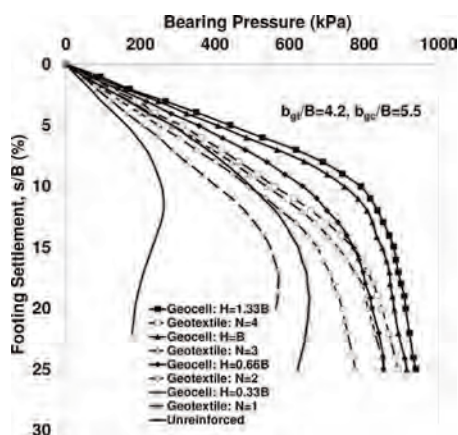
Figure 10.   Variation of bearing pressure with settlement for the geocell and geotextile reinforcement with long width: $b_{gc}/B=4.2$ & $b_{gt}/B=5.5$(Moghaddas Tafreshi & Dawson 2010).

The performance improvement due to the provision of reinforcement is represented using non-dimensional improvement factor of *IF* which compares the bearing pressure of the geotextile or geocell reinforcement bed to that of the unreinforced bed at a given settlement, s_i.

$$IF_{gt} = \frac{q_{gt}}{q_{un.}} \; OR \; IF_{gc} = \frac{q_{gc}}{q_{un.}} \quad s_i/B = 2\%, 4\%, 6\%, 8\%, 10\% \text{ and } 12\% \tag{1}$$

Where q_{un}, q_{gt}, and q_{gc} are respectively the values of bearing pressure of the unreinforced bed, the geotextile reinforced bed and the geocell reinforced bed.

The variation of these two parameters, IF_{gt} and IF_{gc} with footing settlement for long, medium and short reinforcement width are shown in Figure 11. According to this figure, it is evident that for the same mass of geotextile material used in the tests at the settlement level of 4%, the maximum improvement in bearing capacity (*IF*) was obtained as 2.73 and 1.88 with the provision of geocell and the equivalent geotextile reinforcement, respectively (Figure 11a). Therefore, improvement of foundation performance is proved, and it can be concluded that geocell provides more benefits compared to geotextile forms of reinforcement. For amounts of settlement that are tolerated in practical applications, improvements in bearing capacity greater than 200% (*IF_gc>3*) can be achieved with the application of geocell reinforcement, whereas geotextile reinforcement arrangements can only deliver 150% (*IF_gt>2.5*) for these two quantities, respectively.
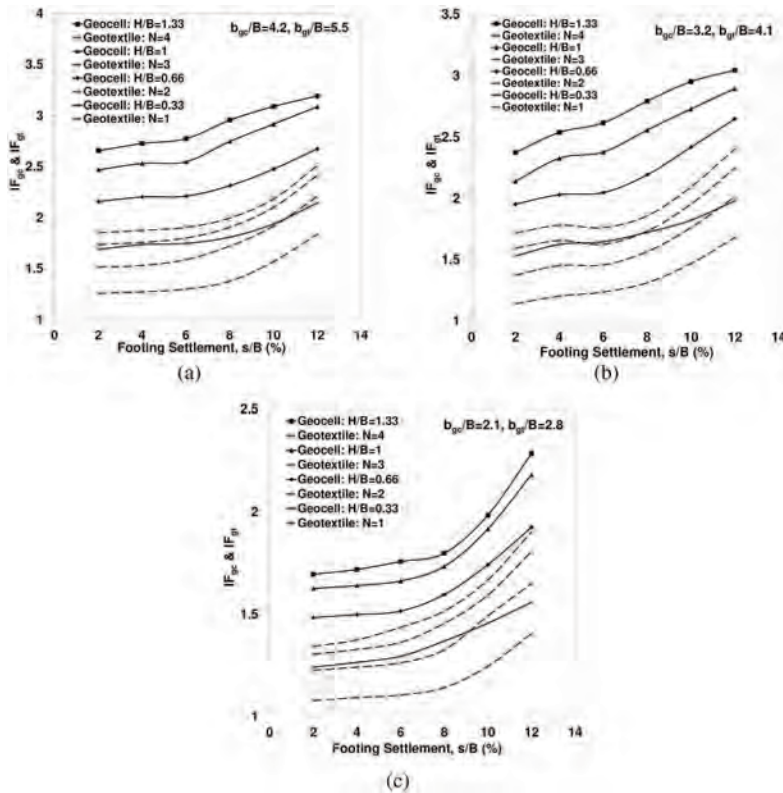
Figure 11. Variation of the bearing capacity improvement factor (*IF*) with footing settlement for the geocell and geotextile reinforcement, (a) Long width (b_g/B=4.2 & b_p/B=5.5), (b) Medium width (b_g/B=3.2 & b_p/B=4.1) and (c) Short width (b_g/B=2.1 & b_p/B=2.8), (Moghaddas Tafreshi & Dawson 2010).

6.1.2 *Comparison of multiple geocell and geotextile reinforcement layers*

The previous research (Moghaddas Tafreshi & Dawson 2010) showed that geocell reinforcement can be significantly more effective than a geotextile reinforcement at the same mass of material, in improving the behaviour of foundation beds. Geosynthetic inclusions will be most effective if used in the zone significantly stressed by the footing load, traffic load, etc. – which may be over a depth of 1 or 2 diameters beneath the loading surface width/diameter. Since the heights of commercially produced geocells for soil reinforcement are usually standard and most manufacturers of geocell produce them for reinforcement purpose only at heights less than 200 mm, the use of a thick geocell layer beneath the footing is impossible. Even if it were, such a thick geocell layer would likely make compaction of cell-fill extremely difficult, probably negating any reinforcement benefit (Tavakoli Mehrjardi et al. 2013). Hence, the use of several thin layers of geocell (say, three or four) with vertical spacing between successive layers of geocell is a practical alternative and might be a beneficial means of reinforcing the soil beneath a footings and roads.

Moghaddas Tafreshi et al. (2016) performed a series of laboratory model tests on a model circular footing with 112.8 mm diameter (D), supported on multi-layered of geocell-reinforced and multi-layered geotextile-reinforced sand beds. Figure 12 shows the layout tests and parameters used for evaluation of such multi-layered geotextile and geocell reinforced systems. In a previous study by Moghaddas Tafreshi & Dawson (2010) and regarding the model geometry in Figure 12, the optimum values of b_{gc}, b_{gt}, u_{gc} and u_{gt} in non-dimensional form with respect to footing diameter (D) were $b_{gc}/D = 3.2$, $b_{gt}/D = 4.1$, $u_{gc}/D=0.1$ and $u_{gt}/D=0.32$. The same values were used and kept constant in the tests described here. The pocket size (d) of the geocell used was kept constant ($d=50$ mm), while the geocell was used at a thickness (H_g) of 25 mm. The optimum vertical spacing of geocell and geotextile reinforcement layers are approximately 0.36 and 0.4 times footing diameter ($h_{gc}/D = 0.36$ and $h_{gt}/D = 0.4$), respectively which not reported here as detailed. The properties and classification of soil, geotextile and geocell reinforcement are as detailed in the previous section and The performance improvement due to the provision of reinforcement is represented using non-dimensional improvement factor IF_{gt} and IF_{gc} as given in Equation (1).
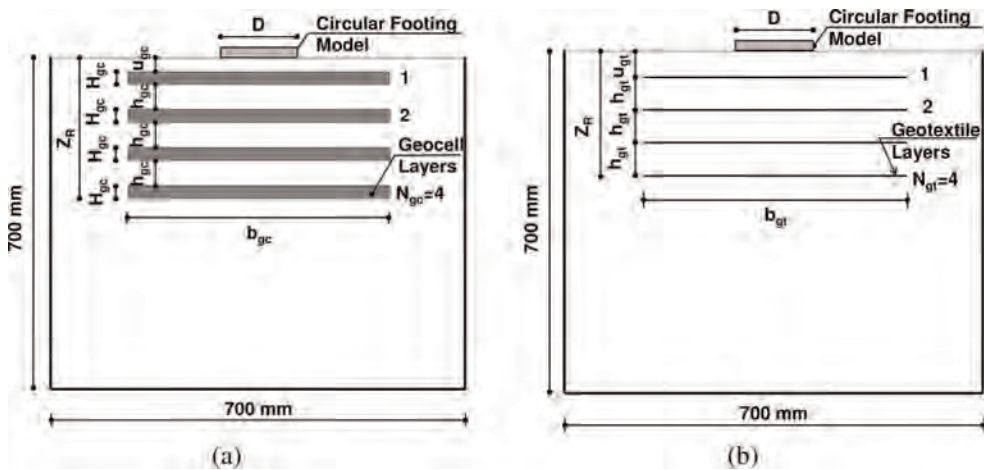
Figure 12. Layout of the multi-layered (a) geocell-reinforced system, (b) geotextile-reinforced system (Moghaddas Tafreshi et al. 2016).

Figure 13 presents the bearing pressure-settlement behaviour of geocell and geotextile reinforced foundations when the layers of geocell and geotextile were placed at their optimum spacings. For any matching pair of geocell and geotextile reinforcement ($N_{gc}=N_{gt}=1$,

etc.), the width of geocell and geotextile reinforcement are kept constant (as before, at b_{gc}/D= 3.2, b_{gt}/D= 4.1, respectively) and the masses of geosynthetic material are kept the same within each pairing. It may be observed that, with increasing the layers of reinforcement (increase in the mass of the geocell and geotextile reinforcement and consequently the increase in the depth of the reinforced zone, Z_R) both stiffness and bearing pressure (bearing pressure at a specified settlement) increase considerably. In the case of the unreinforced soil, it is apparent from Figure 13 that the peak bearing pressure has taken place at a footing settlement equal to approximately 13% of footing diameter while in case of both the geocell- and geotextile-reinforced soil, no clear failure point is evident. For the reinforced soil, beyond a footing settlement level of s/D=8-14%, there is a noticeable reduction in the slope of the pressure-settlement curve (the ratio $\Delta q / \Delta(s/D)$ reduces). Beyond this stage, the slope of the moderately and heavily reinforced cases remains almost constant while the footing bearing pressure continuously, but gradually, increases as further mobilization of its reinforcement and anchorage is exploited.
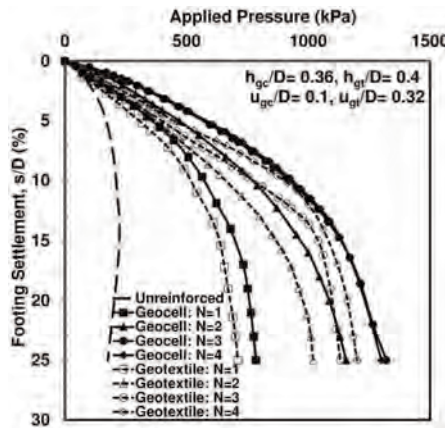
Figure 13.   Variation of bearing pressure with settlement for the geocell and geotextile reinforcement (h_g/D=0.36, h_p/D=0.4)- (Moghaddas Tafreshi et al. 2016).

Figure 14a shows the improvement in bearing pressure (IF_{gt} and IF_{gc}) with the number of reinforcement layers at three levels of settlement (s/D=4%, 8%, 12%) when the layers of geocell and geotextile were placed at optimum values of h_{gc}/D (= 0.36) and h_{gt}/D (= 0.4). In all situations, the values of IF_{gt} and IF_{gc} are higher at higher footing settlement for both reinforcement types (attributable to greater mobilization of tensile strain in the reinforcement layers and to the confinement provided between layers by the reinforcement).

For the multi-layered geocell, no significant improvement in performance is observed when the number of geocell layers are more than three ($N_{gc} \geq 3$). Therefore, when three layers of geocell are located at the optimum value of h_g/D (=0.36), the maximum zone of soil that can usefully be reinforced extends to a depth of approximately 1.48D (Z_R= 1.48D). In contrast, Figure 14a shows that the performance improvement due to the provision of geotextile reinforcement may continue beyond 4 layers (N_{gt}>4 with reinforcement zone of Z_R>1.52D). This comparison indicates that the effective reinforcement zone beneath the footing base is smaller for geocell reinforcement usage (for N_{gc}=3 with reinforcement zone of Z_R=1.48D) compared to that of the effective geotextile reinforcement zone (N_{gt}>4 with reinforcement zone of Z_R>1.52D). These findings serve to confirm that the reinforcing mechanism of the geocell facilitates a broader load distribution area and a shallower depth in comparison to the 2D reinforced bed.

Figure 14a also shows that improvement in bearing pressure (IF) for all the cases with the same number of geocell and geotextile reinforcement layers (and, thus, the same mass of geotextile material), is greater for geocell reinforcement than for geotextile reinforcement, irrespective of settlement ratio of the footing. For example, for $N_{gc} = N_{gt} = 3$ and a settlement of $s/D = 4\%$, the geocell installation improves performance 84% more than the comparable geotextile. Alternatively, by comparing, for example, the improvement due to two layers of geocell reinforcement (N_{gc}=2) with the improvement due to four layers of geotextile reinforcement (N_{gt}=4) at a settlement ratio of 4%, both are shown to have a similar bearing pressure (Figure 14a), yet the geocell installation contains half the mass of material. Also, the reinforcement zone depth beneath the footing (Z_R) for four layers of geotextile reinforcement (Z_R= 1.52D) are approximately 1.68 times bigger than two layers of geocell (Z_R= 0.9D).

For many practical purposes, performance of reinforced systems at low footing settlement ratios, s/D (say, less than 2%) is critical. For the tests described here, this is the subject of Figure 14b. Again, for the same number of layers (i.e. with the same mass and area) of geocell and geotextile used, the multi-layered geocell reinforcement system is both stiffer and more effective than the system with multi-layered geotextile reinforcement system and benefit of the geocell reinforcement is gained at very low settlement ratios ($S/D = 0.4\%$) whereas, in the case of geotextile reinforcement, the benefit only appears at footing settlement ratios of around 1-1.5%. At low settlements, apparently before the geotextile has attracted loading to itself, geotextile installations may actually lead to a softer response than when unreinforced. The cause of this is uncertain but is probably indicative of a lower geotextile-soil interface friction than soil-soil friction at a point in the loading sequence before the geotextile has been tensioned and is able to deliver benefit. Similar results were observed in the pressure-settlement of geotextile and geogrid reinforcement (Madhavi Latha & Somwanshi 2009b) and of geocell reinforcement (Dash et al. 2001, 2003). It is likely that the better performance at low settlement levels of the multi-layered geocell, compared with that of the multi-layered geotextile, is due to the geocell system gaining its resistance from the soil confinement that occurs when localized hoop stresses are developed in the walls of cells close (vertically and horizontally) to the footing. In a geotextile reinforcement system, reinforcing action requires outward shear stress to be developed in the horizontal plane between the geotextile and soil throughout a zone whose size is controlled by the load spreading achieved

Figure 14. Variation of IF_{gc} and IF_{gt} with (a) the number of reinforcement layers (N_{gc} & N_{gt}) at different levels of settlement (s/D=4%, 8% and 12%), (b) low footing settlement (s/D) for different number of reinforcement layers (N_{gc}= N_{gt} =1, 2, 3, and 4)- (Moghaddas Tafreshi et al. 2016).

in the soil between footing and the uppermost geotextile layer. Such shear strains are not thought to be necessary in the geocell system, as localized compression alone will be sufficient to generate the hoop strain.

Overall, the results show that the geocell system provides a better performance than does the geotextile system, so that the same or greater improvement in vertical stiffness and much shallower required zone of reinforcement can always be gained by significantly less geotextile material employed in an arrangement of geocell layers than in geotextile sheets. Whether this is also associated with an economic benefit will depend on the fabrication costs of the geocell material, the reinforcement zone depth beneath the footing (i.e., excavation and backfilling) and on any difference in soil backfill material and procedure.

6.2 *Buried pipes protection by geosynthetics*

In many cases, buried pipes, whether located in shallow or deep trench backfill, are constructed using flexible materials like uPVC (unplasticized polyvinyl chloride) and HDPE (high density polyethylene). It is crucial to ensure a prolonged service life and protect these pipes from stress caused by static and repetitive loading, such as traffic loads at the ground surface. Therefore, careful consideration must be given to the arrangement of backfill materials. To guarantee the safety of buried pipes under various loading conditions, it is essential to thoroughly understand their behavior, as well as that of the surrounding construction materials. By employing geosynthetics, it is possible to mitigate pipe deformation and minimize transferred pressure onto the buried pipe, while keeping trench settlement within acceptable limits.

6.2.1 *Buried pipes response in geogrid-reinforced trench*

The testing tank was a rigid steel box 1000 mm in length, 1000 mm in height, and 220 mm in width, encompassing the model pipe inside a geogrid-reinforced trench filled with a soil of predetermined uniform density as shown in Figure 15a (Moghaddas Tafreshi & Khalaj 2008). The test trench was constructed 550 mm wide and 220 mm long. The trench width was selected to meet the recommendations of BSI (1980) and ASTM D2321-08. The BSI (1980) and ASTM D2321-08 recommend the minimum trench width as $D+300$ mm and $1.25D +300$ mm (where D is the pipe diameter in mm), respectively.

Figure 15.   (a) Schematic layout of the model trench including pipe, geogrid layers, and geometric parameters (unit in mm), (b) General view of the testing apparatus (Moghaddas Tafreshi & Khalaj 2008).

To allow the visual observations of the sand-pipe system, as well as the photo scanning, the front face of the tank has been made of a plexiglass, which can be removed during the preparation stage. A circular hole of 50 mm diameter has been provided in the center of the back face of the tank to accommodate the displacement transducers to detect the radial deflections of the model pipe. Figure 15a shows the schematic layout of the model trench including pipe, geogrid layers, and geometric parameters trench and Figure 15b shows the general view of the testing apparatus.

Two zones of soil are prepared in the test tank. To simulate the natural ground (at bedding and two sides of the trench) in zone A, a granular soil with grain sizes between 0.08 and 20 mm was prepared by the compaction method. This soil is classified as SP in the unified soil classification system. A uniform silica sand in zone B is prepared as the main trench by the raining technique. The properties and classification of soil in zone B is as detailed in section 6.6.1 (Figure 8a). In order to study the effect of the soil density on the behaviour of the buried pipe, three different relative densities of soil trench: 42%, 57%, and 72% were selected.

Based on the dimensions of the model test, the plastic pipes with 110 mm external diameter, 4.03 mm thickness and 210 mm length, made of polyethylene (HDPE: High density polyethylene) was employed. The HDPE geogrid was used to reinforce the soil mass over the pipe. This geogrid has an aperture size of 27×27 mm, thickness of 5.2 mm, area weight of 695 g/m^2 and ultimate tensile strength of 5.8 kN/m. To investigate the effect of embedment depth of pipe and geogrid reinforcement, four burial depths of $1.5D$, $2D$, $2.5D$ and $3D$ and one to five geogrid layers were examined. All the tests were carried out under repeated loads with an amplitude of 550 kN/m^2 and frequency of 0.33 Hz which imposed through a rectangular plate of 100×220 mm located at the center of the trench surface.

Figure 16 shows the typical trends of pipe deformation in term of change in ΔD (percent vertical diameter change) of the pipe and SSS (Settlement of Soil Surface) with the time under repeated loading. This figure shows that, the rate of change of peak ΔD (or SSS) and residual ΔD (or SSS) reduce as the number of cycles increase, and a small reduction in amplitude [i.e., peak ΔD (or SSS) minus residual] is also apparent. It shows that, the variation of ΔD is stabled after short time (almost 400 sec) whereas the variation of SSS tend to be continued. This constant value of ΔD reaches after few passes of the load. This indicates that the early process of reorientation of particles in the side fill of the pipe, causing local side fill stiffening, ceases relative rapidly and the system reaches an elastic stability. The reason of continuing the value of SSS relates to confining effect of the soil surface.
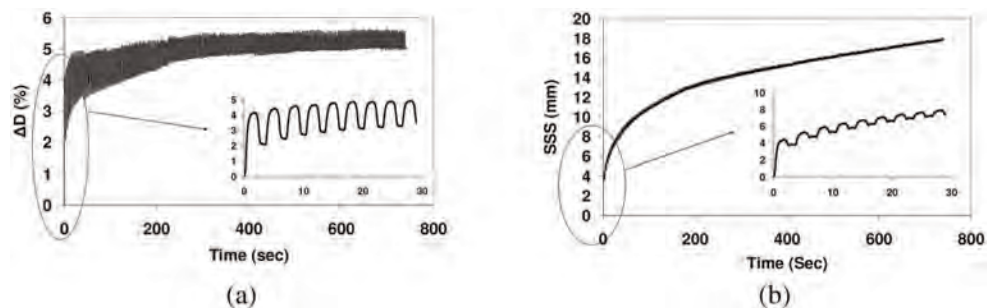
Figure 16. Typical trend of ΔD and SSS during repeated load: (a) ΔD and (b) SSS (Moghaddas Tafreshi & Khalaj 2008).

The influence of the soil reinforcement on the maximum ΔD and SSS at different relative density and embedment depth are shown in Figure 17 and Figure 18, respectively. As expected, the value of ΔD and SSS decrease with increase in the reinforcement layers, embedment depth of pipe and soil relative density.
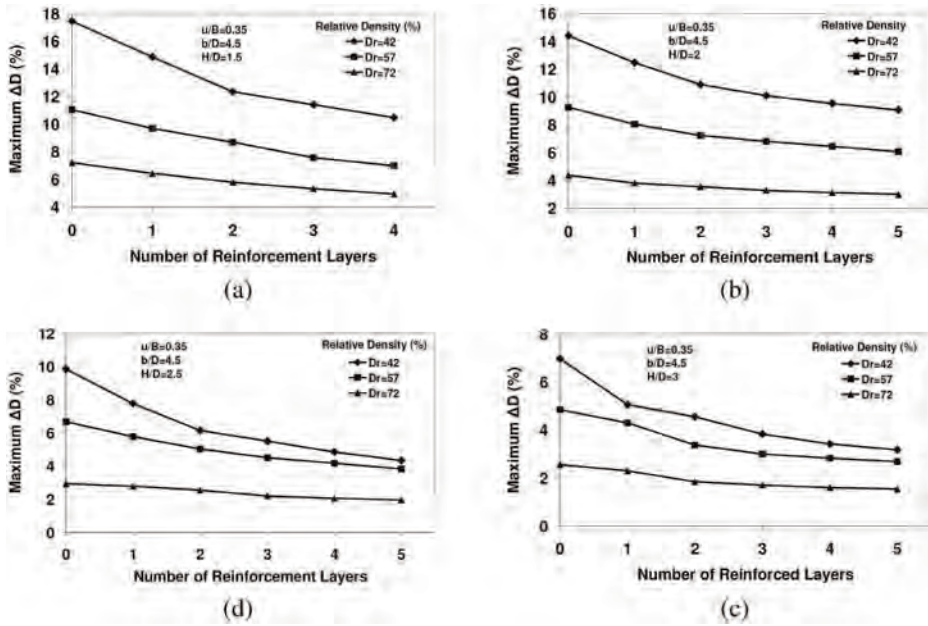
Figure 17. Variations of the maximum ΔD with number of reinforced layers for (a) H/D=1.5, (b) H/D=2, (c) H/D=2.5 and (d) H/D=3 (Moghaddas Tafreshi & Khalaj 2008).
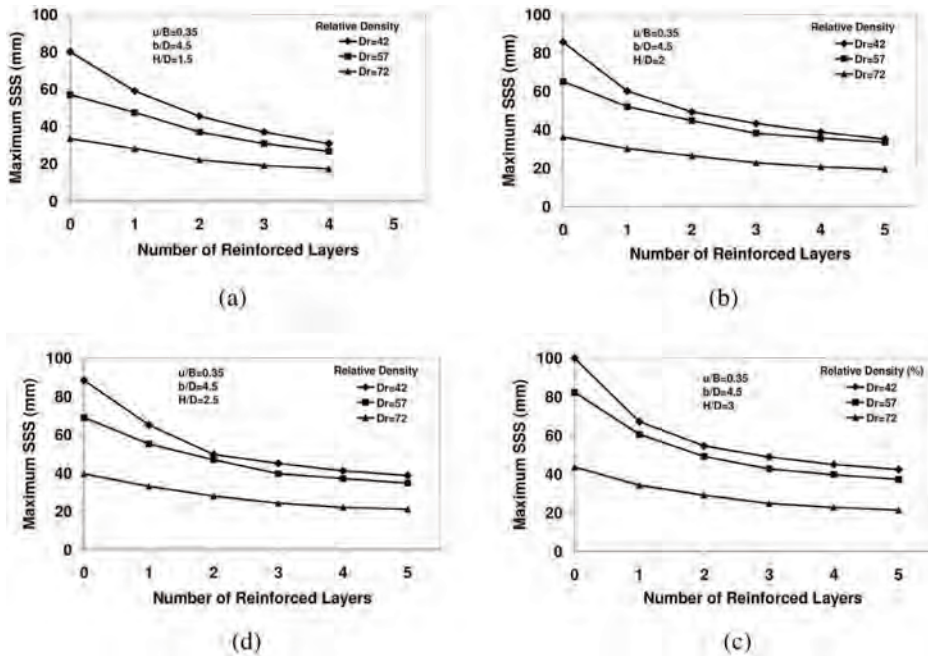
Figure 18. Variations of the maximum SSS with number of reinforced layers for (a) H/D=1.5, (b) H/D=2, (c) H/D=2.5 and (d) H/D=3 (Moghaddas Tafreshi & Khalaj 2008).

It can be observed that the decrease in ΔD and *SSS* due to additional layers of reinforcement begin to converge at around the fourth layer and almost constant at the fifth layer of reinforcement. The reason is that the reinforcement considerably increases the stiffness of reinforced trench compared with unreinforced trench. This matter is similar to enhancement of the soil density which increases the stiffness of the backfill or embedded depth of pipe which causes more soil available for load sharing in unreinforced sand. Consider, for example in $2.5D$ of embedment depth and relative density of 42%, ΔD reduces 21% at one layer of reinforcement, whereas there is 56% reduction at five layers of reinforcement. Similar pattern is observed for variation of *SSS* with the number of reinforced layers.

Figure 19 shows the trench deformation at three different conditions corresponding to unreinforced and reinforced sand with two and five layers of geogrid at the end of tests. The movements of soil layers and settlement of soil surface are clearly shown in this figure by using the colored lines in the front face of the trench. This figure implies that with increase in the reinforcement layers, the soil surface settlement is reduced significantly.
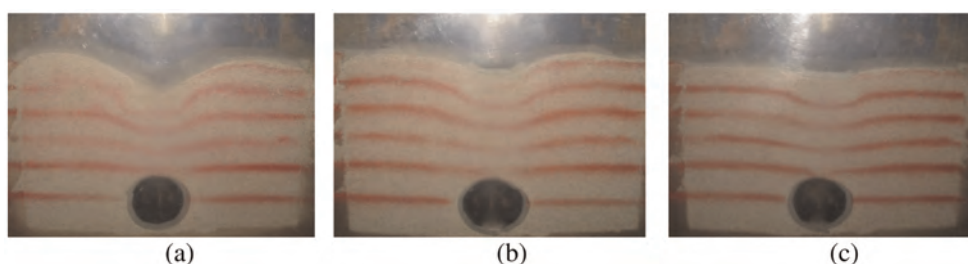
Figure 19.   Photograph of trench deformation at the end of tests under embedment depth of 2D and relative density of 42% (a) unreinforced sand, (b) reinforced trench with 2 layers, (c) reinforced trench with 5 layers (Moghaddas Tafreshi & Khalaj 2008).

6.2.2   *Buried pipes response in geocell-reinforced trench*

Figure 20 schematically shows the full-scale model test of buried pipe in geocell-reinforced trench. The model of the test containing the pipe and geocell layer was prepared in a test pit with plan dimensions of 2200×2200 mm and depth of 1000 mm (Moghaddas Tafreshi et al. 2020). The test trench was constructed 750 mm wide and 750 mm deep, as shown in Figure 20, and 1750 mm long. The trench width was selected to meet the recommendations of BSI (1980) and ASTM D2321-08 (see section 6.2.1). The maximum buried depth of the pipe was selected as two times the pipe's diameter ($2D=500$ mm), as proposed by Moghaddas Tafreshi & Tavakoli Mehrjardi (2018), being an optimized value of burial depth for a pipe embedded in geogrid-reinforced soil.

To simulate the loads imposed by traffic, loading, unloading and reloading were imposed through a circular plate located at the centre of the trench surface. In all tests, 150 cycles of repeated loading with amplitude of 800 kPa and frequency of 0.33 Hz were applied to the loading plate. The diameter of the loading plate (250 mm) and the maximum applied pressure of 800 kPa were chosen to replicate that of a heavy vehicle half-axle (40 kN) as used on a common heavy trailer (mean tyre pressure 792 kPa) as recommended by Brito et al. (2009).

In order to simulate likely usage conditions, a granular soil was used around the two sides of the pipe and to cover the crown and to fill the geocell pockets (in geocell-reinforced installations), as shown in Figure 20. The soil has a maximum grain size and mean grain size of 20 mm and 4.3 mm, respectively and a specific gravity of 2.66 ($G_s=2.66$). According to the Unified Soil Classification System, this soil is classified as well-graded sand with letter symbol "SW" which satisfies the grain size limits for pipe backfill materials according to ASTM D 2321-08. The maximum dry unit weight and the optimum moisture content of this
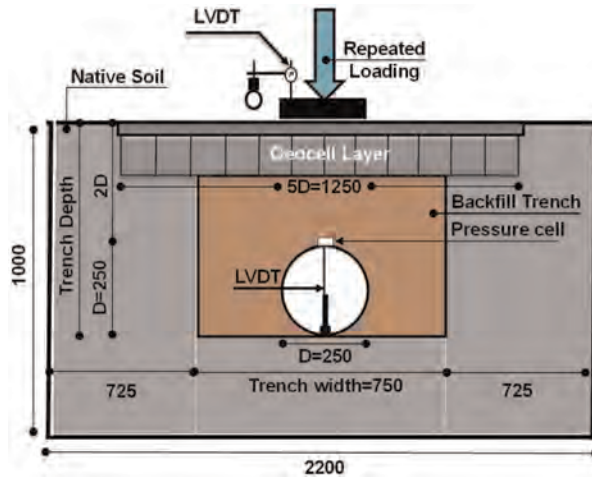
Figure 20. Schematic view of model test, including pipe, geocell layer, instrumentation and geometric parameters (unit in mm) (Moghaddas Tafreshi et al. 2020).

soil were about 20.42 kN/m3 and 5.1%, respectively. The angle of internal friction (φ) of the soil, obtained by consolidated undrained triaxial compression tests of specimens at a wet unit weight of 19.72 kN/m3 and a moisture content of 5% (corresponding to 92% of maximum dry unit weight, similar to the compacted unit weight of soil layers in backfill was 40.5°. In all the tests, the unreinforced soil layers around both sides of the pipe and over the pipe were prepared, respectively at wet unit weight of 17 and 19.72 kN/m^3. The wet unit weight of soil in geocell layer with pocket size of 55×55 mm^2 and 110×110 mm^2 were about 19.20 and 18.53 kN/m^3, respectively.

The geocell layer with the described properties in section 6.1.1, was used in two pocket sizes of 55×55 mm^2 and 110×110 mm^2 and one height of 100 mm. When spread out, it occupied an area of 1250×1250 mm^2 in plane (5 times the loading plate in each direction), centered on the axis of loading. A high-density polyethylene pipe (HDPE 100), designed to withstand a pressure of 4 bar, having an outer diameter (D) of 250 mm, a wall thickness (t) of 4 mm and, thus, a Standard Dimension Ratio (SDR) = D/t =40 was selected. Based on the manufacturer, this pipe has an elastic modulus of 1000 MPa, a Poisson's ratio of 0.3 and a weight per unit length of 4.83 kg/m. A pipe length of 1740 mm, approximately equal to the length of the trench in the full-scale model test was chosen.

The data measurement system was developed to read and record the applied repeated load, loading plate settlement, pipe deformation and soil pressure automatically. An S-shaped load cell, with a full-scale capacity of 100 kN, was used to precisely measure the applied repeated load. To measure the settlement of the loading plate and the pipe defor-mation during loading, unloading and reloading, respectively one LVDTs and six LVDTs (linear variable differential transducers) were installed on the loading plate and inside the pipe. Figure 21 provides a schematic of the LVDTs inside the pipe in the middle and along the pipe's axis at distances of 150, 300, 450 and 600 mm from the mid-point of the pipe's length, a photograph of pipe installation and defining the vertical pipe deflection meanings. The soil pressure on the crown of the pipe (as shown in Figure 20) was monitored and measured by one soil pressure cell with a diameter of 50 mm.

Figure 22a-b shows the typical trends of the vertical diametral strain of the pipe (ΔD: reduction in vertical diameter divided by the pipe diameter) and the soil surface settlement (SSS) with the number of load cycles during the repeated loading. As seen in this figure, the rate of increase in ΔD (or SSS) decreases as the number of load cycles increase. It illustrates
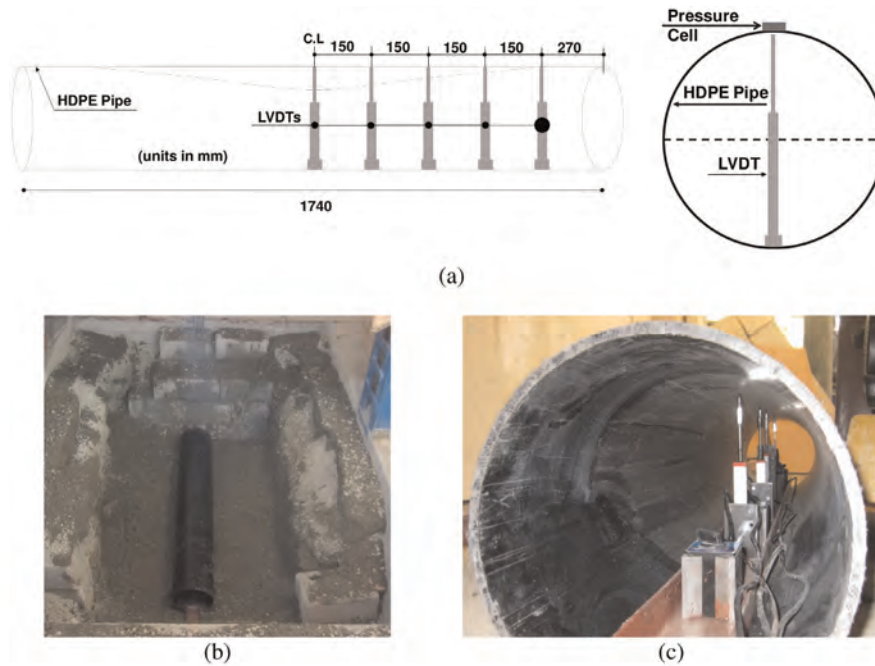
Figure 21.   (a & b) Schematic installation of LVDTs inside the pipe, (c & d) Photograph view of pipe and steel U channel solid base, magnet base/rod and LVDTs inside the pipe (Moghaddas Tafreshi et al. 2020).

that, in this condition of test and due to 150 load cycles, the variation of ΔD and SSS becomes approximately stable, and it can be anticipated to reach a fully stabilized condition with only a few additional cycles of load. This may be attributed to the early process of reorientation of particles in the side fill of the pipe and beneath the loading, causing local side fill stiffening, but which ceases relative rapidly allowing the system to reach elastic stability (Faragher et al. 2000) (i.e., a shakedown condition).

The pressure-SSS or pressure-ΔD plots derived from these tests are shown in Figure 22c-d. Although initial plastic strain occurs, it is clear that for repeated loads on the soil surface, a steady response condition was approximately achieved when the load path formed a closed hysteresis loop, indicating only a small amount of energy lost in the system. The other fact seen in Figure 22, associated with the general behavior of the buried pipes subjected to repeated loads, is the large proportion of the pipe deformation/soil surface settlement at the end of the first pulse compared with its total pipe deformation/soil surface settlement due to many, later, load cycles. Again, this helps to support the conjecture that the first pulse is largely causing compactive action on, i.e., large plastic strain in, the surrounding soils. In this case, 30 or 27% of the total ΔD or SSS, respectively, occurs during the first cycle. A similar behaviour is obtained for variation of pressure on the pipe crown as measured by soil pressure cell.

Figure 23 compares the response of the buried pipe in the unreinforced and geocell-reinforced systems through 150 cycles of repeated loading. Both soil surface settlement, SSS (rut depth on soil surface) and vertical pipe diameter, ΔD change are smaller when the geocell is in place, evidence of beneficial stiffening and load-spreading abilities of the geocell installation under repeated loading. As seen in Figure 23a, the soil surface settlement of the reinforced installation, at the last load cycle decreased by 25% to 45%, respectively, for small and large pocket geocell installations (compared to the unreinforced installation). From
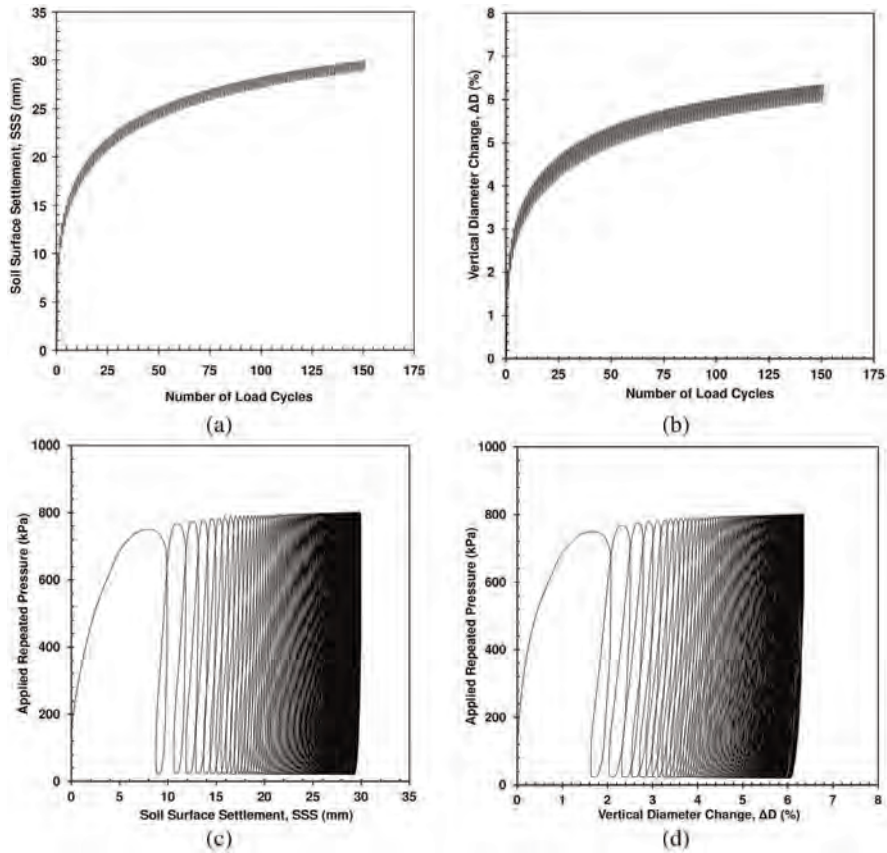
Figure 22.   Typical trend of (a) *SSS* with load cycles, (b) Δ*D* with load cycles, (c) hysteresis curve of *SSS*, (d) hysteresis curve of Δ*D* (Moghaddas Tafreshi et al. 2020).

Figure 23b, the values of Δ*D* of the pipe at the end of load cycling for unreinforced and geocell-reinforced tests with small and large geocell pocket sizes were obtained as 8.74%, 7.12% and 6.35%, respectively. These values indicate an improvement in Δ*D* by about 27.4% due to the large pocket geocell reinforcement. Thus, the competent performance of the geocell reinforced system in reducing the pipe deformation is evidenced as well as that in decreasing the soil surface settlement.

   To gain a better assessment of the pipe deformation, the variation of the pipe's vertical deflection at its crown, along the pipe's longitudinal axis (at distances of zero, 150, 300, 450 and 600 mm from the middle of pipe's length) at the end of load cycling is presented in Figure 23c. The zero-value on the horizontal axis of this figure indicates the point on the crown beneath the center of the loading surface and the axis indicates the distance along the pipe's axis from zero point. As expected, the deflection of the pipe's crown decreases away from the centre of loading for both unreinforced and reinforced systems. From Figure 23c, for the buried pipe in unreinforced backfill, the vertical deflection of pipe (Δ*D*) at the distances of zero, 150, 300 and 450 mm from the middle of pipe length were about 8.74%, 6.52%, 3.89%, 1.63% and 0.23%. The corresponding values for geocell-reinforced system with small pocket size are about 7.12%, 5.56%, 3.62%, 1.28% and 0.19% and for geocell-reinforced system with large pocket size are about 6.35%, 4.86%, 3.18%, 1.16% and 0.15%. It indicates that using the geocell layer beneath the soil surface, rendered the buried pipe system
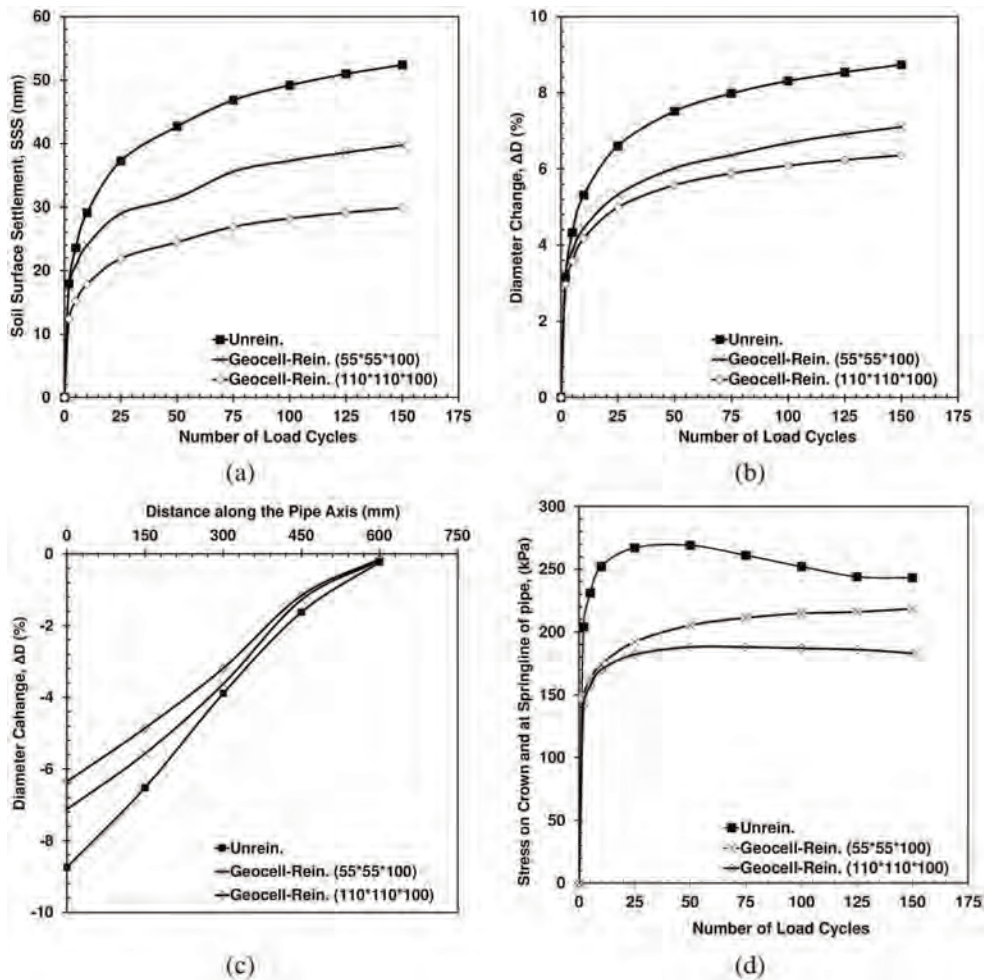
Figure 23. Comparison between geocell-reinforced and unreinforced installations for (a) *SSS*, (b) Δ*D* (c) pipe deformation in longitudinal axis, and (d) Soil pressure on crown of pipe (Moghaddas Tafreshi et al. 2020).

considerably protected. As can be seen in Figure 23c, there was a non-linear variation of pipe crown deformation along the pipe's longitudinal axis, and it converges to an insignificant value over 600 mm from the centre of the loaded area.

Figure 23d demonstrates the variation of the measured pressure on the crown with load cycles, for both unreinforced and geocell-reinforced systems. The readings show that, in the last cycle of loading, the transferred stress on the crown of the pipe was about 75% and 86% of the values in the unreinforced installation, respectively, for large and small pocket size geocell. However, Figure 23d indicates that the observed reduction in pipe deflection in Figure 23b could be attributed to a lower transferred pressure on the pipe crown. It is assumed that this reflects improved load spreading achieved by the geocell which is spreading load away from the crown (with a matching reduction in deflection there) and spreading it somewhat to the pipe margins. There, it is assumed, passive, horizontal earth pressure is now developed by smaller pipe deflections than before, due to the better com-pacted soil that has resulted from the increase in vertical load that has been spread to it. The

improvement in the behaviour of pipes due to provision of reinforcement is in the line with the finding of Moghaddas Tafreshi & Khalaj (2008), Tavakoli Mehrjardi et al. (2012), Hegde & Sitharam (2015) and Elshesheny et al. (2019).

Figure 23 shows that the $110 \times 110 \times 100$ mm geocell installation delivers greater benefit, for all tests, than does the $55 \times 55 \times 50$ mm geocell arrangement. It proved impossible to achieve as great a density of pocket infill in the small pockets as in the large - despite preparing and compacting the infill soil in the same manner. Probably, the greater number of vertical pocket sides found in the smaller geocell than in its larger 'brother' offered a greater hindrance to compaction. A further factor may be the greater number of (inevitable) break-ups between otherwise interlocked soil particles. These reductions in density and in stone-stone interaction are unavoidable, as noted by previous authors (Tavakoli Mehrjardi et al. 2013).

6.3 *Geosynthetic-reinforced flexible pavement*

Geosynthetics are commonly employed in pavement applications to fulfill various functions such as filtration, separation, sealing, drainage, and reinforcement. In this section, the focus lies on the role of soil reinforcement in increasing pavement bearing pressure and reducing settlement, which is important. Geotextile, geogrid, and geocell are commonly used as reinforcement elements in transportation geotechnical applications (Bueno et al. 1987). The enhanced performance of pavements attributed to geosynthetic reinforcement can be attributed to the factors discussed in sections 2–5. The results presented in this section are derived from full-scale experiments aimed at demonstrating the effectiveness of multi-layered geocell reinforcement in reducing road deformations caused by traffic loads.

6.3.1 *Cyclic response of multi-layered geocell-reinforced flexible pavement*

In order to showcase the capabilities of geosynthetics in enhancing the strength and minimizing deformation in pavement foundations, this section will delve into the results of a comprehensive full-scale model test (Moghaddas Tafreshi et al. 2013). The test specifically focuses on the utilization of multiple layers of geocells within the foundation bed under cyclic loads. The findings from this study hold significant potential for application in pavement foundation systems.

The backfill soil was a sandy soil passing through the 38 mm sieve (Figure 24a) with a specific gravity, G_s, of 2.65. According to the Unified Soil Classification System, the soil is classified as well graded sand with the letter symbol *SW*. The maximum dry density was about 20.62 kN/m^3, which corresponds to an optimum moisture content of 5.7%. The angle of internal friction (φ) of sand obtained through triaxial compression tests at a wet density of 19.58 kN/m^3 (corresponding to 90% of maximum dry density) was 40.5°.

The natural ground soil, at the bottom and four side walls of the test pit, has a maximum particle size of about 20 mm (Figure 24a) and a specific gravity, G_s, of 2.62. This soil is classified as SP in the Unified Soil Classification System. The wet density and the natural moisture content of this soil were measured as 17.9 kN/m^3 (it corresponds to 90% of maximum dry density of 20.25 kN/m^3) and 9%, respectively. The angle of internal friction (φ) of the natural soil at a wet density of 17.9 kN/m^3 was 32.5°. The dimensions of the excavated test pit relative to the loading plate diameter are sufficient to minimize boundary effects. The natural ground soils were selected so as not be excessively soft and weak. In this way the assessment of reinforcing benefit from the installations investigated might be conservative. However, the use of a softer subgrade might show the benefits of rubber-soil with geocells to be even better.

The geocell layers with the described properties in section 6.1.1, were used in pocket size of 110×110 mm^2 and height of 100 mm and spread out in plane to 5 times the loading plate in

each direction), centred on the axis of loading plate. Figure 24 shows particle size distribution curves for backfill and natural soils and a view of geocell layer spread over soil in the test pit.

(a)   (b)
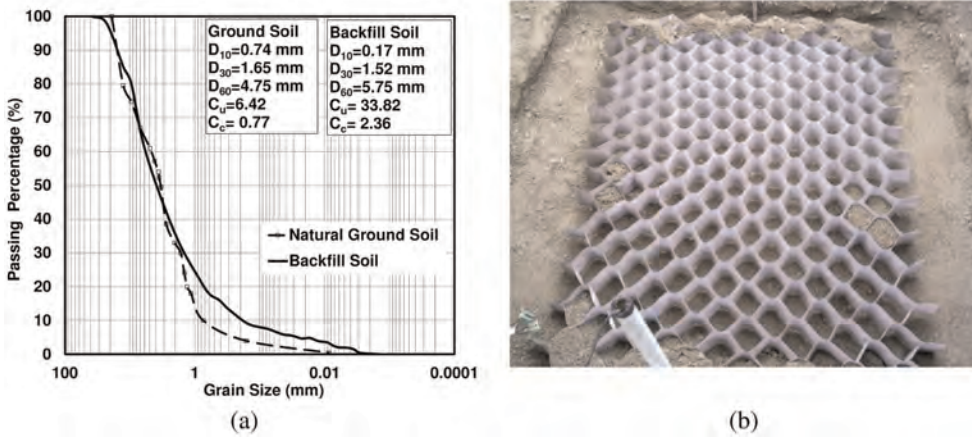
Figure 24. (a) Particle size distribution curves for backfill and natural soils (b) A view of geocell layer spread over soil in the test pit (Moghaddas Tafreshi et al. 2013).

Figure 25a shows the schematic cross-section of the full-scale model test set-up of the foundation bed, its geometry and data measurement system (dial gauges and soil pressure cells). All plate load tests on the steel rigid circular plate of 300 mm in diameter were conducted in an outdoor test pit, measuring 2000 mm × 2000 mm in plan, and 700 mm in depth. A photograph of the test installation prior to testing, showing the reaction beam, load plate, hydraulic jack and three dial gauges is presented as Figure 25b. In all the tests, the unreinforced layers and geocell reinforced layers were compacted with a walk-behind vibrating plate compactor at an optimum moisture content of 5.7% with two and three passes, respectively to achieve the dry density of about 18.56 and 18.2 kN/m^3.

(a)   (b)
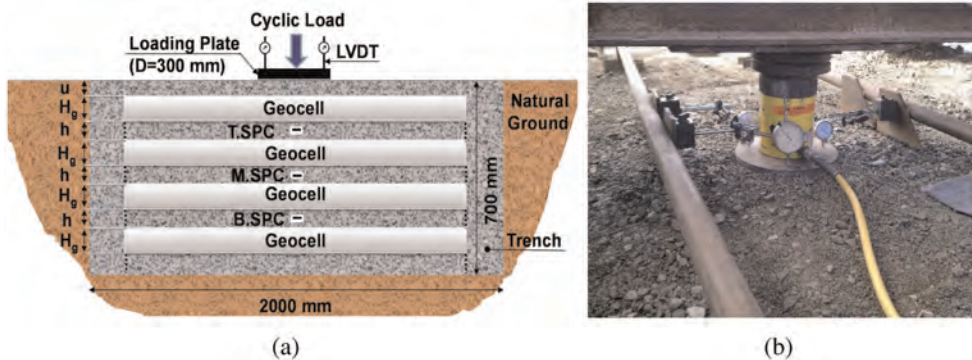
Figure 25. (a) Schematic cross-section of the test set-up (not to scale), "T.SPC", "M.SPC", and "B. SPC" indicate the location of soil pressure cells, (b) Photograph of test installation prior to loading include reaction beam, load plate, hydraulic jack and three dial gauges (Moghaddas Tafreshi et al. 2013).

In order to simulate the effect of wheel loading, unloading and reloading, the maximum applied pressure of 792 kPa (i.e., a heavy vehicle half-axle with "Super-Single" tire, as used on a common heavy 6 axles trailer) (Brito et al. 2009), was divided into two stages being 400 and 800 kPa to simulate half and full traffic loadings. For each stage, fifteen loading and unloading cycles were applied through the plate at a rate of 1.5 kPa per second.

The optimum depth of the first layer of geocell layer beneath the loading plate (u), and the vertical spacing of the geocell layers (h), are obtained approximately 0.2 times the loading plate diameter ($u/D=h/D=0.2$) which not detailed here. To investigate the effect of the number of geocell layers on the deformation response of pavement, the unreinforced test and geocell-reinforced tests conducted by varying the number of geocell layers (N_g=1, 2, 3, 4), when the layers of geocell were placed at the optimum values of u/D and h/D.

The variation of the loading plate deformation (including the accumulated residual (plastic) deformation and resilient (elastic rebound) displacement) with the number of load cycles for the unreinforced system and the multi-layered geocell reinforced system with one, two, three, and four layers of geocell (N_g=1, 2, 3, 4), when the layers of geocell were placed at the optimum values of u/D and h/D ($u/D=h/D=0.2$), is shown in Figure 26a. Also, the residual plastic deformation of the unreinforced and reinforced bases with the number of loading cycles is shown in Figure 26b. This figure shows that for the unreinforced and reinforced bases, an initial, rapid total deformation (Figure 26a) and rapid residual deformation (Figure 26b) during the first load applications is followed by secondary deformation that develops at a slower rate. Both the total and plastic deformations caused by the first cycle of applied load form a large portion of the final deformation after all cycles. Overall, in most of the tests performed on the unreinforced and the geocell reinforced foundation, the initial, rapid deformation that took place due to the first cycle of loading gave rise to between 25% and 70% of the accumulated plastic deformation. This ratio is greater for the unreinforced foundation than for the reinforced foundation. The actual proportion appears to depend on the mass of reinforcement and on the magnitude of the applied cyclic load.

Figure 26 shows that the total and residual deformations of the unreinforced pavement foundation material tend to increase with the number of load cycles. There is a non-stabilizing response, eventually leading to plastic failure, particularly at higher levels of
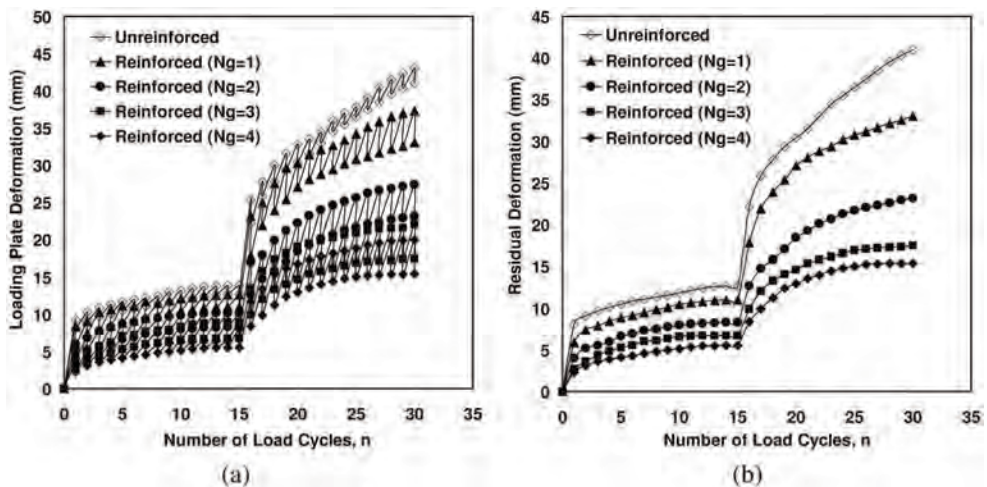
Figure 26. Variation of (a) loading plate deformation, and (b) residual deformation with number of applied load cycles for the unreinforced and geocell reinforced systems with one, two, three, and four layers of geocell. The fifteen first cycles and the fifteen second cycles were applied with amplitudes of 400 and 800 kPa, respectively (Moghaddas Tafreshi et al. 2013).

cyclic loads (i.e., 800 kPa). It should be noted that a large deformation in these tests is not the primary means of judging unsuitability of the arrangements under test but, rather, a non-stabilizing response. Large deformations could largely be dealt with in practice by compaction, whereas instability responses are destructive.

For the reinforced bases, regardless of the number of geocell layers, the rate of change of both total and the residual deformation of the loaded surface reduces as the number of load cycles increases, so that their response has become, approximately, stable after fifteen load cycles (of both 400 and 800 kPa applied load), particularly for the reinforced bases with three and four layers of geocell. The performance of geocell reinforcement in decreasing the deformations may be attributed to the superior confinement offered by the geocell layers in all directions. Thus, the multi-cell geometry allows the soil in the cells to develop a passive resistance that increases the soil's bearing capacity and decreases the deformations within the pavement foundation. This behavior is a consequence of the shakedown process as the granular structure of the sand becomes arranged into a progressively more stable arrangement better able to behave resiliently without undergoing plastic deformation. It implies that the reinforced system as compared with unreinforced system (Figure 26) is storing energy (and releasing it in resilient recovery) rather than the energy being used to cause further damage. This stabilizing response suggests that the early process of reorientation of particles inside the geocell layers, causing local fill stiffening, ceases relative rapidly and the system then reaches a "plastic shakedown" condition, in which subsequent deformation is fully recovered in each cycle. In such a case no yield condition is reached at conventional stress levels. The final deformation value can be referred to either as the "maximum deformation" or the "shakedown deformation (settlement)" (Werkmeister et al. 2005). The behavioral patterns observed in these tests (Figure 26) is in-line with those observed in the repeated load testing of unreinforced granular materials as observed by several authors (Werkmeister et al. 2005) and as predicted from mechanical interaction considerations (García-Rojo and Herrmann 2005). Thakur et al. (2012) reported similar results of the total and residual deformations with number of loading cycles and with height of single geocell-reinforced bed.

The variation of maximum measured pressure with the number of load cycles, inside the foundation at the three levels of 190 mm (T.SPC), 350 mm (M.SPC), and 510 mm (B.SPC) beneath the center of loading plate (Figure 25a) for the unreinforced system and the multi-layered geocell reinforced system is illustrated in Figure 27. The readings of the three soil pressure cells for unreinforced and reinforced bases show an immediate large increase in the vertical stress when the first cycle of loading is applied and then a further, smaller increase over the next 6-8 cycles of loading, thereafter stabilizing to a constant value. This pattern is observed irrespective of applied pressure or of cell depth.

The figure also demonstrates the performance of geocell layers, as anticipated, in reducing the pressure transferred through the pavement foundation. For instance, as can be seen in Figure 27c, with increase in the number of geocell layers from one layer to three, the vertical stress transferred to a depth of 510 mm beneath the center of loading surface, as measured by the bottom soil pressure cell ("B.SPC"), almost halves. For example, under the applied cyclic pressure of 800 kPa, at the end of the load cycles (cycle number 30), the stress measured at 510 mm depth ("B.SPC") is about 284.5, 223.5, 159.7, 125.2 kPa for unreinforced and the reinforced pavement foundations with one, two and three layers of geocell, respectively. This comparison illustrates the excellent performance of the geocell reinforcement, so that the pressure at a depth of 510 mm decreases to about 35.6%, 27.9%, 20%, and 15.7% of the applied surface pressure (=800 kPa) for the same sequence of constructions. Thus, as reinforcing geocell layers are added, the effective load spreading continues to improve, consequently delivering a better performance, as compared with unreinforced base. It confirms the pressure distribution in depth (beneath the footing) as shown in Figure 7, which describes for the 3D (geocell) reinforced bed, the wider area and less depth of pressure distribution are contributed by the geocell due to its reinforcing mechanism as compared to the unreinforced bed. On the whole, the data presented in Figures 26 and 27 show that multiple geocell layers, particularly the use
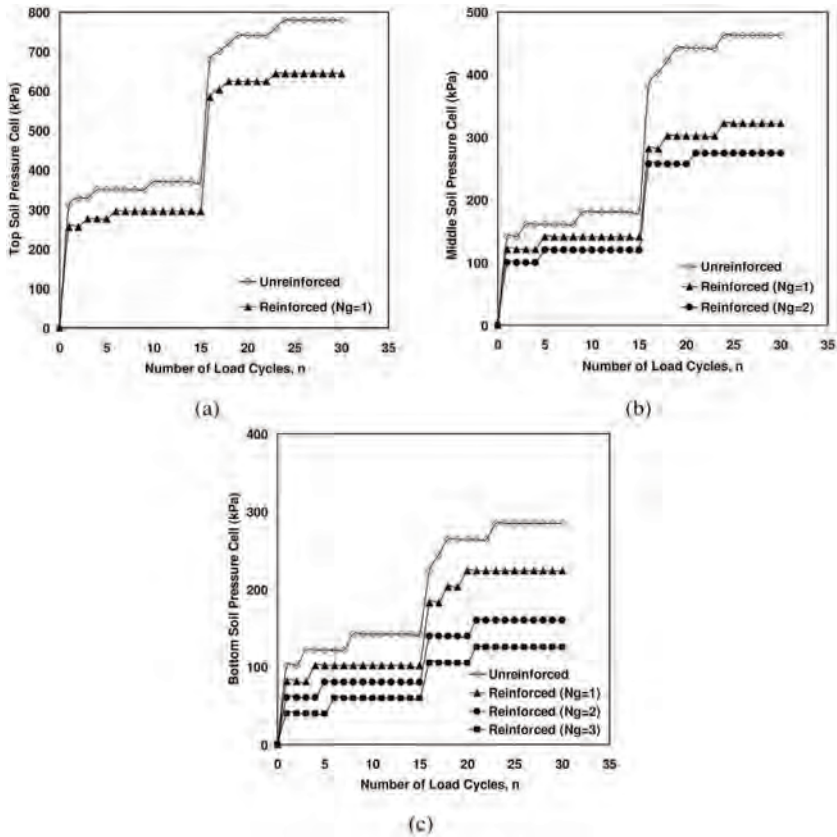
Figure 27. Variation of transferred pressure with number of applied load cycles at different depths in the geocell-reinforced and unreinforced pavement foundations (a) at a depth of 190 mm (T.SPC), (b) at a depth of 350 mm (M.SPC), and (c) at a depth of 510 mm (B.SPC). The fifteen first cycles and the fifteen second cycles were applied with amplitudes of 400 and 800 kPa, respectively (Moghaddas Tafreshi et al. 2013).

of three and four layers of geocell, are able to limit the soil surface deformation and the soil pressure through the depth of the reinforced pavement foundation. Consequently, an increase in road life may be anticipated under the same heavy traffic loading.

Considering both the deformation and stress effect, it appears that, cell-pocket structure of the geocell layer prevents the encased soil from easily moving away from the point of load application. This is probably achieved by hoop confinement provided by the pocket walls. Thereby the infill cannot easily spread laterally, hence the shear strength of the composite system is increased.

This mechanism would allow the geocell layer to act like a soft plate with high flexural stiffness, spreading the applied load over an extended area, and decreasing the stress at depth in the pavement foundation (Moghaddas Tafreshi & Dawson 2012; Thakur et al. 2012).

7 CONCLUSIONS

This paper presents an overview of the soil-reinforcement interaction and the reinforcing mechanism of 2D and 3D reinforcements in enhancing the performance of foundation beds.

It also provides a summary of research findings from experimental studies on the application of 2D and 3D geosynthetics for protecting footings, buried pipes, roads, and pavements. These findings serve as a valuable reference for future studies in this field. Based on the analysis and discussion of the presented research, the following conclusions can be drawn:

- The optimal depth of the topmost layer of 2D reinforcement is approximately 0.33-0.4 times the width or diameter of the footing. In contrast, the depth to the top of the 3D reinforcement should be around 0.1-0.2 times the width or diameter of the footing.
- The optimal width of 3D reinforcement is approximately 4 times the width or diameter of the footing, while for 2D reinforcement, it is about 5 times the width or diameter of the footing. The smaller required width of 3D reinforcement is due to its superior anchorage compared to 2D reinforcement.
- The optimal spacing between reinforcement layers for 2D and 3D reinforcements is approximately 0.35 and 0.2 times the width or diameter of the footing, respectively.
- The effective reinforcement zone beneath the footing base is smaller when using 3D reinforcement (less than 1.5 times the footing width/diameter) compared to the effective zone for 2D reinforcement (greater than 1.5 times the footing width/diameter). This difference in reinforcement zones confirms the better reinforcing mechanism of the geocell that facilitates a broader load distribution area and a shallower depth in comparison to the 2D reinforced bed.
- By employing a lesser quantity of 3D reinforcement, such as geocell, compared to 2D reinforcement, such as geotextile, a significant improvement in bearing pressure and footing settlement can be achieved.
- For buried pipes, the safety of the system depends on factors such as embedment depth, backfill quality, and the amount of reinforcement in the backfill trench. The use of geogrid and geocell reinforcement demonstrated beneficial performance on the buried pipe system. Adding reinforcement layers above the pipe reduced vertical deflection, soil surface settlement, and pressure on the pipe crown.
- In road and pavement applications, the inclusion of geocell layers helps prevent punching shear or rutting that can occur in unreinforced surfaces. It also leads to a significant reduction in vertical stress spread through the pavement foundation by distributing the load over a wider area.

Advancements in understanding the technical aspects of geosynthetic reinforcement instill confidence in societies, encouraging widespread application of these materials in various areas, including the stabilization and reinforcement of footings, pavements, buried pipes, underground utilities, railway and road embankments, slopes, and retaining walls.

REFERENCES

American Society for Testing and Materials. 2008. Standard Practice for Underground Installation of Thermoplastic Pipe for Sewers and Other Gravity-flow Applications. *ASTM D* 2321–08.

Amiri, Z., Moghaddas Tafreshi, S. N., Dawson, A. R. 2023. Vibration Response of Machine Foundations Protected by use of Adjacent Multi-layer Geocells. *Geotextiles and Geomembranes*, 51(4): 15–35

Avesani Neto, J. O., Bueno, B. S., Futai M. M. 2013. A Bearing Capacity Calculation Method for Soil Reinforced with a Geocell. *Geosynthetics International*, 20(3): 129–142.

Binquet, J., Lee, K.L., 1975. Bearing Capacity Tests on Reinforced Earth Slabs. *Journal of Geotechnical Engineering ASCE* 101 (12): 1241–1255

BS8006. 1995. *British Standard: Code of Practice for Strengthened/Reinforced Soils and Other Fills.*

Britto, A. M. 1979. *Thin-walled Buried Pipes. Ph.D. thesis*, Cambridge University, UK.

Bueno, B. D. S. 1987. *The Behavior of Thin-walled Pipes in Trenches*. Ph.D. thesis, Civil Eng. Dept., Leeds University, UK.

Chen QM, Abu-Farsakh M. 2015. Ultimate Bearing Capacity Analysis of Strip Footings on Reinforced Soil Foundation. *Soils and Foundations*. 55(1): 74–85

Dash, S.K, Krishnaswamy, N.R., Rajagopal, K., 2001. Bearing Capacity of Strip Footings Supported on Geocell-reinforced Sand. *Geotextiles and Geomembranes* 19 (4): 235–256.

Dash, S.K, Sireesh S, Sitharam T.G., 2003. Model Studies on Circular Footing Supported on Geocell Reinforced Sand Underlain by Soft Clay. *Geotextiles and Geomembranes* 21 (4): 197–219.

Dash, S. K., Rajagopal, K. & Krishnaswamy, N. R. 2007. Behaviour of Geocell Reinforced Sand Beds Under Strip Loading. *Canadian Geotechnical Journal*, 44(7): 905–916.

Elshesheny, A., Mohamed, M., Sheehan, T., 2019. Buried Flexible Pipes Behavior in Unreinforced And Reinforced Soils Under Cyclic Loading. *Geosynthetics International*. 26 (2): 184–205.

Faragher, E., Feleming, P.R., Rogers, C.D.F. 2000. Analysis of Repeated-load Field Testing of Embedded Plastic Pipes. *Transportation Research Record, 1514, Transportation Research Board, Washington, D.C.*: 271–277.

García-Rojo, R., Herrmann, H.J., 2005. Shakedown of Unbound Granular Material. *Granular Matter* 7 (2): 109–118.

Guo, X., Zhang, H., Liu, L. 2020. Planar Geosynthetic-reinforced Soil *Foundations: A Review. SN Applied Sciences*, 2(11): 2074.

Han, J., Yang, X., Leshchinsky, D. & Parsons, R. L. 2008. Behavior of Geocell-reinforced Sand Under a Vertical Load. *Transportation Research Record*, 2045: 95–101.

Hegde, A.M., Sitharam, T.G. 2015. Three-Dimensional Numerical Analysis Of Geocell-Reinforced Soft Clay Beds By Considering The Actual Geometry Of Geocell Pockets. *Canadian Geotechnical Journal*, 52(9): 1396–1407.

Inti, S., Tandon, V., 2021. Design of Geocell Reinforced Roads through Fragility Modelling. *Geotextiles and Geomembranes* 49 (5): 1085–1094.

Kief, O., Schary, Y., Pokharel, S.K. 2014. *High Modulus Tough-Cells for Sustainable Highway Infrastructure Indian Geotechnical Journal*, Springer. *September*.

Madhavi Latha, G.M., Somwanshi, A., 2009a. Bearing Capacity of Square Footings on Geosynthetic Reinforced Sand. *Geotextiles and Geomembranes* 27 (4): 281–294.

Madhavi Latha, G. & Somwanshi, A. 2009b. Effect of Reinforcement Form on the Performance of Square Footings on Sand. *Geotextiles and Geomembranes*, 27(4): 409–422.

Meyerhof, G., Hanna, A. 1978. Ultimate Bearing Capacity of Foundations on Layered Soils Under Inclined Load. *Canadian Geotechnical Journal*, 15(4): 565–572

Moghaddas Tafreshi, S.N., Khalaj, O. 2008. Laboratory Tests of Buried Plastic Pipes in Reinforced Sand under Repeated-Load. *Geotextiles and Geomembranes*, 26 (2): 145–163.

Moghaddas Tafreshi, S.N., Tavakoli Mehrjardi, G. 2008. *The Use of Neural Network to Predict the Behavior of Small Plastic Pipes Embedded in Reinforced Sand and Surface Settlement under Repeated-Load. Engineering Applications of Artificial Intelligence*, Elsevier, 21 (6): 883–894.

Moghaddas Tafreshi, S. N., Dawson, A. R. 2010. Comparison of Bearing Capacity of a Strip Footing on Sand with Geocell and with Planar Forms of Geotextile Reinforcement. *Geotextiles and Geomembranes*, 28(1): 72–84.

Moghaddas Tafreshi, S. N., Khalaj, O., Dawson, A. R. 2013. Pilot-scale Load Tests of a Combined Multi-layered Geocell and Rubber-reinforced Foundation. *Geosynthetics International*, 20(3): 143–161.

Moghaddas Tafreshi, S. N., Sharifi, P., Dawson, A. R. 2016. Performance of Circular Footings on Sand by Use of Multiple-geocell or-planar Geotextile Reinforcing Layers. *Soils and Foundations*, 56(6): 984–997.

Moghaddas Tafreshi, S.N., Joz Darabi, N., Dawson, A.R., Azizian, M. 2020. Combining EPS Geofoam With Geocell To Reduce Buried Pipe Loads And Trench Surface Rutting, *Geotextiles and Geomembranes*, 48 (3): 400–418.

Pokharel, S.K., Han, J., Leshchinsky, D., Parsons, R.L., Halahmi, I., 2010. Investigation of Factors Influencing Behavior of Single Geocell-reinforced Bases under Static Loading. *Geotextiles and Geomembranes* 28 (6): 570–578.

Rajabian, A., Shukla, S.K., 2023. Stability Analysis of Anchor-Reinforced Soil Slopes with Taylor's Stability Chart. *International Journal of Geomechanics*, 23(2)

Rajagopal, K., Krishnaswamy, N.R., Madhavi Latha, G., 1999. Behaviour of Sand Confined with Single and Multiple Geocells. *Geotextiles and Geomembranes*, 8 (1): 55–62.

Schary, Y., 2019. *Neoloy—Developing a Novel Polymeric Alloy for Geocells. Book Chapter*, Chapter 3: 63–76, (Springer)

Sitharam, T.G., Hegde, A., 2013. Design and Construction of Geocell Foundation to Support Embankment on Soft Settled Red Mud. *Geotextiles and Geomembranes*, 41: 55–63.

Sharma R, Chen QM, Abu-Farsakh M, Yoon S 2009 Analytical Modelling of Geogrid Reinforced Soil Foundation. *Geotextiles and Geomembranes*, 27:63–72

Shukla, S. K. 2012. Reinforced Soil Engineering – Basic Concepts. Proceeding of One day International Workshop on Reinforced Soil and Geosynthetic Engineering: 2–13, Punjab, India.

Tavakoli Mehrjardi, Gh., Moghaddas Tafreshi, S.N., Dawson, A.R. 2012. Combined use of Geocell Reinforcement and Rubber Soil Mixtures to Improve Performance of Buried Pipes. *Geotextiles and Geomembranes*, 34 (October): 116–130.

Tavakoli Mehrjardi, Gh., Moghaddas Tafreshi, S.N., Dawson, A.R. 2013. Pipe Response in a Geocell Reinforced Trench and Compaction Considerations. *Geosynthetics International*, 20(2): 105–118.

Tavakoli Mehrjardi, Gh., Motarjemi, F. 2018. Interfacial Properties of Geocell-reinforced Granular Soils. *Geotextiles and Geomembranes*, 46(4): 384–395.

Thakur, J.K., Han, J., Pokharel, S.K., Parsons, R.L, 2012. Performance of Geocell-reinforced Recycled Asphalt Pavement (RAP) Bases Over Weak Subgrade under Cyclic Plate Loading. *Geotextiles and Geomembrane.* 35(December): 14–24.

Wayne, M. H., Han, J., & Akins, K. 1998. *The Design of Geosynthetic Reinforced Foundations*. Paper Presented at the Geosynthetics in Foundation Reinforcement and Erosion Control Systems.

Wehbi, M., Nogy, L., 2022. Development of a Simplified Design Approach for Shallow Ballasted Track Forms with Geocells Reinforced Sub-Ballast. *International Journal of Rail Transportation* 10 (5): 631–654.

Werkmeister, S., Dawson, A.R., Wellner, F., 2005. Permanent Deformation Behaviour of Granular Materials: The Shakedown Theory. *Transportation Research Board* 6(1): 31–57.

Yang, X., Han, J., Pokharel, S.K., Manandhar, C., Parsons, R.L., Leshchinsky, D., Halahmi, I. 2012. Accelerated Pavement Testing of Unpaved Roads with Geocell-reinforced Sand Bases. *Geotextiles and Geomembranes*, 32(June): 95–103.

Zhang, L., Zhao, M., Shi, C., Zhao, H. 2010. Bearing Capacity of Geocell Reinforcement in Embankment Engineering, *Geotextiles and Geomembranes*: 28, 475–482.

Zhou, H.B., Wen, X.J. 2008. Model Studies on Geogrid- or Geocell-reinforced Sand Mattress on Soft Soil. *Geotextile and Geomembranes*: 26, 231–238.

Sustainability with geosynthetics

Geosynthetic damage due to installation stresses in ultra-light weight foamed glass aggregate versus conventional aggregate

G.R. Koerner
Geosynthetic Institute (GSI) Folsom, PA, USA

T. Loux & A. Filshill
Aero Aggregates of North America, LLC, Eddystone, PA, USA

J. Schuller
Rowan University Glassboro, NJ, USA

ABSTRACT: Several large-scale laboratory tests were conducted on multiple geosynthetic specimens to assess damage effects from ultra-light weight foamed glass aggregates (UL-FGA) versus AASHTO #57 stone. When geotextile or geogrid design strengths are needed for geosynthetics used in separation or reinforcement applications, one needs to define the long-term design allowable strength. This value utilized in design, is arrived at by first determining the ultimate wide strip tensile strength and then reducing this value to an allowable one by the applying partial factors of safety for creep potential, installation damage and degradation potential. Favorable results were realized with UL-FGA compared to AASHTO #57 stone.

1 INTRODUCTION

Lightweight fill, including geofoam and expanded shale, are becoming increasingly popular in the United States in terms of construction. UL-FGA is a new member to this group. With its rise starting in Europe in the late 20th century, UL-FGA quickly became a sustainable alternative to traditional lightweight aggregate fills; not only is it made from 100% post-consumer recycled glass, but it also increases the lifetime of other materials within the construction project. Benefits of UL-FGA are that it is extremely lightweight and highly insulating (Aaboe & Oiseth 2004); UL-FGA is also closed-cell, making it non-absorbent, as well as slightly buoyant in water. Lastly, the unique shape of each piece of UL-FGA allows water to drain around it, which prevents the buildup of pore water pressures in the layer. These properties make UL-FGA a viable option for civil engineering projects where soft soil, utilities, or other sensitive materials are unavoidable (Loux *et al.* 2019, 2022) as well as where sand or other small, lightweight particles would not be best suited due to the need for draining. Specifically, when working with geosynthetics that can be easily damaged during the installation of aggregates, UL-FGA is a great option.

2 GEOSYNTHETICS PRODUCTION, INSTALLATION, AND PROPERTIES

There are many types of geosynthetics, but the two types used in these tests and discussed in this report are geotextiles and geogrids.

Geotextiles are custom-made depending on their intended use. A majority of geotextiles are made from polypropylene (95 percent), and use one of five principal fiber types: monofilament, multifilament, staple fiber yarn, slit-film monofilament, or slit-firm multifilament. After this, the fibers are then made into either woven or nonwoven fabrics. Geotextiles

usually have a mass per unit area between 150 and 750 grams per square meter, and usually have a thickness between 0.25 and 3.5 millimeters. The strength of geotextiles can vary between 20 and 60 kilonewtons per meter, depending on the fabric. Geotextiles are most commonly used for separation and filtration (Koerner 2016).

Geogrids are most commonly used for reinforcement of soils. There are three types of geogrids: homogeneous, coated yarn, and laser-bonded. The homogeneous variety is made by punching holes into sheets of either high density polyethylene for unidirectional or polypropylene for bidirectional, then drawing the sheets under controlled circumstances to avoid fracture until a grid is achieved. The coated yarn variety is made from polyester yarn which is woven into an open structure; junctions are either knitted together or physically intertwined to create a grid before being coated with polyvinyl chloride or latex for stability. Lastly, the laser-bonded variety is made by joining straps of polyester or polypropylene together using either lasers or ultrasonic welding. Geogrids can have a mass per unit area anywhere between 200 and 1000 grams per square meter, and a percent open area anywhere between 40 and 95 percent. Properties such as strength, creep, and degradation depend largely on which type of geogrid is being considered (Koerner 2016).

The long term design allowable strength (LTDA) for geotextiles and geogrids is arrived at by first determining the ultimate wide strip tensile strength (using ASTM D4595 or ASTM D6637) and then reducing this value to an allowable one by applying partial factors of safety as in the following equation 1 below:

$$T_{all} = T_{ult} * (1/(FS_{cr} * FS_{id} * FS_{cd})) \tag{1}$$

where T_{all} = the long-term design allowable load (lb/in or lb/ft); T_{ult} = the ultimate wide strip tensile strength (lb/in or lb/ft); FS_{cr} = the partial factor of safety for creep potential; FS_{id} = the partial factor of safety for installation damage; and FS_{cd} = the partial factor of safety for degradation potential.

Regarding the partial factor of safety for installation damage, it is well known how reinforcement geosynthetic behave with conventional soil and aggregate. Installation damage is the loss of strength properties resulting from the act of installation. In some situations, where aggressive backfill and heavy equipment are used in construction, the resultant loss of strength can be significant. Cases have been reported where only 30% of the original strength properties remain after installation (AASHTO 1990). Although this high loss level is unusual, it points out the need to address installation conditions.

It should be clearly pointed out that the range of partial factor of safety for installation damage is usually 1.1 to 1.6 for conventional geosynthetic materials installed in AASHTO #57 stone with moderate ground pressure equipment. The design engineer can control several variables which impact installation survivability conditions, including the choice of backfill and installation equipment. Specifications requiring sand backfill will reduce the installation damage significantly. However, this option does reduce ability for water to drain and the strength of the fill. Furthermore, light ground pressure equipment and greater lift thickness will reduce installation stresses. Unfortunately, neither is possible when a 90 to 95% requirement of standard proctor is desired for the fill (ASTM D698 2021).

3   TESTING PROCEDURE

The Geosynthetic Institute, or GSI, recently conducted installation survivability tests with UL-FGA manufactures by Aero Aggregates and AASHTO #57 aggregate. Test specimens were cut from geotextile and geogrid samples expose according to ASTM D5818; Standard Practice for Exposure and Retrieval of Samples to Evaluate Installation Damage of Geosynthetics. The UL-FGA exposure and retrieval was conducted at Aero Aggregates' plant in Eddystone, PA (Site 1) or the Philadelphia International Airport Remain Overnight

Apron (PHL RON) project in Philadelphia (Site 2). The AASHTO #57 exposure and retrieval was conducted at GSI in Folsom, PA (Site 3).

Either ASTM D4595: Test Method for Determining Tensile Properties of Geotextiles by the Wide-Width Strip Method or ASTM D6637: Test Method for Determining Tensile Properties of Geogrids by the Single or Multi-Rib Tensile Method was performed on the retrieved and as received, or new, materials at GSI in Folsom, PA.

Four total batches of each sample were tested, one as received (i.e. new) and one after being exposed at each of the three sites. The unexposed sample was used as the baseline for calculating the strength reduction factor. The samples that were exposed were installed under a sample of each aggregate at the designated location, and the aggregates were compacted over top of them, as per the manufacturer's instructions. Both the geogrids and the geotextiles were restrained, so they were not allowed to float or move through the aggregate. After installation was complete, the samples were left for a brief period of time before being exhumed. The geosynthetics were only left for a few minutes after installation, as survivability after installation is being tested; if it were left for a longer period of time, it would be a durability test. Upon being removed from the aggregate, the geosynthetics were visually inspected for any cracks, tears, or punctures. Lastly, these samples, as well as the new samples, were sent to the Geosynthetic Institute for strength testing, as well as further evaluation and analysis.

Figures 1–6 respectively show samples being installed, as well as the different aggregates and installment equipment, at Aero Aggregates, GSI and the PHL RON project.

Figure 1.   Photograph of UL-FGA installation.

Figure 2.   Close-up of UL-FGA and geogrid.

Figure 3.   Photo of AASHTO #57 installation.

Figure 4.   Photograph of AASHTO #57.
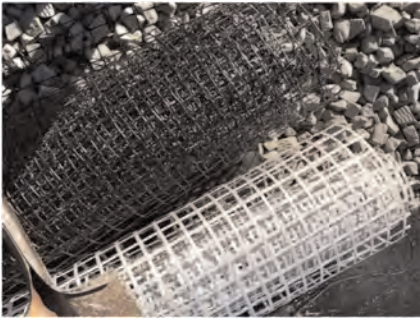
Figure 5.   Photo of GS installed at PHL Ron.

Figure 6.   Photograph of PHL Ron installation.

After both the exposed and the new materials were received at the Geosynthetic Institute, testing was completed to determine the break load, break strength, break deflection, and break strain. Specifically, ASTM D4595 was followed to test the geotextiles, and ASTM D6637 was followed to test the geogrids. Both tests utilize a Constant Rate of Extension Tensile testing machine; ASTM D4595 elongates a 200 by 200 millimeter rectangular specimen to failure at a rate of 10 percent per minute, whereas ASTM D6637 elongates a section of a geogrid (either 1, 3, or 7 ribs) to failure at a rate of 10 percent per minute. All materials were tested in the machine direction, and twenty specimens were tested for each of the four batches of samples. After testing was concluded, the average, standard deviation, and the coefficient of variation were calculated for each sample. Lastly, the strength reduction factor was calculated to determine, on average, how much strength was lost in each batch of samples.

4   RESULTS

Table 1 summarizes the strength reduction factors, or the results of the material testing and analysis, for the geosynthetics from all three sites. For the purpose of anonymity, the geosynthetics is not identified. The strength reduction factor (SRF) was determined by using the Equation 2 below:

$$SRF \; = \; F_{rec} \, / \, F_{exp} \tag{2}$$

where SRF = the strength reduction factor; F_{rec} is the average break load of the as received (new) material; and F_{exp} is the average break load of the exposed material.

Table 1.   Strength reduction results from material testing.

Geosynthetic Material Tested	SRF for AASHTO #57 exposed at GSI (Site 3)	SRF for UL-FGA at Aero Aggregates (Site 1)	SRF for UL-RGA exposed at PHL RON (Site 2)
Geotextile A	1.8	1.3	1.1
Geotextile B	1.7	1.2	1.7
BX Geogrid A	1.6	1.1	1.2
BX Geogrid B	1.4	1.0	1.1
UX Geogrid A	1.6	1.3	1.2

5 DISCUSSION

As can be seen from the data above, UL-FGA causes much less damage to geosynthetics upon installation. Each SRF is less for the materials exposed to UL-FGA compared to those exposed to AASHTO #57. The geosynthetics exposed to AASHTO #57 are, therefore, weaker than those exposed to be UL-FGA. Specifically, when AASHTO #57 was installed over the geosynthetics, strength was lost from the damage, making the geosynthetic 1.4 to 1.8 times weaker; however, when UL-FGA was installed over geosynthetics, little to no strength was lost, making it only 1.0 to 1.3 times weaker, with the exception of geotextile B at PHL RON, which yielded a SRF of 1.7. This overall trend can mainly be attributed to how lightweight UL-FGA is compared to AASHTO #57, as well as the care taken to install UL-FGA in relatively thick lifts, per the recommended installation procedure.

It is also worth noting that, with the exception of geotextile B at PHL RON, all the SRFs for the UL-FGA are within the rang 1.0 to 1.3, showing consistency both throughout testing and installation as well as within the production and performance of the UL-GFA. Potential reasoning for this outlier could be mishandling during the exhumation of the geotextile; the PHL RON site had active construction activities occurring at the time and the authors were conscious of contractor's time – and work progression. Ultimately, this outlier is not a cause for concern given the trend for the other geosynthetic materials, and the SRF calculated for geotextile B at Aero Aggregates. Consistency within the product is important when discussing survivability because less frequent checking and replacing of the material is needed.

Since UL-FGA is so lightweight, it causes less damage upon installation, which is one of the major benefits to using it as backfill compared to regular aggregates. Also, since a very specific procedure is recommended when installing UL-FGA, additional care is taken not to damage the geosynthetic material underneath. In terms of survivability, this is important because it will allow the geosynthetics to perform at a high level for longer, since little to no strength is lost during installation. When material strength is lost, it is not as efficient, which means that more material must be used to achieve the same long-term design performance. Taking care not to damage materials during installation leads to an increase in survivability of the whole system, which means less frequent repairs and less cost to maintain or fix the system down the line.

6 CONCLUSION

UL-FGA is a lightweight aggregate that is used as a backfill in many construction and other civil engineering projects. It is favorable due to its extreme lightweight, high insulating, and draining properties. Additionally, UL-FGA is installed in such a way that helps limit damage to the material underneath it, which is important when fragile material is being covered. Specifically, when using geosynthetics in construction and other civil engineering projects, use of a lightweight aggregate such as UL-FGA is appropriate in order to maintain the strength and integrity of both the aggregate and the geosynthetic; this increases the survivability of the entire system. As can be seen from the results of the testing discussed in this report, UL-FGA causes significantly less installation damage to the geosynthetic material being used than AASHTO #57 does, which increases its ability to perform well and survive longer. Installation of UL-FGA only made the geosynthetics 1.0 to 1.3 times weaker, whereas installation of AASHTO #57 made the geosynthetics 1.4 to 1.8 times weaker. When discussing survivability, it is paramount to maintain the strength and integrity of materials, especially during installation, so that the material can survive and perform well for longer.

ACKNOWLEDGEMENT

REFERENCES

Aaboe, R., and Oiseth, E. 2004. Foamed Glass: An Alternative Lightweight and Insulating Material. In M. Limbachiya and J. Roberts (eds), *Sustainable Waste Management and Recycling: Glass Waste*. 167–176. London: Thomas Telford Publishing.

AASHTO Task Force 27.1990. *In Situ Soil Improvement Techniques*. Washington, DC: AASHTO.

ASTM D698. 2021. *Standard Test Methods for Laboratory Compaction Characteristics of Soil Using Standard Effort*. Conshohocken, PA: ASTM International.

Koerner, R. M. 2016. *Designing with Geosynthetics*, 6th ed., Vol. 1. Xlibris.

Loux, T.A., Filshill, A., and Zhang, Z. 2019. Foamed Glass Aggregate Lightweight Fill Over Compressible Soils. *Geo St. John's 2019*. The Canadian Geotechnical Society.

Loux, T., McInnes, S., Crawford, R., and Filshill, A. 2022. Design and Construction of a Geosynthetic-Reinforced MSE Structure with Foamed Glass Aggregate Lightweight Backfill. *Proceedings of the 7th European Geosynthetics Conference*, Warsaw, Poland, 4-7 September 2022.

Contribution to the study of mechanical degradation of geosynthetic products in a saline environment

L. Naga, M. Chikhaoui* & L. Djerbal

LEEGO Laboratory, Faculty of civil engineering, University of Science and Technology Houari Boumediene, Algeria

ABSTRACT: The durability of geosynthetics used in aggressive environments can be affected by many degrading agents. This is why this paper is devoted to the study of the mechanical resistance of a geogrid based on polypropylene with respect to sulfuric acid (to create a medium rich in sulfur). To do this, the geogrid was subjected to an immersion test in the laboratory, considering different concentrations of sulfuric acid (in this case: 4% (0.8 mol.L^{-1}) 10% (1.2 mol .L^{-1}) and 16% (3.2 mol.L^{-1})). The damage caused by the accelerated degradation test was evaluated through the analysis of the results of the tensile test carried out on intact and degraded samples. The results show that the maximum tensile strength, as well as the tensile strength at 2%, 5% and 10% strain of the geogrid, did not undergo significant changes after the immersion tests regardless of the concentration. sulfuric acid. However, the corresponding strain to the maximum tensile strength underwent an increase in particular for acid concentrations greater than or equal to 1.2 mol.L-1. This result clearly shows the effect of the aggressive environment on the behavior of the geogrid is well as the observation of irreversible damage after only 1 month of immersion in sulfuric acid.

1 INTRODUCTION

Geosynthetics are products based on synthetic or natural polymers, used to fulfill several functions in the construction of numerous civil engineering infrastructures such as roads, tunnels, retaining structures, dams and coastal protection (Müller et Saathoff 2015). These relatively new products offer many advantages over the traditional product and technique: facilitate construction even in unfavorable conditions, reduce construction costs, increase the life of the structure.

Nowadays, there are different types of geosynthetics fulfilling different service requirements of the work (Shukla 2016), geogrids, are part of this large family of products, which are widely used for the reinforcement of slopes, walls, roads and foundations.

During the lifetime of the structure, the geosynthetic product can be in prolonged contact with several degradation agents (Greenwood *et al.* 2012; Hsuan *et al.* 2008) insofar as the lifetime required for a structure can be extremely long (up to one century in civil engineering) which can negatively alter the chemical, physical and mechanical behavior of geosynthetics by reducing their functional life (Bartolomeo 2003). These undesirable modifications are mainly related to the type of polymer used and the application conditions of the geosynthetic.

The polymers used for the production of geosynthetics (such as polyolefins, polyester or polyamides) generally suffer during prolonged contact with aggressive liquids from problems of extraction of chemical additives or gain mass by absorption of solution (physical aging).

---

*Corresponding Author: mch_gcg16@yahoo.ca

In addition, the absorbed solutions can interact with the polymer chains of the geosynthetics (chemical aging) (Kay *et al.* 2004; Koerner *et al.* 2007; Santvoort 2017). Polypropylene is extremely resistant to the inorganic environment (José Ricardo Carneiro, Morais, et Lopes 2018; Gulec, Benson, et Edil 2005; Jose Ricardo Carneiro, Almeida, et Lopes 2019; José Ricardo Carneiro, Almeida, et Lopes 2018; José Ricardo Carneiro, Almeida, et Lopes 2014). However, it is susceptible to being affected by oxidizing agents such as sulfuric acid, halogens, etc. Remember that additives added to improve the properties of polypropylene can be attacked by aggressive chemicals to which PP is resistant (Tripathi 2002).

The main objective of this research is to study the resistance of a PP geogrid to sulfuric acid. For this, an accelerated degradation test in the laboratory has been developed, in order to evaluate the resistance of the product in an environment rich in sulfur. The main indices adopted in this work are based on the results of the tensile test carried out on intact samples and subjected to degradation in different concentrations of sulfuric acid for 1 month. The evolution of the test parameters (tensile strength and tensile strain) according to different concentrations of sulfuric acid will be developed and studied.

2 EXPERIMENTAL DESCRIPTION

2.1 *Geogrid*

In this work, an extruded biaxial geogrid made-up from polypropylene with a minimum of 2% carbon black (percentage by weight), see Figure 1 below.

Figure 1. Visual aspect of intact biaxial geogrid (ruler in centimeters).

The main characteristics of the geogrid are summarized in Table 1.

2.2 *Immersion test*

The geogrid product was immersed, at a constant temperature of 80°C, in different concentrations of dilute sulfuric acid: 4%, 10%,16% (The stock solution has a purity of 95%). The immersion tests were carried out in the dark (the sample is protected from UV rays) and lasted 1 month.

Table 1. Main characteristics of the geogrid (reference specimens).

Parameters	Quantity
Structure	Extruded geogrid
Polymers	Polypropylene
Minimum carbon black content	2%
Tensile strength at 2% strain (MD-CMD)[a]	9.10 ($\pm$0.28) - 10.47 ($\pm$0.73) KN/m
Tensile strength at 5% strain (MD-CMD)[a]	18.07 ($\pm$0.06) - 20.92 ($\pm$1.36) KN/m
Tensile strength at 10% strain (MD-CMD)[a]	28.15 ($\pm$0.22) - 32.22 ($\pm$1.66) KN/m
Ultimate tensile strength (MD-CMD)[a]	32.89 ($\pm$1.07) - 36.18 ($\pm$1.04) KN/m
Elongation at ultimate tensile strength (MD-CMD)[a]	17.90 ($\pm$0.54) - 15.77 ($\pm$0.58) %
Unit area mass[b]	0.33kg/m^2

In brackets are the 95% confidence intervals.
[a]Determined according to ASTM 6637 (ASTM 6637).
[b]Determined according to ASTM 3776 (ASTM D3776).
MD: machine direction – CMD : cross-machine direction.

The composition of the solution was checked by measuring the pH. The monitoring results showed that the concentration of the solutions changes slightly over time. In order to keep a stable concentration, the solution was replaced every 15 days.

After collection, the specimens were rinsed with deionized water and wiped with water-absorbent paper towels. All specimens were conditioned at 23°C and 65% RH for at least 24 h prior to testing.

2.3 *Evaluation of the damage suffered by the geogrid*

The damage suffered by the geogrid product (during degradation tests) was evaluated by tensile tests according to (ASTM 6637), to determine the changes in the tensile properties of the geogrid under the effect of an accelerated aging treatment. The tensile tests were carried out on the Instron universal testing machine equipped with a 250 kN load cell (Figure 2).

Figure 2. Tensile test machine.

The method used in this study is to perform tensile tests on a single rib in the cross-machine direction only, each tensile test included a minimum of 5 specimens with a length equivalent to the distance between 3 junctions in the direction of the test.

Maximum tensile strength (MTS in KN/m) and corresponding strains at the maximum tensile strength ε_{ML} (%), The tensile strength at 2% (TS 2% in KN/m), at 5% (TS 5 % in KN/m) and at 10% (TS 10% in KN/m) were obtained from the load versus strain curves for a single rib (Figure 3) converted over the entire unit width (1m). The deformation was determined by expressing the relative displacement of the jaws as a percentage of the original length (120 mm). Results are shown with a 95% confidence interval.
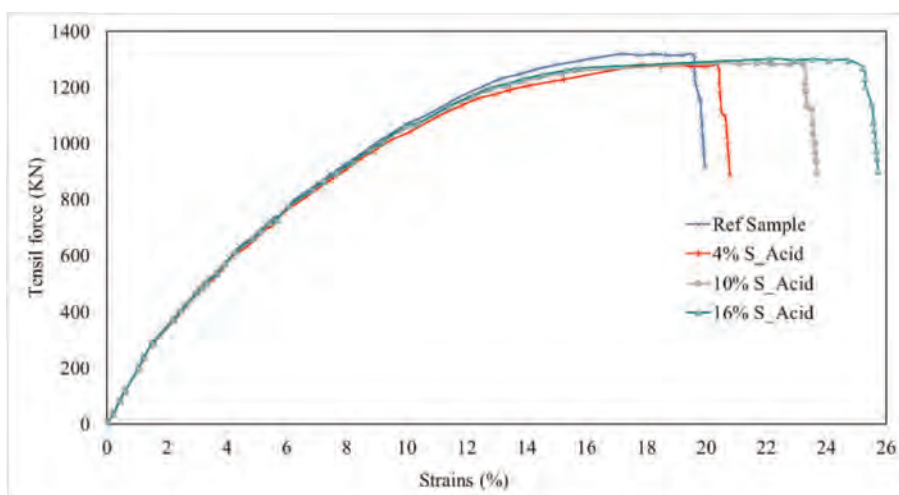
Figure 3.   Rib tensile force-strain curves obtained before and after the immersion tests.

3   RESULTS AND DISCUSSION

The maximum tensile strength as well as the tensile strength at 2%, 5% and 10% strain of geogrid did not undergo significant changes after the immersion tests and this whatever the sulfuric acid concentration. Moreover, the small decreases in these terms show the negative effect of the aggressive environment on the long-term behavior of the geogrid, particularly in the event of prolonged contact with aggressive substances. In addition, the results obtained confirm good tensile strength for an immersion time not exceeding 1 month.

However, the minor variations observed in these parameters (between 0.64% and 7.27%) are not statically significant and can be attributed to the heterogeneity of the geogrid product resulting from their manufacturing process. It is necessary to increase the immersion time and to vary the products in order to better quantify the effect of sulfuric acid on the mechanical resistance of the geogrid. In terms of tensile strain corresponding to the maximum tensile strength, the results obtained clearly show a significant increase of approximately 10% and 16% corresponding respectively to concentrations of (1.2 mol.L^{-1}) and (3.2 mol.L^{-1}) of H_2SO_4 (Figure 4) after only one month of immersion.

The change in strain at maximum strength after immersion in sulfuric acid may have several possible explanations:

– High temperature immersion tests favored the extraction of carbon black, or a chemical interaction that occurs between sulfuric acid and carbon black which reduces their
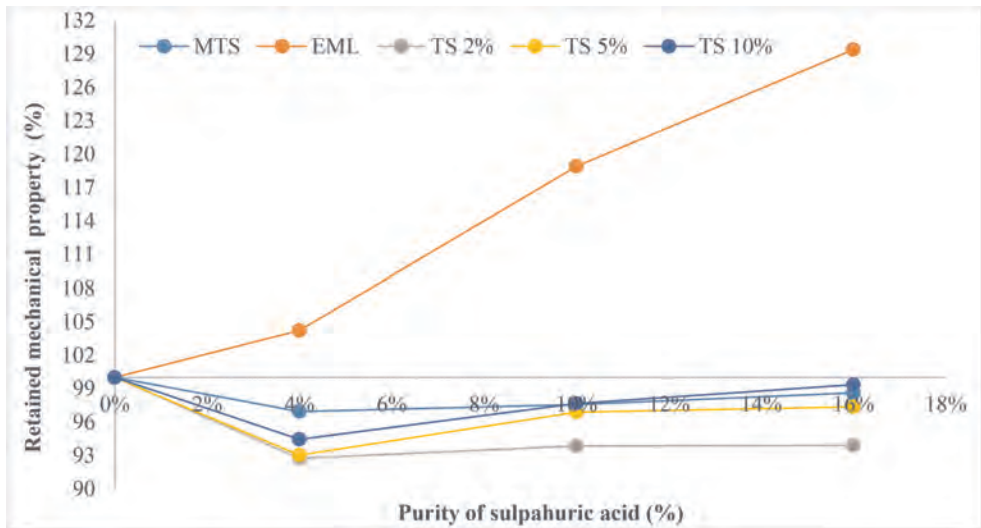
Figure 4. Retained mechanical property against purity of sulfuric acid.

stiffening effect and makes them more deformable (the carbon black in addition to their protective role against UV, it improves the mechanical behavior of certain polymers by increasing their rigidity (Donnet *et al.* 1993).

– Appearance of the plasticization phenomenon of PP under the effect of sulfuric acid. Moreover, two or more of the preceding phenomena could have occurred simultaneously. Further research will be addressed in our future work to clarify previous hypotheses through thermal and chemical analyses. (No previous studies were found in the literature on this subject).

4 CONCLUSION

The main objective of the research work carried out in this paper is to identify the mechanical behavior of a geogrid product subjected to an accelerated aging test at the laboratory level. Tensile tests were performed on undamaged samples immersed in different concentrations of sulfuric acid (the most dominant chemical compound of selected aggressive soil). for one month at a temperature of 80°C.

The test results show a slight influence of sulfuric acid, for an immersion time not exceeding 1 month, on the tensile strength (maximum or which corresponds to 2% 5% 10% strain). Moreover, the strain corresponding to the maximum tensile strength increased by up to 16% at relatively high acid concentrations. Some hypotheses have been put forward to explain this increase. However, additional research is needed to better understand the problem and identify the causes of degradation through a microstructural study.

The results presented in this study correspond to particular degradation conditions and to the specific characteristics of the geogrid (the geosynthetic structure and its physical properties, base polymer used, type of stabilizer) and cannot be generalized at this state of knowledge. to other geosynthetic products.

ACKNOWLEDGEMENT

REFERENCES

ASTM 6637. 2015. *Test Method for Determining Tensile Properties of Geogrids by the Single or Multi-Rib Tensile Method*. ASTM International. doi:10.1520/D6637-11.

ASTM D3776. 2020. *Test Methods for Mass Per Unit Area (Weight) of Fabric*. ASTM International. doi:10.1520/D3776_D3776M-20.

Bartolomeo, Philippe. 2003. Vers une Prévision de la Durée de vie des Polymères Géosynthétiques. *Bulletin des Laboratoires des Ponts et Chaussées*, 23.

Carneiro, José Ricardo, Paulo Joaquim Almeida, et Maria de Lurdes Lopes. 2014. Some Synergisms in the Laboratory Degradation of a Polypropylene Geotextile *Construction and Building Materials* 73 (décembre): 586–591. doi:10.1016/j.conbuildmat.2014.10.001.

Carneiro, José Ricardo, Paulo Joaquim Almeida, et Maria de Lurdes Lopes. 2018. Laboratory Evaluation of Interactions in the Degradation of a Polypropylene Geotextile in Marine Environments *Advances in Materials Science and Engineering* 2018: 1–10. doi:10.1155/2018/9182658.

Carneiro, Jose Ricardo, Paulo Joaquim Almeida, et Maria de Lurdes Lopes. 2019. Effect of Acids and Alkalis on the Resistance of a Polypropylene Geotextile against Thermo-Oxidation *Journal of Construction Research* 1 (1). doi:10.30564/jcr.v1i1.152.

Carneiro, José Ricardo, Miguel Morais, et Maria de Lurdes Lopes. 2018. Degradation of Polypropylene Geotextiles with Different Chemical Stabilisations in Marine Environments *Construction and Building Materials* 165 (mars): 877–886. doi:10.1016/j.conbuildmat.2018.01.067.

Donnet, Jean-Baptiste, Roop Chand Bansal, et Meng-Jiao Wang, éd. 1993. *Carbon Black: Science and Technology*. 2nd ed., rev.expanded. New York: Dekker.

Greenwood, J.H, H.F Schroeder, et W. Voskamp. 2012. *Durability of Geosynthetics*. CUR Building&Infrastructure. Vol. 243. Building with Knowledge, CUR committee C 187. Netherlands: Stichting CURNET, Gouda. https://www.geosynthetica.com/wp-content/uploads/Publication243_Durability_C187.pdf.

Gulec, S. B., C. H. Benson, et T. B. Edil. 2005. Effect of Acidic Mine Drainage on the Mechanical and Hydraulic Properties of Three Geosynthetics *Journal of Geotechnical and Geoenvironmental Engineering* 131 (8): 937–950. doi:10.1061/(ASCE)1090-0241(2005)131:8(937).

Hsuan, Y G, H F Schroeder, K Rowe, W Müller, J Greenwood, D Cazzuffi, et R M Koerner. 2008. Long-Term Performance and Lifetime Prediction of Geosynthetics. *In Proceedings of the 4th European Conference on Geosynthetics*, 41.

Kay, Dominique, Eric Blond, et Jacek Mlynarek. 2004. GEOSYNTHETICS DURABILITY: A POLYMER CHEMISTRY ISSUE. *In Proceedings of the 57th Canadian Geotechnical Conference*, 14.

Koerner, G.R., Y.G. Hsuan, et R.M. Koerner. 2007. The Durability of Geosynthetics. In *Geosynthetics in Civil Engineering*, 36–65. Elsevier. doi:10.1533/9781845692490.1.36.

Müller, Werner W, et Fokke Saathoff. 2015. Geosynthetics in Geoenvironmental Engineering *Science and Technology of Advanced Materials* 16 (3): 034605. doi:10.1088/1468-6996/16/3/034605.

Santvoort, G.P.T.M.van, éd. 2017. *Geosynthetics in Civil Engineering*. 1re éd. Routledge. doi:10.1201/9780203753378.

Shukla, Sanjay Kumar. 2016. *An Introduction to Geosynthetic Engineering*. Boca Raton: CRC Press/Taylor & Francis Group.

Tripathi, Devesh. 2002. *Practical Guide to Polypropylene*. First published. Rapra Practical Guide Series. Shawbury, UK: RAPRA Technology Ltd.

In search of an alternative surfactant for stress cracking tests for HDPE geomembranes

G.R. Koerner

Geosynthetic Institute, Folsom, Pennsylvania, USA

ABSTRACT: Igepal CO-630 is referenced in ASTM & CEN norms-test methods as the reagent for the stress cracking test. Unfortunately, it has now been listed as a priority pollutant by several counties because of a benzene ring in its formulation. As a result, it is no longer available for laboratory use in several locations, particularly in Europe (EU) and Canada. This event has manifested itself over the past several years. Obviously, our industry is searching for an alternative surfactant for this important performance test which can be used and is available globally. This paper will describe the search and round robin tests which lead to an alternative surfactant that conceivably will fill the need internationally.

1 INTRODUCTION

Improved stress cracking resistance in high density polyethylene (HDPE) geomembranes has been a quest of our industry for many years. The Geosynthetic Institute (GSI) has been working in this area since the mid 1980's. GRI GM13 standard specification for HDPE geomembranes has moved the ASTM D5397 (appendix) single point notch constant tension load result requirement from 200 to 300 and finally to 500 hours over the last thirty years. It is interesting to note that some current HDPE geomembrane formulations have Single Point – Notch Constant Tension Load Test (SP-NCTL) values greater than 1,000 hours.

The European Union no longer allows the sale of Rhodia Solvay Group Igepal CO-630 to anyone in production industries (i.e., large quantities) due to ecological and health issues. This is apparently a REACH directive, not a law. As such, GSI has been tasked with finding a replacement for the surfactant used in several stress cracking tests. Trying to be proactive, we know that there are hundreds of commercially available non-ionic surfactants in the family of detergents. The task is daunting but necessary.

2 PROCEDURES

The stress crack test method developed in the late 1980s Koerner, R. M., Halse, Y. H. and Lord, A. E. Jr. (1990) is used to determine failure times from which the susceptibility of polyolefin geomembrane is evaluated for durability in use. The test is run under a constant tensile load condition and an accelerated environmental condition as described in ASTM D5397 "Standard Test Method for Evaluation of Stress Crack Resistance of Polyolefin Geomembranes Using the Notched Constant Tensile Load Test". One can generate the entire stress crack curve, which requires measurement of the failure time associated with a given test specimen at a specified tensile load level. Results from a series of such tests utilizing a range of load levels can be used to construct a stress-time plot on a log-log axis for the geomembrane. We did not generate complete curves for this investigation. In contrast, we only conducted SP-NCTL tests per the

appendix of the standard. This stress crack test utilizes five (5) ASTM D1833 Type "L" specimens. One determines the thickness and yield stress of the geomembrane and then notches it 20% of its nominal thickness (i.e. resulting in a ligament 80% of the no minal thickness). We run the SPNCTL test at 30% of the yield stress and record the failure time in hours. The apparatus used for the stress cracking test is shown in Figures 1 and 2.

Figure 1.   Frame and specimens.

Figure 2.   Immersion baths.

The notching of the specimens for this test is critical. One should use a precision (i.e., rigid) notching apparatus like the one shown in Figure 3 to control the notch depth to plus or minus 0.01mm (0.5 mil). The blade in the notcher should be a single-edged razor made of carbon steel. The profile of the blade should be like that of an arrow rather that a chisel point. The sharpness of the point is critical to the cleanliness of the cut, which affects the results of the test significantly. It is highly recommended that double honed razor blades are used in the notcher for no more than twenty specimens. It is also important that the notched depth is controlled by verification. This is typically done optically in cross section and plan view (pre and posttest). A photograph of a notch specimen pretest is shown in cross section in Figure 4 and in the end-plan view posttest in Figure 5.

Figure 3.   Notching.
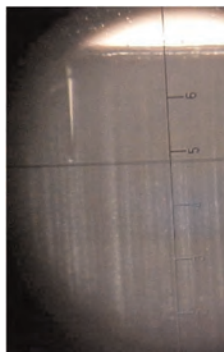
Figure 4.   Verifying sharpness.
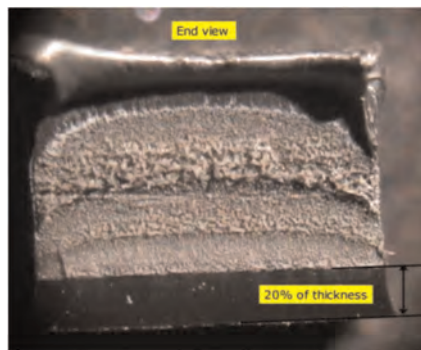
Figure 5.   Verifying notch depth.

A group of surfactants were used for this investigation. The group included four (4) surfactants, which were chosen based on efficacy and availability. Efficacy is critical as explained by Bobsein, R. L. (1998). The surfactants used were as follows:

- IGEPAL CO-630 (10% by volume) at 50 degrees Celsius
- Solvay: Rhodasurf LA-9 (10% by volume) at 50 degrees Celsius
- DOW: Tergitol 15-S-15 (5 % by mass) at 70 degrees Celsius
- BASF: Dehyton PL (10% by volume) at 70 degrees Celsius

In addition, we implemented a group of five (5) geomembranes for this investigation in the round robin test program. The geomembranes were chosen based on their association with the GAI-LAP proficiency test program. Each had a known stress crack resistance that was developed by several international laboratories. The geomembranes used were as follows:

- GM-71, ADS pipe resin, (SP-NCTL = 3 hours +/−2)
- GM-72, NSC 60 mil UC resin, (SP-NCTL = 165 hours +/−24)
- GM-73, SOLMAX CP Chem resin, (SP-NCTL = >500 hours)
- GM-74, Well researched Field failure, (SP-NCTL = 375 hours +/−67)
- GM-75, Layfield DOW Bimodal resin, (SP-NCTL = >1,000 hours)

3 TEST RESULTS

3.1 *Round Robin #1*

Three sets of round robin tests were run in three different laboratories. Testing included three surfactants and five different geomembranes. The results of the first-round robin are presented in Table 1.

Table 1. Round robin #1 results (all entries are in hours).

GM Number	Lab 1 Igepal	Lab 2 Igepal	Lab 3 Igepal	Lab 1 Rhodasurf	Lab 2 Rhodasurf	Lab 3 Rhodasurf	Lab 1 Tergitol	Lab 2 Tergitol	Lab 3 Tergitol
GM-71	1	2	2	2	5	27	2	3	1
GM-72	141	192	144	>500	410	>500	>800	315	278
GM-73	>800	>1000	>1000	>500	>1000	>500	>800	>500	372
GM-74	554	525	565	>500	487	>500	>800	267	400
GM-75	>800	>1000	492	>500	>500	>500	>800	230	241

In short, the results look poor. Originally six labs were solicited and sent samples, but only three labs ended up participating. In addition, the availability of some surfactants during the COVID pandemic was a challenge and there were supply chain issues experienced by some labs. As can be seen form Table 1, there is little consistency in results beyond Igepal CO-630. Lastly we found that the Rhodasurf is unavailable to many labs and its stability at elevated temperature over long test times is an issue.

3.2 *Round Robin #2*

The second-round robin results were better than the first. We had six labs participating, testing only two surfactants. It should also be noted that we arrived at 5 % by mass criteria

after much experimentation in GSI's laboratory. During the testing, we found that the DOW Tergitol 15-S-15 (5 % by mass) at 70 degrees Celsius is a bit of a challenge to work with. Tergitol is a solid at room temperature and needs to be diluted in very hot water before entering the stress cracking bath, which questions its viability as a replacement surfactant for Igepal.

The results of the second-round robin test are presented in Table 2. Six laboratories participated in the activity utilizing two surfactants and five different geomembranes.

Table 2.   Round Robin #2 results (all entries are in hours)

GM Number	Lab 1 Igepal	Lab 2 Igepal	Lab 3 Igepal	Lab 4 Igepal	Lab 5 Igepal	Lab 6 Igepal	Lab 1 Tergitol	Lab 2 Tergitol	Lab 3 Tergitol	Lab 4 Tergitol	Lab 5 Tergitol	Lab 6 Tergitol
GM-71	2	1	2	2	2	3	2	3	1	1	1	1
GM-72	141	192	144	139	152	139	508	315	278	267	411	524
GM-73	>800	>1000	>1000	–	>1000	>500	>800	>500	372	334	>500	325
GM-74	554	525	565	488	624	629	>800	267	400	>500	>500	>500
GM-75	>800	>1000	492	316	>1000	470	>800	230	241	224	>500	>500

3.3   *Round Robin #3*

The results of the third-round robin are presented in Table 3. Five laboratories participated in the activity utilizing two surfactants and five different geomembranes.

Table 3.   Round Robin #3 results (all entries are in hours).

GM Number	Labi Igepal	Lab 2 Igepal	Lab 3 Igepal	Lab 4 Igepal	Lab 5 Igepal	Labi Dehyton	Lab 2 Dehyton	Lab 3 Dehyton	Lab 4 IDehyton	Lab 5 Dehyton
GM-71	2	1	3	1	4	6	5	4	7	11
GM-72	141	192	144	139	152	215	225	290	275	342
GM-73	>1000	>1000	>1000	–	>1000	>500	>500	>500	>500	>500
GM-74	554	525	565	488	611	697	753	822	>500	783
GM-75	>800	>1000	492	316	>1000	>1000	>1000	>1000	>500	>500

The results of the third-round robin test look pretty good. However, I wish the alternative surfactant, Dehyton PL would shorten the time horizon for the test and not lengthen it. This was the case even at elevated temperatures. It should be pointed out that all results are averages from sets of five (5) specimens for round robin testing run per SPNCTL in the appendix of the ASTM D5397 standard. It also should be made very clear that the 10% Igepal CO-630° was tested at 50 degrees Celsius, where the BASF 10% Dehyton PL was tested at 70°degrees Celsius as a result of different cloud point numbers given by the manufacturers.

4   DISCUSSION

We can divide what was learned from these studies into two sections: lessons learned from the study results, and lessons learned regarding procedural issues. The major takeaway from the results of the concluded studies is that between-participant variation plays a larger role than within-participant variation in the standard uncertainty. In most of the cases, good

notching is imperative for repeatable stress cracking results. The variation in characteristics between participants was statistically significant, even when using the same raw materials and machine settings. This leads to the conclusion that unknown variables exist between participants (or there are unknown machine differences, e.g., age of machine, maintenance, calibration, history, etc.) that were not adequately controlled.

Looking toward future round robins, it appears that increasing the number of participants, or at least the number of machines, will have a larger effect on reducing the standard uncertainty in the consensus values rather than by having each participant produce more samples. The difficulty with the results is that while the variability in the results is clear, the causes of the variability are not. Without specific knowledge of which aspects are to blame, there is no quantitative basis for modifying the standard to produce more consistent results. This top-down approach illustrates that there are unknown sources of unknown variability in the testing, which is troubling.

One common take away from all three round robin studies is that the procedure is vitally important. It is clear from these different studies that the procedure must address more issues than stress level and notch depth. Running a stress crack test is much more than, machine calibrations, setup, material handling, operation and maintenance of the immersion bath. A robust round robin plan must address all these areas to avoid confusion and assumptions by the different participants. Furthermore, a more focused study using only one material, notch by a single laboratory may be needed going forward to identify an alternative surfactant to IGEPAL CO-630.

"Planning the ILS" section of ASTM E691-13 is broken into seven subsections: ILS membership, basic design, test method, participating laboratories, materials, number of test results per material, and protocol. The ILS membership discusses the scope and details of the study and assigns a coordinator, and a statistician. Similarly, the basic design section notes the importance of keeping the design simple. The remaining sections require consideration specific to the test method in question. We realize that a detailed round robin study defined by ASTM ILS does not allow for an abbreviation like having only one material and letting one central lab do all the notching. However, it is important to note that this is a complicated test with many variables. After three attempts at conducting round robin studies, it is still not unequivocally clear that an alternative surfactant to IGEPAL CO-630 has been identified for ASTM D5397.

To our knowledge, all known substitute surfactants to date have unique characteristics that will affect stress cracking in HDPE GMs differently. Unfortunately, we know of no REACH (EU) compliant surfactant that has the same SP-NCTL signature as Igepal CO-630 to use with polyethylene geomembranes common to our industry. As stated by Sheirs, J (2022), "Unfortunately, Igepal CO-630 will become harder to purchase with restricted supply in many countries because it can cause long-lasting harmful effects to aquatic life. Alternative surfactants should have physiochemical properties like Igepal CO-630, should be readily soluble, should be easy to remove, should have a similar critical micelle concentration (CMC), should be eco-friendly and should not degrade to toxic phenolic metabolites." This is an onerous list of conditions that are proving difficult to attain.

Therefore, our work here is ongoing and in need of a new direction. Perhaps the work with strain hardening modulus referenced by Engelsing, K. and Zanzinger, H. (2012) will change the paradigm of our industry away from actual accelerated aging performance tests to a mechanical index test.

5 CONCLUSION

After extensive round robin testing, it has been determined that no known REACH directive compliant surfactant has the equivalent efficacy as Igepal CO-630 for ASTM D5397 testing. Therefore, if performing this test with an alternative surfactant one will have to first

determine a correlation between the substitute-alternative surfactant and Igepal CO-630. Comparative experiments will have to show a correlation coefficient greater than 0.9 as well as a coefficient of variation within any given SP-NCTL data set of less than 5 for validation on a specimen set of at least thirty (30) data points. At which point an effectiveness ratio may be used to extrapolate results between the substitute-alternative surfactant and Igepal CO-630.

ACKNOWLEDGMENT

REFERENCES

ASTM D1833, "Standard Test Method for Odor of Petroleum Wax," *ASTM International*, 100 Barr Harbor Drive, PO Box C700, West Conshohocken, PA 19428-2959 USA

ASTM D5397, "Standard Test Method for Evaluation of Stress Crack Resistance of Polyolefin Geomembranes Using Notched Constant Tensile Load Test," *ASTM International*, 100 Barr Harbor Drive, PO Box C700, West Conshohocken, PA 19428-2959 USA

ASTM E691, "Standard Practice for Conducting an Interlaboratory Study to Determine the Precision of a Test Method," *ASTM International*, 100 Barr Harbor Drive, PO Box C700, West Conshohocken, PA 19428-2959 USA

Bobstein, R.L. (1998), "Factors Influencing SP-NCTL Test Results, "*Proc. GRI-12 Conference on Lessons Learned from Geosynthetic Case Histories,* G.R. Koerner, Y.G. Hsuan, T.Y. Soong and R.M. Koerner, Eds., GII Publ., Folsom, PA, pp. 46-57

Engelsing, K. and Zanzinger, H. (2012), "A New Accelerated Test Method for Stress Crack Resistance of HDPE Geomembranes," *Geo12-FW-036, Proceedings of GeoAmericas 2012 Conference*, May 1-4, 2012, Lima, Peru (on CD).

Koerner, R. M., Halse, Y. H. and Lord, A. E. Jr. (1990), "Stress Cracking of Semi-Crystalline Geomembranes," *Chapter 11 in Geomembranes: Identification and Performance Testing, RILEM TC-130.*

Sheirs, J (2022), "Alternative Stress Cracking Surfactants" *Geosynthetic Magazine – Industry News, IFAI-ATA* https://geosyntheticsmagazine.com/2022/02/09/alternative-stress-cracking-surfactants-identified-for-hdpe-geomembrane-testing/

Life cycle analysis of an innovative reinforcement geosynthetic coupled with a detection and monitoring warning system

M. Riot
Afitexinov, Champhol, France

P. Delmas
Independant Expert, PHD HDR, Fontenay le Fleury, France

T. Monnet
Afitexinov, Cessieu, France

ABSTRACT: The use of reinforcement geosynthetics to prevent localized collapses over cavities is now relatively common. During the REGIC research project, an innovative geosynthetic solution has been developed. It includes a specific reinforcement geosynthetic coupled with an autonomous and remote warning device to detect, to locate and then monitor a localized collapse or sinkhole. This study identifies technically and environmentally the implementation conditions of this innovative instrumented geosynthetic solution compared to the traditional solution. The Life Cycle Analysis is realized to carry out this comparison from an environmental point of view. The results, including a sensitivity analysis aim to provide information on the environmental performance of the developed instrumented solution in a R&D framework. This detailed analysis is extended to most current other possible solutions with same level of performance and safety. This life cycle analysis finally resulted in the publication of an EPD® for the geosynthetic range concerned.

1 INTRODUCTION

The coupling of an auscultation and warning system to a reinforcement geosynthetic is a judicious innovative solution in case of sensitive structures like areas with high risk of soil subsidence. Although there exist already some reference studies on the Life Cycle Assessment of solutions incorporating geosynthetics, it seems important to evaluate the influence of auscultation and warning system on the environmental impact and to compare it with other currently used solutions as concrete solution. During the REGIC (Reinforcement using Intelligent Geosynthetics over Natural or Anthropic Cavities) research project, an innovative and warming geosynthetic solution has been developed. The Life Cycle Analysis is realized to carry out this comparison from an environmental point of view. It presents a sensitivity analysis for identifying the most influencing parameters; it is then extended to other solutions offering the same level of performance and security to the Owner.

2 OBJECTIVE AND SCOPE OF THE STUDY

The data of this study is based on the characteristics of a real construction site in Lille (France). It concerns the reinforcement above a 2 m diameter cavity. The solutions require

zero residual settlement for a service life of 100 years. Different technical solutions and monitoring and warning methods are proposed:

– Reference solution: concrete slab with a 16 m^2 and 25 cm thick of concrete. A volume of 24 m^3 of soil is excavated for pouring the 4 m^3 concrete slab. Then 20 m^3 of soil is covering the concrete slab and 4 m^3 is deposited. The slab is reinforced with 50 kg/m^3 of iron. Monitoring is planned with a visit every 7 years.
– Solution (a) - Reinforcement by geosynthetic without auscultation: This is designed in accordance with standard NF XP G 38065, for a service life of 100 years with zero residual settlement on the surface. Monitoring by the project owner is planned with a visit every 7 years. This geosynthetic will be called FPET-600.
– Solution (b) - Reinforcement by geosynthetic FPET-600 with automatic monitoring and inspection: As the same design as the solution (a) but with instrumented monitoring. Monitoring by the project owner is planned with a visit every 7 years.
– Solution (c) - Optimised reinforcement geosynthetic FPET-150-I with automatic monitoring and inspection: As the same design as other solutions but with optimized characteristics. Monitoring by the project owner is planned with a visit every 7 years. The optimization considers the reduction of the intervention time of the project owner linked to the alert system.
– Solution (d) - Pre-instrumented geosynthetic without a warning system: It allows the measurement of possible deformations of the geosynthetic but assumes a follow-up by the project owner through an annual visit.

3 LIFE CYCLE ASSESSMENT

The Life Cycle Assessment (LCA) study is conducted based on the standards ISO 14040, ISO 14044 and ISO 14025. In accordance with the European standard EN 15804 + A1, the "cut-off" approach is applied to the systems studied. This means that the materials resulting from recycling or reuse are considered free of any environmental impact. In order to be able to compare the different solutions, it is necessary to determine a Functional Unit (FU) common to all the products compared and defined in the ISO 14044 standard as "the quantified performance of a product system, intended to be used as a reference unit in an LCA". The FU will be used to weight and base the results of this LCA on a common basis in order to make optimal choices.

In this LCA, the functional unit considered is the following: Reinforcement of a cavity of 2 m diameter for 100 years.

The surface to be covered (64 m^2, to take into account the lateral anchors) is excavated to a depth of 1.5 m. A volume of 95.4 m^3 is excavated. The machinery used for the earthworks is estimated on the basis of (Suer P. & Andersson-Sköld, Y. 2011) which considers the use of a hydraulic excavator and a compactor. The same volume of soil is excavated and backfilled.

3.1 *Production data*

As the concrete slab is produced on site, only the production of geosynthetics, whether instrumented or not, is considered. For geosynthetic solutions, the production data is based on that of the factory in Saint-Didier-de-la-Tour (France) for the year 2019. They include raw material consumption including losses related to the manufacture of geosynthetics, consumption by suppliers of reinforcement yarns, considering the energy mix of the country where these yarns are manufactured and the consumption for assembly at the Saint-Didier-de-la-Tour plant (France). They also include packaging consumption, production waste and transport stage.

In the case of instrumented geosynthetics, the production of optical fibres should also be considered. For the purposes of this study, it is assumed that one metre of optical fibre is

required for the design of 1 m^2 of instrumented geotextile and the data is based on the data provided by (Unger & Gough 2008).

3.2 *Data for the completion of the project*

The construction data considers the phasing and quantities defined in paragraph 2.

The data from the operation phase considers the different scenarios defined in 2. For this study, it was assumed that an average distance of 100 km was covered during the visits to the structure. For the scenarios based on instrumented solutions, the use phase requires to consider the electricity consumption of the monitoring system, or even the use of a measurement box. The electrical consumption depends on the type of box, depending on the type of optic fibre used. For the present study, a box for Bragg gratings was considered, with a 15 minutes per day were devoted to measurements. In the case of a connection to the electrical network, the site being in Lille, the French mix was used. For data transfer, sending and storage of emails, different options were considered. The electrical consumption required for the transmission and storage of emails is taken from the studies (Pflueger 2010) and (Schmidt *et al.* 2009). The data on the Bragg grating measurement box takes into account different electronic components with a weight of 800 g. The steel casing was heavier than normal (7 kg) to allow for the later integration of components such as batteries and solar panels. The lifetime of the electronic components is estimated at 7 years.

As the use of the geosynthetics, or the concrete slab, is considered permanent (100 years), no end of life is considered in the analysis.

4 ENVIRONMENTAL IMPACT ASSESSMENT AND SENSITIVITY ANALYSIS

For the assessment of environmental impact, the indicators selected are those recommended by the EN 15804 + A1 standard for environmental declarations of construction products, to which is added the cumulative energy consumption.

For a complete sensitivity analysis to optimize the impact of the system, the study carried out in the framework of the research project integrated the influence of the following parameters:

– energy consumption for monitoring;
– the power source of the monitoring box: solar panels or others;
– the duration of daily use of the monitoring system
– the service life of the structure;
– the duration of storage of the e-mails sent by the box;
– the size of the site;
– the end of life of the geotextiles: in the case of a short-term application (e.g., reinforcement of cavities in a mining activity), next to the excavation and transport activities, a treatment by incineration can avoid the consumption of fossil resources.
– the country of implementation of the structure; in addition to the transport from the production plant to the construction site, this has an impact on the electricity mix used for monitoring and on the impact of alternative solutions.

4.1 *Impact on the cumulative energy consumption*

The global LCA analysis assesses environmental impact through several categories of impacts such as global warming, cumulative energy consumption, photochemical oxidation, resource depletion, water consumption, ozone depletion, etc. In this article we focus on the environmental impact on the cumulative energy consumption.

The cumulative energy consumption of the concrete slab solution is 20.8 GJ/FU, compared to 13.6 GJ/FU for the non-instrumented geosynthetic reinforcement solution (a) and 34.1 GJ/FU for the instrumented geosynthetic reinforcement solution (b) (Figure 1).
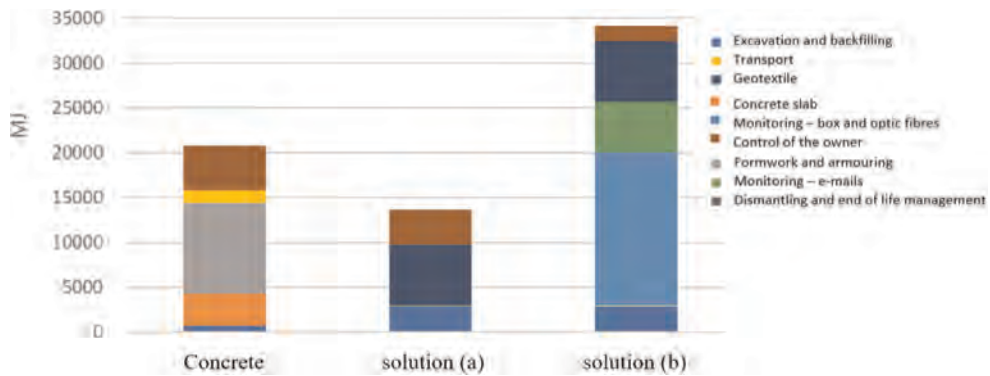
Figure 1. Comparison of the impact on cumulative energy consumption of the 3 reinforcement scenarios.

The instrumented geosynthetic reinforcement solution (b) requires the most energy resources over its life cycle. The impacts of the 'concrete slab' and non-instrumented geotextile (a) solutions are respectively 39 % and 60 % lower.

For the "concrete slab", the first contributor corresponds to the production of the reinforcement (48 %). The second is related to the project owner's travel (24 %), followed by the production of the concrete (17 %). For the non-instructed geosynthetic (a), the first contributor is linked to the production of the product (50 % of the total impact); this is mainly due to PET fibres. The second contributor is related to the project owner's travel (29 %), followed by earthworks (21 %).

For the instrumented geosynthetic (b): the first contributor is linked to the production of the monitoring and warning box (approximately 50 %), followed by the production of the geosynthetic and the transfer and storage of emails. The impact of the monitoring, assessment, and warning system ("box and optic fibre") is 60 % attributable to the production of the box and 40 % to electricity consumption.

The mechanical dimensions of the non-instrumented (a) and instrumented (b) geosynthetics are identical, which is debatable insofar as it does not consider the important contribution to safety made by the monitoring and warning system. Moreover, the high level of consumption related to the monitoring and warning system reveals a significant potential for optimization of the system design. Possible improvements include the power consumption of the monitoring and alert system, its type of power supply (electrical, solar, etc.), the daily duration of monitoring (geosynthetic measurement), the daily duration of the connection to the monitoring server (permanent, one-off in case of a local alert, etc.) and the storage of e-mails (in the cloud, locally).

4.2 Trends in the evolution of Life Cycle Assessment as a function of reinforcement design parameters

The parametric study carried out in this research project has enabled the following trends to be identified: First of all, in the case of a solution with an instrumented geosynthetic (b) with an associated monitoring and warning system:

– as the service life of the structure increases, the daily duration of monitoring has a significant impact on the cumulative energy consumption;
– reducing the storage of emails on the cloud to 1 week instead of 1 year significantly reduces the environmental impact;
– the power consumption of the monitoring box has little impact on the results;
– the electricity mix of the country where the instrumented geosynthetic solution is implemented has a strong impact on its environmental performance.

Then, by comparing of the "concrete slab" and instrumented geosynthetic solution (b) with an associated monitoring and warning system:

– the increase in the service life of the structure has a greater influence on the environmental impact of the "concrete slab" solution than on that of the instrumented geosynthetic with an associated monitoring and warning system;
– similarly, the larger the area of the structure treated, the lower the environmental impact of
– the instrumented geosynthetic solution with an associated monitoring and warning system compared to the concrete slab solution.

5   COMPARISON OF DIFFERENT SOLUTIONS ACCORDING TO THE LEVEL OF SAFETY ENVISAGED AS A FUNCTION OF THE RISK OF THE STRUCTURE

This section summarizes how, for a given level of safety, it is advisable to adapt the design of the geosynthetic reinforcement according to the use, or not, of a monitoring and warning system. It is important to analyse structures that are comparable in terms of safety and technically justifiable.

The following comparison (Figures 2, 3 and 4) is based on the example of a potential cavity, similar to the one presented in paragraph 2 and considering different hypotheses of risk evolution:

– The cavity is not likely to expand beyond the nominal diameter: If it is considered that there is no risk of the cavity enlarging beyond the nominal diameter, the competing solutions may be the "concrete slab" solution and a non-instrumented geosynthetic (a). For these two solutions, it was planned that the project owner would carry out a monitoring visit every 7 years.
– The risk of the cavity expanding beyond the nominal diameter is not well known but a priori is not very high: Considering that the risk of the cavity expanding beyond the nominal diameter is not well known but not very high at least at the beginning, the competing solutions can be the "concrete slab" solution and an instrumented geosynthetic with an optical sensor but without continuous monitoring (d). This geosynthetic solution allows for modular monitoring, punctual at the beginning (e.g. one measurement per year) which can be accelerated over time and can even be converted into continuous monitoring if things get worse.
– Analysis of the impact on the environment of the different solutions according to the hypotheses of risk regarding the cavity: For this analysis, assumptions were made for the electricity consumption of one hour per measurement, if the optic fibre measurement is carried out punctually; however, in the case of continuous monitoring, solar panels are systematically used. We also consider the daily transmission of measurement data to the central server, without online storage, except in the event of an alert.
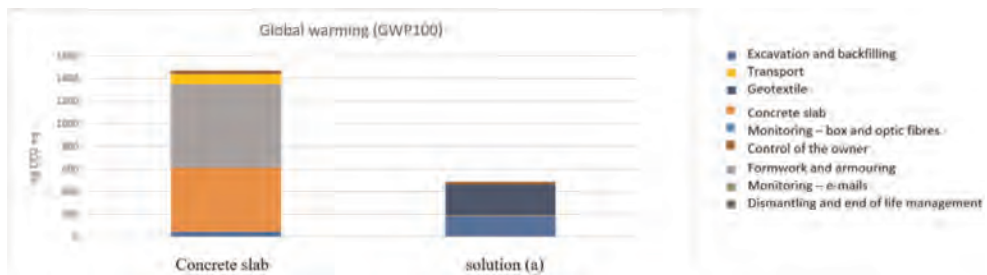
Figure 2. The cavity is not likely to expand beyond the nominal diameter.
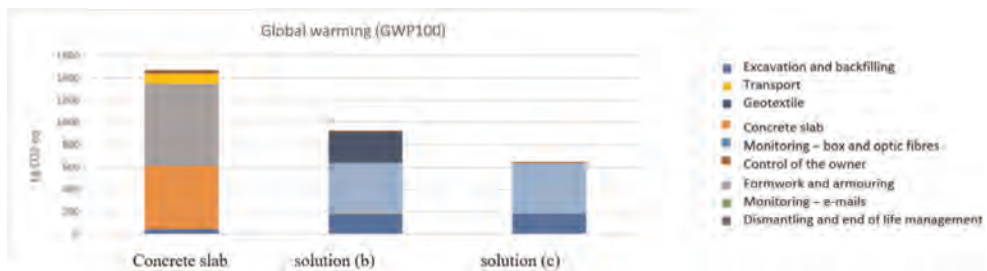
Figure 3. The cavity may present a non-negligible risk of expanding beyond the nominal diameter.
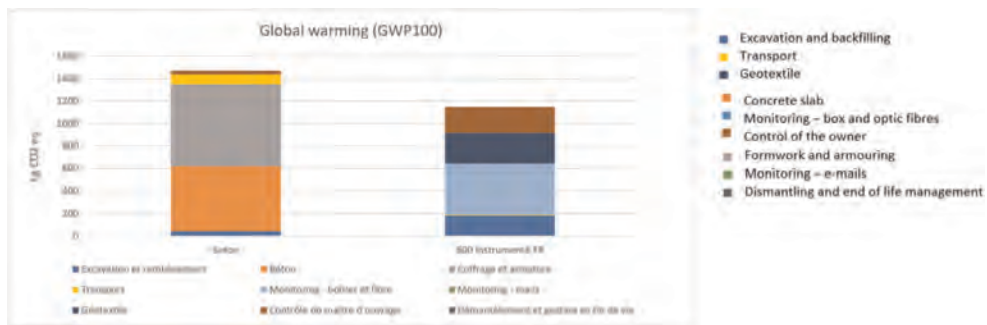
Figure 4. The risk of the cavity enlarging beyond the nominal diameter is unknown but not very high at least at the beginning.

6 CONCLUSION

The analysis of the Life Cycle Assessment of solutions integrating instrumented geosynthetics, with monitoring and warning devices, showed how important this assessment was to optimize the design of the reinforcement system, especially for sensitive structures such as those above areas at high risk of localized collapse. It was possible to evaluate and quantify the influence of the different design parameters of the system (geosynthetic, instrumentation, monitoring and warning system) on the impact on cumulative energy consumption.

The tool developed shows that it is possible to adapt and optimize the treatment and monitoring solution for an area at high risk of localized collapse according to the level of risk linked to the potential evolution of the cavity.

The addition of instrumentation and an optimized monitoring system is particularly relevant from an LCA point of view as well as from a safety and technical aspects. This study validates the expected benefits of this innovative instrumented geosynthetic solution compared to the traditional reinforcement solution, under optimized conditions adapted to each site, as in this case in the Lille region on a 2 m diameter cavity.

This Life Cycle Assessment has finally led to the publication of an EPD® Environmental Product Declaration for the range of geosynthetics concerned, which provides data on the environmental impact of the geosynthetic. This document presents the data in a standardized format for comparison with other solutions on the market.

REFERENCES

ISO 14040. 2006. Environmental Management. Life Cycle Assessment. *Principles and framework*.

ISO 14044. 2006. Environmental Management. Life Cycle Assessment. *Requirements and guidelines*.

ISO 14025. 2010. Environmental Labels and Declarations. Type III Environmental Declarations. *Principles and procedures*.

EN 15804 + A1. 2016. Contribution of Construction Works to Sustainable Development. Environmental Product Declarations. *Rules for construction product categories*.

NF XP G 38-065. 2020. Geosynthetics, GTX & GTP. *Reinforcement of the Base of Embankments in Areas at Risk of Collapse. Justification of the Dimensioning and Design Elements*. AFNOR: 50.

Pflueger J. 2010. Understanding Data Center Energy Intensity, *A Dell Technical White Paper*.

Schmidt, Anders, Nanja Hedal Kløverpris. 2009. *Environmental Impacts from Digital Solutions as an Alternative to Conventional Paper-Based Solutions*.

Suer P., Andersson-Sköld, Y. 2011. Biofuel or Excavation? *Life Cycle Assessment (LCA) of Soil Remediation Options. Biomass and Bioenergy 35* (2): 969–81. https://doi.org/10.1016/J.BIOMBIOE.2010.11.022.

Unger N., Gough O. 2008. Life Cycle Considerations about Optic Fibre Cable and Copper Cable Systems: A Case Study. *Journal of Cleaner Production* 16 (14): 1517–25. https://doi.org/10.1016/J.JCLEPRO.2007.08.016.

Valorisation of C&D waste as backfill material of geosynthetic reinforced structures – study of the long-term behaviour

Castorina S. Vieira, Fernanda B. Ferreira, Paulo M. Pereira,
Maria de Lurdes Lopes & A. Topa Gomes
CONSTRUCT, Department of Civil Engineering, Faculty of Engineering, University of Porto, Porto, Portugal

Sérgio Madeira & Nuno Cristelo
Department of Engineering, University of Trás-os-Montes e Alto Douro, Vila Real, Portugal

ABSTRACT: This paper presents an overview of the research project CDW_LongTerm - Valorisation of Construction and Demolition Wastes in geosynthetic reinforced structures - Prediction of long-term behaviour and summarizes its main conclusions. Mixed fine-grain recycled aggregates obtained from non-selected C&D waste, with low market acceptance for other applications such as pavement base layers and concrete production, were used in this study. Changes on the geotechnical and geoenvironmental behaviour of recycled C&D materials induced by real weather conditions and other agents (such as, compaction or wet-drying cycles), the durability and creep behaviour of the geosynthetics, the long-term behaviour of geosynthetic/C&D material interfaces and the long-term performance of a full-scale model have been studied. In general, the results show an acceptable long-term performance of the materials, of the recycled C&D materials/geosynthetic interfaces and of full-scale model.

1 INTRODUCTION

Waste generation and its efficient management is currently recognised as a key area of concern within the construction industry. In fact, construction and demolition (C&D) waste is one of the heaviest and most voluminous waste streams generated worldwide, accounting for over 35% of all waste produced in the European Union, EU (EC 2020). On the other hand, the responsible use of natural resources is among the fundamental pillars for the sustainable development demanded to modern societies. Since the construction sector is one of the main contributors to the consumption of natural resources, the use of alternative (recycled) materials in the construction and rehabilitation of civil infrastructure can make a significant contribution towards sustainable development.

In 2015, the European Commission (EC) presented the EU Circular Economy Action Plan to help European businesses and consumers to make the transition to a circular economy, where resources are used in a more sustainable way. C&D was among the priority sectors identified in this Circular Economy Package, because of the vast amounts produced across the EU and their high potential to be reused and recycled. More recently, a new EU Circular Economy Action Plan for a cleaner and more competitive Europe has been launched, in which Construction and Buildings (with special reference to C&D waste) is among the key priority value chains (EC 2020).

In recent decades, several studies on the use of recycled C&D wastes in a variety of civil engineering works have been reported in the literature with encouraging results (e.g. Arulrajah *et al.* 2013; Ferreira *et al.* 2021; Lu *et al.* 2021; Santos *et al.* 2014; Vieira *et al.*

2016). However, most of these previous studies have investigated the short-term response of recycled C&D materials, and hence the knowledge about their long-term behaviour, as well as the overall long-term response of the structures where they are used is still limited.

In this context, the CDW_LongTerm research project focuses on the use of recycled C&D waste as an alternative backfill material for geosynthetic-reinforced structures (such as embankments and retaining walls), with special emphasis on the long-term response. As opposed to the majority of previous related studies, this research involves mixed recycled aggregates obtained from non-selected C&D wastes (the materials actually available on the Portuguese market). One of the main aims of this project is to demonstrate that geosynthetic-reinforced structures built with C&D materials are durable and fully capable of maintaining satisfactory performance throughout the design working life. This, in turn, will increase the confidence of owners, designers and constructors in the usage of recycled C&D wastes and promote the valorisation of waste materials, thus contributing towards the implementation of circular economy in the construction sector.

2 OVERVIEW OF THE RESEARCH PROJECT

The valorisation of recycled C&D waste as filling material, particularly in geosynthetic-reinforced structures, where it is possible to reach large heights and very steep slopes, represents significant economic and environmental benefits. On the one hand, the valorisation of C&D wastes contributes to achieve the recycling targets set out by the European Commission and prevents these wastes from ending up in landfills, and on the other hand, it avoids the environmental and economic costs related to the extraction of large volumes of borrow soils.

The research project CDW_LongTerm has dealt with the study of the long-term behaviour of geosynthetic-reinforced structures (GRS) constructed with recycled C&D materials. Thus, changes on the physical, mechanical and environmental properties of recycled C&D materials were studied, the durability and creep behaviour of geosynthetics after exposure to recycled C&D materials and the long-term behaviour of the interfaces between the geosynthetics and the recycled materials were assessed, and the overall performance of a full-scale instrumented geosynthetic-reinforced structure, as well as its numerical model were also carried out.

The long-term behaviour of geosynthetics when inserted into recycled C&D materials was investigated by exposing the geosynthetics to the recycled wastes under real environmental conditions (Figure 1a) and under artificial conditions (wet-dry cycling tests, Figure 1b). After
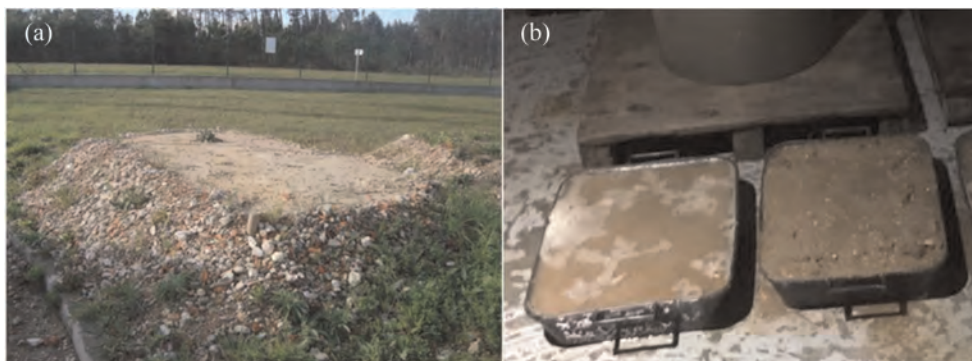
Figure 1. Exposure of the geosynthetics to the recycled C& D wastes: (a) under real environmental conditions; (b) wetting-drying cycles.

exposure the geosynthetic samples were subjected to tensile and creep tests to characterise the effects on the short-term and long-term behaviour, respectively. Scanning Electron Microscope (SEM) analyses were carried out on intact and exhumed samples.

An extensive laboratory test programme has been conducted involving conventional and multistage direct shear and pullout tests to investigate the long-term response of recycled C&D waste-geosynthetic interfaces.

The direct shear tests were performed using a large-scale direct shear test apparatus (Vieira el al. 2013). Apart from conventional direct shear tests, two types of multistage tests were also carried out to simulate the effects of creep (Figure 2a) and stress relaxation (Figure 2b) at the interfaces (i.e. time-dependent behaviour).
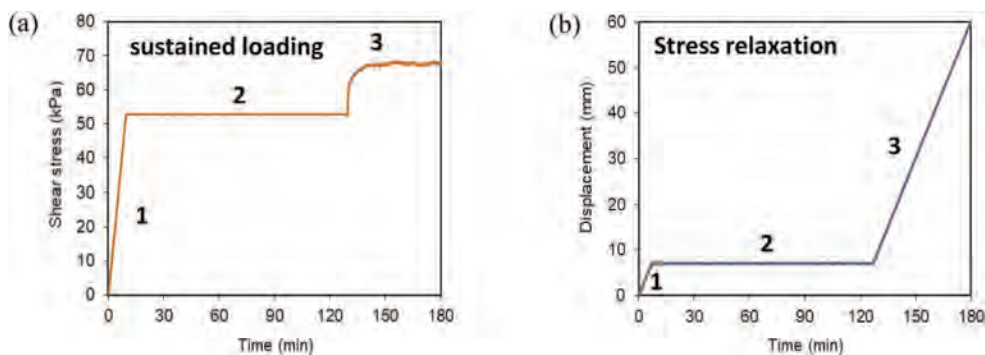
Figure 2. Different setups of the multistage direct shear tests: (a) sustained loading; (b) stress relaxation.

Sustained load pullout tests were also carried out on recycled C&D material/geogrid interfaces on a large scale apparatus (dimensions in plan of 1.53m x 1.0m and 0.8 m high). The test procedure is similar to the one schematically shown in Figure 2(a), although much longer: the pullout force was applied under load controlled model until a predefined value (equal to 40% or 70% of the pullout resistance under monotonic loading), in a second stage the pullout force was held constant for a predefined time slot (30 or 120 minutes), during which the geogrid pullout displacement was monitored and in the last stage, the test proceeded until the failure of the interface.

A full-scale experimental embankment with two geosynthetic-reinforced slopes has been constructed using recycled C&D materials as backfill material (Figure 3a). The full-scale

Figure 3. Full-scale instrumented geosynthetic-reinforced structure: (a) during construction; (b) readings on the inclinometers; (c) pressure cells readings.

instrumented model consists of a 3.1 m high, 10.4 m long and 3.0 m wide geosynthetic-reinforced embankment composed of two wrapped-face slopes with a face inclination of 63.4° with the horizontal (batter of 1H:2V). Fine-grained recycled C&D materials were sourced from a Portuguese recycling plant and used as backfill. The southern slope was reinforced with a uniaxial woven geogrid, GGR3 (Figure 5c) and a uniaxial geocomposite reinforcement, GCR2 (Figure 5e) was used to reinforce the northern slope. The geosynthetic reinforced structure was built in a reinforced masonry block container with a reinforced concrete foundation.

To monitor the performance of the geosynthetic-reinforced structure. geotechnical instrumentation was installed during its construction. Specifically, the instrumentation system included: 4 inclinometer casings, 4 magnetic extensometers (with a total of 20 magnetic targets), 2 soil settlement gauges, 10 earth pressure cells, 35 electrical strain gauges attached to the geogrid, 12 mechanical extensometers (tell-tales) attached to the geocomposite, 4 settlement plates and 50 survey points at the slope faces and on the side walls. Figures 3(b) and 3(c) illustrates the collection of some readings during a monitoring campaign. In order to assess the long-term performance of the reinforced structure, the monitoring process is expected to remain for several years beyond the project end. Additional information regarding the full-scale model, instrumentation and monitoring can be found in Vieira *et al.* (2023).

The numerical modelling of the behaviour of the full-scale geosynthetic-reinforced structure was also performed using the three-dimensional explicit finite-difference software FLAC 3D (*Itasca Consulting Group, Inc.*). Five 0.6 m thick layers of recycled C&D material were simulated with the geosynthetic reinforcement layers placed at the appropriate locations along the height of the lateral slopes. The slopes were modelled with wrap-around facing, resembling actual field conditions.

3 MATERIALS

The fine grained recycled C&D materials used in the current research consisted of the finer fraction (0–10 mm) obtained during the recycling process of C&D wastes. The materials used in the project were obtained from three different batches (i.e. collected from the recycling plant at different times, but after being subjected to the same recycling process) and consisted mainly of soil, unbound and hydraulically bound aggregates, concrete and mortar products. Figure 4 illustrates the type of recycled material used in this study.

Figure 4.   Visual appearance of the recycled materials used in the study.

Figure 5 presents the photographic views of the geosynthetics tested in CDW_LongTerm project. It should be mentioned that not all the geosynthetics were subjected to the same test or exposure conditions.
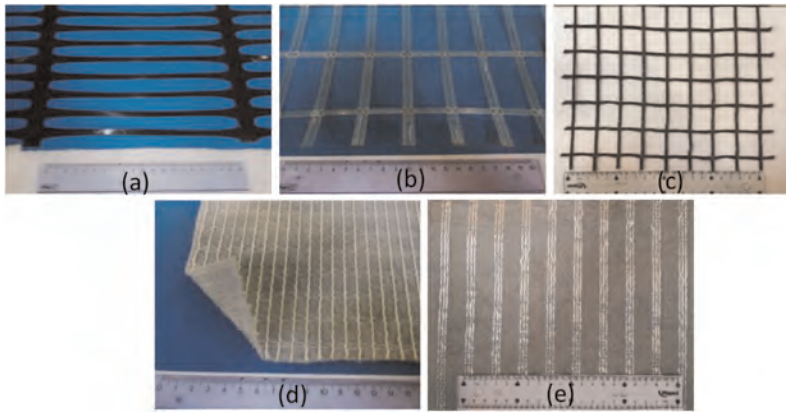
Figure 5.   Geosynthetics used in the study (ruler in centimetres): (a) uniaxial high-density polyethylene geogrid (GGR1); (b) polyester welded geogrid (GGR2); (c) polyester woven geogrid (GGR3); (d) geocomposite reinforcement 1 (GCR1); (e) geocomposite reinforcement 2 (GCR2).

4   RESULTS AND DISCUSSION

Figure 6 presents the effects on the tensile strength of geosynthetics GGR1, GGR2 and GCR1 (Figure 6a) and on their tensile stiffness for 2% of strain (Figure 6b) of different exposure conditions (specimens immediately exhumed, exposure to recycled C&D material, exposure to soil).
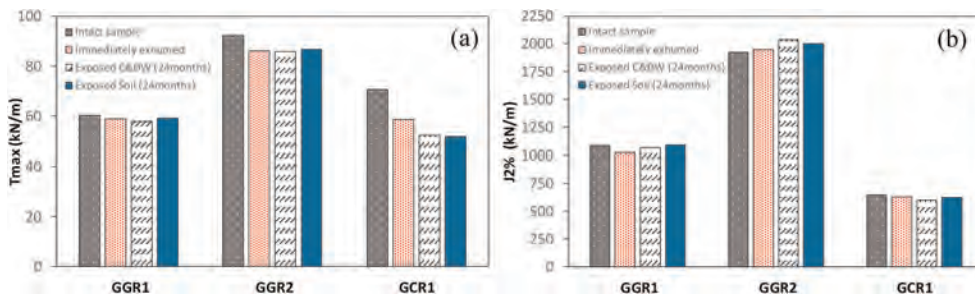
Figure 6.   Effects of exposure of geosynthetics to a recycled C&D waste and other conditions: (a) on maximum tensile strength; (b) tensile stiffness at 2% strain.

From Figure 6 it can be concluded that the effects of exposure to recycled C&D material and to soil are similar and, with the exception of geotextile GCR1, in general the tensile strength after immediate exhumation is close to that obtained after exposure for 24 months. The loss of tensile strength of GCR1 is most likely due to the less effective binding of the PET yarns to the nonwoven geotextile, caused by handling during installation, rather than damage induced by the compaction or exposure to the filling materials.

Figure 7 shows the creep behaviour of intact specimens (as provided by the manufacturer) of the geocomposite GCR1 (Figure 5d) and of specimens that were previously exposed to the recycled C&D waste for a period of 24 months.

When subjected to the same tensile force, the intact specimens exhibited higher tensile strength properties than the exhumed specimens However, the estimate of the long-term available strength, considering the extrapolation of the creep rupture curves, for the

242

specimens that were previously exposed to recycled C&D waste will be more optimistic when compared to the intact specimens (higher retained strength), (Figure 7). This finding suggests that the conventional approach (use of intact specimens) to estimate the long-term tensile strength of geosynthetics through creep rupture tests is a conservative procedure (Ferreira *et al.* 2022).
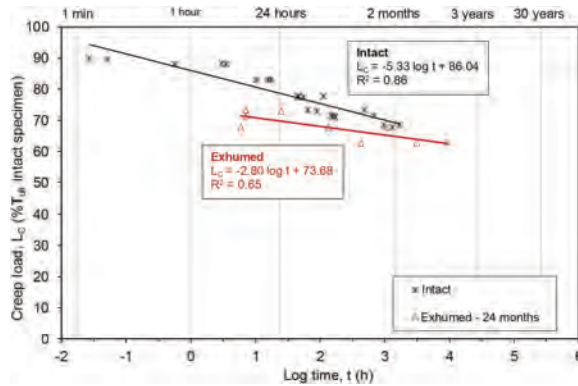
Figure 7.   Applied creep loads *vs* time to rupture and associated rupture curves (modified from Ferreira *et al.* 2022).

Figure 8 compares the results of conventional and stress relaxation direct shear tests (Figure 2b) to characterize recycled C&D material/geotextile GCR2 interface. As shown in Figure 8, and for the test conditions analysed in this project, the effect of stress relaxation on the interface behaviour was almost negligible, implying that the conventional large-scale direct shear tests can be considered suitable to characterise the long-term interface strength properties under direct shear mode (Ferreira *et al.* 2021).
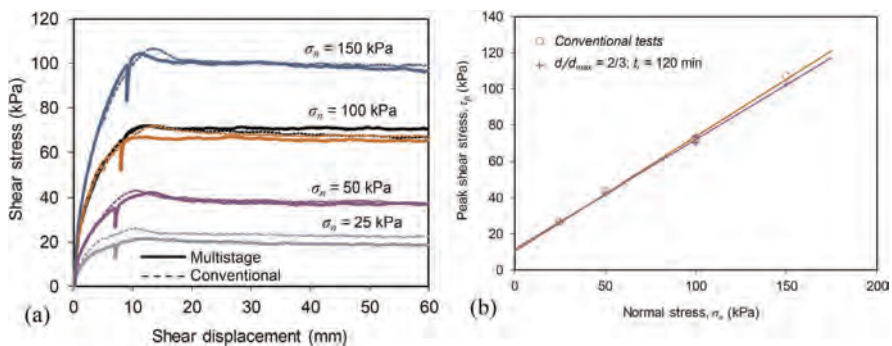
Figure 8.   Results of conventional and multistage (stress relaxation) direct shear tests to characterize recycled C&D material/GCR2 interface (adapted from Ferreira *et al.* 2021): (a) shear stress-shear displacement curves; (b) interface failure envelopes.

5   MAIN CONCLUSIONS

The main goal of the research project CDW_LongTerm was to demonstrate the good long-term performance of geosynthetic-reinforced structures constructed with recycled C&D wastes, reducing the barriers on the use of alternative materials and giving an important

contribution to the reduction of human carbon footprint. Based on the results obtained in the extensive laboratory programme and the satisfactory behaviour of the full-scale geosynthetic-reinforced structure (even though it has been subjected to very adverse weather conditions - at least one extremely rainy winter) it is considered that these objectives have been achieved.

Among the main conclusions of this study, the following must be highlighted:

- Laboratory leaching tests carried out on all the recycled C&D materials have shown that only the sulphates exceeds the maximum value established by the European legislation for inert landfill. All the other pollutants are significantly below the limits.
- In general, the changes induced by the compaction procedures, weather conditions and adverse artificial conditions on the physical and mechanical behaviour of the recycled C&D materials are not significant.
- The effects of stress relaxation and sustained loading on interfaces direct shear strength and pullout resistance can be considered almost negligible, which suggests that good performance can be expected in the long term.

ACKNOWLEDGEMENTS

REFERENCES

Arulrajah, A., J. Piratheepan, M. M. Disfani, and M. W. Bo. 2013. "Geotechnical and Geoenvironmental Properties of Recycled Construction and Demolition Materials in Pavement Subbase Applications." *Journal of Materials in Civil Engineering*. 25 (8): 1077–1088.

EC 2020. *"EU Circular Economy Action Plan"*. European Commission. Accessed November 2022. https://ec.europa.eu/environment/circular-economy/.

Ferreira, F. B., Pereira, P. M., Vieira, C. S. & Lopes, M. L. 2021. Time-dependent Response of a Recycled C&D Material – geotextile Interface under Direct Shear Mode. *Materials*, 14, 3070.

Ferreira, F. B., Pereira, P. M., Vieira, C. S. & Lopes, M. L. 2022. Long-term Tensile Behavior of a High-Strength Geotextile after Exposure to Recycled Construction and Demolition Materials. *Journal of Materials in Civil Engineering*, 34, 04022046.

Lu, C., J. Chen, C. Gu, J. Wang, Y. Cai, T. Zhang, and G. lin. 2021. "Resilient and Permanent Deformation Behaviors of Construction and Demolition Wastes in Unbound Pavement Base and Subbase Applications." *Transportation Geotechnics*. 28.

Santos, E., E. Palmeira, and R. Bathurst. 2014. "Performance of Two Geosynthetic Reinforced Walls with Recycled Construction Waste Backfill and Constructed on Collapsible Ground." *Geosynthetics International*. 21 (4): 256–269.

Vieira, C. S., Ferreira, F. B., Pereira, P. M., Madeira, S., Cristelo, N. & Lopes, M. L. 2023. *Construction and Monitoring of a Full-scale Model of a Geosynthetic Reinforced Embankment Built with Recycled C&D Materials*. submitted to Journal.

Vieira, C. S., Lopes, M. L. & Caldeira, L. M. 2013. Sand–geotextile Interface Characterisation Through Monotonic and Cyclic Direct Shear Tests. *Geosynthetics International*, 20, 26–38.

Vieira, C. S., P. M. Pereira, and M. L. Lopes. 2016. "Recycled Construction and Demolition Wastes as Filling Material for Geosynthetic Reinforced Structures. Interface Properties." *Journal of Cleaner Production*. 124: 299–311.

Study of the damage induced by recycled aggregates coming from Construction and Demolition Waste (C&DW) on the short-term tensile behaviour of a PET geogrid

P.M. Pereira & C.S. Vieira
CONSTRUCT, Department of Civil Engineering, Faculty of Engineering (FEUP), University of Porto, Porto, Portugal

ABSTRACT: The valorisation of Construction and Demolition Wastes (C&DW) is nowadays an imperative since it reduces the use of natural resources and avoids congesting landfills with these inert materials. The use of C&DW in geotechnical works, such as geosynthetic reinforced structures, is an interesting alternative from an economic and environmental perspective. This paper presents the mechanical, chemical and environmental degradation induced by fine grain recycled aggregate coming from C&DW on the short-term tensile behaviour of a uniaxial geogrid manufactured of extruded polyester (PET). In order to study the chemical and environmental degradation a damage trial embankment was constructed using C&DW as filling material. The damage caused by the mechanical actions during installation was also simulated by mechanical damage under repeated loading tests. Wide width tensile tests were carried out on geogrid samples exhumed from the trial embankment after 12 months of exposure, on laboratory damaged samples and on intact samples. Their short-term tensile behaviour is compared. Scanning electron microscope (SEM) images of intact and exhumed specimens are also presented.

1 INTRODUCTION

Minimizing the consumption of non-renewable natural resources for the production of construction materials is considered one of the key aspects to achieve sustainability in the construction sector. The recovery of construction and demolition waste (C&DW) as aggregate is an efficient way to achieve this purpose. Adopting and implementing this principle is particularly relevant for an industry that consumes more raw materials than any other economic activity and produces huge amounts of waste.

Considering the need to find new ways of avoiding landfilling of inert waste and preserving natural resources, recent studies have been carried out on the reuse of recycled aggregates from C&DW in geosynthetic reinforced structures (Arulrajah *et al*. 2014; Soleimanbeigi *et al*. 2019; Santos *et al*. 2013; Vieira & Pereira 2015; Vieira & Pereira 2021; Vieira *et al*. 2016). However, one of the main issues regarding the use of geosynthetics in contact with alternative materials is their durability.

The damage caused by mechanical actions during installation and the chemical and biological degradation are important issues to be considered in geosynthetics behaviour. The changes in their physical, mechanical and hydraulic properties, induced by the above-mentioned degradation processes, can control the performance of the structures where these materials are used.

Within the framework of a research project damage trial embankments have been constructed to study degradation induced by recycled C&DW on different geosynthetics. The

exhumation of geosynthetic samples from these embankments was done after 6, 12 and 24 months of exposure.

The results herein presented are related to polyester (PET) geogrid samples exhumed after 12 months of exposure to recycled C&DW. The mechanical damage induced by this recycled material on the geogrid was simulated by laboratory installation damage tests.

2 MATERIALS AND METHODS

The geosynthetic used in this study was a uniaxial geogrid manufactured of extruded polyester (PET) (Figure 1a) with aperture dimensions of 30 mm × 73 mm. To minimize the influence of external factors all the samples (intact - as provided by the manufacturers, damaged in the laboratory and exhumed samples) were taken from the same roll of material and tested using the same methods and equipment.
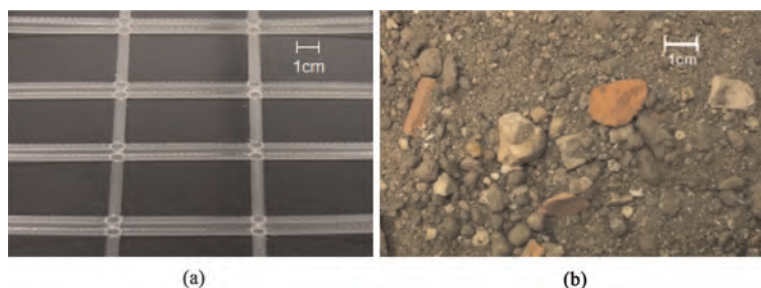
Figure 1.   Visual appearance of the material: (a) PET geogrid. (b) recycled aggregate from C&DW.

To study the chemical and environmental degradation induced by a recycled aggregate coming from C&DW (or recycled C&DW) on the short-term tensile behaviour of the geosynthetics, damage trial embankments were constructed. The damage trial embankments were constructed using fine grain recycled C&DW coming mainly from maintenance works or demolitions of small buildings and cleaning of lands with illegal deposition of C&DW (Figure 1b). The particle size determined by sieving and sedimentation is represented in Figure 2a. The predominant constituents of this fine grain recycled C&DW used are concrete, masonry, unbound aggregates, natural stones, as well as, a significant portion of soil (Figure 2b). These recycled materials were provided by a Portuguese Recycling plant located in Centre region.
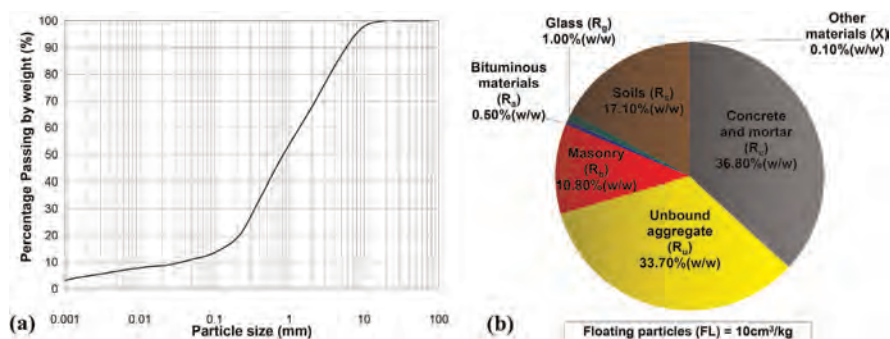
Figure 2.   Recycled aggregate from C&DW: (a) particle size distribution; (b) portions of constituents.

After cleaning the foundation from the existing vegetation, a 5 cm-thick layer was placed and compacted and the geosynthetic samples of the first level were carefully positioned without overlapping. Geosynthetic samples were then covered with a first layer of recycled C&DW placed manually to prevent mechanical damage. Additional quantities of filling material were disposed, evenly spread and compacted to reach a lift with final thickness of approximately 0.20 m (Figure 3a). To minimize the installation mechanical damage on the geosynthetics, a lightweight compaction process was adopted (forward compaction plate with weight of 94 kg). Details on embankment construction are available in Vieira & Pereira (2015).

The tensile behaviour of exhumed specimens presented in this paper is related to geogrid samples exhumed after 12 months of installation (Figure 3b). The samples were carefully exhumed to prevent additional damage, being the material just above the geosynthetics removed carefully with the hands.
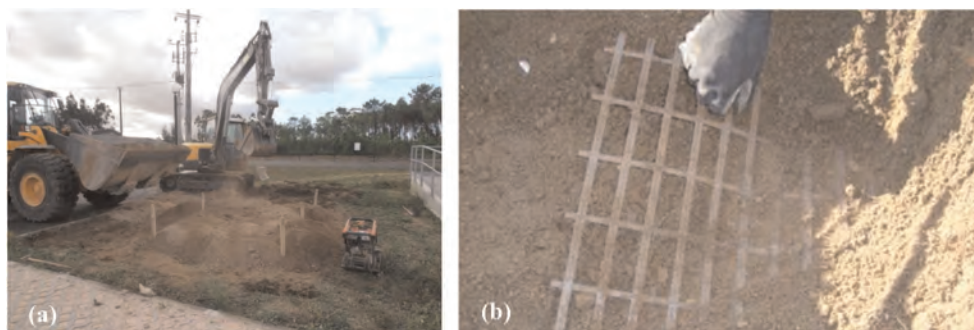
Figure 3. Study of the degradation induced by recycled C&DW on PET geogrid: (a) trial embankments construction; (b) geogrid specimens' exhumation.

SEM analyses were performed using a high resolution Environmental Scanning Electron Microscope with X-Ray Microanalysis and Electron Backscattered Diffraction analysis (Quanta 400 FEG ESEM / EDAX Genesis X4M) from the Materials Centre of University of Porto.

Laboratory installation damage tests were also carried out, using recycled aggregate from C&DW similar to the one used in the embankments construction (coming from the same batch), to study the mechanical damage induced by these recycled materials on the geogrid tensile behaviour.

The mechanical damage tests were performed using a laboratory prototype developed at the University of Porto (Lopes & Lopes 2003). The apparatus is composed by a rigid container (300 mm × 300 mm × 150 mm) divided in two boxes (where the geogrid and the recycled aggregate from C&DW were placed), a loading plate and a hydraulic compression system.

The geogrid specimens were cut with a width of 200 mm (5 longitudinal bars) and length of 380 mm. Each specimen was placed between two layers of C&DW and submitted to repeated loading. The layer placed under the specimen consisted in two sublayers (each 37.5 mm high) compacted by a flat plate loaded to a pressure of 200 ± 2 kPa, during 60 s, over the whole area of the test container. The layer placed over the specimen consisted in loose recycled C&DW with 75 mm high. Each specimen was subjected to dynamic loading (ranging between 5 ± 0.5 and 500 ± 10 kPa) at a frequency of 1 Hz and for 200 cycles. Finished the loading, the specimen was removed carefully from the test container, avoiding additional damage.

Tensile tests carried out on intact (as provided by the manufacturers), exhumed and damaged specimens were performed in accordance with the European Standard EN ISO 10319 (2015). Five specimens (for each condition) and a strain rate of 20%/min. were used.

3 RESULTS AND DISCUSSION

3.1 *Specimens exhumed from the embankment*

Although the preliminary visual inspections of the exhumed samples have not revealed significant damages. Scanning Electron Microscope (SEM) analyses were carried out to evaluate potential damages in more detail

Figure 4 illustrates SEM images (at 100 × magnification) of intact (Figure 4a) and exhumed specimens of geogrid (Figure 4b). From the analysis of Figure 4 it is visible that small particles of the backfill material have stuck to the geogrid but there is no relevant damage in the exhumed geogrid. Load-strain curves of exhumed geogrid specimens resulting from tensile tests are illustrated in Figure 5a. The mean curve is also represented. The maximum tensile strength (T_{max}), the geogrid strain for T_{max} (ε_{Tmax}), the secant stiffness modulus at strain of 2% ($J_{2\%}$) and the secant stiffness modulus at ε_{Tmax} (J_{Tmax}) for the five specimens are summarized in Table 1. The mean values of these parameters and the 95% confidence intervals assuming a Student's t-distribution were also included in Table 1. Analysing Figure 5a and Table 1 it is clear the low variability of the results.
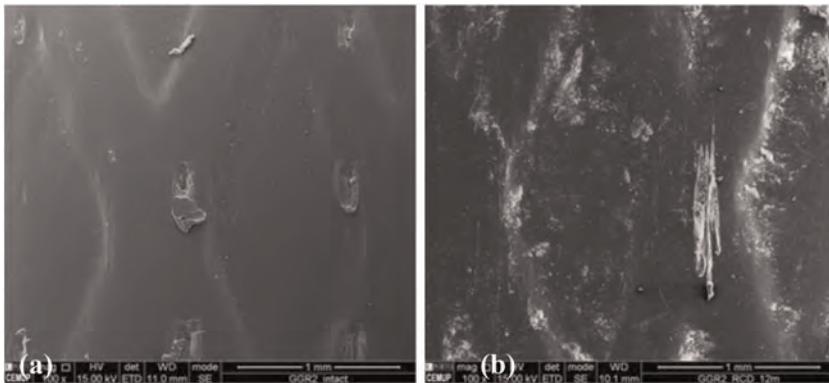
Figure 4. SEM images of PET geogrid specimens (× 100): (a) intact; (b) exhumed after 12 months.
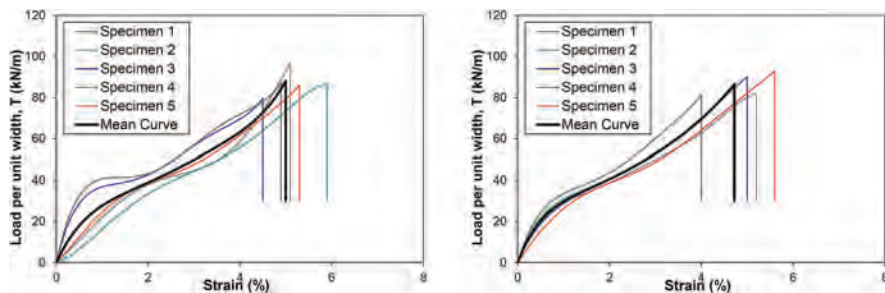
Figure 5. Load-strain curves of tensile tests performed on: (a) exhumed geogrid specimens; (b) geogrid specimens damaged in laboratory.

Table 1. Summary of results of tensile tests carried out on exhumed geogrid specimens.

	T_{max} (kN/m)	ε_{Tmax} (%)	$J_{2\%}$ (kN/m)	J_{Tmax} (kN/m)
Specimen 1	97.5	5.1	1892	1908
Specimen 2	87.8	5.9	1366	1489
Specimen 3	79.3	4.5	2134	1750
Specimen 4	86.5	4.9	2164	1747
Specimen 5	85.7	5.3	1925	1618
Mean value	87.4	5.2	1896	1703
Confidence interval of 95%	87.4 ± 8.1	5.2 ± 0.6	1896 ± 397	1703 ± 196

The tensile behaviour of exhumed and intact specimens will be compared and discussed in section 3.3.

3.2 Specimens damaged in laboratory

After the laboratory mechanical damage tests the specimens were subjected to tensile load tests following similar procedures to those used for intact or exhumed specimens. The load-strain curves of damaged geogrid specimens, as well as the mean curve corresponding to the 5 samples are represented in Figure 5b. Table 2 summarizes the values of maximum tensile strength (T_{max}), geogrid strain for T_{max} (ε_{Tmax}), secant stiffness modulus at strain of 2% ($J_{2\%}$) and at ε_{Tmax} (J_{Tmax}). The mean values of these parameters and the 95% confidence intervals assuming a Student's t-distribution were also tabulated.

Table 2. Summary of results of tensile tests carried out on geogrid specimens damaged in laboratory.

	T_{max} (kN/m)	ε_{Tmax} (%)	$J_{2\%}$ (kN/m)	J_{Tmax} (kN/m)
Specimen 1	82.1	5.2	1941	1579
Specimen 2	85.9	4.7	2048	1829
Specimen 3	90.8	5.0	2024	1817
Specimen 4	80.3	4.0	2180	2008
Specimen 5	91.0	5.5	1931	1641
Mean value	86.0	4.9	2025	1775
Confidence interval of 95%	86.0 ± 6.1	4.9 ± 0.7	2025 ± 125	1775 ± 211

3.3 Comparison and discussion of results

The tensile behaviour of intact specimens was reported in a previous publication (Vieira & Pereira 2021). Table 3 summarises the main results. The tensile strength reached in laboratory tests of intact specimens exceeded the mean value provided by the manufacturer. It should also be noted that the maximum tensile force is achieved for a low value of strain (5.6%), meaning that it is a geogrid of high tensile stiffness (around 2025 kN/m for 2% of strain). The comparison of these results with those presented in Tables 1 and 2 points out that of the loss of strength caused either by the exposure to the recycled C&DW for 12 months or by the laboratory installation damage tests is very small (loss of 5% and 7% on average, respectively).

Figure 6 compares the mean curves for intact, exhumed and damaged specimens. The shape of curves is quite similar but the coordinates at failure were shifted. Figure 6 enhances the little influence of this damage processes on the tensile behaviour of this geogrid. It should also be emphasized that the geogrid tensile strength after 12 months of exposure to C&DW and laboratory damage remains higher than its nominal value (80 kN/m).

Table 3. Summary of results of tensile tests carried out on intact geogrid specimens (Vieira & Pereira 2021).

	T_{max} (kN/m)	ε_{Tmax} (%)	$J_{2\%}$ (kN/m)	J_{Tmax} (kN/m)
Specimen 1	89.9	5.5	2037	1635
Specimen 2	100.7	5.8	2078	1736
Specimen 3	82.1	5.2	1942	1579
Specimen 4	91.0	5.5	1931	1641
Specimen 5	97.9	6.0	1971	1631
Mean value	92.3	5.6	1992	1645
Confidence interval of 95%	92.3 ± 9.1	5.6 ± 0.4	1992 ± 79	1645 ± 71
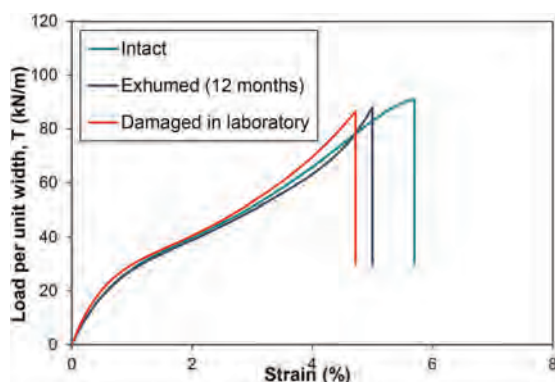
Figure 6. Comparison of mean load-strain curves of intact, damaged in the laboratory and exhumed specimens.

The geogrid tensile stiffness for very small strains (initial stiffness) did not change significantly while an increase on the secant stiffness modulus at ε_{Tmax} (J_{Tmax}) is noticeable. The increase on the secant stiffness was slightly higher in samples damaged in laboratory than in samples exposed 12 months to the recycled aggregate from C&DW.

The damage on geosynthetics used as reinforcement is currently quantified by the retained values of relevant parameters, such as, the tensile strength, the strain at maximum load or the secant stiffness modulus. The retained value of the parameter X can be defined as the ratio between the mean value of the parameter X for damaged or exhumed specimens and the corresponding mean value for intact specimens.

The mean values of the retained tensile strength, R_T, retained peak strain, $R\varepsilon$, and retained secant modulus at 2% of strain, $R_{J2\%}$ are presented in Table 4. As previously mentioned, the mechanical damage induced in laboratory was slightly more pronounced than the effects of exposure for 12 months.

Table 4. Mean values of retained tensile strength, R_T, retained peak strain, $R\varepsilon$, and retained secant modulus, $R_{J2\%}$.

Exhumed after 12 months			Mechanical damaged		
R_T (%)	$R\varepsilon$ (%)	$R_{J2\%}$ (%)	R_T (%)	$R\varepsilon$ (%)	$R_{J2\%}$ (%)
94.7	92.9	95.2	93.2	87.5	101.7

4 CONCLUSIONS

The mechanical, chemical and environmental degradation induced by fine grain recycled C&DW on the short-term tensile behaviour of an extruded uniaxial PET geogrid was presented. The research herein reported has shown that the mechanical damage induced in the laboratory is more aggressive than that caused during trial embankments construction. That means that, it is possible to consider that the installation damage during the construction of the trial embankments was, as expected, insignificant and therefore, the damages recorded on exhumed specimens could be attributed to the chemical and environmental degradation.

Results of tensile tests carried out on exhumed specimens have shown that the exposure of this geogrid to fine grain C&DW under real atmospheric conditions for 12 months did not induce geogrid degradation.

Despite the fact that the exposure period of the geogrid to the recycled C&DW was very short compared to the lifetime of the structures, this study allows us to conclude that it is not expected that the use of recycled materials will induce the degradation of geogrids.

REFERENCES

Arulrajah, A., Rahman, M., Piratheepan, J., Bo, M. & Imteaz, M. 2014. Evaluation of Interface Shear Strength Properties of Geogrid-Reinforced Construction and Demolition Materials Using a Modified Large-Scale Direct Shear Testing Apparatus. *J. Mater. Civ. Eng.* 26 (5): 974–982.

EN ISO 10319 2015. Geosynthetics - Wide width tensile test. CEN.

Lopes, M.P. & Lopes, M.L. 2003. Equipment to Carry out Laboratory Damage During Installation Tests on Geosynthetics. *Journal of the Portuguese Geotechnical Society* 98: 7–24 (in Portuguese).

Santos, E.C.G., Palmeira, E.M. & Bathurst R.J. 2013 Behaviour of a Geogrid Reinforced Wall Built with Recycled Construction and Demolition Waste Backfill on a Collapsible Foundation. *Geotext. Geomembr.* 39 (August 2013): 9–19.

Soleimanbeigi, A., Tanyu, B. F., Aydilek, A. H., Florio, P., Abbaspour, A., Dayioglu, A. Y., & Likos W. J. 2019. Evaluation of Recycled Concrete Aggregate Backfill for Geosynthetic-reinforced MSE walls. *Geosynth. Int.* 26 (4): 396–412.

Vieira, C.S. & Pereira, P.M. 2015. Damage Induced by Recycled Construction and Demolition Wastes on the Short-term Tensile Behaviour of Two Geosynthetics. *Transp. Geotech.* 4: 64–75.

Vieira, C.S. & Pereira, P.M. 2021. Short-term Tensile Behaviour of Three Geosynthetics After Exposure to Recycled Construction and Demolition materials. *Constr. Build. Mater.* 273, (1 March 2021): 122031.

Vieira, C.S., Pereira, P.M. & Lopes, M.L. 2016. Recycled Construction and Demolition Wastes as Filling Material for Geosynthetic Reinforced Structures. Interface Properties. *J. Clean. Prod.* 124: 299–311.

Mechanically Stabilized Tire Derived Aggregate (MSTDA) retaining walls

J.S. McCartney*
Department of Structural Engineering, University of California, San Diego, CA, USA

ABSTRACT: Waste tires have been used in a variety of forms in civil engineering applications as a lightweight fill, insulation layer, or drainage layer. This approach to recycling and reusing waste tires has significant environmental benefits over other methods of disposal or incineration due to the quantity of waste tires generated by society. Although many civil engineering applications have used waste tire shreds mixed with mineral soils, there are advantages to using shredded tires in monolithic layers. For example, a greater number of waste tires can be recycled when using monolithic layers and there are lower construction costs associated with avoiding mixing with soils. Further, monolithic layers of tire shreds have similar shearing properties to soils, superior thermal insulating properties, excellent drainage, and high damping ratio. When shredded tires are used in a monolithic layer a civil engineering application they are referred to as tire-derived aggregate (TDA). This paper focuses on the use of TDA as a backfill material in the construction of internally stabilized retaining walls referred to as "Mechanically Stabilized TDA" or MSTDA retaining walls.

1 INTRODUCTION

There is an urgent need for sustainable reuse of "End of Life Tires" (ELTs) due to the large number of tires being generated by society and the lack of environmentally friendly disposal options. The number of ELTs generated each year in the US has increased by approximately 18% over the past decade [1]. Historically, these waste tires would be sent to stockpiles as they are not accepted by most landfills. However, stockpiles have risks associated with tire fires and act as a breeding ground for disease spreading insects and rodents. As tires are combustible and can be used as fuel source when mixed with coal, approximately 36% of ELTs are used as a fuel source [2]. However, there are environmental concerns with this strategy as burning ELTs release toxic air pollutants [3]. Because of these concerns, CalRecycle seeks to reuse or recycle 75% of waste tires. An effective and environmentally friendly approach for reducing ELT stockpiles is the reuse of waste tires as an alternative backfill material in civil engineering applications. This includes use as a lightweight embankment fill, in landslide repair/slope stabilization, as insulation layers for landfill clay liners, as alternative drainage layers in landfills, as a retaining wall backfill, as stress reduction backfill over pipes, as storm water infiltration gallery media, and as vibration mitigation layers for foundations and railroads embankments [e.g., 4–19]. Through the reuse of waste tires in civil engineering applications, the quantity of stockpiled waste tires has reduced from 800 million in the mid-1990's to 200 million today [3]. Approximately 5.1% of waste tires were reused in civil engineering applications in the US [1], while 3.0% were reused

---

*Corresponding Author: mccartney@ucsd.edu

in civil engineering applications in California [2]. The percentage of waste tires reused in civil engineering applications is increasing each year.

An advantage of reusing waste tires in civil engineering applications is that both older tires from stockpiles and freshly recycled tires are suitable. While early studies investigated tire shreds mixed with soils, the cost associated with mixing and the reduction in the volume of tires reused increases the cost of this approach. Instead, it most economical to reuse tire shreds in civil engineering applications is as a monolithic layer. In this case, the shredded tires are referred to as tire-derived aggregate (TDA) to emphasize that they are similar to a granular aggregate. Due to the growing popularity of reusing waste tires in the form of TDA, ASTM D6270 [20] was developed to provide guidance on the classification of TDA and how it should be used in different civil engineering applications to minimize the likelihood of self-heating. Self-heating was encountered in large TDA fills in the 1990s without provisions for drainage control or in the amount of exposed steel. Two categories of TDA are permitted in ASTM D6270: Type A TDA, with particle sizes ranging from 75 to 100 mm, and Type B TDA, with particle sizes ranging from 150 to 300 mm. Both types of TDA have limits on the amount of sidewall tire pieces and the quantity of particles having exposed steel wire. However, Type B TDA requires less processing than Type A TDA and is therefore more cost effective and has less exposed steel due to the larger particle sizes. ASTM D6270 limits the height of fills constructed using Type B TDA to 3 m (approximately 10 ft), while it limits the height of fills constructed using Type A TDA to 1 m (3 ft). Further, ASTM D6270 requires that monolithic layers of TDA be encapsulated with inorganic mineral soil to help dissipate heat and isolate the TDA from exposure to water.

The use of TDA as backfill in civil engineering applications not only helps reduce stockpiles and reuse waste tires, but TDA also has favourable engineering properties. For example, the total unit weight of TDA is 5 to 9 kN/m^3, which is about one-third to one-half that of most granular backfill soils. Despite this low total unit weight that is less than that of water (9.8 kN/m^3), the tire shreds are heavier than water (specific gravity of approximately 1.15) and will not float when submerged. Its low total unit weight makes TDA favourable for use as a fill above deformable subgrade soil or on soils with global stability issues. In addition to the lower unit weight, TDA has shear strength that is comparable to soils [21], a hydraulic conductivity of 0.01 m/s (on the same order of magnitude to gravel), a thermal conductivity of approximately 0.17 W/mK, which is approximately 8 times smaller than most soils, and a high damping ratio that provide TDA with favourable cyclic shearing properties [22]. Differences between TDA and granular backfills are that TDA may deform more than soils upon loading, and that the displacement at peak shear strength is greater than in dense backfill soils. These differences in deformation response require careful consideration in the construction of civil engineering infrastructure with TDA backfill to accommodate the more flexible response of TDA to external loading but can be overcome with careful planning and design.

TDA has been widely used as a backfill in gravity-type, reinforced concrete retaining walls [11–16]. These gravity retaining walls with TDA backfill had good performance in terms of lateral earth pressures exerted on the retaining wall. However, recent civil engineering applications in California have explored the approach of creating internally reinforced TDA walls that are similar to Mechanically Stabilized Earth (MSE) walls, referred to herein as Mechanically Stabilized TDA (MSTDA) walls. Internally reinforced retaining walls have lower material costs and faster construction times. Like MSE walls, MSTDA walls are fill-type retaining walls that are used when to provide a change in grade, lane widening, or repair of slope instability. MSTDA walls have a unique feature over gravity-type retaining walls in that the weight of the TDA backfill will not induce as large a stress on the underlying subgrade material. This can be advantageous in areas with compressible subgrade soils or when there is global instability influenced by the weight of the retaining wall. McCartney [23] presented a design methodology for MSTDA walls that built upon MSE wall design methodologies [24] incorporating experimental data on TDA deformation and shearing

properties. This paper presents a summary of an MSTDA wall design and design details from MSTDA projects.

2 TYPICAL MSTDA CONFIGURATIONS AND DESIGN CONCEPTS

Like MSE walls, MSTDA walls have a wide range of possible geometric configurations, facing types, reinforcement types, and heights. However, based on current practice in California, the most common type of MSTDA walls involves a horizontal back-slope used to support a roadway, flexible gabion-style facing elements, extensible geosynthetic reinforcements, and granular backfill within the gabions and overlying a reinforced TDA layer, as shown in Figure 1(a). Although the wall height is typically a major design choice in MSE walls, the height of MSTDA walls is typically governed by a reinforced TDA layer having a maximum thickness of 3 m (10 ft) overlain by a granular soil layer having a thickness of 0.8 to 2.0 m according to recommendations in ASTM D6270-20, with a total wall height of 3.8 to 5.0 m (12.5 to 16.4 ft). It is possible to construct a taller MSTDA wall by including multiple layers of TDA separated by granular backfill layers, an approach used in a TDA embankment at the Dixon Landing Interchange in Milpitas, CA [14]. It is clear from the typical design configurations in Figure 1(a) that geosynthetics are used as separation layers, reinforcements, filters, and drains. The definitions of the nominal loads in an MSTDA wall with a gabion facing are shown in Figure 1(b). The internal and external stability of this wall under static and earthquake loading must be considered for different factored load and resistance combinations.
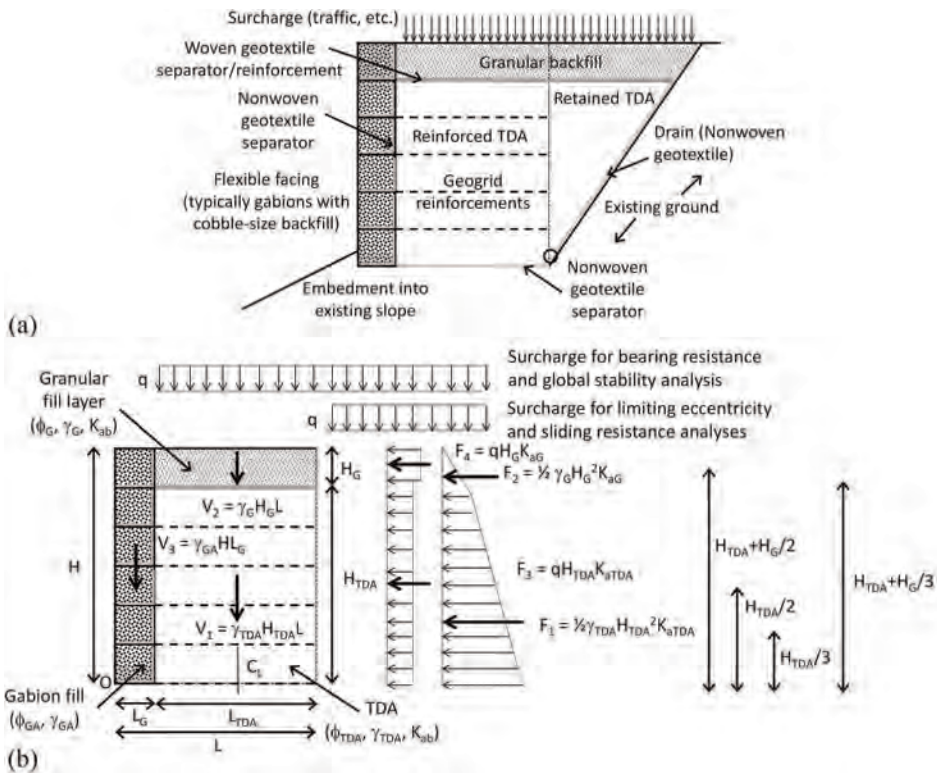
Figure 1. (a) Typical MSTDA configuration; (b) Definition of nominal loads.

3 TDA PROPERTIES AND TDA-GEOSYNTHETIC INTERACTION

Several studies have recently been conducted at the University of California San Diego focused on understanding the shear strength, deformation, and geosynthetic interaction of Type B TDA. Testing materials with large particle sizes requires the use of a large testing device, which was summarized by Fox et al. [25]. This type of TDA is recommended for use in MSTDA walls due to the greater permissible layer height and because it requires less processing to manufacture. Two critical properties of TDA are shown in Figure 2, including the volume change of Type B TDA during application of high stresses [21] and the shear strength of TDA and TDA interfaces [21,26]. TDA has a nonlinear compression curve which can be represented approximately using a bi-log linear relationship as shown in Figure 2(a), and also has a nonlinear failure envelope, with a secant friction angle of 30.2° at a normal stress of 100 kPa decreasing at a rate of 14.4° per log cycle of normal stress at failure.
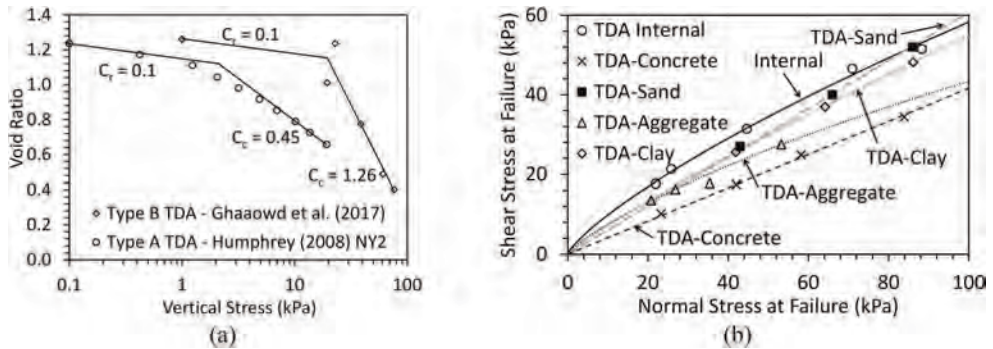
Figure 2. Key properties of TDA: (a) Compression curve; (b) Failure envelope.

TDA-geogrid interaction was studied using large scale pullout tests by Ghaaowd and McCartney [26]. The pullout factor is a key component to the internal stability calculations of MSTDA walls. Ghaaowd and McCartney [26] tested the pullout of 3 geogrids, Tensar UX1100 (GGA), Miragrid 5XT (GGB) and Tensar BX1500 (GGC). The pullout-displacement curves for GGB are shown in Figure 3(a), and the pullout factor versus vertical stress is shown in Figure 3(b). GGB had a combination of high pullout resistance under a wide range of vertical stresses and was used in the design calculations.
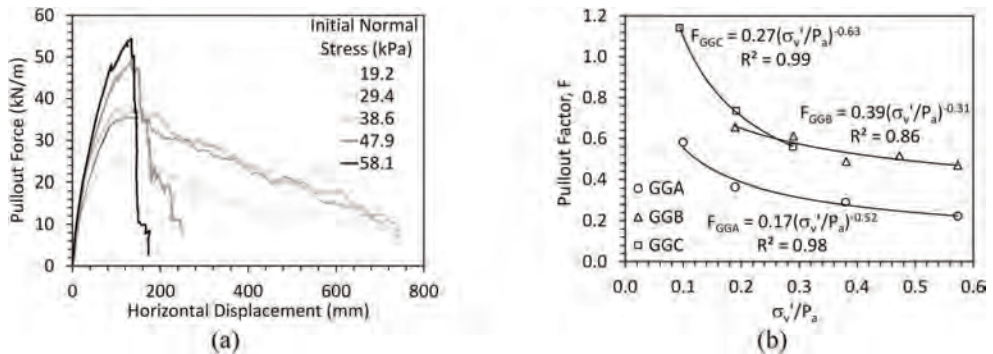
Figure 3. Pullout results from Ghaaowd and McCartney [26]: (a) Pullout force from TDA vs. displacement for GGB; (b) Pullout factors for three geogrids as a function of vertical stress.

255

4   MSTDA WALL DESIGN OUTCOMES

McCartney [23] summarized the design requirements of an MSTDA wall with a TDA fill height of 3 m and an overlying granular fill of 1.2 m, supporting both a pavement section and a heavy traffic surcharge, as shown in Figure 4. The wall was designed for expected earthquake conditions near Santa Barbara, CA. The TDA was reinforced with geogrid GGB with the pullout factor relationship shown in Figure 3(b). Based on the design steps considered in McCartney [23], the TDA reinforcement length was found to be 5 m, mainly to resist the earthquake loading at the site. An interesting aspect of the design was the consideration of the overbuild requirements for the TDA due to its high compressibility. An analysis was performed to consider the required overbuild for a range of granular fill thicknesses overlying the TDA layer along with the surcharge from traffic and the pavement section. When the 3 m TDA fill was split into 10 lifts, each lift should be overbuilt by a certain amount to ensure that the final fill height will be 3 m, as shown in Figure 5(a). The compression of the TDA will lead to an increase in TDA unit weight as shown in Figure 5 (b), which will change the effective stress profile and the stress-dependent friction angle of the TDA used in the analysis, as summarized by McCartney [23]. Overall, the design features of
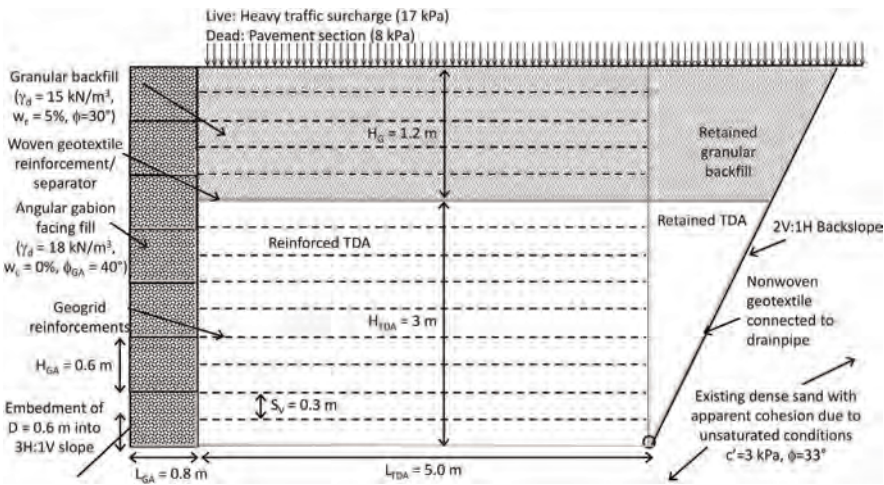
Figure 4.   Final MSTDA wall configuration accounting for all design checks.
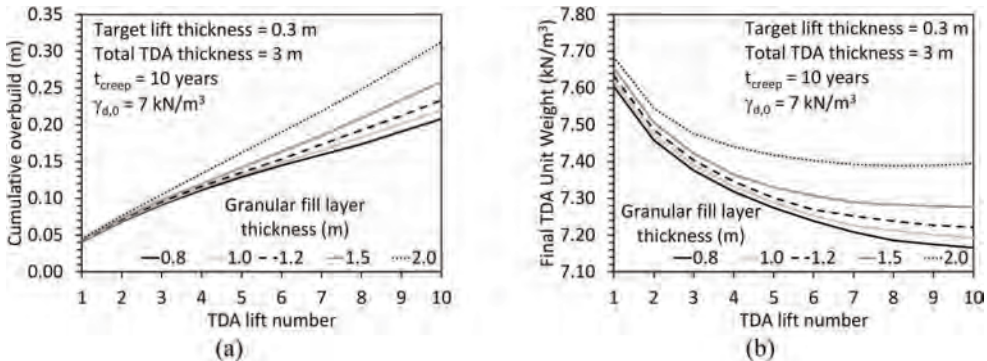
Figure 5.   (a) Overbuild calculations for TDA to reach target TDA fill height; (b) Final TDA unit weights after compression under overlying lifts.

this wall are consistent with those encountered in an MSTDA wall constructed on the Ortega Ridge road near Montecito, California. Design drawings and construction photographs of this MSTDA wall are provided in McCartney [23].

5   CONCLUSIONS

This paper introduces the concept of Mechanically Stabilized TDA (MSTDA) walls, and notes some of the key TDA properties and design considerations necessary to ensure the stability and serviceability of these walls. TDA has similar mechanical properties to soils albeit with greater compressibility that should be considered in the wall design through appropriate overbuild.

REFERENCES

[1]   USTMA. 2019 U.S. Scrap Tire Management Summary. 2020. Washington, D.C.

[2]   CalRecycle. 2020. *California Waste Tire Market Report: 2019*. DRRR-2020-1691. California Department of Resources Recycling and Recovery (CalRecycle). Sacramento, CA.

[3]   Cheng, D.X., Zhang, K., Cavender, Z., Giles, M., Thor, J., and Joslin, K. 2021. *Tire Derived Aggregate Handbook*. 3rd Ed. California Department of Resources Recycling and Recovery.

[4]   Bosscher, P.J., Edil, T.B., and Eldin, N. 1993. "Construction and Performance of Shredded Waste Tire Test Embankment." *Transportation Research Record*. **1345**, 44–52.

[5]   Bosscher, P.J., Edil, T.B., and Kuraoka, S. 1997. "Design of Highway Embankments using Tire Chips." *Journal of Geotechnical and Geoenvironmental Engineering*. **123**(4), 295–304.

[6]   Dickson, T.H., Dwyer, D.F., Humphrey, D.N. 2001. "Prototype Tire-shred Embankment Construction." *Transportation Research Record*, **1755**, 160–167.

[7]   Finney, B.A. and Maeda, R.K. 2016. *Evaluation of Tire Derived Aggregate as a media for Stormwater Treatment*. DRRR-01625. CalRecycle, Sacramento, CA.

[8]   Geisler, E., Cody, W.K., and Niemi, M.K. 1989. "Tires for Subgrade Support." *Annual Conference on Forest Engineering*, Coeur D'Alene, ID. 1–5.

[9]   Ahmed, I. and Lovell, C.W. 1993. "Rubber Soils as Lightweight Geomaterials." *Transportation Research Record*. **1422**, 61–70.

[10]   Hoppe, E.J. 1998. "Field Study of Shredded-tire Embankment." *Transportation Research Record* **1619**, 47–54.

[11]   Humphrey, D.N., Sandford, T.C., Cribbs, M.M., Gharegrat, H., and Manion, W.P. 1992. *Tire Chips as Lightweight Backfill for Retaining Walls - Phase I*. New England Consortium, 137 pp.

[12]   Humphrey, D., Sandford, T., Cribbs, M., and Manion, W. 1993. "Shear Strength and Compressibility of Tire Chips for use as Retaining Wall Backfill." *Trans. Res. Rec.* **1422**, 29–35.

[13]   Humphrey, D.N., Whetten, N., Weaver, J., Recker, K., Cosgrove, T.A. 1998. "Tire Shreds as Lightweight Fill for Embankments and Retaining Walls." *Prof. Conference on Recycled Materials in Geotechnical Applications*. GSP 79, ASCE, Reston, Virginia. 51–65.

[14]   Humphrey, D.N. 2008. "Tire Derived Aggregate as Lightweight Fill for Embankments and Retaining Walls." *Scrap Tire Derived Geomaterials – Opportunities and Challenges*. Hazarika and Yasuhara (eds). Taylor and Francis, London. 59–81.

[15]   Tandon, V., Velazco, D.A., Nazarian, S., and Picornell, M. 2007. "Performance Monitoring of Embankments Containing Tire Chips: Case Study." *J. Perf. of Const. Facilities.* **21**(3), 207–214.

[16]   Tweedie, J.J., Humphrey, D.N., and Sandford, T.C. 1998a. "Full Scale Field Trials of Tire Shreds as Lightweight Retaining Wall Backfill, At-rest Conditions." *Transportation Res. Rec.* **1619**, 64–71.

[17]   Tweedie, J.J., Humphrey, D.N., and Sandford, T.C. 1998b. "Tire Shreds as Retaining Wall Backfill, Active Conditions." *J. of Geotechnical and Geoenvironmental Eng.* **124**(11), 1061–1070.

[18]   Xiao, M., Bowen, J., Graham, M., and Larralde, J. 2012. "Comparison of Seismic Responses of Geosynthetically-reinforced Walls with Tire-derived Aggregates and Granular Backfills." *J. of Materials in Civil Eng.* **24**(11), 1368–1377.

[19]   Mahgoub, A. and El Naggar, H. 2019. "Using TDA as an Engineered Stress-reduction Fill Over Preexisting Buried Pipes." *J. of Pipeline Systems Engineering and Practice.* **10**(1), 04018034.

[20]   ASTM D6270-20. 2020. *Standard Practice for Use of Scrap Tires in Civil Engineering Applications.* ASTM International, West Conshohocken, PA.

[21]   Ghaaowd, I., McCartney, J.S., Thielmann, S., Sanders, M. and Fox, P.J. 2017. "Shearing Behavior of Tire Derived Aggregate with Large Particle Sizes. I: Internal and Concrete Interface Direct Shear Behavior." *Journal of Geotechnical and Geoenvironmental Eng*. **143**(10), 04017078.

[22]   McCartney, J.S., Ghaaowd, I., Fox, P.J., Sanders, M., Thielmann, S., and Sander, A. 2017. "Shearing Behavior of Tire Derived Aggregate with Large Particle Sizes. II: Cyclic Simple Shear Behavior." *ASCE Journal of Geotechnical and Geoenvironmental Eng*. **143**(10), 04017079.

[23]   McCartney, J.S. 2021. Design of Mechanically Stabilized Tire Derived Aggregate (MSTDA) Retaining Walls. SSRP 01/22. 97 p.

[24]   Berg, R.R., Christopher, B.R. and Samtani, N.C., 2009. *Design of Mechanically Stabilized Earth Walls and Reinforced Soil Slopes – Volume I*. FHWA-NHI-10-024. Federal Highway Administration, Washington, DC.

[25]   Fox, P.J., Thielmann, S.S., Sanders, M.J., Latham, C., Ghaaowd, I., and McCartney, J.S. 2018. "Large-scale Combination Direct Shear/simple Shear Device for Tire-derived Aggregate." *ASTM Geotechnical Testing Journal*. **41**(2), 340–353.

[26]   Ghaaowd, I., Fox, P.J. and McCartney, J.S. 2020. "Shearing Behavior of the Interfaces between tire Derived Aggregate and Three Soil Materials." *ASCE J. of Mat. in Civil Eng*. **32**(6), 04020120.

[27]   Ghaaowd, I. and McCartney, J.S. 2020. "Pullout of Geogrids from Tire Derived Aggregate with Large Particle Size." *Geosynthetics International*. **27**(6), 671–684.

Pavement rehabilitation with polymeric reinforcing grids – economic and environmental benefits

Fabiana Leite-Gembus & Andreas Elsing
Huesker Synthetic GmbH, Gescher, Germany

Luis Eduardo Russo
Huesker Srl, Trieste, Italy

ABSTRACT: For more than 50 years, asphalt reinforcing grids manufactured with polymeric fibres have been used to delay or even prevent the development of reflective cracking in pavement rehabilitation. Their positive performance has contributed to increase maintenance periods and to provide substantial economic and environmental benefits, reducing traffic disruptions and the use of exhaustible resources. This paper will present results of recent researches, which show the importance of some factors and their respective influence in the durability and performance of reinforced asphalt overlays, such as interlayer bonding and grid resistance to installation damage. Through practical experiences will be demonstrated the effect of the asphalt reinforcement on the long-term asset pavement performance. Additionally, a cost comparison and a detailed description of the calculation of CO_2 emissions savings between a reinforced and a not reinforced rehabilitation solution is given.

Keywords: asphalt reinforcement grid, pavement rehabilitation, long-term performance, cost reduction, CO_2 emission

1 INTRODUCTION

The need for sustainable designs and construction methods has become a debated topic due to the growing concerns over global warming, climate change and the finite nature of resources. These events are causing increased pressure on the construction industry to reduce their environmental impact. Therefore, sustainable construction procedures and green building technologies are playing an important role in pavement rehabilitation.

Asphalt reinforcing grids have been used all over the world to delay the development of reflective cracks in asphalt layers and to extend the service life of rehabilitated pavements (Montestruque 2002; Monser *et al.* 2010). This solution has not only the positive effect that the maintenance costs per year are reduced but also the amount of carbon emissions can be significantly decreased.

The use of appropriate asphalt reinforcement should ideally be considered for future maintenance and rehabilitation surfacing contracts, which have a history of cracking at surface. Currently there are several types of geosynthetic products available in the market, which are made of different raw materials (e.g., polyester, glass fiber, polyvinyl alcohol, carbon fiber and polypropylene). It is not disputed that each of these systems has a positive effect in the battle against reflective cracking (Norambuena-Contreras & Gonzalez-Torres 2015; Vanelstraete & Francken 1996). However, there are differences in the behavior and effectiveness of each system.

The objective of this paper is to present important required characteristics for the asphalt reinforcement, so that a good performance and durable pavement rehabilitation can be achieved. Typical applications for the use of asphalt reinforcement, described by basic theory and practical experiences, will be demonstrated. Finally, a simplified comparison to estimate the carbon dioxide (CO_2) savings between a conventional and a reinforced pavement rehabilitation is presented.

2 REFLECTIVE CRACKING AND ASPHALT INTERLAYERS

A conventional rehabilitation of a cracked flexible pavement involves milling off the existing top layer and installing a new asphalt course, but cracks are still present in the existing (old) asphalt layers. As a result of the horizontal and vertical movements at the crack tip, the cracks will propagate rapidly to the top of the rehabilitated pavement. This phenomenon is called reflective cracking and is a serious challenge associated with pavement rehabilitation, as it allows water infiltration in the structure, causing stripping in the asphalt layers and weakening in the base and subgrade (Elseifi 2015).

To delay the propagation of cracks is the use of geosynthetic asphalt interlayers between the old pavement and the new overlay one of the most popular methods among new techniques recommended (Nejad *et al.* 2016). Basically, there are three types of geosynthetics designed for pavement rehabilitation: geotextiles (nonwovens or paving fabric), geogrids (grids) and geocomposites. To further improve confidence in the utilization of these materials, there is since 2008 mandatory CE marking for the products in Europe. According to the European standard EN 15381, an asphalt interlayer can fulfill three tasks: reinforcement, stress relief and/or interlayer barrier.

While the stress relief function concerns to soft products (as nonwovens) to dissipate strain energy by deforming itself, the reinforcement function regards stiff products (as grids) to compensate the lack of asphalt concrete tensile strength (Elseifi 2015). In providing reinforcement, the grid structurally strengthens the pavement section by changing the response of the pavement to loading (Koerner 2012). The reinforcement increases the resistance of the overlay to high tensile stresses and distributes them over a larger area, thereby reducing the peak shear stresses at the edges of the cracks in the existing old pavement.

Many products have been promoted as a reinforcement when in fact these products serve only as moisture barrier or stress relief layer. Designers should have a clear understanding of the limitations all the different asphalt interlayer products offer in terms of position and stress-strain characteristics within the pavement structure (Asphalt Academy 2008). Asphalt reinforcement grids made of polyester (PET) have been used for more than 50 years to control reflective cracking in asphalt layers. The wider benefits of polymeric grids in delaying reflective cracking were discussed in previously publications (Elsing & Horgan 2019; Leite-Gembus *et al.* 2020; Russo 2011) and as the example shown in the following.

3 PRATICAL EXPERIENCE

In 2006 the Olympic Winter Games took place in Torino, Italy. Prior to this major event the "Corso Giovanni Agnelli", which is one of the main roads passing the Olympic Stadium, was greatly in need of rehabilitation. The existing asphalt pavement showed severe cracking where almost every joint from underlying concrete slabs had reflected through the asphalt overlay. Therefore, the city of Torino decided to carry out a rehabilitation. Over a length of approx. 500m a bituminous coated polyester (PET) asphalt reinforcement grid was used. In order to obtain a comparison, a second area was rehabilitated without reinforcement (Russo & Simini 2011).

In June 2005 the reinforced area was rehabilitated. After milling off the existing asphalt wearing course, an asphalt levelling course was laid on the concrete slabs. The polyester asphalt reinforcement grid was then installed in accordance with the manufacturer's installation guidelines (Figure 1a) and was covered with a 40 mm layer of asphalt wearing course. Two weeks later, the second area was rehabilitated without reinforcement. Here a new 50mm asphalt layer was installed directly on top of the concrete slabs (without reinforcement), also after milling off the existing wearing course (Figure 1b).

Figure 1. Installation of the HaTelit C 40/17 asphalt reinforcement (a) and asphalt placement on unreinforced section (b) (June 2005).

In May 2006 the first assessment of the road took place. The reinforced area did not show any cracking, however in the unreinforced area, first signs of cracking were visible over the expansion joints of the concrete base. In July 2009, some 4 years after the rehabilitation, the second assessment of the road took place. At that time the reinforced area still did not show any cracking (Figure 2a). In contrast, almost every expansion joint from the concrete slabs had reflected through the new overlay in the unreinforced area (Figure 2b).

Figure 2. HaTelit C 40/17 reinforced area without cracks (a) and unreinforced section presenting reflective cracking (b) (July 2009).

Due to the widespread crack pattern in the unreinforced section, in August 2010, five years after the rehabilitation, the unreinforced section had to be again repaired. The asphalt

layer was removed and in the sequence an asphalt overlay was placed. Overall condition of the pavement in the reinforced section was very good, showing no reflective cracking, despite Corso Agnelli is always under intensive traffic. In 2015, a third resurfacing of the unreinforced section was carried out. The asphalt layer was once more in bad condition, presenting significative reflective cracking. The reinforced section was still in good condition; however, the first ones barely visible cracks could be seen. In 2019, after 14 years from the first mentioned rehabilitation, the whole section was presenting reflective cracking and in need of remediation works.

This example has proven in the practice that the use of a polyester asphalt reinforcement grid can considerably delay the propagation of reflective cracks. The unreinforced section presented the first cracks already 10-11 months after the rehabilitation, demonstrating how reflective cracking can cause a premature failure of the asphalt overlay. The poor performance of this section has resulted in additional maintenance costs and in the need of complete rehabilitation every 4-5 of road operation. Conversely, the reinforced section has received no maintenance during 14 years of traffic operation, leading to significant cost savings. Based on the difference of required rehabilitation intervals and the overall performance, it is possible to conclude that the polyester asphalt reinforcement grid achieved an improvement factor of 3 with respect to the life time of the rehabilitation. Considering the gain in reflective cracking resistance of the asphalt overlay, the improvement factor observed in this case was well above 5.

4 EMBODIED ENERGY (EE) AND EMBODIED CO2 (ECO2)

Since the 1980's sustainability has been used in the sense of human sustainability on planet Earth and this has resulted in the most widely quoted definition of sustainability and sustainable development, that of the Brundtland Commission of the United Nations: "Sustainable development is development that meets the needs of the present without compromising the ability of future generations to meet their own needs." (United Nations General Assembly 1987)

In the context of the construction industry this does mean that different construction techniques and designs for a specific project are compared for their ECO2 as an indicator for their sustainability. As a matter of fact, the ECO2 is only one criterion beside social and economic considerations. Recent commitments signed at Cop26 in Glasgow saw many countries signing up to net zero carbon emissions by 2050. By assessing and quantifying the embodied energy (EE) and embodied carbon dioxide (ECO2) for the materials used on site without considering the individual transport distances and their installation. The authors of this paper appreciate that this comparison is not in line with the typical "cradle to grave" approaches used in this field, but it has been previously shown that the following comparison is sufficiently detailed to compare the two construction techniques without compromising on the accuracy of the results.

The ECO2 values ("Carbon Footprint") used in the following are taken from the latest Inventory of Carbon & Energy (ICE) V2.0. The University of Bath has created the ICE embodied energy & embodied carbon database which is the freely available (Hammond & Jones 2011). The aim of this work is to create an inventory of embodied energy and carbon coefficients for building materials. The data base is structured into 34 main material groups (i.e. aggregates, aluminum, asphalt, etc.).

The amount of embodied carbon dioxide per kg of material can vary significantly. The more processing and energy that is required to achieve the final product the higher is the ECO_2. Energy intensive processes like the production of cement are producing a high amount of CO2. Cement manufacturing releases CO2 in the atmosphere both directly when calcium carbonate is heated, producing lime and carbon dioxide, and also indirectly through the use of energy if its production involves the emission of CO2.

Based on a specific Environmental Product Declaration (EPD) the embodied CO2 for HaTelit C 40/17 eco asphalt reinforcement, made of recycled PET, has been assessed and externally verified as 1.05 kg ECO2/m^2 of material (3.88 kg ECO2/kg of material). This assessment is based on a cradle to grave approach and thus exceeds the system boundaries for the examples presented in in Table 3.

4.1 Comparison of embodied carbon dioxide for reinforced and unreinforced asphalt overlays

The report "Sustainable geosystems in civil engineering applications" commissioned by the Waste and Resource Action Plan (WRAP 2010) has analysed geosystems as alternatives to standard designs used by civil engineers.

Parallel to geosystems for ground engineering the report has identified that "Reinforcement of the asphaltic or bound layers can increase the life of the surface layers, again by contributing to a strengthening of the bound layers. Such strengthening increases their ability to resist cyclic fatigue, thermal stresses during extremes of winter and summer temperatures, as well as increasing resistance to near-surface crack propagation." (WRAP 2010). The report clearly identifies that asphalt reinforcements can extend pavement life by limiting reflective cracking and thus providing more sustainable pavements consequently. This paper aims to demonstrate the above referenced effect by comparing the ECO2 based on the material consumption per year of lifetime of two construction techniques. One construction technique is the conventional rehabilitation of cracked overlays by milling and repaving, the second is a rehabilitation using polyester asphalt reinforcement in the same process.

The example chosen for this comparison is a typical rehabilitation project with 5,000 m^2 of cracked wearing course to be replaced. Although the project size does not have any effect on the relative saving of ECO$_2$ it helps to give a better assessment for the saving potential (Table 1).

Table 1. Basis for calculation.

Job size	5,000 m^2
Asphalt thickness to be replaced	40 mm
Density of asphalt	2,500 kg/m^3 (compacted)
Bituminous emulsion (70%)	0.3 kg/m^2 (unreinforced)
Bituminous emulsion (70%)	1.0 kg/m^2 (reinforced)[a]
PET asphalt reinforcing grid	0.27 kg/m^2 (made of recycled polyester)
Improvement factor	3 [-][b]
Design life (unreinforced):	4 years[c]

[a]Required amount of bituminous emulsion for HaTelit asphalt reinforcement over milled surfaces acc. to manufacturer's recommendations.
[b]The improvement factor of 3 for the life time of reinforced asphalt as compared to unreinforced asphalt has been selected
[c]The design life of the unreinforced asphalt overlay has been chosen as 4 years since a typical crack propagation rate of approx. 10 mm / year would result in cracks reaching the surface of the new overlay after 4 years. The crack propagation rate of approx. 10 mm / year is of course project specific and could vary.

In the comparison in Table 2 it can be seen that a conventional (unreinforced) rehabilitation method results in 7.72 kg embodied CO2 per m^2 for the materials used. The alternative design using a PET asphalt reinforcement results in 9.04 kg embodied CO2 per m^2 due to the additional asphalt reinforcement and a higher amount of bituminous emulsion.

Table 2. Comparative calculation of embodied carbon dioxide (ECO$_2$).

Material	Material consumption	kg embodied CO$_2$ per kg of material	embodied CO$_2$ in kg/m^2	
			unreinforced	PET grid reinforced
Asphalt ($\sim$25 kg/cm)	100 kg/m^2	0.076	7.60	7.60
Bituminous emulsion (70%, 0.3 kg/m^2)	0.21 kg/m^2	0.55	0.12	–
Bituminous emulsion (70%, 1.0 kg/m^2)	0.70 kg/m^2	0.55	–	0.39
HaTelit C 40/17 eco asphalt reinforcement	0.27 kg/m^2	3.88	–	1.05
Total embodied CO$_2$ for rehabilitation	kg/m^2		7.72	9.04
Improvement factor	[-]		1	3
Design life (improved)	years		4	12
Total embodied CO$_2$ per year design life	kg/m^2/year		1.93	0.75
CO$_2$ saving per m^2 and year of design life				61%
Total CO$_2$ saving for improved design life				70,800 kg

The comparison of the ECO2 for the rehabilitation project has to be put into relation with the design life. The design life for the unreinforced overlay is set to 4 years until first cracking is likely to have reached the surface again. The reinforced overlay on the other side would last at least 3 times longer, i.e. 12 years.

The result is a saving of 61 % of ECO$_2$ per m^2 and year of design life for the HaTelit reinforced overlay as compared to the unreinforced overlay. For a project of 5,000 m^2 to be repaved this would mean a total ECO$_2$ saving of 70,800 kg based on the significantly improved design life of 12 years.

Many conscientious manufacturers provide Environmental Product Declaration (EPD) for their products and thus provide a basis for project owners to assess all potential environmental impacts of a product, system or solution during its entire life cycle (cradle to grave). Such EPDs are independently assessed and verified as per ISO 14025 and EN 15804. On this basis individual products, systems or construction methods can be compared for their environmental impact during initial construction and over the full service life of the infrastructure asset as shown here.

5 CONCLUSIONS

Reflective cracking occurs in cracked asphalt or concrete pavements rehabilitated with a simple asphalt overlay. To delay the development of reflective cracks, an asphalt reinforcement interlayer can be placed before the new asphalt wearing course. The presented research results and case study has shown that the use of an asphalt reinforcement made of high tenacity polyester (PET) in pavement rehabilitation can be advantageous, significantly improving the resistance to reflective cracking of the structure. This increase in service life has a number of financial and social economic benefits. The increased uptake of these asphalt reinforcement products, in particular those produced from recycled polyester, will help support the move towards a more circular economy and achieve net zero carbon emissions in the future.

REFERENCES

Asphalt Academy. 2008. Technical Guideline: *Asphalt Reinforcement for Road Construction*. TG 3, First Edition, South Africa.

Elseifi, M. 2015. Presentation 2: Mitigation Strategies for Reflective Cracking in Pavements. TRB Webinar - Mechanisms and Mitigation Strategies for Reflective Cracking in Rehabilitated Pavements, August 24.

Elsing, A. & Horgan, G. 2019. Determining Key Influence Factors of a Durable Asphalt Reinforcement. *18th Annual International Conference on Highways, Airports Pavement Engineering, Infrastructures & Asphalt Technology*, Liverpool.

EN 15381:2008. *Geotextile and Geotextile-related Products - Characteristics Required for use in Pavements and Asphalt Overlays.*

Hammond, G. & Jones, C. 2011. *ICE Inventory of Carbon and Energy V 2.0*. Sustainable Energy Research Team (SERT), Department of Mechanical Engineering, University of Bath, UK.

Koerner, R. M. 2012. *Designing with Geosynthetics*. Xlibris Corporation.

Leite-Gembus, F.; Elsing, A.; Amo, P. 2020. Asphalt Reinforcement Interlayers as Reflective Cracking Mitigation System in Rehabilitated Pavements. *7th Euroasphalt & Eurobitume Congress*. Madrid, Spain.

Monser, C. A.; Montestruque, G. E.; Silva, A. E. F. 2010. Evaluation of an Airport Pavement After Almost 8 Years of Overlay Rehabilitation with a Polyester Geogrid Asphalt Reinforcement. *9th International Conference on Geosynthetics*, Brazil.

Montestruque, G. E. 2002. *Contribuição Para a Elaboração de Método de Projeto de Restauração de Pavimentos Asfálticos Utilizando Geossintéticos em Sistemas Anti-Reflexão de Trincas* (in portuguese). Ph. D.-thesis, Technological Institute of Aeronautics, São José dos Campos, Brazil.

Nejad, F. M.; Asadi, S.; Fallah, S.; Vadood, M. 2016. Statistical-experimental study of Geosynthetics Performance on Reflection Cracking Phenomenon. *Geotextiles and Geomembranes*, 44: 178–187.

Norambuena-Contreras, J. & Gonzalez-Torre, I. 2015. Influence of Geosynthetic Type on Retarding Cracking in Asphalt Pavements. *Construction and Building Materials*, 78: 421–429.

Russo, L.E. 2011. Rinforzo di Pavimentazioni con Geogriglie in Poliestere. *XXIV Convegno Nazionale sui Geosintetici* (in italian). Bologna, Italy.

Russo, L.E. & Simini, A. 2011. L'efficacia del rinforzo con griglia sintetica nel ripristino di corso Agnelli a Torino (in italian). *Strade & Autostrade* 3–2011.

United Nations General Assembly. 1987. *Report of the World Commission on Environment and Development: Our Common Future*, Transmitted to the General Assembly as an Annex to document A/42/427 - Development and International Co-operation: Environment; Our Common Future.

Vanelstraete, A. & Francken L. 1996. Laboratory Testing and Numerical Modelling of Overlay Systems on Cement Concrete Slabs. *Proceedings of the 3rd International RILEM Conference*, Maastricht, Netherlands.

WRAP Waste and Resource Action Plan. 2010. *Sustainable Geosystems in Civil Engineering Applications*. UK.

Improving the resistance of asphalt mixtures against fatigue cracking with an interlayer (review paper)

H. Ghadi

CEO, Geoparsian Geosynthetic Producer Co., Islamic Republic of Iran

A. Ghollasimood

Ph.D. Candidate in Geomechanical Engineering, Shiraz University, Shiraz, Iran

H. Pakniyat

M.Sc. in Geotechnical Engineering, Noshirvani University of Technology, Babol, Iran

H. Khansari

M.Sc. in Highway and Transportation Engineering, Islamic Azad University, Tehran, Iran

H. Eskandari

B.Sc. in Mining Exploration Engineering, Shahrood University of Technology, Shahrood, Iran

ABSTRACT: Asphalt mixtures overlays are applied to an existing road pavement (flexible or rigid) when the structural or functional conditions of the pavement have reached an unacceptable level of deterioration. Most of the overlays are designed against fatigue and rutting failure mechanisms. Pavements that are structurally sound after the placement of the overlay and that are adequately designed against rutting and fatigue distresses may show cracking patterns after a short period of time that is similar to those that existed in the old pavement. This distress is known as "reflective cracking." Although reflective cracking is the most common failure mechanisms in rehabilitated pavements, it is rarely considered in the overlay design.

1   INTRODUCTION

During the last decades, the number of vehicles per citizen as well as the traffic speed and load has dramatically increased. This sudden and somehow unplanned overloading has strongly shortened the life of pavements and increased its cost of maintenance and risks to users (Polacco *et al.* 2015). In order to limit the deterioration of road networks, it is necessary to improve the quality and performance of asphalt pavements and designed to be resistance to fatigue and/or rutting failure mechanisms and mitigating reflection cracking. One of the most common techniques used to rehabilitate severely cracked pavements (load associated fatigue cracking, thermal cracking) consists in placing a Hot Mix Asphalt (HMA) overlay on the existing pavement (Romeo *et al.* 2014). Rarely this approach is a long-term efficient solution since deficiencies in the old pavement are very rapidly reflected at the surface as a result of the combined effects of thermally induced stresses and traffic loading.

The ability to distinguish crack resistance behavior and rank mixture performance in the laboratory can be a crucial asset to pavement engineers and also can serve in forensic analysis of pavement failures. In recent years, interlayer systems have received considerable

attention as viable solutions to the problem of improving flexible pavement resistance to reflection cracking in asphalt overlays, as well as to extend the pavement's fatigue life (Al-Qadi *et al*. 2003; Romeo & Montepara 2012).

2 LITERATURE REVIEW

The attempt to provide tensile reinforcement for asphalt pavements goes back to 1950s. At the beginning, all attempts to do so experience installation difficulties in laying the mesh flat but, later, with new technology (Marienfeld & Guram 1999). There was evidence of possible benefits related to the use of interlayers in road construction. The reason for the continued interest in interlayer systems is that, in terms of the mechanics of the materials, interlayers theoretically can reduce the occurrence of reflective cracking in AC overlays. Nowadays, interlayers can be used for both long-term road and cost-effective maintenance (Brown 2006). In particular, the reinforcement function in a continuum body is obtained by the insertion of reinforcing materials able to improve the mechanical properties of the continuum body. The reinforcement function in bound layers can be summarized in:

1. The extension of fatigue life or reduction of layers' thicknesses,
2. The elimination or limitation of reflective cracking,
3. The reduction of rutting and permanent deformation,
4. Interlayer systems to control reflective cracking.

Several remedial techniques have been used to control reflective cracking, including placing a thin layer or an interlayer system at the interface between the old and new layers, rubblizing the existing concrete pavement, crack-sealing the existing pavement, and increasing the thickness of the hot mix asphalt (HMA) overlay. Among these techniques, interlayer systems have been the most effective in controlling reflective cracking (Figure 1). Interlayer systems, which are relatively thin layers placed between HMA overlay and existing pavements, have two different mechanisms to delay reflective cracking:

1. By absorbing strain energy which occurs in HMA overlay;
2. By reinforcing the low tensile strength HMA overlay.

The efficiency of the interlayer depends on the appropriate selection of the interlayer system type, the interlayer conditions, correct installation, and the conditions and characteristics of the existing pavement and HMA overlay (Button & Lytton 2007).
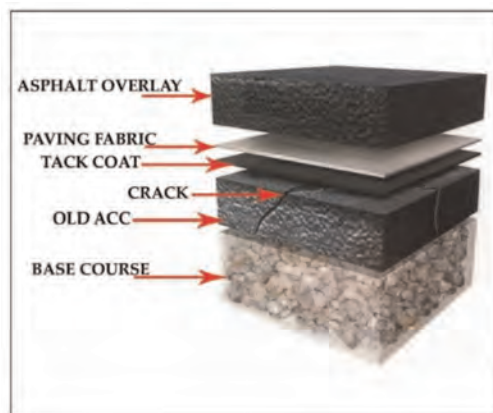
Figure 1. Use of interlayers in mitigation of reflective cracking in asphalt overlays.

High modulus geogrids, such as fiberglass grids, are commonly used as reinforcing materials to control and retard reflective cracking in asphalt pavements. High modulus polypropylene grids, glass fabrics, and glass grids are classified as reinforcing geosynthetics and, if constructed properly, can redirect the reflective cracks along the interface and retard their progress (Lytton 1989). Grids are designed to have high modulus values at low strain levels so that they can engage in reinforcing the system and transfer loads throughout the grid system before the protected pavement layer fails in tension. Interlayer characteristics, including the interlayer bond, play an important role in the structural stiffness of the pavement system and in the distribution of the stress and strain within the pavement; thus, the long-term performance of pavements and cracking patterns depend on the interlayer bond and interlayer conditions (Canestrari *et al.* 2005). The retardation effect of fiberglass grids, which is an important mechanism that affects the performance and life cycle of the pavement, needs to be assessed and, if possible, quantified. To understand the various effects of interlayer systems more fully and to be able to predict the performance of reinforced pavements that incorporate different interlayer conditions, it is necessary to investigate the ways that different interlayer conditions affect the damage mechanisms, crack propagation rates, and crack patterns in the pavement structure.

3 GEOSYNTHETICS

The prevention of reflective cracking in asphalt overlays was one of the earliest applications involving geosynthetics in paved roads. Reflective cracks can occur in new flexible pavement overlays where pre-existing cracks are located within the old paved road. Reflective cracking may be triggered by bending and/or shear stresses induced by repeated traffic loads, as well as by tensile stresses caused by thermal variations (Button & Lytton 2003). Figure 2 shows the development of stresses resulting from lateral movements induced by flexing of the paved road located directly below the traffic load. Such stresses may end up causing a reflective crack that propagates through the new pavement overlay, making it susceptible to early failure facilitated by moisture intrusion.
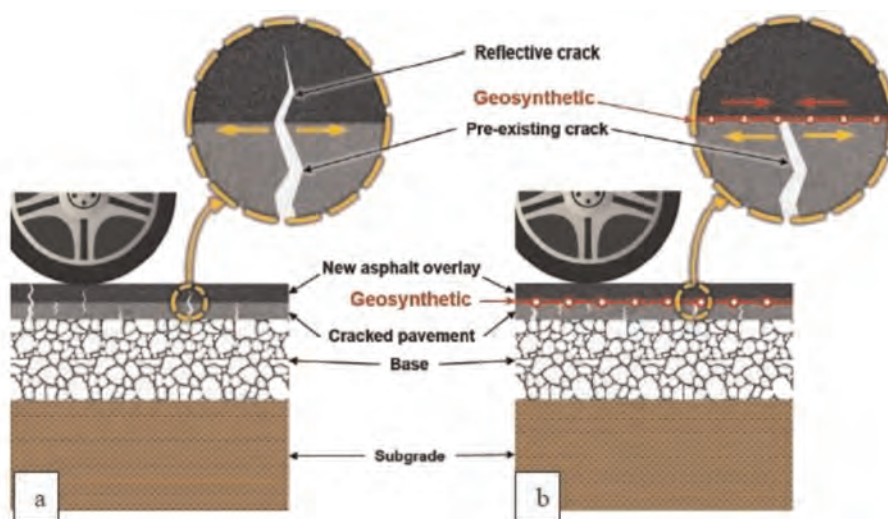
Figure 2.   Use of geosynthetics in mitigation of reflective cracking in asphalt overlays: (a) roadway designed without geosynthetics, (b) roadway designed with geosynthetics (Zornberg 2017).

(Perkins & Ismeik 1997) illustrates the three reinforcement mechanisms geosynthetics can provide for roadways: lateral restraint, modified failure surface, and tensioned membrane. They explained how interlocking and friction between the geosynthetic and the soil provides a lateral restraint for the aggregate base layer. Under repeated loads, the aggregate base layer tends to spread laterally; however, if the geosynthetic is placed at a depth of high lateral strain, the shear stress in the soil can be transferred to tensile stress in the geosynthetic. If the geosynthetic used is stiff, it will act to restrain the lateral spreading and result in a stiffer road.

Geosynthetics are divided into seven major categories: geotextile, also known as paving fabric; geogrid; fiberglass; geocell; geomembrane; geonet; and geocomposite. Geotextile, geogrid, fiberglass, and geocomposite have been tested as reflection cracking control treatments by acting as reinforcement or as a strain energy absorber, also known as stress relieving layer. The effectiveness of these products as crack control treatments has been mixed and was reported to depend on many factors including the installation procedure and conditions of the existing pavement. Table 1 introduces the major types of geosynthetics that have been evaluated to control reflection cracking.

Table 1. Major types of crack control Geosynthetics.

Geosynthetics	Performance
Geogrids or Grid-reinforced	Reinforcement
Polyester geogrids	Reinforcement
Fiber glass geogrids	Reinforcement
Carbon geogrids	Reinforcement
Biaxial grids	Reinforcement
Geonets	Reinforcement
Paving fabric	Stress relief
Geocomposite	Stress relief
Woven geojute mat	Stress relief
Geotextile	Stress relief

4 EVALUATING EFFECT OF USING INTERLAYERS ON PERFORMANCE OF FLEXIBLE PAVEMENTS

Evaluation of the effectiveness of various antireflective cracking alternatives is a significant task and mainly realised by three methods: field project observation, finite element model (FEM) simulation and laboratory simulation. In addition to Digital image correlation (DIC) appears the most suited image processing technique for asphalt mixture investigation since it has shown to adequately detect anisotropies and heterogeneities typical of bituminous materials, i.e. defect or cracks within the skeleton.

4.1 Digital Image Correlation (DIC)

Digital Image Correlation (DIC) was used to track and measure the deformations, displacements, and strains on the surface of the specimens and especially at areas around the interlayer. Digital image correlation (DIC) appears the most suited image processing technique for asphalt mixture investigation since it has shown to adequately detect anisotropies and heterogeneities typical of bituminous materials, i.e. defect or cracks within the skeleton. Kim and Wen (Fallah & Khodaii 2015) first proposed the use of a DIC technique as a possible displacement/ strain measurement method for asphalt mixtures. They applied the DIC technique to determine the proper gauge length for a 100-mm diameter IDT specimen. Safavizadeh and Kim (Abe N. 2000; Anderson 2017; Smith 1983), Romeo and Montepara (Perkins & Ismeik 1997), used digital imaging techniques to evaluate the microstructure of

Grid-Reinforced asphalt Specimens, as well as Strain localization and damage distribution. They found that the most important advantages of using DIC for asphalt mixture testing can be summarized as follows:

1. It is a noncontact technique; this reduces setup timing and mounting errors;
2. It provides pointwise analysis pinpointing the location of crack initiation;
3. It accounts for non-uniform strain distributions (i.e. fracture process zone);
4. It provides flexibility since it allows a ''back analysis'' of the resulting strain field over an area of finite extent, preventing to mount multiple sensors in different locations.

4.2 *Modeling of interlayers- reinforced flexible pavements*

The finite element method (FEM) currently offers the level of sophistication needed to analyze a pavement section under applied wheel and environmental loading conditions. Numerical modeling is a useful tool for understanding the crack initiation and propagation in asphalt mixtures. Currently, two different numerical methods are employed. One is the finite element method and the other is the discrete element have been widely used to study the cracking behavior of homogeneous materials.

A mechanistic model based on the FEM is currently best suited to evaluate the effectiveness and benefits of including geosynthetic reinforcement in flexible pavements for improving the response behavior. (Eiksund *et al.* 2002) developed a 2-D axisymmetric finite element model for geogrid-reinforced flexible pavements using the ABAQUS^{TM} program. The Coulomb interface friction contact was used to model the soil/ aggregate–geosynthetic interface. The researchers examined the ability of the linear elastic constitutive models considering cross-anisotropic characterization of the unbound aggregate layer. They reported that the predicted pavement responses were affected by the material and numerical model properties such as reinforcement tensile stiffness and contact interface friction properties. The geogrid reinforcement limited lateral strains throughout the pavement section, and thus decreased pavement critical responses. The improvement from geogrid reinforcement was higher when a cross-anisotropic model was used in the unbound aggregate base. (Kwon *et al.* 2005) used the finite element method for modeling geogrid interface behavior, and reported that the predicted pavement responses obtained from 3-D ABAQUSTM analyses. FEMs of specimens with and without the stress-absorbing interlayer were constructed in accordance with the HWTT by finite element software ABAQUS, respectively (Kwon *et al.* 2005).

5 COST EFFECTIVENESS OF INTERLAYERS IN FLEXIBLE PAVEMENTS

Life-cycle costing can consider many cost components, particularly initial construction costs, maintenance costs, user costs (vehicle damage, user delay in work zones), and salvage value. Life-cycle costs were computed for two analysis cases, containing the following groups of cost components:

- Case 1 (neglecting maintenance and milling costs):
  – Hot mix asphalt overlay cost, in-place (material plus construction costs), and
  – In-place reflective crack control cost.

- Case 2 (maintenance and milling costs included):
  – Hot mix asphalt overlay cost, in-place (material plus construction costs),
  – In-place reflective crack control cost,
  – Periodic crack-sealing costs, and
  – Milling costs (removal of previous overlay lift).

The in-place costs of geosynthetics and other interlayers to address reflection cracking are influenced by (a) the specific product used, (b) the quantity to be placed, (c) local experience

with its installation, (d) local labor costs, and (e) the general condition of the market place. The in-place cost of fabrics has fallen significantly since the early 1980s, apparently because of stiff competition and perhaps improved contractor experience and acceptance of geosynthetics. In 1991, NCHRP Synthesis 171 offered the following rule of thumb: The in-place cost of a full-width paving fabric is roughly equivalent to the cost of approximately 0.5 in. to 0.6 in. of asphalt concrete.

Interlayer systems have been successfully used as a cost-effective method to alleviate reflective cracking (Baek *et al*. 2009). A study performed by (Morian *et al*. 2004) in Pennsylvania evaluated the performance and cost-effectiveness of cold-in-place recycling and SAMI in 49 sections. Results showed that the use of SAMI and cold in-place recycling improved pavement service life when compared to normal milling and leveling rehabilitation procedures (Heitzman 1992). While cold-in-place recycling extended the overlay service life by four to five years, the use of SAMI increased pavement service life by two years and proved to be cost-effective when compared to conventional leveling and milling procedures. Further, the application of the overlay when the pavement is in fair condition proved more cost-effective as compared to its application when the pavement reaches a poor condition. (Herbst *et al*. 1993) reported that overlays using stress-absorbing interlayers typically cost about 10 percent more than a conventional overlay. A few authors have reported that geotextiles are cost-effective treatments for prolonging overlay life (Collios 1993, Zapata 1958). A few more have reported that geotextiles are not cost effective for use on both flexible (Maurer *et al*. 1989, Button 1989) and rigid (Allen 1985; Heins 1992; Maurer *et al*. 1989) pavements. The economic justification of the geotextile must be derived from a combination of:

- An increase in pavement serviceability due to reduced reflective cracks,
- An increase in pavement life,
- A decrease in pavement maintenance costs, and
- An increase in structural capacity due to dryer base and subgrade.

REFERENCES

Abe N., H. M., Maruyama T., Ooba K. *An Examination on the Factor Which Affects Reflective Cracking*. In: A. O. Abd El Halim, D. A. T. & Mohamed, A. E. H. H., Eds. Fourth International Rilem Conference On Reflective Cracking In Pavements - Research In Practice, 2000.

Al-Qadi, I. L., Elseifi, M. & Leonard, D. J. A. P. T. 2003. Development of an Overlay Design Model for Reflective Cracking with and Without Steel Reinforcing Nettings. 72, 388–423.

Allen, H. 1985. Methods and Materials for Reducing Crack Reflectance. Final Report.

Anderson, T. L. 2017. *Fracture Mechanics: Fundamentals and Applications*, Crc Press.

Baek, J., Wang, H. & Al-Qadi, I. L. 2009. *Numerical Modeling and Life Cycle Cost Analysis of Hot-Mix Asphalt Overlay with Steel Netting Interlayer System For Airport Pavements*.

Brown, S. Reinforcement of Pavements with Steel Meshes and Geosynthetics: Keynote Presentation. *Cost Action 348 Dissemination International Symposium*, London, 2006.

Button, J. W. & Lytton, R. L. 2003. *Guidelines for Using Geosynthetics with Hma Overlays to Reduce Reflective Cracking*, Texas Transportation Institute, Texas A & M University.

Button, J. W. & Lytton, R. L. J. T. R. R. 2007. Guidelines For Using Geosynthetics with Hot-Mix Asphalt Overlays to Reduce Reflective Cracking. 2004, 111–119.

Button, J. W. J. T. R. R. 1989. *Overlay Construction and Performance Using Geotextiles*.

Canestrari, F., Ferrotti, G., Partl, M. N. & Santagata, E. J. T. R. R. 2005. *Advanced Testing and Characterization of Interlayer Shear Resistance*. 1929, 69–78.

Collios. 1993. Design and First Application of Geotextiles Against Reflective Cracking in Greece. *2nd International Rilem Conference*, 1993. London.

Eiksund, G., Hoff, I., Svanø, G., Watn, A., Cuelho, E., Perkins, S., Christopher, B. & Schwartz, C. 2002. Material Models for Reinforced Unbound Aggregate. *Bearing Capacity of Roads, Railways and Airfields*. Crc Press.

Fallah, S. & Khodaii, A. 2015. Reinforcing Overlay to Reduce Reflection Cracking; An Experimental Investigation. *Geotextiles And Geomembranes*, 43, 216–227.

Heins, D. 1992. *A Study on the Use of Fabric to Retard Reflective Cracking Over Widening Joints*. Interim Report.

Heitzman, M. J. T. R. R. 1992. Design and Construction of Asphalt Paving Materials with Crumb Rubber Modifier. 1339.

Herbst, G., Kirchknopf, H. & Litzka, J. Asphalt Overlay on Crack-Sealed Concrete Pavements Using Stress Distributing Media. Reflective Cracking in Pavements. State of the Art and Design Recommendations. *Proceedings of the Second (March 10-12, 1993) International Rilem Conference*, Liege, Belgium, 1993.

Kwon, J., Tutumluer, E. & Kim, M. J. G. I. 2005. *Development of A Mechanistic Model for Geosynthetic-Reinforced Flexible Pavements*. 12, 310–320.

Lytton, R. L. 1989. Use of Geotextiles for Reinforcement and Strain Relief in Asphalt Concrete. *Geotextiles And Geomembranes*, 8, 217–237.

Marienfeld, M. L. & Guram, S. K. 1999. Overview of Field Installation Procedures for Paving Fabrics in North America. *Geotextiles And Geomembranes*, 17, 105–120.

Maurer, D. A., Malasheskie, G. J. J. G. & Geomembranes 1989. *Field Performance of Fabrics and Fibers to Retard Reflective Cracking*. 8, 239–267.

Morian, D. A., Oswalt, J. & Deodhar, A. J. T. R. R. 2004. *Experience with Cold in-place Recycling as a Reflective Crack Control Technique: Twenty Years Later*. 1869, 47–55.

Perkins, S. W. & Ismeik, M. J. G. I. 1997. *A Synthesis and Evaluation of Geosynthetic-Reinforced Base Layers in Flexible Pavements-Part I*. 4, 549–604.

Polacco, G., Filippi, S., Merusi, F. & Stastna, G. 2015. A Review of the Fundamentals of Polymer-Modified Asphalts: Asphalt/Polymer Interactions and Principles of Compatibility. *Advances in Colloid and Interface Science*, 224, 72–112.

Romeo, E., Freddi, F. & Montepara, A. 2014. Mechanical Behaviour of Surface Layer Fibreglass-Reinforced Flexible Pavements. *International Journal Of Pavement Engineering*, 15, 95–109.

Romeo, E. & Montepara, A. 2012. Characterization of Reinforced Asphalt Pavement Cracking Behavior Using Flexural Analysis. *Procedia - Social And Behavioral Sciences*, 53, 356–365.

Smith, R. D. J. T. R. R. 1983. *Laboratory Testing of Fabric Interlayers for Asphalt Concrete Paving*: Interim Report.

Zapata 1958. *Experimental Fabrics On I-94 Bl*, City Of Kalamazoo.

Zornberg, J. G. 2017. Functions and Applications of Geosynthetics in Roadways. *Procedia Engineering*, 189, 298–306.

Investigation of the effect of using geogrids on the performance of the road in pavements constructed with reduced layer thicknesses

S. Terzi & M. Saltan
Süleyman Demirel University, Turkey

S. Gökova
Burdur Mehmet Akif Ersoy University, Turkey

F. Erkmen
Komsa Engineering, Turkey

E. Tutumluer
University of Illinois at Urbana-Champaign, USA

M. Karaşahin
Istanbul Gelisim University, Turkey

V.E. Uz
İzmir Institute of Technology, Turkey

O. Pekcan
Middle East Technical University, Turkey

M.V. Taciroğlu
Mersin University, Turkey

Ş. Çömez, A. Sağlık, M. Komut, Ş. Altıok & E. Yalçın
General Directorate of Highways, Turkey

ABSTRACT: In this study, the structural performance of road pavements with reduced layer thicknesses at different rates using geogrids was examined, and the benefits of geogrids in preventing rutting were investigated. Within the scope of the study, a total of 16 test sections of 50 meters in length, 12 with geogrids and four without geogrids, were constructed on the Adana - Kozan road determined by the General Directorate of Highways of Turkey (KGM). The constructed sections were divided into two, and besides the reference sections, two types of geogrids with different geometric structures were used in successive sections. Some layer thicknesses used in the study were determined following the specification, and the other part was determined through a pavement design program. In addition, to compare the effect of using geogrids in different locations on the pavement performance in the application sections, the geogrid was used in two positions, on the subbase layer and between the base layer. Data from the load, displacement and temperature sensors placed between the layers during the construction phase and on-site Heavy Weight Deflectometer (HWD) data at certain time intervals were used to observe the structural performances of the constructed pavement sections. In addition, GPS and IRI measurements are made regularly. The traffic values of the trial section are also monitored. Examining the obtained data aims to compare the economic gain achieved by reducing the layer thicknesses, the cost to be spent for the geogrid, and to make cost-benefit analyses.

Keywords: Highway pavement, geogrid, geosynthetics.

1 INTRODUCTION

This study examines structural performance by using geogrids in highway pavements and providing economic gain by reducing layer thicknesses. Kind of gains are obtained with the use of geogrid that will arise as a result of the achievement of the purpose of this study, and how these gains change with the place of geogrid in the pavement will be parameters that the outputs of the study can determine. The road pavement is expected to have excellent structural performance and comfort and be economical. When these parameters are taken into account, in addition to all the positive outputs to be obtained as a result of the study, the use of geogrid allows for a reduction in layer thicknesses, which means saving enormous amounts of labor, materials and natural resources.

The development of geosynthetics, a polymeric material, has brought about positive changes in geotechnical engineering (Das 2021). Geosynthetics are synthetic products widely used to solve many civil engineering problems and provide one or more functions such as protection, separation, filtration, erosion control, drainage and reinforcement (Giroud & Han 2004; Han J. & Thakur 2015). Specific properties are needed for geosynthetics to undertake different uses in different applications and perform various functions. First of all, it is necessary to know which of the functions, as mentioned earlier, are needed in order to determine the reason for the application. It should be determined which type of geosynthetic will be used and which properties will be according to the conditions where the application will be made (McGown & Brown 2008).

In terms of the applications of geosynthetics, roads can be considered in two categories as paved and unpaved roads (Wasti 2007). Yang *et al.* (2012), it has been observed that the use of geosynthetics has a significant effect on providing durability and reducing permanent deformations on unpaved roads.

Geosynthetics in road pavements started with woven and non-woven geotextiles with unscientific methods. While these materials had some advantages with their separation and filtering functions, they were ineffective for stabilisation (Brown *et al.* 1982). Due to the low stiffness of the geotextiles and their weak interaction with the surrounding materials, they cannot reduce the stresses accumulated during repeated loads. Later, Chan *et al.* (1989) used a medium stiffness geogrid in their work. Showed that a much more tightly woven geotextile reduced rutting depth in pavements with granular layers. Geogrids can reinforce unpaved roads (Benmebarek *et al.* 2013; Calvarano *et al.* 2016; Calvarano *et al.* 2017; Gabr 1998; Tingle & Webster 2003). One of the main reasons for the plastic deformations on the surface under cyclic loads is the inability to reduce the stresses reaching the granular layers and the subgrade. Minimizing the stresses that can reach the lower layers would be necessary (Dawson *et al.* 1994; Harianto 2022). Geogrids minimize the stresses that can reach the lower layers by interlocking and strengthening according to their region (Ibrahim *et al.* 2017). Using geogrid enables carrying the maximum load with minimum stress and increasing the elastic modulus of the place where it is used (Geosynthetic materials Association 2000; Laughs *et al.* 2009; Tensar Corporation 2017).

When geosynthetics are used between the subgrade and foundation layers, it ensures the separation of the two layers and prevents the mixing of granular foundation materials with the subgrade. In addition, geosynthetics used between the subgrade and the base layer increase the bearing capacity of the subgrade and strengthen the layers applied to it (Giroud & Han 2004).

2 CONSTRUCTION OF TEST SECTIONS

As a result of the preliminary studies, base, and subbase layer thicknesses were determined, some following the specifications, as shown in Table 1, and some by reducing as a result of modeling and analysis made in pavement design software.

Table 1. The layer thicknesses used in the study and the sections where the layer thickness is reduced.

Application Sections		1	2	3	4	5	6	7	8	9	10	11	12	13	14	15	16
Layers and Thickness (cm)	Binder	11	11	11	11	11	11	11	11	7	7	7	7	7	7	7	7
	Bituminous Base	0	0	0	0	0	0	0	0	9	9	9	9	9	9	9	9
	Base Granular	15	15	15	20	20	20	20	20	10	10	10	20	20	20	20	20
	Subbase Granular	15	15	15	20	20	20	20	20	15	15	15	20	20	20	20	20

Base and subbase layers are applied by decreasing their thickness at sections 1, 2, 3, 9, 10, and 11, as shown in Table 1. After the first eight sections, the thickness of the binder layer was reduced by 4 cm to 7 cm, and a 9 cm thick bituminous base course was applied to the 10 cm aggregate base course. It is planned to evaluate the data obtained from type-1 and type-2 geogrids by comparing the plastic deformations in the sections where the layer thicknesses are reduced. In addition, productivity analyses could be made by comparing the sections prepared without using geogrids with the same layer thicknesses and using type-1 and type-2 geogrids in the study.

Type-1 and type-2 geogrids are applied in the sections:

- In sections 1, 2, 3, 4, 9, 10, 14, and 15, between the base and sub-base layers,
- Sections 6, 7, 12, and 13 were placed in the middle of the base layer (Figure 1).

As a result of the positive results that can be seen in the sections where the use of geogrid reduces the layer thicknesses, it is foreseen that the amount of material to be used in similar applications and the labor force will be reduced. Thus, both time and economic gain are provided. The sensors to be used in the study, their number and equipment were determined, and their procurement was carried out by the General Directorate of Highways (KGM). After the region where the test sections will be applied has been determined in line with the purpose of the application, the construction process has been completed, and the process of obtaining data from the sensors has been started. Basic information such as road profiles, geogrid layouts, sensor types, and placements are shown in Figure 1.
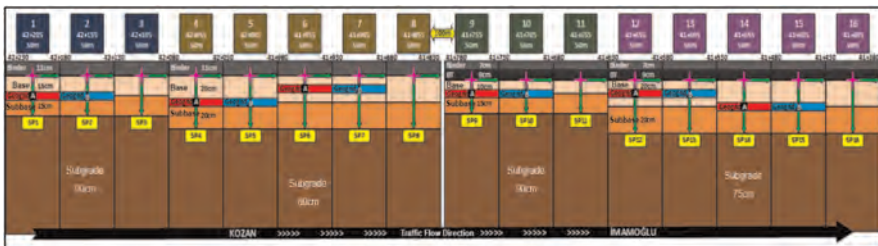
Figure 1. Schematic representation of the trial road.

The test road, built 850 meters, has the following elements:

- Four different road sections
- Two types of geogrids
- 8-channel fibre optic data acquisition device
- 16 test sections and measuring stations
- Dedicated server and control board
- 92 sensors

Types and numbers of sensors used at measuring points are:

- Sixteen soil pressure sensors (They are placed on the subgrades to determine the stresses reaching the subgrades).
- Sixteen vertical displacement sensors (placed in each section to determine the vertical displacements between the subgrade and the surface layer).
- Sixteen horizontal displacement sensors (They are placed under the coating layer to determine the horizontal displacements).
- Sixteen transverse and longitudinal strain sensors (For cable-type strain gauges to be placed on the pavement surface, channels were opened using an asphalt cutter, and cable-type strain gauges sensors were placed in these channels fixed with bitumen).
- Twelve temperature sensors (Channels were opened for temperature sensors to be placed on the subgrade, subbase layer, base layer and surface layer interface, and the sensors were placed and fixed).

Geogrids, which will be used in the construction of the test sections and which form the basis of the study, were determined in line with the purpose of use, and samples were obtained from the companies. After the strength tests of these samples were carried out in the laboratory, two different types of geogrids (Type-1 and Type-2) suitable for the study were shipped to the construction site in rolls. The biaxial and triaxial geogrids that are being provided by the two different companies feature rib openings that are 40 mm by 40 mm. The fiber optic sensors and data collection systems provided for monitoring the structural performance of the test road made within the scope of the study were tested in the Accelerated Pavement Test Device available in the Civil Engineering Transportation Laboratory of Süleyman Demirel University for trial purposes before the field application to be made. After the applicability of the relevant equipment was seen, all equipment was brought to the area where the application would be made, and assembly processes were carried out.

3 EVALUATION OF MEASUREMENT DATA

The performance of the road was also evaluated by on-site heavyweight deflectometer (HWD) tests performed at certain time intervals. There were no significant differences in the measurements made at different time intervals, but the conditions of the layer thicknesses and the sections using geogrids could be observed. It also provides information on the effects of two different geogrids on pavement performance (Figure 2).
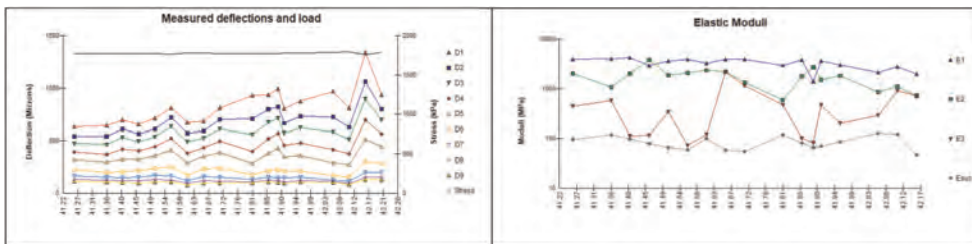
Figure 2.   Heavyweight deflectometer (HWD) test results at different sections.

In order to determine the performance and road comfort, IRI (International Roughness Index) values were obtained by measuring the unevenness of the test road. Four years after the road was opened to traffic, the values obtained as a result of the tests

carried out to determine the unevenness were examined, and the conditions of the sections with and without geogrid were evaluated. It was observed that the unevenness values obtained from the sections without using geogrid were higher than the sections using geogrid (Table 2).

Table 2. Measurement of the International Roughness Index (IRI) of trial sections.

| Trial Sections | IRI | Layer Thicknesses | | | | With geogrid / without geogrid | Geogrid Location |
		Subgrade	Subbase	Base	HMA		
1	2.49	90cm	15cm	15cm	11cm	Type A Geogrid	Between Base and Subbase
2	2.38	90cm	15cm	15cm	11cm	Type B Geogrid	Between Base and Subbase
3	3.8	90cm	15cm	15cm	11cm	Without Geogrid	- - - - - - - -
4	2.23	80cm	20cm	20cm	11cm	Type A Geogrid	Between Base and Subbase
5	1.39	80cm	20cm	20cm	11cm	Type B Geogrid	Between Base and Subbase
6	1.45	80cm	20cm	20cm	11cm	Type A Geogrid	Middle of the Base
7	1.31	80cm	20cm	20cm	11cm	Type B Geogrid	Middle of the Base
8	1.56	80cm	20cm	20cm	11cm	Without Geogrid	- - - - - - - -
9	1.09	90cm	15cm	10cm	16cm	Type A Geogrid	Between Base and Subbase
10	1.06	90cm	15cm	10cm	16cm	Type B Geogrid	Between Base and Subbase
11	1.47	90cm	15cm	10cm	16cm	Without Geogrid	- - - - - - - -
12	1.22	75cm	20cm	20cm	16cm	Type A Geogrid	Middle of the Base
13	1.23	75cm	20cm	20cm	16cm	Type B Geogrid	Middle of the Base
14	1.17	75cm	20cm	20cm	16cm	Type A Geogrid	Between Base and Subbase
15	1.22	75cm	20cm	20cm	16cm	Type B Geogrid	Between Base and Subbase
16	1.48	75cm	20cm	20cm	16cm	Without Geogrid	- - - - - - - -

While making IRI measurements, road sections are photographed separately, and the resulting deterioration is visually examined. In the image in Figure 3, when the rut settlement differences between section 7 with geogrid and section 8 without geogrid are observed, the rut settlement formed in the section without geogrid can be seen more clearly.

Figure 3. The difference in plastic deformations in the seventh and eighth sections.

4 RESULTS

This study carefully determined the principles be applied for the test sections and the materials used. The study aims to reduce construction costs by reducing layer thicknesses using geogrids. In order to increase the efficiency of the work carried out for the purpose and to prevent the adverse effects that may occur afterward, the materials to be used, their settlements and how they will give results were determined by conducting experiments in the Transportation Laboratory of Süleyman Demirel University before the construction started. Some of the pavement layer thicknesses used in the study were determined following the KGM (General Directorate of Highways of Turkey) specification, and the other part was determined using pavement design software.

Following the stages determined in the light of the data obtained as a result of the experiments, the application was carried out on the 850 m road section on the Adana - Kozan road. When the last data obtained are examined, since there is no significant deterioration in the trial sections, tests continue to be carried out at specific periods to see the performance of the applied geogrids. However, when the final IRI data is examined, it was observed that the IRI values obtained from the sections without using geogrid were larger than those used geogrid. This shows that the deterioration occurs more rapidly in sections with no geogrid. In the following periods, the data obtained from the test sections will be taken and analyzed, and the effects of different types of geogrids according to layer thickness will continue to be examined.

ACKNOWLEDGEMENTS

REFERENCES

Benmebarek, S., Remadna, MS & Belounar, L. 2013. Numerical Modeling of Reinforced Unpaved Roads by Geogrid, *The Online Journal of Science and Technology*, Vol.3, No.2, pp.109–115.

Brown, S.F., Jones, C.P.D. & Broderick, B.V. 1982. Use of Non-woven Fabrics in Permanent road Pavements, *Proceedings of the Institution of Civil Engineers*, Vol.2, No.73, pp.541–563.

Calvarano, LS, Plamara, R., Leonardi, G. & Moraci, N. 2016. Unpaved Road Reinforced with Geosynthetics, VI Italian Conference of Researchers in Geotechnical Engineering, Geotechnical Engineering in Multidisciplinary Research: from Microscale to Regional Scale, CNRIG2016, Vol.158, pp.296–301, Italy.

Calvarano, LS, Leonardi, G. & Plamara, R. 2017. *Finite Element Modeling of Unpaved Road Reinforced with Geosynthetics, Transportation Geotechnics and Geoecology,* TGG 2017, Vol.189, pp.99–104, Saint Petersburg, Russia.

Chan, F.W.K, Barksdale, R.D & Brown, S.F. 1989. Aggregate Base Reinforcement of Surfaced Pavements, *Geotextiles and Geomembranes*, Vol.8, No.3, pp.165–189.

Das, M., Mohanty, M. & Das, S. 2021. Multi-objective Optimum Design of Geosynthetic Reinforced Soil Foundation Using Genetic Algorithm. 10.1016/B978-0-12-821205-9.00018-6.

Gabr, M. & Dodson, R.E. 1998. *Stress Distribution in Geogrid Reinforced Foundations, Geo-Congress'98*, Geotechnical Special Publication, Vol.76, pp.62–76, Reston, VA

Geosynthetic Materials Association. 2000. *Geosynthetic Reinforcement of the Aggregate Base/subbase Courses of Pavement Structures*, GMA White Paper II, prepared for AASHTO Committee 4E.

Giroud, J.P & Han, J. 2004. Design Method for Geogrid-Reinforced Unpaved Roads – Part I: Theoretical Development. *ASCE Journal of Geotechnical and Geoenvironmental Engineering*, 130(8), (776–786)

Han, J., & Thakur, J.K. 2015. Sustainable Roadway Construction using Recycled Aggregates with Geosynthetics. *Sustainable cities and Society*, *14*, 342–350.

Harianto, T. 2022. Performance of Subbase Layer with Geogrid Reinforcement and Zeolite-Waterglass Stabilization. *civil engineering Journal*, *8* (02).

Ibrahim, E.M., El-Badawy, S.M., Ibrahim, M.H., Gabr, A. & Azam, A. 2017. Effect of Geogrid Reinforcement on Flexible Pavements, *Innovative Infrastructure Solutions*. 2 (1–15), Chen DH; ElZahaby KM (Ed), Springer International Publishing

McGown, A. & Brown, S.F. 2008 Applications of Reinforced Soil for Transport Infrastructure. *Advances in Transportation Geotechnics* (27–36), Ellis, Yu, McDowell, Dawson and Thom (Ed), CRC Press, 786s, Nottingham, UK.

Tensar International Corporation. 2017. *Evaluating Unpaved Road Research*, Tensar Search Report, pp.112.

Tingle, J.S. & Webster, S.L. 2003. Review of Corps of Engineers Design of Geosynthetic Reinforced Unpaved Roads, Transportation Research Record. *TRB 2003 Annual Meeting*, Vol.24, Washington, DC

Wasti, Y. 2007 Geosynthetics – Theory and Practice. Middle East Technical University. Ankara.

Yang, X., Han, J., Pokharel, S.K., Manandhar, C., Parsons, R.L., Leshchinsky, D. & Halahmi, I. 2012. Accelerated Pavement Testing of Unpaved Roads with Geocell-reinforced Sand Bases, *Geotextiles and Geomembranes*, Vol.32, pp.95–103.

Carbon footprint of HDPE geomembrane *vs.* traditional waterproofing barrier

J.M. Muñoz
Sotrafa S.A. Almería, Spain

ABSTRACT: Lowering the Carbon Footprint is one of the most important reasons for using HDPE geomembrane instead of traditional ways of waterproofing such as compacted clay. An HDPE liner in 1.5 mm thickness could give similar watertight properties as using 0.60 m of high quality and homogeneous compacted clay with lower permeability than $1 \times 10\text{-}11$ m/sec (ASTM D 5887). Based on several scientific surveys, and when considering all resources and energy needed to install both products as a waterproofing barrier, the geosynthetic option (HDPE Geomembrane 1.5 mm) means a lower carbon dioxide equivalent, therefore it is a more environmentally friendly solution.

1   INTRODUCTION

The transition to a carbon neutral economy is a move to which most countries, as well as thousands of companies and a large part of civil society, are committed.

One of the ways to achieve this objective is to replace traditional waterproofing systems (clay-based) with a geosynthetic barrier, such as HDPE Geomembrane.

1.1   *Features of HDPE geomembrane and its carbon footprint*

The main component of HDPE is the monomer ethylene, which is polymerized to form polyethylene. The main catalysts are aluminum trialkylitatanium tetrachloride and chromium oxide.

The polymerization of ethylene and co-monomers into HDPE occur in a reactor in the presence of hydrogen at a temperature of up to 110° Celsius degrees (230 degrees Fahrenheit). The resulting HDPE powder is then fed into a pelletizer to produce pellets.

Then, SOTRAFA, as a manufacturer with the latest calandering (flat die) technology, manufactures ALVATECH HDPE Geomembrane from these pellets. The ALVATECH HDPE constantly retains its outstanding features whether it is a dry or wet season.

2   GHG IDENTIFICATION AND CO2 EQUIVALENTS

The GHGs (**G**reen**h**ouse **G**as protocol) included in the calculation were the three (3) primary GHGs, namely carbon dioxide, methane, and nitrous oxide. Each of these gases has a different Global Warming Potential (GWP), which is a measure of how much the given mass of a greenhouse gas contributes to global warming or climate change.

Carbon dioxide issues a GWP of 1.0. by definition. To quantitively include the contributions of methane and nitrous oxide to the overall impact, the mass of the methane and nitrous oxide emissions are multiplied by their respective GWP factors and then added to the

mass emissions of carbon dioxide to calculate a "carbon dioxide equivalent" mass emission. For purposes of this paper, the GWPs were taken from the values listed in the USEPA regulations "Mandatory Reporting of Greenhouse Gas Emissions" (USEPA 2010). The GWPs for the GHGs considered in this analysis are:

1. Carbon Dioxide = 1.0 GWP 1 kg CO_2 eq/Kg CO_2
2. Methane = 21.0 GWP 21 Kg CO_2 eq/Kg CH_4
3. Nitrous Oxide = 310.0 GWP 310 kg CO_2 eq/kg N_2O

Using the relative GWPs of the GHGs, the mass of carbon dioxide equivalents (CO_2eq) was calculated as follows:

$$kg\ CO2 + (21.0\ x\ kg\ CH4) + (310.0\ x\ kg\ N2O) = kg\ CO2eq \qquad (1)$$
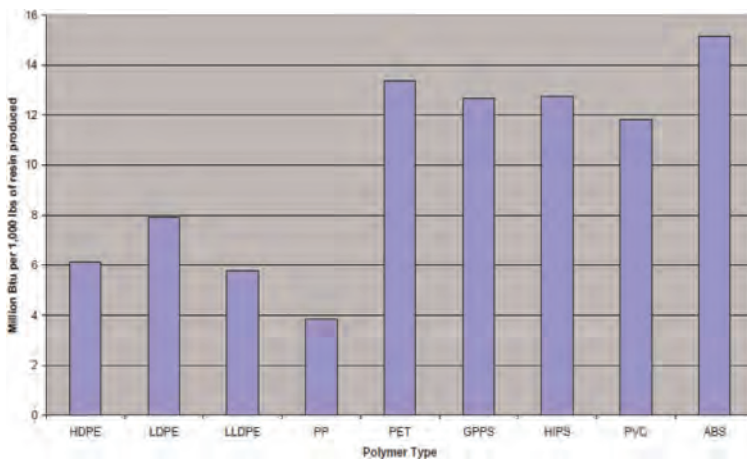
Figure 1.   Energy required for production of common packaging polymers.
6 million Btu = 156 liters fuel equivalent = 1,758 KW*hour
(Franklin Associates, a Division of ERG 2007).
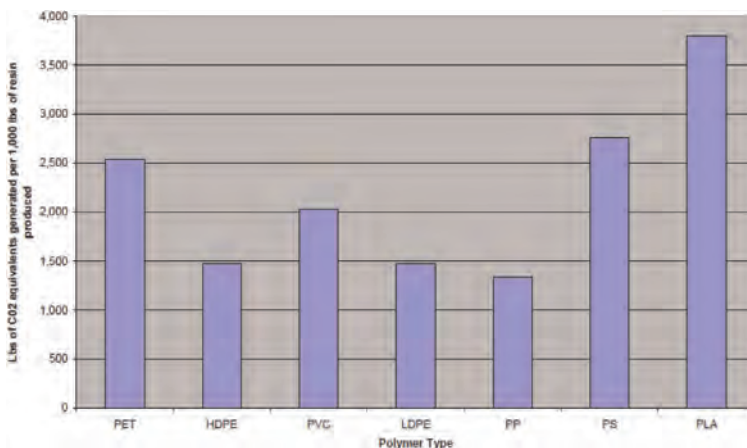
Figure 2.   Greenhouse gas emissions generated in polymer production.
(Franklin & Vink et al. 2007)

281

Assumption

The energy, water, and waste information from the extraction of the raw materials (oil or natural gas) through to production of HDPE pellets and then the manufacture of geo-membrane HDPE:

1. 1.5 mm thick HDPE geomembrane, with density 940 Kg/m3
2. HDPE carbon footprint is 1.60 Kg CO2/kg polyethylene (ICE 2008).

$$940 \ Kg/m3 \ x \ 0.0015 \ m \ x \ 10,000 \ m2/hectare \ x \ 1.15(waste \ and \ overlaps)$$

$$= 16,215 \ Kgr \ HDPE/hectare \tag{2}$$

$$E = 16,215 \ Kg \ HDPE/Ha \ x \ 1.60 \ Kg \ CO2/kg \ HDPE => 25,944 \ Kg \ CO2 \ eq/hectare \tag{3}$$

Assumed Transport: 15,600 sqm/truck, 1,000 km from manufacturing plant to project site.

1. 10.15 kg CO2/ gal diesel $\times$ gal/3.785 liters = 2.68 Kg CO2 /liter diesel
2. 0.26 g N2O/gal diesel $\times$ gal/3.785 liters $\times$ 0.31 kg CO2 eq/g N2O = 0.021 kg CO2 eq/ liter diesel
3. 1.44 g CH4/gal diesel $\times$ gal/3.785 liters $\times$ 0.021 kg CO2 eq/g CH4 = 0.008 kg CO2 eq/ liter diesel

Transport by road - transport emissions:

$$E = TMT \ x \ (EF \ CO2 + 0.021 \cdot EF \ CH4 + 0.310 \cdot EF \ N2O) \tag{4}$$

$$E = TMT \ x \ (0.972 + (0.021 \ x \ 0.0035) + (0.310 \ x \ 0.0027)) $$

$$= TM \ x \ 0.298 \ Kg \ CO2 \ eq/ton - mile \tag{5}$$

Where:

1. E = Total CO_2 equivalent emissions (kg)
2. TMT = Miles Travelled
3. EF CO_2 = CO_2 emission factor (0.297 kg CO_2/ton-mile)
4. EF CH_4 = CH_4 emission factor (0.0035 gr CH_4/ton-mile)
5. EF N_2O = N_2O emission factor (0.0027 g N_2O/ton-mile)

Converting to Metric Units:

$$0.298 \ kg \ CO2/ton - mile \ x \ 1,102 \ tons/tonne \ x \ mile/1.61 \ km = 0.204 \ kg \ CO2/tonne - km \tag{6}$$

$$E = TKT \ x \ 0.204 \ kg \ CO2 \ eq/tonne - km \tag{7}$$

Where:

1. E = Total CO_2 equivalent emissions (kg)
2. TKT = tonne – kilometers Travelled

Distance from Manufacturing Plant (Sotrafa) to Project Site (Hypothetical) = 1,000 km

– Typical Loaded truck weight: 15,455 kg/truck + 15,600 sqm $\times$ 1.5 $\times$ 0.94/truck = 37,451 kg/truck
– 0.641 truck/hectare

$$E = (1,000 \; km \; x \; 37,451 \; kg/truck \; x \; tonne/1,000 \; kg \; x \; 0.641 \; truck/hectare) \\ x \; 0.204 \; kg \;\; CO2 \; eq/tonne - km \tag{8}$$

$$E = 4,897.24 \; Kg \; CO2 \; eq/hectare \tag{9}$$

3 FEATURES OF COMPACTED CLAY LINERS AND ITS CARBON FOOTPRINT

Compacted clay liners have been historically used as barrier layers in water lagoons and waste containment facilities. Common regulatory requirements for compacted clay liners are a minimum thickness of 0.6 meters, with a maximum hydraulic conductivity of 1×10^{-11} m/sec.

Table 1. Summary of geomembrane HDPE 1.5mm carbon footprint.

Process Step	Kg CO_2 eq/Ha	Assumptions
Manufacturing Geomembrane HDPE 1,5mm	25,944	From ICE 1.6a (polyethylene) = 1.6 tonnes CO_2/tonne PE
Transport to site	4,897	1,000km from Manufacturing Plant to site
TOTAL	30,841	Kg CO_2 eq/10,000 sqm

The process:

Clay at source is excavated using standard construction equipment, which also loads the material onto tri-axle dump trucks for transport to the site. Each truck is assumed to have a capacity of 15 m^3 of loose clay. Using a compaction factor of 1.38, it is estimated that over 550 truckloads of clay would be needed to construct a 0.6-meter-thick compacted clay liner over a one-hectare area.

The distance from the source to the job site is, of course, site-specific and can vary greatly. For the purpose of this analysis, a distance of 16 km (10 miles) was assumed. Since transport from the clay source and the project site is such a large component of the overall carbon emissions, the sensitivity of the overall carbon footprint to changes in this site-specific variable is investigated later in this study.

4 CONCLUSION

Considering everything mentioned above, this study clearly demonstrates the huge advantage of using geosynthetics over traditional materials. When it comes down to waterproofing, ALVATECH HDPE Geomembrane in 1.5 mm is by far the best choice, as not only does it ensure outstanding long-term features (high chemical resistance and strong mechanical properties) but it is also a much more environmentally friendly solution.

It has 3 times less carbon footprint, even when using good quality clay transported 16 km from extraction source to site, as this can be compared with geomembrane HDPE supplied by truck and travelling 1,000 km from manufacturing plant to site.

That is why ALVATECH HDPE is being installed in a wide range of applications for cover and ground protection in demanding industries such as mining, oil, landfills, waste-water treatment and irrigation lagoons.

Table 2. Summary of compacted clay liner carbon footprint.

Step	Kg CO_2 eq/Ha	Assumptions
Excavate clay at Source	2,656	CAT 329 Excavator, Operation 40 hours/ha. Assume 24,5 litres/hr fuel consumption, based on medium work application and medium engine load factor (CAT performance handbook)
Haul Clay to Job Site	93,527	Assume site is 16km from source, and 552 truckloads (each carrying 15m^3 of clay) are needed Process to cover 1 hectare.
Construct Clay liner CAT D6 Bulldozer	2,789	Operation 40 hours/ha. Assume 25,7 litres/hr diesel fuel consumption
Construct Clay liner CAT 815 Sheepsfoot compactor	4,553	Operation 40 hours/ha. Assume 42 litres/hr diesel fuel consumption
Construct Clay liner CAT 815 Smooth drum compactor	4,553	Operation 40 hours/ha. Assume 42 litres/hr diesel fuel consumption
38,000 litres water truck	1,518	Operation 40 hours/ha. Assume 14 litres/hr diesel fuel consumption
TOTAL	109,593	Kg CO_2 eq/10.000 sqm lined area with compacted clay

Ultimately, we hope you find it interesting, and we appreciate your consideration on the limitations of our research, as we are aware that there are some recent and interesting studies that incorporate the calculation of geomembrane life cycle and water footprint, among others.

Vertical drainage of compressible soils subjected to artesian pressure under the Moroccan high-speed railway line

A.H. Mridakh
Department of Mines, Mines School of Rabat, Resources Valorization, Environment and sustainable Development Research Team (RVESD), Morocco

H. Ejjaaouani
Laboratoire Public D'Essais et D'Etudes, Casablanca, Morocco

ABSTRACT: Due to the environmental concerns, sustainable soil improvement methods are considered an essential part of the modern infrastructure development. Today's environmental sustainability policy often expects noise-free, chemical-free and low-carbon processes, while being economical. In this context, the application of prefabricated vertical drains (PVD) with preloading is considered a sustainable soil improvement Method. However, the presence of some unique hydraulic systems such as the artesian pressure and its effect on geo-structures is rarely discussed in the literature. Furthermore, the effect of the artesian pressure on the PVD's performance is one of the most important questions that needs to be addressed. For that, a numerical modeling approach is used to study the performance of a well instrumented section of the high-speed line Embankment, over a shallow artesian aquifer in Drader compressible area, Morocco. In addition, a comparison between the performance of PVD-Preloading system with and without the artesian pressure is presented.

1 INTRODUCTION

The presence of artesian pressure in Drader area under the Moroccan High-speed railway line was first noticed during the subsoil in situ investigation campaign. However, its presence is known by early geological and hydrogeological investigations (Cirac 1985; Combe 1963). A few case studies have mentioned the subject of artesian pressure induced head (Kim 2008; Kim & Do 2010) in the literature. Meanwhile, recently Mridakh *et al* (2022) investigated the dispositional characteristics of Drader under artesian pressure. Mridakh *et al* (2022) investigated the deposition and the artesian aquifers (shallow and deep) location, soil characteristics, soft soil compressibility and behavior. He also reported that artesian pressure from shallow aquifer had affected the deformation magnitude and rate.

In a similar case study in Busan marine clay, Nakdong river, south Korea; Kim and Do (2010) examined the leaching effect on the compressibility indexes. Kim *et al* (2018) studied the soft soil in a large one-dimensional column test in the laboratory with and without artesian pressure. In addition, Kim *et al* (2018) matched the predicted settlement from Busan marine clay with measured settlement from the field.

To understand the effect of artesian pressure on the PVD (Prefabricated vertical drains) performance in Drader basin, Morocco; we investigated the consolidation behavior in a well instrumented embankment section. For that, a series of artesian pressure mean values were performed based on sessional artesian pressure variation, from which we included only a selected value of an artesian pressure of 40 kPa that was drawn from the study. We compared the measured settlement and lateral movement with the predicted settlement and lateral movement with and without artesian pressure effect.

2 SITE DESCRIPTION AND MONITORING

2.1 *Site description*

Drader area is located in the N-W region of Morocco (Figure 1). It is marked by marine and continental deposits, formed during the recent Plio-quaternary epoch (Cirac 1985; Le coz 1964). Plio-quaternary soft soil deposits are mainly present in Drader area the central part between two hills (Lalla Zahra hill *et al*. 2022), in form of blackish compressible soils and loose sands (Combe 1963). From the tectonic structures and sedimentary mode, the deposition configuration has been described as a lacustrine deposition environment.
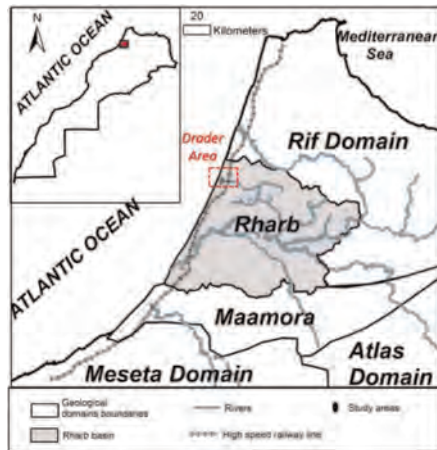
Figure 1.   Location of the high-speed railway line.

2.2 *Data-base*

The data-base collected during the geotechnical investigation campaigns used a number of boreholes, CPT's (Figure 2) to identify subsoil layers to construct a comprehensive cross-section (Figure 2, Mridakh *et al* 2022). Samples from boreholes were prepared for laboratory testing, such as oedometer tests (for obtaining modified compressibility index λ^* and the modified swelling index K^*), direct shear tests, density, water content.
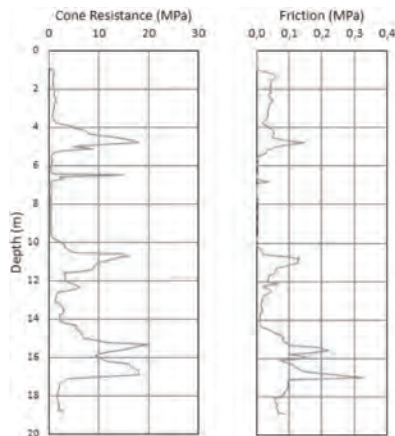
Figure 2.   Soil characteristics variation based on CPT measurement.

As shown in Figure 2, the choice of the laboratory test is based on CPT's, and borehole logs. The maximum resistance shown in Figure 2 indicate sandy layers, and low cone resistance values identify soft soil layers where oedometer tests have been performed.

2.3 Field monitoring

The cross-section in Figure 3 shows the instrumentation equipment installed under the selected embankment section, such as settlement cells (SC), inclinometers (INC), interstitial pressure sensors (IPS). The embankment construction was done during 3 phases; phase 1 for constructing 5 m embankment, phase 2 attaining 9 m height, phase 3 to reach 10 m height plus 1.5 m surcharge (30KPa). In addition, Figure 3 shows the PVD arrangement under the embankment with 25 m depth and 1 m spacing.
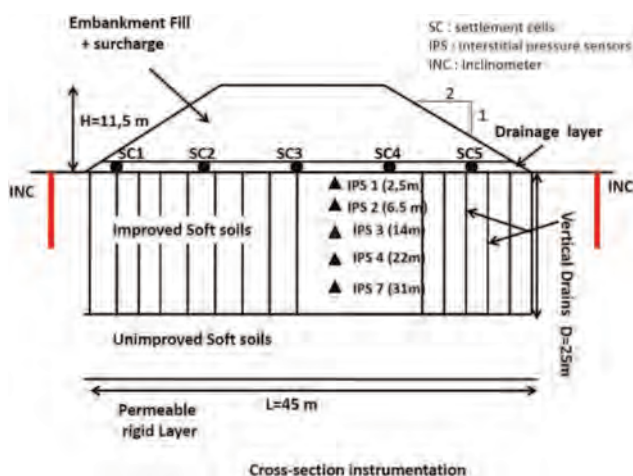
Figure 3.   Field monitoring and PVD's arrangement.

3   NUMERICAL MODELING

3.1   Constitutive models

The constitutive models are selected based on the embankment-soft soils types used in the lithological model, to precisely capture the overall soil behavior during the embankment construction. Herein, we used 3 constitutive models such as Mohr-Coulomb model for sand layers (the embankment and layer 1 see Table 2), soft soil model (SSM) for sandy silts, soft soil creep (SSCM) for clay layers.

3.2   Input parameters

The input parameters indicated in Table 1, shows the PVD configuration and parameter and Table 2 the subsoil input parameters.

Table 1.   The parameters of PVD-improved soft soil ground.

s (m)	r_s (m)	r_w (m)	d_s/d_w	k_h/k_s	D_e/d_w	q_w ($m^3/year$)
1	0.15	0.03	4,4	20	17	100

Table 2. The input parameters of SSM and SSCM in numerical analysis.

Layer	Depth (m)	K^*	λ^*	μ^*	μ^*/λ^*	k_h (m/day)	k_v (m/day)	k_{ve} (m/day)
L1	0–1	–	–	–	–	2.5E-2	2.5E-2	1.0E-1
L2	1–3.5	0.020	0.08	1.80E-3	0.022	2.6E-4	1.3E-4	1.0E-2
L3	3.5–5.5	0.006	0.03	–	–	2.0E-3	1.4E-3	6.4E-2
L4	5.5–10.5	0.016	0.07	1.9E-3	0.027	3.0E-4	4.3E-4	3.5E-4
L5	10.5–13	0.04	0.02	–	–	5.5E-4	3.7E-4	2.1E-2
L6	13–14	0.020	0.07	1.6E-3	0.023	1.2E-5	6.0E-6	1.0E-5
L7	14–17	0.006	0.02	–	–	8.3E-3	5.5E-3	1.5E-1
L8	17–18.5	0.04	0.09	1.2E-3	0.017	1.3E-4	1.9E-4	1.1E-2
L9	18.5–38	–	–	–	–	2.5E-2	2.5E-2	1.0E-1

The equivalent vertical permeability parameter (k_{ve}) values present in Table 2, represent a method developed by Chai *et al.* (2001). The k_{ve} is calculated based on the following expression:

$$k_{ve} = \left(1 + \frac{2.5l^2}{\mu D_e^2}\frac{k_h}{k_v}\right)k_v \qquad (1)$$

Where l = drainage length, D_e = diameter of unit, k_h, k_v = horizontal and vertical hydraulic conductivity respectively. The parameter μ is calculated by the following expression:

$$\mu = \ln\frac{n}{s} + \frac{k_h}{k_s}\ln(s) - \frac{3}{4} + \pi\frac{2l^2 k_h}{3q_w} \qquad (2)$$

Where $n = D_e/D_w$ (d_w = diameter of vertical drain); $s = D_s/D_w$ (d_s = diameter of smear zone), k_s = horizontal hydraulic conductivity in the smear zone; q_w = discharge capacity of the PVD . r_w and r_s are the radius of the mandrel and the smear zone respectively.

4 RESULTS AND DISCUSSIONS

To apply the artesian pressure effect in the numerical model, we assumed that the artesian pressure is acting upward on soft soil layer layer above the confined aquifer, and the artesian pressure is decreasing linearly in the upward direction until reaching the top layer. Figure 4 shows the estimated effective stress and pore pressure distribution when applying a selected AP of 40 KPa.

Figure 5 shows a comparison of vertical deformation from numerical analysis and measured results in three positions, under the embankment centerline, crest and slope (BT3, BT4 and BT5 respectively). The numerical results of the PVD improved deposits using an artesian pressure has shown a good agreement with the measured settlements under the embankment centerline, crest and slope when including the 40 KPa artesian pressure in the analysis. Whereas when excluding the artesian pressure, the model under predicts the settlement in all position under the embankment. Hence, the artesian pressure has an important effect on consolidation in regard of the PVD improved Drader area deposits. Therefore, the artesian pressure interferes with PVD effect on speeding up the consolidation by increasing the artesian pressure played an inversed role, by decreasing the undrained shear strength, which affects the performance of the PVD role during the embankment construction.
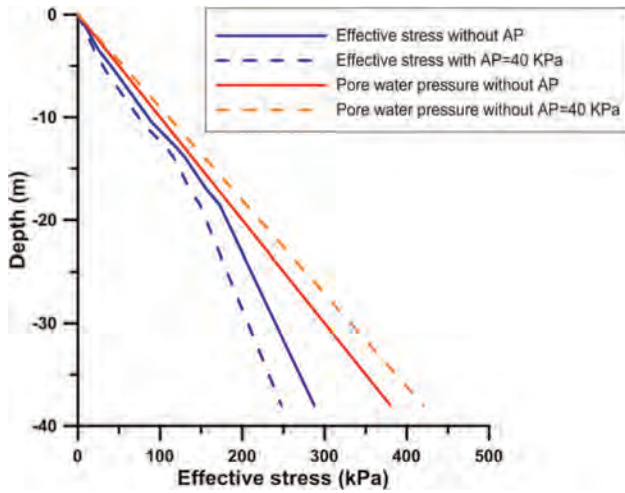
Figure 4. Distribution of mean pore pressure and resulting effective stress as a function of depth.
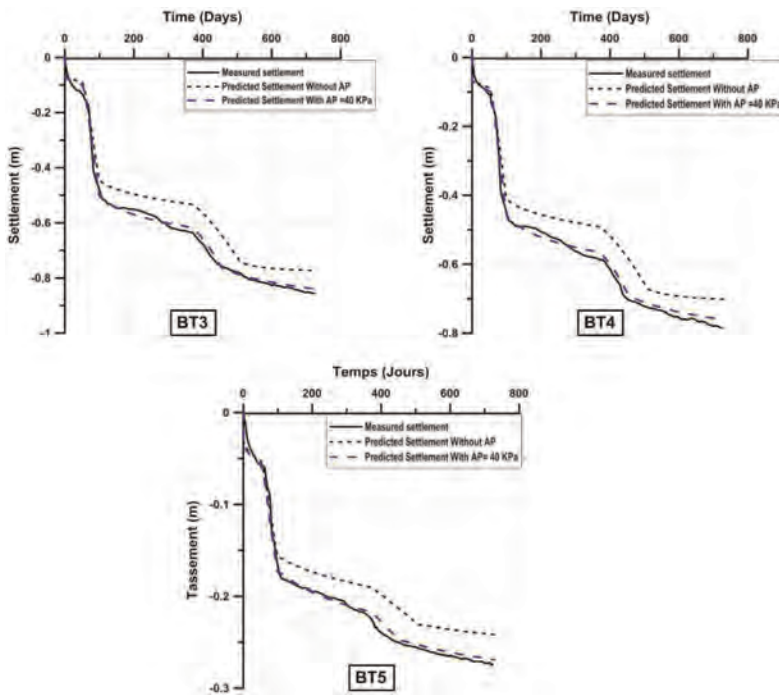
Figure 5. Measured and predicted settlements under the embankment.

Figure 6 shows a comparison between the predicted lateral movement and the measured results for the whole embankment construction period. The predicted lateral movement when including the artesian pressure of 40 KPa showed a fairly close agreement with the measured results. Hence, including the artesian pressure in the numerical model is of a big importance for predicting accurate lateral movement values under the embankment Toe.
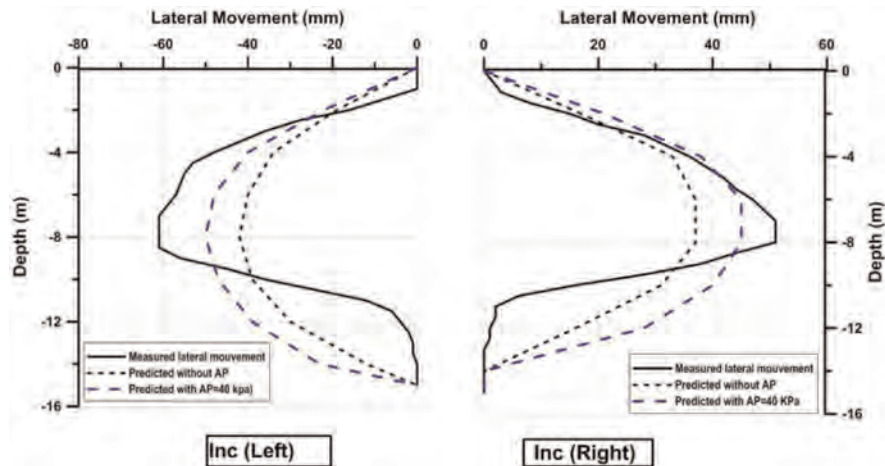
Figure 6. Measured and predicted lateral movements.

5 CONCLUSIONS

This paper describes a detailed numerical analysis that was conducted to analyze the effect of artesian pressure on the consolidation behavior of a PVD improved subsoils in Drader area under the Moroccan High-speed-railway line. The subsequent conclusion can be presented:

1. The consolidation process in the PVD improved Drader area, was affected by the artesian pressure upward flow.
2. PVD effect on consolidation was negatively affected by the artesian pressure. Meaning that, the soil supposed to gain more shear strength when using PVD's and also speeding up the consolidation process. However, the artesian pressure players an important role on decreasing the Shear strength of the subsoil, thus increasing deformations during the embankment construction.
3. When including artesian pressure in the numerical analysis, the predicted vertical and lateral deformation were in good agreement with the measured in situ deformation.

REFERENCES

Combe, M. 1963. *Etude Hydrogéologique de la Région de Lalla Mimouna*, Kénitra: Office National des Irrigation.

Chai, J.C. & Miur. N. 2001. Investigation of Factors Affecting Vertical Drain Behavior. *J. Geotech. Geoenviron. Eng.*, 125(3), 216–226.

Cirac, P 1985. Le Bassin Sud-rifain Occidental au Néogène Supérieur. Evolution de Ladynamique Sédimentaire et de la Paléogéographie au Cours D'une Phase Decomblement. Thèse de doctorat d'état. Université Bordeaux I.

Kim, Y. T. & T. H. Do. 2010. Effect of Leaching on the Compressibility of Busan clay. *Geotech. Eng. KSCE J. Civ. Eng.* 14 (3): 291–297.

Kim, YT. Nguyen. BP. Yun. DH. Effect of Artesian Pressure on Consolidation Behavior of Drainage-installed Marine Clay Deposit. *ASCE's J Mater Civ Eng* 2018 ;30(8):04018156. 1–13.

Le Coz. J 1964. Le Rharb. Fellahs et colons. Etude de Géographie Régionale. Inframar 1. Rabat p.481.

Mridakh, A.H. Ejjaaouani. H. Nguyen. B.P. Lahlou. F. H. Labien. H. 2022. Soft Soil Behavior Under High-Speed Railway Embankment Loading Using Numerical Modelling, "*Geotechnical and Geological Engineering*", vol. 40, pp. 2751–2767.

Climate change and extreme weather conditions: Applications of geosynthetics securing flood defenses and coastal protection

R.H. (Rijk) Gerritsen
Naue Prosé Geotechniek B.V., The Netherlands

A. (Adam) Bezuijen
University Ghent, Belgium
Deltares Delft, The Netherlands

C. (Kees) Dorst
Dowaco, The Netherlands

ABSTRACT: This article presents an overview of climate change research, predictions of global sea level rise, the increasing effects on coastal and riverine areas all over the world and furthermore an extensive overview of geosynthetic applications for flood defenses and coastal protection. Sea level rise, an important consequence of climate change, will lead undeniably to increasing problems concerning the safety against flooding and major challenges in design and construction of embankments. Where coastal and riverine areas are highly populated or have high economic value (business areas/industrial sites), flood protection schemes will require increasing efforts and capital investments. For climate adaption of flood defenses the application of geosynthetics can be of major importance. Building with geosynthetics is highly sustainable and enables the use of local less suitable soils. This results in reducing the use of primary granular building material, limiting transport distances and most importantly: decreasing substantial CO_2 emission. Other distinctive aspects are increasing construction speed, optimized building cost efficiency and reducing the amount of required space. Geosynthetics can be applied to ensure stability (embankments with reinforced soil and geogrids), top soil erosion control (3D structural mats, reinforced grass), coastal protection (sand-filled elements with bags, tubes or containers), controlling water level differences (drainage mats) or sealing levees (Geosynthetic Clay Liners - GCL). Implementing geosynthetics to meet one of these various functions to levees or coastal protection can give a considerable boost to the ambitions of global flood protection programs. For the big challenge to climate adaption geosynthetics will contribute to adapt safe and resilient living areas for humanity.

1 INTRODUCTION

The consequenses of global warming are evident and undeniable. More extreme weather conditions as well signs of sea level rise can be seen all around the world. The global sea levels have risen about 0.20 m during the last 100 years. However, the speed is increasing and research predicts 0.70 m sea level rise in 2100 with appr. 66% reliability [1]. Due to climate change also other hydraulic conditions are changing rapidly, with heavier rainfall conditions, more severe storm conditions, higher river discharges, increased flow velocities and wave overtopping. As billions of people are living in low laying areas near rivers and coastlines this will give major challenges to secure and improve flood defenses and flood

protection schemes worldwide. Inevitable some living areas will be abandoned. All these threats influence already political decisions on transferring societies to more sustainable living. In the coming decades, huge improvement operations have to be initiated to keep as far as possible human living areas safe and resilient to climate change.

2   CLIMATE CHANGE IMPACT

2.1   *Sea level rise*

Sea level rise is one of the consequences of global warming. This relation is almost universally accepted today. The effect and consequences for people on earth are enormous. The IPCC (Intergovernmental Panel on Climate Change) has made global assessments of possible scenarios with predictions of sea level rise between 0.3 m and 1.5 m up to 2150 depending on the climate scenario [1]. A combination of measurements and predictions of sea level rise is given in Figure 1. A probabilistic study from 2017 indicates that with accelerated land ice loss in Antarctica the projected sea level rise could even increase to 1.8 m in 2100 (median value, scenario DP16, [4]). To compare, global sea level rise over the past 100 years was about 0.2 metres. Evaluations of measured sea levels between 1993 and 2018 in Australia show an increase of about 0.08 m over the last 25 years, already showing an accelerating trend (Australian Government Meteorological Office [5]). This presents clearly the major challenges in reinforcing or realising new flood defenses.
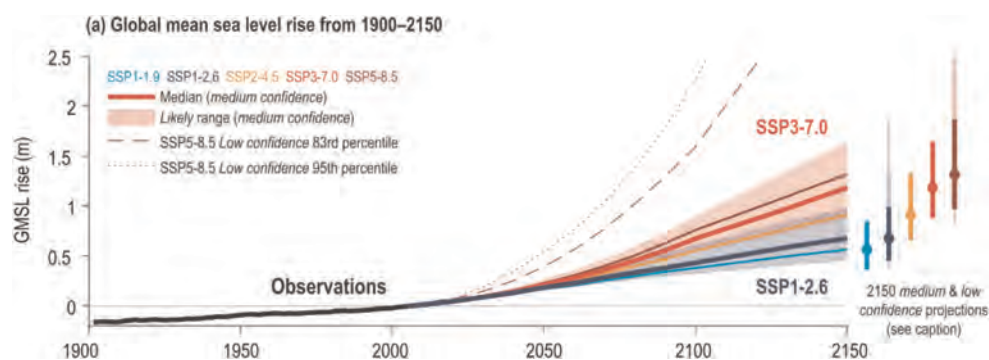
Figure 1.   Projected global mean sea level rise under different SSP scenarios in timeframe 1950-2150 given in different colours and reliability range by IPCC (Box TS.4 Sea Level, [1]).

2.2   *Impact climate change*

The predictions of sea level rise obviously contain uncertainties, but even if values reach only half the predicted values, this already will have significant consequences for the safety, liveability and sustainability of residential, commercial and agricultural areas. Effects such as dune and beach erosion along coastlines as a result of high-water conditions will become increasingly frequent and intense (see Figure 2). The costs of maintaining coastlines will increase rapidly. Furthermore, sea level rise will lead to an increase in saline seepage. This salinization of groundwater will have considerable consequences for agricultural production in coastal areas. For the Netherlands the possible consequences of accelerated sea level rise have been charted [6]. Considerably more beach nourishment is to be expected, structural measures to maintain the fresh water supply and water safety, higher and wider flood defenses, and considerably higher frequencies in closing storm surge barriers like the Eastern Scheldt barrier in The Netherlands. In addition to increased sea levels, there are also other

climate effects, like more extreme weather conditions having longer periods of intense drought or on the contrary more severe rainfall. Extreme discharges in the large European rivers such as the Meuse, Rhine, Donau and Volga will be higher and more frequent. The opposite is also possible: in 2018 large areas of Europe experienced a period of extreme drought with virtually no precipitation between the months of May and November [8]. In 2022 there was again exposure with sever droughts between April and August, resulting in extreme low river levels in large parts of Europe. Dehydration can have disastrous consequences to flood defenses. Extreme droughts affects deterioration and disappearance of peat layers and crack formation in impermeable clay layers [7]. The extreme droughts caused the major collapse of a peat levee near Wilnis NL in 2003 (Figure 3), resulting in flooding of the residential area behind and major capital damage.

Figure 2. Severe dune erosion after storm surge, Egmond aan Zee lighthouse, The Netherlands.

Figure 3. Arial picture peat levee collapse, caused by dehydration during extreme draught, 2003 Wilnis Netherlands.

2.3 *Impact damage or protection measures*

The global damage costs as a result of flooding's due to sea level rise are expected to increase enormously. A study published in 2018 [2] shows that at 0.86 cm sea level rise (RCP8.5 scenario, median value) and without additional measures for flood defenses, the worldwide estimated annual flood damage costs in the year 2100 are 11600 billion Euro/year. If measures are taken to improve coastal protection, these annual damage costs could be reduced by about a factor 10. But the amount still remains enormous, indicating that the impact of sea level rise and consequential costs of flooding will be very high for all coastal areas worldwide.

By Deltares a study is done to look on the possible effects of accelerated sea level rises [6]. One effect is beach nourishment. The current situation involves the annual implementation of 12 million m^3 of sand on or in front of the beaches in The Netherlands to protect the existing coastline coasting appr. 42–60 million Euro. With a sea level rise of 15 mm/year there is a quantity needed 4 to 5 times as much, which could already be reached in 2050. In case of acceleration the amount and costs for maintaining the shoreline will be unprecedental. Another effect is the time period of protective measures. From the 90's safety measures could be taken with a functional lifetime of appr. 65 years. In case of acceleration this would be around 2060 reduced to a period of 20 years and upto the year 2100 even reduced to 10 years cycle. This would mean that steps for climate adaption will become increasingly difficult based on planning, efforts and financial costs. This results to an infeasible task living and fighting against rising water. Drastic measures and building methods to strengthen levees and coastlines will be needed.

Table 1. Amount of sand annually needed and related costs beach nourishment in The Netherlands [6].

Sea level rising speed (mm/year)	Required volume of sand (million m3/year)	Cost of beach nourishment (million Euros)
2	8	28–40 €
3	12 (current *)	42–60 €
5	20	70–100 €
12,5	50	175–250 €
30	120	420–600 €
40	160	560–800 €
60	240	840–1200 €

* current situation 12 million m^3 annual required sand for protecting the existing NL coastline.

3 GEOSYNTHETIC APPLICATIONS IN FLOOD DEFENSES

3.1 *Functions and applications to flood defenses*

For flood defenses, geosynthetics can contribute to many functions, like erosion protection, reinforcement, separation, sealing, drainage and filtration. The potential contribution using geosynthetics in levee reinforcements is considerable. For a long time, the construction of flood defenses has been focused on traditional methods using natural materials like sand, clay and stones [9]. However, increased safety requirements, preservation of landscape and buildings, rising sea levels and other climate effects continuously increase the complexity of levee reinforcements. Alternative and innovative techniques are increasingly seen as necessary and highly desirable, given the challenges for levee reinforcements in time. Also financial budgets for flood control will be more under pressure. Figure 4 shows a cross section of a flood defence construction, with multiple geosynthetics for various functions. These multiple geosynthetic applications in flood defences reduce the use of primary soil building materials, stimulate the use of locally available soil and reduce the environmental impact by a significant lower CO_2 emission.

Figure 4. Systematic section of a high-performance flood defence construction with soil reinforcement, geosynthetic clay liner as a barrier, nonwoven geotextile for filtration and separation and erosion control products on the embankments.

To ensure flood security levels the speed and frequency of levee reinforcements will increase in the coming decades. Knowing this, it is very important that the design is made in such a way that the structure as easily as possible can be adapted during the next dyke

reinforcement. In doing so, (geosynthetic) materials should also be easily removable from the ground again or structures which are extendable.

Embedding geosynthetics on larger scale into designs can result in a better, faster and/or cheaper construction of new flood defenses, levee reinforcements or coastal protections. This could give a considerable boost to the ambitions of global flood protection programs. Large-scale application with high performance geosynthetic building material in flood defenses has major potential. This paper illustrates the potential and added value of engineered materials to flood defenses to support the use of these alternative materials by designers, contractors and authorities.

3.2 Geotextile filter constructions under stone revetments

3.2.1 Single nonwoven filter systems

Construction of hydraulic filters can traditionally be done by using rock gradings in multiple layers according to filter rules concerning soil gradings, properties and hydraulic wave conditions. Doing so, traditional filtersystems can result in construction layers of 1–2.5 meter thickness. In lot's of countries rock is not widely available, and the rock must be transported over far distances. Single non-woven filter systems can be installed on the profiled subsoil and can fully replace the bottom filter layer. This can save between 0.3–1.0 m of granular filtermaterial. Beside these savings also CO_2-emissions can be reduced with appr. 40–50% due to far lesser transport of materials. Due to the easiness of installation and cost efficiency. Geosynthetic filtersystems in rock revetments are widely used in hydraulic engineering projects. In Figure 5 an example is given of the construction of rock revetment, placed on a nonwoven filter. For the application it's very important to consider the filter rules and add adequate robustness to avoid damage by dropping stones (see paragraph 3.2.4).

Figure 5.   Filter construction using a non-woven geotextile underneath a rock top layer.

Figure 6.   Fascine mattress with geotextile filter layer and brushwood wickerwork as a filter construction underneath riprap.

3.2.2 Fascine mattress applications

A fascine mattress is a floating filter system which is prefabricated on land, towed onto the water to the construction site and submerged on location by controlled rock dumping. Initially, fascine mattresses were completely built up with natural materials, using willow branches and reed. Developments with geosynthetics made it possible to replace the reed and most of the willow branches by a geotextile since '70's. Willow branches are attached to the loops of the geotextile, making a square pattern (see Figure 6). This pattern stabilizes the fascine mattress for moving the fascine mattress into position. As towing and positioning by cranes can initiate large forces to the geotextile attention should be paid to the robustness of the materials used.

3.2.3 Sand mattress applications

A sand mattress is a geocomposite, existing of 2 layers of non-woven with a sand fill in between. By needle punching a firm heavy product is obtained for underwater installation. A sandmattress is delivered on rolls and can directly be installed from the slopes of banks into the water. Installation can be done by rolling out using a crane with a long reach, equipped with a hydraulic spreader bar (see Figure 7).

Figure 7.   Installation of geocomposite sandmattress as filter layer below a stone revetment.

3.2.4 Rock dumping impact on geotextiles

Rock dumping on the geotextiles can cause serious damage. Various innovation and research programs are running to understand failure mechanisms of filter systems and improve design and application rules. Example is a CROW working group for geotextiles in rock revetments, active since 2019. This working group initiates field- and laboratory tests to understand the behaviour of geosynthetics with the energy impact by dropping stones. Multiple fieldtrial drop tests are done to analize the failure mechanism and dependency of the subsoil (clean loose sand, stiffer layering or intermixed with gravels). This is illustrated in Figures 8 and 9. Before the performance and failure mechanisms are also tested with laboratory research in Ghent [13,19].

Figure 8.   Fieldtrial drop tests with selected stone classes on nonwoven geotextile and analysis of failure mechanism and test conditions subsoil.

Figure 9.   Fieldtrial drop tests with selected stone classes on nonwoven geotextile and analysis of failure mechanism and test conditions subsoil.

Figure 10.   Drop tests with standardized stone shapes and weight on composite geotextiles (woven/non-woven) at Ghent University.

These imply large scale droptests in laboratory conditions to single products and geocomposites (woven/nonwoven) with standardized stone shapes and weights (Figure 10). All data will be analyzed and embedded to an update of the NL design guide on geotextile filtersystems in rock revetments. See also Bezuijen [22].

3.3   Water barriers with Geosynthetic Clay Liners (GCL)

Traditionally, natural clay has been used to create artificial low permeable layers in flood defenses, both for the construction of the entire levee, sealing embankments or sealing the foreshore. In order to obtain adequate water retardation and erosion resistance, this clay must meet high requirements. Erosion-resistant clay is becoming increasingly scarce near project sites and often has to be transported from far away regions. This results in increasing construction costs and environmental impact. As an alternative to a thick layer of natural clay, it's possible to implement a Geosynthetic Clay Liner (GCL) to river levees. These mats with a thickness of approximately 1 cm, consist of multilayer high-quality geotextiles with bentonite powder in between. GCL's can be used to seal the foreland as an anti piping measure, or the levee itself. In addition to cost savings, the application of GCLs offers other major advantages to the use of clay: sustainability (energy requirement and CO_2 emissions for transport), construction speed (less deep excavation, no dewatering required), more use of near-site soil and less soil investigation required. Due to the swelling capacity of the bentonite, the mat is self-healing to a certain extent. Leakage through small holes (in the order of centimeters) for instance caused by mice or root growth will be stopped by swelling of the bentonite.

In Germany multiple projects with GCL's on flood defenses have been executed in the last decades, like along the Oder levee. The introduction of GCL's to in The Netherlands is done in 2 pilot projects initiated by Water Authority Limburg NL, being the levee reinforcement in Beesel and Neer. In Beesel the GCL is applied on the crest and slopes of the levee to replace a natural clay layer (see Figure 11). At the project in Neer the seepage length is extended by using GCL's to prevent piping (Figure 12).

Figure 11.   Installation Geosynthetic Clay Liner (GCL) on a levee reinforcement to replace a 1 meter thick clay layer (Beesel Netherlands).

Figure 12.   Horizontal installed Geosynthetic Clay Liner (GCL) in the levee foreland to enlarge the seepage length from the flood defense base.

3.4   Geosynthetic Sand Containers (GSC's) for coastal protection and anti-scour

One of the oldest applications of geotextiles in flood defenses is large geobag elements filled with sand. In 1957 these were already used to seal the Pluimpot, a small estuary near Tholen, The Netherlands. In the following years geotextile elements were further developed. Small elements like geobags can be filled on site and installed on beaches to stabilize the coastline

(Figure 13). Sand filled geotextile bags can also be used in deeper water to prevent scouring or to fill-up (big) scourholes. Scouring can occur in riverbeds by floods with extreme discharges, in harbours or by hydraulic turbulence to structures like dams and outlet structures. An example is the North Sea flood barrage in the river Eider (Germany), were major scouring was detected. After extensive research on the remedial measure to be taken, it was decided to fill the scourhole with 48.000 sandfilled geotextile bags to stabilize the underwater slope.

Geotextile elements are regularly used as breakwaters, dune foot defense structures, erosion protection or water retaining structures. These applications are used globally. The use of geotextile elements in coastal or flood defense structures could substantially reduce the risks and effects of beach and dune erosion. This may reduce the number of beach nourishments, cost and maintenance frequency of beaches and dunes after severe storms. Much literature is available on the application of geotextile sandfilled elements. A good overview of possibilities, research and calculations is given in several publications [16, 17 and 18].

In the area of Lubmin on the Baltic Sea, the existing coastline with sand dunes has been severely impacted by multiple storm surges. A solution is being implemented with a hidden underground protection using Geotextile Sand Containers (GSC). To reinforce approximately 2 kilometers of coastline, in total 34,000 sandfilled elements were installed. The elements weigh approximately 1.4 tonnes each and are used to construct the underground coastal defence structure below the beach surface. The bags are laid in two rows, inclined to the long side and stacked in an offset manner (see Figure 14). Being covered with sand, the structure is no disturbing factor in the landscape. Also important is that after implementating the hidden protection measure the beach area has no restrictions for tourism and beachlife.
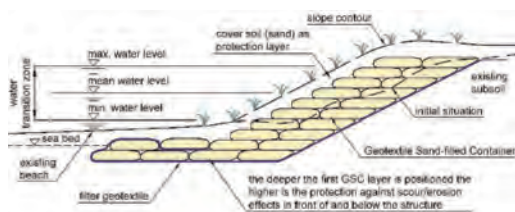
Figure 13. Schematic cross-section dune protection with Geotextile Sand Containers (GSC) underground structure, covering with beach sand and planting with helm grass.

Figure 14. Installation of Geotextile Sand Containers as coastal protection measure in the dune core of the sandy beach, Ludmin Germany.

3.5 *Erosion protection with 3D structure mats*

As a result of climate change there are higher waterlevels, currents, waves or heavy rain to be expected. Based on this more robust and intelligent erosion protection systems of flood defences will become increasingly important. Water levels will rise and the question is whether we can continue to build fully flood-resistant structures, or whether a certain degree of water spillover should be accepted. In the case of overflow levee structures, robust erosion protection is key.

Embankments can be protected against erosion in a natural way by a good (grass) vegetation with a clay under layer. This requires deep and good grass rooting of which the development takes in general at least two growing seasons. In The Netherlands it is mostly accepted that the turf has insufficient strength in the first months or even years, relying on

the erosion resistance of the underlying clay layer. Also additional measures are taken at floods by installing so called cramming mats (geotextiles) over young turf to protect these from erosion. In other countries the requirements for initial strength of vegetated slopes at embankments are often higher. For example anchored three-dimensional geosynthetic structure mats are often used in America, but this application is also increasing to the European continent.

These 3D structure mats can be used to reinforce the top soil layer on embankments (see Figure 15). This mat provides protection of the bare soil or early vegetation, thus providing extra resistance to erosion. This prevents grass seed or young vegetation from being washed away, thus ensuring homogeneous germination. The effect of this is the development of a better-quality grass vegetation. In addition, the structure mat provides a permanent reinforcement of the top layer in the root zone. This may be necessary at locations where higher loads are expected, such as wave action, overtopping water and currents. In addition, the mat provides reinforcement in the case of a poor subsoil (grass on sand conditions) or where local damage can occur (animal burrows, sheep pathways, bicycle tracks, along stairs, structures, side's road pavements on the crest, etc.). During wave overtopping tests carried out on vegetated embankment slopes, it was observed that accelerated failure can occur in the event of local damage to the grass vegetation [20]. Extensive tests [21] were carried out to determine the erosion resistance including HPTRM (high performance turf reinforcement mats).

Figure 15. Installation of a reinforced High Performance Turf Reinforcement Mat (HPTRM) for slope protection.

In case of desirable rapid vegetation development, the choice can be made not to use grass seeds, but to apply hydro-mulching. In this process, a mixture of grass seed, nutrients and organic fibers is sprayed hydraulically into a 3D structure mat. For hydro-seeding or -mulching, attention must be paid to the quality of the seeds, nutrients and structure mat as all components have a major influence on obtaining a well-covered slope. Related to climate change seeds are to be chosen that are suitable for the changing climate conditions (more intense periodes wet and dry conditions). Research is also done to use different herb-mixtures, which stimulate also bio-diversity to levees.

Special attention should be paid to all types of transitions on slopes as often the loads are higher and the strength is less. In The Netherlands field tests on reinforced transitions are planned.

3.6 *Soil reinforcement for stability and steep slopes*

Raising embankments on soft soils can cause stability problems. A regularly applied solution is the installation of high strength soil reinforcement below the embankment. High strength

reinforcement can be in the range of 300–1500 kN/m and can exist of woven-fabric, knitting or high-strength geogrids.

At the Oder levee along the German-Polish border a levee stretch with a length of 3 kilometres was reconstructed to withstand more extreme flood conditions. Soil investigations below the dyke stretch revealed relatively deep soft layers of peat, organic silt and clay. In order to ensure sufficient stability of the new dyke, a high strength geogrid of 1000 kN/m was installed as basal reinforcement (Figure 16).

Figure 16.   Installation of high strength geogrids as basal reinforcement below the flood defence at the Oder dike, Germany.

Another application of geogrids to flood defenses is the realisation of steep slopes to reduce area use. Next to many flood defenses there are existing structures, like houses. In case of levee crest raising the footbase of the flood defence would be enlarged also. In case of space shortage, vertical constructive elements are designed to flood defenses, like sheet pile or concrete walls. When hard constructions like sheet piling are used in a levee, calculations show that these are heavily loaded, because this is a relatively stiff (settlement free) structure within the more flexible soil body.

As alternative steep slopes or even vertical retaining walls to flood defenses can be realized using geogrid reinforced soil structures. A description of implementation of geogrid reinforcement to flood defences is described in [11]. A comprehensive overview of possibilities, research and calculations is included in a publication on retaining structures of reinforced soil [15]. Retaining walls using geosynthetic reinforcement are generally flexible and are able to deform together with subsoil settlements. This makes geosynthetics ultimate suitable for levee reinforcements to soft soil areas. By using Finite Element Models (FEM) the effect between forces, deformation and interaction between soil and geosynthetics can be determined in detail. Due to the interaction, geosynthetics constructions behave as a block stabilization with considerable redistribution capacity. Another consideration is from research in Japan it is observed that reinforced soil structures behave very stable during earthquakes and big hydraulic impacts like tsunami's [14].

3.7   *Geosynthetic 3D composite drainage systems at levee structures*

As a result of higher water levels outside the levee and subsidence in the polders, the hydraulic loads on flood defenses will increase. The increase of the hydraulic head will have a negative effect on the stability of flood defenses. The hydraulic pressures can be positively influenced by using geosynthetic drainage systems, described in a publication of drainage techniques to levee structures [10]. Figure 17 shows the installation on a slope with a

geocomposite drainage system and a Geosynthetic Clay Liner (GCL) on top. Levee drainage can be useful to avoid failure mechanisms such as macro and micro stability, but also piping. Examples of drainage are vertical wells, gravel boxes, horizontal drains or geosynthetic drainage mats. These drainage mats consist of geosynthetic 3D structure composites, which must be pressure-stable under the given conditions. These drainage mats can be installed vertically (for example as toe drainage), horizontally (partly under the embankment core or berm) or on the slope. This is illustrated in Figure 18.

Figure 17. Geosynthetic drainage composite mat (white color) with a Geosynthetic Clay Liner (GCL, light brown) on top as sealing system.
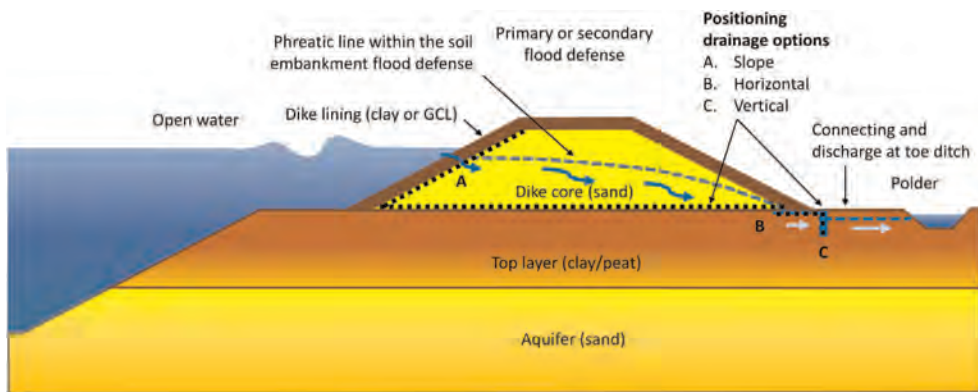
Figure 18. Schematic cross-section with freatic head in a river levee and options to decrease that phreatic head applying geosynthetic drainage systems, at slope (A), horizontal (B) and vertical (C).

4 CONCLUSIONS

Climate change will have significant effects on flood defenses globally. Aspects such as sea level rise and extreme weather conditions will have major consequences for the safety, quality of life and sustainability of residential, industrial and agricultural areas. In the coming decades huge and costly operations to flood defenses have to be initiated to keep local areas, larger regions or full countries safe and sustainable.

This article discusses the problems and effects of climate change and the potential positive role that geosynthetics can play in new or existing coastal and riverine flood defense systems: more sustainable, faster and/or cheaper construction. There are also major challenges in making (future-proof) designs with geosynthetics in embankments. Levees must be adaptable for subsequent levee reinforcements, in which case applied geosynthetics in the levee should not be an obstacle. When adapting future flood defences, geosynthetics should then be easily removable, re-usable or recyclable. In some application areas geosynthetics in flood defenses are still in an initial stage of development. Development of integrated concepts with geosynthetics offers a major potential to flood protection. Implementing geosynthetics to levees or coastal protection can give a considerable boost to global flood protection programs. For the big challenge to climate adaption geosynthetics can contribute to adapt safe and resilient living areas for humanity.

Table 2.   Reference and copyright to figures.

Reference and copyright	Figure number
IPCC / Deltares	1
Rijkswaterstaat, beeldbank	2
Rene Oudehoorn	3
Adam Bezuijen, Gent University / Deltares	10
Kees Dorst, Dowaco	6
Rijk Gerritsen, Naue Prosé Geotechniek B.V.	8, 9, 18
Naue GmbH & Co. KG	4, 5, 7, 11 t/m 17

REFERENCES

[1]   Bezuijen A, (2023) *Field Tests on the Impact of Stones on Geotextile Compared with Theory*, 12th ICG Roma.
[2]   Bezuijen A, Izadi E, 2018, Damage of Geotextile Due to Impact of Stones, *11th International Conference on Geosynthetic*.
[3]   Bezuijen, A., Vastenburg, E.W. November 14, 2012, *Geosystems: Design Rules And Applications*, CRC Press.
[4]   CUR/CROW, 2018, *Kerende Constructies van Gewapende Grond*, CUR-rapport 198, CROW.
[5]   De Vries, H, Katsman, C, Drijfhout S, November 2014, *Constructing Scenarios of Regional Sea Level Change Using Global Temperature Pathways*, Royal Netherlands Meteorological Institue (KNMI), De Bilt.
[6]   Dijkwerkers, September 2018, *Handboek Dijkenbouw*, Uitvoering Versterking en Nieuwbouw, Hoogwaterbeschermingsprogramma (HWBP), Utrecht.
[7]   Haasnoot M. e.a., September 2018, *Mogelijke Gevolgen Van Versnelde Zeespiegelstijging Voor Het Deltaprogramma, Een Verkenning*, Deltares report 11202230-005-0002, Delft.
[8]   Infram, 24 juni 2011, *Overslagproeven en Oploopproef Tholen*, Projectbureau Zeeweringen, Factual Report, referentie 10i092.
[9]   IPCC, 27th February 2022, *Intergovernmental Panel on Climate Change, Technical Summary*, IPCC_AR6_WGII_Technical_Summary.pdf.

[10] Izadi E, Decraene T, De Strijcker S, Bezuijen A, Vinckier D, 2018, A Laboratory Investigation on the Impact Resistance of a Woven Geotextile *Geotextiles and Geomembranes* 46 (1), 91–100.

[11] Jevrejeva, S, Jackson, Grindsted, A, e.a. June 2018, Flood Damage Costs Under the Sea Level Rise with Warming of 1.5°C and 2°C, *Environmental Research Letters*.

[12] Koninklijk Nederlands Meteorologisch Instituut (KNMI), Ministry from Infrastructure and Water Authorities, 31 August 2018, KNMI 2018 warmste-zomer-in-drie-eeuwen.

[13] Kuwano, J., Mohri, Y. *et al.*, 2018, Geosynthetics for Natural Disaster Prevention and Mitigation – Japan's Challenge, Keynote Lecture, *11th International Conference on Geosynthetics*, Seoul.

[14] Le Bars D, Drijfhout S, De Vries, H. April 2017, A High-End Sea Level Rise Probabilistic Projection Including Rapid Antarctic Ice Sheet Mass Loss, *Environmental Research Letters*, KNMI, De Bilt.

[15] Onderzoekscommissie Wilnis, Wat Wilnis ons leert, December 2004, *Over Technische, Bestuurlijke En Juridische Aspecten Van Dijkverschuiving Bij Langdurige Droogte*.

[16] Pilarczyk, K.W. 2000, *Geosynthetics and Geosystems in Hydraulic and Coastal Engineering*, A.A. Balkema, Rotterdam.

[17] POV Macrostabiliteit en de POV-Piping, May 2018, *POV Drainagetechnieken, Hoogwater bescherming programma* (HWBP), Utrecht.

[18] POV Macrostabiliteit, September 2018, POVM Grondverbeteringen, *Hoogwater Beschermingsprogramma* (HWBP), Utrecht.

[19] SBR CUR net, March 2017, *Ontwerprichtlijn Geotextielen Onder Steenbekleding*, SBR CUR net, Delft.

[20] State of the climate 2018, CSIRO, Australian Government bureau of Meteorology.

[21] US Army Corps of Engineers, October, 2013, Greater New Orleans Hurricane and Storm Damage Risk Reduction System, Levee Armoring Research Documentation Report.

[22] Young C Kim, Oumeraci, e.a. February 2018, *Handbook of Coastal En Ocean Engineering*, in 2 volumes expanded edition.

Integrating engineered and nature-based solutions for riverbank stabilization

D. Loizeaux, J. Hill, M. Patton & J. Hoilman
Solmax, Chattanooga, Tennessee, USA

ABSTRACT: Adding resilience to flood defense structures is critical to mitigating the impacts of climate change and natural disasters. Integrating engineered erosion control systems with nature-based infrastructure provides an effective solution for hazard mitigation that yields environmental and economic benefits. This presentation will highlight how Engineered Earth Armoring Systems can be combined with vegetation to provide resilient and long-term flood mitigation. It will also highlight fieldwork from a bank stabilization project on the Des Moines River. Palo Alto is the 13th largest agricultural producing county in Iowa, with an estimated $468,000,000 in crops and livestock reported in 2017. The West Fork of the Des Moines River cuts diagonally through the County, providing drainage for approximately 4,660 square kilometers of farmland. During rain events, the river would often flood this area, causing erosion on an upstream bend. The flooding impacted nearby roadways and a historic bridge, resulting in a nearly 40-kilometer detour for travelers. Between 2006 and 2019, flooding events caused severe bank erosion to occur on the river bend. Along roughly 215 linear meters of riverbank, up to 65 m of horizontal erosion occurred, losing over 1.25 hectares to erosion within this timeframe. If an erosion control solution was not implemented, then the historic bridge and surrounding roadway would continue to be at risk. The Sioux City Natural Resource Conservation Service (NRCS) and Palo Alto County originally considered the use of rock riprap or gabion hard armoring to control the erosion, but ultimately looked for a more cost-effective, nature-based solution. A combination of the Engineered Earth Armoring Systems was used to stabilize the bank and protect against scour, erosion, and surficial slope instability while promoting vegetation.

1 INTRODUCTION

Palo Alto is the 13th largest agricultural producing county in Iowa, with an estimated $468,000,000 in crops and livestock reported in 2017. On average, each farm in Palo Alto County covers about 175 hectares and each acre is essential for the farm's livelihood. Simply put, land is important and losing it to erosion is not an option.

The West Fork of the Des Moines River cuts diagonally through Palo Alto County, providing drainage for approximately 4,660 square kilometers of farmland. 485th Avenue and 425th Street intersect along the West Fork of the Des Moines River and are connected by the Kirby-Flynn Bridge, a historic pin-connected Pratt high-truss bridge dating back to 1881. During rain events, the Des Moines River would often flood in this area, causing erosion on an upstream bend and flood waters to inundate the bridge, resulting in a nearly 40-kilometer detour for travelers.

Between 2006 and 2019, flooding events caused severe bank erosion to occur on the river bend just upstream of the Kirby-Flynn Bridge. On this roughly 215 linear meters of riverbank, up to 65 m of horizontal erosion occurred, losing over 1.25 hectares to erosion

within this timeframe (Figure 1). If an erosion control solution was not implemented, then the historic bridge and surrounding roadway would continue to be at risk. The NRCS and Palo Alto County originally considered the use of rock riprap or gabion hard armoring to control the erosion, but ultimately looked for a more cost effective, nature-based solution.

Figure 1.   Erosion along West Fork of Des Moines River in 2020 upstream of the Kirby-Flynn bridge.

2   ENVIRONMENTAL CONSIDERATIONS

The West Fork of the Des Moines River flows generally southeast across western Iowa converging with the East Fork at the Frank A. Gotch Park south of Humboldt, IA. The project site is located approximately at river mile 44.5 of the West Fork of the Des Moines River which is environmentally regulated by the by the Iowa Department of Natural Resources (IA DNR). The IA DNR is responsible for managing fish and wildlife programs, ensuring the health of Iowa's forests and prairies, and providing recreational opportunities in Iowa's state parks. Additionally, the DNR carries out state and federal laws that protect air, land, and water through technical assistance, permitting and compliance programs.

To ensure compliance, the IA DNR Water Quality Monitoring and Assessment Section assess streams, creeks, waterbodies, etc. to determine if they are meeting state and Federal water quality standards. The IA DNR does not list the West Fork in the vicinity of the project location as a 303(d) impaired stream, meaning that its pollution does not exceed the standards for one or more water quality criteria.

A great variety of wildlife are common along the West Fork, including herons, shorebirds, songbirds, owls, hawks, eagles, beavers, and turtles. Per IA DNR, several threatened and endangered species including birds, fish, insects, plants and reptiles are located in Palo Alto County. Wildlife are particularly abundant as the river flows through several wildlife management areas including the Brushy Bayou Wildlife Area located approximately 2.4 kilometers upstream of the project site. Additional recreation areas including the West Fork Wetlands are located downstream of the project area. The West Fork Wetlands provide an excellent habitat for ducks and geese, wild turkeys, many fur bearing animals as well as non-game species.

Using satellite photos of the project site from 2006 to 2019, the right descending bank has eroded as much as 65 linear meters horizontally into the adjacent agricultural fields (Figure 2). From these same photos, it was determined that approximately 1.25 hectares of land was lost to erosion over the 13 years. Using an average vertical height of 1.8 m over this area yields nearly 2,300 CM of soil loss. This volume would equate to almost 8 hectares of stream bed covered in 30 cm of soil.
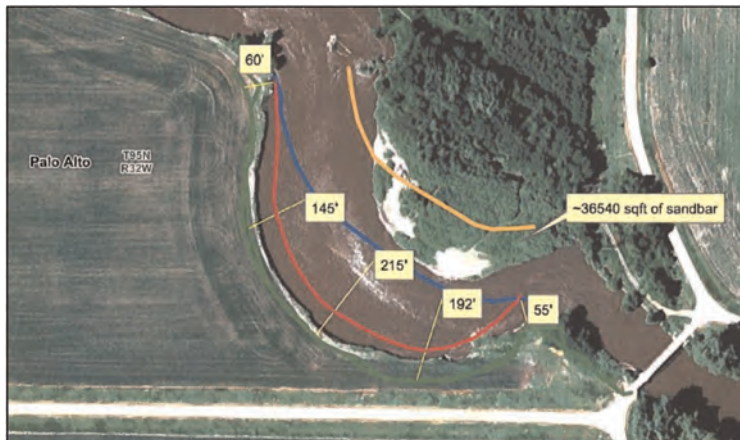
Figure 2.   Des Moines Riverbank Erosion: Blue 2006, red 2016, green 2019.

3 HYDRAULIC DESIGN

From 2006 to 2019, 1.25 hectares of streambank was lost to erosion. The design goal of the project was to restore the channel back to its 2006 alignment. The NRCS provided design criteria that protection would be needed for whichever was greater between ½ of the height of the bank or the 5-year storm event. In 1984, the United States Army Corp of Engineers (USACE) performed a study on the West Fork of the Des Moines River. In that study, storm flows were developed for the 2-year, 5-year, and 10-year storm events. The results from that study can be found below in Table 1.

Table 1.   Storm events for design.

Storm Event	Flow Rate (m^3/s)	Flow Depth (m)
2-year	56.9	2.03
5-year	131.4	3.29
10-year	207.6	4.19

The bank was measured to have a maximum height of 4.9 m. Therefore, for this design, the 5-year storm event depth of 3.3 m controlled the portion of the slope that would require protection. In order to protect the riverbank, Palo Alto County chose to use a combination of the SCOURLOK® and ARMORMAX® Engineered Earth Armoring Solutions.

SCOURLOK is a solution designed to resist extreme hydraulic and non-hydraulic stresses and provide riverbank stabilization that can be vegetated. SCOURLOK is constructed of PYRAMAT® 75 High Performance Turf Reinforcement Mat (HPTRM) and interlocking, zinc coated carbon steel baskets lined with GEOTEX® nonwoven geotextile. The vegetative pockets and tops of SCOURLOK are designed to be filled with organic growth media for vegetation. SCOURLOK provides permanent erosion protection from the time of initial construction. The 1.2 m high by 0.9 m wide SCOURLOK units can be stacked and offset for various configurations and can be filled with on-site soil or granular fill, depending on the suitability of the soil. SCOURLOK has superior ultraviolet (UV) resistance, strength, and durability withstanding the most demanding environments.

ARMORMAX 75 is an Engineered Earth Armoring System used for erosion control and surficial slope stability applications. It is composed of two components: PYRAMAT 75

306

HPTRM and Engineered Earth Anchors. The PYRAMAT 75 component provides resistance to erosion and distributes the load amongst the anchors. The anchor component is specifically designed and tested for compatibility and performance with HPTRM and works to permanently secure the PYRAMAT 75 HPTRM as well as increase erosion resistance.

Two SCOURLOK units were placed along the 2006 alignment to provide enough height to provide protection for the 2-year storm events, which occur more frequently. A 12 m wide floodplain bench, protected by ARMORMAX 75, extended behind the first section of SCOURLOK to provide increased erosion resistance above the 2-year events. An additional SCOURLOK unit was placed at the edge of the 12 m floodplain bench to provide protection for the 5-year storm events. The ARMORMAX system utilized above the second tier of SCOURLOK helped provide increased erosion resistance for the 5-year and 10-year events. This riverbank SCOURLOK and ARMORMAX engineered earth armoring configuration is depicted in Figure 3.
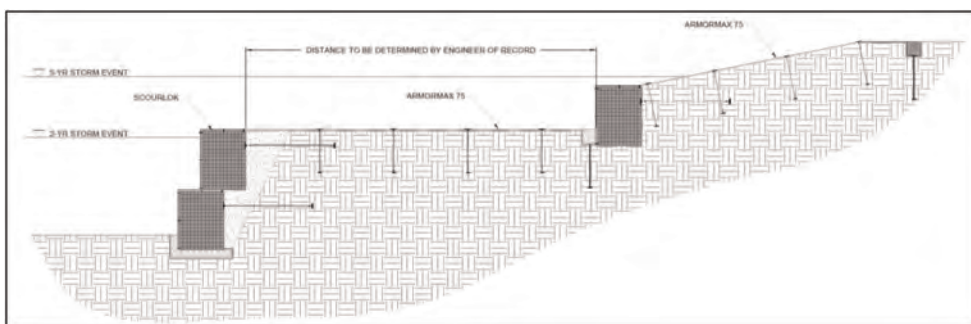
Figure 3.   SCOURLOK / ARMORMAX Riverbank cross-section configuration.

4   GEOTECHNICAL EVALUATION

From a geotechnical perspective, the stability of a slope or wall is a complex interaction of soil layers and the pore water pressure within those layers. Understanding the soil layers within a given project site, and the overall subsurface characteristics of the area, will allow a licensed geotechnical engineer to be less conservative with the design and get a more accurate factor of safety (FS). The calculated FS is a ratio of resisting forces (such as the friction angle of the soil) to driving forces (such as weight/gravity). A FS value less than 1.0 means the slope or wall is unstable and failure is imminent, while a FS value greater than 1.0 means the wall is stable and some outside force will have to interact with the area to cause a failure. Knowing what types of soil comprise a given slope or wall is imperative to calculating an accurate FS.

When evaluating the proposed bank stabilization solution, the soil information available consisted of an NRCS soil map that depicted the soil type to be Wabash silty clay for the project area. This was incorporated into the design as a low strength clay, using an angle of internal friction (ϕ) of 23 degrees and a cohesion (c) of 0 kPa for conservative purposes. The clay on site was classified as an MH/CH which is a high-plasticity clay or silt. This highly plastic material is not self-consolidating and hard to compact, so it was deemed unsuitable for infill within the SCOURLOK units. A suitable fill material would need to be imported for the infill of the units.

Since this project involved the design of SCOURLOK and ARMORMAX, it was best to start the design of the wall or earth retaining structure with SCOURLOK first. The design of an earth retaining structure incorporates three separate analyses. The first two analyses are base sliding and overturning, which follow Coulomb's theory for lateral earth pressure. The

weight of the SCOURLOK wall needs to resist the driving force generated by the weight of the retained soil and any external forces. The third analysis is for bearing capacity to evaluate the foundation soil when the SCOURLOK wall is placed on top of it. Typically, the FS targets for base sliding, overturning, and bearing capacity are 1.5, 2.0, and 2.0 respectively.

For the bank stabilization of the Des Moines River in Palo Alto, two separate SCOURLOK configurations were considered as previously depicted in Figure 3 for the different size storm events. Each configuration considered the Wabash silty clay as the foundation and retained soil, and a more self-consolidating, free draining soil as the infill in the SCOURLOK units. The first was a 1-1 configuration used for the 2-year event, incorporating 1.8 m long Engineered Earth Anchors in each cell and a flat slope above (Figure 4). The factors of safety for this configuration were as follows: 1.57 for base sliding, 2.89 for overturning and 2.19 for bearing capacity. The second was a 1-unit configuration for the 5-year event, incorporating 1.8 m long B2 anchors in each cell and a 5H:1V slope above (Figure 5). The factors of safety for this configuration were as follows: 1.85 for base sliding, 4.14 for overturning and 2.78 for bearing capacity. Both configurations met all three target factors of safety.
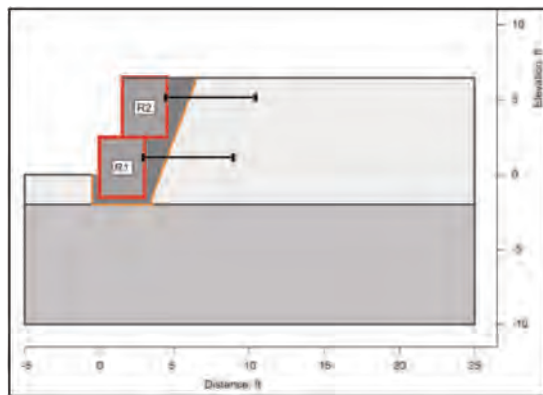
Figure 4.   1-1 Anchored SCOURLOK configuration.
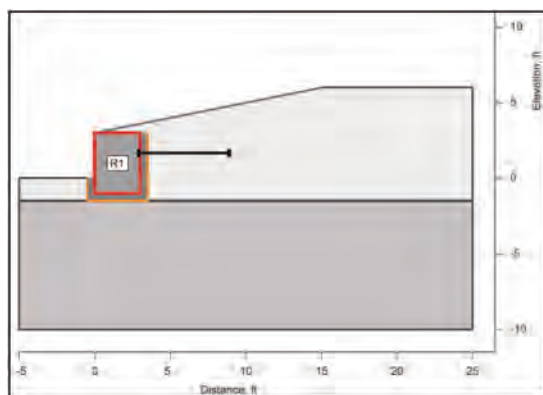
Figure 5.   1-Unit anchored SCOURLOK configuration.

When arriving on site for the installation, the Wabash silty clay was found to only be present on the surface of the soil. Most of the soil on site consisted of free draining sand.

While this caused some unexpected challenges during the installation process, the increase in the retained soils overall internal angle of friction added to the FS for the gravity wall calculations. The highly plastic clay described in the NRCS soil map was expected to aid more in water retention during construction than the sand that was on found on site. Instead of water coming into the project area from one location, the river, water was coming into the area from all directions. While the installation conditions were different than originally assumed, SCOURLOK was able to be installed due to its flexibility in application (Figure 6). While the installation had its challenges, the SCOURLOK system was designed to meet these challenges as it can be used in a wide range of environments and situations.

Figure 6.   Installation conditions for SCOURLOK.

5   SOLUTION AND INSTALLATION

Installation of the bank stabilization solution began in November 2020, beginning with the lower 1-1 section of SCOURLOK. Once the lower section was completed, the upper 1-unit section of SCOURLOK was then installed, followed by the ARMORMAX system between the SCOURLOK sections and along the above sloped area (Figure 7). The contractor was able to use material from a sand bar to fill the SCOURLOK units, providing an efficient installation and minimizing the import of any fill or rock. "Propex provided a high level of technical direction to ensure a successful project even with a contractor who was unfamiliar with the SCOURLOK product. We feel the project will stop the severe erosion that had been occurring on the riverbank and will save the bridge that would be in danger of washing out otherwise," said Rick Hopper, Director of Engineering at Jacobson-Westergard & Associates. The

Figure 7.   Installation of SCOURLOK and ARMORMAX, January 2021.

installation was completed by February 2021 and vegetation had begun to establish by the summer of 2021.

The SCOURLOK and ARMORMAX Engineered Earth Armoring Solutions have been able to provide a vegetated, nature-based solution for severe riverbank erosion. The systems have been engaged several times during flow events since installation and are performing as designed. Their durability and ability to incorporate reinforced vegetation will allow for a long term, environmentally friendly solution (Figures 8, 9, and 10).

Figure 8.   Vegetated SCOURLOK and ARMORMAX performance, July 2021.

Figure 9.   SCOURLOK and ARMORMAX performance during frozen conditions, January 2022.

Figure 10.   SCOURLOK and ARMORMAX performance during flood conditions, May 2022.

Comparative life cycle assessment of geosynthetics versus conventional construction materials in infrastructure, filter function in a river construction, a study on behalf of the EAGM

H. Ehrenberg
Naue GmbH & Co. KG, Espelkamp, Germany, on behalf of EAGM

ABSTRACT: The European Association of Geosynthetic product Manufacturers (EAGM) commissioned ETH Zürich and ESU-services Ltd. to quantify the environmental performance of commonly applied construction materials (such as concrete, cement, lime, or gravel) versus geosynthetics for 4 cases. Geosynthetic materials are used in many different applications in civil and underground engineering. In most cases, the use of geosynthetic material beneficially replaces the use of other construction materials. To this end, a set of comparative life cycle assessment studies are carried out, concentrating on various functions or application cases. The environmental performance of geosynthetics is compared to the performance of competing construction materials used. Further new cases have been evaluated since 2020. This paper presents the results of a case with a filtration function (the construction of a filter, where geosynthetics are used, is compared to the case of a mineral filter) in a river construction with a typical geotextile filter in comparison to a gravel/sand filter. The study shows benefits in sustainable constructions using geosynthetics.

1 INTRODUCTION

Geosynthetic materials are used in civil engineering in many different areas. In most cases, the use of geosynthetics replaces or improves the use of other materials. For the first time in 2010, the European Association of Geosynthetic Materials Manufacturers (EAGM) commissioned ETH Zürich and ESU-services Ltd. to quantify the environmental impact of commonly used construction materials (such as concrete, cement, lime, or gravel) compared to geosynthetics in civil engineering.

To this end, a series of comparative life cycle assessment (LCA) studies were conducted focusing on different use cases, namely filtration, foundation-stabilised road, landfill construction, and slope stabilisation structures. The environmental performance of geosynthetics and competing construction materials was compared.

In 2018, it was verified if the obtained results were still up to date or whether the study needs to be renewed. EAGM commissioned treeze Ltd (the successor company of ESU-services Ltd) with the review.

The assessment confirms the timeliness of the study. The full study, including the results of the critical reviews, is available at: http://www.eagm.eu/. The latest results were presented in detail at EUROGEO 7 in Warsaw in 2022. In 2021 and 2022, another study was prepared based on the findings, which are presented in detail below.

2 FILTRATION FUNCTION INFRASTRUCTURE IN A RIVER CONSTRUCTION

This paper presents the results of a case with a filtration function (the construction of a filter where geosynthetics are used is compared to the case of a mineral filter) in a river construction

with a typical geotextile filter in comparison to a gravel/sand filter. The study shows benefits in sustainable constructions using geosynthetics. treeze Ltd. evaluated the study.

The life cycle assessments carried out within this study follow a cradle-to-grave approach. The product systems of the waterway analysed encompass the extraction of the raw materials, their processing into building materials, the construction and disposal of the waterway (infrastructure element, see Figure 1). Operation and maintenance of the waterways are excluded. Transport processes and infrastructure are included. All processes describe average European conditions.
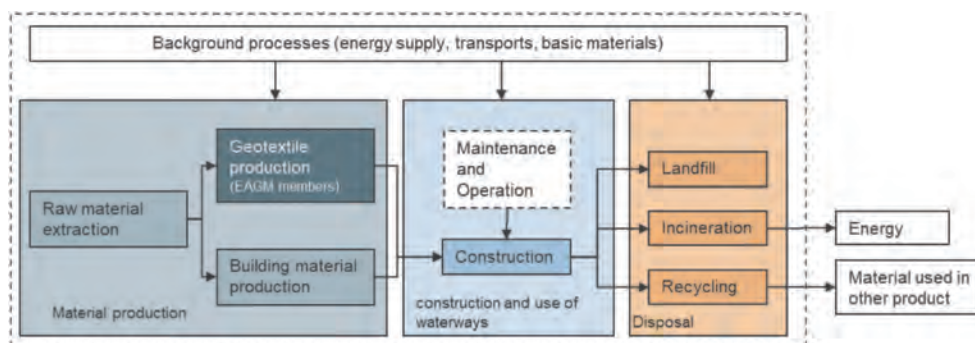
Figure 1. Simplified process flow chart showing the most important process steps. Maintenance and operation of the infrastructure element are not included in the system boundaries.

The lifetime of the waterways is expected to be the same (100 years) for both options assessed in this study.

7 European producers, all members of the EAGM, provided data on the production of geosynthetic materials. The required data were collected by means of prepared questionnaires. An industry expert provided data on construction and de-construction efforts. The primary source of background inventory data used in this study is UVEK LCI data DQRv2:2022. The LCA software SimaPro v 9.3.0.3 was used to model and calculate the life cycle based environmental impacts.

The first seven environmental impact category indicators form part of the Environmental Footprint method v3.0 published by the European Commission (2017). The cumulative non-renewable energy demand is based on the approach published by Frischknecht *et al.* (2015).

– climate change (greenhouse gas emissions),
– photochemical ozone formation (summer smog),
– particulate formation,
– acidification,
– freshwater eutrophication,
– land use impacts,
– abiotic resource depletion (minerals and metals)
– cumulative energy demand (primary energy consumption), non-renewable

Sensitivity and uncertainty analyses were carried out to learn more about the stability of the comparative results. Not included are:

– Operation and maintenance of the infrastructure element (e.g. shipping, cleaning) because these activities do not differ between the alternatives;
– Manufacturing equipment (machinery) at the geosynthetics manufacturer's site, because of its minor importance (see e.g. Frischknecht *et al.* 2007);

– Operation of the storage of raw and geosynthetic materials at the manufacturer's site because the energy consumption is considered negligible;
– Packaging of the geosynthetics because they are of minor importance (less than 3% of mass contribution);
– Efforts and emissions of thorough end-of-life cleaning (decontamination) of the filter materials because of missing information and empirical data.

The study refers to the year 2019. Foreground data about geosynthetic materials gathered by questionnaires refer to 2019 or, in a few exceptional cases, 2018. Data available about further material inputs and the use of machinery are somewhat older. The characterisation of the waterway analysed represents current best practices. Age differences are discussed in the data quality section of the results chapters.

All data refer to European conditions. Some background data referring to Switzerland are used to estimate European conditions, particularly regarding landfilling and incineration of wastes.

3 EVALUATED CASES

The waterways assessed in this report are defined in a way that they represent commonly applied new constructions. Nevertheless, construction methods may vary from one EU member state to the other. Thus, the case should be perceived as an exemplary model of the common and frequent application of geosynthetic materials in waterways. The functional unit is 1 meter of an inland waterway with a width of about 34 meters (water level, see Figure 2). The upper layer consists of water stones in both cases. The filter layer is either gravel/sand of two times 20 cm (left side see Figure 2) or a geosynthetic filter (right side see Figure 2).
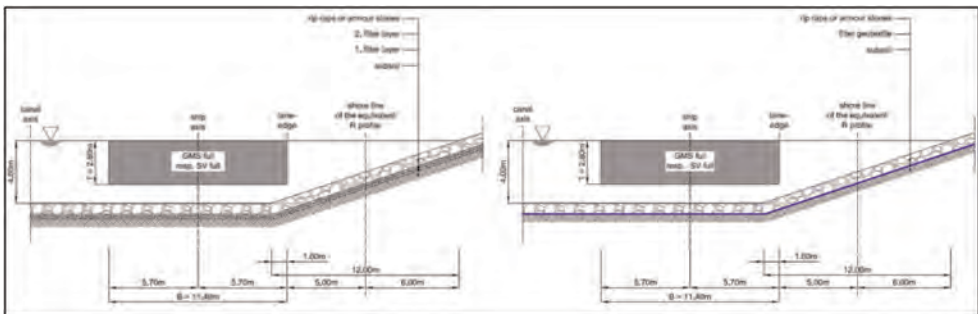
Figure 2.   Cross-section of the waterway analysed in this study (left: gravel filter; right: geosynthetics filter).

The two alternatives are defined such that they can be considered technically equivalent or at least comparable. The geosynthetics used represent a mix of different brands suited for waterways. Scenario 2 and 3 include a typical geosynthetic as used in Germany in this application. The conventional systems represent the most common type of construction.

3.1 *Base scenario*

The base scenario shows a geosynthetic filter with a specific weight of 350 g/m^2 and a shipping distance of mineral material (water stones and gravel/sand filters) of 20 km. Based

on the evaluation with 7 manufacturers of the EAGM for the year 2019, the delivery distances and the type of transports are determined.

For the raw materials, an average distance of 820 km was evaluated, with a weighted distribution of 600 km per truck and 220 km per ship.

For the nonwovens, an average distance of 795 km was evaluated, typically by truck (62%) and in special cases by train (38%).

Alternatives to the base scenario are described in detail in the following Table 1.

Table 1.   Overview of different scenarios.

	Unit	Base	Scenario 1	Scenario 2	Scenario 3
Geosynthetics basis weight	g/m^2	**350**	350	750	
Distance supply of mineral materials	km	**20**	50	20	50

3.2 *General information*

The calculated nonwoven geosynthetics used in waterways construction are made from polypropylene staple fibres and have a specific weight of about 350 g/m^2. In some countries like Germany, geosynthetics with a specific weight of 750 g/m^2 are used. The life cycle inventory of manufacture of nonwoven geosynthetics is based on data and information provided by seven European manufacturers. They collected data on consumption of raw materials, working materials, packaging materials, fuel, steam and electricity consumption, water consumption and release, pollutants emissions to air and water, wastes (including the kind of treatment), supply and delivery logistics, as well as land use and infrastructure (such as factory halls and office buildings). Production volume weighted average datasets on the manufacture of nonwoven geosynthetics with a specific weight of 350 g/m^2 and 750 g/m^2 were established.

The material demand of gravel/sand was determined by Norbert Kunz, BAW (Bundesanstalt für Wasserbau, Germany; Federal Waterways Engineering and Research Institute, Germany) based on the regular cross-section of a typical inland waterway. The material additionally excavated is assumed to be shipped to a landfill site over a distance of 20 km.

4 RESULTS OF THE SCENARIOS

4.1 *Detailed results base scenario*

Figure 3 shows the comparison of all impact categories and gives in detail the proportion of each construction / production step.

For example, the first part shows

– in the first line the highest proportion of greenhouse gas emissions with e.g. roughly 30% (light blue) for the construction efforts and
– in the second line the highest proportion of greenhouse gas emissions with e.g. roughly 20% (brown) for the deconstruction efforts

In general, the first line (greenhouse gas emissions) shows that the geosynthetic construction method reduces the production of greenhouse gas emissions by more than 25% compared to the classic construction method.

The results for the scenarios 1, 2 and 3 are similar and can be seen in detail at www.eagm.eu.
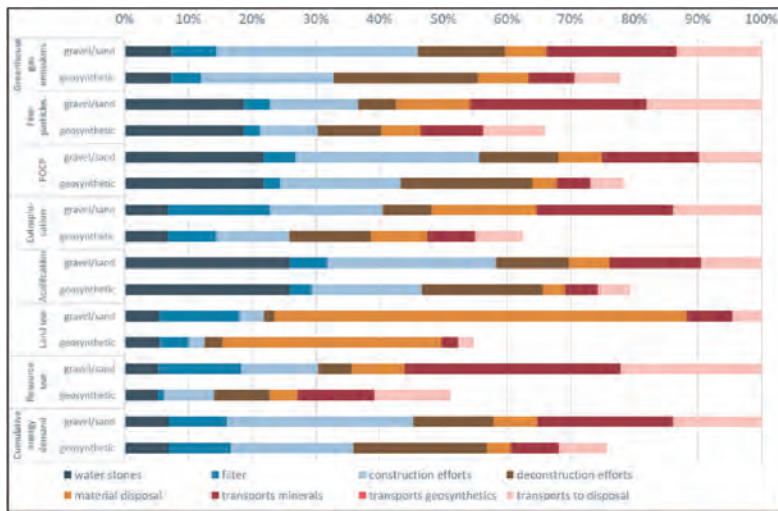
Figure 3.   Environmental impacts and their main contributors caused by 1 m of the inland waterway (width of about 34 m, water surface) relative to the environmental impacts of the waterway with gravel/ sand (which equal to 100%); base scenario.

5   SUMMARY OF RESULTS

Two significant impacts discussed in the last years are climate change (greenhouse gas / CO_2 emissions) and cumulated energy demand. In the last years, the saving of natural resources, e.g. minerals (abiotic resource depletion), is coming more in mind.

Figure 4 shows that the use of a filter nonwoven leads to lower impacts compared to the classic construction with a mineral filter layer in the base scenario.
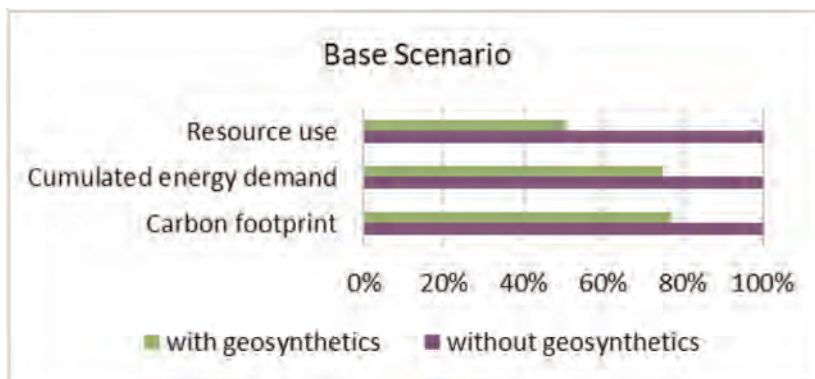
Figure 4.   Relative differences in resource use, cumulated energy demand and carbon footprint; base scenario (details see Table 1, 350 g/m^2 geosynthetic, 20 km transportation distance for minerals).

The results for the scenarios 1, 2 and 3 are similar and show that the use of a filter nonwoven in all three above-mentioned impact categories leads to lower impacts compared to the classic construction with a mineral filter layer in all four evaluated scenarios. The results can be seen in detail at www.eagm.eu.

6 CONCLUSION

Given the goal in the European Climate Law of the European Union to become climate neutral by 2050, a further and substantial reduction in greenhouse gas emissions and other impacts is required. This involves low CO_2 construction equipment and freight transports, and the reduction in greenhouse gas emissions during the manufacture and disposal of geosynthetic materials. Filters constructed in Europe may differ in cross-section and materials used. Thus, generalised assumptions were necessary to model a filter layer of a typical channel.

In this study, the environmental impacts of construction and deconstruction of two different alternatives for inland waterways were quantified and assessed. The results show that the alternative with a geosynthetic filter causes up to 50% less environmental impact than the alternative with a gravel/sand filter. Even with the least favourable alternative for geosynthetic filters with a relatively heavy geosynthetic (750 g/m^2) and in comparison, a rather short transport distances (20 km) for the mineral components, emissions are reduced when using the geosynthetic filters.

Furthermore, it was shown that the use of geosynthetics means a high saving of natural resources, as minerals such as sand and gravel from a mineral filter are saved.

REFERENCES

Ehrenberg, H. & Mermet, J.P. 2012. Comparative Life Cycle Assessment of Geosynthetics versus Conventional Construction Materials, a Study on behalf of the EAGM, General, *Proc. EUROGEO 5*, Valencia, Spain.

Elsing, A. & Fraser, I. 2012. Comparative Life Cycle Assessment of Geosynthetics versus Conventional Construction Materials, a Study on behalf of the EAGM, Case 2, Foundation Stabilisation, *Proc. EUROGEO 5*, Valencia, Spain.

Fraser, I. & Elsing, A. 2012. Comparative Life Cycle Assessment of Geosynthetics versus Conventional Construction Materials, a Study on behalf of the EAGM, Case 4, Soil Retaining Wall, *Proc. EUROGEO 5*, Valencia, Spain.

Frischknecht, R. 2022. Comparative Environmental Life Cycle Assessment of Waterways, a Study on behalf of the EAGM, Uster, Schweiz.

Frischknecht, R., Büsser-Knöpfel, S., Itten, R., Stucki, M. & Wallbaum, H. 2013. Comparative Life Cycle Assessment of Geosynthetics versus Conventional Filter Layer, *Proc. 18th International Conference on Soil Mechanics and Geotechnical Engineering*, Uster, Schweiz.

Frischknecht R., Wyss F., Büsser Knöpfel S., Lützkendorf T. and Balouktsi M. 2015. Cumulative Energy Demand in LCA: The Energy Harvested Approach. *In: The International Journal of Life Cycle Assessment*, Retrieved from: http://dx.doi.org/10.1007/s11367-015-0897-4.

Frischknecht, R., Büsser-Knöpfel, S., Itten, R., Stucki, M. & Wallbaum, H. 2013. Comparative Life Cycle Assessment of Geosynthetics versus Concrete Retaining Wall, *Proc. 18th International Conference on Soil Mechanics and Geotechnical Engineering*, Uster, Schweiz.

Frischknecht R., Jungbluth N., Althaus H.-J., Doka G., Dones R., Heck T., Hellweg S., Hischier R., Nemecek T., Rebitzer G. and Spielmann M. 2007. *Overview and Methodology*. Ecoinvent report No. 1, v2.0. Swiss Centre for Life Cycle Inventories, Dübendorf, CH, Retrieved from: www.ecoinvent.org.

Laidié, N. & Shercliff, D. 2012. Comparative Life Cycle Assessment of Geosynthetics versus Conventional Construction Materials, a study on behalf of the EAGM, Case 1, Filter Function, *Proc. EUROGEO 5*, Valencia, Spain.

Stolz, P. & Frischknecht, R. 2019. Comparative Life Cycle Assessment of Geosynthetics versus Conventional Construction Materials, treeze Ltd. commissioned by European Association of Geosynthetic product Manufacturers (EAGM), Uster and Zürich, Switzerland.

Werth, K. & Höhny, S. 2012. Comparative Life Cycle Assessment of Geosynthetics versus Conventional Construction Materials, a study on behalf of the EAGM, Case 3, Landfill Construction Drainage Layer, *Proc. EUROGEO 5*, Valencia, Spain.

Displacement-based design method to increase sustainability of pile-supported embankments: Practical application

V. Mangraviti
Chalmers University of Technology, Gothenburg, Sweden

ABSTRACT: Concrete piles and geosynthetic reinforcements are commonly used to reduce settlements at the top of embankments. The use of geosynthetic layers at the embankment bottom leads to several advantages: (i) faster construction, (ii) better control of differential settlements and (iii) a fewer number of piles is needed for equal admissible settlements at the embankment top. Because of the latter point, the use of geosynthetic reinforcement reduces the Embodied Carbon related to concrete. Unfortunately, since existing design methods for Geosynthetic-Reinforced and Pile-Supported embankments do not allow to calculate settlements at the embankment top, they cannot be used to optimize the number of concrete piles to increase sustainability. In this note, an innovative model for assessing settlements induced by the embankment construction process is applied to the preliminary design stage of a practical example. The mass of CO_2 saved by using geosynthetics and optimizing the number of piles is calculated.

1 INTRODUCTION

Civil engineering is enormously contributing to the consumption of both global energy reserves and raw materials such as gravel, sand, and water (Dixit *et al.* 2010). In a context where all civil engineers can have a major influence towards a more sustainable development, geotechnical engineers have a crucial role in highly increasing the sustainability of a project. In fact, geotechnical engineering is one of the key fields contributing to a sustainable development, since it faces a challenging dichotomy between delivering project goals (environmental, economic, and social) and maintaining sustainability (Abreu *et al.* 2008).

From a practical point of view, the exploitation of increasingly large areas of territory has led also to the construction of infrastructures under difficult geological and geotechnical conditions, requiring geotechnical engineers to find new (and not always "environmentally friendly") solutions. As an example, embankments for major infrastructures are more often realized in areas where soils are deformable and, to avoid unacceptable settlements, concrete piles are commonly employed as settlement reducers. Such "geo-structures", composed of embankment, foundation soil and concrete piles, are named Conventional Pile-Supported Embankments (CPSE). The rigid inclusion (i.e. the pile) causes the development of the "arching effect", that reduces the portion of embankment load transferred to the soft soil (alleviating differential settlements within the embankment), while stresses flow through the piles towards more competent soil layers. Depending on both the overall length of the infrastructure to be realized and the mechanical properties of the ground to improve, CPSE may require the installation of a huge number of concrete piles along different kilometers of infrastructure, leading to a huge outflow of both economic and environmental resources.

To further reduce settlements in CPSE, geosynthetic reinforcements (GR) are often installed at the bottom of the embankment. Studies on Geosynthetic-Reinforced Pile-Supported

Embankments (GRPSE) have proven that the GR effectively increase the arching effect, leading to both a reduction of differential settlements as well as a reduction in the number of piles needed. This latter aspect is fundamental to increase the sustainability of the project, by reducing the Embodied Carbon (EC, which is defined as the carbon dioxide emitted during the manufacturing, transport, construction and the "end of life" of a material) related to concrete piles.

According to the actual standards (BS8006-1, 2010; EBGEO, 2010), the design of GRPSE is carried out in Ultimate Limit State (ULS) conditions, leading to extremely conservative estimation of the loads applied on GR and piles (Bhasi & Rajagopal 2015). Despite the very simplistic approach suggested by the standards, it is hard to use those methods to optimize the design of both piles and GR to reduce the number of piles (and EC) needed for GRPSE.

Furthermore, the standards do not allow for the estimation of settlements at the top of the embankment, even though King *et al.* (2017) recently stated that the assessment of settlements to ensure the serviceability of the infrastructure over its all lifetime is necessary. In this perspective, (Mangraviti *et al.* 2022) developed a displacement-based (DB) method for the estimation of settlements at the top of the embankment during the construction of GRPSE under drained conditions, validated against field tests in (Mangraviti *et al.* 2023a). The simplified method proposed by the authors applies for smooth end-bearing concrete piles located in the central part of the embankment. Based on this new DB method, Mangraviti (2022) conceived a simplified DB procedure to optimize the design of GRPSE (i.e. pile spacing and GR stiffness) in a preliminary design stage.

In this note, the procedure developed by Mangraviti (2022) is introduced (§2) and a practical application of the procedure is presented (§3), together with some concluding remarks (§4).

2 DB PROCEDURE TO INCREASE SUSTAINABILITY OF GRPSE

In this study, settlements induced by the embankment construction process in GRPSE (Figure 1a) are considered. When studying the mechanical behavior of the central part of the embankment, it is common in the literature to consider as representative one central axisymmetric cell. The representative unit cell (Figure 1b) of diameter s, assumed to be equal to the pile spacing (different values can be considered in case of squared pile pattern) includes: (i) one pile of diameter d and length l, (ii) a homogeneous soft soil stratum of thickness l resting on a rigid bedrock, (iii) an embankment of which height h evolves during the construction process and (iv) the geosynthetic reinforcement laid at the embankment base. The pile shaft is assumed to be smooth (leading to a conservative estimation of settlements), and the construction process is assumed to occur under drained conditions.
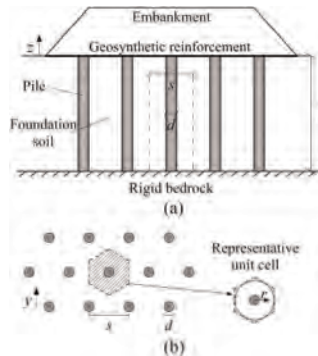
Figure 1.   (a) Geosynthetic-reinforced and pile-supported embankment and (b) representative unit cell.

In Mangraviti et al., (2023b), the mechanical response of the representative unit cell was modelled with finite difference numerical analyses by using simple constitutive models: the pile was assumed to be elastic, the GR was modelled as an elastic isotropic membrane (of axial tensile stiffness J) and the soil was modelled with non-associated elastic-perfectly plastic constitutive relationship with a Mohr-Coulomb failure criterion. This constitutive modelling, despite of its simplicity, can capture the main aspects of the mechanical processes taking place in the representative unit cell, which are:

a) the arching effect, that is the stress transfer mechanism towards piles occurring within the embankment (Terzaghi 1936);
b) the plane of equal settlements, that is the plane above which differential settlements are negligible (McGuire 2011);
c) the process height, that is the height of the portion of embankment where plastic shear strain accumulate during construction (di Prisco et al. 2020).

It is worth mentioning that, when the construction process is considered, the plane of equal settlements is where the increments of differential settlements are nil, even though differential settlements are larger than zero (Mangraviti et al. 2023b). According to di Prisco et al. (2020), differential settlements in CPSE stop increasing during construction when the height of the embankment is larger than a critical height value (h^*). The non-dimensional critical height (H^*) value is:

$$H^* = \frac{h^*}{d} = \frac{1}{2} \sqrt{ \left[\frac{E_{oed,e}}{E_{oed,f}} \frac{l\,d}{s^2} \right]^2 + \frac{(s/d)^2 - 1}{\overline{k}\,\tan\phi'_{ss}} \left(\frac{E_{oed,e}}{E_{oed,f}} \frac{l\,d}{s^2} \right) } - \frac{1}{2} \left(\frac{E_{oed,e}}{E_{oed,f}} \frac{l\,d}{s^2} \right) \tag{1}$$

where $\overline{k}$ is a parameter uniquely depending on the dilatancy angle of the embankment ($\overline{k}$ = 0.83 for dilatancy angle equal to zero); $E_{oed,e}$ and $E_{oed,f}$ are the oedometric moduli of the embankment and foundation soil, respectively. ϕ'_{ss} is the embankment friction angle in simple shear:

$$\tan\phi'_{ss} = \frac{\cos\psi_e \sin\phi'_e}{1 - \sin\psi_e \sin\phi'_e} \tag{2}$$

Equation 1 gives a conservative estimation of H^* in case of GRPSE (Mangraviti et al. 2022).

In the design practice, it is convenient (and strongly recommended by the current standards) to keep differential settlements at the top of the embankment in the r-direction (r defined in Figure 1b) negligible, by having an embankment higher than the critical height value ($u_{t,\text{diff}} = 0$, if $h > h^*$). Under this conditions, differential settlements at the top of a GRPSE induced by the application of a distributed load Δq are always nil, regardless of the value of Δq (Figure 2). However, average settlements at long term ($u_{t,av}$ in Figure 2) due to Δq are larger than zero (Mangraviti et al. 2023c) and need to be evaluated. In fact, also average settlements can be problematic when becoming differential settlements in the y-direction (y defined in Figure 1b). In this paper, average and differential settlements at the embankment top are defined as:

$$u_{t,av} = \frac{u_{t,f}\,(s^2 - d^2) + u_{t,p}\,d^2}{s^2} \quad \text{and} \quad u_{t,diff} = u_{t,f} - u_{t,p} \tag{3}$$

where:

$$u_{t,p} = \frac{2\pi \int_0^{d/2} u_t(r)\,dr}{\pi d^2/4} \quad \text{and} \quad u_{t,f} = \frac{2\pi \int_{d/2}^{s/2} u_t(r)\,dr}{\pi(s^2 - d^2)/4} \tag{4}$$
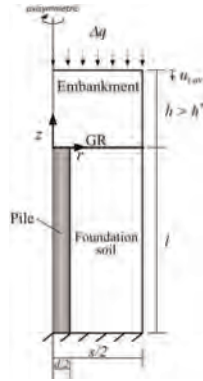
Figure 2.   Problem geometry.

are the weighted average values of u_t above the pile ($0 < r < d/2$) and the foundation soil ($d/2 < r < s/2$), respectively. u_t are the vertical displacements accumulated during construction at the top of the embankment.

In engineering practice, engineers might be requested to design GRPSE in a way that settlements at the top of the embankment would be less than an admissible value ($u_{t,av}^{amm}$). By assuming that the increment of average settlement induced by Δq is equal to the value of $u_{t,av}^{amm}$ for the project, the efficiency of GRPSE in terms of settlements can be defined as:

$$efficiency = 1 - \frac{u_{t,av}^{amm}}{u^*} \tag{5}$$

where u^* is the increment of average settlements at the top of the embankment that would be induced by Δq if nor piles neither GR were installed:

$$u^* = q\left(\frac{l}{E_{oed,f}} + \frac{h}{E_{oed,e}}\right). \tag{6}$$

Usually, $h/E_{oed,e} \to 0$ since the embankment soil is very stiff.

Mangraviti (2022) used the meta-model by Mangraviti *et al.* (2022, 2023a) to define efficiency isolines in the $s/d - (Jl)/(E_{oed,f}\,d^2)$ non-dimensional plane (Figure 3). The plot reported in Figure 3 refers to friction angle and dilatancy angle of the embankment equal to $\phi'_e = 40°$ and $\psi_e = 0$, respectively. During a preliminary design stage, efficiency isolines can be a very effective tool to optimize pile spacing (s) and GR stiffness (J) considering the required
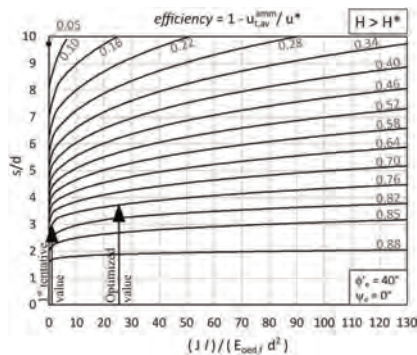
Figure 3.   Mangraviti (2022): non-dimensional efficiency isolines for $H (= h/d) > H^* (= h^*/d)$, $\phi'_e = 40°$ and $\psi_e = 0$.

320

average settlement at the top ($u_{t,av}^{amm}$). In fact, by calculating the efficiency (Eqs. 5,6), one isoline is individuated in Figure 3 and, knowing the mechanical properties of the foundation soil ($E_{oed,f}$) and its thickness (l), the value of s and J can be chosen in order to get the larger value of pile spacing to reduce the number of concrete piles.

3 RESULTS

The case from Feng *et al.* (2017) of a GRPSE, with $h = 5$ m and built for 3.5 km of linear infrastructure, is here considered. The homogeneous foundation soil deposit of thickness $l = 16$ m has mechanical properties chosen as average values from Feng *et al.* (2017) (Table 1). A conservative estimation of GRPSE response is obtained by considering cohesionless soils.

Table 1. Materials mechanical properties for GRPSE.

	Unit weight kN/m^3	Young modulus MPa	Poisson ratio -	Oedometric modulus MPa	Friction angle °	Cohesion kPa	Dilatancy angle °
Foundation soil	19.2	10.2	0.3	13.69	24	0	0
Embankment soil	18	40	0.3	53.85	40	0	0

A uniformly distributed vertical load $\Delta q = 12.5$ kPa is applied at the top of the embankment (Figure 2) and the resulting admissible settlement at the top of the embankment is 3.5 mm.

The piles have $d = 0.5$ m, whereas the spacing needs to be designed together with the stiffness of the GR. The procedure previously described to optimize the design of GRPSE is here used to increase s and J in order to improve the sustainability of the project.

To identify the isoline corresponding to this case, the *efficiency* $= 1 - 0.0035/(12.5 \times 16/13690) = 0.76$ (Eq. 5) is calculated. A first tentative value of J is chosen (Table 2) and, by entering the plot in Figure 3 with $Jl/(E_{oed,f}d^2) = 120 \times 16/(13690 \times 0.5^2) = 0.6$ value, a pile spacing of $s = 1.4$ m is found on the isoline of *efficiency* $= 0.76$. Knowing s, the value of critical height is calculated (Eq. 1) to verify that $h^*(= 1.4m) > h(= 5m)$. The same procedure is used for one higher value of J ("optimized value" in Table 2), and the number of piles needed in the central part of the embankment along 3.5 km in this case results in 658 piles less than the first tentative case.

To calculate the tons of CO_2 saved by choosing the optimized option, an average value of EC (generally measured in mass of CO_2 emitted per mass of material) of concrete is considered (Table 3). Knowing the mass of concrete needed for each pile (7.9 t) and the tons of

Table 2. Optimizing the preliminary design of GRPSE.

	GR axial stiffness, J kN/m	Pile spacing, s m	Number of piles in 3.5 km –
First tentative value	120	1.4	2501
Optimized value	5000	1.9	1843

Table 3. Reinforced concrete mass and EC.

	Embodied Carbon, EC tCO$_2$/t	Mass kg/m^2
Concrete	1.08 (Koerner 2019)	2500

CO_2 emitted for each pile (1.08 tCO_2/t × 7.9 t = 8.5 tCO_2), the total amount of CO_2 saved by reducing the number of piles is calculated (8.5 tCO_2 × 658 = 5580 tCO_2).

4 CONCLUSIONS

In this paper, an innovative and simplified displacement-based method to design Geosynthetic-Reinforced and Pile-Supported Embankments in a preliminary stage was presented. The methodology was applied to a practical example, where two different configurations of pile spacing and stiffness of the geosynthetic reinforcement were considered. The mass of CO_2 emitted was calculated for both the cases, and the optimized design led to reducing the number of piles needed in the project, by reducing the mass of CO_2 emitted (related to concrete piles) of 26%.

ACKNOWLEDGEMENTS

REFERENCES

Abreu, D.G., Jefferson, I., Braithwaite, P.A., Chapman, D.N., 2008. *Why is Sustainability Important in Geotechnical Engineering?* In: GeoCongress 2008. American Society of Civil Engineers, Reston, VA, pp. 821–828.

Bhasi, A., Rajagopal, K., 2015. Geosynthetic-Reinforced Piled Embankments: Comparison of Numerical and Analytical Methods. *Int. J. Geomech.* 15, 04014074.

BS8006-1, 2010. Code of practice for strengthened/reinforced soils and other fills.

di Prisco, C., Flessati, L., Frigerio, G., Galli, A., 2020. Mathematical Modelling of the Mechanical Response of Earth Embankments on Piled Foundations. *Géotechnique* 70, 755–773.

Dixit, M.K., Fernández-Solís, J.L., Lavy, S., Culp, C.H., 2010. Identification of Parameters for Embodied Energy Measurement: A Literature Review. *Energy Build.* 42, 1238–1247.

EBGEO, 2010. *Empfehlungen für den Entwurf und die Berechnung von Erdkörpern mit Bewehrungen aus Geokunststoffen – EBGEO.* Wiley-VCH Verlag GmbH & Co. KGaA, Weinheim, Germany.

Feng, S.J., Ai, S.G., Chen, H.X., 2017. Estimation of Arching Effect in Geosynthetic-reinforced Structures. *Comput. Geotech.* 87, 188–197.

King, D.J., Bouazza, A., Gniel, J.R., Rowe, R.K., Bui, H.H., 2017. Serviceability Design for Geosynthetic Reinforced Column Supported Embankments. *Geotext. Geomembranes* 45, 261–279.

Koerner, G.R., 2019. *Relative Sustainability (i.e., Embodied Carbon) Calculations With Respect to Applications Using Traditional Materials Versus Geosynthetics.*

Mangraviti, V., 2022. *Displacement-Based Design of Geosynthetic-Reinforced Pile-Supported Embankments to Increase Sustainability.* In: Antonelli, M., Della Vecchia, G. (Eds.). Springer International Publishing, Cham, pp. 83–96.

Mangraviti, V., Flessati, L., di Prisco, C., 2022. A Rheological Model for Georeinforced Embankments Based on Piled Foundations. *IOP Conf. Ser. Mater. Sci. Eng.* 1260, 012014.

Mangraviti, V., Flessati, L., di Prisco, C., 2023a. Mathematical Modelling of the Mechanical Response of Geosynthetic-reinforced and Pile-supported Embankments. *Numer. Anal. Methods Geomech. Under revi.*

Mangraviti, V., Flessati, L., di Prisco, C., 2023b. Geosynthetic-reinforced and Pile-supported Embankments: Theoretical Discussion of Finite Elements Numerical Analyses Results. *Eur. J. Environ. Civ. Eng.*

Mangraviti, V., Flessati, L., di Prisco, C., 2023c. Basal Reinforced Earth Embankments on Piled Foundations: The Role of Embankment Construction Process. In: *International Conference on Geosynthetics.* Under Review, Rome.

McGuire, M.P., 2011. *Critical Height and Surface Deformation of Column-supported Embankments.* Virginia Polytechnic Institute and State University.

Terzaghi, 1936. Stress Distribution in Dry and in Saturated Sand Above a Yielding Trap-Door. In: *International Society for Soil Mechanics and Geotechnical Engineering.* pp. 536–537.

Polyolefinic geosynthetics as key components in future energy systems – A case study and perspective

H. Wetzel
PlanEnergi, Skørping, Denmark

L. Peham
Institute of Polymeric Materials and Testing, University of Linz, Linz, Austria

P.A. Sørensen
PlanEnergi, Skørping, Denmark

G.M. Wallner
Institute of Polymeric Materials and Testing, University of Linz, Linz, Austria

ABSTRACT: Pit Thermal Energy Storages sealed with geomembranes have proven to be vital applications for long term storage of solar thermal energy or excess heat in large volumes at affordable costs. Energy content and its utilization depends on the system integration, so does the temperature profile, which impacts the liner material lifetime. During the transformation of energy systems a thorough demand for energy storage can be expected in the future. The project in Høje Taastrup vastly increases scope of functions as permanent high temperatures ($\geq 90°C$) enable more advanced operation strategies with additional measurable economic outcomes for operators. For lifetime prediction of liner materials, a methodological approach was implemented based on micro-specimen. Due to the reduction of specimen thickness an acceleration factor of up to 20 was achieved. The best performing novel PP-HTR liner material revealed a predicted lifetime of up to 35 years at a temperature loading profile ranging from 60 – 90°C.

1 INTRODUCTION

The implementation of low carbon climate action plans expectably leads to an increase of renewable energies within the next decades. Fifty percent of the European energy demand is used for heating and cooling including domestic hot water and space heating. While 66% of the thermal energy is produced by fossil fuels, only 13% comes from renewable energy sources (Mathiesen 2017). Efficient integration of renewables is challenging due to its fluctuating production times (Dyrelund 2016), however for future energy systems combining heating and cooling (CHP) sector with the electricity and/or transport sectors results in the most effective and economical solution (Lund 2014). Latest experiences show that it will become essential to stabilize the smart grid with other energy carriers, leading to a smart energy system in which energy storage plays an important role. Electrical storage as an evident solution is costly and limited in its capabilities (Heller 2019). Water can therefore be an alternative carrier for thermal energy. It has a high thermal capacity, is non-toxic and easily available almost everywhere.

Many CHP plants in district heating networks, i.e., use thermal energy storages (TES) in form of steel tanks to increase flexibility in short-term storage and supply. The water

temperatures are typically either close to 100°C (unpressurized) or, in a few cases, beyond (pressurized tank) (Sørensen 2013). In Denmark, pit thermal energy storage (PTES) is typically used for long term thermal storage, since it can be charged and discharged quickly besides be employed for short-term storages (Pauschinger 2020), hence an alternative to steel tanks.

2 PIT THERMAL ENERGY STORAGE (PTES)

Since the 1980's PTES have been developed in Denmark (Pauschinger 2020) with projects of a volume up to 220,000 m^3. The structure is a large inverted truncated pyramid with an inclination of 1:2 to 1:1.5. The sides, the bottom and the water surface are typically covered with a geomembrane, made of either polyethylene (PE) or polypropylene (PP). A standard for pit designs to reduce costs is considering a soil balance by using the excavated soil from the storage's bottom as surrounding embankments (Kallesøe 2019). Favorable geotechnical conditions made this an obvious approach in Denmark. After filling with water, the floating geomembrane gets covered with thermally insulating materials. The exchange of thermal energy takes place through diffusers connected via pipes to a nearby pumpstation with heat exchangers and grid connection. Water temperatures inside can reach up to 90°C, depending on the system integration of the storage.

2.1 PTES as seasonal storage

The energy utilization cycle in a PTES used as a seasonal storage is based on a surplus of thermal energy production in summer (i.e., solar thermal, waste heat) compared to a low heat demand at the same time. This surplus is stored over time (charge) and utilized in winter (discharge). The temperature profile reaches up to 90°C for a limited period during the year (Figure 1). Beside energy independence and price stability for connected customers, this shift of otherwise unutilized thermal energy creates an opportunity for transition to a circular carbon energy future. Tests according to the test method (hot water of i.e., 110°C on one side of a liner sample, air on the other) developed at the Danish Technological Institute (DTI) showed that service life of high temperature resistant HDPE liners achieve more than 20 years in a seasonal temperature profile (Jensen 2014; Paranovska 2016). To further accelerate the ageing process a novel methodological approach was implemented, based on micro-specimen (Grabmann 2017; Grabmayer 2014 & 2015; Peham 2022; Wallner 2016). Depending on the polyolefinic liner material, a test acceleration factor of up to 20 was proven to shorten the oven ageing exposure time at elevated temperatures significantly.

2.2 PTES as buffer storage – the case study Høje Taastrup, Copenhagen

The Energy Technology Development and Demonstration Program Denmark (EUDP) invested 1.3 Mio€ in the FLEX_TES (Flexible Thermal Energy Storage) project, which is a new 70,000 m^3 pit storage constructed in Høje Taastrup, Copenhagen. It acts as a buffer storage with a capacity of 3300 MWh. The PTES is linked to a transmission line that connects different heat producers (4 CHP plants – 2050 MW, 3 waste incineration plants – 400 MW, reserve and peak load power plants – 1.900 MW, 2 TES – 660 MW) in the greater area of Copenhagen with the local district heating network in the city. With an amount of 20 to 25 energy utilization cycles per year and permanent 90°C in the uppermost water level (Figure 1), it is designed to optimize the heat- and electricity production of the connected power plants.
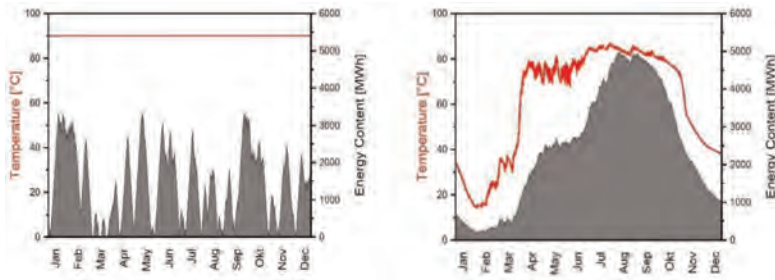
Figure 1. Comparison of water surface temperature and energy content inside a storage over the course of a year. Forecast for the multifunctional PTES in Høje Taastrup for 2025 by Ea Energy Analyses during the project FFH50 using Balmorel Power System Model (left panel) and actual measurements of the seasonal PTES in Dronninglund in 2019 by PlanEnergi (right panel).

The storage adds value due to the additional production of the most efficient CHP and waste incineration plants, saved peak loads and bypass operation. This has an expressive impact especially during winter months and an optimization of the CHP plants with respect to the electricity market price. Annual operational benefits are estimated between € 800k – € 900k, whilst further benefits in the business case are expected. This particular project aims for the development and demonstration of PTES as a more advanced and flexible manner compared to all other plants before, expecting using PTES as flexible weekly or daily storage. The Technology Readiness Level for the FLEX_TES project brings the application PTES as accumulation tank from TRL 6/7 to 8 (Bruus 2019). Implementation costs of the storage in Høje Taastrup are in the range of 71 €/m^3 water volume. For larger volumes (500,000 m^3 and more) calculations show approximate investment costs of 40 €/m^3 for both PTES used as seasonal and as multifunctional or buffer storage. In comparison, Danish experiences show that a steel tank of a similar capacity like the PTES in Høje Taastrup can be implemented at costs in the range of 133 €/m^3 (Bruus 2019).

3 LIFETIME ESTIMATIONS FOR POLYMER LINERS

Due to significantly higher operating temperatures (Figure 1), more durable liner materials are of utmost importance for PTES buffer storages. To develop and screen novel liner material formulations in a highly accelerated manner, a testing approach based on miniaturized specimen has been implemented at the Institute of Polymeric Materials and Testing (University of Linz, AT). Methodological approach

First, liner materials are extruded to sheets with a thickness of 2 mm. Second, strips with a width of 20 mm are cut and positioned in a CNC milling machine (Figure 2 left). Micro-sized specimen with thickness ranging from 50 to 500 μm are prepared using a home-built cutting tool. These specimens are clamped onto a sample holder and exposed to hot air or water in a convection oven (Figure 2 middle). For water exposure, micro-specimens are positioned in autoclaves and filled with deionized water. After defined exposure intervals, specimens are removed and characterized by tensile testing (Figure 2 right). As sensitive ageing indicator strain-at-break values are deduced (Kahlen 2010; Wallner 2004). Ultimate mechanical failure is achieved when strain-at-break drops below strain-at-yield ($\varepsilon_b < \varepsilon_y$). At the yield point of semi-crystalline polymeric materials, usually inter-spherulitic voiding is initiated. In the post-yield regime, failure of the spherulites and rearrangement of crystal lamellae associated with fibrillation takes place (Maier

325

2005). The considered ultimate failure criterion strain-at-break below strain-at-yield indicates failure due to critical degradation and chain scission of inter-spherulitic tie molecules (Grabmann 2017).
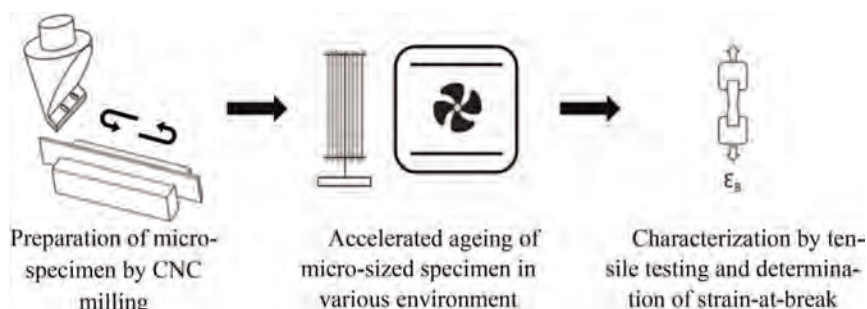
Figure 2. Methodological approach for accelerated ageing testing of polyolefin micro-specimen.

3.1 Lifetime assessment

For lifetime estimation an approach based on cumulative damages is used (Wallner 2016). The lifetime assessment is based on various inputs: the simulation of temperature loading profiles, the extrapolation of experimental aging data from elevated to service-relevant temperatures, the extrapolation of specimen thickness to the liner thickness and the accumulation of damages at different temperature levels. Exposure temperatures range from 65 to 135°C. For lifetime estimation, a high- and low-temperature loading profile was considered with temperatures ranging from 60 to 90°C and 35 to 80°C, respectively (van Helden 2021).

3.2 Results

In Figure 3, the effect of exposure temperature in air and specimen thickness on the strain-at-break values of a selected PP-R grade is depicted. Failure times are indicated by open symbols. Depending on the polyolefin grade, the temperature rises by 20°C resulting in 3 to 5 times shorter endurance times. Due to the diffusion limited oxidation (DLO, Celina 2013), semicrystalline polyolefins degrade by a factor of 2 to 20 faster when the specimen thickness is reduced from 2 mm to 50 μm. Based on the extrapolation of temperature and thickness effects to service relevant levels, estimated failure times can be calculated. Considering this endurance times as a cumulative damage model including seasonal temperature loading profiles used to ascertain lifetime estimations.
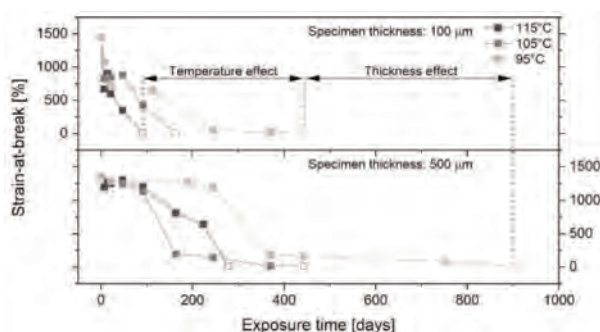
Figure 3. Effect of air temperature and specimen thickness on strain at break values of a random propylene copolymer (PP-R) reference grade.

It was shown by Grabmann (2018) that the ageing behavior of PE liner materials is more critical in hot water. In contrast, novel PP-R liner materials are more prone to degradation in hot air than in water. Overall, a much better ageing performance was ascertained for novel PP-R formulations compared to well established PE liner materials.

Predicted lifetime values are stated in Table 1. All lifetime value of 15 years was obtained for PE liners used in conventional PTES (low temperature profile). This value is about 5 years lower than the lifetime estimated by Paranovska (2016). The deviation could be attributed to differences in the experimental setup, the calculation procedure, and the investigated PE grade. While established PE liners (PE-HTR) can only be used in low temperature thermal energy storages, PP-R is suited for both applications. Replacing the PE liner with a conventional PP-R liner increases the lifetime by a factor of more than 2, from 15 to 34 years at a low temperature loading profile. Additional stabilization is improving the endurance time by a further factor of 1.7. At a high temperature loading profile, lifetime values of 20 and 35 years were deduced for PP-R and optimized PP-HTR grades, respectively.

Table 1.   Lifetime predictions for PE, PP-R and PP-HTR for high- and low-temperature profiles.

Predicted lifetime [years] for a 2 mm liner Temperature profile/Polymer grade	High 60–90°C	Low 35–80°C
PE-HTR		15
PP-R	20	34
PP-HTR	35	

4   PERSPECTIVE

According to Hay (2022) the district heating production in Germany, i.e., mainly is done by CHP plants consuming 82% of fossil fuels. For heat generation without CHP process 75% fossil fuels as energy source are used. The vulnerability and dependence on fossil fuels for energy production has moved into the political spotlight, especially since February 2022, in the course of partly drastic price increases for the end consumer.

The decarbonization of heat supply by substituting of heat generation systems requires adjustment of the system operating parameters. The current supply temperatures of networks in Germany are between 90 and 112°C in average with maximum peaks up to 140°C. In the future a significant reduction of supply temperatures for large network temperatures of < 100°C and for smaller ones < 80°C are to be expected (Hay 2022). Since the area of most European cities will increase (Alberti 2019), existing district heating networks can be expected to grow and new ones to be established.

Due to the relatively low investment cost per m^3 of water volume, the integration of a PTES into future systems can also have potential for electricity storage by converting the electrical into thermal energy (Power to Heat, P2H), i.e., for wind farms to prevent grid overloads (energinet.dk). Thermal energy can be utilized in district heating networks, combined with heat pumps for mutual benefits amongst different stakeholders. Another possibility is the combination with an Organic Rankine Cycle (ORC) turbine and a cold thermal storage, as recently built in a CSP plant in Carwarp, Australia (Bellini 2021).

In the application there is not only a perspective for geomembranes but also for reinforced soil. For thermal stratification purposes it is beneficial to reach a certain water column (i.e., 16 m depth in Høje Taastrup). Difficulties can occur in areas with a low groundwater level, as groundwater can cause heat loss especially when it is floating. Unfavorable soil conditions on the other hand can lead to increased costs if disposal or purchase of soil is required. Soil reinforcement and steeper slopes can address these matters and furthermore lead to an

improved surface/volume ratio. This, according to the Danish Energy Agency (2018), is a "characteristic figure for the heat loss per amount of stored energy". Additionally, the potential location area can be optimized, a practical approach similar as to increase volume in landfills (Cazzuffi 2021).

Further potential for polyolefins in PTES also exists for geotextiles and geocomposites as protective layers to the ground, as well as inside the lid construction, in where a combination of polymers can be used to address the different challenges: water tightness, water vapor handling, release of oxygen from the water side, entrance of oxygen into the water or rain/snow on the floating surface.

5 SUMMARY

Storage will expectably become an essential part of future energy systems, for both thermal and electrical energy. The storage technology PTES has been developed to a high level of maturity and offers scalability to extremely large volumes at attractive costs compared to other technologies to date. The application scenarios increase enormously if a PTES can be used as a multifunctional or buffer storage instead of a seasonal one. Operation strategies for such demand permanent high temperatures inside; a stressful environment partially beyond temperature operation ranges for typical geosynthetic products. To meet service life and operational requirements of the FLEX_TES in Høje Taastrup a PP-HTR liner with enhanced durability has been chosen.

For lifetime estimation a cumulative damage approach was implemented. Based on micro-specimen ageing studies were carried out at various environmental conditions at temperatures ranging from 95 to 135°C. The lifetime could be improved by a factor of more than 2 by replacing the PE liner by a PP-R liner. Additional stabilization allows for further increase of the estimated lifetime by a factor of 1.7 resulting in an endurance time of 35 years.

REFERENCES

Alberti, V., Alonso Raposo, M., Attardo, C., Auteri, D. *et al.* 2019. *The Future of Cities.* Publications Office of the European Union. Luxembourg.

Bellini, E., Carroll, D. 2021. Australian Massive Solar + Storage Project Combines Sun-tracking Mirrors, Gallium Arsenide Modules and Thermal Storage. *PV Magazine*

Bruus, F., Sørensen, P.A. 2019. New Thermal Heat Storage in Greater Copenhagen Hot Cool Magazine 4/2019.

Cazzuffi, D., Recalcati, P. 2021. Landfills Volume Increase with Reinforced Soil Embankments: Basic Theory and Case Studies, Detritus, Volume 15 – 2021, pages 113–119

Celina, M.C. 2013. Review of Polymer Oxidation and its Relationship with Materials Performance and Lifetime Prediction, *Polymer Degradation and Stability* 98: 2419–2429.

Danish Energy Agency, 2018. Technology Data for Energy Storage.

Dyrelund, A., Ulbjerg, F. 2016. Large Thermal Storages – a Vital Part of the District Heating System. *Hot Cool Magazine* 1/2016.

Energinet.dk. 2016. Technical Regulation 325 for Wind Power Plants Above 11 kW Revision 4, Section 5.2.3 Constraint Functions.

Grabmann, M.K., Wallner, G.M., Maringer, L., Buchberger, W., Nitsche, D. 2017. Hot Air Aging Behavior of Polypropylene Random Copolymers. *Journal of Applied Polymer Science* 136: 47350.

Grabmann, M. K., Wallner, G. M., Grabmayer, K., Buchberger, W., Nitsche, D. 2018. Effect of Thickness and Temperature on the Global Aging Behavior of Polypropylene Random Copolymers for Seasonal Thermal Energy Storages. *Solar Energy* 172: 152–157.

Grabmayer, K., Wallner, G.M., Beißmann, S., Braun, U., Steffen, R., Nitsche, D., Röder, B., Buchberger, W., Lang, R.W. 2014. Accelerated Aging of Polyethylene Materials at High Oxygen Pressure Characterized by Photoluminescence Spectroscopy and Established Aging Characterization Methods, *Polymer Degradation and Stability*, 109: 40–49.

Grabmayer, K., Beißmann S., Wallner, G. M., Nitsche, D. 2015. Characterization of the Influence of Specimen Thickness on the Aging Behavior of a Polypropylene Based Model Compound. *Polymer Degradation and Stability* 111: 185–193.

Hay, S., Heiler, D., Kallert, A.M., Lottis, D., Ziegler, R., Weidlich, I., Dollhopf, S. 2022. Fernwärmenetze im Kontext Nationaler Klimaziele: Potentiale für „Urban Turn". Eine Studie des AGFW, *Der Energieeffizienzverband für Wärme, Kälte und KWK e.*V.

Heller, A. 2019. From seasonal to smart energy storage. Hot Cool Magazine 4/2019.

Jensen, M.V. 2014. Seasonal pit heat storages – Guidelines for Materials & Construction, IEA-SHC TECH SHEET 45.B.3.2, Task 45 Large Systems.

Kahlen, S., Jerabek, M., Wallner, G.M., Lang, R.W. 2010. Characterization of Physical and Chemical Aging of Polymeric Solar Materials by Mechanical Testing, *Polymer Testing*, 29: 72–81.

Kallesøe, A.J., Vangkilde-Pedersen, T. 2019. HEATSTORE Underground Thermal Energy Storage (UTES) – State-of-the-art, *Example Cases and Lessons Learned.*

Lund, H., Hvelplund, F., Østergaard, P., Möller, B., Mathiesen, B.V., Connolly, D., Andersen, A.N. 2014. Renewable Energy Systems 2nd Edition, Chapter 6 – Analysis: *Smart Energy Systems and Infrastructures.*

Maier, G.A., Wallner, G. M., Lang, R.W., Fratzl, P. 2005. Structural Changes during Plastic Deformation at Crack Tips in PVDF Films: A Scanning X-ray Scattering Study. *Journal of Macromolecules* 38: 6099–6105.

Mathiesen, B.V. 2017. *Heating and Cooling: Facts and Figures;* https://heatroadmap.eu/heating-and-cooling-energy-demand-profiles/ (accessed 09.2022).

Paranovska, I., Pedersen, S., 2016. Lifetime Determination for Polymer Liners for Seasonal Thermal Storage.

Pauschinger T., Schmidt, T., Sørensen, P.A., Snijders, A., Djebbar, R., Boulter, R., Thornton, J. 2020. *Design Aspects for Large-Scale Aquifer and Pit Thermal Energy Storage for District Heating and Cooling*, IEA DHC Annex XII.

Peham. L., Wallner, G. M., Grabmann, M., Nitsche, D. 2022. Long-term Behaviour of Welded Polypropylene Liners for Pit Thermal Energy Storages. *Energy Storage* 50: 104689.

Sørensen, P.A. *et al.* 2013. *Udredning Vedrørende Varmelagringsteknologier Og Store Varmepumper Til Brug I Fjernvarmesystemet.* online: https://ens.dk/sites/ens.dk/files/Forskning_og_udvikling/ udredning_om_ var-melagringsteknologier_og_store_varmepumper_i_fjernvarmesystemet_nov_2013.pdf. accessed 13. 12.2022.

van Helden, W., Wallner, G. M., *et al.* 2021. Saisonale Speicher zur Erhöhung des Anteils erneuerbarer Energien für Distrikte. Final report – giga_TES-project

Wallner, G.M., Weigl, C., Leitgeb, R., Lang, R.W. 2004. Polymer Films for Solar Energy Applications– Thermoanalytical and Mechanical Characterisation of Ageing Behaviour, *Polymer Degradation and Stability*, 85: 1065–1070.

Wallner, G.M., Povacz, M., Hausner, R., Lang, R.W. 2016. Lifetime Modeling of Polypropylene Absorber Materials for Overheating Protected Hot Water Collectors, *Solar Energy*, 125: 324–331.

How the use of cementitious geocomposites in tunnels will reduce our impact on the planet?

Paul Guinard
ESTP Civil Engineer
Director Civil Engineering, SOPREMA Group
President of the Geomembranes French Producers Association (APRODEG)

ABSTRACT: During the PVC geomembrane installation for waterproofing of tunnels and structures and in order to mechanically protect the product, we usually pour a 6 cm thick slab of concrete. This screed allows the installation of reinforcement bars for the internal structure.

After dynamic and static tests, we realized that we could use cementitious geocomposites instead of this on site poured concrete. In fact, the presence of a big quantity of poly-propylene fibers in the product offers a subsequent resistance which is sufficient in most of the cases.

It has a real impact on resiliency as the use of this type of product instead of a thick concrete slab is reducing: 1. the depth for the digging and 2. the quantity of concrete poured on site.

The example of this use in tunneling applications demonstrates it can be used in many other situations for protection: basins, basements, buried structures, temporary protection ... offering on each project a reduction of energy compared to traditional solutions.

1 PRESENTATION

The awareness of recent years concerning our environmental responsibility and the worrying studies in terms of the carbon footprint of our achievements has pushed us, for several years now, to embrace our environmental responsibility and to develop viable solutions to reduce the environmental impact on our way to build.

A recent study (Carbone 4 for FNTP - Fédération Nationale des Travaux Publics = French Federation for Civil Works: acteurspourlaplanete.fntp.fr/actualites/travaux-publics-quel-est-le-cout-carbone-des-chantiers/) shows that the construction of infrastructures in France emits approximately 23 million tons of CO2eq per year. This corresponds to 3.5% of France's carbon emissions. Among these emissions, around 14.5 million tons of CO2eq are generated by products, raw materials, and land use.

There are many ways to approach this challenge, but the simplest of them is to reduce the quantities of materials used. In the construction of tunnels, between 60 and 80% of embodied carbon is contained in the concrete linings (International Tunnelling Association - IATTech). Solutions to reduce the quantity of concrete or the thickness used are therefore among the most interesting to limit the carbon footprint of our projects.

During the studies conducted by SOPREMA Group, we realized that the use of cementitious geocomposites made it possible to significantly reduce the quantities of concrete used to protect our PVC geomembranes under rafts.

This article describes the materials used and compares the methods both from an environmental and a financial point of view.

2 CEMENTITIOUS GEOCOMPOSITE

In recent years, we have seen some new geosynthetic solutions for many different applications often relative to soil reinforcement and water management. The cementitious geocomposite is an innovative type of product which can be used in many applications and offers the possibility of new domains to geosynthetics uses.

Depending on the area or the producer, they are named geocomposite or mats but are all grouped in the family of GCCM: (Geosynthetic Cementitious Geocomposite Mats).

2.1 *Concrete in rolls*

The concept of a GCCM is simple: to deliver and install a layer of concrete in a new way.

Use of this product allows to deliver on site, only rolls made from geosynthetics containing a sand and cement mixture which once hydrated will form a thin layer of fiber reinforced concrete.

It is concrete delivered in rolls!

It can be used in many applications in which erosion control or mechanical protection are required: on slopes, for ditches and canals lining, as a protection of geomembranes or as a temporary protection and many other applications as concrete blinding, reinforcement support, temporary support, etc …

There are different ways to produce GCCM: needle punching, injection of cement within a prefabricated matrix … The importance is to create a regular cementitious layer on the full surface of the product embedded between geotextiles.

For our application, we used a TILTEX® which is produced as follows:

- A non-woven geotextile in 100% polypropylene fibers is placed in the production line.
- The requested quantity of mixture sand/cement is placed on this first layer.
- These two layers are covered by a second layer of a non-woven geotextile in polypropylene.
- All is then maintained by an intense needling made in line to allow the fibers to bind the two geotextile layers together, strengthen the base of the mortar and make the product workable. A mesh of polypropylene fibers is then dragged between carrier and cover layers allowing cohesion between them and thus giving an excellent hold to the product.
- The products are then cut, rolled and packed.
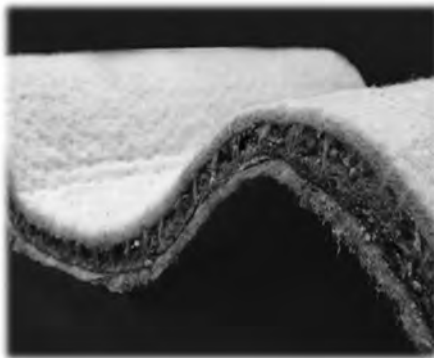
Figure 1.   Sectional view of a cementitious geocomposite.

The amount of sand / cement mixture placed between the geotextiles is chosen according to the desired product applications: mechanical resistance (to puncture for example), resistance to erosion ... For protection applications, we are using geocomposites containing 10 or 12 kg/m^2 of mixture. This offers products from 10 mm to 12 mm thick.

The geocomposite is produced in maximum 5 m width and different dimensions (width and length) and are proposed in order to adapt to the requirement of the projects (size, installation method, accesses ...):

- 5 m × 20 ml and 2.5m × 20ml for large flat surfaces or slopes.
- 1 m × 5 ml for small applications or difficult accesses.

2.2 Installation

The cementitious geocomposite rolls are delivered directly on site. They are individually wrapped in a watertight plastic protection covering the roll and sealed at the ends. Depending on the weight of the rolls, they are unloaded with the use of lifting straps predisposed on each roll (for large ones) or in pallets (for small or medium size ones). Handling of large or medium size rolls must be done using a lifting device and a suitable lifting beam. For small rolls, it is possible to handle them with 2 or 3 people using a pin placed in the roll core.

Once unpacked, the geocomposite is positioned by unrolling it directly on the prepared substrate or on the geomembrane to protect. As the product is flexible, it is easy to install it with the desired shape. An overlap of the ends of 0,10 to 0,20 m ensures the continuity of protection.

Of course, the product can be cut to fit specific dimensions or shapes. Providing it is not hydrated, it remains flexible and can be repositioned.

Once the layer has been positioned correctly, hydration by abundant watering is necessary to set the concrete. It is set by spraying water without pressure directly on the whole surface of the product. The prescribed quantities of water are at least 0.5 liter per m^2 and per kg of sand / cement mixture. In case of strong wind or hot temperature, further watering may be essential. It is necessary that the surface geotextile be kept wet for 48 hours.

About 48 hours after the completion of the hydration, the concrete will be hardened enough for the geocomposite to fulfill its role of protection.

3 USE AS WATERPROOFING PROTECTIVE SCREED

3.1 Traditional and GCCM solutions to protect PVC geomembranes in tunnel

The use of PVC geomembrane waterproofing systems under the foundation rafts requires a protection between the waterproofing layer and the reinforcement bars of the raft. This protection allows the implementation of the reinforcements without damaging the geomembrane. Traditionally, this protection is made of lean mix concrete to a thickness of 6 cm. The proposed alternative is to use the geocomposite, which is much easier and quicker to implement, especially on inclined areas, and allows a sufficient level of protection.

Figure 2.   3D view of the alternative with geocomposite as protection screed.

This alternative presents both savings in the quantities of concrete used but also the ground to be excavated under the raft. The savings are as follow:

- The 6cm of lean mix concrete poured on site for the protection screed are removed.
- As the geocomposite has a thickness of only 1 cm, it affords a reduction in the excavated depth of 5 cm which can be important for urban projects.

Not only this can have an economic advantage (depending on the location, the depth, the type of ground, etc.), but it also has a significant impact on the CO_2 emissions of the projects.

3.2 Are GCCM sufficient to protect geomembrane?

The resistance of the cementitious geocomposite is mainly due to the presence of a high density of polypropylene fibers in the concrete part which give both good strength and excellent puncture resistance (static and dynamic).

We saw multiple advantages to use this product to protect a geomembrane placed under the raft, but we had first to prove its resistance for this specific use. We then made specific tests in order to comply with each respective requirements for this application.

The first step is to use the appropriate CE marking of this type of product as it is mandatory to apply it in Europe. The EN 13256 (Geotextiles and geotextile-related products – Characteristics required for use in the construction of tunnels and underground structures) has been used with the function Protection (P).

In the DoPs (Declaration of Performances) and in the technical data sheet, it is important to detail if the values are measured before or after hydration.

Table 1. Example of declared performances.

Essential characteristics	Characteristics	Before or after hydration
Thickness (mm)	EN 9863-1	Before hydration
Mass per unit area (kg/m2)	EN 14196	Before hydration
Maximum tensile strength MD/CMD (kN/m)	EN 10319	Before hydration
Elongation at break MD/CMD (%)	EN 10319	Before hydration
Static puncture resistance (CBR) (N)	EN 12236	After hydration
Dynamic puncture resistance (mm)	EN 13433	After hydration

The requirement of the CE marking as geocomposite with the appropriate standards needs the assessment and the verification of constancy of performance of the product in a system 2+. It means the initial values have to be controlled by a notified body which is accredited for these types of products.

The second step was to ensure that the product protects the PVC geomembrane sufficiently. For this we carried out two series of specific tests:

- Compressive strength:
  To validate the quality of the cement/sand mixture used, its process of integration in the geocomposite and of hydration, we confirmed the value of the compressive strength with the two used standards: EN 13791 and ASTM C109-2.
- Dynamic puncture:
  The most representative way to evaluate the level of protection the GCCM offers to a geomembrane is the one proposed by the French standard NF P 84-506. This test is highly demanding but ensures the required level of protection against any puncture due to the application of backfills or reinforcement bars.

This test simulates a dynamic shock by the drop of a specific impact tool on a specimen composed by a geomembrane (or the system used as waterproofing barrier) protected by the geocomposite. The energy of the system is set at the specified value (named Class II, I or 0) depending on the required protection level. Impacts may cause the tool to penetrate through the protection and into the membrane. The integrity of the membrane is then checked by vacuum tests.

To be used in applications under any type of backfills or reinforcement, the requirement is to have a protection of class 0 (which correspond of an impact of 14,75 Joules) (AFTES Guidelines on "Design of protection barriers to geomembrane waterproofing systems", June 2004 – www.aftes-asso.fr).

In our case, the geocomposite TILTEX 10 passed the test with not only a class 0 but also under the same test with double impact on the same position. To be sure to reach a sufficient protection on every project, we decided to use this geocomposite thickness as a minimum.

The use of this product as an alternative to protect PVC geomembranes has been validated and is now authorized in many underground projects.

3.3 *Case study – grand paris project – line 16*

As an example, the geocomposite $10kg/m^2$ has been used as a protection screed on waterproofing PVC geomembranes full system in the following project:

Site: Mandella well, Paris metro new line 16 (France)
Owner: Société du Grand Paris
Surface: 4,500 m^2 installed

Figure 3.   Geocomposite installed on the PVC geomembrane in Paris Line 16.

We found multiple benefits in this solution:

• Easy and quick to install even with difficult access or on slopes.
• No need to be cast on joints and along the compartmentalization.
• Less digging (the bottom level is 5 cm higher).
• Less concrete used …

Depending on the project, this solution will afford both economic and environmental advantages to the designers.

4 CARBON FOOTPRINT

What does "carbon footprint" mean?

According to the French Ministry of Ecological Transition, the carbon footprint is an "indicator estimating the quantity of greenhouse gases emitted to satisfy consumption in the broad sense (goods, services, use of infrastructure) of an individual, a population, a territory or an activity, taking into account emissions related to imports and exports regardless of where these goods and services are produced (domestic production or imports)."

It therefore takes stock of the carbon emissions associated with goods or services produced on a national scale, but also those that we import each year.

For simplicity and homogenization, we use a single standard related to CO2 for all greenhouse gases (there are in fact 6 of them: Carbon Dioxide (CO2), Methane (CH4), Hydrofluorocarbon (HFC), Protoxide of Nitrogen (N2O), Perfluorocarbon (PFC) and Sulfur Hexafluoride (SF6)).

We speak of "CO2 equivalent", or "CO2e" (or sometimes even "CO2eq").

One of the big advantages of using the carbon footprint is that, in the case of calculating the carbon impact of a product, we must consider its entire "life cycle", from the research & development phase to that of its final production (also including its packaging up to the recycling stage). Indeed, the carbon footprint of materials used in the world of construction is calculated by considering all the stages of their life cycle:

- Production: supply of raw materials, transport from the manufacturer and manufacturing.
- Construction: transport of construction and implementation.
- Use: use, maintenance, repair, replacement, rehabilitation, use of energy or water.
- End of life: dismantling, transport, waste treatment and disposal.

The carbon footprint is therefore measured by considering the quantity of CO2 emitted by a unit of product used (liters of gasoline, m2 of surface, kg of steel, m3 of concrete, etc.).

If the carbon footprint, which does not take into account pollution, the extinction of biodiversity, etc., is not perfect, it remains a very interesting, indisputable and important tool to use because it makes it possible to quickly measure the impact of our climate activities.

To give a realistic idea of the significance of the carbon footprint, you may consider that an adult tree absorbs an average of 50 kilos of CO2 per year (it depends on its species, its age, its size or even the climate but it is a medium range ...).

5 COMPARATIVE IMPACTS

In order to compare the impact of our two solutions, we can add up all the carbon footprints relating to each element of the construction.

These data are available either in material-specific documents (based on the dedicated protocol and the EN15804 standard) or in databases giving average values. For example, the French INIES database (available free of charge on the internet www.inies.fr) makes it possible to find most of the data related to the average carbon footprints of materials.

To carry out this comparison we are going to base it on a metro station of approximately 2.000 m^2 located in Paris (the location is necessary to include the transportation of the GCCM, but we will have an approx. same result for all cities in Europe) and consider only the elements that differ between the 2 solutions

Traditional solution:

- Lean mix concrete:
  Quantity: 6 cm on 2.000 m^2 = 120 m^3
  Medium carbon footprint = 180 kgCO2eq/m^3

Total: 21.600 kgCO2eq

Note: The carbon footprint of concrete depends on their dosage and varies from 150 to 400 kgCO2eq/m3. Here we have taken the average value for lean concrete as presented in the INIES base (www.inies.fr). If we have a project with difficult access, long distance from a concrete central or with a deep raft, we will have to consider a higher rate of CO2eq.

<u>Solution with use of GCCM:</u>

- GCCM:
  Quantity: 2.000m^2
  Carbon footprint = 3.13 kgCO2eq/m^2 (value issue from the "Carbon Footprint Report" of TILTEX 10)

  <div align="right">Sub Total: 6.260 kgCo2eq</div>

- Transport of the GCCM:
  Quantity: 1.250km for 2.000 m^2 of product which weighs 10 kg/m^2
  Medium carbon footprint = 0.076 kgCO2eq/t/km

  <div align="right">Sub-Total: 1900 kgCO2eq</div>

Note: We considered the installation impact as negligeable as it includes only unrolling and watering.

- Reduction of the excavated volume:
  Quantity: 5 cm less on 2.000 m^2 = -100 m^3
  Medium carbon footprint = 0.82 kgCO2eq/m^3

  <div align="right">Sub-Total: -820 kgCO2eq</div>

- Transport of the excavated volume:
  Quantity: 100 m^3 (or 250 tons) on 20 km
  Medium carbon footprint = 0.76 kgCO2eq/t/km

  <div align="right">Sub-Total: -3.800 kgCO2eq</div>

Note: We consider the excavated ground with a small depth (which can be important in many metro stations in cities) and to be directly re-used on another project. If it is not the case, we will have to consider a higher medium CO2eq and a treatment and storage additional CO2eq.

<div align="right">Total: 3.540 kgCO2eq</div>

6 CONCLUSION

As presented in this article, the alternative use of cement geocomposites to replace protections made of lean mix concrete above PVC geomembrane waterproofing not only creates financial savings but also greatly limits the environmental impact of our works.

For example, for an underground station with a plane surface of 2000 m^2, the use of a geocomposite allows a reduction of its carbon footprint by more than 18,000 kgCO2eq (it divides by 6 the impact due to the protection).

For the record, it means that for each metro station built, this excessive CO2eq corresponds to the average absorption of a 360 adult trees forest in one year.

This study has been performed for a protection on PVC geomembrane within a tunnelling application, but the same GCCM can be used on basins, basements, buried structures or landfills with similar positive environmental impact.

If this is not enough to save it, it helps to limit our impact on our planet.

How an enhanced lateral drainage geosynthetic provides resilience to civil structures

R.B. Laprade, P.Eng. & J.M. Lostumbo, P.E.
Solmax, Jefferson, Georgia, USA

ABSTRACT: According to The Resilience Shift, infrastructure resilience is defined as the ability to withstand, adapt to changing conditions, and recover positively from shocks and stresses (The Resilience Shift, 2020). Four properties are associated with engineering resilience: (1) Robustness to withstand unforeseen demands; (2) Redundancy to tolerate the loss or damage to a component; (3) Resourcefulness to identify a problem and to respond effectively; and (4) Rapidity to restore functionality quickly. This paper will examine the contribution of a unique enhanced lateral drainage reinforcement geosynthetic (ELDRG) towards the resilience of current and future infrastructure projects, especially roadways and working surfaces. Research summaries will demonstrate how the ELDRG is incorporated in civil projects to provide separation and mechanical stabilization as well as moisture management in saturated and unsaturated conditions. We will also show how to quantify the mechanical and hydraulic benefits of this moisture management system in pavement designs.

1 INTRODUCTION

Resilience and sustainability go hand in hand. The ability to satisfy our immediate demands without compromising the welfare of others in the future is what is meant by sustainability (Brundtland 1987). A system's resilience is its ability to withstand stress while maintaining its essential structure and function (Walker & Salt 2006). In essence, resilience prioritizes the processes that lead to these outcomes while sustainability emphasizes the outcomes.

Bruneau *et al.* (2003) consider engineering resilience as desired outcomes that are reached through measurements of improvement when looking at roads and other civil constructions. The targeted outcomes are: (1) Robustness, which is the capacity to resist a specific degree of stress or demand without degrading or losing function; and (2) Rapidity, which is the capacity to fulfil priorities and complete tasks quickly to stem losses and prevent disruption in the future. The units of improvement are: (3) Redundancy: the extent to which elements, systems, or other units of analysis exist that are substitutable in the event of a disruption; and (4) Resourcefulness: the ability to identify problems, prioritize, and mobilize resources when conditions exist that threaten to disrupt some element, system, or other unit of analysis. These are the four R's of resilience.

Geotechnical engineering serves as the basis for the design of project components such as roadways and foundations. Due to it being at the start of many projects, geotechnics presents a huge opportunity for resilient development methods. To that end, an improved lateral drainage reinforcement geosynthetic is now available, providing the functions required for roadway and civil applications (separation, filtration, reinforcement), as well as unique moisture management capabilities that move the needle toward structures that have all four R's of resilience.

2 ENHANCED LATERAL DRAINAGE REINFORCEMENT GEOSYNTHETIC (ELDRG)

The ELDRG is a woven high-modulus geotextile made primarily of polypropylene resin, which provides strength and reinforcement. The polar hydrophilic (naturally attracted to water molecules) and hygroscopic (absorbs moisture from the air) yarns interwoven within the non-polar hydrophobic (repels water molecules) polypropylene yarns provide the enhanced lateral drainage capability.

2.1 Saturated vs. Unsaturated water flow

There are several traditional methods to remove water from roadways. The primary route is through surface runoff from a paved roadway. Water does, however, find its way into aggregate base and subbase materials through infiltration through cracks and joints in the asphalt or concrete surface, as well as through roadway shoulders. The rate of drainage in such cases is determined by the quality of the aggregate materials. This method only considers water in saturated ground conditions. In unsaturated conditions with negative pore water pressures, the effectiveness of an aggregate base in removing water is greatly reduced. Polypropylene nonwoven geotextiles and geocomposites excel at draining water in saturated conditions. However, due to the hydrophobic nature of their polymer constituents and large pore sizes, their efficiency is significantly reduced in unsaturated soils.

Zhang *et al.* (2009) performed rainfall infiltration soil column tests in which they compared the drainage performance and behaviour of saturated columns of silt that were underlain by four different geosynthetics; two woven geotextiles, one geocomposite and the ELDRG. The results of the tests are depicted in Figure 1. The ELDRG removed significantly more water than the other geosynthetics. According to the researchers, "differences in moisture content distributions in the soil columns are therefore mainly caused by unsaturated water flow induced by suction head difference." This is a significant conclusion because, at the time of writing, the ELDRG is the only geosynthetic available capable of removing water in unsaturated conditions.
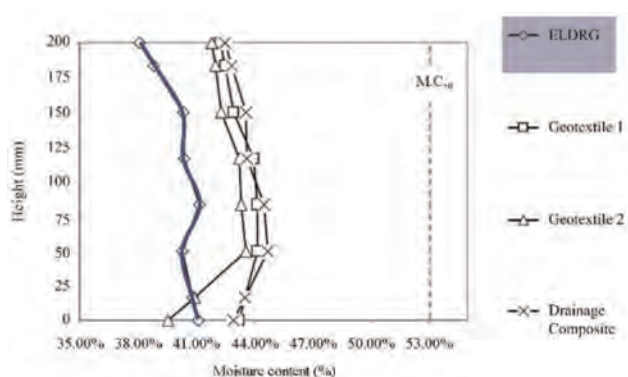
Figure 1.   Rain infiltration tests (Zhang *et al.* 2009).

2.2 Air entry value for the ELDRG

Lin *et al.* (2019) determined that the ELDRG's inner-yarn air entry value is approximately 250 kPa and that of a nonwoven geotextile is less than 1 kPa. This means that the ELDRG can draw water out of any soil until the reduced moisture content causes the suction value to reach 250 kPa. The Soil Water Characteristic Curves for various soils, as well as the

Geosynthetic Water Characteristic Curves for the ELDRG, are shown in Figure 2. To illustrate the significance of these curves, the ELDRG can reduce the moisture content of fully saturated silt from approximately 20% to 10%. Suction is inherent in clays, particularly those with high plasticity indices. This means that the overall moisture reduction is lower than it is in non-cohesive silts and sands. However, Budhu (2011) claims that for every 1% decrease in moisture content, the undrained shear strength of fine-grained soils can increase by about 20%. According to this statement, a 3% to 4% decrease in moisture content in cohesive soils has a major impact on the soil's bearing capacity.
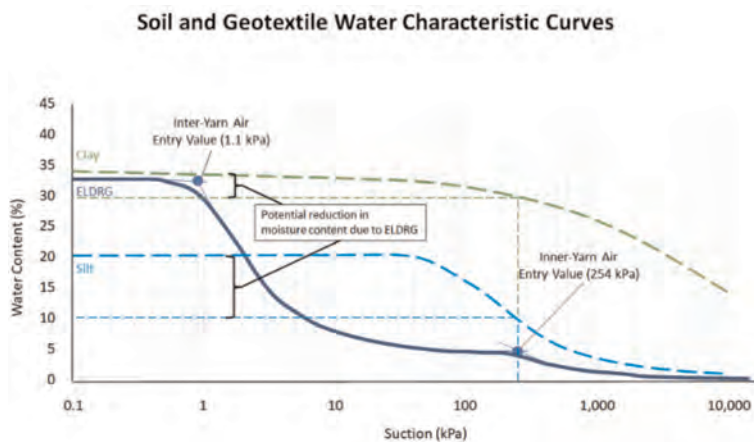
Figure 2. Soil and geotextile water characteristic curves (Lin *et al.* 2019).

3 THE FOUR R'S OF RESILIENCE AND ELDRG RESEARCH

3.1 *Robustness*

The ability of a system to withstand unforeseen demands without degradation or loss of function is referred to as robustness. The ELDRG provides robustness by mechanically stabilizing soft subgrades, extending the life of the overlying roadway while minimizing rutting. This geosynthetic can also reduce differential movement caused by (1) freeze-thaw cycles in frost-susceptible soils and (2) shrinking and swelling of expansive clays due to its hydraulic stabilization ability.

3.1.1 *Frost susceptible soils on the Dalton Highway – Alaska, USA*
Beaver Slide is an unpaved section of the Dalton Highway in Alaska, located at Mile 110.5. It has an 11% downward gradient looking north. Since its construction in 1974, frost boils and soft areas have appeared during the spring thaw, healed during dry summer periods but reappeared after a heavy rain. The soft areas vanished when the ground froze during the winter. Previous conventional repair efforts were ineffective.

A 20-metre ELDRG test section was constructed in August 2010 (Zhang *et al.* 2012). The section was excavated to a depth of one metre, and two layers of ELDRG were placed at different elevations. Moisture and temperature probes were placed throughout the section, above, between, and beneath the layers of ELDRG. Since the installation, hourly probe readings have been recorded and will continue until the end of 2023. Water within the roadway freezes between October and April, and the system goes hydraulically dormant. At the time of freezing, the materials in the upper 0.6 m of the road section are below saturation levels, which is 26% volumetric moisture content. Since soils are unsaturated when they

freeze, no ice lenses form, mitigating seasonal frost heave and subsequent spring thaw weakening of the subgrade. Figure 3 depicts the temperature and moisture contour graphs on May 22, 2011. The top 1.2 m of the roadway has thawed while the soils in this section of the roadway have remained unsaturated. Every year, the Beaver Slide is inspected, especially during the spring thaw. The surface failures that had existed since the roadway's construction have vanished since the installation of the ELDRG.
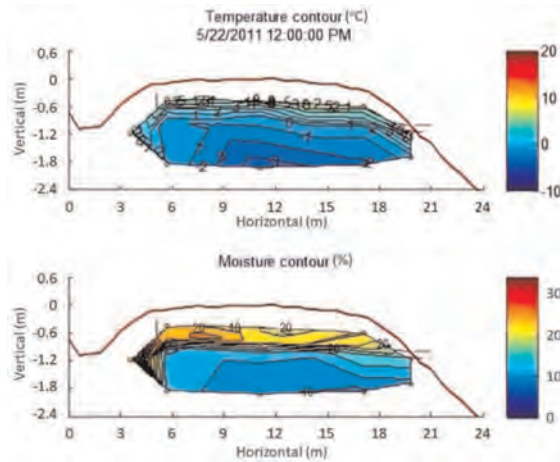
Figure 3.   Contour Plots (May 22, 2011).

3.2   *Rapidity*

The ability of a system to quickly restore function after a disruption is referred to as rapidity.

3.2.1   *Effect of water on the resilient modulus of a granular base and pavement deformation*
The primary mechanical property required in both the Mechanistic-Empirical Pavement Design Guide (MEPDG) and AASHTO pavement designs is resilient modulus. Water entering the granular base of a roadway can have a significant negative impact on its resilient modulus. Lin *et al.* (2019) demonstrated, using tri-axial testing, that decreasing an aggregate base's moisture content by 2% from optimal compaction levels could increase its resilient modulus several times. (Figure 4).
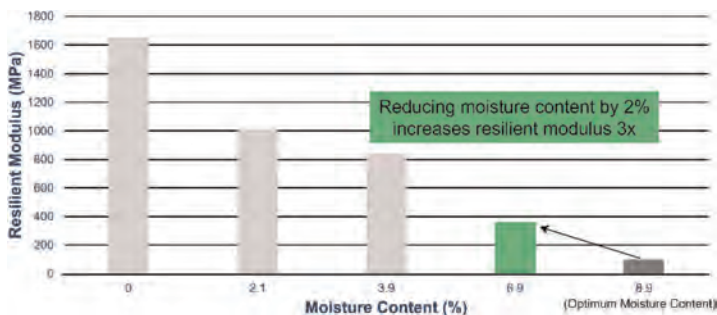
Figure 4.   Resilient modulus vs. Moisture content (Lin *et al.* 2019).

Guo *et al.* (2018) used large-scale cyclic plate loading tests with simulated rainfall to determine the ELDRG's improved lateral drainage ability. Each test section had a 0.9-meter-thick subgrade layer (CBRs of 3% and 5%) and a 0.3-meter-thick base course layer. They included a control section (no geosynthetic), a second test section with a high-modulus woven geosynthetic with similar physical properties to the ELDRG but without the moisture management yarns, and a third with the ELDRG. Moisture and pressure sensors were installed throughout the box. The researchers used simulated rainfall for 24 hours, then waited six days before conducting their cyclic plate loading tests, which included 1000 loading cycles. This cycle was repeated twice with different wait times between rainfalls and testing. Moisture content in the ELDRG test sections was reduced by up to 2% compared to the control and other geotextile sections. Permanent deformation was reduced in the ELDRG section by more than 70% compared to the other sections.

3.3 *Redundancy*

The extent to which elements, systems, or other units of analysis are substitutable, meaning they are capable of satisfying functional requirements in the event of disruption, degradation, or loss of functionality, is referred to as redundancy. Water drainage within a roadway structure is thought to be accomplished by a "free draining" base course placed on a crowned subgrade, typically constructed with a 2% to 3% crossfall. Ideally, this approach is sufficient to ensure a roadway's longevity. What happens if the subgrade is not strong enough to support the structure? Water may accumulate in the subgrade ruts, exacerbating the problem. Similar issues can arise in granular base/sub-base materials with fines contamination. Water will worsen the situation by interfering with free drainage. The inclusion of the ELDRG into such structures provides redundancy on two levels. First, the mechanical stabilisation benefits can compensate for the weaker supporting subgrade, reducing premature rutting. Second, the additional lateral drainage of the ELDRG provides water removal redundancy.

3.4 *Resourcefulness*

When conditions threaten to disrupt some element, system, or other unit of analysis, resourcefulness refers to the ability to identify problems, establish priorities, and mobilize resources. Moisture is the most common cause of premature roadway deterioration. It is easy to conclude that a system capable of removing excess water from such civil structures while also preventing rutting and surface cracking is an especially useful addition. The ELDRG is a particularly resourceful means that designers and owners can include in their roadway assets owing to its previously mentioned exceptional ability to remove moisture in both saturated and unsaturated conditions.

4 QUANTIFYING THE MECHANICAL AND HYDRAULIC BENEFITS OF THE ELDRG

Quantifying both the mechanical and hydraulic gains of the ELDRG in roadway design methodologies is important. The moisture content of unbound aggregate base has a significant impact on the material's resilient and permanent strains. Based on previous research, Lekarp *et al.* (2000) concluded that a high degree of saturation combined with low permeability results in high pore pressure and low effective stress, and thus low stiffness, strength, and deformation resistance.

4.1 *Flexible asphalt pavements*

One of most used design methods for flexible pavements in North America is the AASHTO Guide for Design of Pavement Structures (AASHTO 1993). A structural coefficient

incorporates the resilient modulus of the aggregate base, and a drainage coefficient considers the effect of moisture on the aggregate base within the methodology. Flexible pavement designs have included geosynthetics since the early 1980s. Lacina *et al.* (2015) evaluated high-modulus woven geotextiles in full-scale accelerated load frame pavement testing. The tests quantified the mechanical benefits provided by high-modulus woven geotextiles, including the ELRDG, in base reinforcement applications at various traffic levels and sub-grade conditions. This research yielded Geosynthetic Structural Coefficient (GSC) values that can be applied to the structural number of the granular layer directly overlying the geosynthetic. This approach also complies with AASHTO R50-09 (2009), which states that "because the benefits of geosynthetic reinforced pavement structures may not be derived theoretically, test sections are necessary to obtain benefit quantification."

Guo *et al.* (2017) investigated the hydraulic characteristics of the ELDRG through a series of demonstration, water tank removal, small box, and soil column tests. They also conducted six large-scale cyclic plate loading tests with rainfall simulations to assess the impact of the ELDRG on the permanent deformation of base courses and subgrades. This research provided design guidelines incorporating the ELDRG's water content reduction benefit, allowing for further modification of the 1993 AASHTO Pavement Design Guide. This work enables designers to generate a Hydraulic Improvement Factor (HIF) by incorporating local precipitation data for any geographical location in North America. It is determined by the following factors: (1) the frequency and duration of saturation rain events, (2) seasonal temperatures, (3) traffic load expectancy, and (4) the structural integrity of the granular layer overlying the ELDRG. Figure 5 depicts an example of HIF values for specific subgrade and traffic loading conditions in North America.

1.01 – 1.05	
1.06 – 1.10	
1.11 – 1.15	
1.15 – 1.20	
1.21 – 1.25	

Subgrade CBR = 6.0
< 1,000,000 ESALs
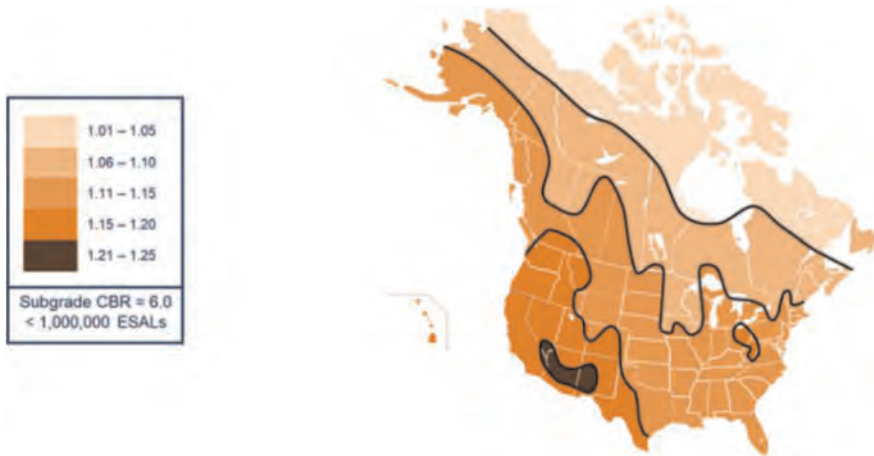
Figure 5. Hydraulic Improvement Factors in North America for ELDRG.

5 CONCLUSIONS

There is a growing need for more resilient construction practices. New ideas and innovative solutions must be developed and implemented to meet the limited natural and financial resources that various levels of government and owners face. The ELDRG is an example of looking at things differently. Designers now have a highly effective tool which removes water in unsaturated conditions. Lacina *et al.* (2015) showed that high-modulus woven geotextiles provide mechanical stabilization to soils having low bearing capacity. As a high-modulus woven geotextile, the ELDRG provides mechanical stabilization and, uniquely, it also

provides quantifiable hydraulic stabilization to roadway designs. The ELDRG has a decade plus proven history of solving moisture-related problems in expansive clays, frost-susceptible soils, areas with high-water tables and other applications where moisture can affect civil structures.

REFERENCES

American Association of State Highway and Transportation Officials. 1993. *AASHTO Guide for Design of Pavement Structures*. The Association.

AASHTO Designation: M 288-21. 2021. *Standard Specification for Geosynthetic Specification for Highway Applications*. American Association of State Highway and Transportation Officials.

AASHTO Designation: R50-09. 2009. *Geosynthetic Reinforcement of the Aggregate Base Course of Flexible Pavement Structures*. American Association of State Highway and Transportation Officials.

Brundtland, G. 1987. *Report of the World Commission on Our Common* Future, United Nations General Assembly Document A/42/427.

Bruneau, M., Chang, S., Eguchi, R., Lee, G., O'Rourke, T., Reinhorn, A., Shinozuka, M., Tierney, K., Wallace, W. & Von Winterfeldt, D. 2003. *A Framework to Quantitatively Assess and Enhance the Seismic Resilience of Communities*. EARTHQ SPECTRA. 19. 10.1193/ 1.1623497.

Budhu, M. 2011. *Soil Mechanics and Foundations*, *3rd Edition*. Hoboken: John Wiley & Sons, Inc.

Lacina, B., Sack, R., and Odgers, B. 2015. *Flexible Pavement Reinforcement using Geotextiles*. 2015 Geosynthetics Conference.

Lekarp, F., Isacsson, U. and Dawson, A. 2000. State of the art: Resilient response of unbound aggregates, *Journal of Transportation Engineering*, 126(1), 66–83.

Lin, C., Zhang, X. and Han, J. 2019. Comprehensive Material Characterizations of Pavement Structure Installed with Wicking Fabrics. *Journal of Materials in Civil Engineering*, Vol. 31, No. 2, 2019, p. 04018372. http://ascelibrary.org/doi/10.1061/%28ASCE%29MT.1943-5533.0002587.

Walker, B. & Salt, D. 2006. *Resilience thinking: Sustaining Ecosystems and People in a Changing World*. Washington, DC: Island Press.

What Is Critical Infrastructure? Why Is Resilience Important? (2020, October 20) The Resilience Shift. www.resilienceshift.org/work-with-us/faqs

Zhang, X., Presler, W. 2012 *Use of H₂Ri Wicking Fabric to Prevent Frost Boils in the Dalton Highway Beaver Slide area – Final Project Report*. Department of Civil and Environmental Engineering, University of Alaska, AK.

Sand-rubber mixtures under one-dimensional cyclic loading

S. Ozkan, E. Ibraim & A. Diambra
University of Bristol, Bristol, UK

ABSTRACT: The number of scrap tyres is growing all around the world due to increasing number of vehicles. This creates significant environmental and economic concerns. Recycling and reusing scrap tyres in engineering projects is an alternative way to deal with these concerns. Recycled tyres are commonly mixed with soils in different proportions. This paper presents a series of laboratory experiments on sand-rubber mixtures (tested with seven different volumetric rubber fractions ranging from 0% (pure sand) to 100% (pure rubber)) under one-dimensional cyclic loading at different stress levels. It is aimed to investigate the behaviour and response of mixture with increasing rubber fraction under different cycle loads. The results indicate that one-dimensional characteristics of mixtures depends on rubber fraction. The applied cycle load also affects the response of mixtures. The results of cyclic oedometer tests were analysed and the effect of applied vertical stress on the remanent deformation were discussed.

1   INTRODUCTION

Increasing number of scrap tyres causes significant environmental concerns globally. Recently, recycling scrap tyres through use in civil engineering projects has become an effective way to deal with their environmental effects. Additionally, the inclusion of scrap tyres in their shredded form into civil engineering materials creates alternative solutions to meet the demand for construction industry (Hazarika *et al.* 2010). As rubber is a soft, elastic material and has high damping properties, sand-rubber mixtures (SRM) are also used in playgrounds and sport facilities as a soft surface material and in railways, pavement and road embankments (Edil & Bosscher 1994; Edincliler *et al.* 2010). Rubber is also used in retaining walls as a lightweight backfill material (Lee *et al.*, 1999; Tweedie *et al.* 1998) and in structures to reduce the vibration (Feng & Sutter 2000). In geotechnical engineering, it has also been observed that mixing rubber particles obtained from scrap tyres with granular soils can help improving soil properties such as bearing capacity and settlement problems (Ahmed 1993; Tatlisoz *et al.* 1997). The engineering properties of SRM have extensively been studied in laboratory. most of the research has mainly focused on the characterization of the compressibility (Attom *et al.* 2007; Fu *et al.* 2014; Lee *et al.* 2007; Trouzine *et al.* 2012) and the monotonic strain-stress-strength behaviour of various combinations of soils, rubber types and particle size dimensions (Edil & Bosscher 1994; Rouhanifar *et al.* 2020; Sheikh *et al.* 2013; Zornberg *et al.* 2004). Rubber content, rubber particle size with respect to the size of the host granular soil and rubber particle shape have been found as key parameters in controlling the response of SRM (Kim & Santamarina 2008). A comprehensive summary of a range of experimental studies including the physical characteristics of the mixture materials used as well as the testing conditions and main outcomes is given by (Fu *et al.* 2017). However, the investigation of the cyclic behaviour of SRM is relatively limited (Mashiri 2014; Tsang *et al.* 2012; Uchimura *et al.* 2008). The undrained cyclic triaxial test results show

that the excess porewater pressure ratio decreases with increasing rubber content in the mixtures (Ahmed 1993) which also results in increasing liquefaction resistance with increasing volumetric fraction of tyre chips in the mixtures as observed from dynamic experimental work on sand-tyre chips mixtures (Tsang *et al.* 2012; Uchimura *et al.* 2008).

This paper presents the results obtained from laboratory-based research on the mechanical response of SRM under strain-controlled one-dimensional loading, including successive cyclic loading at different stress levels. The effect of the rubber content on the cyclic response of SRM is particularly investigated. The aim of this work is a fundamental investigation revealing insights into the internal interaction mechanisms between a rigid particle material, sand, and a soft particle material, rubber, to integrate into a constitutive model rather than optimising the amount of rubber content for engineering applications. In this respect, the particle size distribution of both sand and rubber materials are chosen to be identical. Test on pure sand and pure rubber complete the experimental programme.

2 MATERIALS AND METHODS

2.1 *Materials and sample fabrication*

Leighton Buzzard sand (D_{50} = 1.57, G_s = 2.65) is mixed with rubber material (G_s = 1.04, (Rouhanifar 2017)), both materials having the same particle size distributions (Figure 1) to remove any effect of sand/rubber particle size contrast as observed in the previous studies (Kim & Santamarina 2008; Lee *et al.* 2007). The rubber material was sieved, the particles separated and then remixed in such a way to obtain the same particle size distribution as that of the sand. Leighton Buzzard sand is mixed it with rubber material in seven different volumetric fractions (F_R):0 (pure sand), 10, 20, 30, 50, 70, and 100% (pure rubber). Volumetric fraction of rubber (F_R) is defined as the ratio of rubber volume to total solid volume of the mixtures as shown by the relation 1.

$$F_R = \frac{V_{Rubber}}{V_{Rubber} + V_{Sand}} \qquad (1)$$

where V_{Rubber} and V_{Sand} are volume of rubber and volume of sand, respectively.
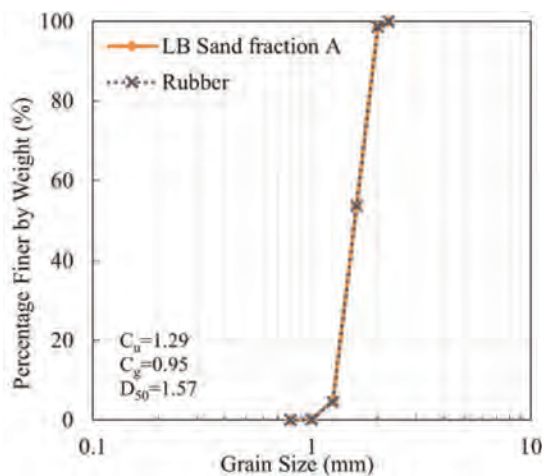
Figure 1.   Particle size distribution for sand and rubber materials obtained from sieve analysis.

345

A steel cylinder (75 mm diameter and 60 mm height) was used for sample fabrication. Sand and rubber materials were initially mixed in dry conditions and then 10% water by the dry weight of sand only was added to all mixtures. Each sample was prepared in two volumetrically equal layers and compacted to required height to obtain a target fabrication void ratio of 0.64, except the sample at $F_R = 100\%$, for which this target void ratio was impractical to be reached in which case a single rubber layer was considered. The list of all the tests, including the sample characteristics like, F_R, initial height, the actual fabrication void ratio, e_f, and the axial displacement rate employed in this study are presented in Table 1. A study of the effect of the axial displacement rate conducted by the authors as part of this research showed that no discernible effect on the one-dimensional behaviour were observed for displacement rate ranges given in Table 1. In the name of the tests, the number represents the values of volumetric fraction of the rubber, F_R. When the sample fabrication process was completed, the top cap was carefully placed on top of the sample, and the one-dimensional test was ready to be conducted.

Table 1. Initial sample properties and testing conditions.

Sample	F_R%	Initial Height mm	Void Ratio (e_f)	Displacement Rate mm/min
SR0	0	57.93	0.644	0.1
SR10	10	57.84	0.642	0.5
SR20	20	57.94	0.644	0.5
SR30	30	57.85	0.642	1.0
SR50	50	57.98	0.645	1.0
SR70	70	58.17	0.651	1.0
SR100	100	34.27	0.881	1.0

2.2 *Experimental set-up*

A constant strain rate loading device was used for the cyclic oedometer tests. A load cell with 10 kN maximum load capacity was employed with a LVDT of 25 mm range for the axial displacement measurements. Three unload-reload cycles at different level of stress of approximately 200, 800 and 2400 (maximum load) kPa were applied for each sample. Once the reloading was applied for the third cycle, the samples were all fully unloaded.

3 EXPERIMENTAL RESULTS AND ANALYSIS

The results of the experimental work are presented in terms of void ratio-axial stress relationship (Figure 2). Making abstraction of the unload-reload cycles, the overall void ratio-axial stress Envelopes move further downwards as the rubber content is increased so the overall volumetric strains at a given stress level tend to increase with the addition of rubber. increasing rubber content induces further deformability and compressibility of the mixture (Kim & Santamarina 2008; Sheikh *et al*. 2013). As discussed by Fu *et al*. (2017) and Fonseca *et al*. (2019), the increased compressibility of the mixture is the result of the low shear modulus of the rubber, and it is the soft rubber distortion, not its compression, that increases the global volume change. As the stress level increases, the rubber particles deform further at the contacts with the rigid sand particles (or similar rubber particles) and, given the fact that the rubber is incompressible, a fraction of the porous space is filled by the deformed rubber particles, hence the increased reduction of the global void ratio, as also discussed by Platzer *et al*. (2018). For both the sand soil and the sand-rubber soil mixtures, unique normal compression lines can be defined especially the limits of the highest pressures. The values of

the compression indices, C_c, resulted from the estimation of the gradient of this normal compression lines function of the rubber fraction, F_R, are given in Figure 3. A steady increase of C_c values with the rubber fraction is recorded, although the increase rate seems to be slightly reduced for rubber contents lower than 20% or higher than 50%. However, at high rubber contents, over 50%, the one-dimensional compression path envelopes gently change into a convex curvature in the void ratio-vertical stress semi-logarithmic plane as similarly observed by Lee *et al.* (2010), Fu *et al.* (2014) and Fonseca *et al.* (2019). This is the effect of the saturation of the voids filled by the rubber grains and thus a clear sign of advanced levels of rubber distortion and rubber saturation of the void spaces.
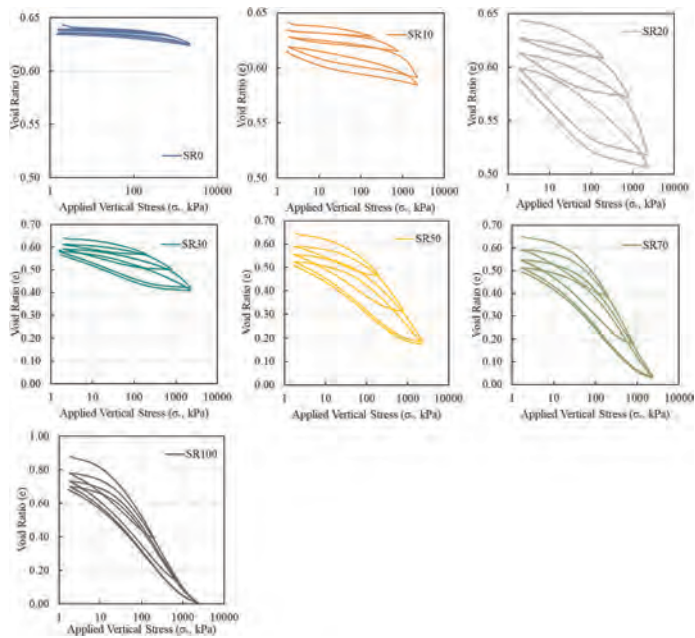
Figure 2.   The void ratio-stress relationship for sand-rubber mixtures with different load cycles.
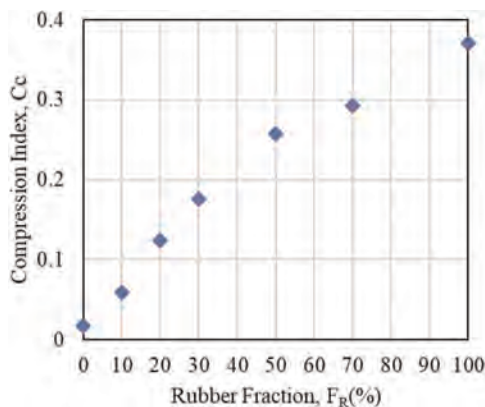
Figure 3.   Compression indexes against rubber fraction.

For the unloading-reloading cycles, the sand shows, as expected, low levels of strain recovery, although the recovery of axial strain is marginally higher for higher axial stress, though not visible at the y-axis scale shown in Figure 2 (SR0). However, the effect of rubber contents on the unloading-reloading cycles is very pronounced. For the sample with 10% rubber content, the unload-reload cycles appear linear for the first two cycles while for the cycle at the highest stress level, 2.4MPa, the unloading shows two distinct linear parts with different slopes, one up to an unloading axial stress of 50kPa and one with a higher gradient up to the full removal of the loading. The last cycle for the SR10 sample shows development of hysteresis. Hysteresis loops are further observed for all sand-rubber mixtures irrespective of the level of axial stress from which the cycles are conducted. Qualitatively, the energy dissipation estimation based on simple visual observation of the hysteresis loops shows that the energy dissipation increases with both the axial stress level, for a given rubber content, and with the rubber content, for a given unloading stress level. The bi-linear unloading paths observed in the semi-logarithmic axes are much more discernible for SR20 and SR30 specimens, while the samples with higher rubber contents, over 50%, the swelling paths have a distinct S-shape.

The effects of adding rubber and for one rubber content the effect of stress level from which the unloading is executed on the cyclic response can be compared by means of swelling index, C_s, Figures 4a and b, respectively. For the sand-rubber mixtures, the C_s values were chosen for the straight part of the swelling curve at the highest gradient. C_s increases with the rubber content, but the variation is linear for both swelling at 2.4MPa and non-linear for the cycles at 200 and 800 kPa (Figure 4a). The C_s variation with the stress level seems to be linear for rubber contents up to 20%, but non-linear for higher F_R values wheat higher increase gradients for pressures up to 800kPa and slower rate of increase for the pressure ranges up to 2.4MPa (Figure 4b). Overall, and based on the values of the void ratio at the end of the unloading cycle, it seems that the sand-rubber structure exhibits higher particle re-arrangements during the initial stage of the loading. As the pressure and the contact area between rubber-rubber and rubber-sand particle increases, the ability of the particles to re-arrange is reduced hence the highest values of C_s indices. As observed by Fonseca et al. (2019), the energy dissipation by unloading at higher stresses can only be explained in terms of the changes of void ratio. Humphrey et al. (1993), Edil and Bosscher (1994) and Bosscher et al. (1997) also showed that rubber-soil mixtures develop substantial initial plastic defor-mations under one-dimensional compression loading, and once the mixture is loaded to a level of reduced void ratio, the behaviour is controlled more by the elastic properties. However, the permanent deformation at the end of each cycle increases with increasing rubber fraction which is in good agreement with previous research by Sheikh et al. (2013).
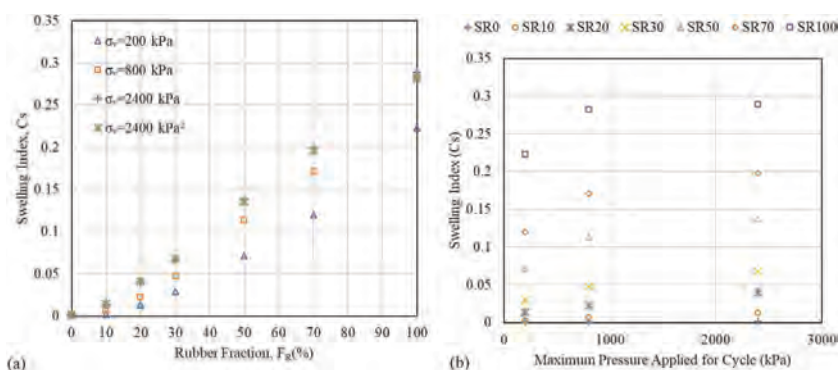
Figure 4. Swelling indexes for all samples plotted a) against rubber fraction for each stress level, and b) against stress at each cycle for rubber fractions.

4 CONCLUSIONS AND RECOMMENDATIONS

The main results of 1-D loading with different unloading-reloading cycles at different stress levels for sand and sand-rubber mixtures of different rubber contents can be summarised as follows:

− Trouble content is the dominant factor controlling both C_c and C_s indices and so the ratio of elastic to plastic strains in compression as well as in unloading.
− The plastic deformation at the end of unloading is related to the applied stress level and rubber fraction.
− The plastic strain seems to be higher following the first unloading, sign of particle rearrangement, and much more reduced for the subsequent cycles, sign of reduced ability of the particles to re-arrange.

Based on the results, it seems that a clear distinction can be made between sand-like behaviour and rubber-like behaviour of the sand-rubber mixtures, and this would correspond to a F_R value of about 20%. Further research is currently conducted for the development of a constitutive model which would include modelling features to reflect the interaction mechanisms revealed by the 1-D loading and unloading-reloading cycles.

REFERENCES

Ahmed, I. 1993. *Laboratory Study on Properties of Rubber Soils*. Phd Thesis, Purdue University.

Attom, M., Khedaywi, T. & Sameer, A. M. 2007. The Effect of Shredded Waste Tire on the Shear Strength, Swelling and Comprssibility Properties of the Clayey Soil. *Journal of Solid Waste Technology and Management* 33 (4).

Bosscher, P. J., Edil, T. B. & Kuraoka, S. 1997. Design of Highway Embankments Using Tire Chips. *Journal of Geotechnical and Geoenvironmental Engineering*, 123, 295–304.

Edil, T. B. & Bosscher, P. J. 1994. Engineering Properties of Tire Chips and Soil Mixtures. *Geotechnical Testing Journal*, 17, 453–464.

Edincliler, A., Baykal, G. & Saygili, A. 2010. Influence of Different Processing Techniques on the Mechanical Properties of Used Tires in Embankment Construction. *Waste Management*, 30, 1073–1080.

Feng, Z. Y. & Sutter, K. G. 2000. Dynamic Properties of Granulated Rubber/Sand Mixtures. *Geotechnical Testing Journal*, 23, 338–344.

Fonseca, J., Riaz, A., Bernal-Sanchez, J., Barreto, D., Mcdougall, J., Miranda-Manzanares, M., Marinell, A. & Dimitriadi, V. 2019. Particle–Scale Interactions and Energy Dissipation Mechanisms in Sand–Rubber Mixtures. *Géotechnique Letter* 9, 263–268.

Fu, R., Coop, M. R. & Li, X. Q. 2014. The Mechanics of A Compressive Sand Mixed with Tyre Rubber. *Géotechnique Letter*, 4, 238–243.

Fu, R., Coop, M. R. & Li, X. Q. 2017. Influence of Particle Type on the Mechanics of Sand–Rubber Mixtures. *Journal of Geotechnical and Geoenvironmental Engineering*, 143 (9).

Hazarika, H., Yasuhara, K., Kikuchi, Y., Karmokar, A. K. & Mitarai, Y. 2010. Multifaceted Potentials of Tire-Derived Three Dimensional Geosynthetics in Geotechnical Applications and Their Evaluation. *Geotextiles and Geomembranes*, 28, 303–315.

Humphrey, D. N., Sandford, T.C., Cribbs, M.M. & Manion, W.P. 1993. *Shear Strength and Compressibilty of Tire Chips for Use as Retaining Wall Backfill Transportation Reseacrh Record*

Kim, H. K. & Santamarina, J. 2008. Sand-Rubber Mixtures (Large Rubber Chips). *Canadian Geotechnical Journal*, 45, 1457–1466.

Lee, C., Truong, Q. H. & Lee, J. S. 2010. Cementation and Bond Degradation of Rubber-Sand Mixtures. *Canadian Geotechnical Journal*, 47, 763–774.

Lee, J. H., Salgado, R., Bernal, A. & Lovell, C. W. 1999. Shredded Tires and Rubber-Sand as Lightweight Backfill. *Journal of Geotechnical and Geoenvironmental Engineering*, 125, 132–141.

Lee, J. S., Dodds, J. & Santamarina, J. C. 2007. Behavior of Rigid-Soft Particle Mixtures. *Journal of Materials in Civil Engineering*, 19, 179–184.

Mashiri, M. S. 2014. Monotonic and Cyclic Behaviour of Sand-Tyre Chip (Stch) Mixtures. Phd, University Of Wollongong.

Platzer, A., Rouhanifar, S., Richard, P., Cazacliu, B. & Ibraim, E. 2018. Sand–Rubber Mixtures Undergoing Isotropic Loading: Derivation and Experimental Probing of A Physical Model. *Granular Matter*, 20:81.

Rouhanifar, S. 2017. *Mechanics of Soft-Rigid Soil Mixtures*. Phd, University Of Bristol.

Rouhanifar, S., Afrazi, M., Fakhimi, A. & Yazdani, M. 2020. Strength and Deformation Behaviour of Sand-Rubber Mixture. *International Journal of Geotechnical Engineering*, 15 (9), 1078–1092.

Sheikh, M. N., Mashiri, M. S., Vinod, J. S. & Tsang, H. H. 2013. Shear and Compressibility Behavior of Sand-Tire Crumb Mixtures. *Journal of Materials in Civil Engineering*, 25, 1366–1374.

Tatlisoz, N., Benson, C. H. & Edil, T. B. 1997. Effect of Fines on Mechanical Properties of Soil-Tire Chip Mixtures. *Testing Soil Mixed with Waste or Recycled Materials*, 1275, 93–108.

Trouzine, H., Bekhiti, M. & Asroun, A. 2012. Effects of Scrap Tyre Rubber Fibre on Swelling Behaviour of Two Clayey Soils In Algeria. *Geosynthetics International*, 19, 124–132.

Tsang, H. H., Lo, S. H., Xu, X. & Sheikh, M. N. 2012. Seismic Isolation for Low-to-Medium-Rise Buildings Using Granulated Rubber-Soil Mixtures: Numerical Study. *Earthquake Engineering & Structural Dynamics*, 41, 2009–2024.

Tweedie, J. J., Humphrey, D. N. & Sandford, T. C. 1998. Tire Shreds as Lightweight Retaining Wall Backfill: Active Conditions. *Journal of Geotechnical and Geoenvironmental Engineering*, 124, 1061–1070.

Uchimura, T., Chi, N. A., Nirmalan, S., Sato, T., Meidani, M. & Towhata, I. 2008. Shaking Table Tests on Effect of Tire Chips and Sand Mixture in Increasing Liquefaction Resistance and Mitigating Uplift of Pipe. *Scrap Tire Derived Geomaterials: Opportunities and Challenges*, 179–186.

Zornberg, J. G., Cabral, A. R. & Viratjandr, C. 2004. Behaviour of Tire Shred-Sand Mixtures. *Canadian Geotechnical Journal*, 41, 227–241.

The sustainable approach to design a noise bund: Paragon Park, Coventry, Warwickshire, UK

Luckeet Rathod*
Geosynthetics Ltd, UK
International Geosynthetics Society IGS
Design Engineer

ABSTRACT: The Paragon Park phase 3 project consisted of constructing a 9.5m high noise bund, 400m in length between a new housing development and a metal recycling facility located in Coventry, Stoney Stanton Road which is in a densely populated area. One challenging aspect of the project was the soil conditions and the fill material, where site won material was to be considered to reduce the overall cost therefore avoiding the use of imported material which would also reduce the disturbance to the local community and travelers during the day. The face of the bund was also a challenge as the client wanted an aesthetic face therefore, we had to consider what possible solutions could be installed on the 70-degree steep face. The bund was built on top of a well prepared and compacted started layer and the site won material was used for the build-up of the bund with multiple layers of geogrid at various length to reduce the material cost. Within the face a rivel mesh system was used to keep the topsoil soil retained at the face with the use of the erosion control mat wraparound and help achieve the 70 degrees as each layer was constructed to achieve the total height of 9.5m. The key elements used to construct the bund: Geotextile Ekotex (nonwoven) used for separation between the different soil materials used for the project, Geogrid Strata to strengthen each layer of the bund, Erosion Control Landlok to achieve a vegetated face and a rivel mesh system to help achieve a 70deg face throughout each layer of buildup.The project was designed using the programs of Reslope and Ressa following the British Standards BS8006:2010 internal stability, Partial Factors and Interaction Factors.

1 INTRODUCTION

1.1 Site description

The Paragon Park project (Phase 3) is a site located at Foleshill Road in Coventry, Warwickshire, United Kingdom. It covers approximately 22 hectares that includes four site landfills in the northeast, a metal recycling yard in the south close to the redevelopment proposal. The redevelopment proposal was to create a residential and commercial/ industrial development on top the landfill areas

The site is underlain by variable thicknesses of made ground that overlays weathered clay and mudstone. Sandstone is expected to be present at depths of 15–20m bgl. Site won material was proposed to be used to help reduce wastage and unnecessary engineering fill import.

*Corresponding Author: Luckeet@geosyn.co.uk

1.2 Project introduction

Phase 3 for the Paragon Park project was to develop a series of low-rise houses and flats in associated soft standing areas. The site formed was to be constructed primarily of cut and fill site won material. A reinforced soil acoustic bund was requested to be designed between a metal recycling facility and a new housing development so that it can provide a noise and visual barrier whilst also being visually aesthetic.

The reason of why geosynthetic material was used for this project was to reduce the overall cost, material and carbon footprint used for the bund's construction with the site won material.

Figure 1.   Cargo containers separating recycling facility & Housing development (prior to bund construction).

Design Considerations

1.3 Noise bund geometry

The geometry for the noise bund was to be designed following the considerations below:

- Maximum height = 9.5m
- Slope angle at face (towards the recycling facility) = 70°
- Slope angle behind the face = 1V:2H
- Running Length (approx.) = 400m

1.4 Soil parameters and surcharges

The surcharge considered due to the fence being installed on top of the reinforced noise bund was a static dead load of 10kPa (unfactored) over the crest, which expands 3m.

Table 1.   Soil properties used in calculations.

Soil Type	Soil Description	Soil Class	Friction Angle $\phi'(°)$	Unit Weight γ (kN/m³)	Cohesion C' (kpa)
Reinforced Fill	Site won material: Dark brown very clayey sandy Gravel and slightly gravelly Clay	Class 2A/2C (Stoney Cohesive Fill)	30	18	0
Backfill	site won material: Very clayey sandy Gravel and slightly gravelly Stoney Cohesive Fill	Class 2A/2C	30	18	0

(*continued*)

Table 1. Continued

Soil Type	Soil Description	Soil Class	Friction Angle $\phi'(°)$	Unit Weight γ (kN/m^3)	Cohesion C' (kpa)
Starter Layer	Prepared subgrade compacted selected granular material	Class 6F2/6F5	35	18	0
Foundation Soil	Existing soil Firm becoming stiff slightly silty slightly gravelly CLAY	Existing Soil	30	18	0

- Surcharge (landscape) = 10kPa
  In order to perform the calculations, we used the following properties for the soil:
- Groundwater: Has been recorded at shallow depth within 2m of ground level across the site, therefore a value of 0.1 has been used for the pore-water conditions Ru taken it into account for the slope stability analysis calculations.

1.5 Sustainable site won reinforced fill properties

One important aspect for this project was to use the existing cuts of the site won soil as the fill for the Reinforced Soil Bund instead of importing engineered fill. This is so that the carbon content can be reduced by less traffic within the densely populated area from construction vehicles travelling to site as site entrance is on a main road.

Materials

The table and pie chart displayed below show the total CO_2e emissions associated with materials purchased for the contract.

Materials, Transport, Energy and Waste Emissions

This table and pie chart show the total CO_2e emissions associated with materials compared to materials transport, energy use, business and employee transport and waste

Category	CO$_2$e Emissions
Fencing / RRS / barriers	0.000
Drainage	0.000
Earthworks	161.627
Pavements	0.000
Street furniture	0.000
Civil Structures	64.015
Bulk Materials	867.362
Total	**1,093.003**

Category	CO$_2$e Emissions
Materials Total	1,093.003
Materials Transport	2,221.745
Energy Use	0.000
Business and Employee transport	0.000
Waste	0.000
Total	**3,314.748**

national highways

Figure 2. Option 1) carbon footprint calculation of the reinforced soil bund with geogrids.

Imported fill was also used for the construction of the bund of which 80,000m^3 was imported from other sites located close by. The hydrocarbon and heavy metal contaminated fill would be treated and graded on site prior to its re-use for the bund. This helped avoid the import of Engineered fill that would have been used for the bund, preventing the material to be processed, graded & transported from further away. With the material being site-won the cost of import engineered fill has been reduced which sped up the construction.

The re-use of the imported material that otherwise would have gone to waste has sustainability benefits as found from calculating the total CO_2e emissions associated with the materials used for the bund was performed using the National highways carbon tool (Figure 2 & 3), considering the principles of PAS 2080:2016 to quantify, promote and deliver a low carbon solution for the project.

The analysis compared the emissions of a conventional solution using imported granular Class 6I/6J fill material to a solution using the site won & re-used fill. The following results were found (*Geosynthetics* 2021):

- 10,990 lorry loads were saved versus an unreinforced solution
- 61% reduction in land required versus an unreinforced solution
- 4,527T (58%) reduction of CO_2e versus a traditional unreinforced solution

Materials

The table and pie chart displayed below show the total CO_2e emissions associated with materials purchased for the contract.

Category	CO$_2$e Emissions
Fencing / RRS / barriers	0.000
Drainage	0.000
Earthworks	1.104
Pavements	0.000
Street furniture	0.000
Civil Structures	0.000
Bulk Materials	3,120.968
Total	**3,122.072**

Materials, Transport, Energy and Waste Emissions

This table and pie chart show the total CO_2e emissions associated with materials compared to materials transport, energy use, business and employee transport and waste

Category	CO$_2$e Emissions
Materials Total	3,122.072
Materials Transport	3,434.133
Energy Use	0.000
Business and Employee transport	0.000
Waste	1,285.796
Total	**7,842.001**

Figure 3.   Option 2) carbon footprint calculation of traditional reinforced soil bund without geogrids.

2 SUSTAINABLE NOISE BUND SOLUTION

2.1 *Design method and standards*

The design for the internal and external stability of the reinforced soil bund was in accordance with BS8006:2010 and the global stability was in accordance with Eurocode 7 (BS EN 1997-1) for the design approaches 1 and 2. The final design proposal consisted of uniaxial Stratagrids of 60kN/m and 40kN/m as primary reinforcement with the use of compacted site won stoney cohesive material Class 2C. The total running length of the noise bund is approximately 400m with a maximum height of 9.5m and a slope angle of 70 degrees facing towards the metal recycling facility and an angle of 26 degrees towards the new housing development.

Figure 4.   Aerial shot of the completed bund.

2.2 *Sustainable noise bund design*

Below shows the detail of the solution for the bund:

- Maximum height = 9.5m
- Slope angle at face (towards the recycling facility) = 70 deg
- Slope angle behind the face = 1V:2H
- Running Length (approx.) = 400m
- Surcharge (landscape) = 10kPa
- Geogrid Reinforcement (300/600mm spacing) = 23 layers
  - 6 Layers of Geogrid strata SG 60kN/m, spacing 500mm, length 7.10m + 1.32m (wrap around)
  - 5 Layers of Geogrid strata SG 60kN/m, spacing 600mm, length 6.10m + 1.63m (wrap around)
  - 7 Layers of Geogrid strata SG 40kN/m, spacing 600mm, length 4.70m + 1.63m (wrap around)
  - 1 Layers of Geogrid strata SG 40kN/m, spacing 600mm, length 3.70m + 1.63m (wrap around)

- 800mm starter layer compacted with selected granular material of class 6F2/6F5 with a layer of Geotextile wrapped around for separation.
- Reinforced fill material = Compacted site won soil class 2C (Stoney Cohesive Fill)
- Retained fill = Site won soil Class 2C (Stoney Cohesive Fill)
- Foundation soil = Made Ground Cu = 10 – 25 kPa
- Facing = each layer of 600mm compacted fill is covered with Landlok TRM (wrap around on the face) to protect the face from erosion and to avoid any wash-out of the fill material on the face.
- External Formwork = steel mesh A252, height = 700mm, length = 800mm to achieve a slope angle of 70deg
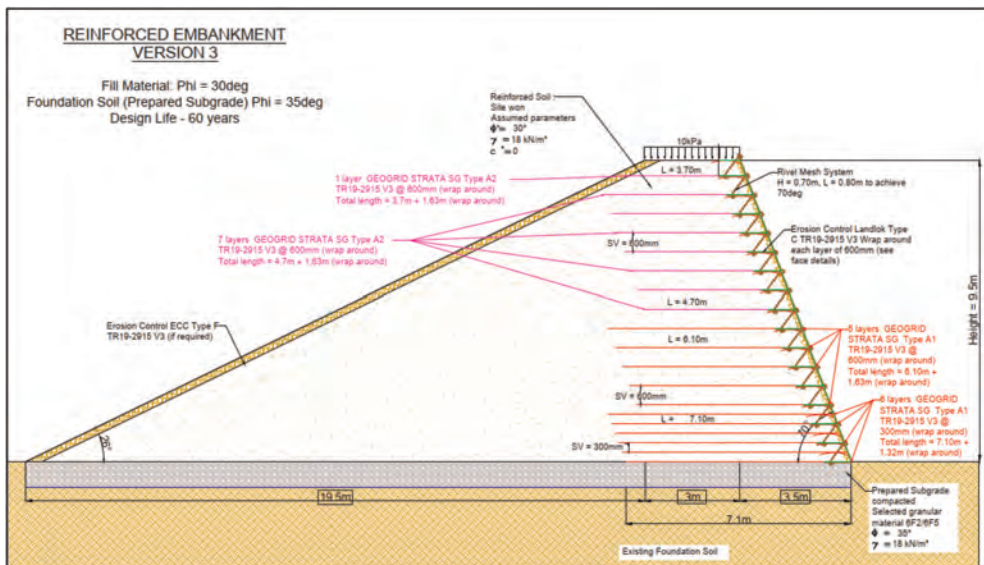
Figure 5.   Cross-section design of bund.

3   CONCLUSIONS

The use of Geogrids vastly helped in the reduction of CO_2 during construction of the bund using site won and locally imported material from other projects by reducing the time taken within the construction process, reducing on-site excavation, placement, importing fill material, testing of the material which was done on site and transportation. This resulted in less fuel consumption, travel and congestion within this area, which is densely populated, therefore reducing the emissions that would have been released into the atmosphere. As these were reduced it sped up the construction process due to not having to wait for material to be tested or being brought to site.

Geogrids helped use the existing material as they would help spread the load and make the poor soil become workable in compacted layers, instead of having been excavated and transported away whereas if Engineered fill was to be used, it would have to be imported from further locations and possibly multiple, depending on resources. Again, this would

have increased the duration of the project which consequently would have increased the CO_2 emissions emitted.

Reduction of aggregate usage, quarrying, dredging, extraction, transport, excavation, finance and waste take place when designing with a sustainable approach with the use of Geosynthetic material.

"Geosynthetics make infrastructure more sustainable. They extend the service life of roads, reduce the use of aggregates, conserve and protect water, minimize land disturbance and control soil erosion." For further research and evidence of the environmental impact and the sustainability of using geosynthetics in construction projects further supporting documents can be found (*IGS sustainability papers to feature at Italy Conference* 2022)

REFERENCES

British Standard, BS8006-1:2010. *Code of Practice for the Strengthened/Reinforced Soils and other Fills.* British Standard Institution, London. UK

British Standard, BS8002:1994. Code of Practice for Earth Retaining Structures. British Standard Institution, London. UK

British Standard, BS EN 1997-1:2004. Eurocode 7. Geotechnical Design – Part1. British Standard Institution, London. UK

British Standard, PD 6694-1:2011. Recommendations for the Design of Structures Subject to Traffic Loading to BS EN 1997-1:2004. British Standard Institution, London.

Emblen, E. (2019) *"Paragon Park Coventry – Materials Estimate."* Leicestershire: Geosynthetics Ltd.

Geosynthetics Ltd (2021) *Paragon Park Visual & Acoustic Bund.* Leicester, Leicestershire: Geosynthetics Ltd. Available at: https://www.geosyn.co.uk/downloads (Accessed: November 15, 2022).

IGS Sustainability Papers to Feature at Italy Conference (2022) IGS. The International Geosynthetics Society. Available at: https://www.geosyntheticssociety.org/sustainability/ (Accessed: November 15, 2022).

Strata, Use of Geogrids for Soil Reinforcement. 2015. Manual for Reinforced Walls and Slopes, Embankment on Soft Soils and Foundation Reinforcement.

UK Koerner, R. 2005. *Designing with Geosynthetics* 5th Edition, Pearson. USA.

GRS retaining structure with paper industry waste as backfill material

S. Lenart, K. Fifer Bizjak & B. Likar
Slovenian National Building and Civil Engineering Institute (ZAG), Ljubljana, Slovenia

ABSTRACT: Deinking sludge ash (DSA) and deinking sludge (DS) represent the main waste from recycled deinking paper pulp production in a paper industry. Their mixtures were used in this research to develop a composite with the proper geomechanical properties for the backfill of GRS retaining structure. Several mixtures with different contents of DS and DSA were initially tested to develop an optimal composite. The chosen composite was used as a backfill material of the retaining wall structure built in the south part of Slovenia, near the railway line, for landslide stabilization. All laboratory and field tests confirmed the required physical characteristics are being reached.

1 INTRODUCTION

1.1 *Residues of the deinking paper industry*

Enormous amount of paper production result also in significant waste generation - 11 million tonnes of solid waste are generated per year in Europe (Garside *et al* 2019). Approximately 70% of this waste is from paper recycling, for example, deinking sludge (Monte *et al* 2009). Recycled paper residues are a potential material that could be substituted for virgin raw materials from a technical and economical point of view (Watkins *et al* 2012). Examples of pulp and paper industry residue implementation have been presented by other authors (Ferreira *et al* 2019; Gabriel *et al* 2017; Saeli *et al* 2019), but in general, most paper industry waste is burned in power plant boilers or landfilled. The production process with different fillers, pigments, and coagulates influences the type of paper ash. Also, the technology and temperature in the boilers have an effect (Fernandez *et al* 2010).

On the other hand, according to information published by the European Aggregate Association (UEPG 2018), the demand for European aggregates is 3 billion tonnes annually. About half of natural (virgin) material is consumed by the construction industry. Undoubtedly, virgin material that are used in various applications in the building sector in huge quantities, particularly for earthworks, can partially be substituted by other materials, such as recycled industrial material, including material made from paper industry waste. However, the mechanical and environment criteria for recycled materials according to the national legislation must be satisfied.

1.2 *Use of residues from deinking paper industry for construction purpose*

The existing published researches on the use of residues from deinking paper industry in construction works relates to laboratory testing. A mixture of sand, paper fly ash, paper sludge, and cement has been used in laboratory research (Wu *et al* 2018). The mixture reached a compressive strength of 0.8 MPa, which is high enough for use as a backfill material for a foundation structure, a structural fill, or a hydraulically bound layer in a road structure. Some published researches present also the field test results. For instance, a road

subgrade was stabilized in a length of 250 m with a mixture of paper sludge and cement in Portugal (Lisbona *et al* 2012). The installed mixture achieved an unconfined compressive strength of 4.5 MPa.

Paper sludge ash is also used in the cement industry as supplementary cementitious material in mortar (Sadique *et al* 2019; Vegas *et al* 2009), concrete manufacturing (Vashistha *et al* 2019), and the brick industry (Singh & Kumar 2017).

Practitioners find it difficult to decide to use recycled material in construction due to a lack of knowledge about the material, technology of installation, high cost of production, and often a negative attitude towards all new materials (UEPG 2018). Thus, the objective of the presented research was to develop a composite backfill material, consisted from the residue of paper industry production and test it in laboratory as well on the field with a pilot structure. A new composite should have high enough unconfined compressive strength and shear properties to be used as a backfill in geotechnical structures (e.g. retaining walls etc), but at the same time it should allow elastic deformation before cracking. Results published in the literature deal mostly with paper sludge ash and deinking sludge used in different mixtures with soil and other binders. It was an aim of a research also to evaluate the time effect upon the hydration process and the effectiveness of a material compaction in real environment. Geomechanical characteristics of the composite to be used as a backfill material were also evaluated in order to support future design of similar earth structures.

2 STABILITY PROBLEM TO BE SOLVED

There was an unstable slope near the railway line between Ljubljana and Novo mesto at a village Mirna Peč in Slovenia (Figure 1). Slope has been monitored for years and it was estimated that it presents a general danger to railway line. The instability of the slope was already evident during the geological-geomechanical mapping of the site. The existing telephone poles along the railway layout were unstable, the road above the slope is severely cracked and individual stone blocks are frequently unstable and inclined towards the railway line. Thus, the stabilization of slope was necessary. It was decided to construct a retaining wall along the railway line for that purpose.

Figure 1.   Unstable slope near railway line in Mirna Peč (Slovenia).

The landslide was stabilised with a retaining wall structure consisting from gabion facing and geosynthetic reinforced backfill of paper industry waste. Figure 2 presents the proposed solution with general results from FEM analysis. The input for the later are presented in the next section.
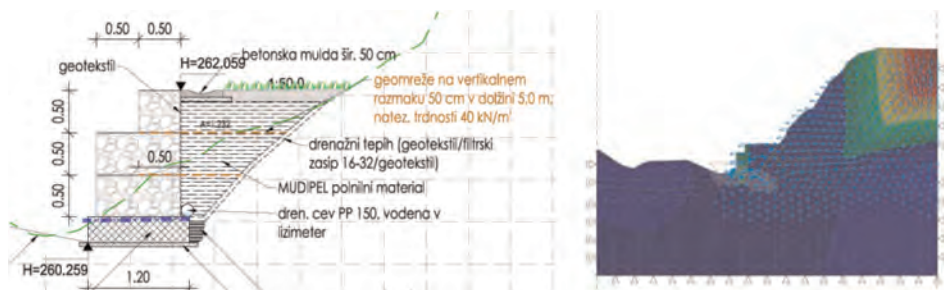
Figure 2. Proposed solution with retaining structure (left) and FE numerical model of structure (right).

3 MATERIALS

3.1 Deinking Sludge Ash (DSA) and Deinking Sludge (DS)

DSA and DS were two raw materials used in the research. They represent the main waste from recycled deinking paper pulp production at a paper industry company, VIPAP Videm Krško d.d., in Slovenia. The DSA is a combustion residue formed in a steam boiler during the incineration of DS. It consists of a mixture of bottom ash (approx. 90 wt %) and fly ash (approx. 10 wt %). VIPAP recycles around 600 tonnes of paper daily. Annually, 25,000 tonnes of DSA and 67,000 tonnes of DS are produced.

In order to design a backfill material for a retaining wall structure for the stabilization of a landslide near a railway line, several mixtures consisting of different ratios of DSA and DS were tested. Among them, two mixtures with sufficiently good geomechanical characteristics and suitable properties for compaction and installation were tested in the laboratory. Mixing proportions of the investigated mixture composites Mixtures were designated as D80/20 and D70/30, according to the composites dry mass mixing ratio DSA/DS in percentages.

3.2 Reinforcement geosynthetic

A polymer PET geogrid was used as a geosynthtetic used for reinforcing the backfill of retaining structure. The aperture size was 30 mm and tensile strength in two perpendicular directions was equal to 42 kN/m. The spacing between geosynthetic reinforcement was 50 cm.

4 TESTING

4.1 Laboratory testing of raw materials

The physical and mechanical properties of DSA and DS are presented in Table 1. DSA is a dry material, while the water content of DS ranges between 45% and 50%. In comparison with DS, the specific gravity of DSA was higher for about 20%. A standard Proctor test (SPP) showed that the optimal water content (w_{opt}) and maximal dry density ($\gamma_{d,max}$) were higher for DS. The unconfined compressive strength of DSA is between 300 and 500 kPa, which is in the range of very stiff soil according to the criteria for virgin materials. DS is a softer material in the range of stiff soil. Both materials are nonplastic.

Table 1. Physical and mechanical properties of raw materials.

Property	DSA	DS
Initial Moisture Content (w) (%)	0	45–50
Specific Gravity (γs) (Mg/m$_3$)	2.64	2.15
Optimum Water Content (wopt) (%)	51	56.5
Maximum Dry density ($\gamma_{d,max}$) (Mg/m$_3$)	0.99	0.89
Unconfined compressive strength after compaction (qu) (MPa)	0.3–0.5	0.22
Liquid Limit (LL) (%)		
Plastic Limit (PL) (%)	Nonplastic	Nonplastic
Particle Size Distribution		
Particle (>2.5 mm) (%)	0	–
Particle (0.063–2.5 mm) (%)	13.3	–
Particle (0.002–0.063 mm) (%)	75.59	–
Particle (<0.002 mm) (%)	11.11	–
D10 (mm)	0.002	–
D50 (mm)	0.02–0.06	–
D90 (mm)	0.4–0.8	–

4.2 Laboratory testing of composites

The components were mixed in a 20 L planetary mixer. Two kilograms were mixed for 2 min until a homogeneous mixture was obtained. Mixtures were compacted at the maximum dry density. In order to prevent evaporation, the composites were stored and cured in a climatic chamber at 90% RH and 22 °C. Compressive strength was tested immediately after compaction and after one, four, seven, 28, and 50 days of curing. The composite specimens were exposed to 12 cycles of freezing at −23 °C and thawing at 20 °C in a climate chamber during the freezing/thawing tests.

Similarly also the shear characteristics of the composites were tested directly after compaction and after seven days of curing. Additionally, the permeability of the composite was tested in a triaxial cell under a pressure of 50 kPa.

In order to investigate the impact of the transport time to the construction site, the time delay between mixing and compacting was taken into account. The tests were performed with two different testing procedures:

- The material was moistened to the maximum water content (w_{max}) and cured in the open air,
- The material was moistened to the optimal water content (w_{opt}) and cured in closed boxes.

After moistening and mixing, the mixtures were compacted in the following time intervals: immediately, and after 4, 8 and 24 h. After seven days, an unconfined compressive strength test was performed on each specimen.

Figure 3 left shows an increase of unconfined compressive strength with increasing of curing time. Furthermore, one can observe also a decrease of unconfined compressive strength, q_u with a higher quantity of DS in the composites. The tests performed immediately after compaction showed relatively similar values of qu (0.2–0.3 MPa), independent of the composition. After one day of curing, composites with higher percentages of DSA showed higher q_u values, accounting for the more intense hydration process in those composites.

The results (Figure 3 right) exhibit also a decrease of q_u with an increasing delay between mixing and compacting. Although a water content w_{max}, which is above the optimal one, w_{opt} causes lower q_u if specimen is compacted immediately after the mixing, the hydration process dries the mixtures and after 4 h resulted in a lower q_u for mixtures with a lower water content (w_{opt}). After 24 h, almost no difference could be observed in qu. Based on the results,

it can be concluded that the mixture compacted immediately must be moistened to the w_{opt}. For a mixture that will be compacted after 4 h due to transport, it is more appropriate to moisten it to the w_{max}.
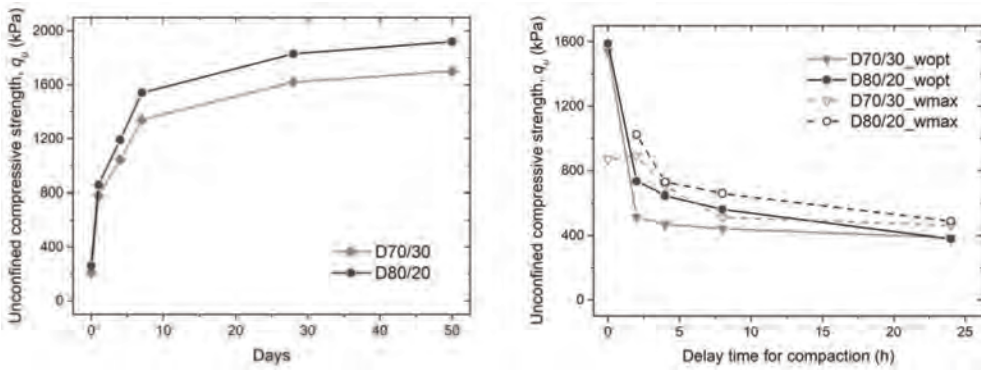
Figure 3. Uniaxial compressive tests results for two composites with curing time (left) and with delay in compaction time (right).

The results of these tests are essential to determine the methods of mixing, transport, and installation of the mixture on the construction site and to assess the maximum distance between the composite production site and the composite construction site.

5 RETAINING STRUCTURE

5.1 *Construction*

A 50 m long retaining structure was built with the use of paper industry waste as backfill material in the south part of Slovenia. The composite D70/30 was used. Construction works were executed in August 2018. Retaining structure consisted gabion facing made from iron mesh and recycled gravel material (reused ballast material) and geosynthetic reinforced paper industry waste composite as a backfill. The structure with inclinometer measurements after completion of all construction works is presented in the Figure 4.

Figure 4. Retaining structure after completion (left) and horizontal displacements in borehole above the retaining wall (right).

5.2 *Field test and monitoring results*

The compaction tests of the installed composite D70/30 were performed at every installed layer (Figure 6). Results shows that only the first three layers were compacted below 95% $\gamma_{d,max}$. The reason for the lower compactness in the first layers is a low compaction of ground under the composite. In all other layers, a higher compaction degree was measured. Measurements confirmed that the composite can be installed according the requirements of the technical specifications.
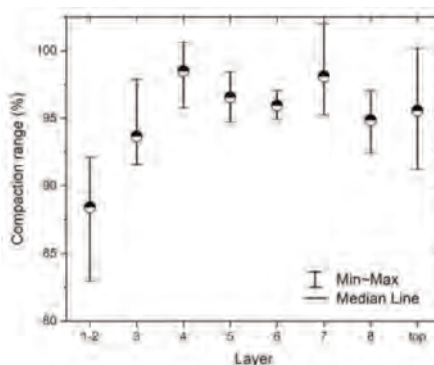
Figure 6.   Results of the measurements with the neutron probe.

Results of shear tests of the samples taken from the composite at the construction site are presented in Table 2. They are similar to the results from the preliminary laboratory investigation and exhibit significant improvements due to hydration with time.

Table 2.   Shear properties of the compacted composite.

ShearProp.	Laboratory Results		Demo Field		
	Immediately	After 7 Days	Immediately	After 7 Days	After 28 Days
F (°)	44	45	37	40	45
c (kPa)	12	42	35	45	200

6   CONCLUSION

The geosynthetic reinforced retaining structure made of gabion facing and backfill from waste materials from the paper industry represents a successful practical example of the use of residues of the deinking paper industry. Development of composite for backfill material was supported by extensive laboratory testing, which enables use of proper composition of waste materials to achieve desired deformation properties. Furthermore, it gave also required information regarding proper composite mixing and installation, which were finally confirmed by field quality control tests.

REFERENCES

Ferreira, I.A.; Fraga, M.C.; Godina, R.; Barreiros, M.S.; Carvalho, H. (2019). A Proposed Index of the Implementation and Maturity of Circular Economy Practices—The Case of the Pulp and Paper Industries of Portugal and Spain. *Sustainability*, 11, 1722; doi:10.3390/su11061722.

Fernández, R.; Nebreda, B.; Vigil de la Villa, R.; García, R.; Frías, M. (2010). Mineralogical and Chemical Evolution of Hydrated Phases in the Pozzolanic Reaction of Calcined Paper Sludge. *Cem. Concr. Compos.*, 32, 775–782.

Gabriel, M.; Schöggl, J.P.; Posch, A. (2017). Early Front-End Innovation Decisions for Self-Organized Industrial Symbiosis Dynamics—A Case Study on Lignin Utilization. *Sustainability*, 9, 515; doi:10.3390/su9040515.

Garside, M. Paper Industry—Statistics & Facts. (2019) *Statista*. Available online: https://www.statista.com/topics/1701/paper-industry/Published (accessed on 4 January 2021).

Lisbona, A.; Vegas, I.; Ainchil, J.; Riso, C. (2012). Soil Stabilization with Calcined Paper Sludge: Laboratory and Field Tests. *J. Mater. Civ. Eng.*, 24, 666–673, doi:10.1061/(ASCE)MT.1943-5533.0000437.

Monte, M.C.; Fuente, E.; Blanco, A.; Negro, C. (2009). Waste Management from Pulp and Paper Production in the European Union. *Waste Manag.* 2009, 29, 293–308.

Sadique, M.; Al-Nageim, H.; Atherton, W.; Seton, L.; Dempster, N. (2019). Analytical Investigation of Hydration Mechanism of a Non-Portland Binder with Waste Paper Sludge Ash. *Constr. Build. Mater.*, 211, 80–87, doi:10.1016/j.conbuildmat.2019.03.232.

Saeli, M.; Senff, L.; Tobaldi, D.M.; La Scalia, G.; Seabra, M.P.; Labrincha, J.A. (2019). Innovative Recycling of Lime Slaker Grits from Paper-Pulp Industry Reused as Aggregate in Ambient Cured Biomass Fly Ash-Based Geopolymers for Sustainable Con-struction Material. *Sustainability*, 11, 3481; doi:10.3390/su11123481.

Singh, D.; Kumar, A. (2017). Performance Evaluation and Geo-Characterization of Municipal Solid Waste Incineration Ash Material Amended with Cement and Fibre. *Int. J. Geosynth. Ground Eng.*, 3, 16, doi:10.1007/s40891-017-0094-6.

Vashistha, P.; Kumar, V.; Singh, S.K.; Dutt, D.; Tomar, G.; Yadav, P. (2019). Valorization of Paper Mill Lime Sludge via Application in Building Construction Materials: A Review. *Constr. Build. Mater.*, 211, 371–382.

Vegas, I.; Urreta, J.; Frias, M.; Garcia, R. (2009). Freeze–thaw Resistance of Blended Cements Containing Calcined Paper Sludge. *Constr. Build. Mater.*, 23, 2862–2868, doi:10.1016/j.conbuildmat.2009.02.034.

Watkins, E.; Hogg, D.; Mitsios, A.; Mudgal, S.; Neubauer, A.; Reisinger, H.; Troeltzsch, J.; Van Acoleyen, M. (2012). *Use of Economic Instruments and Waste Management Performances*; Bio Intelligence Service S.A.S: Paris, France, 2012.

Wu, H.; Yin, J.; Bai, S. (2013). Experimental Investigation of Utilizing Industrial Waste and Byproduct Material in Controlled Low Strength Materials (CLMS). Adv. Mater. Res., 639–640, 299–203.

UEPG (2018). *Annual Review 2017–2018*; UEPG: Brussels, Belgium.

Analysis of the generation of plastic debris and microplastics from geosynthetics

F. Fontana
Geosynthetics Consultant, Valbrenta, Italy

P. Rimoldi
Civil Engineering Consultant, Milan, Italy

M. Scotto & M. Vicari
Officine Maccaferri Spa, Bologna, Italy

ABSTRACT: The uncontrolled generation and dispersion of plastic debris and microplastics in the environment and particularly in the oceans has become a global problem. The present paper intends to critically analyse the source and quantities of microplastic debris produced by geosynthetics vs the environmental benefits afforded by geosynthetics. The paper considers the environmental innovation in the geosynthetics industry. Some fake news which associate geosynthetics to detrimental effects like the generation of plastic debris and microplastics are critically analysed. It is shown that in reality the advantages of geosynthetics are much larger than disadvantages, while detrimental effects are absolutely minimal. The conclusions highlight the undisputable fact that the generation of plastic debris and microplastics from geosynthetics is very limited, and lower than the quantities of microplastics generated by alternative solutions.

1 INTRODUCTION

The uncontrolled generation and dispersion of plastic debris and microplastics in the environment and particularly in the oceans has become a global problem. On one hand, environmental associations, social media, government agencies are claiming more and more attention to this problem, which risks to compromise the flora and fauna of all oceans, seas, lakes and rivers in the world. On the other hand, the same stakeholders and even the scientific community produce everyday fake news and sometimes unreasonable alerts about the amount and toxicity of plastic debris in the oceans. Also geosynthetics are sometimes associated with the production of such plastic debris and microplastics. The present paper intends to critically analyse the source and quantities of plastic debris produced by geosynthetics vs the environmental benefits afforded by geosynthetics.

2 MICROPLASTICS IN GENERAL

2.1 *What are microplastics?*

At present there is no normative definition of microplastics (MP), while MP are generally considered as plastic particles of different polymer composition, the size of which is < 5 mm,

for two or three dimensions. Nowadays, the following classification is increasingly found in publications:

- Macroplastics: particles with size > 5 mm in at least 2 dimensions
- Large microplastics: particles with size of 1 mm – 5 mm
- Small microplastics: particles with size of 1 µm - 1 mm

  Microplastics can be classified into two categories (Ebbert *et al.* 2020):

- Primary MP: plastic particles whose size already meets the size criterion for microplastics (< 5 mm) during their production and deliberately introduced on the market (e.g. particles in the toothpaste or skin scrubbers), or involuntarily introduced into the environment (e.g. granules and pellets). This category is said to represent from 15 to 30% of MP in the oceans and are expected to increase at a rhythm from 0.8 to 2.5 millions tons per year. Figure 1 (from Heß *et al.* 2018) shows possible forms of primary microplastics.
- Secondary MP: particles produced by the progressive fragmentation of macroplastics, separated by mechanical processes (e.g. abrasion), chemical degradation or UV exposure. As it can be seen in Figure 2, Image C, fibres also fall under secondary microplastics. According to Heß *et al.* (2018), the fibres come mainly from synthetic textiles, nets or ropes. Beer *et al* (2018) has looked at the microplastic accumulation in the Baltic Sea over the past 30 years: the fibres found in this study also originate from the wash water and were mainly found near large cities.
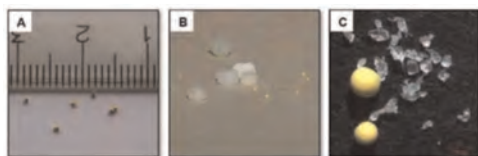
Figure 1. Primary microplastics (a: microbeads; b: raw pellets compared to microbeads; c: comparison between round microbeads and primary microplastics from cosmetics production) (from Heß *et al.* 2018).
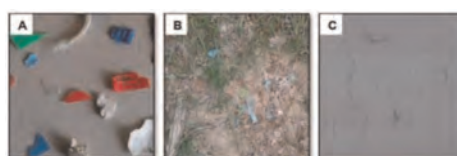
Figure 2. Secondary microplastics (a and b: decomposition products of larger plastic parts; c: textile fibers) (from Heß *et al.* 2018).

2.2 *Where do plastics in open waters come from?*

Independent data shows that most plastic waste entering the environment is a result of poor waste management. In contrast to many consumer plastics, geosynthetics do not normally degrade and can be fully recovered and recycled at the end of their service life.

Marine plastic waste is derived from a huge variety of different sources reflecting the widespread and diverse uses of plastics. The EC's own figures (NOC, 2021) estimate that the origin of microplastics has the following statistical distribution (Figure 3): tires consumption: 48%; pellets: 28%; naval paintings: 10%; textile fibres (fibres released during laundering): 8%, road markings: (7%). Single use consumer plastics such as carrier bags and plastic bottles also contribute. The distribution of microplastic lost to the environment is dominated by elastomers (likely derived from tires), while macroplastic losses correlate with polymers commonly used in packaging including LDPE, HDPE and PP, and those most commonly produced overall.

Heß *et al.* (2018) estimated that of the 117 g per head per year ascribed to German construction sites, 90 g is due to demolition work; 25 g due to on-site processing of plastics, and 1.7 g due to losses from insulating materials. Hence the amount of microplastics released on construction sites is 10 times smaller than the main emitter, tire abrasion. Geosynthetics are not even mentioned.
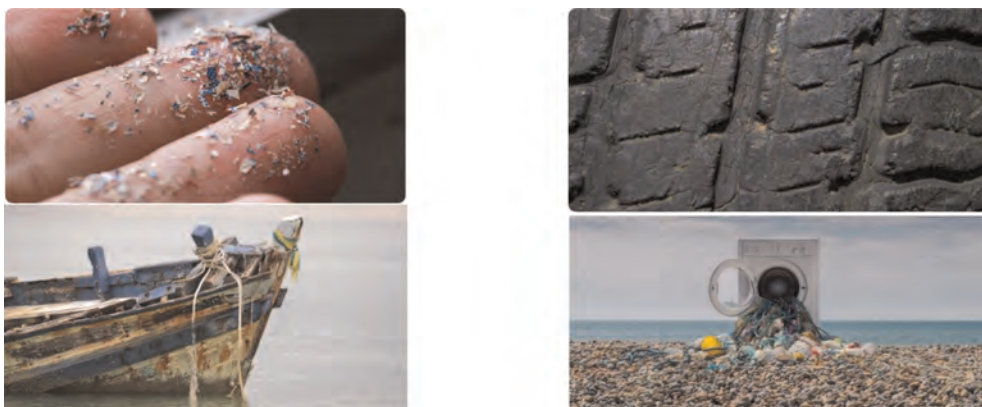
Figure 3.   Main MP in oceans: pellets, tires, naval paintings, textile fibres released during laundering.

WWF (2022) clearly identifies the pathways of macroplastics into the ocean: it has to be noted there is no indication of any source from coastal protection structures.

2.3   *How are microplastics in the ocean produced?*

The aging of plastic items and particles will significantly alter their behaviour and fate due, for example, to loss of plasticisers and other chemical additives, fragmentation and degradation, and biofouling. Loss of additives can lead to change in colour, altered shape and embrittlement of plastics, ultimately leading to their degradation. At near-ambient temperatures chemical degradation typically involves either oxidation (involving O_2) or hydrolysis (involving H_2O), both of which can be accelerated by microbial action, heat and light. There are three important processes that impact the extent and speed of marine plastic degradation:

1. Bacterial and other organism colonisation of the surface of plastic particles will both physically
2. degrade the particles and generate biofilms which may produce enzymes that erode the surface.
3. Abiotic hydrolysis of functional groups, like esters, carbonates, and amides, can sever the large macromolecules which make up polymers, reducing their molecular weight.
4. Exposure to UV radiation and oxygen causes photodegradation, also reducing molecular weight, causing cracking that produces microplastics. This process produces aldehydes and ketones, further encouraging the development of biofilms. Physical weathering will also enhance interactions with organic pollutants, potentially making them more hazardous.

Therefore, when examining marine plastic waste, it is crucial to understand not only the sources and pathways of plastics, but also the chemistry of the plastics involved. Furthermore, the sorption of pollutants onto plastic particles is not the same across different types of plastics.

2.4   *Need to distinguish the types of plastic*

There are thousands of types of plastics with different polymer compositions, additives and characteristics that may be classified in different ways, based on their chemical composition, application and thermosetting properties. The physical characteristics of plastics can broadly be divided into two categories: 1) thermoplastics (which can be remelted and remoulded) and 2) thermosets (which cannot return to their original state once set). Additives within plastics give them their inherent properties, but are not chemically bound to the polymer's chemical structure

and can thus leach out over time, changing the properties of the plastic as it ages. The more commonly used polymers are high density polyethylene (HDPE), polyvinyl chloride (PVC), low density polyethylene (LDPE), polypropylene (PP), polystyrene (PS), nylon (polyamide, PA), and polyethylene terephthalate (PET). The distinct physical and chemical properties of plastics play an important role in determining the extent and rate of transformations (e.g. fragmentation, degradation, aggregation) and interactions (biofouling, ingestion, sorption of other pollutants) for different plastics in the ocean, and thus their persistence and impact on the biota within it. The impacts on biota and the ecosystem will depend on their composition, concentration, routes and time of exposure, as well as the state of organisms exposed (e.g. age and level of nutrition), all of which require intensive in situ and laboratory-based assessments, as they are currently at the very early stage of being quantified and understood.

2.5 *How are microplastics measured?*

Two methods have been proposed to count and measure microplastics: 1) number of pieces; 2) by weight. The most common techniques to reliably identify MPs seem to be spectroscopic (infrared (IR) spectroscopy and micro-Raman spectroscopy (RM)) or thermal degradation methods.

While the mass-based thermo-analytical methods can determine the overall mass of different polymer types, the spectroscopic methods provide information on the polymer type, number, size and size distribution, and morphology for each analysed plastic particles and MPs in a sample. Spectroscopic methods seem particularly well suited for gathering these characteristics, because they permit a direct enumeration of potential MPs and in contrast with colorimetric methods (use of dye) or morphological methods (e.g., scanning electron microscopy, SEM) they should be capable of specifically determining their identity through a complete spectral pattern recognition.

Anyway JRC, Joint Research Centre of the European Government, organized two years of interlaboratory investigation with 98 labs involved all around the world, with comparison with contextual studies in Norway (34 labs) and America (40 labs); this research got discouraging results, since the z-scores show a very poor reliability and reproducibility of the current methods.

Hence standardisation and reliability of methods are still a long way to reach, and a challenging task for the international technical community.

3   MICROPLASTICS AND GEOSYNTHETICS

3.1 *Effects of microplastics from geosynthetics*

WWF (2022) found that 190 marine species out of 2788 show some effects of MP with different importance and depending on the type of polymers.

According to Scholz *et al* (2021), ecotoxicity tests were performed to evaluate the geosynthetic leachate ecotoxicity: a combination of bioassays was applied, where both acute and chronic tests and organisms representing two trophic levels were used. The loss of additives, such as plasticizers and antioxidants, during the ageing of geotextiles potentially can add to the concentrations of hazardous substances in the water. Another consideration is that the base structure forming polymers gradually degrades to microplastic particles, and as such can be ingested by heterotrophs or interfere with algal photosynthesis. However, ecotoxicological test results in this research did not show significant toxicity of geotextile leachates to water organisms. In case of microalgae, the test samples showed even nutritive properties, as an increase in microalgae concentration was observed during the 72 h of the test. Currently, there is limited research in the field of geosynthetic ecotoxicity, but a study evaluating the environmental safety of construction

products also found that geosynthetic PET multifilament yarns and polyamide mono-filament with Polypropylene fleece coating have low toxicity. A lethal concentration (LC50) was calculated only for specific amphipods. However, the LC50 at 83% and 89% concentrations can be considered as very low toxicity. As geosynthetics in hydraulic engineering are exposed to intensive water exchange, no toxic effects in the environment could be observed.

3.2 *Beware fake news*

The two article by Bai *et al* (2022.a and 2022.b) are a dramatic example of fake news about microplastics derived from geosynthetics, even presented as scientific data. Instead, these papers lack any scientific rigor where the authors wrongly evaluate that geotextiles are a high-volume source of ocean microplastics. In facts, the numerical values, assumptions made and conclusions drawn in the papers are seriously flawed (NOC, 2021) and result in unrealistic amounts (Dixon, 2017). A first element to support this statement is related with the assumptions made regarding the mass per unit area of geotextile and the lifetime of geotextiles. A second element is related to the amount of exposed geotextiles (to UV). Those statements are supported by the developments here presented.

1 - Mass per unit area of geotextiles

Bai *et al* (2022.b) mention the following assumptions:

- An amount of fibres released in the range 0.696 to 2.267×10^6 particles per square millimetre or 0.696 to 2.267×10^{12} particles per square meter
- A typical linear density of 0.03 mg per mm, thus 3×10^{-5} kg/m
- An assumed average fibre length of 100 nm per particle

Therefore, although not outlined in the paper, the author calculates a production rate, PR, in kg of microplastics per m^2 of geotextile due to exposure in the range:

$$0.696 \times 10^{12} \times 3 \times 10^{-5} \times 100 \times 10^{-9} \ \leq PR \leq 2.267 \times 10^{12} \times 3 \times 10^{-5} \times 100 \times 10^{-9} \quad (1)$$

$$\text{Thus}: \ 2.088 \leq PR \leq 6.801 \quad (2)$$

Those figures are unrealistic for two reasons:

- According to Eq. (2), each m^2 of geotextile would produce from 2 to 6.8 kg of MP! But most geotextiles manufactured are far less than 2 kg/m^2 (Heerten 2012) and therefore there is not enough geotextile mass available to produce this amount of microplastics.
- Even if the geotextiles were of sufficient mass, this calculation estimates that the entire mass of the geotextile would degrade to 100% microplastics within 1 year, which is totally unrealistic (Koerner 2012).

2 - Amount of geotextiles exposed to UV

The paper Bai *et al* (2022.b) states that, at present, the quantity of geotextiles used globally has reached 14 billions square meters, out of which only 2% are natural fibres. Due to different degradation mechanisms of various types of geotextiles, only the number of microfibers released by PET geotextiles under coastal reclamation was estimated. PET geotextile production is assumed to account for up to 5% of the total production of geotextiles worldwide. Geotextiles used for drainage in coastal reclamation areas are assumed to account for 17% of the global market share in 2019. Based on the assumptions mentioned above, the authors obtain an amount of PET geotextiles used globally and exposed equal to 116,620,000 m^2.

Combining with the previous estimates from Equations 2, the authors obtain a Global Microplastics Production discharged every year into the environment from PET geotextiles only as presented in Equation (3):

$$\frac{2.088 - 6.801 \text{kg}}{\text{m}^2}/\text{year} \times \frac{1 \text{ton}}{1000 \text{kg}} 116,620,000 \text{m}^2 = 0.24 - 0.79 \text{ million tons/year} \quad (3)$$

It is not possible to agree on those figures (Freedonia 2020). Indeed, to perform these calculations, the authors assume that all geotextiles used in drainage applications (17%), made of PET (5%), are used exposed and in coastal protection applications, degrading to 100% MP.

Instead, extremely small quantities of geotextile are used for drainage in coastal reclamation areas. A small quantity of geotextile is used in the applications of erosion control (Rimoldi2021) and other coastal protections (Boucher 2017). A vast majority of these materials are buried or otherwise protected by covering (Koerner 2012). The authors make an inadmissible error in both extending their research from one site with specific conditions to global quantities of emissions; moreover, the assumptions and claims made in the document are inconsistent and unacceptable.

As comparison, the correct figures can be derived from Ebbert *et al.* (2020): a total of around 360 million tons of plastic are produced worldwide every year. The proportion of technical textiles made from synthetic filament fibres is 34.5 million tons or 9.6%. The proportion of the quantities processed in the construction industry is again significantly lower at only 1.4%. In hydraulic engineering, physical decomposition processes can occur, e.g. in the case of products exposed to the free flow due to sediment carried along in the water. However, this still includes a large proportion of textiles used in building construction (75% of the 1.4%). This includes gardening and landscaping textiles and a fifth of total amount used in building construction. Accordingly, the actual share of geotextiles, industrial and agricultural textiles is less than 1 million tons.

These figures can help to clarify that the proportion of geotextiles in relation to the total amount of plastic produced is very small.

It is clear that Bai *et al* (2022.a and 2022.b) figures of the global production of MP from geosynthetics are dramatically wrong, being 1 million to 1 billion times bigger than the reality!

3.3 *Life cycle*

It is clear that the whole geosynthetics industry do not produce any primary MP.
The issue of secondary MP depends on two main factors:

- Time gap between physical life and service life
- Exposure, during the service, or at the end of the life, to the degradation factors: oxydation, UV, temperature, abrasion, chemicals.

3.4 *Benefits of geosynthetics*

From Scholz *et al* (2021): the application of geosynthetics in coastal protection has huge economic benefits, such as savings via substitutions of or reductions in selected soil materials, ease of installation, increased speed of construction, life cycle cost savings through improved performance (by increased longevity or reduction in maintenance), and improved sustainability in terms of conserving natural environments as compared to alternative designs. It is commonly accepted that geosynthetics which are adequately stabilized with antioxidants (e.g., sterically hindered amines) will last in underwater constructions with limited oxygen supply and temperatures at constantly low levels for at least 100 years.

When used to line containment units, geotextiles hold sand fill, which results in a stable mass-gravity unit that is erosion resistant and structurally sound. They answer the growing concern over the environment and the concomitant restrictions in mining and quarrying. In addition, by allowing the use of locally available natural materials, high transportation costs and the associated pollution are avoided, An interesting element is that artificial reefs and submerged breakwaters made from geotextile tubes, geobags, and geogrid-assembled marine mattresses units provide a safe, injury-free environment for humans in close proximity to populated beaches. Geotextile containers also attract an abundance of marine plants and life soon after construction, making such living breakwater a prime marine habitat (Phillips 2013, see Figure 5). Moreover, there are many cases where geosynthetic structures enable the preservation of endangered species: several studies have shown that geosynthetics provide new habitats, proving to be effective for future preservation activities and offering safe solutions that fully integrate into the surrounding environment. Geotextiles are placed on glaciers to protect the ice against high temperatures and solar radiation, thus reducing and retarding the melting rate of snow and ice (Figure 5). Geosynthetics reduce freshwater losses from irrigation canals in water-stressed regions and play a critical role in water and wastewater treatment plants. Compared to other construction materials, their carbon footprint is typically 65% lower. They protect lives and livelihoods by reinforcing slopes and underpinning vital infrastructure. Geosynthetics offer a durable, reliable and resource-light means to protect vulnerable coastal zones from erosion. They also help to contain millions of tons of plastics wastes stored in landfill every year.

Figure 5.   Examples of living breakwaters with geosynthetic (from Phillips, 2013) and of geotextiles for protecting glaciers.

As shown above, the major source of MP comes from tires: hence geosynthetics, being light and non-voluminous products requiring an average of 50 times less trucks for transport compared to granular materials, afford to save million tons of microplastics which would be generated by thousands of trucks of clay or gravel or concrete consuming the tires.

3.5   *Risk of microplastics release*

It is important to fully consider the entire lifecycle benefits of all products that use synthetic materials in their manufacture. It is inappropriate to compare single-use consumer plastics, which decompose rapidly and are often disposed of irresponsibly, with high-quality durable engineering products that deliver long-lasting benefits to entire communities. Geosynthetics present a negligible environmental risk, and where risk exists at all, it is a rare occurrence within the highly regulated disciplines of civil and environmental engineering. Potential examples such as the use of incorrectly specified products or misguided installation and

maintenance practices are addressed through high technical and professional standards in the industry.

Geosynthetics are destined to a service life cycle designed to be as long as their physical life.

They allow to reduce the use of materials destined to undetermined service lives, and extremely expensive in environmental terms (like concrete, gravel, sand)

It is evident that, for 99% of the applications, geosynthetics are installed underground or under water with limited or absent problems of oxygen, without UV, without high temperatures, and without heavy mechanical or chemical actions.

Geosynthetics are made with the best polymers for obtaining very high durability and very long service life, with UV protection additives and antioxidant additives.

In literature the reported cases of supposed or possible MP release from geosynthetics are very few and essentially related to wrong design or wrong choice of the products.

From Scholz *et al* (2021): only the improper installation of the geotextiles and the lack of service and maintenance after extreme weather events could cause the failure of the engineered structures and, as a result, the pollution of the environment by remnants of geosynthetic materials. The successful application of geosynthetics in coastal protection depends on the selection of suitable materials and proper installation and maintenance.

From Scholz *et al* (2021): the field study performed at the shore of Kaliningrad Oblast (Russia) demonstrated that remnants of geosynthetic materials that are used in coastal protection structures (geotextiles, geocells, geogrids, plastic coating from gabions, and geotextile big bags) were found in the environment and were the mostly visible litter on the beach.

But it has to be noted that litter is not, or not yet, microplastic!

It is evident that the found objects could be attributed to unsuitable material selection and improper waste management. Considering that any damage, even partial, of the coastal protective constructions using geosynthetic material could lead to the littering of the beach or the sea, specific attention is needed for the maintenance of such constructions.

The base structure forming polymers gradually degrades to microplastic particles, and as such can be ingested by heterotrophs or interfere with algal photosynthesis. However, ecotoxicological test results did not show significant toxicity of geotextile leachates to water organisms. In case of microalgae, the test samples showed even nutritive properties, as an increase in microalgae concentration was observed. Moreover, a study evaluating the environmental safety of construction products also found that geotextiles made of PET multifilament yarns and polyamide monofilament with PP fleece coating, have low toxicity.

All this means that for geosynthetics there is very low or even negligible environmental risks from microplastics release.

4 ENVIRONMENTAL INNOVATION IN THE GEOSYNTHETICS INDUSTRY

Innovative research has been focusing on biodegradable polymers of natural origin, like cellulose fibres, viscose fibres and others, including poly(lactic acid) or polylactide (PLA), to reduce the use of plastics. Among the fully biodegradable polymers, PLA seems to be one of the most promising. PLA is a thermoplastic, high-strength and high-modulus polymer that has already been used on large-scale production and commercialized for a wide range of fields.

Biopolymer ensures several advantages in terms of sustainability and eco-compatibility: (i) they derive from renewable agriculture-based resources; (ii) they decompose into non-toxic substances, as water, carbon dioxide and humus; (iii) they degrade quite slowly; (iv) they are recyclable and compostable. In addition, some biopolymer based products can be reinforced with a wide variety of natural fibers such as bamboo, coir, cotton, flax, hemp, jute, kenaf, ramie, sisal.

Geosynthetics from biopolymers are used at present for short term applications, but their use in combination with live plants, where the root system development initially supports and then gradually substitutes the biodegradable products in soil reinforcement. Moreover, biopolymer can be used as environmentally friendly coating for polymer coated wire products.

Another innovation is the use of recycled polymers: one of the largest applications is the production of woven geogrids and nonwoven geotextiles from shredded polyester (PET) bottles; billions PET cold drinks bottles are used annually to produce geosynthetics with recycled polymers.

Hence innovative companies are raising the bar on the use of recycled content in the manufacture of high-quality geosynthetic materials.

Other geosynthetic companies are implementing new methods to offset carbon emissions, while other companies are developing new techniques for the greener disposal of geosynthetics and withdrawal of the products at the end of the service life in case of temporary applications.

These initiatives are having a huge positive socio-economic impact, including lowering greenhouse gas emissions during construction, longer-lasting engineering solutions and more effective waste management.

5 CONCLUSIONS

Geosynthetics, like any material, have an impact on the environment, yet this impact is much smaller than the alternatives.

The examples and measures shown in the paper make it clear on one hand that the use of geosynthetics is accompanied by a saving in microplastic emissions and, on the other hand, that greenhouse gas emissions are significantly reduced. Geosynthetics are therefore not only advanced materials but also ecologically sustainable building materials, provided they are manufactured, correctly designed and installed, and recycled in a sustainable manner.

The paper considers the recent use of biopolymers and of recycled polymers, which represent an important step towards decarbonised geosynthetics and polymer coated wire products.

Fake news available even in scientific literature, reporting non-scientific and sometimes catastrophic data, have been critically analysed.

In conclusions we highlight the undisputable fact that the generation of plastic debris and microplastics from geosynthetics is negligible and surely not worth of any negative evaluation vs the technical and environmental advantages provided by these products.

Hence, Geosynthetics are a part of the solution and not of the problem: geosynthetics are convenient products that improve the ecological and economical future of our planet.

REFERENCES

Bai, X., Li, C., Ma, L., Xin, P., Li, F., Xu, Z. (2022.a). Quantitative Analysis of Microplastics in Coastal Tidal-flat Reclamation in Dongtai, China. *Front. Environ. Sci. Eng.* 2022, 16(8): 107.

Bai, X., Li, F., Ma, L., Li, C. (2022.b). Weathering of Geotextiles Under Ultraviolet Exposure: A Neglected Source of Microfibers from Coastal Reclamation. *Science of The Total Environment*, Volume 804, 15 January 2022, 150168

Beer, S., Garm, A., Huwer, B., Dierking, J., Gissel Nielsen, T. (2018). No Increase in Marine Microplastic Concentration Over the Last Three Decades – A Case Study from the Baltic Sea; *Science of the Total Environment* Volume 621, 15 April 2018, Pages 1272–1279

Boucher, J. & Friot, D. *Primary Microplastics in the Oceans: A Global Evaluation of Sources.* 10, (IUCN Gland, Switzerland, 2017). https://portals.iucn.org/library/sites/library/files/documents/2017-002-En.pdf

Dixon, N., Fowmes, G., Frost, M. (2017). "Global Challenges, Geosynthetic Solutions and Counting Carbon". *Geosynthetics International*, 24, pp. 451–464.

Freedonia Group: Industry Study #3834 *Global Geosynthetics*, 2020.

Ebbert, S, Wilke, M., Hessing, C., Elsing, A., Detert, O. (2020). Microplastics - How a Manufacturer of Geosynthetics and Technical Textiles Deals with the Topic. *Proc. Contaminated Sites* 2020. Karlsruhe, Germany.

Heerten, G. (2012). "Reduction of Climate-damaging Gases in Geotechnical Engineering by Use of Geosynthetics". *Geotextiles and Geomembranes*, 30, pp. 43–49.

Heß, M., Diehl, P., Mayer, J., Rahm, H., Reifenhäuser, W., Stark, J., Schwaiger J. (2018). Mikroplastik in Binnengewässern Süd- und Westdeutschlands Bundesländerübergreifende Untersuchungen in Baden-Württemberg, Bayern, Hessen, Nordrhein-Westfalen und Rheinland-Pfalz Teil 1: Kunststoffpartikel in der oberflächennahen Wasserphase (in German)

JRC (2021. *Current status of the Quantification of Microplastics in Water - Results of a JRC/BAM inter-Laboratory Comparison Study on PET in water*. Publications Office of the European Union, Luxembourg

Koerner, R. M. (2012), *Designing with Geosynthetics*, 6th Edition, Xlibris Publ. Co.,

NOC, National Oceanography Centre (2021). Sources, Amounts & Pathways of Plastics Entering the Global Ocean. https://noc.ac.uk/files/documents/science/report-plastics-entering-the-global-ocean-noci-december-2021.pdf

Phillips, J. (2013). Adaptive Management Strategies for Resilient Coastlines: A Case Study on the Ft. Pierce, FL Breakwater Project. USACE Workshop, November 21, 2013.

Rimoldi, P., Shamrock, J., Kawalec, J., Touze, N. (2021) "Sustainable Use of Geosynthetics in Dykes", *Sustainability*, 13(8), https://doi.org/10.3390/su13084445.

Scholz, P.; Putna-Nimane, I.; Barda, I.; Liepina-Leimane, I.; Strode, E.; Kileso, A.; Esiukova, E.; Chubarenko, B.; Purina, I.; Simon, F.-G. Environmental (2021). *Impact of Geosynthetics in Coastal Protection. Materials* 2021, 14, 634. https://doi.org/10.3390/ma14030634

WWF (2022). Impacts of Plastic Pollution in the Oceans on Marine Species, Biodiversity and Ecosystems. https://wwfint.awsassets.panda.org/downloads/wwf_impacts_of_plastic_pollution_on_biodivesity.pdf

Some current topics regarding geomembrane liners and floating covers for water storage reservoirs

M.A. Sadlier*
Geosynthetic Consultants, Australia

ABSTRACT: Current issues in the renovation of water supply reservoirs by the replacement of old geomembrane liner and floating cover systems with new systems are discussed. Topics include sampling and testing, underdrain systems, material choices, floating cover access for maintenance and the impact of conductive geotextiles on leakage rates.

1   BACKGROUND

In Australia and New Zealand many water storages and service reservoirs were renovated around the year 2000 and were fitted with geomembrane liners and floating covers based on flexible polypropylene (fPP). These fPP materials whether reinforced or not reinforced have suffered greatly from degradation as a result of their exposure to solar radiation and exposure to chlorine compounds in the stored water.

As a result there has been a need to inspect, sample and evaluate these materials and their state of degradation. This has also generated a lot of work to renovate these reservoirs and fit them with new liners and floating cover systems.

Aspects of the work including material selections were discussed by Sadlier and Frobel (2018) and this paper discusses other contemporary aspects of these reservoir renovation works.

2   SAMPLING AND TESTING

The liners and cover materials are generally in operating clear water reservoirs containing treated and usually disinfected water. Because the aged fPP materials have become difficult to clean and seam properly there has been a reluctance to take larger samples that would require substantial repair that may affect the operation of the facility. Larger samples provide an opportunity for tensile, tear, puncture and other mechanical testing.

In many cases smaller and less obtrusive samples have been taken from weld flaps and under perimeter batten bar fixings (See Figures 1 and 2) and this has required the use of tests such as Oxidation Induction Time (OIT) and High Pressure Oxidation Induction Time (HPOIT). These analytical tests use small samples the size of a thumbnail to assess the remaining anti-oxidant capacity of the material and the OIT method is applicable to materials with mainly phenolic anti-oxidants and the lower temperature HPOIT is applicable to materials with mainly hindered amine anti-oxidants.

The fPP materials generally used hindered amine anti-oxidants and that makes the HPOIT test the appropriate method to use. Although not often specified at the time these

---

*Corresponding Author: sadlierma@gmail.com

Figure 1.   A small cover material sample taken from a ballast tube partly under a batten bar.

Figure 2.   A small liner material sample taken from under a batten bar. This floating cover had many small marked holes which had been caused by embers from a grass fire.

fPP materials generally had HPOIT values in the order of 100 to 150 minutes when new and we often see values now of around 50 minutes in sheltered samples and less than 30 minutes in exposed samples. At these low HPOIT values it is clear that these fPP materials are close to the end of their useful life.

3 LINER UNDERDRAIN SYSTEMS

Many of these reservoirs were originally constructed in fairly rural settings on the periphery of cities and towns and as populations grow they are often being encroached upon by urban environments. This has driven a need for demonstrated control of water leakage and this has resulted in these renovations seeing more and more use of double liner systems for better leakage control.

In some cases an existing concrete liner might be utilised and in others the old liner might be sufficiently effective to function as a secondary liner. There have been other projects where a choice has been made to install a complete new double liner system. See example in Figure 3.

Figure 3. A reservoir with the old discoloured fPP liner being used as a secondary liner. The white material on the floor is a drainage geocomposite and the black material on the slopes and the floor is a conductive non-woven geotextile with a unit mass of about 350 gsm.

These double liner systems have an underdrain system based on a geonet or geocomposite drainage layer and will often make use of conductive materials such as special conductive geotextiles to facilitate electronic leak location surveys. When conductive geotextiles based on graphene coated needled non-woven geotextile fabrics are used and heavier grades are available, they may be adequate for drainage on slopes without the need for a geonet as well as providing the other protective cushioning benefits of a heavy non-woven geotextile.

Where a reservoir has an existing gravity underdrain pipe under the embankment that will be tested and utilised if effective. However, because of the difficulties involved with properly grouting the annulus around a pipe new under embankment bores are not used and a down the slope pipe with a bore pump installation is used instead. See Figure 4.

The conductive geotextiles based on needled non-woven geotextiles are quite robust and easily installed with overlaps seamed by a wedge welder. However, supply situations have occasionally made them unavailable, and a few projects have used a needle punched composite with a 150 gsm non-woven geotextile base and a thin conductive film of polyethylene. This has required a separate drainage layer and has been much less robust than the heavier conductive non-woven geotextile.

Figure 4. An underdrain water extraction system with a down the slope pipe with a bore pump.

Figure 5. Holes in a conductive composite made by workers walking on it. These required patching to ensure adequate conductivity.

4 GEOMEMBRANE LINER AND COVER MATERIALS

Whilst high density polyethylene (HDPE) might be expected to dominate as the liner material of choice due to its cost advantages there other materials being used such as 1.1 mm thick reinforced polyvinyl chloride with elvalloy plasticisers (PVC/Elvalloys). Bitumen geo-membranes and coated fabric geomembranes are being considered if a new secondary liner is required.

All of these materials lie a lot flatter on the underdrain or subgrade with less wrinkles than HDPE and this has a positive influence on the quality of the subsequent work on primary liners and floating covers. Sometimes on sites with tight access the narrower (2-3 m wide) rolls are helpful and larger panels can be fabricated if required.

For the floating covers the PVC/Elvalloys are often being used in a 1.5 mm thick grade and reinforced chlorosulphonated polyethylene (CSPE) is still preferred on occasions. The PVC/Elvalloy materials are formulated to be suitable for both potable water and direct sunlight exposure. There are other PVC materials for water reservoir floating covers that have different formulations for the top and bottom coating layers.

A detailed discussion of the available materials was given by Sadlier and Frobel (2018) and will not be repeated here.

The fPP materials have not been considered recently because of their poor performance in the past. However there is now some interest in the newer formulations of fPP driven partly by the cost advantages offered and partly by the availability now of extended accelerated UV testing by QUV of up to 40,000 hrs. This interest has so far only extended to putting some large sample materials out at existing reservoirs for both water and sunlight field exposure and evaluation.

5 FLOATING COVER ISSUES

Access onto covers for maintenance remains a concern. Access is needed for water sampling and to clear leaves and other debris from the pumps or foot valves in floating sumps. The anti-skid surfaces on the walkways are much better than previously but there is still a reluctance to have personnel working on the cover.

Although there are openings for surface water release the ponding of surface water can be clearly seen along with the associated collection of leaves and debris.

Figure 6 is an example of a cover with floats for tensioning each side of the ballast lines and additional floats for walkways. These often have openings in the float paths intended to allow surface water to move around and enter the ballasted trench area for collection and removal. Prevailing winds can cause the water to pond and windblown dirt and soil collect at those locations and make the ponding worse.

Figure 6.   A floating cover with foam floats for tensioning and other floats for access walkways.

Especially on older floating covers there is a reluctance for personnel to use the access walkways to remove the leaves, soil and debris. There is also a reluctance to empty the reservoirs in order to carry out necessary maintenance and cleaning. In Figure 7 it can be seen how this can lead to substantial growth of undesirable vegetation.

Figure 7. A 30 year old CSPE cover where a lack of maintenance has allowed vegetation to grow.

6 LEAKAGE RATES

Based on North American data Peggs and Giroud (2014) suggested a range of action leakage rates for water supply reservoirs which included a suggestion for an expectation of leakage of around 2600 litres/hectare/day for a water depth of about 5 m.

A collection of ten of the recent renovation projects in South East Australia discussed above have seen PVC/Elvalloy geomembrane liners installed over geocomposite drain systems with existing compacted clayey soils, concrete liner or old geomembrane retained as a reasonably effective form of secondary liner. In terms of surface area the reservoir sizes have ranged from 3000 sqm to 10,000 sqm with effective depths of in the range of 4 to 8 m.

The majority of them used a conductive geotextile to facilitate an electronic leak location survey by the Spark or Arc Method (ASTM D7240 or ASTM D7953 respectively) and others had water introduced to enable a dipole water puddle or water lance leak location survey (ASTM D7002 or ASTM D 7703 respectively). All had independent third party quality assurance inspections.

Due to privacy concerns, we are not able to publish exact details but observed leakage rates were all less than 150 litres/hectare/day and in about half the cases less than 100 litres/hectare/day. Whilst these adapted secondary liners might not have been perfect these leakage rates are indicative of what can be achieved with good quality control and a conductive geotextile to facilitate an electronic leak location survey.

Points of weakness for leakage in renovation of these old reservoirs are seen to be the old concrete structures and the geomembrane liner fixings to the old structures such as shown in Figure 8. The concrete can be cracked, porous and rough providing a poor surface for an underwater batten fixing. Sometimes surface grinding of the concrete is enough but on other structures a coating with something like a smooth sprayed polyurethane is required and there are other structures that are best replaced.
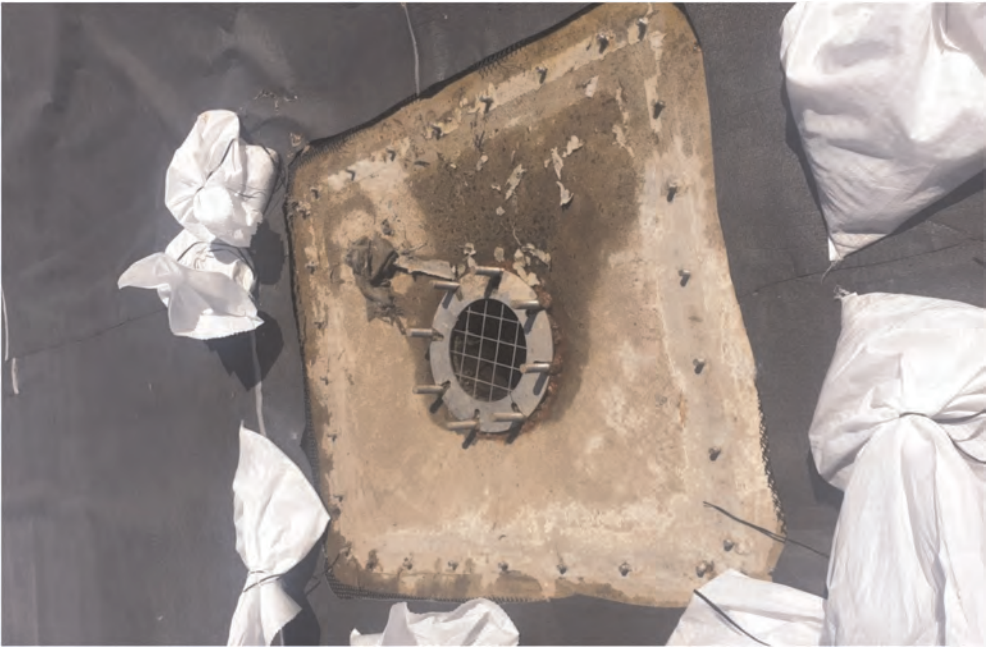
Figure 8.   An old concrete structure for a scour outlet.

7   CONCLUSIONS

This paper has discussed a number of contemporary issues in the renovation of existing water supply reservoirs by the installation of new geomembrane liners and floating covers. Topics have included:

- Sampling and evaluation of existing materials
- Underdrain systems and options for removal of leakage water
- Liner and cover materials
- Cover design, access and maintenance
- Conductive geotextiles and the impact on leakage rates

REFERENCES

Peggs I.D. and Giroud J.P. (2014) "Action Leakage Rate for Reservoir Geomembrane Liners" *10th International Conference on Geosynthetics – Proceedings 10ICG*, Berlin Germany, September 2014

Sadlier, M.A. (2017). "Geosynthetics in Mining and Environmental Applications" *Invited Lecture for Geosintetik 2017*, Jakarta Indonesia, October 2017

Sadlier, M.A. and Frobel R.K. (2014) "Material Selection For Reservoir Floating Covers". *10th International Conference on Geosynthetics – Proceedings 10th International Conference on Geosynthetics*, Berlin 2014.

Sadlier, M.A. and Frobel R.K. (2018) "Current Developments and Trends for Water Reservoir Renovation with Geosynthetics" *11th International Conference on Geosynthetics – Proceedings 11ICG*, Seoul, South Korea, October 2018

Sadlier M.A, Scheirs, J, Hay, B. (2014) "Enhanced HDPE and Subgrade Requirements" *10th International Conference on Geosynthetics – Proceedings 10ICG*, Berlin Germany, September 2014

Performance of turbidity curtains in a mine waste dump drainage system

L.G.M. Macedo
Department of Mining Engineering, Federal Center of Technician Education of Minas Gerais, Araxá, Minas Gerais, Brazil

M.G.A. Gardoni
Department of Transportation and Geotechnical Engineering, Federal University of Minas Gerais, Campus Pampulha, Belo Horizonte, Minas Gerais, Brazil

E.M. Palmeira
Department of Civil and Environmental Engineering, University of Brasilia, Campus Universitário Darcy Ribeiro Asa Norte., Brasília, Federal District, Brazil

ABSTRACT: In the mining plant, it is usual to direct rainwater to the nearest water bodies to reduce the accumulation and infiltration of water into the mining structures. However, little is discussed to minimize turbidity in the generated effluent, using downstream dam structures, that stabilize and reduce the turbidity of this effluent. Due to the environmental incidents of recent years, environmental agencies are imposing restrictions on projects for new dam structures. Because of this, mining has sought other technologies to solve the problem of fine sediments in water bodies. In this context, turbidity curtains act as filters and deflectors of suspended sediments, favouring turbidity reduction. The objective of this study was to analyse the performance of two turbidity curtains, installed downstream of a waste rock dump at a phosphate mine in Alto Paranaiba, Brazil, to investigate the performance of these structures when subjected to high peak flows. The results obtained in this study confirmed the effectiveness of the curtains and will support the design of new structures for future sediment containments.

1   INTRODUCTION

The turbidity curtains are vertical, flexible structures that extend downward from the water surface to a specified water depth and are designed to contain or deflect suspended sediments or turbidity in the water column (Francingues & Palermo 2005). These structures are supposed to divert sediment-laden currents towards the bed, thereby reducing the time particles take to settle and the horizontal range of influence of the suspended sediment (Radermacher *et al.* 2016).

The present work evaluated the possibility of incorporating turbidity curtains into the drainage system of a waste rock dump, still in the construction phase, in a phosphate rock mine in Alto Paranaiba, in Minas Gerais, Brazil. The area has a rainfall distribution concentrated in a restricted period of the year (rainy period), with a high solid carrying potential. Not been able to construct a dam to contain the sediments at the site, the investigation of other engineering solutions capable of reducing turbidity of the effluent is necessary.

The present study aimed at reducing the turbidity of the effluent generated by the drainage system of the waste rock dump by installing turbidity curtains in the receiving pond of this effluent. A hypothetical deductive method is used to evaluate the performance of the curtains in reducing turbidity as well as if they will survive the adverse conditions of working with peak flows.

2 MATERIAL AND METHODS

2.1 *Materials*

2.1.1 *Curtains*

The irregular rainfall regime makes it very hard to control the input flow in the pond. Thus, it can be assumed that the main risk associated with the experiment is the possibility of the curtains to collapse, either by the rupture of the tension cable, rupture of the woven geotextile or detachment of the anchorages due to flow peaks resulting from heavy rainfall.

Peak effluent flow can promote currents with high speeds, causing an increase in the risk of rupture or failure of the installed devices. The curtains in the present case-history were installed in two parallel sections, with an angle of approximately 45° to the flow direction. The geometry was of a labyrinthine type to increase the probability of the installed curtain to resist to the mechanical effects of weather variations and strains during the rainy seasons of 2021-2022.

The labyrinth configuration of the curtains was adopted due to the risk of rupture of the structure. The mining company did not receive installation support from the curtain manufacturing company, which yielded to an installation in a more effective configuration as suggested in the literature (Francingues & Palermo 2005; Johanson 1978).

In places where the curtains can be exposed to high hydraulic loads, it is suggested to adopt a tension cable to dissipate the loads at the anchorage points. As this was one of the risks identified at the beginning of the project, it was decided to adopt an upper-tension cable anchored to the edges of the structure. The anchor points consist of 2.8 m long train tracks, with columns in the ground to a depth of 2.0 m (Francingues & Palermo 2005; Palermo 2006; Palermo *et al.* 2008)

The turbidity curtains are formed by panels 5000 mm long and 3000 mm high, composing the curtain skirt with a minimum free edge of 300 mm. The core of the curtain is composed of a woven geotextile, made of high tenacity polypropylene strips, high tensile strength, high permeability, low creep, and anti-UV treated. The fabric provides high permeability to liquids but with rather low apparent pore openings, yielding to high solids retention. On the upper part of the curtains, handles were installed to provide more agility and ease in its movement and launch, as well as greater ergonomic and operational safety for its operators. The ballast of the turbidity curtain is composed by a chain of links with a minimum diameter of 9.0 mm, hot-galvanized steel with a minimum breaking load of 25 kN. Standard ASTM naval aluminum connectors were used, connectable through a pin-lock system, shackle, upper handles, and ultralight floats of expanded polyethylene. The technical specifications of the curtains are listed in Table 1. Figure 1 shows a schematic drawing of the curtains used.

Table 1. Technical specifications of the woven geotextile.

Component	Properties	Technical specifications	Unit	Method
WOVEN GEOTEXTILE	Raw Material - Woven Geotextile	Ultra-stabilized PP anti-UV laminates		
	Mass per unit area	$\geq$ 440	g/m^2	ISO 9864
	Tensile strength - longitudinal and transverse	105	kN/m	NBR ISO 10.319
	Deformation at nominal strength	$\leq 10\%$	%	NBR ISO 10.319
	Hydraulic conductivity	2×10^{-3} m/s	m/s	NBR ISO 11.058
	Filtration opening size	0.24mm	mm	NBR ISO 12.956
	Permeability	20×10^{-3}	m/s	
	UV resistance (residual after 4,300h of exposure)	$> 80\%$	%	DIN EN 12.224
	Circumferential and bottom seams	Overlocked, six high tenacity polyester sewing threads		
	Edge seams	Prayer type, six rows of high tenacity polyester seams and a reinforced seam		
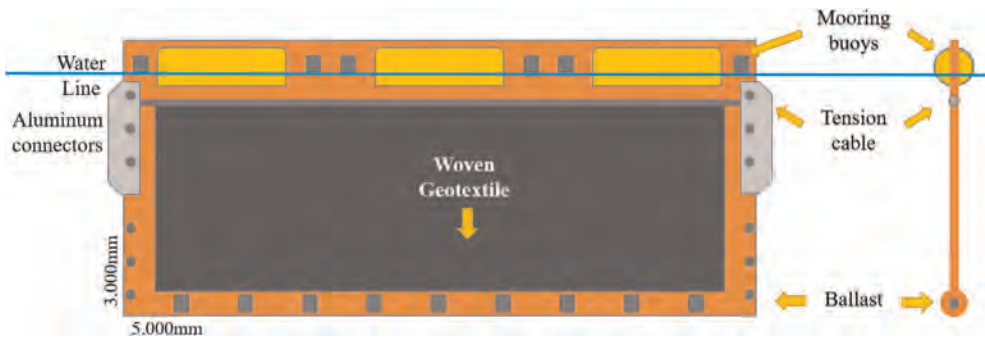
Figure 1. Schematic drawing of the curtains.

2.1.2 *Drainage system*

The waste rock dump of the mining facility has a surface area of 93.5 ha with little vegetation cover and it is currently in operation. The slope revegetation process is in its initial phase and covers less than 11.8% of the area. The surface drainage system conducts the water collected from the berms to the channels and to the hydraulic stairs. The effluents are conducted from the peripherical channels to an effluent containment structure, called "the pond", which is approximately 230 m long, 45 m wide in average, with a depth of 9 m and a 15 m wide spillway (Figure 2).
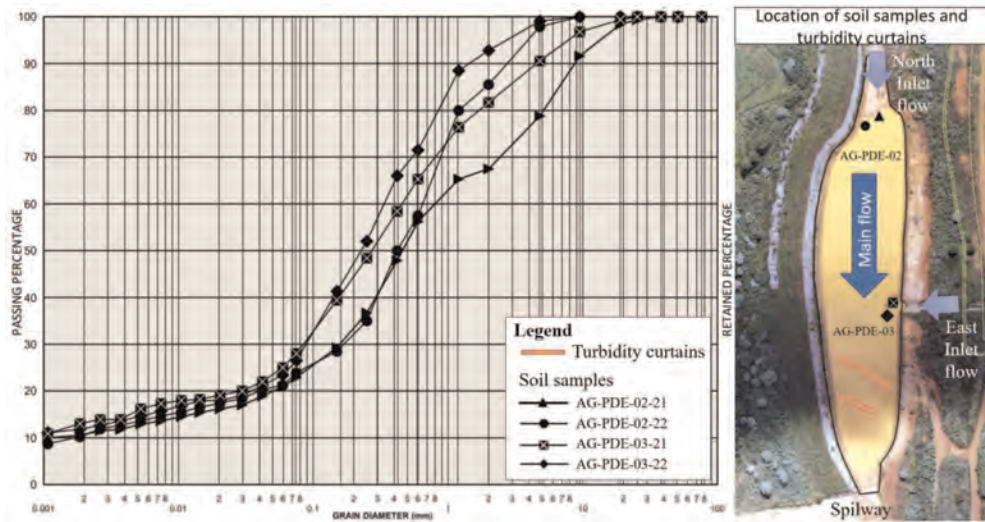
Figure 2. Grain size distribution curves of the soils.

The waste material is composed by a high amount of weather-resistant minerals, with reddish sand-clay characteristics, sometimes with the presence of peat or massive sand-clay materials, grading to levels of sand-clay granulation, orange or orange-red color, interspersed with altered levels of magnetite with medium to coarse grain sizes. The material is mechanically disposed in the waste rock dump, spread, and compacted without the addition of any kind of chemical product that may alter its physicochemical characteristics.

2.1.3 Sedimented material

During the dry season, the containment structure allowed the collection of samples of sedimented material from the last rainy season. So, four samples were collected for characterization tests, two collected in 2021, before the installation of the curtains, and another two samples in 2022, after the curtains have been installed, at the same location. Both samples were collected at the entrance of the sediment containment structure, upstream of the curtains, being the typical sediments in the effluent to be filtered of deflected by the curtains. Typical grain size distribution curves of the materials collected are presented in Figure 2, and the main particle diameters listed in Table 2.

Table 2. Main particle diameters.

Sample	D10 (mm)	D30 (mm)	D60 (mm)
AG-PDE-02-21	0.0011	0.16	0.70
AG-PDE-02-22	0.0019	0.20	0.70
AG-PDE-03-21	0.0010	0.08	0.43
AG-PDE-03-22	0.0010	0.01	0.40

To collect the samples, first the area was cleaned to avoid contamination with organic matter, such as leaves and roots. The collected samples were classified as disturbed because they did not preserve their original structure.

The granulometric curves obtained present a similar shape, however the samples collected in the east inlet flow present finer granulometry then the samples collected in the north flow inlet.

2.1.4 Effluent analysis

For each effluent specimen, the turbidity parameters were analyzed using the YSI Professional Plus PRO-DSS portable multi-parameter probe. This is a multi-parameter portable instrument for water quality and can measure several critical parameters, depending on the sensor installed, such as dissolved oxygen (optical), turbidity, pH, ORP, conductivity, specific conductivity, salinity, TDS, resistivity, ammonium, chloride, nitrate, depth, temperature, and it also has a GPS. In the present study, probes were used to determine the following parameters: turbidity (NTU); temperature (°C); dissolved oxygen (%); conductivity (μs/cm); total suspended solids (TSS-mg/L); pH; ORP.

Effluent turbidity analyses were carried out to evaluate the efficiency of the turbidity curtains. Three samples were collected weekly during the rainy season (Figure 3). One sample was collected upstream (point A) of the curtains, another between curtains (point B), and the third downstream of the curtains (point C), but all on the west bank and perpendicular to the main flow within the effluent containment structure (pond). The analysis was associated with rainfall parameters. After that, it was possible to calculate the efficiency of the barriers by the following equation 1 (Oliveira *et al*. 2018, 2020):

$$E_i = \frac{(T_b - T_a)}{T_a} \tag{1}$$

where E_i = efficiency at point i; T_b = turbidity before the point; T_a = turbidity after the point.
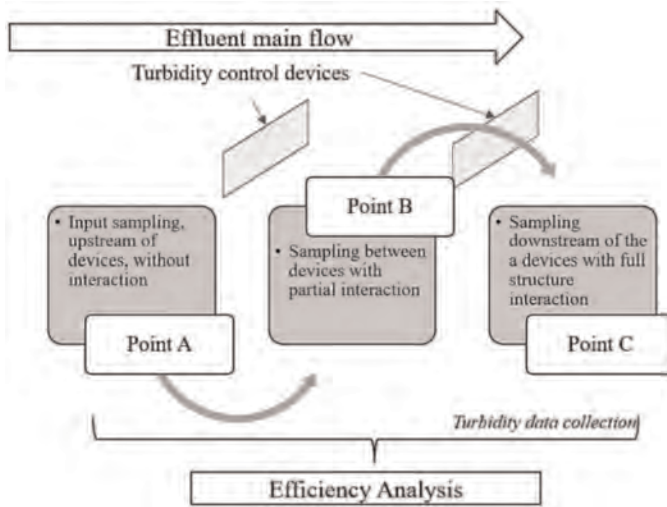
Figure 3. Flowchart of the project's data collection.

3 RESULTS AND DISCUSSION

Over the first 30 days of the experiment, it was possible to identify a significant reduction in the efficiency of the curtains. The curtains showed effectiveness above expectations for the designed conditions after the first month of the experiment with an efficiency of 92.19% (constant flow in a lotic environment). When the energy drops, the pond stops spilling, changing the flow regime to lentic. At this moment, the flow is governed by gravity, and the pond becomes exposed to external factors, like temperature and winds. These factors reduced the efficiency of the curtains, at the end of the first month to 60.83%. During the 2021-2022 rainy season, 148 turbidity samples were collected. The average efficiency obtained through out the study are summarized in Figure 4 as a function of the spillage process of the structure and sample location, either between the curtains or downstream of the curtains. The change of the flow direction caused by winds, associated with a maze configuration, favours the process of homogenization of the residual fluid in the pond, reducing the efficiency of the curtains. In these cases, the wind can suspend sediments, increasing the turbidity in the water body, besides imposing hydraulic loads from waves on the mooring cables and floats, which can cause structural failure (Francingues & Palermo 2005; Radermacher 2013).
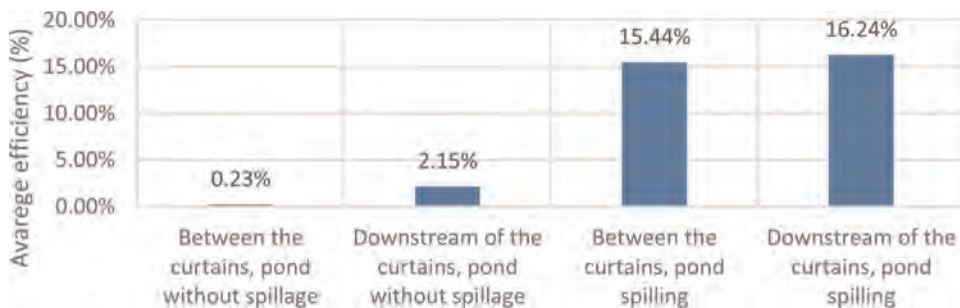
Figure 4. Average efficiency of turbidity curtains throughout the study.

386

4 CONCLUSIONS

This paper presented the results of an investigation on the use of curtains to reduce the turbidity of the effluent of the drainage system of a waste rock dump at a mining plant. The curtains resisted the rainy season, without damage and promoted satisfactory turbidity reductions of the effluent generated by the drainage system, which demonstrates the potential of this type of solution. However, the geometry used was a crucial factor in reducing the efficiency of the system with time and this study suggests the need for a change in the installation geometry of the curtains to a closed "U" geometry (Francingues & Thompson 2006; Johanson 1978; NYSDOT 1996; Pilarczyk 2000) before the 2022-2023 rainy season to increase the efficiency of the system.

REFERENCES

Francingues, N. R., & M. R. Palermo. 2005. "Silt Curtains as a Dredging Project Management Practice." *ERDC TN-DOER-E21, September*, 1–18.

Francingues, N. R., & D. W. Thompson. 2006. "Control of Resuspended Sediments in Dredging Projects." Pp. 243–54 *in 26th Annual WEDA Conference*. San Diego: WEDA.

Johanson, Edward E. 1978. "*An Analysis of the Functional Capabilities and Performance of Silt Curtains.*" JFB Scientific Corporation, Wilmington.

NYSDOT. 1996. *Temporary Soil Erosion and Sediment Control Specifications*. Nova Iorque.

Oliveira, Eduardo Paniguel, Rafael Brito de Moura, Caio Pompeu Cavalieri, and Rafael de Oliveira Tiezzi. 2020. "Evaluation of Silt Curtain in the Reduction of Suspended Solids." *Geotextiles and Geomembranes* 48 (6):983–88. doi: 10.1016/j.geotexmem.2020.07.001.

Oliveira, Eduardo Paniguel, Rafael Brito de Moura, Diego de Souza Sardinha, Paulo Henrique Bretanha Junker Menezes, Alexandre Silveira, and Rafael de Oliveira Tiezzi. 2018. "*Experimental Evaluation and Development for Tests of Floating Barriers Aiming at Containment of Suspended Solids.*" *Magazine DAE* 66 (213):36–47. doi: 10.4322/dae.2018.030.

Palermo, Michael R. 2006. "Design Sequence for Environmental Dredging." in *26th Annual WEDA Conference*. San Diego: WEDA.

Palermo, Michael R., Paul R. Schroeder, Trudy J. Estes, and Norman R. Francingues. 2008. *Technical Guidelines for Environmental Dredging of Contaminated Sediments*. Vicksburg.

Pilarczyk, Krystian W. 2000. *Geosynthetics and Geosystems in Hydraulic and Coastal Engineering*. Vol. 1. 1st ed. New York: Taylor & Francis.

Radermacher, Max. 2013. *Effectiveness of Silt Screens*. Delft.

Radermacher, Max, Lynyrd de Wit, Johan C. Winterwerp, and Wim S. J. Uijttewaal. 2016. "Efficiency of Hanging Silt Curtains in Crossflow." *Journal of Waterway, Port, Coastal, and Ocean Engineering* 142(1): 1–31. doi: 10.1061/(asce)ww.1943-5460.0000315.

Geosynthetics properties and testing

A comparison of particle motions in reinforced and unreinforced triaxial specimens of transparent sand

D.H. Marx, K. Kumar & J.G. Zornberg
The University of Texas at Austin, Austin, Texas, USA

ABSTRACT: This study investigated particle displacement and rotation (motion) in reinforced triaxial tests conducted on transparent sand. Individual particles were segmented from laser-illuminated sections through the specimens by using a neural network. State boundary lines between probable and improbable particle motions were drawn. The reinforced specimen was found to be stronger than the unreinforced, despite having a similar volumetric strain response. Measurement of the particle motions showed that the centre of the unreinforced specimen gradually shifted outwards under applied load. This applied an additional moment to the specimen. The reinforcement restricted the outwards movement of the specimen, resulting in a higher strength. These results also suggest that at a given applied axial strain, particle rotation increases with increasing lateral restraint.

1 INTRODUCTION

Conventional soil-geosynthetic interaction tests focuses on macro-scale behaviour. Pullout tests, direct shear tests and reinforced triaxial tests all measure the behaviour of the soil-geosynthetic composite, rather than the interaction of individual particles with the geosynthetic. However, it is only by studying the motions of individual particles that the mechanisms of soil-geosynthetic interaction can be fully understood.

Monotonic triaxial tests were done on transparent sand to investigate the effect of geosynthetic inclusions on the displacement and rotation (motions) of individual particles. The motions were compared at relatively large strains induced by monotonic loading. Thus, the mechanism of interaction was assumed to be similar to a geogrid providing reinforcement. The experimental setup, image analysis implemented to the track particles, and the mechanisms observed are discussed in the following sections.

2 METHODOLOGY

2.1 Experimental setup

The experimental setup shown in Figure 1 was used for the triaxial tests on transparent sand. The setup consists of an imaging frame attached to a regular triaxial cell, load frame and volume pumps. The pumps and loading frame are not shown in Figure 1. Two lasers with a wavelength of 638 nm, placed at 60° to each other, were used to illuminate sections through the specimens. Cameras fitted with 50 mm prime lenses captured images of the specimen every 0.02% axial strain. Oil was used both to saturate the specimens for transparency and as a confining fluid.
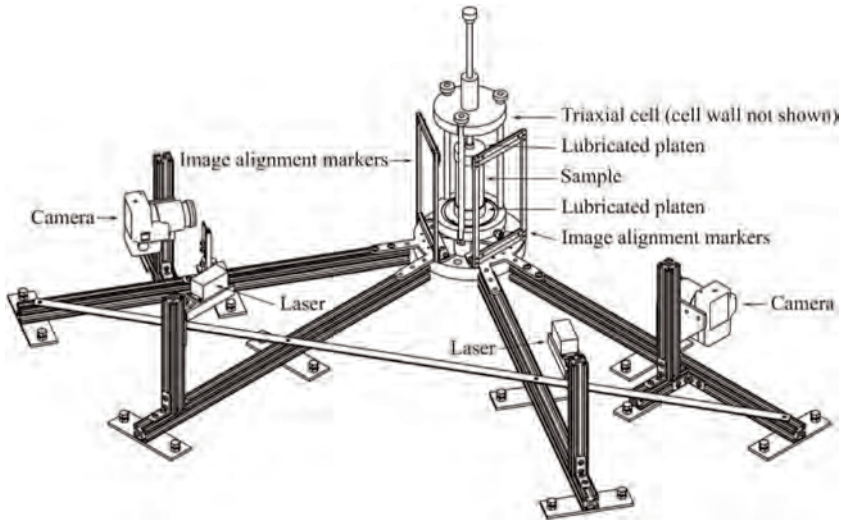
Figure 1. Experimental setup used to measure particle motions in triaxial tests on transparent sand (from Marx *et al*. 2023).

A custom, transparent silicone membrane was used for the tests. The frictional restraint of the platens was reduced by placing two layers of silicone lubricated with vacuum grease at either end. A drainage pipe protruded through silicone layers. Further discussions of the experimental setup can be found in Marx & Zornberg (2022b) and Marx *et al*. (2023).

2.2   *Materials*

The transparent sand tested in this study consisted of fused quartz saturated with a mixture of mineral oils. The fused quartz was uniformly graded with a D_{50} of 2.9 mm and compacted to its maximum density. A mixture of 52% Puretol 7 Special and 48% Paraflex HT4, both manufactured by Petro-Canada, was used to saturate the specimens (Peng & Zornberg 2019).

The honeycomb inclusion shown in Figure 2 was used to reinforce one of the specimens. The inclusion was water jet cut from a sheet of 3 mm thick polypropylene used in the manufacturing of integrally formed geogrids. A honeycomb shape was selected for the inclusions as it provides axisymmetric confinement, which is compatible with the stress state in a triaxial test. The ratio between aperture size and D_{50} was 4.7.

2.3   *Testing program*

Three groups of specimens were tested for this study: 1) two repeat unreinforced specimens consolidated to 25 kPa (U-25a and U-25b), used to validate the repeatability of the experimental setup, 2) a honeycomb-reinforced specimen consolidated to 25 kPa (H-25) and 3) an unreinforced specimen consolidated to 50 kPa effective stress (U-50). The U-50 specimen was used to compare the effect of reinforcement with that of increased confining stress.

All the specimens were back pressure saturated to 300 kPa before consolidation and had B-values of 0.99. The specimens were sheared at a rate of 6% axial strain per hour. This relatively slow rate of shear was necessitated by the constrained drainage through the lubricated platens and the slow shutter speed used to capture the images.

3 IMAGE ANALYSIS

The images of the laser-illuminated sections through the specimens were captured in a 14-bit raw format. Subsequently, the images were demosaiced, the dynamic range compressed and corrections for lens distortion and distortion by the triaxial cell was applied, as outlined in Marx & Zornberg (2022b) and Marx *et al.* (2023). A typical post-processed image from a section through the specimen in shown in Figure 3a.
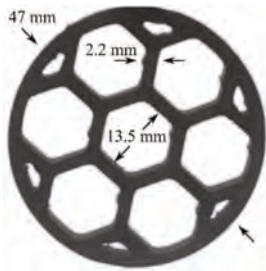
Figure 2. Honeycomb inclusion used for reinforcement.
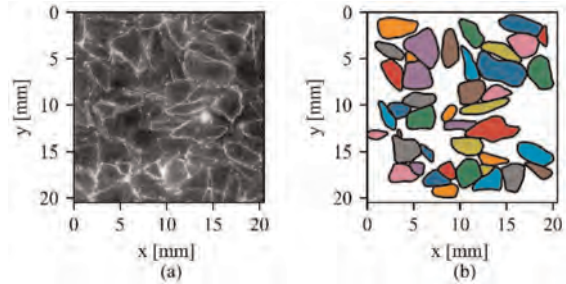
Figure 3. Typical result of image segmentation: a) original image and b) segmented particles.

A local measurement of axial strain was required as the global measurements included the compression of the lubricated platens. Digital Image Correlation (DIC) is an optical measurement technique that tracks regions of pixels (patches) from one image to another. By using the DIC software developed by Stanier *et al* (2016) it was possible to measure the displacement of the top and the bottom of the specimen and calculate the axial strain, as discussed in Marx & Zornberg (2022a).

The DIC measurements provides a continuum displacement field across the specimens. To investigate the motions of individual particles the images first had to be segmented. Analytical segmentation techniques failed due to inconsistent internal lightning, image noise and heterogeneous particle outlines. Consequently, a neural network was trained to segment the individual particles. The network, Cellpose (Stringer *et al.* 2021), was originally developed to segment biological tissue. By implementing transfer learning the network was able to segment fused quartz particles as shown in Figure 3b. The rotation and displacement, i.e. the motions, of the particles were subsequently tracked through successive images. The details of the image segmentation and particle tracking can be found in Marx *et al.* (2023).

4 STRESS-STRAIN RESULTS

The deviatoric stress-axial strain measurements for the four specimens are shown in Figure 4a. Standard area corrections (Head 2014) and membrane corrections (Ducan & Seed 1967) were applied.

The two unreinforced tests (U-25a and U-25b) show good correlation, illustrating the repeatability of the testing setup. Increasing the confining strength to 50 kPa (specimen U-50) resulted in a corresponding increase in strength. When reinforcing a specimen tested at 25 kPa confining stress its strength increased.

In Figure 4b the volumetric strain of the specimens is shown as a function of axial strain. All specimens contracted initially followed by dilation. Both the control specimens and the reinforced specimen tested at 25 kPa confining stress showed similar dilative behaviour up to
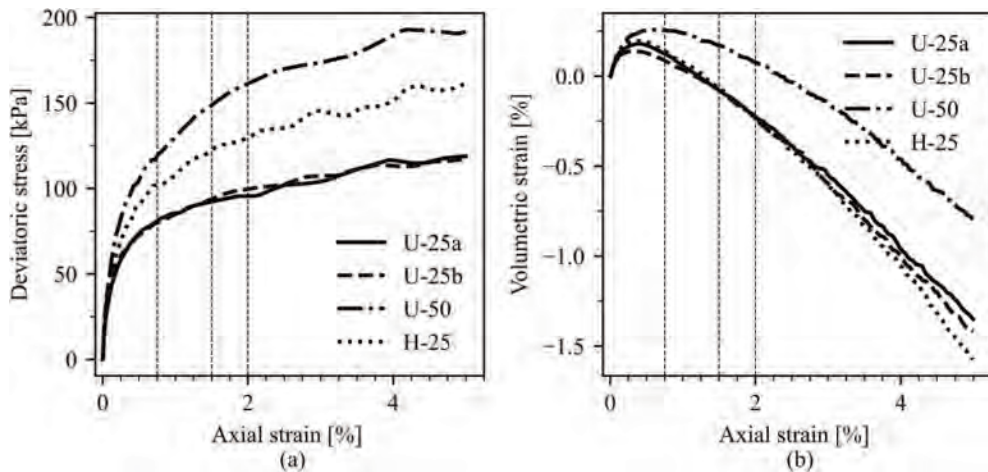
Figure 4.   Stress-strain results of the triaxial tests: a) deviatoric stress b) volumetric strain.

approximately 3% axial strain. Only when the confining stress was increased to 50 kPa did the rate of dilation decrease. In the following section the particle motions will be analysed to determine why the control specimens were weaker than the reinforced, despite displaying similar volumetric strain behaviour.

5   PARTICLE MOTIONS

5.1   Motions state boundary line

The particles in the centre 50 mm of one of the control specimens are shown in Figure 5a and b. In Figure 5a the particles are shaded by their horizontal displacement at 1.5% axial strain. In Figure 5b the particles are shaded by their absolute rotation. The displacement measurements clearly show the specimen expanding laterally. In contrast, the particle rotations are more haphazard in nature.

Marx et al. (2023) proposed that a boundary exists between probable and improbable particle states (i.e. displacement-rotation pairs). Under stable loading conditions a particle that displace significantly will not rotate significantly as well and vice versa. Consequently, when plotting all the absolute particle rotations against displacements in Figure 5c the state boundary follows the shape of a triangle.

The apex of the triangle was set at 2.5 MADs (Median of all Absolute Deviations from the median) away from the median rotation. Similarly, the base covers ±2.5 MAD from the median horizontal displacement. The MAD, a descriptor from the field of robust statistics (Rousseeuw & Hubert 2018), was used due to the large scatter in the rotation measurements. In addition, the median absolute rotation and median horizontal displacement is also indicated on the figure.

The median displacement is -0.12 mm indicating that in additional to expanding laterally the specimen is also moving towards the left at 1.5% axial strain. The maximum probable rotation is 6.5° and the range of probable displacements is [-0.46 mm, 0.22 mm] for a total range of 0.68 mm.

5.2   Comparison of probable motions across different levels of strain

In Figure 6 the ranges of probable motions are compared across three levels of strain for the four specimens. Firstly, in Figure 6a the displacement range is compared. The greater
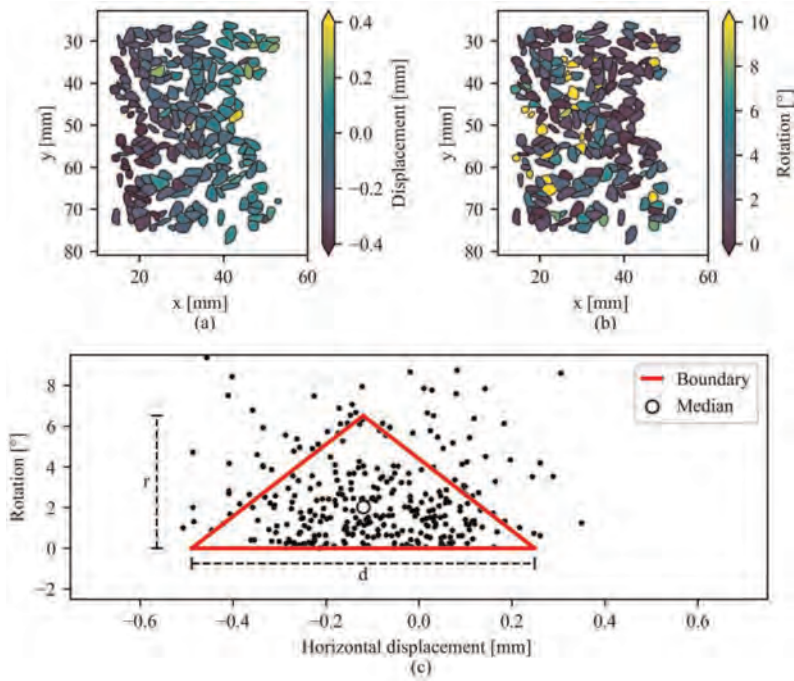
Figure 5. Particle motions for U-25b at 2% axial strain a) horizontal displacements, b) rotations and c) rotation-displacement pairs with state boundary and medians shown.
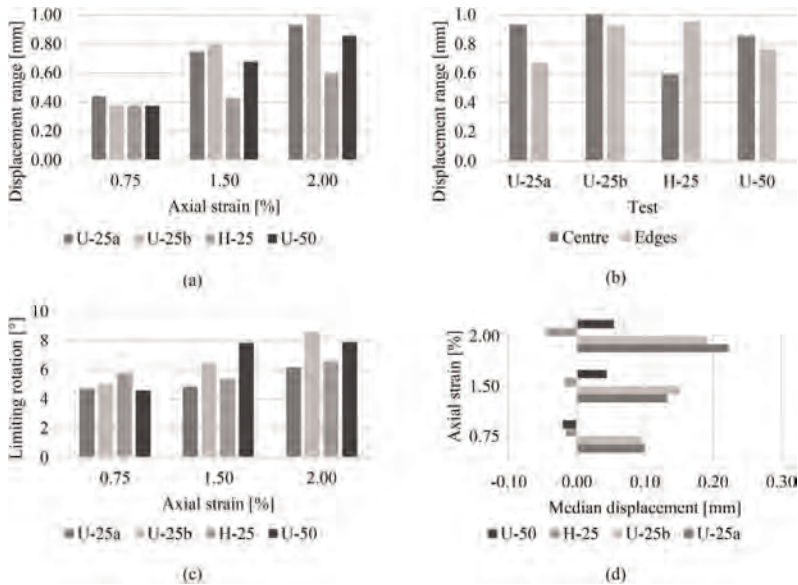
Figure 6. Summary for particle motion boundaries: a) horizontal displacement range (centre 50 mm), b) comparison between the horizontal displacement range at the centre of the specimens and their edges, c) maximum probable rotation (centre 50 mm), and d) median horizontal displacement (centre 50 mm).

confining stress of the U-50 specimen results in reduced lateral displacement compared to the U-25 specimens. Despite the similar volumetric strain response for U-25 and H-25 at a given axial strain, the H-25 specimen has a more limited displacement range. This is due the lateral deformation being distributed between the two halves of the reinforced specimen.

In Figure 6b the displacement range of the centre 50 mm of the specimen is compared with the displacement range of the outer two quarters. The extremities of the reinforced specimen displaced more than the centre, indicating that the lubricated platens were effective in preventing artificial restraint. In addition, the increased displacement at the ends balances the reduced displacement in the centre, to result in a net volumetric strain similar to the control specimens. However, the lubricated platens were not perfect as apparent from the reduced displacement at the edges of the control specimens when compared to the centre.

The resolution of the rotation measurements is coarse relative to the magnitude of the particle rotation. Thus, the difference in the limiting rotation between the specimens is less severe as shown in Figure 6c. However, in general the limiting rotation was greater for U-50 which has greater lateral restraint due to increased confining stress. When a fixed axial strain is applied to a specimen a particle can either move, compress, or crush. Both compression and crushing are unlikely for the stress considered in this study. For a specimen under low lateral restraint particles sliding apart provide the path of the least resistance. When particle displacement is restrained (e.g. by reinforcement) rotation of the particle may be a more efficient mechanism of deformation. Thus, the increase in particle rotation for the U-50 specimens when compared to the U-25 specimens, at the same level of axial strain.

Figure 6d reveals the mechanism producing the difference in strength between U-25 and H-25, despite both specimens having the same volumetric strain behaviour. The figure shows the median displacement for the centre 50 mm of particles each of the unreinforced specimens for three levels of axial strain. For the reinforced specimen the median displacement is shown for the centre 25 mm of upper half and the centre 25 mm of the lower half (i.e. a total of 50 mm of the specimen). The direction of the displacement is extraneous. However, the difference in magnitude is significant. The large median displacement of the two control specimens (U-25-a and b) indicates that the body of particles has shifted significantly away from the central axis the test setup. Thus, an additional moment was applied to the control specimens, which resulted in a lower strength. In the reinforced specimen the inclusion restricted this lateral shift.

The control specimen tested at 50 kPa confining stress also experienced a lateral shift. However, due to the increased confining stress along the length of the specimen U-50 remained stronger than the reinforced specimen tested at 25 kPa (H-25).

6 CONCLUSIONS

This study investigated some of the mechanisms of soil-geogrid interaction present in reinforced triaxial specimens of transparent sand. The effects of increased confinement, whether due to reinforcement or due to increased cell pressure, was measured in terms of the observed particles motions (displacement and rotation). Both the reinforced and unreinforced specimens tested at 25 kPa confining stress had the same volumetric response. However, the reinforced specimen was stronger. Investigation of the particle movements found that the difference in strength was due to a gradual lateral shift in the central axis of the control specimen. This shift resulted in an additional moment being applied to the specimen, and thus a lower strength was measured. Initial results indicate that when the lateral movement of the particles was constrained, particle rotation increased for a given applied axial strain.

REFERENCES

Duncan, J.M., Seed, H.B., 1967. Corrections for Strength Test Data. *Journal of the Soil Mechanics and Foundations Division* 93, 121–137.

Head, K.H., 2014. *Manual of Soil Laboratory Testing*, 3rd ed.

Marx, D.H, Zornberg, J.G., 2022a. Strain Localization in a Triaxial Extension Test on Transparent Sand. *Proceedings of the 7th International Young Geotechnical Engineers Conference*, Sydney, Australia.

Marx, D.H, Zornberg, J.G., 2022b. Shear Band Measurement in Transparent Sand. *Proceedings of the 20th International Conference on Soil Mechanics and Geotechnical Engineering*, Sydney, Australia.

Marx, D.H., Kumar, K. & Zornberg, J.G. 2023. *Evaluation of Particle Motions in Stabilized Triaxial Specimens of Transparent Sand using Deep Learning Segmentation*. Manuscript under review.

Peng, X., Zornberg, J.G., 2019. Evaluation of Soil-geogrid Interaction using Transparent Soil with Laser Illumination. *Geosynthetics International* 26, 206–221

Rousseeuw, P.J., Hubert, M., 2018. Anomaly Detection by Robust Statistics. *WIREs Data Mining and Knowledge Discovery* 8

Stanier, S.A., Blaber, J., Take, W.A., White, D.J., 2016. Improved Image-based Deformation Measurement for Geotechnical Applications. *Canadian Geotechnical Journal* 53, 727–739

Stringer, C., Wang, T., Michaelos, M., Pachitariu, M., 2021. Cellpose: A Generalist Algorithm for Cellular Segmentation. *Nature Methods* 18, 100–106

Chemical characterization of geomembranes by mass spectrometry

Leonardo A. Valentin, Clever A. Valentin, Marcelo Kobelnik & Jefferson Lins da Silva
São Carlos School of Engineering (EESC), University of São Paulo (USP), São Carlos, Brazil

ABSTRACT: Geomembrane is a type of material used in civil engineering and environmental engineering works for the protection and recovery of environment. Five geomembranes commercially obtained from three Brazilian companies were chemically characterized in order to evaluate the chromatographic profile and differentiate them and the results contribute to create a database and evaluate the geomembranes after periods in different applications. The GC/MS technique and multivariate analysis tools were applied. 211 compounds were selected for SVOCs and 59 compounds for VOCs. Considering the 211 compounds, 159 met the p-value criterion < 0.05. For the 159 compounds 130 met the cut-off criterion of 2.0 for the fold change analysis and were considered in the study. Regarding VOCs compounds, of the 59 compounds considered, 25 met the p-value criteria < 0.05 and 15 for the cut-off 2.0 criteria for fold change analysis. The combination of chromatographic determination with multivariate analysis was applied and showed to be an excellent tool for chemical characterization and the differentiation between the five groups can be observed. This information can be useful for use of these techniques in routine for material quality control and for geosynthetics database.

1 INTRODUCTION

With the considerable advance of Chemistry and recent analytical instrumentation, a large number of substances became the target of investigations, making it possible to study their properties and classify them, according to their chemical structures (Hanton 2000; Korner *et al*. 1992). The classification of materials is very extensive and is related with concept of matter where any type of liquid or solid substance can be considered a material (Zarbin 2007).

Interest with composition and structure of materials soared that a new branch of chemistry studies was established, the "Materials Chemistry" (Zarbin 2007). The materials used in Civil Engineering, with emphasis on polymeric materials, are classified as geosynthetic and cover various types of polymers with functions in civil construction activity. A geosynthetic that stands out in works for environmental protection and recovery are geomembranes, especially those of polyethylene type, which are analyzed in this research.

The characterization of materials uses instrumental analysis techniques aimed at understanding different aspects related to composition (molecular mass, oxidation number, etc.) and structure (chemical bonds, crystalline phase, etc.) that are directly linked to chemical properties and physical, and these properties are linked to other properties such as mechanical, optical, catalytic, etc. (Skoog; Holler & Nieman 2009).

For geomembranes, regarding the most common instruments used, we can highlight spectroscopy in ultraviolet/visible (UV/Vis) region, infrared (IR) spectroscopy, X-ray diffraction, thermal analysis TG (thermogravimetric) and DTA (differential thermal analysis), DSC (differential scanning calorimetry) and DMA (dynamic mechanical analysis), chromatography and MS (Mass Spectrometry) (Ahari *et al*. 2019; Hanton 2000; Paiva *et al*. 2010; Valentin *et al*. 2018).

The characterization of different materials is found in literature using MS, being widely applied to biomaterials such as photoresins, polyphenols, PEGs, and others. The characterization of these materials by MS is used in order to elucidate the molecular mass through the identification of the molecular ion, in addition with information obtained by fragmentation (Figueiredo 2014).

Although several studies on geomembranes using instrumentation are found, most have focused on qualitative, quantitative determination or even focusing on standards such as international (ISO), German (DIN), French (AFNOR) and American (ASTM). For the characterization using chromatography with MS and mainly associated with the use of multivariate statistics, only few publications are found in literature.

Regarding multivariate analysis, we can reveal constituents that are important through various interferences and interactions (Wold *et al*. 2001). Multivariate, unlike classical statistics, considers several variables simultaneously. Although multivariate ANOVA (MANOVA) is available, other multivariate analytical methods have the advantage of being able to take collinearity into account (Gelad 2003; Naes et. al. 2002). Research with multivariate analysis covers a wide area with different methods that can be applied in different fields of science and technology (Naes et. al. 2002; Valentin *et al*. 2020).

In a previous study, four geomembranes were analyzed for TG, DTA, DSC and DMA (Valentin *et al* 2018). The different samples showed different thermogravimetric behavior. For the mechanical properties, it was observed that the density and carbon black data had compatible values between samples. The values obtained for tensile, tear and puncture tests are linked to material thickness and showed that commercial samples have values much higher than those recommended. With these results obtained, we realize the importance of chemical characterization of these materials (Valentin *et al*. 2018).

Therefore, the main objective of this study was to chemically characterize five geomembranes commercially obtained from three Brazilian companies, four of which have already been analyzed by Valentin *et al.* (2018) considering thermo-analytical analyses. The second point is to check if the results can contribute to create a database and evaluate the geomembranes after periods in different applications. The MS technique was used for these characterizations and multivariate analysis tools were applied to determine and process the results.

2 MATERIALS AND METHODS

2.1 *Materials*

The geomembrane samples were obtained from coils manufactured by three Brazilian companies, referred to A, B, C, D and E. Each of geomembranes has a different thickness being: A = 2.0 mm, B = 1.90 mm, C = 1.50 mm, D = 0.80 mm and E = 0.75 mm, all with smooth surface. The criterion for choice of samples were good reputation and representativeness of manufacturers, diversity of thicknesses and also the types of application for materials. Samples were collected directly on site and all of them are virgin samples. For the chromatographic determinations, specimens cut in format of tapes with length of 20 mm and thickness of 4 mm were used. The samples were used for determinations of volatile (VOC) and semi-volatile (SVOC) compounds in sufficient quantity for triplicate determinations. For both types of determinations, 22 mL vials with screw caps were used. The solvent used for this study was GC/MS grade Dichloromethane obtained from J T Baker Chemical Co (New Jersey, USA).

2.2 *Methods*

The chemical characterization for compounds was carried out in two steps. First, the samples were analyzed via headspace (HS) coupled to gas chromatograph with mass spectrometer (GC/MS) for volatile compounds. For the second stage, the same GC/MS was used

with liquid injection after extraction (sample preparation) of compounds for determination of semivolatiles.

2.2.1 *Determination of volatile compounds by HS-GC/MS*

Volatile compounds VOC were analyzed according to Castro, *et al.* (2014). For volatile compounds, samples (2 g) were transferred to 22 ml vials and sealed. After that, vials were taken to the CTC Combpal autosampler (CTC Analyticss, Zwinge, Switzerland) and analyzed in headspace (HS) mode by gas chromatograph coupled to mass spectrometer (GC/MS, model 7890) (Agilent Technologies, Inc., Palo Alto, USA) with S / SL inlet and MS single quadrupole model 5977A in scan mode (SCAN). The capillary column used was Agilent Technologies DB-5 (95% dimethylpolyixane and 5% phenyl, 30 m, 0.25 mm, 0.25 µm). The temperature ramp was 35 °C / 5 min, followed by 250 °C to 3 °C / min and holding 5 min at 250 °C. The inlet temperature was 250 °C throughout the run and the rate of carrier gas flow was 1.2 mL/min using helium. For mass spectrometer the source temperature was kept at 230 °C. The EI ionization source was kept at 70 eV. The mass range (m/z) used was 33-400. The parameters used for extraction of compounds in CTC were incubation oven temperature at 120 °C for 8 minutes and the syringe operating at the same temperature. The compounds were also deconvoluted using "Mass Hunter Qualitative" version B.10.00. Then the compounds were identified using the NIST library (National Institute of Standards and Technology) in ID Browser window, including mass and formula. The criteria used for comparison with the NIST library to identify compounds was a minimum score of 80%. All analyzes were performed in triplicate.

2.2.2 *Determination of semi-volatile compounds by GC/MS*

The semi-volatile compounds SVOC were analyzed according to Watanabe, *et al.*, (2007). For semi-volatile compounds, samples (2 g) were transferred to 22 ml vials, sealed and filled with 10 ml of dichloromethane. Then the samples were taken to ultrasound with heating at 60 ° C for 10 minutes. Then, a volume of 1 mL was transferred to vial and then taken to the CTC Combpal autosampler (CTC Analyticss, Zwinge, Switzerland) and analyzed using liquid injection mode by gas chromatograph coupled to mass spectrometer (GC /MS, model 7890) (Agilent Technologies, Inc., Palo Alto, USA) with S / SL inlet and MS model single quadrupole 5977A in scan mode (SCAN). The capillary column used was Agilent Technologies DB-5 (95% dimethylpolyixane and 5% phenyl, 30 m, 0.25 mm, 0.25 µm). The ramp temperature was 35 °C / 5 min, followed by 250 °C to 3 °C / min and holding 5 min at 250 °C. The inlet temperature was 250 °C throughout the run and the rate of carrier gas flow was 1.2 mL/min with a 1:10 split ratio using helium. For the mass spectrometer the source temperature was kept at 230 °C. The EI ionization source was kept at 70 eV. The mass range (m/z) used was 33-500. The compounds were also deconvoluted using "Mass Hunter Qualitative" version B.10.00. Then the compounds were identified using the NIST library (National Institute of Standards and Technology) in ID Browser window, including mass and formula. The criteria used for comparison with the NIST library to identify compounds was a minimum score of 80%. All analyzes were performed in triplicate.

2.2.3 *Statistic*

Initially, all identified compounds (VOCs and SVOCs) were evaluated in MassProfinder 10.0 software (Agilent Technologies, Inc., Palo Alto, USA) to verify the presence of false positives compounds and confirm the spectral fidelity among all samples. In Profinder we have some algorithms that allow find and confirm the identity of compounds. The algorithm used for VOCs and SVOCs was Batch Target Feature Extraction, where we initially selected the library and parameters to be used for identification. Then we define the tolerance percentage for identification followed by signal integrator, spectrum extraction and post-processing filters. Profinder also compare samples and blanks for verification of false positives. Finally, all data were converted to cef format and exported to Mass Profiler Professional MPP 15.1 software

(Agilent Technologies, Inc., Palo Alto, USA) where the statistical tools were applied. With MPP software, samples were separated in groups and analyzed using multivariate tools. In the first step, the significance analysis was performed, to verify if selected groups after defining a value of $p < 0.05$ to reject the null hypothesis. Principal Component Analysis (PCA) was used as a complementary technique to identify the variables and separate the geomembrane groups according to clusters. Fold change was also applied as measure to assess the change between the first group and the subsequent group with ratio between the two measures with variation of unfolding between the groups.

3   RESULTS

The results of chromatographic determinations for VOC and SVOC observed for five types of samples showed satisfactory results for significance analysis. After the interpretation performed using the massprofinder software and the application of criteria, 211 compounds were selected for SVOCs and 59 compounds for VOCs. For the 211 selected compounds, 159 met the p-value criterion < 0.05. For the 159 compounds 130 met the cut-off criterion of 2.0 for the fold change analysis and were considered. For the VOCs compounds, for the 59 compounds considered, 25 met the p-value criteria < 0.05 and only 15 for the cut-off 2.0 criteria for fold change analysis. Thus, the selected compounds were used for processing and plotted on 3D graph to first examine the values by PCA Figure 1. In the PCA graph we can clearly see the good separation of groups for five samples showing the difference obtained after applying the criteria for choosing compounds.
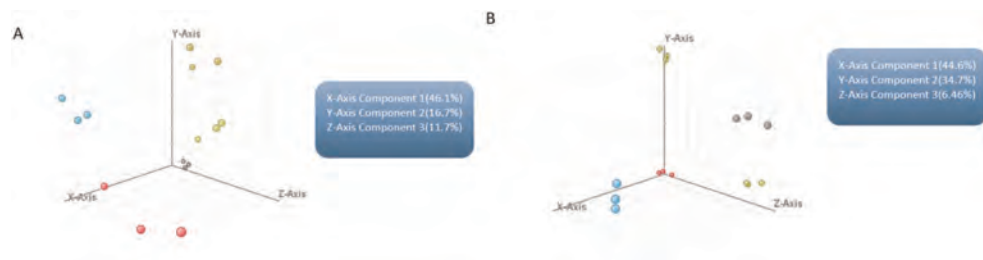
Figure 1.   3D representation for the PCA result in VOC (A) and SVOC (B).

4   DISCUSSION

The five commercial geomembranes samples with different thicknesses were chemically analyzed. The objective was identify the VOCs and SVOCs compounds that could characterize the samples using gas chromatograph instrument with mass spectrometer and multivariate tools (Costa *et al.* 2017; Crotty *et al.* 2016; Kusch P. & Knupp G 2002, 2004; Vilaplana *et al.* 2010). First, five samples were selected to complement a study carried out by our group considering other types of analysis. This first step was very interesting considering the type of information acquired in terms of chemical and physical characteristics for five samples studied. A second important aspect was obtain a chromatographic profile (Figures 2 and 3) for determinations in terms of VOCs and SVOCs compounds, which enables us to carry out future studies for other geomembranes in terms of degradation, aging, evaluation after pre-established times or even for quality control (Blanco *et al.* 2012).

For chromatograms shown above we can observe that for VOCs compounds (Figure 2), the difference between the five samples, mainly for general intensity of compounds. Other details are some peaks found around 7.5 min that are observed only for samples A, B and E. For samples of SVOCs (Figure 4), we can observe a very different profile around 19 min, where there are several candidates for markers. Another detail is the presence for sample D, compounds around 20.5 min, showing the real difference between the groups studied.
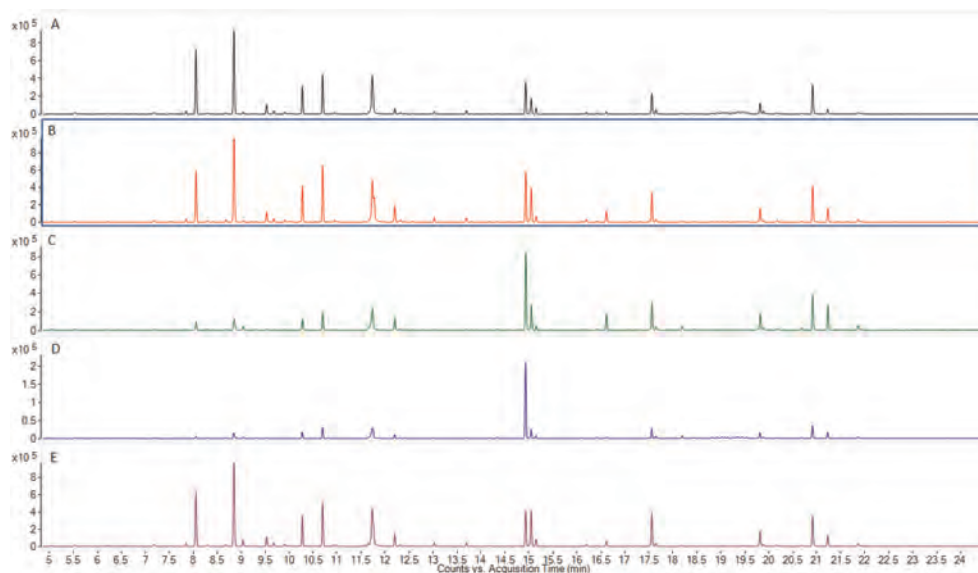
Figure 2.   Chromatograms generated for determination of VOCs compounds for five samples.

Another highlight for this study was being able to propose and develop analytical methodologies, since just few information for this subject is found in literature, mainly using instrumentation (GC/MS) combined with chemometric analysis. (Camacho W. & Karlsson S. 2000; Ciucanu *et al*. 2002)

For data analysis, the use of statistical tools such as PCA, cluster analysis, fold change, significance analysis, among others, were fundamental to determine which compounds could be considered in this study (Shenton *et al*. 2000). In the literature the compounds commonly identified by GC/MS in geomembranes for VOCs are Benzene, 1-1-(1,2-cyclobutanedkyl)bis, Styrene, Ethylbenzene, Candinene, Benzaldehyde, Isocumene, Tetradecane, Cumene, Diethylphthalate, Acetophenone, Diphenylether, tridecane, benzene, (1-methylpropyl), dodecane, nonanal, pentadecane, heptadecane, 1,3-dephenylpropane, benzene, 1-methyl-4-propyl, octadecane, octane, 1,1-oxybis, n-Heptadecanol-1, undecane, among others (Castro *et al*. 2014). For SVOCs, polymer or alloy, oil or plasticizers, carbon black, inorganics, antidegradants, sulfur, among others (Rolin & Rigo 1991).

The use of specific software such as massprofiler to create the criteria for acceptance of peaks found proved to be a fundamental step for this study. Often times, the use of only retention time or molecular ion can lead to use of false positives, which can generate inconsistent data about the actual characteristics of samples. The MPP software also deserves great attention in our study since, with the use of this tool, it was possible to practically and accurately use the data generated by instrument without the need for intermediate steps, such as the use of excel sheets, which they can generate errors and cause distortion of results. In addition to this issue, the possibility of analyzing all data with all

statistical tools proved to be very useful and complete allowing for an accurate interpretation of all compounds (Kumar *et al* 2014; Geladi 2003).

Regarding analytical instrumentation, the use of GC/MS technique was a powerful tool where we had an excellent chromatographic separation, the precise determination of masses and fragments for compounds, allowing the identification through comparison with NIST library (Garrigós *et al*. 2004). For determination of volatiles, the use of CTC with the headspace technique was extremely important where the sampler performed all the work of incubation, extraction and injection of volatilized sample (Wang *et al*. 2019). For SVOC compounds, through a simple sample preparation step, the liquid injection of solvent also brought complete information of entire profile called fingerprint.

The dichloromethane solvent presented a great extraction power for geomembranes where, combined with ultrasound and heating, it resulted in a powerful extraction for SVOC compounds (Smith, & Taylor 2002)

Finally, the combination of chromatographic techniques with chemometrics tools generated valuable results where compounds called markers were determined and selected and can be used in future studies for geomembranes, geosynthetics or related materials.

5   CONCLUSIONS

It was possible to identify a chemical profile to characterize the VOCs and SVOCs compounds using chromatographic techniques coupled with mass spectrometry. The combination of chromatographic determination with multivariate analysis proved to be an excellent tool for chemical characterization and the differentiation between groups could be observed. This information can be useful for use of these techniques in routine for material quality control and also for the creation of a specific database for geosynthetics in general.

REFERENCES

Ahari, M.; Touze-Foltz, N.; Mazéas, L. Sorption of Chlorophenols on Geotextile of the Geosynthetic Clay Liners. *Environmental Engineering Research* 2020; 25(2): 163–170.

Blanco, M.; Castillo, F.; Soriano, J.; Noval, A. M.; Touze-Foltz, N. *Comparative Study of Three Different Kinds of Geomembranes (PVC-P, HDPE, EPDM) used in the Waterproofing of Reservoirs*. Eurogeo 5, Sep 2012, Valencia, Spain. p. 46–54.

Camacho, W.; Karlsson, S. Quality-determination of Recycled Plastic Packaging Waste by Identification of Contaminants by GC–MS After Microwave Assisted Extraction (MAE). *Polymer Degradation Stability*, 2000, v.71, p. 123–134.

Crotty, S.; Gerislioglu, S.; Endres, K. J.; Wesndemiotis, C.; Schubert, U.S. Polymer Architectures via Mass Spectrometry and Hyphenated *Techniques: A Review, Anal. Chem. Acta* 932 (2016) 1–21.

Ciucanu, I.; Kaykhaii, M.; Montero, l.; Pawliszyn, J.; Szubra, J. Continuous Monitoring of Thermooxidative Degradation Products of Polystyrene by Membrane Extraction with Sorbent Interface and Gas Chromatography. *Journal of Chromatographic Science*, 2002, v. 40, p. 350–354.

Figueiredo, T. G. B.; Camposb, M. I.; Sousa, L. S.; da Silva J.R; Druziana, J. I. Produção E Caracterização De Polihidroxialcanoatos Obtidos Por Fermentação Da Glicerina Bruta Residual Do Biodiesel. *Quim. Nova*, 2014, Vol. 37, No. 7, 1111–1117.

Garrigós, M. C.; Marín, M. L.; Cantó, A.; Sánchez, A. Determination of Residual Styrene Monomer in Polystyrene Granules by Gas Chromatography–mass Spectrometry. *Journal of Chromatography A*, 2004 v. 1061, p. 211–216.

Geladi, P. Chemometrics in Spectroscopy. Part I. Classical Chemometrics. *Spectrochimica Acta Part B*, 2003, v.58, p.767–782.

Hanton, S. D. Mass Spectrometry of Polymers and Polymer Surfaces. *Chem. Rev.* 2001, 101,527–569.

Koerner, R.M., Lord, A.E., JR & Hsuan, Y.H. Arrhenius Modelling to Predict Geosynthetic Degradation Geotextiles and 277 Geomembranes. 1992 pp 151–183.

Kusch, P.; Knupp, G. Analysis of Residual Styrene Monomer and Other Volatile Organic Compounds in Expanded Polystyrene by Headspace Solid-phase Microextraction Followed by Gas Chromatography and Gas Chromatography/mass Spectrometry. *Journal of Separation Science*, 2002 v. 25, p. 539–542.

Kumar, N.; Bansal, A.; Sarma, G.S.; Rawal, R. Chemometrics Tools used in Analytical Chemistry: An Overview. *Talanta*, 2014, vol 123, pages 186–199.

Naes, T.; Isaksson, T.; Fearn, T.; Davies, T. User-friendly Guide to Multivariate Calibration and Classification. *Chemometrics*, 2002, v.17, p.571–572.

Paiva, D. L.; Lampman, G. N.; Kriz, G. S.; Vyvyan, K. J.; *Introdução à Espectroscopia, 1a ed.; Cengage Learning, - Tradução da Quarta Edição Americana*: São Paulo, SP, 2010.

Pajaro-Castro, N.; Caballero-Gallardo, K.; Olivero-Verbel, J. Identification of Volatile Organic Compounds (VOCs) in Plastic Products using Gas Chromatography and Mass Spectrometry (GC/MS). *Rev. Ambient. Água*, 2014, vol 9, n4, Taubaté.

Rollin, A.L. & Rigo, J.M. *Geomembranes: Identification and Performance Testing – Report of Technical Committee 103 – MGH – Mechanical and Hidraulic Testing of Geomembranes – RILEM*, Rollin, A.L. & Rigo, J.M., eds., Chapman and Hall, Cambridge, Great Britain, 1991.

Shenton, M. J.; Herman, H.; Stevens, G. C. Using Spectroscopy with Chemometrics to Measure Polymer Molar Mass. *Polymer International*, 2000, v.49, Issue 9, 1007–1013.

Smith, S. H.; Taylor, L. T. Extraction of Various Additives from Polystyrene and their Subsequent Analysis. *Chromatographia*, 2002, v. 56, p. 165–169.

Skoog, D. A.; Holler, F. J.; Nieman, T. A.; Princípios de Análise Instrumental, 6ª ed., Bookman: São Paulo, SP, 2009.

Valentin, C. A.; da Silva, J. L.; Kobelnik, M., Ribeiro, C.A. Thermoanalytical and Dynamic Mechanical Analysis of Commercial Geomembranes used for Fluid Retention of Leaching in Sanitary Landfills. *Journal of Thermal Analysis and Calorimetry*, 2018, v.136, pag 471–481.

Valentin, L.; Barroso, L.P.; Barbosa R. M.; de Paulo G. A.; Castro I. A. Chemical Typicality of South American Red Wines Classified According to Their Volatile and Phenolic Compounds using Multivariate Analysis. *Food Chem*. 2020, vol 302.

Vilaplana, F.; Martínez-sanz, M.; Ribes-greus, A.; Karlsson, S. Emission Pattern of Semi-volatile Organic Compounds from Recycled Styrenic Polymers using Headspace Solid-phase Microextraction Gas Chromatography–Mass Spectrometry. *Journal of Chromatograpy A*, 2010, v. 1217, p. 359–367.

Vinicius, C., C.; Aquino, F. W. B.; Paranhos, C. M.; Pereira-Filho, E. R. - Identification and Classification of Polymer e-waste Using Laserinduced Breakdown Spectroscopy (LIBS) and Chemometric Tools. *Polymer Testing* 59 (2017) 390–395.

Wang, Q.; Zuo, X.; Xia, M.; Xie, H.; He, F.; Shen, S.; Bouazza, A.; Zhu, L. Field Investigation of Temporal Variation of Volatile Organic Compounds at a Landfill in Hangzhou, China. *Environ Sci Pollut Res Int*. 2019 Jun;26 (18):18162–18180

Watanabe M, Nakata C, Wu W, Kawamoto K, Noma Y. Characterization of Semi-volatile Organic Compounds Emitted During Heating of Nitrogen-containing Plastics at Low Temperature. *Chemosphere*. 2007 v.68 (11):2063–72.

Wold, S.; Sjöstrom, M.; Eriksson, L. PLS-regression: A Basic Tool of Chemometrics. *Chemometrics and Intelligent Laboratory Systems*, 2001, v.58, p.109–130.

Zarbin, A. J. G. Química de (nano) Materiais. *Quim. Nova*, 2007 Vol. 30, No. 6, 1469–1479.

Geomembrane integrity surveys of 30 liquid containment storages and their contribution to high quality installation outcomes

G. Fairhead
Fabtech, Adelaide, Australia

A. Bouazza
Monash University, Melbourne, Australia

ABSTRACT: There have been significant developments in the accuracy, speed and availability of integrity surveys over recent years. Geomembrane electrical integrity surveys have become a commonly used tool to assist in achieving low installed geomembrane defect rates and, accordingly, low seepage rates. This paper examines several recent projects where the correlation between defect rates, construction methods, and quality control strategies is reported. The database analysed includes a significant number of containment systems that were subjected to geomembrane integrity surveys quantifying the as-installed and post-survey quality levels. This data provides valuable insight into and contemporary benchmark for achievable defect rates in liquid containment storages.

1 INTRODUCTION

The use of geomembranes (GMBs) in lining systems has become a norm in modern waste containment facilities to cater for a large spectrum of waste, including municipal solid waste (MSW), hazardous waste (HW), mining waste, leachates from MSW and HW, liquors from mining and oil and gas industries and also in resource recovery such as heap leach pads. In typical liner configurations, the GMB is an excellent barrier to the migration of fluids, provided it is devoid of defects and free of wrinkles. However, defects in the geomembrane can occur, even with carefully controlled manufacture, and damage can be found even in sites where strict construction quality control (CQC) and construction quality assurance (CQA) programs have been put in place (e.g., Bouazza *et al.* 2002; Rowe 2005). Not surprisingly, tremendous efforts have been made in the past decade to implement various leak detection technologies to minimise leakages through geomembranes (Gilson-Beck 2019; Gilson 2021). This paper presents a short survey of leakage detection outcomes on leachate and liquors ponds lined with geomembranes as part of the lining systems.

2 ELECTRONIC LEAK DETECTION METHODS

There are a range of electrical leak location (ELL) methods available for conducting leak detection on geomembranes. ELL methods can be divided into two overarching categories: bare and covered geomembrane methods (Gilson-Beck 2019). Bare methods are conducted prior to covering the primary geomembrane. These include high voltage methods of Arc and Spark testing, as well as water-based methods such as water puddle and water lance techniques. Covered methods, such as dipole testing, are conducted during or after commissioning when the system is in operation. Both covered and uncovered methods are taken to

have relatively equal accuracy, however, Gilson-Beck (2019) warns that there is a greater risk of inaccuracy associated with the covered methods. The risk is introduced due to the sensitivity of the instrumentation and the greater reliance on operator skill and methodology. Despite this caveat, the present work assumes equal accuracy across the methods. The assumption is made, as the data was collected by highly skilled technicians, and there was an even distribution of techniques across the data set.

3 STUDY BACKGROUND

Various electrical leak location (ELL) methods were used in the current work. They included arc testing, water lance testing and dipole testing. These tests were conducted on thirty ponds of various sizes in Australia as part of a construction quality assurance program between 2012 and 2021. The ponds were constructed to store potable water, irrigation water, landfill leachate, minerals processing liquors, coal seam gas brines, petro-chemical liquors, and wastewater treatment liquids, respectively.

The lining system configurations and sizes of the ponds are given in Table 1, together with the type of ELL methods conducted on the geomembrane for each site. All the tests were conducted on the primary geomembrane except where indicated.

Table 1. Summary of liquid containment storages surveyed between 2012 and 2021.

Site Number	Area (m²)	Lining system configuration	Layer inspected	Test method
1	21107	GMB primary-Conductive geotextile-Geonet leak detection-GMB secondary	Primary	Arc testing
2	6702	GMB Primary- conductive geotextile GCD leak detection	Primary	Arc testing
3	5200	GMB Primary-conductive geotextile GCD leak detection	Primary	Arc testing
4	4658	GMB Primary-conductive geotextile-GCD leak detection	Primary	Arc testing
5	6,05	GMB Primary-conductive geotextile GCD leak detection	Primary	Arc testing
6	20439	GMB Primary-conductive geotextile GCD leak detection	Primary	Arc testing
7	21650	GMB primary-Conductive geotextile Geonet leak detection-Secondary GMB	Primary	Water Lance Testing
8	4000	GMB Primary-GCD leak detection	Primary	Water Lance
9	14000	GMB Primary GCD leak detection	Primary	Water Lance Testing
10	9000	GMB Primary	Primary	Water Lance testing
11	47670	GMB primary-Secondary GMB-Geonet leak detection	Primary	Water Lance Testing
12	50000	GMB Primary on subgrade	Primary	Water Lance testing
13	8000	GMB Primary on subgrade	Primary	Water Lance testing
14	12600	GMB Primary	Primary	Water Lance Testing
15	7125	Double Lining system	Secondary	Water Lance Testing
16	32000	GMB Primary-GCD leak detection	Primary	Water Lance Testing
17	15555	GMB Primary	Primary	Dipole floor Water Lance walls
18	2940	GMB Primary-GCL Secondary	Primary	Dipole floor Water Lance walls
19	75000	GMB Primary-GCD leak detection GCL Secondary	Primary	Dipole Testing

(continued)

Table 1. Continued

Site Number	Area (m²)	Lining system configuration	Layer inspected	Test method
20	75000	GMB Primary-GCD leak detection GCL Secondary	Primary	Dipole floor Water Lance walls
21	65000	GMB Primary GCD Leak Detection	Primary	Dipole Testing
22	75000	GMB Primary-GCD leak detection GCL Secondary	Primary	Dipole floor Water Lance walls
23	75000	GMB Primary-GCD leak detection GCL Secondary	Primary	Dipole floor Water Lance walls
24	3920	GMB Primary	Primary	Dipole floor Water Lance walls
25	64000	GMB Primary-GCD leak detection GCL Secondary	Primary	Dipole floor Water Lance walls
26	44000	GMB Primary-GCD leak detection GCL Secondary	Primary	Dipole floor Water Lance walls
27	104000	Double Lining system	Pipe Penetrations	Water Lance Testing
28	10000	GMB Primary	Primary	Water Lance
29	14617	GMB Primary-GCD leak detection-Concrete secondary	Primary	Water Lance
30	27000	GMB Primary	Primary	Water Lance Testing

*GMB=geomembrane, GCD-Geocomposite drain, GCL=geosynthetic clay liner

4   RESULTS AND DISCUSSION

The survey on the detection of localised defects in geomembranes conducted in the current work indicated that most defects occurred during the installation phase, generally from construction activities. A total of 120 defects were recorded over 921888 m² of liner tested.

These defects included inadequate seams (18%), mechanical damage (61%) and animal damage caused by kangaroos (18%), as indicated in Figure 1. Interestingly, it was noted that relatively fewer defects were detected from 2017 through 2021 compared to 2012-2016, indicating improved installation methods and construction protocols.
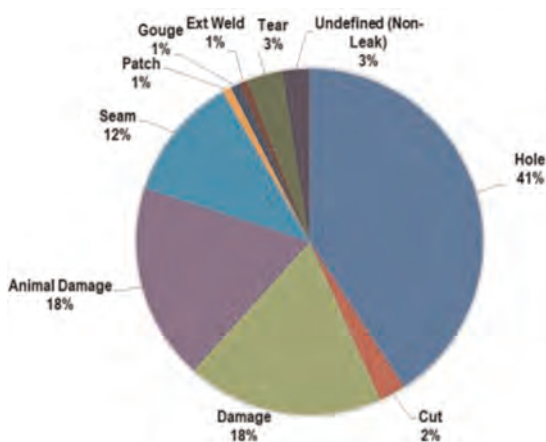
Figure 1.   Cause and type of defects in geomembrane liners.

Another interesting aspect related to geomembrane defects is the leak density per liner area (i.e., the number of defects per hectare or m^2). The results of the survey shown in Figure 2 indicate that the frequency of defects is low (from 0 to 12 defects per hectare), with 24 sites experiencing only a frequency of defects ranging from 0 to 3 defects per hectare which confirms that the construction protocols adopted for these sites minimised the number of defects to the level that regulators consider acceptable. The average frequency for the 30 surveyed sites was 1.3 defects per hectare which is representative of the standard achievable with competent installation and thorough construction quality assurance.
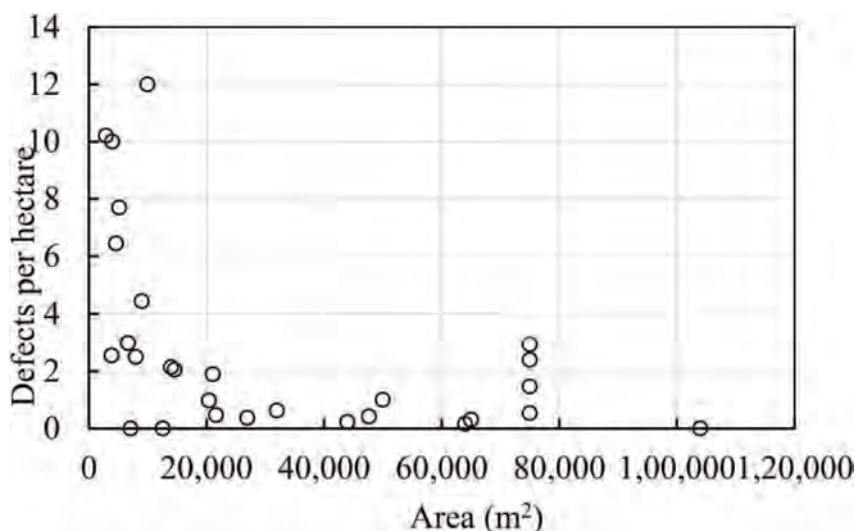
Figure 2.   Variation of defect density versus area surveyed.

The above observations reinforce the fact that the application of a thorough quality assurance program substantially reduces the frequency of defects in a geomembrane liner. It is interesting to note that the density of leaks tended to decrease as the surveyed area increased. Colucci & Lavagnolo (1995) and Charpentier *et al.* (2016) pointed out that larger installations tend to have better construction quality programs aided further by the simplicity of the installation: whereas smaller sites have proportionally more complex features to deal with.

5   CONCLUSIONS

This paper examined the integrity of geomembrane liners used in 30 liquid containment storages using various electrical leak detection methods. The analysis of the database of the electrical integrity surveys conducted between 2012 and 2021 showed that the average frequency for the 30 surveyed sites was 1.3 defects per hectare. This indicates that a thorough quality assurance program substantially reduces the frequency of defects in a geomembrane liner. Furthermore, there were indications that fewer defects were detected from 2017 through 2021 compared to 2012-2016, indicating improved installation methods and construction protocols.

REFERENCES

Bouazza, A., Zornberg, J. G., & Adam, D. 2002. Geosynthetics in Waste Containment Facilities: Recent Advances. *Proc. Int. Geosynthetics Conf., Nice, France*, September 22-27, A.A. Balkema, Vol. 2: 445–510.

Charpentier, C., Jacquelin, T., Rollin, A. L., & Bremner, H. 2016. Statistics on ELL Surveys Compared to the Overall Geomembrane Covered Area in the Province of Quebec in 2014. *Proc. 3rd PanAmerican Conference on Geosynthetics, Miami, USA*: 520–529.

Colluci, P. & Lavagnolo, M.C. 1995. Three Years Field Experience in Electrical Control of Synthetic Landfill Liners. *Proc. 5th Intern Symp on* Landfills, Cagliari, Italy, vol 1: 437–451.

Gilson-Beck, A. 2019. Controlling Leakage Through Installed Geomembranes using Electrical Leak Location. *Geotextiles and Geomembranes*, 47(5):697–710.

Gilson, A. 2021. Advancements in Field Testing for Locating Geomembrane Installation Damage. *International Journal of Geosynthetics and Ground Engineering*, 7(3):1–12.

Rowe, R. K. 2005. Long-term Performance of Contaminant Barrier Systems. *Geotechnique*, 55(9):631–678.

Triaxial compression tests on the stress-strain responses of geocell-reinforced normally-consolidated clay

Fei Song*, Wangsheng Chen* & Yawei Nie*

Institute of Geotechnical Engineering, School of Highway Engineering, Chang'an University, Xi'an, P.R. China

ABSTRACT: Experimental and theoretical investigations on the stress-strain responses of geocell-reinforced clay are very limited. In this paper, a series of conventional triaxial compression tests were conducted on the geocell-reinforced normally consolidated clay to investigate the reinforcement effects and validate the effectiveness of the proposed method. The study results show that the geocell-reinforced normally consolidated clay exhibits strain-hardening. The reinforcement effect on the clay increases with increase of the axial strain and the reduction of the confining pressure. The predicted stress-strain responses via the analytical method proposed in this study are in good agreement with those measured in the tests, showing the effectiveness of the proposed method.

1 INTRODUCTION

Geocell is a three-dimensional geosynthetic material which was originally developed in the late 1970s. Due to its excellent mechanical properties, geocell-reinforced soil has been widely used in engineering construction. Bathurst and Karpurapu (1993), Rajagopal *et al.* (1999), Madhavi Latha and Murthy (2007), Wu and Hong (2009), Chen *et al.* (2013), Chen *et al.* (2018), Xue *et al.* (2019), Song *et al.* (2019) performed triaxial compression tests to study the stress-strain responses of the geocell-reinforced soil and geotextile-encapsulated sand columns. Their research results show that the confining effect of the cell on the infilled soil can be equivalent to the increment of confining pressure, which can improve the strength and stiffness of the backfill. In addition, the cohesion of the infilled soil caused by the confinement of the cell is called apparent cohesion, while the internal friction angle of reinforced soil is basically the same as that of unreinforced soil. On the basis of the analysis of the test results, Song *et al.* (2020, 2022) proposed an analytical method for the stress-strain response of geocell reinforced soil by employing the soil response in the triaxial stress condition and the thin cylinder theories, and verified the validity of the analytical method via the common and large-scale triaxial compression test results of the reinforced soil. However, the infilled soil in the above experiments and theoretical studies are all sand and granular materials, and the analytical model of the stress-strain responses of geocell-reinforced clay is still not systematically studied.

In order to solve the above problems, a series of triaxial tests of unreinforced normally-consolidated clay and geocell reinforced normally consolidated clay were carried out by using GDS triaxial apparatus in this study. The stress-strain relationships under different confining pressures were measured. The differences between the unreinforced and the geocell-reinforced soil were compared, and the mechanism and influencing factors of geocell reinforcement for infilled clay soil were revealed and discussed. The validity of the proposed theoretical model for the geocell reinforced normally-consolidated clay was verified by the triaxial compression test results.

---

*Corresponding Authors: songf1980@163.com, 460308421@qq.com and 987511710@qq.com

2 TRIAXIAL TEST OF REINFORCED NORMALLY CONSOLIDATED CLAY

2.1 *Test instruments and materials*

A static triaxial apparatus produced by the British GDS Company was employed in this study. The triaxial test system is composed of a microcomputer control system, a confining pressure chamber, two controllers (1MPa back pressure controller and 2MPa confining pressure controller), and a measurement system (axial load, confining pressure, axial deformation, pore pressure, and volume strain measurement devices). The basic physical properties of silty clay used in the test are shown in Table 1. In the tests, the silty clay was remolded to be two kinds of soil samples. One is with the moisture content of 21% and the natural density of 2.01g/cm^3, while the other is with the moisture content of 25% and the natural density of 1.94g/cm^3. The remolded clay sample was prepared by the moisture tamping method.

Table 1. Physical properties of the backfill used in the test.

Specific gravity, G_s	Liquid limit(%)	Plastic limit(%)	Optimum moisture content(%)	Maximum dry density(g/cm^3)
2.67	29.5	18.1	16.0	1.66

In this study with references to the research experiences of Madhavi Latha and Murthy (2007), and based on the similarity of strength and stiffness of geocell-reinforced soil, a circular model geocell is fabricated by using PE material, with a thickness of 0.12mm, a diameter of 39mm and a height of 26.6mm, as shown in Figure 1(a). The triaxial specimen has a diameter of about 39.1mm and a height of about 80mm, and it is composed of three circular geocells stacked along the height direction, as shown in Figure 1(b). The tensile stress-strain curve of the geocell strip was tested per ASTM D 882-12 (2012), as shown in Figure 2.

Figure 1. Geocell and the reinforced silty clay specimen.
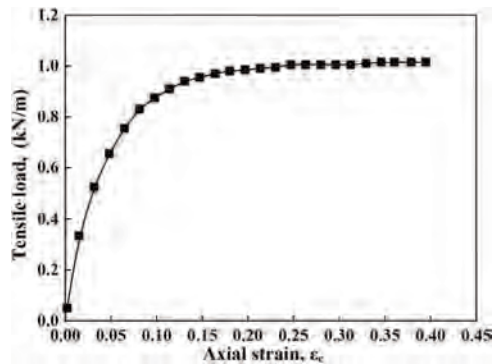
Figure 2. Tensile load-strain curve of geocell sheet.

2.2 *Test scheme and results*

According to ASTM 4767-11(Reapproved 2020), the prepared remolded clay sample was saturated by the vacuum saturation method, so the saturation reached more than 95%.

Triaxial consolidated drained shear tests were carried out on unreinforced clay and geocell-reinforced clay. The axial shear strain rate is 0.012%/min. The measured stress-strain relationships of unreinforced and reinforced soil in the tests were shown in Figure 3.

(a) ρ=2.01g/cm^3 (b) ρ=1.94 g/cm^3
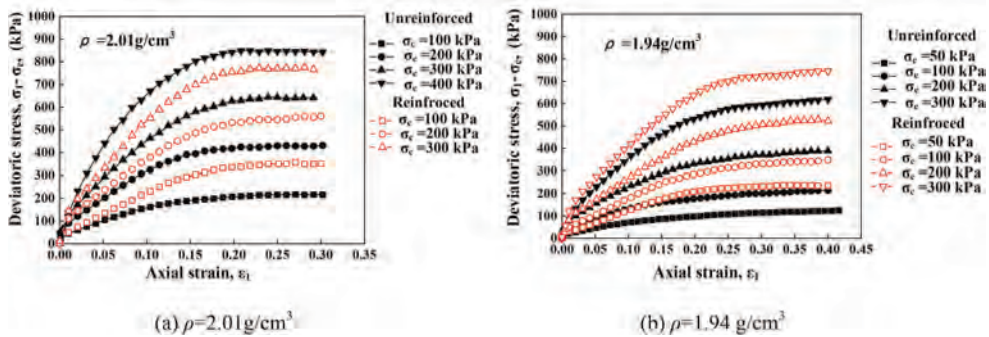
Figure 3.   Stress-strain curves of unreinforced and reinforced clay specimens.

In order to study the increase in the stiffness of the infilled soil due to geocell reinforcement, the ratio of the secant modulus of the reinforced clay to that of the unreinforced clay is defined as the modulus enhancement coefficient η_E, expressed as:

$$\eta_E = \frac{E_{sr}}{E_{su}} \tag{1}$$

in which E_{sr} and E_{su} are the secant modulus of the reinforced clay and that of unreinforced clay, respectively.

According to Figure 3, the relationship between the modulus enhancement coefficient and the axial strain was calculated as shown in Figure 4. It can be seen from Figure 4 that when the axial strain is small, the modulus enhancement coefficient is close to 1, indicating that the cell reinforcement effect is not obvious, and the modulus enhancement coefficient increases gradually with the increase of the axial strain. For example, when the confining pressure is 100kPa, the modulus enhancement coefficient increases from 1.03 to 1.81 with the axial strain increasing from 0.05 to 0.3. The is probably because that with the increase of axial strain, the gradually increasing lateral strain of the infilled soil in the cell leads to the

(a) ρ=2.01g/cm^3 (b) ρ=1.94g/cm^3
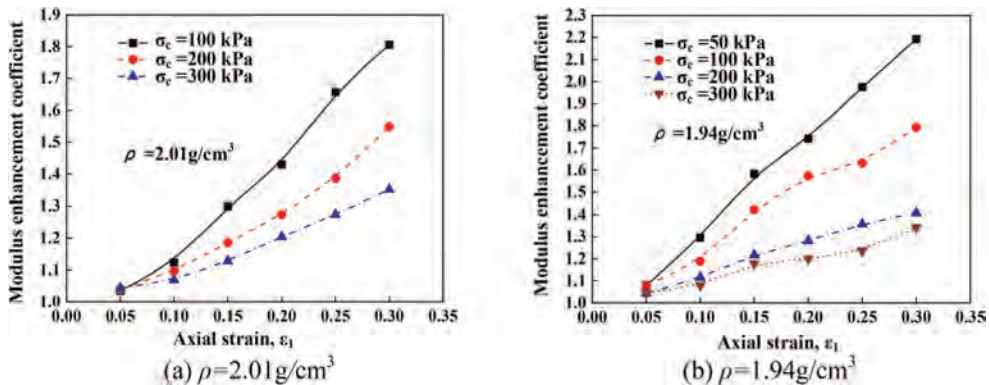
Figure 4.   Variation of modulus enhancement coefficient with the axial strain.

enlargement of the circumferential tensile strain and tensile force of the cell. Thus, the additional confining pressure provided by the cell to the filler will gradually increase with the increase of axial strain of the reinforced soil. In addition, for the same axial strain, the modulus enhancement coefficient decreases gradually with the increase of the confining pressure. For example, for $\varepsilon_1=0.3$，when the confining pressure increases from 100kPa to 300kPa, the modulus enhancement coefficient decreases from 1.81 to 1.35. This is because the volumetric contraction trend of the infilled soil is more obvious under high confining pressure, and its lateral strain is relatively smaller. Therefore, the tensile strain and stress of the geocell are smaller, resulting in smaller confining pressure provided by the cell under high confining pressure.

According to the peak deviator stress in Figure 3, the Mohr circle in Figure 5 can be obtained. It can be seen from Figure 5 that the failure envelope of normally-consolidated clay basically passes through the origin, and the apparent cohesion increases due to the confining pressure of the cell, but the internal friction angle remains basically unchanged. This is basically the same as that of cell-reinforced sand and gravel materials (Bathurst & Karpurapu 1993; Chen et al. 2013; Rajagopal et al. 1999; Song et al. 2019).
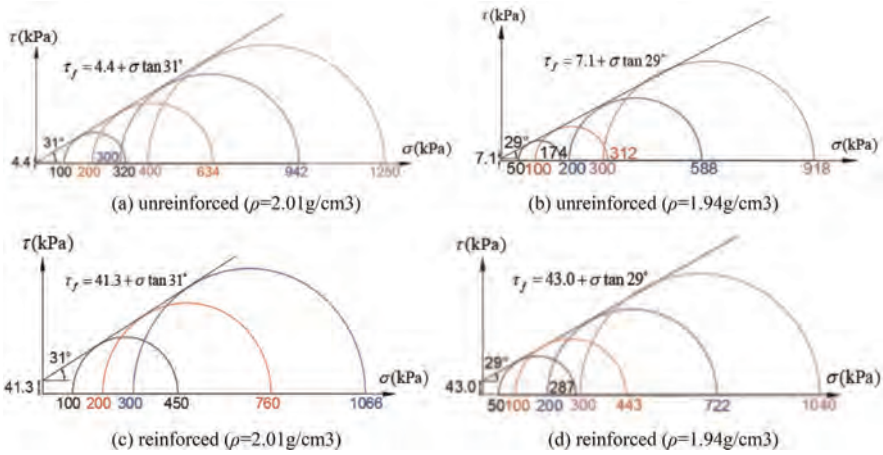
Figure 5.   Mohr circles of unreinforced and reinforced clay.

3   ANALYTICAL MODEL

An analytical method for predicting the stress-strain response of geocell-reinforced granular soil in the triaxial stress state was developed by Song et al. (2020, 2022). In their method, the relationship between the horizontal and vertical stress increments of the backfill can be expressed as:

$$d\sigma_1 = md\sigma_3 + E_t d\varepsilon_1 \qquad (2)$$

where σ_1 and σ_3 are the major and minor principal stresses of the infilled soil in the geocell, respectively, and ε_1 is the axial strain of the soil. $d\sigma_3 = d\sigma_g + d\sigma_c$, in which σ_g is the additional confining pressure provided by the geocell to the infilled soil and σ_c is the minor principal stress of the geocell-reinforced soil. m can be expressed as follows:

$$m = \dfrac{\dfrac{\partial f}{\partial q} - \dfrac{2}{3}\dfrac{\partial f}{\partial p}}{\dfrac{\partial f}{\partial q} + \dfrac{1}{3}\dfrac{\partial f}{\partial p}} \qquad (3)$$

413

in which p and q are the mean principal stress and deviatoric stress, which can be expressed as $p=(\sigma_1+2\sigma_3)/3$ and $q=\sigma_1-\sigma_3$, respectively, in the triaxial stress state. f is the yield function of the infilled soil. In this study, for the normally-consolidated clay, the modified Cam-clay yield function is adopted and then Eq. (3) can be expressed as:

$$m = \frac{1 - \frac{2\omega}{3}}{1 + \frac{\omega}{3}}$$ (4)

$$\omega = \frac{M^2 - \eta^2}{2\eta}$$ (5)

$$\eta = \frac{q}{p}$$ (6)

$$M = \frac{6 \sin \varphi_{cr}}{3 - \sin \varphi_{cr}}$$ (7)

in which φ_{cr} is the residual friction angle of the soil.

E_t in Eq. (2) is the tangent modulus in the nonlinear elastic stress-strain relationship (Duncan *et al.* 1980) and can be expressed as:

$$E_t = kp_a\left(\frac{\sigma_3}{p_a}\right)^n \left[1 - \frac{R_f(\sigma_1 - \sigma_3)(1 - \sin \varphi)}{2c \cos \varphi + 2\sigma_3 \sin \varphi}\right]^2$$ (8)

where k is the modulus number of the hyperbolic model, n is the modulus exponent, R_f is the failure ratio of the soil, and p_a is the atmospheric pressure. c and φ are the cohesion and friction angle of the soil, respectively.

The incremental expression of confining pressure formed by the confining constraint of the cell on the filler is as follows:

$$d\sigma_g = \frac{2M_t}{D_\varepsilon}\frac{d\varepsilon_c}{(1 - \varepsilon_1)}$$ (9)

where M_t is the tangent modulus of the geocell strip, ε_c is the circumferential strain of the cell when the geocell-reinforced soil reaches the axial strain ε_1, D_ε is the equivalent diameter of the geocell when the axial strain of the reinforced soil reaches ε_1. They are determined by equations (10) and (11) respectively (Chen *et al.* 2013):

$$\varepsilon_c = \sqrt{\frac{(1 - \varepsilon_v)}{(1 - \varepsilon_1)}} - 1$$ (10)

$$D_\varepsilon = D_0 \sqrt{\frac{(1 - \varepsilon_v)}{(1 - \varepsilon_1)}}$$ (11)

where D_0 is the original equivalent diameter of the geocell pocket and ε_v is the volume change of the filler. For the normally-consolidated clay, the volumetric change is contraction, which can be estimated via the modified Cam-clay stress-dilatancy relationship and expressed as (Roscoe & Burland 1968):

$$d\varepsilon_v = \frac{3(M^2 - \eta^2)}{M^2 - \eta(\eta - 6)}d\varepsilon_1$$ (12)

On the basis of the above derivation, the stress-strain responses of the geocell-reinforced clay can be obtained according to the procedure proposed by Song *et al.* (2020). In the analysis, the soil parameters include k, n, R_f, c, φ, and φ_{cr}, which can be determined by three conventional triaxial compression tests under different confining pressures. The parameters of geosynthetics include equivalent diameter, D_0, estimated by measuring the pocket size, and the tangent modulus, M_t, determined by tensile load tests.

4 VALIDATION OF THE MODEL

The validity of the proposed analytical method for predicting the stress-strain responses of geocell-reinforced normally-consolidated clay was verified via triaxial test results in this study. The parameters of the clay were calibrated from the triaxial test results and listed in Table 2. The comparison between the prediction results via the theoretical method based on the above parameters and the experimental ones is shown in Figure 6, and the agreement between the calculated curves and the measured ones proves the validity of the above parameters.

Table 2. Parameters of the clay in the analysis.

Density of clay, ρ, g/cm^3	k	n	R_f	c (kPa)	φ (°)	φ_{cr} (°)
2.01	52.2	0.970	0.890	4.4	31	31
1.94	25.6	0.953	0.729	7.1	29	29
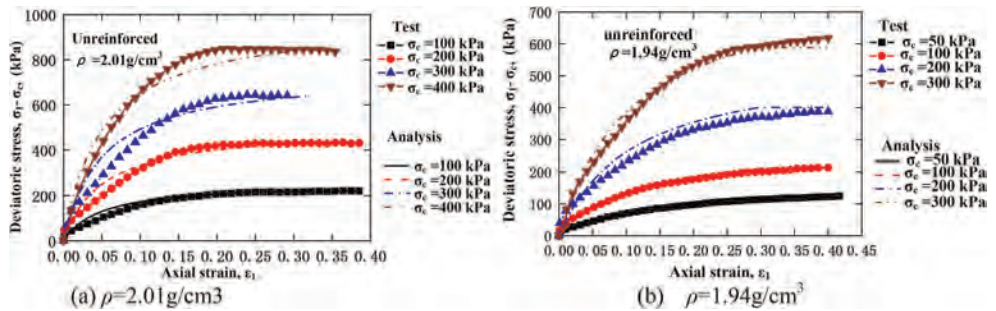
Figure 6. Calibration of calculation parameters of unreinforced soil.

Based on the fitting of the tensile curve in Figure 2, the tangent modulus of the cell strip can be obtained as follows:

$$\frac{M_t}{M_{tref}} = 7G_0\varepsilon_c^6 + 6G_1\varepsilon_c^5 + 5G_2\varepsilon_c^4 + 4G_3\varepsilon_c^3 + 3G_4\varepsilon_c^2 + 2G_5\varepsilon_c + G_6 \qquad (13)$$

in which, G_0, G_1, G_2, G_3, G_4, G_5, and G_6 are 37605.76, -59332.02, 38152.04, -12991.258, 2575.89, -313.52, 24.06 and 0.00392. Since ε_c is dimensionless, the reference tangent modulus M_{tref} is defined here as 1kN/m. The initial equivalent circle diameter D_0 of the cell is 39mm.

The parameters of the above backfill and geocell were substituted into the analytical method proposed in this paper, and the incremental analysis was carried out to obtain the stress-strain responses of geocell-reinforced normally-consolidated clay under different confining pressures, as shown in Figure 7. In order to facilitate comparison, the experimental

results were also superimposed in the figure. The predicted stress-strain responses of reinforced soil were close to the experimentally measured results, which verifies the effectiveness and reliability of the proposed analytical method.

(a) $\rho = 2.01 \text{g/cm}^3$

(b) $\rho = 1.94 \text{g/cm}^3$
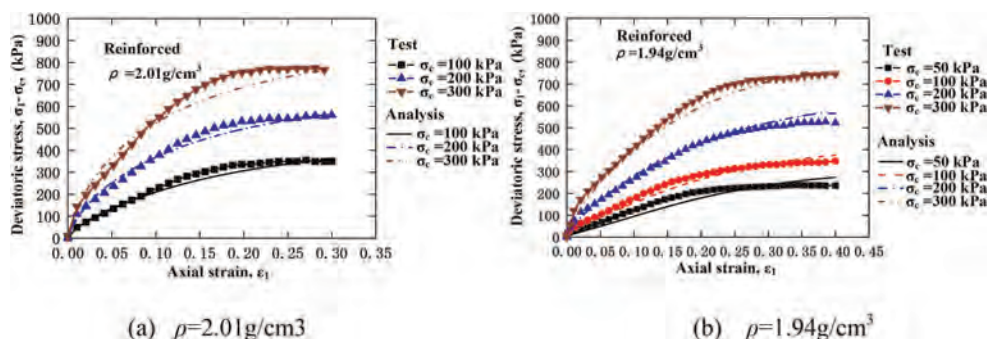
Figure 7.   Validation of the proposed method via triaxial compression test results.

5   CONCLUSION

In this paper, a series of triaxial compression tests were conducted to investigate the stress-strain responses of geocell-reinforced normally consolidated clay. On the basis of the analysis of the test results and the theoretical derivation, the following preliminary conclusions were drawn:

(1) The stress-strain relationship of the geocell-reinforced normally consolidated clay was strain-hardening. Similar to the granular soil, the internal friction angle after reinforcement was basically unchanged, but the apparent cohesion can be improved significantly and the reinforcement effect increases gradually with the increase of axial strain.

(2) By employing the Duncan Chang hyperbolic model, modified Cam-clay yield function and dilatancy equation, an analytical method for predicting the stress-strain responses of geocell reinforced normally-consolidated clay was derived. The proposed method was theoretically rigorous, and the parameters of the geocell and soil required for the calculation have clear physical meanings and can be obtained through routine tests.

(3) The validity of the proposed analytical method was verified by the triaxial compression tests of geocell-reinforced normally consolidated clay in this study.

REFERENCES

ASTM D882-12, 2012. Standard Test Method for Tensile Properties of Thin Plastic Sheeting. *ASTM International*, West Conshohocken, PA, USA.

ASTM 4767-11, 2020. Standard Test Method for Consolidated Undrained Triaxial Compression Test for Cohesive Soils. *American Society for Testing and Materials*, West Conshohocken, Pennsylvania, USA.

Bathurst R. J., Karpurapu R., 1993. Large-scale Triaxial Compression Testing of Geocell-reinforced Granular Soils. *Geotechnical Testing Journal*, 16(3), 296–303.

Chen, J. F., Wang, X.T., Xue, J.F., Zeng, Y., Feng S. Z., 2018. Uniaxial Compression Behaviour of Geotextile Encased Stone Columns. *Geotextiles and Geomembranes*, 46(3), 277–283.

Chen R. H., Huang Y. W., Huang, F. C., 2013. Confinement Effect of Geocells on Sand Samples Under Triaxial Compression. *Geotextiles and Geomembranes*, 37(3), 35–44.

Duncan, J. M., Byrne, P., Wong, K. S., Mabry, P., 1980. Strength, Stress Strain and Bulk Modulus Parameters for Finite Element Analyses of Stresses and Movements in Soil Masses. *Geotechnical Engineering Research Report*, No. UCB/GT/80-01, University of California-Berkeley, Berkeley. CA.

Madhavi Latha G. and Murthy V. S. 2007. Effects of Reinforcement Form on the Behaviour of Geosynthetic Reinforced Sand. *Geotextiles and Geomembranes*, 25(3): 23–32.

Rajagopal, K., Krishnaswamy, N. R., Madhavi, Latha G., 1999. Behavior of Sand Confined with Single and Multiple Geocells. *Geotextiles and Geomembranes*, 17(3): 171–184.

Roscoe K. H., Burland J. B., 1968. *On the Generalised Stress-strain Behavior of 'wet' clay*. In: Heyman J, Leckie FA, editors. Engineering Plasticity. Cam-clay, England: Cam-clay University Press, 535–609.

Song F., Liu H. B., Yang B. Q., Zhao J., 2019. Large-scale Triaxial Compression Tests of Geocell-reinforced Sand. *Geosynthetics International*, 26(4), 388–395.

Song F., Jin Y. T., Liu H. B. and Liu J. 2020. Analyzing the Deformation and Failure of Geosynthetic-encased Granular Soil in the Triaxial Stress Condition. *Geotextiles and Geomembranes*, 48(6):886–896.

Song F., Chen W. S., Nie Y. W. and Ma L. Q. 2022. Evaluation of Required Stiffness and Strength of Cellular Geosynthetics. *Geosynthetics International*, 29(3): 217–228.

Wu, C. S., Hong, Y. S., 2009. Laboratory Tests on Geosynthetic-encapsulated Sand Columns. *Geotextiles and Geomembranes*, 27(2), 107–120.

Xue, J. F., Liu, Z. Y., Chen, J. F., 2019. Triaxial Compressive Behavior of Geotextile Encased Stone Columns. *Computers and Geotechnics*, 108, 53–60.

Soil-geosynthetic interface shear behaviour: Insights from inclined plane and direct shear tests

F.B. Ferreira
CONSTRUCT, Faculty of Engineering, University of Porto, Porto, Portugal

J. Fernandes
Mota-Engil Engenharia e Construção África, SA

C.S. Vieira & M.L. Lopes
CONSTRUCT, Faculty of Engineering, University of Porto, Porto, Portugal

ABSTRACT: The assessment of soil-geosynthetic interface shear strength properties is essential for the safe design of geosynthetic-reinforced soil systems. In this study, a series of inclined plane and direct shear tests was carried out to evaluate the shear strength parameters of the interfaces between a residual soil from granite and two different geosynthetics: an extruded geogrid and a geocomposite reinforcement. The influence of soil moisture content was analysed under inclined plane and direct shear modes by compacting the soil at the optimum moisture content (w_{opt}) and 2% wet of the w_{opt}. The direct shear test results show that the increase in soil moisture content may lead to a considerable reduction in the apparent cohesion of the soil-geosynthetic interface. In general, higher shear stresses were reached at the interface involving the geocomposite reinforcement. Moreover, the interface shear strength parameters established from direct shear test results generally exceeded those obtained by inclined plane tests, particularly in terms of the apparent cohesion value.

1 INTRODUCTION

Understanding the shear behaviour of soil-geosynthetic interfaces is of the utmost relevance for the safe design of geosynthetic-reinforced systems. One of the major benefits from the use of geosynthetics as reinforcement elements in geotechnical structures is the possibility of using lower quality locally available backfill materials, such as cohesive and/or residual soils and recycled waste materials, particularly in cases where higher quality granular soils are not readily available. However, low quality soils are often more susceptible to the detrimental effects of moisture content increase, and thus the influence of moisture content on the behaviour of soil-geosynthetic interfaces involving these soils should be thoroughly evaluated (Ferreira *et al.* 2013, 2015).

The direct shear test is commonly used to investigate the shear strength properties of soil-geosynthetic interfaces subjected to relatively high normal stresses. The inclined plane test can alternatively be used to assess the interface shear strength under lower confining pressures. This method is particularly well suited to study the interaction between soils and geosynthetics when these materials are installed on inclined plane surfaces (e.g. erosion protection systems and landfill liner/cover systems), since it can more accurately reproduce the slippage that may occur on slopes (Ferreira *et al.* 2014; Lopes *et al.* 2014).

The main aim of the present study is to characterise the shear behaviour of the interfaces between a locally available residual soil from granite and two geosynthetics, specifically a

uniaxial extruded geogrid and a uniaxial geocomposite reinforcement, by using two distinct test methods (the inclined plane and the direct shear test), while establishing a comparison between the interface shear strength parameters estimated from both methods. Special care was taken to ensure that the specimen preparation was identical for both types of test to avoid any external factors that could hamper the comparison of results. The influence of soil moisture content and geosynthetic type on the soil-geosynthetic interface shear strength under inclined plane and direct shear modes is also evaluated and discussed in this paper.

2 MATERIALS AND METHODS

2.1 *Materials*

The soil used in this study was a locally available residual soil from granite with the particle size distribution curve presented in Figure 1a. This soil is classified as well-graded sand with silt and gravel (SW-SM) according to the Unified Soil Classification System. The maximum dry unit weight and optimum moisture content ($w = w_{opt}$) obtained from the Modified Proctor test (CEN 2010) are 18.9 kN/m^3 and 11.5%, respectively. The internal soil strength was evaluated by large-scale direct shear tests. For $w = w_{opt}$ and dry unit weight of 17.5 kN/m^3, the soil shear strength can be characterised by a friction angle of 42.4° and cohesion of 13.6 kPa.
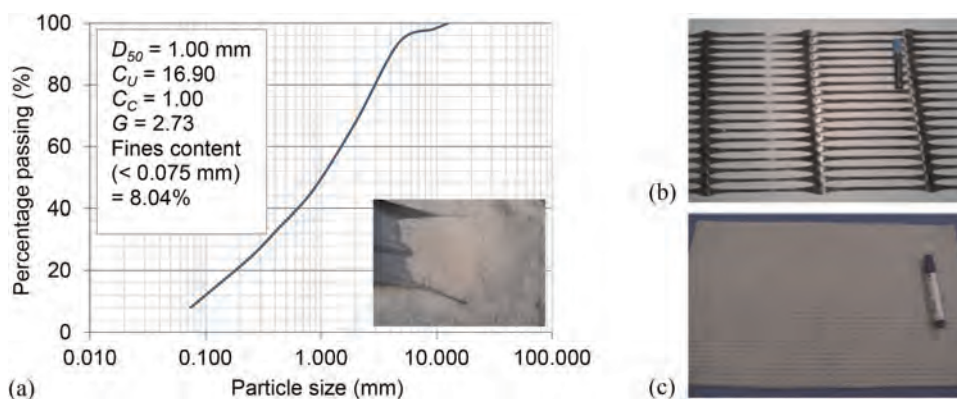
Figure 1. (a) Particle size distribution curve of the residual soil from granite; (b) GGR; (c) GCR.

Two commercially-available geosynthetics were employed, specifically a uniaxial extruded geogrid (GGR) manufactured from high-density polyethylene, with a mean grid size of 22×235 mm (Figure 1b), and a uniaxial geocomposite reinforcement (GCR), consisting of a continuous filament nonwoven polypropylene geotextile reinforced with high modulus polyester yarns (Figure 1c). The tensile load-strain behaviour of the geosynthetics was assessed by wide-width tensile tests following the EN ISO 10319:2015 (CEN 2015). The average values of maximum tensile strength (T_{max}), strain at maximum load (ε_{Tmax}) and secant stiffness at 5% strain ($J_{5\%}$) for the geogrid (machine direction) were 52.2 kN/m, 12.4% and 509.8 kN/m, respectively. For the geocomposite, the corresponding values were 54.6 kN/m, 10.6% and 600.9 kN/m, respectively.

2.2 *Test devices and methods*

Two prototype test facilities were used to carry out the experimental programme: an inclined plane test device and a large-scale direct shear test device. The inclined plane device is

composed of a rigid lower box (510 mm × 350 mm in plan and 80 mm high), a rigid upper box (300 mm × 300 mm in plan and 80 mm high) and a rigid base (620 mm × 430 mm in plan and 10 mm high). According to the EN ISO 12957-2:2005 (CEN 2005), the test can be conducted by using a rigid support for the geosynthetic or with the lower box filled with soil. The tests reported herein were performed using the latter method. During the tests, the base plane was raised at a rate of 0.5°/min and the relative displacement between the upper box and the geosynthetic was monitored. The vertical force was applied by weights transmitted to a rigid steel plate installed over the soil specimen. To ensure that the vertical force approximately passed through the centre of gravity of the upper box, two wedges inclined 1:2 were placed on its front and back walls. The vertical stress (σ_v) was applied for 60 min prior to raising the base plane. Further details about the device, instrumentation and test procedures can be found elsewhere (Ferreira *et al.* 2014; Lopes *et al.* 2014).

The direct shear test device consists essentially of a steel shear box (including upper and lower boxes), a support structure, hydraulic actuators and respective power unit, an electric cabinet and a set of displacement and pressure transducers. The internal dimensions of the upper and lower boxes are 600 mm × 300 mm in plan and 50 mm height, and 800 mm × 340 mm in plan and 100 mm height, respectively. The tests may be performed according to the method of constant or reduced contact area. The present tests were conducted according to the latter method by placing a rigid ring inside the lower box, which enabled equally sized upper and lower halves to be filled with soil. Prior to shearing, the normal stress was applied to the specimens by a rigid metal plate for a period of 60 min. Following the EN ISO 12957-1:2018 (CEN 2018), a constant displacement rate of 1 mm/min was used. A detailed description of the test facility and procedures can be found in Vieira *et al.* (2013) and Ferreira *et al.* (2013, 2015).

2.3 *Test programme*

A series of inclined plane (IPT) and direct shear tests (DST) was carried out to estimate the shear strength parameters of the interfaces between the residual soil from granite and the geosynthetics. The IPT were performed under vertical stresses (σ_v) of 5, 10 and 25 kPa, as recommended by the EN ISO 12957-2:2005 (CEN 2005), and each test was carried out twice under identical conditions. The DST were conducted under normal stresses (σ_n) of 25, 50, 100 and 150 kPa. Soil dry unit weight was kept constant in all of the tests (17.5 kN/m³). The interface shear strength variation associated with an increase in soil moisture content (w), which may potentially occur under field conditions, was evaluated under inclined plane and direct shear modes by compacting the soil at the optimum moisture content (w_{opt} = 11.5%) and 2% wet of the w_{opt} (w =13.5%).

3 RESULTS AND DISCUSSION

3.1 *Influence of soil moisture content*

Figures 2a, b present the evolution of the upper box displacement with the inclination of the shear box from inclined plane tests on the soil-GGR and soil-GCR interfaces performed under σ_v =10 kPa and different soil moisture contents *(w_{opt} and w_{opt} + 2%)*. It can be observed that the influence of soil moisture content on the soil-geosynthetic interface shear strength under inclined plane mode was more significant when the geogrid was used (Figure 2a). For this interface, the slipping angle of the upper box (i.e. the inclination leading to the displacement of 50 mm) increased with the moisture content, implying that the moisture content increase (from w_{opt} to w_{opt} + *2%)* produced a beneficial effect on the interface shear strength. However, for the interface involving the geocomposite reinforcement (Figure 2b), the variation in soil moisture content did not significantly influence the slipping angle, and hence the interface shear strength. This is possibly associated with the structure and moisture absorption capacity of this geosynthetic.
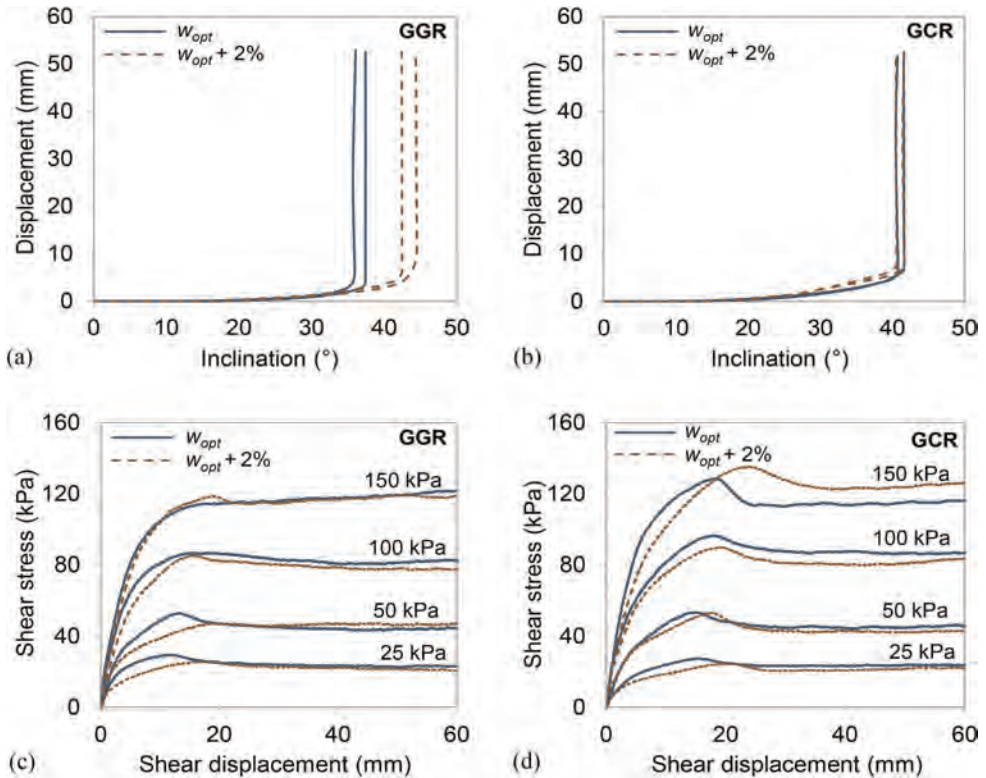
Figure 2. Influence of soil moisture content on soil-geosynthetic interface behaviour: (a) inclined plane tests on soil-GGR interface (σ_v = 10kPa); (b) inclined plane tests on soil-GCR interface (σ_v = 10kPa); (c) direct shear tests on soil-GGR interface; (d) direct shear tests on soil-GCR interface.

Figures 2c, d compare the shear stress-shear displacement behaviour of the soil-GGR and soil-GCR interfaces obtained from direct shear tests carried out under different soil moisture conditions (w_{opt} and w_{opt} +2%). For the soil-GGR interface (Figure 2c), the increase in moisture content led to a considerable reduction in the maximum interface shear strength under lower normal stress values (by up to 11.5% for σ_n=25 kPa). When subjected to higher normal stresses (σ_n=100 and 150 kPa), the influence of soil moisture content on the maximum interface shear strength was almost negligible. Similarly, the maximum shear strength of the soil-GCR interface (Figure 2d) also tended to reduce with increasing moisture content (by up to 10.5% for σ_n=25 kPa).

3.2 Influence of geosynthetic type

The influence of geosynthetic type on the soil-geosynthetic interface behaviour under inclined plane and direct shear modes is illustrated in Figure 3. It is noteworthy that the same type of support for the geosynthetic was used in all of the tests (i.e. lower box filled with soil) to enable the comparison of results. The inclined plane test data show that, when the soil moisture content is equal to w_{opt}, the slipping angles achieved at the interface involving the GCR were greater than those for the interface involving the GGR (Figure 3a). However, when the moisture content was increased (Figure 3b), the slipping angles were similar for both interfaces.
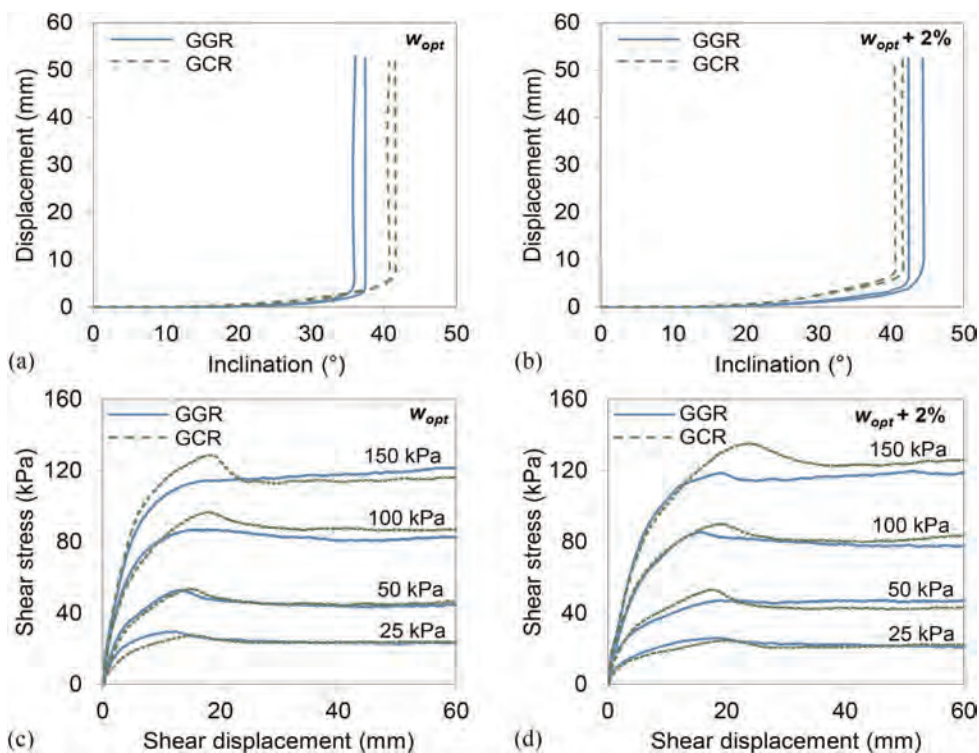
Figure 3. Influence of geosynthetic type on soil-geosynthetic interface behaviour: (a) inclined plane tests for $w = w_{opt}$ ($\sigma_v = 10$kPa); (b) inclined plane tests for $w = w_{opt} +2\%$ ($\sigma_v = 10$kPa); (c) direct shear tests for $w = w_{opt}$; (d) direct shear tests for $w = w_{opt} +2\%$.

The results from the direct shear tests, shown in Figures 3c, d indicate that the maximum shear stresses reached at the soil-GCR interface generally exceeded those at the soil-GGR interface, regardless of moisture content. In addition, the increase in the maximum interface shear strength attributed to the use of the geocomposite became more pronounced as the normal stress was progressively increased. The higher values of shear stress reached for the interface with the geocomposite may be associated with the higher surface roughness of this geosynthetic, comparatively with the geogrid, which promoted higher mobilisation of frictional resistance during shearing.

3.3 *Inclined plane test versus direct shear test*

Soil-geosynthetic interface shear strength parameters are generally estimated from direct shear tests by fitting a straight line through the plot of peak shear stress versus normal stress, which represents the interface shear strength envelope. Based on the Mohr-Coulomb failure criterion, the shear strength parameters, specifically the interface friction angle (δ) and apparent cohesion (c_a) are derived. A comparable analysis may be performed from the inclined plane test results, taking into account the shear stress and normal stress acting at the interface when failure occurs (i.e. at the base inclination leading to a relative displacement of 50 mm) (Ferreira *et al.* 2016).

Figure 4 compares the shear strength envelopes and associated shear strength parameters estimated from inclined plane and direct shear tests on the soil-GGR (Figures 4a, b) and soil-GCR (Figures 4c, d) interfaces under different soil moisture conditions (w_{opt} and $w_{opt} + 2\%$).

These results show that the shear strength parameters obtained from direct shear tests were generally higher than those estimated from inclined plane tests for a specific interface. The interface friction angles derived from the direct shear tests slightly exceeded those from the inclined plane tests (by up to 5%). On the other hand, the values of the interface apparent cohesion determined from the inclined plane tests did not exceed 1.7 kPa, whereas the values obtained from the direct shear tests were significantly higher. The above findings are consistent with previous studies on soil-geosynthetic (Izgin & Wasti 1998, Ferreira *et al.* 2016) and geosynthetic-geosynthetic interfaces (Girard *et al.* 1990; Wasti & Özdüzgün 2001), in which the interface shear strength parameters derived from direct shear tests exceeded those from inclined plane tests conducted on an identical interface. This indicates that the extrapolation of the linear interface shear strength envelope established from direct shear test results for normal stresses below the range over which the tests are conducted may be nonconservative. Therefore, in cases where the soil-geosynthetic interface is expected to be subjected to low normal loads during construction or throughout the service life of the structure (e.g. erosion protection systems and landfill liner/cover systems), the inclined plane test should be used for more accurate prediction of the soil-geosynthetic interface shear strength.
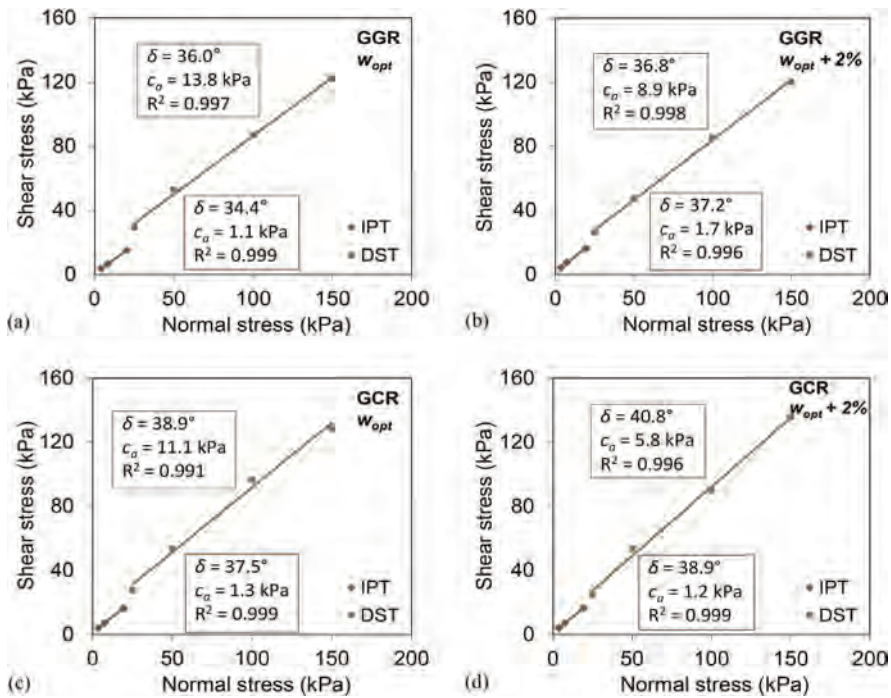
Figure 4. Comparison of soil-geosynthetic interface shear strength envelopes from inclined plane and direct shear tests: (a) soil-GGR interface ($w = w_{opt}$); (b) soil-GGR interface ($w = w_{opt} + 2\%$); (c) soil-GCR interface ($w = w_{opt}$); (d) soil-GCR interface ($w = w_{opt} + 2\%$).

4 CONCLUSIONS

A series of inclined plane and direct shear tests was conducted to investigate the effect of soil moisture content and geosynthetic type on the soil-geosynthetic interface shear strength and to compare the shear strength parameters estimated on the basis of the aforementioned test methods.

Under inclined plane shear mode, the increase in soil moisture content from w_{opt} to $w_{op} + 2\%$ did not induce any reduction in the soil-geosynthetic interface shear strength. However, under direct shear test conditions, the interface shear strength tended to reduce with increasing moisture content, particularly under lower normal stress values. Maximum shear strength reductions of 11.5% and 10.5% were obtained for the interfaces with the GGR and the GCR, respectively.

In general, higher shear stress values were reached at the interface involving the geocomposite reinforcement, regardless of soil moisture content, which may be attributed to the rougher surface of this geosynthetic, in comparison to that of the geogrid.

The interface shear strength parameters obtained from the direct shear tests generally exceeded those from the inclined plane tests conducted on the same interface. While the values of friction angle determined from the direct shear tests were only slightly higher (by up to 5%) than those estimated from the inclined plane tests, the apparent cohesion values were significantly greater when derived from the former method.

ACKNOWLEDGEMENTS

REFERENCES

CEN 2005. EN ISO 12957-2:2005. *Geosynthetics - Determination of Friction Characteristics - Part 2: Inclined Plane Test*. CEN, Brussels, Belgium.

CEN 2010. EN 13286-2:2010. *Unbound and Hydraulically Bound Mixtures - Part 2: Test Methods for Laboratory Reference Density and Water Content - Proctor Compaction*. CEN, Brussels, Belgium.

CEN 2015. EN ISO 10319:2015. *Geosynthetics - Wide-width Tensile Test*. CEN, Brussels, Belgium.

CEN 2018. EN ISO 12957-1:2018. *Geosynthetics - Determination of friction characteristics - Part 1: Direct shear test*. CEN, Brussels, Belgium.

Ferreira, F.B., Carneiro, J.R., Vieira, C.S. & Lopes, M.L. 2014. Soil-geogrid Interaction in the Inclined Plane Shear Movement. *Proc. of 10th Intern. Conference on Geosynthetics, Berlin, 21-25 September 2014*.

Ferreira, F.B., Vieira, C.S. & Lopes, M.L. 2013. Analysis of Soil-geosynthetic Interfaces Shear Strength Through Direct Shear Tests. *Proc. of International Symposium on Design and Practice of Geosynthetic-Reinforced Soil Structures, Bologna, 14-16 October 2013*: 44–53.

Ferreira, F.B., Vieira, C.S. & Lopes, M.L. 2015. Direct Shear Behaviour of Residual Soil–Geosynthetic Interfaces–Influence of Soil Moisture Content, Soil Density and Geosynthetic Type. *Geosynthetics International* 22(3): 257–272.

Ferreira, F.B., Vieira, C.S. & Lopes, M.L. 2016. Soil-geosynthetic Interface Strength Properties from Inclined Plane and Direct Shear Tests - A Comparative Analysis. *Proc. of 6th Asian Regional Conference on Geosynthetics, New Delhi, 8-11 November 2016:* 925–937.

Girard, H., Fischer, S. & Alonso, E. 1990. Problems of Friction Posed by the Use of Geomembranes on Dam Slopes-examples and Measurements. *Geotextiles and Geomembranes* 9(2): 129–143.

Izgin, M. & Wasti, Y. 1998. Geomembrane-sand Interface Frictional Properties as Determined by Inclined Board and Shear Box Tests. *Geotextiles and Geomembranes* 16(4): 207–219.

Lopes, M.L., Ferreira, F.B., Carneiro, J.R. & Vieira, C.S. 2014. Soil-geosynthetic Inclined Plane Shear Behavior: Influence of Soil Moisture Content and Geosynthetic Type. *International Journal of Geotechnical Engineering* 8(3): 335–342.

Vieira, C.S., Lopes, M.L. & Caldeira, L.M. 2013. Sand–geotextile Interface Characterisation Through Monotonic and Cyclic Direct Shear Tests. *Geosynthetics International* 20(1): 26–38.

Wasti, Y. & Özdüzgün, Z.B. 2001. Geomembrane-geotextile Interface Shear Properties as Determined by Inclined Board and Direct Shear Box Tests. *Geotextiles and Geomembranes* 19(1): 45–57.

The effect of soil on the shear strength of geosynthetic interfaces

P. Pavanello & P. Carrubba
Dipartimento ICEA, Università degli Studi di Padova, Padova, Italy

ABSTRACT: In landfill cover systems, a geogrid or reinforced geomat is often used, placed just above the upper drainage geocomposite, to ensure the stability of the topsoil. In these cases, a specific interface occurs, which could be defined as a mixed interface, as there is a simultaneous contact between two geosynthetics and between the geosynthetics and the soil. The paper presents some preliminary results of a research on the interface shear strength of two interfaces of this type, corresponding to the contact between a drainage geocomposite and a geogrid or a reinforced geomat. A series of tests were carried out with a not standard direct shear device, operating at increased shear stress, to compare the response of the soil-less interface with that measured in the presence of the soil. The results showed how the presence of soil leads to an increase in the shear strength compared to the condition without soil and they also highlighted how the influence of soil on the behavior of the interface depends on the type of reinforcement used.

1 INTRODUCTION

In composite landfill cover systems, where geosynthetic materials are generally widely used, the problem of ensuring the stability of the topsoil frequently arises. To resolve this issue, a geogrid or a reinforced geomat is often inserted into the stratigraphy to reinforce and stabilize the upper layer of soil (Cortellazzo *et al.* 2022). Moreover, if the thickness of the soil is considerable or if the inclination of the slope is steep, it may be necessary to insert a further layer of reinforcement inside the soil, at half the thickness of the layer. For practical reasons, during the construction phase the first geogrid/geomat is generally placed immediately above the drainage geocomposite, which has the function of removing rainwater, and is subsequently covered with the soil. In these cases, among the various interfaces between geosynthetics that must be considered in stability analyses, there is also a unique interface corresponding to the contact between the geogrid/geomat and the draining geocomposite. The peculiarity of this interface is represented by the fact that it is a mixed type or hybrid interface, in which not only two different types of geosynthetic are in contact with each other but there is also the simultaneous presence of the soil. It is therefore neither a geosynthetic-geosynthetic interface, nor a geosynthetic-soil interface.

While many studies are available for both geosynthetic-geosynthetic (Carbone *et al.* 2015; Frost & Lee 2001; Pavanello *et al.* 2018; Stark *et al.* 2015) and geosynthetic-soil interfaces (Bacas *et al.* 2015; Moraci *et al.* 2014; Palmeira 2009), for these types of mixed contacts there is little information in the literature and the present study illustrates some preliminary results obtained at the geotechnical laboratory of the University of Padua by means of an experimental apparatus for shear tests at low confinement stress.

2 THE EXPERIMENTAL DEVICE

This study was carried out by means of an experimental device of new design, conceptually similar to a classical direct shear but with a different method of application of the shear stress and able to perform tests at very low normal stress (Pavanello *et al.* 2022).

The apparatus is composed of a steel box, having sides of 0.30 m × 0.30 m, which can slide over a horizontal surface. The first geosynthetic specimen is fixed to the base of the box, while the second is fixed over the horizontal plane. The box has no bottom and can be filled either with rigid steel plates or with soil. It is connected, via a steel cable, to a counterweight of variable weight (Figure 1): a load cell, placed between the box and the cable, allows to measure at any moment the value of the horizontal force acting on the mobile box.
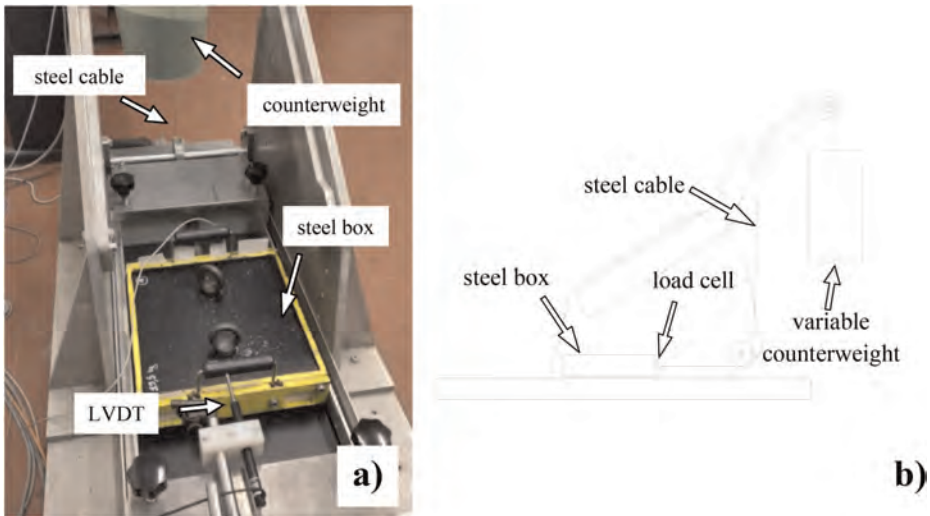
Figure 1.   The direct shear apparatus: a) view from the top and b) sketch.

The instrumentation is completed by a linear variable displacement transducer (LVDT) which allows to detect the displacements of the box as a function of the applied shear stress. Indeed, during the test, the weight of the counterweight gradually increases over time, until the sliding box reaches a minimum displacement of 50 mm. The weight varies gradually by means of a simple mechanism, similar to an hourglass, which makes sand slide from an upper container into the counterweight at a constant speed. Under the hypothesis of a static condition, the mobilized friction angle can be evaluated, time by time, by means of the following simple equation:

$$\tan \varphi = \frac{H}{W} \qquad (1)$$

being H the measured horizontal force applied to the box and W its weight. In analogy with the standard direct shear, the interface friction is generally evaluated in correspondence to a displacement of 50 mm.

Referring to the differences with the standard direct shear test, it should be noted that in the standard device the displacement increases at a constant imposed speed of 1 mm/min while the response of the interface is detected in terms of opposing force, equal to the friction mobilized at the contact surface. Conversely, in the apparatus adopted in this research, the shear stress gradually increases, depending on the weight of the counterweight, while the

displacements of the interface are measured. In summary, in the first case a displacement is imposed and a stress is detected while in the second case a stress is imposed and a displacement is detected.

This latter approach is much closer to the real kinematics involved in the sliding of an interface over a slope and allows to highlight different behaviors of the interfaces that would not be so evident with the usual direct shear test (Pavanello *et al.* 2021).

3 TESTED MATERIALS AND SOIL

The experimental investigation examined the contact between a drainage geocomposite and a geogrid and the contact between the same drainage geocomposite with a reinforced geomat (Figure 2). The drainage geocomposite is formed by a three-dimensional high density polyethylene (HDPE) geonet coupled to two nonwoven geotextiles in polypropylene (PP). Its overall thickness at 2 kPa is equal to 6.4 mm and the tensile strength in the machine direction is 21.5 kN/m. The geogrid is made of polyethylene coated with pvc. It has meshes with a open size of 20x24 mm, mass per unit area of 367 g/m^2 and peak tensile strength of 85 kN/m in the longitudinal direction. Lastly, the reinforced geomat is a composite made by a woven geogrid from high tenacity polyester multifilament yarns protected by a polymeric coating and joined to a multifilamet polyolefin three-dimensional mat. The nominal thickness is of 7 mm and the mass per unit area is of 380 g/m^2; its tensile strength is equal to 25 kN/m in the machine direction.
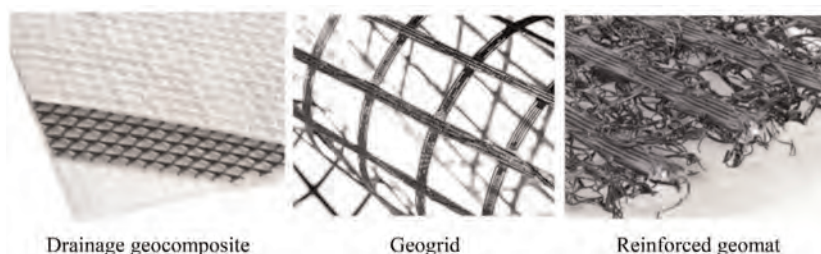
Figure 2.   The geosynthetics involved in the experimentation.

Both the interfaces were previously tested without the soil and after with the soil (Figure 3). In the first case, the normal load was applied by means of steel plates placed inside the upper box. Conversely, in the case of test with soil, it was placed inside the box and a steel plate was added on the top of the layer of soil, to increase the confining stress. The tests were carried out under a normal stress of 5 kPa, for the condition without the soil, and of about 4 kPa in the case of presence of soil.
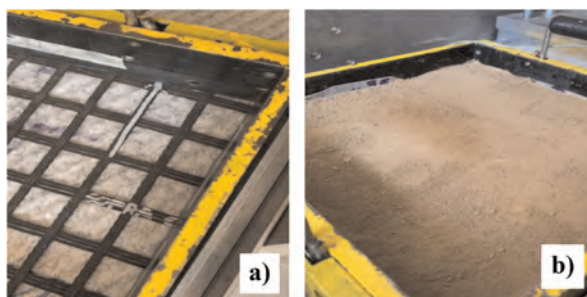
Figure 3.   Preparation of the box for the test a) without soil and b) with soil.

Referring to the selection of the soil, it must be considered that in general the material used to cover landfills does not have to meet very stringent requirements. For this reason, rather varied soils can be used, due to their availability in the area of the site, and consequently it is very difficult to identify a typical soil for these applications. In this research, a silty soil with traces of sand was used, as evidenced by the particle size distribution curve shown in Figure 4. The preliminary characterization tests indicated a liquid limit value of $W_L = 34\%$ and a plastic limit value of $W_P = 22\%$, while the standard Proctor test provided an optimum water content for the compaction of $W_{opt} = 14\%$.
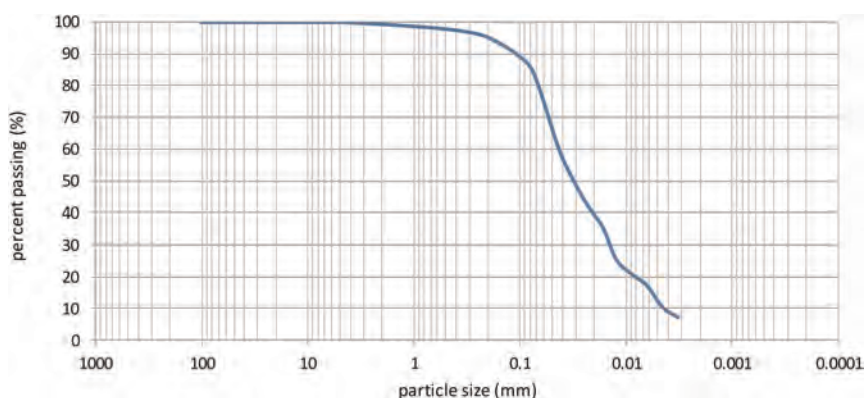
Figure 4.   Particle size distribution of the tested soil.

Considering this data, the tests were performed with various water contents, ranging from approximately 9% up to 18%. In the preparation phase of each test, the dry soil was preliminarily hydrated. Subsequently, it was placed in the box, in three thin layers, and each layer was manually compacted by a variable number of blows, with a wooden pestle. In this way, tests with various densities and water content of the soil were performed.

4   RESULTS

The first results relate to tests conducted on the interfaces without soil (Figure 5). In detail, Figure 5a shows an example of the increasing horizontal force, applied to the upper box, as a function of the time and the corresponding displacements of the two interfaces. Figure 5b shows the corresponding values of the mobilized angle of friction versus the displacement, as obtained by means of Equation 1. The two combinations of materials show a slightly different failure kinematics. It can be observed that the GMT/GCD contact is characterized by a very marked "gradual sliding" behavior (Pavanello et al. 2021): there is no a well-defined limit force value, beyond which the sliding is triggered and, on the contrary, the motion starts very slowly in correspondence with rather low force values and then gradually evolves as the applied shear stress increases. The behavior of the other interface, the GGR/GCD, albeit still characterized by a gradual sliding component, appears to have a much more restricted evolution range. As already highlighted in previous studies (Pavanello et al. 2021), the type of sliding behavior influences the criteria for defining the available static friction angle which in the case of "gradual" behavior, is more difficult to determine or in other words presents more uncertainty.
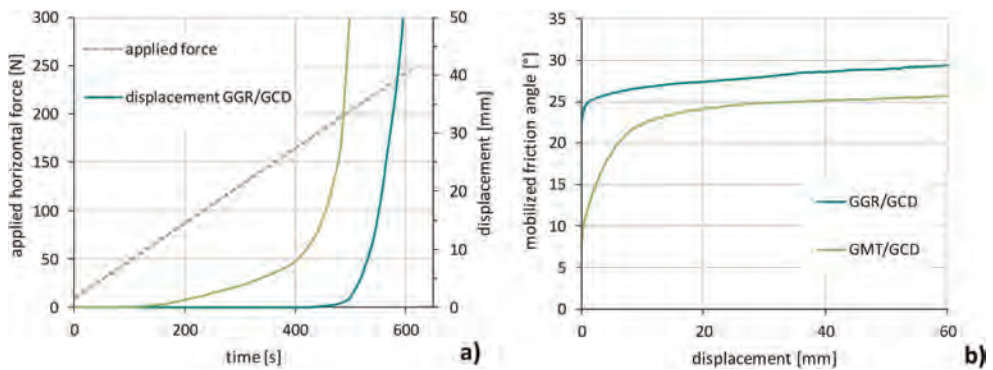
Figure 5. Results of the shear tests on the interfaces without soil: a) development of displacements as function of the time and of the applied horizontal force; b) mobilized friction angle versus displacement.

One of the aims of this research was to understand how much the presence of the soil can influence this type of interfaces, both in terms of the variation of the friction angle and in terms of the possible variation of the behaviour, i.e. the sliding mode. For this purpose, the shear tests were repeated also with the presence of soil at the interface and the related results are shown in Figure 6, compared to the results of the previous case without the soil. Figure 6a reports the case of the GGR/GCD contact, while the results for the interface GMT/GCD are shown in Figure 6b.
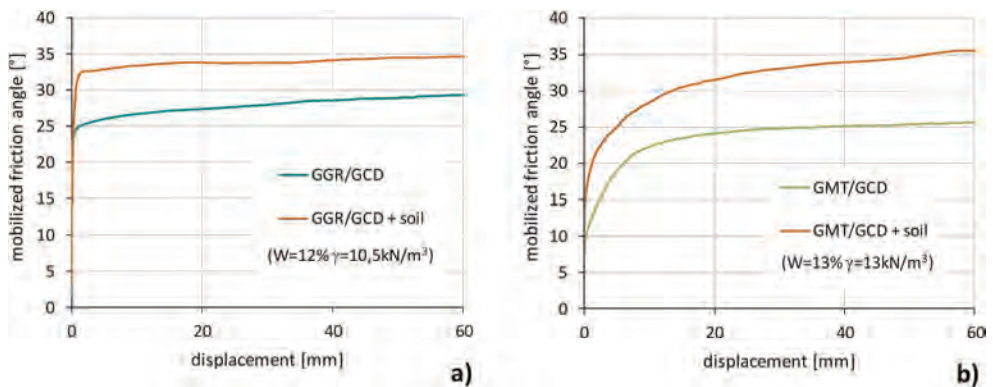
Figure 6. Comparison of the results of the shear tests for the interfaces with and without soil: a) GGR/GCD interface; b) GMT/GCD interface.

In both cases, a significant increase in the friction developed at the interface is observed thanks to the presence of soil particles. In the case of the first interface, GGR/GCD, the behavior evolves towards sudden sliding, with the sliding developing quite clearly when a limit value of the mobilized friction is reached. Differently, in the case of the GMT/GCD contact, the behavior remains of the "gradual sliding" type, with a wide range of friction values mobilized as a function of the displacement. To investigate the influence of soil properties on the interface shear strength, the tests were repeated with different values of water content and soil density. A graphical summary of the results obtained is shown in Figure 7 in terms of friction angle as a function of the wet density of the soil and of its water content. Given the gradual sliding behaviour of the GMT/GCD interface, the friction angle

was evaluated at a displacement of 1 mm, instead of using the usual reference of 50 mm. The figure shows that there is no obvious correlation between water content and interface friction angle. Furthermore, regarding the influence of the compaction level, the two interfaces reveal a different behavior. In the case of contact with the geogrid, a certain dependence on the volume weight of the soil can be observed, with interface friction values increasing as the density of the soil increases (Figure 7a). On the contrary, in the case of contact with the geomat, the data show a relevant scattering and it is not possible to identify an analogous correlation between the values of the angle of friction and the degree of compaction (Figure 7b).
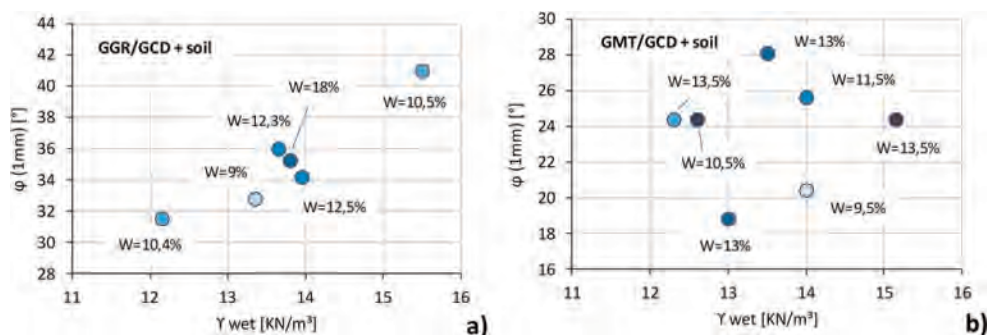
Figure 7.   Interface friction angle versus wet density and water content of the soil: a) GGR/GCD interface; b) GMT/GCD interface.

The set of data collected shows that for the interface with the geogrid, characterized by large openings between the meshes, the soil plays an important role in the formation of interface friction. In fact, not only does the shear resistance show an increase with respect to the case of an interface without soil, but the sliding kinematics itself changes, passing from a "gradual sliding" type behavior to a "sudden sliding" type one. Furthermore, precisely because of the extent of the contact between the soil and the geodrain, the interface shear strength depends on the mechanical properties of the soil and can be indirectly related to its level of compaction.

Conversely, in the case of the reinforced geomat, only a fraction of the soil can cross the geomat and come into contact with the drainage geocomposite. Consequently, while also in this case a general increase in the friction angle is observed, there is no modification of the sliding mechanism, which remains of the "gradual sliding" type even with the presence of the soil. Furthermore, the values of water content and soil compaction do not seem to significantly influence the results, probably due to the interaction with the geomat rather than with the interface.

5   CONCLUSION

The research analyzed the behavior of mixed interfaces, i.e. interfaces in which there is simultaneous contact between two geosynthetics and between the geosynthetics and the soil. Two interfaces were considered, generated by the contact between a drainage geocomposite and respectively a geogrid and a reinforced geomat. The results showed in both cases an increase in the interface shear strength between the test case with soil compared to the condition without soil. However, they also highlighted a different role played by the terrain at the two interfaces. In fact, while in the case of the geogrid the behavior changes passing from the case without soil to the one with soil, this does not happen for the interface with the reinforced geomat.

These investigations, although preliminary, allow some interesting conclusions to be drawn: the first is that in the absence of information on the soil that will be used on site, the tests conducted on geosynthetics without the soil are in any case a valid and certainly precautionary reference. The second observation is that the "gradual sliding" behavior observed for some interfaces without soil can remain so even in the presence of soil. This circumstance implies the need for a careful and prudent evaluation of the available friction in the design phase.

REFERENCES

Bacas, B. M., Cañizal, J., & Konietzky, H. 2015. Shear Strength Behavior of Geotextile/geomembrane Interfaces. *Journal of Rock Mechanics and Geotechnical Engineering*, 7, 638–645.

Carbone, L., Gourc, J.P., Carrubba, P., Pavanello, P., Moraci, N. 2015. Dry Friction Behaviour of a Geosynthetic Interface Using Inclined Plane and Shaking Table Tests. *Geotextiles Geomembr.*, 43, 293–306.

Cortellazzo, G., Russo, L. E., Busana, S., Carbone, L., Favaretti, M., Hangen, H. 2022. Field Trial of a Reinforced Landfill Cover System: Performance and Failure. *Geotextiles and Geomembranes*, 50, 655–667.

Frost, J. D., & Lee, S. W. 2001. Microscale Study of Geomembrane-Geotextile Interactions. *Geosynthetics International*, 8(6), 577–597.

Moraci, N., Cardile, G., Gioffré, D., Mandaglio, M.C., Calvarano, L.S., Carbone, L. 2014. Soil Geosynthetic Interaction: Design Parameters From Experimental and Theoretical *Analysis. Transp. Infrastruct. Geotechnol.*, 2, 165–227.

Palmeira, E.M. 2009. Soil–Geosynthetic Interaction: Modelling and Analysis. *Geotextiles and Geomembranes*, 27, 368–390.

Pavanello, P., Carrubba, P., Moraci, N., Pezzano, P. 2018. Some Aspects Concerning the Laboratory Evaluation of Geosynthetic Interface Friction. *11th International Conference on Geosynthetics 2018,* Seoul (Korea), 16–21 September 2018, 2, 1344–1351.

Pavanello, P.; Carrubba, P.; Moraci, N. 2021. The Characterisation of Geosynthetic Interface Friction by Means of the Inclined Plane Test. *Geotextiles and Geomembranes*, 49, 257–275.

Pavanello, P., Carrubba, P., Moraci, N. 2022. Geosynthetic Interface Friction at Low Normal Stress: Two Approaches with Increasing Shear Loading. *Applied Sciences*, 12(3), 1065.

Stark, T. D., Niazi, F. S., Keuscher, T. C. 2015. Strength Envelopes from Single and Multi Geosynthetic Interface Tests. *Geotechnical and Geological Engineering*, 33(5), 1351–1367.

Response of diagonally enhanced geocells to significant planar tensile loads

K. Fakharian, M. Kashkooli & A. Pilban
Department of Civil & Environmental Engineering, Amirkabir University of Technology, Tehran, Iran

ABSTRACT: Geocells have been used as basal reinforcement in improvement of foundation soils, embankments and highway subgrades to increase bearing capacity and reduce total and differential settlements. Attempts have been made in engineering practice to somehow reduce the extensibility of the geocells whenever they are subjected to considerable tensile forces. This paper presents pullout test results on conventional (ordinary) and diagonally enhanced geocells under different surcharge pressures to evaluate feasibility of their applications when subjected to significant planar forces. Extensive pullout tests on scaled geocells embedded in silica sand are performed to investigate the effects of improvements on load-deformation response, strength and stiffness. Conventional web-shaped geocells are having a small stiffness when subjected to planar tension attributed to deformability of webs. Therefore, conventional geocells may not function properly when subjected to tensile forces along the main plane in service. A special geocell is fabricated in this study, similar to tendoned geocells, through adding diagonal members along the induced tensile load to overcome the shortcomings of conventional geocells. The test results have shown that both the stiffness and ultimate resistance of the diagonally enhanced geocells have significantly improved with respect to the conventional ones.

1 INTRODUCTION

A geocell is a three-dimensional cellular structure that can be filled with soil, gravel, or other materials and is made of high-density polyethylene (HDPE). Geocells have been used as basal reinforcement for improving the foundation soils, embankments and highway subgrades to increase bearing capacity and reduce total and differential settlements. Recent studies have presented the advantages of conventional diamond-web geocells with respect to planar reinforcements in certain applications (Fakher & Jones 2001; Tafreshi & Dawson 2010; Choudhary *et al.* 2020).

The reinforcement elements contribute to improving the soil characteristics including strength and stiffness on one hand, and their frictional interaction with soil on the other hand, to increase the stability and reducing the deformability of the soil structure system. Figure 1 shows typical examples of soil reinforcement under foundations and slope protection. The deformed geocell reinforced mattress of Figure 1a clearly shows the role of tensile load (T) along the geocell plane under a surcharge pressure and the shear stress transfer mechanism below and above the geocell. Figure 1b shows a steep soil slope protected with geocell from erosion. It is evident that both tensile stiffness and shear stress transfer are contributing to stability of the reinforced slope with geocells during the service life.

Attempts have been made in engineering practice to somehow reduce the extensibility of the geocells whenever they are subjected to considerable tensile forces. One example is nailing the geocell into ground to prevent sliding. Also, tendon type supports along the
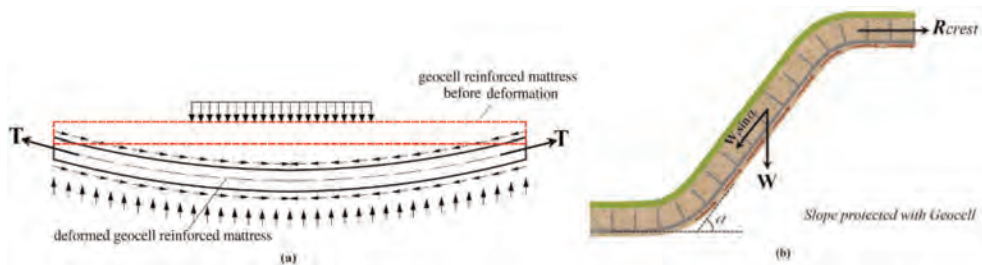
Figure 1.   Example applications of geocells subjected to planar tensile forces: (a) Planar tensile forces (T) in a geocell mattress (Zhang et al 2012), (b) a Slope protected by geocell subjected to downward tensile.

tensile load plane have been added for anchoring the protected geocell layer to the crest of slope and also reducing the geocell longitudinal deformability (Senf 2010). The tendons are being installed diagonally after spreading the geocell in the field in every other web or one tendon per several webs.

The same idea of tendoned geocells and adding diagonal members is further studied here to expand the applications in engineering practice as well as identifying the interactive response with soil when subjected to tensile planar force. The main idea of modifying the common geocells was adding longitudinal members along the tensile load while they are connected at nodes, to enhance its load carrying capacity as wells as reducing the extensibility of geocells. The enhanced product does not function planar and still the multi-dimensional nature of geocell prevails while it is improved against the tensile loads.

A well-known testing apparatus capable of evaluating the tensile resistance/stiffness and interactive shear transfer mechanism is the large-scale pullout box. Most of the reported studies in literature using pullout box are limited to planar reinforcements such as geogrides and geotextiles. The reported data on pullout tests on 3D cellular reinforcement, however, are very limited. Khedkar & Mandal (2009) carried out pullout tests on 3D square webs with various heights and proved their advantages with respect to planar reinforcement, but their experiments were limited to using metal reinforcements. Han *et al.* (2013a,b) reported initial low stiffness and high deformability of diamond-web polymeric geocells. Their results indicated that pullout resistance increases with soil grain size and cell height. In their studies, however, the vertical surcharge was limited to the soil weight and no external pressure was applied onto the soil top.

The main objective of this study is to evaluate the tensile deformability and interaction response of conventional and diagonally enhanced geocells with soil using pullout tests. The longitudinal members are added to conventional diamond-web geocells to enhance their performance for applications in which tensile forces in service are considerable. Pullout behavior of "conventional" and "diagonally enhanced" geocells are carried out under various surcharges and then compared with similar pullout test results of geogrides.

2   TEST EQUIPMENT, MATERIALS, AND EXPERIMENTS

2.1   *Pullout apparatus*

The automated pullout box of Amirkabir University of Technology developed by Nayeri & Fakharian (2009, 2010) was used with some modifications, to carry out the experiments of this study. The schematics of the apparatus and more details are presented by Fakharian & Pilban (2021).

2.2 Soil

The soil used in this study was a crushed angular poorly graded silica sand (SP) with D_{50} of 1.15 mm, supplied from Firuzkuh mine located east of Tehran. Many studies have used different grades of this sand for research purposes and its properties have been well-documented. The sand was deposited through uniform pluviation from 20 cm elevation to obtain a relative density of 45%.

2.3 Conventional and diagonally enhanced geocells

Other than conventional geocells having diamond-shape cells, a special geocell was also fabricated for situations that planar longitudinal forces are significant. For this purpose, longitudinal members were embedded diagonally with the patterns shown in Figure 2. The special geocells are referred in this paper as "diagonally enhanced geocells". This is while diamond-shape webs are referred as "conventional geocells". The conventional geocells are named D25. Three types of diagonally enhanced geocells are fabricated with 3, 5 and 9 longitudinal members, named H25-3, H25-5 and T25, respectively, as shown in Figure 2. The height and length of all reinforcements are considered 25 mm and 720 mm, respectively.

The size of the fabricated geocell was reduced to fit in the common pullout boxes. Polypropylene strips with 1.5 mm thickness and having an ultimate tensile strength of 61 kN/m were adopted.

For comparison purposes of 3D reinforcements with planar reinforcements, extruded HDPE uniaxial Geogrids supplied by Tenax under names TT45 and TT120 were also used. The used Geogrids are having ultimate tensile strengths of 45 and 120 kN/m, respectively, referred to as GG1 and GG2 in this study.
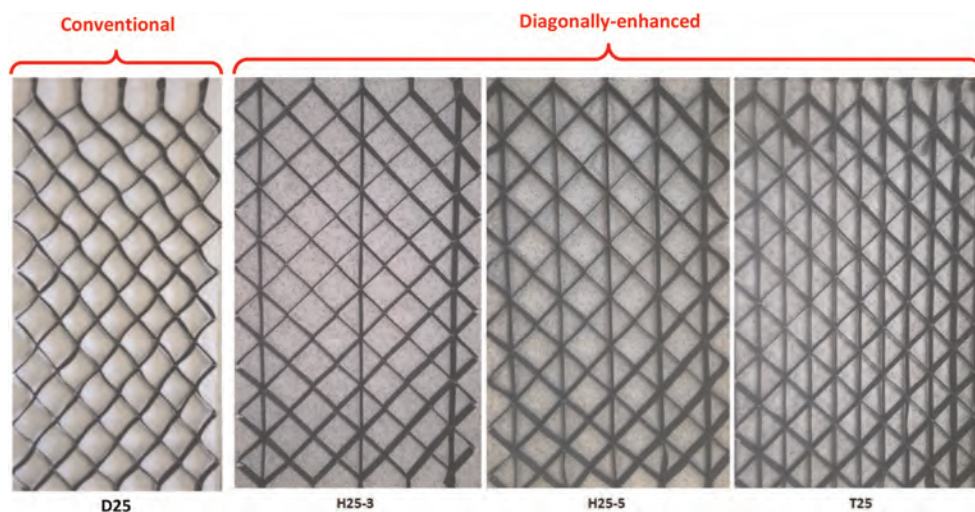
Figure 2. Conventional diamond-shape geocell (D25) and diagonally enhanced geocells developed in this research having 3 (H25-3), 5 (H25-5) and 9 (T25) longitudinal members.

2.4 Sample preparation and test outline

Sample preparations and testing procedures are discussed in details by Fakharian & Pilban (2021). The maximum surcharge pressure used in this study was 33 kPa. With increase in surcharge, the strain hardening response prevails and hence the peak and post-peak of load-frontal displacement graphs cannot be reached within the 90 mm stroke of the apparatus. Pressures starting from zero up to 30 kPa with 10 kPa increments were specified.

3 PULLOUT TESTS RESULTS

The presented results include deformation and load distribution patterns as well as load-frontal displacement along different types of reinforcement at the end of test under different surcharges. Pullout behavior of reinforced elements is usually comprised of a strain-hardening portion first until reaching a peak load. If the displacement is continued, depending on reinforcement property, soil density and magnitude of normal pressure, post-peak softening may or may not be experienced until a steady state is reached. It is pointed out that the passive resistance is mobilized through relative displacement between side walls and soil inside the webs. In the following, the pullout test results are presented for conventional and diagonally enhanced geocells as well as planar geogrids and comparisons are made.

3.1 *Deformation and load transfer patterns*

The main objective of this study is evaluating the tensile response of a diagonally enhanced geocell when subjected to tensile forces along the geocell plane. Deformability of conventional and diagonally enhanced geocells at different stages of tensile force are schematically presented in Figure 3. The conventional geocells simply benefit their 3-Dimentional behavior (confinement and reduction of lateral movement of the soil inside the cells) that leads to an increase in bearing capacity of foundations and reduction of total and differential settlements. When conventional geocells are subjected to tension, however, the cells adjacent to the tensile force point at the front are deformed first and thus the displacements cannot distribute along the reinforcement, resulting in no interaction along the specimen with upper and lower soils. In other words, interactions only occur near the loading point and no extension is observed along the reinforcement. Therefore, both initial stiffness and pullout resistance become very small. To overcome this shortcoming, longitudinal members were added to webs aligned with tensile force direction. Deformation mode of the diagonally enhanced geocell compared to conventional geocell represents a rapid and simultaneous tensile load transfer mechanism between webs along the loading, as observed in Figure 3. The main difference in the conventional and enhanced geocells, is the extent of deformability and the load transfer mechanism between the cells.
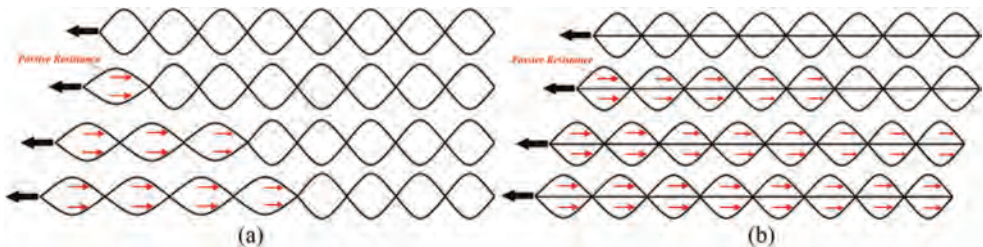
Figure 3.   Plan view of deformation patterns and gradual mobilization of passive resistance during pullout: (a) along the typical diamond-shape (conventional); (b) along diagonally enhanced geocell.

3.2 *Load-frontal displacement and pullout force*

The load-frontal displacement and relative movements of the nodes of different geocells under different surcharge pressures 3, 13, 23 and 33 kPa are compared with each other. In general, according to the load-frontal displacement responses, as anticipated, the pullout resistance and stiffness have increased under higher surcharges.

Figure 4 presents variations of pullout force versus frontal displacement along conventional geocells, diagonally enhanced geocells with 3, 5 and 11 longitudinal members—respectively
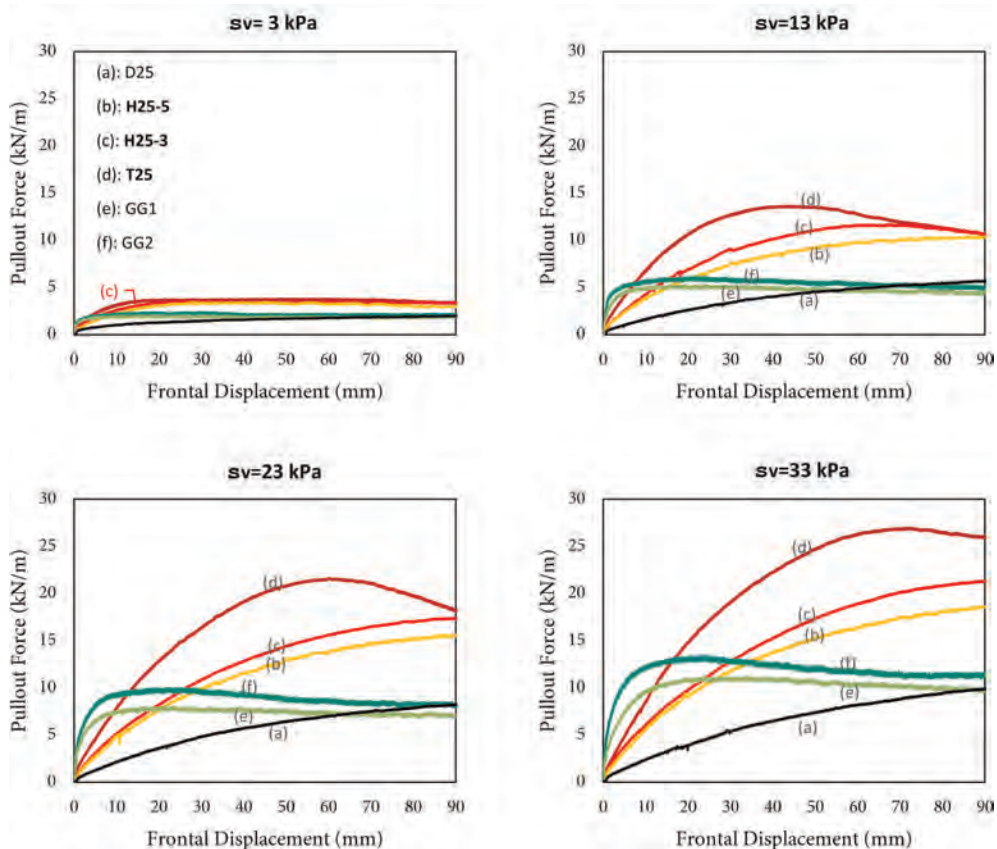
Figure 4. Pullout force versus frontal displacement for "geocells" (D25, H25-3, H25-5 and T25) and "geogrids" (GG1 and GG2) under different surcharges 3, 13, 23 and 33 kPa.

referred to as H25-3, H25-5 and T25—and two types of geogrids. The conventional geocells have shown initial low stiffness and strain-hardening response in such a way that up to the end of the test at 90 mm, no peak was observed. This is understood to be attributed to high extensibility of the diamond-shape conventional geocells. The results show that with increase in number of longitudinal members, the geocell has become stiffer, the relative movements along the specimen are shown to become more uniform and the pullout resistance has increased. The added longitudinal members are contributing to distribute the tensile force more evenly along the specimen and hence the entire geocell has contributed to increasing the interaction between soil and webs. In other words, the longitudinal members are transferring the frontal displacement to the end of the reinforcement (along the specimen) because of their tensile strength; then, the relative displacement between soil inside the cells and above/below leads to frictional and passive resistances along the entire length of reinforcement. (See Figure 3).

The pullout strength of all three types of diagonally enhanced geocells are greater than the geogrides. This is while the initial stiffness of both geogrides are greater than the diagonally enhanced geocells. The difference in strength is due to the fact that geocells are having a much higher passive resistance because of their height. But since the geocell webs are more deformable than extruded geogrides, their stiffness are smaller. The conventional geocell is having a much smaller stiffness than geogrides and diagonally enhanced geocells owing to its

much larger elongation subjected to tensile planar loads. The concept of the soil interaction mechanism inside the webs of geocells is not too different than contribution of the transverse ribs of geogrids. The passive resistance of the ribs is the result of the geogrid movement along the tensile load and the trapped soil inside reacts the movement of the passive rib as it is in frictional contact with the soil above and the soil below it. The thickness of the soil inside the geogrid is much smaller than the geocells though. Besides, geogrid webs are a kind of more rigid as compared to geocells in terms of compressive deformation during the pullout. That is why geogrids have exhibited initially stiffer response compared to (even) diagonally enhanced geocells (Figure 4).

Figure 5 presents the maximum pullout force variations with surcharge pressure for all the specimen types. It is noticed that the differences between pullout resistances of diagonally enhanced geocells with respect to geogrides have become more pronounced with increase in surcharge pressure. The maximum pullout resistance of conventional geocell is almost the same as geogrides, but a much higher deformation has been required to mobilize the pullout resistance.
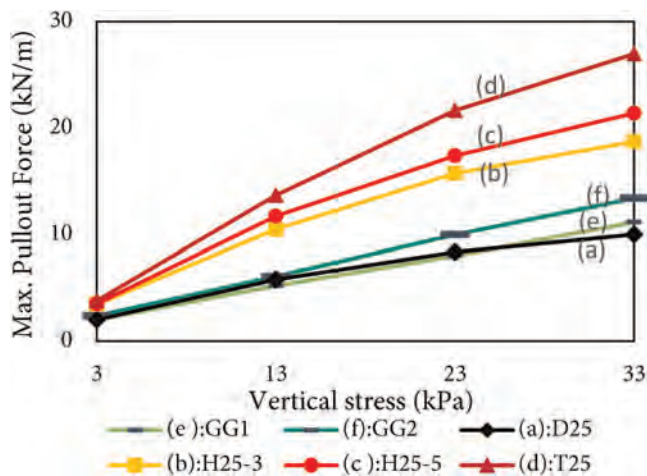
Figure 5. Variations of maximum pullout force with surcharge pressure for different geocells and geogrids.

4 CONCLUSIONS

The most important findings of the study are summarized as follows.

The added longitudinal members in "diagonally enhanced geocells" contribute to transfer the tensile load towards the end of the specimen more evenly as compared to "conventional geocells". As the geocell moves relative to the soil along the specimen simultaneously, the interaction with soil is stronger resulting in higher strength and stiffness. The diagonally enhanced geocells are having higher pullout resistance.

With increase in number of added longitudinal members, the deformability reduces and pullout resistance increases, resulting in more efficient geocells whenever higher longitudinal loads are present in practice.

The extruded geogrids are having an initially stiffer response with respect to diagonally enhanced geocells. However, the pullout resistance of diagonally enhanced geocells are considerably higher than geogrids, providing slightly higher flexibility and hence damping properties when subjected to seismic excitations.

REFERENCES

Choudhary, A.K. & Dash, S.K. 2020. Influence of Soil Density on Performamce of Geocell-reinforced Vertical Anchor in Sand. *Geosythetics International*, https://doi.org/10.1680/jgein.20.00047

Fakharian, K. & Pilban, A. 2021. Pullout tests on Diagonally Enhanced Geocells Embedded in Sand to Improve Load-deformation Response Subjected to Significant Planar Tensile Loads. *Geotext. Geomembr*. 49, No. 2, 1229–1244

Fakher, A. & Jones, C. 2001. When the Bending Stiffness of Geosynthetic Reinforcement is Important. *Geosynthetics International*, 8 (5), 445–460.

Han, X., Kiyota, T. & Tatsuoka, F. 2013a. Pullout Resistance of Geocell Placed as Reinforcement in Gravelly Soil Backfill. *Proceedings of the 10th International Conference on Urban Earthquake Engineering*, Tokyo Institute of Technology, Tokyo.

Han, X., Kiyota, T. & Tatsuoka, F. 2013b. Interaction Mechanism Between Geocell Reinforcement and Gravelly Soil by Pullout Tests. *Bulletin of Earth Resistance Structures*. 46: 53–62.

Khedkar, M. & Mandal, J. 2009. Pullout Behaviour of Cellular Reinforcements. *Geotextiles and Geomembranes*, 27(4), 262–271.

Nayeri, A. & Fakharian, K., 2009. Study on Pullout Behavior of Uniaxial HDPE Geogrids Under Monotonic and Cyclic Loads. *International Journal of Civil Engineering*, Vol. 7, No. 4, pp. 211–223.

Nayeri, A. & Fakharian, K. 2010. Design and Development of Cyclic Pullout Test Apparatus. *Amirkabir Journal of Civil Engineering (AMIRKABIR)*, 41, 137–146.

Senf, D. F. 2010. Creating Sustainable Vegetated Covers Over Difficult Slopes. *Proceedings, American Society of Mining and Reclamation*, 1040–1058.

Tafreshi, S.M. & Dawson, A. 2010. Comparison of Bearing Capacity of a Strip Footing on Sand with Geocell and With Planar Forms of Geotextile Reinforcement. *Geotextiles and Geomembranes*, 28 (1), 72–84.

Zhang, L., Zhao, M., Shi, C. & Zhao, H. 2012. Nonlinear Analysis of a Geocell Mattress on an Elastic–Plastic Foundation. *Computers and Geotechnics*. 42, 204–211.

Mathematical modeling of geotextiles durability exposed to weather

B.M.C. Urashima & L.D. Ferreira
Federal University of Ouro Preto, Ouro Preto, Minas Gerais, Brazil

D.C. Urashima & M.G.A. Guimarães
Federal Center for Technological Education of Minas Gerais, Varginha, Minas Gerais, Brazil

ABSTRACT: This article uses mathematical modeling to present a complementary approach for determining the failure over the geosynthetic's lifetime. Its relevance is in developing an exponential mathematical model to evaluate the durability of polypropylene woven geotextiles exposed in the field since exposure to the environment is of considerable complexity. It was found that the sum of resistance losses of the isolated periods cannot be considered equivalent to resistance loss for the total exposure period due to the accumulation of damages that the material subject. There was also a greater loss in the second exposure cycle compared to the first, justified by the damage that the polymer matrix structure had already accumulated during winter and spring. It was concluded that the durability of intact geosynthetics exposed to weathering factors presents itself differently due to different atmospheric dynamics since each period or season presented its peculiarities.

1 INTRODUCTION

Studies show that the world population is estimated at more than 7.4 billion people; among these, one in ten people does not have access to drinkable water, and one in three people does not have access to primary hygiene conditions. At the same time, natural disasters are recorded more frequently than in the past due to climate change. In this context, the United Nations (UN) in 2016, established a program to encourage sustainable development called Agenda 2030, which presents 17 sustainable development goals (SDGs) to assist and guide the decisions of nations (Dixon *et al.* 2017; Touze 2021).

Geosynthetics can be used in water treatment, food production, economic growth, fishing activities, and renewable energy production. In other words, such materials fulfillment of the 17 sustainable development goals established by the UN (Müller & Wohlecke 2017; Mirhaji *et al.* 2019).

Geosynthetics can be grouped into geotextiles, products related to geotextiles, geosynthetic barriers, and geocomposites (ISO TS 13434 2020). The increase in the use of these materials occurs due to multiple factors, such as the reduction in the environmental impact generated in the construction, operation, and service life of these works about conventional projects. Another factor is the easy installation, transport, and potential for emergency solutions. It makes these materials a reference for their technological appeal and for minimizing environmental damage (Blond *et al.* 2019; Chang *et al.* 2019; Chang & Feng 2021; Jahan *et al.* 2018).

The effects of the geosynthetic application environment on its design service life and, consequently, on its failure probability must be evaluated through appropriate tests, which require determining the material's primary functions and associated degradation processes (ASTM D5819 2022; Troost *et al.* 1994).

This paper presents a complementary approach to evaluate geosynthetics' durability. The present work proposes to evaluate the durability of polypropylene woven geotextiles in the field by submitting them to the weather. The results will be evaluated using statistical tools to validate modeling that considers damage accumulation in geotextiles exposed to the weather over time. This approach makes it possible to better understand the specific behavioral pattern of the material.

2 METHODOLOGY

The case study was the fundamental base for developing the mathematical modeling presented in this article. Two types of polypropylene woven geotextiles made for this research were used. Both were similar in their physical and mechanical characteristics but differing in the percentage of additive against UV radiation (HALS type). GLH (Geotextile with Lowest HALS) and GHH (Geotextile with Higher HALS) were analyzed. The UV radiation protection additive percentage in GHH was twice greater than in GLH, and both percentages were lower than 1%. Table 1 shows the physical and mechanical properties obtained by the GLH and GHH geotextiles.

Table 1. Properties of the polypropylene woven geotextiles (GLH and GHH).

Parameters	GLH**	GHH**
Mass per unit area (ISO 9864 2005)	273.0 g/m^2 (1.3%)	458.0 g/m^2 (0.8%)
Thickness (ISO 9863-1 2016)	0.96 mm (4.8 %)	1.62 mm (1.5 %)
Ultimate tensile strength (ASTM D 5035 2019)[*]	57.5 kN/m (1.7%)	55.8 kN/m (2.0%)

*Mechanical property in the machine direction (MD), **Confidence interval (CI), with 95% of confidence level.

The materials were submitted to weathering according to ISO 877-1 (2009a) and ISO 877-2 (2009b). The field was in the state of Minas Gerais, Brazil. Two exposure cycles were evaluated. The first started on December 21, 2016 (early summer) and ended on December 20, 2017 (late spring). The second was on June 21, 2018 (early winter) until June 20, 2019 (late autumn). GLH and GHH were exposed to the weather of each weather station individually and cumulatively.

The meteorological data from exposure periods was obtained through a meteorological station installed on field. An estimation of the 4.2% UV radiation of global solar radiation (UV/G) was adopted in the durability tests (Escobedo *et al.* 2009; Escobedo *et al.* 2011; Escobedo *et al.* 2014).

Graphs were developed based on the tensile strength data over the exposure time to validate a durability modeling, considering the aging until the degradation of the material, that is, the end of its service life. An exponential mathematical model, using the R^2 statistical analysis, was applied. The number of specimens allows for obtaining tensile strength results with an expected error of up to 1%.

3 RESULTS AND DISCUSSIONS

Table 2 presents the percentage loss of strength values for geotextiles exposed in the first cycle and Table 3 for geotextiles exposed in the second cycle. Confidence intervals were constructed for the aged geotextiles' strip tensile strength test results. This approach was based on the t-student statistical analysis, with a 95% confidence level, allowing the extrapolation of sample data for the population, with a 5% significance level (Tables 4 and 5).

After the first cycle, GHH showed less loss of tensile strength than GLH. It is in line with the percentages of additives against UV radiation used the in each geotextile. The confidence intervals explain that, for the first cycle, the percentage of the strength of geotextiles exposed to summer+autumn is only equivalent to the loss of material exposed to summer; that is,

Table 2. Percentage loss of strength values for geotextiles exposed in first cycle.

Period	GLH%	GHH%
Summer (Su.)	27.4	14.6
Autumn (Au.)	5.0	9.4
Winter (Wi.)	6.2	1.0
Spring (Sp.)	5.6	13.0
Su.+Au.	22.1	13.6
Su.+Au.+Wi.	28.6	21.0
Su.+Au.+Wi.+Sp.	31.3	22.1

Table 3. Percentage loss of strength values for geotextiles exposed in second cycle.

Period	GLH%	GHH%
Summer (Su.)	17.5	16.1
Autumn (Au.)	16.8	20.8
Winter (Wi.)	20.0	19.7
Spring (Sp.)	15.3	14.0
Su.+Au.	32.6	22.3
Su.+Au.+Wi.	40.1	31.3
Su.+Au.+Wi.+Sp.	41.8	34.3

Table 4. Confidence intervals for the aged geotextiles' strip tensile strength in first cycle.

Period	GLH			GHH		
	LL* kN/m	Mean kN/m	UL** kN/m	LL* kN/m	Mean kN/m	UL** kN/m
Intact material	54.7	55.8	56.9	56.8	57.5	58.2
Summer (Su.)	45.9	47.6	49.3	39.2	41.7	44.2
Autumn (Au.)	48.8	50.5	52.2	52.9	54.6	56.3
Winter (Wi.)	54.3	55.2	56.1	51.6	54.0	56.4
Spring (Sp.)	46.0	48.5	51.0	53.2	54.3	55.4
Su.+Au.	47.3	48.2	49.1	42.8	44.8	46.7
Su.+Au.+Wi.	43.2	44.0	43.2	39.4	41.1	42.8
Su.+Au.+Wi.+Sp	42.0	43.4	44.8	37.6	39.5	41.4

*LL: lower limit and **UL: upper limit.

autumn did not significantly affect geotextiles. The geotextiles also showed expected behavior in the second cycle, considering the accumulated time. GLH exhibited a greater loss of tensile strength when compared to GHH.

The distinct behavior of geotextiles in the face of both climatic cycles is highlighted. GLH and GHH, in the first cycle, showed a loss of strength in summer. However, analyzing the first cycle total exposure time, these losses were smaller than the second cycle losses. It is believed that the highest magnitude value occurred in the second cycle due to the polymer matrix structure accumulated damage during winter and spring. When these samples were exposed to atmospheric dynamics during the summer season, as part of their structure had already been compromised, the loss of strength was significantly higher than in the first cycle.

Table 5. Confidence intervals for the aged geotextiles' strip tensile strength in second cycle.

Period	GLH			GHH		
	LL* kN/m	Mean kN/m	UL** kN/m	LL* kN/m	Mean kN/m	UL** kN/m
Intact material	54.7	55.8	56.9	56.8	57.5	58.2
Summer (Su.)	45.6	46.8	48.0	45.8	47.5	49.1
Autumn (Au.)	42.0	44.2	46.4	45.3	47.9	50.4
Winter (Wi.)	43.2	44.8	46.3	41.5	46.0	50.5
Spring (Sp.)	46.2	48.0	49.7	48.2	48.7	49.2
Su.+Au.	33.2	35.6	37.9	37.9	38.8	39.6
Su.+Au.+Wi.	31.1	34.5	37.9	32.5	34.5	36.4
Su.+Au.+Wi.+Sp	32.0	33.5	34.9	31.1	33.5	35.8

*LL: lower limit and **UL: upper limit.

Therefore, regarding the exposure to climatic seasons individually, it is noted that the greatest losses of tensile strength occurred after the summer and spring. In addition, it is noticed that the percentage of losses after total exposure is not equivalent to the sum of the losses in each climatic season. This fact is probably due to changes in the polymeric material structure that occur during exposure and directly influence its behavior. The polymer structure and behavior after exposure to one weather station differ when the material is exposed to other weather seasons, for example.

As expected, it was found that the durability of intact geosynthetics exposed to weathering factors presents itself differently if exposed to the same factors but with different atmospheric dynamics since each period or season presented its peculiarities.

Table 6 presents the estimated UV radiation incidence values and precipitation in the climatic seasons first cycle. Table 7 presents the estimated for the second cycle. It is observed that summer and spring presented high values of radiation and precipitation. This fact explains the higher percentage losses of geotextiles' tensile strength after exposure in these periods individually.

Table 6. Local UV radiation and precipitation values on first cycle.

Period	Number of days -	Estimated UV radiation MJ/m^2	Precipitation mm
Summer	90	76.0	342.4
Autumn	92	40.0	165.4
Winter	93	74.0	17.8
Spring	90	65.0	545.8
Total	365	255.0	1071.4

Table 7. Local UV radiation and precipitation values on second cycle.

Period	Number of days -	Estimated UV radiation MJ/m^2	Precipitation mm
Winter	90	64.0	169.0
Spring	92	63.0	412.2
Summer	93	65.0	504.9
Autumn	90	63.0	62.0
Total	365	255.0	1148.1

It is important to note that the percentage losses of strength were smaller in both cases, even in winter, presenting a similar UV radiation in summer and spring. The joint action of UV radiation and precipitation could be fundamental in the behavior of the exposed material. Therefore, Maxwell's model (2005) becomes less accurate in estimating the damage suffered since it only considers the action of UV radiation in isolation.

Another point to be noted is that during the winter and autumn seasons, days with little rain were predominant for both exposure cycles, thus creating a protective layer of dust on the exposed materials.

Graphs were obtained to validate a durability modeling, considering the degradation until its service life. As shown in Figures 1 and 2, the durability of geotextiles subject to weathering could be represented in terms of time versus tensile strength by an exponential mathematical model according to Equation 1.

$$R = Ke^{-(Y).X} \tag{1}$$

where R = tensile strength (kN/m); K = coefficient dependent on the strength characteristics of the intact material (kN/m), that is, the average value, within its lower and upper limits of the IC; X = exposure time (in days); Y = 10^{-4} to 10^{-3} (depending on the effect of weather, damage accumulation and protection level of material's polymer matrix-additives).
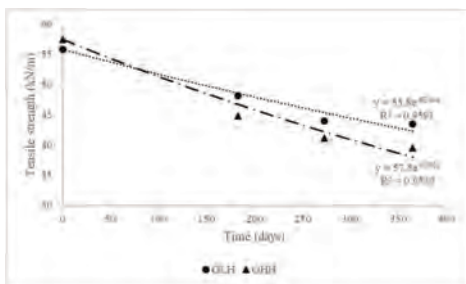
Figure 1.   Model considering the first cycle.   Figure 2.   Model considering the second cycle.
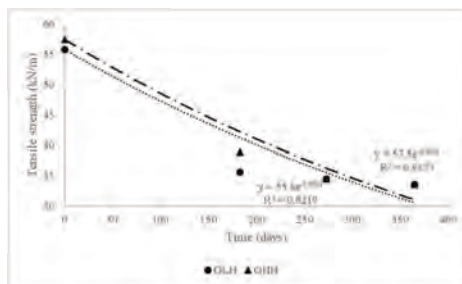
4   CONCLUSIONS

It was possible to verify a greater degradation of geotextiles in the summer climatic season compared to other seasons, even when the highest incidence of UV radiation did not occur in this season, as it was in the second cycle, where the highest incidence occurred in winter. This behavior is due to the sum between the weather, precipitation, and UV radiation.

In the first cycle, even with a greater volume of precipitation during the spring compared to summer, the incidence of UV irradiation was lower and, consequently, the loss of tensile strength. That is, the atmospheric dynamics of the field can directly influence the long-term geosynthetics' behavior in situations exposed to the weather.

GLH showed higher average values of tensile strength loss than GHH, probably due to the lower HALS-type additive concentration.

An exponential mathematical model could be determined to evaluate the geotextiles' durability, an adaptation of the exponential proposal of Maxwell (2005), which deals with the tensile strength in function only of UV radiation. The model proposed in this article seems promising, considering the atmospheric dynamics involved over exposure time. Therefore, the results are for research purposes and are not used in dimensioning parameters.

In order to improve the work developed in this paper, it is proposed to carry out more in-depth statistical analyses, such as, for example, adherence tests, since the R-squared coefficient could show greater adherence to the model.

REFERENCES

ASTM D 5035. 2019. *Standard Test Method for Breaking Force and Elongation of Textile Fabrics (Strip Method)*. ASTM International, West Conshohocken, PA, USA.

ASTM D 5819. 2022. *Standard Guide for Selecting Test Methods for Experimental Evaluation of Geosynthetic Durability*. ASTM International, West Conshohocken, PA, USA.

Blond, E., Boyle, S., Ferrara, M., Herlin, B., Plusquellec, H., Rimoldi, P.& Stark, T. 2019. Applications of Geosynthetics to Irrigation, Drainage and Agriculture. Irrigation and Drainage 68: 67–83.

Chang J.Y. & Feng S.J. 2021. Dynamic Shear Behaviors of Textured Geomembrane/nonwoven Geotextile Interface Under Cyclic Loading. Geotextiles and Geomembranes 49 (2): 388–398.

Chang, I., Lee, M. & Cho, G. 2019. Global CO_2 Emission-Related Geotechnical Engineering Hazards and the Mission for Sustainable Geotechnical Engineering. Energies 12 (13): 1–21.

Dixon, N., Fowmes, G. & Frost, M. 2017. Global Challenges, Geosynthetic Solutions and Counting Carbon. Geosynthetics International 24 (5): 451–464.

Escobedo, J.F., Gomes, E.M., Oliveira, A.P. & Soares, J. 2009. Modeling Hourly and Daily Fractions of UV, Par and Nir to Global Solar Radiation Under Various Sky Conditions at Botucatu, Brazil. Applied Energy 86: 299–309.

Escobedo, J.F., Gomes, E.M., Oliveira, A.P. & Soares, J. 2011. Ratios of UV, PAR and NIR Components to Global Solar Radiation Measured at Botucatu Site in Brazil. Renewable Energy 36: 169–178.

Escobedo, J.F., Rodrigues, D., Dal Pai, A., Oliveira, A.P. & Soares, J. 2012. Irradiações UV, PAR e IV Médias Mensais em Botucatu/SP/Brasil. Avances em Energías Renovables y Medio Ambiente 16: 85–92.

ISO 877-1. 2009a. Plastics – Methods of Exposure to Solar Radiation – Part 1: General Guidance. International Organization for Standardization, Brussels, Belgium.

ISO 877-2. 2009b. Plastics - Methods of Exposure to Solar Radiation – Part 2: Direct Weathering and exposure Behind Window Glass. International Organization for Standardization, Brussels, Belgium.

ISO 9863-1. 2016. Geosynthetics - Determination of Thickness at Specified Pressures - Part 1: Single layers. International Organization for Standardization, Brussels, Belgium.

ISO 9864. 2005. Geosynthetics - Test Method for the Determination of Mass Per Unit Area of Geotextiles and Geotextiles-related Products. International Organization for Standardization, Brussels, Belgium.

International Organization for Standardization 2020. *ISO TS 13434: Geosynthetics — Guidelines for the Assessment of Durability*. International Organization for Standardization, Brussels, Belgium.

Jahan, I., Wood, M., Lake, C. B. & Gagnon, G. A. 2018. Using a Geotextile with Flocculated Filter Backwash Water and its Impact on Aluminum Concentrations. Geotextiles and Geomembranes 46 (2018): 759–769.

Maxwell, A.S., Broughton, W.R., Dean, G. & Sims, G.D. 2005. Review of Accelerated Ageing Methods and Lifetime Prediction Techniques for Polymeric Materials. *National Physical Laboratory*: NPL REPORT DEPC MPR 016.

Mirhaji V., Jafarian, Y., Baziar, M. H. & Jafari, M. K. 2019. Evaluating Seismic In-soil Isolation of MSW Landfill using Geosynthetic Iners in Shaking Table Test: Case Study of Tehran Kahrizak Landfill. Sharif Journal of Civil Engineering 35.2 (1.2): 105–113.

Müller, W. W. & Wöhlecke, A. 2017. Zero Leakage? Landfill Liner and Capping Systems in Germany. Journal of Environmental Geotechnics 6 (3): 1–9.

Touze, N. 2021. Healing the World: A Geosynthetics Solution. Geosynthetics International 28 (1): 1–31.

Troost, G.H., den Hoedt, G., Risseeuw, P., Voskamp, W. & Schmidt, H. M. 1994. Durability of a 13-year Old Test Embankment Reinforced with Polyester Woven Fabric. In *Fifth international conference on geotextiles, geomembranes and related products*, Singapore, 5-9 September 1994. Singapore.

Geosynthetics initial creep behavior parameters as a function of the load level applied in ramp and hold tests

Mateus P. Fleury
São Carlos School of Engineering (EESC), University of São Paulo (USP), São Carlos, Brazil
Mauá Institute of Technology (IMT), São Caetano do Sul, Brazil

Clever A. Valentin & Jefferson Lins da Silva
São Carlos School of Engineering (EESC), University of São Paulo (USP), São Carlos, Brazil

ABSTRACT: Long-term analysis of geosynthetics is mandatory in the design phase. Once the performance of creep-rupture tests is too time-consuming, adopting temperature to accelerate the geosynthetics creep behavior is an attractive solution. The ASTM D 6992 provides guidelines to perform accelerated creep rupture tests in geosynthetics and recommends adopting ramp and hold tests to help assess the initial creep rupture behavior. Thus, this paper aims to assess the initial creep behavior of two geogrids and two non-woven geotextiles. A universal testing machine was used to perform ramp and hold tests. The specimens were loaded (at a similar load condition to the ones adopted in the accelerated creep rupture tests) to load levels ranging between 10% and 90 % of the geosynthetic ultimate tensile strength. Each load level was maintained for 3,600s and 10,800s for geogrids and non-woven geotextiles, in this order. Three specimens were tested for each load level and a best-fit equation was used to obtain the initial creep train rate and the initial axial strain of the mean curve obtained. The results revealed a higher development of creep strains for the non-woven geotextile than the geogrids. The effects of the non-woven geotextile mass per unit area, and the polymer type of the geogrids were pointed out. The results help to identify and compare the initial axial strain of these geosynthetics after the performance of the accelerated creep rupture tests.

1   INTRODUCTION

Once the service life of geosynthetic-reinforced soil structures can reach 100 years (Wu & Helwany 1996), assessing geosynthetics' long-term behavior is mandatory in the design phase (Allen & Bathurst 1996, 1994). Since the early 1980s, geosynthetics' elongation analysis under sustained axial load, which means the creep behavior, has been used to assess their long-term durability (Andrawes *et al.* 1984; Den Hoedt 1988; França & Bueno 2011; Greenwood 1990; Thornton *et al.* 1997; Zornberg *et al.* 2004). Under this condition, reinforcement reaches rupture under excessive elongation. However, to obtain the reduction factor for creep behavior used in the design, twelve specimens must show failure (rupture) at three (or more) load levels. To deal with these too time-consuming tests, Thornton *et al.* (1998) developed a test method (stepped isothermal method; SIM) that uses the temperature to catalyze geosynthetics' creep behavior.

ASTM D 6992 (2016) specifies the geosynthetic materials' accelerated creep and creep-rupture method using SIM. The standard recommends adopting a very short creep test (100 to 1000s; called ramp and hold (R+H) test) to complement the results obtained from SIM tests. This test can be used to i) estimate the initial parameters of creep curves (at load/strain

levels appropriate for the SIM results) and ii) establish the range of strains that the geosynthetics experience after a short response under a given load.

As non-woven geotextiles and geogrids can be adopted as reinforcement elements (Koerner 2005), this paper aims to report the results of R+H tests performed using four geosynthetics (two geogrids (GGR) and two non-woven needle-punched geotextile s (GTXnw)). R+H tests were performed at three specimens at each load level (ranging from 10 to 90% of the geosynthetics ultimate tensile strength, T_{ult}). This paper is part of a comprehensive study on the durability of geosynthetics, where accelerated creep rupture tests using SIM are being performed in undamaged and damaged samples to assess the synergisms between different degradation mechanisms. The results reported herein help to analyze the SIM test results performed in undamaged (virgin or as received by the manufacturers) specimens tested for the whole project.

2 MATERIALS AND METHODS

2.1 Geosynthetics

This study investigates four geosynthetics: two poly(ethylene) terephthalate (PET) non-woven needle-punched geotextiles (GTXnw1 and GTXnw2) and two woven geogrids (one made of PET yarns – GGR1, and the other one made of polyvinyl alcohol (PVA) fibers – GGR2). It should be mentioned that non-woven geotextiles are the most versatile geosynthetic materials that were used as reinforcement in Brazil's first geosynthetic reinforced soil structure. Moreover, Koerner (2005) highlighted the three reinforcement mechanisms (membrane, shear and anchorage) when geotextiles are used as reinforcement elements. Thus, both geogrids and geotextiles can be used in geosynthetics-reinforced soil structures. Table 1 shows some properties and characteristics of the materials according to the manufacturers' specifications. The study investigated two non-woven needle-punched geotextiles to assess the effect of the mass per unit area in the materials behavior.

Table 1. Characteristics and properties of the geosynthetics investigated.

Properties / Characteristics	Unit	GTXnw1	GTXnw2	GGR1	GGR2
Tensile strength MD*	kN/m	12.0	18.0	35.0	35.0
Elongation at break MD*	%	> 70%	> 70%	≤ 10	≤ 6
Mass per unit area	g/m^2	250	500	n.a**	n.a**
Open size	mm	n.a**	n.a**	20 x 20	20 x 30
Manufacturer	-	A	A	B	B

Notes: * Machine direction; ** not applicable

2.2 Test program

Tensile tests were performed in ten geogrids and geotextile specimens following the recommendation of ASTM D 6637 (2015) and ASTM D 4595 (2005), respectively. GGRs specimens (100 mm width – three longitudinal elements – x 500 mm wide) were tested using a load cell of 250 kN, roller clamp system, a strain rate of 10%/min and the strains were measured by a video-extensometer with infrared. GTXnws' specimens (200 mm width per 300 mm wide) were tested using a load cell of 30kN, pneumatic jaw clamps, a strain rate of 10%/min and the strains measured by displacing the upper clamp (the jaw clamp system adopted avoided the specimens slippage).

In the comprehensive project of the study, the SIM tests were performed using dead weights to apply the tensile loads to the specimens. The dead weights were applied to the specimens using an elevation table constructed for this application. Due to the equipment's limitation, the

specimens are loaded at a strain rate of 90mm/min. Thus, the geosynthetics specimens were also tested in the universal testing machines using the strain rate of 90mm/min.

The geosynthetics T_{ult} values obtained after tensile tests with the strain rate of 90mm/min were used as a reference value to calculate the loads adopted in the R+H tests. The tests were performed at 10% to 90% (load steps of 10%) of each geosynthetic's T_{ult} value. Three specimens were tested for each load level, and a mean curve was obtained. The time under sustained load was equal to 3600 s (1 hour) for geogrids, and 10,000 s (3 hours) for GTXnws – both periods were higher than the one recommended by ASTM D 6992 (2016). For the mean curve, a best-fit equation (Equation 1) was used to obtain the initial axial strain (ε_0) and the initial creep strain rate ($\dot{\varepsilon}_0$). This procedure was made just for the section under sustained axial tensile load, which means the loading section was not considered. This process was made for each geosynthetic and for the mean curve obtained by each load level applied.

$$e_t = \dot{\varepsilon}_0 . \ln(t) + e_0 \qquad (1)$$

where e_t is the total strain (percentual) at a given time t (in seconds).

3 RESULTS AND DISCUSSION

Figure 1 shows the results of the R+H tests performed in the geosynthetics. For non-woven geotextiles made of PET fibers, the increase in the material's T_ult value decreases the levels of strain experienced. The non-woven geotextile with a lower T_ult value (GTXnw1, Figure 1a)
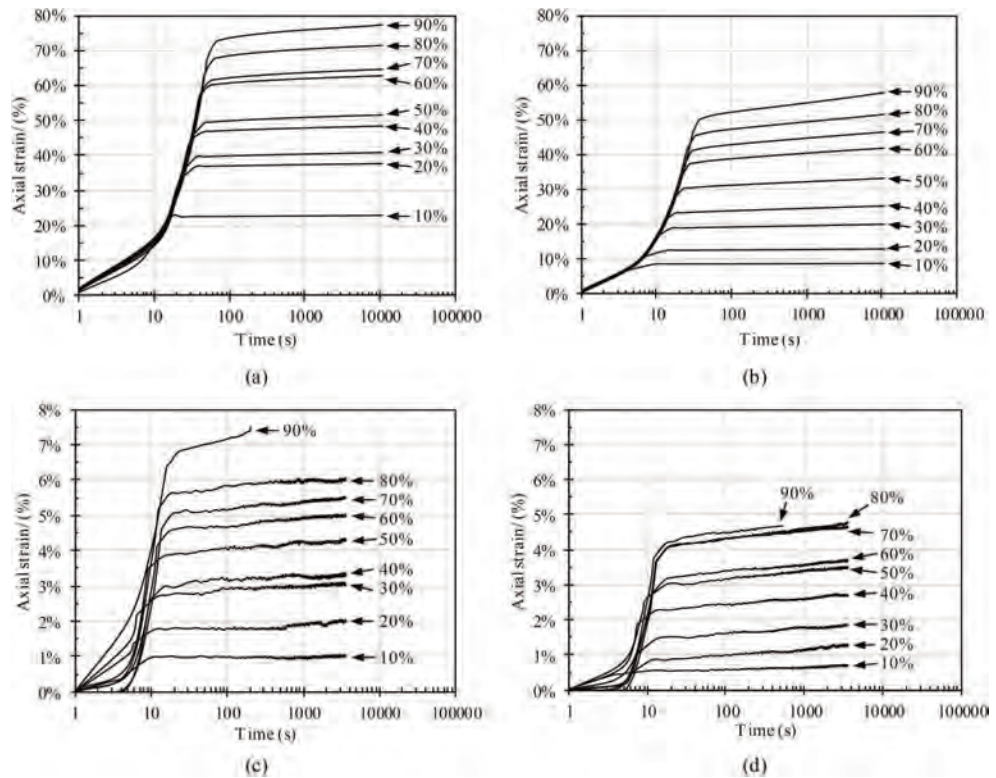
Figure 1. Evolution of the short-term creep behavior for different load levels applied in a) GTXnw1, b) GTXnw2, c) GGR1 and d) GGR2.

shows higher strain levels in its short-term creep behavior than the one with the higher T_ult values (GTXnw2, Figure 1b). Figure 1b shows that GTXnw2 exhibits a gradual evolution of the initial creep behavior. However, GTXnw1 exhibits a very similar initial creep behavior for the load levels of 20% and 30%, 40% and 50%, and 60% and 70% (Figure 1a).

In the case of the geogrids investigated, the lower elongation at break of the geogrid manufactured with PVA filaments (GGR2; Table 1) can be pointed out as the reason for their lower strain levels experienced (Figure 1c) compared to the ones obtained by the PET geogrid (GGR1, Figure 1d). GGR1 exhibited a similar initial creep behavior when tested under the load levels of 30% and 40%, whereas the GGR2 experienced a negligible difference in the initial creep behavior for the load levels of 70% and 80% and a similar behavior at load levels of 50% and 60%.

Figure 1 also demonstrates that the geogrids are more susceptible to rupture under sustained axial load than the non-woven geotextiles. At the load level of 90% of T_{ult}, both geogrids reach rupture before 480s (eight minutes), whereas the non-woven geotextiles did not fail after 10,800 s (three days).

Figure 2 shows the parameters obtained from the geosynthetic's initial creep behavior as a function of the load level applied. Power model equations best fitted the geosynthetics results for the initial creep strain rate ($\dot{\epsilon}_0$; Figure 2a). The best-fit equations provided an excellent coefficient of determination (R^2) for the geotextile materials ($R^2 > 0.995$), but the geogrids show reasonable R^2 values (between 0.58 and 0.79). The geosynthetics results for the initial axial strain (e_0; Figure 2b) exhibited excellent R^2 values (higher than 0.94) for linear best-fit equations.

Although GTXnw2 exhibited lower e_0 values (Figure 1b) than GTXnw1, it demonstrated a significant increase in $\dot{\epsilon}_0$ values (Figure 2a) for load levels higher than 50% of T_{ult}. However, up to this load level (50% of T_{ult}) the geotextiles experienced similar $\dot{\epsilon}_0$ values. In terms of the geogrids results, the GGR1 had $\dot{\epsilon}_0$ and ε_0 values higher than GGR2. As previously mentioned, the lower strain values obtained for the GGR2 material compared to GGR1 are expected due to the lower elongation at the break of GGR2.
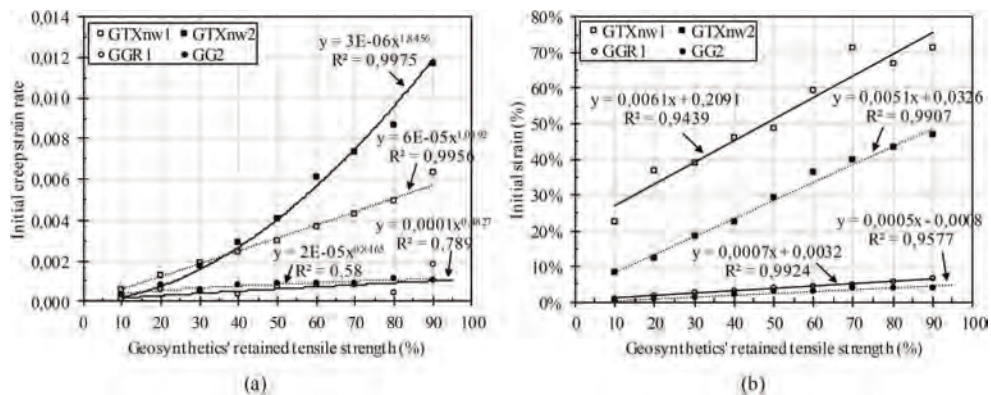
Figure 2. Evolution of the short-term creep behavior for different load levels applied in a) GTXnw1, b) GTXnw2, c) GGR1 and d) GGR2.

4 CONCLUSIONS

This paper assesses the initial creep behavior of four geosynthetics materials through the ramp and hold tests using load levels ranging from 10% to 90% of each geosynthetic ultimate tensile strength. The results reported in the study indicated that the non-woven geotextile with higher mass per unit area exhibited a lower initial strain. However, the initial creep strain rate was significantly higher than the non-woven geotextile with a lower mass per unit

area. Due to the PVA geogrid's lower elongation at break, it experienced lower initial axial strain and initial creep strain rates than the one made with PET fibers. Based on the geosynthetics' strain levels reported in this paper, the results of the first step of accelerated creep rupture tests performed in the same geosynthetics can be better assessed to obtain the material's creep rupture behavior with more reliability.

REFERENCES

Allen, T.M. & Bathurst, R.J. 1996. Combined Allowable Strength Reduction Factor for Geosynthetic creep and Installation Damage. *Geosynthetics international* 3(3): 407–439.

Allen, T.M. & Bathurst, R.J. 1994. Characterization of Geosynthetics Load-strain Behavior After Installation Damage. *Geosynthetics International* 1: 181–199.

Andrawes, K.Z., McGown, A. & Kabir, M.H. 1984. Uniaxial Strength Testing of Woven and Nonwoven Geotextiles. *Geotextiles and Geomembranes* 1: 41–56.

ASTM D 6992-16: *Accelerated Tensile Creep and Creep-rupture of Geosynthetic Materials based on Time-temperature Superposition using the Stepped Isothermal Method*. West Conshohocken, PA, USA.

ASTM D 6637-15: *Standard Test Method for Determining Tensile Properties of Geogrids by the Single or Multi-rib Tensile Method*. West Conshohocken, PA, USA.

ASTM D 4595-05: *Standard Test Method for Tensile Properties of Geotextiles by the Wide-width Strip Method*. West Conshohocken, PA, USA.

Den Hoedt, G. 1988. Principles of Creep and Relaxation, in: *Durability of Geotextiles*. London: Chapman and Hall.

França, F.A.N. & Bueno, B.S. 2011. Creep Behavior of Geosynthetics using Confined-accelerated Tests. *Geosynthetics International* 18: 242–254.

Greenwood, J.H. 1990. The Creep of Geotextiles, in: Den Hoedt, G. (Ed.), *4th International Conference on Geotextile, Geomembranes and Related Products*. Hauge: Balkema.

Koerner, R.M. 2005. Designing with Geotextiles, in: *Designing with Geosynthetics*. New Jersey: Prentice Hall.

Thornton, J., Allen, S.R. & Thomas, R. 1997. Approaches for the Prediction of Long Term Viscoelastic Properties of Geosynthetics From Short-term Tests, in: *Geosynthetics '97 Conference*. California: Industrial Fabrics Association International.

Thornton, J.S., Allen, S.R., Thomas, R.W. & Sandri, D. 1998. *The Stepped Isothermal Method for Time-temperature Superposition and its Application to Creep Data on Polyester Yarn*, in: Rowe, R.K. (Ed.), *Sixth International Conference on Geosynthetics*. Atlanta: Industrial Fabrics Association International.

Wu, J.T.H. & Helwany, S.M.B. 1996. A Performance Test for Assessment of Long-term Creep Behavior of Soil-geosynthetic Composites. *Geosynthetics International* 3: 107–124.

Zornberg, J.G., Byler, B.R. & Knudsen, J.W. 2004. Creep of Geotextiles using Time–temperature Superposition Methods. *Journal of Geotechnical and Geoenvironmental Engineering* 130: 1158–1168.

The impact of specimen preparation and ageing on oxidative induction time of HDPE geomembranes

G. Fairhead
Fabtech Australia, Adelaide, Australia

W.P. Hornsey
TRI Australasia, Gold Coast, Australia

ABSTRACT: The polyethylene geomembrane industry continues to evolve and enhance material formulations to meet the challenges of demanding containment systems. There is increasing interest in characterising these geomembranes when used in critical containment applications and this is often accompanied with increased quality assurance testing. A key test used to indicate the likely durability of a polyethylene geomembrane is to measure its Oxidative Induction Time (OIT) according to either ASTM D8117 for Standard OIT or ASTM D5885 for High Pressure OIT. These tests can be undertaken on new un-aged samples, materials that have been artificially laboratory aged, or specimens exhumed from the field. Particularly with more advanced polyethylene formulations the specimen preparation procedure for OIT testing can affect the measured OIT result, making the comparison of different geomembrane formulations and the comparison of new and aged test results problematic. This paper reports on a systematic examination of different specimen preparation procedures on the measured OIT result for several different geomembrane formulations, multi-layer geomembranes and aged geomembranes. Specimen preparation procedure was also observed to have a significant effect on OIT test repeatability. Results are analysed and suggestions made regarding specimen preparation procedures for advanced geomembranes.

1 INTRODUCTION

1.1 *Measurement of antioxidant levels*

High Density Polyethylene (HDPE) typically comprises a base polyethylene resin, carbon black to resist UV ageing, and additives primarily to resist oxidative ageing of the geomembrane (antioxidants). The presence and performance of antioxidants is measured according to ASTM D8117 (Standard-Oxidative Induction Time, S-OIT) and ASTM D5885 (High Pressure-Oxidative Induction Time, HP-OIT). Minimum requirements for OIT are set out in the industry reference standard published by the Geosynthetics Research Institute's standard GRI GM13. OIT measurements are also used to characterise the durability performance of Geomembranes by comparing OIT results for un-aged material and material that has been subjected to accelerated ageing in a laboratory, usually aged in air at elevated temperatures, UV exposure or synthetic liquors at elevated temperatures accelerating expected service conditions. Comparison of OIT results from in-service assets with their original as manufactured levels allows estimations of residual geomembrane life to be made.

OIT testing is widely used in material quality acceptance plans. It is therefore important that the test procedure correctly characterises the geomembrane properties to avoid incorrect acceptance or rejection of material. Also, when undertaking project specific testing to select a geomembrane material, predictions of geomembrane life will be less reliable if the sample preparation process is influencing the test results.

1.2 *Variability in results*

The ASTM D5885 estimates that precision of HP-OIT testing inter-laboratory reproducibility is 25% and repeatability is 6.5%. In this study of multi-layer geomembranes, repeatability has been observed to be significantly greater than 6.5%. Previous studies (Fairhead & Hornsey 2020) on monolayer homogeneous geomembranes have shown that test variables can be controlled and repeatability improved. Recently the ASTM standards for S-OIT (ASTM D8117) and HP-OIT (ASTM 5885) testing up-dated test protocols to mandate three replicates at zero and 90 days of ageing to improve the utility of OIT measurements, reflective of the issues explored in this paper.

Data from a continuous manufactured lot of geomembrane is summarised as a graph (HP-OIT minutes) in Figure 1. Eleven samples were taken as part of a quality acceptance programme and tested for HP-OIT in the un-aged condition and when air aged with tests at 30, 60 and 90 days in an oven at 85 deg C. Variability in results is evident in the results. When combining the results, a more consistent ageing characteristic is apparent. Relying on a limited data, which is more typical of industry quality acceptance standards and candidate material testing comparisons would not characterise this material well.
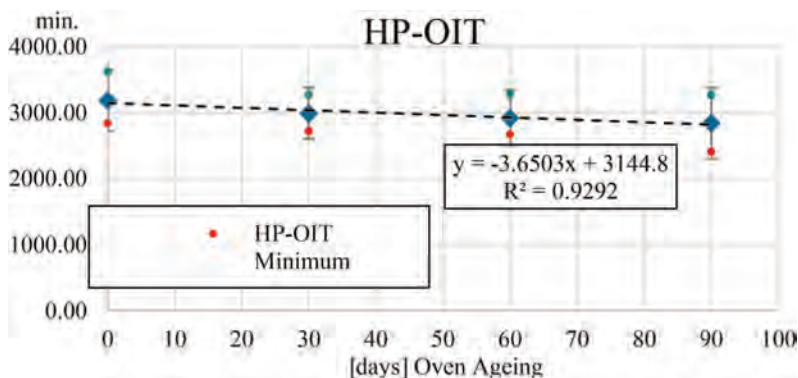
Figure 1.   Averaged HP-OIT results for eleven samples from a production lot when oven aged in air at 85 deg C.

1.3 *Multi-layer geomembranes*

Geomembrane manufacturing equipment can produce sheets from a single extruder and die or with multiple extruders allowing two or more layers of material within the sheet. If the same raw materials are used in multiple extruders a mono-layer geomembrane is produced, or by introducing different materials a multi-layer geomembrane is produced, with the capability to create unique properties. Conductive geomembranes have a thin outer skin containing a high percentage of carbon black. White geomembranes have a proportion of black material and a proportion of white, the ratio varies according to the manufacturing process and product performance requirements. The two layers have different additive packages, usually the white layer has a more highly fortified package than the black layer.

Table 1.   HP-OIT properties of a multi-layer black/white geomembrane.

Layer	HP-OIT [min.]
White	9646
Black	878
Full profile	3577

Multi-layer membranes are also designed to combine different properties such as chemically durable HDPE outer surfaces with a more flexible LLDPE core. An example of a multilayer geomembrane shown if Table 1 shows significantly different additive package performance for the black layer and the white layer as measured by HP-OIT testing.

1.4 *Plaquing of samples*

For both S-OIT & HP-OIT tests the relevant standards require the as-received specimens to be pressed into a thin sheet of 0.25mm ±0.015mm, for polyolefin geomembranes this requires the introduction of temperature and pressure to reduce the original thickness of between 1mm to 3mm.

1.5 *Homogenisation of aged samples*

With aged samples where the outer layers of the geomembrane may have lost a significant portion of the antioxidant package the interpretation of the results can become challenging as double exotherm reactions can occur as the outer layers burn off sooner than the core where the antioxidant package has remained relatively intact. It therefore becomes a subjective analysis of the results depending on how the technician or designer interprets the Heat Flow (W/g) graph. ASTM D5885 was updated to allow the homogenisation of aged samples in order to remove the double exotherm reaction. Three options for homogenisation are allowed namely, Torque Rheometer, Cryogenic Grinder and Two Roll mill. This paper reports on materials homogenised using the cryogenic grinding and mechanical grinding methods. Note while mechanical grinding method does not comply with the standard, many laboratories use this method due the equipment costs of the other methods.

When multilayer geomembrane (black/white) samples are not homogenised or plaqued adequately, two clearly recognisable exotherm peaks present in OIT testing. Industry does not have a uniform view on if the first or second peak is more useful to characterise the specimen and therefore should be reported. When a multi-layer sample is property homogenised, a single energy peak should present in OIT testing.

Additive loss occurs by diffusion, according to Fick's law, with a rate dependent on the crystalline structure of the geomembrane resin combined with the effectiveness of antioxidative additives resisting the oxidizing environment. HDPE geomembrane samples from a brine storage in Queensland, Australia, were tested after 8 years in service. UV exposed samples had been subjected to high UV loading and ambient temperatures while the brine exposed samples experienced moderate temperatures with a strong oxidizing alkaline environment. Samples were HP-OIT tested across the material section profile, at the top (exposed) surface, core, and bottom surface, Table 2. The UV exposed sample has the lowest HP-OIT values in the top surface which would have been exposed to UV and thermal degradation, while the remainder of the sheet would only be exposed to thermal degradation. The brine exposed sample would have experienced highly oxidative brine on the top surface. The lower surface would have limited thermal degradation and limited available oxygen. Degradation would be largely single sided; this is apparent from the measured HP-OIT values.

Table 2. HP-OIT measurements across the geomembrane profile for service aged geomembranes aged for 8 years in a brine storage containment.

Exposure		HP-OIT [min.]			
			Aged		
Duration	Type	Unaged	Top	Core	Bottom
8 Years	UV	600	334	474	392
8 Years	Brine	600	258	448	500

2 PLAQUING PROCESS

OIT test standards require samples to be compression molded (often referred to as plaquing) and test specimens extracted from these plaques. In the authors experience this aspect of the test standard is not uniformly adhered to by industry. The two test standards, ASTM D8117 and D5885 differ slightly in their requirements for the preparation of specimens. ASTM D8117 requires the samples compression molded at 160°C but does give a time period for which the sample should be exposed, the confining pressure under which it should be confined, or the how the specimens should be contained.

ASTM D5885 references ASTM D4703 Practice for compression molding thermoplastic materials into test Specimens, Plaques or Sheets states that the temperature for HDPE should be molded at between 155 &177°C under 5MPa pressure for a flash mold with a preheat time of 5 minutes and a full pressure time of 2 minutes.

2.1 Plaquing trials – Homogenous geomembranes

Process optimisation trials were undertaken seeking to improve OIT test repeatability. A series of plaquing tests were undertaken to assess the effect of temperature-time history on the measured OIT values, Figure 2. A compression mould consistent with ASTM D4703 was manufactured and a single geomembrane formulation tested to reduce test variables. Small quantities of un-aged geomembrane were compression moulded (plaqued) according to the standard.

Mould dwell time and mould temperature were varied and OIT measurements recorded. Mould dwell time was varied from 2 minutes to 8 minutes and mould temperature from 125 deg C to 177 deg C. From over 100 tests no coherent correlation was observed between mould dwell time or mould temperature and OIT measurements. It was expected that increasing temperature and time would accelerate oxidation of the geomembrane and therefore reduce measured values of OIT. This characteristic was not evident for the temperature-time histories examined and for this specific geomembrane formulation. The result may be formulation specific and a more significant relationship with temperature history with other geomembranes with different antioxidant packages.
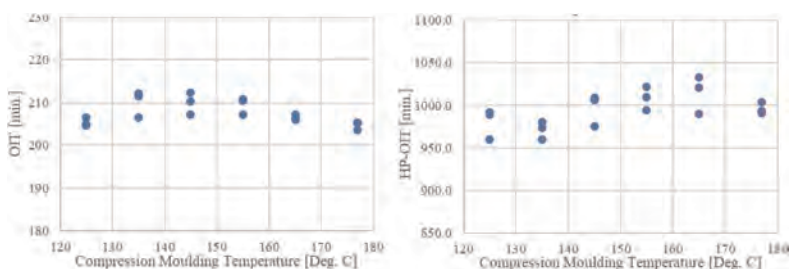
Figure 2.   Compression mould temperature trials evaluating the effect on OIT measurements. Left S-OIT, Right HP-OIT.

2.2 Test consistency

A homogeneous geomembrane was subjected to an oven ageing study according to ASTM D5721. Consistent with previous studies (ASTM D3895 2019) multiple-frequency ageing tests were undertaken. The results were coherent, allowing the geomembrane ageing characteristic to be compared with the technical requirement or compared with other material formulations.

By comparison samples of a multilayer (black/white) geomembrane from two different rolls having been oven aged in air exhibited variable HP-OIT results, Figure 3. Test samples were
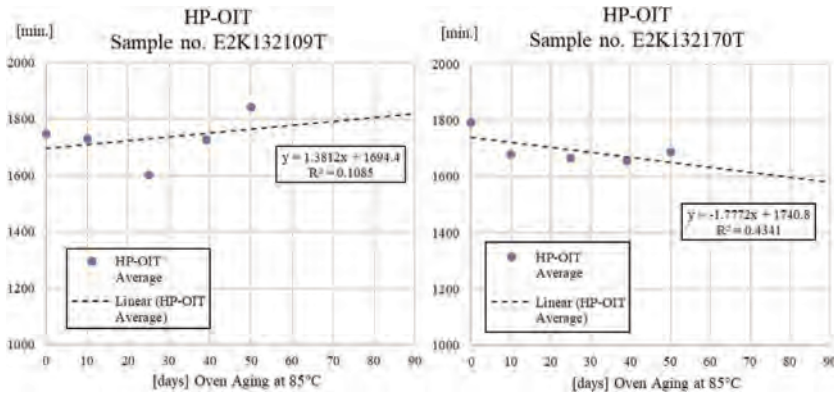
Figure 3. Oven ageing measurements for two samples of multi-layer geomembrane.

homogenised and plaqued prior to HP-OIT testing. All of the OIT exotherms generated were smooth with a single dominant exotherm peak. Variability between tests results at different ageing durations makes it difficult to determine the underlying ageing characteristic of this geomembrane formulation. These results confirm that it can be unreliable to rely on data from single test age points to characterise durability, multiple tests are beneficial.

2.3 Multi-layer geomembranes

In the case of multi-layer geomembranes simply plaquing the geomembrane is not possible due to the different melting point of the different layer will result in different ratios of layers within the plaque. This is not visible to the naked eye with a multi-layer black geomembrane; however, it is quite evident with a Black/White geomembranes, Figure 4 shows the distribution of the layers when plaquing without homogenisation.

Figure 4 clearly shows that simply plaquing a multilayer geomembrane is not acceptable as the ratio of each of the layers would not be representative of the actual product. In the case of multilayer geomembranes, they should be treated the same way as an aged sample requiring homogenisation prior to testing.
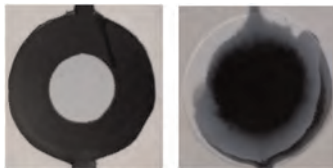
Figure 4. Plaqued Black/White geomembranes. Left: 80% Black–20% White, Right: 5% Black–95% White.

3 SAMPLE HOMOGINISATION

There are conflicting requirements when homogenising samples. A "coarsely" ground sample will have a lower surface area to volume ratio which, when the ground material is plaqued, will oxidise less than a "finely" ground sample. Conversely a finely ground sample will ensure homogenisation and repeatable results while a coarsely ground sample will not. Using the black/white geomembrane allowed two-dimensional uniformity of the homogenised and plaqued samples to be visually observed. Samples of a geomembrane with a profile of 70% black and 30% white material, were homogenised in a cryogenic impact grinding machine
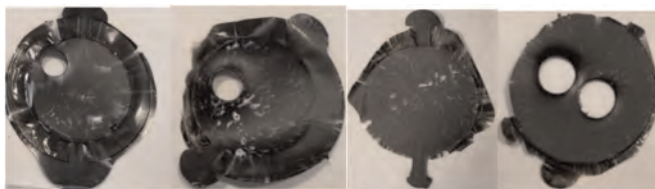
Figure 5.   Visual homogenisation for different impact grind settings. Left to right, 300, 600, 1200, 2400 impacts.

and the ground material plaqued. The level of grinding was increased until a visually homogeneous plaque was produced, Figure 5.

For this grinding equipment the least amount of pulverisation that produced a visually homogenised sample was 2,400 impacts. HP-OIT repeatability with this sample preparation was approximately 4.5%. HP-OIT tests on samples with less than 2,400 impacts were less repeatable with values up to 20%. From visual observations reduced repeatability was directly related to unsatisfactory homogenisation of the two layers of material which had significantly different HP-OIT characteristics.

4   CONCLUSIONS

Geomembrane manufactures continual innovation to provide improved material performance challenge existing test procedures. Increasing use of multi-layer geomembranes in critical applications which usually have elevated levels of durability testing is increasing the importance of S-OIT and HP-OIT test repeatability. This study has examined the effects of sample preparation on S-OIT and HP-OIT test repeatability. Several different geomembranes formulations have been included in the study, results may be more or less significant for other geomembrane formulations. A single homogenisation procedure has been assessed, being low temperature impact grinding. From this work.

- Plaquing time/temperature history did not have a strong influence on measured OIT results for the geomembranes evaluated.
- Black/White multi-layer geomembranes allowed qualitative assessment of homogenisation.
- OIT measurements of samples with non-homogeneous structures are sensitive to the sample preparation procedure. This applies to multi-layer geomembranes, where the properties of layers are significantly different to aged material samples.
- An optimised sample preparation procedure has been developed which improved test repeatability.
- With multilayer geomembranes where one layer contains the bulk of the antioxidant package effective homogenisation must be carried out to obtain results which can be used to determine loss over time correlation.

REFERENCES

ASTM D3895 (2019) *Oxidative-Induction Time of Polyolefins by Differential Scanning Calorimetry*
ASTM D4703 (2016) *Practice for Compression Molding Thermoplastic Materials into Test Specimens, Plaques or Sheets*
ASTM D 5721 (2022) *Air-Oven Aging of Polyolefin Geomembranes*
ASTM D5885 (2017) *Oxidative Induction Time of Polyolefin Geosynthetics by High-Pressure Differential Scanning Calorimetry*
ASTM D8117 (2021) *Oxidative Induction Time of Polyolefin Geosynthetics by Differential Scanning Calorimetry*
Fairhead G & Hornsey W. P. (2020) *Predicting HDPE OIT Aging Performance from a Revised Short Duration Test*, 4th Pan American Conference on Geosynthetics, Rio De Janeiro, Brazil, 26-29 April 2020

At the limit of liner puncture resistance for high-capacity leach pads projects

A. León Saavedra
Axios Ingeniería SpA, Santiago, Chile
IGS Chilean Chapter, President 2022–2023

1 INTRODUCTION

The Liner system in leach pads projects is especially valuable and implies a considerable part of the capital expenditure for these types of projects. As well as the overliner material, sometimes represent a big challenge to find a nearby and adequate material source capacity. The overliner must meet specific geotechnical properties to provide drainage and liner protection, been critical a controlled maximum coarse size and sieve distribution to avoid puncture failure in the liner system and provide efficient drainage.

This paper includes the summary of two recent studies developed for one of the biggest copper leaching operations in Chile, consisting in an expansion of the secondary leaching process with more than 168 million tons capacity and 120 m maximum high of the leached ore deposit, and a Low-Grade Oxide dump leach expansion of 85 m high, with large surface of lining and high demand of overliner material where natural sources are almost unavailable.

2 METHODOLOGY

Large Scale Puncture test (ASTM D5514 Modified) were developed with the collaboration of Geo-logic Associates in USA. The objective consisted of studying the influence of the overliner materials and subgrade on a geomembrane by applying a normal load equivalent to the heap leach's maximum height.

The test configuration is shown in Figure 1(a) and its conditions are as follows:

- As a variation of the referred ASTM standard where a hydrostatic compression is applied, in this test the ore vertical load is simulated by a hydraulic pressure frame in a large scale direct shear test box. In that way it is possible to generate the liner contact effect in both sides under the load and, is closer to the specifics conditions in this type of projects.
- The test was carried out on a square hydraulic press of 12″x12″.
- Normal stress was applied at a speed of 70 kPa per minute for 48 hrs. up to the maximum specified load. For this test, the maximum load was 2400 kPa, which equivalent to 120 m ore height.
- The overliner material was placed under the middle of the test box at 1.85 ton/m3 of dry density (corresponding to 95% maximum dry density) and a moisture content of 3.0%.
- The subgrade was moisture conditioned near optimum moisture and compacted until no yielding was observed under pressure.
- Coarse material larger than 2″ were in contact with the geomembrane during the test.
- The textured side of the geomembrane is placed in contact with the subgrade material layer (Figure 1(b)).
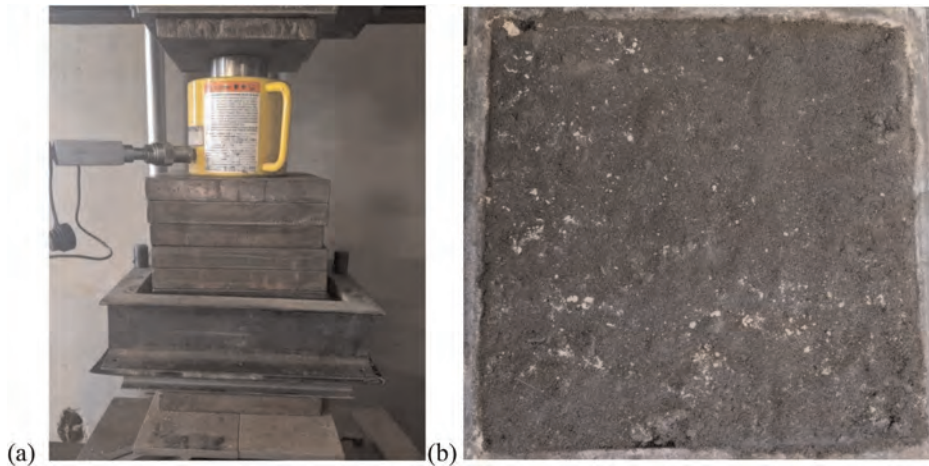
Figure 1.   (a) Large scale puncture test configuration. (b) Subgrade material.

3   INCREASE IN OVERSIZE MATERIAL CONTENT

This analysis aims to verify the feasibility of using old leached crushed ore material as overliner on the geomembrane, by analyzing large scale puncture tests for loads equivalent to up to 120 m on an 80 mils (2 mm) HDPE geomembrane, considering an increase of coarse size overliner material between $2'' - 3''$. Previously, the project specified an overliner material with maximum particle size of 1 ½″ and coarse material over this size represent approximately 40% from the sources available, and a high cost of selection process.

3.1   *Overliner alternative sieve analysis*

The sample of the proposed material had a 5% of coarse size ($>2''$) and high fine content (16% under #200 sieve) according to the project specifications. Due to the major coarse content, the material may present a behavior that could generate puncture failures in the geomembrane. In addition, it could allow the migration of fine particles from the leached ore during the irrigation process. Figure 2 shows the leached ore sample used as overliner in the Large Scale Puncture test and Figure 3 shows its grain-size curve.

Figure 2.   Overliner used in puncture test (Leached ore sample).
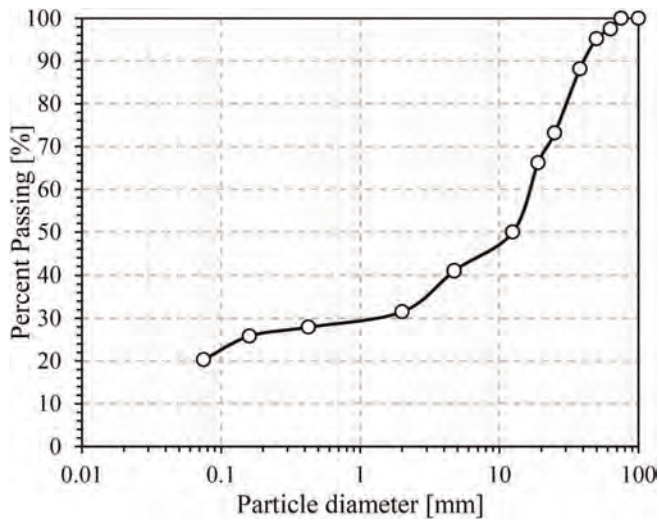
Figure 3.   Overliner grain-size curve.

3.2 *Large scale puncture content test*

Figure 4 shows the 2 mm HDPE geomembrane after the large scale puncture test results, from which no puncture failures were observed in the geomembrane, showing only small yielding areas (plastic flow not recoverable after removal of the load). This is a normal response to the load level reached.
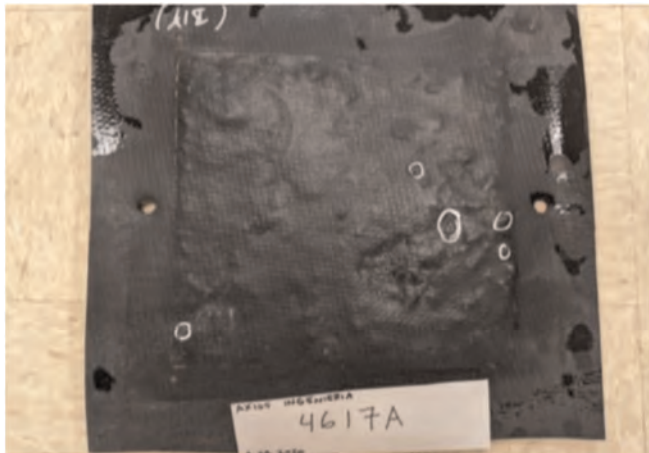
Figure 4.   2mm HDPE Geomembrane after puncture test.

4   PUNCTURE RESISTANCE VS LOAD INCREASE

Because of the lack of additional approved areas to stack more secondary leached ore, the current operation looked to reuse abandoned phases of the deposit to load additional fresh ore. Based on this, the objective was to determine the maximum height that the current Leached ore deposit can reach so as not to affect the integrity of the liner system and the drainage system due to the overload. The integrity of the liner material subjected to an

increase in load was analyzed by the performing different large scale puncture tests using an overliner material of 2″ maximum coarse size and normal stresses increments to up to 235 m ore height.

4.1 Large scale puncture test verification

4.1.1 Overliner sieve analysis

Same old leached ore material of previous test was used as overliner material (Figure 5), which complied with the grain-size specifications of the project. The sample's sieve analysis curve is shown in Figure 6.

Figure 5. Overliner material used in large scale puncture test.
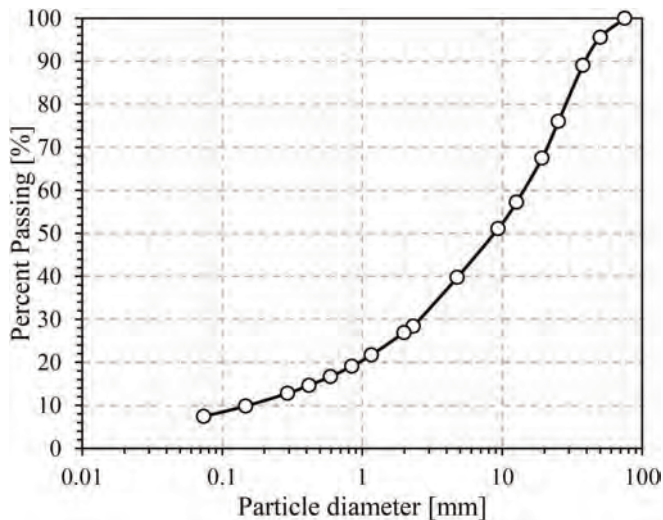
Figure 6. Overliner materials sieve analysis curve.

4.1.2 Large scale puncture test results

The large-scale puncture tests results are shown in Figure 7 and summarized in Table 1. These show that, for heights lower than 180 m for 1.5 mm HDPE geomembranes and 185 m
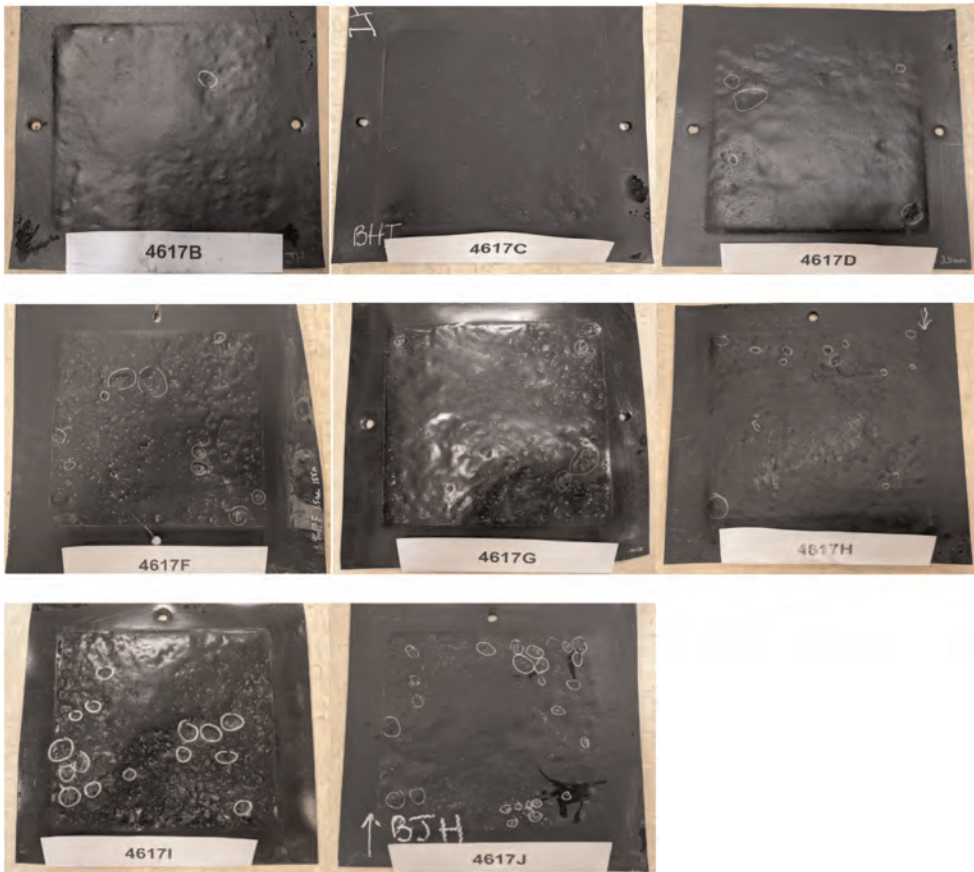
Figure 7.   HDPE geomembranes after large scale puncture test.

Table 1.   Large scale puncture tests results.

Test ID	HDPE Geomembrane thickness (mm)	Equivalent Height (m)	Yielding	Puncture
4617B	1.5	140	Mild	Not observed
4617C	2.0	155	Mild	Not observed
4617D	2.5	165	Mild	Not observed
4617F	1.5	155	Moderated	Not observed
4617G	2.0	185	Mild	Not observed
4617H	1.5	180	Moderated	Not observed
4617I	2.0	235	Major	Not observed
4617J	1.5	225	Major	Not observed

for 2.0 mm, the geomembranes developed between mild and moderate yield, in addition to not generating puncture failure of the material.

On the other hand, tests 4617I and 4617J show major yielding for the 2.0 mm and 1.5 mm HDPE geomembranes when reaching equivalent heights of 235 m and 225 m respectively, which is expected due to the considerable increase in the applied normal load.

460

5 CONCLUSION

The current study assessed the feasibility of using granular materials with a maximum particle size greater than 2″ as overliner, as well as the viability of increasing the vertical load to which the liner is subjected. It is important to consider that these analyses were based solely on the integrity of the liner system under higher vertical loads and did not evaluate specific variables of each project that may affect its overall slopes stability.

Regarding the increase in the coarse material content in the overliner, the puncture test results verified that despite the major coarse size (2″ to 3″), the leached ore used as overliner did not generate punctures in the geomembrane. There was minor yielding in the contact side that generated observable amount of plastic flow which does not recover after removal of the pressure.

Therefore, it is concluded that the overliner material proposed with a maximum size of 3″ at an equivalent vertical load of 120 m would not generate punctures in the geomembrane currently considered in the dump leach project, since the portion of 3″ coarse size does not exceed 5% retained on 2″ sieve, the material must be well graded with sand and gravels content, and fine fraction under #200 sieve with maximum of 4%, to avoid migration of fine particles from the ore during the leaching process.

The puncture tests results showed that, for heights below 185 m for the 2.0 mm and 180 m for 1.5 mm HDPE geomembranes, respectively, also showed a mild to moderate yielding, in addition to not generating puncture failure.

On the other hand, tests equivalent to load heights of 235 m and 225 m showed a major yielding for 2.0 mm and 1.5 mm HDPE geomembranes respectively. From these results, it is determined that, although there is no puncture failure observed in the HDPE geomembranes considering these height increases, they are probably very close at the limit of the puncture failure with an increase in load or yielding over time.

It is important to note that the original project was developed 20 years ago, while the HDPE geomembranes tested for this study were of current manufacture, so it could be concluded that present HDPE geomembrane material developments are delivering a better performance.

Finally, it can be said that the tested HDPE geomembranes obtained high puncture resistant and low to moderate deformation for the 1.5 mm liner thickness cases up to 155 m total ore height equivalent load, as well as for the 2.0 mm up to 185 m. Comparing this results to the resistances and deformations that were obtained under theoretical calculations, the assessed HDPE geomembranes can offer better resistance than what was expected, demonstrating the improvement in technology and components that the materials used for their manufacture have had in the last years.

REFERENCES

ASTM D5514M *Standard Test Method for Large Scale Hydrostatic Puncture Testing of Geosynthetics*
Godoy, C. & Paredes, L. 2011. *Estudio Experimental de Punzonamiento en Geomembranas en Interfaces de Depósitos de Minerales.*
Geomembrane Protection. *Design Manual – GSE*, Narejo – Corcoran
GM13-*Test Methods, Test Properties and Testing Frequency for High Density Polyethylene (HDPE) Smooth and Textured Geomembranes*
Koerner, Robert M. 2005. *Design with Geosynthetics*, 5th ed.

Designing and analysis of carbon fiber reinforced grid materials for application to seismic resistance improvement

H.Y. Jeon
Department of Chemical Engineering, Inha University, Incheon, South Korea

K.H. Nam
GSI-Korea, Incheon, South Korea

ABSTRACT: Carbon fiber geogrid usable as geosynthetics reinforcement was fabricated, and seismic resistance, which affects the stability of the soil structure when constructed on a soil structure, was analyzed through SIM (stepped isothermal test) creep test. Seismic resistance was tested by simulating seismic event circumstance at 40. 60. 80% of UTS (ultimate tensile strength) of carbon fiber geogrid, and it is seen that seismic simulated event has no effect on long-term property of carbon fiber geogrid.

1 INTRODUCTION

The geosynthetics reinforcement method is one of the seismic performance reinforcement methods, and has the advantage of being able to have various shapes depending on the weight of the material, the convenience of construction, and the fiber material and physical properties. Carbon fiber has properties such as high strength, high elasticity, light weight, excellent durability and construction method, and waterproof effect, so it can be used as an earthquake-resistant reinforcing material. The carbon fiber geogrid can be used as a one-way or two-way load member depending on the high strength and structure of the carbon fiber, so no additional process is required and equipment investment costs are reduced. In addition, carbon fiber geogrid can be applied to the manufacturing of concrete composite panels for construction depending on various factors such as optimization of weaving preparation process, composition of coating resin and coating conditions.

In this study, a creep test was conducted to examine the seismic resistance of carbon fiber geogrids to earthquakes that would occur when applied to underground structures. The SIM (stepped isothermal method) creep test method was applied, and the seismic resistance was explained by the creep behavior analysis by simulation considering the Effects of sudden loads that may occur in seismic situations.

2 EXPERIMENTAL

Carbon fiber for geogrid was made by the double covering process. To make carbon fiber geogrid, unidirectional design system was used and the specification of carbon fiber geogrid is shown in Table 1.

Table 2 shows the seismic simulated SIM creep test condition. Seismic resistance by the SIM creep test was used as a creep test. Five isothermal temperatures of 23, 37, 51, 65, 79 °C were applied to the SIM creep test procedure. The seismic simulation creep test is conducted

Table 1. Specification of carbon fiber geogrid.

Composition	Specification (Warp/weft) (Denier)	Ultimate tensile strength (UTS)(kN/m)	Tensile strain (%)
Carbon fiber	4000/573	87.8	1.2

Table 2. Seismic simulated SIM creep test condition.

Test Item	Test Condition
Temperature (°C)	23, 37, 51, 65, 79
Loading level (%) of UTS	40, 50, 60
Isothermal duration	1.5 hrs
Seismic simulated loading level (%) of UTS	80,90,100
Seismic simulated duration	1 min
Additional loading time	Midway through from 23°C to 79°C

for 1.5 hours by applying a creep load corresponding to 40 to 60% of the ultimate tensile strength (UTS) of the geogrid at the test temperature. Then, a creep test was conducted by applying a seismic condition sudden load (80 to 100% of the maximum tensile strength) for 1 minute, and then the overall creep behavior of the geogrid was analyzed. This test was carried out in 5 temperature ranges (23, 37, 51, 65, 79°C) respectively.

3 RESULTS AND DISCUSSION

Figure 1 shows the creep strain vs. log time at various stress conditions. The creep strain increases linearly with log time and creep rupture was detected at 70~100% of creep loads. After graphically showing the result of creep rupture with applied stress over rupture time,
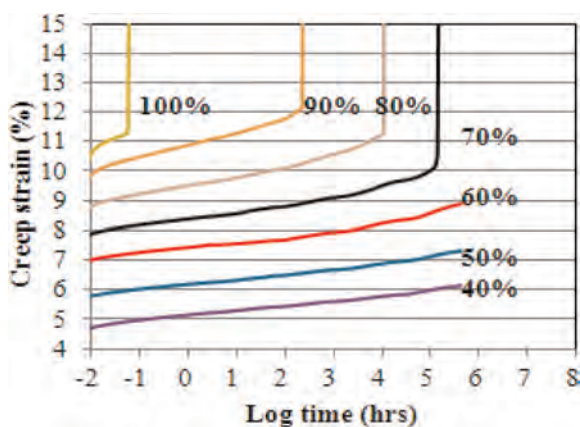
Figure 1. Creep properties of carbon geogrid.

the applied stress at 106 hours of design term was obtained through regression analysis and the reduction factor was obtained by the comparison of this value with the UTS.

Creep strain exhibits an initial decrease at each elevated temperature step. The final strain was approximately 7.9%, similar value as that obtained from the application of the seismic load midway through 23°C temperature step. Creep strain decreased after seismic event cause of recovery force, after that strain increased again. After same condition of seismic event in different times, strain finally overlapped. Normally, seismic event has no effect on long-term property but in specific condition, a seismic event may reduce the creep property of carbon geogrid.
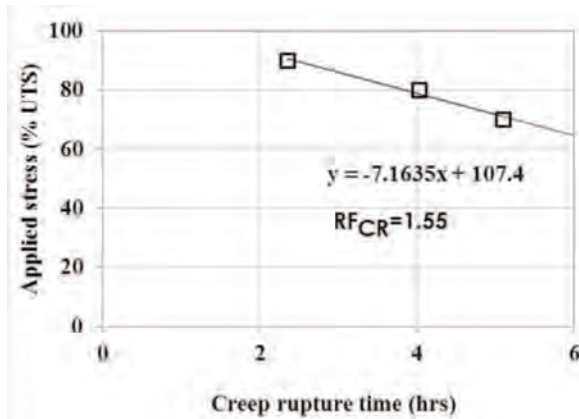
Figure 2.   Plot of applied stress vs. creep rupture time.

Figure 2 shows regression analysis diagram and it is observed that the data follows a linear trend and the reduction factor was 1.55.

Creep response resulting from the application of the seismic load midway through the 23°C is shown in Figure 3 (a). Temperature was gradually increased from 23°C to 79°C and the seismic load produced an immediate strain of approximately 5.6% at initial stage. At this
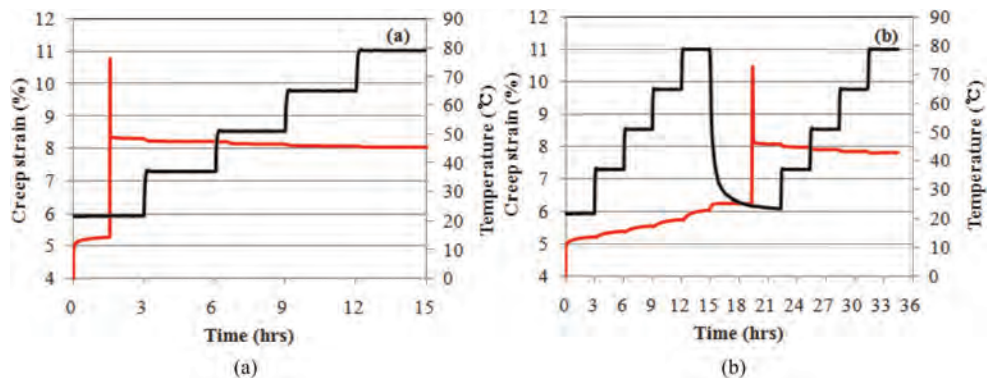
Figure 3.   Creep strain vs. time curves for a seismic SIM creep test; (a) 100% of UTS applied for 1 min midway through the 23°C (b) 100% of UTS applied for 1 min after the 79°C.

moment, the strain recovery is 2.6% after removal the creep load. It is apparent that there is no effect on the creep response after 1.5 hour without regard to temperature till 79°C. The final strain was approximately 8%. The creep response of the application of the seismic load after the 79°C is shown in Figure 3 (b).

Creep strain exhibits an initial decrease at each elevated temperature step. The final strain was approximately 7.9%, similar value as that obtained from the application of the seismic load midway through 23°C. Creep strain slightly decreased at 40% of UTS until reaching the 65°C, after seismic event and began to increase after the 79°C. Creep strain rate is very slow after the seismic event, so the recovery force leads to long-term shrinkage. Creep strain slightly decreased at 50% of UTS until 103 hours, after which it increased. Creep strain rate at 50% UTS occurs at a greater rate than observed in the test at 40% of UTS after same seismic event. The time for shrinkage rebound for the test at 50% of UTS is shorter than that for the test at 40% of UTS. In contrast, creep strain increased at 101 hours for the test at 60% of UTS.

Figures 4 and 5 show the creep strain vs. log time curves for seismic SIM creep test, using a constant load of 40, 50% and 60% of UTS. It can be seen that the results of applying the seismic simulated loads corresponding to 80, 90, and 100% of UTS at 79°C for 1 minute are almost similar to those at 23°C as shown in Figure 3.
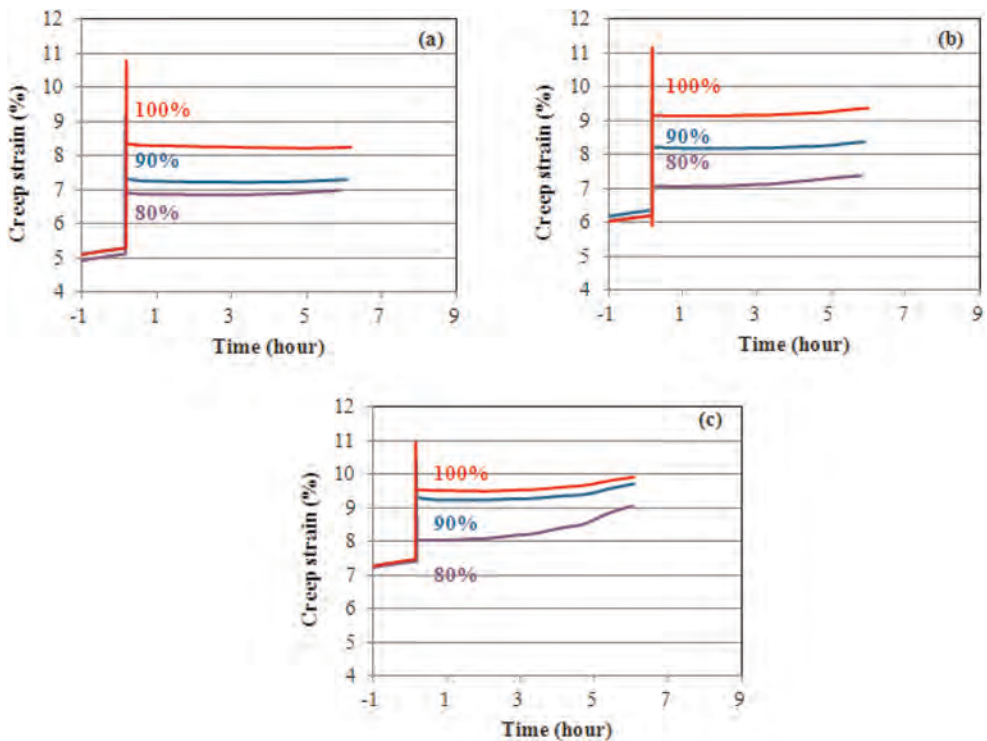
Figure 4.   Creep strain vs. log time curves for seismic SIM creep test; for creep load as (a) 40%, (b) 50%, (c) 60% of UTS and for simulated seismic load equivalent to 80, 90 and 100% of UTS for 1 min midway at 23°C.
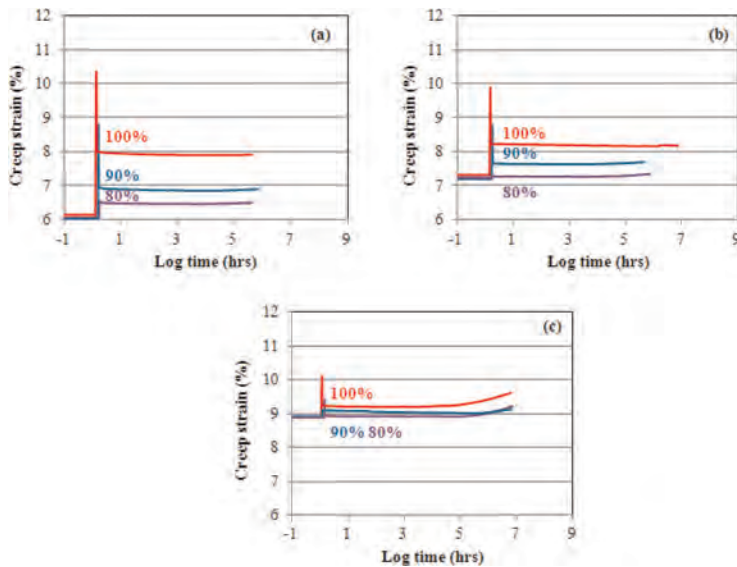
Figure 5. Creep strain vs. log time curves for seismic SIM creep test; for creep load as (a) 40%, (b) 50%, (c) 60% of UTS and for simulated seismic load equivalent to 80, 90 and 100% of UTS for 1 min midway at 79°C.

4 CONCLUSIONS

Creep properties of carbon fiber geogrid during a simulated seismic event were evaluated using the simulated SIM creep test method. Creep strain decreased after seismic event cause of recovery force, after that strain increased again. In general, seismic event has no effect on long-term property of carbon fiber geogrid in specific condition, a seismic event may reduce the creep property of a geogrid. Through the further study, we will make the hybrid carbon fiber geogrid to improve the seismic resistance, and evaluate the long-term performance and durability.

ACKNOWLEDGMENTS

REFERENCES

Jones C.J. F.P, Clarke D, 2007. The Residual Strength of Geosynthetic Reinforcement Subjected to Accelerated Creep Testing and Simulated Seismic Events, *Geotextiles and Geomembranes*, 25(3), 155–169.

Koerner R.M, 2012. *Designing with Geosynthetics*, Xlibris Corporation, 6th Edition, Indiana, USA.

Lin C.W, Lin J.H, 2005. Manufacture and Application of High-Performance Geogrids with PP/PET Composite Covered Yarn, *Textile Research Journal*, 75(6), 453–457.

Michael A.P, Hamilton H.R, Ansleym M.H, 2005. *Concrete Confinement Using Carbon Fiber Reinforced Polymer Grid*, American Concrete Institute, SP230-56, 230, 991–1010.

Nicola M, Filippo M, 1997. Behavior of Geogrids Under Cyclic Loads, *Proceedings of Geosynthetics'97*, 961–976.

Volmer X, 2014. *Creating architecture with CFRC: Introducing carbon fibre composite as structural material*, *Master thesis* Delft University of Technology, Delft, Netherland.

Xiao Y, Wu H, 2000. Compressive Behavior of Concrete Confined by Carbon Fiber Composite Jackets, *Journal of materials in civil engineering*, 12(2), 139–146.

Geogrids in cold climates: Insights from in-isolation tensile tests at low temperatures

R.L.E. Desbrousses & M.A. Meguid
McGill University, Montreal, QC, Canada

ABSTRACT: Geogrids are used to reinforce ballasted railway embankments thanks to their high tensile strength and strong mechanical interlock with the granular material encountered in railway substructures. Railway tracks built in seasonally cold regions must also be designed to withstand harsh environmental conditions such as freezing and thawing cycles and the corresponding frost heave and thaw softening. In that context, it is crucial to understand how extreme temperature variations affect the performance of geogrids and their ability to fulfil their functions within a railway embankment. To do so, an experimental campaign is devised to assess how temperature changes in the range of -30°C to 20°C affect the tensile strength of a polymeric geogrid and a geogrid composite designed for use in ballasted railway tracks.

1 INTRODUCTION

Geogrids are sheets of polymeric material that consist of large openings called apertures bordered by longitudinal and transverse ribs (Desbrousses & Meguid 2021; Desbrousses *et al.* 2021; Koerner 2005). They are commonly used to reinforce earth structures such as retaining walls, slopes, embankments, paved and unpaved roads, railroad substructures, etc. owing to their ability to develop a strong mechanical bond with the soil in which they are placed (Desbrousses & Meguid 2021; Han & Jiang 2013; Jewell *et al.* 1984; Jewell 1988; Shokr *et al.* 2022). Because geogrids tend to be placed at a shallow depth below the ground surface, the temperature fluctuations associated with seasonal weather changes may cause variations in ground temperature and correspondingly impact the temperature of geogrid reinforcements, particularly since maximum ground temperature variations occur near the ground surface (Kim & Kim 2020; Segrestin & Jailloux 1988; Zarnani *et al.* 2011). Geogrids are typically made with polymeric materials called thermoplastics that exhibit temperature-dependent mechanical properties characterized by a brittle behavior at low temperatures and a ductile behavior at elevated temperatures, high-lighting the need to assess how temperature fluctuations affect the mechanical properties of geogrids.

Several studies have been devoted to examining the effect of temperature on the mechanical properties of polymeric geogrids. Kongkitkul *et al.* (2012), Chantachot *et al.* (2016, 2017), and Kasozi *et al.* (2014) investigated how elevated temperatures affect the tensile strength of polymeric geogrids and reported that a rise in temperature is usually followed by a reduction in the ultimate tensile strength and an increase in the ultimate strain of a polymeric geogrid, providing evidence that such materials become more ductile at high temperatures. On the other hand, Bonthron and Jonsson (2017) studied the impact of subjecting polymeric geogrids to low temperatures ranging from 20°C to -20°C on their tensile strength and concluded that polymeric geogrids tend to develop greater tensile forces at smaller strains as the temperature decreases. Shokr *et al.* (2022) examined the effect of

temperatures typical of seasonally cold climates ranging from -30°C to 40°C on the tensile strength of a fiberglass geogrid. Their findings demonstrated that the geogrid exhibited brittle and ductile responses to loading over the range of tested temperatures, emphasizing the influence temperature wields over the behaviour of geogrids.

Given that polymeric geosynthetics have temperature-dependent mechanical properties, this study seeks to examine the behavior of a biaxial polypropylene geogrid and a polymeric geocomposite in cold climates by performing in-isolation single rib tensile tests on the two materials at temperatures ranging from 20°C to -30°C. These two geosynthetics are designed and used to reinforce ballasted railway tracks resting on weak saturated sub-grades located in seasonally cold regions (Bhat & Tomas 2017).

2 METHODOLOGY

2.1 Testing program and experimental setup

This study seeks to investigate the effect of temperature on the tensile strength of a biaxial polymeric geogrid and a polymeric geocomposite. The tensile strength of the two geosynthetics is determined using single rib tensile tests as described in Method A of ASTM D6637. The tensile strength of the geogrid and geocomposite is determined at temperatures ranging from -30°C to 20°C in 10°C increments.

The tensile tests are performed in an MTS universal testing machine fitted with a 5kN load cell to monitor the tensile loads applied to the singe rib samples. The samples are held in place during the tests using two wedge action grips as shown in Figure 1. The elongation of the samples is recorded with a clip-on extensometer with a 25mm gauge length designed to operate at temperatures ranging from -100°C to 150°C. To perform experiments in a temperature-controlled environment, the testing machine is equipped with a temperature chamber with cooling and heating capabilities that completely encloses the wedge grips and the single rib sample being tested. The environmental chamber is connected to an analog temperature controller that regulates the opening and closing of a valve that links a tank of liquid nitrogen to the environmental chamber. Upon inputting a target temperature, e.g.
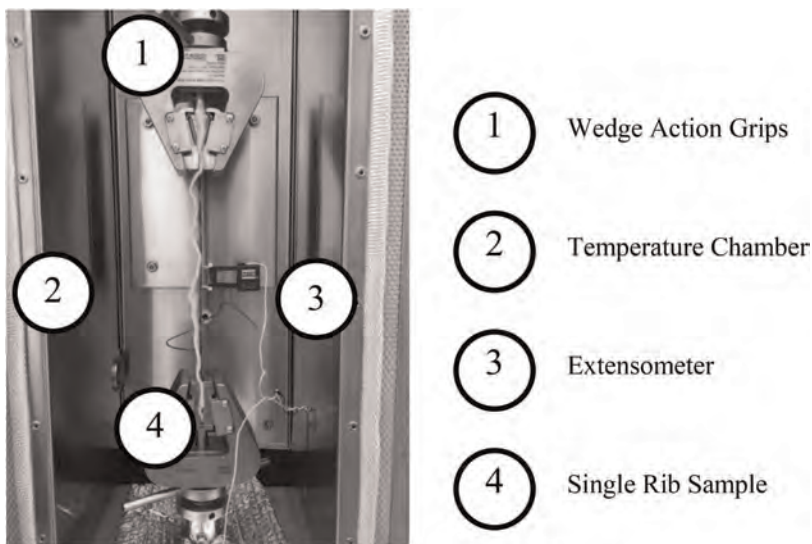
Figure 1. MTS testing machine and its temperature chamber.

-30°C, into the controller, an electrical signal is sent to the valve, triggering its opening and allowing liquid nitrogen to flow into the chamber. A thermocouple located within the environmental chamber monitors its temperature and sends a feedback signal to the controller to adjust the valve's opening and closing to maintain a steady temperature. The tensile test is initiated once the thermocouple detects that the environmental chamber's temperature has reached the desired setpoint.

2.2 Materials

The geosynthetics considered in this study are a biaxial polypropylene geogrid and a geo-composite composed of a biaxial polypropylene geogrid heat-bonded to a non-woven polyester geotextile manufactured by Titan Environmental (Titan Environmental Containment 2020, 2021). The mechanical properties of both materials as reported by the manufacturer are summarized in Table 1. It is noteworthy that both materials have identical properties in the machine and cross-machine directions. The two geosynthetics are shown in Figure 2.

Table 1. Material properties of the geogrid and geocomposite.

	Biaxial geogrid	Geocomposite
Material	Polypropylene	Polypropylene (Geogrid) Polyester (Geotextile)
Aperture size (mm)	57	38
Ultimate tensile strength (kN/m)	30	30
Tensile strength at 2% strain (kN/m)	11	12
Tensile strength at 5% strain (kN/m)	21	22
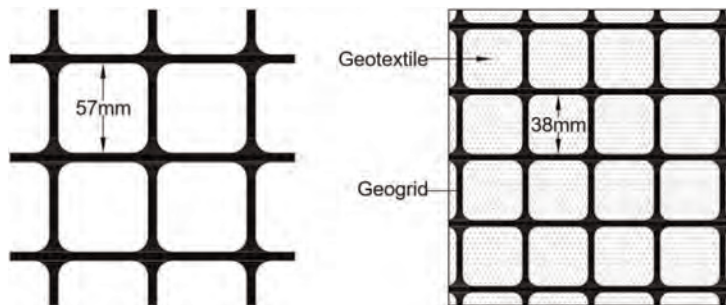
Figure 2. Biaxial geogrid (left) and geocomposite (right).

3 RESULTS

3.1 Biaxial geogrid

The average load-strain curves of the biaxial polypropylene geogrid at temperatures ranging from -30°C to 20°C are shown in Figure 3. The load-strain curve obtained at 20°C is used as a reference against which the other curves are compared given that it corresponds to the standard testing temperature given in ASTM D6637. The load-strain curves suggest that exposure to temperatures below 20°C translates into the geogrid exhibiting an increasing
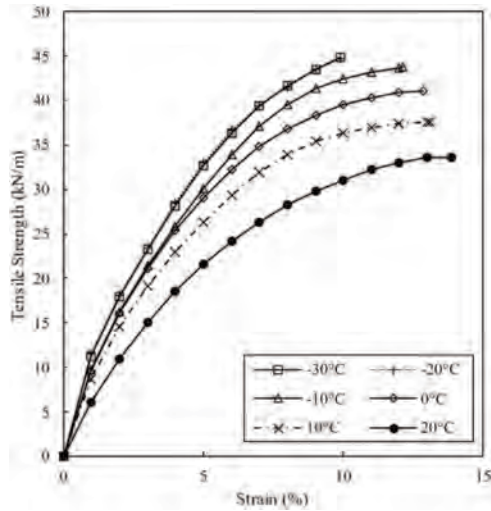
Figure 3. Load-strain curves of the biaxial geogrid at temperatures ranging from -30°C to 20°C.

brittle behavior as the temperature decreases. Indeed, the curves show that as the testing temperature decreases, larger tensile forces are mobilized at a given strain. This is attributed to the geogrid being made from polypropylene, i.e., a thermoplastic polymer that exhibits a soft and ductile behavior at elevated temperatures and a stiff and brittle response to loading at low temperatures.

At failure, geogrid samples exposed to low temperatures develop an ultimate tensile strength that exceeds the one obtained at 20°C at a strain level that is smaller than at the reference temperature. The largest gains in ultimate tensile strength are recorded at -20°C and -30°C, with the tensile strengths being about 33% greater than at 20°C. Additionally, the biggest reduction in ultimate tensile strain also happens at -20°C and -30°C, with the ultimate strain at the two temperatures being about 28.5% smaller than at 20°C. It is noteworthy that the load-strain curves at -20°C and -30°C are very similar and contrast with the gradual stiffening of the load-strain response observed at 10°C, 0°C, and -10°C. This behavioral difference is caused by the testing temperature reaching and going below polypropylene's glass transition temperature.

3.2 Geocomposite

The geocomposite's average load-strain curves at temperatures ranging from -30°C to 20°C are plotted in Figure 4. The experimental data suggests that the geocomposite becomes increasingly brittle as testing temperatures drop below 20°C. Indeed, temperature drops to 10°C, 0°C, -10°C, -20°C, and -30°C result in ultimate strains that are 8.9%, 20.9%, 21.8%, 33.7%, and 32.2% smaller than the one at 20°C respectively. However, it is important to point out that the ultimate tensile strength appears to be relatively insensitive to temperature changes with a maximum increase in ultimate tensile strength of 3.4% being recorded at -30°C.

3.3 Comparison

Figure 5 shows the normalized tensile strength of the geogrid and geocomposite at the 2%, 5%, and ultimate strain level. The tensile strength of each material is normalized by dividing its tensile strength (T) at the relevant strain level and temperature by its ultimate tensile strength at 20°C ($T_{ult@20°C}$). For example, at -30°C, the geogrid has a tensile strength of 17.99kN/m at 2% strain which, when divided by the geogrid's ultimate tensile strength of
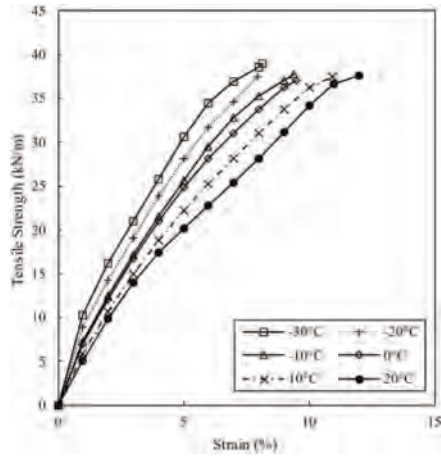
Figure 4.   Load-strain curves of the geocomposite at temperatures ranging from -30°C to 20°C.
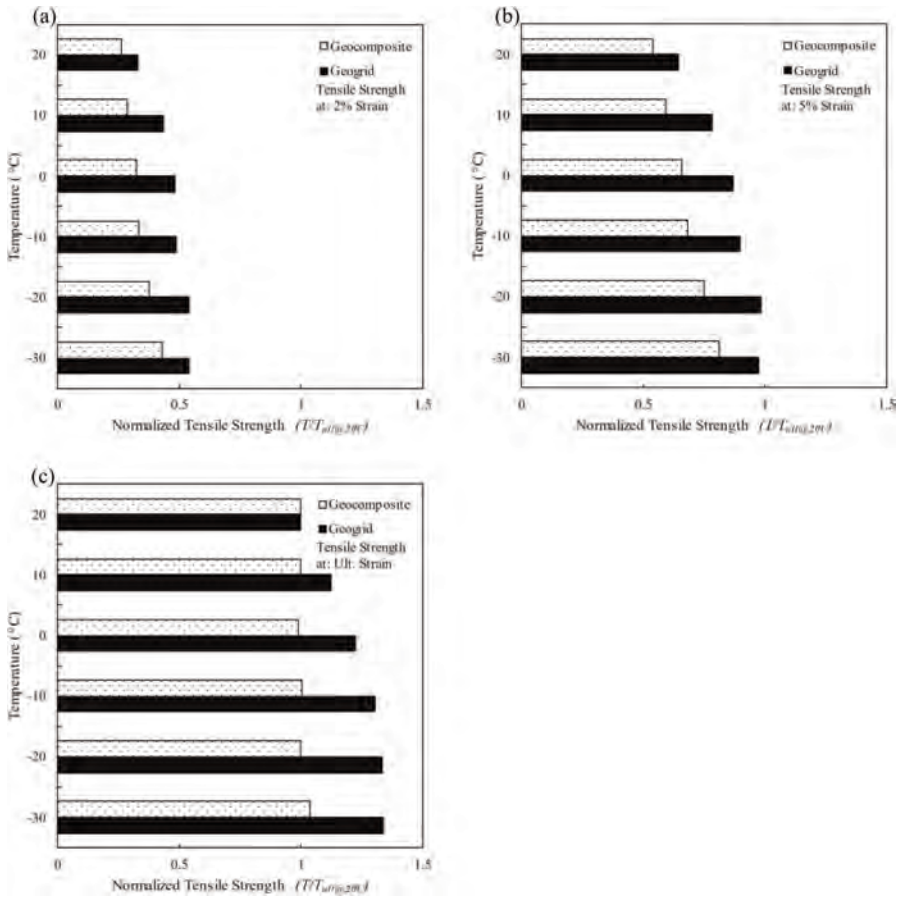
Figure 5.   Normalized tensile strength at (a) 2%, (b) 5%, and (c) ultimate strain for the geogrid and geocomposite.

33.55kN/m at 20°C, gives a normalized tensile strength of 0.54 at 2% strain. As shown in Figure 5a, the biaxial geogrid appears to be more sensitive to exposure to temperatures below 20°C than the geocomposite at 2% strain. Compared to the tensile strength obtained at 20°C at the 2% strain level, temperatures of 10°C and -30°C result in tensile strength increases of 32.6% and 63.4% in the geogrid against only 8.6% and 44.2% in the geocomposite. A similar trend is observed at 5% strain (Figure 5b) with exposure to temperatures of 10°C and -30°C leading to increases in tensile strength compared to that recorded at 20°C of 22.1% and 51.4% in the geogrid compared to 9.7% and 39.4% in the geocomposite. The trend observed at the 2% and 5% strain level is exacerbated at the ultimate strain level where the geocomposite appears to experience negligible fluctuations in its ultimate tensile strength as a result of temperature changes. This is in stark contrast with the considerable increases in ultimate tensile strength that occur in the geogrid across the range of temperatures shown in Figure 5c. While the ultimate tensile strength of the geocomposite only experiences a maximum increase of 3.4% at -30°C compared to that at 20°C, the geogrid exhibits tensile strengths at -20°C and -30°C that are about 33% greater than at 20°C.

4   CONCLUSIONS

This paper seeks to capture features of the behavior of geogrids in cold climates by performing in-isolation tensile tests on a biaxial polypropylene geogrid and a polymeric geocomposite at temperatures ranging from 20°C to -30°C. The key findings are as follows:

- The biaxial geogrid exhibits an increasingly brittle response to tensile loading when exposed to temperatures below 20°C characterized by higher tensile forces being mobilized at smaller strains
- The geogrid develops a maximum ultimate tensile strength at -20°C and -30°C that is about 33% greater than its ultimate strength at 20°C. This is accompanied by an ultimate strain that is 28.5% smaller than at the reference temperature
- The geocomposite becomes increasingly brittle when subjected to temperatures smaller than 20°C. However, while its ultimate strain decreases with decreasing temperature, its ultimate tensile strength appears to be insensitive to temperature changes
- The geogrid experiences more pronounced changes to its tensile load-strain response than the geocomposite as the testing temperature changes at 2%, 5%, and ultimate strain

REFERENCES

Bhat, S. and Tomas, J. (2017) 'Railroad Subgrade Stabilization using Biaxial Geogrid-Geotextile Composite – A Case Study', in Paredes, L. et al. (eds) *First International Conference on Technology and Application of Geotextiles*. Santiago, Chile: Gecamin, pp. 1–7.

Bonthron, B. and Jonsson, C. (2017) *Geogrids in cold climate*. Lulea University of Technology.

Chantachot, T., Kongkitkul, W. and Tatsuoka, F. (2016) 'Load-strain-time Behavours of Two Polymer Geogrids Affected by Temperature', *International Journal of GEOMATE*, 10(3), pp. 1869–1876. doi: 10.21660/2016.21.5192.

Chantachot, T., Kongkitkul, W. and Tatsuoka, F. (2017) 'Effects of Temperature on Elastic Stiffness of a HDPE Geogrid and its Model Simulation', *International Journal of GEOMATE*, 12(32), pp. 94–100. doi: 10.21660/2017.32.6620.

Desbrousses, R. L. E. and Meguid, M. A. (2021) 'On the Analysis and Design of Reinforced Railway Embankments in Cold Climate: A Review', in Tighe, S., Walbridge, S., and Henderson, V. (eds) *CSCE 2021 Annual Conference*. Niagara Falls, ON, Canada: Springer, pp. 588–598.

Desbrousses, R. L. E., Meguid, M. A. and Bhat, S. (2021) 'Effect of Temperature on the Mechanical Properties of Two Polymeric Geogrid Materials', *Geosynthetics International*, pp. 1–31. doi: 10.1680/jgein.21.00032a.

Han, J. and Jiang, Y. (2013) 'Use of Geosynthetics for Performance Enhancement of Earth Structures in Cold Regions', *Sciences in Cold and Arid Regions*, 5(5), p. 517. doi: 10.3724/SP.J.1226.2013.00517.

Jewell, R. A. et al. (1984) *'Interaction Between Soil and Geogrids.'*, pp. 18–30.

Jewell, R. A. (1988) 'The Mechanics of Reinforced Embankments on Soft Soils', *Geotextiles and Geomembranes*, 7(4), pp. 237–273. doi: 10.1016/0266-1144(88)90001-5.

Kasozi, A. M., Siddharthan, R. V. and Mahamud, R. (2014) 'MSE Wall Geogrid Tensile Strength at High Temperature Sites', *Environmental Geotechnics*, 3(1), pp. 4–16. doi: 10.1680/envgeo.13.00073.

Kim, U. J. and Kim, D. S. (2020) 'Load Sharing Characteristics of Rigid Facing Walls with Geogrid Reinforced Railway Subgrade During and After Construction', *Geotextiles and Geomembranes*, 48(6), pp. 940–949. doi: 10.1016/j.geotexmem.2020.08.002.

Koerner, R. M. (2005) *Designing with Geosynthetics*. Fifth. Upper Saddle River, NJ: Pearson Education.

Kongkitkul, W. et al. (2012) 'Effects of Temperature on the Rupture Strength and Elastic Stiffness of Geogrids', *Geosynthetics International*, 19(2), pp. 106–123. doi: 10.1680/gein.2012.19.2.106.

Segrestin, P. and Jailloux, J. M. (1988) 'Temperature in Soils and its Effect on the Ageing of Synthetic Materials', *Geotextiles and Geomembranes*, 7(1–2), pp. 51–69. doi: 10.1016/0266-1144(88)90018-0.

Shokr, M., Meguid, M. A. and Bhat, S. (2022) 'Experimental Investigation of the Tensile Response of Stiff Fiberglass Geogrid Under Varying Temperatures', *International Journal of Geosynthetics and Ground Engineering*, 8(1). doi: 10.1007/s40891-022-00361-7.

Titan Environmental Containment (2020) *Titan Rail Grid 30*.

Titan Environmental Containment (2021) *Swamp Grid 30*.

Zarnani, S., Scott, J. D. and Sego, D. C. (2011) 'Effect of Soil Temperature Changes on Geogrid Strains', *Canadian Geotechnical Journal*, 48(8), pp. 1287–1294. doi: 10.1139/t11-035.

Effect of UV radiation exposure on HDPE geomembrane properties

R.K. Anjana
Former Graduate Student, Indian Institute of Technology Madras, Chennai, India

S. Keerthana
Research Scholar, Indian Institute of Technology Madras, Chennai, India

D.N. Arnepalli
Professor, Indian Institute of Technology Madras, Chennai, India

ABSTRACT: This study investigates the resulting changes in the properties of a high-density polyethylene geomembrane (HDPE GMB) subjected to an accelerated UV (ultraviolet) ageing test. A commercially available GMB having a nominal thickness of 1.5 mm was exposed to UV radiation for varying durations for three years using an Atlas make UV weatherometer. Properties including thickness, density, melt flow index, tensile behaviour, oxidative induction time (OIT), crystallinity and microstructural changes using Fourier transform infrared (FTIR) spectroscopy were studied. The results showed that the thickness of GMB was not affected by UV radiation. However, density and melt flow index of the GMB showed a significant variation. At the end of 26095 hours of exposure, OIT was reduced by more than half the value of the initial OIT. The degradation by cross-linking was verified from FTIR spectra which showed an increased crystalline content against the ageing time.

1 INTRODUCTION

The high-density polyethylene geomembranes (HDPE GMBs) have become an integral part of the modern composite liner of engineered landfills. It has been the material of choice for most landfill liners because of its good physical, mechanical, and endurance properties (Rowe *et al.* 2010). In general, the durability of GMB mainly depends on the ageing rate of the liner material. Among all, the ageing of GMB is primarily governed by the exposure conditions pervading its service life. In landfill applications, the GMB may be exposed to different exposure conditions such as ultraviolet (UV) radiation, thermal, oxidative, and chemical exposures (Lavoie *et al.* 2020).

When the GMB is used as a basal and cover liner of a landfill, it may be exposed to UV radiation for short-term and long-term durations, respectively. Improper liner installation methods, delay in protecting GMB liner, and the formation of a whale/hippos may result in the exposure of GMB to UV radiation even for years (Anjana *et al.* 2023). It can trigger photodegradation and imparts discoloration, brittleness, and stress cracking in the liner material (Arnepalli & Rejoice 2012). This leads to damage to GMB and causes a reduction in the engineering properties of the material. The prolonged exposure to UV radiation may lead to the progressive degradation of polymeric liner material and alter its properties. These changes impair the geosynthetic material and eventually affect the service life of the GMB (Hsuan & Koerner 1995).

Ageing due to UV exposure is known to affect the physical and mechanical properties of the GMB (Arnepalli & Rejoice 2013a, b). Therefore, it is paramount to understand the behaviour of GMB under UV exposure conditions to ascertain its long-term performance in adequately providing the containment function. Given this, the present study aims to evaluate the effect of UV ageing on the depletion of properties of HDPE GMB subjected to

26095 hours (approximately three years) of exposure to UV radiation using a UV weatherometer in the laboratory. The present study focuses on the variation in the physical, mechanical, and endurance attributes of the GMB, including thickness, density, melt flow index, tensile behaviour, oxidative induction time (OIT), crystallinity, and microstructural changes examined using Fourier transform infrared (FTIR) spectroscopy.

2 MATERIALS AND METHODS

2.1 Geomembranes

A black smooth 1.5 mm-thick HDPE GMB was used in this study. Table 1 shows the featured properties of the selected GMB (Anjana *et al*. 2023).

Table 1. Properties of GMB used in this study.

Properties	Reference method	Values (Unit)
Thickness	ASTM D5199	1.51 ± 0.01 (mm)
Density	-	0.961 ± 0.001 (g / cm^3)
Melt flow rate	ASTM D1238	0.145 ± 0.001 (g / 10 min)
Oxidative induction time	ASTM D3895	132 (min)
Crystallinity	ASTM E794	49 (%)

2.2 Accelerated UV ageing test

The GMB specimens were exposed to UV radiation in the laboratory using an Atlas make UV Weatherometer. The samples were exposed to fluorescent UV light using UVA-340 lamps under controlled environmental conditions, according to ASTM G154. The exposure cycles of eight-hour UV radiation at 0.89 W / m^2 and four-hour condensation were followed. To study the effect of long-term UV exposure on GMB properties, the samples were subjected to 26095 hours (nearly three years) of accelerated ageing. The GMB samples were retrieved at various time intervals of UV ageing and tested for their desired properties.

2.3 Thickness

The thickness of the GMB was determined using a thickness measurement device by following the guidelines presented in ASTM D5199. The thickness was measured after applying a pressure of 20 kPa for 5 seconds against the specimen by means of a presser foot. The value was recorded to the nearest 0.02 mm, and the average thickness of ten samples was reported.

2.4 Density

The helium gas pycnometer (Quantochrome, USA) was used to measure the density of the GMB. The pycnometer measures the solid volume of the sample by displacing it with helium gas. From the known weight and the solid volume of the sample, the density of the GMB was determined.

2.5 Melt flow index

A fully automated melt flow indexer was used to perform the test according to ASTM D1238. As per the codal provisions, procedure-A was used to determine the melt flow index of a thermoplastic material. The molten polymer of the GMB was extruded through an orifice under an applied load of 2.16 kg and 190 °C. The mass of molten polymer extruded in 10 minutes (in grams of material / 10 min) is expressed as the melt flow index.

2.6 Oxidative Induction Time (OIT)

The standard OIT test was carried out according to ASTM D3895 using a Netzsch DSC 200 differential scanning calorimeter (DSC). The known sample weight was initially heated to

200 °C from room temperature at 10 °C / min in an inert nitrogen atmosphere. The sample was then maintained at the isothermal condition for 5 minutes, following which oxygen was introduced at 35 kPa pressure. The test was terminated after an oxidative reaction peak was observed. The OIT was calculated as the time elapsed between introducing oxygen and the arrival of the oxidative reaction peak.

2.7 *Tensile strength test*

A tensile testing machine (ZwickRoell, Germany) equipped with pincer grips and a video extensometer was employed to assess the tensile properties of the GMB as per ASTM D6693. The dog bone specimens were cut from the GMB using a die cutter and tested at a strain rate of 50 mm / min. The variations in tensile properties such as yield strength, break strength, yield strain and break strain for various UV ageing durations were determined.

2.8 *Crystallinity of polymer*

The crystallinity of the polymer was determined as per ASTM E794 using a Netzsch DSC 200 differential scanning calorimeter (DSC). A known sample weight was heated to 200 °C at 10 °C / min in an inert nitrogen atmosphere to obtain the crystallization melt curve. The crystallinity of the polymer is defined as the ratio of heat of fusion of GMB specimen and the heat of fusion of 100% crystalline HDPE polymer. The heat of fusion of 100% crystalline HDPE polymer, i.e., 293 J / g (Brandrup *et al.* 1999), was used to calculate the percent crystallinity of the samples.

2.9 *Fourier transform infrared (FTIR) spectroscopy*

The FTIR analysis was performed using a Perkin Elmer Spectrum 100 in the spectral range from 4000 cm^{-1} to 400 cm^{-1}, 128 scans at 4 cm^{-1} resolution. The test was conducted on virgin and aged GMBs to study the surface-level molecular changes owing to UV radiation. Further, the spectrum was obtained on the UV irradiated side of the aged GMB, labelled as the exposed side, and the other side on which UV light was not exposed, labelled as the unexposed side.

3 RESULT AND DISCUSSIONS

3.1 *Thickness, density, melt flow index, oxidative induction time, and crystallinity*

The thickness of a GMB is one of the important properties since it significantly affects the service life of a GMB (Rowe *et al.* 2010). The thickness of the GMB was measured at various durations of UV exposure. The results indicated that the thickness of the aged GMB was invariable for the complete duration of UV testing. There was no considerable change in the GMB thickness with UV ageing time. This implies that exposure to UV radiation does not affect or have an insignificant effect on the GMB thickness.

A notable change was observed in the density of GMB upon UV exposure (Table 2). When the ageing duration increased, the density of GMB decreased. For instance, the density of GMB reduced from 0.961 to 0.945 at the end of 11200 hours of exposure. This decrease in density reflects the localized change in the crystallinity or extraction of additives or absorption of solvents (Anjana *et al.* 2023).

The melt flow index measures the rate of extrusion of molten GMB resin. It is a useful measure for assessing the change in molecular weight of the polymer (Park *et al.* 2013). The degradation caused by cross-linking results in an increase in molecular weight, and chain scission causes a decrease in molecular weight (Hsuan & Koerner 1995). Table 2 shows the variation of the melt flow index with respect to ageing time. The melt flow index reduced for up to 11200 hours of ageing time and then increased. These characteristic changes denote the degradation of polymer caused by both cross-linking and chain scission reactions due to UV exposure. Thus, it can be inferred that UV exposure can deplete the GMB properties by one or more of the degradative reactions depending on the extent of exposure time (Guillet 1972; Anjana *et al.* 2023).

Table 2. Variation of GMB properties at various UV ageing durations*.

Ageing time hours	Density g / cm³	Melt flow index g / 10 minutes	Oxidative induction time minutes	Crystallinity %
0	0.961	0.145	132	49
90	0.956	0.141	132	46
1000	0.95	0.139	111	52
3000	0.949	0.138	94.8	65
9000	0.95	0.132	80	54
11200	0.9447	0.130	–	51
13803	0.9577	0.137	65	51
26095	0.9533	0.138	55	56

*From (Anjana *et al.* 2023)

Oxidative induction time (OIT) indicates the amount of antioxidants in the GMB. From Table 2, OIT was found to reduce with the increase in UV ageing time. At the end of 26095 hours of UV exposure, the OIT was reduced by a factor of 0.42 from its initial value. The relationship between OIT and ageing time was linear, and the depletion of antioxidants followed a first-order exponential decay. Hence, the above trend of reducing OIT against ageing time confirms that antioxidant depletion is proportional to the level of deterioration caused due to UV exposure.

The role of crystallinity is essential in explaining the GMB behaviour upon UV exposure as it affects mechanical and chemical resistance. When the crystallinity of GMB is high, its stiffness and chemical resistance would be high (Scheirs 2009). The crystallinity determined using DSC denotes the overall crystallinity in the bulk of a material. It is clear from Table 2 that UV ageing has resulted in an overall increase in the crystallinity of the polymer. The crystallinity increase with the increasing ageing duration can be attributed to the post-crystallization of polymer molecules due to UV exposure (Anjana *et al.* 2023). This observation is similar to the melt flow index test results, where the cross-linking reactions led to an increased crystallinity of polymeric GMB.

3.2 *Tensile properties*

Table 3 shows the tensile properties of GMB in the machine direction as a function of UV exposure. The GMB did not exhibit a distinct trend in the increase or decrease of the tensile properties. However, the overall increase in the tensile properties can be attributed to the crystallinity changes in the polymer due to UV ageing. The increase in tensile strength and the decrease in yield strain indicates the occurrence of cross-linking and oxidative degradations (Anjana *et al.* 2023). Similar behaviour was noted for cross-machine direction as well.

Table 3. Variation of tensile properties with UV exposure*.

Ageing time hours	Yield strength kN / m	Break strength kN / m	Yield strain %	Break strain %
0	28.18	26.33	18	542
90	27.7	32.15	18	669
1000	27.1	30.1	17	649
3000	28	36	19	753
9000	29.98	44.35	16	913
11200	31.55	48.14	17	800
13803	32.09	37.59	14	869
26095	32.98	40.25	15	889

*From (Anjana *et al.* 2023)

3.3 *Fourier transform infrared (FTIR) spectroscopy*

FTIR analysis was performed on virgin and aged GMB in view of studying the molecular changes due to UV ageing. The methylene functional group peaks are the prominent features

of HDPE GMB and are found at wave numbers 2915, 2848, 1472, 1462, 729 and 719 cm^{-1}. The peaks at 1462 and 1472 cm^{-1} correspond to the methylene deformation vibrations in the amorphous and crystalline regions, respectively (Anjana *et al*. 2023). Figure 1 shows the spectra of virgin and aged GMBs of exposed sides.
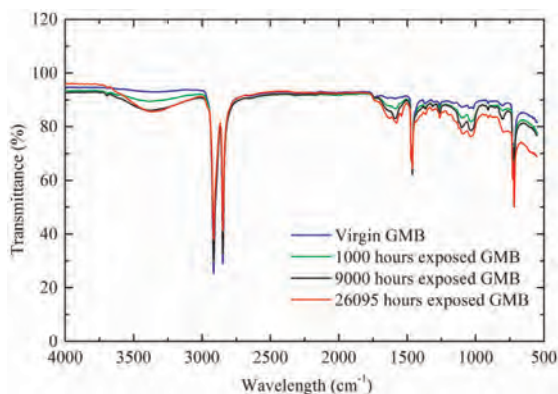
Figure 1. FTIR spectra of virgin and aged GMBs at varying UV ageing durations.

With the increasing duration of UV ageing, the peak corresponding to crystalline content was increased and the amorphous content was decreased. The variation of peak intensity in this region reflects the crystallinity increase in the polymer due to cross-linking reactions. This finding supports the results obtained in other tests of GMB properties. Thus, quantifying crystalline content in polymer becomes essential to validate those observations. Hence, the method described by Zerbi *et al*. (1989) was used to determine the crystalline content as per Equation 1 below:

$$Crystalline\ content\ = \left\{ 100 - \frac{[1 - (I_a/I_b)]/1.233}{1 + (I_a/I_b)} \right\} \times 100 \qquad (1)$$

where I_a and I_b denote the peak intensities of bands at 1472 and 1462 cm^{-1}, respectively. The crystalline content determined using Equation 1 represents the surface-level modification. The spectra were collected on both exposed and unexposed sides of aged GMB and their corresponding crystalline content was calculated (Table 4). The values were found to be higher for the aged GMB relative to the virgin GMB. Further, the crystalline content on the exposed side was greater than that of the unexposed side in the aged GMB. There was a significant difference in the crystalline content of exposed and unexposed sides beyond 1000 hours of ageing. These results imply that with the increasing duration of UV ageing, there is an increase in the crystalline content. This shows the evidence for cross-linking reactions, as the same was also witnessed in the other tests (Anjana *et al*. 2023).

Table 4. Variation of crystalline content with UV exposure*.

Crystalline content (%)	Ageing time (hours)									
	0	48	90	400	1000	3000	9000	11200	13803	26095
Virgin GMB	88	88	88	88	88	88	88	88	88	88
Exposed side	90.05	91.03	91.91	91.66	91.98	93.41	94.4	95.48	95.55	95.8
Unexposed side	88.62	90.4	91.74	91.28	91.89	91.45	91.97	91.71	90.95	92.4

*From (Anjana *et al*. 2023)

4 CONCLUSIONS

The study investigated the effect of accelerated UV ageing on the properties of HDPE GMB exposed to UV radiation for three years. The variation of GMB properties such as thickness, density, melt flow index, tensile behaviour, OIT, crystallinity and FTIR spectra with varying exposure durations have been studied in detail. The results showed an inappreciable variation in the thickness of GMB with UV ageing time. However, the effect of UV degradation was considerable, as evidenced by the changes in density, melt index and tensile behaviour of GMB. The reduced density, increased tensile properties and reduced melt index values dictate the occurrence of cross-linking reactions. The standard OIT decreased significantly as the ageing duration increased. This can be attributed to antioxidant depletion owing to oxidative degradation. The FTIR spectra showed that the crystalline content measured at the exposed GMB surface increased with the increasing UV ageing duration. This suggests that due to UV ageing, the GMB is more prone to surface-level damage and the evidence for cross-linking reactions depicts superficial degradation. The reported findings are confined only to the tested exposure conditions, and based on the above findings, it can be concluded that the depletion of GMB properties depends on the severity and extent of UV ageing.

REFERENCES

Anjana, R.K., Keerthana, S. & Arnepalli, D.N. 2023. Coupled Effect of UV Ageing and Temperature on the Diffusive Transport of Aqueous, Vapour and Gaseous Organic Contaminants Through HDPE Geomembrane. *Geotextiles and Geomembranes* 51(2): 316–329.

Arnepalli, D.N. & Rejoice, A.A. 2012. Durability and Long-Term Performance of High Density Polyethylene Geomembrane. *Proceedings of ASCE Conference on Geosynthetic Lining Solution and Related Issues, 25 February*. Bangalore.

Arnepalli, D.N. & Rejoice, A.A. 2013a. Evaluation of Geosynthetic Liner Long-Term Performance Under Landfill Conditions. *Proceedings of Geopractices*, Hyderabad, India.

Arnepalli, D.N. & Rejoice, A.A. 2013b. Service Life and Long-Term Performance of Geosynthetic Liners Under Simulated Landfill Conditions. *Proceedings of Geosynthetics India - 2013*, New Delhi, India.

ASTM D1238 2004. Standard Test Method for Melt Flow Rates of Thermoplastics by Extrusion Plastometer. ASTM International, West Conshohocken, Philadelphia, USA.

ASTM D3895 2014. Standard Test Method for Oxidative-Induction Time of Polyolefins by Differential Scanning Calorimetry. ASTM International, West Conshohocken, Philadelphia, USA.

ASTM D5199 2006. Standard Test Method for Measuring the Nominal Thickness of Geosynthetics. ASTM International, West Conshohocken, Philadelphia, USA.

ASTM D6693 2001. Standard Test Method for Determining Tensile Properties of Non-reinforced Polyethylene and Non-reinforced Flexible Polypropylene Geomembrane. ASTM International, West Conshohocken, Philadelphia, USA.

ASTM E794 2012. Standard Test Method for Melting and Crystallization Temperatures by Thermal Analysis. ASTM International, West Conshohocken, Philadelphia, USA.

ASTM G154 2016. Standard Practice for Operating Fluorescent Light Apparatus for UV Exposure of Non-Metallic Materials. ASTM International, West Conshohocken, Philadelphia, USA.

Brandrup, J., Immergut, E.H. & Grulke, E.A. 1999. *Polymer Handbook*. John Wiley & Sons.

Guillet, J.E. 1972. Fundamental Processes in the UV Degradation and Stabilization of Polymers. *Pure Applied Chemistry* 1(30): 135–144.

Hsuan, Y.G. & Koerner, R.M. 1995. Long Term Durability of HDPE Geomembrane: part i - Depletion of Antioxidant. *GRI Report* 16: 35.

Lavoie, F.L., Kobelnik, M., Valentin, C.A. & Silva, J.L.D. 2020. Durability of HDPE Geomembranes: an Overview. *Química Nova* 43(5): 656–667.

Park, Y.M., Khan, B.A. & Jeon, H.Y. 2013. Analysis of Degradation Behaviors of Geomembrane by Accelerated Test under UV Exposure Conditions. *Polymer Korea* 37(1): 5–14.

Rowe, R.K., Islam, M.Z. & Hsuan, Y.G. 2010. Effects of Thickness on the Aging of HDPE Geomembranes. *Journal of Geotechnical and Geoenvironmental Engineering* 136(2): 299–309.

Scheirs, J. 2009. *A Guide to Polymeric Geomembrane: A Practical Approach*. John Wiley & Sons.

Zerbi, G., Gallino, G., Del, F.N. & Baini, L. 1989. Structural Depth Profiling in Polyethylene by Multiple Internal Reflection Infra-red Spectroscopy. *Polymer* 30(12): 2324–2327.

Prediction of the vertical permeability coefficient of needle-punched nonwoven geotextiles

K.Y. Li, X.W. Tang*, J.X. Liang, W.K. Lin, T.Q. Wang & Q.Q. Xiang
Research Center of Coastal and Urban Geotechnical Engineering, Zhejiang University, Hangzhou, P.R. China
Engineering Research Center of Urban Underground Space Development of Zhejiang Province, Hangzhou, P.R. China

ABSTRACT: The vertical permeability coefficient is an important hydraulic characteristic index of needle-punched nonwoven geotextiles. A theoretical model has been proposed to predict the vertical permeability coefficient of nonwoven geotextiles, considering the fiber orientation distribution characteristics. The permeability coefficient and parameters of four needle-punched nonwoven geotextiles were obtained from the literature and image analysis. By comparing the predicted results of the permeability model with the experimental results, it is confirmed that the permeability model proposed in this paper was validated with thicker nonwoven geotextiles.

1 INTRODUCTION

Geotextiles have been widely used as filtration materials in civil engineering, water conservancy, port and environment and other engineering construction (Lee & Douglas 2012; Touze-Foltz *et al.* 2016; Yang *et al.* 2019). The vertical permeability coefficient of nonwoven geotextiles is an important hydraulic parameter used in the design of road separations, the design of dam filter layers and the selection of drainage design (Fatema & Bhatia 2021; Zhang *et al.* 2013).

In the current standards, such as ASTM D4491M-15 (2015), BS 6906: Part 3 (1989), and GB/T 15789-2016 (2016), the vertical permeability coefficient of nonwoven geotextiles requires time and energy consumption. The number of samples to be tested should be at least five, and the samples should be soaked in the water container until saturated. Furthermore, the experimental vertical permeability test cannot help to understand the permeability mechanism of nonwoven geotextiles.

Therefore, accurate prediction of permeability of nonwoven geotextiles by understanding the relationship between the pore characteristic and permeability. This study proposed a theoretical model to predict the vertical permeability coefficient of nonwoven geotextiles, considering the influences of fiber orientation distribution. Four geotextiles from the literature were used to calculate their permeability to determine the validity of the model proposed in this study.

2 THEORETICAL MODEL

2.1 *Analytical solution of pore size distribution*

Nonwoven geotextile is a three-dimensional structure consisting of fibers arranged in a planar direction. The structure and morphology of the pores in nonwovens are very

---

*Corresponding Author: tangxiaowu@zju.edu.cn

complex. Some analytical models for predicting the pore size distribution of nonwoven geotextiles have been found in the literature (Faure *et al.* 1986, 1990; Lombard *et al.* 1989). Faure *et al.* (1986, 1990) proposed a cumulative probability expression of a polygon inscribed circle based on the Poisson polyhedra theory. Lombard *et al.* (1989) calculated the pore size distribution by extending the definition of the effective thickness of the analytical model by Faure *et al.* Rawal *et al.* (2010, 2011) developed an analytical model for predicting the pore size distribution of nonwoven geotextiles combining the effects of fiber orientation. The cumulative probability $F(r)$ of a particle with a diameter r passing through the layers of nonwoven geotextiles is shown below:

$$F(r) = 1 - \left[\left(1 + \omega r + \frac{\omega^2 r^2}{2} \right) e^{-\omega r} \right]^N \tag{1}$$

where

$$\omega = \frac{4 V_f K_\alpha}{\pi d_f} \tag{2}$$

$$V_f = \frac{\mu_g}{\rho_f T_g} \tag{3}$$

$$K_\alpha = \int_{-\frac{\pi}{2}}^{\frac{\pi}{2}} |\cos \varphi| \chi(\varphi) d\varphi \tag{4}$$

$$N = \frac{T_g}{d_f} \tag{5}$$

where ω is the scale parameter; N is the number of layers; V_f is the volume fraction of fiber; K_α is the directional parameter; d_f is the fiber diameter; μ_g is the mass per unit area; ρ_f is the fiber density; T_g is the thickness of geotextile; and $\chi(\varphi)$ is the distribution function of fiber orientation (φ). The details of the parameters can be found in the literature (Rawal *et al.* 2010, 2011).

2.2 Permeability model of nonwoven geotextile

Nonwoven geotextiles can be seen as porous materials composed of a bundle of tortuous capillary tubes with variable cross-sectional areas. Therefore, the cumulative probability function proposed by Rawal *et al.* (2010, 2011) can well describe the distribution of the pore channels. The probability density function $f(r)$ can be obtained,

$$f(r) = F(r)' = \frac{1}{2} \omega^3 N r^2 (1 + \omega r + \frac{\omega^2 r^2}{2})^{N-1} \cdot e^{-\omega r N} \tag{6}$$

Based on the Hagen-Poiseian equation, the flow rate $q(r)$ of a single r pore-sized tube can be modified as follows (Denn 1980):

$$q(r) = \frac{\pi}{128} \frac{\Delta P}{L_t r} \frac{r^4}{\mu} \tag{7}$$

where $L_t(r)$ is the tortuous length of the pore channels, ΔP is the pressure gradient, and μ is the dynamic viscosity. Yu and Cheng (2002) reported that the tortuous length of the pore channels $L_t(r)$ can be expressed as the equation of the diameter and fractal dimension:

$$L_t(r) = L_0^{D_T} r^{1-D_T} \tag{8}$$

where L_0 is the straight length of pore channels, it can be assumed to equal to the thickness of geotextile T_g. D_T is the tortuosity fractal dimension. $1 < D_T < 2$ presents the tortuosity of flow through a porous media capillary tube. When $D_T = 1$, the capillary tube is straight and when $D_T = 2$, the capillary tube is too torturous to fill the whole surface.

The flow rate per unit area $v(r)$ of a single tube can be taken as:

$$v(r) = \frac{q(r)}{\frac{1}{4}\pi r^2} = \frac{\pi \Delta P r^4}{128 \cdot T_g^{D_T} r^{1-D_T} \mu} \cdot \frac{4}{\pi r^2} = \frac{\Delta P r^{1+D_T}}{32 T_g^{D_T} \cdot \mu} \tag{9}$$

The total flow Q is given by integrating the products of Equation (6) and (9),

$$Q = \phi_{eff} A \int_{r_{min}}^{r_{max}} v(r) f(r) dr$$

$$= \frac{\phi_{eff} \Delta P A \omega^3 N}{64 \cdot \mu \cdot T_g^{D_T}} \int_{r_{min}}^{r_{max}} r^{3+D_T} \cdot \left(1 + \omega r + \frac{\omega^2 r^2}{2}\right)^{N-1} \cdot e^{-\omega r N} dr \tag{10}$$

where A is the flow area, r_{max} is the maximum pore size, r_{min} is the minimum pore size, and ϕ_{eff} is the effective porosity of nonwoven geotextile which can be expressed as:

$$\phi_{eff} = 1 - \frac{\mu_g}{\rho_f T_g} \tag{11}$$

In nonwoven geotextiles, the ratio of r_{min} to r_{max} is usually less than 0.01, so the Equation (10) can be simplified accordingly,

$$Q = \frac{\phi_{eff} \Delta P A \omega^3 N}{64 \cdot \mu \cdot T_g^{D_T}} \int_0^{r_{max}} r^{3+D_T} \cdot \left(1 + \omega r + \frac{\omega^2 r^2}{2}\right)^{N-1} \cdot e^{-\omega r N} dr \tag{12}$$

Based on Equation (11) and Darcy's law (Yu and Cheng 2002), the permeability coefficient model of nonwoven geotextiles can be calculated,

$$k = \frac{\rho g Q T_g}{\Delta P A} = \frac{\phi_{eff} \omega^3 \rho g N}{64 \cdot \mu \cdot T_g^{D_T-1}} \int_0^{r_{max}} r^{3+D_T} \cdot \left(1 + \omega r + \frac{\omega^2 r^2}{2}\right)^{N-1} \cdot e^{-\omega r N} dr \tag{13}$$

where ρ is the density of water, g is the gravitational acceleration.

3   EXPERIMENTAL PROCEDURE

In Equation (12), the permeability coefficient of nonwoven geotextile is in terms of the maximum pore size r_{max}, directional parameter K_α, fiber diameter d_f, tortuosity fractal dimension D_T, the mass per unit area μ_g, fiber density ρ_f, and the thickness of geotextile T_g, that is $k = k$ (r_{max}, K_α, d_f, D_T, μ_g, ρ_f, T_g).

3.1   Digital image analysis

The digital image method has been used in several studies to measure pore and fiber characteristics of nonwoven geotextiles due to the advantages of fast processing speed, high accuracy, and not damaging the specimen (Aydilek et al. 2002; e Silva et al. 2019). Therefore, the pore size and fractal parameters of the nonwoven geotextiles sample were obtained using image analysis.

Images of the geotextiles were obtained using scanning electron microscopy (SEM). Firstly, to make the pores and fiber boundaries of geotextiles clear and easy to identify, the image brightness and contrast of the geotextiles were adjusted to ensure sufficient contrast between interests. The optimal threshold values were calculated using Otsu's method (Otsu 1979). The resulting images were then converted into a binary format, where the pore pixel intensity and fiber intensity were set to 1 (pure white) and 0 (pure black), respectively.

Lastly, several required parameters can be determined through statistical analysis, including maximum pore size r_{max}, directional parameter K_α, and fiber diameter d_f. The procedures were as follows:

(1) The equivalent hydraulic diameter of the nonwoven geotextile pore was obtained based on hydrodynamic theory by converting the pores of the geotextile into circular channels as follow:

$$r = \frac{4A_p}{S_p} \tag{13}$$

where A_p is the pore area, S_p is the pore perimeter. Thus, the maximum pore size r_{max} can be obtained.

(2) The edge of the fibers was smoothed using median filtering and erosion operation. Then, the orientation distribution of the fibers was obtained statistically by fitting the pore edges with the Hough transform. The directional parameter Kα can be calculated by the proportion of lines for 10° orientation angle interval with respect to machine direction.

(3) The fiber diameters df of nonwoven geotextiles were manually recognized by drawing lines on the fibers using FSCapture. More than 100 fibers were need in this statistical work.

3.2 Determination of pore tortuosity fractal dimension D_T

Several studies have tended to determine the pore tortuosity fractal dimension D_T. Shen *et al.* (2018) calculated the value of D_T using a theoretical equation. Liu *et al.* (2011) used the box-counting method to obtain the value of D_T of nonwoven geotextile. Here, the box-counting method was recommended to be applied in this study.

It is tough to obtain the actual vertical percolation path of nonwoven geotextiles by experiment. It was assumed that the nonwoven geotextiles have the same pore size distribution in two and three dimensions. Thus, surface morphology images of nonwoven geotextiles were used to present the actual pathway of the longitudinal capillary tubes. First, the digital image analysis mentioned above was performed to convert the image into binary. Then, the binary image is divided by numerous square boxes with side *a*. The number $N(a)$ of boxes required to cover the whole area is counted. The side of the square box *a* was changed, and the above operation was repeated. Finally, the slope of the linear fitted line on the double logarithmic plot of *log(a)* and *log N(a)* was obtained.

3.3 Determination of physical properties

The physical properties of the nonwoven geotextiles, the mass per unit area μ_g and the thickness of geotextile T_g, were determined according to ASTM D5261-10 (2018) and ASTM D5199-12 (2012), respectively. The data of fiber density ρ_f can be obtained from manufacturers.

4 RESULTS

The data of the needle-punched nonwoven geotextile samples were obtained from Liu *et al.* (2011). The physical and fractal properties of the samples are presented in Table 1. Comparations of theoretical and experimental values of the permeability coefficient of

Table 1. Properties of nonwoven geotextiles.

Samples	r_{max}* (μm)	K_α*	d_f (μm)	D_T	μ_g (mm)	ρ_f (kg/m^3)	T_g (mm)
Sample 1	148.4	0.6378	20.0	1.061	172.37	1380	1.499
Sample 2	339.2	0.6599	20.6	1.065	354.39	1380	3.966
Sample 3	283.2	0.6362	21.2	1.073	526.61	1380	5.781
Sample 4	447.0	0.6432	19.9	1.058	591.88	1380	5.833

*These two parameters were determined using the SEM images of nonwoven samples (Liu *et al.*, 2011) in this study.

Table 2. The theoretical and experimental value of permeability coefficient of nonwoven geotextiles.

Samples	Experimental value (cm/s)	Theoretical value (cm/s)	Relative error (%)
Sample 1	0.18	0.19	5.55
Sample 2	0.43	0.39	9.30
Sample 3	0.41	0.30	26.83
Sample 4	0.34	0.20	41.18

nonwoven geotextiles are shown in Table 2. The experimental values were obtained from Liu *et al.* (2011), while the predicted values were calculated using Equation (13) and the parameters specified in Table 1.

The values of the predicted permeability coefficient compared well with the experimental permeability coefficient. For sample 1 and sample 2, the error rates between the experimental and the calculated value are 5.55% and 9.30%, respectively. Nevertheless, sample 3 and sample 4 show some differences. The difference between the two values ranges from 26.83% to 41.18%.

This discrepancy may be due to the fact that nonwoven geotextiles are complex porous structures. SEM image analysis can only be carried out on the surface layer of the geotextile, not on the deep layer. The pores within the geotextile cannot be adequately analyzed. Furthermore, Giroud (2010) claimed that the reliability of a nonwoven geotextile filter is a function of the number of constrictions in the filtration path. Constriction means a "window" delimited by three or more fibers through which soil particles could migrate. The number of constrictions of thicker geotextiles is larger than those of thinner geotextiles, which are more unpredictable. Therefore, the model proposed in this study (i. e. Equation (13)) is less applicable for thick geotextiles sample 3 and sample 4, which are more suitable for nonwoven geotextiles with low thicknesses.

5 CONCLUSIONS

A permeability model has been proposed to predict the vertical permeability coefficient of needle-punched nonwoven geotextiles. The fiber orientation distribution characteristics are considered in this model. The model involves the maximum pore size r_{max}, directional parameter K_α, fiber diameter d_f, tortuosity fractal dimension D_T, the mass per unit area μ_g, fiber density ρ_f, and the thickness of geotextile T_g. The permeability coefficient and parameters of nonwoven geotextiles are determined from the literature. The tortuosity fractal dimension and directional parameter are calculated by image analysis in this study. Comparison between the experimental and theoretical results shows that the model was validated with thin geotextiles but not as well for thicker geotextiles.

REFERENCES

ASTM D4491M-15. 2015. Standard Test Methods for Water Permeability of Geotextiles by Permittivity. *ASTM International*, West Conshohocken, PA.

ASTM D5199-12. 2012. Standard Test Method for Measuring the Nominal Thickness of Geosynthetics. *ASTM International*, West Conshohocken, PA.

ASTM D5261-10. 2018. Standard Test Method for Measuring Mass Per Unit Area of Geotextiles. *ASTM International*, West Conshohocken, PA.

Aydilek, A.H., Oguz, S.H. & Edil, T.B. 2002. Digital Image Analysis to Determine Pore Size Distribution of Nonwoven Geotextiles. *Journal of Computing in Civil Engineering* 16(4): 280–290.

BS 6906: Part 3. 1989. Determination of Water Flow Normal to the Plane of the Geotextile Under a Constant Head. *British Standard Institution*, London, UK.

Denn, M.M. 1980. *in: Process Fluid Mechanics*, Prentice-Hall, Englewood Cliff, NJ, p. 35.

e Silva, R.A., Negri, R.G. & de Mattos Vidal, D. 2019. A New Image-Based Technique for Measuring Pore Size Distribution of Nonwoven Geotextiles. *Geosynthetics International* 26(3): 261–272.

Fatema, N. & Bhatia, S. 2021. Role of Geotextiles Pore Size Distribution in Dewatering Tests. *Geosynthetics International* 28(1): 80–94.

Faure, Y.H. 1986. Theoretical and Experimental Determination of the Filtration Opening Size. *In: Proceedings of the Third International Conference on Geotextiles*: 1275–1280. Vienna: Austria.

Faure, Y.H., Gourc, J.P. & Gendrin, P. 1990. Structural Study of Porometry and Filtration Opening Size of Geotextiles. In Ian D. Peggs (eds), *Geosynthetics: Microstructure and Performance*: 102–119. ASTM Special Technical Publication.

GB/T 15789-2016. 2016. Geotextiles and Geotextile-Related Products—Determination of Water Permeability Characteristics Normal to the Plane, Without Load. *Standardization Administration of the People's Republic of China*, Beijing, China.

Giroud, J.P., 2010, "Development of Criteria for Geotextiles and Granular Filters", Prestigious Lecture, *Proceedings of the 9th International Conference on Geosynthetics*, Guarujá, Brazil, May 2010, Vol. 1, 45–64.

Lee, E.C. & Douglas, R.S. 2012. Geotextile Tubes as Submerged Dykes for Shoreline Management in Malaysia. *Geotextiles and Geomembranes* 30: 8–15.

Liu, L., Ji, L., Guo, F. & Yu, J. 2011. Prediction of the Vertical Permeability of Needle-Punched Nonwoven Geotextiles by Fractal Geometry Theory. *Geosynthetics International* 18(4): 169–177.

Lombard, G., Rollin, A. & Wolff, C. 1989. Theoretical and Experimental Opening Sizes of Heat-Bonded Geotextiles. *Textile Research Journal* 59: 208–217.

Otsu, N., 1979. A Threshold Selection Method From Gray-Level Histograms. *IEEE Transactions on Systems, Man, and Cybernetics: Systems* 9 (1), 62–66.

Rawal, A. & Agrahari, S. K. 2010. Pore Size Characteristics of Nonwoven Structures Under Uniaxial Tensile Loading. *Journal of Materials Science* 46(13): 4487–4493.

Rawal, A.2010. Structural Analysis of Pore Size Distribution of Nonwovens. *Journal of the Textile Institute* 101(4): 350–359.

Shen, X., Li, L., Cui, W. & Feng, Y. 2002. Improvement of Fractal Model for Porosity and Permeability in Porous Materials. *International Journal of Heat Mass Transfer* 121(2018): 1307–1315.

Touze-Foltz, N., Bannour, H., Barral, C. & Stoltz, G. 2016. A Review of the Performance of Geosynthetics for Environmental Protection. *Geotextiles and Geomembranes* 44(5): 656–672.

Yang, Y.H., Wei, Z.A., Gao, G.S., Yang, Y., Wang, H., Zhuang, S.N. & Lu, T. 2019. A Case Study on Utilizing Geotextile Tubes for Tailings Dams Construction in China. *Geotextiles and Geomembranes* 47(2): 187–192.

Yu, B.M. & Cheng, P. 2002. A Fractal Model for Permeability of Bi-Dispersed Porous Media. *International Journal of Heat Mass Transfer* 45(14): 2983–2993.

Zhang, Y.P., Liu, W.C., Shao, W.Y. & Yang, Y. 2013. Experimental Study on Water Permittivity of Woven Polypropylene Geotextile Under Tension. *Geotextiles and Geomembranes* 37: 10–15.

The evolution of geosynthetic hydraulic performance measurement

S.R. Allen
The TRI Environmental Group, Austin, USA

ABSTRACT: The growth of geosynthetic hydraulic product types, structures, and associated performance has been impressive. Geosynthetics routinely replace traditional materials such as soil and stone layers to provide for important engineering functions including drainage, filtration and erosion and sediment control, all while providing greener engineering options resulting in lower carbon footprints. The growth of product structures and performance behaviors has challenged the standardization community to keep pace with measurement technologies appropriate to capture both short and long term product performance. Along the way, many testing tools and measurement procedures have been developed, and many more are in development.This paper reviews many of the geosynthetic hydraulic structures and their specific applications. The important work ISO TC221 and ASTM International Committee D35 to standardize measurement technologies will be presented, including selected summary descriptions for:

- ISO 18198, Determination of long-term flow of geosynthetic drains
- ISO 12958-1, Determination of water flow capacity in their plane - Part 1: Index test
- ISO 12958-2, Determination of water flow capacity in their plane - Part 2: Performance test
- ASTM D4716, Standard Test Method for Determining the (In-plane) Flow Rate per Unit Width and Hydraulic Transmissivity of a Geosynthetic Using a Constant Head
- ISO TC 18228-8, Design using geosynthetics - Part 8: Surface erosion control
- ASTM D6459, Standard Test Method for Determination of Rolled Erosion Control Product (RECP) Performance in Protecting Hillslopes from Rainfall-Induced Erosion
- ASTM D 6460. Standard Test Method for Determination of Rolled Erosion Control Product (RECP) Performance in Protecting Earthen Channels from Stormwater-Induced Erosion

Also discussed is the significance of test water management, the use of alternative permeants such as leachates and air, and the accelerated "aging" of drainage systems in an effort to predict long term performance.

1 INTRODUCTION

Geosynthetics that provide desired hydraulic performance comprise a variety of manufactured products that include geotextiles as well as several three-dimensional structures. While the primary function of most geotextiles in hydraulic drainage applications is filtration, the ability of geosynthetic porous structures to provide hydraulic performance is impressive, and include products such as geonets, cuspated cores, geomats, geospacers, multilinear drains and drainage liners.

The majority of planar geosynthetic drains are geocomposites with geotextiles laminated to a drainage core and it is common to consider the drainage behavior of the geocomposite as a whole rather than the behavior of the component parts in isolation. Examples of geosynthetic products are included in Figure 1.
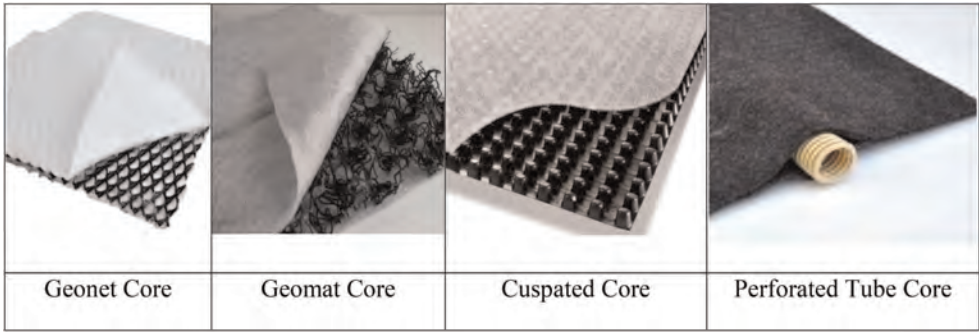
Figure 1.   Examples of drainage cores (from ISOTS18198-08).

When geotextiles are used for surface erosion resistance and associated filtration, woven or nonwoven geotextiles are common for both vertical applications of soil retention and dewatering applications.

Figure 2.   Examples of vertical surface erosion control products.

Also included in the geosynthetic contributions to hydraulic performance is the very important application of surface erosion control. Three-dimensional product rolls can protect the soil against rainfall splash and runoff by keeping in place soil particles. Moreover, they can increase the shear resistance of the root system several times over. The synthetic structure of geosynthetics work quite well with a variety of natural or bio-material fills that can serve to encourage vegetative growth. The permanent geosynthetic erosion and revegetation materials then provide erosion control, and aid in vegetative growth, eventually becoming entangled with the vegetation to provide reinforcement to the root system and enhanced hydraulic shear resistance.

Finally, some geosynthetics can provide vertical flow in dewatering or targeted drainage applications. Prefabricated vertical drains (PVDs) are typically constructed of an accordion shaped core, or other channeled structure and wrapped in a geotextile filter. These products are used successfully to dewater and accelerate consolidation of wet or saturated soils. They have also been used successfully to drain perched pregnant solutions trapped in mining leach piles after chemical digestion. By piecing the ground, or leach pad, with special installation equipment, PVDs can be placed in specific locations for application success.

Cuspated core vertical drains are common in housing or industrial building construction to drain away subsurface waters from the foundation.

Geomat   Vegetated light geogrid   Pre-filled geomat

Figure 3. Examples of three-dimensional planar products provide surface erosion control (from ISO TR 128228-8).
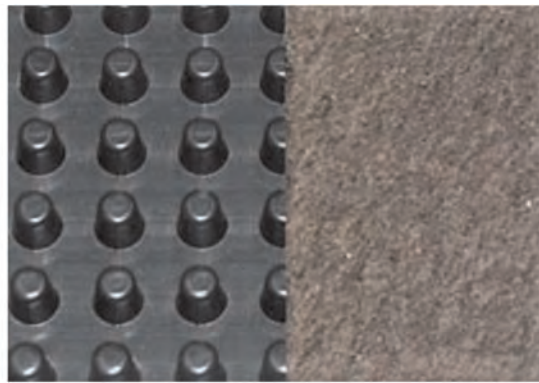
PVD   Wall-Drain

Figure 4. Example of prefabricated vertical drain (PVD (left) and cuspated core drain (right).

2 GEOSYNTHETIC PERFORMANCE MEASUREMENTS

The following sections will look at some of the very important geosynthetic hydraulic measurements specific to our industry and the contributions of resource standards and laboratory investigations.

2.1 Planar drainage

Throughout geosynthetic drainage product development, the evaluation of performance has been necessarily focused on flow capacity, resistance to short-term compression and collapse, characteristics of the filter, and long term behavior or the drainage system. Recently, key guidance documents have been standardized by the International Standards Organization (ISO) Technical Committeee (TC) 221 on geosynthetics that are relevant to geosynthetic drainage systems. They are as follows.

- SO/TR 18228-3, Design using geosynthetics — Part 3: Filtration
- ISO/DTR 18228-4, Design using geosynthetics — Part 4: Drainage

These documents provide great benefit to all those wanting a comprehensive summary of the specific parameters for using geosynthetic drains and their components (filters and cores). They each reference the relevant test procedures needed to characterize the hydraulic properties of geosynthetics. Of special importance is the measurement of planar flow properties outlined in two ISO standards,

- ISO 12958-1, Geotextiles and geotextile-related products — Determination of water flow capacity in their plane — Part 1: Index test
- ISO 12958-2, Geotextiles and geotextile-related products — Determination of water flow capacity in their plane — Part 2: Performance test

ASTM International has also standardized this measurement via ASTM D4716, *Standard Test Method for Determining the (In-plane) Flow Rate per Unit Width and Hydraulic Transmissivity of a Geosynthetic Using a Constant Head*. In all of these standards, the basic procedure involves the use of a flow box capable of holding a planar drainage sample under an applied normal compressive load. Hydraulic energy is established via an applied gradient by controlling the upstream water reservoir height relative to the downstream water height.
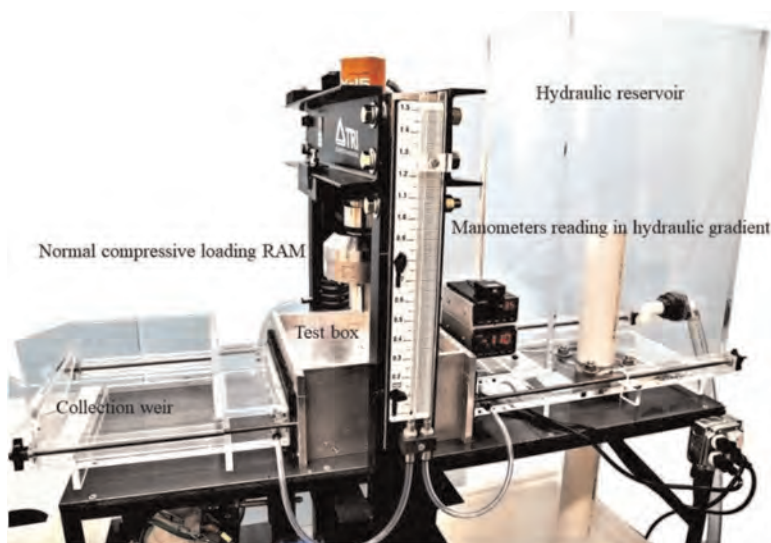
Figure 5.   Example of ISO 18228 and ASTM D4716 test apparatus.

The figure below shows a typical planar test apparatus.
The discharge capacity of the geosynthetic drain can be given in terms of:

- Specific flow rate = discharge per unit width in the geosynthetic drain, under a specified hydraulic gradient:

$$Q = q \quad \beta \tag{1}$$

Some users of flow tests desire to index the discharge rate per unit width to the applied hydraulic energy or hydraulic gradient at which flow is measured. In this case:
- Hydraulic transmissivity = discharge per unit width of the geocomposite and per unit of hydraulic gradient.

$$\theta = (q \quad \beta)/i \tag{2}$$

489

The concepts of transmissivity and flow capacity were developed specifically to avoid consideration of the thickness as it is often difficult to specifically define the thickness of a geosynthetic drain under load in application. Transmissivity is equal to flow rate only at a gradient of 1. Note also that the numerical value of transmissivity can be very different than the numerical value of the specific flow rate at small hydraulic gradients (e.g. at i = 0.1 transmissivity is 10 times the specific flow rate).

(a)

(b)

(c)

(d)
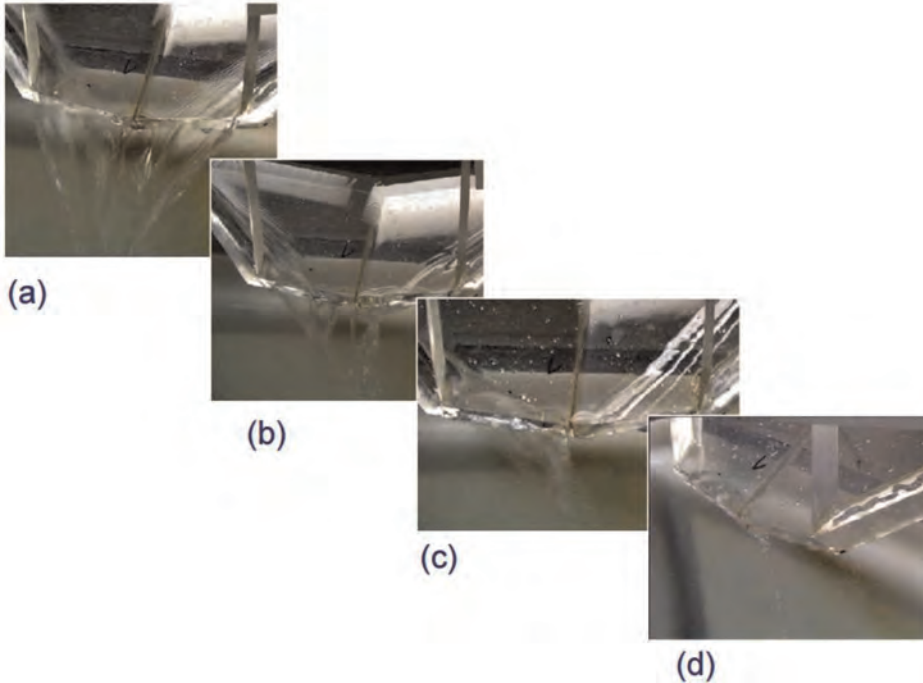
Figure 6. Example of time under load on discharge rate at (a) 1 hour, (b) 24 hours, (c) (48 hours), (d) 100 hours, for an 8.9 mm geocomposite under 172 kPa compressive stress and a gradient of 0.33.
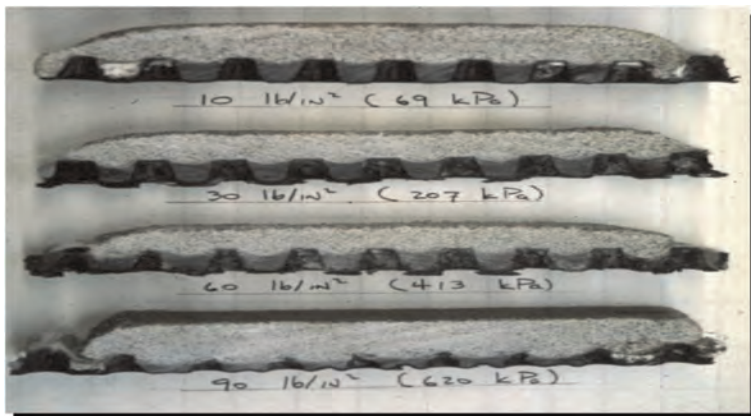
Figure 7. Example of filter geotextile intrusion under various compressive loads (courtesy of the Geosynthetic Institute).

It is well established that geosynthetic drains under load have a reduced flow capacity relative to the unloaded condition related to both the magnitude of compressive loading as well as associated changes in the three-dimensional drainage core structure. This change in structure is related to compression of the core and intrusion of the filter geotextile. Further, in addition to short-term response to load, or ductile deformation, additional change is time-dependent. The available long-term flow related to these phenomena and the reductions of flow related to chemical and biological clogging of the drain can be determined per ISO/DTR 18228-4 as follows.

$$Q_a = Q_L \ / \ (RF_{in} \ \cdot \ RF_{cr-Q} \ \cdot \ RF_{cc} \ \cdot \ RF_{bc} \ \cdot \ RF_L) \qquad (3)$$

where,

Q_a is available long-term flow rate for the geocomposite;

Q_L is the short-term flow rate obtained from laboratory tests with the appropriate boundary

conditions;

RF_{in} is the Reduction Factor for the intrusion of filter geotextiles into the draining core due to tensile creep of the gtx, occurring after the short-term test;

RF_{cr-Q} is the Reduction Factor for the compressive creep of the geocomposite;

RF_{cc} is the Reduction Factor for chemical clogging of the draining core;

RF_{bc} is the Reduction Factor for biological clogging of the draining core;

RF_L is the Reduction Factor for overall uncertainties on laboratory data and field conditions.

As the time-dependent resistance to vertical deformation or compression of planar geo-synthetic drains is paramount to the understanding of RF_{cr} and the related long term flow capacity, there have been several efforts to accelerate this measurement to provide confidence in drainage design and reduce the time necessary to realize this long term deformation. Conveniently, a summary of the most common procedures is included in ISO 18198.

Significantly, one accelerated procedure using a combination of the Stepped Isothermal Method (SIM) and subsequent thickness-dependent hydraulic discharge capacity testing is referencd in ISO 18198 and now standardized in ASTM D4716. In this test SIM is used to measure and document the time-dependent thickness reduction of the geosynthetic drain using ASTM D7361 and then subsequent design flow testing at a specific thickness associated with the anticipated service life instead at a specific load representing the intended product application is carried out. As shown in Figure 10, this testing requires a vertical displacement driven compression control mechanism with LVDTs and a feedback loop for thickness control. This assembly also requires hydraulic testing apparatus capable of affecting the desired thicknesses of the geosynthetic drainage core during flow testing.

Another feature of this testing is the possibility of incorporating site-specific conditions into the test via the use of anticipated in-situ soils and other geosynthetic products. As the site-specific materials are represented in the test, geotextile intrusion and compressive creep are modelled and may not need to be applied during the determination of long-term flow capacity, although this should be confirmed on a given drain and geotextile filter configuration. In addition, because the flow testing is short-term in nature, measurements of flow at different loading conditions through the service life of the geosynthetic drain may be visited and numerous specimens may be measured to provide greater confidence in developed measurements.

2.2 *Air as a permeant*

Another interesting development in the ongoing effort to make drainage capacity measurements easier and more accurate is the use of air as a permeant. The use of air as a permeant has already been well established and standardized in ASTM International in the geotextile

Key
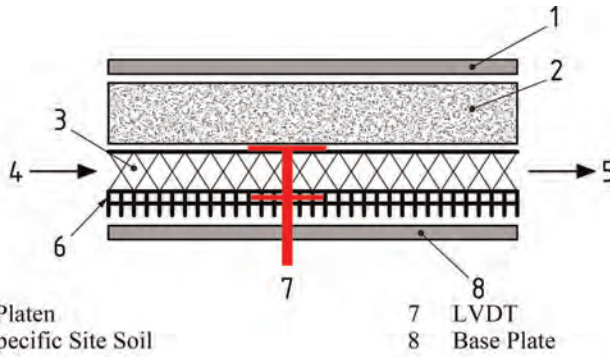
1 Loading Platen
2 Project Specific Site Soil
3 GCO Drain
4 Inflow
5 Outflow
6 GBR-P (textured)

7 LVDT
8 Base Plate

(a)   Example "profiled" flow test with thickness measuring LVDT

b) Flow test box with LVDT displacement measuring ports

(c) LVDT(s) housed in sleeve

d) Top disk to rest on top of drain

e) Final placement of top disk adjacent to drain

Figure 8.   Example thickness-dependent flow test configuration.

filtration measurements of permeability normal to the plane, or permittivity, and also opening size measurements to identify the opening size at which 95% of particles are retained. The advantages of air are many including the lack of need for temperature correction factors as air is much faster and quicker to condition and maintain than the temperature of water, and the lack of need to battle water quality issues as sediment, air and other contaminants can interfere with flow measurements. While yet to be standardized for planar flow measurements, the use of air in planar flow measurements is actively being investigated as an enhanced measurement approach.

The typical test apparatus is fitted with an upstream source of air that is introduced into the reservoir. Air flow rate is captured as a function of time and converted to hydraulic flow results using the same principles as permittivity tests, that is, using the mass density and viscosity of water and air.

2.3   *Erosion control*

Very important in the development of erosion control information and technology resources is the recently published ISO TR18228-8, Surface Erosion Control. This resource document
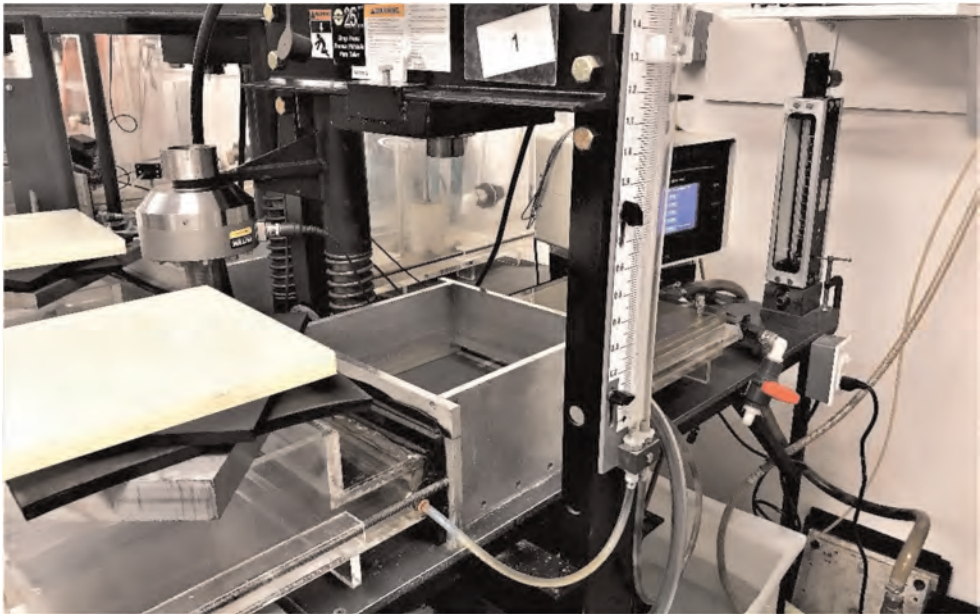
Figure 9.   Example hydraulic discharge capacity flow apparatus using air as a permeant.

provides a summary of relevant geosynthetic products and their erosion control measurements. Significantly, it also provides several tables of related reference data such as design factors related to topography, rainfall intensity and other relevant information.

Fundamental to the understanding of the performance of many of our planar geomeshes, turf reinforcement mats and similar products is performance testing. An erosion control product can shield the underlying soil from raindrop impact energy, yes, but we also want to provide for vegetative germination and growth, thus we need porosity and some level of openness. A product can also absorb and retain rainwater to hold it in place and gradually release it thereby prohibiting its damage to the soil, but we may also not want the product or the sol underneath it to become too saturated as it may become too heavy with water creating internal or even surface instability.

Observation of hundreds of large-scale performance tests lead to an understanding that erosion control products appear to fall into one of three general categories of field performance:

- Those that encourage infiltration as the primary mechanism to limit erosion;
- Those that block rainfall impact but rely on their anchor pattern/frequency to reduce erosion inducing runoff;
- Those that armor the slope against both rainfall impact and infiltration, leading to high percentages of runoff.

These competing needs are what is designed for in each product, and provide the performance as observed during testing. Erosion control products that cause excessive amounts of precipitation to infiltrate and remain in the slope rather than running off the slope may cause the soil to become supersaturated and unable to hold itself onto the slope. This causes a "mass wasting" phenomenon.

These large- scale performance phenomenon require large-scale tests to measure. Two tests referenced in ISO TR 18228-8 are the following.

1. ASTM D6459,Standard Test Method for Determination of Rolled Erosion Control Product (RECP) Performance in Protecting Hillslopes from Rainfall-Induced Erosion

493

2. ASTM D6460,Standard Test Method for Determination of Rolled Erosion Control Product (RECP) Performance in Protecting Earthen Channels from Stormwater-Induced Erosion

The slope erosion test is performed on one bare soil control and three replicate geosynthetic protected soil slopes at 3H:1V slope. Rainfall is simulated at target intensities of 50, 100 and 150 mm per hour, which are applied in sequence for 20 minutes each. Runoff from each slope is collected and soil loss is measured. From this data, an appropriate C-factor (for use in the RUSLE equation) can be calculated by comparing the geosynthetic protected soil loss to the soil loss of the bare soil control. Rain intensity, test duration and test soil variables may be investigated as desired.

(a) (b)

Figure 10. (a) The standard plot is a 3 to 1 slope with a down slope length of 12.2 m and a width of 2.3 m, and (b) calibrated rain delivery system.

For channel erosion the test is conducted in a rectangular flume with at least four sequential increasing flows applied for 30 minutes each (unvegetated conditions) or 60 minutes each (vegetated conditions). Unvegetated geosynthetic protected channel testing is typically performed in a 10% slope flume. Vegetated geosynthetic protected channel tests are typically performed in a 20% slope flume. The limiting or permissible shear stress is defined as the shear stress necessary to cause an average of 13 mm of cumulative soil loss over the entire subject test area.

There has been discussion in erosion standardization working groups about tilting bed test facilities. This test equipment has the ability to quickly change and test different slope angles. The tilting bed slope test configuration has been successfully used to isolate the surface dynamics from surface-depth slope stability issues, and thus has been shown in this limited context to segregate between surface-treatment technologies. These slope testing protocols often employ tilting beds that allow for the soil layer to drain from below. This prevents the soil layer from becoming saturated under heavy rainfall simulations. This also creates a soil condition that cannot exist in the real world. In addition, testing protocols using test slopes that are shorter and narrower may have index utility, while limiting the extent to which natural erosion mechanisms can develop, such as rills, rivulets and grooves.

Global erosion phenomenon, including infiltration and associated hydraulic loading, warrant the use of large – real world slope tests, such as ASTM D 6459, for field performance investigations.

While tilting bed test apparatus have utility for kinetic energy related studies, there are many times when the primary indicator of differences in the erosion control treatments is whether mass wasting occurs or not. For this reason, most large-scale users, like transportation related authorities, specify using real world slope tests.

In ASTM D6460 testing a rectangular or trapezoidal cross section channel may be used; however, a rectangular channel is recommended for consistency of construction and explicit computation of shear stress. A rectangular cross section must be 0.61 m minimum in width. The test channels are a minimum of 12.2 m in length.

Figure 11.   Large-scale channel erosion testing facility.

Test plots are constructed and then channel flow is initiated gradually (over about 5 minutes) into the channel and, using a velocity meter, the flow is monitored until it becomes steady. This flow is allowed to continue for 30 minutes (unvegetated) or 1 hour (vegetated). Velocity and water surface measurements are taken at all cross-sections during the last 10 minutes. With the flow stopped and without stepping into the tested channel, new measurements to top-of-soil are made to establish erosion caused by the chosen test flow. The process is repeated at somewhat higher shear/flow levels until all required data is
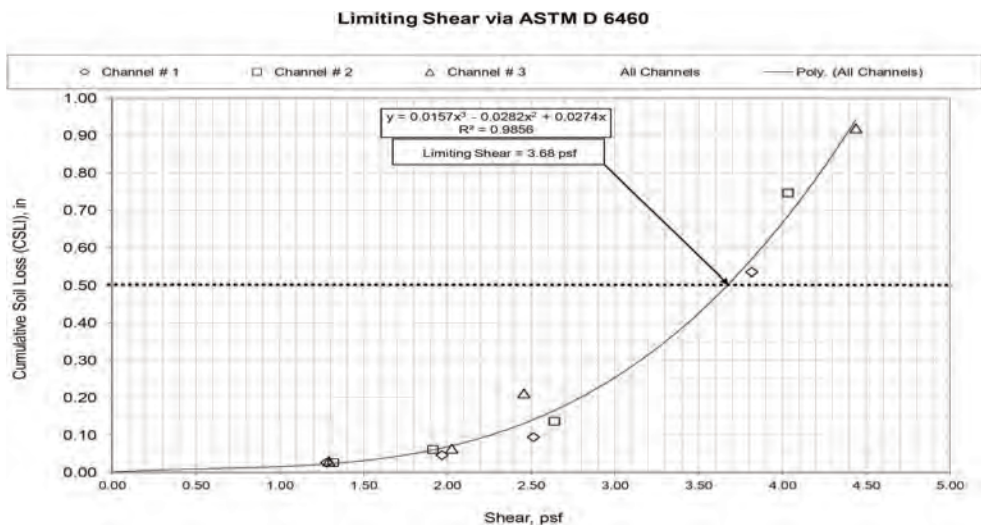
Figure 12.   Example large-scale channel erosion testing results.

collected. If a vegetative component is incorporated into the testing, quantification of the vegetative stand density is performed using a count box. The time-of-growth, type of seed, seed density (i.e. # seeds/sm), and other related info is documented. Channels are prepared identically to unvegetated channels and serve as the basis for the testing.

Test variables such as test vegetation used, growth time, test flow time and depth, etc. may be modified as desired to investigate specific site conditions.

In the figure above, the hydraulic shear results are plotted with an equation fit applied. From this the shear stress associated with a 0.5 inches or 13 mm of soil loss is determined as the limiting shear stress. This same measurement exercise can be performed on unvegetated, partially vegetated or fully vegetated channels with geosynhetic root reinforcement benefits demonstrated.

3 CONCLUSIONS

The geosynthetic industry has responded impressively with the development of measurement tools and standardized procedures and guides to propel and support the wonderful contributions that geosynthetics deliver to drainage and erosion control applications. It is important for industry participants to know of these documents and resources and to assist our expanding community of design engineers familiar, and unfamiliar, with geosynthetic design.

REFERENCES

ASTM D4716, Standard Test Method for Determining the (In-Plane) Flow Rate Per Unit Width and Hydraulic Transmissivity of a Geosynthetic Using a Constant Head

ASTM D7361, Standard Test Method for Accelerated Compressive Creep of Geosynthetic Materials Based on Time-Temperature Superposition Using the Stepped Isothermal Method

ISO 12958-1, Geotextiles and Geotextile-Related Products — Determination of Water Flow Capacity in their Plane. Part 1 – Index Test.

ISO 12958-2, Geotextiles and Geotextile-Related Products — Determination of Water Flow Capacity in their Plane. Part 2 – Performance Test.

ISO TR-18228-4, Design Using Geosynthetics — Part 4: Drainage

ISO/TR 18228-8, ISO TC 221/ WG 6, Design Using Geosynthetics: Part 8: – Surface Erosion Control

Moore, I.D. e Burch, G.J., (1986b), Physical Basis of the Length-Slope Factor in the Universal Soil Loss Equation. *In: Soil Science Society America Journal*, 50, 1294–1298. 48

Sprague, C.J. (2008), "Slope Erosion Testing – Identifying "Critical" Parameters", Conf. XXXIX, International Erosion Control Assoc., Orlando, FL, (Digital Proceedings).

Investigation and comparison of inlet port design strengths

S.H. Chew & J.M. Soh
National University of Singapore, Singapore

Y.C. Tan, H.M.A. Yim, J.W.A. Quek, D.J. Lim & S. Kee
Housing & Development Board, Singapore

ABSTRACT: Geotextile tube is a popular solution for dewatering applications. During the dewatering process, infill material is pumped into the geotextile tubes through the inlet port at high pressures, and thus significant amount of tension forces can be developed at the inlet port sleeve and connecting parts of the tube. Geotextile tearing could occur at these locations during high pressure pumping. Therefore, it is important to determine its resistance to tearing and the factors that affect its tearing strength. So far, only limited studies have been done on this aspect. Hence, a new tensile test setup was developed to simulate the application of tensile forces on the inlet port sleeve and surrounding geotextile material during slurry pumping. The setup consists of a housing to clamp a portion of the geotextile tube body, and a circular drum that connects to the inlet port sleeve. Strain gauges were installed on the critical locations on the geotextile test specimen both on body and inlet port sleeve. Several types of inlet port designs were tested, and the critical tearing strength of these inlet ports were analysed. Test results suggest that the seam design connecting the inlet sleeve and geotextile body is a key factor in deciding the critical tearing strength of an inlet port design.

1 INTRODUCTION

Geotextile tubes is a popular solution in dewatering applications (Lawson 2008). Infill material such as soft soil slurries and sludge material are pumped into the tube through the inlet port at high pressures and left to dewater (Figure 1). As a result of high-pressure pumping, significant amounts of tension could be developed on the inlet port sleeve and parts of the geotextile tube body. While the inlet port sleeve itself is usually made from high strength geotextile material, tensile force is exerted on the seam connection between the sleeve and geotextile body, and the area on the geotextile body around the inlet port during high pressure pumping. Hence, the inlet port becomes a possible area of failure (Figure 2). If
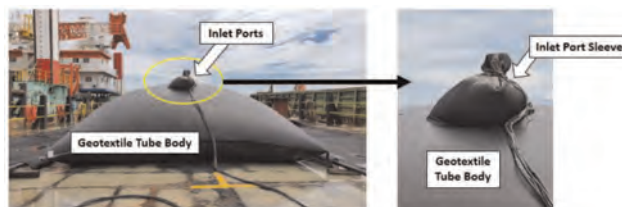
Figure 1. Geotextile tube being infilled on site.
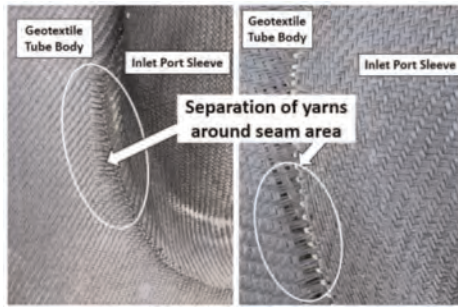
Figure 2. Separation of yarns around seam observed on-site due to tensions during pumping.

significant tearing occurs, the leakage (or piping) of infill material could result in environmental contamination and wastage of materials. The resistance of various geotextile tube components during high pressure pumping is not widely studied. Thus, a laboratory testing setup was designed and constructed to investigate the tearing capacity of inlet port designs, and the key components that contribute to the tearing strength.

2 METHODOLOGY

2.1 *Test specimen and material properties*

The sample tested is a geotextile using high-tenacity polypropylene multifilament yarns, which are woven into a stable network such that the yarns retain their relative position. This is one of the high strength woven geotextile commonly used in the construction of geotextile tubes. This type of woven geotextile was used for both the body of the geotextile tube and the sleeve of the inlet port. A picture of the geotextile material is shown in Figure 3(a). There are 3 main components of the inlet port specimen: (1) Inlet port sleeve; (2) Geotextile tube body; and (3) Seam design connecting components 1 and 2. The properties of the geotextile material used to make the test specimen, expressed in Machine Direction (MD) and Cross Machine Direction (CD), are listed in Table 1. The inlet port sleeve used geotextile A and had lower strength, but higher flexibility, which was required for infilling operations. The geotextile tube body was made from geotextile B, which had higher strength. The design of inlet port sleeve and geotextile tube body can affect the tearing strength. Two different inlet port seam designs (i.e. J-Seam and Butterfly Seam) as illustrated in Figure 3(b) were tested. In total, 3 different configurations were tested to investigate the effect geotextile grades and seam designs on the resistance of the inlet port to tearing. The configurations of the specimen tested in this paper are presented in Table 2.
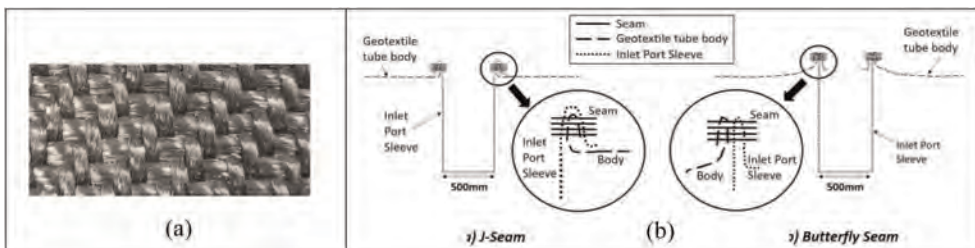
Figure 3. (a) Geotextile material; and (b) Seam designs.

Table 1. Geotextile properties.

Property	Units	Geotextile A (For Sleeve)	Geotextile B (For Body of Geotextile Tube)	Standard
Wide Width Tensile Strength (MD/CD)	kN/ m	130/130	200/200	ISO 10319
Strain at Break (MD/CD)	%	10/10	12/10	ISO 10319

Table 2. Test specimen configurations.

Test ID	Seam Design	Inlet Port Sleeve	Geotextile Tube Body	Inlet Port Diameter (mm)
T1	J-Seam	Geotextile A	Geotextile A	500
T2		Geotextile A	Geotextile B	
T3	Butterfly Seam	Geotextile A	Geotextile B	

2.2 Testing setup and procedure

A test apparatus capable of testing a full-scale inlet port was designed and constructed in the Geotechnical Laboratory at the National University of Singapore (NUS) (Eng & Chew 2014), shown in Figure 4. The test specimen was fixed at 2 points onto the test apparatus: (1) The geotextile tube body was fixed to a 1000 mm diameter circular steel frame using clamps, and (2) The 500 mm diameter inlet port sleeve was fixed around a hanging steel drum. A hydraulic piston, connected to the extension rod, was pushed downwards, exerting a downward force onto the hanging steel drum; thus, exerting a tensile force onto the sleeve of the inlet port specimen. As the maximum travel distance of the piston was 300 mm, multiple pushes may be done (with additions of extension rods) before the tearing conditions were observed.

While previous tests had focused on the ultimate seam strength of the inlet port (Eng & Chew 2014), this parameter may not be the most critical condition in the context of on-site
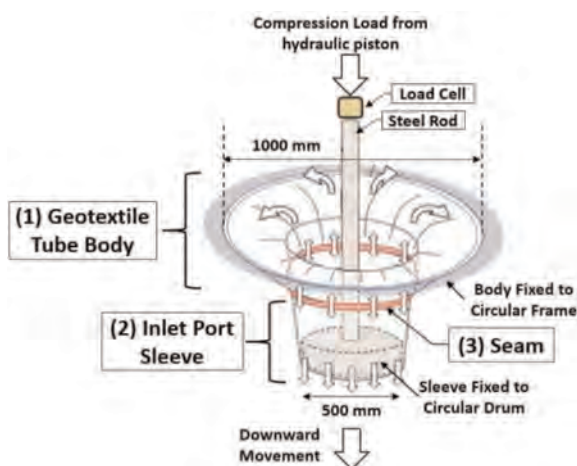
Figure 4. Illustration of inlet port strength test apparatus in NUS (adapted from Eng & Chew 2014).
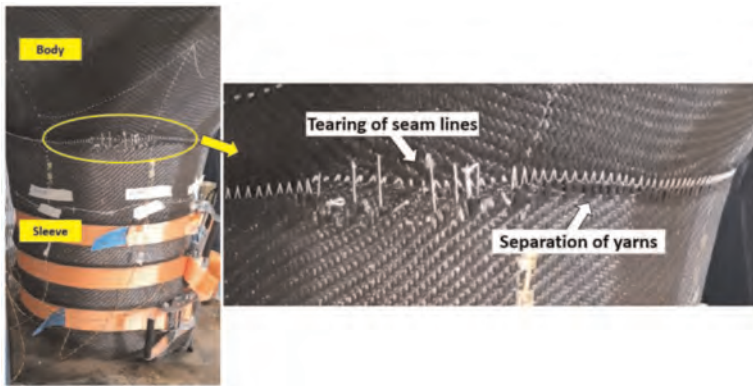
Figure 5.   Critical tearing during inlet port loading test.
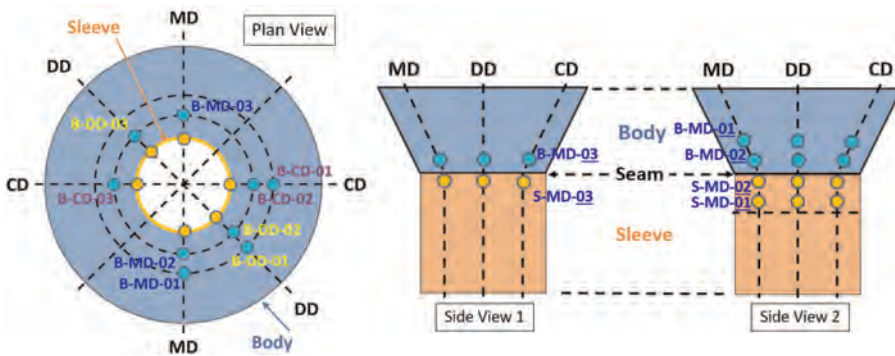
Figure 6.   Strain gauge layout on inlet port specimen when loaded onto test apparatus.

pumping of fine infill material, as any slight tear that occurs before total failure may result in leakage of infill material. Thus, in this paper the term "Critical Tearing Strength" (in kN/m) is introduced, and is defined as the force at which the following conditions were observed during the test: (1) Tearing of seam lines; and (2) Apparent separation of geotextile yarns around the seam area that will result in leakage of infill materials during pumping. An example of the conditions observed when critical tearing strength was reached is shown in Figure 5.

The test specimens were extensively instrumented with 18 strain gauges, using the strain gauge method proposed by Chew *et al.* (2000), with 9 gauges each on both the geotextile of the sleeve and body. Strain gauges were installed in the Machine Direction (MD), Cross Machine Direction (CD) and the Diagonal Direction (DD). Figure 6 shows the layout of strain gauges installed on the body and sleeve. A load cell was also attached to monitor the load applied on the geotextile specimen.

3   RESULTS AND ANALYSIS

Figures 7, 8 and 9 shows the load cell and geotextile strain gauge results for Tests T1, T2 and T3 respectively during the inlet port loading test. The readings from the strain gauges were converted to tensile force (kN/m) using the tensile force-strain relationship of the geotextiles
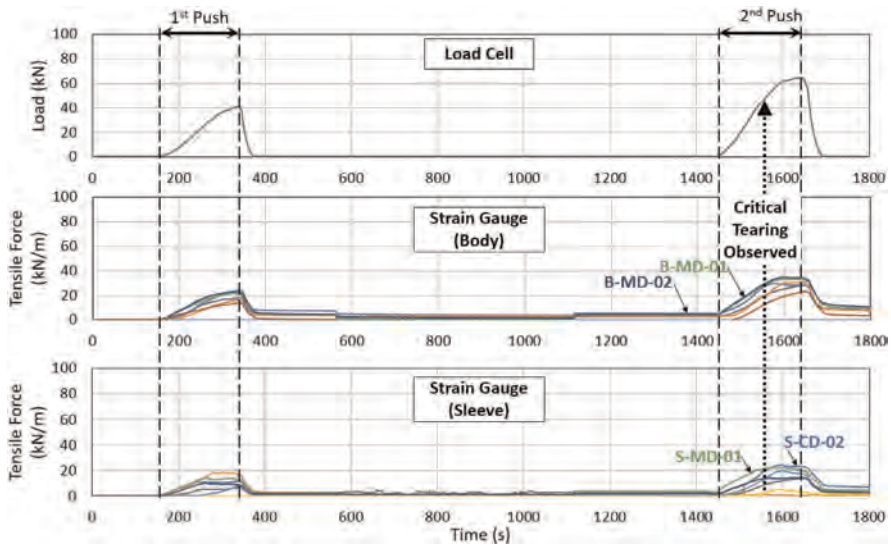
Figure 7. Results of inlet port test T1.
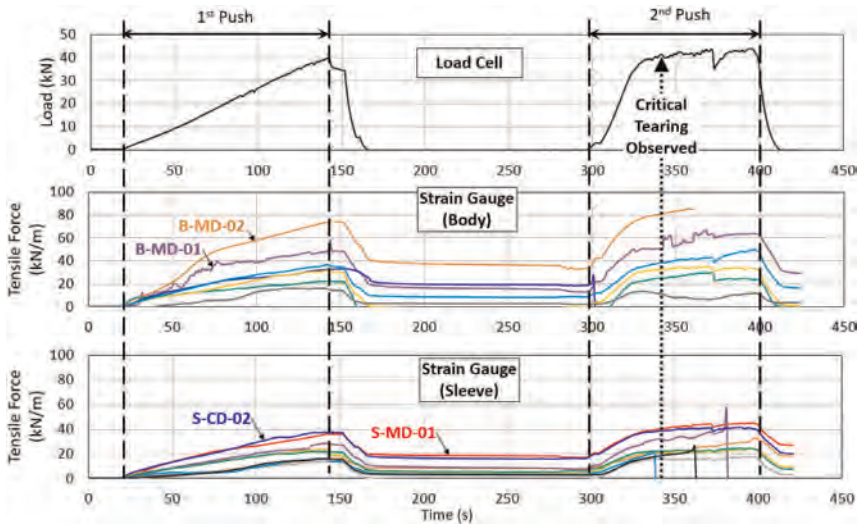
Figure 8. Results of inlet port test T2.

calibrated prior to the test. Key results from strain gauges were highlighted. Finally, the point where critical tearing was observed was also marked on the graphs. When downward pushing load was applied to the geotextile via the hydraulic piston, there was a corresponding increase in the strain gauge readings at various locations of the geotextile. This suggested that the loading force from the hydraulic piston was transferred to the inlet port specimen effectively. All three test results showed good agreement between the readings from the load cell and strain gauges.

For Test T1, "critical tearing" condition was observed when vertical load reached 47 kN. The pushing continued until a vertical load of about 62 kN. On the geotextile body, the
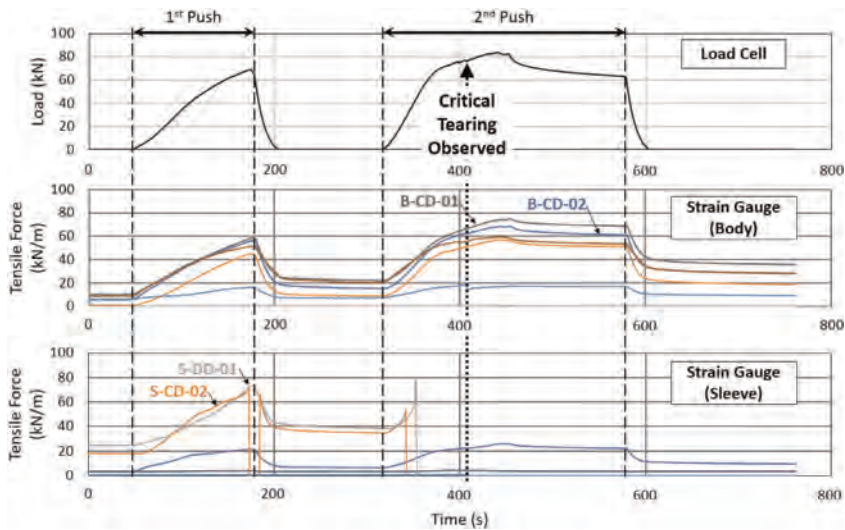
Figure 9. Results of inlet port test T3.

largest tension developed at the "critical tearing" stage was in the MD direction at 36 kN/m (28% of ultimate strength of the geotextile material). Strain gauges in other directions on the body registered maximum tensions between 25–35 kN/m at this "critical tearing" stage. On the sleeve portion, the strain gauges registered tensions between 2–22 kN/m (17% of ultimate strength of the geotextile material) at this "critical tearing" stage, with the largest tensions developing along both CD and MD directions.

"Critical tearing" conditions were observed at a vertical load of 43 kN for Test T2. At the point of "critical tearing", the largest tensile forces developed on the body was observed at MD direction at 80 kN/m (40% of ultimate strength of the geotextile material), and at the sleeve was in the CD and MD direction at around 42 kN/m (32% of ultimate strength of the geotextile material). Compared to Test T1, the range of tensions registered at "critical tearing" in Test T2 was much larger than that in Test T1, especially on the body geotextile with a range of 15–85 kN/m.

Finally, the "critical tearing" conditions of Test T3 were observed at a vertical load of 82 kN. On the geotextile body, the largest tension developed at this "critical tearing" stage was in MD direction at 64 kN/m (32% of ultimate strength of the geotextile material) and around 70 kN/m (54% of ultimate strength of the geotextile material) along CD and DD direction on the inlet port sleeve. The range of tensions observed on the geotextile body at "critical tearing" stage was relatively small, between 55–75 kN/m. Table 3 shows a summary of the test results on the 3 inlet port tests.

Table 3. Summary of inlet port loading test results.

Test ID	Seam Design	Geotextile Tube Body	Inlet Port Sleeve	Tearing force observed for 500mm Diameter Specimen (kN)	Critical Tearing Strength (kN/m)*
T1	J-Seam	A	A	47	30.0
T2		B	A	43	27.5
T3	Butterfly Seam	B	A	78	50.0

*Based on the circumference of the 500 mm diameter inlet port

Comparing the results of Test T1 and T2, "critical tearing strength" of Test T1 was slightly higher than Test T2, likely due to its more uniform distribution of tension as compared to Test T2. However, overall "critical tearing strengths" of both Test T1 and T2 were relatively close. The results from these 2 tests suggested that varying sleeve and body geotextile grade configurations in this manner had minimal effect on the "critical tearing strength" of the inlet port specimen.

On the other hand, comparing the results of Test T1 & T2 (J-Seam) to Test T3 (Butterfly Seam), it could be observed that Test T3 obviously had a much larger "critical tearing strength". This was likely due to the difference in the seam design. Furthermore, it was also observed in all three tests that tearing of the geotextile occurred only at the seam area, and not on the greater geotextile material elsewhere. This illustrated that this tearing was very localized, or at least at the "critical tearing stage", did not propagate to the whole geotextile piece.

4 CONCLUSION

Based on the inlet port tests conducted and analysed in this paper, key findings were:

1. The grade of geotextile material used for the inlet port sleeve and geotextile tube body as configured in the manner shown in this paper has minimal effect on the "critical tearing strength" of the inlet port.
2. The seam design had a more significant effect on the "critical tearing strength" of the inlet port.
3. The seam is the most critical component of the inlet port design. The failure of the inlet port specimen was limited only at the seam, and no failure of the geotextile material itself was observed. The critical tearing at the seams also did not propagate to other parts of the geotextile piece.

It should be noted that the result presented here are for the specific geotextile material tested.

ACKNOWLEDGEMENT

REFERENCES

Chew S.H., Wong W.K., Ng C.C., Tan S.A., and Karunaratne G.P. (2000). *Strain Gauging Geotextile Using External Gauge Attachment Methods*, ASTM STP 1379, USA.

Eng, Z.X. & Chew, S.H. (2014) A Laboratory Full-Scale Tensile Test of Geotextile Tube Inlet Port. *The 10th International Conference on Geosynthetics*, 2014.

Lawson, C.R. (2008) Geotextile Containment for Hydraulic and Environmental Engineering. *Geosynthetics International* 15, 2008: 382–427.

PVC geomembrane seams: Influence of the testing speed on peel and shear test results

M. Barroso
Laboratório Nacional de Engenharia Civil, Lisbon, Portugal

M.G. Lopes
Instituto Superior de Engenharia de Lisboa, Lisbon, Portugal

ABSTRACT: The PVC geomembranes are the most commonly used in dams. The success of geomembranes as barrier depends on field seams quality. Seams have to be evaluated in terms of continuity and mechanical strength, the latter being assessed by peel and shear tests. These tests are generally carried out according to the ASTM D 6392, which, for PVC geomembranes, recommends a testing speed of 50 mm/min, for peel test, and 500 mm/min, for shear test. However, in field, sometimes it is not possible to attain the testing speed suggested for shear test. This raises questions about the acceptance of seams. To address this issue, two thermally bonded PVC geomembrane seams were tested to peel and shear strength at testing speeds ranging from 50 to 500 mm/min. The results showed that shear and peel strengths tend to increase with the testing speed.

1   INTRODUCTION

Geomembranes have been applied to dams since the 1950s. In the first applications, a wide variety of geomembranes were used. Then, based on experience acquired in early applications, as well as developments in research, testing and manufacturing, the best performing geomembranes have progressively become more popular (Cazzuffi *et al.* 2010). Currently, polyvinyl chloride (PVC) geomembranes are the most commonly used in dams (ICOLD 2010).

The performance of geomembranes as barriers in dams depends on field seams quality. PVC geomembrane field seams are typically made by thermal fusion (hot air or hot wedge). For that it is necessary to melt the polymer at the sheet surface using a heat source. The heat can be transferred to the sheets to be welded from hot air or a hot wedge. A hot air welder uses an air blower that blows heated air from an electrical element between the two sheets to be bonded by melting an interface strip. A hot wedge welder generates the heat energy necessary to melt the sheets at the interface by electrical elements placed directly between two sheets. Pressure is applied to the top and/or bottom sheets of the geomembrane, forcing together the two surfaces to form a continuous bond (Stark *et al.* 2004).

Dual-track and single-track seams can be made. Both types of seams allow destructive and non-destructive testing to assess seams quality in terms of continuity and mechanical strength.

Mechanical strength is typically evaluated based on peel and shear tests. For PVC geomembranes thicker than 1.5 mm, these tests are generally carried out according to ASTM D 6392 standard, which recommends a testing speed of 50 mm/min, for peel test, and 500 mm/min, for shear test. However, in field, sometimes it is not possible to attain the testing speed

suggested for shear test, mainly due to limitations of the testing machines routinely used. This raises questions about the acceptance of seams.

To address this issue, two thermal fusion seams were tested to peel and shear strength at testing speeds ranging from 50 to 550 mm/min, based on test procedure described in the ASTM 6392 standard.

The locus-of-break codes of the seams, according the same ASTM standard, were also addressed in order to discuss its usefulness within the acceptance criteria for PVC geomembranes.

2 EXPERMENTAL WORK

2.1 *Materials*

Two commercially available PVC geomembranes were used in this study, hereafter referred to as geomembrane A (1.5 mm thick) and geomembrane B (2.0 mm thick). Their main properties are summarized in Table 1, according to Technical Data Sheets provided by the supplier.

Table 1. Main geomembranes properties based on technical data sheets.

Property	Geomembrane A	Geomembrane B
Color (upper /down side)	orange/black	orange/black
Thickness (EN 1849-2)(mm)	1.5 (-5/+10%)	2.0 (-5/+10%)
Mass per unit area (EN 1849-2) (g/m^2)	2055 (-5/+10%)	2740 (-5/+10%)
Tensile strength at break (EN ISO 527-1 and 3, specimen type 5, 100mm/min) (kN/m^2)	$\geq 1.5\times10^4$	$\geq 1.5\times10^4$
Elongation at break (EN ISO 527-1 and 3, specimen type 5, 100 mm/min) (%)	≥ 250	≥ 250
Tear resistance (ISO 34, method B, 500mm/min) (kN/m)	≥ 45	≥ 45
Puncture resistance (EN ISO 12236) (kN)	2 ($\pm$0.25)	2.3 ($\pm$0.25)
Foldability at low temperature (EN 495-5)	Not failure at -25ºC	Not failure at -25ºC

Dual-track seam samples, welded by hot air, were made from geomembranes A and B. From each seam sample, specimens were cut such that the seams were perpendicular to the longer dimension of the strip sample. Specimens were die cut using a 25 mm wide by 150 mm long die. (Figure 1).
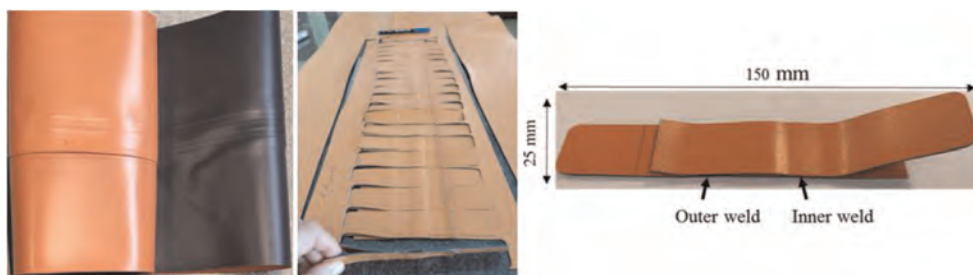
Figure 1. Dual-track geomembrane seam sample and seam specimen.

2.2 Testing procedure

Tests were carried out based on the ASTM D 6392, but at different testing speeds of besides the one indicated in this standard, 50 mm/min, for peel test, and 500 mm/min, for shear test.

The ASTM D 6392 standard was used rather than ASTM D 7408 since the latter covers just PVC geomembranes in thickness of 0.25 through 1.52 mm.

Testing speeds used were as follows: 50, 100, 150, 200, 250, 300, 350, 400, 450, 500 and 550 mm/min.

Although on ASTM standard recommends to test five specimens to peel and five specimens to shear, in this study, for each testing speed, twenty specimens were tested to shear and ten specimens were tested to peel. A smaller number of specimens were tested to peel because the length of the sample did not allow to cut a larger number of specimens.

Specimens were pulled out as shown in Figure 2, for peel and shear test, respectively. In peel test, inner and outer welds were tested from outside towards the air channel.
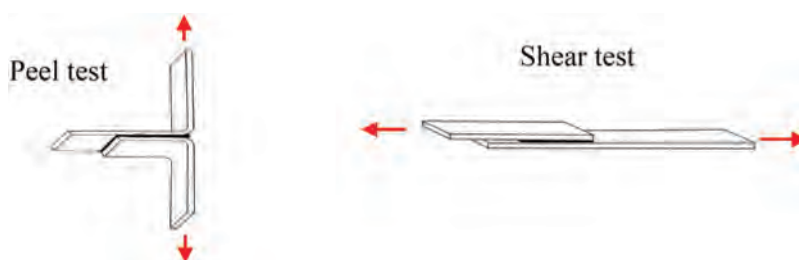
Figure 2.   Scheme of the peel and shear test.

In total, 880 tests were carried out: 440 peel (10 specimens×11 testing speeds×2 welds×2 geomembranes) and 440 shear tests (20 specimens×11 testing speeds×2 geomembranes).

Minimum values of peel strength and shear strength of 2.6 kN/m and 20kN/m, respectively, are typically required for field seams of PVC geomembranes up to 1.5 mm thick (FGI 2017). For thicker geomembranes, to the best of the authors' knowledge, there are no general acceptance criteria.

In addition to peel and shear strengths, locus-of-break codes, as per their description in ASTM D 6392 (Figure 3), were recorded. Typically, AD and AD BRK break > 25% codes are unacceptable, in peel and shear modes.
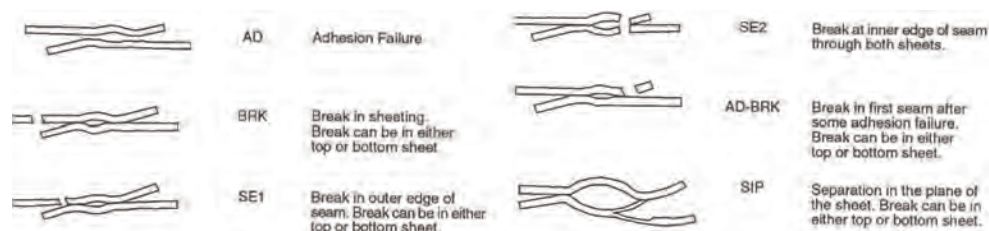
Figure 3.   Locus-of-break codes for seam strength in shear and peel modes (ASTM D 6392).

3 RESULTS AND DISCUSSION

3.1 *Influence of the testing speed on shear strength*

Figures 4 and 5 present the results of shear strength as function of testing speed, for geomembranes A and B. The shear strength values correspond to the average of the 20 test specimens tested, per each testing speed.

Graphs contain error bars corresponding to the standard error. The standard error value was calculated from the standard deviation expanded to a confidence level of 95%, using the t-Student distribution. In the discussion presented below, it is assumed that differences in tests results are only significant when they are higher than the standard errors associated with the measurements.

Results depicted in Figures 4 and 5 show that shear strength tends to increase as testing speed increases from 50 to 550 mm/min. The increase was 3.2 kN/m, for geomembrane A, and 3.3 kN/m, for geomembrane B.

Results obtained in this study are consistent with the results reported by Lopes & Barroso (2022). These authors tested a PVC geomembrane seam (2.5 mm thick) at testing speeds of
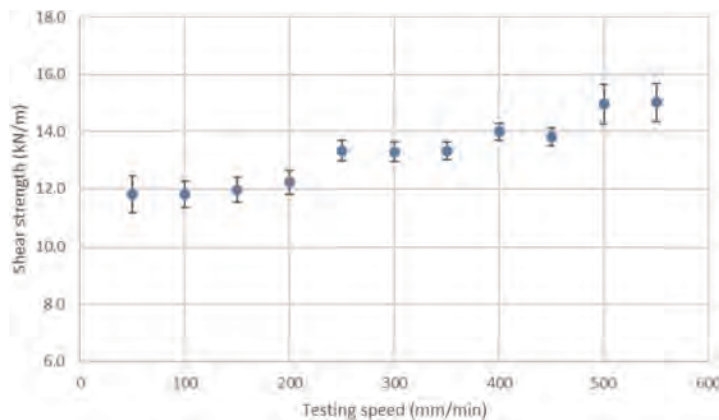
Figure 4.   Geomembrane A (1.5 mm): Effect of testing speed on seam shear strength.
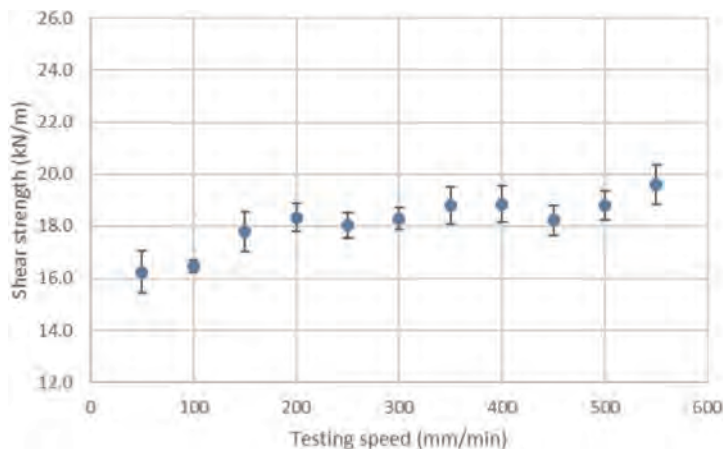
Figure 5.   Geomembrane B (2.0 mm): Effect of testing speed on seam shear strength.

100 mm/min and 500 mm/min. They tested 40 specimens, 20 at a testing speed of 100 mm/min and 20 at a testing speed of 500 mm/min, using a constant machine cross head speed. They found that shear strength was, approximately, 3.0 kN/m higher for testing speeds of 500 mm/min.

For geomembrane A, shear strength of dual-track seam ranged from 11.8 kN/m and 15.0 kN/m. These values are significantly lower than the minimum of 20.0 kN/m suggested on acceptance criteria by FGI (2017), raising questions about the seam quality.

For geomembrane B, shear strength ranged from 16.3 and 19.6 kN/m. These values are not compared with acceptance criteria proposed by FGI (2017), as they include only geomembranes up to 1.5 mm thick.

3.2 Influence of the testing speed on peel strength

Regarding peel strength, Figures 6 and 7 present the effect of testing speed obtained for the seams of geomembranes A and B, respectively. The peel strength values correspond to the average of the 10 test specimens tested, per each testing speed. As for shear strength, graphs also include the error bars corresponding to the standard error.

Peel strength shows a slight increase with the increase of the testing speed from 50 to 550 mm/min, for geomembranes A and B. This happens for both welds (inner and outer).

Geomembrane A shows systematically higher peel strength in the outer weld than in inner weld. This trend does not occur for geomembrane B, inner and outer welds presented similar strengths.
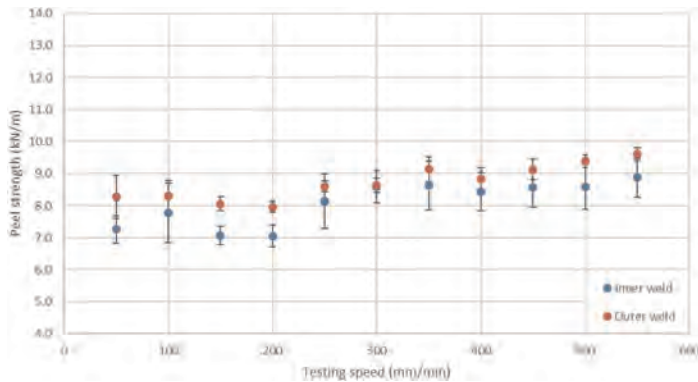
Figure 6.   Geomembrane A (1.5 mm): Effect of testing speed on seam peel strength.
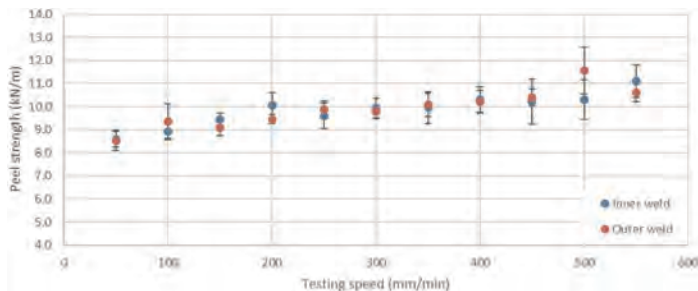
Figure 7.   Geomembrane B (2.0 mm): Effect of testing speed on peel shear strength.

Taking into account the standard error estimated, results obtained suggest that testing speed has a small influence on peel strength.

For geomembrane A, results obtained for peel strength of dual-track seam ranged from 7.1 kN/m and 8.9 kN/m, for inner weld, and ranged from 8.0 kN/m and 9.6 kN/m, for outer weld. These values are significantly higher than the minimum of 2.6 kN/m suggested on acceptance criteria of FGI (2017), which raises questions about the suitability of the value required as a minimum.

For geomembrane B, peel strength ranged from 8.6 kN/m and 11.1 kN/m, for inner weld, and ranged from 8.5 kN/m and 11.6 kN/m, for outer weld. Minimum values for geomembranes thicker than 1.5 mm are not included in criteria by FGI (2017).

3.3 *Locus-of-break codes for the peel and shear modes*

Locus-of-break codes for the peel (inner and outer welds) and shear modes as per their description in ASTM D 6392 (see Figure 3), were recorded for each specimens.

Table 2 summarizes the results obtained in peel test. In shear test, all specimens exhibited SE break. This means that the 440 tested specimens exhibited SE break.

As can be seen in Table 2, most of the breaks were type SE (break in outer or in inner edge of the seam). A large number of AD breaks were also obtained. Regarding the SIP breaks, it was found that the separation occurred at the interface between the two layers that comprise the geomembrane, distinguished by different colors (orange and black).

Table 2. Locus-of-break codes for seam strength peel mode (based on ASTM D 6392).

Locus-of-break codes	Geomembrane A*		Geomembrane B*	
	inner weld	outer weld	inner weld	outer weld
AD	34	–	51	11
BRK	–	–	–	–
SE1	73	107	54	80
SE2	–	–	–	–
AD-BRK	–	–	–	–
SIP	3	–	5	–

* For some specimens it was impossible to fully grip them across its width. For geomembrane A, 217 of 220 specimens were tested; for geomembrane B, 201 of 220 specimens were tested.

The usefulness of break type analysis for PVC geomembranes has been questioned by several authors. For example, Rohe (2011) refer that an important difference between PVC and high density polyethylene (HDPE) seam testing is that failure does not have to occur in the PVC sheet on either side of the seam (FTB). FTB is the requirement that the bond of the seam is stronger than the parent film and the film itself fails before the seam fails. This requirement applies to HDPE films because they have such a small window of functional elongation. When the HDPE material only elongates 50% before it breaks, it is very important that the seam never comes apart. PVC geomembrane has a completely different molecular structure, which gives it excellent elongation properties. While the PVC material does thin out as it is elongated, it does not exhibit any yield point typical with polyethylene. At 200% elongation the 1.0 mm PVC geomembrane did not exhibit any failures in peel or shear mode. PVC only requires that the shear and peel strengths exceed a minimum specified value.

Results obtained in this study tend to confirm that the type of rupture does not provide additional useful information about the quality of seams. Thus, its usefulness raises some doubts. However, due to the limited number of PVC geomembranes tested, more research is necessary to confirm this judgment.

4 CONCLUSIONS

In this work, the influence of testing speed on peel and shear strength of PVC geomembrane seams was studied. This issue is important because, in field, it is not always possible to carry out these tests at the standard testing speed, raising questions on their acceptance.

The results showed that shear and peel strengths tend to increase with the testing speed. However, the increase of testing speed has higher impact on shear strength than on peel strength. More research seems to be necessary to confirm this trend.

REFERENCES

ASTM D 6392. Standard Test Method for Determining the Integrity of Nonreinforced Geomembrane Seams Produced Using Thermo-Fusion Methods, *American Society for Testing and Materials*, West Conshohocken, Pennsylvania, USA.

Cazzuffi, D.A., Giroud, J.P., Scuero, A. & Vaschetti, G. 2010. Geosynthetic Barriers Systems for Dams. *9th International Conference on Geosythetics*, Guarujá, Brazil, 23-27 may 2010, pp. 115–163.

FGI (Fabricated Geomembrane Institute) 2017. *PVC Geomembrane Material Specification 1117*, University of Illinois, Urbana, IL.

ICOLD 2010. Geomembrane Sealing Systems for Dams. *Bulletin 135 of the International Commission on Large Dams*, Paris, France.

Lopes, M.G. & Barroso, M. 2022. PVC Geomembranes in Dams: Influence of Test Temperature on Seams Peel and Shear Strength. *7th European Geosynthetics Conference*, EuroGeo7, Warsaw, Poland, 4-7 september2022, pp. 795–802.

Rohe, D.S. 2011. *PVC Geomembrane Research Negates Film Tearing Bond Requirement*. Geo-Frontiers Congress 2011, March 13-16 Dallas, U.S.

Sanfona, P.; Barroso, M. & Fontul, S. 2019. Influência da Temperatura no Controlo Das Soldaduras de Geomembranas de PVC. *Revista Geotecnia No 147*, Novembro 2019; pp. 3–13; http://doi.org/10.24849/j. geot.2019.147.01 (in Portuguese).

Stark, T. D., Choi, H. & Thomas, R. W. 2004. Low Temperature Air Channel Testing of Thermally Bonded PVC Seams. *Geosynthetics International*, 11, No. 6, 481–490.

Experiments on the cyclic shear behavior of staggered assembly of soilbags

F. Jia
State Key Laboratory of Simulation and Regulation of Water Cycle in River Basin, China Institute of Water Resources and Hydropower Research, Beijing, China

S. Chen
China Water Resources Beifang Investigation, Design and Research Co. Ltd, Tianjin, China

S.H. Liu
College of Water Conservancy and Hydropower Engineering, Hohai University, Nanjing, China

ABSTRACT: A series of large-scale direct shear tests and cyclic shear tests were conducted on the staggered stacking soilbags. The influences of the number of cyclic shears, vertical stress, and amplitude of shear displacement during the cyclic shearing process on the dynamic deformation characteristics and shear strength of the staggered stacked geotechnical bags were explored. The results show that the shear failure of the interface between the soilbags before and after the cyclic shear basically conforms to the Mohr-Coulomb failure criterion. Under low vertical stress condition, the dynamic parameters of the interface between the soilbags change slightly as the number of cycles increases. As the vertical stress increases, the dynamic shear modulus of the interface between the soilbags increases, while the damping ratio remains unchanged. As the amplitude of horizontal shear displacement increases, the damping ratio of the interface between soilbags gradually goes up, and the dynamic shear modulus decreases. After the cyclic shear test, the increase in the shear strength of the interface between the soilbags increases with the rise of the vertical stress.

1 GENERAL INSTRUCTIONS

Soilbag is a kind of reinforced soil material widely used in building foundation (Matsuoka & Liu 2003, 2006), highway subgrade (Liu 2017), embankment (Martinelli *et al*. 2011), channel (Li *et al*. 2014), slope (Huang *et al*. 2008; Liu *et al*. 2015), retaining wall (Liu *et al*. 2018a, 2018b, 2020; Wang *et al*. 2015) and other projects. It has the characteristics of high compressive strength, local materials, energy conservation, environmental protection, economy and practicality. As a flexible foundation reinforcement material, soilbags not only have high compressive strength, but also have significant seismic isolation effect (Jia *et al*. 2020; Liu *et al*. 2014, 2015; Wang *et al*. 2014). In order to improve the overall stability of soilbag assemblies, staggered stacking is usually used in engineering field. Many scholars have studied the shear characteristics of the interface between layers of soilbags under static condition: Liu *et al*. (2016) conducted direct shear tests of soilbags with four different arrangements using a large indoor direct shear apparatus, and found that the arrangement of horizontal and vertical interlacing can significantly improve the equivalent friction coefficient between layers of soilbags. Fan *et al*. (2020) studied the interlayer friction characteristics of vertically staggered soilbags under different vertical loads through a series of direct shear tests.

The soilbags structure not only bears permanent loads, but also may be subjected to seismic and traffic loads. Therefore, the dynamic characteristics of soilbags have gradually attracted the attention of the academic community. In order to study the damping effect of soilbags, Wang *et al.* (2011, 2019) carried out a series of shaking table tests on soilbags and their materials by using electric shaking table tests, explored the damping effect of soilbags under different input frequencies and different vibration accelerations. They found that the greater the frequency and acceleration, the better the damping effect of soilbags. And this mechanism of soilbag is also researched by using discrete element method. Li *et al.* (2015) carried out a series of vertical stacked soilbag cyclic shear tests using a large cyclic shear tester to study the impact of different bag filling materials on the damping and energy dissipation effect of soilbags, and found that the particle size and grading had little impact on the damping and energy dissipation effect of soilbags. However, the current research on the dynamic characteristics of soilbags mainly focuses on the vertical layered soilbags, which cannot reflect the stacking situation of soilbags in actual projects. Therefore, it is important to study the dynamic characteristics of staggered soilbags and the interlaminar shear strength characteristics before and after cyclic loading to explore the seismic isolation effect of soilbags.

In this paper, a series of cyclic shear tests were carried out on staggered stacked soilbags by using a large cyclic shear system to explore the effects of different vertical stresses, different shear displacements and other factors on the cyclic shear characteristics of the interface between staggered stacked soilbags. The direct shear test was conducted immediately after the completion of the cyclic shear test to obtain the variation law of the interlaminar shear strength of staggered stacked soilbags before and after cyclic shear. It is expected to provide reference for the design of soilbag foundation, retaining wall and other projects.

2 TEST APPARATUS AND TEST MATERIALS

2.2 *Test apparatus*

The instrument used in the test is a large cyclic shear test system developed by Hohai University. The test system is mainly composed of three parts: loading system, measurement system and acquisition system, as shown in Figure 1. The horizontal loading system is composed of screws and flexible chains driven by motors on both sides, and the motor provides a horizontal movement rate of 2mm/min. The vertical loading system applies the vertical load by placing a certain number of weights on the loading plate. The mass of each weight is 50 kg. The measuring system consists of LTR-1 tension-compression sensor installed on the horizontal loading system and DTH-A-100 displacement sensor installed on the loading plate. The acquisition system is the UCAM-60B static data acquisition instrument. The tension-compression sensor and displacement sensor are connected to the static data acquisition instrument for synchronous data acquisition.

In this test, in order to ensure the continuity of horizontal shear force and the stability of vertical load during horizontal loading, as well as avoid the impact of shear and volume deformation in the upper soilbag on the interface characteristics (Chen *et al.* 2020), a "π" shaped
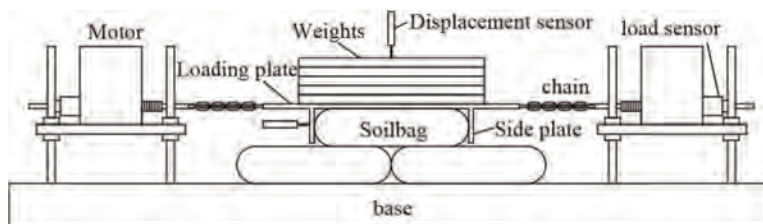
Figure 1. Cyclic shear test device for soilbags.

loading plate as shown in Figure 1 was designed. The width of the loading plate is slightly larger than that of the soilbag, which is convenient for stacking weights and installing connecting buckles. Both ends of the loading plate are connected with the horizontal loading system through flexible chains, so that the stably applied horizontal load can be obtained. Two vertical baffles with the same width as the soilbag are installed at the lower part of the loading plate. During the loading process, both sides of the soilbag are close to the vertical baffle, which can continuously and stably transfer the horizontal load on the loading plate to the lower soilbag.

2.2 Test material

The geotextile woven bag used in the test is a black polypropylene (PP) woven bag with a size of 80cm × 55cm and weight of 108g/m². The ultimate tensile strength in warp and weft is 19.46kN/m and 18.55kN/m respectively, and the ultimate elongation in warp and weft is 20.15% and 19.17% respectively. The filling volume is about 35kg, with a size of 52cm*48cm*12cm.

3 TEST SCHEME

The study is focused on the influence of cyclic shear number, vertical stress, shear displacement amplitude and other factors on the dynamic characteristics of staggered stacked soilbags, as well as the change rule of the interlayer shear strength of the soilbags before and after cyclic shear. The direct shear test and cyclic shear test of staggered stacked soilbags were carried out respectively, and the direct shear test was carried out immediately after the cyclic shear test. Firstly, the direct shear tests of staggered stacked soilbags under four different vertical stresses are carried out, and the reasonable range of the ultimate shear displacement amplitude of soilbags during the cyclic shear test is determined according to the test results. Then, the control variable method is used to carry out the cyclic shear test of staggered stacked soilbags under different cyclic shear times, different shear displacement amplitudes and different vertical stresses. The direct shear test is carried out on the samples immediately after the completion of the cyclic shear test, so as to obtain the change rule of the interfacial shear strength of staggered stacked soilbags before and after the cyclic shear. Table 2 shows the working condition setting of shear test. During the test, in order to ensure

Table 2. Testing conditions.

Test type	Vertical stress/kPa	Shear displacement amplitude/mm	Number of cycles
Direct shear test	4	–	–
	8		
	12		
	16		
Direct shear test after cyclic shear	4	5	4
	8	5	4
	12	2.5	4
		5	1
			2
			3
			4
		7.5	4
		10	4
	16	5	4

the continuous and stable shear process and reduce the influence of stress and strain rate on the test results (Cen *et al.* 2019; Xu *et al.* 2013), the direct shear rate and cyclic shear rate are both set to 2 mm/min. The loading process of cyclic shear displacement is shown in Figure 3.
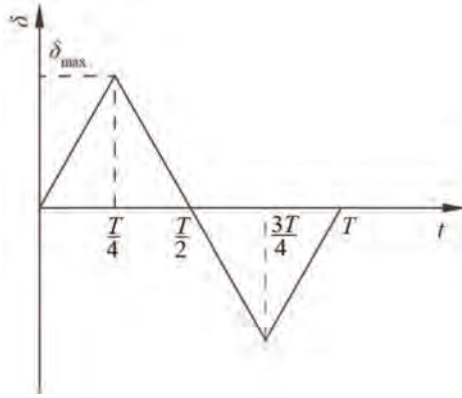
Figure 3. Loading process of the cyclic-shear tests.

4 TEST RESULTS AND ANALYSIS

The dynamic shear modulus G and damping ratio λ are two key parameters in the dynamic design of soilbag structures. According to the peak shear stress and corresponding shear displacement amplitude in Figure 4, the dynamic shear modulus and damping ratio of the soilbag assembly can be calculated by the following formula:

$$G = \frac{\tau_c}{\gamma_c} \tag{1}$$

$$\lambda = \frac{A_L}{\pi S_{\triangle abc}} \tag{2}$$

where τ_c and γ_c are the shear stress and shear strain at the top of the hysteresis loop, respectively; A_L is the area of hysteresis loop, $S_{\triangle abc}$ is the area of $\triangle abc$.
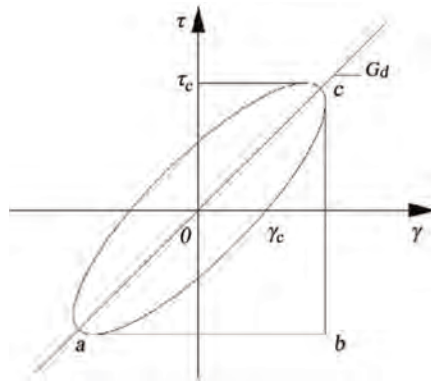
Figure 4. Schematic diagram of ideal hysteresis loop in cyclic shear test.

Figure 5 shows the comparison of the results of the direct shear test and the direct shear test after cyclic shear of staggered stacked soilbags under different vertical stresses when the
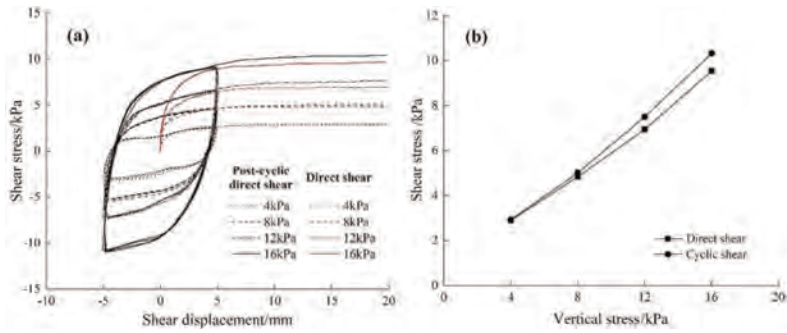
Figure 5. Results of direct shear tests and post-cyclic direct shear tests under different vertical stresses: (a) shear stress versus shear displacement; (b) shear stress versus vertical stress.

horizontal shear displacement amplitude is 5 mm and the number of cycles is 4. In the cyclic shear test stage, after the first cyclic shear is completed, the interfacial shear strength of soilbags increases significantly. In the second and subsequent cyclic shear processes, the interfacial strength basically does not increase, and gradually tends to be stable. In addition, it can be found from the figure that the relationship curve between shear stress and shear displacement is basically consistent with the direct shear test in the first quarter of the shear cycle before the cyclic shear test.

Under different vertical stresses, during the direct shear test after cyclic shear and direct shear test, the peak shear stress of the interface between layers of the soilbag increases with the increase of the vertical stress, and basically presents a positive correlation trend, indicating that the interface between layers of the soilbag basically conforms to the Mohr Coulomb failure criterion under the process of the cyclic shear test. With the increase of vertical stress, the difference between the peak shear strength of direct shear test after cyclic shear and that of direct shear test also grows gradually. It shows that after cyclic shear, the shear strength of the interface between staggered stacking soilbags gradually goes up, and the greater the vertical stress, the greater the increase of the shear strength of the interface between layers of soilbags. This is mainly due to the strengthening of the embedding effect between the staggered stacked soilbags during the cyclic shear process.

Figure 6 shows the direct shear test results of staggered stacked soilbags after cyclic shear under different horizontal shear displacement amplitudes when the vertical stress is 12kPa
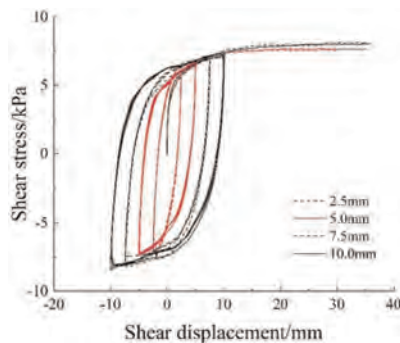
Figure 6. Shear stress-shear displacement relation of post-cyclic direct shear tests under different shear displacement amplitudes.

515

and the number of cycles is 4. Under the same vertical stress, the apex of the hysteresis loop with smaller shear displacement amplitude falls on the path of the hysteresis loop with larger shear displacement amplitude, which indicates that the amplitude of the horizontal shear displacement has little effect on the peak shear strength of the interface between staggered stacked soilbags. This is mainly because there is always a good anchoring effect between the upper and lower soilbags during the cyclic shear process, this further shows that the staggered stacking soilbag composite structure has good recoverability in the shear process. It can also be found that the peak shear strength of interlaminar interface of staggered soilbags after cyclic shear is little affected by the amplitude of horizontal shear displacement.

5 CONCLUSIONS

In this paper, the direct shear test, cyclic shear test and direct shear test after cyclic shear are carried out for staggered stacked soilbags by using a large indoor cyclic shear tester. The shear characteristics of the interface between layers of soilbags under different vertical stresses, cyclic shear displacement amplitudes and other conditions are studied. The main conclusions are as follows:

(1) Before and after cyclic shear, the interlaminar shear stress increases with the increase of vertical stress.
(2) The shear strength of the soilbag assembly increases greatly after the first cyclic shear, and the interlaminar shear strength of the soilbag increases little after the cyclic shear continues.
(3) The greater the vertical stress is, the greater the difference between the direct shear strength after cyclic shear and the direct shear test strength is, and the two basically show a positive correlation trend. The increment of direct shear strength after cyclic shear mainly depends on the increment of shear strength after the first cycle.

REFERENCES

Cen, W. J., Bauer E., Wen L. S., *et al.* 2019. Experimental Investigations and Constitutive Modeling of Cyclic Interface Shearing between HDPE Geomembrane and Sandy Gravel. *Geotextiles and Geomembranes*, 47 (2), 269–279.

Chen S., Liu S., Lu Y., *et al.* Experimental Study on the Cyclic Shear Behavior of the Single Soilbag Proceedings of the 10th National Conference on Geosynthetics Conference. Chengdu: *Southwest Jiaotong University*, 2020: 489–494. (in Chinese)

Fan Kewei., Liu Sihong., Liao Jie., *et al.* Experimental Studies on Shearing Characteristics of the Pebbles–filled Soil bags. *Rock and Soil Mechanics*, 2020,41(2):477–484. (in Chinese)

Huang C. C., Matsushima K., Mohri Y., *et al.* 2008. Corrigendum to Analysis of Sand Slopes Stabilized with Facing of Soil Bags with Extended Reinforcement Strips *Geosynthetics International*, 15(4): 232–245.

Jia F., Liu S. H., Shen C. M., *et al.* Predicting Strength of Soilbags Under Cyclic Compression. *Geosynthetics International*, 2020, 27(6): 646–654.

Li L. J., Liu S., Xu X. D., *et al.* Experimental Study of Effects of Soil Fills on Dynamic Characteristics Parameters of Soil-bag. *Rock and Soil Mechanics*,2015,36(1):131–136. (in Chinese)

Li Z., Sheng J.B., Liu S.H., *et al.* 2014. Model tests on frost heave-prevented channels using soilbags. *Chinese Journal of Geotechnical Engineering*, 36(8), 1455–1463. (in Chinese)

Liu S. H, Gao J. J, Wang Y. Q., *et al.* Experimental Study on Vibration Reduction by using Soilbags. *Geotextiles and Geomembranes*, 2014, 42(1): 52–62.

Liu S. H., Fan K. W., Chen X. L., *et al.* 2016. Experimental Studies on Interface Friction Characteristics of Soilbags. *Chinese Journal of Geotechnical Engineering*, 38(10):1874–1880. (in Chinese)

Liu S. H., Gao J. J. & Wang Y. Q., 2015. Mechanism Analysis and Experimental Study of Vibration Reduction and Isolation Effect of Soilbag. *Rock and Soil Mechanics*, 36(2), 325–332. (in Chinese)

Liu S. H., Jia F., Chen X. L., *et al.* 2018b. Shaking Table Model Test on a Retaining Wall of Soilbags. *Yanshilixue Yu Gongcheng Xuebao/Chinese Journal of Rock Mechanics and Engineering*, 37, 4338–4347. (in Chinese)

Liu S. H., Jia F., Chen X. L., *et al*. 2020. Experimental Study on Seismic Response of Soilbags-built Retaining Wall. *Geotextiles and Geomembranes*.

Liu S. H., Jia F., Shen C. M., *et al.* 2018a. Strength Characteristics of Soilbags Under Inclined Loads. *Geotextiles and Geomembranes*, 46(1), 1–10.

Liu S., Lu Y., Weng L., *et al*. 2015. Field Study of Treatment for Expansive Soil/rock Channel Slope with Soilbags. *Geotextiles and Geomembranes*, 43(4), 283–292.

Liu S.H. 2017. *The Principle and Application of Soilbags*. Beijing: Science Press, 36–45.

Martinelli L., Zanuttigh B., Nigris N.D., *et al.* 2011. Sand Bag Barriers for Coastal Protection along the Emilia Romagna littoral, Northern Adriatic Sea, Italy. *Geotextiles and Geomembranes*, 29(4), 370–380.

Matsuoka H. & Liu S.H. 2003. New Earth Reinforcement Method by Soilbags ("Donow"). *Soils and Foundations*, 43(6):173–188.

Matsuoka H. & Liu S.H. 2006. *A New Earth Reinforcement Method using Soilbags*. The Netherlands: Taylor and Francis, 23–25.

Wang L.J. , Liu, S. H. & Zhou B., 2015. Experimental Study on the Inclusion of Soilbags in Retaining Walls Constructed in Expansive Soils. *Geotextiles and Geomembranes*, 43(1), 89–96.

Wang Y .Q., Li X., Liu K., *et al.* Experiments and DEM analysis on Vibration Reduction of Soilbags. *Geosynthetics International*, 2019,26(5):551–562.

Wang Y. Q. & Wang L. J., 2014. Numerical Simulation of Vibration Reduction and Energy Dissipation of Soilbags. *Rock and Soil Mechanics*. (in Chinese)

Wang Y., Liu S., Lin S., *et al.* 2011. Vibrating Platform Test Study of Vibration Reduction Effect of Soil Bag. *Water Resources and Power*, 2(3), 401–407. (in Chinese)

Xu, C., Chen H. S. & Shi Z. L., 2013. Research on the Mechanical Behavior of Soil-reinforcement Interface by Horizontal Cyclic Shear Test. *Rock and Soil Mechanics*, 34(6), 1553–1559. (in Chinese)

Designing with geosynthetic cementitious composite mats – the importance of managing risk by using ASTM D8364-21 'standard specification for GCCM materials'

L. Church
Concrete Canvas Ltd, UK

N. Brusa
Tailor Engineering, Italy

ABSTRACT: Geosynthetic Cementitious Composite Mats (GCCMs) are factory-assembled geosynthetic composites consisting of a cementitious material contained within layers of geosynthetics that becomes hardened when hydrated, and are primarily used to replace conventional concrete for erosion control and weed suppression applications. GCCMs are unique geosynthetic materials as their properties change from flexible to rigid once cured and in service. The cured cementitious layer also provides inherent physical properties to the GCCM including its compressive strength, initial (1st crack) flexural strength and abrasion resistance. Assessing the performance of the cementitious layer within a GCCM typically falls outside the scope of conventional geosynthetic test standards. Similarly, testing of GCCM cementitious materials to conventional concrete standards at optimum water/cement ratios can also be unrealistic of in service GCCM performance, as the water applied in hydration is not controlled and GCCMs often cure in immersed conditions, increasing the water/cement ratio and decreasing the compressive strength of the cementitious layer. If a designer does not understand the test conditions that GCCM manufacturers have used to report their physical properties, there is a risk that they can specify an unsuitable GCCM material for their project. ASTM D8364 'Standard Specification for GCCM Materials' was published in March 2021 and provides assurance to designers of GCCM applications. This paper provides an assessment of ASTM D8364, reviewing the GCCM performance properties listed in the Classifications for GCCMs table and the importance of testing to the specified standards. Particular focus is given to why all GCCMs specimens should be cured by hydration by full immersion to ADTM D8030 and why the compressive strength should be determined to the GCCM specific test methodology in ASTM D8329. By specifying GCCM Classification Types to ASTM D8364, designers can protect themselves from using GCCM test data that may not be representative of in field GCCM performance.

1 INTRODUCTION

Geosynthetic Cementitious Composite Mats (GCCMs) are a relatively unique geosynthetic material, as unlike most geosynthetics their properties change from flexible in deployment, to rigid once hydrated and cured as illustrated in Figure 1. Many GCCMs consist of top and bottom geosynthetic layers, which are connected to constrain a cementitious material within. GCCMs are supplied in roll format, installed, and then hydrated in-situ. The cementitious material cures to form a thin, rigid cementitious layer. GCCMs are typically used to replace conventional poured, precast, and sprayed concretes for surface erosion control applications, including channel lining, slope protection, berm lining, culvert lining and concrete remediation, providing a robust and low-maintenance surface erosion control solution.
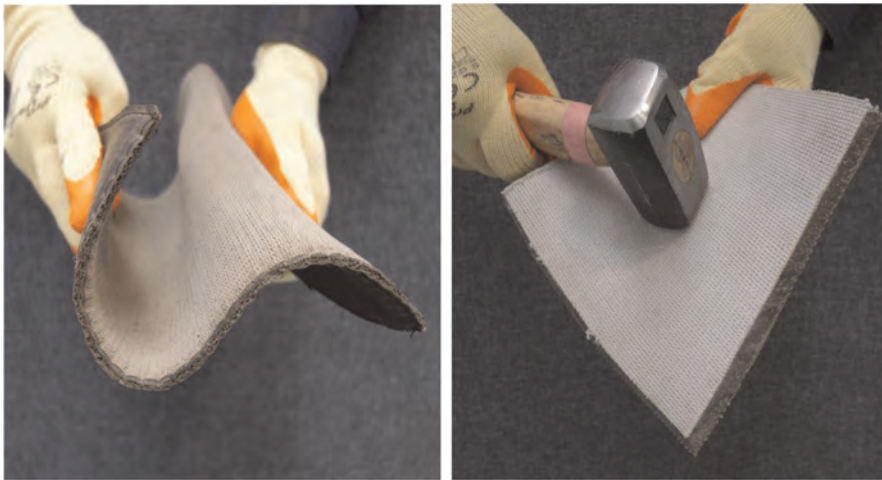
Figure 1. The change of GCCM properties on curing from flexible to rigid means that when assessing GCCM properties, appropriate test methods should be used to determine the cured, in-service GCCM cementitious layer performance.

GCCMs are therefore a composite construction product, combining both geosynthetic and cementitious materials, both of which possess very different physical properties. Geosynthetics are typically buried and their performance is often assessed according to their tensile performance, whereas hardened cementitious materials are often exposed and their performance is typically assessed by their compressive strength, which is typically correlated with durability characteristics such as abrasion resistance, freeze thaw resistance and resistance to chemical attack.

GCCMs are the only geosynthetic to contain cementitious material so traditional geosynthetic test standards do not include methods for understanding the performance of the cementitious material contained within a GCCM, such as compressive strength. It is important therefore to test the properties of the cured cementitious material so that the behaviour of the GCCM as a hardened composite can be understood. It is also necessary to ensure the cementitious material is cured at a water/cement ratio that is representative of field (in-service) hydration and not controlled in the laboratory to an artificially low ratio. If a design relies on performance property data determined under artificially controlled laboratory conditions, the engineer is potentially at risk of under designing their GCCM structure which could potentially lead to in-service failure.

Both the uncured (pre-set, soft and flexible) and cured (post-set, hardened and rigid) properties need to be reported to understand the realistic GCCM capabilities in both deployment and in-service respectively.

2 GCCM SPECIFIC STANDARD DEVELOPMENT

ASTM International Standards Organisation and its D35 Geosynthetics Committee has recognised GCCMs as a geosynthetic product, defining them in ASTM D4439 'Standard Terminology for Geosynthetics' as: a factory-assembled geosynthetic composite consisting of a cementitious material contained within a layer or layers of geosynthetic materials that becomes hardened when hydrated. To address the shortfalls in testing GCCMs using pre-existing geosynthetic or concrete standards, since 2015 the ASTM International Standards Organisation has published several standards specifically for GCCMs. They include (in order of publication):

- ASTM D8030 'Standard Practice for Sample Preparation for GCCM'
- ASTM D8058 'Standard Test Method for Determining the Flexural Strength of a GCCM Using the Three-Point Bending Test'
- ASTM D8329 'Standard Test Method for Determination of Water/Cementitious Materials Ratio for GCCMs and Measurement of the Compressive Strength of the Cementitious Material Contained Within'
- ASTM D8364 'Standard Specification for GCCM materials'

These standards have been created to ensure that repeatable testing and reporting of GCCM properties is conducted on specimens that have been prepared in a manner that is consistent with their use in the field, so the test results are representative of GCCMs installed in real-world operating conditions. Note there are currently no GCCM specific EN or ISO standards for sample preparation or physical property testing.

3 ASTM D8364 – STANDARD SPECIFICATION FOR GCCM MATERIALS

In March 2021, ASTM International published ASTM D8364/D8364M-21: 'Standard Specification for Geosynthetic Cementitious Composite Mat (GCCM) Materials'. ASTM D8364 is currently the only internationally recognised standard for specifying GCCMs and lists typical GCCM erosion control applications by three Classification Types: Type I, Type II, and Type III.

Type I GCCMs are described as being typically used to control wind and rain erosion, not used in constant water flow, and therefore have the lowest requirements for abrasion, wear and loading of the classes. They are installed over supporting subgrades such as concrete or rock. The most common Type I uses are for slope protection, berm lining and weed suppression applications.

Type II GCCMs are described as being typically used to provide erosion protection to hydraulic structures and therefore have greater requirements for abrasion, wear, and loading. They can be installed over medium dense subgrades such as clays or compacted soils. The most common Type II uses are for channel lining, culvert lining and armouring of hydraulic structure applications.

Type III GCCMs are described as being typically used on loose subgrades where additional flexural strength is required. They can be specified to provide greater durability and resistance to abrasion, wear, impact, and loading compared to Type I and Type II GCCMs when used in the same application.

The required physical properties for each type of GCCM is presented in Table 1 of ASTM D8364. The table lists the required minimum mean average performance values of each GCCM Type, based wherever possible on GCCM specific standard test methods, or by using modified geosynthetic or concrete tests methodologies in order to represent in-field performance of a GCCM product when used in typical erosion control applications.

The typical dimensional properties such as thickness, mass per unit area and density are listed first. Importantly, GCCM Types are not differentiated by thickness as both Type II and Type III GCCMs are required to have a minimum thickness of 7mm. Therefore, a thicker GCCM may not necessarily provide superior durability to a thinner GCCM when used in the same application. In Table 1 the cured, in-service performance of each GCCM Type is differentiated based on the flexural strength (initial breaking load), compressive strength, pyramid puncture resistance and tensile strength. The use of ASTM D8364 can therefore help ensure the quality and performance of a GCCM is suitable for the intended application, helping protect against project failures.

It is important that the ASTM D8364 specified test methods are used, as other non-GCCM tests could potentially be manipulated to give artificially high results. An example of this is when testing for compressive strength by using ASTM C109, preparing cubes by using

an artificially low water/ cement ratio that is not representative of field hydration conditions, instead of using ASTM D8329 (specified in ASTM D8364), which was developed specifically for GCCM materials and discussed in detail in chapter 5.

To ensure the reported cured GCCM values are representative of the in-service GCCM product, ASTM D8364 specifies that the GCCM test specimens must be prepared in accordance with ASTM D8030 prior to performance testing.

4 ASTM D8030 – STANDARD PRACTICE FOR SAMPLE PREPARATION FOR GCCMS

In virtually all concrete based materials the water/cement ratio governs the final compressive strength of the cured product. This is discussed in BR331-Design of Normal Concrete Mixes: second edition: 'A major factor in providing durable concrete is the production of a dense, impermeable concrete, having an adequate cement content and low free-water/ cement ratio, which is fully compacted and properly cured'. Therefore, if the water/cement ratio is too high, the compressive strength of the cured concrete will be extremely weak.

It is therefore important to control the water/cement ratio of all concrete materials to ensure they cure to provide the required GCCM durability. For conventional concretes, the addition of water is carefully controlled when batching. This is not so simple for GCCMs, as by their ASTM D4439 definition they are supplied in a flexible, uncured state and only harden when hydrated, which can only take place once the GCCM has been installed.

This means the GCCM manufacturer cannot directly control the quantity of water used by the installer when hydrating and must rely on the quality and structure of the GCCM to consistently limit the water/cement ratio. GCCMs are often used to line channels and culverts that naturally contain horizontal or concave surfaces that will pool water, so it is therefore likely that even if hydrated by spraying, some parts of a GCCM will cure under fully immersed conditions as illustrated in Figure 2. Immersed curing results in the highest water/cement ratio the GCCMs will be subjected to, resulting in the lowest in-service compressive strength and (according to BR331) the poorest durability of the cementitious material. It is critical that the performance of a construction material is assessed based on the physical properties present at the weakest point in the structure, as a failure will usually occur at this location. It is therefore critical to understand the in-service performance of GCCMs that have been hydrated by full immersion.

Figure 2. GCCM hydrated by surface spraying resulting in pooling water in the invert. These parts of the GCCM structure cure in immersed conditions.

ASTM D8030 specifies the procedure for the hydration and curing of GCCM material for subsequent physical property testing. This standard specifies that GCCMs are hydrated by full immersion for 24 hours to represent in-field hydration conditions.

Hydration of GCCM test specimens by surface spraying is not permitted in ASTM D8030. Spraying using a limited quantity of water can produce misleading physical property test results, as the water/ cement ratio can be lower than in parts of the GCCM structure that will cure under the immersed conditions. Using ASTM D8030 will therefore provide cured test specimens that represent worst case in-service cementitious material properties, such as compressive strength.

5 CEMENTITIOUS MATERIAL PERFORMANCE – GCCM COMPRESSIVE STRENGTH TO ASTM D8329

Conventional concrete compressive strength testing (for example ASTM C109) is conducted by casting a cube of cementitious material (typically 50 or 100mm in size) and loading it to failure. Since GCCMs cannot be cast into cubes, the cementitious material must be removed from the GCCM and cast into a cube at the appropriate water/cement ratio prior to load testing.

ASTM C109 and other non-GCCM concrete standards are usually designed for mixed concretes using a pre-determined water/cement ratio, which can be significantly lower than the GCCMs exhibit in actual use, so test results to this standard may not represent real world GCCM performance.

When testing for GCCM compressive strength, it is essential that the water/cement ratio used in the cube testing is representative of the ratio achieved during hydration of the GCCM on site. ASTM D8329 is specific to GCCMs as it determines the representative water/ cementitious materials ratio of a GCCM when hydrated by immersion. This water/ cementitious materials ratio is then used to prepare cube specimens for compressive strength testing.

The water/cementitious materials ratio is not the same as the water/cement ratio of a GCCM. If the cementitious material contains a high percentage of sand, aggregate or other additives, a low water/cementitious material ratio obtained using ASTM D8329 may still result in a high water/cement ratio. It is therefore important when determining the compressive strength of a GCCM that the cementitious material is extracted directly from the unset GCCM test sample so that the formulation is representative of the actual product. Testing of a powder sample only may not be accurate.

ASTM D8364 specifies that when tested at a water/cementitious materials ratio determined to ASTM D8329, Type I, II and III GCCMs to have a minimum 28-day compressive strength of 40, 50 and 60MPa respectively.

6 GCCM TENSILE STRENGTH

The Ultimate Tensile Strength (UTS) of a GCCM is primarily governed by the geosynthetic components within the composite. As cementitious materials typically have lower tensile strength than geosynthetics, when testing the tensile strength of a cured GCCM, multiple cracks will typically form in the cementitious material at low strains, transferring loads to the reinforcing fibres until the UTS of the GCCM is reached.

ASTM D8364 requires three tensile strength properties to be reported. The first is the UTS, or final strength of the GCCM its uncured state. Uncured tensile strength at fast loading rates is required when installing the GCCM as it might be suspended, stressed, and dragged on the job site. Once the GCCM has cured and is in service, the material may be stressed at perimeter and intermediate anchors when resisting hydraulic shear forces or wind uplift, which would be at a slower rate of strain. Two cured tensile strength properties must be reported; the Initial Tensile Strength when the cementitious material first cracks, and the

Final Tensile Strength (UTS) of the GCCM. Note the cementitious material could have cracked and effectively failed long before reaching the UTS, so designers need to be mindful when using tensile strength values in their designs and Initial Tensile Strength values are typically recommended for anchorage design.

It should also be noted that the top geosynthetic layer in a GCCM may be exposed to degradation from abrasion, especially in watercourse lining applications with high levels of sedimentation or debris impact, and UV exposure (depending on the composition of the geo-synthetic layer). Several GCCM manufacturers describe their top surface geosynthetic layer to be sacrificial. It is therefore important that reported tensile strength values take account of the effects of environmental degradation, or top geosynthetic layer removal. At the time of writing, the ASTM International Standards Organisation is developing a GCCM specific tensile strength test methodology, which proposes to establish long-term Initial and Final Tensile Strength values by removing the top geosynthetic layer from the cured GCCM material prior to testing.

7 ABRASION RESISTANCE

Abrasive conditions typically occur in GCCM hydraulic applications (such as channelling works or culvert remediation) where the top surface of the lining is subject to a range of water flow velocities and bed loads of silt, sand or cobbles during storm events. These actions can wear the surface of the GCCM and abrasion resistance is therefore an essential property of cured GCCMs.

Since the major contributor to abrasion resistance in GCCMs is the cementitious layer, there are no relevant test methods from within the existing library of geosynthetic standards. GCCM abrasion resistance is therefore best characterised using ASTM C1353 "Test Method Using Taber Abraser for Abrasion Resistance", a simple abrasion test using a rotary plat-form abrader.

The GCCM test specimen is placed in the abrader, two grinding discs are loaded on the top surface of the specimen, which is spun for a defined number of cycles to abrade the GCCM surface. In ASTM D8364, ASTM C1353 is modified to record the depth of wear of the cementitious material after every 1,000 cycles. A low depth of wear represents good abrasion resistance; a higher depth of wear represents a lower resistance to abrasion, meaning over the same duration, more of the GCCM will be abraded away under the same sediment flow conditions. ASTM D8364 specifies that all GCCMs must have a maximum depth of wear of 0.3mm/1000 cycles when tested to ASTM C1353 (modified).

8 SCPECIFICATION OF GCCMS

ASTM D8364 provides a simple way to specify GCCMs for erosion control applications. Using this standard ensures appropriate performance levels are defined and helps to protect Clients, Designers, and Installers against project failures, particularly given the typical life-span of GCCM surface erosion control projects and the likelihood of significant storm events. Designers can specify a GCCM classification Type in accordance with ASTM D8364, and insist that manufacturers provide independent test data showing that their material meets the minimum performance properties when tested to the specified test stan-dards. By using Table 1 of ASTM D8364 Engineers can have the confidence that the design values they are using are representative of in-service GCCM performance.

Where necessary, customers can conduct their own GCCM material testing either them-selves or by engaging test houses to verify properties to GCCM standards, such as ASTM D8058 1-day Flexural Strength and ASTM D8329 28-day Compressive Strength. When engaging a test laboratory, testing should always begin with samples of soft (uncured) material so that the test house can cure the material in accordance with ASTM D8030.

9 CONCLUSIONS

ASTM D8364 is an essential tool for all GCCMs users because it is simple. ASTM D8364 makes specifying the right product easier for the designer whilst ensuring they meet minimum performance requirements, helping to prevent project failures. It is safe, as specifying GCCM Classification Types to ASTM D8364 protects specifiers from designing with GCCM test data that may not be representative of in field GCCM performance, helping ensure the GCCM is suitable for the intended application. And finally, it is secure, as purchasing GCCM's that comply with ASTM D8364 protects contractors and clients from being misled by performance data using inappropriate non-GCCM specific standards that may not represent the performance that can be achieved in the field.

REFERENCES

ASTM C 109/C109M-16a. Standard Test Method for Compressive Strength of Hydraulic Cement Mortars (Using 2-in. or [50-mm] Cube Specimens), *American Society for Testing and Materials*, West Conshohocken, Pennsylvania, USA.

ASTM C 1353/C1353M-15a. Standard Test Method for Abrasion Resistance of Dimension Stone Subjected to Foot Traffic Using a Rotary Platform Abraser, *American Society for Testing and Materials*, West Conshohocken, Pennsylvania, USA.

ASTM D 4439-20. Standard Terminology for Geosynthetics, *American Society for Testing and Materials*, West Conshohocken, Pennsylvania, USA.

ASTM D 8030/D8030M-19. Standard Practice for Sample Preparation for GCCM, *American Society for Testing and Materials*, West Conshohocken, Pennsylvania, USA.

ASTM D 8058-19. Standard Test Method for Determining the Flexural Strength of a Geosynthetic Cementitious Composite Mat (GCCM) Using the Three-Point Bending Test, *American Society for Testing and Materials*, West Conshohocken, Pennsylvania, USA.

ASTM D 8329-21. Standard Test Method for Determination of Water/Cementitious Materials Ratio for GCCMs and Measurement of the Compressive Strength of the Cementitious Material Contained Within, *American Society for Testing and Materials*, West Conshohocken, Pennsylvania, USA.

ASTM D 8364/D8364M-21. Standard Specification for GCCM Materials, *American Society for Testing and Materials*, West Conshohocken, Pennsylvania, USA.

Kujawski, M., Church, L.K., Crawford, W. 2022. Use of ASTM D8058 Flexural Strength Test Method to Assess Overall GCCM Performance, *EuroGeo7*, Warsaw, Publication TBC.

Teychenne, D.C., Franklin, R.E. & Erntroy, H.C. 1997. *REP BR 331 Design of Normal Concrete Mixes*. 2nd edition. Bracknell: BRE.

Geotextiles used for separation and filtration in UL-FGA applications

T.A. Loux & C.R. Calabria
Aero Aggregates of North America, LLC, Eddystone, PA, USA

M. McGuire
Lafayette College, Easton, PA, USA

A. Filshill
Aero Aggregates of North America, LLC, Eddystone, PA, USA

ABSTRACT: Ultra-lightweight foamed glass aggregate (UL-FGA) is a lightweight and insulating fill material used in the construction of retaining structures, embankments and general grade-raising fill, bridge abutments, and foundation slabs throughout Europe as well as in North America. UL-FGA is granular material that has dry bulk densities ranging from 180–240 kg/m^3 and a closed cell structure which provides good insulation properties and minimal water absorption. This sustainable material has a favorable carbon footprint in part because it is manufactured using recycled glass cullet. Most UL-FGA applications require a separation geotextile fabric to be installed in conjunction with the UL-FGA as the geotextile is critical in maintaining the UL-FGA layer's ultra-lightweight and highly insulating properties over the design life of the project. Additionally, there are UL-FGA applications where the UL-FGA layer is providing water storage and thus the filtration characteristics of the geotextile need to be understood. This paper summarizes the characteristics of geotextiles serving the separation and/or filtration functions in various UL-FGA applications over the design life of the project.

1 INTRODUCTION

Ultra-lightweight foamed glass aggregate (UL-FGA) has been a commercially manufactured product since the 1990s. The primary raw material used for production of UL-FGA is recycled glass. Closed-cell UL-FGA is used as an insulation or lightweight fill layer on infrastructure, commercial, and residential construction projects. It is also utilized as retaining wall or bridge abutment backfill where the low density and high friction angle (40-55 degrees) [Auvinen 2013; Arulrajah *et al.* 2015; Loux *et al.* 2019b; Swan *et al.* 2016] reduce lateral earth pressures significantly compared to normal weight fill. While the direct material cost of UL-FGA per unit volume is generally higher than mined aggregates in most of the U.S., it is competitive with other types of lightweight or insulating fill (e.g. expanded shale, clay, or slate, cellular concrete, and expanded or extruded polystyrene). Details regarding the history, manufacturing of closed-cell foamed glass aggregate via the dry-process of foaming, and applications are documented in the literature (e.g., Aabøe *et al.* 2005; Loux *et al.* 2019a; Zegowitz 2010).

The low density of UL-FGA permits large single truckload quantities of approximately 75 m^3 per load in North America (Loux *et al.* 2019a) and up to 120 m^3 per load in Europe. This is a major advantage compared to shipping in dump trucks that typically hold between 8 and 12 m^3 per load, decreasing the amount of truck traffic at the project site (Auvinen *et al.* 2013), and it makes UL-FGA an economically feasible option even for project locations that are a significant distance from the manufacturing plant (Loux *et al.* 2019a).

UL-FGA is placed and compacted according to a method specification. While the exact recommendations vary by supplier, typical procedures recommend compaction with tracked equipment (having between 30 to 50 kPa ground pressure) at 0.6 to 1 m thick lifts or with a vibratory plate compactor (50 to 200 kg) at 0.3 to 0.5 m thick lifts (Loux et al. 2019a). A roller is not used to compact UL-FGA in most applications. The compaction factor, defined as the ratio of bulk to in-place volume, for dry-process UL-FGA, will vary slightly based on the placement and compaction procedures. McGuire et al. (2021) reports a compaction factor of 1.08 to 1.20, excluding the effects of compaction due to leveling each lift, and Aabøe et al. (2005) reports values between 1.2 and 1.3. Therefore, an average compaction factor of approximately 1.25 is reasonable for estimating purposes.

2 UL-FGA PROPERTIES

2.1 Density

The low density of UL-FGA drives many of the uses and application for the product. Most dry-process UL-FGA has bulk densities between approximately 180 and 240 kg/m^3. Once the 1.25:1 compaction factor and moisture content of approximately 25% by mass, or 6% by volume, is accounted for, the in-place density falls between approximately 281 and 375 kg/m^3. (Auvinen et al. 2013; Arulrajah 2015; Loux et al. 2019a).

2.2 Gradation

As manufactured, UL-FGA has nominal particle sizes between approximately 10 and 60 mm with up to 15% by mass allowed under or over these limits. Some crushing occurs when the UL-FGA layer is placed and compacted resulting in an overall decrease in particle size; however, this particle breakage does not typically generate significant fines and any fines that are created are nonplastic. Typically, both the pre- and post-compaction gradation yields a GP classification per the Unified Soil Classification System criteria (Arulrajah 2015; Loux et al. 2019a).

2.3 Particle shape

Immediately after production, UL-FGA has sharp edges and may have a blocky particle shape. However, due to material handling and the temperature equalization process, delivered material will have rounded edges and is frequently more subangular in shape. The placement and compaction process tends to increase angularity due to the particle breakage of the blockier pieces that occurs as the material is seated. There is no evidence that changes to particle shape during handling, placement, and compaction elevate the potential for damage to geotextiles, which the authors speculate is due to the offsetting effects of increased angularity by particle fracture and decreased angularity from crushing of particle corners.

2.4 Permeability

Constant head permeability testing on UL-FGA indicates a permeability on the order of 1 cm/sec (Loux et al. 2019a) and accessible porosity for flow is approximately 38% or higher (Loux and Filshill 2021). This permeability result aligns with other similarly classified coarse aggregates (U.S. Department of Agriculture 1984).

2.5 pH

The chemical composition of UL-FGA is derived from the container (soda-lime) glass that is used in manufacturing. As such, there is a significant amount of sodium (an alkali element) ions in the internal structure of UL-FGA. pH testing methods for soils and aggregates subject samples to a liquid water bath for a given amount of time. Typical pH testing results

on powdered UL-FGA is between 10-11 (Arulrajah 2015); however, modified test methods that maintain the in-service gradation yield results closer to 9 (Loux *et al.* 2019b). The reason for this difference is the significant role that particle surface area plays in the dealkalization process that is occurring in the glass during a pH test.

3 GEOTEXTILES

3.1 *Definition and functions*

ASTM D4439 defines a geotextiles as "a permeable geosynthetic comprised solely of textiles." Geotextiles are used with foundation, soil, rock, earth, or any other geotechnical engineering-related material as an integral part of a human-made product, structure, or system. The original use of geotextiles was as a replacement for granular filters; thus, their early moniker of "filter fabrics" was born. In recent years, approximately 95% of geotextiles are manufactured from the polymer polypropylene (Koerner 2016). Geotextiles may be described by their fiber type (monofilament, multifilament, staple fiber yarn, slit-film monofilament, or slit-film multifilament) and method of fabric construction (most commonly woven or nonwoven for geosynthetics). Koerner (2016) provides a thorough discussion of geotextile manufacturing methods and types.

The major functions that geotextiles may serve include separation, filtration, drainage, and reinforcement. The separation function involves keeping dissimilar materials from mixing and can be seen when geotextiles are used between subgrade and stone bases in paved/unpaved roadways. When placing a coarse aggregate on fine-grained soils without a fabric, there are two mechanisms that occur over time. First, the finer soil particles enter the voids of the coarse aggregate and decrease its permeability. Secondly, the coarse aggregate intrudes into the finer soil, thereby decreasing the strength of the coarse aggregate (Koerner 2016).

The filtration function allows for cross-plane flow and the use of geotextiles in lieu of granular filters is a primary example. In this function, there is a balance between allowing adequate flow rates across the plane of the geotextile while limiting the migration of the finer soil across the plane of the geotextile and into the coarse aggregate. There are many approaches to soil-retention design. Most methods compare the soil particle sizes to the O_{95} value (the 95% opening size) for the geotextile. ASTM D4751 employs a dry-sieving process to determine the O_{95}, referred to as the apparent opening size (AOS) in this testing. While the O_{95} and AOS refer to the same pore size, the O_{95} is the corresponding sieve opening in millimeters while the AOS is the U.S. Standard sieve number. Outside of the U.S., wet or hydrodynamic sieving is commonly used to determine the O_{95}, referred to as the filtration opening size (FOS) in these tests (Koerner 2016).

The drainage function represents supporting in-plane flow and an example use may be as a drainage blanket beneath a surcharge fill or railroad ballast. Lastly, the reinforcement function serves to enhance the strength of weak soils or other materials. Geotextile-reinforced walls and slopes are an example of geotextiles serving this function (Koerner 2016). This paper limits discussion to the first two functions, separation and filtration, in applications where geotextiles will be in contact with UL-FGA.

3.2 *Design and construction considerations*

3.2.1 *Abrasion/installation damage*

Polypropylene fibers have been shown to have good abrasion resistance compared to other polymers (Galanti 1964). For applications of geotextiles in contact with UL-FGA, the installation damage caused by the placement of UL-FGA compared to a mined coarse aggregate, such as AASHTO #57 stone, is decreased for most geotextiles and geogrids (Koerner *et al.* 2023).

3.2.2 Clogging

The simplified design procedure proposed by AASHTO for filtration design considers the percentage of soil passing the No. 200 sieve (0.074 mm opening size). If the fine-grained soil has ≤ 50% passing the No. 200 sieve, then the required O_{95} for the fabric is < 0.60 mm. If the fine-grained soil has > 50% passing the No. 200 sieve, then the required O_{95} for the fabric is < 0.30 mm (Koerner 2016). After handling, placement, and compaction, the percentage of UL-FGA passing the No. 200 sieve is far below 50%, therefore, the O_{95} sizing is expected to be controlled by the subgrade soil.

3.2.3 Chemical compatibility/ UV degradation

The most popular polymer for geotextile production, polypropylene, is exceptionally chemically resistant (Galanti 1964) and is stable within a pH range of 2 through 13. Since UL-FGA is expected to exhibit an in-service pH between 9-10, insignificant impacts on chemical degradation of the polymer are expected due to contact with the UL-FGA. Most polypropylene geotextiles are produced with a UV stabilization package that is proprietary and specific to the manufacturer (Koerner 2016). However, even with this additional protection from UV degradation, there will be practical limits to the UV exposure for the geotextile. In particular, nonwoven geotextiles, because of the very small fiber sizes, uncovered exposure time is generally limited to 14 days. Contact between UL-FGA and the geotextile is not expected to pose unique impacts to UV resistance as compared with mined aggregates.

3.2.4 Overlap/seaming

Most UL-FGA applications require a separation geotextile fabric to be installed to completely surround the UL-FGA where it is in contact with another granular material. The geotextile is critical in maintaining the UL-FGA layer's ultra-light weight and high insulating properties over the design life of the project. In order to construct the geotextile so that it is a continuous wrap around the UL-FGA layer, the roll edges may be either overlapped or seamed together. A standard overlap distance of 0.3 m is sufficient in most cases. If significant movement is expected, as with soft subgrade soil, the overlap distance may be increased to ensure continuous coverage at the geotextile-UL-FGA interface.

3.2.5 Cover soil

UL-FGA is typically covered in service to ensure that the layer remains intact during the design life of the project. As such, the top and sides of the UL-FGA layer usually have cover soil or rip rap placed on the geotextile wrap of the UL-FGA. It is important to evaluate the veneer stability of the cover soil based on the steepness of the slope and the properties of the proposed cover material.

3.2.6 Design by specification

A common specification used in the U.S. for geotextiles on highway projects is AASHTO M 288. This specification is intended to ensure good long-term performance of geotextiles in the applications of subsurface drainage, separation, stabilization, erosion control, temporary silt fence, and paving fabrics. Suitable geotextiles must meet requirements for material quality and be able to withstand installation without excessive damage.

This specification sets forth general requirements for three geotextile classes – Class 1, Class 2, and Class 3; Class 1 geotextiles have the highest strength requirements and Class 3 geotextiles have the lowest strength requirements. High-strength geotextiles, e.g. those belonging to Class 1, can survive harsh installation conditions better than low-strength geotextiles, e.g. those belonging to Class 3. Thus, as the requirements for survivability decrease, a higher Class of geotextile, by number, may be used. The survivability requirements of the geotextile are a function of the subgrade conditions, the ground pressure from construction equipment, and the lift thickness as shown in Table 1. As subgrade conditions improve and lower ground pressure equipment is used, the survivability requirements for the

Table 1. Required degree of survivability as a function of subgrade conditions, construction equipment ground pressure, and lift thickness (Class 1, 2, and 3 properties are given in Table 2; Class 1+ properties are higher than Class 1, but not defined here and, if used, must be specified by the purchaser)[a] (adapted from AASHTO M 288).

	Low Ground-Pressure Equipment ≤25 kPa (3.6 psi)	Medium Ground-Pressure Equipment > 25 to ≤50 kPa (>3.6 to ≤7.3 psi)	High Ground-Pressure Equipment >50 kPa (>7.3 psi)
Subgrade has been cleared of all obstacles except grass, weeds, leaves, and fine wood debris. Surface is smooth and level so that any shallow depressions and humps do not exceed 450 mm (18 in.) in depth or height. All larger depressions are filled. Alternatively, a smooth working table may be placed.	Low (Class 3)	Moderate (Class 2)	High (Class 1)
Subgrade has been cleared of obstacles larger than small to moderate-sized tree limbs and rocks. Tree trunks and stumps should be removed or covered with a partial working table. Depressions and humps should not exceed 450 mm (18 in.) in depth or height. Larger depressions should be filled.	Moderate (Class 2)	High (Class 1)	Very High (Class 1+)
Minimal site preparation is required. Trees may be felled, delimbed, and left in place. Stumps should be cut to project not more than ±150 mm (±6 in.) above subgrade. Geotextile may be draped directly over the tree trunks, stumps, large depressions and humps, holes, stream channels, and large boulders. Items should be removed only if placing the geotextile and cover material over them will distort the finished road surface.	High (Class 1)	Very High (Class 1+)	Not Recommended

[a]Recommendations are for 150 to 300 mm (6 to 12 in.) initial lift thickness. For other initial lift thicknesses:
1. >300 to 450 mm (12 to 18 in.): reduce survivability requirement one level (i.e., increase Class number by one level);
2. >450 to 600 mm (18 to 24 in.): reduce survivability requirement two levels (i.e., increase Class number by two levels);
3. >600 mm (24 in.): reduce survivability requirement three levels (i.e., increase Class number by three levels). For special construction techniques such as prerutting, increase the geotextile survivability requirement one level. Placement of excessive initial cover material thickness may cause bearing failure of the soft subgrade.

geotextile are lessened. Similarly, greater initial lift thicknesses are expected to impart more uniform stresses to the geotextile during installation and lower the survivability/strength requirements. Table 2 lists the geotextile strength properties requirements for Class 1, 2, and 3 geotextiles.

The equipment commonly utilized for UL-FGA placement is within the "Medium Ground Pressure" category in Table 1. The survivability/ geotextile Class recommendations within Table 1 are based on a 150 to 300 mm initial lift thickness, and the footnote recommends a one-level reduction in the survivability requirement (thus, an increase in the Class number by one) for initial lift thicknesses >300 mm to 450 mm, a two-level reduction in the survivability requirement (thus, an increase in the Class number by two) for initial lift thicknesses >450 mm to 600 mm, and a three-level reduction in the survivability requirement

Table 2. Geotextile strength property requirements (AASHTO M 288).

	Test Methods	Units	Geotextile Class [a,b,f]					
			Class 1 (severe)		Class 2 (typical)		Class 3 (moderate)	
			woven[c]	nonwoven[c]	woven[c]	nonwoven[c]	woven[c]	nonwoven[c]
Grab strength	ASTM D4632	N	1400	900	1100	700	800	500
Sewn seam Strength [d]	ASTM D4632	N	1260	810	990	630	720	450
Tear strength	ASTM D4533	N	500	350	400[e]	250	300	180
Puncture strength	ASTM D6241	N	2750	1925	2200	1375	1650	990

[a]Required geotextile class is designated by the indicated application. The severity of installation conditions for the application generally dictates the required geotextile class. Class 1 is specified for more severe or harsh installation conditions where there is a greater potential for geotextile damage, and Classes 2 and 3 are specified for less severe conditions.
[b]All numeric values represent MARV (Minimum Average Roll Value) in the weaker principal direction.
[c]Woven corresponds to elongation <50% and nonwoven corresponds to elongation $\geq$ 50% as measured in accordance with ASTM D 4632.
[d]When sewn seams are required.
[e]The required MARV tear strength for woven monofilament geotextiles is 250 N.
[f]Minimum property values for permittivity, AOS, and UV stability are based on geotextile application.

(thus, an increase in the Class number by three) for initial lift thicknesses >600 mm. Also, it is noted the recommendations in Table 1 are based on the use of normal-weight mineral aggregates (e.g., AASHTO #57 stone) or fill as the initial lift materials. Given the unit weight and low installation damage expected from UL-FGA, the authors suggest that an additional one-level class reduction beyond the survivability requirements shown in Table 1, including the allowance for initial lift thickness, may be warranted for UL-FGA. For example, if subgrade conditions, installation equipment, and the initial lift thickness lead to the recommendation of a Class 2 geotextile based on mined aggregate or normal weight fill as the initial lift material, a Class 3 textile may be used when UL-FGA is the initial lift material and all other conditions remain unchanged.

Beyond the survivability requirements for the geotextile, other properties of the geotextile are relevant in the different applications covered within the AASHTO M 288 specification. For subsurface drainage and separation geotextiles, the authors do not recommend any deviation from the requirements in the AASHTO M288 specification when UL-FGA is used in lieu of mined aggregate or normal weight fill.

4 CONCLUSIONS

Ultra-lightweight foamed glass aggregate is manufactured from recycled glass and has a combination of physical and engineering properties that include low unit weight, high friction angle, high permeability, and high porosity. Both the pre- and post-compaction gradations yield a GP classification per the USCS criteria. Approximately 95% of geotextiles manufactured today use polypropylene fibers, which have been shown to have good abrasion resistance compared to other polymers and be stable within a pH range of 2 through 13. UL-FGA has an in-service service pH between 9-10, thus insignificant chemical degradation

is expected due to the UL-FGA. For applications of geotextiles in contact with UL-FGA, the installation damage caused by the placement of UL-FGA compared to a mined coarse aggregate, such as AASHTO #57 stone, is expected to decrease for most geotextiles. Accordingly, the authors recommend increasing the Class number by one level, i.e. lower the survivability requirement one level, for geotextiles when used with UL-FGA as the initial lift material.

REFERENCES

Aabøe, R., Øiseth, E., Hagglund, J. 2005. Granulated Foam Glass for Civil Engineering Applications. *Recycled Materials in Road and Airfield Pavements.*

AASHTO M 288. 2011. *Standard Specification for Geotextile Specification for Highway Applications.* Washington, D.C.: American Association of State Highway and Transportation Officials.

Arulrajah, A., Disfani, M.M., Maghoolpilehrood, F., Horpibulsuk, S., Udonchai, A. Monzur, I., and Du Y.-J. 2015. Engineering and Environmental Properties of Foamed Recycled Glass as a Lightweight Engineering Material. *Journal of Cleaner Production*, 94: 369–375.

ASTM D4439. 2020. *Standard Terminology for Geosynthetics.* Conshohocken, PA: ASTM International.

ASTM D4751. 2021. *Standard Test Methods for Determining Apparent Opening Size of a Geotextile.* Conshohocken, PA: ASTM International.

Auvinen, T., Pekkala, J., and Forsman, J. 2013. *Covering the Highway E12 in the Centre of Hämeenlinna – Innovative Use of Foamed Glass as Light Weight Material of Approach Embankment.* The XXVIII International Baltic Road Conference.

Galanti, A.V. 1964. *Polypropylene Fibers.* Thesis. Newark College of Engineering, Newark, NJ.

Koerner, R.M. 2016. *Designing with Geosynthetics*, 6th ed., Vol. 1. Xlibris.

Koerner, G.R., Filshill, A., Loux, T.A., and Schuller, J.C. 2023. Geosynthetic Damage Due to Installation Stresses in Ultra-Lightweight Foamed Glass Aggregate Versus Conventional Aggregate. *Proc. Of the 12th International Conference on Geosynthetics*, 17-21 Sept 2023, Rome, Italy. In press.

Loux, T.A., and Filshill, A. 2021. *Foamed Glass Aggregate for Resilient Waterfront Construction.* Geo-Extreme 2021. Reston, VA: ASCE.

Loux, T.A., Filshill, A., and Zhang, Z. 2019a. *Foamed Glass Aggregate Lightweight Fill Over Compressible Soils.* Geo St. John's 2019. The Canadian Geotechnical Society.

Loux, T.A., Swan, Jr., R.H., Yuan, Z., and Filshill, A. 2019b. Pullout Testing of Geogrids, Geostraps and Steel Strips Embedded in Foamed Glass Aggregate. *Geosynthetics* 2019. 728–737. Industrial Fabrics Association International.

McGuire, M.P., Loux, T.A., and VandenBerge, D.R. 2021. Field-Scale Tests to Evaluate Foamed Glass Aggregate Compaction. *IFCEE* 2021, GSP 326. 157-168. Reston, VA: ASCE.

Swan, R, Yeom, S., Sjoblom, K.J., Stark, T., and Filshill, A. 2016. *Engineering Properties of Foamed Recycled Glass as a Lightweight Fill.* Geo-Chicago, GSP 272. 11-22. Reston, VA: ASCE.

U.S. Department of Agriculture, Soil Conservation Service, *Engineering Division.* 1984. Soil Mechanics Note No. 9 Permeability of Selected Clean Sands and Gravels. March 1984.

Zegowitz, A. 2010. *Cellular Glass Aggregate Serving as Thermal Insulation and a Drainage Layer.* Thermal Performance of Exterior Envelopes of Whole Buildings XI, Florida, USA: ASHRAE.

Measurement uncertainty in testing bentonite index properties

B. Kovačević Zelić & I. Dobrilović
Faculty of Mining, Geology and Petroleum Engineering, University of Zagreb, Zagreb, Croatia

D. Kosić
Hrvatske vode, Zagreb, Croatia

A. Vrbaški
Faculty of Mining, Geology and Petroleum Engineering, University of Zagreb, Zagreb, Croatia

ABSTRACT: Geosynthetic clay liners (GCLs) are factory-manufactured products used in various applications mainly for containment purposes. The type of construction, as well as the anticipated function determine the technical requirements that GCLs must fulfil. There are many laboratory test methods that can be used for the characterization of GCLs. Among other tests, the swell index test and the Enslin-Neff water-adsorption test are used for quality control in manufacturing and as performance indicators for the mineral component, i.e. bentonite clay. The paper presents the findings of within-laboratory evaluation of measurement uncertainty in bentonite swell index and water-adsorption testing, and the evaluation of some requirements of the standard test method, such as the influence of time and temperature of drying for the sample preparation phase or the influence of different observers. No statistically significant deviations from normality were found for the Enslin-Neff water-adsorption test. The F-test and t-test were performed to compare variances and means for the same observer at two drying temperatures, as well as for two observers at the same temperature, with some differences. The results of the detailed statistical analysis indicate that the assessment of the measurement uncertainty type A was properly estimated.

1 INTRODUCTION

Geosynthetic clay liners (GCLs) are factory-manufactured assembled products consisting of geosynthetic and mineral components (usually natural sodium bentonites or sodium activated bentonites). They are increasingly used in geotechnical, hydrotechnical, mining and environmental applications as hydraulic barriers. The type of construction, as well as the anticipated function determine the technical requirements that GCLs as a composite material must fulfil. The mineral component that provides the sealing function continuously undergoes quality control, from the production and construction phase (MQC, MQA, CQC and CQA) to the end of its lifespan (long-term properties or durability).

The list of different testing methods for GCL components and the final product has been growing since 1990s. Within the framework of ASTM more than fifteen standards are active, covering mainly laboratory testing methods for the determination of physical, index, mechanical and hydraulic characteristics, but also guides and practices for storage, installation and quality control. The same trend of an increasing number of standard testing methods for GCLs can be found in the EU as well. With the given quality control measurements and standardization of testing methods the confidence among producers, designers and users can be properly established.

It is assumed that the exceptionally good swelling properties of the mineral component (bentonite) guarantee the sealing function and self-healing potential as well. There are many

laboratory test methods that can be used for the characterization of bentonites. It is common practice to perform chemical and mineralogical characterization of bentonites especially in the production phase. For practical civil engineering applications, physical and index testings of bentonites are more acceptable as they are used in everyday practice of geotechnical laboratories, are simple to perform and are relatively cheap. Besides, various correlations between index and other engineering properties are commonly used for the prediction of design parameters.

Among other tests, the swell index test (ASTM D5890) and Enslin-Neff water adsorption test (DIN 18132) are almost inevitably used for quality control in manufacturing and as the performance indicator for the mineral component i.e. bentonite clay. To assist the users of GCL products, ASTM developed two standards (ASTM D 5889 and ASTM D 6495), in which various properties are listed, together with the appropriate test methods and testing frequencies that should be applied as part of MQC and/or CQA.

Besides, the compatibility of the GCLs mineral component with various liquids or soils can be derived by performing swell index (ASTM D 5890) and fluid loss (ASTM D 5891) tests in accordance with ASTM D 6141. If the GCLs mineral component preserves its swelling properties when site-specific liquid or some other testing fluid is used instead of water, then it is assumed that it is chemically compatible. Otherwise, additional, more time-consuming and expensive testings may be warranted in order to prove its sealing properties (Erickson & Jasionek 2004).

In view of the above, index testing is inevitable and very often performed in the GCLs production phase, then during the construction phase until the end of the lifespan of its various structures. This paper presents the findings of the within-laboratory evaluation of measurement uncertainty in bentonite swell index and water-adsorption testing, and the evaluation of some requirements of the standard test methods, such as the influence of drying time and temperature in the sample preparation phase or the influence of different observers.

2 MATERIALS AND METHODS

Sodium activated bentonite, which is used as drilling mud in petroleum engineering and as a waterproof barrier in civil engineering applications, was chosen from a local producer. In order to evaluate the homogeneity of bentonite samples, Atterberg limits test were conducted on six representative samples from the same batch delivered by the producer in the same form as for commercial purposes i.e. in a bag (total mass of 30 kg). The range of obtained liquid limit values, w_L were between 380% and 391% with a standard deviation of 3.9%, and for the plastic limit, w_P were between 42% and 45% with a standard deviation of 0.9%, thus confirming the homogeneity of the tested samples.

The swell index test (ASTM D5890) and Enslin-Neff water adsorption test (DIN 18132) were performed on 120 samples in total for both methods (30 samples with the drying temperature of 60°C or 105°C each, and 30 samples by the first and the second observer each). The results for both methods with statistical analysis are presented in the next section. The ASTM D5890 standard test method appeared in a revised version in 2019 providing the expected precision for within- and inter-laboratory repeatability and reproducibility limits in terms of coefficients of variation. Previous research also showed that test results are mainly influenced by the careful addition of bentonite into the glass cylinder. In other words, the influence of the examiner seems to be the most important one (Olsta et al. 2004).

The water adsorption test was originally proposed by Enslin in 1933 and improved several times later on. Today it is mainly used in the clay industry, civil engineering and soil science under the name Enslin-Neff method (Kaufhold & Dohrmann 2008). In Germany this method is standardized (DIN 18132). Many authors have identified that the reproducibility of the Enslin-Neff method is strongly influenced by the laboratory ambient conditions, particularly temperature and relative humidity. This test is broadly accepted also as a quick method for the estimation of the mineral composition of clay materials, since

montmorillonites (bentonites) possess a large swelling capacity, as opposed to kaolinites or other clay minerals. For environmental applications, sodium bentonites or sodium activated bentonites are used for the production of GCLs as a hydraulic barrier. This test can, therefore, be used for the manufacturing quality control of the mineral component in the GCLs production stage, but also as a simple and quick method for construction quality control purposes or the estimation of long-term properties (DGGT 1993, 2002).

3 RESULTS AND STATISTICAL ANALYSES

According to the JCGM 100 "uncertainty (of measurement) is a parameter, associated with the result of a measurement, that characterizes the dispersion of the values that could reasonably be attributed to the measurand". In this paper, the type A evaluation of uncertainty is used which is based on the statistical analysis of laboratory data sets. The uncertainty in measurements is expressed using the arithmetic mean, standard deviation and coefficient of variation. The coefficient of variation as the relative standard deviation is a dimensionless measure of variability which enables comparing the precision of different methods.

As mentioned before, the swell index test (ASTM D5890) and Enslin-Neff water adsorption test (DIN 18132) were performed. Type III reagent water was used in all tests. The results of the measurement were determined on the basis of laboratory data sets obtained under repeatability conditions, r (the same: measurement procedure, observer, measuring instrument, conditions at the same location) and under reproducibility conditions, R (the changed parameter was the observer and drying temperature for the sample preparation).

The swell index test results are summarized in Table 1 for 120 tests in total, performed by two observers and by using two drying temperatures in the sample preparation phase.

Table 1. Swell index test results (in ml/2 g).

Statistical parameter*	Units	1st observer	2nd observer	1st observer	2nd observer
		Drying temperature for sample preparation			
		60°C		105°C	
min/max $value$	ml	22.5/24.5	24.0/25.0	24.0/24.5	24.0/24.5
$\overline{x}$	ml	23.7	24.5	24.4	24.3
$s_r = \left(\dfrac{\sum_{k=1}^{n}(x_k-\overline{x})^2}{n-1} \right)^{1/2}$	ml	0.59	0.31	0.33	0.24
$u_r = \frac{s_r}{\sqrt{n}}$	ml	0.11	0.06	0.06	0.04
$CV_r = \frac{s_r}{\overline{x}} \cdot 100$	%	2.49	1.25	1.37	0.99
$r = 2\sqrt{2}s_r$	ml	1.65	0.86	0.94	0.67
$\overline{x}$	ml	24.08		24.41	
$s_R = \left(\dfrac{\sum_{k=1}^{2n}(x_k-\overline{x})^2}{2n-1} \right)^{1/2}$	ml	0.64		0.30	
$u_R = \frac{s_R}{\sqrt{2n}}$	ml	0.08		0.04	
$CV_R = \frac{s_R}{\overline{x}} \cdot 100$	%	2.65		1.22	
$R = 2\sqrt{2}s_R$	ml	1.79		0.83	
$U_{rel} = \frac{u_R}{\overline{x}} \cdot 100$	%	0.34		0.16	

*NOTES: s - standard deviation, u - standard uncertainty, CV - coefficient of variation, U_{rel} - relative uncertainty, r - repeatability, R - reproducibility, n=30.

Table 2. Enslin-Neff water adsorption test results, w_A (in %).

Statistical parameter*	Units	1st observer	2nd observer	1st observer	2nd observer
		— Drying temperature for sample preparation			
		60°C		105°C	
min/max *value*	%	377.5/700.0	477.5/720.0	477.5/737.5	460.0/647.5
$\overline{x}$	%	540.1	569.0	586.4	559.9
$s_r = \left(\dfrac{\sum_{k=1}^{n}(x_k-\overline{x})^2}{n-1}\right)^{1/2}$	%	73.46	52.05	51.81	41.67
$u_r = \frac{s_r}{\sqrt{n}}$	%	13.41	9.50	9.46	7.61
$CV_r = \frac{s_r}{\overline{x}}\cdot 100$	%	13.60	9.15	8.84	7.44
$r = 2\sqrt{2}s_r$	%	205.69	145.74	145.07	116.68
$\overline{x}$	%	554.55		573.13	
$s_R = \left(\dfrac{\sum_{k=1}^{2n}(x_k-\overline{x})^2}{2n-1}\right)^{1/2}$	%	64.78		48.48	
$u_R = \frac{s_R}{\sqrt{2n}}$	%	8.36		6.26	
$CV_R = \frac{s_R}{\overline{x}}\cdot 100$	%	11.68		8.46	
$R = 2\sqrt{2}s_R$	%	181.39		135.75	
$U_{rel} = \frac{u_R}{\overline{x}}\cdot 100$	%	1.51		1.09	

*NOTES: s - standard deviation, u - standard uncertainty, CV - coefficient of variation, U_{rel} - relative uncertainty, r - repeatability, R - reproducibility, n=30.

An inter-laboratory study of the test was performed in 1999 (ASTM D5890) for seven clay samples and ten laboratories, showing the within-laboratory repeatability limit, CV_r % of 2-5%. The statistical analyses of our laboratory data sets showed a CV_r % from 1 to 2.5, which is in line with the ASTM D5890 precision requirement.

As the test results are presented according to the standard requirements to the nearest 0.5 ml, they do not follow the normal distribution, and it was impossible to perform the standard statistical analyses. Nevertheless, at the drying temperature of 60° the results obtained by the first observer are more dispersed (indicated by a greater standard deviation) compared to the results of the second observer, which also leads to a relatively high reproducibility; this difference between the two observers is smaller at the temperature of 105°. The results of the detailed statistical analysis indicate that the assessment of the measurement uncertainty type A was properly estimated. Also, the calculated relative uncertainty, U_{rel}, shows that the measurement uncertainty was reasonably estimated.

The water adsorption test results are summarized in Table 2 for 120 tests in total, performed under the same conditions as mentioned for the swell index testing.

Figure 1 summarizes all test results, for both observers and drying temperatures. Figures 2 and 3 show the comparison between two observers under the same drying temperature, 60°C or 105°C, respectively.

At both drying temperatures the results obtained by the first observer are slightly smaller and more dispersed compared to the results of the second observer; this difference between the two observers is slightly more visible at the temperature of 105°.

The Shapiro-Wilk test for normality was performed in the R programming language for the measurement results for each observer and each drying temperature, as well as the combined results for each temperature. No statistically significant deviations from normality
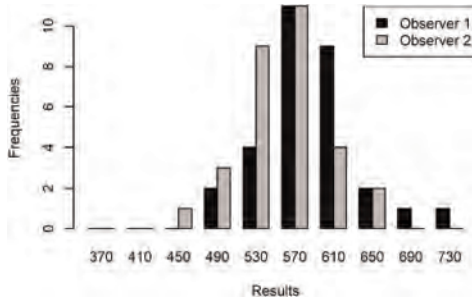
Figure 1. Water adsorption test results for two observers under two drying temperatures.
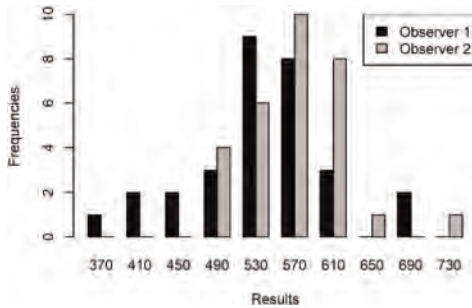
Figure 2. Water adsorption results for two observers and the drying temperature of 60°C.
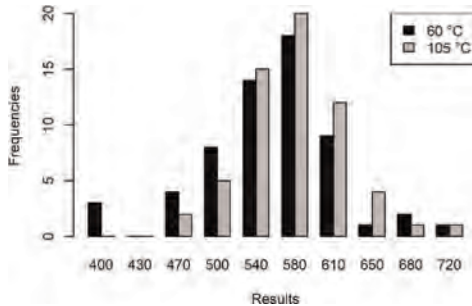
Figure 3. Water adsorption results for two observers and the drying temperature of 105°C.

were found at significance level of 5% for all data sets. The F-test and t-test were performed in R to compare variances and means for the same observer at two drying temperatures, as well as for two observers at the same temperature. There were no significant differences found at 5% significance level, except for the first observer at two temperatures (the mean is smaller at 60°) and for two observers at the temperature of 105°C (the mean is larger for the first observer). A certain difference in variability between the two temperatures was observed by testing at the 5% significance level for combined results of the two observers (the variability is larger at 60°), while no statistically significant difference was found between their means.

As for the swell index test, the results of the detailed statistical analysis indicate that the assessment of the measurement uncertainty type A was properly estimated, giving a slightly

higher relative uncertainty, U_{rel}, which is probably due to the greater influence of the laboratory ambient conditions.

4 DISCUSSION AND CONCLUSION

The mineral component of GCL determines its hydraulic conductivity and sealing function. In the production stage, the clay mineral component (bentonite) can be obtained from various producers and deposits, with variable composition and quality. The swell index test (ASTM D5890) and water adsorption test (DIN 18132) are commonly used as simple and quick testing methods for the QC and QA in the production and construction stage, as well as for the control of the durability of GCLs in various structures and environments.

To examine the sensitivity of the swell index and water adsorption regarding variations in the test procedure, 120 tests were performed for both methods by two observers, using two temperatures ($60°C$ and $105°C$) in the sample preparation phase. All tests were performed in the same laboratory that was not conditioned (air temperature and relative humidity was changeable) intentionally to mimic the practice in many commercial laboratories.

Our test results and statistical analysis showed that statistically significant deviations from normality for all data sets were not found at the significance level of 5%. The F-test and t-test were performed in R to compare variances and means for the same observer at two drying temperatures, as well as for two observers at the same temperature. There were no significant differences found at the 5% significance level, except for the first observer at two temperatures; for two observers at the temperature of $105°C$, and between the two temperatures for combined results of the two observers.

The results of the detailed statistical analysis indicate that the assessment of the measurement uncertainty type A was properly estimated for both testing methods. Also, the calculated relative uncertainty, U_{rel} for the swell index test shows that the measurement uncertainty was reasonably estimated. A slightly higher relative uncertainty for the water adsorption test was probably caused by a greater influence of the laboratory ambient conditions. To conclude, our research showed that even in a non-conditioned laboratory, reproducibility and repeatability for the swell index and water adsorption test results can be obtained.

REFERENCES

DGGT 1993 *Geotechnics of Landfill Design and Remedial Works - Technical Recommendations – GLR*, 2nd ed. (Berlin: Ernst & Sohn)

DGGT 2002 *Empfehlungen zur Anwendung Geosynthetischer Tondichtungsbahnen, EAG-GTD*, (Berlin: Ernst & Sohn)

Erickson RB and Jesionek KS 2004 *ASTM STP 1456*, ed R E Mackey and K von Maubeuge (ASTM International) pp. 75–91

JCGM 100:2008 *Evaluation of Measurement Data: Guide to the Expression of Uncertainty in Measurement*. https://www.bipm.org/en/committees/jc/jcgm/publications

Kaufhold S and Dohrmann R 2008 *Clays and Clay Minerals* **56/6** 686

Olsta JT, Chung JH and Daniel DE 2004 *ASTM STP 1456*, ed R E Mackey and K von Maubeuge (ASTM International) pp. 3–10

Shear strength prediction of fiber–reinforced soils based on direct shear test results

I.N. Markou, E.D. Evangelou & D.G. Chalkos
Democritus University of Thrace, Xanthi, Greece

ABSTRACT: The present study aims at the development of a model for the shear strength prediction of any type of soil reinforced with synthetic fibers of circular cross-section. A database was created from the available literature comprising experimental results of direct shear tests conducted in soils ranging from sands to clays, reinforced with polypropylene and nylon fibers. The shear stress at failure of fiber-reinforced soils was correlated to independent variables pertinent to the soil, fiber, and laboratory test by performing multivariable ordinary linear regression analyses of the experimental results with suitable statistical software. The model with the best performance exhibits a coefficient of multiple determination, R^2, equal to 0.96 and estimates successfully the experimental results used for model testing at a rate equal to 77%. The predictions of the shear strength parameters of fiber-reinforced soils, based on the proposed model, are in reasonable agreement with the measured values after applying appropriate reduction factors.

1 INTRODUCTION

Soil reinforcement with geogrids, geotextiles, metal strips, fibers etc. is an effective technique for increasing the strength and stability of the soil in various applications, including retaining structures, embankments, foundations, slopes and pavements. As the fiber inclusions bring several technical, economic and environmental benefits, in recent years, a great deal of interest has been created worldwide on the potential applications of fibers within the soils and other similar materials, such as coal ashes and mine tailings (Shukla 2017). Fibers are generally available in natural, synthetic and waste forms. Synthetic fibers made of polymers, such as polypropylene, polyester and polyethylene, are superior to natural fibers in terms of mechanical behavior, standardization and durability over time. Nevertheless, natural fibers emanating from various plants are used in countries where they are available in large amounts. Utilization of waste fibers in constructions can solve their disposal problems in a cost-effective and environmentally friendly manner.

Over the past 30–35 years, the laboratory and field research studies have shown that the use of fibers as a tension-resisting element and/or an admixture causes significant modification and improvement in the engineering properties (strength, stiffness, permeability, compressibility, etc.) of soils and other similar materials (Shukla 2017). The improvement of soil shear strength due to fiber reinforcement is investigated in the laboratory using mainly direct shear and triaxial compression tests (e.g. Anagnostopoulos *et al.* 2014; Atom & Al-Tamini 2010; Benziane *et al.* 2019; Chen 2010; Diab *et al.* 2016; Esna-Ashari & Asadi 2008; Falorca & Pinto 2011; Hejazi *et al.* 2014; Kar *et al.* 2010; Lirer *et al.* 2011; Mirzababaei *et al.* 2018; Pradhan *et al.* 2012; Santiago *et al.* 2013; Zaimoglu & Yetimoglu 2012). Test results have shown that the strength of fiber-reinforced soil depends on several factors such as: fiber content, fiber geometric characteristics, confining pressure or normal

stress and soil characteristics. The trustworthy prediction of the shear strength of fiber-reinforced soils can facilitate the reliable design and enhance the utilization of fiber-reinforced soils in civil engineering projects. As a result, attempts have been made to develop models for the estimation of the strength of fiber-reinforced soil, either by analytical solutions (Michalowski & Cermák 2003; Michalowski 2008; Shukla 2017; Zornberg & Li 2003) or by statistical processing (Dutta &Venkatappa 2007; Lirer *et al.* 2011; Maliakal & Thiyyakkandi 2013; Ranjan *et al.* 1996; Sivakumar Babu & Vasudevan 2008). In most cases, the development of these models was based solely on the experimental results of the same research effort and the produced models refer to specific type of soil, i.e. sand or clay. Also, some of these models cannot be applied easily as they employ parameters difficult to determine.

The abovementioned information indicates that a practical tool, applicable to any type of soil and based on simple parameters pertinent to the soil and fiber, could be an efficient means for shear strength prediction of fiber-reinforced soils. The study reported herein aims toward the development of a prediction tool having these characteristics. Accordingly, this presentation includes: (a) the database created for the purposes of this investigation, comprising shear strength measurements from direct shear tests conducted on various fiber-reinforced soils and found in the literature, (b) development of the new prediction model by performing multivariable ordinary (conventional) linear regression analyses of the obtained experimental results, and (c) documentation of model performance.

2 EXPERIMENTAL MEASUREMENTS

The first step for the development of the strength prediction model was the selection of the variables. The dependent variable should be quantified efficiently and the independent variables should represent factors affecting substantially the shear strength of fiber-reinforced soil. All variables should not hinge on specific materials and procedures. Accordingly, the shear stress at failure, $\tau_{f,r}$, determined by direct shear testing on fiber-reinforced soil was chosen as the dependent variable. Although the cohesion, c, and the friction angle, φ, are generally used for the quantification of shear strength, they were not used as dependent variables because their determination results from test series limiting in this way the number of the available measurements. The dependent variable was correlated to five independent variables pertinent to the soil, the fiber and the testing procedure.

The normal stress, σ_n, used in the direct shear tests was the first independent variable because it has been observed that its increase has a beneficial effect on the strength of fiber-reinforced soil (Qu *et al.* 2013). Due to the large number of factors affecting the behavior of soils, it was decided for simplicity reasons to use the shear stress at failure, $\tau_{f,u}$, of the unreinforced soil as the sole, independent variable representing the soil. The increase of the fiber content in the soil leads to an increase of shear strength up to a limit. Beyond this limit, further increase of fiber content causes an increase of the porosity of fiber-reinforced soil and, as a result, a decrease of its shear strength (Hoare 1979). The fiber cross-section and dimensions (e.g. diameter and length) are also important since they determine the contact surface of the fibers with the surrounding soil (Gray & Al-Refeai 1986). For that reason, the aspect ratio, A_r, (ratio of the fiber length to the fiber diameter) affects the shear strength of fiber-reinforced soil (Sadek *et al.* 2010). Another factor influencing the mechanism of soil reinforcement is the tensile strength of the fiber (Zornberg & Li 2003). Based on this information, the selected independent variables for the fibers are: the content, w_f, (percentage of fibers by weight of dry soil), the tensile strength, $\sigma_{y,f}$, and the aspect ratio, A_r.

For statistical processing, at least 20 measurements are needed for each independent variable used in the model (Coakes & Steed 1999; Field 2009; Harrel 2002). Taking into consideration that the cross-section type of the fiber affects the strength of fiber-reinforced soil, it was decided to use in this study the measurements obtained from direct shear tests

Table 1. Data of selected research studies based on direct shear tests.

				Fiber characteristics				Direct shear tests		
									Shear stress at failure	
				Aspect ratio	Tensile strength	Fiber content		Normal stress	Unreinforced soil	Reinforced soil
Reference	Number of tests	Soil type	Material*	A_r	$\sigma_{y,f}$ (MPa)	w_f (%)	Type	σ_n (kPa)	$\tau_{f,u}$ (kPa)	$\tau_{f,r}$ (kPa)
[1]	17	Soft clay	P	312–594	600	0.25–0.5	CD	50–200	27–98	49–139
[2]	59	Sandy silt Silty clay	P	400–480	400–500	0.3–1.1	CU CD	50–200	26–151	39–221
[3]	2	Silty sand	P	545–864	375	0.1–0.2	CD	49–98	73–113	88–121
[4]	5	Sand	P	781–1563	200	0.25–1	CD	110	106	125–190
[5]	45	Clay	P	75–125	120	0.1–0.5	UU	100–300	92–191	103–457
[6]	8	High plasticity silt	P	240	360	0.25–1	CD	50–200	131–288	160–331
[7]	15	Clay	P	75	120	0.1–0.5	UU	100–300	91–190	103–366
[8]	12	Sandy soil	P	84–385	250–1004	1–4	UU	28–110	9–40	14–62
[9]	56	Sandy silt	N	667–2000	1500	0.2–1	UU	50–300	70–295	75–390

*P: Polypropylene, N: Nylon.

conducted on soil specimens reinforced with not crimped fibers of circular cross-section. This preference was dictated by the insufficient number of the available measurements obtained for fibers of other cross-section geometries. After an extensive literature review, the available for statistical analysis set of 219 measurements of the shear strength of fiber-reinforced soils, ranging from sands to clays and including values for all abovementioned independent variables, is presented in Table 1. These measurements were obtained from unconsolidated–undrained (UU), consolidated–undrained (CU) and consolidated–drained (CD) direct shear tests reported by Mirzababaei *et al.* 2018 [1], Anagnostopoulos *et al.* 2014 [2], Hejazi *et al.* 2014 [3], Falorca & Pinto 2011 [4], Pradhan *et al.* 2012 [5], Zaimoglu & Yetimoglu 2012 [6], Kar *et al.* 2010 [7], Atom & Al-Tamini 2010 [8] and Esna-Ashari & Asadi 2008 [9], and indicate shear strength increase of the soil due to fiber reinforcement. A percentage nearly equal to 80% (180 measurements) of the data presented in Table 1 was used for the generation of the model, whereas the remaining 39 measurements (≈20%) were used for the evaluation of the prediction efficiency of the model. This partitioning was made with extreme care in order to maintain the homogeneity and the representativeness of the two samples.

3 DEVELOPMENT AND EFFICIENCY OF MODEL

The preparation of the set of measurements and the selection of the dependent and independent variables were followed by the statistical analysis using the multivariable ordinary linear regression (MVOLR) method. A large number of analyses were performed using a special statistical software in an attempt to develop a model for predicting the value of the shear stress at failure of fiber-reinforced soil, $\tau_{f,r}$, based on the results of direct shear tests. A model developed by applying the multivariable ordinary linear regression method to a set of data, has the following form:

$$y = \alpha_0 + \alpha_1 x_1 + \alpha_2 x_2 + \cdots + \alpha_n x_n \tag{1}$$

where y is the dependent variable, $\alpha_0, \alpha_1, \ldots, \alpha_n$ are the partial coefficients and $x_1, x_2, \ldots, x_n$ are the independent variables.

For statistical purposes, the data must be checked for independence and regularity of observations, linearity between dependent and independent variables, equality of

dispersion as well as for the assumption of multi-collinearity and singularity (Norusis 2002). The verification of independence was carried out by using the Durbin – Watson index, which should attain values between 1.0 and 3.0 (Field 2009). The regularity, linearity and dispersion equality were checked using the relevant graphs provided by the software. The existence of multi-collinearity and singularity is not desirable in the analyses and was checked by using the eigenvalue of the covariance matrix, the condition index, the tolerance interval and the variance inflation factor. During the analyses, extreme and impact observations were checked with appropriate indicators. More specifically, the Mahanobis distance and the Leverage measure were used for extreme values, whereas the Cook distance, DfFits and DfBetas indicators were used for impact observations. Finally, the levels of statistical significance (p-value) for each variable as well as the value of t-statistics were checked in all analyses. The p-value must be lower than 5% and the absolute value of t-statistics must be greater than 2. Apart from the aforementioned statistical checks, the credibility of models was also attested by the high values of the coefficient of multiple determination, R^2.

The resulting models were also tested for their prediction efficiency utilizing, as stated above, a percentage approximately equal to 20% of the total set of measurements. The predicted values, $\tau_{f,r,predicted}$, of the shear stress at failure of fiber-reinforced soil were estimated by applying the models to these testing measurements. The deviation, Δ (%), of the predicted values from the experimental values, $\tau_{f,r,measured}$, was then calculated as follows:

$$\Delta\ (\%) = \frac{\tau_{f,r,measured} - \tau_{f,r,predicted}}{\tau_{f,r,measured}} \cdot 100 \tag{2}$$

The predicted values presenting deviation equal to or less than $\pm 20\%$ are considered acceptable. By finding the total number of acceptable values, the prediction efficiency of each model was obtained for the testing measurements as follows:

$$Efficiency\ (\%) = \frac{total\ number\ of\ acceptable\ values}{total\ number\ of\ measurements} \cdot 100 \tag{3}$$

The different combinations and variations of the aforementioned independent variables led to the examination of numerous models. Two types of analyses were performed, one including the constant term, α_0, (Equation 1) in the model and another one without the constant term so as to find the optimal equation. As a result, the model exhibiting the highest coefficient of multiple determination, R^2, the best statistical characteristics and the largest prediction efficiency is:

$$\left(\frac{\tau_{f,r}}{\sigma_n}\right) = 0.001 * \left(\frac{Ar}{\sigma_n}\right)^{1.75} - 3.958 * 10^{-5}\left(\frac{\sigma_{y,f}}{\sigma_n}\right)^{0.95} + 3.636 * \left(\frac{w_f}{\sigma_n}\right)^{0.75} + 1.462 * \left(\frac{\tau_{f,u}}{\sigma_n}\right)^{0.85} \tag{4}$$

This best model does not include constant term and is statistically acceptable as all p-values are lower than 5% and all absolute values of t-statistics are greater than 2. The model presents a value of the coefficient of multiple determination, R^2, equal to 0.96 indicating satisfactory conformity to the experimental measurements. The prediction efficiency of the model, computed with the Equations 2 and 3, is also satisfactory as it is equal to 77%. The performance of the proposed model is also depicted in Figure 1 where the estimated values of shear stress at failure of fiber-reinforced soil, $\tau_{f,r}$, are compared to those determined experimentally. It is confirmed that 30 (77%) of the 39 predicted values lie within the area set by the acceptable deviation of $\pm 20\%$ from the testing measurements.
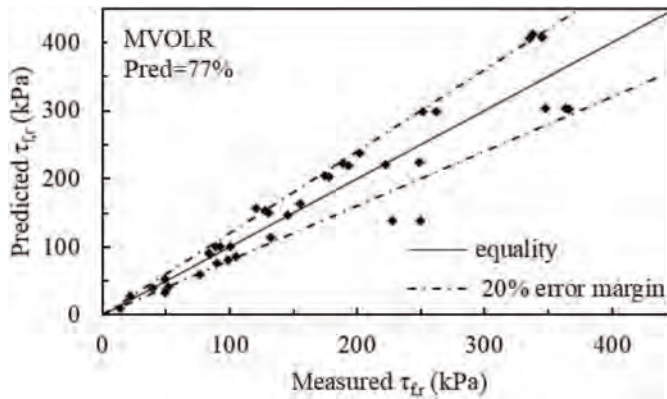
Figure 1.   Performance of prediction model (testing data).

4   ESTIMATION OF SHEAR STRENGTH PARAMETERS

The shear strength of soil is generally used in the design of geotechnical engineering projects in terms of cohesion, c, and friction angle, φ. Therefore, it was decided to evaluate the effectiveness of the proposed model in the prediction of shear strength parameters of fiber-reinforced soil as well. For this purpose, the 74 cases of failure envelopes resulted from direct shear tests conducted on various fiber-reinforced soils were collected from the available literature and the corresponding values of shear strength parameters are summarized in Table 2. The numbering of references in Table 2 coincides with that of Table 1. Subsequently, estimated values of shear stress at failure, $\tau_{f,r}$, were obtained by applying Equation 4 to these 74 cases and were utilized for plotting the estimated linear failure envelopes and determining the predicted values of cohesion, c, and friction angle, φ, of the fiber-reinforced soils.

The predicted values of shear strength parameters are compared in Figure 2 to those determined experimentally. It is easily observed that the proposed model overestimates the friction angle values and the cohesion values up to 25 kPa (initial values in Figure 2).

Table 2.   Shear strength parameter values of fiber-reinforced soils.

Reference	Soil type	Fiber material	Test type	Number of failure envelopes	Shear strength parameters	
					Cohesion c (kPa)	Friction angle φ (°)
[1]	Soft clay	Polypropylene	CD	5	29–52	22–27
[2]	Sandy silt	Polypropylene	CU	3	8–20	38–45
[2]	Silty clay	Polypropylene	CD	9	5–33	22–39
[2]	Silty clay	Polypropylene	CU	9	6–13	29–39
[3]	Silty sand	Polypropylene	CD	9	46–64	28–34
[5]	Clay	Polypropylene	UU	15	50–165	27–46
[6]	High plasti-city silt	Polypropylene	CD	4	79–142	26–49
[7]	Clay	Polypropylene	UU	5	100–130	25–42
[9]	Sandy silt	Nylon	UU	15	27–58	43–49
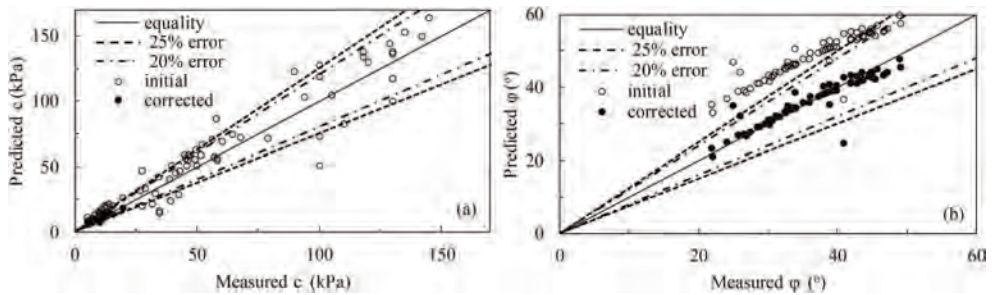
Figure 2. Comparison between predicted and measured values of shear strength parameters.

Consequently, the overestimated values of friction angle and cohesion were reduced by 12° and 30%, respectively, and the corrected values are also presented in Figure 2 in comparison with the measured values of shear strength parameters. It can be observed that, after correction, 49 (66%) cohesion values and 71 (96%) friction angle values lie within the area set by the acceptable deviation of ±20% from the measured values. In 48 (65%) of the 74 cases, the corrected values of both shear strength parameters lie simultaneously within the area set by the acceptable deviation of ±20% from the measured values. If the acceptable deviation from the measured values is increased to ±25%, 54 (73%) of the cohesion values, 72 (97%) of the friction angle values and 53 (72%) cases for both shear strength parameters are considered as estimated effectively by the proposed model.

5 CONCLUSIONS

Based on the results obtained in the investigation reported herein and within the limitations posed by the number of experimental measurements used, the following conclusions may be drawn:

- The model developed for the estimation of the shear stress at failure of fiber-reinforced soil using the multivariable ordinary linear regression method exhibits satisfactory performance as it presents value of the coefficient of multiple determination, R^2, equal to 0.96 and prediction efficiency equal to 77%. It is anticipated that this model can be further improved if the database of available measurements is enhanced with additional direct shear test results.
- The shear strength estimations of the proposed model lead to overestimated values of friction angle and of cohesion up to 25 kPa. By applying appropriate reduction factors to the overestimated values of shear strength parameters, the corrected values are in reasonable agreement with those determined experimentally.

REFERENCES

Anagnostopoulos, C.A., Tzetzis, D., & Berketis, K. 2014. Evaluation of the Shear Strength Behavior of Polypropylene and Carbon Fibre Reinforced Cohesive Soils. *Research Journal of Applied Sciences, Engineering and Technology* 7(20): 4327–4342.

Atom, M.F. & Al-Tamini, A.K. 2010. Effects of Polypropylene Fibers on the Shear Strength of Sandy Soil. *International Journal of Geosciences*, pp 44–50.

Benziane, M.M., Della, N., Denine, S., Sert, S. & Nouri, S. 2019. Effect of Randomly Distributed Polypropylene Fiber Reinforcement on the Shear Behavior of Sandy Soil. *Studia Geotechnica et Mechanica* 41(3): 151–159.

Chen, C.-W. 2010. Triaxial Compression and Extension Tests for Fiber-reinforced Silty Sand. *GeoShanghai 2010 Int. Conf. - Ground Improvement and Geosynthetics*, GSP no. 207, pp 367–375.

Coakes, S.J. & Steed, L.G. 1999. *SPSS Without Anguish.* New York, USA: Wiley & Sons.

Diab, A.A., Sadek, S., Najar, S. & Daya, M.H.A. 2016. Undrained Shear Strength Characteristics of Compacted Clay Reinforced with Natural Hemp Fibers. *International Journal of Geotechnical Engineering* 20(10): 1–8.

Dutta, R.K. & Venkatappa, R.G. 2007. Regression Models for Predicting the Behavior of Sand Reinforced with Waste Plastic. *Turkish Journal of Engineering and Environmental Sciences* 31: 119–126.

Esna-Ashari, M. & Asadi, M. 2008. A Study on Shear Strength and Deformation of Sandy Soil Reinforced with Tire Cord Wastes. *Proc. 4th Asian Conf. on Geosynthetics*, pp 355–359.

Falorca, I.M.C.F.G. & Pinto, M.I.M. 2011. Effect of Short, Randomly Distributed Polypropylene Microfibers on Shear Strength Behavior of Soils. *Geosynthetics International* 18(1): 1–11.

Field, A. 2009. *Discovering Statistics using SPSS.* London: SAGE Publications.

Gray, D. & Al-Refeai, T. 1986. Behavior of Fabric-versus Fiber-reinforced Sand. *Journal of Geotechnical Engineering* 112(8): 804–820.

Harrel, F.E. 2002. *Regression Modeling Strategies: With Applications to Linear Models, Logistic Regression, and Survival Analysis.* New York, USA: Springer.

Hejazi, S.M., Baghulizadeh, A.R., Nateghi, M. & Mardani, M. 2014. Shear Modelling of Polypropylene-Fiber-reinforced Soil Composite Using Electrical Conductivity Contour Technique. *Journal of Industrial Textiles* 45(1): 133–151.

Hoare, D.J. 1979. Laboratory Study of Granular Soils Reinforced with Randomly Oriented Discrete Fibers. *C.R. Coll. Int. Reinforcement des Sols. Paris*, pp 47–52.

Kar, R.K., Pradhan, P.K. & Naik, A. 2010. Strength Characteristics of Randomly Distributed Fiber-reinforced Soil. *International Journal of Earth Sciences and Engineering* 3(3): 434–440.

Lirer, S., Flora, A. & Consoli, N.C. 2011. On the Strength of Fibre-reinforced Soils. *Soils and Foundations* 51 (4): 601–609.

Maliakal, T. & Thiyyakkandi, S. 2013. Influence of Randomly Distributed Coir Fibers on Shear Strength of Clay. *Geotechnical and Geological Engineering* 31: 425–433.

Michalowski, R.L, & Cermák, J. 2003. Triaxial Compression of Sand Reinforced with Fibers. *Journal of Geotechnical and Geoenvironmental Engineering* 129: 125–136.

Michalowski, R.L. 2008. Limit Analysis with Anisotropic Fibre-reinforced Soil. *Geotechnique* 58(6): 489–501.

Mirzababaei, M., Arulrajah, A., Haque, A., Nibalkar, S. & Mohajerani, A. 2018. Effect of Fiber Reinforcement on Shear Strength and Void Ratio of Soft Clay. *Geosynthetics International* 25(4): 471–480.

Norusis, M. 2002. *SPSS 11.0. Guide to Data Analysis.* USA: Prentice Hall.

Pradhan, P.K., Kar, R.K. & Naik, A. 2012. Effect of Random Inclusion of Polypropylene Fibers on Strength Characteristics of Cohesive Soil. *Geotechnical and Geological Engineering* 30: 15–25.

Qu, J., Li, C. & Liu, B. 2013. Effect of Random Inclusion of Wheat Straw Fibers on Shear Strength Characteristics of Shanghai Cohesive Soil. *Geotechnical and Geological Engineering* 31: 511–518.

Ranjan, G., Vasan, R. & Charan, H. 1996. Probabilistic Analysis of Randomly Distributed Fiber-reinforced Soil. *Journal of Geotechnical Engineering* 122(6): 419–426.

Sadek, S., Najjar, S.S. & Freiha, F. 2010. Shear Strength of Fiber-reinforced Sands. *Journal of Geotechnical and Geoenvironmental Engineering* 136: 490–499.

Santiago, G.A., Franco, C., Consoli, N.C. & Botaro, V.R. 2013. Study of Mechanical Behavior of Sand Soil Reinforced with Carua Treated Fibers with Asphalt. *Material Science Forum* 730–732: 319–324.

Shukla, S.K. 2017. *Fundamentals of Fibre-reinforced Soil Engineering.* Singapore: Springer.

Sivakumar Babu, G.L. & Vasudevan, A.K. 2008. Strength and Stiffness Response of Coir Fiber-reinforced Tropical Soil. *Journal of Materials in Civil Engineering* 20: 571–577.

Zaimoglu, A.S. & Yetimoglu, T. 2012. Strength Behavior of Fine Grained Soil Reinforced with Randomly Distributed Polypropylene Fibers. *Geotechnical and Geological Engineering* 30: 197–203.

Zornberg, J.G. & Li, C. 2003. Design of Fiber-reinforced Soil. *Proc. 12th Panamerican Conf. on Soil Mechanics and Geotechnical Engineering* 2: 2193–2200.

Reduction in geosynthetics ultimate tensile strength caused by the dropping of recycled backfilling materials

Mateus P. Fleury
São Carlos School of Engineering (EESC), University of São Paulo (USP), São Carlos, Brazil
Mauá Institute of Technology (IMT), São Caetano do Sul, Brazil

Mateus A. Lima & Jefferson Lins da Silva
São Carlos School of Engineering (EESC), University of São Paulo (USP), São Carlos, Brazil

Eder C.G. Santos
School of Civil and Environmental Engineering (EECA), Federal University of Goiás (UFG),
Goiânia, Brazil

ABSTRACT: To handle the sustainable construction required by the modern world, designers of geosynthetic reinforced soil structures should search for alternative backfill materials, such as recycled materials. Since installation damage is responsible for significant changes in geosynthetic stress-strain behavior, the ones caused by the recycled ones must be carefully assessed and quantified. This study aims to assess the damage to geosynthetics caused by the backfill material-dropping process. Four geosynthetics (two geogrids and two non-woven geotextiles) and five types of recycled aggregates (with different grain–size distributions) were tested. The experimental program consists of laying the geosynthetic on the area of the recycling plant and the individual launching of the tested backfill materials (using a backhoe loader) from two drop heights: 1.0 m and 2.0 m. The geosynthetic samples were then exhumed to obtain specimens, perform wide-width tensile tests, and assess their ultimate tensile strength. The geotextiles experienced reductions in the property of interest for all scenarios investigated. These reductions were higher than the ones experienced by the geogrids. Within some limitations, the results show that the damage increased as the maximum grain size of the backfill increased. Further investigations are required using sophisticated statistical analysis adopting a broader database.

1 INTRODUCTION

The geosynthetic properties along a structure lifetime must meet the ones established in the design phase. For geosynthetic reinforced soil (GRS) structures, three independent mechanisms that affect the durability of geosynthetics are required for design and have led to several investigations: i) installation damage (e.g., Austin 1997; Huang & Wang 2007; Hufenus et al. 2005; Lim & McCartney 2013; Paula et al. 2004; Pinho-Lopes et al. 2018; Richardson 1998), ii) creep behavior (e.g., (Andrawes et al. 1984; den Hoedt 1988; França & Bueno 2011; Greenwood 1990; Thornton et al. 1997; Zornberg et al. 2004), and iii) lifetime degradation (e.g., (Cassidy et al. 1992; Elias et al. 1998; Halse et al. 1988, 1987; Mathur et al. 1994)). However, one must consider specific work conditions to assess the geosynthetic durability.

According to Huffenus et al. (2005), the immediate reduction caused by the installation activities is the most relevant mechanism affecting the reinforcement element durability of a

GRS structure. The investigations into this mechanism encompass the damage caused by the backfill material drop and its posterior compaction. However, the influence of the backfill material drop process height has been addressed by a few studies, particularly when using recycled aggregates. Barbosa and Santos (2013) observed the visual damage caused by the drop of recycled construction and demolition waste (RCDW) from different heights (1.0 m and 2.0 m) on a PET geogrid and concluded that no visual damage occurred as the drop height increased. Fleury et al. (2019) reported a slight reduction in geogrid ultimate tensile strength due to the dropping process from 1.0 m and 2.0 m (maximum reduction factor – RF_{Drop} – equal to 1.11) and highlighted no direct association between the drop height and RF_{Drop} values. In another study, Barbosa et al. (2016) showed higher values of RF_{Drop} for the drop from 2.0 m (1.21) than from 1.0 m (1.11) for a non-woven geotextile.

These previous investigations have shown that the backfill material drop height may compromise the geosynthetic durability, and therefore must be investigated. This paper aims to assess the damage caused by different recycled aggregates (backfill material) on geosynthetic ultimate tensile strength. Moreover, this paper investigates if there is any correlation between the backfill grain size distribution and the reduction factor obtained.

2 MATERIALS AND METHODS

2.1 Geosynthetics

This study tested four poly(ethylene) terephthalate (PET) geosynthetics: two non-woven needle-punched geotextiles (GTXnw1 and GTXnw2) and two geogrids (GGR1 and GGR2). In Brazil, the geogrids are mainly used for the construction of reinforced soil structures. The non-woven geotextiles were chosen to quantify how the geotextiles' mass per unit area (M_A) influences the materials' survivability to the damage caused by the backfill drop. Table 1 shows some properties and characteristics of the materials according to their manufacturer's catalogues.

Table 1. Characteristics and properties of the geosynthetics investigated.

Properties / Characteristics	Unit	GTXnw1	GTXnw1	GGR1	GGR2
Tensile strength MD*	kN/m	6.0	14.0	35.0	55.0
Elongation at break MD*	%	>70	>70	≤10	≤10
Mass per unit area	g/m^2	130	300	n.a**	n.a**
Open size	mm	n.a**	n.a**	20 x 20	20 x 20
Manufacturer	–	A	A	B	B

Notes: * Machine direction; ** not applicable.

2.2 Backfill materials

Recycled construction and demolition waste (RCDW) was provided by a recycling plant located in Aparecida de Goiânia-GO, Brazil. After a sorting and doubled-stage crushing process (jaw crusher), the recycled aggregates were sieved to obtain materials classified according to their grain size (d) ranges: i) gravel A (GA; $d > 19$ mm), ii) gravel B (GB; 19 mm $< d < 9.5$ mm), iii) gravel C (GC; 9.5 mm $< d < 4.8$ mm) and iv) sand (SA; $d < 4.8$ mm). With the mixture of equal volumes of GA, GB, GC and SA, the recycling plant produced graded gravel (GG) material, which is the material most in demand nowadays. Figure 1 shows the grain size distribution curves of the materials investigated, and some characteristics are presented in Table 2.
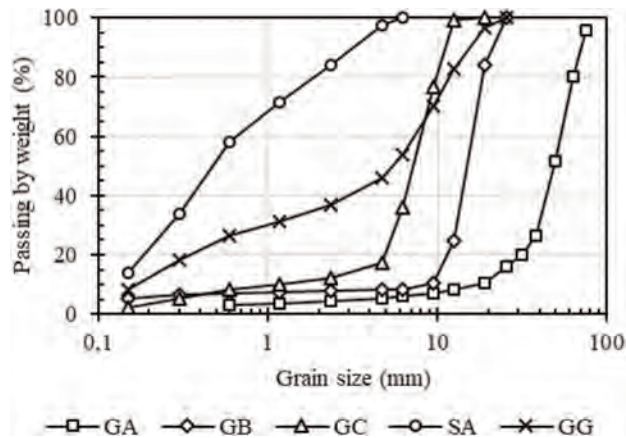
Figure 1.   Grain size curves of RCDW.

Table 2.   Characteristics and properties of the RCDW.

Characteristic / Property	RCDW				
	GA	GB	GC	SA	GG
Fine grained specific unit weight (kN/m^3)	n.a[a]	n.a[a]	26.0	25.8	25.9
Coarse grained specific unit weight (kN/m^3)	n.t[b]	22.8	24.3	n.a[a]	23.1
Coefficient of curvature (C_C)	1.8	3.3	5.5	0.8	1.0
Coefficient of uniformity (C_U)	3.1	4.1	12.0	4.9	43.4
Classification (ASTM D 2487-06)	GP[c]	GP[c]	GP[c]	SP[d]	GW[e]
Shape index	n.t[b]	2.0	2.1	n.t[b]	2.1

Note: [a] not applicable; [b] not tested; [c] poorly-graded gravel; [d] poorly-graded sand; [e] well-graded gravel.

2.3   Damage simulation

The present study assesses the damage caused by the backfill drop, and does not consider the damage that could be due to the backfill compaction. The in-field tests were carried out near the recycling plant operation area. Firstly, loose gravel and strange materials (e.g., wood and metal) present on the surface (compacted RCDW) were removed manually. Afterward, geosynthetic samples (1.0 m long and 2.4 m wide) were laid over the flat surface. The backhoe loader was used to drop the backfill material (one at a time) from 1.0 m or 2.0 m height (considering the bottom part of the shell). After dropping the backfill over the whole area, the geosynthetics samples were exhumed carefully with a hoe and shovel – avoiding any additional damage.

After exhuming the samples, ten specimens were obtained from the damaged and undamaged samples (virgin condition as received from the manufacturers). The geotextile specimens (300 mm long and 200 mm wide) were tested accordingly to ASTM D 4595 (2005) using a universal testing machine with a load cell of 30 kN and pneumatic jaw clamps at a strain rate of 10%/min. The geogrid specimens (800 mm long and 200 mm wide) were tested following ASTM D 6637 (2015) using another universal testing machine with a load cell of 250 kN and roller clamps, at a strain rate of 10%/min. From the tests, the specimen ultimate tensile strength was obtained, which is the property of interest of this study. The laboratory test program comprises 240 samples.

The geosynthetic damage was quantified by reduction factors related to the drop process (RF_{Drop}; Equation 1), calculated as the rate between the geosynthetic undamaged ultimate tensile strength (T_{UND}; reference value) and its damaged ultimate tensile strength (T_{DAM}) for each backfill material investigated. RF lower than the unity (1.00) was considered 1.00 as these values should not be adopted for design purposes. This procedure is similar to the one adopted to quantify installation damage.

$$RF_{Drop} = \frac{T_{UND}}{T_{DAM}} \tag{1}$$

3 RESULTS AND DISCUSSION

Table 3 shows the mean ultimate tensile strength values obtained after ten tests performed in undamaged and damaged specimens. For both non-woven geotextiles tested (GTXnw1 and GTXnw2) and for GGR1, all damaged scenarios reduced the tensile strength reference value. The GGR2 shows unexpected results: the drop of the GG material from a 1.0 m height and the drop of GB, GC and SA materials from a 2.0 m height led to an increase in the tested material ultimate tensile strength compared to its undamaged value. Some authors (Huang & Chiou 2006; Paula et al. 2004) indicated that these increases result from fiber rearrangement due to the damage caused. However, no tests have been performed to validate this assumption, which requires further investigations to understand the increases reported.

In terms of RF_{Drop}, Figure 2 shows that the non-woven geotextiles exhibited RF_{Drop} values higher than 1.10 regardless of the drop height and backfill material dropped. On the other hand, the geogrids exhibited RF_{Drop} values lower than 1.10. Generally, this difference can be attributed to the materials' different structures. Due to the geogrid open area, their contact area with the material is smaller than the non-woven one leading to minor damage occurrences due to the backfill drop. However, further investigations are required to assess geotextiles and geogrids with a similar ultimate tensile strength to derive further conclusions. Except when the GC backfill was dropped, the GGR1 showed higher RF_{Drop} values than GGR2, indicating the geogrids with higher ultimate tensile strength may be more resistant to damage.

In general, GTXnw1 exhibited higher RF_{Drop} values than GTXnw2. This may indicate that the increase in the geotextile mass per unit area decreases the material sensitivity to the damage caused by the backfill drop. However, for GA and GG backfill materials, GTXnw2

Table 3.   Geosynthetic ultimate tensile strength for undamaged and damaged conditions.

Condition	Drop height	Backfill	GTXnw1	GTXnw2	GGR1	GGR2
Undamaged	n.a[a]	n.a[a]	3.91	17.83	29.74	44.54
Damaged	1.0m	GA	3.00	16.06	27.45	41.59
		GB	3.18	15.26	28.39	44.38
		GC	3.07	15.20	29.22	42.86
		SA	n.t[b]	16.30	27.68	44.03
		GG	3.37	14.06	27.42	47.70
	2.0m	GA	2.93	12.76	26.86	40.91
		GB	3.30	15.20	28.12	45.40
		GC	3.49	15.92	29.38	44.98
		SA	3.32	15.98	28.22	45,10
		GG	3.32	14.06	28.03	43.18

Note: [a] not applied; [b] not tested.

exhibited higher RF_{Drop} values than GTXnw1, which contradicts the previous information. Thus, it should be considered that the increase in the geotextile mass per unit area improved its resistance to mechanical damage caused by RCDW as previously reported by Palmeira (2018).

Figure 2 also indicates that the damage caused by the backfill material drop from a 2.0 m height was similar to those caused by a drop of 1.0 m height. This finding matches the results reported by Barbosa & Santos (2013) and Fleury et al. (2019).

To verify possible relationship between the backfill grain size distribution and the RF_{Drop} values obtained, the RF_{Drop} values were plotted as a function of i) the maximum grain size (D_{max}; Figure 3a), ii) the grain size corresponding to 50% passing material (D_{50}; Figure 3b), iii) coefficient of curvature (C_c), and iv) coefficient of uniformity (C_u). The best-fit equations obtained from these plots are indicated in Figure 3. One must be aware that the figure joins the data obtained for different geogrids and different geotextiles in two groups: GGRs and GTXnws, respectively, which tries to join the data obtained from materials of the same type but different characteristics (mechanical and physical). Considering these limitations, Figure 3 shows that there is a tendency to increase the RF_{Drop} values as the D_{max} or the D_{50} increases but without a good coefficient of determination (R^2) –values remaining below 40% for all cases. However, despite these limitations, Figure 3 corroborates that the tested geogrids are more resistant to damage than the tested geotextiles.
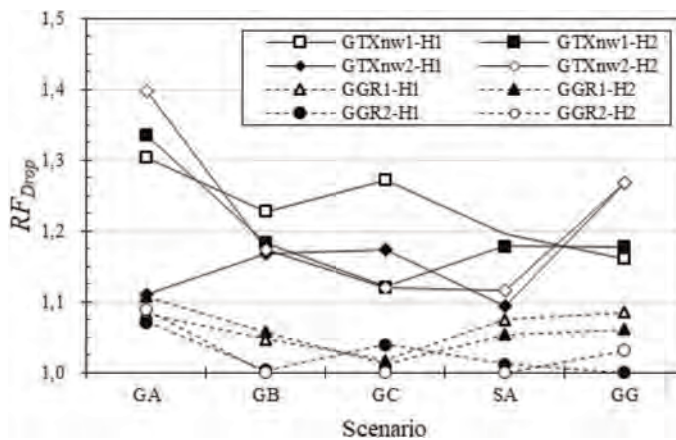
Figure 2.   Reduction factors of each geosyntehtic related to the drop height and backfill material.
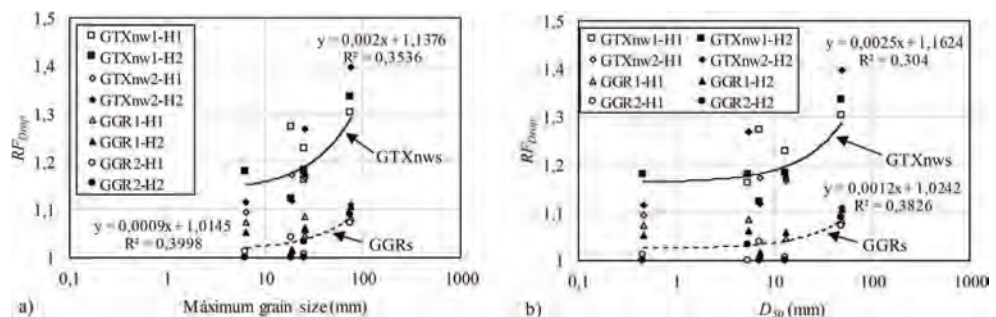
Figure 3.   Relationship between the reduction factor and a) the maximum grain size, and b) the grain size corresponding to 50% passing material.

4 CONCLUSIONS

This paper assesses the geosynthetic damage caused by the backfill material drop from an experimental in-field test. The results reported in the study indicated that the backfill drop should be considered in the design phase as it could be responsible for a decrease in the geosynthetic' ultimate tensile strength. The tested geogrids have shown to be more resistant to the damage caused by the drop height than non-woven geotextiles. Possibly, their different structure is responsible for the different results obtained. As expected, the increase in the geotextile's mass per unit area increases its survivability to the damage induced. On the other hand, as the geogrid ultimate tensile strength increased, they became more resistant to damage. Despite testing five different backfill materials, further studies are needed to validate any relationship between the grain size distribution of the backfill and the reduction factors. Even with a low coefficient of determination, it was observed that the damage tends to be higher as the RCDW maximum grain size increase, similar to conventional materials. Further investigations are required to assess and understand the factor that affects the damage caused by the backfill material drop, mainly when they consist of non-conventional materials. Investigations using sophisticated statistical analysis should be used considering a broader database.

REFERENCES

Andrawes, K.Z., McGown, A. & Kabir, M.H., 1984. Uniaxial Strength Testing of Woven and Nonwoven Geotextiles. *Geotexiles and Geomembranes* 1: 41–56.

ASTM D 6637-15: Standard Test Method for Determining Tensile Properties of Geogrids by the Single or Multi-rib Tensile Method. ASTM International, West Conshohocken, PA, USA.

ASTM D 4595-05: Standard Test Method for Tensile Properties of Geotextiles by the Wide-Width Strip Method. ASTM International, West Conshohocken, PA, USA.

Austin, R.A. 1997. The Effect of Installation Activities and Fire Exposure on Geogrid Performance. *Geotextiles and Geomembranes* 15: 367–376.

Barbosa, F.A.S. & Santos, E.C.G. 2013. *Geogrid Mechanical Damages Due to Recycled Construction and Demolition Wastes*, in: Cossu R., H.P., Kjeldsen, P., Matsufuji, Y., Reinhart, D., Stegmann, R. (Eds.), 14th International Waste Management and Landfill Symposium. International WasteWorking Group (IWWG), Sardegna, Italy.

Barbosa, F.A.S., Silva, E.M. & Santos, E.C.G. 2016. Polypropylene (PP) Geosynthetics Strength Reduction Due Installation Damages Caused by Construction and Demolition Waste (RCDW) [in Portuguese], in: Simões, G.F., Ávila, J.P. (Eds.), *16th Brazilian Conference of Soils Mechanics and Geotechnical Engineering - COBRAMSEG 2016, Belo Horizonte, Brazil.* Brazilian Association of Soil Mechanics and Geotechnical Engineering (ABMS).

Cassidy, P.E., Mores, M., Kerwick, D.J., Koeck, D.J., Verschoor, K.L. & White, D.F. 1992. Chemical Resistance of Geosynthetic Materials. *Geotextile and Geomembranes* 11: 61–98.

Den Hoedt, G. 1988. Principles of Creep and Relaxation, in: *Durability of Geotextiles*. London: Chapman and Hall, pp. 25–28.

Elias, V., Salman, A. & Goulias, D. 1998. The Effect of pH, Resing Properties, and Manufacturing Process on Laboratory Degradation of Polyester Geosynthetics. *Geosynthetics Intternational* 5: 459–490.

Fleury, M.P., Santos, E.C.G., Lins da Silva, J. & Palmeira, E.M. 2019. Geogrid Installation Damage Caused by Recycled Construction and Demolition Waste. *Geosynthetics Internatioanl* 26: 641–656.

França, F.A.N. & Bueno, B.S. 2011. Creep Behavior of Geosynthetics Using Confined-Accelerated Tests. *Geosynthetics International* 18: 242–254.

Greenwood, J.H. 1990. The Creep of Geotextiles, in: Den Hoedt, G. (Ed.), *4th International Conference on Geotextile, Geomembranes and Related Products.* Hauge: Balkema.

Halse, Y., Koerner, R.M. & Lord Jr, A.E. 1988. Effect of High Alkalinity Levels on Geotextiles. Part 2: NaOH Solution. *Geotextextiles and Geomembranes* 6: 295–305.

Halse, Y., Koerner, R.M. & Lord Jr, A.E. 1987. Effect of High Levels of Alkalinity on Geotextiles. Part 1: Ca (OH)$_2$ Solutions. *Geotextextiles and Geomembranes* 5: 261–282.

Huang, C.-C. & Chiou, S.-L. 2006. Investigation of Installation Damage of Some Geogrids Using Laboratory Tests. *Geosynthetics International* 13: 23–35.

Huang, C.-C. & Wang, Z. 2007. Installation Damage of Geogrids: Influence of Load Intensity. *Geosynthetics International* 14: 65–75.

Hufenus, R., Rüegger, R., Flum, D. & Sterba, I.J. 2005. Strength Reduction Factors Due to Installation Damage of Reinforcing Geosynthetics. *Geotextiles and Geomembranes* 23: 401–424.

Lim, S.Y. & McCartney, J.S. 2013. Evaluation of Effect of Backfill Particle Size on Installation Damage Reduction Factors for Geogrids. *Geosynthetics International* 20: 62–72.

Mathur, A., Netravali, A.N. & Rourke, T.D.O. 1994. Chemical Aging Effects on the physio-Mechanical Properties o f Polyester and Polypropylene Geotextiles. *Geotextile and Geomembranes* 13: 591–626.

Palmeira, E.M. 2018. *Geosynthetics in Geotechnics and the Environment [In Portuguese]* (1st ed.) São Paulo: Oficina de Textos.

Paula, A.M., Pinho-Lopes, M. & Lopes, M.L. 2004. Damage During Installation Laboratory Test: Influence of the Type of Granular Material, in: Geotechnik, Z. (Ed.), *Third European Geosynthetics Conference.* Munich.

Pinho-Lopes, M., Paula, A.M. & Lopes, M.L. 2018. Long-Term Response and Design of Two Geosynthetics: Effect of Field Installation Damage. *Geosynthetics International* 25: 98–117.

Richardson, G.N. 1998. Field Evaluation of Geosynthetic Survivability in Aggregate Aoad Base. *Geotechnical and Fabrics Reports* 16: 34–38.

Thornton, J.., Allen, S.R. & Thomas, R. 1997. Approaches for the Prediction of Long Term Viscoelastic Properties of Geosynthetics from Short Tem Tests, in: *Geosynthetics '97 Conference*. California: Industrial Fabrics Association International.

Zornberg, J.G., Byler, B.R. & Knudsen, J.W. 2004. Creep of Geotextiles Using Time–Temperature Superposition Methods. *Journal of Geotechnical and Geoenvironmental Engineering* 130: 1158–1168.

The inclined plane compression test: A new technique to assess the interface shear-strength properties of polyethylene geomembranes

E. Blond
Eric Blond Consultant Inc., Montreal, Canada

D. Beaumier
CTT Group, St-Hyacinthe, Canada

C. Tarnowski
Solmax, Hamburg, Germany

ABSTRACT: Geomembranes can be produced with or without surface texture. This choice is generally driven by design requirements, in particular the slope stability, but also the safety of users and wildlife. Overall, a bit less than half of textured geomembranes worldwide are produced by coextrusion, a bit more than a third are embossed, and a bit less than a fifth are sprayed with polyethylene filaments. For coextruded textures, Blond & Elie (2006) have shown that there is a correlation between the height of the asperity, measured by ASTM D7466, and the shear-strength properties of the interface between the geomembrane and an adjacent material. Adesokan & Blond (2018) have shown that the density of asperity may also further influence the interface shear-strength properties. However, there is little information available on the performance of the two other texturing techniques frequently used for geomembranes, i.e., embossing the surface, or spraying it with polyethylene particles. Finally, there is a consensus on the limited performance of ASTM D7466 to adequately predict the performance of geomembranes with an embossed or a spray-on texture. In this document, the various techniques used to create a surface texture on a polyethylene geomembrane are described. The results of an experimental program aiming at measuring their shear-strength properties against a geotextile is presented. A new technique to qualify the performance of textured geomembranes is proposed, which can be used to generate an intrinsic property of the geomembrane, and which can also be used in manufacturing quality control to certify the geomembrane / geotextile interface friction angle.

1 INTRODUCTION

ISO 12957-1 and 12957-2 standards are used to characterize the behavior of interfaces including at least one geosynthetic. ISO 12957-2 is conducted using a tilt table, to model interfaces exposed to low normal stresses, to assess the interface friction properties at peak. ISO 12957-1 test is performed with a direct shear box under any normal stress to assess the interface friction properties at peak as well as at large deformation.

When specifying geosynthetics, a notable problem is the cumbersome nature of interface shear tests, which makes it very difficult to use them in construction quality assurance programs – as well as for manufacturing quality assurance. Current practice is to focus on an intrinsic property of the materials known to provide information which can be connected to the friction behavior of the interface. This approach is common practice for textures manufactured using blown film coextrusion process (Blond 2006), and recent attempts were

made for calendared textures (Adeleke 2020). Unfortunately these methods are only applicable to specific manufacturing technologies, and they remain indirect methods. In this project, a novel approach is proposed to assess the interface friction properties of any type of geomembrane, disregarding their structure and their manufacturing technique.

2 SURFACE CHARACTERISTICS OF TEXTURED GEOMEMBRANES

2.1 *State of the art*

The surface of polyethylene geomembranes can be textured to provide it with sufficient frictional properties. Figure 4 describes two types of texture commonly found on the market. The shear strength which can be developed between this surface and another material is thus influenced by a surface characteristic, i.e., by an intrinsic property of the geomembrane.

a) Cx Basic   b) Cx Rough   c) Cx Dense   d) Cx X-Rough   e) SO Standard   f) SO Dense
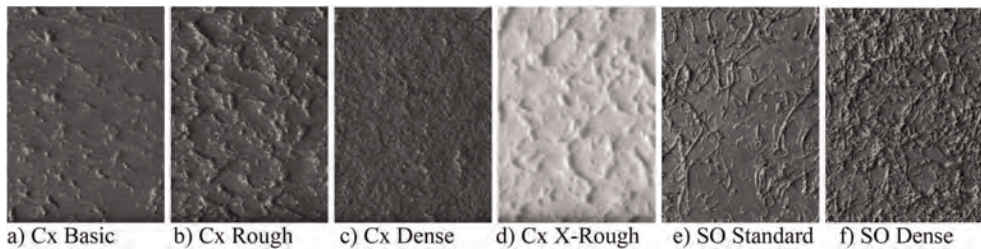
Figure 1.   Texture of polyethylene geomembranes (surface: 20 ×27 mm; Cx: coextruded, SO: Spray-on).

Blond & Elie (2006) have observed that for geomembranes with a texture produced by coextrusion in a blown film process (Figures 1-a, 1-b, 1-d), there is a relation between the shear strength and the asperity height, measured by the ASTM D7466 test (equivalent to the GRI GM12 test method referenced by Blond and Elie).

Adesokan and Blond (2018) have shown that in addition to asperity height, the density of asperities (Figure 1-c) also influences the shear strength of interfaces involving a geomembrane. Their study was focusing on the coextruded, blown film texturing process. However, no method for characterizing texture density is referenced by Adesokan.

Adeleke (2020) demonstrated that the height of the studs manufactured by calendaring as well as their density affect the maximum friction properties of calendared geomembranes. He also suggested that surface roughness may also impact the measured properties at large deformation. However, no standard test method is referenced by this author to characterize these properties. The height of the studs as well as their density are defined by the characteristics of the calendar roll used during manufacturing. Because of the relatively low density of the studs and the ease of visual identification, they can indeed be characterized using a ruler to measure their density, a caliper to measure their diameter, and the depth gauge described in ASTM D7466 to measure their height. However, surface roughness cannot be measured using a standard test method.

For geomembranes where the texture is sprayed on the surface of a smooth geomembrane (Figure 1-e, 1-f), experience shows that friction properties are influenced by the density of the texture, which also influences the height of 'asperities' as measured applying test method ASTM D7466, despite this test was developed for another type of manufacturing process. A more appropriate technique would be to determine the spray-on 'density', reflecting the quantity of filaments projected on the surface per unit area. This property is controlled during production by varying the quantity of polymer sprayed per unit area, using a proprietary process. However, there is no test method available to measure this characteristic once production is completed, and it would be difficult to assess in Construction Quality Control.

2.2 *Summary of relevant features of geomembrane textures*

Adeleke's findings are generally consistent with those of Adesokan, and they are consistent as well with field observations: the higher the asperity density and the asperity height: the 'rougher' the surface and the higher the shear strength developed at the interface.

Introducing the concept of 'roughness' (more than isolating or combining height or density) allows to extend this observation to spray-on textures: the rougher the spray-on texture, the higher friction properties can be developed at the interface.

However, it is not possible to determine a universal correlation between an indicative geometrical property of the surface texture, regardless of its morphology, and the shear strength that the geomembrane will exhibit against a given material. Furthermore, the morphology of the texture is not the only parameter that will affect shear strength: adhesion properties specific to each polymer – in particular the surface energy – will also affect the shear strength that can be developed against a given product.

Overall, it can be concluded that it is NOT possible to determine a physical property (such as asperity height) that could be measured on any type of texture (coextruded, calendared or sprayed), which could provide enough information to estimate even roughly the shear-strength performance of a textured geomembrane. The two methods currently available, based on asperity height measurement (ASTM D7466) or geometrical characterization of the texture (Adeleke's method), can only be used effectively on the material for which they were respectively developed, and cannot be extended to other manufacturing techniques.

3 NEW APPROACH FOR CHARACTERIZING THE SURFACE PROPERTIES OF GEOMEMBRANES

Blond (2022) provides more details on the development of the test developed to improve manufacturing quality control of spray-on texture, where the geomembrane is tested against itself. The general principle of the test is to replicate the conditions prevailing onsite by applying a vertical force (mimicking the gravity-controlled weight of a soil overburden) on the interface installed with a pre-set angle. The upper side of the tested interface is connected to a load cell, while the lower side rests on a carriage free to move horizontally (Figure 2-a).
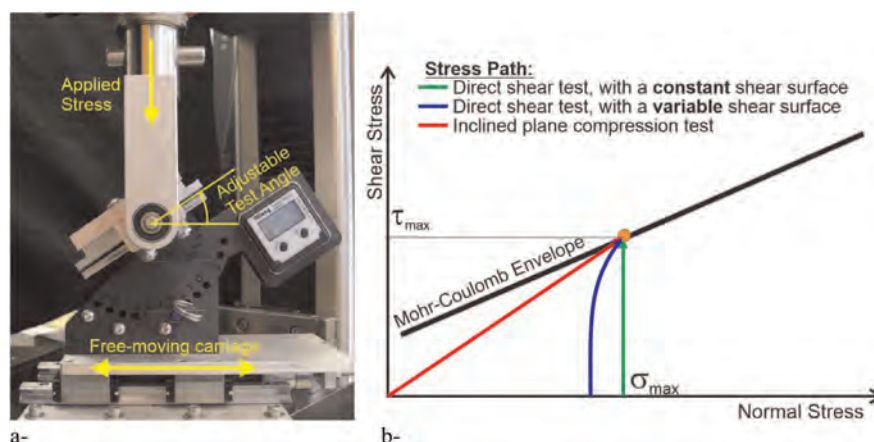
Figure 2. Inclined plane compression test setup, stress paths reflecting the three methods which can be used to characterize friction properties of geomembrane interfaces.

With a fixed angle, the normal stress and the tangential stress increase proportionally as the vertical force increases. The maximum shear stress sustained by the interface 'τ_a' and the

corresponding normal stress 'σ_α' can be calculated using Equations 1, where 'α' is the (fixed) angle of the interface, 'F' the force applied, and 'S' the contact area:

$$\sigma_\alpha = \frac{F \cdot \cos \alpha}{S} \quad and \quad \tau_\alpha = \frac{F \cdot \cos \alpha}{S} \tag{1}$$

Practically, the 'Inclined Plane Compression Test' measures the vertical stress which must be applied on a given interface, installed at a given angle, to reach a failure, instead of looking for a maximum angle measured using an indirect method as with a direct shear test. With this approach, the modulus of the applied force 'F' is a value which directly reflects a gravity-controlled loading of the interface – such as the weight of an overburden soil. It can therefore be associated to a maximum service load which the interface at a given angle can carry before a failure is observed.

One of the most important conceptual differences between this test and direct shear tests such as ISO 12957-1 resides in the stress path followed by the interface until it reaches failure, which are illustrated in Figure 2-b:

- In a direct shear test with a constant shear surface (e.g., ASTM D5321 or ISO 12957-2), the normal stress is set and remains constant throughout the test. The shear stress increases until the Mohr-Coulomb failure envelope is reached. It is a displacement-controlled test, i.e. the rate of application of the shear stress is not controlled.
- If the direct shear test is performed using a variable shear surface, as for direct shear testing of soils (e.g., ASTM D3080), the normal stress increases throughout the test because of the reduction of shear surface. It is a displacement-controlled test as well, where the rate of increase of the shear stress is not controlled. the shear stress must be corrected to account for the reduction of the shear surface as the test progresses.
- With the proposed inclined plane compression test, both normal and shear stresses increase proportionally: the stress path follows an angle which is the same as the inclined plane angle. This stress path reflects the mechanism that would typically prevail onsite. A maximum force is achieved when the stress path reaches the Mohr Coulomb envelope of the interface. This mechanism cannot take place (i.e., an infinite force is reached) when the angle of the test (of the slope) is such that the stress path never reaches the Mohr-Coulomb envelope.

The details of device depicted on Figure 2-a will be revealed in a standard test method, to be published. However, the following details can be highlighted:

- Both platens are covered with an abrasive surface to exhibit a higher shear strength than the one being observed. No anchoring of the specimens should be necessary.
- The upper plate is articulated to ensure parallelism of the two surfaces. The rotation axis of the upper plate is in the same plane of the interface, to avoid the development of parasitic torque during the test.
- A magnet sets and restrains displacement carriage in a predefined location at the beginning of the test. Its force is adjusted to ensure the test surfaces are in contact with one another when the vertical force increases, eliminating parasitic effect of the curvature of the specimens.
- The speed of vertical displacement was set at 10 mm/min until a peak is observed or the capacity of the equipment is reached.
- Once a test is completed under a given angle, the test can be repeated using different angles, until a very high force is measured (when the angle is reduced) or a neglectable force is measured (when the angle is increased).

Testing one interface under a given angle requires up to 2 minutes per replicate (once specimens cut and the system calibrated), which was found an acceptable duration for Manufacturing Quality Control.
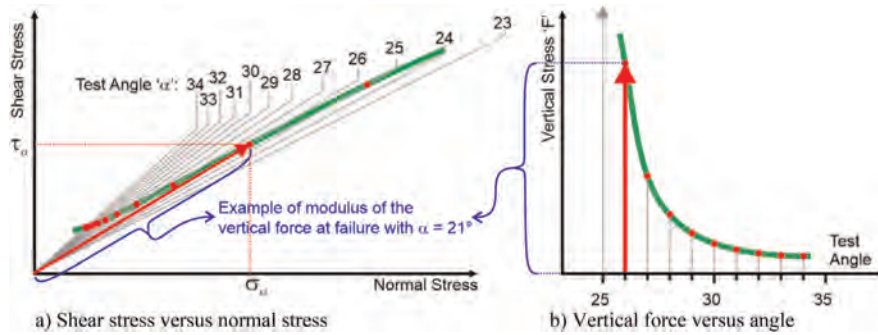
Figure 3. Idealized behavior of an interface during a series of inclined plane compression tests.

The idealized behavior of an interface is described on Figure 3. For each test angle, the stress path is a straight line starting from the origin and defined by the test angle, ending on the Mohr-Coulomb envelope of the interface, i.e., where slippage occurs. On Figure 3-a, the stress path is illustrated with a red arrow for the test angle '26°'.

The modulus of the vertical force 'F' required to reach failure is plotted against the test angle on Figure 3-b. This format is, in fact, simpler to report as it is the direct output from the dynamometer, and it can be set considering a friction angle which should be sustained by the interface (before any reduction factors are applied).

Blond (2022) reports a good correlation between results obtained using this novel procedure with those obtained using a direct shear box per ASTM D5321, when testing a medium-density, or a high-density spray-on texture against itself. This validation was however limited to 400 kPa, which is the capacity of the direct shear box used.

4 EVALUATION OF GEOTEXTILE / GEOMEMBRANE INTERFACES

Geotextile / geomembrane interfaces are frequently considered the critical part of a project with respect to interfaces stability. It was therefore decided to investigate if the Inclined Plane Compression Test can be used to assess the properties of such interfaces. Several geomembranes exhibiting different textures were tested against a non-woven, needle-punched continuous filament geotextile with a mass per unit area of 800 g/m^2. Both the IPCT and direct shear tests were used.

Figure 4 presents the (α, F) relation for these tests (i.e., using the presentation strategy exposed on Figure 3-b). Figure 5-a presents the Mohr-Coulomb envelopes obtained with both the IPCT and Direct Shear. Figure 5-b presents the angle for which a force of 3,000N or 8,000N can be applied on the tested interface without slippage, along with the tangent friction angle obtained using a direct shear test, and the asperity height, for each texture. The 3,000N and 8,000N values were selected looking at Figure 4 and choosing the region located immediately above what appears to be an inflexion of the 'Force versus Angle' curve, i.e., the limit where a reduction the test angle by just 1° leads to a significantly higher force.

Based on these observations, the inclined plane compression test appears as a promising technique to evaluate the geotextile / geomembrane interface friction properties. When using the shear surface used in this project (50 mm width x 120 mm length), it allows evaluation of the behavior of interfaces under very high normal loads, i.e., up to ~12 to 14 MPa using a 20kN load cell.

The stress path used to run the test mimics normal operating conditions of geosynthetic interface exposed to a vertical, static load, and the result can be expressed as a service load (i.e., weight of the overburden) under predetermined operating conditions. Hence, this test
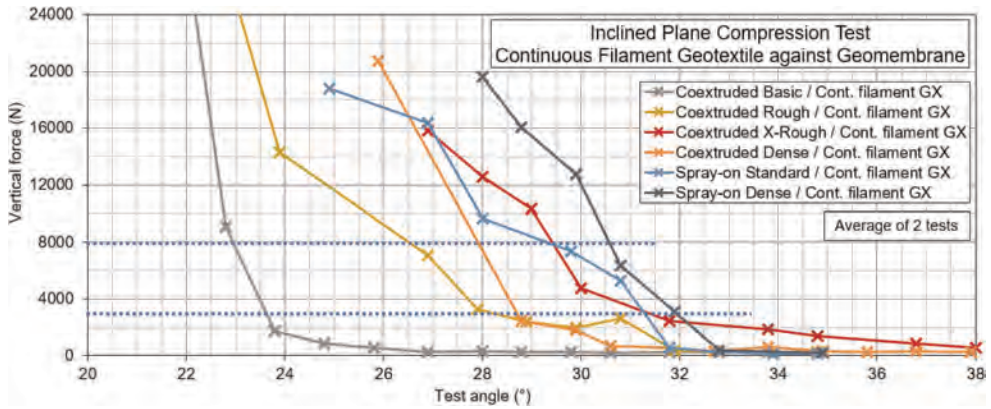
Figure 4. Inclined plane test results, geomembrane tested against a geotextile.
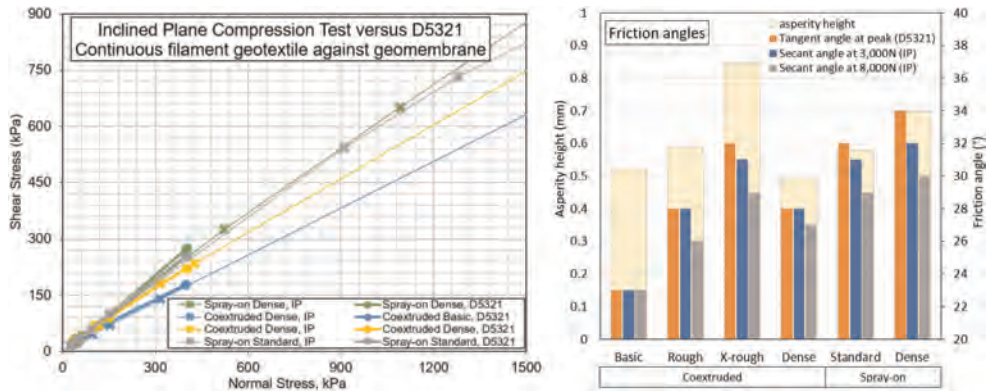
Figure 5. Inclined plane test results, geomembrane tested against a geotextile.

could offer a better opportunity to quantify the serviceability of a structure using safety factors.

The simplicity and rapidity of the test makes it a good candidate for manufacturing quality control of geosynthetic interfaces, with geotextile / geomembrane friction properties becoming a feature that could be consistently assessed on a project-by-project basis as very low cost.

5 CONCLUSION

The proposed Inclined Plane Compression Test provides an opportunity to rapidly assess the surface friction properties of a geomembrane by testing the surface of the geomembrane against itself, as shown by Blond (2022). In addition, the test also offers the possibility to evaluate the behavior of geomembrane/geotextile interfaces. Under a similar normal stress, results were found to be comparable to those obtained using a direct shear box, per ISO 12957-2.

Moreover, the test allows characterization of the Mohr-Coulomb Envelope up to very high normal loads, much higher than the loads which can be reached using direct shear boxes currently available on the market.

This test offers the possibility to measure the stress necessary to reach the failure of an interface under a specific angle. This approach offers an opportunity to define a Safety Factor applicable to a service load for a given service condition = slope angle. This approach could improve the understanding of failure mechanisms and offer a new approach to define a safety factor applicable to the stability of an interface.

ACKNOWLEDGEMENTS

REFERENCES

Adeleke, D. 2020. *An Investigation into the Effects of Asperities on Geomembrane/Geotextile Interface Shear Characteristics*, Master Thesis, University of Cape Town, Faculty Of Engineering And Built Environment, Department Of Civil Engineering

Adesokan D, Blond E. 2018. Asperity Height or Asperity Concentration: What Matters More For Interface Shear Resistance on Textured Polyethylene (PE) Geomembranes?; *Proceedings of the XIth international Conference on Geosynthetics*, Sept 16-21 2018, Coex, Seoul, Korea

ASTM D5321-21: *Standard Test Method for Determining the Shear Strength of Soil-Geosynthetic and Geosynthetic-Geosynthetic Interfaces by Direct Shear*

ASTM D7466-10(2015)e1: *Standard Test Method for Measuring Asperity Height of Textured Geomembranes*

Blond E., Beaumier D. 2022. *Caracterisation Des propriétés de Frottement Des Géomembranes Texturées.* Compte-Rendu Des 13èmes Rencontres Géosynthétiques – du 5 au 7 Avril 2022, Saint-Malo

Blond E., Elie G. 2006. Interface Shear-Strength Properties of Textured Polyethylene Geomembranes. *Proceedings of the 59th Annual Conference of the Canadian Geotechnical Society*, Saskatoon, October 2005.

ISO 12957-1 (2018): *Géosynthétiques — Détermination des Caractéristiques de Frottement — Partie 1*: Essai de Cisaillement Direct

Koerner R. 2012. *Designing with Geosynthetics*, 6th Edition, Volume 2, ISBN (Ebook) 978-1465345264

Chemico-osmotic efficiency of geosynthetic clay liners: Testing apparatus and preliminary results

D. Bernardo, J. Domizi, E. Fratalocchi & F. Mazzieri
Marche Technical University, Ancona, Italy

ABSTRACT: The membrane behaviour of conventional and enhanced Geosynthetic Clay Liners is regarded with interest for applications in barrier systems as the presence of chemical osmosis improves the GCL containment properties. With the purpose of assessing the existence and persistence of chemico-osmotic behavior in GCLs, an apparatus able to perform chemico-osmotic diffusion tests on GCLs and soils has been developed. The paper describes the main features of the systems and preliminary results obtained using conventional and polymer-amended GCLs and a 20 mM KCl solution. The measured osmotic efficiency and solute diffusion coefficients were close to results in the literature on similar GCL materials and similar testing conditions, proving the system reliability.

1 INTRODUCTION

The ability of bentonite-based geosynthetic clay liners (GCLs) to act as semipermeable membranes that is, inhibit the passage of ions while allowing the migration of water (chemical osmosis) is well recognized (Kang & Shackelford 2009; Malusis et al. 2001; Mazzieri et al. 2010). The restriction of solute transport is usually partial and the degree to which a soil inhibits the entry of ions into the pore has been traditionally quantified in terms of the chemico-osmotic efficiency coefficient, ω (Shackelford 20139. Chemico-osmotic diffusion tests have been widely used to determine the ω coefficient of soils and geosynthetic clay liners (GCLs). The most commonly adopted testing condition has been the closed-system approach (Malusis et al. 2001). which consists in generating a steady-state chemical gradient across a saturated specimen while preventing the hydraulic flow through the specimen. If the soil has semipermeable membrane properties, a differential pressure will arise across the specimen. The absence of volume change in closed-system chemico-osmotic testing is ensured by using rigid-wall cells and preventing the vertical swell by a locked-in-place rigid piston (Di Emidio 2010; Malusis et al. 2001). However, in rigid-wall cells, specimen shrinkage is possible, resulting in short-circuiting and destruction of membrane behavior (Bonhoff & Shackelford 2013; Scalia et al. 2018).

The paper presents a recently developed rigid-wall cell for diffusion and chemico-osmotic testing of GCLs or soils, with allows applying strain-controlled condition to the test specimen, either by a locked-in-place piston, similarly to the testing approach in Malusis et al. (2001), or by using a load cell, similarly to the testing approach described in Dominijanni et al. (2019). The latter setup enables monitoring the total vertical stress during the test and helps identify possible anomalies (e.g. vanishing total stress) yet allowing relatively small strains ($< 1\%$). The paper also reports the results of preliminary tests performed on two different GCLs materials with the purpose of comparison with literature data to check the system reliability and to highlight the possible influence of the testing approach on the determined membrane properties.

2 MATERIALS AND METHODS

2.1 *Chemo-osmotic diffusion apparatus and testing*

Figure 1 shows a drawing of the apparatus, conceptually similar to that described in Malusis et al. (2001). The principle of the test is to induce a steady-state chemical gradient across a saturated soil specimen, while preventing the hydraulic flow. The concentration gradient is induced by circulating equal volume rates of solutions of different concentrations at the specimen boundaries. This is obtained by equipping a double-syringe pump with two metallic cylinders. The syringe plunger separates the cylinder in two compartments, hydraulically connected to a porous disk lying on top or beneath the specimen in the testing cell, such that the solution is infused by the plunger displacement at one side of the porous plate and withdrawn at the other side.

The rigid-wall cell consists of a lower plexiglass mould housing the soil specimen and an upper plexiglass pressure chamber, hydraulically isolated from the specimen chamber by a sealed rigid piston. Plexiglass was preferred over stainless steel for being non-conductive. The specimen mould is 100 mm in diameter and 100 mm in height. The solutions are circulated through the porous stones by the two drainage lines connected to the cylinders, while a third drainage line connects the porous plates and a differential pressure transducer. The liquid pressures generated at specimens top and base during circulation are also monitored by means of in-line relative pressure transducers.

The rigid piston is free to move downwards or upwards under a given stress applied to the upper chamber, during the consolidation or swelling stage of the specimens. During the circulation stage the piston can be locked-in -place by blocking the rod against a rigid steel frame ("no-strain" condition). Alternatively, a stiff load-cell (LCM411-500-USBH Load Cell, AEP Transducers, Italy) can be interposed between the piston rod and the steel frame, which allows monitoring the total stress acting on the specimen during the chemico-osmotic test. As the load cell undergoes some deformation in measuring the applied load ($\approx$0.2 mm/KN), the volume
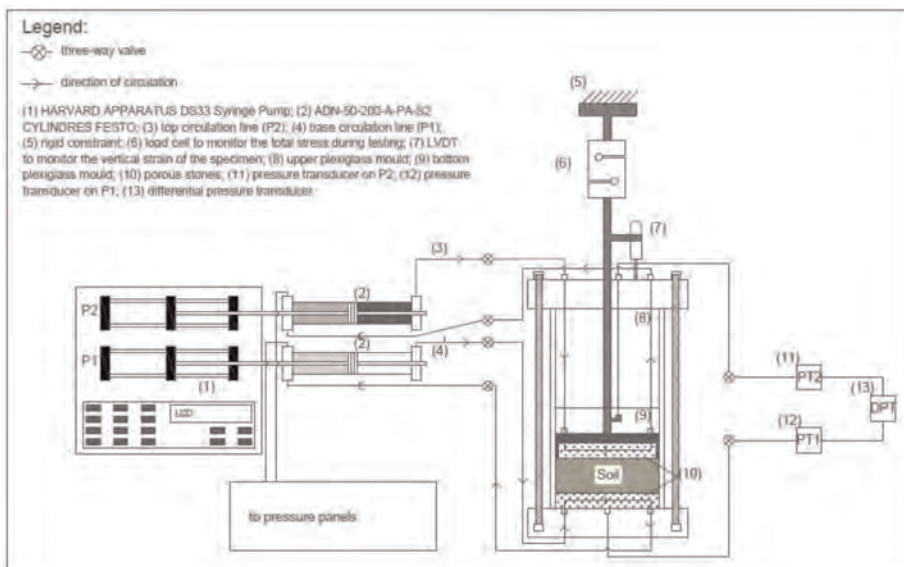
Figure 1. Schematic of the circulation apparatus and rigid-wall cell for chemico-osmotic diffusion tests.

change of the specimen is in principle not prevented for the latter testing condition ("small-strain" condition). A displacement transducer (LVDT) firmly attached to sliding rod of the piston allows monitoring any volume change during the preliminary consolidation or swelling phase of the specimen as well as during the chemico-osmotic diffusion stage.

A closed-system chemico-osmotic diffusion test consists in measuring the pressure difference induced across a soil or GCL specimen as a result of prohibiting the chemico-osmotic flux q of solution (Keijzer et al. 1999). The chemic-osmotic coefficient is determined as follows:

$$\omega = \left(\frac{\Delta P}{\Delta \pi}\right)_{q=0} \tag{1}$$

where ΔP = the liquid pressure difference across the specimen and $\Delta \pi$ = the theoretical pressure difference across an "ideal" semipermeable membrane separating dilute solutions of a single electrolyte, which can be computed using the van't Hoff Equation:

$$\Delta \pi = \nu RT \Delta C \tag{2}$$

where ν = the number of ions per molecule of the salt, R = the universal gas constant [8.314 J mol^{-1}°K^{-1}], T = the absolute temperature, ΔC = the concentration solute difference across the membrane.

As the restriction of solutes through the porous medium is usually partial, diffusive flux occurs in response to the induced concentration gradient until a steady-state diffusion condition is reached. Monitoring the outflow and inflow solute concentrations allows determining the solute steady-state diffusive molar mass flux J (Malusis et al. 2001) and the effective diffusion coefficient is experimentally determined as:

$$D^* = H \frac{J}{n(C_{t,av} - C_{b,av})} \tag{3}$$

where $C_{t,av}$ = the average solute concentration at top boundary, $C_{b,av}$ = the average solute concentration at the base boundary, H = the specimen thickness, and n = the total soil porosity. In case of a salt solutions and nil electrical current density, in the absence of membrane behaviour the measured diffusion coefficient at steady-state is the effective salt diffusion coefficient D_s^*. In the presence of membrane behavior the effective diffusion coefficient D^*, can be related to the salt diffusion coefficient, as follows (Manassero & Dominijanni 2003):

$$D^* = (1 - \omega)D_s^* = (1 - \omega)\tau_m D_{so} \tag{4}$$

where τ_m is the matrix (geometric) tortuosity and D_{so} is the salt diffusion coefficient in free solution.

2.2 Materials

Two different geosynthetic clay liner products (GCL-1 and GCL-2), previously used in other studies on chemico-osmotic behavior were used in this study to compare the results obtained with the testing apparatus with literature data. GCL-1 is a conventional needle-punched product (Bentomat®), consisting of a cover nonwoven polypropylene geotextile (0.3 kg/m^2) and a carrier woven polypropylene geotextile (0.2 kg/m^2), encapsulating a nominal unit mass of 4.2 kg/m^2 of granular natural sodium bentonite. Physical and chemical properties of GCL products with the same trade name are reported in Malusis & Shackelford (2002). GCL-2 is a product known as Dense Prehydrated (DPH) GCL

(Rawell, UK). The product type used in this study comprises a 4.6 mm thick layer of prehydrated and vacuum-extruded bentonite interposed between a perforated polyester geotextile (17 g/m^2) and a HDPE layer, that was removed before testing, as the bentonite core only was expected to exhibit chemico-osmotic behavior. The HDPE layer it is not firmly bonded to the bentonite layer and was easily peeled by hand. The bentonite of DPH GCLs is known to be amended with polymers (Na-Polyacrylate and Na-Carboxymethyl Cellulose) during manufacturing. Physical and chemical properties of the GCL are reported in Mazzieri & Di Emidio (2015).

2.3 Testing procedure and program

The liquids used in this study were distilled water (DW) and a 20 mM solution of potassium chloride (KCl). The salt solution was prepared by dissolving analytical grade KCl in DW. Circular GCL specimens (diameter =100 mm) were carefully cut from larger sheets and first permeated with DW to reduce the concentration of soluble salts, increase saturation and measure the initial hydraulic conductivity (k). Preliminary hydration and permeation were carried out in flexible-wall permeameters (FWP) under an average isotropic effective stress σ'_i=34.5 kPa (as per ASTM D5887); after 4-6 months of permeation, the specimen was transferred to the rigid-wall cell, paying attention to prevent gaps in the contact between the soil and the cell walls. Then, the GCL specimens were again permeated with DW (i=90-120) in the rigid-wall cell, primarily to check for sidewall leakage. After permeation, the piston was locked for the "no-strain" testing approach, whereas the load cell was interposed between the piston rod and the rigid steel frame for the "small-strain" approach. The upper cell was depressurized and DW was first circulated as input solution at both boundaries of the specimen to establish the baseline differential pressure. The circulation rate was set to 4.8×10^{-10} m^3/s in all tests to enable comparison with previous studies (Malusis & Shackelford 2002; Malusis & Danyarov 2016). After about 7 days of circulation with DW, the chemico-osmotic stage of the tests was initiated by circulating the 20 mM KCl solution as input solution at the top while continuing circulation of DW at the base. During circulation, the inflow and outflow solutions were collected with periodic refills (on average every 48 hours) to monitor the progress of electrical conductivity, EC, and for subsequent analysis of concentrations. At the end of chemico-osmotic testing, the GCLs specimens were permeated with the 20 mM KCl solution to check for specimen shrinkage and increase in k with respect to permeation with DW. Finally, the moisture content of the specimen was measured to check the final degree of saturation. Both GCLs were tested by adopting the two testing approaches and the 20 mM KCl source solution. In the case of the "small-strain" test on GCL-1 the source solution was subsequently increased (multi-stage test). The present paper reports on the first stage of testing only.

3 RESULTS AND DISCUSSION

3.1 Chemico-osmotic coefficient and diffusion coefficients

Figure 2 and Figure 3 show the differential pressured $\Delta P = (P_{top} - P_{base})$ during circulation of DW and of the 20 mM KCl solution for the tests performed adopting the conventional "no-strain" approach (Figure 2a and 3a) and the "small-strain" testing approach (Figure 2b and 3b) for GCL-1 and GCL-2 respectively.).

The average value of ΔP during circulation with DW was assumed as the baseline value, ΔP_{DW}. Input of 20 mM KCl solution in the top circulation loop determined in all tests an almost immediate increase in ΔP. The steady-state value of differential pressure during KCl circulation, ΔP_{KCl}, was estimated for each test considering the overall trend, as the
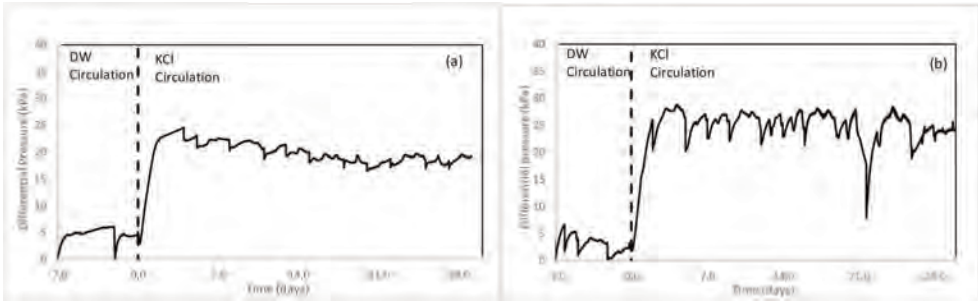
Figure 2. GCL-1. Differential pressure measured across the specimen: (a) with the conventional (no-strain) testing approach; (b) with the novel (small-strain) testing approach.
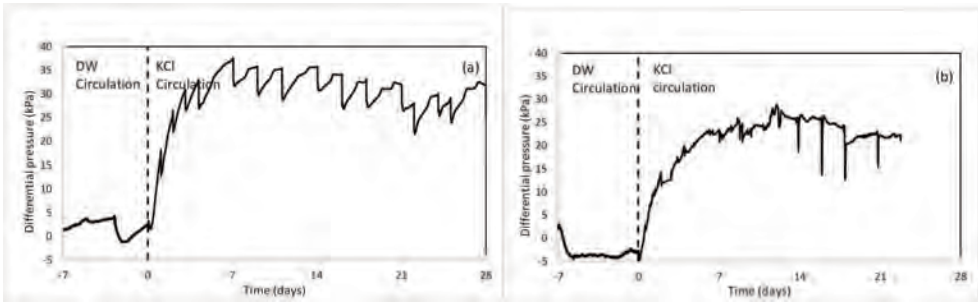
Figure 3. GCL-2. Differential pressure measured across the specimen: (a) under the conventional (no-strain) testing approach; (b) under the novel (small-strain) testing approach.

instantaneous ΔP values are affected by the sampling and refilling operations and to some extent by room temperature variations as well. The chemico-osmotic coefficient ω was the calculated as follows:

$$\omega = \frac{\Delta P_e}{\Delta \pi_{av}} = \frac{\Delta P_{KCl} - \Delta P_{DW}}{\Delta \pi_{av}} \tag{5}$$

Where ΔP_e= the effective differential pressure and $\Delta \pi_{av}$ = the theoretical averge osmotic pressure difference calculated with Equation. 2 from the average KCl concentration difference $\Delta C_{av}=C_{t,av}-C_{b,av}$ between the top and base boundary at steady-state, determined from concentration measurements (Table 1). In the case of GCL-1 (SS), the concentrations were estimated by correlation with the *EC*, as the chemical analyses are not yet available. Application of Equation. 3 to the calculated steady-state molar fluxes of the solutes gives the D^* values reported in Table 1.

The values of ω and D^* coefficients obtained in this study are for both GCLs in the range expected from the literature. For example, using the no-strain approach and GCL-1 at similar total porosity (n=0.79), Malusis et al. (2002) obtained ω=0.32 (vs. ω=0.16 obtained in this study). Malusis & Danyarov (2016) obtained ω=0.57 and D^*=0.45×10^{-10}m^2/s on a similar GCL-2 product (vs. ω=0.33 and D^*=0.59×10^{-10}m^2/s in this study). Therefore, while full reproducibility of literature data was not expected due to several influencing factors (e.g. difference in GCL properties over different production lots, details of testing procedure etc.) the capability of the apparatus of producing tests results reasonably close to literature data under similar conditions can be considered satisfactory. The ω and D^* values determined with the "no-strain" and the "small-strain" testing conditions are also relatively close;

Table 1. Summary of membrane/diffusion test results for GCLs specimens.

Test conditions		Membrane/diffusion test results									
Sample [-]	Strain [-]	$C_{ot,}$ [mM]	L [mm]	n [-]	ΔP_e [kPa]	$C_{b,av}$ [mM]	$C_{t,av}$ [mM]	$\Delta \pi_{av}$ [kPa]	ω [-]	D^* [10^{-10}m^2/s]	k_{DW} - k_{KCl} [$\times 10^{-12}$m/s]
GCL-1	NS	21.4	10.5	0.77	14	1.56	19.3	88.0	0.16	1.50	8.5 - 3.5
GCL-1	SS	20.0*	10.4	0.77	23	1.62*	17.9*	80.7*	0.29*	1.73*	7.3 - 4.6**
GCL-2	NS	21.4	7.0	0.77	31	1.04	20.0	94.4	0.33	0.59	3.8 - 2.0
GCL-2	SS	21.0	7.3	0.78	27	1.67	19.5	87.2	0.31	1.00	2.1 - 3.3

*= estimated by EC; **= measured at the end of subsequent test stages (multistage test)

however, the available data do not allow identifying a systematic influence of the testing approach on the obtained results.

The total vertical stress acting on the specimen during the test, monitored with the "small-strain" testing option is shown in Figure 4a (GCL-1) and Figure 4b (GCL-2). Circulation of DW gradually reduced the content of soluble salt at the specimen boundaries, thus increasing the osmotic pressure difference between the internal pore water and the external bulk solution, which contributes to the increase in swelling pressure (Dominjanni et al. 2019). Conversely, circulation of 0.02 M KCl at the top boundary (and consequent migration of ions into the GCLs) determined a gradual decrease in total stress, associated with the reduction in double-layer repulsion and osmotic pressure difference. Indeed, the observed change in total stress with boundary concentrations can be related by physical modelling of chemico-osmotic phenomena in clays to intrinsic properties of the solid skeleton such as the fixed charge concentration (Guarena et al. 2022). Application of theoretical models to the interpretation of the obtained results is among the further objectives of this study.
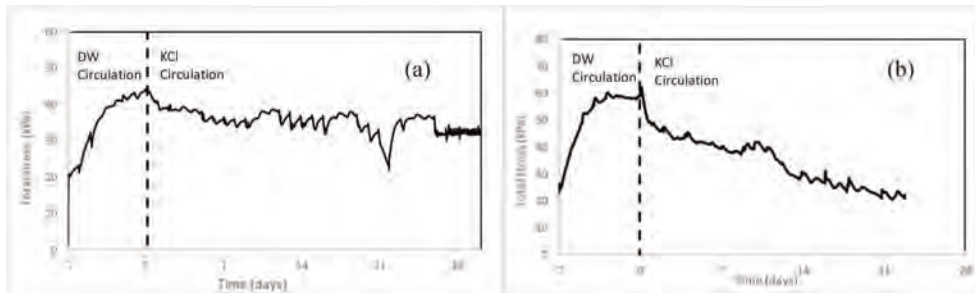
Figure 4. Total vertical stress acting on the specimens during the chemico-osmotic tests with the "small-strain" approach: (a) GCL 1; (b) GCL-2.

4 CONCLUSIONS

Chemico-osmotic diffusion tests have been widely used to determine the chemico-osmotic coefficient (ω) geosynthetic clay liners (GCLs). The most common testing approach has utilized rigid-wall cells under no-strain conditions (testing specimens confined by a locked piston.) A modified rigid-wall cell has been recently developed, which allows conducting the test either under the no-strain condition or using a load cell, that allows monitoring the total stress during the test with relatively small strain of the test specimen ($<1\%$ in this study). Preliminary tests implementing the two testing approaches have been performed on

conventional and Dense Prehydrated GCLs. The values of chemico-osmotic coefficients obtained with the two testing approaches were for all tests in the range expected from the literature. Although the available data are still limited, the modified approach offers a more complete picture of the specimen behavior in response to chemical exposure and allows determining on the same specimen the relevant parameters for advanced theoretical modeling of chemico-osmotic phenomena in GCLs.

REFERENCES

Bonhoff, G. & Shackelford. C.D. 2013. Improving Membrane Performance Via Bentonite Polymer Nanocomposite. *Applied Clay Science* 86. 83–98.

Di Emidio, G. .2010. "*Hydraulic and Chemico-osmotic Performance of Polymer-Treated Clays*" PhD dissertation. Ghent University. Belgium. 249 p.

Dominijanni, A. Guarena, N. Manassero, M. 2019. Strain-Controlled Oedometer Test for the Measurement of the Chemico-Osmotic Properties of Bentonites. – *Proc. 17th. ECSMGE 2019. Reykjavik, 1-6 September 2019*

Guarena, N. Dominijanni, A. Manassero, M. 2022. The Role of Diffusion Induced Electro-osmosis in the Coupling Between Hydraulic and Ionic Fluxes Through Semipermeable Clay Soil. *Soils and foundations*, 101177

Kang, J.-B.& Shackelford, C.D. 2009. Clay Membrane Testing Using a Flexible-Wall Cell Under Closed-System Boundary Conditions. *Applied Clay Science* 44(1-2) 43–58.

Keijzer Th., Kleingeld P.J. and Loch. J.P.G. (1999). "Chemical Osmosis in Compacted Clayey Material and the Prediction of Water Transport." *Engineering Geology*. 53. 151–159.

Malusis, M.A. Shackelford, C.D. & Olsen. H.W. 2001. A Laboratory Apparatus to Measure the Chemico-Osmotic Efficiency for Clay Soils. *Geotechnical Testing Journal* 24 229–242.

Malusis, M. & Shackelford, C.D. 2002. Chemico-Osmotic Efficiency of a Geosynthetic Clay Liner. *Journal of Geotechnical and Geoenvironmental Engineering*. 128. 97–106.

Malusis, M.A. & Daniyarov, A.S. 2016. Membrane Efficiency and Diffusive Tortuosity of a Dense Prehydrated Geosynthetic Clay Liner." *Geotextiles and Geomembranes*. 44. 719–730.

Manassero, M. & Dominijanni, A. 2003. Modelling the Osmosis Effect on Solute Migration Through Porous Media. *Géotechnique*. 53.481–492.

Mazzieri, F., Di Emidio, G.& Van Impe, P.O. 2010. Diffusion of Calcium Chloride in Modified Bentonite: Impact on Osmotic Efficiency and Hydraulic Conductivity. *Clays and Clay minerals*. 58(3) 351–363.

Mazzieri F., Di Emidio G. 2015. Hydraulic Conductivity of a Dense Prehydrated Geosynthetic Clay Liner *Geosynthetics International*. 22(1) 138–148.

Scalia, J.IV Bareither, C.A. & Shackelford, C.D. 2018. Advancing the Use of Geosynthetic Clay Liners as Barriers" *Geotechnical Engineering Journal of the SEAGS & AGSSEA*. 49(4) 100–113.

A practical isochronous stiffness model for analysis and design of reinforced soil structures

R.J. Bathurst
GeoEngineering Centre at Queen's-RMC, Royal Military College of Canada, Kingston, Canada

F.M. Naftchali
GeoEngineering Centre at Queen's-RMC, Queen's University Kingston, Canada

ABSTRACT: Geosynthetic reinforcement materials such as geogrids, geotextiles and polymer straps are rate-dependent materials which means that their mechanical tensile properties are most often time-, load- and strain-dependent. Nevertheless, analytical and numerical analyses of geosynthetic reinforced soil walls, slopes, thin fills and embankments under operational (serviceability) conditions are most often carried out using a single-value estimate of the reinforcement stiffness consistent with the notion of a single equivalent elastic modulus for the reinforcement material. This paper describes a two-component hyperbolic isochronous stiffness model that accounts for time-dependent changes in reinforcement stiffness due to creep. The model for the reinforcement can be used in numerical and analytical modelling of reinforced soil structures under operational (serviceability) conditions corresponding to low tensile loads and strains.

1 INTRODUCTION

Geosynthetic reinforcement materials are rate-dependent materials, which means they exhibit time- and strain-level-dependent behaviour under load to different degrees depending on the product. This introduces challenges for numerical and analytical models used to design reinforced soil structures where the reinforcement is most often assumed as a linear-elastic plastic material with constant stiffness. The first attempt to account for time-dependent strain (creep) under load is the seminal work of McGown et al. (1984a,b) who introduced the concept of isochronous load-strain curves deduced from constant load in-isolation tensile tests carried out on specimens of geosynthetic material. This paper describes a simple two-parameter isochronous tensile load-strain hyperbolic model for these materials that can be used to estimate the stiffness of the reinforcement at low tensile strain and load expected under operational conditions. The model has application to geosynthetic reinforced soil applications such as reinforced fills over voids, reinforced slopes and embankments, geosynthetic-reinforced pile-supported embankments, geosynthetic-encased columns, internal stability of geosynthetic mechanically stabilized earth (MSE) and the estimation of MSE wall deflections. The application of the model is limited to estimating the stiffness of the reinforcement at low tensile strain and load levels expected under operational (serviceability) conditions, as opposed to ultimate limit state conditions.

2 HYPERBOLIC MODEL FOR ISOCHRONOUS STIFFNESS

The procedure to construct isochronous stiffness curves is illustrated in Figure 1. Creep tests are first carried out at different constant loads as illustrated in Figure 1a. From these data,
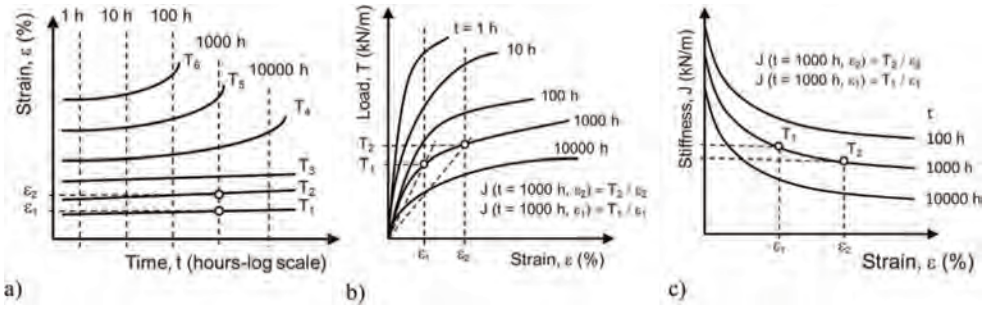
Figure 1. Interpretation of load-strain-time data from: a) constant-load creep tests; b) isochronous load-strain curves showing secant stiffness, and; c) isochronous secant stiffness curves.

isochronous curves are constructed (Figure 1b). Finally, isochronous stiffness curves are plotted as shown in Figure 1c. Isochronous stiffness values can be used in analytical and numerical modelling to describe the tensile load in a polymeric reinforcement material using a single-value equivalent stiffness as follows:

$$T(\varepsilon, t) = J(\varepsilon, t) \times \varepsilon \qquad (1)$$

Here, $T(\varepsilon,t)$ is the strain-dependent tensile load at isochronous time t, ε is strain, and $J(\varepsilon,t)$ is the isochronous stiffness. Bathurst & Naftchali (2021) proposed the following two-parameter hyperbolic model to describe isochronous load-strain curves (Figure 1b):

$$T(\varepsilon, t) = \frac{\varepsilon}{\frac{1}{J_o(t)} + \frac{1}{\chi(t)}\varepsilon} \qquad (2)$$

from which the secant stiffness $J(\varepsilon,t)$ values shown in Figure 1c follow as:

$$J(\varepsilon, t) = \frac{1}{\frac{1}{J_o(t)} + \frac{1}{\chi(t)}\varepsilon} \qquad (3)$$

Here, $J_o(t)$ is the initial stiffness at zero strain for isochronous time t, and $\chi(t)$ is a parameter that captures the curvature of the isochronous curve. These parameters are determined by non-linear regression fitting to the curves in Figure 1c. Equation 3 can accommodate both linear elastic and non-linear (creep) stiffness behaviour. For instance, for steel grids and strips, $J_o(t) = E \times A$ where E is the elastic modulus of steel and A is the cross-section area per meter width of a continuous sheet of steel grid reinforcement or the width of a single strip, and $1/\chi(t) = 0$.

3 DATABASE OF CREEP TESTS

A total of 606 creep tests from 89 different products falling into seven different categories were collected by Bathurst & Naftchali (2021) from AASHTO National Transportation Product Evaluation Program (NTPEP) reports in the USA (see NTPEP 2019a, b) and from the research literature. Only data sets with a minimum of three creep curves at different low load levels were included in the database. A summary of the database appears in Table 1.

Table 1. Summary of reinforcement types in the database of Bathurst & Naftchali (2021).

Reinforcement type	Number of data groups (product lines)	Number of data sets (products in a product line)	Number of creep tests	Ultimate tensile strength, T_{ult} [a] (kN/ m) [b] or (kN/strap) [c]
HDPE punched and drawn geo-grid	9	19	148	38 – 177 [b]
PET woven and knitted geogrid	12	38	257	17 – 807 [b]
PP punched and drawn geogrid	5	7	37	12 – 39 [b]
PP woven geo-textile	3	4	22	51 – 155 [b]
PET woven geo-textile	3	8	56	53 – 1030 [b]
PET nonwoven geotextile	1	1	3	25 [b]
PET strap	4	12	83	28 – 156 [c]
$\sum$ =	37	89	606	12 – 1030 [b]

Notes: [a] Based on in-solation tensile test carried out at 10% strain per minute (ASTM D4595-17, ASTM D6637/D6637M-15). [b] T_{ult} values are reported as load/unit width of specimen (kN/m). [c] T_{ult} values reported as load/strap (kN/strap).

4 RESULTS

Figure 2a shows stiffness values for a typical HDPE geogrid used as soil reinforcement for MSE walls. The isochronous stiffness curves can be seen to converge with increasing time and strain. The data in Figure 2b are for a biaxial PP geogrid which is often used as secondary reinforcement in MSE walls and slopes, and to reinforce road base layers. This material has the same positive curvature as the HDPE geogrid but is less stiff. Figure 2c shows stiffness curves for a PET woven geotextile. This material has negative curvature which is ascribed to the macro-structure of the material tightening up during tensioning. A similar behaviour can be seen in Figure 2d for a PET strap material (geostrip) comprised of parallel-aligned bundles of PET filaments protected by a polyethylene sheath. The PET bundles also tighten up during tensioning. This material is used as soil reinforcement in MSE walls.

Product-specific isochronous curves such as those reproduced here can be used in numerical and analytical models for different reinforced soil applications. Most often, iso-chronous curves at 1000 h suffice for practical purposes because reinforced soil structures typically reach constant load equilibrium under operational conditions within this time frame. Isochronous curve approximations for a wide range of reinforcement products can be reproduced from tables of $J_o(t)$ and $\chi(t)$ values for different times and strain levels found in the supplemental material to the paper by Bathurst & Naftchali (2021). Values of $J_o(t)$ and $1/\chi(t)$ for different products are plotted against isochronous time in Figure 3. The data in Figure 3a show that with the exception of the PET strap material, $J_o(t)$ decreases with increasing isochronous time. The trend is reasonably well captured using a power function. The two HDPE geogrid products show the greatest sensitivity to isochronous time. From a practical point of view, values of $J_o(t)$ at 1000 hours are sufficiently accurate for design lives of 1000 h or greater for the reasons given earlier. The curvature of the isochronous curves expressed as $1/\chi(t)$ in Figure 3b can be seen to be sensibly constant with time, with the exception of the PP geogrid and PET woven geogrid.
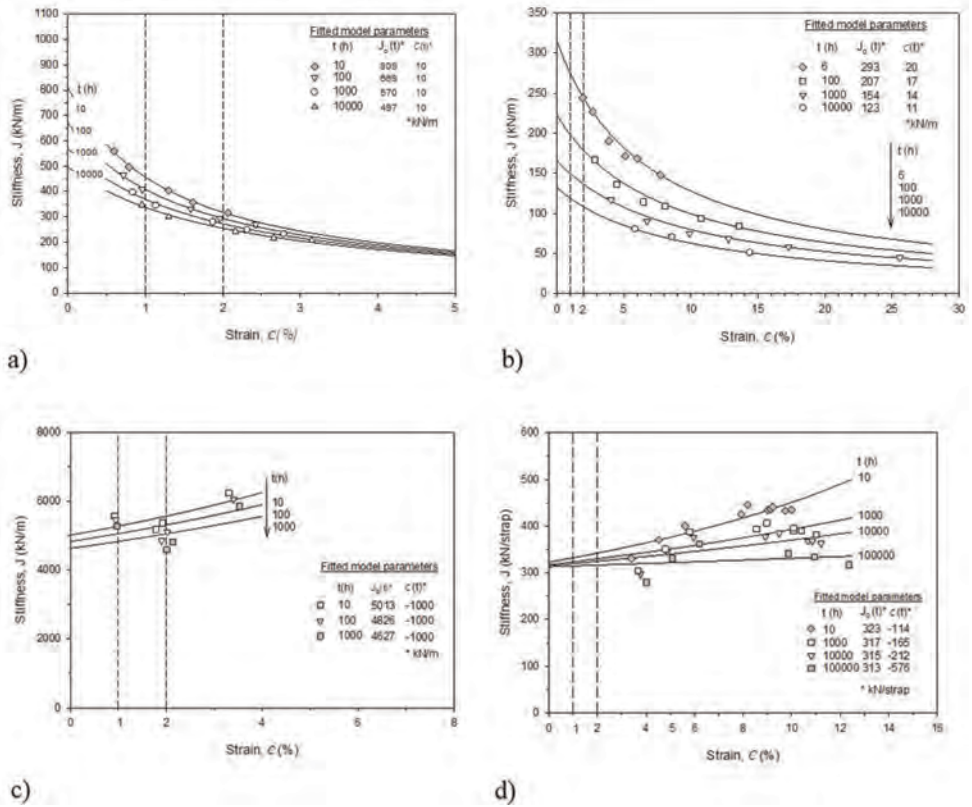
Figure 2. Secant stiffness versus strain and isochronous time for: a) uniaxial HDPE geogrid product; b) biaxial PP geogrid product; c) PET woven geotextile product, and; d) PET strap product. Note: Negative $\chi(t)$ values have been capped at –1000 kN/m.
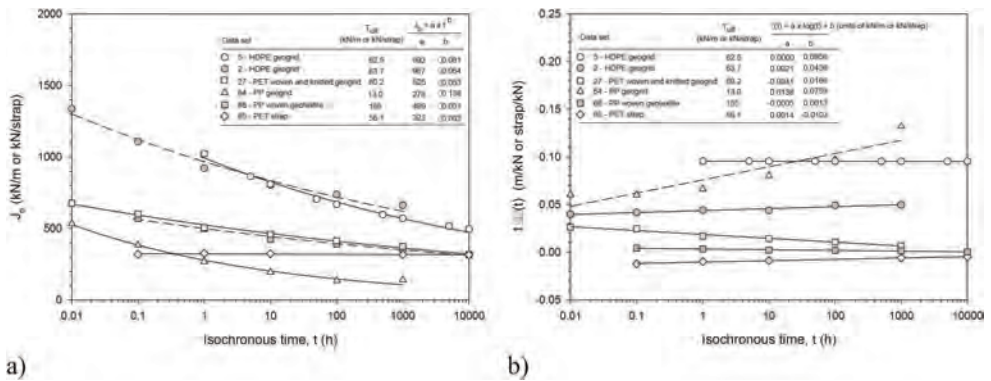
Figure 3. Example plots of hyperbolic model parameters versus isochronous time t: a) J_o, and; b) $1/\chi$ (data from Bathurst & Naftchali 2021).

5 USEFUL APPROXIMATIONS

For many geosynthetic reinforcement products in use today, constant-load creep data are not available or, if creep tests have been performed, the data at low strains expected at operational conditions in the field were not recorded. Bathurst & Naftchali (2021) collected isochronous secant stiffness values and ultimate tensile strength (T_{ult}) values for each product in their data-base. Values of T_{ult} were determined in accordance with ASTM D4595-17 and ASTM D6637/D6637M-15 methods of test. The isochronous stiffness values for strains of 1%, 2% and 5% at 1000 h were found to be reasonably well represented by a simple linear function of the form:

$$J(\varepsilon, t) = R \times T_{ult} \tag{4}$$

where, R is a dimensionless constant. This equation is in accordance with the observation that for products falling within the same product line, the stiffness of the reinforcement increases in direct proportion to its strength, which would appear to be reasonable. This relationship was observed to be true across product lines of similar type for practical purposes as shown in Figure 4.
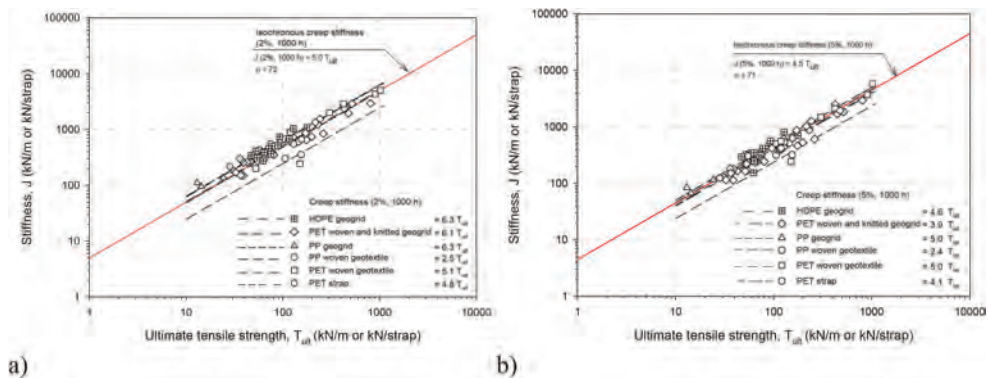
Figure 4. 1000-h isochronous creep stiffness versus ultimate tensile strength for: a) ε = 2%, and; b) ε = 5%. Note: n = number of data points (data from Bathurst & Naftchali 2021).

The data are presented using logarithmic axes because of the wide range in magnitude of stiffness and strength values. Only product data from the six reinforcement categories with sufficient data points are presented. The plots show that average values of coefficient R = 5.0 and 4.5 for ε = 2% and 5%. However, within each plot the product type-specific R values vary widely as shown in the figure legends. The average R values shown here are useful for preliminary sensitivity analyses for different reinforced soil applications. As candidate solutions become more refined during design, the values for R based on product type can be used and finally, if available, product-specific isochronous stiffness data of the type shown earlier in Figure 1 can be used. The data in Figure 4 are also useful for numerical modelling purposes to ensure that the stiffness of the reinforcement used in calculations matches the expected strength of the material. This check is often missed in the numerical modelling research literature.

6 EXAMPLE

An unsurcharged vertical MSE wall of height H_w, constructed with layers of the same PET woven geogrid reinforcement having constant length and placed with uniform vertical

spacing (S_v) is illustrated in Figure 5a. The wall outward deformation Δh at layer depth z below the crest of the wall can be computed as (Jewell & Milligan 1989):

$$\Delta_h = \frac{K_a S_v \gamma z (H_w - z)}{3(\mathrm{J} \times S_r)} \left[\tan\left(45° - \frac{\psi}{2}\right) + 2\tan(90° - \phi) \right] \qquad (5)$$

Here, Δh is the incremental wall displacement taken with respect to the time the layer is placed in the wall during construction. Hence, this moving datum displacement should not be confused with the wall final (end of construction) vertical out-of-alignment taken with respect to the toe of the wall. Other parameters are K_a = active earth pressure coefficient, S_r = reinforcement coverage ratio, γ = soil unit weight, ϕ = friction angle from direct shear tests, Ψ = dilatancy angle $\sim \phi - 30° \geq 0$, and J is the nominal reinforcement stiffness. For continuous sheet reinforcement $S_r = 1$, and for sheets of reinforcement placed with a gap or space between rolls, S_r is the fraction of the reinforcement layer that is continuous per unit length in the running wall direction. Figure 5b shows that the maximum outward deformation of the wall decreases with increasing stiffness of the reinforcement. The shaded range in the plot captures specified or anticipated values for well-constructed walls collected by Bathurst et al. (2010) from a survey of codes and design guidelines from different jurisdictions.
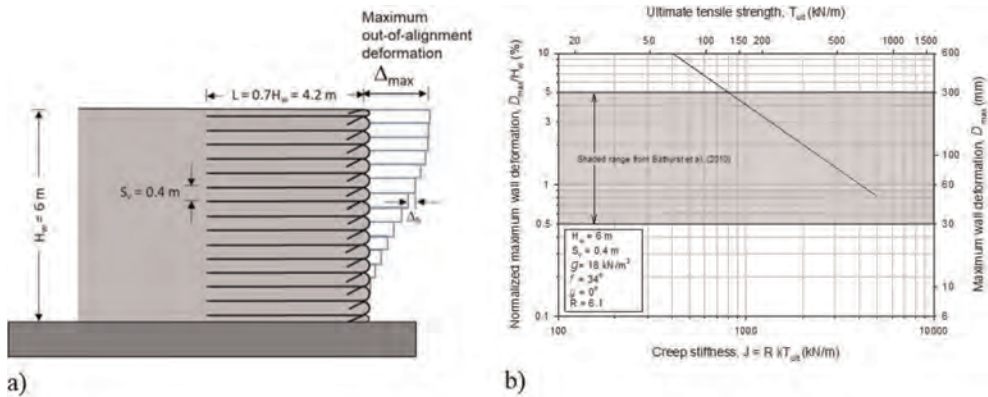
Figure 5.   a) Schematic of 6 m-high MSE wall with wrapped-face and 15 reinforcement layers, and; b) maximum horizontal wall deformation versus design isochronous secant stiffness [J(ε = 2%, 1000 h)] using Equation 4 with R = 6.1 for PET woven geogrid (Bathurst & Naftchali 2023).

7 CONCLUSIONS

This paper gives a brief review of a simple two-parameter hyperbolic isochronous tensile stiffness model developed by Bathurst & Naftchali (2021). The paper provides guidance to designers and researchers for the selection of constant stiffness values at different strain levels and elapsed time for use in analytical and numerical reinforced soil applications where: 1) the reinforcement is treated as a linear elastic-plastic material, and; 2) load levels are low enough that reinforcement strains are reasonably linear with logarithm of time, and creep to failure is not possible over the design life of the structure. The paper provides useful approximations for the magnitude of secant stiffness as a linear function of ultimate tensile strength, based on analysis of a large database of constant-load creep tests compiled by the authors. Finally, the reader is directed to the papers by Bathurst & Naftchali (2021, 2023) for a deeper treatment of the subject and other examples using the hyperbolic model for design of MSE walls and reinforced fills over a void.

REFERENCES

ASTM D4595-17. Standard Test Method for Tensile Properties of Geotextiles by the Wide-Width Strip Method. *ASTM*, West Conshohocken, PA, USA.

ASTM D6637/D6637M-15. Standard Test Method for Determining Tensile Properties of Geogrids by the Single or Multi-Rib Tensile Method. *ASTM*, West Conshohocken, PA, USA.

Bathurst, R.J., Miyata, Y. & Allen, T.M. 2010. Facing Displacements in Geosynthetic Reinforced Soil Walls. *Earth Retention Conference 3 (ER2010), ASCE Geo-Institute*, 18 p.

Bathurst, R.J. & Naftchali, F.M. 2021. Geosynthetic Reinforcement Stiffness for Analytical and Numerical Modelling of Reinforced Soil Structures. Geotextiles & Geomembranes, 49(4): 921–940.

Bathurst, R.J. & Naftchali, F. 2023. Influence of Uncertainty in Geosynthetic Stiffness on Deterministic and Probabilistic Analyses Using Analytical Solutions for Three Reinforced Soil Problems. Geotextiles & Geomembranes, 51(1): 117–130.

Jewell, R.A. & Milligan, G.W.E. 1989. Deformation Calculation for Reinforced Soil Walls. In: *Proc. 12th Int Conf on Soil Mech and Found Engineering. Taylor & Francis*, p. 1259–1262.

McGown, A., Z Andrawes, K., Yeo, K.C. & Dubois, D. 1984a. The Load-Strain-Time Behaviour of Tensar Geogrids. *In Polymer Grid Reinforcement. Thomas Telford Publishing*, p. 11–17.

McGown, A., Paine, N., Dubois, D., Andrews, K.Z. & Jewell, R.A. 1984b. Use of Geogrid Properties in Limit Equilibrium Analysis. *In Polymer Grid Reinforcement*. Thomas Telford, p. 31–36.

NTPEP. 2019a. National Transportation Product Evaluation Program (NTPEP). Use and Application of NTPEP Geosynthetic Reinforcement Test Results. *American Association of State Highway and Transportation Officials (AASHTO)*, Washington, DC, USA. (Accessed Online 30/05/2019).

NTPEP. 2019b. National Transportation Product Evaluation Program (NTPEP) DataMine – Geosynthetic Reinforcement (REGEO). *American Association of State Highway and Transportation Officials (AASHTO)*, Washington, DC, USA. (Accessed Online 30/05/2019).

Effect of welding quality from dual track wedge welding on post-weld geomembrane oxidative induction time

J.W.B. Silva & R. Kerry Rowe
GeoEngineering Centre at Queen's-RMC, Department of Civil Engineering, Queen's University, Canada

ABSTRACT: Geomembranes sheets used in fluid containment applications are welded together in situ using a dual track hot wedge welder or extrusion welding. In dual track wedge welding, overheating can occur in the weld and still meet typical acceptance standards based on peel and shear strength. However, this overheating depletes antioxidants and contribute to a potential reduction in the service life of the geomembrane in the heat-affected zone (HAZ) and junction zone (JZ) adjacent to the weld. This study examines the relationship between the welding quality and thickness on the production of the weld and any reduction in standard oxidative induction time (Std-OIT) for four HDPE geomembranes. The paper describes ageing tests being conducted on these different welds to evaluate the impact of ageing on the rate of antioxidants depletion during welding on the aging of the junction zone relative to the parent material.

1 INTRODUCTION

The composite liners using a geomembrane over a geosynthetic clay liner (GCL) are extensively used to minimize the migration of contaminants from solid waste landfill facilities (Abdelaal et al. 2019; Abdelaal & Rowe 2019; McWatters et al. 2020; Rowe 2005). However, the correct performance of the composite liners lies on the correct choice and installation of the materials with a service life that will need to exceed the contaminating lifespan (centuries). Previous studies have examined the degradation rates and service life of HDPE geomembranes for a wide variety of conditions (Abdelaal & Rowe 2019; Ewais et al. 2014; Li et al. 2021; McWatters et al. 2020; Morsy & Rowe 2020). Geomembranes are known to age at varying rates depending on the material, time, exposure medium, temperature, and strain, with brittle failure, or stress cracking, being the final failure mechanism. Researchers have examined the durability of HDPE geomembranes focusing on sheet durability. However, one of the essential processes involving the use of geomembranes as barriers, namely the welding of panels together, has been neglected in most studies. Available evidence suggests that the welds/seam are the most consistent weak point (Francey & Rowe 2021; Giroud 2005; Kavazanjian et al. 2017; Peggs et al. 2014; Rowe & Shoaib 2017, 2018; Zhang et al. 2017). Thus, this paper will follow on form the limited work to date by examining the effect of welding on the rate of antioxidant depletion in the junction zone (JZ) relative to the parent material for four different geomembrane thickness welded with two different sets of welding parameters. The junction zone (JZ) represents the intermediate area between the weld zone (WZ) and heat affected sheet zone (HAZ) as shown in Figure 1.

1.1 Seams

The wide use of HDPE geomembranes requires the application of weld techniques to construct a uniform barrier. There are different methods of geomembrane welding: extrusion fillet welding, extrusion flat welding, dual track wedge weld, and hot air welding. The current practices commonly use the dual track wedge and the extrusion welds due to the fast process and control. The dual track wedge welding consists of applying pressure to two parallel tracks of heated geomembrane and forming two welds with an air channel between the two. This air channel can be used to perform integrity tests after the welding process. During the welding process, the technician can change the machine's speed, temperature, and pressure based on environmental conditions and the thickness of geomembrane. These parameters should be validated using destructive tests and trial seams. If these welding parameters are not correctly defined, poor seams and localized defects can occur as the result of over or under-heating the weld itself (Elton & Peggs 2002; Müller 2007; Scheirs 2009; Zhang et al. 2017). The current definition of a good and bad geomembrane weld is based on the ASTM 6392 recommendations and German DVS 2225-4. However, while these guidelines are useful for construction monitoring, they have limited applicability with respect to the long-term performance of seams. There has been a paucity of studies examining the durability of HDPE seams, with a few notable exceptions. Rowe & Shoaib (2013, 2017) found that the heat-affected zone (HAZ) represents a critical location of the weld with respect to ageing, with faster antioxidant depletion. Kavazanjian et al. (2017) experimentally showed the level of strain concentration that occurs at seams. Francey & Rowe (2021) analyzed the stress crack resistance of HDPE seams exposed to synthetic leachate at 85°C and demonstrated that the stress crack resistance of seams is affected by the welding parameters and why these can make a weld the critical weaker point with respect to liner durability.

1.2 Ageing process and immersion tests

Oven immersion tests are commonly used to examine the stages of geomembrane degradation and to allow extrapolation of HDPE geomembrane behaviour at any site-specific temperature (Abdelaal et al. 2019; Abdelaal & Rowe 2019; Hsuan & Koerner 1998; McWatters et al. 2020; Morsy & Rowe 2020; Rowe et al. 2009, 2010a; Sangam & Rowe 2002). The exposure to elevated temperatures and synthetic MSW leachates reduce the time to chemical degradation of geomembranes. During these tests, three stages can be observed: (a) antioxidant depletion (Stage I), where antioxidants in the geomembrane have just depleted to a residual value; (b) induction period (Stage II), where additives have been fully depleted but mechanical degradation has not yet occurred; and (c) reduction in mechanical properties (Stage III), where thermo-oxidative degradation leads to a reduction in mechanical properties (Hsuan & Koerner 1998; Rowe & Sangam 2002). The life service of the geomembrane can be improved with either a change in the additives to increase Stage I or the resin to increase Stages II & III. However, the focus in both cases is on increasing the service life of the sheet. The portion of the sheet that is welded is subject to elevated temperatures to melt the geomembrane and produce the weld, with the normal wedge temperature ranging between 350-560°C; much higher than the effective temperature range of common antioxidants (Hsuan & Koener 1998). The implications of this are not well understood.

2 MATERIAL AND EXPERIMENTAL PROCEDURE

2.1 Geomembrane properties

Table 1 presents the initial properties of four HDPE geomembranes examined. These geomembranes were dual wedge-welded by an experienced technician at ambient temperature (20°C) using two different machines: DemTech ProWedge (DPW) and Leister G7 (G7). The welding parameters are presented in Table 2, following the guidelines of the welding machine

manufacturer and the qualification tests (peel and shear). "Good" and "Inferior" welds were prepared, changing the properties to produce rippling for the inferior welding quality.

Table 1.   Initial properties of HDPE geomembranes.

Index Property Geomembrane	Initial Value			
	MxC10	MxC15	MxC20	MxC24
Thickness (mm)	1.0	1.5	2.0	2.4
Std-OIT (min)	155	160	162	162
HLMI (g/10min)	17.3±0.6	15.3±0.2	15.7±0.7	16.3±1.1

Table 2.   Initial properties of HDPE seams.

Geomembrane Welding quality	MxC10		MxC15		MxC20		MxC24	
	Good	Inferior	Good	Inferior	Good	Inferior	Good	Inferior
Welding Speed (m/min)	3.0	1.8	5.5	3.7	5.0	2.6	3.2	1.6
Wedge Temperature (°C)	400	460	400	460	400	455	420	460
Welding Pressure (N)	-*	-*	1060	1060	1200	1200	1300	1300
Sheet ayay form weld-OIT (min)	155	155	160	160	162	162	162	162
Std-OIT (min) JZ (see Figure 1)	157	147	161	157	156	160	160	161
Std-OIT (min) WZ (see Figure 1)	153	153	161	157	161	161	149	154
Average Weld Thickness (mm)	1.90±0.07	1.69±0.09	2.40±0.05	2.03±0.12	3.35±0.17	2.93±0.12	3.90±0.07	3.11±0.06
Thickness reduction (mm)	0.1	0.31	0.6	0.97	0.65	1.07	0.9	1.69
Thickness reduction (T_R) limits (mm)		-	$0.6 \leq T_R \leq 0.8$		$0.4 \leq T_R \leq 0.8$		$0.4 \leq T_R \leq 0.8$	

*Welded with DPW which does not quantify pressure but has a number of specific settings.

2.2   Qualification tests

After the welding, the welds were tested following the current North American guideline (ASTM 6392). The criteria defined by ASTM D6392 require a specified value for peel and shear strength and elongation. For all four geomembranes and two welding qualities examined the seams passed the tests. Thus, seams welded considered to have inferior quality passed the usual quality control tests despite evidence of overheating in the form of rippling. Additionally, to the ASTM 6392 guidelines, the seams were evaluated by the DVS 2225-4 which has a thickness reduction criterion for the weld. The welds produced with inferior welding quality did not meet this criterion. For MxC10 it was not possible to produce a viable weld with a thickness reduction higher than 0.3.

2.3   Immersion test

After the welding process, qualification tests the four geomembranes were cut in coupons (190 ×95 mm) and immersed in synthetic leachate in 4-litre glass jars. The coupons were separated by 5 mm glass rods to ensure exposure to the fluid on both sides of geomembrane coupons. They were all incubated at 75°C and 85°C where chemical degradation requires a

short time. These samples were used to extract specimens for OIT tests at different times of ageing. The synthetic leachate solution used in this research is based on studies conducted by Rowe et al. (2009), Abdelaal et al. (2014b), and Rowe & Shoiab (2013, 2017). This solution is based on the chemical analyze conduct for the Keele Valley landfill, in Ontario, Canada (Rowe et al. 2009). Rowe and Shoiab (2017) conducted research using this leachate to examine the long-term durability of HDPE seams.

As a result of chemical degradation, there can be a loss of antioxidants or stabilizers from the geomembrane. To evaluate this change Std-OIT tests were performed using a TA instruments Q-200 series differential scanning calorimeter (DSC). The OIT specimens were taken at the three locations shown in Figure 1: (1) The Sheet Away from the Weld (SAW), where the geomembrane is unaffected by the welding process; (2) The Welded Zone (WZ) below the nip rollers which has experienced some thickness reduction (see Table 2); and (3) The Junction Zone (JZ) adjacent to the weld that includes some squeeze-out fused to and integral with the sheet on neither side by heat of the welding process and having a thickness greater than either the sheet or the Welded zone (WZ). This is the first study to examine the JZ; others have focused on the HAZ.
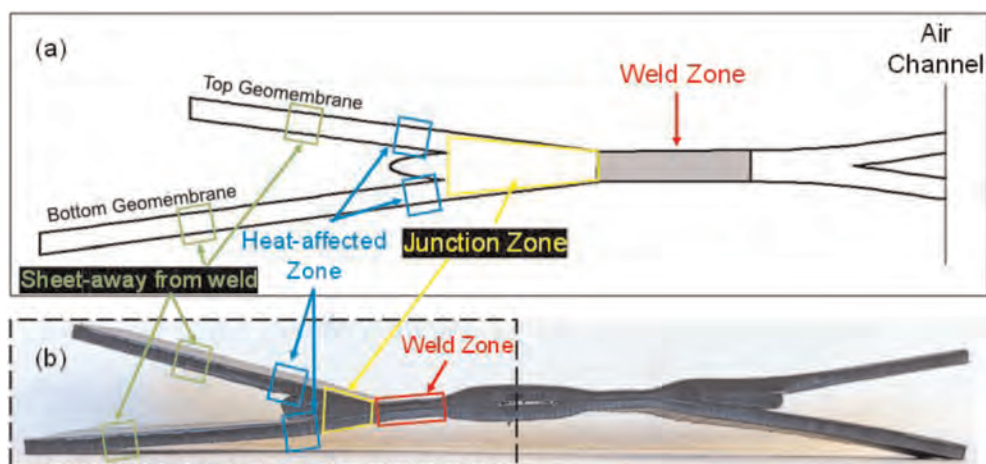
Figure 1.   Cross-section of typical HDPE dual track fusion weld (a) Schematic magnification of main zones, (b) Entire cross-section of the weld.

3   PRELIMINARY RESULTS

Std-OIT depletion was examined for four different geomembranes and two welding qualities, during the tests three different areas were analyzed for 16 weeks and two immersion temperatures (75°C and 85°C). Figure 2 presents Std-OIT results for MxC10 and MxC15 for both welding quality parameters with time, normalized by dividing the values by the initial (virgin) material values immediately after welding.

The observed results for MxC20 and MxC24 were similar to those shown in Figure 2 for thinner geomembranes. Based on these preliminary results the STD-OIT depletion of the antioxidants was fastest in SAW, next in the WZ and slowest in the JZ. This general trend was found for all the thicknesses for both sets of welding quality parameters and both immersion temperatures analyzed. The difference in welding quality is evident from faster Std-OIT depletion for the inferior welds than for the good welds. This effect decreased slightly with an increase in geomembrane thickness.
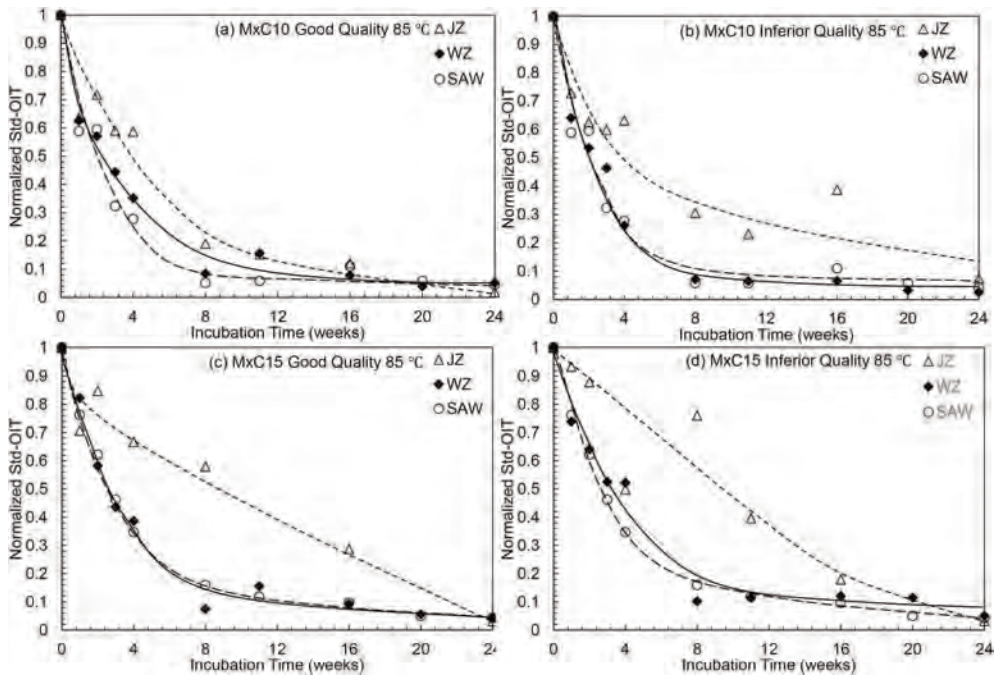
Figure 2. Normalized variation Std-OIT with incubation time at three locations immersed in leachate at 85 °C (a) MxC10-Good weld, (b) MxC10-Inferior weld, (c) MxC15-Good weld, and (d) MxC15-Inferior weld. Note: SAW is the same for good and poor for each GMB thickness and can be used as a reference curve.

The slower depletion of the junction zone (JZ) compared with weld (WZ) and the parental sheet (SAW) is attributed to the difference in geomembrane thickness at each location because an increase in thickness results in a longer path for the outward diffusion of anti-oxidants (Rowe et al. 2010, Rowe et al. 2014, Rowe & Ewais 2014). The fast depletion of SAW than WZ is in agreement with the findings of Rowe & Shoaib (2017) and Rowe & Shoaib (2018). Also, it is important to highlight that this study and Rowe & Shoaib (2017, 2018) used different HDPE geomembranes with different additives packages and properties. Longer incubation times are needed to more accurately compare the JZ and HAZ in terms of antioxidant depletion.

4 CONCLUSIONS

This paper has reported an examination of the effect of geomembrane thickness and welding quality on the Std-OIT depletion for three different regions of the weld. The preliminary results suggest the following conclusions for the four different geomembranes and two welding quality parameters examined in this paper.

- Std-OIT depletion was fastest for the SAW and WZ and slowest for JZ, showing that for the material and data analyzed to date, the JZ is not a critical zone with respect to antioxidant depletion.
- Welding quality appears to have a significative effect on the Std-OIT depletion rate for all the geomembrane and temperatures studied. The influence of welding quality on results appears to be reduced with increasing geomembrane thickness.

- The inferior welding quality that visibly presented some sign of overheating and rippling met typical QA/QC peel and shear test requirements.

These preliminary findings will be re-examined as more data becomes available.

ACKNOWLEDGMENTS

REFERENCES

Abdelaal, F. B., Rowe, R. K., and Islam, M. Z. (2014). "Effect of Leachate Composition on the Long-term Performance of a HDPE Geomembrane." *Geotextiles and Geomembranes*, 42(4), 348–362.

Abdelaal, F., and Rowe, R. (2019). "Degradation of an HDPE Geomembrane Without HALS in Chlorinated Water." *Geosynthetics International*, 26(4), 354–370.

Abdelaal, F., Morsy, M., and Rowe, R. K. (2019). "Long-term Performance of a HDPE Geomembrane Stabilized with HALS in Chlorinated Water." *Geotextiles and Geomembranes*, 47(6), 815–830.

ASTM (2012). "Standard Test Method for Determining the Integrity of Nonreinforced Geomembrane Seams Produced Using Thermo-Fusion Methods." *American Society for Testing and Materials* D6392, West Conshohocken, PA.

ASTM (2014). "Standard Test Method for Oxidative-Induction Time of Polyolefins by Differential Scanning Calorimetry." *American Society for Testing and Materials* D3895, West Conshohocken, PA, USA.

DVS 2225-3. "*Welding of Linging Membranes Made of Polyethylene (PE) for the Protection of Groundwater.*"German Welding Society, Düsseldorf, Germany.

Elton, D. J., & Peggs, I. (2002). Geomembrane Research Needs. *Geosynthetics International*, 9(3), 283–300.

Ewais, A. M. R., Rowe, R. K., & Scheirs, J. (2014). Degradation Behaviour of HDPE Geomembranes with High and Low Initial High-Pressure Oxidative Induction Time. *Geotextiles and Geomembranes*, 42(2), 111–126.

Francey, W., & Rowe, R. K. (2021). Stress Crack Resistance of Unaged High-Density Polyethylene Geomembrane Fusion Seams. *Geosynthetics International*, 1–46.

Giroud, J. P. 2005. Quantification of Geosynthetic Behavior. *Geosynthetics International*, 12, No. 1.

GRI-GM19. "*Seam Strength and Related Properties of Thermally Bonded Polyolefin Geomembranes.*"Geosynthetic Research Institute, PA, USA.

GRI-GM13. "*Standard Specification for test Methods, Test Properties, and Testing Frequency for High Density Polyethylene (HDPE) Smooth and Textured Geomembranes.*"Geosynthetic Research Institute, PA, USA.

Hsuan, Y., and Koerner, R. (1998). "Antioxidant Depletion Lifetime in High Density Polyethylene Geomembranes." *Journal of Geotechnical and Geoenvironmental Engineering*, 124(6), 532–541.

Kavazanjian, E., Andresen, J., and Gutierrez, A. (2017). "Experimental Evaluation of HDPE Geomembrane Seam Strain Concentrations." *Geosynthetics International*, 24(4), 333–342.

Li, W., Xu, Y., Huang, Q., Liu, Y., and Liu, J. (2021). "Antioxidant depletion Patterns of High-Density Polyethylene Geomembranes in Landfills Under Different Exposure Conditions." *Waste Management*, 121, 365–372.

Müller, W. W. (2007). *HDPE Geomembranes in Geotechnics*, Springer.

McWatters, R., Rowe, R., Di Battista, V., Sfiligoj, B., Wilkins, D., and Spedding, T. (2020). "Exhumation and Performance of an Antarctic Composite Barrier System After 4 years Exposure." *Canadian Geotechnical Journal*, 57(8), 1130–1152.

Morsy, M., and Rowe, R. K. (2020). "Effect of Texturing on the Longevity of High-Density Polyethylene (HDPE) Geomembranes in Municipal Solid Waste Landfills." *Canadian Geotechnical Journal*, 57(1), 61–72.

Peggs, I., Gassner, F., Scheirs, J., Tan, D., Arango, A., and Burkard, B. (2014). "Is There a Resurgence of Stress Cracking in HDPE Geomembranes." *Proc., Proceedings of the 10th International Conference on Geosynthetics*, Berlin.

Rowe, R. K., and Sangam, H. P. (2002). "Durability of HDPE Geomembranes." *Geotextiles and Geomembranes*, 20(2), 77–95.

Rowe, R.K., 2005. Long-term Performance of Contaminant Barrier Systems. 45th Rankine Lecture. *Geotechnique 55* (9), 631–678.

Rowe, R. K., Rimal, S., & Sangam, H. (2009). Ageing of HDPE Geomembrane Exposed to Air, Water and Leachate at Different Temperatures. *Geotextiles and Geomembranes*, 27(2), 137–151.

Rowe, R. K., Islam, M. Z., & Hsuan, Y. G. (2010). Effects of Thickness on the Aging of HDPE geomembranes. *Journal of Geotechnical and Geoenvironmental Engineering*, 136(2), 299–309.

Rowe, K., & Shoaib, M. (2013). Durability and Long-term Strength of Seams in HDPE Geomembranes. 66th Canadi-an Geotechnical Conference, *GeoMontreal 2013*, Montreal, Canada - October 2013.

Rowe, R. K., Abdelaal, F. B., & Islam, M. Z. (2014). Aging of High-Density Polyethylene Geomembranes of Three Different Thicknesses. *Journal of Geotechnical and Geoenvironmental Engineering*, 140(5), 04014005.

Rowe, R. K., & Ewais, A. M. R. (2014). Antioxidant Depletion from Five Geomembranes of Same Resin but of Different Thicknesses Immersed in Leachate. *Geotextiles and Geomembranes*, 42(5), 540–554.

Rowe, R. K., and Shoaib, M. (2017). "Long-term Performance of High-Density Polyethylene (HDPE) Geomembrane Seams in Municipal Solid Waste (MSW) Leachate." *Canadian Geotechnical Journal*, 54 (12), 1623–1636.

Rowe, R. K., and Francey, W. (2018). "Effect of Dual Track Wedge Welding at 30°C Ambient Temperature on Post-Weld Geomembrane Oxidative Induction Time." *11th International Conference on Geosynthetics*, Seoul, Korea, September

Rowe, R. K., and Shoaib, M. (2018). "Durability of HDPE Geomembrane Seams Immersed in Brine for Three Years." *Journal of Geotechnical and Geoenvironmental Engineering*, 144(2), 04017114.

Scheirs, J. (2009). *A Guide to Polymeric Geomembranes: A Practical Approach*, John Wiley & Sons.

Zhang, L., Bouazza, A., Rowe, R., and Scheirs, J. (2017). "Effect of Welding Parameters on Properties of HDPE Geomembrane Seams." *Geosynthetics International*, 24(4), 408–418.

Roughness based prediction of geofoam interfaces with concrete

P.G. Sreekantan
Geotechnical Engineering Division, CSIR-Central Road Research Institute, New Delhi, India

G.V. Ramana
Department of Civil Engineering, Indian Institute of Technology Delhi, Hauz Khas, New Delhi, India

ABSTRACT: Geofoam is a popular lightweight material block, used for the structural filling for the construction of vertical approach embankments of road bridges over soft subsoils. The design of such embankments is driven by the differential settlement, as the overall settlement of the geofoam blocks is lower than the fascia wall. Thus, the critical interface is the geofoam blocks with the concrete fascia wall. In the present study, an attempt has been made to determine the geofoam-concrete interface characteristics using a series of interface tests in a direct shear box. Geofoam with varying densities and concrete with varying roughness were utilised for the study. Based on the observed test results, a non-linear model for predicting interface friction angle with the roughness index was derived. This study can be utilised for the design and site quality assurance based on the roughness index of the concrete retaining wall cast at the site.

1 INTRODUCTION

Expanded Polystyrene blocks, also known as "Geofoam," are rigid cellular foam blocks used in various geotechnical engineering applications. Since these foams are typically 20-100 times lighter than soil (ASTM D6817, 2021), they are commonly used as lightweight fill. Since its first application by the Norwegian Public Roads Administration for preventing excessive settlement in 1972 (Aabøe et al. 2019), geofoams were popularly used for the construction of road embankments resting over soft soil. (Farnsworth et al. 2008; Puppala et al. 2019). In the past decade, it has also been used for the construction of vertical approach embankments for road bridges over soft subsoils as structural fill material (Bartlett et al. 2012; Stuedlein & Negussey 2013). However, the fascia wall of such embankments undergoes considerable elastic and consolidation settlement. This generates differential movement at the geofoam-concrete interface, leading to the development of interface shear stress. The estimation of this interface shear resistance is important for the accurate numerical modelling and design of such walls. Apart from this, to increase the stiffness of the geofoam subgrade, it is a common practice to provide a cast in situ load distribution slab over the geofoam blocks (Stark et al., 2004). In this case, the quantification of the geofoam-concrete interface is essential for the translational sliding failure analysis.

Various researchers (AbdelSalam & Azzam 2016; Khan & Meguid 2019; Özer & Akay 2022; Sheeley & Negussey 2000) have evaluated the interface shear behaviour between geofoam and concrete. Some have used cast-in-situ concrete, whereas others have used precast concrete. The reported interface friction values varied between 25° to 48°, whereas the friction coefficient varied from 0.5 to 2.3. This variation can be attributed to the variation in the roughness of concrete and geofoam (Özer & Akay 2022). However, none of these researchers quantified the roughness parameters of concrete blocks used in the testing. In the case of monolithic materials, the mechanism of friction is also influenced by the hardness of both sliding materials. Geofoam

and concrete being dissimilar materials, the difference in hardness influence the interface friction parameters. No research is available to date quantifying the friction parameters with respect to the roughness or hardness of geofoam and concrete. Such a study will give a generalized approach for evaluating and predicting such interface friction coefficients.

The main objective of this paper is to study the interface frictional behaviour of geofoam and concrete with varying roughness indexes and study the correlation between the friction parameters and the relative roughness values of the geofoam-concrete interface. Such a correlation, if established shall be useful for any concrete surface, irrespective of cast-in-situ or precast. The results obtained from the direct shear tests for the interface were used for arriving at this correlation. To obtain a generalized prediction model for the geofoam-concrete interface, the influence of the roughness of both materials is incorporated using a relative roughness (R') parameter. Additionally, to evaluate the mechanism of shearing, the relative hardness between the materials was also estimated.

2 MATERIALS AND TESTING METHOD

Expanded polystyrene (EPS) geofoam blocks manufactured by two Indian companies E-Pack Polymers Pvt. Ltd. and Shree Insupac Ltd., were used for the present study. Geofoam blocks namely 15D, 20D, 25D and 30D having respective nominal densities of 15 kg/m^3, 20 kg/m^3, 25 kg/m^3, and 30 kg/m^3, were collected. Cubical specimens of size 60 mm × 60 mm × 12.5mm were cut out from the blocks using a hot wire. The measured mechanical properties of various geofoam types are listed in Table 1. The surface roughness profiles of the geofoam specimens were measured using an advanced stylus profiler having an accuracy of 8 nm, as shown in Figure 1a. The roughness profile was measured at three locations of each specimen over an evaluation length of 12.5mm. The measuring force of the stylus needle was maintained at 4 mN throughout the measurement. A typical surface roughness profile for each type of geofoam is indicated in Figure 1b. The roughness profiles indicate that the maximum and the mean surface asperity decreases with the increase in geofoam density. This can be attributed to the decrease in bead size and the increase in bead density with increasing density. The arithmetic average and the root mean square of the difference between the peak and valleys of the surface profile is represented by average roughness, R_a and R_q respectively, which is indicated in Table 2.

Table 1. Mechanical properties of the geofoam.

Property		Test Method	Geofoam Type			
			15D	20D	25D	30D
Apparent Density, (kg/m^3)		ASTM D1622 (2020)	14.17-17.36	18.20-22.78	24.20-27.43	33.63-34.71
Avg. Density, γ (kg/m^3)			15.76	20.50	25.8	34.17
Compressive resistance (kPa) at strain	1% (σ_1)	ASTM D1621 (2016)	27	29	44	66
	Yield (σ_y)		72	105	126	167
	10% (σ_{10})		87	119	141	198
Elastic Modulus, E_i (MPa)			2.73	2.93	4.45	6.63
Monoblock cohesion, C_b (kPa)		ASTM D5321 (2021)	21.6	31.6	40.3	42.5
Monoblock internal friction, φ_b (°)			6.7	15.5	20.5	24.2

The different plain cement concrete blocks were cast using varying mix proportions of water, cement, fine aggregate and coarse aggregate to obtain different roughness. The roughness profiles of concrete blocks were measured using the sand patch method (ASTM E1845, 2015). Three different concrete blocks with average roughness ranging from 0.6 mm to 1.1 mm were cast and cured for 7 days before testing. The hardness of the materials was measured using Shore hardness durometers. Shore A tester was used for geofoam blocks, while Shore D tester was used for
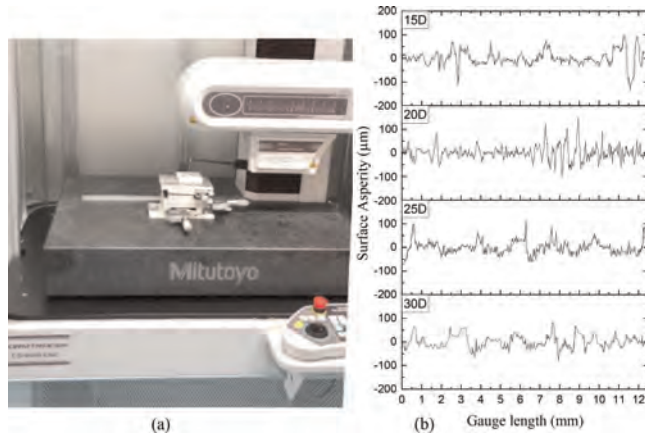
Figure 1.   a) Roughness measurement using stylus profiler, b) Roughness profile of geofoam with varying density (kg/m^3).

Table 2.   Properties of the materials used.

Property		15D	20D	25D	30D	C1	C2	C3
Roughness	R_a (μm)	22.79	22.01	21.23	21.65	626	828	1013
	R_q (μm)	28.85	28.46	27.81	26.36			
Hardness, H	Shore A	2	5	6	12	–	–	–
	Shore D	–	–	–	–	55	77	81
Classification			Extra Soft		Soft		Extra Hard	

concrete blocks. The measured values are indicated in Table 2. Geofoam can be classified as extra soft to soft material, while all the concrete specimens are extra hard materials.

The interface shear tests were conducted in a direct shear testing equipment with concrete and geofoam blocks of size 60 mm × 60 mm ×12.5 mm each. Since both the concrete and geofoam are rigid blocks, the scale and edge effect of the shear box is not anticipated on the friction behaviour. This test has the advantage of maintaining the horizontal load application at the same level of interface, minimizing any eccentricity. The concrete blocks and geofoam blocks were placed at the bottom and top boxes respectively. This ensured maintaining the same horizontal interface throughout testing. Tests were performed at a strain rate of 1mm/min, under three different normal stresses (18 kPa, 28 kPa and 48 kPa), which are well within the elastic limits of the geofoam.

3   RESULTS AND DISCUSSIONS

3.1   *General response*

The typical variation of friction coefficient with respect to shear strain is indicated in Figure 2. It can be observed that with the increase in the normal stress, the friction coefficient reduces leading to the disappearance of the peak. This can be attributed to the flattening of micro-indentations of geofoam with the increase in normal stress. It can also be observed that with the increase in the roughness of concrete, the peak friction coefficient increases. Residual friction coefficient increases from 0.50 to 0.54, when the roughness of concrete increases from 0.6 mm to 1.0 mm. The local ploughing of geofoam strands leads to the formation of a peak friction coefficient and is more evident with increasing roughness of the concrete. After attaining peak stress, the geofoam strands undergo micro-cutting, which is
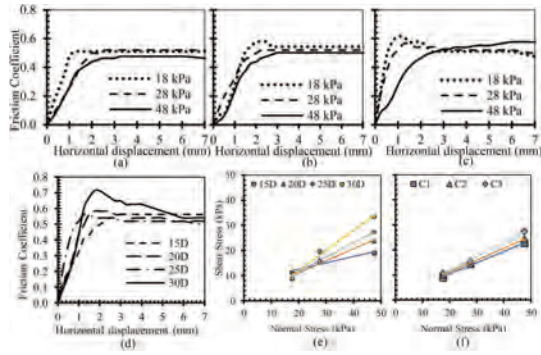
Figure 2. Variation of friction coefficient of 25D geofoam grade under different normal stress for varying concrete roughness (a) C_1 (b) C_2 (c) C_3; (d) Variation of friction coefficient with C_3 concrete and varying geofoam grades at 25kPa normal stress; Failure envelopes for varying (e) geofoam grades (f) concrete grades.

followed by sliding along the concrete surface. Thus, residual stress may be attributed to the sliding mechanism only.

From Figure 2d, it can be inferred that for the same concrete grade and normal stress, the friction coefficient increases with the geofoam density. This can be attributed to the increased yield strength of the strands with the increase in geofoam density. Increase in yield strength results in the increased effort by the concrete for ploughing the geofoam strands. The formation of peak friction coefficient is also evident with the increase in geofoam density, indicating the ploughing mechanism. The extent of ploughing is influenced by the relative hardness of the sliding materials. With the increase in geofoam density, hardness also increases leading to increased effort in shearing. However, at large strains, the friction coefficient attains a nearly constant value of 0.53 for all the geofoam grades. Even though the roughness of geofoam decreases with increasing density, its effect is not visible in the friction coefficient. It can be inferred that the effect of geofoam density is more than the roughness of geofoam, and the initial resisting force arises from the ploughing resistance of the geofoam rather than sliding.

Thus, the friction mechanism of the geofoam concrete interface can be classified into three distinctive phenomena namely, ploughing in the elastic range, micro-cutting during yielding and sliding during large strains. The main parameters governing the friction behaviour are

Table 3. Comparison of experimental results with literature.

Reference	Interface size (mm × mm)	Concrete type	GF density (kg/m³)	Normal Stress (kPa)	Adhesion, C_a (kPa)	Friction angle, φ (kPa)	Friction coefficient, μ	
							Peak	Residual
Sheeley & Negussey (2000)	100 × 100	Cast-in-situ	19	32	–	–	2.38	1.56
AbdelSalam & Azzam (2016)	100 × 100	Precast smooth	19	10-30	4.3	26	0.49	0.49
		Precast rough			0.3	44	0.96	0.96
Khan & Meguid (2019)	99.5 × 99.5	Cast-in-situ	15	18-54	11	37	1.2	1.2
			22		7	41	1.1	1.1
			39		1	48	1.2	1.2
Özer & Akay (2022)	100 × 100	Precast	19	10-40	–	42.8	0.9	0.6
			29		–	43.1	0.95	0.8
		Cast-in-situ	19		31.5	23.7	1.2	>1.2
			29		50.5	37.2	2.2	>2.2
Present Study	60 × 60	Cast-in-situ	15	18-48	7.6	14	0.53	0.53
			20		1.4	26	0.53	0.45
			25		0.5	29	0.58	0.53
			30		0	38	0.64	0.56

the roughness of concrete, normal stress and the geofoam density. Figure 2e and 2f indicate that the slope of the failure envelope increases with the increase in the geofoam density and roughness of the concrete respectively. The results obtained are lower than the other reported studies as indicated in Table 3. Some of the studies (Sheeley & Negussey 2000; Özer & Akay 2022) adopted two different sizes of top and bottom blocks. They also positioned the concrete blocks over the relatively larger-sized geofoam blocks. This might have resulted in the additional passive resistance from the uncompressed zone of the geofoam blocks while shearing, leading to a higher friction coefficient.

3.2 Prediction models

A generalized prediction model is developed based on non-dimensional parameters. The roughness and hardness of the materials were non-dimensionalised using relative roughness and relative hardness indexes as given in Equations 1 and 2. Since ploughing of the geofoam peaks is the major influencing factor on the friction behaviour, the roughness parameter which accurately quantifies the localized peaks of surface asperity needs to be utilized for developing prediction models. Consequently, the roughness parameter R_q of geofoam is chosen for deriving the relative roughness index. However, in the case of concrete, average roughness obtained from the sand patch method was utilized for the same.

$$R' = \frac{R_c}{R_{q_g}} \tag{1}$$

$$H' = \frac{H_c}{H_g} \tag{2}$$

where R_c and Rq_g indicate the roughness parameters of concrete and geofoam respectively. H_c and H_g indicate the hardness of concrete and geofoam respectively.

The variation of peak friction coefficient and friction angle with respect to relative roughness is indicated in Figure 3a. As expected, both the friction coefficient and friction angle increase with the increase in relative roughness. It follows an exponential pattern, and the empirical relationship is obtained as given in Equations 3 and 4. This expression shall be used for quick estimation of interface frictional parameters between geofoam and concrete.

$$\mu = 0.43 + 0.07 \quad e^{(R'-22.5)/18.5} \tag{3}$$
$$\varphi = 21 + 2.9 \quad e^{(R'-22.5)/13.9} \tag{4}$$

Additionally, to understand the effect of hardness on the ploughing behaviour, the variation of peak friction coefficient and friction angle with the relative hardness, is shown in Figure 3b. It can be observed that with the increase in relative hardness, both friction coefficient and friction angle reduce and follows a dose-response curve. When the relative hardness is more than 25, the friction coefficient and friction angle attain a minimum value of 0.53 and 14 respectively. However, additional tests for a wider range of relative hardness are required for developing an empirical equation with higher reliability.
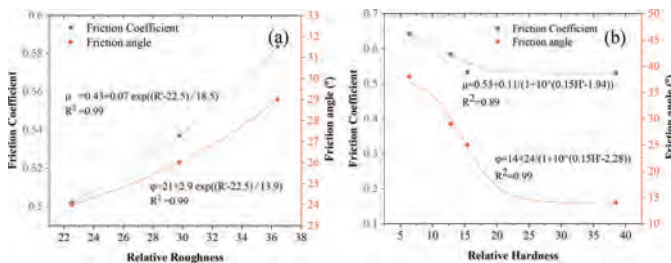
Figure 3. Variation of friction coefficient and friction angle with (a) relative roughness; (b) relative hardness.

4 CONCLUSIONS

The following conclusions can be made for the present study.

– The friction mechanism of the geofoam concrete interface has three distinctive phenomena namely, ploughing in the elastic range, micro-cutting during yielding and sliding during large strains. The friction behaviour is governed by the roughness of the concrete, the normal stress, and the density of the geofoam.
– The peak friction coefficient reduces with the increase in the normal stress due to the flattening of micro-indentations of geofoam. Local ploughing of geofoam strands leads to an increase in the peak friction coefficient with an increase in the concrete roughness and an increase in geofoam density. The extent of ploughing is influenced by the relative hardness of the materials.
– Empirical correlations were developed for the quick estimation of friction parameters for geofoam-concrete interfaces. They indicate that the friction coefficient and friction angle increase exponentially with increasing relative roughness, while decrease with increasing relative hardness. When the relative hardness is more than 25, the friction coefficient and friction angle attain a minimum value of 0.53 and 14 respectively.

REFERENCES

Aabøe, R., Bartlett, S.F., Duškov, M., Frydenlund, T.E., Mandal, J.N., Negussey, D., Özer, A.T., Tsukamoto, H. & Vaslestad, J., 2019. Geofoam Blocks in Civil Engineering Applications. In *5th International Conference on Geofoam Blocks in Construction Applications: Proc. EPS 2018*. 3–38. Springer International Publishing.

AbdelSalam, S. S. & Azzam, S. A. 2016. Reduction of Lateral Pressures on Retaining Walls Using Geofoam Inclusion. Geosynthetics International, 23(6): 395–407.

ASTM D1621. 2016. *Standard Test Method for Compressive Properties of Rigid Cellular Plastics*, *ASTM International*, West Conshohocken, PA

ASTM D1622. 2020. *Standard Test Method for Apparent Density of Rigid Cellular Plastics*, A*STM International*, West Conshohocken, PA

ASTM D6817. 2021. *Standard Specification for Rigid Cellular Polystyrene Geofoam, ASTM International*, West Conshohocken, PA

ASTM D5321. 2021. *Standard Test Method for Determining the Coefficient of Soil and Geosynthetic or Geosynthetic and Geosynthetic Friction by the Direct Shear Method, ASTM International*, West Conshohocken, PA

ASTM E1845. 2015. *Standard Practice for Calculating Pavement Macrotexture Mean Profile Depth, ASTM International*, West Conshohocken, PA

Bartlett, S., Lawton, E. C., Farnsworth, C. B., & Newman, M. P. 2012. Design and Evaluation of Expanded Polystyrene Geofoam Embankments for the I-15 Reconstruction Project, Salt Lake City, Utah (No. UT-12.19). *University of Utah. Dept. of Civil and Env. Eng.* Assessed on 20/12/2021

Farnsworth, C. B., Bartlett, S. F., Negussey, D., & Stuedlein, A. W. 2008. Rapid Construction and Settlement Behavior of Embankment Systems on Soft Foundation Soils. J. Geotech. Geoenviron. Eng., 134(3): 289–301

Meguid, M. A., & Khan, M. I. 2019. On the Role of Geofoam Density on the Interface Shear Behavior of Composite Geosystems. International Journal of Geo-Engineering, 10(1): 1–18.

Özer, A. T., & Akay, O. 2022. Interface Shear Strength of EPS-Concrete Elements of Various Configurations. Journal of Materials in Civil Engineering, 34(6): 04022102.

Puppala, A. J., Ruttanaporamakul, P., & Congress, S. S. C. 2019. Design and Construction of Lightweight EPS Geofoam Embedded Geomaterial Embankment System for Control of Settlements. Geotextiles and Geomembranes, 47(3): 295–305

Sheeley, M., & Negussey, D. 2001. An Investigation of Geofoam Interface Strength Behavior. Geotechnical Special Publication No. 112, *In Soft Ground Technology Conference*, ASCE, Reston, VA, 292–303.

Stark, T. D., Arellano, D., Horvath, J. S., & Leshchinsky, D. 2004. Geofoam Applications in the Design and Construction of Highway Embankments. NCHRP web document, *65*, 792.

Stuedlein, A. W., & Negussey, D. 2013. Use of EPS Geofoam for Support of a Bridge. In Sound Geotechnical Research to Practice: Honoring Robert D. Holtz II, 333–344.

Estimate of the nonwoven geotextile mechanical characteristics starting from the fiber characteristics

Francesco Niccolai*

Ecofibre, Italy

ABSTRACT: The study in question is based on the specific industrial experience made on nonwoven lines consisting mainly of the following manufacturing phases: opening of the fiber, carding , pre-punching, needling 1, needling 2, folding, calandering.

The raw material considered is made of high tenacity polypropylene (PP) fiber. The study starts from the analysis of the fiber resistance trend in reference to the EN ISO 5079 toughness test, in order to characterize the behavior of a mixture of up to three types of fibers. The specific processing characteristic of the production line is represented by the specific mechanical tensile resistance values obtained on the nonwoven geotextiles with reference to EN ISO 10319. Subsequently, the loss of resistance of the mixture due to the different toughness and elongation of the three components of the mixture is determined. Moreover, the weighted resistance values of the individual components of the mixture are calculated in order to determine the toughness of the mixture itself. Starting from the toughness of the mixture, as estimated above, the resistance of the resulting nonwoven geotextiles is linearly obtained. In order to evaluate this model, the values of an historical series of production control tests have been processed.

1 INTRODUCTION

This study refers to the experience made on an industrial plant for the manufacturing of nonwoven needle-punched geotextiles consisting of the following phases:

– opening of the fiber, carding, folding, pre-punching, needling 1, needling 2, calandering
  This plant processes high tenacity polypropylene (PP) fiber starting from staple, that is fiber already cut to size. Hereafter some relevant characteristics of the fiber, i.e. fiber length, title, toughness, elongation, are reported.

Table 1. Some typical values of high tenacity polypropylene (PP) fiber.

Fiber length [mm]	Title [dtex]	Tenacity [cN[dtex]	Elongation [%]
70–90	4.4–6,7	4.8–5.6	70–100

The high tenacity polypropylene fiber is used for the production of nonwoven needle-punched geotextiles which are usually adopted in geotechnical works with different functions as separation, drainage, filtration and protection.

---

*Corresponding Author: f.niccolai@ecofibre.it

The nonwoven needle-punched geotextile is a technical product and is mainly characterized by its mechanical, hydraulic and durability characteristics.

The main mechanical characteristics, as illustrated by Cazzuffi (1996) and Corbet & Cazzuffi (2017), are the following:

– Wide-width tensile strength in reference to the EN ISO 10319 standard
– Static puncture resistance in reference to the EN ISO 12236 standard

The performance of the product on site could directly influence its applicability in specific geotechnical works.

The mechanical characteristics of the product are influenced by a series of factors, as:

– Type of fiber
– Mechanical characteristics of the fiber
– Type of machines used in the manufacturing processes and equipment of the machines
– Parameters used in the machine settings

The purpose of this study is to have a tool to predict the mechanical characteristics of the nonwoven geotextile starting from the tenacity and elongation characteristics of the fibers used in the blends for the realization of the nonwoven. In particular, the relationship between the characteristics of the original fibers and the mechanical characteristics obtained on the finished product, i.e. the nonwoven geotextile, is mainly investigated.

The approach takes into consideration the specific reference characteristics of the finished product, defined on the basis of experience, moreover it models the characteristics of the fiber, and the behavior of the blend in order to define a semi-empirical relationship between the main characteristics of the blend of fibers and the specific tensile strength of the nonwoven geotextile obtained in factory using this blend.

In particular, it is considered the common case that the production of nonwoven geotextile is carried out using fibers from two or three different suppliers, which necessarily have different mechanical characteristics, even if within the limits of acceptability imposed by the company's quality systems.

In order to characterize the performance of the finished product, the specific resistance will be considered: the specific resistance Rs is defined as the tensile strength (kN/m), obtained through EN ISO 10319 test, for every 100 grams per square meter of finished product (100 g/m^2).

Table 2. Abbreviations adopted for fiber parameters and nonwoven geotextile parameters.

Fiber parameters	Nonwoven geotextile parameters
Alfn [%]: Elongation of fiber nth in reference of ENISO10319	Ag [g/m^2]: Areic mass of nonwoven
Fibern [%]: Fiber nth quantity in blend	Rs [kN/m/(100g/m^2)]: Specific tensile strength reference
Tfn [cN/dtex]: Tenacity of fiber nth	Rnw [kN/m] = Ag·Rs/100:
Rt [cN/dtex]: Fiber reference tenacity	Reference tensile strength resistance of nonwoven
Ral [%]/[1% Elongation Difference]: Tenacity loss reference due elongation difference	Tnw [kN/m]: Estimated tensile strength resistance of non woven
RtLossn [%]:Fiber nth tenacity loss respect Rt	Rr [%] = Wrt/Rt: Nonwoven residual resistance respect Rnw
RaLossn [%]/[1% Elongation Difference]: Tenacity loss of fiber nth respect Ral	Rses [kN/m/(100g/m^2)]: Estimated specific tensile strength resistance
Rtfn [%]: Residual tenacity of fiber nth respect Rt	Rstest [kN/m/(100g/m^2)]: Tested specific tensile strength resistance
Wrtn[cN/dtex]: Weighed tenacity of fiber nth	
Wrt [cN/dtex]: Total tenacity of fibers blend	

Furthermore, based on experience, the tenacity Rt of the fiber required to obtain the Rs value will be defined.

This approach makes it possible to avoid analyzing the complexity of the production process, the specific type of line and the particular set of industrial machinery adopted, as well as the specific mechanical, electrical and electronic parameters of each machine, considering only the ability to generate specific tensile strength resistance on the nonwoven geotextile (Figure 1).
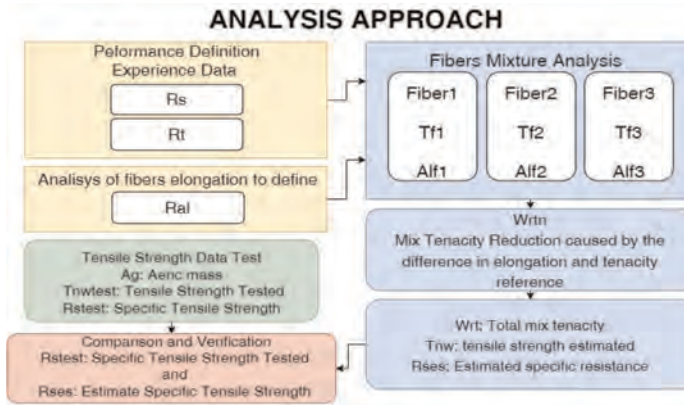
Figure 1. Approach scheme.

2 CONSIDERATIONS ON THE POSSIBLE CORRELATION FIBRE – GEOTEXTILE

2.1 *Nonwoven geotextile*

The nonwoven geotextiles are formed by a set of mechanically bonded fibers and one of the main characteristics is the tensile strength, measured according to the EN ISO 10319 test. They are generally isotropic products, so in this analysis we will assume that the considered products are isotropic : in particular the average between machine and cross-machine direction resistance is adopted as the parameter of reference. In order to define a general and normalized parameter of performance of nonwoven geotextile, a specific tensile strength is defined in kN / m for every 100 g / m2 of nonwoven geotextile. This parameter would be defined considering the optimal processing and the use of fiber with optimal characteristics which will be defined respectively as Rt and Rs. These values are used to characterize the performance of a specific production line beyond any particular characteristic of the plant and of the machines, allowing for considerable simplification. These values may vary between different production plants and could allow for a general application of the estimation method in object.

Some basic assumptions:

– Nonwoven geotextile is an isotropic product
– The tensile strength of the nonwoven geotextile is linearly proportional to the tenacity of the blend of fibers used
– The tensile strength of the nonwoven geotextile is linearly proportional to the mass per unit area of the nonwoven geotextile itself

2.2 *Fiber tensile strength modelling*

Polypropylene fibers have a density of about 0.91g/cm^3; high tenacity fibers are defined fibers with tenacity generally higher than 4.8cN / dtex. The fiber tenacity test is performed

according to EN ISO 5079. The typical curve of a tensile strength test on the fibre is of the type:
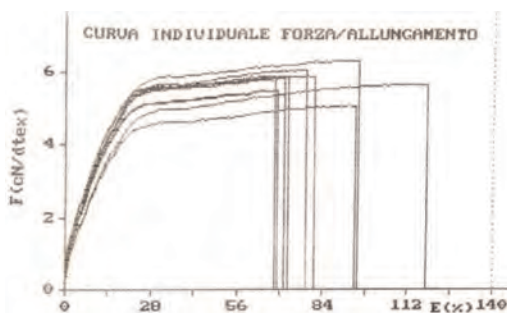
Figure 2.   Fiber tenacity test result example.
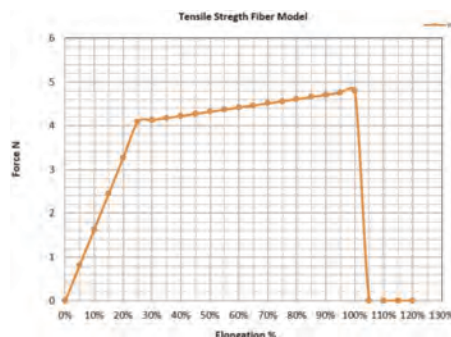
Figure 3.   Fiber model example.

In order to simplify the calculations, the tenacity/elongation curve is modeled through two straight lines, one starting from zero up to the elastic limit and one, in the plastic part, which goes from the elastic limit to the tenacity and elongation at break, as illustrated in Figure 3.

In order to use only the tenacity and elongation data detected by the fiber control tests, the trend of the resistance of the fibers is modeled by setting the elastic limit at an elongation of 25% of the maximum elongation at break. In the same type of modelisation, the yield strength is set at 85% of the maximum detected tenacity.

This simplified approach allows to model the fibers tensile strength trend only by having the values of maximum tensile strength and elongation at break, which are the relevant values in the fiber control tests. This model simplifies the subsequent analysis of the tenacity and elongation characteristics of the blend of fibers consisting of a maximum of three types of fibers.

2.3   *Fibers blend considerations*

A blend of 3 fibers from different suppliers is considered, as it is common to select different types of fibers in this type of manufacturing of nonwoven geotextiles. A further assumption is that the strength of the nonwoven geotextile is linear with respect to the tenacity of the fiber and that the contribution to the total tenacity of the blend of fibers is linear with the percentage of quantity in to the blend of fibers.

To determine the tenacity of the blend of fibers, the following aspects are considered:

– The tenacity of the fibers blend is the sum of the tenacity of the single types of weighted fiber in relation to the quantity in the blend
– The difference in elongation at break between the three types of fibers generate a reducing of total tensile strength of fibers blend
– The difference in overall tenacity of the fibers blend will be compared with the optimal Rt reference value

In order to clarify the behavior of tensile strength resistance of blend of fibers we can make an example, of two fibers. Consider fiber F1 with 100 % of elongation at break and fiber F2 with 80% of elongation at break, we can consider overall tensile strength as the sum of single tensile strength until the fiber F2 arrive at breaking point. Subsequently of this point only the F1 tensile strength contribution remain. So the effect of difference of elongation at break of type of fibers is a decreasing of overall tenacity of fibers blend.
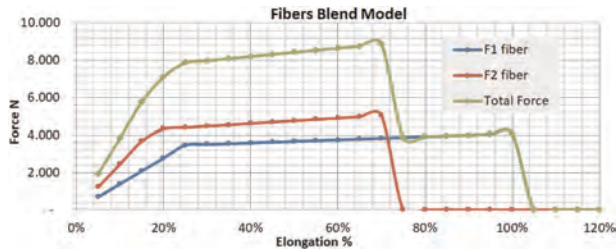
Figure 4.   Example of blend model.

2.4   *Analisys of influence of fibers elongation*

The difference in elongation at break of the fibers in a blend generates an inhomogeneity effect, which reduces the overall strength of the fibers blend, which we will evaluate as a percentage reduction due to the difference in elongation.

In order to calculate the reduction of the tenacity of the blend, we consider two fibers that have extreme characteristics in a typical range of polypropylene fibers, also considering that the fibers that detect greater tenacity generally detect a lower elongation:

– Fiber 1 (F1): tenacity 4.8cN/dtex, elongation 100 %
– Fiber 2 (F2): tenacity 5.6cN/dtex, elongation 70 %

To simplify calculation we propose to mediate the tenacity of F1 and F2 in the linear plastic part of the curve. Through a linear regression equation we can find a relationship that allows us to define the reduction in tenacity in relation of the elongation (Figure 4). Evaluating of angular coefficient of regression line of Av average trend line y = 1,28x + 4,16 we see that the tenacity reduction is 0.0128[cN/dtex] for 1[%] of elongation. In order to obtain a percentage value, we can refer this tenacity with respect of average Av trend line tenacity at 70[%] of elongation that is 5.056[cN/dtex], obtaining 0.0128/5.056 = 0.2532[%]/ [1% difference]. So we assume that the decreasing of tenacity with respect the 1[%] difference of fibers elongation is −0.2532[%]/ [1% difference], note that in hereinafter calculus we round the value Ral = −0.26[%]/ [1% difference]

This value mean that if we found a difference of 10% in elongation between two fibres, the fiber that has the higher elongation contribute to the fibers blend tenacity loosing 2.6 % of tenacity.

We consider the effect of reducing tenacity due to the difference in elongation at break, for the types of fibers contained in the blend calculating the tenacity loss for fiber nth with respect of the fiber that has the lowest elongation as following:

$$RalLoss_n = [Alf_n − min(Alf1, Alf2, Alf3)] \cdot Ral \ \ [\%] \tag{1}$$
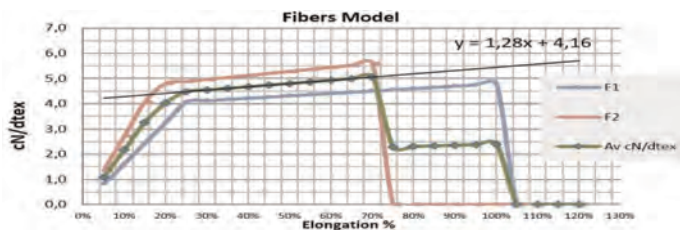
Figure 5.   Fibers model with two fibers with limit characteristics.

For example, if we have fiber F1 with 100 % of elongation at break and fiber F2 with 80% of elongation at break, we obtain a value of reduction in tenacity of fiber F1, RalossF1 = Rt·(−5.2%)

We will obtain as results: RalLoss1, RalLoss2, RalLoss3 the reduction in tenacity due to the difference in elongation of each type of fiber compared to the one that has the lowest elongation.

2.5 *Analisys of influence of tenacity fibers difference with respect of the reference tenacity*

Let us now consider the percentage reduction effect of the tenacity of the blend of fibers, due to the difference between the tenacity of the three types of fibers with respect the reference tenacity detected by experience in reference of the fiber control tests and tensile strength test data on nowvoven geotextiles. Following fiber nth tenacity percentage respect of the reference tenacity Rt (Equation 2):

$$RtLossn \ [\%] = \frac{Tfn}{Rt} - 1 \tag{2}$$

We will get the reduction values for each fiber: RtLoss1, RtLoss2, RtLoss3.

2.6 *Estimation of nonwoven geotextile tensile strength*

In order to estimate tensile strength resistance of nonwoven geotextiles we consider RaLossn and RtLossn and we calculate the residual tenacity of the fiber nth, Rtfn:

$$Rtfn = 1 + (RaLossn + RtLossn) \ [\%] \tag{3}$$

Subsequently we'll calculate the weighted tenacity of fiber nth considering also the percentage quantity of fiber included in blend of fibers (Equation 4).

$$Wrtn = Rtfn \cdot Rt \cdot Fibern \ \ [cN/dtex] \tag{4}$$

And finally we can obtain total tenacity of blend of fibers as:

$$Wrt = Wrt1 + Wrt2 + Wrt3 \ \ [cN/dtex] \tag{5}$$

The total blend tenacity Wrt can be compared with Rt fiber reference tenacity, and remembering assumption:

"The tensile strength of the nonwoven geotextile is linearly proportional to the tenacity of the blend of fibers used" in Equation (6) it's possible to calculate the tensile strength of non woven geotextile making a proportion with blend of fibers tenacity and fiber tenacity reference, multiplied by reference tensile strength tenacity of non woven geotextile

$$Rnw = Ag \cdot Rs/100 \tag{6}$$

In this way we find the nonwoven tensile strength resistance in relation of tenacity of fibers blend.

$$Tnw = \frac{Wrt}{Rt} \cdot Rnw \ [kN/m] \tag{7}$$

So we arrive to find the estimated specific tensile strength resistance dividing by mass per unit area:

$$Rses = \frac{Tnw}{Ag} = \frac{1}{Ag} \frac{Wrt}{Rt} \quad Rnw = \frac{1}{Ag} \frac{Wrt}{Rt} \quad \frac{Ag}{100} \frac{Rs}{Rt} = \frac{Wrt}{Rt} \frac{Rs}{100} \ [kN/m]/[100g/m^2] \tag{8}$$

The specific tensile strength resistance Rses can be compared with reference specific tensile strength resistance Rs to understand if the process is in line with expectation or not.

Table 3. Resistance estimation example (with equation reference).

Parameters	Value			Blend Fibers			
Ag [g/m^2]	200			**Fiber 1**	**Fiber 2**	**Fiber 3**	**(Equation.)**
Rs [kN/m/(100g/m^2)]	8.0		Fibern [%]	35	32	33	
Rnw [kN/m]	16		Alfn [%]	90	80	70	
Rt [cN/dtex]	5.2		Tfn [cN/ dtex]	4.8	5.0	5.2	
Ral [%]/[1% DeltaE-long.]	−0.26		RaLossn [%]	−5.2	−2.6	−0.0	(1)
			RtLossn [%]	−7.69	−3.85	−0.0	(2)
			Rtfn [%]	87.1	93.6	100.0	(3)
			Wtrn	1.5854	1.5567	1.7160	(4)
	Wrt [cN/ dtex]		**Rr[%]**	**Tnw [kN/ m]**		**Rses[kN/m/(100g/ m^2)]**	
Results	4.858	(5)	93.42	14.95	(7)	7.474	(8)

2.7 Statistical analisys

In order to test the model we made a statistical analisys on 105 tensile strength test results made by Ecofibre's internal laboratory. The analisys compares Rses, the specific tensile strength resistance of nonwoven estimated by this model and the specific tensile strength resistance of nonwoven calculated by tensile strength tests results Rstest.
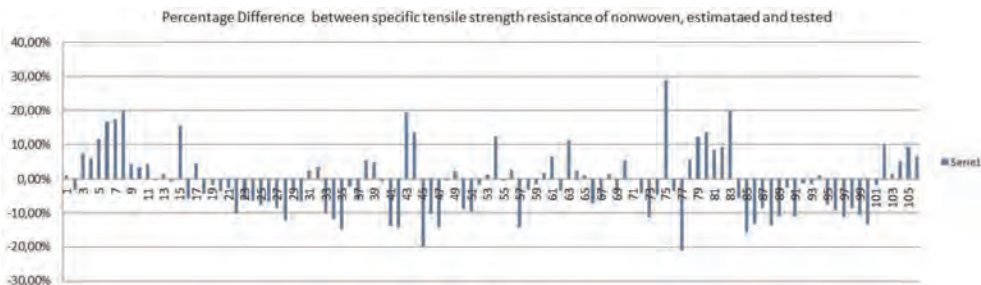
Figure 6. Data of percentage difference between specific tensile strength estimated and tested.

Table 4. STATISTICAL PARAMETER of percentage difference between specific tensile strength comparison between estimated and tested values on 105 samples.

Rses[kN/m/(100g/m^2)] difference from expected	
Average	−1.036 [%]
Max	29.05 [%]
Min	−21.00 [%]
Dev.Standard	9.47 [%]
IC95[%]	1.31 [%]
IC99[%]	1.72 [%]
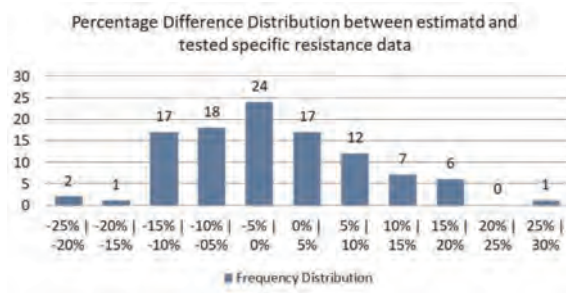
Figure 7. Percentage difference distribution.

Hereinafter the comparison of specific resistance distribution estimated by the model is given in Figure 8, while the actual values obtained by test results are illustrated in Figure 9.
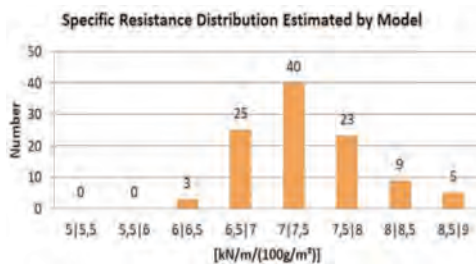
Figure 8. Specific tensile strength by model.
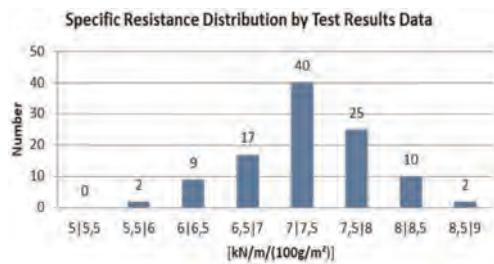
Figure 9. Specific tensile strength by test results.

Table 5. STATISTICAL PARAMETERS in reference of distribution in (Figure 8) and (Figure 9) [kN/m/(100g/m^2].

Statistical Parameters Graph (Figure 8)		Statistical Parameters Graph (Figure 9)	
Average	7.40	Average	7.29
Max	8.93	Max	8.95
Min	6.19	Min	5.92
Dev.Standard	0.55	Dev.Standard	0.59
Kurtosis	0.73	Kurtosis	−0.13
IC95[%]	7.66 [%]	IC95[%]	8.19 [%]
IC99[%]	10.06 [%]	IC99[%]	10.76 [%]

We can see that the shape and frequencies of the distributions are very similar, so it could mean that the model is representative. Considering also that the reference of specific tensile strength is fixed as the optimized value obtainable from the process, we may think that the slightly greater dispersion of data of testing could be due to non-optimal processing.

An example of smartphone app in development is also reported in Figure 10.

This simplified method could be implemented in app or other software to have a simple tool to be used to predict nonwoven tensile strength result in reference of fibers used to produce it, and it could permit also to optimize the selection of the original fibers. Also the
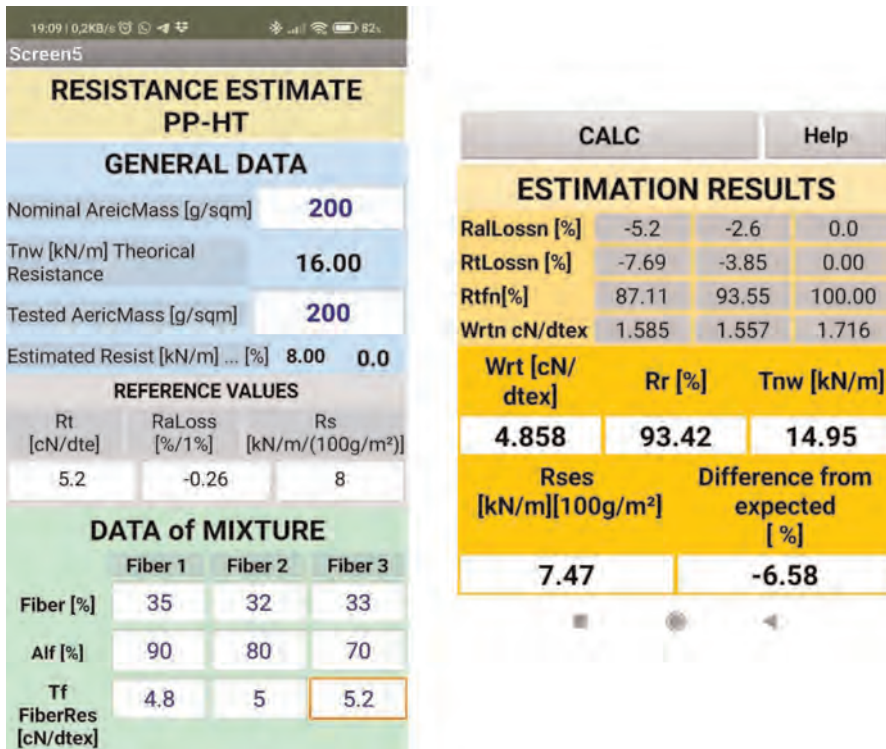
Figure 10. Screenshot of the smartphone app under development.

method could give indications about the efficiency of line of nonwoven production giving reference values to be compared with tested performance of nonwoven produced, in order to understand and continuously check the performance of the machinery setup.

Concluding we can say that this approach, that surely may be improved, could represent an interesting tool for people that work in nonwoven production plants – in particular for management and quality assurance phases – in order to estimate and verify the main results of process.

REFERENCES

Cazzuffi, D. (1996). *Evolution of European Standardization on Geotextiles, with Special Reference to Mechanical Tests. Proceedings "Index 96" Nonwoven Congress – Construction Session*, Geneva, Switzerland, 1–15.

Corbet, S. & Cazzuffi, D. (2017). CEN/TC189 and ISO/TC 221 – European and International Standards for Geosynthetics: the Current Developments. *Proceedings International Conference on Soil Mechanics and Geotechnical Engineering*, Seoul, South Korea, 2493–2496.

Soil-geosynthetic interaction

Experimental and numerical investigations on the pullout behaviour of coir geotextile

N. Kumar, M.S. Narayanan, S. Thasneem & R.K. Kandasami
Department of Civil Engineering, IIT Madras, Chennai, India

ABSTRACT: The pullout mechanism (typically due to friction and bearing) is influenced by the type of reinforcing material and the soil properties. To an extent, the interfacial behaviour of coir geotextiles with the surrounding matrix is affected by the low stiffness of the material. In this study, in order to quantify the soil-coir geotextile interaction, a series of pullout experiments were carried out with geotextiles having different mass density. For a particular normal stress, it was observed that geotextiles with higher mass density exhibit higher shear resistance during pullout. Further, for the coir geotextile having a specific mass density, a better shear mobilization was realized at a particular normal load. In order to predict the soil-coir geotextile interaction behaviour precisely, a three dimensional (3D) numerical model was developed in this study. Using an appropriate constitutive law for the geo-material and contact law for soil-geotextile interface, the numerical model was validated with the experimental results. This numerical model will be helpful in quantifying the extent of shear mobilization under different boundary conditions.

1 INTRODUCTION

Geotextiles are increasingly becoming an essential product for many geotechnical applications. Conventional forms of geotextiles are typically made of petrochemical derivatives such as polypropylene, polyethylene, polyester, and polyvinyl. These geosynthetic materials have good mechanical and durability characteristics however having high initial production cost and being unsustainable. With growing awareness towards utilization of sustainable materials in the construction sector, it is essential to explore alternate natural products (Rawal & Anandjiwala 2006). Natural fibres from plants such as coir, sisal, jute, hemp, flax, bagasse, abaca, bamboo, ramie, pine and many more are extensively available, especially in tropical and subtropical countries (Kumar *et al.* 2022). These natural fibre-based geotextiles have a great potential to substitute synthetic geo-materials owing to their comparable mechanical characteristics and abundant availability. It has been observed that some of the natural fibre-based geotextiles, in addition to being sustainable, exhibit high tensile strength and fracture modulus (Faruk *et al.* 2012). However, durability is the prime concern which inhibits its utilization in many construction projects. Among the various natural fibre-based geotextiles, coir geotextile is the most durable material (Vivek *et al.* 2020). The durability and strength can further be improved by performing physical and chemical treatments (Anggraini *et al.* 2016). Hence, before utilizing these geotextiles extensively in the field, it is important to quantify their suitability for specific applications. Existing studies showed that coir geotextiles could fulfil all the primary functions of synthetic geotextiles and have been successfully used as primary reinforcement layer in retaining walls, soil slopes, embankments of earthen dams, railways and highways and so forth (Lekha 2004). However, when used as a reinforcement, soil-geotextile interfaces act as a potential plane of failure especially during

shear due to pullout. Since the interfacial characteristics of coir geotextiles play a significant role in mobilizing the shear resistance between the reinforcement and the surrounding soil matrix, a comprehensive understanding of these interfaces is essential, especially in applications where the reinforcements are under tension, as shown in Figure 1a. The shear resistance provided by the geotextile is primarily due to two distinct mechanisms i.e., skin friction between the soil-geotextile interface and bearing resistance provided by the soil present in the aperture of the geotextile (Hussein & Meguid 2016). To quantify the interfacial characteristics under controlled conditions, a laboratory experimental technique such as the pullout test (Figure 1b) is widely adopted (Subaida *et al.* 2008). In this study, a suite of experiments was carried out on different grades (based on mass density) of coir geotextiles to quantify the pullout capacity of reinforced earth. Additionally, a three-dimensional numerical model of geotextiles with appropriate constitutive/ contact laws was developed to accurately analyze the interfacial behaviour of reinforced soil. Most numerical studies in the past have used simplified assumptions related to either geosynthetic geometry or the constitutive/contact model. Limited studies have been reported on the 3D numerical modelling of geosynthetics. A realistic three-dimensional modelling will help in accurately predicting the role of interface during the shear and pullout mechanism of geotextiles inside the soil. By using appropriate material and model parameters, the 3D numerical model used in this study was validated with the laboratory pullout experiments.
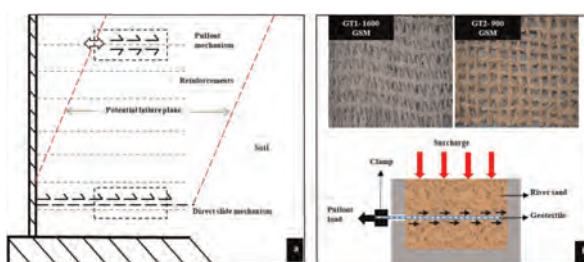
Figure 1   a. Failure mechanism of geo-structure due to weak interfacial characteristics of reinforcements, b. Coir geotextiles with different mass density and the pullout test setup.

2   CHARACTERIZATION OF MATERIALS

2.1   *Coir geotextile*

Coir geotextiles having a mass per unit area of 400, 900, and 1600 g/m^2 were used for the laboratory pullout experiments. Before performing the pullout test, the coir geotextiles having different mass per unit area were characterized to determine the physical and mechanical properties. The summary of various properties of the geotextiles used in this study is shown in Table 1.

Table 1.   Various physical and mechanical properties of coir geotextiles.

Mass density (g/m^2)	1600		900		400	
Direction	Warp	Weft	Warp	Weft	Warp	Weft
Tensile strength* (kN/m)	32.75	30.90	14.25	12.90	6.89	5.26
Failure strain* (%)	30.82	28.38	25.80	23.95	20.62	19.40
Thickness (mm)	4.032 − 4.52		2.55 − 2.96		1.306 − 1.68	
Aperture size (mm)	12.35 × 4.05		17.4 × 9.5		24.5 × 16.5	
Fibres density (g/cm^3)	1.593		1.288		1.202	

*Average values.

2.2 *Tensile strength*

The tensile strength of the coir geotextile was determined as per ASTM D4595 standards. The variation of tensile force with the axial displacement in the warp direction for different mass densities of coir geotextiles is shown in Figure 2. The experimental results indicated that the tensile strength and failure strain of coir geotextile primarily depends on the geotextile's mass per unit area (GSM) and the number of yarns in both directions of geotextiles. Additionally, the geotextiles with higher GSM (mass per unit area) exhibited a higher failure strain and tensile strength compared to lower GSM geotextiles. Furthermore, the tensile strength and failure strain of the coir geotextile in the weft direction was comparatively lesser than in the warp direction.
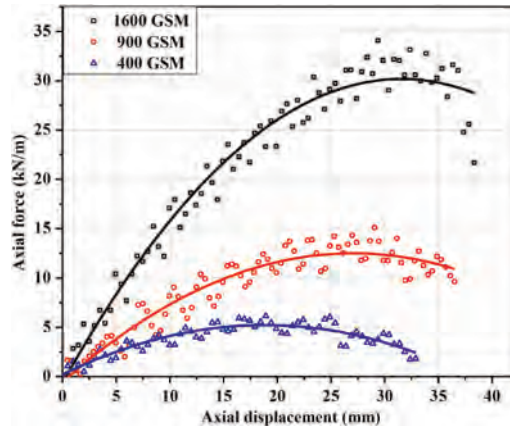
Figure 2. Tensile characteristics of coir geotextiles having different mass density (GSM).

2.3 *Characterization of geo-materials*

The geo-material used in this study to carry out pullout experiments was dry river sand with a specific gravity of 2.69 and a uniformity coefficient of 2.86. The sand has a dry unit weight of 16.73 kN/m^3 and was compacted at a relative density of 80 % to perform the laboratory tests.

3 LABORATORY PULLOUT EXPERIMENTS

The experimental setup consisted of a steel box having a square cross-section of 300 × 300 mm and an overall depth of 230 mm, as shown in Figure 1b. The tangential loading unit consisted of a horizontal actuator and a load cell connected in series with the loading shaft, which was further attached to a clamp to hold the geotextile in a tangential direction. Additionally, the normal load (connected to a load cell having a capacity of 100 kN) was applied on the loading cap through a steel ball which spread the load uniformly over the soil surface. During specimen preparation, sand was pluviated into the box in four layers and compacted adequately to achieve a desired relative density of 80%. A coir geotextile having a width of 200 mm was placed in between the two halves of the box, and enough gap was provided to minimize friction between the steel box edges and the surface of coir geotextile. After carefully placing the geotextile inside the steel box, the gap between the box's upper and lower half was covered by a thick strap to avoid any soil loss from corners during the pullout loading. All the geotextiles were pulled tangentially to the steel box at a

rate of 1 mm/min under a constant normal load of 0.5 kN, 1 kN, 1.5 kN, and 2.0 kN. During the testing process, proper care was taken to make sure the tangential loading unit was coaxial with the geotextile for proper transmission of force along the shearing plane without causing any eccentricity.

3.1 *Results and discussion from laboratory pullout tests*

The shear stress mobilization during the pullout test depended on the geometrical and mechanical properties of coir geotextiles in addition to the boundary stresses. The pullout resistance of geotextile with very closely spaced yarns (1600 GSM) was nearly double that of the open mesh geotextile (400 GSM), as shown in Figure 3a. This pullout behaviour could be due to the high frictional resistance in geotextiles with closely spaced yarns which increases the surface area as well as adequate bearing resistance generated due to high lateral confinement of the soil present inside the apertures. The result shown in Figure 3a illustrates that the pullout resistance has a substantial correlation with the mass density, aperture size and thickness of geotextiles. Further, due to the higher stiffness of closely spaced yarns in geotextiles, the shear mobilization rate was higher than in open mesh/ lower GSM geotextiles. In addition, for any geotextile (irrespective of their mass per unit area), the maximum pullout resistance, shear displacement, and shear mobilization rate depended on the specific set of normal loads (Figure 3b). With the increase in normal load (up to a certain extent), the maximum pullout resistance increased while the corresponding displacement decreased. However, when geotextiles with low mass density were subjected to a very high normal load, only the coir geotextiles were stressed, leading to tearing failure before shear mobilization could occur. Experimental results for 900 GSM demonstrated that, at a very low normal load (0.5 kN), large displacement was observed before reaching the peak capacity; this could be due to lesser frictional resistance and lower confinement of soil inside the aperture of the coir geotextile, which allows the geotextiles to move in tangential direction without mobilizing peak shear resistance. Hence, an optimum normal load should be applied over the coir geotextile reinforced soil to mobilize their peak shear resistance within the permissible limit of displacement. This study showed that the maximum pullout resistance within the permissible displacement limit occurred at 1 kN of normal load (Figure 3b) for 900 GSM coir geotextiles. However, this observation needs to be validated with further laboratory experiments and field tests.
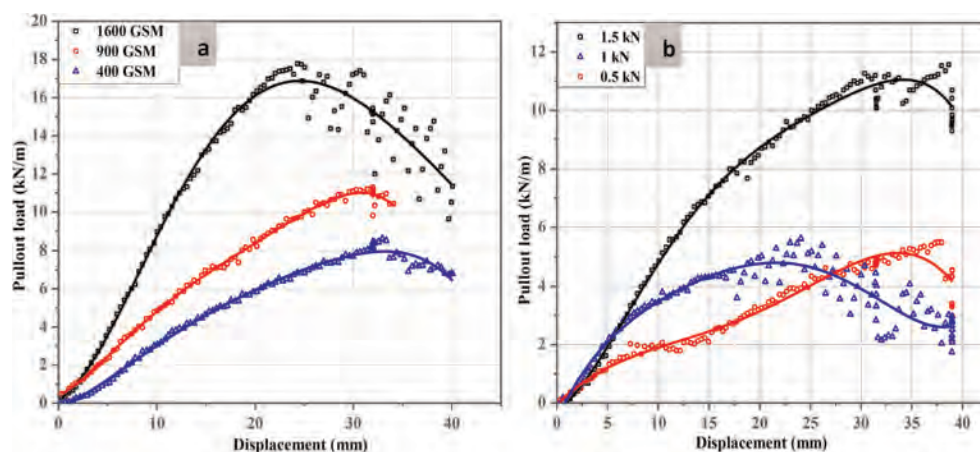
Figures 3   a, b. Pullout characteristics for different grades of coir geotextile at different normal loads.

4 FINITE ELEMENT MODELLING OF GEOTEXTILE REINFORCED SOIL BED

A three-dimensional finite element model was developed using ABAQUS (Figure 4) to simulate the pullout test for determining the interfacial characteristics. All the geometrical and mechanical parameters of the geotextile were fixed based on the experimental results obtained from the laboratory tests.
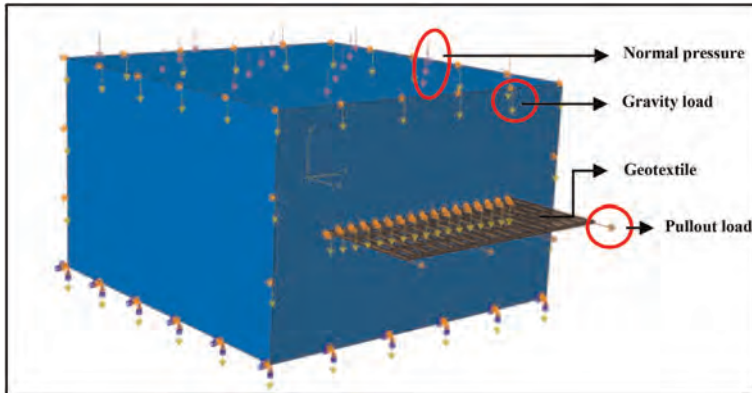
Figure 4.   Different loadings and boundary conditions in numerical model.

4.1   *Geometrical modelling and validation*

A coir geotextile of 900 GSM was used for simulating the pullout experiment. Due to the difficulties in meshing the realistic woven geometry of coir geotextiles, the geotextile geometry was modelled as a cuboidal structure with rigid joints while retaining the aperture size and dimensions. Both the soil and geotextile were discretized using eight-noded linear brick elements (C3D8). The model was simulated using 157,373 elements. The soil-geotextile interface was modelled using the ABAQUS inbuilt Master-Slave contact pair technique with surface-to-surface contact discretization. The part with the coarser mesh (i.e., soil) was considered the master surface, and the one with the finer mesh (i.e., geotextile) was considered the slave surface. The master-slave model incorporated both tangential and normal behaviour between the soil and geotextile. The tangential behaviour was based on the Coulomb friction law, which used two input parameters, friction coefficient ($\mu = 0.74$) and a tolerance parameter ($E_{slip} = 0.005$). The normal behaviour, based on the contact pressure-overclosure model, was incorporated using two models; the hard contact model and the linear softened contact model. The hard contact model, which does not allow the penetration of the geotextile into the soil, was used for both the horizontal sides of the geotextile as well as the vertical sides of longitudinal yarns. A linear softened contact model was used for the vertical sides of transverse yarns since the geotextile penetrates into the soil when subjected to pullout force. The boundary conditions of the model were defined such that the base is fixed, and the sides of the soil model are allowed to move only in the vertical direction (roller support). Initially, geostatic loading was applied to the whole model. Further, a normal pressure of 11 kPa (a total of 1 kN normal load) was applied at the top surface, followed by a velocity-controlled pullout load at the rate of 1 mm/min. The properties of the coir geotextile were obtained from the uniaxial tensile test performed in the laboratory. A non-linear elastic-plastic constitutive law based on the Von Mises failure criterion was used for the geotextile. The soil was modelled using the elastic-plastic Mohr-Coulomb model, which involves five input parameters, as shown in Table 2.

Table 2. Input parameters for validation of numerical model.

Density (kg/m^3)	E (MPa)	μ	Φ°	Ψ°	C (kPa)
1681	50	0.3	39.39	9.38	11.79

The numerical results were validated against the experimental data (Figure 5a) obtained from the laboratory pullout tests. From the displacement profile, the shear mobilization was observed for a considerable length of geotextile inside the soil box (Figure 5b). This model accurately predicted the pullout response until a certain displacement. The slight deviation in the pullout resistance at higher displacement can be attributed to the simplification of geotextile geometry, choice of joints in the numerical model, interface friction/contact parameters, as well as the low stiffness response of geotextiles. Additional studies are required to accurately quantify the pullout mechanism i.e., individual contribution of friction and bearing towards the pullout behaviour.
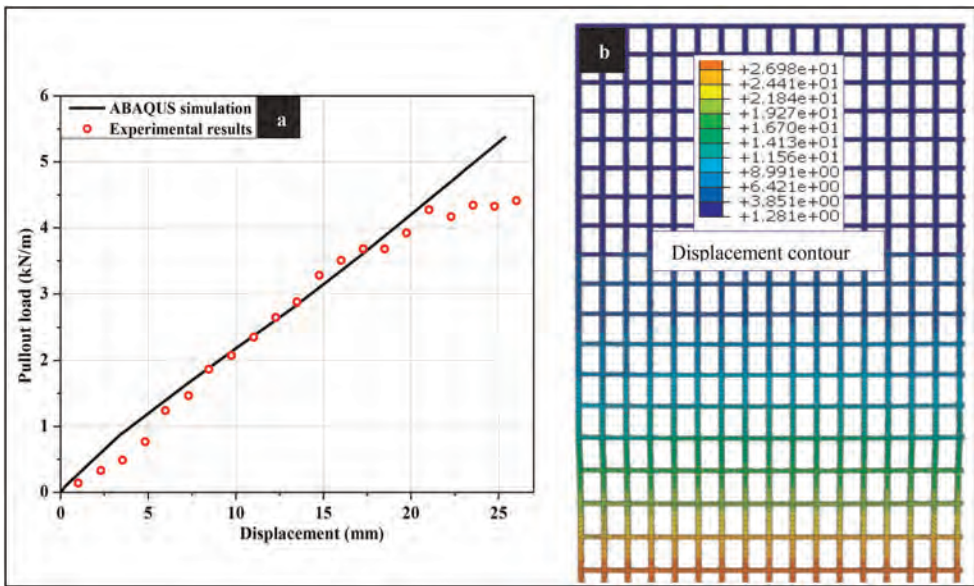
Figure 5 a. Validation of the simulation with the pullout experimental results, b. Displacement contours of the coir geotextile inside the soil during pullout.

5 CONCLUSIONS

- Pullout resistance of coir geotextiles was observed to be dependent on the mass density of the coir geotextile and the magnitude of normal load applied to it. Further, the extent of shear mobilization during pullout depended on the strength and stiffness of coir geotextiles
- Shear mobilization rate and maximum pullout resistance of coir geotextiles depended on the optimal normal load. A higher normal load led to maximum stretching of geotextile between the clamp and the face of the box during the pullout test without mobilizing the peak shear resistance in the soil

- The numerical model was successful in predicting the load-displacement response of coir geotextiles subjected to pullout until a displacement of 22 mm. Realistic geometry needs to be considered for predicting the pullout behaviour under large displacement.

REFERENCES

Anggraini, V., Asadi, A., Farzadnia, N., Jahangirian, H. & Huat, B.B., 2016. Reinforcement Benefits of Nanomodified Coir Fiber in Lime-Treated Marine Clay. *Journal of Materials in Civil Engineering*, *28*(6), p.06016005.

Faruk, O., Bledzki, A.K., Fink, H.P. & Sain, M., 2012. Biocomposites Reinforced with Natural Fibers: 2000–2010. *Progress in polymer science*, *37*(11), pp.1552–1596.

Hussein, M.G. & Meguid, M.A., 2016. A Three-Dimensional Finite Element Approach for Modeling Biaxial Geogrid with Application to Geogrid-Reinforced Soils. *Geotextiles and Geomembranes*, *44*(3), pp.295–307.

Kumar, N., Kandasami, R.K. & Singh, S., 2022. Effective Utilization of Natural Fibres (coir and Jute) for Sustainable Low-Volume Rural Road Construction–A Critical Review. *Construction and Building Materials*, *347*, p.128606.

Lekha, K.R., 2004. Field Instrumentation and Monitoring of Soil Erosion in Coir Geotextile Stabilised Slopes—A Case Study. *Geotextiles and geomembranes*, *22*(5), pp.399–413.

Rawal, A. & Anandjiwala, R., 2007. Comparative Study Between Needlepunched Nonwoven Geotextile Structures Made from Flax and Polyester Fibres. *Geotextiles and Geomembranes*, *25*(1), pp.61–65.

Subaida, E.A., Chandrakaran, S. & Sankar, N., 2008. Experimental Investigations on Tensile and Pullout Behaviour of Woven Coir Geotextiles. *Geotextiles and Geomembranes*, *26*(5), pp.384–392.

Vivek, Dutta, R.K. & Parti, R., 2020. Application Potential of Treated Coir Geotextiles in Unpaved Roads. *Journal of Natural Fibers*, *17*(10), pp.1454–1467.

Influence of the surface roughness on the interface shear strength

G.L.S. Araújo*
University of Brasilia, Brazil

N.P. Sanchez*
Geotechnical Consultant

E.M. Palmeira*
University of Brasilia, Brazil

ABSTRACT: The interface shear strength between geomembranes and other materials plays an important role in waste landfills and has been investigated over the years. Although prior investigations regarding different types of used materials, just a few publications were found concerning the geomembrane´s surface. This paper presents a study which shows several roughness parameters of one smooth and three textured geomembranes and tries to relate them to the interface shear strength. The results showed a great potential of these parameters to help understanding how the geomembrane surface contributes to the interface shear strength.

1 INTRODUCTION

Geomembranes have been used as impermeable material in geotechnical constructions such as waste landfills and water transportation canals and the shear strength between them and overlaying materials has a paramount function in order to avoid the sliding of the latter over the geomembrane. Laboratory tests can be performed to estimate interface friction angle (ϕ_i) and the adhesion (a) values of the interfaces. In this context, the direct shear test can overestimate the obtained values for low applied normal stresses. One technique which can be used to reduce this problem is the investigation of these interfaces by means of inclined ramp tests (Palmeira & Viana 2003; Pitanga et al. 2009). Large-scale experiments were conducted by Briançon et al. (2002) and the results were compared to ramp tests. The authors found close obtained values when comparing field and laboratory experiments, therefore showing satisfactory results for the ramp tests.

Besides the type of experiment, many factors can affect the obtained values such as the geomembrane asperity height, and polymer. Regarding the granular overlying material, the results can vary depending on the granular material density, particle shape and its grain size distribution (Abdelaal & Solanki 2021; Bacas et al. 2011; Palmeira & Viana 2003; Pitanga et al. 2009). In this context, the geomembrane surface has also a potential influence on the interface strength.

In the recent years, several investigations have shown that the geomembrane surface can also impact on the interface shear strength based on the micro and macroroughness distribution (Vangla & Gali 2016). Recently, the current devices that can measure roughness characteristics have been improved so that more parameters can be obtained.

This paper shows the results of inclined plane tests of four geomembranes (one smooth and three textured) in contact with sand. Additionally, several bidimensional roughness

---

*Corresponding Authors: gregorio@unb.br, nelsonwerpnsn@gmail.com and palmeira@unb.br

parameters were evaluated to understand how they could influence on the interface shear strength. The results of the surface parameters were compared to the interface shear strength to imply which one has the best relation to the geomembrane-soil resistance.

2 ROUGHNESS PARAMETERS

Several surface parameters are specified by the ISO 4287 (1997). In this investigation, four parameters are associated to the surface height (Figure 1): (i) the Maximum Height of the Profile (R_z), (ii) the Total Height of the Profile (R_t), (iii) the Arithmetical Mean Deviation of the Assessed Profile (R_a) and (iv) the Mean Height of Profile Elements (R_c). It is important to point out that in the analysis there is a difference between the sampling length and the evaluation length: the first one is measured in each parallel line drawn in the surface and the evaluation length is defined as the sum of "n" sampling lengths. In this study, ten sampling lengths were used.
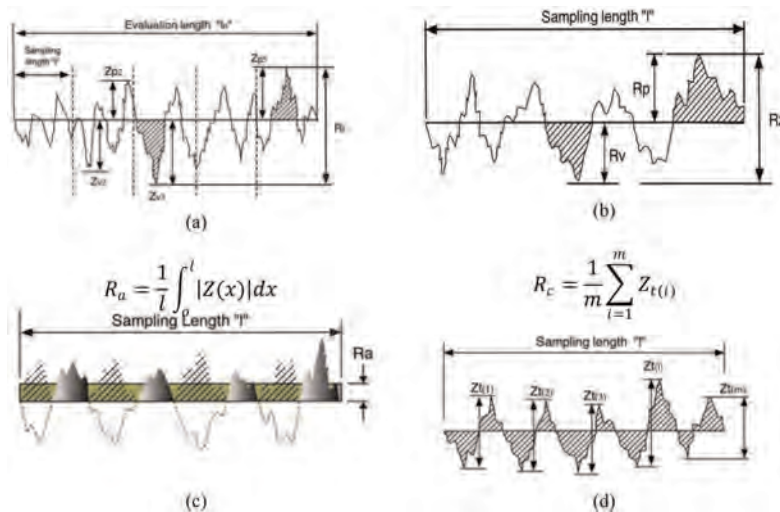
Figure 1. Investigated bidimensional roughness parameters: (a) R_t, (b) R_z, (c) R_a and (d) R_c.

3 MATERIALS AND EQUIPMENTS USED

Four High Density Polyethylene (HDPE) geomembranes were used in the tests as impermeable material: one smooth, two blown film textured and one flat die textured and they are illustrated in Figure 2.

As overlying material, a 50-mm thick medium uniform sand was placed, lifted in two layers for compaction control. The material had angular grain sizes ranging from 0.16 mm to 2 mm and according to the Unified Soil Classification System (USCS -ASTM D2487-17e1 2017), it was classified as poorly graded (SP). For the experiments, a relative density (Dr) of 57% was adopted, which resulted in a peak friction angle of 39°. Table 1 summarizes the main properties of the used materials.

The used inclined plane apparatus was composed by a metal frame structure with a rigid base which has a hinge at one extremity and a hook at the other side (Figure 3a) with a large box (1.90 m long and 0.50 m wide) over it. Prior the tests, sandpaper was glued to the ramp surface to increase friction with the lower geomembrane face. Then, the geomembrane was
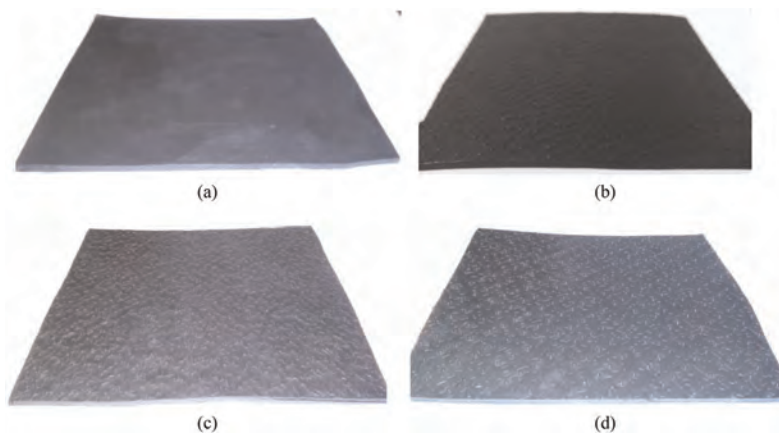
Figure 2. Inclined plane tests: (a) GM-S, (b) GM-T1, (c) GM-T2 and (d) GM-T3.

Table 1. Main properties of used materials.

Sand				
D_{10} (mm)[1]	0.16			
D_{50} (mm) [1]	0.43			
D_{85} (mm) [1]	1.1			
Friction angle (degrees)[2]	39			
Geomembranes				
	GM-S	GM-T1	GM-T2	GM-T3
Polymer	HDPE	HDPE	HDPE	HDPE
Thickness (mm) [5]	2.0	2.0	2.0	2.20
Asperity height [6]	-	0.32	0.52	0.63
Density (g/m^3)[7]	0.94	0.95	0.94	0.98
Tensile strength (MPa)[8]	30.9	17.8	17.8	16.2
Tensile strain at maximum tensile strength (%)[4]	729.2	544.7	556.4	546.0

Notes: [1] ASTM D6913/ D6913M-17, [2] ASTM D3080/D3080M (2011), [3] ASTM D5261 – 10 (2018), [4] ASTM D4595 – 17 (2017), [5] ASTM D5199-12 (2019), [6] ASTM D7466-08 (2008), [7] ASTM D1505-18 (2018) and [8] ASTM D4885-01 (2018).

rested on the sandpaper. The tested side as interface was the outer side of geomembrane´s roll. This represents the typical situation of canal constructions for water supply, where the geomembrane is commonly in contact with a soil layer.

The test strain rate adopted to raise the plane was $3 \pm 0.5°$ / minute and the experiments were finished when the box displacement reached 50 mm (ISO 12957-2, 2005). Rollers underneath the ramp´s box were used to minimize the friction between it and the base of the ramp. Concrete blocks were used as surcharge to provide normal stresses of 1 kPa, 3 kPa and 5 kPa (Sánchez 2018). Two displacements transducers and one load cell were used to measure box displacement and the geomembrane tensile force. As sandpaper was used on the ramp base, measured forces were equal to zero.

In order to characterize the geomembranes surface, Olympus LEXT OLS4100 3D digital microscope was used. The apparatus has a high sensibility detector which can obtain the position and estimating the superficial height of this point, regardless of the surface texture (Figure 3b). Firstly, based on previous analysis, a 10x magnification was chosen as standard

for the surface survey, since it provided satisfactory results within a test duration of six hours. Then, the cutoff wavelength was defined following ISO 4287 (1997). The lateral borders of the specimens were removed in order to reduce the influence of handling and sample cutting implying in an initial specimen size of 20 mm. All the tests were performed using virgin samples.

In this investigation, the number of profiles used for the measurements in each sample is equal to ten. Over any of the ten profiles, each point has an abscissa x and an ordinate $Z(x)$, where $Z(x)$ refers to the point´s elevation or depression. For bidimensional measurements, the sample was divided into ten randomly chosen profiles to guarantee better statistical variability. Although the microscope can also obtain 3D surface distribution, this paper will discuss the results of 2D parameters only.
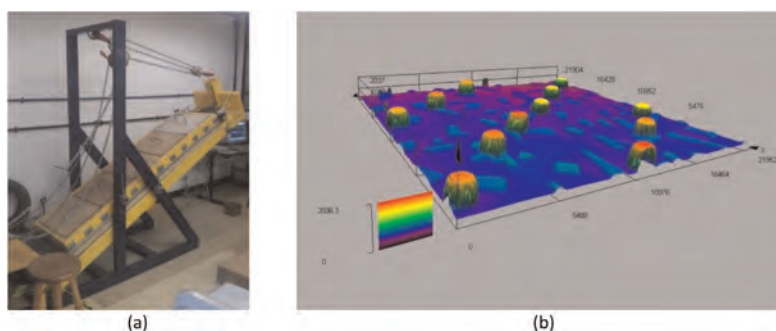
Figure 3.   Inclined plane tests: (a) overview and (b) Tridimensional image obtained by the microscope of a flat die manufactured geomembrane.

4   RESULTS

Figure 4a presents the results of inclined plane tests and it is possible to notice that the presence of the texture increases the interface shear strength. However, no further rises were observed when the asperity height increased from GM-T1 to GM-T3, which is probably due to the relation between the grain size and the asperity height Afzali-Nejad et al., (2017). The results may also be influenced by the soil density: it is expected that higher densities should have led to increases of the friction angle if the sand had a different relative density Dejong, Westgate (2005).

Figure 4b illustrates how the roughness parameters herein analyzed varied among the geomembranes analyzed. The Maximum Height of the Profile (R_z) showed an increasing for the external side regarding the asperity height. Nonetheless, this trend is not observed for the shear resistance. Therefore, this surface parameter is not considered adequate to predict the interface shear strength. On the other hand, the Total Height of the Profile (R_t) presented similar behavior, also not being considered satisfactory to be related to the interface shear resistance. For both R_t and R_z parameters, it is important to point out that they have their values defined locally and it not measured throughout the sample length. For this reason, average values are considered more adequate.

The Arithmetical Mean Deviation of the Assessed Profile (R_a) also indicated an increasing value with the asperity height rise. Nevertheless, when the asperity height raised from 0.32 mm (GM-T1) to 0.52 mm (GM-T2) no significant change in the R_a value was observed. This finding may be due to the observed variability of the topography concerning the two geomembranes (Figure 1) and the parameter calculation, which is based on the ordinate module. Furthermore, R_a presented the lowest values among the four parameters investigated and this is related to the way that it is calculated: only considering positive values as

shown in Figure 1c and therefore is not considering the presence of valleys. Due to the way that R_a is calculated, it is not considered adequate to related to the interface shear strength. Goodhand et al. (2015) examined different surfaces and concluded that they exhibited unsimilar topographies although they had the same value of R_a.

The Mean Height of Profile Elements (R_c) depicted similar trends comparing to R_a, with average values higher than R_a and lower than R_t and R_c. It is important to clarify that R_c is calculated based on an average value over the sampling length, which is different the way of R_t and R_z are calculated. Therefore, R_t and R_z might have measured values out of trend when comparing to the overall surface distribution leading to higher values. As R_c uses an average value which considers peaks and valleys, it may be used to applied to estimate the interface friction angle when considering other parameters Araujo et al., (2022). It also possible to observe that the smooth geomembrane exhibited larger values of R_z and R_t than R_a and R_c. This likely occurred due to existent indentations prior to the surface measurements that increased the first two cited roughness parameters, once they are estimated locally.
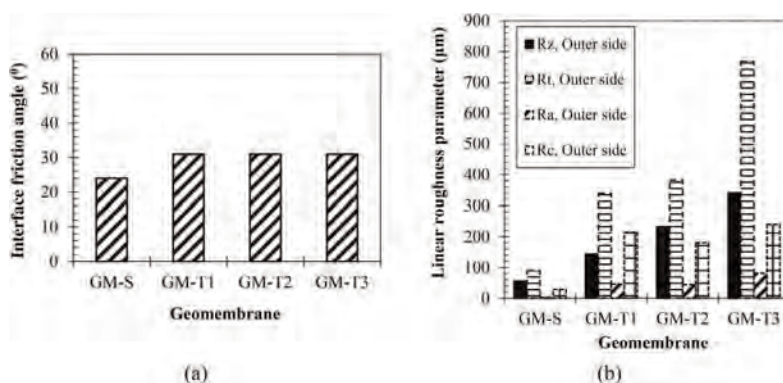
Figure 4.   Results obtained: (a) Interface friction angles and (b) Analyzed Roughness parameters.

5   CONCLUSIONS

In this investigation, ramp tests were performed in order to measure the interface shear strength between geomembranes and different materials for low normal stresses. Bidimensional roughness parameters were also measured to evaluate how they may interfere on the interface resistance. Based on the results, the following conclusions could be made:

- The ramp tests showed that, for the interfaces applying sand, providing asperities to the geomembrane increased the interface shear strength. However, increasing the asperities height does not raise this resistance significantly.
- Depending on the parameter analyzed, it is not possible to relate it to the interface shear strength and this is due to how the parameter is calculated.
- Among the four bidimensional roughness parameters investigated, the R_c average value was considered the most adequate to be related to the interface shear strength, once it had the tendency which could be more directly related to the interface resistance.

REFERENCES

Abdelaal, F.B., & Solanki, R. 2021. Effect of Geotextile Ageing and Geomembrane Surface Roughness on the Geomembrane-Geotextile Interfaces for Heap Leaching Applications. *Geotextile and Geomembranes*. 50 (1): 55–68. https://doi.org/10.1016/j.geotexmem.2021.09.001

Afzali-Nejad, A., Lashkari, A., & Shourijeh, P. T. 2017. Influence of Particle Shape on the Shear Strength and Dilation of Sand-woven Geotextile Interfaces. *Geotextile and Geomembranes*. 45(1):54–66. https://doi.org/10.1016/j.geotexmem.2016.07.005

Araujo, G.L.S., Sanchez, N.P., Palmeira, E.M, & Gardoni, M.G. 2022. Influence of Micro and Macroroughness of Geomembrane Surfaces on Soil-Geomembrane and Geotextile-Geomembrane interface Strength. *Geotextile and Geomembranes* 50(4):751–763.

ASTM D1505-18. 2018. *Standard Test Method for Density of Plastics by the Density-Gradient Technique*, ASTM International, West Conshohocken, PA

ASTM D3080/D3080M. 2011. *Standard Test Method for Direct Shear Test of Soils Under Consolidated Drained Conditions*. ASTM International, West Conshohocken, PA.

ASTM D4595-17. 2017. *Standard Test Method for Tensile Properties of Geotextiles by the Wide-Width Strip Method*, ASTM International, West Conshohocken, PA.

ASTM D4885-01. 2018. *Standard Test Method for Determining Performance Strength of Geomembranes by the Wide Strip Tensile Method*, ASTM International, West Conshohocken, PA.

ASTM D5199-129. 2019. *Standard Test Method for Measuring the Nominal Thickness of Geosynthetics*, ASTM International, West Conshohocken, PA.

ASTM D5261-10. 2018. *Standard Test Method for Measuring Mass per Unit Area of Geotextiles*, ASTM International, West Conshohocken, PA, 2018.

ASTM D6913/ D6913M-17. 2017. *Standard Test Methods for Particle-Size Distribution (Gradation) of Soils Using Sieve Analysis*. ASTM International, West Conshohocken, PA.

ASTM 7466-08. 2008. *Standard Test Method for Measuring the Asperity Height of Textured Geomembrane*, ASTM International, West Conshohocken, PA.

Briançon, L., Girard, H., & Poulain, D. 2002. Slope Stability of Lining Systems—Experimental Modeling of Friction at Geosynthetic Interfaces. *Geotextile and Geomembranes* 20(3):147–172. https://doi.org/10.1016/S0266-1144(02)00009-2.

Hebeler, G.L., Frost, J.D., & Myers, T. 2005. Quantifying Hook and Loop Interaction in Textured Geomembrane–Geotextile Systems. *Geotextile and Geomembranes* 23(1):77–105.

ISO 4287 (1997). Geometrical Product Specifications (GPS) — *Surface Texture: Profile Method — Terms, Definitions and Surface Texture Parameters*. 25p.

ISO 12957-2 (2005). Geosynthetics — Determination of Friction Characteristics — *Part 2: Inclined Plane test*. 10 p.

Bacas, B.M., Konietzky, H., Berini, J.C., & Sagaseta, C. 2011. A New Constitutive Model for Textured Geomembrane/Geotextile Interfaces. *Geotextile and Geomembranes* 29(2):137–148. https://doi.org/10.1016/j.geotexmem.2010.10.014

Dejong, J.T., & Westgate, Z.J. 2005. Role of Overconsolidation on Sand-Geomembrane Interface Response and Material Damage Evolution. *Geotextile and Geomembranes* 23(6):486–12. https://doi.org/10.1016/j.geotexmem.2005.04.001

Goodhand, M.N, Walton, K., Blunt, L., Lung. H. W., Miller, R. & Marsden, R. 2015. The Limitations of "Ra" to Describe Surface Roughness. In: *Proceeedings of the ASME Turbo Expo 2015: Turbine Technical Conference and Exposition*. https://doi.org/10.1115/1.4032280

Palmeira, E.M., & Viana, H.N.L. 2003. Effectiveness of Geogrids as Inclusions in Cover Soils of Slopes of Waste Disposal Areas. *Geotextile and Geomembranes* 21(5):317–337. https://doi.org/10.1016/S0266-1144(03)00030-X

Pitanga, H.N., Gourc, J.-P., & Vilar, O.M.. 2009. Interface Shear Strength of Geosynthetics: Evaluation and Analysis of Inclined Plane ests. *Geotextile and Geomembranes* 27(6):435–446. https://doi.org/10.1016/j.geotexmem.2009.05.003

Sanchéz, N.P. 2018. Study of Some Aspects that Influences on the Adherence Between Geosynthetics and Different Materials. PhD Dissertation. Graduate program on Geotechnics, University of Brasilia. Department of Civil and Environmental Engineering. 168 p. (In Portuguese).

Vangla, P., & Gali, M.L., 2016. Shear Behavior of Sand-Smooth Geomembrane Interfaces Through Micro-Topographical Analysis. *Geotextile and Geomembranes* 44(4):592–603. https://doi.org/10.1016/j.geotexmem.2016.04.001

Modelling single & multi-layer soil-geosynthetic interface behaviour from large direct shear tests

S.S. Muluti
University of Namibia, Ongwediva, Oshana Region, Namibia
University of Cape Town, Cape Town, Western Cape, South Africa

D. Kalumba & L. Sobhee-Beetul
University of Cape Town, Cape Town, Western Cape, South Africa

C.D.R. Aza-Gnandji
University of Abomey-Calavi, Abomey-Calavi, Benin
University of Illinois at Urbana-Champaign, Illinois, USA

ABSTRACT: To predict the performance of engineered structures such as composite liner systems in landfills, constitutive modelling of soil–geosynthetic interfaces is required. This paper presents a numerical model that was developed to simulate the shear stress versus shear displacement responses of single and multi-layer soil-geosynthetic interfaces. A series of large direct shear tests were initially carried out to investigate the behaviour of the interface of a typical composite liner system made up of compacted clay and three geosynthetics: Geotextile (GTX), Geomembrane (GMB), and Geosynthetic Clay Liner (GCL). The numerical model developed in MATLAB R2022a was then utilised to simulate the behaviour of the soil-geosynthetic interfaces using the experimental data. The shear stress–displacement response of the soil-geosynthetic interfaces was modelled by dividing it into two parts: pre-peak and post-peak behaviour. The modelling parameters were then determined based on the results of the large direct shear tests performed on these interfaces. Subsequently, the shear stress–displacement response of the interfaces was evaluated and compared with the experimental results. For both single and multi-layer soil-geosynthetic interfaces, the predicted shear stress–displacement response was shown to be in good agreement with the experimental results.

1 INTRODUCTION

Multiple interfaces exist in geotechnical structures such as composite liner systems in landfills, which consist of compacted soil with low permeability and geosynthetic materials (Feng & Cheng 2014; Guler 2017). Therefore, several interface planes are introduced into the system, potentially causing instability along the slope, and eventually leading to failure. Shear strength between soils and geosynthetics has been identified as a significant challenge in landfill designs. The shear strength of each material layer and the different interfaces between contact layers in the system influences the stability of these liner systems (Feng & Cheng 2014; Stark et al. 2012). The interface shear behaviour of these components can be determined from various laboratory tests using direct shear, ring-shear, inclined plane and pull-out apparatus (Moraci et al. 2014). However, direct shear is frequently used to assess the interface shear behaviour between soils and geosynthetics (Lings & Dietz 2004).

A landfill liner system is made up of several interfaces that must be tested as a single system to fully comprehend the shear strength characteristics of the entire composite liner system (Adeleke et al. 2021; Sikwanda et al. 2019). Using a Large Direct Shear Apparatus (LDSA), two methods of determining the interface shear strengths can be employed, namely, single and multi-layer interface shear testing (Stark et al. 2015; Shenthan et al. 2019). The behaviour of geosynthetic reinforced structures such as landfills is strongly influenced by soil-geosynthetic interaction. For the theoretical and numerical analysis of soil-geosynthetic interaction problem, constitutive modelling of soil-geosynthetic interfaces plays a major role in geotechnical engineering. Thus, a series of direct shear tests using the LDSA were performed to numerically study the soil-geosynthetic interface shear behaviour of components of a typical liner system.

2 EXPERIMENTAL STUDY

2.1 Test materials

The soil used for this study was a reddish-brown clay, which was sourced from Durban, South Africa. The clay was consistent, and simple to work with, allowing the results obtained to be replicated. It was found to have a plasticity index of 30.2 % and based on the Unified Soil Classification System (USCS), it was characterized as a lean clay with sand (group symbol – CL). The clay's specific gravity was found to be 2.8, and its Maximum Dry Density (MDD) and Optimum Moisture Content (OMC) were reported to be 1.6 Mg/m^3 and 24.3% respectively.

Three types of geosynthetics, namely Geotextile (GTX), Geomembrane (GMB), and Geosynthetic Clay Liner (GCL), were used for this study. The 6.4 mm thick GTX had a mass per unit area of 1080 g/m^2, a static puncture strength of 11.7 kN, a permeability of 0.0026 m/s and 50 – 80 % of elongation at break. The GMB, on the other hand, was a 2 mm thick, 2.5% carbon black, Double Textured (DT) High Density Polyethylene (HDPE), with a formulated density of 0.94 g/cm^3. The reinforced GCL was composed of a white polypropylene non-woven GTX cover, a middle layer of light brown, dry sodium bentonite powder with 0% moisture content, and a bottom layer of polypropylene slit film woven GTX carrier. The Minimum Average Roll Value (MARV) was 200, 3700, and 110 g/m^2 for the cover, bentonite, and carrier layer, respectively.

2.2 Test procedures

The automated *ShearTrac-III* Large Direct Shear Apparatus (LDSA) was used in this work. The apparatus was composed of a top (static) shear box with plane dimensions of 305 × 305 mm and a depth of 100 mm and a lower (moving) shear box with plane dimensions of 460 × 355 mm and a depth of 100 mm. The procedures followed to perform both single and multi-layer interfaces tests are briefly summarized and discussed below. More detailed information on the test apparatus and procedures followed can be found in Muluti et al. (2023).

The geosynthetics were cut into rectangles with sizes of 300 × 420 mm and 300 × 520 mm to fit the top and bottom shear boxes of the LDSA, respectively, and placed parallel to the Machine Direction (MD) during testing. As shown in Figure 1(a), for single interface testing, the GTX was fixed to the bottom shear box using bolts and a clamping device. For multi-layer interface testing, on the other hand, one geosynthetic was fastened to the bottom shear box using bolts and a clamping device, and the other geosynthetics were laid on top of the clamped geosynthetic without being clamped, as can be seen in Figure 1(b) and (c). This was done to allow failure to occur at the weakest interface during interface shearing. Then, clay mixed with water quantity corresponding to the OMC, was placed in layers, and compacted to a density close to its MDD.
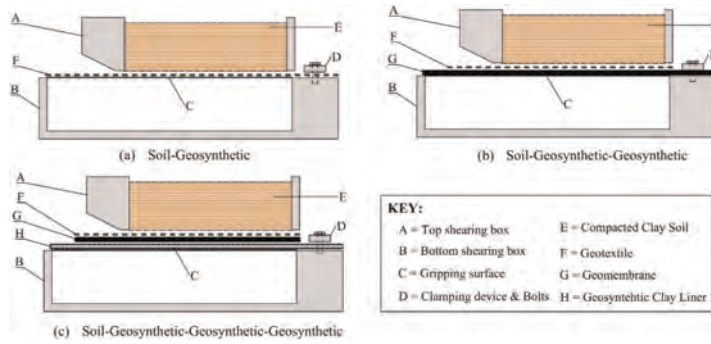
Figure 1. Single and multi-layer interface shear test configurations.

The tests were conducted at increasing normal stresses of 50, 100, 200, and 400 kPa, with a Shearing Displacement Rate (SDR) of 0.1 mm/min. These normal stresses were selected to simulate the increasing load of waste during the landfill design life. At the end of each test, the equipment automatically generated the variation of the shear stress against the shear displacement for each applied normal stress which was subsequently used during data processing and analysis.

2.3 Test results

The shear stress versus shear displacement curves from both the single-layer and multi-layer interface tests are shown in Figure 2. The measured shear stress responses were non-linear for all the interfaces. The CLAY-GTX-GMB interface showed a fast reduction in shear strength after the peak shear stress was reached for the fourth applied normal stress (400 kPa). This behaviour was again obtained when this test was repeated. This observation may possibly have been due to the transfer of the shear stress within the system. It was also observed that for the CLAY-GTX-GMB-GCL, there was a gradual decrease in shear stresses at applied stresses of 200 and 400 kPa, with continuous progress in horizontal displacement to approach the Large Displacement (LD). More detailed information on the results of the other geosynthetic-geosynthetic single interfaces (i.e. GTX-GMB and GMB-GCL) are available for comparison in Muluti et al. (2023). Moreover, the peak and LD strength envelopes for the three interfaces are shown in Figure 3. The peak secant friction angles for the CLAY-GTX interface were 37°, 36°, 35° and 32° for the corresponding applied normal stresses of 50, 100, 200 and 400 kPa. Similarly, they were 40°, 38°, 35° and 28° for the CLAY-GTX-GMB, and 36°, 35°, 33° and 29° for the CLAY-GTX-GMB-GCL interface respectively. On the other hand, LD secant friction angles for the CLAY-GTX interface were 32°, 31°, 29° and 25° for the applied normal stress 50, 100, 200 and 400 kPa respectively. Likewise, they were 39°, 36°, 30° and 16° for the CLAY-GTX-GMB, and 25°, 24°, 22° and 18° for the CLAY-GTX-GMB-GCL interface respectively. These values of peak and LD secant friction angles decreased generally with the increasing applied normal stresses.
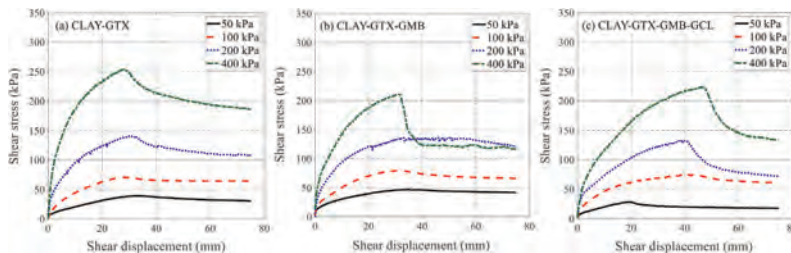
Figure 2. Shear stress versus shear displacement for single and multi-layer interfaces.
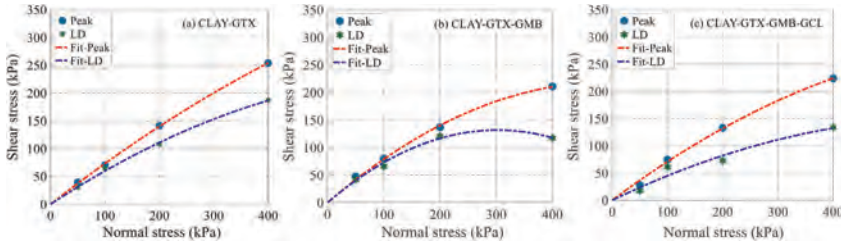
Figure 3. Shear stress versus normal stress for single and multi-layer soil-geosynthetic interfaces.

3 MODELING OF INTERFACE SHEAR BEHAVIOR

The complete shear stress - displacement behaviour of the interfaces was considered and modelled by breaking it up into two segments, namely, a pre-peak and post-peak behaviour as illustrated in Figure 4. The numerical models developed by Anubhav and Basudhar (2010) and Aza-Gnandji et al. (2019) to account for the nonlinearity of the failure envelopes was utilized to simulate the shear stress-displacement behaviour of the single and multi-layer interfaces. In the simulations, the peak and LD (residual) shear stresses were computed from the nonlinear failure envelopes shown in Figure 3.
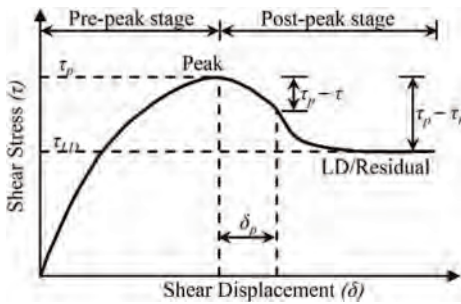
Figure 4. Generalized stress–displacement relationship for clay–geosynthetic interface.
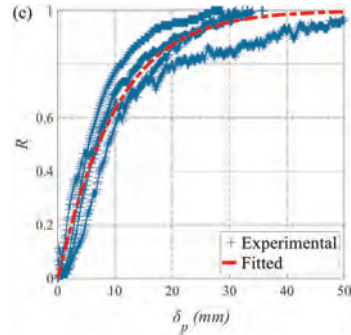
Figure 5. Residual factor vs plastic displacement for CLAY-GTX-GMB-GCL interface.

3.1 Pre-peak behaviour

It can be seen from Figure 4 that the initial shear stiffness depends on the normal stress and the tangent shear modulus varies with the displacement. The approach suggested by Duncan and Chang (1970) and Duncan et al. (1980), which was modified by Anubhav and Basudhar (2010), was used to predict the pre-peak behaviour. Before shear stress reaches peak shear strength, the relationship between shear stress and shear displacement of the interface can typically be modelled by a hyperbolic equation:

$$\tau = \frac{\delta}{\frac{1}{E_i} + \frac{\delta}{\tau_{ult}}} \tag{1}$$

Where τ = shear stress; δ = horizontal displacement; E_i = initial tangent shear modulus; and τ_{ult} = ultimate shear stress.

For soil-geosynthetic interfaces, an increase in normal stress will result in steeper shear stress-relative displacement curves and a higher strength and thus, the values of E_i and τ_{ult}

increase with increasing normal stress. The following equation was used to express the variation of E_i with σ_n (Janbu 1963):

$$E_i = K \cdot P_a \left(\frac{\sigma_n}{P_a}\right)^n \tag{2}$$

Where σ_n = applied normal stress; K = modulus number (dimensionless number); n = modulus exponent (dimensionless number); and P_a = atmospheric pressure. The variation of the ultimate shear stress (τ_{ult}) with the normal stress was considered by relating it with the peak shear stress (τ_p) as follows:

$$\tau_p = R_f \cdot \tau_{ult} \tag{3}$$

Where R_f = failure ratio, which is always less than one (1) since τ_p is always smaller than τ_{ult}. To obtain the values of the coefficients K, n and R_f, the procedure explained in the research of Duncan et al. (1980) was followed for their determination.

3.2 Post-peak behaviour

The tested interfaces in this research showed a post-peak strain softening behaviour like the general curve shown in Figure 4. The strain-softening behaviour has been modelled using the method modified by Anubhav and Basudhar (2010) which accounts for the slow decrease of the shear strength in the initial stages after the peak. Initially, the relationship between the reduction factor (R) and the shear displacement (δ) is established. Then, the reduction factor (R) is defined by the post-peak reduction ($\tau_p - \tau$) in shear stress normalized by the shear stress reduction from peak to the LD or residual value ($\tau_p - \tau_{LD}$):

$$R = \frac{\tau_p - \tau}{\tau_p - \tau_{LD}} \tag{4}$$

Where τ_p = peak shear strength; τ_{LD} = LD/residual shear strength and τ = shear stress obtained after the peak shear stress is reached. From the experimental observation of clay–GTX interfaces, relationship between plastic shear displacement (δ_p) and residual factor (normalized shear strength degradation, R value ranging from 0 to 1) was proposed by Anubhav and Basudhar (2010) to be represented as follows:

$$R = 1 - \exp\left(-A \cdot \delta_p^z\right) \tag{5}$$

To simulate the post-peak behaviour, the two parameters, A and z, were obtained through a non-linear regression analysis using a code developed in MATLAB R2022a. This was achieved by first plotting the residual factors against experimental data as a function of the previously defined plastic shear displacement (δ_p). Then these residual factors were correlated with the fitted curves defined by Equation 5. Good fits were obtained during the analyses, as shown in Figure 5 for the CLAY–GTX-GMB-GCL interface data. Table 1 shows a summary of the model parameter values obtained.

Table 1. Values of model parameters for pre-peak and post-peak behaviour.

Interface	Pre-peak parameters			Post-peak parameters	
	K	R_f	n	A	z
CLAY – GTX	74.32	0.688	1.4	0.069	1.022
CLAY – GTX – GMB	103.83	0.759	0.8	0.081	0.974
CLAY – GTX – GMB – GCL	67.72	0.675	0.8	0.088	1.051

4 SIMULATION OF SHEAR DISPLACEMENT BEHAVIOR

From Figure 6, it can be observed that the numerical data obtained through a back-fitting analysis performed in MATLAB R2022a, exhibited good agreement with the experimental results, although, they could not well fit them for the high normal stress 400 kPa. Nevertheless, the model was able to reproduce the shear behaviour of the soil–geosynthetic interfaces involving the clay and the three geosynthetics over the entire range of normal stresses used in the experiments. In addition, the numerical method that was originally developed for the analysis of sand-geotextile interfaces has demonstrated a good agreement of effectiveness in simulating the shear stress versus shear displacement responses of the interface between the tested single and multi-layer clay-geosynthetics considered in this work.
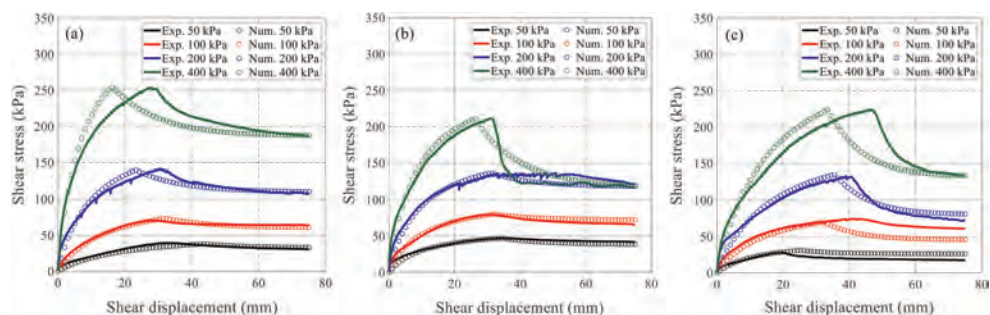
Figure 6. Experimental vs. numerical stress-displacement curves for: (a) CLAY-GTX, (b) CLAY-GTX-GMB, and (c) CLAY-GTX-GMB-GCL.

5 CONCLUSIONS

This study investigated the numerical modelling of single and multi-layer clay-geosynthetic interfaces. The results of the LDSA on the three interfaces revealed that the stress–displacement behaviour of the interfaces could be divided into two zones: pre-peak and post-peak behaviour. The shear displacement necessary to mobilize the peak shear strength increased with higher applied normal stress, and it was lower for the single interfaces compared to that of the muti-layer interfaces. Over the entire range of normal stresses used in the experiments, the stress-displacement response of the interfaces predicted using the proposed model exhibited good agreement with the experimental data. It is therefore possible to consider using this numerical approach for the analysis of interface behaviour along geosynthetic materials that may exhibit similar behaviour based on the results of this work.

REFERENCES

Adeleke, D., Kalumba, D., Nolutshungu, L., Oriokot, J. and Martinez, A. (2021) 'The Influence of Asperities and Surface Roughness on Geomembrane/Geotextile Interface Friction Angle', *International Journal of Geosynthetics and Ground Engineering*, 7(2), pp. 1–12.

Anubhav and Basudhar, P. K. (2010) 'Modeling of Soil-woven Geotextile Interface Behavior from Direct Shear Test Results', *Geotextiles and Geomembranes*, pp. 403–408.

Aza-Gnandji, R., Kalumba, D. and Gbaguidi, V. (2019) 'Modelling the Geomembrane – Fly ash Interface Behaviour', *Proceedings of the XVII European Conference on Soil Mechanics and Geotechnical Engineering (ECSMGE)-2019*, pp. 1–8.

Duncan, J. M., Byrne, P., Wong, K. S. and Mabry, P. (1980) 'Strength, Stress-Strain and Bulk Modulus Parameters for Finite Element Analysis of Stress and Movements in soil Masses', *Thin Solid Films*, 379. doi: 10.1016/S0040-6090(00)01559-5.

Duncan, J. M. and Chang, C.-Y. (1970) 'Nonlinear Analysis of Stress and Strain in Soils', *Journal of Soil Mechanics and foundations Division*, 96(SM5), pp. 1629–1653.

Feng, S.-J. and Cheng, D. (2014) 'Shear Strength between Soil/Geomembrane and Geotextile/Geomembrane Interfaces', (May), pp. 558–569.

Guler, E. (2017) 'A Material Which Started a New Era in Geotechnical Engineering: Geosynthetics', *Innovative Infrastructure Solutions*, 2(1), pp. 1–21.

Janbu, N. (1963) 'Soil Compressibility as Determined by Oedometer and Triaxial Tests', in *Proceedings of the European Conference on Soil Mechanics and Foundation Engineering*. Wiesbaden, Germany, pp. 19–25.

Lings, M. L. and Dietz, M. S. (2004) 'An Improved Direct Shear Apparatus for Sand', *Geotechnique*, 54(4), pp. 245–256.

Moraci, N., Cardile, G., Gioffrè, D., Mandaglio, M. C., Calvarano, L. S. and Carbone, L. (2014) 'Soil Geosynthetic Interaction: Design Parameters from Experimental and Theoretical Analysis', *Transportation Infrastructure Geotechnology*, 1(2), pp. 165–227.

Muluti, S. S., Kalumba, D., Sobhee-Beetul, L. and Chebet, F. C. (2023) 'Shear Strength of Soil-Geosynthetic and Geosynthetic-Geosynthetic Interfaces Using Large Direct Shear Testing', *Under Review to be Submitted to the International Journal of Geosynthetics and Ground Engineering*.

Shenthan, T., Khilnani, K. and Stark, T. D. (2019) *'Case Histories of Multi-Layer Interface Tests for Composite Liners and Comparison to Single Interface Tests'*, 1, pp. 1–17.

Sikwanda, C., Kalumba, D. and Nolutshungu, L. (2019) 'A Comparison of Single and Multi-Interface Shear Strengths at Geosynthetic/Geosynthetic Interface', Proceedings of the 17th African Regional Conference on Soil Mechanics and Geotechnical Engineering., (October), pp. 77–81.

Stark, T. D., Choi, H., Lee, C. and Queen, B. (2012) 'Compacted Soil Liner Interface Strength Importance', *Journal of Geotechnical and Geoenvironmental Engineering*, 138(4), pp. 544–550.

Stark, T. D., Niazi, F. S. and Keuscher, T. C. (2015) 'Strength Envelopes from Single and Multi Geosynthetic Interface Tests', *Geotechnical and Geological Engineering*, 33(5), pp. 1351–1367.

Long-term pullout tests to analyse the soil-geogrid interaction

M. Pisano, G. Cardile & N. Moraci
Mediterranea University of Reggio Calabria, Italy

P. Recalcati
TENAX S.p.A., Italy

ABSTRACT: One of the most important aspects regarding the design of geosynthetic-reinforced soil structures is to predict the long-term behaviour of reinforcements and interfaces. The paper describes a new large-scale laboratory apparatus capable of investigating the behaviour under pullout conditions of a geosynthetic reinforcement embedded in a compacted granular soil, and subjected to sustained tensile loading. By using the long-term pullout test results, the writers suggest a procedure for the determination of the interface parameter necessary to design the length of the reinforcement in the anchorage zone that can take into account the viscous effects of the polymeric material arising under serviceability conditions during the design working life.

1 INTRODUCTION

The viscous nature of geosynthetics leads to a reduction of their tensile resistance due to the development of tensile creep strains in the reinforcements during the working life of the structure they are embedded into. Although both experimental measurements on full scale walls (Bathurst et al. 2005; Carrubba et al. 2000) and laboratory tests (Tatsuoka 2008) have shown that these tensile strains are limited when the reinforcement is placed in contact with soil, the viscous behaviour may reflect on the soil-geosynthetic interface response under serviceability conditions. In fact, since the stress-strain state of the reinforcement in the anchorage zone varies over time, the interface parameters currently obtained from standard pullout tests may be not conservative. As this aspect neither has yet been investigated in scientific literature nor considered in the design of civil and environmental engineering works, further in-depth research seems useful.

To this effect, the Authors designed and assembled a new large-scale prototype pullout apparatus capable of studying the variation over time of geosynthetic strains that occur under sustainable tensile loading due to interaction with soil. After describing the long-term pullout apparatus and the developed test procedure, the paper shows the preliminary results obtained from tests carried out on geogrids embedded in a compacted granular soil.

2 EXPERIMENTAL STUDY

2.1 *Apparatus*

In this research, the Authors (Cardile et al. 2021) have developed a large-scale prototype apparatus (Figure 1) equipped with a completely mechanical system for the application of a constant tensile load over time, capable of simulating the strain state variation that arises

due to the geosynthetic pullout mechanism in the anchorage zone of a geosynthetic-reinforced soil (GRS) structure (Bathurst & Ezzein 2015; Bergado et al. 1993; Cardile et al. 2014, 2017a, 2019, 2020; Di Filippo et al. 2019; Jewell 1990; Palmeira 2009; Pisano et al. 2018, 2019; Wang et al. 2016). The long-term pullout apparatus consists of: a large rigid steel box (625x400x1700 mm) to reduce scale effects (Moraci & Recalcati 2006; Moraci et al. 2017), with walls covered with Teflon films; a pair of metal sleeves (200 mm long) positioned in the slot on the front wall; an internal system to clamp the geosynthetic; a pneumatic system for the application of vertical loads (flexible rubber membrane filled with air); a reserve tank to compensate for lack of air in the case of suspension of the electricity supply; a mechanical system (Figure 2) for the application of the horizontal load (potential maximum force equal to 70 kN) made up of weights, gear wheels and pulleys (theoretical transmission ratio of 10:1); six rotary variable displacement transducers (RVDT) for the measurement of the geosynthetic displacements; and a system for data acquisition.

Figure 1.   Large-scale prototype apparatus for long-term pullout tests.
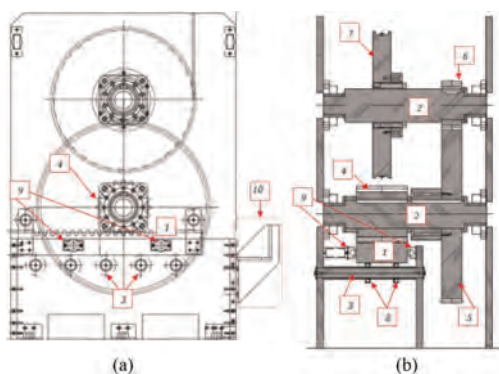
Figure 2.   Longitudinal (a) and transverse (b) cross-sections of the system for the application of pullout load. 1) Gear rack; 2) Main axles; 3) Axles in support of gear rack; 4) Gearwheel 1; 5) Gearwheel 2; 6) Gearwheel 3; 7) Pulley; 8) Bearing in support of gear rack; 9) Gear rack lateral supports; 10) Shock absorber for gear rack.

2.2   *Test materials and procedure*

The first long-term pullout tests on two twin apparatus were carried out on two identical specimens of geosynthetic (330x1200 mm) embedded within a compacted granular soil classified as SW and A1-b according to ASTM D2487 (2017) and UNI EN ISO 14688-1

(2018). The compaction of soil inside the pullout box was performed until reaching a dry unit weight value equal to 95% of the maximum dry unit weight obtained by AASHTO T 99 (2015) Standard Proctor compaction tests. The values of the soil peak shear-strength angle ϕ'_P were obtained by direct shear tests performed on compacted soil specimens ($\phi'_P = 52° \div 44°$ for $\sigma'_v = 10 \div 100$ kPa).

The geosynthetic used in the long-term pullout tests is a high-density polyethylene (HDPE) uniaxial extruded geogrid, whose geometric characteristics are listed in Table 1. Wide-width tensile tests (Cardile et al. 2016, 2017b) were carried out to investigate its mechanical behaviour according to UNI EN ISO 10319, 2015 (Table 2).

Table 1.   Geometric characteristics of the geogrid used in this research.

Geosynthetic			Uniaxial Extruded Geogrid High-Density Polyethylene
Polymer			(HDPE)
S	(mm)	*Spacing between two consecutive bearing members of geogrid*	240
W_T	(mm)	*Width of bar portion between two nodes*	4.4
B_T	(mm)	*Thickness of bar portion between two nodes*	4.5
W_R	(mm)	*Node width*	15.2
B_R	(mm)	*Node thickness*	6.8

Table 2.   Wide-width tensile test results of geogrid used in this research.

$T_{max\ (ISO)}$	(kN/m)	at $\varepsilon'=20\%$ per minute	159
$\varepsilon_{max\ (ISO)}$	(%)	at $\varepsilon'=20\%$ per minute	12.2
$J_{sec\ 2\%\ (ISO)}$	(kN/m)	at $\varepsilon'=20\%$ per minute	2454

A procedure to make the long-term pullout tests repeated, reproducible and without scale effects was developed. The first step consists of covering the internal walls of the pullout box with Teflon; then, the lower half of the pullout box is filled with the selected soil, which is compacted by layers of small thickness to the desired dry unit weight value; the geosynthetic specimen is clamped and positioned on the lower layer of the compacted soil; the upper half of the pullout box is filled and the soil compacted according to the procedure followed previously for the lower half; the flexible air-bag is put in place and the pullout box is closed using a rigid steel plate; the pneumatic system is connected to the air-bag; the desired confinement pressure is applied and the data acquisition software is set; the clamp system is connected to the horizontal force application device; and the test is launched.

The long-term pullout tests are carried out at controlled temperature and humidity conditions by applying a vertical effective stress equal to $\sigma'_v = 50$ kPa to both soil-geogrid specimens. The sustained pullout loads P applied on the two twin apparatus are equal to 50% and 70% of the peak pullout resistance P_R obtained by a pullout test performed, according to ASTM D6706–01 (2013), on the same interface at constant rate of displacement (CRD) equal to 1 mm per minute and at the same vertical effective stress.

3   ANALYSIS OF TEST RESULTS

The design of geosynthetic-reinforced soil walls and slopes is commonly performed using Limit Equilibrium methods for which it is necessary to determine the apparent coefficient of friction between soil and geosynthetic, $\mu_{s/GSY}$. This coefficient allows determining the

reinforcement length (and consequently the reinforced block size), and it is generally used considering its peak value (calculated from the peak pullout resistance P_R obtained by standard pullout tests). In light of the fact that creep/relaxation phenomena affect the deformation of geosynthetics over time, it is useful to analyse to what extent the apparent coefficient of friction mobilised at the interface should be reduced in order to take these phenomena into account. The coefficient is defined as follows:

$$\mu_{s/GSY} = \frac{P}{2 \cdot L_R \cdot \sigma'_v} \tag{1}$$

with P being the sustained pullout load and L_R the reinforcement length.

To investigate the influence of the viscous behaviour on the interface under serviceability conditions, isochronous curves on the $\mu_{s/GSY}$-ε_{conf} plane were built, where ε_{conf} are the strains calculated along the geogrid portion closer to the clamp, (i.e. in the most stressed segment, which goes from the first confined section to the first transverse bar). $\mu_{s/GSY}$ values starting from the two different levels of the sustained load investigated experimentally ($P = 50\% \ P_R$ and $70\% \ P_R$) were computed, in order to plot the isochrones. For each value, the ε_{conf} strains mobilised at set times (t=1 h, 10 h, 100 h, 1000 h, 10000 h) were also calculated. Thereafter, curve fitting was used on the pairs of $\mu_{s/GSY}$-ε_{conf} values thus obtained, leading to the isochronous trend shown in Figure 3. By looking at the trend in the figure, it can be stated that it is generally almost linear providing no local rupture phenomena or tertiary creep take place.
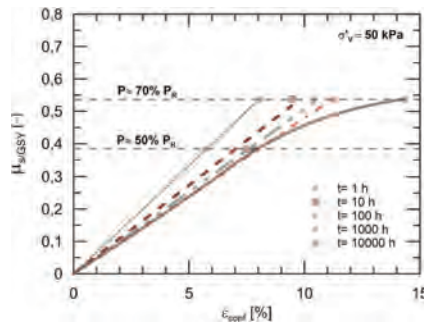
Figure 3. Isochronous interaction curves under long-term pullout conditions (modified from Cardile et al. 2021).

As might be expected, the graph shows that the reinforcement strains in the anchorage zone increase continuously just as the $\mu_{s/GSY}$ value that provides stability to the structure over time has been mobilised, and this applies to each reinforcement layer (therefore, for varying the vertical effective stress). While the tensile strains grow, it is important to check whether the final value achieved (i.e. at the design working life) is compatible with the serviceability of the structure.

Additionally, moving from one time in logarithmic scale to the next, the cumulative strains decrease significantly over time for a given coefficient of friction (i.e. P), with the exception of the isochrone at $t = 10000$ h. In this case a deviation from the trend can be noted. This different behaviour might be connected to local phenomena, such as a local damage caused by the clamping system or a local flaw in the material, leading to the rupture of one or more longitudinal ribs. In fact, by comparing the tensile strain increments obtained for the two different loading levels when time ranges from 1000 h to 10000 h, it can be seen that for tests carried out at $P = 50\% \ P_R$ the strain increment is nil, oppositely to what happens for tests carried out at $P = 70\% \ P_R$, where the strain increment is equal to 27%.

The construction of these curves, obtained for different vertical effective stresses, could help in design structure because they allow the designer to choose an apparent coefficient of friction that also considers the long-term behaviour of the geosynthetics. If design methods focusing on

the ultimate limit state are used (Cardile & Pisano 2020), the design parameter $\mu_{s/GSY}$ could be chosen through the $\mu_{s/GSY}$-ε_{conf} isochronous curves so as to also take into account the serviceability limit state. Specifically, the design procedure (Figure 4) would consist in entering in an isochronous $\mu_{s/GSY}$-ε_{conf} graph (plotted for a given vertical effective stress) with a horizontal segment representing the allowable strain value for a certain structure. When the segment touches both the curve of the strain occurring at the end of the selected design working life and that of the strain at the end of construction, the corresponding coefficient value in the vertical axis can be read (long-term creep apparent coefficient of friction $\mu^{LTC}_{s/GSY}$). The allowable strain could be obtained by evaluating the correlation between the strain of the most stressed segment of the reinforcement and the actual deformation of the structure (e.g. horizontal deformation of GRS wall facing) for each layer of reinforcement by means of numerical analyses and/or measurements on full-scale walls, thus determining threshold values to ensure that the most commonly used design methods investigating the ultimate limit state (e.g. Limit Equilibrium design) also take into account the serviceability limit state.
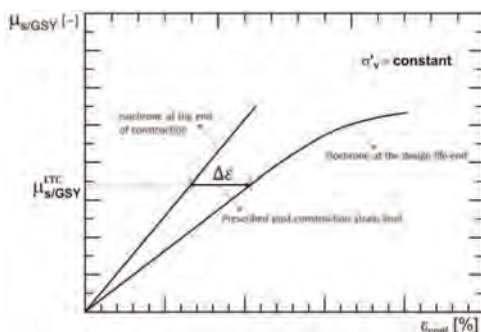
Figure 4.   Long-term apparent coefficient of friction assessed at a prescribed limiting value of post-construction strain in reinforcement by using isochronous curves (modified from Cardile et al. 2021).

4   CONCLUSIONS

The paper illustrates a new large-scale prototype apparatus capable of analysing the pullout behaviour of a soil-geogrid interface subjected to a tensile load kept constant over time.

The first results obtained allowed the Authors to build isochronous curves that link the apparent coefficient of friction mobilised at the interface under long-term pullout conditions to the geosynthetic confined strains occurring when a tensile load is kept constant over time. These isochronous curves demonstrate that the choice of the interface parameter currently being done could lead to tensile strains that are not compatible with the serviceability of the structure. Therefore, their construction could help the designer to choose an apparent coefficient of friction at the interface that also takes the long-term behaviour of the geosynthetics into account. For this purpose, the Authors propose a procedure to ensure that the limit equilibrium analysis (which investigates the ultimate limit state) could also bear in mind aspects regarding the serviceability limit state.

REFERENCES

AASHTO T 99 2015. *Standard Method of Test for Moisture-Density Relations of Soils Using a 2.5-kg (5.5-lb) Rammer and a 305-mm (12-in.) Drop.* American Association of State Highway and Transportation Officials *(AASHTO)*, Washington, DC, USA.

ASTM D2487 2017. Standard Practice for Classification of Soils for Engineering Purposes (Unified Soil Classification System). *ASTM International*, West Conshohocken, PA, USA.

ASTM D5262–07 2016. Standard Test Method for Evaluating the Unconfined Tension Creep and Creep Rupture Behavior of Geosynthetics. *ASTM International*, West Conshohocken, PA, USA.

ASTM D6706–01 2013. Standard Test Method for Measuring Geosynthetic Pullout Resistance in Soil. *ASTM International*, West Conshohocken, PA, USA.

Bathurst, R.J., Allen, T.M., Walters, D. 2005. Reinforcement Loads in Geosynthetic Walls and the Case for a New Working Stress Design Method. *Geotextiles and Geomembranes* 23: 287–322.

Bathurst, R.J. & Ezzein, F.M. 2015. Geogrid Pullout Load-Strain Behaviour and Modelling using a Transparent Granular Soil. *Geosynthetics International* 23 (4): 271–286.

Bergado, D.T., Shivashankar, R., Alfaro, M.C., Chai, J.-C., Balasubramaniam, A.S. 1993. Interaction Behaviour of Steel Grid Reinforcements in a Clayey Sand. *Géotechnique* 43: 589–603.

Cardile, G., Calvarano, L.S., Gioffrè, D., Moraci, N. 2014. Experimental Evaluation of the Pullout Active Length of Different Geogrids. In *Proceedings of the 10th International Conference on Geosynthetics 2014, ICG 2014*, Code 110984.

Cardile, G., Moraci, N., Pisano, M. 2016. In-Air Tensile Load-Strain Behaviour of HDPE Geogrids Under Cyclic Loading. *Procedia Engineering* 158: 266–271.

Cardile, G., Gioffrè, D., Moraci, N., Calvarano, L.S. 2017a. Modelling Interference Between the Geogrid Bearing Members Under Pullout Loading Conditions. *Geotextiles and Geomembranes* 45 (3): 169–177.

Cardile, G., Moraci, N., Pisano, M. 2017b. Tensile Behaviour of an HDPE Geogrid Under Cyclic Loading: Experimental Results and Empirical Modelling. *Geosynthetics International* 24 (1): 95–112.

Cardile, G. & Pisano, M. 2020. Advances in Soil Reinforcement with Geosynthetics: from Laboratory Tests to Design Practice. *Rivista Italiana di Geotecnica* 54 (3): 52–82.

Cardile, G., Pisano, M., Moraci, N. 2019. The Influence of a Cyclic Loading History on Soil-Geogrid Interaction Under Pullout Condition. *Geotextiles and Geomembranes* 47 (4): 552–565.

Cardile, G., Pisano, M., Moraci N. 2020. A Predictive Model for Pullout Bearing Resistance of Geogrids Embedded in a Granular Soil. In *Proceedings of the 7th edition of the Italian National Congress of Geotechnical Researchers* (Calvetti, F., Cotecchia, F., Galli, A., Jommi, C. eds), *Springer International Publishing, Cham, Lecture Notes in Civil Engineering*, vol. 40, pp. 438–445.

Cardile, G., Pisano, M., Recalcati, P., Moraci, N. 2021. A New Apparatus for the Study of Pullout Behaviour of Soil-Geosynthetic Interfaces Under Sustained Load Over Time. *Geotextiles and Geomembranes* 49: 1519–1528.

Carrubba, P., Montanelli, F., Moraci, N. 2000. Long Term Behaviour of an Instrumented Wall Reinforced with Geogrids. In *Proceedings of the 2nd European Geosynthetics Conference*, pp. 125–129.

Di Filippo, G., Biondi, G., Moraci, N. 2019. Seismic Performance of Geosynthetic-Reinforced Retaining Walls: Experimental Tests vs Numerical Predictions. In *Proceedings of the 7th lnternational Conference on Earthquake Geotechnical Engineering* (Silvestri, F., Moraci, N. eds), *CRC Press, Boca Raton, London, New York*, pp. 2120–2127.

Jewell, R.A. 1990. Reinforcement Bond Capacity. *Géotechnique* 40: 513–518.

Moraci, N., Cardile, G., Pisano, M. 2017. Soil-Geosynthetic Interface Behaviour in the Anchorage Zone [Comportamento All'interfaccia Terreno-Geosintetico Nella Zona Di Ancoraggio]. *Rivista Italiana di Geotecnica* 51 (1): 5–25.

Moraci, N. & Recalcati, P. 2006. Factors Affecting the Pullout Behaviour of Extruded Geogrids Embedded in Compacted Granular Soil. *Geotextiles and Geomembranes* 24 (4): 220–242.

Palmeira, E.M. 2009. Soil-Geosynthetic Interaction: Modelling and Analysis. *Geotextiles and Geomembranes* 27 (5): 368–390.

Pisano, M., Cardile, G., Moraci, N. 2018. The Influence of Cyclic Loading Histories on Soil-Geogrid Interface Behaviour Under Pullout Conditions. In *Proceedings of the 11th International Conference on Geosynthetics 2018, ICG 2018*, vol. 4, pp. 2543–2548.

Pisano, M., Cardile, G., Moraci N. 2019. Soil-Geogrid Interface Behaviour Under Cyclic Pullout Conditions. In *Proceedings of the 7th lnternational Conference on Earthquake Geotechnical Engineering* (Silvestri, F., Moraci, N. eds), *CRC Press, Boca Raton, London, New York*, pp. 4507–4514.

Tatsuoka F. 2008. Geosynthetics Engineering, Combining Two Engineering Disciplines. Special Lecture in *Proceedings of GeoSynthetics Asia*, pp. 1–35.

UNI EN ISO 10319 2015. *Geosynthetics – Wide-Width Tensile Test. - Geosintetici - Prova di Trazione a Banda Larga*. Ente Nazionale Italiano di Unificazione, Milano.

UNI EN ISO 13431 2002. *Geotessili e Prodotti Affini - Determinazione Delle Proprietà di Viscosità a Trazione (Tensile Creep) e Comportamento a Rottura (Creep Rupture)*. Ente Nazionale Italiano di Unificazione, Milano.

UNI EN ISO 14688-1 2018. *Indagini e Prove Geotecniche - Identificazione e Classificazione Dei terreni - Parte 1: Identificazione e Descrizione*. Ente Nazionale Italiano di Unificazione, Milano.

Wang, Z., Jacobs, F., Ziegler, M. 2016. Experimental and DEM Investigation of Geogrid-soil Interaction Under Pullout Loads. *Geotextiles and Geomembranes* 44 (3): 230–246.

Effect of backfill gradation on bearing capacity of a Geosynthetic-Reinforced Soil (GRS) mass

Zhen Zhang, Wijit Itthiwongkul, Yunlong Chen, Guanbao Ye & Chao Xu
Department of Geotechnical Engineering, Tongji University, Shanghai, China

Jie Han
Department of Civil, Environmental, and Architectural Engineering, The University of Kansas, Lawrence, KS, USA

ABSTRACT: Geosynthetic-reinforced soil (GRS) structure has been received much attention recently due to its advantages of less over-excavation, ease of construction, cost-effective and excellent performance in practice. The backfill gradation may influence the bearing capacity of GRS mass. This paper conducts a series of model tests under plane strain condition using transparent soil to investigate the effect of backfill gradation on the bearing capacity of GRS mass. The particle image velocimetry (PIV) technique was adopted to monitor the deformation field change in the backfills during testing. The results showed that the maximum aggregate size of backfill affected the bearing capacity of the GRS mass, while the test with well-graded aggregates yielded larger bearing capacity than that with poor-graded aggregates although both backfill had the same maximum aggregate size. Moreover, the well-graded aggregates reduced the deformation of GRS mass.

1 INTRODUCTION

Geosynthetic Reinforced Soil (GRS) generally refers to densely reinforced soil with reinforcement, which behaves as a macroscopically uniform and anisotropic composite material (Adams & Nicks 2018). In practice, the reinforcement spacing is commonly less than or equal to 300 mm. Many studies have shown that RGS composite structure has high bearing capacity and coordinated deformation capacity (Barrett & Ruckman 2007), is easy to construct, and clearly offers both social and economic benefits (Aub-Farsakh et al. 2017; Sagherbfar et al. 2017).

The main factors influencing the bearing capacity of GRS composite include the reinforcement spacing, reinforcement strength, and backfill properties, as well as some external factors, such as the width of bearing plate and setback distance (Xiao et al. 2015). The FHWA design and construction guidelines for geosynthetic reinforced soil abutments and integrated bridge systems (Adams & Nicks 2018) considers the most internal influence factors in calculation of bearing capacity,

$$q_{ult} = (0.7^{(Sv/6d_{max})} \frac{Tf}{Sv}) Kp \tag{1}$$

where S_v is the reinforcement spacing; T_f is the ultimate tensile strength of reinforcement; K_p is the coefficient of Rankine passive earth pressure, and d_{max} is the maximum particle size of backfills. However, in terms of particle size of backfill, this method only considers d_{max} against the influence of bearing capacity.

Nicks and Adams (2013) found that the well-graded backfill is considerably stiffer than the poorly-graded backfill, although both backfills had the same maximum particle size. Nicks et al. (2016) further indicated that the load-bearing performance of GRS composite is not only affected by the maximum particle size of the backfill, but also by the gradation of backfill. This paper presents a series of plane strain model test to investigate the effect of backfill gradation on bearing capacity of a GRS mass. Transparent soil combined with particle image velocimetry (PIV) technique was used to monitor the load-bearing performance of GRS model as the applied load creased.

2 MODEL TEST

2.1 *Test setup and test plan*

Figure 1 shows the setup of the model test. The model box had the inside dimensions of model box are 700 mm (length) × 100 mm (width) × 650 mm (height). The model box was made of 20 mm-thick Plexiglas panel and fixed by steel frames. The Plexiglas panel allows visual observation and photogrammetry of the soil particle movements during the test.

This study considered a GRS mass under a plane strain condition, which had dimensions of 300 mm (length) × 100 mm (width) × 600 mm (height). Considering the size of the mode box, the size effect of $n = 3$ was given for the model test. Six model tests were designed by carrying out the plane strain condition of GRS mass with different gradations of backfill. According to the FHWA design guidance (Adams & Nicks 2018), the reinforcement spacing of the GRS composite is not more than 300 mm. As a result, the model test had a reinforcement spacing of 100 mm. A hydraulic jack was connected to a loading plate, applying load on the top of the GRS mass. During the loading test, a load increment of 85 kPa was applied at each stage until the GRS mass was failed.

Figure 1 also illustrates the layout of the instruments. Two linear variable differential transducers (LVDT) and a load cell were installed to record the vertical displacement of the loading plate and the applied load during the test. Two high-intensity lasers (650 nm, 150 mW) were placed on the same plane at both sides of the box as shown in Figure 1, producing speckles on the laser-lighted plane. A Canon 6D digital camera with a resolution of 26 megapixels was positioned right in front of the model box to properly focus on and visualize the analysis area. The Geo-PIV technique (Stanier et al. 2015) was adopted to determine incremental displacements and strains by comparing the successive pairs of photographs during the test.
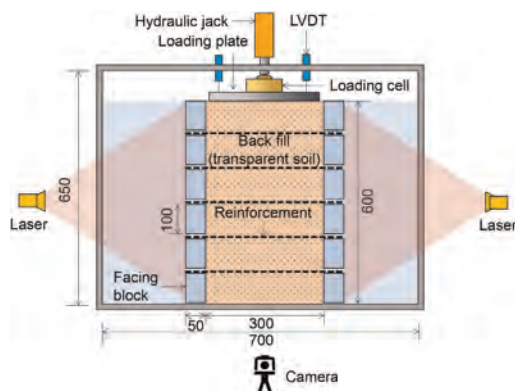
Figure 1.   Setup of model test.

2.2 *Materials and preparation*

Transparent soil technology is one type of modern technology for simulating natural soil, which can be able to visually observe the deformation and seepage inside the soil. Therefore, this study adopted the transparent soil as the backfill. The transparent soil in this study was a mixture of high purity fused quartz particles and industrial white oil. The white oils of Nos. 3 and 15 were mixed at a volume ratio of 1.5:1, and the refractive index of the mixed oil was equal to 1.4584 at 25°C, which was the same as the refractive index of the quartz and sand. The maximum and minimum dry density of transparent soil were 1.41 g/cm^3 and 1.22 g/cm^3, respectively. Its internal friction angle was 43° by the direct shear test. The facing blocks were made of transparent plexiglass blocks of 100 mm (length) $\times$ 100 mm (width) $\times$ 50 mm (thickness). This study selected the grey polyamide mesh as geosynthetic reinforcement. The ultimate tensile strength (T_{ult}) was 10.1 kN/m at a strain of 2.93% based on the tension test. Each model test had 5 layers of reinforcement in the GRS mass.

The first layer of facing block was placed on the base of the model box. The prepared white oil mixture was poured into the model box, and then the weighted fused quartz particles were gently placed into the model box. The fused quartz particles were compacted manually by a steel hammer to a compaction degree of 95% with a lift thickness of 100 mm, which is equivalent to the height of the facing block. The compaction was controlled by the mass and volume in each lift. After the soil placement was complete, a reinforcement layer was directly placed on the top surface of the backfill, and a frictional connection between the reinforcement and the facing block was considered. These procedures were repeated until to the desired fill height.

The FHWA design guidelines recommend a particle size range of 0.39 mm to 25.4 mm, and the proportions of different particle size ranges are shown in Table 1 The modified analogy method proposed by Lowe (1964) was used to ensure the similarity of the gradation of the backfill as below:

$$\frac{D^b - D^b_{min}}{D^m - D^m_{min}} = \frac{D^b_{max} - D^b_{min}}{D^m_{max} - D^m_{min}} = A \tag{2}$$

in which, D^b is the prototype particle size, D^m is the corresponding similar model particle size, and the subscripts, min and max, represent maximum and minimum; A is the similarity ratio of the test. Accordingly, the calculated model particle size range is shown in Table 1. Table 2 shows the particle size distribution of backfill in the six model tests. The test No.1 followed the FHWA recommended particle size gradation, which is also referred to as the standard test, while the other five tests had backfills different from the FHWA recommended particle size gradation.

Table 1. Particle size and gradation of FHWA and model.

	Particle size (mm)			
FHWA	25.4 (94-100%)	9.5 (72-63%)	2 (32-41%)	0.39 (14-24%)
Model	8	3	0.7	0.2

Table 2. Gradation of backfills in the model test.

Test	8-3 mm (%)	3-0.7 mm (%)	0.7-0.2 mm (%)	<0.2 mm (%)	C_u	C_c
1	30	25	25	20	20.80	0.77
2	30	25	45	0	6.88	0.45
3	30	25	0	45	42.57	0.18
4	0	55	25	20	13.27	1.21
5	55	0	25	20	43.64	0.37
6	30	50	0	20	25.40	5.30

3 RESULT AND ANALYSIS

3.1 Standard test

Figure 2 shows the variation of the vertical displacement at the top surface with the increase of the applied load. The vertical displacement the GRS mass basically follows a linear trend, however as the load exceeded 850 kPa, the vertical displacement rapidly increased, followed by the failure of the GRS mass.
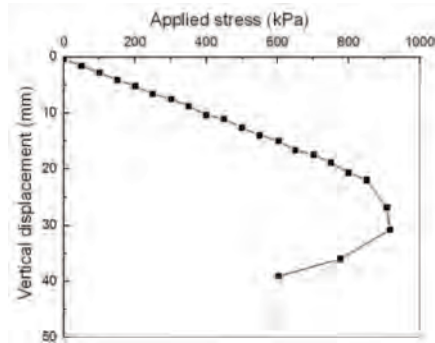
Figure 2.   Applied load versus vertical displacement.

Figure 3(a) shows the lateral displacement of the backfills at different load stage measured by the PIV technique at a distance of 20 mm from the facing block. The lateral displacement of the backfills show an overall decrease with depth. The backfills near the reinforcement had small lateral displacement as they were restrained by the reinforcement. When the applied load reached 900 kPa, the lateral displacement of the reinforced soil had a surge increase. Figure 3(b) shows the vertical displacement along the depth at the center profile of the GRS mass. The vertical displacement in the GRS mass decreased gradually along the depth, and there was a sudden change in the vertical displacement of the GRS composite at the location of the reinforcement.
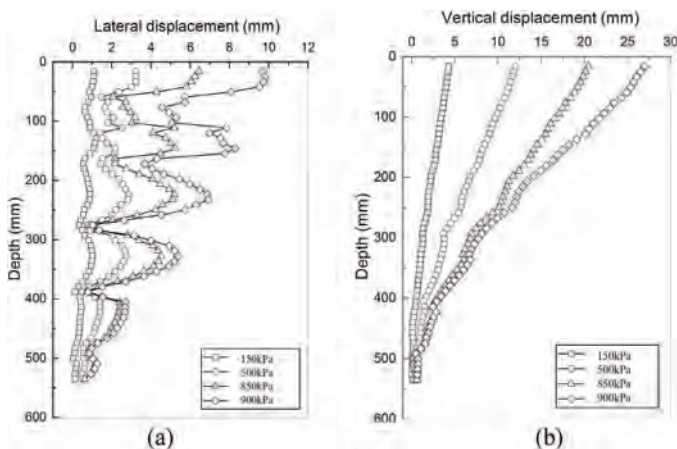
Figure 3.   Deformation of GRS standard test: (a) horizontal displacement; (b) vertical displacement.

3.2 *Failure pattern*

Figure 4 shows the broken locations of the reinforcement in each test, as well as the angle of the failure plane against the horizontal plane. The GRS composite failed mostly due to the shear rupture surface through the reinforcement, resulting in the broken of the reinforcement. The broken location of the reinforcement mostly appeared inside the composite or at the connection between the reinforcement and the facing block. The GRS mass failed by shear and finally slid out along the interface between the reinforcement and the facing block, but the shear damage varied in range and mode in each test. For the Test Nos. 1, 2, 4 and 6, the slip surface developed as a straight line and then sheared out from the interface between the block and the reinforcement. The test No. 5 had a bilinear slip plane, i.e., the upper part was steeper than the lower part. The angle of the measured slip plane to the horizontal plane basically confirms to the Rankine slip surface.
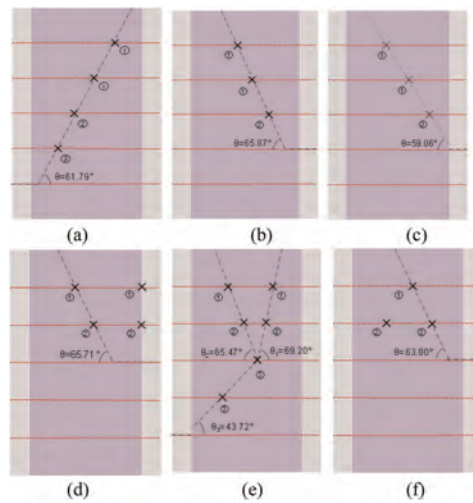
Figure 4.   Failure mode: (a) Test 1; (b) Test 2; (c) Test 3; (d) Test 4; (e) Test 5; (f) Test 6.

3.3 *Bearing capacity*

Figure 5 shows the variation of the bearing capacity of the GRS composite with the non-uniformity and curvature coefficient. There tends to be an increase in the bearing capacity as the non-uniformity coefficient increased. However, as the curvature coefficient increased, the bearing capacity gradually decreased. The non-uniformity coefficient increased from 6.88 to
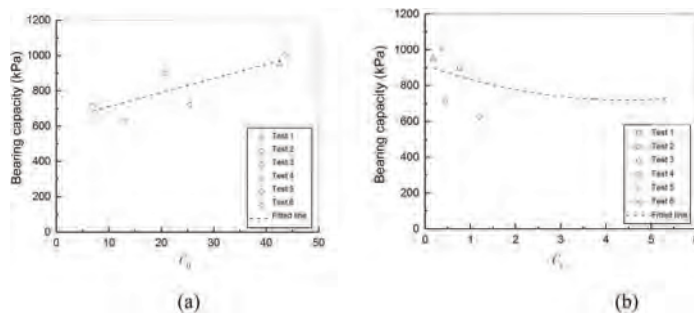
Figure 5.   Influence of gradation on bearing capacity: (a) non-uniformity coefficient; (b) curvature coefficient.

43.64, and the bearing capacity increased by approximately 40%. The curvature coefficient increased from 0.18 to 5.30, and the bearing capacity decreased by about 22%. It can be seen that the particle size gradation of the backfill has a significant effect on the bearing capacity of the GRS composite, rather than being influenced by the maximum particle size only.

4 CONCLUSION

(1) The reinforcement plays a significant part in preventing the deformation of GRS composite, especially in the case of horizontal deformation. The broken location of the reinforcement mostly occurred inside the composite or at the connection between the reinforcement and the facing block. The angle of the slip surface to the horizontal plane was in basic agreement with the Rankine failure plane.
(2) The gradation of the backfill has a significant influence on the bearing capacity of the GRS composite. Moreover, the non-uniformity coefficient of backfill increased from 6.88 to 43.64, and the failure load increased by approximately 40%; on the other hand, the curvature coefficient increased from 0.18 to 5.30, while the failure load decreased by around 22%.

REFERENCES

Abu-Farsakh M, Sagherbfar M, Ardah A, *et. al.* 2017. A Case Study on Evaluating the Performance of a Geosyn-thetic Reinforced Soil Integrated Bridge System (GRS-IBS). *Geotechnical Frontiers*, 12–22.

Adams, M., Nicks J. 2018. Design and Construction Guidelines for Geosynthetic Reinforced Soil Abutments and Integrated Bridge Systems. *FHWA-HRT-17-080*. Federal Highway Administration, McLean, VA.

Barrett R K, Ruckman A C. 2007. GRS-A New Era in Reinforced Soil Technology. *Geosynthetics in Reinforce-ment and Hydraulic Applications: ASCE Geotechnical Special Publication* No.165. Denver, Colorado, USA:ASCE, 153–164.

Lowe J. 1964. Shear Strength of Coarse Embankment Dam Materials. *Proc. 8th Int. Congr. Large Dams 3*, Edimbourg, UK, 1964:745–761.

Nicks J E, Adams M T, Ooi P, *et al.* 2013. Geosynthetic Reinforced Soil Performance Testing: Axial Load Deformation Relationship. *Final Report, FHWAHRT-13-066*. Federal Highway Administration, McLean, VA. 2013.

Nicks J E, Esmaili D, Adams M T. 2016. Deformations of Geosynthetic Reinforced Soil Under Bridge Service Loads. *Geotextiles and Geomembranes*, 44(4):641–653.

Sagherbfar M, Abu-Farsakh M, Ardah A, *et. al.* 2017. Full-Scale Testing of Geosynthetic Reinforced Soil Integrated Bridge system. *Transportation Research Record Journal of the Transportation Research Board*, 2656:40–52.

Sagherbfar M, Abu-Farsakh M, Ardah A, *et. al.* 2017. Performance Monitoring of Geosynthetic Reinforcede Soil Integrated Bridge system (GRS-IBS) in Louisiana. *Geotextiles and Geomembranes*, 45(2):34–47.

Stanier S.A., Blaber J., Take W.A., *et al.* 2015. Improved Image-based Deformation Measurement for Geotechnical Applications. *Canadian Geotechnical Journal*, 53(5):727–739.

Wu J.T.H., Pham T.Q. 2013. Load-Carrying Capacity and Required Reinforcement Strength of Closely Spaced Soil-Geosynthetic Composites. *Journal of Geotechnical and Geoenvironmental Engineering*, 139 (9):1468–1476.

Pullout performance of anchored earth systems

K. Nell
TerraTech Consulting Ltd, Ireland
Formerly Postgraduate Student, Faculty of Engineering & Design, Atlantic Technological University Sligo, Ireland

P.J. Naughton
Faculty of Engineering & Design, Atlantic Technological University Sligo, Ireland

ABSTRACT: Anchored earth is a derivative of reinforced soil. The pullout resistance and corresponding displacement of square mild steel anchor plates 100mm x 100mm, 200mm x 200mm and 300mm x 300mm, was investigated. Good repeatability of the pullout resistance – displacement was observed. However, both the peak pullout resistance and corresponding displacement indicated some scatter. Early stiffness of the tendon and anchors at displacements less than 10mm was observed. Once the peak resistance was achieved, tendon and anchor capacities reduced. The peak pullout resistance increased with the area of plate anchor. The smallest plates (100mm x 100mm) reached peak resistance at displacement less than 5mm, the large plates (200mm x 200mm and 300mm x 300mm) reached peak at similar values between 10 – 30mm. The peak pullout resistance for the 200mm x 200mm and 300mm x 300mm was found to reduce as the in-situ vertical stress in the wall increased.

1 INTRODUCTION

Anchored earth technology has been used to construct retaining walls for over 100 years (Jones 1996). The system consists of a facing element and a connecting rod or tendon that connects the facing system to an anchor located in the retained fill, Figure 1(a). Anchored earth systems differ from conventional steel and geosynthetic reinforced wall technologies in that the resistance to outward movement is mobilised, primarily, as passive resistance against the anchor plate, rather than friction along the reinforcement element (Jones 1996).

Jones (1996) reported on early anchored earth technologies, including an array of wooden timber reinforcement units developed in the USA (Munster 1925). A French engineer also developed a ladder wall in 1932, which consisted of precast concrete facing units, selected stone fill and ties with steel anchor plates (Coyne 1945). The ladder system allowed the facing units to move relative to each other to accommodate settlement.

The first anchored earth wall in the UK was constructed in 1984 (Snowdon et al. 1986). The wall, 6m high and 86m long, formed part of the A660 Otley bypass in West Yorkshire, UK. Different types of anchors, including plate anchors and anchor heads, were utilised on that project.

In this study, the pullout behaviour of plate anchors was investigated in a full-scale trial wall. Three plate anchor face dimensions of 100mm x 100mm, 200mm x 200m and 300mm x 300mm were investigated. The data was assessed in terms of peak pullout resistance, stiffness of the pullout response and the impact of both plate size and in-situ vertical effective stress on the behaviour of the plate anchors.

The test wall was constructed in Co. Offaly, Ireland, at the Lusmagh Quarry owned by Banagher Precast Concrete Ltd. The wall was 6.75m high, Figure 1(b), and faced with 0.14m

thick concrete panels. The panels were 1.5m x 1.5m in face area, with a full panel having four anchor connections.

2 METHODOLOGY

The wall was reinforced with 4.65m long high tensile steel tendons, 16mm in diameter, connected to steel anchor plates placed at 0.75m horizontal and vertical centres.

The anchor plates comprised of 10mm thick mild steel (S275) of different face dimensions: 100mm x 100m, 200mm x 200mm and 300mm x 300mm. The plates sizes used at each location are summarised in Table 1 The numbered locations on the front of the wall are shown in Figure 2(a), with a cross section of the wall shown in Figure 2(b). Kentledge, in the form of large concrete blocks, was placed on top of the wall to increase the vertical stress in the retained fill by 20kPa. The backfill consisted of Class 6I/6J fill (2013) compacted in accordance with the Specification for Road Works, Series 600 (2013). Class 6I/6J is a well graded backfill with a maximum particle size of 125mm and with less than 15% passing the 63μm sieve size.
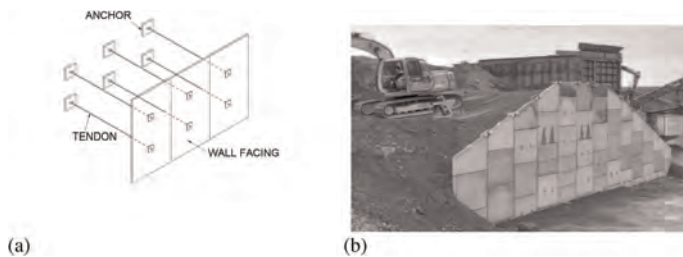
Figure 1. (a) Schematic of an anchored earth structure and (b) Image of 6.75m high test wall constructed as part of this study.

Table 1. Plate sizes at different locations in the wall.

Plate size	Location number
100mm x 100mm	1, 2, 9, 10
200mm x 200mm	5–8, 11–18, 23–26
300mm x 300mm	19–22, 27–32
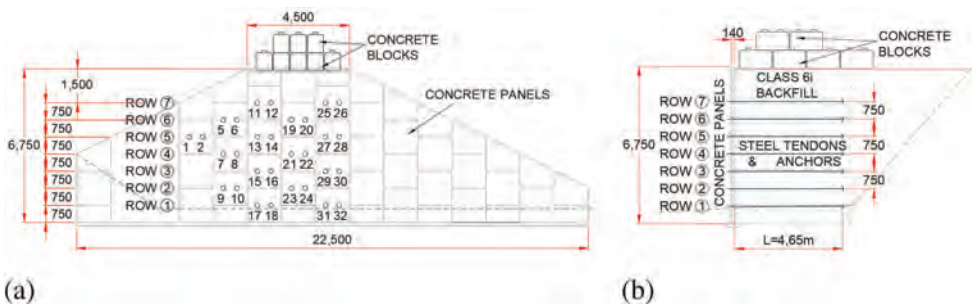
Figure 2. (a) Front elevation of test wall and (b) Cross section through the test wall.

2.1 Backfill properties & construction of the wall

Compaction testing on the Class 6I/6J backfill was in accordance with BS1377-1 (2016). The optimum moisture content was determined as 6.5%, with a maximum dry weight density of 22.3kN/m^3. Large shear box testing was conducted in accordance with BS 1377-7 (1990). The moisture content was 4.5%, with a dry weight density of 19.6kN/m^3, corresponding to 88% of maximum dry density. The peak angle of friction was 47.8° with an apparent cohesion of 8kPa.

Figure 3(a) indicates the construction of the wall. The fill was placed and compacted in 150mm layers, using Method 2 of Series 600 (Anon 2013). During the construction process, the steel tendons connected to the anchors were left protruding through the wall face to facilitate testing, Figure 3(b).
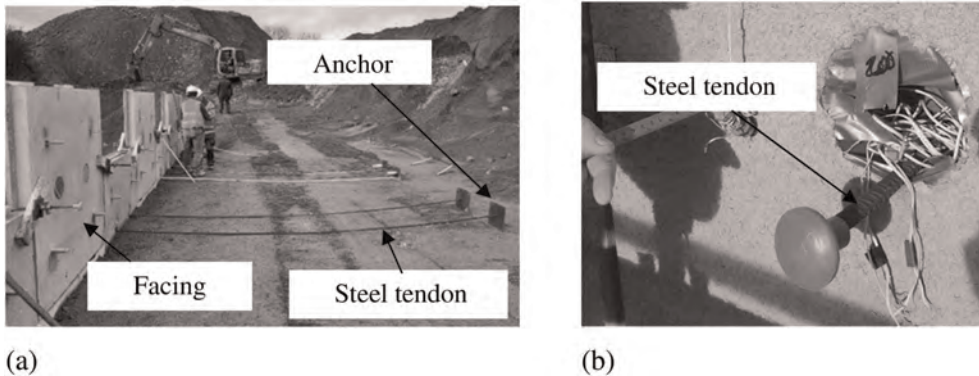
Figure 3. (a) Construction of test wall, including installation of anchors and (b) Anchor tendon protruding at face of wall through preformed hole in facing panel.

2.2 Pullout testing

A 20-tonne jack was used in the pullout testing. The tendons and threaded bars were joined using bespoke steel slotted 'H' connectors which provided sufficient strength to prevent slippage between the components, Figure 4(a). The threaded bar was welded to the end of the 'H' connector, that passed through the hole in the centre of the jack and was locked off with a loading plate and wing nut. The displacement of the anchor/tendon was measured using a long-stroke linear voltage displacement transducer (LVDT). The experimental setup during a test is indicated in Figure 4(b).
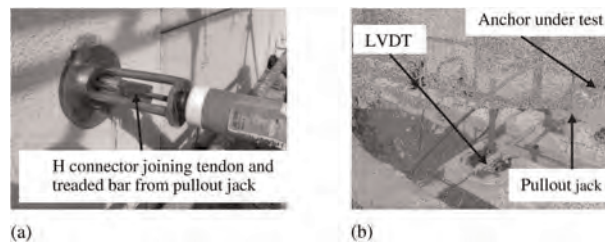
Figure 4. (a) Connection between jack and anchor tendon during a test and (b) Experimental setup for conducting pullout testing.

A preload of 0.5kN, corresponding to 1% of the tensile strength of the test tendon, was applied. Pullout testing was conducted at 2mm/minute with pullout resistance and displacement recorded at 1-minute intervals. The horizontal displacements and loads were automatically logged by a Hydrotechnic Multi System 5060 data logger.

3   RESULTS & DISCUSSION

In total, 30 pullout tests were conducted. Figure 5(a) presents four pullout test results plotted against displacement for the anchors on Row 6: Anchors 5, 6, 19, and 20. Good repeatability with early stiffness, up to a displacement of 10mm, was observed. There was some scatter in the observed peak pullout resistance, with peak resistance varying between 65 – 85kN and corresponding displacement varying from 20 – 37mm.
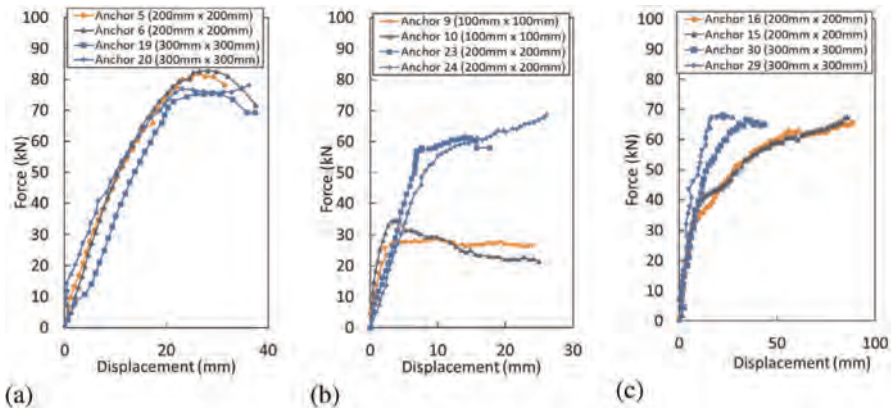
Figure 5.   Pullout test data for (a) Row 6, (b) Anchors 9, 10, 23 and 24, (c) Row 3, Anchors 15 & 16.

3.1   *Impact of plate size on pullout resistance*

Figure 5(b) shows the displacement relationship for 100mm x 100mm (Anchors 9 & 10) and 200mm x 200mm (Anchors 23 & 24) anchors at Row 2 in the wall. Good repeatability in comparable data was observed. The 100mm x 100mm anchors appear to have a slightly stiffer response at small displacement than the larger 200mm x 200mm anchors. The smaller anchors also display a definite peak pullout, with the post peak behaviour displaying a plastic response or some softening. The 200mm x 200mm plates, in contrast, did not have a definite peak value and the force – displacement curve hardened at higher displacement.

Figure 5(c) presents the pullout resistance – displacement data for Row 3, Anchors 15 & 16 (200mm x 200mm plates) and Anchors 29 & 30 (300mm x 300mm plates). Good repeatability was found. The stiffness of the anchors on Row 3 was similar at low displacements. The 100mm x 100mm plates reached peak resistance at a lower displacement than the 200mm x 200mm at the same elevation in the wall. In Row 3, both plate sizes, 200mm x 200mm and 300mm x 300mm, had comparable displacements at peak pullout resistance.

The peak pullout resistance and corresponding displacement for each anchor is summarized in Table 2 In Row 2, the 200mm x 200mm plates had a higher peak pullout resistance at a slightly larger displacement compared with the 100mm x 100mm plates. However, the increase in peak pullout resistance was not proportional to the increase in the cross-sectional area of the plate. Similarly for Row 3, the larger 300mm x 300mm plates had a higher peak pullout resistance than the 200mm x 200mm plates, but again increased resistance was not proportional to the increase in plate area.

Table 2. Summary of peak pullout resistance and corresponding displacement for anchors on Rows 2 & 3.

Row	Anchor No	Plate size (mm x mm)	Peak pullout force (kN)	Displacement at peak pullout force (mm)
2	9	100 ×100	28	4
	10	100 ×100	45	4
	23	200 ×200	58	7
	24	200 ×200	54	9
3	15	200 ×200	48	15
	16	200 ×200	54	24
	29	300 ×300	68	18
	30	300 ×300	76	16

3.2 Impact of vertical stress on pullout resistance

The impact of vertical stress on pullout resistance was assessed by comparing the pullout resistance of similar sized plates located at different elevations in the wall.

Figures 6(a) & 6(b) show the respective pullout resistance – displacement relationship for the 200mm x 200mm plates located in Rows 1 – 7 inclusive and 300mm x 300mm plates located in Rows 3 – 6 inclusive. Both plate sizes displayed a linear and similar value of stiffness for a displacement less than 10mm.

Figure 7 presents the relationship between peak pullout resistance and in-situ vertical effective stress. Overall, and irrespective of plate size, a reduction in peak pullout resistance with increased in-situ vertical effective stress was observed. The reduction in pullout resistance with increased vertical stress, while counterintuitive, was not unexpected. Pullout testing (Weldu et al. 2015) on inextensible steel reinforcement had found enhanced interaction between the reinforcement elements and the surrounding soil at low normal stress, which is attributed to dilation in the well compacted granular fill near the top of the wall (Weldu et al. 2015).
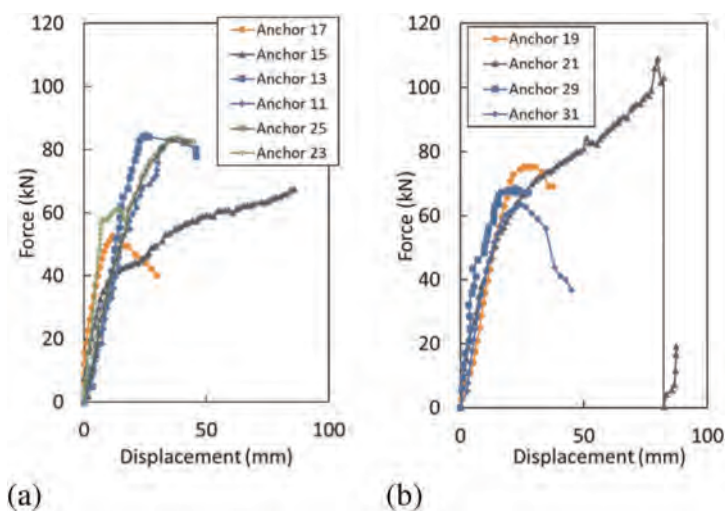
Figure 6. Pullout test data for (a) 200mm x 200mm plates and (b) 300mm x 300mm plates.
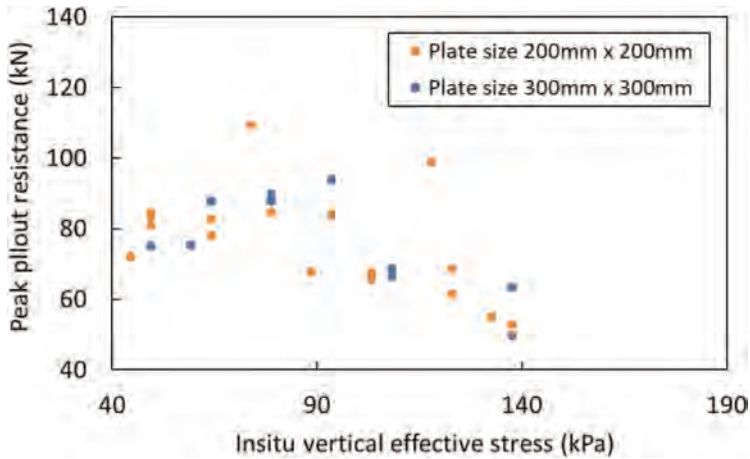
Figure 7. Relationship between pullout resistance and insitu vertical effective stress for (a) 200mm x 200mm plates and (b) 300mm x 300mm plates.
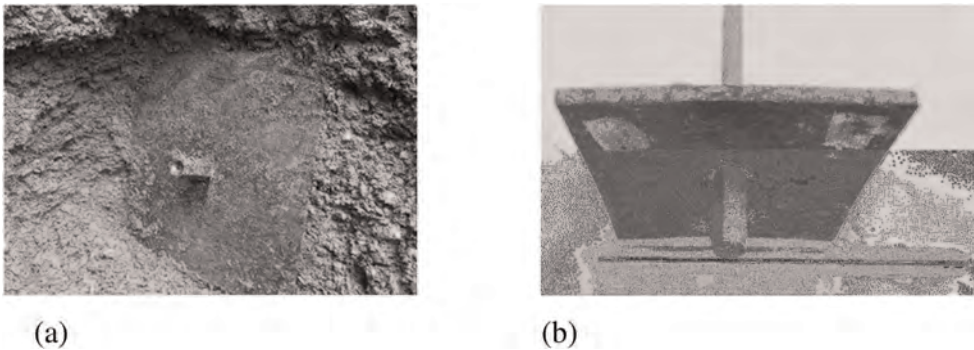
Figure 8. (a) Exhumed Anchor 28 and (b) Deformed Anchor 14 following exhumation.

Typically, the interaction between the soil and inextensible reinforcement reduces with vertical stress to a depth of 6m and then remains relatively constant (BS 8006-1:2010+A1, 2016).

3.3 Anchor post-construction excavation and inspection

The backfill behind the top three anchors (Rows 5, 6 & 7) was excavated. The granular backfill was well compacted, cemented, and difficult to excavate with a spade. The plates were intact and well embedded into the granular backfill, Figure 8(a). Row 5 contained all plate sizes. The 100mm x100mm plates (Anchors 1 & 2) when exhumed had rotated by approximately 45 degrees from the vertical. The 200mm x 200mm (Anchor 13) & the 300mm x 300mm plates (Anchors 27 & 8) displayed evidence of slight deformation. However, Anchor 14 (200mm x 200mm) displayed noticeable bending and deflection - approximately 12mm at the centre of the plate, Figure 8(b).

4 CONCLUSION

This study presents pullout testing on a 6.75m high trial anchored earth wall. The wall was reinforced with three different size plate anchors which were connected to the concrete facing units by high tensile steel tendons. Kentledge of 20kPa was applied to the top of the wall.

Good repeatability of the pullout resistance – displacement curves, particularly at displacement less than 10mm, was observed in all tests conducted. The post peak behaviour was also found to vary, with softening, plastic displacement and hardening all observed. The smaller 100mm x 100mm plate failed at small displacements, less than 5mm, while the displacement at peak resistance for the 200mm x 200mm and 300mm x 300m plates was largely consistent and was in the range of 10 – 30mm. The peak pullout resistance was found to be not proportional to the anchor plate size as the area of the anchor plate increased. This anomaly may be the result of poor backfill compaction around the plate, the vertical alignment of larger plates or the slack of the tendon during the installation. The peak pullout resistance also varied with insitu vertical stress, reducing as the vertical stress increased. This response is in keeping with pullout testing on inextensible steel reinforcement reported in the literature (Weldu et al. 2015). The measured displacement of the anchor may be attributed to elastic deflection of the tendon & anchor plate. However, further analysis of the data is required. The passive resistance of the backfill was secondary to the mechanical properties of the tendons and anchor plates used in this study when high quality granular backfill was used.

When the horizontal deflection was limited to 10 – 20mm, the horizontal force that the anchor could resist was 30 – 60kN, depending on the anchor size. The working resistance of the anchor is considered the best approach to take in analysing pullout data.

REFERENCES

BS 8006-1:2010+A1. 2016. *Code of Practice for Strengthened/Reinforced Soils and Other Fills*. BSI:London.
BS1377-1. 2016. *Methods of Test for Soils for Civil Engineering Purposes - General Requirements and Sample Preparation*. BSI:London.
BS1377-7. 1990. *Methods of Test for Soils for Civil Engineering Purposes - Shear Strength Tests (Total Stress)*. BSI:London.
Coyne, M.A. 1945. Murs De Soutenement Et Murs De Quai à Echelle. Le Genie Civil, May.
Jones, C.J.F.P. 1996. *Earth Reinforcement and Soil Structures*. Third ed. Thomas Telford: London.
Munster, A. 1925. United States Patent Specification No 1762343.
Snowdon, R.A., Darley, P. & Barratt, D.A. 1986. An Anchored Earth Retaining Wall on the Otley Bypass: Construction and Early Performance. *Transport and Road Research Laboratory, Research report 62*:UK.
Specification for Road Works, Series 600, 2013 CC-SPW-00600, Transport Infrastructure Ireland.
Weldu, M.T., Han, J., Rahmaninezhad, M.S., Parsons, R.L. & Kakrasul, J.I., 2015 Pullout Resistance of Mechanically Stabilized Earth Wall Steel Strip Reinforcement in Uniform Aggregate, *Report No K-TRAN: KU-14-7*, University of Kansas.

Development of stability analysis of reinforced soil by rigid-plastic finite element method

Y. Yamakuri
Chuo University, Tokyo, Japan

E. Sakon & S. Kobayashi
Kanazawa University, Kanazawa, Japan

ABSTRACT: A rigid plastic finite element method for a stability analysis of a reinforced soil is discussed in this article. In the literature, deformation constraints such as no-length change or no-angle change between FEM nodes were introduced as internal constraints to model the interaction between reinforced members (RMs) and surrounding soils. It is noteworthy that this implementation requires no meshing of RMs. This idea can be extended to more general cases, such as one-directional-resistant (tensile only) RMs and slippage of RMs from soils, by using the duality of the limit theorems (upper bound and lower bound theorems). A mathematical framework of rigid-plastic finite element method with finite strengths of RMs and bonding between RMs and soils is presented. Some numerical examples are also demonstrated to show the ability of the proposed method.

1 INTRODUCTION

To increase the strength and stiffness of soil, reinforcement members such as anchors and geotextiles are placed in the ground. The stability of reinforced soil structures is assessed using traditional rigid-plastic analysis methods such as the limit equilibrium method and slope analysis. In these analysis methods, the resistance force of reinforcement is often assumed and a specific value is given before the analysis is conducted. However, the resistance force of reinforcement is essentially the value that should be obtained as the solution to the boundary value problem. If the predicted value differs from the actual resistance force exhibited significantly, the accuracy of the stability evaluation will be decreased.

The rigid-plastic finite element method (RPFEM) based on the limit theorem is one of the numerical analysis methods to evaluate the stability of soil structures. Several studies have applied RPFEM to reinforced soil problems. Otani et al. (1998) modeled the reinforcement and surrounding soil layers as a single composite material. Asaoka et al. (1994) and Kodaka et al. (1995) modeled the deformation constraint effect of the reinforcement by imposing linear constraints on the nodal displacement velocity of the ground mesh. Since only the ground mesh is used, the physical mesh of the reinforcement is not necessary. However, the reinforcement strength is assumed to be sufficiently large that the reinforcement does not yield.

The authors have developed a RPFEM based on a hybrid-type formulation (Kobayashi 2005; Yamakuri et al. 2020). The advantage of the developed analysis method is that it can handle inequality constraints. In other words, the anisotropy of the reinforcement strength and the adhesion strength between the reinforcement and the ground can be taken into account. In this paper, a stability analysis method for reinforced soil problems is developed

by extending the methods of Asaoka et al. (1994) and Kodaka et al. (1995) to consider the strength of the reinforcement and the adhesion strength between the reinforcement and the ground. Bearing capacity analyses of shallow foundations are conducted as numerical experiments to demonstrate the characteristics of the proposed method.
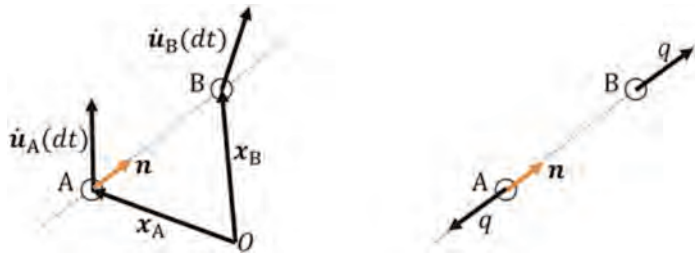
Figure 1.   Concept of "no-length change condition" (Asaoka et al. 1994; Kodaka et al. 1995).
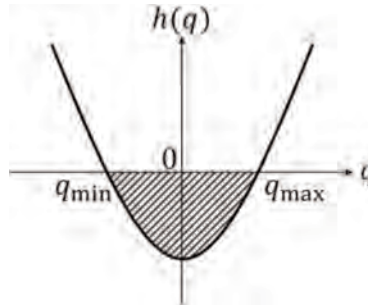
Figure 2.   Inequality constraint condition of the confining force by reinforcement strength.

2   FORMULATION OF REINFORCED SOIL PROBLEMS BY RIGID PLASTIC FINITE ELEMENT METHOD

2.1   *Modeling of reinforcement member*

Asaoka et al. (1994) and Kodaka et al. (1995) proposed linear constraint conditions (invariant length between two nodes of the ground mesh in contact with the reinforcement members) to express the deformation constraint effect of reinforcement members such as anchors and geotextiles. It is called the "no-length change condition".

Figure 1 shows the concept of "no-length change condition". If we ignore the geometric nonlinearity and linearly approximate the ``no-length change condition" between node A and node B, we can derive the condition that the elongation velocity between AB is zero.

$$\boldsymbol{n} \cdot (\dot{\boldsymbol{u}}_B - \dot{\boldsymbol{u}}_A) = 0, \quad \boldsymbol{n} = (\boldsymbol{x}_B - \boldsymbol{x}_A)/|\boldsymbol{x}_B - \boldsymbol{x}_A| \tag{1}$$

where $\boldsymbol{n}$ is the unit vector in the AB direction. $\dot{\boldsymbol{u}}_A$ and $\dot{\boldsymbol{u}}_B$ are the nodal displacement velocities corresponding to node A and node B, respectively.

When the above constraint conditions are imposed on multiple two-node pairs in a three-dimensional ground mesh, Eq. (1) can be transformed and summarized in the following expression.

$$\boldsymbol{D}_r \dot{\boldsymbol{u}}_N = 0 \tag{2}$$

where $\boldsymbol{D}_r$ is a $n_r \times 3n_n$ matrix. n_r and n_n are the number of no-length change conditions and nodes, respectively. $\dot{\boldsymbol{u}}_N$ is a vector that summarizes all nodal displacement velocity fields.

According to the duality of the problem, the confining forces q act to maintain "no-length change condition". The positive direction of the confining force q is shown in Figure 1.

$$\boldsymbol{D}_r^T \boldsymbol{q} = \boldsymbol{f}_r \tag{3}$$

where $\boldsymbol{q}$ is a vector that summarizes all confining forces.

2.2 Modeling of reinforcement strength

To treat a finite reinforcement strength, the following inequality constraints on the confining force are introduced.

$$q_{min} \le q \le q_{max} \tag{4}$$
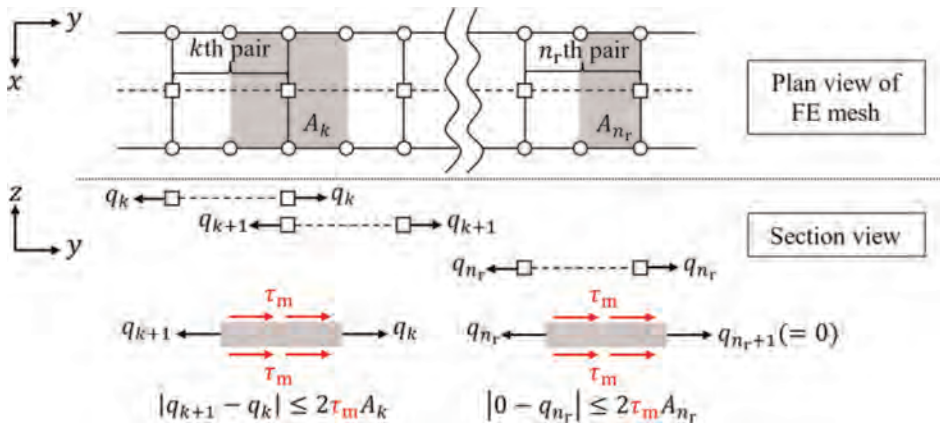
Figure 3. Concept of sticking/slipping interaction between reinforcement members and surrounding soils.

Note in Figure 1 that q_{max} corresponds to the absolute value of the reinforcement strength in the compression direction q_c, and q_{min} corresponds to the absolute value of the reinforcement strength in the tensile direction q_t multiplied by the negative sign.

For notational simplicity, Eq. (4) is expressed in the following form using the convex function $h(q)$ as shown in Figure 2.

$$h_k(q_k) \le 0, \quad k = 1, \cdots, \quad n_r \tag{5}$$

where the lower subscription denotes the kth two-node pair.

2.3 Modeling of sticking/slipping interaction between reinforcement members and surrounding soils

In this study, a novel modelling of a stick/slip interaction between reinforcement members and surrounding soils is proposed as shown in Figure 3. It should be noted that the proposed model can be embedded in a ground mesh, i.e., the deformation constraints by the reinforcement members can be expressed as confining forces acting on the nodes of the ground mesh.

It is assumed that the uniform plane strain behavior of reinforcement member in the x direction. 20-noded hexahedral elements per depth are used in this study as shown in the plan view.

A change in confining forces between adjacent two segments $(q_{k+1} - q_k)$ is related to share stress τ_{m}. $|q_{k+1} - q_k| = 2\tau_{\mathrm{m}}A_k$ is satisfied because the shear resistance force acts on both sides of the reinforcement member. Where A_k is a representative cross-section.

The maximum difference between the confining forces is defined as the adhesion strength, s. In the case of clayey soil, it can be assumed that the adhesion strength per side, i.e., $s/2$ is related to the cohesion c and the contact area A. The reduction parameter $w(0 \leq w \leq 1)$ reflects the bounding condition of the interface between the ground and the reinforcement member; $w = 0$ for a perfectly smooth case and $w = 1$ is for a perfectly rough one. Thus, the following equation can be derived.

$$s/2 = wcA, \quad 0 \leq w \leq 1 \tag{6}$$

Therefore, $|q_{k+1} - q_k|$ and adhesion strength s_k satisfies the following inequality constraints:

$$2\tau_{\mathrm{m}}A_k = |q_{k+1} - q_k| \leq s_k, \quad k = 1, \cdots, \quad n_{\mathrm{r}} - 1 \tag{7a}$$

$$2\tau_{\mathrm{m}}A_0 = |q_1 - q_0| \leq s_0 \tag{7b}$$

$$2\tau_{\mathrm{m}}A_{n_{\mathrm{r}}} = |q_{n_{\mathrm{r}}+1} - q_{n_{\mathrm{r}}}| \leq s_{n_{\mathrm{r}}} \tag{7c}$$

where $k = 0$ and n_{r} means the edge of the reinforcement member. When q_0 or $q_{n_{\mathrm{r}}}$ is zero, the constraint condition corresponds to the free-edge condition. When q_0 or $q_{n_{\mathrm{r}}}$ is unconstrained, the constraint condition corresponds to the fix-edge condition. If the equality holds in Eq. (7), the slippage between the reinforcement member and the ground occurs.

The deformation constraint conditions considering the interaction force model are summarized and expressed in the following form:

$$g_k(\boldsymbol{q}) \leq 0, \quad k = 0, \cdots, \quad n_{\mathrm{r}} \tag{8}$$

2.4 Lagrangian of reinforced soil problems based on the lower bound theorem

The lower bound theorem is to maximize a load factor α under satisfying the equilibrium equation and failure criterion. The Lagrangian for reinforced soil problems based on the lower bound theorem is expressed as follows:

$$L = \begin{cases} \alpha + \boldsymbol{\mu} \cdot (\boldsymbol{B}^T\boldsymbol{\sigma} - \alpha\Gamma_0 - \Gamma_{\mathrm{c}} - \boldsymbol{D}_{\mathrm{d}}^T\boldsymbol{p} - \boldsymbol{D}_{\mathrm{r}}^T\boldsymbol{q}) - \boldsymbol{\lambda} \cdot \boldsymbol{f}(\boldsymbol{\sigma}) \\ -\sum\limits_{k=1}^{n_{\mathrm{r}}} \omega_k h_k(q_k) - \sum\limits_{k=0}^{n_{\mathrm{r}}} \psi_k g_k(\boldsymbol{q}) \quad (\boldsymbol{\lambda} \geq \boldsymbol{0}, \quad \omega_k, \quad \psi_k \geq 0) \\ +\infty \quad \text{(otherwise)} \end{cases} \tag{9}$$

where variables $\boldsymbol{\mu}$, $\boldsymbol{\lambda}$, ω_k and ψ_k are Lagrangian multipliers. The physical meaning of the right-hand side of Eq. (9) is as follows. The first term shows a load factor α. The second term is an equilibrium equation where $\boldsymbol{\sigma}$ are stresses at the integration points, Γ_0 is a reference load, Γ_{c} is a constant load such as body force, $\boldsymbol{p}$ are nodal forces on the Dirichlet boundaries. The third term is a failure criterion where $\boldsymbol{f}$ are yield function at the integration points. The fourth term is an inequality constraint condition of reinforcement strength. The fifth term is an inequality constraint condition of the interaction of reinforcement members and surrounding soils.

2.5 *Karush-Kuhn-Tucker conditions (KKT conditions)*

The following Karush-Kuhn-Tucker conditions (KKT conditions) are obtained from the Lagrangian (Eq. (9)).

$$\text{Equilibrium}: \quad \boldsymbol{B}^T\boldsymbol{\sigma} = \alpha\Gamma_0 + \Gamma_c + \boldsymbol{D}_d^T\boldsymbol{p} + \boldsymbol{D}_r^T\boldsymbol{q} \tag{10a}$$

$$\text{External work rate}: \quad 1 - \boldsymbol{\mu}\cdot\Gamma_0 = 0 \tag{10b}$$

$$\text{Dirichlet boundary}: \quad \boldsymbol{D}_d\boldsymbol{\mu} = \boldsymbol{0} \tag{10c}$$

$$\text{Flow rule}: \quad \boldsymbol{B}\boldsymbol{\mu} = \left(\frac{\partial f}{\partial\sigma}\right)^T\lambda \tag{10d}$$

$$\text{Complementarity}: \quad \lambda\cdot f(\sigma) = 0, \quad \lambda \geq \boldsymbol{0}, \quad f(\sigma) \leq \boldsymbol{0} \tag{10e}$$

In addition, the following terms regarding the deformation constraint conditions hold for all constraints k.

$$\text{Nodal velocities of ground mesh}: \quad (\boldsymbol{D}_r\boldsymbol{\mu})_k = -\omega_k\frac{\partial h_k(q_k)}{\partial q} - \psi_k\frac{\partial g_k(q_k)}{\partial q} \tag{10f}$$

$$\text{Complementarity}: \quad \omega_k h_k(q_k) = 0, \quad \omega_k \geq 0, \quad h_k(q_k) \leq 0 \tag{10g}$$

$$\text{Complementarity}: \quad \psi_k g_k(\boldsymbol{q}) = 0, \quad \psi_k \geq 0, \quad g_k(\boldsymbol{q}) \leq 0 \tag{10h}$$

In this paper, we used the commercial optimization solver "Gurobi Optimizer" to solve Eq. (9) as a primal problem.

3 NUMERICAL EXAMPLES

3.1 *Bearing capacity of footing on reinforced soil*

A series of bearing capacity analyses on weightless c, $\phi = 0$ soils were conducted to demonstrate the proposed method. The von-Mises model was used as the failure criterion for the geomaterial, and the inequality constraint $I_1 \leq 0$ was imposed on the first invariant I_1 of the stress tensor to express the tension cut-off (Yamakuri et al. 2020).

Figure 4 shows a 3D FE mesh (number of nodes:18,687 and number of elements: 2,592) and boundary conditions. A rigid-rough footing was assumed under the plane strain condition.
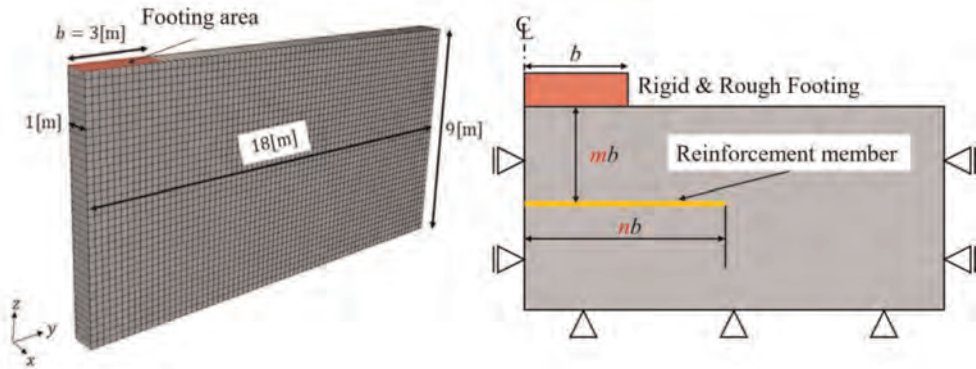
Figure 4.　Finite element mesh and boundary conditions.

(a) Reduction parameter $w = 0.2$ (b) Reduction parameter $w = 0.5$ (c) Reduction parameter $w = 1.0$
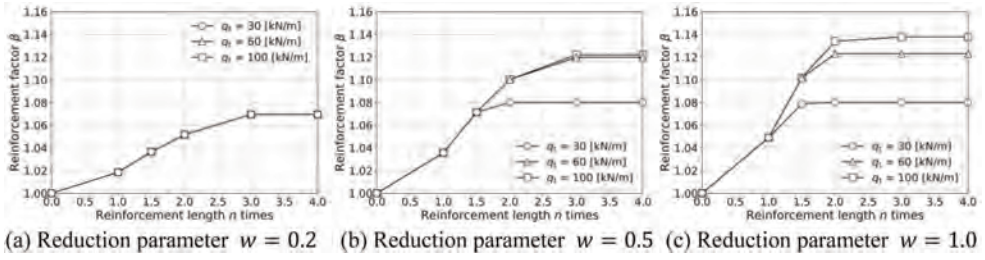
Figure 5. Relation of reinforcement effect β and reinforcement length n (at burial depth $m = 0.5$, with no compressive strength $q_c = 0$ [kN/m]).

The reinforcement member was placed as shown in Figure 4. The reinforcement was assumed to be a geotextile, and the parameters were set as follows. The reinforcement depth m was set to 0.5 and the reinforcement compressive strength q_c was set to 0. The reinforcement length n, reinforcement tensile strength q_t and reduction parameter $w (0 \leq w \leq 1)$ which represents a shear strength of the interface; $w = 0$ is a perfectly smooth case and $w = 1$ is perfectly rough, for example. These parameters were all varied.

To summarize the numerical results, the reinforcement factor β was defined as,

$$\beta = q_u^* / q_u \qquad (11)$$

where q_u^* is an ultimate bearing capacity of reinforced soil and q_u is an ultimate bearing capacity of normal ground.

3.2 Numerical results

Figure 5 shows the numerical results. It can be seen from Figure 5(a) that the reinforcement factor depends on the reinforcement length only and the adhesion strength is dominant. When $w \geq 0.5$, it can be seen from Figure 5(b), (c) that not only the reinforcement length but also reinforcement tensile strength contributes to the reinforcement effect. In any of the reduction parameters, the reinforcement effect converges if the reinforcement length $n \geq 2$. The ultimate bearing capacity increased by up to approximately 14% over that before reinforcement.

Figure 6 shows the distributions of equivalent plastic strain rate. As shown in Figure 6(a), The obtained failure mechanism of normal ground was in good agreement with the Prandtl's solution. When $w = 0.2$, there is no significant difference between the failure mechanisms of reinforced soil and normal ground. On the other hand, when $w = 1.0$, the failure zone is expanded more than that of $w = 0.2$ and contributes to the bearing capacity.

The difference in ultimate bearing capacity due to the reinforcement condition is not so significant, and the reinforcement effect β is at most 1.14.

(a) Reduction parameter $w = 0.2$ (b) Reduction parameter $w = 0.5$ (c) Reduction parameter $w = 1.0$
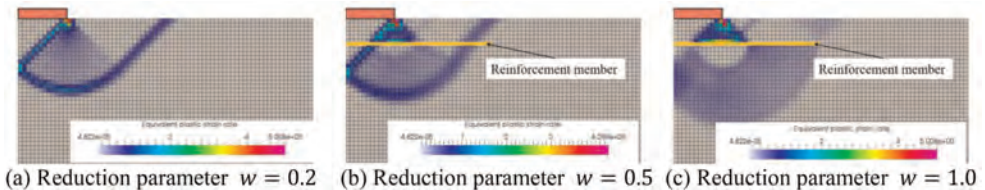
Figure 6. Distribution of equivalent plastic strain rate (with length $n = 3$ at burial depth $m = 0.5$, with no compressive strength $q_c = 0$ [kN/m] and finite tensile strength $q_t = 100$ [kN/m]).

This is because the target ground is a c, $\phi = 0$ soil (i.e., clayey soil). However, it was found that the failure mechanism occurring in the ground varied greatly depending on adhesion strength.

4 CONCLUSIONS

A mathematical framework of rigid-plastic finite element method with finite strengths of reinforcement members and bonding between reinforcement members and surrounding soils is presented and discussed in this article. By using the duality of the limit theorems, no-length change constraint condition can be extended to more general cases of one-directional resistant (tensile only) reinforcement or finite / anisotropic strength of reinforcement members. To be specific, the authors have proposed a new Lagrangian function by introducing inequality constraints of Lagrangian multipliers corresponding to deformation constraints. A similar approach can be used for a sticking/slipping interaction between reinforcement members and surrounding soils. It should be noted that this modeling requires no specific meshing of reinforcement members and only FE mesh of a ground is necessary.

A series of numerical analysis for the bearing capacity of a shallow footing resting on reinforced ground was conducted to demonstrate the ability of the proposed method. Besides the influences of geometry, such as length and burial depth of reinforcement members, the influences of strengths of reinforcement members and interfaces between reinforcements and soils on the bearing capacity are observed in the numerical results. Failure mechanism is also greatly affected by the geometry and strengths. From the practical point of view, this modelling can express behaviors of sheet-like reinforcement members with no compressive strength and pull-out of reinforcement members.

REFERENCES

Asaoka, A., Kodaka, T., & Pokharel, G. 1994. Stability Analysis of Reinforced Soil Structures using Rigid Plastic Finite Element Method. *Soils and Foundations* 34(1), 107–118.

Gurobi Optimization, LCC. 2022. Gurobi Optimizer Reference Manual., https://www.gurobi.com/doc-umentation/9.5/refman/index.html.

Kobayashi, S. I. 2005. Hybrid Type Rigid Plastic Finite Element Analysis for Bearing Capacity Characteristics of Surface Uniform Loading. *Soils and Foundations* 45(2), 17–27.

Kodaka, T., Asaoka, A., & Pokharel, G. 1995. Model Tests and Theoretical Analysis of Reinforced Soil Slopes with Facing Panels. *Soils and Foundations* 35(1), 133–145.

Otani, J., Ochiai, H., & Yamamoto, K. 1998. Bearing Capacity Analysis of Reinforced Foundations on Cohesive Soil. *Geotextiles and Geomembranes* 16(4), 195–206.

Yamakuri, Y., Kobayashi, S. I., Saito, J. 2020. The Influence of Tensile Strength of Soils on the Bearing Capacity Analysis by Rigid Plastic Finite Element Method, *Journal of Japan Society of Civil Engineers, Ser. A2 (Applied Mechanics)*, 76(2), I 225–I 236 (in Japanese).

Use of bi-modulus geosynthetics for the reinforcement of cohesive backfill on cavities

M. Delli Carpini
Afitexinov, France

F. Emeriault & P. Villard
Université Grenoble Alpes, France

M. Riot
Afitexinov, France

L. Briançon
INSA, Lyon

P. Delmas
Independent expert

M. Al Heib
INERIS, France

ABSTRACT: The results of an experimental campaign of reinforcement of thin cohesive soil embankments in the case of cavity collapse are presented. In particular, the aim is to test the effectiveness of a new type of bi-stiffness geosynthetic. A coupled DEM-FEM numerical model is validated based on these results and allows a better understanding of the soil-geosynthetic interaction phenomena mobilized during the collapse. Comparison between the numerical and experimental results obtained with the two types of reinforcement (mono-stiffness and reversed bi-modulus) make it possible to underline the interest of the innovative product developed.

1 INTRODUCTION

The collapse of an underground cavity represents a major potential risk of ground movements, affecting the safety of the concerned infrastructures as well as people.

In order to limit the risks associated with a collapse of the embankment, a solution of reinforcement of embankments above a cavity by a geosynthetic sheet is generally adopted. During the collapse of the soil surface, the geosynthetic reinforcement is able, by deforming, to transfer the vertical load related to the weight of the collapsed soil and the overloads towards the edges of the cavity, by limiting the surface deflections to acceptable values. Numerous experimental works such as the RAFAEL project (Villard et al. 2022), the GeoInov project (Huckert 2015) and numerical studies (Le Hello 2007; Potts 2007; Pham et al. 2018; Villard et al. 2009) have led to an understanding of the load transfer mechanisms that develop within reinforced granular layers in particular when the tensile behavior of the geosynthetic reinforcement is assumed to be linear elastic and characterized by a single stiffness. On the other hand, knowledge on the load transfer mechanism for cohesive soils is still limited. Based on full-scale experiments, an analytical design formulation has

been proposed for such cohesive soils by Huckert (2015) and has been evaluated and partially validated by Hassoun (2019) through an experimental campaign on a small-scale laboratory setup.

To fill the existing gaps and to complete the current knowledge on the behavior of reinforced embankments made of cohesive soil, an experimental campaign has been conducted in the framework of the REGIC (Reinforcement by Intelligent Geosynthetics over Cavities) research project. The objective is to test innovative reinforcement solutions in the specific case of the reinforcement of a cohesive soil layer. This innovative reinforcement process, patented by the company Afitexinov under the name of "reversed bi-modulus" geosynthetics, ensures that the reinforcement layer has two tensile stiffnesses which are activated one after the other, the first being weaker than the second (unlike the "bi-modulus" for which the first is higher than the second). This new type of "reversed bi-modulus" reinforcement makes it possible to detect the beginning of a rupture of the soil layer (by means of an integrated optic fiber and thanks to the first low stiffness of the geosynthetics) while guaranteeing the same level of safety as a geosynthetic with only one stiffness (thanks to the second high stiffness mobilized after the threshold of deformation necessary to the detection of the movements related to the cavity).

The experiments carried out allowed the analysis of the behavior of the reinforced embankments during the opening of cavities 1 and 2 m in diameter, then during a progressive loading phase until the final collapse of the soil layer on the geosynthetic reinforcement.

In order to analyze the interaction behavior of the geosynthetic sheet (single- or bi-modulus) with the cohesive soil, during the opening of the cavity, the collapse of the soil on the sheet, and the loading phase, a numerical study, complementary to the experiments, using a coupled DEM-FEM numerical model has been conducted. This numerical model has been tested and validated in the case of a classical reinforcement (Delli Carpini et al. 2020).

The aim of this paper is to highlight, through the numerical study, the interest and specificities of the new "reversed bi-modulus" technology and to compare it to the classical solution of the single-stiffness geosynthetic.

2 THE EXPERIMENTAL CAMPAIGN

The experimental campaign, carried out in La Tour-du-Pin (France), consisted in the realization of 3 full scale tests for which backfills 0.5 or 0.75 m thick were implemented. For each test, three cavity openings were tested with a size of 1 m then 2 m in diameter and when the backfill did not reach failure under its own weight, an incremental loading was applied until collapse.

For this type of experimentation, different void generation mechanisms have been used for granular soils. One of the most commonly used techniques is the emptying of a cavity filled with materials. For example, Bridle and Jenner (1997) adopted emptying by sand suction, while in the RAFAEL project (Villard et al. 2002) clay balls were used. Another alternative is to implement inflatable pads or air chambers (Huckert 2015).

In this campaign, the cavity was filled with washed rolled gravel. A trap door device between two chambers allows to drain the aggregates from the upper chamber to the lower chamber and thus to create a cavity under the geosynthetic. In order to obtain a progressive opening, an inner cylinder was also placed in the upper chamber, in order to obtain a first cavity of 1 m in diameter when the central trap door is opened. The cylinder falls into the lower chamber when the four outer hatches are opened to create a cavity of 2 m in diameter.

After the installation of the opening device, the geosynthetic sheet was placed, equipped with backscattering fiber optic sensors that allows a distributed measurement of the deformation on the length of the optical fiber. After the placement of the cohesive soil and before the opening of the cavity, the compaction of the backfill (in 2 layers of 0.25 m) is controlled with a light dynamic penetrometer which allowed to conclude that the compaction is not

homogeneous on the backfill depth H = 0.50 m. Indeed, the surface layer of 0.10 m appeared denser than the rest of the backfill and this for both layers. After the opening of the cavities, the backfill was overloaded with steel plates of 80 kg each, placed on a steel cube 0.5 m in width and 38 kg in weight. The deformations obtained with the optical fiber will be presented when comparing with the numerical results.

2.1 *The materials*

Two coherent soils were used for the realization of the test plots: a sand treated with 1% of lime and a silty soil. Only the tests carried out on the 0.5 m thick treated sand will be presented here.

Preliminary Proctor compaction tests showed that the Proctor Normal optimum is obtained for the following conditions: an optimum water content equal to 16.7% and an optimum dry density γd_OPN of 16.3 kN/m3. In order to complete the characterization of this material which is in unsaturated condition and is loaded in a quick way, three triaxial Unconsolidated - Undrained tests (UU tests) as well as flexural tests were carried out on, following the same procedure as for the preliminary tests. The parameters are summarized in Table 1. These characteristics will be taken into account for the numerical back analysis of the full-scale tests.

Table 1. Treated sand main mechanical properties measured in laboratory tests.

	γ_d (kN/m^3)	w (%)	c_{uu} (kPa)	φ_{uu} (°)	σ_t (kPa)
Limed sand	15	16-18	18.93	34.9	$\sim$ 15

Two cavities were opened for each of the two full scale tests using the lime treated sand: cavity N°1 concerns a reinforcement sheet with reversed bi-modulus behavior, cavity N°2 was opened under a conventional reinforcement sheet (monostiffness). The monostiffness geosynthetic is composed of PVA cords with a breaking strength T = 165 kN/m and a stiffness Jsp = 2395 kN/m in the X direction (production), the non-woven support brings a low stiffness in the perpendicular Y direction (estimated at 30 kN/m). The reversed bi-modulus geosynthetic consists of PVA cords with a breaking strength of 45 kN/m in the weft direction and a breaking strength of 131 kN/m in the production direction. From standardized tensile tests performed on this product, it was determined that, in the reinforcement direction, the reversed bi-modulus geosynthetic has an initial stiffness Jsp_1=750 kN/m up to a threshold strain value of 1.5% (a strain value that allows the detection of cavity-related movements and remains well above the minimum strains that can be detected by fiber optics), and beyond that, a second stiffness Jsp_2= 2500 kN/m up to failure. An anchoring by simple covering of the sheet by the backfill allows the tensioning of the sheet above the cavity.

3 NUMERICAL MODEL

The numerical modelling (Figure 1) is based on the SDEC numerical code (Donzé 1997) that is coupling the Discrete Element Method (DEM) to model the soil and the Finite Element Method (FEM) to represent the reinforcement layer simultaneously. The DEM considers a set of particles interacting at the contact points, which makes it possible to describe the behaviour of soils under large deformations (shear, overturning or global rotation) and their failure by blocks, such as those observed for cohesive soils during the collapse of the soil
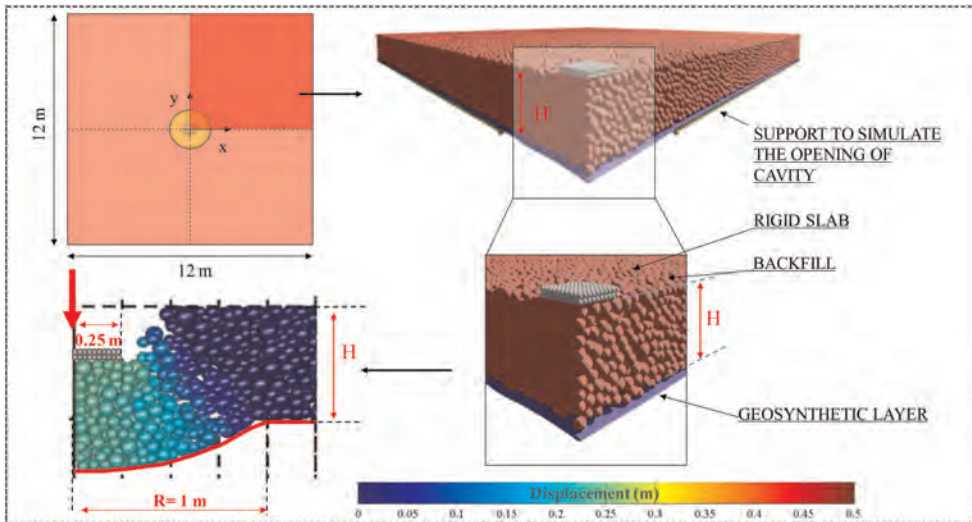
Figure 1. Geometry of the numerical model.

layer on the geosynthetics sheet. The embankment consists of several spheres of different diameters placed in a volume of 6 m x 6 m (boundary conditions with a minimum impact on the behaviour of the part of the backfill close to the cavity) x 0.5 m, corresponding to a quarter of the model for symmetry reasons. To represent the cohesive soil, the soil particles are linked together at their contact points by cohesive bonds (normal and tangential adhesion). The forces between particles are subjected to a Mohr-Coulomb type criterion (Delli Carpini 2021).

The contact micro-parameters that allow to reproduce the macroscopic behavior of the cohesive granular material (cohesion of 19 kPa, internal friction angle of 35° and tensile strength of 15 kPa, as identified by triaxial UU tests and bending tests) are: $c = Tn = 60$ kPa and $\phi = 40°$ (c is the microscopic contact shear resistance, Tn the microscopic contact resistance to traction and ϕ the microscopic contact friction angle). A thin geosynthetic layer, modelled by deformable 3-nodes triangular finite elements and which are assembled together to form a continuous sheet, is positioned below the embankment. The elements of the sheet interact with the soil particles by contact forces defined at the point of contact. The behaviour of the fibre's system is described in details by Delli Carpini (2021).

Some of the spheres in the support are moved downwards at a constant speed to create the void under the backfill and to simulate the opening of the cavity. After the cavity is fully opened, a loading procedure is applied by means of a rigid slab consisting of two layers of bounded spheres. Once the slab is in contact with the backfill surface, the actual loading test begins. A uniformly distributed load is progressively applied to the slab until the backfill breaks.

For the geosynthetic, the values of the numerical parameters retained are deduced from the average stiffnesses obtained during tensile tests. Figure 2 shows the good match between the experimental results and the numerical modelling of the tensile tests carried out in the production direction on the single-stiffness geosynthetic sheet (a) and the reversed bi-modulus geosynthetic sheet (b). A tensile stiffness in the perpendicular direction of 30 kN/m was considered for both products. In the absence of experimental friction test results, a friction angle of 30° was used to numerically characterize the soil/geosynthetic interface.

646
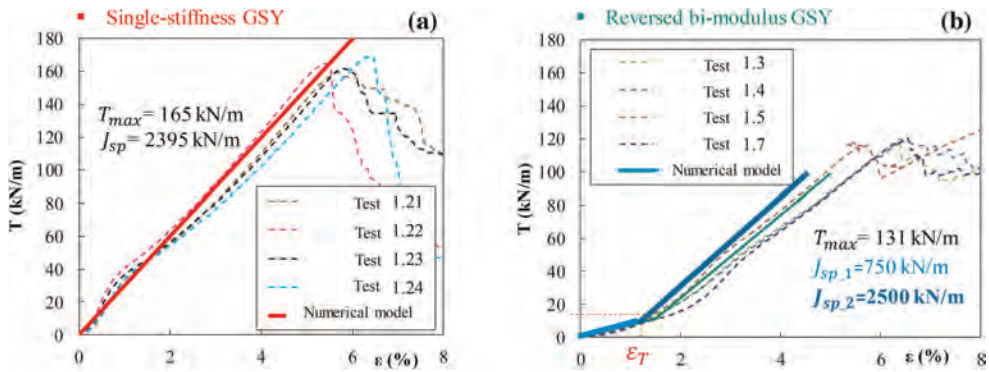
Figure 2. Stress-strain curve of tensile tests performed on single-stiffness (a) and reversed bi-modulus (b) geosynthetic sheets. Comparison with numerical modeling.

4 RESULTS OF COMPARISONS WITH EXPERIMENTAL MEASUREMENTS

A comparison with experimental results available for the 0.5 m backfill made of treated sand is used to test the validity of the numerical model (single-stiffness geosynthetic and reversed bi-modulus geosynthetics).

Several main phases can be highlighted during the test: opening of the cavity, rupture of the soil layer, collapse and stabilization of the cohesive block on the sheet, deformation of the sheet during loading. In this article, we would like to focus our attention on the failure of the cavity to better understand the different behaviour from a single stiffness and a reversed bi-modulus geosynthetics. The analysis of the shape of the collapsed block and the deformations of the geosynthetic layer are important elements that allow the evaluation of the relevance of the numerical model.

For the numerical model, the cohesive soil layer collapses for a loading force of 16 kN for the single-stiffness reinforcement and a loading force of 16.7 kN for the reversed bi-modulus reinforcement. The numerical values obtained for both types of reinforcement are higher than the failure force obtained during the full scale tests: F = 4.30 kN and 12.14 kN for the two tests done. The difference between the values can be attributed to the uncertainties on the real experimental mechanical characteristics of the backfill, related to the non-homogeneous compaction in depth of the soil layer for both tests. However, the shape of the collapsing rigid block of soil is similar between the experimental observation and numerical result, as Figure 3 shows. As it can be seen in Figure 4a, in both cases tested (mono-modulus or reversed bi-modulus geotextiles), the maximal vertical displacements of the reinforcement after collapse of the cohesive soil are rather similar (dn,v = 250 mm approximately).

Figures 4b and c show the deformations of the geosynthetic along the entire length of the model (12 m), during stabilization of the cohesive block on the sheet, after its collapse. The comparison shows in particular that the reversed bi-modulus geosynthetic undergoes a greater maximum deformation than the single-stiffness one, but that it is less stressed in the anchorage zones due to its low initial stiffness. On the other hand, the results obtained at the collapse of the soil layer are very comparable to the experimental measurements. For the single-stiffness reinforcement, the maximum numerical strain value $\varepsilon = 1.5\%$ is close to the experimental value $\varepsilon = 1.46\%$. Similarly, for the reversed bi-modulus reinforcement, the numerical value of deformation ($\varepsilon = 2.07\%$) is comparable to the experimental value ($\varepsilon = 1.96\%$).

Nevertheless, in the anchorage zone, the experimental measurements are bigger than the numerical results. This difference is due to the slippage of the measuring device from the geosynthetics.
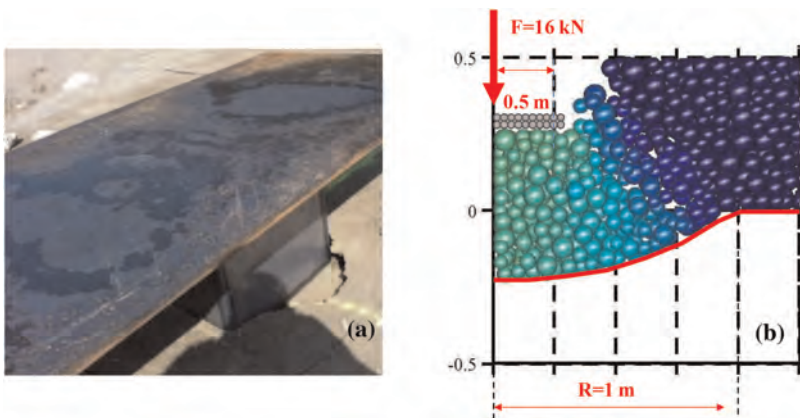
Figure 3. Shape of the collapse soil. Comparison between experimental observation (a) and numerical model (b).
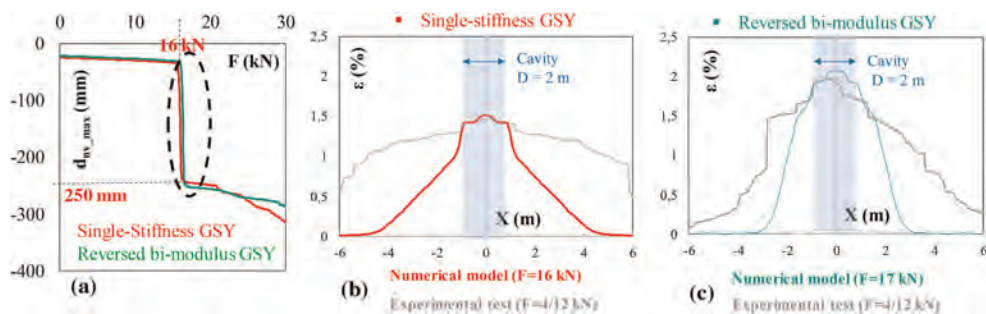
Figure 4. Displacement vs loading force (a), deformation of the geosynthetic at the collapse : (b) single-stiffness model (red curve) and (c) reversed bi-modulus model (green curve).

The numerical model clearly shows the different behaviour of the two types of reinforcement, especially in the anchorage zone, which leads to higher deformation values at the center of the cavity for the reversed bi-modulus geosynthetic, even though similar vertical displacements are obtained for the two products. After collapse of the soil on the sheet, the reversed bi-modulus geosynthetic leads to lower deformation of the sheet. This result confirms that the reversed bi-modulus reinforcement fulfils its function: the large initial deformations activate the warning signal transmitted by the optical fibres inserted in the product, while the high stiffness mobilised later ensures global deflections of the sheet.

5 CONCLUSIONS

The presence of a cavity in the subsoil represents a risk of collapse of the overlying soil that can be reduced by the installation of geosynthetic layer. In this context, different geosynthetic reinforcement products (single stiffness or reversed bi-modulus) associated with cohesive backfills were tested in the framework of the REGIC project. The instrumented reversed bi-modulus geosynthetic allows, in a first step, to activate the warning system based on deformation measurements by optical fibers installed on the sheet as soon as a threshold movement of the ground can be recorded. The second stiffness, much larger than the first

one, allows to contain the deformations and to limit the displacements of the sheet and the soil surface. In spite of the inherent limitations of the experiments and the numerical model used, it can be concluded that qualitatively the numerical model correctly represents the behavior of reinforced cohesive embankments (conventional geosynthetic, single stiffness and reversed bi-modulus geosynthetic). The difference between the two types of reinforcement highlighted during the experimental campaign is also confirmed by the numerical results, i.e. larger deformation values at the center of the cavity for the reversed bi-modulus sheet despite similar vertical displacements for the two products. As expected, the large initial deformations activate the warning signal while the high stiffness mobilized later limits the surface settlements during loading.

On the basis of the observations made, the numerical model, used also by Delli Carpini (2021) for parametric studies, will lead to an improvement of the existing design methods.

REFERENCES

Bridle, R. J., Jenner C. G. 1997. Polymer Geogrids for Bridging Mining Voids. *Geosynthetics International*. ICE Publishing, 4(1), 33–50.

Delli Carpini M., Emeriault F., Briançon L., Villard P., Mengue E., Leguernevel G. 2020. Etude du Comportement des Remblais Cohesifs Renforcés par Géosynthétique. *Journées Nationales de Géotechniques de l'Ingénieur*, 1–8.

Donzé F. V. 1997. Spherical Discrete Element Code. *Discrete E. Universite du Quebec a Montreal*.

Hassoun M. 2019. *Modélisation Physique du Renforcement par Géosynthétique des Remblais Granulaires et Cohésifs sur Cavités*. Thèse de Doctorat. Communité Université Grenoble Alpes.

Huckert A. 2015 *Approche Expérimentale du Dimensionnement d'une Couche de Sol Traité Renforcée Par Géosynthétique sur Cavités Potentielles*. Thèse de Doctorat. Université Grenoble Alpes.

Le Hello B. 2007 *Embankment on Piles Reinforced by Geosynthetic Sheet - True Scale Experimental Study and Numerical Analysis*. Thèse de Doctorat. Université Joseph-Fourier - Grenoble I.

Pham M. T., Briançon L., Dias D., Abdelkader A. 2018. Investigation of Load Transfer Mechanisms in Granular Platforms Reinforced by Geosynthetics Above Cavities. *Geotextiles and Geomembranes*. Elsevier, 46(5), 611–624.

Potts V. 2007 *Geosynthetic Reinforced Fill as a Load Transfer Platform to Bridge Voids*. University of London.

Villard P., Chevalier B., Le Hello B., Combe G. 2009. Coupling between Finite and Discrete Element Methods for the Modelling of Earth Structures Reinforced by Geosynthetic. *Computers and Geotechnics*, 36(5), 709–717.

Villard P., Gourc, J.-P., Blivet J.-C., 2002. Prévention des Risques d'effondrement de Surface Liés à la Présence de Cavités Souterraines: Une Solution de Renforcement par Géosynthétique des Remblais Routiers et Ferroviaires, *Rev. Fr. Geotech.*, 99, 23–34.

Laboratory testing of geosynthetics-reinforced soils under freeze-thaw cycles and mechanical plate loading

M. Huang & C. Lin
University of Victoria, Victoria, British Columbia, Canada

S. Pokharel
Stratum Logics, Acheson, Alberta, Canada

ABSTRACT: As part of an endeavor to develop a laboratory scale device for testing freeze-thaw behaviors of geosynthetics-reinforced soils, this study synthesizes outcomes from a survey of plate loading apparatuses developed in various labs in different countries. The survey specifically investigated the setup of each component, loading mechanism, instrumentation, and materials tested. The functions of the apparatuses and the implications of the test results are examined. The results from the survey were utilized to develop a new model test apparatus capable of performing freeze-thaw and plate loading tests. The apparatus was further upgraded to incorporate a water supply system. The preliminary tests based on the open system were conducted, and the results are discussed.

1 INTRODUCTION

Freeze and thaw action is the major cause of the dysfunction of roads due to expansion of water during freezing and formation of segregated ice lenes as well as the weakening during thawing. In freezing process, the formation of ice lenses is developed as pore water is forced to migrate to freezing fringe under the suction induced by the unidirectional freezing. In thawing process, after the upper frozen layer is thawed, the melted water is trapped in the thawed layer as the water is restrained in the lower frozen layer. The excess pore water pressure weakens the soil interparticle contact, resulting in a markable drop in the strength of base courses and subgrades. Pavements in the seasonal cold area, therefore, are prone to the distress by the traffic loads at the thawed seasons.

To ensure durability of road in cold regions, it is critical to implement varying measures to mitigate freeze-thaw damages. Among the available solutions, geosynthetics stabilization/ reinforcement can improve the freeze-thaw resistance of pavements. Limited field tests (Henry *et al.* 2005; Pokharel *et al.* 2017) indicated that the freeze-thaw performance could be improved when the base courses were stabilized / reinforced by geocells. In contrast to scarcity of field tests, the laboratory model tests on the freeze-thaw behavior of geosynthetics-reinforced bases are even less. This is probably attributed to the limited efforts for developing the model test apparatus. Extensive laboratory model tests, namely plate loading tests, have been widely conducted to investigate geosynthetics-reinforced bases, in which the apparatus consists of a box filled with compacted soils and a loading frame applying static or dynamic loads on soils. However, this apparatus is unable to run freeze-thaw tests.

This paper provides a synthesis of plate loading tests on geosynthetics-reinforced soils without considering freeze-thaw effects. On the basis of this review, a custom-made model test apparatus capable of performing both freeze-thaw and plate loading tests is introduced.

For the freeze-thaw tests, both closed and open systems can be accommodated. The test results based on the closed system have been reported by Huang *et al.* (2021, 2023). Here, the test results in an open system are discussed.

2 REVIEW OF PLATE LOADING TEST APPARATUS

Plate loading tests have been widely conducted to investigate the performance of geosynthetics-reinforced bases, from which static or dynamic responses such as load-movement curves and stress distribution in the soil can be measured. These results can be used to directly quantify the geosynthetics stabilization / reinforcement functions as well as calibrate the design parameters for geosynthetics reinforced bases (Han 2015). Table 1 summarizes the typical features of the plate loading test apparatus reported in literature. It shows that the apparatus in general includes a square box with the side length ranging from 600 to 3000 mm and a circular loading plate with the diameter ranging from 150 to 300 mm. For design purpose, the plate diameter is recommended to be 300 mm to properly simulate the tire contact with pavements (Han 2015). The choice of side length of the box should ensure the minimal boundary effect on the soil responses under plate loading.

Table 1. Summary of plate loading test devices for geosynthetics-reinforced soils.

References	Box dimension (length × width) mm × mm	Plate loading diameter mm	Loading type	Instrumentation
Al-Qadi *et al.* (1994)	3100 × 1800	300	Cyclic	LVDT
DeMerchant *et al.* (2002)	2200 × 3200	305	Static	LVDT
Pokharel *et al.* (2010)	605 × 605	150	Static	Dial gauge
Thakur *et al.* (2012)	2200 × 2000	300	Cyclic	LVDT, pressure cell, strain gauge
Tanyu *et al.* (2013)	3000 × 3000	250	Cyclic	LVDT, strain gauge
Mehrjardi *et al.* (2019)	1200 × 700	80/120/150	Static	Dial gauge

To investigate the mechanical properties of geosynthetics-reinforced bases, the apparatus may come with actuators that can apply static load, dynamic load or both. The static plate loading tests normally follow a quick test procedure. Plate loads are incrementally applied to the test soils and maintained for three to five minutes until the displacement reaches stable. The applied load (or pressure) and the displacement are monitored and the load-displacement curves allow for estimating the stiffness and ultimate bearing pressure of unreinforced and reinforced bases. The stiffness is defined as the slope of the initial portion of the curve (DeMerchant *et al.* 2002; Pokharel *et al.* 2010), and the ultimate bearing pressure is determined as the pressure corresponding to the inflection displacement point before failure (Mehrjardi *et al.* 2019; Pokharel *et al.* 2010).

For the dynamic loading tests, appropriate loading magnitude and frequency as well as waveforms need to be considered to simulate traffic loads. Table 2 shows the loads applied during the plate loading tests. As it is shown in the table, the magnitude ranges 550 to 710 kPa, frequency 0.5 to 1 Hz, and the maximum number of cycles 800 to 1000. During the tests, the cumulative deformation is monitored using displacement sensors such as linear variable displacement transducers (LVDTs). Pressure cells are also placed at the interface of base courses and subgrade to monitor the distributed stress on the subgrade during the cyclic loading, which allows for evaluating the geosynthetic stabilization effect. Sometimes, strain gauges are attached on geosynthetics materials to evaluate the geosynthetic reinforcement effect.

Table 2. Summary of cyclic plate loading in model tests.

References	Applied load kPa	Loading frequency Hz	Maximum loading cycles
Al-Qadi *et al.* (1994)	550	0.50	800
Thakur *et al.* (2012)	550	0.77	100
Tanyu *et al.* (2013)	710	1.00	1000

3 MODEL TESTS ON GEOCELL-REINFORCED SOILS IN AN OPEN SYSTEM

The existing model test apparatuses are designed to investigate the mechanical responses of geosynthetics-reinforced bases in room temperature. Limited model tests are concerned with the mechanical responses of the bases under freeze-thaw cycles. To advance the research in this area, the authors have dedicated to develop a new model test apparatus that can perform freeze-thaw tests and plate loading tests by adapting the existing plate loading model apparatus to incorporating the freeze-thaw function. Some essential features of this new apparatus will be described later in this section, while the details are contained in Huang *et al.* (2021). It is noted that the apparatus only includes the closed system (i.e. no water supply during the freeze-thaw process). This section introduces the apparatus that has been further upgraded to include the open system (i.e. the water supply is provided during the freeze-thaw cycles). Some preliminary results obtained in the open system are also presented.

3.1 *Model test apparatus*

This new model test apparatus consists of a freeze-thaw component, a plate loading component and a rail connecting component (Huang *et al.* 2021). The freeze-thaw component is made up of an aluminum square box with the side of 750 mm, a cooling plate with the dimensions of 745 × 745 mm, thermal insulation foams, and a chiller connecting to the cooling plate. During freeze-thaw process, the cooling plate, placed on the surface of the soils, can freeze or thaw soils by adjusting the coolant temperature in the chiller. To achieve unidirectional top-down freezing process, which is consistent with the natural phenomenon, a thermal sink is created by four aluminum angles which connect box walls and the cooling plate. Box walls serve as the temperature barrier to prevent soils from absorbing ambient heat, so the thickness of the insulation foams could be reduced to 51 mm under the normal environment. In thawing process, four aluminum angles are removed to prevent soils from absorbing excessive heat. Therefore, one-directional freeze and thaw is imposed to the soils. Plate loading tests are conducted right after freeze-thaw tests. The static loading system has a loading plate with the diameter of 150 mm, which is attached to a hydraulic cylinder with the maximum load of 109 kN.

The above features do not include the water supply. The apparatus is therefore upgraded to include a water supply component mounted to the box bottom. A valve is set to control the water ingress and egress during the freeze-thaw processes. The water supply component is the Marriott type tank as shown in Figure 1, which enables setting and fixing the water levels at the source (simulating groundwater level). Scientific Commodities® porous sheets with the thickness of 6.4 mm are placed at the box bottom to distribute water uniformly at the bottom.

3.2 *Test materials and experimental instrumentation*

3.2.1 *Materials*

Geocells used in this study were nano-polymeric alloy (NPA) Type-C geocells manufactured by PRS®. The tensile strength of ribs and seams was both 19 kN/m. The geocell ribs were
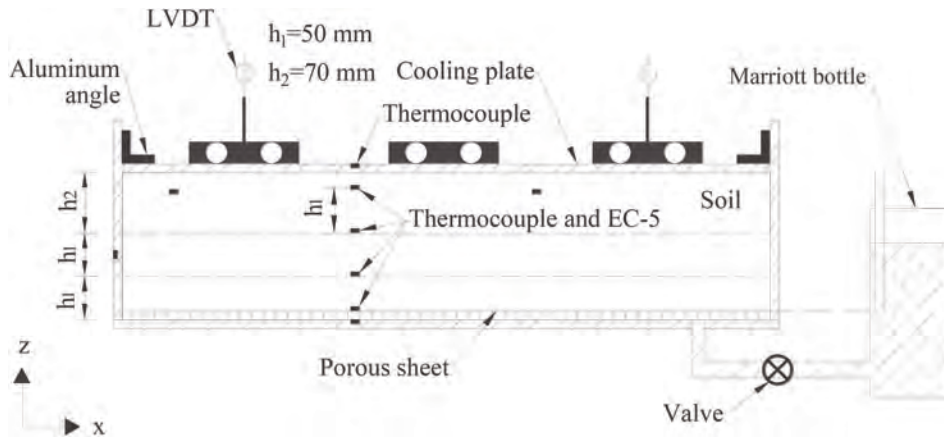
Figure 1. Setup of freeze-thaw system with water supply component and instrumentation plan.

150 mm in height and were perforated. The opening dimension of a single geocell was 245 mm × 210 mm when it was unfolded. The basic properties of this material are presented in Huang *et al.* (2021).

Base courses consisted of a mixture of 95% sand and 5% kaolin. The sands were classified as poorly graded sand (SP) according to the Unified Soil Classification System (USCS) with the specific gravity of 2.7, and the kaolin was commercial EPK kaolin manufactured by Edgar Minerals®. The mixture was thus a poorly graded sand with clay (SP-SC) having the mean particle size (D_{50}) of 0.674 mm with the coefficient of uniformity and curvature of 5.7 and 1.1, respectively. The maximum dry density and the optimum moisture content were determined to be 1970 kg/m^3 and 11.7%, respectively, according to the standard Proctor compaction test (ASTM D698).

3.2.2 *Soil preparation and instrument installation*

Four model tests were performed to investigate the freeze-thaw behavior of geocell-reinforced soils under an open system. In each test, soils were compacted to the maximum dry density and the optimum moisture content per standard Proctor compaction test as described previously. The compaction was carried out in four lifts, with 50 mm for the first three lifts and 20 mm for the last lift. The added mass of soils at each lift of the compaction was calculated by the soil density times the volume of each lift. The target level of compaction degree was achieved by controlling the added mass and the determined thickness of soils. After the complete of the compaction at each lift, the soil surface was scratched to improve the bonding between soil layers and minimize the layered effect in soils. T-type thermocouples were placed on the soil surface immediately after the compaction of each of the first three lifts to monitor the soil temperature during freeze-thaw cycles. T-type thermocouples were also embedded into the box wall, box bottom, top surface of the porous sheet and the cooling plate to monitor the temperature changes at these locations.

After the completion of soil compaction, the soil surface was covered with a plastic sheet to avoid water loss and the valve at the box bottom was switched on to supply water. This circumstance was kept for one night to achieve the hydraulic equilibrium in the soils. The freeze-thaw test was then performed. Figure 2a shows the setup of the freeze-thaw tests on soils. The cooling plate was placed on the soil surface. The box and the cooling plate were wrapped by the insulation foams. In the freezing process, the chiller temperature was set as −20°C. The soils were gradually frozen from the surface to the bottom. When the temperature of the box bottom reached −5°C, the freezing process was terminated. Immediately

Figure 2. Photographs: (a) freeze-thaw tests and (b) plate loading tests.

after that, the valve was switched off and the four aluminum angles were removed. The chiller temperature was then set to 20°C to initiate thawing process. The cooling plate heated soils from the surface to the bottom. When the temperature of the box bottom was 15°C, the thawing process was finished. This concluded one freeze-thaw cycle. The above procedure was repeated until the predefined freeze-thaw cycles were reached. During the freeze-thaw tests, National Instruments® datalogger was used to record the readings of T-type thermocouples and LVDTs every 30 minutes. The accuracy of T-type thermocouple and LVDT was 1°C and 0.01 mm, respectively. The four model tests included zero and five freeze-thaw cycles for unreinforced bases and zero and four freeze-thaw cycles for reinforced bases.

Static plate loading tests as shown in Figure 2b were conducted after the freeze-thaw cycles. The circular plate fixed to a load cell was placed at the center of the soil surface. The load exerted by the hydraulic cylinder was measured by the load cell and recorded by the datalogger PASCO® 550 Universal Interface. Load was applied in an increment of 62 kPa on the soils and maintained for five minutes. The incremental pressure was applied until the soil failed and then it was unloaded to zero. During the loading-unloading process, the plate movement was monitored using three dial gauges mounted on the plate perimeter at an angular spacing of spaced 120°. The accuracy of the load cell and dial gauge was 1 kPa and 0.025 mm, respectively.

3.3 Test results

Since the model apparatus was upgraded recently, only limited freeze-thaw tests were conducted. Here, the preliminary results are reported, including soil heave / settlement during freeze-thaw cycles and mechanical load-movement curves during plate loading tests.

3.3.1 Evolution of soil movement during freeze-thaw cycles

Figures 3a-b present the evolution of the soil movement in unreinforced and reinforced bases during freeze-thaw cycles. Included in the figures are the time histories of temperature in the cooling plate, soils, and the box bottom. The data of soil movement (e.g. heave) and soil temperature were the averaged readings of LVDTs and T-type thermocouples, respectively. The plateau of soil movement was achieved when the box bottom temperature reached $-5°C$ in the freezing process and 15°C in the thawing process. The maximum soil movement and the difference between two plateaus within the same freeze-thaw cycle were the peak heave and thaw settlement.

Figures 3c-d present variations of peak heave and thaw settlement with freeze-thaw cycles. They experienced the largest increase at the 2nd freeze-thaw cycle in both the
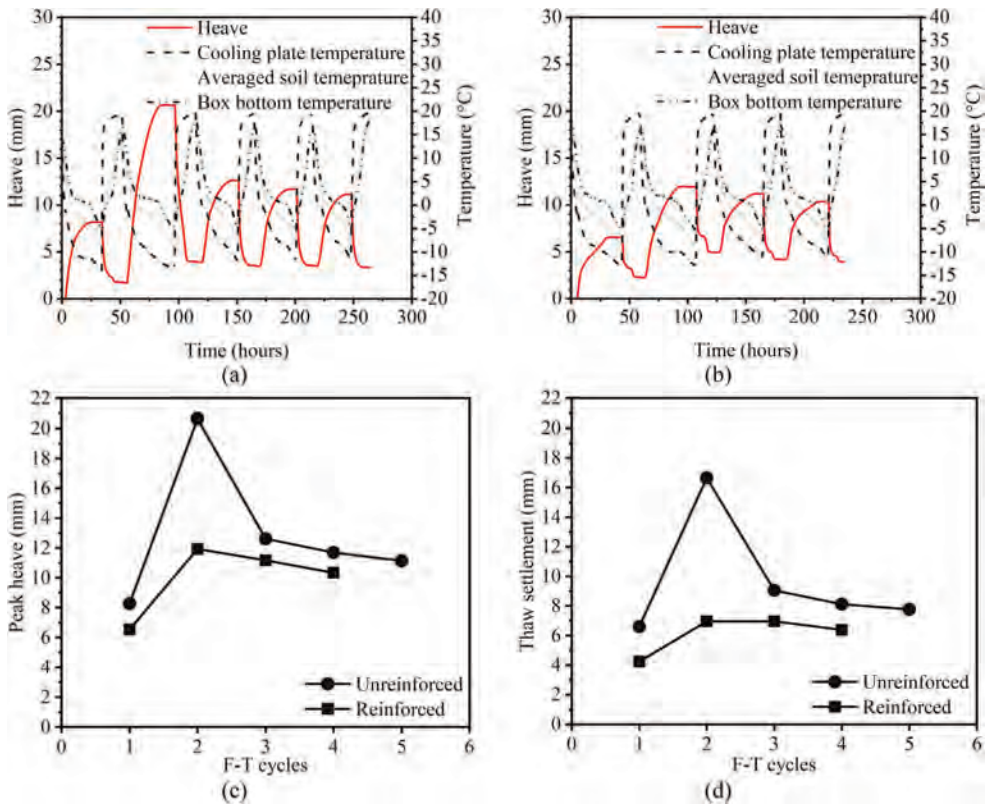
Figure 3. (a) Evolution of soil movement and temperature in unreinforced soils, (b) evolution of soil movement and temperature in reinforced soils, (c) peak heave and (d) thaw settlement.

unreinforced and reinforced soils, followed by a slight decrease for reinforced base but a drastic decrease for unreinforced bases in the further freeze-thaw cycles. The inclusion of geocell significantly reduced the soil heave by 42% and the thaw settlement 42% and 58%, respectively after one freeze-thaw cycle. After four freeze-thaw cycles, the peak heave and thaw settlement were reduced by 12% and 21%, respectively, due to the geocell reinforcement.

3.3.2 *Plate loading test results*

The plate loading tests were performed right after the freeze-thaw cycles. Figure 4 shows the pressure-displacement curves of the unreinforced and reinforced soils after the freeze-thaw cycles.

It is evident that the freeze-thaw effect significantly reduced the mechanical properties of both unreinforced and reinforced bases. After five freeze-thaw cycles, the stiffness and ultimate bearing pressure of the unreinforced bases were decreased by 82% and 88%, respectively. The corresponding values of reinforced soils were 88% and 90%. Figure 4 confirms that the effectiveness of geocell stabilization and reinforcement in improving the mechanical properties. The geocell increased the stiffness and ultimate bearing pressure by 148% and 117%, respectively without freeze-thaw cycles. The comparison of the results after freeze-thaw cycles is not possible as the reinforced bases experienced one cycle less than the unreinforced bases.

655
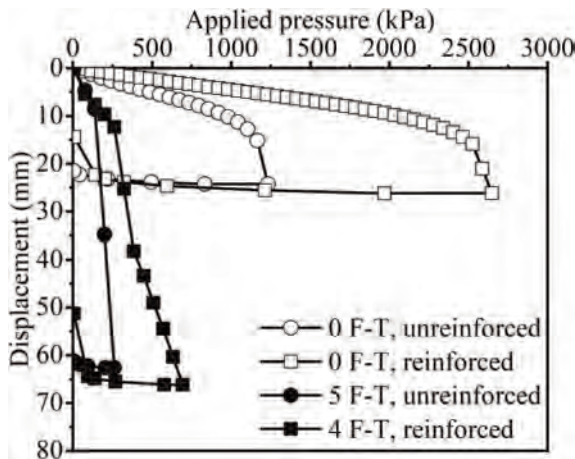
Figure 4. Load-movement curves for unreinforced and reinforced bases.

4 CONCLUSIONS

This paper presents a survey of existing plate loading test apparatuses on geosynthetics-reinforced soils. A customized model test apparatus capable of performing freeze-thaw and plate loading tests has been developed. This study further improves the apparatus to include the water supply system, and with this upgraded apparatus, some preliminary tests using the open system were conducted. The following conclusions are draw from this study:

(1) The largest peak heave and thaw settlement occurred at the second freeze-thaw cycle in both unreinforced and reinforced bases in the open system.
(2) The inclusion of geocells reduced the peak heave and thaw settlement by 42% and 58% after the second freeze-thaw cycle. After four freeze-thaw cycles, the reduction due to geocell reinforcement was lowered to 12% and 21%.
(3) The geocell reinforcement could improve the stiffness and ultimate bearing pressure by 148% and 117% respectively without freeze-thaw cycles.
(4) The unexpected early termination of freeze-thaw cycles for the reinforced bases rendered the comparison of plate loading test results between reinforced and unreinforced bases impossible at this stage. More open system tests for comparable freeze-thaw cycles will be performed in the future.

REFERENCES

Al-Qadi, I.L., Brandon, T.L., Valentine, R.J. & Lacina, B.A., Smith, T.E. 1994. Laboratory Evaluation of Geosynthetic-reinforced Pavement Sections. *Transportation Research Record* (1439): 25–31.
DeMerchant, M.R., Valsangkar, A.J. & Schriver, A.B. 2002. Plate Load Tests on Geogrid-reinforced Expanded Shale Lightweight Aggregate. *Geotextiles and Geomembranes* 20(3): 173–190.
Han, J. 2015. *Principles and Practice of Ground Improvement*. Hoboken: John Wiley & Sons.
Henry, K.S., Olson, J.P., Farrington, S.P. & Lens, J. 2005. *Improved Performance of Unpaved Roads During Spring Thaw*. Research Report, US Army Corps of Engineers, Engineer Research and Development Center.
Huang, M., Lin, C. & Pokharel, S. 2023. Freeze-Thaw Behavior of Geocell-Reinforced Bases Considering Different Fines Contents. *Geosynthetics International*: 1–18.
Huang, M., Lin, C., Pokharel, S., Tura, A. & Mukhopadhyaya, P. 2021. Model Tests of Freeze-Thaw Behavior of Geocell-Reinforced Soils. *Geotextiles and Geomembranes* 49(3): 669–687.

Mehrjardi, G.T., Behrad, R. & Tafreshi, S.M. 2019. Scale Effect on the Behavior of Geocell-reinforced soil. *Geotextiles and Geomembranes* 47(2): 154–163.

Pokharel, S., Han, J., Leshchinsky, D., Parsons, R.L. & Halahmi, I. 2010. Investigation of Factors Influencing Behavior of Single Geocell-reinforced Bases Under Static Loading. *Geotextiles and Geomembranes* 28(6): 570–578.

Pokharel, S., Norouzi, M. & Breault, M. 2017. New Advances in Novel Polymeric Alloy Geocell-Reinforced Base Course for Paved Roads. *2017 Conference of The Transportation Association of Canada*, 24–27 September 2017. St. John's, Newfoundland, Canada: 1–16.

Tanyu, B.F., Aydilek, A.H., Lau, A.W., Edil, T.B. & Benson, C.H. 2013. Laboratory Evaluation of geocell-reinforced Gravel Subbase Over Poor Subgrades. *Geosynthetics International* 20(2): 47–61.

Thakur, J.K., Han, J., Pokharel, S.K. & Parsons, R.L. 2012. Performance of Geocell-reinforced Recycled Asphalt Pavement (RAP) Bases Over Weak Subgrade under Cyclic Plate Loading. *Geotextiles and Geomembranes* 35: 14–24.

Numerical modeling and evaluation of passive grout-anchors in geotextile bags

D. Stathas, J. Glover, S. Braun-Badertscher & I. Lifa
Institute for Construction in Alpine Regions IBAR, University of Applied Sciences Graubünden, Chur, Switzerland

ABSTRACT: Passive grout-anchors are used in as the foundations of rockfall and avalanche barriers. In regions of high ground porosity, grout losses can increase construction costs and impact the environment negatively. Geotextile bags are applied to control grout losses. However, the complex interactions between geotextile bags, grout, and ground are little understood. This study investigates the behaviour of passive anchors in geotextile bags (PAGB) under tension loads in pull-out laboratory tests. The pull-out tests have been subsequently simulated numerically to provide modelling guidelines for design engineers. In summary, PAGB could provide a sustainable solution to anchoring problems in terrain with high porosity. Geotextile permeability has strong influence on the bonding strength and should be considered for optimal PAGB design. Multiple interfaces can be modelled, with a single interface element, using conventional Mohr-Coulomb models and properties acquired from laboratory pull-out tests.

1 INTRODUCTION

Passive anchors in geotextile bags (PAGB) are applied to foundations in porous terrain for rockfall and avalanche barriers in mountainous terrain. Their intended function is to contain grout around the anchor tendon ensuring full grout coverage and associated corrosion protection. The geotextile bags are installed into a borehole surrounding the steel tendon, spacer and a perforated (>50% shading) metal tube for wall support. The anchor is then filled with grout through an injection tube (Figure 1). On construction projects with high grout losses, anchor boreholes can be impossible to fill leading to high costs through construction delays, material waste and associated negative environmental impact. The use of PAGB is thus a common go-to solution for grout loss during construction projects in porous ground. PAGB solutions are available in a range of different geotextiles with varying properties thought to control grout loss. For example, impermeable elastic geotextile bags that allow the grouted column to mold to borehole topography, especially in voids. While other geotextiles offer more rigid meshed fabrics with sufficient opening to allow grout to bond with the surrounding aggregate. However, the application of PAGB remains unregulated and without a best practice guide.

In the framework of a research project commissioned by the Swiss expert commission for avalanche and rockfall (EKLS), the influence of geotextile bags on anchor pullout strength of anchors was investigated. The performance of common PAGB solutions were assessed through 1) analysis of a pull-out testing database of test anchors from construction projects, 2) a full-scale field experiment, 3) laboratory pull-out experiments and 4) numerical modelling. The research presented herein focuses on the laboratory and numerical investigations. An overview of the geotextile bags investigated are presented in Table 1.
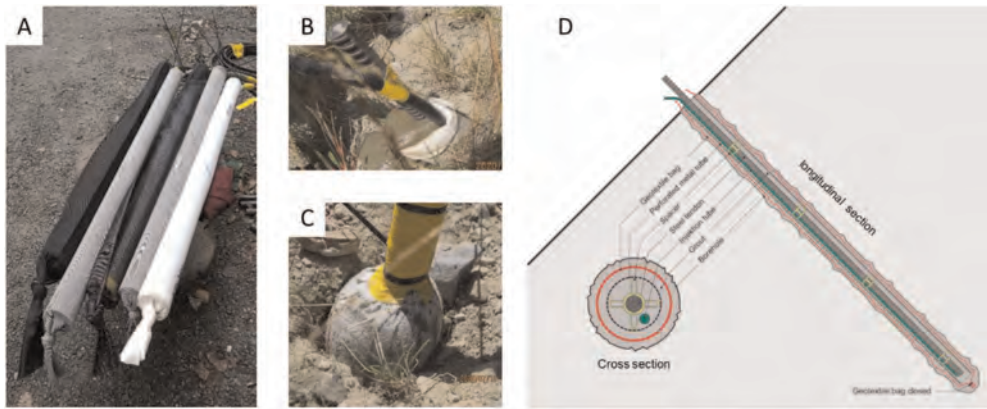
Figure 1. A) Different types of PAGB before installation B) PAGB after installation during grouting C) PAGB after installation and grouting D) PAGB components.

Table 1. Geotextile bags basic properties and description.

Bag ID	Mass [g/m^2]	Opening Size* [mm]	Strength MD/CMD** [kN/m]	Elongation at break MD/ CMD** [%]	Water Perme-ability* [l/m^{2}s]	Geotextile Bag description
A	222	0.20	33/28	33/20	96	woven geotextile / MD mono-filaments (PE) / CMD multifila-ments (PP)
B	900	n.a.***	34/7	74/181	111	knitted polyacryl fabric / multifilaments in both direc-tions (seamless)
C	228	n.a.***	7/2	106/196	102	seamless knitwear unknown fibres
D	166	n.a***	12/12	54/54	51	nonwoven geotextile (PP) sta-ple fibres
E	258	1.15	24/27	24/30	234	woven geogrid / MD and CMD PET multifilaments / PVC coating
F	145	0.55	21/26	41/20	207	woven geotextile / MD monofilaments (PE) / CMD tapes (PP)

*Average values.
**MD: Machine direction / CMD: Cross machine direction.
***n.a.: not applicable, practical impermeable for the grout used in the current study (d$_{max}$ = 0.9mm).

2 ANCHOR PULL-OUT TESTING

The laboratory pull-out experiments were designed to determine the bond strength of PAGBs within a porous ∅ 8 – 32 mm gravel. The test cylinder arrangement consisted of a 0.5 m DN400 pipe section containing a 400 mm aggregate layer in which a 115 mm hole-space was formed and PAGB samples including anchor tendon grouted (Grout maximal grain size d$_{max}$ = 0.9mm) to a depth of 0.4 m. A covering 370 mm ring plate with inner diameter D$_i$ = 150 mm and 100 mm thickness was placed on the aggregate surface (Figures 2 & 3).

The test model was then placed in a universal testing machine and bespoke testing frame to exert the resultant compression load on the ring plate during PAGB anchor pull-out at a rate
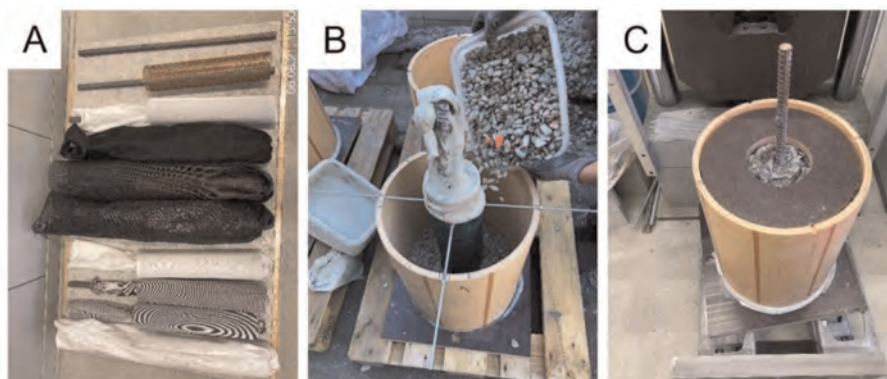
Figure 2. A) samples with anchor tendon and geotextile bag prepared for grouting, B) preparation of the gravel layer and hole-space, C) application of the ring plate.
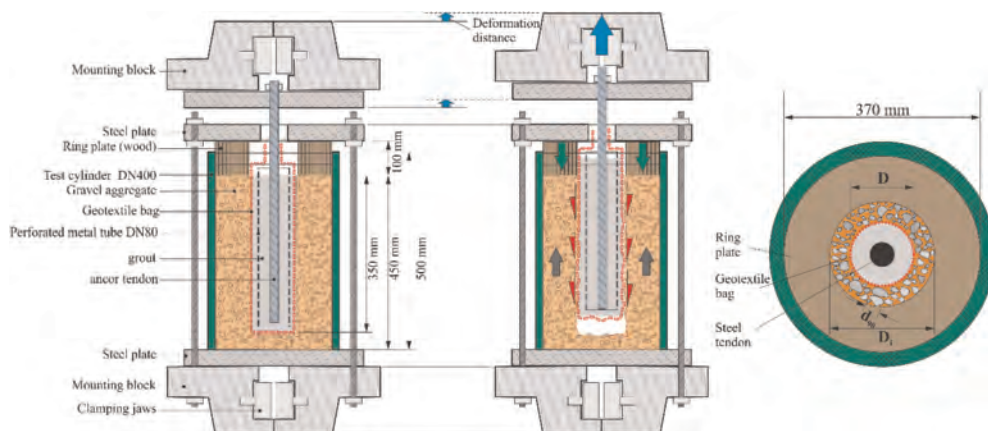
Figure 3. Schematic test configuration showing the PAGB sample grouted in the test cylinder gravel and set in the UTM test frame indicating pull-out kinematics.

of 0.1 kN/s. The ring plate forces the anchor to shear along the grouted anchor column and aggregate interface, testing bond strength (Figure 3). And thus excludes the surrounding aggregate as principal determinant of pull-out resistance. Force deformation curves of the PAGBs are used to develop a FE model of the experiments. A comparative plot of results from the pull-out experiments and numerical modelling are presented in the following section.

3 NUMERICAL MODELING

3.1 Introduction

Finite element (FE) models are applied in research and practice to design grouted anchor systems and estimate their pull-out resistance and displacements (O'Kelly B.C. *et al.* 2014; Zhou W.H. *et al.* 2011). A reliable simulation is based on verifiable modeling parameters. In practice simple models are required to reduce the problem complexity and computation effort. The modeling approach applied in this study to simulate the pull-out behavior of a PAGB uses common material models and the practice-oriented FE Software Optum G2

(Krabbenhøft K. *et al.* 2016). Optum G2 is a commercial FE software for geotechnical studies (Oberhollenzer S. *et al.* 2018; Stathas *et al.* 2021). The feature of axis-symmetry analysis was used to simplify the three-dimensional case of PAGB and solve it in a two-dimensional (2D) FE environment. The PAGB and aggregate contact surface was simulated with an interface feature using Mohr-Coulomb material model properties and associated flow rule which is commonly applied in practice. Data from the laboratory tests described in the previous chapter, were used to determine input material parameters of the FEM model, such as the bonding force τ_A [kN/m^2] and Elasticity modulus of the PAGB interface. Following chapters present the definition of material parameters, FEM analysis and comparison with the data acquired from the laboratory tests.

3.2 *Finite element model of pull-out test*

3.2.1 *Test cylinder and gravel*

The geometry of the test cylinder was replicated based on scan data from the pull-out specimens and adjusted for axis-symmetry analysis to the FE model. Figure 4 shows the dimensions and fixations of the FE Model. The test cylinder was modelled as a rigid material by fixing its base in x- and y-direction (radius and height). The ring plate placed on the aggregate surface during the pull-out tests inducing shear along the PAGB-aggregate interface is fixed in y-direction (height) of the FE model constraining upward movement of the aggregate. The PAGB is pulled out through the 150 mm diameter shear hole of the ring plate. The free space (Figure 4) between PAGB and ring plate varies depending on the anchor diameter obtained from scans of the laboratory samples. The aggregate in the test cylinder was modelled as a Mohr-Coulomb material with a friction angle of $\varphi_{Aggr} = 35°$ and modulus of elasticity $E_{Aggr} = 12$ MPa (Loose). The surface between the test cylinder and the gravel was also modelled as a Mohr-Coulomb material with a friction angle of $\varphi_{Aggr/cylinder} = 10°$ (approx. φ_{Aggr} /3). The Unit-weight of the aggregate is 18 kN/m^3.
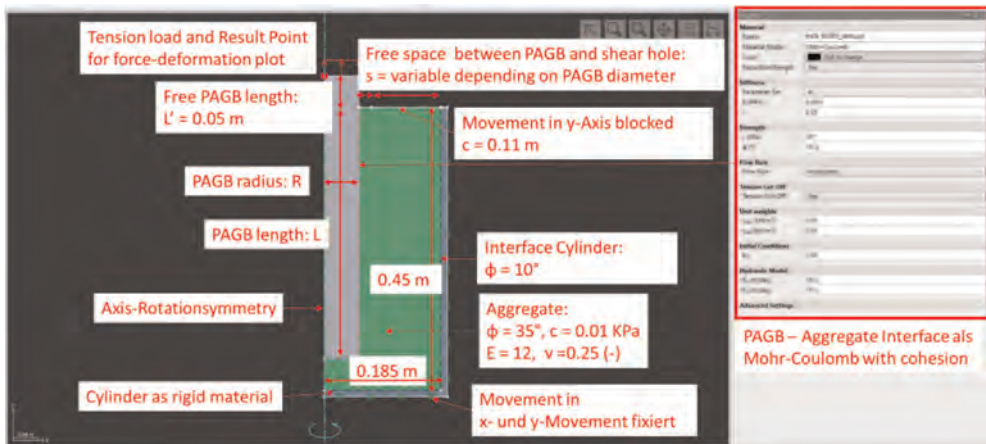
Figure 4.   FE model of pull-out test.

3.2.2 *Pull out anchors*

The PAGB specimens from the laboratory tests were scanned to acquire geometry data. The scan data were used to determine the PAGB dimensions in the FEM Model and in combination with the recorded force-travel data estimate the strength parameters of the Interface MC Model. The steel anchor-grout body of the PAGB was modelled as elastic material with a weight of 25 kN/m^3. The elastic modulus of the PAGB [E_A] can be estimated from the

elastic modulus of grout [E_G: 14,500 MPa] and steel [E_S: 205,000 MPa], and accounts for the deformation compatibility of the two elements, following equation (1):

$$E_A = \frac{E_s \cdot A_S + E_G \cdot A_G}{A_S + A_G} \qquad (1)$$

where E_A = modulus of elasticity anchor system [MPa]; E_S = modulus of elasticity of steel bars [MPa]; E_G = modulus of elasticity mortar [MPa]; A_S = Surface area of steel bar [m²]; A_G = mortar surface [m²].

During the pull-out tests, tensile force and vertical displacement data were recorded. The critical maximum force for PAGB from the Pull-out tests was set for a vertical displacement of 24 mm. This strength value [F_{24}] together with the topographic scan-data were used to calculate the bond strength of the PAGB according to equation (2):

$$\tau_A = \frac{F_{24}}{2 \cdot \pi R \cdot L} \qquad (2)$$

where: τ_A = bonding strength [kN/m²]; F_{24} = maximum pull-out force at 24 mm travel [kN]; R = anchor radius = ½ anchor diameter D [m]; L = anchor length [m].

The anchor-gravel interface was set as a Mohr-Coulomb material with a cohesion equal to the bonding force. The modulus of elasticity was calculated from equation (3) according to Stathas et al. 2021:

$$E_{int.} = \frac{\left[2(1 + v)\frac{t_{FEM}}{\delta} \tau_A \right]}{1000} \qquad (3)$$

where: $E_{int.}$ = E-modulus of the grout-aggregate interface [MPa]; v = Poissons number, here 0.25 [-]; t_{FEM} = interface thickness in FEM, here 1 mm; δ = displacement, here 24 mm; τ_A = bonding strength force anchor [kN/m²]; 1000 = Conversion of E-modulus units from kPa to MPa. Table 2 summarizes the critical input parameters resp. properties of the numerical PAGB for each geotextile bag.

Table 2. PAGB model parameters for the various geotextile bags.

Geotextile Bag	Radius R [mm]	Length L [m]	E-Modul E_A [MPa]	Max. Pull-out Force F_{24} [kN]	Bonding Strength τ_A [kN/m²]	E-Modul Interface $E_{int.}$ [MPa]
A	55	0.40	20,800	1.75	13	0.0013
B	50	0.40	22,100	10.22	81	0.0085
C	45	0.40	23,900	11.29	100	0.0104
D	55	0.40	20,800	12.95	94	0.0098
E	65	0.45	19,000	37.31	203	0.0211
F	73	0.45	18,400	71.61	347	0.0361

3.3 A multiplier elastoplastic analysis

Multiplier Elastoplastic Analysis is an integrated analysis feature in Optum G2 which allows the calculation of the ultimate load of a system by incremental load increase while computing system deformation at each load step. This type of analysis is suited to the laboratory pull-out tests. Using the "Result Point" feature of OptumG2, force-displacement diagrams were generated for the top of the PAGB and compared with the laboratory tests.

For each geotextile bag a FE Model was created and a multiplier elastoplastic analysis carried out. Figure 5a shows the force-displacement diagram for each geotextile bag with a dashed line. In the same figure, the corresponding laboratory data from the pull-out tests for 10, 20 and 24 mm deformation are shown with continuous lines.

The results from the FE numerical simulation show good agreement with the laboratory tests validating the input model parameters. The numerical simulation also allows an examination of the pull-out test failure mode. The primary shear plane is developed along the PAGB-aggregate interface, while a secondary slip surface is developed starting from the PAGB anchor bottom and reaches the test cylinder wall with some inclination (Figure 5b).

4   SUMMARY AND CONCLUSIONS

In this study different types of geotextile bags were used to prepare short passive anchors and investigate their pull-out performance in laboratory experiments. Subsequently the pull-out tests were simulated numerically using the recorded physical data. From the physical tests and numerical simulations, the following conclusions can be drawn:

- PAGB pull-out strength strongly depends on the bonding strength of the grout column to the surrounding aggregate which is governed by the passage of grout through the geo-textile membrane.
- For grout bags that prevent grout from seeping through the bag membrane and bonding with the aggregate, the pull-out strength is very low.
- The radial pressure and topographic molding of grout columns seen in impermeable grout bags offer insufficient bond strength to obtain reasonable pull-out strengths.
- Geotextile bags that permit sufficient grout to pass through the geotextile membrane and bond to the aggregate, pull-out strengths are higher and can be recommended for use in porous ground.
- PAGB can be modelled numerically using and an interface element following the MC parameters.
- The elasticity modulus and the bonding strength can be estimated from pull-out tests conducted in the laboratory for use with this numerical model.
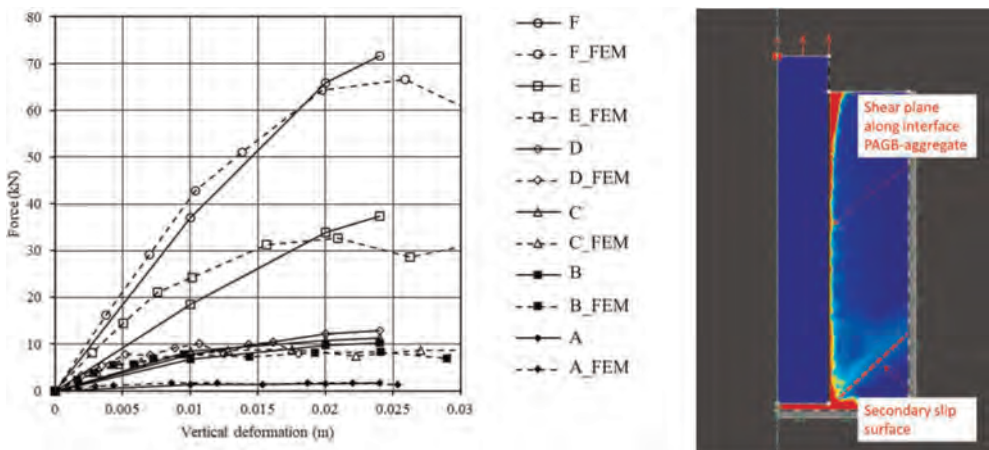
Figure 5.   Force-deformation curves of numerical (dashed lines) and physical (continuous lines) pull-out test (left) and Failure mode of numerical pull-out simulations(right).

REFERENCES

Krabbenhøft, K., Lymain, A.V. & Krabbenhøft, J. 2016. *OptumG2: Theory*. Newcastle, Australia: Optum Computational Engineering.

Lifa, I., Glover, J., Stathas, D., Braun, S., Lucas, D. & Crivelli, P. 2022. *Tragverhalten von Geotextilsäcken bei Ankern im Lawinen- und Steinschlagverbau.*

Oberhollenzer, S., Tschuchnigg, F. & Schweiger, H.F. 2018. Finite Element Analyses of Slope Stability Problems using Non-associated Plasticity. *Journal of Rock Mechanics and Geotechnical Engineering* 10: 1091–1101.

O'Kelly, B.C., Brinkgreveb, R.B.J. & Sivakumar, V. 2014. Pullout Resistance of Granular Anchors in Clay for Undrained Condition. *Soils and Foundations* 54: 1145–1158.

Stathas, D., Wang, J.P. & Ling, H.I. 2021. Behavior of Concave Segmental Soil Retaining Wall Using Porcupine Blocks. *Int. J. Geomech.* 21(8): 04021138

Zhou, W.H., Yin, J.H. & Hong, C.Y. 2011. Finite Element Modelling of Pullout Testing on a Soil Nail in a Pullout Box Under Different Overburden and Grouting Pressures. *Can. Geotech. J.* 48: 557–567.

Investigation of one-dimensional compression behavior of rubber chips mixed soil: Calculation of volumetric compression amount in the densest particle arrangement

T. Kimata
Osaka Metropolitan University, Sakai, Osaka, Japan

N. Kobayashi
Ehime University, Matsuyama, Ehime, Japan

ABSTRACT: This study aims to estimate the compressive properties resulting from the deformation of elastic particles as a foundation for constructing a model of soil mixed with elastic particles such as rubber chips. To determine these compressive components, a series of one-dimensional compression tests were conducted using rubber and aluminum chips. After that, the calculating method of these compression amounts was examined, considering the geometrical deformation of the component particles. The results indicated that if the specimen is in the densest particle arrangement state and the skeletal structure is not disrupted by compression, each compressive component of the mixture could be predicted with almost perfect accuracy.

1 INTRODUCTION

Efforts to promote a society that values recycling have made resource recycling a significant area of research. Geotechnical engineering research has focused on investigating the feasibility of using certain waste materials, such as scrap tire chips, expanded polystyrene waste, and scrap glass, as geomaterials (Kubo et al. 2004; Kohata et al. 2011; Hazarika et al. 2010; Yasufuku et al. 2000). The authors have also examined the potential for crushed expanded plastic waste to be utilized as a lightweight mixed soil, as its strength parameters, such as internal friction angle, were found to be nearly unaffected (Kimata et al. 2001), thereby demonstrating the material's viability for this purpose.

However, adding high-deformability materials, such as rubber or expanded plastic, to soil can lead to significant distortion. Similarly, layering of flexible geosynthetics in the ground can pose deformation issues. The authors examined the microscopic mechanisms of compressive deformation to understand the deformation properties of soil mixed with deformable particles. Specifically, the amount of mixed soil compression was assumed to consisted of ordinary soil compression (i.e., the amount of compression assuming no deformable particles in the soil skeleton) and an added compression amount due to the deformation of the deformable particles. The latter was further classified into the following three components: (a) a component resulting from the compression of the deformable particles themselves, (b) a component from the reduction in pore space volume caused by the deformation of the deformable particles, and (c) a component from the volume change in the pore space caused by the further rearrangement of the deformed particles. The authors conducted a one-dimensional rod-stack model compression test using aluminum rods and rubber or expanded polystyrene rods to predict each component introduced by the deformable particles. The test showed that a relatively simple model that considered the geometric deformation relationship during compression in

the two-dimensional cross-section of a rod-stack model could almost successfully predict the compressive components (a) and (b) (Kimata et al. 2010, 2013).

In this study, one-dimensional compression tests on a mixture of rubber and aluminum chips were conducted, to extend the previous research to three-dimensional conditions. The specimens were prepared in a state of 100% relative density (referred to as the densest state) to avoid disturbing the arrangement of particles. Accordingly, it is regarded that the generation of compressive component (c) due to particle movement within the skeleton is limited, and only the compressive components (a) and (b) can be considered. The basic three-dimensional compression behavior of the mixture was then determined, and the compressive component was modeled from a geometric standpoint.

2 SPECIMENS AND TESTING METHOD

2.1 Specimens

In this study, aluminum chips (equivalent to soil particles) and nitrile rubber chips with densities of 2.69g/cm^3 and 1.38g/cm^3, respectively, were used, and both chips have a diameter and length of 3 mm. The specimens were prepared by mixing these chips and packing them into an acrylic cylinder with an inner diameter of 50 mm and a height of 100 mm, in the densest state. The mixing ratio was defined as the volume ratio of rubber chips to all chips. The "Test Method for Minimum and Maximum Densities of Sands" (The Japanese Geotechnical Society 2015) was used as a reference to achieve the densest state. The chips were divided into 10 layers, and each layer was horizontally hit from all sides 100 times, resulting in a void ratio of approximately 0.52, considered the densest condition without altering the particle arrangement.

2.2 Testing method

A specimen was prepared, and a one-dimensional compression test was conducted using the apparatus shown in Figure 1, which includes an acrylic cylinder. One notable feature of this apparatus is that it saturates the specimen's pore space with water and measures the drainage from the pore space, which allows the volume change of the pore space to be quantified independently from the volume change caused by the compression of the entire specimen. The double negative pressure technique was used to saturate the samples with deaerated water. Compression tests were conducted at slow axial strain rates ranging from 0.1% to 0.4%/min based on the specimen stiffness until the axial stress reached approximately 500 kPa to avoid crushing the rubber chip.
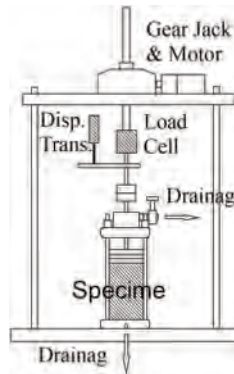
Figure 1. One-dimensional compression test apparatus.

3 TEST RESULTS

3.1 Concept of compressive component

After considering the findings of the earlier research, three deformable particle compressive components that need to be included were identified, as previously described. In the experiments, the volumetric strain resulting from the compression of the rubber chip was compared to the volumetric strain of the entire specimen and the pore space (corresponding to the amount of drainage) and became the component (a). Since the skeleton was kept in its densest state to avoid disturbing the arrangement of the particles, the component (c) related to the particle arrangement was not expected to occur. Therefore, only the component (b), the reduction in pore space resulting from particle deformation, was considered the cause of the drainage from the specimen. As a result, it is possible to focus on the components (a) and (b) among the components added due to deformable particles in this experiment.

3.2 Test results

The results of one-dimensional compression tests are presented in Figure 2, with filled marks indicating total volumetric strain and white marks indicating volumetric strain in the pore space, and the legend is the mixing ratio of the specimens. This figure shows that an increase in compressive stress increases the volumetric strains for all specimens. As the specimens were compacted to their densest state, there should be little volumetric compaction in ordinary soil. This result emphasizes the importance of anticipating soil compression levels when deformable particles are present. Furthermore, it is evident from this graph that volumetric compression of the rubber chips themselves accounts for a small portion of the volumetric strain, which is caused by component (b) (white plot), representing the volume change in the pore space.
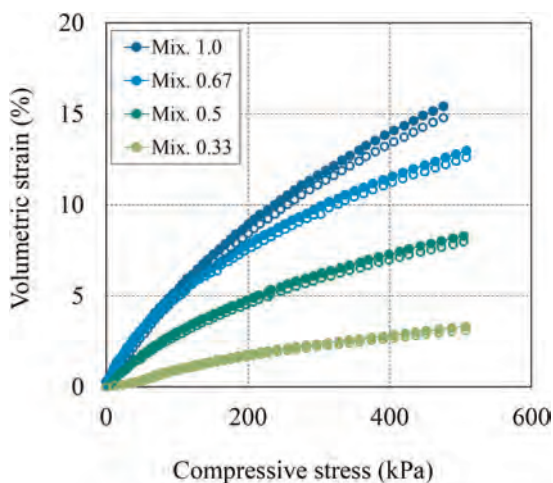
Figure 2. Volumetric strains of overall and pore space of specimens.

Figure 3 illustrates the component (a) calculated from the test results, assuming zero volume change for the aluminum chip. It indicates that even at a mixing ratio of 1.0 (rubber chips only), the volumetric strain does not exceed 1%. This outcome is reasonable since rubber is generally regarded as nearly incompressible, with a Poisson's ratio close to 0.5.

667
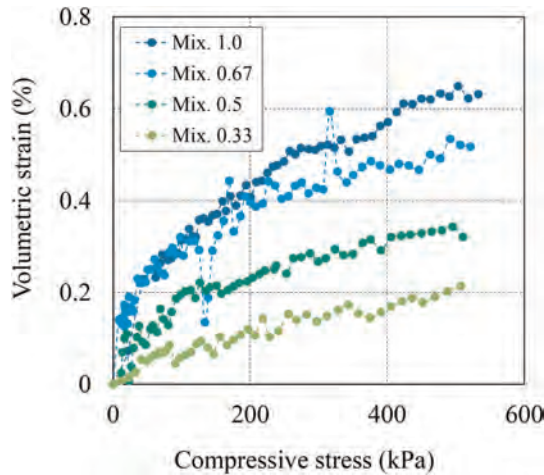
Figure 3. Volumetric strain caused by rubber chips, component (a).

4 MODELING OF COMPRESSION AMOUNT

4.1 *Modeling method*

Based on earlier research, it was found that the geometrical consideration of the deformation and movement of rod elements in a two-dimensional cross-section can accurately represent the one-dimensional compression of the rod-stack model using rubber and aluminum rods (Kimata et al. 2010). The elastic modulus and Poisson's ratio of the rubber rod element are used to calculate the deformation and movement of the circular cross-section when compression, and developed a method to determine and assess the amount of compression of the rubber rod and the amount of volumetric change in pore space resulting from the change in cross-sectional area. This method can be extended to a three-dimensional approach for this current research.

Dealing with cylinder contact presents a challenge when using a cylinder-based model. The study examined various configurations, including the intersecting of two cylinders sideways. The findings revealed that the model shown in Figure 4 provided the results closest to the experimental data. Therefore, this section elaborates on the details of the study, which was conducted based on this particular model.
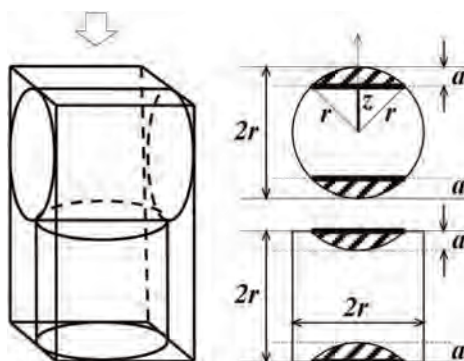
Figure 4. Geometric image of compression (rubber chips).

In this figure, two cylinders are present, each with a diameter and height of $2r$, and are enclosed within a rectangular prism with a dimension of $2r \times 2r \times 4r$ (length $\times$ width $\times$ height). The volume change, denoted as ΔV_1, resulting from the compression of one side of the horizontal cylinder by a, and the volume change, denoted as ΔV_2, resulting from the compression of the vertical cylinder by a, are represented by Equation (1) and (2), respectively.

$$\Delta V_1 = 2r \left\{ r^2 \cdot \sin^{-1} \left(\frac{\sqrt{2ar - a^2}}{r} \right) - (r - a)\sqrt{2ar - a^2} \right\} \tag{1}$$

$$\Delta V_2 = \pi \cdot a \cdot r^2 \tag{2}$$

In the case of rubber chips, compression occurs at all contact points, whereas with rubber and aluminum chips, it only occurs at the contact points on the rubber chip side. The compressive component (a) of volumetric stain due to rubber chips was calculated by considering the contact points on the rubber chip side based on the mixing ratio to calculate the volumetric strain resulting from the compression of rubber chips. The calculation also considered the lateral expansion of rubber due to Poisson's ratio. The compressive deformation of the rubber chip was determined by referring to experimental results for a mixing ratio of 1.0 (rubber only) and incorporating the converted axial strain value into the calculation. As the rubber chip was slightly compressed according to the experiment, Poisson's ratio was estimated to be 0.46 in the calculations.

4.2 Comparison with experimental results

Based on the theory presented in the previous section, Figure 5 illustrates the compressive component (a) caused by rubber chips. In this figure, the solid lines display the calculated values, while the experimental results are shown by marks (only mixing ratios of 1.0 and 0.5 are presented for clarity). Upon examining this figure, it can be observed that the calculated values are generally close to the experimental results. However, there are still some specific issues, such as an area where the volumetric strain increases in the initial stage. Consequently, modeling of the compressive components will continue in the future based on this line of reasoning.
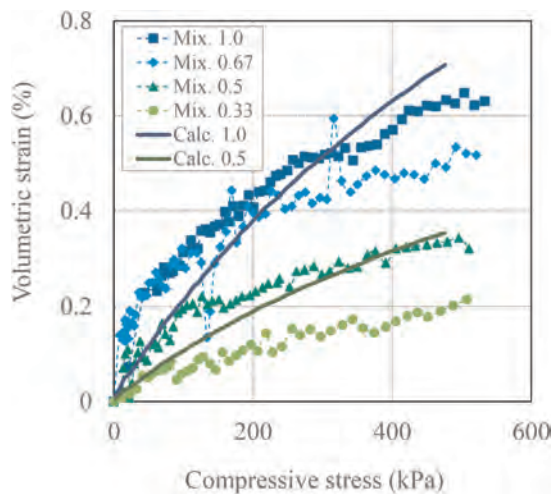
Figure 5.   Prediction of compressive component (a).

4.3 *Overall volumetric strain*

Finally, the overall volumetric strain of the mixture was predicted using the cylindrical model. The volume of the mixture pushed in by compression was first calculated using the overall volumetric strain at a mixing ratio of 1.0, which was used to determine the volume of compressive deformation of the chips. The compressive stress at that time was then back-calculated using the elastic modulus of rubber, which was found to be 4.0 MPa for NBR70 based on the material of the rubber chip used. For mixtures with ratios other than 1.0 (including aluminum chips), the overall volumetric strain was calculated using the same method as for the compressive component (a) discussed earlier. The existence ratio of the contact state between the rubber and the aluminum chips was considered when calculating the overall volumetric strain since it is possible to obtain the compressive stress applied to the rubber chips and the amount of compressive deformation from the above calculation.

Figure 6 shows the results where the experimental data are represented by markers (filled markers indicate the whole space, while white markers indicate the pore space). The solid and dashed lines indicate the calculated values for the whole and pore spaces. Only the
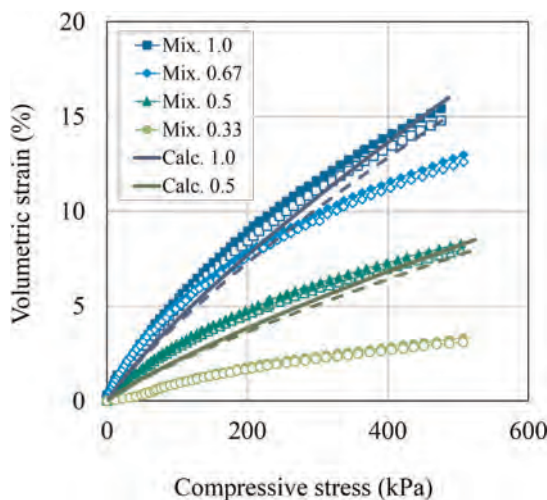
Figure 6.   Prediction of overall and pore space volumetric strain.

mixing ratios of 1.0 and 0.5 are shown for clarity purposes. The figure shows that the experimental results can be roughly predicted, similar to the compressive component (a). Thus, even with a basic geometric model of the mixture's compression behavior, it is possible to predict the volumetric strain caused by compression.

5   CONCLUSIONS

In this study, the compressive mechanism of a mixture of rubber and aluminum chips packed in the densest state was evaluated using a one-dimensional compression test, and a geometric approach to calculate the amount of compression was examined. The results showed that, despite the relatively small volumetric compression of the rubber chip itself, the deformation of the rubber chip caused a significant volumetric change in the pore space of the mixture. A simple cylindrical model was proposed to calculate the amount of compression, and the calculated values were found to be consistent with experimental outcomes. Future research

should investigate the factors influencing particle mobility. Overall, a model for the compression characteristics of soil mixed with deformable particles, such as rubber chips, has been established.

ACKNOWLEDGEMENTS

REFERENCES

Hazarika, H., Yasuhara, K., Kikuchi, Y., Karmokar, A.K. & Mitarai, Y. 2010. Multifaceted Potentials of Tire-derived Three-dimensional Geosynthetics in Geotechnical Applications and their Evaluation. *Geotextiles and Geo-membranes* 28(3): 303–315.

Kimata, T., Ohno, T. & Kuwabara, T. 2001. Mechanical Properties of Soils Mixed with Crushed Expanded plastic Wastes - Shear Strength Properties of Compacted Materials. *Transactions of the Japanese Society of Irrigation Drainage and Reclamation Engineering* 213: 93–100 (in Japanese, with English abstracts).

Kimata, T., Shimada, K. & Masaki, Y. 2010. Consideration of the Compressibility of Soil Mixed with Deformable Particles - Classification of the Compressive Components by using Rod-stack Model Tests. *Geomechanics and Geotechnics: From Micro to Macro (Proc. of IS-Shanghai 2010)* 1: 113–116.

Kimata, T., Kitaguchi, S. & Mori, S. 2013. The Compressibility of Soil Mixed with Elastic Particles-Estimation of the Compressive Components by using Rubber Rod-stack Model Tests. *Geosynthetics Engineering Journal* 28: 207–212 (in Japanese, with English abstracts).

Kohata, Y., Ito, K. & Koyama, Y. 2011. Effect of Cement Content on Shear Properties of Liquid Stabilized Soil Reinforced by Fiber Material. *Geosynthetics Engineering Journal* 26: 95–100 (in Japanese, with English abstracts).

Kubo, T., Makiuchi, K. & Minegishi, K. 2004. The Friction Characteristic between Lightweight Embankment Materials with Mixing Formed Scrap Glass and Geogrid. *Geosynthetics Engineering Journal* 19: 225–230 (in Japanese, with English abstracts).

Yasufuku, N., Ochiai, H., Omine, K. & Suetsugu, D. 2000. Geotechnical Utilization of Sand with Waste Expand-ed Polystyrene. *ISRM International Symposium 2000, Melbourne, Australia, November 2000.* Paper number: ISRM-IS-2000-347.

Confinement effects of geocell under direct shear conditions

S. Miyamoto & Y. Miyata
National Defense Academy, Yokosuka, Japan

ABSTRACT: In this study, the confinement effects of geocells were investigated using medium-scale direct shear tests. The shear box had a transparent sidewall to view the soil deformation in the box, and the soil strain localization behavior was visualized using particle image velocimetry. In a series of tests, the interface shear strength between geocell-reinforced and unreinforced soil was investigated and compared with the soil shear strength. The test results showed evidence that the interface shear resistance is higher than the soil shear strength because the geocell confines soil shear and volumetric deformation. Moreover, a simple empirical formulation of the interface shear resistance was proposed based on the Taylor-Bishop energy correction formula.

1 INTRODUCTION

Rapid road construction techniques are important in the recovery and reconstruction stages of disaster areas. In such road construction under time constraints, it is important to use on-site soil as much as possible and avoid using heavy construction machines. In this study, the authors focused on reinforcement technology for base foundations using geocells to solve this engineering problem. Figure 1 shows an overview of geocell technology. A geocell is a reinforcing material consisting of polymeric sheets bonded thermally at regular intervals. A geocell is deployed on-site by constructing a honeycomb structure that is filled with on-site
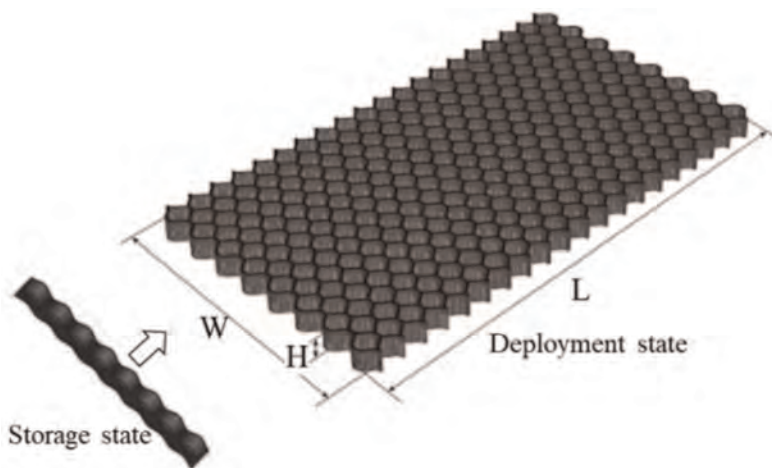
Figure 1. Overview of a geocell.

soil to form a reinforced foundation. Figure 2 shows the effects of geocell reinforcement. Geocells can reduce the sinking of passing vehicles and prevent slip failure of the base foundation.

To design a geocell-reinforced foundation, various limit states should be considered. The internal stability of geocell-reinforced foundations has been investigated by several researchers (ex. Bathurst & Jarrett 1988). However, the external stability has not been investigated sufficiently, especially the slippage between the reinforced layer and unreinforced surface layer when the reinforced layer behaves as a quasi-rigid body.
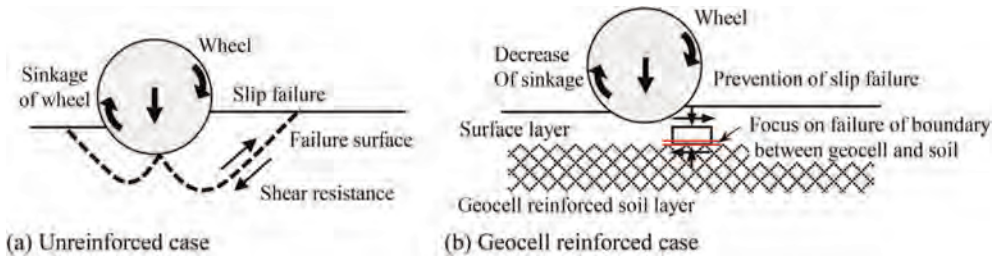
Figure 2.   Effects of geocell reinforcement.
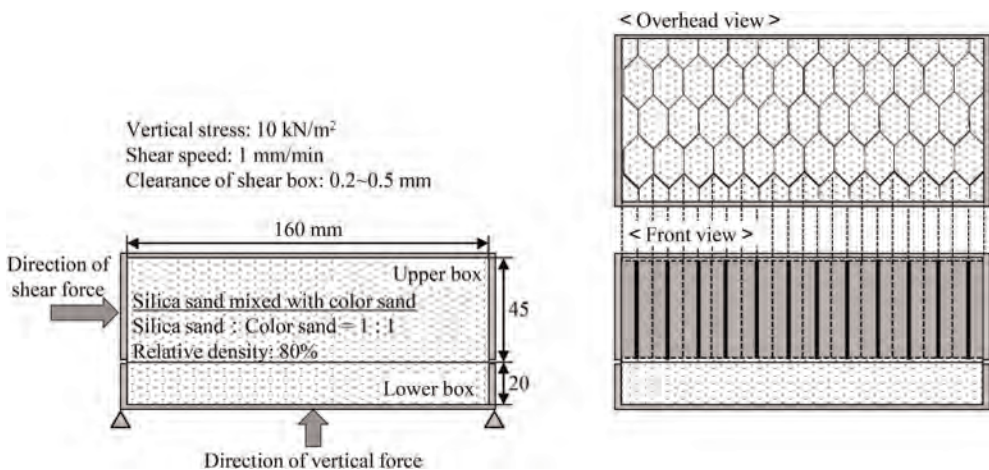
Figure 3.   Physical model overview of geocell-reinforced soil.

In this study, the interface shear resistance between geocell-reinforced and unreinforced soils was investigated using direct shear tests compared to unreinforced soil. The deformation of the reinforced/unreinforced soil was visualized using the particle image velocimetry (PIV) technique (Miyamoto & Miyata 2022), and the mechanism of the interface shear resistance was investigated (Miyamoto & Miyata 2021). Based on the results, an evaluation equation for the interface shear resistance between the geocell-reinforced layer and unreinforced surface layer is proposed.

2   EXPERIMENTAL METHODS AND CONDITIONS

A medium-sized direct shear test apparatus was used for a series of physical model tests (Miyamoto & Miyata 2021). Figure 3 shows a physical model of the geocell-reinforced soil

in this study. The shear box was rectangular with a length of 1600 mm and depth of 90 mm, and it was divided into an upper and lower box by height: 45 and 20 mm, respectively. The sides of the shear box were made of acrylic to visualize the deformation of the reinforced/unreinforced soil. Geocell-reinforced soil was set in the upper box, and the unreinforced soil layer was set in the lower box. Horizontal loading was applied to the upper box at a rate of 1 mm/min under constant vertical pressure. The vertical stress σ_v was set to $\sigma_v=10$ kN/m^2 by considering the actual height of the geocell-reinforced layer and the weight of the light vehicle. Silica sand with an average grain size of 0.32 mm was used as the soil sample. The specimens were prepared by mixing commercially available colored silica sand, which was colored black with a special dye at a ratio of 50%. The prototype of the geocell was prepared by a PET polymer sheet with a stiffness of 71.8 kN/m at 5% strain. The specimen was prepared by compacting air-dried colored sand mixtures with a relative density of $D_r = 80$ % using 8-mm-diameter round bars. For the reinforced soil layer, a geocell was placed 2 mm above the top of the lower box to allow for smooth shearing.

3 EXPERIMENTAL RESULTS AND DISCUSSION

The shear stress τ and vertical displacement v–d relationships with shear displacement d obtained from the direct shear tests are shown in Figure 4. In the unreinforced case, τ reached its peak value at $d = 5$ mm and did not reach the residual state in which v remained constant at a large shear displacement. In the reinforced case, greater shear resistance and a steeper initial slope of the τ–d relationship were observed than in the unreinforced case. The shear stress peaked at a small shear displacement, and the vertical displacement was smaller than that of the unreinforced case. After the peak shear stress was reached, the vertical displacement was almost constant when the shear resistance reached a residual state.
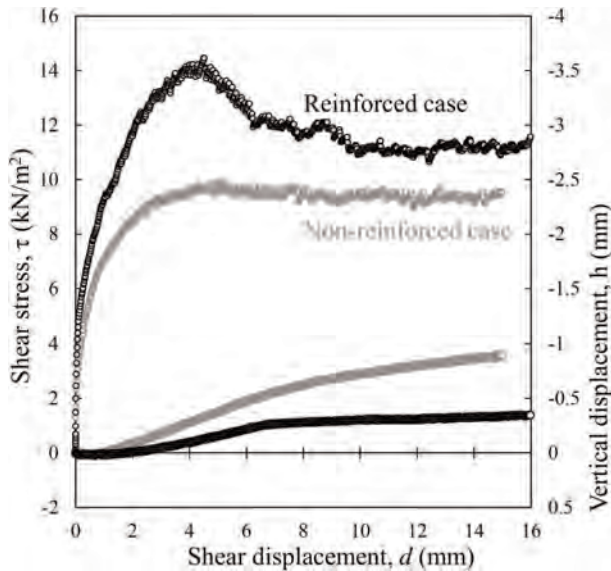
Figure 4.   Shear stress, shear displacement, and vertical displacement relationships.

Figures 5(a) and (b) show the results of the PIV analysis used to visualize the deformation of the specimens for the unreinforced and reinforced cases, respectively. In the unreinforced case, the shear strain was concentrated near the boundaries of the upper and lower shear
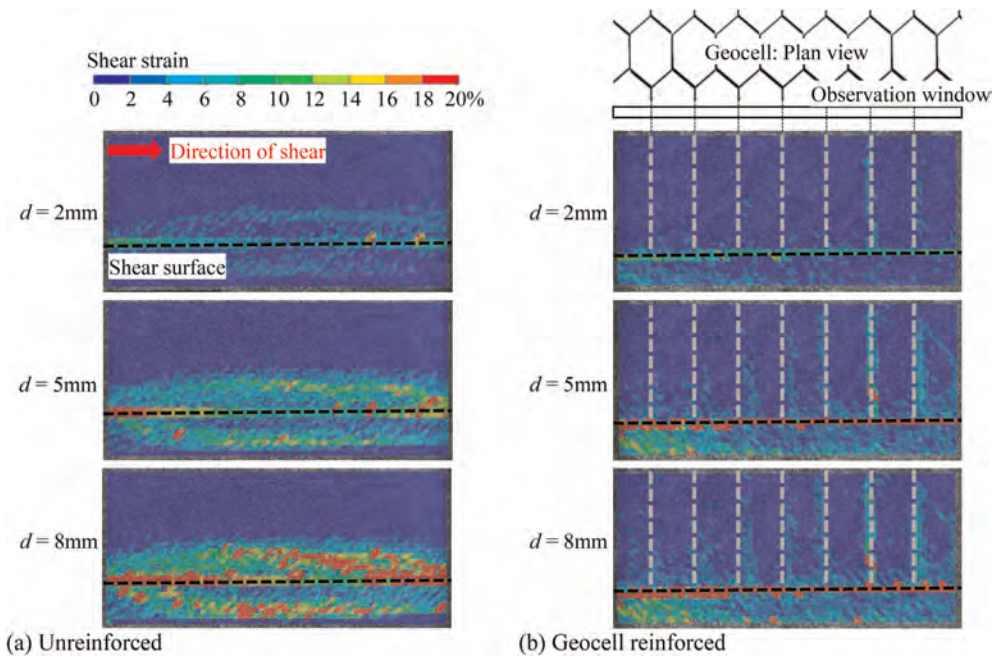
Figure 5. Development of shear displacement in soil.
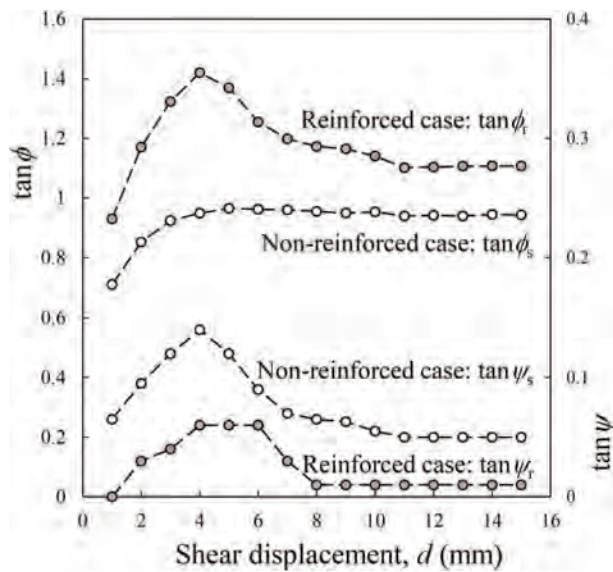
Figure 6. Mobilizations of tan ϕ and tan ψ.

boxes with an increase in the shear displacement, as previously reported. In the reinforced case, shear strain occurred near the boundaries of the upper and lower shear boxes and at the boundaries between the geocell and filled soil. No local deformation of the soil in the geocells was observed. It can be considered that the geocells constrained the soil dilatancy, which increased the shear resistance in the geocell region.
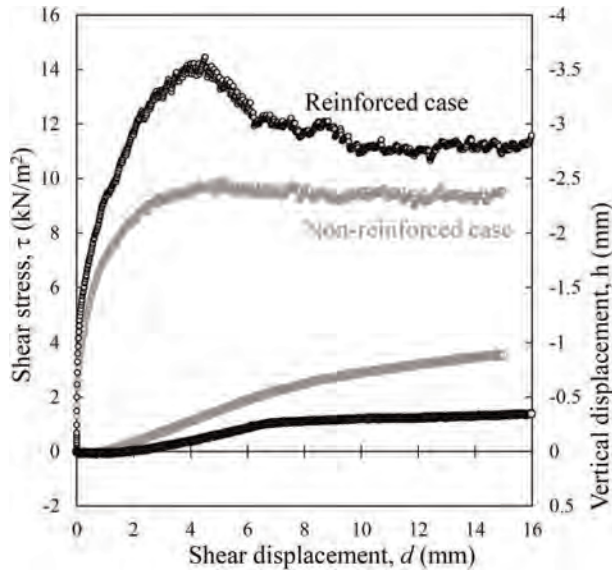
Figure 7.   Back calculated confinement effect parameter, λ.

Based on the above results, the shear resistance between the geocell-reinforced layer and the supporting foundation was investigated. The shear resistance τ_r of the two layers can be expressed using the following equation:

$$\tau_r = \sigma_v \tan \phi_r \tag{1}$$

where ϕ_r is the shear-resistance angle of the two layers. In the above equation, $\tan\phi_r$ can be expressed as follows, based on the Taylor-Bishop energy equation for soil dilatancy (Taylor, 1948).

$$\tan \phi_r = \tan \phi_s + \lambda \tan \psi_s, \tag{2}$$

where ϕ_s is the shear-resistance angle of the soil, ψ_s is the dilatancy angle of the soil, and λ is the confinement effect parameter that shows the increase in the shear resistance owing to the geocell constraining the soil dilatancy.

When evaluating the shear resistance between the geocell-reinforced and surface layers, it is difficult to evaluate the coefficient λ using a simple theory. Here, the authors performed a back calculation of λ using the test results. The estimated $\tan\phi_s$ and $\tan\psi_s$ for the unreinforced and reinforced cases are shown in Figure 6. The coefficient λ is almost constant regardless of the shear displacement and can be evaluated as $\lambda = 3.4$ in this analysis, as illustrated in Figure 7.

4   CONCLUSION

The confinement effects of the geocell were investigated by conducting medium-scale direct-shear tests. The results of this study are as follows:

(1) The interface shear resistance between the geocell-reinforced and unreinforced soil was higher than the soil shear strength.
(2) The geocell confined the soil shear deformation, that is, dilatancy.
(3) Interface shear resistance can be determined using a simple empirical formulation. The proposed equation is based on the Taylor-Bishop energy correction formula. It is

expressed by the shear resistance and dilatancy angles of the soil, the ratio of the cell confinement area to the total shear area, and an empirical coefficient on the dilatancy confinement.

The present evaluation was limited in that the test results were based on a single vertical stress condition. To validate the proposed method, future research should be done to perform laboratory tests under wide vertical stress conditions and investigate under full-scale test conditions.

REFERENCES

Bathurst, R.J. & Jarrett, P.M. 1988. Large-scale Model Tests of Geocomposite Mattresses Over Peat Subgrades. *Journal of Transportation Research Board* Vol.1188: pp.28–36.
Miyamoto, S. & Miyata, Y. 2022. Experimental Investigation on Ground Displacement Measurement in Geotechnical Physical Modeling using PIV Technique. Japan. *Journal of JSCE* Ser. A-2 Vol.78 No.1: pp.1–10 (in Japanese).
Miyamoto, S. & Miyata, Y. 2021. Deployable Geocell Reinforcement for Road Restoration and Laboratory Testing of Reinforcing Effects. Japan. *Journal of JSCE* Ser. C Vol.77 No.2: pp.118–128 (in Japanese).
Taylor D. W. 1948. *Fundamentals of Soil Mechanics.* New York: John Wiley & Sons.

Micromechanical investigation of geogrid-reinforced granular soil

G. Stocco & A. Pol
Department ICEA, University of Padova, Padova, Italy

O. Detert & L. Carbone
Huesker GmbH, Germany

C. Lackner
3G Gruppe Geotechnik Graz ZT GmbH, Österreich

F. Gabrieli
Department ICEA, University of Padova, Padova, Italy

ABSTRACT: Geogrids are widely used as a soil reinforcement technique in many engineering applications, however a detailed study of the mutual interaction between these structures and the granular soil is complex and generally faced only with specific laboratory tests. In the last decades, the recourse to numerical methodologies has experienced large growth, and among the different methods, the discrete element method (DEM) has proven its reliability in understanding both the micro and macro aspects of the soil-geogrid interaction. In this study, 3D discrete element simulations of pull-out tests are performed. The shape of the numerical geogrid and the contact properties of its elements are calibrated using the results of laboratory tests referring to a real PET woven geogrid. The geogrid mechanical properties investigated control its strength and stiffness. Their role and influence on pullout behaviour are investigated in different soil conditions regarding the confinement stress, the soil particle size and shape. The granular soil is modelled using both spheres and clumps to simulate different fine-graded gravels.

1 INTRODUCTION

Geogrids are specifically designed polymer materials used in many geotechnical applications: from earth-reinforced retaining walls to ground and foundation improvement in embankments (Koerner 2012; Moraci *et al.* 2014). Their mechanical behaviour is related to a combination of the mechanical properties of the geogrids themselves and to the mutual interaction with the soil in which these structures are embedded. For this reason, different geogrids may be proposed for different soil types in order to enhance the mechanical coupling between the reinforcing materials and the soil around them. Focusing on their use with coarse granular soils like rock fragments, gravel and coarse sand, the standard experimental and numerical approaches to study their behaviour appear more complex since the size of the grains is of the same order of magnitude as the mesh opening size and width of the elementary members. This reflects on several aspects that must be accounted for: the grains apply puncture loads on the product with possible indentation problems; the interlocking effect is enhanced by the sharpness and angularity of grains; local damage and failures of single strands are possible; soil compaction effort becomes a relevant variable; pretension and bending stiffness of the geogrid starts to play a relevant role.

These effects, even at a local scale, may have a great impact on the performance of these structures and cannot be studied efficiently with a continuum-based approach. In order to face this problem, in this work a discrete element modelling approach was adopted to describe a

real PET woven geogrid. The strands of the mesh are represented as chains of bonded spherical particles while the grains are modelled both as spherical and angular particles to study the effect of the grain shape on the macro-scale mechanical response of the mesh.

The mechanical properties of these bonds have been calibrated on the base of simple laboratory tests. Finally, pull-out tests on different configurations have been considered.

2 NUMERICAL MODEL

2.1 *Geogrid*

Mesh grids can be numerically modelled with DEM using different approaches: node-wire-based, cylinder-wire-based, and bonded-particles-based (Gabrieli *et al.* 2017). The first approach is the simplest: mesh grids are represented as a collection of nodes joined by user-defined long-range interactions taking into account the tensile forces in the elastic and plastic domain. This approach has been proven to provide very good results to model steel wire meshes, especially for mainly tensile problems, like puncture and plate bearing capacity (Gabrieli *et al.* 2018; Pol & Gabrieli 2022) but it fails in reproducing problems where the real shape of the grid element and its bending stiffness plays a relevant role. The cylinder-wire-based approach may be more realistic in terms of shape description and contact detection but cylinders must be split into many parts to describe the flexural properties of the strands and problems may arise to correctly describe a variable-section mesh fiber or strands with cross-sections different than circular, with an increase of the computational cost (Pol *et al.* 2018). The bonded-particles approach is the most accurate and can be viewed as an extension of the cylinder-wire-based approach with a cylinder length equal to zero. It can take into account the fiber tensile strength and bending stiffness. Moreover, different geometrical shapes of the fibers can be reconstructed and also frictional properties at the interface are more realistic (Miao *et al.* 2014).

In this work, a PET woven geogrid has been modelled with the bonded-particles approach as a collection of spherical particles having different particles size and joined together by means of normal, tangential and rotational bonds. This permits (a) to control the tensile and bending properties of the strands (b) to simulate the variable cross-section of transversal fibers and (c) the real spiral geometry of the longitudinal strands. The DEM open-source code Yade has been used for the simulations (Šmilauer *et al.* 2015).

The geogrid considered in this work is the coated woven PET geogrid Fortrac® by Huesker (Figure 1). Longitudinal members are twisted while transverse ribs are constituted by fibers knitted together to form an irregular flexible sheet and maximize the frictional and bonding effect. The mesh opening size is 2 cm in both directions. The thickness of the grid is about 3 mm.
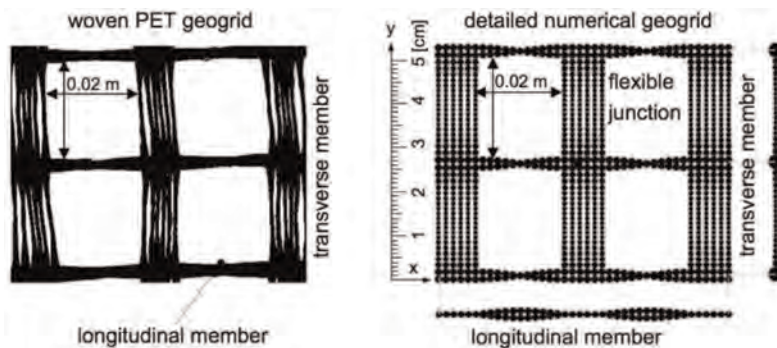
Figure 1. Woven PET geogrid Fortrac® by Huesker and its numerical model (modified from Dijak 2012).

In order to calibrate the contact mechanical properties of the spheres constituting the geogrid, laboratory tensile and bending tests in longitudinal and transversal directions have been considered. The tensile response of the geogrid in the longitudinal direction and the result of one bending test are reported in Figure 2. The geogrid reacts mainly elastically up to a brittle failure representing the maximum tensile strength. From sensitivity analyses, the Young modulus, and the bond cohesion at the contact mainly control its tensile stiffness and strength while the Young modulus and the rotational stiffness at the contact rule the bending response. The final calibrated mechanical properties of the particles composing the mesh grid are reported in Table 1.
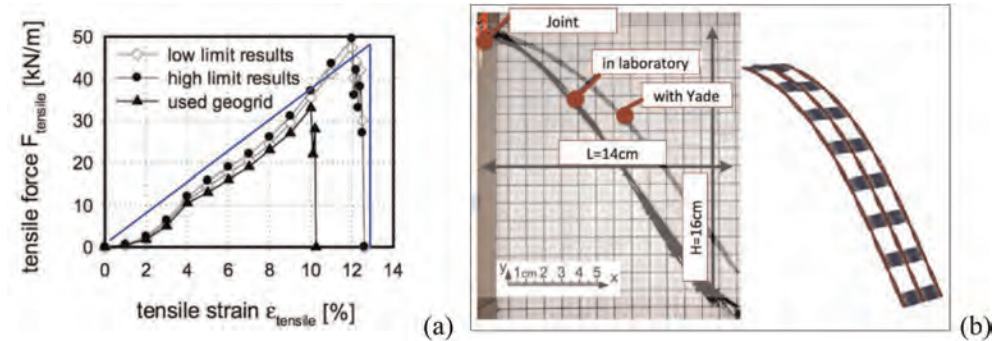
Figure 2. (a) Result of real (black curves) and simulated (blue curves) tensile tests with the geogrid (modified from Lackner 2012) (b) lateral view of a cantilever bending test (modified from Dijak 2012).

Table 1. Particle's characteristics and mechanical properties at the contact for the geogrid model.

Particle size mm	Young modulus Pa	Normal and tangential strength Pa	Rotational stiffness
0.5–0.78	3.5e9	8.7e8	0.02

2.2 Granular soil

Two types of soils have been considered in this work: a coarse granular soil constituted by spherical particles (soil A) and a more realistic granular soil with angular particles (soil B). The first soil type facilitates the study of the interaction mechanism keeping low the complexity and computational cost of the simulations.

The shape of the angular particles has been obtained through photogrammetric 3d reconstruction of a sample of some real grains. Then, the external surface of the grains have been used as containers to fill the volume with a set of spheres clumped together that mimic the irregular shape (see Figure 2). The algorithm used for this purpose is the power crust (Amenta et al. 2001) which allows controlling the number of spheres to be used in the sphere-filling procedure to create the clump and the ratio between the coarsest and the finest sphere.
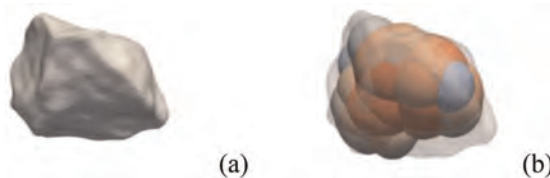
Figure 3. (a) Example of the 3d surface reconstruction of one sample grain and (b) corresponding clump generation by applying the sphere-filling procedure.

The micromechanical properties of the grains have been calibrated from previous laboratory tests (Zarattini *et al.* 2019) and are reported in Table 2.

Table 2. Particle's characteristics and mechanical properties at the contact.

	Particle type	Particle size mm	Solid density kg/m^3	Young modulus Pa	Poisson ratio	Friction angle °
Soil A	spheres	6, 10, 16, 22	2700	1e8	0.2	40
Soil B	clumps	16	2700	1e8	0.2	40

3   PULL-OUT TEST SIMULATION

A numerical pullout box has been built with dimensions 0.3 x 0.1 x 0.35 m considering the criteria suggested in the literature (ASTM 2001; Konietzky *et al.* 2004; Moraci & Recalcati 2006; Palmeira 2009). The smaller transverse dimension of 0.1 m is compensated by periodic boundary conditions that allow simulating an infinite-width geogrid and infinite box. The height of 0.35 m (about 0.3 m after the compression) is the minimum recommended in literature to allow the development of the bearing effect (Konietzky *et al.* 2004). The upper rigid plate applies the desired vertical stress. Its friction angle is set equal to 25° to simulate the steel-soil contact friction angle. The other facets (front, back and bottom) have a friction angle decreased to 6° to reduce their influence as suggested in the literature and carried out in the laboratory with lubrication (Palmeira & Milligan 1989; Palmeira 2009). The length of the geogrid specimen is 295 mm. Figure 4a shows the dimensions of the pullout apparatus and the position of the geogrid.
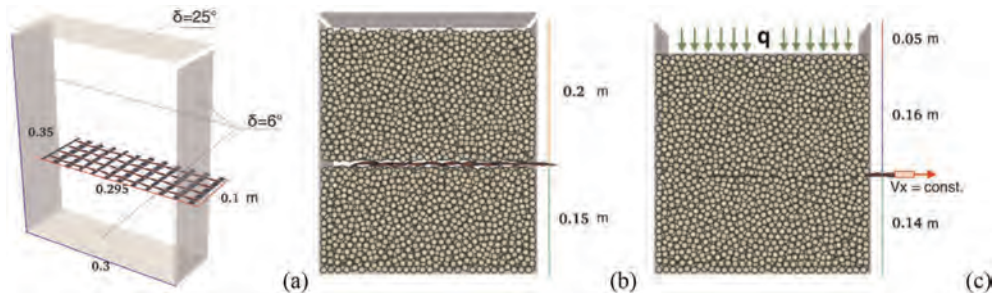
Figure 4.   (a) Sketch of the pullout box and grid; (b) initial soil packing with cut and geogrid positioning; (c) application of the vertical load and beginning of the pullout test.

The compacted granular soil is created by a gravity-pluviation procedure starting from a cloud of particles inside a tall prismatic box without the geogrid. After the deposition, the granular soil reaches a porosity of about 0.4 – 0.45. The geogrid is imported and left to adapt to the irregular soil surface in a thin cut inside the soil (Figure 4b). A variable vertical velocity through a PI controller function is applied to the plate in order to exert constant vertical pressure. When the vertical stress reaches a stable value under a threshold of 2%, a constant horizontal displacement rate of 0.05 m/s is applied to the clamp, thus starting the pullout test (Figure 4c).

4 RESULTS

Before the beginning of the test, due to the medium-low flexural stiffness of this geogrid, the soil particles slightly bent the transversal and longitudinal members with benefits in terms of initial interlocking. After pulling the geogrid, the mobilized frictional resistance starts to increase almost linearly with deformation and a quite large volume of soil is involved in a convective motion especially considering Soil A (Figure 5a). Moreover, the large flexibility of transversal members helps the geogrid to trap particles in the mesh openings and to facilitate the development of the bearing resistance mechanisms. The latter can be seen in the bent and stressed transversal elements close to the front wall of the box (Figure 5b). At the end of the test, the geogrid slides (sliding failure mechanism) or breaks close to the front wall (yielding failure mechanism) where the longitudinal fibers experience the highest tensile stresses.
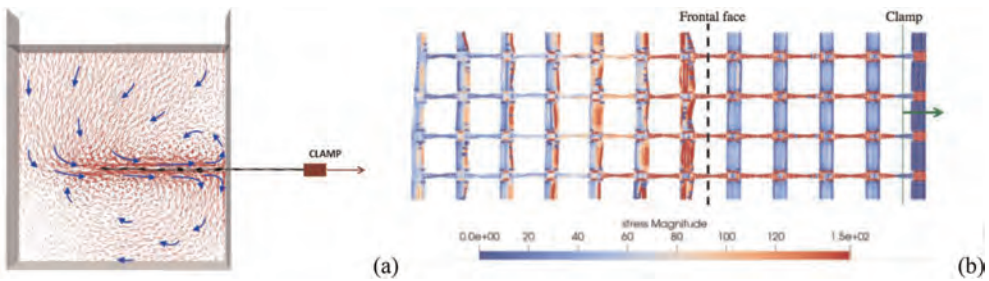
Figure 5. (a) Lateral view of the typical soil displacement field during the pullout test carried out with soil type A; (b) Top view of the tensile stress distribution in the geogrid before the failure.

4.1 *Effect of the confinement stress*

The first set of simulations was carried out by modifying the vertical stress (i.e. the soil thickness z above the geogrid) using the soil A (spheres). The results in terms of tensile force vs longitudinal strain are reported in Figure 6. A transition from a sliding failure to a yielding failure is visible increasing the thickness of the soil: at low vertical stresses (z < 2 m;
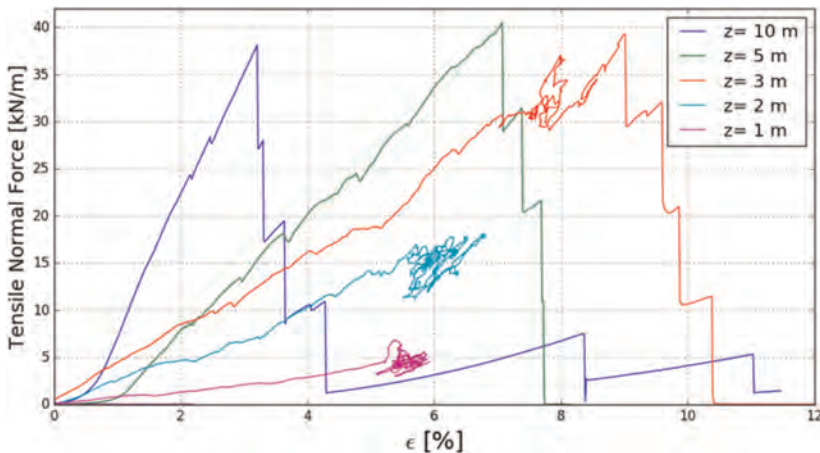
Figure 6. Numerical results of pull-out tests varying the vertical stress.

$\sigma_v > 30$ kPa) the typical geogrid failure mode is characterized by sliding while increasing the vertical stress ($z > 3$ m; $\sigma_v > 45$ kPa) the geogrid failure is of the yielding type. The maximum yielding strength at failure is 10% lower than the tensile strength of the geogrid evaluated without the soil (compare Figures 2a and 6) due to the inhomogeneous tensile stress distribution in the geogrid fibers. Moreover, it is more or less constant (for $z > 3$ m) but with very different maximum elongation values.

4.2 *Effect of the grain size and shape*

The second group of tests have been performed using soil A (i.e., spheres with different grain sizes) and soil B (clumps characterized by one diameter), keeping a constant vertical stress σ_v = 30 kPa, corresponding to a soil thickness z=2 m. In all cases, the reinforcement does not reach the yielding point but starts to slide. The maximum shear strength seems to be independent of the grain size but smaller particles provide better results in terms of maximum elongation (Figure 7a).
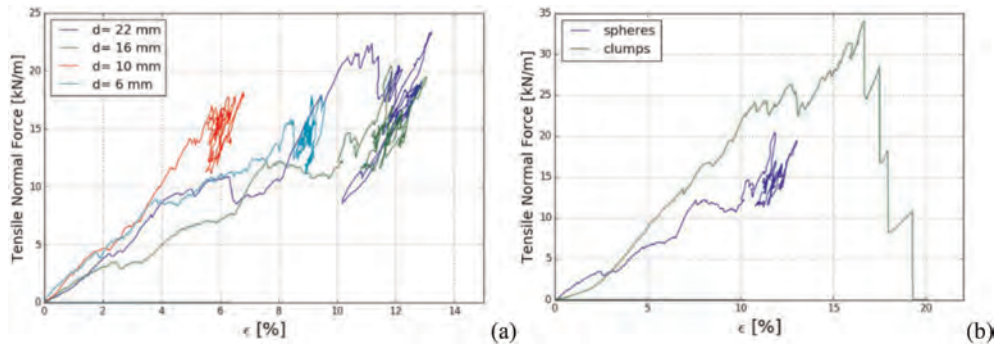
Figure 7.   (a) Numerical results of pull-out tests varying the grain size (Soil A) (b) Comparison of numerical results using the different grain shape (Soil A and B) (d=16mm).

Comparing the results of the simulations carried out using soil A and B (i.e. spheres and clumps with the same mean diameter d = 16 mm) at the same vertical stress, the pullout response moves from a sliding failure to a yielding failure mechanism with a maximum tensile strength that is 25% lower than the tensile force obtained without the soil. However, the overall tensile stiffness is higher than in the case of spheres. The use of angular particles (i.e. clumps) in place of spheres has the same effect of increasing the particle size: The contact force network is less homogeneous and local effects prevail.

5   CONCLUSIONS

The interaction mechanism of a flexible geogrid with coarse soil is investigated using the discrete element method and considering a pullout test configuration. The frictional and bearing behaviour can be noticed in the stress distribution on the geogrid members. The use of a micromechanical approach allows for considering a real interlocking between the geogrid and the grains. Moreover, local effects like puncturing, local failures and bending are taken into account. The numerical results show the important effect of stress confinement in the transition from a sliding-prone failure to a yielding-type failure condition. The coupling with coarse soil having a grain size larger than the geogrid opening size increases the chance of premature failure. The use of angular particles allows for considering more realistic

conditions with an increased rotational frustration of the particles and overall stiffer behaviour of the soil-reinforcement interaction.

REFERENCES

Amenta, N., Choi, S., & Kolluri, R. K. 2001. The Power Crust, Unions of Balls, and the Medial Axis Transform. *Computational Geometry*, 19(2–3): 127–153.

ASTM D6706-01, 2001. Standard Test Method for Measuring Geosynthetic Pullout Resistance in Soil. *Annual Book of ASTM Standards*. ASTM International, West Conshohocken, USA. http://www.astm.org.

Dijak, M. 2012. *Dreidimensionale Numerische Modellierung von Laborversuchen mit Geokunststoffen unter Verwendung der Diskreten Elemente Methode*. Master thesis, Graz University of Technology, Institute of Soil Mechanics and Foundation Engineering (in German).

Gabrieli, F., Pol, A. & Thoeni, K., 2017. *Comparison of Two DEM Strategies for Modelling Cortical Meshes. In PARTICLES V: proceedings of the V International Conference on Particle-Based Methods: fundamentals and applications* (pp. 489–496). CIMNE.

Gabrieli, F., Pol, A., Thoeni, K. & Mazzon, N., 2018. Particle-based Modelling of Cortical Meshes for Soil Retaining Applications. In *Numerical Methods in Geotechnical Engineering IX* (pp. 391–397). CRC Press.

Koerner, R.M., 2012. *Designing with Geosynthetics*-Vol. 1. Xlibris Corporation.

Konietzky, H., te Kamp, L., Groeger, T. & Jenner, C., 2004. Use of DEM to Model the Interlocking Effect of Geogrids under Static and Cyclic Loading. *Numerical modeling in micromechanics via particle methods*, pp. 3–12.

Lackner, C. 2012. *Prestressed Reinforced Soil Concept, Investigations and Recommendations*, PhD thesis, Technical University Graz, Graz, Austria.

Miao, C.-x., Zheng, J.-j., Cui, M.-j., Xie, M.-x. & Zhao, J.-b. 2014. Discrete Element Simulation of Interface Characteristic and Frictional Properties of Triaxial Geogrid. *Rock and Soil Mechanics*, 35 (1): 423–430.

Moraci, N. & Recalcati, P. 2006: Factors Affecting the Pullout Behaviour of Extruded Geogrids Embedded in a Compacted Granular Soil. *Geotextiles and Geomembranes*, 24(4): 220– 242.

Moraci, N., Cardile, G., Gioffrè, D., Mandaglio, M.C., Calvarano, L.S. & Carbone, L., 2014. Soil Geosynthetic Interaction: Design Parameters from Experimental and Theoretical Analysis. *Transportation Infrastructure Geotechnology*, 1(2): 165–227.

Palmeira, E.M. & Milligan, G.W., 1989. Large Scale Direct Shear Tests on Reinforced Soil. *Soils and Foundations*, 29(1): 18–30.

Palmeira, E.M. 2009. Soil–geosynthetic Interaction: Modelling and Analysis. *Geotextiles and Geomembranes*, 27(5): 368–390.

Pol, A., Gabrieli, F., Thoeni, K. & Mazzon, N. 2018. *Discrete Element Modelling of a Soil-mesh Interaction Problem*. In *ISRM European Rock Mechanics Symposium-EUROCK 2018*. OnePetro.

Pol, A. & Gabrieli, F., 2022. Anchor Plate Bearing Capacity in Flexible Mesh Facings. *Soils and Foundations*, 62(6), p.101222.

Šmilauer et al. 2015. DEM formulation. In Yade Documentation 2nd ed. The Yade Project , DOI 10.5281/zenodo.34044 (http://yade-dem.org/doc/)

Zarattini, F., Pol, A., Schenato, L., Tecca, P. R., Deganutti, A. M., Garcia-Ruiz, A., Soriano-Amat, M., Gonzàlez-Herràez, M., Martins, H. F., Pasuto, A., Palmieri, L., & Gabrieli, F. 2019. Preliminary Numerical and Experimental Tests for the Study of Vibration Signals in Dry Granular Flows. *6th International Conference on Particle-Based Methods. Fundamentals and Applications, Particles 2019*, 305–312.

Experimental evaluation of the pullout resistance of geostrips within sands and recycled Construction and Demolition Waste (CDW)

A.G. Corrales
University of Brasília, Brazil
University of Costa Rica, Costa Rica

G.L.S. Araújo
University of Brasília, Brazil

ABSTRACT: The massive generation of construction waste is one of the priority urban environmental problems in recent years, causing losses in urban populations' quality of life, where 54% of the world population currently lives (84.3% of the Brazilian population) (IBGE, 2019). In this context, this paper presents the results of an experimental investigation on the interaction between synthetic strips with sand and low-cost alternative material (recycled Construction and Demolition Waste). The objective is to determine their possible suitability as landfill material in Mechanically Stabilized Earth retaining structures. Large-scale reinforcement pullout tests were carried out. Based on the results, it was possible to carry out a comparative analysis of the mobilized resistance, allowing to determine design parameters. The experiments also showed favorable results, and the CDW can be considered a viable option for partial and/or total replacement of commonly used natural materials.

1 INTRODUCTION

In Brazil, CDW from construction works, renovations, demolitions, and excavations represent up to 70% (by mass) of total solid waste (Angulo *et al.* 2022). Only in Brasília (Brazilian capital), more than 6,200 t/day of CDW are generated and most of which are deposited in more than a thousand irregular deposition points (Brazilian Federal District Government 2016), causing the loss of ecosystems, contamination of natural resources such as air, water and soil, and deterioration of the landscape. The growing production of CDW and an increasing demand for materials for civil construction works makes necessary to reuse the CDW material.

Overall, reinforced soil standards suggest the use of good-quality granular soils as backfill material. However, there is often no availability of this type of material, therefore, several researches have been developed using unconventional materials, such as fine-grained soils (Araujo *et al.* 2021; Pierozan *et al* 2022), tire derived aggregates (Arulrajah *et al.* 2019; Ghaaowd1 & McCartney 2020; Zhang *et al.* 2020), industrial wastes (Mashifana & Sithole 2021; Mymrin *et al.* 2021; Pant *et al.* 2019) and recycled construction waste (Mandloi *et al.* 2022; Ok *et al.* 2023; Vieira 2020).

In this context, the present study comparatively analyzes the mechanical behavior of soils reinforced with synthetic strips in Mechanically Stabilized Earth Retaining Walls, using natural sands and CDW as backfill materials, through large-scale pullout tests, to determine its suitability as a backfill material.

2 INTRODUCTION MATERIALS AND METHODS

2.1 *Backfill and reinforcing materials*

In this research, natural sand, CDW sand, and CDW gravel were used as filling materials. The natural sand it was used, as a reference backfill material, usually used in earth structures. Figure 1 presents the particle size distribution curves and Table 1 presents the main geotechnical properties of the tested materials, as well as some compaction properties adopted for the pullout tests. As reinforcing elements, 50mm wide and 3 mm thick smooth synthetic strips were used, with maximum strength of 45kN, composed by polyester fibers (PET) with a low-density polyethylene coating (LDPE).
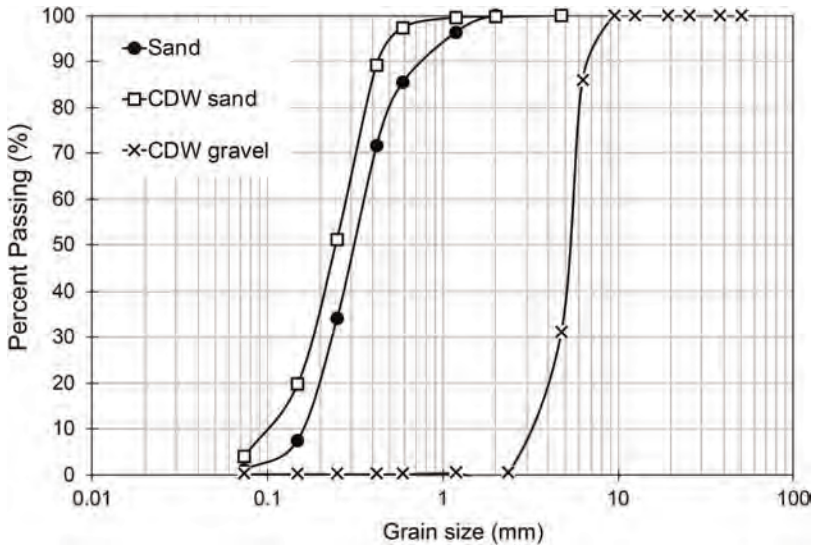
Figure 1.   Particle size distribution curves.

Table 1.   Physical and engineering properties of the materials.

Geotechnical Properties	Sand	CDW sand	CDW gravel
Grain specific gravity, G_s	2.71	2.68	2.66
Effective particle size, D_{10} (mm)	0.17	0.10	3.29
Fine content (%)	0.9	3.9	0.0
Coefficient of curvature, C_c	0.98	1.17	1.23
Uniformity coefficient, C_u	2.19	2.87	1.73
Unified soil classification system	SP	SP	GP
Relative density, DR (%)	96.3	96.1	95.2
Void ratio, test, $e_{95\%}$	0.67	0.61	0.82
Maximum dry unit weight, $\rho_{d\ 95\%}$ (g/cm^3)	1.63	1.66	1.56
Friction Angle, ϕ (°)	35	33	45
Cohesion, c (kPa)	0	3.7	0

2.2 *Test equipment*

The laboratory pullout test instrumented apparatus consists of three components (Figure 2): (1) the pullout box (Figure 3a), (2) a vertical load application system, and (3) a horizontal load application system (Figure 3b). The pullout box was designed and built for Palmeira

(1996) as recommended by D6706-01 (ASTM 2013). It is made of steel plates and consists of a rectangular cross-section box, with internal dimensions equal to 570 mm high, 900 mm wide, 1450 mm long, and a reaction structure for the application of horizontal loads. The horizontal load application system (pull-out system) is composed by a reinforcement-load transfer system connection element, a mobile load transfer system, a hydraulic cylinder, and a manual hydraulic jack. On the other hand, the vertical stress system consists of a lid with a rubber bag, an air-water interface system and a vertical reaction frame.
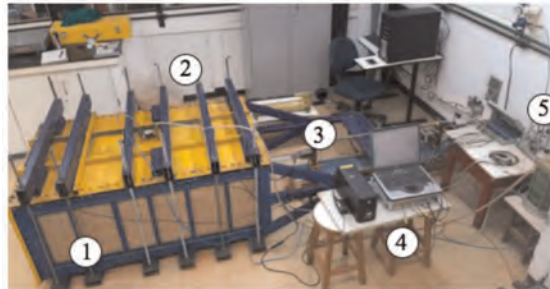
Figure 2.   Overview of pullout test apparatus and data acquisition systems. 1) pullout box; 2) vertical load application system; 3) horizontal load application system; 4) Spider acquisition system and 5) LYNX acquisition system.
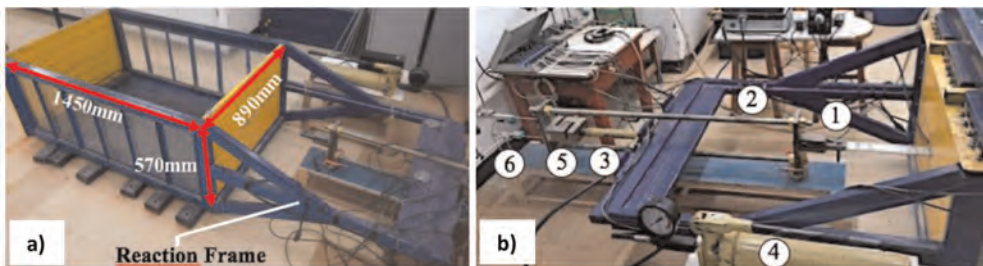
Figure 3.   Overview of pullout test; (a) pullout box and (b) horizontal load application system. *1) reinforcement-load transfer; 2) load transfer system; 3) hydraulic cylinder; 4) manual hydraulic jack; 5) Load cell and 6) displacement transducers.

The instrumentation of the tests was consisted by (1) two displacement transducers, to control the rate of displacement of the reinforcements during pullout, to control the rate of displacement of the reinforcements during pullout, (2) one load cell, (3) four pressure cells and (4) three displacement transducers, to measure the axial deformation of the reinforcement elements. For recording and converting the sensors' analog readings into digital readings, the Spider-8.0 and LYNX data acquisition systems was used.

In order to avoid friction between the granular material and the box walls, lubricant was spread over the surface. The lower half of the pullout box is filled in 3 layers of 9cm thick compacted (CR>95%, as recommended by NBR 19286 (ABNT 2021). Then, the reinforcement is installed in the middle of the soil box in pairs, one parallel to the other and separated by 50 mm. The anchored length of the strips was equal to 1225 mm. The upper half of the box was filled using the same procedure as in the lower part. The upper lid with a rubber bag was installed and then the vertical frame was assembled. After the assembly, the normal stress (equal to 12.5 kPa, 25 kPa and 50 kPa) was applied and the pull-out force was applied with a strain rate equal to 1mm/min (ASTM D6706-01 2013).

3 RESULTS AND DISCUSSION

3.1 *Pullout test*

The results from pullout tests of geostrips with the normal stresses of 12.5 kPa, 25 kPa e 50 kPa are presented below. The variation of pullout force with the reinforcement displacement can be observed in Figure 4. The maximum pullout force ($F_{max.}$) or peak resistance (red triangles) is also shown.
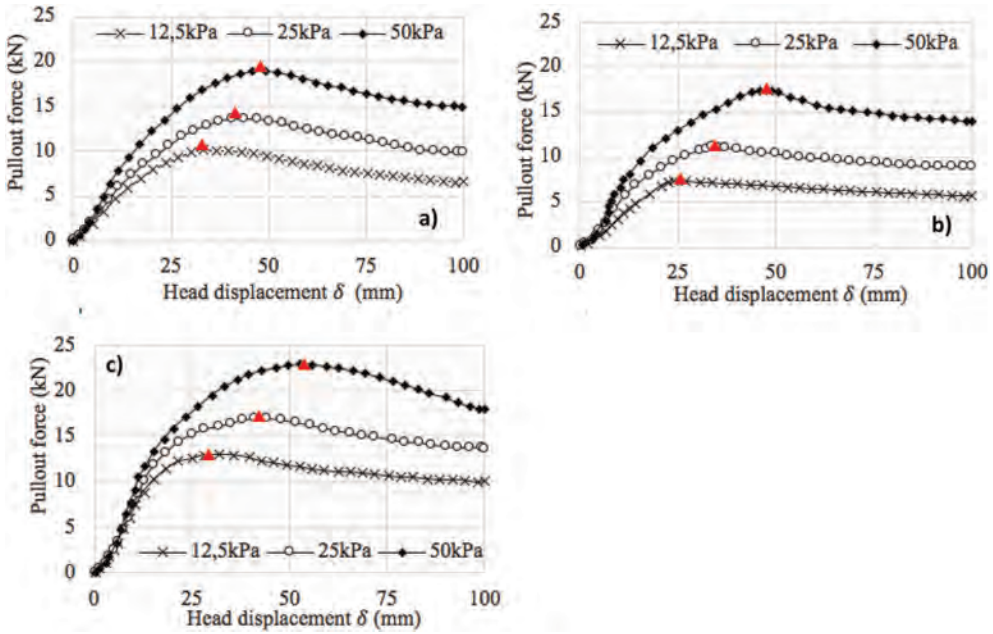
Figure 4.   Pullout tests with a) Sand, b) CDW sand, and c) CDW grave.

From the maximum pullout force, the value of the pullout friction factors (f'^*) can be obtained according to the AASHTO (2012) standard, based on the hypothesis that the pullout strength is uniformly developed on both sides of the reinforcement along its length (Equation 1):

$$f'^* = \frac{F_{max.}}{w_g \times \phi \times C \times L_e \times \sigma_v} \tag{1}$$

where w_g = width of the geosynthetic; L_e= reinforcement length in the resisting zone; Φ = resistance factor for reinforcement pullout (0.90 for Service Limit State (SLS) and 1.00 for Ultimate Limit State (ULS)); α = scale effect correction factor (1 for geostrips); and σ_n= vertical overburden stress at the reinforcement level and C is the overall reinforcement surface area geometry factor (2 for strips).

The variation of the maximum pullout resistance as a function of vertical overburden stress and the pullout friction factors (f'^*) with the overburden thickness are shown in Figure 5.

As expected, the value of the pullout resistance for the three materials increases with increasing confining levels, and the value of the pullout friction factor for the three materials decreases with increasing overburden thickness, according to ABNT (2021), due to the influence of the material dilation in the vicinity of the frame.
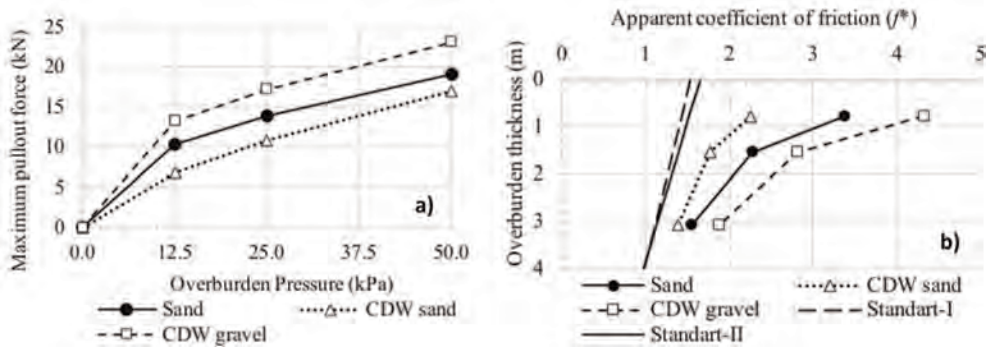
Figure 5. a) Maximum pullout force and b) Pullout friction factors (f^*) from laboratory tests.

3.2 Design standard

For comparison purposes, the values of the pullout friction factor (f^*) proposed by the French Standard (Norme Française 2009) were estimated. According to this standard, for class A (draining) materials the value of f^* varies linearly with the depth (z) and is given by Equation 2:

$$f^* = f_0^* \times \left(1 - \frac{z}{z_0}\right) + f_1^*\left(\frac{z}{z_0}\right), \; for \;\; z < 6m \qquad (2)$$

where, z_0 = depth at which there is no longer any dilation effect (6.0m); f_0^* = coefficient as a function of the uniformity coefficient (1.1 for $C_u < 2$ and 1.3 for $C_u > 2$); and f_1^* = coefficient as a function of the internal friction angle of the embankment, and is given by Equation 3:

$$f_1^* = 0,9 \times \tan\varphi' \qquad (3)$$

Table 3 presents the values of the apparent pullout friction factors calculated from the pullout tests (f^*) and estimated according to the French standard f^* (Norme Française 2009).

Table 3. Apparent friction coefficients calculated and estimated according to Norme Française (2009).

Geotechnic Material	Pullout Test			Coefficients	
	Normal stress (kPa)	Overburden thickness (m)	Max. pullout force (kN)	f^*	f^*
Sand	12.5	0.77	10.35	3.28	1.23
	25	1.54	13.92	2.27	1.17
	50	3.07	19.04	1.55	1.04
CDW sand	12.5	0.77	6.90	2.25	1.26
	25	1.54	10.80	1.76	1.21
	50	3.07	17.00	1.39	1.13
CDW gravel	12.5	0.77	13.24	4.32	1.10
	25	1.54	17.23	2.81	1.09
	50	3.07	23.08	1.88	1.08

It can be observed that the values obtained of the friction coefficients from laboratory tests are greater than the calculated according to the procedures established by the reinforced soil standard and design manuals. This was expected, once standards are conservative because they consider different types of soils.

4 CONCLUSIONS

In this study, large-scale pullout tests were carried out, using natural sand and two types of recycled construction and demolition waste as backfill materials and smooth synthetic strips as reinforcement elements, aiming at investigating the possibility of using CDW as backfill alternative material in mechanically stabilized walls. The findings of this study are summarized below:

(1) The maximum pullout resistance increased with the normal applied stress, while the pullout resistance factor, f^*, decreased. These tendencies were more pronounced under low overburden-pressure conditions.
(2) The CDW gravel friction coefficient was significantly greater than those obtained in sandy materials, once this material presented better geotechnical properties.
(3) The lowest pullout resistance values were obtained for the CDW sand, showing that the internal friction angle had a greater effect on the pullout resistance.
(4) The pullout resistance factors calculated for all materials used in this study were higher than the default f^* values recommended by the French standard (Norme Française, 2009) and design manuals (The Reinforced Earth Company 1995).
(5) The tested materials have excellent granulometric properties and excellent mechanical behavior in terms of pullout resistance and therefore are suitable to be used as backfill material in mechanically stabilized walls.

REFERENCES

Angulo, S.C., Oliveira, L.S. & Machado, L. 2022: *ABRECON 2020 Sectorial Survey- The Recycling of Construction and Demolition Waste in Brazil* – São Paulo, 104 p.

American Society for Testing and Materials, *ASTM D6706- 01. 2013*: *Standard Test Method for Measuring Geosynthetic Pullout Resistance in Soil*. Pennsylvania, USA, 8 p.

American Association of State Highway and Transportation Officials, AASHTO. 2012. *AASHTO LRFD Bridge Design Specifications*. Washington, USA, 6 ed., 1661 p.

Araujo, G.L.S., Moreno, J.A.S. & Zornberg, J.G. 2021. Shear Behavior of Mixtures Involving Tropical Soils and Tire Shreds. *Construction and Building Materials* 276: 122061.

Arulrajah, A., Mohammadinia, A., Maghool, F., Horpibulsuk, S. 2019. Tire Derived Aggregates as a Supplementary Material with Recycled Demolition Concrete for Pavement Applications. *Journal of Cleaner Production* 230: 129–136.

Barreto, L.S.S. 2014. *Environmental and Economic Life Cycle Assessment of Construction and Demolition Waste Management*, Master's Thesis, Florianópolis, 138 p.

Brazilian Association of Technical Standards- ABNT NBR 19286. 2021. *Mechanically Stabilized Earth Walls - Specification*. Rio de Janeiro, Brazil, 22 p.

Brazilian Federal District Government, GDF. 2016. Urban Cleaning Service-SLU. *Report on Urban Cleaning Services and Solid Waste Management in the Federal District (2015)*, Brasília, Brazil, 90 p.

Brazilian Institute of Geography and Statistics, IBGE. 2019. *Resident Population Estimates for Municipalities and Federation Units, Report, Population Co-ordination and Social Indicators*, Rio de Janeiro, Brazil,16 p.

Ghaaowd, I. & J. S. Mccartney, J.S. 2020. Pullout of Geogrids from Tire-derived Aggregate Having Large Particle Size. Technical Note- *Geosynthetics International* 27 (6): 671–684.

Mandloi, P., Hegde, A. & Sarkar, S. 2022. Performance Assessment of Mechanically Stabilised Earth Walls with Sustainable Backfills. *Engineering Sustainability* 175 (6): 302–318.

Mashifana, T. & Sithole, T. 2021. Clean Production of Sustainable Backfill Material from Waste Gold Tailings and Slag. *Journal of Cleaner Production* 308: 127357.

Mymrin, V., Pedroso, D.E., Pedroso, C.L., Avanci, M.A., Rolim, P.H.B., Carvalho, K.Q. & Catai, R.E. 2021. Physical-chemical Processes of Sustainable Construction Materials Structure Formation with Iron Ore Processing Tailings and Aluminum Anodizing Sludge. *Construction and Building Materials*, 298: 123698.

Norme Française. 2009. *NF P94-270. Geotechnical Calculation – Retaining Structures – Reinforced and Massive Backfills in Nailed Soil*. CSTB Éditions, France, 205 p.

Ok, B., Sarici, T., Demir, A., Talaslioglu, T. & Yildiz, A. 2023. Investigation of Construction and Demolition Materials Reinforced by Geosynthetics. *Engineering Sustainability*.

Palmeira, E.M. 1996. *Design and Construction of a Full-scale Pullout Box*. Research Report, Geotechnical Pos-Graduation Program. Brasilia, Brazil.

Pant, A., Datta, M. & Ramana, G.V. 2019. Bottom Ash as a Backfill Material in Reinforced Soil Strutures. *Geotextiles and Geomembranes* 47(4): 514–521.

Pierozan, R.C., Araujo, G.L.S., Palmeira, E.M., Romanel, C. & Zornberg, J.G. (2022). Interface Pullout Resistance of Polymeric Strips Embedded in Marginal Tropical Soils. *Geotextiles and Geomembranes*, 50: 20–39.

The Reinforced Earth Company. 1995. *Apparent Coefficient of Friction, f* to be Used in the Design of Reinforced Earth® Structures*. Technical Bulletin: MSE-6. Virginia, USA, 14 p.

Vieira, C.S. 2020. Valorization of Fine-grain Construction and Demolition (C&D) Waste in Geosynthetic Reinforced Structures. *Waste and Biomass Valorization* 11(4):1615–1626.

Zhang, H., Yuan, X., Liu, Y., Wu, J., Song, X. & He, F. 2020. Experimental Study on the Pullout Behavior of Scrap Tire Strips and Their Application as Soil Reinforcement. *Construction and Building Materials* 254, 1–11.

Laboratory study and meso-mechanical analysis of geogrid-reinforced sand under variable angle shear

MengXi Zhang, Hao Zhu & Cen Li
Shanghai University, Shanghai, China

ABSTRACT: In this paper, a series of laboratory tests were carried out through large direct shear apparatus, and the variation law of shear strength with different geogrid reinforcement angles was analysed. Using discrete element simulation, the influence of different placement angles on the meso-characteristics of geogrid reinforced soil is analysed from the perspectives of force chain evolution, geogrid deformation, shear band and particle displacement. The results show that when geogrid is placed at 60°, the shear strength is the highest and the tensile performance is fully exerted, which effectively prevents the displacement of soil. The force chain is concentrated and passes through the middle of the geogrid. The movement of soil particles in the lower box leads to the compression of the longitudinal ribs of geogrid placed at 120°, which fails to prevent the movement of soil particles, and the force chains are scattered due to the compression of soil.

Keywords: Geogrid, Direct shear tests, Discrete element simulation, Force chain

1 INTRODUCTION

Since geosynthetic-reinforced soil was first applied to engineering practice in 1970 (Leflaive 1988), this kind of reinforcement technology has received attention and been widely adopted with obvious advantages of low cost, high efficiency and good servicea-bility (Jia *et al*. 2021). A large number of research have been done on the performance of geosynthetic-reinforced structure under different conditions through field and laboratory tests and achieved remarkable results (Korini *et al*. 2021; Xue *et al*. 2014). Furthermore, the interface characteristics and the meso-reinforcement mechanism analysis through nu-merical simulation are also becoming new research focuses (Chen *et al*. 2021; Esmaeili *et al*. 2018; Grabowski *et al*. 2021).

At present, most of the interface characteristics analysis is based on the experimental study of geosynthetics placed in parallel to simulate the actual construction environment such as subgrade or slope. But the potential failure surface of reinforced soil often forms an angle with geosynthetics, which affects the performance of materials. For example, geogrid can effectively limit the displacement of soil due to its excellent tensile performance, but too large shear angle will also make it in compression, which will affect the reinforcement effect (Baadiga *et al*. 2021). Therefore, it is necessary to study the interface characteristics of geogrid reinforced soil under the condition of variable angle. In addition, for soil, a granular material, discrete element simulation has unique advantages in the analysis of interface characteristics between geosynthetics and soil, and provides a key data source for evaluating meso-performance and improving design methods (Liu *et al*. 2022). Feng *et al*. (2017) used discrete element simulation to analyse the direct shear behavior of the interface between geomembrane and sand, and proved that surface roughness and normal stress are important factors affecting the interface shear behavior. Wang *et al*. (2018) conducted a discrete

element model for rubber and sand mixtures, and analysed the parameters such as particle displacement, void ratio, stress state and force chain in the shearing process.

In this study, a large shear test of sand reinforced with geogrid at different angles is carried out. The influence of geogrid reinforcement angles on shear characteristics is ana-lysed from shear strength, cohesion and internal friction angle. In the mesoscopic analysis, the deformation, force chain evolution and particle displacement of sand reinforced with geogrid at different angles are studied through discrete element simulation. The conclusions drawn from this study provide a new idea for the research of geosynthetics.

2   EXPERIMENTAL SETUP

2.1   *Materials*

A sand was used in this study, with uniformity coefficient (Cu) of 2.78 and curvature co-efficient (Cc) of 1.14. Figure 1 shows the particle size distribution curve of the sand. which is then classified as poorly graded sand (SP) in accordance with ASTM D2487. A geogrid was used as the reinforcement material, and the tensile-strength test as per ASTM D6637 was carried out to obtain the technical indices, as shown in Table 1.
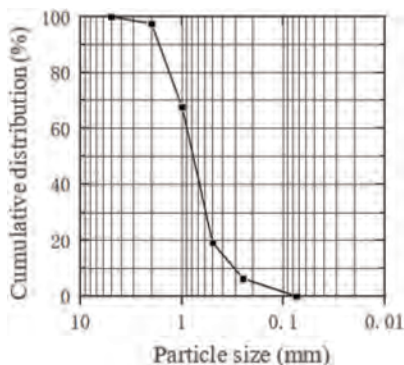
Figure 1.   Particle size distribution of test sand.

Table 1.   Technical indices of the geogrid.

Parameter	Value
Aperture size (mm)	40 × 40
Thickness (mm)	1.6
Tensile strength at 2% strain (kN/m)	10
Tensile strength at 6% strain (kN/m)	14
Ultimate tensile strength (kN/m)	17

2.2   *Test system*

The test system consists of direct shear instrument and data collection device, as shown in Figure 2. The dimensions of upper shear box are 300 mm × 300 mm × 100 mm, and 400 mm × 300 mm × 100 mm for the bottom shear box. The vertical stress was controlled by an air pump, which kept stable in the shearing process. The displacement is detected by a displacement meter, and the maximum range is 10 mm.
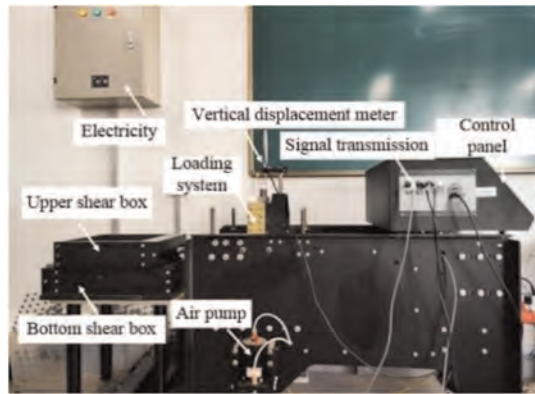
Figure 2. Schematic diagram of direct shear test system.

2.3 *Test procedures*

In order to analyse the relationship between shear stress and displacement of geogrid reinforced at different angles, the interface characteristics of specimens were tested under vertical stress of 50 kPa, 100 kPa, 150 kPa and 200 kPa, respectively. Samples were prepared by layered filling method. Sand was filled every 20 mm and compacted to the relative density (Dr=0.8). By changing the relative angle between geogrid and shear box, five different test conditions were designed, as shown in Figure 3. During the test, the upper shear box was fixed, and the shear plane was formed by moving the bottom shear box.
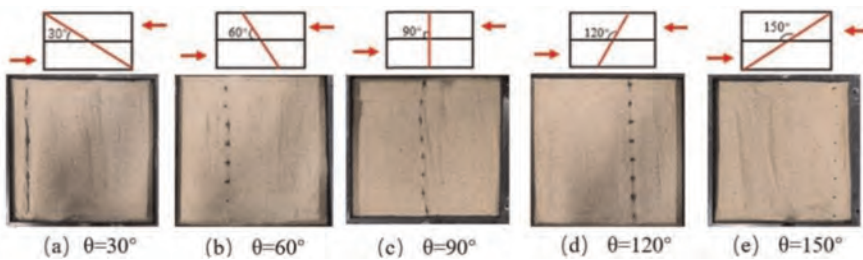
Figure 3. Schematic diagram of different arrangement angles of geogrid.

3 EXPERIMENTAL RESULTS

3.1 *Shear strength*

The shear stress-displacement curves for sand reinforced by geogrid, with five arrangement angles, under different normal stress, as shown in Figure 4. It can be seen that with the increase of shear displacement, the shear stress of all samples increases rapidly at the initial stage and then remains relatively stable after reaching the peak stress. In addition, the arrangement angle of geogrid has great influence on shear strength. The shear strength of the soil strengthened by geogrid arranged at 60° is the highest, and the geogrid gives full play to its tensile strength. However, when the arrangement angle is larger than 90°, the geogrid is mainly in a compressed state and leads to the decrease of reinforcement effect. Figure 5 shows the fitting lines for peak shear strength and vertical stress. The sample with best reinforcement effect when the arrangement angle is 60° has the maximum cohesion and internal friction angle, which are 25.2 kPa and 38.7° respectively.
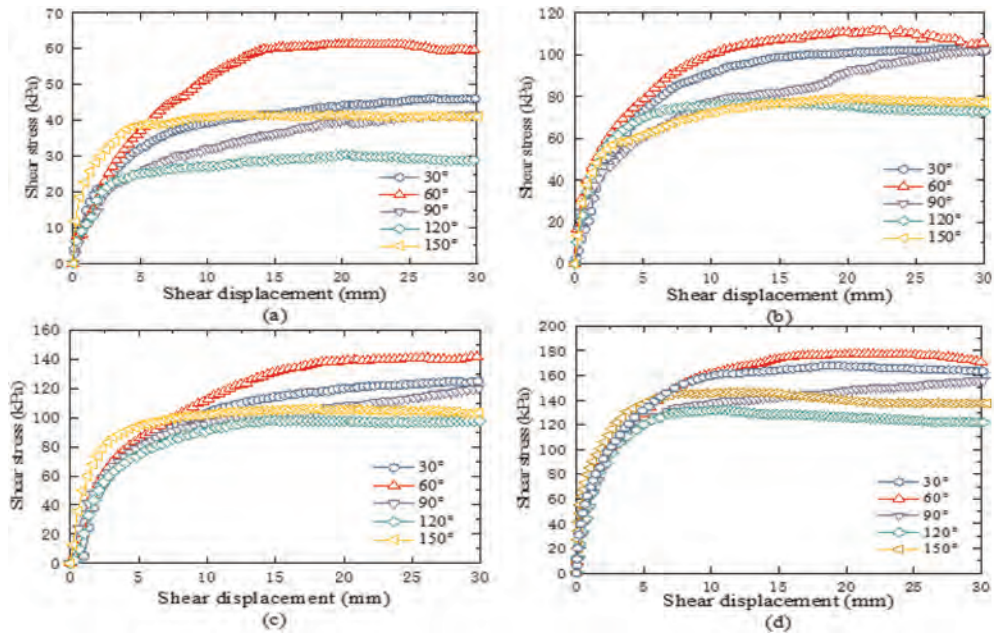
Figure 4. Shear stress-displacement curves for sand reinforced by geogrid at different angles under different vertical stress (a) 50 kPa, (b) 100 kPa, (c) 150 kPa, and (d) 200 kPa.
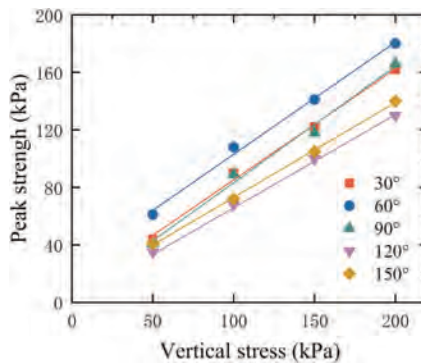
Figure 5. Fitting lines for peak strength and vertical stress under different geogrid arrangement angles.

4 NUMERICAL SIMULATIONS

4.1 *Model development*

The meso-characteristics during shear process are helpful to analyse the mechanism of reinforced soil. In this study, PFC^{3D} is used for discrete element simulation, which provides a powerful supplement for indoor shear test. The wall was generated to simulate the shear box, and its size was consistent with the experiment. In order to effectively simulate the friction and embedment between sand and reinforcement, the structured triangular cluster particles (clump) were used. The particle density of sand is 2600 kg/m^3. Both normal contact stiffness

and tangential contact stiffness are 3×10^5 N/m. The particle range of sand is 0.5-2 mm. The porosity is 0.4 and the friction factor is 0.2.

Geogrid was built by circular particles and big balls were used at nodes. The parallel bonding model was used for geogrid, and the tensile properties of geogrid were fitted by macroscopic tensile-strain relationship. The arrangement scheme of geogrid is the same as the experimental design. The numerical sample model is shown in Figure 6(a). The particle density of geogrid is 1800 kg/m^3. Both normal contact stiffness and tangential contact stiffness are 1×10^5 N/m. Both parallel bonding normal stiffness and parallel bonding tangential stiffness are 6×10^8 N/m. The particle range is 0.75-1.5 mm. The friction factor is 0.3. By numerical simulation, the macroscopic shear characteristics of the experiment were matched. Figure 6(b) shows the comparison of shear test and simulation results for different angles of geogrid under vertical stress of 200 kPa. Solid marks represent test results, and hollow marks represent simulation results. The curves show that the experimental and simulation results are very close, showing a good match.
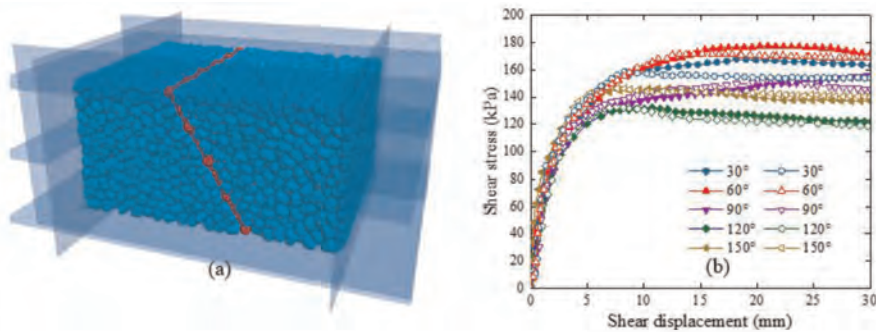
Figure 6. Discrete element simulation (a) Numerical model (b) The comparison curve of shear test and simulation results for different angles of geogrid under vertical stress of 200 kPa.

4.2 Force chain

The characteristics of load transfer between reinforcement and soil particles can be reflected from the distribution of force chain network. Figure 7 shows the evolution of force chain network of samples with different geogrid reinforcement angles under the vertical stress of 200 kPa. In order to save space, 60°, 90° and 120° are selected for analysis. Black indicates the compression state, and red indicates the tension state. It can be seen that under the action of shear stress, a strong chain penetrating the geogrid is formed in the soil. The geogrid with reinforcement angles of 60° and 90° are obviously stretched and deformed in different degrees. and the force chain remains stable. However, the geogrid with reinforcement angle of 120° is mainly subjected to compressive stress, and the force chain is broken and dispersed, which shows the shear zone characteristics on the shear plane.
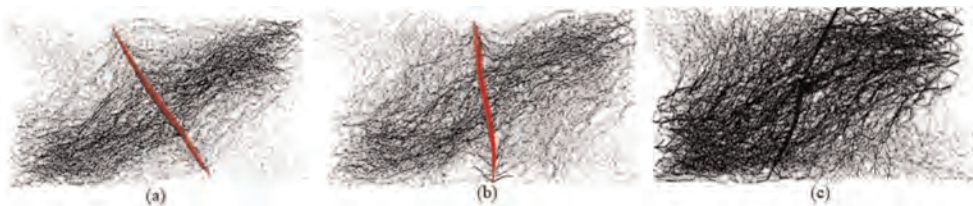
Figure 7. Force chain network of samples with different geogrid reinforcement angles under the vertical stress of 200 kPa (a) 60°, (b) 90°, and (c) 120°.

4.3 Geogrid deformation

Figure 8 shows a schematic diagram of geogrid deformation with different angles under vertical stress of 200 kPa. Red represents tension, black represents compression, and the thickness of force chain represents force value. It can be seen that when geogrid is reinforced at 60°, the tensile force near the shear zone is larger, and the force chain is thicker. The direction of geogrid arranged at 90° is quite different from the shear direction, but with the movement of particles, the angle of geogrid gradually deflects, and the longitudinal ribs tend to deflect downward. The geogrid arranged at 120° is obviously more deformed at both sides due to compression. It is worth noting that under all conditions, the transverse ribs of geogrid are generally in tension. This shows that whether the whole stress state of geogrid is tension or compression, the displacement of soil particles will be limited by the transverse ribs of geogrid.
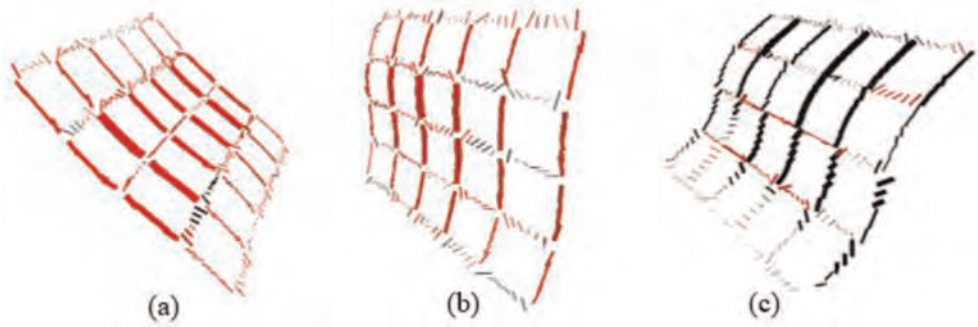
Figure 8.　Schematic diagram of geogrid deformation with different angles under vertical stress of 200 kPa (a) 60°, (b) 90°, and (c) 120°.

4.4 Displacement field

Generally speaking, it is difficult to observe the internal displacement of the sample in the actual direct shear test. In this paper, the displacement field of soil particles and geogrid is clearly reflected by discrete element simulation, as shown in Figure 9. Different geogrid angles have great influence on the results. The lower part of the sample with geogrid placed at 60° has a small particle displacement around the geogrid and hinder the movement of the lower soil. Therefore, the tensile performance of the geogrid can be fully utilized. The upper box soil prevents the geogrid from being pulled out, which leads to the increase of vertical stress. However, when the geogrid is placed at 90° and 120°, the movement of soil particles in the lower box causes the longitudinal rib of geogrid to be compressed, which fails to effectively prevent the movement of soil particles.
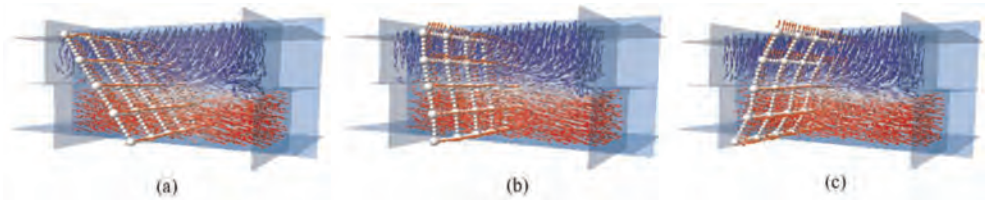
Figure 9.　Displacement field of samples with geogrid placed at different angles under vertical stress of 200 kPa (a) 60°, (b) 90°, and (c) 120°.

5 CONCLUSIONS

In this study, the influence of geogrid angle on the shear characteristics of reinforced soil was studied by using large-scale direct shear apparatus, and a discrete element simulation was carried out to analyse meso-characteristics. The conclusions can be summarized as follows:

1. In the laboratory test, the geogrid with less than 90° is helpful to exert its tensile performance. The shear strength of soil strengthened by geogrid at 60° is the highest. When the arrangement angle is larger than 90°, the geogrid is mainly in a compressed state and leads to the decrease of reinforcement effect.
2. The force chain of samples reinforced by geogrid with reinforcement angles of 60° is thicker passes through the geogrid. However, the geogrid with reinforcement angle of 120° is deformed greatly, mainly bears compressive stress, and the force chain breaks and disperses, showing the characteristics of shear band on the shear plane.
3. The tensile property of geogrid with an angle of 60° can be fully utilized, and the movement of soil particles can be effectively prevented. However, when the geogrid is placed at 90° and 120°, the movement of soil particles in the lower box causes the longitudinal ribs of geogrid to be compressed, which fails to effectively prevent the movement of soil particles.

REFERENCES

ASTM, 2011. *Standard Practice for Classification of Soils for Engineering Purposes. D2487*. West Conshohocken, PA.

ASTM, 2015. *Standard Test Method for Determining Tensile Properties of Geogrids by the Single of Multi-Rib Tensile Method. D6637*. West Conshohocken, PA.

Baadiga, R., Saride, S., Balunaini, U., et al. 2021. Influence of Tensile Strength of Geogrid and Subgrade Modulus on Layer Coefficients of Granular Bases. *Transportation Geotechnics*, 29, 100557.

Chen, J.F., Guo, X.P., Sun, R., et al. 2021. Physical and Numerical Modelling of Strip Footing on Geogrid Reinforced Transparent Sand. *Geotextiles and Geomembranes*, 49, 399–412.

Esmaeili, M., Naderi, B., Neyestanaki, H.K., et al. 2018. Investigating the Effect of Geogrid on Stabilization of High Railway Embankments. *Soils and Foundations*, 58, 319–332.

Feng, S.J., Liu, X., Chen, H.X., et al. 2017. Micro-mechanical Analysis of Geomembrane-sand Interactions using DEM. *Computers and Geotechnics*, 94, 58–71.

Grabowski, A., Nitka, M., Tejcman, J. 2021. 3D DEM Simulations of Monotonic Interface Behaviour between Cohesionless Sand and Rigid Wall of Different Roughness. *Acta Geotechnica*, 16, 1001–1026.

Jia, M.C., Zhu, W.K., Xu, C. 2021. Performance of a 33m High Geogrid Reinforced Soil Embankment without Concrete Panel. *Geotextiles and Geomembranes*, 49, 122–129.

Korini, O., Bost, M., Rajot, J.P., et al. 2021. The Influence of Geosynthetics Design on the Behavior of Reinforced Soil Embankments Subjected to Rockfall Impacts. *Engineering Geology*, 286, 106054.

Leflaive, E. 1988. Durability of Geotextiles: The French experience. *Geotextiles and Geomembranes, 7 (Nos. 1–2)*, 23–31.

Liu, F.Y., Fu, J., Wang, J., et al. 2022. I Effect of the Particle Size Ratio on Macro- and Mesoscopic Shear Characteristics of the Geogrid-reinforced Rubber and Sand Mixture Interface. *Geotextiles and Geomembranes*, 50, 779–793.

Wang, C., Deng, A., Taheri, A. 2018. Three-dimensional Discrete Element Modeling of Direct Shear Test for Granular Rubber-sand. *Computers and Geotechnics*, 97, 204–216.

Xue, J.F., Chen, J.F., Liu, J.X., et al. 2014. Instability of a Geogrid Reinforced Soil Wall on Thick Soft Shanghai Clay with Prefabricated Vertical Drains: Case Study. *Geotextiles and Geomembranes*, 42 (4), 302–311.

Modelling temperature dependent behavior of soil-polyethylene contact surfaces

Ö. Bilgin
University of Dayton, Dayton, Ohio, USA

B. Shah
Clayton Concrete, Edison, New Jersey, USA

ABSTRACT: Polyethylene has temperature dependent properties. As a thermoplastic material, it softens on heating and hardens on cooling. This behavior affects the contact surface areas of materials made out of polyethylene, such as geomembranes, adjacent to other materials. Interface strength properties depend on the contact area and stress at the interface. Since the soil-geomembrane interfaces are relatively weak and potentially form the critical failure planes, modeling temperature dependent soil-polyethylene contact surfaces is important. A theoretical model to determine soil-polyethylene contact areas was developed during this study and presented in this paper.

Keywords: Polyethylene, geomembrane, contact surfaces, interfaces, temperature effects, thermal properties

1 INTRODUCTION

Polyethylene is one of the most widely used materials in geosynthetics and in their civil engineering applications. For example, polyethylene material is used in 70% of the geomembranes, which are relatively thin and impervious sheets of polymeric materials used primarily in hydraulic structures, e.g. reservoirs and canals, and landfills as impervious boundary for liquid and/or gas containment (Koerner 2005). Some of the example applications of geomembranes are: as liners for potable water, radioactive and hazardous waste liquid, solar ponds, agriculture industry, aquiculture industry, waste conveyance canals, solid-waste landfills; as covers for solid-waste landfills; as cutoffs within zoned earth dams for seepage control; as linings for emergency spillways; as waterproofing liners within tunnels and pipelines; as waterproof facing of dams; as a barrier to odors from landfills, to vapors (such as radon) beneath buildings; to control expansive soils and frost-susceptible soils; and to shield sinkhole-susceptible areas from flowing water (Koerner 2005).

The interfaces between soil and polyethylene material these materials are relatively weak and constitute critical potential failure planes. Therefore, the soil-geomembrane contact surfaces and interface shear behavior is critical to an overall performance of the structure in majority of the applications listed above. With the increased use of geosynthetic materials in civil and geotechnical engineering applications, interface shear behavior between sand and geosynthetic materials have been investigated by several researchers. Studies showed that the interface shear depends on soil properties (such as composition, grain size, water content, and density) and geosynthetic properties (such as tensile strength, modulus, surface roughness, surface hardness) as well as the loading conditions (Bilgin & Stewart 2006; Bilgin & Stewart 2009; Dove & Frost 1999; Dove & Jarrett 2002; DeJong & Westgate 2005; Dove *et al.* 2006; Martin *et al.* 1984; O'Rourke *et al.* 1990; Saxena & Wong 1984; Williams & Houlihan 1987).

The polyethylene has also temperature dependent properties. Temperature-induced changes in the modulus of polyethylene material are significant. For example, between 0 and 50°C, the modulus of the polyethylene increases by nearly a factor of two, with higher modulus at lower temperatures. Therefore, the soil-geomembrane interface shear strength will be affected by the temperature, since the interface shear depends on the geosnythetic material's modulus as mentioned earlier.

The objective of this study was to develop a model for the temperature dependent contact surface areas of soil-polyethylene interfaces. The model developed and the effect of temperature and its variations on the soil-polyethylene contact surface areas is presented in this paper.

2 EFFECT OF TEMPERATURE ON POLYETHYLENE

Polyethylene has temperature dependent properties. The operating temperatures of geosynthetics made out of polyethylene used in civil engineering applications are well below the melting temperature and well above the glass transition temperatures. However, the geosynthetics are exposed to different temperatures in the applications that they are used and during their design life. Within the operating temperatures, temperature dependent properties of polymers affect the behavior of geosynthetics. The modulus of polyethylene changes nearly by a factor of two between 0 and 50°C, with higher modulus at lower temperatures as shown in Figure 1 (Bilgin 2007). The modulus of medium density polyethylene (MDPE) is approximately 80% of the high density polyethylene (HDPE).
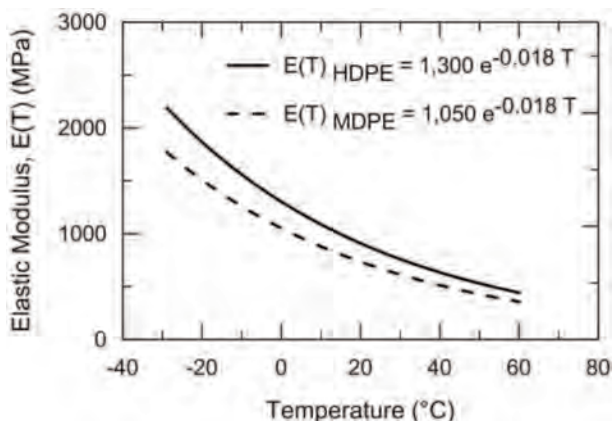
Figure 1. Temperature dependent modulus of high density (HDPE) and medium density (MDPE) polyethylene (after Bilgin *et al.* 2007).

Geomembranes are used as a part of liner systems in modern landfills. The studies showed that significant amount of heat is generated in landfills, resulting in long–term elevated waste temperatures (Lefebvre *et al.* 2000; Yesiller *et al.* 2005). As much as 87°C temperatures were measured inside a landfill (Klein 2001). These high temperatures will affect the modulus of elasticity of the polyethylene materials significantly which will affect the soil-geomembrane contact surface areas and the interface shear strength characteristics.

3 CONTACT AND FRICTION BETWEEN SURFACES

A friction behavior of smooth geomembrane-particle interfaces has been studied in details and the shear mechanisms involved has been discussed by Dove & Frost (1999). A frictional

force between two solid surfaces is proportional to the normal force at the surface. The constant of proportionality is defined as coefficient of friction, μ, and given by:

$$\mu = \tan \delta = \frac{F}{W} \quad \text{or} \quad \mu = \tan \delta = \frac{\tau}{\sigma} \tag{1}$$

where δ = interface friction angle; F = friction force; W = normal force; τ = shear stress; and σ = normal stress. These equations are used commonly in geotechnical engineering and holds reasonably well for the materials involved. However, it is not valid for many materials since their friction coefficients can vary with normal load.

The friction force, F, is governed by two fundamental shear strength components (Adamson 1982; Briscoe 1992; Bowden & Tabor 1956; Shooter & Tabor 1952), adhesion and plowing, or plastic deformation components, and it is given as:

$$F = F_{adhesion} + F_{plowing} \tag{2}$$

The adhesion component is identified as microscale process formed because of the pressing of two materials at the contacts and becoming like one continuous material. It is given as:

$$F_{adhesion} = \tau_a \ A_c \tag{3}$$

where τ_a = material shear strength at points of contact; and A_c = real contact area between two materials. It has been reported that τ_a is the bulk shear strength of the softer material and can be stress level dependent (Stachowiak & Batchelor 1993).

The plowing component is given as:

$$F_{plowing} = \tau_p \ A_p \tag{4}$$

where τ_p = bulk strength of the softer material; and A_p = cross-sectional area of plowed track.

The contact area, A_c, for the elastic contact conditions is given by Hertz as (Adams 1992):

$$A_c = \pi \left(\frac{3WR}{4E'} \right)^{2/3} \tag{5}$$

where W = applied load; R = mean radius of curvature = $(1/r_1 + 1/r_2)^{-1}$; where r_1 and r_2 are the particle radii; and E' = composite elastic modulus given by:

$$E' = \left(\frac{1-v_1^2}{E_1} + \frac{1-v_2^2}{E_2} \right)^{-1} \tag{6}$$

where E_1 and E_2 = modulus of elasticity of each material; and v_1 and v_2 = Poisson's ratio of each material.

4 MODELLING TEMPERATURE DEPENDENT CONTACT SURFACE AREA

As previously discussed, the modulus of polyethylene is temperature dependent and this will affect the soil-geomembrane contact surface area as schematically shown in Figure 2. Figure 2(a) shows the soil particles and the geomembranes before the contact, i.e. just before the loading. For better visualization uniform grain size and orderly packed configuration is shown, although in reality the grain sizes and particle configurations vary. While Figure 2(b) shows the penetration of soil particles into the geomembrane due the soil weight (plus surcharges, if any) right after the placement of the soil at relatively lower temperatures, Figure 2 (c) shows the increased penetration and the contact area at relatively higher temperatures. For this study, a smooth under-support to the geomembrane is assumed. Another soil layer below the geomembrane (depending on geomembrane thickness, size of soil particles, and orientation of soil particles), could cause waviness along the geomembrane and could affect the mean radius of curvature, R, given in Equation 5.
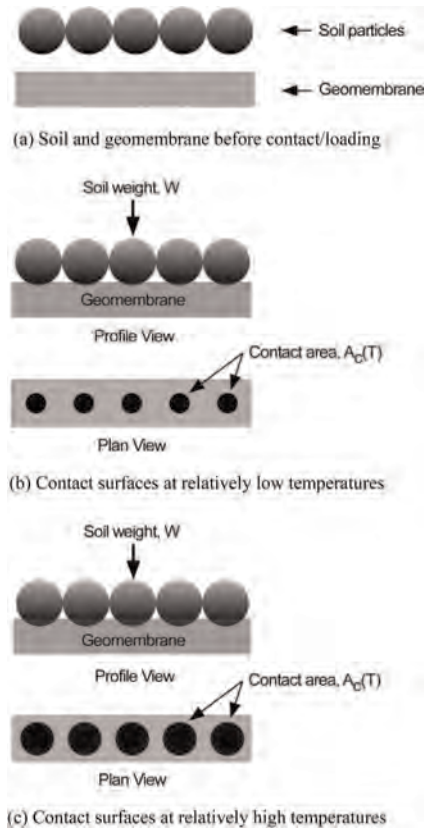
Figure 2.   Effect of temperature on soil-geomembrane contact area: (a) Soil grains and geomembranes before construction, (b) Penetration of soil particles and contact area of the soil grains on the geomembrane surface at relatively low temperatures, and (c) At relatively high temperatures.

To account for the temperature dependent behavior of polyethylene, the contact area given by the Hertz equation (Equation 5) can be modified as:

$$A_c(T) = \pi \left(\frac{3WR}{4E'(T)} \right)^{2/3} \tag{7}$$

where $A_c(T)$ = temperature-dependent contact area; and $E'(T)$ = temperature-dependent composite elastic modulus that can be given as:

$$E'(T) = \left(\frac{1 - v_1^2}{E_1} + \frac{1 - v_2^2}{E_2(T)} \right)^{-1} \tag{8}$$

where $E_2(T)$ = temperature-dependent modulus of polyethylene (Figure 1) in contact with soil particles. The modulus of soil particles, E_1, can be assumed to be constant during the service life of the structure.

The effect of temperature on the soil-polyethylene interface contact surface area using the proposed modified Hertz equation (Equation 7) is given in Figure 3. The temperature-dependent composite section modulus, $E'(T)$, for the soil-geomembrane interface calculated using Equation 8 is shown in Figure 3(a). The modulus and Poisson's ratio of 72,000 MPa
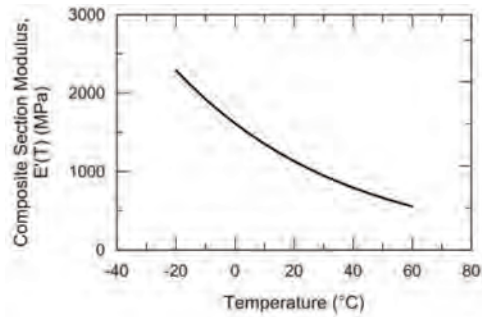
(a) Composite section modulus of soil-geomembrane interface
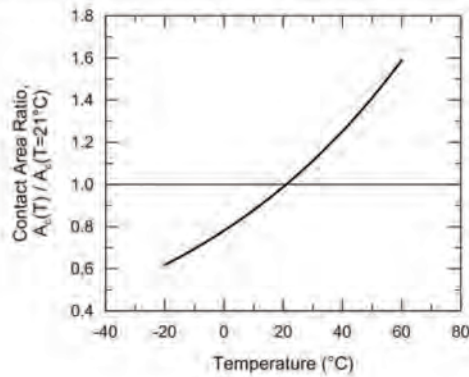
(b) Change in soil-geomembrane contact area at the interface

Figure 3.   Effect of temperature on the soil-geomembrane contact area: (a) Temperature-dependent composite modulus of the interface, and (b) Contact area ratio (contact area at any temperature over the contact area at 21°C).

and 0.17, respectively, (for quartz) were used for the soil particles. The change in the contact area is shown as the ratio of temperature-dependent contact area, $A_c(T)$, (Equation 7) to the reference contact area, $A_c(T = 21°C)$ as:

$$\text{Contact Area Ratio} = \frac{A_c(T)}{A_c(T = 21°C)} \tag{9}$$

Figure 3 shows that temperature increase of approximately 40°C, with respect to reference temperature of 21°C, will results in 60% increase in the soil-geomembrane contact area. On the other hand, a decrease of approximately 40°C will result in 38% drop in the contact surface area.

5   CONCLUSIONS

Many of the geomembrane materials have temperature-dependent properties. In this paper, the effect of temperature on the soil-polyethylene material contact area was studied using a theoretical approach. An existing model used for the contact area between surfaces has been modified to include the temperature-dependent material property of geomembranes. The results show that the contact area at the interface can change significantly (as much as 60%

with respect to baseline temperature of 21°C or as much as 150% within the range of temperatures (−20 to 60°C) investigated during this study.

REFERENCES

Adams, M.J. (1992). "*Friction of Granular Non-metals.*" Fundamentals of Friction: Macroscopic and Microscopic Processes, I.L. Singler and H.M. Pollock, eds., Kluwer, Dordrecht, The Netherlands: 183–207.

Adamson, A.W. (1982). *Physical Chemistry of Surfaces*. Wiley, NY.

Bilgin, Ö. and Stewart, H.E. (2006). "Effect of Temperature on Surface Hardness and Soil Interface Shear Resistance of Geosynthetics." *Proc., 8th International Conference on Geosynthetics*, Vol. 1, Yokohama, Japan: 251–254.

Bilgin, Ö. and Stewart, H.E. (2009). "Design Guidelines for Polyethylene Pipe Interface Shear Resistance." *J. of Geotechnical and Geoenvironmental Engineering*, ASCE. 135(6): 809–818.

Bilgin, Ö., Stewart, H.E., and O'Rourke, T.D. (2007). "Thermal and Mechanical Properties of Polyethylene Pipes." *J. of Materials in Civil Engineering*, ASCE. 19(12): 1043–1052.

Bowden, F.P. and Tabor, D. (1956). *Friction and Lubrication*. Methuen, London.

Briscoe, B.J. (1992). "*Friction of Organic Polymers.*" Fundamentals of Friction: Macroscopic and Microscopic Processes, I. L. Singler and H. M. Pollock, eds., Kluwer, Dordrecht, The Netherlands: 167–182.

DeJong, J.T. and Westgate, Z.J. (2005). "Role of Overconsolidation on Sand-geomembrane Interface Response and Material Damage Evolution." *Geotextiles and Geomembranes*. 23: 486–512.

Dove, J.E., Bents, D.D., Wang, J., and Gao, B. (2006). "Particle-scale Surface Interactions of Non-dilative Interface Systems." *Geotextiles and Geomembranes*. 24: 156–168.

Dove, J.E. and Frost, J.D. (1999). "Peak Friction Behavior of Smooth Geomembrane-particle Interfaces." *J. of Geotechnical and Geoenvironmental Engineering*, ASCE. 125(7): 544–555.

Dove, J.E. and Jarrett, J.B. (2002). "Behavior of Dilative Sand Interfaces in a Geotribology Framework." *J. of Geotechnical and Geoenvironmental Engineering*, ASCE. 128(1): 25–37.

Klein R, Baumann T, Kahapka E, Niessner R., (2001). Temperature Development in a Modern Municipal Solid Waste Incineration (MSWI) Bottom ash Landfill with Regard to Sustainable Waste Management. *Journal of Hazardous Materials, 2001 May 30*;83(3):265–80.

Koerner, R.M. (2005). *Designing with Geosynthetics*, Fifth Edition, *Pearson Prentice Hall*, New Jersey.

Lefebvre, X., Lanini, S., and Houi, D. (2000). "The Role of Aerobic Activity on Refuse Temperature Rise, Landfill Experimental Study." *Waste Management & Research*, Vol. 18, 444–452.

Martin, J.P., Koerner, R.M., and Whitty, J.E. (1984). "Experimental Friction Evaluation of Slippage between Geomembranes, Geotextiles, and Soils." Proc. of International Conference on Geomembranes, Denver, CO: 191–196.

O'Rourke, T.D., Druschel, S.J., and Netravali, A.N. (1990). "Shear Strength Characteristics of Sand-polymer Interfaces." *J. of Geotechnical Engineering*, ASCE. 116: 451–469.

Saxena, S.K. and Wong, Y.T. (1984). "Friction Characteristics of a Geomembrane." *Proc. of International Conference on Geomembranes*, Denver, CO: 187–190.

Shooter, K.V. and Tabor, D. (1952). "The Frictional Properties of Plastics." *Proc., Phys. Soc., Ser. B*. 65: 661–671.

Stachowiak, G.W. and Batchelor, A.W. (1993). *Engineering Tribology*. *Elsevier Science*, Amsterdam.

Yesiller, N., Hanson, J.L., and Liu, W-L. (2005). Heat Generation in Municipal Solid Waste Landfills, *Journal of Geotechnical and Geoenvironmental Engineering*, Vol. 131, No. 11, 1330–1344.

Williams, N.D. and Houlihan, M.F. (1987). "Evaluation of Interface Friction Properties between Geosynthetics and Soils." *Geosynthetics '87 Conference*, 616–627.

Machine learning for soil-geosynthetic interface shear strength analysis

T.T. Abenezer*, G.L.S. Araújo*, F. Evangelista Jr.* & R.M.S. Gomes*
University of Brasilia, Brazil

ABSTRACT: This paper presents geosynthetic interface friction angle prediction by using the Random Forest algorithm. A number of 495 interfaces consisting geomembrane and cohesionless soil and fourteen influencing parameters for each interface are used. In the analysis the Pearson's correlation coefficient is used to measure the linear interdependence between each pair made by input-input and input-output parameters. After the linear analysis, an optimized Random Forest has been initialized to make a prediction of the interface friction angle. Random Forest splits the implemented data into training and testing sets and it is observed only for 3% of the training set and 6% of the testing set the estimation has exceeded $\pm 5°$ from the actual records. R^2 measures shows strong coherence between predicted and laboratory study friction angles by resulting $R^2 = 0.93$ for training and $R^2 = 0.92$ for testing set. Thus, the Random Forest has forecasted interface friction angle adequately.

1 INTRODUCTION

Several soil structures and waste disposal areas can be constructed by single or multilayer of geosynthetics for filtration, drainage containment or reinforcement. The interaction between geosynthetic layers and the reinforced soil is an important section for determining the overall structure stability. Laboratory experiments are the main practice to study geosynthetic interface strength and direct shear test, medium size direct shear test, and inclined plane (ramp) test are the most practiced ones. Several authors states that interface shear strength can be affected by some critical factors like type of test equipment, applied normal stress, the strain rate, contact area between interface components, type of geosynthetics, thickness of geomembrane, asperity height of geomembrane, relative density of reinforced soil, specific gravity of soil, coefficient of curvature, coefficient of uniformity, D_{50} and friction angle of soil (Araujo *et al.* 2022; Bacas *et al.* 2015; Carbone *et al.* 2015; Choudhary *et al.* 2016; Cen *et al.* 2018; Lashkari & Jamali 2021; Pavanello 2021, 2022; Sánchez 2018; Vangla *et al.* 2017).

Based on the finding of these practical laboratory results it is possible to build a prediction model by using Machine Learning algorithms. Machine Learning algorithms are set to learn from an available data and trained to make a projection of a certain parameter. In this study Random Forest regression will be initialized to predict geomembrane-sand interface shear strength. Some researchers applied Random Forest to geotechnical engineering parameters analysis (Dutta *et al.* 2019; Ly *et al.* 2020; Pham *et al.* 2020; Zhang *et al.* 2019, 2021, 2022; Zhou *et al.* 2019).

Although there are investigations over the years on the topic, there is a need to improve the interface shear strength determination between geomembranes and other materials, and

---

*Corresponding Authors: abenitefera@gmail.com, gregorio.unb.br, fejr@unb.br and raisla.gomes@aluno.unb.br

Machine Learning has great potential for this application. A number of 495 interfaces from three test types (conventional direct shear, medium size direct shear and inclined plane tests) and 14 influencing factors for each interface are recorded. The impact type and level of each parameter can be determined by the other factors in the test. To measure the inter-dependence between the variables their corresponding values corelated by Pearson's correlation. The Pearson's correlation coefficient results are indicating that, the influence level between most parameters is not considerably strong. These values indicate the nonlinearity of the database and the need of a multivariate algorithm for studying this type of interface. This investigation aims at evaluating Random Forest algorithm of Machine Learning, projecting interface shear strength. To improve the performance of Random Forest, a powerful minimizer tool called Differential Evolution is applied.

2 DATA ANALYSIS

The laboratory results from the three different test types compiled together to build single prediction model. In this work, 495 interface friction angles from different works of literature are accumulated and employed in the regression analysis. The types of studies and the number of samples they provided are listed in Table 1.

Table 1. Types of data providing studies.

No.	Type of studies	No. of samples
1	Dissertations/Theses	103
2	Research papers from journals	357
3	Manufacturing companies' results	35

3 APPLIED METHODS

3.1 *Pearson's correlation measures*

The influence of each considered interface component on the interface friction angle, may vary depending on the other involved strands. For example; the level of the effect of the applied normal stress on the interface shear strength outcome depends by other parameters such as the sliding velocity of the upper box in the inclined plane test (Carbone *et al.* 2015; Lashkari 2021; Pavanello *et al.* 2021; Sánchez 2018). This is due to when the ramp proceeds on tilting, the upper box tends to slide quickly and the applied stress level tends to decrease. These inter-correlations between the affecting elements and the friction angle and among the input variables are analyzed by Pearson's coefficient.

The Pearson coefficient (ρ) is a type of correlation coefficient that represents the linear relationship between two variables that are measured on the same interval or ratio scale. It is a measure of the strength of the association between two continuous variables. Its value ranges between -1 to 1 and a value close to |1| indicates higher influence level and when it is closer to 0 it shows lower interdependence between the observed parameters. In this study the value $\bar{\rho} \geq |0.2|$ is considered as indication of the presence of a certain influence level (Pant & Ramana 2021).

3.2 *Performance measures*

Two performance assessment criteria namely Coefficient of Determination (R^2) and Root Mean Square Error (RMSE) are used to evaluate the prediction capability of the Random

Forest algorithm. R^2 measures how much variability in dependent variable can be explained by the model and presents the linear correlation between the actual and predicted outputs. Values of R^2 range from 0 to 1, and higher value close to 1 indicates a better accuracy and lower values closer to 0 indicates poor prediction.

$$R^2 = 1 - \frac{SS_{Residuals}}{SS_{Total}} \tag{1}$$

Where $SS_{Residuals}$ = the sum of square of residuals; SS_{Total} = the sum of the square of the observed variable.

While, the root mean square error (RMSE) is defined as the square root of differences between predicted and observed values. The RMSE estimates the magnitude of the errors which are known as "residuals". RMSE is a standard way to measure the error of a model in predicting quantitative data and its lower value indicates a better performance of the model.

$$RMSE = \sqrt{\frac{1}{n}\sum_{i=1}^{n}\left(y_i - \widehat{y_i}\right)^2} \tag{2}$$

where y_i = the observed variable $\widehat{y_i}$ = dependent or prediction variable.

3.3 Random Forest (RF)

RF is developed by Breiman, (2001) and it is a supervised machine learning algorithm which is constructed from decision trees and used to solve regression problems. RF is implemented based on bagging decision trees by employing random split selection and it extracts multiple sub-sample sets from the original sample set, each of them independently forms a decision tree. A five-fold cross-validation method is applied during random sampling, where 4/5 of the selected features will be utilized for training the model and 1/5 of the randomly selected features applied for testing the performance. Thus, the database is split in to 80% for training and 20% for testing purpose and decision trees randomly select features to split nodes internally to form a random forest. For the regression algorithm, the prediction result is the average of all decision tree output results (Zhang *et al*. 2021). Number of trees, maximum depth of trees and minimum number of samples to split a node are called hyperparameters of a RF. A proper optimization of hyperparameters leads to a more accurate prediction of the algorithm (Zhou *et al*. 2019). To optimize the RF hyperparameters, Differential Evolution, which is a powerful minimizer adopted in this study (Pierre *et al*. 2021).

3.4 Differential Evolution (DE)

Differential Evolution (DE) is a heuristic approach for the global optimization of nonlinear and non-differentiable continuous space functions (Storn & Price 1997). It starts with an initial population of candidate solutions. These candidate solutions are iteratively improved by introducing mutations into the population, and retaining the fittest candidate solutions that yield a lower objective function value. DE can handle nonlinear and non-differentiable multi-dimensional objective functions, while requiring very few control parameters to steer the minimization. These characteristics make the algorithm easier and more practical to use. The algorithm works in two phases, i.e., (i) Initialization: population is generated randomly and, (ii) Evolution: the generated population goes through mutation, crossover and selection processes which are repeated until a termination criterion is met. The RF hyperparameters which are the number of trees, maximum depth and minimum number of samples to split a node are the populations for the DE application. These hyperparameters are optimized by the mutation, crossover and selection steps of DE. The number of trees optimized to 103, the maximum depth in each tree is 30 and the minimum number of samples to split a node are determined as 4.

4 RESULTS

4.1 *Linear correlation results*

The influence extent of each considered interface parameter on its adjacent pair is analyzed by Pearson's correlation coefficient results. There are 44 pairs of variables which are showing the presence of influence among the total 105 pairs of variables analyzed herein. Of the 44 pairs, 37 pairs show moderate, 6 of them are showing strong and one of them is showing very strong linear correlations. This designates that 58% of the total pairs have negligible linear relationships. If the ruling observation focuses only on the Pearson's coefficient results it can mislead to a stipulation of a lack of influence between studied variables. However, the analysis can be interpreted as an implication of non-linearity between the pairs (Spanos 2003).

4.2 *Optimized RF results*

The prediction performance of RF is assessed by calculating R^2 and RMSE. As shown in Figure 1, the interface friction angle estimation for the training data resulted in $R^2 = 0.93$ and RMSE = 1.94. And for prediction of the testing set, it is measured $R^2 = 0.92$ and RMSE = 2.09. This indicates a good agreement and less residual error between interface friction angle from RF estimation and laboratory test results. In civil and geotechnical engineering parameters prediction utilizing ML algorithms, $R^2 > 0.90$ is considered as an indication of a very good fit (Dutta *et al*. 2019; Farooq *et al*. 2020; Liu *et al*. 2020; Zhang *et al*. 2021). Figure 1 shows most of the predicted friction angles varied less than ±10%, and few of them are exceeded ±10% and prediction exhibited ±20% error is very rare, either on training or testing set.
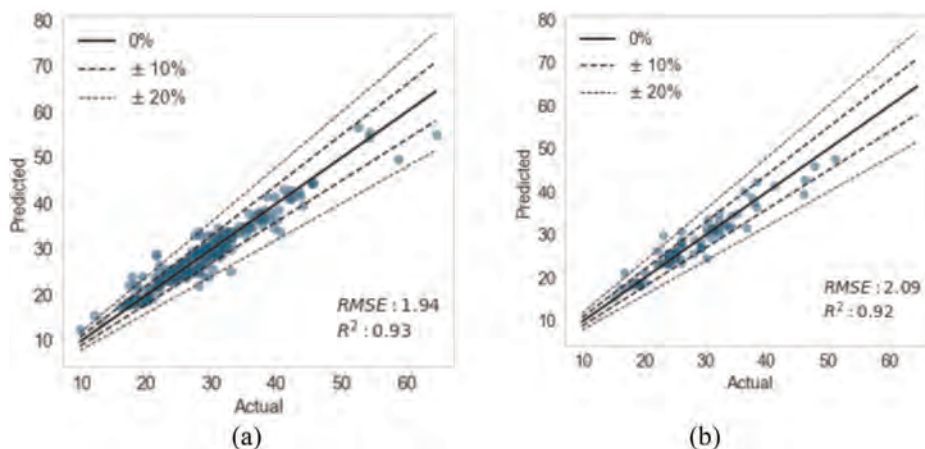
Figure 1. Optimized RF prediction performance measures (a) training set, (b) testing set.

Furthermore, the performance of the RF algorithm was performed by determining residual errors. Figure 2 shows that the actual laboratory results (O marks) and the predicted interface friction angles (X marks) obtained by the RF model are in strong agreement. From the total interfaces, 80% of the samples are utilized in the training set. As shown in Figure 2a from 396 predicted interface shear strength, only for 12 of them the friction angle has a ±5° variation from laboratory test results. For the remaining 384 interfaces the difference between interface friction angles of RF estimation and actual laboratory test is lower than 5°. As aforementioned, 20% of the data is utilized in the testing set and Figure 2b shows that from 99 predicted interfaces, only for 8 of them the friction angle has outlined a ±5°

difference from the literatures. For the remaining 91 interfaces, the difference between predicted and actual laboratory test friction angles remained lower than 5°.
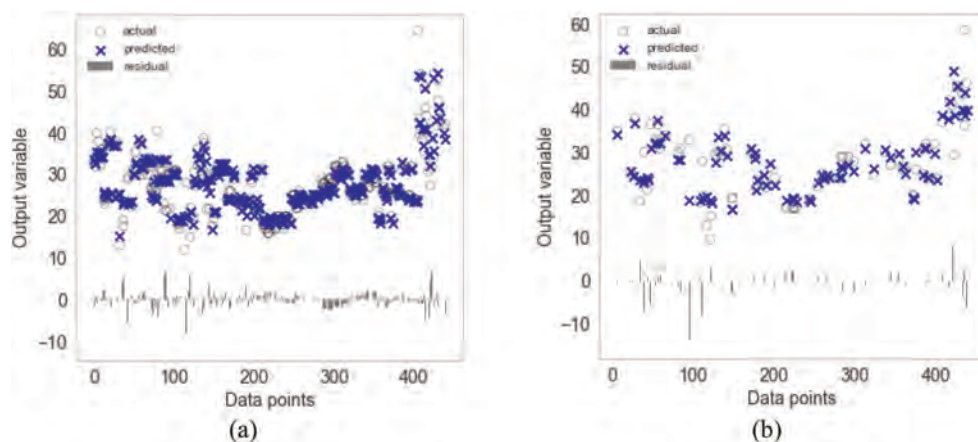
Figure 2. Predicted, actual and residual values for interface friction angle by RF model: (a) training set, (b) testing set.

5 CONCLUSIONS

This paper initiates a discussion about the application of Random Forest for geomembrane interface shear strength analysis. A total number of 495 interface friction angles and 14 influencing factors for each interface are used to create the data set. Based on the analysis and results the following conclusions are driven;

- Pearson's correlation coefficient measurements showed limitations for the utilized database by resulting for 58% of the total 105 pairs, $\overline{\rho} < |0.2|$.
- The optimized Random Forest regression algorithm predicted geomembrane-sand interface friction angle adequately by resulting $R^2 = 0.93$ for training and $R^2 = 0.92$ for testing set.
- The Random Forest regression model functioned better with the nonlinearity of the data and delivered a prediction in strong coherence with laboratory test results.

REFERENCES

Afzali-Nejad, A., Lashkari, A., & Shourijeh, P.T. 2017. Influence of Particle Shape on the Shear Strength and Dilation of Sand-woven Geotextile Interfaces. Geotextile and Geomembrane 45 (1): 54–66.

Araujo, G.L.S., Sánchez, N.P., Palmeira, E.M., & Maria, G.G.A. 2022. Influence of Micro and Macroroughness of Geomembrane Surfaces on Soil-geomembrane and Geotextile Interface Strength. Geotextiles and Geomembrane 50 (4): 751–763.

Bacas, B.M., Cañizal, J., & Konietzky, H. 2015. Frictional Behavior of Three Critical Geosynthetic Interfaces. Geosynthetics International 22 (5): 355–365.

Breiman, L. 2001. Random Forests. Machine Learning 45 (1): 5–32.

Carbone, L., Gourc, J.P., Carrubba, P., Pavanello, P., & Moraci, N. 2015. Dry Friction Behavior of a Geosynthetic Interface using Inclined Plane and Shaking Table Tests. Geotextile and Geomembranes 43 (4): 293–306.

Choudhary, A., K., & Krishna, A., M. 2016. Experimental Investigation of Interface Behavior of Different Types of Granular Soil/Geosynthetics. International Journal of Geosynthetic and Ground Engineering 2(4): 1–11.

Cen, W., Wang, H. & Sun, Y. 2018. Laboratory Investigation of Shear Behavior of High-Density Polyethylene Geomembrane Interfaces. Polymers 10(734).

Dutta, R.K., Gnananandarao, T. & Sharma, A. 2019. Application of Random Forest Regression in the Prediction of Ultimate Bearing Capacity of Strip Footing Resting on Dense Sand Overlying Loose Sand Deposit. Journal of Soft Computing in Civil Engineering (3–4): 28–40.

Frost, D.J., Kim, D. & Lee, S.W. 2012. Microscale Geomembrane-granular Material Interactions. KSCE Journal of Civil Engineering, 16(1): 79–92.

Izgin, M. & Wasti, Y. 1997. Geomembrane—sand Frictional Interface Properties as Determined by Inclined Board and Shear Box Tests.

Koutsourais, M. M., Sprague, C. J. & Pucetas, R.C. 1991. Interfacial Friction Study of Cap and Liner Components for Landfill Design. Geotextiles and Geomembranes 10 (1): 531–548.

Lashkari, A. & Jamali, V. 2021. Global and Local Sand–geosynthetic Interface Behavior. Géotechnique 71 (4): 346–367.

Lima Júnior, N.R. 2000. Estudo da Interação Solo-geossintético em Obras de Proteção Ambiental com o uso do Equipamento de Plano Inclinado. Dissertação de Mestrado: Universidade de Brasília. Brasil. 148p.

Liu J. & Qiao, S. 2015. The Image Segmentation Algorithm Based on Differential Evolution Particle Swarm Optimization Fuzzy C-Means Clustering. Computer Science and Information Systems 12(2):873–893.

Lopes, C.P.F.C. 2001. *Study of Soil and Geosynthetic Interaction by Shear Tests and Incline Plane Tests.* MSc Dissertation, *Civil Engineering University of Porto. Portugal.* 186p.

Mello, L.G.R. 2001. Estudo da Interação Solo-geossintético em Taludes de Obras de Provisão de Resíduos. Dissertação de Mestrado Universidade de Brasília. Brasil,137p.

Nortene Plásticos: *Research Data from Nortene Plásticos*, Sao Paulo, Brazil. *Av. Dr. Dib Sauaia Neto, 4628 - Vila Industrial, Barueri - SP*, 06455–050.

O'Rourke, T.D., Druschel, S.J. & Netravali, A.N. 1990. Shear Strength Characteristics of Sand-polymer Interfaces. Journal of Geotechnical Engineering 116(3): 451–469.

Palmeira, E.M., Lima Junior, N.R., Viana, H.N.L. & Mello, L.G.R. 2004. Large Scale Ramp Test for the Study of Soil-geosynthetic Interaction in Slope of Waste Disposal Areas. *Euro-Geo 3 Munich Germany*.

Pant, A. & Ramana, G.V. 2021. Novel Application of Machine Learning for Estimation of Pullout Coefficient of Geogrid. Thomas Telford Ltd. Geosynthetics International 1072–6349.

Pham, B. T., Qi, C., Ho, L. S., Nguyen-Thoi, T., Al-Ansari, N., Nguyen, M. D., Nguyen, H.D., Ly, H., Le, H. V. & Prakash, I. 2020. A Novel Hybrid Soft Computing Model using Random Forest and Particle Swarm Optimization for Estimation of Undrained Shear Strength of Soil. Sustainability 12 (2218).

Pavanello, P.C. & Moraci, N. 2021. The Characterization of Geosynthetic Interface Friction by Means of the Inclined Plane Test. Geotextiles and Geomembranes 49:257–275.

Pavanello, P., Carruba, P. & Moraci, N. 2022. Geosynthetic Interface Friction at Low Normal Stress: Two Approaches with Increasing Shear Loading. Applied Science 12(1065).

Pierre, G. A. N., Shui-Long, S., Annan, Z., & Giuseppe, M. 2021. Artificial Neural Network Optimized by Differential Evolution for Predicting Diameters of Jet Grouted Columns. Journal of Rock Mechanics and Geotechnical Engineering (13):1500–1512.

Rebelo, K.M.W. 2003. *Resistência de Interface Entre Geomembranas e Solos Através do teste de Cisalhamento em anel.* Masters' dissertation: *University of São Paulo Engineering School of São Carlos.*126 p.

Sanchéz, N.P. 2018. *Study of Some Aspects that Influences on the Adherence between Geosynthetics and Different Materials.* PhD Dissertation. Graduate program on Geotech-nics, *University of Brasilia. Department of Civil and Environmental Engineering*. 168 p. (In Portuguese).

Schober, P., Boer, C., Schwarte, L. A. 2018. Correlation Coefficients: Appropriate Use and Interpretation. Anesthesia and Analgesia 126 (5): 1763–1768.

Storn, R., & Price, K. 1997. Differential Evolution – A Simple and Heuristic for Global Optimization Over Continuous Spaces. Journal of global optimization (11): 341–359.

Spanos, A. 2003. Probability Theory and Statistical Inference: Econometric Modeling with Observational Data. *Cambridge University Press* (Virtual Publishing). 844p.

Swinscow, T. D.V. 1997. *Statistics at Square One*. Revised by M J Campbell. University of Southampton, Copyright BMJ Publishing Group.

Viana, H.N.L. 2007. *Estudos da Estabilidade e Condutividade Hidráulica de Sistemas de Revestimento Convencional E Alternativos Para Obras de Eliminação de Resíduos.* Tese de Doutorado. Universidade de Brasília. Brasil. 259p.

Zhang, W., Wu, C., Li, Y., Wang, L. & Samui, P. 2019. Assessment of Pile Drivability Using Random Forest Regression and Multivariate Adaptive Regression Splines. Georisk: Assessment and Management of Risk for Engineered Systems and Geohazards (15): 27–40.

Zhang, W., Wu, C., Zhong, H., Li, Y., & Wang, L. 2021. Prediction Undrained Shear Strength using Extreme Gradient Boosting and Random Forest on Bayesian optimization. Geoscience Frontiers (12): 469–477.

Durability and long term performance

Durability of HDPE geomembranes under different challenging exposure conditions

Darren Webb*
Regional Executive, WSP Australia Pty Ltd, Melbourne, Victoria, Australia

Fred Gassner*
Technical Director, WSP Australia Pty Ltd, Melbourne, Victoria, Australia

Gareth Phillips*
Principal Engineer, WSP Australia Pty Ltd, Melbourne, Victoria, Australia

ABSTRACT: Understanding the life expectancy and performance characteristics of geo-synthetic products is critical in the design of containment and storage systems. Standard testing methods do not enable assessment of the expected long-term performance of products exposed to challenging exposure conditions such as those related to storage of unique solid and liquid waste by-products generated by industrial and mining sectors. Therefore, the adoption of alternate approaches for assessment of material durability under anticipated exposure conditions is necessary. Accelerated exposure testing programmes were undertaken on several different HDPE geomembrane product samples to assess the material performance under different expected service conditions. The laboratory testing programmes included the simulation of a very high pH environment, very low pH environment and extreme UV exposure conditions. The results were used to assess the expected performance of the candidate products proposed by manufacturers for use in different applications. The outcomes of the testing indicated significant variability in expected long term durability under the different assessed conditions for the different HDPE geomembrane products. These results indicate the need for this type of testing to provide evidence to support the choice of geomembrane materials for applications involving exposure to challenging conditions.

1 INTRODUCTION

The industrial and mining sectors require liquids, solids and semi-solid by-products to be stored and contained long term in order to mitigate the environment impact of the industrial and mining processes. The design of these containment facilities typically requires a composite lining system and include a geomembrane liner underlain by a mineral liner. Initial commercial selection for the geomembrane liner resulted in a preference to use HDPE for the geomembrane liner, if technically viable. The HDPE geomembrane is a key component of the lining system and must be designed to perform long term when subjected to the by-products.

WSP Golder has designed containment systems for a range of industrial and mining applications subjected to a variety of by-products and a range of climatic conditions. The HDPE geomembrane selection process requires careful consideration as the operating

---

*Corresponding Authors: darren.webb@wsp.com, fred.gassner@wsp.com and grphillips01@gmail.com

conditions (including chemical characteristics and environmental conditions) for each application vary.

This paper intends to demonstrate importance of adopting a thorough geomembrane selection process as experience shows that different products perform differently when subjected to challenging environmental conditions and chemical characteristics.

2   TYPICAL GEOMEMBRANE SELECTION METHODOLOGY

Geomembranes used in containment systems are often selected based on data sheets supplied by the geomembrane manufactures related to indicative durability to some mono-chemicals, and material properties relative to Geosynthetics Research Institute (GRI) nominated properties outlined in GRI 2019. The GRI nominated properties have been developed to reflect the material properties of materials available from a range of geomembrane manufacturers and experiences. The nominated properties are intended to be a starting point for consideration and should be refined to suit the intended application based on the specific project conditions and performance requirements.

Industrial and mining by-products can be unique and the combination of various chemical and operating conditions of the by-product containment facilities are unlikely to have been considered during the development of the GRI documents. The GRI documents do not provide an indication of service life. Manufacturers may have chemical resistance information for some conditions however, these are unlikely to represent the complete by-product chemistry and the information can become outdated as resin properties are re-engineered over time.

3   SERVICE CONIDITIONS

3.1   *Acidic liquid storage pond*

The acidic storage pond is located in an arid area with ambient temperatures recorded between 6°C and 48.5°C. The Average monthly Solar UV Index at the location is greater than 6 between September and April and peaks at over 12 during summer (Australian Government Bureau of Meteorology 2019).

The acidic liquid is a by-product of the processing of ore and contains high concentrations of dissolved solids (mainly heavy metals with some organics) and has a low pH.

To assess which HDPE geomembrane products could perform when subjected to the acidic storage pond's service conditions for the required design service life of at least 20 years, a laboratory testing programme was developed to simulate the service conditions.

3.2   *Caustic solid containment facility*

The caustic containment facility is required to contain by-product of alumina refining which is delivered to the storage facility and has potential to generate leachate to which the geomembrane liner would be exposed. The containment facility liner system is intended to be buried and covered with a sand layer with limited UV exposure during the construction period and expected minor temperature variation during service conditions.

A 2mm thickness HDPE geomembrane was nominated for inclusion in the liner system for the facility. To assess which HDPE geomembrane products could perform when subjected to long term exposure to the leachate a laboratory immersion and testing programme was developed.

4   CANDIATE PRODUCT SHORTLISTING

To help establish a 'shortlist' of candidate products for inclusion in the testing program key geomembrane manufacturers were approached to nominate proposed products. The

manufacturers approached were provided with a description of expected service conditions to assist them in nominating a product that they considered to be most suitable for the application. The products proposed typically comprised specialist 'high performance' geomembrane products or 'special runs' with a formulation developed specific to the application. A total of 4 products were selected for laboratory testing for each application.

5 LABORATOR TESTING REGIME

A laboratory testing regime was designed to simulate accelerated aging of the various products in the acidic and caustic service conditions. The programme was informed by the research published by Rowe *et al*. for selecting geomembranes (Rowe *et al*. 2019) and included:

5.1 *Ageing of candidate samples*

The candidate samples were immersed in representative liquids or leachates from the by-products recovered from the sites to replicate the expected service conditions. The candidate samples were immersed for up to 90 days at three temperatures (55°C, 70°C and 85°C for the acidic exposed samples and 50°C, 75°C and 90°C for the caustic exposed samples) in general accordance with ASTM D5322 and ASTM D5747. Samples were recovered from the immersion liquid and subjected to laboratory testing to assess changes in the materials.

In order to estimate the service life of the candidate materials, extrapolation of the OIT depletion time at various temperature was undertaken using the Arrhenius equation. The Arrhenius extrapolation of the various temperature data enabled the prediction of the degradation rates of the geomembrane products, which were applied to the estimated service temperature and informed a service life assessment.

5.2 *Representative field conditions*

For the acidic liquid storage pond the geomembrane liner will be subjected to varying temperatures and UV exposure depending on its location within the lining system and its environmental exposure. The climatic data was therefore assessed to estimate representative operating temperatures for the geomembrane and estimate of UV exposure where appropriate. Where the geomembrane was expected to remain submerged a representative service temperature of 25°C was adopted based on temperature measurements recorded on existing ponds at site.

Published field measurements by Take 2015, *et al* has shown that the temperature of exposed polyethylene geomembrane is linked to exposure to UV radiation/sun. So, for the exposed geomembrane on the upper portion of the slopes and embankments crests of the pond the service temperature was estimated by utilising the UV Index data published by the Bureau of Meteorology for the site. Based on research by Rowe & Ewais 2014, the daily, monthly and annual UV index trends were correlated to the temperature of black HDPE geomembrane to develop a degradation ratio of the geomembrane. This approach indicated a representative service temperature of 40°C for the site conditions which resulted in an equivalent degradation rate of the geomembrane considering diurnal and seasonal variations.

For the caustic exposure project the liner will be covered and not subject to solar radiation or elevated temperature effects so a constant representation temperature of 25 °C was adopted.

6 ASSESSMENT OF AGEING EFFECTS

The aged geomembrane samples underwent a range of laboratory tests which included the following:

- Both standard (S) and high pressure (HP) oxidative induction time (OIT) testing in accordance with ASTM D3895 and ASTM D5885 respectively. Samples were tested

pre-immersion and after immersion to estimate the retention rates of antioxidants and stabilisers. Samples were recovered and tested periodically throughout the 90 days testing.

- Geomembrane stress crack resistance (SCR) was considered critical to the performance of the geomembrane as experience indicates HDPE geomembrane becomes crack sensitive as it degrades over time. Therefore, the SCR of the candidate geomembrane samples was also assessed periodically throughout the testing process. Notched Constant Tensile Load (NTCL) SCR testing was undertaken in accordance with ASTM 5397 on parent geomembrane samples prior to immersion and after immersion for 90 days at 55°C. For the acid exposed samples Strain Hardening modulus (SHM) testing was also undertaken in accordance with DIN EN 17096 on parent geomembrane samples prior to immersion and periodically throughout the 90 days of immersion at each temperature. The values of the Strain Hardening test results were correlated to the NTCL SCR method for the various samples to estimate a stress crack resistance value in hours.
- Tensile testing of the candidate products was undertaken in accordance with ASTM D6693 prior to immersion and periodically throughout the 90 days. Tensile testing of the candidate geomembrane products was intended to provide an early indication of any performance issues. Testing on samples of welded seams subjected to the immersion tests were also carried out to assess any early changes in mechanical behaviour of the samples.
- Carbonyl Index testing of the caustic exposed candidate products was undertaken in accordance with a modified ASTM F2102 method prior to immersion and periodically throughout the 90 days to detect oxidised groups in the samples

6.1 *Outcomes of laboratory testing of samples immersed in acidic conditions*

6.1.1 *SOIT*
Based on the results of the SOIT testing the following observations were made:

- The initial SOIT values varied between 250 minutes and 150 minutes.
- The retained SOIT values after 90 days immersion at 55°C varied between 70% and 90%
- The retained SOIT values after 90 days immersion at 70°C varied between 40% and 90%
- The retained SOIT values after 90 days immersion at 85°C varied between 2% and 52%

The depletion rates of retained OIT over time at different immersion temperatures varied significantly between the different geomembrane samples.

6.1.2 *HPOIT*
Based on the HPOIT testing results the following observations were made:

- The initial HPOIT values varied between 500 minutes to 1800 minutes.
- The retained HPOIT values after 90 days immersion at 55°C varied between 80% and 100%
- The retained HPOIT values after 90 days immersion at 70°C varied between 50% and 100%
- The retained HPOIT values after 90 days immersion at 85°C varied between 20% and 85%

The depletion rates of retained HPOIT over time at different immersion temperatures varied less than the SOIT results significantly between the different geomembrane samples. The HPOIT values of some products returned erratic results, so those results were considered to be secondary indicators only.

6.1.3 *Stress crack resistance*
The following observations were made related to SCR testing:

- The rate of change of SCR of the different samples varied significantly. The SCR of some samples reduced by more than 50 % over the immersion period, while others only reducing by approximately 20 %.

- Some samples resulted in apparent increased SCR with time. Research undertaken by Rowe *et al.*, indicates such changes in the SCR trend of some samples is explained by the initial stages of material relaxation after manufacture before stabilising for an extended period of time, which is referred to as the equilibrium SCR (Rowe *et al.* 2019).

6.1.4 *Oven aging and UV exposure testing*
Samples were also exposed to oven aging and UV testing in accordance with ASTM D 7238 and ASTM D 5721. The UV energy applied in the ASTM test method was correlated to the measured UV energy of the site, to interpolate the test results relative to site conditions. The results of these tests were adopted as an initial screening method for potential samples.

6.2 *Outcomes of laboratory testing of samples immersed in caustic conditions*

6.2.1 *SOIT*
Based on the results of the SOIT testing the following observations were made:

- The initial SOIT values varied between 165 minutes and 291 minutes.
- The retained SOIT values after 84 days immersion at 50°C varied between 85% and 95%
- The retained SOIT values after 84 days immersion at 70°C varied between 39% and 82%
- The retained SOIT values after 84 days immersion at 90°C varied between 8% and 52%

The depletion rates of retained OIT over time at different immersion temperatures varied significantly between the different geomembrane samples.

6.2.2 *HPOIT*
Based on the HPOIT testing results the following observations were made:

- The initial HP-OIT values varied between 165 minutes and 291 minutes.
- The retained HP-OIT values after 84 days immersion at 50°C varied between 69% and 102%
- The retained HP-OIT values after 84 days immersion at 70°C varied between 25% and 99%
- The retained HP-OIT values after 84 days immersion at 90°C varied between 14% and 104%

The depletion rates of retained HPOIT over time at different immersion temperatures varied more significantly than the SOIT results between the different geomembrane samples. Some samples showed no reduction in HPOIT during the testing period.

6.2.3 *NTCL*
The following observations were made related to SCR testing:

- The rate of change of SCR of the different samples varied significantly. The SCR of some samples reduced by more than 95 % over the immersion period, while others showed no reduction to the limits of testing (1000 hours).
- Result of testing for some samples returned higher results for 90°C immersed samples than 50°C and 70°C immersed samples

7 FINDINGS

7.1 *SOIT and HPOIT depletion*

The testing results were used to estimate the rate at which the SOIT properties and HPOIT properties reduced in each geomembrane product (i.e. the depletion rate). The SOIT and HPOIT degradation rates varied for each candidate product.

Using the Arrhenius method, the degradation rates of each product were extrapolated to assess the times to when the stabilisers and antioxidants were considered to no longer providing benefits. Based on the degradation rates developed for each product, the time for each geomembrane product to achieve residual values was estimated for the representative service temperatures, referred to as Stage 1 in the HDPE geomembrane degradation model developed by (Hsuan & Koerner 1998).

7.2 The assessment indicated the following

7.2.1 Acid exposure samples

- A number of the geomembrane candidate products when subjected to pond floor service conditions would retain their stabilisers and antioxidants for at least 20 years, meeting the design life requirements.
- The estimated time for effective depletion of the SOIT and HPOIT stabilisers varied between 1 year and 20 years at a representative service temperature of 40°C for the exposed slopes and crest areas. Only a couple of geomembrane candidate products were considered to meet the required design life.

7.2.2 Mechanical and physical properties

The results of the stress crack resistance, seam strength and tensile properties testing were considered to assess whether changes in the physical and mechanical properties of the geomembrane samples had occurred due to the immersion testing.

The SCR test indicated that some of the samples stress crack resistance had reduced substantially during the immersion testing. This was considered to be a reason to exclude the materials for further consideration in the project. None of the samples showed any meaningful changes in the seam or tensile strengths of the samples subject to the effects of the immersion tests.

7.2.3 Caustic exposed samples

- The estimated time for effective depletion of the SOIT and HPOIT stabilisers (to residual values of 1min and 50min respectively) varied between 7 year and 102 years at a representative service temperature of 25°C. Only a couple of geomembrane candidate products were considered to meet the required design life.
- Similar to the acid exposed samples stress crack resistance, seam strength, Carbonyl Index and tensile properties testing were considered to assess whether changes in the physical and mechanical properties of the geomembrane samples had occurred due to the immersion testing. The SCR test indicated that for some products the samples stress crack resistance had reduced substantially during the immersion testing. This was considered to be a reason to exclude the materials for further consideration in the project. None of the samples showed any meaningful changes in Carbonyl Index or the seam or tensile strengths.

8 CONSTRUCTION QUALITY ASSURANCE MEASURE – 'FINGERPRINT' TESTING

Material composition ('fingerprint') testing was undertaken on a sample of the geomembrane product selected for use in construction of the caustic facility to assess the stabiliser and antioxidant package concentrations for this material. This was then compared to the results of material composition testing undertaken on materials supplied for the works to provide increased confidence that the supplied materials have characteristics consistent with the sample subjected to the accelerated exposure immersion testing program.

9 CONCLUDING SUMMARY

The immersion testing with site specific solids or liquids showed that different geosynthetic materials result in very different design lives, depending on the composition of the material. The key message is that HDPE materials varies widely and for many projects site specific immersion and associated durability testing is highly recommended to provide confidence that the material can meet the design life of the liner system. Geomembrane manufacturers are highly unlikely to have durability data for complex exposure conditions of facilities, noting that many facilities are required to store a mixture of materials that in combination can have unexpected impact on the durability of materials.

REFERENCES

Australian Government (2019) *Bureau of Meteorology*. Available at: www.bom.gov.au/jsp/ncc/climate_averages/solar-exposure/index.jsp (Accessed: 25 August 2019).

GRI 2017 - Geosynthetics Institute GRI – GM13 Standard Specification.

Hsuan, Y.G. & Koerner, R.M. 1998. Antioxidant Depletion in High Density Polyethylene Geomembranes. *Journal of Geotechnical and Geoenvironmental Engineering: ASCE*: 532–541.

Rowe et al. 2019. An Approach to High-density Polyethylene (HDPE) Geomembrane Selection for Challenging Design Requirements, *Canadian Geotechnical Journal*, 11 December 2019.

Rowe, K.R. & Ewais, A. M. R. 2014. Antioxidant Depletion from five Geomembranes of Same Resin but of Different Thicknesses Immersed in Leachate. *Geotextile and Geomembranes*, Vol 42, 540–554.

Take, W.A., Rowe, R.K., Brackman, R.W.I., Arnepalli, D.N. 2015. Thermal Exposure Conditions form a Composite Liner with a Black Geomembrane Exposed to Solar Radiation. *Geosynthetics International*, 22(1).

Resiliency of PVC coated polyester geogrid in high pH conditions

L.M. Spencer, Ph.D., P.E. & J. Lostumbo, P.E.
Solmax, Jefferson, Georgia, USA

ABSTRACT: The resilience of mechanically stabilized earth structures in elevated pH backfill conditions have typically been a concern due to the potential for elevated degradation due to hydrolysis. An investigation of the reduction in tensile strength of coated polyester (PET) geogrids exposed to pH of 10 was performed. Arrhenius modeling was used to extrapolate the degradation rate of the geogrid tensile strength to 20°C over a 75-year design life and determine the appropriate reduction factor for durability in higher pH environments. This study also identifies the importance of product specific testing by evaluating two types of PET geogrids and the limitations of only using CEG and molecular weight as guidelines for determining reduction factors. The two geogrid types exhibited distinctly different tensile strength degradation. The disparity in tensile strength degradation confirms the importance of the materials and the geogrid manufacturing processes in selecting appropriate durability reduction factors for field applications.

1   INTRODUCTION

The reuse of crushed concrete as reinforced backfill in MSE walls and reinforced slopes is a sustainable use of otherwise waste material. Utilizing recycled concrete reduces the need for high-quality imported materials, lowering the carbon footprint. However, using recycled concrete necessitates additional product testing to determine the long-term durability of the geogrid reinforcement.

According to the most recent EPA (2020) Advancing Sustainable Material Management 2018 Fact Sheet, 405 million tons of construction and demolition (C&D) concrete waste were generated, with 381 million tons of that being demolition debris. 71 million tons of concrete waste were disposed of in a landfill, while 301 million tons were reused as aggregate. This aggregate can be used as reinforced backfill for MSE walls.

Calcium silicate hydrates (CSH) and calcium hydroxide are produced during the chemical process of cement hydration. The presence of these compounds causes an elevated pH in the concrete structure. When concrete is exposed to air, carbonic acid is formed due to the presence of carbon dioxide (CO_2) in the air and free water within the concrete matrix. The calcium hydroxide then reacts with the carbonic acid to form calcium carbonate. The pH of the concrete decreases as the carbonation front moves through it due to the formation of calcium carbonate (Richardson 2002). Due to the increased surface area exposed to air in a crushed concrete structure versus an intact concrete structure, this carbonation process will accelerate. Even though crushed concrete is exposed to air and has the potential for pH reduction due to carbonation, using crushed concrete as reinforced backfill in MSE walls introduces the possibility of accelerated geogrid degradation due to elevated pH levels.

The mechanism by which polyester tensile strength is lost occurs during the reverse reaction known as hydrolysis. When terephthalic acid and ethylene glycol react, they produce polyethylene terephthalate (PET) and water. Because this is an equilibrium reaction, it is

DOI: 10.1201/9781003386889-81

reversible, so PET can react with water to reverse the reaction and return to ethylene and glycol. This reverse reaction is irreversible. The rate of this reaction is influenced by the carboxyl end group (CEG) concentration, molecular weight, temperature, humidity, and pH of the environment (FHWA 2009; Hsuan *et al.* 2008). The presence of more OH- ions speeds up the hydrolysis reaction when the pH of the environment is higher. The OH- ions will react with the polymer chain, causing the chain to split. This reaction reduces the molecular weight and reduces tensile strength (Elias *et al.* 1998).

The long-term strength loss due to degradation is accounted for by applying reduction factors to the ultimate tensile strength. The tensile strength used in the design of reinforced soil structures is known as the long-term design strength (LTDS). This value is derived from product-specific testing and is calculated by Equation 1 in accordance with AASHTO R69 (AASHTO 2015).

$$LTDS = \frac{T_{ult}}{RF_{CR} \times RF_{ID} \times RF_D} \tag{1}$$

where T_{ult} = ultimate tensile strength (MARV); RF_{CR} = reduction factor for creep; RF_{ID} = reduction factor for installation damage; and RF_D = reduction factor for durability.

The tests to determine the reduction factors are performed by third-party accredited laboratories. They involve measuring the strength loss due to creep, the strength loss over time caused by supporting a sustained load, and installation damage, the abrasion and strength loss due to backfill soil compacted over the geogrid. The reduction factor for durability, on the other hand, is a default reduction factor established by the Federal Highway Administration (FHWA) based on the material properties of the polyester yarn used to construct the PET geogrid and the pH of the soil backfill.

Polyesters with a higher molecular weight and lower CEG are less prone to hydrolysis (Elias *et al.* 1998). To minimize strength losses due to hydrolysis over the design life of the structure, the FHWA recommends PET geogrids have a minimum molecular weight of 25,000 and a maximum CEG of 30. FHWA also restricts the use of PET geogrids to soils with a pH less than 9, based in part on Elias' testing of a specific PVC coated PET geogrid (1998). FHWA 09-087 (FHWA 2009) does, however, allow for product-specific testing for the use of coated PET geogrids outside of the outlined yarn properties or in pH conditions other than 3 to 9.

The test program conducted by Elias (1998) used a PVC coated polyester geogrid with a CEG of 26.7 and a molecular weight of 30,200. The rate of strength degradation that occurred in the Elias testing for a pH of 10 and 12, was 0.17% per year and 1.61% per year, respectively.

2 MATERIALS AND METHODS

This paper outlines the testing performed on two PVC coated high tenacity polyester uni-axial geogrids (Geogrid A and Geogrid B). The PET geogrids are manufactured by different companies, therefore used different polyester yarn, different PVC coating, and different construction methods. The physical properties of the Elias PET geogrid and Geogrids A and B from this study are in Table 1. The geogrid was exposed to high pH aqueous solutions at elevated temperatures over time to determine the 75 to 100-year design life durability reduction factor to be used in the LTDS calculation per AASHTO R69 (AASHTO 2015).

Table 1. Physical properties of Elias (1998) and Geogrids A & B in this study.

Geogrid Tested	Geogrid Description	Carboxyl End Group (CEG) (meq/kg)	Average Molecular Weight	Mass/Unit (g/m^2)
Elias (P-6)	PVC-coated PET Fiber	26.7	30,200	334
Geogrid A	PVC-coated PET Fiber	15.2	34,855	271
Geogrid B	PVC-coated PET Fiber	14.2	33,320	280

Geogrid A & B were tested in accordance with ISO/TR 20432 and ISO/TS 13434. The PET geogrid samples were immersed in aqueous solutions held at a pH of 11.4. The aqueous pH solution was maintained at three temperatures: 40°C, 50°C, and 60°C. In each temperature environment, 35 samples were exposed. At predetermined time intervals, samples were removed from the aqueous solution and subjected to single rib tensile strength tests per ASTM D6637.

Geogrid coupons were hand cut from the geogrid roll with scissors; each coupon was 7 ribs wide and 42 inches long. The coupons were distributed among the chemical solutions and test temperatures. The samples were rolled loosely within the glass jars to allow for contact with the immersion chemical solution. The geogrid's cut ends were not covered and were exposed to the solution.

Preparation of the elevated pH solution began by calculating the amount of powdered calcium hydroxide necessary to produce the desired pH level of 11.4. Calcium hydroxide was weighed using an analytical balance and mixed with a placed in a small container. A drill mounted "paint" mixer was used to mix a specified volume of water and the measured calcium hydroxide powder. Once mixed, the pH of the solution was measured with a digital pH meter to confirm that the pH was correct. The calcium hydroxide solution was poured into the specimen jars, the jars were filled completely to limit headspace then sealed. Sealed jars were then placed in temperature chambers with fans and heaters located within the temperature chamber. The heaters were controlled with digital temperature controllers to maintain consistent temperatures during the full geogrid exposure time. Specimen jars were checked at least weekly and additional pH solution was added if needed and the jars were resealed. Solutions were replaced with new solution prepared as described above at each test interval.

Specimen coupons were removed at each test interval. The coupons were rinsed with water and then allowed to dry and condition at laboratory temperature for at least 48 hours. Single rib tensile properties were measured in accordance with ASTM D6637, Method A.

Multiple samples were taken at each elapsed time period for each temperature environment. Each sample underwent tensile strength testing to determine the strength loss in comparison to the baseline ultimate strength. The number of samples used in calculating the average tensile strength loss for a particular time/temperature environment varied from 3 to 5 samples.

A summary of the number of coupons obtained at each time interval is in Table 2. Three to five samples were pulled and tested at each time interval to determine the average strength loss. Where lower sample numbers were used to determine the average strength, it was to keep the limited number of samples remaining in the aqueous solution for later time interval pulls.

Table 2. Samples taken at each time interval to calculate the average tensile strength loss.

	Number of Samples to Determine to determine average tensile strength loss for 40°C/50°C/60°C						
Elapsed Time (months)	1	2	4	10	16	26	37
Geogrid A	5/5/5	5/5/5	5/5/5	5/5/5	5/5/5	5/5/5	3/3/3
Geogrid B	5/5/5	5/5/5	5/5/5	4/4/4	5/5/5	5/5/5	3/3/3

The data used in the Arrhenius modeling plots was the average tensile strength loss of the samples taken at that specific time and temperature. This research has been ongoing for over three years. By exposing the samples to the pH solution at higher temperatures, the time-temperature superposition principle can be used to extrapolate the tensile strength loss due to hydrolysis to 20°C over a longer time period, in this case 75 years (FHWA 2009).

3 RESULTS AND DISCUSSION

3.1 *Test results*

Arrhenius plots were created for each tested geogrid to determine the time required to achieve a specific strength loss extrapolated to 20°C (FHWA 2009). The average tensile strength retained obtained from single rib tensile tests of the exposed geogrid is plotted on a natural log scale versus time, as shown in Figure 1. The fit lines for each temperature obtained from this plot are used to determine the time to a certain percentage strength loss.
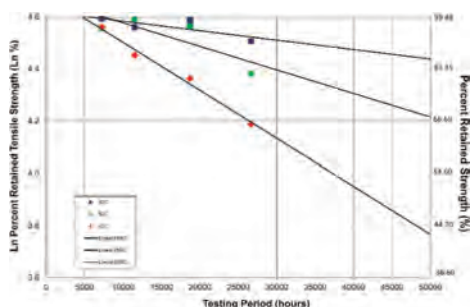
Figure 1.   Average tensile strength retained for Geogrid A in pH 11.4.

To extrapolate the time to reach a specific percent retained strength (of tensile ultimate strength) at 20°C, Arrhenius plots, a log plot of the time to reach a specific percent strength retained versus the inverse of absolute temperature (1/K), were developed for a range of percent strength retained values. An example plot of Geogrid A at 80% strength retained at a pH of 11.4 is shown in Figure 2.
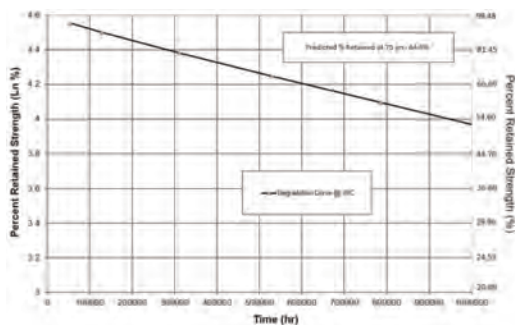
Figure 2.   Arrhenius plot for Geogrid A at 80% strength retained at pH 11.4.

Arrhenius plots for Geogrid A were developed for retained strengths ranging from 95% retained to 20% retained, and Geogrid B plots were developed for retained strengths from 90% to 10% retained. These were used to determine the time to reach that specific retained strength at 20°C. The results were then compiled to obtain a degradation curve for a pH value of 11.4. The degradation curve plots the natural log of percent strength retained versus time at the reference temperature of 20°C. The degradation curve for Geogrid A is shown in Figure 3 and for Geogrid B in Figure 4. The reduction factor for durability in a pH environment of 11.4 is determined from these degradation curves and can be used in the calculation of LTDS. This
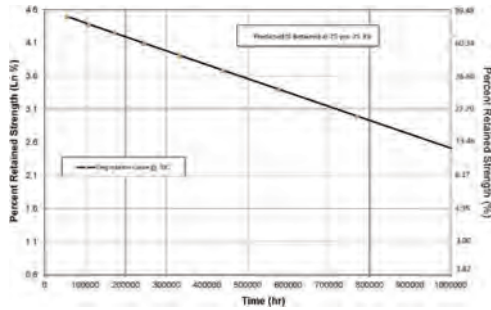
Figure 3. Degradation curve of Geogrid A in pH 11.4.
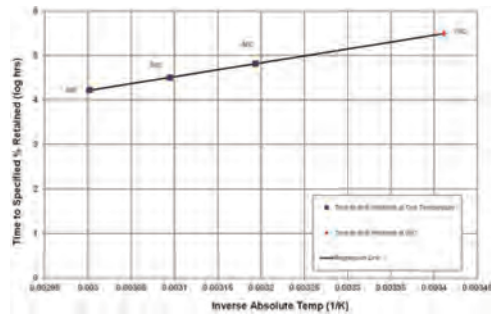
Figure 4. Degradation curve of Geogrid B in pH 11.4.

testing allows the reduction factor to be determined at different design life periods, up to 1,000,000 hours (114 years).

To calculate the reduction factor for durability, the design life should be known. An example reduction factor calculation is outlined using a design life of 75-years. The percent retained strength for Geogrid A at a pH of 11.4 at 75-years (657,000 hours) is 64.8%. The calculation for the 75-year design life of Geogrid A at a pH of 11.4 reduction factor for durability is shown in Equation 2.

$$RF_{DpH11.4} = \frac{100\%}{64.8\%} = 1.54$$ (2)

The percent retained of Geogrid B at a design life of 75-years at a pH of 11.4 was 25.3%, which equates to a reduction factor for durability for Geogrid B of 3.96.

3.2 Discussion

For reference, the Elias (1998) study showed a strength loss of 0.17%/year for the pH 10 solution, which is a strength loss of 12.75% over a 75-year period. The pH 12 solution loss was 1.61%/year, meaning there is no strength retained after approximately 62 years. However, it is difficult to compare to the Elias (1998) test results to the degradation in this testing program due to the different pH values.

Geogrid A had similar, albeit slightly higher, CEG and molecular weight with a lower mass/unit area than Geogrid B but had a marked greater resistance to elevated pH degradation. This indicates that more than just the physical properties of the polyester yarn used in the geogrid construction affects the degradation rate. This indicates the manufacturing

process, including the PVC coating, is important in determining the durability of coated polyester geogrid to elevated pH environments.

ISO 20432 (2007) notes that laboratory assessment of hydrolysis of polyesters should be performed on uncoated yarns; however, it also says, "Take care that the conditions during the accelerated tests are representative of those in service. There should be no change in the mechanism of degradation or in the physical structure of the material; and no barrier layers should form or be present that might retard the degradation process in a manner that does not occur in service." The method of testing uncoated polyester yarn is not representative of field conditions and as indicated in this study would discount the degradation resistance with the PVC coating. Further, Elias (1998) used PVC coated polyester in the accelerated durability testing that was used in the determination of the FHWA acceptable pH range.

The current test procedure is overly conservative and does not consider how carbonation will change the pH of the backfill overtime. To more accurately determine the tensile strength loss of in-service polyester geogrid, future testing should evaluate how to incorporate installation damage on coated polyester geogrid in accelerated durability testing.

4 CONCLUSIONS

The study evaluated the resistance of two different PVC coated polyester geogrids to strength loss due to elevated pH conditions. The reduction factor for durability for a pH of 11.4 and a 75-year design life for Geogrid A is 1.54 and for Geogrid B is 3.96. The CEG and molecular weight of the two geogrid samples were similar, thus indicating more than the physical properties of the polyester yarn determine the degradation rate. Therefore, degradation curves obtained from accelerated durability testing are only applicable for the specific geogrid and pH environment tested. The current degradation testing procedure does not adequately model the in-service condition and the method of testing uncoated polyester geogrid is overly conservative in comparison to field conditions.

REFERENCES

AASHTO (American Association of State Highway and Transportation Officials). 2015. *AASHTO R 69-15, Standard Practice for Determination of Long-Term Design Strength for Geosynthetic Reinforcement*. Washington, D.C.:AASHTO.

ASTM D6637/D6637M-15. 2015. *Standard Test Method for Determining Tensile Properties of Geogrids by the Single of Multi-Rib Tensile Method*. West Conshohocken: ASTM International.

Elias, V., Salman, A., and Goulias, D. 1998. The Effect of pH, Resin Properties, and Manufacturing Process on Laboratory Degradation of Polyester Geosynthetics. *Geosynthetics International*, 5(5): 459–490.

EPA (United States Environmental Protection Agency). 2020. *Advancing Sustainable Materials Management: 2018 Fact Sheet, Assessing Trends in Materials Generation and Management in the United States December 2020*.

FHWA (U.S. Department of Transportation Federal Highway Administration). 2009. *FHWA-NHI-09-087 Corrosion/Degradation of Soil Reinforcements for Mechanically Stabilized Earth Walls and Reinforced Soil Slopes*. Washington, D.C.: NHI.

Hsuan, Y.G., Schroeder, H.F., Rowe, K., Muller, W., Greenwood, J., Cazzuffi, D., and Koerner, R.M. 2008. Long-term Performance and Lifetime Prediction of Geosynthetics. *EuroGeo 4 Keynote Paper*.

ISO (International Organization for Standardization). 2020. *Geosynthetics – Guidelines for the Assessment of Durability*. (ISO/TS 13434).

ISO (International Organization for Standardization). 2007 *Guidelines for the Determination of the Long-term Strength of Geosynthetics for Soil Reinforcement*. (ISO/TR 20432).

Richardson, M.G. 2002. *Fundamentals of Durable Reinforced Concrete* (1st ed.). CRC Press.

Interaction between the PVC-P and HDPE geomembranes used in the waterproofing and re-waterproofing of a reservoir

B. Mateo, A. Leiro & R. Solera
CEDEX, Madrid, Spain

T. Vara & D. Cabrera
BALTEN, Tenerife, Spain

ABSTRACT: The Buen Paso reservoir, located in the island of Tenerife (Spain), was waterproofed with a PVC-P geomembrane with a polyester fabric. After 66 months, due to its poor condition, caused by a rapid loss of plasticizer, it was decided to re-waterproof the reservoir with a HDPE geomembrane, which was placed directly over the PVC-P geomembrane, without any kind of geosynthetic between them. The placement of the two geomembranes, in direct contact, makes the Buen Paso reservoir an opportunity to study the possible interaction between the two materials. To study the possible interaction between HDPE and PVC-P geomembranes, samples of the PVC-P geomembrane were extracted under the HDPE geomembrane and the content of plasticizer was determined. In addition, migration tests were performed on HDPE samples according to the UNE-EN ISO 177 standard. It has been proven that the PVC-P geomembrane has continued losing plasticizer and the migration of plasticizer to the HDPE geomembrane.

1 INTRODUCTION

The Buen Paso reservoir was built in 1989. It is located on the island of Tenerife (Spain) and has a capacity of 150,788 m^3. The reservoir was waterproofed with a PVC-P geomembrane reinforced with a 1.2 mm thick polyester thread fabric, which originally met of the requirements demanded at that time for this type of material. Once installed, periodic monitoring was carried out, the results of which led to the deduction, 66 months after its placement, that the reservoir had to be re-waterproofed due to its state of deterioration.

The re-waterproofing was carried out in 1995 with a HDPE geomembrane, which was placed directly over the PVC geomembrane, without any type of separating geosynthetic material.

Keeping the old geomembrane can be an extra element of protection against mechanical actions of the support, but it is necessary to guarantee that there are no chemical interactions between both materials (Aguiar 2015). In the case of the Buen Paso reservoir, considering the location of the reservoir, on an island, the removal of the vinyl material was difficult and made the work considerably more expensive, so it was decided to leave the old sheet, and place the new geomembrane above it.

The placement of another PVC-P geomembrane was discarded, due to the tendency of the plasticizers of the upper layer to migrate to the lower one, as has been experimentally verified in other reservoirs in Spain (Blanco *et al.* 2006) so it was decided to use an HDPE geomembrane.

The re-waterproofing was carried out with a 2-mm-thick HDPE geomembrane that was anchored at the crest under a perimeter ditch and at the berm and bottom using curb-type concrete ballasts. No type of geosynthetic material was placed between the two

DOI: 10.1201/9781003386889-82

geomembranes as a separator, since at that time it was considered that there would not be interaction between the two materials.

In Spain there are several references to reservoirs that were initially waterproofed with a PVC-P geomembrane and later re-waterproofed with an HDPE geomembrane (García 2004; Méndez *et al*. 2008), but these cases differ from the Buen Paso reservoir in that a geotextile was placed between the two geomembranes. The case of the Buen Paso reservoir, with the geomembranes in direct contact, is an opportunity to study the interaction between both materials.

2 PREVIOUS STUDIOS OF THE GEOMEMBRANES OF BUEN PASO RESERVOIR

The Central Laboratory for Structures and Materials of CEDEX has been studying the performance of the waterproofing system of Buen Paso reservoir since its construction, both initial PVC geomembrane and HDPE re-waterproofing one. This study includes carrying out a series of tests on samples taken from the reservoir over time.

2.1 *Performance of the PVC-P geomembrane*

In the case of the PVC geomembrane, one of the most important tests that have been carried out over time is the determination of the loss of plasticizer, since it is the main cause of deterioration. Although the PVC-P geomembrane initially met the requirements for its use in waterproofing reservoirs, a continuous and rapid loss of plasticizers was observed. After 66 months from its installation, the loss experienced was 56.3% at the crest and 55% in the intermittent zone of the northern slope of the reservoir (Figure 1).
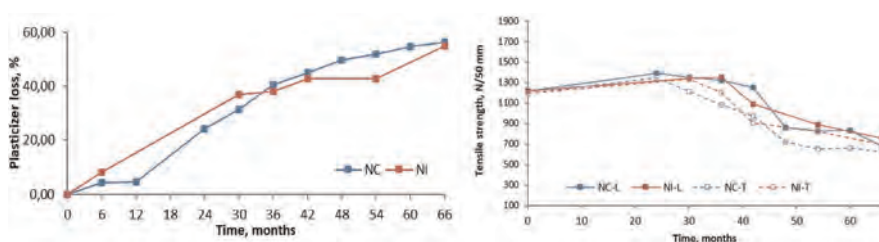
Figure 1. Loss of plasticizer and decrease of tensile strength of the PVC-P geomembrane over time. NC: North Crest, NI: North Intermediate, L: longitudinal, T: transverse.

The loss of plasticizer led to a decrease in mechanical resistance (Figure 1) and elongation, as well as the detection of failures in the bending tests at low temperatures and dynamic impact. Simultaneously, the samples began to show deterioration symptoms, such as cracks, changes in color, and loss of resin, leaving the reinforcement of polyester threads exposed to the air.

The nature of the plasticizer was determined by IR spectroscopy and gas chromatography-mass spectrometry techniques. The plasticizer used in the geomembrane was bis(2-ethylhexyl) phthalate, which has a molecular weight of 390.56 g/mol, lower than the value of 400 g/mol, recommended to ensure the durability of geomembranes, and a branched structure, which makes it highly prone to migration, especially in the air. This was the cause of the great loss of plasticizer and the rapid degradation of the geomembrane.

2.2 *Performance of the HDPE geomembrane*

Once the re-waterproofing was carried out with the HDPE geomembrane, placed over the PVC-P one, follow-up controls continued in the new geomembrane. Characterization tests

were periodically carried out on samples extracted from the reservoir, which included tensile strength and elongation, static and dynamic impact, oxidation induction time (OIT), and resistance to stress cracking.

216 months after its installation, the geomembrane continued to meet the requirements for use in waterproofing with respect to the physical and mechanical characteristics, but cracks began to appear in the crest area of the reservoir, where the change in direction of the geomembrane occurs and it is subjected to the greatest stress. The cracks were found at the top of both slopes, although to a greater extent on the north slope (Figure 2).

Figure 2. Crest zone of the Buen Paso reservoir, where the geomembrane changes direction and cracks are detected, and examples of cracks.

The values of stress cracking resistance obtained were very low: 24 h in north crest and 26 h in south crest, not meeting the value required by the regulations (336 hours). The values of the OIT were also lower than 100 minutes, minimum value required, in all areas of the reservoir.

3 STUDY OF THE INTERACTION BETWEEN PVC-P AND HDPE GEOMEMBRANES

In the areas where the cracks appeared, a series of symptoms were detected that could indicated that some type of interaction may be occurring between the HDPE and PVC-P geomembranes. When the first cracks were detected, it was observed that the temperature between the geomembranes was very high. Subsequently, a system of breathing tubes was installed in the crest zone and even so, temperatures above 50ºC were recorded. Also, oily spots appeared around some cracks. For this reason, a series of tests were carried out aimed at studying the influence of the presence of the PVC-P geomembrane under the HDPE geomembrane, to determine the possible interaction between them and verify how this interaction could affect to the durability of the reservoir's waterproofing system.

216 months after the installation of the HDPE geomembrane, when cracks began to be detected in the northern crest, samples of the PVC-P geomembrane were taken from the crest and intermittent areas of the northern slope. They were also extracted at 258 months, in this case from the north and south crest zones, since there are currently cracks in the crest of both slopes, although mainly in the north. In addition to check the state of degradation of the PVC-P geomembrane, the plasticizer content and the HDPE geomembrane migration test were performed on the extracted samples according to the UNE-EN ISO 177 (AENOR 2001) standard.

3.1 *State of the PVC-P geomembrane*

Figure 3 provides the poor condition of the PVC-P geomembrane once the sample of the HDPE geomembrane was extracted, in the north crest.

Figure 3. Appearance of the PVC-P geomembrane under the HDPE geomembrane in the crest area of the north slope at 216 months.

The sample from the coronation was in worse condition than that from the intermittent zone. In both samples, the external face (in contact with the HDPE geomembrane) shows a greater state of degradation than the internal face and higher than that shown by the geomembrane before re-waterproofing.

258 months after the re-waterproofing, the PVC-P geomembrane was once again sampled. On this occasion, the extraction has been carried out in the crest area of the north and south slopes. Figure 4 corresponds to the sample from the crest of the north slope.

Figure 4. PVC-P geomembrane sample extracted from the north slope crest 258 months after re-waterproofing. A: external face, in contact with the HDPE geomembrane, B: internal face, in contact with the geotextile, C: detail of the state of the external face of the geomembrane.

The sample shows a higher state of degradation on the external face, in contact with the HDPE geomembrane. It presents a state of stiffness and deterioration superior to that shown by the sample extracted from the same area at 216 months and as can be seen in Figure 4 C, the polyester threads are almost completely separated of the resin and very deteriorated.

3.2 *Loss of plasticizer*

The extraction of the plasticizer was carried out using Soxtec equipment. Figure 5 provides the results of the loss of plasticizer experienced by each sample of PVC-P geomembrane, before and after re-waterproofing with the HDPE geomembrane. In the case of the sample from the crest of the southern slope, the evolution over time is unknown because no sample had previously been taken from this area of the reservoir.
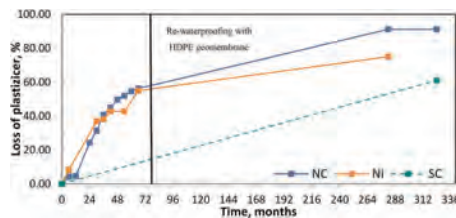
Figure 5. Evolution of the loss of plasticizer experienced by the samples of the PVC-P geomembrane. NC: North crest, NI: North intermediate, SC: South crest.

3.3 *Plasticizer migration test to HDPE geomembrane*

The study of the plasticizer migration from the PVC-P geomembrane to the HDPE geo-membrane was carried out using the UNE-EN ISO 177 (AENOR 2001) standard test. In this test, the set of test pieces, on which a 5 kg weight is placed, is heated to 70 °C (Figure 6). PVC-P geomembrane samples extracted after re-waterproofing were used, at 216 and 258 months, with different plasticizer contents, and HDPE geomembrane samples extracted from the north slope at 216 months. Various combinations were made with them to determine the influence of the plasticizer content. Table 1 presents the combinations studied.

Figure 6. Plasticizer migration test. Arrangement of the test pieces in the combination that includes a separator geotextile, for carrying out the plasticizer migration test.

Table 1. Combinations of HDPE and PVC-P geomembranes samples used to perform the plasticizer migration test. NC: north crest, NI: intermittent north zone, NF: north bottom, SC: south crest.

	Samples of PVC-P geomembrane (extracted under HDPE geomembrane)	
Samples of HDPE geomembrane (extracted at 216 months)	Plasticizer content, %	Zone/Extraction time
North crest	3,8	North crest / 216 months
North crest	10,0	North intermittent/ 216 months
North bottom	10,0	North intermittent/ 216 months
North crest	14,9	South crest / 258 months
North crest+ Geotextile	14,9	South crest / 258 months

In the last combination, a polypropylene geotextile was placed as a separation between each HDPE geomembrane specimen and the PVC-P specimen, as shown in Figure 6. In the rest of the combinations, the PVC-P geomembrane specimen was in direct contact with the HDPE specimens.

The measurement of plasticizer migration is considered as the mass loss of the PVC-P specimen. If the migration to HDPE is complete, it will coincide with the increase in mass of the HDPE geomembrane specimens, although a difference is normally observed in the weights that coincides with the loss of volatile substances. To study the progress of migration as a function of time, the specimens were weighed at different intervals. The results are presented in Figure 7.

It can be seen in Figure 7 that the higher the plasticizer content of the PVC-P geomembrane sample, the greater the tendency to migrate to the HDPE geomembrane and
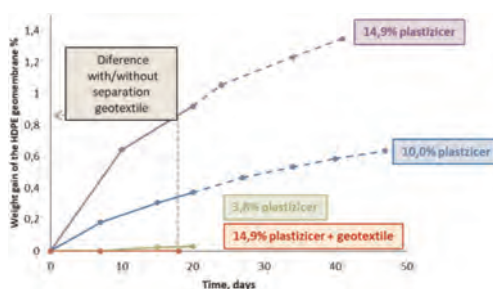
Figure 7. Weight gain experienced by the HDPE geomembrane depending on the plasticizer percentage of the PVC-P geomembrane sample.

consequently the increase in weight of the HDPE geomembrane. There is always a loss corresponding to volatile substances, which may be a part of the plasticizer that migrates into the air. This loss decreases as the plasticizer content of the PVC-P sample increases.

These results indicate that there is interaction between the two geomembranes, producing the migration of plasticizer from the PVC-P geomembrane to the HDPE one.

To verify the effectiveness of the interposition between the geomembranes of a protection barrier, in the last combination studied, two non-woven polypropylene geotextile test tubes have been placed between them, as shown in Figure 6. The HDPE specimens in this case practically do not experience weight variation, thus confirming the effectiveness of the geotextile as a barrier to prevent interaction between the geomembranes.

3.4 Discussion of the results

After re-waterproofing of the Buen Paso reservoir, although the PVC-P geomembrane has been covered by the HDPE geomembrane, it has continued to lose plasticizer, as indicated by the results of plasticizer loss obtained in samples taken from various areas of the reservoir. It has been observed that the higher the plasticizer content, the greater the tendency to migrate to the HDPE geomembrane, so probably the greatest migration occurred during the first months after re-waterproofing.

The interaction between both geomembranes, which has led to the migration of plasticizer, as well as the high temperatures recorded between the two sheets, has been able to influence the degradation of both geomembranes, mainly on the crest of the north slope. The PVC-P geomembrane has continued to deteriorate under the HDPE geomembrane, as has been verified by checking the condition of the extracted samples. Likewise, because of the interaction between the geomembranes and the migration of plasticizers, the degradation of the HDPE geomembrane has accelerated, favoring the appearance of cracking due to "stress cracking".

4 CONCLUSIONS

- After re-waterproofing the Buen Paso reservoir with a HDPE geomembrane, which was placed in direct contact with the initial geomembrane of PVC-P, the PVC-P geomembrane has continued to lose plasticizer and deteriorate under the HDPE geomembrane.
- The migration of plasticizer from the PVC-P geomembrane to the HDPE geomembrane has been confirmed, observing that the higher the plasticizer content, the greater the tendency to migrate.
- The use of a geotextile between the HDPE and PVC-P geomembranes would have delayed the interaction between them and therefore the migration of plasticizers from the PVC-P to the HDPE geomembranes.

REFERENCES

Aguiar, E. 2015. Reposición de Pantallas de Impermeabilización de Balsas Con Materiales Geosintéticos. *Geosintec2*, Madrid.

AENOR 2001. UNE-EN ISO 177. *Plásticos*. Determinación de la Migración de Plastificantes.

Blanco, M.; Castillo, F. & Aguiar, E. 2006. Comportamiento de los Plastificantes Utilizados Como Aditivos del Poli(Cloruro de Vinilo) Plastificado Usado Como Geomembrana en Obras Hidráulicas. *Revista de Plásticos Modernos*, 603, 246–250.

Brydson 1995 *Plastics Materials*. Sixth edition. Butterworth Heinemann, Oxford, UK.

García, M. 2004. Reimpermeabilización del Embalse de Sa Rota. *Jornadas Sobre Impermeabilización Con Materiales Sintéticos*. La Palma.

Méndez, C.; González, J.M.; Zapata, F. & Gómez-Nieves, A. 2008. Reimpermeabilización de Balsas de Riego en la Provincia de Alicante. *Cinco Casos Particulares. 2º Congreso Nacional de Impermeabilización: Edificación y Obra Pública*, 737–748. Palma de Mallorca.

Investigations on degradability of cotton samples buried in different soil conditions (case study)

Gh. Tavakoli Mehrjardi
Department of Civil Engineering, Faculty of Engineering, Kharazmi University, Tehran, Iran
Institute of Geomechanics and Underground Technology, RWTH Aachen, Germany

R. Fuentes
Institute of Geomechanics and Underground Technology, RWTH Aachen, Germany

K. Heins & T. Gries
Institut für Textiltechnik, RWTH Aachen, Germany

ABSTRACT: The aim of this research was to compare the performance of cotton textiles when exposed to different environmental conditions namely categories "A" to "G", herein. The testing method complied with standard soil burial methods. The tensile strength of the cotton samples was examined after one week buried in different soil conditions, including gravel only (without compost), top soil only, top soil with 3, 6, 10 and 30% compost. Also, to investigate the effect of water drainage, the top soil with undrained condition was considered. Generally speaking the tensile strength of the samples was reduced due to biodegradation after one-week exposure. Moreover, the results highlighted the important role of water in degradation of the samples. Moreover, the reduction in tensile strength of the buried specimen were very low (few percent) for small percentage of compost and therefore, the presence of 30% compost in soil was resulted in 75% tensile strength reduction for the proposed cotton samples.

1 INTRODUCTION

The successful use of geosynthetics, as one of the most important constructing materials in geotechnical projects such as embankments over soft subgrades, road construction, slopes, retaining walls and railroads have been (Cardile *et al.* 2017; Moghaddas Tafreshi *et al.* 2011, 2015; Tavakoli Mehrjardi & Sardehaei 2017; Tavakoli Mehrjardi & Moghaddas Tafreshi 2020; Tavakoli Mehrjardi *et al.* 2012, 2013, 2015, 2016, 2018, 2019, 2020). Todays, geosynthetics are mostly made of Petro-based polypropylene (PP) or polyethylene terephthalate (PET). The dependence on petroleum as a raw material is controversial from social, political and ecological points of view. Therefore, bio-based biodegradable textiles can play a pivotal role in different types of temporary and even permanent earthwork structures such as traffic routes, shorelines and especially on slopes to be re-cultivated in opencast mines. For example, newly constructed, unvegetated slopes and embankments are protected against erosion due to wind and precipitation. The use of geotextiles increases the shear and flow resistance of the mostly uncompacted upper soil layer against surface erosion. This ensures the initial erosion protection until this function is taken over by natural vegetation after two to three vegetation periods.

Since the bio-degradable textiles should be designed for applications ending up in or on soil, therefore the durability and degradability of the textiles should be investigated towards passing the time. Several International Standards specify test methods to determine the

ultimate aerobic or anaerobic biodegradation of textiles in aqueous or compost conditions (DIN EN 12225, ISO 17556, ISO 11721-1, 2). DIN EN 12225 mentions that if the requirements for appropriate functioning of the geosynthetics demand proof of microbiological resistance or if they are manufactured from newly developed polymers whose resistance is in any doubt, the soil burial test should be performed. In order to examine the biodegradability of a bio-degradable textile by the soil burial test, the suitability of soil, in terms of the soil biological activity, should be firstly assessed by testing cotton fabrics. This study aims to discuss about the effect of compost percentage in degradability of a cotton-like textile buried in soil. Moreover, we will inspect the applicability of the current standard.

2 TEST MATERIALS

2.1 *Soils*

Two types of soils as filling materials with the medium grain size (D_{50}) of 60 and 8 mm were considered. A few technical parameters of the soils are tabulated in Table 1.

Table 1. Technical properties of soils used for burial test.

Characteristic	Unit	Testing Method	Gravel	Top Soil
Finer than 0.002 mm	%	DIN 18123	0.5	10
Specific Gravity	——		2.67	2.65
Loss on ignition	%	DIN 18128	0.73	2.76
Carbonate content	%	DIN 18129	1.58	0.53
Calcite content	%		0.58	0.43
Dolomite content	%		1	0.11
Lime content	——		Very low in lime	Lime-free
Soil Type	——	DIN 4022	S/G	U,s,t`,fg`

2.2 *Cottons*

Woven cotton fabric (bleached and de-sized) with the nominal mass per unit area 235 g/m^2 was utilized.

2.3 *Compost*

A kind of humus compost (plant materials from gardening and landscaping) with grading size of 0-10 mm, was utilized. The compost includes different types of nutrients, notably nitrogen = 0.65 %, phosphate = 0.25, potassium oxide = 0.48 %, zinc = 0.012%, Iron = 0.60%, Manganese = 0.02 %. The C/N ratio of the compost was 20:1.

3 TEST SETUP, INSTRUMENTATION AND TEST PROCEDURES

In this study, two steps including burying stage and tensile tests were carried out. In order to exposing the cotton samples to the soil environment, According to DIN EN 12225, ten strip specimens of the cotton fabric were buried and kept in each of the testing soils for a period of seven days. Testing soils were included with gravel only (without compost), top soil only, top soil with 3, 6, and 10% compost. All the soils were drained from the bottom of the boxes. Also, to investigate the effect of drainage, the top soil with undrained condition was

considered. The top soil-compost composite was obtained by mixing the soil with relevant percentage (by weight) of compost at the natural moisture content. Moreover, five control strip specimens were stored at temperature (24) °C and relative humidity (40 ± 10) %. After seven days, the buried specimens were exhumed and submerged in an ethanol-water solution (70:30) for 300 s. Then, all the specimens were dried for 72 h in the room atmosphere. Figure 1 illustrates two selective photos for this stage.

Figure 1.   Photos for soil burial test (a) buried sample, and (b) dried samples.

After drying the samples, the tensile strength of the specimens should be assessed. As shown in Figure 2, the tests were performed on a tensile testing machine under standard climate conditions in accordance with DIN EN ISO 139. The clamping length at the start position is 50 mm. A pre-load of 5 N was applied. The specimens were loaded at a rate of 25 mm/min up to a force cut-off threshold of 75% of the maximum load.
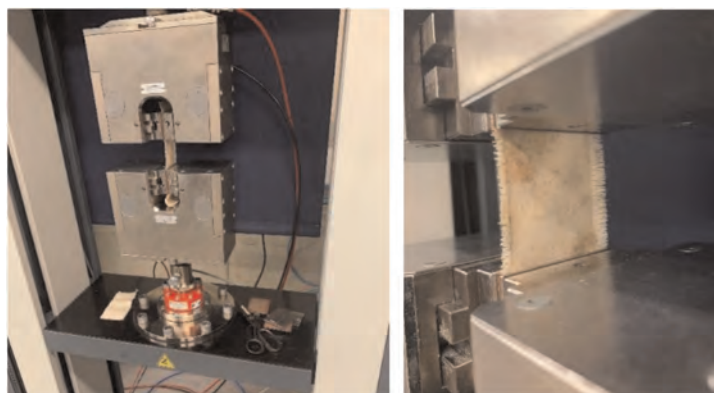
Figure 2.   Photos for tensile tests.

4   RESULTS AND DISCUSSIONS

As it mentioned, 70 tensile tests divided in seven categories were carried out. Figure 3 illustrates the force-elongation plots for categories "A" and "D". As can be seen, the samples reached a peak strength at different strain levels and then, the tensile force dropped suddenly, ending up to the breakage state.

Table 2 presents the variation of different parameters, notably the weight of the samples after exhumation, PH of the soils, and tensile strength of the samples for the examined

categories. At it can be seen, the PH of all samples were in the range 6.80 to 6.95 which were quite similar for all the categories. Moreover, the weight of the samples for all categories, apart from category "D", were similar (7.9 g) and a bit more in comparison with the weight of virgin samples (7.6 g in category "A"). Based on the obtained values and visual inspection of the samples after exhumation and also, considering three scenarios for calculation of the mean value of peak tensile strength (refer to footnote of Table 2 and Figure 4), the following hints can be pointed out:

- Some samples in specified categories including "B", "D" and "G" witnessed clamp failure during tensile tests, giving rise to a kind of pre-mature failure. Therefore, from technical
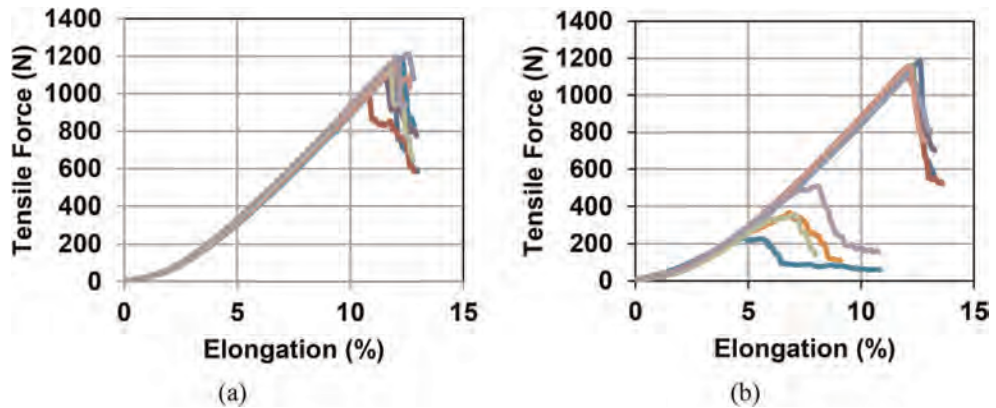
Figure 3.   The force-elongation curves of the tensile tests for categories (a) "A" (b) "D"

Table 2.   A summary of testing results of the examined categories.

Category	Testing Conditions	Weight (g)	PH	Min-Max[1]	Tensile Strength (N) Mean value[1]	Mean value[2]	Mean value[3]	Reduced Strength[1] (%)	Reduced Strength[3] (%)
A	Virgin	7.6	——	1008–1213	1139 (0)[4]	1139	1139	0	0
B	Gravel	7.9	6.79	1080–1154	1107 (4)	1075	1107	2.8	2.8
C	Drained Top Soil	7.9	6.89	960–1183	1100 (0)	1100	1100	3.4	3.4
D	Top Soil + 3%C	7.5	6.82	232–1159	749 (4)	833	1132	34.2	0.6
E	Top Soil + 6%C	7.9	6.85	1128–1226	1155 (0)	1155	1155	-1.4	-1.4
F	Top Soil + 10%C	7.9	6.94	618–1170	1066 (0)	1066	1122	6.4	1.5
G	Undrained Top Soil	7.9	6.79	1046–1125	1085 (8)	1005	1085	4.7	4.7

Notes
[1]Clamp failures excluded.
[2]Clamp failures included.
[3]Clamp failures and out of range data excluded.
[4]Number of tests witnessed clamp failure (out of 10 tests for each category).
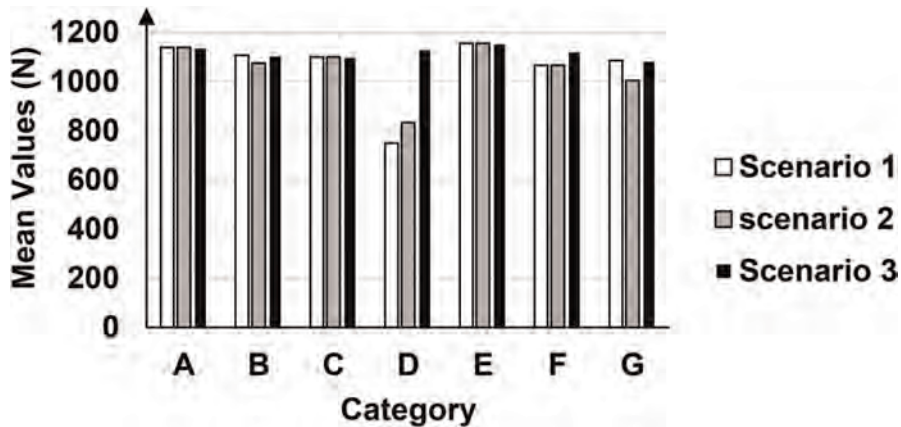
Figure 4.   Mean values of tensile strength for different categories and scenarios.

point of view, the results of the tests having clamp failure should be excluded so as to have an impair comparison.

- According to Table 2, the tensile strength of the samples, apart from category "E", was reduced due to degradation after one-week exposure. Be that as it may, the reduction ranges are not as high as it should be for a degrading soil. In effect, according to DIN EN 12225, the tensile strength of the cotton strips shall be ≤ 25 % of the original tensile strength after exposure for 7 days. However, this level of degradation cannot be expected even with mixing the natural soil with ten percent of compost. In the line with this claim, Margariti (2020) showed that there was no change in the thread diameters of the cotton textile samples before and after burial in soil.

- Category "G" in comparison with category "C" experienced the largest number of premature failure. This matter highlights the important role of water in degradation of the samples.

- Amongst all, category "D" (top soil mixed with three percent of compost) faced the highest reduction in tensile strength. Although the specimens adsorbed fine materials, the weight of the samples in this category was smaller than the others. Based on visual inspection, color difference (red color) was detected in few buried samples of this category which can be due to presence of few degrading grains in the soil or compost. Tomšič et al. (2007) stated that the smaller the color change, the more slowly the samples are degraded (Arshad et al. 2014).

- A significantly higher standard deviation can also be seen. The ratio of the standard deviation to the mean value of the maximum force is 2-6 %. In order to consider the data with enough precision, in one of the scenarios, the data being out of range in comparison with the other values in the same category was removed. In this scenario, the test results with clamp failure were also disregarded. Considering this scenario, which can be more reasonable, samples in category "D" had roughly the same reduction factor as others had.

As a whole, following the soil burial testing method prescribed by the standards, it was understood that the examined admixtures of soil and compost did not cause a considerable reduction on the tensile strength of the cotton samples. According to DIN EN 12225, since the tensile strength reduction was less than 75%, the biological activity of the soil was enhanced by increasing the percentage of the compost to 30% and the samples were exhumed and examined after one and two weeks. As Figure 5 shows, the tensile strength of the samples was decreased about 74% and 95% for the samples with one- and two-week exhumation.
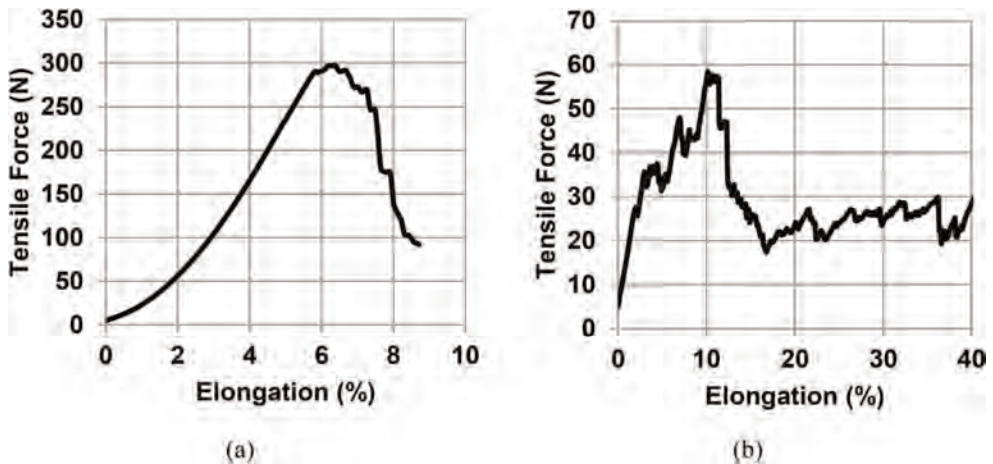
Figure 5.   Mean values of tensile strength for different categories and scenarios.

5 CONCLUSIONS

The biodegradation of cotton samples under the attack of microorganisms present in different soils was studied by using standard burial method where textile materials were directly buried for a period of seven days. Visual observations and tensile tests on the samples after exhumation revealed that:

- The tensile strength of the samples was reduced due to degradation after one-week exposure.
- Samples subjected to undrained condition experienced the largest number of pre-mature failure. This highlights the important role of water in degradation of the samples.
- The reduction in tensile strength of the buried specimen were very low (few percent) for small percentage of compost and therefore, the presence of 30% compost in soil was resulted in 75% tensile strength reduction for the proposed cotton samples.

REFERENCES

Arshad, K., Skrifvars, M., Vivod, V., Valh, J.V., Vončina, B. 2014. Biodegradation of Natural Textile Materials in Soil. *Tekstilec* 57(2),118–132. DOI: 10.14502/Tekstilec2014.57.118-132

Brigita, T., Simončič, B., Orel, B., Vilčnik, A., Spreizer, H. 2007. Biodegradability of Cellulose Fabric Modified by Imidazolidinone. *Carbohydrate Polymers* 69 (3): 478–488

Cardile, G., Moraci, N., Pisano, M. 2017. Tensile Behaviour of an HDPE Geogrid Under Cyclic Loading: Experimental Results and Empirical Modelling. *Geosynthetics Internaltional* 24 (1), 95–112.

Deutsches Institut für Normung (DIN) 1987. Subsoil and Groundwater; Classification and Description of Soil and Rock; Borehole Logging of Soil and Rock not Involving Continuous Core Sample Recovery. *DIN* 4022.

Deutsches Institut für Normung (DIN) 2002. Soil - Investigation and Testing- Determination of Ignition Loss. *DIN* 18128.

Deutsches Institut für Normung (DIN) 2011. Soil, Investigation and Testing- Determination of Grain-size Distribution. *DIN* 18123.

Deutsches Institut für Normung (DIN) 2011. Soil, Investigation and Testing- Determination of Lime Content. *DIN* 18129.

European Committee for Standardization 2019. Geosynthetics – Method for Determining the Microbiological Resistance by a Soil Burial Test; German and English version. *DIN EN* 12225.

Margariti, C. 2020. The Effects of Micro-organisms in Simulated Soil Burial on Cellulosic and Proteinaceous Textiles and the Morphology of the Fibres. *Studies in Conservation*. https://doi.org/10.1080/00393630.2020.1812245

Moghaddas Tafreshi S.N., Shaghaghi T., Tavakoli Mehrjardi, Gh., Dawson A.R., Ghadrdan M. 2015. A Simplified Method for Predicting the Settlement of Circular Footings on Multi-layered Geocell-reinforced Non-cohesive Soils, *Geotextiles and Geomembranes*, 43(4), 332–344.

Moghadas Tafreshi, S.N., Tavakoli Mehrjardi, Gh., Ahmadi, M. 2011. Experimental and Numerical investigation on Circular Footing Subjected to Incremental Cyclic Loads. *International Journal of Civil Engineering*, 9 (4), 265–274.

Tavakoli Mehrjardi, Gh., Amjadi Sardehaei, E. 2017. Design Graphs to Estimate Reduction Factor of Nonwoven Geotextiles Due to Installation Process. *European Journal of Environmental and Civil Engineering*, DOI: 10.1080/19648189.2017.1327897, 1–14.

Tavakoli Mehrjardi, Gh., Ghanbari, A., Mehdizadeh, H. 2016. Experimental Study on the Behavior of Geogrid-reinforced Slopes with Respect to Aggregate size. *Geotextiles and Geomembranes* 44 (6), 862–871.

Tavakoli Mehrjardi, Gh., Azizi, A., Haji-Azizi, A. and Asadollahfardi, G.R. 2020. Evaluating and Improving the Construction and Demolition Waste Technical Properties to Use in Road Construction. *Transportation Geotechnics*, 23, 1–13.

Tavakoli Mehrjardi, Gh., Khazaei, M. 2017. Scale Effect on the Behavior of Geogrid-Reinforced Soil under Repeated Loads. *Geotextiles and Geomembranes* 45(6), 603–615.

Tavakoli Mehrjardi, Gh. and Moghaddas Tafreshi, S.N. 2020. *Geocell-Reinforced Foundations, Geocells, Advances and Applications*. Springer, 77–131.

Tavakoli Mehrjardi, Gh., Moghadas Tafreshi, S.N., Dawson, A.R. 2012. Combined Use of Geocell Reinforcement and Rubber-soil Mixtures to Improve Performance of Buried Pipes. *Geotextiles and Geomembranes* 34, 116–130.

Tavakoli Mehrjardi, Gh., Moghaddas Tafreshi, S.N., Dawson, A.R. 2013. Pipe Response in a Geocell Reinforced Trench and Compaction Considerations. *Geosynthetics International* 20(2), 105–118.

Tavakoli Mehrjardi, Gh., Moghadas Tafreshi, S.N., Dawson, A.R. 2015. Numerical analysis on Buried Pipes Protected by Combination of Geocell Reinforcement and Rubber-soil Mixture. *International Journal of Civil Engineering* 13 (2B), 90–104.

Tavakoli Mehrjardi, Gh., Motarjemi, F. 2018. Interfacial Properties of Geocell-reinforced Granular Soils. *Geotextiles and Geomembranes* 46(4), 384–395.

Tavakoli Mehrjardi, Gh., Behrad, R. and Moghaddas Tafreshi, S. N. 2019. Scale Effect on the Behavior of Geocell-Reinforced Soil. *Geotextiles and Geomembranes*, 47(2), 154–163.

The International Organization for Standardization (ISO) 2001. Textiles — Determination of Resistance of Cellulose-containing Textiles to Microorganisms — Soil Burial Test — Part 1: Assessment of Rot-retardant Finishing. *ISO* 11721–1.

The International Organization for Standardization (ISO) 2003. Textiles — Determination of resistance of Cellulose-containing Textiles to Microorganisms — Soil Burial Test — Part 2: Identification of Long-term Resistance of a Rot Retardant Finish. *ISO* 11721–2.

The International Organization for Standardization (ISO) 2019. Plastics — Determination of the Ultimate Aerobic Biodegradability of Plastic Materials in Soil by Measuring the Oxygen Demand in a Respirometer or the Amount of Carbon Dioxide Evolved. *ISO* 17556.

White polyethylene geomembrane: Forensic and laboratory evidence for superior durability

B. Ramsey
Boyd Ramsey Consulting LLC, Houston, TX, USA

A. Maskal
Solmax, Visalia, CA, USA

ABSTRACT: White Polyethylene Geomembranes have been available in the market for over two decades and have been used broadly, often exposed (uncovered) in demanding and sensitive applications. The performance of these materials has far exceeded the initial (circa 1990's) exceptions. There is increasing evidence that the durability and lifespan of a white geomembrane in an exposed application is longer, not only than projections, but perhaps longer than that of traditional black colored geomembranes of comparable composition. This paper presents data in support of that hypothesis and reaches the conclusion that in exposed applications, white surfaced geomembrane is the material of choice, based on durability as well as other pertinent considerations. Data and evidence from forensic evaluations as well as laboratory testing for durability is presented and new estimates on lifespan are presented.

1   INTRODUCTION

White Polyethylene Geomembranes have been available in the market for over two decades and have been used broadly, often exposed (uncovered) in demanding and sensitive applications. The performance of these materials has far exceeded the initial (circa 1990's) exceptions. There is increasing evidence that the durability and lifespan of a white geomembrane in an exposed application is perhaps longer, not only than projections, but perhaps longer than that of traditional black colored geomembranes of comparable composition. This paper presents data in support of that hypothesis and in fact, reaches the conclusion that in exposed application, white surfaced geomembrane is the material or choice, based on durability as well as other pertinent considerations. Data and evidence from forensic evaluations as well as laboratory testing for durability is presented and new estimates on lifespan are presented.

2   FORENSIC EVALUATIONS

The successful performance of white geomembranes in the field has been well established. Perhaps Cowlitz County, Washington (Thiel) is the most complete forensic examination, however, the Polk County, Florida site (Roberts and separately, Ramsey) (green surfaced, with very similar stabilization) has also been extensively documented. The Palo Verde Nuclear Generating Station has been one of the largest users of white geomembrane as reported by Eichelberger. Samples from each of these sites have been included in this study, as well as others. Further information on the performance of white geomembrane can be found in Rentz and other references. In general, white geomembrane materials present multiple benefits as

contrasted with traditional black geomembrane, these include improved damage detection, fewer and smaller wrinkles / less thermal expansion and contraction and expanded installation windows and improved safety and handling. Nearly all of these are on outcome of the lower temperature of the white geomembrane as a result of reflection of sunlight as contrasted with the exceptionally high absorption of solar energy of black materials.

3   SAMPLE IDENTIFICATION

The materials used in this examination came from various locations and climates around the world. The details of the samples reported are listed below:

Sample A – Polk County, Florida, USA 1.5 mm exposed green landfill cap. Sample exposed outdoors for 21 years at Latitude 27° North tropical environment

Sample B- Polk County, Florida, USA 1.5 mm exposed green landfill cap. Sample from original installation, but stored in a warehouse, aged 21 years but no UV/solar exposure

Sample C- Toowoomba, Queensland, Australia. 1.0 mm white geomembrane from an exposed outdoor evaporation pond in service since 2012 at Latitude 27° South, warm and temperate environment

Sample D – Cowlitz Country, Washington, USA 1.5 mm exposed white geomembrane from an exposed outdoor pond in service since 1993 at Latitude 46° North, Mild Mediterranean climate

Sample G- Palo Verde Nuclear Generating Station, Phoenix AZ, USA 2.0 mm sample from 1999 installation, but stored in a warehouse, aged but no UV/solar exposure.

Sample H – Commercial sample from 2013, 1.5 mm white geomembrane, but stored in a warehouse, aged but no UV/solar exposure

Sample J – Commercial sample from 2020, 1.5 mm white geomembrane, stored in a warehouse, no UV/solar exposure

Sample K – Commercial sample from 2020, 2.0 mm black geomembrane, stored in a warehouse, no UV/solar exposure

Sample M – Commercial sample from 2013, 2.0 mm white conductive geomembrane, but stored in a warehouse, aged but no UV/solar exposure.

In the presentation of data, the samples can be delineated into three groups: Those materials that have been exposed in-service (A, 21 years C, 8 years and D, 25 years). Those materials that have aged, but have not been exposed in-service (B, 21 years G, 21 years M and H, 7 years). Those materials that can be considered "new" – manufactured recently with no exposure in-service (J and K).

4   TEMPERATURES OF EXPOSED GEOMEMBRANE

There is existing literature and studies on the temperature differentials of black and white geomembranes exposed to the environment. Koerner (G.) in "Temperature Behavior of Field Deployed HDPE Geomembranes," addresses both the overall difference and the seasonality in the northern hemisphere (Latitude 40° North). Rentz reports a temperature delta (Black vs. White geomembrane) of 22°C at the Queen's University Queen's University Environmental Liner Test Site II (QUELTS II) in August at Latitude 44° North. Cadwallader reports a 25° temperature differential, presumably at Latitude 36° North. Further, Cadwallader includes the assumption proven in this paper:" Advantages of maintain a lower geomembrane temperature are also evident in long term aging tests." Pelte reports the largest differential of 35°C at latitude 45° North. Pelte also conducted laboratory scale testing demonstrating greater differentials in the temperature response of black and white geomembranes, both polyethylene and polyvinylchloride.

The author also has significant field experience in evaluating the temperature of geomembranes that comes in the form of both personal observation and the recording of weld/seaming activity temperatures.

Taking this all under consideration, for the purposes of this evaluation a temperature differential of 25°C is used to estimate the temperature difference / behavior of white vs. black polyethylene geomembranes when exposed to the environment.

5 SPECIFICATION OF DURABILITY CRITERIA

When the Geosynthetics Institute originally (June 1997) created the specification "GRI GM-13" consideration was given to durability. Similar to the other properties of the specification, multiple "successful" materials were tested, these values reported and a requirement was negotiated in relation to the performance of existing materials that were known to be functioning well. For durability considerations, this was agreed to be the retention of Oxidative Induction Time (OIT), proposed to represent the length of the "Stage A" of geosynthetic lifespan as reported by Hsuan and Koerner. The parties involved in the discussions were all participants in the geosynthetic and geomembrane industry, with manufacturers, design and quality engineers and major consumers all represented. This group agreed that the retention of OIT with the values enumerated within the specification should be acceptable. The long-term success and the broad global use of the specification proves this decision to be correct and this characteristic has become a reliable indication of durability performance.

For High Pressure OIT, this value is a minimum initial HP-OIT of 400 minutes with the retention of HP-OIT of 80% of the initial value after oven aging at 85°C for 90 days. The specifics of this testing are included in ASTM specifications: ASTM D 5885 and D 5721 respectively. To comply with GM-13, a geomembrane material needs to have a reduction rate for HP-OIT during Oven aging at 85°C of less than 0.89 minutes/day over a 90-day period. This performance level has served the geomembrane industry well in the following decades and is one of the basis for comparison in this paper's evaluation.

6 LABORATORY EVALUATION PROGRAM

The material sample listed above were subjected to Oven Aging in a modified fashion, generally as directed by GM-13 and ASTM 5721. The modification was a reduction in the oven temperature to reflect the difference in field temperatures as discussed above. The oven aging was conducted at 60°C. The oven aging was conducted at the Geosynthetic Institute, Folsom, PA in the summer of 2021. Samples of the materials as initially received, and after 30, 60 and 90 days of oven aging were tested for HP-OIT. This testing was conducted at the Solmax laboratory in Rechlin, Germany. This laboratory is certified within the GAI-LAP (Geosynthetic Accreditation Institute-Laboratory Accreditation Program) to conduct this test as well as multiple other certifications.

There have been recent significant changes to the HP-OIT testing document published by ASTM (5885). These relate primarily to sample preparation and are not completely addressed here. However, it is important to understand how the data reported herein was generated. The samples tested here were tested in the "as-is" condition. That is, a section was taken from the entire thickness of the sample, weighted and tested for HP-OIT properties as it existed at that point. No grinding, homogenization, plaque preparation or other alteration of the samples occurred prior to testing. In the opinion of the authors, this most directly reflects the "real-world" conditions in which these materials are used.

Further to sample preparation and testing, it should be noted how the values reported were calculated. In multi-layer geomembrane materials, it is common for the different layers to be stabilizer with different varieties of stabilizer, different levels of stabilizer, or both. In

HP-OIT testing, this can manifest itself in results that contain "shoulders" as indicated in Figure 1 below. This contrasts with other results that are more indicative of Figure 2.
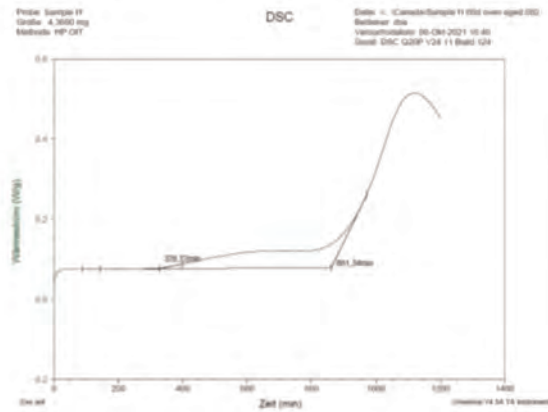
Figure 1.   HP-OIT with shoulder.
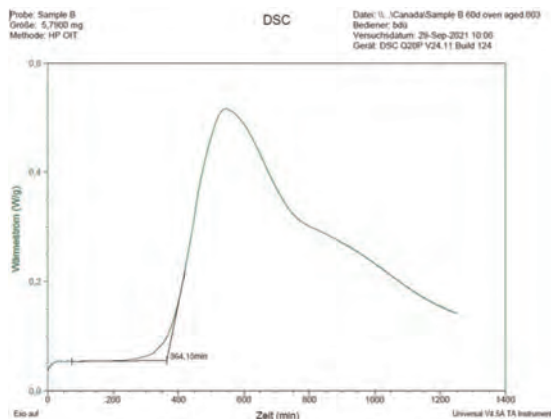
Figure 2.   HP-OIT with no shoulder.

In this examination, small shoulders such as shown above in Figure 1 were ignored and the much larger exothermic reaction demonstrated by the large steeply sloped curve to the right was used to calculate the HP-OIT value for that sample. In some cases, retesting was done to validate results that appeared inconsistent or unexpected. In every case, no data points were discarded and the values reported below are the results of one, or the average of two test results.

The author is sympathetic to the attempts to improve the reliability and repeatability of the HP-OIT test by requiring sample homogenization. Striving to reduce testing variation is a good thing. However, in this case, and generally, the benefit of testing the material in the condition and state that it is actually used in greatly outweighs the need to reduce variation. One would not endeavor to try to explain to a design engineer, owner, or other stakeholder that rather than simply taking a section of material and testing it, it was justifiable to significantly modify the material prior to testing.

7 RESULTS

The results are reported below in three tables and three graphs: Figure 3 lists the numerical values for HP-OIT test results. Figure 4 lists these same results but in the format of a percentage of original OIT retained. Figure 5 presents the rate of reduction of HP-OIT as compared with the GM-13 requirements and discussed above.

Tested Values	T = zero days	T = 30 days	T = 60 days	T = 90 days
A (green)	110	108	107	97
B (green)	427	337	367	371
C	651	644	604	634
D	329	325	309	264
G	506	529	518	541
H	900	896	784	832
J	502	461	424	420
K (black)	1776	1771	1659	1756
M	520	551	506	519

Figure 3. HP-OIT test results (numerical values).

% retained	T = zero	T = 30 days	T = 60 days	T = 90 days
A (green)	100%	98%	97%	88%
B (green)	100%	79%	86%	87%
C	100%	99%	93%	97%
D	100%	99%	94%	80%
G	100%	105%	102%	107%
H	100%	100%	87%	92%
J	100%	92%	84%	84%
K (black)	100%	100%	93%	99%
M	100%	106%	97%	100%

Figure 4. HP-OIT test results (percentage retained).

Tested Values	OIT loss (Min/day)	GM-13 requirement (Min/day)	Delta (Min/day)
A (green)	0.14	0.89	0.75
B (green)	0.62	0.89	0.27
C	0.19	0.89	0.70
D	0.72	0.89	0.17
G	-		
H	0.76	0.89	0.13
J	0.91	0.89	-0.02
K (black)			
M	0.01	0.89	0.88

Figure 5. Rate of sample OIT loss relative to GM-13 requirement.

The average rate of OIT loss for the seven colored samples was 0.48 minutes /day as compared with the GM-13 requirement of 0.89 minutes per day – an improvement of almost 50%

The result is that materials tested exceed the specification requirement for HP-OIT retention albeit at a lower temperature. However, as lower daily temperature is clearly a feature of the non-black/white materials, the author is confident that this is a clear, logical, and now demonstrated contributor to extended lifespan. This has been demonstrated across multiple locations, multiple materials and different applications. Exposed white surfaced polyethylene geomembrane materials should be expected to last longer than black surfaced materials in so far as the effects of temperature.

8   APPLICATION OF RESULTS TO CURRENT LIFESPAN PROJECTIONS

In the Koerner (R.M.) Keynote lecture at the 2016 GeoAmericas event, held in Miami, Florida a detailed analysis and calculation was presented for the estimated lifespan of exposed polyethylene geomembranes. One of the metrics used to estimate lifespan, in addition to OIT, was the retention of physical properties, specifically tensile strength and tensile elongation. These properties were used to prepare (Koerner) figure 19C (below) which lists the predicted lifespan of materials at a range of field temperatures. Using this data and the temperature ranges and impacts from the Koerner work and extending the results demonstrated in this paper, one can reason that the daily temperature reductions of white materials would add an additional 17 years of lifespan (correlating to 20 degrees Celsius of temperature reduction) for white polyethylene geomembrane materials as compared with black in an exposed application.

A second methodology for quantification of lifespan extension is the rate of OIT reduction as demonstrated in Figure 5. This decrease in the rate of stabilizer consumption would indicate an extension of the "Stage A" decomposition, as modeled in Koerner's text, Designing with Geosynthetics and multiple other publications. Again, drawing on data presented in the Koerner Miami 2016 Keynote address, Koerner presents an estimate of 207 years for Stage A for standard commercial materials, similar to materials evaluated in support of the GM-13 HP-OIT retention requirement(s), in Figure 6. The data developed and presented here indicates that the rate of HP-OIT retention for white materials at field temperatures is 53% of the specification requirement. This methodology would indicate a Stage

Site Temperature (°C)	Halflife (months)	Halflife (yrs)
80	177.3	14.77
70	280.3	23.36
60	383.4	31.95
50	486.5	40.54
40	589.6	49.13
30	692.7	57.72
20	795.7	66.31

c) Halflife field predictions in Phoenix, Arizona down to 20°C
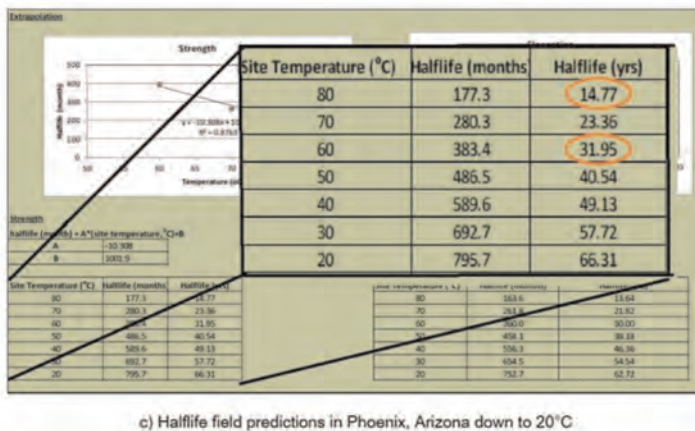
Figure 6.   Copy of Figure (19 C) from Koerner Miami lecture.

A time of approximately 300 years, as compared with the 207-year estimate. The author does not suggest that this is an accurate absolute value, but clearly the materials examined here have performed significantly longer than was initially anticipated.

Clearly these estimations come with many caveats as there are multiple factors effecting lifespan. However, the results of testing of exposed forensic samples, field evaluations reported in literature, as well as the modeling and testing contained in this paper demonstrate consistently that white surface polyethylene geomembranes have lower temperatures in the field and this results in improved lifespan and durability.

9   CONCLUSIONS

What has been presented is a combination of forensic field evaluations, public literature information and in a new addition to the industry knowledge, the behavior of white surface polyethylene geomembranes in retention of HP-OIT at a temperature that reflects field exposure temperatures. This data and information all imply and support the hypothesis that these materials will have a longer lifespan than that of the equivalent black geomembrane materials. Literature suggests that this improvement is approximately 17 years and possibly more in terms of lifespan.

ACKNOWLEDGEMENTS AND APPRECIATION

REFERENCES

ASTM D5721, "*Standard Practice for Air-Oven Aging of Polyolefin Geomembranes*", American Society for Testing and Materials, West Conshohocken, Pennsylvania, USA.

ASTM D5885, "Standard Test Method for Oxidative Induction Time of Polyolefin Geosynthetics by High-Pressure Differential Scanning Calorimetry", *American Society for Testing and Materials*, West Conshohocken, Pennsylvania, USA.

Cadwallader, M., Cranston, M., and Peggs, I. D. (1993). "White-surfaced HDPE Geomembranes: Assessing their Significance to Liner Design and Installation." *Proc., Geosynthetics' 93, Industrial Fabrics Association International*, St. Paul, MN, 1065–1079.

Case, Mark E., Koerner, George R., Koerner, Robert M., Hsuan, Yick (2010), Case History of a 16-Year Old Exposed HDPE Geomembrane Cover, *Proceedings of 9th International Conference on Geosynthetics*, Guarujá, Brazil

Eichelberger, C., Hersh, G. and Pittawala, S. (2013, Oct.) "Geosynthetics: The Solution for Managing Nuclear Power Generation Water Supply in an Arid Environment" *Geosynthetics Magazine*, Oct. 2013.

Fischer, R., & Ketola, W. (1994). "Surface Temperatures of Materials in Exterior Exposures and Artificial Accelerated Tests". *Materials Science*, DOI:10.1520/STP18174S

Giroud, J.P. and Morel, N., (1992) "Analysis of Geomembrane Wrinkles" *Geotextiles and Geomembranes* Volume 11, Issue 3, 1992, Pages 255–276

Gleason, M.H., Houlihan, M.F., and Palutis, J.R., (2001) "Exposed Geomembrane Cover Systems: Technology Summary," *Proceedings of the Sixth International Conference on Geosynthetics*, Portland, Oregon, February, 2001, pp. 905–918.

GRI – GM13 Standard Specification for "*Test Methods, Test Properties and Testing Frequency for High Density Polyethylene (HDPE) Smooth and Textured Geomembranes*", The Geosynthetic Institute, Folsom, PA, USA

Hsuan, Y.G., and Koerner, R.M. (1998). "Antioxidant Depletion Lifetime in High Density Polyethylene Geomembranes". *Journal of Geotechnical and Geoenvironmental Engineering, ASCE*, 124(6): 532–541. doi:10.1061/(ASCE)1090-0241

Ivy, N., (2002), *HDPE Geomembrane After 20 years of Service*, GFR Magazine June/July 2002

Jafari, N.H. *et.al.*, (January 2014) "Service Life of HDPE Geomembranes Subjected to Elevated Temperatures", *Journal of Hazardous, Toxic, and Radioactive Waste, American Society of Civil Engineers.* DOI: 10.1061/(ASCE)HZ.2153-5515.0000188

Koerner, G. R. and Koerner, R. M., (1995) "Temperature Behavior of Field Deployed HDPE Geomembranes," *Proc. Geosynthetics '95*, IFAI, St. Paul, MN, pp. 921–937.

Koerner, R. (2016) "Lifetime Predictions of Exposed Geotextiles and Geomembranes" *Proceedings of GeoAmericas 2016 3rd Pan-American Conference on Geosynthetics*, Miami, FL USA

Koerner, R. (2012) *"Designing with Geosynthetics"* 6th Edition, Xlibris Press, 2012

Koerner R. *et al.* "*GRI White Paper #6 on Geomembrane Lifetime Prediction: Unexposed and Exposed Conditions*", Geosynthetic Institute, Folsom, PA Website: http://www.geosynthetic-institute.org/ Accessed September 4, 2020.

Koerner R. *et al.* "*GRI Report #44 Exposed Lifetime Predictions of 19-Different Geosynthetics in the Laboratory and in Phoenix, Arizona*" Geosynthetic Institute, Folsom, PA Website: http://www.geosynthetic-institute.org/ accessed September 4, 2020.

Koerner, R. M., Koerner, G. R. and Hsuan, Y. G., (2005) "Lifetime Prediction of Exposed Geomembranes," *Proceedings of the GRI-18 Conference on "Geosynthetics Research & Development In-Progress"* at GeoFrontiers, January 26, 2005, GII Publication, Folsom, PA.

Pelte, T., Pierson, P., and Gourc, J.P. (1994). "Thermal Analysis of Geomembranes Exposed to Solar Radiation". *Geosynthetics International*, 1(1): 21–44

Ramsey B., (2016, Sept.) "*13-Year Study of Exposed, Green Geomembrane Cover*", Geosynthetica.com Web Reference: https://www.geosynthetica.com/13-year-exposed-green-geomembrane/ Accessed November 15, 2021.

Rentz, A.K., *et al.*, (August 2007) "Comparison of Wrinkles in White and Black HDPE Geomembranes", *Geosynthetics International*, Volume 14 Issue 4, pp. 219–227

Roberts, M., Bonilla, V., Kelner, R., and Choate, A. (April 2005), "*Exposed Geomembrane Liner Cap Takes on Three Hurricanes in Polk County, South Central Florida*" 2005 March/April, MSW Management, pp. 72–77. Web reference: http://www.erosioncontrol.biz/MSW/Articles/The_EGC_Takes_On_Three_Hurricanes_in_Polk_County_1545.aspx

Rowe, R.K. *et al.* (2009) "Ageing of HDPE Geomembrane Exposed to air, Water and Leachate at Different Temperatures" *Geotextiles and Geomembranes* vol. 27 (2009) pg. 137–151.

Rowe, R.K., and Ewais, A.M.R., (2014) "Ageing of Exposed Geomembranes at Locations with Different Climatological Conditions", *Canadian Geotechnical Journal*, 25 August 2014, https://doi.org/10.1139/cgj-2014-0131

Suits, L.D. and Hsuan, G., (1992), Technical Note: Assessing the Photo-degradation of Geosynthetics by Outdoor Exposure and Laboratory Weatherometer", *Geotextiles and Geomembranes* 11 pp. 255–276.

Take W.A. *et al.*, (2003) "Quantifying Geomembrane Wrinkles Using Aerial Photography and Digital image Processing", *Geotextiles and Geomembranes* 21, 111–122.

Take, W.A. *et al.*, (2015) "Thermal Exposure Conditions for a Composite Liner with a Black Geomembrane Exposed to Solar Radiation", *Geosynthetics International*, Volume 22 Issue 1, February 2015, pp. 93–109

Tarnowski, C., and Baldauf, S. (2006). "*Ageing Resistance of HDPE-geomembranes – Evaluation of long-term Behavior Under Consideration of Project Experiences*". In Geosynthetics. Edited by J. Kuwano and J. Kosaki. Millpress, Rotterdam, N.L.D., pp. 359–362.

Thiel R., (2019, Feb.) "A Leachate Pond Geomembrane After 25 years of Service", *Geosynthetics Magazine*, Feb, 2019.

Thiel, R., Purdy, S. and Yazdani, R. (2003), "Case History of Exposed Geomembrane Cover for Bioreactor Landfill," Session D06, *Proceedings of the Sardinia Conference*, 2003.

Thomas, R.W., and Ancelet, C.R. (1993). "The Effect of Temperature, Pressure and Oven Ageing on the High Pressure Oxidative Induction Time of Different Types of Stabilizers. *In the Proceedings of the Geosynthetics '93 Conference*, IFAI, St.Paul, Minn. pp. 915–924.

Yako, M. A., Koerner, G. R., Hsuan, Y. G. and Koerner, R. M. (2010), "Case History of a 20-Year Old Exposed HDPE Surface Impoundment Liner," *9th ICG*, Brazil.

Durability of geogrid reinforcement from a sloped retaining wall after 25 years in-service

R.J. Fannin
University of British Columbia, UBC, Vancouver, British Columbia, Canada

V.S. Quinteros
Norwegian Geotechnical Institute, NGI, Oslo, Norway
Department of Civil Engineering and Energy Technology, Oslo Metropolitan University, Norway

ABSTRACT: This study presents a durability assessment of geogrid samples that were exhumed from a sloped retaining wall 25 years after completion of construction. The durability assessment is based on visual inspection and a series of index and strength tests, focusing on the identification of possible physical damage and/or degradation. The assessment lends confidence in the use of isochronous load-strain-time data for predicting the long-term strain of geogrid reinforced soil structures for design practice. This research belongs to the few well-documented long-term studies on geogrid durability.

1 INTRODUCTION

The determination of a long-term value of tensile strength for stability analysis of a geosynthetic reinforced soil structure involves use of a separate reduction factor to account for (i) the potential for damage of the reinforcement during installation and (ii) the durability of the reinforcement over the service life of the structure. The two factors account for any strength loss that may occur and appear in design guidelines and codes of practice (see for example, BS-8006). A limited number of field trials have sought to quantify durability from strength testing of specimens retrieved after long-term burial. They encounter a common difficulty in being able to distinguish between strength loss due to installation damage and change in strength arising from material durability, see for example Harney and Holtz (2006), Wayne *et al.* (1997), Onodera *et al.* (2004), and Jenner and Nimmesgern (2002).

Given a very limited body of data on geosynthetics after more than 20 years in-service, and recognizing that differentiation between a strength change due to installation damage and durability has not always been feasible, this contribution reports on the durability of geogrid exhumed from a sloped reinforced soil wall near Oslo, Norway, about 25 years after completion of construction. Little or no installation damage was anticipated in the geogrid reinforcement because of the practices used in construction of this instrumented research structure. Accordingly, the objectives of this study are to (i) assess exhumed samples for installation damage based on visual observations, (ii) quantify any changes in material properties in terms of geometry, composition, and tensile strength from isochronous load-strain testing, and (iii) based on the findings, comment upon the implications for consideration of durability in design practice.

2 THE NORWEGIAN SLOPED REINFORCED SOIL WALL

The structure is located 25 km northeast of Oslo, Norway. The steep (2V:1H) sloped wall is 20 m long and 4.8 m high (see Figure 1). It comprises two sections, termed Sections 'J' and

'N', each of which is 10 m long and with a different arrangement and spacing of Tensar SR 55 geogrid reinforcement (Fannin & Hermann 1990).
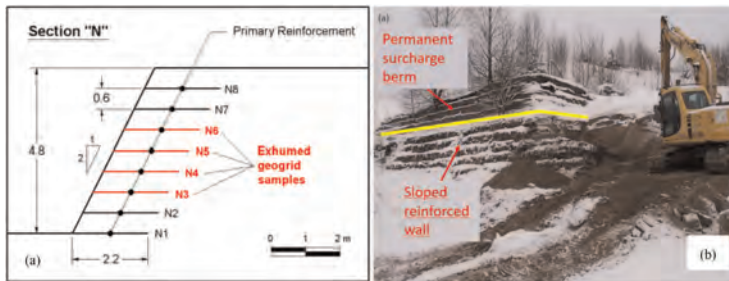
Figure 1. Section "N": (a) exhumed geogrid layers and (b) preparation for field sampling activities.

2.1 Construction details

The sloped wall seats into an existing slope in a borrow pit used by the local road authority. The backfill is a uniformly graded clean sand with trace of fine gravel, with median grain size d_{50} = 0.2 mm and coefficient of uniformity C_u = 2.6, obtained from the same borrow source. Construction took place in July 1987. Backfill sand was placed using a front-end loader, prior to spreading with a mini excavator to a minimum loose lift-thickness of approximately 350 mm. Thereafter it was moisture-conditioned to a water content $5 \leq w \leq 10\%$, and compacted using a vibrating plate to a thickness of approximately 300 mm and dry density greater than 92% of the maximum value from the Standard Proctor test (ASTM D698).

Eight layers of uniaxial geogrid were used in Section 'N' (termed layers N1 to N8, see Figure 1a). They were placed at a uniform vertical spacing of 0.6 m that equates to two finished compaction lifts. The length L = 2.2 m of the geogrid reinforcement does not satisfy modern design guidance: it was purposely chosen for Section 'N' as a parametric variable for investigation in the original field trial that predated regulatory design guidance by several years.

The front-end loader was not permitted to drive on the reinforced soil zone, and the mini-excavator was only permitted to move onto that zone after pushing a loose layer of backfill sand over it to a working-platform thickness of 350 mm. The commensurate supervision of all equipment operation afforded little or no opportunity for construction-related installation damage.

2.2 Service life

Following a month of self-weight loading commencing in July 1987, a single load-unload cycle of surcharge loading was applied to the crest of the structure over a period of nearly 2 months using water-tanks that were filled in August 1987 and subsequently emptied and removed in September 1987. Permanent surcharge loading was subsequently imposed on the sloped wall by means of a 3 m high berm that was constructed in October 1987 and then left in place. Upon completion, instrumentation established a maximum tensile load per unit width $T_{max} \approx 1.4$ kN/m the lowermost (N1) layer of geogrid, and values of $2.1 \leq T_{max} \leq 3.0$ kN/m in the other (N2 to N8) layers above it; the companion values of maximum tensile strain were in the general range $0.2 \leq \varepsilon_{max} \leq 0.8\%$. Although the force mobilized in the geogrid layers is relatively small, it was demonstrated entirely consistent with a geotechnical analysis informed by the frictional strength of the sand backfill (Fannin & Hermann 1990). The average temperature in the reinforced soil zone varied between 7 and 9°C, depending on location, with the near surface locations experiencing a seasonal range between 0 and 20°C. Long-term performance monitoring over a period of 10 years established that the tensile force per unit width in each layer remained essentially constant. The associated strain

exhibited a time-dependent increase: the invaluable time-series record of field data for independent measurements of load-strain-time to almost 90,000 h was found very consistent with laboratory creep test data for the geogrid to 100,000 h (Fannin 2001).

3 FIELD SAMPLING

A program of field sampling was conducted about 25 years after completion of construction in February 2013. Section 'N' was selected for sampling of the backfill sand and geogrid reinforcement because the site layout provides for easier access to that end-location of the structure.

3.1 Soil

Excavation proceeded in a 'top-down' direction from the crest of the structure near the lateral toe of the surcharge berm (see Figure 1b). Three grab samples of soil were taken at the mid-height between layers N8-N7, N7-N6, and N6-N5, respectively (see Figure 1a). At the time of construction, the backfill soil was classified as a uniformly graded sand with trace gravel and trace silt. Scanning Electron Micrograph (SEM) images of sand in the grab samples (see Figure 2a) suggests a generally angular to very angular grain shape. XRD analysis established the mineralogy as approximately 70% quartz, 20% feldspar, 5% mica, and 5% others. Index testing to ASTM 4972 established a pH of 8.3, believed consistent with the predominantly silicate content of the sand.
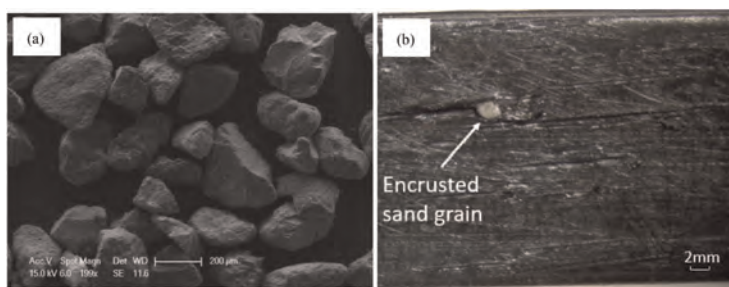
Figure 2. Sampled materials (a) sand grains and (b) geogrid reinforcement.

3.2 Geogrid

The backfill sand was carefully removed by machine-excavation, in a series of horizontal cuts. When the backfill cover thickness reduced to approximately 15 cm, the rest was then removed by hand-excavation using a shovel to move the bulk of the sand, and a combination of spade and soft-sweep push-broom to remove all of the remaining sand and expose the top surface of a geogrid layer for sampling. Four layers, N6 to N3 (see Figure 1a), were exhumed from the structure. The backfill was frozen to over a distance of approximately 0.75 m into the reinforced soil zone behind the slope-face, thus field exhumation yielded samples of geogrid reinforcement that were approximately 1.25 m long and 1.0 m wide. Hand-held visual assessment established no evidence, on any of the geogrid samples, of adverse damage that could be attributed to installation at the time of construction in 1987 or the process of field sampling.

SEM inspection of the N6 specimens (Quinteros 2014) identified a high frequency of low magnitude abrasions: they took the form of surficial scratches of variable length, typically less than 0.1 mm deep. A very low frequency of medium-size abrasions was detected: they took the form of pits and gouges that were typically 2 to 15 mm long and 0.2 to 0.5 mm deep (see Figure 2b). The absence of any damage is attributed to the supervision of all equipment

operation resulting in no opportunity for installation-related damage during construction of the instrumented field-trial.

4 CHARACTERIZATION OF THE GEOGRID AFTER 25 YEARS IN-SERVICE

The exhumed geogrid was characterized with reference to geometry, material composition, and analysis of its load-strain-time response in creep testing. Creep test data for the exhumed specimens are compared directly with typical data for the same product reported by the manufacturer. Given the absence of any observed installation damage, the methodology enables an assessment of material durability.

4.1 Tensile strength

Rapid loading creep (RLC) tests were performed to ISO 13431:1999 at the Tensar International laboratory at Atlanta, USA, with oversight by an independent third-party inspector. Test specimens were taken from the exhumed samples of layer N3 and N5 geogrid material. A constant tensile load per unit width of 8.8, 15.4, 17.8, 19.8, or 24.2 kN/m was applied to five layer N3 specimens, and a loading magnitude of 8.8, 17.8 or 24.2 kN/m to three layer N5 specimens. The RLC tests were performed at a constant temperature of T = $20 \pm 2°C$, and all eight specimens were loaded to a total elapsed time of 10,000 h. The tests yield load-strain-time data, and are presented in the form of isochronous curves at t = 1, 10, 100, 1,000, and 10,000 h (see Figure 3).
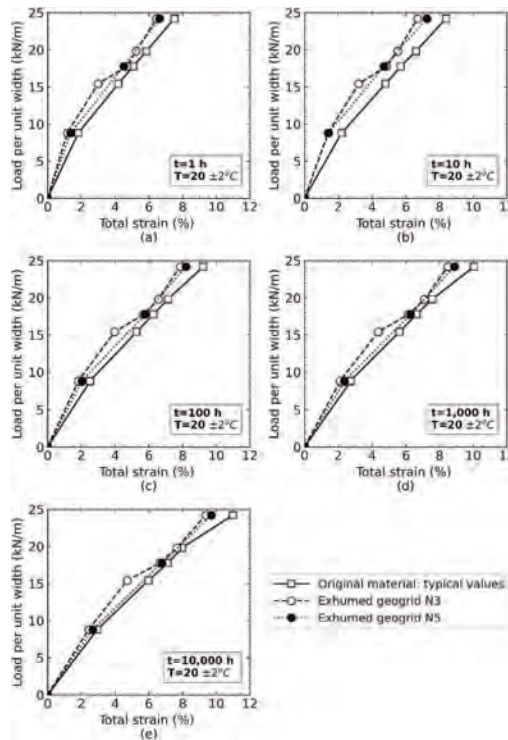
Figure 3. Isochronous load-strain curves: typical values for original material and results for exhumed layer N3 and N5 test specimens.

There is generally good agreement in the load-strain response with time for the exhumed N3 and N5 specimens. For example, at the largest magnitude of load per unit width (24.2 kN/m), the difference in total strain between the N3 and N5 test specimens is: 0.1% strain at t = 1 h; 0.5% strain at t = 10 h; 0.3% strain at 100 h; 0.3% strain at 1,000 h; and 0.2% strain at 10,000 h.

A comparison of the isochronous curves of the current study with curves reported by the manufacturer for the same Tensar SR55 geogrid product, termed herein typical values, indicates a plotting position for the exhumed N3 and N5 material that is consistently associated with relatively smaller values of total strain (see Figure 3). To investigate further the nature of the difference between the measured values for the exhumed field material and typical values for the same product, the magnitude of strain increment between isochronous load-strain curves was calculated for RLC test data on the exhumed material ($\Delta\varepsilon_{exh}$) and from the typical curves for original product type ($\Delta\varepsilon_{typ}$) as illustrated schematically in Figure 4a.
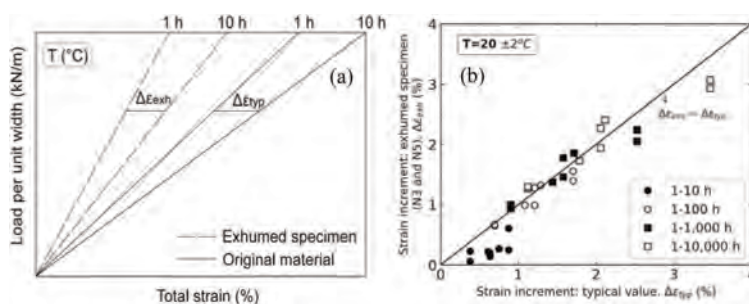
Figure 4. RLC test data: (a) schematic illustration of strain increment $\Delta\varepsilon$ (t = 1 to t = 10 h) and (b) comparison of data for field samples with typical values for the original product.

Results are reported for the four increments of 1 to 10, 1 to 100, 1 to 1,000, and 1 to 10,000 h (see Figure 4b). Strain increments for specimens of the exhumed geogrid at 1 to 10 h exhibit the least good agreement, while the data for increments of 1 to 100, 1 to 1,000, and 1 to 10,000 h are in good agreement with the typical values. The 32 data points establish $\Delta\varepsilon_{exh}$ = 1.03·$\Delta\varepsilon_{typ}$. Strain increments in rapid load creep testing of the exhumed specimens are thus believed very similar to those for the original product type. Taken collectively the evidence in Figure 3 and Figure 4 suggest the isochronous load-strain response of the exhumed geogrid compares very well with the typical behaviour reported by the manufacturer. The finding implies no degradation of strength or stiffness of the geogrid over the 25 year service life in the sloped reinforced soil wall at the Skedsmo location, near Oslo, Norway.

The British Standard (BS-8006) gives explicit consideration to a serviceability limit state, which is expressed as a limit value on the magnitude of permissible post-construction strain over the service life of a structure. Isochronous load-strain curves are used for purposes of estimating the post-construction strain in a reinforced soil retaining structure. The difference between 'the end of construction total strain' and 'the design life total strain' defines the strain increment of interest. The observed excellent agreement between strain increments in this study for exhumed and original uniaxial geogrid reinforcement lends strong support to the use of isochronous load strain curves for estimating long-term values of reinforcement strain in design to BS-8006.

5 CONCLUSIONS

Geogrid samples were exhumed from a sloped wall structure to investigate the material durability after 25 years in-service. Based on the results of this study, following conclusions are drawn:

(a) visual inspection and microscopic imaging revealed no installation damage of any significance, a finding that is attributed to the good quality of the backfill soil and the close inspection of all construction activities for this research structure. Accordingly, it is reasonable to compare properties of the exhumed material with typical values for the original product and attribute any changes to durability phenomena over the service life of the structure near Oslo, Norway;

(b) rapid loading creep test data to 10,000 h show excellent agreement between incremental strain in specimens of the exhumed geogrid and typical values for the original product type, with a finding of $\Delta\varepsilon_{exh} = 1.03 \cdot \Delta\varepsilon_{typ}$ that implies no degradation of strength or stiffness of the sampled geogrid;

(c) in the absence of any installation damage, the excellent agreement in rapid loading creep test data is believed indicative of no concern for durability manifesting itself as degradation in the strength or stiffness of the geogrid reinforcement after an elapsed time of 25 years; and,

(d) the finding lends confidence to the use of isochronous load-strain-time data for predicting the long-term tensile strain of geogrid in reinforced soil structures.

ACKNOWLEDGEMENTS

REFERENCES

ASTM Standard D698. (1942). Laboratory Compaction Characteristics of Soil Using Standard Effort (12 400 ft-lbf/ft3 (600 kN-m/m3)). ASTM International, West Conshohocken, PA.

ASTM Standard D4972. (2007). Standard Test Method for pH of Soils. *ASTM International*, West Conshohocken, PA.

British Standard Institute (BSI). (2010). *Code of Practice for Strengthened/Reinforced Soils and Other Fills*. BS, 8006-1:2020+A1:2016.

Fannin, R.J. (2001). Long-Term Variations of Force and Strain in a Steep Geogrid Reinforced Soil Slope, *Geosynthetics International*, 8(1): 81–96.

Fannin, R.J. and Hermann, S. (1990). Performance Data for a Sloped Reinforced Soil Wall, *Canadian Geotechnical Journal*, 27(5): 676–686.

Harney, M. and Holtz, R.D. (2006). *Mechanical Properties of Geotextile Reinforcement, 30 years After Installation, 8th International Conference on Geosynthetics*, Yokohama, Japan, International Geosynthetics Society, 1041–1044.

Jenner, C., and Nimmesgern, M. (2002). Geogrid Reinforced Railway Embankment – Excavation After Ten Years of Loading, *Geosynthetics 7th ICG – Delmas*, Gourc and Girad (eds). Swets & Zeitlinger, Lisse. ISBN 90 5809 523 1.

ISO 13431 (1999). *Geotextiles and Geotextile-related Products — Determination of Tensile Creep and Creep Rupture Behaviour*. International Organization for Standardization.

Onodera, S., Hirai, T., Hazama, A., and Itagaki, S. (2004). *Long-term Durability of Geogrids Laid in Reinforced Soil Wall*. Third Geosynthetics Conference, EuroGeo3, Munich, Germany.

Quinteros, V.S. (2014). *Observations on the Mobilization of Strength in Reinforced Soil Structures*. M.A.Sc. Thesis. University of British Columbia, Vancouver, Canada. DOI: 10.14288/1.0165550

Wayne, M., Bright, D., Berg, R.R., and Fishman, K. (1997). Tanque Verde Retaining Wall Structure: Revised After 11 years. *Geotextiles and Geomembranes*, 15(4-6): 223–233.

Comparison between the environmental stress-crack resistance of unaged and aged HDPE and LLDPE geomembranes

R.A. e Silva

Department of Civil Engineering, Queen's University, GeoEngineering Centre at Queen's-RMC, Kingston (ON), Canada

M.S. Morsy

Geotechnical Engineering Group, Structural Engineering Department, Ain Shams University, Cairo, Egypt

F.B. Abdelaal & R.K. Rowe

Department of Civil Engineering, GeoEngineering Centre at Queen's-RMC, Queen's University, Kingston (ON), Canada

ABSTRACT: High-density (HDPE) and linear low-density polyethylene (LLDPE) geomembranes are used in barrier systems in various containment applications. The former is known for its better chemical resistance, while the latter is known for its higher stress-crack resistance (SCR). The SCR of high-density polyethylene is well defined in the literature, but the SCR of LLDPE as well as its failure mechanism are rarely addressed. This paper thus investigates the SCR of LLDPE versus HDPE geomembranes based on the fractured plane of unaged and aged specimens examined using the single-point notched constant load tensile test method. The GMBs were aged using a synthetic heap leaching solution with pH 13.5 at 85°C. Failed specimens are analyzed using scanning electron microscopy, after which the differences in fracture surface for both LLDPE and HDPE resins are discussed. The relationship between SCR, tensile break elongation, and melt flow index is also presented for the geomembranes examined.

1 INTRODUCTION

Stress-crack resistance (SCR) and its failure mechanism are some of the primary factors controlling the service-life of geomembranes (GMB). Environmental stress-cracking, in particular, arises when polyethylene geomembranes are exposed to sustained tensile stresses in the presence of fluids (e.g., municipal solid waste leachate or heap leaching liquors), and is a serious problem for base liners in geoenvironmental applications (Choi *et al.* 2009; Rowe *et al.* 2019).

High-density (HDPE) and linear low-density (LLDPE) polyethylene GMBs are typically chosen as the primary liners in these applications, but they do not have similar SCR. While the increased resin density of HDPE GMBs implies better chemical resistance and hardness, it increases the potential for stress cracking. For LLDPEs, the high side chain branching of the polymer molecule gives them more flexibility and a relatively higher off-roll SCR compared to HDPE (Brown *et al.* 1991; Lustiger & Markham 1983; Scheirs 2009). There are several methods for assessing the SCR for a broad range of polymeric materials (Robeson 2013), among which the notched constant tensile load test (NCTL; ASTM D5397) is well accepted and commonly used both in industry and research.

Examining crack growth and propagation can be very useful in identifying fracture mechanisms such as brittle, semi-brittle and ductile, and this becomes especially important in the case of GMBs with very different SCR values being exposed to high levels of stress in the field. Nevertheless, the morphology of slow crack propagation has not yet been clarified for LLDPE GMBs tested using the NCTL method and thus it is still not clear how the fracture mechanisms change as the polymer density varies for both unaged and aged conditions. To fill this gap, this paper investigates the fracture surface of HDPE and LLDPE GMBs based on a microscopical analysis of the cross-section of broken SCR specimens from unaged and aged samples.

2 EXPERIMENTAL INVESTIGATION

2.1 Geomembranes examined

Two commercially available 1.5 mm thick smooth black HDPE and LLDPE GMBs were investigated in this study and are denoted as MxC15 and LxD15, respectively (Table 1). The two GMBs were produced by the same manufacturer using the blown film method. The performance of these two GMBs in different geoenvironmental applications has been extensively investigated (Abdelaal et al. 2012; Abdelaal & Rowe 2014; Abdelaal et al. 2011; Morsy et al. 2021; Rowe et al. 2019).

Table 1. Initial properties of the GMBs examined.

Property	Unit		
Designator	–	MxC15	LxD15
Type	–	HDPE	LLDPE
Nominal thickness (ASTM D5199, 2012)	mm	1.5	1.5
Resin density[1] (ASTM D1505, 2018)	g/cm^3	0.936	0.924
SCR (ASTM D5397, 2019)	hours	800 $\pm$ 90[2]	18,700 (24,000-15,000)[3]
HLMI(ASTM D1238, 2020)	g/10min	15.2 + 0.8	13.4 $\pm$ 0.8
Type V Break Elongation[4] (ASTM D6693, 2020)	%	800 $\pm$ 16.5	980 $\pm$ 34

Notes
[1]Provided by GMB manufacturer based on their results.
[2]Standard deviation.
[3](Maximum-minimum) SCR readings.
[4]Measured in the cross-machine direction.

One could challenge the assessment of SCR from LLDPE since it may not display a clear yielding point, as is the case of HDPE (e.g., Krishnaswamy & Lamborn 2000). However, the resin density of LxD15 is at the upper bound of the LLDPE density range (0.919–0.925 g/cm^3; ASTM D883) and yields in a similar manner as medium density polyethylene.

2.2 Oven ageing and immersion solutions

Two-sided exposure tests (ASTM D5322, 2017) were used to investigate how the SCR value and morphology change with ageing. This immersion technique consists of placing 200 x 95 mm GMB coupons in 4 L vessels filled with synthetic chemical solutions that mimic the effluents found in field conditions. The vessels were incubated in a forced air

oven at an elevated temperature of 85°C to accelerate the ageing of the GMBs. Coupons were separated with glass rods to ensure that the chemical solution is in full contact with the GMBs. Samples were then periodically extracted at different incubation durations to assess changes in the SCR over time.

The incubation fluid was an extremely basic solution (pH = 13.5) simulating the extreme alkalinity found in pregnant liquors for gold and silver heap leaching (Abdelaal & Rowe 2017). This solution was prepared by mixing de-ionized water with a trace metal solution and inorganic salts and was titrated with a 15 mol sodium hydroxide solution to achieve the target pH.

2.3 *Single-Point Notched Constant Tensile Load Test (SP-NCTL)*

Both SCR and morphology of slow crack growth were assessed using the single-point notched constant tensile load test (SP-NCTL, ASTM D5397). In this test method, an engineered defect (notch) is made on one surface of a dumbbell-shaped specimen such that the ligament thickness (i.e., the portion of GMB uncut under the notch) is 80% of the nominal thickness of the specimen. The notched specimen is subjected to a load equal to 30% of the initial GMB yield strength in a stainless-steel tank filled with a 10% (v/v) solution of Igepal CO-630 in water at 50 $\pm$ 1°C. The SCR value is then taken as the elapsed time to failure. After failure, the specimens were examined using scanning electron (SEM) microscopy.

3 RESULTS AND DISCUSSION

3.1 *Slow crack growth in unaged GMBs*

In all the SEM micrographs presented below the direction of crack propagation is from bottom to top. The fractured plane of an unaged HDPE specimen with a SCR of 750 h had generally a three-phase morphology (Figure 1a). Zone A is a relatively small region in the vicinity of the notched area (i.e., ahead of the crack tip) where crazing effectively began at lower stress levels. There was a non-uniform fiber pullout across that area, suggesting that the fibers of the craze being formed did not rupture immediately after loading. Once this rupture occurred, crack growth transitioned into a zone of relatively less pullout (Zone B) characteristic of brittle failure (Chen 2014; Francey & Rowe 2021; Lu *et al*. 1991). This surface fracture appearance was more dominant than that observed at the other two zones, indicating that the failure mechanism of the examined HDPE GMB was predominantly brittle. As the crack extended and the cross-sectional area of the specimen was increasingly reduced, the applied load exceeded the yield strength of the GMB, which in turn led to large fibre deformations and failure in a ductile manner, i.e., Zone C (Francey & Rowe 2021). The lengths of Zones A, B and C measured from the SEM micrograph were approximately 130 μm, 410 μm and 290 μm, respectively.

The SCR morphology of an unaged LLDPE specimen that failed after 17,100 h in the NCTL test was quite different (Figure 1b). Near the razor blade cut and at the base of the craze (using the aforementioned designation, Zone A), there was a strong continuous film instead of the fibrous structure observed from the HDPE specimen. This suggests that the time required to engage a crack in the first craze was considerably greater (e.g., Lu *et al*. 1992). The region of brittle failure (Zone B) was characterized by several short, thin fibers uniformly distributed and of somewhat uniform length and orientation. Finally, Zone C still showed ductile, long-fibrous structures, but the fibres were less distinguishable than Zone B when compared with HDPE. Zones A, B and C in this case had approximate measured lengths of 230 μm, 275 μm and 400 μm, respectively.
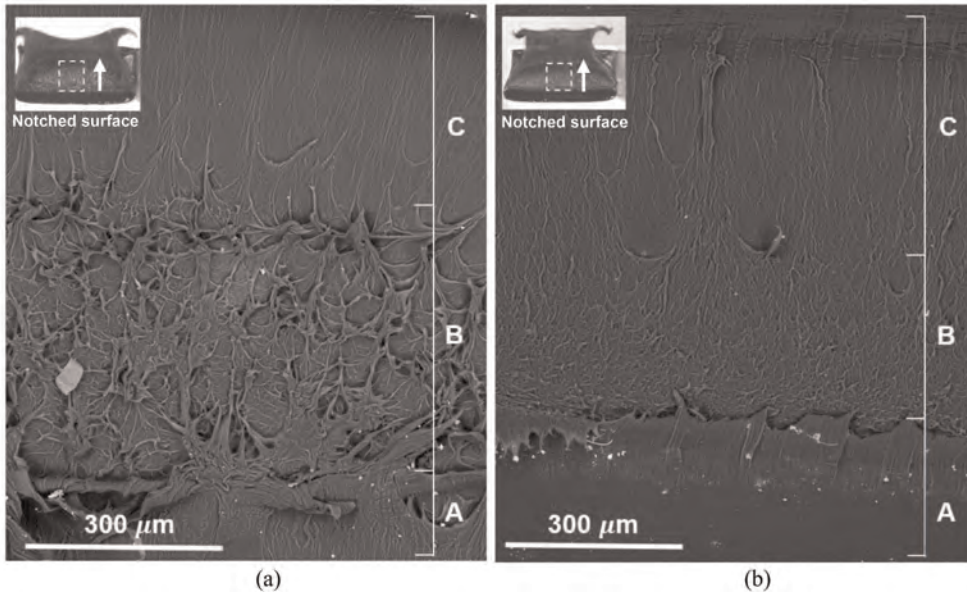
Figure 1. SEM micrographs of the fracture surface from: (a) an unaged HDPE specimen (SCR_o = 750 h); and (b) an unaged LLDPE specimen (SCR_o = 17,100 h).

3.2 *Effect of ageing on the morphology of crack growth*

Ageing can significantly reduce the environmental SCR of polyethylene GMBs due to the relaxation of residual stresses and changes in the semi-crystalline structure (i.e., physical ageing), and/or due to oxidative degradation (Ewais & Rowe 2014; Koerner *et al.* 2017; Morsy & Rowe 2020). Thus, the surface fracture morphology for aged specimens is also expected to change (Figures 2a and 2b).
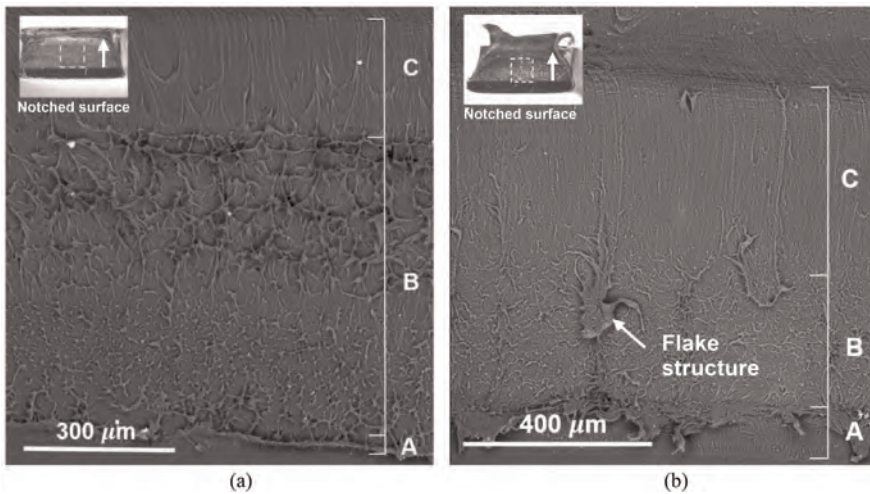
Figure 2. SEM micrographs of the fracture surface from: (a) a HDPE specimen aged for 6.8 years (SCR_{7years} = 5 h; $SCR_{7years}/SCR_0 < 0.01$); and (b) a LLDPE specimen aged for 4 years (SCR_{4years} = 617 h; SCR_{4years}/SCR_0 = 0.03).

For the HDPE specimen aged for almost 7 years in the synthetic heap leaching solution at 85°C (SCR$_{7years}$ = 5 h), fibre length was significantly reduced in Zones A and B (Figure 2a), although the number of residual fibres was greater. While these shorter, isolated fibres increased relative to the unaged specimen, their resistance to crack propagation became considerably lower. The least affected region appears to be Zone C. This implies that, even in a highly aged HDPE specimen there was a portion of the material experiencing ductile failure (Scheirs 2009). The lengths of Zones A, B and C after ageing were approximately 35 μ m, 590 μm and 235 μm, respectively.

In the LLDPE specimen aged for 4 years (SCR$_{4years}$ = 617 h; Figure 2b), initiation of crack growth was marked by a non-uniform long-fibrous detachment between Zones A and B very similar to that of the unaged HDPE specimen. Zone B displayed an increased number of long, thick fibres and flake structures that were not observed in the unaged specimen. The morphology of Zone C, once again, did not seem to be significantly affected. Zones A, B and C were 110 μm, 275 μm and 395 μm in length, respectively.

3.3 Ageing of other physical and mechanical properties

The SCR of the aged HDPE and LLDPE specimens are compared with the high-load melt index (HLMI) and tensile break elongation values at the same incubation duration (Table 2). The HDPE GMB retained 40% of its initial tensile break elongation after 7 years of ageing. The extremely low melt index value indicates the domination of cross-linking oxidative reactions. The generation of a more "tightly packed" structure due to excessive cross-linking makes the polymer more susceptible to brittle failure (Lustiger 1985), which might explain the short fibre structure depicted in Figure 2a.

Table 2. Physical/mechanical properties of HDPE and LLDPE GMBs after ageing.

Property	Percent retained (%)	
	MxC15 (aged for 7 years)	LxD15 (aged for 4 years)
SCR[1] (ASTM D5397, 2019)	0.6	3.3
HLMI[2] (ASTM D1238, 2020)	10.5	131.2
Type V Break Elongation[2] (ASTM D6693, 2020)	39.6	14.8

Notes
[1]Value from one single specimen
[2]Mean value

Even with less ageing time than the HDPE GMB, the LLDPE GMB lost 85% of its break elongation and 97% of its SCR. This was accompanied by a significant increase in HLMI, which implies chain scission reactions typically dominant in LLDPE GMBs (Morsy *et al.* 2021). Despite the extremely large reduction in SCR and break elongation, the GMB was still able to retain some flexibility, as depicted by the short to long-fibrous fracture surface (Figure 2b) and by the pullout of material in the macroscopic view of the specimen (Figure 2b, top left corner).

4 CONCLUSIONS

The environmental SCR performance of HDPE and LLDPE GMBs has been investigated. Unaged specimens as well as those aged in synthetic mining leachate at 85°C were tested

using the single-point notched constant tensile load (NCTL) testing method. Broken specimens were recovered from the SCR test and were further analyzed by scanning microscopy to investigate the differences in failure mechanisms. The SCR results from aged specimens were then compared to the melt index and tensile break elongation values at the same incubation duration. For the GMBs and test conditions (e.g., ageing temperature, incubation fluid) investigated in this paper, the following conclusions can be reached:

- LLDPE had an initial very high SCR but after 4-years ageing it had reduced to 3% of its initial value.
- The fractured plane of SCR specimens tested in the NCTL test generally displays a three-phase morphology, namely: (1) a small zone of relatively longer pullout in the vicinity of the notch, or Zone A, (2) an intermediate zone wherein brittle failure dominates (Zone B), and (3) a zone of ductile failure (Zone C). The main difference in brittle failure between unaged HDPE and LLDPE was the length, orientation, and distribution of fibres.
- The length of the aforementioned zones is markedly different between HDPE and LLDPE. In the unaged HDPE, Zone B was 40% longer than Zone C in the direction of crack propagation, while the unaged LLDPE had Zone B only about two-thirds the length of Zone C. For the aged HDPE specimen, Zone B was 150% longer than Zone C. In the aged LLDPE, the length of Zones B and C remained the same as the unaged condition. In other words, the large decrease in SCR of the LLDPE GMB mainly reflects the change in morphology of Zone A.
- The morphology of Zone A from a 4-year aged LLDPE specimen is relatively similar to its HDPE counterpart in an unaged condition.

ACKNOWLEDGMENTS

REFERENCES

Abdelaal, F. B. & Rowe, K. R. 2017. Effect of High pH Found in Low-level Radioactive Waste Leachates on the Antioxidant Depletion of a HDPE Geomembrane. *Journal of Hazardous, Toxic, and Radioactive Waste*, *21*(1), 1–15.

Abdelaal, F. B. & Rowe, R. K. 2014. Antioxidant Depletion from a LLDPE Geomembrane in an Extremely High pH Solution. *Geosynthetics Mining Solutions*, 225–236.

Abdelaal, F. B., Rowe, R. K., Smith, M., Brachman, R. W. I. & Thiel, R. 2012. Antioxidant Depletion from HDPE and LLDPE Geomembranes Without HALS in an Extremely Low pH Solution. *2nd Pan American Geosynthetics Conference*, 1–9.

Abdelaal, F. B, Rowe, R. K., Smith, M. & Thiel, R. 2011. OIT Depletion in HDPE Geomembranes Used in Contact with Solutions Having Very High and Low pH. *Pan-American CGS Geotechnical Conference*, 1–7.

ASTM D1238 2020. *Standard Test Method for Melt Flow Rates of Thermoplastics by Extrusion Plastometer.*.

ASTM D1505 2018. *Standard Test Method for Density of Plastics by the Density-Gradient Technique.*

ASTM D5199 2012. *Standard Test Method for Measuring the Nominal Thickness of Geosynthetics.*

ASTM D5322 2017. *Standard Practice for Laboratory Immersion Procedures for Evaluating the Chemical Resistance of Geosynthetics to Liquids.*

ASTM D6693 2020. *Standard Test Method for Determining Tensile Properties of Nonreinforced Polyethylene and Nonreinforced Flexible Polypropylene Geomembranes.*

ASTM D883 2020. *Standard Terminology Relating to Plastics.*

Brown, N., Lu, X., Huang, Y. & Qian, R. 1991. Slow Crack Growth in Polyehtylene - a Review. *Makromolekulare Chemie. Macromolecular Symposia*, *41*, 55–67.

Chen, Y. 2014. Investigations of Environmental Stress Cracking Resistance of HDPE/EVA and LDPE/EVA blends. *Journal of Applied Polymer Science*, *131*(4), 1–8.

Choi, B., Weinhold, J., Reuschle, D. & Kapur, M. 2009. Modeling of the Fracture Mechanism of HDPE Subjected to Environmental Stress Crack Resistance Test. *Polymer Engineer*, *49*(11), 2085–2091.

Ewais, A. M. R. & Rowe, R. K. 2014. Effect of Aging on the Stress Crack Resistance of an HDPE Geomembrane. *Polymer Degradation and Stability*, *109*, 194–208.

Francey, W. & Rowe, R. K. 2021. Stress Crack Resistance of Unaged High-density Polyethylene Geomembrane Fusion Seams. *Geosynthetics International (Ahead of Print)*, 1–15.

Koerner, R. M., Hsuan, Y. G. & Koerner, G. R. 2017. Lifetime Predictions of Exposed Geotextiles and Geomembranes. *Geosynthetics International*, *24*(2), 198–212.

Krishnaswamy, R. K. & Lamborn, M. J. 2000. Tensile Properties of Linear Low Density Polyethylene (LLDPE) Blown Films. *Polymer Engineering and Science*, *40*(11), 2385–2396.

Lu, X., Mcghie, A. & Brown, N. 1992. The Dependence of Slow Crack Growth in a Polyethylene Copolymer on Test Temperature and Morphology. *Journal of Polymer Science Part B: Polymer Physics*, *30*, 1207–1214.

Lu, X., Qian, R. & Brown, N. 1991. Discontinuous Crack Growth in Polyethylene Under a Constant Load. *Journal of Materials Science*, *26*(4), 917–924.

Lustiger, A. 1985. *The Molecular Mechanisms of Slow Crack Growth in Polyethylene. PhD Thesis. Drexel University*.

Lustiger, A. & Markham, R. L. 1983. Importance of Tie Molecules in Preventing Polyethylene Fracture Under Long-term Loading Conditions. *Polymer*, *24*(12), 1647–1654.

Morsy, M. S. & Rowe, R. K. 2020. Stress Crack-resistance of Textured Geomembranes. *Pan American Conference on Geosynthetics*, 1–6.

Morsy, M. S., Rowe, R. K. & Abdelaal, F. B. 2021. Longevity of Twelve Geomembranes in Chlorinated Water. *Canadian Geotechnical Journal*, *58*, 479–495.

Robeson, L. M. 2013. Environmental Stress Cracking: a Review. *Polymer Engineering and Science*, *53*(3), 453–467.

Rowe, R. K., Morsy, M. S. & Ewais, A. M. R. 2019. Representative Stress Crack Resistance of Polyolefin Geomembranes Used in Waste Management. *Waste Management*, *100*, 18–27.

Scheirs, J. 2009. *A Guide to Polymeric Geomembranes: a Practical Approach* (1st ed.). John Wiley and Sons Ltd.

Evaluation of durability of PVC-P geomembranes for tunnel waterproofing with laboratory tests

A. Luciani
TECNE – SYSTRA SWS Advanced Tunneling, Turin, Italy

ABSTRACT: Durability of waterproofing systems used in tunnels is of main importance because water highly influences durability, effectiveness and maintenance costs of underground structures. PVC-P geomembranes are one of the most applied technologies for tunnel waterproofing, nonetheless there is a lack of knowledge on their durability in underground applications. Even if long-term durability of PVC-P geomembranes has been analysed for outdoor applications (e.g. dams, roofs), few information are available for applications in underground conditions. In this paper the durability of two commercial PVC-P geomembranes for tunnelling applications is analysed based on the results on laboratory tests. Plasticizer absorption tests and mechanical tests are performed on the commercial geomembranes and on eight formulations of PVC-P specifically produced. The results of those tests permit to study the long-term degradation due to plasticizer loss and extrapolate the losses in time. Finally, an end-of-life time for the geomembranes has been defined merging mechanical requirements for the membrane and the long-term evolution of the degradation of the properties.

1 INTRODUCTION

Water is renown as one of the main causes of damages to underground structures and of their maintenance costs. Therefore, the use of effective and durable waterproofing systems is of overwhelming importance for tunnels. In conventional tunnelling, the waterproofing system is nowadays constituted by a geomembrane installed in between the primary and the final concrete lining (Luciani & Peila 2019).

The design life span for new tunnels is of about 100 years and, in some cases, it can rise to 150 years. This request, combined with the inner surface quality requirement of absence of leakages and moisture spots, point out the importance of durability of waterproofing system. Moreover, since waterproofing is installed behind the concrete lining of the tunnel, it is difficult or almost impossible to perform maintenance or substitute it. As a consequence, the durability requirement on waterproofing systems for tunnel applications has to be the same of the whole tunnel (i.e. 100 years). Nevertheless, there is a clear lack of knowledge on the durability of waterproofing membranes used in underground structures.

In this study the durability of plasticized PVC (PVC-P) geomembranes is analysed. PVC-P geomembranes are one of the most used material for underground applications.

Durability of PVC-P has been analysed in many applications (e.g. waterproofing of roofs, dams, channels) (Blanco *et al*. 2012; Cazzuffi 1995, 2016; Newman *et al*. 2004; Stark *et al*. 2005) but there are almost none studies on underground applications.

Moreover, there are also few reported cases in scientific literature of geomembranes naturally aged in underground applications for 30–40 years (Maehner *et al*. 2018; Usman & Galler 2014) while data for longer times do not yet exist. Therefore, the study of durability of geomembranes in these applications are still based on accelerated tests (Luciani *et al*. 2020).

2 PVC-P DEGRADATION IN TUNNELS

PVC degradation is mainly caused by dehydrochlorination, i.e. the loss of gaseous hydro-chloride from the PVC chain. The energy needed to initiate the degradation process comes from heat or ultraviolet (UV) rays. However, in underground applications, high temperatures or UV rays are absent, and so this phenomenon can be neglected.

Consequently, the main degradation phenomenon occurring to PVC-P in underground is the loss of plasticiser. Plasticizer is not chemically bonded to the polymer chain and so, during the life of the material, migrates from the geomembrane into the surface and then in the surrounding environment (Marcilla *et al.*, 2004; Storey *et al.*, 1989).

The plasticizer content is defined by the concentration expressed as percentage by weight. The loss of plasticizer is described with the plasticizer loss ratio P_L (Benneton 1994) defined as

$$P_L(t) = \frac{M_{P_0} - M_P(t)}{M_{P_0}} \tag{1}$$

with M_{P_0} the initial mass of plasticizer and $M_P(t)$ the mass of plasticizer at time t.

The study of durability of PVC-P waterproofing geomembranes consists in evaluating the evolution of this phenomenon with time and its impact on the mechanical properties of the material.

3 PLASTICIZER LOSS EVALUATION

The degradation of geomembranes is sometimes extrapolated on the long term with Arrhenius' equation. This equation permits to evaluate with accelerated tests at different temperatures a rate constant of the phenomenon. However, this simple correlation implies a constant rate of the phenomenon with time that is not realistic for the case of plasticizer loss, where the rate is dependent on the gradient of concentration between the geomembrane and the environment. Moreover, in PVC-P the rate is also influenced by the plasticizer content because as the plasticizer content reduces it becomes more difficult to the plasticizer to diffuse in the now stiffer matrix.

Since plasticizer loss can be analysed as a mono-dimensional diffusion problem, in order to have a better evaluation of the physical phenomenon, the evaluation of plasticizer loss can be performed using Fick's law of diffusion

$$\frac{\partial c(x,t)}{\partial t} = D \frac{\partial^2 c(x,t)}{\partial x^2} \tag{2}$$

with $c(x,t)$ the value of plasticizer concentration at time t and in the coordinate x inside the thickness of the membrane and D is the diffusion coefficient.

In tunnel applications, one side of the membrane is constantly cleaned by the flow of the water drained from the rock mass, and therefore it is possible to consider the plasticizer concentration on the external surface always equal to zero. On the other side of the geomembrane, in contact with concrete, diffusion is considered negligible. As an initial condition the concentration in all the points of the geomembrane is set constant as the initial value.

Solving Equation (2) in the given boundary and initial condition it is possible to obtain the concentration at any time inside the membrane as

$$c(x,t) = -\sum_{n=1}^{\infty} C_0 \frac{4}{(2n-1)\pi} e^{-D\left(\frac{2n-1}{2L}\pi\right)^2 t} \sin\left(\frac{2n-1}{2L}\pi x\right) \tag{3}$$

One of the factors governing the computation is the diffusion coefficient D, that must be dependent on the concentration and temperature in order to account for PVC-P behaviour.

To evaluate the dependence of D on these parameters, plasticizer absorption tests have been performed.

4 PLASTICIZER ABSORPTION TESTS

4.1 *Test procedure and materials*

Plasticizer absorption tests permit to evaluate diffusion coefficient of plasticizer in a geomembrane. Small specimens of geomembrane of regular and known surface are cut with a metallic hollow cutter, cleaned on the surface, dried in a desiccator and weighted. Specimens are then immersed in plasticizer at a specific temperature and the change of weight is measured overtime. The diffusion coefficient is obtained by fitting the data of weight-time curve with the diffusion law (Griffiths *et al*. 1984; Storey *et al*. 1989).

Tests have been performed at 4 different temperatures: 20°C, 45°C, 60°C and 75°C.

Since the study aims to evaluate the durability of waterproofing geomembranes used in underground applications, two commercial geomembranes have been considered: geomembrane A, that is a 2 mm PVC-P coloured geomembrane with filler, and geomembrane B, a 2 mm PVC-P translucent geomembrane without filler.

In addition to these commercial materials, 8 specifically produced geomembranes have been testes. These geomembranes have been formulated with different plasticizer contents, with and without filler. The production of both geomembranes with and without filler aims to evaluate the parameters for both commercial geomembranes. Table 1 summarises the composition of the 10 tested materials. For materials A and B, Table 1 reports the sum of the content of PVC and stabilizer because separated values are not available.

The plasticizer used for the tests is the same used to produce the geomembranes.

Table 1. Tested materials composition.

Material	PVC (%)	Stabilizers (%)	Plasticizer (%)	Filler (%)
A	56.0		24.0	20.0
B	73.3		26.7	0.0
1	67.4	2.6	30.0	0.0
2	72.4	2.6	25.0	0.0
3	77.4	2.6	20.0	0.0
4	82.4	2.6	15.0	0.0
5	47.4	2.6	30.0	20.0
6	52.4	2.6	25.0	20.0
7	57.4	2.6	20.0	20.0
8	62.4	2.6	15.0	20.0

4.2 *Results*

From the analysis of the results on the same material at different temperature, an exponential relation between diffusion coefficient D and temperature T has been observed, analogous to Arrhenius' equation. The correlation can be expressed as

$$D(T) = D_0 \cdot e^{-\frac{E_A}{RT}}$$ (4)

where D_0 is a constant, E_A is the activation energy, R the gas constant and T is the temperature.

Similarly, from the results of absorption tests performed at the same temperature on geo-membranes with different initial plasticizer content, the dependence of diffusion coefficient on plasticizer content has been evaluated. In this case a potential law has been obtained:

$$D(c) = D_1 \cdot c^b \qquad (5)$$

where D_1 and b are constants, and c is the content of plasticizer.

The values of diffusion coefficient obtained for material A is in good agreement with the ones of the geomembranes with filler, and the one of material B with the ones of geomem-branes without filler, thus confirming that the results of the tests can be applied to the two commercial geomembranes.

Diffusion coefficient for materials with filler are higher than the ones of materials without filler, confirming that the degradation of geomembranes without any filler is slower. Figure 1 and Figure 2 show examples of the results obtained in terms of temperature and con-centration correlation. Figure 2 also compares the results for the two commercial geomem-branes (A and B) and the 8 specifically produced geomembranes: Material A fits very well with the results of geomembrane with filler, while material B has a slightly worse fit.
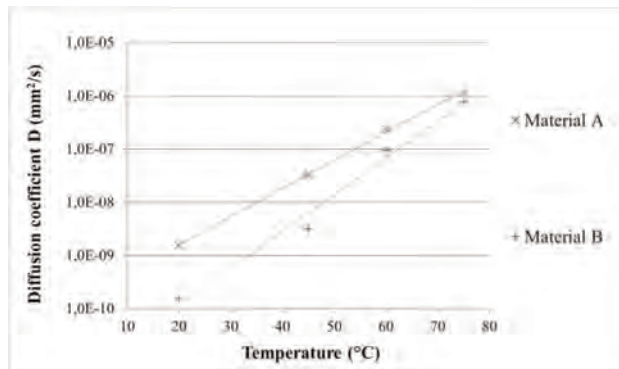
Figure 1. Results of plasticizer absorption tests of the two commercial geomembranes (y axis in log scale).
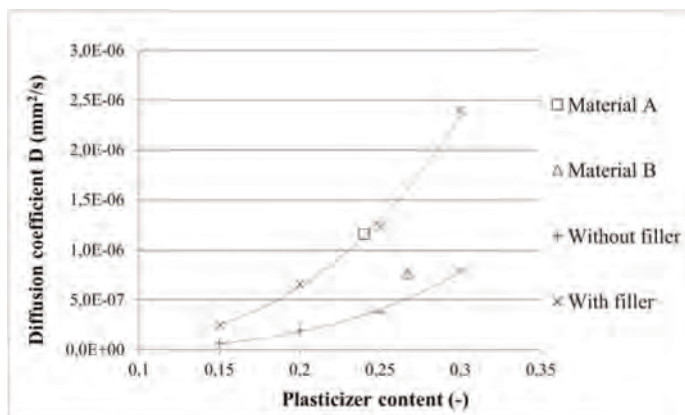
Figure 2. Results of plasticizer absorption tests at 75°C.

4.3 *Long-term extrapolation of plasticizer loss*

Using Equations (3), (4) and (5), it is possible to evaluate the variation of concentration with time at different temperatures and the plasticizer loss ratio.

Table 2 reports the diffusion coefficients used in the extrapolation, as derived from the plasticizer absorption tests results.

Table 2.   Diffusion coefficients for 15°C extrapolation.

Material	D_1 (mm^2/s)	b $(-)$
A	$7.47 \ 10^{-7}$	4.94
B	$2.44 \ 10^{-8}$	4.94

Figure 3 reports the results of the extrapolation in terms of plasticizer loss ratio for the two commercial geomembranes at 15°C. This temperature has been chosen as representative of the site temperature for shallow and urban tunnels in ordinary conditions.

The rate of degradation is relatively high in the first years and reduces with time.
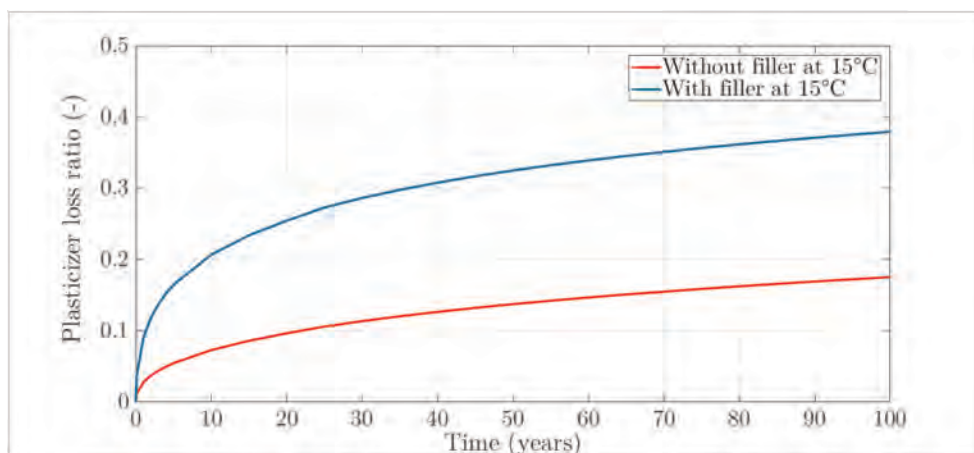
Figure 3.   Long-term extrapolation of plasticizer loss of the two commercial geomembranes at 15°C.

5   PLASTICIZER LOSS EFFECT ON GEOMEMBRANES

As plasticizer content changes within the geomembrane its mechanical properties change. The mechanical properties of the 10 materials used in the absorption tests have been tested.

With the reduction of plasticizer content, Shore A hardness, tensile strength and elastic modulus of the geomembrane increases. On the contrary, elongation at break reduces.

Figure 4 shows the results of tensile tests. It is evident that as the plasticizer content reaches values of about 15–20% the behaviour of the geomembrane passes from a soft-rubber like to a hardening elasto-plastic one with an evident yielding point. This means that for certain values of elongation of the geomembranes a plastic irreversible deformation occurs, causing the reduction of the section. For both geomembranes with and without filler,

this occurs for a plasticizer content of about 15% and the yielding point is reached for a deformation of about 6%.

Moreover, plasticizer loss causes the shrinkage of the geomembrane that creates tensile stresses in the geomembrane with time. Shrinkage progress with plasticizer loss can be evaluated with the correlation proposed by Giroud (1995).
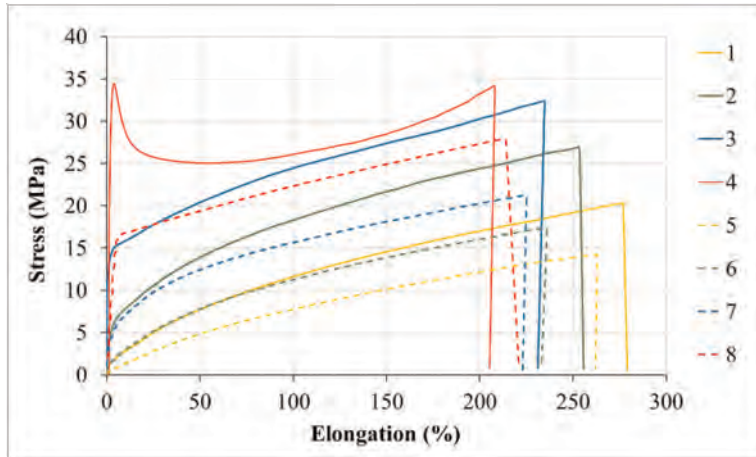
Figure 4.   Tensile tests results on the 8 produced geomembranes.

6   DURABILITY ASSESSMENT

Benneton (1994) suggested that the end of effectiveness of a waterproofing PVC-P geo-membrane can be defined at the moment when the plasticizer loss ratio is equal to 0.5. However, the author does not give any explication about the origin of this assumption.

In order to define a performance-based end-of-life threshold, it is needed to establish a correlation between the action on the geomembrane and the mechanical properties during the life of the structure.

Once the tunnel is built, the waterproofing geomembrane is in perfect contact with the two concrete lining (with protection layers installed to avoid that some unevenness of the concrete can damage the geomembrane). On the long term, the geomembrane only transmits the geological load to the final concrete lining. This load is constant and uniform on the surface of the geomembrane, therefore there is not a specific request for mechanical properties. In case of any unpredicted unevenness (e.g. voids in the lining, protruding elements), the deformation of the geomembrane would be very small and compatible with the elastic behaviour of the geomembrane. Furthermore, as shown, with degradation tensile strength and surface hardness increase reducing the risk of penetration of external grains.

The only consequence of plasticizer loss that seems to affect the effectiveness of the water-proofing geomembrane is shrinkage, that, in association with the more rigid behaviour of the material with lower plasticizer content, can induce plastic deformations. Plasticization is not necessarily a limit condition for the effectiveness of the geomembrane but represents a change of behaviour and causes the reduction of thickness and possible opening of small holes.

Therefore, in order to be on the safe side, the end-of-life value for the geomembrane is defined as the limit value of plasticizer loss ratio resulting in a plastic deformation of the geomembrane. For the tested materials this means or the 15% of plasticizer content, or an elongation due to shrinkage higher than 6%. For both commercial geomembranes tested the

lower of these two values correspond to a plasticizer loss ratio of about 0.45, slightly lower than Benneton's limit.

From Figure 3, it is possible to state that both the commercial geomembranes tested are still within the defined end-of-life limit of plasticizer loss ratio after 100 years in an urban tunnel at 15°C.

7 CONCLUSIONS

The need of having effective underground structures calls for the request of durability of 100 years of the PVC-P geomembranes used for waterproofing.

Plasticizer loss from the geomembrane, that is the main degradation phenomenon in tunnel application, can be described has a diffusion problem. Through plasticizer absorption tests on 10 materials, the dependence of diffusion coefficient on temperature and concentration has been defined and an equation predicting the phenomenon has been proposed.

On the base of conservative evaluation on the possible consequences of shrinkage of the geomembrane, a threshold value of 0.45 has been defined for the plasticizer loss ratio as end-of-life value of the two commercial geomembranes analysed.

Both the commercial geomembranes tested fulfil this requirement for an application of 100 years in a shallow tunnel, thus confirming the capacity of the used materials to achieve the required goal during the life of the structure.

REFERENCES

Benneton, J. 1994. PVC-P Geomembrane Behaviour in a Ten Years Water Laboratory Immersion Test. *In 5th International Conference on Geosynthetics*, 1105–1108.

Blanco, M., Leiro, A., Soriano, J., Crespo, M., Zornberg, J., Aguiar, E., Pargada, L. 2012. Long-term Performance of the Laguna de Barlovento Reservoir Waterproofing Using a PVC-P Geomembrane. *Eurogeo*.

Cazzuffi, D. 1995. Évaluation du Comportement de Différent Types de Géosynthétiques Prélevés Sur Canaux de l'Enel. In *Comptes Rendus du Colloque Sur les Geotextiles Et Les Geomembranes–Rencontres,* 95, 9–15.

Giroud, J. 1995. Evaluation of PVC Geomembrane Shrinkage Due to Plasticizer Loss. *Geosynthetics International*, 2 (6), 1099–1113.

Griffiths, P., Krikor, K., Park, G. 1984. Diffusion of Additives and Plasticizers in Poly (Vinyl Chloride)-III Diffusion of Three Phthalate Plasticizers in Poly (Vinyl Chloride). *In Polymer additives*, 249–260.

Luciani, A. & Peila, D. 2019. Tunnel Waterproofing: Available Technologies and Evaluation Through Risk Analysis. *International Journal of Civil Engineering*, 17 (1), 45–59.-

Luciani, A., Todaro, C., Martinelli, D., Peila, D. 2020. Long-term Durability Assessment of PVC-P Waterproofing Geomembranes Through Laboratory Tests. *Tunnelling and Underground Space Technology*, 103.

Maehner, D., Peter, C., Sauerlaender, B. 2018. *Langzeitverhalten von Kunststoffdichtungsbahnen*. Tunnel, 37 (1).

Marcilla, A., Garcia, S., Garcia-Quesada, J. 2004. Study of the Migration of PVC Plasticizers. *Journal of Analytical and Applied Pyrolysis*, 71 (2), 457–463.

Newman, E., Stark, T., Rohe, F., Diebel, P. 2004. Thirty-year Durability of a 20-mil PVC Geomembrane. *Journal of Vinyl and Additive Technology*, 10 (4), 168–173.

Stark, T., Choi, H., Diebel, P. 2005. Influence of Plasticizer Molecular Weight on Plasticizer Retention in PVC Geomembranes. *Geosynthetics International*, 12 (1), 1–12.

Storey, R. F., Mauritz, K. A., Cox, B. D. 1989. Diffusion of Various Dialkyl Phthalate Plasticizers in PVC. *Macromolecules*, 22 (1), 289–294.

Usman, M. & Galler, R. 2014. Ageing and Degradation of PVC Geomembrane Liners in Tunnels. In *Proceedings of the International conference on Chemical, Civil and Environmental Engineering*, Singapore, November 2014.

Effect of aged geomembrane extrusion welding on antioxidant depletion

M.M. Ali & R.K. Rowe
GeoEngineering Centre at Queen's-RMC, Department of Civil Engineering, Queen's University, Kingston, Ontario, Canada

ABSTRACT: High-density polyethylene geomembranes (HDPE GMBs) are in-situ welded to create an "impermeable seal". Extrusion welds are primarily used for repairs, curves, and other welds not accessible to fusion welding machines. A welding rod which is fed into the extrusion machine is made from the same raw materials for adherence/compatibility requirements between the two materials. The examined geomembrane was welded using preheat and barrel temperatures of 230°C and 250°C, respectively. In a municipal solid waste (MSW) landfill, an extrusion weld facing upward will be in contact with leachate that can lead to chemical degradation. In this paper, the antioxidant depletion rate from welding bead and HDPE GMB sheet away from welding immersed in MSW landfill simulation is examined over an 11-month period at 85°C, 75°C, and 65°C. Preliminary results shows that antioxidant depletion rate of the welding bead was faster than that for the GMB sheet material at lower temperatures (i.e. 65°C)

1 INTRODUCTION

High-density polyethylene geomembranes (HDPE GMBs) are an essential component of the landfill barrier system (Abdelaal *et al.* 2019; Hsuan *et al.* 2008; Morsy *et al.* 2021;). The primary function of the GMBs is to prevent the leakage of fluids and gasses over the lifespan of the landfills, which may reach from decades to centuries (Rowe *et al.* 2004; Scheirs 2009). HDPE is usually selected due to its high resistance to chemical degradation compared to other polymeric geomembranes (Koerner *et al.* 2017; Scheirs 2009). HDPE GMBs consist of 96 to 97.5% of polyethlene resin, 2 to 3% carbon black, and 0.5 to 1% of other additives (i.e., stabilizers and antioxidants) (Hsuan & Koerner 1998). The additives delayed the polymer thermo-oxidative degradation which may occur during the manufacture process, installation, and ageing (Hsuan & Koerner 1998; Scheirs 2009). During installation, HDPE GMBs rolls are welded in-situ to create continuous impermeable seal using high welding temperatures. There has not been any previous study focused on examining the effect of extrusion welding on oxidative and chemical degradation.

There are two common methods of geomembrane welding: Fusion welding and extrusion welding (Müller 2007; Scheirs 2009). Fusion welding is used for the majority of the geomembrane welding length. Extrusion welding is used for welding patches, repairs, curves, and inaccessible areas by fusion weld machines (Scheirs 2009). Although numerous studies identified welds as a weak point of the HDPE GMBs liner system (Francey & Rowe 2022a,b, c; Halse *et al.* 1990; Peggs *et al.* 2014; Rowe & Shoaib 2017, 2018), there are no studies examining the long-term performance of extrusion welding compared GMBs sheet material.

HDPE GMBs ageing follows three stages until failure is reached (Hsuan & Koerner 1998): antioxidant depletion (Stage I), where the antioxidant is depleted without a reduction

in the mechanical properties; induction time (Stage II), where it occurs after full depletion of the antioxidants package, and there is no change in the mechanical properties; reduction in mechanical and physical properties (Stage III), where the oxidative reactions start leading to a reduction in the mechanical and physical properties. Some work has been performed on the effect of fusion welding on the long-term behaviour of the welds. However, no studies have been performed on the effect of extrusion welds on the longevity of the welds. This study presents the preliminary results of antioxidant depletion (Stage I) for extrusion welding based on the standard oxidation time test results (Std-OIT).

2 MATERIAL

One 1.5mm HDPE GMB, denoted by MwA15, with a Std-OIT of 165± 2 (min) was examined.

The extrusion welding of MwA15 was conducted on a landfill site by a licensed geosynthetic installer on a summer day using a Demtech. The geomembrane surface was prepared by grinding the surface to remove the oxidative layers and the additive blooms. The welding machine was fed by extrusion rods made from the same geomembrane materials. The GMB sheets were preheated with hot air to reduce the heat required and increase the size of the molten bead (extrudate).

The preheating was used to avoid the thermal shock that would weaken the polymeric structure along the edge of the weld. Afterwards, the welding rod was softened, mixed in the heated barrel, and pushed out on the GMB surface. The GMB sheet was melted and mixed with the molten bead and then cooled and solidified (Peggs *et al*. 2019). The welded zone has random and isotropic microstructure (Peggs *et al*. 2019). The examined extrusion welding preheats and barrel temperatures were 220°C and 230°C, respectively.

Extrusion welds contain weld beads and flashing (squeeze out) (Figures 1 and 2). Toward the terminal of the extrusion, welding is heat affected zone, which has a similar thickness to the sheet and is subjected to high welding temperatures. The flashing (squeeze out) zones are located toward the extrusion welding extremities, which is the result of the extrudate molten polymer exiting the weld zone during welding (Figures 1 and 2).
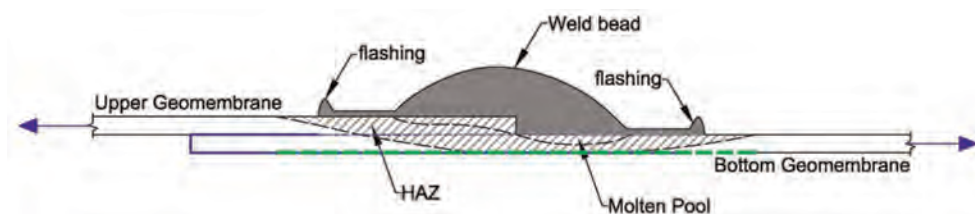
Figure 1.   Cross-section of typical HDPE extrusion weld.
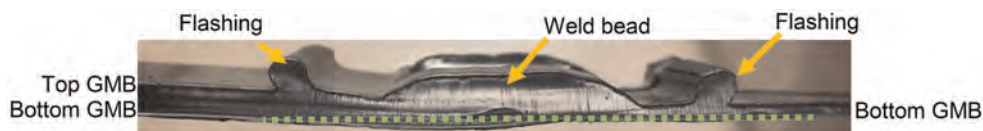
Figure 2.   Photographic cross-section view of HDPE extrusion weld.

3 EXPERIMENTAL PROCEDURE

3.1 Jar immersion

Immersion tests were used to accelerate the ageing of the GMB extrusion welds in the laboratory. In the immersion test method, 90×170 mm welded coupons were immersed in 3.5L glass jars filled with simulated municipal solid waste leachate (MSW-Leachate 3; Abdelaal *et al.* 2014). The welded GMB coupons were separated using a glass rod to ensure that the coupons would be in contact with the leachate from both sides. The jars were placed at three different temperatures (85°C, 75°C, and 65°C). The GMB was sampled from the welding area and GMB sheet at different incubation times to monitor the change in Std-OIT with time.

3.2 Differential Scanning Calorimetry (DSC)

To assess the depletion of antioxidants, Std-OIT tests were conducted using a TA instruments Q-2000 series differential scanning calorimeter (ASTM D3895). First, test specimens were cut from the welding bead and sheet material. Then, the specimens were placed at the center of the aluminium pan and loaded into the DSC machine for testing. Hsuan and Koerner (1998) found that this depletion rate can be classified as a first-order decay model. The initial Std-OIT, depletion rate and residual Std-OIT are used to describe the change of Std-OIT with time for extrudate bead and SAW as follows:

$$OIT_t = OIT_o\, e^{-st} \tag{1}$$

Taking the natural logarithm of both sides of [1] gives:

$$\ln(OIT_t/OIT_o) - st \tag{2}$$

where OIT_t is the Std-OIT during ageing at time t (min); OIT_o is the initial Std-OIT (min); s is the antioxidant depletion rate (month^{-1}); t is the incubation time (month).

4 RESULTS

4.1 Unaged Std-OIT

Std-OIT was examined for aged and unaged GMB sheets and post-welding bead zone. The unaged Std-OIT of welding rod material was measured before feeding it into the welding machine to investigate the effect of welding temperature on the pre-welding bead. The measured unaged Std-OIT of welding rod material (348±16 min) was more than twice the Std-OIT of the unaged sheet material (165± 2 min). The high Std-OIT value of unaged pre-welded rods was due to using a high antioxidant package to decrease the effect of the high welding temperature on the possibility of reduction of Std-OIT of the unaged post-welded area. After welding, the Std-OIT of the extrudate bead was 181± 1 min, and this follows from it being twice initially and ~10% finally (after welding) above that of the sheet away from the weld (SAW). The post welding Std-OIT of the sheet and extrudate bead were higher than the minimum requirement (100 min) indicated by GRI-GM 13.

4.2 Depletion in oxidative induction time

The Std-OIT obtained from specimens taken from extrudate bead and sheet material immersed in MSW Leachate at three different temperatures (85°C, 75°C and 65°C) over 12 months of immersion were normalized based with respect to the initial Std-OIT value and plotted for the two locations examined in (Figure 3). The depletion was fastest in the GMB

sheet material and slowest at the welding bead (where the geomembrane was thick) at 85°C (Figure 3). The depletion rates decreased with decreasing the temperature (Figure 3). At low temperatures (i.e., 65°C), the rate of depletion of the extrudate bead area (where the extrudate rod was molten and pushed into the geomembrane during the welding process) was faster than at the geomembrane sheet away from welding (SAW) (Figure 3).
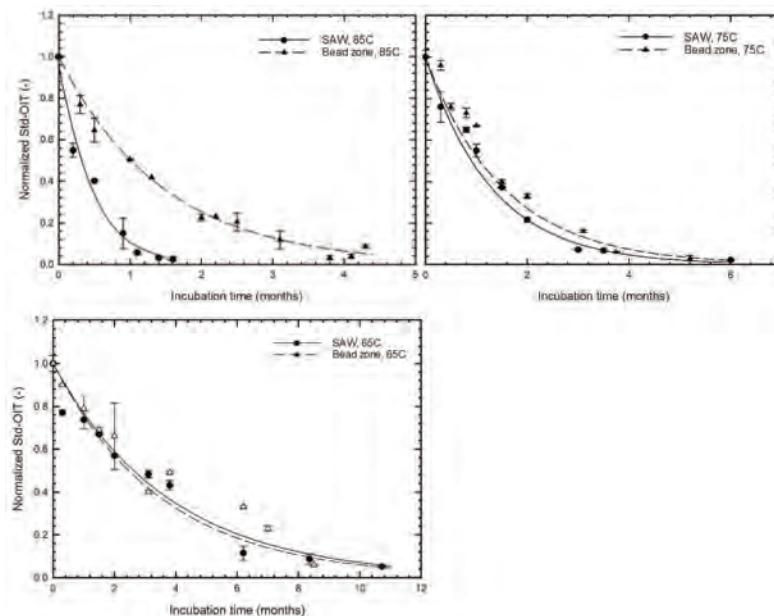
Figure 3.   Normalized variation of Std-OIT of bead zone and sheet material with incubation time at two locations immersed in Leachate 3 at 85°C, 75°C, and 65°C.

The welding bead Std-OIT depleted to residual after four months at 85°C, five months at 75°C, and 10.5 months at 65°C. The sheet material Std-OIT depleted after 1.5 months at 85°C, five months at 75°C, and ten months at 65°C. Despite the higher initial Std-OIT of the extruding rod, the depletion rate was slow for the welding bead at 65°C, and the fastest rate was for the welding bead area at 85°C com to the pared sheet away from welding (SAW).

A trend of exponential decay was observed at all temperatures (Figure 3). Figure 4 is plotted as ln (normalized Std-OIT) to allow linear regression to be conducted.
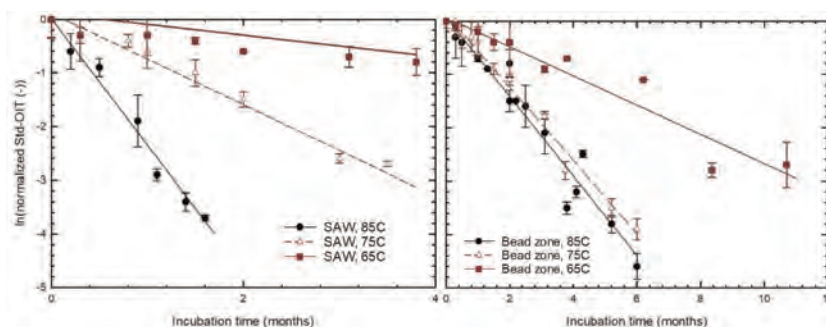
Figure 4.   Linear regression of ln (Std-OIT (min)) depletion of sheet material and bead zone, aged at 85°C, 75°C, and 65°C.

Arrhenius model was used to predict the Std-OIT depletion rates at lower temperatures (i.e., typical landfill temperature). The predicted (based on Eqs. 1 and 2) Std-OIT depletion times are summarized in Table 1, which shows that the time to antioxidant depletion was lowest for the extrudate bead at lower temperatures.

Table 1. Predicted time to Std-OIT deletion in bead and sheet away from the weld (SAW).

| Temp. (°C) | Predicted Depletion time (years) | |
	Bead (220°C/230°C)	SAW
85	0.4	0.16
75	0.6	0.4
65	0.9	1.2
55	1.4	3.6
40	3	21
35	3.9	40
30	5.2	76

The predicted Std-OIT depletion time in MSW Leachate 3 at a typical landfill temperature of 30°C–40°C (Rowe 2005) was 5.2 to 3 years for the extrudate bead and 76 to 21 years for the geomembrane sheet material. The examined geomembrane showed a depletion rate in the extrudate bead (≥ 7 times) faster than in the sheet material. The depletion rates incubated in jars for sheet material have been shown to be substantially faster than in a composite liner system and may be 3.4-fold (or more; (Rowe *et al*. 2010, 2020) greater than in immersion tests (e.g., as given in Table 1) The same comparison has no been done for welds but that depletion can also be expected to be much slower than in Table 1in the filed, however the relative trend is suspected to be similar.

5 CONCLUSIONS

This paper has focused on the effect of extrusion welding on the antioxidant depletion from extrusion welds for a 1.5 mm HDPE GMB used in municipal soil waste applications. The extrusion welds performed on sheet at a temperature of 37°C for a combination of pre-heating and barrel temperatures of 220°C and 230°C. Accelerated ageing tests at 85°C, 75°C, and 65°C were conducted to increase the antioxidant depletion rate and the Arrhenius model was then used to predict the antioxidant depletion rate expected in the field. For the conditions considered, the following preliminary conclusions have been reached for the GMB sheet and extrudate bead:

(1) The unaged post-welding Std-OIT of the extrudate bead was higher than the same for SAW for the GMB examined.
(2) At a test temperature of 85°C, the Std-OIT depletion rate of the extrudate bead was slower than SAW immersed in MSW Leachate; this is attributed to the greater thickness of the extrudate bead compared to the SAW.
(3) The Std-OIT depletion rate of the extrudate bead was faster than SAW at a lower temperature (i.e. 65°C).
(4) The predicted antioxidant depletion times to the residual value for the GMB immersed in MSW leachate at a temperature of 35°C was 3.9 years for welding bead and 40 years for the geomembrane sheet (and probably 3-4 times longer in a full barrier system).

This paper only reported antioxidant depletion detected by Std-OIT test for one geo-membrane and one welding combination. An examination of the effect of different welding parameter combination on antioxidant depletion of welding bead and heat affected zone is important. Additionally, the effect of extrusion welding on physical and mechanical properties needs to be examined for unaged and aged extrusion welds specimens.

ACKNOWLEDGEMENTS

REFERENCES

Abdelaal, F. B., Rowe, R. K., Smith, M., & Thiel, R. 2011. OIT Depletion in HDPE Geomembranes Used in Contact With Solutions Having Very High and Low pH. In *Proceedings of the 14th Pan-American Conference. Soil Mechanics and Geotechnical Engineering*, Toronto, Ontario: 2–6.

Abdelaal, F.B., Rowe, R.K. & Islam, M.Z. 2014. Effect of Leachate Composition on the Long-term Performance of a HDPE Geomembrane. *Geotextile and Geomembranes* 42: 348–362.

ASTM D3895. *Standard Test Method for Oxidative Induction Time of Polyolefins by Differential Scanning Calorimetry*. Annual Book of ASTM Standards, Philadelphia, USA

ASTM D5199. *Standard Test Method for Measuring the Nominal Thickness of Geosynthetics.* Annual Book of ASTM Standards, Philadelphia, USA.

ASTM D 6392. *Standard Test Method for Determining the Integrity of No Reinforced Geomembrane Seams Produced Using Thermo-fusion Methods*. Annual Book of ASTM Standards, Philadelphia, USA.

Ewais, A. M. R., Rowe, R. K., Brachman, R. W. I., & Arnepalli, D. N. 2014. Service Life of a HDPE GMB Under Simulated Landfill Conditions. *J Geotech. Geoenviron.* 140(11): 04014060.

Francey, W. & Rowe, R.K. 2022a. Stress Crack Resistance of Unaged HDPE Geomembrane Fusion Seams. *Geosynthetic International*.

Francey, W. & Rowe, R.K. 2022b. Long-term Stress Crack Resistance of HDPE Fusion Seams Aged at 85°C in Synthetic Leachate. *Can. Geotech. J*, in press

Francey, W. & Rowe, R.K. 2022c. Thickness Reduction - Squeeze-out Std-OIT Loss Relationship for HDPE Geomembrane Fusion Seams. *Geotext. Geomembr.*, in press

Giroud, J. P. 2005. Quantification of Geosynthetic Behaviour. *Geosynthetics International*

GRI-GM13. 2003. *Standard Specification for Test Properties, Testing Frequency and Recommended Warrant for HDPE Smooth and Textured Geomembranes*. GRI, Folsom, Pennsylvania, USA.

GRI-GM19. 2005. Standard Specification for Seam Strength and Related Properties of Thermally Bonded Polyolefin Geomembranes. GRI, Folsom, Pennsylvania, USA.

Hsuan, Y. G. & Koerner, R. M. 1998. Antioxidant Depletion Lifetime in High-Density Polyethylene Geomembranes. *ASCE J Geotech. Geoenviron.* 124(6): 532–541.

Kavazanjian, E., Andresen, J. & Gutierrez, A. 2017. Experimental Evaluation of HDPE Geomembrane Seam Strain Concentrations. *Geosynth. Int*.

Müller, W.W 2007. Welding of HDPE Geomembranes. *HDPE Geomembranes in Geotechnics* 2007: 379–420.

Müller, W. & Jacob, I. 2003. Oxidative Resistance of High-density Polyethylene Geomembranes. *Polymer Degradation and Stability* 79(1): 161–172.

Rowe, R.K., & Sangam, H.P. 2002. Durability of HDPE Geomembranes. *Geotextile and Geomembrane* 20(2): 77–95.

Rowe, R. K., Quigley, R. M., Brachman, R. W. I. & Booker, J. R. 2004. *Barrier Systems for Waste Disposal Facilities*, E & FN Spon, London.

Rowe, R.K., Islam, M.Z. & Hsuan, Y.G. 2008. Leachate Chemical Composition Effects on OIT Depletion HDPE GMB. *Geosynthetic International* 15: 136–151.

Rowe, R. K., Rimal, S., & Sangam, H. 2009. Ageing of HDPE Geomembrane Exposed to Air, Water and Leachate at Different Temperatures. *Geotextile and Geomembrane* 7(2): 137–151.

Rowe, R.K, Islam, M.Z. & Hsuan, Y.G. 2010. Effect of Thickness on the Ageing of HDPE Geomembranes. *ASCE J Geotech. Geoenviron*. 136(2): 299–309.

Rowe, R.K., Islam, M.Z., Brachman, R.W.I., Arnepalli, D.N. & Ewais, A.R. 2010. Antioxidant Depletion from an HDPE Geomembrane Under Simulated Landfill Conditions. *ASCE J Geotech. Geoenviron*. 136: (7): 930–939.

Rowe, R.K., & Shoaib, M. 2017. Long-term Performance HDPE Geomembrane Seams in MSW Leachate. *Can. Geotech. J*. 54(12): 1623–1636.

Rowe, R.K. & Shoaib, M. 2018. Durability of HDPE Geomembrane Seams Immersed in Brine for Three Years. *J Geotech. Geoenviron*. 144(2).

Rowe, R.K., Abdelaal, F.B., Zafari, M. Morsy, M.S. & Priyanto, D.G. 2020. An Approach to Geomembrane Selection for Challenging Design Requirements, *Can. Geotech. J.*, 57(10):1550–1565.

Peggs, I. D. 2019. Impact of Microstructure on HDPE Geomembrane Seaming and Vice Versa. *Geosynthetics*. Houston, TX, USA.

Sangam, H.P. & Rowe, R.K. 2002. Durability of HDPE Geomembranes - A Review. *Geotextile and Geomembrane* 20(2): 77–95.

Scheirs, J. 2009. *A Guide to Polymeric Geomembranes: A Practical Approach*. Australia: John Wiley and Sons, Ltd.

Zhang, L., Bouazza, A., Rowe, R. K., & Scheirs, J. 2017. Effect of Welding Parameters on Properties of HDPE Geomembrane Seams. *Geosynthetics International* 1(11).

Determination of the reduction factors applied to polymeric coated steel woven wire mesh reinforcement in new Eurocodes

P. Rimoldi
Civil Engineering Consultant, Milan, Italy

M. Vicari & F. Trovato
Officine Maccaferri SpA, Bologna, Italy

ABSTRACT: The new norm prEN 1997-3 (at present under discussion in CEN TC 250), that is the new EuroCode for Geotechnical Design, is introducing specific rules for the design of reinforced fill structures. Polymeric coated woven steel wire mesh reinforcement is treated in specific clauses, with Reduction Factors suited to this peculiar type of reinforcement. In facts a product with a metallic core and polymeric coating exhibits different properties than Geosynthetics and fully metallic reinforcements. The present paper is aimed at presenting the durability criteria for woven steel wire mesh reinforcement and the way to derive the specific Reduction Factors proposed in new EuroCode. For design purposes it is required to address the concept of durability following mechanical and chemical damage. In practical terms this means that installation damage, as well as chemical degradation tests, are required for defining the Reduction Factors which need to be accounted for to reduce the tensile strength from the characteristic value to the design value. The paper presents the specific approach to durability for woven steel wire mesh reinforcement, for defining the Reduction Factors for design of reinforced fill structures.

1 INTRODUCTION

1.1 *Products presently used for soil reinforcement*

The products presently used for soil reinforcement can be classified in three homogeneous classes:

– Geosynthetics (GSY, purely polymeric products): the tensile resistant elements are polymeric;
– Polymeric coated steel woven wire meshes: the tensile resistant elements are metallic, made of steel wires, which shall be metallic coated (typically with zinc aluminium alloys) and polymeric coated (i.e. with PVC, PE, PA6 or other polymers);
– Purely metallic products: the tensile resistant elements are metallic, usually made of steel, which may be metallic coated (zinc, zinc – aluminium, etc.).

The durability of polymeric coated steel woven wire meshes should be addressed with specific criteria, which consider the mode of development of corrosion in the metallic core when the product is placed in soil; the set criteria shall be subject to laboratory testing for the definition of the durability and of the Reduction Factors for design of reinforced fill structures.

Polymeric coated steel meshes show a totally different behaviour than fully polymeric geosynthetics; as example, the installation damage will produce the following effects:

– On geogrid made up of polyester yarns with polymeric coating: the polyester yarns (tensile resistant elements) will be immediately damaged to a lesser or larger extent;
– On steel wire mesh with metallic and polymeric coating: the steel wires (tensile resistant elements) will suffer negligible immediate damage, while the polymeric coating may get damaged at multiple points; in points where only light scratches or bruises occurred on the polymeric coating, the metallic coated steel wire will not be exposed to outside environment (the compacted soil), hence the steel wire will not suffer damages even in the long term; only in points where the polymeric coating suffered nicks exposing the metallic coated steel wire to the surrounding compacted soil the tensile resistant elements may suffer long term damage, due to oxidation produced by contact with the chemicals contained in the soil.

By analysing existing norms, like EN 10223-3, EN 14475, and ISO/TS 20432, it appears that different approaches should be used for the two classes of products; the approach to the durability of polymeric coated steel meshes for soil reinforcement still needs to be defined.

2   POLYMERIC COATED STEEL WOVEN WIRE MESHES IN NEW EUROCODES

The new EuroCode EN 1997-3 (at present under discussion in CEN TC 250) will include provisions for polymeric coated steel woven wire meshes within Section 9 on Reinforced fill structures, and in particular:

– Reinforcement in the form of polymeric coated woven wire mesh should comply with EN 10223-3.
– Polymeric coated steel woven wire meshes should be treated with a zinc-aluminium alloy coating (Zn95Al5 or Zn90Al10) conforming to EN 10244-2.
– The minimum coating unit weight shall comply with Class A of Table 2 of EN 10244-2:2009 and be further protected (according to EN 10245-1) by a:
    – PVC coating conforming to EN 10245-2; or
    – PE coating conforming to EN 10245-3; or
    – PET coating conforming to EN 10245-4; or
    – PA coating conforming to EN 10245-5.

– The characteristic tensile strength of polymeric coated steel woven wire mesh reinforcement shall be determined in accordance with EN ISO 10319.

With reference to the topic of the present paper, the most important provision requires that the representative tensile resistance $R_{t,rep,el}$ of a polymeric coated woven wire mesh reinforcing element shall be determined from Formula (1):

$$R_{t,rep,el} = \eta_{pwm} \cdot T_k \qquad (1)$$

where:
    T_k is the characteristic tensile strength of the reinforcing element;
    η_{pwm} is a reduction factor accounting for anticipated loss of strength with time and other influences.
    The value of the reduction factor for tensile strength of steel woven wire meshes, η_{pwm} shall be determined from Formula (2):

$$\eta_{pwm} = \eta_{dmg} \cdot \eta_{cor} \qquad (2)$$

where:

η_{dmg} is a reduction factor accounting for the adverse effects of mechanical damage during transportation, installation, and execution;

η_{cor} is a reduction factor accounting for the adverse effects of degradation of the element by corrosion over the design service life of the structure.

It has to be noted that:

– The value η_{dmg} can be assessed by testing in accordance with EN 17738, as the ratio of the tensile strength of damaged specimens divided by the tensile strength of the undamaged specimens. Note that damage to the coating does not decrease the tensile strength in the short term and is accounted for in the determination of η_{cor}, as it will induce corrosion of the exposed wire.

– The determination of η_{cor} shall account for the long term effect of corrosion of the steel wires due to the local loss of protection caused by mechanical and chemical damage to the polymeric coatings, exposing the wires (with or without zinc-aluminium alloy) to the surrounding environment.

– The polymeric and the zinc-aluminium alloy coating have no structural function, since theirs only purpose is to protect the metallic wires.

– The value of η_{cor} is based on the residual strength of the product ignoring the wires that are exposed and assumed to be ineffective due to loss of polymeric coating. This assumes that the coating does not degrade chemically up to a level such that its protective function is lost over the design service life.

3 DURABILITY OF POLYMERIC COATED STEEL WOVEN WIRE MESHES

3.1 *Effect of mechanical damage on the tensile strength*

Mechanical damage, which affects the tensile strength of polymer coated steel wire meshes, can develop basically during installation, due to friction of the coarse aggregates during compaction of the soil layers; it is related to possible scratches, cuts, bruises, consequent to the mechanical friction of the sharp edges of stones during compaction of coarse soil.

The test for installation damage on double twisted steel wire meshes, according to the full scale procedure specified in EN 17738, is used to define η_{dmg}, but it can be also used as reference for determination of the mechanical resistance of the polymeric coating.

The application of this procedures allows determining the percentage of wires with polymeric coating damage (nicks exposing steel wire) caused by mechanical compaction, which can be used to define η_{cor}.

3.2 *Service life of polymeric coated steel mesh geosynthetics*

To provide the longest corrosion protection to the steel wire mesh, the steel wire is galvanized with a Zn+Al alloy (metallic coating), and additionally coated with a polymer of required characteristics.

The durability of polymeric coated steel wire meshes placed in soil relies primarily on the durability of the polymeric coating:

– the expected service life of the steel wire can be assumed to be at least equal to the expected service life of the polymeric coating if the coating remains intact or just slightly damaged, that is when in no point the metallic wire is exposed to the external environment;

– only at points where physical and/or chemical and/or thermal degradation of the polymeric coating occurs, then the metallic coating of the wires will start to rust and corrode.

Hence the lower limit of durability can be identified in the situation when local damages to the polymeric coating occur: where the metallic wire is exposed to the external environment then rust and corrosion start to develop.

When the polymeric coating is damaged and the metallic coated wire get exposed to the outside environment (usually the compacted soil), corrosion of the steel wire may be produced by the chemical composition of such environment, and corrosion may propagate along the wire.

In this situation two phenomena need to be considered:

(1) diffusion of corrosion along the wire starting from the point where the polymeric coating is damaged;
(2) accelerated corrosion due to differences of electric potential between adjacent points of damage along the same wire or between points of damage along different wires.

3.3 Corrosion of the steel wire

The constant exposure to outside environment always occurs (even without damage) at the ends of the steel wire mesh panels, where the full cross-section of the steel wire is in contact with the surrounding environment. Hence this is surely the worst case, since corrosion will affect the whole cross section of the wire since the beginning. Therefore the evaluation of corrosion propagation can be made by using end cut wires as reference specimens and referring to the corrosion spread test defined in ASTM A975-21. The procedure consists of immersing 250 mm long wire samples in a 5 % solution of HCl by weight. Samples are removed from the solution and analysed after 100, 500, 1000, 1500, 2500 hours of immersion. The polymer coating shall be removed, and the length of the corroded wire measured. The part of the wire with reduced diameter is considered as corroded. The average corrosion lengths measured versus time plot shall show the maximum length after which there is no more increase in length with time: this maximum length measured shall be always less than a mesh repetition.

The corrosion spread test allows to verify that the corrosion, when exposed to such an aggressive environment (pH = 0.137), does not progress further with time and that it remains confined within the size of a mesh only.

Tests using ASTM A975-21 procedure on Maccaferri Polimac coated steel wire mesh have shown that the maximum corrosion length (mm) is always less than a mesh repetition and has the tendency to reach a plateau after approx. 1500 h, as shown in Figure 1. As the length of corrosion penetration is less than half the twisted length, then corrosion occurring in one wire will not affect any other wire of the hexagonal mesh; in this case the effect of corrosion will be limited to the single wire where damage occurred.
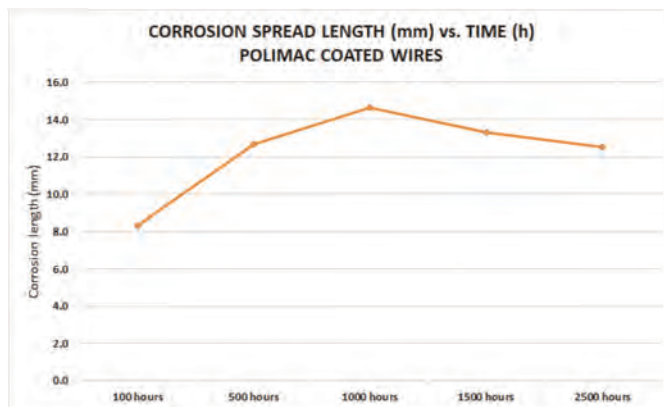
Figure 1.   Length of the corrosion penetration along the polymer (POLIMAC) coated steel wire at pH = 0.137.

The corrosion spread test is focused on the evidence that very low pH (acid environment with pH lower than 0.2) produces the highest corrosion rates in steel, while very high pH (alkaline environment) has negligible effects on corrosion; this is consistent with the common experience that concrete, that is a highly alkaline material, does not produce corrosion of steel bars, rather it protects the steel from corrosion.

As for the possible corrosion due to differences of electric potential between two points (i.e., stray currents near railway tracks), being the polymeric coating of steel wires dielectric, it provides electrical insulation to the steel wire itself and avoids electrical connections between adjacent wires, hence corrosion cannot occur if the polymeric coating is not deeply damaged.

Since the general criteria for setting durability of a geosynthetic at X years is that the minimum retained strength shall be 50 % after X years, the evaluation of the durability of polymeric coated steel wire mesh geosynthetics will require the evaluation of the number of wires which can be considered as instantly corroded at the points where the polymeric coating is damaged and the steel wire is exposed. Hence in this case the effect of installation damage can be evaluated by the following procedure, which is consistent with ISO/TS 13434:2007 "Geosynthetics – Guidelines for the assessment of durability" (Figure 2):

– perform the installation damage procedure;
– retrieve the damaged specimens;
– carry out a visual and microscopic inspection for setting the points where the steel wire became exposed;
– cut the steel wires at the points where they were exposed (taking into account that multiple damages on the same steel wire will be counted as one wire exposed);
– perform tensile tests according to ISO 10319:2015 on the reference specimens and the damaged specimens;
– the ratio between the tensile strength of specimens with the damaged wire cut to that of specimens with no cuts provides the minimum retained strength.

Figure 2.   Procedure for installation damage of metallic geosynthetics: a) fill compaction on the sample; b) retrieving sample and identifying local damages; c) microscopic examination to assess exposure of the metallic core; d) indicating points where the metallic core is exposed.

For practical purposes the steel wire can be considered as totally corroded in very short time at the point of coating damage; that is, the steel wire can be considered as instantly corroded or, which is the same, it can be considered as totally cut and not contributing

anymore to the tensile strength of the steel mesh: this conservative assumption allows to include the effect of mechanical damages into the η_{cor} partial factor.

Tests according to the above procedure performed on the steel mesh of Maccaferri Terramesh units (8x10 mesh type and 2.7 mm diameter wire, coated with Polimac), provided the values of η_{cor} listed in Table 1.

Table 1. Results of installation damage tests on the steel mesh of Maccaferri Terramesh units (8x10 mesh type and 2.7 diameter wire, coated with Polimac).

Fill material	Maximum particle size (mm)	η_{cor}
Crushed stones	<200	0.820
Coarse gravel	<38	0.869
Sandy gravel	<9.5	0.952
Sands	<2	1.000
Silts and clays	<0.06	1.000

3.4 Chemicals resistance of the polymeric coating of steel wires

The chemical resistance of steel wires depends on the environment where they work during their service life. Considering the chemicals usually occurring in natural soils and their concentration, it is evident that the polymeric coating of steel wires mesh geosynthetics will suffer very little or even negligible degradation even over very long time. Moreover, the polymeric coating has no structural function, since it has only to provide protection to the steel wire. Hence the durability of the polymeric coating shall be evaluated taking into account its function: its service life shall be considered as the maximum time when it is still able to provide protection to the steel wire.

The resistance of the polymeric coating over time can be predicted by accelerating the ageing effect of the plastic specimens in a rigorously constant and replicable environment (oven), testing degradation by monitoring the variation of the property, the reduction of which will have an effect on the wire protection.

Tests to assess the long-term resistance of polymer coatings shall be performed according to EN 60216-8, where an extrapolation of service life is made by accelerating polymer degradation in oven at various temperatures and then using an Arrhenius plot extrapolation to predict degradation at the ambient temperature.

In the Arrhenius regression method the logarithms of the mean times to end point are plotted versus the reciprocal values of the exposure temperatures. The intersection of this curve with the inverse of the selected reference temperature (20°C) provides the service life T_{pc} (Figure 3).
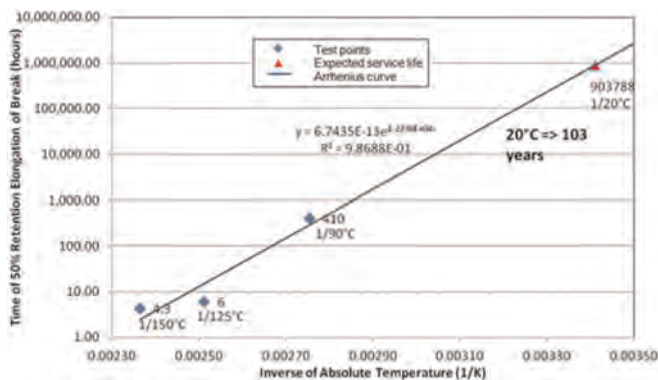
Figure 3. Arrhenius plot for the Terramesh polymeric coating to determine its expected service life at 20°C.

4 CONCLUSIONS

The metallic core of polymeric coated woven steel meshes exhibits different properties than purely polymeric geosynthetics. Therefore, the durability of woven steel meshes needs to be addressed in a peculiar way.

In the present paper the Authors have proposed a rational procedure for assessing the durability of polymeric coated woven steel meshes, for the definition of the Reduction Factor η_{pwm} that will be required for design of reinforced fill structures according to the new EuroCode.

REFERENCES

ASTM A975-21. *Double-Twisted Hexagonal Mesh Gabions and Revet Mattresses (Metallic-Coated Steel Wire or Metallic-Coated Steel Wire With Poly(Vinyl Chloride) (PVC) Coating)*.

EN 10223-3. *Steel Wire and Wire Products for Fencing and Netting. Part 3: Hexagonal Steel Wire Mesh Products for Civil Engineering Purposes*

EN 10244-2. *Steel Wire and Wire Products – Non-ferrous Metallic Coatings on Steel Wire – Zinc or Zinc Alloy Coatings.*

EN 10245-1. *Steel Wire and Wire Products. Organic Coatings on Steel Wire. General Rules*

EN 10245-2. *Steel Wire and Wire Products. Organic Coatings on Steel Wire. PVC Finished Wire*

EN 10245-3. *Steel Wire and Wire Products. Organic coatings on steel wire. PE coated wire*

EN 10245-4. *Steel Wire and Wire Products. Organic coatings on steel wire. Polyester coated wire*

EN 10245-5. *Steel Wire and Wire Products. Organic coatings on steel wire. Polyamide coated wire*

EN 10319. *Geosynthetics — Wide-width Tensile Test*

EN 14475. *Execution of Special Geotechnical Works – Reinforced Fill*

EN 60216-8. *Electrical Insulating Materials – Thermal Endurance Properties – Part 8: Instructions for Calculating Thermal Endurance Characteristics using Simplified Procedures*

EN 17738. *Geotextiles and Geotextile Related Products — Damage During Installation Procedure — Full Scale Test*

ISO/TS 20432. *Guidelines for the Determination of the Long-term Strength of Geosynthetics for Soil Reinforcement*

prEN 1997-3. *Eurocode 7 – Geotechnical Design – Part 3: Geotechnical Structures*. Under Discussion in CEN TC 250

Risks and alternatives to the use of PET reinforcements in treated backfills

M. Aressy
Terre Armée, Rueil Malmaison, France

R. Lozano
Reinforced Earth Company, Sterling VA, USA

ABSTRACT: The increasing demand to reuse excavation materials, to use soil in place or materials with high fine contents in the construction of Mechanically Stabilized Earth structures leads to the extensive application of soil stabilization technics such as lime, cement or fly ash treatment.

Soil treatment is an economical solution to exploit poor in-situ materials that cannot be implemented in their natural state. The treatment improves, in short terms, the physical parameters of the soils allowing its workability. However, such treatments also modify the chemical parameters of soil such as alkalinity in durable manner. The pH will remain well above 10 for very long period even at low dosage. Most of the MSE structure reinforced with geosynthetic uses PET based products. It is well established that PET is only suited for soil having pH ranging from 4 to 9. In highly alkaline environment, the degradation mechanism is strongly accelerated particularly when mechanical stresses are applied on the material. Then using PET in treated backfill is a clear risk for a structure integrity.In this paper, we will propose an extensive review of treatment technics detailing the gradual transformation of the soil alkalinity with time, then we will provide technical data showing the performances of PET reinforcement materials when exposed to alkalinity in the conditions of reinforcement applications, finally we will propose alternative solution such as the use of PVA reinforcement material and present their performances.

1 INTRODUCTION

Soil treatment is used to improve or stabilize soils addressing the handling and compacting problems resulting from high plasticity or high-water content found in backfills with elevated quantities of clay or Limestone.

Soil treatment principally involves mixing the soil with a binder to improve its geo-mechanical performance. Binders are mainly lime or cement, resulting in a strong and durable increase in soil alkalinity. The main compound impacting the mechanical and physicochemical properties is calcium hydroxide ($Ca(OH)_2$) (IDRRIM 2015). MSE structures are designed to perform 75 to 120 years depending on the codes, therefore the reinforcement used should be adequately selected.

Often, PET reinforcement is suggested for use in lime-treated backfills. While this option appears economically attractive, it goes against recommendations in international codes and is highly risky for the structure's integrity (L. Van Schoors 2013) (V. Elias 1998).

This paper will focus on lime treatment as it is the most common binder, introducing the treatment's requirements, mechanisms, and long-term properties in MSE structures context. We will also emphasize physico-chemical changes, particularly the alkalinity built up, which directly impacts the choice of reinforcements.

Then, we will provide a condensed literature review of the PET yarns hydrolysis degradation focusing on the influence of alkalinity, the impact of lime on the degradation, and its kinetic. We will provide technical evidence PET based reinforcement is not compatible with treated backfills.

Finally, we will introduce PVAl yarns, presenting some durability results obtained under various conditions and demonstrating why PVAl based reinforcements are the best high stiffness alternative product when construction is done with treated backfill.

2 PRINCIPLES OF LIME TREATMENT FOR MSE STRUCTURES

2.1 *Soil requirements*

Adding lime to soil induces several chemical reactions between the soil particles and the lime. Nevertheless, some geotechnical parameters shall be satisfied to ensure an optimal process:

- The presence of fine particles: Passing at $80 \mu m > 25\%$.
- The Plasticity Index (PI): PI > 10.

In addition, some chemical components that may have adverse consequences on lime treatment shall be limited (IDRRIM 2015):

- The organic matter which may consume the lime. Organic content shall not exceed 1% by weight.
- The chlorides can accelerate the lime treatment and induce swellings by forming chloroaluminates. Chlorides shall not exceed 2000 ppm.
- The sulfate and sulfides in soils (in the form of gypsum or pyrite) can induce ettringite formation, causing considerable swellings. The total soluble sulfate content shall not exceed 3000 ppm.
- The presence of phosphates and nitrates can slow down the curing process. They shall not exceed 1200 ppm.

2.2 *Soil-lime reaction*

Lime includes all products manufactured from the decarbonization of calcitic or dolomitic limestone:

- Quicklime is the product of the calcination of limestone.
- Hydrated lime is obtained from the hydration of quicklime.
- Precipitated calcium carbonate.

When mixed with soil, different reactions occur following chronological order (Figure 1).
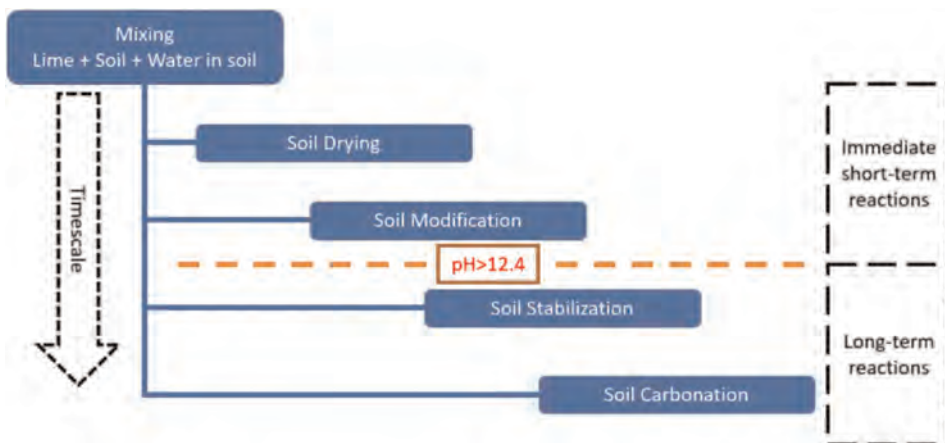
Figure 1.   Chronology of lime/soil reactions.

Short-term actions consist of soil drying, soil modification, and improving the workability and compaction characteristics. In contrast, long-term actions consist of soil stabilization and carbonation, improving the soil's mechanical behavior.

2.3 Soil drying

When the soil is mixed with lime, immediate action is to induce the reduction of the water content. The lime is a dry product, and its addition to soil increases the total mixture weight, whereas the water weight does not change, reducing water content. When using quicklime, the water in the soil activates the hydration of the calcium oxide, thus consuming water. The exothermic reaction induces further water consumption through evaporation (Equation 1).

$$CaO + H_2O \rightarrow Ca(OH)_2 + Heat\ Release \tag{1}$$

2.4 Soil modification

Soil modification is a step in the stabilization process or can be achieved alone using a limited amount of lime. The so-called "lime modification optimum" (LMO) can be determined using the soil-lime pH test described in ASTM D6276. Generally, the LMO lies between 1 wt% to 3 wt% and draws the line between short-term and long-term actions of the treatment or soil modification and stabilization (DigueELITE 2015).

The soil modification mechanism is based on the flocculation process. In the presence of water, hydrated lime or calcium hydroxide will ionize, leading to Calcium (Ca2+) ions and Hydroxyl (OH-) ions (Equation 2)

$$Ca(OH)_2 \rightarrow Ca^{2+} + 2OH \tag{2}$$

The presence of Ca^{2+} in great quantity induces a cation exchange with the soil particles leading to the saturation of the surfaces of the particles with calcium. This mechanism reduces the repulsions forces between the particles and disturbs the water adsorption mechanism. Consequently, the soil particles agglomerate, forming larger and stronger particles.

This modification of the soil induces an instantaneous improvement of the treated fill's physical properties. The following consequences are generally observed:

- Textural change: the fill grading curve changes there are fewer fine particles.
- Plasticity: changes of the Atterberg limits, decrease of the PI.
- Swell potential: significant reduction in swell potential
- Shrinkage: decrease of shrinkage potential
- Compaction characteristics: Modification of the Proctor curve

All these short-term improvements occur in a matter of hours after treatment and facilitate construction. The use of soil modification as the primary process solely concerns granular or intermediate backfills that are too wet or high plasticity, preventing workability and optimal compaction in their natural state. The minimal lime content for soil modification results from the targeted treated soil's immediate bearing index value to be reached. Table 1 gives a range of values for the type of soil. (SETRA 2000).

Table 1. Immediate bearing index values.

Type of soil	Immediate bearing index value after treatment
Granular	15 to 30
Intermediate	7 to 15

2.5 Soil stabilization

In soil stabilization, the treatment influences the long-term performances of the material. The geomechanical characteristics are modified to get a sustainable strength gain and a permanent stability. Here, the quantity of lime added is sufficiently high (superior to the LMO) to generate long-term pozzolanic reactions between the calcium of the lime and the silica and alumina from the soil particles (Equation 3 and 4).

$$Ca(OH)_2 + SiO_2 + H_2O \underset{pH>12.4}{\rightarrow} Calcium\ Silicate\ Hydrate\ (CSH) \tag{3}$$

$$Ca(OH)_2 + Al_2O_3 + H_2O \underset{pH>12.4}{\rightarrow} Calcium\ Aluninate\ Hydrate\ (CAH) \tag{4}$$
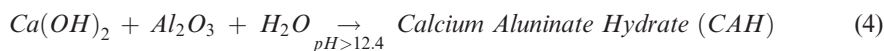
The pozzolanic reactions form cementitious products enhancing the shear strength and the stiffness of materials. The lime treatment progressively increases the soil cohesion but has little impact on the friction angle (G. Herrier April 2013). This stabilization process is possible when the silica and the alumina become soluble. The solubilization only happens at elevated pH (pH > 12.4). As lime is a strong alkaline, the treatment increases the pH of the soil. However, to achieve a pH of 12.4, enough lime, superior to the LMO, shall be added. Because of the heterogeneity of the soil mass, lime is always added in excess compared to the LMO value determined to ensure the treatment's durability.

2.6 Carbonation reaction

Finally, a carbonation reaction occurs during the life of structure, the remaining calcium hydroxide reacts with the carbon dioxide present in the soil forming cementitious products, furthering improving the cohesion of the fill.

2.7 Treatment's durability

Chemical stabilization significantly changes the geotechnical characteristics of the treated backfill to achieve long-term permanent strength and stability. External factors can alter the design performance along the service life. Therefore, the durability of soil stabilization shall be considered at the formulation; this often results in adding an excess of lime to cover the uncertainties.

Indeed, the long-term strength gain can be considered durable only when the chemical stabilization mechanism remains active; this means keeping the pozzolanic reactions active. If there is enough calcium hydroxide in the soil, the pH will remain sufficiently high to ensure the solubility of silica and alumina. Thus, the pozzolanic reaction will continue.

One of the primary impacting environmental factors is hydraulic solicitations. These can be found in retaining structures with hydraulic exposure or structures exposed continuously penetration of rain. The presence of water and its circulation inside a stabilized backfill alter the long-term performance by leaching out the calcium hydroxide, which ultimately will reduce the pH and alter the cementitious compounds, inhibiting pozzolanic reactions, and deleteriously changing soil properties.

Whilst, proper drainage management is always highly recommended, to obtain a durable treatment in MSE structures as it necessary to prevent water circulation inside the treated backfill (fully integrated drainage system, a properly designed barrier at the top of the structure, etc.). It should be noted that drainage management is also essential to avoid contamination of adjacent areas, soil treatment use chemical additives that are deleterious to vegetation growth.

2.8 Long-term properties: pH gradual transformation

Treatment of long-term properties has been the subject of numerous studies. It was shown that long-term changes are observed in the soil's physicochemical and mechanical properties,

whether the treatment is done for modification/workability or stabilization. In the scope of MSE structures and the choice of reinforcement, a stable pH in the soil should lead to different reinforcement choices dues to materials compatibility.

Daniele *et al.* (Deneele D. 2016) presented an accelerated leaching study comparing lime-treated silty soil with 1wt% and 3wt%. The pH of these soils after a percolation protocol equivalent to about 11.5 years of heavy water circulation presented values of 9 and 12, respectively. The non-treated soil sample kept a constant pH of 8. De Bel and al. (De Bel R. 2013) who followed the pH evolution of a silty soil over two years showing a stable pH value between 11.5 and 12. Also C. Jung and al. (Jung C. 2008), studied six structures aged from 5 to 11 years old, measuring pH values at different depths. An average pH value of around 10.5 was obtained for all structures, with none of the structures showing a pH lower than 9 at any depth.

All those studies demonstrate that lime-treatment impact the long-term physico-chemical characteristic of the soil and particularly its alkalinity, which can be expected to present a pH>9 whether the treatment is done for modification (short-term) or stabilization (long-term).

3 PET REINFORCEMENT DURABILITY: ALKALINE ENVIRONMENT CONSIDERATIONS

It is well established that PET degradation is hydrolysis. Polyester hydrolysis occurs following two different mechanisms depending on the exposition environment (Van Schoors 2007).

The two environmental conditions considered in MSE structures applications are:

- Acid or neutral environment $1 \leq pH \leq 9$.
- Alkaline environment pH>9.

In acidic or neutral environments, hydrolysis occurs under a mechanism called internal hydrolysis well described in the literature. The water molecules diffuse into the polymer matrix leading to a homogeneous degradation of the polyester chains through a random chain scission process. This induces a reduction of the mechanical properties at a moderate rate after a considerable induction period.

In alkaline environment, the hydrolysis mechanism strongly differs. The reaction is catalyzed by hydroxyl anions (OH-) which transforms the esters functions into alcohol and carboxylate ions. Carboxylate ions can then recombine with cations (such as Na^+, Ca^{2+}, ...) to form carboxylate salts.
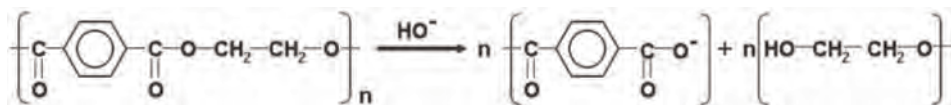
Figure 2.   PET alkaline hydrolysis.

Elias and al. theorized this degradation mechanism (V. Elias 1998). They stated that the molecular split described in Figure 2 modifies the polyester's dielectric properties, creating a barrier that hydroxyl ions cannot penetrate. As a result, the hydrolysis intensity at the fiber surface is increased, creating shorter polymer chains that can later be dissolved in the solution, ultimately leading to a drop in the fibers' diameters. This phenomenon can be assimilated to surface erosion of the fibers occurring at a very fast rate. The rate of alkaline hydrolysis also highly depends on the type of environment and the type of cations present.

Figure 3 shows the results of hydrolysis exposure test carried out at 23°C and 50°C over 15 years in various solutions (K.L. Nait Ali 2009). Two alkaline compounds were used in this
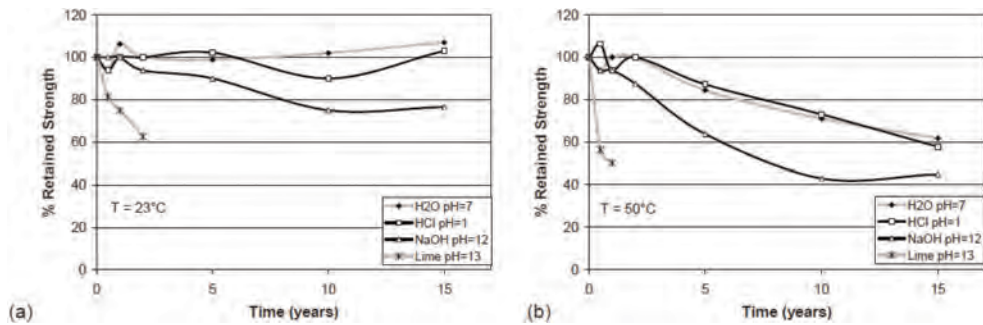
Figure 3. Hydrolytic degradation of PET yarns in various media (1<pH<13) at (a) 23°C and (b) 50°C over 15 years.

study sodium hydroxide and calcium hydroxide (or lime). Despite the difference of one point in pH value, it is easily noticeable that the ageing in calcium hydroxide is much faster than in sodium hydroxide. The results show that at 23°C PET yarns lose about 40% of strength when exposed to saturated lime solution in only 2 years. The fast degradation rate observed in lime is not only the result of calcium hydroxide being a very strong di-base (carrying two hydroxyl) but also to the presence of Ca^{2+} cations which accelerate the surface hydrolysis rate (H.F Schroeder 2000).

The results show that lime or calcium hydroxide is highly damaging to PET yarns, even at low temperatures. Indeed, at 23°C after two years, the yarn lost almost 40% of its original strength.

Other papers reported that tensile loading of PET yarns further accelerates the hydrolysis rate, particularly when subjected to alkaline hydrolysis. Finally, given the recommended level of compaction in MSE structures, the use of PET based reinforcement products, even if protected with a coating, will lead to yarns being exposed to the surrounding environment and thus to strong alkalinity. This is reminded in many standards but often ignored. The combination of all these remarks highlight that PET reinforcement products are not well suited to lime-treated backfill, and the risk involved in doing so is incredibly high for the reinforcement and, ultimately, for the structure. Other polymers such as polyolefin-based reinforcements provide good chemical compatibility but lack good stiffness and long-term creep performance. It is possible to consider aramid-based reinforcement but, their cost effectiveness and chemical compatibility is limited.

4 PVAL: A HIGH STIFFNESS ALTERNATIVE

PVAl yarns are known to degrade following an oxidation mechanism (Sakurada 1985). While oxidation mechanism can be accelerated in acidic environments, exposition of PVAl fibers to alkaline environments has never shown a considerable impact on the mechanical strength even after a long time of exposure at elevated temperatures (L.K. Nait Ali 2014) (Y. Bian 2018) (M. Nishiyama 2006).

Its chemical behavior associated with its high stiffness (twice as compared to PET yarns) combined with a reasonable cost makes PVAl reinforcement products the best alternative material for MSE structures where treated backfills will be used.

To fully understand the degradation mechanism of PVAl yarns, a durability study exposing yarns to three different solutions (H_2SO_4 pH = 2.4, distilled water pH = 7, and sodium hydroxide pH = 12). Aging conditions were conformed to EN 14030. In this study, the tensile properties were followed as a function of time, and the results are presented in
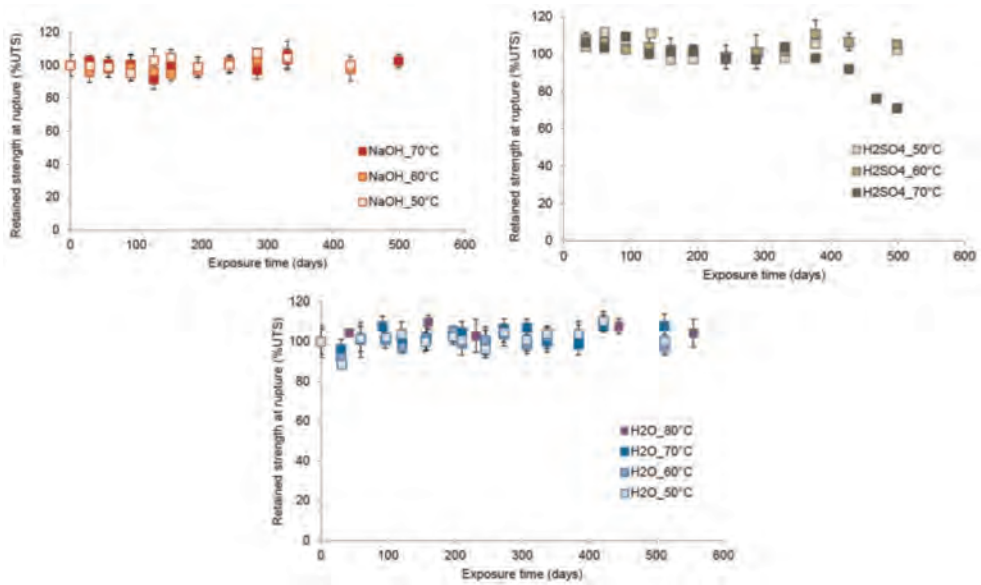
Figure 4. Progression of the retained strength at break of PVAl aged yarns as a function of exposure time in NaOH, H2SO4 and H2O.

Figure 4. Part of this data was presented in a previous paper (Y. Bian 2018). The results are in Figure 4.

The results clearly show that an alkaline environment does not impact the tensile properties of PVAl yarns even after an extended exposition period (more than 500 days) at elevated temperatures. As expected, PVAl oxidation will only be accelerated when exposed to a strong acidic medium.

As a matter of comparison, we exposed PVAl yarn and PET yarn to a solution of saturated lime at a temperature of 80°C for about ten days (Figure 5). The picture clearly shows the difference in behavior between PVAl and PET yarn. While the PET yarn is degraded, PVAl yarn shows a slight color change due to heat exposure (Y. Bian 2018), but no loss in strength.

Figure 5. Comparison between PVAl and PET yarn exposed to a saturated lime solution at 80°C.

These results clearly show that PVAl yarns are well suited to provide long-term performances when exposed to strong alkaline and thus compatible with treated soils such as lime-treated fills.

5 CONCLUSIONS

Where high and long-term stiffness is required, PET yarns-based geotextile reinforcements are preferred to other materials in MSE structure design. PET yarns benefit from excellent mechanical properties and good chemical resistance (as long as pH<9) at a particularly attractive cost.

In this paper, we have shown that when designing a MSE structure with treated backfill PET based reinforcement is not well adapted, and the risk involved in using this type of material is extremely high for the structure's durability, even if these products are coated for installation damage protection.

Alternatively, we propose that PVAl yarns-based reinforcement is an ideal candidate for MSE structure construction, combining chemical compatibility, high stiffness, and long-term mechanical performances.

REFERENCES

Bian Y., Aressy M., Colin X. "Polyvinyl Alcohol Yarns Long Term Properties Assessments. Part II : Chemical durability." 11th ICG . Seoul, 2018.

De Bel R., Gomes Correia A., Duvigneaud P.H., François B., Herrier G., and Verbrugge J.C. "*Evolution Mécanique et Physico-chimique à Long Terme d'un sol Limoneux Traité à la Chaux.*". Paris, 2013.

Deneele D., Le Runigo B., Cuic Y.J., Cuisinier O., Ferbere V. "Experimental Assessment Regarding Leaching of Lime-treated Silt." *Construction and Building Materials* 112 (2016): 1032–1040.

DigueELITE. "Utilisation des Sols Traités À la Chaux Dans les Ouvrages Hydrauliques." 2015.

Elias V., Salman A., Goulias D. "The Effect of pH, Resin Properties and Manufacturing Process on Laboratory Degradation of Polyester Geosynthetics." *Geosynthtics International* 5, no. 5 (1998): 459–490.

Herrier G., Puiatti D., Chevalier C., Froumentin M., Bonelli S., *et al.* "Lime treatment : New Perspectives for the Use of Silty and Clayey Soils in Earthen Hydraulic Structures." *9th ICOLD European Club Symposium*. Venice, Italy, 2013.

IDRRIM. "Enseignement de TerDOUEST, Proposition de Compléments Au Guide Traitement Des Sols." 2015.

Jung C., Bobet A. "Post-construction evaluation of lime-treated soils." Indiana DOT USA, 2008.

Nait Ali K.L., Thomas R.W., Anderson P.L, Freitag N. "Hydrolysis Testing of High Tenacity Poly(ethylene terephthalate) – Results from 15 Years of Exposure." *Geosynthetics*. Salt Lake City, 2009.

Nait Ali L.K., Thomas R., Freitag N. "Polyvinyl Alcohol Physical Behaviour and Chemical Durability." *10th ICG*. Berlin, 2014.

Nishiyama M., Yamamoto R., Hoshiro H. "Long-term Durability of Kuralon (PVA fiber) in Alkaline Condition." 10th IIBCC. Sao Paulo, 2006.

Sakurada, I. Polyvinyl Alcohol Fibers. New York: International Science and Technology Series 6, 1985.

Schroeder H.F., Bahr H., Kneip G., Lorenz E., Schmucking I., Steifert I. "Long-term Resistance of PET Geofibers to Inner and Outer Hydrolysis." *China International Nonwovens/Techtextiles Conference*. Beijin, 2000.

SETRA. "Traitements des Sols à la Chaux et/ou Aux Liants Hydrauliques. Application à la Réalisation Des Remblais et Des Couches de Forme." 2000.

Van Schoors, I. Nour, S. Moscardelli, N. Barberis, D. Lozach, M. Khay. "Comparaison Des Propriétés Des Fibres d'un Géotextile Polyester Vieilli en Laboratoire Et Dans Des Sols Traités." 9ème Rencontres Géosynthétiques. Dijon, 2013.

Van Schoors, L. Viellissement Hydrolitique des Géotextiles Polyester (polyéthylène téréphtalate) - Etat de l'art. BLPC n 270–271, 2007.

Feedback from the bituminous geomembrane (BGM) implemented 20 years ago at the Galaube dam

N. Pepin & L. Deroo
ISL Ingénierie, France

B. Breul
Axter, France

B. Gasc
Institution des Eaux de la Montagne Noire, France

ABSTRACT: The Galaube dam is a 40 m high French rockfill dam commissioned in 2001. The upstream facing is ensured by a 4.6 mm thick bituminous geomembrane (BGM) directly laid on a cold mix layer and an impregnated layer gavel.

During construction, control measurements were first carried out in the factory. The BGM was then installed by vertical strips, in one piece, from top to bottom. Welds were subject to a strict quality control plan and all defect immediately rectified.

After 20 years of operation, the hydraulic behavior of the dam shows that piezometry is low and leakage through the membrane is deemed to be negligible. The dam has settled very few in practice and has already undergone its first filling and a complete emptying in 2007. No defects have been identified and almost no maintenance operations carried out. The design and construction of the upstream facing has been very successful.

1 INTRODUCTION

The Galaube dam on the Alzeau river, located in the communes of Lacombe (Aude department, France) and Arfons (Tarn department, France), was built in 1999-2000. It is operated by the Institution des Eaux de la Montagne Noire and was designed to store and regulate water resources for drinking water, irrigation and navigation on the Canal du Midi.

The dam is a rockfill dam with a tight upstream facing. The maximum height of the structure on the natural ground is 33 m. It creates a reservoir with a volume of 7.7 hm^3 below the normal reservoir level of 720.5 m NGF. The structure is class A according to French legislation on the safety of hydraulic structures.

The purpose of this article is to analyze the behavior of the dam after more than 20 years of operation, and more particularly of the bituminous geomembrane (BGM) which ensures the upstream sealing of the structure. We summarize the reasons for the choice of a rockfill dam, then describe the characteristics of the structure and its waterproofing membrane. Finally, we analyze the hydraulic and mechanical behavior of the dam. Our study indicates that the BGM waterproofing system is very effective.

2 CHARACTERSITICS OF THE DAM AND DESIGN OF THE UPSTREAM FACING

2.1 *Initial design options at the Galaube dam*

Two possibilities were studied and compared at the Basic Preliminary Design stage for the Galaube dam: a roller-compacted concrete dam (RCC) or a rockfill dam with an upstream face. The rockfill dam was finally selected by the project designers because it made the most of the poor foundation and could be easily adapted to the lack of watertight materials by adding a specific watertight component.

Two solutions were possible, depending on the position of the watertight component: an upstream facing or a central core dam, either with an asphalt core or a plastic concrete core. The rockfill dam solution with an upstream facing was considered the most suitable for the Galaube dam because of the following advantages: it was less expensive (in this case), there were lower risks of internal erosion of the sandy gouges of the foundation thanks to a better connection with the granite foundation, there was better handling of the interface with hydraulic galleries and, construction schedule was more flexible.

2.2 *Design of the upstream facing*

2.2.1 *Cross-section of the dam*
The typical cross-section of the dam is shown in Figure 1. The rockfill consists of two main zones:

– an upstream zone with a horizontal width of 3 m (Zone 2), consisting of a material with a grain size of 0/150 mm, ensuring a triple function: *i)* a transition zone between the rockfill and the support layers of the geomembrane, *ii)* a semi-permeable zone limiting leaks in the event of a localized defect on the upstream facing, and *iii)* the creation of a contrast in permeability with the downstream rockfill. The latter contributes to the lowering of the water line in the event of accidental loading by damage to the upstream facing or accidental impounding during construction.
– the compacted rock fill 0/500 mm (zone 3).
– the reinforced concrete plinth is founded and anchored on fresh or slightly weathered granite. A grout curtain ensures that percolations in the foundation are cut off.

Prior to the placement of any material of the upstream facing, the upstream slope of the dam embankment was compacted with two static rollers of 4 tons each, specially designed and manufactured, and pulled from the dam crest. This compaction complemented the previous compaction of the backfill.
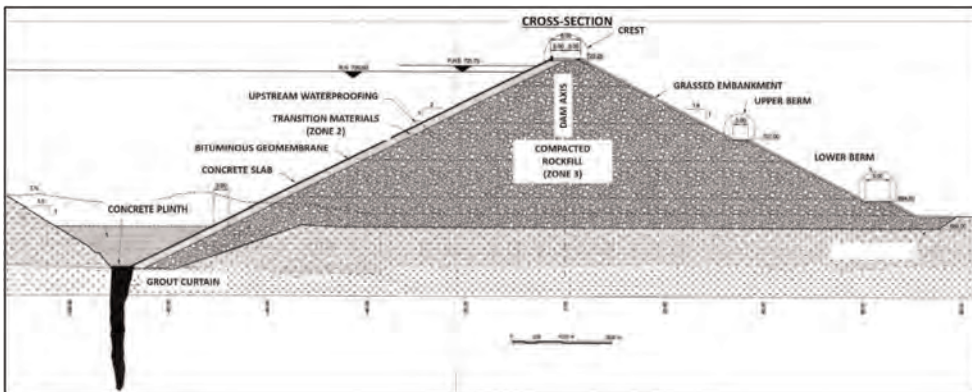
Figure 1. Typical cross-section of La Galaube dam (ISL).

2.2.2 Technical specifications of the upstream facing

The typical cross-section of the upstream facing of the Galaube dam is shown in Figure 2.
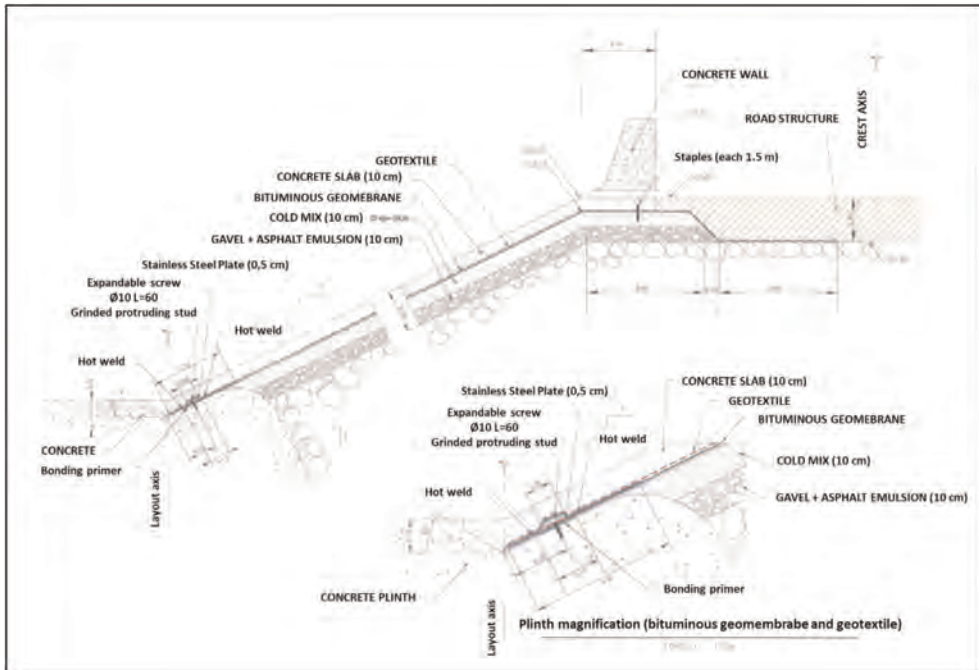
Figure 2. Typical cross-section of the upstream facing.

2.2.2.1 Membrane supporting layers

The membrane supporting layer consists of two sub-layers:

– a layer of gravel, with a grain size of 0/20 mm, with a minimum thickness of 10 cm impregnated with bitumen. It is designed to absorb most of the irregularities in the flatness of the dam body and those that may occur because of prior compaction of the slope.
– a cold semi-permeable asphalt mix layer with a nominal thickness of 10 cm and permeability between $0,75 \times 10^{-6}$ et $1,25 \ 10^{-6}$ m/s. The controlled breaking behaviour of the emulsion was selected so that the cold asphalt mix manoeuvrability was ensured throughout the implementation and compaction phases.

2.2.2.2 Bituminous geomembrane

The upstream facing of the dam is ensured by a 4.6 mm thick "Coletanche NTP3" bituminous geomembrane with the following data:

– Mass per unit area of 5.5 kg/m2
– High tensile strength in both directions: 28 kN/m in longitudinal direction, 20 in transverse direction, together with more than 70 % elongation at break, according to French standard NF P 84-50
– High resistance to puncture: 500 N according to French standard NF P 84-507
– tensile/shear joint strength greater than 75% of the tensile strength in the current part, according to French standard NF P 84-502.1.

A series of measurements on each of the components was carried out in the factory for each laid strip. The membrane was laid directly on the cold mix layer without the

interposition of a geotextile and by following a detailed installation drawing. The membrane was unrolled from top to bottom and each strip was laid in one piece from the crest attachment to the weld on the concrete plinth. Horizontal joints were not permitted.

Welds were performed according to the procedure recommended by the geomembrane manufacturer. The minimum overlap to be achieved by welding was 20 cm. Welds should only be carried out on perfectly clean surfaces, free of dust, moisture, and grease. A continuous control of all the welds between the strips was carried out. For the Galaube dam, the weld quality was checked by a continuous non-destructive device called CAC 94. This machine had a measure wheel, which included 24 ultrasonic sensors that could detect flaws of a minimum surface of 0.8×0.5 cm at the interface between the two geomembranes, on a 21 cm wide strip. If a section of welds showed defects, repairs had to be carried out immediately. A wider patch with at least 30 cm around the flaw was then applied, hot welded and checked again.

The concrete plinth was anchored into the rock foundation. The geomembrane was fastened to the plinth at the foot of the slope and along the whole periphery of the impervious face. It was hot-welded on the 2H/1V sloping part of the concrete surface, which has been previously covered with a tack-primer, then anchored with stainless steel plates bolted into the plinth, each 15 cm.

At the crest, the geomembrane was clamped using metal staples spaced 1.5 m apart, driven into the cold mix asphalt layer and into the concrete slabs overlying the membrane. The membrane was flipped under the road structure over a length of 0.80 m.

For the cconnection to concrete structures, the materials used were the same as those used for fixing to the concrete plinth.

2.2.2.3   Geotextile

A geotextile was placed above the BGM: it provided a puncture protection function when the protective slabs were laid and now ensures a drainage function for the underside of these slabs. The geotextile presented a mass per unit area of 500 g/m^2 (NF G 38-013), a tensile strength of 20 kN/m (NF G 38-014), and a transmissivity higher than 10^{-6} m^2/s (NF G 38-018).

2.2.2.4   Concrete slabs

The dimensions of the protective slabs for the geomembrane were 5 m width (horizontal) and 10 m length (along the slope). The concrete (35 MPa standard compressive strength) was cast in place. The anti-cracking device was made of polypropylene fibres (0.4% by volume) which tensile strength had to be greater than or equal to 500 MPa.

Horizontal joints were continuous and consisted of simple concrete interfaces. Vertical joints were staggered and designed as dilatation joints and filled with a strip of expanded polystyrene type material of about 20 mm. After concreting and hardening of the second panel, they were cleared of the joint material and left open.

The horizontal and vertical joints between minimum and maximum water level were filled with a flexible mastic to prevent the joints from being filled with silt and vegetation.

3   FEEDBACK ON THE MONITORING OF THE UPSTREAM FACING

3.1   Analysis of the hydraulic behavior of the dam

The filling of the reservoir took place in two seasons. In June 2001, the reservoir reached a maximum level of 710.94; the level then progressively decreased until it reached 704.50 in December 2001. In February 2002, the reservoir exceeded the maximum level reached in 2001. The normal reservoir level of 720.50 was finally reached in June 2002. The reservoir had an average annual tidal range of 15 m until the 2007 drawdown. Afterwards, the range has been about 5 to 10 m until today.

The piezometry at the downstream foot of the plinth (Figures 3 and 6) appears to be well draw down with a low (less than 30%) to very low (less than 10%) dependence on the reservoir level. Only PF03 piezometer shows particularly sensitive to the level of the reservoir
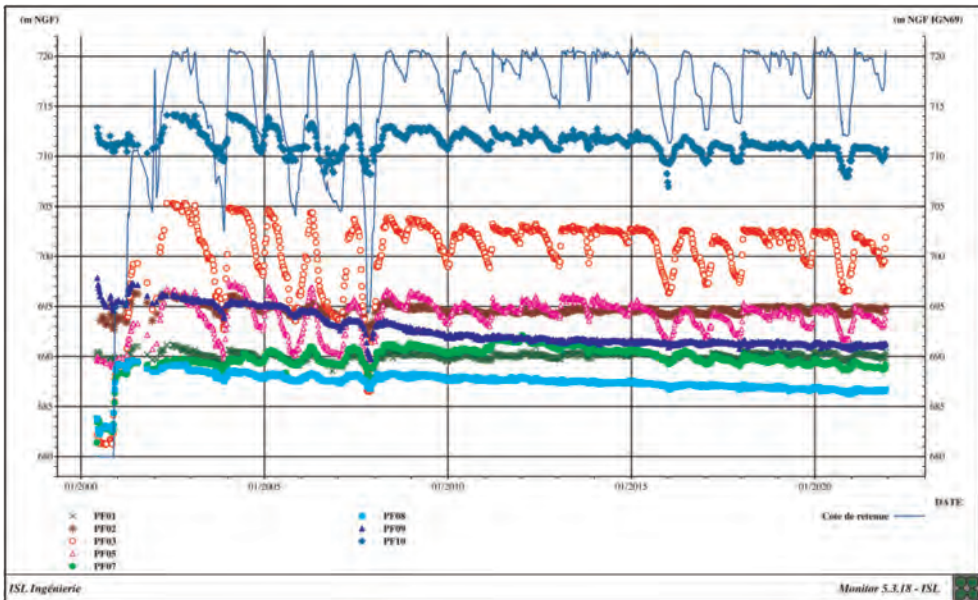
Figure 3.   Time evolution of the piezometric levels in the foundation, downstream of the plinth.

and reacts by faithfully reproducing the reservoir curve. This singular behavior, detected immediately after the first filling, is not reproduced by its neighbors (PF07 and PF08). As PF03 is drilled in a zone where the rock is of good quality and low permeability, it is likely that PF03 measures a singularity of piezometry, for example by capturing a fine fissure, where pressures can become high due to the low permeability of the medium. Watertightness of the geomembrane is therefore not in question.

Overall, the analysis of piezometric levels downstream of the plinth over the period 2001–2021, shows that they are constantly decreasing since impound, on average by about −10 cm/year. It is most certainly a consequence of the progressive sealing of the upstream foot of the dam in connection with the progressive silting of the reservoir.

In the axis of the dam (Figure 4), PF06 and PR03 were apparently above the piezometric level at the first filling but they have shown a continuous decrease since then confirming the very good behaviour of the upstream facing. The piezometry at the bottom of the valley (Figure 4, PR01, PR02, PF04), is quite homogeneous under 690 m NGF, which corresponds to the foundation level of the dam in this area. The rockfill, which is very draining, does not allow piezometry to develop.

Regarding the piezometry downstream of the dam (Figure 5), only the piezometers at the top of the bank (PD01, PG01 and PG02) reacted to first filling and show now a strong dependence on the reservoir level. These piezometers are the closest to the reservoir and they are located in an area (the upper bank) where the foundation is permeable (upper left bank made up of deeply altered granite, and upper right bank where there is an interface between the granite foundation of the dam and the shale that overhangs it). All these piezometers are traditionally influenced by weather conditions, especially the heaviest rainfall events which lead to reversible peaks.

With respects to the leakage flows, the absolute value of the measured flows at the end of impoundment was of the same order of magnitude as what had been observed on other dams of the same type in France. Given the greater height of the Galaube dam, and especially the greater dammed surface area than that of these previous dams, the level of measured runoff was considered satisfactory (0.7 liters per hour and per square meter of facing). Leakage
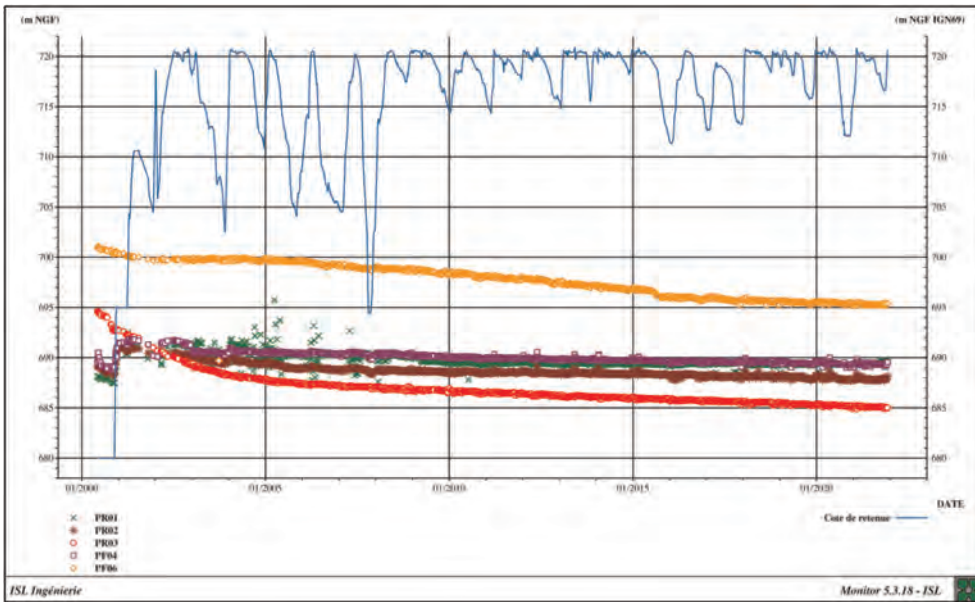
Figure 4. Time evolution of the piezometric levels at the interface of the dam body and the foundation.
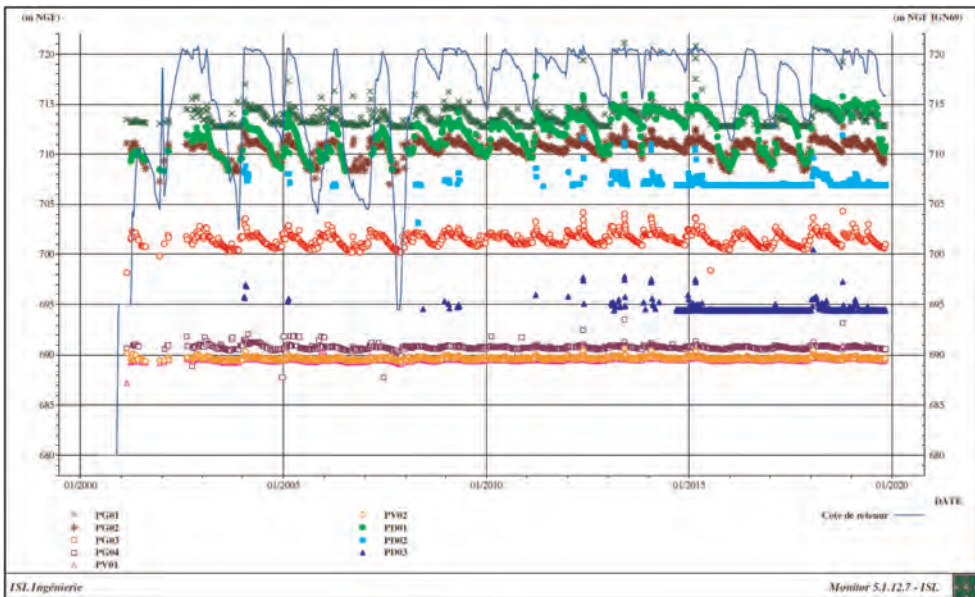
Figure 5. Time evolution of piezometric levels downstream of the dam and on the riverbank.

rates have remained generally moderate – on average about 20 l/min for the flow drained by the drainage gallery – which is well correlated to the reservoir level and increases significantly above 720 m NGF. The flow drained by the temporary diversion tunnel on the left bank – on average about 60 l/min – is also dependent on the reservoir level, but it has a higher dispersion, mainly due to rainfall.
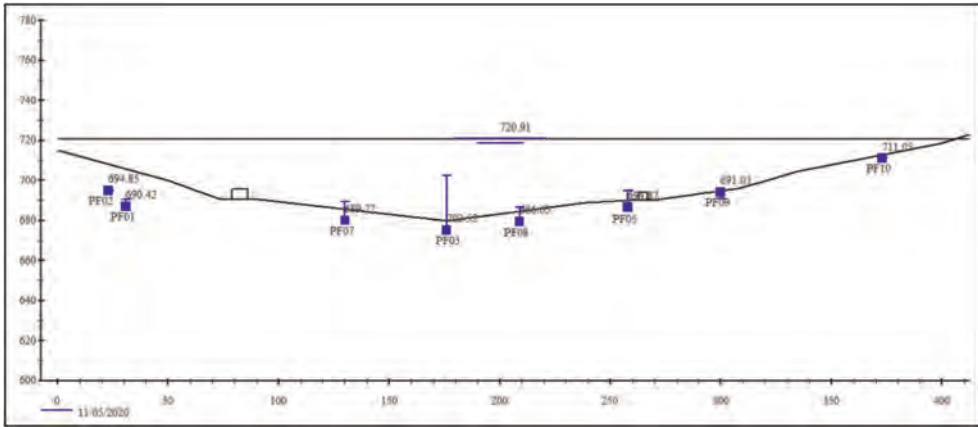
Figure 6. Maximum piezometry in the foundation - downstream of the plinth (period 2018-2019).

The monitoring of leakage flows over the period 2001–2021 shows a continued favourable downward trend of almost −2 l/min/year. This confirms the good watertightness of the upstream facing and the absence of leaks.

3.2 *Analysis of the mechanical behaviour of the concrete plinth and upstream facing*

3.2.1 *Deformations of the upstream facing*

Calculations of the deformation of the dam's upstream facing under the effect of the structure's own weight and the water pressure exerted by the reservoir were carried out in 1996 when the dam was designed.

The calculated deformations of the facing during the operation of the reservoir show that the most stressed area of the membrane is located near the plinth where the differential settlements created by the variation in the height of the embankment cause the geomembrane to be put under tension.

Careful excavation and plinth geometry aimed to limit discontinuities in the upstream facing foundation to limit localized differential settlement. The same applies to the connection of the facing to the upstream structure and to the spillway, where 0.5H/1V facing slopes have been provided to limit membrane extension deformations. These slopes also made it possible to ensure satisfactory compaction in the entering angles near the concrete facings.

The expected membrane deformations – of the order of a few millimetres per metre at most – are negligible compared to the specified elongations at failure of the membrane, which are greater than 40%. The weight of sediment in the lower part of the upstream facing does not seem to be able to alter these conclusions. The deformations generated by the incremental vertical stress (of the same order of magnitude as those calculated under the effect of hydrostatic pressure alone) are in fact considered negligible compared to those generated by possible differential settlement of the fill, which are themselves considered very unlikely in view of the deformations:

– The proven behavior of the structure: it has settled very few in practice (cumulative settlement less than 4 cm at the crest, i.e. less than 0.1% of the total height of the dam) and less than most upstream facing rockfill structures of the same type (see comparison in the graphs on Figure 7 and Figure 8 with 11 well compacted dams, i.e. with materials of medium to high quality $20 < RC < 70$ MPa) ;
– The precautions taken during the construction phase to compact the rockfill, in particular: a maximum layer thickness of 80 cm, a minimum of 8 passes (one way) of a heavy smooth

795
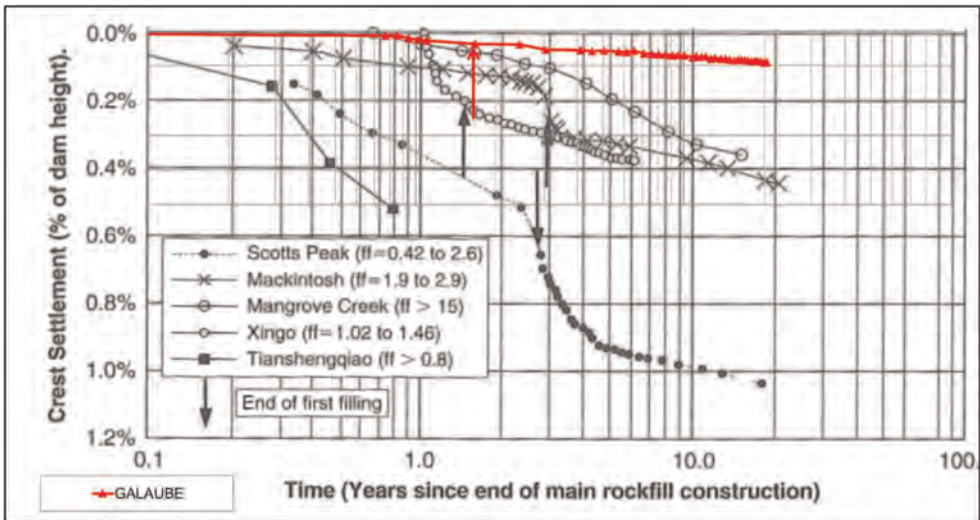
Figure 7.   Comparison of maximum crest settlements in relation to 5 dams of the same type, some of which were sensitive to first filling.
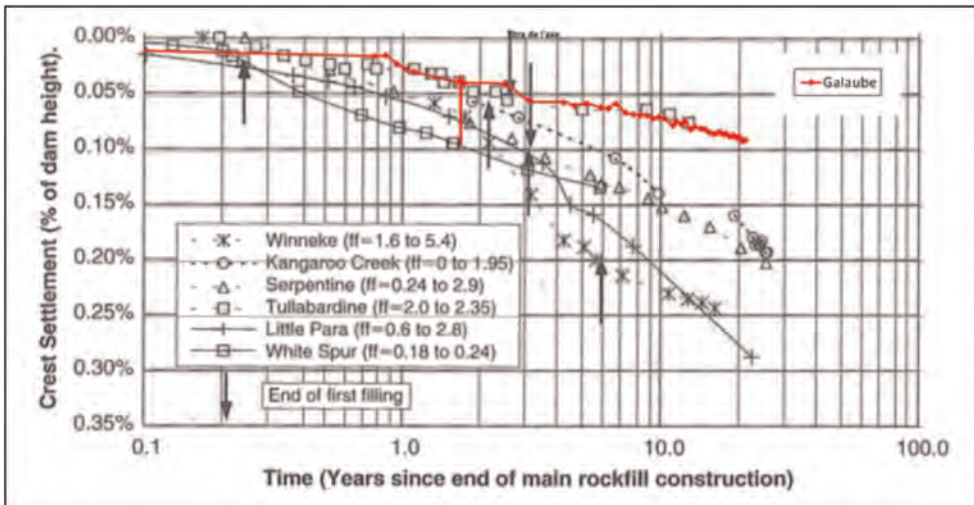
Figure 8.   Comparison of maximum crest settlements in relation to 6 other dams of the same type.

vibratory roll, a travel speed of less than 3 km/h, specific compaction in the vicinity of concrete structures (using mechanical tampers), specific compaction in the vicinity of the plinth with a backfill built directly above the structure to ensure optimal compaction, the excess volume being removed before the membrane support layers are placed, and a strict control plan, particularly in the transition zones under the upstream facing (geometry, granulometry, density weight and permeability).

3.2.2   *Effect of welding*
The welding of geomembrane panels is an essential aspect for the success of their implementation as an impermeable barrier. For the Galaube dam, the geomembrane was installed

by vertical strips in a single piece, so there are no horizontal joints. The vertical joints were subjected to a strict quality control plan. All welding defects were immediately rectified by welding a piece of geomembrane that was larger than the identified defect. One should thus expect criteria at break close to those of the geomembrane itself (elongation at break $\geq 60\%$).

3.3.3 Risk of puncturing

Geomembranes, especially polymeric geomembranes, placed on any type of aggressive rough substrate or soil containing stones, pieces of wood or other debris are vulnerable to puncturing stresses, which may cause leakage. ICOLD Bulletin No. 135 states that "*the lining with a needle-punched non-woven geotextile, whether above or below, improves puncture resistance quite impressively.*" The risk of puncture can occur at three different points in the life of the liner:

– During the installation of the geomembrane (tool falls, snags and wear caused by site workers and equipment, etc.),
– During the installation of the covering layer (the most crucial step, regardless of the sealing system),
– After impounding, due to the hydrostatic pressure pushing the geomembrane against protrusions of the support.

From this point of view, the Galaube dam has many favourable factors:

– A geotextile is placed above the membrane: it provides a function of protection against puncturing during the installation of the protection slabs and a function of drainage of the underside of these slabs.
– The bituminous membrane is laid directly on the cold mix layer without the interposition of a geotextile because the layer is smooth (gravel with a regular grading curve of between 0 and 10 mm) and is itself laid on a transition layer consisting of a 20 mm minus well-graded gravel.
– The dam has already undergone its first filling, a complete emptying in 2007, as well as 20 years of service without any observed defects.

3.2.4 Ageing of the geomembrane

Geomembranes are sensitive to UV radiation, thermal, biological or chemical aggression. However, ICOLD Bulletin No. 135 states that: "*It goes without saying that the lifetime of protected geomembranes will be much longer than that of exposed geomembranes. It seems reasonable to expect a geomembrane protected by a permanent concrete layer to have a life expectancy of more than 200 years.*"

At the present time, there is no reason to suspect any issue with the BGM of the Galaube dam; leakage through the geomembrane is deemed to be negligible.

3.3 Lessons from 2007 drawdown

3.3.1 Behaviour of the dam during the drawdown

The reservoir of the Galaube dam was emptied for the first time in the fall of 2007 as part of the first "five-year" inspection of the dam, which generally takes place 5 to 6 years after the dam is impounded according to French regulations.

The inspection reports n°3 (February 2008) and n°4 (February 2009) prepared by ISL Ingénierie) did not reveal any anomalies in the hydraulic and mechanical behaviour of the structure, which proved to be completely reversible.

It should be noted that a slight elevation of the dam crest was recorded (of the order of 1 to 2 mm and visible on all the height benchmarks on the crest of the dam), during the emptying (cf. Figure 9). This is a mechanical consequence of the decrease in hydrostatic
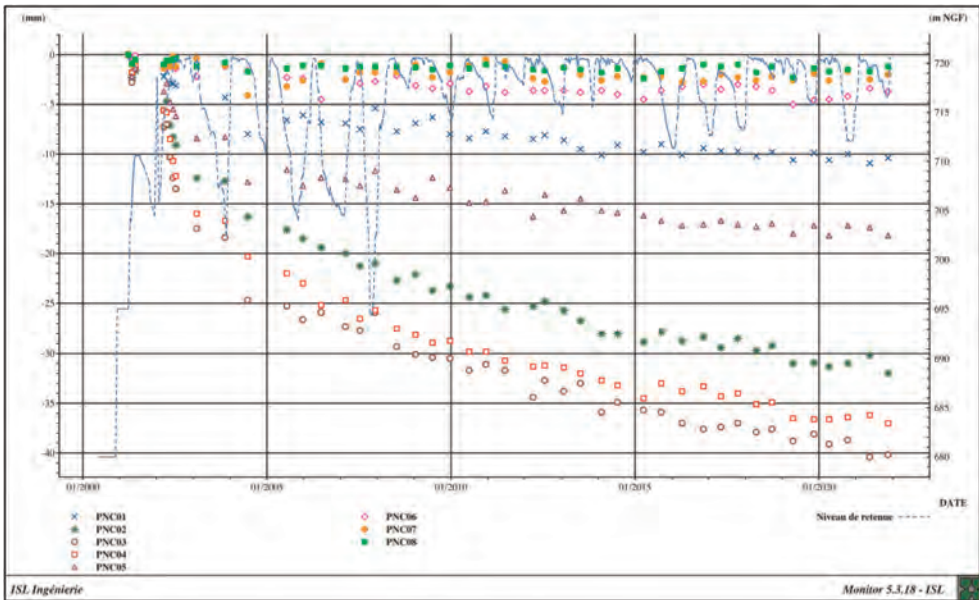
Figure 9. Time evolution of crest elevation measurements.

pressures of the reservoir on the upstream face of the structure (decompression of the rockfill).

It was also checked that the under-pressure behind the facing remained below the hydrostatic pressure exerted by the reservoir on the facing, which did not create a risk of lifting the geomembrane or the concrete protection slabs (cf. Figure 10).
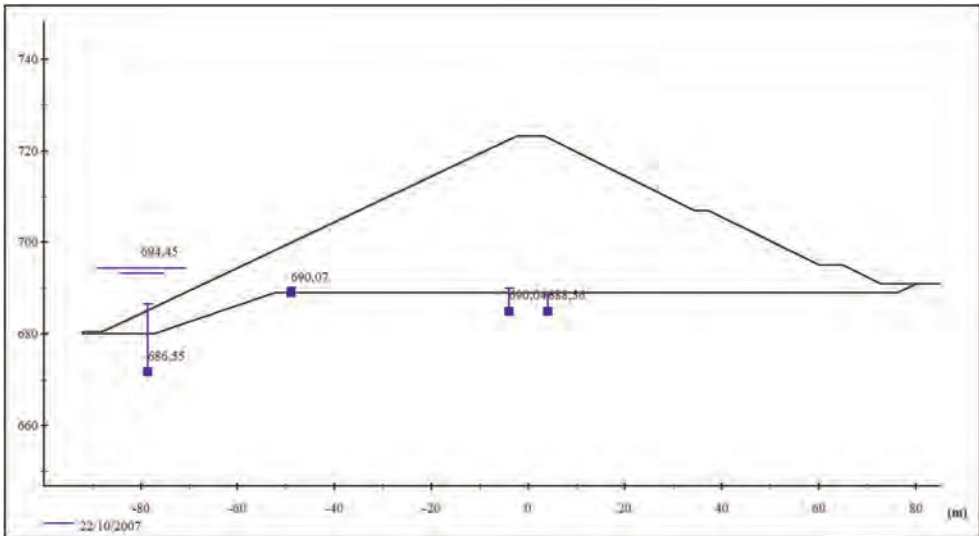
Figure 10. Maximum piezometry downstream of the plinth at the time of the 2007 reservoir emptying.

3.3.2 *Maintenance work carried out on the upstream facing*

The mechanical protection of the facing membrane of the Galaube dam consists of juxtaposed 5 m wide × 10 m long slabs cast in place with a fibre-reinforced concrete. The horizontal joints are parallel and the vertical joints are offset by half a slab. An expansion joint made with expanded polystyrene was present on the periphery of each slab, after the drying and shrinking of the concrete. It was observed that this joint was no longer held and it was torn off by wave action. Silt had begun to settle in this void and vegetation to grow.

A first area in the upper part of the upstream face had been treated during the construction site (a row and a half of slabs vertically and from bank to bank horizontally), but despite this, as the water level was lowered, plant growth began to take root in the unfilled spaces.

The owner and operator of the Galaube dam (IEMN) decided to extend the filling of the joints to the lower slabs with identical product, so that the usual tidal height is now completely treated. The work was carried out as part of the 2007 drawdown.

The horizontal joints have been filled in. For the vertical joints, a gap of approximately 20 cm was left at the bottom of each joint to allow water that had passed behind the plate to drain away as the level of the reservoir was lowered. The product used was cold bituminous mastic applicable even under water: Shell Tixophalte Wet.

This is the only work carried out on the upstream face of the Galaube dam during the first 20 years of the structure's life. Underwater inspections conducted in October 2020 as part of the exhaustive review of the dam thus showed no adverse changes to the upstream facing.

4 CONCLUSION

All the elements presented in this article allow us to affirm that the BGM upstream facing has been very successful at the Galaube dam: great care in the construction of the structure, low piezometry, absence of leaks and no notable disorders for 20 years of operation. It also has a very good record on other French dams, some of them a bit older than the Galaube dam (though not as high).

Of course, every project still requires adaptations and, despite its great success, the Galaube dam design shall probably not be directly applied to other project. The need from adaptations might come from three reasons:

– The design of an upstream facing depends a lot on the nature of the backfill materials and of the foundation.
– At Galaube dam, the rockfill and the foundation were of poor quality, which led to a gentle 2:1 upstream slope; steeper slopes might be considered – but stability of the upstream facing must be checked carefully.
– The Galaube dam design may be considered as "very safe" and could probably be optimized.

Assessment of creep behavior in aged geotextiles

J.L.E. Dias Filho
Department of Geotechnical Engineering, São Carlos School of Engineering (EESC), University of São Paulo (USP), São Carlos, São Paulo, Brazil

ABSTRACT: Considering the exogenous environment of the geotextile application, the characterization is more representative when tests and analysis are performed with sample exposed by sunlight or artificial UV light. Then, this paper aims quantitative evaluation of creep in specimens from field and laboratory degraded conditions. All analysis was done in two different types of geotextiles differing by their weights and composition. Results obtained with the aged specimens were larger than virgin samples and varied according to the base polymer and weight. The behavior of the aged materials did not show rupture results and the deformations were up to 40% greater. Thus, it can be concluded that simulating different conditions of exposure make the results more accurate as the application of geosynthetics in design and this makes the data from the studies more reliable for dimensioning engineering design.

1 INTRODUCTION

Creep is the deformation that occurs in a material subjected to constant stress over time. This test is important for characterizing the durability of geosynthetics, as the results serve as an estimate of the material's useful life. The design involving the use of geosynthetics require long-term performance, it makes sense to characterize materials by this property. Therefore, geosynthetics are often characterized using a standardized creep test (ASTM D5262) under controlled temperature and relative humidity conditions. However, this technique requires the use of expensive long-term testing to obtain a significant creep deformation response, which can take up to 10,080 hours.

There are three stages of creep behavior that can be seen in the measured strain curve as a function of time for the geosynthetic material under constant load for over time. The first stage, also known as the transition phase, is characterized by a decrease in strain rate with time. In the case of secondary stage, the linearity of the curve dominates. Tertiary stage, on the other hand, is characterized by an increase in the creep strain rate, which causes the material to rupture within a short period of time. It is important to highlight that this behavioral pattern will vary depending on the type of polymer (Dias Filho *et al.* 2021; Guimarães *et al.* 2016), the stress level of the specimen (Balakrishnan & Viswanadham 2017; Dias Filho *et al.* 2022), and the rate at which the stress is applied (Bathurst *et al.* 2012; Naftchali & Bathurst 2021). From these variables, the creep curve can acquire a dominant stage. Mathematical models can be characterizing the curve format (Dias Filho *et al.* 2019a; Dias Filho *et al.* 2021; Kongkitkul *et al.* 2014) that allow extrapolation of laboratory-derived data to identify interests such as creep deformation rate relative to temperature or load change and rupture.

The creep test method is designed to determine the unconfined tension creep and creep rupture behavior of geosynthetics under permanent tensile load and constant temperature.

According to ASTM D5262, there are two variants of the creep test: the determination of the creep deformation behavior and the determination of the creep rupture. In this paper, four tests were performed at different load levels from 5% to 60% and test times up to 1008 hours to determine the creep deformation behavior.

Evaluation of alternatives for rapid, precise and representative collection of creep results has been the focus of many papers. These papers investigate the factors that influence the deformation behavior of geosynthetics under constant load. Key methods include: stepped isotherm (SIM) and time-temperature superposition (TTS), which accelerate creep with increasing temperature (Achereiner *et al.* 2013; França & Bueno 2011; Zhao *et al.* 2021); methods to study exposure degradation (Dias Filho *et al.* 2019b; Pinho-Lopes *et al.* 2018); and analysis of the effect of soil confinement on the behavior of geosynthetics (Plácido *et al.* 2018; Nuntapanich *et al.* 2018).

Researcher papers (Liu *et al.* 2017; Zhao *et al.* 2019) reported strain limit data under 10% in structures dimensioned with geosynthetics, which in engineering practice indicates low deformation. It is also important to highlight that several of these geosynthetic design are exposed to the weather, mainly to ultraviolet (UV) radiation. Then, this paper seeks to contribute to the understanding of creep deformation behavior in woven geotextiles by evaluating different conditions testing (field and laboratory) using short-term unconfined creep test.

2 MATERIALS AND METHODS

2.1 *Study material*

Two different mass per unit area of woven geotextiles were selected for testing. As shown in Table 1, tests were performed on monofilament polypropylene (PP) and multifilament polyester (PET) according to American Standard Test Method - ASTM. The geotextile nomenclature is formed by the union of the base polymer and its weigh.

Table 1. Reference values for the nominal characteristics of the woven geotextiles.

Property	Test standard	PET340	PP500
Tensile strength (kN/m)	ASTM D5035-11	52.5 ± 1.6	106.2 ± 2.0
Elongation at rupture (%)	ASTM D5035-11	16.5 ± 1.8	20.1 ± 1.3
Mass per unit area (g/m^2)	ASTM D5261	340 ± 8	500 ± 9
Thickness (mm)	ASTM D5199	0.51 ± 0.02	1.53 ± 0.04

2.2 *Methodology*

The test procedure included characterizing the creep deformation of two selected woven geotextiles. Taking into account the exogenous environment of the application, testing and analysis are performed on representative samples exposed to sunlight or artificial UV light, and traditional tests can then be used to evaluate the effectiveness of virgin samples and other samples exposed to UV damage characterization.

2.2.1 *Outdoor exposure*
Samples were exposed to natural climatic conditions in Campos dos Goytacazes/RJ from August 2013 to August 2015. The test specimens were installed in appropriate exposure racks using suitable holders, which were affixed to the racks. The samples are mounted on support that are inclined 21°48' relative to the horizontal, corresponding to the local latitude, i.e. 21° 48' 14" S and 41° 19' 26" W. The method ensures a higher incidence rate and

therefore a stronger absorption of solar radiation. It was used the ISO TS 13434 and ASTM D5970. The field degradation times for performing the tests specified in the experimental procedure were 360 and 720 days.

The climate characteristics of this site during the natural exposure test were: the highest average temperature was 33°C, the lowest average temperature was 20°C, 14 meters altitude, precipitation in 292 days with the cumulative value of 1487.8 mm, the relative humidity was 81%, the largest irradiation of solar energy accumulated by month was 847.7 MJ/m^2 and 13.44 GJ/m^2 for the total irradiation of solar energy for two years of analysis. Briefly, the ultraviolet radiation was 1.01 GJ/m^2, i.e. a value corresponding to 7.5% of the total cumulative incidence of solar radiation according to ISO TS 13434. Such information was obtained directly from the National Institute of Meteorology - INMET.

2.2.2 *Accelerated UV test*

Samples were degraded by condensation and ultraviolet radiation, simulating natural changes during temperature variation over day, precipitation rain and ultraviolet radiation from the sun. These conditions closely replicate the natural degradation process because they simulate, with greater intensity, the main degradation mechanisms of geosynthetics used in geotechnical design.

The degradation times accelerated in the laboratory to be subjected to the tests set out in the experimental program were 400 and 800 hours. UVB lamps and ASTM D4355 guidelines were used. The UVB lamps disponible at laboratory give a short wavelength output in comparison to field exposure, but promote the degradation of materials quickly.

2.2.3 *Creep test*

Tests are carried out in a laboratory with a controlled room temperature of 20 ± 2 °C and a relative humidity of $65 \pm 5\%$ for a duration of up to 1,080 hours. The creep deformation behavior of two woven geotextile samples was determined at loads of 10%, 20%, 30%, and 40% of the ultimate tensile strength (T) according to ASTM D5262. The creep deformation behavior of the degraded samples was determined over a period of 3 days (Dias Filho *et al.* 2019) at 10% and 20% loads. According with Dias Filho *et al.* (2019), short-term loading tests may be used to extrapolate long-term creep deformation in woven geotextiles.

At scheduled times of 1, 2, 4, 8, 15, 30, and 60 minutes, then at 2, 4, 8, and 24 hours, and finally at 3 days (data collection limited degradation samples), 7, 14, 21, and 42 days, measurements of the displacements in the test samples were taken.

The test specimens were 50 ± 5 mm wide, gripped in the clamps with a gauge length of 25 mm, according to tensile strength strip tests (ASTM D5035-11), which obtained a lateral contraction of less than 10% (NBR 15226). It is important to note that the device basically consists of a grip to hold the sample without slipping and damage, a system to determine the length of the measurement over time and a load to apply the load within a minute system, according to Brazilian standards NBR 15226.

3 RESULTS

Based on the methodology, in order to demonstrate the behavior of the creep deformation of degraded samples, Table 2 shows the evaluation of the variations of the mechanical behavior due to degradation exposure of the material, naturally in the field or accelerated in the laboratory by condensation and ultraviolet radiation.

As can be seen from Table 2, the loss of tensile strength was greater in the polyester. Then, the tests degraded less PP and more PET, as expected for UVB lamp. In the laboratory, results show 66% reduction in tensile strength of PET340 and 16% of PP500. The reductions were 90% for PET340 and 55% for PP500 to exposure time in the field.

Table 2. Retained values of tensile strength and elongation at different UV total irradiation.

| | | | Retained tensile strength/elongation (%/%) | |
| | | UV total irradiation | PET340 | PP500 |
Condition	Time	(GJ/m^2)		
Intact	0	0	100/100	100/100
Laboratory	400 hours	0.14	39/44	90/95
	800 hours	0.28	34/28	84/91
Field	12 months	0.49	21/24	57/59
	24 months	1.01	10/16	45/55

The results test showed that there are no significant changes their stiffness along the stress-strain curve. Observing the deformations in the tests, the PET340 and PP500 samples increased their deformations up to 84% and 45% respectively.

Based on the mechanical characterization of the materials and their behavior according to the degradation conditions presented (Table 2), Table 3 presents an important comparison of the relationship between the tensile loads used in the creep tests (10%T and 20%T), from virgin samples, by tensile strength according to with the conditions found in the tests.

Table 3. Relation tensile load and tensile strength.

| | | 10%T/20%T (%/%) | |
Condition	Time	PET340	PP500
Intact	0	10/20	10/20
Laboratory	400 hours	26/52	11/22
	800 hours	29/59	12/24
Field	12 months	49/97	18/35
	24 months	103/207	22/44

The proportionality between the tensile loads/tensile strength shows that the values of the loads for the creep tests reach the rupture stage. Particularly in polyester, several ratios between load and tension exceed 50%. This explains the nonappearance of some of the creep results in the degraded samples that are shown in Figure 1.

Only one PET340 degraded sample was obtained to the fluence curve (Figure 1a). The sample degraded in the laboratory (400 hour and 10%T) obtained a curve between the results of 20%T and 30%T of the virgin creep test and very close to the value of the tensile loads/tensile strength ratio in Table 3 (26%). The last data collection point may be indicating the beginning of stage 3 of the creep test, where the strain rate over time is no longer linear and increases significantly until failure. In fact, the degradations in the laboratory and in the field greatly altered the other samples, as shown in Table 2. It is also noteworthy that the load in the others degraded specimens exceeds 29% (Table 3), which indicates more than 4% of deformation in virgin samples. This justifies the absence of the other 7 tests in the PET340 samples, since even before counting the deformations, the specimens were lost at the beginning of the test execution.

Figure 1b shows all tests on PP500 samples. The strain rates were all linear and the results were very close to the relation between tensile load and tensile strength according to the condition of Table 3. Among 10%T and 20%T of the creep results in virgin sample, data from samples degraded in the laboratory (400 and 800 hours) and field (12 months) under
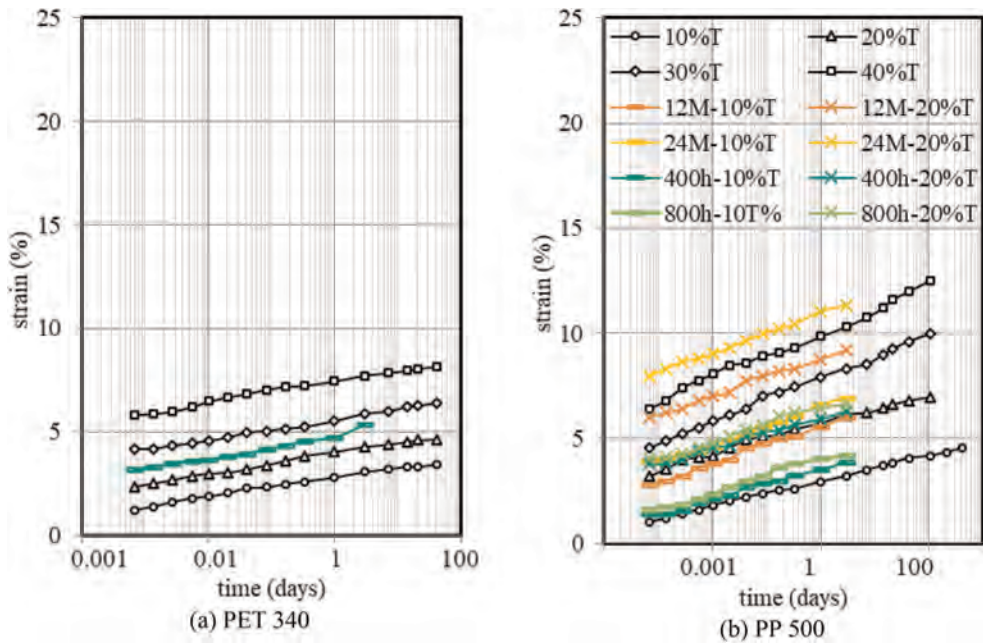
Figure 1. Mean curve of tensile strength (T) and deformation (for geotextile by different conditions. (a) PET 340 (b) PP 500.

10%T are observed. Another set of data were between 20%T and 30%T of the creep results, including samples degraded in the field (24 months) under 10%T, as well as samples degraded in the laboratory (400 and 800 hours) under 20%T. Finally, the data obtained by samples degraded in the field at 12 and 24 months under 20%T was of 30%T-40%T and above 40%T, respectively.

It is important to highlight that these results are a safe and fast way to obtain geotextile de-formations under creep and radiation exposure. In this way, it is possible to estimate the deformations in the field by determining the ultraviolet radiation absorbed over time (Dias Filho *et al.* 2019b) preparing sample by accelerated degradation in the laboratory. Then, the test is carried out as presented in this paper for example (following the 3-day test proposal by Dias Filho *et al.* 2019a). However, it is believed that the deformations will be smaller than those obtained in this paper, since the exposure of the geotextile in the project does not cause accumulated ultraviolet radiation immediately, and consequently, the loading of the geo-textiles as well as the development of creep stage 1 and 2 will be gradual. Therefore, the deformations tend to increase and as the ultraviolet radiation accumulates over time, the response will be a fluence curve that varies between the response of virgin and degraded samples.

4 CONCLUSIONS

The study paper presented fluence results of intact samples and under different conditions of ultraviolet degradation in the field and laboratory.

Evaluation of the data from only 3 days of testing yielded reliable results and according with Dias Filho *et al.* (2019a) can for achieving fast, efficient and findings show that short-term data measurements can be safely extrapolated to obtain long-term durability estimates for the material, in accordance with deformation limits defined by a project.

A susceptibility of polyester to degradation by ultraviolet radiation was also observed in relation to polypropylene. This may be related to the possibility of stabilizers in the PP samples. The retained tensile strength of 10% from PET 340 and 45% from PP500 demonstrate this.

In the creep of samples produced by PET, despite showing generally good creep resistance, the only result indicated an increase in deformations and a possible indication of stage 3, confirming how much radiation degradation actually contributed to this behavior. Meanwhile, PP samples increased their strains according the relation tensile load and tensile strength. The results show that the creep response followed according to the stiffness of the degraded samples.

Finally, this study is relevant because contributes to a discussion of the effect of degradation and creep act in conjunction in routine applications of geosynthetic materials. Therefore, this paper contributes to the study of durability of geotextiles, based on the comparison between the variation of mechanical properties of degraded and virgin material, and which have different applications in civil, geotechnical and environmental projects.

REFERENCES

ABNT NBR 15226, 2005. *Geosynthetics – Determination of Tensile Creep and Creep Rupture Behaviour*. ABNT, Rio de Janeiro, RJ, Brazil.

Achereiner, F., Engelsing, K., Bastian, M. & Heidemeyer, P. 2013. Accelerated Creep Testing of Polymers using the Stepped Isothermal Method. *Polymer Testing*. 32(3): 447–454. https://doi.org/10.1016/j.polymertesting.2013.01.014

ASTM D4355, 2002. Standard Test Method for Deterioration of Geotextiles by Exposure to Light, Moisture and Heat in a Xenon Arc Type Apparatus. *ASTM International*, West Conshohocken, PA, USA.

ASTM D5035-11, 2015. Standard Test Method for Breaking Force and Elongation of Textile Fabrics (Strip Method). *ASTM*, West Conshohocken, PA, USA.

ASTM D5199, 2012. Standard Test Method for Measuring the Nominal Thickness of Geosynthetics. *ASTM*, West Conshohocken, PA, USA.

ASTM D5262, 2017. Standard Test Method for Evaluating the Unconfined Tension Creep and Creep Rupture Behavior of Geosynthetics. *American Society for Testing and Materials*, West Conshohocken, Pennsylvania, USA.

ASTM D5970, 2021. Standard Test Method for Deterioration of Geotextiles from Outdoor Exposure. *American Society for Testing and Materials*, West Conshohocken

Balakrishnan, S. & Viswanadham, B.V.S. 2017. Evaluation of Tensile Load-strain Characteristics of Geogrids Through In-Soil Tensile Tests. *Geotextile and. Geomembranes*. 45(1): 35–44. https://doi.org/10.1016/j.geotexmem.2016.07.002

Bathurst, R.J., Huang, B. & Allen, T.M. 2012. Interpretation of Laboratory Creep Testing for Reliability-Based Analysis and Load and Resistance Factor Design (LRFD) Calibration. *Geosynthics International*. 19 (1), 39–53. https://doi.org/10.1680/gein.2012.19.1.39

Dias Filho, J. L. E., & Maia, P. C. A. 2021. A Non-conventional Durability Test for Simulating Creep of Geosynthetics Under Accelerated Degradation. *International Journal of Geosynthetics and Ground Engineering*. 7:65. https://doi.org/10.1007/s40891-021-00310-w

Dias Filho, J. L. E., Corrêa, B. R. F. & de Almeida Maia, P. C. 2022. Stress-strain Behavior of Geotextile: A Proposed New Indirect Calculation using the Static Puncture Test (CBR test). *Geotextiles and Geomembranes*. 50(1):167–173. https:// doi.org/10.1016/j.geotexmem.2021.10.001

Dias Filho, J. L. E., Maia, P. C. A. & Xavier, G. C. 2019a. A Short-term Model for Extrapolating Unconfined Creep Deformation Data for Woven Geotextiles. *Geotextiles and Geomembranes*, 47(6): 792–797. https:// doi.org/10.1016/j.geotexmem.2019.103492

Dias Filho, J. L. E., Maia, P. C. A. & Xavier, G. C. 2019b. Spectrophotometry as a Tool for Characterizing Durability of Woven Geotextiles. *Geotextiles and Geomembranes*. 47(4): 577–585. https://doi.org/10.1016/j.geotexmem.2019.02.002

França, F.A.N. & Bueno, B.S., 2011. Creep Behavior of Geosynthetics using Confined-accelerated Tests. *Geosynthics International*. 18(5): 242–254. https://doi.org/10.1680/gein.2011.18.5.242

Guimarães M. G. A., Vidal D. M., Urashima D. C. & Castro C. A. C. 2017. Degradation of Polypropylene Woven Geotextile: Tensile Creep and Weathering. *Geosynthics International*. 24(2): 213–223. https://doi.org/10.1680/ jgein.16.00029

INMET, 2105. *Annual Historical Data*. Available in: <https://portal.inmet.gov.br/dadoshistoricos>.

ISO 13434, 2016. *Geotextiles and Geotextile-Related Products - Determination of Tensile Creep and Creep Rupture Behaviour*. ISO, Geneva, Switzerland.

Kongkitkul, W., Chantachot, T. & Tatsuoka, F., 2014. Simulation of Geosynthetic Load-strain-time Behaviour by the Non-linear Three-component Model. *Geosynthetics International*. 21 (4): 244–255. https://doi.org/10.1680/gein.14.00012

Liu, K.W., Rowe, R.K., Su, Q., Liu, B. & Yang, Z., 2017. Long-term Reinforcement Strains for Column Supported Embankments with Viscous Reinforcement by FEM. *Geotextetile and Geomembranes*. 45(4): 307–319. https://doi.org/10.1016/j.geotexmem.2017.04.003

Naftchali, F. M. & Bathurst, R. J. 2021. Influence of Geosynthetic Stiffness on Analytical Solutions for Reinforced Fill Over Void. *Geosynthics International*. 0(0): 1–13. https://doi.org/10.1680/jgein.21.00015a

Nuntapanich, N., Kongkitkul, W., Tatsuoka, F., Jongpradist, P., 2018. Prediction of Creep Behaviour From Load Relaxation Behaviour of Polymer Geogrids. *Geosynthetics International*. 25(3): 334–349. https://doi.org/10.1680/jgein.18.00011

Pinho-Lopes, M., Paula, A.M. & Lopes, M.L., 2018. Long-term Response and Design of Two Geosynthetics: Effect of Field Installation Damage. *Geosynthetics International*. 25(1): 98–117. https://doi.org/10.1680/ jgein.17.00036

Plácido, R., Portelinha, F.H.M. & Futai, M.M. 2018. Field and Laboratory Time-dependent Behaviors of Geotextiles in Reinforced Soil Walls. *Geosynthetics International*. 25(2): 215–229. https://doi.org/10.1680/ jgein.18.00003

Zhao, L.S., Zhou, W.H., Geng, X., Yuen, K.V. & Fatahi, B., 2019. A Closed-form Solution for Column-Supported Embankments with Geosynthetic Reinforcement. *Geotextetile and Geomembranes*. 47 (3):389–401. https://doi.org/10.1016/j.geotexmem.2019.01.006

Zhao, Y., Lu, Z., Yao, H., Hu, H., Li, X., & Tang, Y. (2021). A Fast and Precise Methodology of Creep Master Curve Construction for Geosynthetics Based on Stepped Isothermal Method (SIM). *Geotextiles and Geomembranes*. 49(4): 952–962. https://doi.org/10.1016/j.geotexmem.2021.01.005

Design requirements and long-term performance of multi-component coated GCLs

K.P. von Maubeuge
NAUE GmbH & Co. KG, Espelkamp, Germany

A. Shahkolahi
Global Synthetics, Brisbane, Australia

ABSTRACT: This paper will touch mainly geosynthetic clay liners (GCLs) and the recent development of multi-component GCLs in landfill applications and show their benefits. GCLs are mostly needle-punched, fibre-reinforced composites that combine two durable outer layers and an intermediate uniform core of high-swelling powder sodium bentonite clay, which acts as the barrier component. These uniform needle-punched GCLs form a direction-independent shear strength transferring sealing barrier. When the bentonite core hydrates with fresh water, the bentonite swells and forms a low permeability gel layer, which outperforms traditional, thick compacted clay liners, due to the bentonite's ability to self-seal and re-heal. GCL improvements, since the invention of needle-punched GCLs in 1987 and contribution to the understanding and adoption of GCLs in engineering and construction, have been numerous. This paper will discuss the new GCL technology, the advantages of the polymer coating added to the GCL, the current test results, the applications where such GCL products are ideally used and the necessary design considerations.

1 INSTRUCTIONS

Needle-punched GCLs can be either single component or multi component. In multi-component GCLs, either a thin plastic barrier is attached to one geotextile component of the GCL (Laminated GCL) or a durable polyolefin polymer is firmly coated to the slit-film woven geotextile component of the GCL (Coated GCL). This development enables GCLs to challenge particular site conditions where the use of GCLs has previously been limited. The following definitions are currently being used in GRI-GCL5 specification and ASTM D35 terminology: (a) Multi-component GCL, a GCL with an attached film, coating, or membrane decreasing the hydraulic conductivity or protecting the clay core or both. (b) Laminated GCL, a GCL product with at least one geofilm or geomembrane layer superimposed and bonded to the GCL by an adhesive usually under heat and pressure. (c) Coated GCL, a GCL product with at least one layer of a synthetic substance applied to the GCL as a fluid and allowed to solidify. In general, multicomponent GCLs can be used in all applications where long-term sealing barriers are requested. These applications can include landfill caps and cover systems, landfill base sealing systems near coastal areas, tailing dams or in oil and gas tank farms where hydrocarbons may be present for example.

2 DESIGNING WITH MULTI-COMPONENT GCLS

Although using single component GCLs has solved many challenges and made using clay liners possible in many applications, there are still some potential risks and design challenges

807

related to GCLs including gas permeation, ion exchange, root penetration, bentonite desiccation in low confinement areas or applications with high temperature gradient (e.g. brine ponds, etc.), downslope bentonite erosion, internal erosion and/or bentonite piping, and effect of critical liquids. Multi-component GCLs have been developed to overcome these risks by either reducing or eliminating the risk completely. The multi-component GCL is most effective when at least one of these issues is an important project criterion. With its multiple variables, multi-component GCLs offer economical, long-term barrier solutions that are ideal for a wide range of sealing applications.

When designing with multi-component GCLs to replace a traditional composite lining system, there is a need to focus on specific design issues to ensure the functionality of the final design. These can include but are not limited to the following topics.

2.1 Gas barrier

In applications in which the GCL has to perform immediately as a gas barrier (e.g., landfill cap), the porous bentonite core might not have time to fully hydrate with water and fulfil its sealing performance due to immediate gas migration. Applications of this nature include the waterproofing of underground structures, landfill caps, and other applications in which the GCL is installed over an active source of gas production. The coating/film component of the needle-punched multi-component GCL would act as the gas-impermeable barrier, thus allowing the installation and welding of a geomembrane. In applications where no additional barrier is installed in combination with the GCL, such as where a multi-component GCL is replacing the composite lining system, the coating/film will take over the immediate sealing performance against possible penetrating gas. In both cases the sealing of the coated over-laps of the GCL can easily be carried out with a special bituminous tape.

2.2 Barriers against ion exchange

If there is a supply of free available calcium or magnesium or other polyvalent cations from the surrounding soil, fluids and soils containing leachable cations to the sodium bentonite of a GCL, an ionic exchange within the bentonite can occur over a time in a very short period of time (Egloffstein 2000; Egloffstein et al. 2002). If it does, the clay structure of the GCL core can be affected, which might impact its swelling capacity and the hydraulic conductivity performance. Investigations by Rowe and Abdelatty (2012) has shown considerable increase in the hydraulic conductivity of the GCL within less than a year when in direct contact with the subgrade with high calcium content.

Using calcium bentonite instead as the sealing core in a GCL, even with a higher mass per unit area (e.g., 8 to 10kg), is not a suitable option. Published results (Henken-Mellies 2010; Mueller-Kirchenbauer et al. 2010) have shown that the hydraulic conductivity results of field exposed calcium bentonite are far higher than ion-exchanged sodium bentonite GCLs.

In applications with soils that have a high concentration of free available leachable cations, a coated GCL is an ideal solution. The thin coating, facing the source of exchangeable cations, acts as a barrier and protects the sodium bentonite sealing core of the GCL. A Full-scale field trial was conducted by Hosney and Rowe (2014) on different GCL materials used to line the capping of a tailings dam, to investigate the effect of cation exchange between the tailings and GCL on the long-term performance and hydraulic conductivity of the GCL. Test results on the exhumed GCL products showed no change in the permeability and hydraulic conductivity (K) of the multicomponent GCL with a coating/film facing the tailings, while there was a high increase in the hydraulic conductivity of the normal GCL (without coating/film) due to the Ion exchange with the tailing, which increased the K value of that GCL (GCL A) to higher than acceptable limit in few months.

2.3 *Increasing resistance against bentonite desiccation in low confinement areas*

As the GCL is installed in a dry condition, the performance of the bentonite in the GCL will depend on the hydration of the bentonite. Eberle and von Maubeuge (1998) have reported a moisture content of 100% in less than 24 hours and 140% after 60 days, when placed over sand with a moisture content of approx. 9%.

Low confinement areas include locations with zero confinement such as exposed batters, below geomembrane wrinkles and areas with not enough cover soil to protect the GCL against desiccation. As an example, field and laboratory tests suggest a thickness of 0.75m to 1m for the cover soil in landfill caps and similar application such as tailings dam closures (Hosney & Kerry 2014; Müller-Kirchenbauer *et al.* 2010; von Maubeuge & Lenze 2007). Especially when the GCL is used as a single liner, the thickness of the cover material is suggested to be at least 1m (Müller-Kirchenbauer *et al.* 2010). Hoor and Rowe (2013) research results showed that in a composite liner application, if the liner temperatures is less than 40 degrees, overburden stress is more than 150kpa and there is no wrinkles in the geomembrane, the risk of desiccation will be low. Those results also showed that for lower stresses ($< 100kPa$), desiccation can occur for liner temperature of less than 40 degrees even without wrinkles (due to thermal gradient).

If this is not acceptable for the designed application, a multi-component GCL should be used with the coating facing the direction of expected desiccation. In most cases, this will be the upper side of the GCL. The upside-facing coating of the GCL would prevent moisture escape and allow the bentonite to stay hydrated and act as a barrier, even in arid areas or under very low confining stresses. Boley and Höppner (2014) investigated the desiccation effectiveness of a coated GCL. The initial bentonite water content (prior to saturation) was about 9.3%. After 19 days of saturation, the water content amounted to 133%. After this period, the surrounding conditions were set to constant 40°C and a relative humidity of 40% to allow the investigation of desiccation over a fine sand layer. In the first two weeks after achieving full hydration, a water content loss of approximately 2% was recorded. For the subsequent 213 days the water loss remained nearly constant with an average loss of about 0.11% per week. After 230 days of constant desiccation, the water content was 126.5%. Therefore, during this period a total water loss of 6.5% was noticed. Other than in field where a moisture uptake from the subgrade or from water condensate could occur (due to changing temperature conditions), in these tests there was absolutely no possibility for the bentonite to absorb any additional water, so that these results represent an unrealistic worst-case event.

Due to the mechanism of desiccation protection in multi-component GCLs, these products can be used with less confinement (less total cover soil, e.g. 500mm in a landfill cap) compare to single component GCLs where about 1.0m of cover soil is required. This will not only reduce the cost of supply and placement of cover materials, but also will lead to increase in the landfill volume and capacity in applications such as landfill caps (Figure 10).

2.4 *Root penetration protection*

Roots can penetrate into the GCL seeking water. They can extract water from bentonite. Field investigations by Benson *et al.* (2007) have shown root penetration into the GCL under 760mm of cover soil. Using a multicomponent GCL with the coating against the direction of potential root growth can protect the hydrated bentonite core from root penetration - thus, maintaining a high bentonite moisture content and a high level of safety and performance. Test results in accordance with DIN CEN/TS 14416: Geosynthetic barriers - Test method for determining the resistance to roots which have verified that coated GCLs are resistance against root penetration, even though their overlaps.

2.5 *Increasing resistance against downslope bentonite erosion*

According to full scale field study by Rowe *et al.* (2014), GCLs are at risk of downslope bentonite erosion when used in a composite liner being exposed for few months. This is the process where

the moisture content of the GCL evaporates and concentrates underneath the geomembrane wrinkles during the day (hot hours) and condenses again at night (cold hours) into the GCL surface and washes down the bentonite. Same field investigations and field study by Rowe *et al.* (2014) the only GCL with no evidence of bentonite erosion even after 28 months was the multi-component GCL, with the coating facing upwards (Figure 14). The presence of the coating will prevent moisture evaporation which is the source of downslope bentonite erosion issue.

2.6 *Controlling internal bentonite erosion and piping resistance under high water gradients*

When placed over coarse grain soils or other open structures (such as geonets), a question remains as to whether bentonite extrusion or piping can occur under high hydraulic water conditions. Though needle-punched GCLs with scrim-reinforced nonwovens will provide under laboratory conditions the best performance against bentonite erosion (Rowe & Orsini 2003), the highest safety against this on-site condition involves the attachment of a polymer coating against the slit-film woven side of the GCL. According to *GRI GCL5: Design Considerations for Geosynthetic Clay Liners (GCLs) in Various Applications*, the bentonite erosion issue is somewhat mitigated when using a GM/GCL composite or multicomponent GCL instead of a GCL by itself. Bentonite erosion with the coated side facing against the porous subgrade is now virtually impossible, even under high and extreme hydraulic conditions. The long-term sealing performance of the polymer coated GCL is ensured.

2.7 *Resistance to differential settlements*

Geosynthetic clay liners (GCLs) are hydraulic barriers used as single liners or as apart of a composite lining in various applications, such as landfill caps, base seals, canal liners or in environmental protection applications and in some applications might be subject to settlement. In order to investigate the behavior of GCLs settlement conditions and hydraulic pressure, experiments were performed (Boley & Höppner 2014) using two different GCLs as test materials under different test conditions (saturated or air-dried GCLs, coating facing the water pressure or on the outstream side, GCLs with or without mechanical damages (manual holes), GCLs with or without overlap). The experimental results have showed that GCLs have three different forms of failure: 1) holes forming and expanding; 2) tearing of coating; 3) separation of overlap. In summary, the maximum stretching e_{max} [%] of the GCL in these simulated settlement tests under hydraulic pressure was 13–21% for Coated GCL with 200 g/m2 of coating, 17–22% for Coated GCL with 500 g/m2 of coating, 11–18% for dry GCL, and 16–22% for hydrated GCL.

2.8 *Interface shear stability*

For slope designs, the critical friction plane needs to be investigated with the site materials and is typically confirmed with multiple shear box tests. This is true of nearly all materials considered in slope applications, such as soil, GCLs, other geosynthetics used on slopes, etc.

Where needed, coated GCLs with dimpled/structured surface should be used to provide a high interface friction with the cover layer (Figure 17). Various tests results have confirmed a high interface shear and friction angle between the structured coating and the cover soil, in the range of 30–40 degrees depending on the soil type and testing conditions. Of course, interface friction test needs to be conducted with specific soil for any project individually to determine the exact value. For steeper slopes, the use of geogrid reinforcement can significantly improve the slope friction angle.

2.9 *Durability of the coating*

In most cases it is recommended that the additional barrier component of the GCL can fulfil a long service life. For this reason, the polymer barrier should be manufactured with

a chemically resistant polyethylene resin. According to GRI-GCL3, the geofilm/ geomembrane in its as-received condition should be evaluated for durability via the appropriate GRI specification. The polymer coating ($\geq$ 200g/m^2) should be evaluated by incubation in a forced air oven per ASTM D5721 set at 60°C for 50 days. The minimum percent tensile strength retained at break for either MD or XMD, as measured by ASTM D882, should be reported accordingly and must meet or exceed the specification value (85%).

When in service, the coating of the GCL might be subjected to chemical attacks. This is more likely to happen in a landfill base seal. Therefore, it is important to know the general chemical resistance of this additional polymer barrier to well defined chemicals. Manufacturers need to provide the chemical resistance of the polymeric barrier in at least an independent test report.

3 CONCLUSION

The decisions that designers make about the GCL selection must heavily be influenced by the performance and durability of the system. These decisions start with the overall cross-section (e.g. single lining, composite lining or double lining system).

Geosynthetic clay liners (GCLs) are often used as a stand-alone liner or in combination with a geomembrane, where the GCL replaces thick compacted clay liners due to many advantages. By using a multi-component GCL, the single barrier can be improved by combining the advantages of a polymer and a clay barrier.

A multi-component GCL has add-on values: e.g. root protection, desiccation resistance, gas and water impermeability, downslope erosion protection, internal erosion protection, and Ion exchange protection. While a multi-component GCL improves the overall GCL performance as a single lining system, it opens the possibility to use this type of GCL as a composite lining system. The main advantages are lower installation costs, intimate contact between the clay and the polymer barrier with little till zero transmissivity and likely reducing a shear interface issue between these two barriers (not for glued multi-component GCLs). However, the additional thinner barrier component cannot replace a geomembrane.

REFERENCES

ASTM D882 (2018): Standard Test Method for Tensile Properties of Thin Plastic Sheeting, Annual Book of ASTM Standards, *ASTM International*, West Conshohocken, PA, 2011.

Benson, C., Thorstad, P., Jo, H., and Rock, S. (2007): Hydraulic Performance of Geosynthetic Clay Liners in a Landfill Final Cover." *J. Geotech. Geoenviron. Eng.*, 133(7), 814–827.

Boley, C. and Höppner, R. (2014): The Desiccation Process of Geosynthetic Clay Liners above Different Subsoils and Climatic Changes, *10th ICG*, Berlin, Germany.

DIN CEN/TS 14416: *Geosynthetic Barriers - Test Method for Determining the Resistance to Roots.*

Eberle, M.A. and von Maubeuge, K. (1998): Measuring the In-situ Moisture Content of Geosynthetic Clay Liners (GCLs) using Time Domain Reflectometry (TDR), *6th International Conference on Geosynthetics*, Atlanta, 1: 205–210.

Egloffstein, T. A. (2000): Natural Bentonites–influence of the Ion Exchange and Partial Desiccation on Permeability and Self-healing Capacities of Bentonites used in GCLs, *GRI Conference*.

Egloffstein, T. A., von Maubeuge, K. P., Reuter E. (2002): Application of GCLs in Contact with Leachates or Chemical Solutions, *Proc. 7th ICG*, Nice, France: 813–818.

Ehrenberg, H. and von Maubeuge, K.P. (2008): Long-term Shear Strength Testing with Geosynthetic Clay Liners and Geosynthetic Drainage Mats, *Proceedings of 1st Pan American Geosynthetics Conference and Exhibition*, Cancun, Mexico.

Geosynthetic Research Institute (GRI) (2013): GRI – GCL5 Standard Specification for "*Design Considerations for Geosynthetic Clay Liners (GCLs) in Various Applications*", Folsom, Philadelphia.

Geosynthetic Research Institute (GRI) (2015): GRI - GM18 Standard Specification for *"Test Methods, Test Properties and Testing Frequencies for Flexible Polypropylene (fPP and fPP-R) Nonreinforced and Reinforced Geomembranes"*, Folsom, Philadelphia.

Geosynthetic Research Institute (GRI) (2019): GRI - GCL3 Standard Specification for "*Test Methods, Required Properties, and Testing Frequencies of Geosynthetic Clay Liners (GCLs)*", Folsom, Philadelphia.

Geosynthetic Research Institute (GRI) (2021): GRI - GM13 Standard Specification for "Test Methods, Test Properties and Testing Frequency for High Density Polyethylene (HDPE) *Smooth and Textured Geomembranes*", Folsom, Philadelphia.

Geosynthetic Research Institute (GRI) (2021): GRI - GM17 Standard Specification for "*Test Methods, Test Properties and Testing Frequency for Linear Low Density Polyethylene (LLDPE) Smooth and Textured Geomembranes*", Folsom, Philadelphia.

Heerten G. and Quirk C. M. (2008): Superior Solutions with Geosynthetics in Landfill Capping Applications, *Proc. Fourth European Geosynthetics Conference (EuroGeo4)*, Edinburgh.

Henken-Mellies, W.U. (2010): GCL in a Landfill Final Cover: 10-year Record of a Lysimeter Field Test, *3rd International Symposium on Geosynthetic Clay Liners*, Würzburg, Germany.

Hoor A. and Rowe R.K. (2013): Potential for Desiccation of Geosynthetic Clay Liners used in Barrier Systems, *JGGE* 139(10) 1648–1664

Hosney, M. S. & Rowe, R. K. (2014): Performance of Three GCLs Used for Covering Gold Mine Tailings for 4 Years under Field and Laboratory Exposure Conditions. *Geosynthetics International*, 21, No. 3, 197–212.

Lin L. and Benson C., (2000): Effect of Wet-Dry Cycling on Swelling and Hydraulic Conductivity of GCLs, *Journal of Geotechnical and Geoenvironmental Engineering*, Vol. 126, No. 1. pp 40–49. ASCE, ISSN 1090-0241/00/0001-0040–0049.

Mukunoki T., and Take A., (2016): *Visualization of a Desiccated Geosynthetic Clay Liner Due to Dehumidification using Micro-focused X-ray Computed Tomography*, Japanese Geotechnical Society Special Publication 2(53):1853–1858 DOI: 10.3208/jgssp.JPN-050

Müller-Kirchenbauer, A., Blümel, W. and von Maubeuge, K.P. (2010): Performance of Geosynthetic Clay Liners in Landfill Cap Sealing Systems - Physical Processes in the Bentonite Layer during Drying and Rehydration Periods, *3rd International Symposium on Geosynthetic Clay Liners*, Würzburg, Germany.

Rowe R. K., and Abdelatty Kh. (2012): Effect of a Calcium-Rich Soil on the Performance of an Overlying GCL, *Journal of Geotechnical and Geoenvironmental Engineering*, Vol. 138, No. 4, pp 423–431. ISSN 1090-0241/2012/4-423–431/$25.00.

Rowe R.K., Brachman R.W.I., Take A., Rentz A., Ashe L. E. (2016): Field and Laboratory Observations of Down-slope Bentonite Migration in Exposed Composite Liners, *Geotextiles and Geomembranes* 44 (2016) 686–706.

Rowe, R. K. and Orsini, M. K. (2003): Effect of GCL and Subgrade Type on Internal Erosion in GCLs Under High Gradients, *Geotextiles and Geomembranes*, Vol. 21, Issue 1, pp. 1–24.

Rowe, R.K., Ashe, L., Take, W.A., and Brachman, R.W.I. (2014): Factors Affecting the Down-slope Erosion of Bentonite in a GCL. *Geotextiles and Geomembranes*, 42(5).

Rowe, R.K., Garcia, J.D.D., Brachman, R.W.I. and Hosney, M.S. (2022): Moisture Uptake and Loss of GCLs Subjected to Thermal Cycles From Silty Sand Subgrade, *Geosynthetics International* ISSN 1072–6349.

Schubert, W. R. (1987): Bentonite Matting in Composite Lining System, *Geotechnical Practice for Waste Disposal '87*, ASCE Geotechnical Special Publication (13): 784–796.

Stewart, D., von Maubeuge, K. P. (1997): Cost-effective and Efficient Solutions with GCLs for Sealing Operations in the Mining Industry, *Tailings and Mine Waste '97*, Denver 19.

von Maubeuge, K. P., Coulson, J. and Hedrich, F. (2005): *Landfill Cap Design with Geosynthetic Clay Liners, 6th Landfill seminar*, Institute of Waste, Management of Southern Africa (IWMSA).

von Maubeuge, K. P., Lenze, B., (2007): Landfill Cap Design with Geosynthetic Clay Liners, *2nd Portuguese Seminar on Geosynthetics*, 2007.

Status of existing information on installation requirements for sealing products under Nordic conditions (RoUGH Project)

E. Blond
Eric Blond Consultant, Montreal, Canada

M. Leppänen
Tampere University, Tampere, Finland

P. Delmas
SINTEF Advisor, France

C. Recker
Sintef Community, Münster, Germany

ABSTRACT: This paper is part of a series focusing on the use of geosynthetics in Nordic climates. It focuses on sealing applications, while others in this series are addressing general considerations, and other functions of geosynthetics. In this paper, a review of the main concerns and performance requirements associated to the installation of geosynthetics for sealing applications is first proposed. These are essentially based on a review of the current practice, the interview of several installers specializing in the installation of geosynthetics in cold climates and a literature review. A strategy to assess the suitability of Geosynthetic Barriers in sealing applications under Nordic conditions is then proposed. The proposed requirements were drafted by the authors and approved after revisions by a committee constituted of contributors to the ROUGH project. Guideline on the "Use of GeosyntHetics in Nordic conditions" are being prepared and will be published within the next months by the Nordic country's authorities.

1 INTRODUCTION

Geosynthetic Barriers may be damaged during installation or in service, with numbers of leaks per hectare reported in the literature ranging between 0.25 (Gilson-Becks 2019) and 7 (Nosko 2015) for projects where Electrical Leak Location Surveys were specified and conducted. This number may be even higher where no or insufficient quality control is conducted, as reported by Forget (2005). On the other hand, Phaneuf (2001) suggests that 73% of damages in geosynthetic barriers occurs when the soil layers are placed on top of the geomembranes, 24% occurs during geomembrane installation, and 2% occurs during the post construction phase – i.e., that most damages in geosynthetics barriers take place during installation or soil covering.

These studies do not differentiate the environmental conditions that were prevailing during the installation of the Geosynthetic Barriers. However, it is reasonable to consider that the harsher the environmental conditions, the more likely can the liners be damaged, considering the effects of low temperature on soil and geosynthetic material properties, as well as human factors.

In 2018, several Canadian installers were consulted to obtain their opinion on what are the most critical parameters influencing the risk of damages to geosynthetic liners installed in harsh Nordic conditions. From these observations, a series of recommendations were

developed, focusing on design strategies and preferred geosynthetic material properties. These recommendations were approved by a committee constituted of members of the ROUGH project and will eventually be submitted to authorities of European Nordic Countries for consideration.

2 FACTORS AFFECTING CONSTRUCTION UNDER COLD CLIMATE

This section summarizes the key information obtained while interviewing installers used to work in Northern regions of Canada, interviewed in the first quarter of 2018. The interviews were based on a few generic questions, and a general discussion on how to do things better. The information gathered within each interview was then compiled and structured afterward as presented below. More details are available in the RoUGH project report (2022), accessible through Sintef.

2.1 *Design*

Current practice for the selection of geosynthetic barriers and the design of lining systems typically does not include anything addressing winter installation conditions. Usual design considerations such as soil / geosynthetic interaction, durability and chemical compatibility are approached similarly to what is done for installation under mild environmental conditions. However, soil / geosynthetic interaction may be different when products are frozen, which could affect the design of the structure (slopes, cushions, management of differential settlement, etc.).

2.2 *Contracts and costs*

A clause allowing the installer to stop working with no penalty should be included in geomembrane installation contracts, because of the high risks of delays and unexpected problems. A preferred structure of contracts for winter work is based on time + materials, instead of a lump-sum contract, which is typically preferred in the summertime.

Design-built' contracts are also preferred because they favor the development of teams who become used to work together (general contractor, earth work, geosynthetic installers). Contracts given to the lowest bidder are very likely to generate problems for winter work as this approach favors the use of unexperienced workers, while harsh conditions are anticipated. Although this is applicable to any project, it is more critical when installation is done during the winter.

2.3 *Planning*

Coordination between parties is critical for the success of the project. From a contractual standpoint, the geosynthetic installer is a subcontractor to the general contractor, who typically assigns time slots and defines a master schedule. This schedule must be updated regularly, with a good understanding of the concerns associated with the installation of geosynthetics.

The schedule must consider the risk of weather events and ensure they will not affect installation. For example, if snow falling between preparation of a subgrade and laying of the geomembrane must be removed, it may be necessary to re-do all the earth work after snow removal.

External causes of delay must be avoided. This includes contractual delays, material delivery, QA / QC approval by a third party, or other. Planning must account for more equipment failure.

2.4 *Productivity*

Workable hours may be significantly smaller in winter because of the reduced number of daylight hours and harsh work conditions. Hours worked per week may be as low as

10–15 hours (instead of 40+ hours). An overall productivity of 50% is considered a maximum realistic target, hence a project will typically take twice as much time to complete in winter, as opposed to summer. Most important factors affecting productivity include days cut-off because of bad weather, time needed for the crew to warm up periodically, and a slower welding speed.

2.5 *Packaging, storage and handling*

Existing and well-known good practices such as ASTM D4873 offer adequate guidance: sur-elevation of the storage platform, avoiding direct contact with soil, etc. In addition, geosynthetics must be adequately protected from water to avoid requiring storage in a warm enclosure. An excessive amount of water within a roll of geotextile, geocomposite, or Clay Geosynthetic Barrier (GBR-C) must be avoided. A water-filled, frozen geosynthetic can hardly be unrolled, and may require several weeks to thaw.

Good handling and storage practices must be maintained until the rolls are delivered to their final location, immediately before installation. When feasible, last-minute delivery of the products is preferred to minimize risks of damage caused by sensitive packaging and storage issues.

2.6 *Subgrade condition*

The same criteria apply to both frozen and unfrozen soils, which are typically defined by the size of maximum protrusion or discontinuity of the surface. However, it is not always possible to flatten a subgrade already frozen. Hence, many installers prefer avoiding installation of a Polymeric Geosynthetic Barrier (GBR-P) directly on frozen soil, without a thick cushion layer.

The need to remove snow, especially on already-approved subgrades, is determined on a project-by-project basis. Thin layers of snow, up to about 5 centimeters, are typically left in place to avoid damaging the surface. What often dictates the decision to lay a GBR-P on snow and proceed with welding is the risk of having humidity in the welding area at the time of welding, more than the risk of settlement, which can be handled by providing more slack.

2.7 *Material-related issues*

2.7.1 *Slipperiness*
Smooth polyethylene GBR-P becomes extremely slippery under freezing temperatures. As soon as dampness or snowflakes are observed, it is virtually impossible to walk on a smooth GBR-P. Koerner et al. (2019) conducted preliminary laboratory investigations on smooth HDPE GBR-P tested against geotextiles, which confirmed this higher slipperiness at low temperature.

2.7.2 *Weldability at low temperature*
Welding GBR on a frozen substrate is perceived by installers to be overall easier, as long as water remains frozen. However, it requires more preparation, in particular scraping-off traces of ice from the surface of the GBR, which may affect productivity and accidentally damage the GBR. Pre-heating is sometime recommended, but not always: the release of water vapor must be avoided, as vapor could condensate in the welding area and affect the quality of the weld.

The geosynthetic Institute guide GRI GM9 on the welding of polyethylene geomembranes is often cited in bids and construction guidance. It is typically followed by installers, but the proposed minimum welding temperature is sometimes questioned: several factors other than temperature affect the weldability of geomembranes beyond the temperature itself: wind, humidity, snowflakes, water running down from thawing areas, frost condensate, etc.

Overall, there is a consensus that LLDPE is easier to manipulate and to weld than HDPE.

2.7.3 Stiffness

Stiffness may increase significantly at low temperature for some materials, which can create different problems. This affects the ability of the material to lay flat, adding complexity during installation. HDPE can be installed in winter, but the use of more flexible materials such as LLDPE is typically preferred by installers.

Under cold temperature, HDPE geonets are often stiffer than HDPE geomembranes, which heavily affects their ability to lay flat. They exhibit a 'shape memory': they could either unroll or re-roll in unexpected ways, surprising workers and creating a safety concern. They do now warm-up in the sun as quickly as geomembranes. Possible explanations include a higher resin density, a lower surface exposure to solar radiation, and a larger air supply through the ribs which maintain the temperature close to the air temperature.

Unfolding prefabricated panels made using standard grades of PVC may be extremely difficult at low temperatures, if ever possible. Lay-flat of PVC is very poor at low temperature, and corner folds tend to tear easily. There may still be formulations of PVC material offering better behaviors than others, with types of plasticizers better suited to cold temperature installations. Common grades of PVC – i.e., complying with ASTM D7176 – are not suitable for installation in winter.

2.7.4 Brittleness and cold-cracking resistance

Installers have observed that some HDPE GBR-P tend to have a higher sensitivity to cracking under low temperatures than LLDPE GBR-P, which was confirmed by Cornellier (2014).

Many installers favor the use of bituminous GBR (GBR-B) for winter installation. However, surface cracking may still be observed, depending on the temperature and type of material used.

2.7.5 Thermal contraction

Thermal contraction is a well-documented concern for polymeric GBR-P, with thermal expansion coefficients in the range of 10^{-4} mm/mm/°C. Thermal contraction must be considered for projects extended into winter, whether the GBR-P is to remain exposed, or eventually covered by soil. This usually involves adding enough slack in strategic locations.

GBR-B are considered easier in that regard, given their lower coefficient of thermal expansion.

2.8 Backfilling

Backfilling is not under the scope of the installer. However, it is a critical task with respect to the integrity of the structure. Only aggregates exempt of fines must be used to prevent ice from creating an apparent cohesion in the soil: frozen agglomerates can behave like boulders and damage the geosynthetic during backfilling.

Before backfilling, the geomembrane must be secured against wind uplift, which is typically achieved using 'sandbags', using pea gravels instead of sand to avoid creation of hard blocks of icy sand under freezing temperature – these sandbags also behaving like boulders.

2.9 Health and safety

Worker safety must be proactively managed considering the very harsh work environment. Not only accidents are more likely to happen, but an accident happening under very low temperatures must be treated very quickly as the condition of the injured person can deteriorate quickly. A safety-trained employee must be present on-site at all times.

3 GENERAL RECOMMENDATIONS ON THE DESIGN AND THE SELECTION OF GEOSYNTHETIC PRODUCTS

Following the survey of installers and a literature review, a series of recommendations were developed, focusing on design strategies, considering typical service conditions and performance

requirements needed for a lining system to perform adequately. Preferred geosynthetic material properties applicable to GBR-P, GBR-B and GBR-C are presented in the report of the project. They were approved by a committee constituted of members of the RoUGH project and will eventually be submitted to authorities of European Nordic Countries for consideration.

3.1 *Impact of the environmental conditions on the design of the structure*

ISO/TR 18228-9:2022 provides general concepts which can be used to design a lining system and select an adequate GBR. This Technical Report identifies the installation conditions as one of the factors influencing the design. Indeed, installation in winter implies a low temperature, presence of ice and snow, and freeze / thaw cycles which may influence the selection of the type of sealing product (polymer / type, thickness, finish). Installation conditions will also affect the use of complementary products (especially cushions); the thickness of the soil cover; some details of the design itself, such as the characteristics of the slopes (angle and length, presence of berms), due to lower interface friction properties; the installation process (e.g., scheduling, welding strategy); and the quality assurance program (type of control, approval process, use of leak location).

Geosynthetic Barriers may be damaged during installation or in service, and it is a fair assumption to consider that holes may be present on a structure installed in the wintertime.

To reduce leakage rate into the environment while acknowledging that the GBR is more likely to be damaged if installed during winter, engineered, multi-layered lining systems should be preferred to single liners. These engineered lining systems typically include:

- A geotextile protection layer, or cushion, installed above the geosynthetic lining system to protect it from static or dynamic aggregate puncture during backfilling or in service.
- A compacted clay liner (CCL) or a clay geosynthetic barrier (GBR-C) that will create a composite liner when in contact with the geosynthetic barrier.
- Two geosynthetic barriers separated by a geocomposite drain between the primary (upper) and the secondary (lower) barrier, to create a double lining system. This design reduces the head of liquid prevailing on the secondary liner, hence the flow of liquid released into the environment.

Typical structures of composite, double, and double-composite lining systems are depicted in Figure 1. A more detailed discussion on the benefits and limitations of multi-layered geosynthetic barrier systems can be found in Rowe (2005).
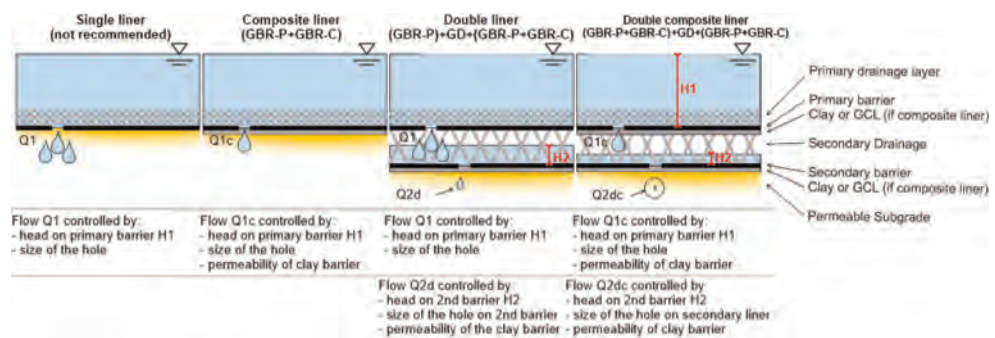
Figure 1. Typical structures of composite and double lining systems.

3.2 *Aspects related to the raw material/structure of the products*

The ease of installation and long-term performance of geosynthetics are partially defined by how much the products will be exposed to cold weather, and at what period of their life:

transportation, storage, installation, and/or during their service life. E.g., if the product is temperature-sensitive but intended to be covered by a thick layer of soil protecting it from cold temperatures immediately after installation, it is theoretically possible to store it at a warm temperature and wait until weather permits its installation and soil cover. The possibility to use a product should therefore be assessed on a case-by-case basis, considering the flexibility of construction schedule and likelihood of encountering extreme environmental events during the projected construction period. Figure 2 summarizes the various issues that must be considered for any given project.

The following classes of service were defined. They reflect the different exposures that could be experienced by the product, once it has been installed under harsh environmental conditions. Each of them reflects a type of stress that may affect the selection of the geosynthetic barrier, and/or that may be mitigated with adequate measures during storage, installation and backfilling.

- Class 1 – Exposed applications: The geosynthetic barrier system is intended to be left exposed in a Nordic environment. It will experience extreme temperatures, temperature cycles, ice and snow, and it will NOT be covered by a material providing a confining stress while in service. Examples of such application include liquid containment or secondary containment structures where the geosynthetic barrier is left exposed.
- Class 2 – Shallow cover: The geosynthetic barrier will be permanently covered by a material providing some confinement stress, but no thermal protection – such as a shallow layer of gravel. The geosynthetic barrier system will be exposed to the same temperature conditions as for Class 1, but the confining stress will prevent temperature-induced contraction/expansion, offer a protection against impact, prevent wind uplift, etc. Examples of such applications include road ditches, as well as ponds where the geosynthetic barrier could be covered by 300 to 500 mm of gravel.
- Class 3 – Fully covered applications: The geosynthetic barrier is intended to be covered by a thick layer of soil and will never be exposed to extreme environmental conditions once installation is completed. In these applications, exposure of the geosynthetic barrier to freezing temperatures is limited to the construction, and its behavior will be essentially independent from the environmental conditions thereafter. Examples of applications include landfills and other waste containment structures where a sufficient thickness of material is installed rapidly, some heap leach pads. Depending on the service and operating conditions of the structure, class 3 may first have to be considered as class 2 for a certain duration.

1. The GBR must preserve its integrity during transportation and storage
2. It must be possible to unroll the GBR in place under freezing temperatures, on a frozen soil subgrade, without damaging it
3. Worker safety must not be affected by a behaviour of the GBR
4. Welding of GBR-P or GBR-B to assemble panels or to repair a tear must be possible under the anticipated environmental conditions.
5. The GBR must not be affected by the installation of the next layer, such as the soil cover (when applicable)
6. The long-term performance of the GBR must not be affected by the installation process
7. The (installed) GBR must exhibit adequate long-term properties when exposed to cold temperatures during service

Figure 2. Issues to consider when selecting geosynthetic barriers installed under freezing temperatures.

4 DISCUSSION AND CONCLUSIONS

Installation of geosynthetic lining systems under harsh Nordic conditions may not always be prevented. In this study, the current practices and concerns associated with such conditions

of installation have been assessed, interviewing those doing the work, and typically holding liability for these projects: the installers. A literature review was also conducted. Based on the information gathered, general recommendations were proposed to maximize the success of these structures.

- Designers should acknowledge there is a higher risk of damage to GBRs when they are installed under harsh conditions. The use of composite and double lining systems should therefore be favored to mitigate these risks, and limit seepage into the environment.
- The integrity of the product must be preserved throughout the installation process. Seven steps were identified as requiring attention, from transportation and storage to the effects of low temperature on the product in the long run.
- The suitability of a product to serve as a barrier when installed in Nordic conditions should be evaluated considering its actual exposure. Three classes of application are proposed: exposed, covered by a shallow layer of soil, or fully covered.

Recommendations were developed and are available in the detailed report of the RoUGH project. They will be used to prepare Guideline on the "Use of GeosyntHetics in Nordic conditions", that will eventually be published by the Nordic country's authorities.

The authors like to have a special thanks the Traffic authority in Finland (FTIA), the Norwegian Public Roads Administration, the Swedish Transport Administration, GRK Infra Oy and the 12 manufacturers for their active participation.

REFERENCES

Cornellier, Tan (2014): A Case Study on the Installation of LLDPE Geomembranes in Cold Weather; *Proceedings of Geosynthetics Mining Solutions* 2014, Vancouver

Delmas P., Want A., Uotinen V.M., Vaslestad J., Griwell F., Recker C. (2023): ROUGH- Recommendations for the Use of GeosyntHetics in Nordic conditions, *Proceedings of the 12th Internal Conference on Geosynthetics*, Roma, September 2023 (in press)

Forget, B., Rollin, A.L., Jacquelin, T., 2005. Lessons learned from 10 Year of Leak Detection Surveys on Geomembranes. In: *Proceedings of the Sardinia Conference*.

Geosynthetic Institute: GRI Guide GRI GM9

Gilson-Beck, A (2019): 'Controlling Leakage Through Installed Geomembranes using Electrical Leak Location', *Geotextiles and Geomembranes*, Vol 47 (2019) 697–710

ISO/TR 18228-9:2022: Design Using Geosynthetics — Part 9: Barriers

Koerner M.R., Koerner G.R., Koerner R.M. (2019): Veneer Instability of a Frozen Geomembrane-to-Geotextile Interface; *Proceedings of the 2019 Geosynthetics Conference*, Houston.

Nosko, V; Crowther J. (2015): "Can the Holy Grail of the Geosynthetics Industry "Zero Leakage" be Achieved by Arc Testing?" *Proceedings of Geosynthetics 2015 Conference*, Portland, Oregon

Rough project, 2022. Recommendations for the Use of GeosyntHetics in Nordic conditions. SINTEF. *Part 1– Tests on damage during installation at low temperatures. Function: reinforcement stabilisation, filtration, drainage, (53 p) & Part 2–Status of existing information on installation requirements for sealing products (GBR-P, GBR-B and GBR-C) under Nordic conditions (45 p)*.

Rowe, R. K. (2005): 'Long-term Performance of Contaminant Barrier Systems', *Géotechnique 55*, No. 9

Reinforced walls and slopes

Impact of geogrid arrangement on the deformational response of geosynthetic reinforced soil – integral bridge systems

D. Naughton
RPS Consulting Engineers, Galway, and formerly Atlantic Technological University, Sligo, Ireland

P.J. Naughton
Atlantic Technological University Sligo, Ireland

ABSTRACT: Plaxis 2D was used to investigate the deformational response of a geosynthetic reinforced soil – integral bridge system with three different geogrid arrangements. The deformational response was found to be independent of the length of geogrid, independent of having secondary geogrid layers directly beneath the bank seat and also independent of vertical geogrid spacing near the base of the wall. The response was found to be only marginally dependent on the direction that the horizontal load was first applied. Applying the horizontal load towards the abutment resulted in inward movement of the wall face and the greatest rotation of the bank seat. Applying the horizontal load away from the abutment resulted in outward movement of the wall face and a slight reduction in the rotation of the bank seat in all models.

1 INTRODUCTION

An integral bridge is a continuous geo-structural system initially developed to overcome some of the problems associated with conventional bridges, i.e., those with expansion joints and bearings (Dicleli 2000). Conventional bridges require periodic maintenance resulting in increased cost and the possibility of extended road closures (Springman *et al.* 1996). However, although integral bridges are relatively cheaper; faster to construct; and require less maintenance, they come with their own problems (Flener 2004). As the structure moves as one unit, temperature fluctuations result in increased earth pressures on the face of the abutment and, over time, settlement of the soil at the abutment-embankment interface. In winter, when temperatures decrease, the superstructure contracts and moves away from the structure, while in summer, when temperatures increase, the superstructure expands and moves towards the soil. This phenomenon of cyclic temperature induced creep, otherwise known as strain ratchetting, can result in much greater earth pressures than the structure was designed for (Horvath 2005).

An alternative to the traditional integral bridge is the geosynthetic reinforced soil – integral bridge system (GRS-IBS). This system is constructed using alternating layers of compacted granular fill and geosynthetic reinforcement, typically in the form of a geogrid. Many GRS-IBS abutments consist of a segmental modular block wall with the bridge beams resting directly on top of the structure, with no bearing or bank seat provided (Adams & Nicks 2018).

The Federal Highways Administration (FHWA) (Adams *et al.* 2011) developed a dedicated design method for GRS-IBS. However, Adams *et al.* (2011) showed that this method was heavily empirically based and only provided a 'recipe' for design.

In this study, the plane-strain modelling software Plaxis 2D, Version 20, (2021) was used to determine the influence that different geogrid arrangements had on the deformational response of a GRS-IBS abutment.

2 METHODOLOGY

2.1 *GRS-IBS abutment validation model and results*

The Plaxis 2D model was initially validated against data from a full-scale instrumented GRS-IBS abutment reported by Ardah *et al.* (2017, 2021) to ensure that the Plaxis 2D model adequately captured the deformational response of a GRS-IBS system. The validation model was discussed in detail by Naughton (2022) and Naughton & Naughton (2022). Overall, reasonable agreement was found between the measured values and those predicted by Plaxis 2D. During validation it was found that fixing the lowest masonry block in both the horizontal and vertical directions, greatly improved the overall correlation with the validation model, but did result in an underestimation of the horizontal deformation at the bottom of the wall. This is discussed in detail by Naughton & Naughton (2022).

2.2 *Parametric study*

A parametric study was conducted to assess the impact the geogrid arrangement in the reinforced block had on the deformational response of a GRS-IBS abutment subject to both vertical and horizontal loading.

The numerical model developed in this study was based on the Maree Michel Bridge reported on by Ardah *et al.* (2017, 2021) and which was used in the validation model. The model consisted of 19 segmental blocks, 400mm wide x 200mm high, forming the abutment wall, Figure 1. Primary geogrid layers, 2.66m long, were placed between each of the segmental blocks, with secondary geogrid layers, 1.6m long, introduced at mid-height vertically at the top six blocks, Figure 1. The segmental blocks were set vertically above a reinforced soil foundation (RSF), which had a width of 2.83m and was 0.46m deep. Foundation soil was present beneath the RSF, with backfill soil extending 9.20m from the back face of the segmental block wall. The water table was not considered during the modelling process in this study. The bank seat was 1.2m wide and located 205mm from the back of the facing blocks.
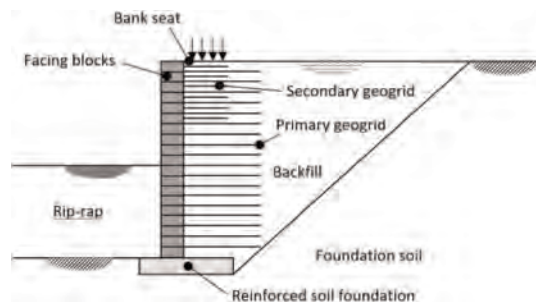
Figure 1.   Schematic of validation model used in this study.

The soil elements of the Plaxis 2D model were developed using a plain-strain model with 15-node triangular elements. The model was horizontally fixed along both the vertical extremities and the base of the model. Additionally, a line displacement was introduced along the lower boundary of the lowest block. This allowed this block to be fixed in place or free to move as required in the modelling process. A medium mesh was used for the model in this study with a tolerated error of 1%. In contrast to Ardah *et al.* (2017, 2021) the wall was wished-in-place.

The Hardening Soil model was used for the backfill soil, the Mohr-Coulomb model for the foundation soil and the Linear Elastic model for the masonry blocks and rip rap at the front of the wall. The geogrid was modelled using geogrid elements in Plaxis 2D, with an elastic normal stiffness, EA, of 600kN/m and an axial tension, NP, of 80kN/m. Interfaces were applied

between the geogrid and backfill soil, the geogrid and facing blocks and at the horizontal interface between facing blocks. The model properties are listed in Table 1. In all models the geogrid layer extended to the front face of the blocks. In this case, the interface between blocks was determined by the geogrid – facing block interaction properties, Table 1. At locations with no geogrid between facing blocks, an interface strength reduction ratio of 0.8 was applied.

The bridge load consisted of a vertical component of 100kN/m and a horizontal component of 85kN/m, determined in accordance with IS EN 1991-2 using Load Model 1 (LM1) (Anon., 2006).

This study investigated three geogrid arrangements, Figure 2. Model 1, Figure 2(a), examined the influence of primary geogrid length on performance. Three lengths of primary geogrid were investigated; notably 1.66m, 2.16m and 2.66m. The secondary geogrid length remained constant at 1.6m. Model 2, Figure 2(b) had the secondary geogrid layers removed. The primary geogrid had a length of 2.66m and was spaced every 0.2m vertically. Model 3, Figure 2 (c) had the secondary geogrid removed and also six alternative layers of primary geogrid at the base of the wall removed. In this model the length of the geogrid was 2.66m, with the layers spaced 0.2m vertically at the top of the wall and 0.4m vertically at the base of the wall.

Table 1. Model parameters for GRS-IBS model.

Material	γ (kN/m^3)	E (MPa)	E_{50}^{ref} (MPa)	E_{oed}^{ref} (MPa)	E_{ur}^{ref} (MPa)	ν	$e_{initial}$	c (kPa)	φ_p (°)	ψ (°)
Facing block	12.5	30000	–	–	–	0	0.5	–	–	–
Backfill	19	–	34	25.6	103.2	0.2	0.5	20	51	21
Foundation soil	18.7	30	–	–	–	0.2	0.5	17.7	27	0
Rip-rap	22	50	–	–	–	0.25	0.5	–	–	–
Geogrid-Backfill Interface	–	–	–	–	–	–	–	8.6	40.4	0
Geogrid / Facing Block Interface	–	–	–	–	–	–	–	7	34	0
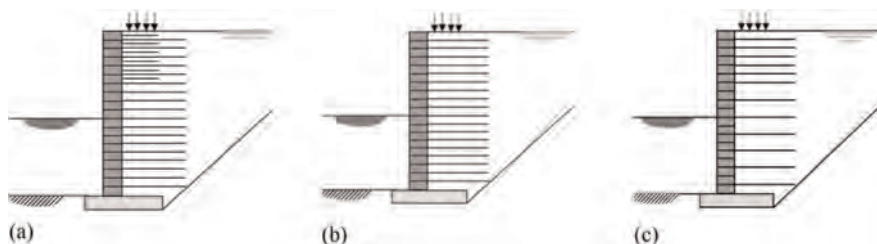
Figure 2. Geogrid Arrangements (a) Model 1, primary and secondary geogrid layers in place, (b) Model 2, secondary geogrid layers removed (c) Model 3, secondary geogrid and six alternative layers of primary geogrid at the base of the wall removed.

During the modelling process a horizontal load was first applied at the location of the bank seat in one direction and then in the other. This was to replicate the cyclic nature of the horizontal loads. The vertical load from the bank seat remained constant throughout the modelling process.

Two cases were examined, Case A and Case B. For Case A, the load was firstly applied towards the abutment and then away from the abutment. For Case B, the reverse occurred with the load firstly applied away from the abutment and then towards the abutment. The model was divided into three phases with Phase 1 (P1) representing pre-loading, with just the vertical load in place and no horizontal load. For Case A, Phase 2 (P2) represented the horizontal load being applied towards the abutment, while Phase 3 (P3) represented the horizontal load being applied away from the abutment. For Case B, P2 and P3 were reversed, with the horizontal load first applied away from the abutment (P3) and then towards the abutment (P2) respectively.

3 RESULTS AND DISCUSSION

The predicted results from the Plaxis models are presented in terms of the horizontal displacement of the wall face and the vertical displacement of the bank seat. For each load phase the displacements refer to the predicted values after application of the loadings for that phase.

3.1 *Impact of primary geogrid length, model 1*

The impact of the primary geogrid length on the deformational response of the structure was investigated for three geogrid lengths, 1.66m, 2.16m and 2.66m. The horizontal displacement of the wall face and vertical displacement of the bank seat are presented in Figure 3(a) and (b) respectively for Case A, where the horizontal load was first applied towards the abutment (P2) and then away from the abutment (P3).

When the horizontal load was applied towards the abutment, the wall face displaced inwards and the bank seat rotated away from the load application direction, Figure 3(a). Overall, very little difference in horizontal and vertical displacements were observed between the shortest and longest primary geogrid lengths (1.66m & 2.66m respectively). Rotation of the bank seat was also largely independent of the geogrid length, Figure 3(b).

When the horizontal load direction was reversed, and it acted away from the abutment (P3), larger horizontal displacements, with outward movement of the wall face, were observed. Shorter geogrid lengths resulted in slightly larger outward horizontal displacements, Figure 3(a). Slightly larger rotations of the bank seat were observed when the load was applied towards the abutment (P2) and smaller rotations when the load was applied away from the abutment (P3), Figure 3(b). However, the rotation of the bank seat only changed marginally when the load direction was reversed.
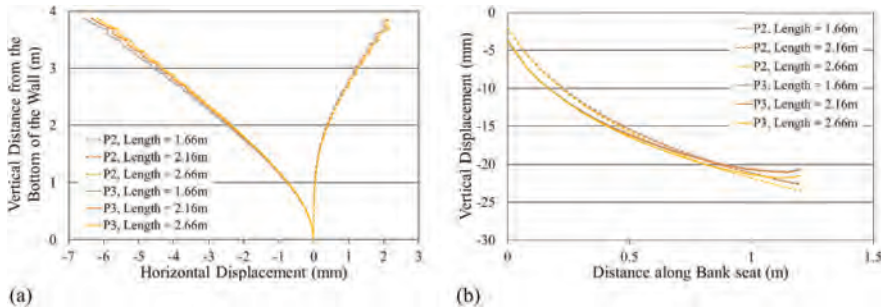
Figure 3. (a) Horizontal displacement for model 1 for Case A and (b) Vertical displacement of bank seat in Model 1 for Case A.

3.2 *Impact of removing secondary geogrid layers, model 2*

The impact of secondary geogrid layers on the deformational response of the structure was investigated in Model 2, Figure 2(b). The six layers of secondary geogrid at the top of the wall were removed and the response compared to that observed in Model 1 which contained the secondary geogrid layers. The horizontal displacement of the wall and the vertical displacement of the bank seat for Case A and B are presented in Figure 4.

Applying the horizontal load towards the abutment in both Case A and B resulted in inward movement of the wall face, Figure 4(a) and rotation of the bank seat, Figure 4(b). When the horizontal load was reversed and acted away from the abutment, outward movement of the wall face was observed accompanied by a slight reduction in the rotation of the bank seat. Removal of the secondary geogrid layers resulted in both a slight reduction in the inward movement of the wall when the horizontal load was applied towards the abutment and a slight reduction in the rotation of the bank seat for all directions of the horizontal

load. Applying the horizontal load away from the abutment resulted in the same outward displacement of the wall for all cases examined. The deformational response of the structure was largely independent of the first direction that the horizontal load was applied.

Overall, the data indicated that there was little advantage in including secondary geogrid layers in the top of the wall directly beneath the bank seat to control horizontal displacement of the wall face and vertical displacement of the bank seat.
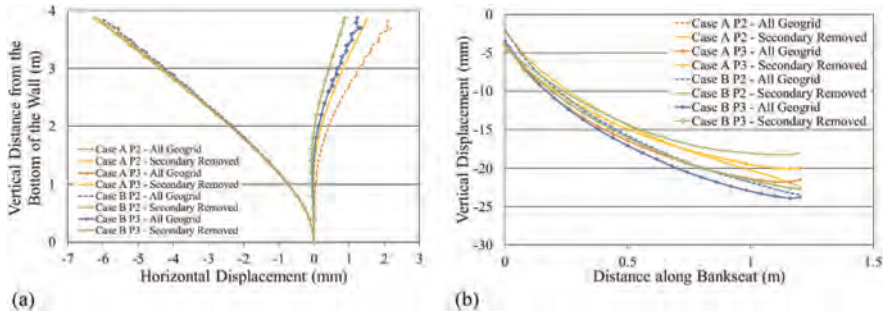
Figure 4. (a) Horizontal displacement for model 2 for Case A and B and (b) Vertical displacement of bank seat in Model 2 for Case A and B.

3.3 *Impact of removing secondary and six alternative layers of primary geogrid at the base of the wall, model 3*

In Model 3 both the secondary geogrid layers and alternative layers of primary geogrid layers near the base of the wall were removed, Figure 2(c). The deformational response of Model 3 was compared with that of Model 1 to assess the impact of removing the geogrid layers. The horizontal displacement of the wall and the vertical displacement of the bank seat for Case A and B are presented in Figure 5.

When the horizontal load was applied away from the abutment almost identical horizontal displacement of the wall face was observed for both Case A and B, Figure 5(a), indicating that the first direction that the horizontal load was applied is not significant in terms of wall displacement. Applying the horizontal load first towards the abutment, Case A, resulted in slightly larger inward displacements of the wall face than Case B. The horizontal displacement of the wall face was largely independent of the number of geogrid layers in the wall.

Like in Model 2, applying the horizontal load towards the abutment resulted in slightly greater rotation of the bank seat, while reversing the direction of the horizontal load resulted in a reduction in the bank seat rotation, Figure 5(b). No significant difference in the rotation
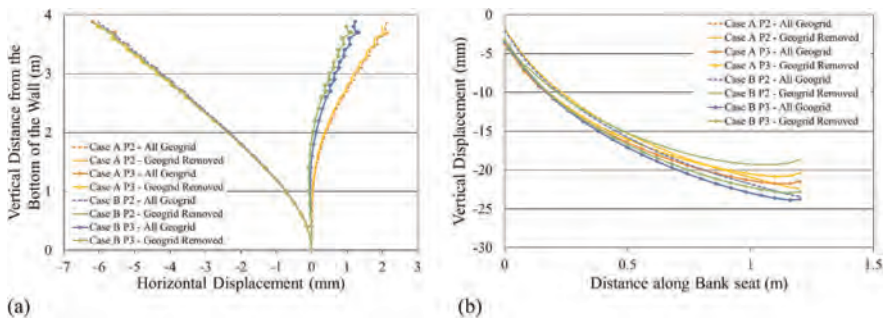
Figure 5. (a) Horizontal displacement for model 3 for Case A and B and (b) Vertical displacement of bank seat in Model 3 for Case A and B.

of the bank seat was observed between Model 1, containing all the geogrid layers, and Model 3, with both the secondary geogrid and alternative layers of primary geogrid removed.

4 CONCLUSIONS

This study investigated the deformational response of a GRS-IBS with different geogrid configurations. The deformational response was assessed in terms of the horizontal displacement of the wall facing and the vertical displacement under the bank seat. Three models were investigated; Model 1 examined the influence of geogrid length, Model 2 the influence of secondary geogrid layers near the top of the wall and Model 3 the impact of removing the secondary geogrid and alternative layers of geogrid near the base of the wall.

Overall, a similar trend was observed in the three models investigated. The deformational response was found to be independent of the length of geogrid, the presence of secondary geogrid layers directly beneath the bank seat and also independent of removing alternative layers of primary geogrid layers near the base of the wall.

The response was also found to be only marginally dependent on the direction that the horizontal load was first applied. Applying the horizontal load towards the abutment resulted in inward movement of the wall face and the greatest rotation of the bank seat. Reversing the direction of the horizontal load, with it acting away from the abutment, resulted in outward movement of the wall face and a slight reduction in the rotation of the bank seat in all models.

REFERENCES

Adams, M. & Nicks, J. 2018. *Design and Construction Guidelines for Geosynthetic Reinforced Soil Abutments and Integrated Bridge Systems*, McLean, VA: Federal Highway Administration.

Adams, M. *et al.*, 2011. *Geosynthetic Reinforced Soil Integrated Bridge System Synthesis Report - FHWA-HRT-11-027*, McLean, VA: Federal Highway Administration.

Anonomus. 2006. *EN 1991-2 Actions on Structures - Part 2: Traffic Loads on Bridges*, European Committee for Standardization, 2006.

Ardah, A., Abu-Farsakh, M. & Voyiadjis, G. 2017. Numerical Evaluation of the Performance of a Geosynthetic Reinforced Soil-Integrated Bridge System (GRS-IBS) under different loading conditions. *Geotextiles and Geomembranes*, 45, pp. 558–569.

Ardah, A., Abu-Farsakh, M. & Voyiadjis, G. 2021. Numerical Parametric Study of Geosynthetic Reinforced Soil Integrated Bridge System (GRS-IBS). *Geotextiles and Geomembranes*, 49, pp. 289–303.

Dicleli, M. 2000. Simplified Model for Computer-Aided Analysis of Integral Bridges. *Journal of Bridge Engineering*, 5(3).

Flener, E. B. 2004. *Soil-Structure Interaction for Integral Bridges and Culverts*, Stockholm: Department of Civil and Architectural Engineering.

Horvath, J. S., 2005. *Integral-Abutment Bridges: Geotechnical Problems and Solutions Using Geosynthetics and Ground Improvement*. Baltimore, Federal Highway Administration (FHwA).

Naughton, D. & Naughton, P.J. 2022. The Influence of Horizontal Load on the Predicted Behaviour of Geosynthetic Reinforced Soil – Integrated Bridge Systems (GRS-IBS). *Proceedings of the Civil Engineering Research in Ireland Conference*, Dublin, 25 – 26 August, page 294 – 299.

Naughton, D. 2022. *A Study on the Effect of Horizontal Loading on Geosynthetic Reinforced Soil Integral Bridge Systems*. MEng thesis, Alantic Technological University, unpublished.

Plaxis 2D. 2021. *Bentley – Plaxis General Information Manual*. Delft, Netherlands: Bentley Systems Inc.

Springman, S., Norrish, A. & Ng, C. 1996. *TRL Report 146 - Cyclic Loading of Sand Behind Integral Bridge Abutments*, Berkshire: Transport Research Laboratory.

Reinforced soil walls/slopes and piling platforms for a causeway route over very soft soils using geogrids–HS2 Thame Valley Viaduct, Aylesbury, United Kingdom

Pablo Vazquez Bernardini & Patricia Guerra-Escobar
Geosynthetics Ltd, Leicestershire, UK

ABSTRACT: The High Speed Two (HS2) is the new high-speed railway for Britain. Thame Valley Viaduct is part of HS2 Phase One from London to West Midlands. In order to cross the Thame River and adjacent flood plain area, The Thame Valley Viaduct made up of 36 spans an overall length of 880m it is proposed. The foundation for the viaduct involves large diameter bored piles. The temporary works to construct the causeway over very soft soils consist of 18no. piling platforms with approximate 15,000m2 and an adjacent haul road connecting the platforms with an overall length of 1,000 m. The ground conditions generally consists of very soft to soft alluvium with undrained shear strengths of 0kPa-36kPa. It is proposed to support the perimeter of the piling platforms with a 45°/70° reinforced soil wall using layers of geogrids wrapped. A design is also required for the 18no. piling platforms.

1 INTRODUCTION

1.1 *Description & location*

The High Speed Two (HS2) is the new high-speed railway for Britain. It will connect eight of Britain's ten largest cities and their regions. Faster, easier and more reliable travel will put more opportunities within reach for millions of people for work, business and leisure.

Thame Valley Viaduct is part of HS2 Phase One from London to West Midlands. The Thame Valley Viaduct is located in the Northern Vale to the north-west of Aylesbury. It travels across the River Thame within a broad, shallow floodplain.

In order to cross the Thame River and adjacent flood plain area, the Thame Valley Viaduct made up of 36 spans an overall length of 880 metres it is proposed. The foundation for the viaduct involves large diameter bored piles. The viaduct will carry HS2 trains at speeds of up to 360km/h between London, Birmingham and the North.

1.2 *Problem geometry*

The design of temporary works to construct the causeway over very soft soils consist of 18no. piling platforms with approximate 15,000m2 and an adjacent haul road connecting the platforms with an overall length of 1,000 metres.

It is proposed to support the perimeter of the piling platforms and the western side of the haul road with a 45° reinforced soil slopes using layers of Biaxial geogrids wrapped around the face with permanent erosion control blanket pinned to the slope face.

The eastern side of the haul road is former via a 70° reinforced soil wall using topsoil filled geotextile bags with horizontal layers of Uniaxial geogrids wraparound in the face. The maximum slope height is 2.5m.

2 DESIGN CONSIDERATIONS

2.1 *Existing ground conditions*

The ground conditions along the causeway route, as revealed by the Ground Investigation Report and borehole logs, generally consists of superficial deposits described as very soft to soft Alluvium/Head Deposits which are encountered to between 1.2m and 4.9m below existing ground level. The Alluvium is generally underlain by firm to stiff Clay of the Ampthill Formation.

SPT "N" values of alluvium were typically 1-8, however close to the northern side of the River Thame, SPT "N" values of 0 were recorded right through the alluvium down to the Ampthill Clay at approximately 4mbgl.

The undrained shear strength for the Alluvium was derived from the results of SPTs with undrained shear strengths between 4.5kPa–36kPa.

It should be noted that SPT "N" values in soft Alluvium are not the most appropriate test requiring correlations to determine the undrained shear strength due to the low blow counts determined in the material and the material sensitivity. Direct methods such as insitu shear vanes or testing on thin wall tube samples will provide more indicative results.

There was no laboratory testing provided to confirm the undrained shear strength of the alluvium and Ampthill Clay at shallow depths. Hand shear vane testing was carried out within the upper 1m of ground at 28no. locations along the causeway. The tests were repeated 3 times at each location and recorded average undrained shear strengths of 19kPa–176kPa.

2.2 *Ground model*

In order to perform the calculations, we have assumed the following geotechnical properties:

Table 1. Ground model used for design.

Description	Location	Unit weight (kN/m^3)	Total Stress Analysis Undrained shear strength–Cu (kPa)	Effective Stress Analysis Effective Angle of Shearing Resistance – Ø'	Effective Cohesion – C' (kPa)
Blended 10/100mm angular Fill	Reinforced/ Retained Fill/ Basal layer	20	–	34°	0
Soft Clay (Alluvium/ Head deposits)	From existing ground level to a maximum depth of 4m bgl.	16	Case 1) 40 (0.75m deep basal starter layer analysis) Case 2) 20 (1.5m deep basal starter layer analysis)	23°	0
Firm Ampthill Clay	4m bgl.	18	50	27°	0

2.3 Existing groundwater conditions

Groundwater was recorded at shallow depths (i.e., <1.0m below existing ground level) according to the borehole logs provided. It should be noted that groundwater levels can be subject to seasonal, tidal and other fluctuations and should not be taken as constant.

The causeway is to be located close to the River Thame and we have been advised that the causeway should be designed for a 1 in 20 year flood event, which is at a level of 70.8m AOD (i.e. 400m below finished haul road/piling platform level).

Analysis has therefore been carried out considering water level at the 1:20 year flood level and also at existing ground level. To allow the floodwater to move freely a series of culverts were proposed crossing the Haul Road in between each piling working platform.

2.4 Surcharges on the piling platform with 45° slopes

To design the 18no. piling platforms with 45° slopes with a maximum height of 2.50m, we have considered a superimpose dead load of 8kPa applied at a distance of 20m from the crest. To take into account the thickness of the granular material for the working platform on top of the wall.

In addition, the 182 tons piling rig Bauer BG45 was considered with an equivalent uniform bearing pressure of 227 kPa at 4.0m spacing with 2no tracks 4.51x1m. The maximum loading considered was approximate 1500 kN.

Construction traffic was considered as a variable load in accordance with Table 2:

Table 2. Summary of variable loads on piling platform with 45° slopes.

Type Traffic	Loading Details (Worst Case)
General Traffic <60 Tons	20kPa over full platform area
Volvo A60 (Laden)	70T load of rear axles over area of 2.14 x 3.884m (85 kPa or 327kN/m over 3.884m) 2no. Wheel point loads of 17.5T over 800x800 bearing area (275kPa) at 3m centres

A minimum 3.0m exclusion zone is to be provided around the edge of the piling platform where no surcharge loading greater than 20kPa is permitted at any time. When the piling rig is operating no plant loading of greater than 15kPa us permitted in this 3m exclusion zone.

2.5 Surcharges on the Haul Road with 70° slopes

To design the Haul Road with 70 slopes with a maximum height of 2.50m and overall length of 1,000 metres, we have considered a superimpose dead load for the road pavement and the safety barriers in accordance with Table 3.

Table 3. Summary of dead loads on Haul Road with 70° slopes.

Item	Width (m)	Slope Crest Setback (m)	Load (kPa)
VCB Foundation Cradle	0.95	0	7.8
VCB	0.45	0.25	15
Road Pavement	11.5	0.70	4.2
Road Pavement Found	11.5	0.70	4.5

Construction traffic was considered as a variable load in accordance with Table 4:

Table 4. Summary of variable loads on Haul Road with 70° slopes.

Type Traffic	Loading Details (Worst Case)
General Traffic <60 Tons	20kPa over full platform area
Cranes up to 750T	99T (6 axles) over 8.6x3m (38kPa or 115kN/m over 3m)
Low Loaders	75T (5 axles) over 6x2.55m (50kPa or 125kN/m over 2.55m)
Bauer BG45 Piling Rig	2no tracks 4.51x1m w/ uniform pressure of 227 kPa at 4m spacing
Volvo A60 (Laden)	70T load of rear axles over area of 2.14 x 3.884m (85 kPa or 327kN/m over 3.884m)
	2no. Wheel point loads of 17.5T over 800x800 bearing area (275kPa) at 3m centres

A minimum 2.5m exclusion zone is to be provided around the edge of the haul road where no surcharge loading greater than 20kPa is permitted at any time.

In addition to the surcharge loads on the surface of the piling platform/ haul road as advised above, a stability check was performed on the proposed Komatsu PC360LC-11 excavator lifting the proposed culverts into place on the starter layer with 2no tracks 3.1×0.7m with uniform pressure of 135 kPa with a maximum 7,100kg lift.

3 DESIGN SOLUTION

3.1 Design method and standards

The design of the Reinforced Soil Wall/Slopes considered the surcharges applied on top and behind the wall, the pressure of the soil at the back and all the properties of the soils (reinforced soil, retained soil, foundation soil). The internal and global stability were considered for the design.

The internal stability design process determined the amount of soil reinforcement required to maintain integrity of the reinforced soil mass and considers tensile and bond failure of the reinforcement. Internal stability checks have been carried out in accordance with the methods allowed in Section 7: Reinforced Slopes, of BS 8006-1:2010+A1:2016 Code of Practice for Strengthened / reinforced soils and other fills. Checks were made for the ultimate limit Combinations A and B and serviceability limit states Combination C.

The global stability analyses were carried out in accordance with BSEN1997-1:2004 – Eurocode7 (EC7) and the UK National Annex. In particular, the analyses are in accordance to BS EN 1997-1 (Eurocode 7) using Design Approach 1, Combination 1 with partial factors on loading and Design Approach 1, Combination 2 with partial factors on soil parameters and variable unfavourable loads. The global stability was performed on the overall structure including the retained soil and the foundation soil using slope stability methods such as Bishop's modified method of slices.

The internal stability analyses were carried out using ReSlope, Geosynthetic Reinforced Steep Slopes from ADAMA Engineering, Inc software version 4.0. Additionally, the internal and global stability analyses were verified using GEO5- MSE Wall, Analysis of mechanically stabilized slopes software version 2021.49.

The depth required for the piling platform has been determined based on the Tenax reinforced soil raft method which uses layers of Tenax biaxial geogrid to improve the load spread through the platform to the subgrade and hence reduce the bearing stress on the subgrade. This method has been verified by experimental testing and experience as advised in TWf guidance 2019 "Design of granular working platforms for construction plant".

3.2 *Final design*

The analysis of the piling working platform and the Haul Road indicated that due the presence of soft superficial deposits in form of Alluvium with Undrained shear strength (Cu) of ≥ 20kPa to <40kPa a minimum 1500mm deep basal starter layer is required, reinforced with layers of Biaxial geogrid Tenax LBO HM4. Additionally, due to the presence of soft soils and to satisfy the global stability analysis in accordance with Eurocode 7, the perimeter of the piling platform requires sheet piling to cut off rotation slips within the Alluvium.

The internal & global stability analysis of the 45° reinforced soil slope supporting the piling platforms requires layers of Biaxial geogrid Tenax LBO HM4 reinforcement at maximum 420mm vertical spacings with a horizontal length of minimum 11.5m.

The analysis of the piling working platform and the Haul Road indicated that due the presence of soft superficial deposits in form of Alluvium with Undrained shear strength (Cu) of ≥ 40kPa a minimum 750mm deep basal starter layer is required, reinforced with layers of Biaxial Tenax LBO HM4. The internal & global stability analysis of the 70° reinforced soil slope supporting the Haul Road requires layers of Uniaxial geogrid Stratagrid SGU60 reinforcement at maximum 420mm vertical spacings with a horizontal length of minimum 8.0m.

4   CONCLUSIONS

The use of geogrids reinforcement was the most cost-effective and environmental solution to construct the temporary causeway to enable the installation of the piles for the Thame Valley Viaduct.

With the Internal Stability analysis, it was possible to determine the required strength of the geogrids, the spacing and the minimum length the layers of reinforcement to meet the equilibrium for each possible failure mechanism. Once the strength, length and spacing of reinforcement were determined, it was required to check the external stability of the reinforced block against overturning, sliding and bearing capacity failure. The use of biaxial geogrid Tenax LBO HM4 improves the load distribution through geogrid-aggregate interlocking mechanism and the use of uniaxial geogrid Stratagrid SGU60 helped to stabilise the 70° & 45° reinforced soil slope.

The geogrid reinforcement solution for a 70° reinforced soil slope supporting the Haul Road and the 45° reinforced soil slope supporting the piling platforms with maximum height of 2.50m, vastly helped in the reduction of CO_2 footprint during construction by reducing the imported reinforced concrete wall, the on-site excavation and reducing the time taken within the construction process.

REFERENCES

BAM Ritchies. 2018 – *Ground Investigation Report. Factual Account Appendix 1.0 Exploratory Hole Logs.* BAX.HS02. P04. Surrey. UK.

BRE. 2004. *Working Platforms for Tracked Plant: Good Practice Guide to the Design, Installation, Maintenance and Repair of Ground-supported Working Platforms.* Watford. UK.

British Standard, BS EN 1997-1:2004. *Eurocode 7. Geotechnical Design – Part1.* British Standard Institution, London. UK

British Standard, BS8002:1994. *Code of Practice for Earth Retaining Structures.* British Standard Institution, London. UK

British Standard, BS8006-1:2010. *Code of Practice for the Strengthened/ Reinforced Soils and other Fills.* British Standard Institution, London. UK

British Standard, PD 6694-1:2011. *Recommendations for the Design of Structures Subject to Traffic Loading to BS EN 1997-1:2004.* British Standard Institution, London. UK

Geoman, 2021. *Temporary Works–Thame Valley Viaduct Reinforced Earth Design*. Reference: 21-6250. Belfast. UK

High Speed Two (HS2) Limited, 2020. *Thame Valley Viaduct Engagement Event*. 1MC06-CEK-IN-PRE-CS04_CL19-000001. UK

Highway Works MCHW. Feb 2016. *Volume 1 Specification for Highway Works Series 600 – Earthworks*. UK

Koerner, R. 2005. *Designing with Geosynthetics* 5th Edition, Pearson. USA.

Leshchinsky D. & Tatsuoka F. 2013. Performance, Design and Redundancy. *Geosynthetics Magazine*.

Strata. 2015. Use of Geogrids for Soil Reinforcement. *Manual for Reinforced Walls and Slopes, Embankment on Soft Soils and Foundation Reinforcement*.

Temporary Works Forum, 2019. *Working Platforms Design of Granular Working Platforms for Construction Plant, A Guide to Good Practice*. London . UK.

TENAX SpA. 2003, *The Design of Reinforced Soil Walls Using Tenax Geogrids*. Vigano, Italy

TENAX SpA. 2011, Reinforced Soil Raft Concept. *Design Guidance*. Vigano, Italy

The use of polyester geotextiles in civil engineering

M. Peroński*, P. Radziemski* & K. Gęsicki*
ViaCon, Poland

ABSTRACT: In the article, the author presents the implementation of construction with the application of polyester woven geotextiles. By using of woven geotextiles, it's possible to reduce significantly the time and the cost of construction. The author presents selected projects to inspire other engineers to use polyester woven geotextiles in their everyday design work or work on the construction side. The application of PES woven geotextiles solves many technical problems while being trivial and easy to build.

1 INTRODUCTION

The technological development of the production of polyester woven geotextiles has made them extremely competitive compared to other geosynthetics. The weaving technology and the production of yarns allow to produce products with very high tensile strengths at a low cost of production. Commonly used are PES woven geotextiles with tensile strength: 100, 200, 300, 600 or 1000 kN/m. A few years ago materials with such parameters were very expensive and produced only on special order. Currently, polyester geotextiles have practically replaced polypropylene or polyethylene geosynthetics on the Polish market due to better mechanical properties and lower production cost.

It should be also noted that polyester woven geotextiles are characterized by a lower elongation at break than polypropylene products. The average elongation at break of polyester woven geotextiles is 10% and polypropylene products 18%. For this reason, designers started more likely to use polyester woven geotextiles. Another reason, why polyester products are designed, is the development of knowledge about them. Today, polyester geotextiles are the so-called qualified geosynthetics. A full range of tests are available, what enable to determine long term design strength, as well as durability and resistance in acid or alkaline environment.

Moreover, these materials are resistant to damage during backfilling (e.g. high static puncture resistance). Therefore, it is very common to use geotextiles together with a crushed backfill aggregate. As a result, geotextiles are widely used in Poland not only in applications with natural aggregate, but also using crushed aggregate backfill. Of course, due to the geological structure of Poland, the backfill is more often made of natural aggregates, which is more available compared to crushed aggregate transported from the mountains – the south of Poland. The above-described features of polyester woven geotextiles caused the use of them in the solutions presented below. Examples of realized projects confirm that technology with use of polyester woven textiles was the best choose from technical and economical point of view.

*Corresponding Authors: mariusz.peronski@viacon.pl, pawel.radziemski@viacon.pl and krzysztof.gesicki@viacon.pl

2 TEMPORARY CONSTRUCTION ON RAILWAY 286

2.1 *Description of the technical problem*

The extension of the Ścinawka Średnia station along the 286 Railway Line assumed the overhaul of the railway viaduct at km 13.665. Due to the lack of consent for the closure of train traffic, the overhaul of the viaduct assumed staging of works – the works were to be completed in half.

First stage (Figure 1) assumed the construction of steel sheet piles GU 16N, 15.0 m and 16.0 m long, with 10m long anchors 116 kN/pcs load capacity each. Then, rebar works were performed in the excavation as a part of the overhaul of the railway viaduct together with the construction of a retaining structure reinforced with polyester woven geotextiles. Retaining structure made of geosynthetics in these case was to provides the stability of the trackway during second stage of works.

Second stage (Figure 2) included the dismantling of the track and transferring the traffic over the retaining structure made of geosynthetics. Then, the excavation works were performed in front of the reinforced soil together with the disassembly of the anchors and further work on the railway viaduct. The sheet piling was not removed.
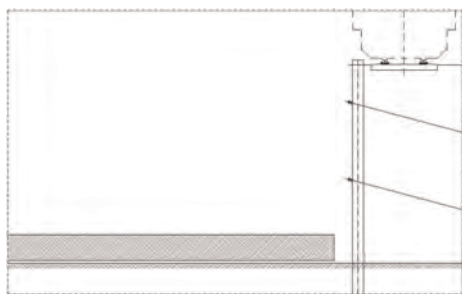
Figure 1.   Stage I.
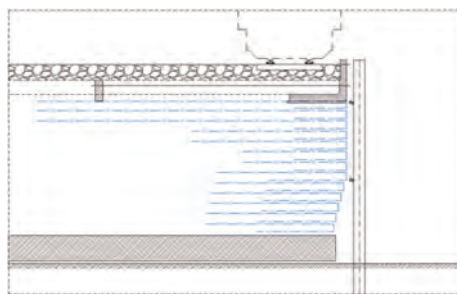
Figure 2.   Stage II.

2.2 *Design assumptions*

It was assumed that the reinforced soil structure will be temporary and that is why the long-term tensile strength has been reduced to only 5 years (through appropriate reduction factors due to creep). Polyester woven geotextile with high tensile strength in MD direction was used. Live load – model LM71 (Figure 3). The height of analysed structure is 6.40m and geometry is according to Figure 2. The backfill was made of non-cohesive soils with a minimum internal friction angle of $\varphi = 35°$. The soil laying below are silty clay soil with internal friction angle $\varphi = 14.2°$ and cohesion 15 kPa.

Figure 3.   Live load example – LM71.

Reinforced soil structure design assumed that the geotextile cannot press the sheet piling. It was based on the assumption that the allowed elongation of the reinforcement could not exceed 2%. After determining the strength in individual reinforcement layers, it was possible to choose the appropriate strength of the geotextiles and finally determine the technological empty space between the sheet piling and the face of the reinforced soil structure. Empty space size was designed to cumulate allowed elongation of geotextile (SLS).

The design was carried out in static condition according to Eurocode 7 (EN 1997-1) using partial safety factor concept. Using this concept, it is assumed that the structure is stable when overdesign factor is ≥ 1. For the stability check it was required to verify the structure using design approach A2 + M2 + R3. The characteristics of PES woven: long term design tensile strength based for 5 years rheological coefficient (temporary structure). Of the attention to difficult structure long term strength has been calculated with safety factor value 1.3. Serviceability Limit State (SLS) was calculated to tensile strength by 2% elongation and reduced to 5 years long term strength.

During calculations, local and global stability of a reinforced soil structure was checked. The following factors were taken into account: overturning, sliding, reinforcement pull-off, ultimate load-bearing capacity of the reinforcement. At the end global stability calculations was checked separately – where critical slip failure was beyond the structure.
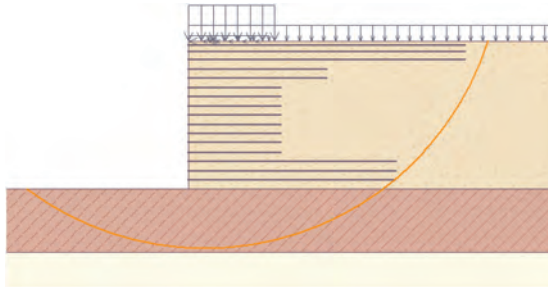
Figure 4.   Critical slip failure.

The calculations were made using the GEO5 – Reinforced Embankments computer program based on the assumptions of the standard: Eurocode 7 and calculation sheets
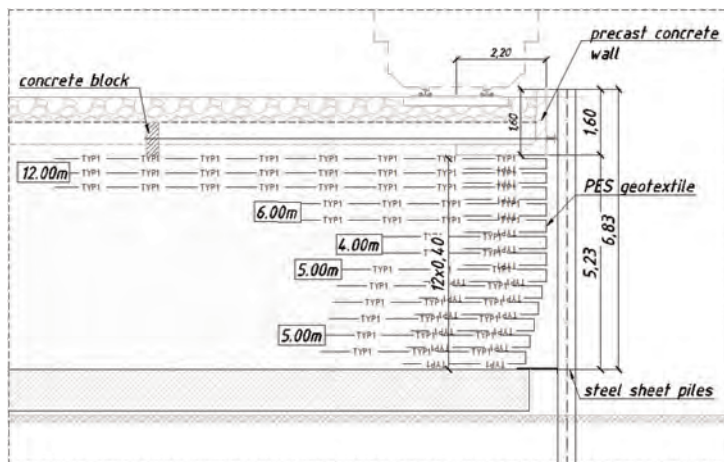
Figure 5.   Temporary retaining.

integrating forces depending on the zone in which the reinforcement is located (zones: active and passive).

A major design problem was the location of the live load next to the face of the retaining structure- the load is shown in Figure 2. To prevent displacements of the rail truck decided to design precast retaining wall a 1.6m height.

The design solution is presented in Figure 5.

2.3 *Summary*

Live load test after end of construction works confirmed the correctness of the assumptions and design calculations. During the test geodetic measurements of the wall and tracks were done. Displacement and track deformation observed were in the limit. The use of soil reinforced with polyester geotextiles made it possible to replace the classic anchoring of the sheet piling in the second stage of works. In this case, it accelerated significantly the construction works and allowed for significant financial savings.

Figure 6.   Construction works.

3   TECHNOLOGICAL ROAD – BYPASS

3.1   *Description of the technical problem*

As part of the construction of a new road viaduct over the Railway Line no. 009 Warszawa Wschodnia – Gdańsk Główny along the road in Tczew, it was necessary to build a bypass road for the construction period. Embankment was designed as a soil reinforced with polyester geotextiles. It was alternative solution to MSEW structure (concrete panels as facing).

3.2   *Design assumptions. Methods of calculation*

It has been assumed that the reinforced embankment will be a temporary structure as bypass around the road for the time of the of the railway viaduct construction. The construction time was planned for 2 years (determining the long term design strength of geotextiles).

In order to optimize the solution, the retaining walls were replaced with a reinforced embankment with a slope angle of $80°$. This solution was cheaper and faster to implement. The normal section through the embankment is shown in Figure 7.

Determining the stability of the embankment, the load with the A-class load was assumed (according to PN-85/ S-10030) The geological condition is good. Subsoil is build of loose sands. For backfill used the same soil but with proper density. Before project calculations existing soil was tested and internal friction angle was determined. The soil properties has shown in Table 1.

Table 1.   Geotechnical characteristics of the soils.

Soil type	Properties		
	Internal friction angle, φ (°)	Cohesion, c (kPa)	Unit weight, γ (kN/m^3)
Subsoil	29	0	18
Backfill	34	0	19.5

3.3   Stability calculations

MSE stability checks were performed using the proprietary software GEO5 – Reinforced Embankments. The most unfavorable cross section was chosen to evaluate the system. During calculation, local and global stability of a reinforced soil structure was checked. The following factors were taken into account: overturning, sliding, reinforcement pull-off, ultimate load-bearing capacity of the reinforcement and displacement. For reinforcement has been used PES geotextile with strength 150/ 50kN/m. MSE wall sliding safety factor is 2.6, overturning safety factor is 3.0 and bearing capacity safety factor 2.1. This calculations does not cover the global stability calculations as the global stability – it was checked separately in GGU Stability program. Stability analysis with circular surfaces according to Bishop's Method showed Factor of Safety of 1.2.

Geometry of structure with vertical specimen of reinforcement has shown in Figure 7.
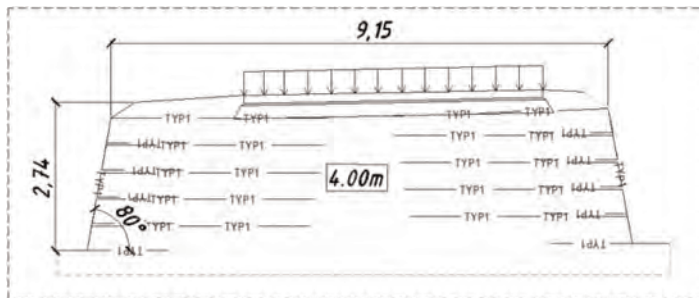
Figure 7.   Geometry of reinforced soil.

After determining the global and local stability, it was analyzed, how to secure the 80°slope. A well-known disadvantage of geosynthetics is the lack of resistance to UV. Polyester woven geotextiles need to be covered in two weeks after installation due to the UV resistance. UV resistance is tested according to EN 12224 standard and declared by the producer. Leaving the half-mattresses rolled up to direct sunlight would damage the reinforcement and damage the structure's stability, either locally or globally.

Several solutions were considered to protect the geotextile against UV, e.g. anti-erosion geomats, precast concrete. Finally, due to the temporary construction, it was decided to protect against UV rays by covering the face with polypropylene geotextile – Figure 8. The solution was not aesthetic, but was extremely cheap and easy to instal.

3.4   Summary

The presented example shows how to speed up works and reduce the costs of implementation. The construction of reinforced soil was done faster and without the need of additional elements: for example the foundation which is required for the construction of retaining

Figure 8. Bypass temporary construction – facing.

walls. Also, the disadvantage of geotextiles, which is the lack of resistance to UV, has been solved. The author hopes that this simple example will point out that these are materials sensitive to UV, which is often forgotten by designers and contractors – without securing geotextiles.

4 SOIL REINFORCEMENT

4.1 Description of the technical problem

As a result of optimization – reducing the costs of the bridge's construction, direct foundation was decided to support the bridge structure. It was possible only after reducing lateral earth pressure to the abutment. Soil reinforced with polyester geotextiles was designed, to take over the earth pressure and not transfer it to the abutment. The project was part of the S-3 Express Road Nowa Sól – Legnica Project.

4.2 Design assumptions. Methods of calculation

In the construction of reinforced soil the following design assumptions were made: high-strength polyester woven geotextiles as reinforcement. Calculations were conducted for each heights of abutment. A class A load was assumed in accordance with PN 85/ S-10030. Cross section with loads has presented in Figure 9. In calculation has been provided loads from: cars, pedestrians and soil weight, concrete plate weight and earth pressure from dead and live loads. Also has been considered horizontal force from brake load.

In calculation has been assumed backfill made of non-cohesive soils with an internal friction angle of minimum $\varphi = 34\,°$, cohesion c = 0kPa and maximum weight $\gamma = 19.0kN/m^3$. An empty space is made between the reinforced soil and the abutment. The calculations were made using the GEO5 – Reinforced embankments computer program based on the assumptions of the standard Eurocode 7 and original calculation sheets integrating forces depending on the zone in which the reinforcement is located (zones: active and passive). After determining the forces in each reinforcement layer, the appropriate strength of the geotextiles was chosen, and then the stress of each reinforcement layer in the active zone was determined. On this basis, the width of the technological space was determined, that will prevent the transmission of the strength to the abutment. During the performed calculations local and global stability of a reinforced soil structure, sliding, reinforcement pull-off, ultimate load-bearing capacity of the reinforcement and displacements was checked. As

840
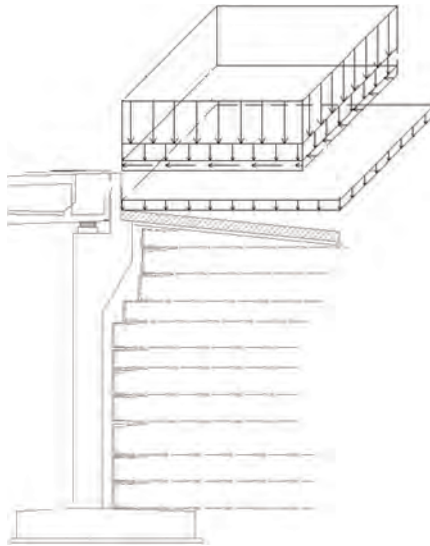
Figure 9. Calculation cross section.

reinforcement has been used PES geotextile with strength from 200 – 400kN/m. MSE wall for that assumptions has factors: sliding safety factor is 1.8, overturning safety factor is 2.0 and bearing capacity safety factor 1.6.
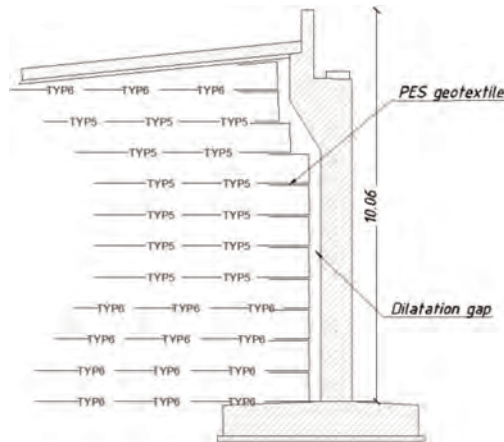
Figure 10. Section of reinforced soil – solution.

According to the requirements for the reinforced soil, the space behind the abutment and the reinforced soil should be made in such a way that during the service live of the structure, after all displacements (construction period, load, rheological effect), the reinforced soil does not come into contact with the abutment and transfer any load. The width of empty space should take into account the following stages: construction stage, service live of structure. Calculation of space between abutment an face of MSE has been considered difference elongation at construction stage and end of predicted service time of structure (100 years). Has been used force by 2% elongation and considered long term material behaviours. Each layer has been calculated and checked displacements. At end has been determinated width of dilatation gap. Elongation length has been considered in active zone L_a.
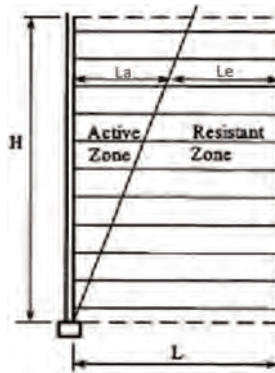
Figure 11. Active zone graph.

5 CONCLUSIONS

The presented projects have shown that the use of polyester woven geotextiles can significantly accelerate and reduce construction costs. The number of designed and implemented soil structures reinforced with polyester woven geotextiles shows that both Designers and as well Contractors have gained confidence in this type of solution.

Finally, it should be underlined that the complicated implementation of reinforced soil is in fact trivial compared with the performance of works that could be avoided thanks to its use. Reinforced soil does not require the use of specialized machines or the work of specialists. Reinforced soil can be made by unskilled workers using basic machines used in earthworks.

Nowadays, when construction sites struggle with the lack of workers, may be very important by choosing the technology of works.

The author, as a popularizer of technical solutions with the use of polyester geotextiles, hopes that the popularity of solutions based on these geosynthetics will increase, and that the constructions themselves will be the best advertisement for them among Designers and new Contractors.

REFERENCES

AASHTO (2010) LRFD Bridge Design Specifications, Customary U.S. Units, 5th Edition. *American Association of State Highway and Transportation Officials*, Washington, DC, USA.

EBGEO (2010) Empfehlungen für den Entwurf und die Berechnung von Erdkörpern mit Bewehrungen aus Geo-kunststoffen. *Deutsche Gesellschaft für Geotechnik e.V. (DGGT)*, Essen, Germany.

Eurocode7: *Geotechnical Design – part 1: EN 1997-1 (2004) General Rules, European Committee for Standardization*, Bruxlles, Belgium.

BS 8006-1 (2010) *Code of Practice for Strengthened/ Reinforced and Other Fills*, British Standards Institution, UK.

Ziegler. M. (2016) Geosynthetic Reinforcement Applications. *EuroGeo6*.

TRA SBR 19 (2019) *Automobilių Kelių Nesurištųjų Mišinių Ir Gruntų, Naudojamų Sluoksniams Be Rišiklių, Tech-Ninių Reikalavimų Aprašas*, Vilnius, Lithuania.

Dynamic response of an innovative reinforced soil embankment subjected to high energy impacts

O. Korini & Y. Bennani
Terre Armée, Rueil-Malmaison, France

ABSTRACT: Rockfall hazard in mountainous areas is often mitigated by placing reinforced soil embankments at the bottom of the slopes. The Terre Armée Company invested in an important research project for designing an innovative reinforced soil embankment, which had vertical facings and a relatively slender shape. High strength geosynthetic reinforcements assured its stability when subjected to impacts. During this project, real scale tests were performed on a 15 m long embankment with rectangular cross section and a foundation width that was almost half of its height. The structure successfully resisted the impacts from concrete blocks travelling with 5 MJ and 2 MJ kinetic energies. The deformed shape of the embankment showed that the internal geogrid reinforcements efficiently engaged a large soil volume far from the impact location. A good mobilization of the geogrids' strength was observed through the strain gauges installed on them, which confirmed the validity of the design.

1 INTRODUCTION

Rockfalls occur when rock blocks are detached from their place on the slope and start to roll or bounce downhill. Being on the surface, these blocks are subjected to atmospheric agents, which eventually degrade the weak links that they have with the base rock. The recent climate changes and the thawing of permanent ice in mountain slopes increase the risk of rockfall in these areas (Allen & Huggel 2013; Kellerer-pirklbauer *et al.* 2012).

Reinforced soil embankments are one of the solutions that engineers employ for mitigating the rockfall risk. Several research projects have been carried out for understanding their behavior under dynamic impacts (Lambert & Bourrier 2013; Maegawa *et al.* 2011; Peila *et al.* 2007). The tests were usually performed on trapezoidal embankments, which had different facings and reinforcement designs. Even though the internal geogrid reinforcements played a role in the deformed shape of the embankment (Peila *et al.* 2007; Ronco *et al.* 2009), their contribution in the impact resistance remains uncertain.

The Terre Armée Company recently invested on a research project concerning rockfall protection embankments. The objective was to produce an optimized slender embankment with a relatively narrow foundation footprint and to quantify the role of the geogrid reinforcements during a dynamic impact. Two experimental campaigns were performed in the framework of this project. The reduced scale campaign provided important conclusions (Korini *et al.* 2021) that were used later on to prepare the real scale tests.

2 EXPERIMENTAL SETUP

2.1 *Test conditions*

The impact tests are performed on a remote site near Chambery, France specially equipped for this purpose. This site was equipped with a crane installed at the top of the cliff, which

served to lift the reinforced concrete blocks for carrying out vertical drop tests. Since a horizontal impact is the most unfavorable for a rockfall protection embankment, another device was necessary to be built. In this context, a large scale pendulum was constructed on the vertical rock slope consisting of a steel beam and cables. The concrete blocks were attached to the pendulum cable and then lifted by the crane to the desired drop height. The potential energy of the lifted rock was fully converted to kinetic energy applied horizontally at the lowest part of the pendulum, where the embankment was foreseen to be built. The new device was able to perform horizontal impacts with a kinetic energy of 5 000 kJ, which corresponds to launching a 12.3 tons concrete block from a height of about 41.4 m.

2.2 Rockfall embankment design

The embankment facings were held vertically by a system of welded steel mesh panels and GeoStrap® reinforcements. The latter were installed in a back to back pattern. For better resistance to the impact, the embankment was equipped with internal geogrid reinforcements. The internal design was chosen after the results of the reduced scale tests (Korini et al. 2021), which showed that the case with geogrids placed horizontally close to the facing had a better performance. For the current tests, the embankment was equipped with additional geogrid reinforcements placed in the back part aiming to reduce the back extrusion during the impact (Figure 1).
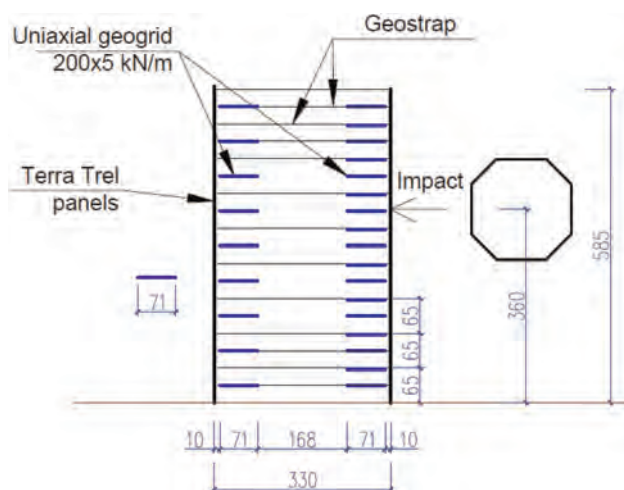
Figure 1.   The cross section design of the embankment.

The embankment was constructed using well graded soil backfill. In this way, a proper soil – geogrid interaction is guaranteed as well as an efficient distribution of the impact effect to a larger soil volume. The geogrids were uniaxial with the working direction installed in the longitudinal embankment direction. The role of the geogrids was to spread the impact load in the lateral direction and preserve the integrity of the embankment.

2.3 Instrumentation

The behavior of the embankment during the impact was monitored with several devices and sensors. Rapid cameras were used to record the impact on both front and back faces of the embankment. Accelerometers were used on the impacting block and in several positions in the backfill for measuring the impact force and internal vibrations. Pressure sensors were installed in the base of the embankment to check the variation of the local pressures. The geogrids' mobilization was monitored with the aid of strain gauges that were glued on the main direction strips.

3 TEST RESULTS

The embankment resisted well to the two impacts despite the important deformations. The rapid cameras (500 images/second) gave the possibility to observe in detail the response of the embankment during the test. Due to the high amount of data provided in this study, only part of the visual observations of the embankment and some of the strain gauges data curves will be presented below.

3.1 Visual observations

The first and strongest impact was directed at the longitudinal center of the 15 m long embankment and at about the upper 2/3 of its height (Figure 2). The displacement recorded at the impact position was about 2.1 m, which represents 63% of the embankment width. This value consists of 1.2 m block penetration and 0.9 m of structural deformation.

During the impact, the embankment exhibited a certain flexibility, which is probably due to its slender shape. After the initial penetration of the block, a longitudinal bending deformation followed that brought closer to each – other the front edges. At the end of the bending, the block lost all the kinetic energy, and the embankment continued to move due to the gained inertia. The final movements consisted of a slight back and forth motion of the whole structure similar to a cantilever structure anchored in the ground.

Figure 2. The deformed shape of the embankment after the 5 000 kJ impact.

3.2 Instrumentation measurements

The strain gauges provided important information concerning the geogrids' mobilization in the embankment. The strain curves may be generally split in three parts, i) an initial rapid oscillation, ii) an increase of the strain up to the peak value and iii) a slow decrease until the residual values (Figures 3 & 4). The front geogrid located at the impact height experienced high temporary strains during the initial moments of the impact, but less residual strains afterwards (Figure 3). Some of the strain gauges failed prematurely (e.g., G-2) without providing useful data.
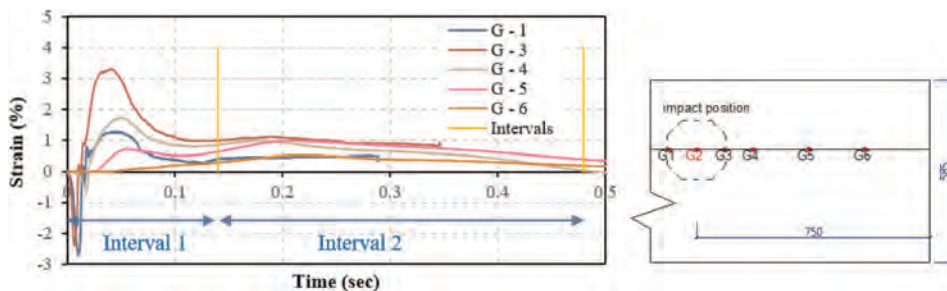
Figure 3. Strain measurements on the front geogrid strip located at depth 0.3 m from the front facing.

The back geogrid experienced quite different mobilization compared to the front geogrid. The initial oscillations were less sudden (the strain rate was lower) compared to the ones of the front geogrids. Moreover, the initial strains were significantly lower while the residual ones were higher (Figure 4). In both cases the strains remained lower than the geogrid maximal allowable strain of 7%, which is calculated considering the relevant reduction factors.
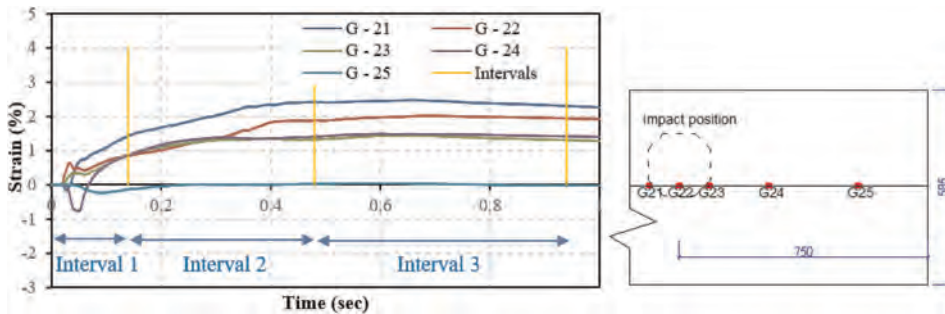
Figure 4.   Strain measurements on the back geogrid strip located at depth 0.4 m from the back facing.

The intervals yellow lines correspond to the significant moments of the embankment's behavior during the impact. The first interval represents the block penetration phase, the second one is the longitudinal bending and the third one is the backward movement of the whole structure. The front geogrids are mobilized during the first and second interval (up to 0.48 s) and show very low residual strains. On the other hand, the back geogrids remain mobilized after the second interval by showing higher residual strains.

The peak strains recorded by the strain gauges present an important variation around the impact position (Figure 5). The strain gauges measurement was limited to 5.3% due to the physical properties of the special glue that was used to stick them to the geogrids. This prevented the recording of higher strain values that could have been reached close to the impact axis.
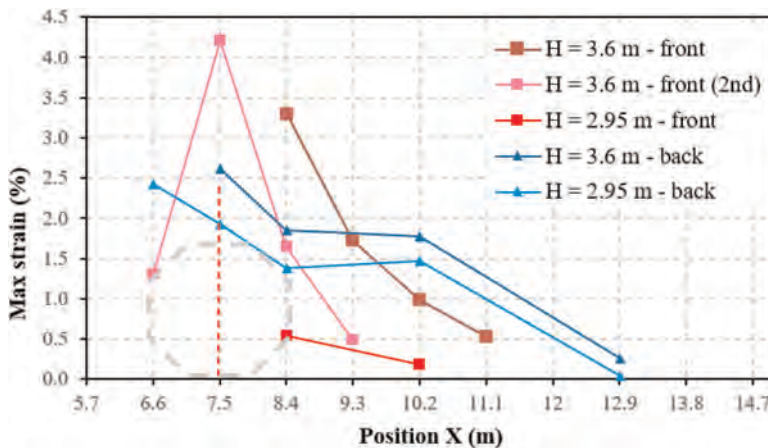
Figure 5.   Peak strain measurements of the strain gauges during the 5 000 kJ impact.

The impact caused some of the strain gauges to fail prematurely, mostly at the impact position. This prevents the creation of a clear picture regarding the peak strains on the monitored geogrids. This is the case for G2 placed at H = 3.6 m on the front geogrid (brown line). However, by observing the trend of the geogrid strip that is installed 0.4 m deeper (pink line), it may be deduced that the G2 peak strain could have been about 6 %. Most of the strain gauges failures happened at low or zero strain values, which means that the loading of the geogrid was not the cause of the failure. The cause was probably the sectioning of the acquisition wires due to the rapid loading.
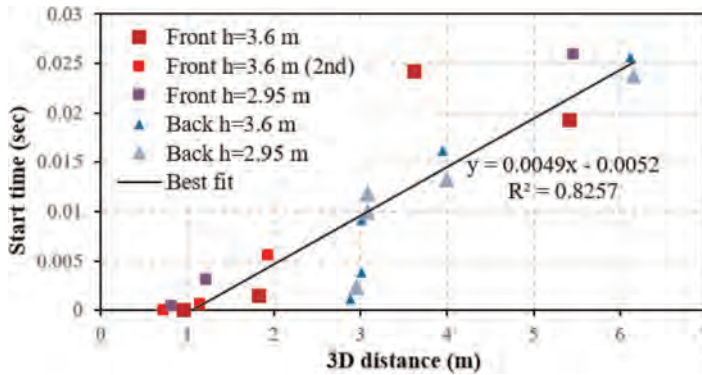
Figure 6.   Determination of the impact wave propagation speed.

4   DISCUSSION OF RESULTS

The embankment dissipated the kinetic energy of the block partly by local plastification at the impact position and partly by structural deformation. During the first moments of the impact the facing steel mesh got quickly disintegrated locally, so its contribution to the impact resistance was not significant. On the other hand, the facing remained intact elsewhere and together with the GeoStrap reinforcements continued to maintain the embankment's structural integrity. This was obvious in the further intervals of the longitudinal and vertical bending of the structure.

The rapid cameras showed the formation of a shear cone in the embankment during the block penetration interval. This is different from the case tested by Peila *et al*. (2007), where horizontal soil layers started to slide at the impact position. The geogrids in Peila's case were continuous sheets that covered all the embankment's width. In our case the internal installation pattern of the geogrids was discontinuous, which prevented the creation of sliding planes and favored a smoother 3D volumetric distribution of the deformations.

The front and back geogrid layers experienced different mobilization (Figures 3 & 4). At the beginning of the impact, most of the strain gauges experienced rapid oscillations with negative sign. This means that they were loaded in compression, which may not seem reasonable for a flexible geogrid. However, these readings could be capturing a physical phenomenon such as an impact (or seismic) wave. Several observations support this claim. Firstly, the negative peaks appear at the initial milliseconds when the block penetration is not significant and the embankment is almost intact. Secondly, the strain gauges continue to measure tensile strains as the block continues to penetrate, which means the gauges were not damaged. Thirdly, the initial peaks have time shifts between them, the oscillation period is higher for the gauges farther from the impact and in some cases the negative peaks have lower amplitude or even switch to positive. The last argument is in line with the seismic waves theory for soils (Kramer 1996).

The impact wave speed may be deduced by the measurements of the strain gauges by considering their initial mobilization time and the distance from the impact position. By plotting these two parameters, a cloud of points is obtained (Figure 6). Considering that a wave has a certain speed in a given medium, a best fit linear curve is proposed. The correlation factor is 0.83, which presents a fairly strong relationship between the plotted parameters. By inversing the slope of the fit curve, it is obtained the average impact wave propagation speed 204 m/s.

5   CONCLUSIONS

An innovative rockfall protection embankment is tested by horizontal impacts with energies up to 5 000 kJ. The embankment behaved as a slender structure due to its low width to

height ratio. Its ability to deform allowed the dissipation of the impact energy by a different mechanism compared to traditional embankments with trapezoidal cross section. Besides the local plastification at the impact position, the structure experienced longitudinal and vertical bending in most of its volume. This structural response was enhanced by the geosynthetic reinforcements, which allowed the distribution of the impact load to a larger soil volume.

The two systems of geosynthetics played a different role in the embankment behavior. The back to back GeoStrap links only guaranteed the structural shape without contributing much to the impact resistance. On the other hand, the geogrid layers got an important mobilization during the impact. The front geogrids contributed more during the initial moments of the impact, while the back ones contributed more after the block penetration interval. The geogrids did not fail during the test due to their ability to deform and also slide in the soil.

The strain gauges installed on the geogrids were able to capture a signal that resembled an impact wave. The rapid initial oscillations presented wave propagation characteristics such as different signal phasing and period depending on the gauge's position. The wave propagation speed was calculated considering the arrival time of the signal for each strain gauge. However, this evaluation needs to be taken with caution since there is the uncertainty whether the wave is transmitted through the soil or through the reinforcement itself.

The impact wave may cause both tensile and compressive strains of the geogrids. If these strains exceed the geogrid's material resistance, they could finally damage it. Consequently, the role of the geogrid in the impact resistance would diminish and the embankment would be more vulnerable. So, the effect of impact (or seismic) waves on geosynthetics is worth investigating in order to prevent undesired situations in relevant engineering applications.

The tested embankment presents an optimized solution compared to traditional rockfall embankments. It may be efficiently used in cases when construction space is limited due to its reduced foundation width.

ACKNOWLEDGEMENTS

REFERENCES

Allen, S. & Huggel, C. 2013. Extremely Warm Temperatures as a Potential Cause of Recent High Mountain Rockfall. *Global and Planetary Change*, *107*:59–69.

Kellerer-pirklbauer, A., Lieb, G. K., Avian, M. & Carrivick, J. 2012. Climate Change and Rock Fall Events in High Mountain Areas: Numerous and Extensive Rock Falls in 2007 at Mittlerer Burgstall, Central Austria. *Geografiska Annaler: Series A, Physical Geography*, *94*(1):59–78.

Korini, O., Bost, M. Rajot, J.-P. Bennani, Y. & Freitag, N. 2021. The Influence of Geosynthetics Design on the Behavior of Reinforced Soil Embankments Subjected to Rockfall Impacts. *Engineering Geology*, *286*:106054.

Kramer, S. L. 1996. *Geotechnical Earthquake Engineering*. Pearson Education India.

Lambert, S. & Bourrier, F. 2013. Design of Rockfall Protection Embankments: A Review. *Engineering Geology*, *154*:77–88.

Maegawa, K., Tetsuya, Y. & Van, P. T. 2011. Experiments on Rockfall Protection Embankments with Geogrids and Cushions *GEOMATE Journal*, *1*(1):19–24.

Peila, D., Oggeri, C. & Castiglia, C. 2007. Ground Reinforced Embankments for Rockfall Protection: Design and Evaluation of Full Scale Tests. *Landslides*, *4*(3):255–265.

Ronco, C., Oggeri, C. & Peila, D. 2009. Design of Reinforced Ground Embankments used for Rockfall Protection. *Natural Hazards and Earth System Sciences*, *9*(4):1189–1199.

Biodegradable formwork for reinforced soil structure

D. Palma
Geoflum Engineering srl, Potenza, Italy

ABSTRACT: Reinforced soil structures and their applications currently represent a key point in the field of the geotechnical engineering. They allow reinforcing soils respecting various environmental aspects. Though widely used, this conventional type of reinforced soil structure hides some drawbacks. One of them is the risk of soil pollution due to the degradation and corrosion of the metallic material making up the conventional formwork currently in use. This also applies to the zinc-coated facing elements which nonetheless release harmful particles of rust into the soil, though later than the classic black facing elements (without zinc-coating). The present invention, covered by a patent, concerns a structure for reinforcing soils made up of a formwork made of bio-degradable natural material, which can be combined both with planar reinforcing elements in metal mesh and with synthetic geogrids.

1 STATE OF THE ART

The reinforced soil structure is an engineering solution that allows combining the soil features with those of the reinforcing elements so obtaining a composite structure capable of resisting to tensile stress, so expanding the scope of earthworks.

Reinforced soil structures and their applications currently represent a key point in the field of the geotechnical engineering. They allow reinforcing soils respecting various environmental aspects.

Reinforced soil structure applies to several areas, as for example road and railway infrastructures, soil protection, mitigation of the hydrogeological instability, hydraulic constructions, river works or rock fall protection works, bridge abutments retaining walls, green elements for street furniture and industrial complexes, noise barriers.

Reinforced soil walls or embankments bring wider benefits than the traditional gravity retaining walls or reinforced concrete retaining walls, mainly because they imply a simple technique that does not need any specialized equipment or staff. For doing this works, it is in fact only necessary to use an excavator, a compactor and poor skilled labour. It is furthermore possible to easily construct very high retaining works able to take significant deformations before reaching their serviceability limit state, so needing no deep foundations and so being particularly suitable for stabilizing landslides. If compared to the rigid concrete structures, they can better bear earthquakes, dynamic traffic loads and impacting loads on them.

Using reinforced soil instead of a traditional reinforced concrete wall has a lower environmental impact, especially in consideration of the green grass growing on the front side, and makes it possible to use filling material collected right there a result of excavation, so considerably reducing the construction costs.

It is worth considering that many countries have laws which forbid (or guidelines suggesting to avoid) the use of steel in certain areas, such as for example some natural parks,

rivers and seas, areas in which slowly it will no longer be possible to use the reinforced earth technique, as it is known today, notwithstanding the aforementioned advantages.

1.1 Conventional reinforced soil's elements

As is well known, reinforced soil structures are made of three elements: the first one is the structural soil (the filling material of the structure); the second one is the reinforcing element (usually a geogrid or an hexagonal double twisted wire mesh, having different levels of corrosion protection); and the last one is the formwork (usually a welded wire steel mesh having a variable spacing and cross section diameter usually about 7 to 8 millimeters, mostly having no corrosion protection, combined with a natural or synthetic anti-erosion component.

1.2 Environmental advantages compared to conventional reinforced soil with lost formwork

Though widely used, this conventional type of reinforced soil structure hides some drawbacks. One of them is the risk of soil pollution due to the degradation and corrosion of the metallic material making up the facing element, that is a lost formwork. This also applies to the zinc-coated facing elements which nonetheless release harmful particles of rust into the soil, though later than the classic black facing elements (without zinc-coating).

A second drawback is the high CO_2 emissions into the atmosphere due to the current steel production standards relating to the only formwork currently in use. A third disad-vantage of conventional formwork are Post-production CO_2 emissions for handling and transporting the steel formworks currently in use: large vehicles are required due to their size and weight (cranes/forklifts and trucks respectively); as a result there are also high transport costs due to the size and weight of the current formworks. Finally, there is often poor greening of the front due to poor maintenance that in Italy notoriously unable to be guaranteed over time.

Accordingly, in consideration of the growing worldwide trend towards maximizing the respect for the environment and reducing the various forms of pollution, the principal aim of the present invention is to provide a reinforced soil structure, embankments and excavation faces comprising a facing element (the formwork) made of a biodegradable and natural origin material in order to avoid the risk of soil and groundwater pollution deriving from the steel degradation and corrosion (the systems currently in use include in fact facing elements, connecting parts and stiffening elements made of steel).

The formwork made of biodegradable material can be one of the ways to eliminate this possible source of pollution.

1.3 Comparison with the reinforced soil made with removable formwork

The primordial technique for making reinforced earth is known as the "extractable formwork" technique. This technique provided that the formwork was used only during the construction phase to give shape to the structure and was immediately extracted before creating the upper reinforcing layer. The formwork typically used consisted of a steel structure with the project inclination closed on the front by a single solid wooden panel.

This type of formwork was obviously reusable, but the technique was clearly much slower to implement on site than the disposable formwork technique (with formwork in electro-welded steel mesh described above) in terms of work surface day. In addition, it required at least two types of highly specialized manpower: from the material installer to the excavator operator who had to be able to extract the formwork with extreme delicacy without deforming or damaging the final work, which is remembered it is made of soil.

This technique has therefore been almost completely abandoned in recent times because it is too expensive in terms of labour, in favor of the lost formwork technique in electro-welded steel mesh, which, while involving the additional cost of steel, allows dras-tic reduction in the workforce.

2 ENVIRONMENTAL INNOVATION

In order to maximize the environmental respect of the reinforced soil currently in use, mitigating the possible sources of pollution they produce, a new formwork was designed and patented.

The environmental innovation is that the formwork is made of biodegradable natural material, in order to eliminate the possible pollution of the soil, and of any aquifers, due to the degradation and corrosion of the steel (with which the facings, the connection and stiffening elements are made) of the similar systems currently in use.

The other main characteristics of the formwork are: a) suitable stiffness demonstrated by fem analysis with which the technical and structural checks are satisfied. b) It is able to maintain the initial shape of the work even after the biodegradation process of the formwork. c) It is made up of light pieces and of reduced length compared to the standards to be "joined" on site with rapid interlocking systems. d) It is of a useful size to easily create curvilinear walls becoming a green technology for landscape projects.

Following image represents one of many results of FEM analysis done, where the maximum deformation of patented formwork is less than 10 mm. More details about FEM analysis and their results will described in the next paper.
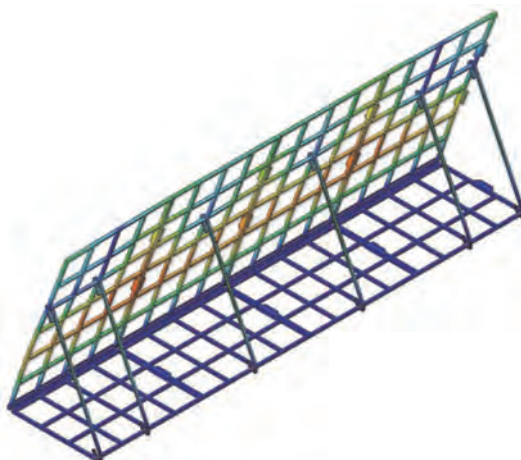
Figure 1.   FEM analysis results of one of the forms of patented formwork made of biodegradable material. Red represents 8 mm of maximum deformation, and blue is zero mm.

2.1 *About the 17 sustainable development goals of the 2030 agenda and about EU green deal for carbon free*

With the Green Deal, Europe wants to become the first continent with zero climate impact by 2050. One goal is reduce CO_2 emissions by at least 55% by 2030 compared to 1990 levels.

As described in paragraph 2.2, the formwork presented here contributes to the achievement of these objectives.

In particular, it should be noted that the bio-formwork in question allows: a) almost total reduction of CO_2 emissions in the production phase. b) Strong reduction of CO_2 emissions from transport, thanks to the reduced weight and size of the elements, which allow them to be transported not only with trucks, as in the version currently in use, but with small vehicles, even by couriers. c) Zeroing of soil and groundwater pollution following the corrosion of the steel formwork currently in use, because the bio-formwork here presented is made of biodegradable natural material. d) a fertilization contribution to the topsoil layer of the reinforced soil, due to the biodegradation of the formwork over time.

About the SDGs, the bio-formwork described above, contributes in different ways to the achievement of the following Sustainable Development goals: 3) Good Health and well-being; 6) Clean water and sanitation; 9) Industry, innovation and infrastructure; 11) Sustainable cities and communities; 12) Responsible cities and communities; 13) Climate action; 14) Life below water; 15) Life on land.

2.2 *The natural formwork patented*

The formwork presented here is protected by patent in the name of the undersigned. The further environmental innovation offered by the system presented here is to create a structure that combines structural reinforcement needs with naturalistic, environmental and green-related needs, through: a) the construction of soil reinforcement structure with a lost formwork made of natural origin material. b) Creation of an intuitive and fast assembly system through simple joints to facilitate installation and eliminate possible installation er-rors. c) Creation of reinforced earth without risks for workers on site, given the absence of spikes or rusty parts and given their lightness.
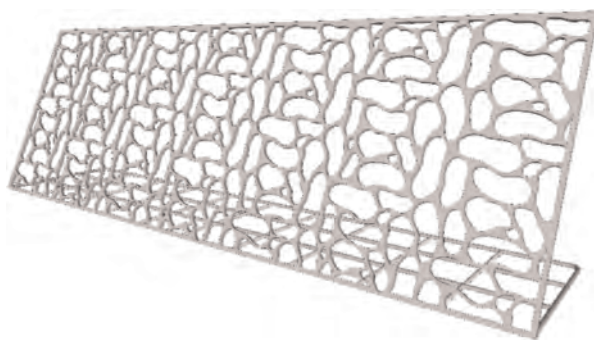
Figure 2.   Example of one of the forms of patented formwork with river stone shape.

This formwork is biodegradable and it is made of natural origin material. The material with which it is made is at the same time capable of conferring suitable rigidity to the face itself, so as to guarantee the maintenance of the right shape to the external wall of the work to be done.

3   CONCLUSIONS

Comparing with the conventional techniques for making reinforced soil, it appears quite clear how the use of the formwork made of natural origin material, as described above, can be considered an innovative method and in step with the times, to construct a new green type of reinforced soil.

This natural formwork is able to eliminate environmental pollution of conventional steel formwork and it is able to improve the landscape insertion of the structure. It indeed mitigate CO_2 emissions in production and transport phases and it does not cause soil pollution because is made of natural origin material. In addition, it is able to offer a fertilization contribution to the topsoil layer of the reinforced soil, due to the biodegradation of the formwork over time.

Finally, it is also able to conjugate the above environmental needs with the technical need of to guarantee the shape of the structure over the time; and with the economic need of to carry it out in a short time and with non highly specialized labour.

The present invention, covered by a patent, concerns a structure for reinforcing soils made up of a formwork made of bio-degradable natural material, which can be combined both with planar reinforcing elements in metal mesh and with synthetic geogrids.

Monitoring and warning system including a double stiffness geosynthetic for the reinforcement of cohesive soil on cavities

M. Riot Verdier
AFITEXINOV, Champhol, France

L. Briançon
INSA Lyon, GEOMAS Laboratory, Villeurbanne, France

T. Monnet
AFITEXINOV, Champhol, France

Ph. Delmas
Geotechnical Expert, Paris, France

ABSTRACT: The use of reinforcement geosynthetics to prevent localized cavity collapses is now relatively common. The communication presents a monitoring solution developed as part of the REGIC research project (Reinforcement using Intelligent Geosynthetic over Natural or Anthropogenic Cavities). It is based on an innovative bi-stiffness instrumented geosynthetic and its integrated autonomous acquisition system, specially designed for use by a non-specialist. Suitable for mitigation and management of the risk of localized collapse, it allows early detection of the development of the collapse phenomenon.

1 INTRODUCTION

Numerous experimental and numerical studies have made it possible to understand the behaviour of geosynthetic reinforcement to prevent collapses of structures in areas at risk of cavities; e.g., Rafael (Villard *et al.* 2002) or GeoInov (Delmas *et al.* 2015) projects.

Recently, the REGIC Project addressed the use of coherent fill soils reinforced with geosynthetics above cavities (Delli Carpini *et al.* 2023). It enabled the design and development of a monitoring system specific to geosynthetic reinforcement over cavities. This complete system, which integrates sensors, geosynthetic and monitoring system, will be named as "geo-auscultation" system; by detecting very small deformations, it allows a monitoring ensuring early detection of the collapse. It can then monitor the structure until the end of the service life, while maintaining a high degree of structural safety.

The design of an operational system for auscultation and warning associated with geosynthetic reinforcement on potential soil subsidence, must consider different possibilities of cavity evolution. Underground voids may collapse gradually or abruptly depending on the configuration of the void and the nature of the overlying soil. The main cases are (Al Heib *et al.* 2021):

the subsidence: continuous depression of the ground above the cavity which causes progressive deformation of the ground without brittle fracture; the extension and amplitude are related to the dimensions of the cavity, its depth and the quality of the overlapping strata; localized collapses: due to failure over a natural or anthropogenic cavity at low depths; size and shape of the cavity varies by configuration, e.g. for gypsum and coarse limestone quarries close to Paris, 90% of cavities have a diameter of less than 5 m.

Geosynthetic reinforcement is a recognized solution for treating localized sinkhole of small diameter up to 5 m. Nevertheless, the use of instrumented geosynthetics combined with the appropriate monitoring system can be an interesting solution for detecting, and/or monitoring, a rise in the cavity that leads to a larger subsidence.

2 BACKGROUND AND BASIS FOR THE DESIGN OF THE CAVITY DETECTION AND WARNING SYSTEM

2.1 *Behaviour of geosynthetic reinforced structures on cavities*

The principle of behaviour of a geosynthetic reinforced structure during the ascent of a cavity at the level of the natural ground and then when the cavity opens under the geosynthetic, is presented in the French standard XP G38065: it is possible to analyse the functioning of a geosynthetic reinforced structure over time, to facilitate the design of the detection, monitoring system.

For simplicity, the same assumptions as in the norm are considered: pulverulent fill soil, cylindrical cavity, progressive opening of the cavity at the surface. It is assumed that the design assumptions are valid until the end of the service life and that the design of the reinforcement is correct. Several periods are distinguished: period (I) corresponds to the installation phase of the geosynthetic and the construction of the embankment; during period (II) the cavity gradually rises to the surface and a subsidence occurs; period (III) corresponds to the opening of the cavity until it's nominal diameter under the geosynthetic; in period (IV) the cavity diameter remains unchanged until the end of the service life before a resumption of progressive opening (period V).

Figure 1 shows an example of possible evolution of the maximum horizontal deformation of the ground at the surface during the ascent of the cavity. The estimation of this change in deformation is based on values obtained by the empirical method of NCB (Al Heib *et al.* 2021).
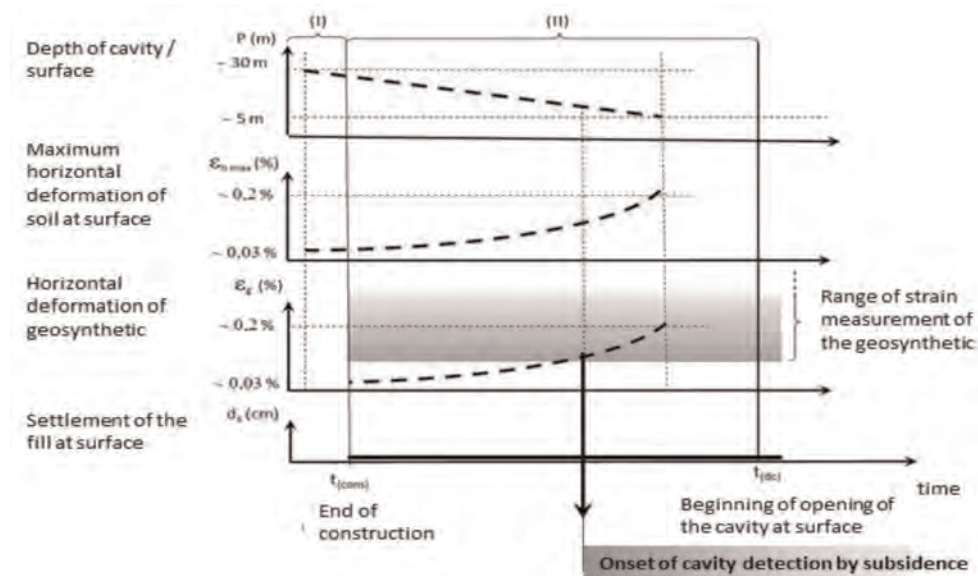
Figure 1.   Schematic diagram of the evolution of horizontal deformations (soil & geosynthetic) and the settlement of the surface of the embankment during the ascent of cavity before opening at the TN.

The absence of slippage between the geosynthetic and the soil is a realistic hypothesis considering the low levels of deformation observed. It is then possible to specify the order of magnitude of the minimum deformation to be measured to allow early detection of the presence of a cavity.

This provides an important criterion for the proper design of instrumented geosynthetics. It should be noted that there was no settlement of the fill surface over this period, which prevents any detection of the cavity using a surface measurement.

The dimensioning methods (XP G38065), and even new modelling tools (Villard *et al.* 2017), make it possible to evaluate the evolution of the deformations of the geosynthetic as well as the settlement observed at the surface during the different phases (III, IV and V). If the geosynthetic is instrumented and its deformation measured, it is possible to deduce the diameter of the cavity and check the level of safety of the structure over time. It should be noted, however, that beyond the maximum measurement threshold of instrumented geosynthetics (limit of sensors), the monitoring of the structure cannot be continued by this technique. This corresponds to a second criterion of the design of the instrumented geosynthetic monitoring system. However, in this phase V, settling at the fill surface is relatively important and allows monitoring of surface settlements.

2.2 *Illustration of the "geo-auscultation" design approach for areas at risk of cavities treated by geosynthetic reinforcement*

As shown in paragraph 2.1, it may be noted that the "monitoring system" and geosynthetic reinforcement are closely linked and must be designed jointly to allow good optimisation.

Solution design begins with the assessment and characterization of the type of potential collapse of the site. This involves specifying whether the cavity location is known or not, whether there is a risk of subsidence or even of sinkhole, and finally assessing the size and shape of the subsidence, or of the sinkhole, and defining the nominal cavity size.

Once these parameters are known and the geotechnical study is finalised, it will be up to the Project Owner (possibly Project Manager) to choose the objectives of the infrastructure's instrumented reinforcement solution:

either a "temporary reinforcement by instrumented geosynthetic" considering that a definitive treatment after detection of the rise of the cavity will be provided;
or a "long-term reinforcement by instrumented geosynthetics": the reinforcement designed (usually for 100 years) is then associated to a "monitoring system" allowing the controlling of the development of the cavity and of the settlement of the surface.

With the definition of these objectives, it is then possible to design the instrumented geosynthetic. It will have to meet the infrastructure stability requirements (mechanical stability, maximum allowable surface settlement) and the monitoring system requirements.

2.3 *Proposal for an innovative "geo-auscultation" system combining monitoring and reinforcement*

It shall be noted that criteria related to design of the monitoring system, mainly those related to the early detection, interfere with the choice of reinforcement geosynthetic.

The requirement to detect at an early stage the subsidence or even the presence of the cavity under the geosynthetic presupposes that the instrumented geosynthetic can deform under very low tensile stresses, which is very often antagonistic with the choice of a high (or even very high) stiffness to meet the reinforcement requirements (low long-term deformations). Even if the measurement accuracy levels of the optical fibre instrumented geosynthetics used are high, they often remain unsuitable for early detection of subsidence during cavity ascent.

To respond to this antinomy, the project has developed a patented innovative reinforcement process based on a "inverted bi-stiffness" geosynthetic. It provides two tensile

stiffnesses that activate one after the other, the first being lower than the second. Combined with a suitable warning system composed by a network of optical fibres, inserted into the geosynthetic during the manufacturing process, this new type of geosynthetic makes it possible to detect small deformations of the soil (thanks to its first lower stiffness) while guaranteeing the same final level of safety as a classical geosynthetic with a single stiffness (the second stiffness more important after the deformation threshold necessary for the detection of movements ensuring this role).

3 DETECTION, AUSCULTATION AND WARNING OF CAVITY BY GEOSYNTHETIC INSTRUMENTED BY "GEO-AUSCULTATION" SYSTEM

Once the preliminary site study has been carried out, with the definition of the cavity type, the knowledge of its possible location or not, the type of expected disorders, their surface extension, and their speeds, it is possible to finalize the design of the solution.

This must consider the temporal objectives of the site Owner (see paragraph 2.3). In order to finalize the specifications of the associated "monitoring system", the following path may be used:

collapse type assessment:
  to be detected, the subsidence, e.g. very progressive opening of a cavity, may require a specific geosynthetic allowing very low deformation measurements (e.g. "inverted bi-stiffness") while a sinkhole with a brutal opening will be less demanding;
  the speed and amplitude of the expected deformations will also be necessary for the definition of the type and frequency of measurements, the processing and the warning system.

spatial location of the collapse in the geometry of the infrastructure:
  the extension of the area to consider will have a major impact on the choice of the type of optical fibres depending if the cavity is located and known, or if potential cavities are not precisely located and may appear under a linear transport infrastructure;
  similarly, the surface extension of the subsidence, or sinkhole, to be detected, will affect the spacing of the optical fibres;

choosing the right optical fibre technology for the site (see types of optical fibres in 3.1).
selection of the geosynthetic product suitable for the chosen optical fibre technology and the type of expected failure;
selection of the appropriate monitoring system (detection/acquisition) for the type of infrastructure, geosynthetic and subsidence type: it depends mainly on the chosen fibre optic technology; an integrated system allowing simple and different auscultation options, is presented in 3.2.

3.1 *Optical fibre sensors used in cavity monitoring*

Distributed (continuous) sensors, Brillouin or Rayleigh are distinguished from the back-scattered signal and distributed (local) sensors, like Bragg sensor. Optical fibres are simultaneously sensitive to temperature and deformation, regardless of the technology used. A fibre not subjected to deformation and placed at the same depth as the geosynthetic allows to realise deformation's measurement corrections.

3.1.1 *Brillouin technology*
Figure 2 shows a schematic drawing of the sensors and the measurement system of the Brillouin technology. The characteristics of the fibre make it particularly suitable for the detection, auscultation, and monitoring of infrastructures where the existence (or presumption) of cavities is known even if they are not localised.
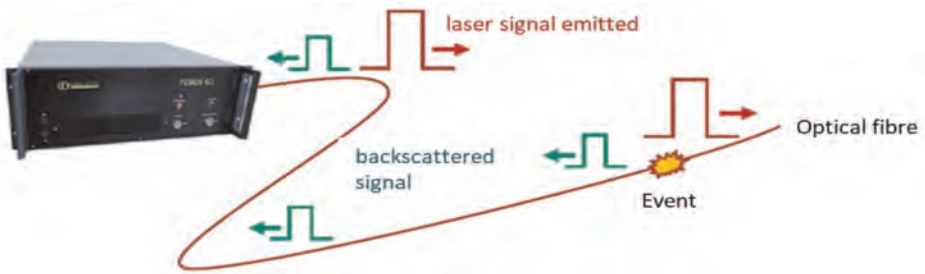
Figure 2. Principle of operation of Brillouin or Rayleigh distributed measure fibres.

3.1.2 *Rayleigh technology*

Although less used in real works than Brillouin technology, this technology can also be used for the detection, auscultation, and monitoring of infrastructure with a limitation, due to its small possible measurement's distance (Figure 2).

3.1.3 *Bragg network technology*

The principle of the Bragg sensors and the associated system are shown in Figures 3 and 4. The use of this technology implies that the wavelengths of each sensor must be chosen

λ_B wavelength reflected by the Bragg sensor
η reflective index
Λ network spacing
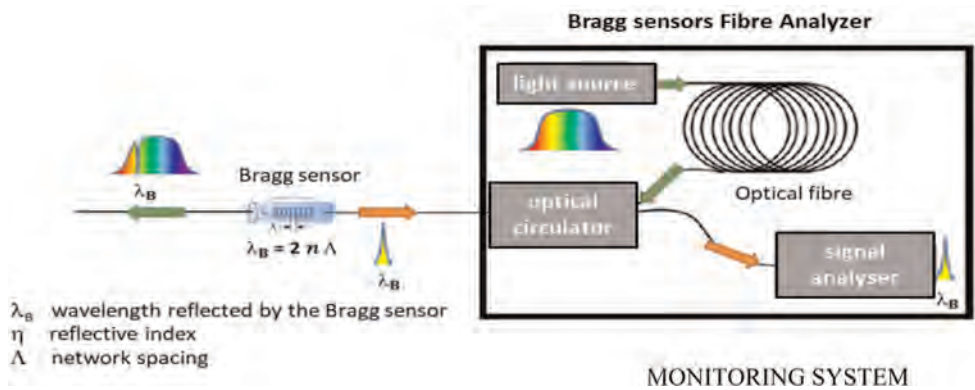
Figure 3 Operating principle of the Bragg network system with analyser.

Figure 4. Operating principle of the measurement chain and monitoring of the integrated survey system.

sufficiently spaced to avoid overlapping when the fibre is deformed. As a result, the number of sensors along the same optical fibre is generally limited to about ten. This makes this technology particularly suitable for the detection, auscultation, and monitoring of infrastructures where the location of the cavity is known or of «punctual» structures (of reduced dimensions). However, increasing the size of the area examined is possible by multiplying the fibre optic lines.

A comparison of the technical characteristics is presented in Table 1. Economically Brillouin or Rayleigh optical fibres cost around ten euros per metre, where fibres with Bragg sensors cost more than six times more. On the other hand, the Bragg sensor analyser is about seven times cheaper than the Brillouin or Rayleigh one's.

In conclusion, depending on the failure mechanisms involved, the treatment objectives and the type of surveillance chosen, the designer has a full range of solutions depending on his objectives and the means available.

Table 1. Comparison of fibre optic sensor specifications for cavity monitoring.

Characteristics	Brillouin scattering	Rayleigh scattering	Bragg network
Spatial resolution	1 m	1 m	8 mm & distance between Braggs
Measurement accuracy	10 $\mu\varepsilon$	1 $\mu\varepsilon$	1 $\mu\varepsilon$
Acquisition time	10 min	1ms	1ms
Distance of measurements	20 km	70 m	10 km
Elongation at failure	5 %	(-)	5 %
Maximum measurement strain	3%	(-)	3 %

4 MONITORING SYSTEM

Once the fibre optic sensor technology, the type of geosynthetic and the timing have been specified, the appropriate monitoring system should be designed to acquire the sensor measurements, process them against the defined thresholds and, if necessary, alerts, or alarms.

Optical fibres are woven into the geosynthetic during the manufacturing process.

The tracking system will obviously need to be able to connect to the site's optical fibres via an optical multiplexer for example.

It will:

perform data acquisition (raw measurements): either in periodic acquisition (with manual backup by a technician) or in continuous acquisition with data sampling, filtering and transfer for processing; in parallel an operation check is carried out with automatic alarm.
preliminary data processing with file concatenation, instrumental correction, amplitude calculation; this phase differentiates between unqualified (miscellaneous) and qualified anomalies (geosynthetic movements);
the data corresponding to qualified anomalies (geosynthetic movements) are then subject to advanced processing: location, extension of movements, exceeding thresholds, etc. this processing allows to trigger if necessary:
alerts to the Client with anomaly report which may result; a change in monitoring mode, on-site intervention, etc.

In parallel, the system must provide for the storage of the catalogue of detected anomalies, monitoring reports and graphs as well as equipment maintenance and progress reports.

In order to facilitate the use of this new "geo-auscultation" technology, which may seem relatively sophisticated for neophytes, Afitexinov has developed the integrated monitoring system called PREDITECT© shown in Figure 4.

In its current version, it meets the above requirements for structures monitored by Bragg sensors. Featuring a 16-way multiplexer, it tracks 128 Bragg networks. It's in situ housing allows continuous data acquisition and ensures their transfer to a specific remote server. Its associated solar panel guarantees a minimum autonomy of 6 months. Once the enclosure is connected to the construction site, the measurements can be carried out either on site, by connecting with a computer or remotely by setting up all the data on the digital platform.

On the remote server, the "integrated monitoring system" ensures all preliminary and advanced processing and, if necessary, enables the Client to trigger configurable alerts.

5 CONCLUSIONS

The use of geosynthetic reinforcement to prevent localized cavity collapses is now common and it was important to provide a technique with reliable measurement, detection, monitoring and warning system. This development, as part of the REGIC research project, has enabled the development of the new "geo-auscultation" technology which is supported by its specific integrated tracking system. The development of an innovative reverse bistiffness geosynthetic has made it possible to extend the measurement range to very small deformations allowing the early detection of subsidence above cavities.

The integrated monitoring system, developed in this framework, adapted specifically to the problem of strain monitoring in areas at risk of collapse, offers Project Managers an easy-to-use and easily configurable tool according to the surveillance objectives.

ACKNOWLEDGEMENT

REFERENCES

Al Heib M., Delmas Ph., Riot M., Emeriault F., Villard P. (2021) Recommandations Pour l'utilisation de Géosynthétique de Renforcement Dans la Mitigation du Risque d'effondrement Localisé, à Paraître.

Delli Carpini M., Emeriault F., Villard P., Riot M., Briançon L., Delmas Ph., Al Heib M. (2023) Use of Bimodulus Geosynthetics for Reinforcement of Cohesive Landfills on Cavities. *12th ICG Roma*.

Delmas Ph., Villard P., Huckert A. (2015). Dimensionnement à Court Terme et à Long Terme de Structure Renforcée Par Géosynthétique sur Cavités Potentielles : Prise en Compte de la Sécurité, CFG, *10ème Rencontres Géosynthétiques*, La Rochelle, pp 13-34.

Villard P., Gourc, J.-P., Blivet J.-C., (2002) Prévention des Risques d'effondrement de Surface Liés à La présence de Cavités Souterraines: Une Solution de Renforcement par Géosynthétique des Remblais Routiers et Ferroviaires, *Rev. Fr. Geotech.*, (99), pp. 23–34

XP G38065, (2020) Géosynthétiques – Géotextiles et Produits Apparentés, Renforcement de la Base de Remblais sur Zones à Risques d'effondrements, Justification du Dimensionnement et Eléments de Conception, *Afnor*, p. 37.

Design and construction of reinforced soil walls for a new highway in Montenegro

P. Rimoldi
Civil Engineering Consultant, Milan, Italy

Y. Han
CCCC Expressway Consultants Co., Ltd. Beijing, China

D. Zhengjie & L. Chen
BOSTD Geosynthetics Ltd., Qingdao, Shandong, China

A. Ricciuti
BOSTD International Ltd, Vaglio Basilicata, Italy

N. Wrigley
NEW Associates, Poole, UK

ABSTRACT: The paper refers to one of the largest reinforced soil walls project in Europe, the Bar-Boljari Highway construction project in Montenegro. The highway runs on hilly terrain with high slopes, hence for a large part the soil has to be excavated upslope, while for the valley side high embankments have to be built to support the road. In order to minimize the height of the embankments, to minimize land occupancy, and to minimize the quantity of excavation at the toe and the quantity of required fill, the valley side was supported by reinforced soil walls, with height up to over 30 m. Segmental wall with uniaxial extruded geogrids connected by special connectors to small size precast concrete blocks for facing has been selected as the technology for this impressive project. The paper presents the overall reinforced soil walls project, the design of the walls in static and seismic conditions, the horizontal displacement analysis, and the construction method, with details of the most challenging situations.

1 INTRODUCTION

The paper refers to one of the largest reinforced soil walls project in Europe, the Bar-Boljari Highway construction project, in Montenegro. The Investor (Government of Montenegro–Ministry of Transport and Maritime Affairs) awarded the contract to the company China Road & Bridge Corporation (CRBC), Montenegro Branch. The highway route from Podgorica to Mateševo is divided into 4 parts, each of length of approx. 10 km.

The highway runs on hilly terrain with high slopes, hence for a large part the soil has to be excavated upslope, while for the valley side high embankments have to be built to support the road. In order to minimize the height of the embankments, to minimize land occupancy, and to minimize the quantity of excavation at the toe and the quantity of required fill, the valley side was supported by reinforced soil walls, with heights from few meters to over 30 m.

DOI: 10.1201/9781003386889-101

2 SELECTION OF REINFORCED SOIL WALLS SYSTEM

2.1 *Segmental walls*

The selection of the wall type has been based on the consideration that construction will be on steep hilly terrain, hence all construction elements shall be light and easy to transport and install. Therefore the following type of wall has been selected: reinforced soil segmental walls with uniaxial extruded geogrids reinforcement connected through special connectors to small size precast concrete blocks for facing.

The characteristics of the elements of this reinforced soil wall system are now explained.

2.2 *Concrete blocks*

The segmental concrete blocks for wall facing are shown in Figure 1: the concrete blocks present a tongue on the bottom face and a groove on the top face, which allows the anchorage of uniaxial extruded geogrids through a specially engineered plastic connector, which ensures that the design strength of geogrids is not impaired at the face. This system affords that the full design strength of geogrids can be considered for their whole length, both in static and seismic conditions.
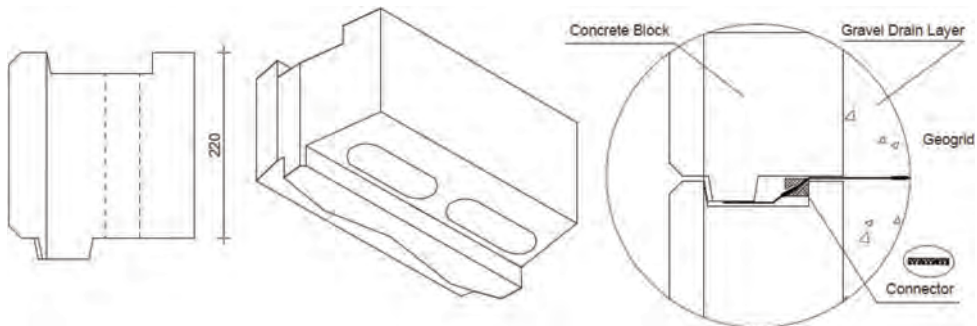
Figure 1.   The concrete blocks: a) Cross section; b) 3-D view; c) Detail of geogrid–block connection.

2.3 *Geogrids*

Geogrids for reinforced soil walls cannot be selected independently from the construction system; in this case geogrids shall fit the connections with the segmental concrete block units. For ensuring that the connection affords 100 % of the design strength of reinforcement, E'GRID uniaxial extruded geogrids (Figure 2.a), produced by BOSTD, were selected. In facts, only this type of geogrid, being an integral product made by drawing a punched HDPE sheet, affords the high junction strength required to be connected to the blocks by the plastic connector through the junctions (Figure 2.a). The geogrids selected for this project afforded ultimate tensile strengths of 60, 95, 125, 170 kN/m, and all geogrids afford a long term design strength > 44 % of ultimate tensile strength.

2.4 *Foundation pad and capping pad*

Reinforced soil walls are inherently flexible structures which can accomodate even differential settlements without impairing their stability. However, the wall system selected for this project presents a segmental concrete blocks facing system, which is in effect a semi-rigid structure. Hence the facing requires a proper foundation to avoid misalignment of concrete blocks which may produce cracking in the facing system. Since the toe of walls is very close

to the slope of the natural terrain, a cast-in-situ concrete foundation pad has been designed, featuring a front upstand which allows simple and firm block alignment and contributes avoiding outward direct sliding of the toe blocks (Figures 2.b and 3.b).

The top of walls has been finished with cast-in-situ capping pads (Figure 3.a), directly on the top row of concrete blocks (Figure 4).

2.5 *Drainage*

A drainage layer has been designed behind the concrete blocks facing for avoiding any water pressure which may impair the stability of the facing system and the connections between geogrids and concrete blocks, as shown in Figure 4.a: a 300 mm wide coarse gravel layer has

Figure 2.   a) Top view of the concrete blocks with the connectors and the uniaxial extruded geogrids; b) Front view of the first row of blocks placed against the tooth of the concrete foundation pad.
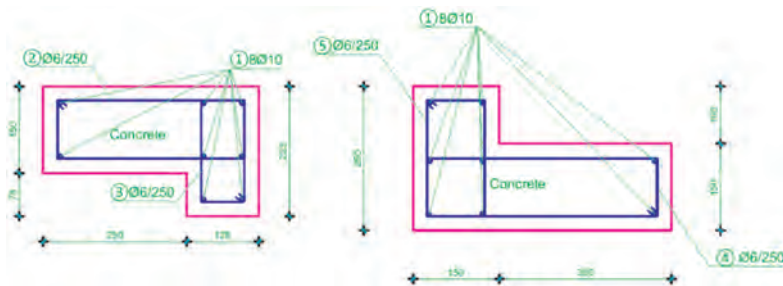
Figure 3.   Detail of cast-in-situ concrete capping pad and concrete foundation pad (all dimensions in mm).
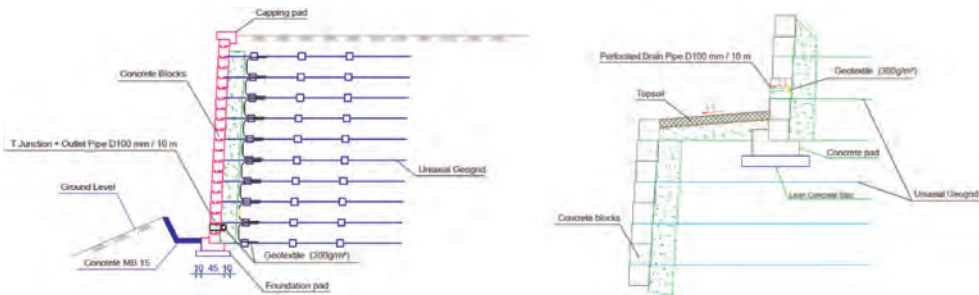
Figure 4.   a) Detail of drainage behind concrete blocks facing; b) Detail of berms.

been specified, with 300 g/m^2 nonwoven geotextiles as filter placed between consecutive geogrid layers. On each berm a horizontal drainage layer has been designed to carry all the rainfall falling on the berm to the vertical drainage layer, as shown in Figure 4.b.

This drainage system and the specification of a self-draining fill allowed to perform the design assuming no pore pressure in the whole reinforced block.

3 OVERVIEW OF PROJECT

The project includes 17 main reinforced soil walls (RSW), with height from few meters to over 30 m. The total length of RSW is 3.5 km, for a total wall face surface of 61,400 m^2; the average wall height is 16.5 m. All walls have been designed with single or multiple tiers: each tier from the top is 6.60 m high and with inclination of 86° on horizontal, with 1.25 m wide berms between tiers. Only the first tier at base has lower height than 6.60 m. Figure 5 shows the cross-section of one of the tallest walls, with height of 30.95 m, composed of 5 tiers; for this wall all geogrid layers have length of 20.10 m.

Geogrid reinforcement is always with the lowest grade (that is 60 kN/m ultimate tensile strength) at top, and increasing strength toward the base. Geogrids are placed every second block, that is with 0.44 m vertical spacing, but for the lower layer of the tallest walls the spacing has been decreased to 0.22 m, as shown in Figure 5.

The highway is always on top of the walls. Whenever possible a shallow embankment has been designed at top, as shown in Figure 5, to move the edge of the highway away from the concrete blocks facing and, in this way, to get the space for placing service pipes and conduits.

For all walls the fill is a selected granular soil with 38° friction angle and high permeability, which allows consideration of the fill as self-draining.
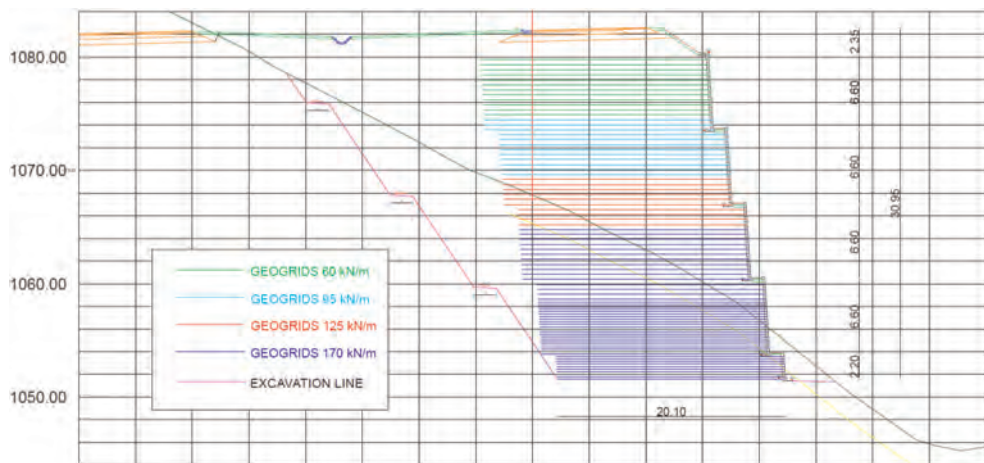
Figure 5. Cross-section of one of the tallest walls.

4 DESIGN OF REINFORCED SOIL WALLS

4.1 *Design approach*

The design process used for designing the reinforced soil structures has been the following:

- Internal stability is first addressed to determine geogrid spacing, geogrid length, and connection to the face, both in static and seismic conditions. This establishes the integrity of the wall.

- External stability against overturning, sliding, and foundation failure is investigated, both in static and seismic conditions, and the internal design is verified or modified accordingly. This establishes that the wall mass will remain stationary.
- Global stability analyses, to ensure that there are no failure mechanisms involving the reinforced soil mass, the soil behind the reinforced fill, and the foundation soil, both in static and seismic conditions. This establishes that the wall mass and the surrounding soil mass will remain stationary.

Eurocode 7 (EN 1997) requires a Limit Equilibrium design approach. A National Annex exists for each Eurocode Part, providing Nationally Determined Parameters. Since a National Annex didn't exist in Montenegro, it was decided to refer to the Italian Norm NTC 2008, since Italian geological, geotechnical, topographical, seismic characteristics are very similar to those in Montenegro.

4.2 *Internal and external stability*

Internal stability analysis addresses the following failure mechanisms: pullout of geogrids; direct sliding along geogrids; geogrids tensile failure; failure of connections between geogrids and segmental blocks. For internal stability of a geogrid reinforced soil wall the tie-back model is assumed, where the failure surface is a straight line starting from the toe and inclined at $(45° + \varphi/2)$, where φ is the friction angle of reinforced fill. To determine the geogrid layers vertical spacing and which grade to use at each level, earth pressures are assumed to be linearly distributed using Rankine active earth pressure conditions for the soil backfill and for the surcharge, even for tiered walls with overall batter $< 20°$. The tie-back model is used also for obtaining the embedment length of geogrid layers in the anchorage zone, L_E, from the pull-out analysis, which is added to the nonacting length of geogrid, L_N, within the active zone for getting the total geogrid length L.

Next, the external stability of the wall mass is considered, which includes overturning, sliding, and bearing capacity analyses. For bearing capacity analysis the Meyerhof distribution of vertical stresses on the foundation (whose width is equal to the geogrids length at base) has been assumed; hence the ultimate bearing capacity has been calculated for each wall height, using the reduced foundation width due to eccentricity, based on the design geotechnical properties of soils.

4.3 *Global stability*

Global stability analyses have been performed as follows:

- Sliding along circular surfaces (rotational stability): for the rotational stability analysis the modified Bishop method (Leshchinsky & Han, 2004) has been used, since this method affords to consider all contribution of forces acting on the slides.
- Horizontal sliding (translational stability): the mass of reinforced soil, and possibly a portion of the soil at its back, can slide as a rigid block along the base or along one of the geogrid layers; hence numerous bilinear surfaces, with a horizontal segment corresponding to increasing portions of each of the geogrid layers and an inclined segment with different angles for each horizontal segment, are therefore investigated; for each bilinear surface the resisting forces and the active forces are calculated, whose ratio provides the Factor of Safety. This is known as the Spencer method (Leshchinsky & Han, 2004).

4.4 *Seismic analyses*

The motion generated by an earthquake at a site depends on the particular local conditions, that is, from the topographic characteristics and stratigraphic deposits of soil and rock masses, and the physical and mechanical properties of the materials. The seismic motion at

the surface of a site, associated with each category of the subsoil, is defined by the maximum acceleration (a_{max}) at the surface. Once the maximum acceleration expected at the bedrock a_g has been defined, it is possible to calculate the seismic coefficients by the following formula:

$$a_{max} = S \cdot a_g = S_S \cdot S_T \cdot a_g \qquad (1)$$

where S_S, S_T are the stratigraphic and topographic amplification coefficients.

The horizontal and vertical seismic coefficients for pseudo-static analyses, K_h and K_v, are:

$$K_h = \beta_m \cdot (a_g/g); \ Kv = \pm 0.5 \cdot K_h \qquad (2)$$

where β_m is the dumping coefficient for reduction of the maximum acceleration at the site.

In the present project the bedrock acceleration a_g varies from site to site, hence from wall to wall, in the range $0.14 \div 0.225$ g.

The definition of seismic parameters was set according to Italian Norm NTC 2008.

4.5 Shear strength of concrete blocks

At the connection between geogrids and concrete blocks the tensile force in the geogrid is resisted by the upstand of the block, against which the plastic connector is butted (Figure 1.c). On the other side of the upstand the fill applies horizontal stresses due to soil thrust.

With reference to Figure 1.c, the base of the upstand is then subjected to shear stresses which may produce breaking of the upstand itself if the shear resistance of concrete is exceeded. Hence the shear strength analysis of concrete blocks is satisfied if:

$$S_{cD} = \tau_{cD} \cdot L \cdot b \geq R1 \cdot S_c \qquad (3)$$

where: S_{cD} is the design shear resistance of concrete (kN/m); S_c is the shear force at the base of the upstand (kN/m); τ_{cD} is the design resisting shear stress of concrete (kPa); L is the length of the upstand = 1.0 m; b is the width of the upstand = 50 mm; R1 is the model factor = Factor of Safety = 1.0,

The shear force S_c at the base of the upstand is:

$$S_c = T_{max} - P_h = T_{max} - \sigma_h \cdot d \qquad (4)$$

where: T_{max} is the maximum tensile strength in the geogrid at connection (kN/m); P_h is the horizontal force applied by soil on the upstand (kN/m); σ_h is the horizontal stress applied by soil on the upstand (kPa); d is the thickness of the upstand = 25 mm.

$$\text{With}: \ \sigma_h = \sigma_v \cdot K_a = \gamma_s \cdot Z \cdot K_a \qquad (5)$$

where: σ_v is the vertical stress applied by soil at the considered elevation (kPa); K_a is the active thrust parameter of fill for factorized friction angle; γ_s is the unit weight of fill = 20.5 kN/m^3; Z is the depth under wall crest.

According to Italian Norm NTC 2008, the shear resistance of concrete is obtained by the formula:

$$\tau_{cD} = 1000 \cdot [1.4 + (R_{ck} - 15)/35]/\gamma_c \qquad (6)$$

where: R_{ck} is the characteristic compressive resistance of concrete blocks (MPa); γ_c is the Reduction Factor for concrete resistance = 1.50.

The maximum tensile force applied to connections is obtained from the stability analyses in seismic conditions carried out for the tallest cross section of each wall.

The calculated Factor of Safety R1 has been always > 1.0 for all walls, thus ensuring that no concrete block of any wall will fail in shear.

4.6 *Horizontal displacements*

The serviceability limit shall refer to post construction displacements, which are equal to the difference between the displacements at 120 years and the displacements at 3 months (at the end of construction); such displacements are due to the tensile creep of the geogrids; hence for the serviceability limit we shall consider:

$$\Delta D_{i,r} = D_{i,k,r}(t = 120 \text{ years}) - D_{i,k,r}(t = 3 \text{ months}) \tag{7}$$

where: $D_{i,k,r}$ is the horizontal displacement of the i-th geogrid layer of tier k; $\Delta D_{i,r}$ is the post construction displacement at the elevation of the i-th geogrid layer of tier k.

According to BS8006: 2010 the serviceability limit for the horizontal strains of the structure of a reinforced soil wall (that is of the whole reinforced block with length L_i, equal to the length of the reinforcing geogrids), with no permanent structural load, is set as:

$$\Delta \varepsilon_{ij \text{ structure, post construction}} \leq 0.01 \, L_i \tag{8}$$

If the differential displacement calculated with Eq. (7) respects the condition in Eq. (8), the serviceability limit on horizontal displacement shall be considered as verified.

The post construction creep strain of the structure, $\Delta \varepsilon_{ij\text{-structure}}$, that is of the whole reinforced block, can be calculated at each geogrid level, by dividing the total post construction displacement (from Eq. 7) by the geogrid length (equal to the width of the reinforced soil block):

$$\Delta \varepsilon_{ij-\text{structure}} = \Delta D_{i,r}/L_i \tag{9}$$

where: L_i = total length of the i-th geogrid (m).

The values of $D_{i,k,\,r}$ (t = 120 years) and of $D_{i,k,\,r}$ (t = 3 months) have been calculated, at each geogrid elevation of each wall, with the method developed by Rimoldi (2018). Figure 6 shows the displacements and strains calculated for a 23.32 m high wall, composed of 4 tiers.

For all walls the condition (8) resulted as satisfied, hence the serviceability limit on horizontal displacement has been verified for all reinforced wall structures of the project.

5 CONSTRUCTION OF REINFORCED SOIL WALLS AND CONCLUSIONS

The construction of the walls was relatively fast and easy, thanks to the modularity and flexibility of the segmental wall system.

Special care had to be applied for the wing walls at the attachment with bridge abutments, where the design layout required either curved or angular connections, as shown in Figure 6. Also widening of the highway at toll stations (Figure 7.a) and the approach to tunnel entrances (Figure 7.b) required specific design details and construction care. The modularity of the construction system allowed to easily address the sudden changes of the wall height, due to the level variability of the hilly terrain (Figure 8.a), and the layout around concrete culverts (Figure 8.b).

The whole project has been completed in July 2022 and the highway was open to the traffic.

All the reinforced soil walls perform very well and their aesthetics has been appreciated, since it merge with the surrounding rocky landscape.

Therefore, this challenging reinforced soil walls project can be considered as completely successful.
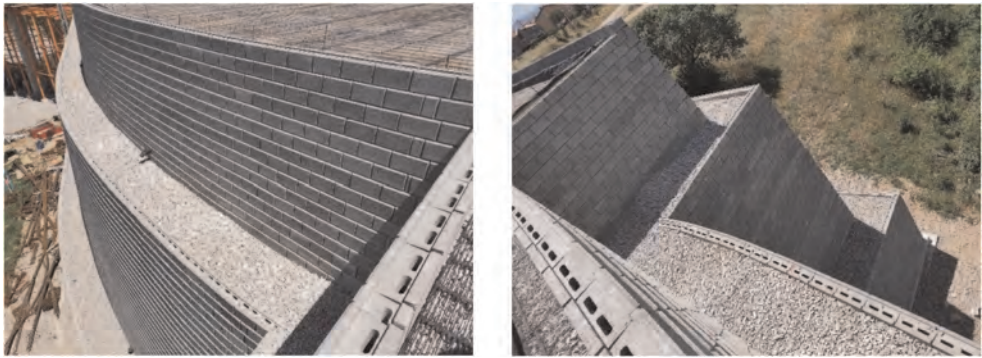
Figure 6.   Connection between wing walls and bridge abutments: a) Curved wing wall; b) Angular wing wall.

Figure 7.   a) Angular wall for highway widening at toll station; b) Wall at tunnel entrance.

Figure 8.   a) Wall with sudden height variation; b) Wall layout around a concrete culvert.

REFERENCES

BS8006:2010. *Code of Practice for Strengthened/reinforced Soils and Other Fills*. BSI. London, UK
EN 1997-1–*Eurocode 7–Geotechnical Design–Part 1: General Rules*. CEN, Bruxelles, Belgium.
Leshchinsky, D. & Han, J. (2004). Geosynthetic Reinforced Multitiered Walls. *Journal of Geotechnical and Geoenvironmental Engineering*, ASCE, 130(12), 2004, 1225–1235.
NTC 2008. *Italian Norm for Constructions*. Italian Offical Gazette Nr 29, 4 February 2008.
Rimoldi, P. (2018). Horizontal Displacements of Reinforced Soil Walls from Limit Equilibrium Calculations. *Proc. 11ICG, 11th Int. Conf. on Geosynthetics*. Seoul, Korea.

Gabion faced reinforced slope with composite reinforcement geotextile, Kandy, Sri Lanka

G.Y.T. Tan
Sarawak Energy Berhad, Kuching, Sarawak, Malaysia

C.J. Jong & J.Y. Tan
TenCate Geosynthetics Asia Sdn. Bhd., Shah Alam, Selangor, Malaysia (A Solmax Company)

ABSTRACT: Kandy, a UNESCO World Heritage Site, is the second largest city in Sri Lanka. The city lies on the 'Kandy' plateau which is mountainous and thickly forested. With the development and population growth in Kandy, it is necessary to construct a wastewater treatment plant which include sludge drying beds. The sludge drying beds which occupy area of about 1.5 acres located in a hilly area on the outskirts of Kandy, namely Gohagoda. To provide the necessary flat platform areas and access road, 250 m length of reinforced soil slopes with slope angle of 65° was constructed on site. The reinforced soil slopes comprise of single tier and two tiers slope with maximum height of 18 m, consisting of gabion facing units with layers of composite reinforcement geotextile. Total 44,000 m^2 of high tenacity composite reinforcement geotextile with characteristic ultimate tensile strength up to 100 kN/m were used in the project.

1 INTRODUCTION

Registered as UNESCO World Heritage Site, Kandy is in the Central province of Sri Lanka and is the second largest city after Colombo. Kandy is both an administrative and religious city housing the Temple of Tooth which is one of the most sacred places of worship in the world. The city is in the Kandy plateau which is mountainous and thickly forested on the island.

Due to city development and rapid increase in population in Kandy, urban issues such as environmental pollution is being concerned. Due to improper disposal of wastewater, the wastewater produced flows through various forms of waterways, deteriorating the water quality that threatens both human beings and environment in Kandy. For example, city's sewerage systems, drainage systems and river are all finally connected to the largest and longest river in Sri Lanka, the Mahaweli River which serves as the main source of raw water locally. To address the water pollution issue in the Mahaweli River, the city of Kandy with collaboration of Kandy Municipal Council (KMC) and National Water Supply and Drainage Board (NWS & DB) together with Japanese International Cooperation Agency (JICA) has introduced a wastewater management project. Figure 1a shows the layout of the overall wastewater management project in Kandy. This project involved the construction of wastewater treatment plant, sludge drying beds, treated effluent disposal system with pipelines, main pump station and maintenance facilities.

Land utilization is a primary concern in this project due to the challenging terrain with limited flat land and access road for construction. Reinforced soil slope (RSS) was designed to support the sludge drying beds (SDB) and access roads which takes up about 1.5 acres of land in Gohagoda. Approximately 250 m length of RSS was proposed in the project (see Figure 1b). The design height of RSS varies from 5.5 m to 10.0 m for single tier slope and up to maximum 18 m combined height with two tiers of slope due to the uneven existing ground terrain.
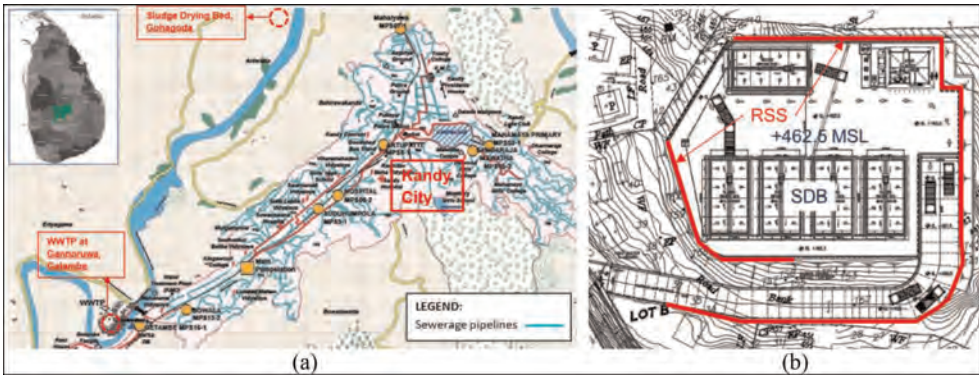
Figure 1. The layout of the overall wastewater management project in Kandy (a) and RSS layout (b).

2 SOIL CONDITIONS & SITE TERRAIN

The location where the newly constructed SDB sit on was a landfill area sitting on uphill, with garbage filling activities carried out in the past. With reference to the soil investigation report, three (3) borehole tests were carried out at site initially, with two (2) additional boreholes being carried out later near to the slope area (see Figure 2). The worst soil profile at site consists of about 3.5m depth of garbage fill layer, followed by a very strong completely weathered rock with SPT-N value greater than 50 (see Table 1). Due to the varying soil profile found at site, a different set of soil parameters were input for the slope designs to ensure the designs are safe and economical.
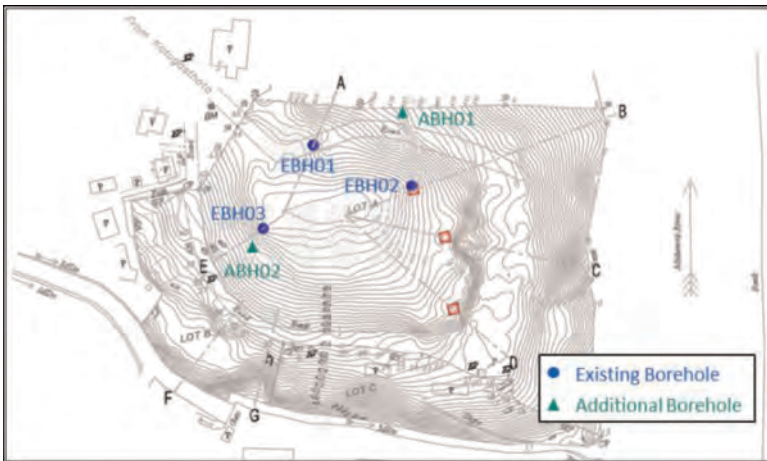
Figure 2. Borehole location and section.

Table 1. Foundation soil properties.

Section	Description	Depth m	Average SPT	Unit weight kN/m^3	Cohesion kPa	Friction angle °
A-A	Highly weathered rock	0.0–5.0	>50	20	10	35
B-B	Garbage fill	0.0–2.0	–	–	–	–

(*continued*)

Table 1. Continued

Section	Description	Depth m	Average SPT	Unit weight kN/m^3	Cohesion kPa	Friction angle °
	Highly weather rock	2.0–7.0	> 50	20	10	35
C-C	Completely weathered rock	0.0–6.0	> 50	20	10	35
D-D	Completely weathered rock	0.0–6.0	> 50	20	10	35
E-E	Garbage fill	0.0–3.5	–	–	–	–
	Highly weathered rock	3.5–13.0	> 50	20	10	35
F-F	Completely weathered rock	0.0–18.0	> 50	20	10	35
G-G	Completely weathered rock	0.0–18.0	> 50	20	10	35

3 REINFORCED SOIL SLOPE SYSTEM

Reinforced soil slope (RSS) is a mechanically stabilized earth structure reinforced with planar reinforcement elements with face inclinations of less than 70 degrees (Berg *et al.* 2009a). Planar reinforcement such as reinforcement geotextiles are typically laid horizontally in multiple layers in a RSS (see Figure 3), providing adequate tensile capacity and stabilizing the slope by transferring destabilized forces from active zone of the slope to resistance zone.
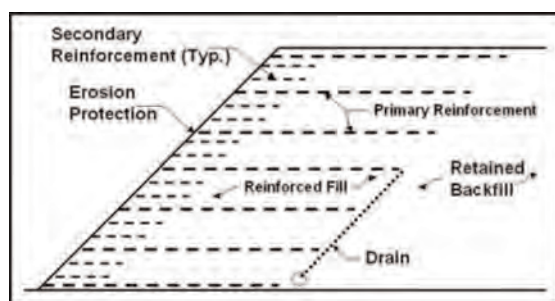
Figure 3. Typical cross section of the reinforced soil slope structure (Berg *et al.* 2009a).

In this project, single tier and two tiers RSS are being constructed with a maximum of 10 m high for the single tier RSS. For the two tiers RSS, a maximum 18 m high with two tiers separated by a 9 m setback distance was constructed. The slope facing angle was formed by stepping each gabion layer approximately half a meter back at each level to create a 65° slope profile.

3.1 Facing system

Gabion facing system is selected for the RSS in this project. The gabion basket is in square size, measuring by 1 m wide by 1 m high by 1 m deep for each basket. The size of rock fills selected to fill up the gabion baskets ranging between 150 mm to 225 mm, with rocks tightly packed into basket to minimize voids.

3.2 Backfill materials

The residual granular soils that are locally available at site are used as the backfill material of the RSS. Utilizing locally available soils not only helps to save cost and time for importing soils, but it also reduces the needs of exporting the excavated soils, especially for a challenging site terrain with difficult access. The selected fills were carefully evaluated to ensure the achievable soil properties meet the project requirements.

3.3 *Reinforcement and filter geotextiles*

Reinforcement and filter geotextiles were used in the construction of the RSS. The reinforcement geotextile used to stabilize the reinforced slope is the Polyfelt® PEC composite reinforcement geotextile made of high modulus polyester yarns knitted to a nonwoven geotextile. The composite reinforcement geotextile combines reinforcement with superior filtration and drainage functionality to enable finer grained soils to be reinforced. The filter geotextile used to wrap drainage aggregates and subsoil pipes is the Polyfelt® TS nonwoven geotextile made of polypropylene continuous filament fibers needle-punched into planar form.

3.4 *Drainage blanket*

The base drain and back drain or often refer as drainage blanket, is designed to collect and remove groundwater from cut slope or behind the reinforced mass and allow infiltration water to preferentially flow toward the back of slope, away from the slope facing (Berg *et al.* 2009a). A typical 300 mm thick drainage blanket is proposed for the RSS. The subsoil pipes are placed within the single size aggregate layer with a nonwoven filter geotextile wrapping both within. To prevent the fines from moving into the subsoil pipes, nonwoven filter geotextile was used to wrap the pipes, protecting it from malfunction due to the potential blockage by the fines. Apart from that, the nonwoven geotextile also protects the subsoil pipes from potential damage from the adjacent aggregates.

4 REINFORCED SOIL SLOPE DESIGN

The design of the RSS using composite reinforcement geotextiles are based on BS 8006-1 (2010). For example, the vertical spacing of the geotextiles and fill material used are proposed according to the strict guidelines stated in the design manual to ensure the structural integrity and workability of the RSS.

4.1 *Soil parameters*

Two soil layers were modelled in the stability analysis, which are the residual granular soil as the backfill soil and weathered rock as the foundation soil. The soil parameters inputted in the analysis are shown in Table 2.

Table 2.   Input soil parameters.

Soil types	Unit weight kN/m^3	Cohesion kPa	Friction angle degrees
Backfill soil	19	0	32
Foundation soil	20	10	35

4.2 *Surcharge loading*

In the design analysis, a uniformly distributed surcharge loading of 20 kPa representing the future traffic loading access to reach the sludge drying bed was adopted on top of the setback platform and the 18 m height finished platform. Dead load such as structure loading was not considered in the RSS design and were taken care by other supporting system.

4.3 *Reinforcement long-term design strength*

Two product grades of the PEC composite reinforcement geotextile were determined and proposed for the RSS based on stability analysis. The lower grade PEC50 was used for the

upper tier whereas the higher grade PEC100 was used for the bottom tier of the RSS. Table 3 shows the long-term design strength of the PEC composite reinforcement geotextile with a design life of 120 years.

Table 3. Long term design strength of PEC composite reinforcement geotextiles used.

Property	Unit	PEC50	PEC100
Characteristic initial strength	kN/m	50	100
Partial factor – creep rupture		1.55	1.55
Partial factor – construction damage		1.02	1.00
Partial factor – environmental effects		1.10	1.10
Long-term design strength (120 years)	kN/m	28.8	58.7

4.4 Stability analyses

Various checking is required to ensure the RSS poses adequate factor of safety against various types of failure. For RSS, the critical design aspects may tend towards internal mode of failures (BS 8006-1 2010). The design was carried out using manual calculation based on BS 8006-1:2010 and with the usage of ReSSA (3.0) software (RESSA 2008). Table 4 shows the various modes of failure considered and the general minimum factor of safety required.

Table 4. Various modes of failure and respective minimum factor of safety required (BS 8006-1 2010, Berg *et al.* 2009b).

Failure mode	Minimum factor of safety
External Stability	
Bearing capacity	1.3
Sliding failure	1.3
Global slip failure	1.3
Internal Stability	
Tensile failure of reinforcement	1.3
Bond failure of reinforcement	1.3
Compound Stability	
Composite slip failure	1.3

4.5 RSS detailing

Figure 4 shows the typical cross section of the single tier maximum 10 m high RSS and two tiers combined maximum 18 m high RSS in this project.
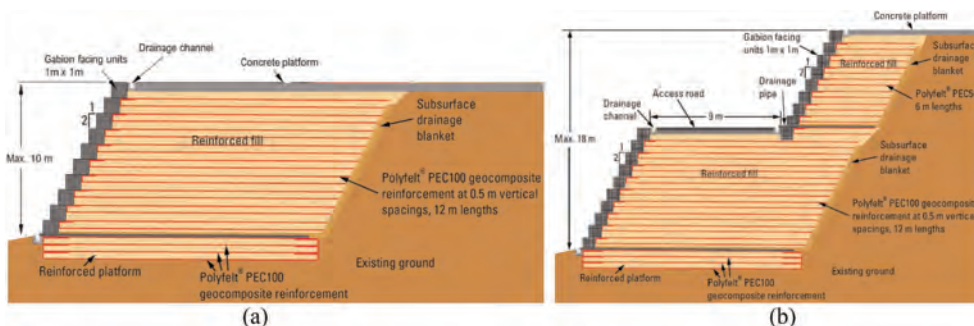
Figure 4. Typical cross section of the proposed single tier RSS (a) and two tiers RSS (b) in Gohagoha.

5 CONSTRUCTION OF REINFORCED SOIL SLOPE SYSTEM

The construction of the RSS began with excavation to form the foundation platform of the RSS at an embedment level of 1.5 m below the base of the RSS. The ground was levelled as flat and smooth as possible for the laying of the first layer of the reinforcement geotextiles. The Polyfelt® PEC composite reinforcement geotextile was precut to length according to the design anchorage length, laid side by side and overlapped with adjacent geotextile panels to ensure the continuity of the reinforcement coverage across the entire slope structure. Once the composite reinforcement geotextile was laid, it was pulled taut and backfill materials were placed over the composite reinforcement geotextile followed by compaction (see Figure 5).

Figure 5.   Placement of backfill soil (left) and compaction of backfill soil (right).

The compaction was carried out with a compaction lift thickness of 0.25 m to achieve a minimum 95% of the optimum dry density based on Standard Proctor method. The composite reinforcement geotextile was installed at 0.5 m vertical spacings. For every unit of gabion baskets installed, a layer of composite reinforcement geotextile is placed under the gabion unit thus creating a frictional connection between the reinforcement and gabion units. At the same time a layer of reinforcement geotextile coincided half-way up the gabion basket was wrapped back towards the backfill materials.

At the base of each tier, a subsurface drainage blanket consisting of single size aggregates wrapped in the Polyfelt® TS nonwoven geotextile was installed (see Figure 6). Along the increased slope height, the drainage blanket was continued up at the back of the slope to intercept any seepage water coming from the back of the slope. A drainage pipe was installed horizontally all the way from the back of the slope to the slope facing. Figure 7 shows the completed RSS with the SDB ready for operation.

Figure 6.   Placement of drainage pipe (left) and drainage blanket at the back of the slope (right).

Figure 7.   Completion of reinforced soil retaining slope.

6   CONCLUSIONS

Without the help of geosynthetics, the slope would have to be constructed at a gentler angle which results in smaller useable land. Geosynthetics reinforced soil slope enables the maximization of land space, and its simple installation allowed the SDB construction to be finished within tight schedule. With the completion of SDB which forms part of the wastewater management project, wastewater can now be processed and cleansed before flowing into the Mahaweli river. Clean water not only improves the health of the public but also assures the sustainability of the environment and natural resources that maintain life forms.

REFERENCES

Berg, R.R., Christopher, B.R. & Samtani, N.C. 2009a. *Design and Construction of Mechanically Stabilized Earth Walls and Reinforced Soil Slopes – Volume I (FHWA Report No. FHWA-NHI-10-024)*. Washington DC: National Highway Institute, Federal Highway Administration, U.S. Department of Transportation.

Berg, R.R., Christopher, B.R. & Samtani, N.C. 2009b. *Design and Construction of Mechanically Stabilized Earth Walls and Reinforced Soil Slopes – Volume II (FHWA Report No. FHWA-NHI-10-025)*. Washington DC: National Highway Institute, Federal Highway Administration, U.S. Department of Transportation.

BS 8006-1 2010. *Code of Practice for Strengthened/Reinforced Soils and Other Fills*. London: British Standards Institution (BSI).

RESSA. 2008. *ReSSA Software Version 3.0*. Delaware: ADAMA Engineering, Inc.

Design and construction of the largest reinforced soil walls project in Cyprus

P. Rimoldi
Civil Engineering Consultant, Milan, Italy

G. Lugli & F. Trovato
Officine Maccaferri Spa, Bologna, Italy

I. Nicolaou
PYS IPSONAS Ltd, Cyprus

ABSTRACT: The paper refers to the design and construction of the largest reinforced soil walls project in Cyprus. The overall project includes reinforced soil wall (RSW) and true bridge abutment structures for the perimeter highway in Lefkosia, the Germasoyeias - Akrountas – Dierona - Arakapa road in Akrounta, the northern bypass of Geroskipou in municipal boundaries Paphos Konia, the Limassol - Saittas Motorway. The project, with a total of 22 RSW with 23,471 m^2 of wall facing, is considered the largest reinforced soil walls application in the country. The walls were designed and built as reinforced fill structures, with precast concrete panel facing elements and polymeric reinforcing strips according to the the Limit Equilibrium design approach and Eurocode 7 (EN 1997). All Cyprus is a seismic area, with peak ground acceleration varying from region to region in the range 0.15–0.25 g. The paper reports the design procedure for the RSW, both in static and seismic conditions. Construction details are introduced and illustrated by photos and sketches.

1 INTRODUCTION

In the last decade the amount of passenger cars per 1000 inhabitants in Cyprus has increased by hundred cars (545 to 645) placing Cyprus on the 7th place among EU, according to Eurostat. Although the amount of passenger cars has increased, the length of motorways and roads in built-up areas has remained almost unchanged over the same period, with increasing traffic problems especially in the capital city Nicosia. This generated the need to build new road infrastructures and improve the existing road network in the island.

For relieving traffic congestion around the city of Nicosia, the Nicosia Orbital Road project is designed to solve the capital's traffic load by creating new roadways. Currently, Phase 1 is under construction and due for completion in 2023, creating 7.5 km of new highway road, 10 km of connecting roads and 3 major junctions.

Limassol - Saittas Motorway is another major project with the aim of expanding the city of Limassol. The project scope is to assist with the suburban development of rural areas and the revitalisation of Troodos Mountain villages and communities. The project is designed in three phases. Phase 1, which is under construction, includes motorway, junctions, and overpasses.

The Germasoyeias - Akrountas - Dierona - Arakapa Rural Road project in Akrounta aims to upgrade 18 km of existing road network to boost the development of the eastern rural communities of Limassol and improve their connection with the city.

In Paphos District, on the west region of the island, the construction of the Paphos – Geroskipou Industrial Area bypass road aims to improve access towards the industrial zone,

previously congested by the merge with the city traffic. The project includes the construction of 6.6 km road network and a bridge overpassing the local stream "Limnaria".

2 THE SELECTED WALL SYSTEM

Retaining structures are heavily demanding in terms of material supplies. Concrete gravity walls, for example, requires large quantities of cement and its production and delivery produce a significant amount of CO_2 emission. Cantilever walls proved to be less demanding than concrete gravity structures, yet not comparable with reinforced soil walls (RSW). The advantages of a reinforced fill structure compared to conventional solutions are even more significant with increasing structure height. The difference among these structures is typically related to the structural components: cast in place walls (CIPW) main element is concrete while RSW rely on reinforcement of soil for supporting loads and superstructures. When possible, in situ soil is used as it is or partially re-worked with selected backfill or chemicals to function as structural fill of the RSW. This entails additional benefits as it represents a further step in achieving circular economy.

When it comes to aesthetics, durability, building installation, and planned settlements, several considerations can lead to the choice of RSW systems. These solutions are often constructed in difficult terrain where massive concrete solutions and traditional construction are not achievable due to site constraints. RSW can withstand extreme loads and mitigate the impacts of high seismic loads thanks to their flexible yet resistant nature. The soil reinforcement elements can be designed to support typical project loads, from traffic to bridge deck, for very long design life (typically 120 years for relevant structures). Once built, the RSW load is spread over a wider foundation area compared to CIPW, therefore RSW can tolerate higher overall and differential settlements, without causing structural damage. RSW walls are versatile, allowing for nearly any geometry and aesthetical customization. Precast concrete panels are relatively thin and can be customized in shape, finishing and colour to fit the architectural requirements. No curing time on site or support structures are needed for these structures, so design and installation are faster than for CIPW. RSW construction does not require skilled labour, even though experience and accuracy are important to guarantee the best results, and the usage of heavy machinery is limited.

The advantages of RSW are also important when it comes to post-construction maintenance. Distress signs can be monitored, and appropriate repair techniques adopted to avoid post-construction concerns and structure instability. Maintenance inspection guidelines detailing expected performance metrics and most appropriate repairs for specific distress observations are often available. Only for shallow RSW costs may become less convenient compared to other wall systems (e.g. CIPW), while significant economic savings has been achieved by using RSW in the construction of retaining walls and bridge abutments (where optimized RSW design leads to shortening the required bridge deck span with clear technical and economic advantages). The polymeric nature and intrinsic flexibility of geosynthetic reinforcement are also a plus when dealing with geometrical obstructions (e.g. pipes, culverts, manholes, etc.), where the geosynthetics layout can be designed to avoid any threat for the structure stability. Moreover, the post-construction deformation of RSW, when subjected to design loads, can be designed to respect the limits indicated by BS8006:2010 guidelines.

Considering all the technical, environmental and economic aspects, RSW has been selected for all the above-described projects in Cyprus. The selected RSW is the MacRes system, developed by Maccaferri, based on precast concrete panel facing elements connected to ParaWeb polymeric geostrips, consisting in discrete bundles of closely packed high strength polyester (PET) filaments, lying parallel to each other, and encased in a tough and durable polyethylene (LLDPE) coating. The geostrips are available in a wide range of tensile strength and width to meet the project design requirements. Geostrips are less demanding than steel reinforcements when dealing with resistivity, water, moisture, chloride ion concentration, temperature, corrosion due to exposure to environment and chemical agents (de-icing salts, etc.).

3 DESIGN OF REINFORCED SOIL STRUCTURES

3.1 *Design approach*

The design process used for designing the reinforced soil structures has been the following:

- Internal stability is first addressed to determine geostrips spacing, length, and tensile strength, and for checking connections to the facing panels, both in static and seismic conditions. This establishes the integrity of the wall.
- External stability against overturning, sliding, and foundation failure is analysed, both in static and seismic conditions, and the internal design is verified or modified accordingly. This establishes that the wall mass will remain stationary.
- Global stability analyses, to ensure that there are no failure mechanisms involving the reinforced soil mass, the soil behind the reinforced fill, and the foundation soil, both in static and seismic conditions.

Eurocode 7 (EN 1997) requires a Limit Equilibrium design approach. A National Annex exists for each Eurocode Part, providing Nationally Determined Parameters. The Cyprus National Annex was integrated with the Italian Norm NTC 2018, since Italian geological, geotechnical, topographical, seismic characteristics are very similar to those in Cyprus.

3.2 *Internal and external stability*

Internal stability analysis addresses the following failure mechanisms: pullout of geostrips; direct sliding along geostrips; geostrips tensile failure; failure of connections between geostrips and concrete facing panels. For internal stability, geostrip are considered as an extensible reinforcement, hence the tie-back model is assumed, where the failure surface is a straight line starting from the toe and inclined at $(45° + \varphi/2)$, where φ is the friction angle of reinforced fill. To determine the geostrips vertical spacing and which grade to use at each level, earth pressures are assumed to be linearly distributed using Rankine active earth pressure conditions for the soil backfill and for the surcharge. The tie-back model is used also for obtaining the length of embedment of the geostrips in the anchorage zone, L_E, from the pull-out analysis, which is added to the length of geostrips within the active zone, L_N, for getting the total geostrip length L. The horizontal spacing of geostrips is varied by increasing or decreasing the number of connections to concrete panel units, ranging from 4 to 6 connections every two panels, that is every 3 m width. Since each geostrip enters and exits the connections at narrow angles, the coverage ratio is calculated considering two geostrips widths for each connection.

Next, the external stability of the wall mass is considered, which includes overturning, sliding, and bearing capacity analyses. The ultimate bearing capacity has been calculated for each wall section, using the Meyerhoff distribution of vertical stresses on the foundation (whose width is equal to the geostrips length at base), using the design geotechnical properties of soils and the design surcharge loads.

3.3 *Global stability*

Global stability analyses have been performed as follows:

– Sliding along circular surfaces (rotational stability): for the rotational stability analysis the modified Bishop method (Leshchinsky & Han 2004) has been used, since this method affords to consider all contribution of forces acting on the slides.
– Horizontal sliding (translational stability): the mass of reinforced soil, and possibly a portion of the soil at its back, can slide as a rigid block along the base or along one of the geostrip layers; hence numerous bilinear surfaces, with a horizontal segment corresponding to increasing portions of each of the geostrip layers and an inclined segment with different angles for each horizontal segment, are therefore investigated; for each bilinear surface the resisting forces and the active forces are calculated, whose ratio provides the Factor of Safety (Leshchinsky & Han 2004).

3.4 Seismic analyses

The motion generated by an earthquake at a site depends on the particular local conditions, that is, from the topographic characteristics and stratigraphic deposits of soil and rock masses, and the physical and mechanical properties of the materials. The seismic motion at the surface of a site, associated with each category of the subsoil, is defined by the maximum acceleration (a_{max}) at the surface. Once the maximum acceleration expected at the bedrock a_g has been defined, it is possible to calculate the seismic coefficients by the following formula:

$$a_{max} = S \cdot a_g = S_S \cdot S_T \cdot a_g \qquad (1)$$

where S_S, S_T are the stratigraphic and topographic amplification coefficients, which were set for each wall according to Italian Norm NTC 2018.

The horizontal and vertical seismic coefficients for pseudo-static analyses, K_h and K_v, are:

$$K_h = \beta_m \cdot (a_g/g); K_v = \pm\, 0.5 \cdot K_h \qquad (2)$$

where β_m is the dumping coefficient for reduction of the maximum acceleration at the site, which was set equal to 0.38 according to Italian Norm NTC 2018.

In the present project the bedrock acceleration a_g varies from site to site, hence from wall to wall, in the range $0.15 \div 0.25$ g.

4 RSW CONSTRUCTION

4.1 Overview

The Cyprus project, with a total of 23,471 m^2 of wall facing, and considering all the 22 RSW that have been built, is considered the largest reinforced soil walls application in the country. This major project has been characterized by the large array of challenges that designers and contractors have tackled for each structure. Different types of RSW were specifically designed to fulfil all the requirements of the sites, space constraints in urban areas, interferences with other infrastructures, and the need of quick and reliable solutions for the many critical geometrical situations; the main types and forms of RSW walls can be classified in 5 categories: simple walls with horizontal or sloping top, trapezoidal walls, back to back walls, true bridge abutments, and overpass and underpass structures. Table 1 presents the inventory for each type of RSW. For this project, the total quantity of geostrips was 778,440 m and the geostrips ultimate tensile strengths were 27 kN; 30 kN; 36 kN; 45 kN; 40 kN; 54 kN; 63 kN; 70 kN. The nominal width of the geostrips vary from 46 to 90 mm and the thickness vary from 1.8 to 2.8 mm.

Table 1. Cyprus project RSW structure inventory.

Wall types	Total facing		Maximum wall height	Geostrip quantity
	m^2	%	m	m
Simple walls [a]	7,007	30%	10.24	227,950
Trapezoidal cross section walls	1,231	5%	7.70	34,460
True abutments [b]	8,220	35%	12.00	306,350
Back-to-back walls	3,711	16%	14.41	92,300
Overpass/Underpass walls	3,302	14%	13.50	117,380

[a]including both horizontal and backslope on top; [b]including the lateral wing wall.

4.2 Simple walls

Simple walls were generally used for the design of highway ramps and retaining walls in Nicosia Orbital Road. The tallest section (H = 9.46 m) with horizontal top was designed for the T6-T7 highway ramp, while the tallest section with sloping top ($H_{backslope}$ = 6.70 m; inclination α = 30°) was reached for the design of the EAC wall (Figure 1). The backslope affected the design, in facts long and closely spaced geostrips with high ultimate tensile strength (UTS) per unit width were required ($L_{geostrip}$ = 13 m; Coverage ratio C = 0.19; UTS = 942 kN/m), according to eccentricity and rotational stability analyses. In addition, a drain channel was provided at the top of the facing behind the top panels, in order to remove water running off the slope and to discharge it at the end of the wall.

Figure 1.   Simple walls: (a) T6-T7 ramp with horizontal top; (b) EAC wall with sloping top.

4.3 Trapezoidal cross section walls

RSW with uneven reinforcement lengths increasing from base to top (known as trapezoidal walls) were adopted for the reconstruction of roadway in Germasogeia – Arakapas area (Figure 2a). This type of reinforcement geometry was the most suitable solution to reduce the amount of excavation works due to the presence of firm ophiolite and dunite rocks (N_{SPT} > 60) encountered after few meters of excavation of the in situ soil. The presence of rock at the back reduces the lateral earth pressure, allowing to shorten the length of the geostrips up to a maximum of L = 0.40 H, where H is the wall height . The flexibility of the polymeric geostrips allowed also to solve some criticalities concerning the presence of large storm drain pipes crossing the wall. Customized panels were designed to fit around the pipe and avoid the washout of the fill through the wall facing. The detail of the drain pipe interference is shown in Figure 2b: a 50 mm thick polystyrene foam was laid around the pipe and the remaining gap between the customized panels and the pipe was filled with concrete or grout.
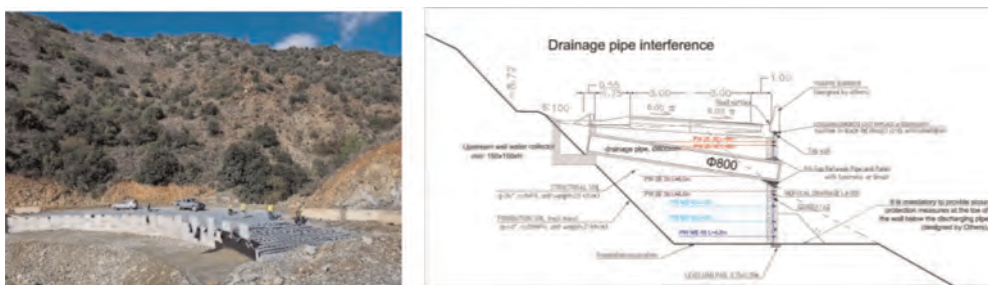
Figure 2.   Trapezoidal wall in mountain area: (a) strips installation; (b) storm pipe interference detail.

4.4 *True bridge abutments*

True bridge abutments are RSW where the concrete bridge seat is placed directly on the reinforced soil block. The structure is therefore directly bearing the loads from the bridge deck (Figure 3a).

Figure 3.   True bridge abutments in Nicosia orbital road: (a) elevation view; (b) cross section.

True abutments were chosen for the construction of the T4, T10 and T17 structures of Nicosia Orbital road for their strategic importance on the viability, where the needs to have a cost effective solution meet also the requirement to keep a tight construction schedule.

It has to be noted that the bridge imposes an extremely high load on the true abutment: as example, for abutment T17 the vertical component of the load on the bridge seat is equal to 13,800 kN, which produces a linear vertical load of 970 kN/m on the abutment and of 5,050 kN/m on the wing wall; moreover, the horizontal component of the load on the bridge seat, perpendicular to the abutment face, is equal to 850 kN.

Considering also that, due to space constraints, the bridge deck was installed very close to the abutment face, a higher density and higher grade of reinforcement (UTS = 801 kN/m, Coverage Ratio C = 0.30) were designed at the top of the structure, while decreasing with depth as the bearing stresses dissipate (Figure 3b). Also the vertical spacing of the geostrips was reduced to S_v = 0.37 m at the top of the abutment, and then increased to S_v = 0.75 m for the bottom layers.

4.5 *Back-to-back walls*

Back to back walls have been mainly used for the design of the long T6A-T6M highway ramp of Limassol – Saittas Motorway. The peculiarity of this application resides in the complexity of the design of a tall and narrow ramp (H_{max} = 14.41 m, width of the ramp = 6.5 m), combined with the presence of horizontal and vertical obstructions, such as manholes, gullies and longitudinal pipes for services. The feasibility of the structure have been made possible thanks to the flexibility of the system and the possibility to lay the geostrips all around the obstruction (Figure 4).
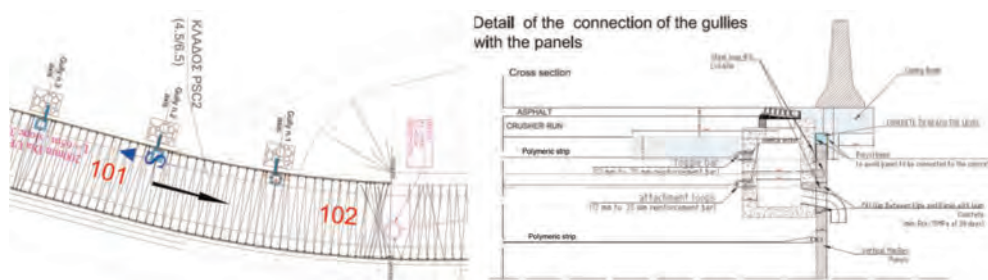
Figure 4.   T6A-T6M ramp: (a) Plan view of geostrips layout; (b) detail of connection of gully with panels.

4.6 Overpass/underpass walls

Overpass and Underpass walls have been mainly designed to allow culverts for pedestrians, cars or water to pass through the structure. The design of these walls was complex because of the height (H_{max} = 13.50 m), high loads and complex geometry of the required panel facing. The Geroskipou Industrial Area bypass is a representative example of such complex geometry: the panels geometry have been designed ad hoc to fit the articulated shape of the culvert while keeping aligned to the curved road alignment (Figure 5).

Figure 5.   Geroskipou bypass road.

5   CONCLUSIONS

The design and construction of the largest reinforced soil walls project in Cyprus has been described, including several types of wall configurations and true bridge abutments in high seismic areas. The RSW were designed and built using a system consisting with precast concrete panel facing elements and polymeric geostrip reinforcements. Construction details have been illustrated by photos and sketches. The construction of the walls has been relatively fast and easy, thanks to the modularity and flexibility of the wall system. All RSW built so far perform very well, therefore this challenging reinforced soil walls project can be considered as completely successful.

REFERENCES

BS8006:2010. *Code of Practice for Strengthened/reinforced Soils and Other Fills*. BSI. London, UK
EN 1997-1 - *Eurocode 7 – Geotechnical Design – Part 1: General Rules*. CEN, Bruxelles, Belgium.
Leshchinsky, D. & Han, J. (2004). Geosynthetic Reinforced Multitiered Walls. *Journal of Geotechnical and Geoenvironmental Engineering, ASCE*, 130(12), 2004, 1225–1235.
NTC 2018. Italian Norm for Constructions. *Italian Official Gazzette Nr 42*, 20 February 2018.

Field instrumentation and preliminary evaluation of a Mechanically Stabilized Earth wall (MSE) with embedded bridge-supporting piles

Qingming Wang & Chao Xu
Department of Geotechnical Engineering, Tongji University, Shanghai, China

Panpan Shen*
Shanghai Investigation, Design & Research Institute Co., Ltd, Shanghai, China

Haoyu Li
Anhui Transport Consulting & Design Institute Co., Ltd, Anhui Hefei, China
Ya Meng & Chongxi Zhao
Department of Geotechnical Engineering, Tongji University, Shanghai, China

ABSTRACT: Mechanically stability earth (MSE) walls have been widely used as bridge abutments due to the advantages of reducing both the construction space saving and the bridge span. This paper presents a case study of an MSE wall with embedded bridge-supporting piles in Anhui, China. Instead of using traditional isolation casing, innovative geogrid treatments were taken to bypass the piles embedded in the MSE wall. The facing deformations, including both lateral displacements and settlement, were monitored for eight months after the completion of construction using a machine vision monitoring system. Monitoring data indicated that both the lateral displacements and settlements of the wall facing increased with time until six months after construction. The rainfall resulted in a small increase of the lateral deformations. In the horizontal direction of facing, both the lateral displacements and settlements at different elevations had an obvious increase from the wing wall to the road centerline. Overall, the deformation of the wall facing was stable and far less than the design limit value, indicating that the MSE wall with embedded bridge-supporting piles showed good service performances after construction.

Keywords: Geosynthetics, Bridge abutment, MSE wall, Pile, Facing deformation

1 INTRODUCTION

Geosynthetic reinforcement has shown great economic benefits in highway, railway and hydraulic engineering applications since its appearance. For the last few decades, due to space constrain t, mechanically stabilized earth (MSE) walls with embedded bridge-supporting piles have been widely used as the transition sections between bridge slabs and approaching embankments. Different from the traditional MSE wall technology, piles are constructed inside the MSE wall to carry the bridge load in this technology. Recent studies show that the use of MSE walls with embedded bridge-supporting piles for highway applications can bring significant savings for the reduction of both bridge span and construction space. (Han *et al.* 2018; Tatsuoka *et al.* 2016). In this technology, the piles are inevitably laterally loaded due to either the thermal expansion of the bridge girders or the active earth

---

*Corresponding Author: shenpanpan@sidri.com

pressures of the retained soil behind the piles. As a retaining structure, the MSE wall itself could limit the lateral deformation of the embedded piles. The interaction mechanism between piles and reinforced soil is still unclear, resulting in a conservative design of the pile diameter. Therefore, researchers have conducted full-scale tests (Pierson *et al.* 2009, 2011; Rollins *et al.* 2022), model tests (Jawad *et al.* 2020, 2021) and numerical analyses (Huang *et al.* 2013, 2014) to investigate the effects of different influencing factors on the responses of MSE walls with embedded piles subjected to lateral loads. However, few cases existed in literature regarding filed monitoring data of MSE walls with embedded piles under service load conditions. As a result, further studies were necessary to have a comprehensive understanding of this special type MSE for further applications.

In this study, a MSE wall with embedded bridge-supporting piles was constructed and monitored in the field. This MSE wall with embedded piles served as a bridge abutment for the Mingguang to Chaohu Highway located in Anhui province in China. This study investigated the facing deformation characteristics of the MSE wall with embedded piles under service loads. This study analyzed the monitored facing deformation of the MSE wall within eight months after construction. Conclusions from these monitoring data could provide references for the design and construction of similar projects in the future.

2 PROJECT DESCRIPTION

2.1 *Site conditions and geometry*

The Mingguang to Chaohu (Ming-Chao) Highway runs through the middle east of Anhui Province in China with a total length of 131 km. The highway has four traffic lanes (two lanes per traffic direction). The mainly geomorphic units crossed by the highway are valley plains and hills. The instrumented MSE wall in this study is located in the section K120 + 173 of the Ming-Chao Highway in Suwan Town in City Hefei. According to the geological survey, the foundation soil mainly consists of three soil stratums. The top layer is Quaternary Holocene silty clay with a bearing capacity of 160 kPa, which is less than the required bearing capacity of the foundation soil (i.e., 200 kPa). The middle layer is Quaternary Upper Pleistocene silty clay with a bearing capacity of 220 kPa. The bottom layer is gravelly argillaceous sandstone with different degrees of weathering. Therefore, the top layer soil was excavated and replaced with 7% lime soil and geogrid reinforced soil cushion. The thickness of the reinforced cushion was 0.6 m with the reinforcement spacing of 0.3 m. The bearing capacity of the treated soil foundation satisfied the design requirement.

The MSE wall had a width of 27 m and a height of H = 5.3 m. The wall facing was composed of modular blocks with dimensions of 0.4 m long × 0.2 m wide × 0.19 m thick. The batter of the wall facing was 2.86° (i.e., the slope ratio of the wall facing was 1:0.05 (vertical: horizontal)). Four steel reinforced concrete piles construed using C35 concrete were embedded inside the MSE wall. Each pile had a diameter of 1.5 m (D = 1.5 m). The distance from the back of the facing top to the center of the pile was 4.05 m. The reinforcement layers used in this project were 9 m long and 1.3 m wide. The vertical spacing of the reinforcement layers was 0.38 m.

2.2 *Materials*

A uniaxial high-density polyethylene (HDPE) geogrid was used as the reinforcement material in the MSE wall and the mechanical properties of the geogrid are listed in Table 1. Graded crushed stones were selected as the backfill material. The maximum particle size of the crush stones was 0.1 m and the friction angle was no less than 35°. Concrete modular blocks with a compressive strength of 107 MPa were used as the facing material of the MSE wall.

Table 1. Mechanical properties of the uniaxial HDPE geogrid.

Item	Value
Ultimate tensile strength (kN/m)	81
Tensile strength at 2% strain (kN/m)	23.2
Tensile strength at 5% strain (kN/m)	41
Ultimate tensile strain (%)	10.5

2.3 Construction

Construction of the MSE wall started on September 12, 2021 and ended with the placement of the bridge girders on late December of 2021. The construction process mainly consisted of ground improvement, the construction of the strip footing, MSE wall, cap beam, and approach roadway, and the placement of the bridge girder. The concrete piles were cast in-place and cured to reach the design strength before the ground improvement. The foundation soil was then excavated and replaced with 7% lime soil and geogrid reinforced soil cushion to improve the bearing capacity. A strip footing using C30 concrete, as shown in Figure 1(a), was cast on top of the reinforced soil cushion before placing modular facing blocks to provide horizontal alignment and to support the modular facing blocks. The strip footing had a thickness of 0.3 m and a width of 0.9 m. The MSE wall was then constructed layer by layer. The bottom layer of the modular blocks was placed on top of the strip footing and levelled with cement mortar. For each layer, the modular facing blocks were placed first, followed by the placement of the backfill soil behind the modular blocks. Before placing the geogrid in each layer, the backfill soil was compacted to a minimum relative compaction of 96% using a large-sized roller compactor and a plate compactor for zones behind the pile shown in Figure 1(b) and near the modular facing blocks respectively.

When placing the geogrid layers into the backfill soil, instead of using traditional isolation casing, innovative geogrid treatments were taken to bypass the piles embedded in the MSE wall as shown in Figure 1(c). Two pieces of geogrid layers were cut into a semi-circle shape to embrace the pile and then connected together using zip-ties. U-nails were used to anchor the geogrid layers with the backfill soil for the purpose of better pre-tensioning. By using plastic connectors to fix the geogrid layers with the sub grooves of the modular facing blocks, all the geogrid layers were mechanically connected with the wall facing as shown in Figure 1(d). At the MSE wall corner where two wall facing intercepted, staggered placing was used to avoid
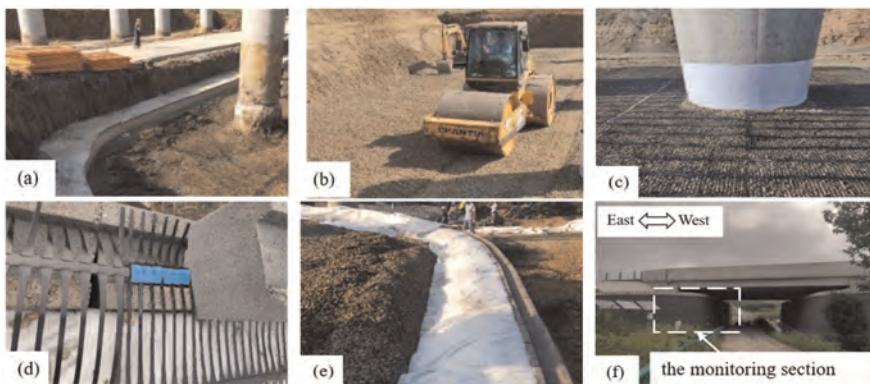
Figure 1. Construction of the MSE wall: (a) Strip footing; (b) Large-sized roller compactor; (c) Geogrid bypass the pile; (d) Connection between geogrid and blocks; (e) Filtration drainage layer; (f) Photo of the bridge supported by the MSE wall with embedded piles after the completion of the construction.

overlapping of geogrid in the same layer. A 0.5 m thick layer composed of geotextile wrapped gravel was set behind the facing as shown in Figure 1(e) to serve as a drainage layer.

After construction of the MSE wall, the cap beam with steel reinforced concrete was cast in-place. The bridge beam and the approach roadway were constructed after the strength of the cap beam concrete reached the design requirements. Figure 1(f) shows a photo of the completed bridge supported by the MSE wall with embedded piles.

2.4 *Instrumentation layout*

In this study, the wall facing deformation was monitored using a machine vision monitoring system, which could achieve a high-precision automatic measurement of the facing deformation. This system mainly composed of a machine vision measurement instrument installed at a stable foundation, a number of targets installed at the surface of the wall facing, a solar power supply system, and a software for data collecting and processing. When the targets changed their coordinates along with the deformed wall facing, the machine vision measurement instrument could process the target image automatically and both the horizontal displacements and the settlements of the facing were measured simultaneously.

Considering the site condition as well as the symmetry of the two walls at different ends of the bridge slabs, the MSE wall located at East was chosen as the monitoring section and targets were installed at this MSE wall. A total of 12 targets (3 rows and 4 columns) were installed on the facing by using expansion screws. Figure 2(a) shows the location of each target. In Figure 2(a), the letters "L" and "P" represent the monitored layer and the position respectively. L1 is located at the bottom of the MSE wall while L3 is located at the top. P1 is located at the position close to the corner of the MSE wall while P4 is located at the road centerline. After the debugging of the monitoring system, the field monitoring of this project started from January 7, 2022. Figure 2 shows the instrument layout and filed installation.
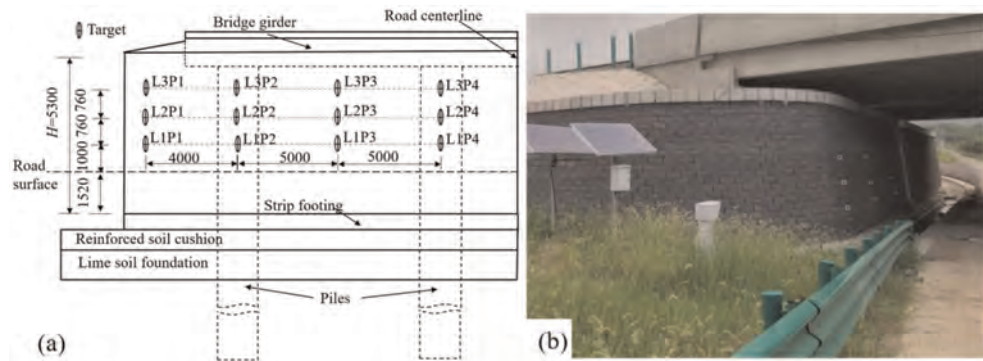
Figure 2. Instrumentation layout: (a) Schematic of the instrument layout (Unit: mm); (b) Filed installation.

3 PRELIMINARY RESULTS

3.1 *Lateral facing displacement*

Figure 3 presents the distributions of lateral facing displacements within eight months after construction. As shown in Figure 3, the lateral facing displacement had an obvious increase within three months after the completion of the construction and then tended to become stable. However, the measured values of the lateral displacements increased again at five

months after construction due to the coming of the rainy season and the rising of air temperature. After the rainy season, the maximum lateral displacement increased approximately 1 mm. Meanwhile, Figure 3 also indicates that the lateral facing displacements increased significantly from the wing wall (i.e., P1) to the road centerline (i.e., P4) in the horizontal direction. The maximum lateral displacements were 5.69mm, 5.84mm, and 5.67mm from the bottom to the top layer respectively, which were less than 0.12% of the wall height and were far below the design limit value. These small lateral displacements indicated that the MSE wall was stable and the use of the geogrid could effectively limit the lateral facing deformation.
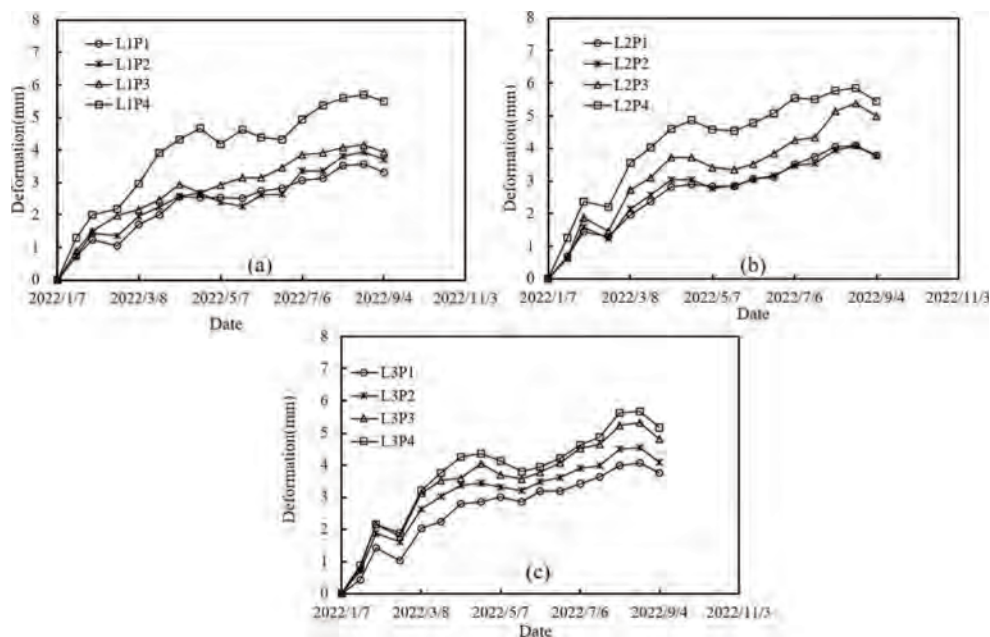
Figure 3.   Distributions of the lateral facing displacements along elevation with time: (a) $z/H = 0.47$; (b) $z/H = 0.62$; (c) $z/H = 0.76$.

3.2   Settlement of the facing

Figure 4 presents the measured facing settlements at different elevations with time. As shown in Figure 4, within the first month after the completion of construction, the facing settlements increased significantly at all measurement points, and then the increments gradually decreased during the following five months. The settlements trended to become stable six months after construction. The maximum settlement at different elevations were approximately the same, which indicated the compression of modular blocks could be ignored and the adjacent block layers were in close contact without large gaps. The measured facing settlements increased significantly from the wing wall to the road centerline in the horizontal direction, which was the same as the distributions of the lateral facing displacements. The maximum facing settlements were 9.8mm, 10.3mm, and 10.4 mm from the bottom to the top layer respectively, which were 0.18%, 0.19%, and 0.19% of the wall height, indicating the bearing capacity of the treated foundation was enough and the strip footing as a supporting structure performed well.
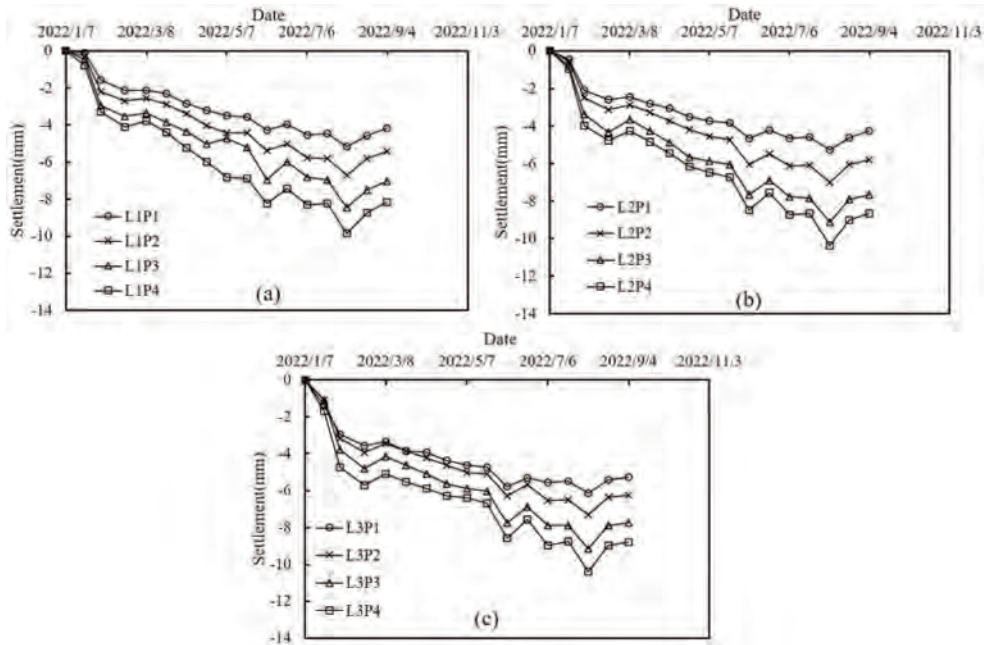
Figure 4. Distributions of facing settlements along elevation with time: (a) $z/H = 0.47$; (b) $z/H = 0.62$; (c) $z/H = 0.76$.

4 CONCLUSION

This study presented field instrumentation and preliminary evaluation of a mechanically-stabilized earth (MSE) wall with embedded bridge-supporting piles serving as a bridge abutment. Instead of using traditional isolation casing, innovative geogrid treatments were taken to bypass the piles embedded in the MSE wall. The wall facing deformations, including both lateral displacements and settlements, were analyzed within eight months after the completion of construction. The following conclusions could be drawn based on the monitoring data:

(1) Overall, the MSE wall with embedded bridge-supporting piles showed good service performance after eight months of the completion of construction. No obvious deformations of the facing were observed, which indicated that the innovative geogrid treatments did not produce an obvious effect on the facing deformation.
(2) The lateral displacements and settlements of the wall facing gradually increased within six months after construction of the MSE wall. In the horizontal direction, both the lateral displacements and settlements of the wall facing increased from the wing wall to the road centerline. Approximately eight months after construction, the maximum lateral displacement of the wall facing was 5.84 mm, which was 0.11% of the wall height. After a rainy season, the lateral displacements had an increment of 1 mm. The maximum settlement of the wall facing was 10.4 mm. The facing settlements at different elevations did not show significant differences.

REFERENCES

Han, J., Jiang, Y. and Xu, C. (2018). Recent Advances in Geosynthetic-reinforced Retaining Walls for Highway Applications, *Frontiers of Structural and Civil Engineering*, 12(2): 239–247.

Huang, J., Bin-Shafique, S., Han, J. and Rahman, M.S. (2014). Modelling of Laterally Loaded Drilled Shaft Group in Mechanically Stabilised Earth Wall. *Proceedings of the ICE-Geotechnical Engineering*, 167(4), 402–414.

Huang, J., Han, J., Parsons, R. and Pierson, M. (2013). Refined Numerical Modeling of a Laterally-loaded Drilled Shaft in an MSE Wall. *Geotextiles and Geomembranes*, 37, 61–73.

Jawad, S., Han, J., Abdulrasool, G. and Al-Naddaf, M. (2021) Responses of Single and Group Piles within MSE Walls Under Static and Cyclic Lateral Loads. *Geotextiles and Geomembranes*, 49(4), 1019–1035.

Jawad, S., Han, J., Al-Naddaf, M. and Abdulrasool, G. (2020). Responses of Laterally Loaded Single Piles within Mechanically Stabilized Earth Walls. *Journal of Geotechnical and Geoenvironmental Engineering*, 146(12), 1–11.

Pierson, M.C., Parsons, R.L., Han, J. and Brennan, J.J. (2011). Laterally Loaded Shaft Group Capacities and Deflections Behind an MSE Wall. *Journal of Geotechnical and Geoenvironmental Engineering*, 137(10), 882–889.

Pierson, M.C., Parsons, R.L., Han, J., Brennan, J.J. and Vulova, C. (2009). Instrumentation of MSE Wall Containing Laterally Loaded Drilled Shafts. *Proceedings of International Foundation Congress and Equipment Expo*, 187, 353–360.

Rollins, K.M., Luna, A., Budd, R., Besendorfer, J., Hatch, C., Han, J. and Gladstone R. (2022). Lateral Pile Resistance, Wall Displacement, and Induced Reinforcement Force for Laterally Loaded Single Piles Near Mechanically Stabilized Earth Walls. *Journal of Geotechnical and Geoenvironmental Engineering*, 148(3), 1–10.

Tatsuoka, F., Tateyama, M., Koda, M., Kojima, K., Yonezawa, T., Shindo, Y. and Tamai, S. (2016). Research and Construction of Geosynthetic-reinforced Soil Integral Bridges, *Transportation Geotechnics*, 8, 4–25.

Mechanical and deformation behavior of geogrid reinforced soil retaining walls using discrete element modeling

Z. Wang
School of Civil Engineering, Shijiazhuang Tiedao University, Shijiazhuang, China
State Key Laboratory of Mechanical Behavior and System Safety of Traffic Engineering Structures, Shijiazhuang Tiedao University, Shijiazhuang, China

M. Shi
School of Civil Engineering, Shijiazhuang Tiedao University, Shijiazhuang, China
Shijiazhuang Vocational College of Finance & Economics, Shijiazhuang, China

G. Yang & H. Wang
School of Civil Engineering, Shijiazhuang Tiedao University, Shijiazhuang, China
State Key Laboratory of Mechanical Behavior and System Safety of Traffic Engineering Structures, Shijiazhuang Tiedao University, Shijiazhuang, China

ABSTRACT: To investigate the geogrid reinforcement mechanisms in the reinforced soil retaining walls, discrete element modeling has been carried out based on the model tests under strip footing loads. The mechanical and deformation behavior of the reinforced soil retaining wall was analyzed at a mesoscopic scale during construction and under strip footing loads. With increasing heights of the retaining wall during the construction period, the strains of geogrids increased. Before applying the footing loads, the contact forces in the retaining wall showed a realistic distribution under gravity and the geogrid strains of lower layers were slightly larger than those of the upper layers. With increasing loads of the strip footing, the vertical settlement of the footing increased gradually. The horizontal deformation of the upper part of the wall facing was larger than the lower part. With increasing footing loads, the strains of geogrids increased, but the increment of geogrid strains was relatively small under the loading conditions in this study. The discrete element modeling results in this study visualize the load transfer between geogrid and soil and quantify the deformation behavior of geogrids in the reinforced soil retaining wall during construction and under strip footing loads.

1 INTRODUCTION

As a kind of flexible retaining structure, the geogrid reinforced soil retaining wall, which has the advantages of saving land, being friendly to the environment, and being low cost, has been widely used in practice (Yang *et al*. 2014). To illustrate the geogrid reinforced mechanisms in reinforced soil retaining walls, many researchers have conducted a series of model tests and field tests (Jia *et al*. 2021; Jiang *et al*. 2016; Sun *et al*. 2019; Santos *et al*. 2014; Viswanadham *et al*. 2017; Yazdandoust & Taimouri 2022).

Numerical simulation is an important supplement to experimental studies. Many researchers also carried out lots of numerical simulations to describe the working mechanisms of reinforced soil retaining walls (Lees & Dobie 2021; Ma *et al*. 2020). Compared to the finite element method (FEM), the discrete element method (DEM) has particular

advantages of capturing detailed insights into the interlocking and interaction between soil and geogrid (Wang *et al.* 2020).

Therefore, this study established a DEM model of a geogrid reinforced soil retaining wall based on laboratory model tests. The horizontal deformation and vertical settlement of the retaining wall were analyzed quantitatively as well as the development of geogrid strains during the construction period and the loading process. The contact force and tensile force chains inside the retaining wall were visualized from a mesoscale level. This study is expected to improve the understanding of the mechanical and deformation behavior of geogrid reinforced soil retaining walls, which provides some theoretical support for the design optimization of reinforced soil retaining walls.

2 EXPERIMENTAL BACKGROUND AND DISCRETE ELEMENT MODELING

The schematic diagram of the reinforced soil retaining wall model in the laboratory tests is shown in Figure 1. The dimensions of the model were 3 m × 1 m × 1.8m (L × W × H) with a slope ratio of 1: 0.05. The vertical spacing of the geogrids was 0.3 m and the length of the geogrid was 2 m. A rigid plate with a width of 0.505 m was placed on top of the reinforced retaining wall. The vertical strip footing loads were applied from 10 kPa to 60 kPa with an increment of 10 kPa. The experimental data such as the horizontal deformation of the wall facing, the vertical settlement of the rigid plate, and the geogrid strains were recorded automatically.
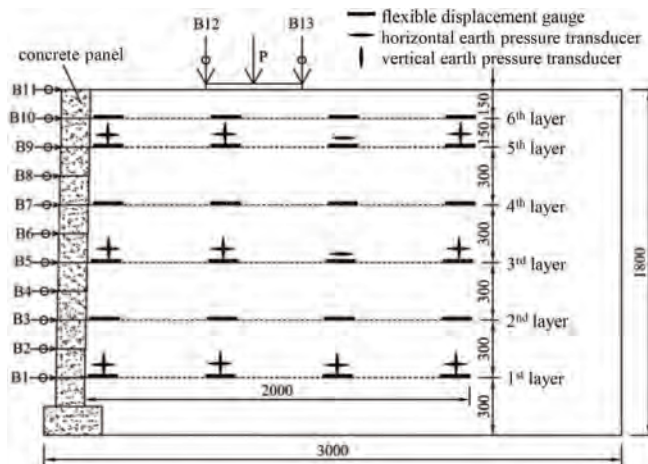
Figure 1. Sketch of reinforced soil retaining wall model test (unit: mm) (after Wang *et al.* 2016).

In the DEM investigations of reinforced soil retaining walls, it is necessary to first determine the mesoscale parameters of geogrid and soil. Based on the experimental data, the mesoscale parameters for geogrids and soils were calibrated by the DEM modeling of geogrid tensile tests and soil direct shear tests, respectively. The corresponding mesoscale parameters were used to establish the DEM model of the reinforced soil retaining wall. A multi-layer compaction method was used in the DEM investigations to build the reinforced soil retaining wall. The 1st layer of soil particles was generated at the bottom of the retaining wall and then the 1st layer of geogrid until the 6th layer of geogrid and the 7th layer of filling soil. In each generation process, the unbalance forces were eliminated after several cycles. A string of vertical bonded particles was used to simulate the facing of the retaining wall and a

rigid wall with a width of 0.505 m was generated on top of the retaining wall as the loading plate. The modeling process was consistent with the construction process of the reinforced soil retaining wall in the model tests. The DEM model of the reinforced soil retaining wall before applying the vertical loads is shown in Figure 2.
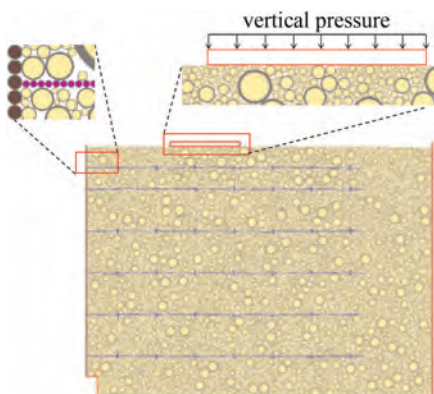
Figure 2.   DEM model of reinforced soil retaining wall before applying the vertical loads.

3   RESULTS AND ANALYSES

3.1   *Accumulated horizontal displacement of wall facing*

The horizontal displacement of facing particles along the vertical height of the retaining wall was recorded and the accumulated horizontal displacement of the wall facing in the DEM simulation is shown in Figure 3a. The corresponding model test results are shown in Figure 3b for comparison. It can be seen from the figure that the horizontal displacements obtained from the DEM simulations were quite similar to those obtained from the laboratory model tests. The horizontal deformation at the upper part of the wall facing was larger than that at the lower part. The accumulated horizontal displacement changed greatly during the initial loading process, while the overall increase amplitude was small in the subsequent loading process. This was mainly due to the sudden vertical pressure on top of the retaining wall, which destroyed the original stability of the structure. Hence, the deformation of the retaining wall was large. With increasing vertical pressure, the reinforcing effects of geogrids were mobilized and the lateral movement of soil particles was restrained by the geogrids, which caused the increase of the accumulated horizontal displacement to be relatively small.
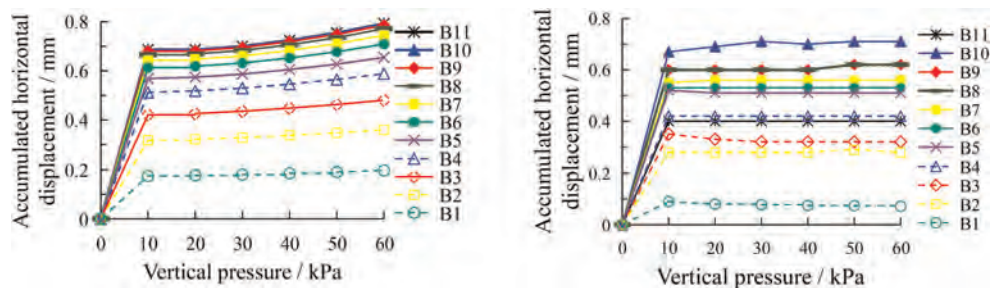
Figure 3.   Accumulated horizontal displacement of wall facing. (a) DEM simulation results (b) Model test results (after Wang *et al.* 2016).
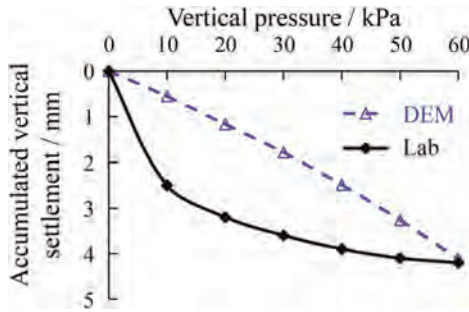
Figure 4.   Comparison of vertical pressure and settlement relations.

3.2   *Vertical settlement of strip footing*

Figure 4 compares the vertical pressure and settlement relations obtained from experimental and DEM investigations. The DEM simulation results showed a linear relationship between the vertical pressure and the settlement, which was different from that obtained from the model tests. Such observation can be explained by the liner model used for soil particles in this study. Nevertheless, the trend of the DEM investigation was the same as that of the model test, i.e. the accumulated vertical settlement increased with increasing vertical pressure and the accumulated vertical settlements at the ultimate pressure of 60 kPa in both experimental and DEM investigations were quite similar. Therefore, it is believed that the DEM models and the mesoscale parameters were rational and further DEM analyses were carried out to investigate the mechanical and deformation behavior of the geogrid reinforced soil retaining wall under strip footing loads.

3.3   *Development of geogrid strain*

3.3.1   *Geogrid strain during the construction period*
The strains of each geogrid layer can be recorded in the DEM investigations during the construction period and the loading process, respectively. Figure 5 shows the strain distribution of the 1st and 6th layers of geogrids during the construction period. The 1st layer of geogrid (bottom) was placed at the lower part of the retaining wall and it experienced 6-times
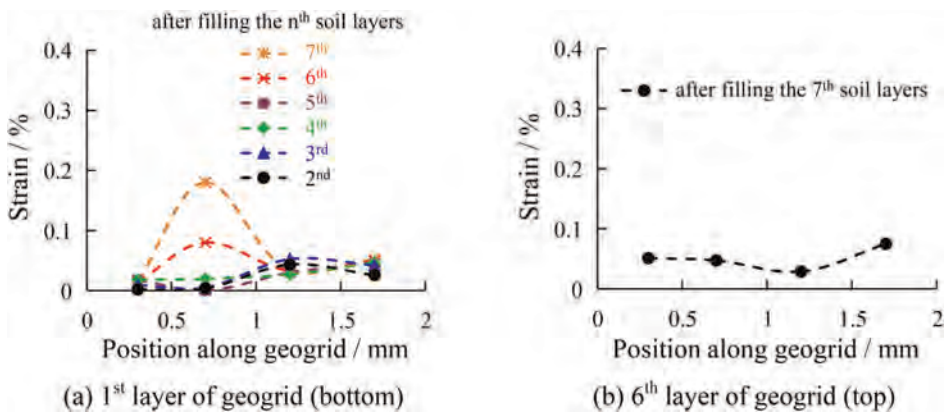
Figure 5.   Distribution of geogrid strain during the construction period. (a) 1st layer of geogrid (bottom) (b) 6th layer of geogrid (top).

892

compaction of the upper soil layers, while the 6th layer of geogrid (top) was placed at the upper part of the retaining wall and it experienced only one-time compaction of the 7th soil layer. It can be seen from the figure that the strain distributions of the 1st layer of geogrid were almost the same under different compaction times of the above soil layers. With increasing compaction times, the geogrid stains increased, as shown in Figure 5a. The geogrid strains in the lower part of the retaining wall (Figure 5a) were larger than those in the upper part (Figure 5b). Such phenomena can be explained by the action of gravity and compaction.

3.3.2 *Geogrid strain during the loading process*

Similarly, the strain distributions of the 1st and 6th layers of geogrids during the loading process were obtained in the DEM investigations, as shown in Figure 6. It can be seen from the figure that the geogrid strains increased with increasing footing pressure. However, the overall increment of the geogrid strain was relatively small, which was less than 0.1 % under the action of each load increase. The vertical loads selected in this study have little influence on the geogrid strains. Since the 6th layer of geogrid (top) was close to the loading plate, the strain increment of the 6th layer of geogrid (top) was greater than that of the 1st layer of geogrid (bottom) during each loading process, especially after the first footing load of 10 kPa by comparing the curves in Figures 5b and 6b. Compared with Figures 5a and 6a, the strains of geogrids in the lower part of the retaining wall mainly occurred during the wall construction period.
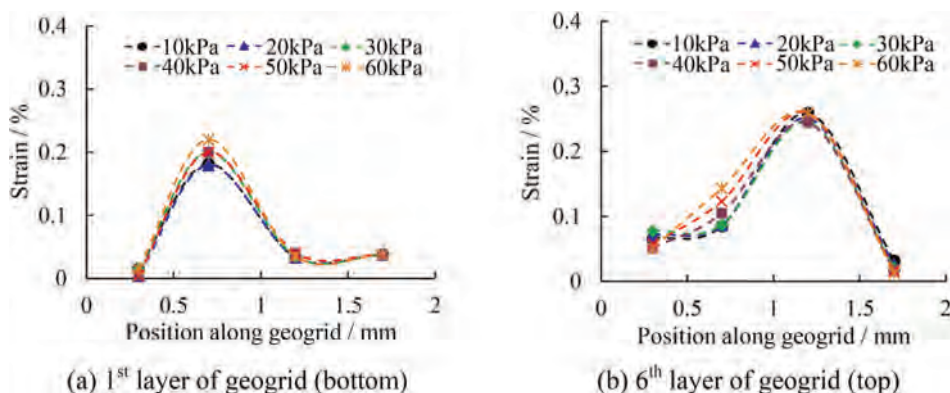
Figure 6. Distribution of geogrid strain under vertical loading. (a) 1st layer of geogrid (bottom) (b) 6th layer of geogrid (top).

3.4 *Development of contact force and tensile force*

Figure 7 shows the development of contact forces among the soil particles and the development of tensile forces along the geogrids in the reinforced soil retaining wall under different vertical loads. The black lines represent the contact forces among the soil particles, while the green lines indicate the tensile forces along the geogrids. The thicknesses of the lines are proportional to the magnitudes. Before applying the vertical load, the distribution of contact forces among the soil particles was following the distribution along gravity, i.e. the contact forces in the lower parts were larger than those in the upper parts as well as the tensile force distributions along the geogrids (Figure 7a). With increasing vertical loads, the contact forces among the soil particles and the tensile forces along the geogrids in the retaining wall increased gradually, especially those below the loading plate. The
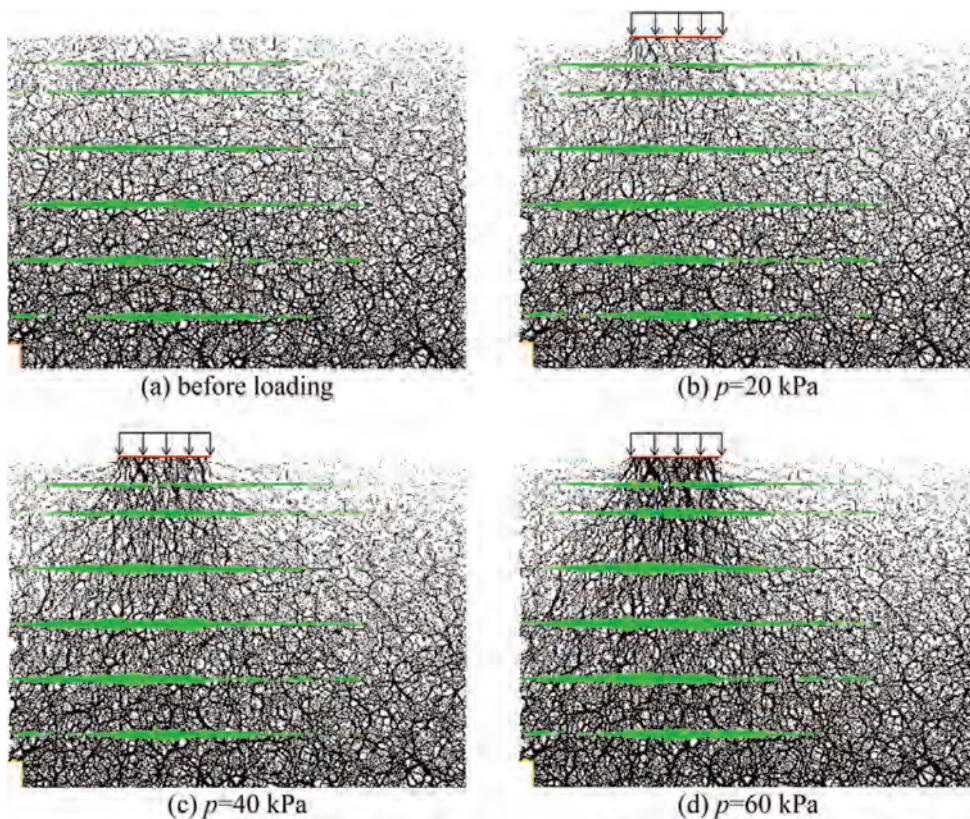
Figure 7. Contact force and tensile force distributions under different loading conditions. (a) before loading (b) p = 20 kPa (c) p = 40 kPa (d) p = 60 kPa.

development of contact forces among the soil particles and tensile forces along the geogrids in this study visualized the load transfer behavior in the geogrid reinforced soil retaining wall under strip footing loads.

4 CONCLUSION

Based on the model tests of geogrid reinforced soil retaining walls, a DEM model was set up and further DEM analyses were carried out to illustrate the mechanical and deformation behavior of the reinforced soil retaining wall under strip footing loads. The main conclusions are as follows:

(1) The horizontal displacements of the wall facing were obtained based on the DEM simulations as well as the vertical settlement of the loading plate on top of the retaining wall. The DEM investigation results showed good agreement with the experimental data, which validated that the DEM models and the corresponding mesoscale parameters were rational.
(2) In the DEM modeling, a multi-layer compaction method was used to build the geogrid reinforced soil retaining wall. With increasing numbers of filling soil layers, the geogrid strains increased. The strains of the geogrids in the lower parts of the retaining wall were mainly generated during the construction period.

(3) Before applying the vertical load, the distribution of contact forces in the retaining wall showed a realistic distribution under gravity. The strains in the lower part of the geogrids were larger than those in the upper parts. With increasing vertical loads, the contact forces below the loading plate increased as well as the tensile forces along geogrids. The vertical loads mainly affected the upper part of the retaining wall in this study.

ACKNOWLEDGEMENTS

REFERENCES

Jia, M., Zhu, W. & Xu, C. 2021. Performance of a 33m High Geogrid Reinforced Soil Embankment without Concrete Panel. *Geotextiles and Geomembranes* 49(1): 122–129.

Jiang, Y., Han, J., Parsons, R.L. & Brennan, J.J. 2016. Field Instrumentation and Evaluation of Modular-block MSE Walls with Secondary Geogrid Layers. *Journal of Geotechnical and Geoenvironmental Engineering* 142(12): 5016002.

Lees, A. & Dobie, M. 2021. Finite Element Modeling of a Mechanically Stabilized Earth Trial Wall. *Transportation Research Record* 2675(10): 1373–1383.

Ma, K., Wang, L., Long, J., Peng, Y. & He, G. 2020. Discrete Element Analysis of Structural Characteristics of Stepped Reinforced Soil Retaining Wall. *Geomatics, Natural Hazards and Risk* 11(1): 1447–1465.

Santos, E.C.G., Palmeira, E.M. & Bathurst, R.J. 2014. Performance of Two Geosynthetic Reinforced Walls with Recycled Construction Waste Backfill and Constructed on Collapsible Ground. *Geosynthetics International* 21(4): 256–269.

Sun, W., Yan, C., Xu, W., Shi, Y., Zhang, Z. & Xie, Y. 2019. Deformation of Geogrid-reinforced Segmental Retaining Wall Due to Insufficient Compaction of Loess Backfill: Case Study in Shaanxi Province, China. *Journal of Performance of Constructed Facilities* 33(6): 04019071.

Viswanadham, B.V.S., Razeghi, H.R., Mamaghanian, J. & Manikumar, C.H.S.G. 2017. Centrifuge Model Study on Geogrid Reinforced Soil Walls with Marginal Backfills with and without Chimney Sand Drain. *Geotextiles and Geomembranes* 45(5): 430–446.

Wang, H., Yang, G., Xiong, B., Wu, L. & Liu, H. 2016. An Experimental Study of the Structural Behavior of Reinforced Soil Retaining Wall with Concrete-block Panel. *Rock and Soil Mechanics* 37(2): 487–498. (in Chinese)

Wang, Z., Jacobs, F., Ziegler, M. & Yang, G. 2020. Visualisation and Quantification of Geogrid Reinforcing Effects Under Strip Footing Loads Using Discrete Element Method. *Geotextiles and Geomembranes* 48(1): 62–70.

Yang, G., Liu, H., Zhou, Y. & Xiong, B. 2014. Post-construction Performance of a Two-tiered Geogrid Reinforced Soil Wall Backfilled with Soil-rock Mixture. *Geotextiles and Geomembranes* 42(2): 91–97.

Yazdandoust, M. & Taimouri, A.B.B. 2022. Performance of Two-tiered Reinforced-soil Retaining Walls Under Strip Footing Load. *Geotextiles and Geomembranes* 50(4): 545–565.

Case study. The geotextile materials application for reinforcing the man-made coastal slopes in the Prymorske village area (Crimea)

O. Trofymchuk & I. Kaliukh
Institute of Telecommunications and Global Information Space, National Academy of Science of Ukraine, Kyiv, Ukraine

ABSTRACT: The boathouses construction in Prymorske village (Crimea, Ukraine) caused the need to undercut the existing Black Sea coastal slopes. It required some additional measures to stabilize the man-made slopes, which were formed as an undercutting result. There was not enough space to make the slopes not steep, so it was recommended to use geotextiles to reinforce them. The PLAXIS software package and the simplified LANDSLIP software with the Bishop and Spencer model were used. The PLAXIS package allowed to perform the direct dynamic calculations of the initial and undercut slopes. Calculated accelerograms of the 7 and 8 points earthquakes were used for calculations. The required breaking strength was provided by geotextile materials with the 130–170 g/m^3 density. The man-made slope reinforcement with synthetic materials should be carried out in layers in every 0.75 m using backfilling with cohesive soil from undercutting the slope with a specific gravity and without compression.

1 INTRODUCTION

The tasks of increasing the slopes stability become increasingly important in the world and in Ukraine (Lacasse 2015), (Jenner *et al.* 2015), (Robertson & Gilchrist 1987). The main reasons for this are the ever-expanding development of landslide territories for construction caused by a shortage of free land areas, as well as the existing landslides activation and the new man-made landslides emergence (Kaliukh *et al.* 2013), (Kaliukh *et al.* 2018), (Voloshkina E. *et al.* 2021)The slopes strengthening is intended to stabilize the soil erosion processes and prevent the soil collapse under its dead weight or sliding due to inertia forces under dynamic effects from industrial explosions during the minerals development, vehicles, seismic and other phenomena (Slyusarenko *et al.* 2009, 2010), (Trofymchuk *et al.* 2018, 2019), (DBN V.1.1-3-97. 1998). The slopes strengthening projects should be chosen taking into account such factors as the slope steepness, loads, the presence or absence of vibrations, as well as the composition of the physical and mechanical characteristics of the slope soil layers. A wide variety of methods have been used to solve the problem of strengthening the embankment slopes, roadbeds or slopes sides and the special synthetic materials (geosynthetics) have been developed for soils reinforcement. The first attempts to increase the soils strength by means of the reinforcement with the use of steel strips, geogrids and geomeshes were undertaken at the beginning of the 20th century, and in the 1960s, with the chemical industry progress, non-woven geotextiles began to be used, and late on the high strength geogrids and geotextiles appeared. In foreign construction practice, the term "geosynthetic materials" was put into practice in the 1990s as a notion that replaced the "geotextile" term (Oliver & Younger 1988). Geotextiles were the first technical textiles and fabrics used in the construction and geotechnics. Geogrids became the next representatives of technical materials. The research of the French scientist A. Vidal

resulted in the development of a new type of material for geotechnics - reinforced soil. Currently, the geosynthetic materials use in construction practice is rapidly increasing, because they have a number of advantages, such as water resistance, biostability, resistance to acid and alkaline environments, resistance to ultraviolet radiation, mechanical resistance, environmental friendliness (due to reducing the natural resources use). Besides, such a property of geosynthetic materials as durability is worth of a special mention.

2 PROBLEM FORMULATION

The execution of works on the boathouses construction in the area of the Vertolit Research Center in Prymorske village, Feodosia district, Autonomous Republic of Crimea, Ukraine, required the existing slopes undercutting. So, it was necessary to provide additional measures to stabilize man-made slopes formed as a result of existing slopes undercutting.

It is known that the slope stabilization works can be performed in various ways, and the expediency of each of them is determined based on the available spaces, reliability and economic feasibility. Making a slope gentle and stable after its undercutting can be recommended as the first and most economical measure. As the Contractor did not have the necessary space to make the slope gentle and stable after undercutting, the use of geosynthetic materials (the second method) was proposed for reinforcing the man-made slopes and ensuring their necessary stability.

The geosynthetic materials could significantly reduce the cost of the initial working project, which provided for the installation of a strengthened landslide protection retaining wall of reinforced concrete. It was assumed that the retaining wall would absorb the landslide pressure and ensure the necessary stability of the new man-made slope. The use of geosynthetic materials envisaged the landslide pressure transfer from the retaining wall to geosynthetic materials. In this way, the effect of "bags with soil placed on top of each other" could create a reinforced wall. This method has obtained a wide application in construction practice, for example, in Pakistan, where an embankment with a vertical slope up to 40 m high was built using geosynthetic materials without any additional reinforced concrete structures. In compliance with this plan, at the first stage the slope stability assessment was carried out in the form of a calculation of its reserve factor, and on that basis the necessary number of interlayers was selected.

3 APPROXIMATE CALCULATIONS

As the first stage, a slopes stability analysis at the boathouses construction site in the area of the Vertolit Research Center in the Prymorske village was performed. The input data for the LANDSLIP software (Trofymchuk *et al.* 2018) consisted of the geometric, physical and mechanical characteristics of the slopes at the construction site provided by the Contractor. Based on the preliminary analysis of the cross-sections of the slopes at the construction site, it was determined that the most serious problems due to the landslides hazard could arise during the existing slopes undercutting along the defined cross-sections. The cutting height just along these cross-sections would be the biggest and reach 6 - 7 m. With this in mind, the further calculations should be carried out for the worst cross-section with extrapolating the results to other cross-sections. Moreover, the recommendations based on the worst calculated cross-section should go into reserve for other cross-sections. First, the initial stability of the existing slope along the worst cross-section was analyzed using the LANDSLIP software. The slope geometry according to that cross-section is presented in Figure 1. As a result of the calculations, the coefficient of the initial slope stability for the cross-section was 3.67. Thus, before the undercutting start, the initial slope was completely stable, which was really observed. In Figure 2 the landslide pressure distribution along the calculated slope width is shown.

According to the geotechnical boring data provided by the Customer, in the cross-sections calculated for the slope soils there are 2 predominant types of the physical and mechanical characteristics of the soils to be cut:

1. Yellowish-brown, greenish, hard-plastic, lumpy clay, strongly swelling, with inclusions of pebbles (ancient landslide deposits) and with the soil density of 1.91 kN/m^3; specific adhesion of 3.24 kN/m^2; internal friction angle of 11°;
2. Yellowish-brown, semi-hard clay with gypsum pockets, strongly swelling with the soil density of 1.93 kN/m^3; specific adhesion of 5.6 kN/m^2; internal friction angle of 21°.

The further calculations are carried out for the case of the first type physical and mechanical characteristics (obtained with a probability of 95%, since they are worse than the indicators obtained with a probability of 85%). These results will be reserved for the case of the second type physical and mechanical characteristics.
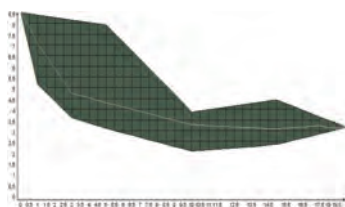
Figure 1. The slope geometry in the boathouse construction area, Prymorske village.
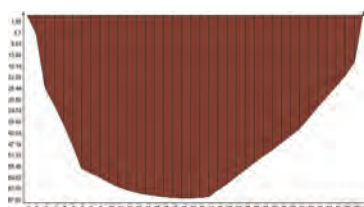
Figure 2. The landslide pressure distribution along the calculated slope width.

That is, a deliberately worse option is assumed. Thus, the sliding slope consists of soil with the following physical and mechanical characteristics: the soil density of 1.91 kN/m^3; specific adhesion of 3.24 kN/m^2; internal friction angle of 11°. Using the Maslov-Berrer and Shahunyants engineering methods (the Bishop and Spencer methods) and the LANDSLIP software package (Trofymchuk *et al.* 2018) the calculations were performed and, in accordance with the requirements of (DBC 49-86. 1988), the minimum tensile strength Rp of geosynthetic materials was determined for one their layer (n = 1):

$$Rp = [3000 - 4000] \text{ N/m}$$

As the geosynthetic materials relative strength under a long-term loading is lower than the nominal value of Rp (depending on the geosynthetic materials type), this lowering can be up to 60%. Therefore, a suitable reserve by Rp is necessary. According to the given breaking load of geosynthetic materials Rp = [3000–4000] N/m, in the discussed case the geotextiles with the density of 150–200 g/m^3 will be the most suitable. The laid material length must be at least 2 m. After the drainage prism is installed, the geosynthetic materials rolls of required length (taking into account the overlap onto the reinforced layer) are rolled out. The residual material is left in a roll on the wall. The rolls should be sewn by width with a stapler. The overlap must be at least 0.1 m. Then the backfilling is carried out with the cohesive clayey soil of a 1910 kg per m^3 bulk weight obtained from slope undercutting and leveling. The reinforced layer is covered with the residual part of the roll at least 2 m from the wall and the cycle is repeated up to an elevation below 1 m from the design soil elevations (Figure 6).

4 REFINED CALCULATION

Due to the fact that in the LANDSLIP software package (Kaliukh *et al.* 2018) the issues of reinforcing the steep slopes and retaining walls are considered on the basis of the approximate formulas and analytical dependencies using the engineering methods of Maslov-Berrer and Shakhunyants (Bishop and Spencer methods), the seismic loads for the slopes stability calculations were taken into account in the form of the appropriate seismic coefficient μ (the supplementary static loads addition according to the Bishop and Spencer methods).

The issue of the calculations improvement based on the more accurate mathematical models and the use of a direct dynamic calculation method with the real accelerograms of the construction site for landslide protection measures (slopes and retaining walls reinforcement design) acquire a national importance. This is due, first of all, to the scale of the phenomenon in Ukraine and the world, and, secondly, to the issues of saving limited resources allocated for landslide protection measures in the country.

Considering these facts, the direct dynamic calculation using the accelerograms based on seismic microzoning of the boathouses construction site in the Vertolit Research Center area, Prymorske village, Feodosia, Autonomous Republic of Crimea, Ukraine, is applied for the existing slopes undercutting based on the software package PLAXIS (2022). The PLAXIS software package is certified in the EU and meets the requirements of the relevant normative documents (Eurocode 7. 2004.). The accelerograms of 7 and 8 points earthquakes are used for the calculations. The preliminary calculations and analysis of the slopes and their undercutting geometry taking into account the physical and mechanical characteristics and seismicity of the construction site show that the greatest landslide hazard can arise when the slope is undercut along a specified cross-section (Figure 1). The further direct dynamic calculations of the stability coefficient of the man-made slope reinforced with geosynthetic materials are carried out using the PLAXIS software (PLAXIS 2022). Two geometric models of the initial and undercut slopes in the PLAXIS software package are shown in Figures 3 and 4.
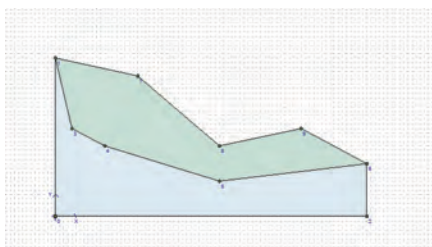
Figure 3.   The initial slope geometric model in the PLAXIS software package.
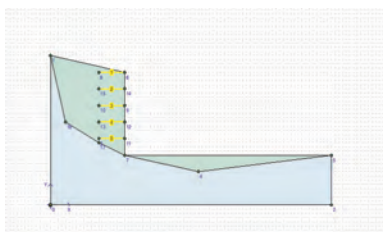
Figure 4.   Geometric model of undercut reinforced slope in the PLAXIS software package.

The calculations were carried out using the preliminary physical and mechanical characteristics. As a result of calculations according to the second group of limit states, the minimum tensile strength Rp of geosynthetic materials is specified for one layer of synthetic materials (n = 1) as Rp = [2500–3500] N/m, which allows to reduce the geosynthetic materials minimum strength up to 30% if compared with the previous case. This made it possible to reduce the minimum density of the geotextile to 130–170 g/m^3, taking into account the appropriate reserve according to Rp.

5   DESIGN AND PRACTICAL EXECUTION OF WORKS

The calculation data were used in the design and arrangement of a landslide protection structure in the area of the boathouses location in Prymorske village, Feodosia city. The step-by-step project for the construction of the landslide protection wall is shown in Figures 5 and 6. The initial and final stages of the landslide protection structure construction are shown in Figure 7(a & b).

6   CONCLUSIONS

1. In the course of the conducted research, modern geosynthetic materials are analyzed in part of their application for ensuring the stability of the man-made soil slope formed as a result of cutting the existing slope. For its reinforcement, it is proposed to use the high strength geosynthetic materials allowing to increase the landslide resistance of soil structures, thereby ensuring the necessary soil stability.
2. Based on the choice of the area most vulnerable to landslide deformations, a graphic model of the slope near the boathouses location in the area of the Vertolit Research

Center, Prymorske village, Feodosia, Autonomous Republic of Crimea, Ukraine, is developed and later on used in the LANDSLIP engineering software for the calculations of the landslide pressure and slope stability coefficient. The calculations show that the undeformed slope is safe with regard to landslides.
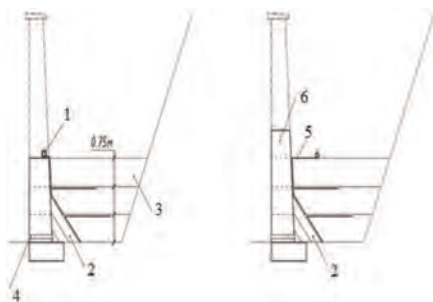
Figure 5.   Stages of the landslide protection wall. construction from geosynthetic materials: 1- sealing roll (2 m); 2 – drainage prism; 3 – reverse filling of the next layer; 4 – drainage pipe; 5 – unrolling of the sealing roll; 6 – the next work section of rubble masonry.
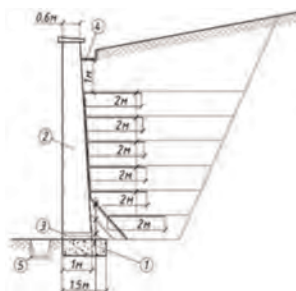
Figure 6.   The final view of the landslide protection. wall reinforced with geosynthetic materials: 1-foundation reinforced concrete pad; 2 – decorative wall of quarry stone; 3 – asbestos cement drainage pipe; 4 – drainage tray; 5 – storm drain.

As a result of serial calculations of various options and their analysis, it is found that for the undercut slopes at the site of boathouses construction, the minimum tensile strength Rp of geosynthetic materials varies in the range of [3000–4000] N/m for one layer of synthetic materials (n = 1). According to the breaking loads given in (DBC 49-86. 1988), geotextiles with the 150–200 g/m^3 density will provide required strength.

3. In the PLAXIS software package a slope graphic model is developed for the most vulnerable to landslide deformations area, Figures 3 and 4. The graphic model is used for the direct dynamic calculations of the landslide pressure and stability coefficient, taking into account the results of construction site microseismic zoning (using real accelerograms). According to refined calculations carried out with the PLAXIS software package, the required tensile strength Rp varies in the range of [2500–3500] N/m. Geotextile having the 100–150 g/m^3 density with one layer of geomaterial meets these requirements. The more advanced model of the PLAXIS software package allows to reduce the geosynthetic material cost due to its density reduction.

4. The man-made slopes reinforcement with geotextile materials should be carried out layer-by-layer in every 0.75 m with the use of backfilling with cohesive soil from undercutting

Figure 7.   The initial and final stages of the landslide protection structure construction during the 2013 summer in the area of the Vertolit Research Center boathouses location (Prymorske village, Feodosia, Autonomous Republic of Crimea, Ukraine): a) – natural slope: b) undercut slope fixed according to the project. The planned monitoring of the reinforced wall was not carried out due to the annexation of Crimea by the Russian Federation in the spring of 2014.

the slope without any compaction, since the backfill soil will be compacted during construction under the weight of the reinforced layers located above. The backfill reinforcement must be carried out up to 1 meter below the design soil levels. The length of geosynthetic material laid in the slope should be at least 2 m (Figure 7).

5. The presented research results define that for the optimal and economical choice of geosynthetic material the need arises for a comprehensive assessment of such factors as the construction site engineering and geological conditions, the type of the erected structure soil material, the loads nature and the environmental conditions. Microseismic zoning is mandatory for the construction sites in earthquake-prone zones.

REFERENCES

Eurocode 7. 2004. *Geotechnical Design*. Part 1. General Rules: EN 1997-1:2004. Retrieved from https://standards.iteh.ai/catalog/standards/cen/5df964dd-bc1e-4649-bd10-a19881574305/en-1997-1-2004

Jenner, C. G., Bassett, R. H. & Bush, D. I. 1988. *The Use of Slip Line Fields to Assess Improvement in Bearing Capacity of Soft Ground Given by a Cellular Foundation Mattress Installed at the Base of an Embankment.*

Kaliukh, I., Fareniuk, G., Fareniuk, I. 2018. Geotechnical Issues of Landslides in Ukraine: Simulation, Monitoring and Protection. In: Wu W., Yu HS. (eds) *Proceedings of China-Europe Conference on Geotechnical Engineering*. Springer Series in Geomechanics and Geoengineering. Springer, Cham, https://doi.org/10.1007/978-3-319-97115-5_124

Kaliukh, I., Senatorov, V., Khavkin, O., Kaliukh, T., & Khavkin, K. 2013. Experimental and Analytic Researches on Technical State, Design and Operation of Reinforced Concrete Antilandslide Structures for Seismic Dangerous Regions of Ukraine. *Proceedings of the fib Symposium on Engineering a Concrete Future: Technology, Modeling and Construction, 22–24 Apr 2013*, Tel-Aviv, Israel: 625–628.

Krivosheev, P., Slyusarenko, Y., Chervinsky, J. 2009. Development of Calculation Methods of Founda-tions on the Pliable Basis in Ukraine. *Proceedings of the 17th International Conference on Soil Mechanics and Geotechnical Engineering: The Academia and Practice of Geotechnical Engineering*, 2: 1818–1821. DOI 10.3233/978-1-60750-031-5-1818

Lacasse, S. 2015. Terzaghi Oration. Protecting Society From Landslides – The Role of the Geotechnical Engineer. *Proc. of the 18th Int. Conf. on Soil Mechanics and Geotechnical Engineering*, 2-6 Sept., Paris, France.

Oliver, T. H. L. & Younger, J. S. 1988. Embankment Construction Over Soft Ground using Geogrid Reinforcement Techniques. *Roads, Highways and Bridges Conference*, September, 1988, Hong Kong: Institute for Internal Research, Singapore.

PLAXIS. 2022. Retrieved from http://www.plaxis.nl/

Robertson, J. & Gilchrist, A. J. 1987. Design and Construction of a Reinforced Embankment Across Soft Lakebed Deposits. M. C Forde (ed.). *Proc. Int. Conf. on Foundations and Tunnels*, vol. 2: 84–92. Edinburgh: Engineering Technics Press.

Slyusarenko, Y., Kryvosheyev, P., Serjogin, J., Kozjavkin, I. 2010. Concrete Structures of the Olym-piyskiy National Sports Complex in Kiev. *Proceedings of the 3rd International fib Congress and Ex-hibition, Incorporating the PCI Annual Convention and Bridge Conference: Think Globally, Build Locally*.

Trofymchuk, O., Lebid, O., Klymenkov, O., Shekhunova, S., & Havrilyuk, R. 2019. Dynamic Certification of Landslide Protection Structures in a Seismically Hazardous Region of Ukraine: Experimental and Analytical Research. *Earthquake Geotechnical Engineering for Protection and Development of Environment and Constructions. Proceedings of the 7th International Conference on Earthquake Geotechnical Engineering, (ICEGE 2019), June 17-20*, Rome, Italy: 5337–5344.

Trofymchuk, O., Kaliukh, I., & Klymenkov, O. 2018. TXT-tool 2.380-1.1: Monitoring and Early Warning System of the Building Constructions of the Livadia Palace, Ukraine. In: *Landslide Dynamics: ISDR-ICL Landslide Interactive Teaching Tools*. Cham: Springer. doi.org/10.1007/978-3-319-57774-6_37

Voloshkina, E., Efimenko, V., Zhukova, O., Chernyshev, D., Korduba, I., Shovkivska, V. 2021. Visual Modeling of the Landslide Slopes Stress-Strain State for the Computer-Aided Design of Retaining Wall Structures. *IEEE 16th Int. Conf. on the Experience of Designing and Application of CAD Sys-tems (CADSM)*: 5/1-5/5. doi: 10.1109/CADSM52681.2021.9385211

Ukraine Building Code. DBN V.1.1-3-97. 1998. Engineering Protection of Territories, Buildings and Facilities From Landslides and Landslips. *The Main Provisions*. Kyiv: Dergbud.

USSR Building Code. DBC 49-86. 1988. Code. Instructions for Increasing the Bearing Capacity of the Subgrade and Pavement using Synthetic Materials. *Minavtodor of Russian Federation*, Moscow: Transport.

Design and construction of hybrid reinforced soil structures

Dave Woods & Graham Horgan
Huesker Ltd, UK

Andreas Ramsauer
Dywidag, UK

Chris Seddon & Sam Deeley
WSP, UK

ABSTRACT: The failure of a historical dry laid masonry gravity wall on a tertiary road in Hereford provided difficulties for the local authority in maintaining traffic access along the existing road with a guaranteed level of stability whilst enabling the retaining wall to be reconstructed with minimal visual impact and upgrading the original vehicular restraint system to meet more exacting modern standards.

This paper will look at the design, construction and detailing of the solution proposed to the client's Engineer WSP by Huesker and Dywidag as well as exploring similar historical solutions to highlight the variety of face finishes achievable and demonstrating the clear advantages hybrid solutions offer to geotechnical asset owners. The paper will also review the limited design advice available for such hybrid solutions and make recommendations for the expansion of existing design codes to specifically address the use of hybrid anchored and reinforced soil solutions.

1 STONE COTTAGE, HEREFORD CASE STUDY

1.1 *Background*

Hereford is a rural County in the West Midlands of England on the border with Wales, it is sparsely populated with the principal businesses being agricultural in nature. The B4224 is a winding rural road linking Hereford to the Forest of Dean, these rural roads are scarcely wide enough for 2 vehicles to pass in places and are generally lined by dense vegetation and mass masonry structures.

On the 16th of February 2020 the aftermath of Storm Dennis following immediately after flooding caused by Strom Ciara caused two slip failures along the road closing it completely between Holme Lacy Bridge and Fownhope. The second of these slip failures at Stone Cottage led to the partial collapse of an unreinforced mass masonry retaining wall approximately 70m long by 5m in height. These failures led to a complete closure of the road to through traffic, requiring lengthy diversions particularly for larger vehicles causing widespread traffic congestion in the area backing up into the county town of Hereford.

1.2 *Developing a solution and facing novel problems*

WSP who had a framework agreement with Hereford Council and Balfour Beatty, their term maintenance contractor were required to develop a solution for the wall failure at Stone

Cottage. In addition to the access constraints posed by the failure itself and the subsequent congestion, the surviving portion of the existing road housed local water, gas and tele-communication services whilst the surviving portions of the masonry parapet wall would clearly not meet modern highway design standards for vehicle containment.

The decision was made to replace the whole 70m length of the partially failed structure including the installation of a reinforced concrete cantilever parapet wall designed to meet current standards. The initial structural options for a wall solution consisted of embedded structures (sheet pile or king post and panel) or in-situ structures (RC cantilever, mass wall such as gabion or reinforced soil). Whilst the embedded structures met the main criteria of retaining the existing services the logistics of accessing the site with the heavy piling equip-ment required made the solutions unsuitable. In situ structures were easier in terms of plant access but the depth of excavation required would have meant the removal of the services and required significant temporary works to facilitate the construction.

A further "novel" problem was becoming apparent during the initial design feasibility stage as the Covid 19 virus took hold in the UK and our first lockdown was announced. Whilst alleviating much of the traffic congestion problem and giving an ideal window to carry out the repair works if a solution could be found the lockdown meant that design meetings were now confined to video conference calls. Through discussions with Huesker Ltd and Dywidag a hybrid solution was proposed which offered the advantages of preser-ving the existing road surface and services with the aesthetic finish of a reinforced soil solution that could be combined with a full reinstatement of the existing masonry facing. A first Teams meeting in mid-April fleshed out this solution resulting in an initial sketch of the solution.
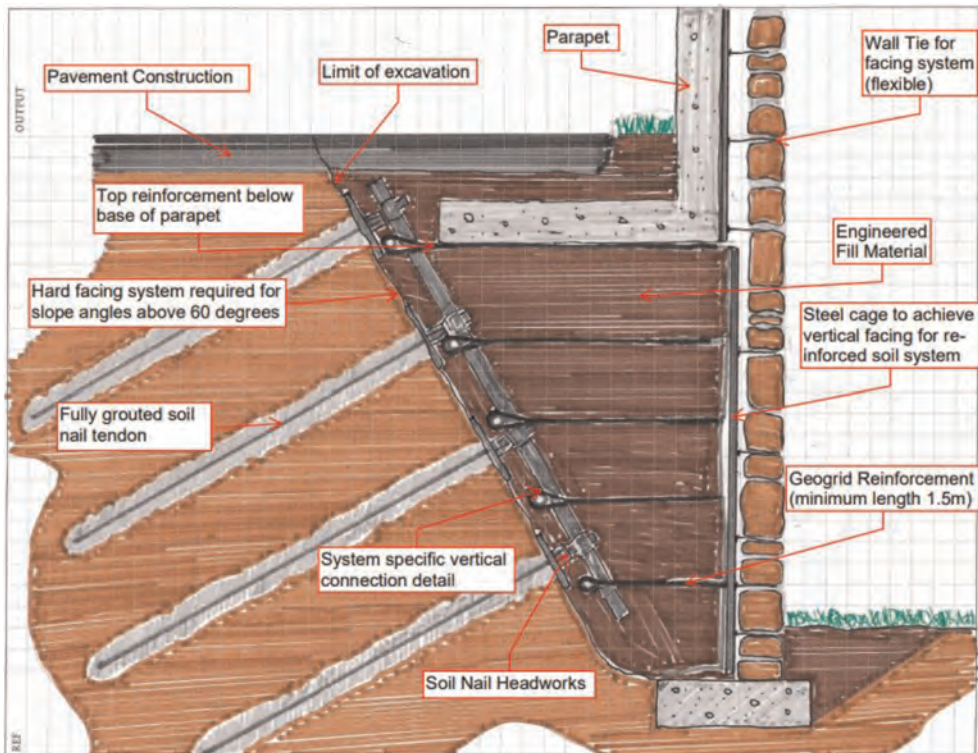
Figure 1. Initial design sketch of hybrid wall concept.

1.3 *A new way of working*

Five remote meetings between of the tripartite design team were required to come up with a final approved solution. For the size and scale of the project had these meetings been face to face involving multiple parties travelling 100s of kilometres the cost implication would have been significant and may have rendered the solution less workable. The new way of remote working however meant that details could be quickly discussed and amended with designs checked so that a final solution could be put forward.

Although a detailed design was agreed relatively quickly approvals and the procurement process meant the construction of the solution did not begin until the start of the UK's third lockdown in January 2021. The construction consisted of removing the failed section of the wall, retaining the masonry for later reuse, and the diversion of the telecom services from the wall edge to the other side of the road and the marking and protection of the existing gas and water services whilst maintain local pedestrian access to the adjacent properties. The road surface and slope was cut back to the construction profile and progressively stabilized by nailing as the works progressed downwards.

A sliding scaffold system was then erected onto the face of the nails along with the normal steel mesh and textile facing to prevent spalling. A vertical reinforced soil structure (RSS) was then built up at a 1.5m offset from the toe of the nailed profile with a vertical galvanized steel mesh formwork to the front face contained a wraparound of geogrid and non-woven textile whilst the tails of the reinforcement were wrapped around 16mm bars located behind the scaffold facing. This "towel rail" connection detail was seated beneath the nail heads so that any movement of the fill during compaction would allow the grids to tension and restrain the RSS face and pass the tensile force into the nails without introducing potential shear forces or moments and without the risk of the towel rail locking out above the nail heads and over tensioning the reinforcement.

This attention to detail produced a flush vertical face to the RSS block to which galvanized sliding masonry anchors were fixed. The RC parapet wall was then cast in-situ above the RSS block with similar masonry anchors cast into the facing. A narrow concrete levelling pad was cast in front of the RSS facing and the existing stone from the failed wall were fixed onto the masonry anchor system to finish the wall in a manner that matched the original structure. The construction by Alun Griffiths was completed ahead of schedule in 13 weeks and the road reopened to traffic 13 months after the initial failure at a cost of £124,000.

The first time the design team physically met was for the interview stage of the Ground Engineering Awards 2022 where the project was nominated in the projects under £500k category and then again for the Awards dinner where the project won its category.

Figure 2.   Wall under construction.

Figure 3.   Finished wall with masonry reattached.

2 HYBRID STRUCTURES

2.1 *Active and passive reinforcement systems*

The concept of reinforced soil is well understood within the field of geotechnical engineering having first been postulated by Casagrande in 1938. When talking of reinforced soil we normally refer to the horizontal layering of strips or sheets of geosynthetic or metallic material within a compacted engineered fill where the reinforcement goes into tension as the fill material is compacted increasing the lateral restraint of the material and reducing the soil's natural tendency to dilate under normal stress. Since the reinforcement is tensioned during compaction it is seen as active reinforcement.

Where an existing soil mass needs stabilising and removal and replacement is impractical or logistically impossible reinforcement can be introduced into the soil either through drilling and grouting or through dynamic insertion of steel bars or carbon or glass fibre rods. In principal soil nails of this nature differ little from soil reinforcement although they are generally inclined downwards from the horizontal. Since the nails will only generate tension through skin friction along the nail/soil or grout/soil interface as the soil begins to move their reinforcement is seen as passive.

The main constraint on the feasibility of reinforced soil solutions in cuttings is insufficient space to excavate and place the reinforced fill mass, this is particularly evident in failed walls and slopes supporting services or access routes, on sites requiring walls and slopes close to boundaries or on sites seeking an aesthetic facing over weathered rock. Similarly when founding reinforced soil slopes or walls on existing shallow embankment slopes to facilitate highway widenings it may be preferable to nail the existing slope rather than excavate significant volumes of fill to place the reinforcement. In such situations it is possible to combine a permanent passive means of stabilising the cut face such as soil nailing, rock bolting or sheet piles with a narrow reinforced soil facing.

2.2 *Design and detailing of hybrid solutions*

Design of both the active and passive reinforcement is typically done by considering the reinforcement affect beyond a series of postulated failure surfaces defined by single or multipart wedges, slip circles or log spirals with partial factors applied to soil and reinforcement properties, interface friction coefficients and applied loads. In the UK this design is generally done in accordance with *BS 8006 Part 1. 2010. Code of practice for strengthened/reinforced soils and other fills* and *BS8006 Part 2. 2011. Code of practice for strengthened/reinforced soils Part 2: Soil nail design.*

Whilst the two design documents explain the design methods for their respective types of reinforced soil well there is no attempt to combine both active and passive reinforcement into a hybrid solution. Some reference to this had previously been included in *Highways Agency. HA68/94. 1994. Design methods for the reinforcement of highway slopes by reinforced soil and soil nailing techniques.*

The approach suggested in HA68/94 consisted of mechanically joining or overlapping the nails and geosynthetic reinforcement at the active/passive interface and matching the vertical spacing of the two systems for simplification of the analysis by the proposed two part wedge method and would apply only to reinforced soil faces shallower than 70°.

Whilst the benching detail and connection shown in HA68/94 suit a steeper RSS built above an existing shallow slope, it is likely that, logistics permitting, the toe of the shallow slope would normally be over-steepened locally to permit the construction of full width reinforced soil rather than nailed whilst the matching of nail and reinforcement layers is generally impractical due to the significant differences in strength between the HT steel bars used for nailing and geosynthetic reinforcement whilst spacings for nails are normally in excess of 1.0m whilst vertical spacings of geosynthetic reinforcement should rarely exceed 0.5m.
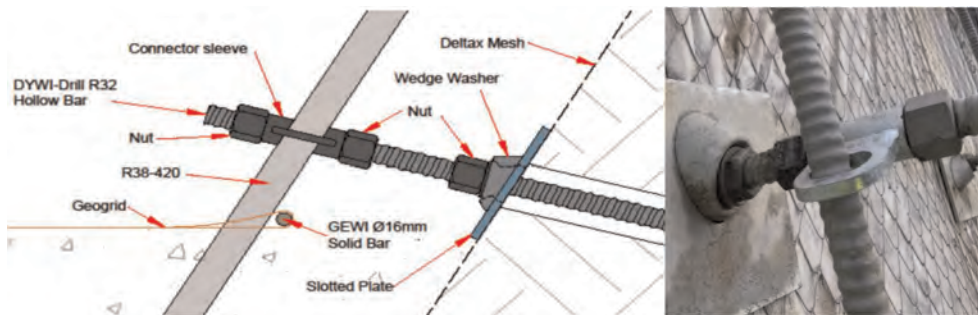
Figure 4.   Detail of nail head connection and "towel rail" geogrid connection behind scaffold bar.

The typical application area for hybrid solutions is usually in far steeper situations against very steep top down nailed or anchored faces. This steeper face lends itself well to a vertical scaffold system fixed to the nail/anchor heads which can then be connected to the reinforcement of the RSS facing with a sliding detail so that moments and shear forces are not transferred into the nail heads but such that the full tensile force from the horizontal reinforcement is transferred via the scaffold facing into the soil nails, this also obviates the need to match the nail and reinforcement spacing enabling them to be designed independently to suit the system.

Initial designs are most simply done using standard single or multi wedge analysis or slip circle analysis for the reinforced soil as if it were a full width normal RSS and similarly the soil nail design should be done independently to stabilize the required cut face. A supplementary check can then be done to ensure the total design load from the geosynthetic reinforcement at the interface does not exceed the total capacity for the soil nails whilst a more detailed global stability analysis can be carried out using staged construction for both the top down nailing process and for the combined nails and reinforced soil facing.

In creating a hybrid facing the narrow reinforced soil zone is typically 1.5m minimum width to facilitate compaction of the fill and a safe working platform, similarly for safety reasons nail heads should be capped to protect workers in close proximity to the face. Since the passive zone with the soil nails is already fully consolidated and the active zone of the reinforced soil block is liable to undergo some vertical compression during compaction, in the order of 5cms for the lowest grid layer decreasing as the wall progresses, the physical connection should be designed to permit sufficient vertical movement to avoid a concentration of forces at the interface and potential shear failure at the nail head. The vertical spacing of the reinforcement is unlikely to coincide exactly with the nail or anchor heads or any lugs connected to a sheet pile facing a vertical bar/ scaffold system attached to the retained face can be created with horizontal connections to the reinforcement formed so that they are capable of sliding vertically without focusing stress in the reinforcement or inducing shear or bending moments at the nail heads.

Ideally the scaffolded face to the nail cutting and the finished face of the reinforced soil should be close to parallel to avoid slackening of the reinforcement during compaction but given the inherent flexibility of the cages and the geogrid/soil interaction the difference between the 70°–80° cut and the vertical cage face produced no perceptible discrepancy from vertical during post construction whilst any minor tolerance issues could have been taken out in the masonry application on the sliding masonry ties to the face to ensure the outer face of the wall was vertical.

2.3   *Pros and cons*

The principal advantages gained through soil nailing the existing soil is the ability to stabilize the face as the works progress in a top-down fashion ensuring existing services and access above the failure are not further jeopardised as the works progress whilst minimizing the need to remove fill from site and import new material for the reconstruction.

The aesthetic finish to a nailed slope is not ideal however usually consisting of exposed nail heads and plates with a retention mesh or textile facing which is typically covered either through the establishment of vegetation or by the application of shotcrete. Since the reinforcement is passive in nature some localized movement of the facing is expected as the earth moves prior to generating skin friction with the nails.

Reinforced Soil Systems offer a wide range of face finishes from grassed or hand planted facings, gabion finishes, modular concrete blocks or panels or masonry which can be used to effectively tie in seamlessly with adjacent structures.

Reinforced Soil Systems require a relatively large footprint in comparison to their height which whilst not a problem when building a new embankment can pose logistical issues when building in cutting supporting existing fill or adjacent to existing site boundaries. With this in mind a hybrid system offers the logistic advantages of nailing in stabilizing the existing fill combined with the aesthetic versatility of the RSS facing for interfacing with other structures.

The introduction of multiple disciplines in the construction process could potentially pose problems but on this scheme the contractor, Alun Griffiths had a geotechnical drilling team and civils team under one company. The sequence of construction is such that the drilling contractor installs the soil nails, temporary mesh and plates and nuts which stabilizes the slope in a temporary as well as permanent state. The slope can in theory, then be left to stand until the civils or earthwork contractor arrives on site. This means there is no real interface problem between the drilling and the earthworks team & the attendant risks of standing time claims usually associated with many trades working closely together in a tight space. The one interface will be in the first excavation of the slope which will need to be done in stages or lifts using an excavator, usually the earthworks contractor followed by the soil nail drilling contractor. This is normal however on all soil nailing schemes requiring co-ordination and management.

2.4 Ageing infrastructure in a changing climate

Innovative solutions like this are likely to become increasingly necessary particularly in countries where their infrastructure is approaching or exceeding original design life and service conditions and the increased frequency of severe weather events risk partial or complete failures of earth retaining structures. The increasing need for resiliant structures to withstand the changing environment and meet modern standards whilst still fitting in alongside existing infrastructure is likely to see more retrofitted repair solutions like the one discussed here being used to minimize the disruption the works cause, reduce the amount of imported material and associated traffic movement and ultimately to create more robust structures.

2.5 Other examples and aesthetic finishes

Reinforced Soil Systems offer a wide range of face finishes from grassed or hand planted facings, gabion finishes to modular concrete blocks or panels or masonry which can be used to effectively tie in seamlessly with adjacent structures.

For steep sloping finishes whilst a simple wraparound with an external demountable formwork might be feasible the ability for sacrificial or galvanized integral mesh falsework to concertina accommodating any vertical compression of the fill lends itself well to the compaction limitations due to the narrow construction zone available when applying a RSS skin to a steep nailed or anchored face and reduces the risk to workers posed by using demountable falsework from a relatively narrow working platform.

The same steel mesh facings can be taken to vertical or near vertical with a galvanized finish to create gabion finished stone facing or provide a facing for post-fix application of masonry or brickwork to match existing structures. Alternatively modular concrete blocks or concrete panels can be constructed as an integral facing to the RSS structure.
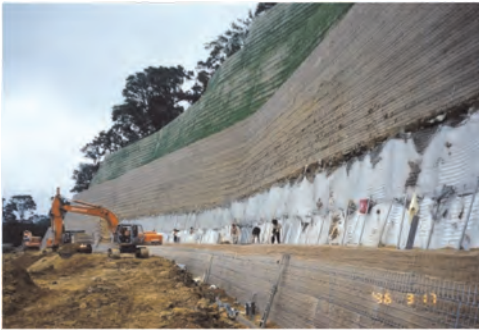
Figure 5. High top-down rock anchored slope with hybrid RSS vegetated slope facing, Taiwan 1996 (AllToffs).

Figure 6. Gabion stone faced wall nailed on left boundary full RSS on adjacent face 1998 (Comtec UK Ltd).

REFERENCES

BSI 2010 BS 8006 Part 1. Code of Practice for Strengthened/reinforced Soils and Other Fills.
BSI 2011 BS 8006 Part 2. Code of Practice for Strengthened/reinforced Soils Part 2: Soil Nail Design.
Highways Agency 1994 HA68/94. Design Methods for the Reinforcement of Highway Slopes by Reinforced Soil and Soil Nailing Techniques.

Lateral earth pressure against geosynthetic reinforced soil-integrated bridge abutment block wall

B. El Refai & P.J. Naughton
Atlantic Technological University Sligo, Sligo, Ireland

ABSTRACT: The deformation and magnitude of the coefficient of earth pressure at locations in a Geosynthetic Reinforced Soil – Integrated Bridge System subjected to self-weight and external vertical and horizontal loads was investigated using Plaxis 2D. The soil mass was found to move outward at all locations under all loading conditions. The application of the external loads increased the outward movement over the full height of the wall. The magnitude of the coefficient of earth pressure varied significantly. Over the middle two-thirds of the wall height the coefficient was close to the active value or between the active and at rest values. At the top and bottom of the wall it was closer to the at rest value. Directly beneath the bank seat the application of the external loads significantly increased the magnitude of the coefficient to higher than the at rest condition.

1 INTRODUCTION

Bridges are essential elements in modern infrastructure. Bridges, in their simplest form, consist of two abutments supporting the bridge deck spanning over an obstacle. In conventional bridge construction, expansion joints and bearings were installed between the bridge deck and the supporting abutments to accommodate relative movement resulting from expansion and contraction of the bridge deck due to temperature changes. Expansion joints require maintenance due to damage from de-icing salts leaking through the deck joints, leading to corrosion and damage of the bridge joints and bearings.

Given the problems with conventional bridges, the concept of physically and structurally connecting the superstructure and abutments to create an integral bridge have become very popular (Carder & Card 1997). For integral bridges the problems associated with joints and bearings are avoided. However, because of the integral connection between the superstructure and the abutment, the abutments are forced to move away from the retained soil when the temperature decreases in winter and the superstructure contracts and move towards the soil when the temperature rises, and the superstructure expands in summer (Horvath 2000).

Geosynthetic Reinforced Soil – Integrated Bridge Systems (GRS-IBS) is an amalgamation of reinforced soil and integral bridge technology with the explicit aim of overcoming several inherent problems with conventional abutment arrangements. These problems include high construction costs, long construction periods, durability and maintenance issues due to water ingress to bridge bearings and joints including differential settlement with the adjoining road construction and low stability in high seismic areas (Abu-Farsakh *et al.* 2018). Unlike conventional integral abutment systems, GRS-IBS involves the placement of the bridge deck directly onto a reinforced soil structure, which is typically a segmental block wall, without the use of vertical piles or bridge bearings.

The Federal Highways Administration (FHWA) (Adams *et al.* 2011) have developed a dedicated design method for GRS-IBS. However, Adams *et al.* (2011) showed that this method was heavily empirically based and provided a 'recipe' for design.

The determination of the tension in the geosynthetic reinforcement is a key design requirement for any GRS. Geosynthetic reinforcement works in tension and creates a

composite material with the surrounding backfill. Current design codes (BS 8006-1 2016; FHWA 2009; NCMA 2020; NF P94-270 2009) tend to use either the coherent gravity or tie back wedge methods to estimate the tension in the geosynthetic reinforcement.

Abu-Farsakh *et al.* (2018) argued that the failure envelopes outlined in BS 8006-1 (2016) failed to cover the true failure patterns within GRS-IBS. Both the BS 8006-1 (2016) and the allowable stress design (ASD) method also disagree on the limit states which occur within a GRS-IBS, (Adams *et al.* 2011).

This study investigated the deformations and lateral earth pressures mobilized in a GRS-IBS abutment.

2 METHODOLOGY

Plaxis 2D, Version 20, (2021) was used to conduct a parametric study investigating the lateral earth pressures in the reinforced soil block of a GRS-IBS abutment subject to both vertical and alternating horizontal load. The GRS-IBS abutment investigated consisted of a reinforced soil segmental block wall with a bridge bank seat resting directly on top of the structure.

The Plaxis 2D model was initially validated against data from a full-scale instrumented GRS wall and GRS-IBS abutment reported by Hatami & Bathurst (2005) and Zheng & Fox (2017) respectively to ensure that the Plaxis 2D model adequately captured the deformational response of GRS-IBS. The validation model was discussed in detail by El Refai & Naughton (2022).

2.1 *Parametric study and geometry*

The model geometry consisted of a 6m high segmental wall with a vertical face. The vertical boundary in the model was 15m both in front of the wall and behind the end of the reinforcement layers. The concrete facing blocks were 0.15m high and 0.3m thick. The blocks were arranged in 40 vertical courses supported on a steel plate. The primary reinforcement had a length of 7m and was spaced every 0.6m vertically, corresponding to every 4th block. In addition, two secondary geogrids of length 4.8m, were installed midway between the topmost geogrid layers in the structure, Figure 1. This reduced the vertical spacing to 0.3m over the top 1.5m of the wall. The wall supported an abutment bank seat which was 2m wide, and 1.4m deep located at 2.5 m from the back of the facing block. The properties of the blocks, bank seat and backfill soil used in the model are presented in Table 1. An interface was created between the blocks themselves, and the blocks and the soil, Table 2. The stiffness, EA, of the geogrid reinforcement was 1500kN/m, corresponding to a polyester geogrid with a short-term strength of approximately 150kN/m.

Table 1. Model parameters for the backfill and facing blocks used in the Plaxis 2D analysis.

Material	γ (kN/m^3)	E_{50}^{ref} (MPa)	E_{oed}^{ref} (MPa)	E_{ur}^{ref} (MPa)	ν	c (kPa)	φ_p (°)	ψ (°)
Backfill	22	50	28	100	0.15	1	44	11
Facing block	16	100	–	–	0.15	–	–	–

Table 2. Backfill – facing block and facing block – facing block interface properties used in the Plaxis 2D model.

Interface	E (MPa)	c (kPa)	φ_p (°)	ψ (°)	Kn (MN/m^3)	Ks (MN/m^3)
Backfill–facing block	50	0	44	11	100	1
Facing block–facing block	100	46	57	0	1000	40
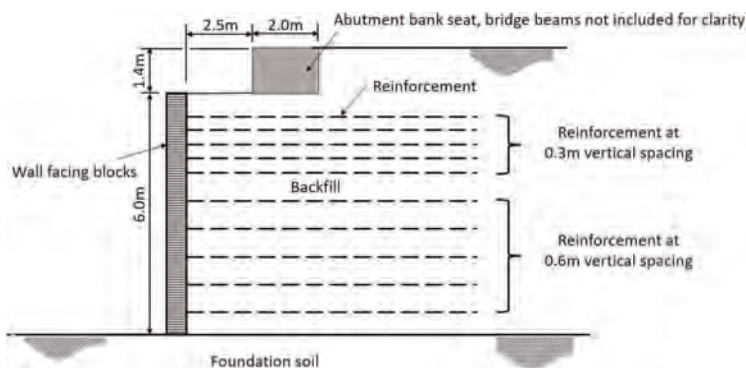
Figure 1. Schematic of GRS-IBS investigated in this study.

The bank seat was supported by a fixed anchor plate at the top of the bank seat representing the bridge beams and was required to restrain the abutment from unconditional outward movement when the bridge loading was activated in the model. The axial stiffness of this fixed anchor plate was 16MN/m, which was selected to limit the horizontal displacement of the bridge beams to 1cm. Without this anchor the GRS wall would have no restraint to horizontal displacement.

2.2 *Model construction and calculation of bridge loads*

Each parametric model was constructed in phases within Plaxis 2D, with an analysis undertaken at each stage. A detailed discussion of each phase is given in El Refai & Naughton (2022).

The vertical and horizontal loads used in this study are shown in Table 3 and were determined from the analysis of a single lane bridge deck, 15m long, supported on a 2m wide and 1.4m high bank seat and were previously discussed by El Refai & Naughton (2022).

In this paper only the results of Phases 2, 9 and 10 are discussed. Phase 2 was the construction phase, where only the facing blocks, the backfill, and the geogrids were activated. Phase 9 applied all the vertical loads (Table 3) together with all the inward, towards the abutment, horizontal loads (Table 3) to the top of the wall. Phase 10 applied all the vertical loads (Table 3) together with the outward, away from the abutment, horizontal loads (Table 3) to the top of the wall.

Table 3. Magnitude of loads used in the analysis.

Load	Self-weight	Variable traffic load	LM1[*]	Shrinkage	Creep	Temperature	Braking force
Vertical (kN)	185.3	31	72	0	0	0	4.3
Horizontal (kN)	123.4	36.6	10.5	−100	−44.2	±73.5	±23

Notes
[*]LM1 model is for tandem axle and general uniformly distributed case in accordance with the design standard for traffic loads on bridges, BS EN 1991-1-1 (2002).

3 RESULTS

The displacement and the coefficient of lateral earth pressure were investigated at three locations in the model during Phases 2, 9 and 10. The first plane was directly behind the facing blocks, the second plane was a vertical section starting at the midpoint of the bank seat base, and the third plane was along the line of maximum tension in the reinforcement layers. The

coefficient of lateral earth pressure, K, was defined in this study as the ratio of the vertical and horizontal stresses extracted from the Plaxis 2D model at each location investigated.

In Phase 2, with just the self-weight of the wall considered, the wall facing bowed outward, with a maximum deflection occurring two-thirds the way up the wall face, Figure 2(a). The application of the vertical and inward horizontal loads, Phase 9, increased the outward movement of the wall. Reversing the direction of the horizontal load, Phase 10, did not impact the deformation of the wall facing. Outward movement of the wall facing was observed during all three phases examined. The magnitude of K immediately behind the wall is shown in Figure 2(b) and was found to be highly variable. The variation of K was almost identical for Phases 2, 9 and 10, with the magnitude of K slightly higher for Phases 9 and 10 following application of the external loads. The magnitude of K was greater than 0.5 at each layer of reinforcement. Between layers of reinforcement the magnitude of K tended towards the coefficient of active earth pressure, K_a. This was in keeping with the outward displacement of the wall observed at this location. Near the top and bottom of the wall between layers of reinforcement, the magnitude of K tended towards the coefficient of earth pressure at rest, K_0. This was contrary to the observed displacement, where outward displacement of the face was observed at the top and bottom of the wall, Figure 2(a).
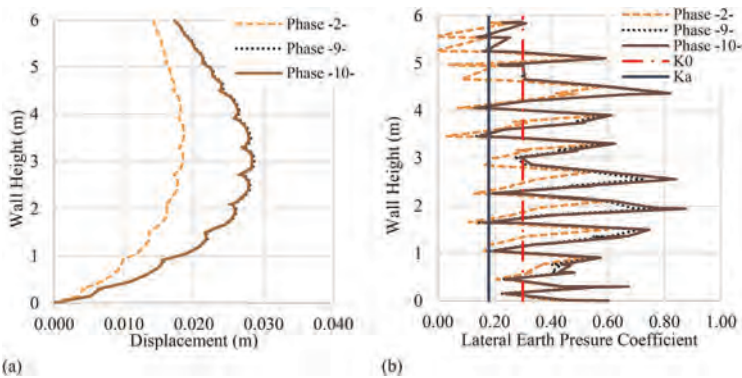
Figure 2. (a) Displacement directly behind the wall & (b) Lateral earth pressure coefficient directly behind the wall.

The displacement at the second plane, a vertical line from the midpoint of the bank seat base, showed outward displacement of the soil mass over the full height, Figure 3(a). In general terms, the displacement increased proportional to the height of the wall, with the maximum displacement observed at the top of the wall in Phases 2, 9 & 10, (18.2mm, 38.8mm & 35.9mm respectively). The application of the vertical load and inward horizontal load, Phase 9, followed by the outward horizontal load, Phase 10, increased the deformation over the full wall height at this location. The value of K at this location is shown in Figure 3 (b), with almost identical values for Phases 2, 9 & 10. The magnitude of K was close to K_a over the middle two-thirds of the wall height and approached K_0 at the very top and very bottom of the wall. The magnitude of K at the top and bottom of the wall was contrary to what was expected based on the predicted displacement at this location, i.e. outward movement of the soil mass.

The displacement along the line of maximum tension is shown in Figure 4(a). Again, outward displacement was observed over the full height, with a maximum value occurring at the top of the wall in Phases 2, 9 & 10 (13.8mm, 31.8mm & 29.9mm respectively). The application of the external loads in Phase 9, followed by Phase 10 resulted in a significant increase in deformation at this location. Very little change was observed in the deformations when the direction of the horizontal load was reversed, Phase 9 followed by Phase 10. The value of K at this location is shown in Figure 4(b), with reasonably good agreement between the magnitude of K over the

bottom two-thirds of the wall height. In the top third of the wall, the magnitude of K for Phases 9 and 10 was approximately double that for Phase 2. The value of K over the bottom two-thirds of the wall height was between K_a and K_0 and approached K_0 at the bottom of the wall. Like the other two locations examined; the magnitude of K was consistent with the predicted displacement over the bottom two-thirds of the wall height. However, at the top and bottom of the wall, the predicted value of K was contrary to the predicted displacement.
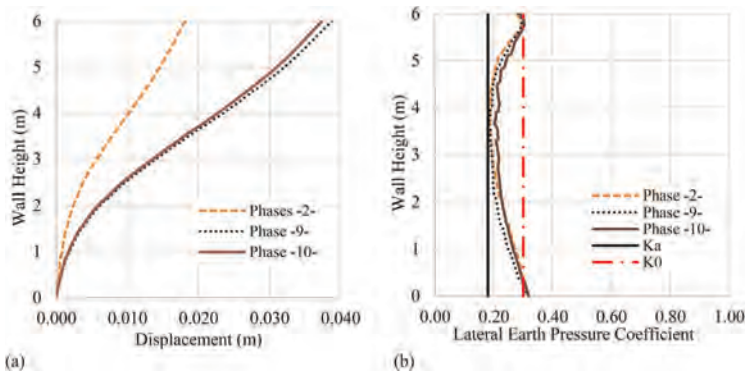
Figure 3. (a) Displacement beneath the bank seat (b) Lateral earth pressure coefficient beneath the bank seat.
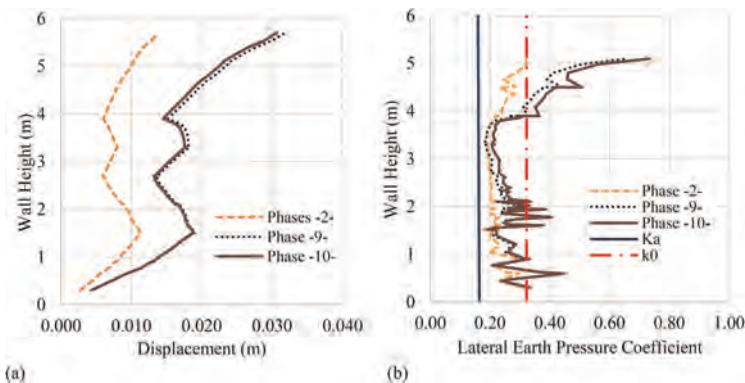
Figure 4. (a) Displacement at line of maximum tension and (b) Lateral earth pressure coefficient at line of maximum tension.

4 CONCLUSIONS

Plaxis 2D was used to predict the behaviour of a GRS-IBS abutment under self-weight of the segmental block wall and the addition of externally applied loads from the bridge deck. The magnitude of displacement and the magnitude of the coefficient of earth pressure were investigated at three locations, behind the wall facing, directly beneath the bank seat and along the line of maximum tension.

The backfill deflected outward at all three locations under all load combinations. The application of the external loads significantly increased the outward displacement. No significant change in displacement was observed when the direction of the external horizontal load switched direction, initially acting towards and then away from the abutment.

913

No consistency was found in the magnitude of K at the three locations examined. Immediately behind the wall face, K was very erratic and had a maximum value at each reinforcement layer, with the magnitude of K > 0.5. In between the reinforcement layers, over the central height of the wall, the magnitude of K tended towards the coefficient of active earth pressure. Near the top and bottom of the wall, K tended towards the at rest coefficient of earth pressure. The magnitude of K when the external loads were applied increased slightly over the case with just the backfill self-weight.

Directly beneath the bank seat, good agreement was found in the magnitude of K. Over the middle two-thirds of the wall height K tended towards the active coefficient, while at the top and bottom of the wall, K tended towards the at rest condition.

Along the line of maximum tension, the value of K, over the lower two-thirds of the wall height was between the active and at rest coefficients. In the top two thirds of the wall height, K tended towards the at rest coefficient of earth pressure for the self-weight only and exceeded the magnitude of K_0 when the external loads were applied.

ACKNOWLEDGEMENTS

REFERENCES

Abu-Farsakh, M., Ardah, A., & Voyiadjis, G. 2018. 3D Finite Element Analysis of the Geosynthetic Reinforced Soil-integrated Bridge System (GRS-IBS) under Different Loading Conditions. *Transportation Geotechnics*: 15, 70–83.

Adams, M., Nicks, J., Stabile, T., Wu, J. T., Schlatter, W., & Hartmann, J. 2011. *Geosynthetic Reinforced Soil Integrated Bridge System, Synthesis Report (No. FHWA-HRT-11-027)*. Federal Highway Administration: United States.

BS EN 1991-1-1. 2002. *Eurocode 1: Actions on Structures - Part 1-1: General Actions - Densities, Self-Weight, Imposed Loads for Buildings*. CEN.

BS 8006-1:2010+A1. 2016). *Code of Practice for Strengthened/Reinforced Soils and Other Fills*. British Standard Institution: London.

Carder, D. R., & Card, G. B. 1997. *Innovative Structural Backfills to Integral Bridge Abutments*. TRL Report 290. Transport Research Laboartory: UK.

El Refai, B.S. & Naughton, P.J. 2022. Numerical Analysis of Stress Concentration Around Bridge Bank Seat in Geosynthetic Reinforced Soil – Integrated Bridge Systems (GRS-IBS). *Proceedings of the 7th European Conference on Geosynthetics, EuroGeo 7, IOP Conf. Series: Materials Science and Engineering 1260* (2022) 012037, IOP Publishing, doi:10.1088/1757-899X/1260/1/012037.

FHWA. 2009. *Design and Construction of Mechanically Stabilized Earth Walls and Reinforced Soil Slopes, FHWA-NHI-10-024*. Federal Highways Administration: USA.

Hatami, K., & Bathurst, R. J. 2005. Development and Verification of a Numerical Model for the Analysis of Geosynthetic-reinforced Soil Segmental Walls under Working Stress Conditions. *Canadian Geotechnical Journal*: 42(4) 1066–1085.

Horvath, J. S. (2000). *Integral-abutment Bridges: Problems and Innovative Solutions using EPS Geofoam and Other Geosynthetics*. Manhattan College Research Report No. CE/GE-00-2: US.

NCMA. 2012. *Design Manual for Segmental Retaining Walls*. National Concrete Masonry Association. 3rd Edition 5th Printing. Virginia, US.

NF P94-270. 2020. *Calcul géotechnique - Ouvrages de soutènement - Remblais Renforcés et Massifs en sol cloué*. AFNOR: France.

Plaxis 2D. 2021. *Bentley – Plaxis General Information Manual*. Delft, Netherlands: Bentley Systems Inc.

Zheng, Y., & Fox, P. J. 2017. Numerical Investigation of the Geosynthetic Reinforced Soil–integrated Bridge System under Static Loading. *Journal of Geotechnical and Geoenvironmental Engineering*, 143(6), 04017008.

Reinforced embankments impacted by landslides: Analytical and numerical modelling

S. Cuomo, A. Di Perna & M. Savino
Geotechnical Engineering Group (GEG), University of Salerno, Italy

L. Frigo
Comune di Chiampo, Vicenza, Italy

M. Martinelli
Deltares, Delft, The Netherlands

ABSTRACT: The paper presents the results of two methods applied to the impact of fast landslides against an artificial barrier reinforced by geosynthetics. The first approach consists in simulating either the fast-moving landslide or the movable barrier through a single mathematical model based on inelastic collision formulation. In a second approach, the maximum expected impact pressure is estimated from the geometric and kinematic features of the impacting landslide mass by using literature impact formulations, and hence a FEM (Finite Element Method) dynamic analysis is performed to assess how the barrier is damaged and/or displaced during the impact. In such a case, a very detailed geometry of the barrier is considered and there is the chance of simulating the local/internal yielding of the structure. The latter is made of granular soil reinforced through geogrids wrapped around the facing, and it is free to move along the contact with the base soil. The landslide is constituted by a rectangular-like shaped volume of saturated soil moving at some meters per second at the impact stage. However, the height of the impact material is necessarily assumed as constant during the landslide-structure impact interaction. Globally, the two approaches provide consistent results as it concerns the Landslide-Structure Interaction (LSI) problem, with some discrepancies depending on the initial landslide velocity and type/geometry of the protection barrier structure.

1 INTRODUCTION

Recent research has outlined the feasibility of geosynthetics reinforced embankments as protection measures against flow-like landslides, especially in the case of debris avalanches, which are unchannalised flows capable to spread laterally upon hitting a rigid-like barrier. The field application has been also verified by means of landslide propagation analyses considering or not the presence of such structure (Cuomo *et al.* 2019).

The geosynthetic reinforcements improve the efficiency of the Deformable Geosynthetics-Reinforced Barrier (DGRB) to withstand the impact forces since they distribute the load in the longitudinal direction (Peila *et al.* 2007). Specifically, the deformation of the barrier nearby the impacted zone causes a tension in the layer oriented along the longitudinal axis of the structure. Moreover, the reinforced layers contain the displacement of the backside facing and thus increases the capability to withstand the impact while the impact force is increased (Lambert & Bourrier 2013). However, geosynthetics can reach the ultimate shear resistance (T_u) bringing the barrier to failure for excessive relative sliding of the layers along the soil-reinforcement interface. Elasto-plastic frictional interfaces are inserted between the granular backfill soil and the geogrids, with strength properties reduced to 80% of those of soil.

Nowadays, the crucial point consists of elaborating methods and procedures to (1) quickly individuate their geometry in the case where different locations for installation can be considered or (2) accurately design such works in the case when the location has been already established.

2 METHODS

2.1 Analytical method

An analytical model is set up where the landslide and the barrier are considered as two colliding bodies (Figure 1). At impact (t = t_{imp}), the approaching flow has mass m_1, length $L_{1,0}$, depth h, unitary width, density ρ_m, and initial velocity $v_{1,0}$. During impact ($t_{imp} < t < T_2$), flow velocity and length change to v_1 and L_1, respectively. The barrier is rigid, with its own mass m_2 and it is free to slide along the base. The frictional contact at the base is equal to $\tan(\delta_b)$, which can be set as the 80% of the strength properties of the subsoil base material (Cuomo *et al.* 2020). The impacted side of the barrier is usually inclined of $\beta = 60° - 80°$. The landslide-barrier interaction is schematized by an inelastic collision. After the impact, the two bodies reach the same velocity v_{CM}, applied in the centre of mass (CM) of the system and can be derived from the conservation of momentum.
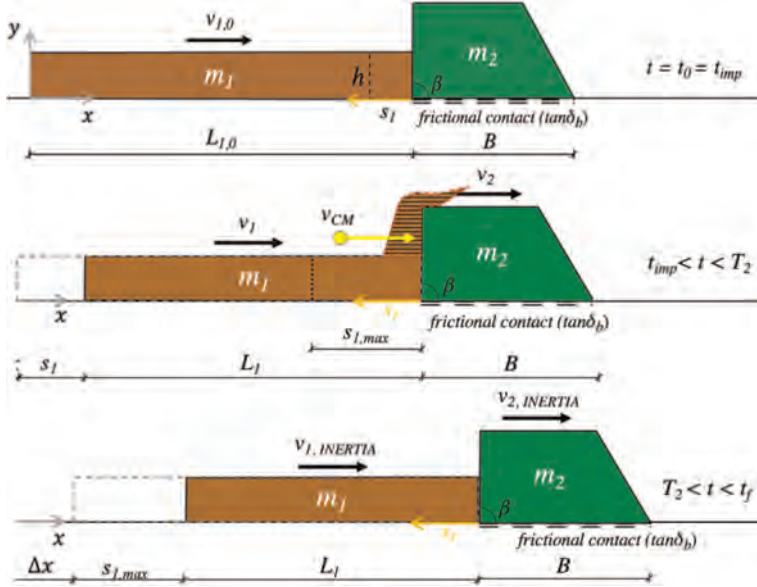
Figure 1. Conceptualization of the impact according to the analytical method.

The impact force F is a spatio-temporal function since the approaching volume of the landslide increases with time until T_1 (Eq. 1) and then diminishes due to the dissipation of flow energy until T_2 (Eq. 2).

$$F(t) = \frac{1}{2}\frac{q_1^2}{K_1}\left(\frac{t}{\tau}\right) \qquad 0 < t \leq T_1 \tag{1}$$

$$F(t) = \frac{1}{2}\frac{q_1^2}{K_1}\left(\frac{T_2 - t}{1 - \tau}\right) \qquad T_1 \leq t < T_2 \tag{2}$$

The quantity s_1 represents the change (shortening) in landslide body after the impact (i.e., $L_{1,0} - L_1$) and it is computed as positive in the direction opposite to the flow movement. Being the impacting mass saturated, the expected behaviour is that a part of the landslide mass will overtop the barrier and the remaining volume will interact with the barrier. The maximum value of s_1 (i.e., $s_{1,max}$) is reached when the impact force is equal to the peak value. This means that only a part of the total volume of the landslide contributes to the interaction with the barrier.

The mathematical steps are reported in Cuomo *et al.* (2022), while the main equations are written below. For more readability, let introduce the quantities K_1 (Eq. 3) and q_1 (Eq. 4). In particular, K_1 is related to the body 1 (landslide) and resembles a change in momentum over space, while the quantities q_1 and T_2 (Eq. 5) are the model primary unknows. For $t_{imp} = 0$, as T_2 and T_1 can be achieved by fixing the ratio $\tau = T_1/T_2$ (e.g., from experimental evidence), the impact dynamics description is complete.

$$K_1 = \left(\frac{m_1 m_2}{m_1 + m_2}\right) \cdot \left(\frac{v_{1,0}}{s_{1,max}}\right) \tag{3}$$

$$q_1 = \frac{3}{4} \frac{K_1 v_{1,0}}{\sqrt{s_{1,max}}} \tag{4}$$

$$T_2 = \frac{8}{3} \frac{s_{1,max}}{v_{1,0}} \tag{5}$$

The barrier acceleration starts growing at $t = t^*$ (Eq. 6) and changes over time, being controlled by the frictional force along the barrier base and by the inertial forces instantly developed in the landslide and in the barrier during sliding. After reached the peak force at $t = T_1$, both landslide and barrier accelerations begin to decrease. It entails that the velocity $v_2(t)$ (Eq. 6) and the displacement $\Delta x(t)$ (Eq. 7) trends over time for the barrier can be approximately computed (if landslide shear stresses along the impacted side of the barrier are neglected). The final displacements of the barrier can be computed through Equation 8.

In this analytical model, two quantities $s_{1,max}$ and τ must be evaluated. From numerical calibrations performed by Cuomo *et al.* (2022) for a set of cases, it emerges that the ratio $\lambda = s_{1,max}/L_{1,0}$ was equal to 0.72 for barriers fixed to the base ground and 0.41 for unfixed barriers. Suggested values for τ are 0.17 (fixed) and 0.25 (unfixed).

$$v_2(t) = \begin{cases} \dfrac{AC}{2}\left(\dfrac{t^2 - t^{*2}}{\tau}\right) - B(t - t^*) & t^* < t \le T_1 \\[2ex] \dfrac{AC}{2}\left(\dfrac{t^2 - 2T_2 t + T_1 T_2}{1 - \tau} - \dfrac{t^{*2}}{\tau}\right) - B(t - t^*) & T_1 < t \le T_2 \\[2ex] t^* = \dfrac{B\tau}{AC} \end{cases} \tag{6}$$

$$\Delta x(t) = \begin{cases} \dfrac{AC}{6}\left(\dfrac{t^3 - 3t^{*2}t + 2t^{*3}}{\tau}\right) - \dfrac{B}{2}(t - t^*)^2 & t^* < t \le T_1 \\[2ex] \dfrac{AC}{6}\left(\dfrac{(T_1 - t)^2(3T_2 - 2T_1 - t)}{1 - \tau}\right) - \dfrac{B}{2}(T_1 - t)^2 - v_2(t = T_1)(T_1 - t) + \Delta x(t = T_1) & T_1 < t \le T_2 \end{cases} \tag{7}$$

$$\Delta x_f = \frac{AC}{6}\left[\frac{(T_1 - t^*)^2(T_1 + 2t^*)}{\tau} + \frac{2(T_2 - T_1)^3}{1 - \tau}\right] - \frac{B}{2}\left[(T_1 - t^*)^2 + (T_2 - T_1)^2\right] \tag{8}$$

where $= \frac{q_1^2}{2K_1 m_2}$; $B = g \tan \delta_b$; $C = \sin \beta + \cos \beta \tan \delta_b$.

2.2 A finite element method approach

Different types of barriers were considered and employed in a numerical model implemented in the Plaxis 2D code.

Barrier B1, whose FEM model is shown in Figure 2, is 6 m high and equipped with 10 geogrids, 0.6 m vertically spaced and wrapped around the facing. This barrier has an equilateral trapezoidal shape with the facing 60° inclined, a top width of 4 m and the base 11 m large. Barrier B2 is 7.5 m high and equipped with 12 geogrids, 0.6 m vertically spaced and wrapped around the facing. This barrier has an equilateral trapezoidal shape with the facing 72° inclined, a top width of 3.63m
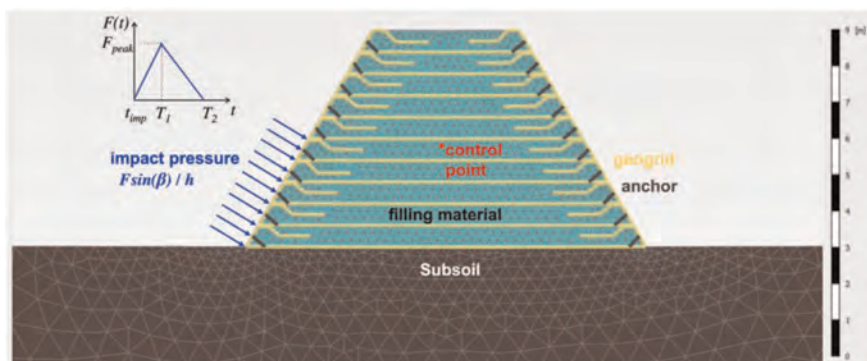
Figure 2. An example of computational domain for FEM analyses (barrier B1).

and the base 8.38 m large. Lastly, barrier B3 is 6 m high and equipped with 10 geogrids, 0.6 m vertically spaced and wrapped around the facing. This barrier has an equilateral trapezoidal shape with the facing 80° inclined, a top width of 6.50 m and the base 8.50 m large. The control point in the core of each structure is individuated for tracking the computed displacements and it is located at the barrier mid-height. The analyses are performed for a unitary width of the barrier, in plane strain conditions.

3 EXAMPLES

3.1 Input data

Some landslide typologies (impact scenarios) are chosen as examples for the analysis of the protection structure. Table 1 reports the geometric features of different types of landslides and barriers for several impact scenarios. In the engineering practice, all these quantities are accurately estimated through specific analyses of landslide triggering and propagation (Cuomo *et al.* 2019, 2021a). The concept of the analyses is to apply the temporal trend of the impact force (obtained from Eqs. 1-2-3-4) along the impacted side of the DGRB modelled in a FEM framework. The pressure distribution along the barrier side simulated in the FEM analyses is assumed as constant. The mechanical properties of the materials employed in the FEM analysis are listed in Table 2.

3.2 Results and discussion

For the nine examples proposed in Table 1, the temporal trend of displacements obtained through the two methods are in many cases in very good agreement (Figure 3).

Table 1. Impact scenarios considered in the analyses.

ID	1	2	3	4	5	6	7	8	9
Landslide	L1	L4	L5	L1	L1	L6	L3	L2	L7
h (m)	3	3	3	3	3	1	4	3	3
$L_{1,0}$ (m)	15	9	21	15	15	45	12	15	15
V_1 (m^3/m)	45	27	63	45	45	45	48	45	45
ρ (kg/m^3)	1,800	1,800	1,800	1,800	1,800	1,800	1,800	1,800	2,120
m_1 (kg)	81,000	48,600	113,400	81,000	81,000	81,000	86,400	81,000	95,400
$v_{1,0}$ (m/s)	10	10	10	10	10	10	10	5	10
Barrier	B1	B1	B1	B3	B2	B1	B1	B1	B1
B (m)	11	11	11	8.5	8.38	11	11	11	11
b (m)	4	4	4	6.5	3.63	4	4	4	4
H (m)	6	6	6	6	7.5	6	6	6	6
β (°)	60	60	60	80	72	60	60	60	60
L_2 (m)	6.95	6.95	6.95	6.08	7.87	6.95	6.95	6.95	6.95
ρ (kg/m^3)	2,000	2,000	2,000	2,000	2,000	2,000	2,000	2,000	2,000
m_2 (kg)	90,000	90,000	90,000	90,000	90,075	90,000	90,000	90,000	90,000
$\tan(\delta_b)$	0.29	0.29	0.29	0.29	0.29	0.29	0.29	0.29	0.29
Impact force computed from the analytical model									
F_{peak} (kN/m)	446	551	375	508	490	149	577	112	485
T_1(s)	0.41	0.25	0.58	0.41	0.41	1.24	0.33	0.82	0.41
T_2 (s)	1.65	0.99	2.31	1.65	1.65	4.96	1.32	1.64	1.65

Table 2. Mechanical properties for the DGRB used in the FEM analyses.

	ρ (kg/m^3)	c' (kPa)	φ' (°)	ψ (°)	K_0 (-)	ν (-)	E (MPa)	T_u (kN/m)	EA (kN/m)	EI (kN/m^2)	α	β
Filling material	1800	0.1	38	0	0.38	0.25	15				0.01	0.001
Subsoil	2000	–	–	–	0.66	0.25	30				0.01	0.001
Geogrids*								100	1000			
Metallic framework									66340	35		
Anchors									21100			

ρ is the density of granular soil; c' is the cohesion; φ' is the friction angle; ψ is the dilatation angle; K_0 is the earth pressure coefficient; ν is the Poisson's ratio; E is the Young modulus; T_u is the ultimate tensile strength of the geogrid; EA is the extensional stiffness; EI is the bending stiffness; α and β are the Rayleigh's coefficients.
*Interface friction assumed equal to 0.8 tan(φ') of the confining material

The numerical method considers the elasto-plastic soil behavior, and the interaction between the filling soil and the geogrids. These features are not considered in the analytical method. However, due to the similarity between the analytical and the FEM displacements, the composite barrier can be schematized as a homogeneous rigid body for the assessment of the final displacements. However, it is worth noting that the influence of pore-water pressure at the impact, recognized as an important factor of LSI (Cuomo et al. 2021), is not considered in these analyses.

The final configurations and the entities of deformations within the barriers are related to the soil-geogrid interaction, which deserves further investigation.

The axial forces (N) along the geogrids have been computed for simulation ID 1 (L1-B1) in Figure 4a and for simulation ID 5 (L1-B2) in Figure 4b. When the peak impact pressure is
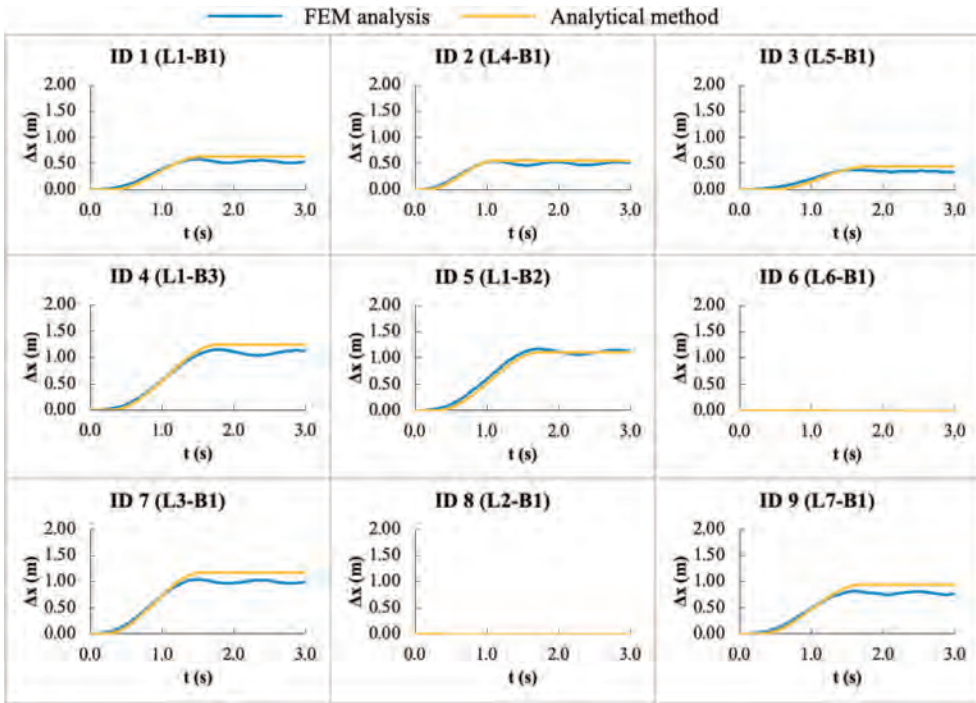
Figure 3. Displacements temporal trend of the DGRB computed with FEM and analytical method.

reached (time equal to T_1), the highest value (N = 10 kN/m) is measured on the valley side (beyond the barrier). Then, the axial forces increase more at time equal to T_2 (N = 18.58–25.88 kN/m). These values are far from the ultimate strength of the geogrids. In both simulations, the occurrence of the peak tensile stress of the geogrids is not the same of the application of peak impact pressure (T_1). This means that the structure is mostly compressed
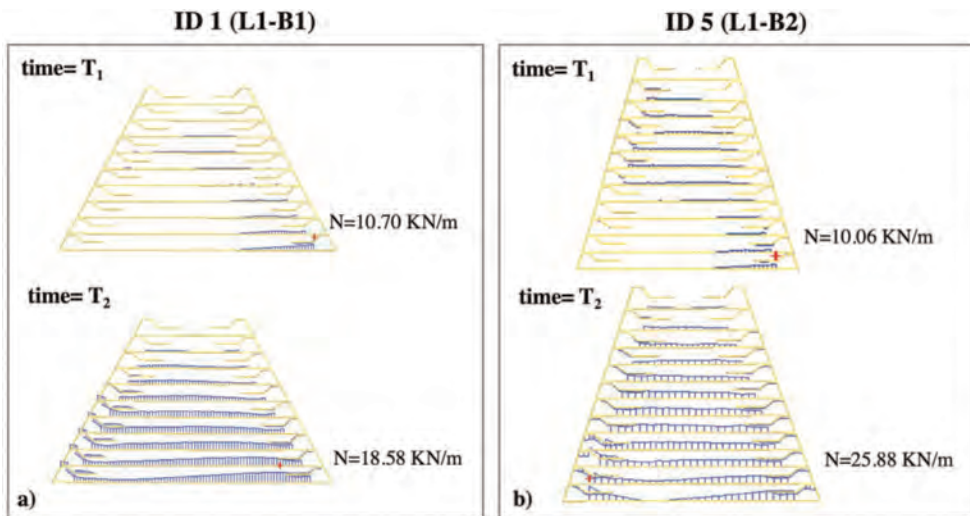
Figure 4. Axial force inside the geogrids: a) ID1; b) ID 5.

until T_1, and the tensile stress within the geogrid is limitedly mobilized; then, the barrier is sheared more and more during the decreasing of the external pressure. Specifically, the peak tensile stress in the bottom geogrid is reached at the rear of the barrier for both configurations, with decreasing values towards the core. This entails that the barrier is mostly compressed at the impact front, and so the geogrids are not pulled out from the base corner where very small tensile stress is mobilized due to the geometrical configuration and the wrap of the geogrid. On the other hand, the rear of the barrier is mostly sheared and so the base geogrid undergoes an extension.

However, more investigation would be needed to understand whether, and in which cases, global stiffness of the barrier may play a role despite the stress in the geogrids still being far from the ultimate state.

4 CONCLUSIONS

Two approaches have been proposed to examine the problem of the interaction of a fast-moving flow-like landslide upon hitting a protection barrier made of geosynthetics reinforced coarse-grained material. The analytical approach fully describes the landslide energy release process and the movement of the barrier. The numerical approach allows including the very detailed layering of the structure and the presence/features of the geosynthetics which contribute to the stiffness of the work. Indeed, the two approaches are complementary rather than alternative, and usable at different stages of the design procedure.

REFERENCES

Cuomo, S., Moretti, S., & Aversa, S. 2019. Effects of Artificial Barriers on the Propagation of Debris Avalanches. *Landslides*, 16(6), 1077–1087.

Cuomo, S., Moretti, S., Frigo, L., & Aversa, S. 2020. Deformation Mechanisms of Deformable Geosynthetics-reinforced Barriers (DGRB) Impacted by Debris Avalanches. *Bulletin of Engineering Geology and the Environment*, 79, 659–672.

Cuomo, S., Di Perna, A., Martinelli, M. 2021. MPM hydro-mechanical Modelling of Flows Impacting Rigid Walls. *Canadian Geotechnical Journal*, 58(11), 1730–1743

Cuomo, S., Di Perna, A., Martinelli, M. 2022. Analytical and Numerical Models of Debris Flow Impact. *Engineering Geology*, 308, 106818.

Lambert, S., & Bourrier, F. 2013. Design of Rockfall Protection Embankments: A Review. *Engineering geology*, 154, 77–88.

Peila, D., Oggeri, C., & Castiglia, C. 2007. Ground Reinforced Embankments for Rockfall Protection: design and Evaluation of Full-scale Tests. *Landslides*, 4(3), 255–265.

Large-scale tests on bearing capacity failure of geogrid-reinforced walls

J. Derksen
Wayss & Freytag Ingenieurbau AG, Special foundations, Düsseldorf, Germany
Formerly: Institute of Geomechanics and Underground Technology, RWTH Aachen University, Germany

R. Fuentes
Institute of Geomechanics and Underground Technology, RWTH Aachen University, Germany

M. Ziegler
ZAI Ziegler und Aulbach Ingenieurgesellschaft mbH, Aschaffenburg, Germany
Formerly: Institute of Geomechanics and Underground Technology, RWTH Aachen University, Germany

O. Detert & H. Hangen
Huesker Synthetic GmbH, Gescher, Germany

ABSTRACT: Retaining structures are one of the most common applications of geosynthetic-reinforced soil (GRS). Most design approaches assume a multi-body failure mechanism below a quasi-monolithically reinforced block for the loss of bearing capacity in the foundation soil. Preliminary small-scale model tests showed that these assumptions are well justified and provided fundamental insights in the bearing capacity failure of GRS walls. However, the small-scale tests suffered from scale effects because the mechanical similarity was not completely fulfilled. Therefore, large-scale tests are additionally presented in this paper using regular geogrids. For this purpose, a 1.2 m high and 1.0 m wide geogrid-reinforced wall with a wrapped-around facing was installed on 2.0 m loose sand as subsoil. Then, a vertical load was applied on top of the reinforced structure. Horizontal and vertical wall deformations were recorded and the kinematic behaviour of the wall footprint at the bottom reinforcing layer was observed through a transparent side window using digital image analysis. Finally, the experimental data are compared to the results of analytical bearing capacity equations, revealing that the reduction of the reinforcement length needs to be considered to conservatively predict the load-bearing capacity.

1   INTRODUCTION

Retaining walls using geosynthetic-reinforced soil (GRS) have proven advantageous performance compared to conventional cantilever or gravity walls in terms of differential settlements, particularly during seismic events due to relatively ductile and flexible behaviour (e.g. Huang B. *et al.* 2010; Tatsuoka *et al.* 1997). On top of the mechanical benefits of GRS to increase load-bearing capacity and reduce deformation, structures with geosynthetics are flexible in geometry, resource-efficient, durable, sustainable, ecologically and economically favourable.

However, the behaviour of GRS retaining walls needs to be carefully considered to enable a safe and economical design (e.g. Allen & Bathurst 2002; Mirmoradi & Ehrlich 2019; Ziegler 2017). For instance, Y. Xie and B. Leshchinsky (2015) confirmed that bearing capacity and overall failures of GRS walls involve complex mechanisms which depend on several factors, e.g. surcharge, reinforcement properties and soil conditions. For the calculation of the load bearing capacity, the design approaches assume a multi-body failure mechanism below a quasi-monolithic reinforced block

(coherent unit) (e.g. British Standard BS 8006; German Standard DIN 4017 in connection with EBGEO 2010). As a result, geogrid-reinforced soil walls are treated similarly to strip foundations and the influence of the reinforced block above the wall footing is not considered. Therefore, a review of the mode of bearing capacity failure is required. For this purpose, small- and large-scale 1g model tests of geogrid-reinforced soil walls have been carried out at the Institute of Geomechanics and Underground Technology (GUT) in RWTH Aachen University under plain strain conditions.

2 MATERIALS

A dry sand was used as a subsoil, fill and backfill material. The particle size distribution is shown in Figure 1a. The uniform graded sand with $d_{50} = 0.5$ mm is classified as "SP" according to the unified soil classification system (ASTM D2487). In the experiments, the subsoil and backfill were installed with approximately 91 % and 100 % of proctor's density (1.725 g/cm^3). In these conditions, the peak friction angle of the sand was determined in triaxial tests for the subsoil as $\phi'_c = {}_0 \approx 34.9°$ and for the backfill to $\phi'_c = {}_0 \approx 43.7°$. The failure envelopes are presented in Figure 1b. Real scale geosynthetic reinforcements were used for the large-scale tests.

The woven biaxial geogrid with an aperture size of 30×30 mm in Figure 1c was made of polyester (PET). The tensile strength and stiffness were determined by the manufacturer to $T_{ult} = 47.9$ kN/m and $J_{0-2\%} \approx 510$ kN/m, respectively.
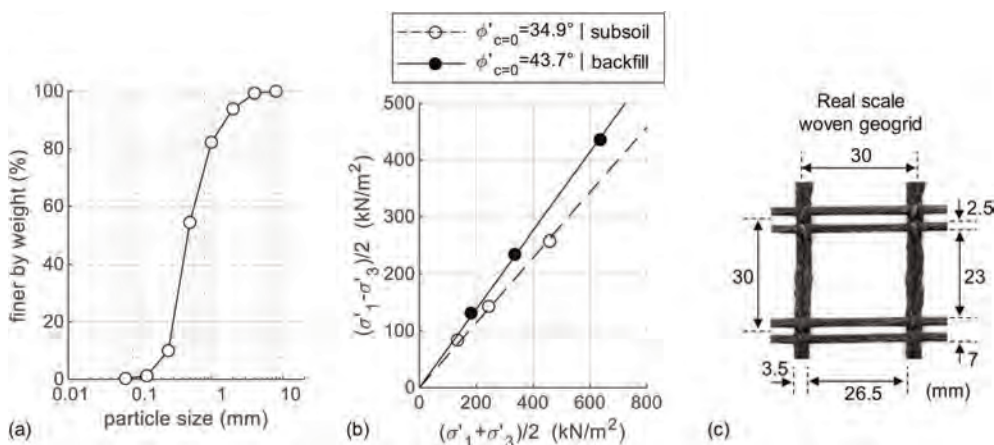
Figure 1. Particle size distribution (a) and triaxial test results (b) of the sand, woven biaxial geogrid (c).

3 PRELIMINARY SMALL-SCALE ANALYSIS

Preliminary small-scale experiments were conducted to analyse the performance and behaviour of GRS walls during bearing capacity failure qualitatively. For this purpose, the geometric scaling factor was chosen to 1/10, whereby a 2 m high prototype wall was represented by 0.20 m high model wall. The reinforcement length was 70 % of the wall height according to common design practice, such as recommended by EBGEO (2010). The wall was constructed with five reinforcement layers, which were wrapped-around the facing. To provoke bearing capacity failure, the wall was seated on a 0.6 m thick layer of subsoil and increasingly loaded on top of the structure.

During the experiment the deformation of the specimen was captured with photographs of a digital camera through the transparent side wall. The displacement field in Figure 2a was calculated by comparing patterns of subsequent taken pictures. Additionally, the changes in direction of the displacement vectors were evaluated, whereby the development of shear bands can be visualized in Figure 2b for a vertical strain $\varepsilon_v = 10\%$, defined as vertical settlement to wall height.
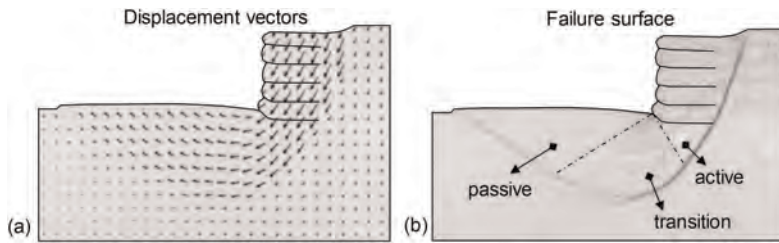
Figure 2.   Total displacements vectors (a) and failure surface (b) in small-scale test.

The mode of failure was characterized by a slip surface running externally around the rein-forced soil block. The retaining wall was pushed into the subsoil and the soil mass in front of the wall was uplifted. The failure was characterised by the loss of bearing capacity of the subsoil that turned into a global failure. The multi-body failure mechanism below the base of the wall con-sisted of an active and passive wedge connected by a transition zone, as illustrated in Figure 2b. The failure pattern in the subsoil was characterised by angles of active and passive failure surfaces of $v_a = 45 + \phi'/2$ and $v_p = 45° - \phi'/2$, corresponding to the assumptions for rigid foundations.

However, the bottom reinforcement layer of the GRS deformed in a curved shape. This flexibility enabled the capability of the structure to mobilize the bearing capacity of the subsoil instead of failing due to overturning or sliding, as observed for comparable con-ventional gravity and cantilever retaining structures, as shown in Derksen *et al*. (2022).

The uniform orientation of the vectors and the shape retention of the wall indicate that the geogrid-reinforced fill acted as a quasi-monolithic, coherent unit. It should be noted that the quasi-monolithic behaviour is expected to suffer when the geogrid spacing becomes too large or the geogrid length too short. Then internal failure modes with shear bands running through the structure are more likely than external modes like bearing capacity failure.

Although the preliminary small-scale tests provided important insights into the bearing capacity failure of GRS walls, the experimental setup suffered from scale effect because the mechanical similarity was not completely fulfilled. For instance, the stress level was by a factor of 10 smaller than for the prototype, influencing the shear strength and in turn also the bearing capacity of the subsoil. Moreover, the small-scale GRS wall was over proportionally stiffer than real scale walls due to the challenge to scale the geosynthetic tensile properties appro-priately. To overcome these drawbacks, large-scale experiments were additionally performed to quantify the ultimate load-bearing capacity and to observe the failure at a larger scale.

4   LARGE-SCALE TESTS

4.1   *Experimental setup*

Figure 3 shows the dimensions of the large-scale experiment for which a geometric scaling factor of 1/1.67 was used, resulting in a wall with a height of 1.2 m that was installed on 2.0 m loose subsoil. The 1.0 m wide wall was constructed using four geogrids with an anchoring length of 0.84 m (70 % of wall height) and a vertical spacing of 0.3 m, corresponding to 0.5 m at prototype scale. Following the small-scale test, the wall was constructed with a wrapped-around facing. A thin nonwoven was used at the face to prevent the sand from running through the geogrid apertures. To minimize friction effects, two layers of Polytetrafluoroethylene (PTFE) foil were installed at each side wall of the testing apparatus. During the test, a vertical load was applied by four actuators, each loading steel plates in a pressure-controlled manner on top of the structure. Linear variable differential transformers (LVDTs) measured the displacements of the wall and the movement of subsoil ground surface in front of the wall. Moreover, photos were taken from the bottom reinforcement layer through the observation window for digital image analysis.
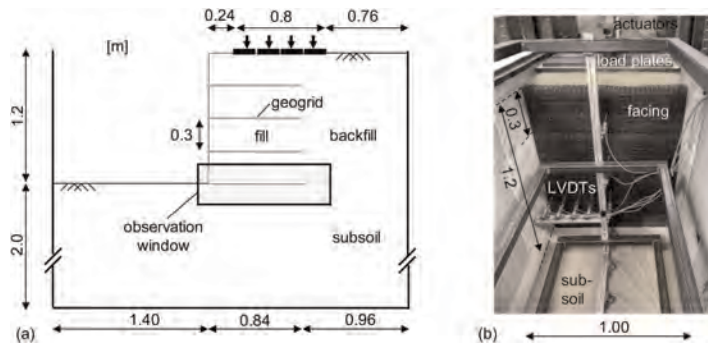
Figure 3.   Experimental setup: sketch of side view (a) and frontal view of wall (b).

4.2   Results

4.2.1   Load-bearing capacity

The load-settlement curve of each of the four actuators and their mean is plotted in Figure 4a. In this paper, the vertical strain $\varepsilon_v = u_y/H_W$ is defined as the ratio of vertical displacements to the initial wall height. Additionally, Figure 4a contains the load-settlement curve of a repetition test of the same wall configuration. The results proved the reproducibility of the large-scale experiment as similar structural response was observed. The curves represent the characteristic load-settlement response of a medium-dense sand in which local failure occurred. In the initial compression stage, all load plates followed the same linear trend. However, larger deviations between the load plates occurred as the vertical strain increased. The vertical stress and deformation gradually increased because the bearing capacity of the subsoil progressively increased during compaction.

Due to the difficulty of determining the ultimate load-bearing capacity at failure, approaches A and B are subsequently presented. Vesic (1963) considered ultimate load-bearing capacity for the local shear mode when the maximum settlement rate was reached. There, the non-linear part of the load-settlement curve turned into a straight line, indicated as point (III) with a failure load of $\sigma_{f,A} = 293$ kN/m^2 in Figure 4a. Moreover, the intersection of the two tangential lines T_1 and T_2 in Figure 4a was used to pinpoint failure following the approach by Adams and Collin (1997). The tangent T_1 described the initial slope of the curve, and tangent T_2 corresponded to the part of the curve where a constant strain rate during shear failure was reached. According to this procedure, bearing capacity failure occurred at vertical load of $\sigma_{f,B} = 249$ kN/m^2 at point (III) in Figure 4a.
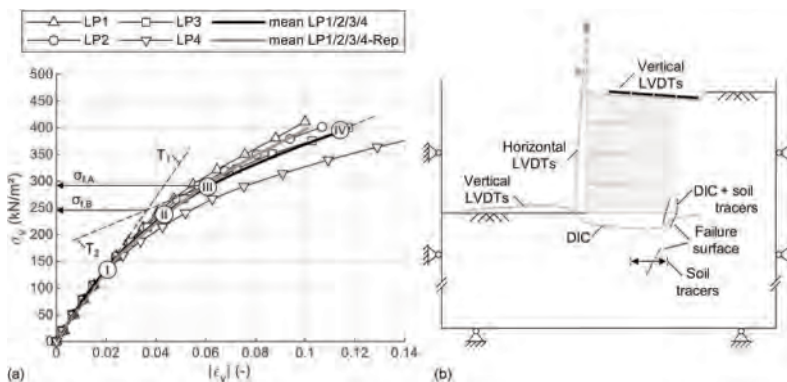
Figure 4.   Load-settlement displacement curve (a) and displacement sketch (b) of large-scale test.

4.2.2 *Wall and subsoil displacements*

The displacement of the wall face was measured with LVDTs for each of the four wrapped-around layers in the centre line of wall. It was observed that the horizontal displacement increased from the top to the bottom layer with increasing load on top of the structure. In conclusion, the geogrid-reinforced block turns backwards to the backfill during failure, as illustrated in the displacement sketch in Figure 4b. At the same time, the subsoil surface in front of the wall was uplifted. The results confirmed that the reinforced block works as a quasi-monolithic, coherent unit what was also found also in the small-scale experiment.

Moreover, Figure 5 presents the results of the DIC analysis in terms of total displacements vectors (a) and failure surface (b). Confirming the findings of the small-scale GRS wall, the failure initially developed at the end of the bottom geogrid layer in Figure 5a, corresponding to a vertical load of $\sigma_{f,B} = 249$ kN/m^2 in Figure 4a. When the reinforced soil block was pushed into the subsoil, the shear bands manifested their presence and were fixed at the end of the bottom geogrid. However, at a vertical load of $\sigma_{f,A} = 293$ kN/m^2 additional shear bands formed, intersecting the bottom geogrid and shortening the reinforcement length relevant for bearing capacity by about 10 % to 0.755 m. It should be noted that the effective reinforcement length relevant to the bearing capacity of the foundation soil was reduced by the intersecting failure line, but the pullout resistance at the rear end of the reinforcement was mobilised as a self-healing process.
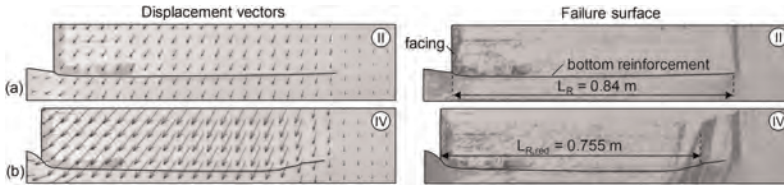
Figure 5.   Total displacements vectors (a) and failure surface (b) in small-scale test.

5   ANALYTICAL CONSIDERATION

The failure pattern in the small-scale and large-scale experiments has revealed that the assumption of a multi-body failure mechanism is justified. Therefore, the bearing capacity was analysed analytically based on the limit-equilibrium equation derived for rigid foundations, as given in equations (1–3). It should be noted that the effect of the reinforcement, e.g. tensile strength and stiffness, are not taken into account because the GRS wall is considered as a monolithic, coherent unit.

$$q_u = i_c \cdot c' \cdot N_c + i_s \cdot s \cdot N_s + i_\gamma \cdot \gamma \cdot B \cdot \frac{1}{2} \cdot N_\gamma \tag{1}$$

$$N_\gamma = 2 \cdot \left(e^{\pi \cdot \tan\phi'} \cdot \tan^2\left(45 + \frac{\phi'}{2}\right) - 1 \right) \cdot \tan\phi' \tag{2}$$

$$i_\gamma = (1 - \tan\delta_{li})^{m+1} \tag{3}$$

To compare the experimental results of the large-scale tests with the analytical approach (without safety factors), the vertical top load, at which limit equilibrium was reached, was determined. It should be noted that for the situation investigated, the eccentricity was shifted towards the backfill. However, the calculation was performed for different effective widths of the reinforced block to illustrate the importance of adequate consideration.

For the initial reinforcement length (B = 0.84 m), the analytical solution ($\sigma_f = 309.1$ kN/m^2) was in good agreement with the experimental capacity obtained with approach A ($\sigma_{f,A} = 293$ kN/m^2) but was 24 % higher than determined with approach B ($\sigma_{f,B} = 249$ kN/m^2). However, when the effective width was reduced to B = 0.755 m according to the experimental observation, the analytically predicted failure ($\sigma_f = 254.1$ kN/m^2) matched with the results of approach B ($\sigma_{f,B} = 249$ kN/m^2). For the width reduced by analytical eccentricity (B = 0.705 m), the analytical solution

underestimated the experimental bearing capacity by 16.8 % and 29.3 % following approaches A and B, respectively. These results show that reducing the reinforcement length to an effective width is crucial to determine a rather conservative load-bearing capacity with the analytical solution.

6 CONCLUSIONS

In this paper, small-scale (1/10) and large-scale (1/1.67) 1g experiments were performed under plain strain conditions to investigate the bearing capacity failure of geogrid-reinforced soil walls. The small-scale model was used to visualize the mode of failure qualitatively. The test results show that the assumption of the geogrid-reinforced soil body as a quasi-monolithic, coherent unit is well justified and that a failure mechanism similar to that of strip foundations occurs below the footing of the wall. However, the small-scale test suffered from scale effects. Therefore, additionally large-scale tests were performed to determine the ultimate load bearing capacity quantitatively. The evolution of shear bands at the base of the wall has shown that the failure surface was initially fixed at the rear end of the reinforced zone, resulting in an effective reinforcement length equal to its full length. However, the effective reinforcement length relevant to the bearing capacity of the subsoil was reduced due to the intersecting failure line. The analytical analysis has shown that a rather conservative load-bearing capacity is predicted by the analytical solution when the reduced reinforcement length is considered.

REFERENCES

Adams, M. T. & Collin, J. G. 1997. Large Model Spread Footing Load Tests on Geosynthetic Reinforced Soil Foundations. *Journal of Geotechnical and Geoenvironmental Engineering*, 123, 66–72.

Allen, T. M. and Bathurst, R. J. 2002. Soil Reinforcement Loads in Geosynthetic Walls at Working Stress Conditions. *Geosynthetics International*, 9(5–6), 525–566.

ASTM D 2487. *Standard Practice for Classification of Soils for Engineering Purposes (Unified Soil Classification System)*, American Society for Testing and Materials, West Conshohocken, Pennsylvania, USA.

BS 8006-1:2010. *Code of Practice for Strengthened/reinforced Soils and Other Fills*, BSI British Standards Institution, London, UK.

Derksen, J., Ziegler, M., Fuentes, R. 2022. Experimental Analysis of Bearing Capacity Failure of Geosynthetic-reinforced Soil Walls. *Geosynthetics International*. In press.

DIN 4017. Baugrund – Berechnung des Grundbruchwiderstandes von Flachgründungen. DIN Deutsches Institut für Normung e. V., Berlin

EBGEO. 2010. *Recommendations for Design and Analysis of Earth Structures using Geosynthetic Reinforcements – EBGEO*, German Geotechnical Society, Ernst & Sohn, Berlin, Germany.

Huang, C. C. & Luo, W. M. 2010. Behavior of Cantilever and Geosynthetic-reinforced Walls on Deformable Foundations. *Geotextiles and Geomembranes*, 28, 448–459.

Mirmoradi, S. H. and Ehrlich, M. 2019. Experimental Evaluation of the Effects of Surcharge Width and Location on Geosynthetic-reinforced Soil Walls. *International Journal of Physical Modelling in Geotechnics*, 19(1), 27–36.

Tatsuoka, F., Tateyama, M., Uchimura, T. & Koseki, J. 1997. Geosynthetic-Reinforced Soil Retaining Walls as Important Permanent Structures 1996 - 1997 Mercer Lecture. *Geosynthetics International*, 4, 81–136.

Vesic, A. B. 1963. *Bearing Capacity of Deep Foundations in Sand*. Highway Research Record.

Xie, Y. & Leshchinsky, B. 2015. MSE Walls as Bridge Abutments: Optimal Reinforcement Density. *Geotextiles and Geomembranes*, 43, 128–138.

Ziegler, M. 2017. Application of Geogrid Reinforced Constructions: History, Recent and Future Developments. *Procedia Engineering*, 172, 42–51.

Geogrid-anchored sheet pile walls under strip footing surcharge loading, small-scale experiments

B. Wittekoek*, S.J.M. van Eekelen* & A. Bezuijen*
Deltares, Delft, The Netherlands

J. Terwindt*
Data Engineer at Scarp DENA, Sweden

P.G. van Duijnen*
GeoTec Solutions, The Netherlands

O. Detert* & J.H. van den Berg*
Huesker Synthetic, Germany
Huesker Synthetic, The Netherlands

D. König*
Ruhr-Universität Bochum, Germany

ABSTRACT: A series of small-scale experiments on geogrid-anchored sheet pile walls (SPWs) under strip footing surcharge loading was conducted at the Deltares laboratory. From the experiments, the following was concluded. Two slip surfaces develop, starting at the edges of the strip footing. These slip surfaces divide the soil behind the SPW into three zones. The paper analyses the contributions of each of these zones to the failure load of the structure. The location of the strip footing surcharge load, the length of the geogrids and the number of geogrid anchors all affect the failure load of the structure. Furthermore, it was found that the slip surface reorients at the intersection with geogrids, and that even very short geogrid anchors contribute to the total resistance.

1 INTRODUCTION

A geogrid-anchored sheet pile wall (SPW) is a relative new application of geogrids (van Duijnen *et al.* 2022; Wittekoek 2020; Wittekoek *et al.* 2022). The system is closely linked to a retaining wall of reinforced soil with a full-height facing as well as to a traditional anchored SPW. However, there are notable differences. The geogrid-anchored SPW has less embedment than a retaining wall of reinforced soil. And contrary to a traditionally anchored SPW, a geogrid anchor is also effective within the active soil wedge when the SPW deforms. This paper looks at small scale experiments, to get a feeling for how the system works. Schoen *et al.* (2023) present numerical analyses on the same structure-type.

---

*Corresponding Authors: britt.wittekoek@deltares.nl, suzanne.vaneekelen@deltares.nl,
adam.bezuijen@ugent.be, jarno.terwindt@gmail.com, pgvanduijnen@geotecsolutions.nl,
detert@huesker.de, joris.vdberg@huesker.nl and diethard.koenig@rub.de

2 SMALL SCALE EXPERIMENTS

Figure 1 shows the test set-up of the small-scale experiments. The 10 mm thick aluminium model-SPW models only the upper part of the embedded part of the SPW. Therefore, the SPW was free to slide along the box bottom. The polypropylene (PP) model-geogrid had a short-term stiffness of 191 kN/m at 2% axial strain and a short-term tensile strength of 16.2 kN/m at a maximum strain of 13.5%. The fill at the active side of the SPW consisted of Baskarp B15 sand. This is a poorly graded sand, densified to a relative density of ~70%. Table 1 lists its properties.
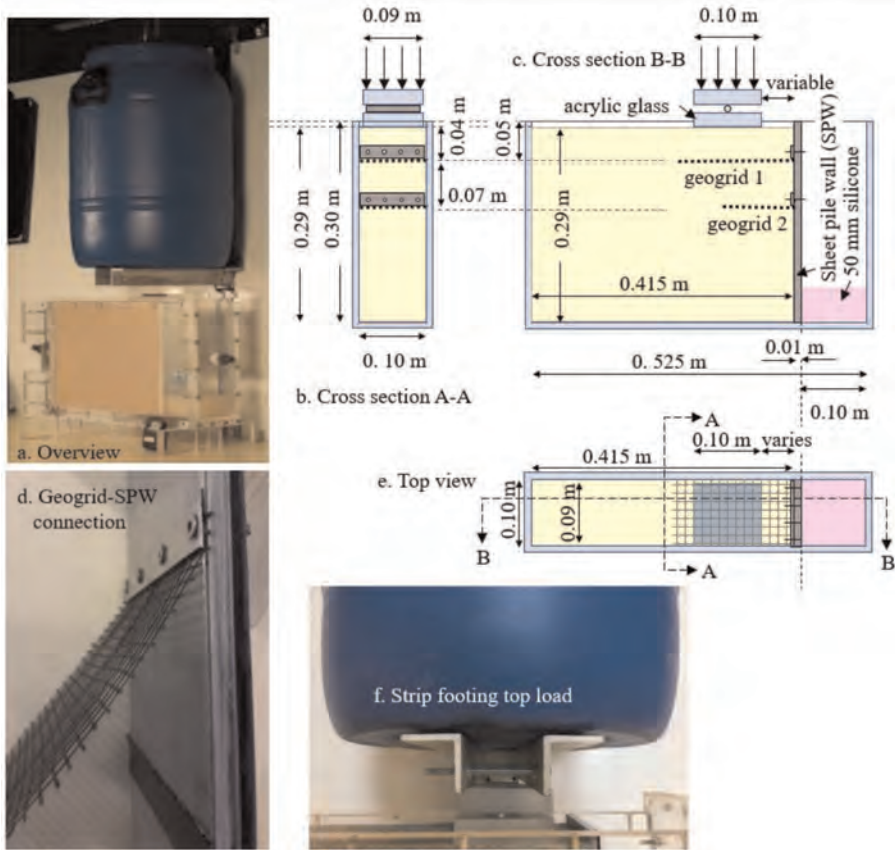
Figure 1.   Test set-up.

Table 1.   Properties baskarp B15 sand.

Parameter	Value	Parameter	Value
Relative density I_D (%)	63–83	Dilatancy angle ψ^{triax} (°)	15
Median particle diameter D_{50} (mm)	0.137	Cohesion c (kPa)	0.6
Coefficient of uniformity D_{60}/D_{10} (−)	1.6	Secant Young's modulus at confining pressure of 100 E_{50}^{ref} (MPa)	72.4
Secant internal friction angle $\varepsilon_{sec}^{triax}$ (°)	45*	Power in power law material stiffness m (−)	0.54
Residual internal friction angle $\varepsilon_{res}^{triax}$ (°)	34	Poisson ratio ν (−)	0.25

*Plane strain value ($^{11}/_9$ · triaxial value).

Table 2. The test series. This paper gives results of the tests with bold-printed numbers. Duplicate tests are denoted by a forward slash.

Test number	12/ 13	14/ 15	16/17/ 45	18/ 19	20/21	22/23	28	30	31	41/ 42	43/ 44	47	48	51	52
Number of geogrids	1	1	1	1	2	2	1	1	1	1	1	0	0	1	1
Length geogrids (mm)	110	110	180	180	180 + 110	180 + 110	60	60	60	180	110	–	–	130	130
Connected to SPW?	Yes	Yes	Yes	Yes	Yes	Yes	Yes	Yes	No	No	No	Yes	Yes	No	Yes
Vertical distance top SPW-geogrid (mm)	50	50	50	50	50 + 120	50 + 120	50	50	50	50	50	–	–	50	50
Horizontal distance surcharge load-SPW (mm)	30	60	30	130	130	30	30	84	30	30	30	84	30	30	30
Relative density fill (%)	67/ 71	73/ 74	68/74/ 76	74/ 73	71/64	74/78	81	78	68	75/ 76	69/ 76	75	71	67	65

A 0.1 m wide silicon block models the passive side. It has a stiffness of 159 kPa up to a strain of at least 8% (8 mm). The strip surcharge load is applied by loading a 0.1 m wide footing with a blue barrel that is filled with water during the test. The soil-wall friction was minimized with a lubricated thin (< 1mm) transparent silicone sheet. Wittekoek *et al.* (2022) analysed how the limited width (100 mm) of the test box and the soil-wall friction affect the results, by, among other things, comparing the results with tests in an eight times wider test box. They found similar slip surfaces, proving that the narrow box results were sufficiently reliable to analyse qualitatively. The movement of the soil and the SPW was tracked using digital photographs, which were acquired with a rate of 0.2 Hz. Soil displacements and strains were subsequently calculated by applying the Particle Image Velocimetry (PIV) technique to the test photos, using the program GeoPIV-GR (Stanier *et al.* 2015). The results matched a number of manually tracked displacements of a number of subsets well.

3 RESULTS SMALL-SCALE EXPERIMENTS

3.1 *The location of the strip surcharge load*

Figure 2 shows how the location of the surcharge load determines the failure mechanism. Two slip surfaces develop from the inner and outer edge of the strip footing towards the SPW. These divide the soil into three different zones. Zone I is enclosed between the SPW and the secondary slip surface 1B and characterized by rigid soil body motions. The active zone II slides along the
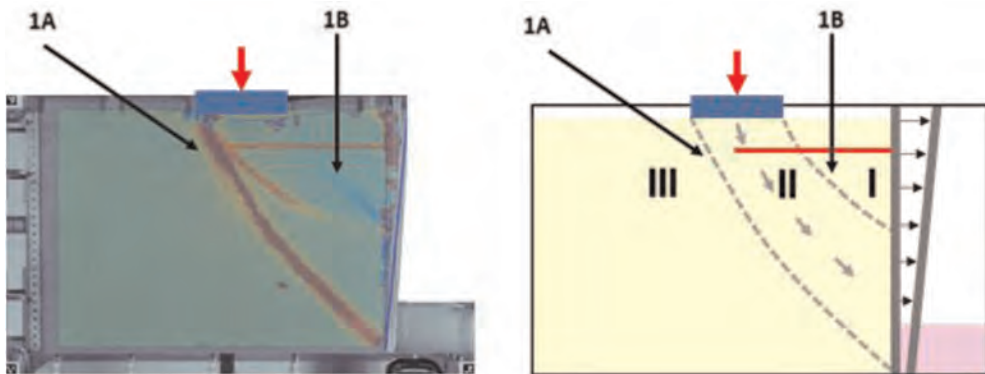
Figure 2. Slip surfaces for a surcharge load of ∼4 kN/m. Test 19. 1A: critical slip surface and 1B: secondary slip surface. The slip surfaces divide the soil in three zones: active zone II between zones I and III.

critical slip surface 1A. Zone III is stable and is located outside the critical slip surface 1A. The third slip surface in Figure 2 only occurred in Test 19, not in duplicate Test 18 or any other test.

Figure 3 shows how the location of the surcharge load affects the total soil displacements close to the SPW. A greater distance between load and SPW results in stiffer behaviour, which is twofold: the wider slip surfaces mobilize more shear resistance and the load is distributed to deeper soil. The difference between Figure 3a and b is remarkable. If the surcharge load is on 84 mm from the SPW, the 60 mm geogrid falls within zone I. Nevertheless, the bearing capacity increases compared to the situation without geogrid. The geogrid therefore has a contribution, although it is located fully in zone I. The position of the surcharge load seems to have less influence for tests with longer geogrids, as shown in Figure 3c and d.
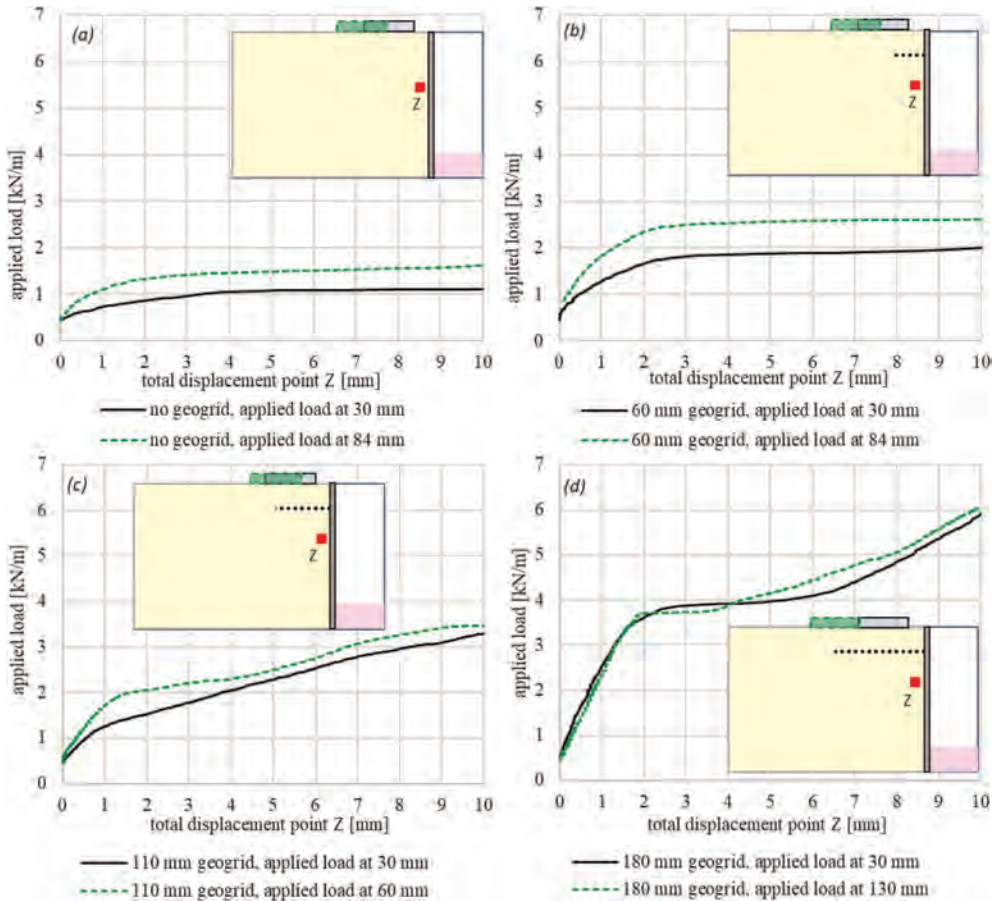
Figure 3. Influence of the location of the surcharge load (a) without geogrid (b) 60 mm geogrid (c) 110 mm geogrid and (d) 180 mm geogrid.

3.2 *Geogrid anchor length*

Figure 4 shows that longer geogrids provide more resistance and therefore the entire system has a higher bearing capacity. The longest geogrid initially behaves stiffer than the shorter geogrids. Figure 4b shows a straight slip surface for all geogrids. Only for the longest geogrid of 180 mm (Test 45), the slip surface crosses the geogrid and a second curved slip surface develops. The initial straight slip surface is therefore not the critical one. The geogrid is activated more efficiently, and the orientation of the slip surface at the intersection with the
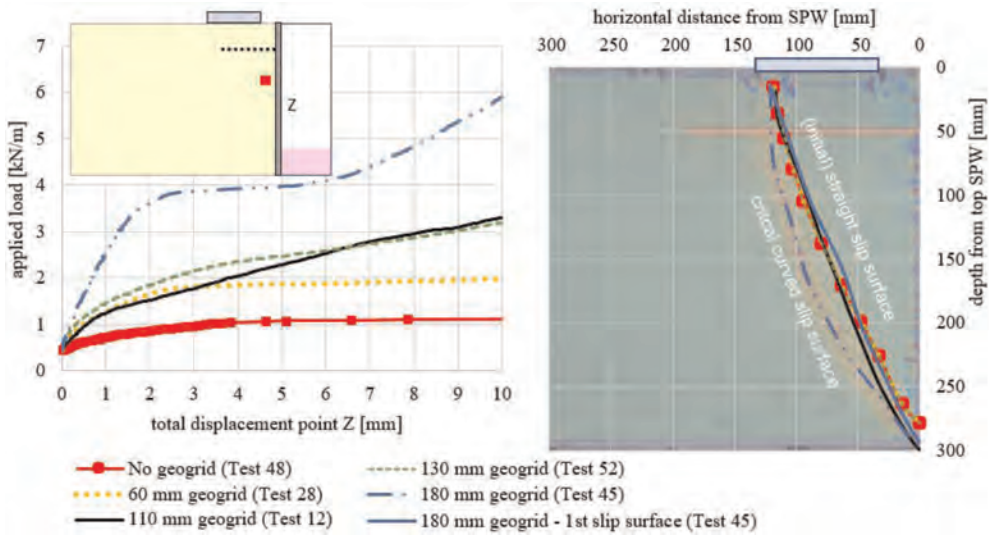
Figure 4. Influence of the geogrid length. Surcharge load on 30 mm from the SPW. The background of the right-hand figure is Test 45 (180 mm geogrid).

geogrid changes. The slip surface therefore becomes longer and curved. This was also found by Ziegler (2010).

3.3 A second geogrid anchor

Figure 5 compares the deformations for the situation with 1 or 2 geogrids. Up to a surcharge load of 3.0 kN/m, the deformations are equal. Above 4.0 kN/m, the SPW slides along the box bottom in both tests. This failure mode is triggered by the relatively high resistance of the geogrid anchor(s). For this higher surcharge load, the second geogrid limits the deformations when the vertical pressure on the geogrids (and therefore the soil-geogrid interface friction) increase. This is in line with the findings of Schoen et al. (2023): they found with 2D FEM calculations that the geogrid anchor is more effective when installed at a lower level. Contrary to expectations, point Z settles more than point Y. The second geogrid increases
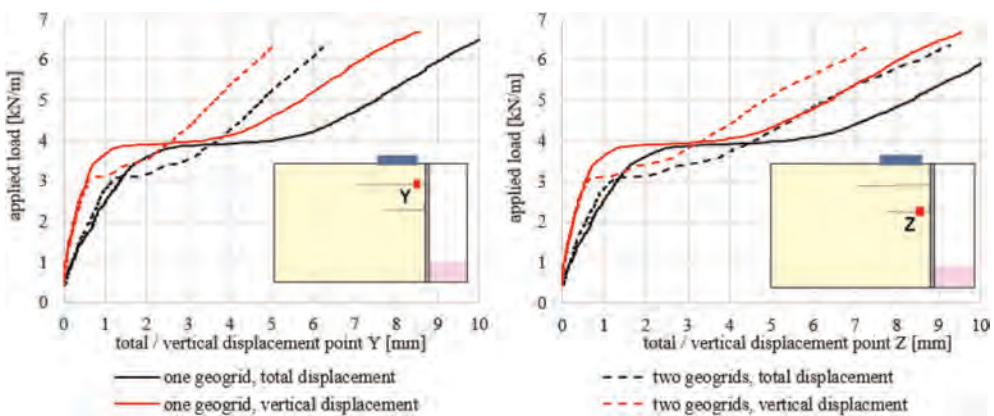
Figure 5. Load-displacement behaviour for 1 or 2 geogrids. Surcharge load on 30 mm from the SPW. Tests 45 and 22. Both tests have a 180 mm geogrid at the same position, Test 22 has a second geogrid (110 mm).
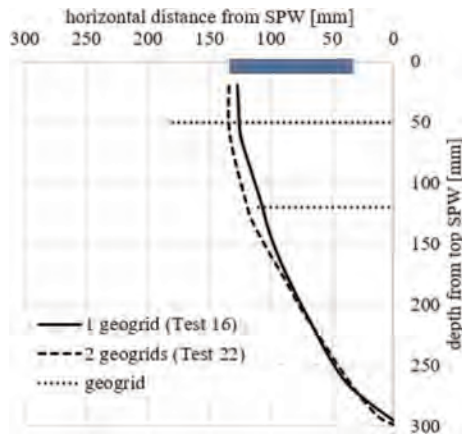
Figure 6. Slip planes for 1 or 2 geogrids.

this difference. Obviously, the geogrids limit the settlement of the soil above. Figure 6 shows how the second geogrid changes the slip surface: it becomes slightly wider and therefore longer as it circumvents the second geogrid.

3.4 Connection geogrid – sheet pile wall

The geogrid was not connected to the SPW in four tests, see Figure 7. We conclude the following:

– Connecting the geogrid increases the failure load.
– Short non-connected geogrids ≤ 130 mm do nearly not contribute to the failure load.
– Short connected geogrids ≤ 130 mm increase the failure load, although they are located in zones I and II only. So, zones I and II are only activated when the geogrid is connected to the SPW and the geogrid has moved downwards with the soil in zone II.
– Short geogrids ≤ 130 mm do not reinforce the soil, because in that case, the situation with short non-connected geogrids would provide more failure load than the situation without geogrid.
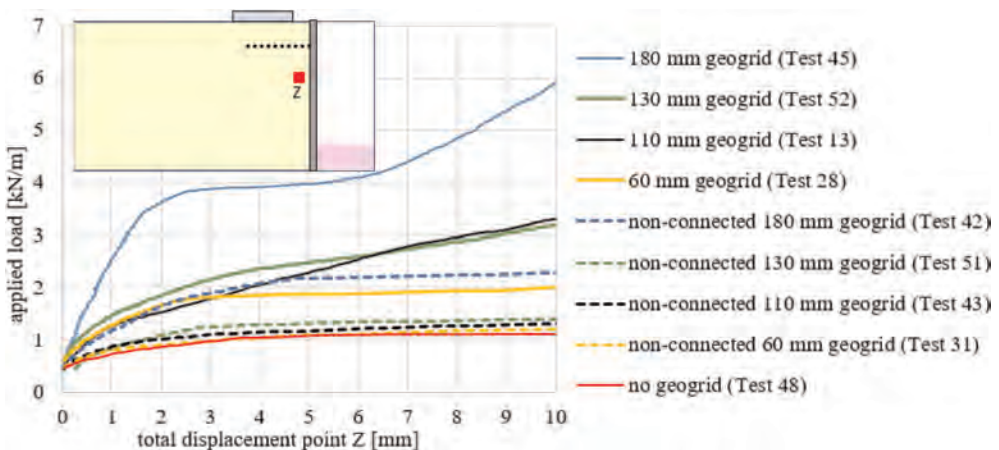
Figure 7. Difference between geogrids that are connected or non-connected to the SPW.

- The increase in failure load due to connecting the geogrids ($\leq$ 130 mm) indicates the presence of the membrane effect.
- The 180 mm geogrid, even if not connected to the SPW, contributes to the total resistance. The failure load results from the pull-out resistance in zones I and III.
- Connecting the 180 mm geogrid activates the rear part of the geogrid (zone III) more effectively and increases the failure load. However, the rear part contributes most to the total resistance at higher load levels while the geogrid is being pulled out by the sliding soil mass in zone II.
- The total resistance of a connected geogrid anchor consists of contributions of the membrane effect (zone I), frictional resistance (zone II) and pull-out resistance (zone III).

4 CONCLUSIONS

A series of small-scale tests of geogrid-anchored SPWs was conducted, leading to the following conclusions. Two slip surfaces develop, starting at the edges of the strip footing. These slip surfaces divide the reinforced fill behind the SPW into three zones: the active zone II, zone III behind the active zone and zone I between SPW and active zone. The paper analyses the contributions of each of these zones to the failure load of the structure. It is concluded that the location of the strip footing surcharge load, the length of the geogrids and the number of geogrid anchors affect the failure load of the structure. Notable findings are the reorientation of the slip surface at the intersection of the critical slip surface with the geogrids and the contribution of a very short geogrid anchor to the total resistance.

ACKNOWLEDGEMENTS

REFERENCES

Schoen, M., König, D., Lavasan, A.A., Wichtmann, T., Hölter, R., Wittekoek, B., van Eekelen, S.J.M., van Duijnen, P.G. & Detert, O. 2023. Numerical Investigation of Geogrid Back-anchored Sheet Pile Walls. *In: proc. 12 ICG*, Rome, Italy.

Stanier, S.A., Blaber, J., Take, W.A. and White, D.J. 2015. Improved Image-based Deformation Measurement for Geotechnical Applications. *Canadian Geotechnical Journal*, 53(5): 727–739, doi: 10.1139/cgj-2015-0253.

van Duijnen, P.G., Detert, O., Lavasan, A.A., van den Berg, J., König, D., Hölger, R., van Eekelen, S.J.M. 2022. Geogrid-anchored Sheet Pile Walls: First Trial Project. *In: proc. Eurogeo7*, Warsaw, Poland.

Wittekoek, B. 2020. *Analysis of the Behaviour of Geogrid-anchored Sheet Pile Walls. Small-scale Experiments and 2D Plaxis Analysis*. MSc thesis TU Delft. https://repository.tudelft.nl/islandora/object/uuid%3A94cf64cc-ff09-4fbe-bde8-42d914b3c7d0.

Wittekoek, B., van Eekelen, S.J.M., Terwindt, J., Korff, M., van Duijnen, P.G., Detert, O. and Bezuijen, A. 2022. Geogrid-anchored Sheet Pile Walls; A Small-scale Experimental and Numerical Study. *Geosynthetics International*. [https://doi.org/10.1680/jgein.22.00501]

Ziegler, M. 2010. *Investigation of the Confining Effect of Geogrid Reinforced Soil with Plane Strain Model Wall Tests*. Aachen, Germany: Rheinische Westfälische Technische Hochschule Aachen (RWTH).

Comparison experiments on geosynthetic-reinforced soil and geogrid-anchored sheet pile walls under strip footing surcharge loads

H. Ahmadi*
Department of Civil Engineering, Faculty of Engineering, University of Maragheh, Maragheh, Iran

B. Wittekoek* & S.J.M. van Eekelen*
Deltares, Delft, The Netherlands

A. Bezuijen*
Ghent University, Belgium
Deltares, The Netherlands

ABSTRACT: Scaled experiments were compared on geosynthetic-reinforced soil walls with a full-height facing (GRSWs) and geogrid-anchored sheet pile walls (SPWs).

A strip footing surcharge load was applied. PIV analyses showed that, in both test series, two slip surfaces developed under the strip footing load: one from the inner edge, the other one from the outer edge of the strip footing. In the GRSWs, the slip surfaces were straight, and the angle with the horizontal was approximately $\pi/4 + \varphi/2$. For the SPWs, the slip surfaces reoriented at the intersection with the geogrids and did not always remain straight.

The GRSW model behaved stiffer than the geogrid-anchored SPW model for relatively high surcharge loads. The SPW-system behaviour was also stiffer when an extra geogrid anchor was installed at a lower level. This indicates that the soil-reinforcement interface frictional behaviour determines the system behaviour more than for example the reinforcement stiffness.

1 INTRODUCTION

In many situations, strip footings are located on the backfill of retaining structures. This paper compares scaled experiments with footings on geosynthetic-reinforced soil walls with a full-height facing (GRSWs) and footings on geogrid-anchored sheet pile walls (SPWs).

The behaviour of GRSWs under a strip footing load has been studied through many full-scale physical models and laboratory model tests, including Ahmadi & Hajialilue-Bonab 2012; Ahmadi & Bezuijen 2018; Allen & Bathurst 2019 and Ahmadi 2020. These studies show that the failure mechanism of a GRSW depends on a number of factors (Ahmadi & Hajialilue-Bonab 2012; Ahmadi 2020 and Ahmadi *et al*. 2021), including: (1) the location of the footing in relation to the wall facing; (2) the type of reinforcement; (3) the number of reinforcement layers; (4) the depth to the first reinforcement layer below the footing; (5) the spacing between reinforcement layers; and (6) the dimensions of the reinforcement compared to the dimensions of the wall.

Research on geogrid-anchored SPWs is scarce. Experiments on scaled models were recently presented by Wittekoek (2020) and Wittekoek *et al*., (2022, 2023).

---

*Corresponding Authors: hamzeh.ahmadi@gmail.com, ha.ahmadi@maragheh.ac.ir, britt.wittekoek@deltares.nl, suzanne.vaneekelen@deltares.nl and adam.bezuijen@ugent.be

Geogrid-anchored SPWs are closely linked to geosynthetic-reinforced soil retaining walls with a full-height facing, as well as to traditionally anchored SPWs. However, there are notable differences causing different soil-structure behaviour. An important difference is that geogrid-anchored SPWs have more passive soil resistance than GRSWs, due to the SPWs' deeper embedment. Furthermore, SPWs have less geogrid layers compared to GRSWs.

Traditional anchors and geogrid-anchors have a different active anchor length, along which resistance is mobilised. Wittekoek (2020) and Wittekoek *et al.* (2022, 2023) proved that a geogrid anchor is also effective within the active soil wedge, when the SPW deforms or moves. This differs from what is normally assumed for traditional anchors.

Purpose of this research is to see how these two systems work. The paper analyses the slip surfaces and load-deformation behaviour of the two construction types.

2   SCALED MODELS FOR THE EXPERIMENTS

2.1   *Geogrid-anchored Sheet Pile Wall (SPW) model*

Figure 1a shows the test set-up of the small-scale experiments for the geogrid-anchored SPW. It has a scale factor of 1/16 compared to the Windpark Krammer project (Van Duijnen *et al.* 2021).

The 10 mm thick aluminium model-SPW modelled only the upper part of the embedded part of the SPW. Therefore, the SPW was free to slide along the box bottom. The polypropylene (PP) model-geogrid had a short-term stiffness of 191 kN/m at 2% axial strain and a short-term tensile strength of 16.2 kN/m at a maximum strain of 13.5%. The backfill at the active side of the SPW consisted of Baskarp B15 sand. This is a poorly graded sand, densified by manual tamping. Table 1 lists the sand properties.

A 0.1 m wide silicon block modelled the passive side. It had a stiffness of 159 kPa up to a strain of at least 8% (8 mm). The strip surcharge load was applied by loading a 0.10 m wide footing with a barrel that was filled with water during the test.
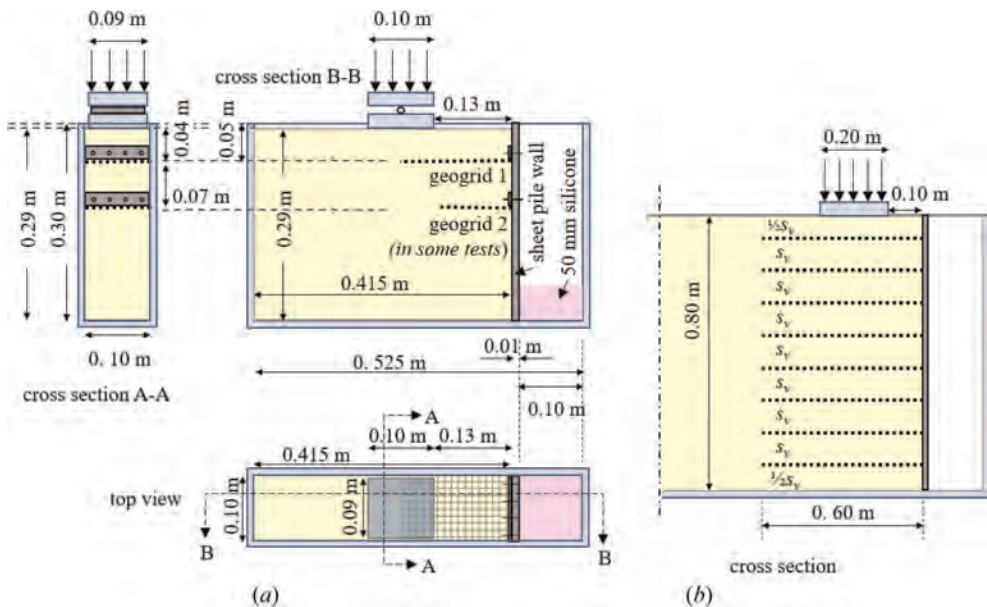
Figure 1.   Test set-up for the small-scale tests considered in this paper: (*a*) geogrid-anchored sheet pile wall (SPW), (*b*) geosynthetic-reinforced soil wall (GRSW).

Table 1. Soil and reinforcement parameters in the geogrid-anchored sheet pile wall (SPW) tests and the geosynthetic-reinforced soil wall (GRSW) tests.

Parameter	Symbol	SPW tests	GRSW tests
Coefficient of uniformity	C_u	1.6 (D_{60}/D_{10})	1.32
Coefficient of curvature	C_c		0.96
Median particle diameter (mm)	D_{50}	0.137	1.5
Unit weight soil (kN/m^3)	γ	15.90	15.72
Relative density (%)	RD	73%	88%
Dilatancy angle (°)	ψ^{triax}	15	
Peak soil friction angle from the direct shear test (°)	φ_d		40.5
Secant soil friction angle from triaxial test (°)	$\varphi_{d,sec}$	36.8	
Residual soil friction angle (°)	φ_r	34	31.15
Estimated plain strain soil friction angle (°) *	φ_{ps}	45*	45.7**
Cohesion-soil (kPa)	C	0.6	0
Reinforcement length (m)	L	0.18	0.6
Short term stiffness reinforcement (kN/m)	J	191 (ε = 2%)	15 (ε < 40%)
Ultimate tensile strength reinforcement (kN/m)	T_u	16.2	8
Flexural rigidity of facing panel (kNm^2/m)	EI	5.8	28 × 10^{-3}

[*]Plane strain value as derived from triaxial test ($^{11}/_9$ · triaxial value)
[**]Plane strain value as derived from direct shear test ($\tan^{-1}(1.2\tan\varphi_d)$).

The soil-wall friction was minimized with a lubricated thin (< 1mm) transparent silicone sheet. Wittekoek *et al*. (2022, 2023) analysed how the limited width (0.1 m) of the test box and the soil-wall friction affected the results. Among other things, by comparing the results with tests in an eight times wider test box. They found similar slip surfaces, proving that the narrow box results were sufficiently reliable to analyse qualitatively.

The movement of the soil and the SPW was tracked using PIV, using the image analysis module for MATLAB, GeoPIV-GR (Stanier *et al*. 2015). The PIV results matched a number of manually tracked displacements of a number of subsets well.

2.2 Geosynthetic-Reinforced Soil Wall (GRSW) model

The GRSW experiments were done on small-scale models. They had a scale factor of 1/5 compared to the full-scale structures evaluated by Ahmadi and Bezuijen (2018). Figure 1b shows the test set-up. The models were 0.8 m high, 0.6 m long and 0.8 m wide. A surcharge load was applied with a hydraulic plunger up to 100 kN/m on a 0.2 m wide strip footing behind the facing of the models.

Table 1 lists the properties of the materials considered in this paper. Sand layers were placed every 0.025 m and compacted by a hand-held electric compactor (a Wacker vibrating plate). Reinforcement layers were placed on the surface of the compacted sand layers, at predetermined depths. Three different reinforcement types were used in this study: a highly extensible nonwoven geotextile, a less deformable geogrid and a woven geotextile. The authors are aware that a nonwoven as this one is not applicable in practical application. Nevertheless, the nonwovens were applied in these experiments to get relatively large deformations and to be able to compare different reinforcement stiffnesses.

3 COMPARING THE SLIP SURFACES FOUND IN THE EXPERIMENTS

3.1 Geogrid-anchored SPW

For the comparison between SPW and GRSW, we focus on SPW-Test 19 of Wittekoek *et al*. (2022, 2023). This test only has one 180 mm geogrid. This maximizes the difference between both systems.

Figure 2 shows the slip surfaces found in the SPW test. Figure 2a shows the soil shear strains after two-third of the test, at a surcharge load of 4 kN/m. The figure shows the general failure mechanism that was found in most geogrid-anchored SPW tests of Wittekoek et al. (2022, 2023). These tests were all subjected to a strip footing surcharge loading. It consists of two slip surfaces which develop from the inner and outer edge of the footing. The outer slip surface goes to the toe of the SPW and does not necessarily have an angle of $^\pi/_4$ $+^\varphi/_2$. It is possible that this would have been different if the SPW had been longer.

The soil first starts to slide along the critical slip surface (labelled 1A in the figure). Then, the secondary slip surface (1B) develops between zones II and I. The unstable soil mass II moves downwards and sideways due to the strip footing load. Soil mass I is enclosed by the unstable soil mass and the SPW. Wittekoek (2020) and Wittekoek et al. (2022, 2023) concluded that the slip surfaces reorient at the intersection with geogrids. This is in line with the findings of Ziegler (2010). In that case, the slip surface does not remain straight, but it becomes more curved and wider as well.

Figure 2b shows that the slip surfaces divide the soil domain behind the wall into three different strain zones:

  I.   a zone with rigid soil body motion between the wall and secondary slip surface;
 II.   an active zone below the strip footing enclosed by the secondary slip surface and the critical slip surface;
III.   the stable soil zone behind the critical slip surface.

The third small slip surface, between 1A and 1B, has been excluded from further analysis since this slip surface was seen in this specific test configuration only. Furthermore, the SPW system was approaching a state of failure prior to the development of this slip surface.

Wittekoek et al. (2022, 2023) analyses in detail the differences in behaviour between zones I, II and II. One of their conclusions is that even very short geogrid anchors, that are located in zone I only, contribute to the failure load of the system. This is because these reinforce the soil at the active side of the wall.

3.2   Geosynthetic-Reinforced Soil Wall (GRSW)

Figure 3 shows shear strains of one of the GRSW tests from Ahmadi (2020) study, which had eight nonwoven geotextile layers and a flexible facing panel. The footing was placed
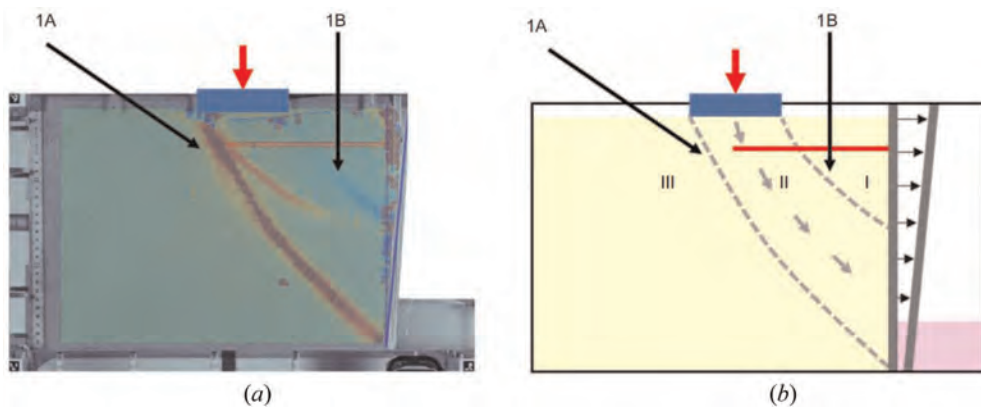
Figure 2.   Slip surfaces in a geogrid-anchored SPW test: (a) soil shear strains (created using PIV) for a test with one 180 mm geogrid anchor and the load positioned 130 mm from the SPW, (b) schematisation of the general failure mechanism and the development of three different strain fields in the backfill behind the SPW. Further explanations in Wittekoek et al. (2022, 2023).
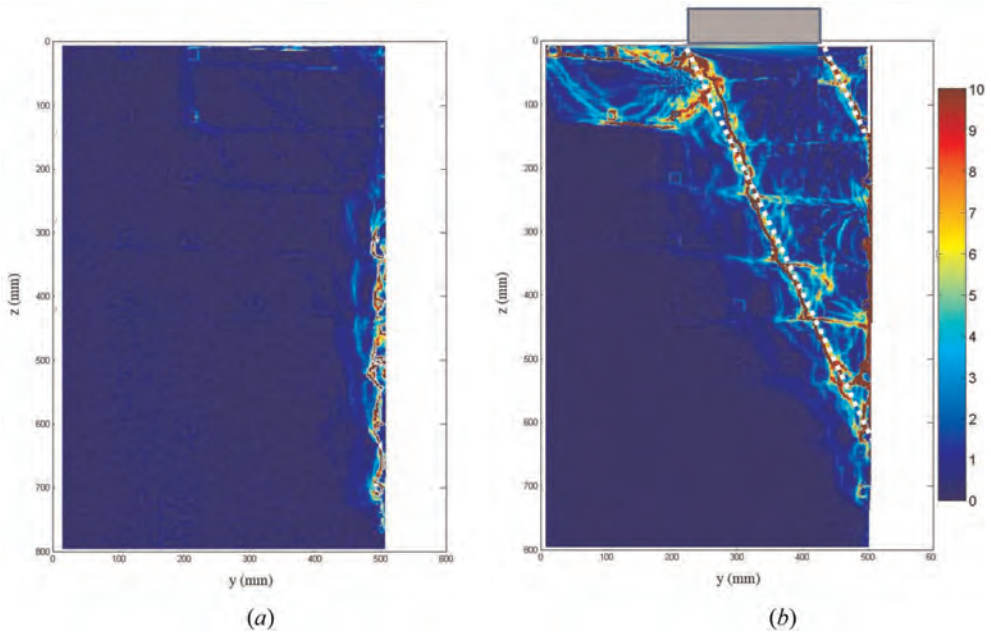
Figure 3. Slip surfaces in a GRSW test, soil shear strains in % obtained from PIV. Test set-up with a flexible facing panel and eight layers of nonwoven reinforcement: (*a*) end of backfill construction step and after releasing struts in front of the wall, (*b*) end of first series of loading steps (Ahmadi 2020).

100 mm from the facing. The pictures show the development of the slip surfaces, that eventually divide the soil into several distinct zones, including the same zones I, II and III as found in Figure 2.

Figure 3a shows the shear zones after removing the struts in front of the wall. Small strains occurred close to the facing, with peaks between the lowest reinforcement layers. This shows the confinement effect of the reinforcement layers, which is in line with the findings of Ruiken *et al*. 2010.

In Figure 3b, after applying a load of 300 kN/m^2, two failure surfaces developed. Similar to the SPW tests, these surfaces originate from the outer and inner edges of the footing. However, in this case, the surfaces are straight and consistently have an angle of $\pi/4 + \varphi/2$, as delineated by the white dashed lines. Also, the slip surfaces both intersect the facing. This shows that the full facing is high enough for the slip surfaces are free to find their location. This is different from the SPW test in Figure 2, as mentioned before.

Figure 3b shows an extra slip surface, on the left-hand side of the footing, over the second layer of reinforcement. The failure pattern is similar to the general shear failure pattern as found under shallow foundations.

4 LOAD-DEFORMATION BEHAVIOUR

Figure 4 compares the measured load-displacement behaviour of the geogrid-anchored SPW and the GRSW. This should be considered as a qualitative comparison to show how the soil-geogrid interface mechanism works between these two different models. The tests are not similar enough to compare quantitatively. However, the scale factor effects should only have limited influence, because the surcharge-induced stresses dominate the stresses in the soil mass and especially under the strip footing load.
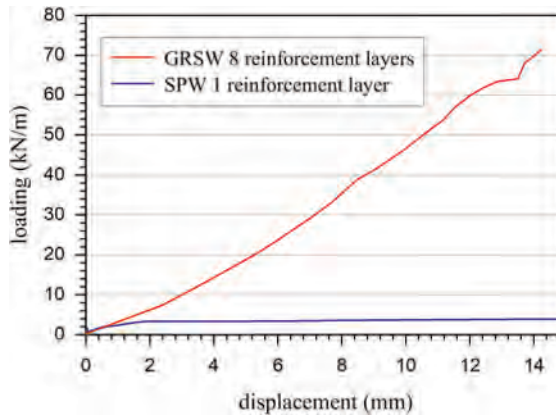
Figure 4.   Comparison load – displacement behaviour of the geogrid-anchored SPW and the GRSW.

The figure indicates that the initial stiffness behaviour of the SPW and the GRSW is comparable. But for higher loading, the GRSW behaves much stiffer than the SPW. Ahmadi (2020) concluded that the stiffness of the reinforcement affects only to a limited extend the stiffness behaviour of the structure, as, the soil-reinforcement interface friction appeared to have more influence.

In addition to that, Wittekoek *et al.* (2022, 2023) found in their test series, that a second geogrid at a lower level only affects the stiffness behaviour for relatively high surcharge loads. These two findings match: the interface friction, and therefore, the vertical pressure on the geogrid apparently is of leading importance. This is also in line with the 2D FEM calculations of Schoen *et al.* (2023), who found that the depth of the geogrid anchor has a large influence on the stiffness behaviour, due to the larger vertical load on the geogrid anchor.

5   CONCLUSIONS

Scaled experiments were compared on geogrid-anchored SPWs and geosynthetic-reinforced soil walls (GRSWs).

For both systems, two slip surfaces developed under the strip footing load: one from the inner and another from the outer edge of the strip footing. The inclination and shape of the slip surfaces differed for the two systems. In the GRSWs, the slip surfaces were straight, with an angle of approximately $\pi/4 + \varphi/2$. For the SPW, the slip surfaces reoriented at the intersection with the geogrids and did not remain straight. The two slip surfaces divide the soil into zones I, II and III. For the SPW, even only one very short geogrid anchor, located fully in zone I, contributed to the failure load of the system.

In the considered scaled experiments, the GRSW behaved stiffer than the geogrid-anchored SPW for relatively high surcharge loads. For lower loadings the difference is less. This confirms the finding that the soil-reinforcement interface friction is leading in the system behaviour, and that this plays a more important role than for example the reinforcement stiffness. So, installing more reinforcement layers increases the ultimate strength of the construction considerably, but has a limited influence on the stiffness behaviour for small deformations.

ACKNOWLEDGEMENTS

REFERENCES

Ahmadi, A., Hajialilue-Bonab, M. 2012. Experimental and Analytical Investigations on Bearing Capacity of Strip Footing in Reinforced Sand Backfill and Flexible Retaining Wall. *Acta Geotechnica*, 7:4, 357–373.

Ahmadi, H., Bezuijen, A. 2018. Full-scale Mechanically Stabilized Earth (MSE) Walls Under Strip Footing Load. *Geotextiles and Geomembranes*, 46(3): 297–311.

Ahmadi, H. 2020. *Geosynthetic-Reinforced Soil Retaining Walls Subjected to Surcharge Loads.* PhD Dissertation, Ghent University, Ghent, Belgium. ISBN: 978-94-6355-342-1.

Ahmadi, H., Bezuijen, A., Zornberg, J. G. 2021. Interaction Mechanisms in Small-scale Model MSE Walls Under the Strip Footing Load. *Geosynthetics International*, 28, No. 3, 238–258.

Allen, T.M., Bathurst, R.J. 2019. Geosynthetic Reinforcement Stiffness Characterization for MSE Wall Design. *Geosynthetics International*, 25(6): 592–610.

Ruiken, A., Ziegler, M., Vollmert, L. & Duzic, I. 2010. *Recent Findings about the Confining Effects of Geogrids from Large Scale Laboratory Testing.* 9 ICG, Guarujá, Brazil.

Schoen, M., König, D., Lavasan, A.A., Wichtmann, T., Hölter, R., Wittekoek, B., van Eekelen, S.J.M., van Duijnen, P.G. & Detert, O. 2023. Numerical Investigation of Geogrid Back-anchored Sheet Pile Walls. *In: proc. 12 ICG*, Rome, Italy.

Stanier, S.A., Blaber, J., Take, W.A. and White, D.J. 2015. Improved Image-based Deformation Measurement for Geotechnical Applications. *Canadian Geotechnical Journal*, 53(5): 727–739, doi: 10.1139/cgj-2015-0253.

van Duijnen, P.G., Detert, O., Lavasan, A., A., van der Berg, J., Hölter, R., König, D. & van Eekelen, S.J.M. 2021. Geogrid-anchored Sheet Pile Walls: Field Test and Numerical Analyses. *In: proc EuroGeo7*, Warsaw, Poland.

Wittekoek, B. 2020. Analysis of the Behaviour of Geogrid-anchored Sheet Pile Walls. *Small-scale Experiments and 2D Plaxis analysis.* MSc thesis TU Delft, Delft, Netherlands.

Wittekoek, B., van Eekelen, S.J.M., Terwindt, J., Korff, M., van Duijnen, P.G., Detert, O. and Bezuijen, A. 2022. Geogrid-anchored Sheet Pile Walls; A Small-scale Experimental and Numerical Study. *Geosynthetics International*. https://doi.org/10.1680/jgein.22.00501.

Wittekoek, B., van Eekelen, S.J.M., Bezuijen, A., Terwindt, J., van Duijnen, P.G., Detert, O., van den Berg, J. H., König, D. 2023. Geogrid-anchored Sheet Pile Walls under Strip Footing Surcharge Loading, Small-scale Experiments. *In: proc. 12ICG*, Rome, Italy.

Ziegler, M. 2010. *Investigation of the Confining Effect of Geogrid Reinforced Soil with Plane Strain Model Wall Tests.* Aachen, Germany: Rheinische Westfälische Technische Hochschule Aachen (RWTH), Aachen, Germany.

Bearing capacity and stability analysis of geocell-reinforced slopes subjected to the footing loading

M.R. Harirsaz
Department of Civil, Environmental and Architectural Engineering, University of Padova, Padova, Italy

A. Ghanbari & Gh. Mehrjardi
Department of Civil Engineering, Faculty of Engineering, Kharazmi University,Tehran, Iran

ABSTRACT: In many cases, the foundations of structures are constructed near the edge of slopes, which may cause a lack of bearing capacity. In recent years, several studies have been carried out on the application of geocell reinforcement to enhance the global stability of slopes. However, there are limited studies on the effect of geocell reinforcement on a slope's stability when the reinforced slope is subjected to footing loadings. In this study, the positive impact of geocell reinforcement on the bearing capacity of strip footings on slopes is discussed. Also, limit equilibrium analysis has been conducted to better investigate the effect of the reinforcement on the potential slip surfaces and factors of safety. The results of the study suggest that geocell reinforcement not only enhances the bearing capacity of the footing located on the slope, but it will also improve the whole stability of the system by forcing the failure planes deeper into the underlying soil.

1 INTRODUCTION

In many cases, the foundations of structures are constructed in marginal ground conditions, which may bring about a lack of bearing capacity. This can include the construction of buildings, roads in hilly regions, and bridge abutments on the top of slopes. The improvement of the bearing capacity of these types of slopes is consequently one of the fundamental issues in foundation engineering practice since such structures are prone to slope failure. Many investigations have indicated that geosynthetic reinforcements can enhance both the ultimate bearing capacity and the settlement characteristics of the foundations located near the slope. (Alamshahi & Hataf 2009; Bathurst *et al.* 2003; EL Sawwaf 2007; Halder & Chakraborty 2018; Kakrasul *et al.* 2020; Moradi *et al.* 2019; Tavakoli Mehrjardi *et al.* 2016).

However, geocell confinement in three dimensions better minimizes the lateral and vertical movements of the soil particles compared to the geogrids and geotextiles. Several studies have investigated the mechanisms and failure modes of geocell-reinforced retaining walls and slopes. Mehdipour *et al.* (2017) and Khorsandiardebili and Ghazavi (2021) provided an analytical approach to calculate the safety factor of geocell-reinforced slopes. Also, Ardakani and Namai (2021) performed a numerical study to evaluate the behavior of geocell-reinforced slopes using FLAC 3D. Chen and Chiu (2008) investigated the behavior of geocell-reinforced retaining walls. Chen *et al.* (2013) showed that the failure modes of the gentler geocell-reinforced walls consist of a few slides passing along the interface between geocell layers, while that of the steep vertical walls revealed both modes of interlayer sliding and overturning failure. Song *et al.* (2018), via centrifuge model tests, found that when the slope inclination is relatively large, the sliding wedge propagates near the slope crest.

Kazemi *et al.* (2022) indicated that the optimum depth of the placement of the first geocell layer for both single and double-layer geocell reinforced slopes was found to be independent of the length of the geocell. Although several studies have been conducted to evaluate the behavior of the geocell-retaining walls under self-weight or surcharge, there are few studies on the effect of footing loading on the stability of the geocell-reinforced slopes. In this study, the positive impact of geocell reinforcement on the bearing capacity of strip footings on slopes is discussed. Also, a numerical study has been conducted to investigate the effect of the reinforcement on the potential slip surfaces and factors of safety.

2 EXPERIMENTAL STUDY

2.1 *Backfill material*

The soil used in this study as backfill material was uniformly graded gravel (GP) with a specific gravity of 2.64 and maximum and minimum dry density of 16.64 and 13.32 kN/m^3. The medium particle size of grains (D_{50}) and effective particle size (D_{10}) are 7 and 3.52 mm respectively. Moreover, the coefficient of uniformity (C_u) and the coefficient of uniformity (C_c) are 2.12 and 1.13.

2.2 *Geocell*

The Geocell used in the tests, made of heat-bonded non-woven geotextile, had a pocket size of 110mm × 110mm and a height (H) of 50 mm, respectively. The pocket size (d_g) is defined as the diameter of an equivalent circular area (d_g = 110mm). The geocell used in the study is made of non-woven polyethylene. The density of the geocell is 0.47 g/cm3. The tensile strength of the strip is 13 kN/m^3 and the elongation is 55% at maximum strength. Figure 1 illustrates a prototype view of the backfill materials and geocell.

2.3 *Performing experiments*

Figure 2(b) shows the schematic of the physical test setup and its attachments consisting of a testing tank, loading system, and data measurement system. The load was transferred to the footing through the hand-operated hydraulic jack and pre-calibrated load cell mounted on the base plate with dimensions of 650 × 150 × 30 mm. In this study, the edge distance (D) of 0.5 B was selected. The hydraulic jack applied the loading via a pre-calibrated load cell with a capacity of 10000 kg and an accuracy of ±0.02% of full scale. All the model-footing tests were performed with a relative density of 70%. In all tests, firstly, soil embankment with the

Figure 1.   A view of installed geocell in the backfill.
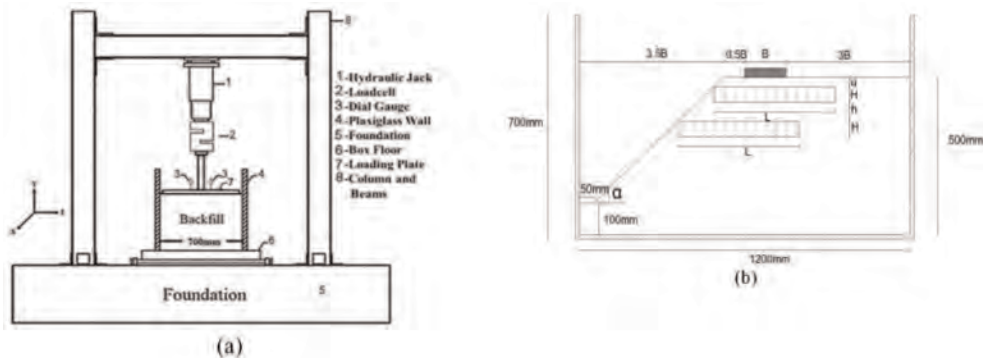
Figure 2. Schematic representation of the test setup (a) Y-Z section, and (b) X-Y section (Not to scale).

plane surface was constructed in layers of 50 mm thickness to reach 500 mm height. Figure 2 (a) shows the geometry of the slope backfill. The embankment was trimmed to achieve a slope backfill with an angle (α) of 40°. Throughout the tests, to investigate any possible rocking or tilting of the footing, settlements were monitored by two dial gauges with an accuracy of 0.01% of the full range (50 mm), located on opposite edges of the loading plate.

3 RESULTS AND DISCUSSION

3.1 *Experimental modeling*

To investigate the impact of geocell reinforcements on the response of the strip footing situated on the sloped backfill, a testing program was established. In this regard, two reinforced experimental tests were performed to examine the behavior of geocell-reinforced slopes using one and two layers of reinforcement in addition to the unreinforced slope condition and a test on the plane surface (plain condition). It should be clarified that the burial depth(u) of the first layer is 0.1B and the vertical distance between the first and the second layer (h) is 0.2B. Also, the length (L) of the geocell in the both single-layered geocell reinforced slope and the double-layer reinforced slope is 3B. In order to consider how much the improvement technique is effective in enhancing slope stability, the factor of slope influence I_f is defined by Equation 1. In this equation $(q)_r$ and $(q)_{un}$ are the bearing pressure of "reinforced" and "slope" backfills for the equivalent settlement ratio, respectively.

$$I_f = \left(\frac{(q)_r}{(q)_{un}} \right) \tag{1}$$

As can be seen in Figure 3 the diagram related to the slope reinforced with one layer of geocell has a significant vertical distance from the unreinforced slope. Table 1 shows the variation of I_f for different settlement ratios for slope reinforced with one and two layers of geocell reinforcement.

As it is indicated in Table 1, for the slope reinforced with one layer, I_f yields the value of 1.41 for S/B = 5% whereas it climbed to 2 for S/B = 15%. It is worth noting that due to the presence of coarse soil grains inside geocells, in larger settlements, the dilation of soil particles will result in better confinement of soil particles, leading to higher relative improvement in bearing capacity.

According to Figure 3 arguably there is a significant gap between the response of the reinforced slope and the plane condition. To lessen this gap, double-layer geocell reinforcement was examined. Figure 3 shows that the double-layer geocell reinforced slope diagram intersects with the plane condition for the range of settlements up to approximately 9 percent indicating
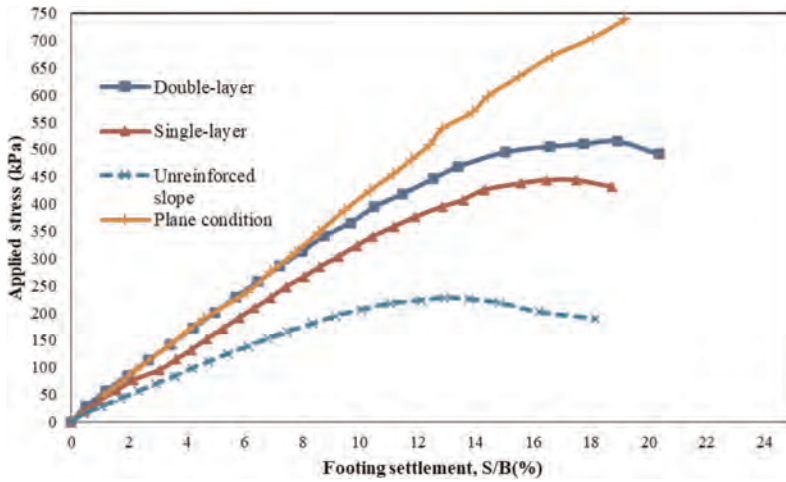
Figure 3. Bearing capacity diagram of geocell reinforced with one and two geocell layers.

Table 1. Improvement factors of the geocell slope reinforced slopes.

Settlement	Single-layer reinforced slope	Double-layer reinforced slope
(I_f) $S/B = 5\%$	1.41	1.73
(I_f) $S/B = 10\%$	1.59	1.84
(I_f) $S/B = 15\%$	2	2.29

that the response of the double-layer system has considerably improved in comparison with the single-layered reinforcement. Table 1 shows that in the case of the double-layer geocell reinforced slope the I_f values for S/B = 0.1 and S/B = 0.15 are 1.84 and 2.26, which are significantly higher than the equivalent values for single-layer reinforced slope. In the case of using two layers of reinforcement, the first layer exerts pressure on the second layer which spread the pressure on the bottom layers. This results in preventing the formation of shallow failure planes, leading to a meaningful increase in the bearing pressure capacity of the slope.

3.2 Limit equilibrium analysis

In order to compare the factor of safety in reinforced and unreinforced conditions a limit equilibrium analysis of the slope condition has been done using the Spencer method. To evaluate the factor of safety of unreinforced slope and single-layer and double-layer geocell reinforced slope, it is necessary to model the geocell layer as a layer with the same friction angle as the granular material and the equivalent cohesion. Madhavi Latha *et al.* (2006) calculated the membrane stresses developed in the walls of the geocell ($\Delta\sigma_3$) using the hoop tension theory (Henkel & Gilbert 1952) to estimate the apparent cohesion. Equation 2 shows the formula to calculate the apparent cohesion due to confinement provided by geocell where K_p is the coefficient of passive earth pressure.

$$C_r = (\Delta\sigma_3/3)\sqrt{K_p} \tag{2}$$

The geocell layer has a friction angle of 43° and equivalent cohesion of 17.33. A surcharge of 200 kN/m^3 was applied on the footing. Figure 4 shows the failure wedge for the unreinforced slope, the reinforced conditions, and also the factors of safety. The factor of safety for the

unreinforced slope is 1.19 which shows medium stability. As can be seen, for reinforced slopes failure wedge tends to form at greater depth compared to unreinforced slopes, which is consistent with previous findings. (Bathurst *et al.* 2003; Mehdipour *et al.* 2013; Tavakoli Mehrjardi *et al.* 2016). Figure 4 depicts that the potential failure surface has been expanded horizontally and vertically for the case of the double-layer geocell reinforced slope yielding a factor of safety of 4.19. This notable increase in the factor of slope stability is because the presence of two geocell-reinforced layers can have a more significant effect on the shear strength characteristics of the slope. To better illustrate this, according to Figure 3 when the double-layer geocell reinforced slope is subjected to the surcharge of 200 kN/m^3 the load bearing capacity of the slope is similar to the plane condition which indicates noticeable stability is predictable in this case.

Considering the fact a small-scale experimental model has been used in this study, it is important to note that in general, small-scale models tend to experience higher stresses than full-scale models which is due to the phenomenon called scale effects. However, for granular soils, the difference in soil stress between a small-scale and full-scale model is less pronounced due to the nature of the soil compared to cohesive soils.
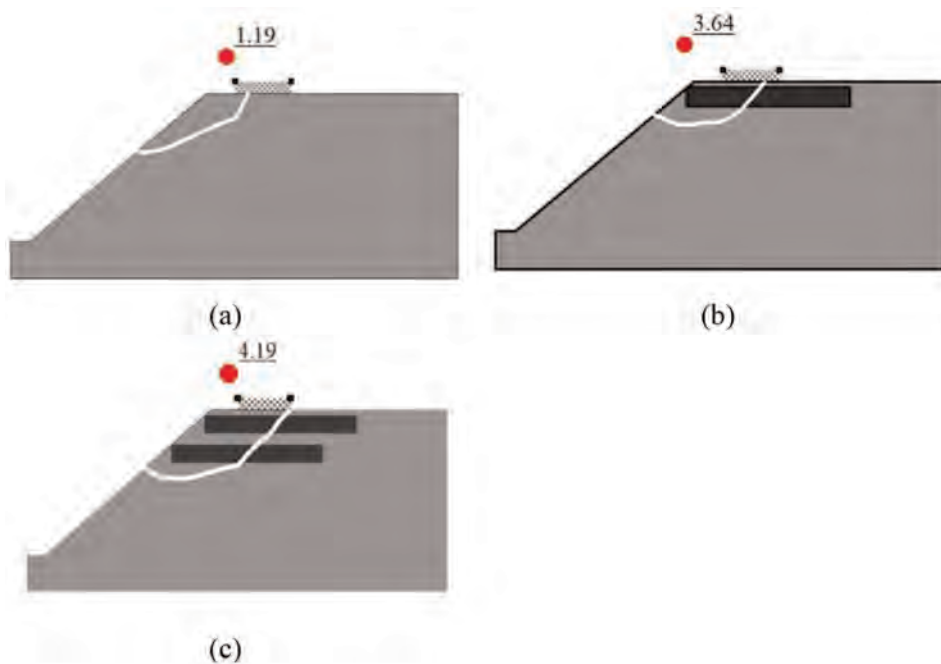
Figure 4. limit equilibrium analysis of the experimental models under the surcharge of 200 kN/m^3. a) Unreinforced slope b) Single-layer reinforced slope c) Double-layer reinforced slope.

4 CONCLUSION

In this article, the behavior of the slopes reinforced with one and two layers of geocell under a surcharge was investigated. The main objective of the experiments was to investigate the effect of using the geocell to improve the bearing capacity and reduction of the settlement of footing located near the slope edge. Also, a numerical study has been conducted to investigate the effect of the reinforcement on the potential slip surfaces and factors of safety. The results of this study are as follows.

Geocell provides anchorage length behind the failure wedge and increases the bearing capacity of soil by reducing the lateral movement of soil particles surrounded by the geocell pockets.

The relative positive impact of the geocell reinforcement in improving the load-bearing behavior of the granular slope increases as the settlement ratio rises due to the mobilization of dilation characteristics of granular backfill material and better lateral confinement of soil grains by geocell in larger pressures.

In the case of the double-layer geocell reinforced slope, the redistribution of pressure over deeper layers of soil causes the load-bearing capacity diagram to intersect with the load-bearing capacity of a plane condition in low settlements.

Geocell reinforcement redistributes the pressure over deeper layers of soil, causing the failure wedge to expand and increasing the factor of safety compared to unreinforced slopes.

As with other studies, the results of this research were influenced by experimental conditions. For instance, the results were obtained for only one type of reinforcement, one type of soil, and one width of the footing. Specific applications should only be made after considering the above limitations. Nevertheless, this study provided insight into the basic mechanism that establishes the behavior of slope reinforced by geocell under static loads, which may be used to guide further studies.

REFERENCES

Alamshahi, S., & Hataf, N. 2009. Bearing Capacity of Strip Footings on Sand Slopes Reinforced with Geogrid and Grid-anchor. *Geotextiles and Geomembranes*, 27(3): 217–226.

Ardakani, A., & Namaei, A. 2021. Numerical Investigation of Geocell Reinforced Slopes Behavior by Considering Geocell Geometry Effect. *Geomechanics and Engineering*, 24(6):589–597.

Bathurst, R. J., Blatz, J. A., & Burger, M. H. 2003. Performance of Instrumented Large-scale Unreinforced and Reinforced Embankments Loaded by a Strip Footing to Failure. *Canadian Geotechnical Journal*, 40(6): 1067–1083.

Chen, R.-H., & Chiu, Y. 2008. Model Tests of Geocell Retaining Structures. *Geotextiles and Geomembranes*, 26(1): 56–70.

Chen, R.-H., Wu, C.-P., Huang, F.-C., & Shen, C.-W. 2013. Numerical Analysis of Geocell-reinforced Retaining Structures. *Geotextiles and Geomembranes*, 39: 51–62.

El Sawwaf , M. A. 2007. Behavior of Strip Footing on Geogrid-reinforced Sand Over a Soft Clay Slope. *Geotextiles and Geomembranes*, 25(1): 50–60.

Halder, K., & Chakraborty, D. 2018. Bearing Capacity of Strip Footing Placed on the Reinforced Soil Slope. *International Journal of Geomechanics*, 18(11): 06018025.

Henkel, D.J. and Gilbert, G.D., 1952. The Effect Measured of the Rubber Membrane on the Triaxial Compression Strength of Clay Samples. *Geotechnique*, 3(1):20–29.

Kakrasul, J. I., Han, J., & Rahmaninezhad, S. M. 2020. Load-deformation Behavior of Geosynthetic-Reinforced Retaining Walls with Limited Fill Space Under Static Footing Loading. *Transportation Infrastructure Geotechnology*, 7(3): 309–331.

Kazemi, K., Arvin, M.R., Hataf, N. and Khademhosseini, A., 2022. Model Studies of Square Footings on Geocell-reinforced Slopes. *Geosynthetics International*, 29(6):576–592.

Khorsandiardebili, N., & Ghazavi, M. 2021. Static Stability Analysis of Geocell-reinforced Slopes. *Geotextiles and Geomembranes*, 49(3): 852–863.

Madhavi Latha, G., Rajagopal, K., & Krishnaswamy, N. R. 2006. Experimental and Theoretical Investigations on Geocell-supported Embankments. *International Journal of Geomechanics*, 6(1): 30–35

Mehdipour, I., Ghazavi, M. and Moayed, R.Z., 2013. Numerical Study on Stability Analysis of Geocell Reinforced Slopes by Considering the Bending Effect. *Geotextiles and Geomembranes*, 37:23–34.

Mehdipour, I., Ghazavi, M., & Ziaie Moayed, R. 2017. Stability Analysis of Geocell-reinforced Slopes using the Limit Equilibrium Horizontal Slice Method. *International Journal of Geomechanics*, 17(9):06017007.

Moradi, G., Abdolmaleki, A., & Soltani, P. 2019. Small-and Large-scale Analysis of Bearing Capacity and Load-settlement Behavior of Rock-soil Slopes Reinforced with Geogrid-box Method. *Geomechanics and Engineering*, 18(3): 315–328.

Song, F., Liu, H., Ma, L., & Hu, H. 2018. Numerical Analysis of Geocell-reinforced Retaining Wall Failure Modes. *Geotextiles and Geomembranes*, 46(3): 284–296.

Tavakoli Mehrjardi, Gh., Ghanbari, A., & Mehdizadeh, H. 2016. Experimental Study on the Behaviour of Geogrid-reinforced Slopes with Respect to Aggregate Size. *Geotextiles and Geomembranes*, 44(6): 862–871

Influence of geometric configuration on the interaction of back-to-back MSE walls under static loading

F. Li, W. Guo & Y. Zheng*
Wuhan University, Wuhan, China

ABSTRACT: Back-to-back mechanically stabilized earth (MSE) walls are commonly used for ramp ways and bridge approaches. The behavior of back-to-back MSE walls is significantly influenced by the geometric configuration, especially the horizontal distance (i.e., width-to-height ratio) of the wall. This paper presents a numerical study on the behavior of back-to-back MSE walls to investigate the influence of horizontal distance on the interaction. Numerical simulations were conducted with different width-to-height ratios. Results indicate the horizontal distance has significant influences on the static behavior of back-to-back MSE walls. The lateral soil thrust behind the reinforced soil zone, the required reinforcement strength, and the vertical toe load generally increase with increasing horizontal distance up to a critical value. The Federal Highway Administration (FHWA) simplified method significantly overestimates the required reinforcement tensile strength, but underestimates the lateral soil thrust for the range of horizontal distances involving interaction between the back-to-back MSE walls.

1 INTRODUCTION

As an important derivative structure of mechanically stabilized earth (MSE) walls, back-to-back MSE walls consist of two opposing MSE walls in a back-to-back configuration. Back-to-back MSE walls can save more space than traditional embankments and are commonly used for ramp ways and bridge approaches (Anderson *et al.* 2018).

The behavior of back-to-back MSE walls is significantly influenced by the geometry. The geometrical configuration of back-to-back MSE walls is typically described in terms of the horizontal distance (D) between the back of the reinforced soil zone of the two MSE walls or the width-to-height ratio (R_{WH}) of the system, which is defined as the system width W divided by the wall height H. In the Federal Highway Administration (FHWA) design guidelines (Berg *et al.* 2009), two cases are considered based on the horizontal distance of the two MSE walls. For Case I, the distance between two MSE walls is large enough so that the two walls do not affect each other and can be designed independently assuming the full active soil thrust could be mobilized. The theoretical critical distance is $D_t = H\tan(45°\text{-}\phi/2)$, which corresponds to the theoretical critical width-to-height ratio $R_t = 1.4 + \tan(45°\text{-}\phi/2)$. For Case II, when the overlapping reinforcement length is greater than $0.3H$, no active soil thrust needs to be considered for external stability. For horizontal distances between Case I and Case II, the active earth thrust can be linearly interpolated from the full active condition to zero. However, no justification is provided for this assumption. Therefore, research is needed to investigate the interaction of back-to-back MSE walls with different horizontal distances.

Several numerical studies have been performed on the static behavior of back-to-back MSE walls (Benmebarek & Djabri 2017; El-Sherbiny *et al.* 2013; Han & Leshchinsky 2010). Han & Leshchinsky (2010) conducted numerical study of back-to-back MSE walls with

---

*Corresponding Author: yzheng@whu.edu.cn

width-to-height ratios R_{WH} ranging from 1.4 to 3.0, and the results indicate that the FHWA design guidelines underestimates the interaction distance. El-Sherbiny *et al*. (2013) found that the interaction effect on failure surface is not significant for horizontal distance greater than $0.5H$. Benmebarek & Djabri (2017) found that the factor of safety increases significantly with increasing overlapping reinforcement length. The above numerical studies generally indicate that ignoring the interaction effect between the back-to-back MSE walls would result in overestimation for the design; however, no quantitative evaluation is provided regarding the interaction of back-to-back MSE walls.

This paper presents a numerical study of the interaction analysis of the static behavior of back-to-back MSE walls. A parametric study is conducted to investigate the effect of width-to-height ratio. Results provide insights regarding the interaction of back-to-back MSE walls in terms of lateral soil thrust, required reinforcement strength, vertical toe load, and factor of safety.

2 NUMERICAL MODEL

A parametric study is performed to evaluate the effect of width-to-height ratio R_{WH} on the static behavior of back-to-back MSE walls with modular block facing. For all the models, the back-to-back MSE walls have a height of $H = 6.0$ m, reinforcement length of $L = 0.7H = 4.2$ m, and vertical spacing of $S_v = 0.6$ m. Only the horizontal distance between the two MSE walls changes, as shown in Table 1, and the corresponding width-to-height ratios range from 0.9 to 4.0.

Table 1. Geometrical configuration of back-to-back MSE walls for baseline case series.

Geometrical Parameter	Value									
Width-to-Height Ratio[1], R_{WH}	0.9	1.1	1.25	1.4	1.65	1.9	2.2	2.5	3.0	4.0
Horizontal Distance, D (m)	−3.0	−1.8	0.9	0	1.5	3.0	4.8	6.6	9.6	15.6

[1]defined as the width of back-to-back MSE walls divided by wall height, W/H.

2.1 *Finite difference grid and boundary conditions*

The finite difference program FLAC was used to investigate the behavior of back-to-back MSE walls at the end of construction. Figure 1 shows the finite difference grid and boundary
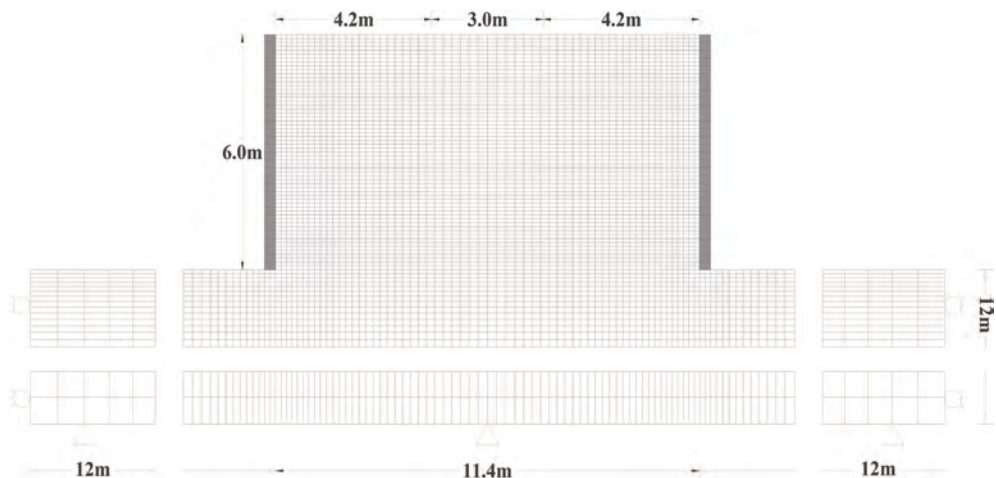
Figure 1. Finite difference grid and boundary conditions of back-to-back MSE walls.

conditions of the back-to-back MSE walls with width-to-height ratio $R_{WH} = 1.9$. The back-to-back MSE walls have a total width $W = 11.4$ m and horizontal distance $D = 3.0$ m between the two opposing MSE walls. The foundation was 12 m ($2H$) depth. The bottom boundary of foundation was fixed in both the horizontal and vertical directions. The left and right sides were fixed in the horizontal direction but free in the vertical direction.

2.2 *Materials interfaces*

The modular blocks were modeled as a linear-elastic material with Young's modulus $E = 31.5$ GPa and Poisson's ratio $\nu = 0.2$. Geogrids were modeled using linearly elastic-plastic cable elements with tensile stiffness $J = 1000$ kN/m. The foundation soil was simulated using a linear elastic-plastic model with $E = 160$ MPa and $\nu = 0.3$, friction angle $\phi = 40°$, and cohesion $c = 0$ kPa. The backfill soil was modeled as a nonlinear elastic-plastic material with the Duncan-Chang hyperbolic relationship and the Mohr–Coulomb failure criterion. This approach has been used successfully in many previous studies on geosynthetic reinforced soil structures (e.g., Zheng & Fox 2016; Zheng *et al.* 2018). The hyperbolic parameters for the backfill soil were selected based on data of granular soils reported by Duncan *et al.* (1980) are listed in Table 2.

The interaction between different materials (e.g., soil-block and block-block) was modeled through interface elements considering Coulomb sliding behavior. The soil interface strength was related to the shear strength parameters of the backfill soil using a strength reduction factor, and the block-block interface parameters were selected based on reported data in the literature. This approach and the parameters were reported by Zheng *et al.* (2018).

Table 2. Parameters for backfill soil.

γ (kN/m^3)	K	K_{ur}	n	R_f	K_b	m	c (kPa)	ϕ (°)	ψ (°)
21.9	1780	2136	0.39	0.67	1300	0.16	0	34	4

2.3 *Modeling procedures*

The numerical model of the back-to-back MSE walls was constructed in stages. The foundation soil was first solved to an equilibrium state under gravitational forces. The walls were constructed in lifts with each lift consisting of facing blocks, soil layer, reinforcements, and interfaces.

3 RESULTS AND DISCUSSION

3.1 *Lateral soil thrust*

Figure 2(a) show the effect of width-to-height ratio R_{WH} on profiles of the lateral soil stress behind the reinforced soil zone. Lateral stresses generally increase with increasing depth, and the maximum values occur near the bottom of the wall. For $R_{WH} \geq 1.9$, lateral soil stresses are essentially similar. The active failure wedge could be fully developed for these cases with large horizontal distances, and the interaction effect between the back-to-back MSE walls is negligible.

Figure 2(b) shows the lateral soil thrust behind the reinforced soil zone. Lateral soil thrust increases significantly from 49.3 kN/m at $R_{WH} = 0.9$ to 89.8 kN/m at $R_{WH} = 1.65$. For these cases, the overlapping reinforcement layers result in strong interaction effect between the two opposing MSE walls. As longer reinforcement layers could provide more anchorage resistance, which would reduce the lateral soil thrust. With increasing horizontal distance, lateral soil thrust further increases mildly to 99.7 kN/m at $R_{WH} = 1.9$, and then remains nearly constant at approximately 100 kN/m for larger distances. The failure wedge could be fully developed for $R_{WH} \geq 1.9$, and the full active soil thrust could be mobilized. Therefore, the interaction effect of the two opposing MSE walls on lateral soil thrust could be ignored for these conditions.
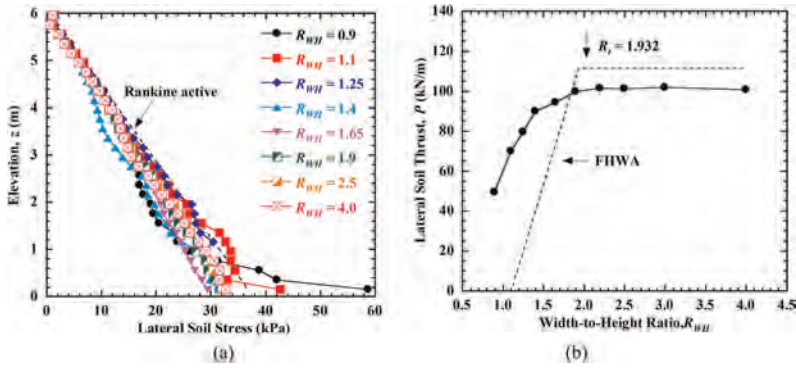
Figure 2. Effect of width-to-height ratio on lateral soil stresses behind reinforced soil zone: (a) lateral soil stress profiles; (b) lateral soil thrust.

3.1 Vertical toe load

The vertical toe load is important for the external stability of MSE walls. The vertical toe load factor is defined as the ratio of the total vertical load divided by the self-weight of wall facing. Figure 3 show the vertical toe load factor for different width-to-height ratios. The vertical toe load factor first increases significantly from 1.85 to 2.02 when the width-to-height ratio increases from 0.9 to 1.65, and then the factors are close to 2.02 for larger ratios. For width-to-height ratio $R_{WH} \leq 1.65$, vertical toe load factors generally increase with increasing distance, but the effect becomes less significant. As the overlapping reinforcement layers could provide anchorage resistance when the horizontal distance is small, which reduce the shear stress on the back of facing and the down drag forces from the connected reinforcements. For the back-to-back MSE walls with $R_{WH} > 1.65$, the vertical toe load factors are nearly constant.
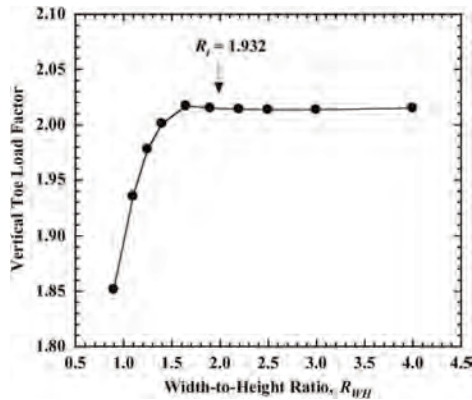
Figure 3. Effect of width-to-height ratio on vertical toe load factor.

3.2 Required reinforcement strength

Figure 4(a) shows the effect of the width-to-height ratio on the maximum reinforcement tensile force profiles, and the reinforcement tensile forces calculated using the FHWA simplified method are also presented for comparison. The maximum tensile force profiles for different width-to-height ratios have similar shapes. The maximum value increases gradually from the top of the wall to the highest value at approximately $z = 1.5$ m, and then decreases slightly toward

the bottom. In addition, the maximum tensile forces generally increase with increasing distance, but the effect becomes less pronounced. The maximum tensile forces are essentially the same for the cases with $R_{WH} \geq 1.65$, and the interaction between the MSE walls has little effect on the internal stability. Simulated maximum tensile forces are close to the calculated values using the simplified method in the upper section but have increasing deviations toward the bottom.

The required reinforcement tensile strength T_{req} is the maximum value of each maximum tensile force profile and is plotted versus the width-to-height ratio in Figure 4(b). The required reinforcement strength increases nonlinearly from 11.3 kN/m to 13.9 kN/m when the width-to-height ratio increases from 0.9 to 1.65, and then remains nearly constant at approximately 14 kN/m for larger ratios. The critical width-to-height ratio for constant required reinforcement strength of the back-to-back MSE walls is approximately 1.65. The calculated required tensile strength using the simplified method is 21.5 kN/m, which is much larger than the simulated maximum values. In addition, the simplified method does not account for the interaction of the back-to-back MSE walls, which would result in even larger overestimation for the cases with smaller width-to-height ratios that involve strong interaction. In general, the simplified method is overconservative for the internal stability design of back-to-back MSE walls.
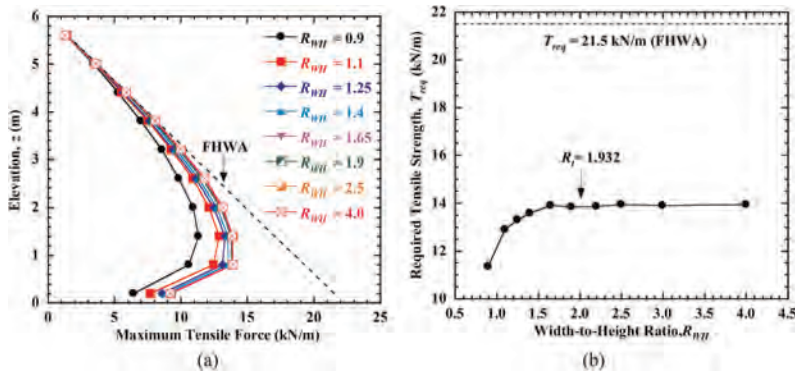
Figure 4. Effect of width-to-height ratio on reinforcement tensile force: (a) maximum tensile force profiles; (b) required tensile strength.
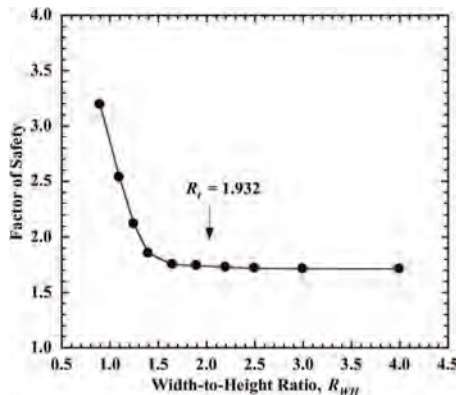
Figure 5. Effect of width-to-height ratio on factor of safety.

3.3 Factor of safety

Figure 5 shows the effect of width-to-height ratio on the factor of safety. The factor of safety against shear failure was obtained using the strength reduction method. The factor of safety

decreases nonlinearly from 3.193 to 1.748 when the width-to-height ratio R_{WH} increases from 0.9 to 1.65, and then remains nearly constant at approximately 1.72 for larger ratios. For the cases with $R_{WH} \leq 1.4$, the overlapping reinforcement layers result in strong interaction effect between the back-to-back MSE walls, and longer overlapping reinforcement could provide more anchorage resistance, resulting in a greater factor of safety. In general, the effect of interaction becomes smaller with increasing horizontal distance, and the interaction could be ignored for horizontal distance greater than a critical value.

4 CONCLUSIONS

This paper presents a numerical study of the interaction analysis of back-to-back MSE walls under static loading. A parametric study was conducted to investigate the effects of horizontal distance on the back-to-back MSE walls. Simulation results indicate that the lateral soil thrust behind the reinforced soil zone, the required reinforcement tensile strength, and the vertical toe load increase nonlinearly with increasing horizontal distance to a critical value, and then remain nearly constant for larger distances. The FHWA simplified method is overconservative for the required reinforcement tensile strength, but underestimates the lateral soil thrust involving interaction of back-to-back MSE walls.

REFERENCES

Anderson, P.L., Gladstone. R.A., Brabant, K., & Sankey, J., 2018. Back-to-back MSE walls – A Comprehensive Understanding. *ASCE IFCEE 2018*, Orlando, FL, 431–447.

Benmebarek, S. & Djabri, M., 2017. FEM to Investigate the Effect of Overlapping-reinforcement on the Performance of Back-to-back Embankment Bridge Approaches under Self-weight. *Transportation Geotechnics*, 11:17–26.

Berg, R.R., Christopher, B.R. & Samtani, N., 2009. *Design and Construction of Mechanically Stabilized Earth Walls and Reinforced Soil Slopes – Volume I.* FHWA-NHI-10-024, DOT, Washington, D.C. U.S.

Duncan, J.M., Byrne, P., Wong, K.S. & Mabry, P., 1980. *Strength, Stress-strain and Bulk Modulus Parameters for Finite Element Analysis of Stresses and Movements in Soil Masses. Report No. UCB/GT/80-01.* University of California, Berkeley, CA.

El-Sherbiny, R., Ibrahim, E. & Salem, A., 2013. Stability of Back-to-back Mechanically Stabilized Earth Walls. *GeoCongress 2013*, San Diego, CA, 555–565.

Han, J. & Leshchinsky, D., 2010. Analysis of Back-to-back Mechanically Stabilized Earth Walls, *Geotextiles and Geomembranes*, 28(3): 262–267.

Zheng, Y. & Fox, P.J., 2016. Numerical Investigation of Geosynthetic-reinforced Soil Bridge Abutments Under Static Loading. *Journal of Geotechnical and Geoenvironmental Engineering*, 142(5): 07016032.

Zheng, Y., Fox, P.J. & McCartney, J.S., 2018. Numerical Simulation of Deformation and Failure Behavior of Geosynthetic Reinforced Soil Bridge Abutments. *Journal of Geotechnical and Geoenvironmental Engineering*, 144(7): 04018037.

Numerical investigation of geogrid back-anchored sheet pile walls

M. Schoen, D. Konig, A.A. Lavasan & T. Wichtmann
Ruhr-Universitat Bochum, Germany

R. Holter
Dr. Spang GmbH Witten, Germany

B. Wittekoek & S.J.M. van Eekelen
Deltares, Delft, The Netherlands

P.G. van Duijnen
GeoTec Solutions, The Netherlands

O. Detert
Huesker Synthetic, Germany

ABSTRACT: In the last decades, geosynthetic reinforcement has been widely used in geotech-nical applications. Recently, geogrid has also been used to back-anchor sheet pile walls. However, this system has not received sufficient attention neither in research nor in construction. Due to the complex interactions between soil, geogrid and sheet pile wall, the applicability of common design guidelines for conventionally back-anchored walls to this particular system has to be proven. To develop a fundamental understanding about the influence of various components of the system on its behaviour, numerical investigations have been conducted within this study. In this paper the influence of geogrid inclination, design of geogrid-sheet pile connection including prestressing and geogrid position on the earth pressure distribution and wall deformation is discussed. The numerical results revealed that the position of geogrid and design of geogrid-sheet pile connection significantly affect the earth pressure distribution. The wall deformations are mainly influenced by the geogrid position.

1 INTRODUCTION

For many years, sheet pile walls have been key construction elements in the design of excavation pits and any types of marine constructions such as ship lock, cofferdams or wharfages. Sheet pile walls can be designed as unsupported walls with fixation in the soil. The use of unsupported sheet pile walls for large retaining heights often leads to large deformations, high embedment depths and thicker sheet pile profile, thus to uneconomical solutions. Therefore, the use of a support system e.g. anchors is selected to obtain a more economical designs. Depending on the boundary conditions, different types of support-systems are possible.

In the case of excavation pits, grouted anchors are often used. In bank construction with backfilled sheet piles, steel anchors with anchored plates or similar constructions are used. A newly alternative to this is the support with a geogrid (Detert *et al*. 2022; Van Duijnen *et al*. 2020, 2022). In this case, individual geogrids are inserted into the soil during backfilling and connected to the sheet pile wall, thus increasing the load-bearing capacity of the sheet pile wall. The advantages of this method are the easy installation as well as the support acting all along the wall, not like punctual support every few meters with anchors. Therefore, it is an economical alternative to other support systems and was therefore used in 2018 in the Netherlands at the Kramer wind park.

However unlike e.g. conventional anchor systems, the geogrid interacts with the soil along its full length. This results in complex interactions that need to be investigated in detail. The aim of this research is to develop a numerical model that can simulate these interactions with the use of the finite element method and can be used to better understand the whole support system. Furthermore, the influence of different design variables, such as anchor length, on the earth pressure distribution and wall deformation will be analyzed in the following chapters.

2 NUMERICAL MODELLING

For a better understanding of the sheet pile wall geogrid system, small-scale tests (Wittekoek *et al*. 2023) and full scale test (Van Duijnen 2022) have been performed. These tests have been simulated using Plaxis 2D and the system behaviour detected from the numerical model was in a good agreement to the laboratory observations (e.g. in Wittekoek *et al*. 2022). Based on these observation, the creation and the main features of the finite element simulation in prototype scale are described in the following section.

2.1 *Finite element model*

Since sheet pile constructions are line structures, a 2D finite element simulation in plain strain is sufficient, wherefore the numerical model was created in finite element code Plaxis 2D. As shown in Figure 1 the sheet pile wall is embedded in a clay soil layer and is supporting a 10 m thick backfill layer of sand. The geogrid is located in this backfill and connected to the wall. The selection of the model dimension was based on the recommendation from EANG (2014). Thus, twice the backfill height was chosen for the lateral distances from the sheet pile wall to the model boundaries. The distance between the bottom of the excavation pit and the bottom edge of the model was also chosen accordingly. The sheet pile wall was modeled as a plate element and the soil as a volume element. An interface was placed between the wall and the soil to allow a realistic sheet pile wall-soil interaction as well as between geogrid and soil. In Plaxis geogrids exist as a structural element, which is a 5 node line element with two degrees of freedom *(ux,uy)* in each node. The only material constant is the elastic axial stiffness *EA*. To realistically account for the membrane effect of the geogrid, the finite element mesh must be updated during the simulation.
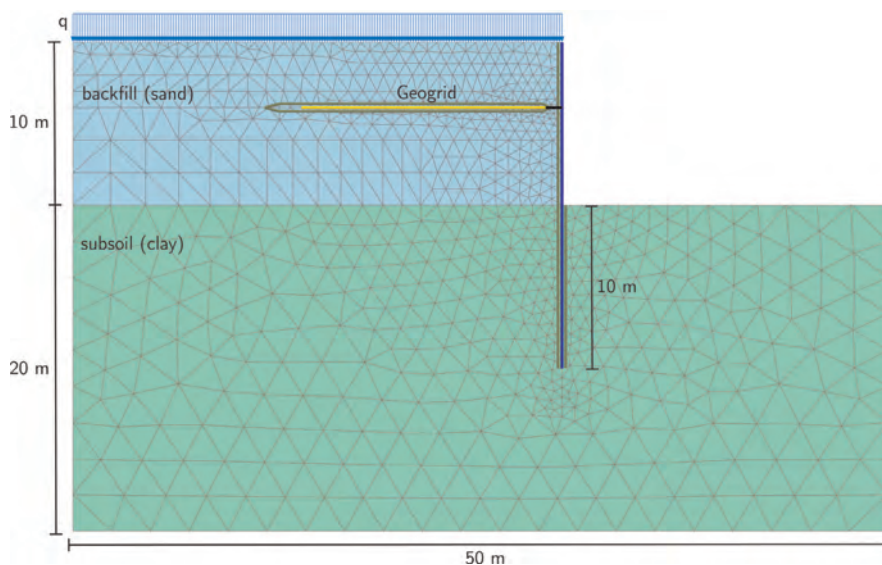
Figure 1.   Finite element model of sheetpile wall with geogrid.

Table 1. Constitutive parameters of hardening soil model used in finite element simulation.

Name	Parameter	Sand	Clay
E_{50}^{ref} (kPa)	Secant stiffness	35000	52500
E_{Oed}^{ref} (kPa)	Tangent stiffness	35000	52500
E_{ur}^{ref} (kPa)	Unloading/reloading stiffness	105000	157500
m (-)	Power coefficient	0.5	0.5
ν_{ur} (-)	Poissons's ratio	0.20	0.20
K_0^{nc} (−)	K_0 value for normal consolidation	0.5	0.6580
R_f (-)	Failure ratio	0.9	0.9
p^{ref} (kPa)	Reference stress for stiffness	100	100

The hardening soil model (Schanz 1998) was used to obtain a more realistic stress-strain behavior of the soil. The hardening soil model has a double hardening yieldsurface, stress-dependent stiffnesses and Mohr-Coulomb (MC) failure criterion. An important detail of the finite element model is the prestressing of the geogrid. On the construction side the geogrid will be inserted and covered with soil, except 1 m close to the sheet pile wall to allow the prestressing. The geogrid is then pulled towards the sheet pile wall using an excavator, where it the wall, creating a prestress. A slight pre-stressing is needed in-situ to allow a force-fit connection to the sheet pile wall, which should prevent the geogrid from slipping under load. In the finite element model two types of geogrid-sheet pile wall connections were simulated. First the installation and the prestressing of the geogrid was performed close to the reality and is shown in Figure 2. Instead of pulling the geogrid, which showed unrealistic results, a spring element between geogrid and sheet pile wall is used to apply the prestressing. Note, along the length of the spring element no interaction between the reinforcement and the soil takes place. Secondly, the geogrid is directly connected to the wall without prestressing.

The construction of the sheet pile wall as well as the installation and prestressing of the geogrids is modeled by the following 12 construction stages/phases:

Phase 1: Applying geostatic pressure on initial soil (clay)
Phase 2: Activation of sheet pile wall and interface
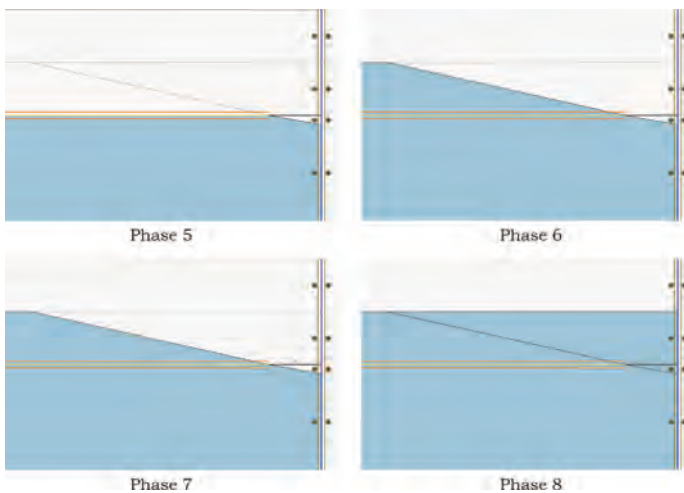
Figure 2. Phases of prestressing of the geogrid in finite element model (Description see text).

Phase 3: Backfilling from -10.0 m to -8.0 m

Phase 4: Backfilling from -8.0 m to -6.0 m

Phase 5: Activation of geogrid with interface and spring (s. Figure 2)

Phase 6: Placing of backfill on the geogrid with a thickness of 1.0 m (Figure 2)

Phase 7: Generate a prestressing force $p = 20$ kN/m in the spring element (Figure 2)

Phase 8: Backfilling the spring - entire area behind the wall is backfilled up to -5.0 m (Figure 2)

Phase 9: Backfilling from -5.0 m to -4.0 m

Phase 10: Backfilling from -4.0 m to -2.0 m

Phase 11: Backfilling from -2.0 m to -0.0 m

Phase 12: Activate uniform load q = 10,0 kN/m

3 RESULTS AND DISCUSSION

The influence of geogrid inclination, geogrid-sheet pile wall connection and the geogrid depth on the resulting earth pressure and wall deformation will be analysed in the following subsections.

3.1 Influence of geogrid inclination

The influence of geogrid inclination in retaining a sheet pile wall is investigated in the following. Therefore, the geogrid position is kept constant at -4 m and only the inclination is varied. Figure 3 shows both, the earth pressure distribution and the related sheet pile deformation for three exemplary geogrids with different inclinations (0%, 4% and 8%) and all prestressed with 20 kN/m. It can be seen that for all three inclinations an almost identical earth pressure develops over the entire height. The magnitude of this is slightly higher than the active theoretical earth pressure within the backfilled area and increases in the area of the sheet pile confinement, so that at the base of the wall the earth pressure generated is as great as the theoretical earth pressure at rest. If the associated displacements of the sheet pile wall are compared, a noticeable difference can be seen. The fact that the use of a geogrid with a greater.
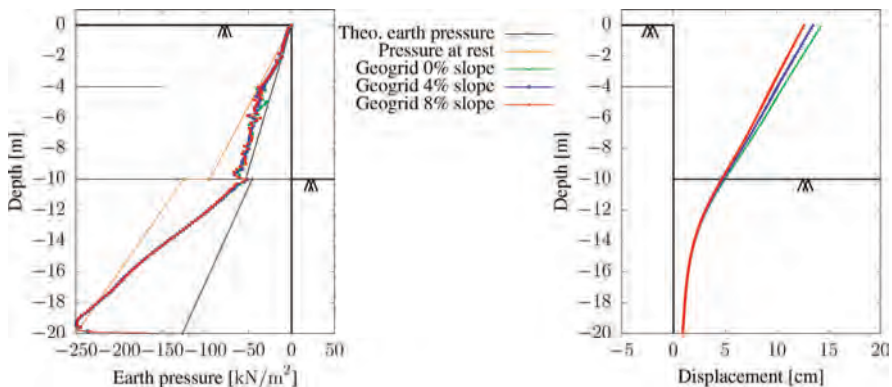
Figure 3. Earth pressure distribution on active side (left) and resulting wall deformation (right) for variation of the geogrid angle in vertical direction.

3.2 Influence of numerical solution for the wall connection

As mentioned before, the pre-stressing on site is needed to connect the geogrid perfectly straight and force-fit to the sheet pile wall. Since this is not necessarily needed for finite element modeling, the influence of the wall connection on the earth pressure distribution as well as on the wall deformation was investigated. As shown in Figure 4, the earth pressure distribution and the wall deformation are very similar. However, it is noticeable that the
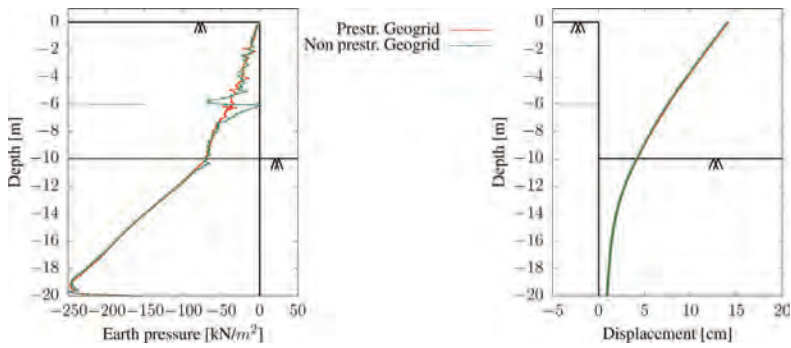
Figure 4. Effect of wall connection for a geogrid at -6 m on earth pressure distribution on active side (left) and resulting wall deformation (right).

calculation without pre-stressing gives jumps in the earth pressure distribution at the height of the geogrid connection. This can be explained by the shielding effect of the geogrid below the connection point. Above the connection point an increase of the earth pressure is visible, which can be explained by local arching effects. The use of a spring eliminates this shielding and arching effects and therefore these jumps are not visible in the earth pressure distribution of the model with prestressing. Which of these wall connection types should be used depends on the in-situ connection of the geogrid to the wall. In the following it is assumed, that the geogrid is installed close to the wall and only a short construction for the connection is designed, so the variant with direct connection is used for further simulations.

3.3 Influence of geogrid position

In order to analyze the influence if the geogrid position, different finite element models of the sheet pile walls retained by geogrids were created, in which the depth of geogrid placement was varied. In this publication only three exemplary variants, with the depths of -6.0 m, -4.0 m and -2.0 m are presented. Figure 5 shows the calculation results of the three models with different insertion depths of the geogrid. The earth pressure distribution in the clay layer is nearly identical in the section between -15.0 m and -20.0 m. In the upper 5 m of clay layer, higher earth pressure occurs for deeper geogrid position, which also occurs in the backfilled area from -7,0 m to -10 m. Above this depth, all three variations generally exhibit an identical earth pressure distribution. When comparing the three variations, it can be seen that the
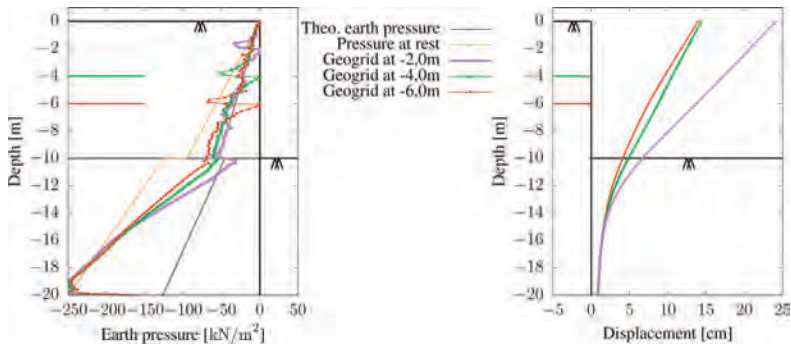
Figure 5. Earth pressure distribution on active side (left) and resulting wall deformation (right) for variation of the geogrid position in vertical direction.

geogrid positions -4 m and -6 m provide an almost identical displacement at the top, whereas the geogrid position -2 m has a significantly higher deformation. To explain this, the wall displacement for all calculation phases of the three variations is shown in Figure 6. Comparing the geogrid positions -4 m and -6 m, shows that the initial deformation prior activating the geogrid in the case of the geogrid at -6 m is lower than at -4 m. As a result, the geogrid with deeper geogrid position is also more loaded, so the maximum geogrid stress for the geogrid at a depth of -6 m is 270.7 kN, 201.2 kN for geogrid at -4 m depth and only 99.7 kN for geogrid at -2 m depth. Nevertheless, in the case of the geogrid position at -4 m, the wall does not deform so much after activation. This can be explained by the more favorable position of the geogrid with respect to the lever arm. In the case of the geogrid position of -2 m, the initial wall deformation is already so high that the geogrid can only reduce the wall deformation to a very limited extent.
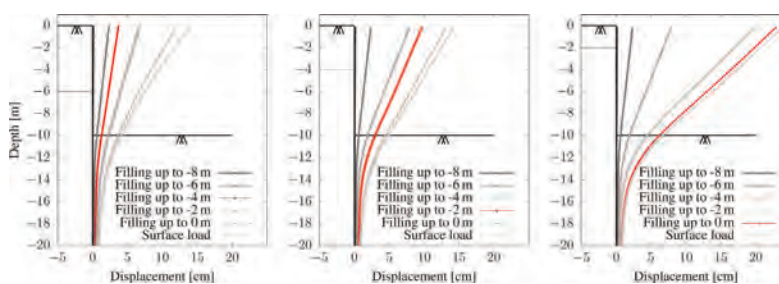
Figure 6. Sheet pile wall deformation for all backfilling phases for Geogrid at -6 m (left), at -4 m (middle) and at -2 m (right).

4 SUMMARY AND OUTLOOK

In the framework of this publication, a finite element model was created that can simulate the behavior of a sheet pile wall back-anchored with geogrids. Different geogrid positions as well as different angles of the geogrids were analyzed. The geogrid position in particular has a great influence on the wall deformation. For a further reduction of the wall deformation, other geogrid positions could be considered in future research.

REFERENCES

EANG 2014. *Empfehlungen des Arbeitskreises Numerik in der Geotechnik - EANG*, Deutsche Gesellschaft fur Geotechnik e. V., Ernst und Sohn.

Detert, O., Lavasan, A. A., van Duijnen, P., van den Berg, J., Holter, R., Konig, D., van Eekelen, S. 2019. Geogrid-Verankerde Damwanden-1. Voorbeeldprojekten en Onderzoek-sopzet, Geogrid-verankerde damwanden: Deel 1: voorbeeldprojecten en onderzoeksopzet. *Geotechniek*, 23(4), 60–65.

Schanz, T. 1998. *Zur Modellierung des mechanischen Verhaltens von Reibungsmaterialien*. Institut fur Geotechnik Stuttgart.

Van Duijnen, P., Detert, O., Lavasan, A. A., van den Berg, J., Konig, D., Holter, R., van Eekelen, S. 2020. Geogrid-verankerde Damwanden: Deel 2: Full Scale Test. *Geotechniek*, 24(1), 53–57.

Van Duijnen, P., Detert, O., Lavasan, A. A., van den Berg, J., Konig, D., Holter, R., van Eekelen, S. 2022. Geogrid-anchored Sheet Pile Walls: First Trial Project. In: proc. Eurogeo7, Warsaw, Poland.

Wittekoek, B., van Eekelen, S., Terwindt, J., Korff, M., van Duijnen, P.G., Detert, O. and Bezuijen, A. 2022. Geogrid-anchored Sheet Pile Walls; A Small-scale Experimental and Numerical Study. *Geosynth Int*.

Wittekoek, B., van Eekelen, S., Bezuijen, A., Terwindt, J., van Duijnen, P., Detert, O., van den Berg, J., Konig, D. 2023. Geogrid-anchored Sheet Pile Walls Under Strip Footing Surcharge Loading, Small-scale Experiments. *In: proc. 12 ICG*, Rome, Italy.

Evaluation of the geosynthetic reinforced structure response to a debris flow impact

D. Gioffrè
University of Pavia, Italy

M. Ciurleo
National Research Council of Italy, Research Institute for Geo-Hydrological Protection (CNR-IRPI), Rende (CS), Italy

M.C. Mandaglio
University of Salerno, Italy

N. Moraci
"Mediterranea" University of Reggio Calabria, Italy

ABSTRACT: Rapid landslides are commonly mitigated by artificial embankments that can be constituted of granular material reinforced by geosynthetics. For their design, the evaluation of debris flow impact force against the structure is a crucial issue. The paper focuses on determining the forces transmitted over time to a geosynthetic reinforced structure and on analyzing its response to the impact in terms of horizontal displacement. The impact force has been evaluated adding the static component, depending on the flowing mass height, to the dynamic component, depending on both the flowing mass height and its velocity. In the analyses of the geosynthetic reinforced structure response, two cases have been considered regarding the soil – geogrid interaction: the first one considers a constant soil shear strength angle along the height of embankment the second one considers the variation of soil shear strength angle along the height.

1 INTRODUCTION

In the last decades, the attention of several scientists focused on debris flow hazard assessment and risk management (Ciurleo *et al.* 2019, 2021, 2022) with a special focus on the design of risk mitigation measures such as sheltering structures. The use of these structures (deformable or rigid) allows to deviate or stop the flow reducing debris flow run-out distance and velocity and, as consequence, its residual destructive power.

In the case of deformable structures, such as geosynthetics reinforced embankments, the design is strictly related to the calculation of the debris flow impact force against the structure and on its response to this force.

Several approaches and empirical formulas are available in scientific literature for the calculation of the impact forces acting on embankments (Armanini 1997; Arattano & Franzi 2003; Calvetti *et al.* 2017; Gioffrè *et al.* 2017; Suda *et al.* 2010). Independently on the adopted approaches and used formulas, only few papers consider the evolution with time of the impact force (Gioffré *et al.* 2017). Gioffrè *et al.* (2017) proposed the evaluation of the impact force adding the static component, which depends on the flowing mass height, to the dynamic component, that depends on both the flowing mass height and its velocity.

Different impact features will result in different response mechanisms of the embankment. In the paper, considering a typical prismatic shape of geosynthetics reinforced embankment,

the impact force according to Gioffrè *et al.* (2017) over the time against the structure has been evaluated. Subsequently, the influence of soil-geogrid interaction properties on the deformative response of the geosynthetics reinforced structure has been analyzed. To do this, FEM numerical analyses have been carried out considering two different cases related to the variation of shear strength angle of the soil along the earth reinforced embankment. The first one with a constant shear strength angle (one layer) along the height and the second one with a variable shear strength angle along the height (four layers).

The deformative response of the structure for these two different configurations has been analyzed and discussed in terms of horizontal displacements.

2 MATERIALS AND METHODS

The evaluation of debris flow impact force with time has been carried out considering a simplified relationship of a fluid-based model proposed by Gioffrè *et al.* (2017). The authors evaluate the impact force with time (F) by adding the static force (F_{stat}) to that dynamic (F_{dyn}). Particularly, F_{stat} and F_{dyn} are respectively calculated as follows:

$$F_{stat}(t) = \frac{1}{2}\gamma K_p S_{stat}^2 w \tag{1}$$

$$F_{dyn}(t) = k\rho v^2 S_{dyn} w \tag{2}$$

where γ is the soil unit weight, K_p is the passive earth pressure coefficient under critical state conditions, and S_{stat} is the static debris flow height, w is the width of storage area, k an empirical coefficient, ρ is the density of the flowing mass and v is the flow velocity, S_{dyn} is the current debris flow height.

Figure 1a shows the trend of debris flow height over the time characterized by a flowing mass that has a height of 1 m at t = 0, increases from t = 0 to t = 18 s with a linear increment and then it increases at t = 18 s. A linear increment of debris flow height has been assumed from 18 s to 30 s when debris flow is over and a debris flow height of 3 m is deposited.

Figure 1b shows the assumed trend of debris flow velocity that is characterized by two peaks of velocity at t = 0 s and t = 18 s respectively equal to 10 m/s and 6 m/s.

The total force (Figure 1) is given by the sum of the two components F_{stat} and F_{dyn} that have been calculated by equations 1 and 2 and considering the trends of debris flow height
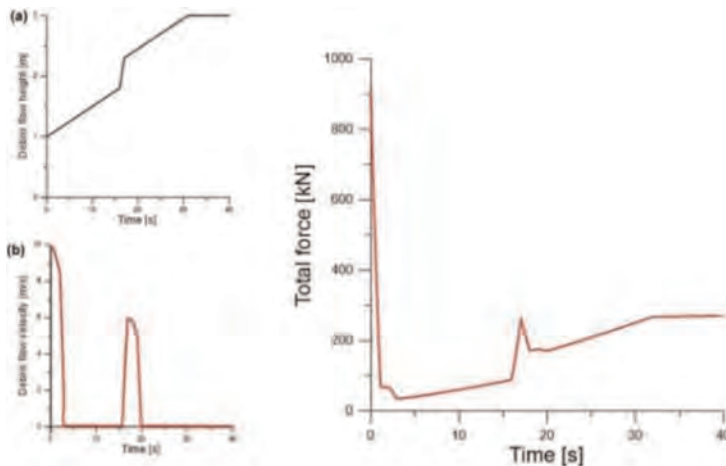
Figure 1.   Debris flow height and velocity trends and total impact force.

and velocity discussed above. The total force shows two peaks of 917 kN and 262 kN respectively at t = 0 s and t = 18 s.

Considering the trend of total impact force so obtained, the points of application of this force over the time on the structure have been evaluated assuming the scheme of accumulation of material behind the earth reinforced embankment without obstacle overtopping shown in Figure 2.

The dynamic component of the total force was assumed to have a rectangular stress distribution and was located at different points in different impact times (t_0 = first impact, t = impact at generic time and t_f = final condition), at t_f the contribution of the dynamic component is equal to 0 (Figure 2).

The static component of the total force was assumed to have a triangular stress distribution that is clearly equal to 0 at t = 0 and gradually increases as the amount of material accumulates beyond the obstacle reaching 3 m (the highest assumed value) at t_f when all material is accumulated (Figure 2).
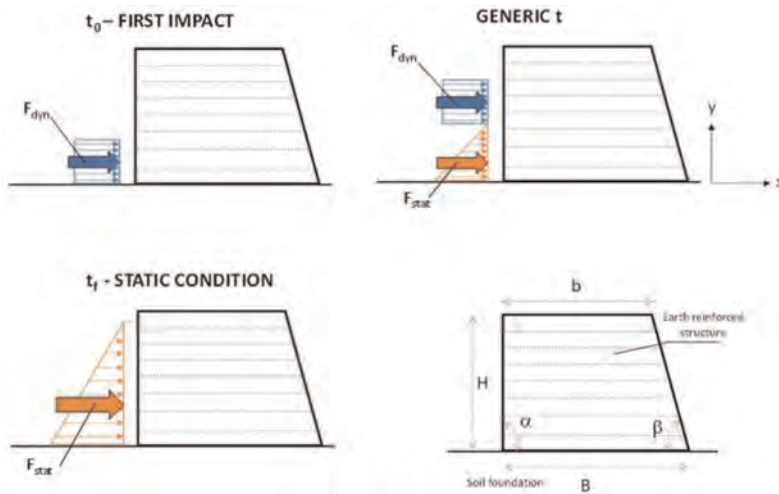
Figure 2. Scheme of static and dynamic force distributions behind the earth reinforced structure.

To evaluate the response of the earth reinforced structure, a typical shape has been considered. Particularly, the structure has a prismatic geometry, the height (H) is equal to 5 m, the top (b) is 6 m large and the base (B) is 8.5 m large, the upstream side slope is 90° (α) and the valley side slope is 63° (β).

The soil that constitutes the earth reinforced structure is a gravel with sand and the geogrid used is a HDPE extruded geogrid with a tensile modulus about equal to 1200 kPa wrapped around the face with 0.50 m vertically spacing.

The characteristics of soil and geogrid are summarised in Tables 1 and 2. Two different cases have been considered (Figure 3) regarding the soil – geogrid interaction, the first one considers a constant soil shear strength angle along the height of embankment (C1 – Table 1) the second one considers the variation of soil shear strength angle along the height (multilayers configuration) (C2 – Table 2). The soil – geogrid interaction has been taken into account in terms of apparent interface coefficient of friction (μ) according to Moraci et al. (2014) and the related assumptions of two cases are reported in Tables 1 and 2. The soil initial shear modulus G_0 has been assumed equal to 280 kN/m^2.

Where γ is the unit weight of soil; c' is the cohesion; φ is the friction angle; ν is the Poisson coefficient; and μ is the apparent interface coefficient of friction.

It is worth to nothing that in C1, only a value of shear strength angle φ and consequently only a value of apparent interface coefficient of friction μ has been considered. In the case

Table 1. Characteristics of soil and geogrid for case C1.

Depth [m]	γ [kN/m^3]	c' [kN/m^2]	φ [°]	v [-]	μ
0–1.25	21	0	48	0.3	0.9
1.25–2.50	21	0	48	0.3	0.9
2.50–3.25	21	0	48	0.3	0.9
3.25–5.00	21	0	48	0.3	0.9

Table 2. Characteristics of soil and geogrid for case C2.

Depth [m]	γ [kN/m^3]	c' [kN/m^2]	φ [°]	v [-]	μ
0–1.25	21	0	52	0.3	1.2
1.25–2.50	21	0	50	0.3	1.0
2.50–3.25	21	0	47	0.3	0.9
3.25–5.00	21	0	44	0.3	0.7
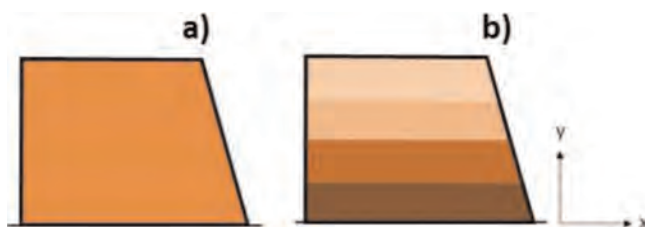
Figure 3. Schematization of the two cases. a) C1 case (Table 1), b) C2 case (Table 2).

C2, different values of shear strength angle φ and so several apparent interface coefficients of friction μ, from the top to the bottom of the structure, have been considered.

The deformative response of the considered earth reinforced structure in C1 and C2 cases has been analyzed by 2D FEM analysis using RS2 – Geoscience (2022).

3 ANALYSES AND RESULTS

The earth reinforced structure has been discretized by triangular elements of about 0.25 m which thicken around geosynthetics and the upstream face (Figure 4).

The FEM analyses have been performed considering drained conditions, a linear elastic-perfectly plastic behavior of the soil and the soil strength parameters and G_0 values reported in Tables 1 and 2. Geogrids have been modelled by means of linear elastic and isotropic elements considering one value or several values of μ depending on the modelled cases as reported in Tables 1 and 2.

FEM results are drawn in terms of horizontal displacements (Figure 5). Figure 5 shows that the maximum horizontal displacement occurs in the downstream top of the structure independently on the analyzed case (one layer – C1; multilayers – C2) and it is equal to $1.3 \cdot 10^{-1}$ m for C1 configuration and $1.8 \cdot 10^{-1}$ m for C2 configuration.

In both cases, the earth reinforced structure slides over the base soil. Particularly, for C1 configuration, the entity of sliding over the base soil assumes values going from 0.093 m (upstream point) to 0.079 m (downstream point) with an average value of 0.088 m. For C2 configuration, the sliding over the base soil assumes values ranging from 0.14 m to 0.11 m (from upstream to downstream points) with an average value of 0.12 m.
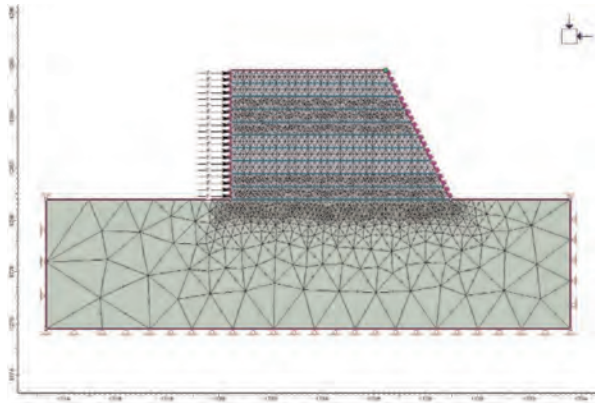
Figure 4.   FEM model.
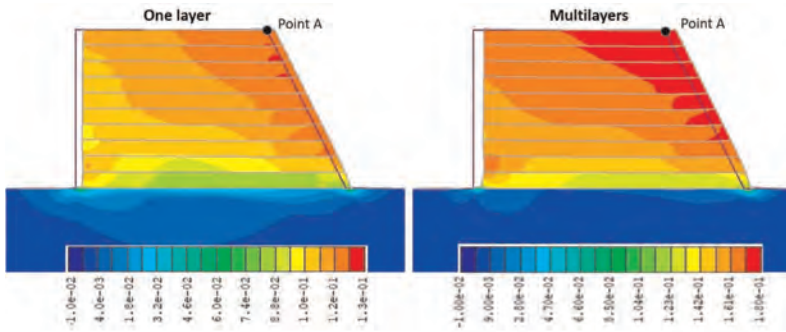
Figure 5.   Horizontal displacements and the control point (point A) used to compare the horizontal displacement vs time.

The maximum horizontal displacement versus time at control point A (located in the downstream top of embankments - Figure 5) for C1 and C2 configurations is shown in Figure 6.
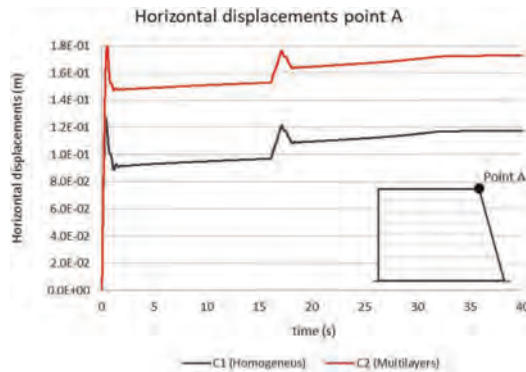
Figure 6.   Point A horizontal displacements vs time.

It worth nothing that, in both cases the trend is characterized by two peaks. The first one appears immediately after the first impact when an instantaneous increase of horizontal displacement has been recorded. The second peak has been recorded around t = 18 s according to second impulse that impacts the earth reinforced structure.

The highest horizontal displacements occur in the C2 configuration that is when the variation of shear strength angle along the depth has been considered (multilayers configuration) (red line in Figure 6).

4 CONCLUSIONS

The obtained results showed that not considering the effect of the variation of soil shear strength angle along the height of an earth reinforced embankment leads to underestimations of horizontal displacements of the structure. So, the design of these structures considering constant the interaction parameter for the overall reinforced soil structure is not precautionary. The knowledge of soil-reinforcement interaction parameters and their evolution over time, that depend on the interface conditions is very important in the design of geo-synthetics reinforced structures. Further investigations are in progress to study in-depth these results assuming values of shear modulus function of applied vertical effective stress, using different soils and geogrids.

REFERENCES

Arattano, M. & Franzi, L. 2003. On the Evaluation of Debris Flows Dynamics by Means of Mathematical Models. *Nat Hazards Earth Syst Sci* 3(6):539–544.

Armanini, A. 1997. *On the Dynamic Impact of Debris Flows*. In: *Recent Developments on Debris Flows*. Springer, Berlin, 208–226.

Calvetti, F., di Prisco, C.G., Vairaktaris, E. 2017. DEM Assessment of Impact Forces of Dry Granular Masses on Rigid Structures. *Acta Geotech.* 12:129–144.

Ciurleo, M., Mandaglio, M.C., Moraci, N. 2019. Landslide Susceptibility Assessment by TRIGRS in a Frequently Affected Shallow Instability Area. *Landslides* 16:175–188.

Ciurleo, M., Mandaglio, M.C., Moraci, N. 2021. A Quantitative Approach for Debris Flow Inception and Propagation Analysis in the Lead up to Risk Management. *Landslides* 18: 2073–2093.

Ciurleo, M., Ferlisi, S., Foresta, V., Mandaglio, M:C., Moraci, N. 2022. Landslide Susceptibility Analysis by Applying TRIGRS to a Reliable Geotechnical Slope Model. *Geosciences* 2022, 12, 18. https:// doi.org/ 10.3390/geosciences12010018

Gioffrè, D., Mandaglio, M.C., di Prisco, C., Moraci, N. 2017. Evaluation of Rapid Landslide Impact Forces Against Sheltering Structures. *Italian Geotechnical Journal* 51(3): 64–76.

Moraci, N., Cardile, G., Gioffrè, D., Mandaglio, M.C., Calvarano, L.S., Carbone, L. 2014. Soil Geosynthetic Interaction: Design Parameters From Experimental and Theoretical Analysis. *Transportation Infrastructure Geotechnology* 1(2):165–227, DOI:10.1007/s40515-014-0007-2, Ed. Springer. Online ISSN 2196-7210. Scopus Index= 2-s2.0-85012816482

RS2 Manual 2022 *Documentation and Theory Overview*. Rocscience www.rocscience.com

Suda, J., Hübl, J., Bergmeister, K. 2010. Design and Construction of High Stressed Concrete Structures as Protection Works for Torrent Control in the Austrian Alps. In: Proceedings of the 3rd international FIB congress, Washington, DC.

Short-term thermo-mechanical numerical modelling of reinforced soil walls with polyester strap reinforcements

A. Moncada & S. Olivella
Department of Civil and Environmental Engineering, Universitat Politècnica de Catalunya·BarcelonaTech (UPC), and International Centre for Numerical Methods in Engineering (CIMNE), Barcelona, Spain

I.P. Damians
Department of Civil and Environmental Engineering, Universitat Politècnica de Catalunya·BarcelonaTech (UPC), International Centre for Numerical Methods in Engineering (CIMNE), and VSL International, Barcelona, Spain

R.J. Bathurst
Royal Military College of Canada, Kingston, Ontario, Canada

ABSTRACT: Polyester (PET) materials have become more common as reinforcement solution in reinforced soil walls (RSW). It has been shown that strength and stiffness of geosynthetics products, including PET, is load-, time-, and temperature-dependent. Consequently, the mechanical response of these materials is influenced by in-soil conditions. The present study describes visco-elastic and visco-plastic constitutive formulations used to model PET strap reinforcement layers in thermo-mechanical finite element models. The models are demonstrated using an idealized 15-meter high RSW with concrete facing panels, including loading due to a road at the top of the structure. Reinforcement model parameters were calibrated using laboratory measured data. Analyses include temperature boundary conditions representing a Mediterranean climate for a 1-year period following end of construction. Calculated stress and strain values were in accordance with values found in the literature. The results of this study are a precursor for the long-term modelling of RSWs under operational conditions subjected to changing atmospheric boundary conditions.

1 INTRODUCTION

Numerical models are being routinely used to predict the behaviour of reinforced soil walls (RSWs) constructed with metallic or geosynthetic reinforcements (e.g., Damians *et al.* 2014; Huang *et al.* 2009; Yu *et al.* 2015, among others). Usually, reinforcement elements are modelled using a single stiffness value. In the case of extensible polymeric reinforcement (Miyata *et al.* 2018), such as polyester (PET), stiffness has proven to be load-, time- and temperature-dependent. Consequently, great care must be taken when choosing a unique stiffness value. Common practice in both numerical and analytical solutions is to obtain a stiffness modulus corresponding to (say) 2% strain and 1000 hours (Allen & Bathurst 2019). This value can be obtained from isochronous stiffness curves based on laboratory measured creep curves as described by Bathurst & Naftchali (2021).

Numerical models typically consider only the in-isolation mechanical behaviour of polymeric reinforcement materials and disregard the effect of hydraulic and thermal in-soil conditions on the mechanical performance of these materials. Temperature dependency implies that under different in-soil conditions, long-term mechanical behaviour of a polymeric reinforcement can vary.

The present work describes visco-elastic and visco-plastic constitutive formulations with temperature and water saturation dependencies used to model PET strap reinforcement

materials. Model parameters were first calibrated using measured creep master curves, followed by a generalization of parameter values using simple power functions. A 2D thermo-mechanical RSW numerical model was used to predict, as a first approach, the short-term behaviour of the structure when subjected to operational (in-service) loading conditions and varying temperature atmospheric conditions. Numerical simulations were carried out using the finite element program CODE_BRIGHT (CODE_BRIGHT 2021; Olivella *et al.* 1996)

2 NUMERICAL MODELLING

2.1 *PET strap reinforcement modelling*

Short-term mechanical behaviour of PET strap reinforcement materials can be approximated using a linear-elastic model. However, because these materials are temperature and moisture dependent, the long-term behaviour requires more complex formulations. The long-term rate of deformation ($d\varepsilon/dt$), or creep, was modelled with a visco-elastic (VE) constitutive model (Eq. 1), and a visco-plastic (VP) constitutive model (Eqs. 2–4).

$$d\varepsilon^{VE}/dt = \left[1/\left(2B(T)\sqrt{S_l}\right)\right](\sigma' - p'I) \tag{1}$$

$$d\varepsilon^{VP}/dt = [\Gamma_0 \exp(-Q/RT)]\langle\Phi(F)\rangle \quad \partial G/\partial\sigma' \tag{2}$$

$$F = \alpha(\eta^*)p' + \left[\cos(\theta) - \alpha(\eta^*)\sin\theta/\sqrt{3}\right]\sqrt{J_2} - \alpha(\eta^*)\delta(\eta^*) \tag{3}$$

$$G = \cos(\theta)\sqrt{J_2} \tag{4}$$

For the VE model, σ' is effective stress, p' is mean stress, I is the identity matrix, S_l is degree of saturation, and B(T) is the elastic fluidity as a function of temperature (T), the universal gas constant (R), and activation energy (Q). In the case of the VP model, Γ_0 is a reference plastic fluidity, F is a function of mean stress (p'), a frictional parameter (δ), a adhesion parameter (α), the lode angle (θ), and the second invariant of the deviatoric stress (J_2), and G is a function of θ and J_2. Parameters δ and α are controlled by a hardening parameter (η^*).

Numerical results were compared with laboratory data reported by Hang-Won & Je-Goo (2020) for different PET strap reinforcement products manufactured by a single manufacturer. Parameters were first calibrated using measured creep master curves constructed from the step isothermal method (ASTM D6992-03 2003) together with simplified 2D axial load model of a single PET strap. Samples were subjected to constant loads ranging from 66% to 80% of the ultimate tensile strength (UTS) for specimen (and grades) rated at 34.2 (i.e., grade 30), 52.9 (grade 50), and 78.2 (grade 70) kN/strap. From the calibration outcomes, simple power functions were used to estimate parameter values and model reinforcement behaviour when subjected to low magnitude axial tensile loads anticipated for PET strap RSWs under operational conditions. Power functions were based on reinforcement grade (UTS) for parameters E, δ, and α, while parameters B and Γ_0 considered reinforcement grade and applied load (as a percentage of UTS). Table 1 shows the range of parameter values depending on reinforcement grade and load conditions using the power functions.

Figure 1 shows the fitted power functions value for elastic modulus E (Figure 1a) and fluidity Γ_o (Figure 1b). E values for each grade are in agreement with those obtained by Allen & Bathurst (2019) and Bathurst & Naftchali (2021) for PET strap reinforcement products after the proper unit conversion (i.e., MPa to kN/strap, considering the proposed geometry). Figure 1c compares the axial strain of measured creep master curves with model (predicted) creep master curves for the grade 50 PET strap reinforcement using the power functions. Results show small discrepancies between measured and modeled results. Axial strain values are underestimated at an earlier stage and present better agreement at a later stage. Parameters were extrapolated for lower axial load conditions to obtain a wide array creep master curves.

Table 1. PET strap reinforcement model parameters based on power law function.

Constitutive model	Parameter	PET strap reinforcement grade		
		Grade 30	Grade 50	Grade 70
Linear-elastic (LE)	Elastic modulus, E [MPa]	211	356	567
	Poisson's ratio, ν [-]	0.2	0.2	0.2
Visco-elastic (VE)	Fluidity, B [$s^{-1}MPa^{-1}$]*	2.70×10^{-43} to 1.60×10^{-13}	1.39×10^{-56} to 3.36×10^{-12}	4.43×10^{-46} to 3.02×10^{-13}
Visco-plastic (VP)	Fluidity, Γ_0 [$s^{-1}MPa^{-m}$]**	1.83×10^{-15} to 2.48×10^{9}	6.24×10^{-14} to 3.89×10^{8}	1.22×10^{-23} to 1.51×10^{8}
	Activation energy, Q [$Jmol^{-1}$]	1.0×10^{5}	1.0×10^{5}	1.0×10^{5}
	Peak and residual parameters for adhesion, α_{peak} and α_{res} [MPa]	2 and 6.8	4.2 and 13.5	6.7 and 21.3
	Peak and residual parameters for friction, δ_{peak} and δ_{res} [°]	0.1 and 1.0	0.1 and 1.0	0.1 and 1.0

*Range of values for a reference temperature of 20°C and loads of 10% to 82% of UTS.
**Range of values corresponding to loads of 10% to 82% of UTS load.

Based on the available experimental data, extrapolating fluidity values using a power law function, values decrease as load decreases, reaching almost zero values, meaning that close to no creep should be expected for lower loads, even after extended periods of time.

Using modelled and measured creep master curves, isochronous stress-strain curves were calculated for 30 and 60 days, and 1, 10, 60, 100, and 120 years. Figure 2 shows isochronous curves for a grade 30 PET strap reinforcement. For loads over 66% of UTS, modelled isochronous curves present an adequate adjustment to laboratory obtained curves for 30- and 60-days, while strains are underestimated for longer periods of time. Measured and modelled isochronous curves did not present any suitable relation from 0 to 60% of UTS. As no measured data was available for loads under 66%, experimental data was approximated by a linear function with respect to the origin. In the case of modelled isochronous curves, extrapolating fluidity values using a power law function results in almost zero values at low loads, meaning that negligible creep can be expected at low load levels.
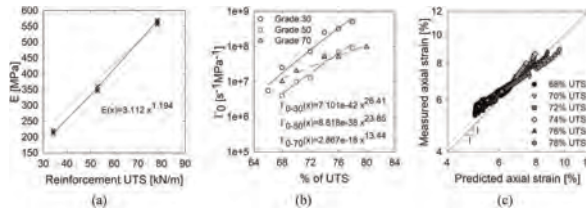
Figure 1. Model parameters for (a) elastic modulus E, (b) fluidity Γ_0, and (c) predicted/measured axial strains comparison.

2.2 RSW numerical model

An idealized 2D, 15-meter-high RSW with PET strap reinforcement layers and concrete facing panels was modelled. A thermo-mechanical (TM) formulation was used. Boundary conditions consisting of daily in-air temperature measurements of a Mediterranean climate (Barcelona, Spain) taken from a weather database (WeatherOnline Ltd.), were applied at all surface boundaries. The dataset mean annual temperature was 17°C. Model geometry includes all relevant structural components, such as the levelling pad at the base of the structure, discrete concrete facing panels, bearing pads between panels, toe front embedment, and equivalent PET strap reinforcement layers (Figure 3). A two-lane road, including a concrete safety barrier was included at the top of the structure. Based on the work of Damians et al. (2022), equivalent continuum interface elements were considered between the reinforced soil and facing elements as
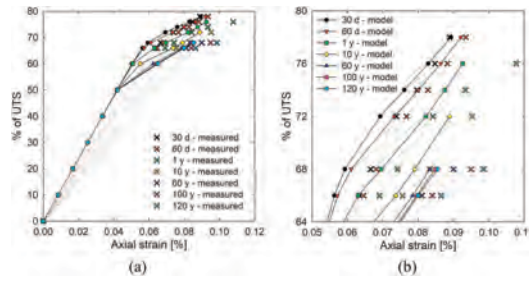
Figure 2.   (a) Measured and predicted stress-strain isochronous curves for grade 30 PET strap reinforcements, and (b) detail for 64% to 80% of UTS curves for 30 and 60 days (d) and 1, 10, 60, 100, and 120 years (y).

well as between soil and reinforcement layer elements. Strength reduction factors of 0.6 and 0.52 were considered for the soil-facing and soil-reinforcement interfaces, respectively.

The soil materials were modelled using a Mohr-Coulomb constitutive model with dilatancy. Parameter values are shown in Table 2 based on the work of Yu *et al.* (2015) and Damians *et al.* (2021), considering plane strain conditions with an equivalent width of 1 m. For numerical stability purposes a small amount of cohesion was considered for all soil materials. The soil within 1 m of the vertical facing was assigned reduced stiffness to account for poorer compaction that is often observed during construction of these types of structures.
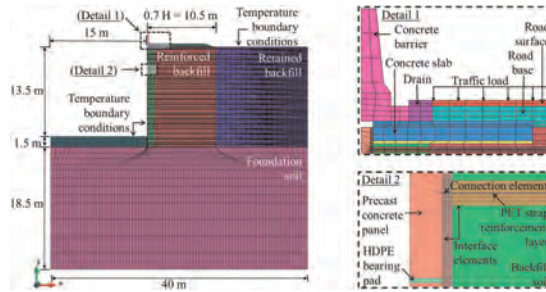
Figure 3.   RSW 2D model domain and finite element mesh geometry detail.

Table 2.   Parameters for mechanical properties of soil materials.

Parameter	Reinforced soil (<1 m)	Reinforced soil (>1 m)	Retained soil	Foundation	Soil-facing interface	Soil-reinforcement interface
Unit weight, γ_n [kN/m³]	19	19	19	19	19	19
Young modulus, E [MPa]	10	20	20	100	4.02	10.20
Poisson's ratio, ν [-]	0.3	0.3	0.3	0.3	0.45	0.45
Cohesion, c [kPa]	1	1	1	5	0.6	1
Friction angle, ϕ [°]	44	44	44	36	30.1	26.6
Dilatancy angle, ψ [°]	14	14	14	6	0	14

Concrete elements used a linear elastic model with E = 32 GPa and $\nu = 0.3$. The road base properties were the same as the reinforced soil (>1 m). The road surface was considered as concrete.

Modelled PET strap reinforcement layers have a coverage ratio of 0.142 (two connections every 2.5 m of wall face in the running length of the wall, two straps per connection, 89 mm-wide straps) including eight grade 30 layers, two grade 50 layers and ten grade 70 layers, from top to bottom of the wall.

Each incremental vertical panel was constructed separately, followed by a 1.5 m-thick soil layer zone, including reinforcement layers, every 10 days. A transient compaction surcharge of

10 kPa was applied over every soil layer during construction to simulate the influence of compaction equipment (see Hatami & Bathurst 2005). The front toe embedment was constructed once the structure achieved a height of 4.5 meters (total of three panels). After construction, a constant vertical pressure of 15 kPa was applied over the road surface for one year.

Thermal dispersion was modelled by Fick´s law, with a horizontal and vertical dispersivity of $d_l = 5$ m and $d_t = 0.5$ m, respectively. Thermal conductivity was modelled using Fourier´s law, with dry and saturated conductivity values of $\gamma_{dry} = 0.5$ W/mK and $\gamma_{sat} = 1$ W/mK for the soil and $\gamma_{dry} = 0.88$ W/mK and $\gamma_{sat} = 1.41$ W/mK for the concrete materials. Solid phase specific heats (c_s) of 1000 $Jkg^{-1}K^{-1}$ and 900 $Jkg^{-1}K^{-1}$ were used for soil and concrete, respectively.

Figure 4a shows the axial tensile loads along the length of layers 5, 8, 11, and 15 (numbered from toe to top of the wall). Maximum loads are obtained near the connection elements. Tensile loads at the free end of each layer approach zero. Figure 4b shows the maximum axial strain and load in each reinforcement layer with respect to wall height. Model outcomes showed tensile loads of up to 8% of UTS. Maximum strains do not exceed 0.8%, which is in agreement with measured maximum reinforcement strain under operational conditions in monitored PET strap field walls (Miyata *et al.* 2018). Tensile loads and strains follow similar distributions, increasing with depth until the two bottom panels. Due to the influence of toe embedment, the lowest reinforcement layers generated attenuated tensile load and strain. Figure 4c shows the maximum load vector for each reinforcement layer, which present a downward direction, attributed to the relative movement of the reinforced backfill with respect to the facing elements. The result is an increased vertical load at the connection and facing elements (see Damians *et al.* 2013, 2016). Computed horizontal facing displacements were less than 5 cm.
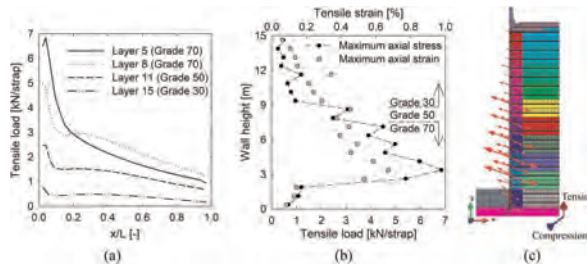
Figure 4. Numerical results after 1 year of service of (a) tensile load in reinforcement layers 5, 8, 11, and 15, (b) maximum tensile load and strain values for all reinforcement layers, and (c) principal stress (load) vector plots in the reinforced soil section.

3 CONCLUSIONS

The present study gives some details of the implementation of visco-elastic and visco-plastic constitutive formulations used to model PET straps reinforcements in an idealized 2D RSW thermo-mechanical finite element model. The constitutive models include temperature and saturation dependencies. Based on calibrations using quality control tensile test records of reinforcement specimens, model parameters were extrapolated to different load levels. The idealized RSW model includes temperature boundary conditions from daily registries of a Mediterranean climate database (Barcelona) and a service traffic load of 15 kPa. The main findings are as follows:

Stiffness values for the numerical model obtained based on laboratory results were in accordance with values in the literature.

Stress-strain isochronous curves were obtained from creep testing and simulated numerically. Long-term (over 1 year) model predictions tended to underestimate measured strain values. Short-term predictions presented an adequate adjustment with measured values over 60% UTS. A lack of data for loads under 60% of UTS resulted in extrapolated fluidity values close to zero, meaning that no creep behaviour will occur. Measured data was extrapolated with respect to the

origin for comparison purposes. For low load values, no suitable relationship between measured and model results was possible.

After 1 year of service, model results are in agreement with similar cases reported in the literature. Reinforcement strains increased with depth up until the four lower-most layers. Maximum reinforcement strains did not exceed 0.8% and axial tensile loads were less than 10% of UTS.

Further work is required in order to predict the long-term behaviour of PET-strap RSWs during service life, along with the influence of hydraulic dependencies in the numerical formulations.

ACKNOWLEDGEMENTS

REFERENCES

Allen, T.M., & Bathurst, R.J. 2019. Geosynthetic Reinforcement Stiffness Characterization for MSE Wall Design. *Geosynthetics International*, 26(6), 592–610.

ASTM D6992-03 2003. *Standard Test Method for Accelerated Tensile Creep and Creep-Rupture of Geosynthetic Materials Based on Time-Temperature Superposition Using the Stepped Isothermal Method.* ASTM International, West Conshohocken, PA, USA.

Bathurst, R.J., & Naftchali, F.M. 2021. Geosynthetic Reinforcement Stiffness for Analytical and Numerical Modelling of Reinforced Soil Structures. *Geotextiles and Geomembranes*, 49(4), 921–940.

CODE_BRIGHT User's Guide. 2021. Department of Civil and Environmental Engineering (DECA), Universitat Politècnica de Catalunya·BarcelonaTech (UPC), and International Center for Numerical Methods in Engineering (CIMNE). https://deca.upc.edu/en/projects/code_bright

Damians, I.P., Bathurst, R.J., Josa, A., Lloret, A., & Albuquerque, P.J.R. 2013. Vertical-facing Loads in Steel-reinforced Soil Walls. *Journal of Geotechnical and Geoenvironmental Engineering*, 139(9), 1419–1432.

Damians, I.P., Bathurst, R.J., Josa, A., & Lloret, A. 2014. Numerical Study of the Influence of Foundation Compressibility and Reinforcement Stiffness on the Behavior of Reinforced Soil Walls. *International Journal of Geotechnical Engineering*, 8(3), 247–259.

Damians, I.P., Bathurst, R.J., Lloret, A., & Josa, A. 2016. Vertical Facing Panel-joint Gap Analysis for Steel-reinforced Soil Walls. *International Journal of Geomechanics*, 16(4), 04015103.

Damians, I.P., Bathurst, R.J., Olivella, S., Lloret, A., & Josa, A. 2021. 3D Modelling of Strip Reinforced MSE Walls. *Acta Geotechnica*, 16(3), 711–730.

Damians, I.P., Olivella, S., Bathurst, R.J., Lloret, A., & Josa, A. 2022. Modeling Soil-facing Interface Interaction with Continuum Element Methodology. *Frontiers in Built Environment*, 8, 842495–1.

Hang-Won, C., & Je-Goo, J. 2020. *Reliability Assessment of Polymeric Straps (FASTEN FS E) for Soil Reinforcement.* M213-19-15189. GECO Industrial Co., Ltd. FITI Testing and Research Institute, Chungbuk, Korea.

Hatami, K., & Bathurst, R.J. 2005. Development and Verification of a Numerical Model for the Analysis of Geosynthetic-reinforced Soil Segmental Walls under Working Stress Conditions. *Canadian Geotechnical Journal*, 42(4), 1066–1085.

Huang, B., Bathurst, R.J., & Hatami, K., 2009. Numerical Study of Reinforced Soil Segmental Walls using three Different Constitutive Soil Models. *Journal of Geotechnical and Geoenvironmental Engineering* 135 (10), 1486–1498.

Miyata, Y., Bathurst, R.J., & Allen, T. M. 2018. Evaluation of Tensile Load Model Accuracy for PET Strap MSE Walls. *Geosynthetics International*, 25(6), 656–671.

Olivella S., Gens A., Carrera J., & Alonso, E. 1996. Numerical Formulation for a Simulator (CODE_BRIGHT) for the Coupled Analysis of Saline Media. *Engineering Computations*, 13(7), 87–112.

Yu, Y., Bathurst, R.J., & Miyata, Y. 2015. Numerical Analysis of a Mechanically Stabilized Earth Wall Reinforced with Steel Strips. *Soils and Foundations*, 55(3), 536–547.

WeatherOnline Ltd. Meteorological Services, viewed on March 2021, https://www.weatheronline.co.uk/

A study on monitoring technique of reinforced soil retaining walls using a single-camera system based on mask R-CNN

Y.S. Ha
Korea Institute of Ocean Science & Technology, Busan, Korea

M.V. Pham
Pukyong National University, Busan, Korea

Y.T. Kim*
Professor, Pukyong National University, Busan, Korea

ABSTRACT: Reinforced soil retaining wall (RSW) frequently collapses due to various causes such as drainage problems owing to heavy rainfall and increase in earth pressure owing to surface load. Therefore, we need technology that can continuously monitor the behavior of the retaining wall. In general, since a depth image between an image and an object cannot be extracted from an image taken from a monocular vision, it is not possible to accurately analyze the three-dimensional behavior of the real space. The behavior of the reinforced soil retaining wall is defined as facing displacement and settlement based on the collapse mechanism of the reinforced soil retaining wall. Mask R-CNN was applied to detect and track the RSW block before and after the behavior, and performances of matching and displacement calculation were evaluated. The errors were distributed in 2.12 mm in laboratory RSW experiment.

1 INSTRUCTION

1.1 *Background*

RSW which is widely used in the world were basically composed of block, geosynthetics, backfill material. Several direct sensors such as displacement sensor, tilt meter, strain gauge were installed to monitor safety of retaining wall, however, it causes lots of control fee, and it can only analyze around the sensors. Therefore, behavior of RSW, which is effected by conditions of geosynthetics and backfill, can be monitored with the movement of blocks. Vision-based technology has strength of low price and possibility of constant monitoring of RSW. The vision-based technologies are not only analyzing behavior but also directly monitoring a RSW in a far distance. The stereo camera system based on two or more cameras or takes images from various location of view. The proposed single camera system processes images from a monocular vision. Many researchers were studied to analyze displacement of slope, retaining wall, and bridge based on three dimensional coordinates with the stereo camera system (Esmaeili *et al.* 2013; Jiang & Jauregui 2010; Oats *et al.* 2017; Sun *et al.* 2022; Zhao *et al.* 2018). However, additional costs were inquired to maintain and process lots of cameras in a stereo camera system. The camera system based on monocular vision has been limitedly studied in analyzing a simple behavior that perpendicular with optical axis. The in-plane displacements were analyzed for the structures such as building, bridge, two-story steel frame, and masonry specimen. (Choi *et al.* 2011; Feng *et al.* 2015; Lee & Sinozuka 2006; Wang *et al.*

---

*Corresponding Author: yuntkim@pknu.ac.kr

DOI: 10.1201/9781003386889-118

2021). In this study, we pro-posed the single camera system that detect blocks and calculates displacement of RSW using mask R-CN with different type of RSW structure.

1.2 *Mask R-CNN*

Vision-based technologies have been gradually developed into image classification, object detection, semantic segmentation, and instance segmentation with the development of deep learning algorithms, Various studies have been conducted to analyze the location of a specific object in an image, such as fast R-CNN, faster R-CNN, sementic segmentation, and instance segmentation based on a convolution neural network (CNN). Mask R-CNN performs fully convolutional networks (FCN) based on the bounding box and classification information estimated by Faster R-CNN, a widely used object detection technique, and performs instance segmentation by estimating the mask without loss of location information. Figure 1 shows the mask R-CNN framework for instance segmentation. Decoupling via per-class binary masks (sigmoid) gives large gains over multinomial masks (softmax). Based on subcell and bilinear interpolation, ROI alignment was used to increase the accuracy compared to ROI pooling. FCNs improve results as they take advantage of explicitly encoding spatial layout than multi-layer perceptrons (MLP, fully-connected) for mask prediction (He *et al.* 2017). Through these various advantages, Mask R-CNN is being used in various fields. Xu *et al.* (2022) conducted comparison study based on faster R-CNN and Mask R-CNN, Performances were compare with different learning rate and figure out optimal learning rare for each case. Tiede *et al.* (2021) made a dwelling map with different type of roof based on mask R-CNN. Jeong *et al.* (2020) utilized the 3D Mask R-CNN approach to localize and segment the high- and low-grade brain tumors from dynamic MRI perfusion images. Wang *et al.* (2020) detected open-pit mines based on improved mask R-CNN and transfer learning. Wang *et al.* (2022) conducted Rural Building roof type recognition from UAV high-resolution Images. Tian *et al.* (2020) suggest road marking detection method based on mask R-CNN Instance Segmentation Model. Mask R-CNN is being used in various fields based on the advantage of being able to detect the exact location of a target based on high-accuracy mask and segmentation information. Therefore, in this study, it is used to detect individual facings of RSW where multiple objects exist in order to detect blocks that are difficult to detect due to changes in conditions during RSW monitoring.
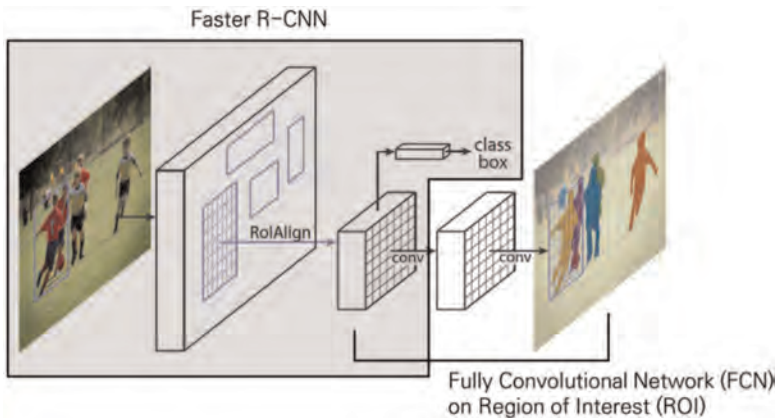
Figure 1.   Mask R-CNN framework for instance segmentation (modified from He *et al.* 2017).

2   EXPERIMENT

2.1 *Laboratory RSW experiment*

The laboratory RSW experiment was performed to evaluate the performance of matching and displacement calculation under controlled conditions in a laboratory. Figure 2 shows an

experimental setup of RSW (650 mm x 270 mm) consisting of 121 blocks. the reference displacements were measured from a total station (Sokkia 510k). The camera was installed with an incident angle of 43 degrees, and distance of 1267 mm. cumulative displacement such as facing displacement and settlement were alternately occurred and analyzed.
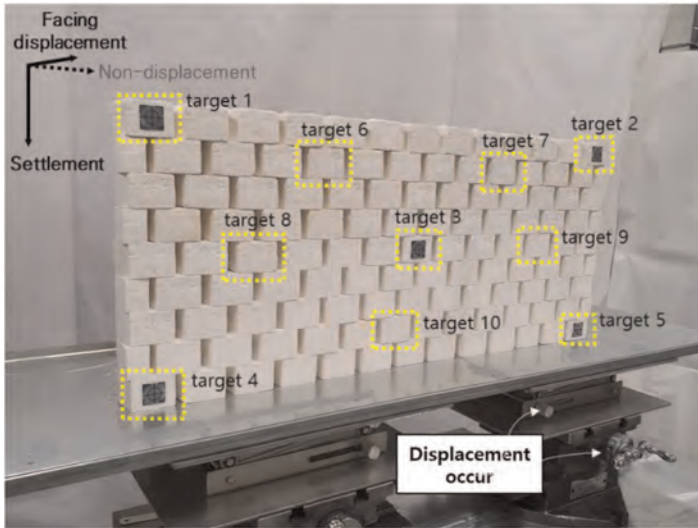
Figure 2. Experimental setup and equally distributed targets in RSW.

3 EXPERIMENTAL RESULT

3.1 *Detection and displacement calculation of block*

Figure 3 shows an example of the blocks trained and detected for the laboratory RSW experiment. 9 images were used for validation, and 2 images are shown in the figure. Each column represents the original image, ground truth, and predicted mask. Table 1 shows the
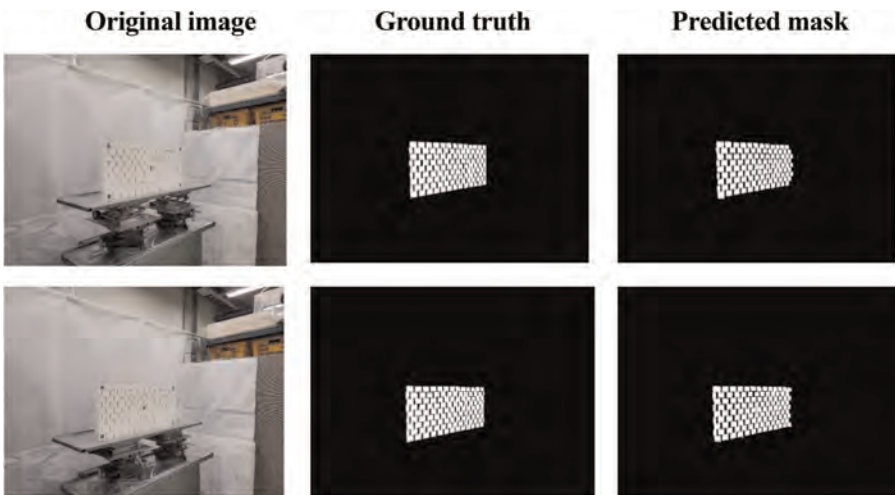
Figure 3. Detection results of mask R-CNN for laboratory RSW experiment.

Table 1. Evaluation result of the trained mask R-CNN for laboratory RSW.

	TP	FP	FN	TN	Precision	Recall	F1_score
1	507,140	24,217	63,126	11,598,285	0.9544	0.8893	0.9207
2	492,566	28,780	53,883	11,617,539	0.9448	0.9014	0.9226
3	98,036	11,950	4,598	79,636	0.8913	0.9552	0.9222
4	99,596	8,014	6,027	45,213	0.9255	0.9429	0.9342
5	92,930	8,129	20,811	211,706	0.9196	0.8170	0.8653
6	74,476	4,085	3,399	75,480	0.9480	0.9564	0.9522
7	27,110	3,242	1,443	22,689	0.8932	0.9495	0.9205
8	33,391	3,603	1,449	42,137	0.9026	0.9584	0.9297
9	47,923	3,832	2,203	207,895	0.9260	0.9561	0.9408
Average					0.9226	0.9187	0.9196
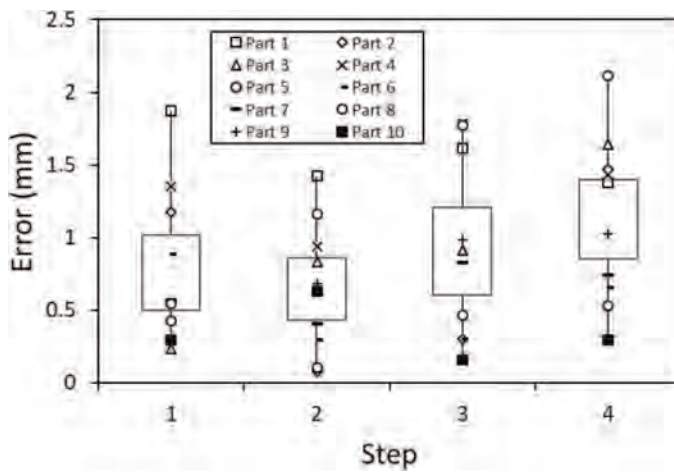
Figure 4. Results of displacement calculation error for laboratory experiment.

precision, recall, and f1 scores for 9 images used for validation. Although blocks could not be detected for some sections for each image, laboratory RSW blocks were detected with precision of 92.28%, recall of 92.51%, and f1 score of 92.31%. Figure 4 shows the results of calculating the behavior based on the detected blocks. In case of using mask R-CNN, since transformation by behavior is not considered, the error does not increase significantly for each behavior step. In addition, the overall performance is excellent with an error within 2.12mm.

4 CONCLUSION

The result based on mask R-CNN showed high performance of detection. However, these results were trained and validated only for laboratory RSW blocks, we need to train and validate for various types of RSW blocks considering the conditions of fields. Regarding displacement calculation performance, the average MREs were 1.39 % in the laboratory RSW experiment, indicating an excellent displacement calculation performance. Based on this result, if more types and behaviors of RSW were considered, the proposed single-camera system can be improved to monitor the behavior of the RSW.

ACKNOWLEDGEMENT

REFERENCES

Choi, H.S.; Cheung, J.H.; Kim, S.H. & Ahn, J.H. 2011. Structural Dynamic Displacement Vision System Using Digital Image Processing, *NDT & E Int.*, 44, 597–608.

Esmaeili, F.; Varshosaz, M. & Ebadi, H. 2013. Displacement Measurement of the Soil Nail Walls by using Close Range Photogrammetry and Introduction of CPDA Method, *Meas.*, 46, 3449–59.

Feng, D.; Feng, M.Q.; Ozer, E. & Fukuda, Y. 2015. A Vision-based Sensor for Noncontact Structural Displacement Measurement, *Sens.*, 15, 16557–75.

Fukuda, Y.; Feng, M.Q.; Narita, Y.S.; Kaneko, I. & Tanaka, T. 2013. Vision-based Displacement Sensor for Monitoring Dynamic Response using Robust Object Search Algorithm, *IEEE Sens. J.*, 13, 4725–32.

He, K., Gkioxari, G., Dollár, P. & Girshick, R. 2017. Mask r-cnn. *In Proceedings of the IEEE International Conference on Computer Vision* (pp. 2961–2969).

Jeong, J., Lei, Y., Kahn, S., Liu, T., Curran, W. J., Shu, H. K., ... & Yang, X. 2020. Brain Tumor Segmentation using 3D Mask R-CNN for Dynamic Susceptibility Contrast Enhanced Perfusion Imaging. *Physics in Medicine & Biology*, 65(18), 185009.

Jiang, R. & Jauregui, D.V. 2010. Development of a Digital Close-range Photogrammetric Bridge Deflection Measurement System, *Meas.*, 43, 1431–38.

Lee, J.J. & Shinozuka, M. 2006. Real-time Displacement Measurement of a Flexible Bridge using Digital Image Processing Techniques, *Exp. Mech.*, 46, 105–14.

Oats, R.C. Escobar-Wolf, R.; Oommen, T. 2017. A Novel Application of Photogrammetry for Retaining Wall Assessment, *Infrastruct.*, 2, 10.

Sun, J.; Peng, B.; Wang, C.C.; Chen, K.; Zhong, B. & Wu, J. 2022. Building Displacement Measurement and Analysis based on UAV images, *Autom. Constr.*, 140, 104367.

Tian, J., Yuan, J., & Liu, H. 2020. Road Marking Detection Based on Mask R-CNN Instance Segmentation Model. *In 2020 International Conference on Computer Vision, Image and Deep Learning (CVIDL)* (pp. 246–249). IEEE.

Tiede, D., Schwendemann, G., Alobaidi, A., Wendt, L., & Lang, S. 2021. Mask R-CNN-based Building Extraction from VHR Satellite Data in Operational Humanitarian Action: An Example Related to Covid-19 Response in Khartoum, Sudan. *Transactions in GIS*, 25(3), 1213–1227.

Wang, C., Chang, L., Zhao, L., & Niu, R. 2020. Automatic Identification and Dynamic Monitoring of Open-pit Mines based on Improved Mask R-CNN and Transfer Learning. *Remote Sensing*, 12(21), 3474.

Wang, J.; Zhao, J.; Liu, Y. & Shan, J. 2021. Vision-based Displacement and Joint Rotation Tracking of Frame Structure Using Feature Mix with Single Consumer-grade Camera, *Struct. Control Health Monit.*, 28, e2832.

Wang, Y., Li, S., Teng, F., Lin, Y., Wang, M., & Cai, H. 2022. Improved Mask R-CNN for Rural Building Roof Type Recognition from Uav High-resolution Images: A Case Study in Hunan Province, China. *Remote Sensing*, 14(2), 265.

Xu, X., Zhao, M., Shi, P., Ren, R., He, X., Wei, X., & Yang, H. 2022. Crack Detection and Comparison Study Based on Faster R-CNN and Mask R-CNN. *Sensors*, 22(3), 1215.

Zhao, S.; Kang, F. & Li, J. 2018. Displacement Monitoring for Slope Stability Evaluation based on Binocular Vision Systems, *Optik*, 171, 658–71.

Influence of different parameters on back-to-back mechanically stabilized earth walls

Khashayar Malekmohammadi
Department of Civil Engineering, Arak Branch, Islamic Azad University, Arak, Iran
Department of Civil and Environmental Engineering, Universitat Politècnica de Catalunya·BarcelonaTech (UPC), Barcelona, Spain

Seyed Hamid Lajevardi*
Department of Civil Engineering, Arak Branch, Islamic Azad University, Arak, Iran

Daniel Dias
Laboratory 3SR, CNRS, Grenoble Alpes University, Grenoble, France
School of Automotive and Transportation Engineering, Hefei University of Technology, Hefei, China

ABSTRACT: Back-to-Back Mechanically Stabilized Earth (MSE) walls can sustain significant loadings and deformations due to the interaction mechanisms which occur between the backfill material and the reinforcement elements. These walls are commonly used in embankments approaching bridges, ramps and railways. The performance of a reinforced wall depends on numerous parameters, including the ones defining the soil, the reinforcement and the soil/reinforcement interaction behavior. The focus of this study is to investigate numerically the behavior of back-to-back mechanically stabilized earth walls considering synthetic and metallic strips. A two-dimensional finite difference numerical modeling is considered. The role of the soil friction angle, the Soil material quality and the wall width to the height ratio are investigated in a parametric study. Their effects on the soil/strip shear displacements and tensile forces on the reinforcements are presented. The behavior of the reinforcement strips in back-to-back reinforced walls strongly depends on the distance between walls and on the soil parameters.

1 INTRODUCTION

The soil resists well to compressive stresses but is less able to resist to shear strength solicitations. Therefore, tensile elements are often used to compensate this weakness. The concept of soil reinforcement was initially expressed by Vidal (1969). Reinforced soils are used in the construction of many geotechnical structures such as retaining walls, embankments, slopes and shallow foundations. The reinforced walls can be integrated in the category of flexible walls, which usually contain three elements an embankment generally made of granular soils, reinforcement elements which can be metallic or synthetic and the wall face usually made of concrete. Utilizing Back-to-back mechanically stabilized earth (MSE) walls are especially prevalent in raising elevation of bridges, ramps and railways. However, these walls are demanding regarding their design, since they require complex geometries like in the FHWA Demonstration Project 82 (Elias & Christopher 1997). In Figure 1, two cases are analyzed regarding the two

---

*Corresponding Author: sh-lajevardi@iau-arak.ac.ir
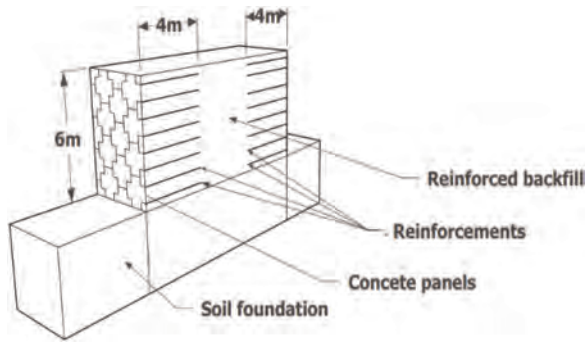
Figure 1. Schematic view of a back-to-back reinforced wall.

back-to-back walls distance. The walls can be designed independently if D (distance between the reinforcements from each other) is greater than H tan (45°-φ/2) where H is the wall height and φ is the backfill friction angle. The effect of the distance, D, between walls (width to height ratio) on the internal and external stability of MSE walls under static conditions was explored. Han & Leshchinsky (2010) conducted back-to-back walls investigations. They indicate that when the two back-to-back walls are far from each other, they perform independently. While, if they are close to each other, they interact with each other. When the ratio is less than one the two walls interact with each other and the earth pressure behind the wall decreases because the failure wedge behind the wall is not fully developed. Thus, the geosynthetic reinforcement tensile forces decrease with decreasing the spacing between walls (El-Sherbiny et al. 2013).

Previous researches on two back-to-back geosynthetic-reinforced soil walls revealed that these walls perform independently when they are far apart and interact with each other when they are close. The location and shape of the critical failure surface would be changed depending on their interaction. Moreover, the distance between the back-to-back walls would affect the maximum geosynthetic tension. Accordingly, the required maximum reinforcement tensile strength slightly decreases in the case of decreasing the distance of the two back-to-back walls (Djabri & Benmobarak 2016). An investigation on the spacing ratio between the two walls to the wall height (W/H) was done (Sasanka et al. 2019). Numerical analysis of the behavior of a reinforced wall using different types of synthetic and metallic strips showed that parameters like the soil friction, the shear interface and the elastic modulus of strips, have an effective role in the wall behavior (Abdelouhab et al. 2009). Numerical studies less considered back-to-back walls, especially when considering two types of reinforcements: Metallic Strips (rigid) and Geosynthetic Strips (flexible). In this article, a stability analysis of back-to-back reinforced walls is carried out using a two-dimensional finite difference code. A parametric analysis considering two types of reinforcements (metallic and synthetic), the effect of the soil friction angle and reinforcement elements distance on the wall displacements, soil/strip shear displacements and reinforcement tensile forces are investigated. In addition, it is shown that for the wall construction that involves static loading conditions, the modified Plastic Hardening model is a good compromise. A full description of this work can be found in the paper by Lajevardi et al. (2021).

2 STUDIED CASE

2.1 Geometry of the wall

The wall is 6 meters high. For both sides of the wall, a concrete face cruciform geometry divided in panels, with 16 reinforcement strips (metallic or synthetic) of 4 m length is used.

The concrete face panels allow to homogenize the displacements of such structures. Using the assumptions of Figure 2, it is possible to consider a 2D model which is representative of the 3D behavior of such structure (Abdelouhab *et al*. 2010). In each wall side, 4 concrete panels in the vertical direction of dimension 1.5 × 1.5 m, are used in the transverse direction. To simplify the model geometry, the three-dimensional shape is converted into a two-dimensional one. The cruciform parts of the concrete parts are then considered as square ones (dimensions of 1.5 × 1.5 m).
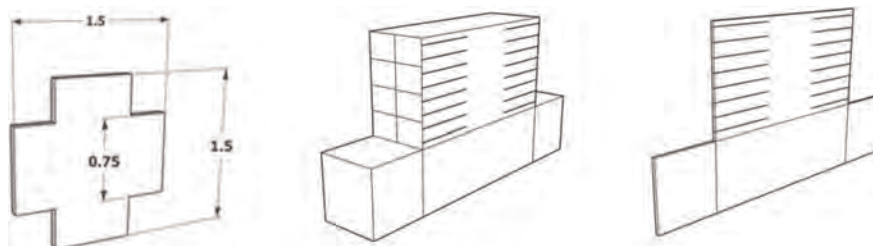
Figure 2.   Three-dimensional view of a back-to-back reinforced wall.

2.2   *Soils*

The system is composed of two types of soils: a reinforced backfill and the soil foundation. In this study, the reinforced backfill soil behavior is simulated by using the Plastic Hardening (PH) constitutive model (Schanz *et al*. 1999). This constitutive model is a shear and volumetric hardening model. The stress-strain relationship is hyperbolic, and a power-law describes the stress-dependent elastic stiffness. Moreover, a shear hardening, a volumetric hardening law and the Mohr-Coulomb failure criterion are included (Itasca Consulting Group 2017). The reinforced backfill soil's parameters for the PH constitutive model (Table 1) were deduced from triaxial tests (Abdelouhab *et al*. 2010).

Table 1.   Reinforced backfill PH input parameters.

Parameter	Value
Volumic weight (kN/m^3)	1580
E_{50} ref[1] (MPa)	50
E_{oed} ref[2] (MPa)	60
E_{ur}[3] (MPa)	145
Failure Ratio	0.7
Cohesion (kPa)	0
Dilatancy angle (°)	6
Friction angle (°)	36

[1]Secant stiffness at half of the ultimate deviatoric stress at the reference pressure; [2]Tangent stiffness in an oedometer test at the reference vertical stress; [3]Elastic unloading-reloading Young's modulus.

2.3   *Concrete face and foundation soil*

The foundation soil (concrete slab) is assumed to behave elastically to minimize the foundation influence on the reinforced soil behavior. The wall face is made up of concrete in the numerical model. This concrete face is simulated using beam structural elements. These elements are resistant to tensile and compressive stresses and to bending moments. They behave as a linear elastic material (Table 2).

Table 2. Parameters for the concrete and the foundation soil.

Parameter	E^1 (MPa)	v^2	Volumic weight (kN/m³) γ
Concrete panel	15000	0.2	2500
Soil foundation	200	0.25	2200

[1]Young modulus; [2] Poisson's ratio

2.4 Concrete panel/soil interface

To simulate the soil/structure interaction, an interface between the concrete panel and soil is defined. The interface elements parameters are related to the soil parameters. The interface shear strength (φ_{int}) is calculated by using a strength reduction factor (R_{int}) Equation 1:

$$tg\varphi_{int} = R_{int} \times tg\varphi_{int} \qquad (1)$$

The interface adhesion (C_{int}) was related to the backfill soil cohesion (C_{Soil}) Equation 2:

$$C_{int} = R_{int} \times C_{soil} \qquad (2)$$

A constant value of R_{int} = 2/3 was assumed (Yu *et al.* 2015). The shear stiffness, normal stiffness and friction angle of this interface are presented in Table 3.

Table 3. Characteristics of the concrete panel/soil interface.

Parameter	Normal stiffness (MPa)	Shear stiffness (MPa)	Interface friction Angle
Concrete panel/soil interface	1000	1000	24

2.5 Reinforcements

Two types of strips reinforcement: a metallic and synthetic strip reinforcement are considered (Lajevardi *et al.* 2021) (Table 4).

Table 4. Reinforcement's characteristics.

Reinforcement	Geosynthetic (GS HA)[1] strip	Metallic strip
Elastic modulus (GPa)	2.5	210
Width (m)	0.1	0.05
Thickness (mm)	3	4
Strip tensile yield-force limit (kN)	70	100
Tensile failure strain limit of the strip (%)	12	10

[1]New geosynthetic strips (GeoStrap High Adherence) used in MSE Walls

The strip structural element implemented in Flac2D is used in the following simulations for the two kind of strip reinforcements. This element has a tensile strength limit. The shear behavior of the soil/reinforcements interface is defined by a nonlinear shear failure envelope, which changes based on the confining pressure.

3 NUMERICAL MODELLING

3.1 *Parametric analysis*

In this section, the behavior of back-to-back walls considering two width to height (W/H) ratios for the two types of strips reinforcement is investigated. The wall height (H) and the reinforcement length (L) are fixed and are respectively equal to 6 and 4 meters. The horizontal distance between the reinforcements from each other (D), which is the variable parameter of this study, is determined by the proposed equation of the FHWA design guideline (FHWA 2007). In this study, the influence of the distance between the reinforcements in the horizontal direction is considered by using two cases. D equal to 0 which is a lower value than the proposed one of the FHWA design guideline and D equal to 10 m which is greater than the FHWA proposed value (Figure 3).
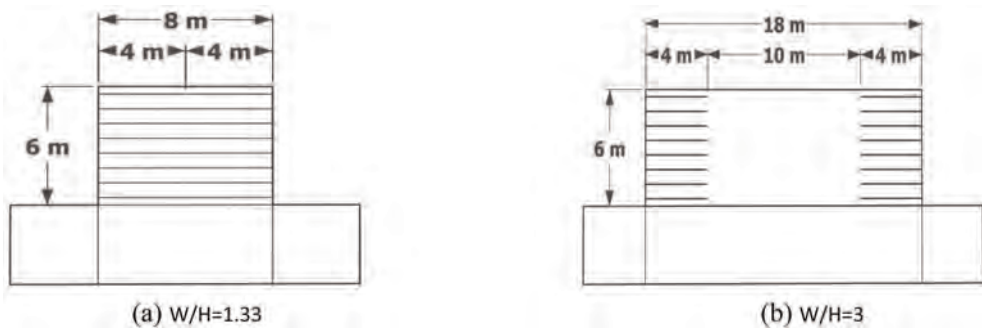
Figure 3.   Geometry of the back-to-back reinforced walls considering different ratios of width (W) to height (H).
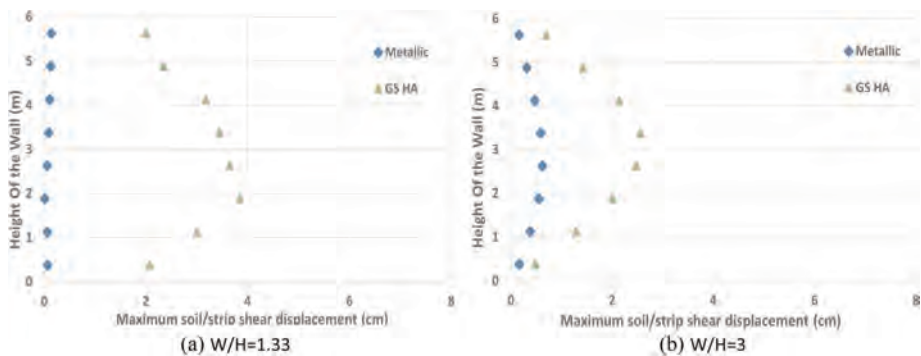
Figure 4.   Soil/strip shear displacements for two strip types and different W/H ratios.

3.1.1 *Influence of the width to height ratio (W/H)*

3.1.1.1 *Soil/strip shear displacements*

The soil/strip shear displacements for the two considered strips started to increase from the bottom of the wall (Figure 4). As the wall height increases, they decrease so that the greatest displacement occurs between the fourth and fifth strips and the lowest between the seventh and the eighth strips.

981

As the reinforcement strip distance (D) increase the values of the soil/strip shear displacements decrease. The distance between reinforcements and the soil/strip shear displacements are directly linked.

3.1.1.2 Tensile force

As shown in Figure 5, the maximum tensile forces occur at the first 2 m of the wall, and then decrease and reach the lowest value at the wall top. In addition the tensile forces on strips decrease with increasing the distance between reinforcements (D).
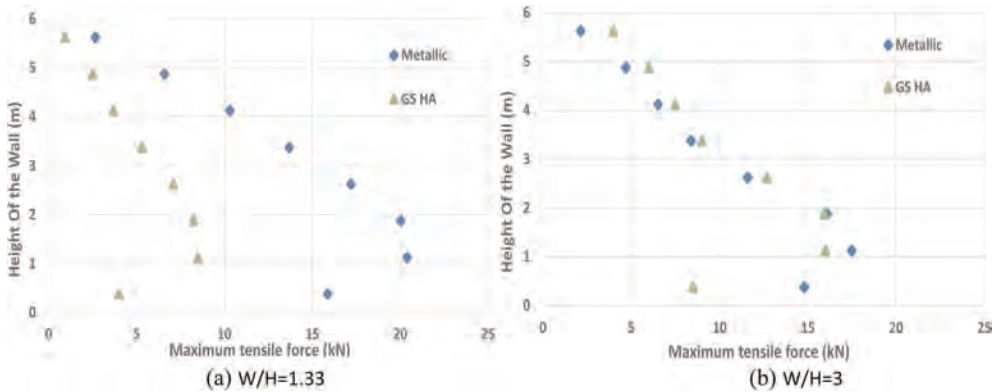
Figure 5.   Tensile force variations on the two strip types and different W/H ratios.

3.1.2 Influence of the friction angle (φ)

The results indicate that the friction angle has a significant influence on the displacement amplitude and on the safety factor of MSE Walls. The results showed that the decrease of the friction angle leads to a wall displacement increase. On the other hand, it leads to a safety factor reduction. The higher safety factor and the lower displacements were related to D = 0. While increasing the distance between strips (D) leads to reduce the safety factor and increases the displacements (Table 5).

Table 5.   Influence of the friction angle.

					% Decrease Fs		% Increase |U|	
Strip	W[1]/H[2]	φ (°)[3]	Fs[4]	|U|[5] (cm)	(36-30)	(30-25)	(36-30)	(30-25)
Metallic	3	36	1.7	1.38	21	19	31.3	35.8
		30	1.3	2.01				
		25	1.1	3.13				
	1.33	36	2.2	0.61	20.6	19	3.2	1.6
		30	1.7	0.63				
		25	1.4	0.64				

[1]width of the wall; [2]Height of the wall; [3]Soil friction angle (°); [4]Factor of safety; [5]Maximal displacement of the reinforced backfill.

4   CONCLUSION

The numerical results show that back-to-back walls with geosynthetic strips have more flexibility than with the metallic ones. This flexibility leads to higher soil/strip interface shear displacements. This is due to the lower rigidity of the geosynthetic strips.

The results of back-to-back reinforced soil walls considering different ratios of width to height indicate that this ratio is directly connected to the tensile forces and it is inversely related to soil/strip interface shear displacements

The results show that the soil friction angle has a significant effect on the behaviour of the back-to-back walls. As this friction angle decreases, the stability of the wall decreases, and the soil/strip shear displacements and the tensile forces on the reinforcement increases.

REFERENCES

Abdelouhab, A.; Dias, D.; Freitag, N. 2009. Physical and Analytical Modelling of Geosynthetic Strip Pullout Behaviour. *Geotextiles and Geomembranes*, 28 (1), 44–53.

Abdelouhab, A.; Dias, D.; Freitag, N. Numerical Analysis of the Behaviour of Mechancally Stabilized Earth Walls Reinforced with Different Types of Strips. 2010. *Geotextiles and Geomembranes*, 29, 116–129

Djabri, M.; Benmebarek, S. 2016. FEM Analysis of Back-to-Back Geosynthetic-Reinforced Soil Retaining Walls. *International Journal of Geosynthetics and Ground Engineering*, 2: 26.

Elias, V.; Christopher, B. R. 1997. *Mechanically Stabilized Earth Walls and Reinforced Soil Slopes Design and Construction Guidelines*, Publication No. FHWA-SA-96–071.

El-Sherbiny, Ibrahim. E.; Salem, A. 2013. Stability of Back-to-Back Mechanically Stabilized Earth Walls. *Proceedings of Geo-congress*. San Diego, California, USA: March, 555–565.

Federal Highway Adinistration. 2009, Design of Mechanically Stabilized Earth Walls and Reinforced Soil Slopes and reinforced soil slope Volume 1, Publication No. FHWA-NHI-10-024.

Han, j.; Leshchinsky, D. Analysis of Back-to-back Mechanically Stabilized Earth Walls. 2010. *Geotextiles and Geomembranes*, 28, 262–267

Itasca Consulting Group.FLAC2D. User's guide, 2017.

Lajevardi, S.H.; Malekmohammadi, K.; Dias, D. 2021. Numerical Study of the Behavior of Back-to-Back Mechanically Stabilized EarthWalls. *Geotechnics*, 1, 18–37.

Sasanka, M. S.; Umashankar, B.; Madhira, R. M. 2019. Reinforcement Tensile Forces in Back-to-Back Retaining Walls. *Geotechnical Applications*, 173–181.

Schanz, T.; Vermeer, P. A.; Bonnie, P. G. R. 1999. The Hardening Soil Model: Formulation and Verification. *Beyond 2000 in Computational Geotechnics – 10 Years of Plaxis*, R.B.J. Brinkgreve, *ed.* Rotterdam: Balkema.

Vidal, H. 1969. The Principle of Reinforced Earth. *Highway Research Record.*

Yu, Y.; Bathurst, R.J.; Miyata, Y. 2015. Numerical Analysis of a Mechanically Stabilized Earth Wall Reinforced with Steel Strips. *Soils and Foundations*, 55, 536–547.

The role of rainwater infiltration on the tensile load in unsaturated geosynthetic reinforced soil layer

M.C. Santos & F.H.M. Portelinha
Federal University of Sao Carlos, Sao Carlos, Sao Carlos, Brazil

ABSTRACT: The comprehension of rainwater infiltration effect into Geosynthetic Mechanically Stabilized Earth (GMSE) walls is required to precisely predict the mobilized tensile loads in design analyses. A laboratory-testing device that simulate a geosynthetic-reinforced layer was used to assess the water infiltration effects in tensile loads mobilized by the reinforcement. The experimental device allows applying a controlled infiltration rate over a reinforced layer and capture the mechanical response from backfill soil to geosynthetic during infiltration. Water content profile, horizontal pressure variations, reinforcement tensile load and strain were provided by the monitoring program. The results demonstrated that the infiltration led to reinforcement strains and loads up to 15% of the ultimate tensile load. In addition, the rates of increases were found to be directly related to the average matric suction of the reinforced-layer.

1 INTRODUCTION

The geotechnical standards guidelines recommend the use of granular soils as backfill material in Geosynthetic Mechanically Stabilized Earth (GMSE) walls. However, the high cost associated with collection and transport of such materials has led to the use of local soils, specifically in tropical areas where lateritic fine-grained soils are abundant (Koerner & Koerner 2011; Ren *et al.* 2022). The main concern about the use of fine-grained materials is the possible strength reduction and large deformations due to decreases in matric suction within the reinforced zone induced by rainwater infiltration. Usually, fine-grained soils are applied in GMSE walls compacted at the optimum moisture content leading to high initial values of matric suction (Portelinha & Zornberg 2017; Vibha & Divya 2021). The unsaturated soil condition improves soil properties, such as strength stiffness and compressibility, as well as the soil-geosynthetic interface shear strength. The unsaturated condition can persist for a long time, depending on the local rainfall events and evaporation rates (Nunes *et al.* 2022; Yang *et al.* 2019). On the other hand, soil condition can be drastically changed by rainfalls, which depends on the intensity, duration and frequency.

Many studies reported the effects of rainfall events on GMSE walls behavior (Wu & Chou 2013; Yoo & Jung, 2006; Yang *et al.* 2018). Vahedifard *et al.* (2017) observed that the infiltration effect is more pronounced in soils with a high initial suction value. Still, the upper part of the soil structure is mostly affected by the rainfall intensity, where the reinforcement loads increased about 60% after an extreme rainfall event. A similar conclusion was assessed by Razeghi *et al.* (2019). The authors reported that the location of maximum reinforcement strains along the wall height followed the progress of infiltration front until a certain depth, which after this point increased for all layers. A large-scale reinforced wall subjected to a moderate rainfall infiltration was investigated by Portelinha & Zornberg (2017) to evaluate the soil structure mechanical response. The authors observed that that the maximum reinforcement strain can significantly increase when infiltration front reached the middle height of the wall. Moreover, the average matric suction measured along the entire wall height was a suitable parameter to assess the infiltration effect in the unsaturated reinforced soil performance.

Here, there is a clearly gap in quantifying the tensile load and strain induced by rainfall events in GMSE walls with unsaturated backfill soils. This paper aims to investigate the hydro-mechanical response of a geogrid reinforcement layer subjected to a rainwater infiltration. The objective is achieved by monitoring the response of an experimental device that properly reproduces the GMSE walls working conditions. Such experiment allows the tensile load-strain quantification in an unsaturated reinforced layer subjected to an infiltration process.

2 EXPERIMENTAL PROGRAM

2.1 *Experimental device*

The experimental device reproduces a reinforced layer of a GMSE wall. The geogrid is indirectly mobilized by the surrounding soil under working stress and plane strain conditions. The geosynthetic reinforced soil system consists in placing a geogrid between two compacted soil layers in a rigid box with internal dimensions of 600 mm × 750 mm × 700 mm (width × length × height), as can be seen in Figure 1.
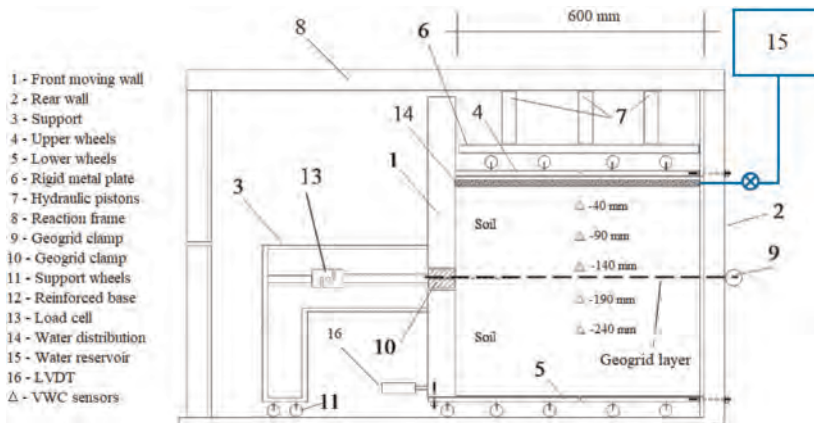
Figure 1.　Geosynthetic reinforcement layer experimental device.

The working principle of the experimental device is applying a vertical surcharge on the top of the reinforced soil system and induces a horizontal stress. While the geosynthetic is strained the internal clamp tends to restrict the movement. The front wall can move freely in the horizontal direction through ball bearings running over rails at the base (plane strain condition). The back and lateral walls are stationary and lubricated with grease to minimize friction along the center plane of the geogrid layer. The vertical surcharge is applied with hydraulic pistons and plates with bearings are used at the base to allow internal soil-geogrid straining.

A Linear Variable Differential Transformer (LVDT) transducer placed outside the front moving wall records the displacement and allows the geogrid strain calculation. The geogrid is attached to a load cell through an internal clamp that measures the reaction force as the front moves. The load cell is connected to a frame attached to the front wall and the relative movement between the front wall and the front geogrid clamp allow the mobilized tensile load to be recorded. A total pressure cell measures the horizontal pressure at the contact between the soil and the front wall. The detail testing apparatus and instrumentation was reported by Portelinha *et al.* (2021).

To simulate a rainfall event an irrigation system was installed over the soil-geogrid layer. The system includes supplying pipes and a 100 mm-thick sand drainage blanket placed on the top. Water was provided by a reservoir with a float switch used to maintain a constant hydraulic

head and the water flow rate was controlled by measuring the output volumetric flow. A vertical display of Volumetric Water Content (VWC) sensors was placed in order to obtain the infiltration process through the unsaturated soil using frequency domain deflection sensors. The location of each VWC sensor is present in Figure 1. Front-wall displacements, geogrid tensile loads, horizontal pressures and VWC were simultaneously measuring during the entire test.

2.2 Materials

The soil used in the experimental test was a high plastic clay with 68% of fines classified as CH according to the Unified Soil Classification System. Consolidated-drained direct shear tests and soil water retention curve (ASTM D5298) for the wetting process were conducted in samples compacted at the optimum water content and at 98% relative to the maximum dry unit weight using the standard Proctor effort. The soil water retention curve experimental data was fitted using the van Genuchten's model (van Genuchten 1980) and the fitting parameters were $\theta s = 0.49$, $\theta r = 4.15 \times 10^{-7}$, $\alpha = 0.016$ and $n = 3.7 \times 10^{-7}$. Figure 2 present the soil water retention curve and Table 1 summarizes the soil characteristics. The reinforcement used was a polyester woven geogrid and Table 2 summarized the physical and mechanical characteristics.

Table 1. Soil characteristics.

Properties	Standard	Value
Clay fraction	ASTM D422	56%
Silt fraction	ASTM D422	12%
Sand fraction	ASTM D422	32%
Specific gravity of solids	ASTM D 7263	2.95
Liquid limit	ASTM D4318	52%
Plastic limit	ASTM D4318	28%
Maximum dry unit weight	ASTM D1557	17.5 kN/m^3
Optimum water content	ASTM D1557	25%
Cohesion (at optimum content)	ASTM D3080	52 kPa
Friction angle (at optimum water content)	ASTM D3080	26°
Saturated hydraulic conductivity	ASTM D5856	3.4×10^{-7} m/s
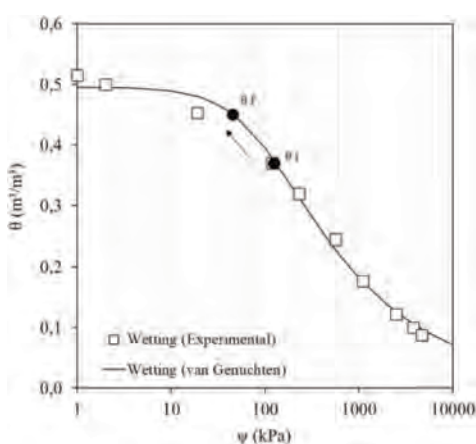
Figure 2. Soil water retention curve and VWC for the initial and final infiltration test conditions.

Table 2. Geogrid characteristics.

Properties	Standard	Value
Thickness	ASTM D5199	1.3 mm
Ultimate tensile strength	ASTM D4595	42 kN/m
Elongation at failure (at 2%)	ASTM D4595	13 %
Tensile strength (at 2%)	ASTM D4595	20 kN/m
Secant tensile strength (at 2%)	ASTM D4595	440 kN/m
MD yarn width	–	3.0 mm
CMD yarn width	–	8.5 mm
MD aperture size	–	27 mm
CMD aperture size	–	19 mm

2.3 Testing procedure

The soil was placed in 50 mm-high layers at 98% relative to the maximum dry unit weight and at optimum water content of 25% compacted with a manual hammer. The initial conditions (void ratio, dry density and water content) were controlled during the compaction phase. The geogrid was embedded between 150-mm-thick soil layers. Then, the upper wheels and a distribution plate were positioned over the top closed the system prior to the application of vertical surcharge.

A conditioning phase was conducted to simulate the operational condition in a GMSE wall before the infiltration test. Vertical surcharges of 30 kPa were applying for 5 min until reaching the final stress value of 180 kPa, which remained constant during the entire experiment. Thus, a water flow rate (q) of 1.3×10^{-7} m/s was applied uniformly over the soil-geogrid layer. The irrigation rate was selected to simulates a moderate rainfall event of 10 mm/day, which represent a ratio with the soil hydraulic conductivity (q/k_s) of 0.38. The experimental test occurred under consolidated drained conditions of soil to simulate rainfall events after the wall construction.

3 RESULTS

The VWC profile is a key factor to determine the hydraulic behavior of geosynthetic-reinforced layers. The sensor readings for the imposed water flow rate of 1.3×10^{-7} m/s is present in Figure 3a. The VWC corresponding to the initial (θ_i), final (θ_f) and saturation
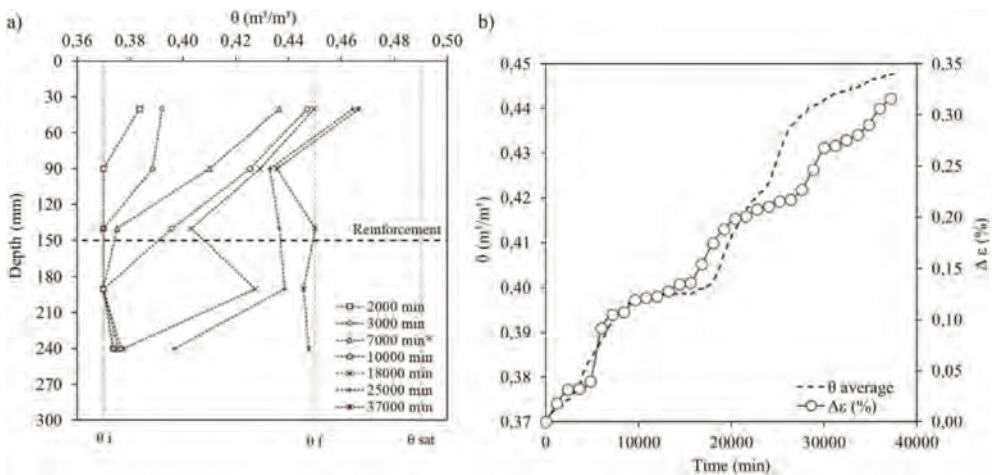
Figure 3. a) VWC profile during the infiltration process in an unsaturated geogrid layer (*infiltration front reached the reinforcement); b) Progression of average VWC and geogrid strains during the infiltration test.

(θ_{sat}) are also plot for comparison reasons. The sensors evidenced a constant infiltration rate over the entire test indicating that the geogrid layer did not affected the infiltration process thanks to the geogrid openings. This fact can be evidence by the sensor located above the geogrid layer after the infiltration front reached the reinforcement depth (7000 min), which registered similar readings to the other sensors. The saturation water content was not reached because the imposed water flow rate was lower than the saturated soil hydraulic conductivity ($q/k_s < 1$).

The coupled hydro-mechanical performance of a geosynthetic-reinforced layer is related to the soil unsaturated condition. Based on the VWC readings, the geogrid-layer hydraulic behavior was evaluated by the average VWC (θ average). Still, the mechanical variations were assessed through the geogrid strain, calculated from the moving front wall displacement divided by the reinforcement length. Figure 3b relates the coupled behavior during the infiltration test. As the infiltration front advanced the geogrid strain increases over the test following the θ average rises. The results demonstrated a correlation between both parameters, since the curves exhibited similar trends. Similar behavior was reported by Portelinha & Zornberg (2017).

The mechanical response of GMSE walls with unsaturated fine-grained soils depends on the earth pressures values. The horizontal pressure variation ($\Delta\sigma_h$) plotted against the average matric suction (ψ average) changes due to the infiltration process is present in Figure 4a. The ψ average was obtained by using the VWC values in the soil water retention curve present in Figure 2. Note that in Figure 2 is plotted the θ_i and θ_f values. Notably, the horizontal earth pressure increased with the progressive reduction in the average matric suction since the begging of the infiltration test. A variation of 28 kPa were registered with a final matric suction of 35 kPa. This behavior can be attributed to the soil stiffness reduction due to the progressive decreases in the matric suction as the infiltration advances. Still, the variation rate in the horizontal earth pressure were higher when the infiltration front advanced from the top to the reinforcement depth, as reported in previous works (Portelinha & Zornberg 2017; Vahedifard *et al*. 2017).
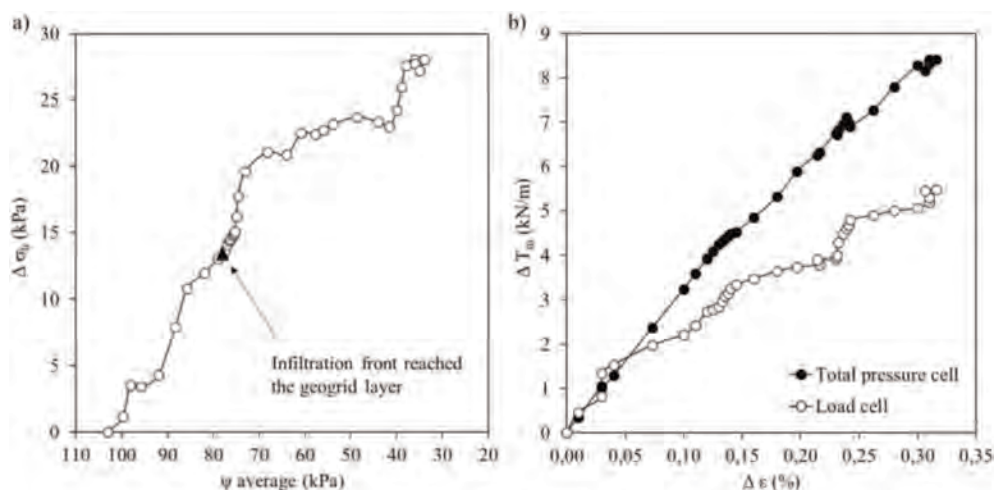
Figure 4. a) Relation between the horizontal pressure variation and average matric suction; b) Tensile load-strain variation relation during the infiltration test.

Figure 4b relates the geogrid strain variation to the tensile load recorded during the infiltration test calculated from the total pressure cell and directly measured by the load cell.

The final tensile load value mobilized by the geogrid was approximately 5.5 kN/m, which corresponded to 15% of the ultimate resistance and it was lower than the back calculated value from the soil response. This fact indicates that the reinforcement did not mobilized the entire horizontal pressure variation caused by the water infiltration. Moreover, the tensile load increment occurred with lower reinforcement strains. This can be possible attributed to the elevate geogrid stiffness combined with the geosynthetic opening, which allowed the surround soil remains continuous even with a reinforcement inclusion. The curves plotted in Figure 4 indicate a relation between the matric suction reduction and the geogrid tensile-strain response under an infiltration state.

4 CONCLUSIONS

An experimental device that simulates the stress transference in GMSE walls was used to evaluate the rainfall infiltration effect in an unsaturated geogrid-reinforced layer. The test was conducted with a constant vertical surcharge and water infiltration rate. The following conclusions can be expressed:

- The infiltration process caused hydraulic-mechanical responses in the unsaturated soil-geogrid layer. The water content elevation generates an increase in the tensile load mobilized by the geogrid (up to 15%) following the matric suction reduction.
- The tensile load increment rate due to the infiltration process was higher when the water front advanced from the top to the geogrid depth. The linear trend of load increases was attributed to the high initial matric suction value (approximately 100 kPa) and to the pattern along the soil water retention curve primary transition (θ_i to θ_f);
- The geogrid did not demonstrated changes in the water flow into the unsaturated backfill soil. This phenomenon can be attributed to the geogrid openings which allowed the surround soil remains continuous even with the reinforcement inclusion.

REFERENCES

ASTM D422. 2011. *Standard Test Method for Particle-size Analyses of Soils*. American Society of Testing Materials, p.8.

ASTM D1557. 2009. Standard Test Methods for Laboratory Compaction Characteristic of Soil Using Modified Effort. American Society of Testing Materials, p. 14.

ASTM D3080. 2009. Standard Test Methods for Direct Shear Test of Soils Under Consolidated Drained Conditions. American Society of Testing Materials, p. 7.

ASTM D4318. 2010. Standard Test Methods for Liquid Limit, Plastic Limit, and Plasticity Index of Soils. American Society for Testing Materials, p. 16.

ASTM D4595. 2017. Standard Test Method for Tensile Properties of Geotextiles by the Wide-Width Strip Method. American Society of Testing Materials, p. 13.

ASTM D5199. 2019. Standard Test Method for Measuring the Nominal Thickness of Geosynthetics. American Society of Testing Materials, p. 4.

ASTM D5261. 2018. Standard Test Method for Measuring Mass per Unit Area of Geotextiles. American Society of Testing Materials, p. 3.

ASTM D5298. 2012. Standard Test Method for Measurement of Soil Potential (Suction) Using Filter Paper. American Society of Testing Materials, p. 6.

ASTM D5856. 2015. Standard Test Method for Measurement of Hydraulic Conductivity of Porous Material Using a Rigid-Wall, Compaction-mold Permeameter. American Society for Testing Materials, p. 9.

ASTM D7263. 2009. Standard Test Methods for Laboratory Determination of Density (Unit Weight) of Soil Specimens. American Society for Testing Materials, p. 7.

Koerner, R.M. & Koerner, G.R. 2011. The Importance of Drainage Control for Geosynthetic Reinforced Mechanically Stabilized Earth Walls. *J. GeoEngineering*, Vol. (6), No. 1, 3–13.

Nunes, G.B., Portelinha, F.H.M., Futai, M.M. & Yoo, C. 2022. Numerical Study of the Impact of Climate Conditions on Stability of Geocomposite and Geogrid Reinforced Soil Walls. Vol (50). 807–824.

Portelinha, F.H.M. & Zornberg, J.G. 2017. Effect of Infiltration on the Performance of an Unsaturated Geotextile-reinforced Soil Wall. *Geotextiles and Geomembranes*. 45 (2017), 211–226.

Portelinha, F.H.M., Santos. M.C. & Futai, M.M. 2021. A Laboratory Device to Evaluate Geosynthetic Load–strain Behaviour in MSE Walls. *Geosynthetics International*. 28, No. 1.

Razeghi, R.R, Viswanadham, B.V.S. & Mamaghanian, J. 2019. Centrifuge and Numerical Model Studies on the Behaviour of Geogrid Reinforced Soil Walls with Marginal Backfills with and without Geocomposite Layers. *Geotextiles and Geomembranes* 47 (2019) 671–684.

Ren, F., Huang, Q. & Chen, J. 2022. Centrifuge Modeling of Geosynthetic-reinforced Soil Retaining Walls Subjected to the Combined Effect of Earthquakes and Rainfall. *Geotextiles and Geomembranes* 50, 470–479.

Vahedifard, F., Tehrani, F.S., Galavi, V., Ragno, E. & AghaKouchak, A. 2017. Resilience of MSE Walls with Marginal Backfill under a Changing Climate: Quantitative Assessment for Extreme Precipitation Events. *J. Geotech. Geoenviron. Eng.* 143 (9).

van Genuchten, M.T., 1980. A Closed-form Equation for Predicting the Hydraulic Conductivity of Unsaturated Soils. *Soil Sci. Soc. Am. J.* Vol (44), No. 5, 892–898.

Vibha, S. & Divya, P.V. 2021. Performance of Geosynthetic Reinforced MSE Walls with Marginal Backfills at the Onset of Rainfall Infiltration. *Int. J. Geosynth. Gr. Eng.* 7, 1–16.

Wu, J.Y. & Chou, N.N. 2013. Forensic Studies of Geosynthetic Reinforced Structures Failures. *J. Perform. Constr. Facil.* 27 (5), 604–613.

Yoo, C. & Jung, H.Y. 2006. Case History of Geosynthetic Reinforced Segmental Retaining Wall Failure. *J. Geotech. Geoenviron. Eng.* 132 (12), 1538–1548.

Yang, K.H., Thuo, J.N., Huynh, V.D.A., Nguyen, T.S. & Portelinha, F.H.M. 2018. Numerical Evaluation of Reinforced Slopes with Various Backfill Reinforcement-drainage Systems Subject to Rainfall Infiltration. *Computers and Geotechnics* 96 (2018) 25–39.

Yang, K.H., Nguyen, T.S. & Leshchinsky. 2019. Performance and Design of Reinforced Slopes Considering Regional Hydrological Conditions. *Geosynthetics International*, Vol. (26), No. 5.

Numerical analysis using FEM on the behavior of reinforced fill structure having geogrid and steel wire mesh as a reinforcing element

Ahsan Rehman Khan & Gemmina Di Emidio
Laboratory of Geotechnics, Department of Civil Engineering, Ghent University, Belgium

ABSTRACT: Nowadays, installation of geosynthetics is an effective and economical way to cater soil stability problems. It also helps in designing reliable, constructible, eco-friendly, cost-effective geotechnical structures. Numerous infrastructures resting on these stabilized soil structures is prone to failure due to collapse which result in financial loss, loss of life and disturbance in the services which may take few years to rebuilt. The aim of this paper is to highlight the importance of geogrid and wire mesh as a reinforcement method in reinforced fill structure. To assess the performance of this soil reinforcement, finite element method analysis was adopted. The geometry model of this reinforced fill structure has dimensions as 10 m height, 20 m wide. The type of geogrid used consist of high tenacity polyester fibers coated with a polyethylene sheath. This research paper explores the use of reinforced fill structures incorporating geogrids and wire mesh as an economical, eco-friendly, and adaptable alternative to conventional methods. These structures offer advantages in terms of minimal labor, low manufacturing costs and easy to install that can be customized to fit the specific requirement of any project. The study concludes that reinforced fill structures using geogrids and wire mesh represent a promising alternative solution for construction projects.

Keywords: Geogrids, Wire mesh, Reinforced fill structure, Soil, Eco-friendly

1 INTRODUCTION

The parameter that effects the tensile loads in MSE walls is the stiffness of a reinforcement (Allen & Bathurst 2019) . By inserting the reinforcing elements in the soil, the stiffness of the soil can be enhanced (Sulovska & Stacho 2021). The effect of soil reinforcement on horizontal and vertical deformation is shown in Figure 1. The behavior of retaining structures is influenced by the various factors that affect their construction, such as the type of compaction, and the degree to which it is applied. In order to avoid failure, proper guidelines are established during the construction process (Koerner & Koerner 2013, 2018). Different case studies have shown that poor or inconsistent compaction can lead to the failure of MSE walls (Mahmood 2009; Tarawneh & Siddiqi 2014).
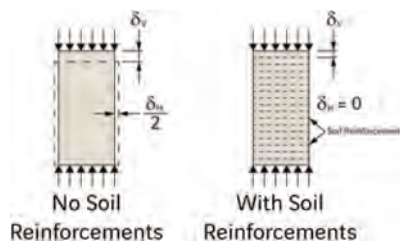
Figure 1. Effect of reinforcement on soil deformation.

Gabion walls, due to their weight, show dominating strength against hydraulic and active soil pressure. The gabions with wire mesh boxes are built by welding or twisting wires and the boxes are filled with course soils (Lin *et al.* 2010). The Gabion walls considered the best stabilization method having 50% less cost (Chikute & Sonar 2019). The reinforced fill structures are also more cost-effective when compared to traditional walls (Uray 2022). Wire mesh has been widely used as a secondary reinforcement for stabilizing earth structures in combination with units that can provide a stone-facing surface for the past few years (Lelli *et al*. 2015). These rectangular boxes are usually manufactured from a combination of steel mesh and stones at the worksite. These materials are commonly used in various infrastructure projects such as airports and roads. Besides stabilization, they can also be utilized for the construction of riverbanks, erosion control measures, and landslide mitigation. Compared to gravity-type retaining structures, reinforced fill boxes offer various economic advantages. They can be used as the wall's height increases (Rimoldi & Scotto 2012). A reinforced fill structure can be constructed using a combination of wire mesh and geogrids, which are commonly used as primary and secondary reinforcement materials respectively. Geogrids, as primary reinforcements, help to prevent the structure from experiencing any potential rupture surfaces. While wire mesh acts as a secondary reinforcement to offer the strength at the facing.

This paper contains the initial part of author's research work. In general, the whole research work is structured around three phases. The initial phase assesses the effectiveness of geogrid and welded wire mesh in terms of stability. The step-by-step procedure of how to model a reinforced fill structure in a simplified way is elaborated. In the second phase of the research, the author aims to predict the long-term performance (creep) of geogrids using finite element method and validate these values with the monitored field data. In the third phase of the research, the author will investigate the long-term pullout test (sustained loading) to predict the performance of geogrid under confined loading based on its design life.

2 METHODOLOGY

Finite element software Plaxis 2D was used here. The model with 15 node elements with plain strain condition was used for the analysis. The stratigraphic feature of the soil can be defined by using the borehole feature. The water table and the location of the soil layers can also be determined by using boreholes. A geogrid was used as a primary reinforcement as it is a slender structure with axial stiffness and axial force and can withstand tension. The gabions with wire mesh were used as a secondary reinforcement to provide erosion control and retention of earth. Also, double twisted wire mesh configuration guarantees the minimum occurrence of strength reduction. The typical steps involved in the analysis of the reinforced fill structure (Edition 2020) are as follows:

- Representation of a Conceptual model
- Specifying boundary, initial, and loading conditions
- Defining geometry
- Specifying the soil, reinforcement, and backfill properties
- Designate specific material model and parameters
- Generation of mesh
- Staged construction development
- Running & verification of the model
- Evaluation of the findings with engineering judgement

2.1 *Constitutive model and material properties*

For the analysis and design of complex geometries, finite element analysis software Plaxis 2D is frequently used nowadays. The tool has the power for the detailed soil response towards construction procedures, boundary conditions & simulating primary loading stiffness, initial stiffness, and unloading/reloading stiffness as per model requirement.

The material properties of the foundation soil & backfill are shown in Table 1, while for geogrid, gabion & wire mesh are listed in Tables 2, 3 and 4 respectively. The model was made using a highly refined mesh.

Table 1. Properties of soil.

Properties	Units	Foundation soil	Backfill soil
Saturated unit weight	kN/m^3	18	18
Unsaturated unit weight	kN/m^3	18	18
Angle of internal friction	Degree	30	35
Cohesion	kN/m^2	1	1
Poisson's ratio	–	0.3	0.3
Reference elastic modulus			
Eref$_{50}$	MPa	60	30
Eref$_{oed}$	MPa	60	30
Eref$_{ur}$	MPa	180	90

Table 2. Properties of geogrid.

Properties	Units	Value
Axial Stiffness (EA)	kN/m^2	3000
Maximum Axial force N$_p$	kN/m	300
Material Type	–	Elastoplastic

Table 3. Properties of gabion.

Properties	Units	Value
Unit weight	kN/m^3	18
Angle of internal friction	Degree	40
Cohesion	kN/m^2	27
Poisson's ratio	–	0.3
Elastic modulus	MPa	40
Material model	–	Mohr-Coulomb

Table 4. Properties of wire-mesh.

Properties	Symbols	Units	Value
Axial stiffness	EA	kN/m	62832
Flexural Rigidity	EI	kN/m^2/m	0.251
Weight	W	kN/m/m	0.023
Poisson's ratio	V	–	0.3
Maximum bending moment	M$_p$	kN/m/m	0.23
Maximum axial force	N$_p$	kN/m	135
Cohesion	C	kN/m^2	27

2.2 Model geometry in Plaxis-3D

The reinforced fill structure modelled in this study has the height of 10 m and base of 20 m as shown in Figure 2, comprises of the following materials components:

- Gabions modelled as soil clusters as shown in Figure 2a
- Welded wire mesh panels modelled as plate elements as shown in Figure 2b
- Geogrids modelled as Elastoplastic (N-ε) geogrid elements as shown in Figure 2c
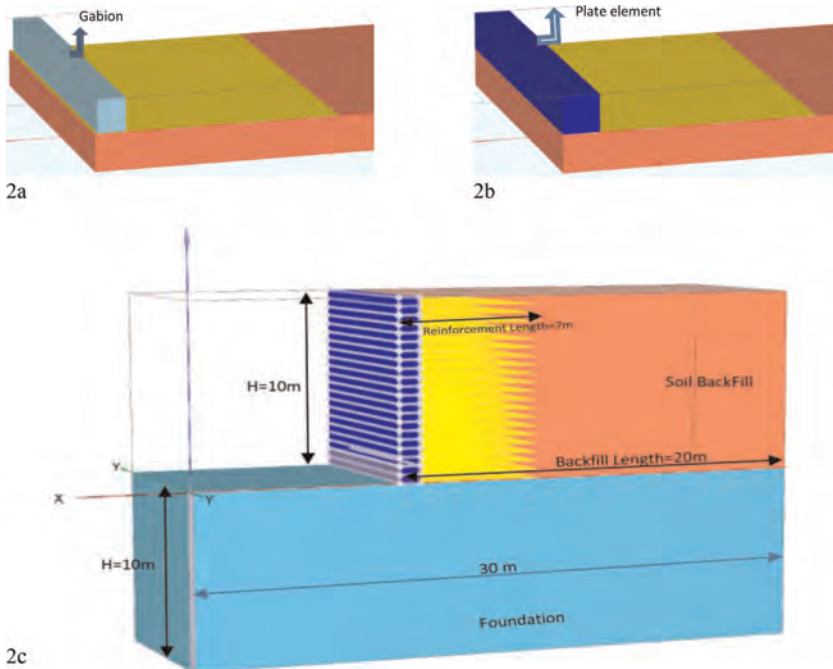
Figure 2. (a and b) Plaxis-3D geometry model and MSE wall components. (c). Plaxis-3D Geometry model and MSE wall components.

2.3 Interface modeling

One of the features of Plaxis 2D is the use of interfaces for modelling soil-structure inter-action. Without an interface the soil & structure are tied together having no relative dis-placement between them. By using an interface, node pairs are introduced at the interface of soil & structure as shown in Figure 3. The interaction is modeled by the various interface elements that are used in the construction process. Here, Table 5 represents the coefficients of friction between the soil & wire mesh and soil & geogrid.
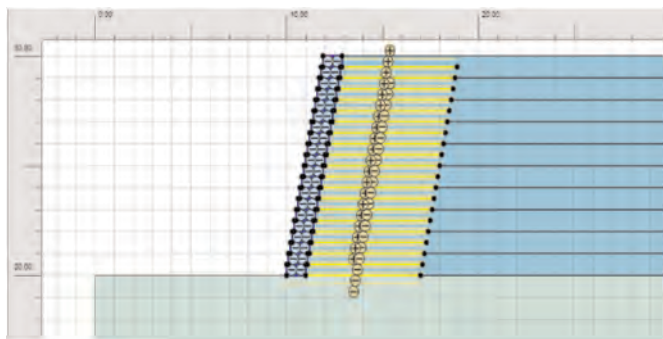
Figure 3. Interaction between soil and reinforcing elements.

994

Table 5. tan δ / tan φ friction coefficients for wire mesh & geogrid.

Soil	tan δ / tan φ (Wire mesh)	tan δ / tan φ (geogrid)
Clay	0.3	0.4
Silt	0.4	0.7
Sand	0.65	0.9
Gravel	0.9	0.9

3 RESULTS AND ANALYSIS

Modeling & analysis was executed using the software known as Plaxis 2D. For the stability assessment of the reinforced fill structure, the base soil and the embankment soil was generalized to be homogeneous with the physical properties. The maximum wall displacement is computed to be around 23 cm as shown in Figure 4. Horizontal and vertical displacement was obtained as 6.3 cm & 23 cm respectively as shown in Figures 5 & 6.

The phi/c reduction method was used for estimating the factor of safety. Both the strength parameters phi (φ) and c are gradually reduced until failure occurs in the soil. The FOS was determined as 1.2 as shown in Figure 7. The required length and spacing of the geogrids used were 7m and 0.5m respectively.
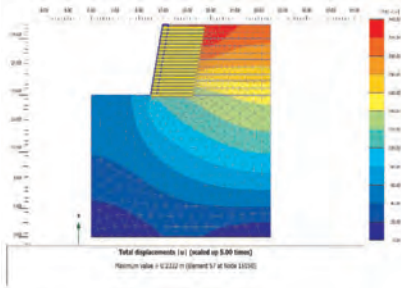
Figure 4. Total displacement.
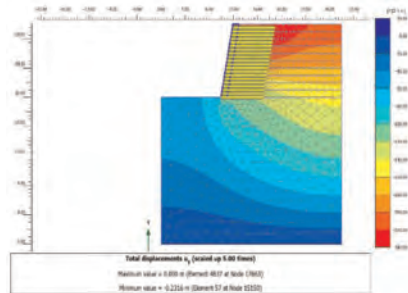
Figure 5. Horizontal displacement.
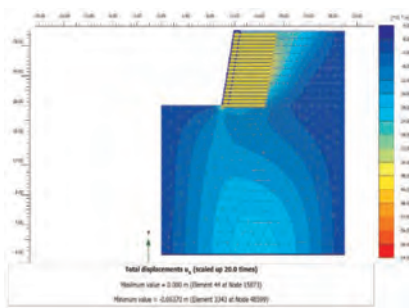
Figure 6. Vertical displacement.
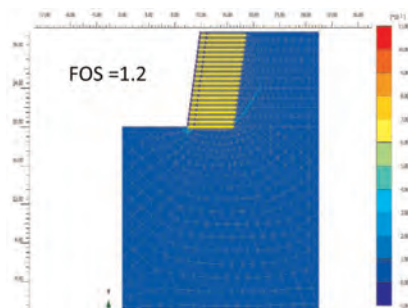
Figure 7. Factor of safety.

4 CONCLUSION

This study is a preliminary research based on first year PhD, about the stability of a reinforced fill structure with geogrids and wire mesh as a reinforcing unit. The reinforcement layer helps spreading the load over a wider area and provides the necessary tensile strength to the surrounding soils. It can be concluded that the use of geogrid and wire mesh can reduce horizontal movement and increase stability in slopes. These reinforcing materials distribute stresses evenly, mitigating the risk of failure. A reinforced fill structure with geogrids and wire mesh are an alternative and economic solution as compared to other conventional solutions as they are easily buildable, adaptive with nature, durable, ecofriendly, and flexible structure.

REFERENCES

Allen, T.M. and Bathurst, R.J. 2019. 'Geosynthetic Reinforcement Stiffness Characterization for MSE Wall Design', *Geosynthetics International*, 26(6), pp. 592–610.

Manual of Plaxis 2D. 2020. 'Plaxis 2D Reference Manual CONNECT Edition V20.02', pp. 1–23.

Koerner, R.M. and Koerner, G.R. 2013. 'A Data Base, Statistics and Recommendations Regarding 171 Failed Geosynthetic Reinforced Mechanically Stabilized Earth (MSE) Walls', *Geotextiles and Geomembranes*, 40, pp. 20–27.

Koerner, R.M. and Koerner, G.R. 2018. 'An Extended Data Base and Recommendations Regarding 320 Failed Geosynthetic Reinforced Mechanically Stabilized Earth (MSE) Walls', *Geotextiles and Geomembranes*, 46(6), pp. 904–912.

Lelli, M., Laneri, R. and Rimoldi, P. 2015. 'Innovative Reinforced Soil Structures for High Walls and Slopes Combining Polymeric and Metallic Reinforcements', *Procedia Engineering*, 125, pp. 397–405.

Lin, Der-guey, *et al.* 2010. "Deformation Analyses of Gabion Structures." *Proceedings of the interpraevent Conference*, 2010, pp. 512–526.

Mahmood, T. 2009. '*Failure Analysis of a Mechanically Stabilized Earth (MSE) Wall Using Finite Element Program Plaxis*', Ph.D. Thesis. The University of Texas at Arlington. Available at : http://hdl.handle.net/10106/1705

Rimoldi, P. and Scotto, M. 2012. 'Hybrid Reinforced Soil Structures for High Walls and Slopes', in *Second Pan American Geosynthetics Conference & Exhibition, GeoAmericas*.

Sulovska, M. and Stacho, J. 2021. 'Analysis of Geogrid Reinforced Structures with a Passive Facing System Using Different Computational Methods', *Civil and Environmental Engineering*, 17(2), pp. 500–512.

Tarawneh, B. and Siddiqi, J. 2014. 'Performance Issues of Mechanically Stabilized Earth Wall Supporting Bridge Abutment', in *Proceedings of 8th international conference on engineering and technology research, Dubai, UAE*, pp. 1–20.

Uray, E. 2022. 'Gabion Structures and Retaining Walls Design Criteria', *Advanced Engineering Science*, 2, pp. 127–134.

Walls, R., Chikute, G.C. and Sonar, I.P. 2019. 'Techno-Economical Analysis of Gabion Retaining Wall Against Conventional Techno-Economical Analysis of Gabion Retaining Wall Against Conventional Retaining Walls', *International Research Journal of Engineering and Technology*, 6(8), pp. 450–457

Probabilistic back analysis of a high geosynthetic-reinforced slope failure

J.F. Chen, R. Sun, M. Peng & N. Bao
Department of Geotechnical Engineering, College of Civil Engineering, Tongji University, Shanghai, China

ABSTRACT: This paper presents a probabilistic back analysis for a geosynthetic reinforced soil slope (GRSS) at Yeager airport considering the uncertainty of statistical parameters of random variables based on the Bayesian network. The response surface method was used to develop the input-out relationship between the random variables and the safety factor of the GRSS. The Markov chain Monte Carlo (MCMC) simulation was used to update the statistical parameters of random variables. The results show that the soften soil strength of soil-rock interface is the main reason of failure of the reinforced soil slope at Yeager airport.

1 INTRODUCTION

The use of reinforcements in the form of geosynthetic materials makes the geostructures (like embankments, retaining walls, engineered landfills and soil slopes) perform well under both static and seismic conditions (Chen *et al*. 2014; Peng *et al*. 2020, 2021; Tatsuoka *et al*. 1997; Yoo & Jung 2004). Even though the geosynthetic-reinforced soil structures (GRSS) have good performance, there are still some failure cases (Koerner & Koerner 2013). Among the reasons to cause failure of the GRSS, the uncertainty of soil and reinforcement parameters is one major reason cannot be ignored. Therefore, it is of great necessity to perform the reliability analysis of the GRSS.

The existing studies on the reliability analysis of the GRSS are composed of reliability analysis under static condition and reliability analysis under seismic condition. In term of reliability analysis of GRSS under static condition, the internal stability reliability analysis (Alhajj *et al*. 2022; Chalermyanont & Benson 2004; Bathurst *et al*. 2020) and external stability reliability analysis (Chalermyanont & Benson 2005; Kim & Salgado 2012; Yang *et al*. 2011) considering the uncertainty of soil and reinforcement parameters was carried out in recent decades. In term of reliability analysis of GRSS under seismic condition, reliability analysis considering the uncertainty of earthquake, soil and reinforcement parameters based on pseudo-static method (Basha & Babu 2010, 2014; Sayed *et al*. 2008) and pseudo-dynamic method (Agarwal *et al*. 2021; Basha & Babu 2009, 2011).

The above studies on the reliability analysis of GRSS ignore the uncertainty of estimated statistical parameters, causing uncertain failure probability or reliability index. Bayesian network provides a probabilistic graphical model representing a set of random variables and their conditional dependencies (e.g. F_S) via a directed acyclic graph (Jensen 2001). It has been proven to be a robust method for reliability analysis to update the random variables (Mahadevan *et al*. 2001). Bozorgzadeh & Bathurst (2019a) used a Bayesian approach to perform internal stability reliability analysis of reinforced soil retaining walls considering the uncertainty in failure probability or reliability index. Bozorgzadeh & Bathurst (2019b) also used Bayesian approach to carry out statistical analysis of load and pullout model bias data for steel strip mechanically stabilized earth walls. The mention-above studies have been investigated clearly the internal stability reliability

analysis of GRSS considering the uncertainty of reliability index (or failure probability) based on the Bayesian method. The overall stability reliability analysis of GRSS considering the uncertainty of reliability index (or failure probability) needs to be further investigated.

In this paper, we constructed a Bayesian network considering F_S to conduct the probabilistic back analysis of a reinforced slope at Yeager airport considering the uncertainty of statistical parameters of random variables. First, the numerical model of reinforced slope at Yeager airport was developed to perform deterministic analysis using the GeoStudio 2018 software (2018). Second, the probabilistic back analysis was conducted based on the Bayesian network considering F_S.

2 DETERMINISTIC ANALYSIS OF A REINFORCED SLOPE AT YEAGER AIRPORT

2.1 *Numerical model*

The geosynthetic-reinforced slope at Yeager airport near Charleston, West Virginia, was constructed in 2007 to support the extension of Runway 5 of the airport. In 2015, the slope failed after 8 years in-service. A GRSS model based on the work of Collin *et al.* (2021) is developed using the GeoStudio 2018 software (2018), as Figure 1 shown.
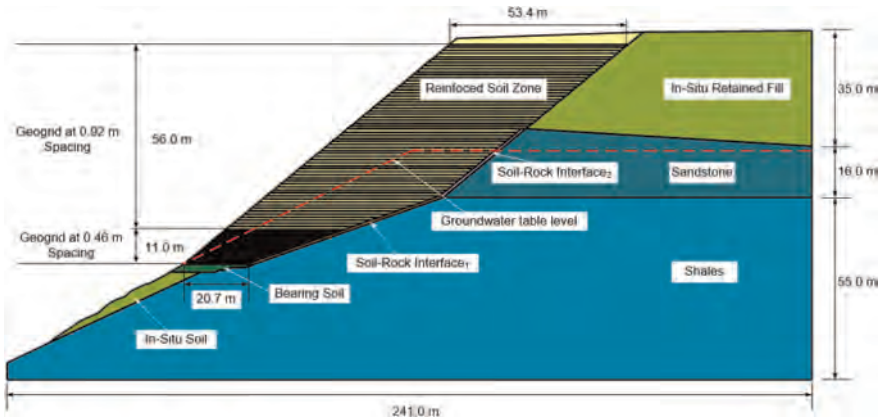
Figure 1.   Geometry of geosynthetic-reinforced soil slope at Yeager airport (adapted from Collin *et al.* 2021).

Table 1.   Inputs of GRSS in the numerical model.

Parameter	c^* (kPa)	ϕ^* (°)	γ^* (kN/m^3)	E^* (MPa)	v^*	A^* (m^2)	H^* (m)
Reinforced soil	0	36	21.2	50	0.3	–	67
In situ retained soil	0	36	21.2	50	0.3	–	67
Bearing soil at slope toe	0	36	21.2	50	0.3	–	67
Soil-rock interface$_1$	0	36	21.2	30	0.3	–	67
Soil-rock interface$_2$	0	36	21.2	30	0.3	–	67
Sandstone	–	–	25	1000	0.3	–	67
Shales	–	–	25	1000	0.3	–	67
Geogrid^1	–	–	–	300	–	0.005	67
Geogrid^2	–	–	–	750	–	0.005	67

Note: $^*c$ is cohesion, ϕ is friction angle, γ is unit weight, E is elastic modulus, v is poison's ratio, A is area, H is the groundwater level.

The soil and the interface between soil and rock was modelled as the Mohr-Coulomb elastic-plastic model and the rock was model as elastic model. The thin soil layer (e.g. Soil-Rock Interface$_1$ and Soil-Rock Interface$_2$ as shown in Figure 1) is used to model the soil-rock interface to evaluate the influence of interaction between the reinforced soil and the sandstone and shales. In the GRSS, two types of uniaxial geogrids were used in the reinforced zone, they were modelled as beam element without moment of inertia. The basic parameters of the soil, and reinforcements are given in Table 1. The cohesion, friction angle, unit weight and poisson's ratio of soil including reinforced soil, in situ retained soil, bearing soil at slope toe and soil-rock interface are 0 kPa, 36°, 21.2 kN/m^3 and 0.3 respectively. The Young's modulus of soil including reinforced soil, in situ retained soil, bearing soil at slope toe and soil-rock interface are 50 MPa and 30 MPa respectively. The unit weight, Young's modulus and poisson's ratio of rock including sandstone and shales are 25 kN/m^3, 1000 MPa and 0.3. The Young's modulus of two types of geogrids are 300 MPa and 750 MPa and the area of geogrid is 0.005 m^2. The groundwater table level is 67 m.

2.2 *Parametric analysis*

Figure 2 illustrates the sensitivity analysis of parameters of soil-rock interface$_1$ and soil-rock interface$_2$ and groundwater table level on the safety factor of GRSS. To make a clear comparison of different factors, the parameters are normalized by the Equation (1).

$$y = \frac{x - x_{\min}}{x_{\max} - x_{\min}} \qquad (1)$$

where y = the normalization parameter; x = the original parameter; $x_{\min}$ = the minimum parameter of original parameters; and $x_{\max}$ = the maximum parameter of original parameters.

It can be seen that the friction angle of soil-interface$_1$ is most sensitive on the F_S of GRSS. The unit weight of soil-interface$_1$ and soil-interface$_2$ have almost no effect on the F_S of GRSS.
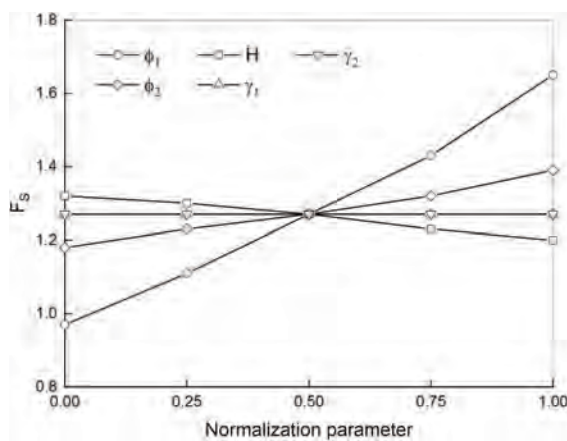
Figure 2. Sensitivity analysis of GRSS at Yeager airport.

3 PROBABILISTIC BACK ANALYSIS OF A REINFORCED SLOPE AT YEAGER AIRPORT

3.1 *Constructing a Bayesian network*

Based on the sensitivity analysis, the friction angle of soil-interface$_1$ and soil-interface$_2$ and the water table level are set as random variables. The friction angle of soil-interface$_1$ and soil-interface$_2$

Table 2. Prior statistics of random variables.

Parameter	$\phi_1(°)$	$\phi_2(°)$	H (m)
Mean	36	36	67
COV	0.1	0.1	0.03
Standard deviation	3.6	3.6	2

is considered to follow lognormal distributions with means and standard deviations of 36° and 3.6°, respectively (Collin *et al.* 2021; Phoon 1999). The groundwater level is important but its location is unclear. In this study, the water table level is considered to follow normal distribution with means and standard deviations of 67 m and 2 m, respectively (Shadabfar *et al.* 2020).

A Bayesian network by considering F_S is constructed to carry out the probabilistic back analysis of the GRSS in this study, as Figure 3 shown. Three random factors are considered, namely the friction angle of soil-rock interface$_1$ (ϕ_1) and soil-rock interface$_2$ (ϕ_2) and the groundwater level (H). The F_S can be calculated by SIGMA/W and SLOPE/W in the GeoStudio 2018 software (2018). The stress-strain relationship is obtained first using SIGMA/W considering the effect of groundwater and the interaction between the soil and reinforcement. The obtained stress of GRSS is then imported into the SLOPE/W to calculate the F_S based on the limit equilibrium method.
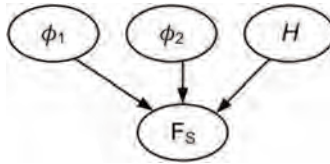
Figure 3. The Bayesian network ϕ_1, ϕ_2 and H of GRSS and F$_S$.

3.2 Response surface function of F_S of GRSS

To improve the efficiency of probabilistic back analysis of GRSS, altogether 125 combinations of ϕ_1, ϕ_2 and H are considered to develop the response surface function of F_S. The F_S model can then be approximated by the following equation:

$$F_S(\phi_1, \phi_2, H) = 0.2425 + 0.0077\phi_1 - 0.0024\phi_2 + 0.0258H + 0.0002\phi_1^2 + 0.0001\phi_2^2 - 0.0003H^2 \tag{2}$$

To check the accuracy of the response surface functions, 25 more points are randomly drawn from the space of θ and the F_S corresponding to these parameters are evaluated with both the numerical simulation and with the response surface function, as shown in Figure 4. It can be seen that the results from the two approaches are close but not exactly the same. Hence, the response surface model error, ε_1, is introduced to characterize the difference between the response surface method and the numerical simulation. The ε_1 is considered to be followed standard normal distribution with mean and standard deviation of 0 and 0.3455, where the standard deviation is estimated by statistical methods. The numerical simulation error ε_2 is also concerned in this study, which is also be modeled as a normally distributed random variable with a mean of 0.05 and a standard deviation of 0.07, according to Christian *et al.* (1994) and Zhang *et al.* (2010).

3.3 Probabilistic back analysis of GRSS based on Bayesian framework

If the F_S is larger than 1, the GRSS is in the safe state, and if F_S is smaller than 1, the GRSS is in the failure state. When the F_S is unity, the GRSS is in the limit state. The F_S is considered
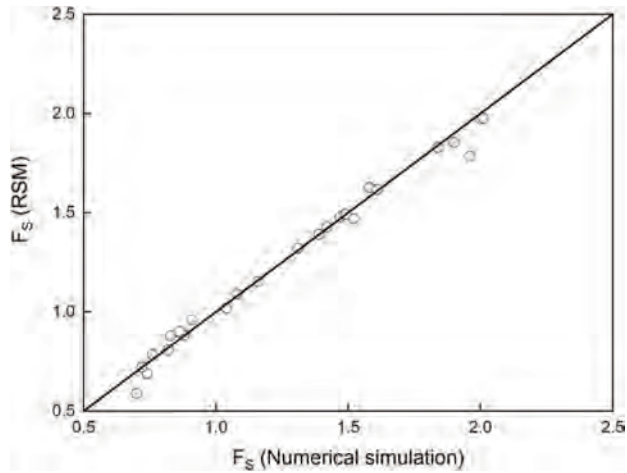
Figure 4. Comparison of F_S calculated using the response surface with those calculated using the numerical simulation.

to be unity in this study as the GRSS failed in the back analysis, which is also be adapted by Zhang *et al.* (2010) and Wang *et al.* (2013) in the back analysis when the slope failed.

The Markov chain Monte Carlo (MCMC) simulation is used to update the random factors in the probabilistic back analysis. It can be seen that the posterior mean values of ϕ_1 and ϕ_2 are much smaller than the prior value from Figure 5, particularly the posterior mean values of ϕ_1, which is
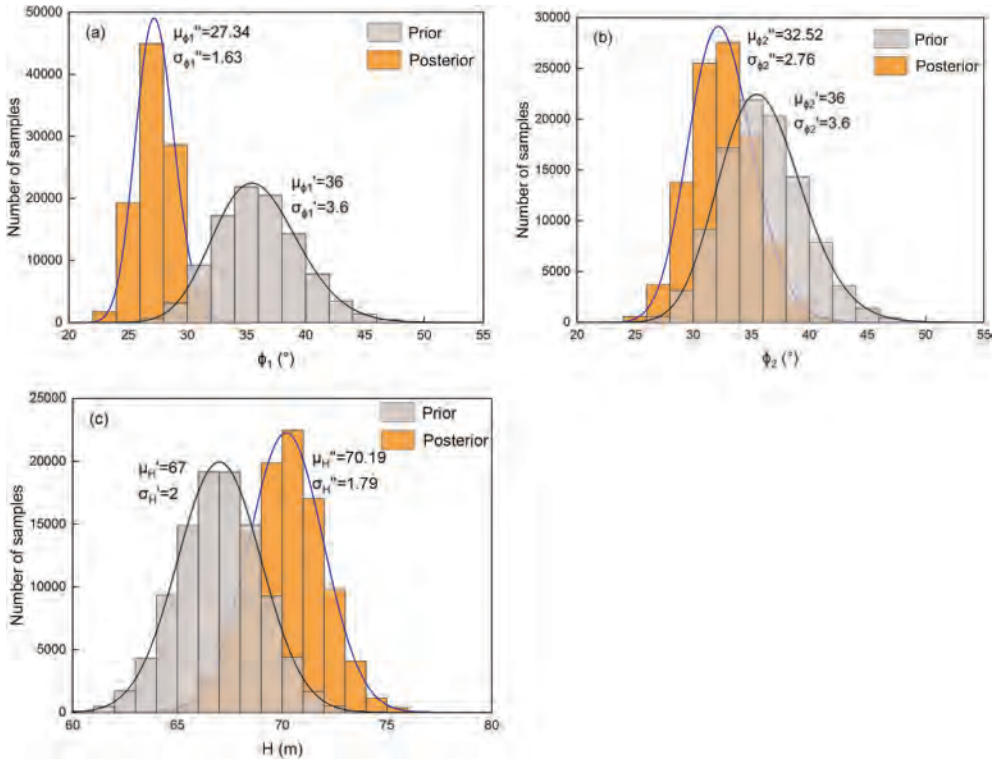
Figure 5. Comparison of distribution of ϕ_1, ϕ_2 and H considering F_S.

0.75 times of the prior value. The posterior mean value of H is larger than the prior value. The standard deviation values of ϕ_1, ϕ_2 and H are a little smaller than the prior values. The prior mean F_S and failure probability of GRSS is 1.27 and 0.16% respectively based on the prior distribution of ϕ_1, ϕ_2 and H. The posterior mean F_S and failure probability of GRSS is 0.98 and 67.89% respectively based on the posterior distribution of ϕ_1, ϕ_2 and H, which is unacceptable level for the safety status of GRSS. It can be found that the decrease of ϕ_1 and ϕ_2 make the posterior failure probability of GRSS significantly increase, which contributes to failure of GRSS.

4 CONCLUSION

This paper conducted a probabilistic back analysis of GRSS considering the uncertainty of statistical parameters of random variables based on the Bayesian network. The uncertainty of friction angle of soil-rock interface and groundwater table level of the reinforced soil slope was considered. Based on the probabilistic back analysis results, the weaken strength of soil-rock interface of the reinforced soil slope at Yeager airport caused significant increase of failure probability of GRSS, making the reinforced soil slope fail. Therefore, the soften soil strength of soil-rock interface is the main reason of failure of the reinforced soil slope at Yeager airport.

REFERENCES

Agarwal, E., Pain, A., Mukhopadhyay, T., Metya, S., Sarkar, S. 2021. Efficient Computational System Reliability Analysis of Reinforced Soil-retaining Structures under Seismic Conditions Including the Effect of Simulated Noise. *Engineering with Computers*: 1–23.

Alhajj Chehade, H., Guo, X., Dias, D., Sadek, M., Jenck, O., Hage Chehade, F. 2022. Reliability Analysis for Internal Seismic Stability of Geosynthetic-reinforced Soil Walls. *Geosynthetics International*: 1–59.

Basha, B.M., Babu, G.S. 2009. Seismic Reliability Assessment of External Stability of Reinforced Soil Walls using Pseudo-dynamic Method. *Geosynthetics International* 16(3): 197–215.

Basha, B.M., Babu, G.S. 2010. Optimum Design for External Seismic Stability of Geosynthetic Reinforced Soil Walls: Reliability Based Approach. *Journal of geotechnical and geoenvironmental engineering* 136(6): 797–812.

Basha, B.M., Babu, G.S. 2011. Seismic Reliability Assessment of Internal Stability of Reinforced Soil Walls using the Pseudo-dynamic Method. *Geosynthetics International* 18(5): 221–241.

Basha, B.M., Babu, G.S. 2014. Reliability-based Load and Resistance Factor Design Approach for External Seismic Stability of Reinforced Soil Walls. *Soil Dynamics and Earthquake Engineering* 60: 8–21.

Bathurst, R.J., Miyata, Y., Allen, T.M. 2020. Deterministic and Probabilistic Assessment of Margins of Safety for Internal Stability of As-built PET Strap Reinforced Soil Walls. *Geotextiles and Geomembranes* 48(6): 780–792.

Bozorgzadeh, N., Bathurst, R.J. 2019a. A Bayesian Approach to Reliability of MSE Walls. *Georisk: Assessment and Management of Risk for Engineered Systems and Geohazards* 15(1): 1–11.

Bozorgzadeh, N., Bathurst, R.J. 2019b. Bayesian Model Checking, Comparison and Selection with Emphasis on Outlier Detection for Geotechnical Reliability-based Design. *Computers and Geotechnics* 116: 103181.

Chalermyanont, T., Benson, C.H. 2004. Reliability-based Design for Internal Stability of Mechanically Stabilized Earth Walls. *Journal of Geotechnical and Geoenvironmental Engineering* 130(2): 163–173.

Chalermyanont, T., Benson, C.H. 2005. Reliability-based Design for External Stability of Mechanically Stabilized Earth Walls. *International Journal of Geomechanics* 5(3): 196–205.

Chen, J.F., Liu, J.X., Xue, J.F., Shi, Z.M. 2014. Stability Analyses of a Reinforced Soil Wall on Soft soils using Strength Reduction Method. *Engineering geology* 177: 83–92.

Christian, J.T., Ladd, C.C., Baecher, G.B. 1994. Reliability Applied to Slope Stability Analysis. *Journal of Geotechnical Engineering* 120(12): 2180–2207.

Collin, J.G., Stark, T.D., Lucarelli, A., Taylor, T.P., Berg, R.R. 2021. Stability and Stress-Deformation Analyses of Reinforced Slope Failure at Yeager Airport. *Journal of Geotechnical and Geoenvironmental Engineering* 147(3): 04020179.

Jensen F.V. 2001. *Bayesian Networks and Decision Graphs*. New York: Springer.

Kim, D., Salgado, R. 2012. Load and Resistance Factors for External Stability Checks of Mechanically Stabilized Earth Walls. *Journal of Geotechnical and Geoenvironmental Engineering* 138(3): 241–251.

Koerner, R.M., Koerner, G.R. 2013. A Data Base, Statistics and Recommendations Regarding 171 Failed Geosynthetic Reinforced Mechanically Stabilized Earth (MSE) Walls. *Geotextiles and Geomembranes* 40: 20–27.

Mahadevan, S., Zhang, R., Smith, N. 2001. Bayesian Networks for System Reliability Reassessment. *Structural Safety* 23(3): 231–251.

Peng, M., Sun, R., Chen, J.F., Rajesh, S., Zhang, L.M., Yu, S.B. 2020. System Reliability Analysis of Geosynthetic Reinforced Soil Slope Considering Local Reinforcement Failure. *Computers and Geotechnics* 123: 103563.

Peng, M., Sun, R., Chen, J.F., Zhang, L.M., Yu, S.B. 2021. Stochastic Seismic Analysis of Geosynthetic-Reinforced Soil Slopes using the Probability Density Evolution Method. *Computers and Geotechnics* 140: 104485.

Phoon, K.K., Kulhawy, F.H. 1999. Characterization of Geotechnical Variability. *Canadian Geotechnical Journal* 36(4): 612–624.

Sayed, S., Dodagoudar, G.R., Rajagopal, K. 2008. Reliability Analysis of Reinforced Soil Walls under Static and Seismic Forces. *Geosynthetics International* 15(4): 246–257.

Shadabfar, M., Huang, H., Kordestani, H., Muho, E.V. 2020. Reliability Analysis of Slope Stability Considering Uncertainty in Water Table Level. *ASCE-ASME Journal of Risk and Uncertainty in Engineering Systems, Part A: Civil Engineering* 6(3): 04020025.

Tatsuoka, F., Tateyama, M., Uchimura, T., Koseki, J. 1997. Geosynthetic-reinforced Soil Retaining Walls as Important Permanent Structures 1996–1997 Mercer Lecture. *Geosynthetics International* 4(2): 81–136.

Wang, L., Hwang, J.H., Luo, Z., Juang, C.H., Xiao, J. 2013. Probabilistic Back Analysis of Slope Failure–A Case Study in Taiwan. *Computers and Geotechnics* 51: 12–23.

Yang, K.H., Ching, J., Zornberg, J.G. 2011. Reliability-based Design for External Stability of Narrow Mechanically Stabilized Earth Walls: Calibration From Centrifuge Tests. *Journal of Geotechnical and Geoenvironmental Engineering* 137(3): 239–253.

Yoo, C., Jung, H.S. 2004. Measured Behavior of a Geosynthetic-reinforced Segmental Retaining Wall in a Tiered Configuration. *Geotextiles and Geomembranes* 22(5): 359–376.

Zhang, L.L., Zhang, J., Zhang, L.M., Tang, W.H. 2010. Back Analysis of Slope Failure with Markov chain Monte Carlo Simulation. *Computers and Geotechnics* 37(7–8): 905–912.

Taylor & Francis
Taylor & Francis Group
http://taylorandfrancis.com

Laboratory study for the new usage of EPS geofoam as a column material

Saeid Bazzazian Bonab*
Department of Civil Engineering, Technical and Vocational University (TVU), Tehran, Iran

Seyed Hamid Lajevardi & Seyed Mohammad Mirhosseini
Department of Civil Engineering, Arak Branch, Islamic Azad University, Arak, Iran

ABSTRACT: Stone column technique is well established to improve soft soil performance. However, an alternative material is proposed to enhance the soft soil performance by reinforcing with geofoam materials. Expanded Polystyrene (EPS) geofoam is a super-weighted geosynthetic material used in various geotechnical engineering applications. This study deals with the innovative use of geofoam as a column material in soft soils to improve bearing capacity. This method has been developed in small-scale laboratory tests and a series of loading tests have been performed on different single floating geofoam columns with two different diameters and a length to diameter ratio of 5. Then, a comparison was made with the results of ordinary stone columns and reinforced stone columns to obtain the advantages of geomofume columns. By considering the bearing capacity, it was found that geofoam columns could be a suitable alternative material to improve the bearing capacity of soft soils. The results showed that the efficiency of geofoam columns is almost similar to ordinary stone columns and geofoam is easy and economical to use.

Keywords: Geosynthetics, Geofoam, Stone Column, Ground Improvement, Laboratory Study

1 INTRODUCTTION

There are various techniques available for improving the soft soil capacity. One of these, is stone columns. Most studies summarized the failure mechanisms of stone columns, including bulging failure, shear failure, and punching failure. However, stone columns may not work well in very soft soil due to the bulging of columns. Encasement materials have been used to minimize the bulging of stone columns and improve their performance (Van Impe 1986). Many studies deal with the stone columns encased with geosynthetics (Murugesan & Rajagopal 2007).

Despite those mentioned above, due to the increasing demand for conventional materials such as stone aggregates as well as the equipment required for construction of stone columns, the use of alternative materials seems necessary. Further, the technique of soil-improvement using geosynthetics is extensively used in the construction of stone columns (Lajevardi *et al*. 2018a, 2018b). In the case of alternative materials, researchers proposed different materials for the construction of columns. The use of a steel bar as reinforcement has been investigated in laboratory studies. The findings show that reinforced stone columns with bars have more stiffness in comparison with ordinary stone columns. (Rezaei *et al*. 2019a).

---

*Corresponding Author: sbazazian@tvu.ac.ir

The newest type of geosynthetics is expanded polystyrene (EPS) geofoam blocks, which is a superlight weight material used for construction purposes. EPS geofoams have been used consistently in roads and as a compressible inclusion behind soil retaining structures as well as a method for protecting buried pipelines (Bartlett *et al.* 2015). It is an elastoplastic hardening material with plastic contractive volume changes under compressive loading, whose behaviour is dependent on the density and confining stress. Further, it has been shown that the volumetric strain and axial compression strain have a linear relation. The growth of both geofoam density and thickness affects the reduction of settlements. However, the changes in the thickness factor of geofoam are more effective than the alteration of the density factor on reducing settlements. Selvakumar and Soundara (2018) conducted one-dimensional swell experiments to evaluate the efficiency of the EPS geofoam column (GC) on the swelling behaviour of expansive soil (Selvakumar & Soundara 2018). The results revealed that by the increase in the diameter of the column, there is a significant reduction in the swelling potential.

The crushed stone aggregate is the most common material used for the construction of the stone column. However, little research has been done on the use of alternative materials as a column material. The previous experimental study as mentioned above has been performed on end-bearing geofoam column using small circular tank (typical CBR sample) and the results were not compared with the other types of columns like ordinary stone columns to obtain its performance. In this study, to introduce a geofoam column as a suitable alternative material to other columns, some laboratory experiments were conducted on floating columns in a large tank. The primary purpose of the study is to evaluate the efficiency of geofoam columns (GCs) with different arrangements. Also, to show the effectiveness of this new approach, the tests were compared with the ordinary stone columns (OSCs) and vertical encasement stone columns (VESCs).

2 LABORATORY MODEL TESTS

2.1 *Material used*

The kaolin clay soil was used as a soil bed. Table 1 represented the properties of kaolin clay soil and stone aggregates features. The properties of geotextile were shown in Table 2. The EPS geofoam blocks with a density of 18.4 kg/m3 (EPS19), were used as a column material. In this case, the geofoam blocks were cut into cylindrical cross sections. Then, one of the geofoam cylinders became a hollow cylinder (Figure 1a), while the other was used as a normal cylinder as shown in Figure 1b. A hollow cylindrical geofoam column had a hole at the middle filled with stone aggregates where a normal solid cylindrical geofoam column had not any hole and it was used without any modifications. As shown in Figure 1c, a cylindrical geotextile was constructed with an overlap of 15 mm geotextile in the length for encasing the column.

Table 1. Properties of the kaolin clay soil and crushed stone aggregates.

Parameter	Kaolin clay	Stone aggregates
Maximum dry unit weight (kN/m^3)	15.5	16.9
Unconfined compression strength (kPa)	30	–
Specific gravity	2.6	2.7
Liquid limit *(%)*	48	–
Plastic limit *(%)*	25	–
Bulk unit weight at 23% moisture content (kN/m^3)	19.1	–
USCS classification symbol	CL	GP

Table 2. Properties of geotextile.

Parameter	Value
Yarn material	Prolypropylene
Ultimate tensile strength (kN/m)	10
Secant stiffness at ultimate Strain (kN/m)	15
Thickness (mm)	1.4
Mass per unit area (gr/m^2)	150

2.2 Experimental model

Similar to some researches (Hamidi *et al.* 2018; Rezaei *et al.* 2019b), a large steel tank with steel rigid loading frame was made. The system of loading was based on displacement control, which contained a hydraulic jack and a rigid loading plate. To achieve the minimum boundary effects on the results of the tests, the steel tank was built in a 1.2 m × 1.2 m × 1 m (Figure 2).

Figure 1. Reinforcement materials: (a) Hollow Geofoam, (b) Normal Geofoam, (c) Geotextile.
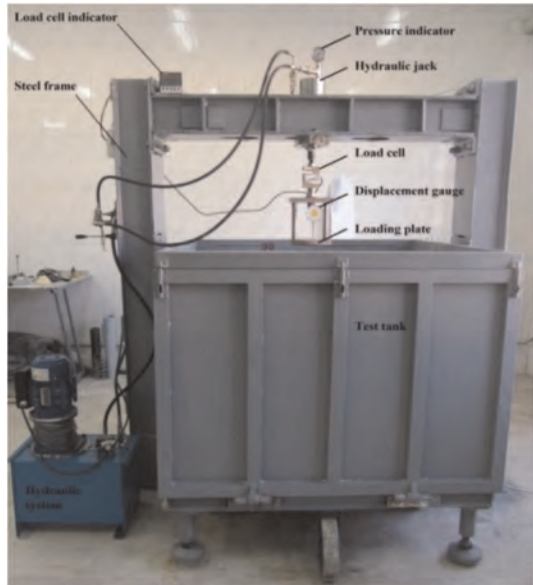
Figure 2. Test tank.

2.3 Experimental procedure

The kaolin clay soil was mixed with a water content of 23% in a container to obtain a homogeneous mixture (corresponding to the unconfined compression strength of 30 kPa). The technique of column construction in the present study is the replacement method. In the case of geofoam columns, after making a borehole in the kaolin clay bed, the geofoam column was simply located into the hole. Moreover, in the case of using a hollow geofoam, the stone aggregate was used to fill the borehole of geofoam column. For encasing vertical geotextile, a thin-walled tube with a diameter equal to the diameter of the geotextile sock

was driven into the hole. Then, the geotextile was located in to the casing and filled with stone aggregates by considering the procedure which was discussed above for OSCs. After that, the casing pulled up while the geotextile left in the place (Bazzazian Bonab *et al.* 2021).

2.4 *Tests conducted*

The columns, which formed in the kaolin clay bed, were subjected to vertical loading through a loading plate displaced at a constant strain rate of 1 mm/min up to a settlement of 50 mm. The loading plate was 2 times larger than the diameter of the columns and had a thickness of 30 mm. The experiments were performed on an unreinforced kaolin clay bed, OSCs, VESCs and GCs (Figures 3 and 4). To evaluate the efficacy of the columns, 11 tests were conducted on two different diameters with the length of 5D, which were installed in kaolin clay bed without ground water level.

As shown in Figure 3, in OSCs, the tests were applied on two diameters (D) and lengths (L), D = 80 mm and L = 400 mm (OSC1) and D = 100 mm and L = 500 mm (OSC2). In VESCs, as the OSCs, two tests were conducted on the stone columns with full-length geotextile encasement with two diameters and lengths (VESC1 and VESC2). The GCs consist of two groups. The first group includes four different tests which were performed using different length of the normal geofoam columns; GC-N1 (D = 80 mm and L = 400 mm), GC-N2 (D = 80 mm and L = 200 mm), GC-N3 (D = 100 mm and L = 500 mm), and GC-N4 (D = 100 mm and L = 250 mm). The second group includes two different tests which were conducted using hollow geofoam columns; GC-H1 (D = 80 mm, L = 400 mm) and GC-H2 (D = 100 mm, L = 500 mm). In this case, there was a hole at the middle of the column with a diameter of 0.5D, which was filled with the aggregates material.
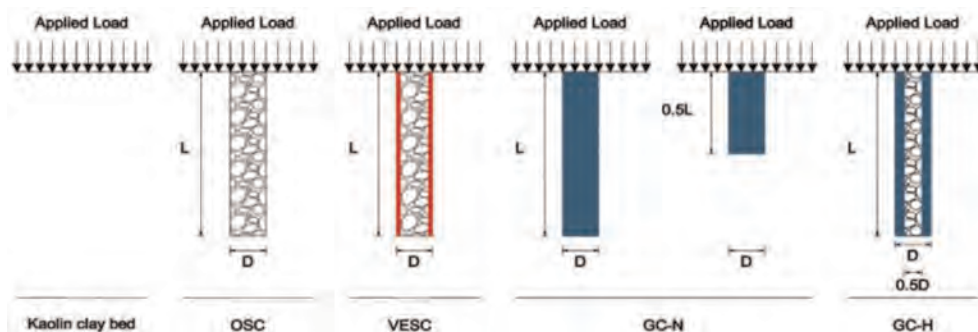
Figure 3.   Schematics of different types of columns testing.
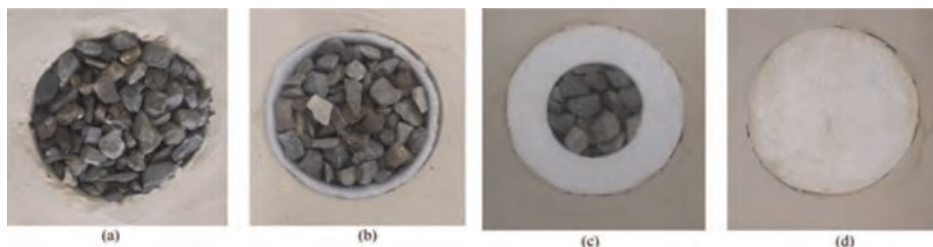
Figure 4.   Different types of column: (a) OSC, (b) VESC, (c) GC-H, (d) GC-N.

3 RESULTS AND DISCUSSION

3.1 *Load-settlement behaviour*

Figures 5(a) and (b) demonstrated the load-settlement behaviour for the columns with the diameter of 80 and 100 mm, respectively up to the settlement of 50 mm. As seen, OSCs, VESCs, and GCs increased the bearing capacity of clay soil. The increase of the bearing capacity for OSC1 (D = 80 mm) and OSC2 (D = 100 mm) were 25.6% and 44.4%, respectively. Also, using VESC1 and VESC2 led to an increase in bearing capacity by 84.8% and 103.7%, respectively. In the case of using geofoam, GC-N1 (D = 80 mm) and GC-N3 (D = 100 mm) led to increase the bearing capacity of the kaolin clay by 33.0% and 40.7%, respectively. The magnitudes of this increase for GC-N2 and GC-H1 (D = 80 mm) was 32.1% and 33.0% while for GC-N4 and GC-H2 (D = 100 mm) was 35.8% and 38.9%, respectively.
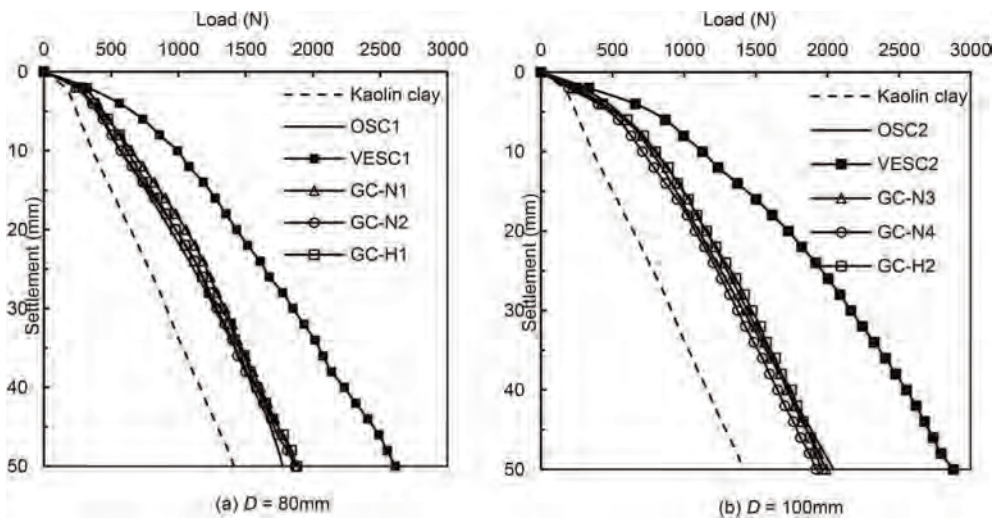
Figure 5.   Variation of load-settlement of kaolin clay bed, OSCs, VESCs and GCs.

According to the results, by using OSCs or GCs instead, the bearing capacity would increase. Encasing OSCs via vertical geotextile reinforcement resulted in a further increase in the bearing capacity of kaolin clay soil. It was because geotextile provides additional confinement, which led to more stiffness of the column. Moreover, the comparison between Figures 5a and 5b for OSCs showed that, by increasing the diameter, the bearing capacity of the clay soil increased by 15.0%. Also, comparing VESC1 with VESC2 showed that upon elevation of the diameter, the bearing capacity rose by 10.3%. Further, the average value of this increase was 4.3% for GCs. The results showed that the increase in the bearing capacity with increasing diameter in VESC is more than twice that of GCs. This is because geotextile has more stiffness, which leads to more confinement than geofoam. Application of VESC1 and VESC2 increased the bearing capacity of the OSC1 and OSC2 by 47.2% and 41.0%, respectively. Therefore, with an increase in the column diameter, the benefit of the encasement decreases. It is because the lateral stresses mobilized in encased stone columns are higher for smaller diameter columns. Based on the experimental study, Bazzazian Bonab *et al.* 2020 also observed that the encasing the stone columns with geotextile, led to increase in the bearing capacity of the stone column by 38% and 32%, respectively for D = 80 and 100 mm. This showed that, encasing the stone columns resulted in more increase in the bearing capacity. Also, the results of the study demonstrated that increasing the column diameter reduced the efficiency of geotextiles as discussed above for the present study.

The effect of the geofoam length was studied for two different lengths. It was seen that with the increase in the length of geofoam from half-length (GC-N2 and GC-N4) to full-length (GC-N1 and GC-N3), the variation of the bearing capacity was negligible. This was because of the deformation mode of OSCs in the form of bulging changes to the small bulging with elastic shortening in both lengths. Therefore, the use of shorter geofoam columns seems sufficient. As observed in Figure 5, the performance of the GC-Hs was almost the same as that of GC-Ns. In other words, filling GCs with stone aggregates did not lead to more increase in the bearing capacity. It might be because GC was not a good element for encasing the stone aggregates.

Comparison of OSCs and GCs showed that the variations of the bearing capacity of the columns for both diameters were negligible. Therefore, the use of GCs instead of OSC led to almost the same results in the bearing capacity of the kaolin clay. From another perspective, the geofoam columns are very easy to install and save both cost and time by eliminating compaction operations. Also, there is not any soil distribution in installation in such cases. Also, the lightness of the geofoam makes it easy to work with and reduces the cost of transportation.

The parameter of the ratio of the area replacement (AR) is defined which offers the percentage of soil replaced by the column materials and obtains from dividing the column area to the loaded area. In order to compare the benefits of geofoam material and geotextile encasement with OSC, the dimensionless parameter (β) is defined, which explained as the ratio of the bearing capacity of the reinforced column (GCs or VESCs) to unreinforced stone column (OSCs). The variations of β with AR for different columns diameters presented in Table 3. As seen, the variation of the β was almost the same for GCs. Thus, by considering the bearing capacity, the performance of the GCs was similar to that of OSCs. In addition, it was found that the β values for VESCs vary within the range of 1.41–1.47. In this case, the elevation of AR leads to decreases in β. So, it means that increasing the column diameter led to a decrease in the efficiency of the reinforcement. Also, as stated for VESCs, in geofoam columns, the column efficiency decreases with increasing the column diameter. As seen in Table 4, with the increase of the AR, the stiffness of the column increases and as a result, the bearing capacity of the column increases.

Table 3. Variation of β with AR.

Diameter (mm)	80	100
AR%	16	25
GC-N1	1.06	–
GC-N3	–	0.97
GC-N2	1.05	–
GC-N4	−0.94	
GC-H1	1.06	–
GC-H2	–	0.96
VESC1	1.47	–
VESC2	–	1.41

Table 4. Details of tests conducted.

	AR	
Type of column	16	25
GC-N1	1.82	–
GC-N3	–	2.24
GC-N2	1.67	–
GC-N4	–	2.05
GC-H1	1.80	–
GC-H2	–	2.28
VESC1	2.79	–
VESC2	–	3.29

4 CONCLUSIONS

- The bearing capacity of geofoam columns (GCs) is almost equal to the bearing capacity of ordinary stone columns (OSCs). However, this amount is smaller than vertical encasement

stone columns (VESC). This shows that the stiffness created by the stone aggregates is the same as the stiffness created by the geofoam materials.

- In VESCs, the reinforcing stone column with geotextile provides additional confinement. Thus, the bulging reduces and the bearing capacity increases. This indicates that the geotextile encasement increases the stiffness of the column.
- The value of β varies in the range of 0.94–1.06 and 1.41– 1.47 for GCs and VESCs, respectively. Therefore, it is concluded that the increase of the area replacement ratio (AR) in the GCs and VESC, lead to decrease in the benefits of the geofoam and geotextile materials.
- The geofoam columns could be a good alternative material because they have the same performance with the ordinary stone columns and are very easy to install and save both cost and time. However, the technique of using geofoam columns is in the beginning and requires additional studies on a real scale condition to understand its behaviour.

REFERENCES

Bartlett, S.F., Lingwall, B.N., Vaslestad, J. 2015. Methods of Protecting Buried Pipelines and Culverts in Transportation Infrastructure using EPS Geofoam. *Geotext Geomembranes* 43:450–461. https://doi.org/10.1016/j.geotexmem.2015.04.019

Bazzazian Bonab, S., Lajevardi, S.H., Saba, H.R., Ghalandarzadeh, A., Mirhosseini, S.M. 2020. "Experimental Studies on Single Reinforced Stone Columns with Various Positions of Geotextile." *Inovativee Infrastructure Solutions* 5 (3): 1–12. https://doi.org/10.1007/s41062-020-00349-0

Bazzazian Bonab, S., Lajevardi, S.H., Saba, H.R., Mirhosseini, S.M. 2021. "The Novel Usage of EPS Geofoam as Column Material: A Laboratory Study." *International Journal of Geosynthetics and Ground Engineering* 7 (1): 1–14. https://doi.org/ 10.1007/s40891-020-00252-9

Hamidi, M., Lajevardi, S.H. 2018. "Experimental Study on the Load-carrying Capacity of Single Stone Columns." *International Journal of Geosynthetics and Ground Engineering* 4 (26): 1–10. https://doi.org/10.1007/s40891-018-0142-x

Lajevardi, S.H., Enami, S., Shamsi, H.R., Hamidi, M. 2018a. "Experimental Study of Single and Groups of Stone Columns Encased by Geotextile." *Amirkabir Journal of Civil Engineering* 50(6): 337–340. https://doi.org/10.22060/CEEJ.2018.12789.5269

Lajevardi, S.H., Shamsi, H.R., Hamidi, M., Enami, S. 2018b. "Numerical and Experimental Studies on Single Stone Columns." *Soil Mechanics and Foundation Engineering* 55 (5): 340–345. https://doi.org/10.1007/s11204-018-9546-9

Mohammad Rezaei, M., Lajevardi, S.H., Saba, H.R., Ghalandarzadeh, A., Zeighamie, E. 2019a. "Laboratory Study on Single Stone Columns Reinforced with Steel Bars and Discs." *International Journal of Geosynthetics and Ground Engineering* 5 (2): 1–14. https://doi.org/10.1007/s40891-019-0154-1

Mohammad Rezaei, M., Lajevardi, S.H., Saba, H.R., Ghalandarzadeh, A., Zeighamie, E. 2019b. "Experimental and Numerical Studies on Load-Carrying Capacity of Single Floating Aggregate Piers Reinforced with Vertical Steel Bars." *Amirkabir Journal of Civil Engineering* In press. http://doi.org/10.22060/CEEJ.2019.15640.5991

Murugesan, S., Rajagopal, K. 2007. "Model Tests on Geosynthetic-encased Stone Columns" *Geosynth Int* 14 (6):346–354. https://doi.org/10.1680/gein.2007.14.6.346

Selvakumar, S., Soundara, B. 2018. The Performance of EPS Geofoam Columns.: An Introduction. *In*: *Proceedings of the 11th Int. Conf. on Geosynthetics*, Seoul, Korea, pp. 47–53.

Van Impe, W.F. 1986. "Improving of the Bearing Capacity of Weak Hydraulic Fills by Means of Geotextiles." *3rd International Conference on Geotextiles.* Vienna, Austria, pp. 1411–6

Influence of layers and stiffness of geosynthetics on the stability and failure modes on embankments over soft ground

Gang Zheng
MOE Key Laboratory of Coast Civil Structure Safety, Tianjin University, Tianjin, China
Department of Civil Engineering, Tianjin University, Tianjin, China

Boyang Xia
Department of Civil Engineering, Tianjin University, Tianjin, China

Haizuo Zhou*
MOE Key Laboratory of Coast Civil Structure Safety, Tianjin University, Tianjin, China
Department of Civil Engineering, Tianjin University, Tianjin, China

Xiaoxuan Yu
Department of Civil Engineering, Tianjin University, Tianjin, China

ABSTRACT: Geosynthetics are widely used on improving embankment stability. However, limited studies have focused on the stability and failure modes of geosynthetic-reinforced embankments with various layers and stiffness of geosynthetics. In this paper, a finite difference approach is used to analyze the ultimate surcharge of embankments and failure mechanism. The results show that the stiffness and layers of geosynthetic both have a positive influence on the embankment stability. A deep-seated failure occurs when the geosynthetic stiffness and layers are low. When the stiffness and layers increase to a certain value, the failure mechanism changes to lateral sliding failure.

Keywords: Numerical analysis, Geosynthetics, Failure mode, Embankment, Stability

1   INTRODUCTION

Embankments on soft clays are often required for building expressways and railways (e.g., Chai *et al.* 2013; UIC 2018; Zhou *et al.* 2020, 2023). The stability of embankments over soft soil has attracted considerable attention (e.g., Sharma & Bolton 1996; Mohapatra & Rajagopal 2017). The application of geosynthetic reinforcements serves as an economical solution for increasing global stability when stabilizing an embankment (e.g., Chai *et al.* 2002; Miao *et al.* 2014; Zheng *et al.* 2021).

The failure mechanisms of embankments reinforced by geosynthetics can be divided into two categories: deep-seated failure (global failure) and lateral sliding failure (surface failure) (Abusharar & Han 2011; Smith & Tatari 2016; Zheng *et al.* 2020). Smith & Tatari (2016) conducted parametric studies of single layer geosynthetic reinforced embankment, the major failure modes were determined and design envelopes of overall stability were presented. However, varying stiffness and layers of geosynthetic reinforcements may have a significant influence on the associated failure mechanism and the embankment's overall stability.

In this study, finite difference numerical modelling is performed to explore the influence of various layers and stiffness on the critical failure modes. The ultimate failure height and the transition of the failure mechanism of the embankment are analyzed.

---

*Corresponding Author: hzzhou@tju.edu.cn

2 NUMERICAL MODELLING

Numerical modelling of the geosynthetic reinforced embankment (GRE) over soft soils is established using the finite difference method implemented through the software FLAC3D (Itasca, 2006; Zheng *et al.* 2018, 2019). A typical numerical modeling section is shown in Figure 1. Embankment with a slope of 3(*H*):2(*V*). The thickness of the soft layer is 15m and the thickness of the silty layer is 5m. One half of the embankment was modeled, and symmetrical boundary conditions were applied along the lateral boundaries, while both the horizontal and vertical displacements were fixed along the bottom boundary.

Soil constitutive models and their baseline material properties are listed in Table 1. The silty clay layer and embankment were represented as linear elastic and perfectly plastic with the Mohr-Coulomb failure criterion. The soft clay layer was modeled with Modified Cam Clay (MCC) model. According to the MCC model and along undrained triaxial compression stress paths, the undrained shear strength (s_u) was determined by the MCC model as shown in Eq. (1) (Chai *et al.* 2013; Liu *et al.* 2007; Zhou *et al.* 2021):

$$c_u = \frac{p'}{2^{1+\Lambda}} M \left(\frac{M^2 + \eta^2}{M^2}\right)^\Lambda (\text{OCR})^\Lambda \tag{1}$$

where $\Lambda = 1-\kappa/\lambda$; $\eta = q/p'$ and overconsolidation ratio (OCR) of 1 in this study.

Geosynthetics were modeled using orthotropic linear elastic structural geogrid elements of the constant strain triangle type (Abusharar & Han 2011; Zheng *et al.* 2019). The geogrid elements can sustain membrane stress but not bending, which reasonably simulate the behavior of the geosynthetic reinforcement layers. A friction coefficient of 0.8 was adopted for geogrid-soil interfaces and the shear stiffness $k_{s,geo}$ between the geosynthetic layer and the surrounding soil was considered as 1/10 of the elastic modulus of the geosynthetic material (Liu *et al.* 2009; Yu *et al.* 2021; Zheng *et al.* 2020, 2021). The properties of the geosynthetic reinforcement are exhibited in Table 3.

The embankment construction process was simulated by placing embankment structure elements layer by layer until the global failure occurs. The thickness of each layer was 0.25m.
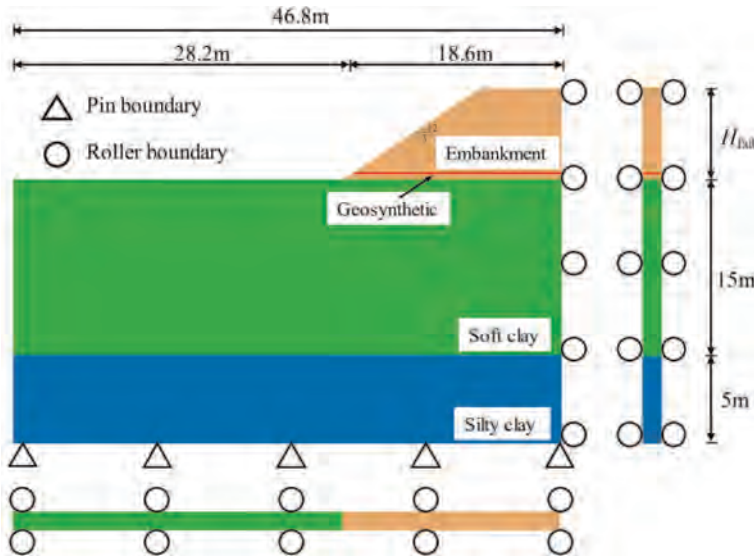
Figure 1.   The configuration of the numerical model.

Table 1. The configuration of the numerical model.

Material	v	c_u(kPa)	E(MPa)	φ (°)	γ(kN/m^3)	λ	κ	M	e_1	σ'_p(kPa)
Embankment	0.3	10	30	32	18	–	–	–	–	–
Soft clay	0.37	–	–	–	18	0.26	0.05	1.02	2.57	σ'_v
Silty clay	0.25	20	37.5	35	19	–	–	–	–	–
Geosynthetic	J = 800, 2000,6000,8000,10000,12000kN/m, v_{geo} = 0.3, c_i = 0.8, t = 2mm, $k_{s,geo}$ = Variable									

Note E = elastic modulus, v = Poisson's ratio of soil, c_u = undrained shear strength, φ = friction angle, γ = unit weight (saturated unit weight for the soil below the ground water table), c_i = interaction coefficient between geosynthetic and the surrounding soil, J = tensile stiffness of geosynthetics, v_{geo} = Poisson's ratio of geosynthetics, t = the thickness of geosynthetics and $k_{s,g}$ = interface shear stiffness between the geosynthetics and the soil.

3 PARAMETRIC STUDY

Figure 2 shows the variation of embankment center settlement with filling height for various geosynthetic tensile stiffnesses. A non-linear variation of foundation settlement can be observed for all the cases. Besides, with the increase in the geosynthetics stiffness from 800kN/m to 12000kN/m, the foundation settlement has decreased from 1.3 to 2.7 times compared with the unreinforced case.
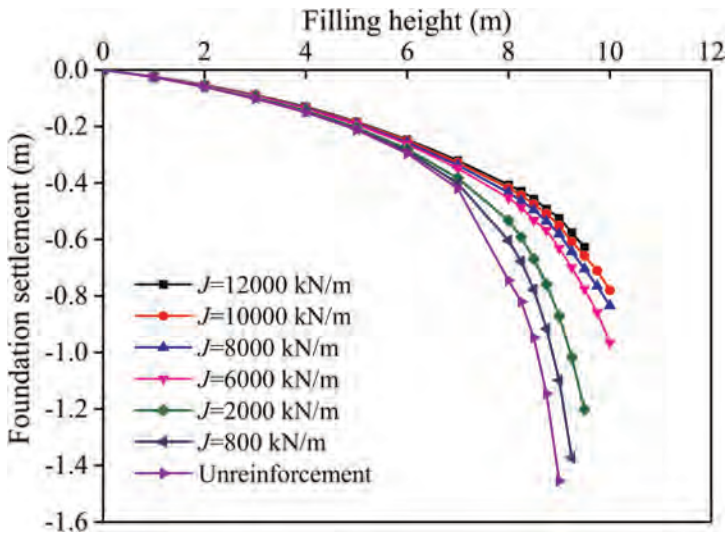
Figure 2. Histories of the vertical settlement of the foundation with various geosynthetic stiffnesses.

Figure 3 illustrates the influence of the number of geosynthetic layers on the settlement of center of the soft foundation (J = 2000kN/m). With an increase in the number of geosynthetic layers, the vertical settlements located at the embankment center are reduced. However, the settlement discrepancy is relatively small at the beginning of the construction process (e.g., $H<6$m) and gradually becomes significant as the embankment height increases. For example, the difference of subsidence between J = 800kN/m and J = 12000kN/m is increased for 16.2% (H = 6m) to 84.9% (H = 9m). This result indicates that compared to adding the number of geosynthetic layers, increasing geosynthetic stiffness is more effective in limiting the global deformation under embankment loading conditions.
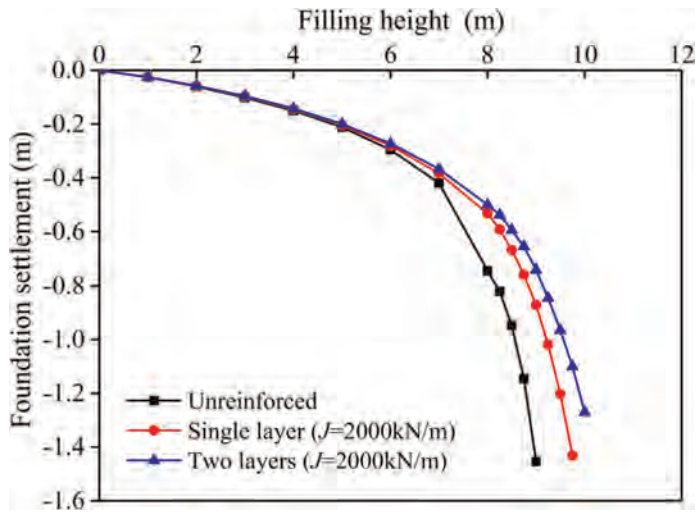
Figure 3. Histories of the vertical settlement of the foundation with numbers of geosynthetic layers.

4 TRANSITION OF THE FAILURE MECHANISM

In this study, the ultimate height of embankment (H_u) is selected as the stability metric. Figure 4 shows the ultimate height corresponding to different stiffness values of single layer geosynthetic. There are two failure mechanisms occurred under embankment loading, which can be described as deep-seated failure and lateral sliding failure (Smith & Tatari 2016; Zheng *et al*. 2019). For a low tensile stiffness reinforcement, a deep-seated failure mechanism is found in the embankment system, and the stability of embankment increases with the increase in the tensile stiffness. Once the tensile stiffness exceeds a certain value ($J = 10000$kN/m), the failure mechanism changes from the deep-seated failure mode to the lateral sliding failure, indicating that the shear strength of the embankment on global stability becomes dominant. In turn, the ultimate height remains constant, representing that the effect of the geosynthetic stiffness is negligible.
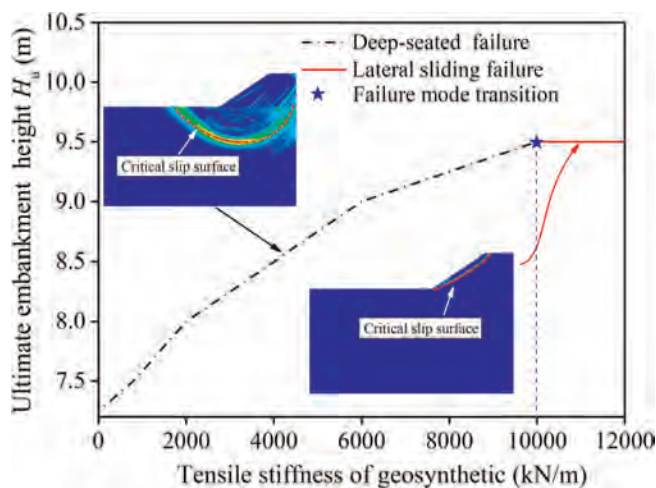
Figure 4. Variation in embankment failure height with geosynthetics stiffnesses.

To further elaborate on the failure mechanisms transition of various geosynthetic tensile stiffnesses, a different number of geosynthetic layers are considered, as shown in Figure 5. It can be seen that in the deep-seated failure mechanism, increasing reinforcement layers effectively improves the global stability. Besides, the threshold value (tensile stiffness J) for the failure mechanisms transition is smaller in the two layers of reinforcements. Similarly, in the lateral sliding failure mechanism, the effect of the number of geosynthetic layers is negligible.
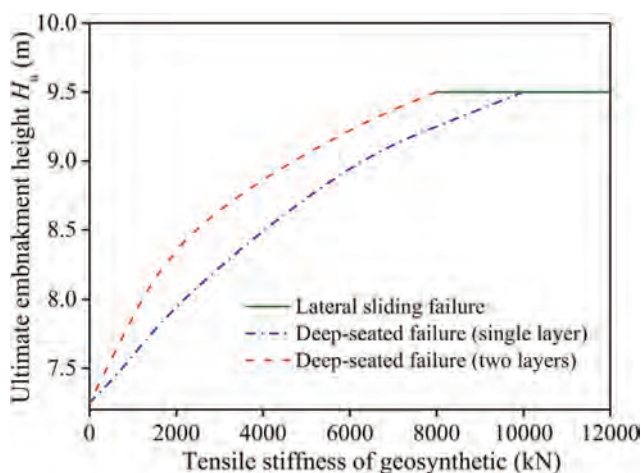
Figure 5. Transition of the critical failure mechanism with different numbers of geosynthetic layers.

5 CONCLUSIONS

A numerical model is adopted to investigate the failure mechanisms and performance of geosynthetic reinforced soft foundations under an embankment load. Various layers and stiffnesses of geosynthetics are considered and discussed. The following conclusions can be drawn:

1. Increasing tensile stiffness and the number of geosynthetic layers result in a better performance to reduce the amount of settlement located at the center of the embankment. Compared to adding the number of geosynthetic layers, increasing geosynthetic stiffness is more effective in limiting the global deformation under embankment loading conditions.
2. The ultimate height of the reinforced embankment increases nonlinearly with the tensile stiffness of geosynthetic, and the deep-seated failure changes to lateral sliding failure as tensile stiffness increases up to a certain critical value. In the lateral sliding failure mechanism, the effect of geosynthetic reinforcement is negligible.
3. Increasing reinforcement layers effectively improve the global stability under the deep-seated failure mechanism. Meanwhile, it reduced the critical value of the failure mechanism transition.

REFERENCES

Abusharar, S. W., & Han, J. (2011). Two-dimensional Deep-seated Slope Stability Analysis of Embankments Over Stone Column-improved Soft Clay. *Engineering Geology*, *120*(1–4), 103–110.

Chai, J. C., Miura, N., & Shen, S. L. (2002). Performance of Embankments with and without Reinforcement on Soft Subsoil. *Canadian Geotechnical Journal*, *39*(4), 838–848.

Chai, J., Igaya, Y., Hino, T., & Carter, J. (2013). Finite Element Simulation of an Embankment on Soft Clay–Case Study. *Computers and Geotechnics*, 48, 117–126.

Liu, C. N., Ho, Y. H., & Huang, J. W. (2009). Large Scale Direct Shear Tests of Soil/PET-yarn Geogrid Interfaces. *Geotextiles and Geomembranes*, 27(1), 19–30.

Liu, H. L., Ng, C. W., & Fei, K. (2007). Performance of a Geogrid-reinforced and Pile-supported Highway Embankment Over Soft Clay: Case Study. *Journal of Geotechnical and Geoenvironmental Engineering*, 133 (12), 1483–1493.

Miao, L., Wang, F., Han, J., & Lv, W. (2014). Benefits of Geosynthetic Reinforcement in Widening of Embankments Subjected to Foundation Differential Settlement. *Geosynthetics International*, 21(5), 321–332.

Mohapatra, S.R., Rajagopal, K., 2017. Undrained Stability Analysis of Embankments Supported on Geosynthetic Encased Granular Columns. *Geosynthetics International*, 24 (5), 465–479.

Railisa. Rail Transport in the World. *Union Internationale Des Chemins de Fer (UIC)*; 2018.

Sharma, J. S., & Bolton, M. D. (1996). Centrifuge Modelling of an Embankment on Soft Clay Reinforced with a Geogrid. *Geotextiles and Geomembranes*, 14(1), 1–17.

Smith, C. C., & Tatari, A. (2016). Limit Analysis of Reinforced Embankments on Soft Soil. *Geotextiles and Geomembranes*, 44(4), 504–514.

Yu, X., Zheng, G., Zhou, H., & Chai, J. (2021). Influence of Geosynthetic Reinforcement on the Progressive Failure of Rigid Columns under an Embankment Load. *Acta Geotechnica*, 16(9), 3005–3012.

Zheng, G., Xia, B., Zhou, H., Zhao, J., Yu, X., Sun, X., & Du, J. (2020). Seismic Bearing Capacity of Strip Footings on Ground Reinforced by Stone Columns using Upper-bound Solutions. *International Journal of Geomechanics*, 20(9), 06020024.

Zheng, G., Yang, X., Zhou, H., & Chai, J. (2019). Numerical Modeling of Progressive Failure of Rigid Piles Under Embankment Load. *Canadian Geotechnical Journal*, 56(1), 23–34.

Zheng, G., Yu, X., Zhou, H., Wang, S., Zhao, J., He, X., & Yang, X. (2020). Stability Analysis of Stone Column-supported and Geosynthetic-reinforced Embankments on Soft Ground. *Geotextiles and Geomembranes*, 48(3), 349–356.

Zheng, G., Yu, X., Zhou, H., Yang, X., Guo, W., & Yang, P. (2021). Influence of Geosynthetic Reinforcement on the Stability of an Embankment with Rigid Columns Embedded in an Inclined Underlying Stratum. *Geotextiles and Geomembranes*, 49(1), 180–187.

Zheng, G., Yang, X., Zhou, H., Du, Y., Sun, J., & Yu, X. (2018). A Simplified Prediction Method for Evaluating Tunnel Displacement Induced by Laterally Adjacent Excavations. *Computers and Geotechnics*, *95*, 119–128.

Zhou, H., Liu, X., Tan, J., Zhao, J., & Zheng, G. (2023). Seismic Fragility Evaluation of Embankments on Liquefiable Soils and Remedial Countermeasures. *Soil Dynamics and Earthquake Engineering*, 164, 107631.

Zhou, H., Xu, H., Yu, X., Guo, Z., Zheng, G., Yang, X., & Tian, Y. (2021). Evaluation of the Bending Failure of Columns Under an Embankment Loading. *International Journal of Geomechanics*, 21(7), 04021112.

Zhou, H., Zheng, G., Liu, J., Yu, X., Yang, X., & Zhang, T. (2019). Performance of Embankments with Rigid Columns Embedded in an Inclined Underlying Stratum: Centrifuge and Numerical Modelling. *Acta Geotechnica*, 14(5), 1571–1584.

Numerical study for the new use of EPS geofoam as a column material

Seyed Mohammad Mirhosseini* & Seyed Hamid Lajevardi
Department of Civil Engineering, Arak Branch, Islamic Azad University, Arak, Iran

Saeid Bazzazian Bonab
Department of Civil Engineering, Technical and Vocational University (TVU), Tehran, Iran

ABSTRACT: A wide range of treatments has been proposed to improve soft soils. However, increasing construction costs and combining with today's environmental considerations will undoubtedly make the need for alternative materials. Expanded Polystyrene (EPS) geofoam is a superlight weight geosynthetic material used in various geotechnical engineering applications. This study deals with the innovative use of geofoam as a column in the soft soil for improving the load-carrying capacity. A series of numerical analysis was carried out on the various single floating geofoam columns with diameters of 80 mm and 100 mm and the length of 400 mm and 500 mm, respectively. Then, the results of the analysis were compared with the results of ordinary stone columns and vertical encasement stone columns with the geotextile to obtain the benefits of geofoam columns. The load-carrying capacity of the geofoam column is almost equal to the load-carrying capacity of an ordinary stone column. However, this amount is smaller than vertical encasement stone columns. The lateral deformation of the columns was investigated for all types of columns. The bulging in geofoam columns is smaller than the ordinary stone column.

Keywords: Geosynthetics, Geofoam, Stone Columns, Ground Improvement, Numerical Analysis

1   INTRODUCTION

There are various techniques available for improving the load-carrying capacity of soft soils. One of these is stone columns. However, due to increasing demand of conventional materials such as stone aggregates as well as the equipment required for construction of stone columns, the use of alternative materials seems necessary. Further, the technique of soil-improvement using geosynthetics is extensively used in the construction of stone columns (Lajevardi *et al.* 2018a, 2018b; Malarvizhi & Ilamparuthi 2007). The newest type of geosynthetics is expanded polystyrene (EPS) geofoam blocks which is a superlight weight material used for construction purposes. EPS geofoams have been used consistently in roads (Beinbrech & Hillmann 1997) and as a compressible inclusion behind soil retaining structures (Ram Rathan Lal *et al.* 2014) as well as a method for protecting buried pipelines (Bartlett *et al.* 2015). It is an elastoplastic hardening material with plastic contractive volume changes under compressive loading (Leo *et al.* 2008) whose behavior is dependent on the density and confining stress. Further, it has been shown that the volumetric strain and axial compression strain have a linear relation (Chun *et al.* 2001). The growth of both geofoam density and thickness affects reduction of settlements. However, the changes in the thickness factor of

---

*Corresponding Author: m-mirhoseini@iau-arak.ac.ir

geofoam are more effective than the alteration of the density factor on reducing settlements. (Abdelrahman & Kamash 2014). Selvakumar and Soundara (2018) have performed a series of one-dimensional swell tests to study the performance of the EPS geofoam column (GEC) on the swelling behavior of expansive soil. The results revealed that by increasing the column diameter, there is a significant reduction in the swelling potential.

There are very limited studies on geofoam columns. In this study, some small-scale laboratory tests were carried out on single floating columns with various diameters. In these tests, columns were installed in kaolin clay bed with no ground water table. The main objective of this study is to investigate the efficiency of geofoam columns (GECs) with various arrangements. Also, to show the effectiveness of this new approach, the tests were compared with the ordinary stone columns (OSCs) and vertical encasement stone columns (VESCs) with geotextile. It was then extended to real columns by performing numerical analyses.

2 LABORATORY MODEL TESTS

2.1 *Material used*

The kaolin clay soil was used as a soil bed. Table 1 represented the properties of kaolin clay soil and stone aggregates features. The EPS geofoam blocks with a density of 18.4 kg/m3 (EPS19), were used as a column material (Bazzazian Bonab et al. 2020).

Table 1. Properties of the kaolin clay soil and crushed stone aggregates.

Parameter	Kaolin clay	Stone aggregates
Maximum dry unit weight (kN/m^3)	15.5	16.9
Minimum dry unit weight (kN/m^3)	–	14.3
Optimum moisture content *(%)*	19	–
Unconfined compression strength (kPa)	30	–
Specific gravity	2.6	2.7
Liquid limit *(%)*	48	–
Plastic limit *(%)*	25	–
Plasticity index *(%)*	23	–
Bulk unit weight at 23% moisture content (kN/m^3)	19.1	–
Bulk unit weight for test at 70% relative density (kN/m^3)	–	16
Internal friction angle at 70% relative density (degree)	–	46
Uniformity coefficient (Cu)	–	2.25
Curvature coefficient (Cc)	–	1.62
USCS classification symbol	CL	GP

2.2 *Experimental model*

Similar to some researches (Hamidi *et al.* 2018; Rezaei *et al.* 2019b), a large steel tank with steel rigid loading frame was made. The system of loading was based on displacement control, which contained a hydraulic jack and a rigid loading plate. More information about the test setup was described by Bazzazian Bonab et al. (2021).

3 NUMERICAL STUDY

The kaolin Numerical modeling is often used to develop and complete experimental modeling, through which engineering problems can be solved and the behavior of materials could

be predicted in both real and field conditions. In this section, axisymmetric finite element model was developed on Plaxis 2D to achieve this purpose. It was calibrated to match the actual laboratory measured response of the column. Then, another series of finite element (FE) models was done to describe the behavior of the columns in real condition (Mohammad Rezaei et al. 2019).

The analyses simulate the same geometry and boundary conditions as in the laboratory tests. Numerical modeling is performed in an axisymmetric form in the half-plane using 15-nodded unstructured mesh. The vertical boundaries were released in the vertical direction with the bottom boundary being fixed.

For loading element, the plate element was placed on the top of the columns and the entire analysis was considered by the displacement control where the maximum settlement was 50 mm. Since the plate was modeled as rigid, the settlement remained uniform beneath the loaded area. The soft soil behavior and Mohr–Coulomb failure criterion were adopted for soil and the crushed stone aggregates, respectively. Also, the elastic-plastic method based on Mohr–Coulomb failure criterion was adopted for geofoam. The material properties used for modeling kaolin clay bed, crushed stone aggregates, geotextile encasement and geofoam are presented in Table 2.

Table 2. The number of officially reported plague cases in the world.

Parameter	Kaolin clay	Crushed stone aggregates	Geofoam	Geotextile
Model type	Soft soil	Moher-column	Moher-column	–
Friction angle, φ (degree)	28	46	2	–
Dilation angle, ψ (degree)	0	16	0	–
Cohesion, C (kPa)	15	1	21	–
Poisson's ratio, v	0.33	0.30	0.10	–
Young's modulus, E (kPa)	–	40000	4000	–
Unit weight, γ (kN/m^3)	19	16	0.18	–
Logarithmic hardening constant for plasticity, λ	0.134	–	–	–
Logarithmic bulk modulus for elastic material behavior, κ	0.40	–	–	–
Secant stiffness, J (kN/m)	–	–	–	15

3.1 Verification

To verify the numerical model developed, a comparison was made between the results of experimental tests and the numerical analysis for 100 mm stone columns (Figure 1) (Bazzazian *et al*. 2020). The comparison showed a good agreement between experimental and numerical results.

3.2 Lateral deformation of the columns

After completion of each test, slurry of plaster was poured into the stone column and allowed to settle for 24 hours to harden. This would prevent dissipation of stone aggregate. Then, the surrounding kaolin clay was removed carefully and whereby a deformed shape of the stone column was obtained where the bulge depth was visible. Figure 2 demonstrates the deformed shapes of OSC and VESC indicating bulging failure mechanism occurring at the depth of D to 2D from top of the column. The bulging in VESC was smaller than that of in
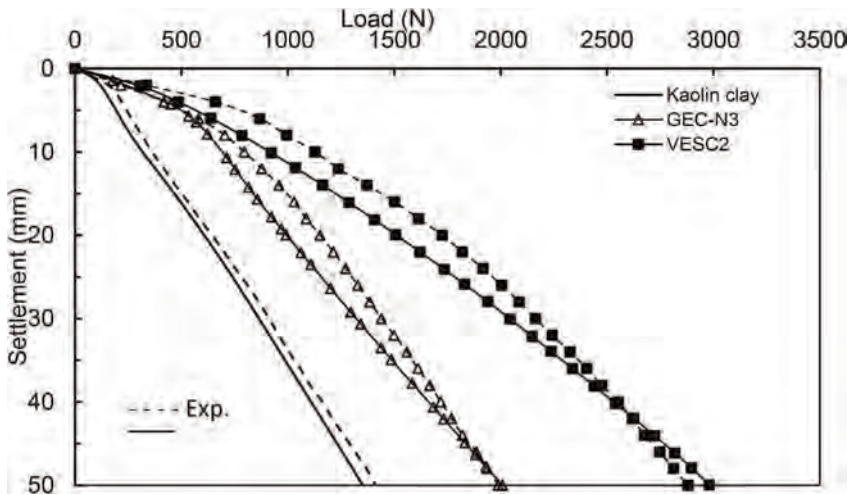
Figure 1. Comparison between numerical analysis and experimental results for D = 100 mm.

(a) OSC   (b) VESC
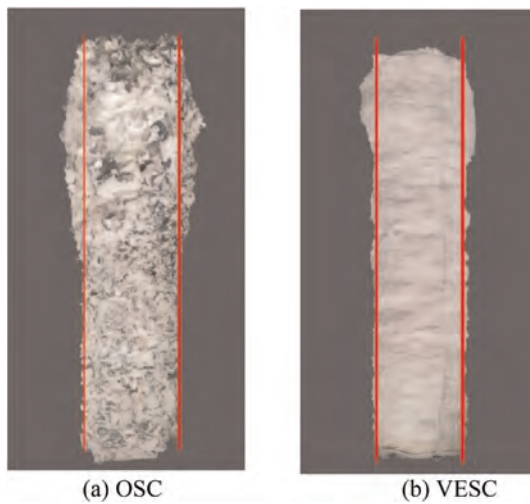
Figure 2. Deformation of columns after test.

OSC. Bulging in reinforced stone columns was reduced due to the additional confinement arising from the reinforcement material.

The lateral deformations of the columns obtained from the experimental and numerical analysis are shown in Figure 3. The bulging in GEC was smaller than that of in OSC and it occurred at the depth of D to 2D from top of the column as with OSC. However, half-length geofoam columns (GEC-N2), fail from punching while full-length geofoam columns (GEC-N1) fail by bulging. Moreover, the bulging in VESC was the smallest.

3.3 Reinforcement ratio

Reinforcement ratio (RR) is defined as the load-carrying capacity of the reinforced stone column to unreinforced stone column. This parameter represents the impact of
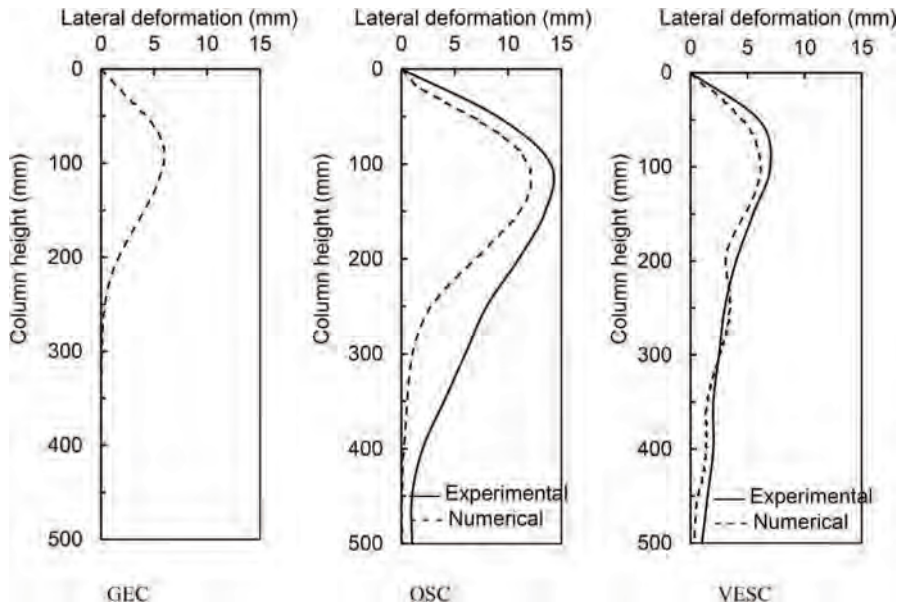
Figure 3.   Lateral deformation of the columns (D = 100 mm).

reinforcement on the load-carrying capacity of stone columns. The ratio of the area replacement (RAR) is a crucial dimensionless parameter which provides the percentage of soft soil replaced by the crushed stone aggregate. It is defined as the area of the stone columns divided by the loaded area. Table 3 presents variations of RR with RAR for various diameters of the columns.

As seen, the variation of the RR is almost the same for GECs. Thus, although GECs enhance the load-carrying capacity of the kaolin clay bed, the performance of the GECs is similar to that of OSCs. It is found that the RR values for VESCs vary within the range of 1.18–1.59. Further, elevation of RAR leads to further increase in RR.

Table 3.   Variation of RR with RAR.

Diameter (mm)		50	60	70	80	90	100	110
RAR %								
Type of arrangement		6.25	9	12.25	16	20.25	25	30.25
RR	GEC-N[*]	1.04	1.05	1.03	1.04	1.03	1.03	1.03
	VESC	1.18	1.27	1.32	1.42	1.49	1.56	1.59

[*]Full-length

3.4   Load ratio

To extend the results of small-scale laboratory tests to large-scale and real conditions, it is necessary to examine the effects of scale in numerical models. Thus, the behaviors of the columns with diameters of 0.80 m and 1.0 m were studied by numerical analysis. Table 4 shows the various values of the load ratio (LR) for real diameters in the 50 mm settlement. As can be seen, the load ratio of numerical modeling has a good agreement with the LR values obtained from experimental tests. Thus, the results of small-scale experimental tests can be used to study the performance of GECs on a real scale.

Table 4. Various values of LR for real diameters.

Column	D (m)	
	0.8	1.0
OSC	1.3	1.54
GEC-N[*]	1.3	1.4
VESC	1.8	2.0

[*]Full-length

Although in the field practices well-established technique has been adopted in the installation of the OSC, but it has some problems. However, this study is an introduction to further studies on the use of geofoam columns. The technique of using geofoam columns is in the beginning and requires additional studies on a real scale condition to understand its behaviour.

4 CONCLUSION

The load-carrying capacity of GEC-N is almost equal to the load-carrying capacity of OSC. However, this amount is smaller than VESC.

The magnitude of the lateral deformation of GECs is between OSCs and VESCs. However, its region is less than both of them. In GECs, it was observed that encasing the stone column in the top of the column plays a fundamental role in the performance of the stone column. The reason is that the bulging failure usually occurs at the depth of D to 2D from the top of the stone columns. So, it might be obvious that half-length geofoam column is more economical than the other types of the group.

The load-carrying capacity of GEC-Ns with half-length and full-length is almost the same. So, using the half-length is recommended. The bulging of GECs is smaller than that of OSCs. The reason could be due to the lateral confinement provided by geofoam. However, in VESCs the bulging failure is very small because the strength of the encasement is high. So, the lateral confinement leads to increase in load-carrying capacity.

The load-carrying capacity of GECs with stone aggregates (GEC-H) and GECs with no stone aggregates (GEC-N) are the same. So, it is not recommended to use GEC-H.

The numerical studies help to predict the behavior of stone column in real condition.

REFERENCES

Abdelrahman, G.E., El Kamash, W.H., 2014. Behavior Improvement of Raft Foundation on Port-Said Soft Clay Utilizing Geofoam. *Conference of Ground Improvement and Geosynthetics*, Geo-Shanghai 2014 May 26-28, 2014, Shanghai, China. https://doi.org/10.1061/9780784413401.055

Bartlett, S.F., Lingwall, B.N., Vaslestad, J., 2015. Method of Protecting Buried Pipelines and Culverts in Transportation Infrastructure using EPS geofoam. *Geotext. Geomembr.* 34 (5), 450–461. https://doi.org/10.1016/j.geotexmem.2015.04.019

Bazzazian Bonab, S., Lajevardi, S.H., Saba, H.R., Ghalandarzadeh, A., Mirhosseini, S.M. 2020. "Experimental Studies on Single Reinforced Stone Columns with Various Positions of Geotextile." *Inovativee Infrastructure Solutions* 5(3): 1–12. https://doi.org/10.1007/s41062-020-00349-0

Bazzazian Bonab, S., Lajevardi, S.H., Saba, H.R., Mirhosseini, S.M. 2021. "The Novel Usage of EPS Geofoam as Column Material: A Laboratory Study." *International Journal of Geosynthetics and Ground Engineering* 7 (1): 1–14. https://doi.org/ 10.1007/s40891-020-00252-9

Beinbrech, G., Hillmann, R., 1997. EPS in Road Construction – Current Situation in Germany. *Geotext. Geomembr.* 15, 39–57. https://doi.org/10.1016/S0266-1144(97)00006-X

Chun, B.S., Lim, H.S., Shin, Y.W., 2001. Application of Constitutive Model to Predict the Behavior of EPS Geofoam. KSCE J. *Civil. Eng*. 5(2). 175–183. https://doi.org/10.1007/BF02829073

Hamidi, M., Lajevardi, S.H., 2018. Experimental Study on the Load Carrying Capacity of Single Stone Columns. *Int. J. Geosynth. Ground. Eng*. 4 (26), 1–10. https://doi.org/10.1007/s40891-018-0142-x

Lajevardi, S.H., Enami, S., Hamidi, M., Shamsi, H.R., 2018a. Experimental Study of Single and Group of Stone Columns Encased by Geotextile. *Amirkabir J. Civil. Eng*. 50 (6), 337–340. https://doi.org/10.22060/CEEJ.2018.12789.5269

Lajevardi, S.H., Shamsi, H.R., Hamidi, M., Enami, S., 2018b. Numerical and Experimental Studies on Single Stone Columns. *Soil Mech. Found. Eng*. 55 (5), 340–345. https://doi.org/10.1007/s11204-018-9546-9

Leo, Ch.L., Kumruzzaman, M., Wong, H., Yin, J.H., 2008. Behavior of EPS Geofoam in True Triaxial Compression Tests. *Geotext. Geomembr*. 26, 175–180. https://doi.org/10.1016/j.geotexmem.2007.10.005

Malarvizhi, S.N., Ilamparuthi, K., 2007. Comparative Study on the Behavior of Encased Stone Column and Conventional Stone Column. *Soil. Found*. 47 (5), 873–885. https://doi.org/10.3208/sandf.47.873

Mohammad Rezaei, M., Lajevardi, S.H., Saba, H.R., Ghalandarzadeh, A., Zeighami, E., 2019. Experimental and Numerical Studies on Load-Carrying Capacity of Single Floating Aggregate Piers Reinforced with Vertical Steel Bars. *Amirkabir J. Civil Eng*. Articles in Press. 10.22060/CEEJ.2019.15640.5991

Ram Rathan Lal, B., Padade, A. H., Mandal, J.N., 2014. Numerical Simulation of EPS Geofoam as Compressible Inclusions in Fly Ash Backfill Retaining Walls. *Ground Improvement and Geosynthetics*, Geo-Shanghai 2014 May 26-28, 2014, Shanghai, China. https://doi.org/10.1061/9780784413401.052

Selvakumar, S., Soundara, B., 2018. The Performance of EPS Geofoam Columns: An Introduction. In: *Proceedings of 11th International Conference on Geosynthetics*: 16-21 September, Seoul, Korea, pp. 47-53.

Cyclic response of geosynthetics-reinforced soil with respect to scale effect

Gh. Tavakoli Mehrjardi*, R. Behrad* & M. Khazaei*
Department of Civil Engineering, Faculty of Engineering, Kharazmi University, Tehran, Iran

ABSTRACT: Existing studies confirmed that the response of geosynthetics-reinforced beds is directly affected by contributory factors, including soil's grains, reinforcement's characteristics, and surface loading geometries. In this paper, a series of plate load tests has been carried out for the further understanding of the behaviour of geocell and geogrid-reinforced soil. The considered variables were included with four different soil grains sizes, two different geocell's opening sizes, two different geogrid's aperture sizes and three different loading plate sizes. As it was expected, the geocell and geogrid-reinforced soil exhibited a few times higher bearing capacity than the unreinforced status, up to 524% and 635%, respectively. The results further focused on the important role of scale effect on the response of reinforced foundations. The optimum nominal aperture size of geocells and geogrids were obtained about 15 and 4 times of medium grain size of soil. Also, it was found that in order to obtain the highest reinforcement benefits, the footing's width should be in the range 13 to 27 (20 in average) times of medium grain size of the backfill. Finally, to provide more stable and reliable geocell-reinforced backfill, it is recommended that the aperture size of geocells and geogrids should be selected smaller than 0.67 and 0.2 times of footing width.

1 INTRODUCTION

Geosynthetics have been successfully utilized as reinforcements in geotechnical projects such as embankments over soft subgrades, road construction, slopes, retaining walls and railroads (Cardile *et al*. 2017; Moghaddas Tafreshi *et al*. 2011, 2015; Tavakoli Mehrjardi & Sardehaei 2017; Tavakoli Mehrjardi & Moghaddas Tafreshi 2020; Tavakoli Mehrjardi *et al*. 2012, 2013, 2015, 2016, 2019, 2020). Many experimental studies in the field of reinforced embankments have been carried out with small or large-scale physical modeling at which the scale effects are rarely fully considered. However, one of the most challengeable matters in this area is how the reduced scale model and prototype model tests can be bridged. Góngora & Palmeira (2016) investigated the performance of unreinforced and backfills reinforced with different types of geosynthetics under cyclic loading. They observed that for the ratio of equal aperture size of geogrids (a_{eq}) to maximum aggregates size (D_{max}) between 0.7 and 1.35, less breakage took place. Also, Brown *et al*. (2007) found out that, for the 50mm ballast that was used, the optimum aperture size was 60–80 mm. Moreover, Cuelho *et al*. (2014) conducted full-scale tests to compare the relative operational performance of geosynthetics used as subgrade stabilization. For the broad graded fill material (coefficient of uniformity, $C_u = 123$), the most efficient a_{eq}/D_{50} ratio was obtained about 3.9.

---

*Corresponding Authors: ghtavakoli@khu.ac.ir, en.raminbehrad.civil@gmail.com and mahdi_khazaii@yahoo.com

There is a serious lack of studies on the response of geocells in soil medium with regard to the geometrical variations. Therefore, development of practical and reliable design methods and specifications for particular applications are still required. Considering the scarcity of studies about the scale effect on the response of geocell and geogrid-reinforced soil, a series of plate load tests has been carried out to investigate the sensitivity of reduced-scale geosynthetic-reinforced soil to variation of prominent key factors, notably loading plate size, soil grain size, and the reinforcements opening size.

2 TEST MATERIALS

2.1 Soils

Four types of uniformly graded soils as backfill materials with the medium grain size (D_{50}) of 3, 6, 12 and 16 mm were considered. The grading of backfill materials which were classified as SP and GP in the Unified Soil Classification System (ASTM D2487-11) is graphically illustrated in Figure 1.
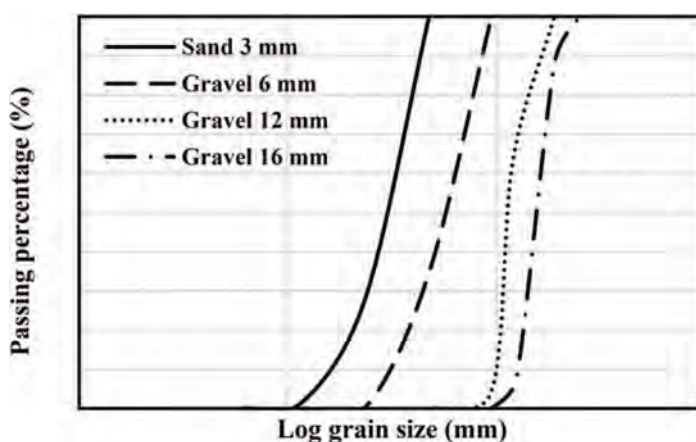
Figure 1.   Grain size distribution curves for backfill materials (Tavakoli Mehrjardi & Khazaei 2017).

2.2 Geocells

Geocells, namely "GC55" and "GC110" had the cell equivalent diameter/height of 55/50 and 110/50 mm, respectively. The provided aspect ratio (defined as the ratio of geocell's cells diameter (b) to the medium grains size (D_{50})) varies from 3.4 to 36.7. The engineering characteristics of the geocells are given in Table 1.

2.3 Geogrids

The geogrids, exploited in the backfill, were made of coated polyester with aperture sizes of 20×20 mm^2 and 25×25 mm^2. The provided aspect ratio (defined as the ratio of geogrid's aperture size (b) to the medium grains size (D_{50})) varies from 1.3 to 8.3. The mechanical characteristics of the geogrids used in this study are given in Table 1.

It should be mentioned that the efforts have been applied to each group of reinforcements that reinforcements provide the same tensile strength, besides having reasonable tensile strength in the considered physical modelling.

Table 1. Technical characteristics of geocells (obtained from the producer).

Reinforcement Type		Cells Size (mm × mm)	Elongation at Failure[*] (%)	Maximum Tensile Strength (kN/m)	Mass per Unit Area (g/m²)
Geocells	GC55	55 × 50	55	13	470
	GC110	110 × 50	55	21	350
Geogrids	R20	20 × 20	11.83	83.62	400
	R25	25 × 25	15.00	80.00	425

3 TEST SETUP, INSTRUMENTATION AND TEST PROCEDURES

Figure 2 shows the schematic representation of the test setup including test box, made of a steel frame, having inside dimensions of 1200 mm × 700 mm in plan (1200 mm in length, in X direction and 700 mm in width, in Z direction) and 700 mm in height (Y direction). Loading, unloading and reloading was chosen to replicate traffic or train loading. The repeated loadings were imposed by a hand-operated hydraulic jack on circular plates with diameters of 80, 120 and 150 mm which were situated at the centre of the soil surface. The loading was divided into four stages which are 200, 400, 600 and 800 kPa to simulate the light to heavy traffic loadings. In the absence of clear-cut failure, loading was stopped at a soil surface settlement of around 0.25 times of the related loading plate's diameter. The soil in dry condition was compacted to achieve 65% relative density of the soils.
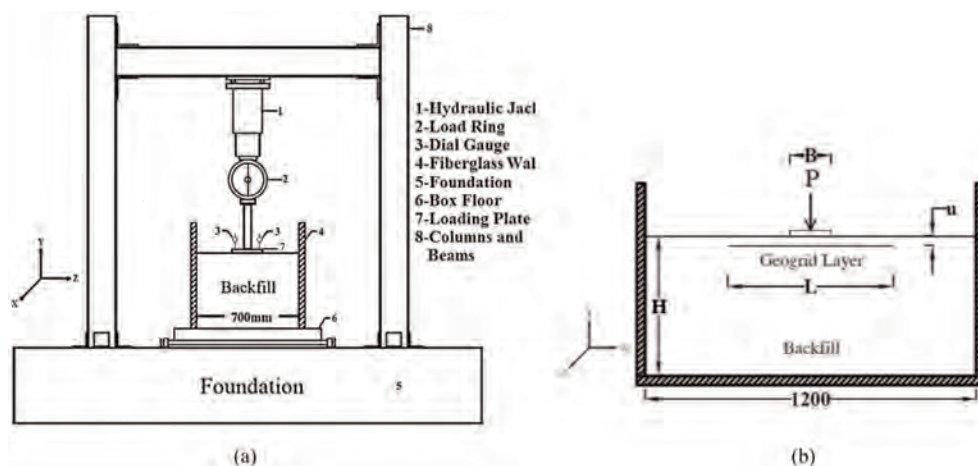
Figure 2. Schematic representation of the test setup (a) Y-Z section, and (b) X-Y section (Not on scale) (Tavakoli Mehrjardi & Khazaei 2017).

According to Table 2, investigated variables were including soil's particle size (sand with D_{50} = 3mm and gravels with D_{50} = 6, 12 and 16mm, namely S3, G6, G12 and G16, respectively), the reinforcement statuses (reinforced (Re) and unreinforced (Ur) conditions) and loading plate size (B = 80, 120 and 150mm). It should be also mentioned that the burial depth of geocells and geogrids (u) was considered 0.1 and 0.2 times of loading plate's diameter (B), respectively. Also, according to Tavakoli Mehrjardi et al. (2013), the width of reinforcements (L) was selected four times of loading plate's diameter.

Table 2. Testing program.

Reinforcing Status	Plate Diameter (mm)	D_{50} (mm)
Unreinforced	80	3, 6, 12, and 16
	120	
	150	
Geocell Reinforcement "GC55" and "GC110"	80	3, 6, 12, and 16
	120	
	150	
Geogrid Reinforcement "R20" and "R25"	80	3, 6, 12, and 16
	120	
	150	

4 RESULTS AND DISCUSSIONS

Owing to reduced size model tests, the results presented in this paper are prone to scale effects. Therefore, further studies using full-scale tests are recommended to verify these observations. However, we can underpin our description of the problem by using dimensional analysis based on a certain amount of background knowledge, tending extrapolation towards the prototype case. The major physical parameters influencing the response of geogrid-reinforced soil systems can be summarized as: B, u, L, D_{50}, γ, E_{soil}, E_{geo}, b; where γ and E_{soil} are unit weight and secant elastic modulus of the backfill, respectively and E_{geo} is opening size of reinforcements. Other parameters have been defined previously. The function (f) that governs the geogrid reinforced backfill systems can be written as Eq. (1).

$$q_u = f(B, u, L, D_{50}, \gamma, E_{soil}, E_{geo}, b) \tag{1}$$

The equation comprises 8 parameters which two of them have fundamental dimensions (i.e. length and force). Therefore, Eq. (1) can be reduced to 6 independent parameters (π_1, π_2, π_3, ..., π_6) and substituted with Eq. (2). As can be seen the obtained non-dimensional parameters could predominantly affect the response of reinforced systems.

$$\frac{q_u}{\gamma B} = f\left(\frac{u}{B}, \frac{h}{B}, \frac{D_{50}}{B}, \frac{\gamma D_{50}}{E_{soil}}, \frac{E_{soil}}{E_{geo}}, \frac{b}{D_{50}}\right) \tag{2}$$

For a prototype footing (p) with diameter n times that of the model (m), Eq. (3) can be considered.

$$\frac{D_p}{D_m} = n \tag{3}$$

For similarity to be maintained, the π terms, both for model and prototype need to be equal. As an example, if a circular footing with diameter of 140 cm is studied. So, it means n = 10 and parameters u, L, D_{50} and b should be considered 10 times of the model parameters. Assuming that the soils used in the model and prototype do have same unit weight, then parameters E_{soil} and $E_{geo.}$ should be considered 10 times of model parameters, as well. In this situation, Eq. (4) can be satisfied to obtain the bearing capacity of prototype system.

$$\left(\frac{q_u}{\gamma B}\right)_m = \left(\frac{q_u}{\gamma B}\right)_p \xrightarrow{yields} (q_u)_p = n(q_u)_m \tag{4}$$

4.1 *The ratio of the aperture size to the medium grains size (b/D_{50})*

Figures 3 and 4 illustrate the effect of the ratio of the aperture size to the medium grains size (b/D_{50}) for both kinds of reinforcements. It is clearly seen that the highest values of BCR in geocell and geogrid-reinforced foundations, irrespective of the loading plate size, is attainable when the ratio b/D_{50} is in the range of 12–18 and 3.3–4.2, respectively. In other words, in the case of larger backfill's particles (left side of the mentioned range), reinforcements/backfill interactions get deteriorated, resulted in reduction in bearing capacity ratio. On the other side, for the smaller backfill's particles or larger aperture size, less stone-stone interactions are provided and therefore, lateral buckling of particles columns in the geocell's plane is encountered and eventually, bearing capacity ratio is reduced, dramatically. Tavakoli Mehrjardi *et al.* (2016), by conducting plate load tests on poor-graded fine and coarse sands and reinforced by geogrids, found out that the ratio of the geogrid apertures sizes to the medium soil grains sizes is a deciding factor in the interaction between soil's grains and geogrid. Moreover, According to Figures 3 and 4, there is an optimum range (b/D_{max}) of 7–11 and 2.1–2.6 for geocell and geogrid-reinforced foundations in which affords the maximum bearing capacity ratio.
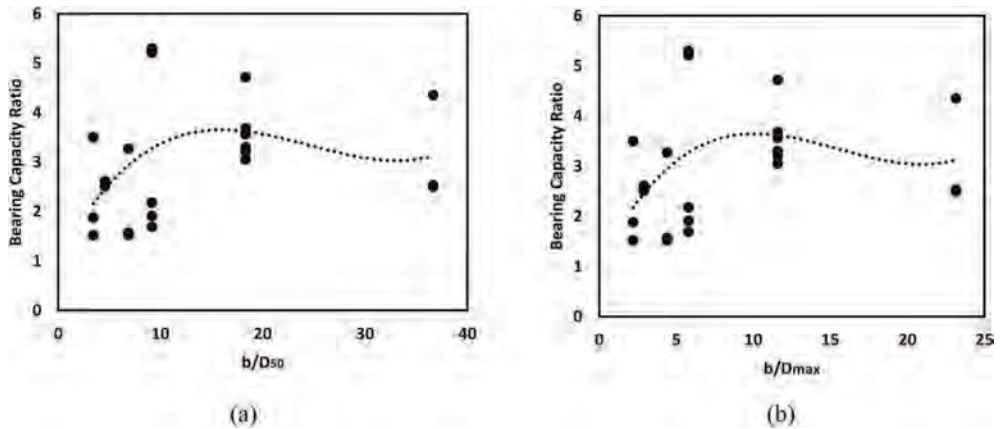
Figure 3. Variation of bearing capacity ratio versus the ratio of the geocell's cells size (b) to (a) the medium grains size (D_{50}), (b) the maximum grains size (D_{max}) (Tavakoli Mehrjardi *et al.* 2019).
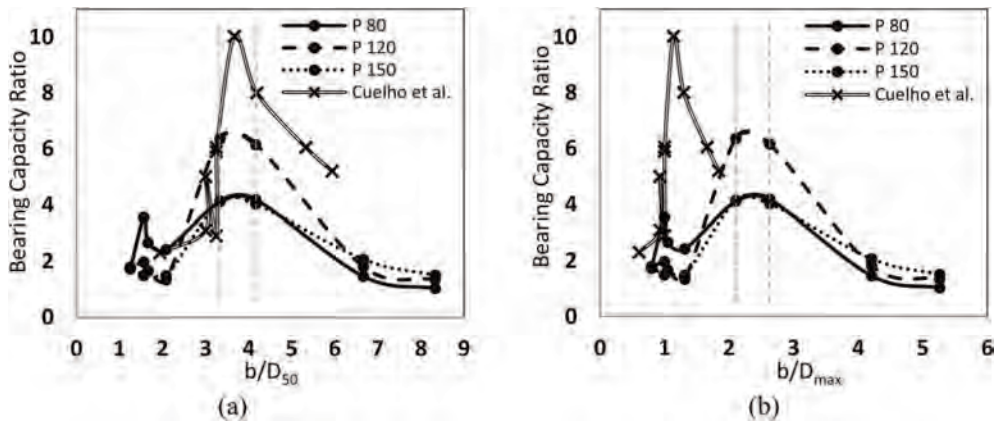
Figure 4. Variation of bearing capacity ratio versus the ratio of the geogrid apertures size (b) to (a) the medium grains size (D_{50}), (b) the maximum grains size (D_{max}) (Tavakoli Mehrjardi & Khazaei 2017).

4.2 The ratio of the loading plate size to the medium grains size (B/D_{50})

With this respect, Figure 5 presents the variation of bearing capacity ratio versus the ratio of the loading plate size to the medium grains size (B/D_{50}) for geocell and geogrid reinforcements. According to the observed variations, the best efficiency of geocell and geogrid reinforcements has been achieved for the optimal amount of B/D_{50} in the range of 13–27 (approximately 20; in average). In the outer of the mentioned optimum range, BCR decreased drastically. In the line with this conclusion, Tavakoli Mehrjardi & Khazaei (2017) observed that in order to obtain the highest benefits from geogrid reinforcement in geogrid-reinforced backfill, the footing's width should be in the range of 13–25 times of medium grain size. Moreover, Hsieh & Mao (2005) reported when the loading plate's diameter was larger than 15 times the D_{50} of the soil test, no marked influence of plate size on surface settlement would be expected.
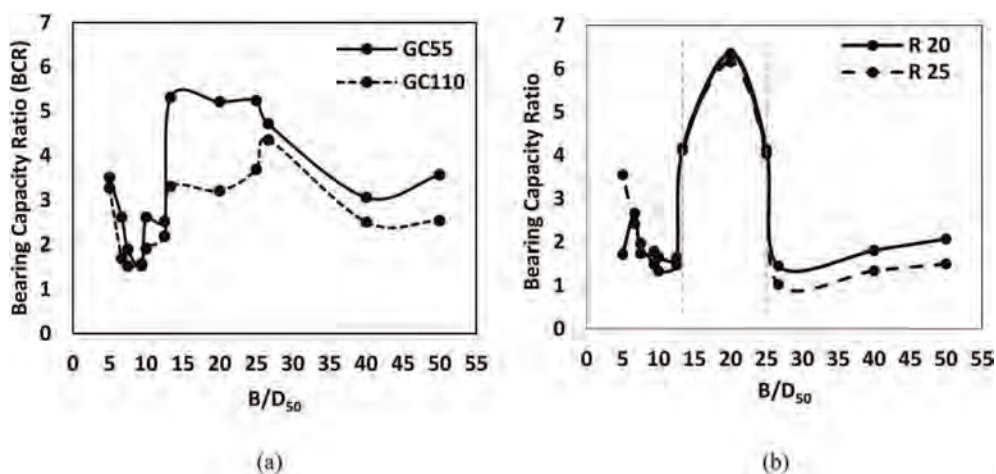
Figure 5. Variation of bearing capacity ratio versus the ratio of the loading plate's diameter (B) to the medium grains size (D_{50}) for a) geocell and b) geogrid reinforcements (Tavakoli Mehrjardi & Khazaei 2017; Tavakoli Mehrjardi et al. 2019).

5 CONCLUSIONS

In this study, a series of repeated plate load tests was performed to investigate the sensitivity of reduced scale geosynthetics-reinforced soil to the contributory factors including loading plate size, soil grains size, and reinforcements apertures size. The detailed conclusions from the acquired results and presented in this paper are:

– Reinforcements are to hold much promise as a strong method to enhance the bearing capacity of foundations. In conditions with appropriate selection of effective parameters, reinforcements could strengthen the unreinforced backfill up to 6.35 times.
– It is recommended that the ratio of aperture size of geocells and geogrids to medium grain size of backfill materials should be selected 15 and 4, respectively.
– In order to obtain the highest benefits of reinforcements, the footing width should be in the range 13 to 27 (20 in average) times of medium grain size of backfill materials.

REFERENCES

American Society for Testing and Materials (ASTM) 2011. Standard Practice for Classification of Soils for Engineering Purposes (Unified Soil Classification System). ASTM D2487-11.

Brown, S.F., Kwan, J., Thom, N.H. 2007. Identifying the Key Parameters that Influence Geogrid Reinforcement of Railway Ballast. *Geotextiles and Geomembranes* 25 (6), 326–335.

Cardile, G., Moraci, N., Pisano, M. 2017. Tensile Behaviour of an HDPE Geogrid under Cyclic Loading: Experimental Results and Empirical Modelling. *Geosynthetics Internaltional* 24 (1), 95–112.

Cuelho, E., Perkins, S., Morris, Z. 2014. Relative Operational Performance of Geosynthetic used as Subgrade Stabilization, Final Project Report, *FHWA/MT-14-002/7712-251*, Research Programs, State of Montana Department of Transportation, Montana, USA.

Góngora, I.A.M.G., Palmeira, E.M. 2016. Assessing the Influence of Some Soil-reinforcement Interaction Parameters on the Performance of a Low Fill on Compressible Subgrade. Part II: Influence of Surface Maintenance. *International Journal of Geosynthetics and Ground Engineering* 2 (1), 18–29.

Hsieh, C., Mao, H.L. 2005. A Bench-scale Performance Test for Evaluation of the Geosynthetic Reinforcement Effects on Granular Base Courses. *ASCE, Geosynthetics Research and Development in Progress, Geo-frontiers*, 1–11.

Moghaddas Tafreshi S.N., Shaghaghi T., Tavakoli Mehrjardi, Gh., Dawson A.R., Ghadrdan M. 2015. A Simplified Method for Predicting the Settlement of Circular Footings on Multi-layered Geocell-reinforced Non-cohesive Soils, *Geotextiles and Geomembranes*, 43(4), 332–344.

Moghadas Tafreshi, S.N., Tavakoli Mehrjardi, Gh., Ahmadi, M. 2011. Experimental and Numerical Investigation on Circular Footing Subjected to Incremental Cyclic Loads. *International Journal of Civil Engineering*, 9 (4), 265–274.

Tavakoli Mehrjardi, Gh., Amjadi Sardehaei, E. 2017. Design Graphs to Estimate Reduction Factor of Nonwoven Geotextiles Due to Installation Process. *European Journal of Environmental and Civil Engineering*, DOI: 10.1080/19648189.2017.1327897, 1–14.

Tavakoli Mehrjardi, Gh., Ghanbari, A., Mehdizadeh, H. 2016. Experimental Study on the Behavior of Geogrid-reinforced Slopes with Respect to Aggregate Size. *Geotextiles and Geomembranes* 44 (6), 862–871.

Tavakoli Mehrjardi, Gh., Azizi, A., Haji-Azizi, A. and Asadollahfardi, G.R. 2020. Evaluating and Improving the Construction and Demolition Waste Technical Properties to Use in Road Construction. *Transportation Geotechnics*, 23, 1–13.

Tavakoli Mehrjardi, Gh., Khazaei, M. 2017. Scale Effect on the Behavior of Geogrid-Reinforced Soil under Repeated Loads. *Geotextiles and Geomembranes* 45(6), 603–615.

Tavakoli Mehrjardi, Gh. and Moghaddas Tafreshi, S.N. 2020. *Geocell-Reinforced Foundations, Geocells, Advances and Applications*. Springer, 77–131.

Tavakoli Mehrjardi, Gh., Moghadas Tafreshi, S.N., Dawson, A.R. 2012. Combined use of Geocell Reinforcement and Rubber-soil Mixtures to Improve Performance of Buried Pipes. *Geotextiles and Geomembranes* 34, 116–130.

Tavakoli Mehrjardi, Gh., Moghaddas Tafreshi, S.N., Dawson, A.R. 2013. Pipe Response in a Geocell Reinforced Trench and Compaction Considerations. *Geosynthetics International* 20(2), 105–118.

Tavakoli Mehrjardi, Gh., Moghadas Tafreshi, S.N., Dawson, A.R. 2015. Numerical analysis on Buried Pipes Protected by Combination of Geocell Reinforcement and Rubber-soil Mixture. *International Journal of Civil Engineering* 13 (2B), 90–104.

Tavakoli Mehrjardi, Gh., Motarjemi, F. 2018. Interfacial Properties of Geocell-reinforced Granular Soils. *Geotextiles and Geomembranes* 46(4), 384–395.

Tavakoli Mehrjardi, Gh., Behrad, R. and Moghaddas Tafreshi, S. N. 2019. Scale Effect on the Behavior of Geocell-Reinforced Soil. *Geotextiles and Geomembranes*, 47(2), 154–163.

Effect of strip footing on the stress-strain behavior of soil-geogrid interaction: A new simple concept

Hussein Ahmad*
Faculty of Civil Engineering, Tishreen University, Latakia, Syria

Ahmad Mahboubi
Faculty of Civil, water and environmental Engineering, Shahid Beheshti University, Tehran, Iran

ABSTRACT: To determine the interface characterization of geogrid inclusion, soil-geogrid interaction is of particular importance. Tensile strength, tensile strain, and interfacial shear stress are all characteristics induced along with geogrid reinforcement. In this paper, a series of small-scale physical modeling has been carried out to investigate the stress-strain behavior and deformation of geogrid after final loading. Therefore, a simplified expression model has been developed to model the behavior of tensile stress-strain of geogrid inclusion. This simple model is similar to the Mohr-Coulomb model that is used in the nonreinforced soil. In general, the results have been confirmed by experimental testing and are consistent with the analytical results. In the main results, it is demonstrated that strains and deflections induced within two layers of geogrid inclusions are less than those induced within one layer. In addition, the tensile force induced in the first geogrid sheet is larger than that in the second geogrid layer.

Keywords: Strip footing, soil-geogrid interaction, stress-strain behavior, Tensile strength.

1 INTRODUCTION

Geogrid-reinforced soils are utilized in foundation building, embankment, railway, and road infrastructure in geotechnically challenging areas with the potential for the formation of failures in weak soils, differential settlement, or localized subsidence. Using the geogrid as a preventative measure, the weak soil and its above infrastructure are supported through the tensile strength created by the geogrid deflection. The deformations are transferred through the geogrid to the soil body with a critical effect on the footing behavior. Among the most obvious and popular methods of strengthening weak soil and reducing settlements under shallow foundations has been the use of geogrid-reinforced soils. The reinforced soil foundation (RSF) bearing capacity has also been investigated by some researchers and some theoretical solutions have been proposed (Binquet & Lee 1975; Chen 2007; Chen & Abu-Farsakh 2015; Huang & Tatsuoka 1990; Huang & Menq 1997; Shukla & Chandra 1994; Sharma *et al*. 2009; Wayne *et al*. 1998). The researchers applied the mode of failure to the reinforced soil and observed the impact of the tensile strain in the geosynthetic element on bearing capacity. Geosynthetics tensile strength is proportional to their tensile modulus. In this work, according to the experimental findings, a simple solution method is presented for a strip footing laid over reinforced fine sand. The analysis concluded that the tensile force

*Corresponding Author: Houssein.ah@gmail.com

produced by any of the reinforcement layers is contained in all of them; therefore, its analytical equation overestimates the usefulness of increased bearing capacity.

McCartney and Cox, 2013 investigated the deformation response of geosynthetic reinforced soil layers for evaluating the strain level needed for mobilizing reinforcement mechanisms over the surface loading. However, there is not much information regarding the magnitude of the strain needed for mobilizing the shear-resisting interface mechanisms. Hence, this work addresses investigating the performance of geogrid-reinforced soils beneath shallow footings to determine the advantages of the reinforcement in decreasing the magnitude and extent of soil deformations against settlement and suggests a proper novel technique. In a geotechnical 1-g model test, physical model tests were conducted to assess the performance of geogrid-reinforced fine sand beneath the strip footing, evaluate these mechanisms, and contribute to comprehending this performance.

2 MATERIALS USED

Sandy soil with fine grains (N.151) was used in the laboratory test. The soil sample was taken from the Firozkoh mountainous area, in northeastern Iran. The grain size was presented in Figure 1 by the soil classification ASTM D422 standard. Using the Unified Soil Classification System (USCS) and based on Figure 1 and Table 1, this soil is categorized as sand-poor-graded soil (SP). The mechanical features of the geogrid-sand interaction coefficient and fine sandy soil were determined by applying six direct shear tests based on ASTM D5321 at a relative density of 40%. The obtained basic properties values were included in Table 1.

Table 1. Soil properties.

Parameter	Value
Cohesion, C (kPa)	15
Specific gravity, G_s	2.68
Residual friction angle, $\phi_{residual}$ (°)	29.33
Peak friction angle, ϕ_{peak} (°)	36.50
Maximum dry density, γ_{dmax} (kN/m^3)	16.61
Minimum diy density, γ_{dmin} (kN/m^3)	14.09
Dry unit weight, γ_d (kN/m^3)	15.00
Relative density, D_r (%)	40
Mean particle size, d_{50} (mm)	0.34
Impact particle size, d_{10} (mm)	0.20
Maximum particle size, d_{max} (mm)	0.60
Minimum particle size, d_{min} (mm)	0.01
Coefficient of curvature, C_c	1.11
Coefficient of uniformity, C_u	1.90
Oedometric modulus, E_{oed} (kPa)	28000
Fine percentage	5
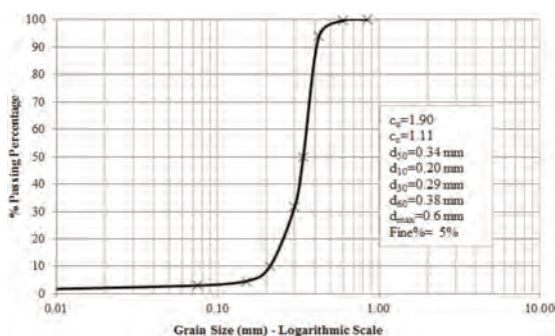
Figure 1. Particle size distribution analysis.

The geogrid CE161 manufactured by an Iranian company, (Ahmad *et al.* 2020) was used here. This material has a thickness of 3.3 mm, an aperture size of 10 mm × 10 mm, and a unit weight of 0.70 kg/m^2. The ultimate tensile strength was assessed to be approximately 6.1 kN/m. Here, one strip footing made of steel material was utilized to perform physical modeling of the footings. The thickness of foundations was considered to be 20 mm; thus, it is viewed as a solid element that is not subjected to scale impact. The footing width is 100 mm. The strip footing length (i.e., 450 mm) is in the same direction as the laboratory model box width but 10 mm less.

3 THE EXPERIMENTAL PROCESS AND TEST ARRANGEMENT

The experimental tests were performed in a rectangular box made of steel with width, length, and height of 500 mm, 1400 mm, and 800 mm, respectively. The horizontal plane of the box was chosen according to the conditions of the plane strain problem. To avoid interfering with the failure surfaces with the model side dimensions, the model length to the footing width ratio of 16 is adequate. Similarly, the height of the soil mass in the model was selected to be up to 800 mm. The box width was equal to the footing width. Additionally, to prevent contact footing with the sandbox wall, the footing length decreased by 5 mm from each side. A pneumatic cylinder equipped with an air compressor was considered as a loading system to provide an air pressure of approximately 10 bars. The system can secure a steady periodic load after applying the pressure circumstances to the soil specimen. The applied force was calculated utilizing a load cell, and the settlement of the footing was measured through two linear variable differential transformers (LVDTs). The test method was performed in compliance with ASTM D 1196 2016, in which the load measurements were implemented and continuously held for three minutes until the settling rate was lower than 0.03 mm/min. the strain distribution along the geogrid was measured by attaching strain gauges on the geogrid at various distances from the center of the footing (x/B = 0, 0.5, 1.5, and 2), as shown in Figure 8b. The increased vertical stresses were measured by placing ten pressure cells under the center of the footing and at these distances from the footing center (x/B = 0.5, 1, 1.5, and 2). The load cell, LVDTs, pressure cells, and strain gauges were all connected to a 20-channel Mutest data logger, which was connected to a desktop computer for monitoring the data readings. For the preparation of the sample, the regular placement of the soil was obtained in the sandbox proportional to the needed relative density using the method of rain sandy soil (Kolbsuzewski 1948). The proper soil unit weight was obtained using a tamper. Figure 2 presents a schematic illustration of this system.
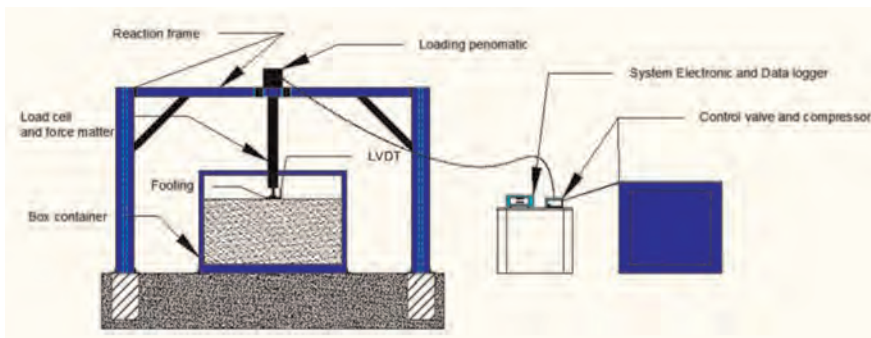
Figure 2. Schematic view of the experimental model study.

4 DISCUSSION OF STRAIN ANALYSIS

Geogrid reinforced soil has numerous uses as a result of its engineering effectiveness and cost. Consequently, it is essential to assess the mechanical performance of reinforced soils. In this regard, plate load tests were carried out for comparison of the mechanical performances of fine sand soil in both reinforced with geogrid and unreinforced status, and the observed results are reported herein. According to Figure 3, the mobilized strain at the midpoint of the interface soil-geogrid interaction was larger than the strain along the geogrid length (the distance increases from the footing center). The mobilized interface strain was largest under the midpoint of the footing center and fell until the distance of 2B from the footing center,

which signifies that the geogrid reinforcement sheet was restricted in the soil mass more strongly than in the folded model, which ensued from the stronger interface parameters. As shown in Figure 3, the deformation of the geogrid sheet was placed after the edge of the foundation up to 150 mm from the middle. It can be reasoned that the mobilized axial load in the geogrid and the interface shear stress between the soil and geogrid are both also localized in the same position. The localized mobilization of the reinforcement forces depends on the failure mode of the soil (Ouria & Mahmoudi 2018; Patra & Shahu 2012). No mobilized interface shear stress occurs in the last 50 mm of the geogrid from either position. Thus, it can be reasoned that only (4B = 400 mm) of the geogrid length had fully interacted with the surrounding soil and participated in the improvement in the carrying capacity.
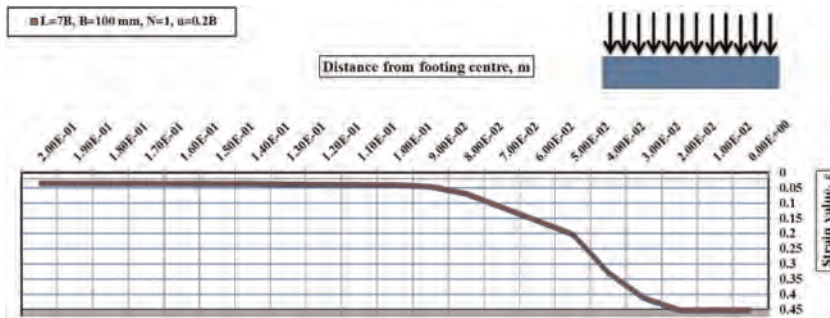
Figure 3.   The two-dimensional strain distributions from the footing center.

5   THE CHARACTERISTICS AND PERFORMANCE OF SOIL-GEOGRID INTERACTIONS

The following Figure 4 shows the linear association between the tensile strength mobilized in the geogrid and the highest deformation created in the geogrid rooted in the soil at different depths. This diagram is based on the findings of the plate loading test. It shows the linear behavior association between tensile strength and greater strain at a certain burial depth. By increasing the burial depth, the tensile strength values decrease, thus reducing the reinforcement deformations. The single geogrid-reinforced soil has a higher deformation value than the strain in the two geogrid layers system. According to these curves, the linear relationship of the tensile force-strain can be expressed as:

$$T_{tot} = J_{mobilized} \times \varepsilon_{\max} + T_{interaction} \qquad (1)$$

This relationship indicates the impact of the reinforcing element and the high performance of the soil-geogrid reaction. The first term shows the impact of the tensile strength resulting from the geogrid (the effect of the opening size and the resistance of the transverse and longitudinal ribs), while the second term represents the effect of the passive frictional force on the interface surface. This finding can be regarded as an original principle to express the modeling of the geogrid-soil system and to represent the performance of reinforced soil under strip foundations. This mechanical linear behavior relationship provides the true impact of the tensile strength assembled when burring the geogrid into the soil. Moreover, it proves the contribution of the resistance force of the interface friction caused by the soil-geogrid mutual reaction. This novel performance of the soil-geogrid contact surface indicates the smaller packed tensile stiffness modulus ($J_{mobilized}$) value of the buried geogrid compared to the geogrid stiffness modulus ($J_{nominal}$) caused by an in-isolation laboratory test. The reduction level in the reinforcement hardness coefficient is associated with the calculation of

deformations occurring in the joint, and the transverse and longitudinal ribs. The distribution of deformations across the length of the geogrid is realistically affected by this event; hence, more than two adjacent nodes are obtained (plastic strain effect) by the concentrated load on the contact surface. This results in the assumption of a new type of geogrid deformation in the soil similar to a trapezoid to some extent. This is not consistent with the hypothesis of (Abu-Farsakh *et al.* 2009; Chen *et al.* 2009), assuming that the triangular kind of strain distribution is under the center of the footing. Thus, in more than two nodes, the maximum value of the tensile strain is equivalent to the length of three aperture sizes of geogrid (on a width five times an open size), as represented in the last two figures. Given the interruption and rupture at the joints or the longitudinal ribs in the weak points exposed to the concentration of stresses, some geogrids reach the condition of occurrence and yield plastic deformation. Considering the triangular distribution of shear stresses on the contact surface in Equation 1, as represented by former researchers, the force-induced interaction at the interface soil-geogrid surface can be assumed to be in Equation 2:

$$T_{interaction} = \frac{1}{2} \quad \tau_{inter} \times L_{geogrid} \times d_{s-g} \qquad (2)$$

where the frictional stress, τ_{inter} (kN/m^2), is mobilized at the interface between the sandy soil and the geogrid reinforcement, $L_{geogrid}$ denotes the effective length of the geogrid reinforcement (m) and ds-g indicates the depth of the general shear zone induced under the strip footing when the geogrid is included in the soil mass (m).

Figure 5 shows the results of the plate load tests. The trend line passing through the experimental points is termed the interaction strength (or failure) envelope, indicating the maximum tensile force of the soil-geogrid interaction at failure (T_{tot}), withstood by the soil without failure, which is mathematically explained in Equation 1. Since numerous
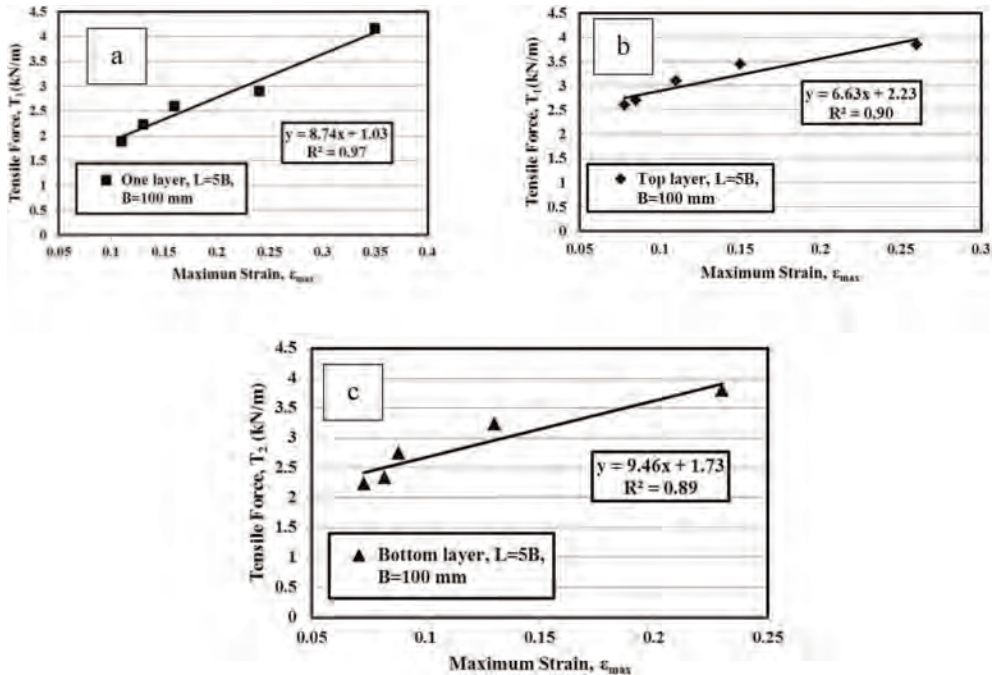
Figure 4.   The tensile force-maximum strain performance of (a) one geogrid layer, (b) upper geogrid layer and (c) lower geogrid layer.
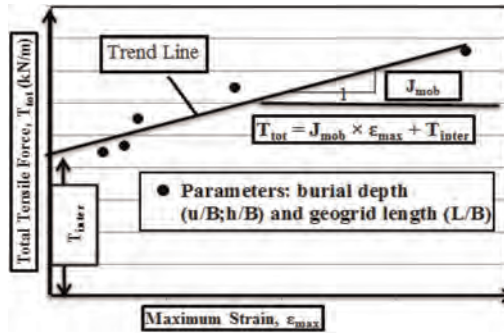
Figure 5. Analysis of data from five plate load tests to obtain the tensile force-strain behavior of the soil-geogrid interaction.

laboratory and field results exist on the experiment of plate loading in reinforced soil in the literature, the following technique can be adopted for modeling the reinforcement in the Soil-Geogrid interface area: (1) The findings of at least five experiments with various depths of burial of the geogrid were confirmed. (2) Mining the total packed tensile force in the geogrid from these curves. (3) Determining the maximum deformation calculated under the center of the footing in the geogrid layer. The maximum deformation values were adopted since they express the highest effective contribution of the geogrid in mobilized tensile strength and transporting the stresses into the soil body. (4) Drawing the linear relationship, the total tensile strength is the geogrid strain, where the horizontal axis exhibits the axis of deformation and the vertical axis shows the tensile strength (kN/m). (5) The intersection point of the straight line with the axis of the total tensile strength is determined. The interfacial shearing force is obtained, representing the role of the interface friction resistance of the soil-geogrid. (6) The slope of the straight line shows the stiffness coefficient of the packed geogrid, representing the real role of the reinforcement in improving the soil resistance and the result of the deflections in the reinforcement. Three principles exist behind the main parameters of this criterion, including the highest deformation, the stiffness reinforcement modulus, and the shear strength interface in the contact zone. This model can be explained and defined in mathematical and numerical analysis by specifying these basic parameters. This could be adopted as a new criterion to represent the soil-geogrid interaction and use this linear association as an inelastic linear model in numerical analyses such as the finite element technique.

6 CONCLUSION

This paper presents an advanced mathematical formula for determining the increased bearing capacity of a strip footing over geogrid-reinforced soil, whether with horizontal or folded geogrid sheets, according to the literature theory of failure. This method helps calculate the reinforcing soil's exact bearing capacity at various depths and demonstrates the effectiveness of the strain-induced soil-geogrid interaction of the reinforcing element to provide the required tensile strength. It was found that the geogrid's effective strain is maximum at the midline of the geogrid layer on a width five times an open size and does not induce at (2–2.5) times the footing width, exceeding the value of the tensile strength will be negligible. Therefore, a new method is proposed to fold the ends of the reinforcing layer to ensure greater efficiency and to reduce settlement and deformations occurring in the soil and reinforcement, respectively. In this novel technique, reinforced soil behaves as a bounded material. A nonelastic linear decay in the geogrid tensile force distributions was found in

geogrid-fine sand for various burial depths as a function of peak normal strain. This reveals that to mobilize the tensile stresses in the geogrid reinforcement layers, larger plastic surface deflections and strains are required. A simple new model was proposed to define the real performance of geogrid-sand interactions in terms of the static plate load test.

REFERENCES

Ahmad, H., Mahboubi, A., Noorzad, A.: Scale Effect Study on the Modulus of Subgrade Reaction of Geogrid-reinforced Soil. *SN Appl. SCI.* 2(4), 394 (2020). https://doi.org/10.1007/s42452-020-2150-4

Abu-Farsakh, M., Chen, Q., Sharma, R., Zhang, X.: Large-scale Model Footing Tests on Geogrid-Reinforced Foundation and Marginal Embankment Soils. *Geotechnical Testing Journal.* 31, 413–423 (2009)

ASTM D 1196: Standard Test Method for Nonrepetitive Static Plate Load Tests of Soils and Flexible Pavement Components, for Use in Evaluation and Design of Airport and Highway Pavements. *American Society for Testing and Material*, ASTM International, Philadelphia, PA, USA (2016)

Binquet, J., Lee, K.L.: Bearing Capacity Analysis of Reinforced Earth Slabs. *Journal of the Geotechnical Engineering Division.* 101, 1257–1276 (1975)

Chen, Q., *An Experimental Study on Characteristics and Behavior of Reinforced Soil Foundation Ph.D. Dissertation.* Louisiana State University (2007).

Chen, Q., Abu-Farsakh, M., Sharma, R.: Experimental and Analytical Studies of Reinforced Crushed Limestone. *Geotext Geomembr.* 27 (5): 357–367 (2009).

Chen, Q., Abu-Farsakh, M.: Ultimate Bearing Capacity Analysis of Strip Footings on Reinforced Soil Foundation. *Soils Found*, 55, 74–85 (2015)

Kolbsuzewski, J.: General Investigation of the Fundamental Factors Controlling Loose Packing of Sands. In: *Proceedings of the 2nd International Conf Soil Mech Found Eng Rotterdam* (4): 47–49 (1948)

Huang, C., Tatsuoka, F.: Bearing Capacity of Reinforced Horizontal Sandy Ground. *Geotext Geomembr*. 9, 51–82 (1990)

Huang, C., Menq, F.: Deep-footing and Wide-slab Effects in Reinforced Sandy Ground. *Journal of Geotechnical and Geoenvironmental Engineering.* 123, 30–36 (1997)

McCartney, J.S., Cox, B.R.: Role of Strain Magnitude on the Deformation Response of Geosynthetic-Reinforced Soil Layers. *Geosynthetics International*, 20, No. 3, 174–190 (2013). http://dx.doi.org/10.1680/gein.13.00010.

Ouria, A., Mahmoudi, A.: Laboratory and Numerical Modeling of Strip Footing on Geotextile-Reinforced Sand with a Cement-treated Interface. *Geotextiles and Geomembranes.* 46(1), 29–39 (2018).

Patra, S., Shahu, J.T.: Pasternak Model for an Oblique Pullout of Inextensible Reinforcements. *J. Geotechnical Geoenvironmental Eng*. 138 (12), 1503–1513 (2012).

Sharma, R., Chen, Q., Abu-Farsakh, M., Yoon, S.: Analytical Modeling of Geogrid Reinforced Soil Foundation. *Geotext Geomembr*. 27, 63–72 (2009)

Shukla, S.K., Chandra, S.: A Generalized Mechanical Model For Geosynthetic-Reinforced Foundation Soil. *Geotext Geomembr*. 13 (12): 813–825 (1994)

Wayne, M.H., Han, J., Akins, K.: The Design of Geosynthetic Reinforced Foundations. *Geosynthetics in Foundation Reinforcement and Erosion Control Systems. ASCE*. 1–18 (1998).

On the practical use of geosynthetics for karts reinforcement

G. Valdeyron, F. Clément, C. Respaud & E. Vedie
Cerema, Bordeaux, Nouvelle-Aquitaine, France

ABSTRACT: The Aquitaine Basin is a sedimentary basin widely compounded by karstic limestones aged from Jurassic to Oligocene series. Throughout years and particularly in future, designers would have to consider resilient structures regarding climate changes that, for instance, emphases karst issues. A methodology based on hydraulic and geological criteria, is provided to assess karst collapse hazard. Applied to a roadway study-case (Departmental Road n°1215), the methodology carries on a set of disposals to ensure the robustness of the design and is about to be published in a Cerema/BRGM guidelines textbook (Cerema & BRGM 2023). Amongst them, a strengthening of the road by a geosynthetics is designed according to the French standards. The importance of the karst diameter and the limiting value of the accepted deformation of the roadway structure, on the required strength resistance of the geosynthetics is enlighten. That confirms the relevance of the methodology to assess a reasonable hazard.

1   DESCRIPTION OF THE DEVELOPMENT AND GEOLOGICAL AND GEOTECHNICAL CONTEXT

1.1   *Roadway infrastructure description*

The project consists in the building of the detour road (called Departmental Road n°1215) of the towns Saint-Aubin Medoc and Taillan-Medoc near Bordeaux (France). The aim of this roadway, expected since approximatively 30 years, is to improve access to the North Medoc area, secure the transit in the town centers and enhance the economical context. The development is 8 km long and composed by 13 structures (2 road bridges, 1 tunnel, and 11 ecological bridges or hydraulic structures). Earthworks consist on two cuttings and two embankments.

1.2   *Geotechnical and geotechnical context*

Two geotechnical units are identified in the vicinity of the project: from top to bottom, recent detrital alluvial deposits of the Garonne or slopes formations, respectively composed by Molasse sands and fine or coarse sands, are underlying the Oligocene marl and limestone which form the geotechnical bedrock of the roadway structures. The limestone of the Oligocene serie is recognized as a karstic complex. During earthworks, a karst collapse appeared on the vicinity of a new built bridge as visible on Figure 1, the groundwater level was measured 5 meters below the bottom of the collapse – it corresponds to the drinking water resource supply to the inhabitants. As it is shown, the landslide appeared in the temporary sanitation infrastructure of the roadway hugely alimented by rainfalls. Explanations of this karstic collapse are summarized in Figure 2. Lateron specific ground investigations were realized in order to identify weathered or fractured zone within the Oligocene limestone. They are first composed by geophysical surveys (electrical resistivity) and inspection

of geophysical irregularities by measurements while drilling (rotational and vertical speed of the drill bit, pressure on the bit, water flow volume, barehole image by camera). Investigation were not carried out on the overall path roadway (8 km) but were restricted to the most exposed area on regards of the karst collapse hazard assessed according to the methodology exposed afterwards. So 9 geophysical surveys of each 150 m long and 20 drillings of 12 m depth were achieved. A sample of the geotechnical model is reported on Figure 3, for instance two representative zones are illustrated: on the left, a clayey zone overlying the karstic limestone, and on the right, a molasse and sandy layer above karstic substratum (zone of the collapse described above).

Figure 1.   Geographical context and RD1215 (in red on left) and karst collapse (on right).
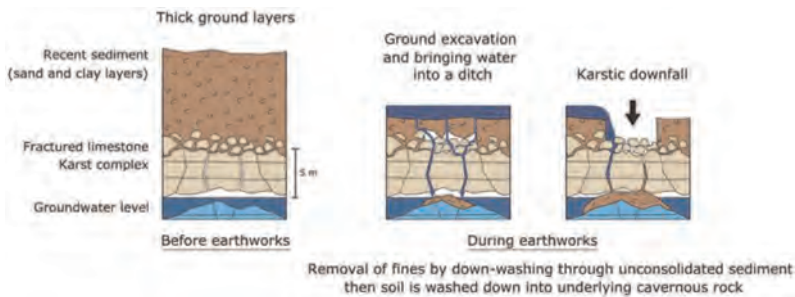
Figure 2.   Kinematics of the karst collapse (2021-02-09).
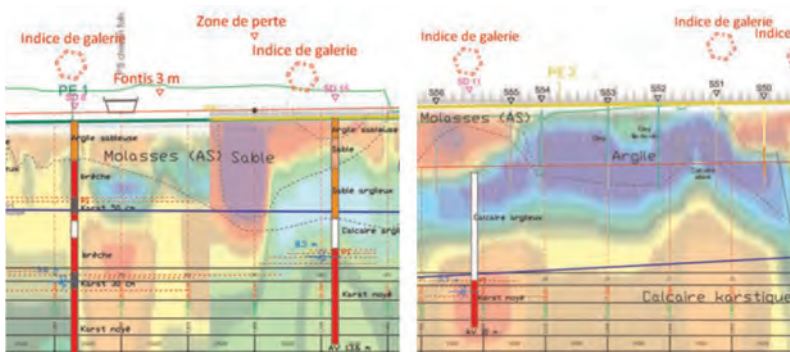
Figure 3.   Geotechnical model (samples) – absence of accessible voids is shown.

2 ASSESSMENT METHODOLOGY FOR KARST HAZARD

2.1 *Mechanisms involved in karstic collapse*

Karst collapses are developing by a cluster of inter-related processes, including suffusion, soil down-washing, soil collapse and rock collapse (Waltham *et al.* 2005), they are illustrated on Figure 4. Each mechanism is initiated by a serie of criteria, which are identified in the methodology. The soil collapse mechanism was clearly identified during the site inspection: eroded/fractured limestone and karstic well are visible on Figure 5b. On ground level the diameter of the hazard depends on the properties of the upper layer of ground: in case of bare karst without soil cover, the diameter is about the karstic well's one. The motion of the upper layer soil grains throughout the karstic substratum initiates the soil down-washing mechanism. Thus, it is highly dependent of the properties of the upper layer (cohesive or not) and the hydrodynamic conditions of the site: soil particles are driven by the hydraulic gradient between the surface and the groundwater level. In case of cohesionless ground surface, the diameter of the collapse depends on the importance of the "hourglass effect" (stability of the slopes of the upper layer). Moreover, the rock collapse corresponds to the rupture of the bedrock of a significant void, it happens when the rockmass is incompetent otherwise when the bedrock has insufficient thickness or when its strength is reduced by fractures.
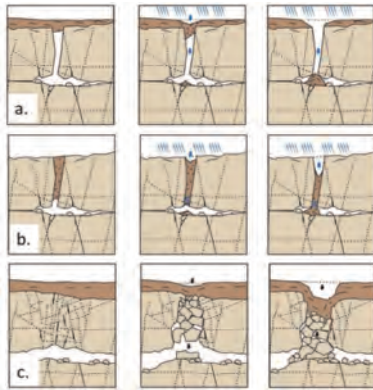
Figure 4. Karstic mechanisms: a. soil down washing, b. soil collapse, c.rock collapse.
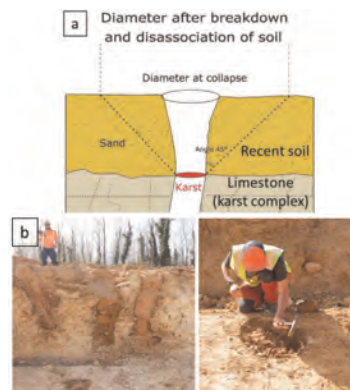
Figure 5. Hourglass effect (a), karstic wells (b).

2.2 *Governing criteria of karstic collapse*

As exposed previously, 3 criteria are supposed to explain and quantify the site predisposition to karstic collapse: strength and quality or level of karstification (voids, fractures, fault) of the rockmass, properties of the upper layer of ground cover and hydrodynamic conditions of the site. For each mechanism, the karstic hazard susceptibility is determined by a set of qualitative criteria matrix developed by the Cerema considering the comparable experience of many roadway infrastructure developments (National Road n°21, 141). For instance, regarding the soil down-washing mechanism (see Figures 6), each predisposition factor is assessed considering the geological knowledge of the site (study desk, comparable experience, geotechnical investigations). In fact, only samples are given here and other matrix, referenced in a handbook (Cerema/BRGM 2023), are needed to evaluate the predisposition. Then, the karstic collapse hazard is assessed by cross-referencing predisposition factors (see Figure 7). According to this methodology, karst hazard is evaluated, within the downfall zone, as "high".

Figure 6. Assessment of karst hazard – susceptibility factors.

Figure 7. Assessment of karst hazard – Soil down-washing (a) and rock collapse (b) within downfall zone.

2.3 Characteristic karst size collapse

Intensity of the landslide depends on the sort of void (fracture, karst well or chamber) but also on the ground cover layer behavior (see Figure 5a). The hourglass effect corresponds to the slope stability of the covering materials and is estimated considering the thickness and the properties (cohesion or not) of the upper layer of ground. In our case, considering the geotechnical model, intensity is assessed as "high". To conclude, the characteristic karst size collapse is combined with the disposition to quality hazard, in our example, it leads to "high" hazard (blue and white boxes on Figure 8), which corresponds to at least 3 meters diameter size hazard (without taking into account of the "hourglass effect" illustrated on Figure 5a).

Figure 8. Assessment of karst hazard – Intensity and collapse size.

3 DESIGN OF REINFORCEMENT

3.1 *Principles of the reinforcement*

The methodology described above was applied to the 8 km long development, depending on the geotechnical model, several homogenous areas (geotechnical units), of about 50 to 200 m long, particularly exposed to karstic mechanisms, could have been identified. Designing a geosynthetic parachute system for a 14 m collapse would not be technically and economically possible, thus the principles of the reinforcement design are based on the mitigation of the susceptibility factors. The reduction of the sensitivity of the bedrock by solid injection for instance was not possible for environmental reasons (risks of pollution of the drinking water resource). Nevertheless, the hydrological factor was enhanced by getting the roadway diches and hydraulic structures impervious. The main issue was to deal with the hourglass effect. The upper layer susceptibility was reduced by an optimization of earthworks: it was decided to reemploy cohesive excavated materials, as much as possible, below the parachute system (see Figure 9), that needed to ensure the chemical compatibility between the geosynthetic and molasses. This action also reduces the amplitude of the hourglass effect. In cuttings, this provision needed an over-excavation of 1 m and a substitution by molasses (cohesive materials). Finally, applying the methodology with principles previously defined, allowed to reduce, after treatment of aggravating factors, the karst hole diameter for initially 14 m to a 5 m residual collapse diameter (including hourglass effect).
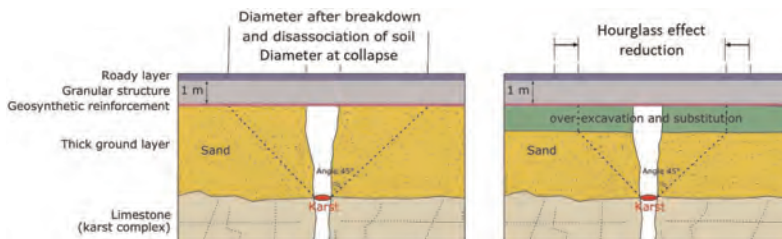
Figure 9.   Predisposition factor reduction and geosynthetics reinforcement.

3.2 *Geosynthetics design*

The design of a geosynthetic parachute system is a compromise between the acceptable settle-ment on surface, the reinforcement depth and the strength of the geosynthetic (Figure 10). Veri-fications are done under Ultimate Limit State (ULS – verification of the resistance) and Serviceability Limit State (SLS – verification of ground deformation and required resistance T_{SLS}). Safety factors are introduced to account for long-term creep, installation damage, effects of environmental conditions. They are defined in standards or calibrated by testing by the producer. A parametric study is carried out in order to identify the importance of the main parameters (H, D, C_e, s – Figure 10), results are plotted on Figure 11. Usually, the SLS resistance is the design case, because of acceptable deformation threshold
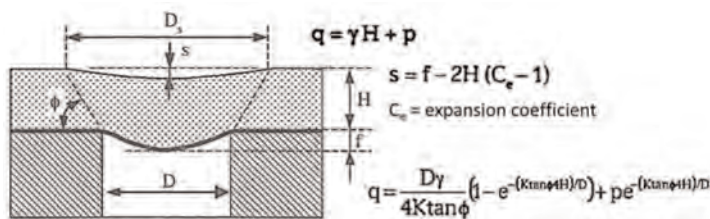
Figure 10.   Geosynthetics for reinforcement karts reinforcement – Rafael method.
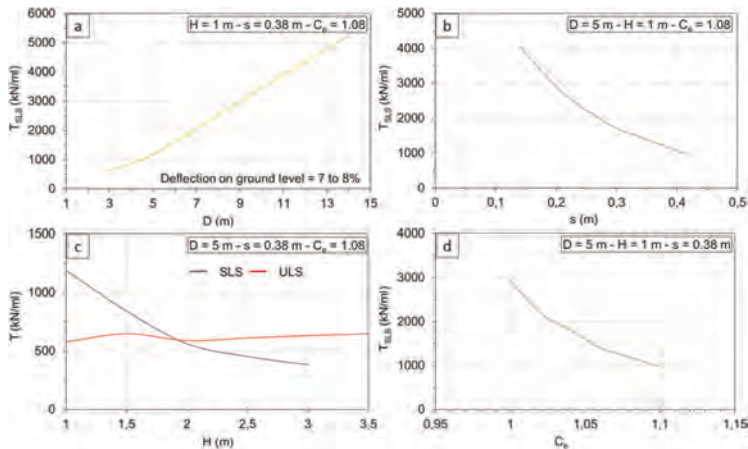
Figure 11.   Geosynthetics design – parametric study.

(11.c). As seeable, expansion coefficient (C_e) of the granular layer has a huge influence on the design, $C_e = 1.08$ was choosen for the verifications (11.d). The assessment of the diameter of collapse (D) and the relevance of the methodology previously exposed is highlighted: it permits to design a reinforcement and reduce hazard from 14 to 5 meters after treatment (by impermeable ditches and sandy layers substitutions) of aggravating factors. For karst reinforcement, acceptable deformations on ground level is a major concern: in our case, the purpose was to prevent an accident by a parachute system, so high deformations were reached (7-8% of ground level deflection). This approach is consistent with the fact that high deformations are needed to mobilize the resistance of the geosynthetics (11.a) and for the ability to quickly detect landslide when occurred. Generally, in order to benefit of the arching effect in the granular layer, which conduce to the reduction of settlement, a layer of granular materials is layered above the geosynthetic with H/D > 0.375. In our case, it would have needed an over-excavation of about 2 meters that was not economically acceptable. Therefore, it was decided to design the reinforcement without taking into account arching effect. To conclude, the characteristic geosynthetic strength needed was about 1200 kN (11.a).

4   CONCLUSION

The proposed approach based on a new methodology to assess karst hazard provides relevant elements for the design reinforcements by evaluation and especially attenuation of the susceptibility factors. Effects of the different reinforcement designs on karst hazard can be easily tested. The method was applied to many roadways and railways infrastructures and permitted an enhanced comprehension of karst phenomena's and the optimization of the reinforcements. In the present study case, the design tensile strength of the geosynthetic is reduced from 5000 kN to 1200 kN by the combination of mitigation actions (on water flow, on the upper layer for example). Moreover, mix of solutions can be adapted on each identified geotechnical units.

REFERENCES

Cerema & BRGM. 2023. *Guide Méthodologique de Détermination de l'aléa Karstique.*
Waltham T., Bell F., Culshaw M. (2005). *Sinkholes and Subsidence: Karst and Cavernous Rocks in Engineering and Construction.*

2D behavior of a granular platform above a soft soil reinforced by rigid inclusions and geogrid subjected to a rolling load traffic

T. Dubreucq, L. Thorel, S. Lerat, A. Jagu & A. Neel
Geotechnical Centrifuge Laboratory, University Gustave Eiffel, Bouguenais, France

ABSTRACT: In a 2D geometry, the effect of rolling loads on a thin granular platform based on a soil reinforced by rigid inclusions, is studied on centrifuged model. Scaled at 1/10th, the physical model consists of a sand Fontainebleau NE34 layer, an analog polystyrene soft soil and spaced vertical metal plates. A strongbox with a transparent face allows image analysis. At a g-level of 10, fatigue tests on a few round-trip cycles were carried out to simulate linear traffic. Perturbations in arching effects in the platform are observed, even with a geogrid reinforcement.

1 INTRODUCTION

In the framework of the French National Research Programme ASIRI+, launched in 2019 (Briançon *et al.* 2020), new research topics have been investigated, including the case of the rolling load. One approach used is the centrifuge modelling. Here, the experimental work in macro-gravity concerns the 2D study of the behavior of thin load transfer platform (LTP) installed on a soft soil reinforced by RI subjected to rolling loads induced by traffic on the platform (Figure 1). The physical model consists of a pavement for rolling load case covering a sandy layer (the granular LTP), possibly reinforced by a geogrid layer, an analog soft soil (geofoam) and spaced vertical metal plates (to simulate RI) installed on a rigid substratum. The rolling load intensity is deduced from the load settlement curves obtained from strip footing loading (Dubreucq *et al.* 2022). Q_p is here the vertical force at top of a RI, and q_{LTP} the pressure beneath the LTP without arching effect as developed further.
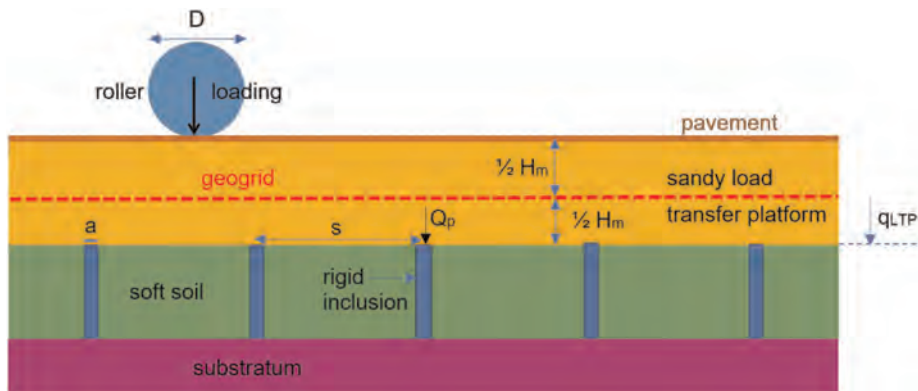
Figure 1. 2D geometry of the physical model – roller in translation.

The 1/10th scale 2D model is placed in a strongbox with a transparent face, under an acceleration of N.g=10×9.81 m/s^2, to visualize the LTP deformations under vertical cyclic rolling load.

The height H_m of the LTP, the spacing s between RI, the width a of a RI and the geogrid elevation (in the middle of LTP) are constant (Figure 1). The 2D geometry is a first step in the understanding of load transfer mechanisms in service state (Lukiantchuki et al. 2018).

2 ROLLING LOAD DESIGN

The strongbox dimensions are L=80 cm long and l =25 cm wide (Figure 2). The 10×g acceleration is applied to the base of the roller. The LTP is a NE 34 Fontainebleau sand. Its thickness H_m is equal to 4 cm (40 cm in prototype scale). The sand (d_{50} = 0.21mm) is moderately dense (density Index: I_d = 0.75). It is implemented by air pluviation in the container to obtain a dry volumic mass of ρ=1648 kg/m^3. Its peak friction angle is 32 degrees with zero effective cohesion. Starting from the strip footing loads, an inverse elastic calculation leads to a modulus of about 10 MPa for the LTP alone.

The 2D RI located every s=10 cm (1 m in prototype scale) consists of flat rigid aluminum plates, laid on a thick rigid aluminum plate to simulate substratum. The RI thickness is a=1 cm (10 cm in prototype scale). The area of the RI over the area of the continuous mesh is thus α =10%. The compressible soil is simulated with a 15.5 kg/m^3 expanded polystyrene (Th.38, Knauf©). Two superimposed 2 cm thick layers (40 cm in prototype scale) are arranged above the substratum. From loading tests of shallow foundations on polystyrene alone, its measured equivalent modulus of 1 MPa is representative of a soft soil in undrained behavior at constant volume, and its measured plasticity stress is about 40 kPa. Compression is followed with mobile marker image analysis. With an zero Poisson's ratio, the polystyrene does not transmit horizontal pressure on the RI when it is compressed. So, there is very few lateral frictions on the RI during loading.
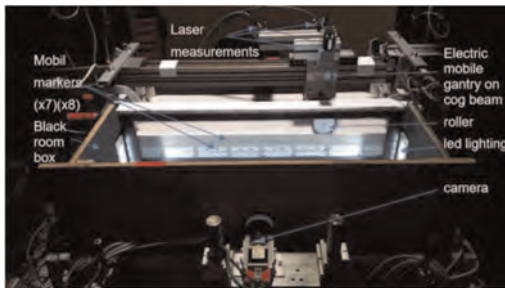
Figure 2. The roller in the transparent-faced strongbox.
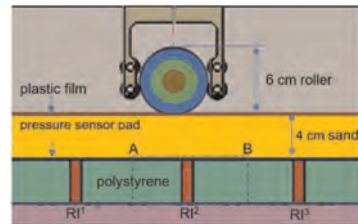
Figure 3. Mobile rolling gantry.

The 2D rolling load consists of an outer steel tube[1] D^1 =6 cm in outside diameter in model scale (Figures 3 and 4), inside which can fit an intermediate tube[2] D^2=4 cm and a rod[3] D^3=2 cm. Their masses are 2.9; 1.8 and 0.6 kg respectively to simulate variable loads up to the critical load measured in static conditions. The roller translation speed is 25 cm/min in model scale. A flexible 0.5 mm thick plastic film is placed on the sand platform to prevent the roller from getting stuck in the sand. In a series of tests, a rectangular fiberglass geogrid (80 cm long and 25 cm wide), with a square mesh of 1.6×1.6 mm^2 and 0.4 mm thick (Windhager©) is placed horizontally in the middle of the LTP layer (Figure 1). Its tensile strength is 10 kN/m (100 kN/m in prototype scale) for a deformation of 1%. So its stiffness is high: J=1 MN/ml in model scale (10 MN/ml, in prototype scale).

The "TactArray" (PPS©) is a 1 mm thick flexible pressure sensor pad (16×32 cells of 1 cm^2), located between the analog soft soil and the LTP. The Figures 3 and 5 show the A-B central mesh of the RI^2 with its soft soil surface S_{soil} equal to $(s\text{-}a).w$, where w is the sensor pad width (w=16 cm), in order to calculate in §.3 the average pressure $q_{average}$ measured by all the pad cells which are inside S_{soil}, and to locate the maximum pressure q_{max} measured among these cells.
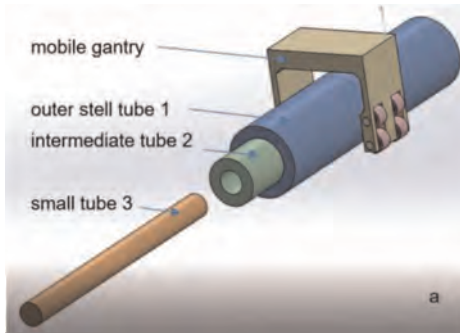
Figure 4.   Drawings of roller design.
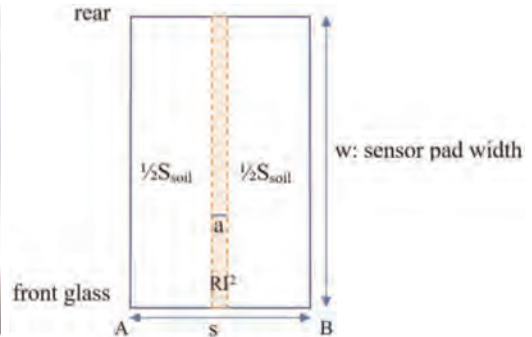
Figure 5.   Central mesh of the RI^2.
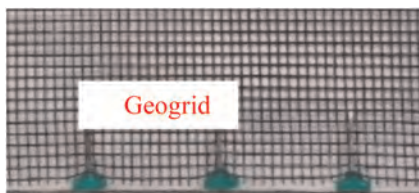
Figure 6.   Details of 3 green flat-headed spikes.
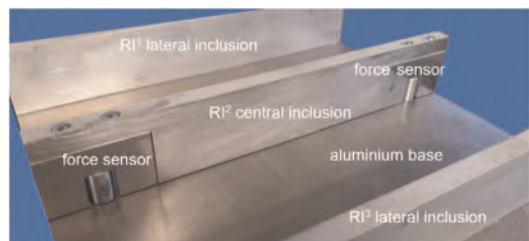
Figure 7.   Location of vertical force sensors.

Figure 6 shows the spikes symmetrically hooked along the longitudinal edge of geogrid, on the side of the glass. An adherence to the glass is provided owing to a film of grease. On Figure 7, two vertical force sensors of 25 daN support the central rigid inclusion RI^2 and are embedded both in the ends of this RI and in the rigid base plate. The surface of the RI's heads is sandblasted to give them a normalized roughness $R_n = R_{max}/d_{50}$ = 0.46 which implies an rough interface friction.

3   RESULTS AND ANALYSIS

The Figure 8 shows the variation without geogrid of the vertical stresses measured by the sensor pad (which is placed on the RI and the polystyrene, Figure 3). During the movement of the roller, before rolling and after 5 round trips of the 2.9 kg roller which is a service load for this foundation.

From scaling laws, model stress and prototype stress on the analog soft soil are equal. The evolution of the vertical stress measured during rolling shows that the localization change of the rolling load induces huge variations on the maximum recorded load, especially at the vertical of each RI. Before rolling, the vertical stress exerted by the roller on the polystyrene after diffusion in the sand is close to that on RI^1 (22 kPa on average). Those on RI^2 and RI^3 are lower (18 kPa on average). This stress distribution over RI before 1st going is due to arching effect in the sandy LTP between two adjacent RI, when the acceleration of the model grows from $1\times$g to $10\times$g, confirmed by a complementary image analysis (not shown here). After the 3rd going, the maximum
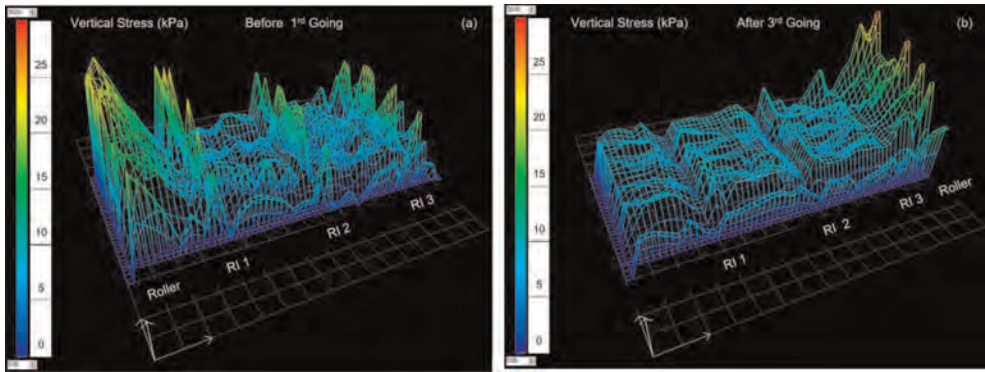
Figure 8.   Vertical stress above the analog soft soil and the 3 RIs: a) before 1st going; b) after 3rd going.

pressure on the analog soft soil can still reach 12 kPa, around an average pressure of 7 to 8 kPa. The stress distribution between RI and polystyrene is now reversed. Following the observed elastic return of the markers in a complementary analysis, the compression then the decompression of the analog soft soil with the rolling can create an "inverse arching effect" above the RIs.

The Figures 9 and 10 show the trajectories over the 5 roller passages (3 going + 2 returns) of mobile marker located in the LTP, above the central IR^2, in cases without and with geogrid in the middle of the LTP. From the scaling laws, the prototype displacement is N=10 times greater.
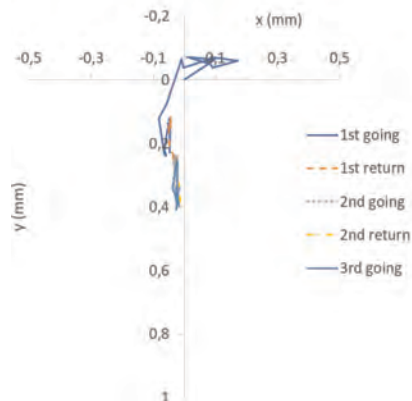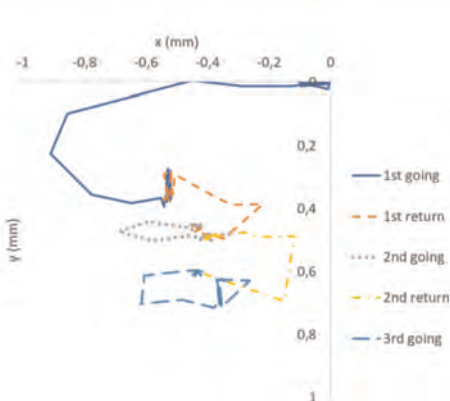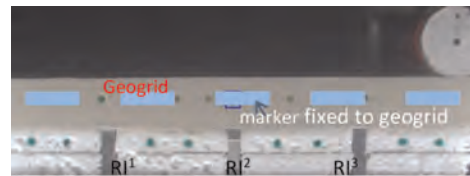
Figure 9.   Trajectory of the central marker.   Figure 10.   Trajectory of the marker fixed to geogrid.

Without the geogrid (Figure 9), the marker moves horizontally in the direction of the translation of the roller when it comes towards the RI2, then in the opposite direction after the roller passes vertically. The horizontal amplitudes decrease over the 5 passages (from 1 to 0.3 mm in model size), as well as for the vertical displacement (from 0.4 to 0.1 mm). The movement of markers between RIs (not represented here) are similar.

With the geogrid (Figure 10), the horizontal displacements of the marker above the RI2 are more or less blocked after the 1st going. Its vertical displacement is half as much. Besides, the geogrid does not reduce the vertical displacements between RIs (not representated here).

The Figure 11 shows the evolution of the vertical load Qp at the top of RI^2, with and without geogrid. From the scaling laws, the load must be multiplied by $Ng^2=100$ for transposition to the prototype scale.
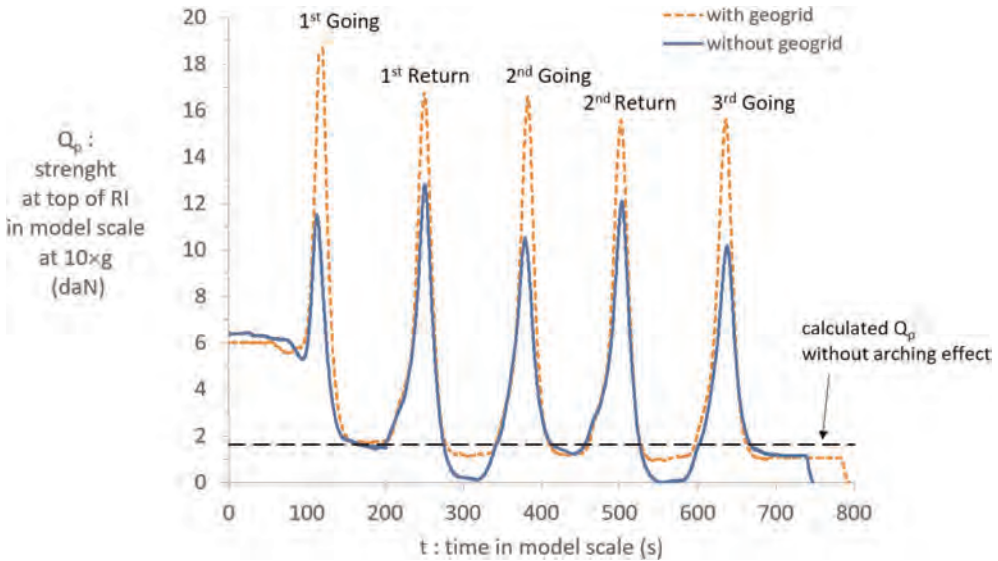
Figure 11. Evolutions of the vertical load at the top of the central RI during the round trips (model scale).

At the "initial" state (t=0s), once the required acceleration has been reached ($10 \times g$), arching effect is visible in both cases with a force concentration about 3.5 times than the calculated load without arching, from the unit weight and the thickness of the LTP, i.e. $\rho.N.g.H_m.l.a = 1.6$ daN here. The rolling load modifies the chain force between the sand grains resulting in variable load transfer.

Without geogrid, the rolling load alternates upwards or downwards in the load transfer with the passages. Thus, the peak load Q_p increases and decreases alternately with the passages, between 10 and 13 daN. This result is related to the alternating movement of the grains of sand located above the RI (Figure 9). The Q_p load is canceled on each return trip. After each going, Q_p approaches by lower value the calculated load without arching effect. This result is in accordance with the stress fall recorded above the RI between the passages (Figure 8). So, the load amplitude on the RI varies alternately on each passage between 9 and 12 daN (+33%).

With the geogrid, the rolling load modifies downwards the load transfer with the passages. The load peak Q_p thus decreases after the 1st going, dropping from 19 to 16 daN, in relation with the loss of initial arching effect (Figure 8). The Q_p load at the head of the RI is always higher than that without geogrid: 17 against 11 daN (+54%) on average at the peaks. The minimum loads between 2 passages also approach by lower value the calculated load of 1.6 daN without arching effect. After the 1st going, the load amplitude varies little over the round trips and remains around 14 daN.

The Figure 12 shows the evolution of the maximum pressure q_{max} and that of the average pressure $q_{average}$ on the analog soft soil inside the RI^2 mesh (Figure 5). From scaling rules, model stress and prototype stress are equal. With or without geogrid, q_{max} presents a double peak before and after the roller passage above the RI^2, for each round trip. The peaks are equal without geogrid (28 kPa) and alternated with geogrid (30/33 kPa).

Between two passages, q_{max} is similar with or without geogrid (12 kPa, see Figure 8). With geogrid, when the roller passes over the RI in return, q_{max} is lower of 3 kPa compared to the going, in connection with the maximum effort Q_p at top of RI (Figure 11).
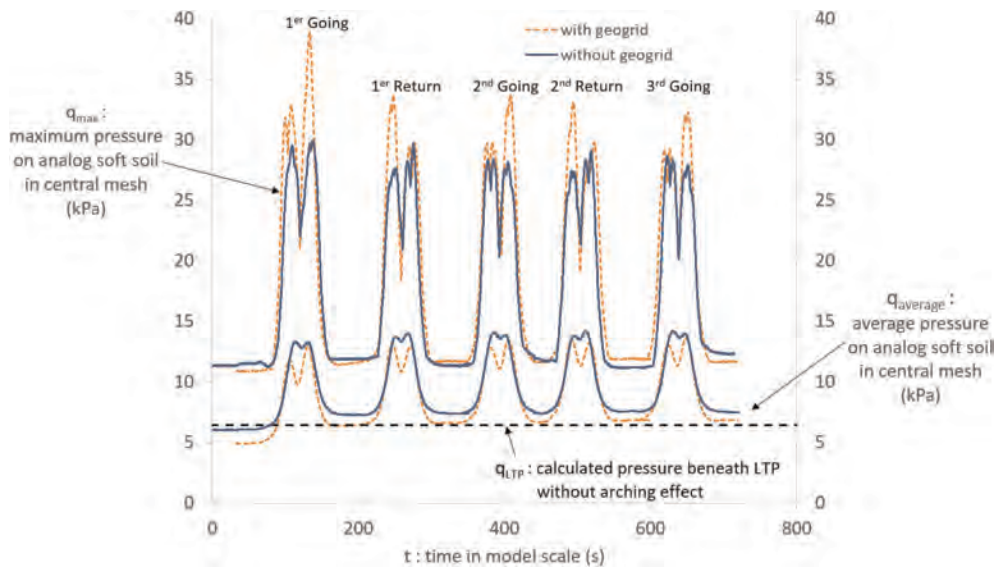
Figure 12. Evolutions of pressure above the analog soft soil beside the central RI[2] during round trips.

Between each going and return, $q_{average}$ approaches by upper value the calculated pressure q_{LTP} beneath LTP without arching effect, i.e. $\rho.N.g.H_m$ = 6.5 kPa, in accordance with the average pressure recorded on the analog soft soil between the passages (Figure 8).

4 CONCLUSIONS

First physical modelling simulations of 2D traffic show an evolution of the load transfer with rolling load and a reversal effect on vertical remaining pressure above inclusions. An additional geogrid reduces the vertical displacement of LTP above the RI, and accentuates the diffusion of the rolling load at depth when crossing, both on the RI whose head is more loaded and somewhat the adjacent analog soft soil. Future tests should include a more rigid pavement to take advantage of this load transfert increase to RI.

REFERENCES

Briançon, L., Thorel, L., Simon, B. 2020. ASIRI+: French National Research Program on soil Reinforcement with Rigid Inclusions. *4th Int. Conf. Transport. Geotech.* (ICTG) Chicago, Illinois, USA Aug.30-Sept. 2. Postponed 24-27 may 2021. Proc. Adv. Transp. Geotech. IV, Lecture Notes in Civil Engng. 165, paper 462. 6p. https://doi.org/10.1007/978-3-030-77234-5_54

Dubreucq, T., Thorel, L., Lerat, S., Jagu, A., Neel, A. 2022. 2D Effect of Rolling Load on a Granular Platform above a Soft Soil Reinforced by Rigid Inclusions. *10th ICPMG*, 19–23 sept. Daejon, Korea.

Lukiantchuki, J.A., Oliveira. J.R.M.S., Pessin, J., Almeida, M.S.S. 2018. Centrifuge Modelling of Traffic Simulation on a Construction Waste Layer. *Int. J. Phys. Mod. in Geotechnics* 18(6): 290–300, https://doi.org/10.1680/jphmg.17.00012

Numerical analysis of low height piled embankments

S. Ahern
Cork County Council, Ireland & Formerly Postgraduate Student Faculty of Engineering & Design, Atlantic Technological University Sligo, Ireland

P.J. Naughton
Faculty of Engineering & Design, Atlantic Technological University Sligo, Ireland

ABSTRACT: A parametric variation using Plaxis 2D showed that the ratio of embankment height to clear spacing between adjacent pile caps and geogrid stiffness were key parameters in the design of low height piled embankments. Increased geogrid stiffness was found to reduce both the geogrid and embankment surface deformations. Geogrid deformations were reciprocated at the embankment surface when the embankment height to clear spacing between pile caps was less than unity. Geogrid tension was not uniform and generally increased with distance from the embankment centre line to the crest of the embankment, before reducing to zero at the embankment toe. Geogrid tension increased with embankment height, with peaks in tension observed at the edge of pile caps; magnitudes 2 – 3 times the mean tension in the geogrid. The geogrid strain was dependent on the geogrid stiffness, with stiffness greater than 5000kN/m resulting in geogrid strain less than 0.5%.

1 INTRODUCTION

A piled embankment consists of piles, usually on a square grid, driven through the unsuitable foundation soil to a firm-bearing stratum. The piles directly reinforce the soft soil and distribute the embankment load onto the firm stratum. Geosynthetic reinforcement is installed over the pile caps at the base of the embankment to further assist in the transfer of load. Low height piled embankments arise where the height of the embankment is less than the clear spacing between adjacent pile caps. Full arching may no longer be mobilised in the embankment fill, with a danger that the embankment surface could imitate the ripple effect occurring at the pile level where the geosynthetic deflects downward between the pile caps.

BS 8006-1 (2016) places a restriction on the design strain in the geosynthetic reinforcement once the height of the embankment is less than 0.7 times the clear spacing between adjacent pile cap edges. In this case the design strain should be less than 3%, significantly less than the 6% design strain allowed for higher embankment heights.

This paper presents data from a plane strain analysis of piled embankments conducted using Plaxis 2D. The Plaxis models are discussed, together with validation of the models against previous studies. The aim of the study is to better understand the performance of low height piled embankments.

2 METHODOLOGY

Plane strain numerical modelling using Plaxis 2D, Version 20, (2021) was used to analyse piled embankments with height, H, ranging from 0.428m to 1.714m. All embankments investigated

had side slopes of one vertical to two horizontal. The model was symmetric about the embankment centre line, requiring only one side of the embankment to be analysed. The piles had a centre to centre spacing, s, of 1.156m with a pile cap diameter, a, of 0.3m, Figure 1. The depth of the foundation soil was 5m. The pile and pile cap geometry together with the depth of the foundation soil were held constant in all analysis. The boundary conditions were fixed along the lower horizontal boundary and horizontally fixed along the vertical left and right boundaries. A tolerated error of 5% was adopted in this study.

2.1 Model parameters

The numerical model for both the validation and parametric variation consisted of embankment fill, geogrid reinforcement, foundation soil and pile and pile caps. In this study the embankment fill was modelled using a Mohr-Coulomb model with the properties given in Table 1. The foundation soil was modelled using the soft soil model in Plaxis, Table 1. The weight density of the foundation soil was 0.39 kN/m^3 and corresponded to the actual value of the material that represented the soft soil in centrifuge modelling reported by Jennings (2012). The geogrid reinforcement was modelled using the geogrid element within Plaxis, which only required the axial stiffness, EA, of the geogrid, Table 1. The piles were modelled using Plaxis embedded beam row elements and were fixed at the lower boundary of the model. The pile caps which were fixed at the top of the piles were modelled as plate elements. The properties of the pile and pile caps are listed in Table 1.
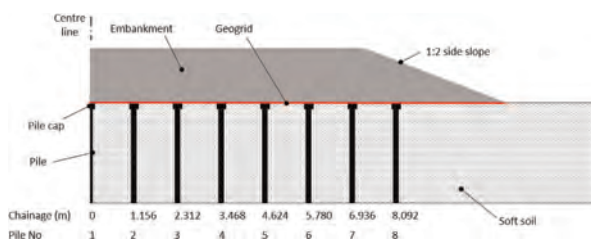
Figure 1. Schematic of model developed in this study.

Table 1. Properties of embankment fill, foundation soil, pile and pile cap used in this study.

Parameter	Embankment fill	Foundation soil	Pile	Pile cap
Youngs modulus (MN/m^2)	20	–	1900	–
Poisson's ratio	0.2	–	–	–
Cohesion (kPa)	1.0	3.0	–	–
Angle of friction (deg)	30	25	–	–
Dilatancy angle (deg)	6.5	0	–	–
Weight density (kN/m^3)	15	0.39	25	–
Modified compression index	–	0.045	–	–
Modified swelling index	–	0.0045	–	–
Width (m)	–	–	0.12	0.3
Centre to centre spacing, out of the plane (m)	–	–	1.156	–
Axial stiffness (GN/m)	–	–	–	3.521
Flexural rigidity (GNm^2/m)	–	–	–	26.9

2.2 Model validation

The model was validated against plane strain physical modelling in the ATU Sligo geotechnical centrifuge and numerical modelling using Plaxis 2D reported by Jennings (2012). The

validation model developed in this study had the material properties listed in Table 1. The embankment height in the validation model was 1.714m, corresponding to a H/(s-a) ratio of 2.0. The geogrid stiffness, EA, was 282kN/m. Overall good agreement was observed between the predicted values and those reported from Plaxis analysis and centrifuge testing by Jennings (2012), Table 2. Based on this data the Plaxis 2D model developed in this study was validated.

Table 2. Comparison of predicted values from this study with data reported by Jennings (2012).

Measurement	This study	Jennings (2012)	
		Plaxis	Centrifuge
Outermost pile displacement (mm)	66	55	45
Vertical deformation of geogrid near embankment toe (mm)	192	160	180

2.3 *Parametric variation*

The parametric variation focused on examining the influence of embankment height and geogrid stiffness on the deformational response of piled embankments. The range of geogrid stiffnesses and embankment heights examined are summarised in Table 3.

Table 3. Embankment heights and geogrid stiffness examined in this study.

Parameter	Geogrid stiffness (kN/m)	Embankment height (m)	H/(s-a) ratio
Range	282 – 15000	0.428 – 1.714	0.5 – 2.0

3 RESULTS AND DISCUSSION

The predicted values from the Plaxis analysis are discussed in terms of the geogrid and embankment surface vertical deformations and the tension and strain in the geogrid.

The vertical settlement of the geogrid increased with higher H/(s-a) ratios, Figure 2(a) for a geogrid stiffness of 282kN/m and Figure 2(b) for a geogrid stiffness of 15000kN/m. In all cases a catenary deflected geogrid shape was observed between adjacent pile caps. The magnitude of vertical displacement increased proportional to the H/(s-a) ratio and inversely proportional to the geogrid stiffness. The deflection of the geogrid with a stiffness of 282kN/m, Figure 2(a), was approximately double that of the geogrid with a stiffness of 15000kN/m, Figure 2(b). The vertical displacement near the outer piles were also greater than that predicted closer to the centre line of the embankment. At higher embankment hights, rotation of the pile caps could be observed, particularly in the outer most piles. At lower H/(s-a) ratios the vertical displacement of the geogrid was relatively flat over a central portion, indicating that the strength/stiffness of the foundation soil was sufficient to restrict the displacement of the geogrid. At higher H/(s-a) ratios the deflected shape was fully curved, indicating that the support from the foundation soil was exceeded. The deflected shape under the side slope where no piles were included was the same for both geogrid stiffnesses.

The predicted vertical deformation at the embankment surface is presented in Figure 3(a) for a geogrid stiffness of 282kN/m and Figure 3(b) for a geogrid stiffness of 15000kN/m. All cases experienced some vertical deformation, with the geogrid with the lower stiffness (282kN/m) experiencing about three times the vertical displacement of the stiffer geogrid (15000kN/m). The deformation of the embankment surface was nonuniform with more settlement occurring closer to the crest of the embankment at chainage 19m, Figure 3. However, for H/(s-a) ratios greater than 1.0, a more uniform deformational response was observed. For
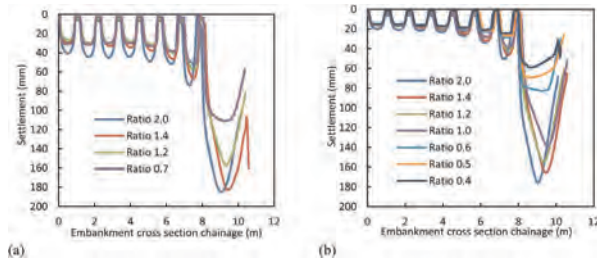
Figure 2.   Settlement of the geogrid for various H/(s-a) ratios and a geogrid stiffness of (a) 282kN/m and (b) 15000kN/m.

lower H/(s-a) ratios, less than 1.0, the surface deformation was more irregular, indicating that at lower embankment heights, the surface deformation may follow that of the geogrid.

The plane of equal settlement is the height above the pile caps were differential settlement ceases in the embankment fill (Naughton 2007). Table 4 summarises the location of the plane of equal settlement, expressed in terms of H/(s-a), from the literature. The plane of equal settlement in BS8006-1 (2016) and Carsslon (1987) was derived from theoretical considerations, Horgan & Sarby (2000), Terzaghi (1936) and Britton & Naughton (2010) from experimental measurements and Lally & Naughton (2012) from numerical analysis. A significant variation in the height of the plane of equal settlement is observed, ranging from 1.16 – 2.45 H/(s-a). In all cases the height of the plane of equal settlement is higher than the value of H/(s-a) determined in this study. One possible explanation for this discrepancy is that this study defined the location of the plane of equal settlement using only embankments surface deformations.
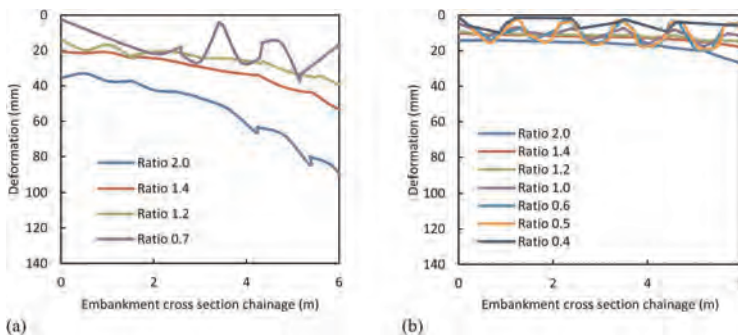
Figure 3.   Surface deformation of embankment for various H/(s-a) ratios and a geogrid stiffness of (a) 282kN/m and (b) 15000kN/m.

Table 4.   Plane of equal settlement expressed in terms of H/(s-a).

| Reference | BS8006-1(2016) | | Carsslon (1987) | Horgan & Sarby (2000) | Terzaghi (1936) | Lally & Naughton (2012) | Britton & Naughton (2010) | This study |
	Marston	Hewlett & Ran-dolph						
H/(s-a)	1.4	1.4	1.87	1.545 – 1.92	2.5	1.16 – 1.47	1.95 – 2.45	1.0

The tension in the geogrid for H/(s-a) ratios between 0.7 – 2.0 are shown in Figure 4(a). Peak tensions were observed at the edge of pile caps. The ratio of peak to mean tension,

Figure 4(b), varied with both location; with larger peaks occurring in the crest of the embankment (chainage 19m), and geogrid stiffness, with the magnitude of peak tension proportional to the geogrid stiffness. Overall, the magnitude of peak tension was 2 – 3 times that of the mean tension. Currently this phenomenon is not considered in design.

The mean tension in the reinforcement increased proportional to geogrid stiffness, Figure 5(a). However, the higher tensions developed at significantly lower reinforcement strains, Figure 5(b). The strain in the reinforcement was relatively uniform over the piled area. The reinforcement strain was inversely proportional to the geogrid stiffness, with the geogrids with stiffnesses of 5000kN/m and 15000kN/m predicting strains less than 0.5%. All predicted geogrid strains were less than the 3% suggested in BS 8006-1(2016). However, it should be noted that for H/(s-a) less than unity, some surface differential settlement may occur at the embankment surface.
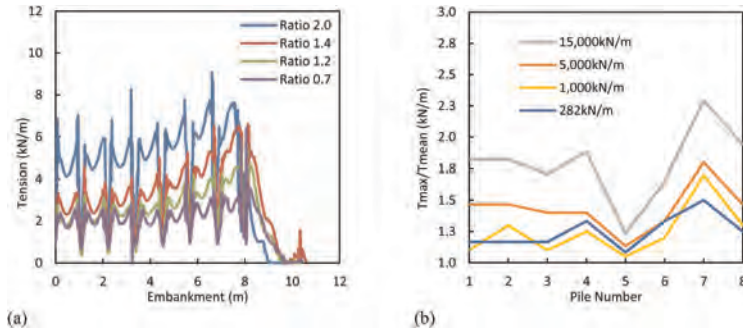
Figure 4.   (a) Geogrid tension for various H/(s-a) ratio and a geogrid stiffness of 282kN/m and (b) ratio of maximum tension to mean tension for H/(s-a) ratio of 2.0 and geogrid stiffness between 282kN/m – 15000kN/m.
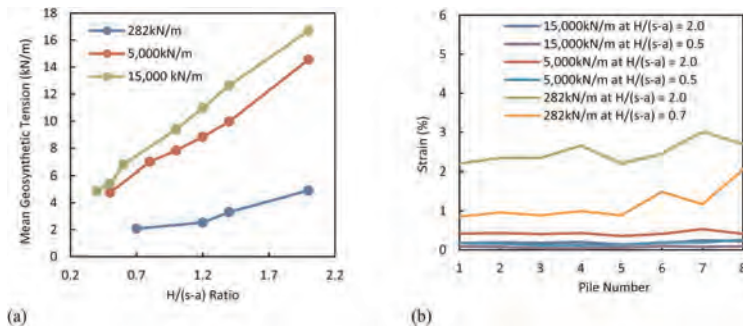
Figure 5.   (a) variation of mean geogrid tension with H/(s-a) and geogrid stiffness and (b) reinforcement strain with location in the embankment, geogrid stiffness and H/(s-a) ratio.

4   IMPLICATIONS FOR DESIGN

Low height embankments, where the height of the embankment to clear spacing between adjacent pile caps is less than 0.7 can be problematic to design. The overriding criteria is to limit differential settlement at the surface of the low height embankment. BS 8006-1 (2016) recommends that the design strain in the geogrid reinforcement should be a maximum of 3%.

The data presented in this paper indicates that both H/(s-a) ratio and geogrid reinforcement stiffness are important factors in the design of low height embankments. Under plane strain conditions limiting the H/(s-a) ratio to a minimum of 1.0 can significantly reduce differential settlement at the surface of the embankment. However, this H/(s-a) is lower than the height determined in other studies for the location of the plane of equal settlement.

Using stiffer geogrid reinforcement will reduce deformation of the geogrid between pile caps, resulting in a reduction in differential settlement at the surface of the embankment. Stiffer geogrid reinforcement will also significantly reduce the strain in the reinforcement to values significantly lower than the 3% maximum value recommended in BS 8006-1 (2016).

However, using higher stiffness geogrid reinforcement will increase the ratio of peak to mean tension in the geogrid at the pile cap. Consideration should be given to careful detailing of the pile cap edge to accommodate this peak tension without damage to the geogrid reinforcement.

5 CONCLUSIONS

Piled embankments are typically used to support road and rail embankments over soft foundation soils. The design of piled embankments is complex and is not yet fully understood. Low height piled embankments, where the height of the embankment is similar to the clear spacing between adjacent pile caps, are known to be difficult to design. The principal design criterion is the serviceability limit state and the requirement to eliminate the differential settlement at the embankment surface.

The impact of embankment height to clear spacing between pile caps and the stiffness of the geogrid reinforcement were investigated under plain strain conditions in Plaxis 2D. The Plaxis 2D numerical models were validated against previous physical and numerical modelling reported by Jennings (2012). A parametric variation showed that the ratio of embankment height to clear spacing between adjacent pile caps and geogrid stiffness were key parameters in the design of low height embankments. Increasing the geogrid stiffness was found to reduce both the vertical geogrid and vertical embankment surface deformations. Piled embankments with low H/(s-a) ratios appeared to receive support from the subsoil, however this diminished for higher H/(s-a) ratios.

Deformations at embankment surface level were reciprocated of the settlement behaviour that occurred at geogrid level for low H/(s-a) ratios, however, when the H/(s-a) ratio was >1.0, the surface deformations were largely uniform and independent of geogrid deformations. H/(s-a) equal to unity is lower than the height of the plane of equal settlement found in other studies.

The tension in the geogrid was not uniform and generally increased with distance from the embankment centre line to the crest of the embankment, before reducing to zero at the embankment toe. Tension in the geogrid increased with embankment height. Isolated peaks in tension were observed at the edge of pile caps, with magnitudes 2 – 3 times the mean tension in the geogrid.

The strain in the geogrid was also dependent on the geogrid stiffness, with geogrid stiffness greater than 5000kN/m resulting in geogrid strain less than 0.5%. Lower stiffness geogrids recorded strain up to approximately 3%.

REFERENCES

Britton, E.J. & Naughton, P.J. 2010. An Experimental Study to Determine the Location of the Critical Height in Piled Embankments. Proc. of the 9th International Conference on Geosynthetics. Guarujá: Brazil.

BS8006-1. 2016. Code of Practice for Strength/reinforced Soils and Other Fills. British Standards Institution: UK.

Carlsson, B. 1987. Armerad Jord – berakningspriniper för – banakar pa Palar. *Linköpig*: Terrarema AB.

Horgan, G. J. & Sarsby, R. W. 2002. The Arching Effect of Soils Over Voids and Piles Incorporating Geosynthetic Reinforcement. *Proc. of the 7th International Conference on Geosynthetics*. Nice: France.

Jennings, K. 2012. *An Investigation of Geosynthetic Reinforced Piled Embankments with Particular Reference to Embankment Extremities*. PhD Thesis, I.T Sligo.

Naughton, P.J. 2007. The Significance of Critical Height in the Design of Piled Embankments. *Proceeding of Geo-Denver 2007*, New Peaks in Geotechnics, ASCE GSP 172, Soil Improvement. Denver: USA.

Plaxis 2D (2021), Bentley – Plaxis General Information Manual. Delft, Netherlands: Bentley Systems Inc.

Russell, D., Naughton, P.J. & Kempton, G. 2003. A New Design Procedure for Piled Embankments. *Proceedings of the 56th Canadian Geotechnical Conference*. Winnipeg: Canada.

Terzaghi, K. 1936. Stress Distribution in Dry and in Saturated Sand above a Yielding Trapdoor. Proc. 1st International Conference on Soil Mechanics and Foundation Engineering, Cambridge: USA.

Soil arching analysis of pile-supported embankment with geosynthetics and verification by centrifuge tests

Bo Li*
Key Laboratory Geotechnical Mechanics and Engineering of the Ministry of Water Resources, Changjiang River Scientific Research Institute, Wuhan, China

Lingwei Chen*
Guangzhou Urban Planning & Design Survey Research Institute, Guangzhou, China

Wenni Deng*
School of Civil Engineering, Southeast University, Nanjing, China

ABSTRACT: Pile-supported earth platforms provide an economical and effective solution for embankments constructed on soft soils, particularly during their rapid construction or when strict control over their deformation is necessary. Based on a three-dimensional assumption of soil arching, an analytical approach is developed to explore the soil arching of the pile-supported earth platform with geosynthetics under the embankment load and uniform pressure. Further, the expression of stress concentration ratio in the pile-supported earth platform with geosynthetics is improved through the analysis of the two regions on top of the pile caps. The results from the in-situ and centrifuge tests are compared with those from the analytical method.

1 INTRODUCTION

Pile-supported embankments with geosynthetics have received considerable attention in soft areas because of their advantages such as rapid construction, easy control of settlements, and suitability for various geological conditions (Magnan 1994). Conventional pile-supported embankments typically have equal-length rigid piles (with caps) floating in the soft soil or embedded in firm soil. Geogrids or geosynthetics are used over the pile head for non-uniform differential settlements between the piles (caps) and the soil. These have been applied to resolve several geotechnical problems such as widening the existing road (Han 2007), bridge approach (Lin & Wong 1999; Reid & Buchanan 1984), subgrade improvement (Jones 1990), and improving the soft ground for constructions (Pinto & Ribeiro 2005).

The main difficulty in their design is assessing the degree of support offered by the pile caps. Terzaghi (1943) defined the "soil arching effect" to measure the degree of support offered by the pile caps. Since then, several researchers have focused on this new ground improvement method through theoretical methods, numerical methods, in-situ tests, physical model tests, etc. Hewlett and Randolph (1988) conducted model tests and developed a three-dimensional theoretical solution based on the dome assumption of soil arching. Low *et al.* (1994) performed four cap-beam model tests with and without geotextile and presented a two-dimensional theoretical analysis. Russell and Pierpoint (1997) and Naughton and Kempton (2005) summarized different analytical methods for modeling the soil arching effect and compared them with the results from three-dimensional numerical analysis. Lin and Wong (1999) performed field measurements of the pressures both on the pile caps and the soil surfaces between the caps, settlements, and

*Corresponding Authors: libo_auliso@126.com, lingweichan@163.com and wdeng@seu.edu.cn

pore-water pressures. Han and Gabr (2002) conducted a numerical study to investigate the pile-soil-geosynthetic interactions by considering the embankment fill height, tensile stiffness of the geosynthetics, and the elastic modulus of the pile material. Cao *et al.* (2007) assessed several existing design methods by comparing the results from the experiments and the numerical and design methods. Chen *et al.* (2004) improved the conventional Hewlett-Randolph three-dimensional soil arch analysis to calculate the efficiency when the soil arch is in the elastic or plastic state. Abusharar *et al.* (2009) calculated the efficiency of the pile support and the tension force of the geosynthetic under universal pressure based on the analysis of Low (1997).

In this paper, based on a three-dimensional assumption of global soil arching, an analytical approach is presented to explore the soil arching effect of the pile-supported embankments with geosynthetics under the embankment load and uniform pressure, as shown in Figure 1. A three-dimensional assumption of soil arching can better reflect real soil arching than using plane strain and axisymmetric geometries. Based on the study by Naughton and Kempton (2005), the geosynthetics is divided into primary and secondary reinforcements. Further, the efficiency expression of pile-supported earth platforms with geosynthetics is improved in the analysis of the two regions on the top of the pile caps. However, owing to the limitations of field testing, it is difficult to conduct in-situ tests to compare the load-sharing ratio of the conventional embankment with equal-length piles. Nevertheless, centrifuge modeling is an effective tool for exploring the mechanism underlying the foundation treatment, as it can simulate a full-scale prototype using a small-scale model by increasing the gravitational acceleration. It even has the advantages of easy management, repeatability, greater control over the test process, and remolded soil properties. Two centrifuge model tests on the pile-supported embankments with uniform piles were conducted to investigate the effect of length ratios on the load-sharing ratio and settlements of the pile-supported embankments. Finally, the proposed analysis method is verified via comparison with the in-situ and centrifuge tests.
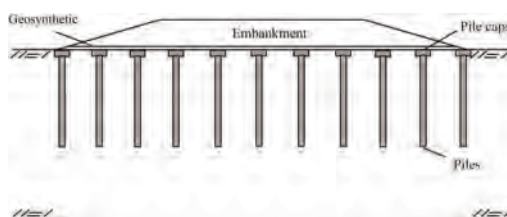
Figure 1.   Pile-supported embankment with geosynthetics.

2   THREE-DIMENSIONAL SOIL ARCHING ANALYSIS

Similar to the three-dimensional analysis reported by Hewlett and Randolph (1988), soil arching is assumed to be a combination of the dome and plane soil arches. Based on the radial equilibrium equations and the boundary condition on the exterior of the soil arch, the equation for the soil arching effect is derived and uniform pressure is assumed. Two separate efficiencies of the soil arch can be calculated when the soil arch fails at either the crown or the pile caps. The lower of the two efficiencies calculated should be used for engineering design.

2.1   *Pile-supported embankment without geosynthetics*

2.1.1   *Crown of the arch*
The vertical stress σ_s acting on the subsoil between the pile caps is given by

$$\sigma_s = \left(q + \gamma H - \frac{\sqrt{2}\gamma s(K_p - 1)}{2K_p - 3} \right)(1 - \delta)^{2(K_p - 1)} + \frac{\gamma(s - b)(2K_p - 2)}{\sqrt{2}(2K_p - 3)} \tag{1}$$

where q is the uniform pressure on the top of the embankment; γ is the unit weight of the embankment fill; H is the embankment height; s is the spacing between the pile caps; b is the

pile cap width, $\delta = b/s$; Kp is the Rankine passive earth pressure coefficient, $Kp=(1+\sin\varphi s)/(1-\sin\varphi s)$; φs is the angle of shearing resistance of the embankment fill.

The following two related terms are used to assess the effect of soil arching:

$$E = 1 - \frac{(s^2 - b^2)}{s^2(\gamma H + q)}\sigma'_s \qquad (2)$$

$$n = \frac{\sigma_p}{\sigma'_s} \qquad (3)$$

where E is the efficiency of the pile-supported embankment; n is the stress concentration ratio. The two terms have different physical meanings. Efficiency indicates the support ratio of the pile caps. The concentration can only show the ratio of pressure acting on the pile caps to that on the soil surface because of the soil arch effect. σ'_s is the mean pressure on the surface of the soil, $\sigma'_s = \alpha\sigma_s$, and α is usually equal to 0.8–1.0 (Low *et al.* 1994). σ_p is the uniform pressure acting on the pile cap and can be obtained using the overall equilibrium equation, as follows:

$$\sigma_p = \frac{1}{b^2}[s^2(\gamma H + q) - (s^2 - b^2)\sigma'_s] \qquad (4)$$

2.1.2 *Pile cap*

One of the four parts of the primary geosynthetics is considered an example that can be simplified as a plane soil arching. As the direction of the radial stress is vertical to that of the fill weight, the arching is considered to be weightless for this simplified case. The pressure acting on the top of the pile cap can be obtained by integrating the tangential force across the cap, which is given by

$$P = 4\int_{(s-b)/2}^{s/2}\sigma_\theta \cdot 2\left(\frac{s}{2} - r\right)dr \qquad (5)$$

where σ_θ is the tangential stress, $\sigma_\theta = K_p\sigma_r$, and σ_r is the radial stress, which is the solution of the plane strain soil arching (Hewlett & Randolph 1988).

2.2 *Pile-supported embankment with geosynthetics*

Low *et al.* (1994) and Abusharar *et al.* (2009) considered soil arching of the pile-supported embankment with geosynthetics in the plane strain case, which could not precisely simulate the real three-dimensional soil arching. Based on the characteristics of its settlement over the elevation of the pile cap, the geosynthetics can be divided into two parts: the primary reinforcement, which is a high-strength reinforcement material that spans between adjacent pile caps; the secondary reinforcement, which covers the entire piled area, as shown in Figure 2 (Naughton & Kempton 2005). Region ② is supposed to be a part of the spherical surface with the equation $x^2+y^2+z^2=R^2$. Region ① can be simplified to be a plane strain case, for which the governing equation is $z = \sqrt{R^2 - \frac{(s-b)^2}{4} - x^2}$ or $z = \sqrt{R^2 - \frac{(s-b)^2}{4} - y^2}$
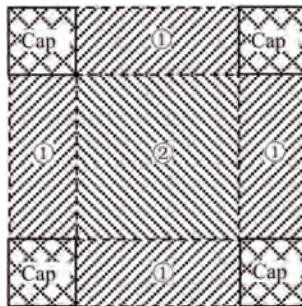
Figure 2.   Plan view of the base of the embankment.

First, region ② is considered the study object. The $y = y_0$ section is considered as an example, which is controlled by $z = \sqrt{R^2 - x^2 - y_0^2}$, as shown in Figure 3. The vertical tension of the geosynthetics at $x = (s - b)/2$ is given by:

$$T_{2z} = 2 \int_0^{\frac{s-b}{2}} K_G \varepsilon_G \sin \theta dy = 2 \int_0^{\frac{s-b}{2}} K_G \frac{l - (s - b)}{s - b} \sin \theta dy \tag{6}$$

where K_g is the tensile stiffness of geosynthetics (kN/m); θ is the angle subtended by the circular arch of the geosynthetics (°), $\theta = \arctan\left(-\frac{s-b}{2} \frac{1}{\sqrt{R^2 - y_0^2}}\right)$ at x=0; l is the deformed length of geosynthetics, $l = 2 \int_0^{\frac{s-b}{2}} \sqrt{1 + \left(\frac{\partial z}{\partial x}\right)^2} dx$.

The reaction of the soft soil below the geosynthetics can be determined by the relation $\sigma - \varepsilon$, which is simplified to exhibit an elastic relationship. Thus, we obtain:

$$F_{R2} = \int_{-\frac{s-b}{2}}^{\frac{s-b}{2}} \int_{-\frac{s-b}{2}}^{\frac{s-b}{2}} \sqrt{R^2 - x^2 - y^2} dx dy \frac{E_s}{D} \tag{7}$$

where D is the depth of soft soil, and E_s is the compression modulus. The vertical equilibrium of region ② requires that:

$$4T_{2z} + F_{R2} = \sigma_s'(s - b)^2 \tag{8}$$

Substituting equations (10) and (11) into equation (12), the value of R is obtained. Subsequently substituting R into equation (10) yields the value of T_{2z}.

Next, region ① of the geosynthetics is considered the study object. Similar to the analysis of region ②, the section parallel to the x-axis is selected, whose governing equation is $z = \sqrt{R^2 - \frac{(s-b)^2}{4} - x^2}$. The reaction of region ① below the geosynthetics is given by:

$$F_{R1} = \int_{-\frac{s-b}{2}}^{\frac{s-b}{2}} \sqrt{R^2 - x^2 - \frac{(s - b)^2}{4}} dx \frac{b}{2} \frac{E_s}{D} \tag{9}$$

The overall equilibrium of region ① requires that:

$$b^2 \sigma_{pG} + bT_{1z} + \frac{b}{2}\left(\frac{E_s}{D} - \lambda\right) \int_{-\frac{s-b}{2}}^{\frac{s-b}{2}} \sqrt{R^2 - x^2 - \frac{(s - b)^2}{4}} dx = \sigma_s'(s - b)\frac{b}{2} + Pb^2/2 + 2T_{2z} \tag{10}$$

The stress concentration ratio of the pile-supported embankment with geosynthetics is defined as the ratio of the average pressure applied on the pile caps to that on the regions ① and ②.
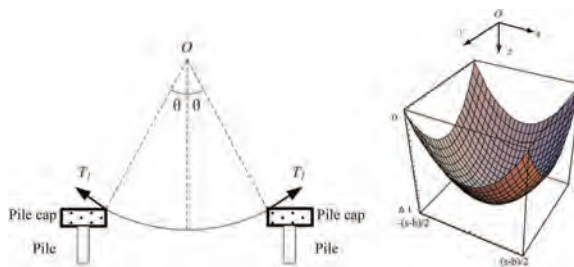
Figure 3.   Settlement analysis of the two regions.

3 VERIFICATION BY CENTRIFUGE TESTS

The load-sharing ratio of a non-uniform pile-supported embankment with geosynthetics was studied through centrifuge tests and three-dimensional numerical analysis (Huang *et al.* 2010). Table 1 demonstrates that four 1:80 scale centrifuge model tests were conducted on the pile-supported embankment with geosynthetics using a 3-m-balanced beam centrifuge at Tongji University.

Table 1. Details of the centrifuge tests.

Test No.	Material Parameters				
	Piles	Length	Total number	Total length (cm)	Saturated soil
1	Uniorm	l = 30 cm	90	2700	$\gamma = 19.5 \text{kN/m}^3$, $c = 1.2\text{kPa}$, $\varphi = 306°$, Water
2	Uniform	l = 23 cm	90	2070	Content = 35.5%, Permeability Coefficient = 5.45×10^{-6} cm/s

Triangular distribution of piles was adopted in the centrifuge tests. Six earth pressure transducers (EPTs) were installed on the top of the piles and the soil between the piles. Four strain gauges were attached to the flank of each of the two piles that were in the middle of the embankment. A rigid plate was located on the top of the sand that can be vertically loaded with the jack when the model box was in the 80-g-centrifugal field. The loading procedure follows four steps: the sand embankment gravity, the rigid plate gravity, and 5000 kN and 9000 kN vertical pressure of the applied loading in sequence.

Table 2 shows the comparison of the stress concentration ratio. There are two stress concentration ratios separately for the long piles and the short ones in Tests 3 and 4. The stress concentration ratio is an important parameter to assess the degree of soil arching and is defined as the pressure applied on the top of the pile to that on the soil. The hybrid method proposed in this study can be used in the analysis of composite embankments with long and short piles as well as for traditional embankments with equal-length piles. The comparison shows that the new method can better predict soil arching in the pile-supported embankment than the Hewlett method.

Table 2. Comparison of the stress concentration ratios.

Test No.	Centrifuge tests With geosynthetics	Finite Element Method With geosynthetics	Present study	
			Without geosynthetics	With geosynthetics
1	38	37	20	34
2	29	20		

4 CONCLUSION

In this study, the three-dimensional soil arching effect was analyzed to examine the incremental generation and progressive failure of arches. Stress concentration ratio of the pile was determined by solving a system of equations, including the equilibrium differential equation, boundary condition equation, and relational expression of the two different soil arching

effect coefficients. The reinforcement tension was calculated by assuming deformed curves considering the presence of geosynthetic reinforcement. Subsequently, a new equilibrium differential equation was established for the elevation of the pile caps. Several improvements were developed in the proposed hybrid analysis method. The deformation and tension of the geosynthetic reinforcements were evaluated in different regions. Furthermore, both the embankment load and uniform pressure were considered to reflect more complicated loading.

ACKNOWLEDGMENTS

REFERENCES

Abusharar, S.W., Zheng, J.J., Chen, B.G., Yin, J.H., 2009. A Simplified Method for Analysis of a Piled Embankment Reinforced with Geosynthetics. *Geotext. Geomembr*. 27, 39–52.

Cao, W.P., Lin, D.S., Chen, Y.M., 2004. Field Tests on Soil Arching of Highway Embankments Reinforced with Rigid Piles and their Comparison with Current Analytical Methods. *Chin. J. Geotech. Eng.* 29, 1577–1581. (in Chinese).

Chen Y., Jia N., Chen R.P., 2004. Soil Arch Analysis of Pile-supported Embankments. *China J. Highway Transp*. 17, 1–6. (in Chinese).

Han, J., Gabr, M.A., 2002. Numerical Analysis of Geosynthetic-reinforced and Pile-supported Earth Platforms Over Soft Soil. *J. Geotech. Geoenviron. Eng.* 128, 44–53.

Han, J., Oztoprak, S., Parsons, R.L., Huang, J., 2007. Numerical Analysis of Foundation Columns to Support Widening of Embankments *Comput. Geotech.* 34, 435–448.

Hewlett, W.J., Randolph, M.F., 1988. Analysis of Piled Embankments. *Ground Eng.* 21, 12–18.

Huang, M.S., Li, B., Cheng, Y., 2010. Centrifuge Tests and Numerical Analysis of Nonuniform Pile-supported Embankments on Load Sharing Ratio. *Chin. J. Rock Mech. Eng.* 29, 2543–2550. (in Chinese).

Jones, C.J.F.P., Lawson, C.R., Ayres, D.J., 1990. Geotextiles Reinforced Piled Embankments. *Proc. 4th Int. Conf. on Geotextiles, Geomembranes and Related Products*, Rotterdam. Balkema, pp. 155–160.

Lin, K.Q., Wong, I.H., 1999. Use of Deep Cement Mixing to Reduce Settlements at Bridge Approaches. *J. Geotech. Geoenviron. Eng.* 125, 309–320.

Low, B.K., Tang, S.K., Choa, V., 1994. Arching in Piled Embankments. *J. Geotech. Engrg.* 120, 1917–1938.

Magnan, J., 1994. Methods to Reduce the Settlement of Embankments on Soft Clay: A Review. *Vertical-Horizontal Deformations of Foundations and Embankments*, ASCE. Geotech. Spec. Publ. 40, 77–91.

Naughton, P.J., Kempton, G.T., 2005. Comparison of Analytical and Numerical Analysis Design Methods for Piled Methods for Piled Embankments. *Contemporary Issues in Foundation Engineering*, ASCE. Geotech. Spec. Publ. 131, 135–144.

Pinto, F., Ribeiro, J.M., 2005. Ground Improvement Solutions Using Jet Grouting Columns. *Proc. 16th Int. Conf. on Soil Mechanics and Geotechnical Engineering*. Millpress Science, Osaka, Japan, pp. 1249–1252.

Reid, W.M., Buchanan, N.M., 1984. Bridge Approach Support Piling. *Piling and Ground Treatment. Thomas Telford Ltd.*, London, pp. 267–274.

Russell, D., Pierpoint, N., 1997. An Assessment of Design Methods for Piled Embankment. *Ground Eng.* 30, 39–44.

Terzaghi, K., 1943. *Theoretical Soil Mechanics*. Wiley, New York.

Full scale experiment of a geosynthetic-reinforced piled embankment

C. Terqueux & J. Racinais
Menard, Orsay, France

L. Briançon
GEOMAS laboratory, INSA Lyon, Université Lyon 1, Villeurbanne, France

A. Pantet
Université Le Havre Nomandie, LOMC, Le Havre, France

P. Gotteland
Fédération Nationale des Travaux Publics, Paris, France

ABSTRACT: This paper presents a full-scale experiment of a geosynthetic-reinforced piled embankment over soft soil. Three tests were carried out in a bench of 8m x 8m x 1m where the type and the position of the geosynthetic were variables. A comprehensive monitoring program was set up in order to follow the stress distribution of the structural elements, the settlement of soil and the strain of the geosynthetics. This work is a part of the cooperative national research project ASIRI+ (2019 - 2024) which gathers about forty organizations and aims at proposing dimensioning rules in the field of soil reinforcement by rigid inclusions. From these experimental results, the understanding of complex mechanisms developed inside the load transfer platform were investigated such as the soil arching, the load efficacy and the differential settlement.

1 INTRODUCTION

Over the past few years, the increasing of urbanization and public works (portion of roads or railways, wind farm reinforcement of quays and dykes, etc.) had led to the construction of geotechnical infrastructure over weak soil with high compressibility. To remedy this problem, new techniques of soil reinforcement have been developed. The French national project ASIRI (2012) set out to define, conduct and interpret the experiments and numerical modelling necessary to understand the mechanisms by which the soil improvement by rigid inclusions works. This technique aims at inserting a network of concrete columns in a soft soil with low bearing capacity in order to transfer the majority of the load to the heads of the inclusions thanks to a granular platform by friction along the pile. The mechanisms developed within the load transfer platform (LTP) called "arching", as well as those due to friction along the inclusion are involved in the complex phenomenon of soil/structure interaction.

With the aim of improving the efficiency of this composite foundation, one or several layers of geosynthetics can be inserted within the granular mattress. The presence of horizontal reinforcement allows a better transfer of the load to the piles through membrane effect. Experimental or numerical investigations of a geosynthetic-reinforced pile-supported embankment have been carried out (Briançon & Simon 2012; Lian *et al.* 2014; Lee *et al.* 2021; Liu *et al.* 2007; Nguyen *et al.* 2022; Sloan 2011; Van Eekelen 2012). However, the number, the type, or the position of geosynthetic in the mattress remains an issue.

As the part of the French national project ASIRI+ (2019 – 2024), which is the extension of ASIRI project, three full-scale tests were carried out in an experimental bench containing 16 rigid inclusions. The soft soil is a three-layer made of sand, rubber granulates and honeycomb cardboard. The objective was to be able to model a two steps settlement, firstly with the compressibility of the rubber granulates and secondly with the biodegradation of the cardboard by water. The first test was conducted without geosynthetic, the second one with one layer of biaxial geotextile and the last one with two layers of crossed monoaxial geogrids.

2 FULL-SCALE TEST MODEL

2.1 *Test model*

As mentioned in the introduction paragraph, three tests were carried out in the experimental bench. The first one was set up without horizontal reinforcement, the second with a biaxial geotextile and the last one with two layers of crossed monoaxial geogrid.

The dimensions of the experimental bench are 8 m x 8 m x 1 m (depth) in which is inserted a square mesh of 16 rigid inclusions. The circular inclusions measure 300 mm diameter and 1 m high. The center-to-center distance between the piles is 2 m. Destructive tests were performed on three concrete samples of 11cm×22 cm after 100 days of pouring. The elastic modulus is 35 GPa. A slab was poured at the bottom of the bench on which were placed the inclusions.

The different layers of materials placed in the experimental bench, as shown in Figure 1, are the following (from the bottom to the top):

- 2.5 cm of duckboard, their role is to allow a water saturation of the Biocofra from below,
- 10 cm of honeycomb cardboard, called Biocofra,
- 50 cm of rubber granulates,
- 38 cm of sand,
- 50 cm of load transfer platform,
- 1.5 m of backfill.

Each layer is separated with a separation geotextile to facilitate dismantling. Those geotextiles have no reinforcing function.
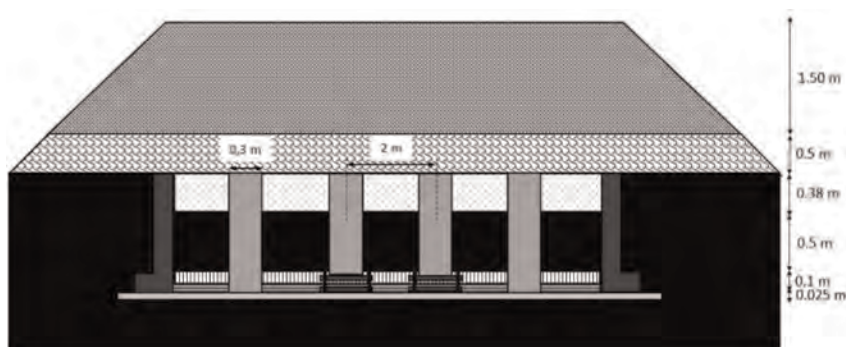
Figure 1. Cross section of the test model.

2.2 *Materials*

As mentioned in the introduction, the soft soil is simulated by three layers made of 10 cm of Biocofra, which correspond of the height of a cardboard, 50 cm of rubbery aggregates from the recycling of used tires (Deltagom) and 38 cm of sand. Laboratory tests in GEOMAS

(INSA Lyon) were performed to characterize the mechanical parameters of each material, referred in Tables 1 and 2.

Table 1. Properties of the soft soil layers.

Parameters	Biocofra	Deltagom	Sand
Unit weight of soil γ (kN/m^3)	–	10	18
Young modulus E_Y (MPa)	–	0,341	35
Cohesion c' (kPa)	–	100	1
Internal friction angle φ' (°)	–	0	32
Compressive strength (kPa)	50	–	–

Table 2. Properties of the LTP and the backfill.

Parameters	Load transfer platform	Backfill
Grain size	0/31.5	0/63
Unit weight of soil γ (kN/m^3)	19	18
Cohesion c' (kPa)	2	8
Internal friction angle φ' (°)	40	33

2.3 Instrumentation

In the case of a full-scale test, the number of rigid inclusions must be sufficient so that the measurement is not affected by edge effects. In the case of a square mesh, 16 inclusions allow a measurement of the central mesh under good conditions (Briançon & Simon 2012). The instrumentation of those tests is therefore concentrated on the four central inclusions.

As shown on Figures 2a and 2b, a total of 8 earth pressure cells were installed. 4 of them were placed directly on the heads of the 4 central inclusions to measure the stress on the pile, their dimensions are equal to the diameter of the inclusion. Three were installed at the center of the mesh on the soil respectively at the top of the Deltagom layer, on the sand and on the LTP. The last earth pressure cell was placed at the right of one inclusion at the top of the

Figure 2. a. Rigid inclusions mesh and sensors positions on the sand; b. Positions of settlement plates, pressure cells and anchor load cells on a cross section.

platform. Twelve settlement plates were installed on the soil, at strategic positions, in order to follow the deformation of the soft soil, to measure the differential settlement and locate the plane of equal settlement in the backfill. Four load cells have been set up at the bottom of the 4 central inclusions to determine the force at the toe.

In the case of test 2 and 3, the geosynthetic layers have been instrumented by a Rayleigh scattering optical fiber which allows a millimetric resolution of the strain.

2.4 Test procedures

After the completion of the installation of the soft soil, the load transfer platform had been setting up alternating a layer of 20 cm of expended material and a compaction until reach 50 cm. The backfill was compacted every 50 cm. This static load was kept constant for one month in order to give way to the formation of arching. After each loading stage, the settlement of the soil, the stress on the pile caps and on the soft ground, and the deflection of the fiber optic were measured.

After a month, water has been injected at the bottom of the bench until it reached the lower part of the Biocofra. The water then migrated by capillarity inside the material allowing its biodegradation. This stage generates an imposed settlement of 7 cm. The evaluation of the stresses, settlements and geosynthetic strain was thus done during these three stages:

- During the installation of the LTP and the backfill,
- During a month of constant static load,
- During the biodegradation of the Biocofra.

3 RESULTS ANALYSIS

3.1 Test 1

The first test, carried out without horizontal reinforcement, was considered as the reference test for the dimensioning of the geosynthetics. Figure 3a shows the evolution of the stress and the settlement on the soft soil during Test 1. The load transfer platform has been set up in two compacted layers of 25 cm. On top of the sand, we measured a stress of 7 kPa after the first 25 cm and 12 kPa after the second layer generating a settlement of 15 mm and 45 mm respectively. This settlement is less at the top of the Deltagom (9 mm and 27 mm) highlighting the deformation of the sand layer. The placement of the backfill generates a stress of 47 kPa at the top of the soft soil, i.e. an increase of 25 kPa. After a month of constant static load, the stress has decreased (load transfer to the inclusion) from 47 kPa to 18 kPa.

Figure 3.   a. Stress and settlement evolution on the soft soil and during test 1; b. Stresses evolution on the pile head and at the toe during test 1.

As the 4 sensors installed on the 4 inclusions head and toe give approximately the same values, an average stress is taken (Figure 3b). As the opposite phenomenon of what happened on the soft soil, during the constant static load of 1 month, the stress on the inclusions is increasing. Moreover, with the generation of a second settlement the stress increases from 847 kPa to 1455 kPa towards the inclusions. The pile efficacy E is a parameter known to assess this technique of soil improvement. It is equal to the load on the pile cap divided by the total load imparted by the embankment over the tributary area of the pile. In the Test 1, E = 71%. The differential settlement on the top of the LTP is not represented in this article but for this test, it is equal to 3 cm.

3.2 *Geosynthetics used for test 2 and test 3*

After this first test, a call for tenders was made to the producers of geosynthetics in order to halve the final soft soil settlement. Two products were selected: 1 biaxial geotextile (formed with 2 monoaxiales geotextile crossed, placed one on top of the other) and 1 monoaxial geogrid. These products are subject to a confidentiality clause, so their exact properties won't be shared in this article. However, the stiffness J (at ε = 2%) is between [6000;7000] kN/m and [5000;6000] kN/m respectively for the geotextile and the geogrid. Table 4 presents the characteristics of the geosynthetics required from producers.

For the second test, 2 layers of superimposed crossed monoaxial geotextile were installed at 10 cm above the pile caps. Concerning the third test, two crossed monoaxial geogrids were installed in the LTP, the first one 10 cm above the pile cap and the second 20 cm above (Figure 4).
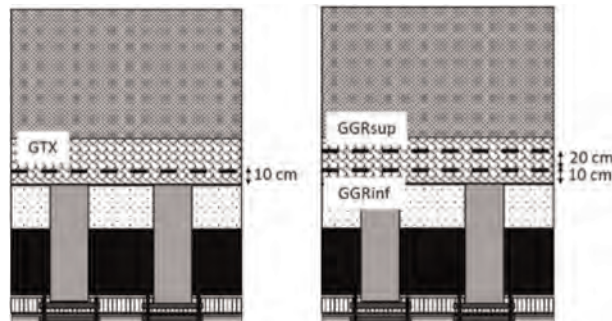
Figure 4.   Positions of the geosynthetics within the LTP for test 2 and test 3.

3.3 *Comparison of the 3 tests*

The load transfer mechanisms are different for all 3 tests. The insertion of horizontal layers in the LTP made it possible to reduce the increase in stress on the ground during the rise of the embankment as shown on Figure 5a. For all 3 tests, the arching is appearing during the month of constant static load as the stress on the soil decreased. Moreover, when comparing the stress variations during dissolution, we note that pad 3 with geogrids allows a better transfer of loads to the inclusions. Even if the stress on the soft soil is limited thanks to geosynthetics, the settlement has not been reduced (Figure 5b). However, we observe a stabilization of the settlement (Δs = 2mm) during the constant static load for Test 3 with geogrids.

At the end of the embankment installation, the loads transferred to the inclusions are higher than in the test without reinforcement as shown on Figure 6a. However, the load transfer mechanisms do not occur at the same time. For the test with geotextiles, the transfer occurs mainly during the constant static load of 1 month, whereas for Test 3 with geogrids
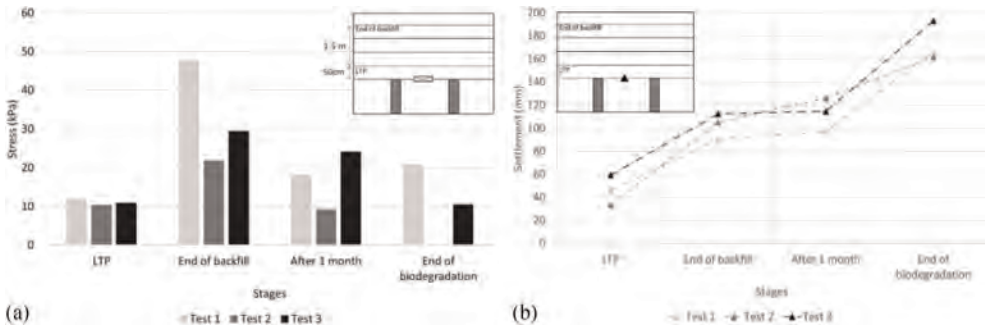
Figure 5.   a. Stress evolution for all 3 tests on the soft soil; b. Settlement evolution on the soft soil.

the transfer occurs mainly during the dissolution (1000 kPa increase towards the heads). By calculating the efficiency at the head of the IR at the end of the dissolution, we obtain respectively E = 67% and E = 93% for the test 2 and the test 3. However, the stress at the bottom of the inclusion is almost equal for plot 2 and 3 (Figure 6b), the load transfer along the inclusion does not occur in the same way for these two tests.
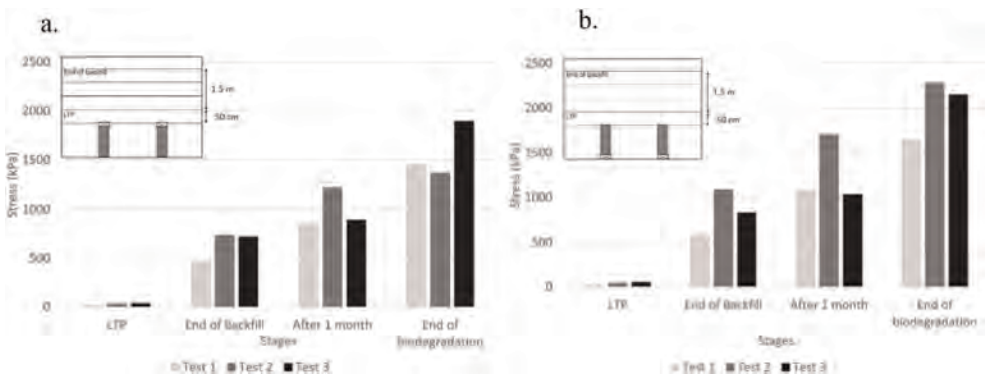
Figure 6.   a. Stress evolution for all 3 tests on the pile cap; b. Stress evolution at the bottom of the inclusion.

Figures 7a and 7b presents the fiber optic strain on an inclusion line; for Test 2, during the installation of the first 50 cm layer of the embankment and after a month; for Test 3, only after a month. Measurements (Figure 7a) indicate deformation on the order of 8000 µdef (0.8%) on the inclusions before dissolution. In test 2, the geotextile sheets were not sufficiently stressed, which did not reduce the settlement of the subsoil. Regarding Test 3 (Figure 7b), fiber optic measurements indicate that the lower geogrid was not stressed during fill placement, with an average deformation at the inclusions of 0 µdef after a month of constant static load. It is conceivable that the reinforcement layers followed the settlement of the soil without coming under tension.

The comparison between the three tests shows that in this configuration the geosynthetics have not brought an upper efficiency than those obtained with the non-reinforced platform. Even this observation is unexpected, other authors have recently led to this conclusion from their experimental studies: Lee et al. (2021) showed approximatively the same efficiency with and without geosynthetic with the same level of settlement, Nguyen et al. (2022) showed a good efficiency of the reinforced granular platform without tension measured inside the geogrid.
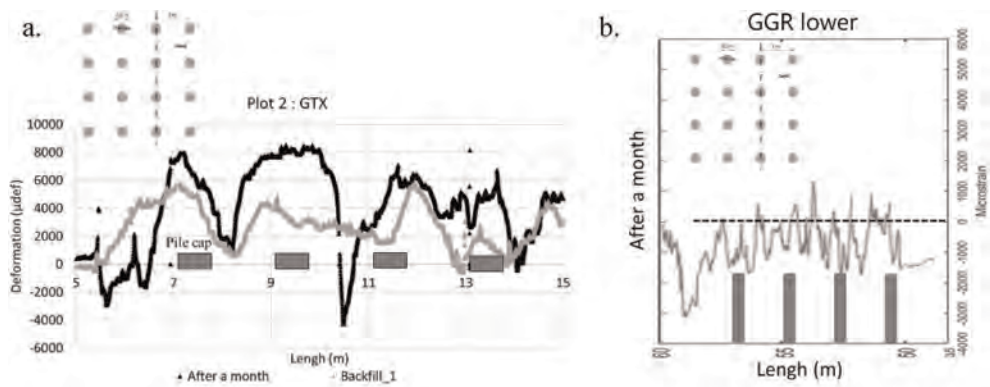
Figure 7. a. Fiber optic deformation on geotextile; b. Fiber optic deformation on lower geogrid.

4 CONCLUSIONS

Three full-scale model tests on a geosynthetic-reinforced pile-supported embankment were conducted. For the three tests, the settlement and load transfer take place during the installation of the embankment. The reference test (Test 1) showed that with a 50 cm load transfer platform under a 1.5 m embankment, an efficiency of 70% is already achieved. Even if the insertion of geosynthetics in the mattress has slightly increased the arching load over the pile caps, the settlement of the subsoil has not been reduced. As the dimensioning of the geosynthetics, perhaps the settlement reductions requested from the producers were not the most realistic and a total reduction in differential settlement should have been requested from the LTP roof. Other tests will be performed in order to verify the measured values of stresses and strains by improving the instrumentation. As the platform is already very efficient without reinforcement, a test with a thinner LTP could be considered.

REFERENCES

ASIRI (French Research Project on Rigid Inclusions) 2013. *Recommendations for the Design, Construction and Control of Rigid Inclusion Ground Improvements.* IREX, Presses des Ponts. Paris.

Briançon, L. & Simon, B. 2012. Performance of pile-supported Embankment Over Soft Soil: Full-scale Experiment. *Journal of Geotechnical and Geoenvironmental Engineering* 138(4): 551–561.

Lee, T. et al. 2021. Lessons from Full-scale Experiments on Piled Embankments with Different Geosynthetic Reinforcements. *KSCE Journal of Civil Engineering* 25(2): 442–450.

Lian, F. et al. 2014. Field Study of Improvement Mechanism of Geogrid-reinforced and Pile-supported Embankment. *Applied Mechanics and Materials* 587: 928–933.

Nguyen, V. D. et al. 2022. Monitoring of an Instrumented Geosynthetic-reinforced Piled Embankment with a Triangular Pile Configuration. *International Journal of Rail Transportation*: 1–23.

Sloan, J. A. 2011. Column-supported Embankments: Full-scale Tests and Design Recommendations. *Docotoral dissertation*, Virginia Tech, Blacksburg, Virginia.

Van Eekelen, S. J. M. et al. 2012. Model Experiments on Piled Embankments. *Part I. Geotextiles and Geomembranes* 32; 69–81.

Four years field measurements in a partly submerged woven geotextile-reinforced pile-supported embankment

S.J.M. van Eekelen* & R.A. Zwaan
Deltares, The Netherlands

A. Nancey
TenCate Geosynthetics, Bezons Cedex, France

M. Hazenkamp
TenCate Geosynthetics, Hengelo, The Netherlands

Y.H. Jung
Kyung Hee University, Giheung-gu, Yongin-si, Gyeonggi-do, Republic of Korea

ABSTRACT: The geosynthetic reinforcement in a pile-supported (GRPS) embankment can be designed using the CUR226 (2016) design guideline. CUR226 has adopted the Concentric Arches (CA) model of Van Eekelen et al. (2013, 2015), which was validated using measurements in field and experiments. The validated use of CUR226 is only possible for conditions that match the conditions of these measurements. This means that the embankmentfill should be positioned above the ground water table, and that at least one layer of the geosynthetic reinforcement should be a geogrid.

This paper describes measurements in a partly submerged piled embankment, reinforced with geotextiles only. The seasonable effect in the measured geotextile strains strongly matches the seasonable temperature variation. However, no correlation with the varying groundwater table was found. The measurements match the calculations with the Concentric Arches model well and remain sufficiently on the safe side. Therefore, the CUR226:2016 design guideline may be used for this type of geotextile-reinforced pile-supported embankments.

1 INTRODUCTION

The design guideline CUR226 (2016) for geosynthetic-reinforced pile-supported (GRPS) embankments adopted the Concentric Arches (CA) model of van Eekelen (2015). This model was validated with more than 100 measurements taken in field and experiments (van Eekelen et al. 2015). These embankments were reinforced with at least one layer of geogrid. Furthermore, all the embankments were unsaturated, and installed above the groundwater table.

Limited research was done on the influence of water in a piled embankment. Briançon and Simon (2012), Sloan (2011), and Van Eekelen et al. (2020) showed that heavy rainfall affects measurements. Song et al. (2018) presented 2D trapdoor tests with sand and concluded that the arching mechanism can degrade. Wang et al. (2019), however, showed that the soil arching strengthened with an increasing water level in full-scale 3D model experiments.

The validated use of CUR226 is only possible for geometries, conditions and materials that match the situation where the measurements for the validation were taken. So, the entire embankment should be positioned above the ground water table, and that at least one layer

---

*Corresponding Author: suzanne.vaneekelen@deltares.nl

of the reinforcement should be a geogrid. If these requirements are not met, measurements should prove that the CA model gives good results for these conditions.

For this purpose, field measurements were done in a partly submerged piled embankment, reinforced with geotextiles only, without geogrids. This paper compares the measured strains with the varying groundwater table and air temperature, and with calculations with the CA model of CUR226.

2 A PARTLY SUBMERGED GEOTEXTILE-REINFORCED PILED EMBANKMENT

Van Eekelen et al. (2022) described the piled embankment that was constructed to connect an industrial area and the regional road N210 in the Netherlands. It was opened on 6 April 2019. Pile caps (0.75 m x 0.75 m), with smooth, rounded edges, were installed on end-bearing prefab concrete piles with an average centre-to-centre spacing of 2.28 m x 2.27 m (across x along the road axis). The basal reinforcement consists of two layers of woven geotextile (TenCate Geolon® PET 400/50). The bottom layer was installed across the road axis, the second layer was installed parallel to the road axis.

Figure 1 shows the monitoring program. Strain transducers E1 to E4 measure the geotextile strain. Pore pressure transducers ppt1 and ppt6 measure the varying groundwater table and ppt7 measures the water level in the adjacent ditch. Furthermore, the air temperature at the test location was measured hourly.
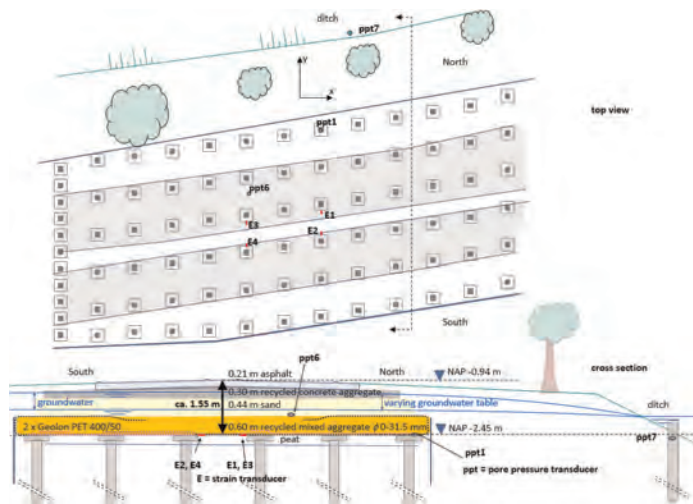
Figure 1.   Lay-out of the geotextile-reinforced piled embankment and the monitoring equipment.

3 MEASUREMENTS

3.1 *Pore pressures and ground water table*

Figure 2 shows the measured pore pressures, translated into groundwater table in m NAP, where NAP is a reference level in the Netherlands. As indicated in the figure, ppt 1 lies on top of a pile cap, and ppt6 lies approximately 0.65 m higher. Therefore, ppt1 lies in saturated soil, well below the groundwater table. However, the groundwater table sometimes drops below ppt6.

Pore pressure transducers are sensitive to air bubbles. Figure 2 nicely shows what can happen if a pore pressure transducer is installed in unsaturated soil. Until June 2020, ppt1 and pp6 match. However, around 1 June 2020, the groundwater table drops below ppt6. This causes an air bubble that disturbs the measurements of ppt6. At this moment, the values of

ppt6 remain well below those of ppt1. In September 2020, the groundwater level passes ppt6 again, the air bubble disappears, and ppt1 and ppt6 match again. In April 2021, the ground-water table passes ppt6 again, resulting in another air bubble that makes the measurements of ppt6 unreliable again. However, it seems plausible that ppt1 continuously gives reliable results; it shows a low water table during the very dry summer of 2022, followed by a rainy period in September 2022. The pore pressure transducer in the ditch was installed in February 2020 and gave reliable results until June 2021 and between November 2021 and March 2022.
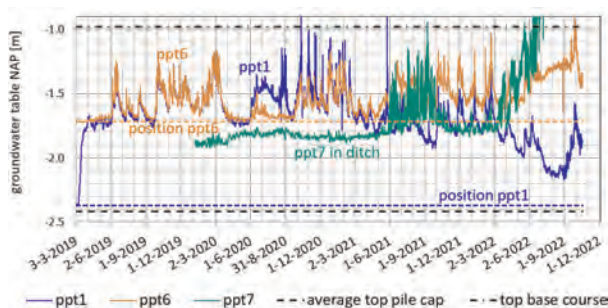
Figure 2.   Measured pore pressures, translated into groundwater table (ppt1, ppt6) ditch water table (ppt7).

3.2   *Geotextile strains compared to groundwater table and average day air temperature*

Figure 3 compares the measured geotextile strains with the measured groundwater table. Strain gauges E1 and E2, that are located on the east-side, give higher values than the two other strain gauges, E3 and E4. The authors cannot explain this difference. All measured strains show a seasonable effect; during the summers, the strains are higher than in the winters. Furthermore, each summer gives slightly higher strains than the previous summer. This can be explained by the creeping behaviour of the geotextile.
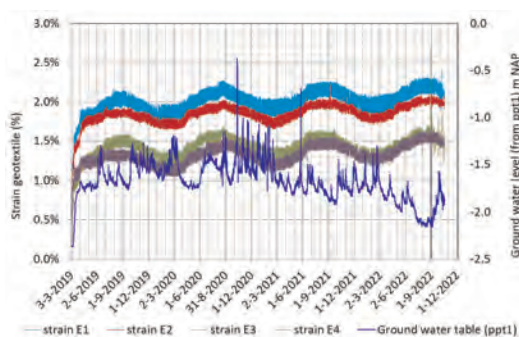
Figure 3.   Comparison measured geotextile strains and to measured groundwater table (ppt1).

The measured strains do not correlate clearly with the groundwater table. Figure 4 zooms in on two four-week-long periods. Figure 4a shows a dry period, without rain resulting in a decreasing groundwater table. Figure 4b shows a wet period, with rainy periods and an increasing ground-water table. The measured strains show a clear daily cycle, which the authors cannot explain. Other papers present a similar daily effect, such as van Eekelen and Bezuijen (2007).

The daily cycle of traffic load, or soil temperature, may have an influence. However, the different strain gauges do not have a peak at the same time of the day. Figure 4b shows an immediate response on rain: the daily cycle is less clear. Possibly, this is caused by the relatively constant and low temperature caused by the rain, which flattens the daily cycle.

Figure 5 shows a clear correlation between the seasonable cycle of the geotextile strains and the average day temperature. The geotextile strain is higher in summer. The thermal expansion of the road surface may play a role in this mechanism.
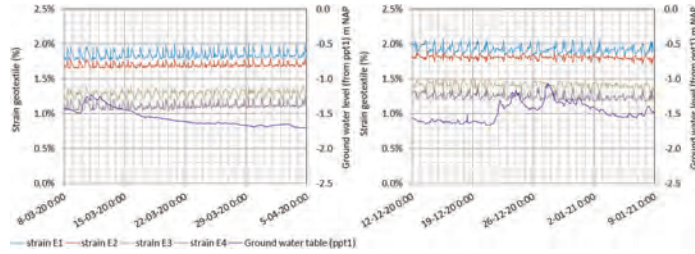
Figure 4. Four-week details of Figure 3; measured geotextile strains and measured groundwater table (a) dry period (no rain) and (b) wet period (several rainy periods).
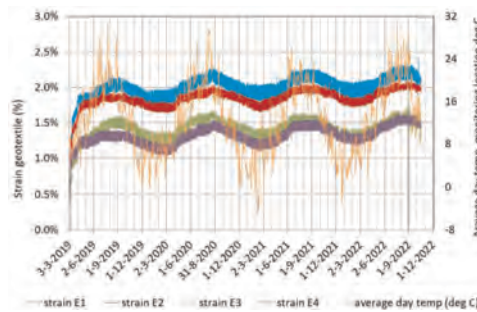
Figure 5. Comparison measured geotextile strains and the day-average of the air temperature which was measured hourly at the field monitoring location.

4 CALCULATIONS WITH THE CONCENTRIC ARCHES MODEL

The geotextile strains were calculated using the CA model (CUR226 2016; van Eekelen 2015). No partial factors were used. Table 1 gives the input parameters that were used. Some remarks:

- For design purposes, the characteristic value of the internal friction angle should be used. For comparison with measurements, the weighted average value of average values for the two soil layers within the soil arch should be used (van Eekelen & Han 2020). For the well-compacted sand layer, an average value of 35° is a good estimation. The 0.6 m aggregate layer below the sand layer consists of mixed concrete and masonry granulate, with a high masonry content. The shape of the grains was sub-angular, and the grain distribution was average to good. An average value for this layer is 36.5° to 38.5°. The weighted average of the friction angle for the two soil layers varies between 35.8° and 36.9°. In the calculations in this paper, the value for the average weighted friction angle was varied between 34° and 38°.
- As usual, we calculate without traffic load when we compare to field measurements. In addition to that, a calculation was conducted with 25% of the design load, to account for the permanent influence of the traffic load on the strains in the geotextile.
- CUR226 (2016) requests to reduce the soil arching for a piled embankment like this one, with a relatively thin embankment, and high traffic load. It is assumed that the soil arching reduces permanently due to the on-going traffic load. The soil arching reduction factor $\kappa = 1.58$ for this configuration and traffic load, as prescribed by Table 2.3 of CUR226.
- It is expected that the calculation with some traffic load and soil arching reduction matches the real situation best.

Table 1. Parameters used for the calculations with the Concentric Arches model[*].

Date	28 Feb '19	1 Mar '19	5 Mar '19	12 Mar '19	24 Apr '19	29 Feb '20	25 Aug '30
Height fill (m)	0.00	0.30	0.60	1.00	1.51	1.51	1.51
Tensile stiffness geotextile (kN/m)	3200	3200	3200	2961	2722	2544	2426

[*]And: centre-to-centre distance piles s_y = 2.28 m, square pile caps width a = 0.75 m, unit weight fill γ = 19 kN/m^3, fill friction angle φ = 34° and 38°, subgrade reaction k = 0 kN/m^3, traffic load p = 0 kPa and 11.5 kPa (25% of the design load), soil arching reduction coefficient κ is 1.0 (no soil arching reduction) and 1.58 (soil arching reduction).

5 COMPARISONS MEASUREMENTS AND CALCULATIONS

Figure 6 compares the measured and calculated geotextile strains. The calculated strains are maximum values at the edge of the pile caps. To safely design with CUR226, the calculated strains should be larger than, or equal to the measured values. The figure shows that the smallest calculated strains agree reasonably with the average values of E1 - E4. All other calculations give higher values than the measured values. This is a safe result.

Figure 7 gives an extension of the validation conducted by van Eekelen et al. (2015). The figure shows that the measurements of E1 and E2 agree well with the calculations, and the measurements of E3 and E4 give lower values than calculated. This is on the safe side. From this we may conclude that the CA model, and therefore the CUR226:2016 design guideline,
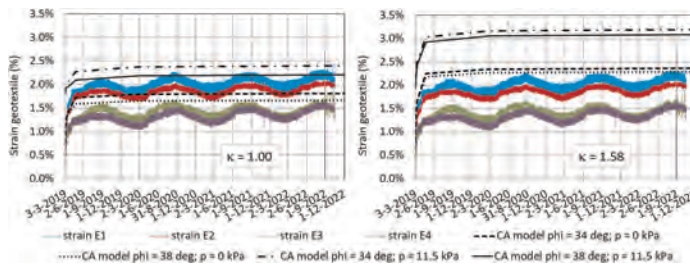
Figure 6. Comparison measured geotextile strains and geotextile strains calculated with the CA model.
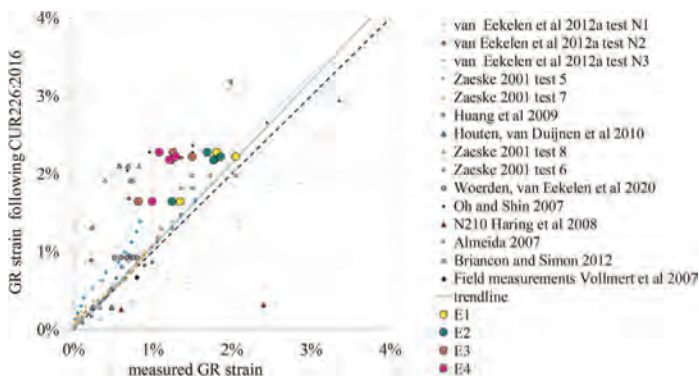
Figure 7. Extension of the validation of the CA model with the new data, with in the calculations: φ = 38°, traffic load = 0 kPa and κ = 1.58.

is applicable for this piled embankment of which the embankment was installed partly below the groundwater table. This conclusion is valid for woven geotextiles as applied in this monitoring project.

6 CONCLUSIONS

Geotextile strains, the varying groundwater table and the air temperature were measured in a geotextile-reinforced piled embankment that was partly submerged. The measured geotextile strains show no correlation with the groundwater level. However, the measured strains have a strong seasonable cycle that match the seasonable cycle in the average day air temperature quite well. This relationship between the air temperature and the geotextile strains may be caused by the thermal expansion of the road surface.

The CA model matches the measurements well. The CUR226:2016 design guideline adopted this CA model. Therefore, the CUR226:2016 is applicable for this type of geotextile-reinforced piled embankment, of which the embankment was installed partly below the groundwater table. This conclusion is valid for the woven geotextiles as applied in this monitoring project.

REFERENCES

Briançon, L. & Simon, B. 2012. Performance of Pile-Supported Embankment over Soft Soil: Full-Scale Experiment. *Journal of Geotechnical and Geoenvironmental Engineering* 138, 551–561. BSI 2015.

CUR226 2016: van Eekelen S.J.M. & Brugman, M.H.A. (Eds.) 2016. *Design Guideline Basal Reinforced Piled Embankments*. CRC Press, Delft, Netherlands.

Sloan, J.A. 2011. *Column-Supported Embankments: Full-Scale Tests and Design Recommendations. PhD Thesis*. Virginia Polytechnic Institute and State University, Blacksburg, Virginia, USA.

Song, J., Chen, K., Li, P., Zhang, Y. & Sun, C. 2018. Soil Arching in Unsaturated Soil with Different Water Table. *Granular Matter* 20, 78.

van Eekelen S.J.M. 2015. *Basal Reinforced Piled Embankments*. PhD Thesis Delft University of Technology, Delft, Netherlands. ISBN 978 94 6203 825 7.

van Eekelen, S.J.M., Van, M.A. & Bezuijen, A. 2007. The Kyoto Road, a Full-scale Test. Measurements and Calculations. In: *the proceedings of ECSMGE14*, Madrid, Spain 1533–1538.

van Eekelen S.J.M., Bezuijen, A., van Tol, A.F. 2013. An Analytical Model for Arching in Piled Embankments. *Geotextiles and Geomembranes* 39, 78–102.

van Eekelen S.J.M., Bezuijen, A. & van Tol A.F. 2015. Validation of Analytical Models for the Design of basal Reinforced Piled Embankments. *Geotextiles and Geomembranes* 43, 56–81.

van Eekelen S.J.M. & Han, J. 2020. Geosynthetic-reinforced Pile-supported Embankments: State of the art. *Geosynthetics International*, 27–2, pp. 112–141. https://doi.org/10.1680/jgein.20.00005

van Eekelen S.J.M., Venmans, A.A.M., Bezuijen, A. & van Tol, A.F. 2020. Long Term Measurements in the Woerden Geosynthetic-reinforced Pile-supported Embankment. *Geosynthetics Int*. 27-2, 142–156.

van Eekelen, S.J.M., Zwaan, R., Nancey, A., Hazekamp, M., Jung, Y.M. 2022. Field Measurements in a partly Submerged Woven Geotextile-reinforced Pile-supported Embankment. Proc. EuroGeo7, Poland. *IOP Conf. Ser.: Mater. Sci.vEng*. 1260 012046. doi:10.1088/1757-899X/1260/1/012046.

Wang, H.L., Chen, R.P., Cheng, W., Qi, S. & Cui, Y.J. 2018. Full-scale Model Study on Variations of Soil Stress in Geosynthetic-reinforced Pile-supported Track Bed with Water Level Change and Cyclic Loading. *Can. Geotech. J.* 56: 60–68 (2019).

Numerical study of the geosynthetics reinforced platforms laid over soft subgrade soil

N. Abou Chaz & P. Villard
Université, Grenoble Alpes, CNRS, Grenoble INP, Grenoble, France

C. Silvani & L. Briançon
INSA Lyon, GEOMAS, Villeurbanne, France

A. Nancey & A. Abdelouhab
Solmax Group, Tencate Geosynthetics France, Bezons, France

ABSTRACT: A DEM-FEM coupled numerical model was used to investigate the behaviour of a platform reinforced by geotextile (GTX) over soft soil subjected to cyclic loading. The ability of the numerical model to consider the settlement of the granular and the subgrade soil surface and the stress transmitted to the top of subgrade layer was established by comparisons with the experimental data for the first loading cycle. A parametric study was carried out using two GTX tensile stiffnesses, one with a medium tensile stiffness and the other with a low tensile stiffness. The comparison between the stress acting on the upper and the lower face of each GTX showed the effect of the tensile stiffness on the tensioned membrane mechanism and confirm the role of the GSY sheet in the numerical model.

1 INTRODUCTION

Poor subgrade is a widespread issue in unpaved roads construction. The geosynthetic (GSY) is considered one of the most innovative solutions since it was used in the late 1970's. Depending on the type of the GSY used, one or many functions among the separation, the reinforcement and the stabilisation can be ensured. Reinforcement takes place in the road structure system when the GSY, which is under tension with a curved shape, transfers the tensile force to the location where it is anchored through the tensioned membrane effect (Figure 1). While the stabilisation is provided to the base course materials when a soil-GSY composite material is formed by interlocking and/or friction and becomes less deformable than the soil.

A few design methods have been presented in the literature and quantifies either the tensioned membrane effect or the confinement mechanism by friction or interlocking between the GSY and the base course material. However, all of these methods have limitations because they have been calibrated on limited GSY and soil parameters and sometimes under static loading rather than cyclic loading. Each method is validated in a range of rut depth which is linked to the mechanism quantified. The most used method has been proposed by Giroud and Han (2004) and accounts for the confinement mechanism by friction or interlocking between the GSY and the base course material with neglection of the tensioned membrane effect. This method is validated when the rut depths ranges between 50 mm and 100 mm and is calibrated on a limited number of GSY.

To highlight the understanding of such mechanisms and to set bases to improve existing design methods, a full-scale experimentation has been recently carried out and investigated the reinforcement performance under cyclic vertical and traffic loadings using two types of

GTXs with different tensile stiffnesses and two base course thicknesses (Abou Chaz et al. 2022). In addition, a numerical model using a Spherical Discrete Elements Code (called SDEC) is used and calibrated based on the experiment results after applying the static load of the first cycle applied experimentally. The confrontation between the numerical model and the experiments carried out for the same purpose is presented below and will allow to give relevant conclusions about the influence of the GTX stiffness on the reinforcement performance.
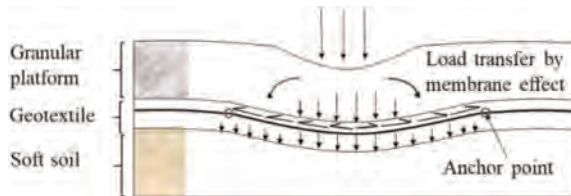
Figure 1.   Tensioned membrane effect mechanism involved in reinforced platform by GSY.

2   THE LABORATORY EXPERIMENT

This section summaries the experiments presented by Abou Chaz et al. (2022), to which the numerical results are compared. The conducted laboratory experiments are developed to investigate the reinforcement performance under vertical loading using two GTXs with different tensile stiffnesses and two base course thicknesses (35 cm and 50 cm).

The experimental box of 2 m long, 1.8 m wide, and 1.1 m high is used to build a 60 cm of subgrade layer thickness, with a CBR around 1%, covered by a compacted granular layer with a thickness equal to 35 cm or 50 cm (Figure 2a). To reinforce the section, a woven GTXs sheet (made of an assembling of polypropylene filaments) is placed at the interface between the soft soil and the granular platform.

The applied cycles are shown in Figure 2b. The frequency of a cycle is 0.77 Hz. The maximum load applied on a circular plate of diameter D (D = 30 cm) is 45 kN, chosen to obtain a pressure equal to 560 kPa which is equivalent to the contact pressure of a wheel. The unpaved road is expected to support 10 000 ESAL passes, with a maximum rutting of 75 mm. Hence, 10 000 cycles are applied to each tested platform.

Each tested section is instrumented with Earth Pressure Cells (EPC), hydraulic settlement sensors (S) and laser displacement sensors (L). The EPCs are placed on the GTX, within and on the top of the subgrade to measure the stress distribution. Each settlement sensor is positioned on an EPC. Laser displacement sensors are fixed to a beam and placed above the circular plate to measure its penetration during the test with a great accuracy.
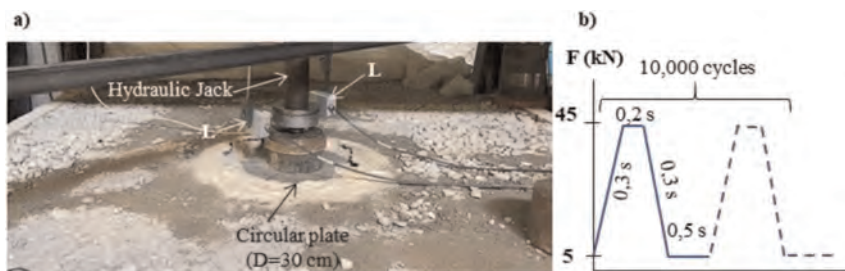
Figure 2.   a) Plate load test setup, b) Cycles applied.

3 THE NUMERICAL MODEL

3.1 *Basic principle of DEM-FEM model*

In this study, a FEM-DEM coupled numerical model (Villard et al. 2009) that considers the discrete nature of the granular material, the fibrous and continuous nature of the GTX and the frictional interaction at the interface (rolling sliding and friction) between the soil particles and the finite elements (used to restore the GTX behaviour) is adopted.

The GTX sheet is modelled by three node triangular finite elements. Each triangular element consists of a set of fibres with various orientations forming a plan. The behaviour of a fibre network is obtained by superposition of behaviours obtained in each fibre direction (no sliding between fibre). The mechanical behaviour of the fibres is non-linear elastic, and the compression elasticity modulus is very low compared to the tensile elasticity modulus (Villard & Giraud 1998). The non-linear force-displacement relation (1) is adopted for each three nodes triangular element used in the iterative process of calculation included in the coupling code.

$$\{F_e\} = \{K_e\} * \{u_e\} + \{R_e\} \tag{1}$$

$\{F_e\}$ are the forces acting on the nodes of an element, $\{u_e\}$ the nodal displacements of the element, $\{K_e\}$ is the elementary matrix of rigidity depending on the final position of the three nodes, and $\{R_e\}$ a corrective vector force resulting from the large displacement formulation.

Within the granular mattress, the discrete elements interact through contact points based on the molecular dynamic method developed by Cundall and Strack (1979). A classical linear elastic contact law and a perfect elastic plastic law are used for the normal interaction and the tangential interaction respectively. The normal component of the contact force F_n is related to the normal overlap u between the grains by the normal stiffness K_n and the incremental tangential component of the force F_t is related to the incremental relative tangential displacement v by the tangential stiffness K_t. The interaction between the particles follows the Coulomb friction law. Thus, the tangential force is limited to a maximum absolute value of $|F_t| \leq \mu F_n$, where μ is the intergranular friction coefficient. The normal contact stiffness (or tangential contact stiffness) between two spheres of radius R_i and R_j, expressed in N/m^2, is defined as follows (2) by a function of the normal rigidity K_{nij} (or tangential rigidity K_{sij}) of the two constitutive materials in contact.

$$K_n = \frac{K_{nij} \left(R_i * R_j \right)}{\left(R_i + R_j \right)} \tag{2}$$

An iterative procedure that alternates successively the resolution of Newton's second law of motion and the actualization of the interaction forces at each contact point is used to solve the problem. The motion equations are integrated using an explicit centred finite difference algorithm involving a time step Δt.

A contact law similar to that used in the DEM method between the grains is used to describe the interaction between the soil particles and the triangular finite elements.

3.2 *Geometry and parameters selected for application to reinforced platform over soft soil*

The used numerical model (Figure 3) is 1.8 m long, 1.8 m wide and 0.36 m deep and includes, from top to bottom:

1. an assembly of clumps (composed of two overlapped and unbreakable spheres of same diameter D with d is the distance between the center of two particles, see Figure 3) describing the behaviour of the granular mattress and interacting through contact points,
2. thin, finite, triangular elements describing the membrane and tension behavior of the GTX,
3. a layer of spheres regularly distributed in a square mesh at the base of the model and associated to springs to represent the supporting soft soil which displace only vertically (no rolling admitted).

Horizontal and vertical frictionless walls are used on the lateral sides to define the boundary conditions. A circular rigid plate (Diameter=0.3 m) made with small spheres is placed at the centre of granular mattress to apply static loading (or cyclic). The incremental load is low enough to avoid dynamic effects.

The granular elements are modelled by means of clusters of two overlapped spheres (Figure 3) in order to approach the mechanical macroscopic behaviour of the experimental soil with respect to a calibration process. A specific method (ERDF method) based on the iterative growth of the particles radii and intergranular friction reduction is used to control the density of the numerical sample. For the calibration process, the micro-mechanical parameters (K_n, K_t and μ) were set in order to obtain vertical displacement of the numerical assembly similar to those measured in the experiment. For this purpose, numerical triaxial tests were performed with a set of microscopic contact friction angle (δ), for several porosities (ranging between 0.3 and 0.41). In the present case a dense state of the numerical assembly is retained to fit the real macroscopic mechanical behaviour. The values of the microscopic contact parameters between the spheres of the granular mattress and the average macroscopic mechanical parameters of the selected numerical model are summarized in Table 1.

The interface friction parameters between the GTXs and the lower subgrade or the upper granular mattress are obtained by pull out tests using a test box $0.5 \times 0.5 \times 0.3$ m^3 while the tensile parameters of the GTX in x and y direction are deduced from traction tests performed by the GTX manufacturer. All these parameters are also presented in Table 1.

Table 1. Numerical parameters describing the different components of the model.

Granular platform parameters		
Normal contact stiffness (MN/m^3)	K_n	100
Tangential contact stiffness to normal contact stiffness	K_s/K_n	1
Micromechanical friction coefficient	$\mu = \tan \delta$	1.11
Peak friction macroscopic angle (°)	Φ_p	46
Young's modulus (MPa)	E	31
Porosity	n	0.34
GTX		
Tensile stiffness in the x direction (kN/m) [0 - 5% strain]	J_x	1200
Tensile stiffness in the y direction (kN/m) [0 - 5% strain]	J_y	1200
Soil-GTX interface friction parameters		
Angle between the clumps and the upper interface of the GTX (°)	$\Phi_{clumps-GTX}$	35
Angle between the subgrade and the lower interface of the GTX (°)	$\Phi_{sphere-GTX}$	25
Lower supporting soil		
Subgrade reaction modulus (MPa/m)	K	3
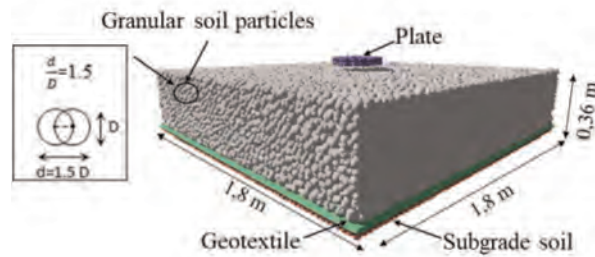
Figure 3. Geometry of the simulated sample and illustration of grain shapes used in simulation.

The subgrade soil rigidity and its evolution with cycles are estimated by experimental cyclic plate load test performed on the subgrade soil placed in a box ($2 \times 1.8 \times 0.6$ m^3). The subgrade reaction modulus retained for the loading phase of the first cycle (that allows to make coincide experimental and numerical vertical displacements of the loading plate) is presented in Table 1.

4   NUMERICAL RESULTS

4.1   *Comparison between the numerical model and the experimental results of the laboratory experiment*

A static load of 40 kN (560 kPa) is applied on a rigid plate placed at the centre of the numerical model. The experimental results of the subgrade and the base course surface settlements obtained after application of the first loading cycle and the calibrated numerical results are plotted in Figure 4a. To evaluate the relevance of the numerical model, Figure 4 b compares the stress measured at the top of subgrade soil at the end of the loading phase of the first cycle to the numerical stress obtained under the GTX. As it can be seen, the relatively good agreement between the experimental and the numerical results of the stress attest to the ability of the numerical tool to well reproduce the experimental behaviour and the possibility to study the mechanism involved in the model.
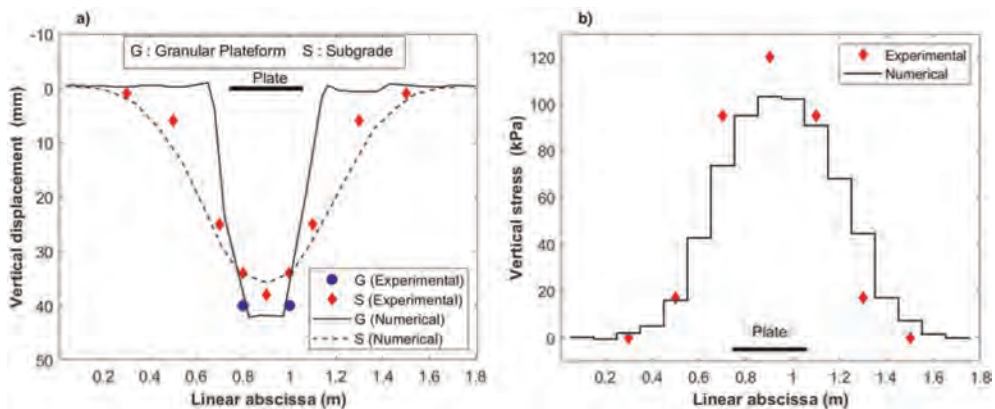
Figure 4.   Comparison between experimental and numerical: a) subgrade and base course surface settlement, b) subgrade surface stress.

4.2   *Numerical analysis of the tensioned membrane effect*

As explained in Figure 1, the tensioned GSY with a curved shape (i.e. out of plane deformation) transfers the load to the location where it is safely anchored. Therefore, the maximum load transmitted to the subgrade is reduced since the loads transmitted to the subgrade are distributed by the geotextile over an area larger than that above the GSY. To clarify this mechanism, called the tensioned membrane effect, two numerical simulations with two different GTX stiffnesses are carried out. The stiffness of the GTX 1 is 1200 kN/m in both directions (Simulation 1), whereas the stiffness of the GTX 2 is 1 kN/m in both directions (Simulation 2). This low value of stiffness is chosen in order to have a non-reinforced model because of the reinforcement GSY should have at least a tensile stiffness equal to 8 kN/m (Hufenus et al. 2006).

The granular mattress parameters are the same as that described in the section 3.2. In the simulation 2, the lower geotextile interface friction angle ($\Phi_{\text{sphere-GTX}}$) is increased to reach 60°, rather than 25° used in the simulation 1, to avoid the geotextile sliding due to its low

stiffness. A subgrade reaction modulus equal to 2 MPa/m is chosen in order to induce a deformation in the GTX more significant than that obtained in the simulation presented in section 4. The same static load of 40 kN (560 kPa) is applied on a rigid plate placed at the center of the numerical model. The maximum subgrade surface settlement obtained with the GTX 1 is 62 mm lower than that obtained with the GTX 2 which is 120 mm. Figure 5a shows that the vertical stress acting on the lower face of the GTX 1 (J=1200 kN/m) is lower than that acting on the upper face in the zone located under the plate, whereas the vertical stress acting on the lower face of the GTX 1 becomes higher than that acting on the upper face in the zone located around the plate. Thus, a part from the stress acting on the upper face of geotextile and located below the circular plate is not transmitted vertically to the top of subgrade, but transmitted by the geotextile to the zone around the plate. However, the stresses acting on the upper and the lower face of the GTX 2 with a low stiffness (J=1 kN/m) are rather similar (Figure 5b). Moreover, it is important to note that the stresses transmitted to the supporting soil are much greater for GTX2 than for GTX1. This shows that the GTX with an enough stiffness has a key role in the load transfer to the top of the subgrade.

The resultant of the vertical stress acting on the lower face of the GTX subtracted from the vertical stress acting on the upper face of the GTX is expressed by $\Delta\sigma_{zz}$ (in kPa) and showed in Figure 6. $\Delta\sigma_{zz}$ is positive in a circular zone with a centre equal to the loading plate centre and a diameter D1 = 1,5D (D is the diameter of the loading plate equal to 0.3 m) and
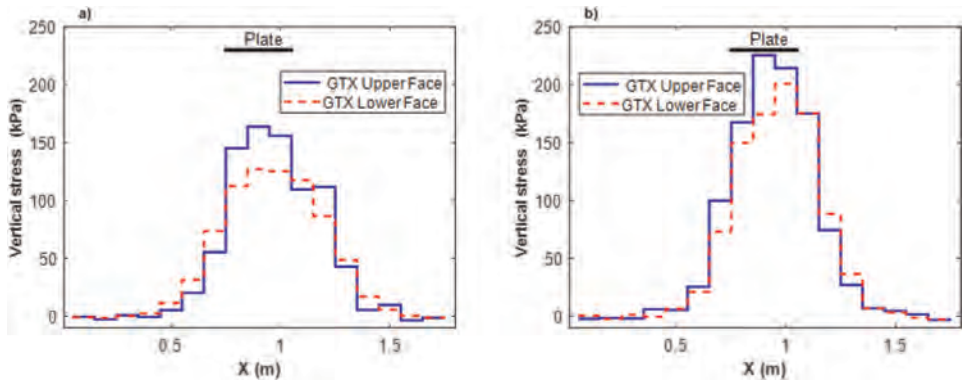
Figure 5.   Vertical stress acting on the upper face and on the lower face of the: a) GSY 1, b) GSY 2.
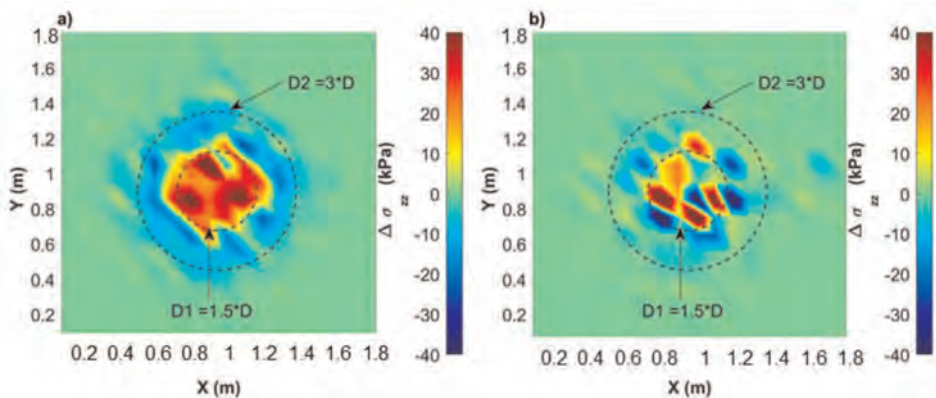
Figure 6.   The resultant of the vertical stress acting on the lower face of the GTX subtracted from the vertical stress acting on the upper face of the GTX: a) case of GTX 1, b) case of GTX 2.

negative in the zone located between the circle with D1=1,5D m and the circle with a diameter D2=3D (Figure 6.a). This means that a part of the stress acting on the upper face of the GTX is transmitted directly to the subgrade and the other part is transmitted by the GTX (tensioned membrane effect) to the adjacent area (1.5D<diameter<3D). Figure 6b shows that the $\Delta\sigma_{zz}$ values, whether positive or negative, obtained with GTX 2 are more important than those obtained with the GTX 1, and concentrated over separate areas so that their sum is less than the entire area referred to with the GTX1. Hence, the GTX 2 with a low stiffness does not show a clear load transmission by membrane effect.

5 CONCLUSION

A numerical tool based on the coupling between DEM and FEM is used to study the behaviour of a granular platform reinforced by GTX over soft soil. It has shown by comparison with the experimental results that the numerical model provides relevant information on the surface settlement, the stress transmitted to top of the subgrade soil for the first loading cycle. The GTX tensile stiffness effect on the load transfer to the top of the subgrade has been demonstrated by a comparison between the stresses acting on the upper and the lower faces of GTX. This comparison points out the tensioned membrane effect mechanism that takes place in this application.

The calibration of this model with further number of cycles is in progress with a calibration of the behaviour law for the soft subgrade soil under cyclic loading. This numerical work will provide access to additional information difficult to be quantified during the experimentation.

REFERENCES

Abou Chaz N., Briançon L., Villard P., Silvani C., Nancey A., Abdelouhab A. 2022. Etude Expérimentale des Plateformes Granulaires Renforcées par Géosynthétique Sur Sol Mou. *11ème JNGG* Lyon 2022.

Cundall, P.A., Strack, O.D.L. 1979. A Discrete Numerical Modelling Method for Granular Assemblies. *Geotechnique* 29 (1): 47–65.

Giroud J. P. & Han J. 2004. Design Method for Geogrid-reinforced Unpaved Roads. II. Calibration and Applications. *Geotechand Geoenv Eng J* 130(8): 787–797.

Hufenus R., Rueegger R., Banjac R., Mayorc P., Springman S.M., Bronnimann R. 2006. Full-scale Field Tests on Geosynthetic Reinforced Unpaved Roads on Soft Subgrade. *Geotex and Geomemb* 24: 21–37.

Villard, P., Chevalier, B., Le Hello, B., Combe, G. 2009. Coupling Between Finite and Discrete Element Methods for the Modelling of Earth Structures Reinforced by Geosynthetics. *Comput. Geotech* 36: 709–717.

Villard, P., Giraud, H. 1998. Three-Dimensional Modelling of the Behaviour of Geotextile Sheets as Membrane. *Text. Res. J.* 68 (11): 797–806.

Numerical study of shear behavior of a geosynthetic encased stone column under direct shear loading

M. Ji, J. Wang & Y. Zheng*
Wuhan University, Wuhan, China

ABSTRACT: Geosynthetic encased stone column (GESC) has higher strength than conventional stone column due to the radial confinement of geosynthetic encasement. This technology has been used for ground improvement in soft soils. In this study, the shear strength behavior of GESC under direct shear loading was investigated using the three-dimensional finite difference program FLAC3D. The stone column and surrounding soil were modeled using the linearly elastic-plastic Mohr-Coulomb model, and the geosynthetic encasement was characterized using linearly elastic elements with isotropic behavior. The model also considered the interaction between geosynthetic encasement and adjacent soils (i.e., stone column and surrounding soil). The shear stress-strain response and the development of longitudinal and circumferential strains of GESC during the shear process were presented and discussed. Simulation results indicated that the geosynthetic encasement can increase the shear resistance of stone column, and the longitudinal strains of GESC are greater than the circumferential strains under direct shear loading.

1 INTRODUCTION

Geosynthetic encased stone column (GESC) technology has been widely used for ground improvement in soft soil foundation and provides many advantages over traditional stone column (SC), including higher bearing capacity and better stability (Castro & Sagaseta 2011; Gniel & Bouazza 2010; Lo *et al.* 2010). In addition, GESC has also been used in the construction of infrastructure, such as embankments and dams (Almeida *et al.* 2015; Alexiew & Raithel 2015). The GESC under the center of the embankment is primarily subjected to vertical loading. Many investigations have studied the bearing characteristics of GESC under vertical loading, which indicate that the geosynthetic encasement significantly improves the bearing capacity and reduces the settlement of stone column (Kadhim *et al.* 2018; Khabbazian *et al.* 2010; Murugesan & Rajagopal 2010; Yoo 2010). The GESC under the toe of the embankment is primarily subjected to lateral loading (Almeida *et al.* 2015; Chen *et al.* 2015). However, research on the GESC under lateral shear loading is limited, and further investigations are needed.

Several experimental and numerical studies have been conducted for the shear behavior of GESC and generally indicate that the geosynthetic encasement increases the shear resistance of stone column under direct shear loading (Cengiz *et al.* 2019; Mohapatra *et al.* 2016). Mohapatra *et al.* (2017) conducted a 3D slope stability analysis through the strength reduction method and found that the geosynthetic encasement improves the factor of safety of embankment slope in soft soil ground improved using stone column. These findings indicate that GESC has better performance over stone column under shear loading conditions. However, the mobilization of shear resistances from the geosynthetic encasement, stone column, and surrounding soil during the shear process has not been studied. Therefore, further investigations are needed to understand the shear reinforcement mechanism of GESC.

---

*Corresponding Author: yzheng@whu.edu.cn

This paper presents a numerical study of the shear strength behavior of GESC model under direct shear loading. The evolution of the shear strength contributions of geosynthetic encasement, stone column, and surrounding soil during the shear process are presented and discussed. Results of this study provide insights on the shear reinforcement mechanism of GESC.

2 NUMERICAL MODEL

In this study, a unit cell model of GESC improved foundation is used to simulate the shear stress-strain response of GESC under direct shear loading using the finite difference program FLAC3D (Itasca Consulting Group 2019).

2.1 Model geometry

Figure 1 shows the geometry and finite difference mesh for the unit cell model of the GESC improved foundation. The GESC has a height of 1.2 m and a diameter of 0.8 m. The geosynthetic encasement wraps around the stone column for the entire length. The unit cell model has a diameter of 2.06 m, which represents a GESC improved ground with a typical area replacement ratio of 15%. This model represents a typical configuration for field conditions. The horizontal shear plane is located at the mid-elevation of the model. The diameter of the lower part below the shear plane was large enough so that the area of the shear plane remains constant during the shear process.
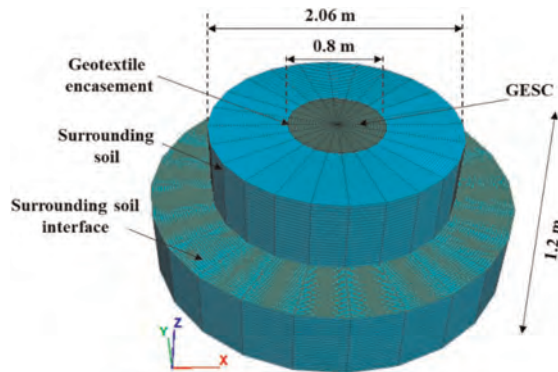
Figure 1. Model configuration for the GESC unit cell model.

2.2 Material models and properties

The column infill material and surrounding soil were modeled using a linearly elastic-plastic material with the Mohr-Coulomb failure criterion. The elastic moduli of the stone column and surrounding soil were selected as 40 MPa and 10 MPa, respectively. The friction angles of the stone column and surrounding soil are 42° and 32°, respectively. The soil parameters used in the simulations are listed in Table 1, corresponding to typical values in field engineering. The geosynthetic encasement was modeled using linearly elastic embedded liner element with isotropic behavior. The liner element was modeled by using the three-node plane-stress Constant Strain Triangle (CST) element. The geosynthetic encasement has tensile stiffness of 4000 kN/m and Poisson's ratio of 0.1.

2.3 Interfaces

The embedded liner element was adopted to simulate the geosynthetic encasement. It provides two links at each node on both sides, which can consider the interaction of geosynthetic encasement with different soils on both sides. The interaction between the geosynthetic encasement

Table 1. Soil parameters.

Property	Column infill	Surrounding soil
Elastic modulus, E (MPa)	40	10
Poisson's ratio, v	0.3	0.3
Friction angle, f (°)	42	32
Apparent cohesion, c (kPa)	1	1

and soils on both sides was simulated through two interfaces, including the surrounding soil-geotextile interface and the column infill-geotextile interface. The horizontal shear plane at the mid-elevation of the unit cell model was modeled using two interfaces for the surrounding soil and the column infill, respectively. These interfaces were predefined in the GESC model to ensure that sliding occurs along the horizontal shear plane. The shear strength parameters of the two interfaces were set as the same strength parameters with the surrounding soil and column infill, respectively. The normal stiffness and shear stiffness of the two interfaces were determined according to the approach suggested by the FLAC manual (Itasca Consulting Group 2019). The normal stiffness and shear stiffness for surrounding soil interface are 0.45 GPa/m, and the normal stiffness and shear stiffness for column infill interface are 1.79 GPa/m.

2.4 Modeling procedures

The direct shear process was simulated in stages. Firstly, the construction of the GESC model under gravitational loading was performed and the horizontal shear plane was set. Then, the embankment loading was modeled by applying a vertical stress of 50 kPa on the top surface of the unit cell model and solved for equilibrium. Figure 2 shows the monitoring points of the GESC, which were arranged on the geosynthetic encasement at an interval of 0.2 m to monitor the development of longitudinal and circumferential strains during the shear process. A shear loading rate of 1×10^{-3} mm/step was applied to the circumferential boundary grid above the shear plane, while the bottom and circumferential boundaries of the lower part below the shear plane were fixed. When the shear strain reaches 20%, the shear loading was stopped.

The unbalanced force at each step were added up first, which is equivalent to the total shear force. The total shear force was then divided by the total area of shear plane, which was taken as the equivalent shear stress on the shear plane (Mohapatra et al. 2017). The shear resistance provided by the geosynthetic encasement was obtained by subtracting the corresponding shear forces generated by the two soil interfaces on the horizontal shear plane (i.e., the surrounding soil interface and the column infill interface) from the total shear force. The shear stresses of surrounding soil, stone column, and geosynthetic encasement are obtained by dividing the
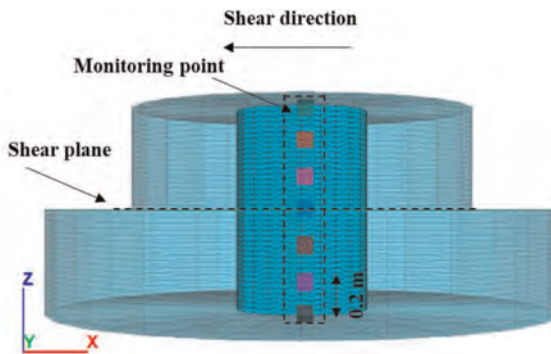
Figure 2. Monitoring point of the GESC unit cell model.

corresponding shear forces by the areas of surrounding soil, stone column, and stone column, respectively. The calculated shear stress for the geosynthetic encasement is contributed by the shear resistance due to the tensile force developed in geosynthetic encasement.

3 RESULTS AND DISCUSSION

Figure 3 shows the development of shear stress and shear strength contribution for the unit cell model. In Figure 3(a), the shear stress of surrounding soil develops very fast in the initial stage, and then reaches stable gradually. When the shear strain reaches 20%, the shear stress of stone column is greater than that of the surrounding soil. The shear resistance contributed by the geosynthetic encasement is much smaller than the surrounding soil and stone column in the initial stage. This is because the shear resistance comes from the mobilized tensile force in geosynthetic encasement in the shear direction, which significantly depends on the development of longitudinal strains. However, the shear resistance provided by the geosynthetic encasement at 20% shear strain is the largest, which indicates that the geosynthetic encasement could provide strong shear resistance for the GESC.

Figure 3(b) shows that with the increase of shear strain, the shear strength contribution of surrounding soil decreases, but those of the stone column and geosynthetic encasement increase. The shear strength mainly comes from the surrounding soil in the initial stage because the shear loading starts from the edge of surrounding soil. The shear strength of the stone column gradually develops with increasing strain, as the shear movement of the surrounding soil drives the stone column to move in the shear direction. Meanwhile, the geosynthetic encasement was deformed by the movement of stone column and surrounding soil, which results in mobilization of longitudinal tensile strains. At 20% shear strain, the shear strength contributions are 59%, 15%, and 26% for the surrounding soil, stone column, and geosynthetic encasement, respectively. The shear strength contribution of surrounding soil is the largest due to the large area (i.e., 85% area of the unit cell), though the shear strength of the surrounding soil is lower than that of the stone column.
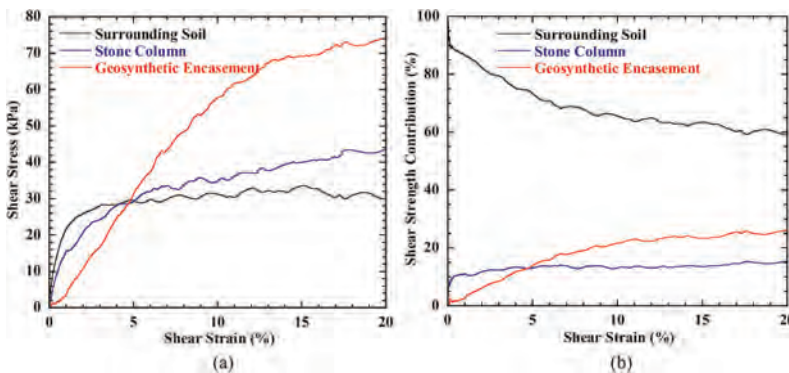
Figure 3. Development of shear stress: (a) shear stress; and (b) shear strength contribution.

The development of longitudinal and circumferential strains of geosynthetic encasement at different elevations are shown in Figure 4. Figure 4(a) shows the development of longitudinal strains with the increase of shear strain. The maximum longitudinal strain of geosynthetic encasement occurs at the shear plane and decreases with the increasing vertical distance from the shear plane. The longitudinal strains of the geosynthetic encasement above the shear plane are larger than those below the shear plane for the same vertical distance from the shear plane, as the upper part is the driving part during shear process. Figure 4(b) shows the development of circumferential strain with increasing shear strain. In general, the

circumferential strains of geosynthetic encasement above the shear plane were affected first in the initial shear stage. As the shear loading continued, the circumferential strain right below the shear plane gradually developed. In general, the circumferential strains near the shear plane increase significantly, especially above the shear plane.
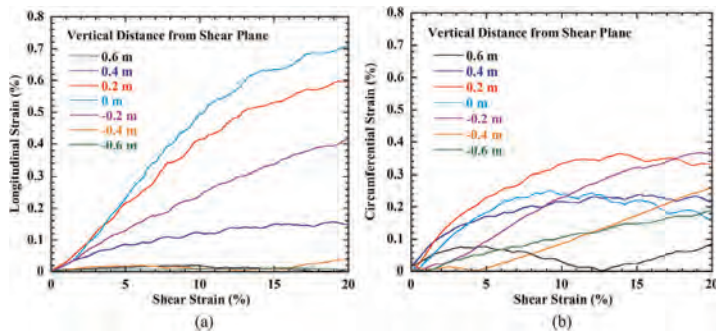
Figure 4.   Development of geosynthetic encasement strain: (a) longitudinal strain; and (b) circumferential strain.

Figure 5 shows the longitudinal and circumferential strains of the geosynthetic encasement with elevation. It can be seen from the figure that within the vertical distance of 0.2 m from the shear plane, the longitudinal strains are greater than the circumferential strains. Moreover, the maximum value of longitudinal strains is approximately twice than that of the circumferential strain, which indicate that the longitudinal tensile rupture is more critical than the circumferential rupture for GESC under shear loading. At the vertical distance further away from the shear plane, the longitudinal strains are slightly smaller than the circumferential strains, as the tensile forces due to shear loading is not obvious at these elevations.
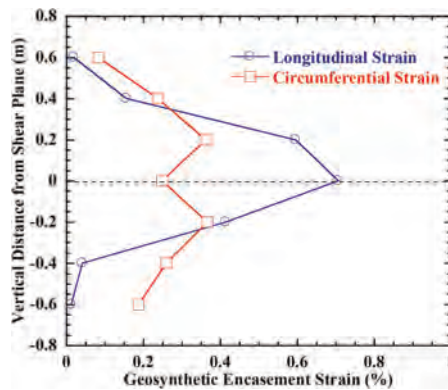
Figure 5.   Geosynthetic encasement strain profiles.

4   CONCLUSIONS

This paper presents a numerical study of the shear strength behavior of GESC under direct shear loading. The backfill soil was characterized using a linear elastic-plastic model and the Mohr-Coulomb failure criterion. Geosynthetic encasement was characterized using linearly elastic elements with isotropic behavior. Two interfaces were included to simulate the horizontal shear planes of the stone column and the surrounding soil. The shear stress-strain

response and the development of longitudinal and circumferential strains of GESC during the shear process were presented and discussed. Simulation results indicate that the geosynthetic encasement can provide shear resistance for stone column from the mobilized tensile force on geosynthetic encasement in the shear direction, which significantly depends on the development of longitudinal strains of geosynthetic encasement. The longitudinal strains are generally much larger than the circumferential strains, which indicates that the longitudinal tensile rupture is more critical than the circumferential rupture for GESC under shear loading.

ACKNOWLEDGEMENTS

REFERENCES

Almeida, M.S.S., Hosseinpour, I, Riccio, M. & Alexiew, D. (2015). Behavior of Geotextile-encased Granular Columns Supporting Test Embankment on Soft Deposit. *Journal of Geotechnical and Geoenvironmental Engineering*, 141(3): 04014116-1–04014116-8.

Alexiew, D. & Raithel, M. (2015). Chapter 17 - geotextile-encased Columns: Case Studies Over Twenty Years. In: Indraratna, B., Chu, J., Rujikiatkamjorn, C. (Eds.), *Ground Improvement Case Histories.* Butterworth-Heinemann, pp. 451–477.

Castro, J. & Sagaseta, C. (2011). Deformation and Consolidation Around Encased Stone Columns. *Geotextiles and Geomembranes*, 29(3), 268–276.

Chen, J.F., Li, L.Y., Xue, J.F. & Feng, S.Z. (2015). Failure Mechanism of Geosynthetic Encased Stone Columns in Soft Soils under Embankment. *Geotextiles and Geomembranes*, 43(5), 424–431.

Cengiz, C., Kilic, I.E. & Guler, E. (2019). On the Shear Failure Mode of Granular Column Embedded Unit Cells Subjected to Static and Cyclic Shear Loads. *Geotextiles and Geomembranes*, 47: 193–202.

FLAC3D Version 6.0 [Computer software], (2019). Itasca Consulting Group, Minneapolis, MN.

Gniel, J. & Bouazza, A. (2010). Construction of Geogrid Encased Granular Columns: A New Pro Posal Based on Laboratory Testing. *Geotextiles and Geomembranes*, 28(1), 108–118.

Khabbazian, M., Kaliakin, V.N. & Meehan, C.L. (2010). Numerical Study of the Effect of Geosynthetic Encasement on the Behaviour of Granular Columns. *Geosynthetics International*, 17(3): 132–143.

Kadhim, S.T., Parsons, R.L. & Han, J. (2018). Three-dimensional Numerical Analysis of Individual Geotextile-encased Sand Columns with Surrounding Loose Sand. *Geotextiles and Geomembranes*, 46: 836–847.

Lo, S.R., Zhang, R. & Mak, J. (2010). Geosynthetic-encased Stone Columns in Soft Clay: A Numerical Study. *Geotextiles and Geomembranes*, 28(3), 292–302.

Murugesan, S. & Rajagopal, K. (2010). Studies on the Behavior of Single and Group of Geosynthetic Encased Stone Columns. *Journal of Geotechnical and Geoenvironmental Engineering*, 136(1): 129–139.

Mohapatra, S.R., Rajagopal, K. & Sharma, J. (2016). Direct Shear Tests on Geosynthetic-encased Granular Columns. *Geotextiles and Geomembranes*. 44(3), 396–405.

Mohapatra, S.R., Rajagopal, K. & Sharma, S. (2017). 3-Dimensional Numerical Modeling of Geosynthetic-encased Granular Columns. *Geotextiles and Geomembranes*, 45: 131–141.

Yoo, C. (2010). Performance of Geosynthetic-encased Stone Columns in Embankment Construction: Numerical Investigation. *Journal of Geotechnical and Geoenvironmental Engineering*, 136(8): 1148–1160.

Physical and numerical study of load transfer mechanism of geotextile-reinforced sand fill over soft marine clay improved by deep cement mixed soil columns

P.C. Wu
The Hong Kong Polytechnic University, Hong Kong SAR, China

J.H. Lin
China Energy Engineering Group Guangdong Electric Power Design Institute Co. Ltd., China

W.Q. Feng
Southern University of Science and Technology, Shenzhen, China

J.H. Yin
The Hong Kong Polytechnic University, Hong Kong SAR, China

ABSTRACT: The Hong Kong International Airport has expanded its existing two-runway system to a three-runway system based on a reclamation project over a seabed of soft marine clay. In the reclamation area, a layer of load transfer platform (LTP) was designed with geosynthetic reinforcement to bridge the overlaid surcharge loadings of reclamation fills and underlaid marine clay improved by deep cement mixing method. In this study, firstly, a small-scale physical model test of geotextile-reinforced sand layer over soft marine clay improved by cement-treated soil columns was performed to investigate the load transfer mechanism among columns, soils, and geotextile under different surcharge loadings. The results from the scaled model test were then adopted to verify the parameters used in a finite element model established using PLAXIS. Furthermore, the finite element model was used to reveal the development of soil arching.

1 INTRODUCTION

The third runway reclamation project of the Hong Kong International Airport has been constructed over a seabed of soft marine clay improved by deep cement mixing (DCM) method. A layer of geosynthetic-reinforced load transfer platform (LTP) was designed in between the reclamation fills and the DCM-treated marine clay seabed (Lee 2016). The consideration of the load transfer mechanism and the design of geosynthetic reinforcements in LTP are similar to geosynthetic-reinforced column-supported (GRCS) embankments. The load transfer in a GRCS embankment is normally related to soil arching effect which develops with the settlement of subsoils or the deflection of geosynthetic reinforcements (Iglesia *et al*. 2014; King *et al*. 2017; Zhang *et al*. 2022). Various theories and models for soil arching in column-supported embankments were proposed based on empirical methods or analytical approaches, among which the semi-spherical arches model proposed by Hewlett and Randolph (1988), multi-shell arches model proposed by Zaesek (2001), and concentric arches (CA) model proposed by van Eekelen *et al*. (2013) have been adopted in British, German, and Dutch design guidelines.

In this study, a small-scale physical model test was conducted on a geotextile-reinforced sand layer over a soft subsoil improved using cement-treated soil columns to investigate the load transfer mechanism and tensile strains of the geotextile reinforcement. In addition, a numerical simulation was performed using PLAXIS software to reveal the development of the soil arching in the geotextile-reinforced sand layer at different stages.

2 EXPERIMENT

2.1 Test setup

The physical model test was conducted in a steel tank with the dimension of 1000 mm (length) × 600 mm (width) × 800 mm (depth). Six prefabricated cement-treated soil columns with a cement content of 20% (in terms of dry mass of soil) were installed in the subsoil of Hong Kong marine deposits (HKMD) overlaid by a geotextile-reinforced sand layer. The subsoil was prepared by consolidating the reconstituted HKMD with the initial water content of 100 % under a uniform load of 5.35 kPa. The columns were subsequently installed using the replacement method adopted by Ho *et al.* (2020). A sand layer (thickness of 350 mm) over the HKMD was filled in seven times with a 50 mm thick sublayer formed each time after compaction. The total weight and volume of sand were controlled to ensure a relative density of 80%. A piece of woven geotextile (secant tensile modulus of 680 and 150 kN/m in longitudinal and transversal directions) was installed 50 mm above the subsoil, as shown in Figure 1. A rigid porous plate was placed on the top of the sand layer to serve as a platform for setting the LVDTs (manufactured by SHOWA) and as a loading plate. Earth pressure cells (EPCs) and porewater pressure transducers (PPTs), manufactured by DMKY, were used to measure the vertical stress and excess porewater pressure at different locations. Fiber Bragg grating (FBG) sensors (manufactured by T&S) were adopted to measure the tensile strain of the geotextile reinforcement. NI PXIE 4331 datalogger was used to record electronic signals from all conventional transducers. FBG-based transducers were connected to Micron Optics SM130 interrogator.
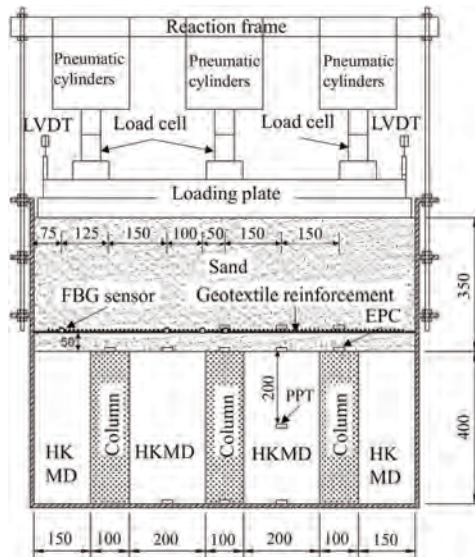
Figure 1.   Schematic diagram of the physical model test (unit in mm).

2.2 Test results

The surcharge loading was applied by pneumatic cylinders following a loading sequence of 10, 20, 40, and 80 kPa. Each loading stage lasted until there was no further change in excess porewater pressure. Figure 2a shows the average surface settlement measured by LVDTs and the actual loading applied to the top of the sand layer measured by load cells. The responses of excess porewater pressure measured by PPTs at the middle and bottom levels of the subsoil are presented in Figure 2b. Rapid dissipation of excess porewater pressure at both

locations can be observed at the very beginning of each loading stage. The accelerated consolidation was mainly because of the mechanical contribution of the columns on loading transfer (Wijerathna *et al*. 2017; Wu *et al*. 2020).

Different terminologies and definitions were proposed to assess the soil arching effect and interpret load transfer mechanisms. In this study, pile (or column) efficacy, proposed by Hewlett and Randolph (1988), is adopted:

$$E = \frac{A + B}{(\gamma H + p)s^2} \tag{1}$$

where A and B represent load parts A and B defined by van Eekelen *et al*. (2013); p is the surcharge loading; s is the center-to-center spacing of columns; γ and H are the unit weight and height of the sand layer. Load parts A and B are calculated as follows:

$$A = \sigma_c^a A_c \tag{2}$$

$$B = \left(\sigma_c^b - \sigma_c^a\right)A_c \tag{3}$$

where σ_c^a and σ_c^b are the average vertical stresses measured by EPCs above and beneath the geotextile reinforcement in column zones; A_c is the area of column zones. Figure 2c presents the values of efficacy with different surcharge loadings. It is found that the efficacy decreases during the process of increasing the surcharge loading. This is because of the partially undrained condition of the subsoil delays the loading transfer. With the consolidation of the subsoil under the given surcharge loading, differential settlements between columns and the surrounding soils increase inducing an increase in the deflection of the geotextile reinforcement, and thus leading to an increase in efficacy. The efficacy of columns after the consolidation slightly increases with the increase of the surcharge loading. This finding agrees with the simulation results from van der Peet and van Eekelen (2014).

Figure 2d presents the maximum tensile strains in both longitudinal (x) and transversal (y) directions of the geotextile reinforcement. The maximum tensile strains under different surcharge loadings can be also calculated according to Dutch design guidelines (van Eekelen & Brugman 2016) and German design guidelines (EBGEO 2010). It is found that the Dutch method gives better predictions in terms of the maximum tensile strains of geotextile reinforcement when the surcharge loading was less than 40 kPa, while German EBGEO method provides closer results to the measured strains under 80 kPa.

3   NUMERICAL SIMULATIONS

3.1   *FE models*

A 3D finite element (FE) model of four quarter columns and HKMD subsoil is built using PLAXIS 3D, as shown in Figure 3. HKMD subsoil is simulated by Soft Soil Creep (SSC) model, cement-treated soil columns are simulated by Mohr-Coulomb (MC) model, the sand layer is simulated by Hardening Soil (HS) model, the geotextile reinforcement is simulated by geogrid elements with elastic properties. Table 1 lists the input parameters for the simulation. Standard boundary conditions with the bottom boundary fixed in all directions, side boundaries normally fixed, and top boundary free are applied to the FE model. Horizontal interfaces are assigned on both sides of the geotextile reinforcement facing to overlaid and underlaid sand layers. A reduction factor of 0.8 is selected to consider the interfacial friction angle between the sand and geotextile reinforcement (Yapage & Liyanapathirana 2018). Vertical interfaces are assigned between DCM columns and HKMD. Similar to the FE models of van der Peet *et al*. (2014), the vertical interfaces are extended 0.1 m into the overlying sand layer. The properties of the extended interface are identical to the

surrounding sand. The FE model is meshed into 55446 10-noded soil (tetrahedrons) elements. In order to consider large deformation and the membrane effect of the geotextile reinforcement, the function of updated generated mesh should be utilized.

3.2 Simulation results

Selected observation points for checking the simulation results are marked in Figure 3. Figure 2a presents the simulated settlement at observation point a, representing the surface settlement. Good agreement can be seen from the simulated settlement and measured settlement. The simulated excess porewater pressures at observation points d and e represent the excess porewater pressures measured by PPTs at the middle and bottom levels, as shown in Figure 2b. Similar to Section 2.2, efficacy can be calculated based on the simulated vertical stresses. It can be seen from Figure 2c that the simulation results agree well with the test results.

The simulated tensile strains of the geotextile reinforcement are calculated as:

$$\varepsilon_{x,y} = \frac{T_{x,y}}{J_{x,y}} \tag{4}$$

where $\varepsilon_{x,y}$, $T_{x,y}$, and $J_{x,y}$ are the tensile strain, force, and stiffness in x and y directions, respectively. Figure 2d shows the comparison between the simulated and measured maximum tensile strains of the geotextile reinforcement under different surcharge loadings. It is found that the FE simulation underestimated the maximum tensile strain. This difference between the simulation and test results might be mainly attributed to that the geotextile reinforcement was treated as a linear elastic material in the FE model.

Table 1. Parameters for different materials.

Material	Model	Parameter
HKMD*	SSC	γ_{sat} = 16.5 kN/m^3; λ^* = 0.107; κ^* = 0.027; μ^* = 0.002037; ν = 0.15; c' = 0.5 kPa; φ' = 24°; $k_{x,y}$ = 7.0×10^{-4} m/day; k_z = 3.5×10^{-4} m/day; POP = 5 kPa
Columns	MC	γ_{sat} = 16.5 kN/m^3; E'_{50} = 40 MPa; ν = 0.25; c' = 80 kPa, φ' = 42°;
Sand**	HS	γ_{sat} = 17.5 kN/m^3; E'_{50} = 30 MPa; E'_{oed} = 20 MPa; E'_{ur} = 90 MPa; m = 0.5; ν = 0.2; c' = 0.1 kPa, φ' = 34.6°; ψ' = 4.6°; POP = 10 kPa; p_{ref} = 100 kPa
Geotextile	Elastic	$J_{x,y}$ = 680,150 kN/m

*The parameters used in SSC model were determined from oedometer and triaxial tests on reconstituted HKMD.
**The parameters used in HS model were determined from CD triaxial tests on sand.

The shape and size of soil arches are usually assumed in different arching models and design guidelines of GRCS embankments (Lee *et al.* 2021). The calculation of load part A highly depends on the shape and size of soil arches. van der Peet *et al.* (2014) considered that the principal stress is parallel to the arches and verified CA model by presenting the directions of principal stress. To investigate soil arching in the physical model test of this study, principal stress directions between two adjacent columns and those between two diagonal columns at different stages are presented in Figure 4. The case with a surcharge loading of 40 kPa is taken as an example to show the difference between the simulation results and CA model in terms of the shape of arches. The arches determined from this study are denoted by dotted curves while the outmost arches determined according to CA model are represented
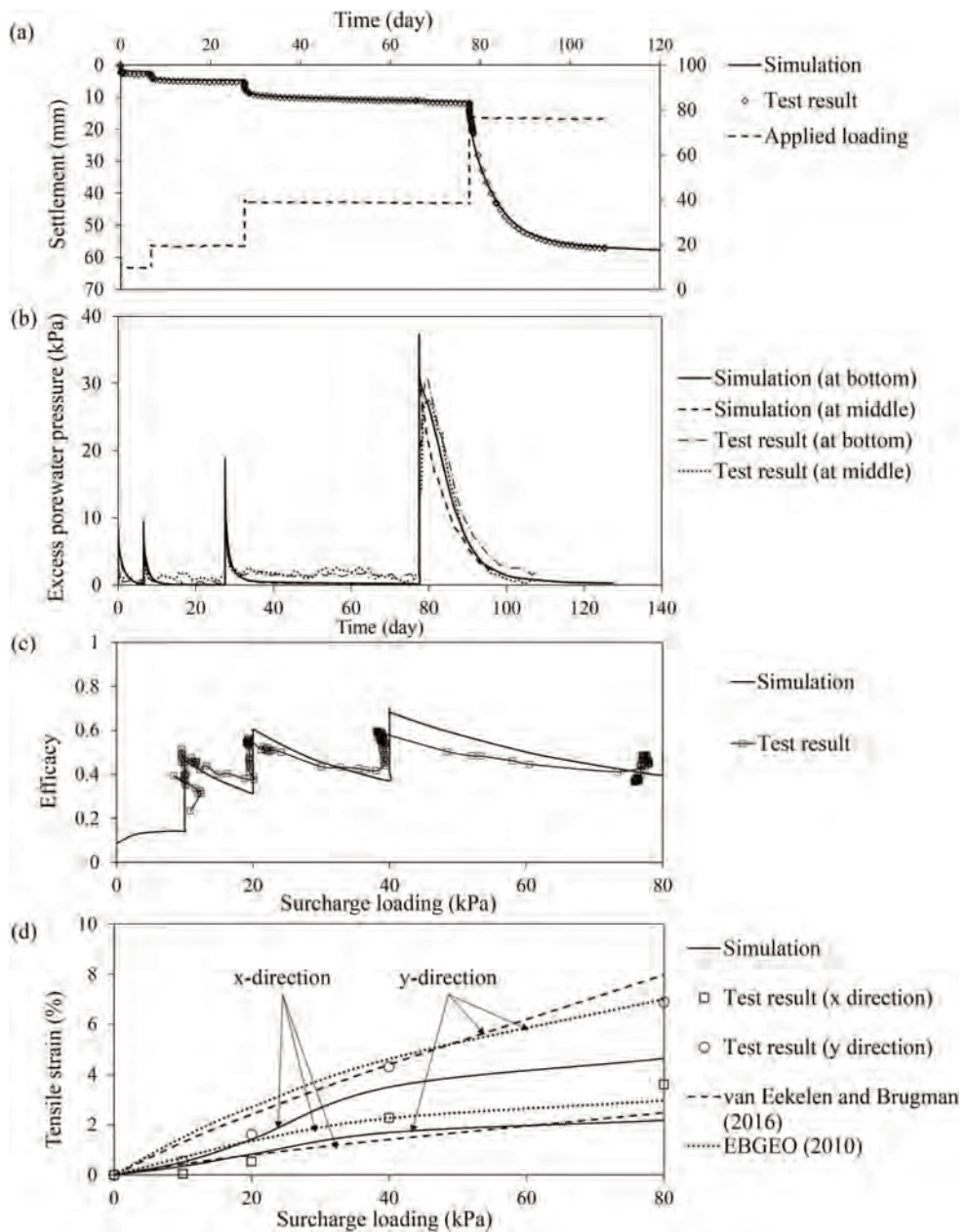
Figure 2. Experimental and numerical results of (a) surface settlement, (b) excess porewater pressures, (c) column efficacy, (d) tensile strains.

by dashed curves. It can be seen from Figures 4a and b that the shape of arches between adjacent columns and between diagonal columns are quite different from those determined by CA model at the loading stage. Triangular arches similar to those shown in Figure 4a were also found by Rui *et al*. (2016) and van Der Peet and van Eekelen (2014) using 2D trapdoor tests and numerical simulation, respectively. After the consolidation of the HKMD
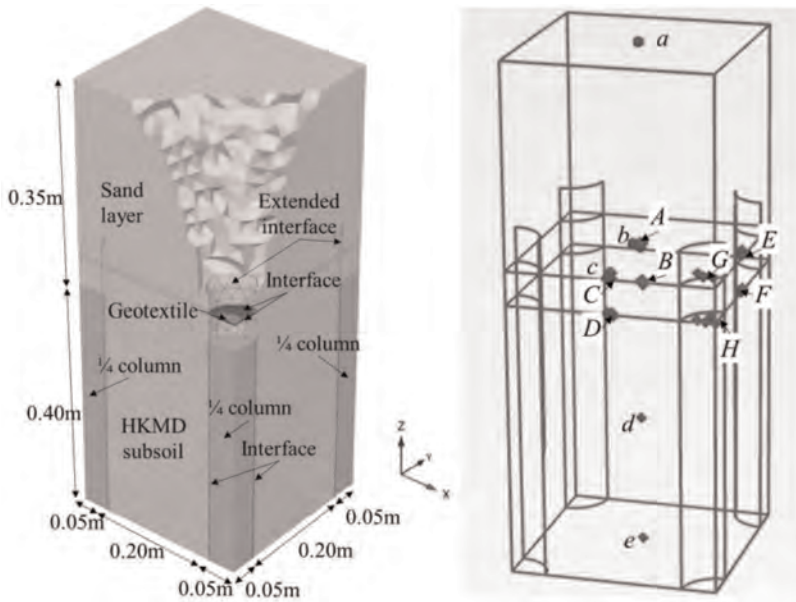
Figure 3. Illustration of the FE model and locations of observation points.
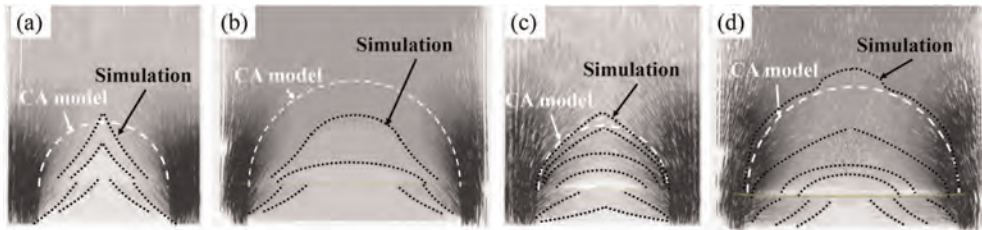
Figure 4. The shape of soil arches: (a) between two adjacent columns at loading stage, (b) between two diagonal columns at loading stage, (c) between two adjacent columns after consolidation, and (d) between two diagonal columns after consolidation.

subsoils, the inner triangular arches between two adjacent columns tended to become concentric semi-circular arches, which agrees with the assumption of CA model about the shape of arches. More clear concentric arches can be also observed between two diagonal columns. Although the outermost arches determined from the simulation results are triangular between two adjacent columns and bell-shaped between two diagonal columns, their sizes are similar to those determined by CA model.

4 CONCLUSIONS

A physical model test on geotextile-reinforced sand fill over soft marine clay improved by DCM columns has been successfully conducted with the measurement of earth pressures and the tensile strains of the geotextile reinforcement. The tensile strains calculated according to Dutch design guidelines agree with the measured data. Soil arching developed during loading stages and after the consolidation of the subsoil was revealed using the verified finite

element method and compared with CA model. Unlike the ideal concentric semi-spherical arches assumed in CA model, the shape of the arches observed in the simulation is more complicated.

ACKNOWLEDGEMENTS

REFERENCES

EBGEO 2010. *Empfehlungen für den Entwurf und die Berechnung von Erdkörpern mit Bewehrungen aus Geokunststoffen e EBGEO*, vol. 2 German Geotechnical Society, Auflage978-3-433-02950-3 (in German). Also available in English: Recommendations for Design and Analysis of Earth Structures using Geosynthetic Reinforcements e EBGEO, 2011. ISBN: 978-3-433-02983-1 and digital in English ISBN: 978-3-433-60093-1.

Hewlett, W. J. 1988. Analysis of Piled Embankment. *Ground Engrg.* 21(3): 12–18.

Ho, T. O., Tsang, D. C., Chen, W. B., & Yin, J.H. 2020. Evaluating the Environmental Impact of Contaminated Sediment Column Stabilized by Deep Cement Mixing. *Chemosphere* 261: 127755.

Iglesia, G.R., Einstein, H.H., & Whitman, R.V. 2014. Investigation of Soil Arching with Centrifuge Tests. *Journal of Geotechnical and Geoenvironmental Engineering* 140(2): 04013005.

King, D.J., Bouazza, A., Gniel, J.R., Rowe, R.K., & Bui, H.H. 2017. Load-transfer Platform Behaviour in Embankments Supported on Semi-rigid Columns: Implications of the Ground Reaction Curve. *Canadian Geotechnical Journal* 54(8): 1158–1175.

Lee D. 2016. Expansion of Hong Kong International Airport into a Three-Runway System, Airport Reclamations – then and now. HKIE YMC Seminar. http://ymc.hkie.org.hk/DocDown.aspx?imgDoc= 151_160120+3RS+Reclamation+(20+Jan+2016).pdf

Lee, T., Van Eekelen, S. J., & Jung, Y. H. 2021. Numerical Verification of the Concentric Arches Model for Geosynthetic-reinforced Pile-supported Embankments: Applicability and Limitations. *Canadian Geotechnical Journal* 58(3): 441–454.

Rui, R., Van Tol, A. F., Xia, Y. Y., Van Eekelen, S. J. M., & Hu, G. 2016. Investigation of Soil-arching Development in Dense Sand by 2D Model Tests. *Geotechnical Testing Journal* 39(3): 415–430.

van der Peet, T. C., & Van Eekelen, S. J. M. 2014. 3D Numerical Analysis of Basal Reinforced Piled Embankments. *In Tenth International Conference on Geosynthetics* (pp. 21–25).

van der Peet, T. C., Van Duijnen, P. G., Van Eekelen, S. J. M., & Brinkgreve, R. B. J. 2014. Validating a New Design Method for Piled Embankments with Plaxis 2D and 3D. *in Plaxis bulletin*.

van Eekelen, S.J.M., Bezuijen, A., & Van Tol, A.F. 2013. An Analytical Model for Arching in Piled Embankments. *Geotextiles and Geomembranes* 39: 78–102.

van Eekelen, S.J., & Brugman, M.H. 2016. *Design Guideline Basal Reinforced Piled Embankments.* CRC Press.

Wijerathna, M., Liyanapathirana, D. S., & Jian Leo, C. 2017. Analytical Solution for the Consolidation Behavior of Deep Cement Mixed Column–improved Ground. *International Journal of Geomechanics* 17(9): 04017065.

Wu, P. C., Feng, W. Q., & Yin, J. H. 2020. Numerical Study of Creep Effects on Settlements and Load Transfer Mechanisms of Soft Soil Improved by Deep Cement Mixed Soil Columns Under Embankment Load. *Geotextiles and Geomembranes* 48(3): 331–348.

Yapage, N., & Liyanapathirana, S. 2018. Behaviour of Geosynthetic Reinforced Column Supported Embankments. *Journal of Engineering, Design and Technology* 16(1): 44–62.

Zaeske, D. 2001. *Zur Wirkungsweise von Unbewehrten und Bewehrten Mineralischen Tragschichten Über Pfahlartigen Gründungselementen*. Fachgebiet u. Versuchsanst. Geotechnik, Univ. Gh Kassel.

Zhang, C., Su, L., & Jiang, G. 2022. Full-scale Model Tests of Load Transfer in Geogrid-reinforced and Floating Pile-supported Embankments. *Geotextiles and Geomembranes* 50(5):896–909.

System efficacy and diffused arching in embankments supported by piles

K. Brzeziński
Warsaw University of Technology, Poland

R.L. Michalowski
University of Michigan, USA

ABSTRACT: A pile support system is a common solution for embankments constructed over soft, normally consolidated fine-grained, or organic soils. Piles are installed to reach the stronger layers of the foundation soil, while the transfer of the embankment load to the piles relies on the development of the stress distribution often referred to as arching. In addition, geosynthetic reinforcement is used in a load transfer platform to enhance the transfer of the load to the piles. A series of numerical simulations (FEM) were carried out to study the formation of arching in embankment fill placed over a square-grid pile support system. The development of the load transfer process was also studied, quantified by the system efficacy. The efficacy of the support system without geosynthetic can easily exceed 80%, but it can be larger than 90% if a geosynthetic-reinforced load transfer platform is used. Numerical simulations provided some insight into the development of the load transfer mechanism, but distinct arching as assumed in many design methods was not detected.

1 INTRODUCTION

Construction of embankments supported by piles is a successful technology used for the development of transportation infrastructure through regions with soft fine-grained or organic soils. Design of such embankment is predicated on inducing soil arching within the lower portion of the embankment, which aids in load transfer from the embankment to the piles. Early efforts to account for soil arch formation are due to Terzaghi (1943), and applications to pile-supported embankments were considered by Hewlett & Randolph (1988). The Distinct Element Method is a good technique to demonstrate development of strong force chains forming a soil arch (Nadukuru & Michalowski 2012), and the literature abounds with papers indicating how to construct a soil arch within a soil mass as part of design procedures. Many of these attempts are variations on the original arch/dome considerations of Hewlett & Randolph (1988).

The practical purpose of studying the process of load transfer is the development of design methods for the pile support systems, so that the required efficacy of the system can be met and the load transferred to the soft soil is minimized. Studies in the area of pile-supported embankments have two foci: improving methods of design (Filz *et al*. 2012; Van Eekelen *et al*. 2013), and gaining better understanding of the load transfer process in granular soils (Brzeziński & Michalowski 2021; King *et al*. 2019). This study will focus on the latter, with special attention paid to the formation of soil arching.

The practical outcome of this study is evaluation of efficacy of the support system, and the factors affecting the efficacy. It is expected that observations of shear strains and stresses in constructed embankments yield some information about the development of the load transfer process, and, in addition, become useful in drawing conclusions regarding the critical embankment height.

Earlier plane strain FEM simulations of a column system with cap beams yielded a reasonable efficacy of the system. They also were found useful in demonstrating the non-compliant columns "attracting" the bulk of the load (Brzeziński & Michalowski 2021).
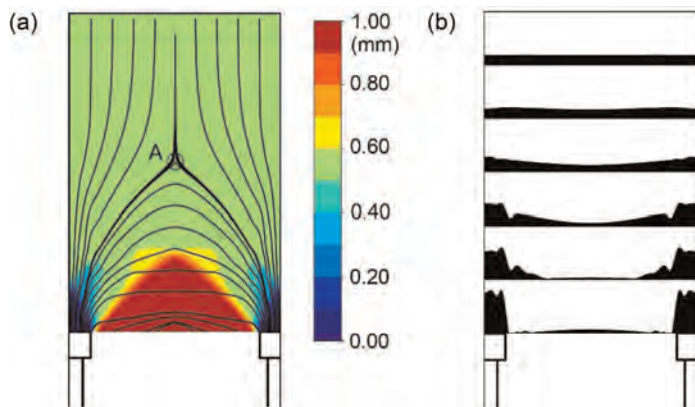
Figure 1. (a) Vertical displacements of the fill associated with 1-mm settlement of the soft soil and trajectories of major principal stresses, and (b) normalized distribution of vertical stress (2D simulation after Brzeziński & Michalowski 2021).

This is demonstrated in Figure 1(b) where the vertical load on horizontal planes is being gradually attracted to the columns as the depth increases. Figure 1(a) indicates the largest vertical displacements immediately above the soft soil, no vertical displacement immediately above the non-compliant columns, and uniform displacements in the upper portion of the embankment. The major principal stress trajectories are shaped in an arch-like structure, but this does not necessarily indicate the formation of a soil arch. Inspection of the stress field did not reveal the existence of a distinct band with increased stresses indicating arch formation, yet a clear divergence of the vertical stress occurs with greatly reduced stress on the soft soil. This phenomenon is now studied through analyses of stress distribution in a three-dimensional support system with piles distributed in a square-grid pattern.

2 SQUARE-GRID PILE SUPPORT MODEL

A periodic cell of the pile support system considered in this study is illustrated in Figure 2(a). Piles are distributed in an $s \times s$ grid (s being the pile spacing).

The cell has four planes of symmetry and its coverage ratio (ratio of pile cap area to the cell area) is

$$\mu = \pi \left(\frac{R}{s} \right)^2 \tag{1}$$

where R is the radius of the pile cap. The geometry of the model cross-section A-A is shown in Figure 2(b). The left and right vertical boundaries are traces of symmetry planes; hence, they coincide with principal directions and will be modeled as shear-free boundaries. The origin of the coordinate system is at the center of the pile at the elevation of the working platform.

The model of the embankment fill is elastic-plastic, with Hook's law describing the deformation prior to reaching the limit state. The plastic state is described by the Mohr-Coulomb criterion

$$f = R_{mc}q - p \tan \phi - c = 0 \tag{2}$$

where $q = \sqrt{3J_2}$ and $p = -I_1/3$, with I_1 being the first invariant of the stress tensor and J_2 being the second invariant of the deviatoric stress tensor, and

$$R_{mc} = \frac{1}{\sqrt{3}\cos\phi}\sin\left(\theta + \frac{\pi}{3}\right) + \frac{1}{3}\cos\left(\theta + \frac{\pi}{3}\right)\tan\phi \qquad (3)$$

with Lode angle θ defined by (J_3 is the third invariant of the deviatoric stress tensor)

$$\cos(3\theta) = \frac{3\sqrt{3}}{2}\frac{J_3}{J_2^{3/2}} \qquad (4)$$

The plastic flow is assumed to be non-associative

$$\dot{\varepsilon}_{ij} = \dot{\lambda}\frac{\partial g(\sigma_{ij})}{\partial\sigma_{ij}} \qquad (5)$$

with plastic potential $g(\sigma_{ij})$ defined by Menetrey & Willam (1995).
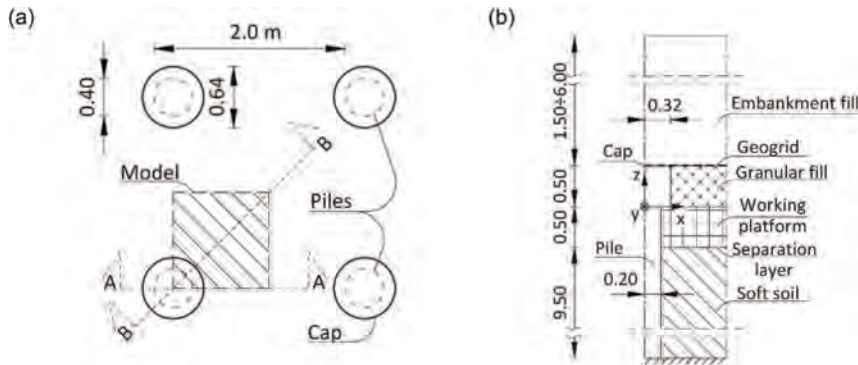
Figure 2. (a) Periodic cell of the pile-support system with pile spacing of $s = 2.0$ m, and (b) section A-A of the symmetric half of the cell.

Material properties of the fill (density ρ, Young's modulus E, Poisson's ratio ν, internal friction angle ϕ, and dilatancy angle ψ) are included in Table 1.

Table 1. Material properties of the embankment fill model.

ρ (kg/m^3)	E (MPa)	ν –	ϕ (°)	ψ (°)
1900	60	0.3	40	10.0

The working platform was modeled as elastic, with a density of 1900 kN/m^3, $E = 60$ MPa, and $\nu = 0.3$. The soft consolidating layer of saturated fine-grain/organic soil was modeled as elastic with density $\rho = 1137$ kN/m^3, $E = 3$ MPa, $\nu = 0.3$, initial void ratio $e = 1.30$, and hydraulic conductivity of $3.5 \cdot 10^{-8}$ m/s. Properties of piles and pile caps are: $\rho = 2400$ kN/m^3, $E = 27$ GPa, and $\nu = 0.16$. The low-stiffness granular fill immediately beneath the geogrid reinforcement was modeled as elastic with $\rho = 1460$ kN/m^3, $E = 3$ MPa, $\nu = 0.3$.

Geogrid reinforcement was assumed to have a strength of 200 kN/m and stiffness of 2000 kN/m. In field conditions, a separation layer (non-woven geotextile) would be placed between the soft consolidating soil and the working platform. This layer, however, is not modeled as it has a negligible influence on the mechanical response of the support system.

3 SIMULATIONS

Simulations were carried out using commercial FEM system ABAQUS. Finite elements used in the model are listed in Table 2.

With the exception of the last column in Table 2, all elements are of the variety of a 20-node brick element. The geogrid is modelled with an 8-node membrane element (M3D8R).

Table 2. ABAQUS elements used in model construction.

	Piles Pile caps	Embankment fill	Working platform	Granular fill layer	Soft subsoil	Geogrid
Model	Elastic	Elastic-plastic	Elastic	Elastic	Elastic consolidating	Elastic tension only
Abaqus Element	C3D20R	C3D20	C3D20R	C3D20RP	C3D20	M3D8R

3.1 Construction process

The embankment construction process is modeled with step-wise increases of the embankment fill in 50-cm lifts, as illustrated in Figure 3. These lifts are added in 7-day intervals.

The results for a given interval are recorded 7 days after application of the load, i.e., just before the next lift is constructed. For example, the results for an instant when the embankment has reached a height of 3 m are collected at 42 days after the start of construction. If 3 m is the final height, then the final results would be collected after an additional 365 days. Construction of the 6-m tall embankment is illustrated in Figure 3. The construction process is considered to end in 84 days (7 days after the construction of the last lift), and the final data is collected in 449 days from the beginning of construction (84 + 365 = 449 days).
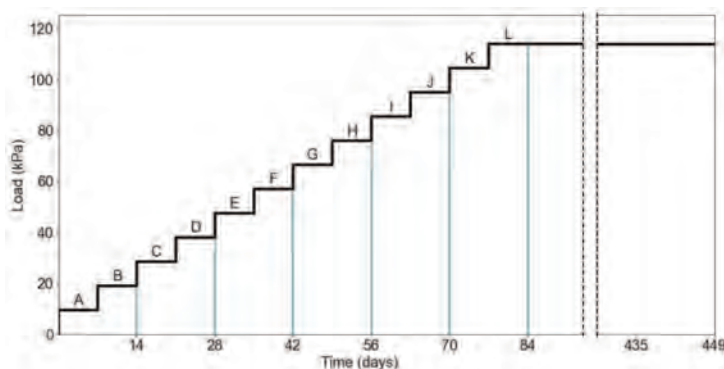
Figure 3. Embankment construction process of a 6-m tall embankment.

3.2 *Development of shear strains and attainment of critical height*

Of particular interest is the development of the load transfer mechanism in the embankment fill and observation of strain localization (*shear banding*), indicative of the embankment fill reaching the limit state.

Graphs in Figure 4(a) show maximum shear strain increments, in a 3-m tall embankment, after 21, 28, 35, 42, and 407 days from the start of construction. The maximum shear strains are shown in cross-section A-A, and Figure 4(b) shows the same in the diagonal cross-section B-B (see Figure 2(a) for sections A-A and B-B). The graphs show the results within the embankment fill above the elevation of the pile cap and the geosynthetic reinforcement. The lower horizontal boundary is supported by the pile cap on the left-hand side and by the geogrid and the layers beneath on the right, as illustrated in Figure 2. Increments of maximum shear strains in the last 7 days are presented in the graphs, except for the last graph in each of the two rows, where the increment includes the strains in the previous 365 days.

Let us concentrate on the results collected from cross-section A-A. The color scale indicates the magnitude of the maximum shear strain increment (or increment of deviatoric strain) at each point in the graphs. The red shows zero shear strain, and it indicates the regions moving approximately as rigid bodies. The color blue shows the maximum shear strain increment of 0.30%, and the regions with a white background are off the scale (larger than 0.30%).

A characteristic feature of the shear strain incremental field is the development of the shear bands indicating a formation of a mechanism. The color scale in Figure 4 indicates the maximum shear strain increments. However, the total maximum shear strains within the shear bands increased from about 4% after the placement of the first 0.5-m layer, to about 12% after embankment reached the height of 3.0 m (maximum shear strain is an invariant quantity for a given strain state). It is clear that once the construction reached the height of
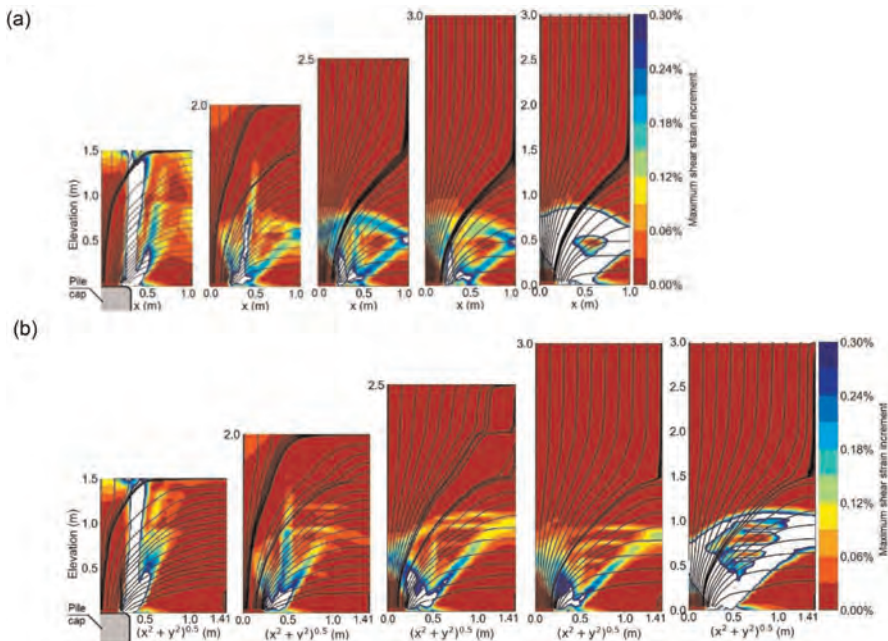
Figure 4. Maximum shear strain increments and trajectories of major principal stresses during construction of a 3-m tall embankment: (a) section A-A at construction times: 21, 28, 35 and 42 days, and the final result after 407 days, and (b) maximum shear strains in section B-B. Pile spacing 2.0 m.

1.50 m, a vertical shear band formed, reaching the embankment top boundary; this shear band separates the almost stationary fill above the pile on the left from the portion resting on the reinforcement and moving downward due to the settlement of the soft soil. The embankment did not reach its critical height yet, and this mechanism is considered a failure mechanism in the fill (loss of integrity of the top surface). Once the construction reaches a 2-m height, the vertical shear band no longer intersects the top boundary, indicating that the embankment has reached its critical height. At the height of 2.5 m a mechanism has formed in the lower portion of the embankment, and it persists through the end of the construction process of the 3-m tall embankment. While this mechanism allows plastic deformation in the lower portion, it does not lead to embankment collapse. A similar process takes place in diagonal section B-B illustrated in Figure 4(b).

The plastic mechanism can be accommodated by the embankment in its lower portion when the embankment height exceeds its critical value, presumably because of a redistribution of stresses in the field above the mechanism, referred to often as *soil arching*. Arching is an elusive concept that is not revealed by the strain field; rather, some specific features in the stress field might indicate whether or not arching has occurred. This will be attempted in Section 3.5.

3.3 Force in the reinforcement

The computational model used in this study makes it possible to monitor the development of the force induced in the geosynthetic reinforcement as the embankment is being constructed.

Figure 5 illustrates the maximum force in the geogrid in embankments with heights: 1.5, 3.0, and 6.0 m, and for a pile spacing of 1.5 and 2.0 m. In all cases, the maximum force was found to be at the edge of pile cap, about 30 cm from its center (pile caps had rounded edges and a radius of 32 cm).

Not surprisingly, the force in the reinforcement was mobilized the least in the low-height embankments, and for the lesser pile spacing. Besides the embankment height and the pile spacing, the magnitude of the maximum force is also sensitive to the reinforcement stiffness and compliance of the layers beneath the reinforcement.

There is a distinct jump (discontinuity) in the maximum force associated with each lift of the fill, and a steady increase in the force during 7-day intervals before the subsequent lift is placed. The increase in the force appears to be linear in the first few weeks following the completion of construction, but the force reaches a plateau sometime within the first year
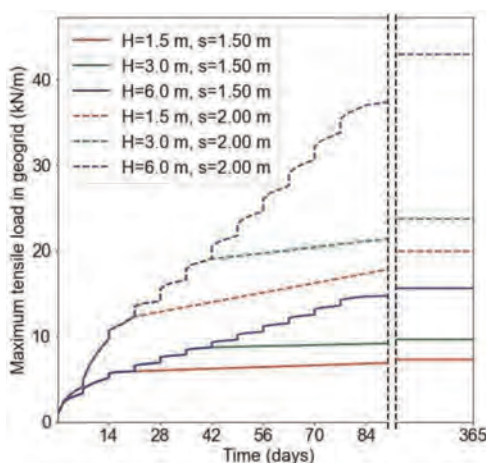
Figure 5.   Maximum force in reinforcement.

after construction. This conclusion, however, may be dependent on the properties of the soft soil, reinforcement stiffness, etc.

One would expect the reinforcement to be more effective if the larger force is mobilized. This conjecture, however, has to be interpreted carefully, because the efficacy of the support system is affected predominantly by the vertical component of the force in reinforcement. Consequently, it is the deflection of the geosynthetic reinforcement that is a key factor in its effectiveness.

The largest force in the reinforcement was mobilized in the tallest, 6-m embankment, with a pile spacing of 2 m. For the properties of the soil and reinforcement used in the simulations, this force was over 35 kN/m at the end of construction (84 days), and it increased to over 40 kN/m in the following year. With the same parameters, but spacing reduced to 1.5 m, the maximum force in reinforcement did not exceed 15 kN/m.

In general, the larger the embankment height and the pile spacing, the larger the force mobilized in the reinforcement.

3.4 *Efficacy of the pile support system*

The effectiveness of the pile support system can be quantified by the ratio of the load carried by the piles to the total load transferred to the subgrade. The latter can be taken as the weight of the embankment fill in a single cell of the support system, and the former is the load transferred to a single pile. This ratio will be referred to as efficacy E_f. Consider polar coordinate system r, θ with the origin at the center of a single pile cap, and R being the radius of the cap. Efficacy E_f can be calculated as

$$E_f = \frac{4 \int_0^{\frac{\pi}{2}} \int_0^R \sigma_{zz} \, dr d\theta}{\rho g s^2 H} \tag{6}$$

where σ_{zz} is the vertical stress on the pile cap, ρ is the mass density of the embankment fill, g is the gravity acceleration, and H is the embankment height.

If the stress caused by the embankment load is transferred uniformly on piles and the soft soil, the efficacy would be equal to coverage area ratio μ in Eq. (1). However, the elastic response of the system, even after the placement of the first lift, causes an instantaneous redistribution of the stress in that layer, producing an increase in efficacy at time $t = 0$.

General observations of the simulation outcomes indicate that efficacy increases with an increase in construction time, and for a fully constructed embankment, the higher the embankment the larger the efficacy. Not surprisingly, the efficacy decreases with the increase in pile spacing, even though the force in the reinforcement increases with the increase in pile spacing.

The development of efficacy is a periodic process defined by the cyclic placement of the lifts of the embankment fill. In the initial stages of construction, placement of a single lift causes a substantial increase in efficacy, but the rate of increase drops after the load is placed. The increments in efficacy associated with consecutive lifts become smaller with increasing embankment height. This is understandable, because the efficacy is defined in terms of the total loads, and the consecutive layers/lifts produce relatively smaller load increments when compared to the total load.

An interesting feature in the increase in efficacy in later cycles (for the 6-m embankment) is a small drop in efficacy at the time of placing the subsequent lift, before it starts increasing again. For example, in the construction process of the 6-m embankment on a 1.5×1.5 m grid of piles, the first drop in efficacy occurred at 21 days, and the placement of all subsequent layers was associated with some initial drop in efficacy. This is because the increase in efficacy develops in time with the settlement of the soft soil, but the placement of the layer (lift) of soil is instantaneous and the load distribution it initially produces is less favorable when compared to the already developed efficacy. This does not happen in the first cycles, where the developed efficacy is still relatively low.

It may be interesting to examine some of the efficacy numbers in Figure 6. The highest final efficacy of all cases shown is achieved by the 6-m embankment with pile spacing of 1.5×1.5 m; the value calculated is $E_f = 0.921$, and the second highest, 0.891 is for the 3-m embankment and 1.5 m pile spacing. It is interesting to notice that the 3-m embankment with 2.0 m pile spacing and the 1.5-m embankment with 1.5 m pile spacing developed almost the same efficacy: 0.819 and 0.823, respectively. Not surprisingly, the lowest efficacy of 0.702 was developed by the 1.5-m embankment and pile spacing of 2.0 m. This is the case where the height of the embankment has not reached the critical value yet, and the plastic mechanism propagates all the way to the top surface, as illustrated in Figure 4.
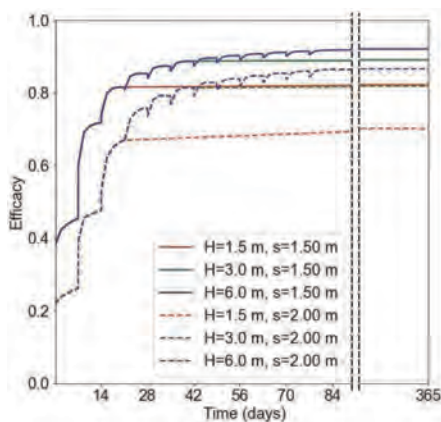
Figure 6. The development of system efficacy.

3.5 *Load transfer and diffused arching*

The current state of knowledge assigns the development of high efficacy of pile support systems to the presence of soil arching, often illustrated as the formation of arches or domes within the embankment fill, spanning the space between the supporting piles. These arches and domes are to carry the elevated amount of load, transferring the bulk of the embankment gravity load to the piles. Successful design methods were developed based on the assumption of soil arching. The reinforcement placed over the system of piles, sometimes referred to as the *load transfer platform*, is to aid in transferring the load to the piles, improving the efficacy of the support system.

Earlier simulations of plane-strain support systems (with cap beams) did not yield evidence for formation of distinct soil arching, but it did reveal an effective stress distribution that produced high efficacy of the system (Brzeziński & Michalowski 2021). We now inspect the distribution of the major principal stresses in the embankment constructed over the square-grid system of piles in an effort to identify features that might indicate the formation of dome-like regions with elevated stresses associated, in many studies, with arching.

Figure 7 illustrates the distribution of the major principal stresses (color scale) and their trajectories (continuous lines in Figures 7(a) and 7(b)). These graphs correspond to the graphs in Figure 4 for a construction time of 42 days. The principal stresses in Figure 7 are normalized with the stress value of $\rho g d$, where d is the depth measured from the top surface of the embankment (ρ - mass density, g - gravity acceleration).

The green-light green indicates the normalized major principal stress value of 1, as it would be in the state of rest, and the stress in the upper 1 m of the fill is consistent with such a distribution. Beneath, however, on the left side (above the pile) the major principal stress
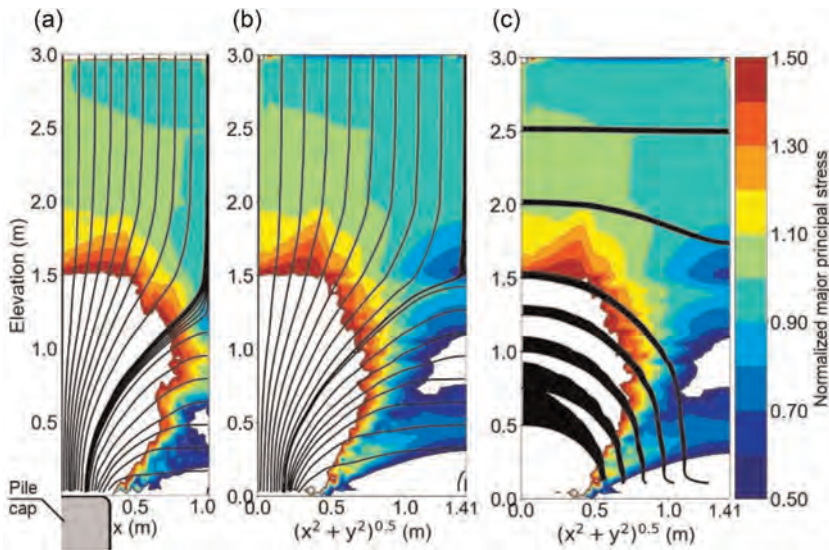
Figure 7. Major principal stresses (normalized) and their trajectories in a 3-m tall embankment: (a) section A-A, (b) section B-B, and (c) plot of the major principal stress magnitudes in section B-B (black bands). Pile spacing 2.0 × 2.0 m.

quickly increases. The areas with the white background are off-the-scale. This time, if the white region borders with dark red, the normalized stress is above 1.5, whereas if the while area borders dark blue, the normalized major principal stress is less than 0.50.

While the stress above the pile increases quickly below the elevation of 2.0 m, the stress on the right side, above the reinforcement and the soft soil beneath, drops. This is more distinct in diagonal section B-B (Figure 7(b)) than section A-A. The pile cap is loaded with much larger traction than the region underlain by the soft soil.

It is demonstrated in both cross-section A-A and B-B that the major principal stress above the pile cap is vertical, but above the soft soil it is horizontal. Hence the preferential load transfer is to the piles, presumably owed to soil arching, and one would expect that arching would approximately follow the major principal stress trajectories.

Figure 7(c) is an edited Figure 7(b), where the lower contours of the black bands coincide with the trajectories of minor principal stresses, and the thickness of the bands indicates the magnitude of the normalized major principal stresses. In the presence of soil arching, one would expect a distinct band in the fill, approximately following the major principal stress trajectories, with elevated stresses that could be identified as a soil arch. Such formation in the stress field, however, was not detected. Understandably, the normalized major principal stresses are uniform in the upper portion of the fill, but they increase significantly in the lower portion, as they approach the left boundary of the model. However, the thickness of the bands increases monotonically, without formation of a distinct "arch" in the stress field.

The efficacy of the system with the geometry in Figure 7 had the final (calculated) efficacy of 0.82, which is a quite respectable value considering that the coverage ratio (Eq. (1)) was only 0.08; i.e., 82% of the gravity load produced by the embankment weight was transferred to 8% of the horizontal area (pile cap area) of the computational cell. That is an effect one would expect to be associated with arching, but a distinct arch was not detected, as was the case in the two-dimensional analysis (Brzeziński & Michalowski 2021). For a lack of a better term, we refer to the effect illustrated in Figure 7(c) as *diffused arching*.

4 CONCLUSIONS

Construction of embankments on the pile support systems has two distinct phases: prior to reaching the critical height, and after the critical height has been reached. The former is characterized by formation of the plastic mechanism with kinematic discontinuity reaching the embankment surface and causing a system failure. The latter is associated with the formation of the plastic mechanism confined to the lower portion of the embankment, which does not cause the collapse of the structure as this mechanism is supported by the piles and the lower layers of the system.

Efficacy of the pile support system is developed in a cyclic process as the sequential layers of embankment fill are being placed. The cyclic increases in efficacy became smaller with the time of construction. The final efficacy of the support system increases with an increase in the embankment height and a decrease in pile spacing. The force in the reinforcement and its effectiveness increases with pile spacing, and is also dependent on reinforcement deflection. The outcomes of simulations with parameters used indicated a maximum efficacy in excess of 0.90.

Arches or domes in the stress field within the embankment fill, commonly referred to as soil arching, were not detected in the simulations. However, the effect of load transfer to stiffer elements of the system was very much present in the simulations, leading to high efficacy of the support systems. The term *diffused arching* was used to describe this type of load transfer.

ACKNOWLEDGEMENTS

REFERENCES

Brzeziński, K. & Michalowski, R. L. 2021. Diffused Arching in Embankments Supported by Non-compliant Columns with Capping Beams. *Comput. Geotech.*, 132, 104031.

Filz, G., Sloan, J., McGuire, M. P., Collin, J. & Smith, M. 2012. "Column-supported Embankments: Settlement and Load Transfer." *Geotechnical Engineering State of the Art and Practice: Keynote Lectures from GeoCongress 2012, Reston, VA*, 54–77.

Hewlett, W. J. & Randolph, M. F. 1988. Analysis of Piled Embankments. *Ground Engineering*, 21(3), 12–18.

King, L., Bouazza, A., Dubsky, S., Rowe, R. K., Gniel, J. & Bui, H. H. 2019. Kinematics of Soil Arching in Piled Embankments. *Géotechnique*, 69(11), 941–958.

Menetrey, P. & Willam, K. 1995. Triaxial Failure Criterion for Concrete and its Generalization. *ACI Structural Journal*, 92(3), 311–318.

Nadukuru, S. S. & Michalowski, R. L. 2012. Arching in Distribution of Active Load on Retaining Walls. *J. Geotech. Geoenviron. Eng.*, 138(5), 575–584.

Terzaghi, K. 1943. *Theoretical Soil Mechanics*, Wiley, New York.

Van Eekelen, S., Bezuijen, A. & Van Tol, A. 2013. An Analytical Model for Arching in Piled Embankments. *Geotextiles and Geomembranes*, 39, 78–102.

Model tests on soil foundation reinforced by geosynthetic encased granular columns subjected to reverse fault movement

J. Chiang & K.-H. Yang
National Taiwan University, Taipei, Taiwan

J.G. Zornberg
The University of Texas at Austin, Texas, USA

E.E. Michel & C.-W. Wu
National Taiwan University, Taipei, Taiwan

ABSTRACT: This paper conducts a 1g model test on soil foundations reinforced by geosynthetic encased granular columns (GECs) across a reverse fault. The aim is to evaluate the effectiveness and reinforcing mechanism of GEC foundations in mitigating the ground surface deformation associated with reverse faulting. For comparison, 1g model tests were also performed on unreinforced and GRS foundations. The test results indicate that GEC foundations can effectively mitigate the ground surface deformation induced by reverse fault movement; compared with the unreinforced foundation, the GEC foundations can reduce the maximum angular distortion at the ground surface by 23.3%–55.6%. A percentage reduction for maximum angular distortion of 23.3% was achieved as the fault offset reached 30% of the foundation height, which mitigates the risk of the surface fault hazards associated with large reverse fault movement.

1 INTRODUCTION

Geosynthetics have been applied in engineering practice to mitigate surface faulting hazards. In central Taiwan, a highway embankment was constructed across the Chelungpu Fault. In the 1999 Chi-Chi earthquake (M_L = 7.3), the vertical surface movement of the Chelungpu Fault reached 2–4 m on average (Chen *et al*. 2001), which resulted in the severe failure of the overlying buildings and infrastructure. The failure of rigid gravity retaining walls was also observed because of the considerable surface rupturing induced by the fault movement. To reduce the risk of a similar event, the Chelungpu Fault was crossed by constructing a ductile highway embankment comprising a geosynthetic-reinforced soil (GRS) wall overlying a GRS foundation.

Yang *et al*. (2020) conducted a series of 1g model tests for investigating the performance of GRS foundations subjected to normal fault movement. The test results revealed that GRS foundations can reduce the fault-induced angular distortion at the ground surface by up to 60% in comparison with unreinforced foundations; this reduction is attributed to the development of the reinforcement tensioned membrane and shear rupture interception effects. Chiang *et al*. (2022) conducted numerical studies to develop design methods for GRS foundations against reinforcement breakage and significant pullout when subjected to normal fault movement. Although studies have validated the benefits of using GRS foundations to mitigate normal fault hazards, the performance of GRS foundations subjected to reverse fault movement has not been understood. Furthermore, GRS foundations might have poor

effectiveness for reducing reverse fault-induced ground deformation because tensile force is not expected to develop in the reinforcement as the hanging wall moves upward. Another type of reinforced foundation, soil foundation reinforced by geosynthetic encased granular columns (GECs), might overcome the deficiencies. In the present study, the performance of GEC foundations in mitigating reverse faulting hazards was evaluated.

In this study, 1g model tests were conducted to investigate the performance of GEC foundations in mitigating the surface hazards associated with reverse faulting. For comparison, 1g model tests were also performed on unreinforced and GRS foundations. A 3-m thick foundation in prototype subjected to a reverse fault displacement up to 90 cm was modeled in the 1g model tests. The effectiveness of GEC foundations and the reinforcing mechanism of geotextile encasement in mitigating ground surface deformation was investigated. The key findings of this study provide valuable information that can be used by engineers to optimize the design of GEC foundations for mitigating reverse faulting hazards.

2   MODEL TESTS

2.1   *Test setup*

The 1g model tests on unreinforced, GRS, and GEC foundations were conducted using a sandbox in the geotechnical research laboratory at National Taiwan University. Figure 1 presents an illustration and overview image of the sandbox and test setup of the 1g model tests. The dimensions of the sandbox were 100 cm × 20 cm × 60 cm (length × width × height). Transparent plexiglass walls were installed on the front and back sides of the sandbox for visual observations during the tests. Thin plastic sheets with lubricant were applied to each plexiglass wall to minimize soil–wall interface friction. The bottom of the sandbox comprised a movable hanging wall and fixed footwall. Reverse fault displacement was generated by moving the hanging wall upward by using a driving motor installed under the sandbox. The initial location of the reverse fault tip was 58 cm from the left boundary, and the fault dip angle was set to 60° in this study.
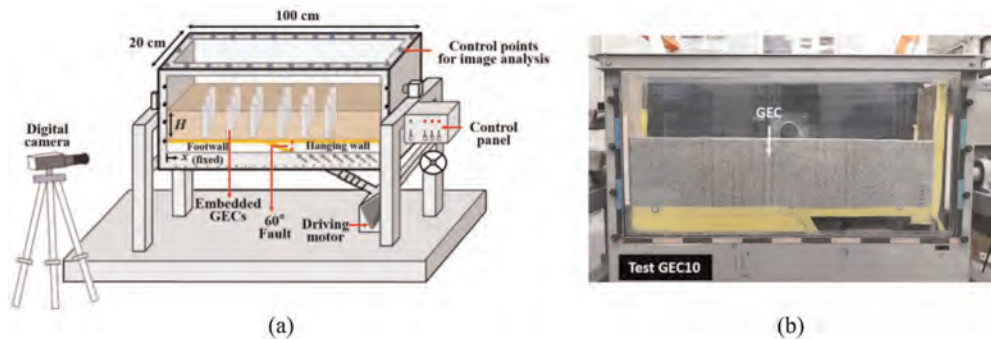
Figure 1.   The sandbox and test setup: (a) illustration; (b) panorama.

2.2   *Material properties*

The soil and reinforcement materials used in the 1g model tests were carefully selected in accordance with the similitude requirements to ensure that the test models and the prototypes have comparable behavior. The material properties adopted in the 1g model tests were scaled down by using scaling factors derived in accordance with Buckingham's theorem

(Buckingham 1914). Table 1 summarizes all the scaling factors and the corresponding values in prototype for the model geometry and material properties. The soil material used in the 1g model tests was uniform quartz sand, which is classified as poorly graded sand (SP) according to the Unified Soil Classification System (USCS). The mean particle size of the test sand was $D_{50} = 0.98$ mm, and the target dry unit weight was $\gamma_d = 15.3$ kN/m^3 at a relative density $D_r = 70\%$. The effective cohesion and peak friction angle of the test sand were $c' = 0$ kN/m2 and $\phi' = 39.2°$, respectively, with confining pressures σ_3 ranged from 50 to 200 kPa; these values were obtained from triaxial consolidated–drained (CD) compression tests (ASTM D7181).

The reinforcement material used in the 1g model tests was nonwoven polypropylene geotextile. The ultimate tensile strength and failure strain of the nonwoven geotextile in the machine direction were $T_{ult} = 0.7$ kN/m and $\varepsilon_f = 32.4\%$, respectively. The tensile stiffness of the nonwoven geotextile in the machine direction at the stress level of 50% of the ultimate tensile strength was $J_{50} = 5.47$ kN/m. For the geotextile encasement used in the GEC foundation test, the nonwoven geotextile in the designated machine direction was oriented along the circumferential direction of the geotextile encasement to develop hoop stress. The sand–geotextile interface friction angle was $\delta' = 27.4°$, and the efficiency factor was calculated to be $E_\phi = \tan \delta'/\tan \phi' = 0.63$.

Table 1. Scaling factors and values based on the similitude requirements.

Parameters	*Scaling factor	Model	Prototype
Geometry			
Foundation height, H (m)	$1/\lambda$	0.2	3.0
Soil parameter			
Target dry unit weight, γ_d (kN/m^3)	1	15.30	15.30
Friction angle, ϕ' (°)	1	39.2	39.2
Reinforcement parameter			
Ultimate tensile strength, T_{ult} (kN/m)	$1/\lambda^2$	0.70	157.5
Stiffness, J_{50} (kN/m)	$1/\lambda^2$	5.47	1231
Interface parameter			
Soil-geosynthetic friction angle, δ'	1	27.4	27.4

[*]Target scaling ratio $\lambda = 15$.

2.3 *Test models and digital image analyses*

The soil layer was constructed with a target relative density $D_r = 70\%$ by using the volume control method. In the GRS foundation test, a layer of planar geotextile was placed on a soil layer, and the process was repeated until the foundation reached $H = 20$ cm. Three layers of planar geotextile were placed in the foundation with a vertical spacing of $S_v = 6.67$ cm. In the GEC foundation tests, low-friction stainless steel tubes with lubricant were penetrated into a full-height soil layer (i.e., $H = 20$ cm) at the desired locations. The location of the outermost GEC installed in the footwall was determined by considering the influential zone of the free-field fault rupture. Each steel tube had a thin-walled tip to minimize its disturbance to the soil layer. The sand inside the steel tubes was extracted using a customized vacuum machine. The geotextile encasement was fabricated in advance and placed into the steel tubes, and the soil material was filled into the encasement and compacted to the target relative density. After the installation was completed, the steel tubes were carefully removed from the soil layer. A 1.5-cm thick soil layer was then constructed on the top of the GEC foundations to

provide overburden pressure. Figure 2 displays an illustration of the GEC foundation test. The diameter of the GECs was $d_c = 3$ cm, corresponding to a diameter of 0.45 m in prototype, and the length-to-diameter ratio of the GECs was $l_c/d_c = 0.67$. Fault displacement was generated after the test models were constructed, and the maximum fault displacement was set to $S = 6$ cm due to the limited displacement capacity of the sandbox. The ratio of fault displacement to foundation height was $S/H = 30\%$.
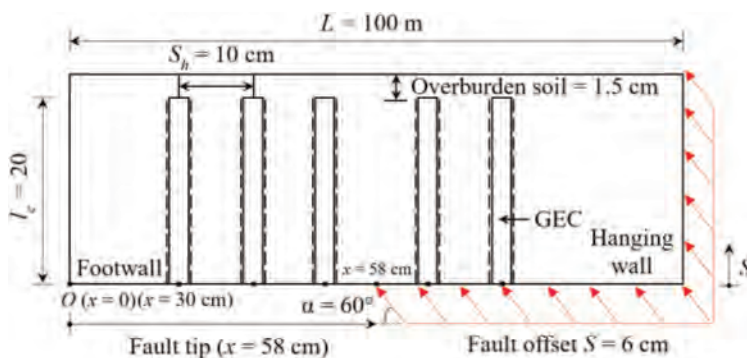
Figure 2. An illustration of the GEC foundation test (not in scale).

During the 1g model tests, charge-coupled device cameras, aimed at the front and top of the sandbox, were used for continuously monitoring the deformation of the test models. The recorded photographic data were analyzed using various digital image analysis (DIA) techniques to obtain the surface displacement profile, maximum angular distortion, and shear rupture propagation for the unreinforced, GRS, and GEC foundations at various fault offset magnitudes. Because the ground surface deformation induced by fault movement critically affects superstructure damage, the maximum angular distortion at the ground surface (β_{max}) was used as a key indicator in this study to evaluate the performance of the unreinforced, GRS, and GEC foundations. Details of the DIA techniques used in this study are provided in the paper of Yang *et al.* (2020).

3 RESULTS AND DISCUSSIONS

3.1 *Unreinforced foundation*

Figure 3a presents a series of test images of the unreinforced foundation subjected to reverse fault movement at fault offsets $S = 1.5$, 3, 4.5, and 6 cm. The test results indicate that the ground surface deformation became pronounced as the reverse fault displacement increased (Figure 3b). The β_{max} at the ground surface were 0.25, 0.76, 0.84, and 0.84 at $S = 1.5$, 3, 4.5, and 6 cm, respectively (Figure 3c). As expected, the β_{max} at the ground surface increased as the fault displacement increased and approached the slope of the peak friction angle of the sand ($\approx \tan \phi = 0.81$) at large fault offsets. The fault influence length was $L_I = 27.7$ cm at $S = 6$ cm.

Figure 3d presents the shear strain contours of the unreinforced foundation subjected to reverse fault movement. The shear rupture propagated upward from the fault tip to the ground surface, and decreased in dip as it approached the ground surface. At $S = 3$ cm ($S/H = 15\%$), the shear rupture broke through the foundation soil, and a surface fault rupture occurred at the ground surface. At this moment, the β_{max} at the ground surface considerably increased from 0.25 to 0.76 (Figure 6a), which indicated a high surface fault hazard risk.
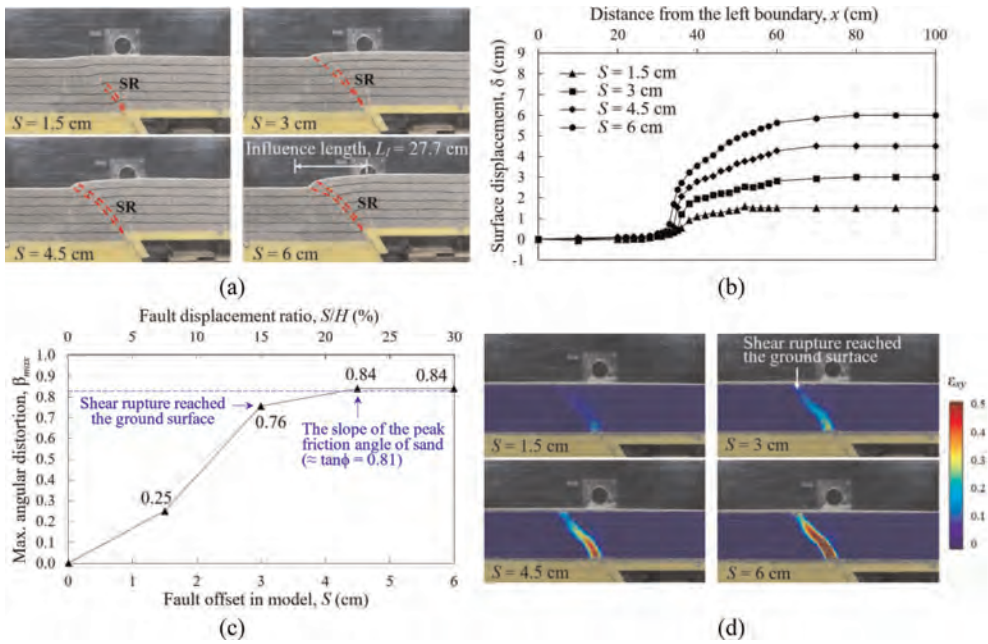
Figure 3. Results of the unreinforced foundation test (Test U) at various fault offsets: (a) test images; (b) surface displacement profiles; (c) maximum angular distortion; (d) shear strain contours.

3.2 GRS foundation

Figure 4a presents a series of test images of the GRS foundation subjected to reverse fault movement at fault offsets S = 1.5, 3, 4.5, and 6 cm. When reverse fault displacement occurred, the ground surface deformed in a similar manner to that of the unreinforced foundation (Figures 3b, 4b). The fault influence length was L_I = 22.1 cm at S = 6 cm, which is similar to the fault influence length for the unreinforced foundation (i.e., L_I = 27.7 cm). The β_{max} values were 0.18, 0.52, 0.74, and 0.84 at S = 1.5, 3, 4.5, and 6 cm, respectively (Figure 4c). The percentage reduction for β_{max} at S = 1.5, 3, 4.5, and 6 cm were R_d = 30.2%, 31.5%, 11.7%, and 0%, respectively, compared with the unreinforced foundation.

The test results revealed that the GRS foundation was effective in reducing β_{max} at relatively small fault offsets S = 1.5 and 3 cm (i.e., a fault displacement ratio $S/H < 15\%$). However, the effectiveness in reducing β_{max} decreased considerably after the shear rupture reached the ground surface (i.e., at S = 3 cm, as shown in Figure 4d). Similar shear strain contours were obtained for the unreinforced and GRS foundations (Figures 3d, 4d) because the mobilization of the reinforcement tensile strain was not developed when the hanging wall was moving upward (i.e., the GRS foundation was compressed).

3.3 GEC foundation

Figure 5a presents a series of test images of the GEC foundation subjected to reverse fault movement at various fault offsets. Stepped surface displacement profiles were observed as the reverse fault displacement increased (Figure 5b). The values of β_{max} were 0.17, 0.34, 0.59, and 0.64 at S = 1.5, 3, 4.5, and 6 cm, respectively (Figure 5c). Compared with the unreinforced foundation, the β_{max} at the ground surface significantly decreased. The percentage reductions for β_{max} at S = 1.5, 3, 4.5, and 6 cm were R_d = 33.3%, 55.6%, 30%, and 23.3%, respectively.

Figure 5d shows the shear strain contour for the GEC foundation subjected to reverse fault movement. Two reinforcing mechanisms, the shear rupture diffusion and diversion
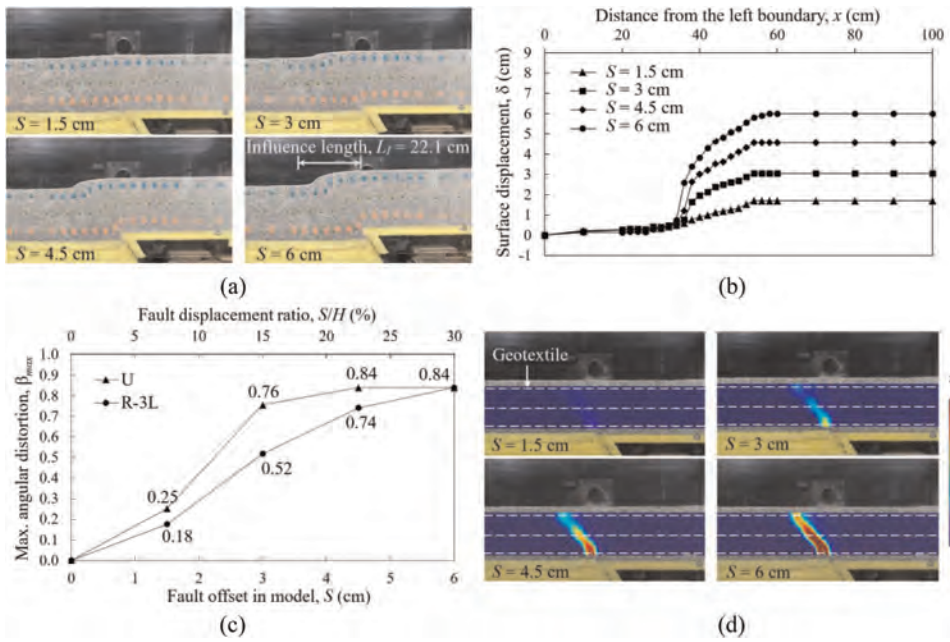
Figure 4. Results of the GRS foundation test (Test R-3L) at various fault offsets: (a) test images; (b) surface displacement profiles; (c) maximum angular distortion; (d) shear strain contours.
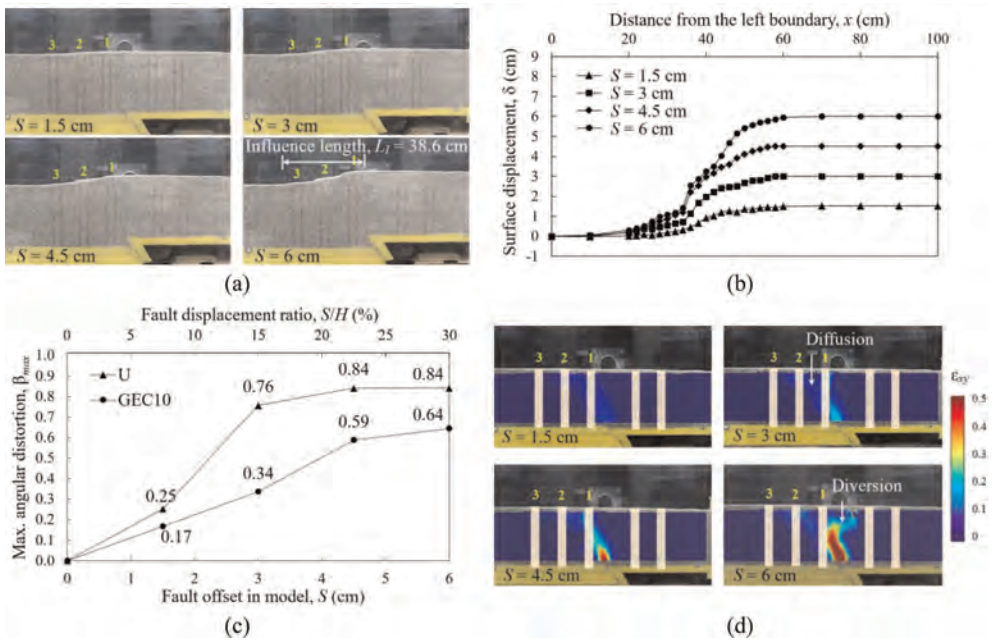
Figure 5. Results of the GEC foundation test (Test GEC10) at various fault offsets: (a) test images; (b) surface displacement profiles; (c) maximum angular distortion; (d) shear strain contours.

effects, were identified. When reverse fault displacement occurred, the fault-induced shear rupture propagated toward the first row of GECs placed in the footwall (indicated by 1 in Figure 5d). The fault-induced shear rupture diffused to the second and third rows of GECs (indicated by 2 and 3 in Figure 5d) during its propagation. The fault influence length was L_I = 38.6 cm at S = 6 cm, which is greater than the fault influence length for the unreinforced foundation (L_I = 27.7 cm). This result indicates that the mobilized tensile strain developed in the geotextile encasement, and the friction developed in the soil–geosynthetic interface effectively spread out the fault-induced shear rupture to a wider influential zone and further decreased the β_{max} at the ground surface. As the fault offset reached S = 6 cm (S/H = 30%), the fault-induced shear rupture was diverted toward the hanging wall, resulting in a considerable decrease in β_{max}. This diversion of the shear rupture was attributed to the increase in the lateral earth pressure acting on the GECs, enhancing the shear strength and bending stiffness of the GECs placed in the footwall. The increases in the shear strength and bending resistance of the GECs eventually diverted the fault-induced shear rupture.

4 CONCLUSIONS

The key findings of this study are as follows:

- For the unreinforced foundation, the β_{max} at the ground surface increased as the fault displacement increased and approached the slope of the peak friction angle of the sand at large fault offsets. At S = 3 cm (S/H = 15%), the shear rupture broke through the foundation soil, and a surface fault rupture occurred at the ground surface. At this moment, the β_{max} at the ground surface increased considerably, which indicated a high surface fault hazard risk.
- The GRS foundation was effective in reducing β_{max} at relatively small fault offsets. However, the GRS foundation was ineffective in reducing β_{max} after the fault-induced shear rupture reached the ground surface, with the R_d value decreasing to 0% at S = 6 cm (S/H = 30%).
- For the GEC foundation, stepped surface displacement profiles were observed as the reverse fault displacement increased. The β_{max} at the ground surface significantly decreased, with the percentage reduction for β_{max} ranging from R_d = 23.3%–55.6%. An R_d value of 23.3% was achieved as the fault offset reached 30% of the foundation height, which mitigates the risk of the surface fault hazards associated with large reverse fault movement. Two reinforcing mechanisms, the shear rupture diffusion and diversion effects, were identified.

REFERENCES

Buckingham, E. 1914. On Physically Similar Systems; Illustrations of the use of Dimensional Equations. *Physical Review* 4(4): 345–376.

Chen, Y.-G., Chen, W.-S., Lee, J.-C., Lee, Y.-H. & Lee, C.-T. 2001. Surface Rupture of 1999 Chi-Chi Earthquake Yields Insights on Active Tectonics of Central Taiwan. *Bulletin of the Seismological Society of America* 91(5): 977–985.

Chiang, J., Yang, K.-H., Chan, Y.-H. & Yuan, C.-L. 2021. Finite Element Analysis and Design Method of Geosynthetic-reinforced Soil Foundation Subjected to Normal Fault Movement. *Computers and Geotechnics* 139: 104412.

Yang, K.-H., Chiang, J., Lai, C.-W., Han, J. & Lin, M.-L. 2020. Performance of Geosynthetic-reinforced Soil Foundation Across a Normal Fault. *Geotextiles and Geomembranes* 48(3): 357–373.

Revisiting the reinforced fill over a void problem considering geosynthetic reinforcement stiffness

F.M. Naftchali
GeoEngineering Centre at Queen's-RMC, Queen's University, Kingston, Canada

R.J. Bathurst
GeoEngineering Centre at Queen's-RMC, Royal Military College of Canada, Kingston, Canada

ABSTRACT: The reinforced void problem is reexamined with special focus on the load-strain-time-dependent behaviour of the geosynthetic reinforcement. In current analytical model approaches, a single-value (constant) estimate of reinforcement stiffness is used for the design of reinforced fills over voids. Hence, the choice of an equivalent (elastic) stiffness value requires careful consideration. A simple hyperbolic stiffness model proposed by the writers is shown to be a useful approximation to the constant-load isochronous creep-strain behaviour of these materials, at least at low load levels, which are applicable to operational (serviceability) conditions of geosynthetic-reinforced soil structures. The paper uses the UK method for the solution of the reinforced fill over a void problem to compute tensile load and strain for a prescribed surface deformation (or maximum reinforcement settlement). An empirical approximation is introduced that links the isochronous stiffness of the reinforcement to its ultimate strength when product-specific creep test results are not available.

1 INTRODUCTION

The problem of a thin reinforced fill spanning a void has been the subject of investigation for many decades including the early seminal work of Giroud *et al.* (1990). The general problem is presented in Figure 1. The void may develop as a result of subsurface pipe failure, collapse
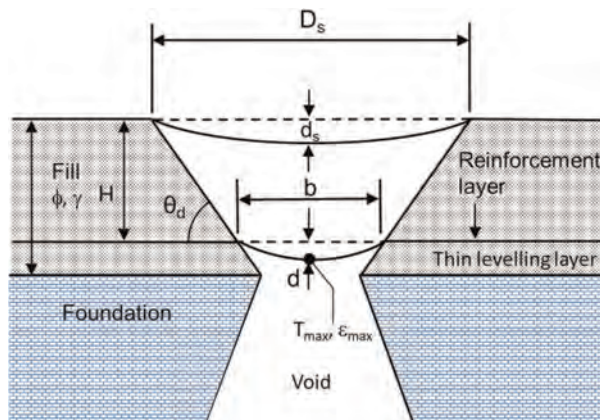
Figure 1. Reinforced thin fill over a long-void shape (width b). Draw angle assumed as $\theta_d = \phi$ using the method of BS 8006-1 (2010).

of mine workings, karstic terrain, openings below landfill liners and thawing in permafrost. The geosynthetic reinforcement prevents collapse of the fill layer into the void. In order to provide sufficient support the reinforcement must not strain excessively, exceed an allowable tensile load and it must have adequate tensile stiffness. Current design methods assume that the stiffness of the reinforcement is linear elastic. In fact, geosynthetic reinforcement products are rate-dependent to different degrees depending on the product type. This means that the stiffness of the reinforcement varies with load, strain, time and temperature. The impact of this so-called "creep" on the design of thin reinforced fills over a void has only been recently addressed by the authors in the journal literature (Naftchali & Bathurst 2023). This paper reviews these developments with special emphasis on the isochronous load-strain stiffness of these materials using a two-component hyperbolic model developed by Bathurst & Naftchali (2021). The analytical framework follows the method found in BS 8006-1 (2010) but without partial factors. To simplify the discussion, a long-void shape with plane strain geometry is assumed and temperature effects are ignored.

2   PRELIMINARIES

The design limit states for the long-void problem of width b are vertical deformation at the elevation of the reinforcement or at the surface (d or d_s), maximum strain in the reinforcement (ε_{max}), maximum tensile load (T_{max}) and mobilized geosynthetic stiffness (J_{mob}). The calculation of maximum strain for a long void is (BS 8006-1 2010):

$$\varepsilon_{max} = \frac{8 \times \left(\dfrac{d_s}{D_s}\right)^2 \left(b + \dfrac{2H}{\tan \theta_d}\right)^4}{3b^4} \tag{1}$$

Here, D_s is the width of the void at the fill surface, d_s is the fill surface deflection, H is the fill height, and γ and ϕ are the bulk unit weight and peak friction angle of the cohesionless granular fill, respectively. Assuming $d = d_s \times D_s/b$ leads to (BS 8006-1 2010):

$$\varepsilon_{max} = \frac{8}{3} \left(\frac{d}{b}\right)^2 \tag{2}$$

Assuming that there is no surcharge at the surface of the fill leads to the maximum tensile load computed as (BS 8006-1 2010):

$$T_{max} = 0.5(\gamma H)b\sqrt{1 + \frac{1}{6\varepsilon_{max}}} \tag{3}$$

The mobilized tensile stiffness now becomes:

$$J_{mob} = T_{max}/\varepsilon_{max} \tag{4}$$

3   ANALYSIS AND DESIGN STEPS

An example flow chart with problem parameters shown in the caption appears in Figure 2. The focus here is on the solid lines. The dashed lines refer to specific products that appear in Table 1 and the example design calculations demonstrated at the end of the paper.
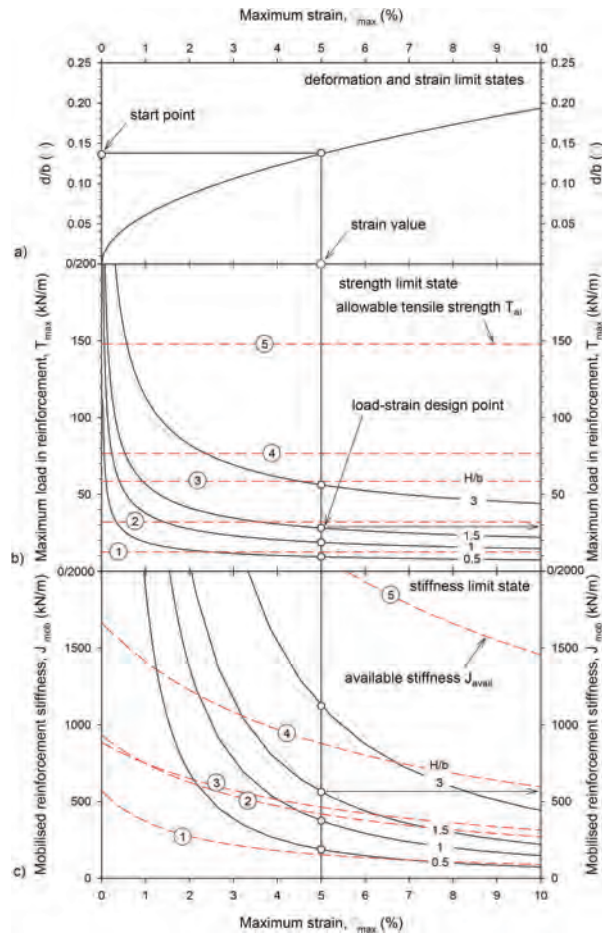
Figure 2.   Flow chart illustrating calculation steps for an unsurcharged reinforced fill layer over a long void using BS 8006-1 (2010) method for: a) deformation and reinforcement strain limit states; b) maximum reinforcement tensile strength limit state, and; c) reinforcement stiffness limit state. Problem parameters: b = 1 m, H = 0.5, 1, 1.5 and 3 m, γ = 18 kN/m^3 and ϕ = 35°.

Table 1.   Candidate reinforcement products for example design.

Number	Data set[*]	Product type	Ultimate strength T_{ult} (kN/m)[**]	Allowable (available) strength $T_{al} = T_{ult}/RF$ (kN/m)	Hyperbolic model parameters $J_o(t)$ (kN/m)	$1/\chi(t)$ (m/kN)
1	5	HDPE punched and drawnu- niaxial geogrid	62.5	12.5	570	0.095
2	42	PET woven and knitted geogrid	96.2	32.1	931	0.026
3	51	PET woven and knitted geogrid	175.6	58.5	886	0.021
4	55	PET woven and knitted geogrid	230	76.7	1666	0.011
5	69	PET woven geotextile	444	159	3792	0.004

Notes
[*]Data set numbers match entries in database collected by Bathurst & Naftchali (2021).
[**]Using ASTM D4595-17 and ASTM D6637/D6637M-15 methods of test.

1117

The design starts with a prescribed maximum vertical deflection (d) at the reinforcement elevation or a maximum permissible tensile strain in the reinforcement (Figure 2a). The strain ε computed using Equation 1 must not exceed a maximum allowable strain, (e.g., $\varepsilon_{max} \leq 5\%$). The solid lines in Figure 2b show solutions for T_{max} for different heights of fill (H) using Equation 3.

The maximum tensile load (T_{max}) must not exceed the maximum allowable tensile strength of the reinforcement (T_{al}) which is the ultimate strength of the reinforcement reduced by factors that account for strength loss due to creep, installation damage and chemical durability mechanisms. Next, Figure 2c shows the mobilized stiffness (J_{mob}) computed using Equation 4. The mobilized stiffness (solid lines in the plot) must not exceed the available isochronous stiffness (J_{avail}) at a strain level equal to ε_{max}.

4 STIFFNESS LIMIT STATE AND CALCULATION OF AVAILABLE REINFORCEMENT STIFFNESS

Figure 3a shows isochronous load-strain curves deduced from constant load (creep) tests carried out on product-specific test specimens using conventional creep test protocols. The curves can be approximated as:

$$T(\varepsilon, t) = J(\varepsilon, t) \times \varepsilon \tag{5}$$

where, $J(\varepsilon,t)$ is the non-linear isochronous secant stiffness. The matching isochronous creep stiffness curves are shown in Figure 3b. Each curve corresponds to a different isochronous time (t).

Bathurst & Naftchali (2021) developed a two-component hyperbolic model to approximate isochronous curves of the type shown in Figure 3. The general form of the equation is:

$$J(\varepsilon, t) = \frac{1}{\frac{1}{J_o(t)} + \frac{1}{\chi(t)}\varepsilon} \tag{6}$$

Parameter $J_o(t)$ is the initial stiffness at zero strain for isochronous time t, and $\chi(t)$ is a parameter that captures the curvature of the isochronous curves in Figure 3. These parameters are determined by non-linear regression fitting to the curves in Figure 3b. The values of $\chi(t)$ are the same for all curves for this particular material based on fitting but this is not the typical situation for all products and isochronous times in the database compiled by Bathurst & Naftchali (2021).

Figure 4 shows the range of $J_o(t)$ and $1/\chi(t)$ (and $\chi(t)$) parameters collected from fitting to creep test results for sheet reinforcement products and an isochronous time of t = 1000 h.

If product-specific data are not available, then the stiffness can be estimated from correlations developed by the authors that describe the isochronous stiffness as a linear function
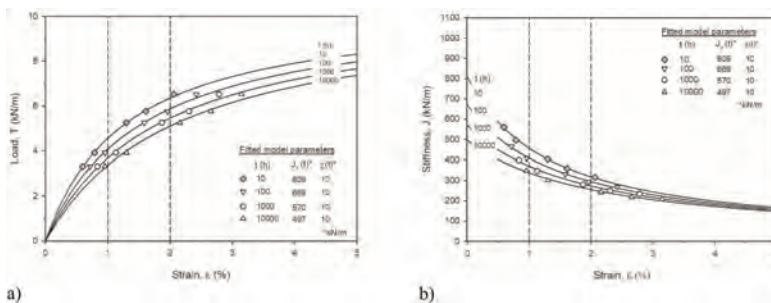
Figure 3. Isochronous: a) load-strain curves, and; b) stiffness curves from constant load (creep) testing of a HDPE punched and drawn uniaxial geogrid. Data from Bathurst & Naftchali (2021).
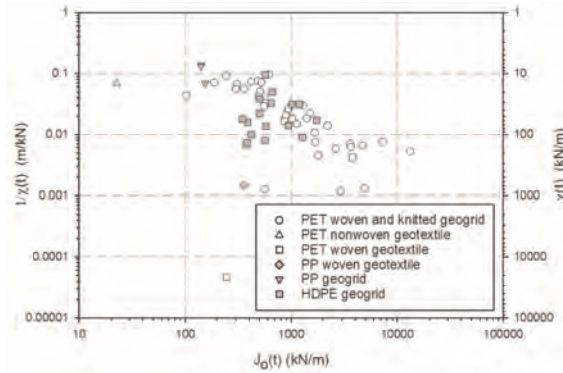
Figure 4. Range of $J_o(t)$ and $\chi(t)$ parameters for geosynthetic sheet reinforcement types at $t = 1000$ h. Data from Bathurst & Naftchali (2021). Data for $\chi(t) > 0$ only.
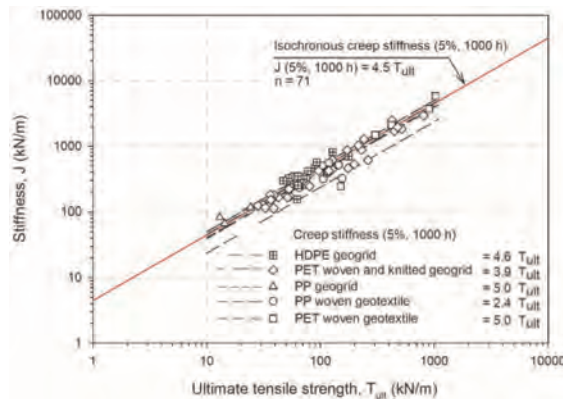
Figure 5. 1000-h isochronous creep stiffness at $\varepsilon = 5\%$ versus ultimate tensile strength for geosynthetic sheet reinforcement types. Data from Bathurst & Naftchali (2021).

of the ultimate strength of the reinforcement (T_{ult}). Examples of such data for a strain of 5% and an isochronous time of 1000 h are shown in Figure 5. Similar plots of the form:

$$J(\varepsilon, t) = R \times T_{ult} \qquad (7)$$

at different strain values are available in the paper by Bathurst & Naftchali (2021) where R is a dimensionless constant. The fit to all (pooled) data with R = 4.5 is also shown in Figure 5 and is useful for preliminary design purposes. However, it is clear that the accuracy of the linear approximation using group data and pooled data is less than the calculation of stiffness J using Equation 6 with product-specific parameters from creep testing.

5 EXAMPLE DESIGN

Candidate products for the design conditions identified in Figure 2 are shown in Table 1. The allowable strengths are computed as $T_{al} = RF \times T_{ult}$ where RF = 3 for PET products and RF = 5 for the HDPE materials. In this example, we assume that there will be a single layer of reinforcement and the maximum allowable tensile strain is 5% in order to keep the reinforcement below a strain level that could lead to creep-to-rupture over the project design

life. The red dashed lines in Figure 2b are T_{al} values for the candidate reinforcement materials. From this figure, it can be seen that all products are satisfactory if the fill height is H = 0.5 m. If the fill height is H = 3 m, then only the three strongest reinforcement materials are adequate. For the stiffness limit state using Figure 2c, and a fill height of H = 0.5 m, four out of five of the reinforcement materials have adequate stiffness. However, for the case with H = 3 m, only the strongest materials in Table 1 will suffice. A strategy to widen the number of design solutions is to use a double layer of reinforcement; doing this will lift the dashed lines in each figure by a factor of two.

An important observation from Figures 2b and 2c is that as the maximum allowable tensile strain becomes less, the demand side for each limit state increases sharply which in turn requires reinforcement products with increasing strength and stiffness. In fact, for very low strains at (say) 2% or less, there may not be practical solutions available unless multiple layers of high-strength and stiffness reinforcement sheet materials are used.

6 CONCLUSIONS

This paper highlights the importance of reinforcement stiffness in the analysis and design for the stiffness limit state for the reinforced fill over a void problem. Two different methods are described to compute the isochronous stiffness of the reinforcement. The first is based on a two-parameter isochronous hyperbolic model with parameters fitted to product-specific creep test results. The second approach uses isochronous stiffness correlations with readily available ultimate strength values for reinforcement products falling into different product categories or, simply using all available (pooled) data. The second approach is useful for preliminary analysis and design and when reinforcement product-specific creep test results are not available.

This paper uses the BS 8006-1 (2010) method as the general approach. However, the three limit states identified in the paper also apply to other similar analytical design methods. The hyperbolic model and correlations discussed above are equally applicable for the resistance side in the load and stiffness limit states discussed in the paper.

ACKNOWLEDGMENT

REFERENCES

ASTM D4595-17. Standard Test Method for Tensile Properties of Geotextiles by the Wide-Width Strip Method. *ASTM*, West Conshohocken, PA, USA.
ASTM D6637/D6637M-15. Standard Test Method for Determining Tensile Properties of Geogrids by the Single or Multi-Rib Tensile Method. *ASTM*, West Conshohocken, PA, USA.
Bathurst, R.J. & Naftchali, F.M. 2021. Geosynthetic Reinforcement Stiffness for Analytical and Numerical Modelling of Reinforced Soil Structures. *Geotextiles and Geomembranes*, 49(4): 921–940.
BS 8006-1. 2010. Code of Practice for Strengthened/reinforced Soils and Other Fills (+A1:2016). *British Standards Institution (BSI)*. UK.
Giroud, J.P., Bonaparte, R., Beech, J.F. & Gross, B.A. 1990. Design of Soil Layer-geosynthetic Systems Overlying Voids. *Geotextiles and Geomembranes*, 9(1): 11–50.
Naftchali, F.M. & Bathurst, R.J. 2023. Influence of Geosynthetic Stiffness on Analytical Aolutions for Reinforced Fill Over Void. *Geosynthetics International*, 30(1): 95–107.

Parametric analysis of a footing on a reinforced soil slope

R. Anjos
RISCO, Department of Civil Engineering, University of Aveiro, Aveiro, Portugal

L. Crescenzo & M. Calvello
Department of Civil Engineering, University of Salerno, Italy

M. Pinho-Lopes
RISCO, Department of Civil Engineering, University of Aveiro, Aveiro, Portugal

ABSTRACT: There are few studies on shallow foundations placed close to the crest of slopes. Many of those studies are based on small scale physical models and include recommendations for the reinforcement layout (usually normalised to the width of the footing, *B*). Such studies have limitations, particularly regarding the unrealistically low stress levels applied. To address such limitations, this paper presents a numerical analysis of a full-scale footing close to the crest of a sandy slope reinforced with geosynthetics, using the finite element method. The parametric analysis focuses on the effect of the depth of the upper reinforcement layer (u) and number of reinforcement layers (n). The response of numerical models reinforced with one layer of geosynthetic was compared to that of the unreinforced model analysed under the same conditions. The installation of a reinforcement at 0.3B allowed a significant increase in the bearing capacity of the shallow foundation. For the same prescribed displacement, the failure mechanism of the reinforced model involved a smaller mass of soil and exhibited more localised shear strains than the unreinforced model. In contrast to what has been reported in the literature for reduced scale models, the optimal depth for one layer of reinforcement was 0.3B (and not 0.5B). This value agrees with recent studies performed in centrifuge and full-scale models. For the optimal depth of reinforcement, adding a second reinforcement layer (equally spaced from the first), led to the maximum bearing capacity improvement: 70% more of the unreinforced model and 38% more of the model with one layer of reinforcement.

1 INTRODUCTION

Geosynthetics have been used to increase the bearing capacity of poor foundation soils and/ or to reduce excessive settlements. In the literature, particular attention has been given to the case of shallow foundations on reinforced soil with a horizontal surface. Few studies have been carried out for the case of shallow foundations on reinforced soil slopes (resting on a horizontal surface above the slope or on the slope itself), mainly considering drained conditions and small scale physical models (1g). Such studies have significant limitations, particularly regarding the unrealistically low stress levels applied. Alternatively, geotechnical centrifuges (Ng) can be used, as they allow inducing realistic stress levels. Such studies have shown that optimum reinforcement layouts obtained from small scale tests (1g) may differ from those obtained using realistic stress fields. For example, for an horizontal soil surface, recent studies [Guo *et al*. 2020; Kyparissis & Pinho-Lopes 2018] showed that the optimal depth of the reinforcement layer (u) is smaller than the value obtained from small scale tests (i.e., 0.3B instead of 0.5B).

Table 1 summarises the optimal reinforcement layout found in the literature and obtained from small scale physical models (1g) for the case of a footing on a reinforced soil slope. To analyse the validity of the optimal layout resulting from 1g models for real-scale structures, herein numerical simulations of a full-scale reinforced soil slope were conducted. The influence of the depth of the upper reinforcement layer and of the number of reinforcement layers was studied.

Table 1. Summary of optimal reinforcement layout from the literature using 1g models.

Reference	u/B^*	$l/B^\#$	$h/B^\&$	n^+	Reinforcement
Lee & Manjunath 2011	0.5	$\lambda^- + 8$	–	–	GGR[1], GTX[2]
Altalhe *et al.* 2015	0.5	6.0	0.3	2	GTX[2]
Baah-Frempong & Shukla 2020	0.5	–	0.5	3	GTX[2]

B = footing width. [*] Depth of 1st layer. [#] Reinforcement length. [&] Spacing between layers. [+] N° of layers. [−] Normalised distance from the crest of the slope to the closest edge of the footing [1] Geogrid. [2] Geotextile

2 PROBLEM ANALYSED

2.1 *Footing close to the crest of a slope*

The problem analysed is a foundation near the crest of a slope in plane strain conditions (Figure 1), set up to encompass an optimal layout identified from the literature. A footing of 1 m width (B) was considered, placed at $\lambda B = 0.2B$ from the crest of the slope. In a parametric analysis, the depth of the first reinforcement layer was set to 0.3B, 0.5B or 0.7B. In addition, a slope with two reinforcement layers was considered: depth of the first layer u =0.3B; spacing between the first and the second layer $h = 0.3B$, which results in a depth of the second reinforcement layer of 0.6B.

The objectives of this work are the following: assessing if the optimal depth of a single reinforcement layer is that obtained from small-scale (1g) tests; analysing the influence of a second layer of reinforcement.
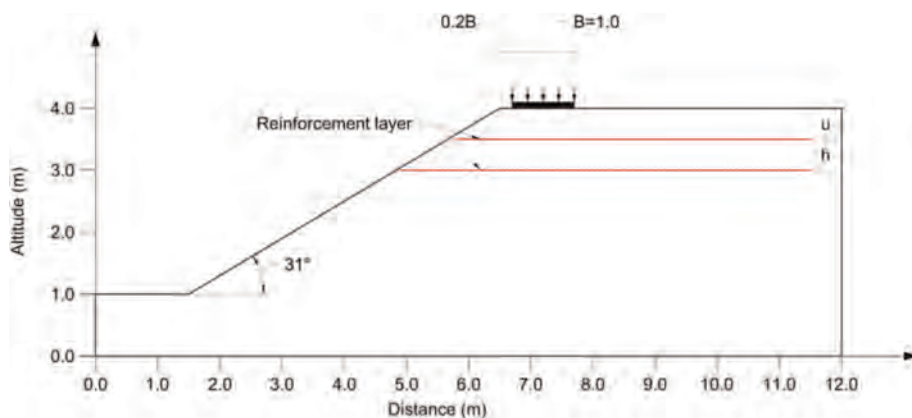
Figure 1. Geometry and dimensions of the problem analysed.

2.2 *Numerical models*

The finite element method was used and the numerical models were prepared using a commercial software (*Plaxis 2D v22*). Five numerical simulations were carried out in plane strain conditions (Table 2).

Table 2. Numerical simulations conducted.

Model	UR	R-03B	R-05B	R-07B	R-03B-06B
N° reinforcement layers	0	1	1	1	2
u/B (h/B)	–	0.3	0.5	0.7	0.3 (0.3)

Figure 2 shows the main characteristics of the numerical model: i) the lowest contour is considered fully fixed; ii) the left and the right vertical boundaries are assumed normally fixed; iii) the footing is modelled as a rigid foundation by applying prescribed incremental displacements by means of a series of plastic phases. The mesh is the same for all the simulations, consisting of a series of 15-node triangular elements, whose dimension is adequate for the assumed geometry and the prescribed boundary conditions. A quality ratio indicator, defined in the software considering the shape of an element reactively to the ideal element, was used to check the initial quality of the mesh, which can be considered good as the lowest value of this ratio is 0.49 (Figure 2). The mesh comprises 10,054 elements and 8441 nodes.
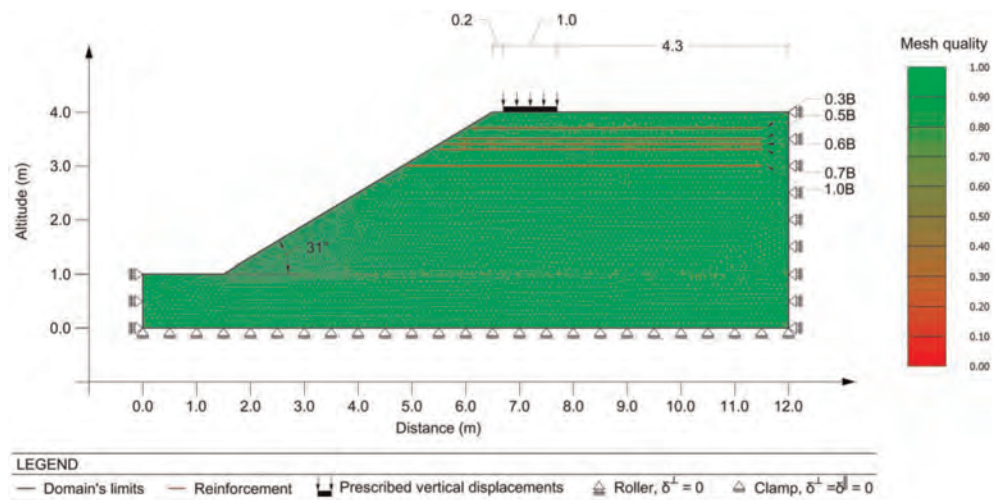
Figure 2. Model boundary conditions and mesh quality ratio.

The soil is considered homogenous, it is modelled using a Mohr-Coulomb constitutive law with properties that can be attributed to a dry sand, as presented in Table 3, wherein: γ_{dry} is the dry soil unit weight; e is the void ratio; $E_{elastic}$ is the elastic stiffness; ν the Poisson's ratio, c' is the effective cohesion (mathematical intercept); ϕ' is the peak angle of friction of the soil. The geosynthetic is modelled using a linear elastic constitutive law represented by its axial stiffness for 2% extension ($EA_{2\%}$). The soil-geosynthetic contact is modelled using

Table 3. Summary table of the material properties.

Material	Constitutive model	Property (unit)	Value
Sand	Mohr-Coulomb	γ_{dry} (kN/m^2)	19.32
		e (-)	0.80
		$E_{elastic}$ (kN/m^2)	7800
		υ (-)	0.3
		c' (kPa)	5.0
		ϕ' (°)	33
Reinforcement	Linear elastic	$EA_{2\%}$ (kN/m)	258
		R_{int} (–)	1.0

interface elements, above and below the geosynthetic, which allow for relative movement of the two materials (soil and geosynthetic). The interface strength is set by means of its ratio to the soil shear strength (R_{int}). Herein, for simplicity, and because no particular reinforcement was modelled, the interface strength corresponded to the soil shear strength. The reinforcement layers extend from near the slope face to 0.50 m from the right boundary of the model.

The initial stress field is applied by gravity loading. The calculation is carried out in phases, by applying successive displacements at the footing considering steps of 0.1% B until a displacement of 1.0% B and then considering steps of 1.0% B up to a cumulative prescribed displacement of 16% B. This led to 25 different plastic calculations phases per simulation.

3 RESULTS AND DISCUSSION

3.1 Summary

The prescribed settlements at the footing are ranging, as mentioned above, from zero to 16% B. The numerical model outputs include the force mobilised at the footing for a given prescribed displacement (Figure 3). In the first four simulations, the maximum prescribed displacement allows to reach a final almost-constant value of this reaction force, which is an indication of a bearing capacity global failure. For the interpretation if the results, despite
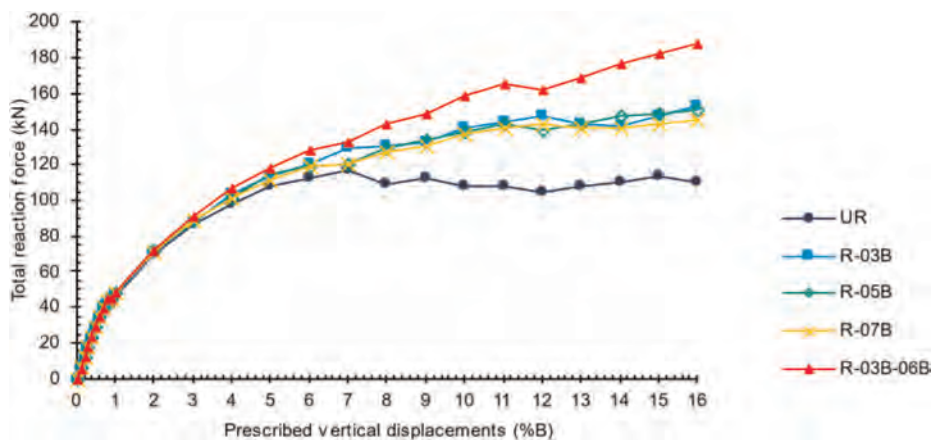
Figure 3. Prescribed displacement vs. total reaction force (Fy) in the five simulations: [UR], [R-03B], [R-05B]; [R-07B] and [R-03B-06B].

the fact that for simulation [R- 03B-06B] the reaction force is still clearly increasing, the bearing capacity of the footing was assumed always equal to the maximum force mobilised and a bearing capacity ratio, BCR (Equation 1), was used to quantify the increase in bearing capacity with the different reinforcement layouts (Binquet & Lee 1975).

$$BCR = \frac{q_{(R)}}{q_{(UR)}} \tag{1}$$

where: $q_{u(R)}$ and $q_{u(UR)}$ are the bearing capacity of the reinforced and unreinforced soil models, respectively.

The numerical models exhibited two different failure mechanisms: FM1, total slope failure mechanism (relatively shallow); FM2, failure surface above the reinforcement layer. Such mechanisms are illustrated in Figure 4, by showing the deviatoric strains of the simulations for a prescribed displacement of 16% B. Table 4 summarises the main results obtained from the numerical models: failure load (maximum force mobilised at the footing); bearing capacity ratio (BCR), and failure mechanism (FM1 or FM2).
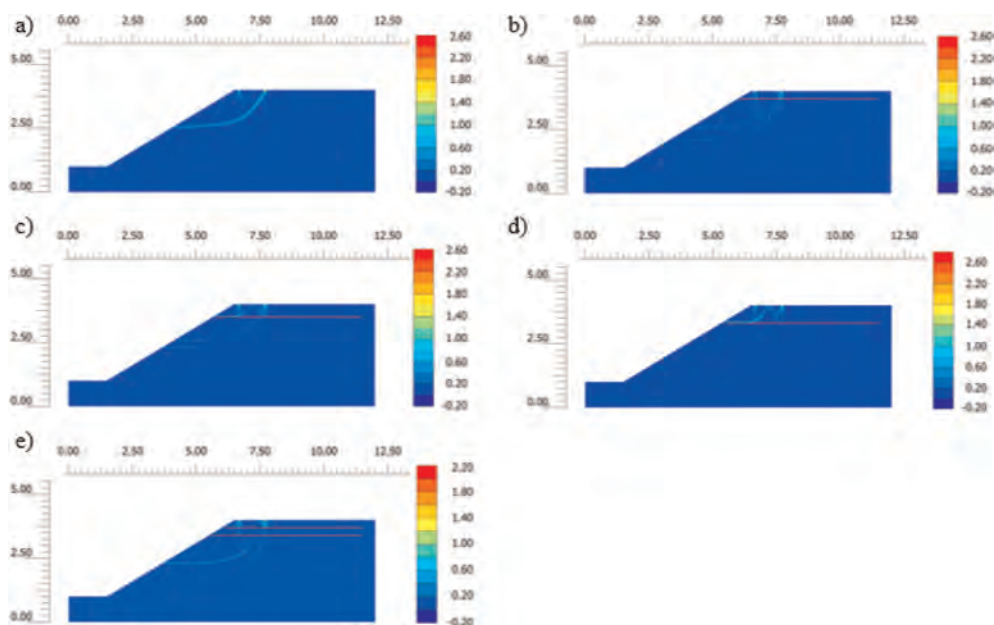
Figure 4. Deviatoric strain for a prescribed displacement of 16% B: a) [UR]; b) [R-03B]; c) [R-05B]; d) [R- 07B]; e) [R-03B-06B].

Table 4. Summary of the main results obtained from the numerical simulations.

Model	UR	R-03B	R-05B	R-07B	R-03B-06B
Failure load (kN/m)	110.1	152.7	150.9	144.7	187.5
BCR (-)	1.00	1.39	1.37	1.31	1.70
Failure mechanism	FM1	FM1	FM1 / FM2	FM2	FM1

The unreinforced model reached the bearing capacity for a prescribed displacement of 8.0% B, which corresponds to a reaction force at the footing of around 110 kN. Considering that the foundation is 1.0 m wide, the bearing capacity reached by the numerical model for the unreinforced condition is equal to 110 kPa.

Figure 5 illustrates the total displacements of the soil slope for different values of the prescribed displacement. Initially, the displacements are mostly in the vicinity of the footing and, as the prescribed displacement increases, a larger mass of soil is affected. For a prescribed displacement of 16% B, a relatively shallow global failure mechanism is formed (FM1). The plastic points (Figure 5) for 8% B and 16% B confirm the failure mechanism already identified.
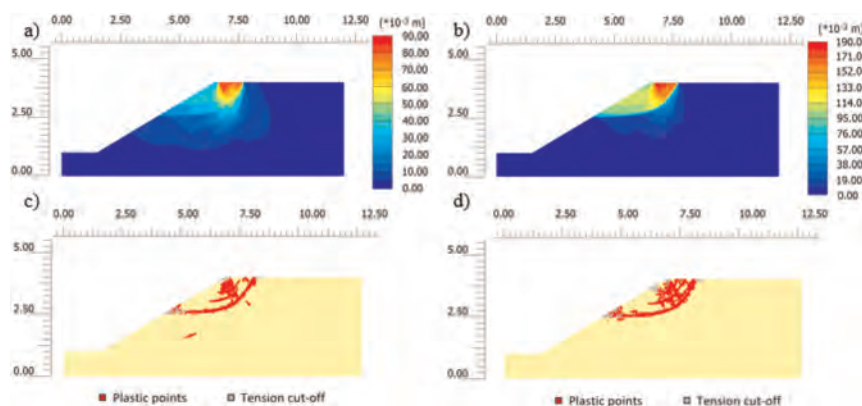
Figure 5. [UR] Total displacement |u|: a) |u| = 8.0%B; d) |u| = 16%B [Note: each subfigure has a different scale for the total displacements]; Plastic points. c) 0.8%B d) 16%B.

3.1.1 Influence of the depth of the reinforcement

One layer of reinforcement resulted in an increased bearing capacity (Table 4): the highest BCR (1.39) was obtained for $u/B = 0.3$ [R-03B]; the lowest BCR (1.31) refers to $u/B = 0.7$ [R-07B]. If the reinforcement layer is placed at a depth of 0.3B or 0.5B there is an increase in the bearing capacity associated with a failure mechanism FM1. For a reinforcement at 0.7B, a different failure mechanism (FM2) is observed, above the reinforcement layer. This means that the reinforcement is too deep to be mobilised, as reported by Chen & Abu-Farsakh (2015).

Nevertheless, for large settlements, [R-03B] exhibited a slightly stiffer behaviour than [R-05B], for this reason a deeper failure surface is observed for [R-03B]. The deviatoric strains for [R-05B] (Figure 4) indicate that several failure surfaces are forming (FM1 / FM2). Relative to the unreinforced model [UR], when a layer of reinforcement is placed at $u = 0.3B$ and $u = 0.5B$, the failure surfaces FM1 have similar dimensions. Thus, contrary to what was observed in small scale models [Altalhe et al. 2015; Baah-Frempong & Shukla 2020; Lee & Manjunath 2011] and for the conditions analysed herein, the optimum depth of the first reinforcement layer is 0.3B.

3.1.2 Influence of the number of reinforcement layers

The installation of a second layer of reinforcement [R-03B-06B] with spacing between layers equal to the depth of the first layer ($h = u = 0.3B$) increased the bearing capacity of the foundation, relatively to the unreinforced model (BCR = 1.70) and when compared to the model reinforced with only one layer [R-03B]. The second reinforcement layer is installed at a depth greater than 0.7B, which has previously been shown to be inefficient. However, as

this is a doubly reinforced model, the deeper layer allows the *deep footing effect* to be optimised (Huang *et al*. 1994). The failure mechanism formed for [R-03B-06B] is qualitatively similar to that of [R-03B], but with a larger volume of soil mobilised, thus presenting higher resistance.

4 CONCLUSIONS

In this paper, the bearing capacity of a strip footing on a reinforced soil slope was analysed. The response of numerical simulations wherein the slope is reinforced with one or two layers of geosynthetic were compared to the numerical simulation of an unreinforced model analysed under the same conditions. The installation of a reinforcement at 0.3B allowed a significant increase in the bearing capacity of a shallow foundation. For the same prescribed displacement, the failure mechanism of the reinforced model involved a smaller mass of soil and exhibited more localised shear strains than the unreinforced model. In contrast to what has been reported in the literature for reduced scale models, the optimal depth for one layer of reinforcement was 0.3B (and not 0.5B). This value agrees with recent studies performed in centrifuge and full-scale models. For the optimal depth of reinforcement, adding a second reinforcement layer (equally spaced form the first), led to the maximum bearing capacity improvement: 70% more of the unreinforced model and 38% more of the model with one layer of reinforcement.

REFERENCES

Altalhe, E. B., Taha, M. R., & Abdrabbo, F. M. (2015). Behavior of Strip Footing on Reinforced Sand Slope. *Journal of Civil Engineering and Management*, *21*(3), 376–383. https://doi.org/10.3846/13923730.2014.890646

Baah-Frempong, E., & Kumar Shukla, S. (2020). Behaviour of a Strip Footing Embedded in a Sand Slope Reinforced with Multilayer Geotextile. *Indian Geotechnical Journal*, *50*(4), 560–576. https://doi.org/10.1007/s40098-019-00393-3

Bentley. (2021). *PLAXIS 2D-Reference Manual*.

Binquet, J., & Lee, K. (1975). Bearing Capacity Analysis of Reinforced Earth Slabs. *ASCE J Soil Mech Found Div*, *101*(GT12), 1257–1276. https://doi.org/https://doi.org/10.1061/AJGEB6.0000220

Chen, Q., & Abu-Farsakh, M. (2015). Ultimate Bearing Capacity Analysis of Strip Footings on Reinforced Soil Foundation. *Soils and Foundations*, *55*(1), 74–85. https://doi.org/10.1016/j.sandf.2014.12.006

Guo, X., Zhang, H., & Liu, L. (2020). Planar Geosynthetic-reinforced Soil Foundations: A Review. *SN Applied Sciences*, *2*(12). https://doi.org/10.1007/S42452-020-03930-5

Huang, C. C., Tatsuoka, F., & Sato, Y. (1994). Failure Mechanisms of Reinforced Sand Slopes Loaded with a Footing. *Soils and Foundations*, *34*(2), 27–40. https://doi.org/10.3208/SANDF1972.34.2_27

Kyparissis, A., & Pinho-Lopes, M. (2018). Bearing Capacity of Reinforced Soil Under A Strip Footing: Centrifuge Tests. *11th International Conference on Geosynthetics 2018, ICG 2018*, *3*, 1918–1926.

Lee, K. M., & Manjunath, V. R. (2011). Experimental and Numerical Studies of Geosynthetic-Reinforced Sand Slopes Loaded with A Footing. *Canadian Geotechnical Journal*, *37*(4), 828–842. https://doi.org/10.1139/t00-016

Pinho-Lopes, M., & Lurdes Lopes, M. (2014). Tensile Properties of Geosynthetics After Installation Damage. *Environmental Geotechnics*, *1*(3), 161–178. https://doi.org/10.1680/ENVGEO.13.00032

Satvati, S, Alimohammadi, H., Rowshanzamir, H, Hejazi, S. (2020). Bearing Capacity of Shallow Footings Reinforced with Braid and Geogrid Adjacent to Soil Slope. *International Journal of Geosynthetics and Ground Engineering*, 6(3), 41. https://doi.org/10.1007/s40891-020-00226-x

Seismic design with geosynthetics

Effectiveness of Geofoam cushion on seismic performance of retaining structures: Numerical study

A. Edinçliler & Y.S. Toksoy
Boğaziçi University, Istanbul, Turkey

E. Danyıldız
Movea Construction Company, Istanbul, Turkey

ABSTRACT: In the last years, EPS Geofoam, which has extremely low density and high compressibility properties, is used to construct earthquake resistant infrastructure in seismic regions. In earthquake prone areas, retaining walls should be designed to resist the excessive dynamic lateral earth pressures. In this study, the effects of EPS geofoam cushion with different densities on seismic performance of retaining wall under two different earthquake motions were determined. Numerical analyses were performed by a finite element analysis program, Plaxis software. Results of parametric analysis were used to evaluate the effectiveness of cushion compared to the model without cushion. Numerical simulations with selected earthquake motions and EPS Geofoam with the different densities are compared. The comparative study showed that the Geofoam cushion can improve the seismic behavior of the retaining wall and the effectiveness of EPS Geofoam is highly dependent on the density of the material and the characteristics of earthquake motions.

1 INTRODUCTION

Earthquakes significantly threaten geotechnical engineering structures such as quay and retaining walls. These structures are likely to suffer excessive deformation or damage from increased earth pressure during the earthquake. However, these structures are the key elements of ports and harbors, transportation system lifelines, and other infrastructural facilities. Therefore, it is necessary to implement a cost effective technique to retrofit such structures, hence enhancing their seismic performance. Inclusion of vertical compressible layers called as cushion can be a solution to increase the stability of the retaining structures in seismic regions. One function of the tire chips cushion is to reduce the load of the retaining structure during earthquake due to the compressibility and energy absorption capacity of the cushion material. Another function is to restrict the permanent displacement of the structure by exploiting the compressibility, the ductility and the energy absorbing capacity of tire chips (Hazarika *et al.* 2008).

Historically, the first use of vertical compressible layers placed against rigid soil retaining wall structures with the aim of reducing the lateral static earth pressures has been reported in the literature by Partos & Kazaniwsky 1987; Horvath 1997; Karpurapu & Bathurst 1992. Expanded polystyrene (EPS) which is also called as Geofoam and tire wastes (tire chips and tire shreds) as cushion materials were studied to attenuate earthquake-induced dynamic earth pressures against rigid walls.

Performed shaking table tests in the literature prove that earthquake induced lateral loads can successfully be diminished by up to 40% on the retaining wall models with compressible

inclusions compared to that of the models with no compressible inclusions (Bathurst *et al.* 2007; Hazarika *et al.* 2003; Zarnani *et al.* 2005; Zarnani & Bathurst 2007;2008).

There are a number of numerical studies in the literature using the finite element model (FEM) code to model rigid wall structures with compressible inclusions. In the studies of Edinçliler and Toksoy (2014, 2017), it is revealed that the existence of a tire waste cushion layer can successfully and efficiently increase the seismic performance of retaining walls. From experiences and knowledge from previous studies, it is known that the dimensions of the seismic cushion affect the dynamic performance of geotechnical structures. In the numerical study performed by Dabiri and Notash (2020), the effects of the geofoam layer behind the cantilever wall on static and dynamic earth pressures have been investigated while considering various parameters such as wall height, wall type (yielding and non-yielding), and geofoam characteristics. According to the tests, as the thickness of inclusion increased, the relative stiffness decreased. The reduction in stiffness resulted in an increase in compressibility of geofoam, which decreased lateral forces against the wall and increased lateral displacement of soil. The geofoam inclusion showed a significant impact on lateral forces under static and dynamic loadings.

The aim of this study is to assess how the EPS geofoam density and earthquake characteristics affect the seismic performance of retaining walls. Three different cushion densities and two different earthquake records were considered throughout the study. Performance criteria have been selected as total displacements, rotations, axial and shear stresses, bending moments, and transmitted accelerations. The results of numerical simulations are compared to an identical retaining wall without a cushion layer. The protective cushion layer provides flexibility, and thereby stability to the structures during earthquakes by absorbing the energy. More importantly, this study is a direct attempt to develop an environmentally friendly, sustainable and earthquake resistant cushion technique that has a reasonably good balance of cost and performance for improving the seismic performance of retaining structures.

2 NUMERICAL STUDY

The aim of this numerical study is to assess the effectiveness of using EPS geofoam behind cantilever type retaining walls for dynamic conditions. Three different geofoam density and two different real earthquake records have been used.

Numerical study has been performed using the PLAXIS 2D Connect Edition. It is known that the thickness (t)/Height (H) ratio of geofoam cushion plays an important role for the stability. Previous studies indicate that the selection of t/H=0.3 increases the dynamic performance of retaining walls (Edinçliler & Toksoy 2018). Thus, the selection of t/H=0.3 has been implemented in the numerical study, where H=5m and t=1.5m. The mesh element distribution was generated as "Fine" for the accuracy of results. The numerical model and the generated mesh are given in Figure 1.
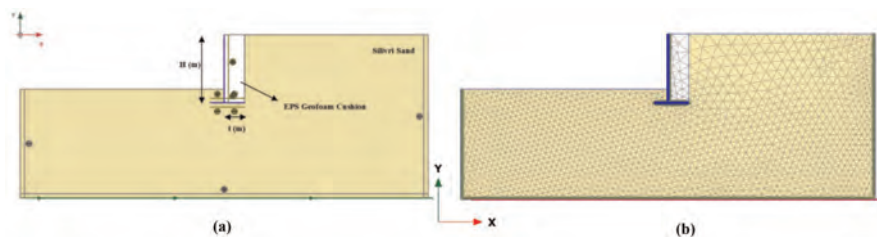
Figure 1.   a) FE model used in this study, b) Generated mesh.

As the cohesionless backfill material, "Silivri Sand" has been used behind the retaining wall. According to the USCS system, the sand material is classified as poorly graded sand (SP) with C_u = 2.29 and C_c = 1.1. The material has been modeled using the Hardening-Soil model with γ = 16.5kN/m^3, $\emptyset$ = 33° and E = 20000kN/m^2.

In order to determine the effect of the density of the EPS geofoam cushion on the dynamic behavior of the retaining wall model, three different cushion densities were selected with respect to the NCHRP (2004) guidelines. Namely, EPS 20, EPS 24 and EPS 32 were used during the study and modeled using the linear elastic soil model.

The retaining wall itself was modelled as a concrete plate element with model parameters of EA=7.5E^6 and EI=1E^6. Model boundaries were selected as compliant base boundary at the bottom of the mesh and free-field boundaries at the left and right end of the mesh due to the nature of the problem. Geofoam properties are given Table 1.

Table 1. Material properties of EPS geofoams.

	EPS 20	EPS 24	EPS 32
γ_{unsat}	0.20 kN/m^3	0.24 kN/m^3	0.32 kN/m^3
E	5000 kN/m^2	7000 kN/m^2	10000 kN/m^2
v'	0.01 kN/m^2	0.01 kN/m^2	0.01 kN/m^2

In order to determine the effect of earthquake characteristics on the seismic response of retaining wall models, two different real earthquake records were used. Records of 1940 El Centro Earthquake and 1995 Kobe Earthquake, which were obtained from KOERI database, are given in Figure 2. Peak ground accelerations and pre-dominant frequencies are 0.36g and 4Hz for the 1940 El Centro Earthquake and 0.68g and 2.1Hz for the Kobe Earthquake motions.
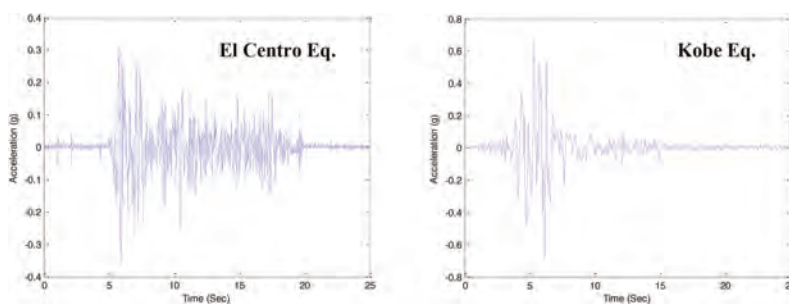
Figure 2. Acceleration time history of the 1940 El Centro and the 1995 Kobe Earthquake motions.

3 RESULTS

Numerical results are presented by means of total displacement of the backfill and the retaining wall model, rotations of the wall due to the combination of the static and dynamic forces, axial and shear forces, bending moments and peak transmitted accelerations. These results were evaluated in detail to obtain the influence of the cushion density in addition to the earthquake characteristics on the dynamic performance of cantilever type retaining walls. Numerical results are given in Tables 2 and 3 for El Centro and Kobe Earthquake motions, respectively.

Compressible vertical cushions behind rigid walls can successfully absorb the additional dynamic forces. Meanwhile, displacements may increase a bit due to the compressible nature of the geomaterial.

Table 2. Numerical results from the El Centro Earthquake motion.

	No Cushion	EPS 20	EPS 24	EPS 32
Total Backfill Displacements (cm)	3.4	5.2	5.2	5.0
Total Wall Displacements (cm)	2.3	3.4	3.4	3.3
Rotations (°)	0.17	0.27	0.27	0.26
Axial Force (kN/m)	74.4	74.9	74.9	74.8
Shear Force (kN/m)	103.9	70.9	71.4	72.0
Bending Moment (kNm/m)	58.8	52.6	53.3	54.5
Peak Transmitted Acceleration (g)	0.34	0.23	0.22	0.22

Table 3. Numerical results from Kobe Earthquake motion.

	No Cushion	EPS 20	EPS 24	EPS 32
Total Backfill Displacements (cm)	30.8	46.1	46.2	45.8
Total Wall Displacements (cm)	22.5	31.7	31.6	31.6
Rotations (°)	1.40	1.90	1.90	1.89
Axial Force (kN/m)	71.8	79.8	75.2	67.4
Shear Force (kN/m)	111.8	91.1	84.2	83.3
Bending Moment (kNm/m)	60.1	72.9	62.2	68.3
Peak Transmitted Acceleration (g)	1.58	0.47	0.44	0.27

The cantilever-type retaining wall model under El Centro Earthquake motions experiences peak values of total backfill and wall displacements due to the dynamic excitations of 3.4cm and 2.3cm in case of no cushion behind the wall. However, when EPS 20 and EPS 24 type cushions are placed behind the wall, total backfill and wall displacements slightly increase to 5.2cm and 3.4cm, respectively (Table 2). It is seen that the increase in EPS geofoam density leads to a minor reduction in displacement values. The retaining wall model with EPS 32 experiences 5.0cm of total backfill and 3.3cm of total wall displacements. Similar seismic behavior was observed when the retaining wall models were subjected to Kobe Earthquake excitations. Total backfill displacement of 30.8cm for no-cushion model increases to 46.1cm in EPS 20 and EPS 24 model and slightly reduces to 45.8cm in EPS 32 model as shown in Figure 3.
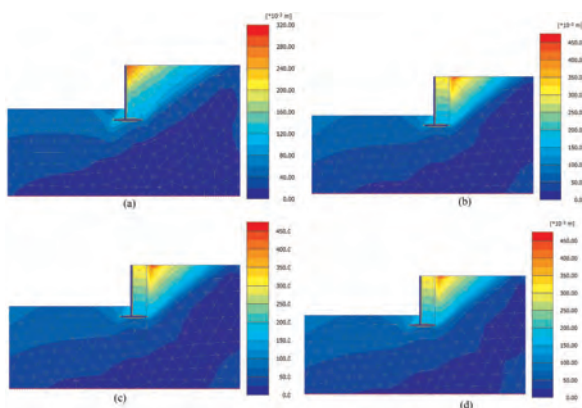
Figure 3. Total displacement distributions under Kobe Earthquake, a) No-cushion case, b) EPS 20 case, c) EPS 24 case and d) EPS 32 case.

Rotations of the wall from normal are directly related to the displacement of the wall and thus they follow the same pattern. Under El Centro Earthquake motions, the wall model with no-cushion rotates 0.17° where the wall model with EPS 20 and EPS 24 cushion rotates 3.4° and the model with EPS 32 cushion rotates 3.3°. Similarly, the 1.40° rotation value in no-cushion case under the Kobe Earthquake motions increases to 1.90° and 1.89° in the retaining wall models with EPS 20, EPS24 and EPS 32 cushions, respectively.

Peak axial forces acting to the retaining wall model under El Centro Earthquake show minor increase with the inclusion of the geofoam layers. The influence of the geofoam density is negligible under the given dynamic motion. Observed peak axial force for no-cushion case is 74.4kN/m where as it is 74.8kN/m for EPS 32 case. Under the Kobe Earthquake motions, peak axial forces in no-cushion case are obtained as 71.8kN/m. However, with the inclusion of the EPS 20, it increases to 79.8kN/m. With the increased cushion density, axial forces slightly decrease under current ground motion. Thus, the obtained axial forces in EPS24 and EPS32 cases are 75.2kN/m and 67.4kN/m, respectively.

Observed peak shear forces acting to the retaining wall models noticeably decrease with the inclusion of the compressible vertical cushions. Shear forces decrease from 103.9kN/m in no-cushion case to 70.9kN/m in EPS 20 case under El Centro Earthquake. Increased cushion density leads to a slight increase in shear forces under current dynamic motion as the obtained shear forces are 71.4kN/m and 72.0kN/m in EPS 24 and EPS 32, respectively. On the contrary of the El Centro Earthquake, increased cushion density leads to a reduction in shear forces under Kobe Earthquake. Obtained results are 111.8kN/m, 91.1kN/m, 84.2kN/m and 83.3kN/m for no-cushion, EPS 20, EPS 24 and EPS 32 cases, respectively.

Obtained results by means of bending moment acting to the wall model are clearly more influenced by the earthquake characteristics than the Geofoam inclusion itself. Under the El Centro Earthquake motions, the inclusion of cushion material decreases the observed bending moments and these values are directly proportional to the increased cushion density as seen in Table 2. The observed peak bending moment value is 58.8kNm/m in the no-cushion case, 52.6kNm/m in EPS 20 case and 54.5 kNm/m in EPS 32 case. Under the Kobe Earthquake excitations, 60.1kNm/m of bending moment value in the no-cushion case increases to 72.9kNm/m in EPS 20 case. However, it is obtained as 62.2kNm/m in EPS 24 case and 68.3kNm/m in EPS 32 case.

Peak transmitted accelerations along the retaining wall model can successfully be decreased by implementing compressible vertical cushions. Under the El Centro Earthquake motions, the peak acceleration value in the no-cushion case is 0.34g. Due to the cushion effect, peak acceleration values successfully decrease to 0.23g in EPS 20 case and to 0.22g in EPS 24 and EPS 32 cases (Table 2). Similarly, when the retaining wall model was subjected to the destructive motions of Kobe Earthquake, observed peak transmitted accelerations in the no-cushion case is 1.58g. Due to the material properties of the EPS geofoam cushion, transmitted accelerations significantly decrease to 0.47g in EPS 20 case, 0.44g in EPS 24 case and to 0.27g in EPS 32 case.

In addition, deviatoric strains, which reflect the deformations which cause a shape change without a volume change, increase from 0.29 in no-cushion case to 0.88 in EPS 20 case, 0.87 in EPS 24 case and 0.83 in EPS 32 case.

4 CONCLUSIONS

Performed numerical analyses with the aim of determining the effectiveness of EPS geofoam cushion reveal that the inclusion of a geofoam layer has a great impact on many aspects of the dynamic performance of the retaining wall.

The inclusion of such ultra-light cushion layers behind rigid walls slightly increases displacements and rotations, absorbs seismic forces and transmits less acceleration to the retaining structure concerned. Peak transmitted accelerations are magnificently reduced by up to 35% and 83% under El Centro and Kobe Earthquakes, respectively. In addition, shear

forces and bending moments acting on the retaining wall model are successfully diminished by up to 32% and 21%, respectively.

EPS geofoam density also has a reasonable impact on the numerical results. Additional total displacements and rotations tend to decrease with the increased geofoam density. Also, peak transmitted accelerations attenuate directly proportional to the cushion density. Axial and shear forces and bending moments are not found to be influenced by the geofoam density directly. The influence of earthquake characteristics on the seismic performance of the retaining wall model is clear. It is seen that the developed model is sensitive to the relatively high peak accelerations and relatively low frequency content of the record that lead to increased displacements therefore higher efficiency of the geofoam cushion layer.

This study is a direct attempt to develop an environmentally friendly, sustainable and earthquake resistant cushion technique that has a reasonably good balance of cost and performance for improving the seismic performance of retaining structures. Obtained numerical results have the potential to encourage researchers and engineers for further applications. It should be noted that presented results and outcomes of this study are only valid for the current model parameters and variables. Authors suggest further studies on this subject.

REFERENCES

Bathurst, R.J., Zarnani, S. & Gaskin, A. (2007). Shaking Table Testing of Geofoam Seismic Buffers. *Soil Dynamics and Earthquake Engineering*, 27:4, 324–332.

Dabiri, R., and N. Hasanpouri Notash, 2020, "Evaluation of Geofoam Effects on Seismic Response in Cantilever Retaining Wall", *Geotechnical and Geological Engineering*, Vol. 38, No. 2, pp. 2097–2116.

Edinçliler, A. & Toksoy, Y.S. (2014). Investigation on Effects of Tire Crumb Cushion on Seismic Performance of Retaining Wall. *TC207 Soil Structure Interaction and Retaining Walls*, 16–18 June, St. Petersburg, Russia.

Edinçliler, A. & Toksoy, Y.S. (2017). Effects of Ground Motion Characteristics on the Seismic Performance of Retaining Walls with Tire Waste Cushion. *16th World Conference on Earthquake Engineering*, 16WCEE 2017 Santiago Chile.

Edinçliler, A. & Toksoy, Y.S. (2018). Effects of Dimensions of Tire Waste Cushion on Seismic Performance of Retaining Wall. *Eurasian Journal of Civil Engineering and Architecture*, 1:(2).

Hazarika, H., Kohama, E. & Sugano, T. (2008). Shaking Table Tests on Waterfront Structures Protected with Tire Chips Cushion, *Journal of Geotechnical and Environmental Engineering. ASCE*, 134–11.

Hazarika, H., Okuzono, S. & Matsuo, Y. (2003). Seismic Stability Enhancement of Rigid Nonyielding Structures. *In: Proceedings of the 13th (2003) International Offshore and Polar Engineering Conference*, Honolulu, HI, USA, 25–30 May 2003, 1244–1249.

Horvath, J.S. (1997). Compressible Inclusion Function of EPS Geofoam. *Geotextiles and Geomembranes*, 15: (1–3), 77–120.

Karpurapu, R. & Bathurst, R.J. (1992). Numerical Investigation of Controlled Yielding of Soil-retaining Wall Structures. *Geotextiles and Geomembranes*, 11, 115–31.

Partos, A.M. & Kazaniwsky, P.M. (1987). Geoboard Reduces Lateral Earth Pressures. *In: Proceedings of Geosynthetics'87, Industrial Fabrics Association International*. New Orleans, LA, USA, 628–39.

Zarnani, S. & Bathurst, R.J. (2008). Numerical Modelling of EPS Seismic Buffer Shaking Table Tests. *Geotextiles and Geomembranes*, 26, 371–383.

Zarnani, S. & Bathurst, R.J. (2007). Experimental Investigation of EPS Geofoam Seismic Buffers using Shaking Table Tests. *Geosynthetics International*, 14:3, 165–177.

Zarnani, S., Bathurst, R.J. & Gaskin, A. (2005). Experimental Investigation of Geofoam Seismic Buffers using a Shaking Table. *In: Proceedings of the North American Geosynthetics Society (NAGS)/GRI19 Conference*, Las Vegas, NV, USA.

Geosynthetic-reinforced soil wall failure encountered in reduced scale shaking table testing

E. Guler
Professor, Bogazici University, Istanbul, Turkey

O. Selek
Former Ph.D. Student, Bogazici University, Istanbul, Turkey

ABSTRACT: An extreme case of model geosynthetic-reinforced soil wall failure encountered during shaking table testing is described in this paper. A ¼ scale, 2 m high model wall with concrete block facing and geotextile reinforcement length of 85 cm was brought to collapse under dynamic loading in which the maximum shaking table acceleration reached 2g. Failure started with the upper facing blocks falling and continued with overturning of the wall face. The test was terminated before the wall fully collapsed. In this paper, the failure mechanism is investigated and the performance of the model is compared to that predicted by design recommendations. The stiffness of geotextile layers and the silt content of the fill are suggested as the reason for the good performance up to such large dynamic loads.

1 INTRODUCTION

To get an insight to the performance of geosynthetic-reinforced soil walls (GRS walls) under seismic loads, a series of reduced-scale shaking table tests were conducted using the shaking table facility at Kandilli Observatory and Earthquake Research Institute (KOERI) of Bogazici University, Istanbul, Turkey. All model GRS walls were constructed on rigid foundation using sand as fill material, a woven geotextile for reinforcement, and concrete facing blocks that have no shear connections but rely only on the interface friction with the geosynthetic. Eight different model setups were tested under El Centro earthquake loading applied at different amplitude scales. The effects of change in peak ground acceleration, reinforcement length, reinforcement spacing, model scale, and treatment of top two facing block layers were evaluated by Guler and Selek (2014). This study concluded that the geotextile reinforced GRS walls with concrete block facing with only frictional connection between facing blocks showed negligibly small permanent displacements. There are many shaking table tests cited in the literature as well investigating geosynthetic reinforced walls (Bathurst *et al.* 2002; El-Emam & Bathurst 2004; Guler & Enunlu 2009; Watanabe *et al.* 2003). However a case with a catastrophic failure is very rare. Therefore to check for the validity of the model and this observation a test has been conducted by applying an extreme acceleration of 2g to a model wall with relatively short reinforcement length. The acceleration of 2g caused failure of the GRS model wall tested. In this paper, this particular incident is reported and the failure mechanism is investigated.

2 LITERATURE REVIEW

Ling *et al.* (2005) performed shaking table tests on 2.8 m high, full-scale model GRS segmental walls with fine-grained sand backfill. The wall face had a 12% batter. For Wall 1,

reinforcement length, was 205 cm and reinforcement spacing was 60 cm. The reinforcement spacing was decreased to 40 cm in Wall 2. In wall 3, reinforcement spacing was 40 cm, and the reinforcement spacing was decreased to 168 cm, but the top reinforcement layer was extended to 252 cm and the vertical component of the Kobe earthquake accelerogram was added to the horizontal component that was applied to the first two walls. After the application of a scaled peak horizontal acceleration of 0.4g, only a hair crack was seen behind the reinforced zone at the surface. After testing with a scaled peak horizontal acceleration of 0.86g, maximum deformation measured was less than 100 mm; large cracks formed behind the reinforced zone at the top, but the cracks were shallow and no distinct failure surface was observed in the backfill during demolition.

Ling *et al.* (2012) performed similar tests using an SM-SC sand with 43.3% fines content. Wall 1 in this study was constructed using the same dimensions of Wall 3 of the previous study; reinforcement spacing was 40 cm, reinforcement length was 168 cm, the top reinforcement layer was extended to 252 cm. In walls 2 and 3, reinforcement spacing was increased to 80 cm and the top reinforcement layer was not extended. In Wall 3, the lips on the blocks were removed to eliminate interlocking between facing blocks. Both the horizontal and vertical components of the Kobe earthquake accelerogram was applied. After shaking with a scaled peak horizontal acceleration of 0.4g (and a vertical acceleration scaled using the same ratio), 3 shakings with a scaled peak horizontal acceleration of 0.8g were applied consecutively. Inclusion of silt, which is generally present in the granular backfill soil used at the site improved performance. There was no visible deformation after the application of 0.4g peak acceleration. After 0.8g peak acceleration, there was only local failure behind the facing blocks at the top. There was no damage to the geogrid reinforcement in any wall configuration.

Parametric studies generally involve models that are validated using shaking table test results. These models are then applied to predict performance under conditions other than those physically tested. In a numerical parametric study of a 6-m high GRS wall with a full-height rigid facing and six reinforcement layers, Bathurst and Hatami (1998) showed that increasing the reinforcement stiffness or the reinforcement length decreased the seismic displacements. Therefore at shaking table tests it is expected that lower deformations are obtained, because considering the height of the model, the stiffness of the reinforcement typically remains above what is common in practice.

3 TEST SETUP

Model scale for the investigated wall was 1/4. Wall height was 2 m and the total reinforcement length including the portion placed between the facing blocks, was 85 cm meaning that the reinforcement length to wall height ratio (L/H) is 0.4. Considering the scale factor, this means that the prototype wall height was 8 m and the prototype reinforcement length was 3.40 m. The geosynthetic reinforcement used was a woven polyester geotextile with tensile strength T_{ult} = 40 kN/m and ultimate strain at failure ε_{ult} = 11 per cent. 10 cm long x5 cm wide x 5 cm high concrete blocks were used to constitute the facing in the model, and the reinforcement was placed with two rows of block layers in between, i.e. the vertical reinforcement spacing, s_v, was 10 cm corresponding to a vertical spacing of 40 cm in the prototype. A general schematic of the model is given in Figure 1). The soil used as backfill was a well-graded sand with silt (SW-SM) with coefficient of uniformity, C_u=9.13 and coefficient of curvature, C_c=1.17. The percentage of fines (mainly silt-size particles) was 6%. The soil was used at its natural water content which was 4.6%.

The model wall was constructed in a steel container with 215 cm height, 278 cm depth, and 53 cm width, which was fixed to the shaking table. The back five centimeters was filled with granular rubber during construction to minimize the reflection of earthquake waves from the back of the steel container. The inner sides of the steel container were greased and
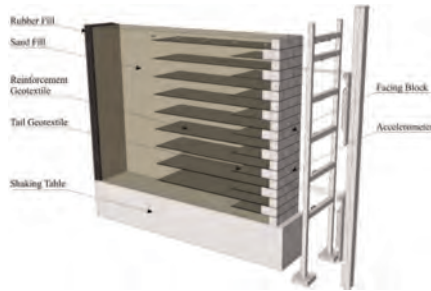
Figure 1.   Schematic of geosynthetic reinforced soil retaining wall model.

lined with floating insulation sheets to minimize the friction at the sides of the wall. Forward movement of the lowest layer of facing blocks was prevented by a steel bar fixed to the base in order to avoid external base sliding due to the low friction between the soil and the steel base because this mode of failure was not considered relevant. Before laying the reinforcement over each layer, the fill was compacted to reach the desired amount of compaction. The dry unit weight of the fill determined from the measurements during demolition was 17.7 kN/m^3. In practice the top two blocks are always tied to each other to prevent the failure of the uppermost block. In the remainder of the experiments reported by Guler and Selek (2014) the top two blocks were always tied to each other. However, for this model to make the model even more vulnerable, only the reinforcing geotextile was placed in between the blocks and no other measure was taken to fix the top two block layers.

The uniaxial shaking table ANCO R-148 at KOERI of Bogazici University was used for testing. Displacement of the shaking table was measured using a long stroke displacement transducer. Optical laser distance sensors were utilized to measure wall face displacements. Two layers of geotextile reinforcement (at 40 cm and 160 cm heights from the base of the model) were instrumented to measure the displacements on the reinforcement and calculate the strains in these reinforcement layers. Accelerometers were placed on the shaking table, on the wall face and in the top soil to measure accelerations at these locations. Further information on the test setup, shaking table used, instruments utilized for measurements can be found in Guler and Selek (2014).

The original North-South component of El Centro Earthquake record was scaled by dividing the time values by 2 for 1:4 scale tests, in accordance with the similitude rules proposed by Iai (1989), which are widely used for shaking table tests conducted in a 1-g gravitational field.

4   RESULTS

Measurements made were explained in detail by Guler and Selek (2014). For the model explained in this paper the measured accelerations increased from bottom to top on the wall face. Accelerations measured by the uppermost accelerometer on face were the highest. Very high amplifications were measured by the uppermost accelerometer on face, indicating high frequency vibrations of the top blocks that were not fixed to the more stable lower blocks.

The lower instrumented geotextile underwent higher strains at a distance of 10-20 cm from the block facing and the strain tended to increase with increasing maximum table acceleration, implying that a potential failure plane passes through this region. There is no such observation for the upper geotextile layer, indicating that the potential failure surface does not pass through the instrumented regions. Considering the actual failure location observed on the top surface of the model, the potential failure surface shown in Figure 2 was deduced, which coincides with the Rankine failure plane.

Figure 2.   Estimated failure plane based on reinforcement strains and top topography.

The shaking table system applied the earthquake record shown in Figure 3 on the model wall. As can be seen there were at least one peak in each direction which was approximately 2g. It can be further seen from the same graph, that the acceleration had several peaks as high as 1.25g. So as a summary it can be stated, that extraordinary accelerations acted on the wall which was constructed to be very weak in terms of reinforcement length. This resulted in failure of the GRS wall and the test was terminated.
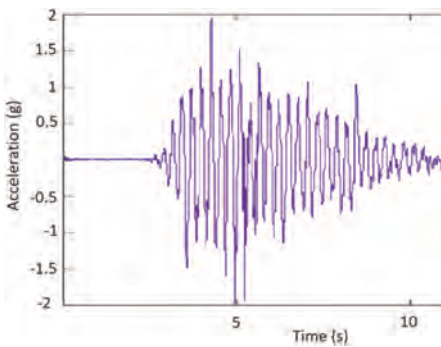
Figure 3.   Acceleration applied to the model wall.
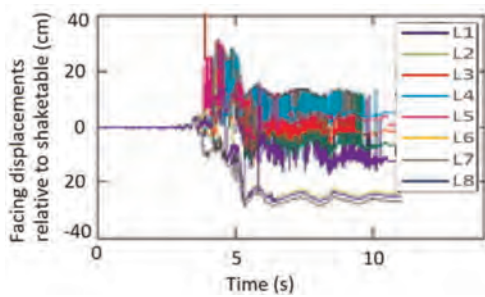
Figure 4.   Facing displacement relative to the shaking table at various elevations.

Figure 4 shows that the face displacements relative to the shaking table, measured at several elevations by the laser displacement sensors. The displacements suddenly reach very high values that are beyond the measuring range when the table acceleration is 1.25g, indicating that at that point facing blocks begin to fall and the GRS wall starts to fail.

Facing blocks from the top four layers fell down before the wall came to a stop. There was sliding between the facing block layers over the 15th layer of reinforcement as can be seen in Figure 5. There was no relative movement between the geotextile reinforcements and the facing blocks in the lower layers. Therefore, the face displacements were determined by measuring the geotextile length protruding from the reference steel box after removal of the facing blocks. The residual face displacements are illustrated on the photograph of the GRS wall face in Figure 5. The relative sliding over geotextile layer 15 is apparent in the photograph. The failure mode seems to be a combination of internal sliding for the upper layers, and external overturning which was actually initiated after the internal sliding started in the upper layers.

The view of the top of the GRS wall after failure is illustrated and dimensioned in Figure 6. The major failure location marked in the figure coincides with the intersection of Rankine plane with the top of GRS wall.

To be able to compare the observed behavior with the behavior to be predicted using state-of-the-art design recommendations, the pseudo-static limit equilibrium design method

Figure 5.   Displaced wall facing after application of extreme acceleration.
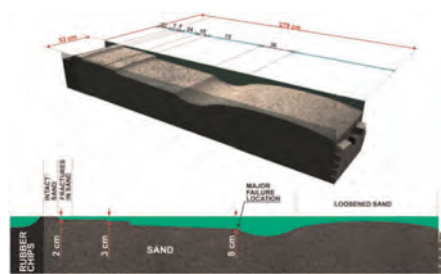
Figure 6.   Topography of model top surface after application of extreme acceleration.

described in FHWA recommendations (Berg *et al.* 2009; Elias *et al.* 2001) was used to calculate the factors of safety against external sliding and overturning failures for different peak ground accelerations. Internal tensile and pullout failures were also investigated for each reinforcement layer according to FHWA recommendations. The dynamic thrust exerted by the retained backfill and the horizontal inertia force on the reinforced mass are added as pseudo-static forces after the static limit equilibrium analysis for external stability is completed. These calculations indicate that an overturning should have occurred when the table acceleration is 0.4g. However, actual deformation leading to failure started only when the table acceleration reached 1.25g. As a result it was concluded that the design guidelines appear to be highly conservative in terms of external stability. Total loads in reinforcement layers were much lower than the allowable tensile load according to the analysis. So it can be said that the predicted and actual results are in agreement when internal stability is considered.

5   CONCLUSIONS

In the study by Guler and Selek (2014), the good performance of the tested configurations with higher L/H ratios encouraged the testing of models with L/H = 0.4 even though FHWA design guidelines recommend a minimum L/H ratio of 0.7 to be maintained. As a result, the extreme case of wall failure described in this paper could be witnessed.

The model GRS wall was tested consecutively under dynamic loading with the maximum table acceleration increasing each time. Maximum accelerations on the GRS wall during testing

increased from bottom to top, compliant with the literature. There were no residual deformations after each dynamic load application until the loading that resulted in failure. The GRS wall started to collapse when the shaking table acceleration reached 1.25g, which is much higher than the maximum acceleration predicted to be accommodated using design guidelines.

The actual failure started with internal sliding between the upper layers and continued with external overturning. Examination of the top of backfill indicated that the major failure location coincides with the Rankine plane. According to the design guidelines, failure by external overturning was to be expected much sooner, namely at 0.4g. Considering the expected and the encountered failure modes, the actual failure mechanism is not easy to predict. As indicated by Ling *et al.* (2005b), increasing the length of the top reinforcement probably would have resulted in a better performance; the local sliding failure at the top layers could be prevented.

The good performance of this model GRS wall with such short reinforcements up to 2g may partly be attributed to the high stiffness of the geotextile layers, which decreased the seismic displacements and partly to the small silt content that is shown to increase performance (Kilic *et al.* 2021). The apparent cohesion resulting from the silt content has more pronounced effects in the low height model walls, so its favorable effect in the prototype cannot be easily established. Although the typical backfill soils used in GRS wall construction are very similar to the backfill used in this study, incorporating the apparent cohesion into design is not recommended.

REFERENCES

Bathurst, R. J. & Hatami, K. (1998). "Seismic Response Analysis of a Geosynthetic Reinforced Soil Retaining Wall." *Geosynthet. Int.*, 5(1&2), 127–166.

Bathurst, R. J., Hatami, K. & Alfaro, M. C. (2002). "Geosynthetic-reinforced Soil Walls and Slopes–Seismic Aspects." *Geosynthet. and Their Applications*, S.K. Shukla, ed., Thomas Telford, London, 327–392.

Berg, R. R., Christopher, B. R. & Samtani, N. C. (2009). "Design of Mechanically Stabilized Earth Walls and Reinforced Soil Slopes – Volume I." *Record No. FHWA-NHI-10-024 FHWA GEC 011-Vol I.*

El-Emam, M. & Bathurst, R. J. (2004). "Experimental Design, Instrumentation and Interpretation of Reinforced Soil Wall Response Using a Shaking Table." *Int. J. Phys. Modell. Geotech.*, 4(4), 13–32.

Elias, V., Christopher, B. R. & Berg, R. R. (2001). "Mechanically Stabilized Earth Walls and Reinforced Soil Slopes, Design and Construction Guidelines." *Publication No. FHWA-NHI-00-043.*

Guler, E. & Enunlu, A. K. (2009). "Investigation of Dynamic Behavior of Geosynthetic Reinforced Soil Retaining Structures Under Earthquake Loads." *Bull Earthq. Eng.*, 7, 737–777.

Guler, E. & Selek, O. (2014). "Reduced-scale Shaking Table Tests on Geosynthetic-reinforced Soil Walls with Modular Facing". *J. Geotech. Geoenviron. Eng. ASCE*, 140(6), 1–11

Iai, S. (1989). "Similitude for Shaking Table Tests on Soil-structure-fluid Model in 1g Gravitational Field." *Rep., Port and Harbour Research Institute*, Vol. 27, No. 3, Japan Ministry of Transport, Tokyo.

Kilic, I. E., Cengiz, C., Edincliler, A. & Guler, E. (2021) "Seismic Behavior of Geosynthetic-reinforced Retaining Walls Backfilled with Cohesive Soil" *Geotextiles and Geomembranes*, 49(5), 1256–1269

Ling, H.I., Leshchinsky, D., Mohri, Y. & Wang, J.P. (2012). "Earthquake Response of Reinforced Segmental Retaining Walls Backfilled with Substantial Percentage of Fines." *J. Geotech. Geoenviron. Eng.*, 138(8), 934–944

Ling, H.I., Mohri, Y., Leshchinsky, D., Burke, C., Matsushima, K. & Liu, H. (2005). "Large-scale Shaking Table Tests on Modular-block Reinforced Soil Retaining Walls." *J. Geotech. Geoenviron. Eng.*, 131(4), 465–476

Watanabe, K., Munaf, Y., Koseki, J., Tateyama, M. & Kojima, K. (2003). "Behaviors of Several Types of Model Retaining Walls Subjected to Irregular Excitation." *Soils and Foundations*, 43(5), 13–27.

Finite difference parametric study of seismic behavior of a GRS bridge abutment

K. Fakharian, M. Kashkooli & S. Nasrolahzadeh
Department of Civil & Environmental Engineering, Amirkabir University of Technology, Tehran, Iran

ABSTRACT: The main objective of this study is to evaluate the influences of different engineering parameters on the seismic response of reinforced bridge abutments. The Founders/Meadows reinforced bridge abutment in Denver Colorado was considered as a case study. In former studies conducted on the same bridge, base isolator was not considered in the model between deck and the deck footing. However, the new finite difference numerical model is comprised of two abutments, one pier in mid-span, concrete deck, and base isolators connecting deck to deck footing. Parameters used in parametric study are related to base isolator, foundation soil, reinforced soil, and input ground motion. Horizontal displacement of facing as well as rotation of deck footing are selected as the main seismic excitation outputs. The overall results show that the response of the two-abutment model with the base isolator is significantly dependent on the base isolator damping, strength of foundation as well as reinforced soils, and frequency of input acceleration wave. The overall response of the GRS bridge abutment subjected to seismic excitations is evaluated and discussed.

1 INTRODUCTION

Reinforced earth walls have been widely used as geotechnical structures in different projects. Reinforced bridge abutments are similar to earth walls except that they carry a surcharge load near the top edge (from the bridge deck) in addition to the soil horizontal pressure behind the reinforced earth zone. Due to significance of bridges as infrastructures, they are expected to remain in service after earthquakes and the destructive effects have to be reduced. Seismic base isolators are used in bridges to notably improve the performance under the seismic excitations. Using base isolators leads to an economical and practical solution mitigating the magnitude of the seismic force by providing both lateral flexibility and energy dissipation through the insertion of the isolation device (Hall *et al.* 1995; Rao & Jangid 2001; Shen *et al.* 2004).

Several numerical and physical modeling studies have been conducted on the response of GRS bridge abutments for static and dynamic loading conditions (For instance: Askari *et al.* 2021; Hatami & Bathurst 2001, 2005, 2006; Fakharian & Kashkooli 2018; Zheng *et al.* 2018). Founders/Meadow segmental bridge abutment was extensively studied for its well-documented field instrumentation data. For instance, Fakharian & Attar (2005, 2007) used FLAC2D v4.0 to simulate the dynamic response of the Founders/Meadows reinforced bridge abutments to seismic excitations. They applied a point load on the top of bridge deck footing to consider the weight of bridge deck. Therefore, the interaction of bridge deck and bridge deck footing were not considered in the analysis. The results showed that the horizontal displacements of the facing increase with number of cycles and reach values at the end of seismic excitations considerably greater than static displacement magnitudes. The

vertical displacement and rotation of the bridge deck footing, however, were not significant. Fakharian & Aghania (2014) continued the study on Founders/Meadows reinforced bridge abutment, incorporating the deck inertia and its interaction with the footing and abutment. The results showed that the horizontal displacement of the top and bottom points of facing were decreased by considering the role of deck. However, one of the instabilities observed in their model was the excessive rotation of the bridge deck footing caused by cyclic horizontal loads, understood to be exerted from bridge deck to the bridge deck footing. The other instability observed was the backward rotation of upper facing segmental blocks of the abutment facing.

Fakharian & Nasrolahzadeh (2017) investigated the influence of base isolators between bridge deck and bridge deck footing in Founders/Meadows reinforced bridge abutments subjected to seismic excitations. They realized that the base isolator significantly contributes to reducing the excessive rotation of the bridge deck footing and the instabilities of upper blocks of footing as reported by Fakharian & Aghania (2014) when no base isolators were installed.

This paper further investigates the behavior of Founders/Meadows reinforced bridge system under seismic excitations considering base isolators between the bridge deck and deck footing. The 70 m long M/F segmental bridge abutment in Denver with one pier in the mid span and base isolators is simulated using FLAC2D v7.0. Post-cyclic facing horizontal deformations and abutment footing deformations are compared with the results of the two-abutment model without considering base isolators (Fakharian & Aghania 2014) and also with single-abutment system (Fakharian & Attar 2005, 2007). Parametric studies of two-abutment model with base isolator are also presented and discussed.

2 FOUNDER/ MEADOWS BRIDGE ABUTMENT

The Founders/Meadows (F/M) bridge abutment constructed and fully instrumented in Denver, Colorado is used for seismic numerical modeling in this study. The Founders/Meadows segmental bridge abutment was completed in 1999 near Denver, by the Colorado Department of Transportation. The plan view and section of the reinforced abutment can be viewed in Abu-Hejleh *et al.* (2000, 2001) and Fakharian & Attar (2007). The bridge deck/ girder load is carried by a strip footing on top of the segmental reinforced abutment. The facing was constructed using solid masonry concrete blocks (toe-to-heel dimension equals to 280 mm and height of 200 mm). Plastic connectors prevent relative slip between the segmental concrete units, and are used to attach the reinforcing geogrids to the facing. The reinforcing geogrids were placed with uniform spacing but varying length. The model geometry and details are generated in FLAC2D v7.0 as shown in Figure 1 with slight differences
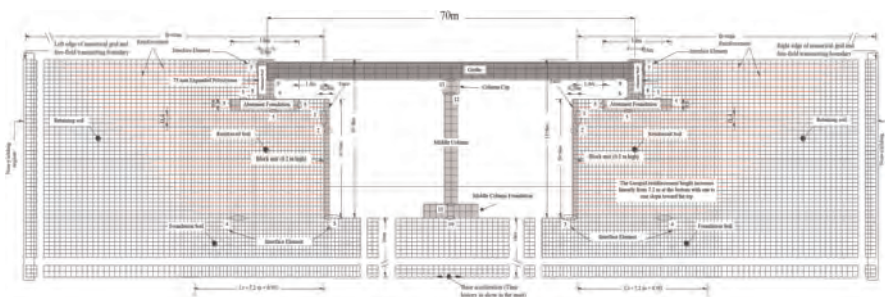
Figure 1. Grid, interface elements and boundary conditions for numerical modeling (FLAC2D v7.0) of the Founders/Meadow segmental bridge abutment.

compared to the prototype, such as changing the facing height (h) from 5.9 m to 6.0 m, geogrid element lengths from 8 to 7.2 m at the base (equivalent to 0.9H, where H is the total height of abutment) and removing the soil beside the facing wall.

3 NUMERICAL MODEL

3.1 Modeling of abutment

The initial condition for the seismic analysis is static stability (end-of-construction) of the system including the initial stresses while resetting all the deformations. The grid geometry is the same throughout the static and seismic analyses, but the boundary conditions and stress-strain relations are different. The soil model is nonlinear elastic (hyperbolic model) with M-C (Mohr-Coulomb) failure criterion under static condition while the softening effects after the peak failure are considered. In the dynamic analysis, a hysteretic nonlinear behavior applying Masing rule in unload/reload process is used (Cai & Bathurst 1995). The reinforcing elements are modeled by elasto-perfectly plastic cable elements with no compressive strength, available in FLAC. The injection layer option around cable elements was used as the interface to simulate the frictional behavior of soil-geogrid. The thickness of this layer was assumed zero and friction angle and cohesion were considered 0.75φ and zero, respectively. The interface element of FLAC was used to model the friction between difference contact surfaces of soil-soil, soil-concrete and concrete-concrete. The interface element is described by shear and normal stiffness, friction, cohesion, sliding and separation. At soil/soil and soil/concrete contact surfaces, the magnitude of the interface friction angle controls the onset of slip. The shear and normal stiffness values for the interface elements were based on the properties of the adjacent materials, as recommended in the FLAC manual. A variable-amplitude sinusoidal harmonic motion was used as an input at the bottom nodes for seismic excitations. More details of the numerical model can be found in Fakharian & Attar (2007).

3.2 Modeling of base isolator

Seismic base isolators (B.I) are material elements used to diffuse the energy induced at the time of the earthquake before being transferred to the structure. In this project, the base isolator type NRB (Natural Rubber Bearing) which is an elastomeric support with low damping was modeled. Cyclic behavior of base isolator can be modeled using nonlinear cyclic relations by applying hysteretic damping in FLAC v7.0. Elastic element with hysteretic behavior is used in order to model the base isolator. The factor used for defining hysteretic behavior in FLAC is Hardin factor (Hardin & Drnevich 1972). Investigation of primary analysis on reinforced abutment system with base isolators carried out by Fakharian & Nasrolahzadeh (2017) showed that damping characteristic of Hardin factor 0.00001 was compatible with laboratory test results, thus Hardin factor of 0.00001 was used in this research.

4 ANALYSIS RESULTS AND DISCUSSION

4.1 Effects of base isolator on seismic behavior

To investigate the performance of the abutment system with base isolator (B.I), comparisons are made with the results of abutment systems without base isolator modeled by Fakharian & Attar (2007) and Fakharian & Aghania (2014). Normalized vertical displacements of the bridge deck footing (rotation of it) and horizontal displacements of the facing are compared in Figures 2a and 2b, respectively. In Figure 2, comparisons are made among three models of
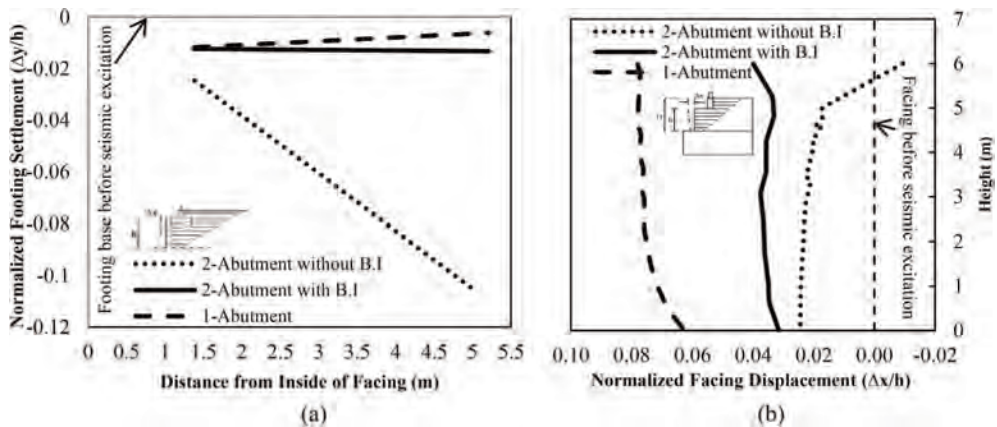
Figure 2. Incremental displacement profiles before and after applying seismic excitations in 1-abutment model and 2-abutment models with and without base isolator: (a) vertical displacement and rotation of bridge deck footing; (b) horizontal displacement of facing.

abutment system to understand the similarities and differences. As shown in Figure 2a, the displacement and rotation of bridge deck footing in both one-abutment and two-abutment models with B.I systems are similar to each other, but the deformations are much lower than the two-abutment model without B.I. Through embedding the base isolator, the performance of bridge deck is isolated from the reinforced abutment. Therefore, the footing is not experiencing excessive rotation due to the impact of bridge deck.

One of the instabilities of the model without the base isolator, as reported by Fakharian & Aghania (2014), was the backward rotation of upper facing blocks of the abutment (Figure 2b). Figure 2b shows that the horizontal displacement of the wall facing in the one-abutment model is almost double of the two-abutment model with B.I. This is attributed to the fact that the other abutment and bridge deck inertia are influencing the wall response to some extent, even with the presence of the base isolator. However, as the performance of the reinforced system is isolated from the bridge deck through embedding the base isolator between bridge deck and footing, the shape and trend of horizontal displacement of facing in the two-abutment model with B.I. is similar to the results of one-abutment model. In fact, with the presence of the base isolator in the system, the interactive effects between bridge deck and foundation wall are reduced.

All the mentioned differences are the result of existence of the base isolator under the bridge deck. In the 2-abutment system without B.I., the deck is directly put on the concrete footing underneath and their horizontal interaction is through the frictional resistance between deck and footing, that is concrete-to-concrete interface. The high frictional resistance between deck and footing has resulted in preventing the footing to experience a significant horizontal movement. In the system with B.I. on the other hand, the frictional interaction of these two elements is isolated and the footing experiences horizontal displacements the same as the underneath reinforced soil. Although the connection effects are ignored in the one-abutment model, the trend of deformations are similar to the two-abutment model with B.I.

4.2 Parametric study

Parametric studies have been carried out in order to investigate the effects of different characteristics on the performance of bridge abutment. Three different parameters were selected among all parameters of different components of abutments, including: damping

factor of base isolator, friction angle of reinforced soil, and input acceleration frequency. Parametric study results in terms of incremental displacement profiles of deck footing as well as facing due to applying seismic excitations in 2-abutment models are shown in Figure 3.

Fakharian & Nasrolahzadeh (2017) showed that damping characteristic of Hardin factor 0.00001 was more compatible with laboratory test results than Hardin factor 0.001. To investigate the effects of this factor, damping of base isolator has decreased with the increase of Hardin coefficient from 0.00001 to 0.1. As shown in Figure 3a, with the increase of
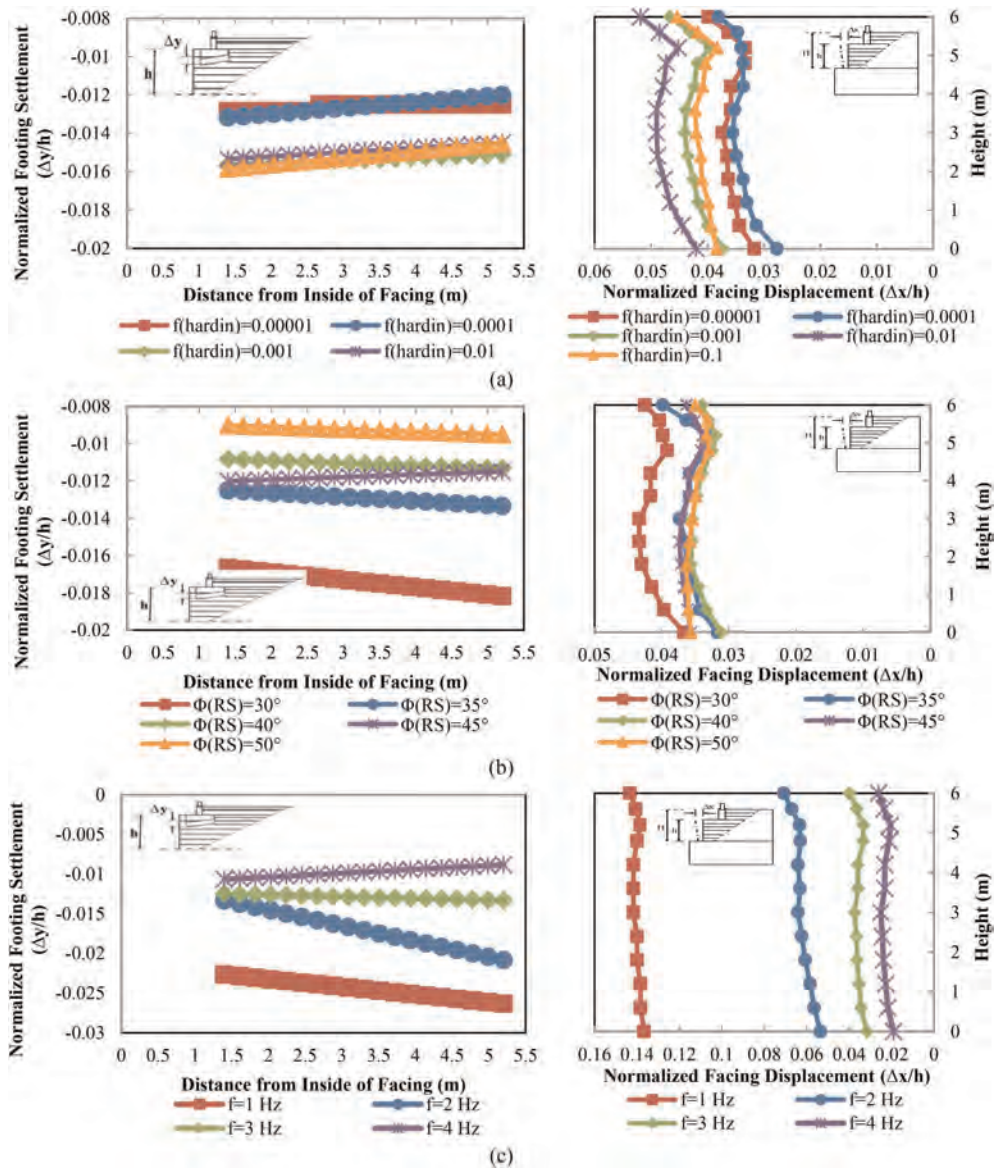
Figure 3. Incremental displacement profiles of deck footing and facing after applying seismic excitations in 2-abutment models with different parameters of: (a) base isolator damping Hardin factor; (b) friction angle of reinforced soil; (c) frequency of input ground motion.

Hardin coefficient of base isolator and consequently a decrease of damping, the horizontal deformation of the facing has increased. As the existence of a base isolator generally separates the performance of the substructure from the bridge deck, it is not expected to have a significant effect on the results and performance of the substructure. According to Figure 3a, the settlement of deck footing has also increased with the increase of Hardin coefficient and the reduction of damping.

The seismic response of the reinforced soil abutment is evaluated by changing the internal friction angle of reinforced soil (φ_{RS}) from 30° (assuming a relatively loose sand) to 50° (assuming very dense sandy gravel). By increasing φ_{RS} of reinforced soil, the resistance of the soil mass increases and the horizontal displacement of the facing decreases (Figure 3b). With increasing φ_{RS} of the reinforced soil, in addition to less movement across the facing height, the facing has undergone less deformations in general and hence has better preserved its straight shape.

The response of the reinforced soil abutment was evaluated by changing the frequency (f) of input wave from 0.5 to 4 Hz (0.5, 1, 2, 3 and 4 Hz). Due to the plastic deformations that occurred under input excitation with the frequency of 0.5 Hz, the entire system has undergone large displacements and it made the results of this analysis unreliable. Therefore, the results of the model with frequency of 0.5 Hz have not been taken into account. In the case that the input wave frequency was equal to 1 Hz, the bridge deck system and the middle column remained stable, but the foundation soil mass was severely deformed. In this case, after applying the harmonic wave for 4 seconds, the analysis became unstable due to large deformations that occurred in the soil mass and the analysis was stopped. This problem can be attributed to resonance occurrence. The natural frequency of the system and resonance is discussed in the following section. As shown in Figure 3c, the greatest change in the horizontal displacement of facing as well as settlement of the deck footing are related to the model with frequency of 1 Hz.

5 CONCLUSIONS

The most important findings of the study are summarized below:

- Embedding a base isolator between bridge deck and footing, the performance of bridge deck and deck footing supported on reinforced wall is isolated. This isolation contributes significantly to improving the stability of the footing as well as the upper blocks of the facing wall.
- If damping of base isolator decreases, the horizontal deformation of the facing increases. Lower damping of the base isolator means that the characteristic of separating the superstructure from substructure is lower and hence the bridge deck will have a greater impact on the substructure.
- The comparison between the 3 analysis types show that the model with base isolator generates the most reliable results, while the model with 2-abutment but without base isolator is the least accurate. The results of the model without considering the interaction of deck (1-abtment) is more close to the 2-abutment model with base isolator. Therefore, it could be used for quick checks and preliminary analysis considering its simplicity.

REFERENCES

Abu-Hejleh, N., Outcalt, S., Wang, T. & Zornberg, J. 2000. Performance of Geosynthetic-Reinforced Walls Supporting the Founders/Meadows Bridge and Approaching Roadway Structures, *Report 1: Design, Materials, Construction, Instrumentation, and Preliminary Results*, Department of Transportation, Colorado, USA.

Abu-Hejleh, N., Outcalt, S., Wang, T. & Zornberg, J. 2001. Performance of Geosynthetic-Reinforced Walls Supporting the Founders/Meadows Bridge and Approaching Roadway Structures, *Report 2: Assessment of the performance and design of the front GRS walls and Recommendations for future GRS abutments*, Department of Transportation, Colorado, USA.

Askari, M., Razeghi, H.R. & Mamaghanian, J. 2021. Numerical Study of Geosynthetic Reinforced Soil Bridge Abutment Performance under Static and Seismic Loading Considering Effects of Bridge Deck. *Geotextiles and Geomembranes*, Volume 49, Issue 5, Pages 1339–1354, ISSN 0266-1144.

Cai, Z. & Bathurst, R.J. 1995. Seismic Response Analysis of Geosynthetic Reinforced Soil Segmental Retaining Walls by Finite Element Method. *Computers and Geotechnics*, Vol. 17, No. 4, pp. 523–546.

Fakharian, K. & Aghania, M. 2014. Numerical Investigation of Deck-abutment Interaction Reinforced by Geogrid Subjected to Seismic Loading, *10th International Conference on Geosynthetics*, Berlin, Germany,3: 288–295.

Fakharian, K. & Attar, I.H. 2005. Effect of Soil Model Type on Seismic Response of Segmental Bridge Abutments, *Soil-Structure Interaction*, Saint Petersburg, Russia.

Fakharian, K. & Attar, I.H. 2007. Static and Seismic Numerical Modeling of Geosynthetic-reinforced Soil Segmental Bridge Abutments. *Geosynthetics International*, 14(4), 228–243.

Fakharian, K. & Kashkooli, M. 2018. Numerical Study of Seismic Behavior of Reinforced Soil Bridge Abutments Located on Soft Clays of Southwest Iran. In *Proceedings of the 11ICG*.

Fakharian, K. & Nasrolahzadeh, S. 2017. Effect of Deck Support on GRS Bridge Abutments Response Subjected to Seismic Loading. *PBD III, July 16-19, 2017*, Vancouver, Canada.

Hall, J.F., Heaton, T.H., Halling, M.W. & Wald, D.J. 1995. Near-source Ground Motion and its Effects on Flexible Buildings. *Earthq. Spectra*, 11: 569–605.

Hardin, B.O. & Drnevich, V.P. Shear Modulus and Damping in Soils. *Journal of Soil Mechanics and Foundation Division, ASCE*, Vol. 98, No. 6, pp. 603–624 and No. 7, pp. 667–691, 1972.

Hatami, K. & Bathurst, R.J. 2001. Modelling Static Response of Reinforced Soil Segmental Retaining Wall using FLAC. *FLAC and Numerical Modelling in Geomechanics*, 223–231.

Hatami, K. & Bathurst, R. J. 2005. Development and Verification of a Numerical Model for the Analysis of Geosynthetic-reinforced Soil Segmental Walls under Working Stress Conditions. *Canadian Geotech. Journal* 42, No. 4, 1066–1085.

Hatami, K. & Bathurst, R.J. 2006. A Numerical Model for Reinforced Soil Segmental Walls under Surcharge Loading, *ASCE Journal of Geotechnical and Geoenviro. Engineering*, Vol. 132, No. 6, pp. 673–684.

Rao, P.B. & Jangid, R.S. 2001. Performance of Sliding Systems under Near-fault Motions, *Nucl. Eng.*, 203: 259–272.

Shen, J., Tsai, M., Chang, K. and Lee, G.C. 2004. Performance of a Seismically Isolated Bridge under Near-fault Earthquake Ground Motions. *ASCE J. Struct. Eng.*, 130: 861–868.

Zheng, Y., McCartney, J.S., Shing, P.B. and Fox, P.J. 2018. Transverse Shaking Table Test of Half-scale Geosynthetic Reinforced Soil Bridge Abutment. *Geosynthetics International*, 25(6), 582–598.

Segmental retaining wall system as approach slab's retaining wall reinforcement on active fault line at the Kretek II Flyover's, Yogyakarta, Indonesia

F. Widhiastuti, N.A. Anindita, D.A. Nurjannah & D.S. Harninto
P.T. Geoforce Indonesia, Central Jakarta, Indonesia

ABSTRACT: The Kretek II Flyover is in Yogyakarta. The location of this flyover is in an earthquake potential area and is on an active fault line that crosses the embankment wall of the flyover. GSRW (Geoforce Segmental Retaining Wall) is an MSEW system that will be used for the construction of the approach slab's retaining wall located on the fault line. In the case of this project, GSRW is installed into 3 segments which were separated by dilated concrete. The purpose of the segment's division is to reduce the damage that will occur to the approach slab if there is movement due to faults. Although the displacement distance and the magnitude of the plane caused by the fault cannot be predicted, the GSRW construction is expected to reduce the damage that will occur, because this system can move independently so that the concrete panels are more flexible against shocks. The global stability was then analyzed using PLAXIS 3D software and yield safety factor 1.792 for static analysis and 1.136 for pseudo-static analysis.

1 INTRODUCTION

The Kretek 2 Flyover located in Bantul, Yogyakarta Special Region (DIY) is part of the Java Southern Cross Road (JJLS) project that connects Samas-Kretek and Kretek-Parangtritis. The location of this flyover is in an earthquake potential area and is on an active fault line that crosses one side of the Kretek Flyover approach slab. The approach slab spans up to 125.5 meters with the height as high as 7 meters. GSRW (Geoforce Segmental Retaining Wall) is the system that will be used for the retaning wall construction of the flyover located on the fault line. GSRW is a Mechanically Stabilized Earth Wall that has a concrete facing and reinforced with Polyester Strip anchored from the facing to the body embankment according to the design calculations.

2 IMPLEMENTATION METHOD OF GEOFORCE SEGMENTAL RETAINING WALL ON ACTIVE FAULT LINE AT THE KRETEK II FLYOVER'S

2.1 *Geoforce Segmental Retaining Wall*

Geoforce Segmental Retaining Wall (GSRW) is an earth retaining wall system that consists of layers of compacted backfill material and facing elements made from high-quality precast concrete, also reinforced with a belt or known as GI Strip. The distinction between GSRW and other products lies in the robustness of the structure which has been tested, the competitiveness of the price compared to a similar segmental product, the fast and easy

Figure 1.   Kretek II Flyover's, Yogyakarta, Indonesia.

installation of the structure that affects the time efficiency of the project, and also the aesthetic side which capable of adding the enticing aspect of the constructed segmental system.

The Geoforce Segmental Retaining system is reinforced with the friction belt made out of high tenacity polyester yarn namely GI-Strip. The strip has been specially designed to generate reinforced belt with high tensile strength and friction coefficient. This component is what makes the structure robust. The selection of the tensile strength type is adjusted with the design calculation from the GSRW construction which will be built. Another advantage from GI-Strip is the high durability of the material, resistance from organic bacteria and acidity from the backfill material. The GSRW system is shown in Figure 2.
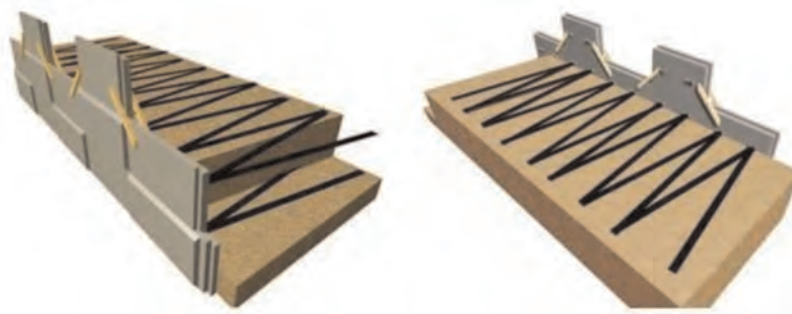
Figure 2.   Typical of geoforce segmental retaining wall system.

2.2   *Geological conditions*

Based on the Geological Map, the Tirtohargo area is a deposit area of the Young Merapi Volcano (Qmi), namely tuff, ash, breccia, agglomerates, and inseparable lava flows. This area is also an area that is on the fault line. Faults are faults in rock that are formed due to forces originating from within the earth such as tectonic and volcanic forces. Faults are areas of discontinuity (discontinuity) in rock, where there has been significant displacement as a result of rock mass movement due to forces from within the earth. The Opak fault is a fault located around the Opak river, in the Special Region of Yogyakarta. According to the research of several experts, based on the direction of movement of the Opak fault, it is included in the Normal Faults fault, which is a fault that occurs due to the maximum compressive force in the vertical direction, causing one of the rock planes to move downward following the fault plane.

Figure 3.   Geological map at Bantul.

2.3   *Implementation method*

The fault line is expected to cross the Geoforce Segmental Retaining Wall structure. However, the distance of the fault shift that will occur cannot be predicted. The fault shift can occur only a few millimeters to tens of kilometers, while the fault planes can also occur ranging in size from a few centimeters to tens of kilometers.
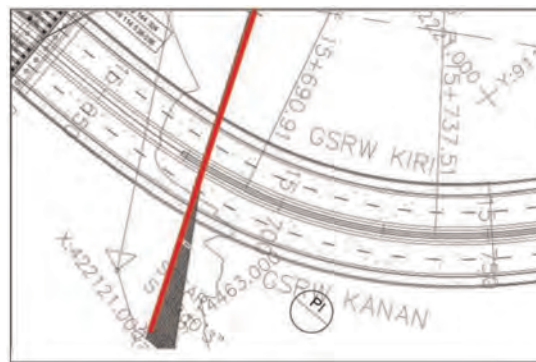
Figure 4.   Faults line in geoforce segmental retaining wall construction.
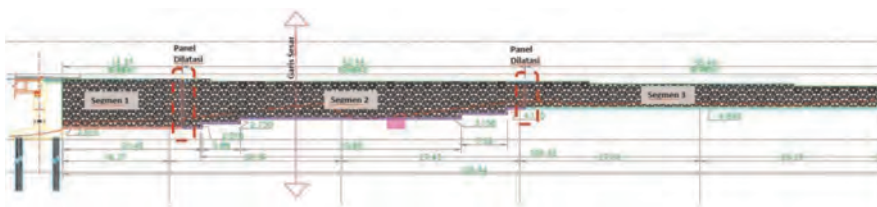
Figure 5.   Segment division.

In the case of GSRW Kretek construction, there are some special things that distinguish it from the implementation of GSRW in general.

GSRW Kretek is divided into 3 segments which are separated by dilated concrete. The purpose of this 3-segment division is to reduce the damage that will occur to the approach slab walls if there is movement due to faults. Segment 2 or the middle segment is the area crossed by the fault line and spaced up to a dozen meters from the line.
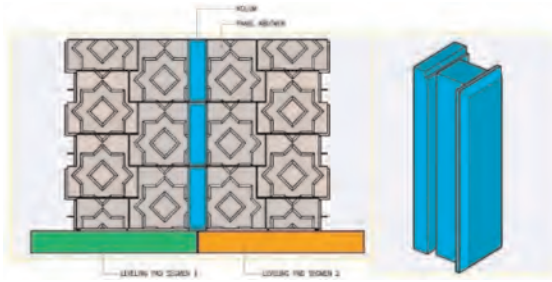
Figure 6.   Dilated column detail.

One of the advantages of using this system, in this case is that the Geoforce Segmental Retaining Wall (GSRW) system can move independently (behaving like a puzzle) so that the panels are flexible against earthquakes or shocks. What can be done when a fault occurs is to repair or replace only the damaged part.

3   DESIGN METHODOLOGY

3.1   *Soil investigation*

Based on the SPT results, it can be concluded that the area is dominated with loose sand material at the surface until the depth of 3 meters. Therefore, a replacement of up to 1.5 until 3 meters was carried out using gravel sand to increase the bearing capacity.
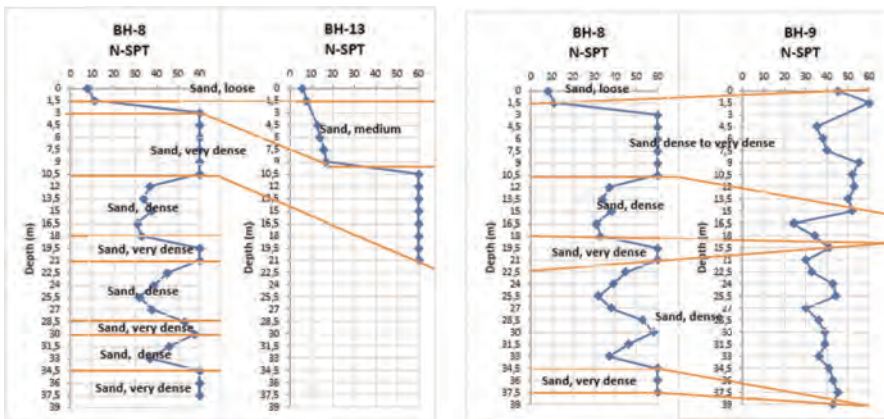
Figure 7.   Soil data profile.

3.2   *Global stability analysis*

Global Stability Analysis is carried out to determine the safety factor of the segmental wall system to be made. To carry out this analysis, the following parameters are used based on interpretation and assumptions of the soil data because the available data are incomplete.

The analysis was carried out using the finite element method with the Plaxis 3D program with soil modeling as follows. The soil parameters are based on assumptions and the closest

available soil data BH 08. The whole system was then assessed with the activation of the 15 kPa traffic load. The soil parameter is as shown in Table 1, as for the geometry model is as shown in Figure 8 and the analysis yield results as shown below in Figures 9 and 10.

Table 1. Soil data parameter with hardening soil model.

Soil type	Υ_{unsat} [kN/m^3]	Υ_{sat} [kN/m^3]	c' [kPa]	φ' degrees	E_{50}^{ref} [kN/m^2]	E_{oed}^{ref} [kN/m^2]	E_{ur}^{ref} [kN/m^2]	Ψ degrees
Sand, loose	16	18	–	27	20000	14000	60000	0
Sand, very dense	19	20	–	37	90000	63000	270000	7
Sand, dense	17	19	–	33	32000	22400	96000	3
Sand, very dense	19	20	–	37	70000	49000	210000	7
Sand, dense	17	20	–	33	32000	22400	96000	3
Sand, very dense	19	20	–	38	54000	37800	162000	8
Fill	17	19	5	35	30000	21000	90000	5
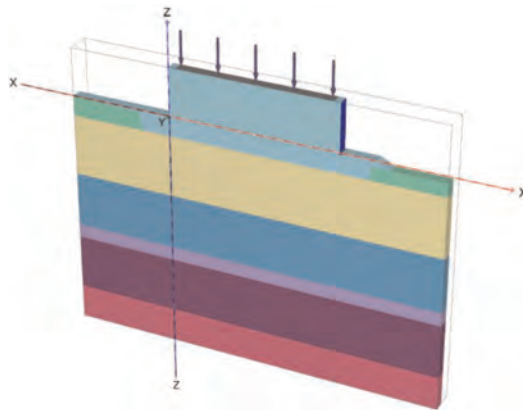
Figure 8. PLAXI 3D model of GSRW of Kretek II.
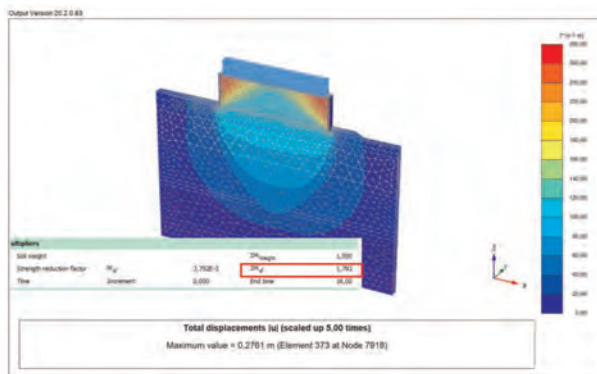
Figure 9. Estimation of static failure mode and safety factor of GSRW of Kretek II.
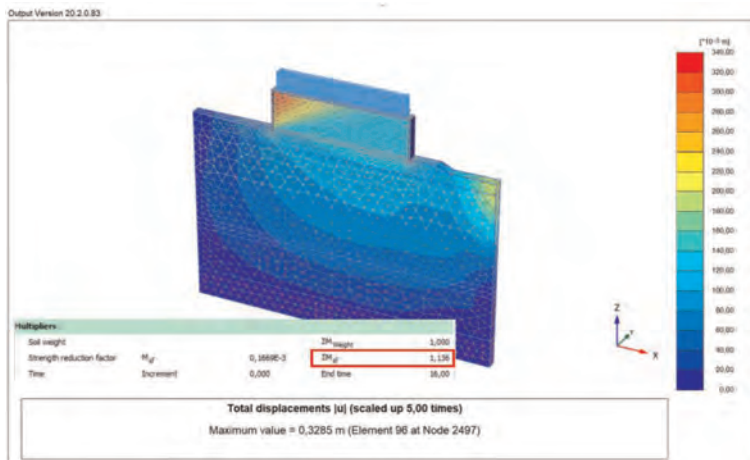
Figure 10. Estimation of pseudo-static failure mode and safety factor of GSRW of Kretek II.

According to Figure 9, the static safety factor for **GSRW** of Kretek II Approach Slab is 1.792. This safety factor fulfills the criteria in Indonesian National Standard for Geotechnical Design Requirements which is above 1.50. After that, the analysis combines with the pseudo-static load which was adopted from design response spectrum in Map of Indonesia Earthquake Sources and Hazards in 2017. The Peak Ground Acceleration value is 0.6 g and multiplied by the amplification factor of 1.0 and 0.5, which results in horizontal acceleration 0.3g. The pseudo-static load analysis yields safety factor 1.136. This safety factor also fulfills the criteria in Indonesian National Standard for Geotechnical Design Requirements for embankment with seismic load which is above 1.10.

4   CONCLUSIONS

GSRW (Geoforce Segmental Retaining Wall) is an MSEW system that will be used for the construction of the flyover wall located on the fault line at the Kretek II flyover. In this case, a replacement of up to 1.5 until 3 meters was carried out using gravel sand to increase the bearing capacity. In the case of this project, GSRW is installed into 3 segments which were separated by dilated concrete. The purpose of the segment's division is to reduce the damage that will occur to the approach slab if there is movement due to faults. Although the displacement distance and the magnitude of the plane caused by the fault cannot be predicted, the GSRW construction is expected to reduce the damage that will occur, because this system can move independently so that the concrete panels are more flexible against shocks. The global stability was then analyzed using PLAXIS 3D software and yield safety factor 1.792 for static analysis and 1.136 for pseudo-static analysis.

REFERENCES

BS8006 (1995). *Code of Practice for Strengthened/Reinforced Soils and Other Fills*. British Standard Institution
Koerner, R. (2005). *Designing with Geosynthetics*. Upper Saddle River: New Jersey.
Badan Standarisasi Nasional. 2017. *SNI 8460:2017. Persyaratan Perancangan Geoteknik*. Jakarta: Badan Standarisasi Nasional.

The evaluation of deformation reduction by geosynthetics sandwiched with gravel layers beneath an embankment during liquefaction of level 2 and level 1

H. Aung*, M. Kubo*, M. Yokoyama* & T. Obata*
Eternal Preserve Ltd, Japan

H. Yokawa*
Chubu University, Kasugai, Japan

ABSTRACT: Roads are permitted to go through some deformation caused by a severe seismic event (so-called Level 2 such as 1996 Kobe and 2011 Tohoku) as long as they could be recovered quickly and easily. The authors have conducted to verify the effect of the countermeasure using geosynthetics sandwiched with gravel layers after a Level 2 seismic event through experiments and dynamic analyses. This countermeasure was found to be effective for maintaining the overall original shape of the embankment by suppressing the stretching of the toe of the embankment. It is legitimate for approach embankments near bridges and box culverts to be designed for a Level 2 seismic event. But because roads are extensive in the longitudinal direction, applying the Level 2 design for the rest of the embankment seems costly, thus Level 1 design approach seems feasible for these locations. Authors have verified the amount of settlement after a Level 1 seismic event (180 gal) by numerical simulations. The authors were able to summarize the settlement levels under various conditions that can be used as reference guidelines for designing embankments.

1 INTRODUCTION

Japan Road Association assigns the required performance for road structures, which are summarized in Table 1. Performance 2 design allows limited deformation that can be easily restored. The Level 1 seismic event is expected to occur once or twice during the service time of the structure (once in 100 years) while the Level 2 seismic event has a very low probability of being experienced by the structure (once in 1000 years).

Importance 1: Highway, national and prefectural roads, roads without alternative routes at the
event of disaster
Importance 2: Not as important as roads classified as Importance 1
Performance 1: Keeps sound condition
Performance 2: Allows limited deformation, easy to restore
Performance 3: Does not totally collapse

The authors conducted research on shallow ground reinforcement structures using geosynthetics. The purpose of this study is to confirm the deformation reduction effect of the embankment over the liquefied ground by the countermeasure. As a result, the effect of

*Corresponding Authors: hla-aung@etp21.co.jp, mikio-kubo2019@etp21.co.jp, masaki-yokoyama@etp21.co.jp, tomoyuki-obata@etp21.co.jp and yokawa@isc.chubu.ac.jp

Table 1. Performance of earthwork structure.

Case	Importance 1	Importance 2
Static loading + traffic	Performance 1	Performance 1
Static loading + rainfall	Performance 1	Performance 1
Level 1 Seismic loading	Performance 1	Performance 2
Level 2 Seismic loading	Performance 2	Performance 3

suppressing settlement of the embankment crest by the countermeasure in this study was not sufficient as expected. However, the effect of suppressing the embankment shoulder and slope toe stretching by the countermeasure was demonstrated, and the effect of retaining the shape of the embankment was confirmed by experiment and reproduction, and predictive analysis.

The guideline of Japan Road Association assigns that important roads must sustain the same performance after a seismic event for structures such as bridges, embankments, box culverts, cut slopes and etc., in order to keep the roadability. Because roads are extensive in the longitudinal direction, applying Level 2 countermeasure for their entire span seems too expensive. Although approach embankments near bridges and other structures should consider severe seismic events, Level 1 design approach seems feasible for the remaining embankments. The authors conducted static numerical simulations of a Level 1 seismic event (180 gal) in order to verify the effectiveness of the countermeasure under various ground conditions.

2 DYNAMIC CENTRIFUGAL MODEL EXPERIMENT

2.1 *Experimental outlines*

A 50G dynamic centrifugal model experiment was conducted using a large-scale dynamic centrifugal load test apparatus at the Public Works Research Institute. The outline of the model of countermeasure is shown in Figure 1.
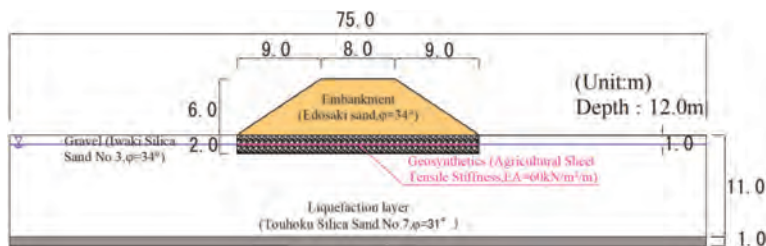
Figure 1. Outline of model ground.

2.2 *Material and seismic wave*

The liquefied layer was prepared by air-drop method using a sand hopper. The target relative density of the liquefied layer was Dr = 50%. A pore water pressure gauge and an accelerometer were set in the middle of the ground. The materials used in the experiment and their properties are shown in Figure 1. The Level 2 seismic wave (1995 Kobe, Japan) was used. The excitation time was 50 sec and the maximum acceleration was 557 gal.

2.3 *Results of dynamic centrifugal model experiment*

2.3.1 *Deformation of embankment*

The settlement of the embankment crest against time for each experiment is shown in Figure 2. The amounts of settlement at the center of the embankment crest and the embankment shoulder at 50 sec are 95 cm and 106 cm in Case 1 and 83 cm and 76 cm in Case 2, respectively. The settlement ratio of with/without the countermeasure is 87% at the center of the embankment crest and 72% at the embankment shoulder. The effect of suppressing settlement of the embankment crest by this method was lower compared to the previous study (Hla Aung 2021). The relation of excess pore water pressure ratio against time is shown in Figure 3. The negative excess pore water pressure ratio which is the same as positive dilatancy occurred during the first 5 sec to 15 sec for the case without the counter-measure, beneath the center of the embankment. This is because the shear deformation occurred at this location which is not compressive deformation by the liquefaction.
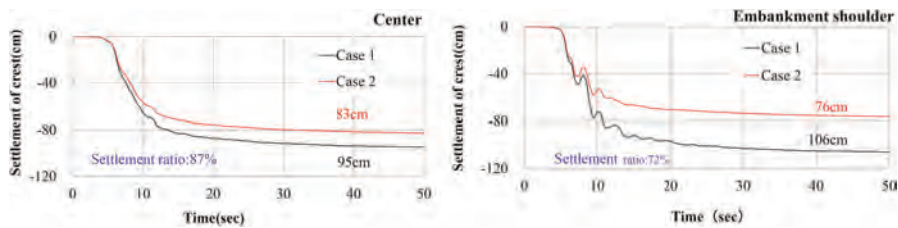
Figure 2.   Relation of embankment crest settlement with times.
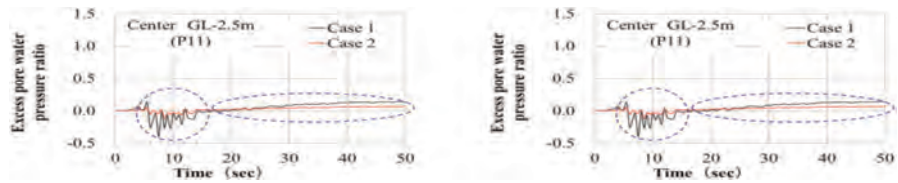
Figure 3.   Relation of excess pore water pressure ratio against times.

2.3.2 *Factor analysis of embankment deformation*

The stretching amount of the embankment shoulders and toes was defined as the amount of widening in the horizontal direction. The lateral displacement of the liquefaction layer was defined as the maximum lateral displacement of the area directly under the embankment. The deformation of the embankment and liquefied ground after a seismic event are shown in
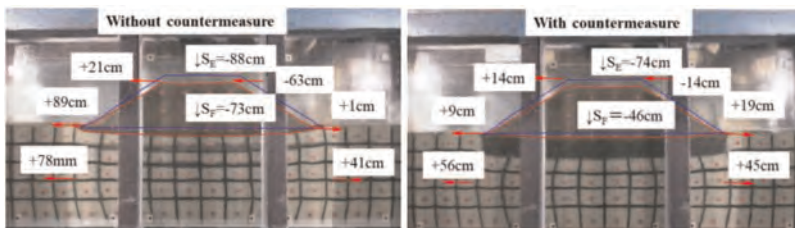
Photo 1.   Deformation after seismic motion.

Photo 1. The stretching amounts of embankment shoulder without and with the counter-measure are -42 cm (21 cm, -63 cm) and 0 cm (14 cm, -14 cm), respectively. The stretching amount of the embankment toe without and with the countermeasure is 90 cm (89 cm, 1 cm) and 28 cm (9 cm, 19 cm), respectively. The embankment shoulder and toe stretching are greatly suppressed. It can be noted that the reduction of the liquefaction-induced deformation of the embankment by the countermeasure.

3 TWO-DIMENSIONAL DYNAMIC EFFECTIVE STRESS ANALYSIS

The 2D dynamic effective stress analysis program, LIQCA2D21, was used to reproduce the experimental results and predictive analyses under multiple conditions.

3.1 *Reproduction analysis*

LIQCA2D21 can reproduce the liquefaction of the ground and evaluate the excess pore water pressure, the deformation of the ground, and the embankment. A preliminary analysis was carried out for the purpose of reproducing the model experiment.

3.1.1 *Analysis conditions*
Analyses cases are Case 1 and Case 2 for without and with the countermeasures. The analysis mesh for Case 2 is shown in Figure 4. A drainage boundary was fixed at a depth of 1 m from the ground surface and the other surfaces are non-drainage boundaries. A 1m non-liquefaction layer was set around the crushed stones because the drainage effect of the crushed stone causes a smaller increase of excessive pore water pressure around the crushed stones and this was verified in the previous study (Hla Aung 2021). By setting the non-liquefaction layer, the analysis well replicated the experimental results.
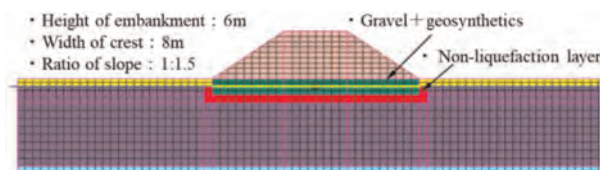
Figure 4.   FEM model.

3.2 *Analysis results*

3.2.1 *Embankment crest settlement*
Figure 5 shows the settlement of the embankment crest against time. The final settlement at the center of the embankment crest shows a larger value than the experiment in Case 1. The
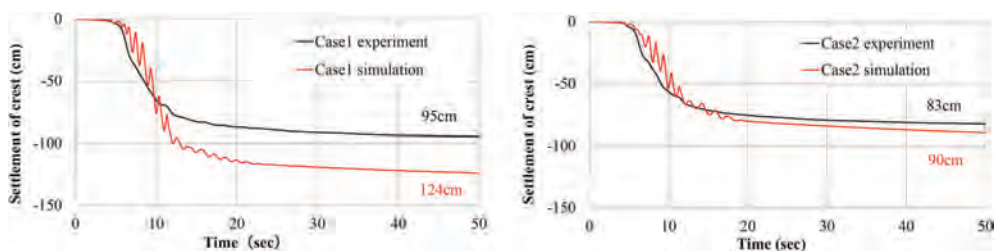
Figure 5.   Relation of embankment settlement against times(Experiment · Simulation).

final settlement amount of the analysis of Case 1 is about 30% larger than the experimental value. Although the embankment settlement value obtained by the analysis is larger than the experimental value, the effect of settlement retention by the countermeasure can be expressed.

Figure 6 shows the relation of excess pore water pressure ratio against time. The excess pore water pressure ratio of the experiment and simulation of Case 1 is close to each other at the initial stage. After 5 sec, the analysis value of excess pore water pressure is about 7 times larger compared to the experiment. These results caused the settlement of analysis to enlarge compared to that of the experiment without the countermeasure shown in Figure 5.
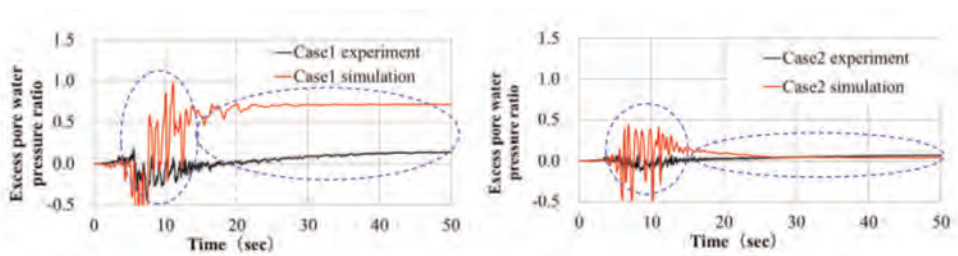
Figure 6.   Relation of excess pore water pressure ratio against times(Experiment · Simulation).

3.2.2 *Deformation retention effect*
Figure 7 shows the deformation of the liquefied ground and embankment at the end of the vibration. The amount of stretching of the toe in Case 1 and Case 2 are 96 cm (57 cm, 39 cm) and 15 cm (10 cm, 5 cm) respectively. According to the above reproduced analysis results, it is possible to analytically confirm the effect of the countermeasures on the deformation reduction of the embankment.
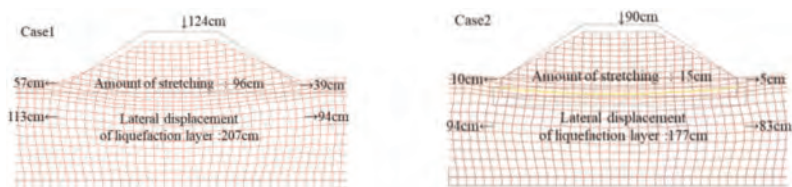
Figure 7.   Deformation after seismic motion.

3.3 *Predictive analyses*

The predictive analyses were performed to verify the effects of the countermeasure under various conditions.

3.3.1 *Analysis conditions*
Analysis conditions are as follows: embankment heights of 2 m, 6 m, and 10 m, and liquefaction thicknesses of 5 m and 10 m. The embankment width and slope are 12 m and 1.5 m, respectively. The relative density of 50% and 70% of the liquefied ground and the Level 2 seismic motion are used in the predictive analysis.

3.3.2 *Analysis results*
The embankment crest settlements are shown in Figure 8. All the results are arranged at the excitation time of 50 sec.
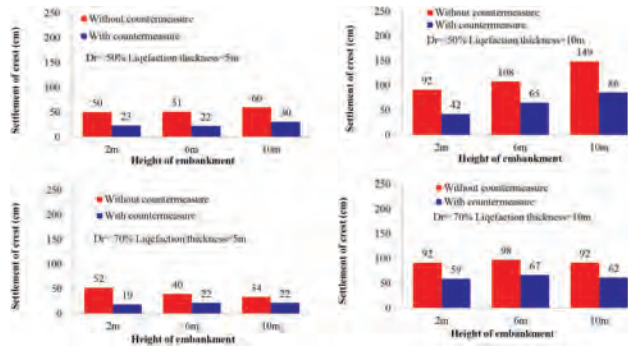
Figure 8.   Settlement of embankment crest.

In the case of the relative density of 50%, the settlement of the embankment crest increases as the embankment height increases. On the other hand, in the case of the relative density of 70%, the amount of settlement does not necessarily increase with the height of the embankment. A height of more than 6 m reveals the phenomena of less settlement occurrence due to the effective stress influences.

Although the effect differs from case to case, the embankment crest settlement ratio (with/ without the countermeasure) is 35% to 68%.

4   THE EFFECTIVENESS OF COUNTERMEASURE KEEPING EMBANKMENT SHAPE

The experiments and dynamic analysis show that the countermeasure refrains the embankment from spreading. It is similar to the deformation pattern IV in Figure 9, which appears in the guideline of road disaster countermeasure handbook published by Japan Road Association. The pattern illustrates the settlement without indifferential settlement and deformation while keeping the overall shape of the embankment. In this case, settlement below 50 cm is enough for a vehicle to pass. But it should be noted that the settlement of approach embankments, similar to Pattern V in Figure 9, must be below 20cm.

Figure 9.   Classification damage patterns.

5   LEVEL 1 SEISMIC EVENT'S STATIC FINITE ELEMENT ANALYSIS

5.1   *Analysis condition and summarized simulation results*

The static finite element analysis program, ALID (Analysis for Liquefaction-Induced Deformation), is used to predict embankment settlement in Level 1 seismic. Analyses are

conducted under various conditions of embankment heights (2 m, 6 m, 10 m), groundwater levels (GL-0 m, 1 m, 2 m), and liquefied ground thickness (3 m, 9 m,15 m).

5.2 *An example of estimation of settlement at the embankment crest*

An example of the estimation of settlements of the 5 m height embankment, under the condition of 1 m no liquefaction layer (groundwater level -1 m) and various liquefaction layers and $RL_{0.2}$, $RL_{0.25}$, are shown in Figure 10.

The settlement of the embankment at the crest of any thickness of liquefaction layers and RL values could be estimated using the two approximate equations shown in Figure 10.

The static finite element analyses results under Level 1 seismic condition (180 gal) simulate the amounts of the settlements. These results will be used as a reference guideline so that the road administrators could obtain the settlement of the embankment with a countermeasure without conducting a static finite element analysis.
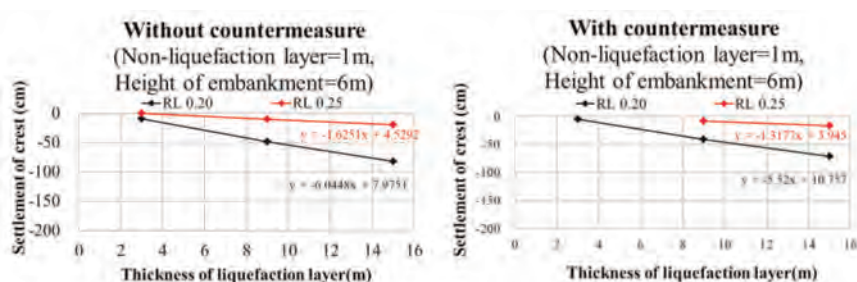
Figure 10.   Settlement prediction for level 1 seismic.

6 CONCLUSIONS

In case of a severe seismic event, Level 2, and for a road that requires Performance 2, geosynthetics sandwiched with gravel layers have been proved as a potential countermeasure that tolerates some deformation that can be restored easily.

Experiments and dynamic finite element analysis show that the countermeasure prevents the stretching of the toe of the embankment.

The static finite element analyses results under Level 1 seismic event (180 gal) simulate the amounts of the settlements. These results will be used as a reference guideline so that the road administrators could obtain the settlement of the embankment with a countermeasure without conducting a static finite element analysis.

REFERENCES

ALID Study Group: Two-dimensional Liquefaction Flow Analysis Program, ALID/WIN Manual 2018 (in Japanese).

Hla Aung, Mikio Kubo, Akihiro Takahashi: Deformation Restriction Measures of Embankment on Liquefiable Ground by Crushed Stones with Geosynthetics, *Japanese Geotechnical Journal*, Vol.16, No.4, PP. 295–305, 2021 (in Japanese).

Japan Road Association: Guidelines for Countermeasures of Road Earthquake Disaster, pp.66&pp.67, 2007 (in Japanese)

Japan Road Association: Guidelines for Soft Ground Countermeasures, pp. 97&pp. 168, 2012 (in Japanese).

LIQCA Research and Development Group: User's Manual for LIQCA2D21 (in Japanese).

Seismic performance assessment of approach embankment MSE wall near Valley Fault System

R.A. Luna, R. Quebral, A. Paulino, J.V. Razon, P.A. Selda & J.M. Tanap
AMH Philippines Inc., Quezon City, Philippines

ABSTRACT: This paper presents the assessment of the adequacy of a Mechanically-Stabilized Earth (MSE) wall, reinforced with steel geostraps, for a bridge approach within Metro Manila, located few kilometers away from the active West Valley Fault (WVF). Performance of the MSE Wall under static and seismic conditions were assessed using two approaches: (1) Limit Equilibrium Method (LEM) by GLE/Morgenstern-Price Method; and (2) Deformation Analysis by Finite Element Method (FEM). The study demonstrates that while inadequate factors of safety under seismic loading may be obtained using LEM, earthquake-induced deformation values are found to be within tolerable limits for lower-hazard design levels. It was also established that designing the geostrap reinforcement to fully withstand higher-hazard ground motions may be uneconomical for the available wall material. Nevertheless, cost-effectiveness of the design may also be achieved by allowing some deformation to the structure in case of higher-level earthquakes, while maintaining serviceability in keeping with current seismic design philosophy.

1 INTRODUCTION

Traffic congestion in Metro Manila, Philippines ranks among the highest in the world, necessitating construction of new roads and bridges to interconnect the various cities within the National Capital Region. Considering the dense urban population, efficient utilization of land is imperative. Thus, the use of vertical Mechanically Stabilized Earth (MSE) Wall for the approach embankment of a bridge is preferred over sloped embankments. Assessment of the seismic response of these walls is also imperative given the susceptibility of Metro Manila to seismic hazards such as ground motion and liquefaction.

This paper presents the slope stability analysis of a 400-meter long bridge with Mechanically Stabilized Earth (MSE) wall, reinforced with steel geostraps, at the approach embankment. Based on the 2021 Fault Map published by Philippine Institute of Volcanology and Seismology (PHIVOLCS), the proposed bridge is located approximately 330 meters from the West Valley Fault (WVF) which can produce a 7.2 magnitude earthquake. The structure was analyzed under both static and pseudo-static (level 1 and 2 earthquakes) conditions. Factors of safety for different soil saturation scenarios were assessed using the Limit Equilibrium Method (LEM). Meanwhile, Deformation Analysis by Finite Element Method (FEM) was used to determine the resulting deformations where the Factors of Safety were found to be inadequate.

2 GEOTECHNICAL EVALUATION AND SEISMIC DESIGN CONSIDERATIONS

2.1 *Idealized subsurface conditions and geotechnical parameters*

The idealized subsurface at the abutments, which were obtained from borehole data, and the corresponding geotechnical parameters for each layer are shown in Table 1.

Table 1. Idealized subsurface conditions.

Depth, m	USCS Classification	SPT N-value	Relative Condition / Consistency	Soil Type	Geotechnical Parameters		
					γ, kN/m^3	S_u, kPa	ϕ, deg
Abutment 1							
0.0 – 3.0	MH / CL	12 – 27	Stiff to Very Stiff	Clay	18	96	0
3.0 – 7.0	CH / MH [SM]	37 – 'refusal'	Hard	Clay	20	196	0
7.0 – 25.0	Rock	'coring'	9% – 55% Recovery RDQ = 0%	Sand	20	0	36
Abutment 2							
0.0 – 4.0	SM / SC-SM / SC	14 – 18	Medium Dense	Sand	18	0	30
4.0 – 9.0	SC / SW / SM	32 – 'refusal'	Dense to Very Dense	Sand	19	0	34
9.0 – 25.0	Rock	'coring'	13% – 67% Recovery RDQ = 0% – 20%	Sand	20	0	36

2.2 *Site class and design accelerations*

Based on the National Structural Code of the Philippines (NSCP) 2015 Table 208–2 and Department of Public Works and Highways (DPWH) – Bridge Seismic Design Standards (BSDS) 2013 Table C3.5–1, the subsurface underlying the bridge site can then be described as stiff soil (site class S_D) or Type II ground. The code-prescribed site class was further verified through a geophysical test data, wherein the average or representative shear wave velocity of the subsurface underlying the area is approximately 259.82 m/s.

Since the bridge location is in close proximity to the West Valley Fault, seismic loading and the consideration of near-source effects are crucial in the design. For bridge structures, DPWH-BSDS 2013 adopts a Performance-Based Design (PBD) approach, wherein two (2) earthquake levels are utilized in the evaluation of displacements and forces/stresses—Level 1 (100-year return period or 53% probability of exceedance in 75 years) and Level 2 (1000-year return period or 7% probability of exceedance in 75 years).

Following the seismic provisions of DPWH-BSDS 2013 Table 3.5.3–1 to Table 3.5.3–3, the recommended seismic parameters for Ground Type II are shown in Table 2.

Table 2. Seismic design parameters considering ground type II.

Earthquake Ground Motion	PGA*	A_S**	S_{DS}***	S_{DI}****
Level 1	0.12	0.19	0.47	0.28
Level 2	0.60	0.53	1.10	0.70

Notes
*PGA: Peak Ground Acceleration Coefficient
**AS: Effective Peak Ground Acceleration Coefficient
***SDS: Design Earthquake Response Spectral Acceleration Coefficient at 0.20-sec period
****$SD1$: Design Earthquake Response Spectral Acceleration Coefficient at 1.0-s period

3 SLOPE STABILITY ANALYSIS

The slope stability analysis (SSA) is done by LEM using the GLE/Morgenstern-Price Method for both circular and non-circular analyses of the embankment/s.

3.1 *Mathematical model*

Figure 1 presents the models of the sections that were analyzed. The sections selected for the analysis are located at the highest elevations within the embankment of each of the bridge
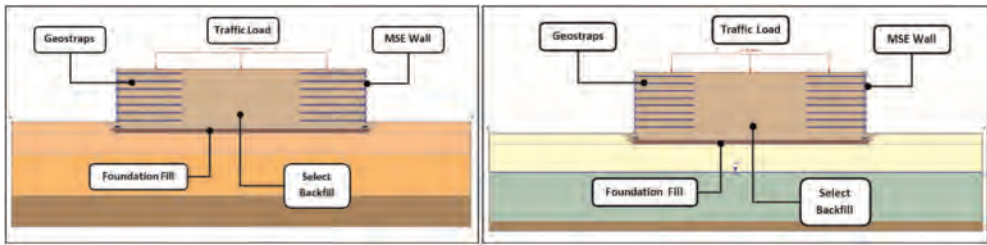
Figure 1. Abutment 1 (left figure) and abutment 2 (right figure) section LEM model.

abutments. These sections are extracted from the conceptual drawings and simplified for the analyses.

The subsurface idealization shown in the LEM models are based on the idealization previously presented in Table 1. Meanwhile, the geotechnical properties for the engineered materials used in the analysis are shown in Table 3. Moreover, the material properties of the geostraps used in the analysis are shown in Table 4.

Table 3. Engineering materials for LEM analysis.

Layer no.	Soil ID	γ, kN/m3	c, kPa	ϕ, deg
Level 1	Select Backfill	18	5	30
Level 2	Foundation Fill	20	5	35

Table 4. Geostrap properties (specified in conceptual drawings).

Length, m	Vertical Spacing, m	Tensile Strength, kN/m
6.13	0.75	29.0 to 55.3

To simulate the traffic load on the approach road upon operation of the bridge, a uniform load of 15.0 kPa is applied on the surface of the model. This live load induces additional surcharge loading to the embankment in the form of lateral earth pressure based on Boussinesq's theory. This may drive the slope to instability or may cause excessive deformation.

Aside from the static lateral earth pressure due to the surrounding structures, earthquakes can induce considerable destabilizing inertial force and permanently degrade the effective shear strength of the soil mass due to the stress and fatigue resulting from the prolonged exposure to cyclic loading. The pseudo-static method is the simplest and most common method in evaluating the stability slopes during earthquakes. Constant seismic coefficients are taken as fractions of the PGA in the idealization. The pseudo-static seismic load induces a horizontal inertial force—$k_h W$, and a vertical inertial force—$k_v W$—where the parameters k_h is the horizontal seismic coefficient, W is the weight of the potential sliding mass, and k_v is the vertical seismic coefficient. Note that the vertical seismic coefficient shall be applied for both upward and downward directions.

In the Philippines, it is common practice to adopt a k_h value taken as half of the surface PGA in accordance with the works of Hynes-Griffin & Franklin in 1994 and Kavazanjian *et al.* in 1997. On the other hand, k_v usually falls within one-fourth (25%) to two-thirds

(66.67%) of its horizontal counterpart. For simplicity, the k_v value was taken as one-half (50%) of k_h.

Based on the seismic provisions of DPWH BSDS 2013, the expected surface PGA is estimated to be 0.53g for the bridge site. The corresponding horizontal and vertical seismic coefficients for both ground motions are summarized in Table 5 for each analysis scenarios.

Table 5. Global slope stability analysis scenarios.

Case	r_u	k_h	k_v	Minimum Allowable FS
1 Long-term static (dry conditions)	0.0	0.0	0.0	1.5
2 Static with moderate porewater pressure	0.2	0.0	0.0	1.3
3 Dry condition with Level 1 earthquake	0.0	0.095g	±0.0475g	1.1
4 Dry condition with Level 2 earthquake	0.0	0.265g	±0.1325g	1.1

3.2 Analysis scenarios

High-intensity rainfall is expected to happen several times a year considering the climate of the Philippines. Conditions wherein pore water pressure build up becoming quite excessive is therefore plausible. The pore water pressure ratio, r_u, is defined as the fraction of pore water pressure to the total vertical pressure exerted by soil. This ratio represents the saturation level of the soil mass in case of a rainfall event. It assumed that adequate drainage is in place at the site which prevents saturation of the soil. As such, only moderate saturation was considered in the analysis. An r_u value of 0.2 would simulate a soil condition of moderately saturated soil. On the other hand, a water surface would be defined for the soils completely below the water table.

An acceptable factor of safety (FS) is based on various considerations such as the recurrent period of rainfall, seismic activity, as well as the assessment of risk or hazard brought about by the slope failure. With these factors considered, recommended factors of safety for static conditions range from 1.3 to 1.5 and a value greater than unity (>1) for earthquake conditions. The minimum allowable FS values for the different analysis scenarios are shown in Table 5.

3.3 Slope stability analysis results

Rocscience Slide 6.0® , a slope stability computer software, was utilized to facilitate calculations for determining the global stability of the embankments. The abutment sections analyzed generally yielded inadequate FS values. FS values for the abutment 1 section under static conditions range from 1.113 to 2.527. Pseudo-static conditions produced FS in the range of 1.239 to 2.263 for Level 1 ground motion and 1.098 to 1.783 for Level 2 earthquake. Abutment 2 section generally produced inadequate FS in all cases considered in the analysis. Table 6 shows the results.

The results of the analysis indicate that the abutment sections have inadequate Factors of Safety under static and Level 2 pseudo-static loading conditions. As such, further analysis is warranted to determine the magnitude of deformations which will be discussed in the following section.

4 DEFORMATION ANALYSIS

The failure surfaces determined from slope stability analysis are not deep-seated in nature. This suggests that localized, shallow failure is more critical than global instability. It should also be noted that the failure planes are typically located along the MSE composite walls.

The primary criterion for designing slope protection systems is the serviceability performance in terms of both vertical deformation (e.g. settlement, heaving) and lateral deflection.

Table 6. Summary of LEM results for approach road embankment of the proposed bridge.

Section	Analysis Type	r_u	Required FS	FS Right Side		FS Left Side	
				Circular	Non-circular	Circular	Non-circular
Abutment 1	Long-term static	0.0	1.5	2.531	1.230	2.527	1.246
	Static with rainfall	0.2	1.3	2.281	1.117	2.283	1.113
	Pseudo-static (Level 1)	0.0	1.1	2.248	1.239	2.263	1.241
	Pseudo-static (Level 2)	0.0	1.1	1.783	1.100	1.720	1.098
Abutment 2	Long-term static	0.0	1.5	1.300	1.019	1.312	0.892
	Static with rainfall	0.2	1.3	1.019	0.772	1.105	0.775
	Pseudo-static (Level 1)	0.0	1.1	1.218	1.042	1.203	0.904
	Pseudo-static (Level 2)	0.0	1.1	0.967	0.787	0.961	0.794

As such, deformation analysis will be performed using FEM to establish both the static and seismic performance of the MSE composite wall. The critical section from LEM was selected for the analysis.

Section 11.10.4 of AASHTO LRFD 2012 details the maximum deformation criteria for MSE walls. For MSE walls with full height precast concrete facing panels, total settlement should be limited to 2.0 in (50 mm) for the seismic conditions. However, given the width of the approach road, it is more crucial to apply this criterion on the road instead of the MSE walls for overall stability. Since lower settlements are expected in normal condition, an allowable settlement of 1.0 in (25 mm) is set for static conditions. The limiting differential settlement should be 1/500.

The maximum allowable lateral displacement of MSE wall, as prescribed by BS 8006 Code of Practice for Strengthened/Reinforced Soils and Other Fills, may be taken as 0.5% of the height of the supported embankment for the static condition. For the pseudo-static case, twice the allowable deflection for the static case or 1% of the height of the supported embankment may be set.

4.1 Soil constitutive model

The primary constitutive model adopted is the Hardening Soil Small-strain (HSS) model (Benz 2007; Schanz et al. 1999). The HSS model is a constitutive model that can vary stiffness depending on the stress state of the soil elements for both small and high strain levels. This is an ideal constitutive model for excavation projects because certain regions of the soil mass may possibly experience different stress state and conditions than those adjacent to them. It should be noted that the HSS model utilizes the Mohr-Coulomb (MC) yield criterion and the model's corresponding shear strength parameters. Due to the lack of advanced lab testing, the HSS parameters were correlated from reported/published values of soil samples with similar relative conditions and/or consistencies to the soil samples obtained from the study area.

PLAXIS, a geotechnical finite element analysis software, was used to obtain the expected deformations. In PLAXIS, the HSS model can generate the Modulus Reduction and Damping Curves by modifying the stiffness model developed by Hardin & Drnevich (1972). The modification revolves around a characteristic shear strain value at 70% stiffness ($\gamma_{0.7}$).

4.2 Deformation analysis results

Table 7 summarizes the deformations obtained from FEM of the critical section at normal (static) conditions. It could be observed that the resulting displacements are well within the tolerable limits.

Table 7. Summary of deformations for approach road embankment (static).

Scenario	Exposed Wall Height, m	Allowable Deformation, mm	Estimated Deformation, mm	Remarks
Left Wall Deflection	6.3	31.5	2.69	Satisfactory
Right Wall Deflection	6.3	31.5	2.67	Satisfactory
Road Settlement	-	25.0	8.57	Satisfactory

Table 8 presents the displacements under pseudo-static loading. Level 1 seismic event would yield tolerable deformations whereas a Level 2 earthquake would produce significant deflection of the embankment walls. A 475-yr earthquake, which has an approximate PGA value of 0.45g, was incorporated in the analysis for comparison, as this seismic design level/loading is adopted on other structures as prescribed by NSCP 2015. Likewise, excessive deformations were also obtained under the 475-year earthquake. As for the road settlement, acceptable values were calculated for all the pseudo-static cases.

The design of the MSE wall of the approach was iterated to come up with a scheme which would decrease the magnitude of the expected deflections. For the geostraps, the vertical spacing installation can be adjusted to 0.60 meters, and their lengths increased to 10 meters. The precast MSE panel was thickness was also adjusted to 200 mm with a compressive strength of 28 MPa.

Table 8. Summary of deformations for approach road embankment (pseudo-static).

Scenario	Exposed Wall Height, m	Allowable Deformation, mm	Estimated Deformation, mm		
			Level 1	Level 2	475-year
Left Wall Deflection	6.3	63.0	55.30	213.90	166.10
Right Wall Deflection	6.3	63.0	60.02	228.70	181.10
Road Settlement	–	50.0	11.95	32.51	27.02

Table 9 presents the resulting deformations from the proposed scheme. Deformations for Static and Level 1 cases are still within the tolerable limit. However, considerable deflections are still expected for the Level 2 and 475-yr earthquake events, albeit at a lesser degree compared to the original scheme (approximately 10 to 30 mm difference). With that, immediate repairs are still warranted if a Level 2 or 475-yr earthquake occur.

Table 9. Resulting deformations from iteration.

Scenario	Estimated Deformation, mm			
	Static	Level 1	Level 2	475–year
Left Wall Deflection	2.24	52.80	195.40	155.70
Right Wall Deflection	2.05	52.77	195.30	155.80
Road Settlement	7.31	6.86	16.56	12.33

5 CONCLUSIONS AND RECOMMENDATIONS

Designing the approach roads for a Level 2 earthquake may be impractical given that excessive deformations are expected. As such, it is proposed to design the approach embankment considering a 475-yr earthquake which minimizes the expected settlement to 25 mm while implementing minimal changes to the original scheme. To achieve this, it is recommended to use 7.0-meter length geostraps, which will be installed at the original vertical spacing of 0.75 m and use a precast MSE wall panel with at least 175 mm thickness. It is important that the internal stability of the geostraps is assessed. It should also be noted that any changes in the original design would require additional costs. As such, evaluation of the cost-effectiveness of the scheme is recommended.

Aside from the proposed scheme, the following are recommended to improve the stability and minimize the possible deformations of the approach embankment: (1) ensure that adequate drainage is implemented during construction to guarantee the relief of porewater pressure and (2) ensure that surface drainage atop the road embankment, as well as at the toe/base, are installed post-construction. Moreover, the construction methodology (staged construction, compaction, quality control and assurance) of the embankment must guarantee stability during various stages of the construction and mitigate slope failures.

REFERENCES

American Association of State Highway and Transportation Officials. 2012. *AASHTO LRFD Bridge Design Specifications*. AASHTO, Washington D.C.

Association of Structural Engineers of the Philippines, Inc. 2015. *National Structural Code of the Philippines 2015 Volume I*. Quezon City, Philippines.

Benz, T. 2007. *Small-Strain Stiffness of Soils and its Numerical Consequences [Doctoral dissertation, University of Stuttgart]*. University of Stuttgart Institute of Geotechnical Engineering.

British Standards Institution. 2010. *BS 8006-1:2010 Code of Practice for Strengthened/reinforced Soils and Other Fills*. BSI Standards Publications, United Kingdom.

Department of Public Works and Highways. 2013. *LRFD Bridge Seismic Design Specifications 1st Edition 2013*. Manila, Philippines.

Hardin, B. O. & Drnevich, V. P. 1972. Shear Modulus and Damping in Soils: Design Equations and Curves. *Journal of the Soil Mechanics and Foundations Division*, *98*(SM7), 667–692.

Hynes-Griffin, M.E. & Franklin, A.G. 1984. *Rationalizing the Seismic Coefficient Method. Miscellaneous Paper GL-84-13*, US Army Engineering Waterways Experiment Station, Vicksburg, Mississippi, USA.

Kavazanjian, E., Matasovic, N., Hadj-Hamou, T. & Sabatini, P.J. 1997. "Design Guidance: Geotechnical Earthquake Engineering for Highways, Design Principles." *Geotechnical Engineering Circular 3*. Federal Highway Administration, Washington DC, USA

Philippine Institute of Volcanology and Seismology. 2021. *Distribution of Active Faults and Trenches in the Philippines*.

Gravel-rubber mixtures as geotechnical seismic isolation systems underneath structures: Large-scale tests vs FEM modelling

G. Abate, A. Fiamingo & M.R. Massimino
Department of Civil Engineering and Architecture, University of Catania, Italy

D. Pitilakis, A. Anastasiadis, A. Vratsikidis & A. Kapouniaris
Department of Civil Engineering, Aristotle University of Thessaloniki, Thessaloniki, Greece

ABSTRACT: According to the sustainable growth, the need for low-cost seismic isolation systems has led to proposals of new projects. The use of granular soils mixed with granulated rubber derived from scrap tires as a layer underlying the foundations of structures represents a solution for the mitigation of seismic risk and the management of waste tires.

Only a few small-scale experimental studies on this subject are available in the literature. The first experimental campaign on a full-scale prototype structure founded on gravel-rubber mixtures (GRMs) with different rubber content per weight was recently carried out in Thessaloniki (Greece). Ambient noise, free- and forced-vibration tests were performed.

This paper shows a comparison between the results achieved during the forced-vibration tests and the results obtained by a non-linear 3D FEM modelling of these tests. This comparison allowed us to investigate the isolation capacity of GRMs and the effects of the rubber content per weight.

1 INTRODUCTION

Over the last decades, seismic isolation has been widely used as an effective strategy in the earthquake-resistant design of structures. The traditional systems, such as elastomeric bearings, sliding elements, and friction-pendulum systems, are quite expensive economically and technically for conventional buildings. In addition, traditional systems produce large volumes of waste both in production and at end-of-life disposal. So, according to the circular economy and sustainable growth, the need for low-cost seismic isolation systems has led to proposals for new projects.

In this context, Geotechnical Seismic Isolation (GSI) is a potential technique to mitigate the effects of seismic motion on superstructures. The main idea is to improve the mechanical properties of the foundation soil and dissipate the seismic motion before reaching the structure (Tsang 2022). Among several materials, soil-rubber mixtures (SRMs) represent an eco-friendly and low-cost solution. The use of end-of-life tires (ELT) for the rubber particles in the mixtures can provide a modern recycling system to reduce the considerable stockpile of scrap tires worldwide. On the other hand, SRMs are considered an affordable alternative for the seismic isolation of conventional structures, especially in developing countries having limited financial resources. SRMs have been investigated in the last years (Anastasiadis *et al*. 2012; Pistolas *et al*. 2018), demonstrating that their use is advantageous due to their good static and dynamic properties. Few small-scale experimental studies are available in the literature. Just one experimental campaign on a full-scale prototype structure founded on three different gravel-rubber mixtures (GRMs) was recently performed in Thessaloniki

(Greece) in the framework of the European Research Program SOFIA-SERA (Abate *et al.* 2022; Pitilakis *et al.* 2021). The three GRMs had variable rubber content per weight, equal to 0%, 10%, 30%, labelled as GRM 100/0, GRM 90/10, and GRM 70/30, respectively. Ambient noise tests and free- and forced-vibration tests were carried out.

This paper shows the main results achieved during the forced-vibration tests and by a 3D FEM modelling of these tests. The performed forced-vibration experiments were carried out in a frequency range of 1-10 Hz to include the fixed- and flexible-base natural frequencies of all three GRM-structure systems. This paper deals with the results concerning the structure founded on the GRM 100/0 and 70/30 layers, subjected to the input frequency equal to 4 Hz and 2.5 Hz, close to the fundamental natural frequency of the systems, using GRM 100/0 and 70/30, respectively.

The foundation soil and the GRMs were modelled by advanced visco-elasto-plastic constitutive model. The structure was modelled by a linear visco-elastic constitutive model.

The numerical results were successfully compared to the experimental ones. Moreover, the numerical simulation allowed to study more in-depth the dynamic behaviour of the GRMs, also considering the shear strains vs the shear stresses in the middle of the GRM layer and represent a valuable tool for future analyses.

2 THE LARGE-SCALE EXPERIMENTAL CAMPAIGN

EuroProteas prototype is the first full-scale model structure in Europe (at the Euroseistest facility, 30km NE of Thessaloniki in Greece), designed to study dynamic soil-structure interaction (DSSI) (Figure 1). It is a perfectly symmetric steel frame, on a reinforced concrete (RC) slab supporting two RC slabs, having the same size as the foundation slab (3.00x3.00x0.40 m). Steel X-braces (section L100×100×10 mm) connect the four steel columns (section QHS150×150×10 mm) in both directions.

The foundation soil was investigated using extensive geotechnical and geophysical surveys, including static and dynamic in-situ and laboratory tests (Pitilakis *et al.* 2018). The subsoil consists of a 7 m thick upper layer of silty clayey sand, which overlies a layer of clayey to silty sand with gravels between 7 and 22 m and, after that, a layer of marly silt to silty sand until the depth of 30 m. More precisely, the soil profile can be subdivided into eight layers, called A, B, C, D1, D2, E1, E2, and F, whose main properties are shown in Table 1. More details are reported in Abate *et al.* (2017). The uppermost 0.50 m of the foundation soil was replaced with three different GRM backfills (Figure 1). The rubber content per mixture weight (p.w.) was fixed equal to 0%, 10%, and 30% for the three foundation mixtures, so labelled as GRM 100/0, GRM 90/10, and GRM 70/30, respectively. The gravel was characterized by $D_{50,G} = 20.76$ mm and $G_{s,G} = 2.67$. The granulated rubber was characterized by
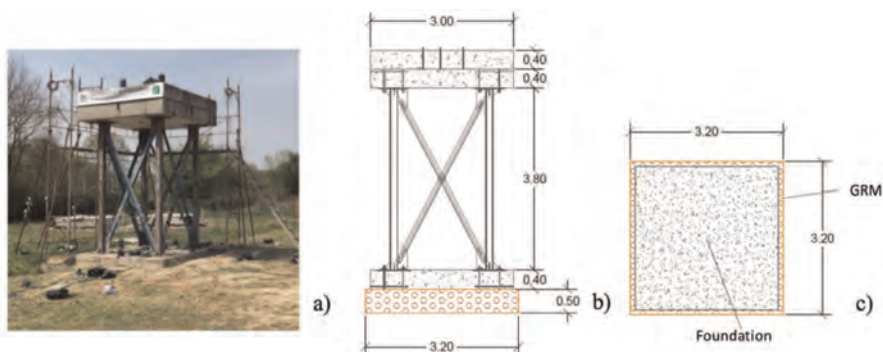
Figure 1. (a) Photo, (b) section and (c) plan view of EuroProteas with the adopted GRM underneath the foundation (lengths in meters).

Table 1. Main properties for EuroProteas subsoil.

Layer	z(m)	V_s (m/s)	G_0 (kPa)	D_0 (%)	γ_d (kN/m^3)
A	0.5–3	100	21407	2.5	21.0
B	3–5	125	32652	3.0	20.5
C	5–8	170	58919	3.0	20.0
D1	8–13	210	89908	2.5	20.0
D2	13–17	210	89908	2.5	20.0
E1	17–20	260	137819	2.5	20.0
E2	20–24	260	137819	2.5	20.0
F	24–30	300	183486	1.7	20.0

$D_{50,R}$ = 3.27 mm and $G_{s,R}$ = 1.10. The ratio $D_{50,R}/D_{50,S}$ is less than unity. As for the mixtures, the main physical properties are reported in Table 2. The V_s values for the GRM's layer were obtained from G_0. The $G/G_0(\gamma)$ and $D(\gamma)$ curves for the mixtures GRM 100/0 and GRM 70/30 were achieved according to Menq equations (2003) and Pistolas ones (2015), respectively. Just the effects of these two mixtures are discussed in the present paper, because the experimental results did not show valuable differences in the behaviour of the analysed system using GRM100/0 and GRM90/10 (Pitilakis *et al*. 2021).

Table 2. Main properties of GRM100/0 and GRM 70/30.

GRM ID	$D_{50,R}/D_{50,R}$	G_s	D_r (%)	γ_d (kN/m^3)	G_0 (kPa)	D_0 (%)	V_s (m/s)
GRM100/0	–	2.67	98	16.2	60044	1.0	192
GRM70/30	0.16	2.19	59–71	11.8	2600	2.7	45

Ambient noise tests, free- and forced-vibration tests were performed at different excitation levels, with and without rubberized soil underneath the foundation. This paper deals with the forced-vibration tests. The input force was applied at the geometrical centre of the structure's roof by an eccentric mass shaker. The produced harmonic force was applied along the structure's principal axis at approximately 30° angle with the magnetic N-S direction. The output force amplitude is adjusted by the eccentricity and the operating frequency according to the equation $F_{sh} = E \cdot (2\pi f)^2$, where F_{sh} is the shaker force (in N), E is the eccentricity of the shaker (in kg-m), and f is the rotational velocity of the shaker (in Hz). The frequency range is 1-10 Hz to include the fixed-base natural frequency (equal to 9.13 Hz) and the flexible-base ones of all three GSI-structure systems (equal to 4.0 Hz and 2.5 Hz, for the systems resting on GRM 100/0 and GRM 70/30, respectively), evaluated by means of the ambient noise tests (Pitilakis *et al*. 2021). The tests characterized by the eccentricity equal to 6.93 kg-m and carried out at 4 Hz and 2.5 Hz, respectively, for the GRM 100-0 and 70-30, are here analysed and numerically simulated being characterized by frequencies next to the first resonant frequencies of the investigated systems. A dense instrumentation scheme was designed to evaluate the response of the structure, the foundation, the GRM layer, and the adjacent soil in the vertical "Z" and horizontal "N" and "E" directions.

3 THE 3D SOIL-GRM-STRUCTURE FEM MODELLING

The above-discussed forced-vibration tests were simulated by a 3D finite element model using the MIDAS FEA-NX (2022) code. Figure 2a shows the mesh of the whole soil-GRM-structure system. The soil layers subdivision was performed according to Table 1, but just the layers from A to E1 were modelled (Figure 2b) to minimize the computational efforts. Free
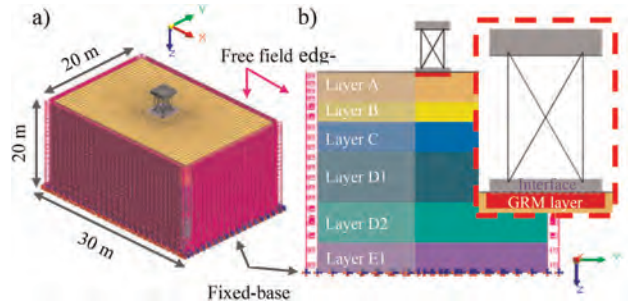
Figure 2. (a) 3D FEM model of the fully coupled soil-GRM-Europroteas structure; (b) details of the mesh.

field edges were defined along the lateral boundaries of the 3D model, to simulate the infinitely far conditions and to prevent the reflection of waves from the model boundaries. Viscous dampers connected the lateral boundaries of the model to the free-field edges. The viscous damper coefficients, according to P and S waves, were calculated automatically by the MIDAS FEA-NX code. The 3D model was fixed at the base. The columns and X-braces were modelled by beam elements. Solid elements were used to model the soil layers and the three slabs. The sizes of the mesh elements were fixed to reproduce all the waveforms of the whole frequency range under study. Contact surfaces were used between the foundation and the GRM to model uplifting and/or sliding phenomena. The Rayleigh damping was considered, evaluating the coefficients α_R and β_R according to the double frequency approach (Fiamingo et al. 2022; Massimino et al. 2019). The natural circular frequencies of the first two modes of the system response (ω_1 and ω_2) were adopted. As for the structure, a damping ratio equal to 3% was assumed for the steel elements and a value of 5% was considered for the concrete slabs. As for the soil, the values of the damping ratio reported in Table 1 were used. A harmonic displacement input was applied at the structure's roof in the x-direction according to the shaker force F_{sh} used during the tests (F_{sh} = 4.38 kN and F_{sh} =1.71 kN for the configuration with GRM100/0 and GRM70/30, respectively). The structure was modelled considering a linear visco-elastic behaviour, assuming E = 31500 MPa, $\nu = 0.2; \gamma =$ 25 kN/m^3 for the concrete slab and E = 210000 MPa, $\nu = 0.3; \gamma$ = 75 kN/m^3 for the steel elements. The GRM layers and the soil layers from A to C were modelled by the visco-elasto-plastic HSsmall constitutive model, whose parameters are reported in Table 3. The HSsmall constitutive model is an isotropic hardening elastoplastic hysteretic model based on

Table 3. Parameters adopted for modelling the GRMs and the soil layers A-C by the HSsmall model.

Parameters	GRM100/00-0.5 m	GRM70/300-0.5 m	Layer A0.5-3.0 m	Layer B3.0-5.0 m	Layer C5.0-8.0 m
G_0^{ref} (kPa)	129912	3715	26491	42392	72353
m	0.40	0.25	0.10	0.3	0.3
γ_{087} (%)	0.0160	0.0842	0.0224	0.0176	0.0176
E_{50}^{ref} (kPa)	30931	885	5519	14131	24118
E_{oed}^{ref} (kPa)	30931	885	5519	14131	24118
E_{ur}^{ref} (kPa)	92794	2654	16557	42392	72353
ν_{ur} (-)	0.25	0.25	0.25	0.25	0.25
K_0 (-)	0.40	0.60	0.46	0.45	0.45
R_f (-)	0.9	0.9	0.9	0.9	0.9
p_{ref} (kPa)	100	100	100	100	100
c (kPa)	2.00	2.00	3.00	20.00	20.00
ϕ (°)	40.1	23.6	33	28	28
ψ (°)	10	0	3	0	0

the combination of the Hardening Soil (HS) model (Schanz *et al.* 1999) with the small-strain overlay model proposed by Benz (2006) and Benz *et al.* (2009). The calibration of the HSsmall constitutive model parameters was performed according to the procedure proposed by Amorosi *et al.* (2016). The soil layers from D1 to E1 were modelled using the Mohr-Coulomb model, adopting the parameters shown in Table 4. This last choice is due to the distance of the soil layers D1-E1 from the structure, where the input is applied, so a sophisticated constitutive model such as the HSsmall one is not necessary.

Table 4. Parameters adopted for modelling the soil layers D1-E1 by the Mohr-Coulomb model.

Parameters	Layer D1 8–13 m	Layer D213–17 m	Layer E117–20 m
E (kPa)	233761	233761	358328
ν (-)	0.30	0.30	0.30
c (kPa)	2.00	20.00	20.00
ϕ (°)	33	28	28
ψ (°)	3	0	0

4 COMPARISON BETWEEN THE EXPERIMENTAL AND NUMERICAL RESULTS

To compare the experimental and numerical results two components of the dynamic motion were investigated: the horizontal response parallel to the direction of shaking (named as "N" direction), and the vertical response (named as "Z" direction). Due to the lack of space only some comparisons are reported in this paper.

Figure 3 shows the numerical and the experimental results at the structure's roof and foundation in terms of acceleration time histories, as well as at the soil surface in terms of velocity time histories. The results deal with the instruments placed along the direction of shaking. Considering the complexity of the analyses, the various uncertainties and not controllable/unexpected factors accompanying in-field testing, the numerical simulations capture very well the experimental response of the structure and the velocities recorded on the soil surface for both the configuration with GRM100/0 and GRM70/30.
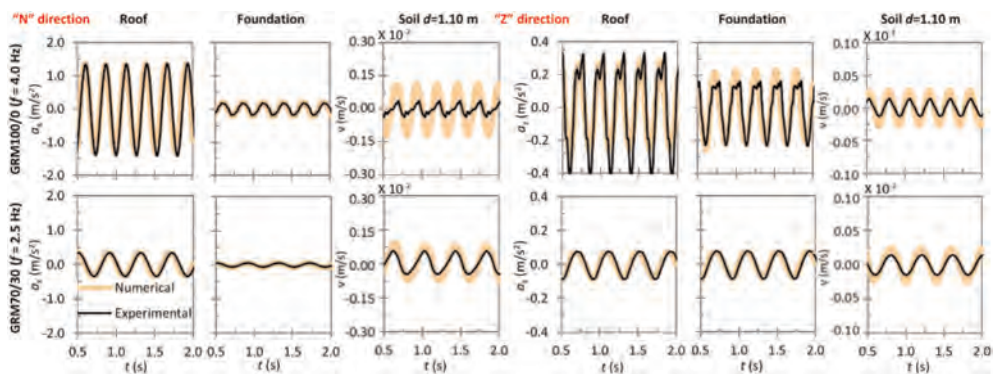
Figure 3. Experimental versus numerical results at the roof and at the foundation in terms of acceleration time histories and on the soil (at 1.10 m from the foundation) in terms of velocity time histories.

5 OTHER NUMERICAL RESULTS

Once the FEM model was validated, the dynamic behaviour of the soil-GRM-structure system was numerically investigated in terms of shear strains (γ_{xz}) versus the shear stresses (τ_{xz}) evaluated in a representative node of the GRMs in front of the foundation, at a depth z = 0.25 m and at the distance of the geometric centre of the foundation equal to x = 1.60 m. Figure 4 shows that γ_{xz} considering the configuration with GRM 100/0 is lower than that with GRM70/30 (0.30% versus 0.50%), due to its low compressibility. On the other hand, the maximum amplitude of τ_{xz} is very amplified for the configuration with GRM100/0 compared to that for the configuration with GRM70/30 (12.5 kN/m^2 versus 5 kN/m^2), due to the higher amplitude of the force applied at the roof. The slope of the loop, for the configuration with GRM70/30, tends to flatten out due to a decrease of the shear modulus compared to that for the configuration with GRM100/0.
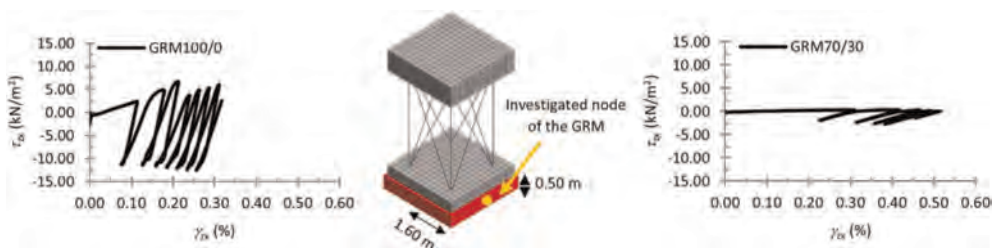
Figure 4. Shear strains versus shear stresses in the middle of the GRMs.

6 CONCLUSIONS

In this paper, advanced nonlinear 3D numerical analyses were carried out to reproduce the forced-vibration tests performed on the prototype structure of EuroProteas in Thessaloniki, Greece, using Gravel-Rubber Mixtures (GRMs) as a means of Geotechnical Seismic Isolation. Two GRM layers with different rubber content per mixture weight (0% and 30%, respectively) were analysed. The experimental response on the structure is well-reproduced by the FEM model. The FEM modelling lightly overestimates the recorded velocities in the soil. As regards the shear strains-stresses curves in the GRMs, investigated only by the FEM model, GRM70/30 provides for a clearly higher maximum level of strains and stresses compared to GRM100/0. The maximum strain level is under the allowable value. The GRM 70/30 clearly act in mitigating the seismic motion before reaching the structure.

REFERENCES

Abate, G., Gatto, M., Massimino, M.R., Pitilakis, D. 2017. Large Scale Soil-foundation-structure Model in Greece: Dynamic Tests vs FEM Simulation, in: M. Papadrakakis, M. Fragiadakis (Eds.), *Proc. 6th Intern. Conf. on Computational Methods in Structural Dynamics and Earthquake Engineering (COMPDYN 2017)*. Eccomas Proceedia, Rhodes Island, Greece: 1347–1359.

Abate, G., Massimino, M.R., Pitilakis, D., Anastasiadis, A., Vratsikidis, A. 2022. Influence of Rubberized Soil Underneath the Foundation of a Structure Investigated by Dynamic Large-scale Tests, in: Mizanur Rahman, Md., Jaksa, M. (Eds), *Proc. 20th Intern. Conf. on Soil Mechanics and Geotechnical Engineering (ICSMGE 2022)*. Australian Geomechanics Society, Sydney, Australia: 1057–1062.

Amorosi, A., Boldini, D., di Lernia, A. 2016. Seismic Ground Response at Lotung: Hysteretic elasto-plastic-based 3D Analyses. *Soil Dyn. Earthq. Eng.* 85: 44–61.

Anastasiadis, A., Senetakis, K., Pitilakis, K., Gargala, C., Karakasi, I. 2012. Dynamic Behavior of sand/rubber Mixtures. Part I: Effect of Rubber Content and Duration of Confinement on Small-strain Shear Modulus and Damping Ratio. *ASTM Special Technical Publication*, 1540 STP: 221–247.

Benz, T., Vermeer P.A., Schwab, R. 2009. A Small-strain Overlay Model. *Int. J. Numer. Anal. Methods Geomech.* 33: 25–44.

Benz, T. 2006. *Small-strain Stiffness of Soil Sand its Numerical Consequences*. Germany (Ph.D. thesis): University of Stuttgart.

Fiamingo, A., Bosco, M., Massimino, M.R. 2022. The Role of Soil in Structure Response of a Building Damaged by the 26 December 2018 Earthquake in Italy. *J. Rock Mech. Geotech. Eng*. (in press).

Massimino, M.R., Abate, G., Grasso, S., Pitilakis, D. 2019. Some Aspects of DSSI in the Dynamic Response of Fully-coupled Soil-structure Systems. *Rivista Italiana di Geotecnica* 2019 (1): 44–70.

Menq, F.Y., 2003. *Dynamic Properties of Sandy and Gravelly Soils*. PhD thesis, University of Texas, Austin.

MIDAS FEA NX, 2022 (v.1.1); CSPFEA—Engineering Solutions: Este, Italy.

Pistolas, G.A. 2015. *Experimental and Numerical Investigation of the Implementation of Recycled Materials Mixtures in the Foundation of Structures for the Improvement of Seismic Behavior*. PhD thesis, Department of Civil Engineering, Aristotle University of Thessaloniki, Greece. (in Greek).

Pistolas, G.A., Anastasiadis, A., Pitilakis, K. 2018. Dynamic Behaviour of Granular Soil Materials Mixed with Granulated Rubber: Effect of Rubber Content and Granularity on the Small-Strain Shear Modulus and Damping Ratio. *Geotech. Geol. Eng.* 36(2): 1267–1281.

Pitilakis, D., Anastasiadis, A., Vratsikidis, A., Kapouniaris, A., Massimino, M.R., Abate, G., Corsico, S. 2021. Large-scale Field Testing of Geotechnical Seismic Isolation of Structures Using Gravel-rubber Mixtures. *Earthq. Eng. Struct. Dyn.* 50(10): 2712–2731.

Pitilakis, D., Rovithis, E., Anastasiadis, A., Vratsikidis, A., Manakou, M. 2018. Field Evidence of SSI From Full-scale Structure Testing. *Soil Dyn. and Earth. Eng*. 112: 89–106.

Schanz, T., Vermeer, P.A., Bonnier, P.G. 1999. The Hardening Soil Model: Formulation and Verification. *Beyond 2000 in computational geotechnics*.

Tsang, H.H. 2022. Analytical Design Models for Geotechnical Seismic Isolation Systems. *Bull. Earthq. Eng*. https://doi.org/10.1007/s10518-022-01469-x.

Influence of geosynthetic interface within a liner system in dynamic analyses of a landfill

D. Gioffrè & C.G. Lai
Department of Civil Engineering and Architecture, University of Pavia, Italy

ABSTRACT: Geosynthetic composites are extensively used in liner systems which are placed beneath the landfill to isolate waste material from the surrounding environment. However, geosynthetics can also be the weak interface, so analyses of seismic response and permanent deformation of landfill should be performed considering the influence of liner interface. This paper investigates the contributing role of the base liner on the seismic behavior of landfills. Based on the results of the site investigation, dynamic analyses of a landfill in Northern Italy were carried out with the finite difference computational platform FLAC-2D. The displacement of the geosynthetics resulting from the seismic loading was estimated along with the potentially induced seismic slip surface taking place at the interfaces. Results indicate that the geosynthetic liner system affects the dynamic response of landfill and that the seismic displacements on the geosynthetics should not be neglected. This paper also discusses results and implications on seismic design of landfills to ensure the integrity of the liner systems as well as the stability of the waste landfill.

1 INTRODUCTION

According to international codes and recommendations, the analysis of the seismic stability conditions of a waste landfill could be conducted using one of the following types of analysis:

a) pseudo-static methods;
b) simplified dynamic methods (displacement-based);
c) advanced dynamic analysis methods.

Methods a) evaluate a global safety coefficient for the slope (landslide section) along a predefined sliding surface and considering a statically applied seismic action in the center of gravity in the unstable rigid body. The magnitude of the pseudo-static inertial force depends on the peak acceleration value expected at the free surface at the study site and on the limit-state considered (return period). Pseudo-static methods do not allow an evaluation of the "performance" of the slope subjected to seismic shaking, a performance defined for example by permanent displacement.

In methods b) and c) the seismic stability is evaluated by comparing the permanent displacement with the admissible displacement defined by codes and recommendations. Therefore, methods b) and c) are based on a performance approach to seismic design. However, while method b) is based on an analysis in which the phases needed to define the seismic input and calculate the permanent displacement are uncoupled (decoupled approach), in method c) these phases are carried out jointly in the same numerical model (coupled approach). Furthermore, in method b) the numerical model used for the evaluation of the permanent displacements is typically carried out by means of a simplified approach that idealizes an unstable rigid body moving on a predefined sliding surface (like in pseudo-static methods).

In method c) the slope is idealized as a deformable body in which the sliding surface is not defined a-priori but it emerges as a narrow zone of intense shearing strain (shear band) during the analysis.

The simplified dynamic method (method b) is approximate and does not allow an accurate evaluation of permanent displacements in the presence of complex geometric configurations such as the presence of berm or embankment along the slope, reinforcement structures, and different types of materials separated by appropriate interfaces.

Furthermore, in systems with significant stiffness and strength differences, the evaluation of permanent displacements requires a coupled approach to account for the dynamic interaction between resistance, deformability, interface and seismic action (Lai *et al*. 2009; Rampello & Callisto 2008).

A liner system generally consists of one or more types of soil and/or geosynthetic materials such as geomembranes, geosynthetic clay liners, geonets and geotextiles. The shear strength of the liner system and the interface friction between the layers determine how susceptible the slope is to lateral movements along a geosynthetic interface in response to forces generated by the waste weight. In fact, sliding along a geosynthetic interface can harm the liner system's containment function. If sliding occurs below the geomembrane at a compacted clay liner/geomembrane interface, the geomembrane will stretch and possibly tear. For these reasons, it is important to assess the performance of the geosynthetic liner system of landfill.

The paper illustrates the seismic stability analysis conducted during the design of the extension to an existing landfill located in the Province of Parma (Northern Italy). The seismic stability analysis of the landfill allowed to evaluate the permanent displacement along the liner system and to reproduce in a satisfactory way the complex interactions that occur between the seismic action and the different elements of the landfill.

2 LANDFILL AND GEOTECHNICAL CHARACTERIZATION

The landfill under study is located in the high hill sector of the Parma Apennines (Italy), in the geological context of the northern Apennine chain. (Figure 1)
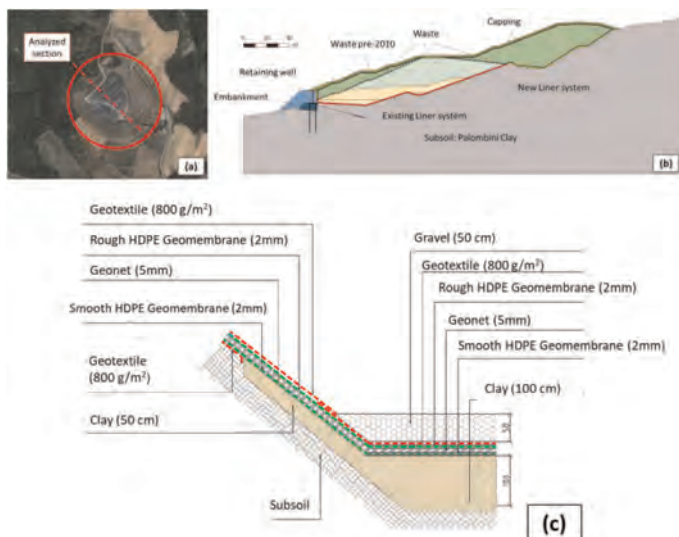
Figure 1. Landfill: (a) Chorography of the site (source "Google Earth"). In the red circle the site of the landfill; (b) Analyzed section; (c) Liner system details.

Starting from an extensive survey campaign, it was possible to accurately define the seismic-stratigraphic model of the landfill and obtain an adequate geotechnical characterization of soil, waste and geosynthetic liner system.

The waterproofing package positioned at the bottom of the landfill is a geocomposite formed by a rough HDPE geomembrane, a draining plastic geonet and a smooth HDPE geomembrane.

The interface shear strength between the several layers of landfill liner has been evaluated using standard direct shear testing of each soil/geosynthetic, soil/waste and geosynthetic/geosynthetic interface.

Table 1 reports the characteristic parameters used in the seismic stability checks of the landfill. Their definition, obtained from a careful analysis of the on-site tests and laboratory tests carried out during the investigation campaigns, is not discussed in detail in this paper (Gioffrè *et al.* 2022).

The existing and the new liner system have been characterized performing several direct shear tests on different interfaces: geotextile - rough HDPE geomembrane; rough HDPE geomembrane -geonet; geonet - smooth HDPE geomembrane; smooth HDPE geomembrane - geotextile. In the numerical model liner systems have been modelled with an interface element which geotechnical parameters (Table 1) are referred to the most critical resistance parameters obtained with direct shear tests on smooth HDPE geomembrane - geotextile interface.

Table 1. Geotechnical parameters using in landfill seismic stability analysis.

Zone[#]	Material	γ[kN/m^3]	Cohesion c'[kPa]	Shear strength angle ϕ' [°]
1	Subsoil (Palombini clay)	20	27	21
2	Embankment	20	50	21
3	Waste pre-2010 with leachate	10	0	24
4	Waste pre-2010	14	0	24
5	Waste	14	8	32
6	Capping	20	15	30
	Interface 1 (Existing liner system)	–	0	10
	Interface 2 (New liner system)	–	0	14

The seismic-stratigraphic model of the landfill was defined with reference to the results of the seismic refraction prospecting (o prospection) for the most superficial part of the landfill (depth $\leq$ 15 m). At greater depths, the values of V_S measured in the MASW tests were used as far as available; in addition, experimental data were extrapolated using a linear interpolation approach.

Figure 2 shows the G/G_{max} decay curves obtained from experimental laboratory tests for soil and waste; G/G_{max} curves for embankment and capping were taken from the literature (Darendeli 2001).

3 NUMERICAL MODEL AND SEISMIC INPUT

Non-linear dynamic analyses were carried out using a 2D numerical model of the landfill implemented in a finite difference computational code (FLAC-2D v8) that is able to consider both large displacements and relative displacement at liner system interfaces.

The model of the cross section of landfill (maximum reservoir section) is made up of 21,160 elements; the elements of the model have dimensions in height between 0.3 and 3.0 m (Figure 3). The dimensions of the elements have been chosen to respect the accuracy
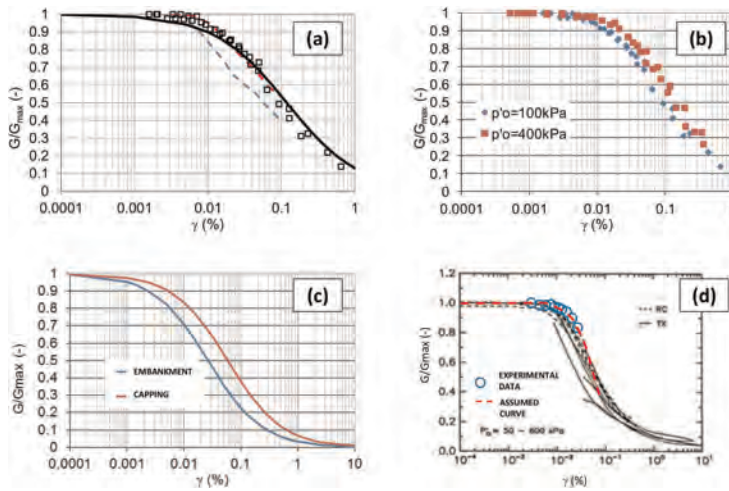
Figure 2. Shear modulus G/G_{max} reduction curves: (a) Experimental curves for waste at the same confining pressure; (b) Experimental curves for waste at different confining pressures; (c) Assumed curves for embankment and capping from Darendeli (2001); (d) Experimental curve for subsoil (Palombini clay).
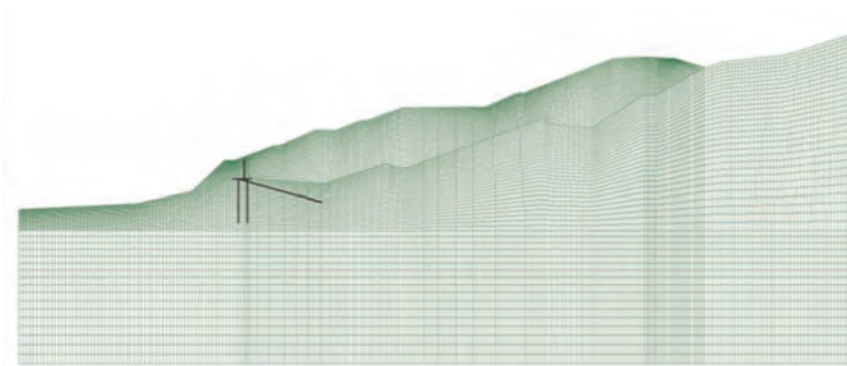
Figure 3. FLAC-2D model.

conditions of Kuhlemeyer and Lysmer (1973), i.e. they are equal to 1/10 of the minimum wavelength, which is a function of the maximum frequency of interest (assumed to be 30 Hz) and of the shear modulus at small deformations of the materials considered.

The constitutive model used for waste is elasto-plastic where the Mohr-Coulomb resistance criterion governs the triggering mechanism(s) of the permanent deformation. The non-linearity of the mechanical behavior is also taken into account by the reduction of the shear modulus G with the level of deformation (hysteretic behavior).

Dynamic analyses have been carried out imposing the following boundary conditions: absorbent conditions at the base and at the lateral edges ("quite boundaries") and free-field conditions along the lateral edges ("free-field boundaries").

Figure 4 shows the elastic acceleration response spectrum of the seven natural spectrum-compatible accelerograms selected for the analyses and the acceleration response spectrum calculated as the average of the selected signals.
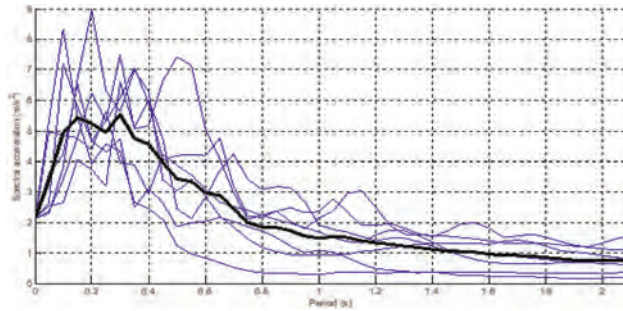
Figure 4. Elastic acceleration response spectrum of the selected signals (thin blue lines) and spectrum-compatible acceleration response spectrum calculated as the average of the selected signals (thick black line).

4 RESULTS OF NUMERICAL ANALYSES

Displacement information is more beneficial than the seismic safety factor when geosynthetics are used because geosynthetics cannot withstand large displacements. Therefore, the design can be modified to ensure that little permanent displacement occurs with geosynthetics. The permanent displacement calculated from the analysis can be used to predict whether the latter will exceed the landfill components' ability to withstand earthquake-induced deformation.

Figure 5 shows the absolute permanent displacement at the end of the dynamic analysis for accelerogram 3 which can be considered representative of the dynamic response of the landfill. It is possible to observe that the interface (liner system) marks a clear separation of the movements between the waste body and the substrate. This result is due to the extremely low shear strength parameters that characterize the contact between the geosynthetics in the waterproofing package.

From Figure 5 it is also possible to observe that the maximum permanent displacements are concentrated in a surface area of the landfill near the embankment.

Considering that the most critical conditions for the stability of the landfill occur along the liner system, the permanent displacements along the interface were also evaluated.
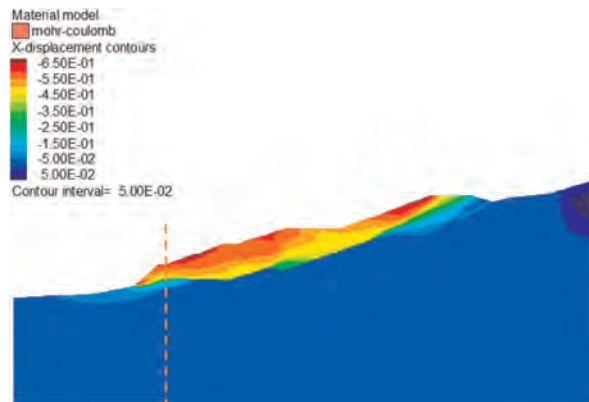
Figure 5. Accelerogram 3: permanent displacement at the end of the analysis (displacements in m).

Table 2. Maximum permanent displacement and maximum permanent displacement along liner system.

Accelerogram	1	2	3	4	5	6	7
Maximum permanent displacement (cm)	15.0	18.0	65.0	27.5	130.0	22.5	8.0
Maximum permanent displacementalong liner system (cm)	12.2	14.5	47.2	21.4	95.2	16.2	4.3

Table 2 reports the horizontal component of the maximum permanent displacement and the maximum permanent displacements along the liner system obtained in the coupled non-linear numerical analyses using the two-dimensional landfill model implemented in FLAC-2D.

Results in Table 2 shows that the accelerogram 5 represents the most severe signal as it is the one associated with the greatest displacements in relation to its duration and its frequency content. The permanent displacements are so significantly greater than those obtained with all the other accelerometric signals, that this accelerogram has been considered an "outlier" signal.

Displacements along the liner system make it possible to carry out the conformity checks that will arise from the comparison between these displacements and the admissible displacement of the geosynthetics present in the waterproofing package.

Figure 6 shows the maximum permanent displacement along the liner system at the end of the dynamic analyses for the different accelerograms used. From Figure 6 it possible to observe that the accelerograms 3 and 5 are those that lead to the greatest permanent displacements along the interface. For all accelerograms, a maximum permanent displacement along the reduced interface is observed at the second tooth located in the upstream part of the landfill.
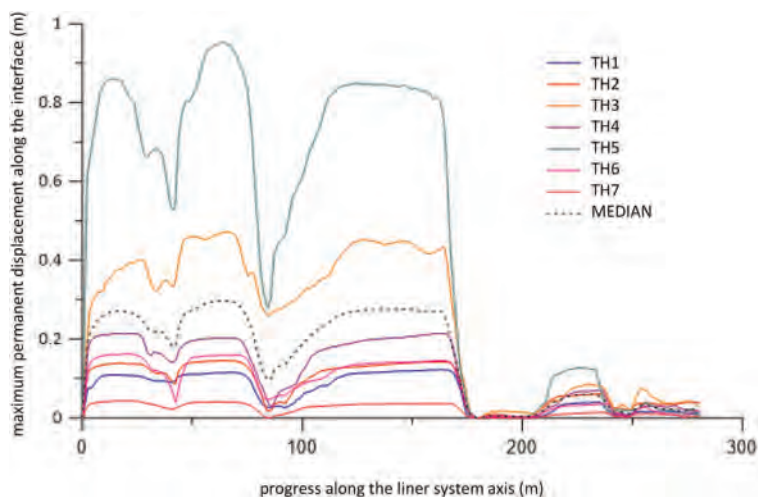
Figure 6. Maximum permanent displacements along the liner system at the end of the two-dimensional dynamic analyses (displacements in m).

5 CONCLUSIONS

The numerical results of the present study lead to the following conclusions: (1) The geotechnical investigation campaigns carried out over the years have made it possible to obtain an excellent geotechnical characterization of waste body, base clay, and liner system; (2) The seismic stability checks of the landfill were carried out by means of non-linear dynamic

analyses which allow to directly calculate the permanent displacement and to reproduce in a satisfactory way the complex interactions that occur between the seismic action and the different elements of the landfill through the mobilization of their strength and deformability. The constitutive model assumed for the waste is of the non-linear hysteretic elastoplastic type with reduction of the shear modulus with the level of deformation and Mohr-Coulomb failure criterion; (3) Permanent displacement data can be used to evaluate the performance of the geosynthetic liner system.

ACKNOWLEDGMENTS

REFERENCES

Darendeli, M. B. 2001. Development of a New Family of Normalized Modulus Reduction and Material Damping Curves, Ph.D. thesis, Univ.of Texas at Austin, Austin, TX.

Kuhlemeyer, R.L. and Lysmer. J. 1973 Finite Element Method Accuracy for Wave Propagation Problems. *Journal of the Soil Dynamics Division*, 99: 421–427.

Lai C.G., Foti S., Rota M. 2009. Input Sismico e Stabilità Geotecnica Dei Siti di Costruzione, Series of Manuals of Aseismic Design, Vol. 6, IUSS Press. ISBN: 9 8-88-6198-035-8.

Gioffrè D., Lai C.G., Zuccolo E. 2023. Analisi di Stabilità Sismica di Una Discarica di Rifiuti Speciali Non Pericolosi a Fornovo di Taro (Parma). Rivista Italiana di Geotecnica 1/2023 (in Italian), *Gennaio-Marzo* 2023, 5–29.

Rampello S., Callisto L. 2008. Stabilità dei Pendii in Condizioni Sismiche. In Opere Geotecniche in Condizioni Sismiche. *XII Ciclo di Conferenze di Meccanica e Ingegneria delle Rocce*: 241–271.

Effect of reinforcement stiffness on a seismically loaded mechanically stabilized earth wall

Berk Turkel
Graduate Research Assistant, Department of Civil, Environmental, and Construction Engineering, University of Central Florida, Orlando, FL, USA

Irem Zeynep Yildirim
Assistant Professor, Department of Civil Engineering, Bogazici University, Bebek, Istanbul, Turkey

Erol Guler
Adjunct Professor, Sid and Reva Dewberry Department of Civil, Environmental and Infrastructure Engineering, George Mason University, Fairfax, VA, USA

ABSTRACT: Compared with rigid retaining systems, Mechanically Stabilized Earth (MSE) walls offer various advantages, such as their cost competitiveness and a higher tolerance for deformations under earthquake loads. Accordingly, MSE walls have become widely popular in the last decades and a thorough understanding of their static and seismic behavior is required for advances in design. In this study, the effect of reinforcement stiffness on the static and seismic response of an MSE wall was investigated by performing two-dimensional finite element analyses. The MSE wall models were excited with a harmonic loading with a frequency content of 4 Hz. In the analysis, geogrids were modeled with two axial reinforcement stiffness values: 600 kN/m and 1200 kN/m. Relative horizontal displacements along the wall height, displacement along the reinforcements, and tensile loads in the geogrids were investigated. The results indicated that the effect of reinforcement stiffness on the MSE wall displacements was less pronounced in the static condition compared with the seismic condition. MSE wall displacements were more visible at about mid-height of the wall in the static case. In the seismic case, the increase in reinforcement stiffness caused a horizontal displacement reduction along the wall height. Doubling the axial reinforcement stiffness increase caused a visible increase in the reinforcement axial forces, in the mid to lower reinforcement levels in the seismic case.

1 INTRODUCTION

In the last decades, the use of Mechanical Stabilized Earth (MSE) wall systems has increased worldwide dramatically due to their economical and aesthetical advantages over conventional retaining walls (AASHTO 2014). MSE walls have especially been preferred in earthquake-prone regions (Koseki *et al.* 2006) as their flexibility help minimize the damage to nearby structures under earthquake load. Researchers have been conducting finite element analyses to evaluate the complex load transfer mechanism and seismic response of reinforced earth wall systems (Fan *et al.* 2020; Kamalzadeh & Pender 2023; Ling *et al.* 2005, 2010; Liu *et al.* 2014; Xu *et al.* 2023). Few researchers studied the effects of axial stiffness (*EA*) of reinforcement on the seismic behavior of MSE walls using numerical analysis and keeping all the other variables constant. Bathurst and Hatami (1998) parametrically varied *EA* values between 500 kN/m and 69,000 kN/m to compute its influence on the reinforced

earth wall displacements under dynamic loading conditions. The authors reported that the higher the reinforcement stiffness values, the lower the wall displacements were, and this effect was more pronounced when EA values were less than 2,000 kN/m. The current study evaluates the effect of stiffness on the MSE wall behavior, focusing on this lower, more critical range of reinforcement stiffness values (i.e., less than 1500 kPa). Accordingly, two types of geogrids with axial stiffness values EA = 600 kN/m and EA = 1200 kN/m were considered for this study. The performance of 8 m high MSE walls was investigated using numerical analyses. The models were excited with a harmonic motion with 0.2g amplitude and a frequency of 4 Hz. Horizontal wall displacements and reinforcement axial forces were evaluated in this study, considering both static (end-of-construction) and seismic conditions.

2 NUMERICAL MODEL

An 8 m high MSE wall model was prepared using the two-dimensional finite element (FE) software PLAXIS 2D (Brinkgreve *et al.* 2010) under plane-strain conditions. Figure 1 shows the general geometry of the analyzed MSE model (Turkel 2019). The wall in Figure 1 has a reinforcement length-to-wall height ratio (L/H) of 1.0 and a reinforcement vertical spacing (S_v) of 0.4 m. The total length of reinforcement is 8.0 m, starting from the front of the facing.
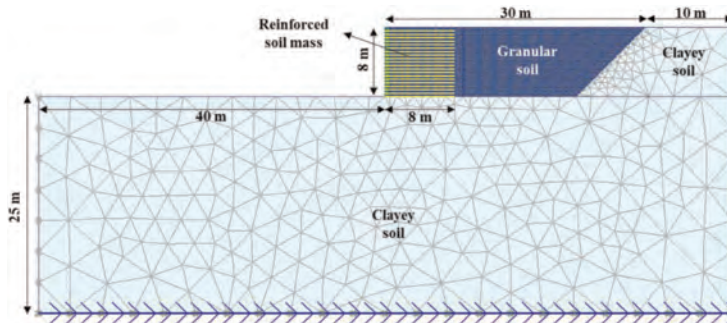
Figure 1.   MSE wall model.

Two different soils: (i) granular soil and (ii) clayey soil were defined in the model. Granular soil was used both in the retained zone and the reinforced soil mass. The material used for the foundation was the same as the natural soil behind the retained zone. The set of material parameters utilized were presented in Table 1. Hardening soil model was used for both the granular and the clayey soil in the model. The groundwater table was assumed to be deep.

Wall facing units were modeled as concrete modular blocks using linear elastic soil elements having a width of 0.5 m and a height of 0.2 m. The modular blocks had a defined elastic modulus of 4,400,000 kPa, Poisson's ratio of 0.17, and a unit weight of 21.8 kN/m³. Reinforcement elements were placed between the concrete modular blocks with vertical reinforcement spacing (S_v) of 0.4 m. Two typical extruded uniaxial geogrids were selected to investigate the effect of reinforcement stiffness on the behavior of the MSE wall. The axial stiffness of the geogrid, which is denoted by EA and defined as the product of the modulus of elasticity and the reinforcement thickness, is used to define the elastic behavior of the geogrids in the models. Axial stiffnesses of these geogrids were calculated as 600 kN/m and 1200 kN/m (International Organization for Standardization 2015). In the FE models, interfaces were incorporated to ensure that the soil-structure interaction in the MSE wall was represented accurately. The strength at all interfaces (i.e., between modular blocks, between the modular blocks and the soils, and between the geogrid and soils) was reduced to 70%.

Table 1. Material parameters used in the model.

Parameter[*]	Description	Granular soil	Clayey soil	Unit
γ_{dry}	Unit Weight (dry)	18	17	kN/m^3
c_{ref}	Cohesion	1	100	kN/m^2
ϕ	Friction angle	34	20	°
E_{50}^{ref}	Secant stiffness	60,000	30,000	kN/m^2
E_{oed}^{ref}	Tangent stiffness	60,000	30,000	kN/m^2
E_{ur}^{ref}	Unloading/ Reloading stiffness	180,000	90,000	kN/m^2

[*]Soil parameters were adopted from Turkel et al. (2020).

The reinforced zone of the MSE wall was modeled using 0.2 m-thick lifts of backfill soil as part of a staged construction approach and a uniform load of 15 kN/m^2 was applied on each lift. In the static condition, a surcharge load of 12 kPa was applied at the end of the staged construction. The average natural frequency of an 8 m high MSE wall was empirically estimated as 4.6 Hz by Turkel et al. (2020). The accelerogram proposed by Bathurst and Hatami (1998) was adapted in this study for harmonic loading. The seismic analyses were performed by applying a harmonic loading at the bottom boundary of the model with a frequency content of 4 Hz (i.e., near the empirically determined natural frequency of the MSE wall). The input duration was set to 5 seconds and the peak ground acceleration (PGA) was 0.2g. The reflection of the seismic waves was avoided by defining absorbent boundaries for the left and right vertical boundaries.

3 NUMERICAL RESULTS

The effect of reinforcement stiffness (i.e., EA = 600 kN/m and 1200 kN/m) on the static and seismic behavior of the 8 m high MSE wall are evaluated and discussed in this section. Figure 2 presents the effect of EA on wall behavior in static condition.

The horizontal face displacements of the MSE wall along its height, which are provided relative to the MSE toe, are shown in Figure 2(a). Horizontal displacements along the wall
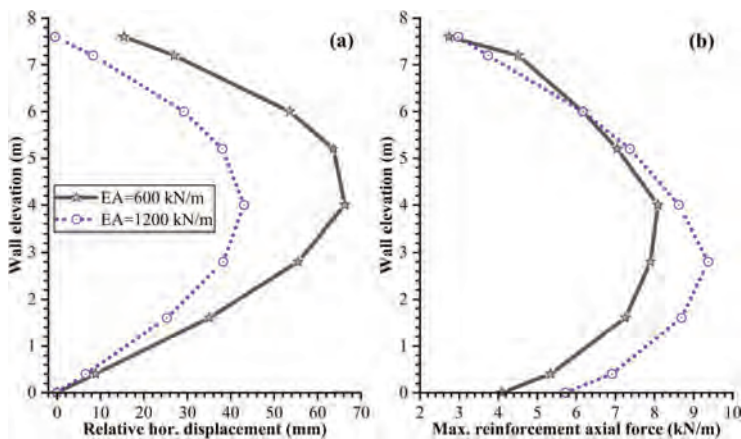
Figure 2. The effect of EA on the wall behavior in the static condition a: (a) relative horizontal displacements and (b) maximum reinforcement axial forces along the wall height.

were reduced by a maximum of 26 mm (from 64 mm to 38 mm) at about the mid-section of the MSE wall when the axial stiffness of the reinforcement was doubled in the static case. Figure 2(b) presents the computed maximum axial force in reinforcements, those obtained from the distribution of the force envelopes. These forces are given with a positive sign indicating tensile loads. The impact of the change in EA was most notable in the lower layers of reinforcements in terms of maximum axial forces. Axial force at the bottom reinforcement increased by approximately 1.6 kN/m (from 4.1 to 5.7 kN/m) when EA was doubled.

Figure 3 presents the effect of EA on MSE wall reinforcement response at selected elevations in the seismic condition. The residual displacements presented in Figure 3(a) are given along the reinforcements (i.e., with distance away from the facing). Note that these displacements are residual or permanent/final deformations that occurred due to seismic loading only (i.e., they are residual) since displacements were reset after the static conditions. On the other hand, displacements provided in Figure 3 are absolute values and not relative to the toe of the wall. Observe how the horizontal displacements increased with wall elevation and the effect of EA became visible at the top of the wall. Figure 3(b) presents the axial forces on the corresponding reinforcements that were obtained from the force envelope distributions. Note that the maximum reinforcement axial force generated along the reinforcement during a seismic loading is the most critical value for the design.
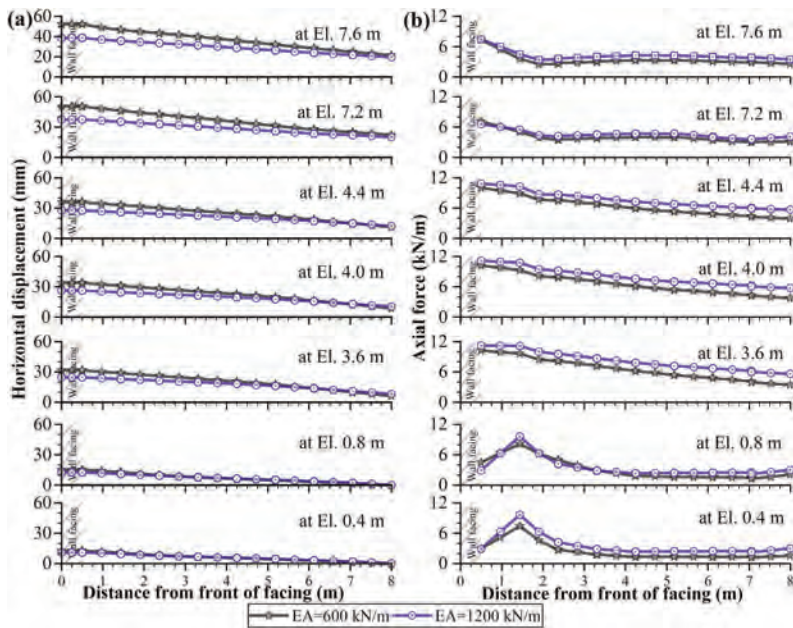
Figure 3. The effect of EA on the response of MSE wall reinforcements at selected elevations in the seismic condition: (a) residual horizontal displacements and (b) axial forces along the reinforcements.

Figure 4 presents the effect of EA on the seismic wall behavior. The computed horizontal displacements along the MSE wall height presented in Figure 4(a) are permanent deformations at the end of the seismic loading with respect to the toe of the MSE wall, and hence they are relative and residual. The increase in EA caused a maximum relative displacement reduction of approximately 12 mm (from 42 to 30 mm) at the top of the wall. The effect of EA on the maximum reinforcement axial forces became significant in the mid to lower reinforcement levels as seen in Figure 4(b). These reinforcement axial forces are the
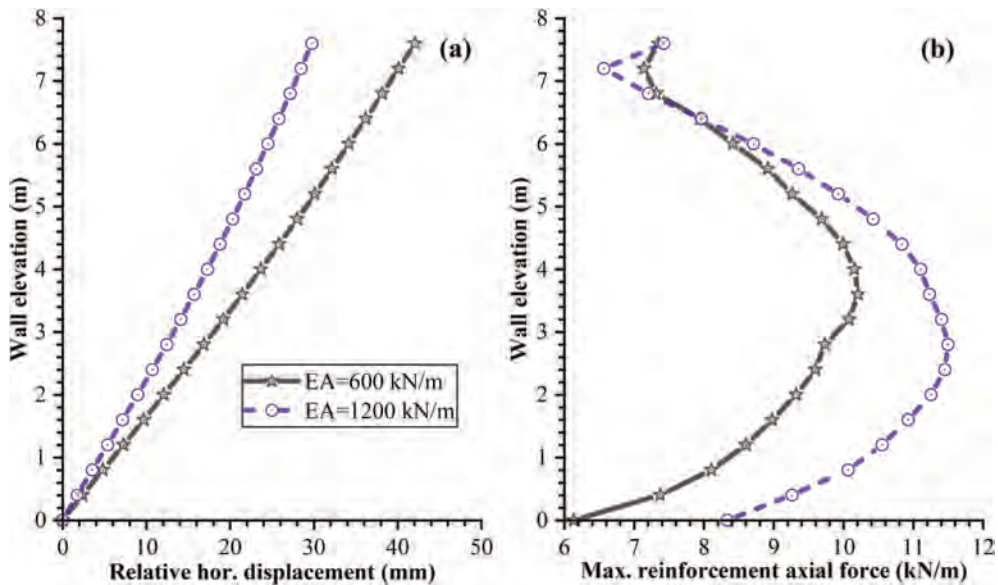
Figure 4. The effect of *EA* on the seismic wall behavior: (a) relative (residual) horizontal displacements and (b) maximum reinforcement axial forces along the wall height.

maximum ones obtained from the envelope. At the bottom of the MSE wall, the maximum axial force of the reinforcement wall was reduced by about 2.2 kN/m (from 8.3 to 6.1 kN/m) when the axial stiffness of the reinforcement was doubled.

4 CONCLUSIONS

A numerical parametric study was undertaken to evaluate the effect of reinforcement axial stiffness (*EA*) on the static and seismic response of an MSE wall. As the effect of *EA* is expected to be more pronounced for lower values of axial stiffness, values of 600 kN/m and 1200 kN/m were assigned for the reinforcements in the FE models. Initially, relative horizontal wall displacements and reinforcement axial forces were investigated in the static condition. Then a harmonic seismic load with a PGA of 0.2g and a frequency content of 4 Hz was applied at the bottom of the models. The results obtained from the seismic analysis were compared and discussed together with the static condition. The following main conclusions were drawn from this study:

- The effect of doubling *EA* was mostly visible at about the mid-section of the wall in the static case when the relative displacements are considered. A maximum relative horizontal displacement reduction of 26 mm was computed at about mid-height of the MSE wall when the *EA* was doubled in the static case.
- Maximum reinforcement axial forces in the lower layers of reinforcements experienced the effect of the change in EA in the static case. Axial forces in the reinforcements at these lower levels experienced a maximum increase of about 1.6 kN/m when *EA* was doubled.
- The effect of *EA* is more pronounced in seismic loading conditions compared with the static condition.
- The increase in *EA* caused a relative displacement reduction along the wall in the seismic case, which was anticipated. The effect was the most prominent with approximately

12 mm of maximum relative displacement reduction at the top of the wall when *EA* was doubled.
- Similar to the observations for the static case, the effect of *EA* on the maximum reinforcement axial forces became significant in the mid to lower reinforcement levels in the seismic case. The maximum axial force of the MSE wall was reduced by about 2.2 kN/m at the bottom of the MSE wall when the axial stiffness of the reinforcement was increased from 600 to 1200 kN/m.

REFERENCES

AASHTO (American Association of State Highway and Transportation Officials). 2014. *AASHTO LRFD Bridge Design Specifications. 7th ed.*, customary U.S. units. Washington, DC: AASHTO.

Bathurst, R. J., and K. Hatami. 1998. "Seismic Response Analysis of a Geosynthetic-Reinforced Soil Retaining Wall." *Geosynthetics International*, 5 (1–2): 127–166. https://doi.org/10.1680/gein.5.0117.

Brinkgreve, R., W. Swolfs, E. Engin, D. Waterman, A. Chesaru, P. Bonnier, and V. Galavi. 2010. *PLAXIS 2D 2010 User Manual*. Delft, Netherlands: Plaxis bv.

Fan, C., H. Liu, J. Cao, and H. I. Ling. 2020. "Responses of Reinforced Soil Retaining Walls Subjected to Horizontal and Vertical Seismic Loadings." *Soil Dynamics and Earthquake Engineering*, 129: 105969. https://doi.org/10.1016/j.soildyn.2019.105969.

International Organization for Standardization. 2015. "ISO 10319 EN ISO 10319 Geosynthetics - Wide-width tensile test - ISO 10319:2015."

Kamalzadeh, A., and M. J. Pender. 2023. "Dynamic Response of Mechanically Stabilised Earth (MSE) Structures: A Numerical Study." *Geotextiles and Geomembranes*, 51 (1): 73–87. https://doi.org/10.1016/j.geotexmem.2022.09.008.

Koseki, J., R. Bathurst, E. Guler, J. Kuwano, and M. Maugeri. 2006. "Seismic Stability of Reinforced Soil Walls." *8th International Conference of Geosynthetics*. Yokohama, Japan.

Ling, H. I., H. Liu, and Y. Mohri. 2005. "Parametric Studies on the Behavior of Reinforced Soil Retaining Walls under Earthquake Loading." *J. Eng. Mech.*, 131(10): 1056–1065. https://doi.org/10.1061/(ASCE)0733-9399(2005)131:10(1056).

Ling, H. I., S. Yang, D. Leshchinsky, H. Liu, and C. Burke. 2010. "Finite-Element Simulations of Full-Scale Modular-Block Reinforced Soil Retaining Walls under Earthquake Loading." *J. Eng. Mech.*, 136 (5): 653–661. https://doi.org/10.1061/(ASCE)EM.1943-7889.0000108.

Liu, H., G. Yang, and H. I. Ling. 2014. "Seismic Response of Multi-Tiered Reinforced Soil Retaining Walls." *Soil Dynamics and Earthquake Engineering*, 61–62: 1–12. https://doi.org/10.1016/j.soildyn.2014.01.012.

Turkel, B. 2019. "Factors Affecting Earthquake Behavior of Mechanically Stabilized Earth Walls." Master's Thesis. Boğaziçi University.

Turkel, B., I. Z. Yildirim, and E. Guler. 2020. "The Effect of Natural Frequency on the Seismic Behavior of an 8 m High MSE Wall." *Geo-Congress 2020: Engineering, Monitoring, and Management of Geotechnical Infrastructure*, 406–415. Minneapolis, Minnesota: Reston, VA: American Society of Civil Engineers. https://doi.org/10.1061/9780784482797.040.

Xu, P., Y. Zhong, K. Hatami, G. Yang, W. Liu, and G. Jiang. 2023. "Influence of reinforcement design on seismic stability of full-height panel MSE walls." *Soil Dynamics and Earthquake Engineering*, 165: 107674. https://doi.org/10.1016/j.soildyn.2022.107674.

A prediction model for the seismic bearing capacity of a shallow foundation positioned on the crest of a geosynthetic reinforced soil structure

E. Ausilio & M.G. Durante
Department of Civil Engineering, University of Calabria, Italy

P. Zimmaro
Department of Environmental Engineering, University of Calabria, Italy
Department of Civil & Environmental Engineering, University of California, Los Angeles, USA

ABSTRACT: Shallow foundations are sometimes built on geosynthetic mechanically stabilized earth (MSE) structures. Such structures are extensively used to support bridge loads and to form approach roads. In recent years many studies provided chart-based solutions to calculate the ultimate bearing capacity of the foundations of MSE structures. Such solutions are provided for different combinations of geotechnical and geometric input parameters. However, such design charts cannot be implemented as part of automated workflows as they contain curves that need to be used on a case-by-case basis. This paper presents a novel method to calculate the seismic bearing capacity of a shallow foundation positioned on the crest of a geosynthetic reinforced soil structure. Such approach is based on a predictive mathematical expression that can be readily used and implemented as part of performance-based design approaches. It relies upon a database of solutions obtained using the upper-bound limit analysis. The proposed expression is valid for static and seismic conditions. Examples are presented illustrating the implementation of this method as part of design procedures of selected foundation systems.

1 INTRODUCTION

Shallow foundations are sometimes built on mechanically stabilized earth (MSE) structures, such as retaining walls and artificial slopes and embankments. Such structures are used quite extensively to support bridge abutments, electrical transmission towers, railways, and road transportation networks. Such reinforcements produce a substantial improvement to the capacity to carry loading by these systems under static and seismic loadings. As a result, the bearing capacity of shallow foundations on sloped fill structures is considerably improved by incorporating geosynthetic reinforcements down to an appropriate depth. Over the past few decades, researchers have studied reinforced soil structures' stability-related applications by means of experimental models, analytical solutions, and numerical approaches. Experimental studies are typically based on the following model types: (1) full-scale structure models (Bathurst *et al*. 2003; Thamm *et al*. 1990; Yoo & Kim 2008), centrifuge model tests (Sommers & Viswanadham 2009), and reduced-scale models (Alamshahi & Hataf 2009; Choudhary *et al*. 2010; El Sawwaf 2007; Hoseini *et al*. 2021; Lee & Manjunath 2000; Mehrjardi *et al*. 2016; Patil *et al*. 2022; Selvadurai & Gnanendran 1989; Turker *et al*. 2014; Xiao *et al*. 2016; Yoo 2001). Such studies focus on the influence of various model input parameter (e.g., footing location and width, geometry of the reinforced soil structure, backfill properties, and reinforcement geometric and spacing characteristics) on the ultimate bearing capacity of such systems.

Several studies present analytical methods to evaluate the bearing capacity and settlement of footings placed on the top of reinforced soil structures. Some of these studies consider a uniformly distributed load (Ausilio 2012; Basha & Basudhar 2010; Jahanandish & Keshavarz 2005; Zhao 1996). Analytical studies on the bearing capacity behavior of a strip footing with loading width placed close to the crest of a reinforced soil structure are limited. The studies of Blatz and Bathurst (2003) and of Haza *et al.* (2000) considered such conditions under static loadings. More recently, Ausilio (2014) used upper-bound limit analyses to develop the seismic bearing capacity of strip footings placed close to the crest of geosynthetic-reinforced MSE structures using a log-spiral mechanism. Furthermore, by using the lower bound finite-element limit analysis technique proposed by Chakraborty & Kuma (2014), Halder & Chakraborty (2019, 2020) presented a series of design charts to compute the bearing capacity of a strip footing placed on the top of a cohesionless soil slope reinforced with layers of reinforcement, also considering the influence of inclined and eccentric loading and the effect of soil dilatancy. Xie *et al.* (2019) proposed a limit equilibrium approach to estimating the bearing capacity of strip footings placed on geosynthetic reinforced soil structures considering five different failure mechanisms. The results of these analyses are presented in a series of normalized design charts accounting for the following input model parameters: footing location and width, geometry of the reinforced soil structure, backfill properties, and reinforcement geometric and spacing characteristics. More recently, Xu *et al.* (2022) used a finite element limit analysis method based on a non-associated flow rule to investigate the load-bearing performance of reinforced slopes.

This body of literature clearly shows that the ultimate bearing capacity of the foundations of MSE structures are influenced by a finite number of geotechnical and geometric input parameters. As a result, many studies focused on providing design charts that can be used by practitioners. However, such design charts cannot be implemented as part of automated workflows as they contain curves that need to be used on a case-by-case basis. In this study we provide a novel mathematical expression to predict the bearing capacity of a shallow foundation positioned on the crest of a geosynthetic reinforced soil structures. It was developed using the nonlinear least squares (NLS) method. The database used to develop this novel expression comprises results from the upper-bound limit analysis used by Ausilio (2014) for a wide variety of input parameter ranges. The proposed mathematical expression can be used in both static and seismic conditions.

2 METHODOLOGY

Ausilio (2014) used the kinematic theorem of the plasticity theory to evaluate the seismic bearing capacity of a strip footing of width B on a geosynthetic reinforced soil slope with angle β at a distance D from the edge (Figure 1). Seismic actions are considered by means of the pseudo-static approach as equivalent horizontal and vertical forces acting on both the foundation and the soil below it. The kinematically admissible mechanism considered in this approach is characterized by a log-spiral failure surface (Ausilio *et al.* 2000), which is assumed to pass through the right edge of the strip footing on the surface of the reinforced slope with r_o which is the radius at initial angle θ_o, while θ_h is the final log-spiral angle (Figure 1). This approach uses three parameters to characterized the soil portion of the MSE system: γ (unit weight), c (soil cohesion) and φ (friction angle).

In this study, a uniformly-placed geosynthetic reinforcement is considered and referenced as an average tensile strength per unit cross-section as:

$$k_T = \frac{T}{d} \tag{1}$$

Figure 1. Geometry of the reinforced soil structure with the log-spiral failure surface (adapted from Ausilio 2014).

where T is the tensile strength of a single the reinforcement layer per unit width, and d is the vertical distance between the layers of the reinforcement layers (Figure 1). By equating the rate of external work to the rate of energy of dissipation, Ausilio (2014) obtained:

$$q = \frac{\frac{1}{2}k_t r_0 \left[\sin^2\theta_h e^{2(\theta_h - \theta_0)tg\varphi} - \sin^2\theta_0 \right] + \frac{cr_0}{2\tan\varphi}\left[e^{2(\theta_h - \theta_0)tg\varphi} - 1 \right] - (1-k_v)\gamma r_0^2 (f_1 - f_2 - f_3) - k_h\gamma r_0^2 (f_4 - f_5 - f_6)}{B\left[(1-k_v)\left(\cos\theta_0 - \frac{B}{2r_0} \right) + k_h\sin\theta_0 \right]}$$

(2)

Where functions $f_1 - f_6$ are dependent on the slope angle (β), the angles defining the position of the failure surface, (θ_o, θ_h) and the soil's friction angle (φ) (Chang *et al.* 1984; Saada *et al.* 2011). Equation 2 provides an upper-bound solution for the ultimate bearing capacity of a footing placed at the crest of a reinforced slope considering a log-spiral failure mechanism. In order to find the best estimation of q, Equation 2 needs to be minimized with respect to angles θ_o and θ_h. Once these angles are found, the limit load is calculated substituting these values into Equation 2. This approach was verified and validated by Ausilio (2014) through comparisons against numerical results and experimental data, respectively.

3 PROPOSED PREDICTION MODEL

In order to obtain a prediction model that can be incorporated as a mathematical expression to predict the ultimate bearing capacity of a strip foundation positioned on the crest of a geosynthetic soil structure, five input parameters are used: (1) the slope angle β; (2) the distance D from the edge; (3) the soil's friction angle φ; (4) the average tensile strength per unit cross-section k_T, and (5) the seismic intensity coefficient k_h. These parameters were identified as the most consequential for this phenomenon by Ausilio (2014) as they influence the slope instability and therefore affect the bearing capacity of a strip foundation. It is convenient to present the results in non-dimensional form and therefore the results are analyzed in term of normalized ultimate bearing capacity ($q/\gamma B$), edge distance (D/B) and non-dimensional geosinthetic factor ($\gamma B/k_t$).

Table 1. Coefficients of the proposed prediction model.

Coefficient	Value	Coefficient	Value	Coefficient	Value
c_1	−0.0043841	c_9	2.1148131	c_{17}	0.0086504
c_2	3.6873746	c_{10}	−0.0092696	c_{18}	1.7032957
c_3	−0.0030405	c_{11}	−0.6479434	c_{19}	1.3902525
c_4	0.0451191	c_{12}	2.6280113	c_{20}	0.026551
c_5	−0.7871863	c_{13}	−1.390382	c_{21}	2.1267126
c_6	0.838201	c_{14}	1.0066753	c_{22}	0.0337078
c_7	0.002757	c_{15}	0.0123847		
c_8	0.0294035	c_{16}	0.8098281		

In this study, data obtained applying the chart-based solution by Ausilio (2014) is fitted using a NLS regression model, in which the sum of the squares of the vertical distances of different points from the regression curve is minimized using the Gauss-Newton algorithm. Appropriate values of all input factors are defined in a way that they uniformly fill the experimental space determined by the following range of input parameters: $D/B = 0.25$–4, $\beta = 30°$–75°, $\phi = 20°$–45°, $\gamma B/k_T = 0.4$–2.75, and $k_h = 0.0$–0.6. The resulting NLS model provides the normalized ultimate bearing capacity ($q/\gamma B$) as (Table 1 provides model coefficient values):

$$\log\left(\frac{q}{\gamma B}\right) = c_1 * \left(\frac{D}{B}\right)^{c_2} + c_3 * \beta + c_4 * \varphi + c_5 * (k_h)^{c_6} + c_7 \frac{D}{B} * \beta + c_8 * \left(\frac{D}{B}\right)^{c_9} * \frac{\gamma B}{K_t} + c_{10}$$

$$* \beta * \frac{\gamma B}{K_t} + c_{11} * \frac{D}{B} * (k_h)^{c_{12}} + c_{13} * \frac{\gamma B}{K_t} * (k_h)^{c_{14}} + c_{15} * \frac{\gamma B}{K_t} * (k_h)^{c_{16}} * \beta$$

$$+ c_{17} * \left(\frac{\gamma B}{K_t}\right)^{c_{18}} * (k_h)^{c_{19}} * \varphi + c_{20} * \left(\frac{\gamma B}{K_t}\right)^{c_{21}} + c_{22}$$

(3)

4 VERIFICATION OF THE PROPOSED PREDICTION MODEL

To verify the reliability of the proposed model (Equation 3), its predictive power is tested against results obtained using the Ausilio et al. (2014) solution (design charts therein and solving Equation 2 for various input parameter permutations). Such verification offers an in-depth evaluation of the reliability of the proposed model and provides similar information, but in a different format, of the residuals analysis performed in the previous section. Representative plots of this verification effort are shown in Figures 2 for a variety of input parameter ranges including the following: $q/\gamma B$ versus $\gamma B/k_T$ for $\beta = 60°$ and $k_h = 0$–0.6 (Figure 2a), and ϕ versus $q/\gamma B$ for $\beta = 60°$ and $k_h = 0$–0.2 (Figure 2b). The comparisons presented in Figure 2 visually confirms that the proposed model is consistent with the solution by Ausilio (2014). Thus, Equation 3 can be reliably used to evaluate the seismic bearing capacity of strip footings placed close to the crest of geosynthetic-reinforced soil structure.

5 APPLICATION OF THE PROPOSED PREDICTION MODEL

In this section, two example applications are proposed to illustrate the use of Equation 3 to evaluate the ultimate bearing capacity of a strip footing resting on reinforced earth structure. Example 1 assumes a 2m-wide strip foundation placed at a distance of 6 m from the edge of a
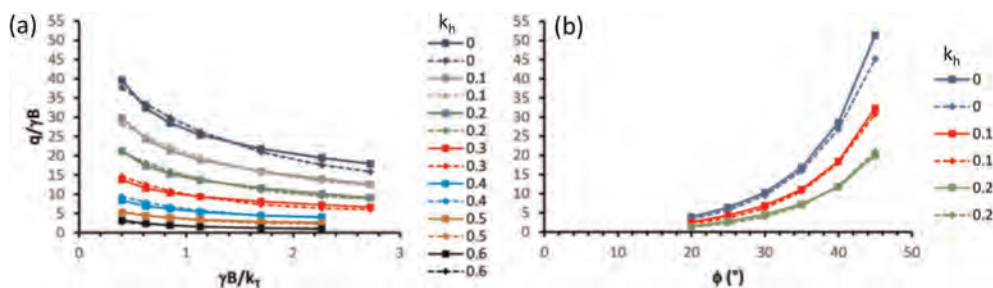
Figure 2. Comparison between the proposed model (dashed lines) and the Ausilio (2014) model (solid lines) for: (a) $\gamma B/k_T$ versus $q/\gamma B$ and (b) ϕ versus $q/\gamma B$. Both comparisons refer to $\beta = 60°$.

slope with an angle of $\beta = 45°$ and soil fill characterized by $\phi = 35°$ and $\gamma = 17$ kN/m^3. The reinforcement used is a strip reinforcement with a tensile limit force of T = 17 kN/m (per strip) and vertical distance of 0.5 m. The static ultimate bearing capacity (i.e., $k_h = 0$) can be calculated as follows: $k_T = T/d = 34$ kPa and $\gamma B/k_T = 1$, then from Equation 3 we obtain: $q/\gamma B = 32.06$ and q = 1,090 kPa. Example 2 Assume the same conditions as in Example 1 but with a seismic excitation summarized by $k_h = 0$. From Equation 3 we obtain $q/\gamma B = 15.20$ and q = 516.80 kPa.

6 DISPLACEMENT-BASED ANALYSIS

The results obtained with the pseudo-static analysis obtained in the previous section, indicate that the reinforcement force required to ensure an adequate bearing capacity could be impracticable for high seismic coefficients. In such circumstances, it is reasonable to accept that the structure is affected by tolerable permanent displacement. The conventional rigid-block analysis procedure originally proposed by Newmark (1965) is usually used to calculate such permanent displacements. In this procedure the earthquake-induced displacement can be obtained by double integration of the equation of motion, which in the case of a rotational failure-mechanism can be expressed in terms of the angular rotation of the failure mass relative to the stable soil. To evaluate the seismic induced permanent displacement, this method requires a scenario ground motion time series and a seismic yield coefficient (k_y) that can be calculated using Equation 3. As an alternative to this formal double integration procedure, empirical relationships can be used to predict the seismic induced permanent displacement of earth structures using the Newmark rigid-block theory. The relationship by Jibson (2007) is widely used in design practice:

$$\log\delta = -2.71 + \log\left[\left(1 - \frac{k_y}{k_{max}}\right)^{2.335} \cdot \left(\frac{k_y}{k_{max}}\right)^{-1.478}\right] + 0.424 \cdot M_w + S\sigma_{\log\delta} \qquad (4)$$

where, k_y is in g (gravity acceleration), k_{max} is the peak acceleration of the rock outcrop motion (in g), δ is the permanent displacement (in cm), $\sigma_{\log\delta}$ is the standard deviation of the logarithm (base 10) of displacement prediction and it is equal to 0.454, M_w is the earthquake moment magnitude, and S is the standardized normal variate. A simplified approach is to consider the displacement evaluated by Equation 4 as that of the unstable soil mass. This value of the seismic displacement is based on the application of the Newmark approach and it is not validated against observed displacements. As a result, it must be viewed as an index of the seismic performance. However, the predicted displacement can still be used effectively for preliminary design purposes. The subsequent step when designing MSE structures is to

decide whether the calculated displacement is acceptable. Such tolerable displacement depends on the characteristics of the geo-reinforced soil structure and what it supports and accordingly, allowable displacement levels must be established using engineering judgment.

Equations 3 and 4 can be used for practical applications in the seismic design where the performance expectations are established in terms of acceptable amount of displacement. Given a set scenario earthquake characterized by M_w and k_{max}, and knowing the width (B) of the footing and its position with respect to edge slope (D), soil (ϕ, γ) and reinforcement (T and d) parameters and the ultimate bearing capacity, k_y can be obtained by trial and error from Equation 3. The permanent displacements can then be calculated using Equation 4. If the displacements are judged to be too high then the process has to be repeated considering a different reinforcement configuration. To show how this procedure works, we propose an example application that assumes a 4m-wide strip foundation, placed at 12 m from the edge of the slope. Additional input parameter are: $\beta = 60°$, $\phi = 35°$, and $\gamma = 17$ kN/m^3. Strip reinforcements with T = 15 kN/m (per strip) are used and installed with a vertical spacing of 0.5 m. The design event is characterized by $M_w = 6.7$ and $k_{max} = 0.57$g. If the target bearing capacity of the footing is 950 kPa, then q/γB = 14 and γB/k_T = 2.26. For these values, a critical acceleration factor $k_y = 0.1$ is obtained from Equation 3. Then Equation 4 provides permanent displacements of 11 and 62 cm for confidence levels of 50% and 95 %, respectively. If these displacements values are not allowable then the process has to be repeated changing T and/or d, to have a greater value of k_T. This procedure, given a scenario event (M_w, and k_{max}), can be applied by calculating k_y as a function of the allowable displacement from Equation 4 and using Equation 3 to derive the value of the bearing capacity.

7 CONCLUSIONS

Geosynthetic reinforced soil structures are popular systems to be employed in modern seismic and static design. Various methods are present in the literature to design these geotechnical systems. However, most of them are based on design charts that are impractical to be applied in automated design workflows. In this paper we present a novel prediction model for the seismic bearing capacity of a shallow foundation positioned on the crest of a geosynthetic reinforced soil structure based on a simple mathematical expression. This model relies upon the upper-bound limit analysis method by Ausilio (2014). After providing a formal verification of this newly-proposed model, we show simple design applications and displacement-based design principles adopting simplified Newmark solutions. Such approaches are particularly useful when implemented as part of performance-based design protocols.

REFERENCES

Alamshahi, S., Hataf, N. 2009. Bearing Capacity of Strip Footings on Sand Slopes Reinforced with Geogrid and Grid-anchor. *Geotextiles and Geomembranes* 27: 217–226.

Ausilio, E., Conte, E., Dente, G. 2000. Seismic Stability Analysis of Reinforced Slopes. *Soil Dynamics and Earthquake Engineering* 19(3): 159–172.

Ausilio, E. 2012. Bearing Capacity of Footings Resting on Georeinforced Soil Structures. *In B. Indraratna, C. Rujikiatkamjorn and J S Vinod (eds), International Conference on Ground Improvement and Ground Control (ICGI 2012), University of Wollongong, Australia 30 October–2 November 2012.*

Ausilio, E. 2014. Seismic Bearing Capacity of Strip Footings Located Close to the Crest of Geosynthetic Reinforced Soil Structures. *Geotech Geol Eng* 32(4): 885–899.

Basha, B.M., Basudhar, P.K. 2010. Pseudo Static Seismic Stability Analysis of Reinforced Soil Structures *Geotech Geol Eng* 28: 745–762.

Bathurst, R.J., Blatz, J.A., Burger, M.H. 2003. Performance of Instrumented Large Scale Unreinforced and Reinforced Loaded by a Strip Footing to Failure. *Canadian Geotechnical Journal* 40(6): 1067–1083.

Blatz, J.A., Bathurst, R.J. 2003. Limit Equilibrium Analysis of Large-scale Reinforced and Unreinforced Embankments Loaded by a Strip Footing. *Canadian Geotechnical Journal* 40(6): 1084–1092.

Chakraborty, D., Kumar, J. 2014. Bearing Capacity of Strip Foundations in Reinforced Soils. *Int J Geomech* 14(1): 45–58.

Chang, C., Chen, W.F., Yao, J.T.P. 1984. Seismic Displacements in Slopes by Limit Analysis. *Journal of Geotechnical Engineering* 110(7): 860–874.

Choudhary, A.K., Jha, J.N., Gill, K.S. 2010. Laboratory Investigation of Bearing Capacity Behaviour of Strip Footing on Reinforced Flyash Slope. *Geotext Geomembranes* 28: 393–402.

El Sawwaf, M.A. 2007. Behavior of Strip Footing on Geogrid-reinforced Sand Over a Soft Clay Slope. *Geotext Geomembranes* 25(1): 50–60.

Halder, K., Chakraborty, D., 2019. Seismic Bearing Capacity of Strip Footing Placed on a Reinforced Slope. *Geosynthet Int* 2(5): 474–484.

Halder, K., Chakraborty, D., 2020. Effect of Inclined and Eccentric Loading on the Bearing Capacity of Strip Footing Placed on the Reinforced Slope. *Soils and Foundations* 60: 791–799.

Haza, E., Gotteland, P., Gourc, J.P. 2000. Design Method for Local Load on a Geosynthetic Reinforced Soil Structure. *Geotech Geol Eng* 18(4): 243–267.

Hoseini, M.H., Noorzad, A.M., Zamanian, M. 2021. Physical Modelling of a Strip Footing on a Geosynthetic Reinforced Soil Wall Containing Tire Shred Subjected to Monotonic and Cyclic Loading. *International Journal of Engineering, Transactions A: Basics* 34(10): 2266–2279.

Jahanandish, M., Keshavarz, A. 2005. Seismic Bearing Capacity of Foundations on Reinforced Soil Slopes. *Geotext Geomembranes* 23(1): 1–25.

Jibson, R.W. 2007. Regression Models for Estimating Coseismic Landslide Displacement. *Eng Geol* 91: 209–218.

Kramer, S.L., Paulsen, S.B. 2004. Seismic Performance Evaluation of Reinforced Slopes. *Geosynthetics International* 11(6): 429–438.

Lee, K.M., Manjunath, V.R. 2000. Experimental and Numerical Studies of Geosynthetic-reinforced Sand Slopes Loaded with A Footing. *Canadian Geotechnical Journal* 37: 828–842.

Mehrjardi, G.T., Ghanbari, A., Mehdizadeh, H. 2016. Experimental Study on the Behaviour of Geogrid-reinforced Slopes with Respect to Aggregate Size. *Geotext Geomembranes* 44(6): 862–871.

Newmark, N.M. 1965. Effects of Earthquakes on Dams and Embankments. *Geotechnique* 15(2): 139–160.

Patil, V.N., Chore, H.S., Sawant, V.A. 2022. Bearing Capacity of Reinforced Embankment Slope Models of Fly Ash and Furnace Slag. *Transportation Infrastructure Geotechnology* 9(5): 673–704.

Saada, Z., Maghous, S., Garnier, D. 2011. Seismic Bearing Capacity of Shallow Foundations Near Rock Slopes using the Generalized Hoek–Brown Criterion. *Int J Numer Anal Meth Geomech* 35:724–748.

Selvadurai, A., Gnanendran, C. 1989. An Experimental Study of a Footing Located on a Sloped Fill: Influence of a Soil Reinforcement Layer. *Canadian Geotechnical Journal* 26(3): 467–473.

Sommers, A.N., Viswanadham, B.V.S. 2009. Centrifuge Model Tests on Behavior of Strip Footing on Geotextile Reinforced Slopes. *Geotext Geomembranes* 27: 497–505.

Thamm, B.R., Krieger, B., Krieger, J. 1990. Full Scale Test on Geotextile Reinforced Retaining Structure, *In Proc. of the 4th International Conference on Geotextiles, Geomembranes and Related Products* The Hague, Netherlands, 1: 3–8.

Turker, E., Sadoglu, E., Cure, E., Uzuner B.A. 2014. Bearing Capacity of Eccentrically Loaded Strip Footings Close to Geotextile-reinforced Sand Slope. *Canadian Geotechnical Journal* 51(8): 884–895.

Xiao, C., Han, J., Zhang, Z. 2016. Experimental Study on Performance of Geosynthetic-reinforced Soil Model Walls on Rigid Foundations Subjected to Static Footing Loading. *Geotext Geomembranes* 44(1): 81–94.

Xie, Y., Leshchinsky, B., Han, J. 2019. Evaluation of Bearing Capacity on Geosynthetic-reinforced Soil Structures Considering Multiple Failure Mechanisms. *Journal of Geotechnical and Geoenvironmental Engineering*, 145(9), 04019040.

Xu, P., Li, T., Hatami, K., Yang, G., Liang, X. 2022. Finite Element Limit Analysis of Load-bearing Performance of Reinforced Slopes using a Non-associated Flow Rule. *Geotext Geomembranes* 50(5): 1020–1035.

Yoo, C. 2001. Laboratory Investigation of Bearing Capacity Behavior of Strip Footing on Geogrid-reinforced Sand Slope. *Geotext Geomembranes* 19: 279–298.

Yoo, C., Kim, S.B. 2008. Performance of a Two-tier Geosynthetic Reinforced Segmental Retaining Wall under a Surcharge Load: Full-scale Load Test and 3D Finite Element Analysis. *Geotext Geomembranes* 26: 460–472.

Zhao, A. 1996. Failure Loads on Geosynthetic Reinforced Soil Structures. *Geotext Geomembranes* 14: 289–300.

On the seismic performance of geosynthetic-reinforced soil retaining walls

G. Di Filippo & G. Biondi
University of Messina, Messina, Italy

N. Moraci
University of Reggio Calabria, Reggio Calabria, Italy

ABSTRACT: Large earthquakes occurring worldwide regularly renew the interest in the analysis of the post-seismic serviceability of Geosynthetic Reinforced Soil Walls (GRSWs). Several post-earthquake reports show that, differently from other types of retaining walls, GRSWs have generally exhibited a satisfactory performance characterized by a ductile behavior against seismic-induced deformations. Similarly, experimental data concerning shaking table and centrifuge tests emphasize the satisfactory seismic performance of GRSWs. In this vein, a simplified displacement-based predictive model, aimed to the evaluation of the seismic performance of GRSWs in terms of magnitude of seismic-induced permanent displacements, was proposed and, using the results of a parametric analyses, the main peculiarities of the seismic performance of GRSWs are discussed in the paper focusing on the possible coupling between the frequency content of the input motion and the vibration frequencies of GRSWs and on the influence of the mechanical properties of reinforcements

1 INTRODUCTION

The use of the earth-reinforced retaining structures has grown progressively in recent decades due to the excellent seismic performance that these geotechnical systems showed even in complex environmental contexts. During most of recent large earthquakes, earth retaining structures reinforced with geosynthetics suffered minor damages with respect to the conventional concrete retaining walls (e.g. Koerner 2000; Tatsuoka 2008) requiring cheaper re-construction costs and ensuring a lower environmental impact. Accordingly, geosynthetic-reinforced soil walls (GRSWs) are nowadays considered a suitable alternative to conventional retaining structures, especially in high seismicity areas (e.g. Moraci 2011; Tatsuoka *et al.* 1997a).

Among the procedures and methods aimed to analyze the seismic performance of GRSWs, simplified dynamic analysis, derived from the pioneer Newmark (1965) sliding block approach, are nowadays widely used also in current practice. The solutions and methods available in the literature were mainly derived modifying the original sliding block approach to account for the main features of the seismic response of GRSWs which is crucially influenced by the soil-geosynthetics interaction under the cyclic and dynamic loading conditions imposed by the ground motion. Available solutions and methos generally belong to two different categories which neglect (e.g. Ausilio *et al.* 2000; Cai & Bathurst 1996; Gaudio *et al.* 2018; Ling *et al.* 1997; Michalowski & You 2000) or account for (e.g. Di Filippo *et al.* 2014, 2019; Paulsen & Kramer 2004) the compliance of the reinforced soil mass and for the deformability of the geosynthetic reinforcements. Available studies also differ in

the assessment of the yield acceleration which has a crucial effect on the evaluation of the earthquake-induced permanent displacements and, thus, on the reliability of the prediction of the post-seismic serviceability condition of GRSWs.

With reference to the case of walls with inclined facing assembled using the wrap-around technique, this paper summarizes the main features of a recently proposed numerical model (Di Filippo *et al.* 2014, 2019) developed to predict the seismic performance of GRSWs in terms of earthquake-induced permanent displacements. Using a set of properly selected input ground motions, a set of numerical analyses have been carried out and the obtained results are presented and discussed in the paper focusing on the influence of the deformability of the reinforced soil mass and of the characteristics of the acceleration records adopted as input in the analyses.

2 PROPOSED NUMERICAL MODEL

The model by Di Filippo *et al.* (2014, 2019) refers to a GRSW of height H, with a face inclination θ and N layers of equally-spaced (s) geosynthetic reinforcement of length L (Figure 1a): γ, φ' and v_s are the unit weight, the angle of shear strength and an average value of the shear wave velocity of the backfill soil (whose profile is described in Figure 1b), respectively; J and, T_u represent the '*in air*' wide-width stiffness and the tensile strength of the reinforcements (Figure 1c, d); δ_i is the friction angle schematizing the shear strength available along the ith soil-geosynthetic interface. The input motion consists of a horizontal acceleration time-history $a(t)$, representing the motion at the base of the GRSW, having peak value $a_{max} = k_{max} \cdot g$.

As in the study by Paulsen & Kramer (2004) the actual GRSW was condensed into a simple rheological model consisting in the 2-degree of freedom (2DOF) system shown in Figure 1e: two masses, m_1 and m_2, define a compliant two-block system schematizing the portion of the actual GRSW involved in the failure mechanism, which has distributed total mass $m = m_1 + m_2$, distributed elasticity and infinite number of degrees of freedom.

Three discrete elements, the compliant two-block system, an elasto-plastic spring and a Coulomb slider, allow reproducing the primary mechanism that characterize the dynamic seismic response of GRSW: *i*) possible amplification of ground motion due to coupling between system and input frequencies; *ii*) possible occurrence of permanent deformations due to soil shearing, to stretching and potential yielding of reinforcements and *iii*), finally, to the possibly occurring pull-out of reinforcements.

Differently from the model by Paulsen & Kramer (2004), the effect of the reinforcement ductility $\chi = \varepsilon_u / \varepsilon_{uy}$ (Figure 1b) can be accounted for in the displacement analysis and proper values of the '*in air*' wide-width stiffness is used herein according to the experimental results
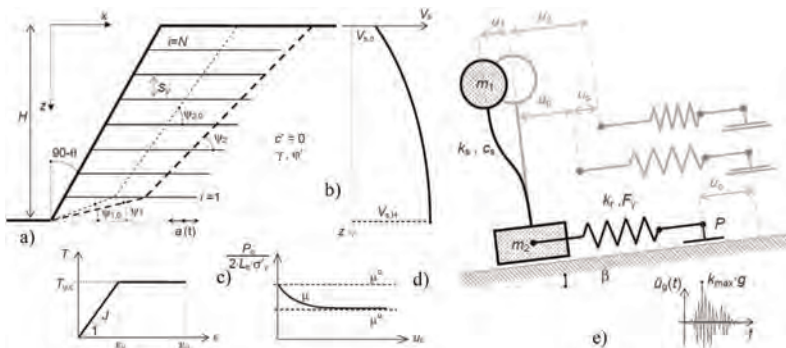
Figure 1.   a-d) reference scheme e) rheological model.

by Cardile *et al.* (2016, 2017). Also, the influence of the static effective stress state and of the soil-geosynthetic interaction under cyclic loading conditions (Moraci *et al.* 2017) are considered for a proper estimate of the interface apparent friction coefficient μ (Figure 1c). Specifically, suitable values of δ_i can be adopted for each layer of geosynthetic reinforcements and the special case $\delta_i = \delta = \varphi$ lead to the assumptions by Paulsen & Kramer (2004). Finally, a proper evaluation of the soil mass involved in the seismic failure mechanism and of the shape function that approximates the fundamental vibration mode of the actual GRSW, are also introduced. Further details on the numerical model can be found in the papers by Biondi & Moraci (2014) and Di Filippo *et al.* (2014).

3 PARAMETRIC ANALYSIS

A first group of parametric analyses were carried out considering two different input motions and several GRSWs schemes. Specifically, two acceleration time-histories (denoted hereafter as records #1 and #2) recorded during the Umbro-Marchigiana 1997 earthquake sequence were considered to define the input motions.

Figure 2 shows the two selected accelerograms (*a*) and the related Fourier Amplitude Spectra (*FAS*), together with some relevant seismic parameters: peak values of the time histories (*PGA*), strong-motion duration (D_{5-95}) and Arias's intensity (I_a). In the numerical analyses presented herein, the accelerograms have been scaled up to 0.8 g and the corresponding values of the relevant seismic parameters are given in brackets in Figure 2b, d.

The two accelerograms are characterized by a different frequency content: a narrow bandwidth (Figure 2a) is apparent for record #1 with a prevalent frequency content concentrated around a predominant frequency $f_p = 6.54$ Hz close to the mean frequency $f_m = 1/T_m = 6.05$ Hz computed starting from the values of the mean period evaluated according to Rathje *et al.* (1998). Conversely, record #2 is characterized by a wide bandwidth (Figure 2c) with a prevalent frequency content concentrated between 2 and 7 Hz; in this case the mean frequency $f_m = 4.98$ Hz is, on average, representative of the significant frequency range. The different frequency content of the two waveforms is also apparent through the acceleration time histories plots (Figure 2b, d).

Different schemes of *GRSWs* have been considered in the analyses. The wall height H range between 6 and 9 m; different values of the soil shear wave velocity ($V_s = 120, 240$ m/s) and of axial stiffness ($J = 550, 850$ kN/m) and tensile strength of the geosynthetic
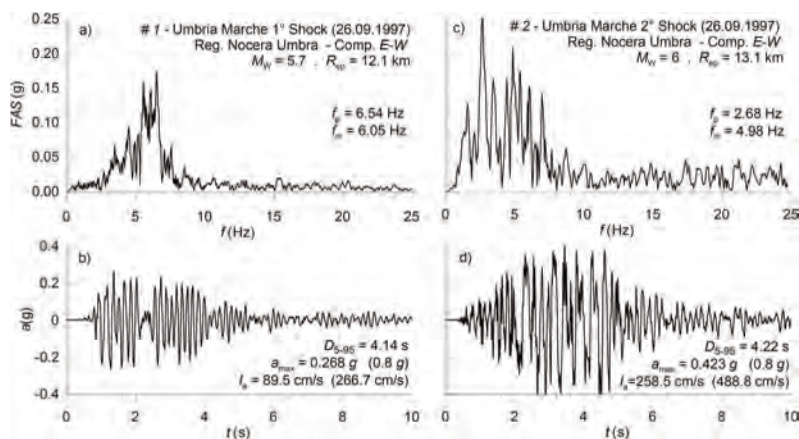
Figure 2. Acceleration records adopted in the numerical analysis as input motions: a,c) Fourier amplitude spectra; b,d) time-histories.

reinforcements (T_u = 18.5, 24.6 kN/m) were also considered in the parametric analyses. In all cases it was assumed s_v = 60 cm, L/H = 0.7, φ' = 35°, γ = 20 kN/m³. Table 1 summarizes the different combinations of the geometrical and mechanical parameters considered in the parametric analyses.

The results of the dynamic analyses carried out using the proposed numerical model, are described herein using a time domain representation. Specifically, the obtained results are presented and discussed in the attempt of highlighting the influence of the wall height H, soil shear stiffness, axial stiffness of the reinforcements and characteristics of the input motions.

Table 1. Parameters of the GRSWs considered in the numerical analyses.

analysis	record	H (m)	V_S (m/s)	J (kN/m3)	T_u (kN/m)
1A	#1	6	120	550	18.5
1B	#1	9	180	550	18.5
2A	#1	6	160	550	18.5
2B	#1	9	240	550	18.5
3A	#1	9	240	850	24.6
3B	#1	9	240	850	18.5
4A	#2	6	160	550	18.5
4B	#2	9	180	550	18.5
4C	#2	9	240	550	18.5
5A	#2	9	240	850	24.6
5B	#2	9	240	850	18.5

3.1 Influence of V_s and H

The results of the analyses relative to the combination of the model parameters denoted as *1B* and *2B* in Table 1 are shown in Figures 3a–d in terms of time histories of displacements (d_1, d_2) of the two masses which characterize the numerical model (Figure 3b, d) and time history of the yield acceleration (Figure 3a, c) superimposed on the input accelerogram (#1). The comparison refers to a wall of height H = 9 m characterized by two different values of the shear waves velocity of the soil and therefore by two different values of the fundamental frequency equal to 5 Hz *1B* (analysis *1B*, V_s = 180 m/s – Figure 3a, b) or 6.67 Hz (analysis *2B*, V_s = 240 m/s – Figure 3c, d). The dynamic response is characterized by final values of the permanent displacements equal to d_2 = 4 cm in the case V_s = 180 m/s (Figure 3b) and d_2 = 8 cm if V_s = 240 m/s (Figure 3d).

The different seismic response is related to the difference coupling effects occurring in the two cases. In the case of analysis *2B* the value of V_s was specifically selected with the aim of providing a fundamental frequency of the system equal to f_s = 6.67 Hz which is almost coinciding with the predominant frequency of the considered input motion (f_p = 6.54 Hz – Figure 2a). For the case V_s = 180 m/s (analysis *1B*, f_s = 5 Hz) the fundamental frequency of the system falls within an interval for which the selected accelerogram is characterized by lower amplitudes (Figure 2a). In both cases (analysis *1B* and *2B*) the response computed for the upper and lower mass of the numerical model leads to a temporal variation of the yield acceleration (a_c in Figure 3a, c); this result cannot be found in conventional (rigid-block) displacement approaches where the deformability of the system and the effects of its dynamic response are not taken into account.

The stabilizing contribution offered by the geosynthetic reinforcements is highlighted by the average increasing trend of the yield acceleration during the seismic motion. The accumulation of permanent displacements involves an increase in the axial forces mobilized in the geosynthetic reinforcements, producing a stabilizing effect which progressively involves the limitation of the cumulative permanent displacements and the increase of the yield acceleration of the system.
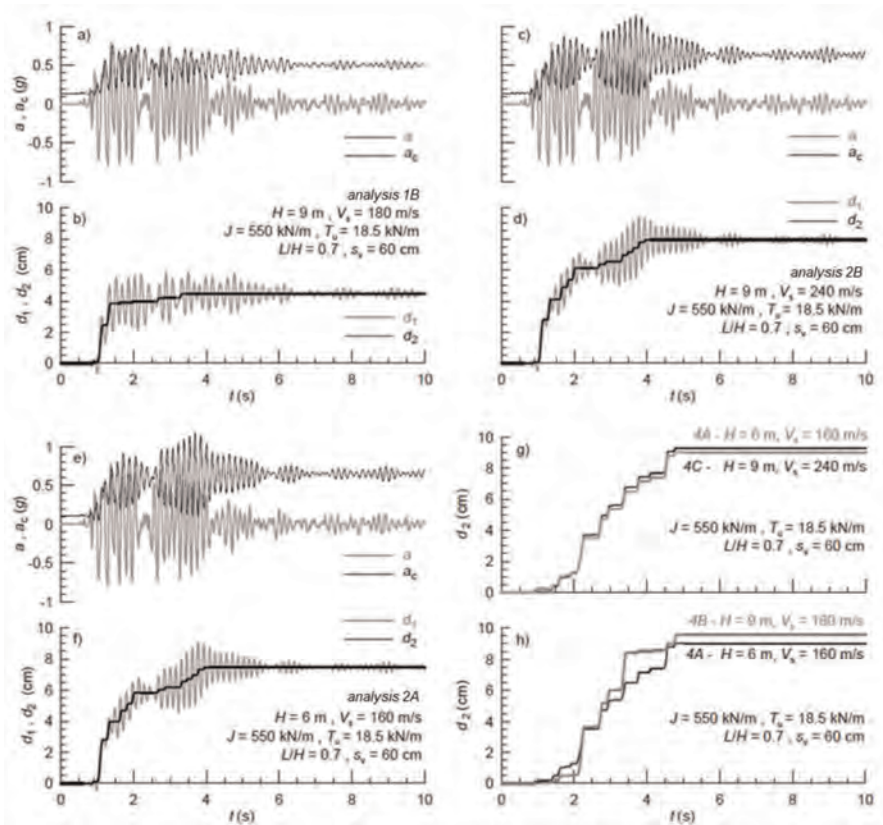
Figure 3. Influence of the *GRSW* compliance on the displacement response.

The dynamic response computed in the analyses *4A* and *4C* is comparable since, in both cases, the systems are characterized by the same fundamental frequency (f_s = 6.67 Hz). Conversely, in more rigid systems (analysis *4A* and *4C*), the occurrence of permanent displacements of the same magnitude as those observed in more deformable systems (analysis *4B*) is mainly attributable to the broadband distribution of the frequency content of accelerogram #2 (Figure 3h).

Similar outcomes can be observed with reference to the comparison of the results relative to the analysis *2B* (Figure 3c, d) and *2A* (Figure 3e, f); the latter (*2A*) differs in the values of the wall height and soil stiffness (Table 1) which, however, were properly selected in order to obtain the same values of the fundamental vibration frequency of the model which is unchanged in comparison with the analysis *2B* (f_s = 6.67 Hz). Figures 3g-h show the results of the analyses carried out for the same systems but using accelerogram #2 (analysis *4A*, *4B* and *4C*). In this case the frequency content of the input motion (Figure 2e) and the values of the model parameters (H, V_s) lead to permanent displacements of about 9 cm for all the systems (Figure 3g).

3.2 *Influence of the reinforcement stiffness*

For the case H = 9 m, V_s = 240 m/s and T_u = 18.5 kN/m Figure 4 shows the influence of the reinforcement stiffness J on the magnitude of seismic-induced permanent displacements.
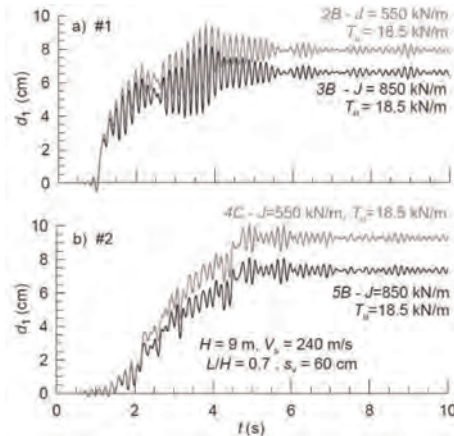
Figure 4. Effect of the stiffness of the reinforcements on permanent displacements.

Specifically, for the accelerograms #1 (Figure 4a) and #2 (Figure 4b) and for two different values of the reinforcement stiffness (J = 550 and 850 kN/m) the computed dynamic responses are shown in terms of displacements d_1 of the upper mass of the numerical model. In the proposed approach, the final value of the displacement time-history represents the permanent displacement of the actual *GRSW*. If the effects of reinforcement deformability are neglected, the two systems (J = 550, 850 kN/m) would be characterized by the same value (constant with time) of the yield acceleration a_c and, thus, the predictions of the permanent displacements would lead to the same result. Conversely, even the same initial value of the yield acceleration (T_u = 18.5 kN/m in both cases), the model characterized by stiffer reinforcements (J = 850 kN/m) exhibits smaller permanent displacements with a reduction of about 15–20% in comparison to the case J = 550 kN/m.

4 CONCLUSIONS

A simplified numerical model was used with the aim of modeling the main mechanisms influencing the seismic response of the geosynthetic-reinforced soil retaining walls (GRSWs) with inclined facing assembled using the wrap-around technique. The seismic performance is evaluated in terms of seismic-induced permanent displacements due to the onset of various plastic mechanisms, also concomitant, caused by the temporary exceeding of the resistances in the soil, in the reinforcements and at the soil-reinforcement interfaces. A set of numerical analyses, carried out in the time domain using actual seismic records as input motions, were presented and discussed in the paper. The analyses show that, due to the possible coupling effects, the amplitude and frequency content of the selected input motion may significantly affect the computed response in terms of permanent displacements. The analysis results also show that, regardless the axial strength, GRSWs equipped with stiffer reinforcements exhibit limited permanent displacements. In the proposed model the better seismic performances are due to the substantial contribution of the reinforcements which modify the fundamental frequencies of the system and limit the amplitudes of the permanent displacements as a consequence of the increase with time of the system yield acceleration.

REFERENCES

Ausilio, E., Conte, E., Dente, G. 2000. Seismic Stability Analysis of Reinforced Slopes. *Soil Dynamics and Earthquake Engineering*: 19(2): 159–172.

Biondi, G. & Moraci, N. 2014. Opere di Sostegno in Terra Rinforzata Soggette ad Azione Sismica: Recenti Esperienze e Previsioni Del Comportamento. Relazione di Panel. In *Associazione Geotecnica Italiana (ed.), XXV Convegno Nazionale di Geotecnica, Baveno, 4–6 giugno, 2014*. Roma: Edizioni AGI.

Cai, Z. & Bathurst, R.J. 1996. Seismic-induced Permanent Displacement of Geosynthetic Reinforced Segmental Retaining Walls. *Canadian Geotechnical Journal*: 33: 937–955.

Cardile, G., Moraci, N., Pisano, M. 2016. In-air Tensile Load-strain Behaviour of HDPE Geogrids Under Cyclic Loading. *Procedia Engineering*: 158: 266–271.

Cardile, G., Moraci, N., Pisano, M. 2017. Tensile Behaviour of an HDPE Geogrid Under Cyclic Loading: Experimental Results and Empirical Modelling. *Geosynthetics International*: 24: 95–112.

Di Filippo, G., Biondi, G., Moraci, N. 2014. Analisi Dinamica Semplificata Della Risposta Sismica di Opere di Sostegno in Terra Rinforzata. In *Associazione Geotecnica Italiana* (ed.), *XXV Convegno Nazionale di Geotecnica, Baveno, 4–6 giugno, 2014*. Roma: Edizioni AGI.

Di Filippo, G., Biondi, G., Moraci, N. 2019. *Seismic Performance of Geosynthetic-reinforced Retaining Walls: Experimental Tests VS Numerical Predictions*. In Francesco Silvestri, Nicola Moraci (eds.), *7ICEGE, Roma, 20–22 Giugno, 2019*. Rotterdam: Balkema.

Gaudio, D., Masini, L., Rampello, S. 2018. A Performance-based Approach to Design Reinforced-earth Retaining Walls. *Geotextiles and Geomembranes*: 46(4): 470–485.

Koerner, R.M. 2000. Emerging and Future Developments of Selected Geosynthetic Applications. The Thirty-Second Terzaghi Lecture. *J. Geotechnical and Geoenvironmental Engineering, ASCE*: 126: 292–306.

Ling, H.I., Leshchinsky, D., Perry, E.B. 1997. Seismic Design and Performance of Geosynthetic-reinforced Soil Structure. *Geotechnique*: 47(5): 933–952.

Michalowski, R.L. & You, L. 2000. Displacement of Reinforced Slopes Subjected to Seismic Loads. *Journal of Geotechnical and Geoenvironmental Engineering*: 126(8): 685–694.

Moraci, N. 2011. Il Rinforzo Dei Terreni Con Geosintetici: Recenti Sviluppi Tecnologici, Progettuali, Normativi. *Relazione Generale. In Associazione Geotecnica Italiana* (ed.), *XXIV Convegno Naz. di Geotecnica; Napoli, 22–24, Giugno 2011*. Roma: Edizioni AGI.

Moraci, N., Cardile, G., Pisano, M. 2017. Soil-geosynthetic Interface Behaviour in the Anchorage Zone. *Rivista italiana di geotecnica*: 51: 5–25.

Paulsen, S.B. & Kramer, S.L. 2004. A Predictive Model for Seismic Displacements of Reinforced Slopes. *Geosynthetics International*: 11(6): 407–428.

Rathje, E.M., Abrahamson, N.A., Bray, J.D., 1998. Simplified Frequency Content Estimates of Earthquakes Ground Motion. *J. Geotechnical and Geoenvironmental Engineering, ASCE*: 124(2): 150–159.

Tatsuoka F. 2008. Geosynthetics Engineering, Combining Two Engineering Disciplines. Special Lecture. In Springer Berlin Heidelberg (ed.), *4th Asian Regional Conference on Geosynthetics*; Shanghai, June 2008. Berlin: Heidelberg.

Tatsuoka, F., Tateyama, M., Koseki, J. 1997a. Geosynthetic-Reinforced Soil Retaining Walls as Important Permanent Structures. Mercer Lecture. *Geosynthetic International*: 4(2): 973–1008.

Unpaved and paved roads

Review of the German geotextile robustness classes (GRK) for separation layers with nonwoven geotextiles using large-scale field tests

H. Zanzinger
SKZ - German Plastics Center, Würzburg, Germany

J. Retzlaff
GEOscope GmbH, Weimar, Germany

R. Kroh
SKZ - German Plastics Center, Würzburg, Germany

ABSTRACT: As part of large-scale field tests, a range of twelve mechanically bonded nonwoven geotextiles from three manufacturers made of polypropylene staple fibres were tested about their robustness against installation loading in their function as separation layers between soft subsoil and coarse-grained base course material ranging from round-grained, sandy gravel to sharp-edged, stony gravel were used for this purpose. Four different installation situations were simulated. The impact by site traffic was controlled based on the ruts resulting from truck crossings. A suction excavator was used to gently reveal the geotextiles.

All samples were visually assessed for damage and then classified. The energy absorption and the derived damaging work were used to evaluate the mechanical changes based on both, wide-width tensile tests and static puncture tests. Half of the exposed samples remained with more than 80% of their original performance. Almost all materials didn't exceed 50% of performance loss after the tests. A classification system should quantify the complexity of the soil-geosynthetic-system for separators. The tests have shown that strength alone is not enough to assess them and to avoid damage. The evasion principle should be followed instead. For this purpose, it is necessary to consider the deformability. The energy absorption together with the minimum elongation ability provides a good basis for this. Against this background, a proposal for an update of the current classification system was made.

1   INTRODUCTION

Empirical classification systems are used for the function of separating soils of different grain sizes with geotextiles. In the current German classification system of the "Merkblatt über die Anwendung von Geokunststoffen im Erdbau des Straßenbaues - M Geok E" (FGSV 2016), a distinction is made between five application cases that consider the influence of the fill material. These are in turn combined with five stress cases resulting from the installation of the geosynthetic and the associated construction operation. This results in 25 possible application combinations, which are nowadays concentrated on three Geotextile Robustness Classes (GRK 3 to GRK 5) and thus describe the loading of the separation layer. The most common are mechanically bonded nonwoven geotextiles (GTX-NW) with staple fibres made of polypropylene. (Bräu *et al*. 2004; Bräu & Laier 1984; Watn & Zeniti 1997) It is important that there must be no holes or damage that would locally disable the filter and separation functions.

2 INVESTIGATIONS

For the investigations of the project, GTX-NWs with and without single-sided thermal treatment were selected. The characteristic as-delivered state (ADS) values for mass per unit area acc. to EN ISO 9864, thickness acc. to EN ISO 9863-1, wide-width tensile strength acc. to EN ISO 10319, static puncture force F_{CBR} acc. to EN ISO 12236, resp. the energy absorption (EA) as integral of the force-strain-line were determined for both tensile tests and CBR tests.

"Energy absorption, uniaxial" $W_{Tensile}$ is based on uniaxial strain whereas "energy absorption, multiaxial" W_{CBR} is based on multiaxial strain ε_{CBR} in a CBR-test (Eq. 1), calculated as the ratio of the increase of the surface area A, here as surface area A of a truncated cone plus the area under the plunger, and the initial area A_0 (Figure 1). Here the plunger penetration displacement was measured at a preload of 1 N.

$$\varepsilon_{CBR} = \left(\frac{A - A_0}{A_0} \right) \cdot 100\% \qquad (1)$$
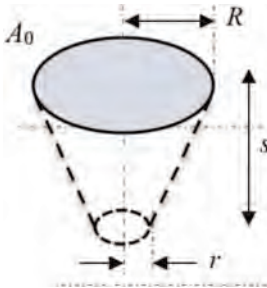
Figure 1. Illustration of the stretched test specimen area in the static puncture test (CBR-test).
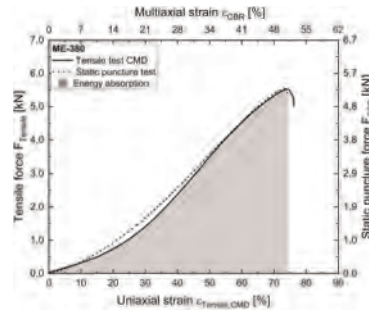
Figure 2. Illustration of tensile force vs uniaxial strain and static puncture force vs multiaxial strain.

Very good correlations between tensile forces and static puncture forces were found for all tested GTX-NWs. As an example (GTX ME 380) diagram shows tensile force $F_{Tensile,CMD}$ plotted on the uniaxial strain $\varepsilon_{Tensile,CMD}$ in cross-machine direction and F_{CBR} on ε_{CBR} (Figure 2).

In order to vary the installation situation of four GRKs, three different fill materials were selected, and these were combined with two different levels of loading due to construction operations. The installation and compaction of the fill material was carried out mechanically. The expected rut depths in the geotextile layer were between 5 cm and 15 cm. Round-grained fill material (sandy gravel) and angular fill material with and without stones (sandy, stony gravel and sand-gravel mixture) were used.

Large-scale test fields (TF) filled with uncompacted quartz sand 0/2 mm not driven on before installation of the GTX-NWs and placement of the base course material are shown on Figure 3.

The bulk material of the sub-base layers was poured onto the TFs with a wheel loader and distributed and levelled with a mobile excavator with a clearing bucket. The sub-base layer was compacted with a single-drum compactor in such a way that the test setup could be driven over with a three-axle truck loaded up to 40 t total weight (Figure 4). After the passes and the measurement of the ruts on the top of the sub-base layers, the top 10 cm to 15 cm of the sub-base layer material was carefully removed with a backhoe. A mobile suction excavator was then used to pick up most of the remaining fill material (Figure 5). The rest was removed manually.

Figure 3.   Four test fields at different stages of installation of GTX-NWs.

Figure 4.   Ruts of a fully loaded truck.

Figure 5.   Removal of fill material with a mobile suction excavator.

3   EVALUATION

All samples taken were subjected to a uniform visual sample approach. Damage was recorded as indentations or holes and cracks and assigned to a defined visual damage factor k_{vis}. Optical damage was found almost exclusively in the area of the ruts. Hardly any optical damage was found "between the wheels" (Figures 6 to 8).

Figure 6.   Stretched sample and relaxed sample after removal of fill material.
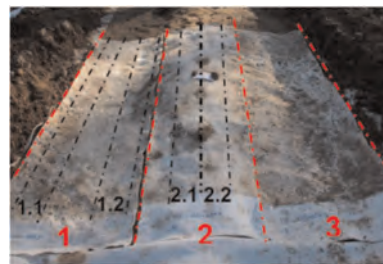
Figure 7.   Samples taken "under the wheels" (sec. 1 and 3) and "between the wheels" (sec. 2).

There was a more or less linear increase in the EA with the increase in the mass per unit area for all samples in the ADS as well as the removed samples. "Under the ruts", the samples showed greater damage here in the form of lower EA than the samples "between the wheels" (Figure 9). There, the GTX-NWs could also be tensioned as a result of the ruts forming on both sides, but the direct compressive load of the coarse grain of the sub-base layer on the GTX-NWs was not present there. The preliminary compaction of the sub-base layer by the single-drum compactor was able to cause the first damage. It was not possible to completely separate these successive influences in retrospect.
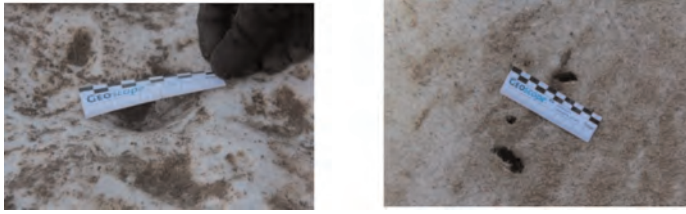
Figure 8.   Damaged samples of an un-treated (left) and of a thermally treated GTX-NW (right).
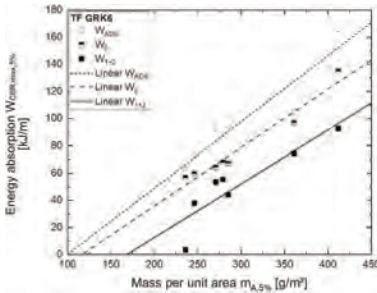
Figure 9.   Example of the EA in ADS W_{ADS}, after damaging "between the wheels" W_0 and after damaging "under the wheels" W_{1+2} shown as EA vs. mass per unit area.
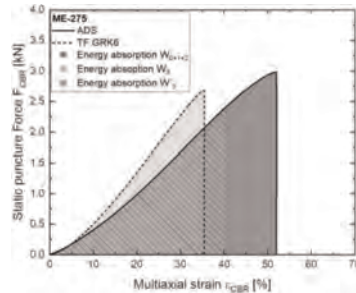
Figure 10.   Illustration of the loss of EA, with EA W_{0+1+2} in ADS and EA W_3 of a damaged specimen. W_3' is equivalent with W_3.

The total damaging work (DW) resulted from the difference between the EA in the ADS W_{0+1+2} and the remaining EA W_3 including the reduction due to the visual damage factor. The "degree of damage" (DoD) was defined as the ratio of the DW and the EA taking into account also the visual findings using k_{vis}. DoD decreased with increasing mass per unit area.

Figure 10 shows the reduction in static puncture force and multiaxial strain of damaged specimens for one example and illustrates the loss of EA, here given as the "areas under the curves".

TF GRK3 showed that DoD was below 20% in 3 out of 5 samples (Figure 11). The other two samples were thermally surface treated and showed DoD between 40% and 50%. The samples in TF GRK4b were very severely damaged. DoD between 40% and 80% were found. In TF GRK5, the 5 lighter GTX-NWs with masses per unit area below 300 g/m² all showed relatively large damage, while the two heavier GTX-NWs only showed damage levels below 20%. All samples from the TF GRK6 showed DoD between 30% and 90%.

The evaluation for "robustness" was carried out for all products. Six of the 12 products met their assigned requirements for a permissible DoD of e.g. 20% in the respective test fields used. Five out of 12 products were installed exclusively in test fields that did not meet their classification. They did not meet the requirements for an allowable DoD of e.g. 20%. One out of 12 products was adequately installed in corresponding test fields according to its classification and did not fulfil the mentioned requirement. In a second observation, a permissible DoD of e.g. 50% was assessed. This criterion, in turn, was met by 11 of 12 products. In principle, it would be desirable that no damage whatsoever occurred to the geotextile separation layers in order to be able to ensure their complete and permanent functionality.

The damage caused by ruts and trucks passing over the surface exceeded the damage caused by backfilling and subsequent compaction with a compactor. Figure 12 shows the increase in DW starting from TF GRK3 on the left up to TF GRK6 on the right side of the diagram. It gives a clear trend of the DW "between the wheels" W_0 and the DW "under the wheels" W_{1+2}.
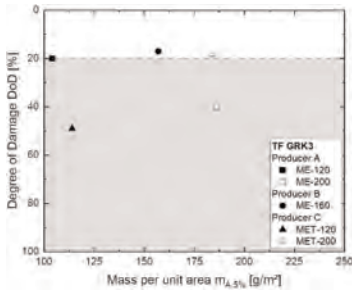
Figure 11. Example of DoD vs mass per unit area for test field TF GRK3.
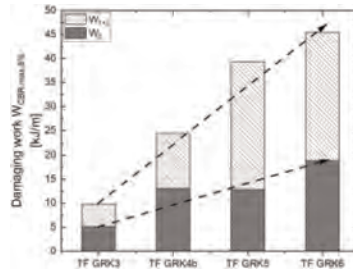
Figure 12. Increase of DW "between the wheels" W_0 and "under the wheels" W_{1+2} shown for four TFs.

The total DW increased in the test fields TF GRK3 and TF GRK4b from approx. 10 to 24 kJ/m, whereby the grain size distribution of the sandy gravel in TF GRK3 and the sand-gravel mixture in TF GRK4 did not show any serious difference. But the grain shapes of the gravel were different. This showed that the grain form of the fill material played an important role in the damage of the geotextiles (Figure 13).
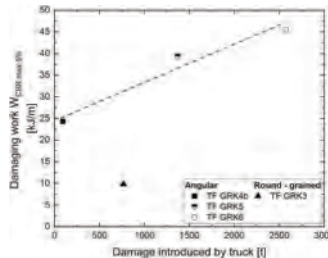
Figure 13. DW vs truck passes.

Another increase in DW from about 40 kJ/m to 45 kJ/m was observed when comparing TF GRK5 and TF GRK6. Here, the identical grain size was used in both TFs. The distinction between these TFs lay in the ruts produced. This again showed that both the construction operation in the form of backfilling and subsequent compaction and the truck passes damaged the GTXs.

A closer look at the stresses caused by the loaded truck passes showed that the effects on the GTX - expressed as DW - due to the grain shape of the angular sand-gravel mixture compared to a round-grained sandy gravel of the filling material was more decisive than the effects of the construction operation. Round or squat grain shapes were obviously less damaging than angular or pointed shapes of the gravel or stones.

The energy introduced by the truck passes correlated with the DW observed for the sharp-edged fill material. The primary selection of GTX separation layers should therefore preferably be based on the existing fill material. The duration and intensity of subsequent construction operations are less predictable. Consequently, the focus should be on sharp-edged fill materials. As a simplified approach, it would be enough to distinguish only between "normal construction operations" and "demanding construction operations".

The GTX-NWs with thermal surface treatment in TF GRK3 resulted in greater DW than the more stretchable products. They were not as good at evading the forces caused by the indentations of the coarse grains. They rather followed the resistance principle. Unlike more "stretchy" GTX filters, which have to safely span the cavities of the core layer in the case of drainage geocomposites, in the case of separation layers between fine-grained subsoil and the coarse fill layer on top of it, it is irrelevant if the GTX-NW deforms into the coarse structure

of the fill material. The essential thing is that this happens without damaging the filter. In cases where the separation function is of primary importance, this evasion principle appears to be more appropriate than the resistance principle.

4 PROPOSAL OF A CLASSIFICATION SYSTEM

Regarding the deformability, an easy pre-selection of GTX-NWs used for the separation function could be the penetration displacement in a CBR-test of at least 53 mm, if the penetration displacement is measured at a preload of 1 N (Figure 14). Furthermore, one could counteract the stress caused by dumping the base course material with limiting the permissible hole diameter of the GTX-NWs in the cone drop test to approx. 20 mm (Figure 15).

Based on the experience of this research project, classification systems should consider the strength and deformability of GTX-NWs. Therefore, the EA and DW should be used to evaluate the robustness. The requirements for the EA result from the fact that the required EA can compensate for the DW without the GTX-NWs being damaged. For "Class 3", this would require an EA based on CBR tests of 60 kJ/m, for "Class 4" 100 kJ/m, for "Class 5" 140 kJ/m and for a "Class 6" 180 kJ/m.
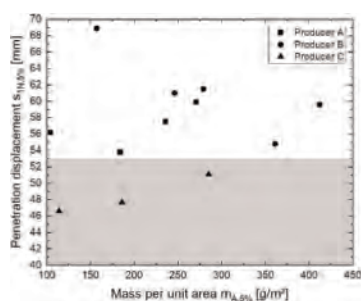
Figure 14. Penetration displacement in the CBR tests vs. mass per unit area.
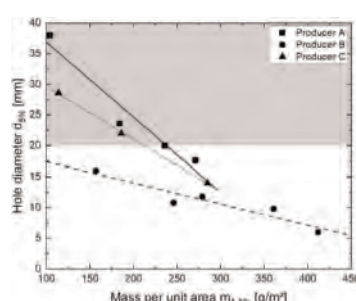
Figure 15. Holes in a cone drop test vs. mass per unit area.

REFERENCES

Bräu, G. & Laier, H. 1984. *Wirkungsweise von Geotextilien als Trennlage unter Tragschichten bei intensiver Verkehrsbeanspruchung*. Forschungsprojekt des BMV/FGSV FE: 05.078.G 84, Bonn, Germany (in German)

Bräu, G., Bauer, A. & Vogt, N. 2004. *Aufstellen Eines Systems für die Anforderungen an Geotextilien hinsichtlich ihrer Beanspruchung beim Einbau*. In: Heft 893, Forschung Straßenbau und Straßenverkehrstechnik, Hrsg. Bundesministerium für Verkehr, Bau- und Wohnungswesen, Bonn, Germany (in German)

Forschungsgesellschaft für Straßen- und Verkehrswesen e.V. (FGSV) 2016. *Merkblatt über die Anwendung von Geokunststoffen im Erdbau des Straßenbaus – M Geok E*, FSGV 535, FGSV-Verlag (in German)

Watn, A. & Zeniti, M. 1997. *Verformung und Einbaubeschädigung von Vliesen bei Gering Tragfähigem Untergrund*. In: 5. Informations- und Vortragsveranstaltung über, Kunststoffe in der Geotechnik", München, 53-60, Germany (in German)

Recommendations for the protection of an earthen embankment from flooding on the Big Almaty Ring Road (BAKAD)

A. Zhussupbekov, N. Aidargaliyeva, A. Tulebekova & A. Yessentayev
L.N.Gumilyov Eurasian National University, Astana, Kazakhstan

ABSTRACT: The problem of construction of the Big Almaty Ring Road (BAKAD) in conditions of the possibility of flooding by ground and external waters is considered. The hydrogeological conditions of this site and general constructive solutions of the embankments, according to the working project, were considered. When designing structures on these collapsible soils, one should consider the possibility of increasing their moisture content by soaking the soil from above from external water sources. Taking this into account, it is necessary to provide for a set of measures, including the elimination of subsidence properties. Having studied the experience of road construction in Kazakhstan, as well as the design data and geological conditions of the project "BAKAD", as well as analyzing the results of laboratory soil studies and the results of field stamp tests. And regarding the test results was recommended constructive technological solution with using geosynthetics materials.

1 INTRODUCTION

The design and construction of civil and industrial buildings and structures on structurally unstable soils are one of the most important and difficult problems today. Such soils include collapsing soils, the feature of which is that these soils have a macroporous structure and exhibit additional deformation, called collapsing when soaking (Kalantari B., Reznik Y.). In this regard, in the design of buildings and structures, there is a need to study the bearing capacity and deformability of soils. Durability, cost, and terms of construction largely depend on the quality of the determination of these properties. Incorrect assessment of the deformability of soils may lead to the construction of unreasonably large foundations or to their excessive collapsing, which may cause an emergency condition of the entire building or structure.

To determine the deformability and bearing capacity of soils there are methods of field soil testing with piles and stamps used. In this regard, in the works, during the construction of buildings and structures on such soils, there are various construction measures to increase the load-bearing capacity of the collapsing soil base proposed. For example, tamping, ground piling, pre-soaking, and reinforcement with vertical elements (Rollins K. *et al.* 1994).

In the Commonwealth of Independent States (CIS), loess soils occupy about 35% of the European and 7% of the Asian parts. In Kazakhstan, loess and loess rocks are distributed mainly in the south and east of the country, which were formed under the influence of cytogenesis processes in the periglacial conditions of the mountain glaciations of the Tien Shan and Pamir.

Technological progress allows the use of artificial and man-made materials for reinforcement. Therefore, the search for new methods and techniques that meet all conditions of construction on collapsing soils is urgent.

2 MATERIAL AND METHODS

2.1 Research object: BAKAD

The road passes through the territories of the Almaty region's Karasay, Ili, and Talgar districts. The "Zero end of the survey" is located on the western side of Almaty city on the 23rd kilometer of the Alma-Ata-Uzyngash highway near the Kyrgauldy village. The end of BAKAD -on the eastern side of Almaty (Kazakhstan), on the 22nd kilometer of the Alma-Ata-Talgar-Yevgeniyevka highway (Figure 1).
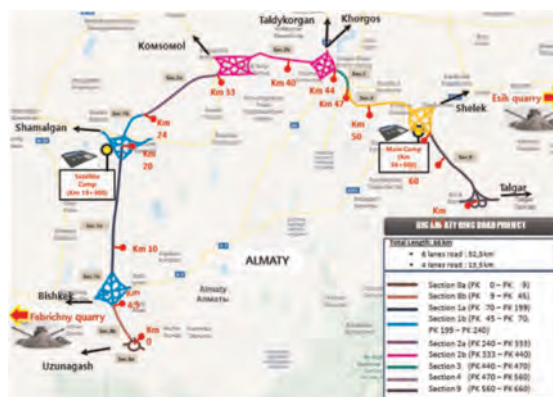
Figure 1.   Location map of BACAD's.

The length of BAKAD is just over 66 kilometers. The route will consist of 21 bridges, 8 two-level interchanges, 18 overpasses, 2 elevated lines, etc. The road will have 4 to 6 lanes, designed for traffic speed up to 150 km/h. According to standard (SP RK, GOST) road belongs to category I a.

2.2 Engineering and geological conditions

Geomorphologically, the surveyed area is located on the gently inclined plain of the Zailiskiy Alatau foothills. The general direction of the plain slope - is the north.

The climate of the district is sharply continental. The climate features of the district are determined by the latitude and the presence of orographic elements on its surface. The combination of climate forcing causes the transformation of hot, dry weather with sharp seasonal and daily fluctuations in air temperatures. Summers are hot, and winters are moderately cold and mild. There are shower rains in spring and summer. Alluvial-proluvial deposits of Quaternary age (Q), represented by loams of different consistency and pebble soils covered with a soil-plant layer, take part in the geological and lithological structure of the site.

Below is a brief description of the engineering and geological conditions of artificial structures. Three wells up to 30.0 m deep were drilled to survey the soils of the overpass, 21 wells 36.0 m deep were drilled to explore the excavation soils, 13 wells 3.0 m deep, and 9 wells 6.0 m deep were drilled along the route axis.

Excavation:

1. EGE-1 - Loam, light hard, brown.

According to compression tests, the loams show collapsing properties from additional loads. Initial collapsible pressure makes 0.062 kg/cm^2. Coefficient of relative collapsing at specific pressure 0.5 kg/cm^2 – from 0.018 to 0.081; at specific pressure 1.0 kg/cm^2 – from

0.041 to 0.130; at specific pressure 2.0 kg/cm^2 – from 0.045 to 0.151; at specific pressure 3.0 kg/cm^2 – from 0.079 to 0.164.

Location line and Overpass bridge:

EGE-1 – Lbelongsoam, light, solid, brown. According to compression tests, the loams show collapsing properties from additional loads. Initial collapsible pressure makes 0.1 kg/cm^2. Coefficient of relative collapsing at specific pressure 0.5 kg/cm^2 – from 0.055 to 0.081; at specific pressure 1.0 kg/cm^2 – from 0.041 to 0.130; at specific pressure 2.0 kg/cm^2 – from 0.045 to 0.151; at specific pressure 3.0 kg/cm^2 – from 0.018 to 0.164. Geotechnical profile as to collapsing capacity belong to the first type.

EGE-2 – Loam, light, low-plastic, brown.

EGE-3 – Loam, light, high-plastic, brown.

EGE-4 – Coarse, brown, low moisture sand.

EGE-5 – Pebble soil with sand aggregate, water-saturated. Standard values of physical and mechanical parameters of strength and deformation properties of loams are given in Tables 1 and 2.

Table 1. Physical and mechanical properties of soils.

Parameter name	EGE-1 recess	EGE-1	EGE-2	EGE-3	EGE-4	EGE-5
		track and over bridge				
Liquid limit, %	25.0	24.1	26.4	24.7	–	–
Plastic limit, %	15.3	14.1	15.1	14.9	–	–
Plasticity index, %	9.7	9.0	11.3	9.8	–	–
Index of liquidity, %	<0	<0	0.38	0.53	–	–
Natural humidity, %	9.7	11.8	19.3	21.1	–	–
Soil particles density, g/sm^3	2.70	2.70	2,71	2.71	–	–
Soil density, g/sm^3	1.57	1.83	1.88	1.93	1.70	1.75
Dry soil density, g/sm^3	1.43	1.65	1,58	1.61	–	–
Void ratio	0.883	0.64	0.718	0.686	–	–
Soil resistance, kPa	325	355	180	100	500	600

Table 2. Normative and calculated values of soil characteristics.

EGE	Unit weight of soil, kN/m^3			Intercept cohesion, kPa			Angle of internal friction, deg.			Modulus of deformation, MPa
	norm	PII	PI	norm	PII	CI	norm	φII	φI	
Recess	1.57	1.57	1.54	21.0 15.0[*]	21.0 15.0[*]	14.0 10.0[*]	21 15[*]	21 15[*]	18 13[*]	13.1 7.4[*]
1	1.83	1.83	1.79	31.0 25.0[*]	31.0 25.0[*]	20.6 16.7[*]	24 19[*]	24 19[*]	21 16[*]	22.6 18.0[*]
2	1.88	1.88	1.84	25.0	25.0	16.6	21	21	17	15.5
3	1.93	1.93	1.89	21.0	21.0	14.0	19	19	15	15.7
4	1.70	1.70	1.67	–	–	–	39 37[*]	39 37[*]	35 34[*]	30.0
5	1.75	1.75	1.72	–	–	–	40 38[*]	40 38[*]	36 34[*]	50.0[*]

[*]Characteristics are given for soils in a water-saturated state.

Normative and calculated values of the intercept cohesion (kPa), the angle of internal friction (degree), and the modulus of deformation (MPa) are shown in Table 4.

The calculated values of the characteristics are given, considering the coefficient of reliability on the ground.

Groundwater during the survey was penetrated at depths of 5.7–12.6 m. Amplitude of oscillations is 1.0–1.5 m. The estimated maximum groundwater level, considering the amplitude of fluctuations in the groundwater level, the influence of irrigation networks

during watering, and the flood period: the first end of February, the beginning of March, and the second end of March, the beginning of April, as well as atmospheric precipitation, should be taken above the measured groundwater level.

2.3 *Stamp tests*

The work was carried out to study the bearing capacity of the embankment and base excavation. The structure of the unit for soil testing by punch includes a stamp; a device for creating and measuring the load on the stamp; an anchoring device (for installations without a load platform); a device for measuring the sediments of the stamp; a device for soaking and control of soil moisture (when testing subsidence soils). The design of the unit provides the possibility of loading the stamp in steps (GOST) of the pressure of 0.01–0.1 MPa, centered transfer of the load on the stamp, and constancy of the pressure at each stage of loading. Stamp loading is carried out by a jack or calibrated weight. The load is measured with an error of no more than 5% of the pressure stage. Deflectometer for measuring stamp settlement are fixed on the reference system. The measuring system provides the measurement of settlements with an error of not more than 0.1 mm. To measure the stamp settlement, it is allowed to use of instruments that provide the measurement of settlements with an error of not more than 0.1 mm. The study of the bearing capacity of the foundation soil was carried out at 6 points of stamp tests. The research was carried out at 3 dry points and 3 wet ones (Zhussupbekov A.). Stamp tests are the most reliable method for determining the deformation modulus, elastic modulus, natural foundations, and structural layers of road pavements. To carry out the tests, a punching machine with a rotary arm was used, acting on the principle of the balance beam provided in Figure 2.
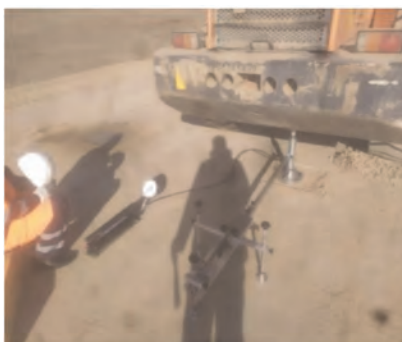
Figure 2. Field test process.

3 RESULTS

Stamping test results are presented in Table 3. Soil collapse is caused by the peculiarities of formation and existence of strata of these soils, because of which they are under consolidated. Under-compaction of loess soils can be maintained throughout the life of the strata unless moisture and load increase. In this case, additional compaction of soil in lower layers under the influence of its weight can take place. Therefore, the foundations formed by collapsing soils should be designed, considering the specific characteristics of such soils. Table 3 presented the compression ratio according to the results of stamp testing.

Soil collapse is caused by the peculiarities of formation and existence of strata of these soils, because of which they are under consolidated. Under-compaction of loess soils can be maintained throughout the life of the strata unless moisture and load increase. In this case,

Table 3. Stamping test.

Soil	Plate diameter, cm	Plate area, cm^2	Plate load, t	Pressure under the plate, kgf/cm^2	Total average plate settlement, $S_{tot.av}$	Deformation modulus, E_{def}, kgf/cm^2	Elastic average plate settlement, mm	Elastic modulus E_{elas}, kgf/cm^2	Coefficient of subgrade, kgf/cm^3
Point №1 Dry soil	30	707	0.71	1	0.6	359.5	0.36	599.1	16.67
			1.41	2	0.98	440.1	0.62	695.7	20.41
			2.12	3	1.4	462.2	0.82	789	21.43
			2.83	4	1.72	501.6	0.98	880.3	23.26
			3.53	5	1.88	573.6	1.2	898.6	26.6
Point №1.1 Wet soil	30	707	0.71	1	2.2	98	0.78	276.5	4.55
			1.41	2	3.82	112.9	1.18	365.5	5.24
			2.2	3	5.74	112.7	1.56	414.8	5.23
			2	4	7.92	108.9	1.96	440.1	5.05
			3.53	5	10.26	105.1	2.22	485.7	4.87
Point №2 Dry soil	30	707	0.71	1	0.8	269.6	0.42	513.5	12.5
			1.41	2	1.52	283.8	0.86	501.6	13.16
			2.12	3	2.18	296.8	1.22	530.3	13.76
			2.83	4	2.74	314.8	1.5	575.1	14.6
			3.53	5	2.94	366.8	1.78	605.8	17.01

additional compaction of soil in lower layers under the influence of its weight can take place. Therefore, the foundations formed by collapsing soils should be designed, considering the specific characteristics of such soils. Table 4 presented the compression ratio according to the results of stamp testing.

Table 4. Results of points.

Point name	Modulus of deformation, MPa	Modulus of elasticity, MPa	Compression ratio
Point1	46.74/ 10.75[*]	39.65/ 39.65[*]	0.99/0.94[*]
Point2	30.64/ 5.54[*]	37.08/ 37.08[*]	0.99/ 0.9[*]
Point3	25.05/ 5.42[*]	41.18/ 31.15[*]	0.99/ 0.9[*]

[*]Characteristics are given for soil at a water-saturated state.

On dry soil:
Average modulus of deformation of the structure for 3 points test is: Ed = 34.14 MP
Average modulus of elasticity of the structure for all 3 points test is Eel = 57.65MPa.
According to the tests carried out, the coefficient of compaction of soil layers the basis ranges from K ≈0.99.
The shape of the graph of general deformations corresponds to the linear dependence of the increment of total deformations on the increase in the load on the base. There is no loss of bearing capacity.
On wet soil:
The average modulus of deformation of the structure for 3 points test is: Ed = 7.24 MPa;
Average modulus of elasticity of the structure for all 3 points test is Eel = 35.96 MPa.
According to the tests carried out, the coefficient of compaction of soil layers in the base fluctuates within K <0.9. The design of the pavement consists of the selection of the most suitable materials based on local resources and the organization of the work, in the
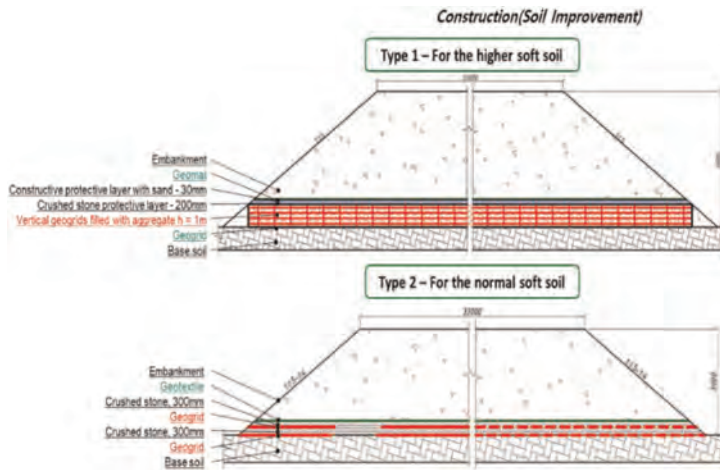
Figure 3. General design solution.

appropriate dimensioning of the individual layers and their placement in depth. Construction solutions for the embankment are presented in Figure 3.

The choice solution of geosynthetic material presented the good filtration properties of geotextile (Tulebekova A.). Also, the economic effect was noted by reinforcing the soil with geosynthetic materials compared with other materials for improving the performance of roads.

4 CONCLUSION

When designing roads and road structures on collapsing soils, it is necessary to:

1. When designing structures on collapsing soils, the possibility of increasing their moisture content due to soaking the soil from external sources (rainwater, meltwater) from above should be considered. Taking this into account, it is necessary to provide a set of measures that include the elimination of subsidence properties (water protection and structural measures).
2. Provide measures to prevent the penetration of surface and anthropogenic water into the foundations.
3. Provide for runoff and channel-regulating structures and measures to prevent flooding and under flooding adjacent to unregulated medium and small rivers and to protect crossings under highways.
4. Provide waterproofing of foundations against aggressive soils. Provide joint corrosion protection for metal and reinforced concrete structures by providing laminated and rustproofing insulation on pipes and other reinforced concrete structures used in bridge construction, recreation, and stop areas buried in the ground, and the use of corrosion-protected, factory-made road signs and signposts.
5. To determine the bearing capacity of the soil foundations of the road highway under construction, one should rely on the results of the field tests (stamp experience). The results of which are as follows for soil at natural moisture, deformation modulus, Ed = 34.14 MPa, for water-saturated soil, deformation modulus, Ed = 7.24 MPa.
6. Lean clay can be used as an artificial embankment if it is well compacted, and a large amount of water is not allowed into the soil.

The following recommendations should be taken into account when strengthening collapsing soil bases with piles: pile foundations in areas with collapsing soils, if soaking of soils is possible, should be used in cases where it is possible to cut through with piles all the layers of collapsing and other clay soils whose strength and deformation characteristics are reduced by soaking; the reasonable choice of a particular geosynthetic material taking into account its physical and mechanical characteristics and functions that it is intended to perform.

REFERENCES

GOST 20276.1-2020. Soils. Plate Bearing Test Methods, Gersevanov Research, Design and Survey and Design and Technological Institute of Foundations and Underground Structures (NIIOSP), Moscow, Russia, p.13.

Kalantari, B. 2013. Foundations on Collapsible Soils: A Review. *Proceedings of the Institution of Civil Engineers: Forensic Engineering*, 166(2), 57–63. doi: https://doi.org/10.1680/feng.12.00016.

Reznik, Y.M. (2007). Influence of Physical Properties on Deformation Characteristics of Collapsible Soils. *Engineering Geology*, 92(1–2), 27–37. doi: https://doi.org/10.1016/j.enggeo.2007.03.001

Rollins, K.M. & Rogers, G.W. 1994. Mitigation Measures for Small Structures on Collapsible Alluvial Soils. *Journal of Geotechnical Engineering*, 120(9), 1533–1553. doi: https://doi.org/10.1061/(ASCE)0733-9410 (1994)120:9(1533)

SP RK 2.03-30-2017*. Construction in Seismic Zones. Introduced. 21.10.2021. - Astana, 2018. - 117 p.

Trofimov, V.T. 2016. On the Results of Engineering Geological Research of Loess-Soil Massifs of Northern Eurasia. *Moscow University Geology Bulletin*, 71(6), 457–461. doi: https://doi.org/10.3103/ S0145875216060119

Tulebekova A., Jumabayev A., Aldungarova A., Zhankina A. 2022. The Use Of Geosynthetics For Strengthening The Soil Base: A Laboratory Experiment To Develop Practical Skills Of Postgraduate Students. *World Transactions on Engineering and Technology Education*, 20(4), 286–291.

Zhu, Y. & Chen, Z. A New Method of Studying Collapsibility of Loess. 2009. *Frontiers of Architecture and Civil Engineering in China*, 3(3), 305–311. doi: https://doi.org/10.1007/s11709-009-0040-3

Zhussupbekov A., Zhankina A., Tulebekova A., Yessentayev A. and Zhumadilov I. Features of the bearing Capacity Estimation of the Collapsing Soil Bases. *International Journal of GEOMATE*, 2022, 22(92), pp. 32–40.

Behaviour of biaxial geogrids in unpaved roads – research from Ireland

C. Reilly
Technological University Dublin, Ireland and Ciaran Reilly & Associates, Mullingar, Ireland

K. Nell
TerraTech Consulting, Portlaoise, Ireland

ABSTRACT: Biaxial geogrids are often used to reinforce unpaved roads over low strength subgrades. By allowing the unsuitable subgrade to remain in place and allowing for reduced road thicknesses, substantial reductions in cost and improvements in performance can be achieved. This paper reviews research undertaken at Technological University Dublin where small model testing boxes and instrumented geogrids have been used in combination with representative samples of weak subgrades and high-quality granular fill to simulate the response of biaxial geogrids to monotonic and cyclic plate loading. It was found that the tensile strain measured in the geogrid under test was only a small fraction of the geogrid's ultimate tensile strain, indicating that the ultimate strength of the geogrid is less important than its interaction with the fill. The magnitude of loading was found to have a more significant effect on displacement than the number of load cycles suffered. It was also found that increasing the number of geogrids in the road had a very significant impact on strain and displacement suffered.

1 INTRODUCTION

Geosynthetic materials, including geotextiles and geogrids, have seen extensive use for the reinforcement of unpaved roads, often for temporary access purposes, over low-strength or otherwise unsuitable subgrades. By allowing the unsuitable subgrade to remain in place and allowing for reduced road thicknesses, the appropriate use of geosynthetics can lead to substantial reductions in the cost while also improving the performance of such unpaved roads (Keller 2016). Other benefits include the reduction of rutting and increased road service life.

Unpaved roads are generally constructed by placing one or more layers of high-quality granular fill over a natural subgrade. The natural subgrade may have been stripped of topsoil or not. When specified, one or more layers of geotextile or geogrid are placed between the subgrade and the granular fill. These geosynthetics can act as separators and reinforcements. A typical reinforced unpaved road cross section is shown in Figure 1.

Many design methods have been proposed for unreinforced and reinforced unpaved roads over the years. A significant body of field test data, where unreinforced unpaved roads and airfields were tested under known loadings, was published in 1970 (Hammitt 1970), and various authors have developed design methods based on these and other data (Giroud & Noiray 1981; Giroud & Han 2004a, 2004b; Jewell 1996; Milligan *et al.* 1989a, 1989b). The majority of these methods take account of the confinement and lateral restraint of the granular particles which interlock with the ribs of the geogrid (Giroud 2009) rather than the
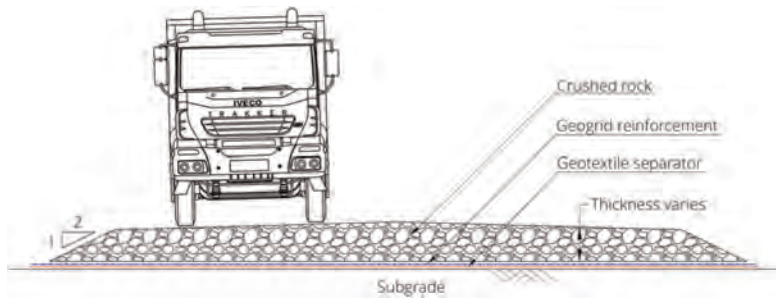
Figure 1. Typical unpaved road cross section.

"tensioned membrane" effect. This is because the deformations required to mobilise the "tensioned membrane" effect are larger than those typically tolerated for roadways.

The Giroud & Han (2004a, 2004b) design method has been widely used to design unpaved roads using biaxial geogrids in Ireland and the UK and, in the authors' experience, has proved suitable. However local experience is important to successful application. Several case histories are presented in Reilly & Nell (2018), although detailed quantitative measurements were not available for these projects. Calvarno *et al.* (2016) report on an analysis of the Giroud & Han design method alongside the more recent Leng & Gabr procedure, with field data also being analysed in the study. It was found the Giroud & Han design method predicted a greater design road thickness than the Leng & Gabr procedure, all other variables being held equal. The field testing found that the Giroud & Han and Leng & Gabr designs formed upper and lower bounds respectively to the measured performance of a road on a subgrade for CBR = 1.3%.

Jas *et al.* (2015a, 2015b) used discrete element modelling, calibrated with laboratory testing in a 1.0m (L) × 1.0m (W) box, to show the response of a geogrid in an unpaved road on a weak subgrade to loading due to a passing wheel. It was shown that the actual tensile stress and strain in the geogrid was very small (less than 0.3 kN/m and around 0.5% respectively) and a small fraction of the geogrid's ultimate capacity, achieved at around 6% strain. It was further concluded that the confinement of the granular particles in the apertures of the geogrid result in a residual stress in the first 8 to 10 cm above the geogrid, a possible explanation of the improved bearing capacity that geogrids provide.

2 RESEARCH ACTIVITIES

2.1 *Research at Technological University Dublin (TU Dublin)*

This paper reviews research conducted by Rutkauskas (2018), Aladwani (2019), and Flaherty (2020) under the supervision of the first author at TU Dublin (Dublin Institute of Technology up to 2019). Two designs of model testing boxes and instrumented biaxial geogrids (Thrace TG3030S) were used in combination with representative samples of weak subgrades and granular fill to simulate the response of biaxial geogrids to monotonic and cyclic plate loading. Testing was carried out with different subgrades, varied loading intensities and cycles, and varying numbers of geogrids in the simulated unpaved road. The granular fill used was locally known as "Clause 804" or "Cl 804" and was a well graded 0/31.5mm crushed rock fill intended as road sub-base. It is considered a high-quality material (Travers & Wyse 2022).

2.2 *Instrumented geogrid with foam subgrade*

Rutkauskas (2018) carried out research involving instrumenting the geogrid with strain gauges to show how the geogrid responded to loading when placed in contact with a weak

subgrade (in this case replicated by a foam used in furniture making) and covered by a surcharge of crushed rock, as would be the case in an unpaved road. The testing box was 0.6m (L) × 0.6m (W) × 0.6m (H) and fabricated from timber. Strain gauges were placed around one junction, located approximately midway in the left-right sense of the geogrid, and at the one third location in the up-down sense of the geogrid. Loading was applied monotonically using a 100mm × 100mm steel plate actuated by a hydraulic ram fitted with a load cell. Tests were carried out as follows:

– No geogrid, 300mm crushed rock directly on the subgrade
– One layer of geogrid on the subgrade, 300mm crushed rock over
– One layer of geogrid on the subgrade, one layer of geogrid at mid-height of the crushed rock

A cross section of the test apparatus is shown in Figure 2.
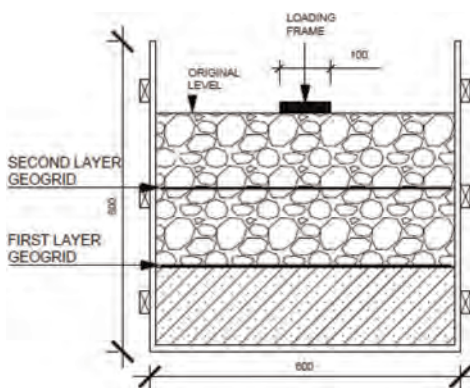
Figure 2.   Testing arrangement for two layers of geogrid. For tests with one layer, the second layer of geogrid was omitted while material thicknesses remained the same (Rutkauskas 2018).

Results of the testing showed that the presence of geogrid increased the loading sustainable for a given displacement, as shown in Figure 3. The load carrying capacity at 40mm defection was increased by 29% for one layer and 83% for two layers, and at 75mm deflection by 29% for one layer and 61% for two layers.
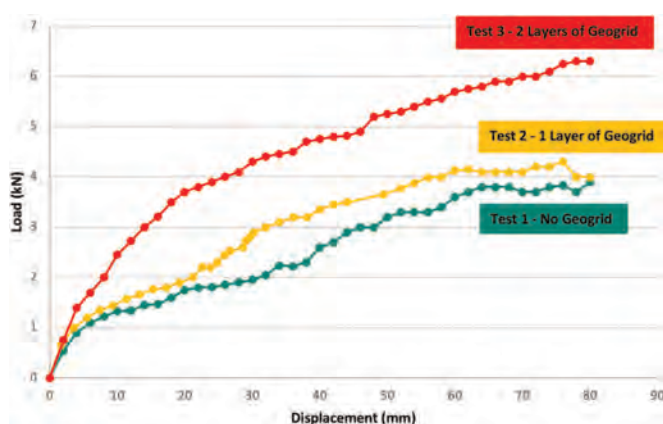
Figure 3.   Loading vs displacement for no geogrid, one layer of geogrid, and two layers of geogrid. (Rutkauskas 2018).

At the end of the test phase at 80kN loading, the plate penetrated the fill by a lesser amount when reinforced; plate penetration was reduced by 5% for one layer and 13% for two layers. Finally, the tensile strain measured was less than 0.31% at the end of the test phase at 80kN for both reinforced cases. For the case with two layers of geogrid, strains measured in the geogrid at mid height were smaller than the strains measured in the geogrid placed on the subgrade (0.13% vs 0.31%. Compression strain was measured in some strain gauges.

The results showed that the tensile strain measured in the geogrid was only a small fraction of the geogrid's ultimate tensile strain. The tensile force per meter in the geogrid was found to be 1.86kN/m for the test with one layer and 2.0kN/m for the test with two layers. These forces are only 6.2% and 6.67% respectively of the ultimate tensile strength of the geogrid of 30kN/m. This finding corresponds with the findings of Jas *et al.* (2015a, 2015b).

2.3 *Instrumented geogrid with natural soil subgrade*

Aladwani (2019) extended this research and built on lessons learned by Rutkauskas (2018), including the use of a more rigid model testing box and a real soft soil (peat) rather than a foam. Aladwani went further in increasing the numbers of geogrid layers used in the model road build up. Up to four layers of geogrid were placed in the model road and their performance assessed.

The testing box was 0.7m (L) × 0.7m (W) × 0.7m (H) and fabricated from mild steel. As a subgrade material, peat obtained from a peatland in the midlands of Ireland was used. Its properties were determined as follows: Von Post H5, unusually low moisture content of 10.5%, and lab vane strength 4.5kPa. The peat was placed and gently compacted to a layer 150mm thick before each test. Testing proceeded to a displacement of 120mm rather than 80mm. Otherwise, testing proceeded largely as per Rutkauskas (2018). The testing arrangement is shown in Figure 4.
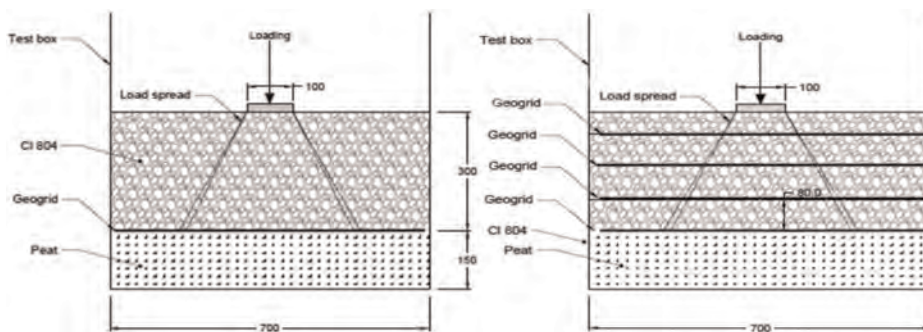
Figure 4.   Testing arrangement (Aladwani 2019).

Results of the testing showed that multiple layers of geogrid, as expected, increased the loading sustainable for a given displacement, as per Rutkauskas (2018). The load carrying capacity at 60mm defection was increased by 245% by increasing geogrid layers from one to four, and at 120mm deflection by 516% for four layers.

At the end of the test phase at 120mm displacement, the loading plate penetrated the fill by a lesser amount when reinforced with four layers as against one layer; plate penetration was reduced by 21% for four layers.

The strain gauge readings showed that the average tensile strain measured was between 0.25% and 0.6% at the end of the test phase at 120mm displacement for both reinforced cases. The greater tensile strain measured by Aladwani as against the strain measured by Rutkauskas is explained by the greater displacement of the loading plate (120mm vs 80mm)

and the use of very soft peat as a subgrade. Again, compression strain was measured in some strain gauges.

The results again showed that the tensile strain measured in the geogrid (0.25 to 0.6%) was only a small fraction of the geogrid's ultimate tensile strain of 9 to 12%, corresponding with the findings of others.

2.4 *Instrumented geogrid with natural soil subgrade subjected to cyclic loading*

Flaherty (2020) built on the previous two studies by introducing cyclic loading conditions to the testing regime. Cyclic loading was intended to replicate traffic passing over the surface above the geogrid and to give a more accurate indication of how the geogrid will perform in a typical unpaved road.

The testing equipment and arrangement were largely the same as used by Aladwani (2019), except that a sheet of non-woven geotextile was introduced to separate the peat from the crushed rock. Thrace S8NW was used, which has a tensile strength of 8kN/m. As a subgrade material, again peat obtained from a peatland in the midlands of Ireland was used. Its properties were determined as follows: moisture content of 75% and lab vane strength 9.4kPa. The peat was placed and gently compacted to a layer 150mm thick before each test.

Tests were carried out as follows:

– one layer of geosynthetic, one layer of geogrid
– one layer of geosynthetic, two layers of geogrid
– one layer of geosynthetic, three layers of geogrid

The cyclic loading regime involved increasing the load intensity from 5kN to 25kN in increments of 5kN. For each 5kN loading phase, four load cycles were applied. Vertical deformation of 120mm was considered as failure. Loading was applied at a rate of 0.5kN per second. Graphs of load vs displacement are shown in Figures 5, 6, and 7.

The results showed that load magnitude has a greater influence on displacement than the number of load cycles. The most significant increases in displacement occur when the load magnitude was increased by 5kN at the start of each new loading phase. After the initial increase the displacement reduced and became more uniform throughout the remainder of each loading phase. The test with three layers of geogrid had the lowest maximum average increase in displacement due to additional load, indicating that increasing the number of geogrid layers improves the roads ability to resist temporary and permanent deformation.

During the unloading phase of each loading cycle, both the displacement and the strain in the bottom layer of geogrid demonstrated the ability to recover. The average strain recovery was 97.5%, and the average displacement recovery was 63%. Displacement recovery was greater as the number of geogrid layers increased, indicating that increasing the number of
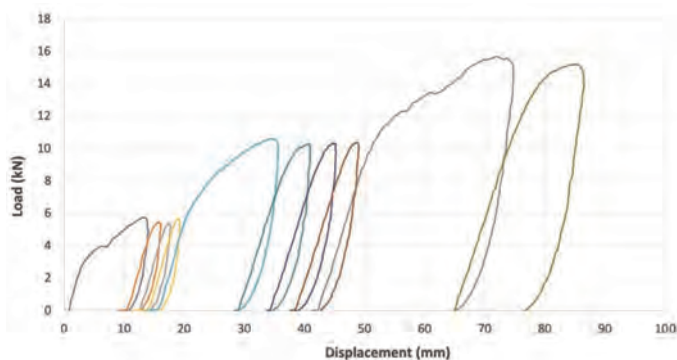
Figure 5.   One layer of geogrid – displacement vs load (Flaherty 2020).
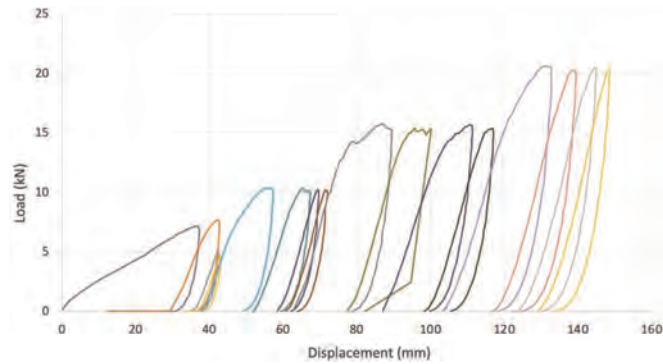
Figure 6.   Two layers of geogrid – displacement vs load (Flaherty 2020).
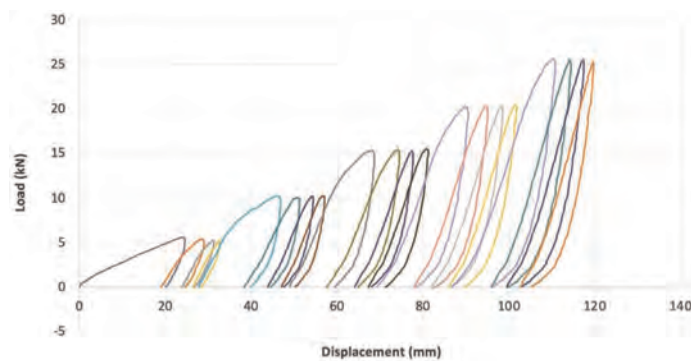
Figure 7.   One layer of geogrid – displacement vs load (Flaherty 2020).

layers of geogrid will help to reduce temporary and permanent deformation and thus increase the life of the road.

The highest strains were recorded at 40mm from the centre of the geogrid, which was directly under the plate load. This suggests that the lateral confinement of the aggregates results in a higher strain under the wheel load. Further research is required to clarify the mechanism causing this.

The results also indicated that lateral confinement occurs earlier when the number of geogrid layers increased. This could be as a result of the top layer of geogrid being closer to the plate load. Further research is required to determine the optimum placement of the geogrid.

3   CONCLUSION

Conclusions drawn from the work are as follows:

– small model testing boxes and instrumented geogrids were used successfully in combination with representative samples of weak subgrades and high-quality granular fill to simulate the response of biaxial geogrids to monotonic and cyclic plate loading;
– it was found that the tensile strain measured in the geogrid under test was only a small fraction of the geogrid's ultimate tensile strain, indicating that the ultimate tensile strength of the geogrid is less important than its interaction with the fill.;
– the magnitude of loading was found to have a more significant effect on road surface displacement than the number of load cycles suffered;

- it was also found that increasing the number of geogrids in the model unpaved road had a very significant positive impact on the strain and displacement suffered;
- further research is required to relate the thickness of the unpaved road in testing to design thicknesses from the design methods commonly in use;
- further work will use increased loading cycles and a larger testing box.

ACKNOWLEDGEMENTS

REFERENCES

Aladwani, A. 2019. *Optimising the Performance of Geogrids in Unpaved Roads*. Bachelor of Engineering (Hons) thesis. Technological University Dublin.

Calvarano, L.S., Palamara, R., Leonardi, G., & Moraci, N. (2016). Unpaved Road Reinforced with Geosynthetics. *Proc. VI Italian Conference of Researchers in Geotechnical Engineering.* Procedia Engineering. Vol. 158, pp. 296–301.

Flaherty, G. 2020. *The Performance of Geogrid-Reinforced Unpaved Roads under Cyclic Loading*. Bachelor of Engineering (Hons) thesis. Technological University Dublin.

Giroud, J.P. 2009. An Assessment of the use of Geogrids in Unpaved Roads and Unpaved Areas. *Proceedings of the Jubilee Symposium on Polymer Geogrid Reinforcement*, Institution of Civil Engineers, London, UK, pp. 23–36.

Giroud, J.P. & Han, J. 2004a. Design Method for Geogrid-Reinforced Unpaved Roads. I: Development of Design Method. *Journal of Geotechnical and Geoenvironmental Engineering*, Vol. 130, No. 8, 775–786.

Giroud, J.P. & Han, J. 2004b. Design Method for Geogrid-Reinforced Unpaved Roads. II. Calibration and Applications. *Journal of Geotechnical and Geoenvironmental Engineering*, Vol. 130, No. 8, 787–797.

Giroud, J.P. & Noiray, L. 1981. Geotextile-reinforced Unpaved Road Design. *J. Geotech. Eng.*, 107(9), pp. 1233–1254.

Hammitt, G.M. 1970. 'Thickness Requirement for Unsurfaced Roads and Airfields, Bare Base Support, Project 3782–65.' *Technical Rep. S-70-5*, U.S. Army Engineer Waterways Experiment Station.

Jas, H., Stahl, M., te Kamp, L., Konietzky, H., & Oliver, T. 2015a. Discrete Element Simulation: Modelling and Analysis of a Geogrid Stabilized Sub-base While Loaded with a Moving Wheel. *Proceedings of the XVI ECSMGE*, pp. 3935–3946. doi:10.1680/ecsmge.606780

Jas, H., Stahl, M., te Kamp, L., Konietzky, H., & Oliver, T. 2015b. Discrete Elements Simulation: Modeling and Calibration of a Plate Load Simulation. *Proceedings of the XVI ECSMGE*, pp. 3941–3946. doi: 10.1680/ecsmge.60678.

Jewell, R.A. 1996. *Soil Reinforcement with Geotextiles*. CIRIA Special Publication 123.

Keller, G.R. 2016. Application of Geosynthetics on Low-volume Roads. *Transportation Geotechnics*. Vol. 8 pp 119–131.

Milligan, G.W E., Jewell, R.A., Houlsby, G.T., & Burd, H.J. 1989a. A New Approach to the Design of Unpaved Roads—Part I. *Ground Eng.*, *Vol* 22, No. 3, pp. 25–29.

Milligan, G.W E., Jewell, R.A., Houlsby, G.T., & Burd, H.J. 1989b. A New Approach to the Design of Unpaved Roads—Part II. *Ground Eng.*, *Vol* 22, No. 8, pp. 37–42.

Reilly, C. and Nell, K. 2018. Geosynthetic Reinforcement for Unpaved Roads – Recent Experience. In: *Proceedings of Civil Engineering Research in Ireland (CERI 2018)*, pp. 252–257. Dublin.

Rutkauskas, A. 2018. *Performance of Geogrids in Soft Soil*. Bachelor of Engineering (Hons) thesis. Dublin Institute of Technology.

Travers, R. & Wyse, E. 2022. Review of Structural Fills in Irish Practice. In: *Proceedings of Civil Engineering Research in Ireland 2022 (CERI2022)*, pp. 279–286. Dublin.

Quantifying geogrid reinforcement mechanism in roadway performance using Cyclic Plate Load (CPL) test

G.S. Ellithy
Assistant Professor, Department of Civil Engineering, Embry-riddle Aeronautical University, Daytona Beach, FL, USA

A. Crippa
Vice President, Tenax Corporation, Baltimore, MD, USA

ABSTRACT: For decades, geogrids have been used successfully to improve performance in both paved and unpaved roadway construction. Even though the current state of practice differentiates between the design methodology incorporating geogrids in paved and unpaved roadways, the true improvement contribution of geogrids is to the base layer, or to the layer that is placed directly on top of it. It has been established that the three reinforcement mechanisms by which geogrids enhance roadway performance are: lateral restraint, bearing capacity increase and membrane tension support. In order to quantify these mechanisms and their contribution to the roadway performance improvement, two Cyclic Plate Load (CPL) tests were carried out, one on a paved section with a hot mix asphalt (HMA) top layer, and the second on an unpaved section. The tests included control and reinforced sections. Each test was instrumented with Linear Variable Differential Transducers (LVDTs) at the surface and subgrade levels that measured the displacements at these levels while the cyclic loads were applied. The paper presents the results in terms of the Reinforcement Improvement Ratio (RIR) which is calculated as the ratio between the number of load cycles of the reinforced section divided by the number of cycles of the control section at the same level of displacement. It was found that RIR is almost identical for surface displacements for both paved and unpaved roadway sections indicating the similar lateral restraint effect of the used product. The bearing capacity increase and membrane tension support vary between paved and unpaved sections depending on the level of displacement at the base course and subgrade contact. The results of those two tests were used to put an emphasis on quantifying the mechanism by which the geogrid contributes to the roadway performance improvement regardless whether it is paved or unpaved. The results could be used empirically to modify the current state of practice for geogrid contribution in paved and unpaved roadways. It should be noted that the terms soil *reinforcement* and soil *stabilization* have been used interchangeably to indicate the above soil improvements using geogrids.

1 INTRODUCTION

As stated by Holtz *et al.* (1998) When an aggregate layer is loaded by a wheel, the aggregate tends to move laterally, as shown in Figure 1a, unless it is restrained by the subgrade or a geosynthetic reinforcement layer. Soft, weak subgrade soils provide very little lateral restraint, so when the aggregate moves laterally, ruts develop on the aggregate surface and also in the subgrade. A geosynthetic layer with good interlocking capabilities, like a geogrid, or frictional ability like a geotextile, can provide tensile resistance to lateral aggregate movement. Bearing capacity increase is another geosynthetic reinforcement mechanism as shown in Figure 5-2b.
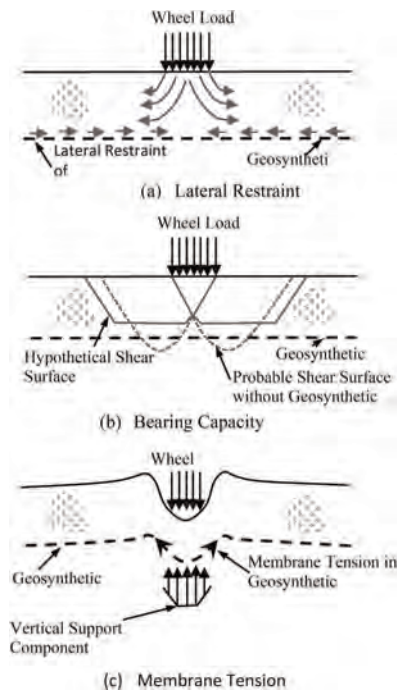
Figure 1. Possible reinforcement functions provided by geosynthetics in roadways: (a) lateral restraint, (b) bearing capacity increase, and (c) membrane tension support (after Haliburton, *et al.*, 1981).

Similar to a footing, the use of geosynthetic reinforcement may force the potential bearing capacity failure surface to follow an alternate higher strength path. A third possible geosynthetic reinforcement function is membrane tension support of wheel loads, Figure 1c. In this case, the wheel load stresses must be great enough to cause plastic deformation and ruts in the subgrade. If the geosynthetic has a sufficiently high tensile modulus, tensile stresses will develop in the reinforcement, and the vertical component of this membrane stress will help support the applied wheel loads. Because tensile stress within the geosynthetic cannot be developed without some elongation, a significant rutting is needed to develop membrane-type support. Therefore, this mechanism is generally present in unpaved roads.

This paper presents the results from two Cyclic Plate Load (CPL) tests, one is performed on a paved section with a hot mix asphalt (HMA) top layer, and the second on an unpaved section. In both tests the California Bearing Ratio (CBR) of the subgrade was 2.0%. The testing conditions for the two tests were almost similar. Each test consisted of a control section and a reinforced section with the a geogrid layer placed on the subgrade where the base course layer was directly compacted on top of it. The tests were performed to investigate the geogrid reinforcement mechanisms in both paved and unpaved roadway sections and quantify these mechanisms if possible using the Reinforcement Improvement Ratio (RIR) which is calculated as the number of load cycles of the reinforced section divided by the number of load cycles of control section at the same displacement level.

2 CYCLIC PLATE LOAD (CPL) APPARATUS

The CPL test apparatus consisted of a rectangular concrete and steel test box that is 1.8 m deep, 2.3 m wide and 2.3 m long (6 ft × 7.5 ft × 7.5 ft). A stiff steel frame bolted to the top of the walls is used as a reaction for the servo-hydraulic actuator that provides the cyclic load to

the test surface. The servo-hydraulic system is programmed to continuously deliver individual load pulses having a trapezoidal shape and at a frequency of 1 Hz. The trapezoidal load pulse consists of four steps: ramp up to maximum load (0.3 s), hold maximum load (0.2 s), ramp down to minimum load (0.3 s), hold at minimum load (0.2 s). Max and min loads were 40 kN (9,000 lb) and 0.44 kN (100 lb), respectively, TRI (2019, 2022). The load was delivered to the road surface through a 2.5- cm (1-in). thick, 30- cm (12-in) diameter steel plate, designed to represent one equivalent single axle load (ESAL). Linear variable differential transducers (LVDTs) were positioned along the centerline of the load plate to measure vertical displacement of the surface as the test progressed, Figure 2. Information from these sensors was used to create a profile of the rut bowl resulting from the applied cyclic load. In addition, a single LVDT was also embedded in the subgrade to monitor displacement at the interface between the subgrade and base course (also the position of the geogrid for the reinforced tests). A data acquisition system was designed to monitor the applied load and displacement of all the LVDTs at a frequency of 25 Hz. From this data, a single max and min value was recorded for each of the sensors every 2 seconds.

Figure 2.   Typical surface sensor setup.

3   MATERIAL PROPERTIES

3.1   *Subgrade*

The subgrade soil was classified as a lean clay with sand (CL) according to the USCS classification system, and had a liquid limit (LL) of 40% and Plasticity Index (PI) of 19%, with an optimum moisture content and dry density of 18.6% and 16 kN/m^3(101.4 lb/ft^3), respectively. Subgrade construction consisted of placing and compacting the subgrade material in six 15-cm (6-in) thick lifts in the CPL box. The subgrade was thoroughly mixed and moisture conditioned to ensure the subgrade was uniform when placed. The target shear strength for the subgrade was 86.5 ± 3 kPa to achieve a California Bearing Ratio (CBR) strength of 2.0 ± 0.1%. This strength corresponded to a moisture content of about 28%. In place shear strength was measured using a hand-held vane shear to ensure consistency and strength during construction. Compaction of the subgrade was accomplished using a jumping jack compactor. The sixth and final layer of the subgrade was leveled to a tolerance of ±2.5 mm using a metal draw bar to cut the surface flat. The surface of the subgrade was covered with plastic during construction to prevent it from drying out.

3.2   *Geogrid*

A 3D structured geogrid was used in the reinforced test section. The geogrid in both tests was placed on the subgrade and the base course was compacted directly on top it. A single piece of geogrid was cut from the roll to fit within the width of the test box The material was cut out in a 45 degree orientation to allow instrumentation wires oriented in the machine and
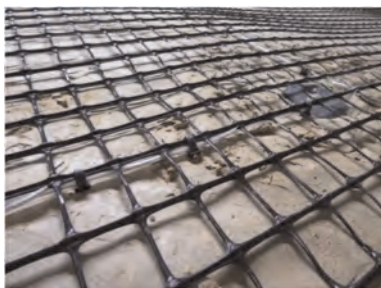
Figure 3. Geogrid instrumentation.

cross-machine directions to exit from the two front corners of the test box. The geogrid was pulled taut to remove any wrinkles and wooden stakes were used to hold the materials in place. A photo of the installed geogrid is shown in Figure 3.

3.3 *Base course*

The base course consisted of crushed granite, and has a gradation as shown in Figure 4. The base course was classified as poorly graded gravel (GP) according to the USACS. It was constructed in four lifts for a total depth of 30 cm (12 inches) and was compacted using a vibrating plate load compactor. The in-place density of the base course was measured using a sand cone device. The dry unit weight averaged 22 kN/m^3 (138 lb/ft^3). The strength CBR of the base course was verified using Dynamic Cone Penetrometer (DCP) and averaged 10%.
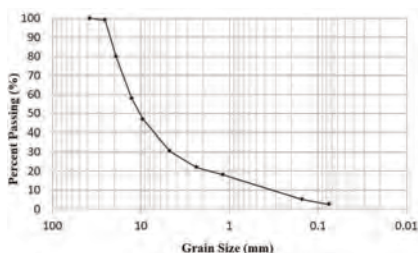
Figure 4. Grain size distribution for the base course.

3.4 *Hot Mix Asphalt (HMA)*

The hot-mix asphalt (HMA) used in the testing of the paved section was purchased from a local HMA plant and stored in steel drums. HMA was installed in two layers, by reheating the mix for each layer, screeding it to a uniform depth and compacting it using a flat vibrating plate compactor. The final mix averaged a density of 19.5 kN/m^3 (124 lb/ ft^3) and a depth of 5.7 cm (2.27 inches).

4 RESULTS AND DISCUSSION

Figure 5 shows the results of the first test which included a 5.7 cm HMA layer (paved section/ Test 1). The results are presented by comparing the number of load cycles corresponding to the same displacement for control and reinforced sections. The compared displacements are those occurring at the surface of the subgrade. The load cycles are compared for the subgrade surface displacement at about 6 mm (0.25 inch), and the Reinforcement
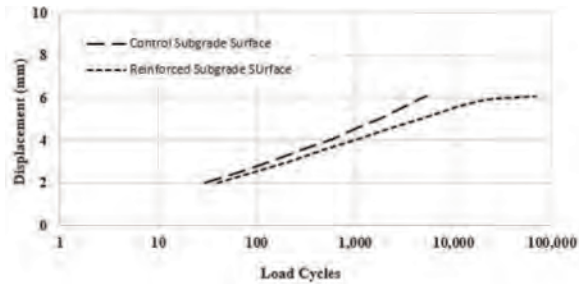
Figure 5.   Subgrade surface displacement response for the paved section (Test 1).

Improvement Ratio (RIR) which is defined as the number of cycles for the reinforced section divided by the number of cycles of the control section, is about 13. An unexpected error occurred while measuring the displacement for the HMA surface and it is not presented in this comparison. As expected, the placement of a geogrid layer as a reinforcement inclusion between the subgrade and base course has significantly contributed to the performance of the paved section and increasing the number of load cycles, which could be translated to increasing design life.

Figure 6 shows the results of the second test which included a base course layer on top of the subgrade (unpaved section/ Test 2). Similar to the paved section, the results are presented by comparing the number of load cycles corresponding to the same displacement for control and reinforced sections. The compared displacements are those occurring at the surface of the base course and the surface of the subgrade. The load cycles are compared for the base course surface displacement at about 100 mm (4 inch), and the ratio is about 12. For the subgrade displacement which is at the level of 50 mm (2 inch), the ratio is also about 27. Similar to the paved section, the placement of a geogrid layer between the subgrade and base course has significantly contributed to increasing the number of load cycles, and hence design life.
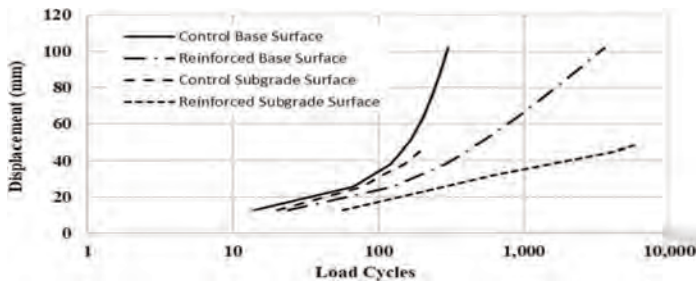
Figure 6.   Base course and subgrade surface displacement response for the unpaved section (Test 2).

It is worth noticing the similarity between Test 1 and Test 2 RIR for the top surface displacements; top of subgrade in Test 1 (RIR = 13) and top of base course in Test 2 (RIR = 12), this indicates that for a given reinforcement level, or a given geogrid or geosynthetic product, the effect is almost identical for the lateral confinement mechanism which is the main mechanism responsible for geogrid reinforcement whether an HMA layer is present or not.

It was observed that the reinforced section in both paved and unpaved sections experiences less heave along the contact between base course and subgrade beyond the deforming area, and hence increase the bearing capacity of the reinforced section. The level of bearing capacity increases different between the paved and unpaved sections. The displacement

1231

along this contact was recorded and will be presented in the final submission of the paper to show the effect of bearing capacity increase mechanism as an effect of geogrid reinforcement.

It could be noticed that the membrane tension support mechanism is more dominant in the unpaved section (Test 2) where the RIR of the subgrade surface displacement is 27, higher than all other calculated RIR values. That is again, an expected result, but now it could be qualified and a clear contribution of the reinforcement through this mechanism can be quantified.

5 SUMMARY AND CONCLUSIONS

This paper summarizes the results from two Cyclic Plate Load (CPL) tests on two roadway sections. Test 1 was on a paved section that included a 5.7- cm thick HMA layer on top of 30- cm thick base course overlying a 2% CBR subgrade. Test 2 was on an unpaved section with configuration similar to Test 1 but without the HMA layer. In both tests, a 3D geogrid was placed at the contact between the base course and the subgrade. To quantify the three mechanisms of reinforcement; lateral restraint, increase in bearing capacity and membrane tension support, results were presented in form of a ratio between the number of load cycles of the reinforced section to that of the control section at the same level of displacement. This ratio is referred to as the Reinforcement Improvement Ratio or RIR. The RIR was calculated for the top surface, top of HMA for Test 1 and top of base course for Test 2, and for top of subgrade for both tests.

It was found that RIR is almost identical for surface displacements for both paved and unpaved roadway sections indicating similar base course lateral restraint effect of the 3D geogrid used in the tests whether the section is paved or unpaved. The bearing capacity increase mechanism varied between paved and unpaved sections depending on the level of displacement at the base course and subgrade contact beyond the deforming area. More data will be presented at the final submission of the paper with regard to this mechanism. RIR of the subgrade surface displacement in Test 2 (unpaved) was 27, higher than all other calculated RIR values. This indicates that the membrane tension support mechanism is more dominant in unpaved sections where high level of displacement leads to elongation in the geogrid which in return increases the resistance to further displacement.

The results of those two tests were used to put an emphasis on quantifying the reinforcement mechanisms by which the geogrid contributes to improvement of roadway performance whether it is paved or unpaved. The results could be used empirically to modify the current state of practice for geogrid contribution in paved and unpaved roadways.

REFERENCES

Han, J. & Asce P.E. (2022) *Experimentally and Mechanistically Quantifying Benefits of Geosynthetics in Improved Road Performance*. Keynote Lectures, Eurogeo 7, Warsaw, Poland.

Holtz, R.D., Christopher, B.R., Berg, R.R. (1998) *Geosynthetics Design and Construction Guidelines*. FHWA HI-95-038

Haliburton, T.A., Lawmaster, I.D. & McGuffey, V.C. (1981) *Use of Engineering Fabrics in Transportation Related Applications*, FHWA DTFH61-80-C-Q0094.

TRI Environmental (2019) *Cyclic Plate Load Testing of Geosynthetic Reinforced Pavement Test Sections*. MAPP-LSM 2019-109

TRI Environmental (2022) *Cyclic Plate Load Test*. MAPP-LSM 2022-002.

The shear bonding of interlayer's effect on rutting parameters of an asphalt overlay

F. Moghadas Nejad, A. Noory & M. Khodadadi
Amirkabir University of Technology, Tehran, Iran

ABSTRACT: Using geosynthetic materials has noticeable effects on reducing the growth of reflective cracks in asphalt pavements. Meanwhile, some other parameters can be changed despite the positive effects and increasing the number of loads that the overlay can tolerate before cracking starts, and reducing the crack growth rate due to the reduction in shear strength between asphalt paving layers. One of the most important effects of changes in shear strength between pavement layers strengthened by geosynthetics is the change in resistance to other failures like rutting. In this study, the shear strength between the pavement layers was measured using the AUT-SFT device. Then, the resistance against rutting was tested for the same samples using a wheel-tracking machine. The results showed that the lower the shear strength of the geosynthetic reinforced specimens, the higher the rut depth in the AUT-SLT machine after the end of 600 load cycles.

1   INTRODUCTION

Hot mixed asphalt (HMA) overlay is a common solution for repairing degraded pavement. In fact, reflection cracks can propagate through the pavement and cause some distress in overlaid systems (Fallah & Khodaii 2015; Gonzalez-Torre *et al.* 2015). Reflective cracks are caused by the displacement of an underlying cracked layer due to shear and tensile stress induced by traffic loads or temperature changes (Amini 2005; Lytton *et al.* 2010). The environment and traffic conditions affect the propagation rate of cracking (Penman & Hook 2008; Sobhan & Tandon 2008). As it is well known, cracks in the lower layer can propagate through the upper layer due to concentrated strain at the top section of the old layer. There is currently no complete solution to prevent this phenomenon, but the occurrence of this cracking can be postponed (Khodaii *et al.* 2009).

Field reports indicate that geosynthetics can delay crack propagation in pavement systems and extend their service life (Shukla & Yin 2004). Some research has been conducted on the delaying solutions for reflection cracking in the overlay using various approaches at the field, experimental, and numerical scales (Austin & Gilchrist 1996; Baek & Al-Qadi 2006; Chen *et al.* 2013; Koerner 2005; Kazimierowicz-Frankowska 2008; Moreno-Navarro *et al.* 2014; Yang *et al.* 2011). Filtration, drainage, reinforcement, separation, and liquid barrier behavior are the primary uses of geosynthetic materials. Geosynthetic material reinforces the pavement structure by altering the pavement's reaction to loads (Koerner 2005). Among the different approaches, using an interlayer at the top of the old layer and the bottom of the overlay can provide better conditions to mitigate and delay the reflective cracking. This interlayer, like geosynthetics (geotextile, geocomposite, and geogrid), reduces stress or reinforces the pavement. Reinforcement occurs when the inter-layer's modulus is higher than that of the top and bottom pavement layers. On the other hand, stress relief happens when the modulus obtains a lower value (De Bondt 2000; Lytton 1989). The overlay's horizontal

tensile stresses created by loading and heat cycling should be reduced using the interlayer (Kim & Buttlar 2002).

Numerous numerical, experimental, and field studies have been conducted to propose various solutions for reducing the reflective cracking rate. The effect of fabric, as the stress relief layer, on pavement performance was evaluated by Amini (2005). It was reported that different factors, such as weather and subgrade conditions, traffic load, overlay thickness, and crack width, can affect pavement crack movement. Penman and Hook showed that the propagation rate of reflective cracking could be changed two-three times based on the glass-fiber geogrid inclusion within the overlay (Penman & Hook 2008). Sobhan & Tandon (2008) analyzed beam samples of asphalt mixture and found that stiff geosynthetic layers create more reflection cracking resistance. Khodaii *et al.* (2009) investigated the effect of different parameters on the propagation of reflection cracks, such as pavement type (asphalt mixture and concrete), the position of geogrids, test temperatures, and crack opening rate. They demonstrated that the position of one-third depth of overlay thickness from the bottom is more appropriate to increase the pavement fatigue life. Siriwardane *et al.* (2010) investigated the effect of glass fiber grids on asphalt pavement. Specifically, the results of their study and Fallah & Khodaii's work (2015) indicate that glass grids provide better pavement resistance to reflective cracking than other materials, such as polyester grids.

In addition, geosynthetics can also be used to reinforce pavements against rutting. Here, we present a summary of the related studies that assess the effects of geosynthetics on the rutting resistance of asphalt mixtures, even though limited research has been conducted regarding the effect of geosynthetics on rutting performance. Rutting distress of asphalt pavement accelerates with increasing the traffic load and pavement temperature (Bertuliene *et al.* 2011). As a result, lateral movement occurs in the pavement and creates a shear failure due to the shear strain (Kim & Park 2013). In addition, other factors, such as the thickness layer and its age, can influence the permanent deformation of the pavement (Abdullah Nur *et al.* 2013).

On the other hand, geosynthetics can reinforce the strength of the pavement against various distresses and changes its rheological model (Huang 1993; Perkins 1999). In this regard, Laurinavičius & Oginskas (2006) evaluated the rutting performance of reinforced pavement layers by geosynthetics and compared it to the control sample (with an equal thickness). They found that the rutting results are correlated with the elastic modulus of pavement, so a higher modulus indicates greater resistance to rutting. Regarding the higher elastic modulus of the reinforced layer, less permanent deformation was experienced. The reason is that geosynthetics reduce the shear strain of the asphalt layer (Laurinavičius & Oginskas 2006). Another study found that pavement reinforced with a smaller aperture geogrid size provides a better rutting resistance (Jenkins *et al.* 2004). The interlocking of asphalt mixture and geogrid contributes to the restraining effect and reduces the settlement of reinforced pavement compared with the control sample (Ling & Liu 2001). A field study was performed to investigate the role of geogrid on the rutting performance of asphalt pavement. The monitoring results proved the efficiency of geosynthetic materials (Sobhan *et al.* 2005). Compared to control samples, Komatsu *et al.* demonstrated that increasing geogrid adhesion to the asphalt mixture and reducing geogrid mesh size increased cutting and crack resistance by 30 and 10 times, respectively (Komatsu *et al.* 1998).

In 2018, Noory *et al.* developed a double shear bonding test named Amirkabir University of Technology Shear Lab Tester (AUT-SLT) for conducting dynamic shear loading on geocomposite-reinforced specimens. The device was able to apply normal load as well as dynamic shear loads (Noory *et al.* 2018). In other research, Noory *et al.* evaluated the effective parameters of shear resistance on the interface in a geocomposite-reinforced pavement. The parameters included product type, effective mesh size of geocomposite, the tensile strength of geocomposite, elongation at break, bitumen retention, and temperature (Noory *et al.* 2019a, 2019b).

Literature shows that different parameters can affect the shear bonding of geosynthetic reinforced overlays. Additionally, little research has been conducted on the effects of such parameters on the rutting resistance of asphalt overlay systems. This study is intended to comprehensively evaluate the effect of the most significant factors contributing to pavement performance through shear bonding strength and rutting phenomena. Here, the shear bonding between overlay and asphalt pavement is measured by the AUT-SLT device, and then the same samples were tested under the wheel track rutting device. An analysis of the results determined that specimens with greater shear bonding between layers were more resistant to rutting and showed less rutting depth.

2 SAMPLE PREPARATION

In order to figure out the relationship between the parameter of the rutting depth and shear bonding between layers of the geosynthetic reinforced specimens, two types of tests and specimens were designed and developed:

– Rutting of a geosynthetic reinforced overlay by a wheel-tracking machine
– Shear bonding between layers by AUT-SLT device

2.1 Rutting test

The specimens for the rutting test were prepared using the Press-BOX device, which applied shear side loading and compression loads from the upper actuator. A wheel-tracking machine is used to simulate the rutting process. The specimens consist of two layers reinforced by geocomposites with two 28 and 111-mm grid sizes. Also, a tack coat was applied at two rates of 0.5 and 1.5 kg/m^2. The specimens were fixed in (Figure 1a). The wheel-tracking machine mold and 600 load cycles were applied (Figure 1b). A side view of specimens is illustrated in Figure 1c. The rut depth was measured using an LVDT installed on the device.
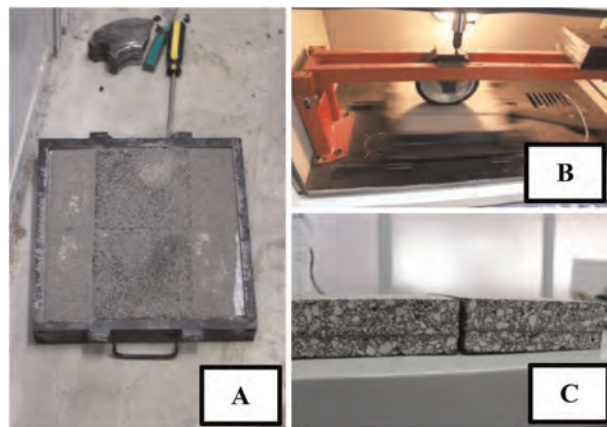
Figure 1. Specimen preparation and rutting test set-up.

2.2 Specimen preparation test

The specimens used in the AUT-SLT device (Amirkabir University of Technology – Shear Lab Tester) are designed and built in three layers, as shown in Figures 2a and 2b. The samples were prepared in Press-BOX mold (Figure 2c), each cut into three samples. A servo-hydraulic actuator conducted the tests at a constant displacement rate of 12.5 mm/min. All the tests were done at two temperatures of 15°C and 30°C.
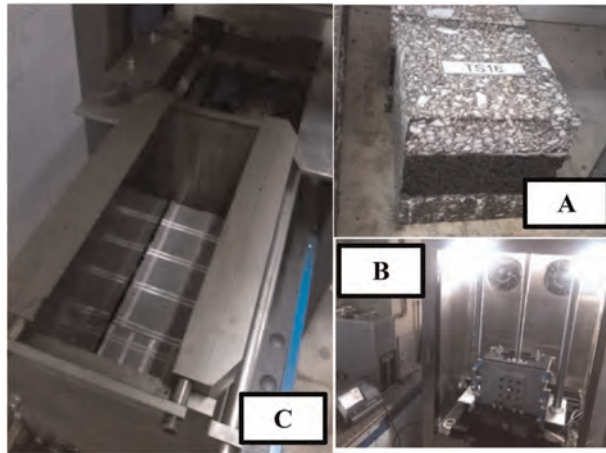
Figure 2. Specimen preparation and rutting test set-up.

Table 1 shows the experimental design of the tests. This analysis considered three factors: temperature, mesh size of the geocomposite, and application rate of the tack coat, all applied at two levels.

Table 1. Experimental design of the tests.

Specimen code	Temperature	GG size	Tack coat application rate
SP1	15	28	0.5
SP2	15	28	1.5
SP3	15	111	0.5
SP4	15	111	1.5
SP5	30	28	0.5
SP6	30	28	1.5
SP7	30	111	0.5
SP8	30	111	1.5

3 TEST RESULTS AND ANALYSIS

Table 2 displays the results of tests performed under predefined conditions.

Table 2. Test results for shear bonding and rutting tests.

Specimen code	Shear test results (kN/m^2)	600 cycles rutting (mm)
SP1	307.5	4.33
SP2	459.6	2.67
SP3	372.2	4.31
SP4	487.9	2.18
SP5	97.6	6.88
SP6	119.8	5.97
SP7	108.6	6.43
SP8	136.5	5.22

Before continuing with the analysis, the Anderson-Darling test was applied to the data to check whether the data was normal. As both rutting and AUT-SLT tests results had a P-Value greater than 0.05, it can be concluded that the test results passed the normality conditions.
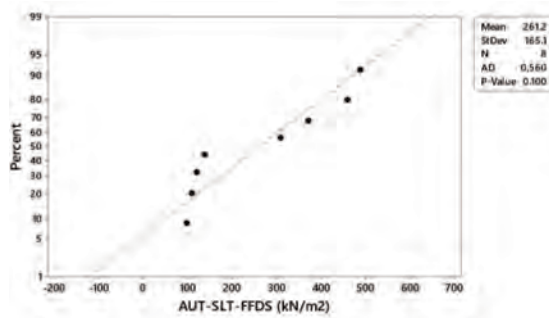
Figure 3. Anderson-Darling test results for AUT-SLT-FFDS (kN.m^2).
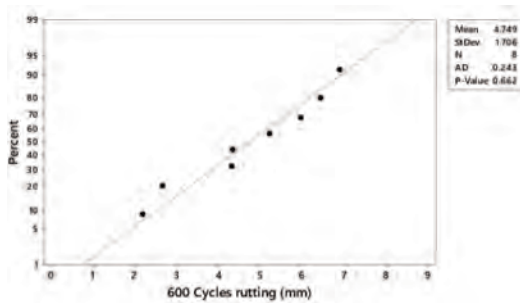
Figure 4. Anderson-Darling test results for 600 cycles rutting depth (mm).

Figures 5 and 6 show that the difference between the lower and higher temperature levels has the greatest influence on both test results but in the opposite direction. As the temperature increases, the amount of rutting increases; on the other hand, the resistance to shear loads decreases. The next effective parameters are tack coat application rate and GG size.
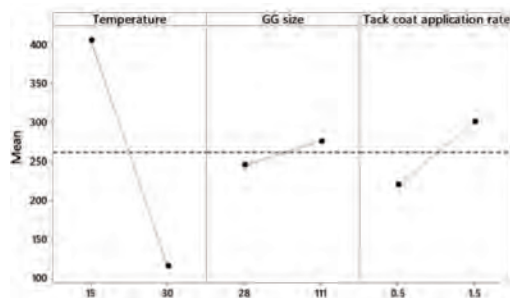
Figure 5. Main effects plot for AUT-SLT results based on the factors.
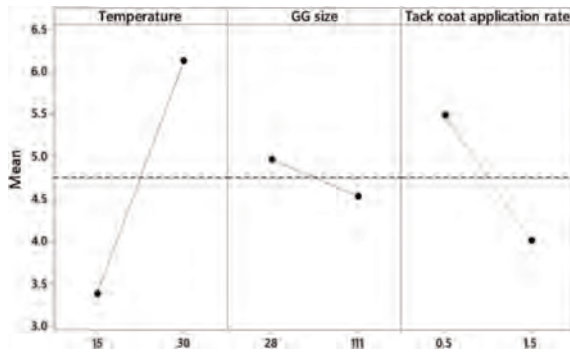
Figure 6. Main effects plot for 600 cycle rutting depth results based on the factors.

The graph of 600 cycles of loading rut depth versus AUT-SLT results is shown in Figure 7. This graph illustrates that rut depth decreases with increasing shear bonding. In other words, the increase in shear bonding can prove a crucial factor in preventing rutting in the studied pavements.

A study of deformed overlays has revealed that the layers slide on top of each other, resulting in a reduction in strength against rutting.
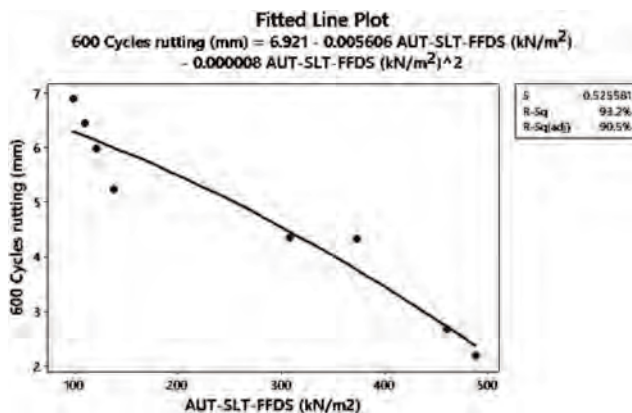
Figure 7. Overlay shear bonding versus rut depth.

4 CONCLUSION

This study tested the shear bonding between layers of a geocomposite-reinforced specimen using AUT-SLT, a double shear test device developed at Amirkabir University of Technology. The rutting effect of the wheel path through pavement was also investigated, and the amount of rut depth was measured. After checking the normality of the data gathered, an analysis of the data was conducted, which resulted in the following conclusions:

− The temperature had the most significant impact both on the shear bonding between layers of a geocomposite-reinforced pavement and the rut depth.
− Tack coat amount was the second significant factor contributing to the dramatic change in shear bonding and rut depth.

- The mesh size of the geocomposite was the third effective parameter affecting shear bonding and rut depth. Greater mesh size can result in better bonding between layers and better action in rutting.
- There is a direct correlation between the shear bonding of layers and the rut depth after 600 wheel paths on the reinforced pavement. It was found that rut depth decreased as shear bonding increased. Consequently, the increase in shear bonding is an important factor in preventing the rutting phenomenon in the studied pavements.

REFERENCES

Abdullah Nur, M., Khattak, M. J. & Bhuyan, M. R.-U.-K. 2013. *'Rutting Model for HMA Overlay Treatment of Composite Pavements'*, International Scholarly Research Notices.

Amini, F. 2005. Potential Applications of Paving Fabrics to Reduce Reflective Cracking, Jackson State University.

Austin, R. & Gilchrist, A. 1996. 'Enhanced Performance of Asphalt Pavements using Geocomposites', *Geotextiles and Geomembranes*, 14(3–4), 175–186.

Baek, J. & Al-Qadi, I. L. 2006. 'Finite Element Method Modeling of Reflective Cracking Initiation and Propagation: Investigation of the Effect of Steel Reinforcement Interlayer on Retarding Reflective Cracking in Hot-mix Asphalt Overlay', *Transportation Research Record*, 1949(1), 32–42.

Bertuliene, L., Oginskas, R. & Bulevicius, M. 2011. *Research of Rut Depth in Asphalt Pavements Reinforced with Geosynthetic Materials*, Translated by Vilnius Gediminas Technical University, Department of Construction Economics, 1039.

Chen, Y., Lopp, G. & Roque, R. 2013. 'Effects of an Asphalt Rubber Membrane Interlayer on Pavement Reflective Cracking Performance', *Journal of Materials in Civil Engineering*, 25(12), 1936–1940.

De Bondt, A. H. 2000. 'Anti-reflective Cracking Design of (reinforced) Asphaltic Overlays'.

Fallah, S. & Khodaii, A. 2015. 'Reinforcing Overlay to Reduce Reflection Cracking; An Experimental Investigation', *Geotextiles and Geomembranes*, 43(3), 216–227.

Gonzalez-Torre, I., Calzada-Perez, M. A., Vega-Zamanillo, A. & Castro-Fresno, D. 2015. 'Evaluation of Reflective Cracking in Pavements using a New Procedure that Combine Loads with Different Frequencies', *Construction and Building Materials*, 75, 368–374.

Huang, Y. H. 1993. *Pavement Analysis and Design*, Pearson Prentice Hall Upper Saddle River, NJ.

Jenkins, K., Dennison, P., Ebels, L. & Mullins, L. 2004. *3-D Polymer Grid Reinforcement of Asphalt for Rut Resistance*, Translated by.

Kazimierowicz-Frankowska, K. 2008. 'Comparison of Stress and Strain States in Pavements with and without Reflective Cracks', *Journal of Transportation Engineering*, 134(11), 483–492.

Khodaii, A., Fallah, S. & Nejad, F. M. 2009. 'Effects of Geosynthetics on Reduction of Reflection Cracking in Asphalt Overlays', *Geotextiles and Geomembranes*, 27(1), 1–8.

Kim, J. & Buttlar, W. G. 2002. 'Analysis of Reflective Crack Control System Involving Reinforcing Grid Over Base-isolating Interlayer Mixture', *Journal of Transportation Engineering*, 128(4), 375–384.

Kim, Y. & Park, T.-S. 2013. 'Reinforcement of Recycled Foamed Asphalt Using Short Polypropylene Fibers', *Advances in Materials Science and Engineering*.

Koerner, R. M. 2005. *Designing with geosynthetics*, Pearson Prentice Hall Upper Saddle River, NJ, USA:.

Komatsu, T., Kikuta, H., Tuji, Y. & Muramatsu, E. 1998. 'Durability Assessment of Geogrid-reinforced Asphalt Concrete', *Geotextiles and Geomembranes*, 16(5), 257–271.

Laurinavičius, A. & Oginskas, R. 2006. 'Experimental Research on the Development of Rutting in Asphalt Concrete Pavements Reinforced with Geosynthetic Materials', *Journal of Civil Engineering and Management*, 12(4), 311–317.

Ling, H. I. & Liu, Z. 2001. 'Performance of Geosynthetic-reinforced Asphalt Pavements', *Journal of Geotechnical and Geoenvironmental Engineering*, 127(2), 177–184.

Lytton, R. L. 1989. 'Use of Geotextiles for Reinforcement and Strain Relief in Asphalt Concrete', *Geotextiles and Geomembranes*, 8(3), 217–237.

Lytton, R. L., Tsai, F.-L., Lee, S. I., Luo, R., Hu, S. & Zhou, F. 2010. Models for Predicting Reflection Cracking of Hot-mix Asphalt Overlays.

Moreno-Navarro, F., Sol-Sánchez, M. & Rubio-Gámez, M. d. C. 2014. 'Reuse of Deconstructed Tires as Anti-reflective Cracking Mat Systems in Asphalt Pavements', *Construction and Building Materials*, 53, 182–189.

Noory, A., Moghadas Nejad, F. & Khodaii, A. 2019a. 'Evaluation of Geocomposite-reinforced Bituminous Pavements with Amirkabir University Shear Field Test', *Road Materials and Pavement Design*, 20(2), 259–279.

Noory, A., Moghadas Nejad, F. & Khodaii, A. 2019b. 'Evaluation of the Effective Parameters on Shear Resistance of Interface in a Geocomposite-reinforced Pavement', *International Journal of Pavement Engineering*, 20(9), 1106–1117.

Noory, A., Nejad, F. M. & Khodaii, A. 2018. 'Effective Parameters on Interface Failure in a Geocomposite Reinforced Multilayered Asphalt System', *Road Materials and Pavement Design*, 19(6), 1458–1475.

Penman, J. & Hook, K. 2008. 'The Use of Geogrids to Retard Reflective Cracking on Airport Runways, Taxiways and Aprons', *Pavement Cracking. Mechanisms, Modeling, Detection, Testing and Case Histories*, 713–720.

Perkins, S. W. 1999. Geosynthetic Reinforcement of Flexible Pavements: Laboratory based Pavement Test Sections, Montana. Department of Transportation.

Shukla, S. & Yin, J. 2004. Functions and Installation of Paving Geosynthetics, 314–321.

Siriwardane, H., Gondle, R. & Kutuk, B. 2010. 'Analysis of Flexible Pavements Reinforced with Geogrids', *Geotechnical and Geological Engineering*, 28, 287–297.

Sobhan, K., Genduso, M. and Tandon, V. 2005. Effects of Geosynthetic Reinforcement on the Propagation of Reflection Cracking and Accumulation of Permanent Deformation in Asphalt Overlays.

Sobhan, K. & Tandon, V. 2008. 'Mitigating Reflection Cracking in Asphalt Overlays using Geosynthetic Reinforcements', *Road Materials and Pavement Design*, 9(3), 367–387.

Yang, J., Yu, B. & Chen, Y. 2011. 'Analysis of the Effect and Mechanism of Conventional Treatment Technologies to Reflective Cracking of Asphalt Pavement with Semi-Rigid Base' in Pavements and Materials: Recent Advances in Design, *Testing and Construction*, 87–96.

Investigating the effects of installation in Nordic conditions on geosynthetics for reinforcement/stabilization: ROUGH project

T.L.H. Oliver
Contech Consulting Ltd (on behalf of Tensar International Ltd.), UK

A. Lavasan
Huesker Synthetic GmbH, Gescher, Germany

J. Klompmaker
Naue GmbH & Co. KG, Germany

C. Recker
Sintef Community, Münster, Germany

Ph. Delmas
Sintef Advisor, France

ABSTRACT: Installation damage tests were carried out on several geosynthetics of various types and from different manufacturers. The testing procedures included conditioning products in a field installation at low temperatures, under specific Nordic conditions (crushed rock, compaction) followed by laboratory tensile testing of the exposed and unexposed geosynthetic samples. The results of the individual tests were evaluated, and the results interpreted anonymously regarding the different geosynthetic versus the typical design approach in similar Nordic conditions at positive temperature.

1 INTRODUCTION

In order to be able to propose recommendations for the use of reinforcement/stabilization geosynthetics in Nordic conditions, an investigation was carried out to collect information and provide data on their behaviour during installation in Nordic conditions (sub-zero temperatures, soil types and working conditions) (Rough project 2022). The investigation included a full-scale trial at a site in Northern Finland, 15 km southeast of Kemi along the E8/E75. The geosynthetics were installed at sub-zero temperatures ($-10°$C) under Nordic conditions, followed by tensile testing of the exhumed materials alongside non-exposed materials at temperatures of $+ 20°$C, $0°$C, $-10°$C and $-20°$C. Installation and recovery of the geosynthetics took place on 5th and 6th February 2020.

The installation replicated a typical subbase/base layer reinforcement/stabilization application. The geosynthetics were installed on a prepared subbase (compacted crushed rock) and a layer of crushed rock then dropped over the geosynthetic and compacted using typical construction plant. The trial was deconstructed, materials were exhumed, and samples taken for testing in the laboratory.

Several geosynthetics have been tested with different product structures and produced with different polymers: polyester woven coated geogrid, polyester strip geogrid, polypropylene strip geogrid, polypropylene punched and extruded geogrids, a polypropylene woven and geocomposites nonwoven with an extruded geogrid or a strip geogrid.

2 CLIMATIC CONDITIONS FOR THE INSTALLATION TRIAL

Temperature was recorded on site and compared with the data provided online by the Finnish Meteorological Institute (www.ilmatieteenlaitos.fi) from the nearest weather station at Kemi Airport (distance 20 km). Temperatures measured on site matched the weather data. For this reason, the data recorded hourly by the Finnish Meteorological Institute is used to indicate the temperatures during the installation conditioning of the geosynthetic products. During installation of the products and compaction of the layers of crushed rock material, the air temperature ranged between $-7°C$ and $-15°C$. No snow needed to be removed from the test section and no snowfall occurred during the installation and filling work. During the deconstruction/recovery of the samples on Thursday the 6th Feb. 2020 temperatures between $-4°C$ and $-7°C$ were recorded.

3 CRUSHED ROCK MATERIAL

The material used for the subbase and base layer was typical for Finnish road construction and unbound granular subbases. Figure 1 displays the particle-size distribution of the material used together with the limit values presented in Finnish guidelines InfraRYL for the base course. The material is named as "KaM 0/56" which means it is crushed rock GO 0/56 mm based on SFS-EN 13242.
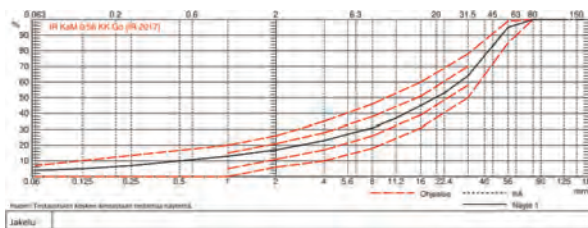
Figure 1.   Particle-size distribution of crushed rock used and the Finnish limit values for subbase material.

4 TRIAL SET UP AND CONSTRUCTION

Construction of the trial sections followed Finnish specifications for road construction. Figure 2 shows the cross section of the setup for field conditioning. An imported fill material was placed and compacted over the entire trial area to level the site and provide a frost protection layer. This was a ferrochrome slag waste product from a nearby steel plant. The slag material had a temperature of approx. $+18°C$ on delivery to site. The temperature dropped to $+6°C$ one night after installation. Material temperatures were checked with a penetration thermometer approx. $5 – 10$ cm below each layer surface.

After placement and compaction of the slag layer, a subbase of 0/56 crushed rock was placed and compacted to a finished layer thickness of 30 cm. The reinforcement/stabilisation geosynthetics were then unrolled into place and finally the base layer of 0/56 crushed rock
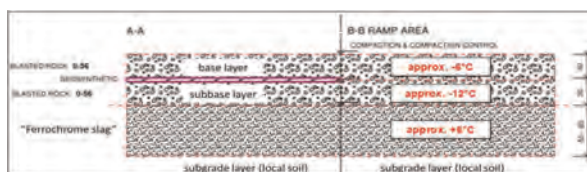
Figure 2.   Cross-section of field trial setup.

was dropped with an excavator bucket on the geosynthetics with a measured height of 1.0 m and compacted to a finished layer thickness of 30 cm.

Compaction was done with a 12.6 ton dynamic roller. Five dynamic roller passes were used for compaction of each layer. Figure 4 shows the compaction level of each layer subsequently checked with a dynamic load plate testing device. During the compaction process the subsoil had a temperature of about – 6°C. Freshly delivered crushed rock material had a temperature of approx. – 6°C. Before installing the geosynthetics, subbase temperatures of about – 12°C were recorded.

Figure 3 shows the layout of the various geosynthetics and the compaction control verification (E_{V2} values). To minimize positional influences, each geogrid product was cut into half and installed at two different locations along the test field. For the subbase layer an average bearing capacity modulus of $E_{V2} = 132$ MN/m^2 was measured. The measured values ranged from $114 – 170$ MN/m^2. The base layer reached a bearing capacity modulus of $E_{V2} = 143$ MN/m^2 in average. The measured values ranged from $92 – 170$ MN/m^2. Before installation of the base layer, the locations of specimens for further laboratory testing were marked. This is to eliminate the possibility of bias by specimen selection. The pre-marked specimen locations can be seen in Figure 4.
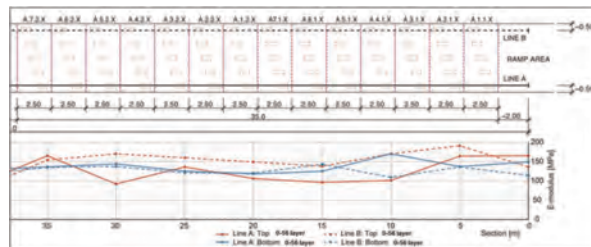
Figure 3.   Arrangement of geogrid samples and results of compaction control (EV2 values).

Figure 4.   Installed geogrid materials with test samples pre-marked before base layer placement.

During installation no heavy equipment drove over the installed geogrid products. The tipping height out of the excavator bucket was controlled to a consistent drop of 1.0 m.

5   RECOVERY OF SAMPLES

Samples needed to be cut from the geogrid specimens for testing and evaluation of installation damage. To avoid additional damage to the samples during recovery a suction

technique was used. The upper 20 cm of the base layer was removed carefully by excavator and the remaining 10cm using a vacuum suction lorry.

After all the base layer had been removed, samples were cut from the previously marked locations and labelled. The marking included the product identifier and location on the installed test setup. For transport to the laboratory, the samples cut out were stacked in a robust wooden box with fabric between to avoid mechanical damage or other degradation during the transport.

6 LABORATORY TESTING

Tests were performed on conditioned samples returned from the field trial ('damaged') and also on samples taken from the same product specimens but not sent to site (non-damaged). Temperature conditioning of the non-damaged samples provided information on the effect of temperature on product behaviour.

6.1 Tensile testing in temperature-controlled environment

The damaged samples from Kemi were tested at + 20°C according to EN ISO 10319 to determine the corresponding evolution of the stress-strain characteristics.

Parallel, tensile testing on non-damaged samples was carried out in a temperature-controlled chamber (Figure 5). The test specimens were temperature conditioned for one hour before testing began. After clamping samples in the test rig, the chamber temperature was allowed to stabilize at the required test temperature before testing commenced. The tests were carried out on single ribs according to EN ISO 10319 to determine stress-strain characteristics.

Non-damaged samples were tested at – 20°C, – 10°C, 0°C and + 20°C.

Figure 5. Single rib tensile testing in a temperature-controlled chamber.

6.2 Results - Influence of temperature on tensile behaviour on non-damaged samples

Results from tensile testing of the non-damaged samples show the influence of temperature on product stiffness. Importantly, all products showed an increase in stiffness with reducing temperature. Using the representation of the reduction factor applied on stiffness ($RF_{ID, J}$) proposed by Allen and Bathurst (1994) the Figure 6 shows its evolution for the range of results for all product types tested.

Considering the average of all products tested, the increase of stiffness is $\geq + 30$ % (20°C to 0°C) $\geq + 40$ % (20°C to – 10°C) and $\geq + 47$ % (20°C to – 20°C).

6.3 Results – Influence of installation on tensile behaviour

Looking at the evolution of the different conditioning steps of the samples helps with the interpretation of the results:
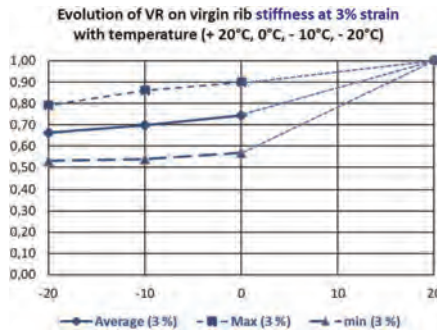
Figure 6.   Effect of temperature on RFID, J (stiffness) - range of data from all products tested.

Samples damaged in Kemi:

– End of manufacturing of the product: temperature $\sim$ + 20°C (positive); undamaged
– Lay down on site in Kemi:temperature −10°C; undamaged
– Backfilling and compaction:temperature −10°C; damaged by installation
– Recovering of damaged samples:temperature −10°C; no extra damaging
– After transport, test in laboratory:temperature $\sim$ + 20°C (positive)

Samples undamaged tested at different temperatures:

– End of manufacturing of the product: temperature $\sim$ + 20°C (positive); undamaged
– Conditioning and testing in laboratory: temperature + 20°C, 0°C, −10°C, −20°C

The laboratory tests on undamaged samples at different temperatures allow evaluation of:

– The tensile strength and the tensile stiffness of the different geosynthetics at −10°C (equivalent to temperature during placement and backfilling and compaction).
– The evolution of tensile strength and the tensile stiffness of the different geosynthetics during the time when they are installed in the soil and submitted to temperature variations. It shall be noted that in this case the surrounding soil is also subjected to the same temperatures; this means that the increase (resp. decrease) of stiffness of the geosynthetics happens parallel to the soil stiffness increase (resp. decrease).

The laboratory tests on the Kemi damaged samples are realized at + 20°C:

– They allow evaluation of the influence of the installation realized at – 10°C on the product when it recovers to a positive temperature (+ 20°C).
– The characteristics (tensile strength, strain, or stiffness) obtained should not be compared with the ones measured at – 10°C on the virgin geosynthetics.

A quite large number of products have been tested in Kemi and considering the severe installation conditions (crushed rock and heavy compaction), some of the products were under-designed for the intended use at conventional conditions and positive temperatures. For this paper, it has been decided to focus only the finding on the geosynthetics which would normally have been used in the same geotechnical conditions at a positive temperature.

Considering the typical subbase/base layer reinforcement/stabilization application, the stiffness is the most important performance related parameter to be considered, not forgetting of course a sufficient robustness (resistance to installation damage).

The tests on the undamaged samples at + 20°C and −10°C show a significant increase in stiffness (Figure 6) as temperatures reduce and it is reasonable to assume that these higher stiffness values were present during installation at −10°C in the Kemi trial. Nevertheless, the effect of installation in Kemi Nordic conditions shows only a small variation of tensile

stiffness (-2% to $+7\%$) compared to the un-damaged samples. This variation is within the test accuracy and can be seen to be minor. The effect of installation in Kemi Nordic conditions measured on tensile strength was found to be a small reduction between 0% and 13%.

7   LABORATORY SIMULATION OF THE EFFECTS OF INSTALLATION AT SUB-ZERO TEMPERATURES

As part of this same study, an attempt was made to simulate installation damage at sub-zero temperatures in the laboratory. Impact conditioning using a specific device with a weight of $1000 \pm 5g$ with a round drop head falling from a height of 50 cm (same energy as defined in EN ISO 13433 - Geosynthetics - Dynamic perforation test) was carried out, on temperature conditioned samples. Single rib tensile testing (on the ribs and the junctions) was then carried out at $+20°C$ on the impact damaged samples. Comparison of the results with those from the actual installation damaged samples from the Kemi trial showed no correlation. It was concluded that while a laboratory method to condition samples that would replicate installation damage effects was desirable, the proposed method was not valid for this purpose.

8   CONCLUSIONS

For the defined Nordic conditions in the Kemi trial (soil type - crushed rock, drop height 1 m, compaction, etc.) geosynthetics correctly designed to have minimal installation damage at more common positive site temperatures (i.e., above zero $°C$)

a) Exhibit no detrimental effect on strength from installation at sub-zero temperatures of –$10°C$.
b) Exhibit no significant difference in stiffness (measured at $+20°C$) following installation at sub-zero temperatures of $-10°C$.

The stiffness of these geosynthetics increased significantly when measured at $-10°C$ compared to $+20°C$ (43% in average). These increased stiffness values will be the expected characteristics when installed in soil at $-10°C$. It should be noted that the soil also exhibits increased stiffness compared to higher temperatures.

REFERENCES

Allen, T.M. and Bathurst, R.J. (1994) Characterization of Geosynthetic Load-strain Behaviour after Installation Damage, *Geosynthetics International*, Vol. 1, No 2, pp. 191–199.
InfraRYL Infrarakentamisen Yleiset Laatuvaatimukset. Maa-, Pohja- ja Kalliorakenteet. Rakennustieto. 2018 - InfraRYL *General Quality Specifications for Infrastructure. Earthworks, foundations and rock structures.*
Rough project, 2022. RecOmmendations for the Use of GeosyntHetics in Nordic conditions. SINTEF. Part 1 - Tests on Damage During Installation at Low Temperatures. Function: Reinforcement Stabilisation, Filtration, Drainage, (53 p) & Part 2 - Status of Existing Information on Installation Requirements for Sealing Products (GBR-P, GBR-B and GBR-C) under Nordic Conditions (45 p)

Reinforcement of local soils for unpaved forest roads: CBR and triaxial tests and estimate of properties

D.M. Carlos
RISCO, Department of Civil Engineering, University of Aveiro, Aveiro, Portugal
CONSTRUCT-GEO, Faculty of Engineering, University of Porto, Porto, Portugal

M. Pinho-Lopes & J. Macedo
RISCO, Department of Civil Engineering, University of Aveiro, Aveiro, Portugal

ABSTRACT: Forest roads are fundamental infrastructures to provide the necessary access to the forest. Most forest roads are unpaved, formed using a superficial layer of unsealed gravel or aggregate, and often local soils or a mix of these two types of material. Herein, two local Portuguese soils were studied, assessing their potential use in unpaved forest roads, namely by including reinforcement with a geocomposite, and by performing CBR and triaxial tests, and estimating key design properties using proposals from the literature. The CBR test results indicate little improvement of the response due to the reinforcement. The triaxial test results show a clear effect of the reinforcement, namely for higher axial strains. The stiffness of the composite material increased relative to the unreinforced soil, particularly for higher strains, and decreased the post-peak softening. The correlations used for estimating the resilient modulus of the soils led to a large scatter of values. Thus, they must be quantified using tests or by proposing adequate relations to other geotechnical properties, extending existing databases.

1   INTRODUCTION

Forest roads are fundamental infrastructures to provide the necessary access to the forest. Their design must be efficient, cost-effective, and compatible with environmental values. Most forest roads are unpaved and, commonly, are formed using a superficial layer of unsealed gravel or aggregate (Institute for Commercial Forestry Research 2005). Such layer spreads the loads, decreasing the stress level at the subgrade and the associated displacement. In some cases, staged construction can be used to ensure higher shear strength, by consolidation of the existing soil (Timber Transport Forum 2020). The superficial layer corresponds to a significant percentage of the total road cost. Thus, adequate design and construction can lead to important savings (construction and maintenance). To perform its functions adequately, a good forest superficial layer should (Dawson 2001): provide a smooth-running surface, promoting efficient driving and low tyre wear; enable low transient (resilient) deformations under the vehicle wheels; lead to insignificant permanent deformation (rutting); minimise dust during dry weather, to provide safe driving conditions, environmentally acceptable air quality and very limited effects on tree growth adjacent to the pavement; enable limited loss of aggregate from the surface, maintaining the pavement thickness. Often, the superficial layer is formed by an aggregate, local soil or a mix of these two types of material. Herein, two local soils were studied, assessing their potential use in unpaved forest roads with a geosynthetic reinforcement, and estimating key design properties.

2 METHODODLOGY

2.1 *Experimental programme*

This paper includes results for two soils, residual soil from granite and fine soil, and one geosynthetic. The response of the reinforced soil was compared to that of the unreinforced soil tested under the same conditions, using triaxial and CBR tests. Table 1 summarises the test programme.

Table 1. Experimental test program.

Test	Soil	N° specimens	Conditions	H (mm)	D (mm)	Reinforcement layer N°	Position (re. top)
CBR	Residual	1	Soaked	125	152	0	–
	Residual	1	Soaked	125	152	1	2H/5
	Fine	1	Soaked	125	152	0	–
	Fine	1	Soaked	125	152	1	2H/5
Triaxial	Residual	3	Dry, UU	140	70	0	–
	Residual	3	Dry, UU	140	70	1	H/2
	Fine	3	Dry, UU	140	70	0	–
	Fine	3	Dry, UU	140	70	1	H/2

2.2 *Materials*

The soils studied represent two possible scenarios for using local materials to build unpaved roads in Portugal. The residual soil from granite is typical of the North of Portugal and was sampled in the region of Porto; the fine soil was collected from a saltpan in the Aveiro lagoon. The main properties of the soils are summarized in Table 2 and Figure 1. The residual soil was a poorly graded sand with silt, while the fine soil was a sandy silt.

Table 2. Properties of the soils studied.

Soil	% fines (%)	D_{50} (mm)	D_{max} (mm)	G_s (–)	γ_{dmax} (kN/m^3)	w_{opt} (%)	I_P (%)
Residual	8	1.000	12.70	2.55	18.88	11.5	11
Fine	65.7	0.023	4.76	2.64	18.10	13.9	10
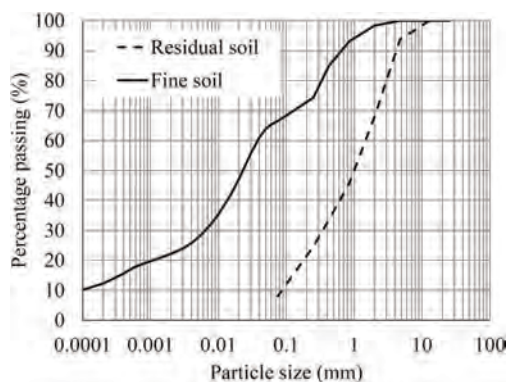
Figure 1. Particle grain size distribution of the soils studied.

A geocomposite, GC, was used, formed by continuous filament non-woven geotextile, reinforced by high tenacity polyester yarns in the machine direction, MD. Some of its nominal properties include: tensile strength and strain of 55 kN/m and 10% in MD; 12 kN/m and 85% in the cross-machine direction; thickness of 2.14 mm; mas per unit area of 325 g/m^2.

2.3 CBR tests

The procedure used for the CBR tests is described in a specification by the *Laboratório Nacional de Engenharia Civil* (LNEC): LNEC E198 (1967). The procedure is very similar to that in ASTM D1883–07 (exceptions for the test velocity and the number of blows used to compaction the soil).

Cylindrical specimens were tested, with diameter D = 152 mm and height H = 125 mm. Each specimen was prepared by assembling 5 layers of soil, 25 mm high each, compacted with 25 blows of a hammer with 4.54 kg of mass and drop height of 457 mm. The soil was prepared to the desired water content (w = w_{opt}, modified Proctor test), and allowed to rest for 24 hours at a standard atmosphere (temperature 20°C; relative humidity 65%) within impermeable containers. Then, the specimens were soaked for 96 hours. The tests were performed applying an axial displacement of 1 mm/min. For the reinforced specimens, a similar procedure was used. The main difference was placing a disc of reinforcement horizontally at 2H/5 from the top of the specimen.

2.4 Triaxial tests

Unconsolidated undrained (UU) compression triaxial tests (ISO/TS 17892-8: 2004) were carried out using the following conditions: cylindrical specimens (70 mm diameter D; 140 mm height H); axial strain rate of 0.7 mm/min; dry specimens; confining stress of 50, 100 and 150 kPa. The residual soil was compacted to a density index, I_D, of 53% (dry unit weight of 14.05 kN/m^3). The fine soil was compacted to a compaction degree of 71% (dry unit weight of 12.85 kN/m^3).

All specimens were assembled in a similar way, by preparing layers of compacted soil (4 layers, 35 mm high each). To achieve the desired soil density, the total mass of soil necessary to remould a soil specimen was quantified and divided by the number of layers; then, each soil layer was build using the relevant mass of soil and compacted to the desired density. The compaction was done manually by vibrating the soil and applying cyclic normal forces to each layer. The reinforced soil specimens included a disc of reinforcement placed horizontally at mid height (H/2 = 70 mm). For these specimens, the mass of soil used to prepare the reinforced soil specimens was adjusted, to consider the volume of soil occupied by the reinforcement layer.

3 RESULTS

3.1 CBR tests

Table 3 summarizes the results of the CBR tests: target water content (w), real water content (w_{real}), CBR value for 2.5 mm and 5.0 mm penetration ($CBR_{2.5}$, $CBR_{5.0}$), maximum force (F_{max}). The force-penetration curves obtained are illustrated in Figure 2.

The results show that the inclusion of the reinforcement layer led to improvement of the response of both soils, when compacted to the optimum water content. The maximum force increased by 6% and 4% for the residual and fine soils, respectively.

Figure 3 shows the improvement factor of each soil reinforced with GC, for different values of the penetration during the CBR tests. For the residual soil, the largest improvement occurred for smaller values of penetration (up to 2.5 mm), while for the fine soil the improvement is more important for larger values of penetration (12.5 mm).

Table 3. Main results of the CBR tests.

Soil	Reinforcement	w (%)	w_{real} (%)	$CBR_{2.5}$ (%)	$CBR_{5.0}$ (%)	F_{max} (kgf)
Residual	–	11.5	11.4	22.1	25.1	1060.3
Residual	GC	11.5	11.0	22.4	25.4	1116.9
Fine	–	13.9	13.8	4.7	4.7	185.8
Fine	GC	13.9	13.6	4.7	4.9	192.9
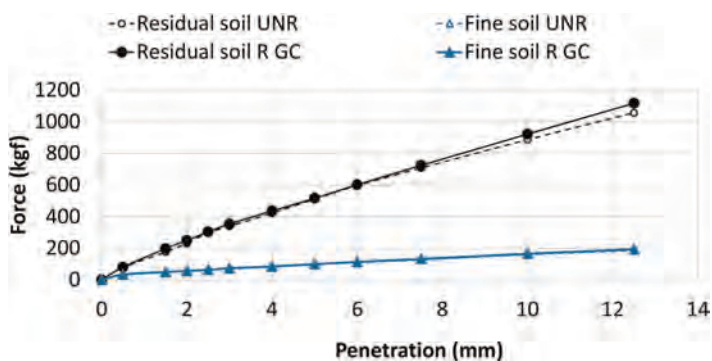
Figure 2. Force-penetration response of residual and fine soils, unreinforced (UNR) and reinforced (R GC).
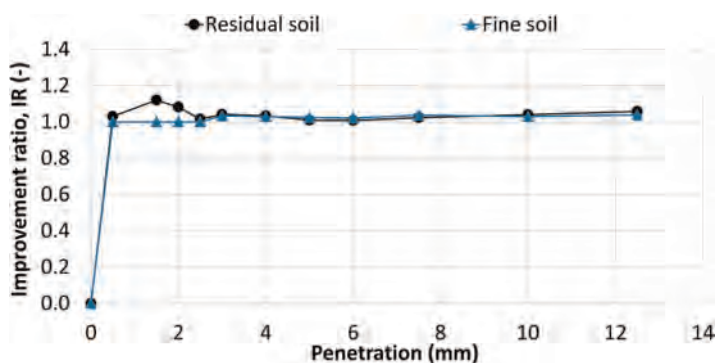
Figure 3. Improvement factor of the specimens of the residual and the fine soils reinforced with GC.

3.2 Triaxial tests

Table 4 summarizes the results of the triaxial tests: deviator stress (q), strain (ε), shear strength parameters (ϕ' and c'), secant stiffness modulus (E). The specimens of fine soil reinforced with GC did not fail; thus, no peak values are included. End of test values are designated as final (subscript fin), as critical state was not always reached. Figure 4 shows the stress-strain curves.

The reinforced soil specimens exhibited a response better than the soil. For the residual soil, the layer of reinforcement at mid-height of the specimens led an increase of peak deviator stress, q_{peak}, from 16% to 31%. The deviator stress at the end of the test increased 34% to 65% for the residual soil and 17% to 27% for the fine soil. Including the

Table 4. Main results of the triaxial tests.

Soil	Reinf.	σ_n (kPa)	q_{max} (kPa)	q_{fin} (kPa)	ε_{qmax} (%)	ε_{qfin} (%)	ϕ'_{peak}; ϕ'_{fin} (°)	c'_{peak}; c'_{fin} (kPa)	E_{50} (MPa)	$E_{\varepsilon\,=\,5\%}$ (MPa)
Residual	–	50	165.2	130.2	11.0	17.0			3.08	2.49
Residual	–	100	294.0	232.9	11.6	17.0	36.6; 32.3	0; 0	4.69	4.21
Residual	–	150	441.4	341.2	10.8	17.0			7.36	6.39
Residual	GC	50	190.8	174.3	15.8	18.1			2.5	2.33
Residual	GC	100	353.8	330.4	13.1	18.0	40.6; 40.0	0; 0	4.64	4.42
Residual	GC	150		576.9	565.2	15.9	18.0		7.11	6.77
Fine	–	50	181.7	170.7	12.6	18.0			7.10	2.87
Fine	–	100	321.8	312.5	13.7	17.3	35.2; 35.5	14.4; 7.9	6.10	4.58
Fine	–	150	454.4	446.9	16.0	18.1			7.30	5.78
Fine	GC	50	–	214.8	–	18.2			4.42[#]	2.90
Fine	GC	100	–	366.5	–	18.1	–; 39.5[*]	–; 6.9[*]	4.75[#]	4.24
Fine	GC	150	–	564.8	–	18.1			6.54[#]	6.22

[*]No failure | [#] E_{50} calculated for 50% of q_{fin}, when the specimens did not fail.
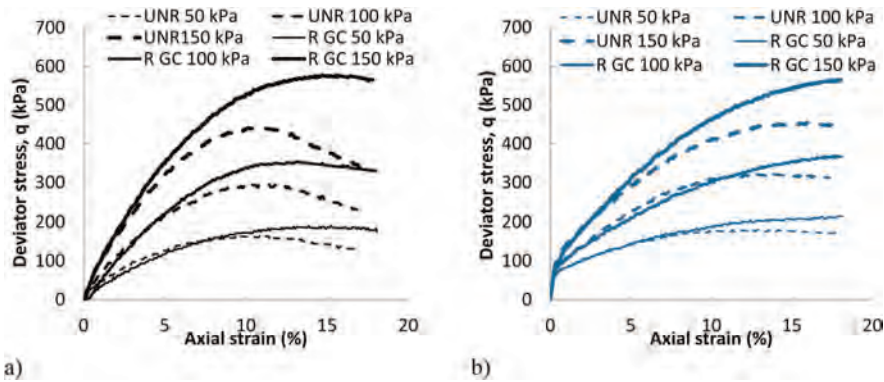
Figure 4. Stress-strain curves for unreinforced soil (UNR) and for soil with reinforcement layer at mid-height (R GC): a) residual soil; b) fine soil.

reinforcement layer changed the failure mechanism (Figure 5) from bulging, maximum at the centre of the specimens (unreinforced soil), to bulging between to top or the base of the specimen and the reinforcement layer (reinforced soil specimens). These changes confirm that the reinforcement was mobilised through friction as extension strains were induced at the centre of the specimens during the triaxial tests.
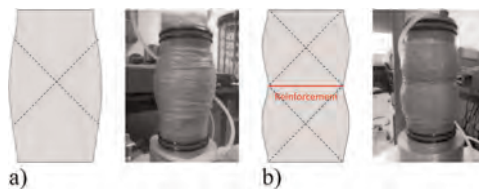
Figure 5. Observed failure mechanisms: a) unreinforced (UNR); b) reinforced (R GC).

4 ESTIMATES OF PROPERTIES RELEVANT FOR THE DESIGN OF UNPAVED ROADS

Mechanistic-empirical methods can be a way forward in achieving widely applicable unpaved roads designs. For that, the resilient modulus, M_R, of the materials is often a key parameter. For many countries where unpaved roads are used, particularly for low-volume roads, it may be challenging to assess the resilient modulus from experimental data. Thus, there are some correlations to other properties that can be used for an initial estimate of M_R. Mallela *et al.* (2009) presented some equations for that purpose, applicable to the design of flexible pavements. The quality of input data depends on the project level: level 1, requires the highest quality of data, obtained from direct testing on the project material; level 2, if a given parameter cannot be obtained from direct test results, it can be correlated to other test results; level 3, for lower volume roadways, where estimated input value for a given parameter are recommended, in the absence of test data. Equations 1 and 2 (level 2) refer to unbound aggregate materials, while Equation 3 (level 2), by AASHTO (1993), is applicable to for subgrade soils, namely fine-grained soils with a soaked CBR of 10. Table 5 shows recommended parameters for level 3, from Mallela *et al.* (2009).

$$M_R(MPa) = 17.6 \times CBR^{0.64} \tag{1}$$

$$CBR = \frac{75}{1 + 0.728(w \times PI)} \tag{2}$$

where PI = plasticity index of the soil and w = % of material passing the 0.075 mm sieve.

$$M_R(MPa) = 10.3 \times CBR \tag{3}$$

The fine soil is estimated to have M_R = 48.6 MPa (Equation 3). The soaked CBR of the soil is 4.7, smaller than the reference value of 10 for applicability of Equation 3. The fine soil can be classified as A-4, which leads to a level 3 estimate M_R = 75.8 MPa. The latter is 56% larger than the first, showing that this approach must be used critically. The residual soil does not meet any of the criteria, thus it is not possible to estimate its resilient modulus.

To promote the use of local soils in unpaved forest roads using mechanistic-empirical design methods, it is necessary to estimate key design parameters. Thus, the resilient modulus of local soils must be quantified using tests or by proposing relations to other geotechnical properties, extending existing databases.

5 CONCLUSIONS

This paper presents data on the shear strength and bearing ratio of two local soils (residual and fine) to assess their potential application in unpaved forest roads. The response of the unreinforced soil was compared to the soil reinforced with a geocomposite, using CBR and triaxial tests data. In addition, properties relevant for the design of unpaved forest roads were derived using proposals from the literature. From the results the following conclusions can be established:

- The CBR test results indicate little improvement of the response due to the reinforcement. The position of the reinforcement (at a depth equal to the width of the plunger used in the CBR test) is one of the causes of the small improvement observed.
- The triaxial test results show a clear effect of the reinforcement, particularly for higher axial strains. The stiffness of the composite material increased relative to the unreinforced soil, namely for higher strains, and decreased the post-peak softening.

Table 5. Recommended resilient modulus for level 3 applications of Mechanistic-Empirical Pavement Design Guide (MEPDG), Malella et al. (2009).

Material category	Base/subbase	Subgrade			
Soil / aggregate	Unbound	A-1[*]	A-4[*]	A-6[*]	A-7[*]
Resilient Modulus, M_R (MPa)	15.2	220.6	75.8	68.9	75.8

[*]AASHTO Soil Classification System (AASHTO M 145 1991)

- Conventional CBR tests may not be adequate for quantifying the mechanical response of the soil-geosynthetic composite.
- The correlations used for estimating the resilient modulus of the soils led to a large scatter of values (56% variation). Thus, they must be quantified using tests or by proposing adequate relations to other geotechnical properties, extending existing databases.

REFERENCES

AASHTO (1993). *Guide for Design of Pavement Structures*. The American Association of State Highway and Transportation Officials, Washington DC.
AASHTO (1991). M 145. *Classification of Soils and Soil-Aggregate Mixtures for Highway Construction Purposes*. The American Association of State Highway and Transportation Officials, Washington DC.
ASTM. (2007e2). D1883. *Standard Test Method for CBR (California Bearing Ratio) of Laboratory-Compacted Soils*.
Dawson, A. R. (2001). Engineering the Forestry Road Pavement. In m *Annual Symp. on Forestry engineering*. Group of the Institute of Agricultural Engineers.
Institute for Commercial Forestry Research (2005). *South African Forest Road Handbook*. Sally Upfold (Editor). 214p.
ISO. 2004. TS 17892-8. Geotechnical Investigation and Testing - Laboratory Testing of Soil. *Part 8: Unconsolidated Undrained Triaxial Test*.
LNEC (1967). E198. *Determinação do CBR*. Especificação LNEC. Lisboa: LNEC.(*in Portuguese*)
Malella, J, Glover, R, Liang, RY and Chou, EY. (2009). Final Report Guidelines for Implementing NCHRP 1-37A M-E Design Procedures in Ohio: Volume 2-Literature Review. (No. FHWA/OH-2009/9B). Ohio. Dept. of Transportation.
Timber Transport Forum (2020). *The design and use of the Structural Pavement of Unsealed Roads. 23p.*

Case study. Experimental and theoretical analysis of reinforcement of weak soils with geogrids at the foundation on the basis of field studies of a road embankment bypassing the city of Reni, Ukraine

L. Gurtina, P. Kharin, R. Plytus & I. Mazur
LLC «UNIPROM», Kyiv, Ukraine

V. Sedin, K. Bikus & V. Kovba
State Higher Education Institution "Prydniprovska State Academy of Civil Engineering and Architecture", Dnipro, Ukraine

Y. Slyusarenko, V. Tytarenko, N. Kosheleva & I. Kaliukh
State Enterprise "The State Research Institute of Building Constructions", Kyiv, Ukraine

ABSTRACT: The methods for design and construction of high embankments on weak bases of geocell mattresses using geogrids have been developed and are successfully used in Ukraine. During construction of the road embankment near the bridge over the railway in Reni, Ukraine, geocell mattresses were used over the section of more than 5 km. The silted marshland, overgrown with reeds, could not serve as a good foundation for the 11 m high embankment. Difficult hydrogeological conditions and the threat of constant floods prompted to use the geocell mattress technology, which made it possible to reduce the cost and time of construction. After the embankment was reinforced with the geocell mattresses, the following was achieved: the total settlement of the embankment base was reduced by 30%; the calculated resistance of the base soil was increased by 25%; the bearing capacity of the base was increased by 33%. The field geodetic observations were carried out to confirm the reliability of the embankment reinforced with the geocell mattresses.

1 INTRODUCTION

The transport structures construction on weak bases creates many problems for designers and builders. Firstly, such construction is always associated with high costs, and secondly, it significantly increases the works execution time. Methods for increasing the base bearing capacity by removing a weak soil and replacing it with stronger materials or by arranging a pile field are not always feasible in practice and, as a rule, are not economically feasible. The modern technologies allow to solve the weak base problem and at the same time significantly reduce the construction time and obtain tangible financial savings (Jenner 1988), (Jewell 1988), (Kaliukh *et al*. 2013, 2021), (Slyusarenko *et al*. 2009, 2010), (Robertson 1987), (Trofymchuk *et al*. 2022), (Voloshkina *et al*. 2021). The base bearing capacity can be increased either by the groundwaters level lowering in water-saturated soils, or by the base soils preliminary compression by pressure (Dobie 2011). Today, the methods have been developed for the design and construction of high embankments on weak bases with the geosynthetic materials use (TENSAR 2023). Most of the calculation methods for the reinforced earthworks are based on limit equilibrium method. In the event of a seismic impact, the additional inertial loads caused by an earthquake are included in the equivalent static

loads and calculated as by the quasi-static analysis methods. The reinforced earthworks calculations shall be performed in two stages (TENSAR 2023). Stage 1 includes the analysis of the overall (external) structure stability, resulting in the determination of the overall dimensions of the reinforced earth structure and the length of the geogrids from reinforced earth with an allowance for the class of consequences (responsibility) of the structure. This is, in fact, the analysis of the gravity retaining wall for shear, overturning, and bearing capacity loss. The analysis of the overall structures strength is performed by the method of circular-arc slip surfaces or by the method of H.M. Shakhunyants (Terzaghi & Peck 1996). Stage 2 refers to the local (internal) strength analysis (a double-wedge method), when the geogrids strength and vertical step, as well as the strength of the geogrids junctions to the cladding are checked. If the structures are built in seismic areas, the stability analysis should consider the seismic actions. The design scheme according to stage 2 is conditionally divided between two wedges, namely, Wedge 1 and Wedge 2 (Figure 1a).

The purpose of the stage 2 analysis is to ensure that the resistance (frictional forces $T_1 + T_2 + T_3$) created by the cladding and soil reinforcement, which is intersected by the Wedge 2, is sufficient to avoid the local (internal) structure stability loss. The horizontal force Z_i required for the balance of two wedges is determined from the balance equation of forces applied to the Wedge 2 (Figure 1b): $Z_i = \sum H_i - \sum V_i \tan(\varphi' - \theta_i)$, where $\sum H_i$ is all horizontal forces sum equal to E_{ah}; $\sum V_i$ is all vertical forces sum equal to $W_i + Q_2 + E_{av}$; φ' is the internal friction angle of the backfill soil, degrees; θ_i is the variable angle of the Wedge 1 and
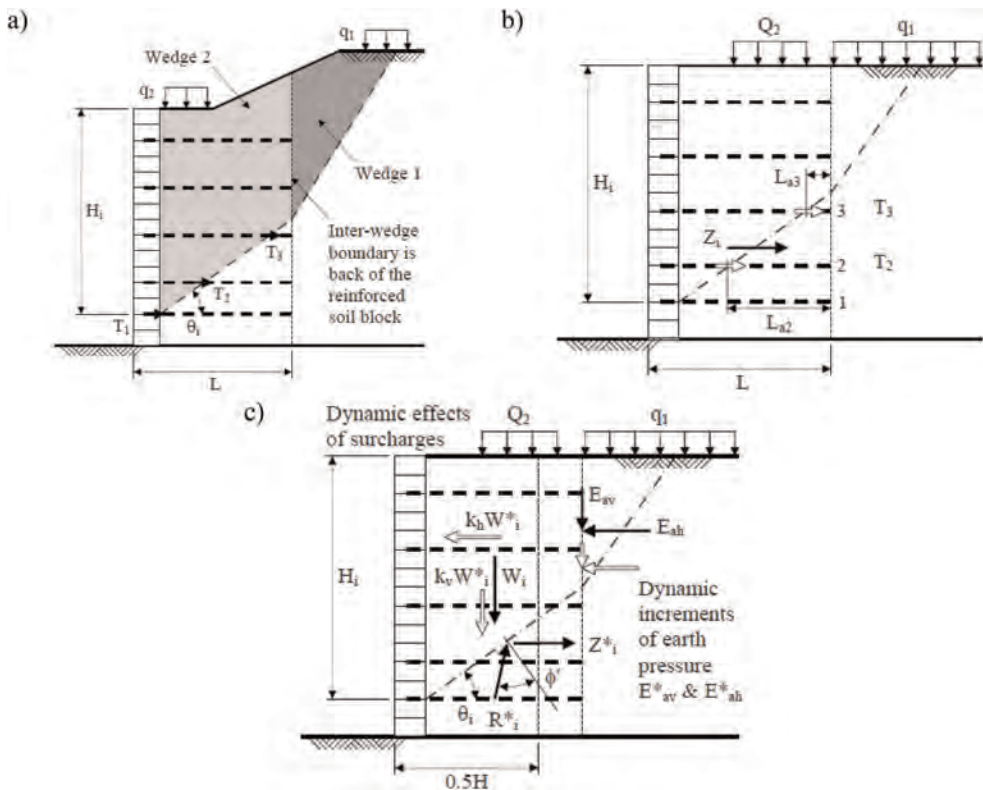
Figure 1. The internal stability analysis according to the stage 2: a - the scheme division into two wedges; b – forces acting on the structure; c – consideration of seismic effects (Dobie 2011). The symbols in Figure 1 correspond to the description of the program code TensarSlope version 1.13 (TENSAR 2023).

Wedge 2 inclination to the horizon, degrees. The analysis procedure for the seismic impact case is like that for static actions (Figure 1b), but with the additional action of seismic forces (Figure 1c). The main difference is the consideration of the additional seismic forces acting on the Wedge 2 (Figure 1c). A geomattress properly formed and placed in the embankment base keeps the overlying soil layers from displacements during the construction process and after its completion, until the base weak soils will gain sufficiently high mechanical characteristics due to consolidation and will stop to plastically deform. The paper purpose is to describe the geocell mattresses use for reinforcing the embankment of the approach to the viaduct over the railway laid through a silty swampy area overgrown with reeds (Bypass of the city of Reni on the km 0 + 000 – km 5 + 600 section with the area seismicity of 7 points on the Richter scale). Due to the complicated hydrological conditions and permanent flooding threat such soil originally could not serve as a good base for an 11-m high embankment. All that was a reason for the geocell mattress technology application by the Odesa highway service (TENSAR 2023). Such a structure was an alternative to the standard methods of the construction on weak soils, such as the soil replacement up to a mineral bed (1), and the pile foundation (2) or overpass (3) arrangement. The geogrids geomattresses in the bases provided a practical solution to the task of the embankments construction on the weak soils bases and promised the significant reduction of works execution time and their costs saving up to 31% compared to other options (TENSAR 2023).

2 MAIN PART

To study the engineering and geological conditions of the construction site at the international highway M15 (E87) Odessa - Reni (bypass of the city of Reni) section between the kilometer posts (KP) of 49 + 60-59 + 20 in the Odessa region, the surveys were carried out as the field, laboratory and office research parts. According to a plan, before the drilling operations start the road embankment base of sandy-loamy material was erected on the site. The natural relief was changed due to the elevations increase by 1.5–3.0 m. Absolute elevations at the wellheads along the road axis were 2.1–4.5 m. For boreholes drilling execution the portable drilling equipment "Geolog-15" was used. During the field works at the site, 6 boreholes of 10-m depth were drilled with soil sampling. In compliance with the general requirements to the soils characteristics determination methods (Ukraine Building Code. DSTU B V.2.1-3-96. 1996), the soils physical and mechanical properties were determined in the geotechnical laboratory, and the groundwaters chemical analysis was performed as well. Based on the office processing of the field and laboratory research data with the use of materials from surveys performed in the area in previous years, the engineering-geological elements (EGE) were defined, and the report was compiled with the corresponding text and graphic appendices. Sandy-argillaceous alluvial-estuarine deposits are the part of the geological succession, and modern Quaternary and Tertiary (ancient deluvium) alluvial and alluvial-estuarine deposits are the part of the site engineering geological structure up to the explored depth of 10.0 m (Figure 2).

If in the soils profile there are the soils belonging to the third category in terms of seismic properties, the site seismic activity should be increased by one point, and for the fourth category of soils in terms of seismic properties the site design seismicity should be determined by microseismic zoning (Ukraine Building Code. DSTU B V.2.1-3-96. 1996). The analysis of the soil physical and mechanical characteristics shows that the natural soils cannot serve as the highway embankment base because these soils deformations under the distributed load from automobile traffic will be very high. The deformations will lead to the road surface destruction. Due to the actual soils physical and mechanical characteristics and other conditions (silty swampy terrain overgrown with reeds), the natural terrain cannot serve as a good base for an 11-m high road embankment. The complicated hydrological conditions and constant flood threat lead to the need of transforming the initial physical and mechanical
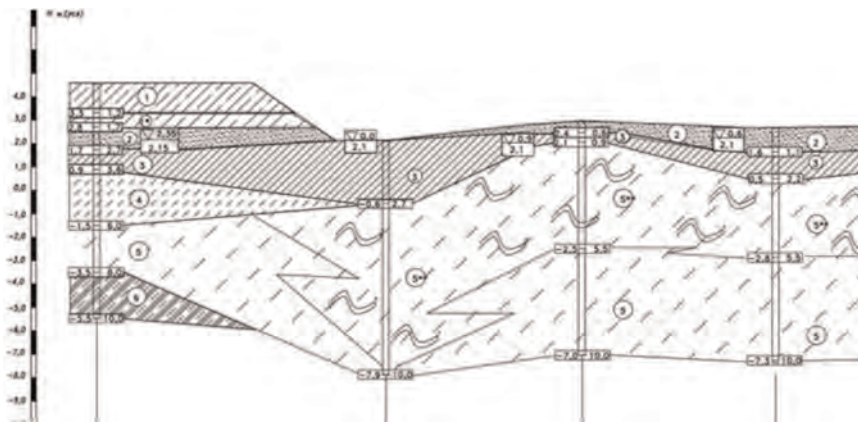
Figure 2. Soil profile and description. Key: Man-made deposits: 1 - Bulk soil: yellow-brown solid loam, backfilling less than 10 years old; 1*- Bulk soil: yellow-brown loam, wet, soft-plastic; 2 - Yellow-gray, fine, dense sand with thin layers of silty sand and gray plastic sandy loam, with rare inclusions of grated shells, saturated with water. Alluvial-deluvial deposits of the floodplain: 3 - Dark gray, beam deluvium, soft-fluid-plastic loam contains biogenic-organic substances and plant roots and has a smell of hydrogen sulfide; 4 - Yellow-brown sandy loam with interlayers of silty plastic sand; 5 - Dark gray silty sandy loam, fluid, organic content; 5* - Gray sandy loamy silt containing fragments of shells, fluid with interlayers of loam and the smell; 5** - Dark gray to black clayey plastic silt with interlayers and lenses of dark gray loam. Tertiary deposits of the upper Neogene: 6 - Yellow-brown soft-plastic loam.

properties of the base soil by means of the soil reinforcement to reduce the deformations of the future highway embankment bases. For this purpose, a TENSAR geocellular mattress is chosen (TENSAR 2023). It is a three-dimensional structure consisting of a TriAx 170 basic hexagonal geogrid laid directly on the weak soil and the vertical cells of RE570 uniaxial geogrids. The slow process of constructing the embankment structure reinforced with geo-mattresses allows to accelerate the rate of the base stability increase with loads applied to the embankment being considered.

3   THE EMBANKMENT STABILITY ANALYSIS

The stability, subsidence and consolidation time of the 11-m high embankment is analyzed in accordance with the EGE data for the borehole No. 1 on the KP-49 road section at the approaches to the viaduct. The embankment subsidence and consolidation time are analyzed for the pressure of 0.20 MPa. The embankment height is 11 m and $\gamma \sim 18$ kN/m^3, P $\approx$ 0.2 MPa. The total embankment subsidence is S = 0.39 m. Some soil layers characteristics taken for the analysis are given in Table 1.

Using the commercial software (program code TensarSlope version 1.13 (TENSAR 2023)), the following types of computations were performed: overall stability analysis for the embankment with a geocellular mattress at its base without any seismic impact (1); overall stability analysis for the embankment with a geocellular mattress at its base under the seismic load action (2); analysis of the embankment base subsidence without reinforcement (3); analysis of stresses reduction along the embankment bottom when the base is reinforced (4); base subsidence analysis in the case of the reinforcement with a geocellular mattress (5); analysis of the embankment base soil consolidation without the base reinforcement (6); base consolidation analysis for the embankment reinforced with a flat mattress (7). In Figure 3 the design scheme of the static analysis is presented.

Table 1. The soil layers characteristics used in the analysis.

№	Soil layer	Layer thickness, (kPa)	φ, (degree)	γ, (kN/m^3)	E, (MPa)	Initial c, (kPa)
0	EGE 2	1	18	19.5	14	4
1	EGE 2a	0.6	18	19.5	14	4
2	EGE 2б	0.4	18	8.4		4
3	EGE 2c	0.4	18	8.4		
4	EGE 3	0.9	10	17.8	10	8
5	EGE 4	2.4	13	19.5	13	4
6	EGE 5	2.4	11	19.2	9	8
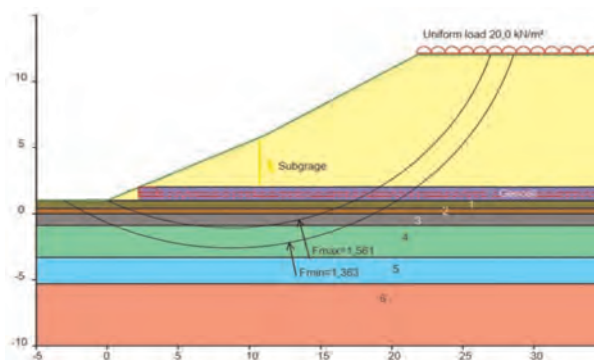
Figure 3. Design scheme of the embankment with a stabilizing geocell mattress (Bishop's method, static analysis): Subgrade – the filled soil according to Table 1 (soil № 0); Geocell – the geocell mattress; 1-6 soils according to Table 1; Fmin/max – the minimum and maximum factors of safety.

The analysis shows that the ratio of the shear moment to the resisting one is 1.363 along the curve No. 1 (Fmin, Figure 3) and 1.561 (Fmax, Figure 3) along the curve No. 2. For a more detailed understanding, the additional seismic analysis (7 points on the Richter scale) is performed. The results of this analysis show that the factor of safety is by $\sim$ 18–20% less than (Fmin, Figure 3), but the minimum factor of safety in the seismic analysis is 1.12, which satisfies the Ukrainian building code (Ukraine Building Code. DBN V.1.1-12:2006. 2006). Such results are achieved due to a geocell mattress arrangement. The principle of the TENSAR geocell structure operation is that in this structure the mechanism of destruction along the circular-arc slip surfaces is not a critical factor. The main criterion of stability is the shear strength of the plastic layer below the geocell, which is maximally mobilized when the Tensar geomattress is used. The geomattress formed and laid in the embankment base keeps the overlying soil layers from displacements during the construction process and after its completion until the base weak soils will gain sufficiently high mechanical characteristics due to consolidation and will stop to plastically deform. The TENSAR geogrid application ensures the subsidence reduction (at least by 33%) and makes it uniform (TENSAR 2023).

4 GEOGRID GEOMATTRESSES ARRANGEMENT ON THE WEAK SOILS OF THE RENY BYPASS ROAD CONSTRUCTION SITE

The geogrid geomattresses installation is performed during two stages. The first one involves the structure formation of interconnected cells consisting of 1-m wide vertical uniaxial plastic geogrids and a horizontal biaxial geogrid as a basic surface (Figure 4). Then at the second
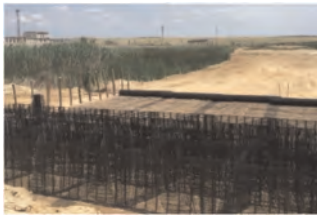
Figure 4.   The geomattresses formation.

Figure 5.   The general view of a geomatttress.

Figure 6.   Geomattress filled with a stone material.

stage the obtained 1-m high structure (Figure 5) is filled in with lumpy natural stone material (Figure 6) to create a rigid base for the deposited embankment.

The mentioned operations are carried out directly at the construction site by rolling out the biaxial geogrid along the day surface of the soil base and parallel to the weak soil layer along the embankment axis with adjacent rolls sheets overlapping by at least 300 mm. To shorten the processes of geogrid laying, subsequent vertical walls installation and geomattress filling with stone material, it is preferable not to stitch horizontal geogrids, but to place them with overlapping (Figure 4). The uniaxial geogrid should be rolled out in a direction perpendicular to the embankment axis and attached to a horizontal grid that operates as the geomattress base. To confirm the operational reliability of the embankment reinforced with geocell mattresses, the in-situ geodetic observations were carried out. The total subsidence of soil layers No. 4 and No. 5 (according to the soil profile (Table 1) was 0.009 m/h, which allowed to construct the 11-m high highway embankment with geocell mattresses in accordance with the requirements of construction standards and regulations in force in Ukraine.

5   RESULTS

The total length of the bypass road around the city of Reni is 6 352 meters. The maximum permissible speed on the road is 90 kilometers per hour, the estimated traffic flow is 7 973 cars per a day, the lane number is 2, their width is 3.75 meters. In 2018, under the OdesaHiprodor and Uniprom LLC project the construction of the international highway M15 (E87) Odesa - Reni part (bypassing the city of Reni) in the Odesa region was completed.

6   CONCLUSIONS

1. The total subsidence of soil layers No. 4 and No. 5 was 0.009 m/year, which made it possible to build the 11-m high road embankment from geocellular mattresses in compliance with the requirements of building codes and regulations in force in Ukraine.
2. The embankment reinforcement with geocellular mattresses allowed to achieve the reduction of the embankment base total subsidence by 30%, the increase of the base soil design strength by 25% and the base bearing capacity growth by 33%. Those effects were obtained due to the embankment soil reinforcement with TENSAR geocellular mattresses and their interaction with the embankment soil.
3. To confirm the operational reliability of the embankment reinforced with geocellular mattresses, the field geodetic observations were carried out, which confirmed the design solutions. In 2019, the President of Ukraine P. Poroshenko put the highway bypassing the city of Reni into operation.

REFERENCES

Dobie, M. J. D. 2011. Internal Stability of Reinforced Soil Structures using a Two-part Wedge Method. 9th Indonesian Geotechnical Conference and 15th Annual Scientific Meeting; Proc. intern. conf., Jakarta, 7-8 December 2011.

Jenner, C. G., Bassett, R. H. & Bush, D. I. 1988. The Use of Slip Line Fields to Assess Improvement in Bearing Capacity of Soft Ground Given by a Cellular Foundation Mattress Installed at the Base of An Embankment. *Geotech. Symp. On Theory and Practice of Earth Reinforcement*; *Proc. intern. symp., Kyushu, 1988.*

Jewell, R.A. 1988. The Mechanics of Reinforced Embankments on Soft Sols. *Geotextiles and Geomembranes* 7: 237–273.

Kaliukh, I., Senatorov, V., Khavkin, O., Kaliukh, T., & Khavkin, K. 2013. Experimental and Analytic Researches on Technical State, Design and Operation of Reinforced Concrete Antilandslide Structures for Seis-mic Dangerous Regions of Ukraine. *fib Symposium on Engineering a Concrete Future: Technology, Modeling and Construction; Proc. intern. symp., Tel-Aviv, 22–24 Apr 2013.*

Kaliukh, I., & Lebid, O. (2021). Constructing the Adaptive Algorithms for Solving Multi-Wave Problems. *Cybern Syst Anal* 57: 938–949. DOI: https://doi.org/10.1007/s10559-021-00419-w

Krivosheev, P., Slyusarenko, Y., Chervinsky, J. 2009. Development of Calculation Methods of Foundations on the Pliable Basis in Ukraine. *17th International Conference on Soil Mechanics and Geotechnical Engineering*: *The Academia and Practice of Geotechnical Engineering; Proc. intern. conf., Alexandria, 5-9 October 2009.* DOI 10.3233/978-1-60750-031-5-1818

Robertson, J., Gilchrist, A.J.T. 1987. Design Construction of a Reinforced Embankment Across Soft Lakebed Deposits. *Intern. Conference on Foundations and Tunnels; Proc. intern. conf., London, 24–26 March 1987.*

Slyusarenko, Y., Kryvosheyev, P., Serjogin, J., Kozjavkin, I. 2010. Concrete Structures of the Olympiyskiy National Sports Complex in Kiev. *3rd International fib Congress and Exhibition, Incorporating the PCI Annual Convention and Bridge Conference: Think Globally, Build Locally; Proc. intern. congr., Washington, 29 May - 2 June 2010.*

TENSAR Access:https://www.tensarcorp.com/

Terzaghi, K., Peck, R.B. 1996. *Soil Mechanics in Engineering Practice*, *3rd Ed.* New York: John Wiley & Sons, Inc.

Trofymchuk, O., Lebid, O., Berchun, V., Berchun, Y., & Kaliukh, I. 2022. Ukraine's Cultural Heritage Objects Within Landslide Hazardous Sites. In: Vayas, I., & Mazzolani, F.M. (Eds.). *Protection of Historical Constructions. PROHITECH 2021, Lecture Notes in Civil Engineering*, *vol. 209*. Cham: Springer. DOI: https://doi.org/10.1007/978-3-030-90788-4_73

Voloshkina, E., Efimenko, V., Zhukova, O., Chernyshev, D., Korduba, I., Shovkivska, V. 2021. Visual Modeling of the Landslide Slopes Stress-Strain State for the Computer-Aided Design of Retaining Wall Structures. *IEEE 16th Int. Conf. on the Experience of Designing and Application of CAD Systems (CADSM)*: 5/1-5/5. doi: 10.1109/CADSM52681.2021.9385211

Ukraine Building Code. DBN V.1.1-12:2006. 2006. *Construction in Seismic Areas of Ukraine*. Access: http://online.budstandart.com/ua/catalog/doc-page.html?id_doc=6614

Ukraine Building Code. DSTU B V.2.1-3-96. 1996. *Foundations and Foundations of Buildings and Structures. Soils. Laboratory tests. Terms*. Access: http://online.budstandart.com/ua/catalog/doc-page?id_doc=4079

Experimental and numerical evaluation on the performance of pervious concrete pavement with geocell base

K. Vinay
Research Scholar, Vellore Institute of Technology (VIT), Vellore, India

M. Muthukumar
Associate Professor, Vellore Institute of Technology (VIT), Vellore, India

ABSTRACT: Pervious pavements are similar to conventional pavements with no fine or little content of fine aggregate. Pervious pavements are considered as sustainable pavements as it controls storm water runoff, mitigate urban heat island effect. The construction of pervious concrete pavement on soft soil subgrade is not feasible unless subgrade soil specially treated with some strengthening material. Geocell is a three-dimensional geosynthetic product that is a promising material to reinforce the soil, there are no prominent studies in the past on application of geocell in the pervious concrete pavement. The present research is focused on the pervious concrete pavement performance using geocell base under the static loading. The series of static plate load tests on geocell reinforced and unreinforced pervious pavements as per the Indian Road Congress standards. The test results have shown that the vertical deformation, was reduced when the pavement is reinforced with geocell.

1   INTRODUCTION

Pervious concrete has been the subject of numerous studies on a variety of topics, including material characterization, mechanical properties, strength qualities, and hydraulic properties. To assess the effectiveness of pervious pavement, field experiments have also been done. Below is a brief summary of these studies.

1.1   *Studies on materials, mechanical and strength properties*

According to the American Concrete Institute (ACI,522R - 2010), the porosity of pervious concrete/asphaltic pavement ranges from 15 to 25%. Usually, single-size aggregates are utilized to make the concrete pervious. To ensure enough voids in pervious concrete, the aggregate size prepared should be between 19 and 9.5mm. The mechanical, permeability, and durability characteristics of pervious concrete pavements are significantly influenced by the physical characteristics, such as shape, size, and size distribution (Keveren *et al*. 2010). The crucial role of the cementing agent is to produce adequate bonding around the aggregates to enhance pervious concrete's durability (Chandrappa & Biligiri 2014). Various cementitious materials, such as fly ash and silica fume as partial replacements, have also been researched in addition to cement. However, after a certain threshold of partial replacement, the strength starts to decline. Additionally, digital imaging techniques were used to investigate how cementing agent coating thickness affected results (Deo & Neithalath 2011). From the studies, it was found that smaller particles had thicker coatings than bigger aggregates and it has been found that when paste thickness increases, characteristics like porosity and permeability decreases.

Several mix designs were also put forth by various researchers based on various principles, but the most prevalent was to give the aggregates enough cement coating (Nguyen *et al.* 2014). According to these investigations, aggregate densities ranged from 1400 to 1800 kg/m^3, and the aggregate to cement ratio ranged from 4:1 to 12:1. The range of the water cement ratio was 0.20 to 0.42.

Realizing that pavement thickness affects pervious concrete, the mechanical and tensile attributes are of utmost significance. Many researchers have looked into these characteristics (Haselbach *et al.* 2005; Huang *et al.* 2009; Yang & Jiang 2002; Yahia & Kabagire 2014). According to the investigations, the strength characteristics can be enhanced to better sustain low traffic roadways. However, there are numerous restrictions on the hydrological properties. Debris and dust cause the pervious concrete pavement to get clogged, which reduces the pervious concrete's ability to withstand infiltration (Haselbach 2010). According to Kayanian *et al.* (2011), the top 25mm of pervious concrete is clogged.

1.2 *Structural integrity of pervious pavements*

In light of the fact that laboratory studies do not accurately reflect how pavement performs in the real world. As a result, a few investigations on the in-service pavement section were also carried out in the field. Geotextiles are used in fields to create a barrier between the subgrade and the aggregate base and the pervious concrete layer. Only a few research on the impact of geotextile on the performance of pervious concrete have been done, according to (Chandrappa & Biligiri 2014). There are not many studies that show the benefits of drainage or structural integrity are improved by the upper geotextile (Scholz 2013). Additionally, the structural stability of conventional concrete and pervious concrete pavements with various foundation conditions was examined (Abit *et al.* 2014). The investigations demonstrate that the structural integrity of pervious concrete pavements is significantly influenced by the aggregate base condition. It was discovered that pervious concrete pavements deflected between 1.7 and 4 times more than normal pavements.

From the literature review it is observed that the permeable concrete pavement system have become an important integral part of sustainable urban drainage system. In contrast, the pervious pavements are associated with clogging problems and are therefore not as much applied in practice. Further from the literatures it is also observed that the structural integrity of pervious pavement largely depends on the base and sub-base conditions. Hence this project aimed at studying to improve the performance of pavements by providing base course using textured geocells, with provision of perforations along the sides. Providing textured geocells the excess water which could not infiltrate will be drained laterally to the ditches through the perforation provided on the geocells. Hence, experimental and numerical investigations have been carried out to study the performance of pervious pavement with and without geocells under undrained conditions.

2 MODEL TEST AND NUMERICAL INVESTIGATION

2.1 *Model studies to evaluate structural integrity of the pervious concrete pavement*

Model test was conducted in a medium scale loading frame designed and fabricated in the laboratory. Subgrade soil was compacted in the test tank of size 1.0m × 1.0m to the desired density. Textured geocells was placed over a compacted soil deposit. The geocells was filled with 20 mm aggregates and compacted to a relative density of 70%. A prefabricated concrete panel of size 1.0m × 1.0m × 0.1m was placed over the geocell/geoweb base. After placing the concrete panel, rainfall is simulated continuously until the subgrade is saturated. The excess water which does not infiltrates in to the subgrade is drained by providing a reservoir on one end of the test tank. The saturation of the subgrade is monitored continuously using

tensiometer placed at three locations placed at top, middle and bottom of the subgrade soil. The saturation is continued for at least 4 days or till the subgrade is fully saturated. After saturation has taken place, load test was carried out to evaluate the structural strength of the pavement. Figure 1 shows the schematic diagram of the laboratory scale model test.
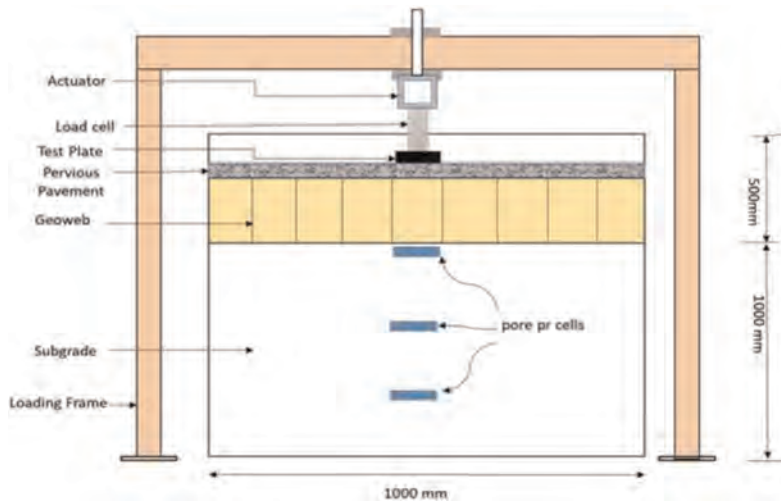
Figure 1.   Schematic diagram of experimental setup.

2.2   *Numerical investigation*

PLAXIS3D, finite element software was used to carry out the numerical analysis. For the purpose of solving this pavement numerical model, the linear strain problem-solving approach was used. The pervious pavement was modelled as a layered structure (Figure 2) and subjected to static loading. A model with a 1 m × 1 m plan was made using a 10-Noded Tetrahedral element.
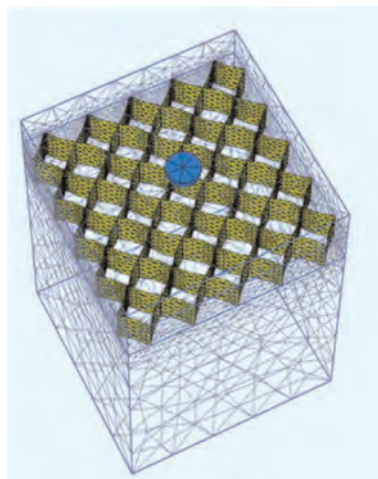
Figure 2.   Numerical Model of the pervious pavement in Plaxis3D.

The load was applied to a rigid circular plate in each model. The loading plate size should be smaller than 1/6th of test tank width to prevent boundary effects (Hegde & Thallak 2016). Therefore, in this investigation, isotropic static compression was applied by positioning a hard plate with a 150mm diameter in the model's centre. Through the robust steel circular plate, 1130 kPa of uniform pressure was applied. Friction at the interface between the soil and the geocell as well as the soil and the geogrid was taken into consideration. The flow coupled deformation computation method was used to analyse the model. The equilibrium of pore water pressures is achieved in each step of the analysis.

2.3 *Model parameters*

The behaviour of sand subgrade soil and geocell composite layer was simulated using the completely elastic Mohr-Coulomb material model. For the clay subgrade, the soft soil model was used, while the linear elastic model was used for the loading plate and pervious concrete. According to IS: 800-2007, the steel plates' qualities were taken into account. According to the guidelines of IRC37-2012, the poisson's ratio of the subgrade soil in the under-drained case is taken into account as 0.3, and in the undrained situation, it is taken into account as 0.49. According to IS: 456-2000, the Young's modulus of pervious concrete is taken into account. Since the porosity of pervious concrete ranges from 15% to 35%, the void ratio is considered to be 0.25.

3 RESULTS AND DISCUSSIONS

Experimental and numerical investigations on the pervious pavement with geocell foundation under drained and undrained conditions were carried out in order to address the effectiveness of structural integrity of pervious pavement under geocell confinement. According to the study, by adding a geocell base, it is possible to reduce vertical displacement. Because of the increased pore pressure caused by the applied pressure in undrained conditions, the shear strength of the subgrade soil is decreased (Figure 3).

Using the geocell under the undrained conditions, the vertical displacement was reduced by over 47%. (From 4.97mm to 2.63mm).The mattressing effect of the geocell, which allows
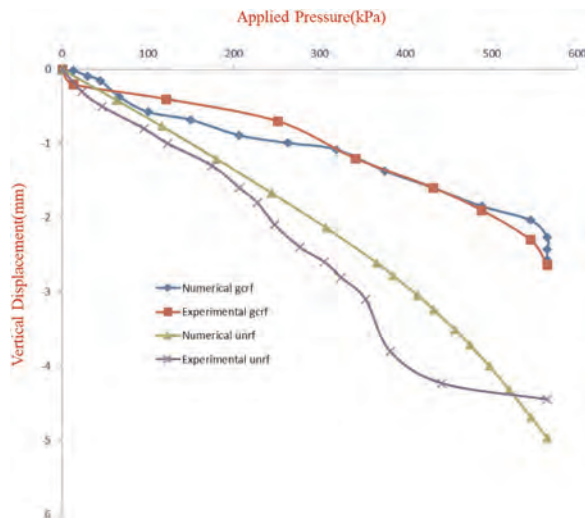
Figure 3. Effect of geocell base on the vertical displacement of the pervious pavements.

for even stress distribution. Figure 3 demonstrates that the geocell not only distributes the stresses but also lessens their intensity over the subgrade.The interconnected geocells function like a wide mat to distribute the applied load across a wider region, thus reducing the pressures on the subgrade. In the area below the loading plate, there was a concentration of the most stress. Additionally, it has been found that the displacement at the top of the geocell is greater than the displacement at the subgrade level. This is because the geocell base's stiffness is aroused, which causes a measurable decrease in the vertical stress on the subgrade.

Geocell is manufactured with different types of polymeric materials, resulting in different order of magnitude of Young's Moduli. The stiffness of geocell plays a major role in parametric studies. Hence FE analyses were carried out to address this issue. The analyses were carried out for the geocell of 15cm height and different stiffness of the geocell. Leshinsky and Ling (2013) reported that the stiffness of the geocell ranges from 0.5GPa to 100GPa. Hence a similar range of geocell stiffness was considered in this parametric study. The analyses inferred that the use of geocell of higher stiffness yielded less reduction in the vertical displacement. This reduction might be significant at larger loading amplitudes, which the current study does not examine. However, the finding in the current study is quite intriguing and helpful that even the geocell with less stiffness is very effective in reducing the vertical displacement of the pervious pavement under any drainage conditions. According to studies on the height of geocell, the strength of the subgrade determines how much influence the height of geocell as a pavement base has. As a result, FE analyses were also carried out to investigate the impact of the geocell's height in both drained and undrained conditions. Under static or dynamic loading beneath the pavement in an undrained condition, excessive pore water pressure typically occurs, leading to increased displacement (Figure 4). As the geocell's height rises, it creates a solid foundation and dissipates stresses, which inhibits the development of pore water pressure in the subgrade. Beyond that point, there is no discernible decrease in the displacement of the pavement when the height of the geocell is raised by five times (from 50mm to 250mm)
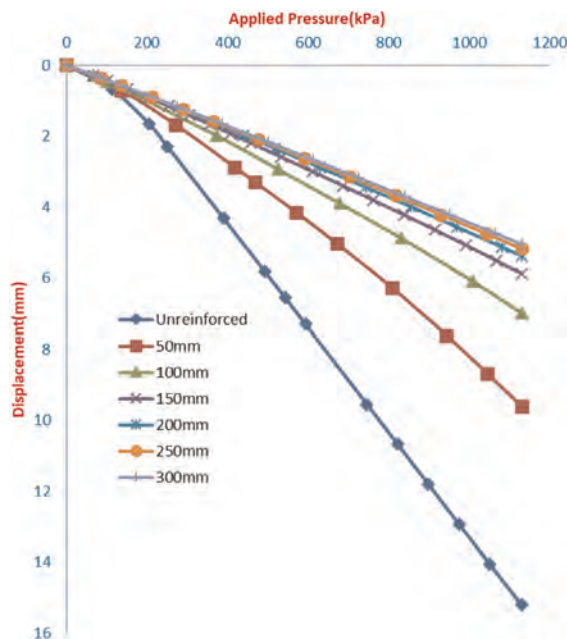
Figure 4. Effect of geocell height on the performance of the pervious pavements.

4 CONCLUSIONS

Through PLAXIS3D modelling, the impact of different parameters on the functionality of pervious pavement is investigated. These conclusions are reached in light of the results.

1. Under an undrained state, the displacement of pervious pavement without geocell confinement is approximately four times larger. It makes intuitive sense that the large decrease in the bearing stratum's shear strength is the cause of this abrupt rise in vertical displacement. The bearing support for the pervious pavement decreases as a result of this loss in shear strength.
2. Providing geocell continues to have a big benefit. The vertical displacement was reduced by over 47% as a result of the installation of a geocell in an undrained environment.
3. The performance of the pervious pavement is greatly influenced by the height of the geocell. When the geocell's height is extended from 50mm to 250mm, the vertical displacement is reduced by 186%. As the strains inside the geocell are released, the pore water pressure in the subgrade under undrained conditions quickly dissipates, providing a firm foundation for the pervious pavement.
4. According to the numerical analysis, adding geocell base improves the pervious pavement's ability to withstand pressure under both drained and undrained conditions. The geocell aids in dispersing stresses over a larger region and in reducing pore water pressure that builds up in undrained circumstances.

REFERENCES

Abite, I. K; Chopra, M; Uju. I., 2014. Evaluation of Mechanical Properties and Structural Integrity of Pervious Concrete Pavement Systems. *Journal of Materials in Civil Engineering*, 26, 1–6.

ACI (2010), Report on Pervious Concrete, *American Concrete Institute. ACI* 522R-10

Chandrappa, A.K and Biligiri, K.P. 2016. Pervious Concrete as a Sustainable Pavement Material – Research Findings and Future Prospects: A State-of-the-art Review. *Construction and Building Materials*. 111, 262–274.

Haselbach, L.M, Valavala, S, Montes, F. 2005. Permeability Predictions for Sand-clogged Portland Cement Pervious Concrete Pavement System, *J. Environmental Management* 81, 42–49.

Haselbach, L.M. 2010. Potential of Clogging of Pervious Concrete Pavement under Extreme Conditions. *Journal of Hrdrol. Engineering*,15, 67–69.

Hegde,A; Thallak,S.G., 2016. Behaviour of Geocell Reinforced Soft Clay Bed Subjected to Incremental Cyclic Loading. *Geomechanics and Geoengineering*, 10(4), 405–422.

Huang, B, Wu, H, Shu, X, Burdette, E.G. 2009. Laboratory Evaluation of Permeability and Strength of Polymer Modified Pervious Concrete. *Construction and Building Materials*. 24, 818–823.

IRC (2012), Guidelines for the Design of Flexible Pavements (third Revision). *IRC*:37-2012

Kayanian, M, Anderson, D, Harvey, J.T, Jones, D and Muhunthan, B. 2011. Permeability Measurement and Scan Imaging to Assess Clogging of Pervious Concrete Pavements in Parking Lots. *Journal of Enviromental Engineering*. 95, 114–123.

Kevern, J.T, Wang, K & Schaefer, V.R. 2010. Effect of Coarse Aggregate on the Freeze-thaw Durability of Pervious Concrete, *Jrl. Of Materials. Civil Engg*. 22(5). 469–495.

Leshchinsky, K; Ling, H.I., 2013. Numerical Modelling of Behaviour of Railway Ballasted Structure with Geocell Confinement. *Geotextiles and Geomembranes*, 36, 33–43.

Nguyen, D.H, Sebaiba, N, Boutouil, M, Leleyter, L, Baurd, F. 2014. A Modified Method for the Design of Pervious Concrete Mix, *Construction & Building Materials*. 73, 271–282.

Scholz, M; Grabowiecki, P., 2007. Review of Permeable Pavement Systems. *Building and Environment*, 42, 3830–3836.

Performance evaluation of three-dimensional geogrid for base stabilization in pavement applications

S. Marelli & P. Recalcati
Tenax SpA, Viganò, LC, Italy

A. Crippa
Tenax Corp., Baltimore, USA

E. Cuelho
TRI Environmental, USA

ABSTRACT: Inclusion of geosynthetic reinforcements within the granular base layer has been shown to substantially improve the overall performance and life of pavements. This effect has been demonstrated in several applications, and the mechanisms through which such an improvement can be achieved have been clearly described for the past 40 years by many authors. However, because of the complexity of the reinforcement mechanisms, quantifying this effect, either in terms of increased design life or reduction of the pavement thickness, is not simple. Because of this, available design methods still rely heavily on empirical test results from large scale lab tests or field trials. The growing need for a sustainable use of plastic materials has led manufacturers to develop innovative geosynthetics capable to give the maximum possible performance with the lowest possible weight. This paper provides an overview of the development of a biaxial geogrid characterized by a three-dimensional shape designed to improve the interaction with the granular aggregate. Multiple laboratory tests were run on various biaxial geogrid designs to evaluate the performance in pavement applications. Laboratory tests included pull-out, composite stiffness tests, cyclic plate load tests, and full-scale rolling wheel load tests using an accelerated pavement tester (APT). This paper summarizes the results of these tests, which showed the advantage of the three-dimensional biaxial geogrids over traditional planar geogrids.

1   INTRODUCTION

Including a geosynthetic reinforcement layer within a granular base layer can substantially improve the strength and extend the life of pavement structures. This effect has been demonstrated in several applications, and the reinforcing mechanisms though which these improvements are achieved are known and have been clearly described over the past several decades by many authors (e.g., Cuelho *et al*. 2014; Hufenus *et al*. 2006; Fannin & Sigurdsson 1996; Tingle & Webster 2003).

   Biaxial geogrids are commonly used for base and subbase reinforcement. The global economic crisis that is affecting the world economy and the construction industry in particular, together with the growing need for a sustainable use of plastic materials, has motivated geogrid manufacturers to optimize the performance of their products by reducing weight and carbon emissions without sacrificing performance, which has led to several recent changes in the structure and geometry of geogrids.

Quantifying performance improvements solely through mechanical means is not easy due to the complexity of reinforcement mechanisms within pavements; therefore, available design methods rely on empirical data from laboratory performance tests. The most widely used road design for geosynthetic-reinforced pavements is based on a modified U.S. AASHTO 1993 design, which relies on empirical performance data from test sections run in accordance with AASHTO R 50-09 and GMA White Paper II (Berg *et al.* 2000). In-air tests on geosynthetics are not necessarily designed to directly quantify these effects; therefore, laboratory tests using geogrids embedded in soil were used to evaluate the effects that various geogrid rib shapes and strengths had on performance.

2 GEOGRID REINFORCEMENT IN PAVEMENTS

Geogrids used in road and rail applications primarily experience loading under plain strain-stress conditions, where the loads imparted in the geogrid perpendicular to the direction of travel (in the cross-machine direction of the geogrid) are significantly greater than loads imparted parallel to the direction of travel (corresponding to the machine direction of the geogrid), as illustrated in Figure 1. The accumulation of stresses in the cross-machine direction of the reinforcement is described in greater detail in Cuelho and Perkins (2016) based on extensive data from full-scale field test sections.
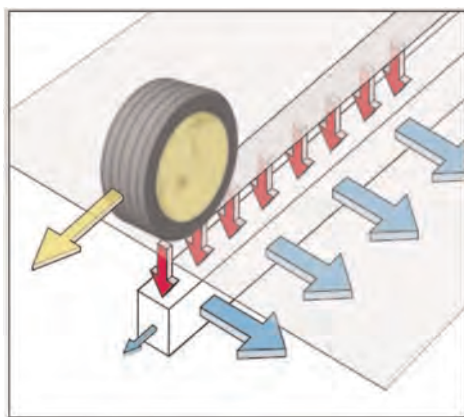
Figure 1.   Geogrid in plain strain-stress condition.

Tensile resistance in all directions is necessary when radial loads are applied; however, in most transportation applications stresses accumulate more significantly in the cross-machine direction of the geogrid (orthogonal to the direction of traffic) due to lateral spreading of the aggregate within the wheel path. Geogrids provide resistance to this movement by interacting with geogrid members oriented in the machine direction, which subsequently transfer stresses into tensile members oriented in the cross-machine direction. Lateral confinement of the aggregate is related to the capability of the geogrid to effectively interact with the aggregate, as illustrated in Figure 2. The shape and stiffness of the individual geogrid ribs and cross-members are important to ensure effective interaction with individual soil particles, resulting in positive stress transfer between the materials and a stiff composite system.

Structural T-beams are commonly used as load-bearing members in steel and reinforced concrete structures because they are able to resist stresses applied in two directions simultaneously. The horizontal member of the T-shaped cross section resists longitudinal stresses
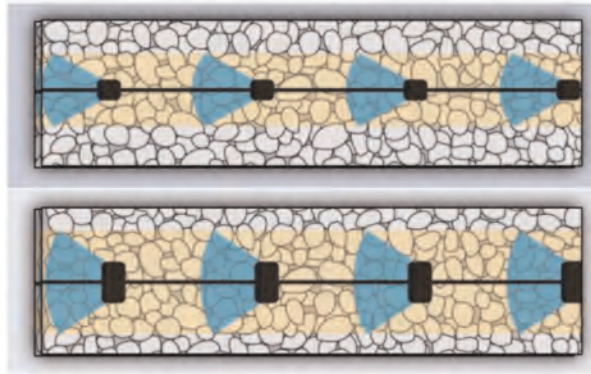
Figure 2.   Illustration of effect of rib height on reinforcement zone of influence.

and horizontal bending moment, while the vertical section of the T-shape resists vertical stresses and bending moments. Utilizing the T-shape for geogrid ribs oriented in the machine direction will allow for greater heights, which will improve its ability to increase the reinforcement zone of influence, but maintain its stiffness to be able to transmit stresses to tensile members.

A series of geogrids were recently designed with modified ribs in the machine direction to improve the interaction with a granular base course in an effort to collect and distribute stresses being transferred by the wheel loads and into tensile members oriented in the cross-machine of the geogrid. Stiffer ribs in the machine direction help restrict horizontal movements of soil particles, thereby increasing confinement. Improving the lateral confinement of the aggregate directly improves the vertical strain resistance (in other words, inhibits rut). Alternate geogrid rib geometries were designed to compare to traditional flat biaxial geogrid ribs. An evaluation of the performance of conventional and redesigned geogrids was made in the lab and using bench-scale and full-scale tests, as described below. The material properties of the geogrids evaluated as part of this study are listed in Table 1. The BX geogrid incorporates the standard horizontal flange, the W-Grid incorporates an upright web, and the T-Grids uses an upside-down T shape, for ribs oriented in the machine direction, as shown in Table 1. T-Grids are ordered from weaker to stronger, T-Grid 1 to T-Grid 4, respectively.

Table 1.   Material properties of geogrids used in this evaluation.

Property	BX (MD/XD)	W-Grid (MD/XD)	T-Grid 1 (MD/XD)	T-Grid 2 (MD/XD)	T-Grid 3 (MD/XD)	T-Grid 4 (MD/XD)
MD Rib Shape						
Mesh Size {mm}	40 / 27	30 / 30	33 / 33	32 / 32	32 / 32	30 / 30
Rib Thickness {mm}	2.9 / 1.6	4.0 / 1.4	3.0 / 1.0	3.3 / 1.2	3.5 / 1.2	4.5 / 1.7
Mass/Area {g/m^2}	380	250	275	300	350	365
2% Strength {kN/m}	10.5 / 10.5	6.0 / 5.0	5.5 / 3.5	6.0 / 5.0	7.5 / 5.0	8.0 / 5.0

3   LABORATORY TESTS

There are a variety of tests that can be used to evaluate the performance of geogrids for roadway applications. AASHTO R50-09 (Standard Practice for Geosynthetic Reinforcement of the Aggregate Base Course of Flexible Pavement Structures) outlines the

necessary steps to effectively incorporate geosynthetics into the design of pavements. Reinforcement benefit in AASHTO R50-09 is defined as the traffic benefit ratio (TBR), which is "the ratio of the number of load cycles of a reinforced pavement structure to reach a defined failure state, to the number of loads for the same unreinforced section to reach the same defined failure state." TBR is most often determined using a Cyclic Plate Load (CPL) test or a Rolling Wheel Load (RWL) test. These tests were originally outlined in the GMA White Paper II (Berg *et al*. 2000). More recently, the CPL test method was codified in ASTM format (ASTM D8462). Other smaller laboratory tests can also be used to evaluate potential benefits of various geogrid designs. The Composite Stiffness (CS) test (Zornberg *et al*. 2012) and the monotonic pullout test (ASTM D6706) were also used in this study to investigate performance improvements of geogrids having ribs that incorporate the structural "T" shape when compared to traditional flat ribs associated with standard biaxial geogrids. Each of these tests was run by TRI Environmental, Inc., and their results on a variety of geogrids is detailed in the subsections below.

3.1 *Standard pullout test*

Monotonic pullout tests (EN 13738:2004) were run at 20 kPa confinement using CEN Standard sand and a 1 mm/min displacement rate to evaluate the pullout resistance of an early prototype of a three-dimensional geogrid (W-Grid) when compared to a conventional biaxial geogrid (BX), the results of which are summarized in Figure 3 (Recalcati 2012). Test results clearly show the effectiveness of the three-dimensional structure; however, the peak resistance is developed at a greater displacement. These results seem to indicate that a geogrid with taller ribs in the machine direction (W-Grid) is able to improve the interaction but may experience deformations larger than conventional biaxial geogrids (BX) that have shallower but wider ribs.
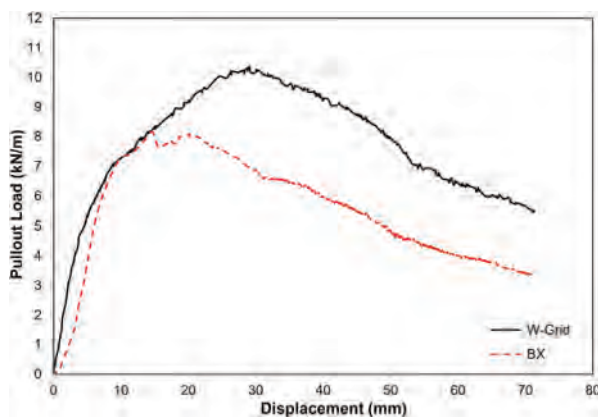
Figure 3.   Pullout test on the first prototype of three dimensional geogrids (Recalcati 2012).

3.2 *Composite stiffness test*

Composite stiffness (CS) tests were performed on two geogrids according to a draft version of the Texas Department of Transportation test procedure (Tex-136-E 2019). This test standard was developed based on research by Zornberg *et al*., (2012) for performance testing of geosynthetic used as reinforcement in pavements. CS tests are performed using a minia-ture pullout device (Figure 4) that applies small displacements to a geogrid embedded in an aggregate while under low-level confinement. The confining aggregate in this testing

Figure 4. Composite stiffness test apparatus (courtesy of TRI Environmental, Inc.).

program consisted of gravel between the 7.35 mm and 4.75 mm sieves and compacted in the test box in a dry state to a density of 1632 kg/m^3, as outlined in the test standard. A constant confining pressure of 20.7 kPa was applied using an air bladder in all tests. The resulting parameters derived from this test, the coefficients of soil-geosynthetic interaction (K_{SGC-1}, K_{SGC-2}, and K_{SGC-3}), are stiffness properties of the soil-geosynthetic composite. The average of these three parameters was used to compare the results from the three geogrids tested, where greater values indicate a stiffer/stronger composite. Three individual specimens were run on each material in the cross-machine direction. The average composite stiffness values were 44, 38, and 23 (kN/m)^2/mm for the T-Grid 3, T-Grid 1, and W-Grid geogrids, respectively, clearly showing the stiffer material shape having a positive influence on this property.

3.3 Cyclic plate load test

Full-scale unpaved CPL tests were conducted on two geogrid-reinforced test sections and one control (unreinforced) test section according to the ASTM D8462 test standard. Development of the ASTM test standard is based on the recommendations outlined in White Paper II (Berg et al. 2000). Tests were performed using a large test apparatus that was 2.3 m by 2.3 m in plan (Figure 5). A road prism was constructed by compacting a 0.9 meter thick layer of lean clay subgrade prepared to a strength of CBR = 2.0%, topped by 250 mm of compacted crushed base course (GP) having a maximum particle size of 25 mm. The geogrid reinforcement in these tests was placed directly atop the subgrade, beneath the base course. A 40 kN cyclic load was applied at a 1 Hz frequency to the surface of the base course using a 305 mm diameter steel plate to evaluate performance. Performance benefit was determined by calculating the TBR associated with 75 mm of vertical displacement (rut) beneath the load plate. Three materials were tested in comparison to the Control, resulting in TBRs of 9.5, 6.1, and 5.7 for the T-Grid 4, T-Grid 2, and BX geogrids, respectively. Performance results from the CPL tests showed the benefit of geogrids having the T-shape over a traditional biaxial geogrid, as well as the benefit of stronger T-shapes.

3.4 Rolling wheel load test

Full-scale paved RWL tests were constructed in an indoor concrete-lined test pit 1.2 m deep by 3.3 m wide and 15 m long and subsequently trafficked using an accelerated pavement
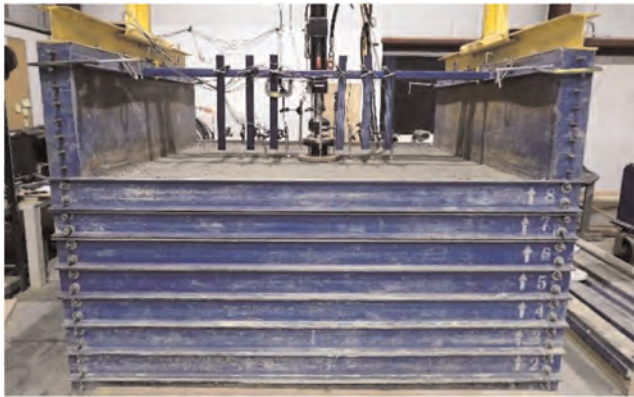
Figure 5.   Cyclic plate load test apparatus (courtesy of TRI Environmental, Inc.).

tester (APT). The subgrade (the same material as the CPL tests outlined above) was prepared and compacted to a final thickness of 0.9 m at a strength of CBR = 2.5%. Geogrids in reinforced test sections were placed directly atop the subgrade. A GW-GM aggregate base course with a maximum particle size of 37.5 mm was prepared and compacted to a total thickness of 312 mm. Hot-mix asphalt was constructed atop the base course at an average thickness of 74 mm. The APT trafficked the test sections (Figure 6) by applying a 40 kN bidirectional load via a dual-wheel assembly. The outcome from these tests, calculated at an average surface rut of 35 mm, resulted in TBRs of 3.2 and 1.9 for the T-Grid 3 and T-Grid 2 geogrids, respectively, showing that a strengthening the T-shape improves performance.

Figure 6.   Rolling wheel load APT (courtesy of TRI Environmental, Inc.).

4   CONCLUSIONS

Traditional biaxial geogrids are commonly used to reinforce the base layers of pavements; however, the growing desire for a sustainable use of plastic materials coupled with the desire to take into proper consideration sustainable civil design has motivated engineers to find more efficient and effective solutions for geogrids used as roadway reinforcement. In the spirit of environmental sensitivity, the structural design of biaxial geogrids was enhanced by stiffening members in the machine direction through the use of T shape in order to optimize and maximize geogrid properties directly linked to better performance. A variety of

interaction tests (pullout, composite stiffness, CPL and APT tests) were used to evaluate their performance when compared to one another.

In general, the results from these tests showed the ability of these geogrid enhancements to improve performance. The following observations were made using the interaction data produced as part of this study.

- Pullout interaction of W-Grid > BX, despite W-Grid being lighter and weaker
- Composite stiffness of T-Grid 3 > T-Grid 1 > W-Grid, despite the same strength in the cross-machine direction
- CPL results of T-Grid 4 > T-Grid 2 > BX, despite weaker strengths in the cross-machine direction
- APT results of T-Grid 3 > T-Grid 2, despite weaker strengths in the cross-machine direction

Additional future tests are planned to add to this analysis to further illustrate the importance of specific geogrid design attributes as well as their impact on the performance of geogrid-reinforced paved and unpaved roads.

REFERENCES

AASHTO R50-09 (2013) *Standard Practice for Geosynthetic Reinforcement of the Aggregate Base Course of Flexible Pavement Structures*, American Association of State Highway and Transportation Officials, Washington, D.C.

ASTM D6706 (2013) *Standard Test Method for Measuring Geosynthetic Pullout Resistance in Soil*, ASTM International, West Conshohocken, PA.

ASTM D8462 (2022) *Standard Test Method for Cyclic Plate Load Tests to Evaluate the Structural Performance of Roadway Test Sections with Geosynthetics*, ASTM International, West Conshohocken, PA.

Berg, R.R., Christopher, B.R. and Perkins, S. (2000) Geosynthetic Reinforcement of the Aggregate Base/ Subbase Courses of Pavement Structures, GMA White Paper II, *Geosynthetics Materials Association*, AASHTO Committee 4e.

Cuelho, E., Perkins, S. and Morris, Z. (2014). Relative Operational Performance of Geosynthetics Used as Subgrade Stabilization, Final Report to the Montana Department of Transportation, FHWA/MT-14-002/ 7712-251, 328 pp.

Cuelho, E., and Perkins, S. (2016) Mechanisms of Reinforcement Benefit from Geosynthetics Used as Subgrade Stabilization, *Proceedings EuroGeo6 Conference*, Ljubljana, Slovenia.

EN-13738:2004 (2004) Geotextiles and Geotextile-Related Products – Determination of Pullout Resistance in Soil, European Committee for Standardization.

Fannin, R.J. and Sigurdsson, O. (1996) "Field Observations on Stabilization of Unpaved Roads with Geosynthetics." *Journal of Geotechnical Engineering*. Vol. 122, no. 7, pp. 544–553.

Hufenus, R., Rueegger, R., Banjac, R., Mayor, P., Springman, S.M., and Bronnimann, R. (2006) Full-Scale Field Tests on Geosynthetic Reinforced Unpaved Roads on Soft Subgrade. *Geotextiles and Geomembranes*. vol. 24, no. 1, pp. 21–37.

Recalcati, P. (2012) Design of Geogrid Reinforced Flexible Pavements and the Evaluation of the Relevant Properties, *Proceedings 5th International Conference Geosynthetics Middle East*.

Tingle, J. and Webster, S. (2003) Corps of Engineers Design of Geosynthetic-Reinforced Unpaved Roads *Transportation Research Record* 1849, pp.193–201.

Zornberg, J.G., Ferreira, J.A.Z. and Roodi, G.H. (2012) Experimental Results on Soil-Geosynthetic Interaction Stiffness, Report FHWA/TX-12/5-4829-01-3, Texas Department of Transportation, Austin, TX, USA.

Evaluation of deformation modulus of unreinforced and reinforced sandy soil layers using LWD device

Duddu Sidhu Ramulu & Kommanamanchi Vamsi
Research Scholar, Department of Civil Engineering, Ecole Centrale School of Engineering, Mahindra University, Hyderabad, India

Chennarapu Hariprasad*
Associate Professor, Department of Civil Engineering, Ecole Centrale School of Engineering, Mahindra University, Hyderabad, India

Balunaini Umashankar
Professor, Department of Civil Engineering, Indian Institute of Technology Hyderabad, Kandi, India

ABSTRACT: Plate load test (PLT) is used frequently to evaluate the elastic modulus (E_{PLT}) of soils. However, this test is cumbersome, time-consuming and requires huge setup for reaction force. While Light Weight Deflectometer (LWD) devices are becoming very popular in earthwork quality control due to their swift evaluation of the deformation modulus (E_{LWD}) and non-destructive in nature. In this study, the effect of two contact pressures (q) to evaluate E_{LWD} were considered for both unreinforced and triaxial geogrid reinforced sandy soils were investigated, in order to successfully implement the use of LWD testing to replace plate load test (PLT). In addition, the correlations were proposed in terms of modulus improvement factors (MIF) of reinforced sandy soils. The findings show very good correlation of MIF obtained from these two tests.

1 INTRODUCTION AND CONTEXTUAL

Mechanical behaviour of unbound granular layers can be determined using a variety of lab and field tests (NCHRP 1-37A 2004). Field tests, such as plate load test (PLT) have some notable drawbacks because it requires large equipment for the reaction force. In-situ load and deformation characteristics are measured by PLT to evaluate elastic modulus (E_{PLT}) of the granular layers (Alshibli *et al*. 2005; DeMerchant *et al*. 2002; Li & Ronald 2005). Mechanical properties of granular layers can be estimated using a variety of laboratory testing methods such as monotonic and repetitive PLT. The limitations of these approaches are there loading patterns, specimen sizes, preparation process and time involved for testing (Consoli *et al*. 2009; Li & Baus 2005). Recent years have seen the development and use of a wide variety of devices to address these problems and provide a quick way to measure modulus (Moshe & Yair 2001; Park & Chung 2003). This implies that there has been a concerted effort to replace the PLT with a quick and portable device such as light weight deflectometer (LWD) (Fleming *et al*. 2007; Nazzal 2014; Sidhu *et al*. 2023; Umashankar *et al*. 2015).

LWD is a non-destructive testing (NDT) device, used for evaluating the deformation modulus (E_{LWD}) of granular layers. Its working principle is based on a dynamic

---

*Corresponding Author: hari.chennarapu@mahindrauniversity.edu.in

portable short impulse plate load bearing-deformation. LWD test has recently gained a lot of attention as a quick and easy way to check the quality of compaction and/or evaluation of modulus. LWD device offers a short duration of impulsive load and provides the same information as PLT but in a dynamic manner (Benedetto et al. 2012; Duddu & Chennarapu 2022; Mooney & Miller 2009; Vennapusa & White 2009). Static and repetitive PLT tests evaluate elastic, resilient modulus respectively and permanent deformations under the plate measured through displacement gauges. Owing to the inherent variability of compacted in-situ granular layers, one should think about the benefits of performing multiple testing points using LWD device rather than single PLT over the course of the project.

According to the literature studies, the elastic moduli (E_{PLT}) obtained from laboratory and field requires expensive setup and needs significant time and effort. These limitations have led authors to carry out the study to provide practicing engineers a new and low-cost approach using LWD device and to establish a reliable moduli and MIF evaluation of reinforced sandy soils that can be used in design of infra projects. In context, the objective of this study was discussed in the following section.

2 OBJECTIVES

The objective of this study is to assess the potential use of LWD device to evaluate: (a) deformation modulus (E_{LWD}) of unreinforced sandy soils for various relative compactions and two plate contact pressures (q) of 0.1 MPa and 0.15 MPa, (b) deformation modulus values of triaxial geogrid reinforced sandy soil for various embedded depth of reinforcements, and (c) modulus improvement factors (MIF) of reinforced sandy soils and to establish correlations between MIF_{LWD} and MIF_{PLT}.

3 MATERIALS

Locally available sandy soil was used to carry out a series of tests and its physical properties was determined as per ASTM specifications as shown in Table 1. Figure 1a shows the particle-size distribution curve of the sandy soil. Triaxial (triangular aperture) polypropylene geogrid reinforcement that satisfies the specification of European Organization for Technical Assessment (EOTA) and BS EN ISO 9001:2015 was selected to reinforce the sandy soils (refer to Figure 1b).

Table 1. Physical properties of sandy soil.

Parameter	Values	Standard (s) used
Coefficient of Uniformity, C_u,	1.26	ASTM D 422
Coefficient of Curvature, C_c	0.99	
Specific gravity, G_s	2.63	ASTM C128
Maximum density, γ_{dmax}, kN/m^3	17.8	ASTM D4253, ASTM D4254
Minimum density, $\gamma_{d\ min}$, kN/m^3	15.6	
Soil Group classification	A-3-a, SP	AASHTO, USCS & ISSCS

4 EXPERIMENTATION

Locally accessible sandy soil was used for testing as unreinforced and reinforced cases for the test configurations with respect to the depth of reinforcement to plate diameter (u/a) ratios of 0.17, 0.25, 0.33, and 0.50. Two different plate load-based testing methods, namely LWD and
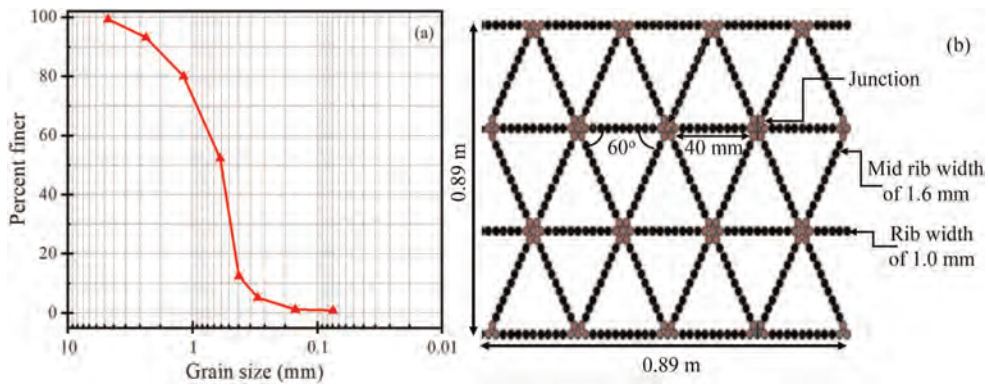
Figure 1. Details of materials used in this study: (a) Particle-size distribution curve of sandy soil, and (b) Schematic view of triaxial geogrid reinforcement.

PLT, were carried out to measure the load deformation responses of the test configurations. Figure 2 represents the LWD device with detailed components and two drop weights of 10 kg and 15 kg to simulate the contact pressures of 0.1 MPa and 0.15 MPa as considered in the study. The considered weights were dropped from a certain height of 0.72 m. The induced impulsive force is transmitted to the center of loading plate and mechanical contact is developed on the surface of sandy soils. An accelerometer is built inside the loading plate, which senses movement, transmits a signal to control unit and deformation of plate will be obtained. The measuring techniques start with the initial three preloading drops allowing for enhancing proper contact between the loading plate and surface of sandy soil. The next three consecutive measuring drops are used to register mean deformation ($\bar{w}$) to evaluate deformation modulus (E_{LWD}) (ASTM E2583, 2015). The E_{LWD} can be calculated by using well-known Boussinesq's elastic solution, Eq. (1), for loading over rigid base resting on an elastic half-space.

$$E_{LWD} = \frac{qr\,(1-r^2)f_r}{w} \tag{1}$$

where, E_{LWD} = Deformation modulus, MPa; q = plate contact pressure (equal to 0.1 MPa and/or 0.15 MPa);

r = Radius of loading plate = 150 mm; v = Poisson's ratio of the sandy soil = 0.25; f_r = Plate rigidity factor (1.65); and $\bar{w}$ = mean deformation mm.
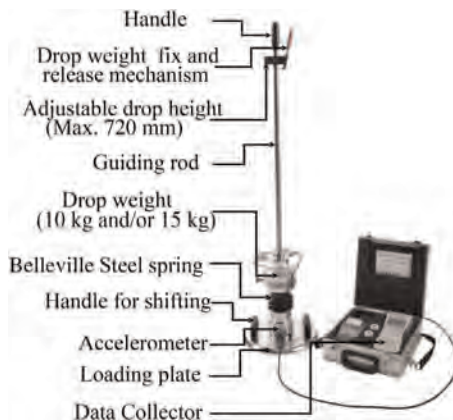
Figure 2. Schematic view of Light Weight Deflectometer (LWD) NDT Device and its components.

Large-scale experiments for PLT were carried out in a test chamber (0.9 m × 0.9 m × 0.9 m in size) using a loading frame of 10-ton capacity and equipped with actuator and load cell. A series of LWD and PLT tests were carried out using a 300 mm diameter circular plate that was placed in the centre of a test chamber, which is 450 mm away from the LSTC walls to ensure that the effects of boundaries were minimal. To achieve a relative density (R_d) of 85%, samples were prepared in layers in the LSTC using pneumatic plate vibratory device. More details of vibratory compaction process can be found in Hariprasad *et al*. (2016). Before compacting the sandy soil layers in LSTC, calibration studies were carried out to prepare a uniformly dense layer to obtain a relative density (R_d) of 45%, 65% and 85%. Relative compaction (RC) was estimated as 89%, 93%, and 97 % respectively from the correlation proposed by Holtz Gibbs (1979).

5   RESULTS AND DISCUSSIONS

Experimental results were represented in terms of deformation modulus (E_{LWD}), elastic modulus (E_{PLT}), and modulus improvement factors (MIF) for various test configurations as mentioned earlier.

5.1   *Influence of compaction and contact pressure on E_{LWD} value*

In the experimentation process, the repeatability tests were conducted to ensure the uniformity of results. Table 2 shows result of deformation modulus values for various relative compaction (RC) levels and contact pressures (q). It was clearly observed that the E_{LWD} value increases with an increase in relative compaction, due to increase in density of sandy soil. For instance, the E_{LWD} increased by 67% as the RC increases from 89% to 97% for the case of unreinforced sandy soil. In addition, due to the change in contact pressure from 0.1 MPa to 0.15 MPa, the LWD measured minimal change in the E_{LWD} value (i.e., variation of 1 to 2.5 MPa). Due to the reason of small increment in the applied contact pressures (i.e., a difference of 0.05 MPa). Similar findings was reported by Fleming *et al*. (2002); Lin *et al*. (2006); Camargo *et al*. (2006). Literature suggests to use the appropriate contact pressure (0.15 MPa) to mobilize elastic-plastic behaviour for reinforced soils and further test results were presented for 0.15 MPa of contact pressure (15 kg drop weight of LWD device).

Table 2.   Deformation modulus (E_{LWD}) for various relative compaction levels and contact pressures.

	E_{LWD}, MPa					
	q = 0.1 MPa	q = 0.15 MPa	q = 0.1 MPa	q = 0.15 MPa	q = 0.1 MPa	q = 0.15 MPa
Test Configurations	RC = 89 %		RC = 93 %		RC = 97 %	
Unreinforced sandy soil	11.41	12.38	17.03	18.02	19.35	20.64

5.2   *Influence of embedded depth of reinforcement on $E_{LWD\ (0.15\ MPa)}$ value*

Table 3 represents the effect of embedded depth (u) of triaxial geogrid reinforcement on deformation modulus of sandy soil for various relative compaction (RC) levels. The deformation modulus (E_{LWD}) of the reinforced sandy soil increases with decrease in u/a ratio for various RC levels. It is due to passive resistance, lateral restraint and radial stiffness offered by the geogrid reinforcement and it will significantly mobilized when placed closely under the loading plate. Hence, a substantial improvement in the $E_{LWD\ (0.15\ MPa)}$ of the reinforced sandy soil was observed at an embedded depth (u) of 50 mm (i.e., embedded depth equal to

Table 3. Deformation modulus (E_{LWD}) for various embedded depth (u) of reinforcements and relative compaction (RC) levels.

Test Configurations	u/a	u, mm	E_{LWD}, MPa					
			q = 0.1 MPa	q = 0.15 MPa	q = 0.1 MPa	q = 0.15 MPa	q = 0.1 MPa	q = 0.15 MPa
			RC = 89 %		RC = 93 %		RC = 97 %	
Triaxial geogrid reinforced sandy soil	0.17	50	16.55	17.68	26.63	27.2	28.09	29.45
	0.25	75	15.43	16.53	22.6	23.87	24.83	27.37
	0.33	100	13.7	15.06	21.3	22.82	23.54	24.32
	0.50	150	12.44	14.09	20.52	21.99	22.08	23.23

one-sixth of the plate diameter) compared to the unreinforced case and other embedded depths (u) of triaxial geogrid reinforcements.

5.3 Modulus improvement factors of geogrid-reinforced sandy soil from LWD and PLT

Modulus Improvement Factor (MIF) is defined as the ratio of reinforced deformation modulus ($E_{LWD(r)}$)/elastic modulus ($E_{PLT(r)}$) to the unreinforced deformation modulus ($E_{LWD(ur)}$)/elastic modulus ($E_{PLT(ur)}$) and can be calculated using Eq. (2).

$$MIF = \frac{E_{LWD(r)} \quad or \quad E_{PLT(r)}}{E_{LWD(ur)} \quad or \quad E_{PLT(ur)}} \tag{2}$$

MIF and E_{LWD} values were represented for the relative compaction of 97% and contact pressure of 0.15 MPa. To compare the $E_{LWD\ (0.15\ MPa)}$ data measured from LWD tests, a plate load tests (PLT) were performed for the same test configurations of unreinforced and reinforced cases. In case of PLT, elastic modulus (E_{PLT}) was calculated at a settlement of 3 mm for both cases and represented in Table 4. MIF values were increased with an inclusion of reinforcement and decreases with an increase in u/a ratio. Improvement in MIF of sandy soil reinforced with triaxial geogrid can be attributed due to passive resistance, lateral restraint resistance offered by reinforcement in the radial directions against applied contact pressure. Figure 3 represents the linear regression analysis for MIF obtained from LWD and PLT and it represents a very good correlation. Equation 3 can be used to calculate the MIF of PLT from MIF of LWD test. The LWD device can be used to calculate the MIF value of reinforcements in the lab and field within a short time.

$$MIF_{PLT} = 0.7635 MIF_{LWD} + 0.2557 \tag{3}$$

Table 4. MIF calculations for $E_{LWD\ (0.15\ MPa)}$ and PLT.

Test Configurations	u/a	u, mm	w̄, mm	E_{LWD}, MPa	E_{PLT}, MPa	MIF	
						LWD	PLT
Unreinforced sandy soil	–	–	1.63	20.64	11.13	–	–
Triaxial geogrid reinforced sandy soil	0.17	50	1.37	29.45	15.30	1.43	1.37
	0.25	75	1.41	27.37	13.50	1.33	1.21
	0.33	100	1.45	24.32	13.05	1.18	1.17
	0.50	150	1.45	23.23	12.52	1.13	1.12
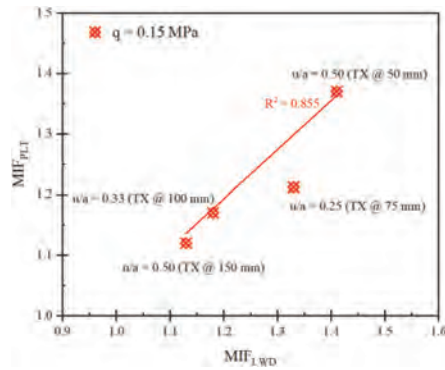
Figure 3. Variation of MIF_{PLT} with MIF_{LWD} for contact pressure of 0.15 MPa.

6 CONCLUSIONS

This study presents the deformation modulus obtained from LWD test for unreinforced and reinforced sandy soils. Deformation modulus (E_{LWD}) values were found to be increased with an increase in compaction levels of sandy soils and minimal change was observed with increase in contact pressures from 0.1 MPa to 0.15 MPa. Due to the incorporation of triaxial geogrid, a substantial improvement in the E_{LWD} of the sandy soil was observed at an embedded depth of 50 mm (i.e., one-sixth of the plate diameter). Hence, it was considered as the optimum depth. Modulus improvement factors were found to be increased with decrease in embedded depth of reinforcement. The developed linear regression model correlates MIF obtained from LWD and PLT tests and was found to be in good agreement ($R^2 = 0.85$). Therefore, LWD device can be used as MIF value evaluating tool for the phases of RC levels and embedded depth of triaxial geogrid reinforcement instead of PLT.

The study is limited to a sandy soil and triaxial type of geogrid reinforcement used in the study. Further scope of this study can be extended to evaluate the E_{LWD} and MIF values for various types of granular soils, aggregates, and geogrids of different apertures.

DATA AVAILABILITY STATEMENT

Some or all data, that support the findings of this study are available from the corresponding author upon reasonable request.

ACKNOWLEDGEMENT

REFERENCES

Alshibli, K.A. Abu-Farsakh, M. & Seyman, E. 2005. Laboratory Evaluation of the Geogauge and Light Falling Weight Deflectometer as Construction Control Tools. *Journal of Materials in Civil Engineering*, 17 (5), ©ASCE, https://doi.org/10.1061/(ASCE)0899-1561(2005)17:5(560).

ASTM E2583-11. 2015. Standard Test Method for Measuring Deflections with a Light Weight Deflectometer. *American Society for Testing and Materials* (ASTM). West Conshohocken, PA, USA.

Benedetto, A. Tosti, F. & Domenico, L, Di. 2012. Elliptic Model for Prediction of Deflections Induced by a Light Falling Weight Deflectometer. *Journal of Terra-mechanics*. 49 (1), pp.1–12.

BS EN ISO 9001: 2015. *Quality Management Systems - Requirements*. 5th Edition. International Standard. Committee Manager ISO/TC 176/SC 2. Sally Swingewood, UK.

Camargo, F. Larsen, B. Chadbourn, B. Roberson, R. & Siekmeier, J. 2006. Intelligent Compaction: A Minnesota Case History. Proc., 54th Annual University of Minnesota Geotechnical Conf., St. Paul, MN.

Consoli, N.C. Rosa,F.D. & Fonini, A. 2009. Plate Load Tests on Compacted Soil Layers Overlaying Weaker Soil. *Journal of Geotechnical and Geoenvironmental Engineering*. 135(12), 1846–1856. https://doi.org/10.1061/(ASCE)GT.1943-5606.0000158.

DeMerchant, M.R. Valsangkar, M.R. & Schriver, A.B. 2002. Plate Load Tests on Geogrid-reinforced Expanded Shale Lightweight Aggregate. *Geotextile and Geomembranes*. 20(3), 173–190. https://doi.org/10.1016/S0266-1144(02)00006-7.

Duddu, S.R. & Chennarapu, H. 2022. Quality Control of Compaction with Lightweight Deflectometer (LWD) Device: A State-of-art. *International Journals of Geo-Engineering. Springer*. 13(6), 1–13. https://doi.org/10.1186/s40703-021-00171-2.

European Organization for Technical Assessment (EOTA) European Assessment Document (EAD) 080002-00-0102. 2011. EOTA Technical report TR41 B.1., TR41 B.2., TR41 B.3., and TR41 B.4.

Fleming, P.R. Frost, M. & Lambert, J. 2007. Review of Lightweight Deflectometer for Routine in situ Assessment of Pavement Material Stiffness. *Transportation Research Record*. 2004(1), 80–87. https://doi.org/10.3141/2004-09.

Fleming, P.R. Lambert, J.P. Frost, M.W. & Rogers, C. 2002. In-situ Assessment of Stiffness Modulus for Highway Foundations During Construction. *9th International Conference on Asphalt Pavements*, Copenhagen, Denmark, August, 2002, pp 12.

Hariprasad, C. Rajashekar, M. & Umashankar, B. 2016. Preparation of Uniform Sand Specimens using Stationary Pluviation and Vibratory Methods. *Geotechnical and Geological Engineering, Springer*. 34(6), 1909–1922, https://doi.org/10.1007/s10706-016-0064-0.

Holtz, W.G. & Gibbs, H.J. 1979. SPT and Relative Density in Coarse Sand. *Journal of the Geotechnical Engineering Division, ASCE* Vol.105, No. GT3, (1979). 439–441.

Li, Tong. and Ronald, L.B. 2005. Nonlinear Parameters for Granular Base Materials from Plate Tests. *Journal of Geotechnical and Geoenvironmental Engineering*. 131(7). https://doi.org/10.1061/(ASCE)1090-0241(2005)131:7(907).

Lin, D.F. Liau, C.C. & Lin, J.D. 2006. Factors Affecting Portable Falling Weight Deflectometer Measurements. *Journal of Geotechnical and Geoenvironmental Engineering*. 132(6), 804–808. https://doi.org/10.1061/(ASCE)1090-0241(2006)132:6(804).

Mooney, A.M. & Miller, P.K. 2009. Analysis of Lightweight Deflectometer Test Based on In Situ Stress and Strain Response. *Journal of Geotechnical and Geoenvironmental Engineering*. 135(2). https://doi.org/10.1061/(ASCE)1090-0241(2009)135:2(199).

Moshe, L. & Yair, G. 2001. Quality Assessment During Road Formation and Foundation Construction: Use of Falling-Weight Deflectometer and Light Drop Weight. *Transportation Research Record*, 1755(1), 69–77. https://doi.org/10.3141/1755-08.

Nazzal, M. Abu-Farsakh, M. Alshibli, E. & Mohammad, L. 2007. Evaluating Light Falling-weight Deflectometer Device for in-situ Measurement of Elastic Modulus of Pavement Layers. *Transportation Research Record*. 2016(1), 13–22. https://doi.org/10.3141/2016-02.

NCHRP 1-37A. 2004. *Mechanistic-Empirical Design of New and Rehabilitated Pavement Structures, Draft Report*, Transportation Research Board, National Research Council, Washington, D.C. USA.

Park, Y.B. & Chung, H.S. 2003. A Comparison of Static and Dynamic Deformation Modulus by Dynamic Plate Test. *Korean Geotech. Soc*. 2003(19):335–342.

Sidhu, R.D. Vamsi, K. Hariprasad, C., & Umashankar, B. 2023. Evaluating Improved Moduli of Geogrid-Stabilized Sandy Soil with a Deflectometer. *Proceedings of the Institution of Civil Engineers (ICE) - Ground Improvement*. Pp 1–34. https://doi.org/10.1680/jgrim.22.00075.

Umashankar, B. Hariprasad, C. & Kumar, G.T. 2015. Compaction Quality Control of Pavement Layers using LWD. *J. Mater. Civil Eng*. 27(7). https://doi.org/10.1061/(ASCE)MT.1943-5533.0001379.

Vennapusa, P, K, R., and White, D, J. (2009). Comparison of Light Weight Deflectometer Measurements for Pavement Foundation Materials. *Geotechnical Test Journal. ASTM International*. 32(3):239–251.

Investigation of variability in large scale laboratory box testing

W. Jeremy Robinson* & Jeb S. Tingle*
US Army Engineer Research and Development Center, Vicksburg, USA

ABSTRACT: The ability to quantify the performance benefits of geosynthetic inclusions in granular pavement layers is a unique challenge. Geosynthetic products in the current market have varying aperture sizes, material types, and manufacturing processes that intend to improve pavement performance through a variety of mechanisms, making quantification of the potential of individual geosynthetic products and the development of a universal design procedure problematic. One approach to quantifying performance benefits is the assessment of geosynthetic inclusions in full-scale testing. While it could be argued that full-scale evaluations provide the most realistic assessment of anticipated performance, full-scale experiments can be logistically burdensome and, at times, cost prohibitive. On the other hand, large-scale laboratory box testing reduces the amount of required materials, reduces required testing time, and reduces required capital investments. Large-scale laboratory box testing has been used for well over 30 years to investigate geosynthetic stabilized pavement structures with well-documented success. However, a comprehensive testing program to assess the repeatability of large-scale laboratory box testing has not been conducted. In the absence of a comprehensive testing program, two historical studies with multiple test items conducted at the U.S. Army Engineer Research and Development Center were selected to assess the repeatability of current large-scale laboratory test procedures. The two historical studies included multiple pavement profiles representative of both a thick airfield pavement subjected to heavy loading conditions and an aggregate-surfaced pavement subjected to highway loading conditions. The assessment of the test procedure included a statistical and engineering evaluation of the reported surface deformation data to estimate repeatability in large-scale box test results and an investigation of potential sources of variability that could influence performance outcomes. The results of these assessments of the large-scale laboratory box experimental procedure represent an initial step to identify expected variability in large-scale box testing.

1 INTRODUCTION

The ability to predict pavement performance with the inclusion of a geosynthetic presents a unique challenge. There are a variety of geosynthetic products on the market that intend to improve pavement performance through mechanisms such as lateral reinforcement of the aggregate base layer, tensioned membrane effect, and bearing capacity improvement. The selection of an appropriate index property that adequately predicts performance is an industry-wide challenge. While some have suggested that certain index properties, i.e., aperture stability and tensile strength, among others, can provide an indication of pavement performance, widespread acceptance of a universal design procedure remains up for debate. An alternative to a universal design-procedure is the evaluation of geosynthetics in a

---

*Corresponding Authors: Jeremy.robinson@usace.army.mil and Jeb.S.Tingle@usace.army.mil

full-scale test section, which could be evaluated at an accelerated pavement test facility or at an in-service pavement. While it could be argued that full-scale evaluations provide the most realistic assessment of performance, full-scale experiments can be logistically burdensome and, at times, cost prohibitive. Alternatively, large-scale laboratory box testing reduces the required amount of materials, testing time, and capital investments. Large-scale laboratory box testing (example shown in Figure 1) is advantageous compared to small-scale laboratory testing, i.e., triaxial cell or direct shear benchtop testing, because more realistic geosynthetic/ pavement interactions can be expected. Tingle *et al.* (2021) recommended standardization of large-scale box testing and presented minimum equipment and instrumentation require- ments. Equipment standardization could improve the effectiveness of data sharing as well as support the ability to construct a shared database of experimental results. However, to the authors' knowledge, a comprehensive testing program to assess the repeatability of large- scale box testing has not been conducted. Like precision and bias statements found in small- scale laboratory test methods, an expected repeatability of large-scale box testing is needed to support data comparisons.

Figure 1.   Example of large-scale laboratory box test setup.

2   OBJECTIVES AND SCOPE

The objective of this paper is to take an initial step in quantifying variability in performance outcomes in large-scale box testing. Two historical studies performed at the U.S. Army Engineer Research and Development Center (ERDC) were found to provide a meaningful amount of data for comparison. The studies represented opposite ends of the pavement spectrum where one study evaluated thick airfield pavements subjected to high-contact pressure aircraft loading conditions, and one study evaluated aggregate-surfaced low- volume pavements subjected to highway loading conditions. Details regarding the airfield experiment can be found in Robinson *et al.* (2019), and details regarding the highway experiment can be found in Tingle and Jersey (2005). The experiments are briefly described in the following subsections.

2.1   *Airfield experiment*

Eleven test items consisting of a 127-mm-thick asphalt layer, a 178-mm-thick crushed limestone base layer, a 305-mm-thick sand subbase layer, and a 3-California Bearing Ratio (CBR) high-plasticity clay subgrade were evaluated. Two distinct phases of the experiment were conducted in which geosynthetics were placed at the subgrade/subbase interface in one phase, and geosynthetics were placed at the base/subbase interface in the second phase. Four unreinforced test items were evaluated with varying layer material properties that included changes in subbase layer material type and changes in subgrade CBR. Loading conditions

consisted of a 128-kN load applied to a 305-mm-diameter steel plate yielding a 1750-kPa contact pressure. Deformation data with load cycles is summarized in Table 1. TI-1, TI-7, and TI-8 had either different material types, different geosynthetic types, or drastically different performance, thus were omitted from the analysis.

Table 1. Summary of deformation data for airfield experiment.

Cycle	TI2	TI3	TI4	TI5	TI6	TI9	TI10	TI11
1	1.4	1.8	1.0	2.3	0.0	0.0	0.0	0.0
100	9.6	10.3	6.2	11.4	10.2	7.1	10.2	6.6
200	11.7	12.3	7.9	14.2	12.3	8.9	13.2	8.1
300	12.9	13.7	8.9	16.0	13.5	10.2	15.2	9.4
500	14.6	15.5	10.4	18.4	15.0	11.4	19.1	10.2
800	16.5	17.5	11.9	21.0	16.6	12.7	22.9	11.4
1,000	17.4	18.6	12.6	22.5	17.5	14.0	25.4	12.2
1,500	19.4	20.8	14.1	25.6	19.2	15.2	30.0	12.7
2,000	21.0	22.6	15.3	28.1	20.7	16.5	35.1	14.0
4,000	26.1	28.1	18.8	35.3	25.2	20.8	49.5	17.8
5,000	28.2	30.4	20.2	38.3	26.4	22.9	55.9	19.1
10,580	33.0	41.9	26.2	52.1	35.6	31.8	ND	26.7
13,500	43.4	49.5	28.8	65.0	41.2	33.0	ND	29.2
18,800	56.0	ND	ND	ND	56.8	39.4	ND	35.6
20,000	61.0	ND	34.1	ND	ND	41.9	ND	36.8

TI = test item; ND = no data; deformation reported in mm.

2.2 *Highway experiment*

The highway experiment consisted of six different aggregate surfaced test items constructed over a very weak high-plasticity clay subgrade. Five of the test items consisted of a 0.36-m-thick crushed limestone aggregate layer over a 1-CBR subgrade. A geogrid, geotextile, and geogrid/geotextile combination were included at the subgrade/aggregate interface. One unreinforced test item with a 0.36-m-thick crushed limestone aggregate layer, referred to as Item 3, was evaluated, and one unreinforced test item with a 0.51-m-thick crushed limestone aggregate layer, referred to as Item 1, was evaluated. A 40-kN load applied to a 305-mm-diameter load plate was targeted, however, the authors noted that the design load was difficult to achieve on the weak pavement layers resulting in varying loading conditions for each test item. Thus, the measured load was used to convert cycles to equivalent single axle loads (ESALs), allowing meaningful performance comparisons to be made. Deformation data with ESALs is summarized in Table 2. Note Item 1 had a thicker aggregate layer and was not included in the analysis.

3 ANALYSIS APPROACH

Permanent deformation data were used to assess the variability for each experiment. A statistical analysis was performed to determine whether the deformation performance between the control test item and the reinforced test items were statistically different. If the performance was not found to be statistically different, then it was assumed that measured performance was within the inherent variability of the box test and could be used to quantify variability. Further, the data were evaluated for practical significance from an engineering standpoint. For example, if the average difference between two test items was 3 mm, i.e.,

Table 2. Summary of deformation data for highway experiment.

Item 2		Item 3		Item 4		Item 5		Item 6	
ESAL	Def.	ESAL	Def.	ESAL	Def.	ESAL	Def.	ESAL	Def.
1	0.0	1	0.0	1	0.0	1	0.0	1	0.0
9	0.0	6	1.9	8	0.8	9	0.4	9	0.4
29	0.0	18	2.5	27	1.1	27	0.4	28	1.0
48	0.5	30	3.1	45	1.5	46	1.0	48	1.8
71	0.4	44	4.0	67	1.8	68	1.1	74	2.6
95	0.6	57	4.6	88	2.1	91	1.5	96	3.4
280	1.5	155	8.0	241	4.1	262	3.5	292	8.9
460	2.0	244	11.1	400	5.8	429	5.0	491	13.5
685	2.8	363	14.4	557	7.5	630	6.6	722	18.1
914	3.4	478	17.4	733	8.9	841	7.8	976	22.5
2,358	6.4	1,336	33.8	1,788	16.8	2,387	14.6	2,917	45.9
3,235	7.6	1,781	40.0	2,353	19.5	3,056	17.0	3,888	54.8
4,086	8.6	2,156	45.1	2,812	21.8	3,860	19.1	4,837	62.5
ND	ND	3,341	55.5	4,017	25.9	5,590	23.3	ND	ND
ND	ND	4,515	63.0	5,071	29.5	ND	ND	ND	ND

ESAL = equivalent single axle load; Def. = deformation (mm); ND = no data

within the accuracy of the measurement technique, then from a practical standpoint the performance of those test items was deemed equivalent.

3.1 Analyses of airfield experiment

Deformation data from the airfield experiment were appropriate for a paired statistical analysis, because data were obtained at the same number of load cycles. A paired t-test was deemed appropriate for the statistical comparison. The results of the statistical analyses (Table 3) indicated that all test items were statistically different from the control test item with the exception of TI6. Further, a practical evaluation of the data, i.e., the average difference between the item of interest (IOI) and the control, found that TI3 had practically equivalent performance. TI5 and TI10 (both containing geosynthetics) were found to have worse performance than the control item, which was not expected, and could be a function

Table 3. Statistical analyses of airfield experiment.

Comparison	n	p-value	Sig.	Average Control (mm)	Average IOI (mm)	Average Difference (mm) (Control-IOI)
TI3	13	0.009	Y	19.6	21.8	−2.1
TI4	13	<0.001	Y	19.6	14.0	5.6
TI5	13	0.001	Y	19.6	26.9	−7.3
TI6	14	0.830	N	22.2	22.2	0.1
TI9	15	0.001	Y	24.8	19.1	5.8
TI10	11	0.011	Y	16.2	25.1	−8.9
TI11	15	<0.001	Y	24.8	16.6	8.2

n = number of observations, Sig. = statistically significant, IOI = item of interest, Y = yes (statistically significant), N = no (not statistically significant)

of box test variability. However, a review of the experimental results indicated that TI5 had a lower subgrade density and a thinner asphalt layer than the control test item. TI10 had approximately 25 mm less base course than the control. These observations could explain the significantly poorer performance of these test items and highlight the importance of implementing strict construction quality control in laboratory box testing, more stringent than would typically be achieved in full-scale construction.

TI2 sustained 3,700 cycles to failure, TI6 sustained 4,100 cycles to failure, and TI3 sustained 3,000 cycles to failure, where failure was defined as 25 mm of permanent deformation. At 25 mm of deformation, the average cycles-to-failure was 3,600, and the standard deviation (SD) was 557 cycles. Coefficient of variation was 15.5%, which was considered relatively low. If a 95% confidence interval (2SD) is considered, then the expected range of cycles to failure was approximately 2,500 to 4,700.

Similarly, at 50 mm of permanent deformation, TI2 sustained 16,990 cycles to failure, TI6 sustained 17,600 cycles to failure, and TI3 sustained 14,000 cycles to failure. Average cycles to 50 mm of permanent deformation was approximately 16,200, and the SD was 1,930 cycles. The 95% confidence interval ranged from 12,350 to 20,050. Coefficient of variation was 11.9% at 50 mm of permanent deformation.

3.2 Analyses of highway experiment

Deformation data from the highway experiment were not found to be appropriate for a paired t-test. Recall that test cycles were converted to ESALs due to variations in load magnitude resulting in reported data at varying traffic levels. Thus, the reported data were first qualified using an F-test to establish if the variances for each sample set were statistically different. The results of an F-test indicated that the variances between the control test item and the other geosynthetic test items were statistically equivalent, indicating a pooled t-test was an appropriate statistical measure of the difference between sample means. The results of the statistical analyses where comparisons are made to Item 3 (Control) are shown in Table 4.

The results of the statistical analyses indicated that Item 4 and Item 6 were statistically equivalent to the control test item. It should be noted that Item 4 would be statistically different from the control at a lower level of confidence, i.e., alpha = 0.10. Further, the average difference between the control and Item 4 was 10.5 mm, which represented a meaningful difference from a practical standpoint. Item 6 was found to perform more closely to the control test item; the average difference between the control and Item 6 was 2.2 mm.

Item 3 sustained 831 ESALs to 25 mm of permanent deformation, and Item 6 required 1,212 ESALs to achieve 25 mm of permanent deformation. To reach 50 mm of permanent deformation, Item 3 required 2,832 ESALs, and Item 6 required 3,557 ESALs.

Item 4 and Item 5 were replicate test items, and both contained a geogrid/geotextile combination; thus, we used these results to evaluate the differences in the test items. A pooled t-test indicated that the average performance difference between the test items was

Table 4. Statistical analyses of highway experiment.

Comparison	N1	N2	p-value	Sig.	Average Control (mm)	Average IOI (mm)	Average Difference (mm) (Control-IOI)
2	15	12	0.007	Y	20.3	2.6	17.7
4	15	15	0.097	N	20.3	9.8	10.5
5	15	14	0.041	Y	20.3	7.2	13.1
6	15	13	0.792	N	20.3	18.1	2.2

N1 = number of observations (control Item 3), N2 = number of observations (reinforced test item), Sig. = statistically significant, IOI = item of interest, Y = yes (statistically significant), N = no (not statistically significant)

not significantly different (p-value = 0.571), and the average difference was 2.5 mm. Item 4 achieved 25 mm of permanent deformation at 3,921 ESALs, and Item 5 achieved 25 mm of permanent deformation at 6,925 ESALs. ESALs required to reach 50 mm of permanent deformation for Item 4 and Item 5 were 22,769 and 31,258, respectively.

4 SUMMARY OF LOAD CYCLE VARIABILITY

The results of a statistical analyses of the experiments described herein provided some meaningful, albeit limited data for the investigation of variability in large-scale box testing. In order to normalize observations from each experiment and summarize variability, the relative percent difference between maximum and minimum cycles to 25-mm and 50-mm failure criteria were determined. Relative percent difference (RPD) is the absolute difference between two values divided by the average of the two values, all multiplied by 100. These calculations were performed on the values from the airfield experiment, the highway experiment, and highway experiment geosynthetic replicate as summarized in Table 5.

It was found that RPD values for the airfield experiment and highway experiment were generally consistent compared to each other. RPDs at 25-mm rut were 31% for the airfield experiment and 37% for the highway experiment, suggesting that the variability observed in the drastically different experiments was similar. In both cases a reduction in RPD was observed from 25-mm rut to 50-mm rut. Notably, the RPDs at 50-mm rut for both experiments were nearly identical, suggesting that variability tends to decrease with an increase in deformation.

RPDs for the replicate geosynthetics (noted as Highway GEO in Table 5) were higher than the other comparisons at both 25-mm rut and 50-mm rut.

These data suggest that if three or more experiments are repeated with the same materials, same construction techniques, and same loading conditions that the coefficient of variation should be below 20%. If only two experiments are repeated with the same materials, then the analyses suggests that the RPD should below 40%.

Table 5. Summary of relative percent difference for analysis data.

Experiment	Minimum	Maximum	Absolute Difference	Average	RPD (%)
Airfield					
25-mm rut	3.000	4,100	1,100	3,550	31.0
50-mm rut	14,000	17,600	3,600	15,800	22.8
Highway					
25-mm rut	831	1,212	381	1,021	37.3
50-mm rut	2,832	3,557	725	3,194	22.7
Highway (GEO)					
25-mm rut	3,921	6,925	3,004	5,423	55.4
50-mm rut	22,769	31,258	8,489	27,013	31.4

RPD = relative percent difference; GEO = geosynthetic

5 CONCLUSIONS

Two laboratory box test experiments conducted at the ERDC were selected to assess the repeatability of performance tests. The experiments represented both heavily-loaded thick airfield pavements and aggregate-surfaced highway pavements providing a range of performance results. The analyses included both a statistical component, i.e., t-test, and a

practical component, i.e., observed differences, to assess similarities in surface deformation performance.

The results of the analyses suggested that variability, i.e., coefficient of variation, was relatively low in the airfield experiment, less than 20%. In the highway experiment, only one test item was found to have similar performance to the control, which limited a variability assessment. These data may suggest that a weaker pavement, in the case of a large-scale laboratory box experiment, may be necessary to obtain meaningful performance differences that could be attributed to geosynthetic inclusion.

A direct comparison of the airfield and highway experiment found that variability was relatively consistent. Relative percent difference was on the order of 35% at 25 mm of deformation and on the order of 22% at 50 mm of deformation. The data suggest that if three or more experiments are repeated, the COV should be expected to be less than 20%, and if two experiments are repeated the RPD should be less than 40%.

The data presented herein represent a limited analysis of anticipated repeatability in large-scale laboratory box testing. While numerous studies have been successfully conducted for well over 30 years at multiple test sites, the absence of a robust assessment of anticipated variability presents difficulty in comparing test results. Thus, we recommend that additional experimentation be conducted to include both with-in laboratory repeatability, as well as a round-robin style assessment of multi-laboratory variability. These data would improve confidence in data sharing and facilitate development of a performance database.

ACKNOWLEDGEMENTS

REFERENCES

Robinson W. J, Mahaffay B. J., Howard I. L., and Norwood G. J. 2019. Cyclic Plate Testing of Geosynthetic-reinforced Airfield Pavements. *Ground Improvement* 172(4):229–243.

Tingle J. S., Robinson W. J., Cuelho E., and Tutumluer E. 2021. Large-scale Laboratory Box Testing as a Performance Test for Geosynthetic Base Reinforcement in Pavement Applications. *Geosynthetics Conference* 2021, ed M Beauregard and J E Nicks (New York: Curran Associates) 386–397.

Tingle J. S. and Jersey S. R. 2005. Cyclic Plate Load Testing of Geosynthetic-reinforced Unbound Aggregate Roads. *Transportation Research Record: Journal of the Transportation Research Board* 1936:60–69.

Effect of asphalt geogrid reinforcement on pavement response considering spatial variability in asphalt layer

L. Xiao & J.F. Xue
School of Engineering & Information Technology, The University of New South Wales, Campbell, Australia

A. Shahkolahi
Global Synthetics Pty Ltd, Virginia, QLD, Australia

ABSTRACT: Base and subgrade spatial variability can induce adverse effects on the structural response of pavements. However, few studies have investigated the impact of the spatial variability of the asphalt layer. The effects of asphalt geogrid reinforcement on pavement performance with spatially variable layers is still unknown, although geogrid reinforcement has been a common practice in pavement engineering. Random finite difference analysis (RFDA) is conducted in this study to evaluate the effect of spatial variability in asphalt layers on pavement responses and determine the effect of geogrid reinforcement under spatial variable situation. Several key conclusions are drawn: (1) the assumption of heterogeneity for the asphalt layer can induce a considerable underprediction of the critical pavement strain; (2) geogrid helps to mitigate the negative impact resulting from the asphalt spatial variability; (3) the low modulus dominating effect amplifies the mean strain of asphalt layer, thereby leading to a better mobilization of the geogrid reinforcement in the probabilistic cases.

1 INTRODUCTION

Spatial variability is one of the main sources of geotechnical uncertainties and has been proven to induce adverse effects on the structural response of pavements. Lua & Sues (1996) presented the first RFEM (random finite element method) application to study the impacts of spatial variability on pavement life. Ali *et al*. (2013) and Vaillancourt *et al*. (2014) investigated the effect of spatially varied modulus in subgrade on pavement responses. Titi *et al*. (2014) investigated the spatial variability of the base layer from FWD (falling weight deflectometer) tests and assessed their impact on pavement performance from existing pavement data. However, compared with studies regarding spatially variable base and subgrade layers, few studies have addressed the impact of spatial variability in the asphalt layer. On the other hand, inclusion of geogrid reinforcement in the asphalt layer has been used as a common practice to improve pavement performance. However, it remains unclear whether the presence of geogrid will aggravate or mitigate the impact caused by spatial variability.

Random finite difference analysis (RFDA) is conducted to: (1) assess the impact of spatial variability in the asphalt layer on the pavement response, (2) determine the role of geogrid reinforcement in the statistical effect of asphalt spatial variability, and (3) explore possible mechanical explanations for the effects of spatial variability and role of geogrid reinforcement. The maximum horizontal tensile strain at the bottom of the asphalt layer (denoted by

ε_h^{ac}) is selected as the critical pavement response variable. Note that, the location of this critical strain might not necessarily occur right below the tire centerline due to the impact of asphalt spatial variability. To avoid coupling effects from different sources of uncertainties, only Young's modulus of the asphalt layer is treated as a spatially varied property. All other parameters are assumed as deterministic.

2 RANDOM FINITE DIFFERENCE METHOD

2.1 Numerical modelling and key influence zone

A typical three-layered pavement structure reported in Austroads (2017) guide is selected as the subject of this study. Figure 1(a) illustrates half of the pavement structure modelled with FLAC2D software. The mesh size is fine enough and further refining of the meshes will not greatly affect the results of the simulation. As shown in the figure, a uniform load of 800 kPa over a 204.8 mm (D) diameter area is used to simulate the tyre pressure. Table 1 lists the material properties.
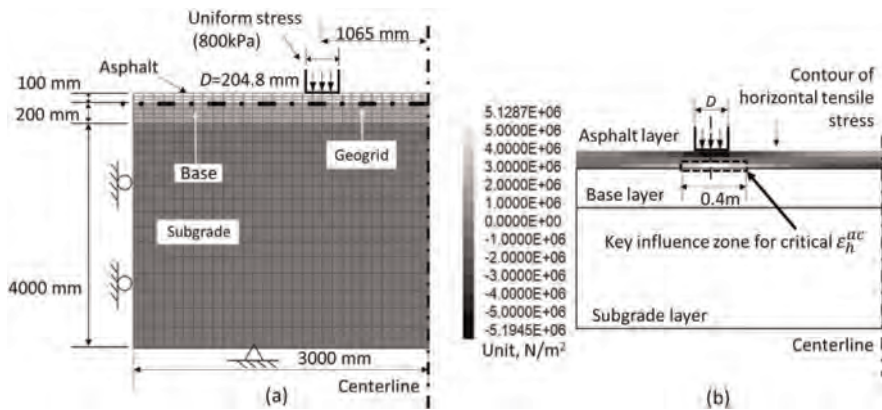
Figure 1.   (a) Finite difference model (not to scale); (b) tensile stresses and key influence zone for ε_h^{ac}.

Table 1.   Material properties of the pavement model.

Material	Asphalt layer	Base layer	Subgrade layer
Constitutive model	Linear elastic	Mohr-Coulomb	Mohr-Coulomb
Thickness	100 mm	200 mm	4000 mm
Young's modulus	2000 MPa	200 MPa	10 MPa
Poisson's ratio	0.40	0.35	0.28
Cohesion	–	5kPa	30 kPa
Friction angle	–	40°	25°
Dilatancy angle	–	20°	0°
Unit weight	24 kN/m^3	20 kN/m^3	18.2 kN/m^3

To investigate whether the presence of geogrid below the asphalt layer will aggravate or mitigate the impact caused by the asphalt spatial variability, a parametric study was conducted by adopting three kinds of geogrid reinforcement (G1, G2, and G3) and one unreinforced (UR) case as reference. The secant stiffnesses (J) at 2% for G1, G2, and G3 are

3000 kN/m, 6000 kN/m, and 9000 kN/m respectively. The geogrids are simulated with geogridSEL in FLAC2D and placed at the interface between the asphalt and base layer. A linear shear behavior is assumed for the interface with cohesion of 30 kPa, friction angle of 45° and shear stiffness of 300 MPa/m.

Figure 1(b) presents the contour of tensile stresses in the asphalt layer of an unreinforced deterministic case. The induced tensile stress in the asphalt layer decreases rapidly with the horizontal distance measured from the centreline of the loading. At about $1D$ away from the centreline of the loading area, the tensile stress reduces to below 40% of the maximum value. Thus, large tensile stress and strain of asphalt layer mainly occur within this $2D$ (about 0.4m) region in the vicinity beneath the loading area. Accordingly, the $2D$ region is determined as the key influence zone for the critical horizontal tensile strain in the asphalt layer (denoted by ε_h^{ac}). As opposed to the deterministic situation, the overall modulus of this key influence zone varies with different realizations in spatial variable situations and therefore leads to different magnitudes of ε_h^{ac}. To measure the overall modulus of the key influence zone, a local modulus, E_{local}, is defined by calculating the arithmetic mean modulus of the 0.4 m wide region.

2.2 Modelling and discretization of random fields

As mentioned above, Young's modulus of the asphalt layer (E) is set as spatially variable. The spatial variability is represented by a continuous and stationary random field generated using the Karhunen–Loève expansion (Huang *et al*. 2001) with Monte-Carlo runs of 100. The lognormal distribution is adopted to characterize the variability of E with its mean μ_E = 2000 MPa, and coefficient of variation COV_E = 30%. The following exponential auto-correlation function, $\rho(x, y)$, is used:

$$\rho(x, y) = \exp\left(\frac{-2|x|}{\delta_x}\right)\exp\left(\frac{-2|y|}{\delta_y}\right) \tag{1}$$

where δ_x and δ_y denote the horizontal and vertical scale of fluctuation (SOF) respectively. In this study, the asphalt modulus is assumed as isotropic random field with $\delta_x = \delta_y$ =0.2 m.

3 RESULTS AND ANALYSIS

3.1 Effect of asphalt spatial variability on the critical tensile strain

Figure 2 presents the relationship of E_{local} versus ε_h^{ac} in the spatially varied (SV) unreinforced pavement. The power regression line shows that the critical stain ε_h^{ac} increases as E_{local} decreases. It is also found that ε_h^{ac} of most realizations (75 out of 100) are larger than the deterministic (DET) value (3.136 millistrain). Furthermore, the number of realizations with ε_h^{ac} greater than the deterministic strain (75 out of 100 realizations) is far more than that with E_{local} smaller than the deterministic modulus (59 out of 100 realizations). The gap between the two numbers is caused by the combined effect of local spatial variability within the influence zone and the low modulus dominating effect (Fenton & Griffiths 2005): the softer areas have a greater influence on the critical strain than stiffer ones do. This effect is manifested by the regression trend in Figure 2 where ε_h^{ac} grows more and more rapidly with decreasing E_{local}.

As shown in Figure 2, the maximum ε_h^{ac} deviates from the deterministic strain much further than the minimum strain does due to the low modulus dominating effect. All these factors make the mean value of ε_h^{ac} in the probabilistic cases higher than their corresponding deterministic ε_h^{ac}. Consequently, assuming the asphalt heterogeneity can induce an underestimation of the critical tensile strain in the asphalt layer and therefore an overprediction of the fatigue life.
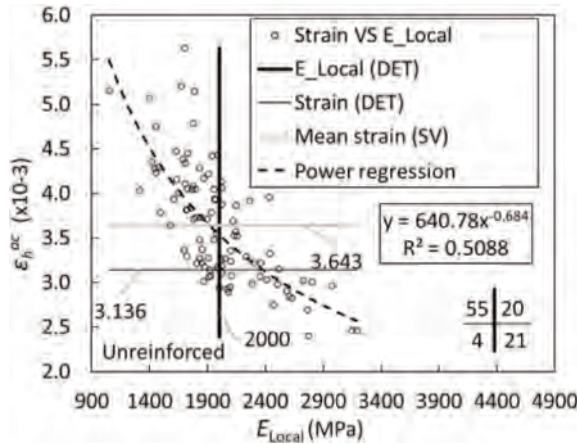
Figure 2.   Relationship of E_{local} versus ε_h^{ac}.

3.2   *Effect of geogrid reinforcement on the statistical result of ε_h^{ac}*

Figure 3(a) shows the statistical distribution of ε_h^{ac} under different reinforcement conditions. Compared with the unreinforced case, the distribution of ε_h^{ac} with reinforcement (G2) is not only left-skewed but also narrower. This is due to the fact that the reinforcement induced reduction in the maximum strain is much greater than that in the minimum strain. Consequently, the geogrid reinforcement is capable of not only decreasing the mean value of ε_h^{ac} but also mitigating the variation in terms of standard deviation.

To quantify the relative increase of the mean strains in spatial variable cases as opposed to the corresponding deterministic strains, an amplification factor R_{mean} is defined:

$$R_{mean} = \left(\frac{\overline{\varepsilon}}{\varepsilon_{\text{det}}} - 1 \right) \times 100\% \tag{2}$$

where $\overline{\varepsilon}$ is the mean value of ε_h^{ac} in a spatial variable (SV) case, and ε_{det} is the corresponding deterministic (DET) strain.

Figure 3(b) shows the value of R_{mean} for four kinds of geogrid reinforcement conditions. It shows that, under the unreinforced situation (UR), the spatial variability of Young's modulus in the asphalt layer can increase the critical strains by 16.1% compared with the
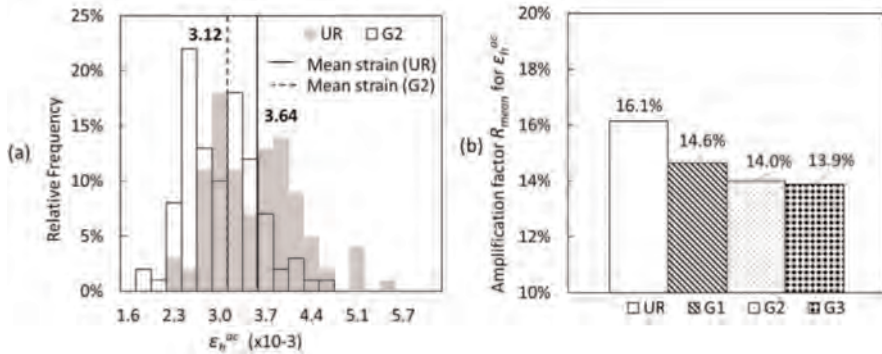
Figure 3.   Effect of geogrid reinforcement: (a) Distribution of critical strain; (b) Amplification factor R_{mean}.

1291

homogenous situation. Another indication is that the presence of geogrid can decrease the amplification factor. And the decreasing effect strengthens but not significantly with the geogrid stiffness. The narrower distributions of ε_h^{ac} and lower R_{mean} in reinforced cases imply that the presence of geogrid can mitigate the negative effect of the asphalt spatial variability, which will be detailed next.

3.3 Statistical and mechanical explanation for the role of geogrid reinforcement

Geogrid reinforcement decreases the critical strain in the asphalt layer in both deterministic and probabilistic analyses. To measure the relative strain reduction resulting from the geogrid reinforcement, a decreasing factor R is defined as the ratio of ε_h^{ac} in the reinforced situations to ε_h^{ac} in the corresponding unreinforced cases. According to this definition, in probabilistic situation, a smaller R suggests a better performance of geogrid reinforcement in mitigating the amplification effect of spatial variation.

Figure 4 shows the relationship of the decreasing factor R under G2 reinforcement in both the spatial variable (SV) case and the deterministic (DET) case. It reveals that the decreasing factor R in most realizations is smaller than that in the deterministic case. Moreover, the minimum R (81.9%) deviates from the deterministic R (87.4%) much further than the maximum R (88.8%) does. All these together contribute to an average decreasing factor R (85.8%) lower than the deterministic R (87.4%). In addition, the linear regression of data in Figure 4 indicates the decreasing factor R is negatively correlated with the asphalt strain level. This is consistent with well established findings that high levels of asphalt stain help to mobilize the geogrid reinforcement (Zornberg 2017).
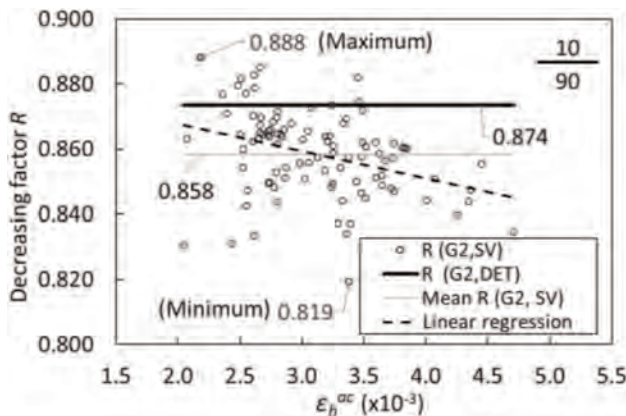
Figure 4. Comparison of decreasing factor R with G2 reinforcement in SV case and DET case.

To mechanically explore the statistical result, the maximum tensile stress of the geogrid (denoted by σ_h^g) is extracted and plotted against the asphalt strain level in Figure 5(a), and against E_{local} in Figure 5(b). As illustrated in Figure 5(a), σ_h^g in most realizations (81 out of 100) is larger than the deterministic σ_h^g of 70.3 MPa. Moreover, the maximum σ_h^g (81.3 MPa) deviates from 70.3 MPa much further than the minimum σ_h^g (64.9MPa) does. All these together lead to an average σ_h^g (72.5MPa) greater than the deterministic σ_h^g. In other words, the geogrid reinforcement is better mobilized owing to the asphalt spatial variability than in homogeneous situation.

The variation of σ_h^g is ultimately induced by the asphalt spatial variability, especially the spatial variability within the key influence zone. As illustrated in Figure 5(b), the power
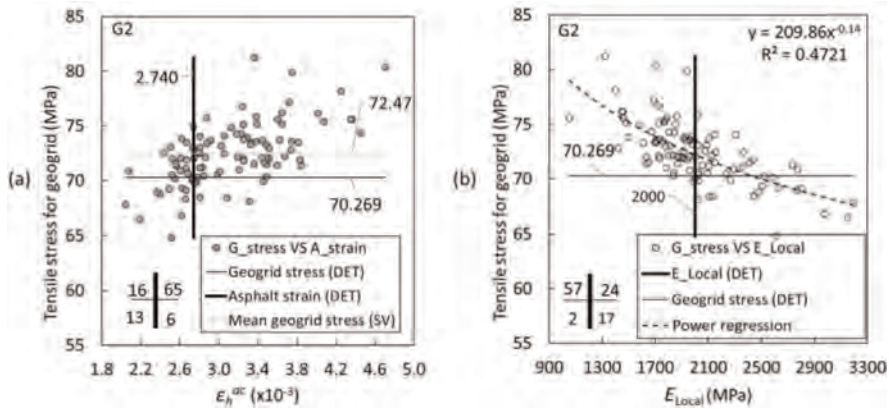
Figure 5. Distribution of the maximum tensile stress of the geogrid (G2): (a) σ_h^g versus ε_h^{ac}; (b) σ_h^g versus E_{local}.

regression trend indicates that σ_h^g grows rapidly as E_{local} decreases, meaning that a soft key influence zone contributes more to the geogrid mobilization than a stiff one does. Another interesting finding is that the number of realizations with σ_h^g greater than the deterministic σ_h^g is far more than the number of the realizations with E_{local} lower than the deterministic Young's modulus (i..e., 2000 MPa). For example, in Figure 5(b), there are 59 out of 100 realizations with E_{local} lower than 2000 MPa, but there are 81 out of 100 realizations with geogrid tensile stress greater than 70.269 MPa. The gap is not caused by the overall modulus (i..e., E_{local}) but by the local spatial variability within the key influence zone.

To demonstrate the effect of local spatial variability on the variation of σ_h^g, three groups of data are extracted from Figure 5(b) and their spatial distributions of Young's modulus within the key influence zone are shown in Figure 6. Each group consists of two realizations with approximate E_{local} but different magnitudes of spatial variability of Young's modulus within the 2D region. For example, with an approximate E_{local} (1700MPa), the spatial variation of Young's modulus in realizaiton No. 62 (R62) is more intense than that in realizaiton No. 69 (R69). In all the groups, a key influence zone with quickly varying modulus always corresponds to a large σ_h^g (or vice versa). This could be explained by the low modulus dominating effect which makes the softer area contributes more to the mobilization of geogrid reinforcement than the stiffer area does. As a result, even under the same E_{local}, the
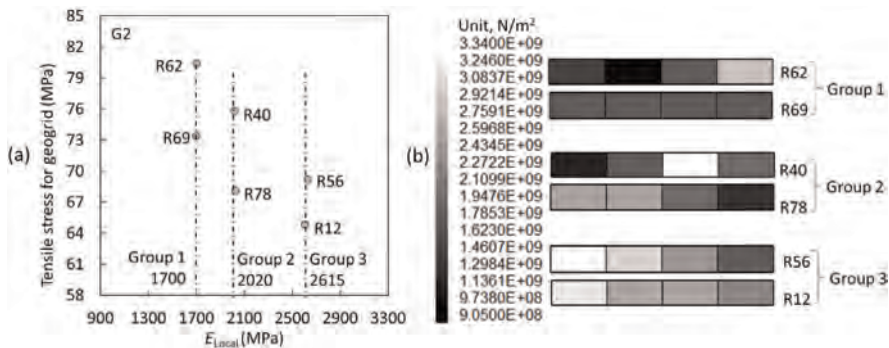
Figure 6. (a) Realizations with approximate E_{local} but different σ_h^g; (b) corresponding distribution of Young's modulus with key influence zone.

geogrid is more fully mobilized by a key influence zone with large local spatial variability than one with less spatial variability.

4 CONCLUSIONS

Based on the analyses, it can be concluded that the asphalt spatial variability can induce a considerable amplication effect on the critical pavement strain and that the geogrid reinforcement can mitigate the adverse effect induced by the spatial variability. On the one hand, the presence of geogrid can decrease the amplification factor R_{mean} and reduce the variation of ε_h^{ac}. The variation of the geogrid stiffness within the selected range in this study makes a marginal difference in mitigating the negative effect. On the other hand, compared with the homogeneous situation, geogrid is more easily mobilized owing to the presence of the asphalt spatial variability. The amplication effect of asphalt spatial variability and the role of geogrid in that effect can be well explained by the low modulus dominating effect.

REFERENCES

Ali, A., Abbas, A., Nazzal, M., & Sett, K. 2013. Incorporation of Subgrade Modulus Spatial Variability in Performance Prediction of Flexible Pavements. 6, 136–140.

Austroads. 2017. Guide to Pavement Technology Part 2: Pavement Structural Design. Sydney, Australia.

Fenton, G. A., & Griffiths, D. V. 2005. Three-dimensional Probabilistic Foundation Settlement. *Journal of Geotechnical and Geoenvironmental Engineering*, 131(2), 232–239.

Huang, S.P., Quek, S.T., Phoon, K.K. 2001. Convergence Study of the Truncated Karhunen–Loeve expansion for Simulation of Stochastic Processes. *Int. J. Numer. Anal. Methods Geomech.* 52 (9), 1029–1043.

Lua, Y. J., & Sues, R. H. 1996. Probabilistic Finite-element Analysis of Airfield Pavements. *Transportation Research Record*, 1540(1), 29–38.

Titi, H. H., Faheem, A., Tabatabai, H., & Tutumluer, E. 2014. Influence of Aggregate Base Layer Variability on Pavement Performance. *Transportation Research Record*, 2457(1), 58–71.

Vaillancourt, M., Houy, L., Perraton, D., & Breysse, D. 2014. Variability of Subgrade Soil Rigidity and its Effects on the Roughness of Flexible Pavements: A Probabilistic Approach. *Materials and Structures*, 48 (11), 3527–3536.

Zornberg, J. G. 2017. Functions and Applications of Geosynthetics In Roadways. *Procedia Engineering*, 189, 298–306.

Evaluation of geocomposite base stabilization on lateritic gravel and granular material bases using accelerated pavement testing

G.O.M. Pedroso
Guaratinguetá Faculty of Engineering and Sciences (FEG), São Paulo State University (UNESP), Guaratinguetá, Brazil

J. Lins da Silva
São Carlos School of Engineering (EESC), University of São Paulo (USP), São Carlos, Brazil

ABSTRACT: This study presents a laboratory study on seven different test configurations subjected to cycling moving wheels load by using an accelerated pavement test. Tests were conducted on lateritic clay mixed with gravel and unbounded granular material at two different thickness, in a geosynthetic stabilized and unstabilized sections. All test sections were constructed on a low CBR clay subgrade. Each pavement section performance was evaluated by measuring the surface rutting and the subgrade vertical pressure at different cycles. Findings indicated that the lateritic gravel base pavement sections had lower surface rutting than the granular base, mainly because the lateritic increases the material stability, delaying the occurrence of damage on the gravel. Furthermore, sections modified with geocomposite were found to have improved performance than the control sections.

1 INTRODUCTION

The use of high-quality crushed aggregates is becoming scarce and expensive, and, in some regions, they are not even found, especially when they are for low to medium traffic volume roads. In this context, it is essential to define alternatives that are both technical and economically viable for pavement construction. The use of geosynthetics can provide an alternative solution. The inclusion of geosynthetic provide tensile reinforcement through frictional interaction with base course materials, reducing applied stresses on the subgrade and preventing excessive permanent deformation (Koerner 2005). Therefore, the geosynthetic with the base/subgrade stabilization function can be a viable option that can extend the pavement service life, minimize maintenance costs, and reduce the demand for crushed aggregates (Palmeira & Antunes 2010).

Many researchers have investigated the performance of geosynthetics in pavement structures (Abu-Farsakh & Chen 2011; Leng & Gabr 2002; Palmeira & Antunes 2010; Qian *et al.* 2013; Tang *et al.* 2008). These studies reported that geosynthetic properties, the location of the geosynthetic, the strength of the subgrade, and the thickness of the base layer affect the geosynthetic effectiveness.

The use of non-conventional and alternative materials in sub-base and base layers to replace conventional granular materials are currently being studied for pavement structures (Rezende *et al.* 2015). Thus, since 1972 it has been common to use lateritic soils mixed with lime or gravel in base and sub-base for low to medium traffic volume in Brazil (Nogami & Villibor 1991). One of the questions is the effectiveness of the geosynthetic when comparing lateritic gravel and unbounded granular material.

This study presents an experimental investigation on the performance of a lateritic clay soil mixed with gravel and an unbound granular material as base materials using a large scale steel box with a moving wheel loading apparatus attached to it. The research scope is to compare these two different materials and the geosynthetic response in the stabilized sections.

2 TEST SETUP AND MATERIALS

2.1 *Materials*

A weak clayed silt subgrade soil classified as high plasticity silt (MH) and A- 7-5, according to the USCS and HRB classification system, was collected near the city of São Carlos, São Paulo, Brazil. Tests were performed, obtaining a CBR of 3.5, 34% moisture content and a density of 1.45 g/cm^3 at Standard Proctor compaction.

A crushed unbounded coarse granular aggregate and a soil-aggregate mixture were used as base materials in this study. The unbound granular base consists of basaltic crushed stone with a dry density of 2.16 g/m^3 at an optimum moisture content of 4.1%. The soil-aggregate is a granulometric stabilized base with 20% of lateritic clay mixed with 80% basaltic crushed stone on a dry mass basis, with a dry density of 2.33 g/m^3 at an optimum moisture content of 6.5%. The lateritic clay was classified as A-6, ML and LG', according to the HRB, USCS and Miniature Compaction Tropical (MCT) systems, respectively. Figure 1 shows the grain size distribution curve of these materials.
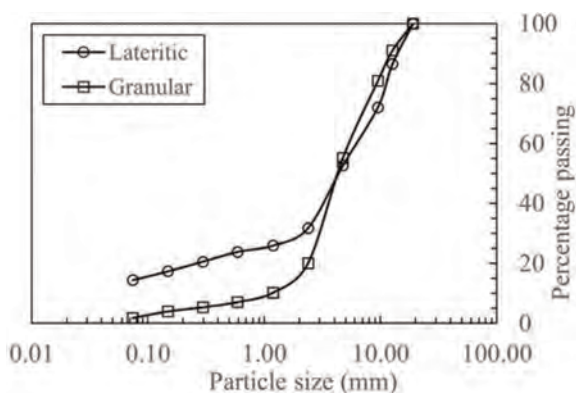
Figure 1.   Particle size distribution curve.

Two types of geosynthetics were used in the tests, a composite geogrid (consisting of a light polypropylene nonwoven geotextile with a polyester geogrid, CGG) and a geogrid (GG) were used to mechanically stabilize the base aggregate. Both geogrids are biaxial and have the same properties. The physical and mechanical properties of the geosynthetics are summarized in Table 1.

2.2 *Test setup*

A large steel testing box with internal dimensions of 1.8 m high, 1.6 m wide, and 1.8 m long available at the University of Sao Paulo was used in this experimental study, as shown in Figure 2. Seven different structures were constructed, and a rolling wheel system, first

Table 1. Physical and mechanical properties of the geosynthetics.

Property	Value	Standard
Nonwoven Geotextile		
Polymer type	PP	–
Mass per unit area (g/m^2)	148	ASTM D5261
Permittivity (s^{-2})	1.71	ASTM D4491
Grab tensile strength (kN)	0.53	ASTM D4632
Geogrid		
Polymer type	PET	–
Aperture size (mm)	25 × 25	–
Tensile strength at 2% strain (kN/m)	11.09	ASTM D6637
Tensile strength at 5% strain (kN/m)	23.35	
Ultimate tensile strength (kN/m)	39.23	
Elongation at break (%)	8.14	

Figure 2. Test setup.

developed by Correia and Zornberg (2016) and modified by Pedroso *et al.* (2022), was used to simulate traffic loading. The testing wheel consists of a one-tire configuration fixed in the centerline of the box, with a diameter of 540 mm and a width of 154 mm that applied unidirectional loading in a tracking length of 1.0 m. The equipment was set to a maximum rate of 600 wheel passes per hour. The wheel load consists of a linear load that increases from 0 to a peak of 16 kN in 0.1 s; then, it is maintained constant through the tracking length. At the end of the tracking length, the load is reduced to zero, the wheel is pulled up and returns to the starting point over 1.5 s.

The pavement performance was evaluated by earth pressure cells, LVDT's and tell tails, as explained in Pedroso *et al.* (2022). Six earth pressure cells with 30 mm diameter installed in pairs at different locations along the experimental section for monitoring the vertical stress distribution. The sensors were placed in the middle of base course, at the top of the subgrade, and 300 mm below the base and subgrade interface.

The surface transversal profile was measured using a manual profilometer. The wheel cycles were stopped, and the profilometer apparatus was installed on the surface, ensuring that all points were aligned. Measurements were made at 0, 100, 500, 1000, 2500, 5000 and 10,000 wheel passes, and then each 10,000 wheel passes. For these experimental conditions, tests were conducted until reaching a total of 100,000 load repetitions or 50 mm surface permanent deformation (half of the base thickness for 100 mm base tests).

Seven stabilized (S) and non-stabilized test sections with two different base materials, lateritic-aggregate (L) and unbond granular (G), and thickness were evaluated. All sections were constructed with the same subgrade and the same bituminous surface treatment. The tests setup, base materials type, stabilized condition, and construction control are specified in Table 2.

Table 2. Test sections, base materials type and stabilized condition.

Test Section	Base material	Thickness (m)	Stabilized condition
LB1	Lateritic-aggregate	0.1	Non-stabilized
LB1S	Lateritic-aggregate	0.1	CGG-interface
GB1	Unbound granular	0.1	Non-stabilized
GB1S	Unbound granular	0.1	CGG-interface
LB2	Lateritic-aggregate	0.2	Non-stabilized
GB2	Unbound granular	0.2	Non-stabilized
GB2S	Unbound granular	0.2	GG-middle of base

3 TEST RESULTS

3.1 *Surface profile*

Figure 3. Shows the surface profile for all seven test sections.

A rut deep and more extensive than the wheel width combined with heave along both sides is formed for the granular base. The repeated wheel shear stress causes a lateral spreading of the granular base material particles. This lateral displacement was one of the main deterioration mechanisms contributing to a thinner and less stiff material while leading to an increase in subgrade deformation. Opposed to the granular base sections, the effect of lateral spreading in lateritic base sections was not a significant deterioration mechanism since the surface profile did not show the formation of a heave beside the wheel path. This behavior is due to the decrease in the number of voids and the increase in density caused by the presence of fines in the soil-aggregate mixture. However, based on the observation after trenching at the end of each test, excess water was observed in the base/subgrade interface and contamination of the base by the subgrade fines. This intermixing are the major deterioration mechanisms for the lateritic base.

3.2 *Vertical stress*

Figure 4 presents the maximum vertical stress for all test sections. The lateritic base, which is more rigid, showed lower vertical stress values at the top of the subgrade. As expected, the maximum vertical stress increased with the number of cycles showing that the repeated wheel loads progressively reduce the base stiffness, which is in agreement with (Qian *et al.* 2013;
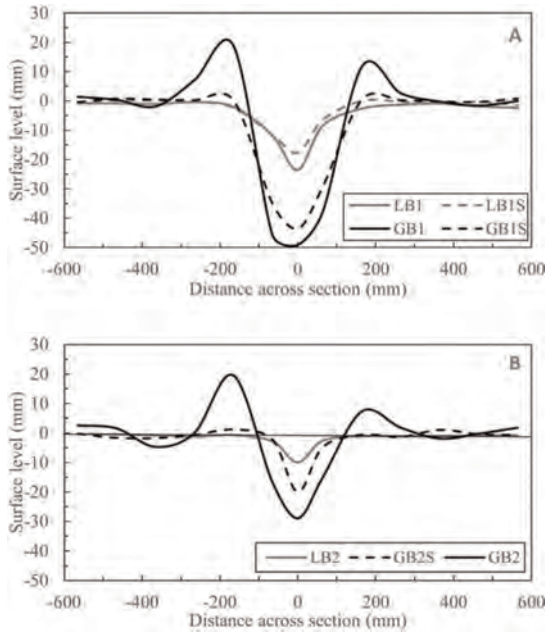
Figure 3.   Surface transversal profile: (a) 10 cm thick base; (b) 20 cm thick base.
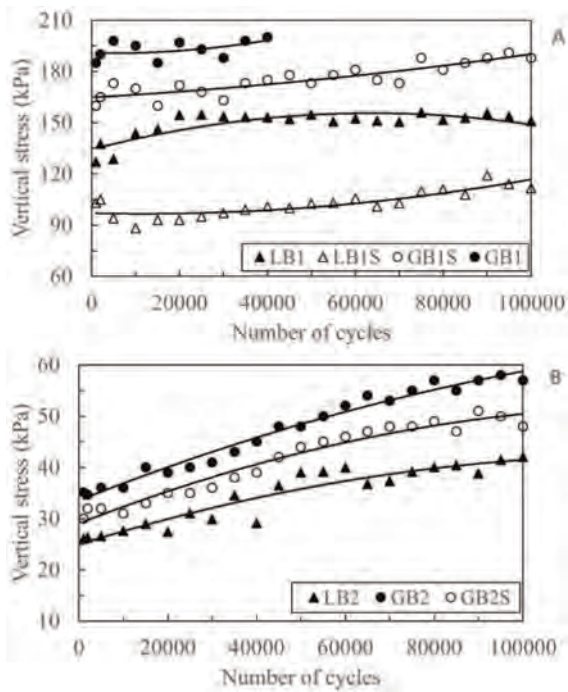
Figure 4.   Maximum vertical stress: (a) 10 cm thick base; (b) 20 cm thick base.

Tang *et al.* 2008). It is noteworthy that the increase in thickness of the base reduces the maximum vertical stress on the subgrade. However, sections with the same permanent deformation do not have the same vertical stress. For example, the GB2 section has lower vertical stress and a higher permanent deformation than LB1S.

The stabilized sections shows that the slope of the curve is less steep, in other words, the increase in vertical stress over the cycles is reduced when compared with the other sections. The same trend was observed for the accumulation of permanent deformation over time. This behavior can be results in the maintain of the base modulus over time.

4 CONCLUSIONS

This paper presented an experimental study on the performance of two base course materials unstabilized and stabilized with geosynthetic at different configurations under a moving wheel load. It can be concluded that the stabilized sections had a superior performance than the unstabilized sections, showing a decrease in superficial rutting and vertical stress at the subgrade. The base coarse deterioration mechanisms were different for the two materials. The primary mechanism for the coarse granular base was the lateral spread. On the other hand, the excess of water and intermixing between materials were the major deterioration mechanisms for the lateritic base. Therefore, the geosynthetic main function had different objectives for each base material.

REFERENCES

Abu-Farsakh, M.Y., Chen, Q. 2011. Evaluation of Geogrid Base Reinforcement in Flexible Pavement using Cyclic Plate Load Testing. *International Journal of Pavement Engineering* 12: 275–288.

Correia, N.S., Zornberg, J.G. 2016. Mechanical Response of Flexible Pavements Enhanced with Geogrid-reinforced Asphalt Overlays. *Geosynthetic International* 23: 183–193.

Koerner, R. M. 2005. *Designing with geosynthetics*. 5th Edition New Jersey: Prentice Hall, 796p.

Leng, J., Gabr, M.A. 2002. Characteristics of Geogrid-reinforced Aggregate under Cyclic Load. *Transportation Research Record: Journal of Transportation Research Board* 1786: 29–35.

Nogami, J.S., Villibor, D.F. 1991. Use of Lateritic Fine-grained Soils in Road Pavement Base Courses. *Geotechnical and Geological Engineering* 9: 167–182.

Palmeira, E.M., Antunes, L.G.S. 2010. Large Scale Tests on Geosynthetic Reinforced Unpaved Roads Subjected to Surface Maintenance. *Geotextiles and Geomembranes* 28: 547–558.

Pedroso, G.O.M., Ramos, G., Lins da Silva, J. 2022. Evaluating Geosynthetic Base Stabilization on Lateritic Gravel and Granular Material Under Cyclic Moving Wheel Loads. *Case Studies in Construction Materials* 16, e00880.

Qian, Y., Han, J., Pokharel, S.K., Parsons, R.L. 2013. Performance of Triangular Aperture Geogrid-reinforced Base Courses Over Weak Subgrade Under Cyclic Loading. *Journal of Materials in Civil Engineering* 25: 1013–1021.

Rezende, L.R., Marques, M.O., da Cunha, N.L. 2015. The Use of Non-conventional Materials in Asphalt Pavements Base. *Road Materials and Pavement Design* 16: 799–814.

Tang, X., Chehab, G.R., Palomino, A. 2008. Evaluation of Geogrids for Stabilizing Weak Pavement Subgrade. *International Journal of Pavement Engineering* 9: 413–429.

Field performance and monitoring of geogrid stabilised/reinforced pavement on soft and expansive subgrade

Amir Shahkolahi & Chaminda Gallage
School of Civil and Environmental Engineering, Queensland University of Technology (QUT), Australia

David Lacy
Foundation Specialist Group (FSG), Australia

Jörg Klompmaker
NAUE GmbH & Co. KG, Germany

ABSTRACT: In order to quantify the effect of geogrid stabilisation/reinforcement, a full-scale pavement field trial was established upon a soft and expansive subgrade. Sections with variable geogrid arrangements were constructed in order to allow the quantitative assessment of geogrid stabilisation/reinforcement; both in terms of their initial contribution to composite insitu stiffness parameters and their benefit to the long-term performance of a pavement. On site testing was completed within all trial sections during the project's construction phase, such that the initial state (strength and stiffness) of performance the subgrade and each pavement layer was adequately characterised. Post construction, ongoing performance monitoring has included the use of embedded pressure cells. An analysis of the first 3 years of monitoring of this full-scale field trial was conducted, with selected results presented herein. The data demonstrates that the inclusion of geogrids successfully improves the bearing capacity of the pavement profile by reducing the traffic imparted vertical pressures being exerted upon the underlying materials. The results also demonstrate that the presence of two geogrid layers (with one placed at the subgrade-subbase interface and one at the subbase-base interface) offer a greater improvement of the bearing capacity than the installation of a single geogrid at the interface of subgrade-subbase materials. Additional observations relate to longitudinal cracking of the pavement, where greater control of cracking has been initially achieved in the test sections where geosynthetic reinforcement was installed.

1 INSTRUCTIONS

Geogrids are used to stabilize and reinforce the roads and improve the bearing capacity of pavements on soft subgrades. Additionally, geogrids installed within granular layers of a pavement formation are frequently used to control environmental distress and limit longitudinal cracking due to expansive subgrades by providing the stiffening, known as the new function of geosynthetic material to control deformations in the soil-geosynthetic composite.

In recent years, "Stiffening" has been introduced by Prof. Jorge Zornberg (2017a,b) as a function of geosynthetics to control pavement deformations (e.g. due to environmental loads) for applications such as pavements on expansive subgrades. "stiffening" refers to development of tensile forces in the geosynthetic material to control deformations in the soil-geosynthetic composite, while "reinforcement" refers to development of tensile forces in the geosynthetic material to maintain or improve the stability of the soil-geosynthetic composite.

Although both functions provide mechanical improvement, the required geosynthetic properties to achieve these functions are slightly different. The key property for "reinforcement" is the geosynthetic tensile strength and stiffness, while the main design parameter for "stiffening" is the stiffness of soil-geosynthetic composite (Zornberg, 2017a,b). Supported by more than 20 years of research and field monitoring, the use of stiffening geosynthetics has now become a standard practice in many countries specially in united states to mitigate cracks and improve pavements life on expansive subgrades. The use of geosynthetics was found to effectively minimise the detrimental effects of expansive soil subgrades on flexible pavements. Geosynthetic-stiffened pavement sections on expansive clay subgrades have showed significantly better field performance than control (non-stiffened) sections or even lime stabilised sections. On the other hand, geogrid-stiffened section with less gravel thickness could perform equal/better to the sections without geogrid and thicker gravel (Roodi & Zornberg 2020; Roodi et al. 2016; Roodi 2016; Zornberg et al. 2012, 2008). This verifies the benefit of geogrid stiffening in reducing the cover thickness for construction on expansive subgrades.

2 FULL SCALE FIELD TRIAL DETAILS

The trial included different sections with different geogrid and gravel combinations. Each test bed is to be 9.0m (length) × 4.85m (width). The main sections for this study are the control section (no reinforcement), single reinforced section and double reinforced section. Pressure cells were installed on top of the subgrade to measure the effect of geogrid stabilization/reinforcement and stiffening (Figure 1).
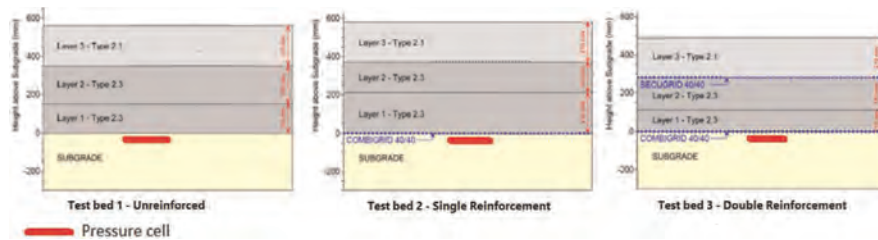
Figure 1.   Test cross sections.

The field was open to local traffic for at least 3 years to make sure the gravel-geogrid interaction and activation of geogrid is occurred. Measurements were conducted after 3 years and results of unreinforced, single reinforced and double reinforced sections were compared to each other.

Geotechnical investigations have shown a black silty clay subgrade with hi plasticity (PI = 86%) with soaked CBR of 2% and CBR swell of 5%. After excavation of the subgrade to the required level, onsite testing was conducted on the subgrade to measure the in-situ subgrade properties. These included DCP, Panda test, FWD and Static Plate Load Test according to DIN 18134:2012-04 (Figure 2). After installing gravel layers, Plate Load Testing was also conducted on top of every granular layer for each section.

Figure 2.   Subgrade preparation and testing.

To monitor the long-term performance of benefit of geogrid reinforcement in single and double reinforced sections, pressure cells were installed during the project and monitored beyond project completion. A total of three test beds were instrumented with pressure cells.

To isolate the study to the effect of geogrid only and provide separation between subgrade and granular layer for all sections, a laid and welded biaxial geogrid-geotextile composite with textured surfacing and with the geotextile integrated between geogrid bars was installed at the subgrade level for reinforced sections and a separation nonwoven geotextile was installed on the subgrade for unreinforced (control) sections. Subbase layers were placed and compacted according to standard installation practice to achieve minimum 98% compaction. Gravel used was type 2.3 according to QLD TMR specification MRTS04 (2021). The thickness of the gravel layer was checked and measured for each subbase layer. Where a second reinforcement layer was planned, a laid and welded biaxial geogrid with structured surfacing was used. A 40mm thin asphalt surfacing was placed and compacted on top of the base course layer. The road was then opened to the public local traffic. Figure 3 shows the placement and compaction of the materials.

Figure 3.   Installation of pressure cell, geocompsoite, geogrid, gravel and asphalt.

After 3 years of local trafficking, a full load water truck was used to apply pressure on the road surface in sections with no reinforcement, single reinforcement and double reinforcement. The water truck stayed on top of the pressure cell point for few minutes, so the pressure cell could have enough time to measure the transferred pressure to the subgrade. The data collecting intervals of the pressure cell was also reduced to few seconds for the time period of the testing. To be able to measure the pressure accurately and apply the load directly on the pressure cell, the exact location of pressure cells was determined and marked on the road surface using a Ground Penetrating Radar (GPR) system.

3   RESULTS & DISCUSSION

3.1   *Strain modulus*

Test result from in-situ Plate Load Testing during construction showed that the improvement in the strain modulus E_{v2} is higher in section with double reinforcement even with a thinner gravel layer compared to section with single reinforced, and both are higher than the unreinforced control section. The improvement has been calculated as E_{V2} on the top of the base layer for each section divided by E_{V2} of subgrade only. Figure 4 shows the results of these test sections.
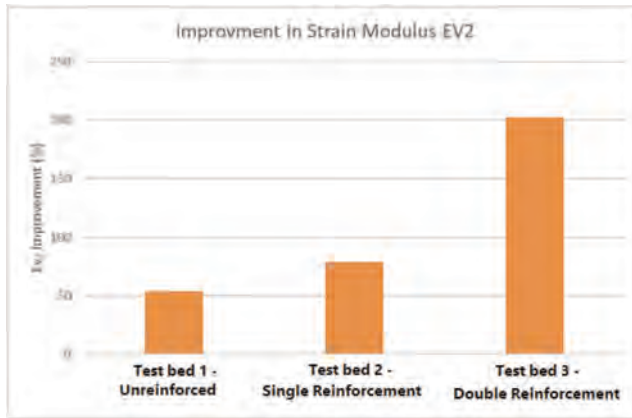
Figure 4. Percentage of increase in Ev2 for different sections.

Results clearly showed that inclusion of one geogrid increases the strain modulus (E_{v2}) v.s. the unreinforced section, and the double reinforcement can increase the strain modulus even more compared to single reinforcement.

3.2 Subgrade deformation

The results from the pressure cell measurements after 3 years were also analysed for the above sections. Results clearly showed that a single reinforcement performed better than unreinforced section, and double reinforcement performed better than single reinforcement in terms of reducing the vertical stresses transferred to the subgrade even with a bit less gravel thickness. This can be due to the better load distribution because of the presence of the geogrid, especially in the double reinforced section compared to the single reinforced section. This can lead to less vertical deformation of the subgrade and longer service life of the pavement in the double reinforced section compared to the single reinforced section. On the
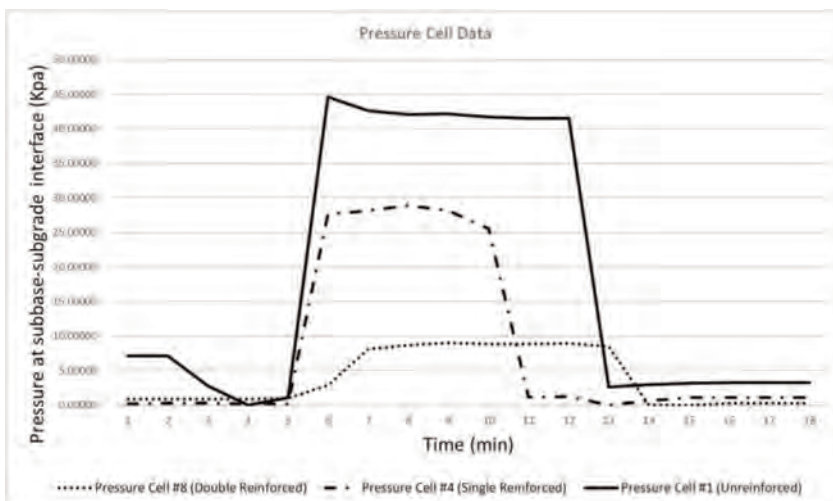
Figure 5. Pressure transferred to the subgrade for different sections.

other hand, the reduction in the vertical stress was higher for double reinforced section with thinner gravel compared to single reinforced and unreinforced sections. This means by using a double reinforcement, the thickness of the pavement can be reduced and still the same or better performance can be achieved.

3.3 *Controlling longitudinal cracks over expansive subgrade*

To study the 'stiffening' effect of the geogrid in controlling the cracks caused by expansive subgrade shrinkage and swell, a single reinforced section was considered between two double reinforced sections in the full-scale field trial to be studied along with the control section with no reinforcement. All sections had the same thickness and subgrade conditions. The single reinforced section had only one layer of geogrid-geotextile composite at the subgrade layer while the double reinforced sections had an extra geogrid within the granular layer. The same geogrid and geocomposite used in other sections were used here. After 3 years under local traffic, longitudinal cracks had developed in the section with no reinforcement. The sections with single and double reinforcement had no cracks on the surface. There was a minor crack in the section with single reinforcement, which was more towards the edge of the cross section in the longitudinal joint with the other road lane. Even this minor crack in the single reinforced section was stopped when reached to the double reinforced sections. Figure 6 shows then results.

Figure 6. Performance of unreinforced (left photo) vs single reinforced and double reinforced sections (right photo) on expansive subgrade.

4 CONCLUSION

In order to quantify the effect of geogrid stabilisation/reinforcement, a full-scale pavement field trial was established upon a soft and expansive subgrade. Sections with variable geogrid arrangements were constructed including control section with no geogrid, single reinforced section with on layer of geogrid-geotextile composite at the subgrade-subbase interface, and double reinforced sections with additional geogrid within the pavement between subbase and base layers. An analysis of the first 3 years of monitoring of this full-scale field trial was conducted. The data demonstrated that the inclusion of geogrids successfully improves the bearing capacity of the pavement profile by reducing the traffic imparted vertical pressures being exerted up-on the underlying materials. The results also demonstrated that inclusion of one geogrid increases the strain modulus (E_{v2}) v.s. the unreinforced section, and the double reinforcement can increase the strain modulus even more compared to single reinforcement. In addition, long term monitoring of longitudinal cracks due to the expansive nature of subgrade shows that the additional geogrid layer within the granular pavement between

subbase and base (stiffening geogrid) can successfully control the longitudinal cracks due to swell-shrinkage of the expansive soil.

REFERENCES

Anderson, P. & Killeavy, M. (1989). Geotextiles and Geogrids: Cost Effective Alternate Materials for Pavement Design and Construction. *Proceedings of the Conference Geosynthetics '89* (pp. 353-360). San Diego, CA, USA.

Barker, W.R. (1987). Open-Graded Bases for Airfield Pavements, Technical Report GL-87-16, USAE Waterways Experiment Station, Vicksburg, MS, USA, 76 p.

Barksdale, R. D., Brown, S. F., & Chan, F. (1989). *Potential Benefits of Geosynthetics in Flexible Pavement Systems (National Cooperative Highway Research Program Report No. 315)*. Washington, DC, USA: Transportation Research Board, National Research Council

Berg, R. R., Christopher, B. R., & Perkins, S. W. (2000). *Geosynthetic Reinforcement of the Aggregate Base/ subbase Courses of Flexible Pavement Structures (GMA white paper II)*. Roseville, MN, USA: Geosynthetic Materials Association.

DIN 18134, German Institute for Standardisation (2012). *Soil-testing Procedures and Testing Equipment - Plate Load Test (DIN 18134)*. Retrieved from https://infostore.saiglobal.com/en-au/standards/din-18134-2012-413157_saig_din_din_935116

Haas R., Walls, J., & Carroll, R.G. (1988). *Geogrid Reinforcement of Granular Bases in Flexible Pavements (Transportation Research Record 1188)*, 19-27. Retrieved from http://onlinepubs.trb.org/Onlinepubs/trr/1988/1188/1188-002.pdf

MRTS04, 2021. Technical Specification MRTS04 General Earthworks, QLD Transport and Main Roads Specifications (TMR), December 2021.

Perkins, S.W., Christopher, B.R., Thom, N., Montestruque, G., Korkiala-Tanttu, L. and Watn, A. Geosynthetics in Pavement Reinforcement Applications, *Proceedings of the 9th International Geosynthetics Conference*, Vol. 1, pp. 165-192, Guaruja, Brazil, May, 2010.

Roodi, G. H., and J. G. Zornberg. 2020. Long-Term Field Evaluation of a Geosynthetic-Stabilized Roadway Founded on Expansive Clays. *Journal of Geotechnical and Geoenvironmental Engineering*, © ASCE, ISSN 1090-0241, 05020001-1 - 05020001-17.

Roodi, G. H., J. R. Phillips, and J. G. Zornberg. 2016. Evaluation of Vertical Deflections in Geosynthetic Reinforced Pavements Constructed on Expansive Subgrades. In *Proc., 3rd Pan-American Conf. on Geosynthetics*, 1970–1987. St. Paul, MN: Industrial Fabrics Association International.

Zornberg, J. G. 2017a. "Functions and Applications of Geosynthetics in Roadways: Part 1." Procedia Eng. 189 (Jan): 298–306. https://doi.org/10.1016/j.proeng.2017.05.048.

Zornberg, J. G. 2017b. Functions and Applications of Geosynthetics in Roadways: Part 2. In Geosynthetics, 34–40. Roseville, MN: Industrial Fabrics Association International.

Zornberg, J. G., J. A. Prozzi, R. Gupta, R. Luo, J. S. McCartney, J. A. Z. Ferreira, and C. Nogueira. 2008. *Validating Mechanisms in Geosynthetic Reinforced Pavements*. FHWA/TX-08/0-4829-1. Austin, TX: Texas DOT.

Zornberg, J. G., J. A. Z. Ferreira, R. Gupta, R. V. Joshi, and G. H. Roodi. 2012. *Geosynthetic-reinforced Unbound Base Courses: Quantification of the Reinforcement Benefits*. FHWA/TX-10/5-4829-1. Austin, TX: Texas DOT.

Delay of crack propagation in 4PB test of double-layered geocomposite reinforced asphalt concrete beams

P. Jaskula, D. Rys, M. Stienns & C. Szydłowski
Faculty of Civil and Environmental Engineering, Gdańsk University of Technology, Gdańsk, Poland

M. Golos
Tensar International Limited, Blackburn, Lancashire, UK

J. Kawalec
Tensar International s.r.o., Cesky Tesin, Czech Republic

ABSTRACT: Geosynthetic reinforcement of asphalt layers has been used for almost several decades but to this day a proper evaluation of influence of these materials on pavement fatigue life is still challenging task, especially for new types of geogrids composites. This paper presents the evaluation of fatigue performance of large sized asphalt concrete beams reinforced with new type of geogrid composite in which hexagonal (multiaxial) polypropylene stiff monolithic paving grid with integral junctions is bonded to the polypropylene non-woven paving fabric. Non reinforced samples were used as a reference. Fatigue testing was performed in the scheme of four-point bending test (4PB-PR) in the controlled strain mode at the constant temperature of +13°C and frequency of 1Hz. The specimens width (170 mm) was selected on the assumption that asphalt layers should cover at least 2 full hexagon pitches of multiaxial geogrid. The distance between axes of the end supports equalled to 740 mm. The distance between axes of the loading supports equalled 247 mm. Test results were analysed in several aspects, including the standardized approach based on stiffness reduction but also with the use of critical strain at one million cycles. The effect of the notch on the fatigue life and the ability of the reinforcement to crack propagation delay was also analysed. Based on the ε_6 critical strain, reinforced samples result in an increase of the critical strain from 30% (notched) to 40% (un-notched).

1 INTRODUCTION

Reinforcement of asphalt with use of geosynthetics is still a globally application where practice is ahead of science. Number of successful installations followed by improvement of asphalt pavements over time reported by various authors [Brown 1985; Canestari *et al*. 2015; Correia 2014; Pasquini *et al*. 2013] are sometimes compared with cases where geosynthetic inclusion did not provided expected performance improvement to the pavement. Mechanism of asphalt reinforcement was subject of research by [Al-Qadi 2006; Graziani *et al*. 2014; Ragni *et al*. 2020; Zieliński 2013; Zofka *et al*. 2017]. This paper is presenting results of implementation of recently developed geocomposite with multiaxial geogrid into double-layered asphalt beams and its impact on delay of fatigue performance under cycled loads. As cracking occurring at the bottom of asphalt layers significantly reduces the fatigue life [Mackiewicz 2013; Spadoni *et al*. 2021], analyzes of the double-layer system with inclusion of a notch were also carried out.

2 MATERIALS USED AND SAMPLES PREPARATION

2.1 Asphalt concretes

Two asphalt concretes were used in this study: bottom layer made of asphalt concrete AC 11 W 35/50 for levelling course, upper layer made of asphalt concrete AC 16 W 35/50 for binder course. Both mixtures were designed and produced in accordance with the European standard EN 13108-1 and the Polish technical guidelines WT-2:2014 for medium traffic load (for the range of 500,000 to 7,300,000 of 100kN ESALs). The mineral mixtures were composed of limestone filler and crushed gneiss/granite fine and coarse aggregate. Neat bitumen classified as 35/50 according to EN 12591 standard was used as a binder.

2.2 Geocomposite with multiaxial geogrid

AX5-GN geocomposite interlayer contains two components, i.e. (1) multiaxial (hexagonal) paving grid with integral junctions bonded to (2) a polypropylene non-woven paving fabric. Unit weight of the grid component is approximately 210 g/m^2. The unit weight of the fabric component is 130 g/m^2. Geocomposite was developed and produced by Tensar International Ltd., Blackburn, UK. Geocomposite interlayer AX5-GN is presented in Figure 1.

The grid is oriented in three directions. The size of hexagon pattern of the hexagonal grid has the nominal value of 80 mm. A geogrid performs the structural reinforcement function (R) of the asphalt interlayer. A geocomposite uses a non-woven fabric that acts as a bonding layer during installation. A non-woven fabric, after installation and saturation with bitumen, also acts as a SAMI layer, which means that it provides a stress relief function (STR). Another functions of the bitumen saturated non-woven fabric is a moisture interlayer barrier (B).
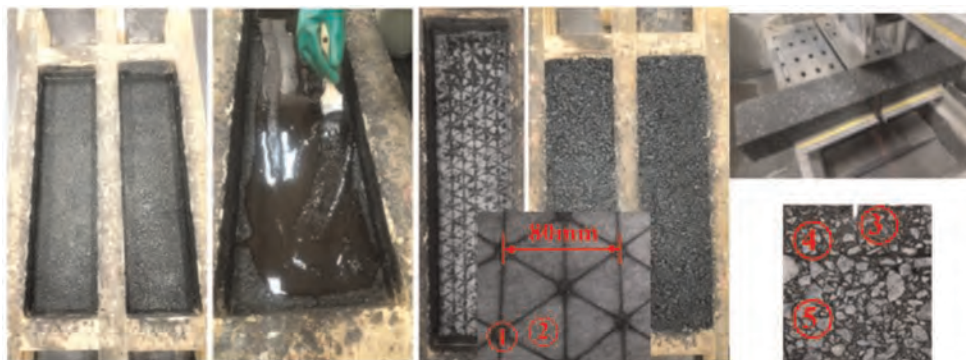
Figure 1. View of the double-layer sample preparation process and notching of beams with circular saw and the view of the middle part of the beam with a cut notch (sample inverted as it was positioned into the 4PB device), 1 – multiaxial (hexagonal) grid, 2 – polypropylene non-woven fabric, 3 – notch 2 × 10 mm, 4 – AC11W, 5 – AC16W.

2.3 Bitumen emulsion

Bitumen emulsion was used as a tack/bond coat for the layer interfaces. The direct shear test method proposed by Leutner was used to assess the interlayer adhesion of asphalt layers.

Based on the previous test results [Jaskula et al. 2021], the following types and amounts of bitumen emulsion for further testing was selected as the most optimal: C69 B3 PU (bitumen emulsion for surface treatments, bitumen content 69%) in quantity of 1.2 kg/m^2 (residue bitumen) for reinforced systems, C60 B3 ZM (bitumen emulsion for layer interfaces,

bitumen content 60%) in quantity of 0.2 kg/m^2 (residue bitumen) for non-reinforced systems. The higher value of the asphalt emulsion in the case of using a geocomposite results from the need to completely infiltrate the non-woven fabric with bitumen. Emulsions for layer interfaces (ZM) were produced from 70/100 bitumen, while emulsions for surface treatments (PU) were produced from 100/150 bitumen.

For the reinforced specimens, shearing failure always occurred at the interface between fabric and the lower asphalt layer and no debonding of the composite was observed, which proves good internal integration of the composite with upper asphalt layer. Introduction of reinforcement composite resulted in 75% reduction of inter-layer bond strength as compared to specimens without reinforcement from 1.5 MPa to 0.4 MPa.

2.4 Samples preparation

The specimens prepared for laboratory testing consisted of two layers of asphalt concrete (AC). They were bonded with bitumen emulsion applied as a tack/bond coat. Reference samples (in which two asphalt layers were used with no reinforcement) and reinforced samples (in which a multiaxial AX5-GN geocomposite was installed in between two asphalt layers) were prepared. The double-layer prismatic specimens preparation process is depicted in Figure 1. They contain the main steps, as: production of timber forms with internal dimensions of 240 × 135 × 1000 mm; laying and compacting of the bottom AC11W asphalt layer (compaction temperature 135 ± 5°C), up to a height of 45 mm after compaction; application of a tack coat of selected bitumen emulsion; installation of composite asphalt interlayer (if applicable); laying and compacting of the upper AC16W asphalt layer (compaction temperature 135 ± 5°C), up to a height of 90 mm after compaction; cutting the test beam from the compacted sample to the final sample with dimensions of 170 × 100 × 850 mm. The final AC11W levelling course thickness of 30 mm and AC16W binder course thickness of 70 mm was obtained. Standard Wacker Neuson walk-behind roller RS 800A was used to compact specimens. The beam samples were notched (2 mm width x 10 mm depth) in the middle of their span, using a high precision notching (circular) saw.

3 METHODOLOGY OF FATIGUE TESTING

3.1 Four-point bending scheme

Fatigue testing was performed in the scheme of four-point bending test (4PB-PR). To reflect actual working conditions of the pavement, the specimens used for a test were significantly larger than those recommended in typical procedures of the fatigue testing: 850 × 170 × 100 mm.

The assumption that the width of the reinforcement placed between asphalt layers must cover at least 2 full hexagon pitches of multiaxial geogrid resulted in a sample width of 170mm.

The test was performed in a climatic chamber at a constant temperature of +13°C, which is the equivalent temperature adopted in the design of flexible pavements in Poland. The scheme of the 4PB test configurations is presented in Figure 2.

Two sets of double-layered beam specimens were used in the 4PB fatigue test: without and with a notch. Fatigue tests on specimens without notches were performed to determine fatigue curves and compare fatigue characteristics of the reinforced systems against systems without reinforcement. Notches were introduced to initiate cracking, thus enabling monitoring of its propagation based on changes in stiffness of the tested systems as well as assessment of the effect of reinforcement on inhibition of crack propagation in asphalt overlay.
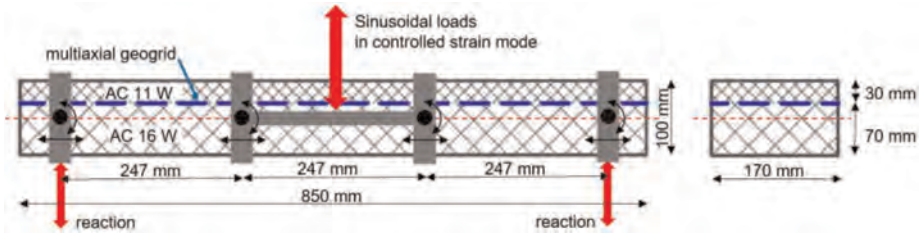
Figure 2. Scheme of the 4PB test configuration.

Beams were exposed to cyclic loading that caused a sinusoidal change in horizontal strain from 0 to the predetermined maximum value equal to 400, 500, 600, 700 and 800 μstrain. A single specimen was tested for each combination of parameters: presence of composite reinforcement of multiaxial geogrid, notching and strain value. Bending was applied in one direction only, and in combination with inverted position of the specimen, the reinforcement functioned in the tension zone. The loading frequency was 1 Hz. The maximum number of applied loading cycles was limited to 300,000, which resulted in a maximum testing time of 84 h per test [Jaskula *et al*. 2021, 2022].

3.2 *Metodology of fatigue life evaluation*

During the fatigue testing in the controlled predetermined strain mode, a gradual decrease in the stiffness modulus of asphalt mixtures occurs during the following load cycles.

The obtained results were analysed in terms of the number of cycles to failure, fatigue curves, strain at one million load cycles and observation of crack delay. A detailed description of monitored parameters is given below [Jaskula *et al*. 2021, 2022]. Stiffness in any given cycle may be calculated from Equation 1:

$$S_i = \frac{\sigma_i}{\varepsilon}$$

(1)

where S_i = stiffness in the i-th cycle of the test; σ_i = maximum tensile stress in the i-th cycle; and ε = maximum strain of the extreme tension fibres of the cross section (constant for controlled strain mode across all cycles).

Fatigue life N_f is a number of cycles required to achieve fatigue failure of the specimen. The most common definition of fatigue failure is the moment when the stiffness S_i is reduced by 50% in comparison of the initial stiffness S_{ini}, measured at 100th cycle.

Fatigue curve is determined by the N_f fatigue life results achieved at various strain levels. The curve enables to estimate fatigue life of the system at any assumed strain level (also outside of the tested range). The general form of the equation of the curve is as follows (Equation 2):

$$\varepsilon = A\left(N_f\right)^b$$

(2)

where ε = tensile strain; A = slope of the fatigue curve; b = coefficient based on the obtained fatigue test results and N_f = fatigue life of the system.

Critical strain at one million load cycles ε_6 means a parameter based on the fatigue curve, equivalent to strain at which fatigue life of the system is one million load cycles. This parameter is used to characterise asphalt mixtures in terms of fatigue resistance. High value of the ε_6 strain indicates better fatigue properties of the mixture (or the entire tested layered system) in comparison with the low ε_6 value.

4 TEST RESULTS

4.1 *Fatigue life evaluation*

For specimens reinforced with geocomposite interlayers, it is visible that the decrease in stiffness modulus in the first phase is more rapid due to lower interlayer bonding. During second phase it is lower compared to reference systems, due to reinforcement. The effect is shown in Figure 3a. In case of inclusion of initial crack, the failure of the system occurs faster in comparison to the plain samples (Figure 3b). Parameters ε_6 were calculated based on fatigue curves and marked in Figure 4. The fatigue models were calculated with the least-square method, and they are presented in Figure 4 as well. Based on equations given in Figure 4, fatigue life can be extrapolated for level of strain, which occur in pavement structure, what is obviously related with some uncertainty.
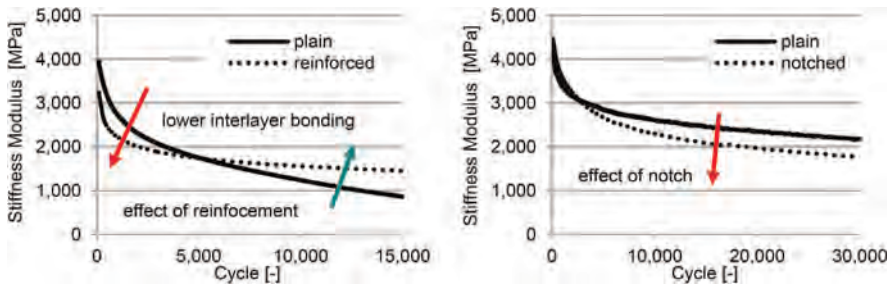
Figure 3. A – schematic influence of reinforcement on fatigue characteristic of un-notched samples, B – schematic influence of inclusion of crack on fatigue characteristics.
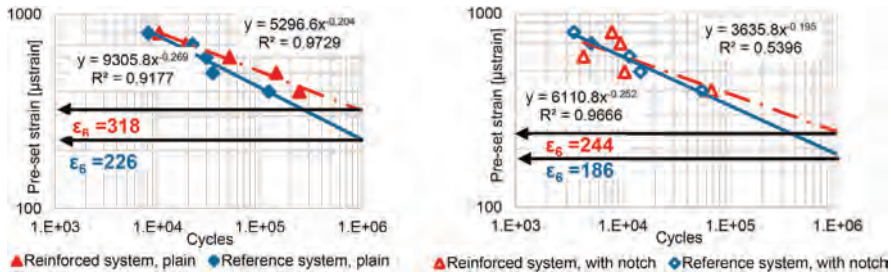
Figure 4. Fatigue model diagrams obtained from the four-point bending test of systems without reinforcement and reinforced with geocomposite of multiaxial geogrid for plain samples: A – samples without notch, B – samples witch notch.

Reinforcement with composite results in an increase in the critical strain by 40% compared to unreinforced systems in case of un-notched specimens. Inclusion of initial crack resulted in decreasing ε_6 parameter in both systems, but it is still clearly noticeable that reinforced system increases in the critical strain by 30%.

4.2 *Delay of crack propagation for notched samples*

A phenomenon of a subsequent flattening of the stiffness curve slope for systems reinforced with geocomposite, which indicates that the process of crack development was relieved, was generally observed. The course of recorded changes in stiffness was compared with the

appearance of cracks in the samples after testing procedure. Images of cracks were presented in Table 1, in order to ensure the visibility of the progressing of the cracks their shapes were marked and highlighted in red.

In the case of systems reinforced with geocomposite, the bitumen saturated fabric starts to dissipate the stresses generated nearby the crack. Inhibition of crack propagation was observed in samples subjected to strain levels of 400, 500 and 600 µstrains, as was depicted in Table 1, hence the composite prevented crack propagation from the lower asphalt layer to the upper asphalt layer for the strain level equal to 600 µstrains. In case of the highest strain levels, i.e., 700 and 800 µstrains, the cracks propagated through the composite interlayer and then into the upper layer. It is suggested, based on the failure mechanism, that a local loss of an inter-layer bonding at the asphalt-composite-asphalt interface would appear. It would lead to the re-initiation of the cracking at the bottom of the upper asphalt layer. Nonetheless, no rupture of the geocomposite components was detected.

Table 1. A comparison of photographs of notched samples after fatigue testing with highlighted cracks.
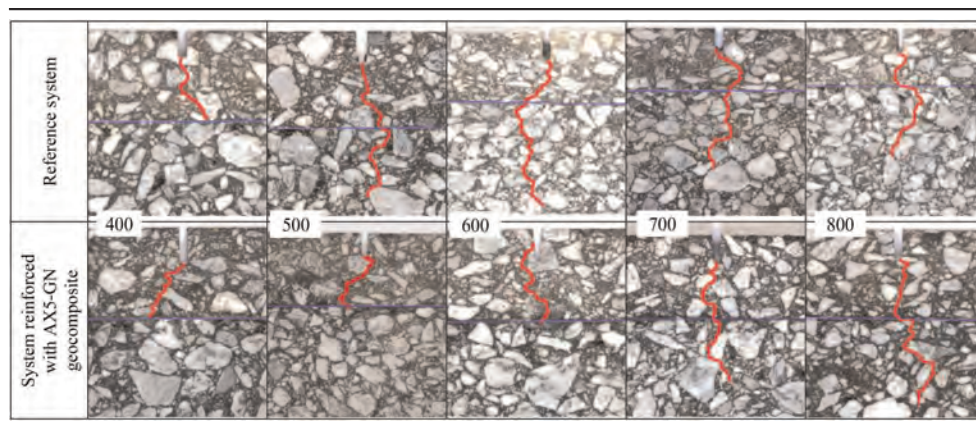
5 CONCLUSIONS

Based on the analysis of the results of the performed fatigue tests carried out on the unreinforced beam samples and samples reinforced with the geocomposite of multiaxial geogrid, the following conclusions can be formulated:

- Enhancing the pavement with the geocomposite noticeably increases its fatigue life. This relative increase strongly depends on the level of horizontal tensile strain at the bottom of the asphalt overlay.
- The effect of asphalt reinforcement is more beneficial in case of new pavements with thick asphalt layers, where one can expect lower tensile strains at the bottom of these layers and fatigue cracks have not been initiated yet. This has been simulated by the tests carried out on plain samples. An increase in ε_6 up to 40% can be achieved, when compares to the control system.
- The effect of asphalt reinforcement is less beneficial in case of rehabilitated pavements, where fatigue cracks have been initiated yet and one can expect higher tensile strains at the bottom of asphalt layers. This process has been simulated by the tests carried out on notched samples. An increase in ε_6 parameter up to 30% can be achieved, when compares to the control system.

- A slight decrease in the initial stiffness modulus of the reinforced systems, as an effect of a reduction in interlayer shearing strength was observed and thus differential movement between asphalt overlay and composite can be expected. However, a 'control de-bonding mechanism' supposed to be a positive effect that provides the function of stress relief as well as SAMI function, created by the bitumen saturated fabric.
- An application of a composite of multiaxial geogrid in the asphalt pavement will significantly delay the occurrence of fatigue cracking and thus extend the pavement durability.

REFERENCES

Al-Qadi, I. L. 2006. Pavement Interlayer System Mechanisms: Separation, Reinforcement, and Reflective Cracking Control. *Chinese Society of Pavement Engineering* (p. 73). Taipei, Taiwan.

Brown, S. F. 1985. Polymer Grid Reinforcement of Asphalt. *Journal of Asphalt Paving Technology*, 54, 18–41.

Correia, N. de S. 2014. *Performance of Flexible Pavements Enhanced Using Geogrid-reinforced Asphalt Overlays*. University of Sao Paulo, Brasil.

Canestrari, F., Belogi, L., Ferrotti, G., & Graziani, A. 2015. Shear and Flexural Characterization of Grid-reinforced Asphalt Pavements and Relation with Field Distress Evolution. *Materials and Structures*, 48(4), 959–975.

Graziani, A., Bocci, E., & Canestrari, F. 2014. Bulk and Shear Characterization of Bituminous Mixtures in the Linear Viscoelastic Domain. *Mechanics of Time-Dependent Materials*.

Jaskula, P., Rys, D., Stienss, M., Szydlowski, C., Golos, M., & Kawalec, J. 2021. Fatigue Performance of Double-Layered Asphalt Concrete Beams Reinforced with New Type of Geocomposites. *Materials*. MDPI, April 2021.

Jaskula, P., Rys, D., Stienss, M., Szydlowski, C., Golos, M., & Kawalec, J. 2022. Laboratory Fatigue Assessment of Large Geocomposite-reinforced Double-layered Asphalt Concrete Beams. *Eleventh International Conference on the Bearing Capacity of Roads, Railways and Airfields*, Trondheim, Norway.

Mackiewicz, P. 2013. Fatigue Tests of Bituminous Mixtures with Inclusion of Initial Cracks. *Journal of Materials in Civil Engineering*. 25. 140–147.

Pasquini, E., Bocci, M., Ferrotti, G., & Canestrari, F. 2013. Laboratory Characterisation and Field Validation of Geogrid-reinforced Asphalt Pavements. *Road Materials and Pavement Design*, 14(1), 37–41.

Ragni, D., Montillo, T., Marradi, A., & Canestrari, F. 2020. Fast Falling Weight Accelerated Pavement Testing and Laboratory Analysis of Asphalt Pavements Reinforced with Geocomposites. *Lecture Notes in Civil Engineering*, 48(May), 417–430.

Spadoni, S., Ingrassia, L. P., Paoloni, G., Virgili, A., & Canestrari, F. 2021. Influence of Geocomposite Properties on the Crack Propagation and Interlayer Bonding of Asphalt Pavements. *Materials*, 14(5310), 1–18.

Zieliński, P. 2013. Investigations of Fatigue of Asphalt Layers with Geosynthetics. *Archives of Civil Engineering*, 59(2), 247–263.

Zofka, A., Maliszewski, M., & Maliszewska, D. 2017. Glass and Carbon Geogrid Reinforcement of Asphalt Mixtures. *Road Materials and Pavement Design*, 18, 471–490.

Experimental study on rainwater infiltration countermeasures by reinforcing base course with geotextile

Mei Akimitsu, Kenichi Sato, Takuro Fujikawa & Chikashi Koga
Department of Civil Engineering, Fukuoka University, Fukuoka, Japan

Yuichiro Wakabayashi & Fuminori Aono
Kiso-Jiban Consultants Co. Ltd, Tokyo, Japan

Masaru Shimazaki & Kazunari Hirakawa
Taisei Rotec Corporation, Tokyo, Japan

Junichi Hironaka, Sousuke Kimura & Kazunari Suzuki
Mitsui Chemicals Industrial Products Co. Ltd, Tokyo, Japan

Yusaku Isobe
IMAGEi Consultant, Tokyo, Japan

ABSTRACT: Asphalt pavements lose their bearing capacity when rainwater infiltrates the base course through cracked and damaged areas in the surface course and binder course. The decrease in base course bearing capacity causes progressive damage because of base course deformation, resulting in early deterioration of the entire pavement structure. Major pavement repairs have been limited to cutting overlays because the cost of pavement maintenance and repair notably drops with increased road stock volume. Thus, an experimental study was conducted to improve the base course durability of asphalt pavement by laying geotextiles to extend the long life of road pavements. As a result, geotextile was found to suppress the reduction of base course bearing capacity even when rainwater infiltrated the pavement.

1   INTRODUCTION

The durable setup life of major national roads and other roads in Japan is 10–15 years. However, asphalt pavements that deteriorate prematurely are increasing because of the increased number of large traffic vehicles and extreme weather conditions. Pavement repair to extend service life necessitates repair work up to the base course layer. Despite the need for costs related to pavement maintenance and repair as the pavement stock increases, the budget for road maintenance and repair is decreasing year by year, along with rising social security costs because of a declining birthrate and an aging population. Therefore, economical and efficient maintenance and management methods are required. Repair work, including a base course, is remarkably more than three times more expensive and four times longer than cutting overlay. Drastic repairs are also difficult to carry out on major national roads and highways in service because of high traffic volumes and strict traffic restrictions.

The general pavement structure of asphalt pavements comprises a lower base course, upper base course, binder course and surface course laid at a specified thickness from the subgrade top, depending on the subgrade strength. Although this structure provides a load-dispersing effect and keeps the road pavement sound, asphalt pavements are thought to

deteriorate over time, rainwater seeps through cracks and pavement joints, and the entire pavement structure begins to deteriorate prematurely because of the reduced bearing capacity of the base course. Therefore, maintaining a sound base course is a key issue that will be essential in the future for extending the service life of pavements and building a sustainable society.

In recent years, research and development have focused on base course reinforcement, especially the reinforcement of base courses using geotextiles (Zomberg *et al.* 2018). Geotextiles are important materials used in constructing soil structures and serve as tensile reinforcement (Takahashi *et al.* 2008; Yamauchi 1986). These have been used in pavement construction in Japan as a countermeasure for the soft base course in road pavements (Hirao *et al.* 1992). However, only a few instances exist in which geotextiles have been used to reinforce base courses. Thus, research on the application of geotextiles to base courses has received much attention. Hirakawa *et al.* (2014) showed that even a single layer of geogrid in the base course can significantly reduce the amount of residual subsidence. They also discovered that when combined with a highly dense base course, progressive residual settlements could be effectively restrained.

In this report, the effects of reinforcing the base course with geotextiles were investigated to understand (1) the effects of soil material and (2) the geotextiles on base course reinforcement during rainwater seepage. The results of constant strain loading tests on the effect of geotextiles laid in a model ground on the bearing capacity characteristics of the base course, which were conducted using a small soil tank test apparatus and two types of geotextiles of different geometries, were presented.

2 EXPERIMENTAL PROCEDURE

2.1 *Experimental materials*

Decomposed granite and crushed stones (C-20) were used as experimental samples. The grain size additive curves are shown in Figure 1. The geotextiles used woven fabrics and triaxial geogrids. An overview of the 2 types of geotextile is presented in Table 1. Woven fabrics are used primarily to improve bearing capacity in soft roadbeds. It is a particularly
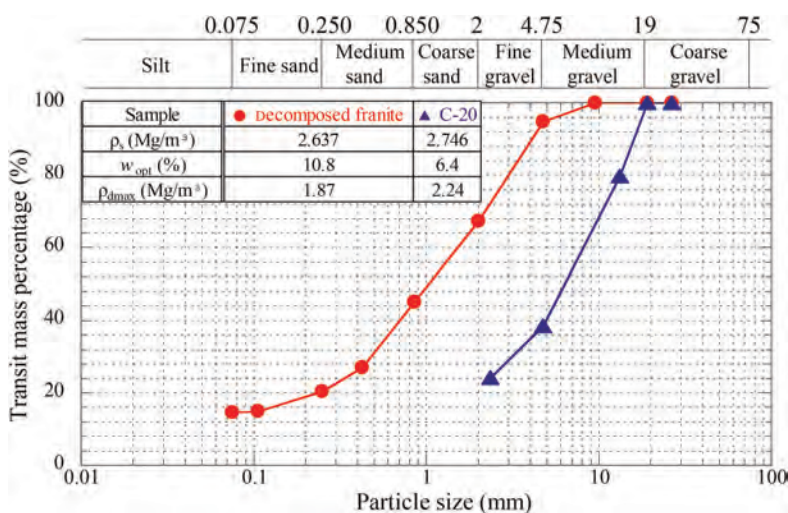
Figure 1.   Grain size accumulation curve.

Table 1. Overview of the geotextiles.

Reinforcement	Woven fabric	Geogrid
Photo		
Tensile strength (kN/m)	89.0	10.0
Wastewater volume (l/min/m²)	3055.5	—

high strength material that combines reinforcement, separation, and drainage. Whereas, geogrid is a reinforcing material with a three-directional stretched shape and excellent restraint effect by interlocking with granular base course material.

2.2 Experimental method

A small soil tank, 90 cm high, 120 cm wide, and 20 cm deep, was used in this study. A schematic diagram of the experimental apparatus is shown in Figure 2. The loading plate was 10 cm wide, 19.8 cm deep, and 2.2 cm thick. A spring (spring constant $k = 3.75$ kN/mm) and plate were placed at the bottom of the small soil tank to determine the base course deformation because of loading. Here, the spring stiffness was set to the maximum strength at which the model ground was not deformed by the dead weight of the soil to be loaded. The model ground was prepared by the tamping method with a thickness of 30 cm under a specified compaction control by density, with the initial water content of the soil sample adjusted. Two layers of 10 cm thickness (1st and 2nd layer) each were compacted in the lower 20 cm of the model ground, and two layers of 5 cm thickness (3rd and 4th layer) were compacted in the upper 10 cm of the model ground to allow geotextiles to be laid at
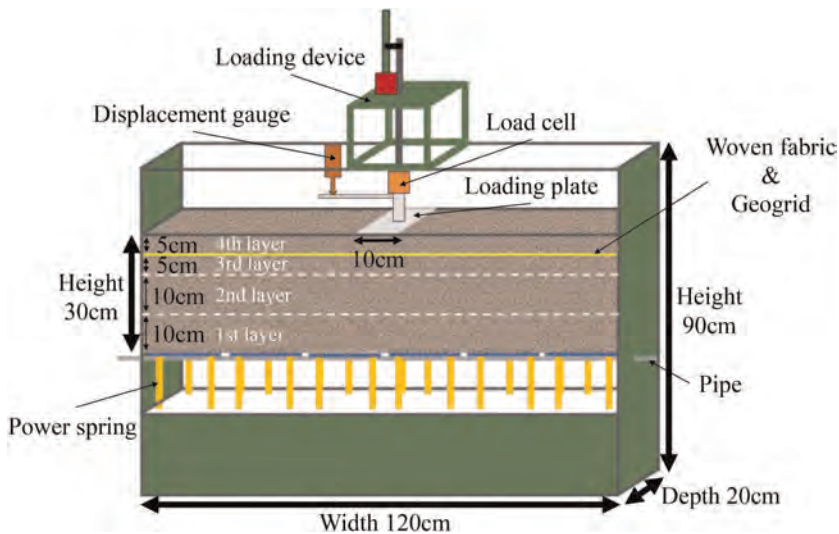
Figure 2. Schematic diagram of the experimental apparatus.

shallower depths. Constant strain loading was carried out with a displacement of 50 mm at a rate of 1 mm/min as the termination condition to determine the characteristics of the base course bearing capacity. In addition, water was sprinkled from the top of the model ground before loading to understand bearing capacity behavior because of rainwater. Water was sprinkled by misting the top 5 cm of the geotextile, and the water content increased by 4% after sprinkling water.

2.3 *Experimental conditions*

The experimental conditions are listed in Table 2. In this study, the method of preparing the model ground differed depending on the sample, with a 95% compaction degree for decomposed granite and 90% for C-20, and the initial water content was set to the optimum water content for both. In addition, the length and depth of the geotextile bedding were standardized.

Table 2. Experimental conditions.

Sample	Initial water content (%)	Degree of compaction (%)	Reinforcement	Laying length (cm)	Laying depth (cm)
Decomposed granite	10.8	95	Unreinforced	–	–
			Woven fabric	120	5
C-20	6.4	90	Geogrid		

3 EXPERIMENTAL RESULTS AND DISCUSSIONS

3.1 *Effect of different soil samples on bearing capacity*

Figures 3(a) and (b) show the loading stress and settlement at the loading plate center from the constant strain loading test. In both soil samples, the loading stress relative to the amount of settlement increased with the geotextile. Here, the ultimate bearing capacity, q_u, is determined from the method of the intersection of the tangent line of the settlement curve at the beginning of the loading with the tangent line of the settlement curve at the end of the loading as shown in Figure 3 (Hirao *et al.* 1992). The ultimate bearing capacity shows that the reinforcing effect of the geotextile is demonstrated regardless of the soil sample.

The results of the bearing capacity reinforcement effect of the geotextile installation, which are calculated as the ratio of the ultimate bearing capacity to the unreinforced ultimate bearing capacity as a percentage increase in bearing capacity, are shown in Figure 4. The effect of support reinforcement by geotextile placement was higher for C-20 than for decomposed granite. This may be due to differences in the frictional and constraining effects of the geotextile because of the differences in grain size width. In addition, when comparing geotextile types for both soil samples, geogrids with lower tensile strength showed higher values than woven fabrics because the geogrids exerted tensile forces in all directions. Thus, the restraining effect was sufficient for crushed stones with large grain sizes, indicating that the bearing reinforcement effect of laying geotextiles was sufficient, irrespective of the geomaterial.

3.2 *Effect of rainwater infiltration on bearing capacity*

In this study, the water was sprinkled from the top of the model ground to assess the base course bearing behavior because of rainwater seepage through cracks in the pavement. Loading tests were conducted using two types of geotextiles and crushed stone (C-20). The
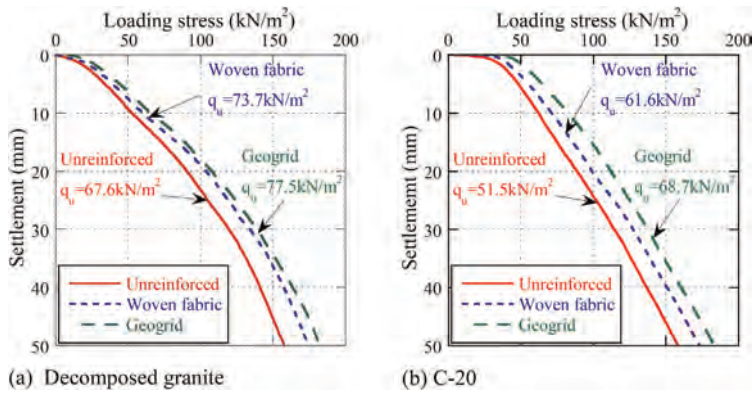
Figure 3. Loading stress and settlement.
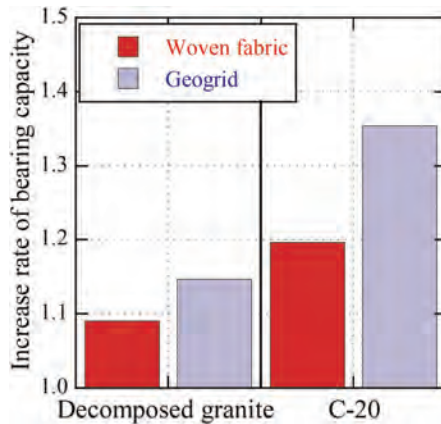
Figure 4. Increase rate of bearing capacity.

loading stress–settlement relationship is shown in Figure 5. As in the case of no sprinkled water, the loading stress relative to the amount of settlement remarkably increased with geotextile laying. Moreover, the effect of sprinkled water on the ultimate bearing capacity is shown in Figure 6. Then, the ultimate bearing capacity remarkably decreased with water sprinkling in both conditions. This may be due to an increase in the degree of saturation of the ground and a decrease in suction because of watering (Figure 7). However, the geotextile-lined ground showed higher values than the unreinforced ground, indicating that geotextiles are effective as a stormwater seepage control measure.

3.3 Understanding bearing capacity behavior over time

In this study, it was assumed that rainwater seeps into the base course and that the seepage water flows down into the ground, and the bearing capacity behavior over time from rainwater seepage was investigated. The experiments were conducted by varying the time between sprinkling water and loading to 0, 6, and 24 h. The effect of the water content state of the model ground because of water sprinkling on the bearing capacity was evaluated by measuring the water content at the end of the loading test. The change in ultimate bearing capacity over time after water sprinkling is shown in Figure 8. Notably, the ultimate bearing
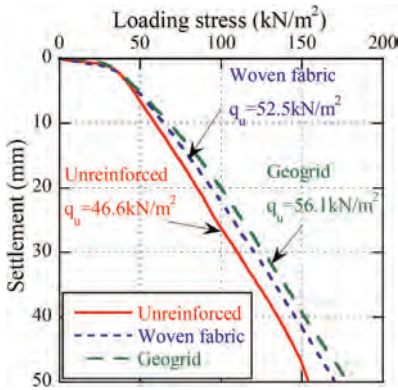
Figure 5. Loading stress and settlement.
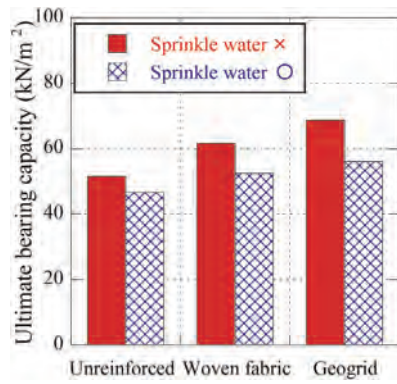
Figure 6. Effect of water infiltration on the ultimate bearing capacity.
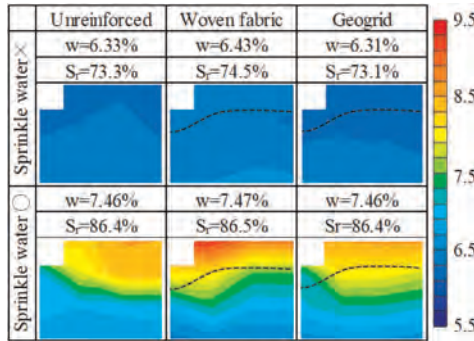
Figure 7. Distribution of water content on water infiltration.

capacity decreased significantly after 6 h of water sprinkling in both conditions and then recovered gradually after 24 h. The geotextile showed a high bearing capacity and recovery because of its reinforcing effect. The water content distribution at the end of the test is shown in Figure 9. The water content was highest at 0 h immediately after water sprinkling, and as
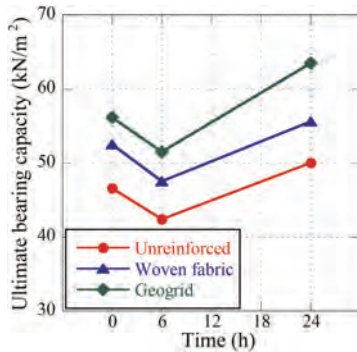
Figure 8. Effect of elapsed time on ultimate bearing capacity.
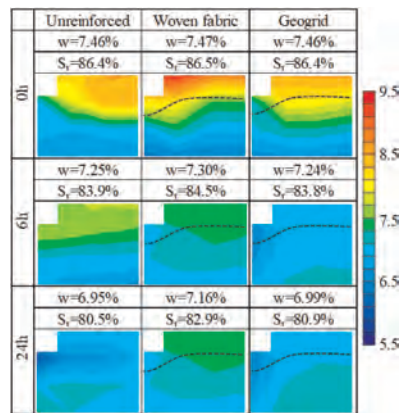
Figure 9. Distribution of water content on elapsed time.

time passed over 6 and 24 h, thecontent decreased as water seeped down into the soil tank. However, the ultimate bearing capacity decreased significantly at 6 h, irrespective of the decrease in water content. This indicates that rainwater seepage through cracks in the road surface largely affects base course bearing capacity, leading to premature pavement degradation. The results also show that geotextile laying is effective in this bearing capacity reduction behavior.

4   CONCLUSIONS

1) The wider the grain size range of the geomaterial and the larger the grain size, the more effective the base course reinforcement by geotextiles.
2) The geotextile's type and shape influence its effectiveness in reinforcing base course bearing capacity.
3) The bearing capacity is once reduced by rainwater seepage, but recovers over time. The reinforcing effect of laying geotextiles is significant, and a high bearing capacity and resilience are demonstrated.
4) The reinforcing effect of geotextile laying on base course bearing capacity results in a longer service life for asphalt pavements.

REFERENCES

Hirakawa, D. & Miyata, Y. (2014). High Stabilization of Asphalt Pavement by Geogrid Reinforcement. *Geosynthetics Engineering Journal* 29, 139–146. (in Japanese).

Hirao, K., Yasuhara, K., Tanahashi, Y., Takaoka, K. & Nishimura, J. (1992). Bearing Capacity Characteristics of Model Soft Ground with Reinforced Geotextilies. *Proceeding of Geotextile Symposium* 7, 1–9. (in Japanese).

Takahashi, Y., Hazama, A., Tachibana, T., Kaneko, K. & Kumagai, K. (2008). Experimental Study on Stability of Reinforced Soil Wall Using a High Strength Geotextile. *Geo-synthetics Engineering Journal* 23, 155–160. (in Japanese).

Yamauchi, T. (1986). Geotextiles, -State of the Art-. *Journal of Japan Society of Civil Engineers* 370(III-5), 27–38. (in Japanese).

Zomberg, J.G., Roodi, H., Sankaranarayanan, S. & Hernandez-Uribe, L. (2018). Geosynthetics in Roadways: Impact in Sustainable Development. *In: Proceedings of the 11th International Conference on Geosynthetics*.

Mechanistic analysis of a pavement with GRC (Geoweb Reinforced Concrete)

J. Schmalbach
Soil Protection, Bogota, Colombia

ABSTRACT: The operation of pavement with GRC (Geoweb reinforced concrete) can be analyzed through a mechanistic methodology of pavement design. This involves modeling the pavement system based on the initial variables, including applied loads, traffic, condition of the subgrade, properties of the concrete, and the Geocell base polymer. To model the pavement, a finite element analysis is used to simulate the behavior of the system. The finite element model can consider the different layers of the pavement, including the subgrade and the GRC layer. The properties of each layer can be specified, including the modulus of elasticity, Poisson's ratio, and thickness. To study fatigue, an analysis of forces and moments is carried out to determine the maximal deformation of the subgrade. The maximum tensile stress in the system is also determined, which is an important factor to understand pavement fatigue. By simulating the behavior of the pavement over time, it is possible to predict the onset of fatigue and determine the expected service life of the pavement. By considering these different variables, it is possible to design a pavement system that is durable, long-lasting, and capable of withstanding the expected loads and traffic conditions. Overall, pavement modeling through a mechanistic methodology of pavement design is a valuable tool for analyzing the behavior of pavement with GRC (Geoweb reinforced concrete) and predicting its performance over time. By taking into account the initial variables and simulating the behavior of the pavement system, it is possible to design and construct pavement that is safe, efficient, and cost-effective.

1 INTRODUCTION

1.1 *Structure*

GRC (Geoweb reinforced concrete) is a system that combines geocell and concrete to create a more efficient and effective way to construct roads and other transportation infrastructure. The system was first developed in Colombia in the 2000s through empirical methods, and formal study of the system began in 2018 by Professor Jie Hann. The key to the GRC system is the combination of geocell and concrete in a way that provides both the necessary flexural and elastic behavior, as well as compressive strength. The geocell provides the necessary flexibility and elasticity that concrete alone would not be able to withstand, while the concrete provides the strength needed to support heavy loads. The geocell also serves as a formwork for concrete, which makes installation faster and easier than other systems. This makes it an attractive option for complex accessibility roads in Pacific islands, as discussed by the World Bank in 2019 (World Bank 2019). Overall, the GRC system offers a promising solution for transportation infrastructure construction. Also, ongoing research and development could lead to even greater improvements in efficiency and effectiveness.

To ensure the long-term viability of GRC as a common construction technology, detailed studies of the technology are needed. By understanding the behavior of GRC pavement over time, it is possible to design and construct sustainable roads that will endure for generations.

One advantage of using GRC technology is that the stiffness of the concrete guarantees longevity, resulting in rigid pavements that have greater endurance and durability over their service life with lower maintenance costs. This is due to their more resilient development and better interaction with the wheel, leading to lower gas consumption per kilometer (Nilson 2001). Furthermore, concrete roads have been shown to perform better in high humidity conditions and over saturated soils, due to their hydraulic binders that are not deteriorated by water in the interface. This assures higher longevity of these types of structures. Overall, GRC technology has the potential to create sustainable and long-lasting roads that offer cost and time savings in construction, as well as improved performance and durability over their service life. Therefore, it is important to continue studying and developing GRC as a common construction technology for generations to come.

1.2 Methodology

The methodology outlined in this paper is aimed at comprehensively understanding the behavior of Geoweb reinforced concrete (GRC) pavements. The steps involved are as follows:

(a) A detailed study of the GRC system's materials, with a focus on understanding the relationship between Geocell Polymer and concrete.
(b) Development of a free-body diagram to analyze the system's loads, stresses, and strains and lay the groundwork for further investigation.
(c) Conducting a large-scale finite element analysis using Ansys software to create a model with a 9x9 matrix of GRC cells and provide design guidelines for GRC pavement designers.
(d) Reviewing existing GRC pavements to identify any shortcomings and gain insights into the failure mechanisms of this pavement type.
(e) Based on the data collected from the previous steps, developing a design approach for GRC pavements.

The primary objective of this paper is to provide a realistic review of the factors that must be considered when designing and building GRC pavements. The findings of this research will be useful for future research and practical applications of this innovative technology.

1.3 State of art

GRC typically consists of two main components: concrete, and geocells. Cement in the concrete acts as a binder to hold the materials together, while aggregates provide strength and stability to the structure. The geocells, on the other hand, are three-dimensional honeycomb-like structures made of high-density polyethylene (HDPE) that serve as a reinforcement to concrete giving the strain capability. The geocells interlock with the concrete, creating a strong composite material that can withstand heavy loads and harsh environmental conditions.

Geocells: Geocells were originally developed in the 1970s by Gary Bach and the US Army Corps, using welded polyethylene sheets to create a honeycomb structure that provided cohesion to soils with no natural stability. This technology was initially used for stabilizing beachheads during wartime landings, but over time, companies like Presto began marketing the product to private firms, leading to the development of the geocell market. Geocells have proven effective in providing cost-effective solutions for heavy load equipment on soft underlayment. (United States Patent nº US6395372 B1 2000).

Concrete: Although concrete has been extensively studied for centuries, with a primary emphasis on enhancing its durability and compression strength, this paper does not intend to explore in detail the tensile properties that are typically considered in the design of conventional concrete pavements. Rather, it focuses on investigating the interplay between concrete and geocell materials in GRC pavements. (World Bank 2019).

Empirical approach: The use of GRC began empirically, with GRC channels being built in Brazil's Amazon River to withstand the heavy equipment required for cleaning the river's muddy banks. Following the success of these channels, GRC was tested for use in road projects

Technical approach: Two distinct approaches have been identified from the projects analyzed and various developments made. The first approach, proposed by Professor Jie Han, involves a rigid slab solved using the Westergaard solution. However, when studying the second state of the slab, a different equation must be implemented due to the relative rigidity radius being less than the length of the concrete cell. The relative rigidity radius is assumed to be equal to the point of push-off test developed by Han. The second approach outlined in this paper evaluates the system in two dimensions by creating a free-body diagram, providing an approach for designing methodology. (Xiaoming Yang 2010).

2 METHODOLOGIC DEVELOPMENT

2.1 *Theoretical approach*

To study GRC, it is essential to begin with a free-body diagram that illustrates the forces present in the system. This diagram provides a clear understanding of where the most significant stresses or strains may occur.

Figure 1 illustrates that the stress in the system will only be in compression for concrete since the geocell will absorb the tractive stresses that may arise in the slab through elastic strain. This shows that the elastic strain caused by the elastic module of the polymer can withstand the strain and return to its original position. The compressive stresses are left for the concrete to withstand, making a high tenacity macro compound comprising a polymer matrix and concrete.
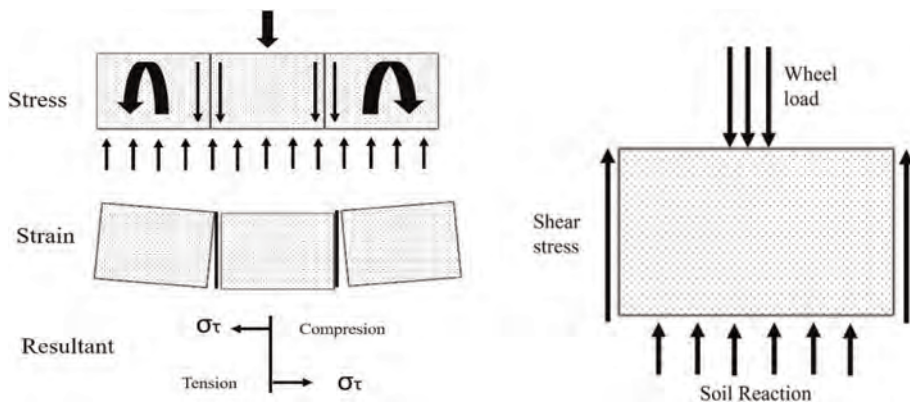
Figure 1. Free corps diagram stresses and strains in GRC system; individual block free corps diagram.

When examining the individual block, there will be a shear stress present in the complete perimeter between the concrete and the geocell. From this point, it is important to analyze stresses and deformations to determine the critical flexural moment that can be present in the concrete block, which is the one that will fail. This ensures that the concrete will not fracture.

To ensure a correct approach, it is important to note that the border elements can transfer shear stress, but they should not transfer torsional stresses. Thus, it can be concluded that:

$$\sum F_y = 0 \therefore R_{soil} + F_{frictionGRC} - P_{wheel} A_{wheel} = 0 \tag{1}$$

$$\sum M = 0 \therefore \quad F_{fCRG} = \frac{240}{N_{wheels}} \frac{h-7}{x \quad Axle} \tag{2}$$

$$M_{crit \quad concrete} = \frac{R_s}{2} \frac{L}{4} + \frac{F_{fCRG}L}{4} + \frac{F_{fCRG}L}{2} - \frac{P_l a^2 \pi}{2} \frac{a}{2} = L\left(\frac{R_s}{8} + \frac{3}{4} F_{fCRG}\right) - \frac{P_l a^3 \pi}{4} \tag{3}$$

$$M_{crit \quad concrete} = L\left(\frac{R_s}{8} + \frac{720}{4} \frac{h-21}{N_{ll}}\right) - \frac{P_l a^3 \pi}{4} \tag{4}$$

By analyzing the critical moment for concrete, it is possible to identify the point at which the concrete will fail. It is important to evaluate the wheel load in three different positions to determine whether the critical point has been identified. Once the moment has been determined, it is possible to calculate the stress at this point in the tension fiber.

$$\sigma_t = \frac{Mc}{I} = \frac{M\frac{h}{2}}{\frac{bh^3}{12}} = \frac{6M}{bh^2} = \frac{\frac{3L}{2}\left(\frac{R_s}{2} + \frac{720}{N_{ll}} \frac{h-21}{N_{ll}}\right) - \frac{3}{2} \frac{P_l a^3 \pi}{2}}{bh^2} \tag{5}$$

The equation shown can be used to determine the maximum possible stress in the system, which identifies the most critical point that the system can be exposed to when modeling the structure in 2D. The equations presented in this paper were developed solely by the author.

2.2 ANSYS model

To model the GRC system using a finite element program, it is important to consider that the honeycomb structure must be transformed into prismatic diamonds to enable the polymer to work within its elastic range with its initial strain, which will arrange the fibers of the structure. The model presented in the paper assumes that the soil is linearly elastic and that the interphase between the concrete and the polymer has the resistance depicted in Figure 2.

The values used for the finite element analysis (FEA) in this study were high density polyethylene (HDPE) and concrete. HDPE had an elastic modulus of 700 MPa, as obtained in a test conducted by the authors in 2018 on strain and stress analysis in a Geoweb cellular confinement cell. The concrete modulus used was 23.4 GPa, corresponding to concrete with a rupture modulus of 24.1 MPa. Boundary conditions were specified by fixing the rotation of the external blocks and using a foundation with known values ranging from 50 MPa/mm to 250 MPa/mm, with variations made every 50 MPa. The simulation utilized a wheel load of 0.69 MPa pressure applied to a circular area with a 12 cm radius to simulate the weight generated by a loaded truck wheel. It is important to note that the results discussed in the study are only a portion of the findings obtained. (Schmalbach 2018).

Based on the finite element solution of the total deformation, it can be observed that the soil deforms more than the slab. This will be further reviewed in the analysis, but it is important to note this initial observation. When analyzing the principal stresses in the
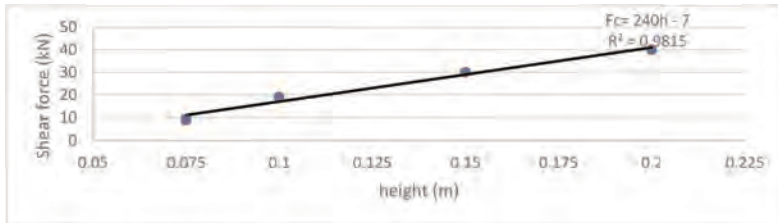
Figure 2. Punch concrete Cell test with GW30 cells redone as the methodology proposed (Han 2012).
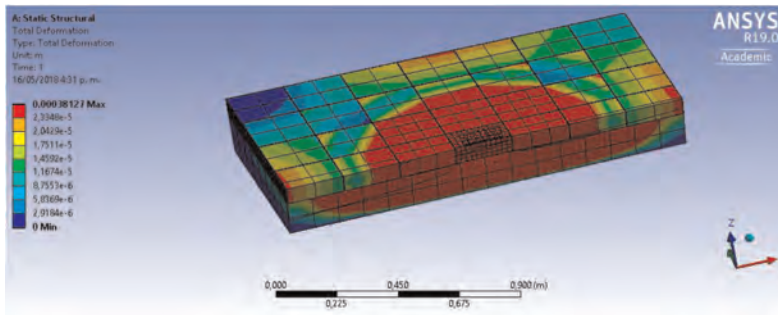
Figure 3. FEA total deformation.
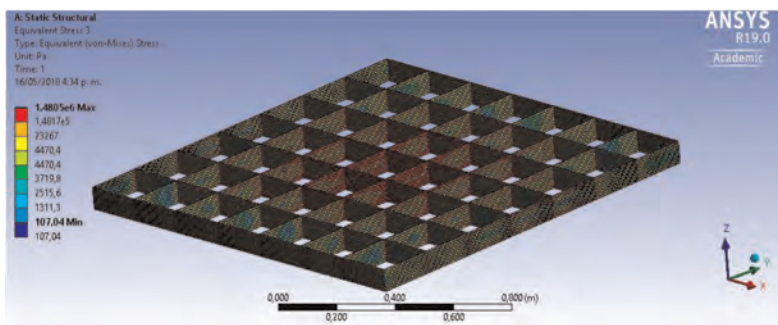
Figure 4. Stress in geocell matrix.
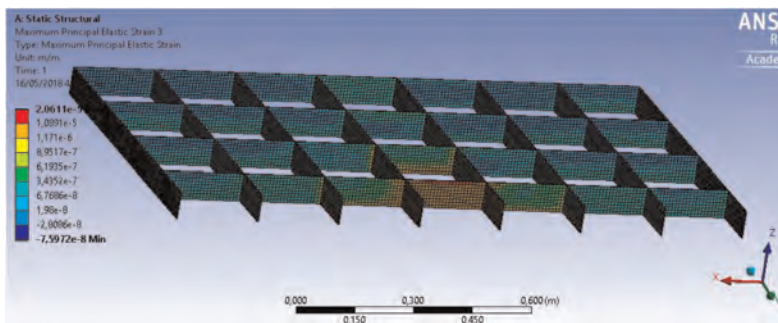
Figure 5. FEA strain in the geocell matrix.

geocell matrix, it can be inferred that they appear in the neutral axis, where compressive and tensile stresses govern the behavior of the evaluated zone in the model. When evaluating strain, the solution highlights the fact that the geocell absorbs stress as a strain, due to the differences in the elastic modulus of the two materials that are working in deformation equivalence. This is demonstrated in Figures 3 to 5.

2.3 *In situ analysis*

It should be emphasized that in Colombia, where GRC has been installed in over one million square meters, cases of deterioration and failure have been observed, with the predominant failure mode being illustrated in Figure 6. This failure mode is caused by the movement of fines underneath the GRC, which generates excessive pressure and degrades the interface between the Geocell and the concrete, resulting in water infiltration. This phenomenon, known as *broad radius rutting*, is characterized by a significant radius of failure, with the wheel paths being noticeably wider than the wheel itself, indicating a failure of the subgrade rather than the rolling layer. When the interface is breached, fines are pumped out of the granular layers, leaving the GRC layer without support. This is a common failure mode for rigid pavements, as evidenced by the AASHTO road test, in which 80% of concrete structures failed due to this type of failure. Adequate design considerations can help mitigate this failure mode.

Figure 6.   Fail presented in a soft soil with high fines and water presence.

3   ANALYSIS

To synthesize, a mechanistic analysis of the GRC system reveals that its monolithic structure generates high-pressure zones with minimal deflection, creating critical issues that require pressure control to avoid deterioration, particularly in low mechanical soil response areas. Two analyses can aid in designing a path that limits deflection, preventing suction caused by pressure in the deflected area and indirectly restraining the total deflection of the geocell to prevent it from reaching the polymer's plastic strain. The geocell must handle significant elastic strains within its elastic range, preventing permanent deformation accumulation that leads to rapid system deterioration. However, a too rigid geocell polymer becomes fragile and fails after only a few loading repetitions. It is crucial to return to equation 5, which determines the allowable stress in the GRC system, either because of the geocell's yield point limit or concrete rupture at a specific point.

4   CONCLUSIONS AND RECOMMENDATIONS

- The failure of the GRC system is caused by excessive deflections allowed in the structure, making the allowable total deflection a crucial designing parameter.

- The finite element analysis and mechanistic analysis show that the geocell can withstand tension stresses, and the tractive stresses are not affecting the concrete. Failure in the field also confirms that the concrete remains intact, while the polymer fails over time
- To better understand the interphase between the two materials, further studies are necessary to develop fatigue curves and predict the system's behavior over time.
- Despite the challenges, GRC pavements can revolutionize the infrastructure industry, offering more durable and cost-effective roads. GRC roads can be the future, particularly in developing countries that need to improve their road systems rapidly and steadily, as the World Bank suggests.
- GRC has proven to be a viable option for pavement construction due to its durability and longevity, as well as its ability to reduce slab thickness, construction time, and costs. Its use in Colombia has been driven by the country's specific geographic and weather conditions, as well as its infrastructure needs. However, further research and development are still needed to fully realize GRC's potential as a sustainable and cost-effective construction material.

REFERENCES

Babu, G. L. (2012). An Approach for Evaluation of Use of Geocells in Flexible Pavements. *Proceedings of Indian Geotechnical Conference*. Dehli.

Bach, G. (1989, Enero 11). *United States Patent No. US4965097 A.*

Bach, G. M. (2000, Noviembre 7). *United States Patent No. US6395372 B1.*

Bortz, B. S. (2011). *Geocell-Reinforced Crushed Stone Base for Low-Volume Roads*. Iowa: Iowa State University.

Cheng, J. (2018). *Geosinthetic Soil Reinforcement Procedures*. Philadelphia: ASTM.

Delatte, N. (2008). *Concrete Pavement Design Construction and Performance*. New York: Taylor & Francis.

Emersleben, A. (2013). *The Use of Sand in Combination with Geocells Instead of Gravel for the Construction of Highly Loaded Acces Roads Over Soft Soil*. Achim: Presto Geossystems.

Hegde, A. (2017). Geocell Reinforced Foundation Beds-past findings, Present Trends and Future Prospects: A State-of-the-art Review. *Construction and Building Materials*, 154(3), 17.

Huang, Y. H. (2004). *Pavement Analysis and Design*. Kentucky: Pearson Prentice Hall.

Laboratoire Central des Ponts et Chausses. (1997). *French Design Manual For Pavements Structures*. Paris: Setra.

Leshchinsky, B. (2013). *Numerical Modeling of Behavior of Railway Ballasted Structure with Geocell Confinement*. Oregon: Oregon State University.

Michael J. Mengelt, T. B. (2000). *Reinforcement of Flexible Pavements Using Geocells*. Wisconsin: Geo Engineering Report.

Myriam R. Pallares M uñoz1, J. A. (2015). Influencia de la Presión de Contacto Sobre Los Parámetros de Diseño de Pavimentos Asfálticos Usando Modelos de Elementos Finitos. *Revista Ingeniería y Región.*, 14(2), 100–112.

Nilson, A. H. (2001). *Diseño de Estructuras de Concreto*. Santafé de Bogotá: Mc Graw Hill.

PRESTOGEO. (2012). *Presto Geosystems*. (Reynolds Consumer Products Inc) Retrieved 11 2, 2017, from https://www.prestogeo.com/

Schmalbach, J. (2018). *Análisis Racional de un Pavimento con CRG (Concreto reforzado con Geoweb)*. Bogotá: Universidad de los Andes.

Sitharam2, A. H. (2014). *Joint Strength and Wall Deformation Characteristics of a Single-Cell Geocell Subjected to Uniaxial Compression*. United States: ASCE.

Sushovan Dutta, S., & Mandal, a. J. (2016). *Numerical Analyses on Cellular Mattress–Reinforced Fly Ash Beds Overlying Soft Clay*. US: ASCE.

Tanyu B. F., A. H. (2013). *Laboratory Evaluation of Geocell-reinforced Gravel Subbase Over Poor Subgrades*. Wisconsin: Geosynthetics International.

World Bank. (2019). *Concrete Pavements for Low-Volume Roads in Pacific Island Countries*. Washington DC: WB.

Xiaoming Yang, J. H. (2010). *Three-dimensional Numerical Modeling of Single Geocell-reinforced sand*. Kansas: Parsons.

Characterization of asphalt mixtures with geosynthetic-reinforced asphalt millings

Ashray Saxena*
Graduate Research Assistant, Department of Civil, Architectural and Environmental Engineering, University of Texas at Austin, Austin, Texas, USA

V. Vinay Kumar*
Postdoctoral Fellow, Department of Civil, Architectural and Environmental Engineering, University of Texas at Austin, Austin, Texas, USA

Natalia S. Correia*
Associate Professor, Federal University of Sao Carlos, Civil Engineering Department, Sao Carlos, Sao Paulo, Brazil

Jorge G. Zornberg*
Professor, Department of Civil, Architectural and Environmental Engineering, University of Texas at Austin, Austin, Texas, USA

ABSTRACT: The incorporation of geosynthetic interlayers during the asphalt overlay construction has proven successful in mitigating the reflective cracking and enhancing the pavement structural capacity. However, milling an asphalt layer reinforced with geosynthetic interlayer is a huge concern, since there is a possibility of geosynthetic interlayers compromising the reclaimed asphalt pavement (RAP) quality and characteristics. On the other hand, inclusion of RAP into the hot mix asphalt (HMA) is a common practice. Hence, it is important to understand the characteristics of RAP collected from geosynthetic-reinforced asphalt layers (referred herein as GRAP) and their influence on the performance of asphalt mixtures. The objective of this study is to understand the characteristics of GRAP and subsequently, investigate the performance of asphalt mixtures with 15% and 30% GRAP contents. Additionally, the performance of asphalt mixtures with 15% and 30% RAP contents, and 100% virgin aggregates (referred as control mixture) was evaluated for comparison with that of asphalt mixtures combining GRAP. The characterization of GRAP and RAP included particle size gradation and binder extraction tests, while the performance evaluation of the asphalt mixtures included indirect tensile strength, and moisture susceptibility tests. Comparison of binder extraction test results revealed that the GRAP samples had binder content slightly higher than that of the RAP samples. While the comparison of indirect tensile strength and moisture susceptibility test results indicated the performance of asphalt mixtures with GRAP similar to that with RAP, where both mixtures outperformed the asphalt mixtures made solely of virgin aggregates. This indicates the potential of incorporating GRAP and RAP up to 30% into the asphalt mixtures without compromising the performance of asphalt mixtures.

1 INTRODUCTION

The search for sustainable and innovative solutions gave rise to a new material in paving works, the reclaimed asphalt pavement. Specifically, during the rehabilitation program, the

*Corresponding Authors: saxena_ashray@utexas.edu, vinay.vasanth@utexas.edu, ncorreia@ufscar.br and zornberg@mail.utexas.edu

pre-existing asphalt layer is either partially or completely milled resulting in tons of aggregate-sized particle material, commonly known as RAP. This material has been transforming paving works in many countries around the world since late 30's. Additionally, with waste reuse and recyclability policies, a great intensification on the utilization of RAP in recent years has been observed. Consequently, there is less waste generation and reduction in the extraction of raw materials required for pavement construction, thereby providing significant environmental and economic benefits.

The Texas Department of Transportation (TxDOT) promotes using RAP on a larger scale in many pavements works, including composition of a new asphalt mix, extra widening of roadways, replacement of granular base course and subbase materials, construction of shoulders, residential driveways, parking lots, bicycle paths, gravel road rehabilitation, trench backfill, and embankment's design. Previous literatures (Plati & Cliatt 2018; Saxena *et al*. 2023) have reported that the pavement containing RAP could perform equally well when used in base course and in some instances better than the conventional granular base course comprising virgin aggregates (VA), in terms of its structural performance.

Additionally, due to the increased binder cost and scarcity of virgin aggregates, the demand for using RAP in asphalt mixtures has increased. In 2010, the utilization of RAP in asphalt mixtures conserved approximately 20.5 million barrels of asphalt binder (NAPA 2011). Moreover, the advantages of using RAP in asphalt mixtures are not limited to only economic and environmental benefits. Research studies (Shu *et al*. 2012; Uribe *et al*. 2022) have shown that the replacement of virgin aggregates with RAP can improve the indirect tensile strength of asphalt mixtures by about 50% and additionally improve the resistance against moisture damage (Shu *et al*. 2012). However, Singh *et al*. (2017) reported that moisture damage of asphalt mixtures containing RAP improves only up to the addition of 30% RAP content, and further increase of RAP content makes the asphalt mix vulnerable to moisture damage.

In recent decades, the incorporation of geosynthetic interlayers during the asphalt overlay construction has proven successful in mitigating reflective cracks and thereby, enhancing the pavement performance (Saride & Kumar 2017, 2019). Thus, it is possible to mill asphalt layers that may include geosynthetic interlayers within them. Therefore, it becomes crucial to conduct experimental research studies to comprehend the characteristics and behavior of RAP obtained from milling such asphalt layers that have been reinforced with geosynthetic interlayers. Although the literature on this topic is very limited, it is important to note that the growing trend of incorporating geosynthetics within asphalt layers may increase the prevalence of RAP containing geosynthetic fragments. Recently, Gu *et al*. (2021) demonstrated that a 30% RAP containing milled polypropylene geotextile fragments presented an excellent resistance to moisture damage, rutting and cracking. In addition, they reported that geosynthetic RAP and control RAP asphalt mixtures had comparable flexibility index values.

In summary, studies on the recyclability of geosynthetic-reinforced asphalt millings are very limited in number, which requires more attention. Hence, this study is undertaken to understand the characteristics of RAP containing geosynthetic fragments (GRAP) and consequently, investigate the performance of asphalt mixtures with 15% and 30% GRAP. Moreover, performance of asphalt mixtures with 15% and 30% RAP contents, and 100% virgin aggregates was determined to answer whether the presence of geosynthetic fragments in RAP has an adverse impact on the quality of asphalt mixtures. The characterization of GRAP and RAP included particle size gradation, and binder extraction tests, while the performance of asphalt mixtures has been investigated through indirect tensile strength, and moisture susceptibility tests.

2   CHARACTERIZATION OF RAP AND GRAP

The RAP with and without geosynthetic fragments were collected during the milling program conducted along the US 70/84 Highway at Muleshoe, TX. The roadway comprised of

a sandy subgrade, 300-mm-thick granular base, and 110-mm-thick asphalt layer that comprised of a 50-mm thick first lift and a 60-mm thick second lift with a paving fabric between them. The paving fabric was a polypropylene nonwoven geotextile used as a stress relieving interlayer to mitigate reflective cracking. The milling process involved two stages: the top 50 mm of the 110 mm thick asphalt layer was first milled to obtain RAP samples, followed by milling of the remaining 60 mm thick asphalt layer (having geosynthetic 10 mm below the first milled surface), to obtain GRAP samples. The collected RAP and GRAP samples were completely dried out in the laboratory and need of crushing them was identified before characterization tests. Specifically, 3 kgs of sample was crushed each time by dropping a modified Proctor hammer weighing about 4.5 kg, from a height of 450 mm for about 100 times. Figure 1 shows the RAP (Figure 1a) and GRAP samples (Figure 1b) collected from the site which were crushed into the laboratory due to their bigger sizes, and crushed GRAP samples (Figure 1c) used in characterization tests.
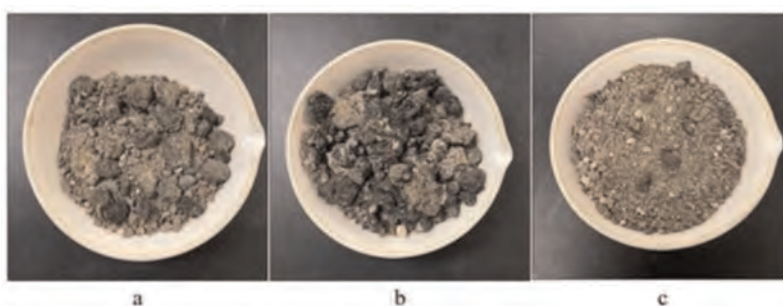
Figure 1. Collected RAP samples: (a) RAP; (b) RAP with geosynthetic fragments (GRAP); and (c) GRAP after crushing process.

The crushed RAP and GRAP samples were first sieved to determine their grain size distribution. Moreover, this analysis allowed for the determination of whether screening of the geosynthetics fragments is required for GRAP samples. Finally, bitumen extraction tests were conducted on RAP and GRAP samples, using centrifuge method with trichloroethylene, per AASHTO T164, to obtain the percentage of binder in the collected samples.

3 MIX DESIGN

The asphalt mixture investigated in this study was a TY-D binder course mix typically used by TxDOT for pavement construction. In order to evaluate the recyclability of GRAP samples as a potential aggregate material for surface course, five different asphalt mixtures are designed. These mixtures included 0% (control mixture), 15% and 30% RAP and GRAP samples. All mixtures were found to fit well within the gradation limits of TY-D surface course mixture, as specified by Item 341 TxDOT. It should be noted that all the specimens were prepared using the same virgin aggregate, procured from the Marble Fall Quarry - Texas Material in Texas. Virgin aggregate used was primarily crushed rock. Moreover, Performance Grade (PG) 64-22 was used as the virgin binder for the sample preparation. In this study, the notation used for mixtures containing only virgin aggregate is VA (control specimen) and mixtures containing RAP and GRAP are respectively denoted as 15-85 RAP/ 30-70 RAP and 15-85 GRAP/30-70 GRAP, where the first term represents the percentage of

RAP or GRAP, the second term represents the percentage of virgin aggregate, and the last term indicates the type of RAP used in a given mixture. An optimum binder content corresponding to 7% air void content for all the prepared mixtures was determind to be 4.45 (VA), 4.10 (15-18 RAP), 4.00 (15-85 GRAP), 3.70 (30-70 RAP), and 3.55 (30-70 GRAP), respectively. This implied that the asphalt mixtures containing GRAP samples require less virgin binder to compose the hot mix asphalt as compared to mixtures containing RAP or virgin aggreagtes.

4 LABORATORY TESTS

4.1 Indirect tensile strength (IDT) test

The indirect tensile strength of asphalt mixtures is used to evaluate their rutting and cracking potential by characterizing the tensile strength and viscoelastic properties of the mixtures. The indirect tensile strength test was performed on five different asphalt mixtures designed herein at different test temperatures (5, 10, 25°C), per ASTM D6931. The cylindrical specimens were prepared in dimensions of 150 mm diameter and 95 mm thickness at a target void content of 7%, using Superpave gyratory compactor. The compacted specimens were then conditioned in a temperature controlled chamber at test temperatures for a period of 24 h prior to testing. Three specimens were prepared for each mix design and tested until failure using a loading rate of 50 mm/min.

4.2 Moisture susceptibility test

Moisture susceptibility tests are conducted to evaluate the moisture-induced deterioration of asphalt mixtures subjected to moisture over extended periods. The moisture susceptibility of the asphalt mixtures is evaluated in terms of tensile strength ratio (TSR), per ASTM D4867. Specifically, tensile strength ratio is defined as the ratio of indirect tensile strength of specimens at wet condition to the indirect tensile strength of specimens at dry condition. Six specimens of 150 mm diameter and 95 mm thickness were prepared for each of the five different asphalt mixtures at a target air void content of 7%, using Superpave gyratory compactor. The specimens (six in number) of each mixture were then separated into sets of three to test them under both dry and wet conditions. The dry condition specimens were conditioned at 25°C for about 2 h prior to testing, while the wet condition specimens were partially saturated through vaccum-saturation until 70% to 80% of the voids were filled with water and then immersed in water bath at 60°C for 24 h. The wet condition specimens after moisture damage were then conditioned at 25°C in a water bath for 2 h before testing. Indirect tensile strength test were conducted on both the dry and wet specimens at a loading rate of 50 mm/min. The load-displacement characteristics were recorded for all the specimens tested and the corresponding maximum load was used to calculate the indirect tensile strength of the respective asphalt mixtures evalauted in this study, which in turn was used to calculate the tensile strenth ratio of the respective asphalt mixtures. A high TSR value (>80%) indicates better resistance to moisture and vice-versa.

5 RESULTS AND DISCUSSIONS

5.1 Characterization of RAP and GRAP

During the sieve analysis of crushed GRAP sample, geosynthetic fragments were observed only up to 12.7 mm sieve, after which no traces of geosynthetics were observed in the mix. This may be due to the fact that geosynthetic particles were bigger in size and the presence of mastic asphalt on their surface has increased their size. Table 1 shows the design gradation of RAP and GRAP samples used for the preparation of asphalt mixtures. Table 1 demonstrates

that the crushed RAP and GRAP samples were almost similar, with no significant change in their volumetric or gradation requirements. On the other hand, while considering the binder extraction test on the collected samples, the binder content of RAP and GRAP samples is determined to be 4.92% and 5.87%, respectively, indicating that there was a difference of 0.95% in binder content for the collected RAP and GRAP samples. The higher binder content of GRAP can be attributed to the application of tack coat during installation of paving interlayer at the site.

Table 1. Design gradation of collected materials.

Sieve size*	Percentage Passing (%)	
	RAP	GRAP
19.05	100	100
12.7 mm	99	99
9.53 mm	90	95
4.75 mm	60	65
2.36 mm	40	44
0.6 mm	20	25
0.3 mm	13	15
0.075 mm	5	5

*Sieve size in millimeters.

5.2 Indirect tensile strength test

5.2.1 Effect of temperature on the indirect tensile strength of asphalt mixtures

The indirect tensile strength for the five different asphalt mixtures evaluated in this study at different test temperatures are reported in Table 2. The results show that the indirect tensile strength of the asphalt mixtures decreases rapidly with increase in test temperature. For example, the indrect tensile strength of 30-70 RAP was reduced by 22% and 65%, when the test temperature changed from 5 to 10°C and 5 to 25°C, respectively. These reduction in indirect tensile strength values was due to the reduction in the viscosity and cohesion of the asphalt binder particles at higher temparature, thereby causing lower resiatnce to tensile forces. Moreover, specimens containing RAP and GRAP samples has shown less reduction in indirect tensile strength value with increasing test temperature compared to control specimens. The reason behind this was the presence of aged binder on the surface of RAP and GRAP samples providing greater stiffness to the mix, which in turn causing higher resistance to tensile stresses.

Table 2. Tensile strength of asphalt mixtures at different temperatures.

Mixture type*	Temperature (°C)		
	5	10	25
VA	2223	1487	589
15–85 RAP	2343	1679	733
15–85 GRAP	2231m	1614	722
30–70 RAP	2722	2113	955
30–70 GRAP	2433m	1826	859

*Tensile strength is in kPa.

5.2.2 *Effect of RAP and GRAP content on the indirect tensile strength of asphalt mixtures*

The indirect tensile strength test results for the specimens containing different percentages of RAP and GRAP samples are reported in Table 2. As can be seen in the table, the average indirect tensile strength value was highest for 30-70 RAP specimen at any given test temperature, followed by 30-70 GRAP, 15-85 RAP, 15-85 GRAP and VA specimens respectively. The higher indirect tensile strength of specimens containing RAP or GRAP samples compared to control specimens was due to the presence of aged asphalt binder on the surface of collected samples, imparting higher stiffness to the asphalt mixtures. Moreover, the indirect tensile strength of control specimen was observed to be 30%, 19%, 11%, and 8% lower than the indirect tensile strength of 30-70 RAP, 30-70 GRAP, 15-85 RAP and 15-85 GRAP, respectively, at test temperature of 10°C. In contrast, no significant difference between the indirect tensile strength of specimens containing RAP and GRAP samples (at any given percentage) were observed. While addition of GRAP samples resulted in lower tensile strength of specimens compared to those containing RAP samples, which can be attribute to the presence of geosynthetic fragments that might have reduce the stiffness of the asphalt mixtures.

5.3 *Moisture susceptibility test*

The moisture susceptibility of the five different asphalt mixtures evaluated in this study was determined in terms of the tensile strength ratio by evaluating the indirect tensile strength of dry and wet specimens. Table 3 shows the moisture susceptibility results (tensile strength ratio values) of the tested specimens. As can be seen in the table, 30-70 RAP specimen has shown the highest TSR value followed by 30-70 GRAP, 15-85 RAP and 15-85 GRAP specimens, respectively. While the control specimen has shown the lowest TSR value. These results indicate that the replacement of VA with RAP or GRAP samples can improve the stability of asphalt mixtures against moisture damage. Specifically, the RAP and GRAP samples contains aged, hardened asphalt binder which increases the stability of asphalt mixtures due to the higher viscosity of aged binder. In addition, oxidized binder is hydrophobic in nature and absorb less water, thus causing RAP and GRAP specimens to absorb less water than control specimens. Moreover, the TSR value of 30-70 RAP and 15-85 RAP was found to be slightly higher than that for 30-70 GRAP and 15-85 GRAP, respectively, because the geosynthetic fragments can absorb moisture. However, asphalt mixtures evaluated in this study, containing either RAP or GRAP samples were found to perform better against moisture damage compared to control specimen.

Table 3. Moisture susceptibility results.

Mixture type	TSR (%)
VA	81
15-85 RAP mm	85
15-85 GRAP m	82
30-70 RAP mm	90
30-70 GRAP mm	87

6 CONCLUSIONS

This study is performed to present the characteristics of RAP containing geosynthetic fragments and its suitability with virgin aggregates as surface course material. The following conclusions can be drawn from this investigation:

(1) The binder content of GRAP samples was observed to be 0.95% higher than that of RAP samples which can attribute to the presence of tack coat used during the installation of geosynthetic interlayer.

(2) The indirect tensile strength of the asphalt mixtures decreases rapidly with increasing test temperature. However, specimens containing RAP and GRAP samples results in less reduction in the indirect tensile strength values with increasing temperature compared to control specimens due to the presence of aged binder.

(3) The addition of RAP and GRAP samples (up to 30% by weight) can improve the indirect tensile strength and moisture susceptibility of the asphalt mixtures compared to control specimens.

REFERENCES

AASHTO T164 (2022). *Standard Method of Test Quantitative Extraction of Asphalt Binder from Asphalt Mixtures*. Washington, DC: American Association of State and Highway Transportation Officials.

ASTM D4867 (2022). Standard Test Method for Effect of Moisture on Asphalt Mixtures. *ASTM International*, West Conshohocken, PA, USA.

ASTM D6931 (2017). Standard Test Method for Indirect Tensile (IDT) Strength of Asphalt Mixtures. *ASTM International*, West Conshohocken, PA, USA.

Gu, F., Andrews, D., & Marienfeld, M. (2021). Evaluation of Bond Strength, Permeability, and Recyclability of Geosynthetic Products. *Geosynthetics Conference*, pp. 362–373.

Marín-Uribe, C. R., & Restrepo-Tamayo, L. M. (2022). Experimental Study of the Tensile Strength of Hot Asphalt Mixtures Measured with Indirect Tensile and Semi-circular Bending Tests. *Construction and Building Materials*, *339*, 127651.

NAPA, 2011. *Mix Production Survey Reclaimed Asphalt Pavement, Reclaimed Asphalt Shingles, Warm-Mix Asphalt Usage: 2009–2010*. Washington, DC: National Asphalt Pavement Association, Technical Report.

Plati, C., & Cliatt, B. (2018). A Sustainability Perspective for Unbound Reclaimed Asphalt Pavement (RAP) as a Pavement Base Material. *Sustainability*, *11*(1), 78.

Saride, S. & Kumar, V. V. (2017). Influence of Geosynthetic-interlayers on the Performance of Asphalt Overlays on Pre-cracked Pavements. *Geotextiles and Geomembranes*, 45, No. 3, 184–196.

Saride, S. & Kumar, V. V. (2019). Estimation of Service Life of Geosynthetic-reinforced Asphalt Overlays From Beam and Large-scale Fatigue Tests. *Journal of Testing and Evaluation*, 47, No. 4, 2693–2716.

Saxena, A., Kumar, V.V., Correia, N.S. & Zornberg, J.G. (2023). Evaluation of Geosynthetic-reinforced Asphalt Milling Characteristics and Suitability as Pavement Base Course. *Geosynthetics Conference, Kansas City, MO*, 324–335.

Shu, X., Huang, B., Shrum, E. D., & Jia, X. (2012). Laboratory Evaluation of Moisture Susceptibility of Foamed Warm Mix Asphalt Containing High Percentages of RAP. *Construction and Building Materials*, *35*, 125–130.

Singh, D., Chitragar, S. F., & Ashish, P. K. (2017). Comparison of Moisture and Fracture Damage Resistance of Hot and Warm Asphalt Mixes Containing Reclaimed Pavement Materials. *Construction and Building Materials*, *157*, 1145–1153.

TxDOT. (2014). *Standard Specifications for Construction and Maintenance of Highways, Streets, and Bridges*. Texas Department of Transportation (TxDOT), Austin, Texas, USA.

Effect of geosynthetics on stability of hidden cavity in base course

J. Kuwano
Saitama University, Japan

R. Kuwano
University of Tokyo, Japan

J. Hashimoto
Saitama University, Japan

R. Terauchi
Saitama City Office, Formerly Saitama University, Japan

ABSTRACT: Road cave-ins associated with hidden cavities are one of key issues in road maintenance. Field model tests were carried out to develop and improve methods of detection, diagnosis, and repair of hidden cavities at the prototype scale test road, 30 m long and 6 m wide. Hidden cavities were made artificially by burying bags filled with fine gravel in well-compacted base course layers. Fine gravel was removed by a vacuum cleaner after the completion of the surface course. FWD tests and plate loading tests were carried out to investigate stability of hidden cavities in base course. A series of laboratory model tests was also carried out to investigate the effect of type of geosynthetics and their depth in the base course on the stability.

1   INTRODUCTION

Road cave-ins associated with hidden cavities are one of key issues in road maintenance. Cavities in ordinary conditions are caused by various factors such as breakage of sewer pipes. Subsurface cavities of this type are formed when subgrade soil particles or subbase materials are washed away into the pipe. A cavity thus formed from a certain depth of the ground expands with time, and when the strength of the pavement is not enough, a sudden cave-in finally occurs. About 5,000 to 10,000 cave-ins are found every year in Japan. Such hidden cavities are usually detected by a ground penetrating radar often mounted on a car which runs as fast as 100 km/hour. Mechanism of cavity formation and stability of the ground have been studied mainly by laboratory model. Mechanism of cavity formation and stability of the ground have been studied mainly by small scale laboratory model tests on clean sand (e.g., Indiketiya *et al.* 2019; Karoui *et al.* 2018; Kuwano & Ohara 2021) but not on crushed stones due to the limitation of model scale. However, experimental study on hidden cavity in prototype scale road pavement is hardly found. This paper reports stability of hidden cavity in base course layer reinforced by geosynthetics through prototype scale field model tests. A series of laboratory model tests was also carried out to investigate the effect of type of geo-synthetics and their depth in the base course on the stability.

2 PROTOTYPE SCALE FIELD MODEL TESTS ON STABILITY OF HIDDEN CAVITY IN BASE COURSE REINFORCED BY GEOSYNTHETICS

2.1 *Test outline*

Field model tests were carried out to develop and improve methods of detection, diagnosis, and repair of hidden cavities at the prototype scale test road, 30 m long and 6 m wide, constructed in the Saitama University campus as shown in Figure 1(a). A cross section of the test road with hidden cavities is shown in Figure 1(b). The test road consisted of 100 mm surface course. Layers below the surface course were 250 mm upper base course with M-30 mechanically stabilized crushed stones ($D=0\sim30$ mm), 100 mm lower base course with C-40 crusher-run stones ($D=0\sim40$ mm), and 200 mm subgrade with decomposed granite sandy soil.
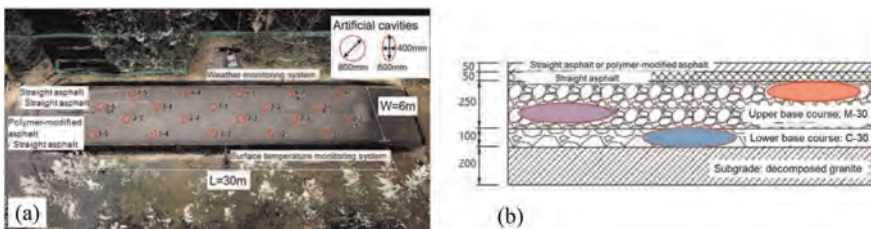
Figure 1.   Prototype scale test road. (a) Aerial view of prototype scale test road. (b) Typical cross section.

Hidden cavities were made artificially by burying bags filled with crushed stone #7 ($D=2.5$-5 mm) in well-compacted base course layers. Fine gravel was removed by a vacuum cleaner through the $\phi=50$ mm hole after the completion of the surface course as shown in Figure 2. About 60% crushed stone #7 could be removed from the buried bags. Although the bags could not be made completely empty, the ceilings, which are key in the stability problem, were thought to be made properly. Size and depth of the cavities were measured by radar. Figure 2(c) is an example of a photograph taken by a borehole camera.

Geogrid TX, geotextiles PET and WF were used. Their rupture strengths are 16 kN/m, 600 kN/m, 80 kN/m, respectively. TX could not be used at the depth of 100 mm, just below the surface course, because TX geogrid melts at the high temperature of about 150 °C when asphalt is used for pavement. Geosynthetics of 2,800 mm×2,800 mm were set at respective depths as summarized in Table 1. Figure 3 shows placement of geotextile PET at 200 mm from the road surface. FWD tests and plate loading (PL) tests were carried out to investigate stability of hidden cavities in base course.
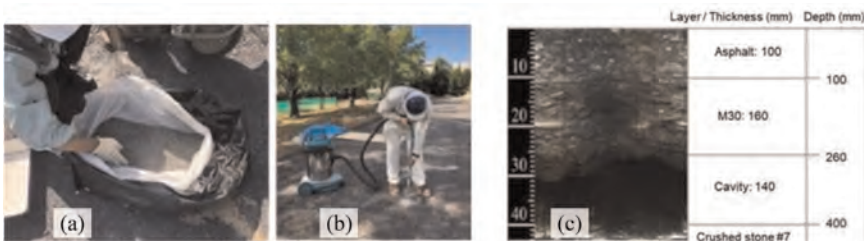
Figure 2.   Formation of a hidden cavity in the base course layer. (a) Crushed stone #7 in a bag. (b) Removal of fine gravels by a vacuum cleaner from the pavement surface.(c) Example of a photograph taken by a borehole camera.

Table 1. Hidden cavity IDs in prototype scale field motel tests.

Depths of cavity and reinforcement	Geogrid TX	Geotextile PET	Geotextile WF	No reinforcement
D100 = D100	—	5–8	—	5–10
D200 = D200	5–6	5–7	—	3–5
D350 > D200	7–6	7–5	7–7	3–3
D350 = D350	5–5	—	—	—

Figure 3. Placement of geotextile PET at 200 mm from the surface of prototype scale model test road.

2.2 *Results of prototype scale field model tests*

Prototype scale field model tests were carried out in some phases. In the first series of tests, only cavities were made without geosynthetics reinforcement in base course layers. Some of the cavities at the shallower depth collapsed due to their deadweights before loading tests. Cavity 5-6 was planned so that the geosynthetics would support the asphalt surface course. As the geogrid TX melts at the temperature of 150 °C, which is expected when asphalt is placed over the base course, only the geotextile PET was placed at the bottom of the asphalt layer at the cavity 5-8. FWD tests and PL (plate loading) tests results at the cavity 5-10 (Cavity@100 mm from the asphalt surface, No geosynthetics) and at the cavity 5-8 (Cavity@100 mm, PET@100 mm). As seen in Figure 4, there was not clear difference in the loading tests results of 5-10 and 5-8 cavities, though the 5-8 cavity was reinforced by the geosynthetics PET. It is probably because the PET was not attached firmly to the bottom of the asphalt layer because it melts at 250 °C and does not have large apertures for good interlocking with aggregate.

When the cavities were at 200 mm deep and the geosynthetics were just above the cavities, FWD deflection and load-settlement relationships of PL test were almost the same for the cavity 5-6 (geogrid TX) and the cavity 5-7 (geotextile) as seen in Figure 5. Those for the cavity 3-5 showed also almost the same, though FWD deflection was slightly high.

When the cavities were deeper at 350 mm but no reinforcement, settlement increased rapidly when the vertical pressure exceeded about 500 kN/m^2 as seen in Figure 6(a). Although this vertical pressure was much higher than the values shown in Figure 5 (cavity@200, reinforcement@200), sudden increase in the settlement indicated that the collapse (road cave-in) took place. According to the observation made in the laboratory model tests, the ceiling of the cavity collapsed with load and deformation, the cavity approached the surface, and resulted in the cave-in of the cavity. On the other hand, when the cavities were at 350 mm and the geosynthetics were at 200 mm, 150 mm above the cavities, sudden increase was not observed to the high vertical pressure of more than 800 kN/m^2 as seen in
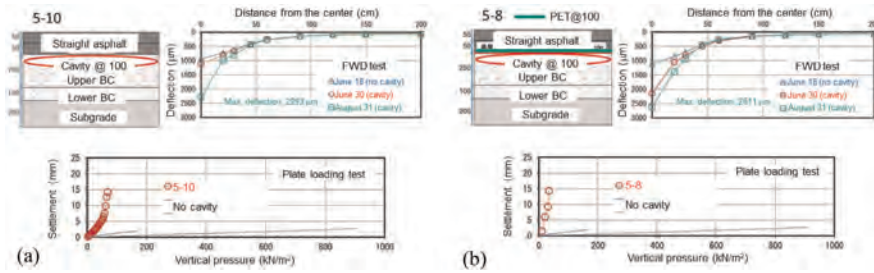
Figure 4. Loading tests on the cavities at 100 mm. (a) 5-10 (No reinforcement). (b) 5-8 (PET at 100 mm).
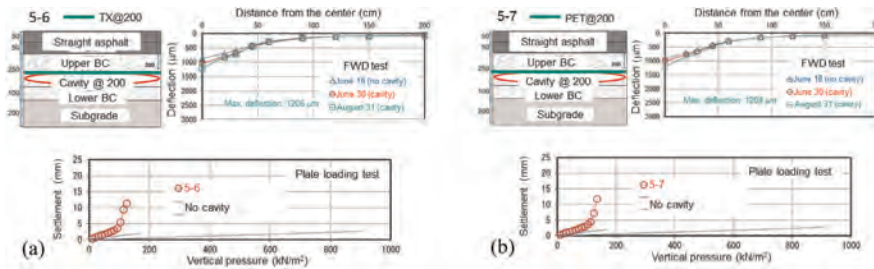
Figure 5. Loading tests on the cavities at 200 mm. (a) 5-6 (TX at 200 mm). (b) 5-7 (PET at 200 mm).
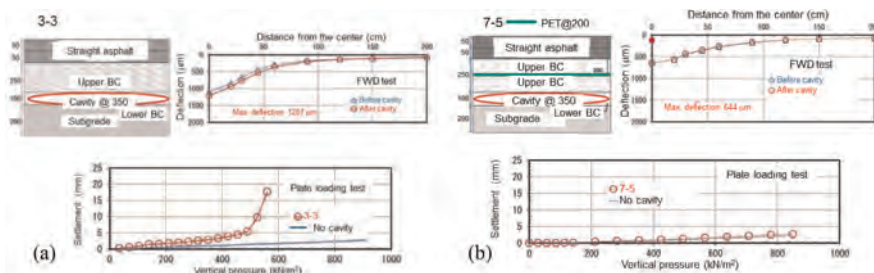
Figure 6. Loading tests on the cavities at 350 mm. (a) 3-3 (No reinforcement). (b) 7-5 (PET at 200 mm).

Figure 6(b). FWD deflections and PL test results were almost the same for the cavities with the geogrid and geotextiles. It is presumed that the pavement is stable enough if the thickness of the base course layer is kept by the geosynthetics.

3 LABORATORY MODEL TESTS ON STABILITY OF HIDDEN CAVITY IN BASE COURSE REINFORCED BY GEOSYNTHETICS

3.1 *Test outline*

In this series of tests, hidden cavities were made in the base course, and surface loading tests were carried out in a large square tank of size 1 m x 1 m in plan and 0.8 m in height. The schematic diagram of the test layout is presented in Figure 7(a). The 350 mm thick model

1338

subgrade of silica sand #5 was placed in the bottom layer and the 300 mm thick base course of compacted C-40 crusher-run stone was placed in the top layer of model ground. This is of a prototype scale of road structure around a cavity. The dry density of base course and subgrade was 1.73 g/cm^3 and 1.55 g/cm^3 respectively. Geogrid TX or geotextile WF, shown in Figure 7(b) and (c), was placed at different depth, d, from the surface of the base course. TXd or WFd indicates a test case reinforced by geogrid or geotextile at the depth d. For example, if geogrid was placed at the depth of 150 mm, the test was identified as TX150. A circular sandbag with a diameter of 120 mm was fully filled with fine gravel to the thickness of 60 mm. It was placed on a funnel (ϕ =130 mm x h=100 mm) at the interface of base course and subgrade. A funnel was connected to a 20 mm hose in the subgrade as shown in Figure 7. The base course was well compacted over the fully filled sandbag. Then, fine gravel in the bag was sucked out by a vacuum cleaner to simulate the cavity formation process in road. The 300 mm base course was made by compacting C-40 crusher-run stones.

Plate loading tests were carried out. Load was increased stepwise until the settlement reached about 100 mm. Besides the monotonic loading tests, some cyclic loading tests were performed. Vertical stress was changed between the minimum stress of 100 kPa and the maximum stress with a period of 10 seconds. The maximum stress was increased stepwise after every 500 cycles. Cyclic loading tests were indicated by "*" such as TX150*. Test cases are summarized in Table 2.
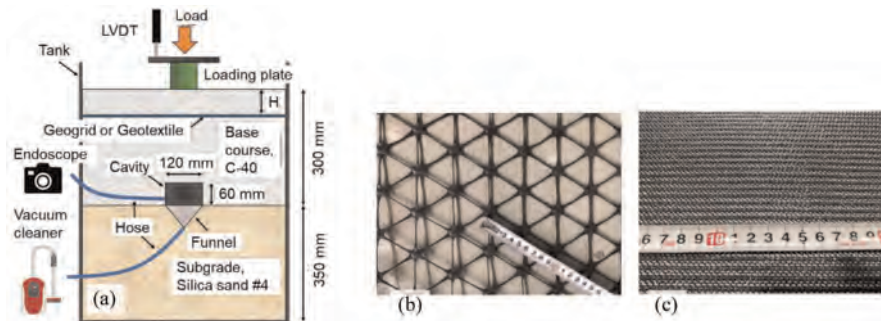
Figure 7.   Outline of laboratory model test. (a) Test setup. (b) Geogrid TX. (c) Geotextile WF.

Table 2.   Test conditions.

Test ID	Reinforcement	Reinforcement depth, d (mm)	Type of loading
NR	No reinforcement	N.A.	Monotonic
TXd	Geogrid TX	d=50, 100, 150, 240	
NR*	No reinforcement	N.A.	Cyclic
TXd*	Geogrid TX	d=50, 100, 150, 240	
WFd	Geotextile WF	d=50, 100, 150, 240	Monotonic

3.2   *Results of laboratory model tests*

Vertical stress – settlement relationships obtained by monotonic loading tests on base course with a cavity are shown in Figure 8(a). The base course layers were reinforced by the geogrid TX at respective depths or without reinforcement (NR). Vertical stress to cause sudden increase of settlement is different for the different depth of geogrid reinforcement. The stress
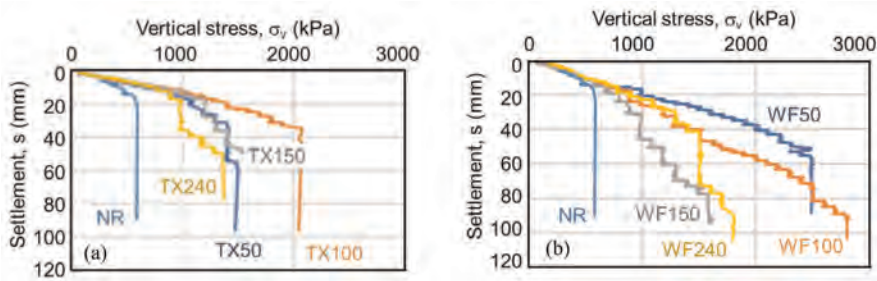
Figure 8.   Monotonic loading test results. (a) Geogrid TX. (b) Geotextile WF.

to cause collapse of the reinforced base course was higher than 1000 kPa and the highest for the base course reinforced at the depth of 100 mm. Figure 8(b) shows the results of monotonic loading tests on the base course layers reinforced by geotextile WF laid at the different depths. Similar to the geogrid cases, base course layers reinforced by geotextile showed higher stability than the base course layer without reinforcement.

Result of cyclic loading test on the model base course without reinforcement, GN*, is shown in Figure 9(a). Settlement increased gradually for the smaller vertical stress. But it increased suddenly and collapsed when the vertical stress reached 900 kPa, as there was a cavity at the depth of 240 mm. This sudden increase of surface settlement was observed also in monotonic loading tests. If TX was laid at the depth of 50 mm or 240 mm (just on the cavity), settlement increased gradually to the maximum stress of around 2000 kPa even after a limited amount of sudden increase at around 900 kPa as shown in Figure 9(b). Geogrid TX changed the base course behavior with a cavity from brittle to ductile. It was also seen for TX100 and TX150.

Figure 10 indicates the vertical stress, σ_v, to cause 20 mm settlement and collapse for the geosynthetics embedded at different depths in the base course. It is seen that the geogrid supported the base course on the cavity better than the geotextile.

Figure 11 shows photographs of endoscope taken in the cavity within the base course (a) WF150 and (b) NR*. Both the pictures were taken when the top of loading cylinder was pushed to the surface of the ground. In the case of WF150, the cavity was still remained though some red C-40 aggregates laid at the ceiling of the cavity dropped to the cavity
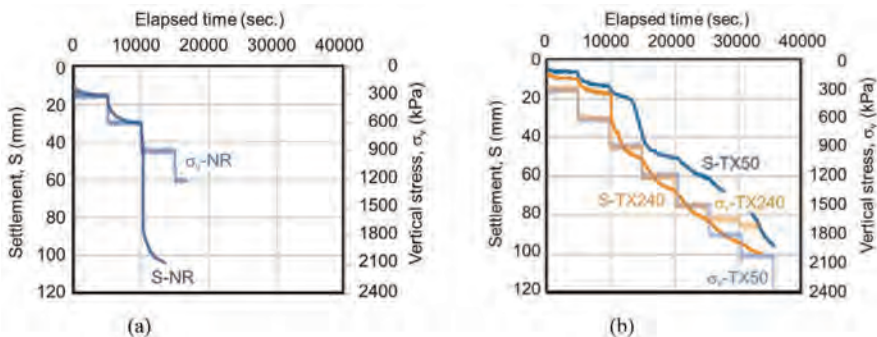
Figure 9.   Cyclic loading test results. (a) No reinforcement. (b) Geogrid TX50 and TX240.
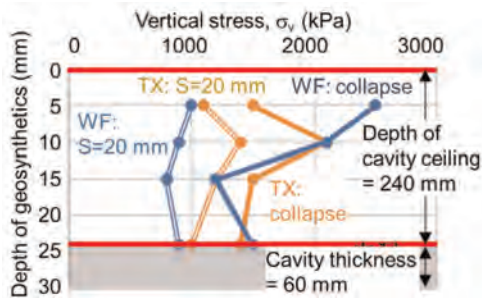
Figure 10. σ_v to cause S=20 mm and collapse.

(a) TX150   (b) NR*
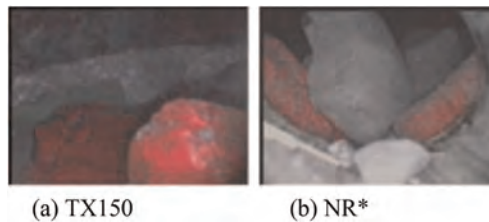
Figure 11. Views in the cavities at the end.

bottom. In the case of NR*, the cavity was filled with the collapsed C-40 aggregate. It indicates that the reinforcement prevented the cavity from collapsing completely.

4 CONCLUSIONS

The following results were obtained from the field and laboratory model tests:

(1) If a cavity without reinforcement is shallow and approaches surface course, the asphalt layer cannot support its own weigh and cave-in occurs.
(2) Effect of reinforcement becomes less obvious when the cavity is shallow.
(3) Geosynthetics contribute more to increase stability of the cavity in base course by maintaining the thickness of well-compacted base course layer above it rather than mechanical reinforcement such as confining effect and tensioned membrane effect (hammock effect).

REFERENCES

Hamanari, K. 2017. Analysis and Consideration of States of Hidden Cavities in Road Pavements. *Proc. 72nd JSCE Annual Conf., Fukuoka, Japan*, 3–495, 989–990 (in Japanese).

Indiketiya, S., Jegatheesan, P., Rajeev, P. and Kuwano, R. 2019. The Influence of Pipe Embedment Material on Sinkhole Formation Due to Erosion Around Defective Sewers. *Transportation Geotechnics* 19, 110–125.

Karoui, T., Jeong, S.Y., Jeong, Y.H. and Kim, D.S. 2018, Experimental Study of Ground Subsidence Mechanism Caused by Sewer Pipe Cracks. *Applied Science* 8(5), 679.

Kuwano, R. and Ohara, Y. 2021. A Study on the Process of Generation, Expansion and Collapse of Subsurface Cavities in Roads. *Geotechnical Engineering Journal, Japanese Geotechnical Society*, 16(4), 307–317 (in Japanese).

Regmi, K.P., Kuwano, J. and Yamato, T. (2020) "Effect of Geosynthetics on Stability of Cavity in Base Course," *Geosynthetics Engineering Journal, JC-IGS*, 35, 115–120.

Using non-destructive testing to evaluate geogrid-stabilised aggregates subject to accelerated traffic loading

C. Yesnik, I. Morozov, I.R. Fleming, H. Soliman, E. Landry &
A. Hammerlindl
University of Saskatchewan, Saskatoon, Saskatchewan, Canada

M.H. Wayne
Tensar International Corporation, Alpharetta, Georgia, USA

A. Lees
Tensar International Corporation, Nicosia, Cyprus

J. Kawalec
Tensar International Limited, Blackburn, UK

ABSTRACT: Roadways include stiff aggregate layers, which support and dissipate traffic loads before reaching the subgrade soil. The aggregate stiffness must be preserved to reduce rutting severity. Geosynthetic-stabilisation can preserve the aggregate stiffness through aggregate-geosynthetic interaction at small strains. The performance of geosynthetic-stabilised roadways depends on the properties of both the geosynthetic and the selected aggregate. A study was completed at the University of Saskatchewan to determine the relative performance of two geogrids used to stabilise two types of aggregate. A recently built full-scale wheel trafficker system applies accelerated traffic loading to 1.5 m wide unsurfaced test sections. Accelerometers were installed on the surface to measure changes in the aggregate stiffness with traffic loading using multichannel analysis of surface waves (MASW). This method facilitates non-destructive measurements of stiffness at numerous depths throughout the aggregate. The average shear wave velocity and rutting performance are presented for each soil-geogrid composite.

1   INTRODUCTION

Rutting is the result of permanent deformations in the road structure and subgrade, which are caused by lateral spreading of the aggregate and bearing capacity failure in the subgrade (Zornberg *et al*. 2017). The subsequent decrease in particle confinement causes the aggregate stiffness to degrade; thus, resulting in less resistance to subgrade shearing and heave (Lees 2017).

The aggregate layers can be stabilised with geosynthetics to help preserve the initial stiffness of the aggregate (Zornberg & Roodi 2021). Through aggregate-geosynthetic interaction, stress transfer is mobilised at small strains/displacements in the geosynthetic which are initiated during construction and initial traffic loading. Effective particle interlock also helps counterbalance any potential bearing capacity failure in the subgrade (Lees 2017). Consequently, the cost and frequency of road maintenance and rehabilitation is decreased.

Geosynthetic stabilisation can also reduce the thickness of aggregate required for design; thus, providing a sustainable solution to preserve non-renewable aggregate resources (Zornberg & Roodi 2021).

Geosynthetic-stabilised roadway design and performance is traditionally evaluated using traffic benefit ratio (TBR) and/or base course reduction (BCR). Geosynthetic manufacturers often provide TBR and BCR values within their product specification sheets. However, these values depend on the interaction between the selected roadway materials and geosynthetic for a given project. Many researchers and transportation agencies have completed independent studies to predict and quantify the stiffness enhancement achieved through geosynthetic stabilisation. These studies are usually completed through index testing, analytical and numerical models, laboratory testing and/or performance testing (e.g. Archer & Wayne 2012; Cuelho *et al*. 2014; Kang *et al*. 2022; Lees 2017; Zornberg & Roodi 2021; Zornberg *et al*. 2017). It is important that the current knowledge base is continually expanded by testing geosynthetics with a variety of aggregates and subgrade soils, subject to traffic loading (Cuelho & Perkins 2017).

The objective of this research is to determine a near-continuous profile of stiffness with depth through the entire aggregate layer, both before and after traffic loading. Traffic loading was applied to unsurfaced road test sections using a full-scale wheel trafficker system. Two types of road base aggregates were used for this study: a locally sourced prairie aggregate, and a high-quality, crushed rock. Two geogrids, with similar aperture geometry and varying rib thickness, and two non-stabilised control sections were assessed. Preliminary estimates of shear wave velocity through geogrid-stabilised and non-stabilised aggregates were obtained directly beneath the applied traffic load using multichannel analysis of surface waves (MASW).

2 SURFACE WAVE ANALYSIS

Of the several types of waves generated during siesmic testing, shear waves are often used to characterize the stiffness of soil. Shear waves can only be transmitted through the soil skeleton, while compression waves can travel through both soil and water. Equation 1 relates the small-strain shear modulus, G_{max}, to the soil density, ρ, and shear wave velocity, V_s (Kang *et al*. 2022).

$$G_{max} = \rho V_s^2 \tag{1}$$

Various seismic techniques can be used to measure V_s within the aggregate layer (Park 2011). Surface wave analysis is a non-destructive test method which maximizes the ease and versatility of sensor installation. This analysis depends on the dispersive nature of surface waves travelling in a vertically heterogenous soil medium. Rayleigh waves are used for surface wave analysis as they are easy to generate and detect, and will disperse in a heterogenous soil profile with varying stiffness (Everett 2013). The Rayleigh wave phase velocity will depend on the soil properties across the entire depth through which the wave travels. Lower wave frequencies (f) provide measurements of V_s at greater depths than higher wave frequencies, which provide measurements of V_s at shallower depths (Park *et al*. 2018), as shown in Figure 1.

MASW has been selected for this research to measure the stiffness profile through the aggregate layer. MASW is an ideal method for analyzing pavement structures, as soil stiffness can be measured at high resolutions over shallow depths (Park *et al*. 2018). MASW also allows for simple detection and separation of multiple modes, as well as mitigation of near-field effects (Olafsdottir *et al*. 2018).
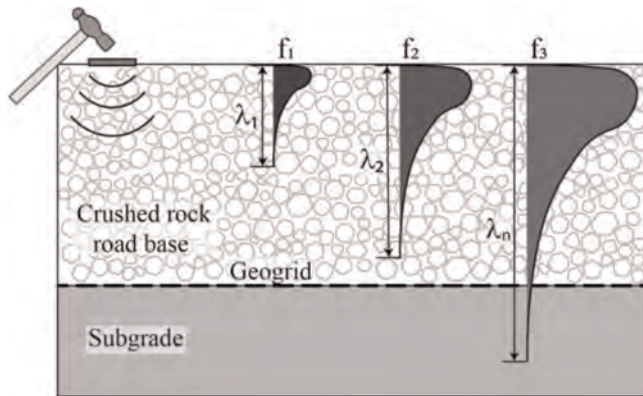
Figure 1. Surface wave analysis through aggregate.

3 EXPERIMENTAL PROGRAM

3.1 *Full-scale wheel trafficker system*

A full-scale wheel trafficker system was built at the University of Saskatchewan, as shown in Figure 2. The system has a structural steel exoskeleton which houses an epoxy-laminated, four-layer marine plywood box. The box dimensions are 6.10 m long by 2.82 m wide, which can accommodate 4 – half-lane test sections per trial. The geogrids were installed in different lane locations for each trial to account for any systematic variability.

A pneumatic loading system provides simulated traffic loading through 2 carriage houses, each equipped with a pneumatic cylinder pressurized to 620.5 kPa. The applied pressure is equal to 40 kN, which is one-half of an equivalent single axle load (ESAL). Two 255/70R22.5 semi-truck tires, each pressurized to 620.5 kPa, apply channelized traffic load to the aggregate surface.

Using an adjustable head reservoir, consistent subgrade conditions (i.e., suction and undrained shear strength) are achieved for each test section. Tensiometers were inserted along the box wall to provide real-time readings of subgrade suctions. A MEXE Cone
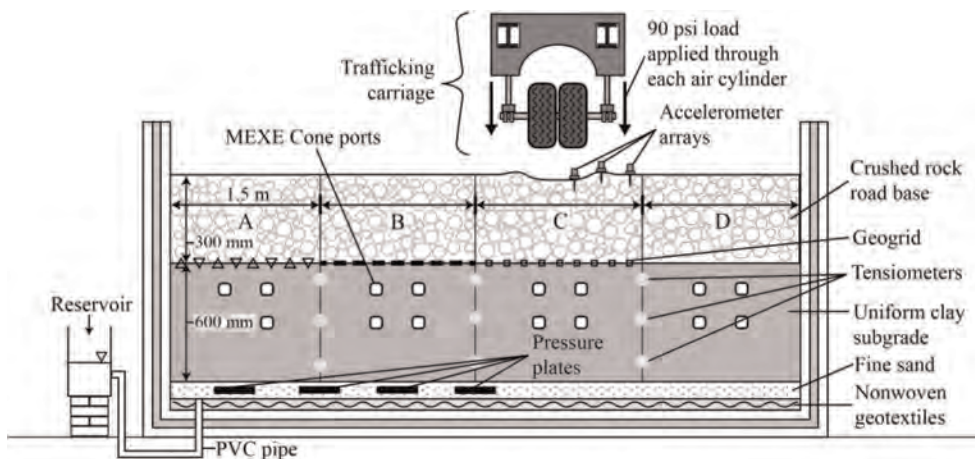
Figure 2. Full-scale wheel trafficker system.

Penetrometer was also used to measure the subgrade California Bearing Ratio (CBR) immediately before and after traffic loading. From the suction and CBR values, the undrained shear strength (Su) is estimated. The design, construction, and operation of this apparatus are detailed further by Landry *et al* (2022).

3.2 Materials

A low-plasticity kaolinite clay subgrade was selected for this research. The clay was purchased as bricks from Plainsman Clays in Medicine Hat, Alberta. Table 1 shows the properties of the clay subgrade. Atterberg testing was completed to obtain the liquid limit and plastic limit of the clay according to ASTM D2487-17. The moisture content, dry density, and Su of the clay was measured immediately after opening the clay samples.

Table 1.   Properties of clay subgrade material.

Characteristics	Values
Liquid Limit (%)	34.5
Plastic Limit (%)	16.9–17.7
Moisture Content (%)	20.8–24.7
Dry Density (kg/m^3)	1520
Undrained Shear Strength, S_u (kPa)	22–43

The Su was measured using a laboratory shear vane. The clay subgrade was hand placed in four lifts (600 mm total) as to minimize any disturbance to the clay. Smoothing and leveling was then carefully completed as to not exceed the bearing capacity of the clay. The clay surface was periodically wetted to prevent desiccation.

Two types of aggregate were selected for this research: Type 32 – crushed gravel (T32-CG), and crushed rock (CR), as shown in Figure 3. The T32-CG is a prairie aggregate,
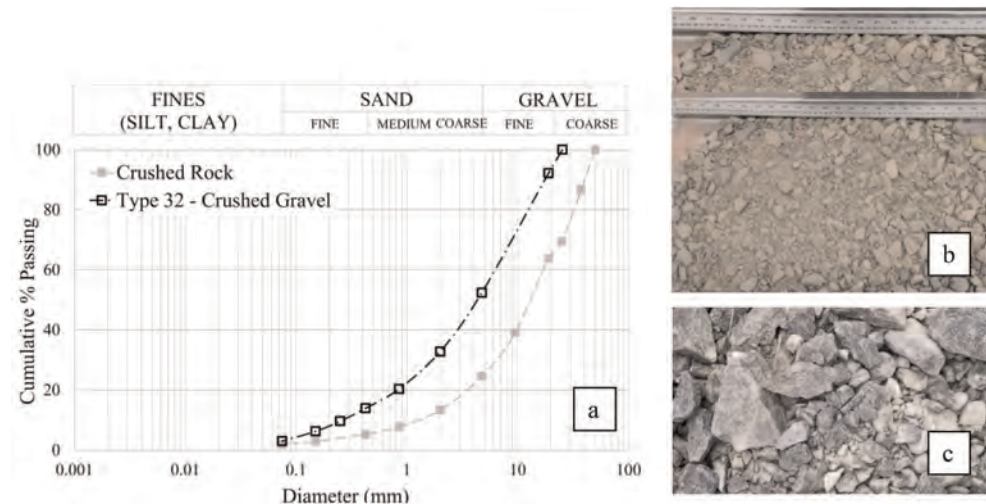
Figure 3.   (a) Grain size distribution (b) Type 32 – Crushed Gravel (T32-CG), and (c) Crushed Rock (CR).

crushed to 90% one-face and 60% two-face fracture. The CR material is a crushed granite bedrock sourced from the Precambrian shield in northern Manitoba, which is intended to represent a high quality, angular aggregate (100% fracture) used by road agencies (where available).

The aggregate is placed and compacted in three 100 mm lifts (300 mm total) using a plate tamper. The maximum dry density (MDD) for the T32-CG and CR is 2100 kg/m^3 and 2350 kg/m^3, respectively. The optimum moisture content for the T32-CG and CR is 8% and 7%, respectively. Compaction was verified through nuclear densometer testing. Each lift was compacted to an average dry density not less than 95% of the aggregate MDD.

In this study, two variable aperture shape geogrids (VASG), GG1 and GG2, were evaluated with each aggregate type. The geogrid properties are identical, with the exception of the node thickness (GG2 > GG1). A control section with no geogrid was also assessed for each aggregate type.

3.3 Instrumentation plan for MASW

The test parameters for MASW must be optimized for each test site. These parameters include the source type/size, source offset, sensor type, number of sensors, and sensor spacing (Ferreira *et al.* 2014). In 2021, a study was completed to inform the equipment requirements and layout for MASW (Yesnik *et al.* 2022). The finalized instrumentation plan is shown in Figure 4.
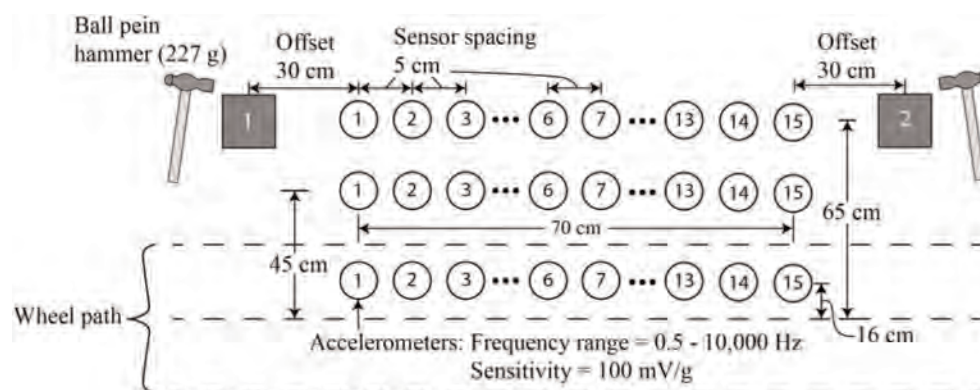
Figure 4. Finalized instrumentation plan for MASW in full-scale wheel trafficker.

4 RESULTS AND DISCUSSION

In Summer 2022, the T32-CG test sections were constructed. For this trial, the average subgrade Su was measured as 22 kPa. To exercise caution in this first trial, and avoid possible failure in the soft clay, each lane was trafficked to only 1200 load cycles at a reduced pneumatic load of 20 kN. MASW was completed at 0, 400, and 1200 load cycles.

In Fall 2022, the CR test sections were constructed. For this second trial, the average subgrade Su was measured as 32 kPa. With stiffer subgrade conditions, each lane was trafficked up to 4000 load cycles (or until reaching 70 mm of rutting) at the full pneumatic load of 40 kN. MASW was completed at 0, 450, 1350, and 4000 load cycles.

To complete MASW, the raw signal transmitted by the hammer strike is recorded by the 15- accelerometer array. Multiple hammer strikes were recorded at each array for every load cycle interval. The raw signal, recorded in the space-time domain (*x-t*), is transformed into the phase slowness-frequency domain (*p-w*) to generate an experimental dispersion image.
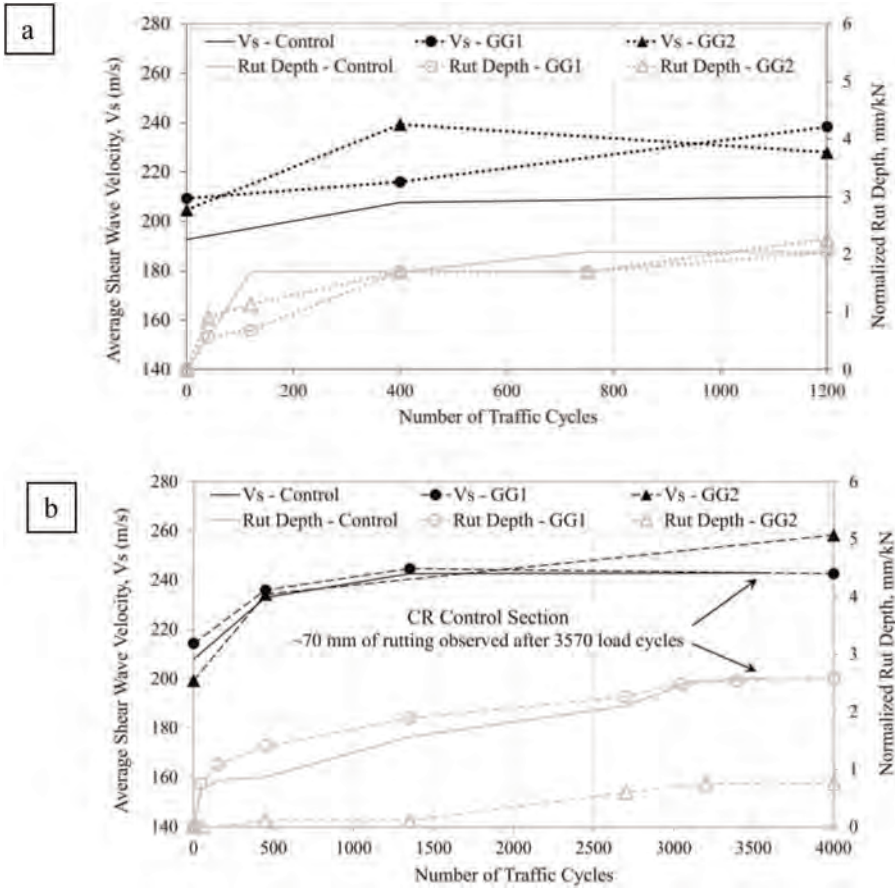
Figure 5. Average V_s and normalized rut depth vs. number of traffic cycles: (a) T32-CG, and (b) CR.

Multichannel data processing is completed using slant stacking in the slowness-frequency method to identify multi-mode dispersion curves (Park *et al*. 1998). Once these experimental modes are selected, inversion analysis is completed to create a profile of V_s and G_{max} with depth in the aggregate. MATLAB is used for all data collection and processing.

The performance of two VASG products used to stabilise T32-CG and CR aggregates, is shown in Figures 5a and 5b, respectively. The control section performance is also shown. MASW was completed for the accelerometer array located in the wheel path. The average V_s was obtained from the velocity model determined through inversion analysis. The rut depth was measured using a rut wedge, and normalized according to the applied traffic load for each trial.

For the geogrid-stabilised T32-CG, there is both a short- and long-term increase in V_s with trafficking. The control section also experiences an initial increase in V_s, which eventually plateaus. The normalized rut depth is initially lower for geogrid-stabilised T32-CG than for the control section, which aligns with the short-term trend in V_s. After long-term trafficking, the rut depth is comparable for all test sections, which varies from the long-term trends in V_s. After 1200 load cycles, the normalized rut depth only varies slightly - ranging from 2 - 2.3 mm/kN.

For the geogrid-stabilised CR, the short-term V_s is comparable to that measured in the control section. With increased trafficking, V_s increases and eventually plateaus for both the

control section and GG1-stabilised CR. However, V_s continues to trend upward with increased trafficking in the GG2-stabilised CR. The normalized rut depths are comparable for both the control section and GG1-stabilised CR; though, rutting is drastically reduced in the GG2-stabilised CR. The rutting performance aligns with the observed trends in V_s for the CR aggregate. After 4000 cycles, the normalized rut depth ranged from 0.8-2.6 mm/kN.

5 CONCLUSIONS

This paper presents an accelerated trafficking device and non-destructive test method to quantitatively assess the stabilisation performance of various aggregate-geogrid composites. The average V_s and normalized rut depths are presented for two trials. The performance of each unsurfaced test section is dependent on the properties of the subgrade, geogrid, and aggregate. Both geogrids mitigate the time-dependent degradation of stiffness (i.e., V_s) in the finer, less fractured T32-CG aggregate. There is a reduced rate of stiffness degradation also observed in the GG2-stabilised CR aggregate. The overall rutting performance over soft clay (after 1200 cycles) was comparable to that of the slightly stiffer clay (after 4000 cycles). Accordingly, the control and monitoring of subgrade strength is important to ensure consistent subgrade conditions during trafficking.

REFERENCES

Archer, S. & Wayne, M.H. 2012. Relevancy of Material Properties in Predicting the Performance of Geogrid-Stabilized Roadways. *Proceedings of Geo-Congress* 2012, 1320–1329.

Cuelho E., Perkins S. & Morris Z. 2014. Relative Operational Performance of Geosynthetics used as Subgrade Stabilization. *Final Report to the Montana Department of Transportation, FHWA/MT-14-002/7712-251*: 328.

Cuelho E. & Perkins, S. 2017. Geosynthetic Subgrade Stabilization – Field Testing and Design Method Calibration. *Transportation Geotechnics*, 10: 22–34.

Everett, M.E. 2013. *Near-Surface Applied Geophysics*. Cambridge: Cambridge University Press.

Ferreira, C., Martins, J.P., & Gomes Correia, A. 2014. Determination of the Small-Strain Stiffness of Hard Soils by Means of Bender Elements and Accelerometers. *Geotechnical and Geological Engineering*, 32(6): 1369–1375.

Kang, M., Qamhia, I.I.A., Tutumluer, E., Flynn, M., Garg, N. and Villafane, W. 2022. Near Geogrid Stiffness Quantification in Airport Pavement Base Layers using Bender Element Field Sensor. *Proceedings of the 4th International Conference on Transportation Geotechnics*, 165: 703–715.

Landry, E., Hammerlindl, A., Fleming, I., & Soliman, H. 2022. Design and Construction of a Full-Scale Traffic Simulating Apparatus Over a Soil-Geosynthetic Composite. Proceedings of GeoCalgary 2022.

Lees, A. 2017. Bearing capacity Of a Stabilised Granular Layer on Clay Subgrade, Proceedings of the 10th International Conference on the Bearing Capacity of Roads, *Railways and Airfields*: 1135–1142.

Olafsdottir, E.A., Erlingsson, S. & Bessason, B. 2018. Tool for Analysis of Multichannel Analysis of Surface Waves (MASW) Field Data and Evaluation of Shear Wave Velocity Profiles of Soils. *Canadian Geotechnical Journal*, 55(2): 217–233.

Park, C.B., Miller, R D. & Xia, J. 1998. Imaging Dispersion Curves of Surface Waves on Multi-channel Record. *SEG Technical Program Expanded Abstracts*: 1377–1380.

Park, C., Richter, J., Rodrigues, R. & Cirone, A. 2018. MASW Applications for Road Construction and Maintenance. *The Leading Edge*, 37(10): 724–730.

Yesnik, C., Morozov, I., Soliman, H., Fleming, I.R., Hammerlindl, A., & Landry, E. 2022. Traffic Induced Changes in Small-Strain Stiffness of Geogrid-Stabilised Aggregate. *Proceedings of GeoCalgary 2022*.

Zornberg, J.G., Roodi, G.H. & Gupta, R. 2017. Stiffness of Soil-Geosynthetic Composite under Small Displacements: I. Model Development. *Journal of Geotechnical and Geoenvironmental Engineering, ASCE*, 143(10): 4017075.

Zornberg, J.G. and Roodi G. H. 2021. Use of Geosynthetics to Mitigate Problems Associated with Expansive Clay Subgrades. *Geosynthetics International*, 28(3): 279–302.

Geogrid reinforced pavement design

W.S. Alexander
Southern Geosynthetics Supplies Pty. Ltd., Australia

D. Alexiew
Dr, Alexiew Geoconsulting, Germany

ABSTRACT: Geogrid reinforcement of pavements is becoming common practice in civil engineering. But in Australia no design method was available that relates directly to Australian pavement design methodology. A design method has been developed that allows rapid, effective geogrid-reinforced pavement design with reference to Austroads pavement design methodology. A case history is presented to demonstrate the usefulness of this method.

1 INTRODUCTION

This procedure evaluates the required thickness of a geosynthetic reinforced bearing layer (base) for permanent roads. It is related to stiffness (bearing capacity, CBR), and not to rut depth.

The procedure is based on Austroads empirical pavement design method (2017) using additionally the Swiss design code, SVG (2003) to model the reinforcing effects of a geosynthetic and Voss R. (1961) to calculate aggregate subbase capping layer thickness. The goal is to reduce the bearing layer thickness resulting for a given situation from Austroads (2017) by application of geosynthetic reinforcement.

2 DESIGN METHOD

In Austroads (2017) Figure 8.4 the required thickness t of a granular layer (base) depends on the CBR of the subbase (subsoil) and on the traffic cycles (DESA). For design traffic of 10^5 to 10^8 axle load cycles (DESA) the relation is given in Figure 8.4 inclusive of the corresponding equation in the form t = t(CBR, DESA). For clarity this t is called here later tAUS.

$$t_{AUS} = [219 - 211.\text{logCBR} + 58.\text{log(CBR)}^2].\text{log(DESA/120) in mm} \qquad (1)$$

The principle of this method is to create a higher CBR than the one available on site at the bottom level of the "Austroad-base", thus reducing the required tAUS above. For this purpose a geosynthetic-reinforced granular layer is being implemented below the "Austroad-base"; it consists of the same fill.

The Swiss Code SVG (2003) defines a procedure how to achieve a second loading plate modulus EV2=45 MPa corresponding to a CBR=11% (BAST2017; SVG 2003) on the surface of a compacted granular layer using reinforcement.

t = [219 – 211(logCBR) + 58(logCBR)^2]log(DESA/120)
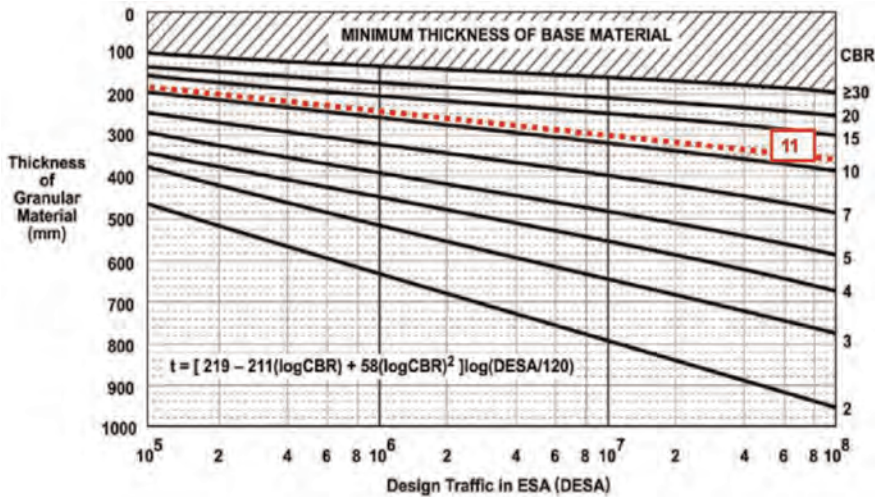
EV2=45 MPa is a kind of benchmark across Europe allowing the application of standard road structural layers above.

Input in SVG (2003) is the CBR of subsoil in the range CBR = 0,5 - 5,0%, and output is the required thickness of the layer.

For CBR>5% reinforcement makes no sense according to SVG (2003): no further thickness reduction. This corresponds approximately to the German State-of-the-Art:
no sense of reinforcement for EV2 >35 MPa (about CBR=7%).

Note that SVG (2003) is product and/or company independent.

It is based on intensive research and trials with different geosynthetics. It is stated therein that the graphs, recommendations etc. are quite conservative.

Note the following preconditions for the reinforcement according to SVG (2003):

P1. The reinforcement has to be biaxial.
P2. The reinforcement has to mobilize a tensile force of F2% >=8 kN/m at 2% strain ε (i.e. a tensile stiffness J2% >=400 kN/m at ε=2%).
P3. This has to be fulfilled in both directions. If it is not the case, the value for the "weaker" direction is decisive.
P4. The minimum Ultimate Tensile Strength (UTS), kN/m, has to be (examples for some typical products):
biaxially stretched geogrid from PP: 25 to 35 kN/m
woven geotextile from PP: 50 to 75 kN/m
woven geogrid from PET: 30 to 45 kN/m etc.

The procedure is using graphs (SVG 2003, Figures 183 & 184). For the purpose of this method the graphs were digitalized, and analytical formulations for the curves were derived. Based on them a Thickness Reduction Factor called here TRFSVG1 was formulated and derived

$$TRF_{SVG1} = t_{SVGR} / t_{SVGNR} \qquad (2)$$

$$t_{SVGR} = t_{SVGNR}. TRF_{SVG1} \text{ in mm} \qquad (2a)$$

1350

$$t_{SVGR}, \text{ in mm, is the thickness of are in forced layer} \qquad (3)$$

$$t_{SVGR}, \text{ in mm, is the thickness of an on} - \text{reinforced layer} \qquad (4)$$

For crushed fill the derivation results in

$$TRF_{SVG1} = 0,0164.CBR^2 - 0,0156.CBR + 0,6662 \qquad (5)$$

For CBR = 0,5 to 5,0% TRFSVG1 varies from 0,66 to 1,0 correspondingly.

The thickness of a non-reinforced layer can be assumed based on Voss (1961). After intensive research and test series Voss published graphs for the required layer thickness of well graded, well compacted gravels (rounded material) to achieve an EV2 from 25 to 250 MPa on the layer surface for an EV2 of subsoil in the range of 5 to 40 MPa (approximately CBR 0,5 to 9%, BAST(2017)).

Although a couple of years has passed, Voss (1961) is still being used and cited due to its basic character e.g. in Grundbau Taschenbuch (2009) or the ZTVE-Series for road construction ZTVE (2006).

For the purpose of this method the Voss-curves were digitalized, and an analytical formulation was derived for the required thickness tVOSS, mm, to achieve EV2 = 45 MPa (CBR= 11%) for CBR of subsoil from 0,5 to 5,0%, see explanations above and SVG (2003):

$$t_{VOSS} = -6,8048.CBR^3 + 88,175.CBR^2 - 402,86.CBR + 844,8 \text{ in mm} \qquad (6)$$

It is obvious due to geomechanical common sense and experience that for a well graded crushed fill the required thickness will be smaller than for rounded gravel as in Voss (1961), and consequently a reduction of tvoss is possible if crushed fill is used.

In SVG (2003) there are graphs for both crushed and rounded fills. Their analysis, comparison and evaluation result in a Thickness Reduction Factor TRFCRUSH if crushed fill is used instead of a rounded one.

$$TRF_{CRUSH} = t_{CRUSH}/t_{VOSS} = 0,8 \qquad (7)$$

$$t_{CRUSH} = t_{VOSS}. \ TRF_{CRUSH} \qquad (7a)$$

$$t_{CRUSH}, \text{ in mm, is the thickness of an on} - \text{reinforced layer from crushed material} \quad (8)$$

$T_{RFCRUSH}$ is almost independent from CBR and can be assumed as constant.

3 DESIGN PROCEDURE SUMMARY

The design can be performed as follows:

a) Calculate tAUS according to Austroad (2017) using Equation (1).
   Note: this is needed only if savings due to an added reinforcement have to be evaluated, see Equation (11) below.
b) Calculate the required layer thickness to achieve a CBR=11% at the level of the bottom of the "Austroad-base" called here tCBR11
   (additionally marked as a red dotted line here in Figure 8.4 from Austroads (2017)).
   2.1 Calculate tVOSS using Equation (6).
   2.2. Calculate tCRUSH using Equation (7) & (7a).
   2.3.

$$\text{Set } t_{SVGNR} = t_{CRUSH} \qquad (9)$$

Figure 1.   Subgrade condition.

Figure 2.   Geogrid with capping layer.

Figure 3.   Installing crushed rock capping layer over geogrid.

Figure 4.   Final pavement ready for asphalt wearing course.

2.4. Calculate TRFSVG[1] using Equation (5).

2.5. Calculate tSVGR using Equation (2a).

2.6. Set tCBR11 = tSVGR.

This is the required thickness of an implemented layer to achieve a CBR=11% at its surface (i.e. at the bottom level of an "Austroad-base" to be installed above).

c) Calculate a new tAUS acc. to Austroad (2017) using Equation (1) for a CBR=11%: This new value is called here tAUS11.

d) Calculate the final new required "reinforced" base thickness tFIN:

$$t_{FIN} \; = \; t_{CBR11} + t_{AUS11}, \; mm \tag{10}$$

Figure 5 Example Design

If from interest, the saving due to the use of reinforcement tSAVING, mm, can be now calculated as:

$$t_{SAVING} = t_{AUS} - t_{FIN}, mm \qquad (11)$$

Note that although this procedure is using mm due to formal reasons (Figure 8.4 in Austroad (2017) is using mm) a precision of 1 mm for a base thickness cannot be practically achieved.

4 EXAMPLE

At the new Essendon FC base, "The Hanger" at Tullamarine, designer Aurecon was faced with a real dilemma. The very soft reactive clay subgrade had repeatedly failed proof-rolling. Traditional options of dig-out and replacement with good quality fill, or in-situ cement-stabilisation were not possible due to the presence of a wide shallow service trench along the middle of the roadway alignment. With very little cover over services no further excavation was possible.

Assuming a design CBR of 1%, and design traffic of 100,000 ESA, the design program solution called for placement of DUX CG30, a 30kN/m biaxial geogrid combined with a non-woven geotextile at subgrade together with a 280mm "stabiliser" layer of crushed rock; this would then provide a working platform with CBR=11% and allow compaction of a second 180mm thick crushed rock pavement layer. The total pavement thickness of 460mm represents a saving of some 200mm, or 30% over traditional design.

To be extra-conservative designer Aurecon opted for reduced thickness of 180mm of cement-treated first lift, followed by 200mm of Class 2 FCR and a wearing course of 40mm AC. Upon setting after a few days the cement increases the strength and stiffness of the first stabiliser layer and provides an improved base for compaction of the second lift. But even on initial placement, before the cement "went off", the grid and 180mm layer virtually eliminated rutting under construction truck traffic.

One of the concerns of the contractor was how to achieve satisfactory compaction of pavement layers. Standard road construction practice requires satisfactory "proof-rolling" of the sub grade, with no visible movement or cracking of the subgrade. Any soft, "unsuitable" areas are dug out and replaced with engineered fill to achieve a typical CBR of 15%. However, when building on very soft soils, construction practice must be modified. Roadbase must be placed more carefully, dump trucks should avoid directly trafficking the grid wherever possible. Materials should be spread with light, low ground- pressure, such as the tracked bobcat such used here.

5 CONCLUSIONS

A design method has been developed to permit design of geogrid-reinforced pavements. The method draws on the Austroads pavement design method, with further input from the Swiss Code SVG for the reinforcing effect of geogrid and the work of Voss relating to aggregaFigure 6. Design Spreadsheet.

te pavement layer thickness. This method assumes a two step procedure, first a geogrid-reinforced subbase capping layer is designed to effectively increase the subgrade bearing strength, then the pavement is designed based on this improved subgrade. For subgrades of CBR<2% up to 30% reduction in total pavement thickness is achieved.

This method was first introduced in 2018 and has been used on numerous projects. Based on this experience the method appears useful and appropriate. One area for further research is regarding the use of cement-treated crushed rock with geogrids.

REFERENCES

Austroads (2017). *Guide to Pavement Technology. Part 2: Pavement Structural Design*. Australia, Sydney, 2017.

BAST (2017). *Berichte der Budesanstalt für Strassenwesen. Baustoffe für Standfeste Bankette. BAST Berichte*, Heft S 107, Deutschland, Bergisch-Gladbach, 2017.

(BAST. German Federal Road Institute. BAST-Reports, Volume S 107).

Grundbau Taschenbuch (2009). *Teil 2: Geotechnische Verfahren*.7. Auflage.

Ernst & Sohn, A Wiley Company, Deutschland, Berlin, 2009. (*Handbook Geotechnics. Part 2: Geotechnical Methods*).

SVG (2003). *Bauen mit Geokunststoffen*. Handbuch. Schweiz, St. Gallen, 2003.

(Constructing with Geosynthetics. Handbook).

Voss R. (1961). *Lagerungsdichte und Tragwerte von Böden bei Straßenbauten*. Straße uns Autobahn, Heft 4, S. 115. Deutschland, Köln, 1961.

(Density and Bearing Values of Soils in Road Construction).

ZTVE-StB 94, 1997 (2006). *Kommentar mit Kompendium Erd- und Felsbau - unter Beruecksichtigung der nationalen und europaeischen Regelwerke*. Ed. R. Floss. Kirschbaum Verlag, Bonn, 2006. (Comments and Compendium Earth and Rockworks under Consideration of National and European Codes).

Taylor & Francis
Taylor & Francis Group
http://taylorandfrancis.com

Railways and other transportation applications

Evaluation of multi-functional composite geotextile's contribution to railway track stabilization through laboratory research

G. Liu & X. Jiang
Southwest Jiaotong University, Chengdu, Sichuan, China

C.J. Jong, T.W. Yee, Q. Lin & S.I.S. Teh
TenCate Geosynthetics Asia Sdn. Bhd., Shah Alam, Selangor, Malaysia (A Solmax Company)

ABSTRACT: Railway has multiple advantages of reliable service, fast and versatile to both passenger and cargo as compared to other modes of transportation infrastructure. However, the efficiency and safety of railway engineering are dependent on the track structure. This paper evaluates the contribution of the multi-functional composite geotextiles to the railway track, through a laboratory test carried out at Southwest Jiaotong University, Chengdu, in collaboration with international industry practitioners. The contributions are assessed through the quantification of the traffic improvement as well as the reduction in ballast and sub-ballast fouling for three sets of simulated cyclic train loading test model, Model 1 as control, with Model 2 and Model 3 using different types of multi-functional composite geotextiles. The findings validate the reduction of vertical deformation and reduction of fouling by using multi-functional composite geotextiles, ultimately allowing the railway track to support additional train traffic and longer lifespan.

1 INTRODUCTION

Railway engineering is a comprehensive industry; comprised of many components including railway track, station, drainage, etc. to ensure the railway smoothly serves the global society without disruption. Among all components, railway track (i.e. track structure and track subgrade as shown in Figure 1) is considered the primary component that governs the efficiency and safety of the railway (Li & Selig 1995; Selig & Li 1994; Tan & Shukla 2012).

The railway track is a more complex field than roadway with a few important considerations including increasing the bearing pressure (capacity) of the subgrade soil,
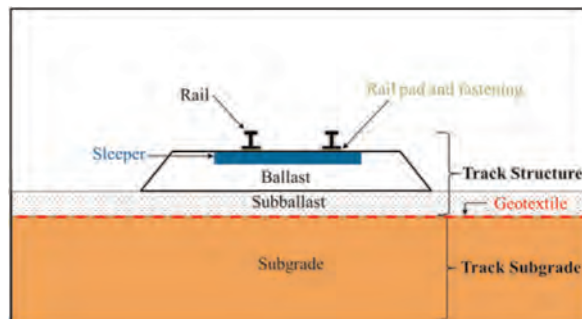
Figure 1. Typical section of railway track.

1359

preventing contamination of the ballast by subgrade fines, dissipating the high pore water pressures built up by cyclic train loadings, and moisture management for expansive or frost heave and thaw susceptible subgrade (adapted from Indraratna *et al*. 2006). It is rarely seen that one geosynthetic type can fit all the above considerations, so multi-functional composite geotextiles are needed. In this paper, the contribution of multi-functional composite geotextiles to the railway track is evaluated through a full scale laboratory model tests. These tests study the vertical deformation behaviour, bearing pressure response, pore pressure variation, and fouling condition of the track structure under cyclic train loadings in different test conditions, for one control section (without geosynthetics) and two reinforced sections (with different composite geotextiles laid below subballast).

2 MODEL TEST

2.1 *Test box and loading apparatus*

The research is conducted at Southwest Jiaotong University (SWJTU) in Chengdu, which is a top research center for the railway engineering industry in China. The test box setup simulates the actual cyclic train loadings exerted on the top surface of 300 mm thick ballast. The loading of 20 tonnes railway axle load on sleeper was simulated using a steel loading plate measuring 1.1 m length and 0.3 m width, which represents half effective areas of the common sleepers utilized in Asia. As a result, the actuated cyclic train loadings were applied in a sinusoidal form with 48 kN as peak load and 4.8 kN as trough load at a frequency of 3 Hz. Besides that, a 20 mm thin rectangular sandbag was laid below the steel loading plate to ensure a uniform loading exerted on the ballast. The test box size was carefully determined through the ABAQUS and Plaxis 3D finite element methods (FEMs), to achieve an optimal box size with the least influence on the test results by the boundary condition. The FEMs suggest that the distance between the edge of the steel loading plate and the steel test box should be kept at a minimum of 0.15 m, and 50 mm thick polystyrene should be added along the inner edge of the steel test box. Meanwhile, the height of the test box should be a minimum of 1.2 m. As a result, the actual steel test box (Figure 2) measured 1.5 m length, 0.7 m width and 1.3 m height, equipped with the mechanism to accommodate the sophisticated requirements of tests was adopted for this research.

The test sections are illustrated in Figure 3, with different types of composite geotextiles laid in between the subballast and subgrade in the reinforced section, and without geosynthetics for a control section. Three loading stages were applied, each to 200,000 cycles of peak load. Stage 1 loading involved the initially prepared subgrade to 90% compaction lifts according to Modified Proctor Test at near optimum moisture content overlaid by 150 mm thick subballast and 300 mm thick ballast, subsequently 200,000 cyclic train loadings were applied. After completion of Stage 1 loading, water was sprayed on the top surface of the ballast to simulate rainfall. The rainfall simulation was applied over a 12 hours period that
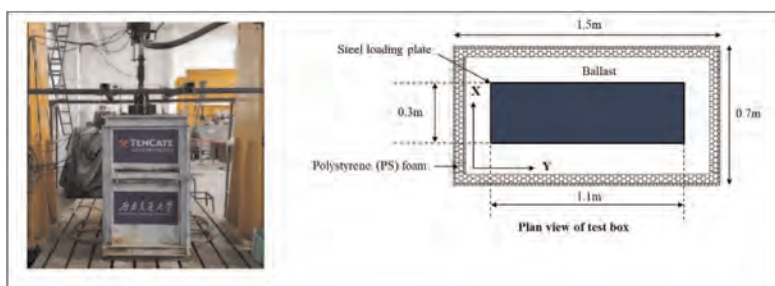
Figure 2. Cyclic train loading test box.

1360
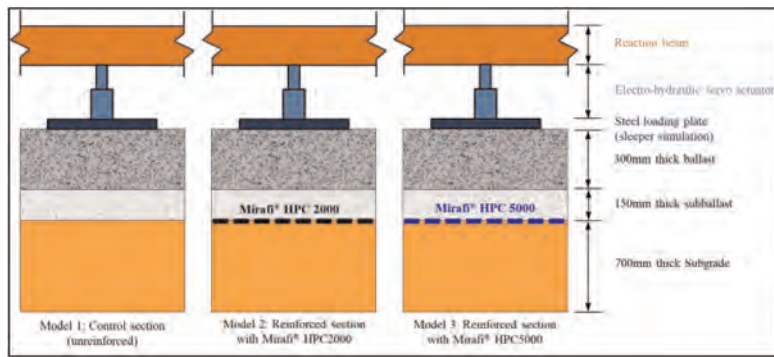
Figure 3. Typical section of steel test box and loading apparatus.

consisted of 6 cycles of 1 hour rainfall and 1 hour rest period. The average rainfall rate is 50 liters/hr. The test box was designed with a side window slot that allowed some water infiltration into subgrade soil while excess water could drain horizontally through the ballast and exit through the side window slot. Stage 2 loading started after 12 hours rest period at the end of the rainfall simulation. At the end of Stage 2 loading, the side window slot was sealed and then the test box was flooded to allow the subgrade soil to be soaked for 10 days until fully saturated. After 10 days, the side window slot was opened to allow excess water in the ballast to be drained off, and the Stage 3 loading was then initiated after that. Upon completion of Stage 3 loading, subballast and ballast were carefully extracted to measure the degree of fouling. The test box was then emptied before a second test was conducted. The second and third tests were identical to the control test, with the only exception of Mirafi® HPC2000 and Mirafi® HPC5000 being placed in between the subgrade and sub-ballast.

2.2 *Instrumentation*

Instrumentations were being installed for a variety of purposes, and properly calibrated before the commencement of tests as shown in Figure 4.
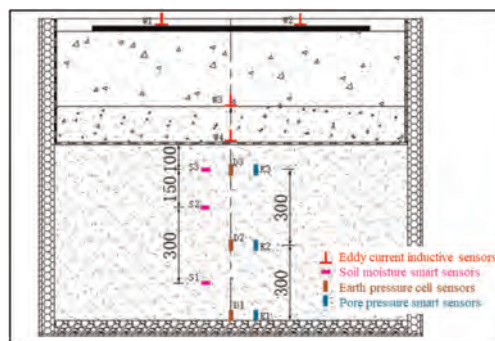
Figure 4. Instrumentations installed in each model.

2.3 *Subgrade soil*

The subgrade used for the test is a synthesized soil consisting of quartz powder (90%) and montmorillonite powder (10%) and is classified as low plasticity clay (CL) under the Unified

Soil Classification System (USCS), with more than 85% soil particles finer than 75 microns, PI = 13.1 and LL = 36. The purpose of using synthesized soil in the research is to ensure the consistency of subgrade conditions for each model. An exercise to calibrate the subgrade CBR against moisture content was also conducted (refer Figure 5).
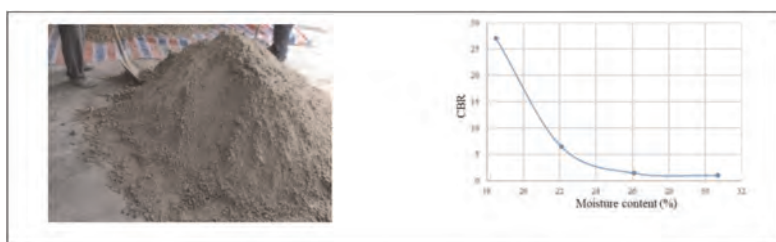
Figure 5.   Subgrade soil and its calibrated CBR vs. moisture content curve.

2.4   *The ballast and sub-ballast*

The ballast and sub-ballast used in the research are both classified as well-graded gravel (GW) under USCS and generally conform to most country standards in Asia (Arema 2010; KTM 2015; RDSO 2007; SNI 2018; TB2897 1998; TB2140 2008). They are stiff basalt and granite, readily available in Sichuan province.

2.5   *Geosynthetics*

TenCate Geosynthetics has invented composite geotextiles (a combination of woven and nonwoven geotextiles mechanically connected by parallel stitching thread at close intervals), namely Mirafi[®] HPC2000 and Mirafi[®] HPC5000 which have a combination of the reinforcement, dynamic separation, drainage and moisture management functions (moisture management function only for Mirafi[®] HPC5000). Their actual test data and photos are shown in Table 1 and Figure 6

Table 1.   Properties of Mirafi[®] HPC composite geotextiles.

Geosynthetics	at 2% strain (kN/m) (MD*/CD**)	Tensile strength at 5% strain (kN/m) (MD*/CD**)	CBR puncture strength (kN)	Peel strength (kN/m) (CD**)	Pore size (mm)	Perme-ability (cm/s)	In-plane flow rate (l/m.h) (MD*/CD**)
Mirafi[®] HPC2000	21.4/38.4	62.8/80.9	12.4	17.3	0.14	0.25	39.2/40
Mirafi[®] HPC5000	11.3/40.7	29.4/101.2	14.5	21.1	0.12	0.21	74.3/87.7
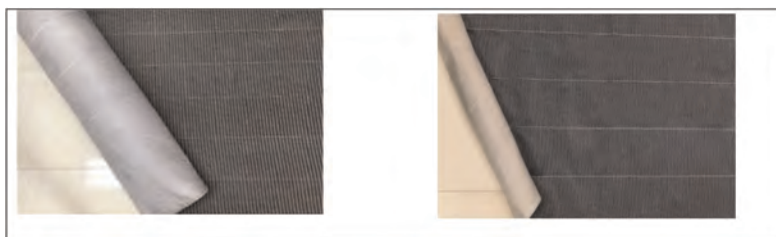
Figure 6.   Mirafi[®] HPC2000 and Mirafi[®] HPC5000 composite geotextile (from left to right).

3 TEST RESULTS AND DISCUSSIONS

3.1 Soil moisture

The subgrade soil moisture contents are summarized in Table 2 as below. The moisture content in Stage 1 was controlled close to OMC, averaged at 17.9%. And then, the moisture content in Stage 2 is determined at the end of 12 hours rest period after rainfall simulation, averaged at 21.2%. Lastly, the moisture content in Stage 3 is determined after 10 days of full saturation averaged at 28.4%. With the average moisture content determined, the CBR for Stage 1, 2 and 3 are estimated as 30, 12 and 1 by using Figure 5.

Table 2. Subgrade moisture content and CBR.

Moisture sensor	Subgrade moisture content at the beginning of cyclic train loadings (%)								
	Stage 1			Stage 2			Stage 3		
M*	M1	M2	M3	M1	M2	M3	M1	M2	M3
Upper (S3**)	17.0	18.2	17.4	25.6	23.2	22.3	32.5	28.4	27.2
Middle (S2**)	18.9	17.7	18.1	19.8	20.5	20.7	26.2	24.4	24.6
Lower (S1**)	17.2	18.3	18.5	19.4	19.6	20.0	31.0	31.6	30.2
Mean (M*)	17.7	18.1	18.0	21.6	21.1	21.0	29.9	28.1	27.3
Mean (Stage)		17.9			21.2			28.4	
CBR (Stage)		30			12			1	

*M= Model; **Refer Figure 4 for details

3.2 Vertical deformation

The vertical deformation is largest at ballast (average of W1 and W2 in Figure 4), followed by subballast (W3 in Figure 4) and least at subgrade (W4 in Figure 4) for all stages and models. This phenomenon is reasonable as the cyclic train loadings induced stress is highest at ballast. The stress reduced gradually when being transferred down to subballast and then subgrade. Besides, the differences in vertical deformation of each model in Stage 1 and Stage 2 are negligible. However, the differences in vertical deformation between each model in Stage 3 are obvious, especially for ballast layer, whereby Model 1 = 49.84 mm, Model 2 = 21.38 mm (reduced by 57.1%) and Model 3 = 19.03 mm (reduced by 61.8%). This phenomenon indicates that the Mirafi® HPC2000 and Mirafi® HPC5000 are effective to minimize the vertical deformation of railway track on low CBR subgrade.
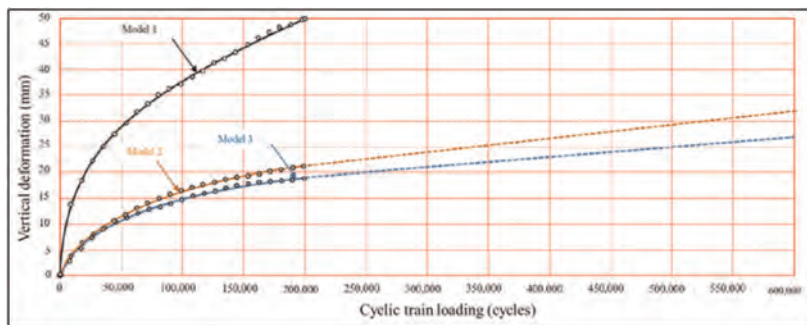
Figure 7. Cumulative plastic vertical deformation prediction at subgrade CBR=1.

By replotting the graph of vertical deformation of all models in Stage 3 (CBR = 1) to a normal scale as shown in Figure 7, the traffic benefit ratio (TBR), which is the train loading cycles of a reinforced section divided by the train loading cycles of a control section to reach the same settlement. The vertical deformation for track structure is normally controlled within 20 mm to 30 mm depending on the individual country's requirement. The train loading cycles and subsequent TBR (average TBR = 8.8 to 13) are tabulated in Table 3.

Table 3. Predicted train cycles and TBR with the inclusion of Mirafi® HPC composite geotextiles.

Test Section	Train cycles			TBR			Average TBR
	20mm	25mm	30mm	20mm	25mm	30mm	
*M1: Control	20,920	37,000	55,870				
*M2: with Mirafi® HPC2000	167,600	335,000	522,450	8	9	9.3	8.8
*M3: with Mirafi® HPC5000	254,590	500,000	745,410	12.2	13.5	13.3	13

*M= Model

3.3 *Ballast and subballast fouling*

Both ballast and subballast were cleaned with water before the test, the fine materials were washed away, and the smallest particle size of subballast is 0.25 mm. As such, the percentage of soil material smaller than 0.25 mm is considered fouling, being assessed at a few locations. After the sampling, the samples were oven-dried and the weight was measured as *m1*. After that, they will be washed in the sieve of 0.25 mm, and then oven-dried again, and the weight is measured as *m2*. The *fouling, μ* is defined as

$$Fouling~(\%),~\mu = (m1 - m2)/m2 \qquad (1)$$

Figure 8 showed the fouling of subballast in all three models at the end of the test, in which the subballast fouling is 3% in Model 1, 1.4% in Model 2 and 0.8% in Model 3. This showed that Mirafi® HPC2000 and Mirafi® HPC5000 composite geotextiles are very effective to prevent subballast fouling (reduced by 53% in Model 2 and 73% in Model 3). For the ballast fouling, it is very minor and there are negligible differences among all the models.

Figure 8. Fouling's observation in Model 1, Model 2 and Model 3 (from left to right).

4 CONCLUSION

In conclusion, this research proves that Mirafi$^{\circledR}$ HPC composite geotextiles effectively reduced vertical deformation and minimized fouling, thus prolonging the service life of railway track.

REFERENCES

AREMA 2010. *Manual for Railway Engineering*. Maryland: American Railway Engineering and Maintenance-of-Way Association.

Indraratna, B., Khabbaz, H., Salim, W. & Christie, D. 2006. Ground Improvement. *Geotechnical Properties of Ballast and the Role of Geosynthetics in Rail Track Stabilisation*. 10 (3): 91–101.

KTM 2015. *Permanent Way Manual*. Kuala Lumpur: Keretapi Tanah Melayu.

Li, D. & Selig, E.T. 1995. *Evaluation of Railway Subgrade Problems. Presented at 74th Annual Meeting of the Transportation Research Board*, Washington, D.C.

RDSO 2007. *Guidelines for Blanket Layer Provision on Track Formation with Emphasis on Heavy Axle Load Train Operation*. Lucknow: Research Designs & Standards Organisation, India.

Selig, E. T. & D. Li 1994. *Track Modulus- its Meaning and Factors Influencing it. Presented at 73rd Annual Meeting of the Transportation Research Board*, Washington, D.C.

SNI 2018. *Spesifikasi Balas*, *Sub Balas dan Lapisan Dasar（subgrade）Untuk Jalur Kereta Api'. Badan Standardisasi Nasional*. Jakarta: Standar Nasional Indonesia.

SWJTU 2020. *Experimental Research of Mirafi$^{\circledR}$ HPC Composite Geotextile- performance improvement on railway track（in Chinese）*. Chengdu: Southwest Jiaotong University.

Tan, S.A. & Shukla, S.K. 2012. *Handbook of Geosynthetic Engineering (2nd edn.)- Chapter 9: Railway tracks*. London: ICE Publishing.

TB2140 2008. *Railway Ballast*. Beijing: China Railway Press.

TB2897 1998. *Sub-ballast for Ballast Bed of Railways*. China: Ministry of Railways.

Reducing the settlement of railway ballast by random fibre reinforcement

E. Ferro
Department of Civil Environmental and Mechanical Engineering, University of Trento, Italy

L. Le Pen
Ramboll, Southampton, UK
School of Engineering, University of Southampton, UK

A. Zervos & W. Powrie
School of Engineering, University of Southampton, UK

ABSTRACT: Random fibre reinforcement of granular soils with flexible polymeric fibres increases their shearing resistance and ductility. However, the potential advantages of fibre reinforcement are not limited to monotonic loading conditions. Recent research has shown that fibre reinforcement has the potential to reduce the permanent settlement of granular materials subject to cyclic loading, such as railway ballast. Ballast is still widely used on railways, as ballasted tracks are still predominant worldwide and are compatible with high-capacity and high-speed applications. Under repeated train passages, ballasted track settles differentially hence costly maintenance operations are required periodically to restore the correct rail level. Full-scale tests in the Southampton Railway Testing Facility (SRTF) have shown that the addition of a moderate amount of thin polyethylene strips to ballast can reduce the permanent settlement with marginal influence on track stiffness, provided that the fibres are sufficiently narrow not to disturb the natural arrangement of the ballast grains. As with fibre reinforced soils, the performance of fibre-reinforced ballast is expected to be influenced by the characteristics of both the host material and reinforcement. This study presents the results of full-scale tests carried out in the SRTF using different materials for the fibres and ballast. The fibres were obtained from polypropylene rope to replicate at a much larger scale the polypropylene filaments often used for the reinforcement of sands. The ballast was coarser and settled significantly less. The design of the reinforcement was informed by packing tests, as suggested by earlier tests using strip fibres. Thin fibres, with a small influence on the packing of the grains, were found to reduce the permanent settlement and had little influence on track stiffness.

1 INTRODUCTION

Reinforcement by randomly-placed flexible polymeric fibres can increase the shear strength of granular materials ranging from sands to gravels, while inhibiting dilation and post-peak strength loss (Ajayi *et al.* 2017b; Diambra *et al.* 2013; Gray & Ohashi 1983; Heineck *et al.* 2005; Lirer *et al.* 2012; Michalowski & Čermák 2003; Santos *et al.* 2010). The reinforcing effect provided by the fibres is attributed to them stretching with the deformation of the soil, hence providing additional confinement (Ajayi *et al.* 2017a; Diambra *et al.* 2010; Gray & Ohashi 1983; Mandolini *et al.* 2019; Michalowski & Čermák 2002). In contrast, at relatively small vertical strains of 1% to 5%, the fibres may reduce the mobilised shear strength (Ajayi *et al.* 2017b; Diambra *et al.* 2013; Heineck *et al.* 2005; Michalowski & Čermák 2003; Santos

et al. 2010). This may be explained by the fibres increasing the void ratio by disrupting the natural packing of the grains (Ajayi *et al.* 2014a; Ferro *et al.* 2022; Lirer *et al.* 2012; Santos *et al.* 2010). Moreover, the fibres require a small initial strain, inversely proportional to the initial density, to become effective (Consoli *et al.* 2009).

Recent research has investigated the potential of fibre reinforcement to improve the performance of railway ballast, as used on most railways (Ajayi *et al.* 2014b; Ferro *et al.* 2022). Modern ballast consists of uniformly-graded, coarse gravel obtained by crushing of high-quality rock, e.g. granite. In response to the stresses induced by the passage of trains, ballast deforms plastically leading to the accumulation of permanent differential track settlements. Costly maintenance operations, e.g. mechanical tamping, are required periodically to restore the correct track level. Considering that ballast settlement is the main source of the overall track settlement (Selig & Waters 1994), fibre reinforcement of ballast, if effective, could extend ballast service life and reduce maintenance costs. Moreover, random fibre reinforcement should be less sensitive to tamping operations than geogrids, also used on railways, which must be placed at a sufficient depth to avoid damage by tamping (Bathurst & Raymond 1987).

Full-scale cyclic tests in the Southampton Railway Testing Facility (SRTF) have shown that, under controlled laboratory conditions, the addition of a moderate proportion of narrow strip fibres can reduce the permanent settlement of ballast by approximately 20% with a negligible influence on the unloading-reloading stiffness. In contrast, excessively wide fibres may increase the settlement and should therefore be avoided, as they disrupt significantly the packing of the ballast grains reducing the initial density of the material (Ferro *et al.* 2022). Wider fibres would anyway be more problematic to mix uniformly with ballast and more prone to segregation during ballast placement.

This paper will present the results from full-size tests carried out in the SRTF to investigate the performance of fibres obtained from polypropylene rope, a scaled-up version of the polypropylene filaments often used as a reinforcement in sands.

2 MATERIALS AND METHODS

The ballast consisted of uniformly-graded, freshly-crushed granite aggregates from Mountsorrel quarry (Leicestershire, UK). The main characteristics and grain size distribution are shown in Figure 1(a), where G_s is the specific gravity, D_{50} is the average grain size, C_u is the coefficient of uniformity, e_{max} is the maximum void ratio; and e_{min} is the minimum void ratio. The fibres were obtained from general purpose three-strand polypropylene rope, of length L_f 300 mm and diameters d_f between 4 mm and 12 mm (Figure 1(b)).
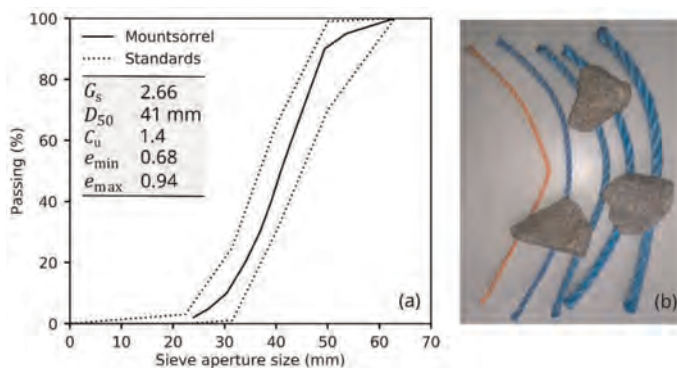
Figure 1. (a) Grain size distribution, standard specification range (Cat. A, BS EN 13450:2002) and key characteristics for Mountsorrel ballast; (b) photo of ballast grains and polypropylene rope fibres with L_f = 300 mm and d_f = 4, 6, 8, 10, 12 mm).

To take account of the relative sizes of the fibres and the grains, the fibre-ballast composite was characterised in terms of fibre/grain ratio N_{fg}, normalised fibre length L_N and normalised fibre diameter d_N (Ajayi *et al.* 2017a):

$$N_{\text{fg}} = N_{\text{f}}/N_{\text{g}} \tag{1}$$

$$L_N = L_{\text{f}}/D_{50} \tag{2}$$

$$d_N = d_{\text{f}}/D_{50} \tag{3}$$

where N_{f} is the number of fibres and N_{fg} is the number grains (calculated as the weight of the ballast divided by the average weight of a single grain, $\sim$0.12 kg). For a given fibre length and diameter, N_{fg} is indicative of the number of grains that can be potentially engaged by each fibre.

The testing apparatus (Figure 2) is a full-size, plane-strain representation of a one-sleeper bay, which has been used previously to investigate the influence of ballast and sleeper interventions on railway track performance (Abadi *et al.* 2018, 2019; Ferro *et al.* 2020; Le Pen & Powrie 2011). The specimens were prepared from bottom to top by placing a 12 mm rubber mat that mimics the resilience of the subgrade, a 30 cm layer of ballast as typical in real railways, a G44 concrete sleeper with two short rail sections for load application, and further 20 cm of ballast to reach the upper surface of the sleeper. The fibre reinforced ballast was prepared by mixing the desired proportions of ballast and fibres manually in buckets, which were then gently poured into the testing rig to avoid fibre segregation. LVDTs were installed at several locations along the sleeper to measure vertical displacements. In each test a cyclic, vertical load representative of a 20-tonne train axle was applied evenly to the rails at 3 Hz for 3 million cycles using a hydraulic actuator. A more detailed description of the testing apparatus and preparation protocols is provided in Ferro *et al.* (2022).
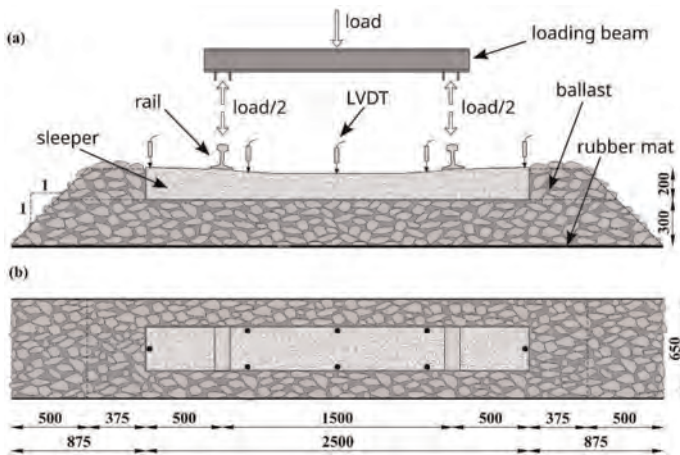
Figure 2.   Schematic of test set-up with dimensions in mm; (a) cross-sectional view; (b) plan view.

3   RESULTS

Results are presented in terms of permanent settlement and resilient deflections for the 4 full-scale tests listed in Table 1.

Table 1. List of tests.

Test	L_N	d_N	N_{fg} (%)
M1	–	–	0
M2	7.1	0.14	7.6
M3	7.1	0.24	7.1
M4	7.1	0.14	13.4

In all the tests L_N was set to 7.1. This gives a fibre length equal to the depth of the ballast bed (300 mm) and should be sufficient to mobilise tension in fibres (Ajayi *et al.* 2017b). Fibre diameters were selected based on the results of the packing tests on the ballast/fibre composite (not reported in this paper, owing to limitations of space). At a given N_{fg}, the fibres with $d_N \leq 0.14$ did not inhibit significantly the packing of the ballast grains, hence were more likely to reduce the ballast settlement under cyclic loading (Ferro *et al.* 2022). For this reason, relatively thin fibres with $d_N = 0.14$ were used in test M2. For comparison, thicker fibres were used in test M3. For the thinner fibres, the effect of the fibre content N_{fg} was also investigated (test M4). The maximum fibre content used ($N_{fg} = 13.4\%$ in test M4) corresponds to approximately 60% of the maximum number of fibres that, based on visual inspection, could be added to ballast without extensive fibre overlapping.

For all the tests, the increase in average permanent settlement of the sleeper (calculated by weighted area) with the logarithm of the number of loading cycle is shown in Figure 4. The thinner fibres with $d_N = 0.14$ reduced the final settlement compared with the baseline test without fibres. At $N_{fg} = 7.1\%$ (test M2) they reduced it by ~10%, at $N_{fg} = 13.4\%$ by ~20% (test M4). This suggests that larger fibre contents may further reduce the settlement. However, previous full-size tests using strip fibres showed that the addition of too many fibres may in fact worsen performance (Ferro *et al.* 2022). The thicker fibres with $d_N = 0.24$ (test M3) were ineffective, increasing (very slightly) the settlement. This was attributed to the fibres disrupting significantly the natural packing of the ballast grains, hence increasing the ballast propensity to exhibit permanent settlement, as already observed for strip fibres (Ferro *et al.* 2022).
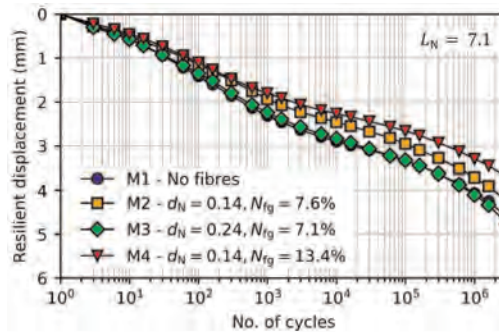
Figure 3. Settlement vs no. of loading cycles.

For each load cycle, the resilient deflections of the sleeper were calculated as the difference between the maximum and minimum displacements. The change in resilient deflection at the middle and at the ends of the sleeper with the logarithm of the number of loading cycles is shown in Figure 4. Overall, the fibres had no adverse effect on resilient deflections. At the middle, their effect was negligible (Figure 4(a)). At the sleeper ends, they reduced the resilient
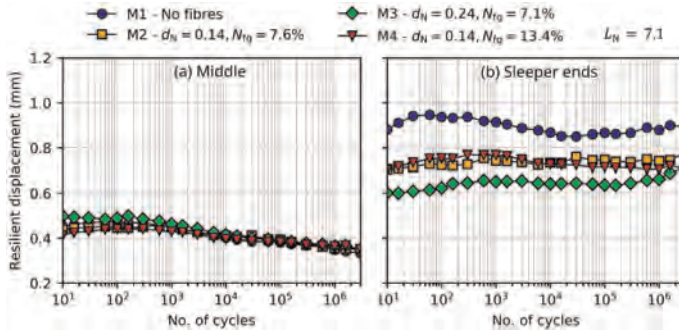
Figure 4. Resilient displacement (a) at the middle of the sleeper and (b) at the sleeper ends, vs no. of loading cycles.

deflections (Figure 4(b)). Therefore, the rope fibres reduced the gapping between the sleeper ends and the ballast, which is responsible for the larger displacements measured at these locations (Ferro *et al*. 2020).

4 CONCLUSIONS AND FINAL REMARKS

Previous full-scale laboratory tests carried out in the Southampton Railway Testing Facility (SRTF) had shown that the addition of narrow, polyethylene strip fibres to ballast can reduce its permanent settlement without affecting significantly its stiffness (Ferro *et al.* 2022). Building on this, further full-size tests were carried out to investigate the potential of a different fibre material, comprising polypropylene rope, and improve understanding of the performance of fibre reinforced ballast. These new tests have shown that:

— relatively thin rope fibres with $d_N = 0.14$ at a content of $N_{fg} = 13.4\%$ reduced the ballast settlement by $\sim$20%
— thicker rope fibres with $d_N = 0.26$ were ineffective; this was attributed to the thicker fibres inhibiting the packing of the ballast grains, hence increasing ballast propensity to settle
— the settlement reduced approximately linearly with increasing fibre content, at least for $N_{fg} \leq 13.4\%$
— ballast stiffness was not adversely affected (reduced) by the addition of fibres and both the thinner and thicker fibres reduced the resilient displacements at the sleeper ends, i.e. they reduced gapping between the sleeper and the ballast.

Qualitatively, the effect of the rope fibres on ballast performance was consistent with that observed for the strip fibres. Neither fibre type adversely impacted the stiffness and both reduced ballast settlement if their dimensions were selected to avoid significant disturbance of the natural arrangement of the ballast grains. Rope fibres may be more effective than strip fibres. Although both types of fibre reduced the settlement by $\sim$20%, the rope fibres improved a particularly good ballast, which on its own exhibited very small settlements. However, further research is required to fully understand the behaviour of fibre reinforcement ballast and evaluate the optimal fibre characteristics for ballast improvement.

ACKNOWLEDGEMENTS

REFERENCES

Abadi, T., Le Pen, L., Zervos, A. & Powrie, W. 2019. Effect of Sleeper Interventions on Railway Track Performance. *Journal of Geotechnical and Geoenvironmental Engineering* 145(4), doi:10.1061/(ASCE) GT.1943-5606.0002022.

Abadi, T., Le Pen, L., Zervos, A. & Powrie, W. 2018. Improving the Performance of Railway Tracks Through Ballast Interventions. *Proceedings of the Institution of Mechanical Engineers, Part F: Journal of Rail and Rapid Transit* 232(2): 337–355, doi: 10.1177/0954409716671545.

Ajayi, O., Le Pen, L., Zervos, A. & Powrie, W. 2017a. A Behavioural Framework for Fibre-reinforced Gravel. *Géotechnique* 67(1): 56–68, doi: 10.1680/jgeot.16.P.023.

Ajayi, O., Le Pen, L., Zervos, A. & Powrie, W. 2014a. Effects of Random Fibre Reinforcement on the Density of Granular Materials. In: K. Soga, K. Kumar, G. Biscontin, & M. Kuo (eds.), *Geomechanics from Micro to Macro: Proceedings of the TC105 ISSMGE International Symposium on Geomechanics from Micro to Macro, Cambridge*, Cambridge, UK, 1-3 Sep 2014. Leiden, the Netherlands: CRC Press/Balkema, https://books.google.it/books?id=fbvNrQEACAAJ.

Ajayi, O., Le Pen, L., Zervos, A. & Powrie, W. 2014b. Feasibility Study of Random Fibre Reinforced Railway Ballast. In: Geotechnical Engineering for Infrastructure and Development; *Proceedings of the 23rd European Young Geotechnical Engineers Conference*, Barcelona, Spain, 2-5 September 2014, https://www.icevirtuallibrary.com/doi/abs/10.1680/ecsmge.60678.vol3.197.

Ajayi, O., Le Pen, L., Zervos, A. & Powrie, W. 2017b. Scaling Relationships for Strip Fibre-reinforced Aggregates. *Canadian Geotechnical Journal* 54(5): 710–719, doi: 10.1139/cgj-2016-0346.

Bathurst, R.J. & Raymond, G.P. 1987. Geogrid reinforcement of Ballasted Track. *Transportation Research Record* 1153: 8–14.

Consoli, N.C., Casagrande, M.D.T., Thome, A., Dalla Rosa, F., et al. 2009. Effect of Relative Density on Plate Loading Tests on Fibre-reinforced Sand. *Geotechnique* 59(5): 471–476, doi: 10.1680/geot.2007.00063.

Diambra, A., Ibraim, E., Muir Wood, D. & Russell, A.R. 2010. Fibre Reinforced Sands: Experiments and Modelling. *Geotextiles and Geomembranes* 28(3): 238–250, doi: 10.1016/j.geotexmem.2009.09.010.

Diambra, A., Ibraim, E., Russell, A.R. & Muir Wood, D. 2013. Fibre Reinforced Sands: From Experiments to Modelling and Beyond. *International Journal for Numerical and Analytical Methods in Geomechanics* 37 (15): 2427–2455, doi: 10.1002/nag.2142.

Ferro, E., Harkness, J. & Le Pen, L. 2020. The Influence of Sleeper Material Characteristics on Railway Track Behaviour: Concrete vs Composite Sleeper. *Transportation Geotechnics* 23 (January 2020): *100348*, doi: 10.1016/j.trgeo.2020.100348.

Ferro, E., Le Pen, L., Zervos, A. & Powrie, W. 2022. Fibre-reinforcement of Railway Ballast to Reduce Track Settlement. *Géotechnique (ahead of print)*, doi: 10.1680/jgeot.21.00421.

Gray, D.H. & Ohashi, H. 1983. Mechanics of Fiber Reinforcement in Sand. *Journal of Geotechnical Engineering* 109(3): 335–353, doi: 10.1061/(ASCE)0733-9410(1983)109:3(335).

Heineck, K.S., Coop, M.R. & Consoli, N.C. 2005. Effect of Microreinforcement of Soils from Very Small to Large Shear Strains. *Journal of Geotechnical and Geoenvironmental Engineering* 131(8): 1024–1033, doi: 10.1061/(ASCE)1090-0241(2005)131:8(1024).

Lirer, S., Flora, A. & Consoli, N.C. 2012. Experimental Evidences of the Effect of Fibres in Reinforcing a Sandy Gravel. *Geotechnical and Geological Engineering* 30(1): 75–83, doi: 10.1007/s10706-011-9450-9.

Mandolini, A., Diambra, A. & Ibraim, E. 2019. Strength Anisotropy of Fibre-reinforced Sands Under Multiaxial Loading. *Géotechnique* 69(3): 203–216, doi: 10.1680/jgeot.17.P.102.

Michalowski, R.L. & Čermák, J. 2002. Strength Anisotropy of Fiber-reinforced Sand. *Computers and Geotechnics* 29(4): 279–299, doi: 10.1016/S0266-352X(01)00032-5.

Michalowski, R.L. & Čermák, J. 2003. Triaxial Compression of Sand Reinforced with Fibers. *Journal of Geotechnical and Geoenvironmental Engineering* 129(2): 125–136, doi: 10.1061/(ASCE)1090-0241(2003) 129:2(125).

Le Pen, L.M. & Powrie, W. 2011. Contribution of Base, Crib, and Shoulder Ballast to the Lateral Sliding Resistance of Railway Track: A Geotechnical Perspective. *Proceedings of the Institution of Mechanical Engineers, Part F: Journal of Rail and Rapid Transit* 225(2): 113–128, doi: 10.1177/0954409710397094.

Santos, S. Dos, Consoli, N.C. & Baudet, B.A. 2010. The Mechanics of Fibre-Reinforced Sand. *Geotechnique* 60(10): 791–799, doi: 10.1680/geot.8.P.159.

Selig, E.T. & Waters, J.M. 1994. *Track Geotechnology and Substructure Management*. London, UK: Thomas Telford Publishing, doi: 10.1680/tgasm.20139.

Bituminous geomembranes used for waterproofing in various transport applications

N. Daly
Axter Coletanche Inc., Montréal, Canada

T. Aguirre
Axter Coletanche Inc., Vancouver, Canada

B. Breul
Axter, Paris, France

ABSTRACT: Bitumen is a natural product, in which its use for waterproofing dates back to ancient times. A bituminous geomembrane (BGM) is manufactured by impregnating a polyester geotextile with an elastomeric bitumen compound. The geotextile provides a high mechanical resistance, while the bitumen provides the waterproofing properties and ensures longevity of the framework by protecting the geotextile. The durability of a BGM is measured in terms of how its key components, their mechanical and low permeable properties are subject to biodegradation by bacteria in various buried applications. Some example project applications in the domain of transportation will be described to illustrate these advantages where the bearing capacity of subgrades of over-consolidated soils can be improved by waterproofing unstable foundations in the presence of water. The infrastructure of the main tarmac runway at St. Georges airport in Utah and a railway track in Nebraska, both in USA will be described.

1 INTRODUCTION

Bitumen is a dense, highly viscous, petroleum-based hydrocarbon that is found in deposits such as oil sands and pitch lakes or it is obtained as a residue of the distillation of crude oil (refined bitumen). This natural substance has been used by humans for a wide variety of tasks and tools for at least the past 40,000 years. It was used in Mesopotamia, 5,000 years ago, to waterproof canals, Babylon gardens, etc. (Schwartz & Hollander 2005).

The first application of an in-situ BGM in transport construction was done to construct aprons for airplanes on low bearing soils, to cover radioactive waste in Texas, USA and a reservoir in the Alps realized with JP. Giroud in 1974.

The first fabrication of BGM in a factory was in France in 1975. This evolution was essentially driven by the need for the ability to control the quality of the product and to have better independence from the weather conditions.

2 BGM STRUCTURE

Bituminous Geomembranes (BGM) have a composite structure consisting mainly of a non-woven polyester long fiber geotextile, impregnated by a compound with a certain mass of elastomeric bitumen (Figure 1). The geotextile provides resistance and bitumen provides watertightness. Every roll manufactured is tested following CEN and ASTM standards for thickness, unit mass, resistance to tearing, static puncture, tensile strength, and elongation.
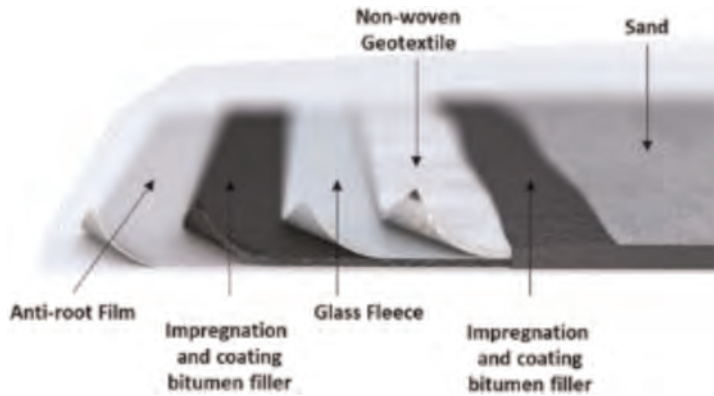
Figure 1. BGM structure.
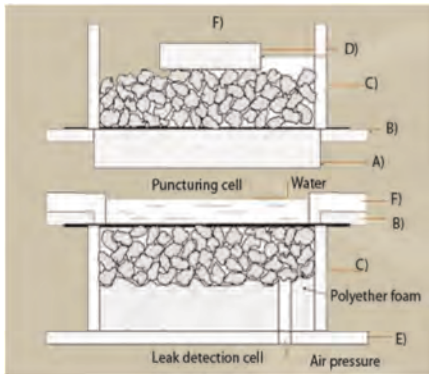
Figure 2a. Apparatus for the test

Figure 2b. BGM after test with aggregates

2.1 *Reasons to use a geomembrane in transport construction application*

The first reason is for waterproofing. Permeability for BGM following ASTM E96 is 6. 10^{-14} m/s. The second reason is for resistance to aggregates puncture (Figure 2a and 2b). Static puncture for BGM following ASTM D4833 ranges from 3.9 kN to 4 kN, while puncture by aggregates following NFP 84-510 ranges from 20 kN to 40 kN.

The third reason is to have a low thermal expansion coefficient to avoid wrinkles during temperature variations. This allows for welding and placing cover materials can be done any time of day with fluctuating temperatures. BGM's low thermal expansion coefficient following ASTM D 696-08 is 0.22. 10^{-2} mm/m/°C, so it remains flat.

3 CASE STUDIES IN TRANSPORT APPLICATIONS

3.1 *Airport, runway reconstruction at the St. George Airport in Utah (USA)*

When the Saint George regional airport in Utah first opened in 2011, it was said the runway would last 20 years, but it only lasted 8 years due to the presence of blue clay under the runway and heavy rains. The runway needed a watertight barrier above the blue clay to avoid contact with water with this soil. This would help maintain the physical and
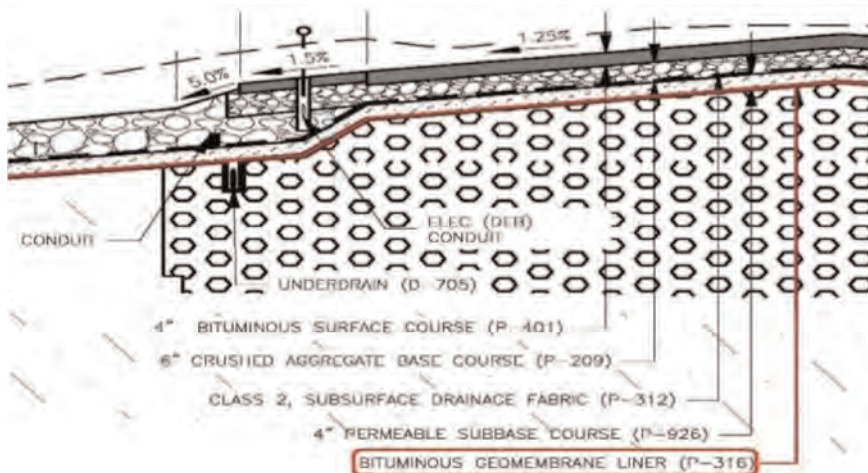
Figure 3.   Cross-section adopted for the reconstruction under the layer of asphalt concrete.

mechanical properties of the runway during varying weather conditions. The consultant had selected to use a BGM liner of 4.8 mm of thickness following ASTM D 5199, in order to accept gravel with high grain size and asphalt (temperature of application: 140°C) to be applied directly on top. See Figure 3 for design cross section.

BGM acted like an umbrella covering the blue clay with a wide overhang to avoid any water getting in contact with the structure supporting the runway. Only 130 calendar days were required to complete the entire project (Figure 4a). Figure 4b shows the large grain size of aggregates directly levelled above the BGM. The work was 200 m wide for over 1,600 m long. A team of six workers installed 6,000 m^2 of BGM per day, with an excavator equipped with a special hydraulic beam working 10-hour days in summer (temperature in the shade up to 40°C), for a total amount of 384,000 m^2 of BGM installed over 4 months.

Figure 4a.   General view of the site.

Figure 4b.   Equipment and material over BGM.

3.2   Use of BGM in railways construction and maintenance

BGM is used to protect railway platforms since it prevents clay from contaminating the ballast with water infiltration. The SNCF (French Railways) tested BGM using a in-house test called Vibrogyr (Figure 5), which simulates pulsed loading on the axles of railway sleepers and its foundation. It checks the puncture resistance of BGM with the aggregates on

Figure 5. Vibrogyr testing simulating rail traffic on ballast by SNCF (French Railways).

the ballast. This test showed that BGM could be placed directly on the platform and covered with ballast, without the need of protective layers.

Under half a sleeper, the ballast rests directly on the clay, under the other half, a BGM 5.6 mm thick following standard ASTM 5199 was placed. After estimated testing equivalent to at least 20 years of traffic on the busiest railroad of the S.N.C.F.(Paris-Tours-Bordeaux), it was found that as-is, the clay migrates into the ballast. If there is a BGM protection layer installed, there is no ballast pollution since some ballast aggregates are embedded inside the BGM without piercing the geomembrane. So BGM was used near Limoges, France in 1974, to shelter rainwater and altered granite substratum, to prevent the contamination of the ballast by clay. The construction site was in a deep trench serving as access to a tunnel. The level of the side ditches could not be changed, and it was therefore not possible to put in place thick layers of gravelly materials. It was noted that BGM had a strong resistance to puncture by these materials. BGM was verified after periods of 5 and 10 years till today. It was then found that the stones of the ballast had become embedded into BGM without piercing it, thus confirming the conclusions of the Vibrogyr test (Potvin 2016). The positive results observed on this test section led to the French Railways SNCF to continue the use of BGM on its railway tracks.

This technique therefore allows to save the cost of a deep stripping, followed by the installation of layers of selected materials. In addition, this geomembrane can be set up during a track and ballast renewal operation, which allows the saving of a prior heavy sanitation site.

3.2.1 High speed european train

East European High Speed Line (LGV Est) is a French high-speed rail line that connects Paris to Strasbourg, Germany and Luxembourg. During construction, engineers must pass over swelling shale soil near Reims. Shale tends to degrade from a hard rock-like material to a fine-grained soil mass. This degradation occurs over a long period of time, and many engineering problems such as settlements and slope failures are evident only several years after construction. The major difference between shale and clay is the lithification and diagenesis experienced by the shale in contrast to the clay, which is affected only by consolidation process. The lithification and diagenesis process affect geotechnical properties like in-situ void ratio, initial shear modulus, cohesion, apparent pre-consolidation stress, and shear strength (Gutierrez et al. 2008). On the other hand, factors that influence the swelling potential are type and amount of clay, initial placement conditions, stress history, nature of pore fluid, and temperature (Nayak & Christensen 1970). The solution found by French railways (SNCF) engineers was to do an umbrella above the shales to avoid any contamination by water by doing a watertight barrier with BGM of 5,6 mm of thickness.

TGV North (Paris-Brussel-Amsterdam-London) crosses a region with the presence of loess and chalk. BGM was used to avoid any diffusion of rainwater and thus avoid any risk of collapse. But this was done only after derailment of a TGV without injury and discovery of caverns under the line already built (Cuiet al. 2008).

3.2.2 *The Burlington Northern and Santa Fe Railway co. (BNSF)*

In Nebraska, the BNSF identified several sections of the existing track requiring refurbishment due to swelling soils (clay). Extensive engineering investigations found that the problem was the result of water in contact with the clay soil causing softening of the clay surface, which lubricated the bottom of the sub ballast. (Hyslip & McCarthy 2000). Under the repeated loading from train traffic, the sub ballast extruded out the sides of the track bed. The sub ballast layer thinned causing the outer rail to settle. In order to improve track performance in the section of track, the clay subgrade required stabilization and protection from further water contact.

Based on the geotechnical investigation, the alternative selected was a BGM of 5.6 mm thick following ASTM D 5199 (Figure 6a). Some of the subgrade clay contained sulfate which in the presence of lime and water could develop a tendency for substantial expansion over a period of time from a process known as "sulfate attack". In the location of this clay type, lime treatment of the clay without eliminating contact with water was unsatisfactory. Also, lime treatment could result in the development of flexural cracks in the stabilized clay. Water entering these cracks would result in the formation of the mud under repeated train loading.

The existing foundation was removed before adding the lime mixed with secure soil in place and BGM. Sub ballast was placed directly on top of the geomembrane without the use of geotextile protection, which BGM allows without a geotextile layer for protection (Figure 6b) (Selig & Waters 1994).
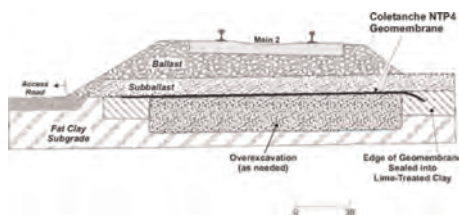
Figure 6a.   Designed cross section for BNSF.

Figure 6b.   Sub ballast placement directly on BGM.

3.3 *Use of BGM in road construction*

Some projects that will be described are for the application of the European Water Law in road construction. The respect of water quality in Europe is managed within the European Water Framework Directive. There is a directive for Ground water: the Groundwater Directive 2006/118/EC has been developed in response to the requirements of Article 17 of the Water Framework Directive. This includes the protection of the quality of groundwater under roads or highways. Vulnerable areas, fractured soils, and nearby water catchment areas, require waterproofing traffic areas and pavement platform areas, to treat water collected in such watertight basins that separate the water from the light pollutants and heavy elements.

3.3.1 *Protection of potable water on an Aquifer in Switzerland under N16 in Switzerland*

Under the N16 highway, there is the aquifer which supplies potable water for the town of Porrentruy, Switzerland with its 10,000 inhabitants. The fear of the Swiss Ministry of Transport was to have a truck carrying benzine, chemical liquid and having an accident by spilling discharges transported and polluting the ground water. So, they covered the complete exit and a superhighway by BGM to protect the aquifer (Figure 7a and 7b).

Figure 7a.   Exit on Swiss motorway N16.

Figure 7b.   Exit covered by BGM.

3.3.2 *Sustaining the ecosystem of a pond near a bypass*

In Ireland, a 3.5-km-long section of highway runs below the water table. Authorities wanted to make sure that the highway did not disturb the hydrogeological conditions and ecosystem of a marsh some 5 km from the Kildare bypass. On average, 30,000 vehicles, 20% of which are heavy trucks, pass through Kildare town every day. A 13-km-long bypass should put an end to the long bottlenecks in Kildare. The highway passes in front of one of the most famous racetracks in Ireland. As such, traffic noise would negatively impact breeding, disturb the horses before the races, and bother the spectators.

The solution was to bury the highway surface so that the berm would act as a natural noise-absorbing wall. Because of this, the highway surface was 4.5 m below the water table over a 3.5 km stretch. Of course, it could not pollute the water table nor interfere with the flow of water.

Technical solutions proposed during the call for tenders, and they chose to go with a BGM after a series of tests performed. See Figures 8a and 8b below for BGM installation.

Figure 8a.   Membrane installation.

Figure 8b.   Membrane over central collector.

4 CONCLUSIONS

The principle in protecting these transport applications is to build an umbrella above water-sensitive soils that avoids clay, gypsum, and inflating shales to be in contact with water. The described examples demonstrate the successful use of a BGM by a proven adequate strength, durability, and low permeability solution over 40 years.

REFERENCES

American Society for Testing and Materials (ASTM) D4833/D4833M. 2020. *Standard Test Method for Index Puncture Resistance of Geomembranes and Related Products*. USA.

American Society for Testing and Materials (ASTM) D5199. 2019. *Standard Test Method for Measuring the Nominal Thickness of Geosynthetics*. USA.

American Society for Testing and Materials (ASTM) D696-08. 2008. *Standard Test Method for Coefficient of Linear Thermal Expansion*. USA.

American Society for Testing and Materials (ASTM) E96. 2000. *Standard Test Methods for Water Vapor Transmission of Materials*. USA.

Antoine P., Cuil Y.J, Delage P., 2008. *Geotechnical Problems Related with Loess Deposits in Northern France*.

Breul, B., Hyslip J.P., Langley, G., Selig, E. 2000. Protecting Railway subgrade with a Reinforced Bituminous Geomembrane. *IGS International Congress*. France, Nice.

Christensen and Nayak, 1970. *Factors that Influence the Swelling Potential are Type and Amount of Clay, Initial Placement Conditions, Stress History, Nature of Pore Fluid, and Temperature*.

Gutierrez, Marte & Nygaard, Runar & Høeg, Kaare & Berre, Toralv, 2008. Normalized Undrained Shear Strength of Clay Shales. *Engineering Geology*. 99. 31–39

Hollander D., Schwartz M., *Annealing, Distilling, Reheating and Recycling Bitumen Processing in the Ancient Near East*

Hyslip, J.P., McCarthy, W.T. 2000. Substructure Investigation and Remediation for High Tonnage Freight Line, *Proceedings of the AREMA 2000 Annual Meeting*. Texas, Dallas.

Kildare Town By-Pass – Technical Visit- 7th International Conference on Geosynthetics John Coppinger, Irish Minister of Public Works

Potvin, R. 2016. *Essai de Fatigue du Vibrogyr sur Géomembrane Coletanche ES4 Axter*. Centre d'essais voie SNCF. France.

Proceedings of International Conference on Problematic Soils, 25-27 May 2005, Eastern Mediterranean University, Famagusta, N. Cyprus

Rencontres 97 CFG Bituminous Geomembrane Protect road Foundation Soil Marcel Rat, Director Laboratory of the French Ministry of Public Works and Gregory Philippon, director of the Ministry of Public Works for the Gard department. Revue RGRA n°762 April 98, BGM: an Answer to the European Water Law

Selig, E.T. and Waters, J.W. 1994. *Track Geotechnology and Substructure Management*, Thomas Telford Publishers. UK, London.

Scetauroute and Réseau Ferré de France, LGV Est European LGV 33, Déblai D38, Chapter 5: Waterproofing Excavation by Geomembrane Ordonnance n° 2022-1611 du 22 décembre 2022, JO du 23 décembre. Directives (UE) 2020/2184 Du Parlement Européen Et Du Conseil du 16 décembre 2020

Reinforced embankments for the Perranporth to Newquay Cycleway project at Newlyn Halt Railway Station, Cornwall, UK

Rozhan Saeed*
Geosynthetics Ltd, UK

ABSTRACT: Perranporth to Newquay Cycleway project is the solution for a ramp construction to be formed on top of an existing historic railway embankment. The ramp is located in tree root protection to provide the approach to footbridges. According to the British Standard BS5837:2012, the design in Tree Root protection areas should not need any excavation and compaction of the soil. The area close to existing tree roots should be protected and undisturbed during construction. Therefore, it is required to use systems to prevent tree and their root during and after construction traffic. A Cellweb system was designed to protect the tree root zone that allows drainage, nutrient and gas exchange necessary for root growth. The system decreases the pressure effect on soil and tree roots by dissipating the loads and transferring laterally to subgrade soil instead vertically. Therefore, the reinforced embankment with a stack Cellweb system filled with clean angular stone was used as a solution for a footbridge that allowed tree roots growth at the same time. The height of the embankment was 1.5m with a slope angle of 70deg. The Rivel Mesh system as a rigidity-formed face was used to achieve slope stability during construction and protect the embankment face against sliding. In the other hand, embankment slope faces were filled with top soil and vegetated. while the face was protected from erosion by covering with Erosion Contol landlok and wrapped around at each layer of soil. The design is included some key elements. Cellweb system to protect tree roots from excavation and compaction also reduces pressure on subgrade soil. Rivel Mesh systems were used to achieve slope side stability. Also, Erosion control landlock was used to protect slope sides against erosion in long term. Geotextile was used as a pollution and separation control and Sleeve-It was used as a supported fence for the ramp.

1   INTRODUCTION

The project is a design for a new ramp on top of an existing historic railway embankment to provide the approach to footbridges at multiple locations on the project to support the new cycleway from Perranporth to Newquay located at Newlyn Halt Railway Station, Cornwall, UK as shown in Figure 1.

The construction of the ramp would require a build-up of approximately 1.5m height in the Tree root Protection Area as shown in Figure 2. Construction of the embankment utilising conventional, compacted subbase materials would prevent continued water permeation and gas exchange between the atmosphere and roots beneath. This may ultimately cause root death, reducing the tree's ability to obtain the water and nutrients that it requires. Therefore, the embankment would need to be constructed using multiple layers of Cellweb.

---

*Corresponding Author: Rozhan.Saeed@geosyn.co.uk

Figure 1. Existing historic railway embankment.
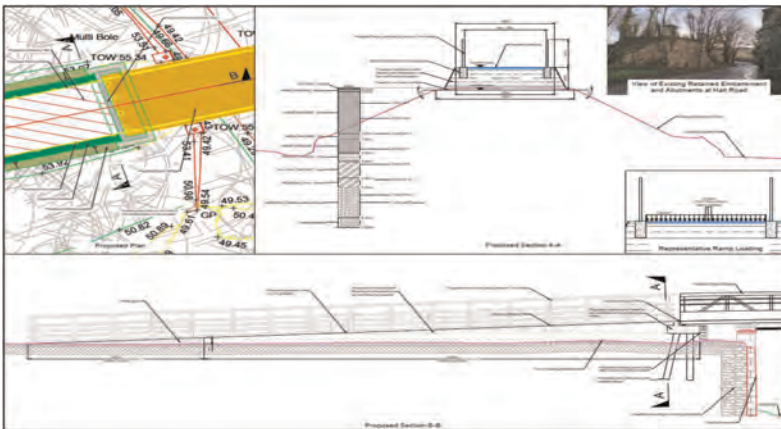
Figure 2. Site plan location and sections of embankment.

This would ensure the continued health of the tree and comply with the arboricultural method statement.

Cellweb TRP is a cellular confinement system used for tree root protection in construction. Cellweb offers a no-dig solution for subbase construction within tree root protection areas. Also, the system prevents the compaction of subgrade soil and allows water permeation and gas exchange between rooting and the environment and atmosphere. The system is filled with clean angular stone which is the confinement material infill to prevent tree roots severance and to allow water and oxygen to go through it. In addition, Nonwoven geotextile is used for separations and pollution control as shown in Figure 3.

Figure 3. Cellweb system with clean angular stone & geotextile for separation beneath it.

2 DESIGN METHODOLOGY

2.1 *Design method and standards*

Initially, the calculation was carried out by using the Cellweb TRP system infill with clean angular material to reduce the pressure on the subgrade and increase bearing capacity. The Cellweb system provides a stable structure to distribute the vertical loads and minimises soil compaction. The structural reinforcement design using Cellweb is based on the guidance provided by Webster (1981) which uses conventional bearing capacity analysis to determine the applied and allowable pressure below the road pavement. However, In this project, Cellweb is used as a multi-layers for building up the embankment and has been checked for slope stability.

The Embankment has been checked according to Standard – EN 1997 – DA1, In the design approach reduction factors are applied to actions and soil parameters as shown in Table 1.

Table 1. Partial factors on actions and soil parameters.

Partial factors on actions (A) Permanent design situation					
		Combination 1		Combination 2	
		Unfavourable	Favourable	Unfavourable	Favourable
Permanent actions :	$\gamma_G =$	1.35 [–]	1.00 [–]	1.00 [–]	1.00 [–]
Variable actions	$\gamma_Q =$	1.50 [–]	0.00 [–]	1.30 [–]	0.00 [–]
Water load :	$\gamma_w =$	1.35 [–]		1.00 [–]	
Partial factors for soil parameters (M) Permanent design situation					
			Combination 1		Combination 2
Partial factor on internal friction :		$\gamma_\phi =$	1.00 [–]		1.25 [–]
Partial factor on effective cohesion :		$\gamma_c =$	1.00 [–]		1.25 [–]
Partial factor on undrained shear strength :		$\gamma_{cu} =$	1.00 [–]		1.40 [–]
Partial factor on Poisson's ratio :		$\gamma_v =$	1.00 [–]		1.00 [–]
Partial factors for variable actions Permanent design situation					
Factor for combination value :		$\psi_0 =$		0.70 [–]	
Factor for frequent value :		$\psi_1 =$		0.50 [–]	
Factor for quasi-permanent value :		$\psi_2 =$		0.30 [–]	

Material of blocks – filling

No.	Name	γ [kN/m³]	φ [°]	c [kPa]
1	Clean Angular Stone 4/20	18.00	35.00	0.00
2	Subbase Type 3	18.00	35.00	0.00

First, the geometry of the embankment was produced and soil property was specified then the embankment was checked for global stability. The stability check included active and passive earth pressure calculation, check for overturning and check for slip stability, the shape of earth wedge and dimensioning check, allowable eccentricity and Bearing capacity of foundation and global slope stability with bishop method as shown in Figure 4.
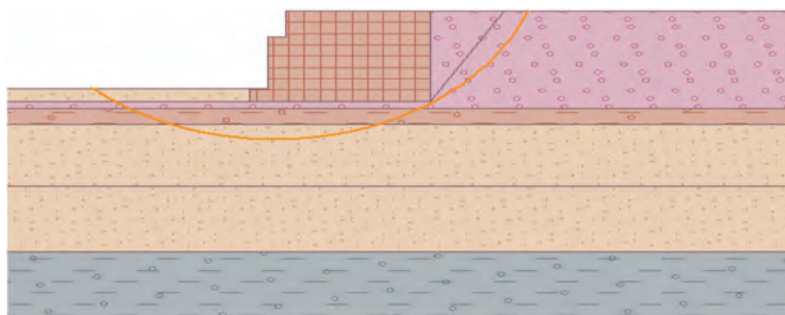
Figure 4. Embankment stability check.

3 DESIGN CONSIDERATIONS

3.1 *Geometry and cross-sections*

The design analysis is based on the worst-case scenario with a maximum height of 1.5m and 70deg slope face. The embankment is along the bridge of around 26m with the different layers of 200mm Cellweb as shown in the following cross-sections. The embankment base width is 6.3m and the path on the top is 4.5m as shown in Figure 5.

Figure 5. Cross section of the embankment.

3.2 *Soil parameters*

The Cellweb infill material shall be a clean angular stone with a size of 20mm to 4mm complying with BS EN 12620. The property of fill material shown below
Cellweb Fill properties:

– Clean angular stone Type 4/20
– Particle sizes: 4mm to 20mm
– Friction angle $\phi' = 35$deg,
– Unit weight $\gamma = 18$kN/m3

The existing embankment was assumed Made of Ground Ballast and stable. The parameters used in the analysis are:
Foundation soil properties:

– Made of Ground Ballast
– Friction angle $\phi' = 30$deg,
– Unit weight $\gamma = 18$kN/m3
– Cohesion C' = 0 kPa

Topsoil and seeded topsoil were used on the face for the vegetated face.

4 DESIGN SOLUTION

The final solution included the results for embankment reinforcement with Cellweb and a vegetated face with a face support framework and erosion control.

In the worst-case scenario, as shown in Figure 6 below, seven layers of 200mm Cellweb were used for the reinforcement which is filled with clean angular stone to protect tree roots protection and as a reinforcement for the build-up embankment up to 1.5m height. However, the layers are reduced along the bridge according to 1:20 slope ramp.
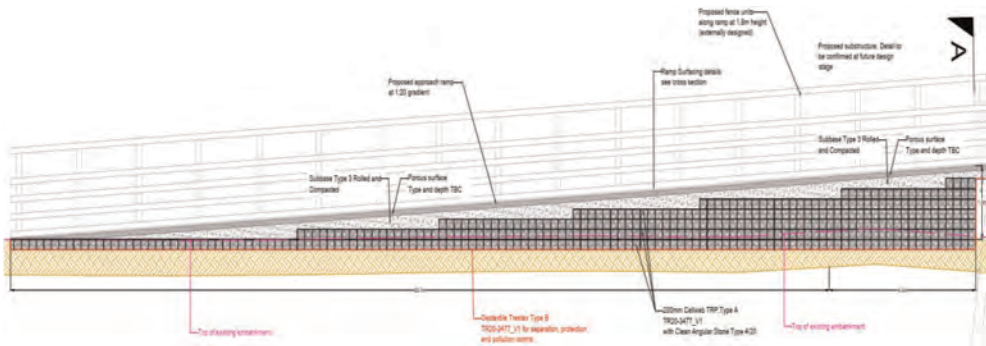
Figure 6. Long section of the reinforcement embankment final solution.

In this project layers of Cellweb have two roles, first as a system to reduce the loads on the tree roots against any compactions while giving permission of water and gas to exchange between roots and the atmosphere. second, Cellweb is used as a reinforcement layer to build up the embankment with a 70deg slope angle. To support the face, the Rivel mesh system has been used to achieve 70deg slope face and Erosion Control Landlok has been used to protect the face form erosions as shown in Figure 7 below.
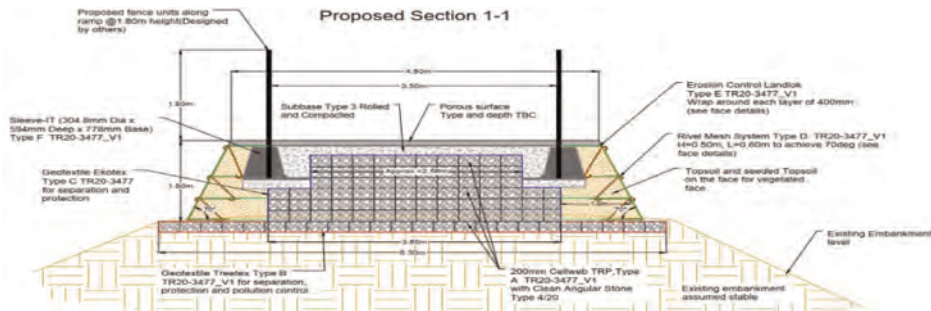
Figure 7. Cross section of the reinforcement embankment final solution.

5 CONCLUSION

The use of reinforced embankments with Cellweb layers and filled with clean angular stone Type 4/20 allowed the construction to build up the new bath on the bridge with no-dig or compactions to the existing embankment to prevent damage to existing tree roots.

The main challenge for the design of the reinforced embankments was to keep the existing embankment to prevent damage and to achieve slop stability of a vegetated face with step angle of 70deg. For this purpose, the Rivel mesh system was used to support slope stability and achieve the angle and erosion control Landlock was used to protect the face from erosions.

In addition, a layer of Geotextile Treetex was used for separations and protections between the existing embankment and the proposed one. Also, between Cellweb layers and the face of the slope.

In conclusion, the beneficial effects of Cellweb system to build up the embankment are as follows:

– Minimizes compaction of the existing embankment.
– No-dig construction solution.
– Allow water and gas exchange between tree roots and the atmosphere.
– Use as a reinforced layer to build the embankment and achieve stability.
– Distribution loads and reduced effect on the existing embankment.

REFERENCES

British Standard, *BS5837:2012 Trees in Relation to Design, Demolition and Construction -Recommendations.* British Standard Institution, London. UK

British Standard, BS8006-1:2010. Code of Practice for the Strengthened/ Reinforced Soils and other Fills. British Standard Institution, London. UK

British Standards Institution (2014) Eurocode 7:Geotechnical design -Part 1: General Rules.BS

Cellweb Tree Root Protection (TRP): System Specially ... – Geosynthetics (n.d.). Available at: https://library.geosyntheticssociety.org/wp-content/uploads/resources/proceedings/122021/S17-03.pdf (Accessed: November 3, 2022).

EN 1997-1:2004 + A1:2013.London: BSI Group.

Geosynthetics (n.d.) Case Study Cellweb Trp Keats Way, Northamptonshire, https://www.geosyn.co.uk/wp-content/uploads/2016/06/Case-Study-Cellweb-TRP-Keats-Way-Extended-CS.pdf. Available at: https://www.geosyn.co.uk/wp-content/uploads/2016/06/Case-Study-Cellweb-TRP-Keats-Way-Extended-CS-1.pdf (Accessed: November 3, 2022).

Geosynthetics (n.d.) Cellweb®Trp – Cellular Confinement System, Geosynthetics. Available at: https://www.geosyn.co.uk/product/cellweb-tree-root-protection (Accessed: November 3, 2022).

Highway Works MCHW. Feb 2016. *Volume 1 Specification for Highway Works Series 600 – Earthworks*. UK

Holtz, R.D. 2001. *Geosynthetics for Soil Reinforcement*. University of Washington Seattle, Washington 98195-2700 USA

Effectiveness of geogrid stabilization of airfield pavements investigated using embedded sensors

Mingu Kang, Han Wang, Issam I.A. Qamhia & Erol Tutumluer
University of Illinois Urbana-Champaign, Urbana, Illinois, USA

Navneet Garg & Wilfredo Villafane
Federal Aviation Administration, Egg Harbor Township, New Jersey, USA

ABSTRACT: This paper focuses on evaluating local stiffness enhancement near a geogrid installed at the base/subbase interface of full-scale pavement test sections at the FAA's national airport pavement test facility (NAPTF) in the USA. The investigated test pavements comprised of the north section stabilized with a square aperture geogrid and the south control section with no geogrid. Inductive coil sensors and pressure cells were embedded in both sections. A full-size dual-tridem gear applied realistic moving wheel loads on the pavement surface. Pavement responses including layer deformations from coil sensors and applied pressure from earth pressure cells were measured during traffic loading. Modulus characteristics of the subbase layer were then estimated based on the sensor measurements during traffic passes. The study findings indicate higher layer stiffness consistently estimated in the geogrid-stabilized pavement section when compared to the values in the control section due to heavy aircraft gear loads.

1 INTRODUCTION

Geogrids used for unbound aggregate stabilization in flexible pavements increase lateral confinement, prevent excessive rutting under vehicular loading, and as a result, extend pavement service life. Despite the widely recognized benefits of geogrid stabilization, the application of geogrids in airport pavements has been limited (Norwood 2019). In the US, the Federal Aviation Administration (FAA) Reauthorization Act of 2018, sec. 525, required FAA, to the extent practicable, to encourage the use of durable, resilient, and sustainable materials and practices, including the use of geosynthetic materials. For decades, FAA has been operating the National Airport Pavement Test Facility (NAPTF) to provide high quality, accelerated pavement test data from rigid and flexible pavements subjected to simulated aircraft traffic. In the NAPTF Construction Cycle 9 (CC9) full-scale pavement tests, a 13.7 m long geosynthetics test section was included as a test item to evaluate related performance improvements of geosynthetics in airport pavements.

Numerous research studies reported that using geogrids to stabilize unbound aggregate layers effectively reduced surface deformation (Al-Qadi *et al*. 2008; Tingle & Jersey 2009). Geogrids installed in unbound base or subbase layers provide lateral restraint through geogrid-aggregate interlocking and create a stiffened zone in the proximity of the geogrid location. Experimental research using various test methods, including dynamic cone penetrometer (DCP) and direct shear tests, have shown that the base/subbase layer became stiffer near the geogrid location (Horvát *et al*. 2013; Kwon & Tutumluer 2009). Furthermore, recent research efforts using innovative bender element (BE) sensors successfully quantified

the stiffness enhancement and the extent of the geogrid-stiffened zone in the vicinity of a geogrid through direct measurement of shear wave velocity (Byun *et al.* 2019; Kang *et al.* 2022a, b).

The objective of the research effort described herein is to quantify localized stiffness characteristics of an unbound aggregate subbase layer installed with two types of embedded sensors, i.e., coil sensors and earth pressure cells, in the NAPTF CC9 geosynthetics experiment subjected to aircraft traffic loading. Comparisons are made between the subbase layer moduli of a geogrid-stabilized section with those of the control section during the accelerated pavement testing, and the performance improvement of the geogrid installed in the unbound aggregate base is highlighted.

2 TEST SECTION

Accelerated pavement testing of two full-scale airport pavement test sections was conducted in the fully enclosed NAPTF; utilized by the FAA to perform airport pavement research. The test track at NAPTF is 274 m (900 ft) long and 18.3 m (60 ft) wide and can accommodate various pavement thicknesses depending on the test objectives. The Construction Cycle 9 (CC9) pavement test sections consisted of 127 mm (5 in.) of P-401 asphalt surface course underlain by 203 mm (8 in.) of P-209 granular base and 737 mm (29 in.) of P-154 granular subbase layers. The paper focuses on the test results obtained from the first 330 vehicle passes for the geosynthetics test item, referred to herein as the low strength flexible conventional (LFC-3), which consists of a north section (LFC-3N) mechanically stabilized with a punched and drawn biaxial geogrid installed at the interface of the base and subbase, and a control section in the south (LFC-3S), which is unstabilized (see Figure 1). The embedded sensors were installed towards the upper part of the subbase layer near the geogrid location.

The properties of the P-154 subbase course, carbonate-based manufactured aggregate screenings, are illustrated in Figure 2. Sieve analysis in accordance with the ASTM C136 procedure was conducted to determine the grain size distribution curve shown in Figure 2(a). The subbase material is classified as A-1-b (stone fragments, gravel, and sand) according to the AASHTO soil classification system, and as SP-SM (poorly graded sand with silt and gravel) according to the Unified Soil Classification System (USCS). The mean grain size (D_{50}) of the aggregate material is 1.42 mm (0.056 in.) and the particle fraction passing No. 200 (0.075 mm) sieve size is 10.2%. As shown in Figure 2(b), the maximum dry density
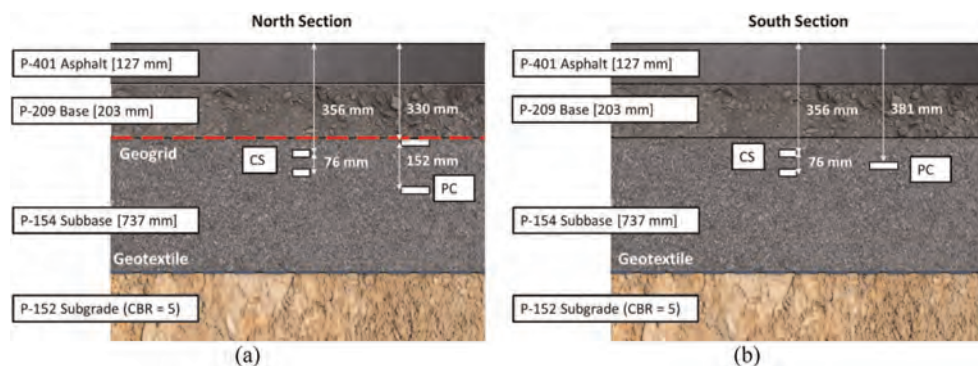
Figure 1. Airport pavement cross-sections of FAA's NAPTF CC9 geosynthetics test item: (a) LFC-3N geogrid stabilized section, (b) LFC-3S unstabilized control section.
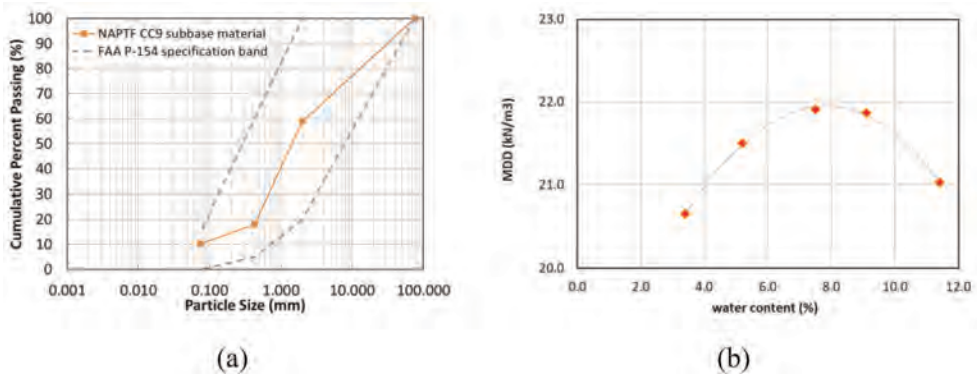
Figure 2. Properties for the P-154 subbase course aggregate: (a) grain size distribution, and (b) moisture-density relationship.

(MDD) and optimum moisture content (OMC) determined by the modified Proctor compaction test (ASTM D1557) were 21.96 kN/m^3 (141 pcf) and 7.9%, respectively.

3 EMBEDDED SENSORS

3.1 Coil sensor

A pair of inductive coil sensors was installed at the top of the subbase layer of both LFC-3N and LFC-3S test sections, as shown in Figure 1. The inductive coil, referred to herein as coil sensor, consists of a transmitter coil and a receiver coil, which are inductive circuits made of a copper wire winding a circular thermoplastic polymer disk [see Figure 3(a)]. A magnetic flux field generated around the transmitter coil by an input alternating current creates an output current to the receiver coil via mutual induction (Greenslade 2016). The distance between the transmitter and receiver coils can be estimated from the magnitude of the received signal using the following parabolic fitting equation.

$$y = ax^2 + bx + c \tag{1}$$

where x is the voltage and y is the relative displacement between coil pairs. The coefficients a, b, and c were obtained from the calibration process using the linear variable differential
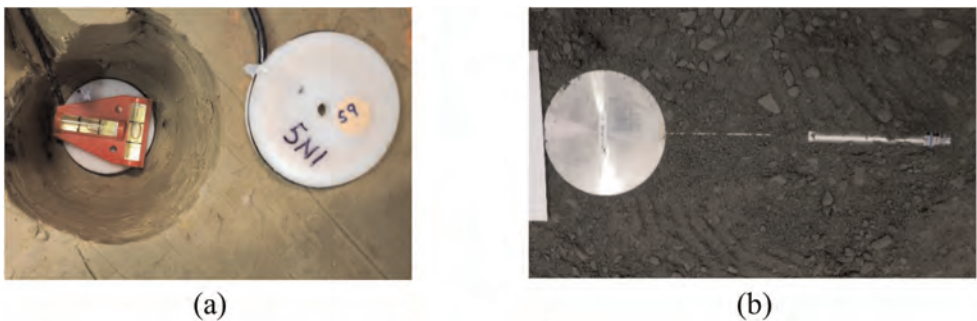
Figure 3. Embedded sensors at NAPTF CC9: (a) Inductive coil pairs, and (b) Pressure cell.

transformers (LVDTs). Therefore, the coil pairs serve as a non-contact strain-measuring sensor that measures the local strain in a certain range. The average resolution of the coil sensors is 75 micro-strain (0.0057mm). Two coil sensor pairs were installed free floating with a target 76.2 mm (3 in.) gap, as recommended by the manufacturer. During each vehicle pass, dynamic pavement deflection responses were monitored using the sensors.

3.2 *Pressure cells*

Pressure cells were installed in the subbase layer, two in LFC-3N and one in LFC-3S sections. Pressure cells measure the dynamic pressure changes in the surrounding material through the internal pressure change in a thin hydraulic fluid cell between the two flat metal plates. A transducer in the pressure cell converts the fluid pressure change into an electrical signal. The output voltage collected by the data acquisition system is converted to a pressure measurement according to an established correlation from the calibration. To minimize local plate deflection due to pressure exerted from surrounding particles, the pressure cells used in this research are equipped with additional thick plates on each side [see Figure 3(b)]. Throughout 330 vehicle passes, dynamic pavement responses, i.e., applied pressure levels, were monitored using pressure cells. The LFC-3N pressure values were calculated by averaging the pressure from the two installed pressure cells in an effort to obtain an accurate estimate of the pressure at the same depth of the coil sensor.

4 TEST PROCEDURE

The National Airport Pavement Test Vehicle (NAPTV) applied a dynamic gear loading of 26.3 tons (58 kips) per wheel using a dual-wheel tridem-axle gear configuration (3D) module; equivalent to a total of 157.8 tons (348 kips) to simulate heavy aircraft gear loading. Figure 4 illustrates the NAPTV gear wander positions consisting of 66 vehicle passes, normally distributed and arranged in nine wander positions with different offset distances. The offsets are the distances from the centerline of the test section to the centerline of the loading module, located midway between the two wheels. The thick red dashed line indicates the pressure cell location at the centerline of the test section, and the blue solid line shows the coil sensor location for each test section. The remaining lines show the centerline of the loading gear at each wander position, which are equally spaced with a 0.26 m (10.2 in.) shift. As illustrated
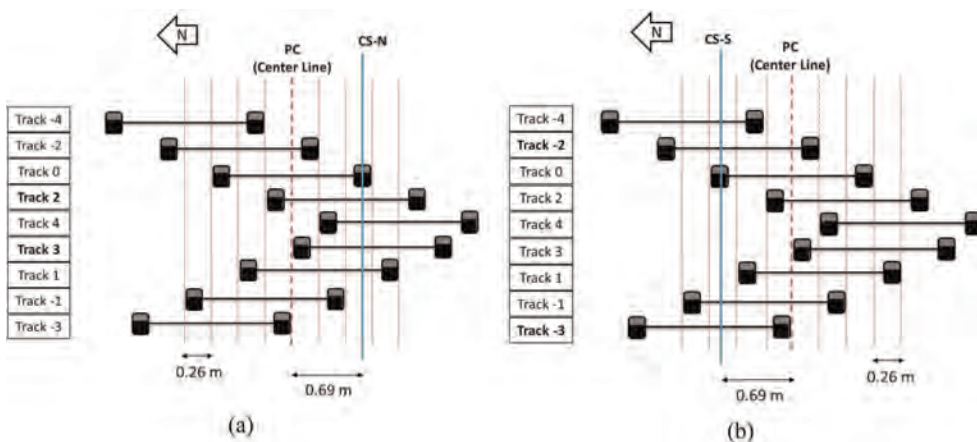
Figure 4.   Traffic loading procedure with wander patterns: (a) LFC-3N, and (b) LFC-3S test sections.

in Figure 4, coil sensors are located at a 0.69 m (2.25 ft) from the centerline, while pressure cells are at the centerline. Data obtained from test tracks 2 and 3 for LFC-3N and from test tracks -2 and -3 for LFC-3S were analyzed and compared considering the identical loading condition at the coil sensor and pressure cell locations. Two passes of the loading module consist of an eastbound passage and a westbound passage at the same offset location. The complete wander pattern consisting of 66 passes is summarized in Table 1. Data from 5 complete wander patterns are presented in this paper.

Table 1. Wander pattern applied with the National Airport Pavement Test Vehicle (NAPTV).

Pass No.	1, 2	3, 4	5, 6	7, 8	9, 10	11, 12	13, 14	15, 16	17, 18	19, 20	21, 22
Track No.	–4	–2	0	2	4	3	1	–1	–3	–4	–2
Pass No.	23, 24	25, 26	27, 28	29, 30	31, 32	33, 34	35, 36	37, 38	39, 40	41, 42	43, 44
Track No.	0	2	4	3	1	–1	–3	3	1	–1	–3
Pass No.	45, 46	47, 48	49, 50	51, 52	53, 54	55, 56	57, 58	59, 60	61, 62	63, 64	65, 66
Track No.	–2	0	2	–2	0	2	1	–1	1	–1	0

5 RESULTS AND DISCUSSION

Figure 5 shows a sample dynamic response from a coil sensor and a pressure cell during pass No. 320 of the traffic testing. The three peaks observed from both sensors correspond to loads from the three wheels of the tridem-axle gear of the NAPTV passing over the sensors. The resilient modulus (M_R) of the unbound aggregate material is determined using the following equation.

$$M_R = \frac{\sigma_d}{\varepsilon_r} \qquad (2)$$

where σ_d is deviator stress, and ε_r is the recoverable resilient strain. Hence, the resilient modulus of the subbase layer can be calculated using the wheel load deviator stress obtained from the pressure cell and the recoverable resilient strain collected from coil sensors.

The stress states induced in the subbase layer will vary as the NAPTV loading is applied at different wander positions. Track 2 of LFC-3N and track -2 of LFC-3S induce the same stress state at the sensor locations. Figure 6(a) shows the resilient moduli estimated from vehicle passes at track 2 of LFC-3N and at track -2 of LFC-3S. Clearly, the estimated

(a) Coil sensor   (b) Pressure cell
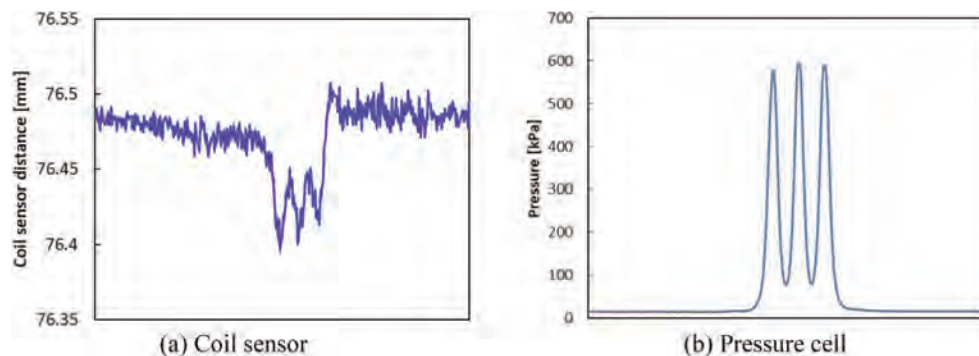
Figure 5. Typical dynamic responses collected from embedded sensors at pass No. 320.

moduli at the geogrid-stabilized section indicate higher values with an average resilient modulus improvement of 68.7%. Therefore, it could be concluded that the geogrid-stabilized subbase layer has higher stiffness near the geogrid location. The authors previously reported that the extent of the geogrid-stiffened zone in the CC9 test section base layer is approximately 102 mm (4 in.) from the geogrid location (Kang *et al.* 2022b). The sensors located within the geogrid-stiffened zone captured the stiffness improvement achieved through geogrid-aggregate interlocking (see Figure 1). Note that the coil sensors were located 0.69 m (2.25 ft) apart from the pressure cell (see Figure 4). Whereas the vertical pressure values were collected near the wheel path, the coil sensor deflections were measured 0.52 m (1.71 ft) apart from the wheel path and thus the estimated moduli values could be higher than the actual values.

Figure 6(b) presents the resilient moduli estimated from vehicle passes at track 3 of LFC-3N and at track -3 of LFC-3S, which have the same stress state. Similarly, the estimated moduli at the geogrid-stabilized section were higher, with an average improvement of
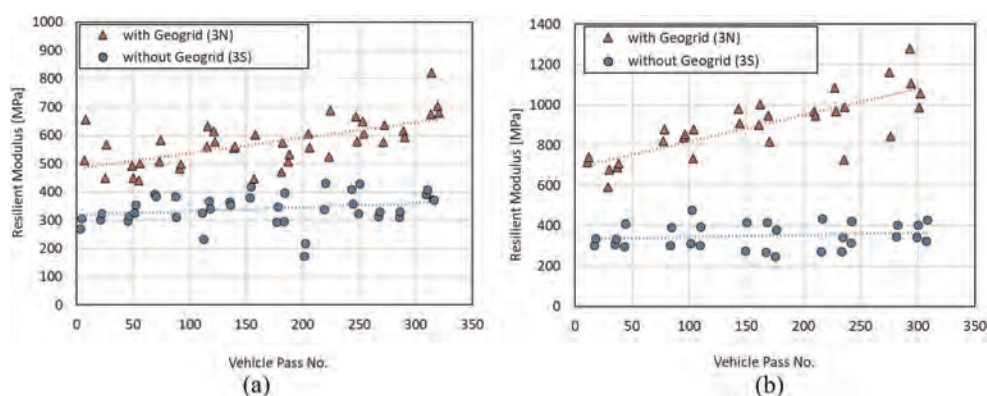
Figure 6. Resilient moduli estimated using embedded sensors: (a) moduli from track 2 of LFC-3N and track -2 of LFC-3S, (b) moduli from track 3 of LFC-3N and track -3 of LFC-3S.

155.3%. The estimated moduli from tracks 3 and -3 were higher than those from track 2 and -2 due to the larger horizontal distance of the coil sensor from the wheel path, which is 0.59 m (1.94 ft), meaning the measured vertical strain is an underestimate of the actual strain at the pressure cell location. Interestingly, the estimated moduli increased as the number of load repetitions increased, especially at the geogrid-stabilized section. This could be attributed to the stabilized unbound aggregate layer by rearranging the aggregate particles during load repetitions, especially during the first few load repetitions (Kang *et al.* 2022a). Han *et al.* (2020) reported that from a falling weight deflectometer (FWD) test performed before and after accelerated pavement testing (APT), the modulus of the unbound base course for a geogrid-stabilized pavement after APT was considerably higher than the unstabilized section owing to the fully mobilized benefit of geogrid. A higher modulus increase observed in the geogrid-stabilized section was likely due to the gradual mobilization of the geogrid during vehicle passes.

6 CONCLUSION

This paper presented recent research findings on geogrid-stabilized airport pavements. The unbound aggregate subbase layer was instrumented with embedded inductive coil sensors

and pressure cells. A full-scale airport pavement test section, including a geogrid-stabilized section and an unstabilized control section were constructed in US Federal Aviation Administration's (FAA's) national airport pavement test facility (NAPTF). The 3D loading module of the national airport pavement test vehicle (NAPTV) applied dynamic gear loading of 26.3 tons (58 kips) per wheel, with a wander pattern consisting of 66 vehicle passes arranged in nine wander positions. Dynamic responses from coil sensors and pressure cells were collected for the first 330 NAPTV passes (5 complete wander sets). The local stiffnesses as resilient moduli at the top of the subbase layer were analyzed with and without geogrid stabilization using the dynamic sensor data.

The estimated subbase moduli from the geogrid-stabilized section were on average 68.7% to 155.3% higher than those for the unstabilized section. A stiffness improvement was therefore achieved within the 102 mm (4 in) geogrid-stiffened zone. The resilient moduli increased as the number of passes increased, especially for the geogrid-stabilized section, which could be attributed to the gradually increasing effect of stabilization during vehicle passes. These research findings clearly demonstrate the benefit of geogrid stabilization in airport pavements through the mechanisms of unbound aggregate base/subbase lateral restraint and stiffness enhancement.

REFERENCES

Al-Qadi, I. L., Dessouky, S. H., Kwon, J. & Tutumluer, E. 2008. Geogrid in Flexible Pavements: Validated Mechanism. Trans. Res. Rec. 2045(1): 102–109.

Byun, Y. H., Tutumluer, E., Feng, B., Kim, J. H. & Wayne, M. H. 2019. Horizontal Stiffness Evaluation of Geogrid-Stabilized Aggregate Using Shear Wave Transducers. Geotext. Geomembr. 47(2): 177–186.

Greenslade, F.R. 2016. Development of a New Pavement Strain Coil Measuring System at CAPTIF. The Roles of Accelerated Pavement Testing in Pavement Sustainability. Springer, Cham. 633–643.

Han, B., Polaczyk, P., Gong, H., Ma, R., Ma, Y., Wei, F., & Huang, B. 2020. Accelerated Pavement Testing to Evaluate the Reinforcement Effect of Geogrids in Flexible Pavements. Trans. Res. Rec. 2674(10): 134–145.

Horvát, F., Fischer, S. & Major, Z. 2013. Evaluation of Railway Track Geometry Stabilization Effect of Geogrid Layers under Ballast on the Basis of Laboratory Multi-level Shear Box Tests. Acta tech. Jaurinensis 6(2): 21–44.

Kang, M., Qamhia, I. I. A., Tutumluer, E., Garg, N. & Villafane, W. 2022a. Airport Pavement Stiffness Monitoring and Assessment of Mechanical Stabilization using Bender Element Field Sensor. Trans. Res. Rec. 2676(8): 542–553.

Kang, M., Qamhia, I. I., Tutumluer, E., Flynn, M., Garg, N. & Villafane, W. 2022b. Near Geogrid Stiffness Quantification in Airport Pavement Base Layers using Bender Element Field Sensor. Advances in Transportation Geotechnics IV. Springer, Cham. 703–715.

Kwon, J., & Tutumluer, E. 2009. Geogrid Base Reinforcement with Aggregate Interlock and Modeling of Associated Stiffness Enhancement in Mechanistic Pavement *Analysis.* Trans. Res. Rec. 2116(1): 85–95.

Norwood, G. J. 2019. *Cyclic Plate Testing of Reinforced Airport Pavements-Phase I: Geogrid*. Final Report No. DOT/FAA/TC-19/3, FAA William J. Hughes Technical Center Aviation Research Division, NJ.

Tingle, J. S. & Jersey, S. R. 2009. Full-scale Evaluation of Geosynthetic-reinforced Aggregate Roads. Trans. Res. Rec. 2116(1): 96–107.

Geosynthetics coated with pure polyurea to create a waterproofing membrane for railways bridge decks

E. De Ambri & C.P. Longoni
Mapei S.p.A., Italy

ABSTRACT: Geosynthetics are materials currently used in the railway's applications. The system developed with the Italian railways infrastructure manager, is using the geosynthetic as a base layer where to spray a pure polyurea membrane, a fast-curing waterproofing product used since decades all over the world to waterproof roofs, decks and hydraulic structures. The system is specifically designed to renovate the waterproofing performance of existent railways bridge decks. Purtop 1000, Mapei pure polyurea membrane, has been tested at a thickness lower than the one prescribed and it has passed all the required tests.

1 INTRODUCTION

Every railway bridge deck needs a waterproofing system to be protected from water which is one of the main causes of structure's decay.

There are a lot of waterproofing technologies suitable to waterproof new railway bridge decks made of concrete or steel; on the contrary it is difficult to find suitable waterproofing systems to renovate existent structures, where fast-track solutions adaptable to different substrate's conditions are required.

In Europe there is still in place the development of new infrastructures, but it is a matter of fact that the renovation market is an upcoming business which will surely increase in the next decades.

With a future wise perspective, in Italy the Italian railways infrastructure manager, developed in the 90's an innovative system to re-waterproof arched bridges. Later this system has been recognized as a valid solution for several kind of railway bridge deck and it has become one of the possible solutions for maintenance works on the Italian railways bridge decks.

The performance expected from the waterproofing layer in such a context are very high because it must keep its performance in a lot of different weather conditions and under multiple stresses (static and dynamic loads, puncture deriving from ballast, friction, etc.). Therefore, a premium waterproofing technology is required to assure watertightness and durability to the structure.

Moreover, the waterproofing system must assure a rapid installation because the service interruption cannot be long in operating infrastructures.

2 THE WATERPROOFING SYSTEM DESIGNED BY RFI (RETE FERROVIARIA ITALIANA)

The specification prescribes the use of resin-based waterproofing product (like polyurethane, polyurea, methacrylate, etc.) free of solvents, plasticizers, inert materials or bitumen. The chemical reaction which leads to the cured waterproofing membrane should last maximum 15 seconds and the waterproofing layer must allow pedestrians' traffic after not more than 5 minutes. Moreover, the product must be spray applied to be fast and to be applied during scheduled service interruptions.

The waterproofing product used for renovations can be the same one used for the new structures, what differs is the application thickness and the layering of the system, as described in the below table.

Table 1. RFI system layering according to the type of deck.

	New decks	Existent decks
Application thickness (mm)	≥ 4	≥ 5
System's layers (bottom-up)	1. Concrete/metal substrate 2. Primer 3. Waterproofing membrane 4. Asphalt-based protection layer	1. Existent structure 2. Geotextile (1500 g/m^2) mechanically fixed to the structure 3. Waterproofing membrane 4. Protective geotextile (800 g/m^2)

The design's logic is increasing the thickness from 4 to 5 mm when the waterproofing membrane is not fully adherent to the structure since it must anyhow withstand all the heavy mechanical actions deriving from the rails' functioning.

Furthermore, it must be also noticed that on new railway bridge decks the membrane protective layer is asphalt-based, and it is poured on the waterproofing membrane's surface at 130°–140°C, adding an additional performance required: the resistance to high temperatures.

2.1 Renovation system's advantages

The system developed more than 20 years ago by RFI is still actual because it presents a lot of advantages.

During renovation works it is always difficult to clearly know before in which conditions the railway bridge deck will be once exposed to be re-waterproofed. Therefore, a system which is using a geotextile, mechanically fixed, as a formwork for the spray applied membrane, prevents problems related to the substrate conditions, such us irregularities or moisture presence. Moreover, such a system can also be laid, properly anchored, on a stone chippings layer, reducing the excavation operations, especially at the sides of the bridge. At the same time such a "detached" system is demanding a high-performance waterproofing product which can withstand the mechanical stresses related to not uniform substrate.

A second important advantage is the absence of joints and/or fixing holes on the waterproofing membrane: the spray applied waterproofing product in fact guarantees seamless joints. Thanks to the chemical adhesion provided by a primer, two layers of product sprayed in different times are monolithically welded one to each other.

Thirdly, the spray application easily follows the geometry of the bridge deck and can easily adapt to the waterproofing details typically present on this kind of structures.

The last important advantage of such a system is the fast-track application. As previously mentioned, the use of the geotextile as a formwork prevents all the problems related to the substrate preparation and at the same time the use of a fast-curing material dramatically reduces the time linked to the waterproofing membrane application. The combination of these two factors allow to work in a night span time without causing service interruption during the day with all the related costs and inconveniences.

2.2 Waterproofing membrane's required characteristics and performance

The specification characterizes the waterproofing membrane through two types of tests: technological tests to be performed on the standard membrane and on an aged one, and functional tests to be performed only on the membrane as it is.

The following table shows the entire test programme and the related requirements.

Table 2. Test programme and requirements.

Test n.	Performance characteristic	Test method	Requirement
Technological tests on the waterproofing membrane			
1	Density	UNI EN ISO 1183-1	$1 \pm 0,1$ g/cm^3
2	IR spectrum	UNI ISO 4650	–
3	Elongation at break:+20°C-30°C	UNI EN 12311-2	$\geq$ 250% $\geq$ 200%
4	Modulus at 100%		> 3 MPa
5	Modulus at 200%		> 5 MPa
6	Tensile strength		> 6 MPa
7	Shore A hardness	UNI ISO 7619-1	$\geq$ 75
8	Tear resistance	UNI EN 12310-2	> 16 N/mm
9	Residual deformation	UNI EN 12311-2	< 7%
10	Abrasion resistance	UNI ISO 4649	< 220 mm^3
11	Adhesion:to concreteto steel	UNI EN 1542	$\geq$ 0,5 N/mm^2 $\geq$ 0,5 N/mm^2
12	Adhesion after 96 h at 70°C: to concreteto steel	UNI EN 1542	$\geq$ 0,5 N/mm^2 $\geq$ 0,5 N/mm^2
13	Overlaps adhesion:to concreteto steel	UNI EN 1542	$\geq$ 4 N/mm^2 $\geq$ 4 N/mm^2
14	Overlaps adhesion after 96 h at 70°C:to concreteto steel	UNI EN 1542	-1%-1%
15	Overlaps tensile strength	UNI EN 12311-1	$\geq$ 6 MPa
16	Overlaps elongation at break		$\geq$ 200%
17	Resistance to dynamic puncture	UNI EN 12691	$\geq$ 1 m
18	Brittleness limit temperature	UNI ISO 812	< -40°C
19	UV resistance after 400 h	UNI EN 1062-11	no cracks
20	Ozone resistance after 96 h at 50 ppcm and 20% traction	UNI EN 1844	no cracks
21	Electrical resistivity:on dry steel (500 V)on wet steel (100 V)	EN 62631-1	$\geq$ 100 MΩ $\geq$ 10 MΩ
22	Solid content: m_S/m_0Water absorption: $(m_A-m_S)/m_S$	UNI EN ISO 325ASTM D 570	$\geq$ 97%$\leq$ 3%
23	Tensile strength	80°C per 14 gg	-5%
24	Tensile strength	NaCl saturated solution for 14 d	-15%
25	Tensile strength	oil ASTM 3 for 14 d	-35%
26	Tensile strength	-30°C for 1 h	-40%
27	Elongation at break	80°C for 14 d	-5%
28	Elongation at break	NaCl saturated solution for 14 d	-5%
29	Elongation at break	oil ASTM 3 for 14 d	-25%
30	Elongation at break	-30°C for 1 h	-40%
31	Abrasion resistance	80°C for 14 d	-10%
32	Shore A hardness	80°C per 14 gg	-10%
33	Shore A hardness	NaCl saturated solution for 14 d	
34	Shore A hardness	oil ASTM 3 for 14 d	
35	Shore A hardness	H$_2$SO$_4$ solution at 20% for 14 d	
Functional tests on the waterproofing membrane			
36	Compressive test of the entire system	RFI	watertightness test (EN 1928) after compressive test
37	Comparative sliding tests	RFI	sliding friction coefficientevaluation

2.3 *Test on the supply and on the applied product*

The specification does impose not only initial tests, but also tests related to the specific supply delivered at the jobsite. For this reason, samples 50×50 cm must be collected on the jobsite to perform the following tests (3 times each): density, tensile strength and elongation at break, Shore A hardness, watertightness test, absorption test at $1°C$ and IR spectrum.

Moreover, also a destructive test must be performed: a piece of the spray applied membrane each 50 m^2 must be cut to check the applied thickness.

2.4 *Execution phases*

The renovation of the waterproofing system implies always the same working phases, specifically:

(a) jobsite's set up;
(b) preparation of the support for the second track and rail's cut of the first one;
(c) rail's removal;
(d) ballast's removal and substrate's regularization;
(e) geotextile (1500 g/m^2) application and fastening;
 (f) waterproofing membrane spray application;
(g) protective geotextile (800 g/m^2) application;
(h) arrangement of the transversal and longitudinal overlaps' protection;
 (i) rail's repositioning, ballast's dumping and tamping.

Figures 1 – 2 – 3   Typical application phases on site.

3   THE MAPEI SYSTEM TO SATISFY RFI'S REQUIREMENTS

Mapei is waterproofing since years Italian railways bridge decks with Purtop 1000, two-component, solvent-free pure polyurea membrane applied by spray with a high-pressure, bi-mixer type pump, to form waterproof coatings on site.

Mapei waterproofing products' range is wide in terms of technologies and within this range Mapei selected polyurea for railways bridge decks as a top-quality solution, fast-track and highly durable.

The company experience in various infrastructures jobsites all over the world (such has tanks, dams, highways bridge decks, etc.) has in fact confirmed the high-level performance of this material. Moreover, a complete set of tests were performed over the years not only to assure its CE marking according to EN 1504-2 ("Products and systems for the protection

and repair of concrete structures - Definitions, requirements, quality control and evaluation of conformity - Part 2: Surface protection systems for concrete") but also to satisfy specific designers' requirements. The R&D department has consequently developed a formula able to withstand all the most severe stresses and conditions, positioning Purtop 1000 as a high technological solution for waterproofing.

In 2019 Mapei has decided to make one step further: it has started a qualifying process together with RFI technicians to apply Purtop 1000 in 3 mm thickness, both in new and existent railways bridge decks. This decision was taken to optimize the price-performance balance of the technology offered to the market, moreover a reduction in thickness is also saving time on site.

3.1 *The pure polyurea chemistry*

A polyurea is the product obtained by the polyaddition reaction of a polyfunctional isocyanate with a polyfunctional amine.
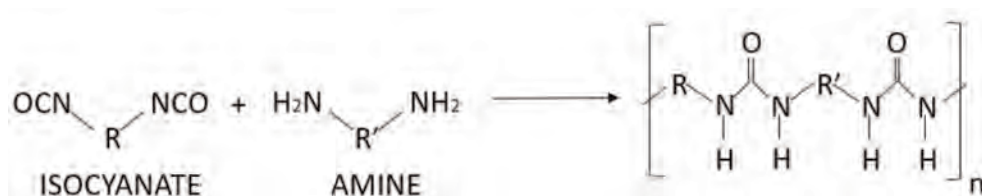
Figure 4. Polyurea reaction.

Thanks to the high reactivity between isocyanates and amines, it is not necessary the use of any catalyst for the reaction and this allows the formation of a continuous film with no bubbles caused by the humidity of the environment (that usually affects the quality of alternatives technologies).

The high reactivity also insures a very fast setting of the product (the pedestrian traffic is possible after only a few minutes and the product gets its final mechanical properties after only 24 hours).

Moreover, the formation of the urea groups leads to a very high number of intermolecular hydrogen bonds, that, after the preliminary selection of the isocyanate and the right mixture of amines, allow to achieve very good mechanical properties, in particular high elasticity, high tensile strength and high tear resistance (the Purtop 1000, for example, has more than 20 MPa as tensile strength, more than 300% of elongation and more than 80 N/mm as tear resistance).

Purtop 1000, as other hot spray polyureas, due to high reactivity of the two components, must be applied by spray, using special pumps, typically with mixing ratio by volume 1:1.

3.2 *Mapei's experience with Purtop 1000*

As already mentioned, Purtop 1000 is CE marked according to EN 1504-2 as a coating for concrete, but a lot of additional tests were performed over the years according to various projects' needs and they all have led to the conviction that the membrane could be applied in 3 mm thickness complying all the requirements of RFI's specification.

Every railway infrastructure is exposed to high temperatures in summer, but especially to low ones in winter and this is the critical condition where the waterproofing coating must maintain its mechanical performance assuring to be able to withstand all the possible loading stresses. Within the European regulatory framework, the EN 1062-7 is classifying coatings according to their crack-bridging ability, both static and dynamic, at different temperatures. As shown in the table below, Purtop 1000 in a thickness between 2 mm and 3 mm is reaching the highest classes at -20°C.

Table 3. Purtop 1000 crack-bridging properties.

Performance characteristic	Test method	Classification	Average samples thickness	Purtop 1000 performance
Static crack-bridging at -20°C	EN 1062-7	from class A1 (> 0.1 mm) to class A5 (> 2.5 mm)	2 mm	A5 > 2,5 mm
Dynamic crack-bridging at -20°C	EN 1062-7	from class B1 to class B4.2	2,9 mm	B4.2 w_o = 0,5 mm w_u = 0,2 mm w_L = ± 0,05 sinus n = 20.000 f = 1 Hz w = 0,3 mm

Another important mechanical characteristic for under ballast applications is the dynamic puncture resistance. Purtop 1000 has been tested by SNCF Réseau (the French rail network manager) according to their internal test method and it has been verified that a 3 mm coating is still continuous and watertight after the dynamical indentation it has been subjected to.

Moreover, for a dam project, Purtop 1000 has been tested, according to the requirements of the designer, in terms of static crack-bridging ability and puncture resistance under a hydrostatic pressure of 25 bar. During this test campaign it has been verified that a 2,16 mm thick sample is assuring the watertightness on an open static crack of 4 mm at 25 bar and that a 2,30 mm thick sample can withstand the puncture of a 5 mm asperity, always under a hydrostatic pressure of 25 bar.

Finally, another important performance, that a waterproofing membrane exposed to the environment should have, is the root penetration resistance, because there is always the possibility that some seeds start germinating in the ballast layer. Purtop 1000 has been tested according to the CEN/TS 14416 ("Geosynthetic barriers - Test method for determining the resistance to roots") method and it has been checked that after two years of roots' action a 2 mm thick film is completely insensitive to this type of stress.

3.3 Obtained results according to RFI specification

Based on the above-mentioned experience, Mapei Spa has approached the test campaign with RFI technicians to qualify the 3 mm thickness according to the specification.

All the tests listed at paragraph 2.2 were successfully passed except for the brittleness limit temperature, which was verified till -38°C and didn't reach the -40°C requirement. Despite this result, polyurea based materials are well-known to be still elastic at low temperature, therefore, the glass transition temperature of Purtop 1000 has also been checked and it has been verified that it is -47,9°C, confirming that the material is still elastic also below -40°C.

The test campaign has led to a fruitful discussion with RFI technicians in order to evaluate alternative test methods for the future, in addition to the ones prescribed by the specification, in order to take into consideration the physical and mechanical properties of each material which is allowed to use for this purpose.

4 CONCLUSIONS

Purtop 1000, pure polyurea membrane spray applied, is suitable to be used as a water-proofing layer for railway bridge decks satisfying the requirements of RFI (Rete Ferroviaria Italiana).

The test campaign which has lasted more than 2 years has verified that this reduced thickness of Purtop 1000 (in comparison to what prescribed by the specification) is able to assure the needed performance both alone and in combination with a geotextile in renovation cases.

This will lead to an improvement in the market because the use of Mapei Purtop 1000 with a reduced thickness is a plus not only from an economical point of view, but also from a practical one: it implies less time to be applied and this is generating a gain also from job-site's timing point of view.

REFERENCE

Rete Ferroviaria Italiana, 30/12/2022. Capitolato Generale Tecnico di Appalto delle Opere Civili – Parte II sezione 12 Ponti, Viadotti, Sottovia e Cavalcavia – RFI DTC SI PS SP IFS 002 F. Roma

Influence of geosynthetics in the structural layers on the railway track geometry

A. Petriaev

Emperor Alexander I St. Petersburg State Transport University, Saint-Petersburg, Russia

ABSTRACT: The paper presents research result of geosynthetics applications in railway structure with focus on ballast and subballast stabilization. Previous investigations have indicated the influence of geosynthetics on ballast bearing capacity and its deformation behavior, but field results of railway track geometry needs to be made. In addition, long-term behavior of stabilized track structure has not clearly indicated yet. In this study the influence of geosynthetics in ballast layer on long-term behavior estimated by the state of the track geometry. For this purpose, rail spotter and track leveling were used. The results have shown that deflection accumulation rate over time on the section with geosynthetics is 1.8 times lower than on the usual one, and the unevenness of track lowering is 1.7 times lower. Ballast stabilization with geomaterials in any case reduces the cost of current maintenance, the most complete difference in labor costs is felt starting from 4 years of post-repair operation.

1 INTRODUCTION

Recent year's information shows that on the railways where the heavy-duty and high-speed trains are being introduced, there is an increase in the number and length of sections of track with limiting train speeds. The appearance of these sections in many cases is due to the inability to ensure the stability of the track geometry.

Recently, geogrids have been increasingly used to strengthen the rail track. The benefits of geogrid reinforcement have been highlighted by some researches (Brown *et al*. 2007; Esmaeili *et al*. 2017; Gobel & Weisemann 1994; Indraratna *et al*. 2011; Ishikawa T. *et al*. 2019; Kwan 2006; Sharpe *et al*. 2006). Geogrids have rigidity, significant tensile strength, high modulus of deformation (low elongation at break), high resistance to temperature, chemical and biological influences and, due to this, are characterized by a long service life. Long-term behavior of track, stabilized by geosynthetics, has a considerable interest.

2 METHODS

Tensar SS30 polypropylene geogrids were laid at a depth of 40 cm under the sleeper during the track overhaul on the top of subgrade, which was presented by fine-grained sand . Granite crushed stone of a 40–65 mm fraction was laid on the top of the geogrid. The influence of geosynthetic materials under the sleepers on the track behavior was assessed by the number of deviation of track geometry from the standard. The evaluation of the track by the track measuring cars was carried out using the WAY software product.

The analysis of the track variations helps to identify problem areas in the sleeper's base. In addition to assessing the state of the track by the number of deviations from the standard, the "average mark" indicator was used to assess the geosynthetics effectiveness. The methodology for determining this indicator is given in the CP515 Instruction. The studies were

carried out at the two railways. The sections of the track were divided into sections, that do not have geosynthetic materials in the base ("standard") and sections that have geosynthetic materials in the base ("geosynthetics"). The evaluation used data for the period from the year following the ballast repairingдевяностотысяч to the tenth year of operation. More than ninety thousand records were used on the state of the track geometry to analyze the railway track. The summative indicator of the geometry state was the adjusted mean of deviations degree (AMDD) indicator. The calculation of the AMDD indicator was carried out according to the next equation:

$$\sum \text{IIst} + 1.35 * \sum \text{IIIst} + 1.71 * \sum \text{IVst}$$

where $\sum$IIst, $\sum$IIIst, $\sum$IVst = amount of railway track geometry deviations of the second, third and fourth degrees according to the instruction CP515.

Deviations that do not require work to eliminate them and the established train speeds do not decrease with such deviations belong to the I-st degree. Grade II also includes deviations that do not require a reduction in the governed trains speed, but affect the smoothness of the rolling stock and the intensity of the disruption of the track. They serve as an indicator of the need for preventive maintenance. The III-rd degree includes deviations, which, if not removed after detection, can significantly worsen the smoothness of train movement and increase the accumulation intensity of residual track deformations and some of them may even develop into deviations that cause a decrease in the train speed during the period before the next measuring car track inspection. Therefore, such deviations are eliminated as a matter of priority. The IVth degree includes deviations that cause an increase in the forces of interaction between the track and the rolling stock to values that can lead to train derailment. Therefore, when deviations of the IV degree are detected, the speed decreases or the movement of trains is closed. The assessment of the track gauge condition for track sections also is determined based on a score assessment of deviations from the standards of the track up-keep. according CP-436 Instruction. The quantitative evaluation of a section is set as the sum of all penalty points issued on a track section, given its length. The average mark of the rail track geometry deviation is set depending on its amplitude and length, the greater the deviation, the greater the value of the score assessment.

3 DISCUSSION

The assessment of the track state at the high-speed railway over time is shown in Figure 1.
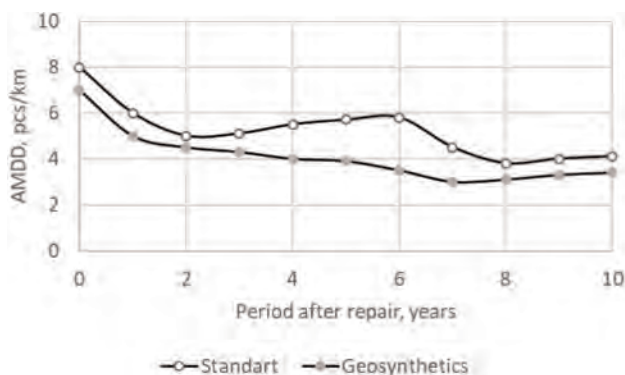
Figure 1. Change in the average value of the AMDD.

The analysis of the obtained dependence clearly shows that the total number of deviations in the post-repair period is steadily decreasing. In the two year after the repair, the track stabilization is going at the same pace, regardless of the presence of geosynthetic material and by the third year of operation, the level of AMDD indicator is on average 4.9 pcs/km. Further, the standard design stabilizes at this value with a slight regression to the to the value 5.9 pcs/km by 6 years of operation. After the track adjusting, it is stabilizing for two years and the level of AMDD indicator reaches a value of 3.95 pcs/km by the by the eighth year. For a railway track with geosynthetic material, the level of AMDD indicator steadily decreases after the repair operation and by the 7th – 10th year reaches a value of 3.45 pcs/km.

Thus, the changes dynamics in the deviations number favorably distinguishes sections of the line with geomaterials.

A graphical representation of the third degree deviations changes dynamics is shown on the Figure 2.
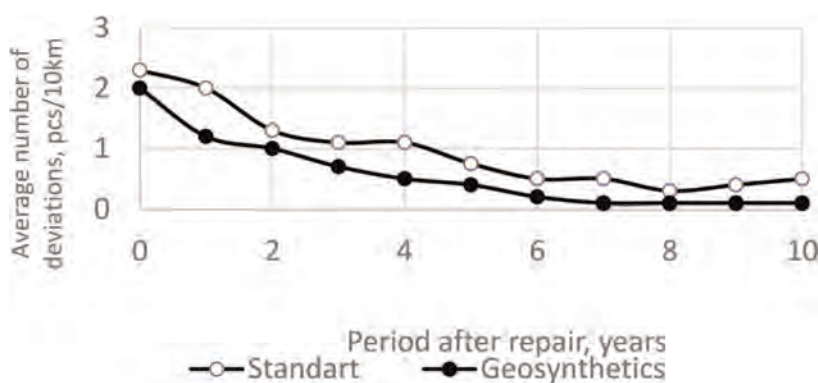
Figure 2. Change in the average number of the third degrees' deviations by year.

Figure 2 clearly shows the effect of laying geomaterials in the sleeper bearing. On the "standard" sections, the same degree of track stabilization is achieved on the two year later compere to the "geosynthetics" sections. Deviations of the third degree, in the sections where geomaterials were laid, for the first year of post-repair operation should be associated with the stabilization of ballast materials after the technology of deep cleaning of crushed stone without removing the track. In addition, it is necessary to pay attention on additional repairs work, which was made on the fourth and seventh years on the "standard" sections.

An additional confirmation of the greater stability of the railway track with geomaterils in the substructure can be the dependences, which are shown in Figure 3.

Despite the fact that the average mark is steadily decreasing during the years after repairing works, the "standard" sections rating is always higher than "geosynthetics" sections. After the fourth year of operation, average mark for sections reinforced with geomaterials is no more than 80% of the same indicator for sections of the track without reinforcement.

To verify the geosynthetics effectiveness, the track stability of heavy-duty railway line was carried out. This line was used by trains with an axle load of 230 kN and speeds up to 80 km/h. The dynamics of changes in indicators of the state of the geometry of the track showed that both for the extracurricular high-speed first line and for the heavy–duty second line, the nature of changes in these indicators is the same.
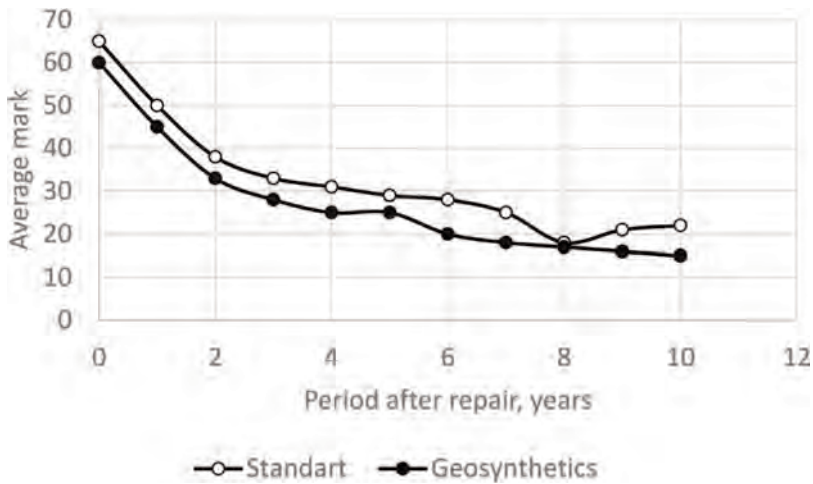
Figure 3. Change in the average Change in the average grade by year by year.

Table 1. Changes in track geometry indicators before and after laying geomaterials.

| | Construction | |
Period	Standart	Geosynthetics
	AMDD indicator, pcs/km	
In the year before the repair	53.2	50.2
For the fifth year after the repair	20.2	14.1
Ratio, before / after	2.6	3.6
	Average mark	
In the year before the repair	90	141
For the fifth year after the repair	40	22
Ratio, before / after	2.3	6.4
	Average number of 3 degrees' deviations, pcs/ 10 km/	
In the year before the repair	6.33	15.6
For the fifth year after the repair	2.27	0.75
Ratio, before / after	2.8	20.8

The assessment generalized results of the track conditions on the second railway are shown in Table 1.

The data from the table show that the use of geomaterials is typical for problematic line sections. A year before the repair on these sections, the AMDD indicator was no more than in the "standard" sections and on the "geosynthetics" sections the number of deviations of the 3rd degree in the pre-repair year was 2.5 times more. Accordingly, the average mark of these sites was more than 1.6 times compared to "standard" sections.

The sections, where the geomaterials were laid demonstrate greater stability. In the fifth year after the repair, the average mark of this sections are 22 units, compared with 40 units for "standard" sections. The presence of third-degree deviations for sections with geosynthetic materials is characterized by an average value of 0.75 pcs / 10km. For "standard" sections, this value is 2.3 pcs/10 km, the values are given for the fifth year of operation after repairing.

To assess the impact of geomaterials on the track settlement five level control operations were carried out on "standard and "geosynthetics" sections. The length of the work section was 408m. The reinforced part was located in the center of the section.

In order to identify the effect of stabilization by geosynthetics on the long-term behavior of the track geometry, high-precision level control of railhead was carried out. After the completion of repair work in 21 days, the average track deformation on the "standard" section was 11 mm, compare to 8 mm at the "geosynthetics" section. After the stabilization of the track for 51 days, the track deformation was 20mm on the "standard" section and 7 mm on the "geosynthetics" section. Such differences in the values of rail deformations may be due to the different time elapsed between the tamping and the leveling work. Thus, at the initial stage of railway track stabilization, the track settlement in the section, stabilized by geosynthetics, decreases by 1.6 times, and after track stabilization by 2.9 times.

Therefore, it can be said that afterwards the track stabilization after repair work, on average, in one day, the track settles are by 0.38 mm on the non-reinforced section and by 0.14 mm on the reinforced one. Thus, the accumulation degree of residual deformations over time at the section, stabilized by geosynthetics, is 2.7 times lower than in the usual one.

The uniformity assessment of the track depression along its length showed that the deformation is more uniform on the reinforced segment of the railway line than on the non-reinforced one. Indeed, within the "standard" section maximum deviation from the average settlement was 9 mm after 21 days and 22 mm after 51 days, which is 2.4 times higher. Consequently, the longer the time interval, the greater the difference in track lowering in individual sections. On the "geosynthetics" section the maximum deviation from the average settlement was 5 mm and 7 mm, respectively, i.e. 1.4 times more. Thus, the subsidence unevenness in the "geosynthetics" section is 1.7 times lower compared to the usual one.

This is one of the positive properties of geomaterials, allowing achieving deflection uniformity in the longitudinal direction, which naturally will not lead to a significant longitudinal profile distortion and of course will reduce the cost of the current maintenance of the railway track by reducing the number of surfacing works by about half.

REFERENCES

Brown, S.F., Kwan, J. & Thom, N.H., 2007. Identifying the Key Parameters that Influence Geogrid Reinforcement of Railway Ballast. *Geotextiles and Geomembranes* 25: 326–335.

CP-436, 2020. Instructions for Assessing the Condition of the Track Gauge by Track Measuring Means and Measures to Ensure the Safety of Train Traffic. *Moscow*: 112.

CP-515, 2013. Instructions for Assessing the Condition of the Track Gauge by Track Measuring Means and Measures to Ensure Traffic Safety. *Moscow*: 57.

Esmaeili, M., Zakeri, J. A, & Babaei, M, 2017. Laboratory and Field Investigation of the Effect of Geogrid-reinforced Ballast on Railway Track Lateral Resistance. *Geotextiles and Geomembranes* 45(2): 23–33.

Gobel, C. H., Weisemann, U. C. & Kirschner R.A.,1994. Effectiveness of a Reinforcing Geogrid in a Railway Subbase under Dynamic Loads. *Geotextiles and Geomembranes* 13(2):91–99.

Indraratna, B., Ngo, N. T. & Rujikiatkamjorn, C., 2011. Behavior of Geogrid-reinforced Ballast Under Various Levels of Fouling. *Geotextiles and Geomembranes* 29(3): 313–322.

Ishikawa, T., Li. T., Yang, T., Tokoro, T. & Tutumluer, E., 2019. Application of the UIUC model for Predicting Ballast Settlement to Unsaturated Ballasts under Moving Wheel Loads. *Transportation Geotechnics* 18: 149–162.

Kwan,C. C. J., 2006. *Geogrid Reinforcement of Railway Ballast*. Thesis, University of Nottingham, UK.: 195.

Sharpe, P., Brough, M. J. & Dixon, J., 2006. Geogrid trials at Coppull Moor on the West Coast Main Line. *Proceedings of Railway foundations conference: Railfound 06, University of Birmingham, UK.*: 375.

Landfills and remediation of contaminated sites

Hydraulic performance of Na CMC-added GCLs permeated with a simulated leachate at different temperatures

H.O. Ozhan*
Civil Engineering Department, Yeditepe University, Inonu Mah., Kayisdagi Cad., Atasehir-Istanbul, Turkey

ABSTRACT: In this study, triaxial permeability and free swell tests were performed on a geosynthetic clay liner (GCL) that had Ca bentonite and was enhanced with the biopolymer, sodium carboxymethyl cellulose (Na CMC) with a concentration of 0.25, 0.5, 1, 2, 5 and 10% by dry mass respectively. The GCL specimens were permeated with a simulated acidic leachate at a temperature of 20, 40, 60 and 80°C. Test results indicated that the temperature increase leaded to an increase in both the permeability and the swell index. As the temperature was increased from 20 to 80°C, the permeability increased by up to 1.5 orders of magnitude. Furthermore, 2% Na CMC was found to be the optimum concentration in the bentonite component of the GCL. 2% Na CMC addition caused the permeability to decrease from 9.81×10^{-7} to 2.24×10^{-8} m/s and the swell index to increase from 8.5 to 13.5 ml/2g at 80°C.

1 INTRODUCTION

Geosynthetic clay liners (GCLs) are barrier materials that are typically placed in landfills and other waste containment areas such as heap leach pads and mine tailings dams (Kang & Shackelford 2010; Rowe & Abdelatty 2012). Due to the biological decomposition of the organic substances in a waste containment area, the temperature of the leachate might exceed 60°C (Reinhart *et al.* 2020) and in some cases, might increase up to 80°C (Bouazza *et al.* 2014). Ishimori and Katsumi (2012) conducted permeability tests on a GCL that consisted of Na bentonite and permeated with 0.4 M NaCl solution. Permeability coefficient of the GCL was measured almost 1 order of magnitude higher at 60°C than at 20°C. Generally, Na bentonite is preferred to be used as the bentonite component of a GCL due to its lower permeability and higher swell index than Ca bentonite. However, polymer-enhanced Ca bentonite can effectively be used as a barrier material in waste containment facilities (Ozhan 2022; Razakamanantsoa *et al.* 2012). The primary reason for adding a polymer to Ca bentonite is to decrease the permeability in order to provide sufficient barrier capability.

Biopolymers are the organic products that are obtained from the bodies of plants or animals. They don't contribute to the carbon emission and thus, don't contaminate the environment. Carboxymethyl cellulose (CMC) is an anionic biopolymer and a derivative of cellulose obtained from the cell walls of plants (Chen 2015). De Camillis *et al.* (2016) performed hydraulic conductivity tests on Na bentonite. The bentonite specimens were enhanced with Na CMC and permeated with seawater. According to the test results, 2% Na CMC addition by dry mass caused approximately 3 orders of magnitude decrease in hydraulic conductivity when the specimens were subjected 4 wet-dry cycles in a permeation period of almost 100 days. Di Emidio *et al.* (2015) conducted hydraulic conductivity tests on Na CMC-added GCLs that consisted of Na bentonite. The GCLs were permeated with CaCl$_2$ solutions during a period of

*Corresponding Author: hakki.ozhan@yeditepe.edu.tr

more than 800 days. Test results indicated that Na CMC enhancement caused decrease in the hydraulic conductivity and increase in the swell index.

One of the primary objectives of this study was to investigate the effect of temperature increase of a simulated leachate on the hydraulic properties of a GCL that was composed of Ca bentonite. The other main objective was to determine the optimum concentration of Na CMC in the Ca bentonite of the GCL in terms of permeability and swell index. For these reasons, triaxial permeability and free swell tests were conducted on the GCLs that were enhanced with 0.25, 0.5, 1, 2, 5 and 10% Na CMC by dry mass respectively. The GCLs were permeated with a simulated leachate for 50 days at a temperature of 20, 40, 60 and 80°C respectively.

2 MATERIALS

The GCL used in this study was manufactured without any reinforcement. The Ca bentonite layer was placed between a woven and a nonwoven geotextile. The woven geotextile component of the GCL was a woven slit-film polypropylene geotextile whereas the nonwoven geotextile had needle-punched polypropylene texture. The bentonite component of the GCL was a powdered Ca bentonite. The engineering properties of the geotextile components of the GCL were listed in Table 1. The Ca bentonite component of the GCL had swell index of 20 ml/2g and montmorillonite content of 85%. The liquid limit and plastic limit of the bentonite were 141 and 41% respectively.

Table 1. Engineering properties of the geotextiles used in the GCL.

Property	Woven Geotextile	Nonwoven Geotextile	Test Method
Mass per unit area (g/m^2)	108	203	ASTM D5261
Apparent opening size (mm)	0.425	0.212	ASTM D4751
Tensile strength (kN/m)	12.2	15.4	ASTM D4595
Elongation (%)	10	45	ASTM D4595

The biopolymer that was added to the bentonite component of the GCL was chosen as Na CMC. CMC is manufactured by the catalytic reaction between cellulose and chloroacetic acid. Na CMC is the salt obtained from CMC. Na CMC is an anionic water-soluble polymer that is primarily used as a thickener and stabilizer in food, textiles, cosmetics and oil. Na CMC has molecular weight and formula of approximately 90000g/mol and $[C_6H_7O_2(OH)_2CH_2COONa]_n$ respectively (Chen 2015).

The fluid that was permeated through the GCL specimens in both the triaxial permeability and the free swell tests was chosen as a simulated leachate that had ion concentrations of 1700 mg/l Mg^{2+}, 240 mg/l Ca^{2+}, 45 mg/l K^+, 27 mg/l Al^{3+}, 5200 mg/l SO_4^{2-}, 430 mg/l NO_3^-. The simulated leachate represented an aggressive acidic leachate that could be collected in a waste containment area. The simulated leachate had pH value of 3.7.

3 TESTING PROCEDURE

3.1 *Triaxial permeability tests*

In order to prepare the GCL specimens, the geotextiles were cut with a diameter of 100 mm. The Ca bentonite that had mass/area of 4800 g/m^2 was placed on the nonwoven geotextile and wetted with tap water homogeneously. Afterwards, the woven geotextile was placed over the bentonite. Both of the geotextiles were bounded to the wetted bentonite without any reinforcement (Ozhan & Guler 2016, 2013; Ozhan 2011). The predetermined amount of Na CMC was poured into deionized water at a temperature of 60°C. Then, the water with the Na CMC was shaken for 30 minutes with a paddle mixer. The predetermined amount of Ca

bentonite was mixed with the Na CMC-added water homogeneously for 3 hours by using a paddle mixer. Then, the mixture was oven-dried for 24 hours at a temperature of 105°C. Afterwards, the dried Na CMC-added Ca bentonite was sieved through #200 sieve (Di Emidio 2010). The Na CMC-enhanced Ca bentonite was also bounded to the geotextile components of the GCL by following the same procedure as described for the Ca bentonite without any polymer addition. The concentration of Na CMC in the bentonite component of the GCL was taken as 0.25, 0.5, 1, 2, 5 and 10% by dry mass respectively.

After the specimen preparation, the GCL was placed in the flexible wall permeameter cell. From top to bottom, the test setup consisted of the top cap, porous stone, filter paper, GCL specimen, filter paper, porous stone and the base cap. The permeameter cell was filled with tap water and then, saturation and consolidation of the GCL specimen were completed by increasing the cell pressure to 550 kPa and the back pressure to 515 kPa. During these stages, the pressures remained constant for a period of 48 hours. Then, the permeation of the simulated leachate from the top of the GCL specimen to the bottom was initiated by increasing the influent pressure at the top to 518 kPa while the effluent pressure was kept constant as 515 kPa (ASTM D 6766 2012). The permeability values of the GCL specimens were measured according to Equation 1 as follows:

$$k = \frac{\Delta Q.L}{\Delta h \cdot \Delta t \cdot A} \tag{1}$$

Where k (m/s) is the coefficient of permeability of the GCL, ΔQ (m^3) is the average of leachate flow rate through the GCL for a specific period time, L (m) is the thickness of the GCL specimen, Δh (m) is the leachate head acting on the GCL, Δt (s) is the period over which the leachate is permeated through the GCL and A (m^2) is the cross-sectional area of the GCL that is perpendicular to the flow.

In order to set the temperature of the leachate to the desired values, the permeameter cell was placed in a stainless steel tank that had heater inside. The tank was filled with the simulated leachate and the permeameter cell was kept in the fluid. Afterwards, the temperature of the leachate was set to 20, 40, 60, and 80°C respectively. The temperature was able to be measured by a digital thermometer that was placed in the outlet tube of the effluent pressure valve.

3.2 *Free swell tests*

For evaluating the hydraulic performance of Na CMC-added GCLs at different temperatures, free swell tests were also conducted on the bentonite components of the GCLs (ASTM D5890 2011). The oven-dried Na CMC-Ca bentonite mixtures were prepared according to Di Emidio (2010). Each mixture that had a mass of 2 g was poured into the graduated cylinder that was filled with the simulated leachate. The swell index (2g/ml) values of the Na CMC-added bentonite specimens were measured after a period of 72 hours due to a possible ongoing swell even after 24 hours (ASTM D5890 2011). Similar to the temperature programming that was conducted in the triaxial permeability tests, the graduated cylinders were also sunk into the water tanks that were filled with the simulated leachate and the temperature of the leachate was set to 20, 40, 60, and 80°C respectively.

4 TEST RESULTS AND DISCUSSION

4.1 *Triaxial permeability tests*

As shown in Figure 1, temperature increase in the simulated leachate leaded to an increase in the permeability of the GCLs. The rate of increase was higher between 20 and 40°C. As a
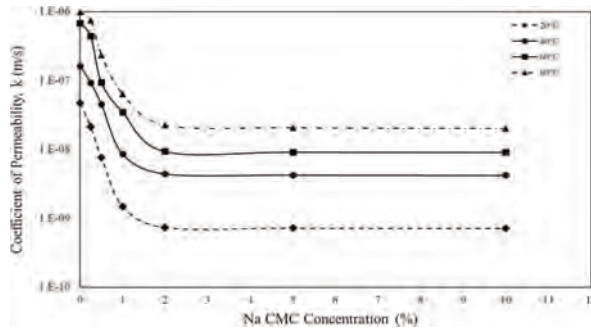
Figure 1. Coefficient of permeability change with respect to Na CMC concentration at different temperatures.

result, when the temperature of the simulated leachate was raised from 20 to 80°C, the permeability of the GCL increased almost 1.5 orders of magnitude. For instance, 2% Na CMC-added GCL had permeability of 7.32×10^{-10} m/s at 20°C whereas the permeability of 2% Na CMC-added GCL was measured as 2.24×10^{-8} m/s at 80°C.

The increase in the permeability of the GCL due to the temperature increase of the simulated leachate can be attributed to the weaker interaction between the leachate and the bentonite grains. Temperature increase might lead to a repulsive zone among the colloids in the leachate (Wang *et al.* 2016). Moreover, the weak interaction between the simulated leachate and the bentonite grains of the GCL might cause the frictional resistance of the leachate to decrease. This behavior can be explained by a decrease in the viscosity of the simulated leachate due to an increase in the temperature (Wang *et al.* 2016).

The optimum Na CMC concentration in the Ca bentonite of the GCL was found to be 2% by dry mass as shown in Figure 1. The permeability of the GCL without Na CMC enhancement decreased by 1.7 orders of magnitude when 2% Na CMC was added to the GCL. However, further increase in Na CMC concentration caused almost no change in permeability. For example, the permeability of the GCL was measured as 9.81×10^{-7} m/s at 80°C. 0.5% and 2% Na CMC-added GCLs had permeability values of 2.34×10^{-7} and 2.24×10^{-8} m/s respectively. However, the permeability of 10% Na CMC-added GCL was measured as 2.01×10^{-8} m/s.

The interaction of Na CMC with the simulated leachate might have resulted in the formation of hydrogels and these hydrogels have the capability to clog the pores among the bentonite grains. The decrease in the permeability of Na CMC-added GCLs can be attributed to the clogging of these pores. 2% of Na CMC by dry mass was found to be the approximate concentration for clogging the pores among the bentonite grains.

As can be seen in Figure 2, the permeability of the tested GCLs increased drastically during the first 20 days of permeation due the ion exchange between the cations in the simulated leachate and the bentonite component of the GCL. The rate of increase in permeability was even higher at higher temperatures. The permeability of 2% Na-CMC-added GCL was almost 1.8 orders of magnitude higher after a permeation period of 20 days at 80°C. Although the rate of increase in permeability decreased as time passed, the permeability of 2% Na CMC-added GCL was measured 0.5 order of magnitude higher at a permeation period of 50 days when compared with that of 20 days as shown in Figure 2. However, the change in the permeability value of the GCL was even lower than 0.1 order of magnitude during the last 10 days of permeation. As a result, a permeation period of 50 days could be considered as the optimum period for the termination of the ion exchange between the bentonite and the simulated leachate. Furthermore, the stable trend after a period of 40-50 days of permeation could indicate that almost no biodegradation occurred within this period. Otherwise, a significant increase in permeability could take place.
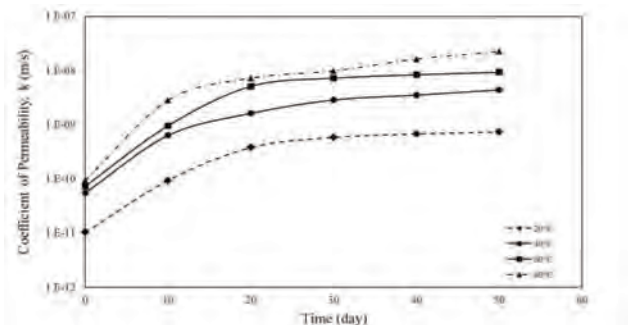
Figure 2. Coefficient of permeability change with respect to time at different temperatures for 2% Na CMC-added GCL.
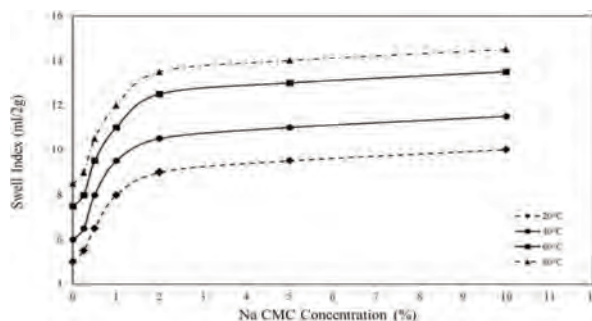
Figure 3. Swell index change with respect to Na CMC concentration.

4.2 Free swell tests

Due to an increase in the temperature of the simulated leachate, the swelling capability of the GCL was enhanced and the rate of increase in the swell index was found to be the highest up to the concentration of 2% Na CMC by mass as shown in Figure 3. The swell index of the GCL without Na CMC enhancement was measured as 8.5 ml/2g at 80°C. 2% Na CMC addition caused the swell index to increase up to 13.5 ml/2g. Finally, the swell index of 10% Na CMC-added GCL was found to be 14.5 ml/2g. On the other hand, 2% Na CMC-added GCL had swell index of 9, 10.5, 12.5 and 13.5 ml/2g at 20, 40, 60 and 80°C respectively. The test results showed that the behavior of the permeability was inversely proportional with that of the swell due to an increase in the temperature of the permeation fluid. This correlation was because of a possible decrease in the viscosity of the permeation fluid that caused both increase in the void size and expansion of the bentonite grains (Ishimori & Katsumi 2012).

5 CONCLUSIONS

An increase in the temperature of the simulated leachate caused the permeability of the GCL to increase. The rate of increase was higher between 20 and 40°C when compared with that between 40 and 60°C or 60 and 80°C. As a result, when the temperature was increased from 20 to 80°C, the permeability increased by a magnitude of almost 1.5 orders.

The deterioration of the hydraulic performance of the GCL was due to the increase in the temperature and also due to the interaction of the GCL with the simulated leachate. Na CMC addition to the GCL resulted in a decrease of 1.7 orders of magnitude in permeability. A concentration of 2% Na CMC by dry mass was found to be the optimum amount.

Due to the increase in the temperature of the simulated leachate, the swell index of the Ca bentonite in the GCL increased.

Na CMC addition leaded to an increase in the swell index of the Ca bentonite. 2% Na CMC addition caused the swell index to increase from 8.5 to 13.5 ml/2g at a temperature of 80°C.

In conclusion, the temperature increase of the simulated leachate deteriorated the hydraulic performance of the GCL by increasing the permeability. Na CMC is an environmentally friendly organic polymer that does not contribute to the carbon footprint. Na CMC addition to the Ca bentonite component of the GCL resulted in an enhancement in the hydraulic performance of the GCL by decreasing the permeability and increasing the swell index even at high temperatures.

REFERENCES

ASTM D5890. 2011. *Standard Test Method for Swell Index of Clay Mineral Component of Geosynthetic Clay Liners*. ASTM International. West Conshohocken, PA: USA.

ASTM D6766. 2012. *Standard Test Ethod for Evaluation of Hydraulic Properties of Geosynthetic Clay Liners Permeated with Potentially Incompatible Aqueous Solutions*. ASTM International. West Conshohocken, PA: USA.

Bouazza, A., Singh, R.M., Rowe, R.K. & Gassner, F. 2014. Heat and Moisture Migration in a Geomembrane-GCL Composite Liner Subjected to High Temperatures and Low Vertical Stresses. *Geotextiles and Geomembranes* 42(5): 555–563.

Chen, J. 2015. Synthetic Textile Fibers: Regenerated Cellulose Fibers. In Textiles and Fashion: *Materials, Design and Technology* (eds), R. Sinclair: 79–95. Amsterdam: Elsevier.

De Camillis, M., Di Emidio, G., Bezuijen, A. & Verastegui-Flores, R.D. 2016. Hydraulic Conductivity and Swelling Ability of a Polymer Modified Bentonite Subjected to Wet-dry Cycles in Seawater. *Geotextiles and Geomembranes* 44(5): 739–747.

Di Emidio, G. 2010. *Hydraulic and Chemico-osmotic Performance of Polymer Treated Clays. Ph.D. dissertation*, Ghent University, Ghent: Belgium.

Di Emidio, G., Mazzieri, F., Verastegui-Flores, R.D., Van Impe, W. & Bezuijen, A. 2015. Polymer-treated Bentonite Clay for Chemical-resistant Geosynthetic Clay Liners. *Geosynthetics International* 22(1): 125–137.

Ishimori, H. & Katsumi, T. 2012. Temperature Effects on the Swelling Capacity and Barrier Performance of Geosynthetic Clay Liners Permeated with Sodium Chloride Solutions. *Geotextiles and Geomembranes* 33: 25–33.

Kang, J.B. & Shackelford, C.D. 2010. Consolidation of a Geosynthetic Clay Liner under Isotropic States of Stress, *Journal of Geotechnical and Geoenvironmental Engineering* 136(1): 253–259.

Ozhan, H.O. 2011. *Internal Erosion of Geosynthetic Clay Liners under High Hydraulic Heads. Ph.D. thesis*, Bogazici University, Istanbul: Turkey.

Ozhan, H.O. & Guler, E. 2013. Use of Perforated base Pedestal to Simulate the Gravel Subbase in Evaluating the Internal Erosion of Geosynthetic Clay Liners. *Geotechnical Testing Journal* 36(3): 418–428.

Ozhan, H.O. & Guler, E. 2016 Factors Affecting Failure by Internal Erosion of Geosynthetic Clay Liners Used in Fresh Water Reservoirs. *Environmental & Engineering Geoscience* 22(2): 157–169.

Ozhan, H.O. 2022. Sodium Carboxymethyl Cellulose-enhanced GCLs in Freshwater Reservoirs. *IOP Conference Series: Materials Science and Engineering*, 7th EuroGeo Conference, IOP Publishing, 1260: 012006.

Razakamanantsoa, A.R., Barast, G. & Djeran-maigre, I. 2012. Hydraulic Performance of Activated Calcium Bentonite Treated by Polyionic Charged Polymer. *Applied Clay Science* 59–60: 103–114.

Reinhart, D., Joslyn, R. & Emrich, C.T. 2020. Characterization of Florida, US Landfills with Elevated Temperatures. *Waste Management* 118: 55–61.

Rowe, R.K. & Abdelatty, K. 2012. Effect of a Calcium-rich Soil on the Performance of an Overlying GCL. *Journal of Geotechnical and Geoenvironmental Engineering* 138(4): 423–431.

Wang, S., Zhu, W., Qian, X., Xu, H. & Fan, X. 2016. Temperature Effects on Non-Darcy Flow of Compacted Clay. *Applied Clay Science* 135: 521–525.

Contaminant transport through landfill composite liners due to geomembrane defects

N. Guarena, A. Dominijanni & M. Manassero
Politecnico di Torino, Torino, Italy

ABSTRACT: Although a number of studies have been devoted to the assessment of the leachate flow rate through defects in geomembranes, which are routinely used in conjunction with low-permeability mineral layers for the lining of waste disposal facilities, relatively little attention has been paid to the mechanisms that control the transport of contaminants. A theoretical framework is here presented to model the advective-diffusive transport of inorganic contaminants through defects of uniform width and infinite length (holed wrinkles, defective seams, etc.), whereby imperfect contact conditions between the geomembrane and the underlying mineral layer are considered, and the mass conservation condition is imposed for both the solvent and the solute phases. Closed-form analytical solutions have been derived to assess the contaminant mass flow rate for the cases of pure advection and pure diffusion, with a view to quantifying the error associated with the simplified calculation approaches that are currently adopted for the performance-based design of landfill composite liners.

1 INTRODUCTION

Composite liners that include a high-density polyethylene (HDPE) geomembrane (GM), placed over a compacted clay layer (CCL), are prescribed throughout the world for the bottom lining systems of waste disposal facilities, with the goal of minimising the migration of contaminants from the waste fill to the surrounding environment. The regulations in force in many countries typically define a set of minimum requirements that have to be satisfied by both the GM and the CCL layers, depending on the type of waste that has to be disposed of in the landfill. In some cases the presence of a natural or engineered attenuation layer (AL), i.e., a layer of soil placed between the composite liner and the underlying aquifer or water resource that needs to be protected, represents an additional requirement.

The use of alternative lining systems, such as those in which the CCL is replaced with a geosynthetic clay liner (GCL), is permitted in most regulations, provided that equivalency with the prescribed composite liner is demonstrated on the basis of a selected performance criterion. Some of the common performance criteria, which are adopted to demonstrate that the proposed alternative liner is equivalent to, or better than, the prescribed composite liner, include: (1) the leachate flow rate under steady-state conditions; (2) the mass flow rate of a given contaminant under steady-state conditions; (3) the time required for the concentration of a given contaminant to reach a specified value at the bottom of the barrier; and (4) the time required for the mass flow rate of a given contaminant to reach a specified value at the bottom of the barrier (Katsumi *et al.* 2001; Manassero *et al.* 2000; Rowe & Brachman 2004; Shackelford 1990).

As far as the first of the aforementioned performance criteria is concerned, which is closely related to the steady-state advective travel time through the composite liner (Shackelford 1993), several approaches have been developed to calculate the leachate flow rate since the pioneering study of Giroud & Bonaparte (1989), who recognised that intact GMs are nearly impervious to the

liquid flow and, therefore, the only accessible pathway by which the leachate can migrate through landfill composite liners is through defects in the GM layer (e.g. defective seams between adjacent panels, punctures caused by sharp materials beneath and above the GM, and tensile failures induced by the landfilling operations). Rowe (1998) and Touze-Foltz *et al.* (1999, 2001) derived analytical solutions for the leakage rate under the assumption that, after infiltration through the GM defect, the contaminated liquid spreads horizontally in the interfacial zone between the GM and the low-permeability mineral layer up to a certain distance from the defect, prior to percolating vertically through the low-permeability mineral layer. The ability of Rowe's (1998) solutions to represent the actual three-dimensional (3D) flow regime within the composite liner was verified numerically by Foose *et al.* (2001a), who observed that analytical and numerical models yield nearly identical results for the values of the hydraulic transmissivity of the interface and the hydraulic conductivity of the low-permeability mineral layer that are representative of field scenarios. Other numerical studies have addressed specific issues, such as the effects related to the spatial variability in the hydraulic transmissivity of the GM/CCL interface (Cartaud *et al.* 2005a), to the change in the degree of saturation of the mineral layer and to the shape of longitudinal defects of finite length in the GM layer (Cartaud *et al.* 2005b; Saidi *et al.* 2006), to the hydraulic interaction between adjacent defects in the GM layer (Saidi *et al.* 2008), and to the different hydraulic properties of the geotextile and bentonite components of GCLs under unsaturated conditions (Bannour *et al.* 2016). Empirical (Giroud 1997; Touze-Foltz & Giroud 2003, 2005) and semi-empirical solutions (Foose *et al.* 2001a; Giroud & Touze-Foltz 2005) were developed using interpolation methods that combine theoretical (both analytical and numerical) and experimental results, thus providing design engineers with simple equations that allow the leachate flow rate to be assessed once a limited number of input parameters (i.e. the hydraulic head on top of the GM, the area of circular defects or the width of longitudinal defects, and the hydraulic conductivity of the mineral layer) and the contact conditions between the GM and the mineral layer are known.

Compared to the numerous attempts that have been made to propose a rational method to assess the leachate flow rate through composite liners, relatively few studies have been aimed at quantifying the advective-diffusive transport of contaminants in the presence of defects in the GM layer. The latter issue is particularly relevant in the case of inorganic compounds, which, unlike many organic compounds, do not readily diffuse through intact portions of the GM layer. Therefore, although the transport of organic compounds can be modelled under the hypothesis of molecular diffusion being the primary migration pathway over the entire surface of the composite liner (Foose 2002; Foose *et al.* 2002) when GMs are installed under strict construction quality assurance conditions (i.e. with a defect frequency ranging from 2.5 to 5 holes/ha, as reported by Rowe (2012)), the transport of inorganic compounds should be recognised as a 3D process that involves migration through the GM defects, through the interfacial zone between the GM and the underlying mineral layer and, finally, through the mineral layer itself, via a combination of advection and diffusion.

A simplified approach to model the advective-diffusive transport of inorganic contaminants through composite liners was proposed by Katsumi *et al.* (2001), who identified an equivalent one-dimensional (1D) system for which analytical solutions to the contaminant breakthrough time and mass flux exist. This approach, which has since been implemented in a number of analytical studies that have dealt with the performance-based design of landfill lining systems, allows both steady-state (Dominijanni & Manassero 2021; Dominijanni *et al.* 2021; Foose 2010; Guarena *et al.* 2020) and transient-state contaminant transport analyses (Foose *et al.* 2001b; Kandris & Pantazidou 2012) to be carried out using typical spreadsheet applications and hand-held calculators, and the equivalence between the prescribed and alternative lining systems to be assessed on the basis of performance criteria (2) to (4), which are preferable over the advective travel time criterion (1) since diffusion is a significant, if not the dominant, transport mechanism through composite liners (Foose *et al.* 2002; Manassero & Shackelford 1994; Shackelford 2014). Furthermore, such an approach may be used as an effective tool to verify the results of more complex (fully 3D) and computationally rigorous numerical models.

Despite its simplicity and versatility, the Katsumi *et al.* (2001) approach is not devoid of drawbacks, the most serious of which can probably be ascribed to the way the equivalent 1D system is defined. Although, on the one hand, satisfaction of the mass conservation condition for the solvent phase is guaranteed with regard to the analytical or empirical model that is selected to calculate the leachate flow rate, on the other, the mass conservation condition for the solute phase is disregarded, and an error is therefore made in the predicted contaminant mass flux relative to the theoretically correct solution. With the aim of covering this modelling gap, a novel theoretical framework is outlined in the present paper, in which the 3D advective-diffusive transport of inorganic contaminants within the composite liner is conceptualised as a horizontal flow along the interface between the GM and the low-permeability mineral layer and then a vertical flow in the low-permeability mineral layer, in a similar way to the reference scheme that was considered by Rowe (1998) with a view to approximating the actual leachate flow network under imperfect contact conditions at the GM/CCL or GM/GCL interface. The error that can arise from the adoption of the Katsumi *et al.* (2001) approach is estimated on the basis of closed-form analytical solutions to the contaminant mass flow rate for the cases of pure advection and pure diffusion, assuming that steady-state conditions have been achieved for both the liquid and solute transport.

2 MODELLING THE ADVECTIVE-DIFFUSIVE TRANSPORT OF INORGANIC CONTAMINANTS THROUGH COMPOSITE LINERS

The containment performance of landfill composite liners is known to be affected by the areal density of wrinkles in the GM layer, whose formation is mostly controlled, during construction of the liner, by the thermal expansion of the GM upon heating by solar radiation, as well as by its placement and protection procedures (Chappel *et al.* 2012; Giroud & Morel 1992; Rowe 2005, 2012). Indeed, because of the greater hydraulic transmissivity of the gap beneath the wrinkles than that associated with the interfacial zone between the GM and the low-permeability mineral layer, contaminants preferentially migrate through holes that are located in correspondence to the wrinkles rather than through holes that occur in flat areas. The following theoretical framework has thus been developed only for the case of a damaged wrinkle, whose width, $2b_w$, is defined as the width of the zone where the GM is not in contact with the underlying mineral layer (Figure 1), as this is the one of the greatest concerns about the problem of assessing the ability of the selected composite liner to limit contaminant transport from the waste fill. Nonetheless, if the liquid and contaminant transport rates are not controlled by the size of the actual holes in the wrinkle, the case of a damaged wrinkle is perfectly analogous to the case of a cut, tear or defective seam of width $2b_w$ occurring in a flat area of the GM layer, so that the two types of defects can collectively be referred to as defects of uniform width. Moreover, if the
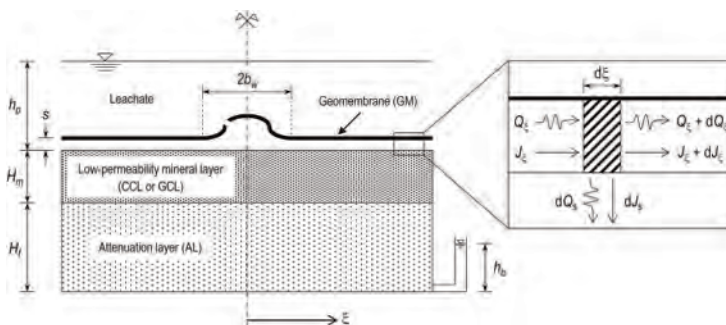
Figure 1. Reference scheme for the liquid and contaminant transport analyses through a composite liner with a defect of uniform width and infinite length in the GM layer and imperfect contact conditions between the GM and the low-permeability mineral layer (not to scale).

length of the defect, L_w, is much greater than its width (i.e. defect of uniform width and infinite length), the liquid and contaminant transport analyses can be treated as two-dimensional problems (Giroud & Touze-Foltz 2005; Touze-Foltz *et al.* 1999).

Provided the spacing between adjacent wrinkles is high enough for their mutual interactions to be neglected, Rowe's (1998) analytical solution to the steady-state hydraulic head profile, h, beneath the GM can be written in the following form:

$$h(\xi) = \begin{cases} h_p & \text{if } \xi \le b_w \\ \left(H_f + H_m - h_b + h_p\right)e^{-\alpha(\xi - b_w)} - \left(H_f + H_m - h_b\right) & \text{if } \xi > b_w \end{cases} \tag{1}$$

The α parameter that appears in Equation 1 is given by:

$$\alpha = \sqrt{\frac{k_s}{(H_f + H_m)\theta_h}} \tag{2}$$

where θ_h is the hydraulic transmissivity of the interfacial zone between the GM and the low-permeability mineral layer, and k_s is the equivalent hydraulic conductivity corresponding to the low-permeability mineral layer (saturated hydraulic conductivity k_m) and the attenuation layer (saturated hydraulic conductivity k_f):

$$k_s = \frac{H_f + H_m}{\frac{H_f}{k_f} + \frac{H_m}{k_m}} \tag{3}$$

The horizontal leachate flow rate in the transmissive layer, Q_ξ, at a distance $\xi > b_w$ from the longitudinal axis of the wrinkle, can be expressed as:

$$Q_\xi(\xi) = L_w i_s \frac{k_s}{\alpha} e^{-\alpha(\xi - b_w)} \tag{4}$$

where i_s is the maximum mean hydraulic gradient through the low-permeability mineral layer and the attenuation layer:

$$i_s = 1 + \frac{h_p - h_b}{H_f + H_m} \tag{5}$$

The vertical leachate flow rate, dQ_s, that infiltrates the strip of the mineral layer between the ξ and $\xi + d\xi$ coordinates can be expressed as:

$$dQ_s(\xi) = \begin{cases} L_w i_s k_s d\xi & \text{if } \xi \le b_w \\ L_w i_s k_s e^{-\alpha(\xi - b_w)} d\xi & \text{if } \xi > b_w \end{cases} \tag{6}$$

and the corresponding vertical volumetric leachate flux, q_s, at a distance ξ from the longitudinal axis of the wrinkle, is obtained directly as the ratio of dQ_s to $L_w d\xi$:

$$q_s(\xi) = \begin{cases} i_s k_s & \text{if } \xi \le b_w \\ i_s k_s e^{-\alpha(\xi - b_w)} & \text{if } \xi > b_w \end{cases} \tag{7}$$

Finally, the leachate flow rate, Q_s, that infiltrates the low-permeability mineral layer at a distance ξ from the longitudinal axis of the wrinkle is given by:

$$Q_s(\xi) = 2b_w L_w i_s k_s \left\{ 1 + \frac{1}{\alpha b_w}\left[1 - e^{-\alpha(\xi - b_w)}\right] \right\} \tag{8}$$

which yields the total leachate flow rate through the damaged wrinkle, Q, if ξ tends to infinity:

$$Q = 2b_w L_w i_s k_s \left(1 + \frac{1}{\alpha b_w}\right) \tag{9}$$

2.1 *Katsumi* et al. *(2001) equivalent 1D system*

The approach that was proposed by Katsumi *et al.* (2001), with the aim of providing a simple calculation tool to analyse the transport of inorganic contaminants through composite liners when the leachate flow is at steady state, consists in computing an equivalent area, A_e, which conducts the same (total) leachate flow rate as the considered defect for the same hydraulic head drop across the composite liner, thereby ensuring that the mass conservation condition for the solvent phase is satisfied:

$$A_e = \frac{Q}{k_s i_s} \tag{10}$$

The equivalent area that is computed according to Equation 10 is here observed to correspond to the definition of the wetted area originally provided by Giroud *et al.* (1992, 1997). Furthermore, if Rowe's (1998) conceptual model is adopted to assess the leachate flow rate, the following expression results from substitution of Equation 9 in Equation 10:

$$A_e = 2b_w L_w \left(1 + \frac{1}{\alpha b_w}\right) \tag{11}$$

and the contaminant mass flow rate through the damaged wrinkle, J_{app}, which approximates the theoretically correct one, can then be obtained from the contaminant mass flux, j_s, which in turn is calculated according to the existing analytical solutions to the partial differential equation that governs the 1D solute transport through multi-layered barriers via advection, diffusion, sorption and degradation:

$$J_{app} = A_e j_s \tag{12}$$

When the contaminant transport is dominated by advection, and steady-state conditions are achieved for both the liquid and the solute transport, the following expression of Equation 12 holds true:

$$J_{app} = 2b_w L_w k_s i_s c_p \left(1 + \frac{1}{\alpha b_w}\right) \tag{13}$$

where c_p is the contaminant concentration in the leachate drainage layer, which is located directly above the GM layer.

If the diffusive component of contaminant transport prevails over the advective one, Equation 12 assumes the following form:

$$J_{app} = 2b_w L_w \Lambda (c_p - c_b) \left(1 + \frac{1}{\alpha b_w}\right) \tag{14}$$

where c_b is the contaminant concentration at the bottom of the composite liner, and Λ is the equivalent diffusivity (Manassero & Shackelford 1994; Manassero *et al.* 2000):

$$\Lambda = \frac{1}{\frac{H_f}{n_f D_f^*} + \frac{H_m}{n_m D_m^*}} \tag{15}$$

being n_m and n_f the porosities of the low-permeability mineral layer and the attenuation layer, respectively, and D_m^* and D_f^* the effective diffusion coefficients of the low-permeability mineral layer and the attenuation layer, respectively, which are obtained as the product of the apparent tortuosity factor (< 1) and the free-solution diffusion coefficient of the contaminant, $D_{s,0}$.

2.2 *Novel theoretical framework*

The theoretical framework outlined in this section should be interpreted as an attempt to overcome the limitations encountered in the Katsumi *et al.* (2001) approach, and to investigate

the extent to which this latter approach approximates the actual transport mechanisms of inorganic contaminants through landfill composite liners with defects in the GM layer.

Satisfaction of the mass conservation condition for the solute phase is guaranteed under steady-state conditions, with reference to the control volume in the interfacial zone between the GM and the low-permeability mineral layer (Figure 1), if the following relationship is verified:

$$dJ_s(\xi) + \frac{dJ_\xi(\xi)}{d\xi}d\xi = 0 \tag{16}$$

The vertical contaminant mass flow rate, dJ_s, that infiltrates the strip of the mineral layer between the ξ and $\xi + d\xi$ coordinates can be expressed as:

$$dJ_s(\xi) = q_s \frac{ce^{\frac{q_s}{\Lambda}} - c_b}{e^{\frac{q_s}{\Lambda}} - 1}L_w d\xi \tag{17}$$

or, substituting Equation 7 in Equation 17, in the following alternative form:

$$dJ_s(\xi) = \begin{cases} i_s k_s \dfrac{c_p e^{\frac{i_s k_s}{\Lambda}} - c_b}{e^{\frac{i_s k_s}{\Lambda}} - 1}L_w d\xi & \text{if } \xi \leq b_w \\[3em] i_s k_s e^{-\alpha(\xi-b_w)} \dfrac{ce^{\frac{i_s k_s}{\Lambda}e^{-\alpha(\xi-b_w)}} - c_b}{e^{\frac{i_s k_s}{\Lambda}e^{-\alpha(\xi-b_w)}} - 1}L_w d\xi & \text{if } \xi > b_w \end{cases} \tag{18}$$

where c is the contaminant concentration beneath the GM.

The horizontal contaminant mass flow rate in the transmissive layer, J_ξ, at a distance $\xi > b_w$ from the longitudinal axis of the wrinkle, can be expressed as:

$$J_\xi(\xi) = Q_\xi c - L_w \theta_d \frac{dc}{d\xi} \tag{19}$$

or, substituting Equation 4 in Equation 19, in the following alternative form:

$$J_\xi(\xi) = L_w i_s \frac{k_s}{\alpha}ce^{-\alpha(\xi-b_w)} - L_w \theta_d \frac{dc}{d\xi} \tag{20}$$

where θ_d is the diffusive transmissivity of the GM/CCL or GM/GCL interface.

Substituting Equations 18 and 20 in Equation 16 and collecting terms yields the following homogeneous, second-order, linear ordinary differential equation with non-constant coefficients:

$$\frac{d^2c}{d\xi^2} - \frac{i_s k_s}{\theta_d \alpha}e^{-\alpha(\xi-b_w)}\frac{dc}{d\xi} - \frac{i_s k_s}{\theta_d}\left[\frac{e^{-\alpha(\xi-b_w)}}{e^{\frac{i_s k_s}{\Lambda}e^{-\alpha(\xi-b_w)}} - 1}\right](c - c_b) = 0 \tag{21}$$

which has to be solved for $b_w \leq \xi < +\infty$ in conjunction with the following set of boundary conditions:

$$\begin{cases} c(b_w) = c_p \\ \lim_{\xi \to +\infty} \dfrac{dc}{d\xi}(\xi) = 0 \end{cases} \tag{22}$$

Once the steady-state contaminant concentration profile beneath the GM has been determined, either analytically or numerically, the contaminant mass flow rate, J_s, that infiltrates the low-permeability mineral layer at a distance ξ from the longitudinal axis of the wrinkle is given by:

$$J_s(\xi) = 2b_w L_w i_s k_s c_p \left\{ \frac{e^{\frac{i_s k_s}{\Lambda}} - \frac{c_b}{c_p}}{e^{\frac{i_s k_s}{\Lambda}} - 1} + \frac{1}{\alpha b_w}\left[1 - \frac{c(\xi)}{c_p}e^{-\alpha(\xi-b_w)}\right] - \frac{\theta_d}{b_w i_s k_s c_p}\left[\frac{dc}{d\xi}(b_w) - \frac{dc}{d\xi}(\xi)\right]\right\} \tag{23}$$

which yields the total contaminant mass flow rate through the damaged wrinkle, J, if ξ tends to infinity:

$$J = 2b_w L_w i_s k_s c_p \left[\frac{e^{\frac{i_s k_s}{\Lambda}} - \frac{c_b}{c_p}}{e^{\frac{i_s k_s}{\Lambda}} - 1} + \frac{1}{\alpha b_w} - \frac{\theta_d}{b_w i_s k_s c_p} \frac{dc}{d\xi}(b_w) \right] \tag{24}$$

2.2.1 Closed-form analytical solution for the case of pure advection

A first case of interest, for which a closed-form analytical solution to the total contaminant mass flow rate is easily obtained, is that of the advection that represents the main transport mechanism through the composite liner. Under such an assumption, Equations 21 and 22 reduce to a condition of constant solute concentration beneath the GM (i.e. $c = c_p$ for $b_w \leq \xi < +\infty$), and the total contaminant mass flow rate through the damaged wrinkle is then given by a relationship that is identical to Equation 13. Therefore, for the limiting case of purely advective transport, the Katsumi *et al.* (2001) approach leads to a prediction of the contaminant mass flow rate that can be regarded as the rigorous one from the mass conservation condition viewpoint, for both the solvent and the solute phases.

2.2.2 Closed-form analytical solution for the case of pure diffusion

When diffusion is the controlling mechanism of contaminant transport, as might be the case of composite liners that include mineral layers with very low hydraulic conductivity values (e.g. GCLs or bentonite-amended CCLs), the steady-state contaminant concentration profile beneath the GM assumes a form that is analogous to the hydraulic head profile given by Equation 1:

$$c(\xi) = \begin{cases} c_p & \text{if } \xi \leq b_w \\ (c_p - c_b)e^{-\beta(\xi - b_w)} + c_b & \text{if } \xi > b_w \end{cases} \tag{25}$$

where:

$$\beta = \sqrt{\frac{\Lambda}{\theta_d}} \tag{26}$$

The following expression can then be derived for the total contaminant mass flow rate through the damaged wrinkle:

$$J = 2b_w L_w \Lambda (c_p - c_b) \left(1 + \frac{1}{\beta b_w} \right) \tag{27}$$

Finally, the error that arises when the Katsumi *et al.* (2001) approach is used, relative to the theoretically correct solution for the limiting case of purely diffusive transport, is assessed by finding the ratio of Equation 27 to Equation 14:

$$\frac{J}{J_{app}} = \frac{1 + \frac{1}{\beta b_w}}{1 + \frac{1}{\alpha b_w}} \tag{28}$$

With the aim of quantifying the aforementioned error for a real pollutant containment scenario, the two landfill composite liners described by Dominijanni & Manassero (2021) have been considered herein, and cadmium (Cd^{2+}) has been selected to represent the inorganic leachate constituent of interest ($D_{s,0} = 7.17 \cdot 10^{-10}$ m²/s). The first lining system consists of a 1.5 mm thick GM and a 1 m thick CCL, which overlies a 3 m thick AL. The second lining system consists of a 1.5 mm thick GM and a 1 cm thick GCL, which overlies a 4 m thick AL. Further details about the physical, hydraulic and transport parameters assigned to the two composite liners can be found in Dominijanni & Manassero (2021), while an

assessment of the diffusive transmissivity, in the absence of experimental studies devoted to its measurement, can be obtained as follows:

$$\theta_d = D_{s,0}s \tag{29}$$

where s is the thickness of the GM/CCL or GM/GCL interface, which in turn can be related to θ_h, if Newton's viscosity law for the flow between two parallel plates applies to the transmissive layer (Giroud & Bonaparte 1989):

$$s = \sqrt[3]{\frac{12\theta_h\mu_w}{\gamma_w}} \tag{30}$$

being γ_w and μ_w the unit weight and viscosity of water, respectively.

The use of Equation 28 leads to a calculated error, J/J_{app}, equal to 0.022 for the composite liner that comprises the CCL, and 0.763 for the composite liner that comprises the GCL, as illustrated in Figure 2. Therefore, the Katsumi et al. (2001) approach overestimates the contaminant mass flow rate for both the considered lining systems, with an error that is greater in the case of the GM + CCL + AL composite liner than in the case of the GM + GCL + AL composite liner. Such an overestimation can be expected, considering the values of the decay constant, β, for the solute concentration profile beneath the GM (Equation 25), which are greater than the corresponding values of the decay constant, α, for the hydraulic head profile (Equation 1) and, thus, cause the footprint of the low-permeability mineral layer, over which contaminant diffusion takes place, to be smaller than the equivalent area that is given by Equation 11.
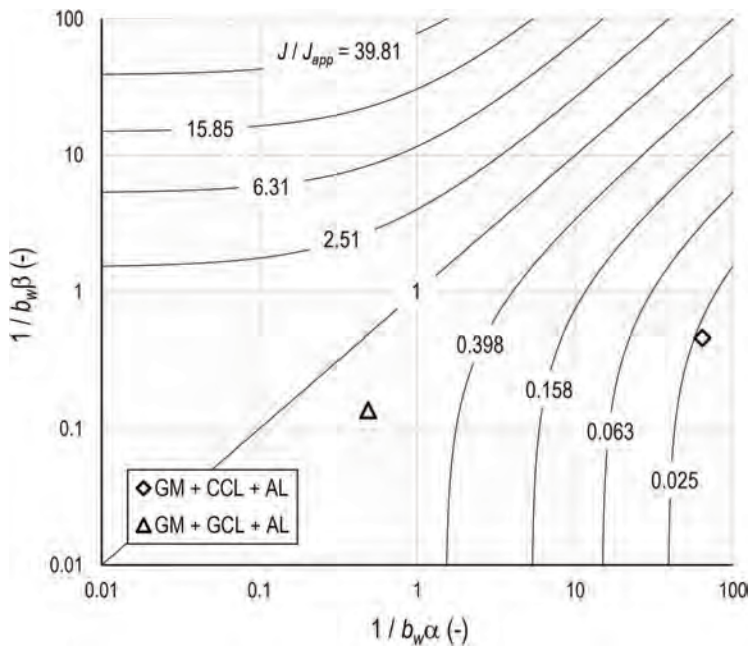
Figure 2. Iso-value curves of the error associated with the use of the Katsumi et al. (2001) approach, which is defined as the ratio of the theoretically correct contaminant mass flow rate, J, to the approximate one, J_{app}, under the hypothesis that diffusion is the controlling transport mechanism. The open symbols refer to the landfill composite liners considered by Dominijanni & Manassero (2021).

3 CONCLUSIONS

An original theoretical framework has been developed to calculate the steady-state mass flow rate of inorganic contaminants through landfill composite liners, which are made up of a GM overlying a low-permeability mineral layer, under the restrictive hypotheses that the transport of both the liquid and the solute only occurs through GM defects of uniform width and infinite length (e.g. holed wrinkles and defective seams), and that all the soil layers maintain fully-saturated conditions, even when negative pore-water pressures build up. The migration pathway within the lining system has been conceptualised as a horizontal flow along the interfacial zone between the GM and the underlying mineral layer, and then as a vertical flow in the mineral layer itself, as in the reference scheme considered by Rowe (1998) for the calculation of the leachate flow rate. Closed-form analytical solutions to the contaminant mass flow rate have been derived for two specific cases, namely pure advection and pure diffusion, with the aim of quantifying the error associated with the use of the simplified calculation approach that was proposed by Katsumi *et al.* (2001). In the case of purely advective transport, the latter approach has been proven to be consistent with the mass conservation condition for both the solvent and the solute phases, while satisfaction of the mass conservation condition for the solute phase is no longer guaranteed when diffusion represents the main transport mechanism, leading to an overestimation of the contaminant mass flow rate if the composite liners described by Dominijanni & Manassero (2021) are considered.

Further research is recommended on the aspects dealt with in the present paper. From a theoretical viewpoint, the possible existence of an analytical expression for the solute concentration profile beneath the GM should be investigated, also considering different defect types (e.g. circular holes in a flat GM), boundary conditions (e.g. parallel interacting damaged wrinkles) and transport properties of the soil layers (e.g. change in the degree of saturation for positive suction heads) from the working hypotheses of this study. Furthermore, the ability of the assumed migration pathway to represent the actual 3D advective-diffusive transport in composite liners should be verified with the aid of computationally rigorous numerical models. From an experimental viewpoint, the development of a laboratory apparatus, which allows the newly introduced θ_d parameter (i.e. the diffusive transmissivity of the GM/CCL or GM/GCL interface) to be measured, is of the utmost importance.

REFERENCES

Bannour, H., Goblet, P., Mendes, M. & Touze-Foltz, N. 2016. Numerical Study of Advective Flow Through Composite Liners. *Environmental Geotechnics* 3(6): 379–385.

Cartaud, F., Goblet, P. & Touze-Foltz, N. 2005a. Numerical Simulation of the Flow in the Interface of a Composite Bottom Liner. *Geotextiles and Geomembranes* 23(6): 513–533.

Cartaud, F., Goblet, P. & Touze-Foltz, N. 2005b. Numerical Study of Advective Flow Through Composite Liners. *Geosynthetics International* 12(6): 299–309.

Chappel, M.J., Brachman, R.W.I., Take, W.A. & Rowe, R.K. 2012. Large-scale Quantification of Wrinkles in a Smooth Black HDPE Geomembrane. *Journal of Geotechnical and Geoenvironmental Engineering* 138(6): 671–679.

Dominijanni, A. & Manassero, M. 2021. Steady-state Analysis of Pollutant Transport to Assess Landfill Liner Performance. *Environmental Geotechnics* 8(7): 480–494.

Dominijanni, A., Guarena, N. & Manassero, M. 2021. Risk Assessment Procedure for the Performance-Based Design of Landfill Lining Systems and Cutoff Walls. *Japanese Geotechnical Society Special Publication* 9(5): 199–204.

Foose, G.J. 2002. Transit-time Design for Diffusion Through Composite Liners. *Journal of Geotechnical and Geoenvironmental Engineering* 128(7): 590–601.

Foose, G.J. 2010. A Steady-state Approach for Evaluating the Impact of Solute Transport Through Composite Liners on Groundwater Quality. *Waste Management* 30(8–9): 1577–1586.

Foose, G.J., Benson, C.H. & Edil, T.B. 2001a. Predicting Leakage through Composite Landfill Liners. *Journal of Geotechnical and Geoenvironmental Engineering* 127(6): 510–520.

Foose, G.J., Benson, C.H. & Edil, T.B. 2001b. Analytical Equations for Predicting Concentration and Mass Flux From Composite Liners. *Geosynthetics International* 8(6): 551–575.

Foose, G.J., Benson, C.H. & Edil, T.B. 2002. Comparison of Solute Transport in Three Composite Liners. *Journal of Geotechnical and Geoenvironmental Engineering* 128(5): 391–403.

Giroud, J.P. 1997. Equations for Calculating the Rate of Liquid Migration Through Composite Liners Due to Geomembrane Defects. *Geosynthetics International* 4(3–4): 335–348.

Giroud, J.P. & Bonaparte, R. 1989. Leakage Through Liners Constructed with Geomembranes - Part II. Composite liners. *Geotextiles and Geomembranes* 8(2): 71–111.

Giroud, J.P. & Morel, N. 1992. Analysis of Geomembrane Wrinkles. *Geotextiles and Geomembranes* 11(3): 255–276.

Giroud, J.P. & Touze-Foltz, N. 2005. Equations for Calculating the Rate of Liquid Flow Through Geomembrane Defects of Uniform Width and Finite or Infinite Length. *Geosynthetics International* 12(4): 191–204.

Giroud, J.P., Badu-Tweneboah, K. & Bonaparte, R. 1992. Rate of Leakage Through a Composite Liner Due to Geomembrane Defects. *Geotextiles and Geomembranes* 11(1): 1–28.

Giroud, J.P., Rad, N.S. & McKelvey, J.A. 1997. Evaluation of the Surface Area of a GCL Hydrated by Leachate Migrating Through Geomembrane Defects. *Geosynthetics International* 4(3–4): 433–462.

Guarena, N., Dominijanni, A. & Manassero, M. 2020. From the Design of Bottom Landfill Liner Systems to the Impact Assessment of Contaminants on Underlying Aquifers. *Innovative Infrastructure Solutions* 5: 2.

Kandris, K. & Pantazidou, M. 2012. Landfill Base Liners: Assessment of Material Equivalency and Impact to Groundwater. *Geotechnical and Geological Engineering* 30(1): 27–44.

Katsumi, T., Benson, C.H., Foose, G.J. & Kamon, M. 2001. Performance-based Design of Landfill Liners. *Engineering Geology* 60(1–4): 139–148.

Manassero, M. & Shackelford, C.D. 1994. The Role of Diffusion in Contaminant Migration Through Soil Barriers. *Rivista Italiana di Geotecnica* 28(1): 5–31.

Manassero, M., Benson, C.H. & Bouazza, A. 2000. Solid Waste Containment Systems. In *Proc. GeoEng2000: An International Conference on Geotechnical & Geological Engineering, Melbourne, 19-24 November 2000*. Lancaster: Technomic Publishing Company.

Rowe, R.K. 1998. Geosynthetics and the Minimization of Contaminant Migration Through Barrier Systems Beneath Solid Waste. In *Proc. 6th Int. Conf. on Geosynthetics, Atlanta, 25-29 March 1998*. Roseville: Industrial Fabrics Association International.

Rowe, R.K. 2005. Long-term Performance of Contaminant Barrier Systems. 45th Rankine Lecture. *Géotechnique* 55(9): 631–678.

Rowe, R.K. 2012. Short and Long-term Leakage Through Composite Liners. 7th Arthur Casagrande Lecture. *Canadian Geotechnical Journal* 49(2): 141–169.

Rowe, R.K. & Brachman, R.W.I. 2004. Assessment of Equivalence of Composite Liners. *Geosynthetics International* 11(4): 273–286.

Saidi, F., Touze-Foltz, N. & Goblet, P. 2006. 2D and 3D Numerical Modelling of Flow Through Composite Liners Involving Partially Saturated GCLs. *Geosynthetics International* 13(6): 265–276.

Saidi, F., Touze-Foltz, N. & Goblet, P. 2008. Numerical Modelling of Advective Flow Through Composite Liners in Case of Two Interacting Adjacent Square Defects in the Geomembrane. *Geotextiles and Geomembranes* 26(2): 196–204.

Shackelford, C.D. 1990. Transit-time Design of Earthen Barriers. *Engineering Geology* 29(1): 79–94.

Shackelford, C.D. 1993. Contaminant Transport. In D.E. Daniel (ed.), *Geotechnical Practice for Waste Disposal*: 33–65. London: Chapman & Hall.

Shackelford, C.D. 2014. The ISSMGE Kerry Rowe Lecture. The Role of Diffusion in Environmental Geotechnics. *Canadian Geotechnical Journal* 51(11): 1219–1242.

Touze-Foltz, N. & Giroud, J.P. 2003. Empirical Equations for Calculating the Rate of Liquid Flow Through Composite Liners Due to Geomembrane Defects. *Geosynthetics International* 10(6): 215–233.

Touze-Foltz, N. & Giroud, J.P. 2005. Empirical Equations for Calculating the Rate of Liquid Flow Through Composite Liners Due to Large Circular Defects in the Geomembrane. *Geosynthetics International* 12(4): 205–207.

Touze-Foltz, N., Rowe, R.K. & Duquennoi, C. 1999. Liquid Flow Through Composite Liners Due to Geomembrane Defects: Analytical Solutions for Axi-symmetric and Two-dimensional Problems. *Geosynthetics International* 6(6): 455–479.

Touze-Foltz, N., Rowe, R.K. & Navarro, N. 2001. Liquid Flow Through Composite Liners Due to Geomembrane Defects: Nonuniform Hydraulic Transmissivity at the Liner Interface. *Geosynthetics International* 8(1): 1–26.

Hydration, desiccation and self-healing capacity of geosynthetic clay liners

W. Lieske
Department of Environment and Urban Planning, City of Herne, Germany

F. Christ
Ruhr-Universität Bochum, Bochum, Germany

K. von Maubeuge
NAUE GmbH & Co. KG, Germany

T. Wichtmann
Ruhr-Universität Bochum, Bochum, Germany

ABSTRACT: Desiccation-induced cracking and associated potential damage of geosynthetic clay liners has been the subject of numerous recent studies. In a previous study by the authors, crack propagation in GCLs was systematically investigated using an X-ray scanner. Based on this, the constitutive relationship between water content and crack intensity factor (CIF) for GCLs under combined impact of drying and wetting with divalent salt solutions has been derived. In the current contribution, the X-ray images of the aforementioned study are examined with respect to their crack width distribution. For this purpose, the experimental results were idealised as a Gaussian distribution and the median and variance were analysed. It was shown that there is a unique relation between median and variance independent of the hydration fluid.

1 BACKGROUND

The increase of drought and sequences of hot days associated with climate change has raised the question of the robustness of clay-based barrier systems under those new boundary conditions. The shrinkage induced by changes in water content and associated cracking can potentially yield cracks that could not be closed by swelling upon rewetting. To investigate this process is particularly complex for geosynthetic clay liners (GCLs) because, on the one hand, the needling and the carrier materials influence the potential cracking of the bentonite filling and, on the other hand, direct investigation of potential cracks through the carrier textiles is not possible.

In a previous study presented by Lieske *et al.* (2020) [2] desiccation-induced cracking in GCLs was investigated using an X-ray scanner. A commercially available GCL was used to prepare four different specimens, hydrated with DI-Water and CaCl$_2$ solutions of different molarity. The X-ray images revealed marked differences in the drying and cracking behaviour of the different specimens. However, based on the analysis of the crack propagation at different water contents it was found, that within the measuring accuracy the crack intensity factor (CIF) was mainly a function of water content, independent of the hydration fluid. The analysis of the CIF over gravimetric water content showed that the shrinkage can be

dedicated to four different stages. The desaturation of a fully saturated GCL is starting with the release of water from large inter-aggregate pores and water that has been absorbed by the geotextile, commonly causing only insignificant shrinkage and, thus, no cracks. In the second stage named linear shrinkage water is released from the inter-aggregate pores and the decrease in water volume is proportional to the decrease in volume. This cracking regime is associated with the most pronounced development of cracks. When the water content falls below a material-specific value, residual shrinkage is observed with a shrinkage much less pronounced than in the linear shrinkage phase. The released water is originating from the intra-aggregate pores and much more energy is needed to remove this water from a sample. The last stage is termed zero-shrinkage where a further water content decrease is not associated with further pore volume reduction.

The study also revealed that with increasing drying, cracks occur that were not closed by swelling upon rehydration. Although the study proves the risk of desiccation-induced damage to GCLs, from an application point of view the question arises, whether the experimental desiccation scenarios can become relevant in practice. GCLs are typically installed as a system with protection and buffer mechanisms which affects the dessication behaviour of the GCL [4,5,7,9]. It is also unclear at which level of desiccation cracks lead to a permanent change in the barrier performance of GCLs [2].

The aim of the present study is to shed more light on the risk of permanent cracks and thus damage to GCLs due to desiccation. The study by [2] was focusing on the crack intensity, i.e. the proportion of the crack area in relation to the entire considerd area. However, this and other studies revealed a wide range in the distribution of cracks [1,2,8]. Considering that large cracks are more likely not to be closed by swelling than smaller ones, it becomes clear that the distribution of cracks might be more important than the total volume of cracks (CIF) for the assessment of potential drying-induced damage. In this paper, the evolution of the crack width distribution of the X-ray experiments presented in [2] is investigated. For this purpose, the crack widths were idealised as normal distributions, and were analysed based on the median and the variance.

2 MATERIALS AND METHODS

The results were obtained from drying tests carried out with commercially available GCLs filled with sodium bentonite. The product data specified by the manufacturer are: Mass per area of 4800 g/m2, a thickness of ≥ 6 mm in the dry state and a hydraulic conductivity $k \leq 3 \cdot 10^{-11}$ m/s in the water-saturated state. Four GCL specimens in the size of 42.5 cm $\times$ 30.5 cm were cut and taped at the corners to prevent loss of bentonite. The raw bentonite was present as granules.

The four GCL specimens were hydrated with DI water (SP1), 0.05 mol/l CaCl2 solution (SP2), a 0.5 mol/l CaCl2 solution (SP3) and a 0.05 mol/l CaCl2 solution after prehydration with DI water (SP4). After hydration, the GCLs were dried in an oven at 30°C. The duration of the drying intervals was increased gradually to achieve different drying intensities. In all experiments, a 3.92 kPa load was applied to the GCLs both during hydration and drying. The profile of the water content of the different GCLs over the duration of the experiment is shown in Figure 1.

After each drying and wetting interval, the samples were examined by means of X-ray imaging. The 2D image of the GCLs obtained in this way was investigated with respect to crack patterns using the digital image processing software PCAS (Particles (Pores) and Cracks Analysis System). It should be noted, however, that the resolution of the device was limited. It was therefore not possible to analyse the GCLs with very fine cracks (e.g. SP3).

The probability density functions f(cw) of the crack widths obtained from the different X-ray images in Figure 2 give an impression of the variability of the detected cracks. The
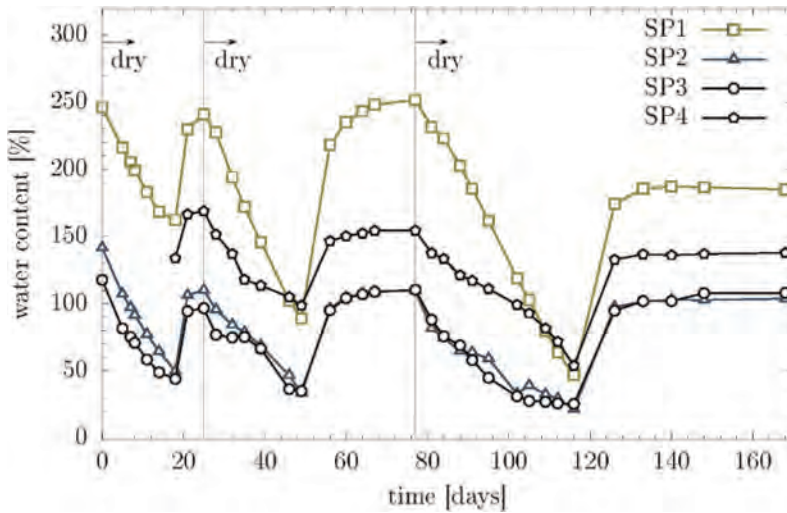
Figure 1. Gravimetric water content over time of the different GCL samples during the drying/wetting cycles.

probability density f(cw) is defined according to equation 1, where n is the total number of cracks and Δn the number of cracks with a width in the interval of Δcw.

$$f(w) = \frac{\Delta n}{n \cdot \Delta cw} \tag{1}$$

The data obtained can be idealised by using the Gaussian distribution (also referred to as normal distribution) given in equation 2, where σ is the median and σ is the variance. The median is giving an impression about the most frequent encountered crack width. The variance μ is a measure of the distribution of the values with respect to the mean value. The larger the value of μ the flatter the Gauss curve, or in other words: the larger the difference between the smallest and the largest encountered crack width.

$$f(x) = \frac{1}{\sqrt{2\pi\sigma^2}} \exp\left(-\frac{(x-\mu)^2}{2\sigma^2}\right) \tag{2}$$

The dashed line in Figure 2 shows the idealised Gaussian curve while the bars represent the experimental data. Even though the Gauss curve has a quite good match with the experimental observations, a certain discrepancy between idealisation and experiment is noticeable, especially for the measured values of SP1 in the relatively wet state (w = 89 \%) and w = 162 \%). This may be attributed to the generally rather fine cracks that could hardly be measured by the device. Vice versa, as the mean crack width increases, the Gaussian distribution of the crack widths becomes more and more pronounced and the fit between experiment and idealisiation gets better.

The importance of the mathematical analysis of the crack distribution for assessing the risk of damage due to drying can be illustrated by means of an example. If a discrete value for a critical crack width cw_{crit} is considered, above which the swelling properties under the given boundary conditions (surcharge load, mineralogical composition of the GCL filling, pore water chemistry, to name just a few) are no longer sufficient to close all cracks induced by drying, then all cracks widths $cw > cw_{crit}$ are associated to an damage of the GCL.
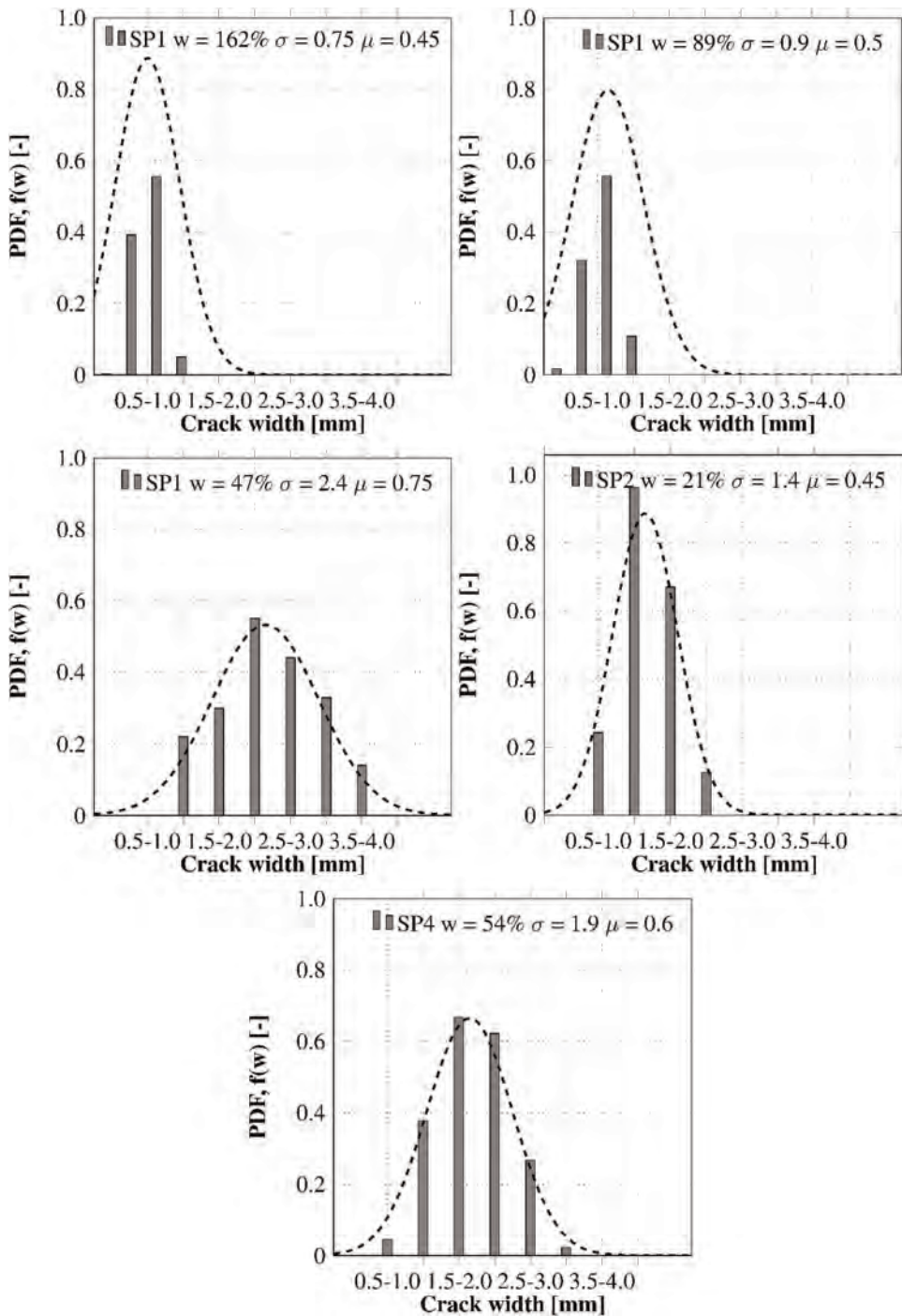
Figure 2. Probability density function of crack width for SP1, SP2 and SP4 at different water contents.

The potential of occuring cracks larger than cw_{crit} is given by the following three σ - μ combinations: (I) $\sigma \ll cw_{crit}$ μ is very high, (II) $\sigma < cw_{crit}$, μ is moderate and, (III) $\sigma > cw_{crit}$ (μ is not decisive in this case). In case (I), the average crack width is clearly below cw_{crit} but due to the wide range of crack widths (μ very high), damaging cracks have also to be expected. In the second case (II), the average crack width is below cw_{crit} but part of the Gaussian curve is located in the area of damage. In case (III) the average crack width is above the damage threshold cw_{crit}. The distribution μ is therefore not decisive for the analysis of the damage in this case.

3 RESULTS AND DISCUSSION

Figure 3 shows the evolution of the mean value μ and the standard deviation σ over the water content, as well as the correlation between σ and μ. Considering only SP1, i.e. the sample hydrated with DI water, an increase of σ with decreasing water content can be observed. Some experimental data given as average crack width in [1] was added in the σ-w plot, supporting the strong correlation between average crack width and water content. This
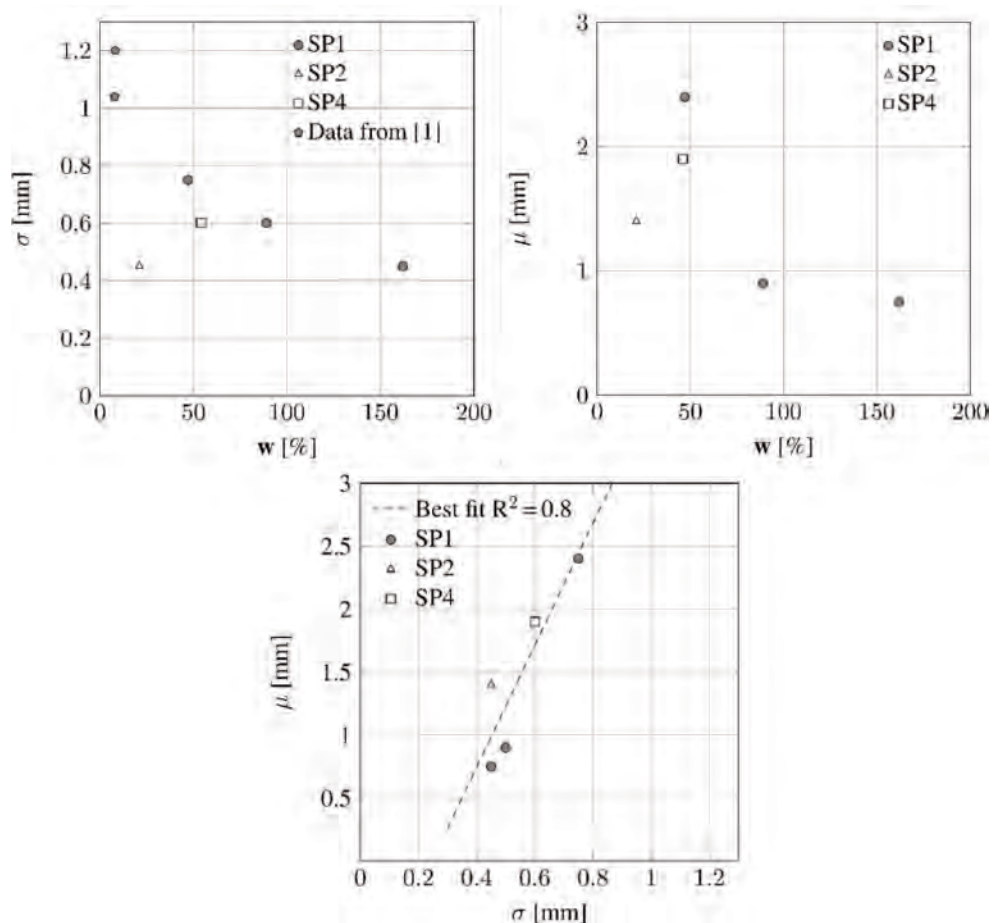
Figure 3. Correlation between σ, μ and w for different specimens.

trend shows that with increasing drying intensity, or decreasing water content, not only the average crack width increases but also the diversity of the crack widths.

When comparing SP1, SP2 and SP3, i.e. samples hydrated with different fluids, the order SP1 > SP3 > SP2 is observed for both μ and σ with similar water content. Dissolved salts cause the clay minerals to aggregate, which leads to a decrease in tensile strength on the macroscale. During drying the decrease in tensile strength manifests itself in the formation of rather fine cracks, since suction-induced stresses lead to cracks at relatively small strains. However, it must be taken into account that this does not provide any information about the number of cracks. The analysis of the CIF in Lieske *et al.* (2020) showed that under the boundary conditions considered, the CIF is only a function of the water content. It follows that for a given water content μ is smaller for a GCL hydrated with a salt solution than for one hydrated with DI water, but at the same time the total number of cracks is larger.

Figure 3(c) shows the relationship between σ and μ. It reveals a strong correlation (coefficient of determination = 0.8), whereas the mean crack width increases, the variability of the cracks also increases, which is mathematically indicated by a flatter Gaussian curve. The σ-w and μ-w plots in Figure 3(a) and (b) show a strong dependence on the hydration fluid, as this affected the tensile strength of the clay. However, the relationship between σ and μ is independent of the hydration fluid for the data considered. For the consideration of the damage potential, this correlation indicates that of the three σ - μ combinations described above that can lead to the formation of permanent cracks, only two are likely. The combination of a mean crack width significantly below the damage threshold and a very flat Gaussian curve as described in (I) seems unlikely in view of the experimental results, since small mean crack widths are associated with a small range of crack widths.

However, at the same time this consideration raises the question of a critical limit value for the crack width cw_{crit}, from which permanent structural damage to the sealing performance of a GCL is likely to occur. This limit is a complex function of material-specific parameters (such as the mineralogy of the GCL fill, mass per m2), installation conditions (load, nature of the surrounding soil) but also the exposure (wet-dry cycles, drying rate, chemistry of the hydration fluid) [1,2,6,8]. Further research is needed to derive such a criterium based on comprehensive understanding of the underlying soil mechanical constitutive relations to include all the aforementioned parameters.

4 CONCLUSION

This contribution is addressing the morphology of drying-induced cracks in GCLs. The global context is the risk assessment of permanent cracks and thus loss of barrier performance caused by extensive drying. Based on the assumption that wide cracks tend to exceed the self-healing capacity of bentonite rather than small ones, the crack width distribution was analysed. For this purpose, the crack width distribution was idealised using a Gaussian distribution and the median (σ) and the variance (μ) were analysed as parameters to describe the crack distribution. Three main observations were made:

– Both, the median and the variance of the Gaussian curves increased with decreasing water content for the samples tested with DI-water only.
– The samples that were hydrated with divalent salt solutions deviated from this trend.
– Regardless of the hydration fluid, there was a clear correlation between μ and σ.

However, these findings are only a first step towards a final risk assessment of drying events. To predict permanent damage, a critical crack width is required, beyond which the swelling capacity of the bentonite filling is no longer capable to fill existing cracks. The derivation of this limit value based on soil mechanics constitutive relations that take into account both material properties and installation boundary conditions is the subject of future research.

REFERENCES

[1] Acikel, A.S., Gates, W.P., Singh, R.M., Bouazza, A., & Rowe, R.K. 2018. Insufficient Initial Hydration of GCLs From Some Subgrades: Factors T and Causes. *Geotextiles and Geomembranes* 46, 770–781.

[2] El-Zein, A., Yu, B. & Ghavam-Nasiri 2019. Insights into Desiccation and Self-Healing of Bentonite in Geosynthetic Clay Liners under Thermal Loads *E3S Web of Conferences*: 92

[3] Lieske, W., Christ, F., Baille, W., Di Emidio, G., & Wichtmann, T. 2020. Suction and Crack Propagation in GCLs Subjected to Drying and Wetting in CaCl2-solutions. *Geotextiles and Geomembranes* 48(6), 973–982.

[4] Müller-Kirchenbauer, A., Blümel, W., & von Maubeuge, K. 2008. Long-term Efficiency of GCLs with Regard to Natural Drying and Wetting Cycles. *EuroGeo4: 4th European geosynthetics conference*: 211.

[5] Müller-Kirchenbauer, A., Blümel, W., & von Maubeuge, K. 2010. Performance of Geosynthetic Clay Liners in Landfill Cap Sealing Systems - Physical Processes in the Bentonite Layer During Drying and Rehydration Periods. *GBR-C 2k10: 3rd International Symposium on Geosynthetic Clay Liners, Würzburg, 15-16 September 2010*.

[6] Rowe, R.K., & Hamdan, S. 2021. Effect of Wet-dry Cycles on Standard & polymer-amended GCLs in Covers Subjected to Flow Over the GCL. *Geotextiles and Geomembranes* 49, 1165–1175.

[7] Southen, J. M., & Rowe, R. K. 2011. Numerical Modelling of Thermally Induced Desiccation of Geosynthetic Clay Liners Observed in Laboratory Experiments. *Geosynthetics International* 18(5), 289–303.

[8] Tang, C.-S., Cui, Y.-J., & Shi, B. 2010. Experiment Evidence on the Temperature Dependence of Desiccation Cracking Behavior of Clayey Soils. *Engineering Geology* 114(3), 261–266.

[9] Yesiller, N., Hanson, J. L., Risken, J. L., Benson, C. H., Abichou, T., & Darius, J. B. 2019. Hydration Fluid and Field Exposure Effects on Moisture-suction Response of Geosynthetic Clay Liners. *Journal of Geotechnical and Geoenvironmental Engineering* 145(4).

The settlement of a municipal solid waste landfill built on collapsible soils

E.D. Olinic*
Faculty of Hydrotechnics, Department of Geotechnics and Foundation Engineering, Technical University of Civil Engineering Bucharest, Bucharest, Romania

T. Olinic*
Faculty of Land Reclamation and Environmental Engineering, Department of Environmental Engineering and Land Reclamation, University of Agronomic Sciences and Veterinary Medicine Bucharest, Bucharest, Romania

ABSTRACT: The paper presents some results of settlement calculations performed after completion of a municipal solid waste landfill built on collapsible soils (sensitive soils). The results of the calculations are compared in the hypothesis of maintaining the conditions of natural moisture content of the collapsible soil and in the hypothesis of flooding the collapsible soil as a result of an imperfect sealing system. Starting from the requirements of the national legislation in force which imposes a slope of at least 1% of the drains that take the leachate from the landfill, after consuming the settling of the deposit, the position of the drain is analyzed to ensure the transport capacity of the leachate from the moment of opening the landfill and until its filling and consumption of the settlement under the load transmitted by the stored waste. Another aspect treated in the paper is related to the tensile effort that may occur in the geosynthetics from the landfill bottom system, as a result of the foundation soil settlement. The settlement calculations were performed according to the Romanian technical norms: "Technical norm for foundation of buildings on moisture – sensitive, collapsible soils, indicative NP 125: 2010" and "Technical norm regarding the determination of characteristic and calculation values of geotechnical parameters, indicative NP 122: 2010", which are correlated to the Eurocode 7.

1 INTRODUCTION

In Romania, collapsible soils cover about 19% of the country's territory (approximately 40.000 km^2) and it is common in the eastern part of the country.

Moisture-sensitive or collapsible soils are unsaturated macroporous cohesive soils that, upon saturation with water, undergo sudden and irreversible changes of the internal structure, reflected by additional settlements with collapsing character and decreases in the values of geotechnical parameters of mechanical behavior (NP 125: 2010).

The design of a municipal solid waste landfill on a collapsible soil is a particular situation due to the fact that several technical regulations that impose certain restrictions must be respected.

On the one hand, the "Technical norm regarding the storage of waste", approved by OMMGA 757/2004 imposes a slope along the drains of at least 1%, drains that collect the leachate both at the time of opening the landfill, as well as after filling it and consuming the settlement of the foundation soil under the load transmitted by the deposited waste.

---

*Corresponding Authors: ernest.olinic@utcb.ro and olinictatiana@gmail.com

Figure 1.   Collapsible soil spreading in Romania (NP 125:2010).

On the other hand, NP 125:2010 "Technical norm for foundation of buildings on moisture – sensitive, collapsible soils" contains two provisions from this point of view: the water supply networks must have a double protection and the calculation of settlement must be performed also in the hypothesis of the flooding of the foundation soil.

2   THE SETTLEMENT EVALUATION FOR COLLAPSIBLE SOILS

In the case of normal consolidated soils, the settlement is evaluated by accepting a linear relationship between stress and deformation (Hooke's law) and is a function of the deformation modulus and the vertical stress due to overload (σ_z). In the case of collapsible soils, the vertical effort due to its weight (in natural conditions and in saturated state) and the total effort due to the construction, respectively the sum between the geological load and the effort due to overload, is evaluated. The settlement is obtained as a difference of the settlements generated by the initial (geological load under natural conditions) and final effort (after flooding the foundation soil and completing of the construction).

Annex 5 from the NP 125: 2010 shows how to calculate the additional settlement caused by saturation by wetting the collapsible soil divided into: additional wetting under geological stress (I_{mg}) and additional wetting by saturation under the load transmitted by the foundation (I_{mp}). Following the calculation steps from the technical norm, it is simulated the flooding of the soil and evaluated its response (I_{mg}) and later the construction on the saturated soil and the evaluation of the total settlement ($I_{mg} + I_{mp}$). The NP 125: 2010 does not present the assessment of the probable settlement after the construction was carried out, in the hypothesis of maintaining the natural moisture content of the foundation soil (s), an extremely important component in choosing the foundation solution.

Figure 2 is a schematic diagram for calculation of the settlement of the collapsible soil, and highlights the efforts of vertical loads required for calculation, while the specific strain is
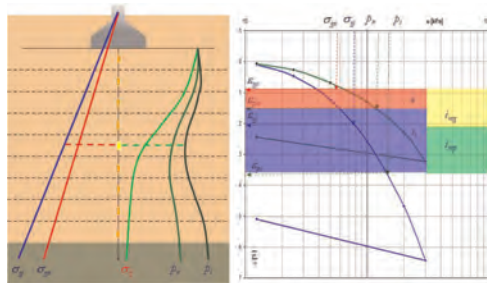
Figure 2.   Scheme for the calculation of the foundation soil settlement for a collapsible soil layer. σ_{gi} - geological stress in saturated conditions, σ_{gn} - geological stress at natural moisture content, σ_z – vertical stress due to surcharge, $p_n = \sigma_z + \sigma_{gn}$ – total vertical stress at natural moisture content, $p_i = \sigma_z + \sigma_{gi}$ – total vertical stress in saturated conditions, ε – specific strain, s – specific settlement at natural moisture conent, s_i – supplementary specific settlement in saturated conditions.

1431

obtained directly from the stress-strain curves, from the tests of compressibility in oedometer of the samples at natural moisture content and the initially saturated samples.

3 CASE STUDY

3.1 *Geotechnical investigation*

For the construction of a municipal solid waste landfill were carried out geotechnical field and laboratory investigations. The size of the landfill is approximately 250×300 m.

According to the geotechnical investigations, it was found that the foundation soil is composed, under a layer of top soil with a thickness of about 70 cm, from a layer of loessoid soil intercepted up to the depth of 13.70 m, followed by a layer of clayey silt – silty clay in a plastic state: medium-soft to stiff. The groundwater was intercepted at a depth of 21 m.

On undisturbed samples from the loess layer, 44 compressibility tests were performed in the oedometer, 27 at natural moisture content and 17 on initially saturated samples, in order to determine the additional settlement caused by the wetting, the structural strength (σ_0) and the behavior of the material under the applied loads.

As a result of the graphic representation of the additional settlement caused by saturation at 300 kPa, depending on the depth (Figure 3), it has been noticed that at the surface, the material records very high values for i_{m300}, which reach even 8 ... 10%, while for depths of 7 to 13 m, this value decreases to 2 ... 5%. As a result, the loess package was divided into 3 layers. Layer 4 is identical from a granulometric point of view but, due to the high natural moisture content, the material has lost its sensitivity to wetting ($i_{m300} = 0 ... 0.5\%$).

For each calculation layer, the characteristic values of the geotechnical parameters necessary for the settlement calculation were determined. Based on the compressibility tests in oedometer, the characteristic values of the specific settlements were determined under the applied loading steps ($\varepsilon_{k\ inf}$, $\varepsilon_{k\ sup}$). For the overestimation of the settlement, only the values $\varepsilon_{k\ sup}$ were selected and the characteristic compression-settlement curves were drawn, for which a function was searched to approximate it.

Figures 4 and 5 shows the upper characteristic curves obtained on natural samples and on initially saturated samples. Also, the functions that approximate the characteristic values of
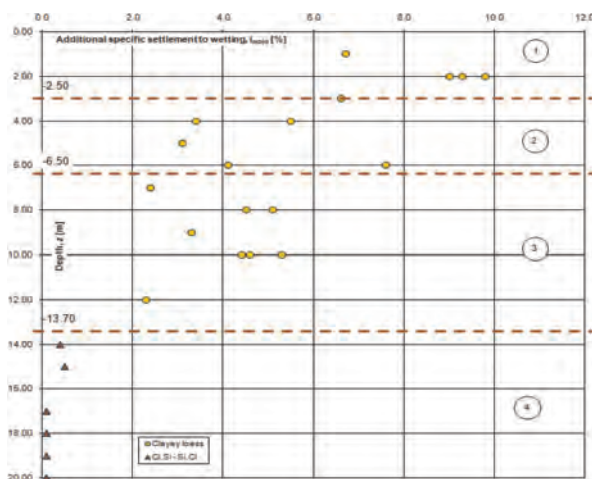
Figure 3. The variation of the additional settlement caused by saturation, im300, depending on the depth.
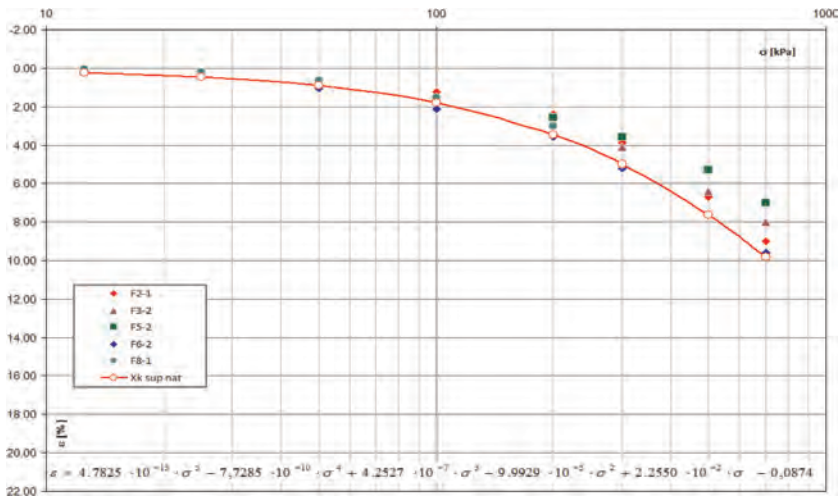
Figure 4. Compression – settlement curves on natural samples from layer 1.
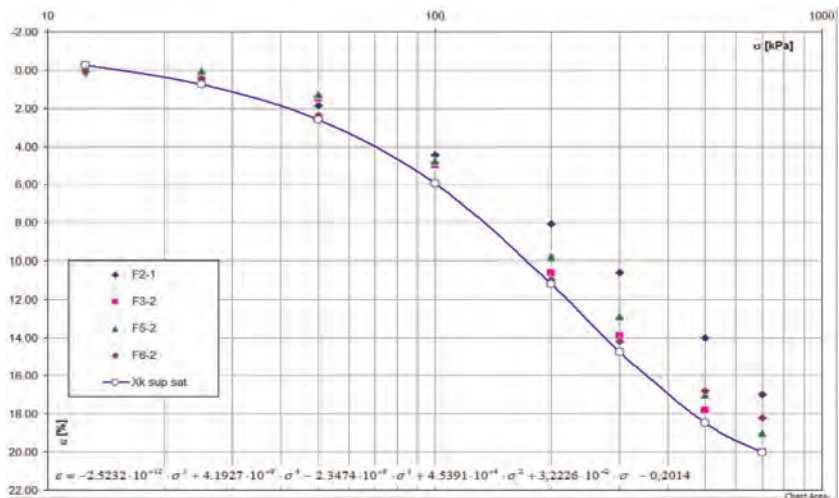
Figure 5. Compression – settlement curves on initially saturated samples from layer 1.

the specific settlement are indicated. These characteristics were determined for each layer but, for example, the values determined for layer 1 are presented graphically.

3.2 *The settlement calculation of the foundation soil*

The settlement of the foundation soil was calculated vertically for 27 points distributed evenly throughout the landfill but also in its vicinity. The load transmitted by the waste was assimilated with two triangular loads (the marginal sections) and a rectangular one (the central section).

The settlement calculations were done iteratively, proposing in an initial phase a slope of 1 % for the landfill base. Figure 6 shows the results of the settlement calculation. Starting from the natural ground level, the designed ground level was calculated to ensure the initial slope of 1% by calculating the settlements, the shape of the base of the landfill was determined after consuming the settlements in case of maintaining the moisture conditions, but also in the hypothesis of saturation of the foundation soil.
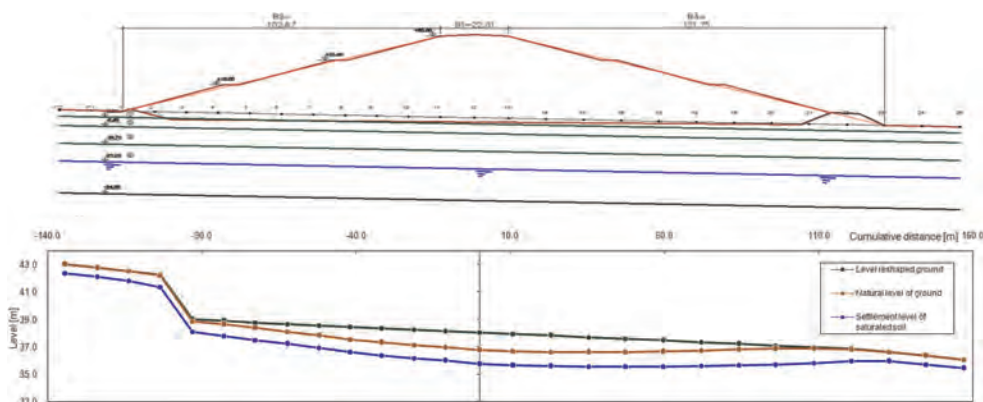
Figure 6.   The settlement calculations with a slope of 1% for the landfill base.

From the calculations performed, we noticed, first of all, the very high values of the settlements in the center of the landfill: 1.3 m in case of maintaining the moisture content of the natural soil and 2.3 m in case of its saturation. It should be mentioned that these values were obtained for a pressure of 360 kPa resulting from the storage height of 30 m and the specific weight of the waste of 12 kN / m^3, evenly distributed over a very large surface (250 × 300 m).

In this initial hypothesis, after the consumption of the settlements, the drain that takes the leachate from the landfill will have for the downstream area a slope of less than 1% and even counter slope in both calculation hypotheses. It turns out that, between sections 13 and 22 of the calculation of the settlement, the slope of the landscaped land will have to be reshaped so that the slope after consuming the settlement is greater than 1%. It turns out that, between sections 13 and 22 of the settlement calculation, the slope of the designed ground level will have to be reshaped, so that the slope after consuming the settlement is higher than 1%.

Figure 7 shows the initial profile of the designed ground level and is imposed, in all sections, a slope higher than 1%, after consuming the settlements. Basically, changes were made between sections 13 and 23. Accepting initially the same settlements of the foundation soil, the slope of the designed ground level was calculated, which varies between 1.6 and 3%, which is why it was modulated in two sectors with slopes of 2 and 3 %.

By reshaping the base of the landfill, excavations of up to 2 m will be carried out, through which the 1st layer of loess will be exceeded, layer which has a high sensitivity to moisture. For this reason, the settlement calculations were remade and the results are presented in Figure 7. It is noted that, by shaping the ground level with slopes of 1, 2 and 3%, during the entire period of operation of the landfill, respectively, from the moment of beggining, until the drainage of the foundation soil is consumed, the drains for taking the leachate will have slopes greater than 1%. If initially the upstream section will have a slope of 1% and the downstream sections of 2 and 3%, after consuming the settlements, the upstream section will have slopes of 2 ... 3% and the downstream sections of 1 ... 2%.
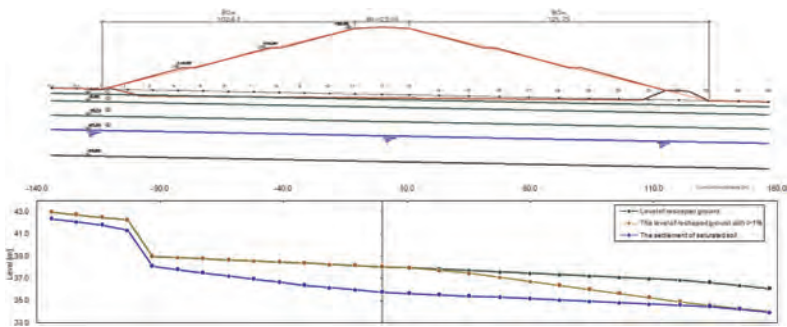
Figure 7. Reshaping the slope of the base of the landfill in order to obtain a slope >1% after consumption of the settlements.

The base of the landfill, shaped with the slopes of 1, 2 and 3% creates a convex surface with a length of 234.82 m. After the consumtion of settlements in natural moisutre content conditions, the profile transforms into a concave surface with a length of 234.84 m and, it the foundation soil becomes saturated, after the consumption of the additiona settlement to wetting, the length of the profile becomes 234.81 m. Therefore, no tensile forces will appear in the geosynthetics from the landfill bottom lining and drainage system due to the initially shape of a convex surface that becomes concave after the consumption of settlements.

4 CONCLUSIONS

By reshaping the designed ground level according to the method described above, the minimum slope of 1% of the drains is ensured for both hypothesis of maintaining the moisture conditions of the foundation soil and in the hypothesis of his saturation.

The maximum settlement of 2.3 m in the central section of the landfill site will not lead to a significant elongation of the geosynthetic materials from the base of the deposit and will not subject them to further tensile efforts.

REFERENCES

NP 125:2010. *Technical Norm Regarding the Foundation of Constructions on Soils Sensitive to Wetting.*
NP 122:2010. *Technical Norm Regarding the Determination of the Characteristic and Calculation Values of the Geotechnical Parameters.*
OMMGA 757/2004. *Technical Norm Regarding Waste Storage.*
Paraschiv, I.E. *The Design of a Municipal Solid Waste Landfill Built on Collapsible Soils.* Master Degree Thesis, Scientific Supervisor: Assoc. Prof. PhD Eng. Ernest-Daniel Olinic, Technical University of Civil Engineering Bucharest, 2016.

Multiple use of geosynthetics in a hazardous waste landfill

M. Bianchi
SCL Ambient, Milan, Italy

P. Ghezzi
Getas Petrogeo, Pisa, Italy

L.E. Russo
HUESKER Srl, Trieste, Italy

ABSTRACT: Bulera's landfill is one of the few authorized landfills for hazardous waste in Italy. In the year 2016 an expansion was decided adding additional volume above the old waste body temporarily covered, for total expected further quantity of 640,500 m^3. The project involved many challenging problems which have been efficiently solved with the use of geo-synthetics. Very restrictive requirements had to be respected for the intermediate barrier system and capping, both from hydraulic and static point of view. To ensure the overall stability of the landfill body reinforced embankments were adopted. Furthermore, road base reinforcements were used to support the traffic of heavy vehicles on soft soils. Erosion control mats were also implemented to protect the slopes of the entire area. The paper illustrates the problems faced and the criteria adopted for the choice of the different solutions with geosynthetics.

1 GENERAL CONTEXT

In 2016 it was decided to expand the Bulera landfill located in the province of Pisa (Italy), intended for the storage of hazardous waste. The expansion consisted in adding a further 640,500 m^3 to be stored on the waste body of the old landfill.

Figure 1. Overview of Bulera's landfill.

To achieve this goal, it was necessary to address many problems which were effectively resolved using geosynthetics. The most important problems faced were the followings:

– The inclined intermediate barrier was, at the same time, the capping of the old waste body and the bottom of the new one. It was necessary to study a multilayer system with geo-synthetics capable to fulfill hydraulic (impermeabilization and drainage), mechanical (protection) and static requirements. With analogous approach also the final capping was designed.

– Since the landfill develops along the side of a hill, different stability problems were analyzed, either global, compound, internal and sliding stability scenarios. From these analyzes it was necessary to implement a steep reinforced slope at the foot of the landfill with the use of high strength geogrids, in order to assure the stability of the additional volume of waste.
– A new reinforced concrete tank for leachate treatment was built and founded on the old waste body saturated with leachate. A geotechnical reclamation of the bottom was therefore studied to assure its stability.
– Due to the presence of soft soils in the entire area, it was necessary to reinforce the base of internal roads with proper reinforcing geocomposites to allow the traffic of heavy vehicles.
– Erosion control mats have been foreseen to protect the slopes of the road embankments and the inclined soil layer above the capping.

2 TECHNICAL PROBLEMS AND SOLUTIONS ACHIEVED WITH GEOSYNTHETICS

2.1 *Geotechnical reclamation of tank foundation*

Before building the new reinforced concrete tank, it was necessary to remove over 10,000 m^3 of existing waste. The excavation, remained open for a long time, was subjected to the action of rains that caused the accumulation of water on the subgrade, which became muddy and difficult for the access of construction vehicles. So, it has been necessary study a geotechnical reclamation of the bottom, keeping the total thickness of the project. The reclamation was characterized by the following phases (Figures 2 and 4):

– Removal of the first ten centimeters of ground material
– Laying of a heavy nonwoven geotextile (1200 gr/m^2) with puncturing resistance $\geq$ 13,000 N.
– Installation of two layers of PET geogrids 80 kN/m overlaid orthogonally only under the base of the tank
– Installation of 40 cm of aggregate layer (size 40 – 70 mm)
– Installation of a second layer of nonwoven geotextile to protect the subsequent barrier system composed by a double layer of a rough bentonite geocomposite, an HDPE rough liner 1.5 mm thick, protected by a further nonwoven geotextile 1200 gr/m^2.

Figure 2. Installation phases of the base reclamation (left to right): 1. Nonwoven and geogrid, 2-3. Aggregate layer, 4-5. Rough bentonite geocomposite, 6. Rough HDPE geomembrane.

2.2 *Reinforced embankment*

To counteract the pressure of the new waste mass acting at the foot of the landfill side, it was necessary to build a reinforced embankment 8 meters high, 250 m long with front inclination of 60°, founded on the existing waste (Figure 3).

The structural design of the embankment was performed according with the Ultimate Limit State method taking in consideration different scenarios: it was analyzed the stability of the overall landfill body, as well as the stability of the new waste mass applied on the intermediate

barrier which represent a potential sliding plane. A critical leachate level was assumed in the calculation model. Internal, compound and global stability analysis were performed under static and seismic conditions. Circular and polygonal sliding surfaces (according with Bishop and Janbu method respectively) were investigated considering different specific scenarios.
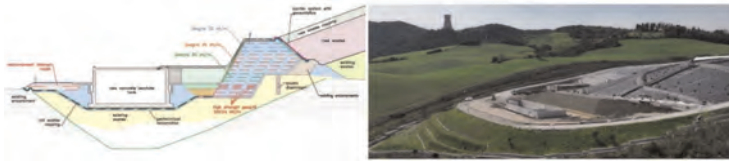
Figure 3.   Typical section and view of the treatment tank and reinforced embankment.

For load combinations and factor of safety the Italian standard NTC 2018 was adopted while, due to the lack of specific Italian regulations for geosynthetic reinforcements, the British Standard BS 8006-1 2020 was used to determine the long term ultimate tensile strength T_D (1) of the geogrids, according with the following formula:

$$T_D = \frac{T_{char}}{RF_{CR} \cdot RF_{ID} \cdot RF_W \cdot RF_{CH} \cdot f_s} \tag{1}$$

The design strength T_D is calculated reducing the short-term characteristic tensile strength (obtained according EN ISO 10319) by reductions factors which take into account the creep (RF_{CR}), the installation damages (RF_{ID}), the weathering (RF_W), the chemical and environmental effects (RF_{CH}) and the extrapolation of data (f_s). As filling soil for the embankment was used clay with permeability $K = 10^{-9}$ m/s, and the geotechnical parameters adopted were: internal friction angle $\phi = 27°$; Cohesion c = 20 kPa; unit weight $\gamma =18.5$ kN/m^3. As reinforcing elements Fortrac T polyester geogrids were used which long term design strengths T_D were obtained using the reduction factors certified by Hapas Certificate 13/H197. As result of the stability calculations geogrids with short term resistance of 600 kN/m (at the base); 80 kN/m and 35 kN/m were adopted, disposed with different anchoring length in layers 60 cm thick (Figure 4).
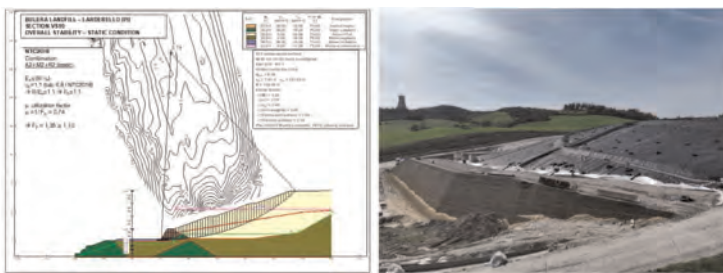
Figure 4.   Stability analysis of one studied scenario and reinforced embankment during construction.

2.3   Reinforcement internal roads

The road subgrade is composed by 1 m. of clay and, below, by old waste deposits. The internal unpaved roads had to be able to allow the continuous passage of heavy vehicles. According to the general project, a total foundation thickness of 50 cm had to be adopted but, due to the poor geotechnical characteristics of the lower layers, it was necessary to implement a base reinforcement in order to keep the road base thickness assuring a proper bearing capacity and to prevent the formation of deep ruts.

To calculate the required strenght of the geosynthetic reinforcement it was considered the load of heavy trucks (50 tons) and, for the underlying layers, the following parameters were adopted:

− For the subgrade it has been adopted an undrained cohesion C_u = 70 kPa.
− For the road sub-base course a sandy gravel 40 cm thick plus a layer of 10 cm of stabilized material was adopted.

The semi-empirical method of Jaecklin & Floss has been used for calculation purposes, obtaining a minimum tensile strength of 26.18 KN/m. For a service life of 20 years, the composite geogrid Basetrac Duo C 65 B15 in polyester (short term strength 65 KN/m) assembled with a polypropylene nonwoven was adopted.(Figure 5).

Figure 5.   Construction phases of internal roads with the use of base geocomposite reinforcement.

2.4 *Bottom barrier system*

The landfill's expansion has been designed adding additional volume above the old waste body temporarily covered. The Tuscan region imposed the construction of an intermediate barrier between the waste of the old landfill and the new ones belonging to the extension. This barrier was to act, at the same time, as a capping for the old landfill and as a bottom of the new one, in accordance with Italian regulation 36/2003 (in force that time) that required, for hazardous waste landfills, a mineral clay layer with permeability $K \leq 10^{-9}$ cm/s and a thickness of minimum 5 m. Due to technical, environmental, and financial issues a 5 m thick barrier was not practicable. The regional authorities allowed the designer to find alternative solutions that could have analogous performance. To overcome this problem, an equivalent mineral barrier system was studied, consisting in one meter layer of clay combined with a special bentonite geocomposite (GCL).

It should be emphasized that the study of barrier systems always involves an accurate analysis of both the hydraulic and static aspects. Both have been taken into consideration with absolute attention in this project. Applying the equivalent criteria it was approved an intermediate multilayer as follow (from bottom to top):

− Old waste
− PP nonwoven geotextile 300 gr/m^2 as separator layer.
− 100 cm of clay with $K \leq 10^{-8}$ m/s
− Bentonite geocomposite with rough surfaces (high internal and external shear strength)
− HDPE rough liner, thickness 2.5 mm
− PP nonwoven geotextile 1200 gr/m^2 as protection layer on the horizontal surfaces
− Drainage composite as drainage and protection layer on slopes
− 50 cm of aggregates as drainage layer on horizontal surfaces
− New waste

So, the mineral barrier system was completed with HDPE liner 2.5 mm, drainage geocomposite and protective geotextiles nonwovens. The equivalence has been demonstrated with two methods (comparison between "flow rates" and application of "Koerner's formula") considering three water heads (H_1 = 0.3 m, H_2 = 0.5 m, H_3 = 1.0 m) so as to be able to identify the minimum technical characteristics required for the geosynthetic clay liner (GCL) adopted. The flow index (q) as well as the other parameters (permeability and thickness after expansion) relating to the bentonite geocomposite (GCL) were determined according to UNI EN 16416. The equivalence calculation criteria between the mineral layer and the geocomposite was based on two methodologies:

− Equivalence of the flow index: expressed in m^3/m^2/s; represents the water flow per unit of surface and time that passes through the layer. This is the closest method to reality because it refers to a physical parameter that can be directly measured in laboratory.

Considering the mineral clay layer 5 m thick and K $\leq 10^{-9}$ m/s, the flow index that was not to be exceeded by the equivalent layer was 1.06 10^{-9} m³/m²/s for H_1 = 0.3 m, 1.1 10^{-9} m³/m²/s for H_2 = 0.5 m and 1.25 10^{-9} m³/m²/s for H_3 = 1.0 m.

- Equivalence through Koerner's method: the input characteristic parameters of the method were used, that is, the permeability and the thickness of the saturated geocomposite after controlled expansion. This value, used in the Koerner method, is obtained from laboratory tests in accordance with UNI EN 16416. According to the Darcy's formula, the permeability needed for the bentonite gecomposite was calculated varying the hydraulic water head, from 0.3 m to 1.0 m, and the GCL thickness after a controlled expansion from, 9 mm to 13 mm.

During the design phase, several materials were examined to evaluate their equivalences as a function of the increasing hydraulic heads, both using the flow rate index and the Koerner method. The equivalence has been proven on all products for H = 0.30 meters while, considering higher water heads levels, the market choice was limited. The final selected material was the GCL Nabento RL-N 5500 F (WB) having the following characteristics: unit weight of sodic bentonite 5500 g/m², minimum thickness before controlled expansion of 9 mm and maximum permeability of K$\leq$ 1.25x10^{-11} m/s for water head of 1 m. Another important performance characteristic of this GCL is its high internal and external shear strength, due to the rough surfaces and the assembly process. These mechanical parameters are relevant since they were considered in the stability analysis of the new waste mass above the inclined intermediate barrier. The barrier system was completed with an HDPE rough liner 2.5 mm thick protected above horizontal surfaces by geotextiles nonwoven of 1200 gr/m² with static puncturing resistance $\geq$ 13,000 N and, along the internal slopes, with a drainage geocomposite (Figure 6). Externally, the 4-meter-high slopes have been protected with the erosion control coconut Bionet HC/40.

Figure 6. Slopes covered, from left to right, with the rough GCL, the HDP liner, drainage geocomposite (slopes) and nonwoven geotextile (bottom).

2.5 *Drainage geocomposites*

The entire design of the landfill expansion comprises the construction of the intermediate barrier and the final capping. No production of biogas is expected so the adopted drainage layers have been foreseen foreseen in two different levels and with two different functions:

- On the intermediate barrier a drainage geocomposite was adopted to be laid only along the slopes of the external and internal embankments (which act as internal cell separators).
- On the capping, over the impermeable barrier, to drain the rain water infiltrated through the covering soil layer.

The drainage geocomposite for the intermediate barrier has two functions: speed up the drainage of the leachate towards the horizontal drainage layer made with 50 cm of aggregates and protect the HDPE geomembrane. At this level, the material is subjected to a pressure of about 320 kPa, corresponding to the pressure of a column of waste up to 20 m thick. For this reason, the drainage geocomposite Pozidrain 6S 500 D, with HDPE cuspated, core was selected since can work effectively with long-term pressures up to 500 kPa.

For the capping, in which the acting pressure is in the order of 20 kPa, was chosen a particular and more economic drainage geocomposite, the Pozidrain G type, which consists of a cuspated HDPE drainage lattice embedded between two layers of non-woven filter/protection geotextile. The draining lattice members provide equal drainage capacity through the longitudinal and

cross ribs. An evaluation of the allowable drainage capacity of the product was done compared with 50 cm of gravel as required by the Italian regulation. The composite also provides protection and, thanks to its irregular structure with windows, the interface friction angle with the cover soil is high, that makes the material suitable to be used on inclined cappings.

2.6 *Final capping*

At present the capping has not been done yet and the design was done with analogous approach of the intermediate barrier. As mentioned above, a specific drainage geocomposite was chosen considering the acting pressure and the inclination of the capping. While, regarding the bentonite geocomposite, a less performing model from a hydraulic point of view was chosen because it was sufficient to comply with regulatory requirements. The characteristic of rough surfaces and high internal and external shear strength was maintained for stability reasons. On the barrier, due to the inclination of the slopes and the interface friction angles between layers, it was necessary to add a tridimensional reinforcement geogrid (Fortrac 3D 120 of 120 kN/m) to assure the veneer stability and prevent the sliding of covering soil layer. For the stability analysis the method developed by Russo (2008) was used. The capping, starting from the waste is as follow:

- Nonwoven weight 300 gr/m^2 to separate the waste.
- 30 cm of clay, K $\leq 10^{-8}$ m/s
- Bentonite geocomposite with K $\leq 5.0\ 10^{-11}$ m/s; 7 mm thick
- HDPE rough liner; 1.5 mm thick
- Drainage geocomposite for rainwater with lattice structure
- Antisliding tridimensional reinforcement geogrid (nominal strength 120 kN/m)
- Topsoil, 1 m thick.
- Bionet for erosion control in coconut fiber to be used only on lateral slopes
- Hydroseeding and bushes.

3 CONCLUSIONS

The design of the extension of Bulera's landfill involved the solution of many challenging problems of diverse nature that have been successfully solved using different types of geosynthetics. The paper describes the most important problems faced and the criteria adopted for the choice of every solution. Each application has been designed and calculated considering the specificity of the context. In this project, a barrier system with 5 m of mineral clay layer was not feasible, so, thanks to the use of geosynthetics, it was possible build a thinner barrier and carry out the work. Product test reports and certificates were essential for the adoption of input reliable data used for design. The versatility and reliability that characterizes geotechnical designs with geosynthetics allowed to find cost effective and sustainable solutions compared with the conventional ones.

REFERENCES

BS 8006-1: 2010. Code of Practice for Strengthened/reinforced Soils and Other Fills. BSI 20 October 2010.
DLgs 13 gennaio 2003, n. 36 Attuazione Della Direttiva 1999/31/CE Relativa Alle Discariche di Rifiuti.
Hapas Certificate, 2014: Fortrac Geosynthetics - Fortrac T and R-T geogrids, Hapas Certificate 13/H197.
Jaecklin, F. & P., Floss, R. 1988. Method for Designing Road Construction on Very Soft Subsoils Using Geotextiles. In *First Congress on Synthetics in Geotechnics, K-GEO 88*. Hamburg.
Koerner, R. M. 2012. *Designing with Geosynthetics*, 6th edition, January 2012. Xlibris Corp.
NTC 2018, Aggiornamento Norme Tecniche per le Costruzioni. D.M 17 January 2018.
Russo, L. E. 2008. Design Method for Cover Soil Stability of Lined Multi-Slope/berm Systems Using Continuous Geogrid Reinforcement. In *The First Pan American Geosynthetics Conference & Exhibition*. Cancun, Mexico.
UNI EN 16416:2013, Geosynthetic clay barriers – Determination of Water Flux Index – Flexible Wall Permeameter Method at Constant Head.

Multi-linear drainage geocomposite for sub-slab depressurization and radon mitigation

E. Vial & M. Vanhée
Afitexinov, Champhol, France

S. Fourmont
Afitex-Texel, Ste Marie, Quebec, Canada

ABSTRACT: Sub-slab Depressurization (SSD) aims to reduce building occupants' exposure to toxic gases from the soil. These gases can either be generated from contaminated soils (like Volatile Organic Compounds or Landfill Gas) or naturally present in the soil (like Radon). The SSD system is composed from the bottom to the top of a separator geotextile, a drainage layer, and a vapor barrier. One or more gas pits are located according to the gas concentration in the area and to the geometry of the building. Because most of the SSD systems are constructed in high-density population areas (e.g., new construction in old industrial zones), the truck traffic and the noise resulting from the excavation works, and the transportation of granular material is a nuisance for residents. It also damages the local road network that is not designed to handle heavy vehicles traffic. This paper presents the sizing and the use of multi-linear drainage geocomposite as part of the SSD system providing separation and gas collection functions. The geocomposite is composed of non-woven geotextile layers incorporating perforated mini-pipes regularly spaced and running the roll length. It is connected to a collector pipe and to the gas pit. It collects the soil gas and reduces the head losses thanks to the high-density network of perforated mini-pipes within the product and the specific fittings used to connect the product to the main collector pipe. The sizing of the geocomposite is done using laboratory tests and software to characterize the flow capacity and the head losses of the system. Multi-linear drainage geocomposites have been found to be efficient for both passive and active SSD systems.

1 INTRODUCTION

The reclamation of industrial brownfield sites or former waste deposit sites for new developments is already common practice in various parts of the world. The infiltration of underground gases poses a serious threat to the safety of the occupants of these reclaimed sites. Gases generated by both waste products (biogas) and contaminated soils (such as volatile organic compounds VOC), and even natural gases like radon produced by the natural decay of uranium and other naturally occurring elements are commonly detected in affected areas. Sub-slab gas collection systems, using a natural permeable layer such as crushed stones paired with draining pipes and vents, are frequently used to prevent gas infiltration into new developments. However, geosynthetic products such as multi-linear drainage geocomposites present an excellent alternative for both passive and active sub-slab gas collection systems.

This technical paper aims to present a comprehensive overview of the installation and performance of such systems, while demonstrating their benefits over conventional approaches to underground gas collection.

2 SUB-SLAB DEPRESSURIZATION SYSTEM

2.1 General description

Sub-slab depressurization (SSD) aims to reduce building occupants' exposure to toxic gases from the soil. A gas collection network is installed under the entire slab and connected to an exhaust pipe, typically 100 mm minimum diameter, installed vertically from below the floor to the roof.

In order to prevent subsurface vapors from entering homes and other buildings, mitigation solutions can be achieved by passive or active SSD. In a passive SSD system, the gas is collected from under the slab by the drainage system to a collector pipe connected to one or several vents, which extracts the gas from the building by natural draft. An active SSD system is created by adding a fan to the drain vent of a passive system to increase the negative pressure applied to the system.

2.2 Gas venting layer

The gas venting layer is constructed using the Draintube multi-linear drainage geocomposite (terminology as per ASTM D4439). It is composed of non-woven geotextiles that are needle-punched together with perforated, corrugated Polypropylene (PP) mini-pipes regularly spaced inside and running the length of the roll. The mini-pipes have two perforations per corrugation at 180° and alternating at 90°. The geocomposite provides the filtration/separation, gas collection and mechanical protection functions with a single product and a single installation.

The mini-pipe components of the geocomposite have a diameter of 25 mm and are typically spaced at 2 m on-center. With this configuration, it exhibits a long-term transmissivity superior or equal to 1×10^{-3} m²/s. This value is measured as per ASTM D4716 or ISO 12958-2 standards, for a hydraulic gradient of 0.02, confined in soil under a normal load of 2400 kPa and a seating time of 1000 hours.

The main characteristic of Draintube multi-linear drainage geocomposites is that they maintain their drainage capacity over time, even under high load (Figure 1). They are not sensitive to creep in compression, nor geotextile intrusion (Blond *et al.* 2010).

Unlike other planar geocomposites, the load transfer mechanism between the overlying and underlying material is only a fraction of the normal load. The mini-pipe component of multi-linear drainage geocomposite is confined by the surrounding soil, thus loads are
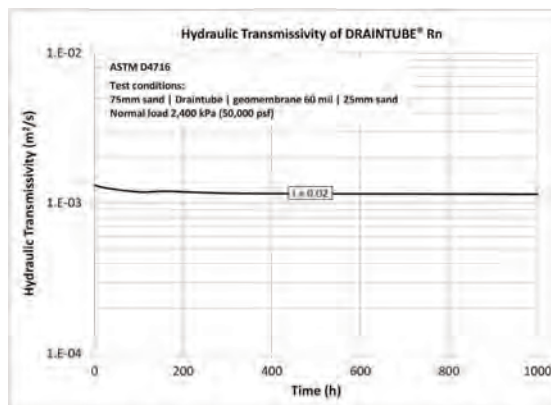
Figure 1. Geocomposite transmissivity under 2400 kPa for 1000 hours (ASTM D4716 / GRI GC15).

calculated using traditional flexible pipe design methodologies. The soil arching effect that applies to other flexible pipes also applies to this type of geocomposite.

2.3 *Gas suction pit*

The number and location of gas suction pits are determined according to the position of the header pipe, the gas concentration and the geometry of the building. Using an active SSD system with a venting layer under the overall surface of the building will decrease the number gas suction pits riequiered.

2.4 *Vapor barrier*

A membrane is typically placed under the concrete slab. It prevents contamination of the underlying layers when the concrete is cast and limits the gas migration through the floor. The performance of the membrane layer is dependent on the composition and thickness of the material, but also on its installation (joints between panels, connection to the walls, etc.).

   The vapor barrier can be installed directly on top of the multi-linear drainage geo-composite. Thanks to its geotextiles layers, the geocomposite mechanically protects the membrane from puncture of the underlying soil. The installation of a protective geotextile may also be required on the vapor barrier to prevent puncture by the overlying layers.

   Multi-layers true gas barrier membranes with an ethylene vinyl alcohol (EVOH) core co-extruded between polyethylene (PE) layers are recommended, especially in presence of VOCs. These types of membrane exhibit much lower gas permeability characteristics by an order of magnitude of 10^3 compared to high density polyethylene (HDPE) membranes (Kelsey 2014).

   Membranes are efficient to prevent gas migration, but should not be used without the depressurization system underneath. Indeed, they exhibit a thickness generally lower than 1.0 mm and they are sensitive to puncture, especially during installation. Moreover, junctions between membrane rolls, and connections to the perimeter walls and any interior slab penetrations, such as columns, etc. are weak points and potential causes of leaks. It is crutial to keep the soil underneath the concrete slab at a pressure lower than inside the building with a gas venting layer like multi-linear drainage geocomposite. In case of leaks, the gas migration will then go from inside to ouside of the building where it is harmlessly vented to the atmosphere.

3 INSTALLATION

3.1 *Gas venting layer*

The installation of the gas venting layer is achieved by unrolling the multi-linear drainage geocomposite on the subgrade such that the mini-pipe components are oriented with the intended flow direction and perpendicular to the main header pipe (Figure 2). Rolls are connected along the side with a minimum overlap of 100 mm and secured using seams, welds, or additional overlap. The connection at the terminating edge of the roll is overlapped such that the upper geotextile layer can be rolled back 150 mm and the end of the next roll inserted into the opening. Mini-pipes are connected using snap coupler fitting.

   In the case of columns or other interior slab penetrations, mini-pipes are diverted along the side of the penetration. If diversion is not possible, additional mini-pipe is positioned to redirect the flow to the next closest mini-pipe. Interior walls are addressed using drainage channels for the mini-pipes.

Figure 2.   Installation of the geocomposite on the subgrade.

3.2   *Connection to the header pipe*

The gas venting layer is connected to one or more header pipes. This is a function of the geometry of the building, and the number of exhausts. These connections are achieved using quick connect connectors that allow the geocomposite mini-pipes to be mechanically attached to the header pipe. These quick connects prevent displacement of the mini-pipes during the installation of the upper layers and reduce the head losses at the connection between the venting layer and the exhaust pipe. This mechanical connection allows for single or double connections of the geocomposite to the header pipe.

Depending on the cross section of the SSD (with or without granular fill), the header pipe may need to be placed in a trench (Figure 3) to prevent intrusion into the thickness of the concrete slab.

Figure 3.   Connection to the header pipe.

1445

3.3 *Vapor barrier*

The vapor barrier is generally delivered in rolls that are unrolled and connected with a 300 mm overlap. Joints between rolls, around penetrations and against the walls are sealed to prevent unwanted gas migration. (Figure 4).

Figure 4. Vapor barrier and geotextile installation.

4 DESIGN AND PERFORMANCE

The aim of the gas venting layer is to migrate the gases to the header pipes and then outside of the building using the exhaust pipes. This exhaust system prevents the accumulation of gas under the slab that could eventually infiltrate into the building. The multi-linear drainage geocomposite is compatible with passive and active SSD.

4.1 *Design software*

A software for the hydraulic design of drainage geocomposite and granular drainage layers , named Lymphea, has been developed by LIRIGM (Laboratoire Interdisciplinaire de Recherche Impliquant la Géologie et la Mécanique) at the University of Grenoble (France) in collaboration with Afitex Group and validated by large scale tests (Faure *et al*. 1995). It has been updated and improved with the contribution of the SAGEOS, CTT Group in Quebec, the CEGEP of Saint-Hyacinthe in Quebec, and the University of Saskatchewan in Alberta (Fourmont *et al*. 2023). The calculation module for gas collection using a multi-linear drainage geocomposite is based on the following flow conditions:

– Gas supply with a homogeneous flow distribution perpendicularly to the geocomposite,
– Horizontal or non-horizontal position of the drainage layer with the flow condition down or reverse to the slope α,

The fluid inside the drainage layer is assumed to flow perpendicular to the perforated mini-pipes. This hypothesis is conservative and reasonably good as the distance between the mini-pipes is 2 m maximum, provided the length of the mini-pipes is generally more than 10 m. The flow per unit area collected by the multi-linear drainage geocomposite is calculated with the software as a function of:

– distance between mini-pipes,
– transmissivity of the geotextile drainage layer itself,

1446

– slope (if any),
– length of drainage (distance to the main collector),
– type of gas (density, dynamic viscosity),
– vacuum (negative pressure) applied to the system.

The software allows for SSD design in passive or active conditions. In passive conditions, the determination of the negative pressure applied to the system is based on the Barometric formula, which is a function of the height of the exhaust pipe.

4.2 *Performance of the geocomposite venting layer*

Figure 5 gives the collected flow rate per unit area as a function of the negative pressure applied, for several lengths of drainage, for a multi-linear drainage geocomposite with the mini-pipe components 25 mm diameter spaced at 2 m centers into the product. Calculations have been conducted using air but can also be done for other gas like methane, radon, or any gas mix. The length of drainage is the maximum drainage length to the header pipe, or the half distance between two header pipes in case the geocomposite is connected at both ends.

As an example, in the case of a passive SSD system under a two-storey building, the applied vacuum into the system is 0.070 kPa (6 m height exhaust pipe) and the multi-linear drainage geocomposite will collect a flow per unit area of 7×10^{-6} m³/s/m² over a maximum length of 25 m to the header pipe. The collected flow is then 1.75×10^{-4} m³/s per linear meter of header pipe.
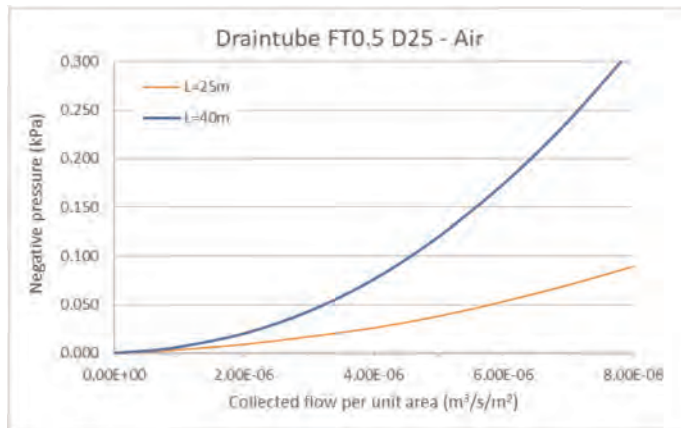
Figure 5. Collected flow per unit area.

As a function of the expected flow of gas to collect, and the vacuum applied into the system, additional header pipes can be installed (to reduce the maximum length of drainage) or the use of a multi-linear drainage geocomposite with a higher density of mini-pipes inside, e.g. mini-pipes on 1 m centers instead of 2 m. The Lymphea software yields the size of the geocomposite based on the project's characteristics.

5 CONCLUSIONS

Draintube multi-linear drainage geocomposite is an effective solution as a gas venting layer in the SSD system. Its dense network of perforated mini-pipes and its mechanical connection

to the header pipe provides a uniform negative pressure under the overall slab of the building. Compared to granular drainage material, the installation of the geocomposite is simple, requiring less excavation works and readily available labor without specialized skills. Additionally, in terms of greenhouse gas emission, social acceptability and economic competitiveness, the system has more positive assets than its conventional counterpart. Multi-linear drainage geocomposites can be used for passive or active sub-slab depressurization systems. A dedicated software is available to calculate the collected flow per unit area as a function of the negative pressure applied, the type of gas and the specific geometry of each project.

In replacement of a granular drainage layer and separation geotextiles, multi-linear drainage geocomposites aim to reduce the Green House Gas emissions while maintaining the same level of effectiveness. Geocomposites save up to 85% of CO_2 equivalent emissions, mostly due to less excavation being needed during installation compared to a granular drainage layer and lighter equipment used in evacuating soil and transporting gravel (Durkheim *et al.* 2010). The geocomposite solution reduces drastically the related costs because there is no soil excavation needed compared to a gravel layer and so no fees for disposal of the excavated polluted soil in a waste facility. It also avoids any problem of supply of granular materials and preserves these natural resources which are not renewable. Because SSD systems are most often required in high-density population areas (e.g. new construction in old industrial zones), the use of a multi-linear drainage geocomposite reduces the social impact on neighboring populations by limiting construction traffic and reducing the duration of the works.

REFERENCES

ASTM D4439. Standard Terminology for Geosynthetics. *ASTM International*. West Conshohocken, Pennsylvania, USA.

ASTM D4716. Standard Test Method for Determining the (In-plane) Flow Rate per Unit Width and Hydraulic Transmissivity of a Geosynthetic Using a Constant Head. *ASTM International*. West Conshohocken, Pennsylvania, USA.

Blond, E., Saunier, P., Ragen, W. 2010. Assessment of the Resistance of Drain Tube Planar Drainage Geocomposites to High Compressive Loads. *9th International Conference on Geosynthetics*, Guarujá, Brazil.

Durkheim, Y., Fourmont, S. 2010. Drainage Geocomposites: A Considerable Potential for the Reduction of Greenhouse Gas Emission. *9th International Conference on Geosynthetics*, Guaruja, Brazil.

Faure, Y.H., Auvin, G. 1995. Gas Drainage by Geocomposites. *Rencontres 95*, Beaunes, France.

Fourmont, S., Decaens, J., Beaumier, D., Riot, M. 2023. Water Drainage and Gas Collection with Geocomposites - Hydraulic Software Development. *12th International Conference on Geosynthetics*, Roma, Italy.

GRI GC15. 2017. Standard Test Method for Determining the Flow Rate per Unit Width of Drainage Geocomposites with Discrete High Flow Components. *Geosynthetic Institute*. Folson, Pennsylvania. USA.

ISO 12958-2. Geotextiles and Geotextile-related Products - Determination of Water Flow Capacity in Their Plane - Part 2: Performance Test. *International Organization for Standardization*. Geneva, Switzerland.

Kelsey, C. 2014. Advances in Barrier Geosynthetics. *Civil and Structural Engineer magazine*, January 2014.

Steinhauser, E., Fourmont, S. 2015. Innovative Approach to Landfill Gas Collection and Control. *Geosynthetics 2015*, Portland, OR, USA.

A medical-triage approach to mitigating risk of geomembrane uplift in high wind events during construction

A.K. Maskal & S.L. Maskal
Solmax Geosynthetics

ABSTRACT: Construction and testing sequences at large facilities can require multiple hectares of geomembrane to remain exposed for some time between installation and placement of cover materials. Winds create uplift pressure that can lift an unballasted geomembrane, creating risks ranging from moving the membrane out of place to complete destruction of an installed geomembrane.

The sloped ridge/valley topography used for drainage and stability in landfill cells often resembles an airfoil shape that creates uplift pressure that enhances risk of uplifting an exposed geomembrane to damage.

Previous efforts have defined the mechanics of wind uplift for exposed geomembranes in smaller pond configurations where geomembranes can remain exposed during their service life. However testing and cover aggregate availability often prevent covering a geomembrane during construction, leaving it at risk of being uplifted, displaced, damaged, or even destroyed in sudden high winds.

This paper re-examines wind uplift mechanics for exposed geomembranes and proposes a potential risk/time-weighted procedure for different topographies to minimize the risk of geomembrane damage and loss due to sudden and extreme wind events that occur during construction.

1 INTRODUCTION

Uplift pressures resulting from wind blowing over surfaces lined with geomembranes have been widely studied, and there are a variety of ballasting and anchoring approaches for exposed geomembranes in widespread successful use throughout the world. The uplift pressure in wind events increases proportionally with the square of wind velocity, leading to uplift pressures in high winds that can far exceed what might be expected by an inexperienced observer. In certain topographies for example, uplift pressures can require on the order of 120 kg/m^2 to resist uplift in 160 km/hr winds (25 lb/ft^2 in 100 mph winds). In properly designed and installed ballasting systems, various combinations of soil ballast and mechanical attachments are routinely used to provide downforce that exceeds the uplift, distributed in such a way that the forces mobilized do not damage the geomembrane.

The performance benefit of installation quality control has also been well established, leading to regulatory requirements for specific tests to be performed and accepted. It is therefore common in many parts of the world to have geomembranes that will ultimately be overlain by cover soil remain uncovered for extended periods while testing is performed. Repairs for failed construction quality assurance tests are typically the responsibility of the geosynthetics installer if a geomembrane is still exposed. However, with the vast majority of geomembrane damage caused by cover soil placement activities, the responsibility for repairs is not so clear if testing is not completed on a completed geomembrane installation prior to placing cover soil.

Standard design practice, experience, and common sense all lead one to observe that high wind speeds occur less frequently than more typical slower wind speeds (for example, at a given site, a 5 m/s wind may be likely to occur several times daily while a 50 m/s wind occurs once in several years). The cost and time needed to place and remove temporary ballast create the need for some amount of judgement of cost vs. risk to determine the amount of temporary ballast needed to resist uplift created by winds that will occur during the relatively short periods that geomembranes remain exposed waiting for testing. For relatively short periods wherein a geomembrane is to remain exposed for testing, it is typically appropriate to use much less ballast than will be needed to anchor a geomembrane to withstand all wind events during its lifetime.

Unfortunately, extreme wind events can happen with little warning. Such wind events occasionally happen during the relatively short periods that sections of geomembranes that remain exposed with only temporary ballast. And on rare occasions, there may not be enough time to place enough ballast to resist the resulting extreme uplift pressures in sudden storms. Large sections of geomembranes can and have been lost to wind damage during such "perfect storms."

2 PREVIOUS WORK

Several methods have been proposed for designing ballast systems based on the work of wind tunnel testing by Dedrick (1973, 1974a, 1974b, 1975), development of practical guidance by Giroud, Pelte, and Bahurst (1995) and several subsequent refinements covering different anchoring approaches and topography details.

3 FIELD OBSERVATIONS DURING CONSTRUCTION

There are several applications where large and relatively flat surfaces are lined with geomembranes such as mine heap leach pads and coal combustion residual landfills. In settings where topography is relatively flat, it is common to grade a larger area into a series of alternating upward and downward slopes separated by alternating parallel ridges and drainage swales (similar to common grading in a flat parking lot). The geomembrane is ultimately covered with drainage geocomposites and/or granular materials. Geomembranes with such topography are nearly universally covered with soil prior to service, so there has been little need for research into wind uplift resistance designs for such cell topographies. However, in these large installations – often in remote areas – installed portions of the geomembrane can remain exposed for extended periods awaiting seam test results, geoelectric leak detection surveys using water-based test methods, and cover soil placement within a larger construction sequence.

One of the authors was called to a facility with this type of cell topography following a major unexpected wind event that included wind speeds in excess of 160 km/hr (100 mi/hr) that led to the loss of approximately 50,000 m^2 (500,000 ft^2) of geomembrane that was awaiting test results in a remote area in the southwestern U.S.

A section of geomembrane covering three pairs of ridges and swales remained uncovered for testing with sandbags in place to resist typical seasonal winds. A strong storm changed direction, blowing over the site with very limited preparation time. The specification prohibited heavy equipment from driving directly on the geomembrane, limiting the amount of ballast that could be placed in the short amount of time before the storm.

The contractor and facility owner reported the direction of the strongest winds perpendicular to the ridges and swales. The geomembrane behaved consistently in the wind direction, generally repeating at each of the three exposed ridge/swale structures – remaining

largely in place on the windward slope, rupturing along each ridge line, sliding downwind on the leeward slope leeward slope, and accumulating as wrinkles in each swale.

Although the slopes were relatively flat (on the order of 5%), the repeated pattern created the opportunity for multiple observations of the effects of downforce and uplift on the type of topography used in large flat landfill settings. These observations included:

- Uplift pressures appeared to have been small enough (and/or downforce adequate) to largely keep the geomembrane in place on the windward slopes, effectively anchoring the windward side of the geomembrane along each ridge;
- Rupturing along the ridgelines implies tensile loading in the leeward direction with maximum magnitude at the ridgeline;
- Some combination of uplift pressure and possibly wind below the geomembrane allowed sliding down the gentle leeward slope;
- Effective anchoring of the entire windward slope "trapped" the geomembrane, causing material that slid downslope to accumulate as large (up to approximately 1m tall) wrinkles and creases at each low swale area.

4   KEY QUESTION

In this case, it was impossible to ballast adequately to save all of the geomembrane, making the loss of some portion of the geomembrane inevitable. However, one might wonder how to use some smaller amount of ballast to most benefit – in other words, how much geomembrane could be saved if a limited amount of ballast were placed optimally. This can be thought of as being analogous to the "triage" prioritization of limited medical resources in an emergency situation. The goal being to save as many lives as possible, which requires (1) having a working understanding of resource capacity and (2) very quickly deciding which patients can be saved using the limited resources. In extreme circumstances, these decisions would involve leaving some patient(s) to die while patients that can be saved are treated.

5   ANALYSIS

The windward slope largely remained in place, so for the purposes of this exercise, it is assumed that the entire leeward slope can be saved without additional ballast. Thus, any available ballast should be used on other areas.

The windward geomembrane was effectively anchored at the ridge, and tensile loads resulting from uplift were clearly greatest at the leeward side of each ridge, so placing additional ballast at the ridge would not likely provide any benefit.

This leaves the leeward slope to be anchored with whatever amount of ballast can be deployed. The remaining question is whether deploying a limited amount of ballast to anchor the upper or lower section of the leeward slope would save more geomembrane. For this, a calculation was performed for an example slope measuring 100m long × 400m wide to determine the amount of geomembrane that can be kept in place with a given amount of ballast. 44 m/s wind speed and 1,600 kg/m^3 cover soil density were used as typical values.

Reference uplift pressure was calculated using the Bernoulli equation:

$$P = 1/2\rho v^2 * C_l \tag{1}$$

where P = uplift pressure; ρ = density of air (1.225 kg/m^3); v = wind velocity (44 m/s), and C_l = coefficient of lift.

It was assumed that coefficient of lift, C_l varies linearly from 0.4 at the bottom of the slope (swale) and 1.0 at the top of the slope (peak), as is typical for calculating slopes in reservoirs

(Giroud 1995). The slope was divided into segments with uplift coefficient changing in this manner. The pressure distribution was calculated for each location up the slope. The amount of ballast mass required to resist the uplift was calculated by dividing the uplift pressure by the acceleration of gravity. The results starting at the top of slope (peak) were calculated as were the results starting at the bottom of the slope (swale), so that the two directions could be compared. A graph of percentage of slope length that can be covered vs amount of ballast was prepared. The results of the calculations are presented as Tables 1, 2, and 3. Results are presented graphically as Figure 1.

Table 1. Ballast needed for each section, starting at the top of slope.

Distance from Peak (m)	C_l (0.4–1)	Pressure Distribution (Pa)	Distributed Ballast (kg/m^2)	Total Ballast Needed	
				(kg/m of width)	(kg)
0			0	0	
6.7	1.00	1186	121	121	48,351
13.3	0.96	1135	116	237	94,629
20.0	0.91	1084	111	347	138,835
26.7	0.87	1033	105	452	180,970
33.3	0.83	983	100	553	221,032
40.0	0.79	932	95	648	259,021
46.7	0.74	881	90	737	294,939
53.3	0.70	830	85	822	328,785
60.0	0.66	779	79	901	360,558
66.7	0.61	728	74	976	390,259
73.3	0.57	678	69	1045	417,888
80.0	0.53	627	64	1109	443,445
86.7	0.49	576	59	1167	466,929
93.3	0.44	525	54	1221	488,342
100.0	0.40	474	48	1269	507,682

Table 2. Ballast needed for each section, starting at the bottom of slope.

Distance from Peak (m)	C_l (0.4–1)	Pressure Distribution (Pa)	Distributed Ballast (kg/m^2)	Total Ballast Needed	
				(kg/m of width)	(kg)
			0	0	0
100.0	0.40	474	48	48	19,340
93.3	0.44	525	54	102	40,753
86.7	0.49	576	59	161	64,237
80.0	0.53	627	64	224	89,794
73.3	0.57	678	69	294	117,423
66.7	0.61	728	74	368	147,124
60.0	0.66	779	79	447	178,897
53.3	0.70	830	85	532	212,743
46.7	0.74	881	90	622	248,661
40.0	0.79	932	95	717	286,650
33.3	0.83	983	100	817	326,712
26.7	0.87	1033	105	922	368,846
20.0	0.91	1084	111	1033	413,053
13.3	0.96	1135	116	1148	459,331
6.7	1.00	1186	121	1269	507,682

Table 3. Comparison of ballast needed starting from top vs bottom of slope.

Starting from Peak		Starting from Swale		Difference	
Distance from Peak (m)	Ballast (kg)	Distance from Peak (m)	Ballast (kg)	(kg)	(% for Section)
0.0	–	100.0	–	–	
6.7	48,351	93.3	19,340	29,010	60%
13.3	94,629	86.7	40,753	53,876	57%
20.0	138,835	80.0	64,237	74,598	54%
26.7	180,970	73.3	89,794	91,176	50%
33.3	221,032	66.7	117,423	103,609	47%
40.0	259,021	60.0	147,124	111,897	43%
46.7	294,939	53.3	178,897	116,042	39%
53.3	328,785	46.7	212,743	116,042	35%
60.0	360,558	40.0	248,661	111,897	31%
66.7	390,259	33.3	286,650	103,609	27%
73.3	417,888	26.7	326,712	91,176	22%
80.0	443,445	20.0	368,846	74,598	17%
86.7	466,929	13.3	413,053	53,876	12%
93.3	488,342	6.7	459,331	29,010	6%
100.0	507,682	0.0	507,682	-	0%
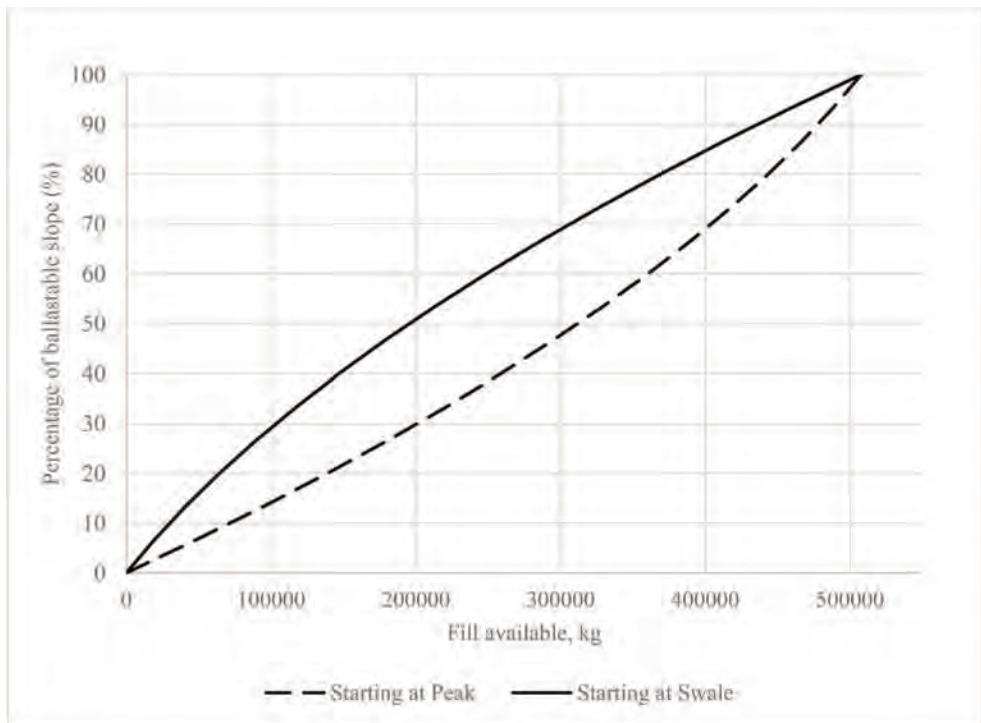
Figure 1. Percentage of ballastable slope vs available fill.

Figure 1. Percentage of slope that can be ballasted using less than half of the ballast needed to secure the entire leeward surface.

6   RESULTS AND CONCLUSIONS

In the example, as much as 60% more surface area can be ballasted using the same amount of soil if ballasting operations start from the bottom of the slope. The additional amount of surface area that can be ballasted with a given amount of soil decreases higher on the slope, but remains higher at all points when starting from the bottom of slope.

It is therefore recommended that when soil quantities and/or time limit the amount of ballast that can be placed before a sudden high wind event and the windspeed and direction can be estimated with some confidence, fill quantity needed for forecasted wind speeds can be calculated using the Bernoulli equation, and ballasting should start at the low and downwind end of each area. The entire exposed geomembrane may not be saved in an extreme wind event, but using this approach will maximize the amount of geomembrane that remains undamaged by developing a ballasting plan with this very quick method. The ballasting quantities need not be calculated in both directions (as they are the same in opposite order). All of the pressures can be calculated in a table, and fill can proceed quickly starting at the bottom of each slope, proceeding up-slope as far as time, resources, and safety allow.

REFERENCES

Giroud, J.P., Pelte, T. and Bathurst, R.J., 1995, "Uplift of Geomembranes by Wind", *Geosynthetics International*, Vol. 2, No. 6, pp. 897–952.

Giroud, J.P., Gleason, M.H. and Zornberg, J.G., 1999, "Design of Geomembrane Anchorage Against Wind Action", *Geosynthetics International*, Vol. 6, No. 6, pp. 481–507.

Yet another excellent reason for locating exposed geomembrane electrical leaks prior to carrying out dipole surveys

C. Charpentier & T. Jacquelin
Groupe Alphard

ABSTRACT: Geomembranes are now part of most designs when dealing with leachates. Good practices suggest performing an electrical leak location survey to ensure imperviousness, or to lower leakage risks to the lower level. Several methods are available for exposed and covered tests, and the relevancy of exposed methods is often questioned: Won't all leaks be found during the covered survey? Tiny leaks such as defects in extrusion seams may be found during dipole survey with ideal conditions but can be hard or even impossible to locate precisely. This scenario has been witnessed in an industrial waste treatment pond as well as in a compost pad leachate pond where a leak area was identified. The protection and drainage layer had been removed, but leak was too small to be noticeable to the naked eye and equipment was inappropriate to investigate any further. This led to a waste of time and uncertainty on all parties regarding the physical and financial responsibility of the defect, whereas a common Water Puddle Leak Location Survey would have located those leaks and they would have been repaired long before the installation of the drainage layer.

1 INTRODUCTION

Geoelectrical Leak Location Methods have been used for decades in all sorts of projects and locations. Technological advances were made to accommodate harsh conditions (weather) and unfavorable specs (ex., double-lined ponds with no conductive layer between both geomembranes). Still, the most limiting factor for most Leak Location projects is the same: budget. The same questions are asked all the time: "why do an exposed survey and then a covered survey? Why not just do the last one?"

Our answer is quite simple: the exposed and covered methods are different, they have a different sensitivity, meaning a Water Puddle Survey will find all defects that occurred during manufacturing, transportation, storage, and installation. A Dipole Survey will find bigger defects like rock punctures, blade and bucket tears, and all big holes made by heavy machinery. Yes, in ideal conditions, a Dipole Survey can be precise enough to find pinholes, but ideal sites are scarce, and it would be unwise to guarantee that level of accuracy in the services proposal, often months before the actual field work starts.

Another great reason to request both methods is to separate responsibility. Once the geomembrane is installed and controlled internally (Quality Control), any defect found will be repaired by the installer at their cost.

From there, all subsequent risks will fall under the general contractor's responsibility such as the installation of a puncture prevention geotextile, an approved way to install the natural material layers and circulating on-site with motorized vehicles. Any additional work due to leaks found with the Dipole Method will be charged to the general contractor, and after that,

any defect and expense will be imputed to the operations department (typically the owner of the site).

On one occasion, a Dipole Survey was conducted on 600 mm of sand. A leak signal was detected, and the area was then excavated. The result was unexpected: the HDPE geomembrane was ripped and there was a sandbag underneath.

This means that the installer forgot to remove the sandbag (often used as a ballast) which resulted in a bump on the geomembrane. The general contractor's heavy machinery had its blade or bucket at approximately 200 mm off the geomembrane, which should have been safe, but in this case, ripped the geomembrane open. Again, this sandbag would have been noticed during a Water Puddle Survey, removed, and patched in no time, with no additional cost.

2 DESCRIPTION OF THE MOST COMMON METHODS

2.1 *Water puddle method (ASTM D7002)*

The Water Puddle Method (WPM) relies on the intrinsic insulation properties of geomembranes for the detection of small perforations (<1 mm^2) in the geomembrane, generally produced at the time of the installation (see following figure). A continuous DC voltage is applied into the metallic Water Puddle structure, and a grounding electrode is placed outside the limits of the geomembrane. In the presence of a leak, the current will pass from the metallic structure, through the defect, into the subgrade and to the grounding electrode, thus producing a visual and auditory signal. This technique requires only a thin film of water on the surface of the geomembrane and provides a validation of the entire exposed surface surveyed.
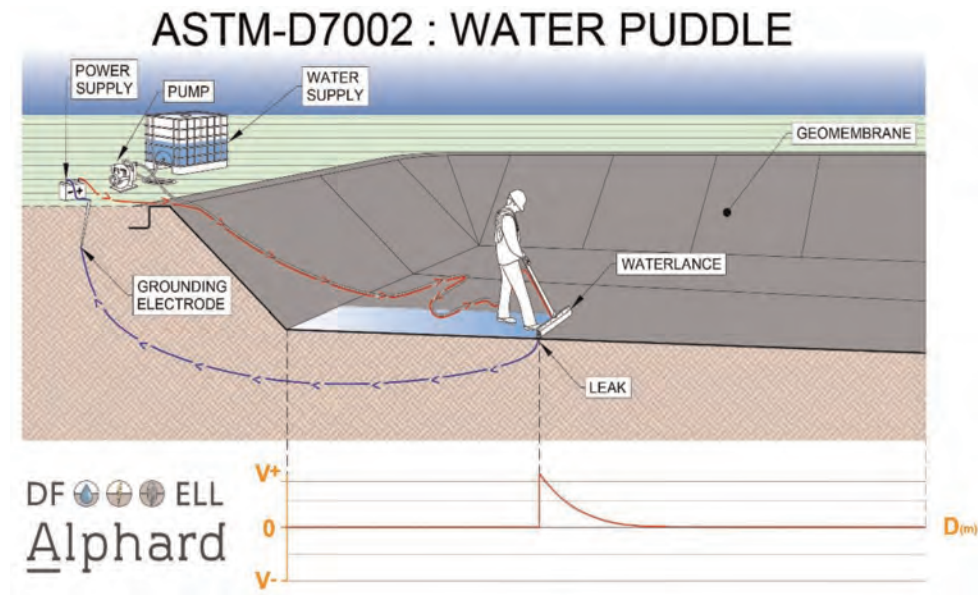
Figure 1. Water puddle method schematic.

2.2 *Dipole method (ASTM D7007)*

The Dipole Geoelectrical Method relies on the geomembranes' intrinsic insulation properties for the detection of perforations created during the installation of the cover material (see following figure).

This means that electrically conductive geomembranes, such as EPDM (Ethylene Propylene Diene Terpolymer), are also incompatible due to their large concentration of carbon black. Other non-plastic barriers that are impermeable but non-isolating, such as a Geocomposite Clay Liner (GCL), prevent Leak Location as well.

To perform a Dipole Survey, a current of approximately 500 V DC (direct current) is injected into the cover material (usually sand, clay, gravel, or crushed stones), and a grounding electrode is placed outside the limits of the geomembrane. Under normal circumstances electricity will flow from a different potential to a ground to discharge and reach equilibrium, however, with a non-conductive geomembrane, it is confined within the cell. If a defect is present, the current will pass through the hole to reach the ground (electrode). This will then generate a distinct electrical signature that can be identified and located by a specialized technician.
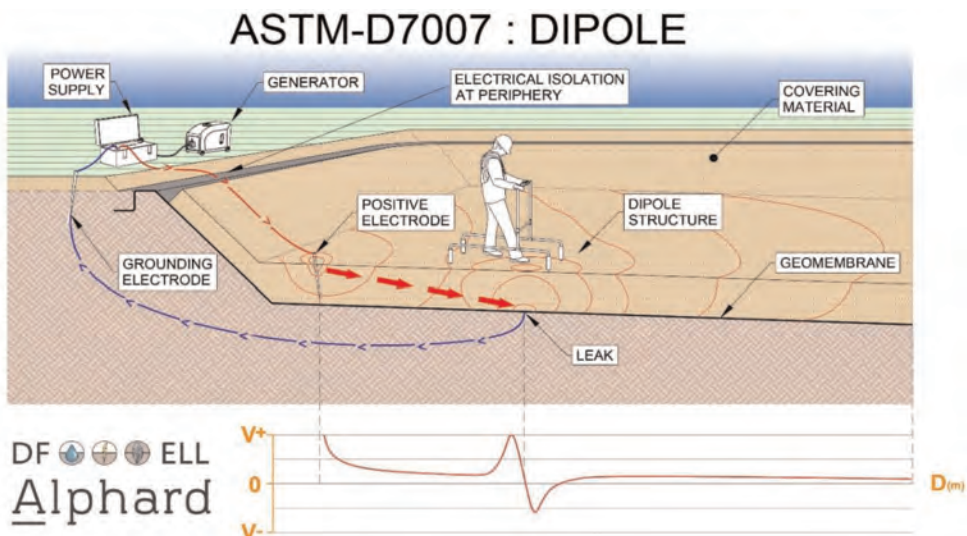
Figure 2.   Dipole method schematic.

3   TYPES OF LEAKS AND CAUSES

Most leaks have obvious causes and can easily be associated with a specific task during construction. Certain defects take the shape of a specific tool or of a power generator leg without its plastic/rubber pad. Sometimes, leaks are aligned in a pattern that can determine which machine caused it, like a faulty track on an excavator, or a pointy stone stuck on a quad tire. Other times, defects on a geomembrane have an unusual shape which really challenges the professionals in finding a cause to adjust construction and lower the risk of creating other similar defects.

Sometimes an extruder gun is put on the liner with the hot end too close to the geomembrane, making it soft, if not liquified.

Damaging effects can also appear by someone walking over waste to access a new cell and getting a piece of scrap metal stuck under their shoe, or any other loose metal on-site like staples or knife blades.

Unless an exposed geomembrane has been in operation for years and has a layer of sediments on it, or because of really bad weather during construction, any defect found should be small or else anybody would have seen and reported it. Therefore, a WPM is expected to find only small defects, faulty extrusion beads, knife cuts, and pinholes.

Our latest WPM statistics show an average of 5.38 leaks/hectare (2.47/acre), which can lead to a considerable flow through a geomembrane depending on the design. The Dipole Method aims to find a 6 mm-wide opening at any place on the site and wherever the Dipole tip lands on a predetermined grid. Site conditions cannot always grant that level of precision and smaller actual holes are not routinely found, meaning a lot of small defects and pinholes are undetected by Dipole Surveys alone.

Of course, big punctures and tears found with the Dipole Method have a far greater impact on imperviousness, it is not implied that the Dipole alone is useless, but it is important to realize not all leaks can be found with a single Dipole Survey based on ASTM D7007. Another standard practice that is used in tandem with the Dipole Method is Electrical Methods for Mapping Leaks in Installed Geomembranes (D8265). This standard has more control on site conditions and data management and implements certain best practices for testing methodology that D7007 lacks. It recognizes that a geomembrane must experience hydraulic head to create an electrically conductive path through the smallest of leaks and that multiple Leak Location Surveys may be required if significant leaks are found during the initial survey, which can reduce testing sensitivity in the same way as poor perimeter isolation. The aim of D8265 is to provide a methodology capable of locating all leaks in a lining system, both large and small.

4 HOW ACCURATE IS THE DIPOLE METHOD

Since the Dipole Method is used to pick up general contractor mistakes or bad geosynthetics leading to holes in a geomembrane, electrical signals are often strong and sharp, so it is easy for an experienced leak locator to start digging less than 500 mm away from the actual hole. That depends on many factors such as the natural material layer's thickness, homogeneity, and peripherical isolation and moisture, to name a few (Gilson-Beck *et al.* 2023). Once the power source is turned off, it is safe to excavate the area where the defect is expected, and the defect is generally easy to spot, there can be bits of torn geomembrane in the area, ripped geotextile, or other geosynthetics, and sometimes, the culprit can be a big pointy rock, a forgotten stake, or trash.

But what happens when there's a perfectly fine drainage geocomposite, a brand-new geotextile, or a geomembrane with no apparent adverse effect? The precise location of a leak relies a lot on a visual inspection of the uncovered geomembrane. If the signal was strong, the surveyor should be confident enough to have the drainage geocomposite or geotextile delicately cut open so the geomembrane can be visually inspected, but what if there is nothing apparent? The excavation might be expanded, but up to what size? If there is a geotextile, it could be watered and a Dipole Survey over it might help locate the signal's origin more precisely but remember that there is no pressure on it anymore, so a pinhole in an extrusion might not have good contact with the wet geotextile.

An installer once had a problem with a third-party Leak Location carrying out the Dipole Method because they had found a signal, excavated the sand, but couldn't locate the defect. They dug about 5 metres in diameter and finally asked the installer to do a 5 metre-wide patch in hopes that it would make the "leak signal go away".

Those small defects and pinholes would be found with Water Puddle equipment, and the repair would be quick and cheap with the installer on-site.

It is rarely the case when the general contractor adds a layer of natural material, so re-mobilizing them has a cost, even if the defect is 2 mm wide. Then, the usual "who is going to pay for that?" happens.

It is too easy to say the leak was left there before the earthworks, or say there's no proof of that, or that it's probably the heavy machinery that put stress on the geomembrane and cracked the extrusion or other tiny physical adverse effect.

5 EXAMPLES OF TINY LEAKS FOUND WITH THE DIPOLE METHOD

The most expensive Dipole Method example yet was a small leak in a toxic waste double-lined cell. As soon as rain started, the amount of water found in the "leak detection layer" was greatly over the tolerated limit.

The owner and general contractor expected a big tear somewhere and proceeded to excavate random sectors to eventually find the leakage area. Every time, a perfectly fine drainage geocomposite was found and the area was considered impervious.

This process went on for months before a Dipole Leak Location Survey was carried out, taking only two days, and a leak signal was identified close to the middle of the cell. After excavation, the drainage geocomposite was intact. A local survey was done over the wet geocomposite to precisely locate the leak, the drainage geocomposite was carefully cut open, and water was pouring out of the wedged seam, on approximately 10 mm in width. A 10 mm^2 hole doesn't sound big but having a drainage geocomposite over AND under the top geomembrane really had a constant flow from top to bottom. Fixing this solved the problem and allowed operations to use the cell.

Another Dipole Survey revealed a leak signal over a 300 mm layer of fine gravel and coarse sand. The center of the anomaly was located at the toe of a slope, which is a typical area for leaks, as bulldozers and such can hardly evaluate the exact depth of the geomembrane right where the slope starts. A tear was expected during excavation, but instead it was a HDPE pipe penetration. Extrusion seams around a small pipe (about 100 mm in diameter) can be very tricky, so the leak signal was probably coming from one point around the penetration, but where? Should the installer grind it all and redo a second layer of extrusion, just to be safe?

It is not smart to grind and weld a perfectly fine water-tight area, and we also try to limit the number of extrusions in general. Studies show that grinding and re-welding weakens the installed HDPE geomembrane (Toepfer 2015). After more observation, a drop of water was found leaking from the side of the extrusion bead. The groundwater was high at that time of the year and there was water pressure from under the geomembrane, which made the repair excessively arduous. It took the liner crew 7 extrusions before completely blocking the electrical signal.

There are many examples like those, where a leak signal is found, an excavation is done, and the geotextile or geomembrane looks intact. We have a little wand we can use that incorporates similar electronics to a Water Puddle detector, to help precisely locate the origin of a leak signature once uncovered. It requires sufficient moisture at the end and amplifies the electrical current going from the cover material (positive voltage from the power source) to a leak (technically zero volts, ground).

6 CONCLUSION

Unless site conditions are ideal (isolated, thin, and homogenous layer), small leaks will not be found.

Another way to phrase the previous sentence would be "not doing a Water Puddle Survey is knowing there are leaks and saving them for the Dipole Survey". That may be a big risk to

take considering conditions at the time of the covered survey might change (precipitations, temperature, schedules) and prevent those small leaks from being found and repaired.

Depending on the site's design, small leaks can lead to a tremendous flow through the geomembrane, and it tends to increase with time due to preferential paths and fine material washed away.

Not all impervious works are critical in terms of water tightness but doing both Leak Location Methods in projects that are critical should be planned and part of good practice. It is also worth mentioning that repairs are far easier to do on a freshly installed clean liner, as opposed to a liner after excavating sand or whatever material sits on the geomembrane, with dirt, moisture, and sometimes not enough room to work effectively (minimal excavation done by the general contractor).

As far as budget and timing go, finding as many leaks as possible during the exposed survey usually allows the installer to repair the defects in a timely manner with no additional costs. Just this point alone could represent more than the cost of a Water Puddle Survey. Our own numbers suggest that a Water Puddle Survey costs approximately 0.5% of a project's global budget. Finding leaks with the Dipole Method means excavations, waiting for the installer to send a small crew, and making repairs in non-ideal conditions. All those additional costs and delays add up quickly, making it a bigger investment than Leak Location on an exposed geomembrane.

Doing a Water Puddle Survey sometimes reveals flaws in the installer's methodology. When those leaks are found in the early stages of a project, it is possible to adjust methods and thus enhance the quality of the job as it goes, instead of having a global portrait of the geomembrane's condition at the end.

REFERENCES

ASTM D 6747. *Standard Guide for Selection of Techniques for Electrical Leak Location of Leaks in Geomembranes, American Society for Testing and Materials*, West Conshohocken, Pennsylvania, USA.

Gilson-Beck, A. & Thiel, R. 2023 *Increasing the Sensitivity of the Dipole Method: A Case Study*, Geosynthetics Conference Proceedings, February 5–8, 2023, Kansas City, Missouri, USA.

Toepfer, G. W. 2015 *Extrusion Welds - The Good, The Bad, and The Ugly Geosynthetics 2015 Conference Proceedings*, February 15–18, Portland, Oregon, USA.

Beck, A. 2016. Best Practices for Groundwater Protection, *GeoAmericas* 2016.

Beck, A. 2015. Available Technologies to Approach Zero Leaks, *Geosynthetics 2015 Conference Proceedings,* Portland, Oregon, February 15–18, 2015.

Beck. A. 2014. Designing to Minimize Geomembrane Leakage, *Geosynthetics Magazine*, August/September Issue.

Darilek, G.T. & Laine, D.L. 1999. *Performance-based Specification of Electrical Leak Location Surveys for Geomembrane Liners*, Geosynthetics '99, Boston, Massachusetts, USA, April 1999, pp. 645–650.

Darilek, G.T. & Laine, D.L., 2010. *Leak Location Surveys, The Past, The Present, The potential*, GSI Annual Meeting 2010.

Forget, B. et al., 2005. *Lessons Learned from 10 Years of Leak Detection Surveys on Geomembranes*, Sardinia Symposium, Sardinia, Italy.

Touze Foltz. N. 2002. *Méthodes de Détection et de Localisation de Défauts Dans Les Géomembranes.* Ingénieries, E A T, 2002, pp. 17–25.

Equivalent intermediate geosynthetic barrier system in a landfill for hazardous waste

M. Bianchi
SCL Ambiente, Milan, Italy

P. Ghezzi
Getas Petrogeo, Pisa, Italy

L.E. Russo
HUESKER Srl, Trieste, Italy

ABSTRACT: Bulera's landfill, located in Larderello, Pisa, is one of the few authorized landfills for hazardous waste in Italy, for over 1 million tons. In 2016 was approved the expansion for further 640,500 m^3 but, even if the pre-existing landfill body was properly insulated, in accordance with the Italian regulations in force that time, was not possible to lay directly new waste on the old one. An intermediate barrier had to be designed which was, at the same time, the capping of the old waste body and the bottom of the new one. The equivalence between the mineral barrier required by the Italian regulations and the alternative barrier package with use of Geosynthetic Clay Liner has been demonstrated with two different methods, considering variable hydraulic heads to fulfill the required performance. The barrier system has been approved by the Tuscany Region and some cells have already been made and tested successfully.

1   GENERAL CONTEXT

In the year 2016 the expansion of the Bulera's Landfill was decided adding additional volume above the old waste body temporarily covered, for total expected further quantity of 640,500 m^3 (Figure 1).

Figure 1.   Overview of Bulera landfill.

The Tuscan region imposed the construction of an intermediate barrier between the waste of the old landfill and the new ones belonging to the extension. This barrier was to act, at the same time, as capping for the old landfill and as bottom of the new one, in accordance with Italian regulation 36/2003 in force that time (legislation superseded by the current DL n. 121-03/09/2020) that required, for hazardous waste landfills, a geological barrier (GB) with permeability $K<10^{-9}$ cm/s and a thickness of minimum 5 m. Due to technical, environmental, and financial reasons a 5 m thick clay barrier was not practicable. The regional authorities allowed the designer to find alternative solutions that could have similar performance. To overcome this obstacle, an equivalent barrier system was studied, consisting in one meter layer of compacted clay combined with special bentonite geocomposite (Geosynthetic Clay Liner - GCL). The entire barrier system was completed with a HDPE geomembrane 2.5 mm, drainage geocomposites and protective geotextiles nonwovens. The equivalence has been demonstrated with two different methods (comparison of "flow rates" and "Koerner's approach") varying the hydraulic heads to be able to identify the minimum characteristics required for the geosynthetic package adopted.

2 STRATIGRAPHIC SCHEME

According with the Italian regulation, the alternative barrier system had to be necessarily equivalent to the following:

– Geological barrier: mineral clay layer with permeability $K<10^{-9}$ m/s and minimum thickness of 5 m

   To obtain the equivalence between the two barrier systems, the flux index was considered the relevant comparison parameter to take in consideration in order to get the same streamed flow through 1 m^2 of surface per unit of time ($m^3/m^2/s$) under analogous conditions. With this purpose, the designers decided to evaluate 3 different hydraulic situations, that is, with water heads of 0.30 m, 0.50 and 1.0 m above the barrier.

   The equivalent designed barrier system proposed to carry out was (bottom up):
– 1m of a compacted clay layer with permeability $K<10^{-9}$ m/s
– bentonite geocomposites with specific performance characteristics for equivalence purposes

   With this regard sodium and calcium bentonite geocomposites have been tested.
   On top of the previous layers, the following layers had to be laid:

– HDPE liner with thickness of 2.5 mm
– protective geotextiles nonwovens with static puncturing resistance CBR $\geq$ 13,000 N

   The flow index (q) as well as the other related parameters (permeability and thickness) of the bentonite geocomposites (GCLs) have been determined according to the UNI EN 16416.

3 CALCULATION METHOD

The calculation criteria for equivalence between the mineral layer and the geocomposite layer was based on two different methodologies:

– Equivalence of the flow index. It is expressed in $m^3/m^2/s$ and represents the water flow per unit of surface that crosses a layer per unit time. This is the method closest to reality because it refers to a physical parameter that can be measured with certainty in laboratory tests.
– Equivalence through Koerner's method. This method requires the following input characteristic parameters: permeability expressed in m/s and thickness of the saturated

geocomposite after controlled expansion expressed in mm. This value is obtained from laboratory tests in accordance with ASTM D5887-09 or UNI EN 16416.

4 RESULTS

4.1 Results with the flow index method

The calculation of the flow index for the geological barrier with a thickness T_{GB} = 5 meters and hydraulic conductivity $K_{GB} = 10^{-9}$ m/s was done considering three different water head levels: a) 0.3 m; b) 0.5 m (which corresponds to the full saturation of the 50 cm thick over-lying drainage layer); c) 1.0 m (considering a more critical scenario). The results are shown in Table 1.

Table 1. Hydraulic gradient and index flux of the geological barrier under different water heads.

Water head	H_1 = 0.3 m	H_2 = 0.5 m	H_3 = 1.0 m
Hydraulic Gradient, $i_{GB} = (H+T_{GB})/T_{GB}$ [-]:	1.06	1.10	1.20
Index Flux q_{GB} [m^3/m^2/s]:	1.06 10^{-9}	1.10 10^{-9}	1.20 10^{-9}

Therefore, the equivalent barrier package must not exceed the flow index obtained for the geological barrier (GB) T_{GB} = 5 m thick, permeability $K_{GB} \leq 1 \times 10^{-9}$ m/s, under the three different water head considered, that is:

- Hydraulic head 0.3 m: maximum flow index q = 1.06 10^{-9} m^3/m^2/s
- Hydraulic head 0.5 m: maximum flow index q = 1.10 10^{-9} m^3/m^2/s
- Hydraulic head 1.0 m: maximum flow index q = 1.20 10^{-9} m^3/m^2/s

4.2 Results with Koerner's method

The essential function assigned to any barrier system is the ability to contain liquids as demanded by the specific project. The Koerner's method is linked to the previous one related to the flow index which, consequently, remains the main reference. The method, in fact, entirely refers to the concept of equivalence between the flow index and, therefore, velocities, but imposes the calculation as a function of the physical characteristics of the product, thickness and permeability, which should be considered according to the real performance values.

The values to be adopted in the calculation are those that can be obtained from certificates issued by independent laboratory tests and supplied by manufacturers to verify and assess the performance of the product: thickness after controlled expansion and actual characteristic permeability. Applying the criteria of equivalent flow rate, considered as water volume flowing through a soil layer per unit area and per unit of time, with the Darcy's formula the required minimum permeability for the GCL is:

$$k_{GCL-required} = k_{GB} \cdot \frac{T_{GCL}}{T_{GB}} \cdot \frac{(H + T_{GB})}{(H + T_{GCL})} \tag{1}$$

The maximum permeability value required for geological barrier (GB) by the Italian norm (Legislative Decree 36/03) in force that time was $k_{CCL} = 1 \times 10^{-9}$ m/s with a minimum thickness of 5 meters. As mentioned before, For Bulera's landfill it was decided to consider

three different hydraulic heads, that is, $H_1 = 0.3$ m; $H_2 = 0.50$ m and $H_3 = 1.0$ m to examine the equivalence with the GCL. Varying the thickness T_{GCL} of the bentonite geocomposite (which, according to Koerner's method, correspond to that after controlled expansion measured during permeability test), the maximum allowable permeability was obtained (see Table 2).

Table 2. Maximum allowable permeability as a function of GCL thickness after controlled expansion.

Thickness mm	max. K allowed [m/s]		
	$H_1 = 0.3$ m	$H_2 = 0.5$ m	$H_3 = 1.0$ m
9.0	3.09×10^{-11}	1.94×10^{-11}	1.07×10^{-11}
10.0	3.42×10^{-11}	2.16×10^{-11}	1.19×10^{-11}
10.5	3.58×10^{-11}	2.26×10^{-11}	1.25×10^{-11}
11.0	3.75×10^{-11}	2.37×10^{-11}	1.31×10^{-11}
11.5	3.91×10^{-11}	2.47×10^{-11}	1.36×10^{-11}
12.0	4.08×10^{-11}	2.58×10^{-11}	1.42×10^{-11}
12.5	4.24×10^{-11}	2.68×10^{-11}	1.48×10^{-11}
13.0	4.40×10^{-11}	2.79×10^{-11}	1.54×10^{-11}

5 SELECTION OF THE GEOSYNTHETIC CLAY LINER

During the selection phase, three different GCLs were investigated (Type A, B and C) on which evaluate the equivalences under different hydraulic heads, both using the flow index and the Koerner method. In Table 3 are shown the minimum performance values obtained by the manufacturer through numerous laboratory tests performed on the three types of geocomposites which allowed to obtain their thicknesses after expansion (average value - standard deviation) and the hydraulic conductivity as tested (average value + standard deviation).

Table 3. Comparative analysis of three GCLs to determine their suitability for equivalence.

GCL			Type A	Type B	Type C
Thickness [mm]	10.5	12	10.5	12.0	12.0
			max K_{GCL} [m/s] obtained from the test set		
			$K_A = 7.83$ E^{-12}	$K_B = 1.90$ E^{-11}	$K_C = 5.73$ E^{-11}
H [m]	$K_{allowed}$ [m/s]		$K_A \leq K_{all}$	$K_B \leq K_{all}$	$K_C \leq K_{all}$
0.3	3.58×10^{-11}	4.08×10^{-11}	OK	OK	NO
0.5	2.26×10^{-11}	2.58×10^{-11}	OK	OK	NO
1.0	1.25×10^{-11}	1.42×10^{-11}	OK	NO	NO

The equivalence has been determined on all products for hydraulic head of H = 0.30 meters while, for higher levels, the market choice is limited.

After carrying out a comparative analysis, the chosen material was Nabento RL-N 5500 F (WB) that fulfill all the required features: minimum unit weight 5000 g/m^2 of sodium bentonite, minimum thickness after controlled expansion of 10.5 mm and permeability values under different hydraulic heads below the maximum permissible. After this investigation, the Tuscan Region authorities decided to establish the minimum parameters that the

geocomposite had to respect in order to carry out Quality Controls of the material supplied on site, and specifically: minimum unit weight of bentonite 5.0 kg/m^2; minimum thickness before expansion T_{GCLmin} = 9 mm; maximum permeability under 1.0 m water head and $K_{max} = 1.25 \times 10^{-11}$ m/s.

Furthermore, it should be emphasized that, for design reasons related to stability issues, not only the hydraulic characteristics were considered in the choice of the GCL, as it was necessary to verify aspects related to the stability of the waste mass, up to 20 m high, placed above a sloping intermediate barrier that was a potential sliding surface. The shear strength at the interface between GCL/clay and GCL/HDPE geomembrane had to be suitable, as well as the internal long-term shear strength of the material. Thanks to the rough surfaces of the selected product and the high internal friction angle value (>36°) was possible to reach shear strengths values higher than the minimum required for every interface. All adopted values for design calculations were supported by a consistent number of laboratory tests and certificates. The stability analyzes carried out are not presented here because they are beyond the scope of this paper, but it is considered appropriate to point out the need to evaluate not only the hydraulic aspects but also the mechanical performances required of the product for the specific work when selecting a GCL.

6 BARRIER SYSTEM CONSTRUCTION

The first cells of the new landfill were constructed in the 2019. The sequence is shown in Figures 2 and 3.

The required performance was assessed trough several laboratory tests. The mineral barrier showed permeability values variable from K< 9.9×10^{-10} m/s to K< 1.2×10^{-10} m/s. The supplied geocomposites were checked through:

– Manufacturer's declaration of conformity
– Test certificates issued by independent laboratories provided by the manufacturer
– Laboratory tests performed by the manufacturer on the supplied production lots
– Laboratory tests performed on samples taken on site (results in Table 4)

Figure 2. GCL and drainage geocomposite rolls stored on flat surfaces to avoid detrimental deformations.

Figure 3. Slopes covered, from left to right, with the rough GCL, the HDP liner, drainage geocomposite (slopes) and nonwoven geotextile (bottom).

Table 4. Comparison between the minimum required values and the laboratory results obtained from 4 GCL samples taken from the site.

	Unit weight UNI EN 14169 gr/m^2	Thickness (dry condition) UNI EN ISO 9863-1 mm	Permeability (under 1 m water head) UNI EN 16416 m/s
Required	≥ 5000	≥ 9.0	$\leq 1.25\ 10^{-11}$
Sample 1	5920	9.51	$7.17\ 10^{-12}$
Sample 2	5940	9.11	$7.24\ 10^{-12}$
Sample 3	6080	9.60	$8.91\ 10^{-12}$
Sample 4	6150	9.25	$8.01\ 10^{-12}$

7 CONCLUSIONS

The construction of impermeable barrier systems in hazardous waste landfills is highly demanding. The 5 m thick layers of mineral clay layer required by law in Italy for the bottom barrier is difficult to fulfill due to technical, environmental, logistic and financial reasons.

The paper describes the possibility to construct a thinner equivalent barrier system making use of special GCLs that must fulfill specific demanding performances related to hydraulic and static issues.

In Bulera's landfill, the equivalent barrier system was designed using a particular GCL which required performance was supported by a consistent number of tests. The equivalence demonstration of the proposed solution allowed the approval by the regional authorities.

During construction, quality control assessments were done through tests made on the material supplied on site which provided positive results, confirming the validity of the adopted technical solution.

REFERENCES

ASTM D5887, *Standard Test Method for Measurement of Index Flux Through Saturated Geosynthetic Clay Liner Specimens Using a Flexible Wall Permeameter*.

Bonaparte, R., Daniel, D. E., Koerner, R. M., *Assessment and Recommendations for Improving the Performance of Waste Containment Systems*. Performed under EPA Cooperative Agreement Number CR-821448-01-0.

BS 8006-1: 2010. *Code of Practice for Strengthened/reinforced Soils and Other Fills*. BSI 20 October 2010.

Council Directive 1999/31/EC of 26April 1999 on the Landfill of Waste (OJ L 182, 16.7.1999 p. 1).

Decreto legislativo 13 gennaio 2003, n. 36 Attuazione Della Direttiva 1999/31/CE Relativa Alle Discariche di rifiuti.

Koerner, R. M. 2012. *Designing with Geosynthetics*, 6th edition, January 2012. Xlibris Corp.

Koerner, R. M., Gartung E., Zanzinger H. 2002. Geosynthetic Clay Liners. In *Proceedings of the International Symposium, Nuremberg, Germany, 16-17 April 2002*

UNI EN 16416:2013, *Geosynthetic Clay Barriers - Determination of Water Flux Index - Flexible Wall Permeameter Method at Constant Head*

Subaqueous sediment capping with a geocomposite containing activated carbon in Sydney (Australia)

S. Niewerth
HUESKER Synthetic GmbH

G. Martins
HUESKER Australia Pty. Ltd.

ABSTRACT: At Kendall Bay in Sydney, the New South Wales Environment Protection Authority issued a sediment remediation declaration for a significantly contaminated area adjacent to a former gasworks facility. Today the disused industrial site has become a modern residential district. Therefore, not only the area on land was redeveloped but also the sediments in the bay. It was determined that remediation was required where the sediments contain total polyaromatic hydrocarbon (PAH) concentrations greater than 25 mg/kg on average and total recoverable hydrocarbon (TRH) of more than 4000 mg/kg on average. To remediate the highly contaminated sediments a subaqueous cap with an active geocomposite filled with activated carbon was built. This geotextile contaminant barrier adsorbs the organic contaminants before they can reach surface water due to diffusion and groundwater discharge. An accumulation of the pollutants in the water of the bay, the benthic and the aquatic organisms is thus prevented over several decades. In addition, the strong odor of organic contaminants is bound by the active geocomposite. The full-scale remediation work was completed from September 2019 until October 2020. In Kendall Bay, it was demonstrated that the installation process can be done quickly and in a variety of aquatic situations, including rivers, harbors, lakes, wetlands, etc.

1 INTRODUCTION

Waterways have been used as transport routes and ports as transshipment points for raw materials, fuels, and residual materials since the beginning of industrialization. In addition, the water also serves as cooling and service water. Accordingly, since the early 19th century, the processing industry and, somewhat later, power plants have settled along river courses. Until the middle of the 20th century, there were no significant requirements for water protection. As a result, contaminated subaqueous sites can be found in industrialized and emerging countries. Not only industry is a source for contamination but also waste dumps, agriculture, infrastructure, or mining. The discharge of pollutants into water bodies inevitably leads to deterioration of water quality and deposition in sediments. In order to reach water quality levels from current directives, such as Australian Water Quality Guidelines or European Water Framework Directive, these sites may need to be remediated.

Modern remediation always focuses on the entire ecosystem and considers all possible interactions resulting from the intervention in the system. Accordingly, extensive knowledge is required not only about the contaminant levels in sediments, but also experience and simulations of impact pathways from sediments to receptors, such as native plants and fish. As an example, the evolution of the pollutant concentration in fish tissue can be considered for different remediation methods. A study done by Patmont *et al.* (2014) compares three remedial options that in principle can be chosen for subaqueous remediation:

1. Monitored natural recovery/attenuation (MNR)
2. Sediment Capping (conventional and active)
3. Dredging

MNR (sometimes also called MNA) based on the principle that a variety of organic pollutants are steadily decomposed by natural processes. The degradation of the substances is continuously monitored in the water and in receptors. If a defined concentration threshold is not exceeded no further technical actions need to be done. Accordingly, this method is the one with the gentlest intervention in the ecosystem. With sediment capping the exposure pathway from the contaminated seabed to the surface water and thus to receptors is interrupted with the help of an isolation layer. Compared with dredging, the method is also gentle with regard to contaminant spills as a result of sediment raising in the water. This technique will be explained more in details in the next chapter. Dredging of contaminated sediments is probably the most common remedial option. With the help of a dredger, the sediments are removed from the seabed, dewatered ex situ and, if necessary, securely refilled, landfilled, or utilized. The advantage obviously lies in the elimination of the source of the pollutant and possibly also in the deepening of the water body. A study on the spillage of pollutants from the three named methods was carried out by Patmont *et al*. (2014). It becomes apparent that dredging work inevitably causes a strong, short-term increase in the concentration of pollutants in receptors (here fish) during and after the construction work. In the long term, the concentration in receptors reaches the same low values as with sediment capping. Next to the long-term development of contaminant concentration there are also many other factors to consider when choosing the best remedial option for a specific site (sediment management plans, functions of waterway for navigation and flood storage, etc.).

2 SEDIMENT CAPPING

2.1 *Conventional capping*

A distinction is often made between a conventional thick layer cap and an active thin layer cap. A conventional cap consists of 1 m or more of sand that is placed on top of the seabed. These clean sediments isolate the contaminated sediments, i.e. avoid a contaminant migration with the pore water in the benthic habitat layer and the surface water. As sand has no sorption capabilities a thick layer is necessary. Not only the weak chemical isolation properties of sand but also construction related uncertainties (mixing of clean and contaminated seabed, placement unevenness, etc.) and influences from the energy water environment (currents, waves, erosion, vessel traffic, etc.) lead to the high thickness, as shown in Figure 1.
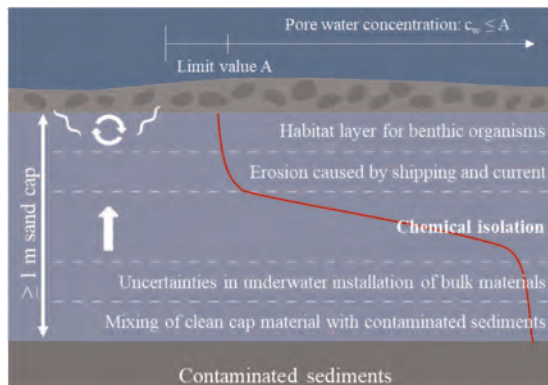

Figure 1.   Design of a conventional thick layer cap (based on Reible & Eek 2017).

Thus, it must be ensured that the minimum thickness for the chemical isolation (∼30 cm) under the habitat layer (∼10 cm) is given even if all uncertainties have been realized, i.e. mixing has taken place, cap is installed uneven, and parts of the cap have eroded.

2.2 *Capping with active geocomposites*

The aim of a thin layer cap with active geocomposites is to reduce the thickness of the cap with the help of geotextiles and sorbents. The latter has the ability to remove contaminants from water whereas the geotextiles function as separation and filtration elements. As uncertainties are drastically reduced the cap thickness is approx. 20–30 cm for a new clean habitat layer and the active geocomposite (∼1 cm). The geotextiles avoid mixing of cap material and the seabed. Also, placement uncertainties and erosion from vessel maneuvering and currents will not occur as the isolation material, i.e. the amendment material, is sandwiched between two layers of geotextiles. These layers are joined by mechanical bonding techniques, such as needle-punching or sewing. Depending on the selection of geotextiles and binder techniques, different properties result for the final product, e.g., tensile strength, elongation, water permeability, etc. In this way, ideal optimal contaminant barriers can be customized. In contrast to sealing systems, such as geomembranes or geosynthetic clay liners, active geocomposites have a comparatively high permeability of k $\geq$ 1,0E-5 m/s. The permeability ensures that the groundwater discharge through the seabed remains unaffected, while the exposure path of the contaminant is interrupted with the help of the sorbents.

To remove contaminants from the pore water, different sorbents can be selected. The choice depends on the affinity of a sorbent towards the target pollutants. Activated carbon for example has a high affinity towards organic pollutants. Those organic contaminants frequently encountered in conjunction with sediments are for example polycyclic aromatic hydrocarbons (PAH), tributyl tin (TBT), or petroleum derived hydrocarbons (TPH). Inorganic pollutants are metals and metalloids, such as chromium, copper, and lead. Most inorganic contaminants are only slightly adsorbed by activated carbon. For the removal of metals, cationic sorbents are more effective.

For the design of a thin active cap a good understanding of the kinetics and the capacity of the amendments is of utmost importance (Niewerth & Wilke 2021). Depending on the annual groundwater discharge and the diffusion rate as well as the pore water concentration the life expectancy can be clearly calculated. Also, the use of professional software tool allows simulations of the cap performance for different designs based on scientifically proven findings. Reible and Eek (2017) published a simulation where different cap designs for isolation of a seabed with a PCB contamination were compared. The result is given in Figure 2. It shows that
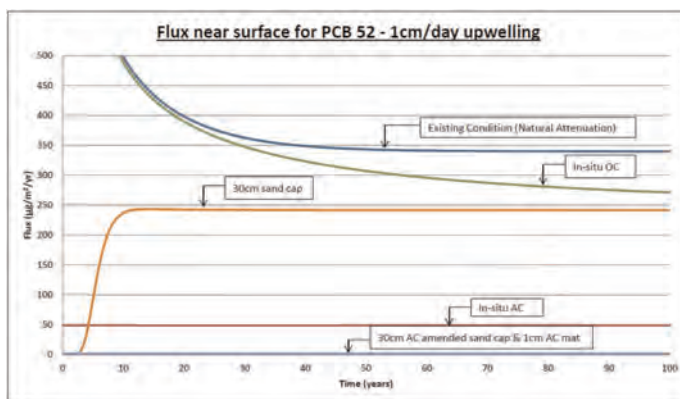

Figure 2.   Simulation of cap performance for different cap designs (Reible & Eek 2017).

the PCB flux in the interface of the cap and the surface water is almost zero with the use of a thin active cap made of an active geocomposite with activated carbon ("1 cm AC mat") underneath a 30 cm sand layer mixed with a certain (unknown) amount of bulk activated carbon. The simulation was done with the help of the CapSim program developed by the Reible Group at Texas Tech University. It shows that the contaminant flux can be drastically reduced with the help of a well designed cap with active geocomposites on the long term.

3   CASE STUDY

From the 1880s until the 1980s a manufactured gas plant operated on the south bank of the Parramatta River approximately 10 km away from the cultural center of Sydney (Australia). Nowadays, the former industrial area has been developed into a modern housing estate as shown in Figure 3. During the time as an industrial area, the Parramatta River was used to ship coal and other production goods to the plant. The century long operation left high levels of polyaromatic hydrocarbons and recoverable hydrocarbons in the sediments. In May 2004, the Environmental Protection Agency of the State of New South Wales therefore declared the bay as a contaminated site in need of remediation. For this, the entire bay was divided into different areas depending on the level of contaminant concentration. The part of the bay which shows the highest concentration ($\leq$ 120 mg/kg PAH) was remediated with a combined method of in-situ stabilization under a thin layer active cap. First, the top layer of the contaminated sediments was stabilized with cement and other additives. Above of the stabilized seabed an active geocomposite with a filling of 3.4 kg/m^2 of activated carbon was installed. Thereupon 30 cm of clean sediments today build the new riverbed of the bay.

Figure 3.   Site remediation in front of modern housing estate (Courtesy of HUESKER Australia).

The work started in 2019 and ends up with the installation of the active cap in 2020. The 45,00 m long and 5,10 m wide active geocomposite was first anchored to the shoreline with the help of sand and armoring stones. Perpendicular to the shoreline they were rolled out from a floating pontoon with an unrolling device. A lowering frame was used to ensure controlled placement and ballasting. In this installation, a crane was used to move the bottomless frame to a precise position on the geocomposite. The weight of the frame pushes the mat down into the shallow riverbed, as shown in Figure 4. A long-arm excavator was then used to fill the frame with approx. 30 cm of sand. It was important that all mats maintained some overlap so that a continuous sorption layer was constructed. Accordingly, care had to be taken to ensure that the sand was applied only after the installation of two mats in the overlap area. Due to the width of 5.10 m, the sand was first be applied in the middle of the mat and finally the overlap area was covered. The installation of the approximately 5.000 m^2

Figure 4. Installation of active geocomposite with bottomless frame (Courtesy of HUESKER Australia).

area was carried out in five weeks, equivalent to 1.000 m^2 of active thin layer capping per week.

The active sediment cap – here in combination with an in-situ stabilization – filters out the contaminants from the uprising pore water and thus prevents accumulation in benthic and aquatic organisms. Moreover, the new residents can enjoy a beautiful view of the entire bay. Strange odors, black sediments, and an oil sheen on the surface of the water are a story of the past.

4 CONCLUSION

Contaminated subaqueous sites result in poor water quality and pose a risk to receptors, such as fish and benthic organisms. Remediation of the seabed is unavoidable at appropriate contaminant concentrations. In addition to removing sediments with a dredger, other remediation techniques are available. With sediment capping the polluted seabed gets isolated from the surface water. Thus, the pollutants transported with the pore water do not reach the surface. A sediment cap has the ability to protect the aquatic environment for many decades. Below the cap, the substances are partially degraded to a certain extent by natural biological and biochemical processes. Caps designed with active geocomposites consists of large-area, thin pollutant filters that adsorb the pollutants and thus represent permanently safe barriers for the pollutants despite a low thickness. A project in Australia demonstrated the successful installation of the products in a polluted bay. A large area was covered and thus secured in a very short time. This shows that the modern remediation technique is gaining relevance in more and more countries.

REFERENCES

Niewerth, S. & Wilke, M. 2021. Remediation of Contaminated Sediments in Surface Waters using active Geocomposites. *GeoResources Journal* 2021(3): 7–13.
Patmont, C. R., Ghosh, U. & LaRosa, P. *et al.* 2014. In Situ Sediment Treatment Using Activated Carbon: A Demonstrated Sediment Cleanup Technology. *In: Integrated Environmental Assessment and Management* 11(2): 195–207.
Reible, D. D. & Eek, E. 2017. Capping Design – Short Course, Part 2, *Ninth International Conference on Remediation and Management of Contaminated Sediments. New Orleans, January 9-12.*

Diffusion and membrane behavior of an exhumed geosynthetic clay liner

S. Tong
Zhejiang University, Hangzhou, China (formerly Villanova University, Pennsylvania, USA)

K.M. Sample-Lord & S.A.B. Rahman
Villanova University, Villanova, Pennsylvania, USA

N. Yesiller & J.L. Hanson
California Polytechnic State University, San Luis Obispo, California, USA

ABSTRACT: A composite bottom liner system consisting of a geomembrane over a geosynthetic clay liner (GCL) was constructed for a municipal solid waste landfill in California, USA, in 2004. The liner system then was left exposed without placement of overlying waste for over a decade. In 2016, samples of the GCL were exhumed from the sideslopes for laboratory testing. To investigate the impact of field exposure on the diffusion and membrane behavior properties of the bentonite, multi-stage through-diffusion tests were performed on the exhumed GCLs and a virgin specimen of the same GCL product. Membrane efficiency coefficients (ω) and effective diffusion coefficients (D^*) were measured for potassium chloride (KCl) source solutions. Preliminary results are presented to assess the impact of the long-term field exposure on diffusion and membrane properties of the GCL. Comparisons are drawn with the existing literature for diffusion and membrane behavior, which to date has been limited to testing of virgin GCLs.

1 INTRODUCTION

Geosynthetic clay liners (GCLs) are widely used as barriers in hydraulic and chemical containment applications (e.g., landfills, impoundments). GCLs have been shown to exhibit low hydraulic conductivity, k, to water (i.e., $< 10^{-10}$ m/s), limiting advective flux of contaminants through the liner (Rowe *et al.* 2004). Laboratory studies have shown that GCLs also exhibit semipermeable membrane behavior and have low effective diffusion coefficients, D^*, further enhancing the long-term performance of the barrier system to restrict migration of contaminants into the environment (e.g., Malusis & Shackelford 2002a; Manassero & Dominijanni 2003).

The existence of membrane behavior in a GCL results in restriction of charged inorganic solutes from entering the pores of the bentonite, thereby reducing the total contaminant flux through the GCL and enhancing the barrier performance (Shackelford 2012). This phenomenon occurs due to electrostatic repulsion of anions from electrical fields surrounding adjacent bentonite particles (Fritz 1986). The membrane behavior of GCLs is quantified by the membrane efficiency coefficient, ω, which ranges from a value of 0 (no solute restriction) to 1.0 or 100% (complete or perfect chemical restriction) (Mitchell 1991). Experimental studies indicated significant membrane behavior in GCLs comprising sodium bentonite (NaB) (e.g., $\omega = 0.7$ in Malusis & Shackelford 2002b). Polymer-enhanced bentonites for GCLs also exhibited membrane behavior (Bohnhoff *et al.* 2014; Di Emidio *et al.* 2015; Tong

& Sample-Lord 2022). In addition, multiple studies on NaB and GCLs measured ω and diffusion simultaneously, and reported an inverse correlation between ω and D^* for chloride (e.g., Dominijanni *et al.* 2013; Shackelford *et al.* 2016).

Experimental diffusion and membrane behavior research to date has focused solely on virgin GCLs (i.e., GCLs that have never been exposed to field conditions). Processes that have been identified to adversely affect GCL performance in the field, such as cation exchange and downslope bentonite migration, may also degrade membrane behavior and diffusion performance. However, aside from the preliminary work of the authors, no known studies have attempted to measure membrane behavior and diffusion properties of GCLs that have been exhumed from field sites. Thus, performance-based modeling capabilities and understanding of coupled flows in clay barriers are limited by current datasets of potentially unrepresentative values of ω and D^* obtained from laboratory testing of virgin GCLs.

The experimental study described in this paper included measurement of ω and D^* for GCL samples exhumed from a liner system in San Luis Obispo, California, USA after 12-years of field exposure. Testing was performed on GCL samples exhumed from the top and bottom of a landfill sideslope, as well as on a virgin GCL that was manufactured during the same time period as the installed liner. Results were compared between the exhumed and virgin specimens under the same testing conditions, as well as values reported in the literature for virgin GCLs that utilized similar testing methodologies.

2 MATERIALS AND METHODS

2.1 *Exhumed and virgin GCL samples*

The virgin and exhumed GCL samples were both Bentomat DN (CETCO, USA). Bentomat DN is a needle-punched nonwoven-nonwoven product made with sodium bentonite. Properties of the GCL determined through conformance testing included a bentonite mass per unit area of 4.9 kg/m^2 and k of 2.8×10^{-11} m/s. The average swell index (SI) reported by the manufacturer was 26.0 mL/2g.

The exhumed samples were obtained from a geomembrane-GCL composite bottom liner system that was installed at a municipal solid waste landfill in San Luis Obispo, California (USA) in 2004. The geomembrane was 1.5 mm-thick black HDPE. The composite liner system was left uncovered for 12 years (Figure 1a), after which point the GCL samples were exhumed in 2016. A utility knife was used to cut a strip sample from the corner of the east and south slopes. For the membrane behavior and diffusion testing program, sub-samples (300 mm x 300 mm) were cut from the strip sample from near the top and bottom of the slope (Figure 1b). Details of the liner exhumation are provided in Hanson and Yesiller (2019).

The SI, bentonite mass per unit area, and k also were measured for GCL samples exhumed from the top and bottom of the slope. The SI of the sample exhumed from the top
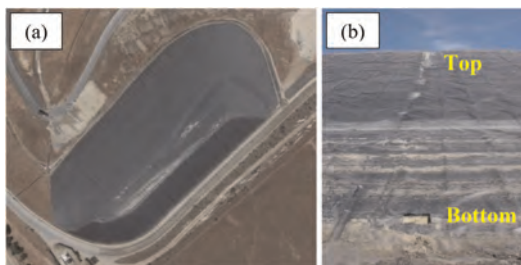

Figure 1. Photographs of: (a) site in San Luis Obispo, California, USA; (b) example "top" and "bottom" of slope exhumed sample locations.

of the slope was 25.5 mL/2g, which was similar to the original *SI* reported by the manufacturer. However, the *SI* of the sample exhumed from the bottom of the slope had decreased to 9.5 mL/2g, suggesting significant cation exchange occurred between the NaB and subsoil for the GCL located near the bottom of the slope over the exposure period. The GCL exhumed from the top of the slope had a bentonite mass per unit area of 3.9 kg/m^2 and average thickness of 6.0 mm. In contrast, the GCL exhumed from the bottom of the slope had a bentonite mass per area of 4.9 kg/m^2 and average thickness of 11.7 mm. These mass/area results supported field observations that significant downslope bentonite erosion had occurred. The *k* of the GCL samples exhumed from both the top ($k = 7.7 \times 10^{-7}$ m/s) and bottom ($k = 1.2 \times 10^{-8}$ m/s) of the slope had increased by 3-4 orders of magnitude above the original values reported from the manufacturer and conformance testing. The increase in *k* for the top sample likely was due to bentonite loss, whereas the increase in *k* for the bottom sample was attributed to reduced swell.

The virgin sample was obtained from a Bentomat DN GCL roll that was manufactured around the same time period as the field installation. This GCL remained stored in a laboratory setting at California Polytechnic State University-San Luis Obispo.

2.2 Diffusion and membrane behavior testing

Membrane efficiency (ω) and chloride effective diffusion coefficients (D^*) were measured simultaneously using a closed-system, through-diffusion apparatus as described in detail in Malusis *et al.* (2001) and depicted in Figure 2. The apparatus includes a hydraulic control system with a double-syringe flow pump to circulate solutions, an acrylic cell to contain the specimen and porous disks, pressure transducers to monitor pressures at the specimen boundaries, and stainless steel connections throughout the apparatus (to prevent corrosion or volume change). The apparatus is used to simultaneously circulate a higher concentration solution across the top boundary of the specimen and a lower concentration solution across the bottom boundary, thus creating a concentration difference (ΔC) across the specimen. If a GCL exhibits membrane behavior, a hydraulic pressure difference (ΔP) will develop across the specimen due to the applied ΔC. The ΔP is measured via pressure transducers at the boundaries of the specimen and used to quantify the membrane efficiency as (Malusis *et al.* 2001):

$$\omega = \frac{\Delta P}{\Delta \pi} \qquad (1)$$

where, $\Delta \pi$ is the theoretical maximum value of ΔP that would result across an ideal membrane subjected to the same ΔC. Values of $\Delta \pi$ for single-salt solutions can be determined in accordance with the van't Hoff expression (Katchalsky & Curran 1965).

In preparation for testing, all specimens were trimmed to a diameter of 71 mm. The test specimen thicknesses for the virgin GCL, GCL exhumed from the top of the slope, and GCL exhumed from the bottom of slope were 7.1 mm, 6.8 mm, and 11.8 mm, respectively. Prior to
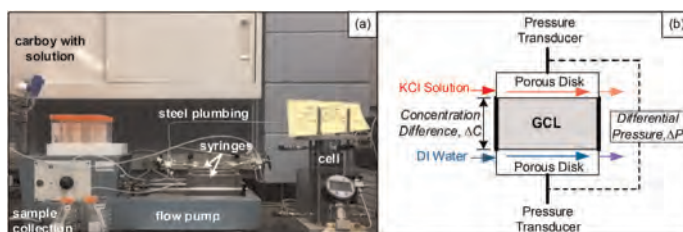

Figure 2. (a) Photograph of one of the closed-system apparatuses to simultaneously measure membrane behavior and diffusion; (b) schematic of conditions within the cell.

introducing salt solution to start the diffusion and membrane behavior testing, deionized water (DIW) was circulated across both boundaries of the specimen. The purpose of this DIW stage is to establish steady baseline conditions before introducing the concentration difference, and measure any initial ΔP that exists across the specimen with $\Delta C = 0$ condition (referred to as the baseline pressure difference, ΔP_o). After completion of the DIW stage, the top solution was switched to 5 mM KCl to commence diffusion and membrane behavior measurements. After steady-state diffusion and pressure conditions were achieved for the 5 mM KCl stage, the top boundary solution was then increased to 10 mM KCl. Each KCl stage typically took three to five weeks to complete.

Recorded ΔP values that developed due to membrane behavior were corrected for ΔP_o (i.e., effective pressure difference, $\Delta P_e = \Delta P - \Delta P_o$) and then used to calculate membrane efficiency in accordance with Equation 1. Samples of the top and bottom boundary outflows were collected every 2 days and subsequently analyzed for EC, pH, temperature, and ion concentrations (Cl^-, K^+, Na^+, Ca^{2+}, Mg^{2+}). The Cl^- concentrations in the bottom boundary outflows were used to determine D^* values based on the commonly used "steady-state method" analysis procedure (e.g., Dutt & Low 1962; Olsen $et\ al$. 1965; Shackelford 1991):

$$D^* = -\left(\frac{L}{n\Delta C}\right)\left(\frac{\Delta m}{A\Delta t}\right) \tag{2}$$

where L is the specimen thickness, A is cross-sectional area, n is porosity, Δt is the time increment over which the liquid outflow sample was collected from the bottom boundary (2 days for this testing), and Δm is the mass of Cl^- that diffused through the specimen over the time interval (calculated as the Cl^- concentration of the outflow sample x volume of the outflow sample).

This paper presents the preliminary results from the first two salt concentration stages (5 mM and 10 mM KCl) for the virgin and exhumed GCLs. The results of the subsequent higher concentration stages (up to 50 mM) are beyond the scope of this paper. The purpose of using KCl (vs. another salt) and solutions within that concentration range was to allow for comparison of the results with most of the literature data for similar tests on virgin GCLs.

3   PRELIMINARY RESULTS

The measured steady-state effective differential pressures (ΔP_e) and calculated membrane efficiency coefficients (ω) for each test stage are presented in Table 1. For all of the specimens, ω decreased as the source salt concentration increased, which has been widely observed in the membrane behavior literature and attributed to diffuse double layer

Table 1.   Summary of membrane behavior test results.

GCL Specimen	Source KCl Concentration, C_o mM	Effective Pressure Difference, ΔP_e kPa	Membrane Efficiency Coefficient, ω %
Virgin	5	10.3	51.2
	10	8.6	23.6
Exhumed from Top of	5	1.0	3.7
Slope	10	2.8	5.3
Exhumed from Bottom	5	2.0	8.9
of Slope	10	0.56	0.95

compression as salt diffuses into the bentonite pores (Di Emidio *et al.* 2015; Dominijanni *et al.* 2018; Fritz 1986; Shackelford *et al.* 2003).

The values of ω for the virgin GCL in Table 1 are consistent with ω ranges reported in the literature for other virgin GCLs. For example, Malusis and Shackelford (2002b) reported ω values of 52 % and 42 % for a similar Bentomat GCL (porosity, $n = 0.86$) from a multi-stage test with 3.9 mM and 8.7 mM KCl concentrations, respectively.

In contrast, values of ω for the exhumed GCLs were substantially lower than those for the virgin GCL in this study. Comparison of ω for the virgin and exhumed GCL specimens is presented graphically in Figure 3. The ω values of the GCL exhumed from the top of the slope were lower than the virgin GCL ω values by factors of 13.8 and 4 for the 5 mM and 10 mM stages, respectively. The reduced ω for the GCL exhumed from the top of the slope was likely due to the lower bentonite mass per area (3.9 kg/m^2), which had been attributed to downslope erosion based on field observations.
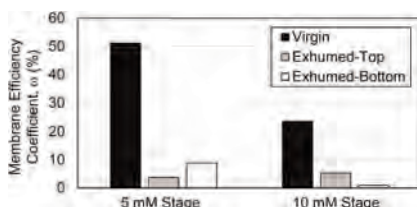

Figure 3.   Membrane efficiency coefficients for the virgin and exhumed GCL specimens.

The ω values of the GCL exhumed from the bottom of the slope were lower than the virgin GCL ω values by factors of 5.7 and 25 for the 5 mM and 10 mM stages, respectively. Unlike the GCL at the top of the slope, the GCL from the bottom of the slope had experienced an increase in bentonite mass per area (4.9 kg/m^2). The increase in bentonite mass per area would have been expected to maintain (or potentially increase) the original membrane behavior. The destruction of membrane behavior for the GCL at the bottom of the slope likely was due to cation exchange. Evidence of cation exchange occurring at the bottom of the slope was supported by the lower *SI*.

Figure 4 presents the ion concentrations measured in the liquid outflow samples collected during the diffusion and membrane behavior tests. As shown in Figure 4a for the virgin GCL and Figure 4b for the exhumed GCL from the top of the slope, the outflow samples had higher concentrations of Na^+ than Ca^{2+} or Mg^{2+}. This observation is consistent with the high *SI* values of the virgin and top GCL (*SI* = 25-26 mL/2g), representative of a bentonite with significant Na^+ occupying the exchange complex. In contrast, Figure 4c for the exhumed GCL from the bottom of the slope shows Na^+ concentrations that are an order of magnitude lower than the Ca^{2+} and Mg^{2+} concentrations. This observation further supports the hypothesis that cation exchange was the primary cause of the reduction in ω for the GCL at the bottom of the slope. Future testing will include measurement of cation exchange capacity and bound cation composition for detailed explanation of the observed behavior.

The concentrations in Figure 4 were used to determine the cumulative mass of Cl^- that had diffused through the specimens with time (normalized to specimen area), as shown in Figure 5. Values of D^* were calculated in accordance with Equation 2. For the 5 mM KCl stage, D^* values for the virgin, top exhumed, and bottom exhumed GCL specimens were 6.29×10^{-11} m^2/s, 2.43×10^{-11} m^2/s, and 1.02×10^{-10} m^2/s. For the 10 mM KCl stage, D^* values for the virgin, top exhumed, and bottom exhumed specimens were 7.97×10^{-11} m^2/s, 3.24×10^{-11} m^2/s, and 1.03×10^{-10} m^2/s.

For all of the specimens, D^* increased as C_o increased, consistent with the literature for diffusion in bentonite and expectations based on diffuse double layer effects. However,
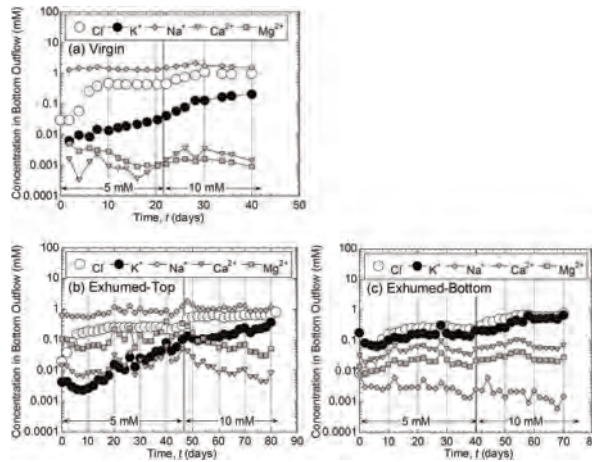
Figure 4. Measured ion concentrations in the bottom outflow samples with time for the (a) virgin GCL specimen, and GCL specimens exhumed from the (b) top and (c) bottom of the slope.
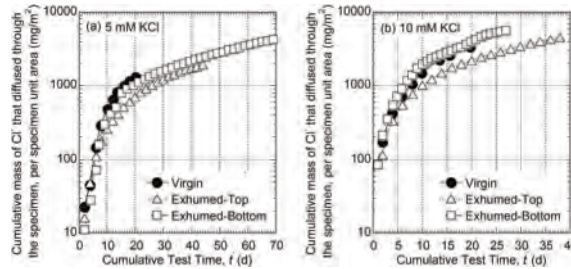
Figure 5. Cumulative mass of chloride (per unit area, per time) that diffused through each of the GCL specimens for the (a) 5 mM and (b) 10 mM test stages.

unlike the membrane behavior results, differences between the D^* values for the virgin GCL versus the exhumed GCLs appeared to be minimal to insignificant. Comparison of D^* values may have been complicated by the presence of other ionic species that were not included in the chemical analysis presented in Figure 4. For example, diffusion of chloride may have been impacted by simultaneous diffusion of other anionic species (e.g., sulfate). Additional testing is required to refine conclusions being drawn regarding the impact of the field exposure on the GCL diffusion properties.

4 CONCLUSIONS

The study represents the first experimental evaluation of coupled membrane behavior and diffusion properties of GCLs exhumed from the field. The membrane behavior was determined to be highly impacted by the field exposure, exhibiting significant decreases in ω, which were attributed to downslope bentonite migration and cation exchange with the subsurface. Impacts of the field exposure on diffusion properties were less apparent, with no consistent trend in D^* observed for the virgin versus exhumed GCL specimens. Further study is underway to confirm the extent of cation exchange that occurred in the bottom GCL and to perform more comprehensive diffusion analysis.

Available data in the literature for ω and D^* values of GCLs are primarily based on laboratory studies of virgin GCLs. The results of this study suggest that predictions of long-term performance using coupled transport models, which consider membrane behavior likely underestimate the total contaminant mass flux transporting through the barrier if virgin GCL properties are used.

REFERENCES

Bohnhoff, G. L., Shackelford, C.D. & Sample-Lord, K.M. 2014. Calcium-resistant Membrane Behavior of Polymerized Bentonite. *J. Geotech. Geoenviron. Eng.* 140(3): 04013029.

Di Emidio, G., Mazzieri, F., Verastegui-Flores, R.-D., Van Impe, W. & Bezuijen, A. 2015. Polymer-treated Bentonite Clay for Chemical-resistant Geosynthetic Clay Liners. *Geosynth. Int.* 22(1): 125–137.

Dominijanni, A., Manassero, M. & Puma, S. 2013. Coupled Chemical-hydraulic-mechanical Behaviour of Bentonites. *Géotechnique* 63(3): 191–205.

Dominijanni, A., Guarena, N. & Manassero, M. 2018. Laboratory Assessment of Semi-permeable Properties of a Natural Sodium Bentonite. *Can. Geotech. J.* 55(11): 1611–1631.

Dutt, G.R. & Low, P.F. 1962. Diffusion of Alkali Chloride in Clay-water Systems. *Soil Sci.* 93: 233–240.

Fritz, S. 1986. Ideality of Clay Membranes in Osmotic Processes: A Review. *Clays and Clay Minerals* 34(2), 214–223.

Hanson, J. L. and Yeşiller, N. 2019. "Assessment of Condition of An Uncovered Geosynthetic Landfill Bottom Liner System," *Proc., Geosynthetics 2019*, IFAI, 1–9.

Katchalsky, A. & Curran, P. F. 1965. *Nonequilibrium Thermodynamics in Biophysics*. Harvard University Press, Cambridge, MA.

Malusis, M. A. & Shackelford, C.D. 2002a. Coupling Effects During Steady-state Solute Diffusion Through a Semipermeable Clay Membrane. *Environ. Sci. Technol.*, 36(6): 1312–1319.

Malusis, M. A. & Shackelford, C.D. 2002b. Chemico-osmotic Efficiency of a Geosynthetic Clay Liner. *J. Geotechnical and Geoenvironmental Eng.* 128(2), 97–106.

Malusis, M. A., Shackelford, C. D. & Olsen, H. W. 2001. A Laboratory Apparatus to Measure Chemico-Osmotic Efficiency Coefficients for Clay Soils. *Geotechnical Testing Journal*, 24(3), 229–242.

Manassero, M. & Dominijanni, A. 2003. Modelling the Osmosis Effect on Solute Migration Through Porous Media. *Géotechnique* 53(5), 481–492.

Mitchell, J. 1991. Conduction Phenomena: From Theory to Geotechnical Practice. *Geotechnique* 41(3), 299–340.

Olsen, S.R., Kemper, W.D. & van Schaik, J.C. 1965. Self-diffusion Coefficients of Phosphorus in Soil Measured by Transient and Steady-state Methods. *Proc. Soil Sci. Soc. Am.*, 29: 154–158.

Rowe, R.K., Quigley, R. M., Brachman, R. & Booker, J.R. 2004. *Barrier Systems for Waste Disposal Facilities*. Taylor & Francis Group, New York, NY.

Shackelford, C.D. 1991. Laboratory Diffusion Testing for Waste Disposal – A Review. *Journal of Contaminant Hydrology*, 7(3): 177–217

Shackelford, C. D. 2012. Membrane Behavior of Engineered Clay Barriers for Geoenvironmental Containment: State of the Art. *Proc. GeoCongress 2012*, 3419–3428. Oakland, California, USA.

Shackelford, C., Meier, A. & Sample-Lord, K. 2016. Limiting Membrane and Diffusion Behavior of A Geosynthetic Clay Liner. *Geotextiles and Geomembranes* 44(5), 707–718.

Shackelford, C., Malusis, M., & Olsen, H. 2003. Clay Membrane Behavior for Geoenvironmental Containment. *Soil and Rock America Conference 2003*, P. J. Culligan, H. H. Einstein, and A. J. Whittle, Eds., Verlag Glückauf GMBH, Essen, Germany, Vol. 1, 767–774.

Tong, S. & Sample-Lord, K. 2022. Coupled Solute Transport Through a Polymer-enhanced Bentonite. *Soils and Foundation* 62(6), 101235.

Review of methods for quantifying polymer loading of enhanced-bentonite geosynthetic clay liners

A. Norris
Stantec Consulting Inc., Denver, Colorado, USA

J. Scalia
Colorado State University, Fort Collins, Colorado, USA

C. Benson
University of Wisconsin, Madison, Wisconsin, USA

C. Shackelford
Colorado State University, Fort Collins, Colorado, USA

ABSTRACT: Geosynthetic clay liners (GCLs) are thin, hydraulic and chemical containment barriers with low hydraulic conductivity ($\leq 3 \times 10^{-11}$ m/s) to water or dilute chemical solutions. However, when used to contain liquids with more aggressive chemistries, the hydraulic conductivity of GCLs can be several orders-of-magnitude higher. Polymer enhanced bentonites are developed for use in GCLs to maintain low hydraulic conductivity upon exposure to liquids with aggressive chemistries. Polymer loading is an important factor affecting the hydraulic conductivity of enhanced-bentonite GCLs (EB-GCLs). Measurements of polymer loading are conducted as part of manufacturing and construction quality assurance/quality control (QA/QC) of EB-GCLs, and to assist in interpreting outcomes of hydraulic conductivity testing of EB-GCLs. Methods used to quantify polymer loading of EB-GCLs are reviewed in this paper, with focus on loss on ignition (LOI) and total carbon (TC) analyses. Both methods may be component methods in that measurement of the parameter of interest (i.e., LOI, TC) is required for the sodium bentonite and polymer components as well as the bentonite-polymer mixture. In addition, composite LOI and TC methods are described whereby the polymer content is determined directly via calibration of measured LOI or TC for an enhanced-bentonite series with different, known polymer contents. Each method can be used without direct measurement of the base materials or calibration for use in QA/QC. Examples are provided from tests conducted with poly(acrylic acid), sodium carboxymethyl cellulose, covalently crosslinked poly(acrylic acid), and a bentonite polymer composite to illustrate the application, accuracy, and limitations of the methods.

1 INTRODUCTION

Enhanced bentonites refer to sodium bentonite that has been amended with polymers such as sodium carboxymethylcellulose or poly(acrylic acid) for use in containment applications involving liquids with aggressive chemistry. These applications include containment solutions with high ionic strengths or extreme pH for which unenhanced sodium bentonite will have an unacceptably high hydraulic conductivity due to limited bentonite swelling. The applicability of enhanced bentonites in geosynthetic clay liners (EB-GCLs) has been documented extensively in the literature (e.g., Chen *et al*. 2019; Scalia *et al*. 2014, 2018; Tian *et al*. 2016a,b).

Polymer quantification of the enhanced bentonites component of EB-GCLs is essential for quality assurance and quality control (QA/QC) in terms of ensuring the correct polymer content and the uniform distribution of the polymer across a manufactured roll. Currently, polymer quantification commonly is performed using a loss-on-ignition (LOI) method, such as described in ASTM D7348-13 (ASTM 2013). Scalia *et al.* (2014) used LOI to determine a polymer content of 28.5 % in an enhanced bentonite referred to as bentonite polymer composite (BPC) by first measuring separately the masses lost on ignition by the system components, viz., the polymer used for enhancement (polyacrylate) and the bentonite (LOI = 74.7 % and 1.6 %, respectively). However, as discussed subsequently, issues exist with LOI methods (Gustitus *et al.* 2021; Norris *et al.* 2022). A second established method used for measuring the organic content in soil samples known as the total carbon (TC) analysis (ASTM D6316, ASTM 2017) also has been evaluated for polymer quantification of the enhanced bentonite component of EB-GCLs (Gustitus *et al.* 2021; Norris *et al.* 2022).

Both LOI and TC analyses can be conducted using component or composite procedures to determine the polymer content of enhanced bentonites. Component procedures rely on measurements conducted on the constituent bentonite and polymer materials individually to determine the polymer content of an enhanced bentonite comprising the same bentonite and polymer (but mixed at an unknown ratio). Composite procedures involve measurements conducted on mixtures of bentonite and polymer (i.e., enhanced bentonites) with known polymer contents to generate a linear calibration that is used to determine the polymer contents of an enhanced bentonite with an unknown ratio of the same bentonite and polymer. Both LOI and TC methods are based on development of calibration curves that are used to determine the polymer content of specimens.

Gustitus *et al.* (2021) identified three potential procedures for quantifying polymer contents in enhanced bentonites that were used for non-hydrated EB-GCLs comprising BPC. These methods were termed component LOI, composite LOI, and composite TC. Norris *et al.* (2022) also reviewed the methods of component LOI and composite TC that were evaluated by Gustitus *et al.* (2021) and developed a component TC method. These methods were evaluated using a range of enhanced bentonites containing different anionic polymer types.

This review combines work by Gustitus *et al.* (2021) and Norris *et al.* (2022) to propose a current best practice for quantification of polymer content of enhanced bentonites comprising EB-GCLs. The results of the component LOI, composite TC, and component TC procedures as described by Gustitus *et al.* (2021) and Norris *et al.* (2022) are compared for use in evaluating the polymer content of EBs

2 LOSS ON IGNITION

2.1 *Loss on ignition method*

Polymer quantification using the component LOI procedure uses known quantities of the polymer enhancements and the base bentonite to develop a known LOI for each individual component of an enhanced bentonite (e.g., Gustitus *et al.* 2021; Norris *et al.* 2022; Scalia *et al.* 2014). A known mass of either a specimen of sodium bentonite or enhanced bentonite with an initial gravimetric water content or a specimen of polymer is oven-dried in a ceramic crucible at 110 °C until no further loss in mass is measured. Specimens are ignited using a muffle furnace, cooled in a desiccator, and the final masses of the specimen and crucible after ignition (m_f) are measured. Then, the specimen LOI is calculated as follows:

$$\text{LOI} = \left(m_i - m_f\right)/\left(m_i - m_c\right) \tag{1}$$

where m_i = initial specimen and crucible mass after drying, and m_c = initial crucible mass. With the measured LOI, the mass fraction of the polymer of an enhanced-bentonite

specimen representing the ratio of polymer mass relative to total mass (i.e., polymer plus bentonite), r_p, is determined from the following relationships:

$$\mathrm{LOI}_p r_p + \mathrm{LOI}_b r_b = \mathrm{LOI}_{eb} \tag{2}$$

and

$$r_p + r_b = 1 \tag{3}$$

where LOI_p = fraction mass loss after ignition of a representative specimen of the polymer component, LOI_b = fraction mass loss after ignition of a representative specimen of the bentonite component, LOI_{eb} = fraction mass loss after ignition of the enhanced bentonite, and r_b = ratio or fraction of bentonite mass to total mass. Based on Equations 2 and 3, the expression for r_p is as follows:

$$r_p = (\mathrm{LOI}_{eb} - \mathrm{LOI}_b)/(\mathrm{LOI}_p - \mathrm{LOI}_{eb}) \tag{4}$$

Polymer quantification using composite LOI analysis is completed by measuring the LOI of mixtures of sodium bentonite and polymer at known polymer loadings to develop a calibration curve, which is specific to a given enhanced bentonite.

2.2 Review of loss on ignition method results

Measured polymer contents using both component and composite LOI from Gustitus *et al.* (2021) and component LOI from Norris *et al.* (2022) are shown versus the actual polymer contents in Figure 1. The results from Norris *et al.* (2022) for the component LOI procedure were consistent with those of Gustitus *et al.* (2021). Residual polymer contents, calculated as the difference between actual polymer content and calculated polymer content and reported in terms of percent dry mass of enhanced bentonite, are shown versus actual polymer content in Figure 2 and summarized in Table 1. The component LOI method results in both underestimation of actual polymer content by up to 2.4 % and overestimation of actual
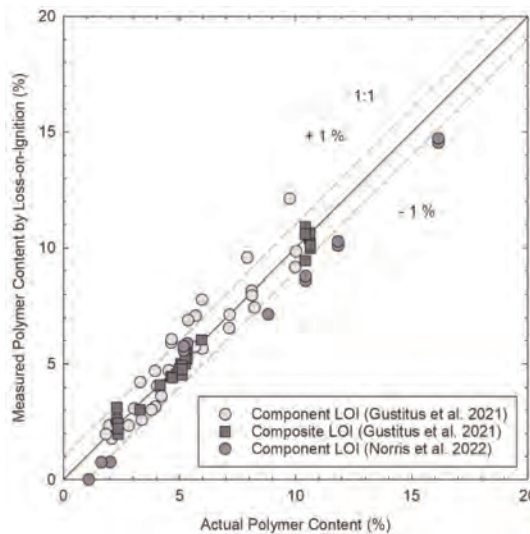
Figure 1.   Measured polymer contents using loss-on-ignition analysis versus actual polymer contents of enhanced bentonites.
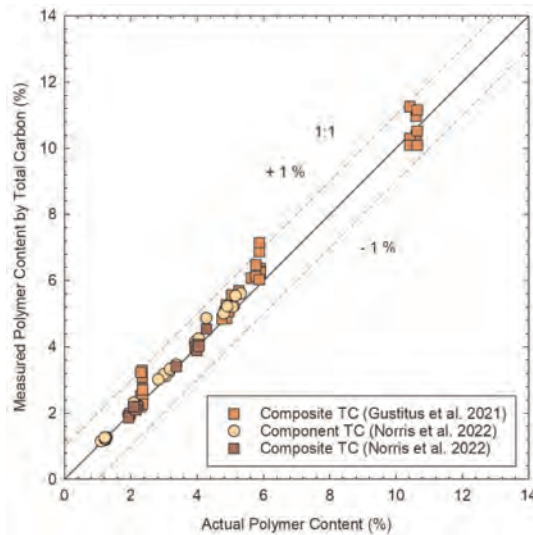
Figure 2. Residual polymer contents (actual minus measured) versus actual polymer contents of enhanced bentonites.

Table 1. Summary of residual polymer contents (= actual – measured) from Gustitus *et al.* (2021) and Norris *et al.* (2022).

Method	Loss-on-Ignition (LOI)		Total Carbon (TC)	
	Component	Composite	Component	Composite
Number of measurements	44	36	30	48
Mean residual polymer content (%)	–0.19	–0.12	0.13	0.26
Standard deviation of residual polymer contents (%)	1.1	0.33	0.14	0.37
95 % confidence interval of residual polymer contents (%)	0.3	0.11	0.05	0.11

polymer content by up 2.6 %, regardless of specimen mass or polymer type, with a residual standard deviation of 1.1 %. The results from the composite LOI method performed were better than those for the component method, but both methods underestimated polymer content by up to 1.0 % and overestimated polymer content by up to 0.8 %, with a residual standard deviation of 0.3 %. The underprediction or overprediction of actual polymer loading versus measured polymer loading of component LOI testing varied depending on the sample tested and the polymer loading.

Gustitus *et al.* (2021) found that polymer quantification via the component LOI method was inaccurate due to changes in the thermal degradation of the polymers tested in a bentonite-polymer mixture. The degree of accuracy of the application of the individually measured polymer loss to the mass loss of the polymer in a bentonite-polymer mixture was shown to depend on the types of thermal degradation reactions the polymer underwent during ignition (endothermic and/or exothermic), which were analyzed via thermogravimetric analysis (TGA) and differential scanning calorimetry (see Gustitus *et al.* 2021). Although TGA is not analogous to LOI (TGA involves ignition under argon, a nonoxidizing environment, whereas LOI involves ignition in a muffle furnace, an oxidizing environment), Gustitus *et al.* (2021) provided

evidence that the difference in masses remaining between polymers heated individually versus polymers heated in bentonite mixtures produced a source of bias that could over- or under-estimate the final polymer content in non-hydrated BPC.

3 TOTAL CARBON ANALYSIS

3.1 *Total carbon analyses methods*

Polymer quantification using the component TC procedure uses known quantities of polymer enhancements and the base bentonite to develop a known TC for each individual component of the enhanced bentonite (Gustitus *et al.* 2021; Norris at al. 2022). A known mass of a specimen of sodium bentonite, enhanced bentonite, or polymer is oven-dried in a ceramic crucible at 110 °C until no further loss in mass is measured. Specimens then are combusted in a calibrated TC analyzer (induction furnace). For component TC analysis, r_p is determined as follows:

$$r_p = (TC_{eb} - TC_b)/(TC_p - TC_b) \qquad (5)$$

where TC_{eb} = measured fraction of total carbon for enhanced bentonite, TC_b = baseline measured fraction of total carbon for sodium bentonite, and TC_p = baseline, measured percent total carbon for polymer. The calculation for r_p is based on the summation of r_b and r_p equal to unity (Equation 3).

As with the composite LOI, the composite TC analysis is conducted by measuring the total carbon of mixtures of sodium bentonite and polymer at known polymer loadings to develop a calibration curve. The developed calibration curve is specific to a given enhanced bentonite.

3.2 *Review of total carbon analyses results*

The resulting measured polymer contents using the composite TC method from Gustitus *et al.* (2021) and both component and composite TC methods from Norris *et al.* (2022) are shown versus the actual polymer contents in Figure 3. Residual polymer contents, calculated

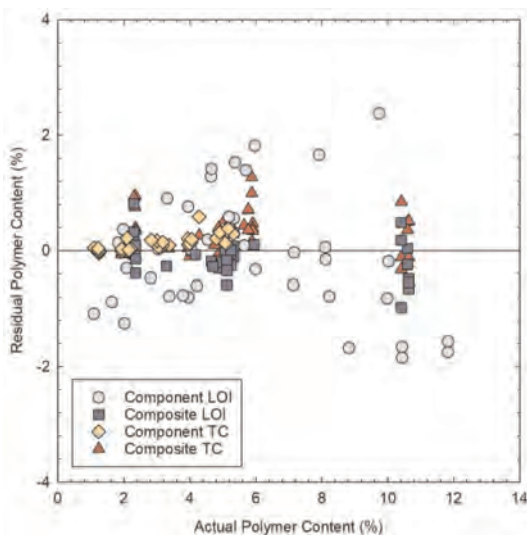Figure 3.   Measured polymer contents using total carbon versus actual polymer contents of enhanced bentonites.

as the difference between actual and calculated polymer contents in terms of percent dry mass of enhanced bentonite, are shown versus actual polymer content in Figure 2 and summarized in Table 1. Comparison of the results in Figures 1 and 3 indicates that polymer quantification by TC provided more accurate prediction of polymer content than by LOI. The composite TC method both underestimated the actual polymer content by up to 1.3 % and overestimated the actual polymer content by up to 0.5 %, with a residual standard deviation of 0.4 %. Unlike the results for polymer quantification by LOI, the component TC method resulted in lower residual polymer contents. The component TC method resulted in underestimation of actual polymer content by up to 0.6 % and overestimation of actual polymer content by less than 0.1 %. Component TC yielded the lowest residual standard deviation of 0.1 %. These results illustrate that, for the materials evaluated in this study, the TC method provided a more accurate method of measuring polymer content of the enhanced bentonites than did the LOI method.

4 CONCLUSIONS AND RECOMMENDATIONS

Measurement of accurate polymer contents is essential for QA/QC of manufactured EB-GCLs. Based on the results of tests conducted by Gustitus *et al.* (2021) and Norris *et al.* (2022), the following recommendations are made. For polymer quantification of non-hydrated enhanced bentonites or EB-GCLs (i.e., initial polymer content), the component TC procedure provided more accurate results. This method requires known TC masses of both polymer and bentonite components. The TC method also can be used solely for QA/QC based on a product-specified TC threshold value representing a minimum polymer content or matching an as-tested product.

REFERENCES

ASTM International. 2013. *Standard Test Methods for Loss on Ignition (LOI) of Solid Combustion Residues*. ASTM D7348-13 (2013). West Conshohocken, PA.

ASTM International. 2017. *Standard Test Methods for Determination of Total, Combustible and Carbonate Carbon in Solid Residues From Coal and Coke*. ASTM D6316-17 (2017). West Conshohocken, PA.

Chen, J., Salihoglu, J., Benson, C., Likos, W., & Edil, T. 2019. Hydraulic Conductivity of Polymer-bentonite Composite Geosynthetic Clay Liners Permeated with Coal Combustion Product Leachate. *Journal of Geotechnical & Geoenvironmental Engineering* Vol. 145, Issue 9 DOI: 10.1061/(ASCE)GT.1943-5606.0002105.

Gustitus, S., Nguyen, D. Chen, J., & Benson, C. 2021. Quantifying Polymer Loading in Polymer-Bentonite Composites using Loss on Ignition and Total Carbon Analyses. *Geotechnical Testing Journal* Vol. 44, Issue 5 DOI: 10.1520/GTJ20200007.

Norris, A., Scalia, J., & Shackelford, C. 2022. Polymer Quantification Methods for Geosynthetic Clay Liners Enhanced with Anionic Polymers. *Geotechnical Testing Journal* Vol. 25, Issue 2 DOI: 10.1520/GTJ20210134.

Scalia, J., Benson, C., Bohnhoff, G., Edil, T., & Shackelford, C. 2014. Long-term Hydraulic Conductivity of Bentonite-polymer Composite Permeated with Aggressive Inorganic Solutions. *Journal of Geotechnical & Geoenvironmental Engineering* Vol.140, Issue 3 DOI: 10.1061/(ASCE)GT.1943-5606.0001040.

Scalia, J., Bohnhoff, C., Shackelford, C., Benson, C., Sample-Lord, K., Malusis, M., & Likos, W. 2018. Enhanced Bentonites for Containment of Inorganic Wastes by GCL. *Geosynthetics International* Vol. 25, Issue 4 DOI: 10.1680/jgein.18.00024.

Tian, K., Benson, C., & Likos, W. 2016a. Hydraulic Conductivity of Geosynthetic Clay Liners to Low-Level Radioactive Waste Leachate. *Journal of Geotechnical & Geoenvironmental Engineering* Vol. 142, Issue 8 DOI: 10.1061/(ASCE)GT.1943-5606.0001495.

Tian, K., Likos, W., & Benson, C. 2016b. Pore-scale Imaging of Polymer-modified Bentonite in Saline Solutions. *In Geo-Chicago 2016: Sustainable Geoenvironmental Systems*, edited byDe, A., Reddy, K., Yesiller, N., Zekkos, D., and Farid, A, Reston, VA: American Society of Civil Engineers.

User guide of design standards for geosynthetics in landfills applications

A. Hérault*
Freudenberg Performance Materials, France

Ph. Delmas*
Chairman of French Standardisation Committee on Geosynthetics, France

ABSTRACT: Geotextiles and geotextile-related products are used in several applications in landfills, particularly for drainage, filtration and reinforcement functions. This paper describes the bottom and side slope applications of waste storage cells as well as capping applications including veneer soil gripping over the slopes. Needed design parameters, to be defined with the project owner, are listed to help designers. Specifications are given to help in establishing relevant requirements in the tender phase. The described specification and product approval processes are based as much as possible on design values to promote competition, product-specific reduction coefficients making the link with characteristic values of the performances. The manuscript provides as well details on test conditions which have to be taken care of by the tender officer.

1 INTRODUCTION

Geosynthetics are construction products covering a large scope of applications in many types of structures. Therefore, they are used by a very large number of end-users and designers who can't be experts in geosynthetics and need help particularly in the case of highly technical applications, sometimes in the context of sensitive projects, especially for human or environmental safety. On top of that, a wide range of materials structures are available on the geosynthetics market to ensure the same function. That's why, when they are faced to new/innovative type of construction materials like geosynthetics, a lack of knowledge leads engineers to be very fearful in the use of alternative solutions and products which don't fulfill initial specifications at 100%. Moreover, in many cases, specifications are a copy paste of a technical data sheet in which all properties are not relevant for the given application, therefore, this prevents free competition without any technical reason. This is neither a win-win situation for the end user nor for the contractor. The information of geosynthetics market players is necessary to open as much as possible the door to all solutions that work well. More familiar users of geosynthetics with a little bit deeper knowledge are indeed more flexible and open to alternative solutions because they are able to understand appropriate designs when available and to skip variations in non-essential product properties.

To help the users of geosynthetics confronted to the complexity linked to the number of existing standards, recommendations and/or guideline, in the design procedure of their structure, the French IGS chapter (Comité Français des Géosynthétiques) has decided to

---

*Corresponding Authors: alain.herault@freudenberg-pm.com and philippe.delmas589@orange.fr

write a series of dedicated fascicles. The goal of these "user guides" is to define the required justifications, including the relevant assumptions and properties to be considered in the design of structures using geosynthetics, in accordance with French and European existing documents and precise the relevant design procedure.

This paper presents a synthesis of the first thematic fascicle for applications of geotextiles and geotextile related products in landfills, which was published in 2021 together with a preliminary fascicle common to all structures using geosynthetics.

2 APPLICATIONS AND REQUIREMENTS

Geotextiles and geotextile-related products are involved with different functions in different construction stages of landfills (Figure 1):

— At the base and on side slopes of the cell for protection, leakage detection and/or leachate drainage, and reinforcement in the case of piggybacking,
— On capping for protection, drainage/filtration of seepage water, biogas and as veneer reinforcement.
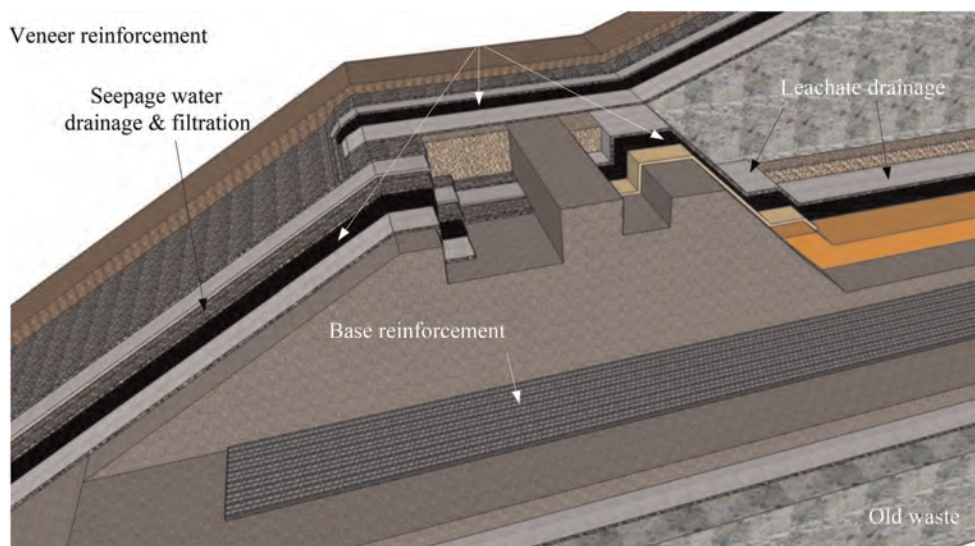
Figure 1.   Applications covered by French design standards.

2.1 *Base and side slopes of the cell*

At the base and on side slopes of the cell, protection of the foundation soil, groundwater and surface water is ensured by a geological barrier known as a "passive safety barrier" consisting of soil layers fulfilling the following criteria:

— At the base of the cell (slope $< 14\%$), from top to bottom, a clay layer with permeability less than or equal to 10^{-9} m/s over at least 1 m thick and a soil layer with permeability less than or equal to 10^{-6} m/s over at least 5 m thick,
— On the side slopes (slope $> 14\%$), a clay layer with permeability less than or equal to 10^{-9} m/s over at least 1 m thick.

At the base of the cell, the geomembrane is in contact with the clay and covered with a granular drainage layer minimum 0.50 m thick with a permeability greater than or equal to 10^{-4} m/s. This drainage layer may, with the agreement of the authorities, be replaced by a hydraulically equivalent leachate collection and drainage system that combines a drainage geocomposite, a puncture resistant geotextile and a layer of granular material of reduced thickness ensuring the required protection function. In some cases, the puncture resistant geotextile can be combined with the drainage geocomposite, always taking care that the protection of the geomembrane is ensured. This drainage layer has to be resistant to mechanical, thermal and chemical stresses throughout the entire time of filling operation, post-operational period and aftercare period. Hydraulic justification of the alternative system by equivalency is described in the French design standard NF G38-061 (AFNOR 2017).

On the side slopes, the geomembrane is covered with protection geotextile and possibly drainage composite or any equivalent system over the entire height.

2.2 *Capping*

The French ministerial decree of 15 February 2016 regarding the landfill of non-hazardous waste specifies that no later than two years after the end of filling operations, any cell shall be covered with a final cover that may include geosynthetics. According to this ministerial decree, this final cover shall consist of the following layers, from the bottom to the top:

— geomembrane;
— seepage drainage layer consisting of either granular material with protective and filtration geotextiles or a geocomposite;
— veneer soil layer.

For waste subject to biodegradation, it is necessary to provide a drainage and gas collection system, its design is not described in this fascicule since it is not yet covered by a design standard.

In the case of sealing by geosynthetics, the design has to consider several failure mechanisms on the slopes. They are all described in this user guide.

2.2.1 *Sliding of the veneer soil layer*

In order to prevent internal or external shearing of the cover soil layer, the project slope angle shall be consistent with the shear characteristics of the cover material, whatever the reinforcement product considered, with or without a three-dimensional structure. Three-dimensional structures ensure the external sliding stability only, at the base of the layer, sometimes confine the layer, but in all cases, the cover soil will come back to its natural slope angle when this one is lower than the project slope angle. The French IGS chapter's guidelines for the use of geosynthetics in erosion control (Comité Français des Géosynthétiques 2003) specify on page 48 (§II.3) the stability level (internal shear) that can be expected for topsoil.

A buildup of water pressure on the base of the cover soil layer due to a lack of drainage, or a design considering a water level in the cover soil, can lead to the cover soil sliding. When needed, it must be taken into account in the design by considering an effective stress that reduces the shear resistance, and by taking into account the destabilizing forces of the flow.

2.2.2 *Tensile break of a geosynthetic*

The tensile stress of the geosynthetic with the highest modulus in the covering structure depends on the slope geometry, dead loads, live loads, and the smoothest interface friction angle. In order to prevent stresses in the geomembrane, the interface with the lowest friction angle, which will be considered in the design, should be located above the geomembrane.

2.2.3 *Anchorage failure*

The geometry of the cover slopes of landfills has to take into account the limitations related to the installation and the stabilization of the cover layer. Particular attention must be paid to the required anchorage at the top of the slope: designer has particularly to check that the available space allows the construction of a suitable anchorage trench, designed in accordance with the French design standard NF G38-067 (AFNOR 2017), while limiting the depth of the trench to comply with the regulations on the maximum depth of the trench admissible without shoring (art. R. 4534-24 of the French Labour Code). This is particularly needed to define the intermediate berm geometry, which should be wide enough to allow the traffic of construction machinery and to anchor the reinforcing geosynthetic of the downstream slope, and therefore prevent lifting of the reinforcing layer.

After warning on some wrong application of design standards, the user guide makes some suggestions to solve anchorage issues on berms.

3   PHASES OF DESIGN AND TENDER

National and European regulations are described in a preliminary fascicle of the user guide that is common to all applications of geotextiles and geotextile-related products. The document reminds in particular the criteria and principles of the Eurocodes such as consequences classes, design working life, geotechnical categories, limit states and combinations of actions, partial factors on actions and reduction coefficients over materials performances. The user guide sets as the target of the design and specification process the definition of the calculation assumptions and the required long-term performance(s) ensuring the proper functionality of the structure until the end of its design working life.

Then, in the tender submission phase, the submitted product performances have to be justified by the manufacturer: long-term performance specification allows each supplier to select the right product in its product portfolio, taking into account its specific reduction coefficients. These reduction coefficients are applied to the short term product performance, while respecting, when relevant, the specific test conditions as defined in some test standards and reminded in this user guide of design standards. These reduction coefficients are a way to take into account durability requirements by checking long term performances of the geosynthetic due to chemical environment, installation damage and tensile creep behavior for the reinforcement products, compressive creep behavior for drainage geocomposites, including filter fleece intrusion in the drainage core.

4   SPECIFICATIONS RESULTING FROM A DESIGN AND RELATED JUSTIFICATIONS

4.1   *Drainage on the base (slope <14%) and side slopes (slope ≥ 14%)*

At the base of the cell, drainage is usually provided by a drainage layer of granular material with a thickness of 0.50 m and a permeability of 10^{-4} m/s. Alternative solution consists in a layer at least 0.30 m thick of the same granular material to ensure the filtration and protection of the underlying geomembrane from the waste, with a drainage geocomposite on the underside that is hydraulically equivalent to the 0.20 m of replaced granular material. Multi-layer geosynthetic system provides as well the needed protection efficiency. On the other hand, the drainage function is often secondary on the sides of cells where the protection function is predominant.

Below are listed for the drainage function the design performances to be specified in the tender texts and to be justified by the contractor and his suppliers.

4.1.1 *Leachate drainage on the base and side slopes*

For the base, the user guide recommends to specify a design water flow capacity higher or equal to the discharge flow capacity of 0.20 m of granular material with a permeability of 10^{-4} m/s. A safety factor of 1.10 has to be applied on the discharge capacity of the geocomposite for leachate drainage. The compressive stress to be considered is calculated with the height of the waste plus the 0.30 m layer of protective drainage material. The hydraulic gradient is given by the slope of the substrate. On the side slopes, the proposed design flow rate is higher than or equal to the discharge flow capacity of 0.50 m of granular material with a permeability of 10^{-4} m/s. These flow rates shall be specified by stating the type of boundary conditions to be applied to measure the performance of the drainage composite, i.e. for this application, rigid plate to simulate a rigid geomembrane on one side and a standardized foam layer according to EN ISO 12958 to simulate a soil layer on the other side.

4.1.2 *Tensile strength and elongation*

They have to be consistent with the installation conditions.

4.1.3 *Durability*

Refer to EN 13252 Annex B for the maximum allowable time of UV exposure and predicted minimal durability. When applicable, indicate the time of extended exposure to weathering and UV or the expected exposure (kLy), together with the required residual tensile strength at the end of the exposure period. A specific study will then be needed to justify the allowable exposure time of the product. The polymers used have to be suitable for usual basic environment (pH > 9) of leachate.

4.2 *Drainage on flat slopes of capping (slope <14%)*

On the flat slopes of capping, four hydraulic design options are suggested:

- usual 0.50 m thick granular drainage layer with a permeability of 10^{-4} m/s can be replaced by a drainage geocomposite which is hydraulically equivalent,
- or consider input flow rate in the drainage composite based on permeability of the topsoil layer,
- or based on volume of rainfall actually reaching the drainage system as a function of the duration of the rainfall event, by considering e.g. a decennial rainfall occurrence, and the slope-dependent infiltration rate,
- last option, the most conservative one which leads to add intermediate collector drains, considers design flow rate based on a decennial rainfall occurrence and a rain duration of one hour with a 50% infiltration rate. The rainfall intensity is determined using the Montana formula, the local coefficients of which can be obtained from the national meteorological authorities. In order to take into account a rainfall event of an exceptional nature, it is proposed to consider a coefficient of 1.5 on the rainfall calculated from Montana's coefficients a and b.

Below are listed for the drainage function the design performances to be specified in the tender texts and to be justified by the contractor and his suppliers.

4.2.1 *Drainage of seepage water on flat slopes*

The design flow rate will be specified with the actual compressive stress of the project and the hydraulic gradient based on the slope angle, preferably without water level in the cover layer. This flow rate shall be specified by stating the type of boundary conditions to be applied to measure the performance of the drainage composite, i.e. for this application, usually rigid plate to simulate a rigid geomembrane on one side and a standardized foam layer according

to EN ISO 12958 to simulate a topsoil layer on the other side. Inappropriate test conditions can lead to major deviations between actual product performances and test results (Touze *et al.* 2014). Due to the new performance test standard EN ISO 12958-2:2020, new boundary conditions provided by project-specific soil layer or standardized sand layer are now available for design performances assessment. The consequences of sand layer boundary conditions over drainage geocomposites performances can vary from one product to another (Stoltz *et al.* 2016).

4.2.2 *Tensile strength and elongation*
They have to be consistent with the installation conditions.

4.2.3 *Durability*
Refer to EN 13252 Annex B for the maximum allowable time of UV exposure and predicted minimal durability, special care has to be taken to determine the time of ultraviolet exposure prior to re-covering.

4.3 *Veneer reinforcement and seepage water drainage on slopes (slope $\geq$ 14%)*

Below are listed for each function the design performances to be specified in the tender texts and to be justified by the contractor and his suppliers.

4.3.1 *Veneer reinforcement*
Design value of the maximum tensile stress in the geosynthetic in accordance with the French design standard NF G38-067 (AFNOR 2017) and post-construction elongation limited to 3% max. between the 10h and design working life isochronous curves. The tensile stress has to be specified together with an assumption on the considered friction angle for the smoothest multi-layer watertight system interface.

4.3.2 *Seepage water drainage*
Similar to §4.2 with the appropriate runoff ratio according to NF G38-061 annex B (AFNOR 2017).

4.4 *Base reinforcement (Piggybacking)*

In order to simulate potential excessive subsidence of the old waste due to the cell extension, a nominal cylindrical subsidence diameter of 1 to 2 m is suggested by the user guide with a maximum elongation of the reinforcement geosynthetic of 3% in the long term to prevent damage of the HDPE geomembrane functionality.

Below are listed the design performances to be specified in the tender texts and to be justified by the contractor and his suppliers.

4.4.1 *Reinforcement*
Design value of the tensile stress at 3% long-term elongation. At the justification stage, it is calculated from the isochronous curve corresponding to the design working life, and the characteristic short-term tensile strength affected by reduction coefficients related to installation damage and durability. The design temperature depends on the cell filling operation conditions and the stored materials.

4.4.2 *Durability*
Refer to EN 13252 Annex B for the maximum allowable time of UV exposure and predicted minimal durability. When applicable, indicate the time of extended exposure to weathering and UV or the expected exposure (kLy), together with the required residual tensile strength

at the end of the exposure period. A specific study will then be needed to justify the allowable exposure time of the product.

5 CONCLUSION

This paper has presented the first thematic fascicle of a series of fascicles under preparation and under publication by the French IGS chapter, devoted to help the users of geosynthetics confronted to the complexity linked to the number of existing standards, recommendations and/or guideline, for the design of their structure. Dealing with the applications of geotextiles and geotextile related products in landfills, this paper shows how to define the required justifications, including the relevant assumptions and properties to be considered in the design of structures using geosynthetics, thus in accordance with French and European existing documents and precising the relevant design procedure.

ACKNOWLEDGMENTS

REFERENCES

AFNOR 2017. NF G38-061 Use of Geotextiles and Geotextiles related Products – Drainage and Filtration Systems – *Justification of Dimensioning and Design Elements*.
AFNOR 2017. NF G38-067 Geosynthetics, Geotextiles and Related Products – Stabilization of a Thin Layer of Soil on Slope – *Justification of Dimensioning and Design Elements*.
Comité Français des Géosynthétiques 2003. *Recommandations Pour l'Utilisation des Géosynthétiques dans la Lutte contre l'Erosion*.
EN ISO 12958 2010. Geotextiles and Geotextile-related Products – Determination of Water Flow Capacity in Their Plane.
EN 13252 2017. Geotextiles and Geotextile Related Products – *Characteristics Required for Use in Drainage Systems*.
Stoltz, G. & Hérault, A. 2016. Long Term Filter Intrusion Phenomenon in Several Types of Drainage Structures. *Proceedings of the 6th Geosynthetics Congress, Ljubljana*: 575–583.
Touze N., Hérault, A., Stoltz, G. 2014. Evaluation of the Decrease in Long Term Water Flow Capacity of Geocomposites due to Filter Intrusion. *Proceedings of the 7th International Congress on environmental geotechnics, Melbourne*: 321–329.

Advanced application of bituminous geomembrane (BGM) for waste capping in Australia

P. Kendall*
National Business Engineer, Axter Australia Pty, Australia

R. McIlwraith*
Director, Axter Australia Pty, Australia

ABSTRACT: A cap is an engineered impermeable barrier designed to cover the top of contaminated waste and prevent precipitation leaching from the waste and into the environment. In landfills, the cap also serves to control gas emissions from the waste. Materials used in a cap must not only survive aggressive installation conditions, but they must also be resilient to the deteriorating effects of long service life and environmental exposure. Bituminous geomembranes (BGMs) have been proposed by various authors as a material well suited to perform the barrier function of a cap in both exposed and unexposed conditions. In Australia, the application of BGMs for capping contaminated waste is growing rapidly. This paper describes three recent successful capping projects designed using a BGM barrier including one mining application and two landfill applications. For each project, the technical background of the site is explained and the important factors of the capping design and installation are described. The examples presented will give designers greater confidence in the use of a BGM as a cap in new and technically challenging applications.

1   INTRODUCTION

1.1   *Waste capping systems*

A waste capping system can have various design features but its primary function is to serve as a barrier to isolate waste from environmental exposure. By restricting the migration of liquid, solid, or gaseous mass into or out of the waste body, the liner plays the critical role of encapsulation. While the focus of this paper is on the liner, the capping system must safely manage the drainage of precipitation onto the barrier and expulsion of gas that may be generated within the waste. Compacted clay, geosynthetic clay liners, polymeric geomembranes, and engineered soil phytocaps are all examples of materials which have been used as hydraulic barriers in waste capping systems.

A wholistic evaluation of liner alternatives, which can include the use of Multi-Criteria Assessments (MCAs), works to optimize the technical, environmental, and economic outcomes of a capping system designs (Paulson 2018). Bituminous geomembranes have gained favor in this wholistic design approach due to their combination of physical properties as well as innovations in safe and measurably controlled electrical hot-air welding installation methods.

---

*Corresponding Authors: pkendall@axter.com.au and RMcIlwraith@axter.com.au

1.2 Bituminous geomembrane for waste capping systems

1.2.1 Composition of BGM

BGMs have multiple components. The crucial components are the bitumen for is hydraulic properties and the geotextile for mechanical properties. The features of the bitumen and geotextile can be controlled for desirable properties. A common configuration of a BGM is shown in Figure 1 which features a needle punched continuous filament non-woven polyester geotextile and Styrene-Butadiene-Styrene (SBS) modified bitumen. The geotextile is fully impregnated with bitumen in the manufacturing process and additional bitumen coats the geotextile. The mass and mechanical properties of the geotextile can vary depending on the grade. Additional elements can be incorporated into the structure of the BGM. These elements include an anti-perforation root barrier film, a glass fiber fleece, and a sand or other mineral surface coating. A removable film can be manufactured as an alternative to the anti-perforation film. The removeable film is removed during installation to reveal a tacky bitumen layer which provides higher frictional properties for installation on steep slopes.
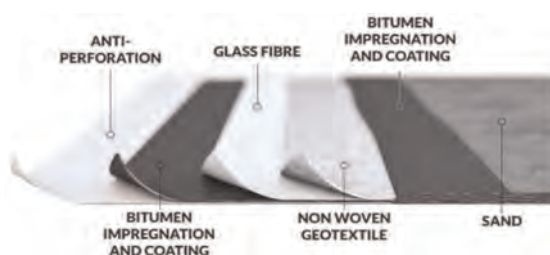

Figure 1. Diagram of a typical BGM composition.

1.2.2 Material properties

Different grades of BGM can be manufactured by varying the reinforcement geotextile and the amount of bitumen incorporated into the liner. In this manner, thickness and mechanical properties can be controlled. Intrinsic properties of the BGM can be identified and measured. The properties outlined in Table 1 describe some of the unique generally applicable properties of BGMs which result in various aspects of their design functionality.

The properties described in Table 1 translate to useful functional features of BGMs. The following is an overview of some of those features:

1.2.2.1 Virtually no thermal wrinkling

BGMs experience virtually no thermal wrinkling due to an extremely low coefficient of thermal expansion (Peggs 2008). Wrinkling of geomembranes can be problematic for installers as well as designers. Many other geomembrane materials such as polyethylene are

Table 1. Typical intrinsic properties of bituminous geomembranes.

Property	Standard	Units	Value
Coefficient of Thermal Expansion	ASTM D 1204-02	$°C^{-1}$	1E-05
Density	ASTM D 792-20	g/cm^3	1.27
Elongation at Break	ASTM D 7275	%	>60
Friction Angle (sand side)	NF EN 495-2	°	39.5
Cold Bending - Lowest Temperature	ASTM D 746	°C	−20
Water permeability	ASTM E 96	m/s	$< 6.10^{-14}$
Gas permeability methane transmission rate	ASTM D 1434-82	$m^3/(m^2.d.atm)$	$< 2.10^{-4}$

known to contract and expand dramatically with temperature. This can lead to extensive wrinkling during day and tensile strain at night if the liner is not covered immediately. Wrinkles prevent intimate contact between the liner and the subgrade which reduce its effectiveness as a barrier (Rowe 1998).

1.2.2.2 Extreme heat or cold exposure
BGMs have been installed in the extreme cold of Northern Canada and Siberia as well as the dry heat of the Australian Pilbara region and Chile's Atacama Desert.

1.2.2.3 Steep slope angles
Steep slope capability allows for more versatile design options and potentially more waste storage volume per unit area of cap. The BGM can be made with a peel off siliconized release paper which reveals a very tacky, high friction angle underside. Higher friction prevents sliding and allows cover soils to be placed at steeper angles. Angles as steep as 1:1.3 have been installed in Australia.

1.2.2.4 High wind resistance
Wind is an important consideration for both designers and installers. The weight of the liner is critical to resist wind uplift (Giroud 1995). BGMs are very dense and heavy with a specific gravity of 1.2 and a thickness of up to 5.6mm. The high weight allows for a safer installation in higher wind conditions and less need for temporary ballasting. For designers, the weight of the BGM is a positive factor to counter wind uplift suction forces.

1.2.2.5 High puncture resistance
BGMs are reinforced geomembranes with a strong polyester continuous filament geotextile imbedded within the liner. The geotextile, combined with the protective bitumen, is very resistant to puncture and abrasion. This makes the material well suited to accommodate the installation process as well as aggressive interfacing materials such an angular drainage aggregate (Blond 2014).

1.2.2.6 Single-layer construction
Unlike other polymeric geomembranes, BGMs do not suffer from the phenomena known as stress cracking. This is due to the geotextile and bitumen composition of the geomembrane. This allows a BGM to interface with aggressive soils and aggregates without the need of additional protection geotextiles. Lab tests have shown that a BGM can withstand extreme pressure over large stones without puncturing (Blond 2014).

1.2.2.7 Storage and installation in a wide range of weather conditions
A BGM can be installed in light rain and damp conditions. Prior to welding, the seams should be dry. A 200mm self-release protection strip, which keeps the seam dry and clean, should be removed prior to welding. The rolls can also be securely stored on site without risk of moisture or UV damage.

1.2.2.8 Strong seams
The BGM is installed with 200mm overlaps and heat welded seams. The weld fuses the bitumen together to form a strong hydraulically sealed barrier. Weld strength can be tested on site or sent to an independent third-party lab.

1.2.2.9 Bond with PE, concrete, and many other materials
Capping applications often interface with a wide variety of infrastructure elements such as concrete spillways, concrete pipe connections, older membrane installations, steel pipe connections and various other structures. Porous materials such as concrete are first coated with a bituminous primer to optimize direct welding to the concrete. For connections to polymer pipes, a bituminous mastic can be applied cold to seal around the pipe and a clamp can secure the BGM to the pipe. To bond to other types of geomembranes, self-adhesive bituminous strips of 0.5m or 1.0m width can be cold bonded to the geomembrane. The BGM can then be welded to the bituminous strip.

2 BGM CAPPING SYSTEMS FOR MINE WASTE IN AUSTRALIA

2.1 Mineral sands mine, Western Australia

2.1.1 Site background

A mining site in Western Australia processed mineral rich sand for over 40 years. Among the valuable minerals extracted from the sand are ilmenite, titanium dioxide, leucoxene, synthetic rutile, zircon, and various rare earth minerals. Mining of mineral sands produces a waste byproduct of a sandy composition. The sand is generally free draining and free of any large aggregate particles. After the processing and mineral extraction, this waste containing acid effluent, neutralized acid effluent, non-magnetic fines, char and iron concentrate can leach contaminants if precipitation is allowed to infiltrate the waste. An impermeable cap shown in Figure 2 was designed to function as the primary mechanism to prevent generation and mobilization of leachate and therefore no basal liner system was incorporated.

Figure 2.   Schematic of mineral sand waste capping solution.

The aggregate-free, processed sand is a forgiving material to serve as a subgrade for the cap liner. The sand waste stockpile was designed with mild slopes of 9° to 14°. The lengths of the slopes were as up to approximately 50m. The site location mean daytime temperatures range from 31°C in February to 17°C in July with an annual average rainfall of 640mm, most of which occurs in the summer months of December to March.

2.1.2 Capping solution

A 500mm cover layer was approved as the favorable system for developing a grassy-herbaceous plant cover for surface erosion control. The 500mm sand cover layer is designed to suffice for 10 years. This 10 year period is the estimated time to complete the full mine waste remediation works and final closure of the facility. The soft sandy interfacing materials combined with the rapid covering of the BGM allowed for a lighter grade of BGM to be used. The liner used was called SC1 with an average thickness of 2.2mm and a reinforcing geotextile of 250gsm. The selection of a thin liner with heavier reinforcement allowed for relatively larger roll dimensions of 5.1m × 140m. Longer rolls are beneficial to installation, particularly on the slopes where transverse welds are not permitted.

The 500mm site won sand layer was designed with 90% maximum dry density compaction. The sand was installed using a GPS assisted D6 Dozer. The dozer traveled along a platform of sand and pushed new stockpiles of sand over the liner. The GPS controlled dozer blade ensured the specified 500mm sand thickness and the dozer weight provided the compaction effort. A construction photo can be seen in Figure 3.
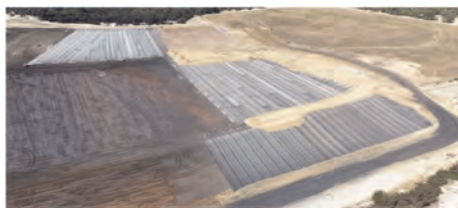

Figure 3.   Aerial image of site during construction.

3 BGM CAPPING SYSTEMS FOR LANDFILL AND MUNICIPLE WASTE

3.1 *Hervey range landfill, Queensland*

3.1.1 *Site background*

A municipal landfill presents a wide variety of dynamic phenomena to account for including stormwater runoff and gas collection to name a few. The material properties if a BGM can be taken advantage of for use on a municipal landfill cap, if the design can overcome the unique restrictions of that type of environment including:

- The BGM must bond to an existing capping system and integrate with various concrete and polymeric components of the landfill.
- The installation of the BGM must be done safely in the potential presence of flammable methane gas.

The site location mean daytime temperatures range from 30°C in February to 10°C in July with a mean annual rainfall of 1019mm.

This landfill was constructed with a regular progression of intermediate waste compartments known as cells. As more waste is deposited into a landfill cell, the cell will eventually reach capacity. At this point, a cap is installed, and a new cell is built to accumulate new waste adjacent to the previous cell. An outline of this cap design is shown in Figure 4. Critical to this sequence is the ability to hydraulicly seal the capping of the new cell to the previous cell. In this case the previous cell was capped with a textured coated Geosynthetic Clay Liner.
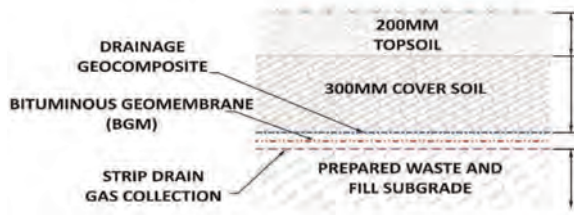

Figure 4.   Schematic of Hervey Range Landfill BGM Cap.

3.1.2 *Capping solution*

One of the motivations for using a BGM on this landfill cap was the ability to bond the liner with an existing capping liner from a previous cap installation in what is known as a piggyback installation. A BGM can be bonded to other membrane materials using a tacky adhesive bitumen strip. The strips used on this site measured 1.0m × 10m. The adhesive strip has a siliconized film which is removed to reveal the tacky bitumen side. The tacky side was bonded to the clean textured polyethylene coated side of a Geosynthetic Clay Liner. A weighted steel roller was used to apply pressure to bond the strip in ambient temperatures. Once the bituminous strip is bonded, the BGM can then be welded to the strip using BGM welding techniques.

The concept of using BGMs in landfill caps, which can have flammable methane gas present, required new developments in welding methods. The conventional gas torch welding methods can pose a risk of fire or explosion if methane gas is detected. Electrically powered hot air welders represent an existing technology which has been in use in the roofing industry for many years. Welding trials at the BGM factory and on replicated local site conditions revealed that these machines could achieve the same or improved performance of conventional torch welding. The use of these welders presents a risk profile similar to wedge welders which have been used on landfill caps successfully for many years.

The schematic in Figure 4 illustrates the various components used in this landfill cap. The BGM served the barrier function. Underneath the BGM was a network of strip drains to collect and expel any gas derived from the waste. Above the BGM was a drainage geo-composite which covered the entire surface of the BGM.

The landfill had various structural protrusions which interfaced with the capping system including concrete and polymeric pipes. For each of these protrusions, there is a process for securing the liner mechanically and sealing it hydraulically. Concrete can be primed with a thin bituminous primer which penetrates the pores of the concrete. The BGM can then be welded directly to the primed surface using a handheld hot air welder if there is a risk of methane gas. A large stainless steel pipe clamp is then tensioned around the concrete pipe. Polymer pipes such as HDPE can be hydraulically sealed without heat by applying a bitumen mastic to a BGM sleeve. The sleeve can be welded to the primary liner and clamped to the pipe using a stainless steel clamp. This process is captured in Figures 5a and 5b.

Figure 5. a) BGM to concrete connection, b) BGM to polymer pipe connection, c) photo during construction d) photo of completed cap with vegetation.

4 BGM CAPPING FORSYSTEMS FOR INDUSTRIAL WASTE

4.1 *Industrial waste at undisclosed site location*

4.1.1 *Site background*

For over 50 years paper was manufactured at this undisclosed industrial site in Australia. The site consisted of 7 hectares of industrial buildings, 30 hectares of wastewater treatment ponds, and 28 hectares of on-site landfill. The site is intended to be remediated to a state suitable for development and public use. Adjacent to the site is a sensitive woodland with a protected koala population. As a result of the long and varied use of the site, many known contaminants have been detected and incorporated into the remediation process. These contaminants include per and polyfluroalkyl substances (PFAS), asbestos, metals, dioxins, polychlorinated biphenyls (PCBs), ash and coal wastes, paper wastes and fuel storage residues. A capping system is critical to prevent the mobilization of any residual contaminants remaining in the solid waste and to make the surface safe and suitable for future use. Due to decomposition of certain waste constituents, the liner was to be installed in the potential presence of methane gas and a gas collection system was incorporated into the capping system. A depiction of the capping system can be seen in Figure 6.
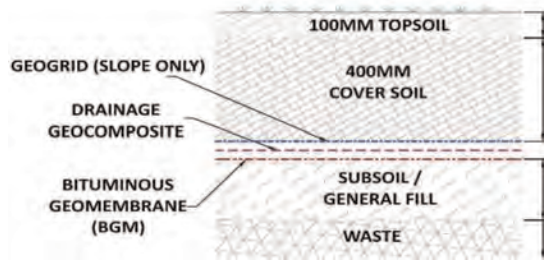
Figure 6.   Schematic of industrial waste site cap profile.

4.1.2 *Capping solution*

A multi-component cap was designed to encapsulate the wide range of waste constituents and account for gas generation. A heavy BGM installed with electrically powered hot air welders was designed to function as the barrier of the capping system. The heavy BGM provides a strong geotextile which provides greater protection against installation damage and a robust barrier for varied future use cases of the cap.

As Figure 6 indicates, a drainage geocomposite was installed above the liner to accumulate and direct stormwater runoff away from the waste body. The drainage geocomposite was composed of a geonet with nonwoven geotextiles on both sides.

For the areas of the cap with higher slope, a geogrid was used to help retain the 500mm of soil covering the cap.

5   CONCLUSION

The three distinct capping projects described above were installed between the years 2020 and 2023 and were designed by three separate engineering design consultants. This snapshot in time highlights the increased adoption of BGM capping systems in Australia. While BGM technology has been in exitance and in use for many decades, innovative installation methods like the hot-air welder have created new application areas for BGMs in caps. A wholistic evaluation of a capping system presents a design engineer with wide variety of barriers including compacted clay and polymeric liners. Consideration of the unique material properties of BGMs in such an evaluation has driven increased usage in waste capping systems in Australia.

REFERENCES

Blond, E. & Breul, B. 2014. Behavior of Bituminous Geomembranes under Elevated-Compression Stress. *Proceedings of Geosynthetics Mining Solutions*. September 8−11, 2014. Vancouver, Canada.

Giroud, J.P., Pelte T., & Bathurst, R.J., 1995. Uplift of Geomembranes by Wind. *Geosynthetics International*, IFAI, Roseville, MN, USA, Vol 2 No 6, pp 897–952.

Paulson, S. 2018. Multi-criteria Assessment of the Landfill Capping Profile, an Innovative Engineering Approach to Select Capping System. *Proceedings of the 11th International Conference on Geosynthetics*. 16–21 September 2018. Seoul, Korea.

Peggs, I.D. 2008. Prefabricated Bituminous Geomembrane: A candidate for Exposed Geomembrane Caps for Landfill Closures. *The First Pan American Geosynthetics Conference & Exhibition*. Cancun.

Rowe, R. K. 1998. Geosynthetics and the Minimization of Contaminant Migration Through Barrier Systems Beneath Solid Waste. *Proceedings of the 6th International Conference on Geosynthetics*, Atlanta, IFAI, St Paul, MN, Vol. 1, pp. 27–103.

Suction behavior of geosynthetic clay liners with polymerized bentonite

M.K. Khan, G.D. Emidio & A. Bezuijen
Laboratory of Geotechnics, Ghent University, Zwijnaarde, Belgium

G.D. Emidio
Pollux Consulting, Evergem, Belgium

ABSTRACT: Geosynthetic clay liners (GCLs) are widely used as a hydraulic barrier due to their low hydraulic conductivity. However, wet and dry cycles by diurnal and seasonal temperature changes and contact with electrolytes induce cracks and compression of the diffuse double layer. This hampers the efficiency of bentonite contained in the GCL. Under this situation, the polymerized bentonite (HYPER clay) has demonstrated better performance against cracking compared to untreated clay. One of the possible reasons for the enhanced efficiency might be the improvement in suction/water retention capacity. Thus, the suction characteristics of the HYPER and untreated clay GCLs were investigated. The paper presents the filter paper total suction test's results of GCLs, along drying and wetting paths, in the form of soil water retention curves and its comparison with the results of the water activity method. Distilled water and seawater were used as wetting solutions. The results showed a higher water retention capacity of HYPER clay GCLs compared to untreated clay. In short, the improved performance of HYPER clay GCLs under wet and dry cycles is partly due to enhanced suction characteristics.

1 INTRODUCTION

Geosynthetic clay liners (GCLs) are 5–10 mm thick and made of a layer of bentonite clay that is either adhered to a geomembrane or sandwiched between two sheets of geotextiles. According to the NF EN ISO 10318-1 standard (AFNOR 2015), a clay geosynthetic barrier is defined as a factory-assembled structure of geosynthetic materials in the form of a sheet in which the barrier function is essentially fulfilled by clay. GCLs experience a variety of environmental conditions throughout their lifespan, including heat gradients and wet-dry cycles. Take *et al.* (2015) demonstrated that the temperature of a GCL composite liner can climb up to 70°C due to daily thermal change when it was directly exposed to solar radiation, while the temperature in brine and solar ponds was even significantly higher, at 90°C (Rowe & Shoaib 2017; Yu & El-Zein 2019), which causes fissures to emerge and thus increases hydraulic conductivity. Furthermore, the influence of ionic solutions must be taken into consideration. The effects of the ionic solution on the GCLs' performance are observed to be more detrimental (Di Emidio *et al.* 2015). In essence, the type of solution and the initial prevention of cracks caused by heat gradients are crucial for the overall efficiency of GCLs.

Sodium carboxymethyl cellulose (Na-CMC) based HYPER clay (HC) GCL was used to study the effects of dry and wet cycles by De Camillis *et al.* (2017). After the fourth wet-dry cycle in seawater (SW), the authors discovered that the hydraulic conductivity of the HC GCLs was three orders of magnitude lower than that of normal GCLs. The changes in the

moisture content of GCLs signify an unsaturated condition. Under these circumstances, permeation is associated with the water retention curve, which is the relationship between suction and water content (WRCs). The increased water retention of HC is anticipated to be one of the factors contributing to its better performance against wet-dry cycles; thus, the study of water retention of GCLs is needed.

The composite structure and broad range of suction to be measured in the case of GCL make it challenging to quantify the water retention behavior. To measure this retention capacity, various approaches have been devised. The vast range of water retention behavior can be conveniently quantified using non-contact filter paper methods (Acikel *et al.* 2015, Risken *et al.* 2016). (Beddoe *et al.* 2010; Hanson *et al.* 2013) measured water retention curves by humidity or vapor evaporation technique, but the technique is time-consuming (Rouf *et al.* 2020). Additionally, approaches based on relative humidity are only considered reliable for the dry end of the water retention curve (Agus & Schanz 2007). Seiphoori *et al.* (2016) investigated GCL's water retention in free swell conditions using the dew point method. The technique was found to be quick and could measure suction at a range of 20 kPa to 110 MPa.

This paper presents insight into WRC of the polymerized HC GCL's WRC and compares it to untreated GCL using non-contact filter paper and dew point method along both wetting and drying paths in deionized water (DW) and seawater (SW).

2   MATERIALS AND METHODS

Sodium bentonite was used, which was treated with sodium CMC to prepare the polymerized clay and subsequently sent to GCL manufacturer to manufacture the prototype needle-punched fiber GCLs (Khan *et al.* 2022).

GCL specimens with a square shape were cut from the prototype roll of UC and HC GCLs for respective wetting and drying paths. The perimeter of the samples was sealed with tape to avoid preferential drying at the edges and loss of the bentonite (Figure 1). For the hydration of the GCLs, DW and SW were used. DW was used as a reference solution, whereas SW represented severe ionic interactions. The properties of the materials are shown in Table 1.

Figure 1.   Filter paper setup for measuring total suction.

For the wetting path of the water retention curve, wetting liquids were added with the help of a sprayer. After the addition of the liquids, the samples were sealed in the plastic bag and left for the homogenization period of 3 weeks. Subsequently, the two filter papers were placed on the mesh, which was placed on the sample, and the samples were sealed in the plastic bag and left for the equilibrium period of 2 weeks (Figure 1). After the equilibrium period, the water content of the filter paper was measured as specified in ASTM-D5298

Table 1. Physical and chemical properties of the materials.

Bentonite	Specific gravity	Plastic limit %	Liquid limit %	CEC meq/100g	Plasticity index	Swell index in SW ml/2g	Swell index in SW ml/2g
UC	2.66	46.9	625.2	85.1	578.3	34	8
HC	2.25	142.5	765.6	56.5	623.1	45	9

GCL		Type		Mass g/m^2		Solution	EC mS/cm
Carrier geotextile		Non-woven		2.25		DW	0.01
Cover geotextile		Woven		1.25		SW	32.7

(2000). Afterward, the additional liquid was added to the sample and the same procedure was repeated.

For the drying path of the water retention curve, the samples were hydrated for 1 month. Lin and Benson (2000) suggested that swelling equilibrium is nearly achieved after 400 h (16.6 days). Therefore, a hydration period of 1 month was chosen for this study. For each subsequent measurement, the sample was dried in the oven at 40°C for 2 h and then left for evaporation through the cover and carrier geotextile at 20°C. Whatman grade 42 filter papers were used, and contamination of the filter papers was avoided by using metal tweezers during handling. The measurement of the filter water content of the filter papers follows the ASTM D 5298 calibration curve. The equations for the ASTM calibration curve are as follows.

$$w_f \leq 45.3\%, \quad Log_{10}(h) = 5.327 - 0.0779 w_f \tag{1}$$

$$w_f > 45.3\%, \quad Log_{10}(h) = 2.412 - 0.0135 w_f \tag{2}$$

where, h = Suction (kPa) and w_f = filter paper water content (%)

The lab calibration curve was also developed, and measurements were compared with that of the ASTM calibration curve. Different samples were used for both wet and dry paths.

For the calibration curve of the filter papers, the humidity sensors, and different solutions of known relative humidity were used. The filter papers were allowed to equilibrate for 7 days with the environment of known relative humidity. The suction was calculated from the water activity by using Eq. 3.

$$h = -\frac{RT\rho}{M} . \ln(R_h) \tag{3}$$

where, h is suction in kilo Pascals (kPa), R is the universal gas constant, which is equals to 8.31 Joule per mole kelvin ($J.mol^{-1}.K^{-1}$), T is the temperature in Kelvin (K), R_h is the relative humidity fraction, ρ is the density of water in kilogram per cubic meter (kg/m^3) at temperature T and M is the molecular weight of the water, which is equals to 0.018 kilogram per mole (kg/mol).

Subsequently, the water content of the filter papers was measured, and curve was plotted as shown in Figure 2. The slope of the second part of the calibration curve (Equation 5) is higher as compared to that of ASTM curve (Equation 2) due to non-contact filter paper measurement (Leong *et al.* 2002), which is desirable for the total suction estimation.
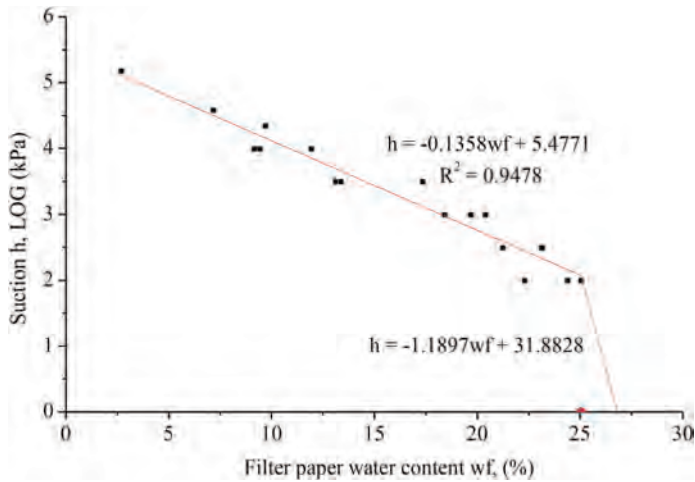
Figure 2. Filter paper lab calibration curve.

The equations for the lab calibration curve are as follows.

$$w_f \leq 25.06\%, \quad Log_{10}(h) = 5.4771 - 0.1358w_f \tag{4}$$

$$w_f > 25.06\%, \quad Log_{10}(h) = 31.8828 - 1.1897w_f \tag{5}$$

where, h = Suction (kPa) and w_f = filter paper water content (%)

For the comparison between the ASTM and lab calibration curve, tests in chilled mirror dew point water activity meter (WAM) were also conducted. The GCLs were cut in accordance with the dimensions of the sample cup (3.64 cm in diameter). For the wetting path of the water retention curve, the sample cups were placed in the 30°C oven and subsequently wetting liquids were added with the help of a sprayer. After the addition of the liquids, the samples were covered with a lid and left for the conditioning period. After every 24 hours, the water activity and temperature were measured with the help of the AQUALAB WAM until the last measurement approximated the preceding measurement. To reach the equilibrium value in the water activity meter for each measurement required 5 to 10 minutes. Afterwards, the additional liquid was added to the sample and the same procedure was repeated until water activity approached the value of 1.

In both filter paper and WAM tests, the samples were allowed to swell freely. Free swelling and shrinkage imply a change in the void ratio. Preferably, the void ratio should be kept constant while quantifying water retention curves since the decrease or increase in void ratio tends to shift the water retention curves upward or downward, respectively (Ghavam-Nasiri *et al.* 2019). However, due to considerable change in the voids of GCL's geotextile and swelling of the clay in GCLs, it is difficult to keep the void ratio constant, or otherwise, accurately measure the volume change of the water retention curve samples. Hence, the present study is limited to free swell conditions.

3 RESULTS AND DISCUSSIONS

3.1 *The effect of clay type on water retention curve*

The total suction results of UC and HC GCLs in terms of gravimetric water content along both wetting and drying path are presented in Figure 3. The Figure shows the suction
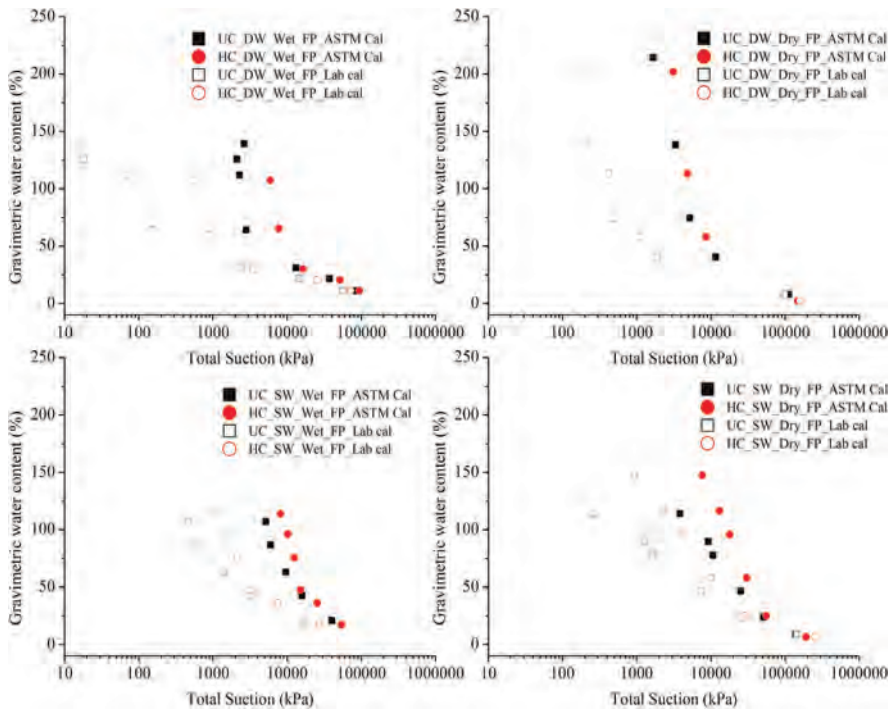
Figure 3.   Gravimetric water retention curves of untreated and Hyper clay GCLs along a) wetting path and b) drying path in deionized water and along c) wetting path and d) drying path in seawater estimated with ASTM and lab calibration curves.

decreases as expected. Besides, the water uptake increases towards lower suction due to increase in swelling. This increase in water uptake is higher in the case of polymerized clay due to higher swelling as depicted by Table 1. At higher suction, greater than 10^5 kPa, the suction of untreated and polymerized GCLs appears approximately similar. In general, HC GCLs showed higher water retention along wetting and drying path for both DW and SW solution.

The suction characteristics are frequently linked to the material's pore size distribution, pore structure, and material composition (Likos & Wayllace 2010). Because of the composite nature of the GCL, which constitutes geotextile and bentonite, trimodal pore structure is evident. Geotextile has apparently large pore/opening size of around 0.1–0.2 mm (Bouazza et al. 2006). Bentonite has been characterized by inter-particle and intra-particle pore sizes of 2–50 nm (Villar & Lloret 2008). Along the wetting path, the bentonite in the GCL went through different suction regimes depending upon the pore sizes starting from dry state to tightly adsorbed state, adsorbed and ultimately to capillary regime (Lu 2016). At lowest suction, the geotextile capillary prevails, which is totally dependent upon its material texture and pore sizes.

In the dry state, the bentonite possesses highest suction, which decreases with the increase in water content and in the tightly adsorbed and adsorbed regime, the suction is found to be greater than 10^4 kPa (Lau et al. 2022). In this regime, surface hydration occurs through hydrogen bonding between the negatively charged bentonite surface and water. The higher hydration energies associated with exchangeable cations in the montmorillonite mineral controls the water retention (Akin & Likos 2016). The positively charged cations attract the dipolar water molecule and layers of dipole water molecules add on and consequently

increase the gravimetric water content. The water in the region of cations and surface of the bentonite is termed as adsorbed water. From the Figure 3, the water content in this regime (at 10^4 kPa) lie in the range of 20 to 50% and descends in the order SW dry path > SW wet path > DW dry path > DW wet path. The higher water content in the drying path can be attributed to hysteresis behavior.

With the further increase in water content, the water starts movement in the interlayer space and establishes capillary connection, which indicates the start of the capillary regime (Acikel *et al.* 2018). This is usually indicated by a sharp rise in water content. Besides, considerable swelling can be observed in this regime. The saturation level in presence of DW is higher compared to that in SW due to compression of the diffuse double layer in SW, which leads to lower swelling and hence lower saturation gravimetric water content. In addition to this, the presence of ions enhances the total suction due to osmotic component of the suction. The osmotic component is more apparent in the case of SW, that is why the transition point of adsorbed to capillary regime lies at the higher water content in SW. For the UC, the SW affected UC more as compared HC since the difference between UC GCL and HC GCL increases for the same suction. The higher water retention of the HC GCL can be attributed to the type of polymer i.e. the Na-CMC which is an anionic polymer that intercalates within the bentonite platelets and results in additional swelling and chemico-osmotic efficiency (Di Emidio 2010) and, ultimately, higher water retention (Khan *et al.* 2022).
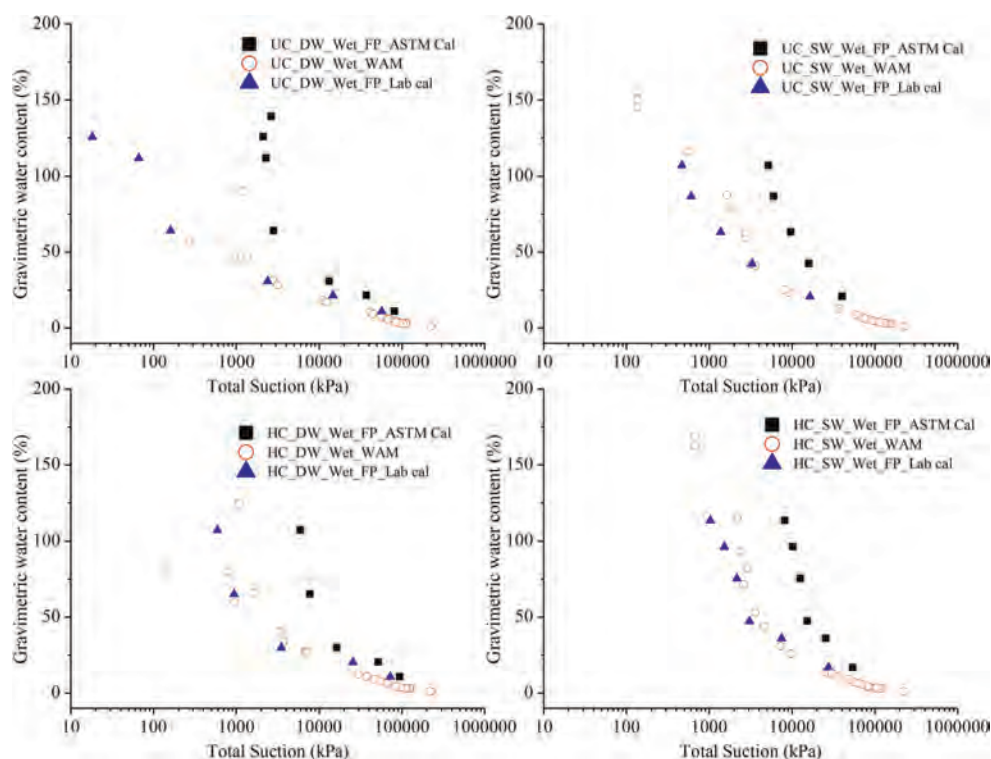

Figure 4. Comparison of water retention curves estimation determined by ASTM and lab calibration curves with the results of water activity method.

3.2 *Comparison of ASTM and lab calibration curve*

The results calculated from ASTM standard calibration curve and lab measured calibration curve of the GCLs along wetting path, and chilled mirror dew point WAM are shown in Figure 4. The Figure demonstrates that the findings of the lab calibration curve closely resemble those of WAM while those of the ASTM calibration curve overestimate the results when compared to lab calibration curve and WAM results. Towards higher suction closer to 10^5 kPa, the filter paper results showed higher value of suction for same water content.

When comparing the filter paper test to the WAM test, the highest difference in the filter paper lab calibration and WAM results was found to be 0.45 log suction (Figure 4b). Besides, an increase of 2.7% and 6% log suction was seen for UC_DW and UC_SW, respectively, at roughly 10^5 kPa. The ASTM calibration curve overestimates more than the lab calibration at lower suction, particularly at suction less than 117 kPa due to the sharp slope of the lab calibration curve (Figure 2). Comparing the results of the ASTM calibration curve to the lab calibration curve, the values for UC DW, UC SW, HC DW, and HC SW are overestimated by around 3 to 163%, 9 to 39%, 2 to 36%, and 6 to 30% log suction, respectively. It is therefore preferable to create a calibration curve for the lab setting while performing the filter paper test.

4 CONCLUSIONS

This study compares the water retention curves of UC and HC GCLs. In comparison to the UC GCL, the HC GCL demonstrated a higher gravimetric water content at a given suction. Besides, the higher ionic strength in seawater increased the osmotic suction of GCLs in both UC and HC and thus enhanced the overall suction. It has also been found that the choice of calibration curve has a substantial impact on the findings. The ASTM calibration curve overestimated the result as compared to lab calibration. Therefore, while conducting the filter paper test method, the lab calibration curve must be generated for accurate results.

In conclusion, the higher water retention of HC GCL would increase its resistance to heat gradients and enable it to act as a long-lasting barrier that would help safeguard subsurface water resources.

REFERENCES

Acikel, A., Gates, W., Singh, R., Bouazza, A., Fredlund, D., and Rowe, R. (2018). "Time-dependent Unsaturated Behaviour of Geosynthetic Clay Liners." *CaGeJ*, 55(12), 1824–1836.

Acikel, A. S., Singh, R. M., Bouazza, A., Gates, W. P., and Rowe, R. K. (2015). "Applicability and Accuracy of the Initially Dry and Initially Wet Contact Filter Paper Tests for Matric Suction Measurement of Geosynthetic Clay Liners." *Geotechnique*, 65(9), 780–787.

AFNOR (2015). "ISO 10318-1:2015(en) Geosynthetics — Part 1: Terms and Definitions."

Agus, S. S., and Schanz, T. (2007). "Errors in Total Suction Measurements." *Experimental Unsaturated Soil Mechanics*, Springer, 59–70.

Akin, I. D., and Likos, W. J. (2016). "Water Vapor Sorption of Polymer-modified Bentonites." *Geo-Chicago* 2016, 508–517.

ASTM-D5298 (2000). "Standard Test Method for Measurement of Soil Potential (suction) using Filter Paper. *American Society for Testing and Materials.*"

Beddoe, R., Take, W., and Rowe, R. (2010). "Development of Suction Measurement Techniques to Quantify the Water Retention Behaviour of GCLs." *Geosynthetics International*, 17(5), 301–312.

Bouazza, A., Freund, M., and Nahlawi, H. (2006). "Water Retention of Nonwoven Polyester Geotextiles." *Polym. Test.*, 25(8), 1038–1043.

De Camillis, M., Di Emidio, G., Bezuijen, A., Flores, D. V., Van Stappen, J., and Cnudde, V. (2017). "Effect of Wet-dry Cycles on Polymer Treated Bentonite in Seawater: Swelling Ability, Hydraulic Conductivity and Crack Analysis." *Applied Clay Science*, 142, 52–59.

Di Emidio, G. (2010). *"Hydraulic and Chemico-osmotic Performance of Polymer Treated Clays."* Ghent University.

Di Emidio, G., Mazzieri, F., Verastegui-Flores, R.-D., Van Impe, W., and Bezuijen, A. (2015). "Polymer-Treated Bentonite Clay for Chemical-resistant Geosynthetic Clay Liners." *Geosynthetics International*, 22(1), 125–137.

Ghavam-Nasiri, A., El-Zein, A., Airey, D., and Rowe, R. K. (2019). "Water Retention of Geosynthetics Clay Liners: Dependence on Void Ratio and Temperature." *Geotextiles and Geomembranes*, 47(2), 255–268.

Hanson, J., Risken, J., and Yesiller, N. "Moisture-suction Relationships for Geosynthetic Clay Liners." *Proc., Proceedings of the 18 th International Conference on Soil Mechanics and Geotechnical Engineering, Paris 2013*, 3025–3028.

Khan, M. K., Di Emidio, G., and Bezuijen, A. (2022). "Water Retention Curves of Untreated and Hyper Clay GCLs using the Filter Paper Method." *Environmental Geotechnics*, 1–11.

Lau, Z. C., Bouazza, A., and Gates, W. P. (2022). "Influence of Polymer Enhancement on Water Uptake, Retention and Barrier Performance of Geosynthetic Clay Liners." *Geotextiles and Geomembranes.*

Leong, E. C., He, L. and Rahardjo, H. (2002). "Factors Affecting the Filter Paper Method for Total and Matric Suction Measurements". *Geotechnical Testing Journal*, 25(3), 322–333.

Likos, W. J., and Wayllace, A. (2010). "Porosity Evolution of Free and Confined Bentonites During Interlayer Hydration." *Clays Clay Miner.*, 58(3), 399–414.

Lin, L.-C., and Benson, C. H. (2000). "Effect of Wet-dry Cycling on Swelling and Hydraulic Conductivity of GCLs." *Journal of Geotechnical and Geoenvironmental Engineering*, 126(1), 40–49.

Lu, N. (2016). "Generalized Soil Water Retention Equation for Adsorption and Capillarity." *Journal of Geotechnical and Geoenvironmental Engineering*, 142(10), 04016051.

Risken, J. L., Hanson, J. L., and Yesiller, N. (2016). "Estimation of Engineering Behavior of Geosynthetic Clay Liners Using Moisture-suction Relationships." *Japanese Geotechnical Society Special Publication*, 2(69), 2373–2378.

Rouf, M. A., Singh, R. M., Bouazza, A., Gates, W. P., and Rowe, R. K. (2020). "Evaluation of a Geosynthetic Clay Liner Water Retention Curve using Vapour Equilibrium Technique." *Unsaturated Soils: Research & Applications*, CRC Press, 1003–1009.

Rowe, R., and Shoaib, M. (2017). "Effect of Brine on Long-term Performance of Four HDPE Geomembranes." *Geosynthetics International*, 24(5), 508–523.

Seiphoori, A., Laloui, L., Ferrari, A., Hassan, M., and Khushefati, W. (2016). "Water Retention and Swelling Behaviour of Granular Bentonites for Application in Geosynthetic Clay Liner (GCL) Systems." *Soils and Foundations*, 56(3), 449–459.

Take, W., Brachman, R., and Rowe, R. (2015). "Observations of Bentonite Erosion From Solar-driven Moisture Migration in GCLs Covered Only by a Black Geomembrane." *Geosynthetics International*, 22(1), 78–92.

Villar, M. V., and Lloret, A. (2008). "Influence of Dry Density and Water Content on the Swelling of a Compacted Bentonite." *Applied Clay Science*, 39(1–2), 38–49.

Yu, B., and El-Zein, A. (2019). "Experimental Investigation of the Effect of Airgaps in Preventing Desiccation of Bentonite in Geosynthetic Clay Liners Exposed to High Temperatures." *Geotextiles and Geomembranes*, 47(2), 142–153.

Permeable contaminant filter for storage and passive decontamination of PFAS-polluted soil

S. Niewerth
HUESKER Synthetic GmbH

T. Walker
HUESKER Inc.

G. Martins
HUESKER Australia Pty. Ltd.

ABSTRACT: For many decades, per- and polyfluoroalkyl substances (PFAS) were used in firefighting foams at airports and military sites. Today, large amounts of soil and consequently groundwater are contaminated with PFAS. Upon reuse of sites, there must be a definite plan on how the contaminated excavated soil will be addressed. Typically, present waste disposal regulations require the soil to be landfilled. However, transport and disposal of enormous amounts of soil make projects expensive and unecological. For storage or reuse of contaminated soil in the vicinity of the excavation innovative contaminant filters are developed. The target is to treat the soil passively, i.e., without labor, energy, or fresh water. Natural precipitation is used to dissolve PFAS from the soil body and transport downwards through the structure. A permeable contaminant filter is placed at the bottom of the stockpile area. This geocomposite consists of a highly effective amendment sandwiched between two layers of geotextiles. The selective agent extracts PFAS from leachate. To develop a long-life contaminant filter, four performance factors must be considered: affinity, kinetics, capacity, and irreversibility. Affinity describes the tendency of the sorbent to uptake particular pollutants. Regarding PFAS, it is essential that long- and short-chain PFAS are included. The kinetics of the amendment determines whether it is possible to reduce contaminant concentrations below the specified permissible threshold while the seepage percolates through the filter at a natural flow rate. The capacity must be greater than the product of the leachate concentration, the total amount of seepage over a defined period, and an appropriate safety factor. Irreversibility precludes subsequent desorption and thus enables long-term safety of the impoundment. Additionally, there are interdependencies between these factors. The determination of the performance factors and their influence on the design concept are presented and discussed in this paper.

1   TECHNICAL STRUCTURES MADE OF POLLUTED SOIL

Technical structures, such as noise barriers, infrastructure embankments, or commercial and industrial areas, are increasingly being constructed from substitute building materials due to soil scarcity and to avoid long transport routes. Among other materials, these are soils with environmentally relevant compounds. When using substitute building material for structures, they must be designed and evaluated such that they do not contribute to soil and groundwater contamination. In Germany, the possibility of reusing contaminated soils for technical structures is linked to the eluate concentration. In case of comparable high

Table 1. German preliminary max. permissible concentrations for corresponding recovery classes (BMUV 2022).

PFAS congeners	RC 1 – unrestricted open replacement (all in $\mu g/l$)	RC 2- restricted open replacement in areas with elevated PFAS concentration	RC 3 – restricted emplacement in technical structures with defined safety measures
Perfluorobutanoic acid, **PFBA**	≤ 10.0	≤ 20.0	≤ 50.0
Perfluorohexanoic acid, **PFHxA**	≤ 6.0	≤ 12.0	≤ 30.0
Perfluorooctanoic acid, **PFOA**	≤ 0.1	≤ 0.2	≤ 1.0
Perfluorononanoic acid, **PFNA**	≤ 0.06	≤ 0.12	≤ 0.6
Perfluorobutane sulfonic acid, **PFBS**	≤ 6.0	≤ 12.0	≤ 30.0
Perfluorohexane sulfonic acid, **PFHxS**	≤ 0.1	≤ 0.2	≤ 1.0
Perfluorooctane sulfonic acid, **PFOS**	≤ 0.1	≤ 0.2	≤ 1.0

concentrations certain containment measures are required. In the Guideline for PFAS Assessment of the German Federal Ministry for the Environment (BMUV 2022) provisional maximum permissible concentrations for PFAS are defined in the 2:1 l/s-eluate. These values result in a recovery classes (RC), which in turn decides on the containment measure to be taken.

The division into the three classes results from the consideration that the concentration in the technical structure is also transported into the subsoil over time. In case of low concentrations, an open replacement is possible since the subsoil is thus only exposed to low concentrations. To avoid the transport of high concentrations of contaminants, the measure used nowadays is the encapsulation of the contaminated soil by means of an impermeable cap. With new technologies, such as permeable contaminant filters, unrestricted open emplacement is possible, even if the eluate concentrations are at RC 3 or higher. The leachate which contains the contaminants is filtered before it continues to percolate into the uncontaminated subsurface at the permissible pollutant concentration of RC 1, as shown in Figure 1.
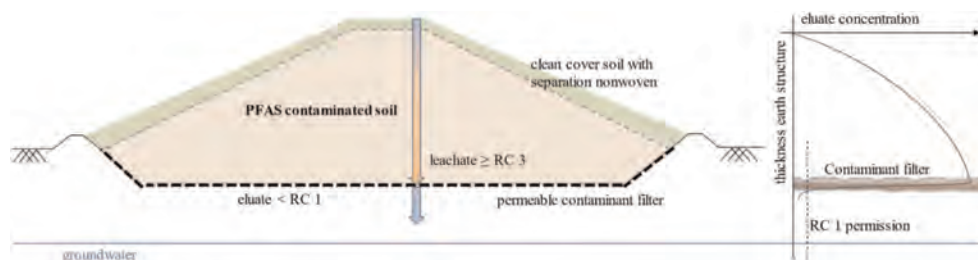

Figure 1. Schematic of technical structure with contaminant filter at the base of the structure and leachate concentration.

In addition to groundwater protection, the advantage of this approach is the successive decontamination of the soil. The infiltration of rainwater into the structure is used specifically to dissolve PFAS compounds. The leachate loads itself with the environmentally relevant components and transports them to the permeable filter. To eliminate the concern of pollutants entering the subsurface, the effective removal of the contaminants and a long-term binding of PFAS to the filter must be proven and ensured. Extensive testing with the newly developed permeable contaminant filters was performed to meet these requirements.

2 GEOCOMPOSITE PERMEABLE CONTAMINANT FILTER

Permeable contaminant filters, or also called active geocomposites, consist of a carrier layer and a cover layer of woven and/or nonwoven geotextiles. The geotextiles serve as a package to permanently stabilize the amendment and thus to install it in the field with a uniform layer thickness. All layers are frictionally joined by needle punching or stich bonding which prevents internal erosion of the fine granular or powder active material. In addition, the fabrics also separates the soil layers. The selection of the most sufficient geotextiles allows the setting of an optimal contact time, which is very crucial for leachate treatment. The core of the geocomposite is composed of an amendment layer, which removes PFAS from infiltrating water. It consists of a highly effective amendment or blend of amendments for PFAS. Since leachate properties can vary widely, project-specific selection of the most effective amendments is again recommended. For designing technical structures four performance factors must be considered:

a) Affinity: Strong tendency to remove long and short chain PFAS.
b) Kinetics: Ability to remove all PFAS below thresholds at usual leachate velocities.
c) Capacity: Quantifiable large amount for pollutant uptake over certain period of time.
d) Irreversibility: Binding between amendment and PFAS that cannot be reversed by natural processes.

A contaminant filter can be characterized as technically effective if a strong affinity and a short contact time result in a high percentage removal of contaminants. If at the same time a high capacity and a strong binding led to a long service life the filter turns out to be economically efficient. The four parameters and their interdependencies were analyzed in laboratory and outdoor tests to understand effectiveness and efficiency.

3 RESULTS FROM LABORATORY AND OUTDOOR TESTS

3.1 *Laboratory tests*

To determine the performance factors, an independent laboratory was commissioned to carry out an extensive test program. Initially, jar tests were conducted in which the amendments are stirred in the leachate for the defined time. At different time points, the sorbents are removed and the water is analyzed for contaminant concentrations. The leachate contained PFBA, PFPeA, PFBS, PFHxA, PFPeS, PFHpA, PFOA, PFHxS, PFOS, and others whereby the individual concentrations of the six congeners shown in Figure 2 were artificially increased. Thus, the concentrations ranged from about 2 μg/l to 15 μg/l per individual compound. A strong uptake of all substances of up to 99.9 % was observed, as shown in Figure 2. In addition to the affinity, a first picture of the kinetics was obtained. It was found that not only the capacity but also the kinetics varies at different concentrations. A very strong removal of all PFAS from the leachate was detected during the first five minutes (a lower duration was not possible in the experiments). It is estimated that about 90% of the treatment success takes place within the first two minutes.
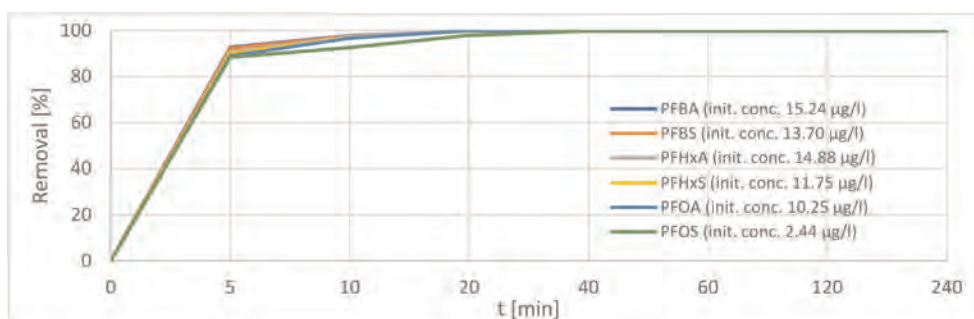
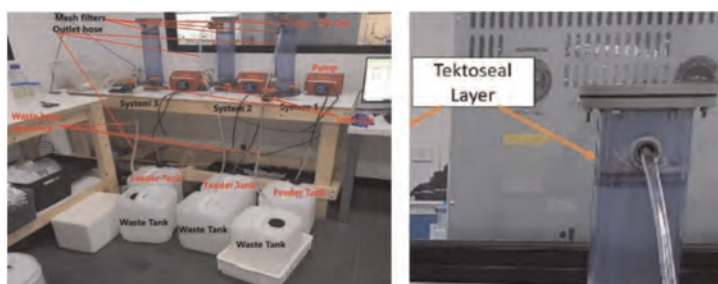Figure 2. Removal of PFAS from leachate in jar tests.

Figure 3. Setup of the column experiments and results at very high concentrations.

Since jar tests confirmed the expectation of high effectiveness, column tests were performed in the next step. These tests more accurately represent the application of geosynthetic contaminant filters in the field than jar tests and are therefore essential. A round sample of the geocomposite was percolated at a defined leachate flow rate in the column shown in Figure 3. Accordingly, a velocity of k = 4.9E-05 m/s was obtained. The eluate was collected in plastic containers and the PFAS concentration was analyzed. The column tests again show a high effectiveness. The test leachate was again spiked with the same six congeners as previously used in the jar tests, but for the column test a concentration of about 1,000 μg/l per congener were added. The reason for this concentration was to determine the capacity limit in a manageable time. Without detecting any breakthrough (maximum capacity not reached), the test was terminated after 7,000 μg/g of PFAS were removed by the amendment. Based on this experiment and confirmed by results from tests of third parties, a capacity of 20,000 μg/g or more can be assumed for very high concentrations. At low concentrations, the expected capacity is correspondingly lower.

Not only the study of the total capacity provides important information for the design of technical structures with contaminant filters, but also the development of the effectiveness as a function of PFAS loading. In Figure 4, the green line represents a theoretical 100% removal of all dissolved PFAS. The orange line shows the actual removal through the filter recorded in the experiments. The result shows that the effectiveness is higher than 99% until the first 110,000 μg of PFAS is sorbed. This corresponds to a capacity of approx. 2,800 μg/g. In the further course, while the concentration remains constant a certain saturation sets in, and consequently the effectiveness decreases. After approx. 250,000 μg of removed PFAS the effectiveness is approximately 75%. This corresponds to a capacity of 7,100 μg/g. After that, however, the capacity limit has not been reached, so that the estimated capacity of 20,000 μg/g to breakthrough seems possible, but only at the expense of efficacy.
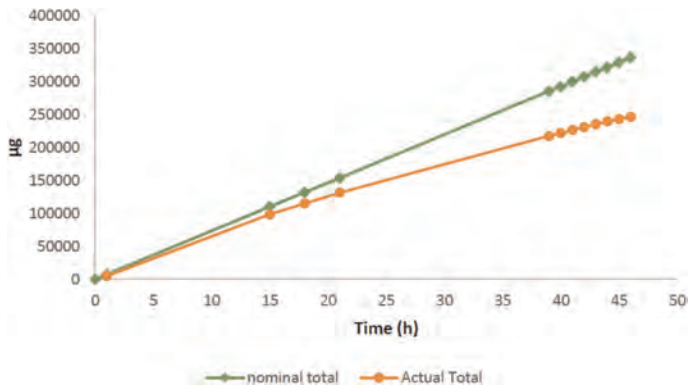
Figure 4. Effectiveness of active geocomposite depending on PFAS loading.

Finally, irreversibility, i.e., the desorption behavior of the amendment, was investigated. For this purpose, the loaded granular agent was placed in a glass with deionized water for a total period of two months and shaken continuously. In this way, it was investigated whether PFAS detach after uptake. The desorption rate was less than 0.1%. Consequently, the binding strength can be described as extremely high.

3.2 Outdoor tests

The success from the laboratory tests was repeated in outdoor tests with PFAS-contaminated soil from a former US airbase in Germany. These series of tests were carried out in close cooperation between HUESKER Synthetic and CDM Smith. Large-scale lysi-meter tests, shown in Figure 5, were build up. Three different rain events were simulated in different 1 m³ HDPE-containers, their effect on PFAS mobilization was investigated and the effectiveness of the active geocomposites was tested. As a control, all rain scenarios were also carried out in a container without the contaminant filter. In the test setup, the active geo-composite was laid out in the bottom of a container that was open at the top. A con-taminated silty sand with a thickness of 0.70 m was placed on top. The leachate produced during the respective rainfall simulations was collected and analyzed at different times. The
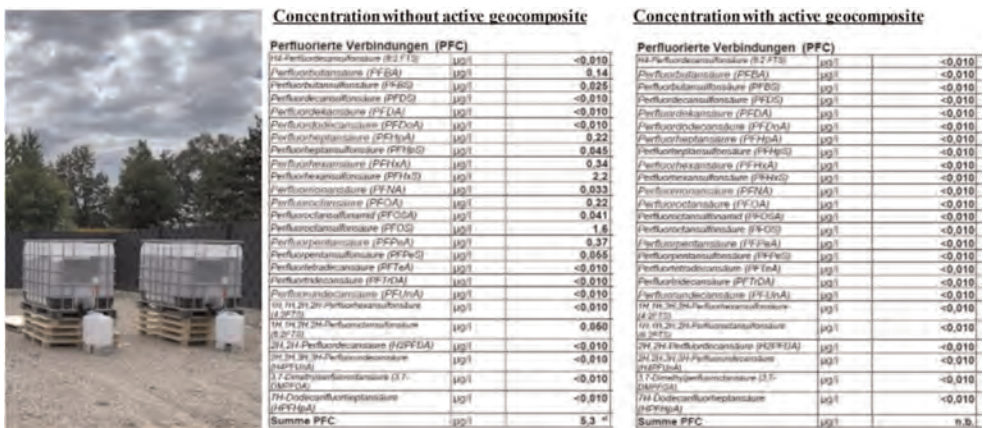

Figure 5. Outdoor trails in HDPE-container and results of rain event 3.

water quantities follow the definitions for moderate, heavy, and extremely heavy rain events according to the German Weather Service (Deutscher Wetterdienst, DWD):

- rain event 1: moderate rain with 10 L/m^2 in 60 minutes
- rain event 2: heavy rain with 30 L/m^2 in 60 minutes
- rain event 3: extremely heavy rain with 50 L/m^2 in 60 minutes

The rainfall simulations led to a mobilization of PFAS from the soil in all test approaches. PFAS levels in the soil leachate averaged about 3–5 μg/l, as shown by the control approach from the container without contaminant filter. These concentrations are also at the level of the analytical laboratory tests of the soil material (10:1 shaking method according to DIN 38414 – S4).

Regardless of the simulated rainfall event, no PFAS were detected in the leachate after filtration by the active geocomposites. The values given in Figure 5 show the result of an extremely heavy rain (rain event 3).

4 DESIGN OF TECHNICAL STRUCTURE

Based on the data obtained from the tests, technical structures can be designed. These structures made of contaminated soils can be noise barriers, infrastructure embankments, utility trenches, etc. If it is ensured that the soil does not have a negative impact on the subsoil and groundwater, it can be used as a building material for these structures.

To design a technical structure with a contaminant filter, information about the leachate velocity is required. It must be verified that the residence time of the leachate in the amendment layer of the contaminant filter is longer than the minimum contact time determined from the column tests. For a road embankment, Finken et al. (2019) used a numerical flow model to calculate the leachate rate based on individual soil layers and infiltration rates, as shown in Figure 6. Comparing the velocities in this technical structure (1.6E-02 m/d) with the flow rates from the outdoor tests, the velocity in the structure is about 68 times lower. Accordingly, the contact time is sufficient to allow significant removal of PFAS by the active geocomposite underneath the embankment.

To evaluate the durability, it must not only be calculated whether the filter works in general, but likewise how long it can be used in the field. For this, a concentration of 10 μg/l total PFAS and an average annual amount of leachate at the interface between the contaminated soil layer and the subsurface of 260 L*m^2/a are used for calculation. The amount of leachate was also taken from Finken et al. (2019) for the structure shown in Figure 6. It is
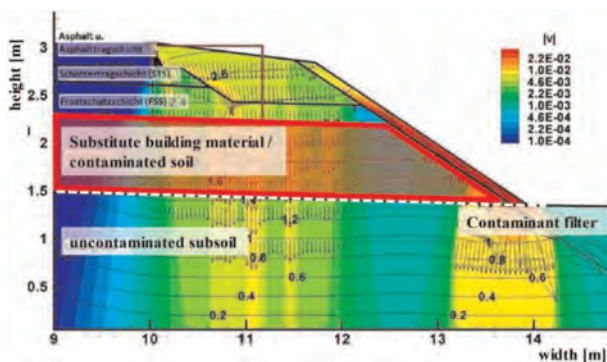

Figure 6.   Leachate rates through a road embankment given in m/d (Finken et al. 2019).

based on an annual precipitation of 859 mm/a and takes into account evaporation and surface runoff.

As described in chapter 3.1 for high PFAS-concentrations a strong effectiveness (almost 100%) is given until a capacity of approx. 2,800 μg/g. However, as the concentration of 10 μg/l is much lower than the concentration in the column tests, the capacity is correspondingly lower. Based on empirical data, the capacity for low concentrations is conservatively estimated to be six to seven times lower. This leads to a capacity of 400 μg/g with almost 100% effectiveness. As described, however, this does not necessarily imply that the capacity limit has been reached. Since it is very likely that other dissolved organic contaminants are also taken up by the amendment, the total capacity is not available for PFAS only. To take this into account, a safety factor of 4 is applied. Accordingly, only 25% of the total capacity is mathematically available for the uptake of PFAS. To reach a sufficient life expectance, an active geocomposite with 3,000 g/m^2 of amendment is chosen. As a result, the service life of the contaminant filter can be estimated at 132 years. This value does not imply that the PFAS concentration is likely to decrease over the years, since the pollutants are discharged from the technical structure with the leachate. For example, if it occurs that the concentration decreases to 9 μg/l after 30 years, the life expectancy increases to 143 years.

5   CONCLUSION

The wide dispersion of PFAS in soil due to their easy solubility and current waste regulations mean that very large excavation quantities must be landfilled or treated ex situ in construction projects on contaminated sites. The reuse of contaminated soil in technical structures represents a solution to avoid long transport distances and disposal. However, sealing these structures results in micro landfills in which the pollutants remain (at best) permanently. Active geocomposites are a new containment and treatment measure. As a permeable filter, the geocomposites are installed underneath the technical structure. It provides a barrier to the contaminants but not to the leachate. In this way, the natural flow path of water is maintained while protecting the clean underground. Since technical structures built in this way are not sealed, precipitation will leach the PFAS over time and direct them into the filter. It must be ensured that the filter effectively removes the substances – i.e., down to the de minimis thresholds – and permanently binds them. The amendment presented in this paper shows very good properties in extensive tests. From a legal point of view, there is the question to be answered if the use of soil with RC 3 leachate is allowed to be used in an open unrestricted emplacement if it is ensured that the concentration underneath the structure is lower than RC 1 values. Since, for example, the German Water Resources Act names the groundwater level as the place of assessment, this question should basically be answered in the affirmative. To control the effectiveness, punctual control shafts can be built. Moreover, first sensor-based eluate measurements already exist and possibly can facilitate the monitoring of the filter under the technical structure soon.

REFERENCES

[BMUV] Federal Ministry for the Environment, Nature Conservation Nuclear Safety and Consumer Protection. 2022. *Guidelines for PFAS assessment*. Berlin. Germany

Finken, M.; Susset, B.; Grathwohl, P. 2019. *Evaluierung der Bewertungsverfahren im Kontext mit der Verwertung mineralischer Abfälle inlauf Böden, Teil II: Modellierung der Stoffmigration und Erarbeitung eines DV-gestützten Leitfadens Stofffreisetzungsverhalten mineralischer Abfälle*. On behalf of the German Environment Protection Agency.

The compatibility of natural and geosynthetic materials for the design of landfill barriers

H. Bannour

Assistant Professor, ISSAT Sousse, University of Sousse, Tunisia

ABSTRACT: Waste disposal facilities (landfills) need to be designed with two distinct and complementary barriers; polymeric and mineral low permeable materials i.e composite liners. In order to prevent contamination of subsoil and groundwater by the leachate provided by wastes, composite liners need to be installed with very strict regulations. Nonetheless, with the luck of natural sites meeting regulations and considering economic and technical concerns, designers used to search for an equivalent design solution on a landfill geographical site by considering alternative materials providing similar protection of the potential environmental impact of wastes on water resources and aquifers. This is where a thin low permeable material such as geosynthetic clay liners (GCLs) or treated soils as polymer-enhanced bentonite–sand mixture (PEBSM) could be added as reinforcement. In this study, analytical and numerical equivalency analyses have been performed on relative concentration evolution of inert contaminant through the geosynthetic reinforced barrier and soil liner in comparison with conventional low permeable soil in the same contamination configuration. Numerical modeling has been used to reproduce contaminant transfers into the entire barrier to the aquifer by SEEP/W and Ctran from Geostudio (2012). In this study, we found that the reinforcement of a non-regulatory passive barrier with a GCL or a PEBSM could provide similar protection level and in some cases enhance it by limiting the evolution of the contaminant migration into the groundwater and subsoil. In conclusion, equivalency is possible for passive barriers through different design solutions; however it is important to pay attention to provide minimum thicknesses of materials to avoid preferential flow paths. This study was inspired from the French guide line for equivalency of landfills passive barrier BRGM/RP-69449-FR (2019). As a result of this study, the proposed methodology for calculating contaminant transport through passive barriers was validated and could provide a reliable tool for other hydraulic applications.

1 INTRODUCTION

Landfills are planned nowadays using a multi-liner approach. Each individual liner allows the environment to be adequately long term protected against aggressive effect of leachate provided by wastes.

Under the EU Landfill directive for Non-hazardous wastes, soil, groundwater, and surface water must be protected by the geological barrier and a composite liner. This latter includes a geomembrane (GMB) and existing low permeable clayey soil or reconstituted one. Essentially, it limits leachate flows and contaminant concentrations in the landfill's environment through its base and sides. It must consist of a mineral layer that satisfies certain hydraulic-conductivity and thickness requirements for the bottom and sides.

The EU Landfill directive defines the following requirements on the geological barrier for non-hazardous waste or compacted clay liner (CCL):

– there must be, from top to bottom, a soil layer with a hydraulic conductivity less or equal than 10^{-9} m/s for at least one meter thick then a soil layer with a permeability less than 10^{-6} m/s for at least 5 meters thick;

– for sides, 1 m thick of the low permeable soil layer presenting a hydraulic conductivity less or equal to 10^{-9} m/s is required.

However, this is a theoretical approach to regulatory design. In a practical point of view, to keep this low hydraulic conductivity at landfill sides, the storage facility must be excavated into the entire deposit with a hydraulic conductivity less than 10^{-9} m/s. This situation is quiet infrequent, and the regulation allows passive barrier reconstruction; when geological barriers don't present local enough specific conditions. Their construction can be completed and reinforced by other materials that provide similar protection. The design of a reinforced passive barrier is justified by an equivalency study that is presented in this paper.

2 EQUIVALENCY JUSTIFICATION ELEMENTS FOR PASSIVE BARRIER

2.1 Qualitative justification for equivalency

If the geological barrier does not naturally provide sufficient regulatory protection, the equivalency study must be conducted by designers after a reliable geological and hydrogeological site modeling.

Ground water is the main target of passive barriers at the bottom of landfills. Indeed, its surface must be kept away from low permeable materials (k < 10^{-9} m/s). For more protection, the distance should be at least 2 m thick.

In terms of potential impact of landfills on ground water resources, two distinguished barriers can be considered equivalent if they offer an equivalent level of ground water protection from a given contaminant migration and concentration. For more security, a minimum thickness of the whole barrier and more specifically of the low permeable material is required. For the whole barrier thickness serves as a security guarantee by reducing risk associated with heterogeneous materials and preferential flow paths.

Currently, equivalency is assured by reinforcing the passive barrier with a thin material exhibiting a low permeability (k < 5×10^{-11} m/s) as a geosynthetic clay liner (GCL) or a treated soil such as a polymer-enhanced bentonite–sand mixture (PEBSM). The permeability is the important parameter that accesses the performance of any lining system. Indeed, the successful association of a low permeable material with a GCL or a PEBSM can reduce significantly the leakage and contaminant migration into the subsoil and the ground water (Rowe & Abdelatty 2012; 2013; Sukumara & Arnepalli 2020). A GCL are defined according to EN ISO 10318 (AFNOR) as a manufactured geosynthetic hydraulic barrier consisting of clay supported by geotextiles or geomembranes, or both, that are held together by needling, stitching, or chemical adhesives. PEBSM is a mixture of a granular material (sand) mixed with a small amount of sodium type bentonite and a minute amount of polymer with certain proportions adopted in many lining and covering applications (Hosny & Rowe 2019)

An alternative solution to conformity requirements is to also increase the thickness and/or reduce the permeability of the attenuation layer (the higher permeable soil) based on the technical and economic conditions of the site.

2.2 Quantitative justification for equivalency and backgrounds

When a quantitative equivalence justification is required, the geological and the hydrogeological data obtained from the site must be used for comparative justification. In addition, the estimation of the contamination level occurring through the barrier and reaching the aquifer is the key providing a quantitative justification of the equivalency for passive barrier.

Indeed, the combination of advective and diffusive transport quantification makes it possible to correctly predict the transport of leachate contaminants in the presence of a hole in the GMB through the composite liner (Rowe & Abdelatty 2012). Advection is provided by the hydraulic gradient across the liner whereas diffusion is provided by concentration gradient.

Furthermore, there is a requirement to calculate the evolution of the relative contaminant concentration C/C_0 into the aquifer and accessing the complete transfer of the contaminant to the environment where:

C is the contaminant concentration through the aquifer as a function of time $[M.L^{-3}]$

C_0 the source concentration through the landfill waste considered as unitary and constant over time represented on the top of the passive barrier $[M.L^{-3}]$.

As a consequence, an easy way to perform equivalency between various distinguished barriers is to compare their relative concentration evolution through the liner.

Then, the purpose of this study is to estimate using a quantitative approach equivalency of various mineral barrier configurations. Numerical modeling using SEEP/W and Ctran from Geostudio make it possible to combine advective flow to diffusive one for the estimation of the level of the contaminant migration (C/C_0) into the aquifer and its corresponding time of occurrence as described in the following case of study for equivalency of mineral barriers.

3 CASES OF STUDY: REINFORMNT JUSTIFICATION BY AN EQUIVALENCY STUDY

3.1 *General features of the composite liners cases and boundary conditions*

9 scenarios cases have been considered for equivalency justification and divided into 3 cases (Table 1 & Figure 1). The two-dimensional multilayers are considered covering a surface of 50 m over a free seepage face representing the aquifer. In the first case (–1–), we considered a soil liner barrier in –a– with a CCL at the top with a hydraulic conductivity k = 1×10^{-09} m/s and a silty soil as an attenuation layer (k = 7×10^{-07} m/s). This barrier could be considered as a regulatory barrier as it satisfies conditions presented in the introduction. It has been considered in –b– a higher permeable soil in the place of the silt represented by silty sand with a hydraulic conductivity equal to 1.2×10^{-5} m/s. As this case is not satisfying the regulation, it has been suggested in that case to reinforce it by the mean of a 0.01 m thick GCL (which hydraulic conductivity is equal to 5×10^{-11} m/s) and in –c– by the mean of a 0.07 m thick PEBSM with the same hydraulic conductivity. In the second case (–2–), we have kept the thickness of the whole regulatory barrier i.e. 6 m and just reducing the thickness of the low permeable soil i.e. the CCL from 1 m to 0.5 m in –b–and –c–. For the third case (–3–), the thickness of the low permeable soil i.e. the CCL has been also reducing to 0.5 m with keeping the same initial thickness of 5 m for the high permeable soil (hydraulic conductivity k < 10^{-6} m/s). The third case has been considered to access the effect of the reduction of the low permeable soil (the CCL) thickness on the contaminant transfer into the whole barrier. Simulations have been performed under 0.3 m hydraulic head and a specific unitary concentration on the top of the multilayered barrier for respectively advection and diffusion.

Table 1. Scenarios of the different cases studied.

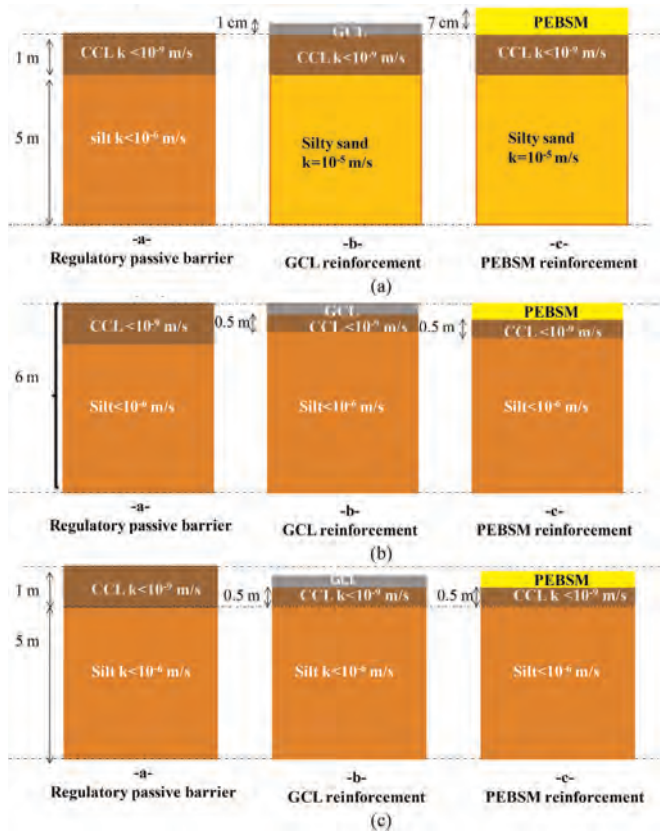| Cases Scenarios	Case –1–			Case –2–			Case –3–		
	–a–	–b–	–c–	–a–	–b–	–c–	–a–	–b–	–c–
GCL	–	1 cm	–	–	1 cm	–	–	1 cm	–
PEBSM	–	–	7cm	–	–	7 cm	–	–	7 cm
CCL	1 m	1 m	1 m	1 m	0.5 m	0.5 m	1 m	0.5 m	0.5 m
Silt	5 m	–	–	5 m	5.49 m	5.43 m	5 m	5 m	5 m
Silty sand	–	5 m	5 m	–	–	–	–	–	–

Figure 1. General features of the passive barrier cases: (a): Case–1–; (b): Case –2–; (c): Case –3–.

3.2 Material properties

The multilayers presented in this study are considered homogeneous and continuous. Interfaces are also considered horizontal. Material properties under saturated and unsaturated condition have been provided from the study of Carsel & Parrish (1988) which characteristics are presented in Table 2.

The chloride solute used in simulation will migrate through the soil and GCL due to two processes: diffusion and advection. The one-dimensional advection-dispersion equation used in Ctran analyses for a homogeneous, isotropic material are defined as:

$$D_i \frac{\partial^2 C}{\partial z^2} - v_z \frac{\partial C}{\partial z} = \frac{\partial C}{\partial t} \qquad (1)$$

C is the concentration $[M.L^{-3}]$; Hydrodynamic dispersion coefficient Di expressed in $[L^2/T]$ for each material layer has been provided according to flow results as follows:

$$D_i = \alpha_i \frac{\inf}{\theta_i} + D_0 \tau_i \qquad (2)$$

Where: α_i is the dispersivity of the layer $[L]$; inf: the infiltration or the ground water velocity $[L/T]$, θ_i the volumetric water content $[L^3/L^3]$; D_0 the contaminant diffusion coefficient in water for a non reactive chloride equal to 2×10^{-09} m^2.s^{-1}.

Table 2. Material properties (Carsel & Parrish 1988).

Material	θ_{sat} (%)	θ_{res} (%)	K_{sat} (m/s)	n	τ
GCL	50	10	5×10^{-11}	-	0.3
PEBSM	50	10	5×10^{-11}	-	0.3
CCL	38	6.8	1×10^{-09}	1.09	0.3
Silt	46	3.4	7×10^{-07}	1.39	0.5
Silty sand	41	6.5	1×10^{-05}	1.89	0.6

The dispersivity α_i is about approximately the tenth of the layer thickness; the volumetric water content θ_i was numerically calculated from the corresponding unsaturated hydraulic conductivity of the layer provided from seepage calculations as follows (van Genuchten 1980):

$$K(\theta) = K_s \theta_D^{0.5} \left(1 - \left(1 - \theta_D^{\left(\frac{n}{n-1}\right)} \right)^{\frac{n-1}{n}} \right)^2 \ with\ \theta_D = \frac{\theta - \theta_r}{\theta_s - \theta_r} \tag{3}$$

Where: $K(\theta)$ [m/s] is the unsaturated hydraulic conductivity under the volumetric water content θ_i [m^3/m^3]; K_s is the saturated hydraulic conductivity; θ_{s_i} is the saturated water content [m/s]; θ_{r_i} is the residual water content [m/s] and n is an experimental parameter.

A constant concentration boundary condition of 1.000 g/m^3 is used to represent the contaminant in the bottom liner. A free exit condition allows mass to leave the domain via advection and dispersion id the concentration C exceeds 0 g/m^3. Sorption was not included in this example.

4 RESULTS AND DISCUSSION

Figure 2 shows the evolution of the relative concentration in an aquifer of a landfill over time. Figure 2(a) represents the results of case –1–, while Figures 2(b) & 2(c) represent the outcomes of cases –2– and –3–.
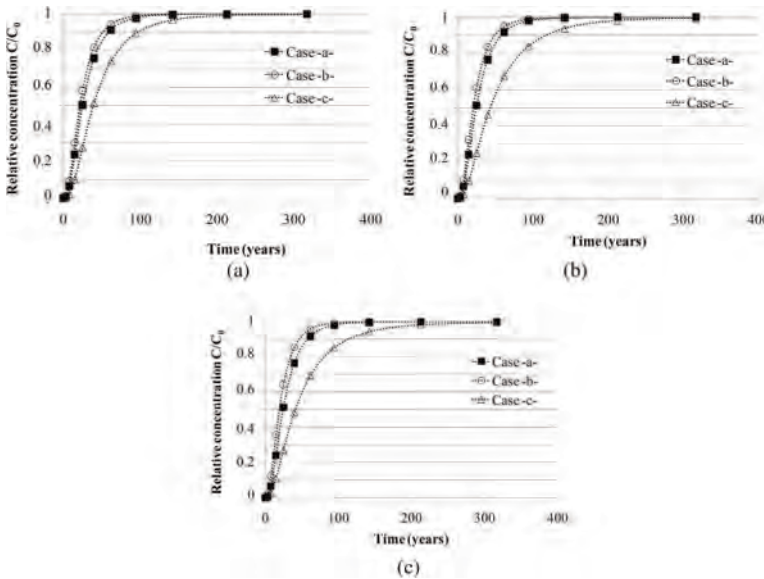

Figure 2. Results of simulation of the evolution of the relative concentration C/C_0 with time through the passive barrier: (a): Case 1; (b); Case 2; (c): Case 3.

In all case studies, numerical simulations showed very similar results in terms of complete contaminant transfer and time to reach it for scenarios –a– and –b–. There is a slightly lower relative concentration evolution with time in scenario –c–. This could be explained by the PEBSM being thicker than the GCL and slowing the contaminant transfer process.

Accordingly, when the regulations could not be met in terms of thickness or hydraulic conductivity of the layer, it appears that reinforcement of the soil barrier with GCL or a thicker material (PEBSM) may be beneficial for the whole barrier and can be used to reduce the contamination of the aquifer over time. In the French guideline, various types of reinforcement configurations for barriers are presented based on numerical and theoretical calculations.

5   CONCLUSION

It is possible to reinforce nonhazardous landfills with low permeable materials when the geological site configuration cannot meet regulatory barrier specifications, for example using geosynthetic clay liners (GCL) or treating soil with polymer enhanced bentonite sand mixtures (PEBSM). Here, a simple and practical methodology is proposed to quantitatively justify equivalency using contaminant migration through a soil barrier. This study was inspired by the French guideline BRGM/RP-69449-FR (2019). Simulations have been conducted for a significant amount of time. The study concluded that in all reinforcement cases, GCLs represent a sufficient equivalent solution for regulations that could not be met (in terms of sufficient thickness or hydraulic conductivity). Additionally, a thicker PEBSM material enhances the barrier's performance. Based on the results of the simulations, this can be regarded as a very significant result, since it reduces risks related to heterogeneous materials and preferential paths. Other hydraulic applications and barrier configurations could be addressed using this methodology.

REFERENCES

AFNOR. EN ISO 10318. *Geosynthetics – Terms and definitions.*
BRGM RP-69449-FR 2019. Recommandation Guideline: Guide de Recommandations Pour la Conception et l'évaluation de Dispositifs d'étanchéité Passive d'installations de Stockage de Déchets-Version 3
Carsel, R. & Parrish, R. 1988. Developing Joint Probability Distribution of Soil Water Retention Characteristics. *Water Resour. Res.* 24(5):755–769.
Hosney, M. & Rowe, R.K. 2019. Polymer-Enhanced Bentonite–Sand To Cover Calcium-Rich Soil. *Environmental Geotechnics* 6(3): 155–16.
Rowe, R.K. & Abdelatty, K. 2012. Modeling Contaminant Transport Through Composite Liner with a Hole in the Geomembrane, *Can. Geotech. J.* 49.
Rowe, R.K. & Abdelatty, K. 2013. Leakage and Contaminant Transport Through a Single Hole in the Geomembrane Component of a Composite Liner. *J. of Geotech. and Geoenv. Eng.* 139.
Sukumara, P.B. & Arnepalli, D. Naidu. 2020. Effect of Biopolymers on Permeability of Sand-bentonite Mixtures. *Journal of Rock Mechanics and Geotechnical Engineering* 12.
van Genuchten, M.T. 1980. A Closed Form Equation for Predicting the Hydraulic Conductivity of Unsaturated Soils. *Soil Science Society of America Journal* 44: 892–898.

A systems engineering and risk assessment-based approach for the design of landfills

A. Dominijanni, N. Guarena & M. Manassero
Politecnico di Torino, Torino, Italy

ABSTRACT: The long-term performance of modern landfills is governed by a set of systems, including the landfill cover and the bottom barrier. In order to minimise the environmental impacts of a landfill, a systems engineering approach may be adopted for the landfill design. Such an approach requires analysing the interactions between the different components of each system involved and then evaluating the response of the entire system assembled to quantify its overall engineering performance. The effectiveness of the lining systems is demonstrated through the verification that the risk for human health and the environment due to pollutant migration is limited to an acceptable level. This risk is quantified through the calculation of the pollutant concentration in the groundwater, which is expected to remain less than some prescribed level at a compliance point. The paper describes a simplified approach to the analysis of pollutant transport, which allows the pollutant concentration in the groundwater to be calculated under different boundary conditions and taking into account the role played by several geosynthetics, such as geonets, geomembranes and geosynthetic clay liners, which are used in landfill lining systems.

1 INTRODUCTION

Modern landfills are required to guarantee the safe disposal of waste for the foreseeable future in order to protect human health and the environment from the harm caused by the release of contaminants. The long-term performance of landfills relies upon the effectiveness of the cover and bottom barrier systems. All the barrier or lining systems include a high-permeability component, which is aimed at collecting and removing the percolating liquids, and a low-permeability component (or liner), which limits liquid infiltration and/or contaminant migration.

Rowe (2011, 2018) pointed out that in order to minimize the environmental impacts of a landfill, a system engineering approach to the design should be adopted. This approach involves decomposing the entire system into subsystems that consist of simpler identifiable components. The performance of the individual components, as well as the interactions between different components of the system, have to be assessed before the response of the entire system can be quantified to obtain its overall engineering performance.

A simplified approach is proposed to model the interaction between the waste, the lining system and the aquifer that is located underneath the landfill. The aquifer represents the natural resource to be protected by limiting the impact due to the migration of contaminants from the waste. As a result, the performance criterion adopted for the design is that the lining system must ensure that the concentrations of pollutants in the groundwater remain less than some prescribed threshold level at a specified compliance point, which is typically a monitoring well that is located downgradient from the landfill. The threshold concentration value of a given pollutant is related to a corresponding risk for human health and the environment

through a toxicological model that takes into account the pollutant features and the exposure paths (Dominijanni & Manassero 2021; Dominijanni *et al.* 2021a).

The lining system typically includes a leachate collection system, which involves a series of perforated pipes in a granular drainage layer that are aimed at minimizing the leachate ponded head. The drainage layer may be replaced by biplanar or triplanar geonets, which are characterized by a high in-plane transmissivity. Geonets are covered with a geotextile on their upper and lower surfaces to preserve their drainage function by preventing direct contact with soil particles. The leachate collection system overlies the low-permeability barrier component, which may consist of compacted clay layers (CCLs) and/or geosynthetic components, such as geomembrane layers (GMLs) and geosynthetic clay layers (GCLs). GMLs can be coupled with CCLs and GCLs to form composite liners that provide optimal groundwater protection performance. Moreover, the aquifer located beneath a landfill is typically separated from the waste not only by these artificial layers but also by a natural foundation or attenuation layer (AL), which plays an important role in limiting contaminant migration (Dominijanni & Manassero 2021).

The interaction analysis between the waste, the lining system and the aquifer can be carried out on the basis of a conceptual model that identifies the leachate produced by the waste with the source of contamination and a monitoring piezometer (which may be real or virtual), placed downstream of the landfill, with the point of compliance, as shown in Figure 1.
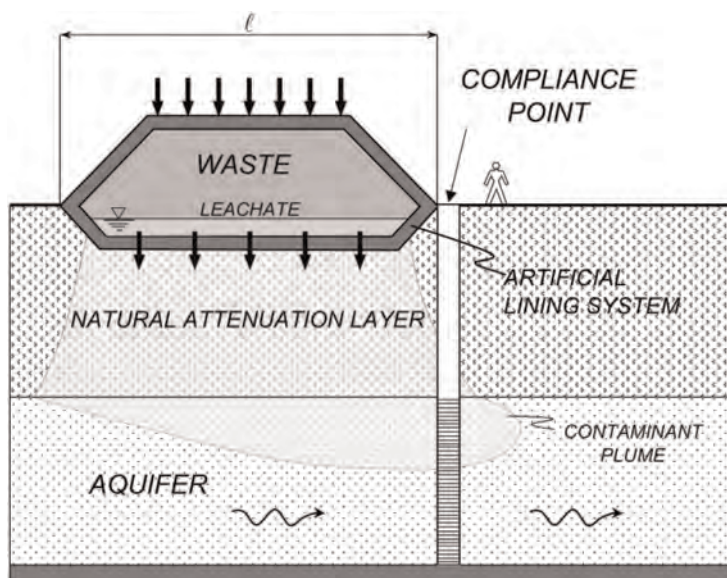

Figure 1.   Reference scheme for the interaction analysis between the waste, the lining system and the aquifer. The pollutant released by the waste migrates vertically through the engineered lining system and the natural attenuation layer up to the underlying aquifer, where pollutant transport becomes horizontal.

2   ASSESSING THE LANDFILL SYSTEMS INTERACTION

The waste, the lining system and the aquifer are considered as control volumes characterized by an internal homogeneous concentration.

The contaminant mass in the waste disposal facility decreases over time due to degradation processes and migration through the barrier system. The mass balance may be expressed as follow:

$$H_w B_l \cdot \frac{dc_l}{dt} = -J_{s,ad} - J_{s,d} - \lambda H_w c_l \tag{1}$$

where H_w is the waste thickness, B_l is the bulk leachate partition coefficient, c_l is the contaminant concentration in the leachate, $J_{s,ad}$ is the contaminant advective flux through the barrier system, $J_{s,d}$ is the contaminant diffusive flux through the barrier system and λ is the decay constant of a linear or first-order decay reaction.

The contaminant migration has been decomposed into a pure advective flux, $J_{s,ad}$, and a pure diffusive flux, $J_{s,d}$, for the sake of simplicity, although the two transport mechanisms are actually coupled in a single advective-diffusive flux. Accepting this modelling simplification allows the advective flux to be expressed as follows:

$$J_{s,ad} = a_w \cdot q \cdot c_l \tag{2}$$

where a_w is the portion of barrier area that is wetted by the leachate and q is the vertical volumetric liquid flux that takes place through the mineral barrier underlying the geomembrane.

The parameter a_w depends on the number, size and shape of the holes in the geomembrane. An empirical equation for the calculation of the leakage rate through a circular hole with a diameter ranging from 100 mm to 600 mm in a geomembrane with imperfect contact with the underlying mineral layer was provided by Giroud (1997):

$$Q = C_q \cdot A_h^{0.1} \cdot h_p^{0.9} \cdot k_{eq}^{0.74} \cdot \left[1 + 0.1 \left(\frac{h_p}{L} \right)^{0.95} \right] \tag{3}$$

where Q is the flow rate, C_q is a dimensionless quality coefficient of the contact between the geomembrane and the underlying mineral layer, which can be assumed equal to 0.21 for good contact conditions and 1.15 for poor contact conditions, A_h is the circular hole area, h_p is the hydraulic head on top of the geomembrane, k_{eq} is the equivalent hydraulic conductivity of the underlying mineral barrier and L is the thickness of the mineral barrier.

The equivalent hydraulic conductivity, k_{eq}, is calculated as the harmonic mean of the hydraulic conductivities of individual layers:

$$k_{eq} = \frac{L}{\sum\limits_{i=1}^{N} \frac{L_i}{k_i}} \tag{4}$$

where k_i and L_i are the hydraulic conductivity and the thickness of the i-th layer, respectively, and N is the number of layers and $L = \sum\limits_{i=1}^{N} L_i$.

The vertical flux through the mineral barrier underlying the geomembrane is given by Darcy's equation:

$$q = k_{eq} \frac{h_p + L}{L} \tag{5}$$

If the holes are assumed to be all equal to each other and their number per unit area is n_h, the wetted portion of the barrier area may be estimated as follows (Dominijanni *et al.* 2021a, b; Giroud 1997; Katsumi *et al.* 2001):

$$a_w = \frac{n_h Q}{q} \tag{6}$$

where Q is the flow rate through a single hole.

In the absence of the geomembrane, the parameter a_w is equal to 1 as the whole barrier area is wetted by the leachate. Instead, the condition $a_w = 0$ corresponds to a geomembrane without holes.

An approximate estimation of the diffusive flux, $J_{s,d}$, in Equation 1 can be obtained by introducing mass transfer coefficients or diffusivities to account for the transport through the barrier system. Under such assumptions, $J_{s,d}$ may be expressed as follows:

$$J_{s,d} = a_w \Lambda_{d,w}(c_l - c_{b,w}) + (1 - a_w)\Lambda_{d,nw}(c_l - c_{b,nw}) \tag{7}$$

where $c_{b,w}$ and $c_{b,nw}$ are the average contaminant concentrations in the barrier system in correspondence to the wetted and non-wetted portions of the landfill barrier, respectively, and $\Lambda_{d,w}$ and $\Lambda_{d,nw}$ are the related diffusivities. $\Lambda_{d,w}$ and $\Lambda_{d,nw}$ are related to the diffusion coefficients of the components of the barrier system as follows:

$$\Lambda_{d,w} = \frac{1}{\sum_{i=1}^{N} \frac{L_i}{n_i D_i^*}} \tag{8}$$

$$\Lambda_{d,nw} = \frac{1}{\frac{L_g}{K_g D_g} + \sum_{i=1}^{N} \frac{L_i}{n_i D_i^*}} \tag{9}$$

where n_i and D_i^* are the porosity and the effective diffusion coefficient of the i-th layer, respectively, L_g is the thickness of the geomembrane, K_g is the partition coefficient between the geomembrane and the contaminant, and D_g is the diffusion coefficient of the geomembrane.

The average concentrations $c_{b,w}$ and $c_{b,nw}$ in the barrier system are found from the contaminant mass balances in the corresponding control volumes:

$$n_b R_{d,b} L \cdot \frac{dc_{b,w}}{dt} = qc_l + \Lambda_{d,w}(c_l - c_{b,w}) - qc_b - \Lambda_{d,w}(c_{b,w} - c_{aq}) - \lambda \cdot n_b R_{d,b} L \cdot c_{b,w} \tag{10}$$

$$n_b R_{d,b} L \cdot \frac{dc_{b,nw}}{dt} = \Lambda_{d,nw}(c_l - c_{b,nw}) - \Lambda_{d,nw}(c_{b,nw} - c_{aq}) - \lambda \cdot n_b R_{d,b} L \cdot c_{b,nw} \tag{11}$$

where n_b is the average porosity of the mineral layers of the barrier system, $R_{d,b}$ is the average retardation factor of the contaminant through the barrier system and c_{aq} is the contaminant concentration in the aquifer that is located underneath the barrier system.

The mass balance of the contaminant in the underlying aquifer allows c_{aq} to be determined:

$$n_{aq} R_{d,aq} L_{aq} \cdot \frac{dc_{aq}}{dt} = a_w qc_{b,w} + a_w \Lambda_{d,w}(c_{b,w} - c_{aq}) + (1 - a_w)\Lambda_{d,nw}(c_{b,nw} - c_{aq}) +$$
$$q_{aq,0} c_{aq,0} - \left(q_{aq,0} + a_w q \frac{\ell}{L_{aq}}\right) c_{aq} - \lambda \cdot n_{aq} R_{d,aq} L_{aq} \cdot c_{aq} \tag{12}$$

where n_{aq}, $R_{d,aq}$ and L_{aq} are the porosity, the retardation factor and the thickness of the aquifer, respectively. $q_{aq,0}$ and $c_{aq,0}$ are the aquifer horizontal specific discharge and the contaminant concentration in the aquifer upstream from the landfill, respectively.

Equations 1, 10, 11 and 12 describe the interaction between the waste, the barrier system and the aquifer. The aquifer represents the natural resource to be protected from the potential harm caused by the contaminant migration from the waste leachate. As a result, the determination of c_{aq} allows the impact of landfill contamination on the potential use of the groundwater to be assessed. For instance, c_{aq} may be compared with a threshold value related to the production of drinkable or irrigation water from a well located in correspondence with the compliance point just downstream from the landfill.

3 APPLICATION EXAMPLE

The following example is provided to illustrate how the previously defined set of equations can be employed in order to assess the effectiveness of a landfill barrier system. The solution of Equations 1, 10, 11 and 12 may be obtained numerically by using the forward Euler method to integrate with respect to the time t, or analytically by using similarity transformations.

The barrier system consists of a composite liner constituted by a 2.5 mm thick geomembrane liner (GML) and a 1 m thick compacted clay liner (CCL), which overlies a 3 m thick attenuation layer (AL), as shown in Figure 2.

The height of the ponded leachate in the leachate removal and collection layer, h_p, is assumed equal to 0.3 m, and the hydraulic head difference between the top of the mineral layers and the bottom of the attenuation layer, is supposed equal to 3 m (Figure 2).

The physical, hydraulic and transport parameters that have been assigned to the geomembrane and the mineral layers are reported in Figure 2 and in Table 1.

The analysis is developed for benzene, which is a common component of municipal solid waste landfill leachates. The release of benzene is assumed to occur from a 30 m-thick waste deposit, which is characterized by a bulk leachate partition coefficient $B_l = 4$. The decay constant λ is calculated from the upper value for the half-life of benzene given by Howard *et al.* (1991), which is 730 days, and results in being equal to $1.1 \cdot 10^{-8}$ s^{-1}.
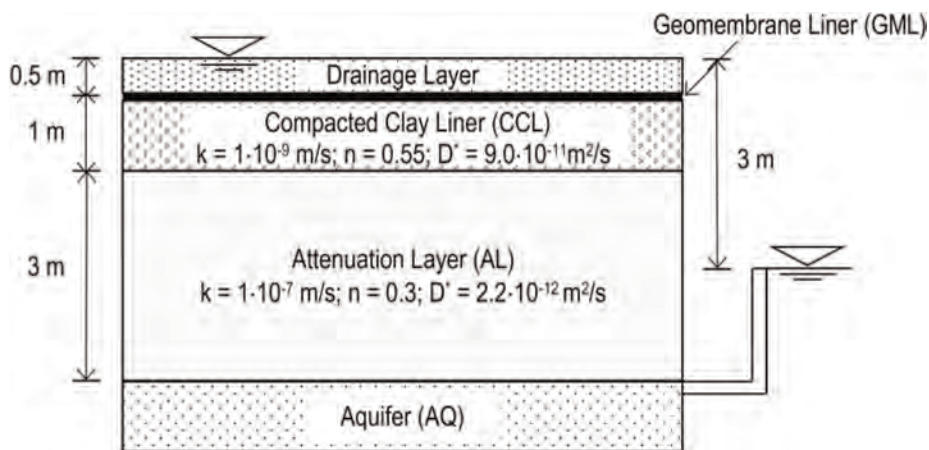

Figure 2. Scheme of the barrier system considered in the example analysis.

Table 1. Physical, hydraulic and transport parameters of the geomembrane and the mineral layers of the barrier system.

Parameter	Mineral layers	
	CCL	AL
Thickness, L (m)	1	3
Hydraulic conductivity, k (m/s)	$1 \cdot 10^{-9}$	$1 \cdot 10^{-7}$
Porosity, n (-)	0.55	0.3
Effective diffusion coefficient, D* (m²/s)	$9.0 \cdot 10^{-11}$	$2.2 \cdot 10^{-10}$
	Geomembrane	
Thickness, L_g (m)	0.0025	
Partition coefficient for benzene, K_g (-)*	30	
Diffusion coefficient for benzene, D_g (m²/s)*	$0.35 \cdot 10^{-12}$	

*data from Sangam and Rowe (2001).

The average porosity n_b of the barrier system is equal to 0.36. The retardation factor $R_{d,b}$, which is estimated from a distribution coefficient $K_d = 1.33$ ml/g (Hrapovic 2001) and an average dry density $\rho_d = 1.6$ g/cm³, results equal to 6.9.

The aquifer located beneath the landfill is assumed to be characterized by a porosity n_{aq} equal to 0.3, a retardation factor $R_{d,aq}$ of 8.1 and a thickness L_{aq} of 10 m. The horizontal groundwater volumetric flux just upstream from the landfill, $q_{aq,0}$, is equal to $1 \cdot 10^{-6}$ m/s (= 31.6 m/ year). The concentration of benzene upstream from the landfill, $c_{aq,0}$, is assumed to be null.

The analysis has been conducted to simulate the decrease in benzene concentration in the leachate released by the waste over time and the simultaneous increase in benzene concentration in the aquifer located beneath the landfill. The obtained results are shown in Figure 3. The benzene concentration in the waste leachate starts from a value of 1,000 mg/l and reduces to a value of about 1 mg/l after 20 years and 10^{-3} mg/l after 40 years. The reduction in benzene concentration is governed by the degradation process, which is modelled as a first-order decay reaction.
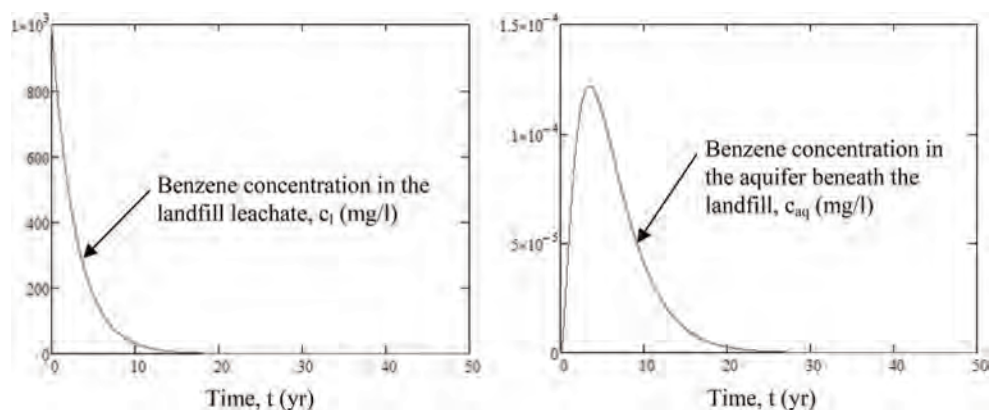

Figure 3. Results of the performed analysis, which show the change in time of the benzene concentration in the landfill leachate, c_l (on the left), and in the aquifer, c_{aq} (on the right).

The analysis takes into account the transport properties of the barrier system, which limits the advective transport through a negligible contribution. Assuming 2 holes/hectare in the geomembrane and poor contact conditions between the geomembrane and the underlying compacted clay liner ($C_q = 1.15$), the portion of the barrier area that results in being wetted is equal to only 0.7%.

The benzene concentration in the aquifer increases up to a peak value that is reached after about 3.5 years. The peak value of about $1.2 \cdot 10^{-4}$ mg/l is lower than the screening value that is indicated by the Italian regulation (10^{-3} mg/l). As a result, the benzene does not appear to cause any harm to the groundwater quality due to the effectiveness of the landfill barrier system.

4 CONCLUSIONS

The proposed approach for modelling the interaction between the waste, the lining system and the aquifer located beneath the landfill allows the impact of contaminant release on the groundwater quality to be assessed. The role played by the geosynthetics and the natural attenuation mechanisms, such as degradation and sorption, in limiting the contaminant migration can therefore be fully appreciated.

REFERENCES

Dominijanni, A. & Manassero, M. 2021. Steady-state Analysis of Pollutant Transport to Assess Landfill Liner Performance. *Environmental Geotechnics* 8(7): 480–494.

Dominijanni, A., Guarena, N. & Manassero, M. 2021a. Risk Assessment Procedure for the Performance-Based Design of Landfill Lining Systems and Cutoff Walls. *Japanese Geotechnical Society Special Publication* 9(5): 199–204.

Dominijanni, A., Guarena, N. & Manassero, M. 2021b. La Progettazione Prestazionale dei Sistemi di Contenimento Degli Inquinanti Nelle Discariche. In *Atti del XXVII Convegno Nazionale di Geotecnica, Reggio Calabria (Italy), 13–15 Luglio 2022*. Roma: Associazione Geotecnica Italiana (*in Italian*).

Giroud, J.P. 1997. Equations for Calculating the Rate of Liquid Migration Through Composite Liners Due to Geomembrane Defects. *Geosynthetics International* 4(3–4): 335–348.

Howard, P.H., Boethling, R.S., Jarvis, W.F., Meylan, W.M. & Michalenko, E.M. 1991. *Handbook of Environmental Degradation Rates*. Chelsea: Lewis Publishers.

Hrapovic, L. 2001. Laboratory Study of Intrinsic Degradation of Organic Pollutants in Compacted Clayey Soil. Ph.D. thesis, The University of Western Ontario: 300 pp.

Katsumi, T., Benson, C.H., Foose, G.J. & Kamon, M. 2001. Performance-based Design of Landfill Liners. *Engineering Geology* 60(1–4): 139–148.

Rowe, R.K. 2011. Systems Engineering the Design and Operations of Municipal Solid Waste Landfills to Minimize Leakage of Contaminants to Groundwater. *Geosynthetics International* 18(6): 391–404.

Rowe, R.K. 2018. Environmental Geotechnics: Looking Back, Looking Forward (16th Croce Lecture). *Rivista Italiana di Geotecnica* 2018(4): 8–40.

Sangam, H.P. & Rowe, R.K. 2001. Migration of Dilute Aqueous Organic Pollutants Through HDPE Geomembranes. *Geotextiles and Geomembranes* 19(6): 329–357.

Geosynthetic sorption sheet—Another function of geosynthetics?

T. Kato, A. Takai, Y. Zhang, L.W. Gathuka & T. Katsumi
Graduate School of Global Environmental Studies, Kyoto University, Kyoto, Japan

Y. Kinoshita
Graduate School of Engineering, Former Student of Kyoto University, Kyoto, Japan

ABSTRACT: This paper discusses a novel geosynthetics sorption sheet that provides both sorption and traditional geosynthetic functions. In particular, the geosynthetic sorption sheet facilitates both water drainage and chemical barrier function. In this paper, batch sorption tests are used to evaluate the sheet's attenuation performance. The results of soil tank tests involving a 110 x 80 x 12 cm tank are also discussed. A key finding was the higher sorbed extent of arsenate compared with arsenite. The sheet absorbed more than 80% of the arsenic when it was contacted for 15 minutes with 0.1 mg/L of arsenate. Based on the soil tank test, ground particles surrounding the sheet are more important to seepage water distribution than the sheet itself.

1   INTRODUCTION

Excavated soils with geogenic contamination such as arsenic (As) or boron (B) are generated from various construction projects since these elements are widely distributed in several geologic strata such as marine clay layers, sedimentary rocks, hydrothermally altered rocks, etc. In Japan, these soils and/or rocks are expected to be used in embankments or other geotechnical applications to reduce the volume of soil disposal as well as to reduce the use of new soil materials. For such application, proper management against geogenic contamination is a primary engineering concern since groundwater contamination due to possible leaching of toxic elements is required to be prevented. Given the importance of developing economical and effective utilization methods for geogenic contaminated soils, effective countermeasures should be established.

Geosynthetic sorption sheets have been developed to contain the toxic elements from geogenic contaminated soils. By being installed below the excavated soils with natural contamination, the geosynthetic sorption sheet is expected to trap the contaminants. It might release the infiltrated water free from contaminants into the base soil layer to prevent groundwater contamination. The geosynthetic sorption sheet consists of sorptive material attached or adhered to the fabric. Several types of sorptive materials, such as hydrotalcite, are applied, and several types of fabric can also be used. Although knowledge has been accumulated on the sorption performance of various kinds of sorptive materials, sorption performances considering the effect of practical conditions, such as preferential flows and overburden pressures, need to be evaluated (Kinoshita *et al.* 2021). Therefore, in this study, the effect of preferential flow in the soil layer overlying the geosynthetic sorption sheet is experimentally evaluated.

2 GEOSYNTHETIC SORPTION SHEET

Utilization of surplus soil is quite important for material recycling. The amount of soil generated from construction work was more than 130 million m^3 in 2018 in Japan (MLIT 2020). Since such a large amount of soil is generated, the soil should be utilized as a geo-material for embankments, fill, etc., while geogenic contaminants are often contained in the excavated soil higher than the environmental standard values (e.g., Kato *et al.* 2023; Tabelin *et al.* 2018). Therefore, proper countermeasures must be taken to prevent contamination of the surrounding environment. However, if such contaminants are of natural origin, the exceeding degree is often within several times the standard value (e.g., Ito & Katsumi 2020; Naka *et al.* 2016). Toward sustainable development, although the standard is exceeded, if the concentration is relatively low, geogenic contaminated soils should be utilized as embankment material with proper countermeasures.

Containment methods using a geomembrane may be an effective way when geogenic contaminated soils are used for embankments. However, the interface between the geomembrane and soils may become a sliding surface. Further, the containment may be an excessive countermeasure, considering the low-concentration toxic chemicals such as the geogenic contaminants.

Geosynthetic sorption sheets have been developed as a promising countermeasure for geogenic contamination (e.g., Kinoshita *et al.* 2021; Miyawaki *et al.* 2022). Herein, the geosynthetic sorption sheet is placed under the excavated soils, as shown in Figure 1. This geosynthetics sorption sheet offers a new function of sorption, in addition to the traditional geosynthetics functions (reinforcement, barrier, drainage, separation, filtration, stabilization). Since the infiltration can be permitted, pore water does not accumulate in the embankment. Furthermore, the upper soil layer can be compacted. Therefore, the stability of the embankment can be maintained. While the sheet is cost-effective and has workability, some challenges remain to be solved. The reliability of the material may decrease in the case of clogging or preferential flow. For instance, when there is preferential flow, a limited area of geosynthetic sorption sheets may be involved in the sorption of toxic chemicals. Furthermore, the sorption kinetics should be investigated since a short contact time is expected for the sheet considering the in-situ condition.
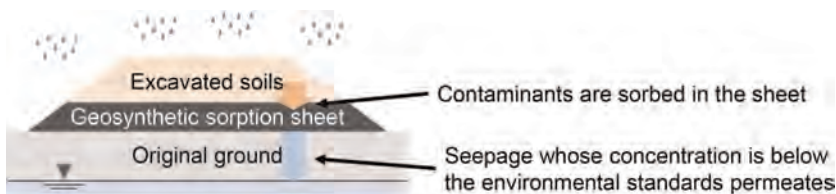

Figure 1. Application of the geosynthetic sorption sheet for geogenic contaminated soils.

3 MATERIALS AND METHODS

3.1 *Materials*

Figure 2 shows the geosynthetics sorption sheet manufactured by TOYOBO CO., LTD used in this study. One side of the sheet is a hydrophilic long-fiber nonwoven fabric coated with an artificial hydrotalcite compound. The hydrotalcite is adjusted to a nano-size of about 10 nm, and 5.0×10^{-2} kg/m^2 of hydrotalcite is coated. The thickness of the sheet is 2.8 mm. The
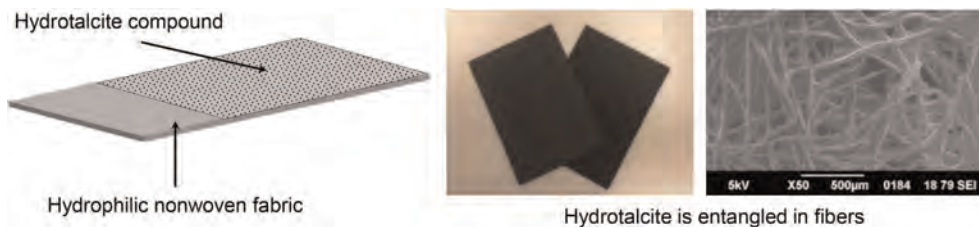
Figure 2.   Geosynthetics sorption sheet used in this study.

hydraulic conductivity is 1.7×10^{-3} m/s (JIS A 1218 2009). The pore size range of the sheet was approximately 10–120 μm, and the average pore size d_{50} was 47 μm.

3.2   Batch sorption tests

Batch sorption tests were conducted to evaluate the sorption performance against arsenic (As) contamination under different contact time to evaluate the sorption kinetics. Figure 3 shows the test setup. Since arsenic mainly exists in the solution as either arsenite [As(III)] or arsenate [As(V)] (Mohan & Pittman 2007), As(III) and As(V) solutions were prepared with the sodium arsenite (NaAsO$_2$) and sodium dihydrogen arsenate (Na$_2$HAsO$_4$ 7H$_2$O) salts, respectively. The salts were dissolved in distilled water to prepare concentrations between 0.1–20 mg/L. A 200 mL of As solution and the geosynthetic sorption sheet cut to 80 mm $\times$ 50 mm were put in a plastic bottle. Afterward, the bottles were horizontally shaken between 5 minutes and 24 hours at 150 rpm using a mechanical shaker (TAITEC TS-10) under room temperature ($\sim$20°C). Three replicate tests were performed for each solution.
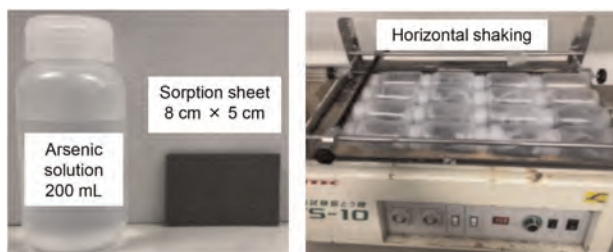

Figure 3.   Set up of the batch sorption tests.

After the sample preparation mentioned above, centrifugation at 3000 rpm for 10 min and filtration with a 0.45 μm membrane filter was carried out to separate the liquid from the solid. The pH of the filtrate was measured using a pH/EC meter (Horiba F-54). The As concentrations were measured using an atomic absorption spectrophotometer (Shimadzu AA-6800). The As removal ratio was calculated using equation (1), shown below:

$$R = \frac{C_0 - C}{C_0} \times 100 \tag{1}$$

where R refers to the removal ratio of As (%), C_0 refers to the As concentrations before the batch sorption tests (mg/L), and C refers to the As concentrations after the batch sorption tests (mg/L).

3.3 Water flow conditions using soil tank tests

Soil tank tests were conducted to evaluate the effect of the preferential flow on the performance of the geosynthetic sorption sheet. The tests were conducted using three different silica sands. Table 1 shows the properties of the silica sands. The soil tank employed was 110-cm wide, 80-cm high, and 12-cm deep, as shown in Figure 4(a). The bottom part of the soil tank consisted of six valleys and water sampling holes (drilled in the bottom of the valley), as shown in Figure 4(b). The seepage water was drained from each water sampling port.

Filter paper was installed at the sampling port at the bottom to prevent the soil particle from flowing out of the tank. Then, the soil layer below the sheet was filled. The air-dried silica sand was filled to achieve a compaction degree of 90%, based on the maximum dry density and optimum water content shown in Table 1. The layer was filled to a height of 1.5 cm from the valley's top, as shown in Figure 4(b). Once the soil layer was filled, the horizontality of the surface layer was confirmed using a level. Next, the geosynthetic sorption sheet cut to 108 cm in width was laid on the soil layer. After that, the same silica sand of the bottom layer was compacted on the geosynthetic sorption sheet with a height of 1 cm. After confirming the horizontality of the top surface of the soil sample using a level, a 3 cm × 3 cm non-woven fabric was laid above the water sampling port (C) to prevent disturbing the silica sand.

After filling the tank with sample, the pump was adjusted to spray water with an intensity of 200 mL/h. Water was sprayed directly above the water sampling port (C), assuming the preferential flow. First, the amount of infiltrated water from each sampling port was measured. Once the difference in the discharged water per hour from the port per hour was less

Table 1. Physical and chemical properties of sand specimens.

| Parameter	Silica sand No. 3	Silica sand No. 5	Silica sand No. 7	Method of measurement
Particle density	2.66 g/cm^3	2.67 g/cm^3	2.749 g/cm^3	JIS A 1202 (2009)
Particle size distribution				JIS A 1204 (2009)
Average particle size	1.4 mm	0.40 mm	0.18 mm	
Coefficient of Uniformity	2.0	1.8	2.4	
Hydraulic conductivity	3.9×10^{-3} m/s	1.3×10^{-3} m/s	1.5×10^{-4} m/s	JIS A 1218 (2009)
Compaction properties				JIS A 1210 (2009)
Optimum water content	12.7%	13.0%	17.1%	
Maximum dry density	2.66 g/cm^3	2.67 g/cm^3	2.749 g/cm^3	
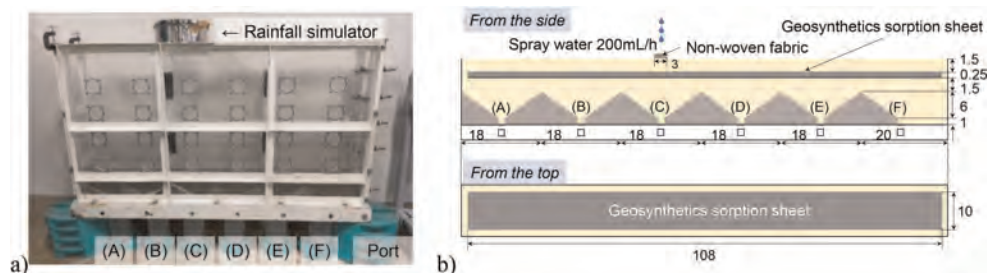
Figure 4. Picture and schematic diagram of the soil tank tests.

than 5%, it was considered that steady state condition was attained. Then, tests were terminated after measuring the amount of water released per hour. The water contents of silica sand near each port were also measured. Each soil tank test was repeated twice.

4 RESULTS AND DISCUSSION

4.1 Arsenic sorption performance

Figure 5 shows the results of the batch sorption tests. The removal ratio of As(V) was higher than that of As(III), as shown in Figure 5(a). This is because more than half of As(III) exists in the neutral region as H_3AsO_3 with no ionic form or $H_2AsO_3^-$ as an anion with a single form (Smedley & Kinniburgh 2002). On the other hand, more than half of As(V) exists in the state of having the divalent anion $HAsO_4^{2-}$ or the monovalent anion $H_2AsO_4^-$. Since the hydrotalcite compound capture arsenic due to anion exchange (Bhaumik et al. 2005), relatively high sorption performance can exhibit for As(V), which shows stronger electric attraction, while the anion exchange was relatively challenging to occur for As(III).

Figure 5(b) shows that the sorption reaction of As reaches nearly equilibrium at 12 hours because almost the same removal ratio is obtained between 12–24 hours. Even though the short contact time is applied, more than 60% of arsenic can be sorbed by the sheet. This result supports the sorption sheet can be one of the promising countermeasures against geogenic contamination. In addition, the higher the initial concentration of arsenic, the lower the removal ratio obtained. Sorption performance of the geosynthetic sorption sheet is affected by the arsenic concentration of leachate, thus the leaching concentration of a given excavated soil should be carefully investigated.

In the case of As(V) with C_0 = 0.1 mg/L, the removal ratio was higher than 80% at the contact time of 15 minutes. Therefore, if the arsenic contained in the leachate is about 0.1 mg/L of As(V), which corresponds to 10 times the environmental standard value in Japan, enough sorption capacity could be performed even with a short contact time of 15 minutes. This result suggests that sufficient sorption performance can be expected even with a thin geosynthetic sorption sheet that cannot ensure a long contact time with the geogenically contaminated seepage.
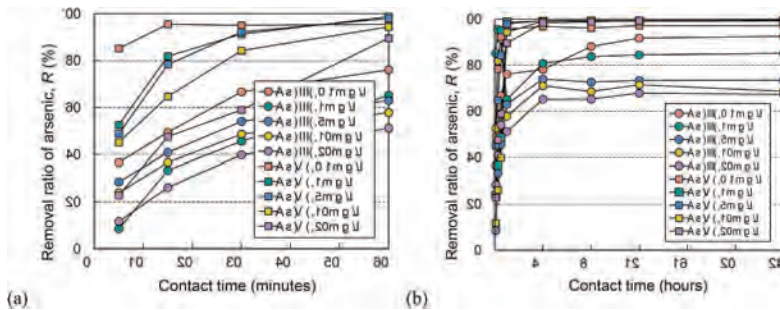

Figure 5. Results of the batch sorption tests of (a) 0–60 minutes, and (b) 0–24 hours.

4.2 Drained seepage from the soil tank tests

Figure 6 shows the amount of drainage per hour from each water sampling port in a steady state when watering is performed. As shown in Figure 6(a), when silica sand No. 3 with a large particle size was used, almost all 200 mL of water sprinkled was drained from the port (C). Judging from Figure 6, the soil tank test was conducted with relatively good
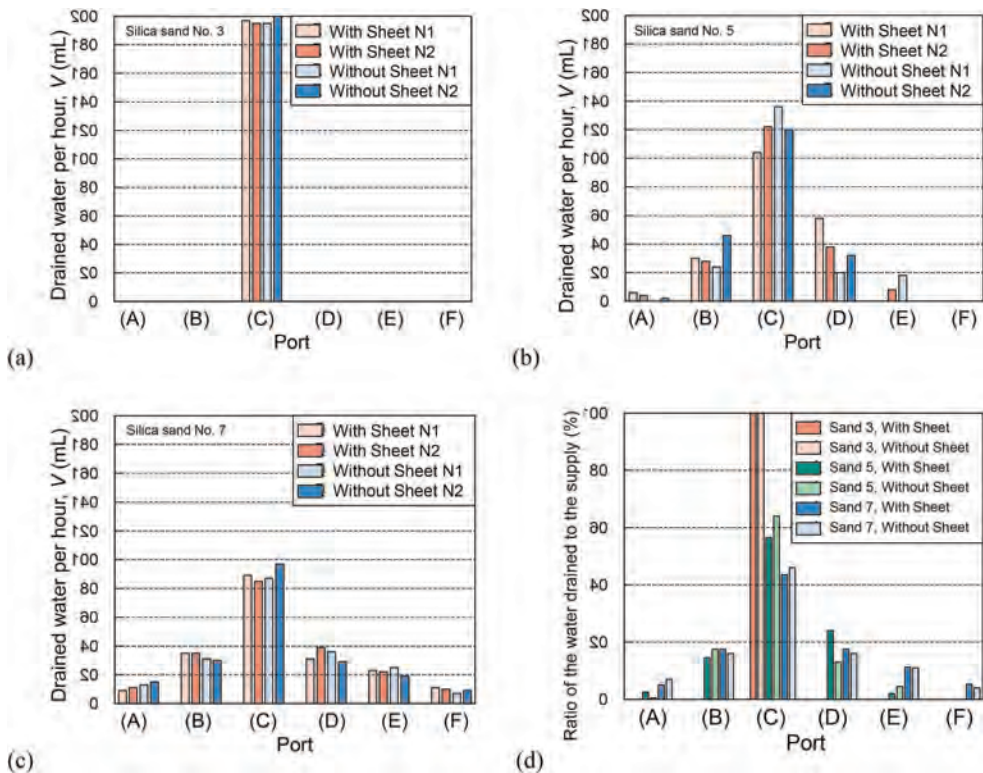
Figure 6. Results of the soil tank tests for (a) Silica sand No.3, (b) Silica sand No.5, (c)) Silica sand No.7, (d) comparison of the effect of installing geosynthetic sorption sheets.

repeatability for duplication. When silica sand No. 5, with a smaller particle size than silica sand No. 3, is used, infiltration water was obtained not only under the watering position (C) but also from (A) to (E), as shown in Figure 6(b). The amount of drainage from (C) was the largest. These results confirmed that a certain amount of infiltrated water could be distributed even with silica sand No. 5, which has a relatively larger grain size than No. 7 and is single-grained soil. As shown in Figure 6(c), when silica sand No. 7, which has a smaller particle size than silica sand No. 5, is used, the amount of drainage from directly below the watering position (C) decreases, and (A) and (E) further increased the amount of water discharged. This result suggested that the infiltration water could be more distributed in the ground with smaller grain sizes.

Figure 6(d) shows the ratio of the amount of drained water from each port. The average value of the test results of two repetitions is shown. For example, focusing on port (C) in Figure 6(d), with silica sand Nos. 5 and 7, the amount of water from (C) was slightly affected by the presence of the sorption sheet, but the difference was not significant. The particle size of the ground surrounding the sheet may affect the seepage water distribution more than the presence the sorption sheet.

5 CONCLUSIONS

When applying geosynthetic sorption sheets, materials that can attenuate contaminants in a short time should be selected. This study revealed that the geosynthetic sorption sheet

exhibits high sorption performance for arsenic even under short contact times. Especially in the case of low concentration, such as geogenic contamination, high sorption performance is expected.

The embankment using geogenically contaminated soils should be constructed to permeate seepage water evenly to the sheets. The seepage water was more distributed in the ground with smaller grain sizes. One reason is that the smaller the soil particles, the greater the suction. Therefore, the surrounding soil layer should be sufficiently compacted when installing a geosynthetic sorption sheet. Further, applying fine-grained soil is recommended so that the soil layer retains pore water for longer periods.

REFERENCES

Bhaumik, A., Samanta, S., and Mal, N.K. 2005. Efficient Removal of Arsenic From Polluted Ground Water using a Layered Double Hydroxide Exchanger. *Indian Journal of Chemistry* 44, 1406–1409.

Ito, H., and Katsumi, T. 2020. Leaching Characteristics of Naturally Derived Toxic Elements From Soils in the Western Osaka area: Considerations from the Analytical Results under the Soil Contamination Countermeasures Act. *Japanese Geotechnical. Journal* 15(1), 119–130. (in Japanese).

Kato, T., Takai, A., Iwata, Y., Gathuka, L.W., and Katsumi, T. 2023. Evaluating Temperature Effects on Leaching Behavior of Geogenic Arsenic and Boron From Crushed Excavated Rocks using Shaking and Nonshaking Batch Tests. *Soils and Foundations*, 63(1), 101274.

JIS A 1202, 2009. *Test Method for Density of Soil Particles*. Japanese Standards Association.

JIS A 1204, 2009. *Test Method for Particle Size Distribution of Soils*. Japanese Standards Association.

JIS A 1210, 2009. *Test Method for Soil Compaction Using a Rammer*. Japanese Standards Association.

JIS A 1218, 2009. *Test Methods for Permeability of Saturated Soils*. Japanese Standards Association.

Kinoshita, Y., Zhang, Y., Kato, T., Gathuka, L.W., Takai, A., and Katsumi, T. 2021. Arsenic Attenuation by Geosynthetics Sorption Sheet Under Different Overburden Pressure Conditions. *Geosynthetics Engineering Journal* 36, 117–124. (in Japanese).

Miyawaki, K, Ishitobi, Y., Fujiyoshi, R., and Shimoda, K. 2022. Evaluation of Adsorption Characteristic by Sheet Adsorption Materials (5). *The 27th Workshop on Groundwater/Soil Contamination and Prevention Countermeasures*, 359–361. (in Japanese).

MLIT (Ministry of Land, Infrastructure, Transport and Tourism). 2020. Results of the Survey on Construction By-products in FY2018. See https://www.mlit.go.jp/report/press/sogo03_hh_000233.html (accessed 12/13/2022). (in Japanese).

Mohan, D., and Pittman Jr. C.U. 2007. Arsenic Removal From Water/wastewater using Adsorbents—A Critical Review. *Journal of Hazardous Materials* 142, 1–53.

Naka, A., Yasutaka, T., Sakanakura, H., Kalbe, U., Watanabe, Y., Inoba, S., Takeo, M., Inui, T., Katsumi, T., Fujikawa, T., Sato, K., Higashino, K., and Someya, M. 2016. Column Percolation Test for Contaminated Soils: Key Factors for Standardization. *Journal of Hazardous Materials* 320, 326–340.

Smedley, P.L., and Kinniburgh, D.G. 2002. A Review of the Source, Behavior and Distribution of Arsenic in Natural Waters. *Applied Geochemistry* 17, 517–568.

Tabelin, C.B., Igarashi, T., Villacorte-Tabelin, M., Park, I., Opiso, E.M., Ito, M., and Hiroyoshi, N. 2018. Arsenic, Selenium, Boron, Lead, Cadmium, Copper, and Zinc in Naturally Contaminated Rocks: A Review of Their Sources, Modes of Enrichment, Mechanisms of Release, and Mitigation Strategies. *Science of the Total Environment* 645, 1522–1553.

Filtration and drainage

Effect of installation under Nordic conditions on drainage geosynthetics: ROUGH project

H. Ehrenberg
Naue GmbH & Co. KG, Germany

C. Recker
Sintef Community, Münster, Germany

Ph. Delmas
Sintef Advisor, France

ABSTRACT: On request of Finnish Transport Infrastructure Agency (Finland), Norwegian Public Roads Administration (Norway) and Swedish Transport Administration (Sweden), Sintef (Norway) has prepared guidelines on the use of geosynthetics in Nordic conditions. The ROUGH project (RecOmmendations for the Use of GeosyntHetics in Nordic conditions) has been realised together with several manufacturers of geosynthetics. The paper focuses on the behaviour of drainage geosynthetics during installation in Nordic conditions. The test conditions included prior storage at Nordic temperatures under which the products were also installed, Nordic conditions such as crushed rock and compaction, followed by laboratory tests of the exposed and unexposed geosynthetic samples.

1 INTRODUCTION

In order to be able to propose recommendations for the use of different kinds of geosynthetics in Nordic conditions, an investigation was carried out to collect information and provide data on their behaviour during installation in Nordic conditions (sub-zero temperatures, soil types and working conditions) (ROUGH project 2022). The investigation included a full-scale trial at a site in Northern Finland, 15 km southeast of Kemi along the E8/E75. Drainage geosynthetics were installed at sub-zero temperatures ($-10°C$) under Nordic conditions, followed by tensile and compressive creep testing of the exhumed materials alongside non-exposed materials at temperatures of $+20°C$, $0°C$, $-10°C$ and $-20°C$. Installation and removal of the geosynthetics took place on 5th and 6th February 2020.

The drainage geosynthetics were installed on the locally available frozen soil. A layer of crushed rock was then dropped over the drainage geosynthetics and compacted using typical construction machinery. The test setup was dismantled, materials were excavated, and samples taken for laboratory tests.

Two different drainage geosynthetics have been tested with different product structures and produced with polyolefin.

2 CLIMATIC CONDITIONS FOR THE INSTALLATION TRIAL

The temperature was recorded on site and compared with the data provided online by the Finnish Meteorological Institute (www.ilmatieteenlaitos.fi) from the nearest weather station at Kemi Airport (distance 20 km). Temperatures measured on site matched the weather data. For

this reason, the data recorded hourly by the Finnish Meteorological Institute were used to indicate the temperatures during the storage on site and installation of the geosynthetic products. During installation of the products and compaction of the layers of crushed rock material, the air temperature ranged between – 7°C and – 15°C. No snow needed to be removed from the test section and no snowfall occurred during the installation and filling work. During the deconstruction/recovery of the samples on Thursday, 6th February 2020, temperatures between – 4°C and – 7°C were recorded.

3 CRUSHED ROCK MATERIAL

The material used for the subgrade was a typical locally available soil which was frozen.

The material used for the base layer was typical for Finnish road construction and unbound granular subbases. Figure 1 displays the particle-size distribution of the material used together with the limit values presented in Finnish guidelines InfraRYL for the base course. The material is named as "KaM 0/56" which means it is crushed rock GO 0/56 mm based on SFS-EN 13242.
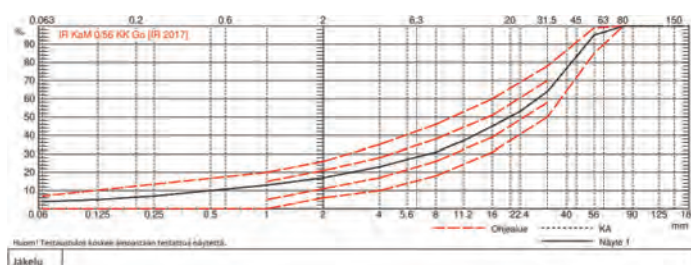

Figure 1.   Particle-size distribution of crushed rock used and the Finnish limit values for base material.

4 TRIAL SETUP AND CONSTRUCTION

Construction of the trial sections followed Finnish specifications for road construction. Figure 2 shows the cross-section of the setup. The material used for the subgrade was a typical locally available, frozen soil. The material temperatures were checked with a penetration thermometer approx. 5 – 10 cm below each layer surface.
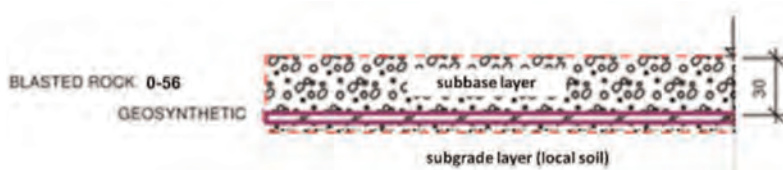

Figure 2.   Cross-section of field trial setup.

In order to minimise positional influences, each product was cut in half and installed at two different locations along the test field. Before installation, the locations of specimens for further laboratory testing were marked. A drawing of the arrangement of the products, and specimens of the products, are given in Figure 3.

TEST SETUP B: DRAINAGE

TOP VIEW AND LOCATION OF SPECIMEN SCALE 1:100

RAMP AREA

RAMP AREA

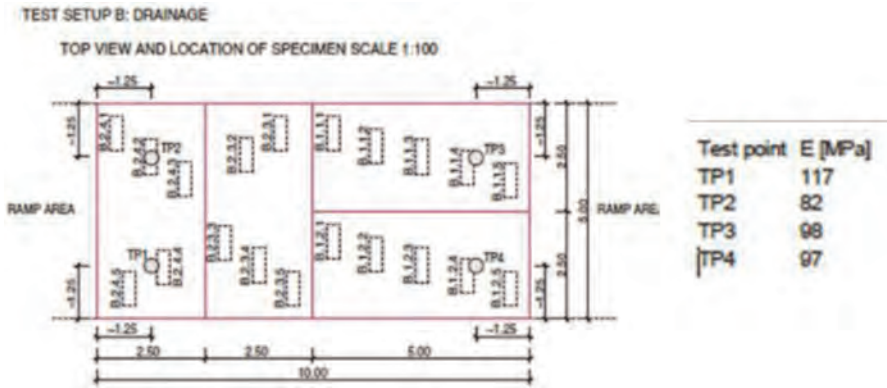| Test point	E [MPa]
TP1	117
TP2	82
TP3	98
TP4	97

Figure 3.   Arrangement of drainage geosynthetic samples.

The drainage geosynthetics were then placed, and finally the base layer of 0/56 crushed rock was dropped with an excavator bucket on the geosynthetics with a measured height of 1.0 m and compacted to a finished layer thickness of 30 cm.

Compaction was done with a 12.6-ton dynamic roller. Five dynamic roller passes were used for compaction of each layer. Compaction control was carried out with a dynamic load plate testing device (a.k.a. portable falling weight deflectometer). The location and results of the compaction control of each layer relative to the sample location were registered. During the compaction process the subsoil had a temperature of about – 6°C. Freshly delivered crushed rock material had a temperature of approx. – 6°C. Before installing the geosynthetics, subbase temperatures of about – 12°C were recorded.

5   RECOVERY OF SAMPLES

Samples needed to be cut from the drainage specimens for testing and evaluation of installation damage. To avoid additional damage to the samples during recovery a suction technique was used. The upper 20 cm of the base layer were removed carefully by excavator as shown in Figure 4 and the remaining 10 cm using a vacuum suction lorry.

Figure 4.   Removing soil with the vacuum / sucking lorry.

Figure 5.   Marked samples for sampling.

After all, the base layer had been removed, samples were cut from the previously marked locations as shown in Figure 5 and labelled. The marking included the product identifier and location in the installed test setup. For transport to the laboratory, the samples cut out were stacked in a robust wooden box with fabric between to avoid mechanical damage or other degradation during the transport.

6 LABORATORY TESTING

Tests were performed on conditioned samples returned from the field trial ('damaged') and on samples taken from the same product specimens not delivered to site ('undamaged'). Temperature conditioning of the undamaged samples provided information on the effect of the temperature on the product behaviour.

6.1 *Testing in temperature-controlled environment*

The damaged samples from Kemi were tested at $+ 20°C$ to determine the corresponding evolution of several characteristics. The tests were focused on the compression behaviour (EN ISO 25619-2) and the hydraulic capacity (EN ISO 12958-1), but also on tensile behaviour (tensile strength and strain acc. EN ISO 10319).

Parallel testing on undamaged samples was carried out in a temperature-controlled chamber as shown in Figure 6. The test specimens were temperature-conditioned for one hour before testing began. After placing the samples in the test rig, the chamber temperature was allowed to stabilise at the required test temperature before testing commenced. The tests were carried out following EN ISI 26619-2 to determine compression strength/strain characteristics.

Non-damaged samples were tested at $– 20°C$, $– 10°C$, $0°C$ and $+ 20°C$.

Figure 6.   Compression test specimen before realisation of test in temperature-controlled chamber. The temperature-controlled chamber can be seen at the back of the photo.

6.2 *Results – Influence of the installation under crushed rock at a temperature of – 10°C on mechanical and hydraulic behaviour of the drainage composites*

Comparison of the tensile strength and strain (20 cm) of the products exposed at Kemi to the installation at $– 10°C$ in crushed rock and tested at $+ 20°C$ in the laboratory versus the "virgin" products shows that the 2 drainage geosynthetics show a similar behaviour when

exposed to the Kemi installation conditions with a reasonable reduction in tensile strength (between ∼ 25 % to ∼ 30 %) and a slightly higher (but still reasonable) reduction in tensile strain (between ∼ 30 % to ∼ 40 %).

Considering the compression behaviour, the 2 products show quite a similar increase of the compression strain when exposed to the Kemi installation conditions (between ∼ 20 % and ∼ 30 %). Whereas the compression strength shows a greater difference between the 2 products, almost no change for 1 product where the other shows a decrease of compression strength of ∼ – 30 %.

The evolution of the drainage waterflow capacity of the products (when exposed, or not, to the Kemi installation conditions) shows a similar decrease on waterflow capacity as on the increase of compression strain (between ∼ 20 % and ∼ 30 %).

6.3 Results – Influence of the temperature (between + 20°C and – 20 °C) on mechanical behaviour of the un-damaged drainage composites.

The tensile tests realised at different temperatures on the undamaged drainage geosynthetics show a quite similar behaviour for the 2 products: a regular increase in the compression strength when the temperature decreases until – 20°C, an increase in the compression strain when the temperature decreases until – 10°C and then remaining constant until – 20°C.

The measurement of the compression strain under 1 MPa is also very interesting to evaluate the evolution of the drainage capacity of the geosynthetic under load. The tests (acc. EN ISO 25619-1) realised at different temperatures (+ 20°C, 0°C, – 10°C, – 20°C) show (Figure 7) almost no influence of the different temperatures on the results (the increase of strains is always ≤ 10 %).
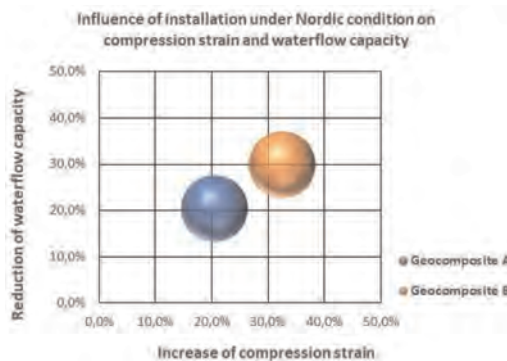

Figure 7. Evolution of the drainage capacity when the products are exposed to the Kemi installation conditions: reduction of waterflow capacity versus increase of compression strain.

7 CONCLUSIONS

When the drainage geosynthetics tested are installed under crushed rock and compacted under normal conditions at – 10°C, the reduction in both tensile strength and tensile strain remains in a reasonable range, which is acceptable for normal use of drainage composites. This means that, if a product is correctly designed for a positive temperature (e.g., + 20°C) for the defined geotechnical conditions of installation (type of soils, drop height, compaction, etc.), no extra installation damage due to negative temperature (−10°C) was observed on the tensile strength and strain.
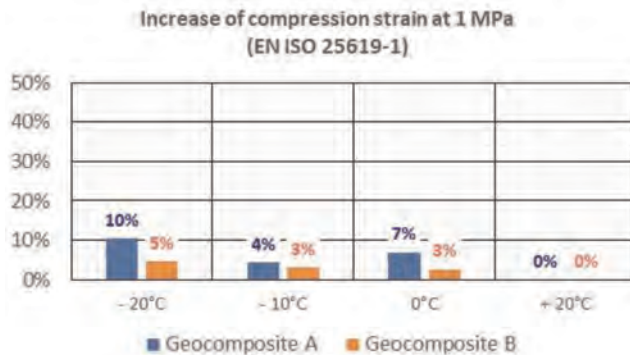
Figure 8. Evolution of the strain at 1 MPa of the products when exposed to different temperatures (+ 20°C, 0°C, – 10°C, – 20°C).

The compression strain at 1 MPa enables a comparison of the behaviour at different temperatures under the same geotechnical conditions. The laboratory tests show that there is almost no influence of strain at 1 MPa at the different temperatures down to – 10°C. As shown on the samples from Kemi ($-10°C$, crushed rock, compaction), a compression strain increase seems related to a similar reduction in water flow capacity.

Thus, it can be expected that the decrease of the water flow capacity linked to low temperature (e.g. – 10°C) should be reduced by only $\sim$ – 4 % to – 5%. The effect of the minus temperature ($-10°C$) on the further hydraulic capacity of the geosynthetic drainage composites appears to be negligeable.

For the defined Nordic conditions in the Kemi study (soil type – gravel, drop height 1 m, compaction, etc.), it is shown for 2 drainage geosynthetics that if these are properly designed to cause minimal installation damage at the usual plus temperatures at the site (i. e. above zero °C), there is no need for extra reduction factors when these products are properly installed at the temperatures below the freezing point of – 10°C.

ACKNOWLEDGEMENTS

REFERENCES

InfraRYL Infrarakentamisen Yleiset Laatuvaatimukset. Maa-, pohja- ja Kalliorakenteet. Rakennustieto. 2018 – InfraRYL *General Quality Specifications for Infrastructure. Earthworks, foundations and rock structures.*

ROUGH project, 2022. RecOmmendations for the Use of GeosyntHetics in Nordic conditions. SINTEF. Part 1 – Tests on Damage During Installation at Low Temperatures. Function: Reinforcement Stabilisation, Filtration, Drainage, (53 p) & Part 2 – Status of Existing Information on Installation Requirements for Sealing Products (GBR-P, GBR-B and GBR-C) Under Nordic Conditions (45 p)

Factors affecting the long-term performance of biplanar geonet-geocomposites

E. Blond
Eric Blond Consultant Inc., Montreal, Canada

A. Maskal
Solmax, Houston, TX, USA

ABSTRACT: Geonet-geocomposites are a common replacement for granular drainage layers, providing drainage, venting, and capillary separation for controlling water content in soils, and controlling hydraulic head around buried structures. This paper describes the mechanisms influencing the long-term compressive properties and flow rate of biplanar geocomposites. For the same structure of product, a relation between the mass per unit area and the capacity of the product to resist sustained stress is quantified using laboratory tests covering aspects such as creep and geotextile intrusion. Results are explained in the context of recent normative developments, i.e., in ISO 18228-4, and ASTM D7931.

1 INTRODUCTION

Drainage geocomposite are widely used to replace granular drainage materials and consequently reduce overall project carbon footprint. HDPE biplanar geonet-geocomposites are the most commonly used geosynthetic drainage products, with the largest number of documented case histories.

However, HDPE can creep, as do most polymers. Therefore, long-term flow capacity of drainage geocomposites must be established, especially for moderate- to high-compressive load applications. These considerations are well-covered in design and specification standards such as ISO 18228-4 and ASTM D7931.

2 IMPACT OF THE STRUCTURE OF BIPLANAR GEONETS ON THEIR PROPERTIES

A drainage geocomposite is comprised of filter geotextiles laminated onto one or both sides of a geonet core. The focus of this paper is biplanar geocomposites in which the geonet core is comprised of two stacked layers of ribs. The ribs within a given layer are parallel to one another and oriented at an angle to the ribs in the other layer. The two layers of ribs are extruded simultaneously to form a monolithic, seamless product as described on Figure 1.

The geonet and the geotextiles both contribute to the performance of a geocomposite. The geonet core is designed to provide compression resistance and to maintain an open structure for carrying water and gases, and the geotextile acts as a filter and supports adjacent materials between the ribs to resist intrusion into that void space.

Wider spacing between ribs allows higher flow capacity within the body of a geonet when used between rigid boundaries. Narrower spacing reducing geotextile span that would allow

Figure 1.   A drainage geocomposite.

the geotextile to sag into the core (i.e., geotextile intrusion, which directly affects its drainage capacity).

Tall/narrow rib shapes provide more open space to accommodate fluid flow, while wider/round ribs have a uniform moment of inertia that resists rollover when placed under compressive load. A slenderness factor can be defined as the ratio between the height and the width of the rib. For a similar mass per unit area, a higher slenderness factor will create a product with higher flow capacity under low normal loads, while a lower slenderness factor will create products with better compressive and creep resistance.

Properties of the geotextile and their lamination onto the geonet core can also affect the geotextile intrusion and consequently the drainage capacity. Higher tensile modulus and lower mass geotextiles generally reduce the amount of intrusion that occurs. The lamination process increases the tensile modulus and confines loose geotextile fibers by calandaring the interior geotextile surface, thereby reducing flow friction from the geotextiles. The lamination process may also slightly increase the crystallinity of the core by way of exposure to a second heating step followed by a (slow) air cooling as opposed to the much faster water quench water cooling used when manufacturing geonets. The thermal history during the lamination process thereby improves the compressive properties of the geonet-geocomposite.

The lamination process involves 2 cylinders between which the geocomposite passes. The distance between these cylinders will affect the shape of the core of the geocomposite, hence its mechanical properties. It will also affect the final thickness of the product, hence its flow rate. Light-weight products with ribs exhibiting a large shape factor may initiate strand rollover during lamination, which can reduce either, or both short- and long-term compressive properties of the geocomposite.

Overall, the long-term hydraulic properties of geonet-geocomposites is the result of a variety of choices which are to be made during the manufacturing process. The most critical ones include the properties of the raw materials (HDPE resin, additives, polypropylene fibers), mechanical properties of the geotextile(s) before lamination, shape of the ribs of the geonet (slenderness factor), distance and angle between the ribs, mass per unit area of the geonet, lamination process and distance between the lamination rolls. However, a range of products is produced from a given extrusion die, varying the mass per unit area of the core. Therefore, when the manufacturing parameters are consistently set from one grade to the other, it is possible to establish trends connecting basic manufacturing parameters such as mass per unit area with the engineering properties of the product.

3   DESIGNING USING ISO 18228-3 OR ASTM D7931

3.1   *Standard and theoretical background*

Long-term flow 'q_{allow}' is assessed using a method first developed by BAM in Germany (reference), adapted by GSI (GRI GC8), and eventually by ASTM D7931 and ISO 18228-4. It is based on a short-term flow test (q_{100}, measured after 100 hours) and reduction factors.

$$q_{allow} = \frac{q_{100}}{RF_{CR} \times RF_{CC} \times RF_{BC} \times RF_{GI} \times RF_{L}} \qquad (1)$$

With:

- q_{100}: Flow rate obtained on the geocomposite after 100 hours seating time using representative normal stress, hydraulic gradient, and boundary conditions.
- RF_{CR}: Reduction Factor for Creep.
- RF_{CC} and RF_{BC}: Reduction Factor for Chemical Clogging and Biological Clogging.
- RF_{GI}: Reduction Factor for (long-term) Geotextile Intrusion, beyond the initial intrusion.
- RF_{L}: Reduction Factor for Laboratory uncertainties.

q_{allow} and q_{100} can be replaced by transmissivity θ_{allow} and θ_{100}. Figure 2 illustrates the effect of creep, geotextile intrusion on the volume of the cavity available for water to circulate, as well as on the differences between the short-term geotextile intrusion, which is already captured in q_{100}, and the long-term geotextile intrusion caused by additional creep of the geotextile.
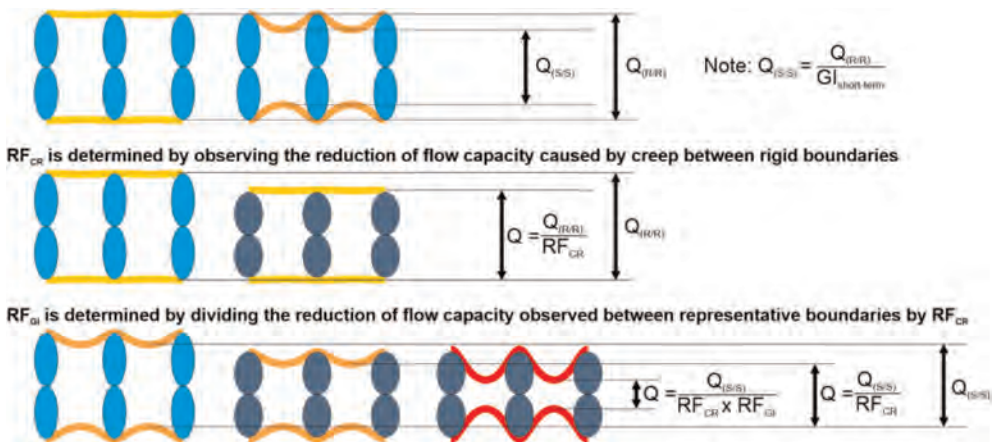

Figure 2.   Distinction between creep, long-term, and short-term geotextile intrusion.

Creep and geotextile intrusion RF are defined using the strategy illustrated on Figure 3:

(1) A creep test accelerated using the Stepped Isothermal Method (SIM) per ASTM D7361, to assess the residual thickness of the core after a given service life. The test must be performed under a test load greater, or equal to the anticipated service load. The change of thickness between 100 hours (i.e., the seating time used in Equation 1) and the service life (typically 100 years) is assessed using the SIM test.
(2) Using a representative short-term compression test, it is possible to define surrogate loads σ_{100h} and σ_{SL} that will compress the core to the thickness reached after 100 hours or the service life.
(3) Using flow capacity tests performed under the surrogate loads σ_{100h} and σ_{SL}, it is possible to assess the effect on the flow capacity of the product of a deformation of the core to a magnitude equivalent to the creep deformation anticipated over a duration of 100 hours, or the Service Life 'SL', using a short-term flow test. To distinguish the effects of the creep of the core to the effects of the long-term geotextile intrusion, 2 tests are considered:
   (a)   A flow test using rigid boundaries, where the flow reduction is only caused by the change of thickness of the core, hence, to the creep of the core. Such a test is

performed to measure $q_{100h(R/R)}$ and $q_{SL(R/R)}$, the short-term flow capacities measured under the surrogate loads σ_{100h} and σ_{SL}.

(b) When boundaries of the geocomposite are not rigid, a flow test using boundaries representative of the anticipated service conditions (i.e., soil / rigid, or soil / soil), where the flow reduction is associated to the change of thickness of the core as well as additional geotextile intrusion into the core caused by creep of the geotextile. Such a test is performed to measure $q_{100h(R/S)}$ and $q_{SL(R/S)}$ (e.g., in the case of Rigid/Soil boundary), which are short-term flow capacities measured under the surrogate loads σ_{100h} and σ_{SL}.

(4) The value of RF_{CR} and RF_{GI} are calculated as follow:

(a) RF_{CR} is obtained by dividing $q_{100h(R/R)}$ and $q_{SL(R/R)}$.

(b) $q_{100(R/S)}$ is reduced by both creep and geotextile intrusion. When dividing $q_{100h(R/S)}$ and $q_{SL(R/S)}$, the value obtained is thus the product of both RF_{CR} and RF_{GI}. Hence, RF_{GI} is obtained by dividing $q_{100h(R/S)}$ and $q_{SL(R/S)}$, and then by dividing the obtained ratio by RF_{CR}.

$$\frac{Q_{100h(R/S)}}{Q_{SL(R/S)}} = RF_{CR(R/S)} \times RF_{GI(R/S)} \tag{2}$$

3.2 Practical approach – assessment of the RF_{CR} and RF_{GI} for a complete line of products

Assessing the value of Reduction Factors applicable to each normal stress, boundary conditions and grade of product likely to be encountered for all possible applications of drainage geocomposites would be extremely costly and time-consuming, should it have to be performed one product at a time. However, it was observed (Blond 2023) that for properties of biplanar geocomposites are correlated to the weight of the specimen when manufactured on the same production line, using the same resin and production parameters, and when the distance between lamination rolls is adjusted to create a thickness proportional to the weight of polyethylene.
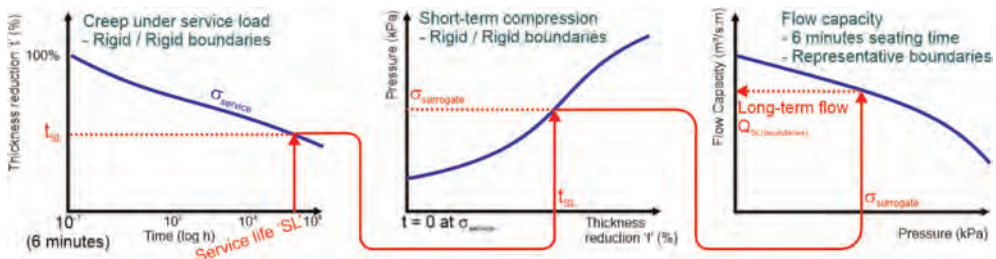

Figure 3. BAM / ISO 18228-4 strategy for determination of the RF.

Based on this observation, it was possible to build a series of abacus, which can be used to establish RF_{CR} and RF_{GI} for any grade of product (i.e., mass per unit area of the core) from a given type of biplanar geocomposite manufactured on a given production line, using 240 g/m^2 geotextiles on each sides, and exhibiting a total mass per unit areas between 1400 and 2400 g/m^2 (including the geotextiles). These abacuses are reflecting experimental data obtained for this specific family of products, using specimens with mass per unit areas covering the range of products:

– Creep deformation versus applied stress, as a function of the total mass per unit area of the geocomposite, for a creep time of 100 hours (i.e., reference flow) and 100 years (i.e., a typical service life) (Figure 4). These abacuses were built by extending the result of a creep test performed to a given load to lower normal loads, considering a linear relation between applied load and creep deformation for a given service life.

– Surrogate load to be considered to reflect a creep deformation of 5, 10 or 15% (i.e., covering a range of typically acceptable creep deformation for a geonet geocomposite, to avoid excessive plastic deformation), as a function of the mass per unit area of the geocomposite. These abacuses were established based on a series of compressive tests where the mass per unit area of the geocomposite was controlled. For each service load considered, the compressive curve was translated to define a zero-deformation corresponding to the thickness of the product under that service load.

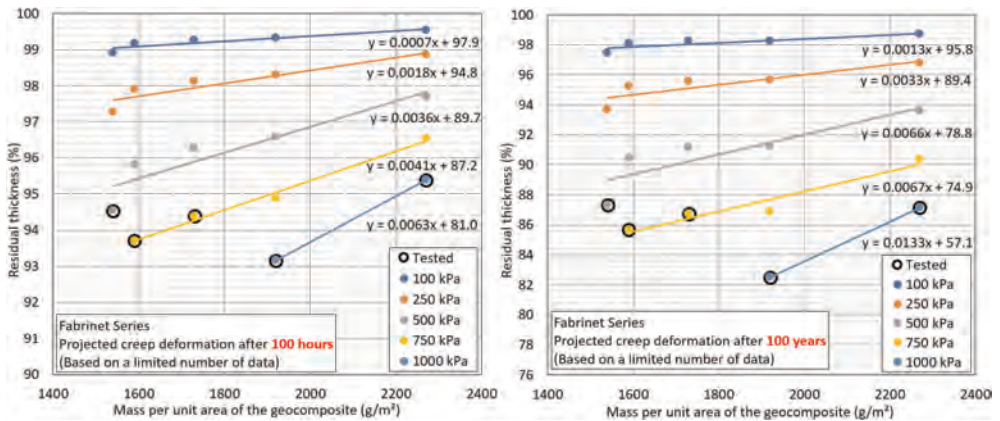– Flow versus mass per unit area, for a variety of normal stresses.

Figure 4.   Creep deformation as a function of the mass per unit area.

Example of use of the abacus for the assessment of a geocomposite with a mass of 1700 g/m^2 (including 2x 240g/m^2 geotextiles) exposed to a load of 500 kPa for 100 years between soil and a geomembrane:

(1) Figure 4 indicates a retained thickness of 95.8% (100 hours) and 90% (100 years), hence creep deformations of 4.2 and 10%.
(2) The surrogate load can be read in Figure 5 as ∼900 kPa (by extrapolation) for 100 hours and 1500 kPa for 100 years.
(3) From Figure 6, it is possible to project the residual flow:
   – Rigid/Rigid boundaries, 1700 g/m^2: ∼$1.1 \cdot 10^{-1}$ l/s/m under 900 kPa (i.e., surrogate load for 100 hours under 500 kPa), and ∼$6 \cdot 10^{-2}$ l/s/m under 1500 kPa (i.e., surrogate load for 100 years under 500 kPa), hence $RF_{CR} = 1.1 \cdot 10^{-1}/6.10^{-2} = 1.8$.
   – Rigid/Sand boundaries, 1700 g/m^2: ∼6.10^{-2} l/s/m under 900 kPa, and ∼$1.6.10^{-2}$ l/s/m under 1500 kPa, hence $RF_{CR}.RF_{GI} = 6.10^{-2}/1.6.10^{-2} = 3.8$.

Therefore, it is possible to conclude that the reduction factors applicable to a 1700 g/m^2 geocomposite exposed to 500 kPa between sand and a geomembrane are: $RF_{CR} = 1.8$ and $RF_{GI} = 2.1$.
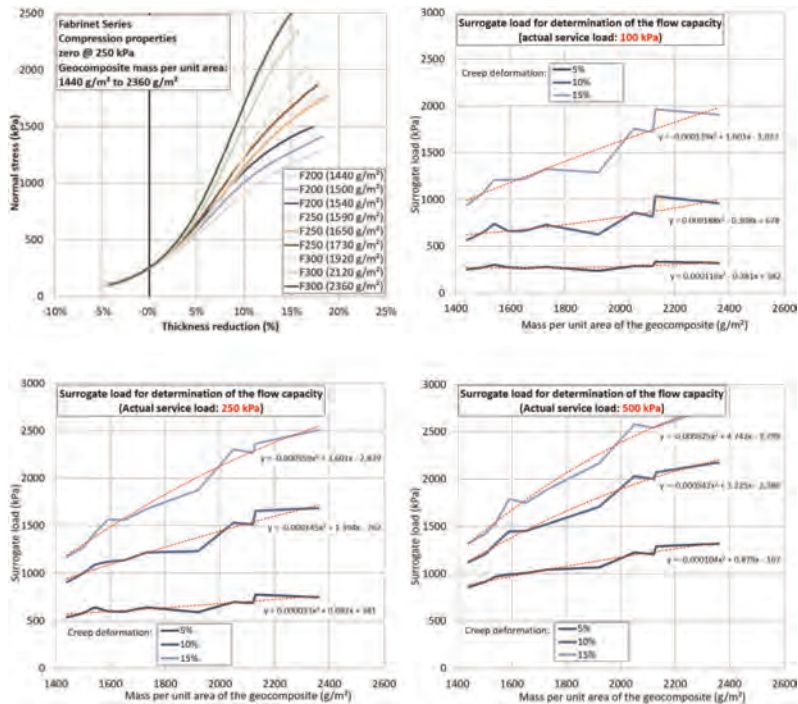
Figure 5.   Compressive behavior, Surrogate load as a function of mass per unit area and flow capacity.

4   DISCUSSION

Using equation 2, the abacus presented on Figures 4, 5 and 6 can be used to establish RF_{CR} (and RF_{GI} when applicable) of a product, based on the mass per unit area of the product, the applied load, and the service life.

These abacuses are only applicable to products manufactured with a specific resin using good manufacturing practices on a specific production line, and for which the thickness is to be proportional to the unit weight when laminating the geotextiles to the core. This can be verified by observing a monotonic and regular change of properties with the mass per unit area, as well as with the normal stress.

Based on data not presented here, it was found that changes made to the morphology of the product during the geotextile lamination process significantly affect the initial thickness of the core and its compression and creep behaviors. It is therefore not possible to extend the use of RF values obtained on a geocomposite to the geonet alone, i.e., not laminated to geotextiles.

5   CONCLUSIONS

Several factors affect the water flow capacity of a drainage geocomposite, and in particular the shape of the ribs, distance between ribs, type of geotextile used, and manufacturing parameters used during the lamination process.

For a given line of products manufactured on the same equipment, using the same resin and extrusion parameters and good manufacturing practices, the mass per unit area of the geonet is considered to be directly correlated to both short- and long-term properties of the product. It is therefore possible to establish a series of abacuses to determine the reduction
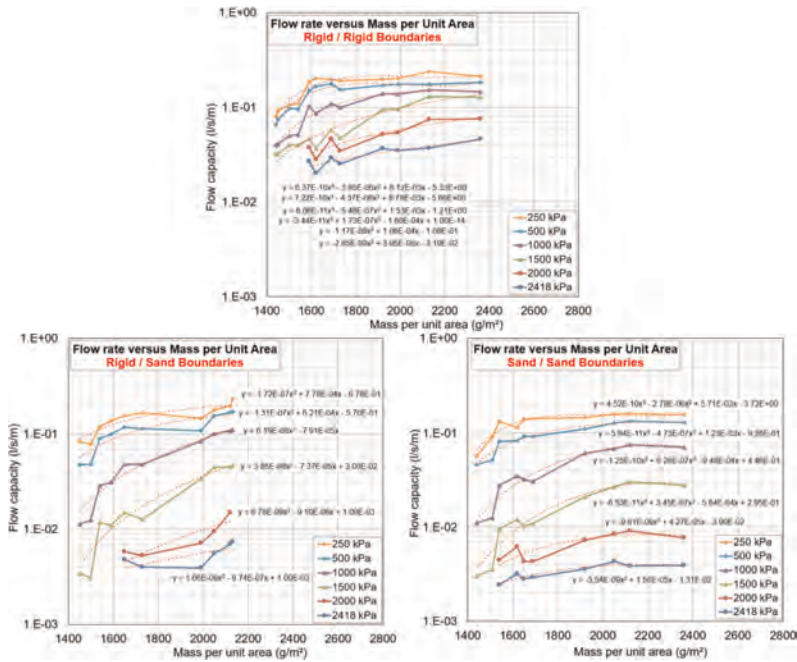
Figure 6. Flow capacity as a function of mass per unit area and applied stress for 3 boundary conditions.

factors which should be used for creep RF_{CR} and geotextile intrusion RF_{GI}, based on the mass per unit area, the applied stress, the service life, and boundary conditions. This approach will facilitate determination of reduction factors adapted to any condition encountered on a project. It can also be used to optimize the mass per unit area of the core to accurately deliver the required long-term flow capacity.

REFERENCES

ASTM D7931-21a: *Standard Guide for Specifying Drainage Geocomposites*

Blond (2023): "*Assessment of the Long-Term Flow Capacity of Solmax Biplanar Geocomposite Drains*", March 2023. Confidential Research Report submitted to Adam Maskal, Solmax.

GRI-GC8. 2001. *Determination of the Allowable Flow Rate of a Drainage Geocomposite*. Geosynthetic Research Institute, Folsom, Pa

ISO/TR 18228-4: *Designing with Geosynthetics – Part 4:* Drainage

Evaluation of biofilm adhesion and development in nonwoven geotextile in contact with wastewater

M.V. Morais, L. Marchiori, J. Sátiro & A. Albuquerque
GeoBioTec and FibEnTech, Universidade da Beira Interior, Covilhã, Portugal

V. Cavaleiro
GeoBioTec, Universidade da Beira Interior, Covilhã, Portugal

ABSTRACT: The contact between wastewater and geotextiles can lead to the development of biofilm due to microorganisms' activity resulting in the decrease of void ratio in the geotextile matrix (bioclogging). This phenomenon reduces the lifespan of geotextiles in works such as sanitary landfills, mining lagoons or wastewater stabilization ponds. However, geotextiles can also promote the removal of wastewater's compounds such as suspended solids, organic compounds, nitrogen (N) and phosphorus (P). The objective of this research is to evaluate the bioclogging evolution in two types of non-woven geotextiles of different weights after contacting with a wastewater. Laboratory experiments were carried out in permeameters colonized with wastewater biomass and fed with domestic synthetic wastewater (300 mg COD/L, 30 mg N-NH$_4$/L, 6 mg P-PO$_4$/L, C/N:4 and C/P:20). The results show rapid biofilm adhesion to both geotextiles and good stabilization conditions of the biofilm, but clogging was not significant for 80 days of contact. Removal of COD, N and P was slightly higher for the GT300 (around 82%, 55% and 36%, respectively), but considered good for both geotextiles.

1 INTRODUCTION

Geosynthetics have been used as drains and filters for some decades, where their high demand comes from a better-quality control in relation to natural materials as they are manufactured materials. Furthermore, the restriction of the use of natural materials is increasing. In addition, they have fast installation even under difficult subsoil conditions, competitive cost, among others (Lopes *et al* 2021; Palmeira 2003).

However, these materials are susceptible to clogging, either by bacterial growth, mineral precipitation and/or by soil migration between their fibers, mainly when applied as filtering materials in wastewater earth-based technologies (e.g. stabilization ponds and constructed wetlands), wastewater infiltration systems (e.g. drains and infiltration ponds for reclaimed water infiltration or soli aquifer treatment), wastewater drainage, mining ponds and sanitary landfills (Morais et al 2022). The contact between wastewater and geotextiles can lead to the development of biofilm due to microorganisms' activity, namely bacteria, with capability of biodegrading organic compounds, N and P (Albuquerque 2003). The biofilm adheres and develops on the fibers of the geotextile and its activity releases by-products that occupy the empty spaces of the geotextile leading to its clogging, called bioclogging (Guo et al 2020; Silva & Lodi 2020). Variations in temperature, organic substrates, inhibitory compounds, oxygen, and nutrients can alter the growth and maintenance of these biofilms. Typically, it can take up to 1000 hours for biological activity to start, grow and reach an equilibrium condition (steady state conditions) after contact with a wastewater (ASTM D1987 2018).

The mesh structure of non-woven geotextiles facilitates good adhesion and stabilization of biofilms, which can grow through the mesh between voids. Therefore, this research aims to evaluate the time that the biofilm and bioclogging take to be installed in the structure of two non-woven geotextiles, with different grammage, and influence the permeability in the media and the removal of organic matter, N and P after contact with wastewater.

2 MATERIAL AND METHODS

2.1 *Laboratory experiments*

Experiments were conducted in two permeameters with an internal diameter of 100 mm and a height of 200 mm, working in vertical flow. Each device has a 10 cm diameter of non-woven geotextile, with different characteristics (Table 1), composed by 100% poly-propylene fibers.

Table 1. Characteristics of the geotextiles.

GTX	Mass per unit area g/m^2	Permeability m/s	Thickness mm
GT120	120	6.3×10^{-2}	1.21
GT300	300	6.3×10^{-2}	2.30

Permeameters were fed with a synthetic domestic effluent (feeding solution). The two columns worked for 20 cycles (each cycle had 4 days), starting with the feeding phase (first day) and finishing with the draining phase (fourth day). Permeability tests were carried out, according to ASTM D1987, at a constant load of 25 cm.

At the beginning of each cycle, the water load in the permeameters was measured and water samples were taken to determine pH, dissolved oxygen (DO), chemical oxygen demand (COD), ammonia nitrogen (NH_4-N) and phosphorus phosphate (PO_4-P). At the end of each cycle, the manometric height in the permeameters was measured and samples of effluent water from the bottom of the permeameters (drained water) were taken for pH, DO, COD, NH_4-N and PO_4-P analysis. The measurements of DO, pH and temperature were carried out through probes CellOx 32 and, SenTix 41 connected to a Multimeter 340i (WTW, Germany). COD, NH_4–N, and PO_4–P were determined by colorimetric method using a RFID model DR3900 UV photometer (Hach, Loveland, USA) and the cuvette tests LCK 114, LCK 303, and LCK 350, respectively. Removal efficiencies were calculated through Eq. (1).

$$\Delta C = \left(\frac{Ci - Ce}{Ci} \right) \quad x \quad 100 \qquad (1)$$

Where ΔC = removal efficiency for parameter C (%); Ci = concentration of parameter C in the feeding solution (influent) (mg/L); Ce = concentration of parameter C in the drained samples (effluent) (mg/L).

2.2 *Synthetic effluent*

The synthetic wastewater was prepared based on the following composition (Albuquerque *et al.* 2012): buffer solution (8.50 g KH_2PO_4 + 21.75 g K_2HPO_4 + 33.40 g $Na_2HPO_4 \cdot 7H_2O$ + 1.70 g NH_4Cl/L), magnesium sulphate solution (22.50 g $MgSO_4 \cdot 7H_2O/L$), calcium chloride solution (36.43 g $CaCl_2 \cdot 2H_2O/L$), iron chloride solution (0.25 g $FeCl_3 \cdot 6H_2O/L$),

oligoelements solution (0.04 g $MnSO_4 \cdot 4H_2O$ + 0.06 g H_3BO3 + 0.04 g $ZnSO_2 \cdot 7H_2O$ + 0.032 g $(NH_4)_6 \cdot Mo_7O_{24} \cdot 4H_2O$ + 0.0555 g EDTA ($C_{10}H_{14}N_2Na_2O_8 \cdot 3H_2O$) + 0.0445 g $FeCl_3 \cdot 6H/L$), sodium acetate solution (20.20 g $C_2H_3O_2Na \cdot 3H_2O/L$, organic source as acetate), ammonia chloride solution (20.30 g $N-NH_4/L$, nitrogen source) and potassium nitrate solution (13.7 g KNO_3/L, as phosphorous solution).

Geotextiles were inoculated with 2 mL of a biomass previously acclimatized during two weeks in a semi-continuous reactor, which contained 6.68 mg/L SSV, 8.42 mg/L TSS, 311.20 mg/L COD, 11.20 mg/L $N-NH_4$, and pH of 7.40. Experiments were performed with the synthetic wastewater (feeding solution) with initial average loads of 450 mg COD/L, 25 mg NH_4-N/L and 19 mg PO_4-P/L. The average temperature during the tests was 20.8°C.

3 RESULTS AND DISCUSSION

Permeability did not change significantly for both geotextiles during the 20 cycles, which would mean bioclogging was not significant for that time of operation (approximately 80 days). Figures 1 to 3 show the evolution of the removal of COD (ΔCOD), NH_4-N (ΔNH_4-N) and PO_4-P (ΔPO_4-P) in the two permeameters. The removal of COD, N and P increased over time in both geotextiles, just after the first cycle, with the highest removals having been observed for the heavier grammage and thickness geotextile (GT300). To analyze the graphics, GT120 is the geotextile with a density of 120g/m^2 and GT300 the one with 300g/m^2.

During the first 5 cycles (20 days operation), there was an increase in COD removal of up to 73% for GT300 and around 28% for GT120 (Figure 1). The stabilization in COD removal (steady-state conditions) appear after the fourth cycle (16 days operation) for GT300 and after the thirteenth cycle (52 days operation) for GT120. From the fifth cycle (20 days operation) to the twentieth cycle (52 days operation), the average COD removal efficiency maintained the same value (around 80%) GT300. In the GT120 the average COD removal efficiency stabilized around the thirteenth cycle (52 days operation) between 65% and 75%.
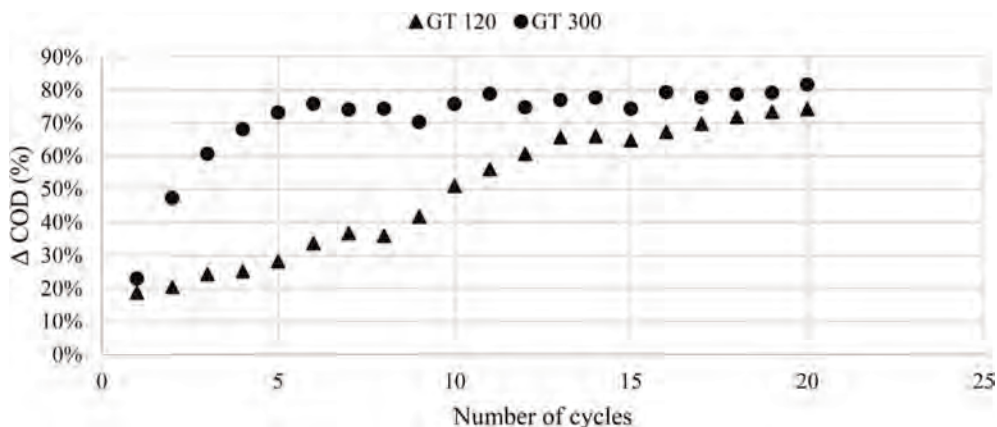
Figure 1. Variation of COD removal in permeameters.

Regarding N removal (Figure 2), as ammonia-nitrogen, the removal efficiency in GT300 ranged from approximately 25% to 40% (30% on average) in the first two cycles (8 days operation) and stabilized after the third cycle (12 days operation). For the GT120, the equilibrium conditions stabilize around the fourteenth cycle (56 days operation), with a greater variation between the fourth and the thirteenth cycles (from 16 to 52 days operation). However, the final average efficiencies for both geotextiles were similar, around 50%.

Figure 2.   Variation of NH$_4$-N removal in permeameters.

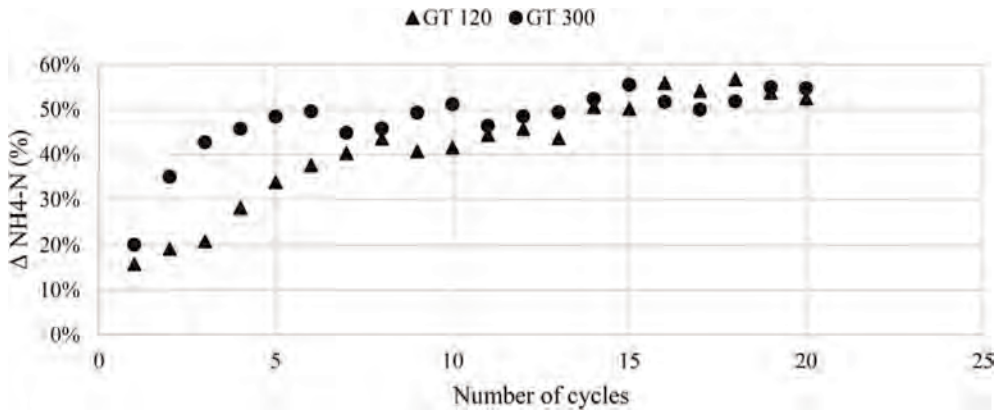The global average removal efficiencies for the 20 cycles (80 days operation) were 74%, 52% and 33% for COD, NH$_4$-N and PO$_4$-P, respectively, for GT120, and 82%, 55% and 36% for GT300. Therefore, the greater removal of organic matter, N and P in GT300 seems to be associated with its greater thickness and grammage, which would have allowed a greater development of biofilm, as observed in Albuquerque et al (2012) for a pozzolana-based partially aerated low-loaded biofilter.

Average phosphorus removal (Figure 3) ranged from 17% in the first 3 cycles (12 days) and stabilized around 31% from the fourth to the tenth cycle. While the behavior of microorganisms in the GT 120 is more linear, reaching stabilization around the fifteenth cycle.
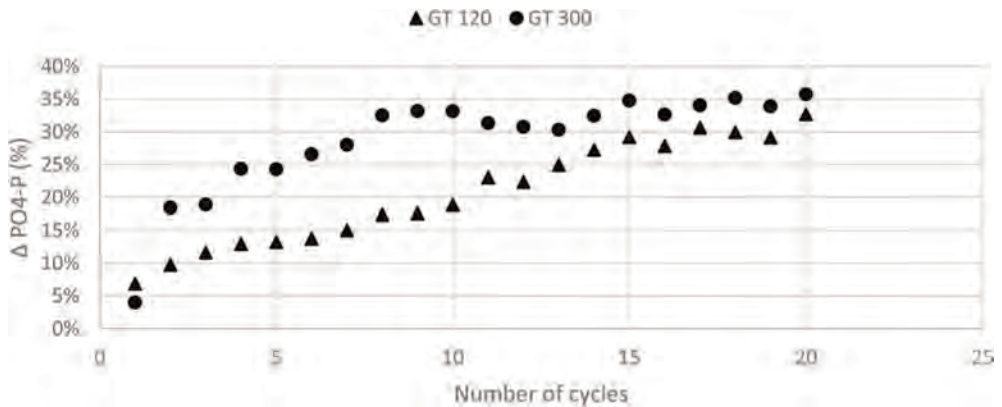
Figure 3.   Variation of PO$_4$-P removal in permeameters.

COD, N and P removal results seem to indicate that the biofilm began to stabilize (i.e., under steady-state conditions) after approximately three cycles (i.e., after 12 days contact with the wastewater) for the geotextile GT300, when the processes of growth and detachment would already be in equilibrium. For the geotextile GT120, growth was slower and more constant, as it was a finer mesh, the detachment conditions last longer, the microorganisms apparently had a greater difficulty in getting into rapid equilibrium since the contact area mesh cross section was smaller.

4 CONCLUSIONS

This preliminary research shows biofilm adhesion and stabilization in a geotextile material placed inside permeameters, highlighting the main points:

- For the 300g/m^2 geotextile, *steady-state* conditions were observed after 5 cycles (20 days), with very good COD (82%) and NH$_4$-N (55%) removal and good PO$_4$-P (36%) removal.
- For the 120g/m^2 geotextile, *steady-state* conditions were observed for only after 10 cycles (40 days), reaching GT300 conditions only around 15 cycles. with very good COD (74%) and NH$_4$-N (52%) removal and good PO$_4$-P (33%) removal,
- The different behaviors between the two geotextiles seems to be because the mesh thickness provides a greater accommodation of microorganisms. More in the GT300 than in the GT120.
- Aerobic heterotrophic oxidation, nitrification and PAOs appear to be the predominant microorganisms in both permeameters.

REFERENCES

Albuquerque A. 2003. *Contribuição Para o Estudo da Remoção de Residuais de Carbono em Filtros Biológicos de Leito Imerso e Fluxo Descendente*. PhD Thesis, University of Beira Interior, Covilhã, Portugal, 469p.

Albuquerque, A., Gonzales-Martinez, A. & Osorio, F. 2012. Effect of Aeration on Steady-state Conditions in Non- and Partially Aerated Low-loaded Biofilter. *International Journal of Environmental Science and Technology* 9(3): 395–408. https://doi.org/10.1007/s13762-012-0073-3

ASTM D1987-18 2018. Standard Test Method for Biological Clogging of Geotextile or Soil/geotextile Filters. *American Society for Testing and Materials* (ASTM), West Conshohocken, USA, 6p.

Guo, C., Wu, J., Zhu, Y., Lin, Z., He, S., Qian, Y., Yang, H., Li H., Mao, W. 2020. Influence of Clogging Substances on Pore Characteristics and Permeability of Geotextile Envelopes of Subsurface Drainage Pipes in Arid Areas. *Geotextiles and Geomembranes* 48(5): 735–746. https://doi.org/10.1016/j.geotexmem.2020.05.006

Lopes, M. da G., Barroso, M., & Neves, J. (1st ed.) 2020. *Geossintéticos em Engenharia Civil: Dimensionamento, Instalação e Casos de Obra*. SPG-LNEC, December de 2020, Lisbon, Portugal, 400p. (978-989-54038-6-8). https://doi.org/10.24849/spg.igs.2021.01

Morais, M. V., Marchiori, L., Albuquerque, A. & Cavaleiro, V. 2022. Simultaneous Application of Physical Methods and Scanning Electron Microscopy for Evaluation of Bioclogging in Geotextiles. *3rd Conference on Testing and Experimentation in Civil Engineering (TEST&E 2022) – Smart Technologies*, 21–23 June 2022, FCT-NOVA, Lisbon, Portugal, 10p.

Palmeira, Ennio Marques 2003. Fatores Condicionantes do Comportamento de Filtros Geotêxteis. *IV Simpósio Brasileiro de Geossintéticos*, 23 May 2023, Porto Alegre, Brazil, Vol. 1, 49–67.

Silva, J. & Lodi, P. 2020. Evaluation of Superficial and Internal Clogging of Geotextiles. *International Journal of Civil Engineering* 18(10): 1125–1137. https://doi.org/10.1007/s40999-020-00524-5

Site testing to assess the performance of filtration/separation geotextiles in cold climate: ROUGH project

K. De Wolf
BontexGeo, Zele, Belgium

A. Bugiel
Dupont de Nemours, Luxemburg, Luxemburg

M. Moeller
Fibertex Nonwovens, Aalborg, Denmark

Ph. Delmas
Sintef Advisor, Sintef, Oslo, Norway

C. Recker
Sintef Community, Münster, Germany

ABSTRACT: The Nordic countries in Europe are faced with specific challenges when it comes to construction. Next to specific soil conditions, these regions are faced with significantly lower temperatures during wintertime than other regions in Europe. To confirm that the current best practices for geosynthetic installation are also applicable to these specific cold conditions or that new guidelines should be implemented for these specific conditions, full scale field testing has been conducted recently within the ROUGH project. A job site in the north of Finland was prepared to perform installation damage testing on nonwoven geotextiles used as filtration/separation geotextile in a drainage trench. Laboratory evaluation of the characteristics before and after installation provides a good view of the impact of installation in Nordic conditions: cold climate and typical Nordic soils.

1 INTRODUCTION

Finland, Norway and Sweden are three Nordic countries that extend beyond the arctic circle. These countries are all subject to some very specific conditions when performing construction works.

One of these conditions is a colder climate compared to other European countries. It is the aim of this study to thoroughly investigate whether the installation of geosynthetics is affected by these Nordic conditions (cold temperature, frozen soils, typical backfill like crushed rock), and, if so, additional guidelines are for example required when installing geosynthetics at sub-zero temperatures.

Geosynthetics are construction materials that are cost-effective and provide a long-term performance, making them very suitable and sustainable materials for use in different construction application, such as road construction, drainage trenches, railways, erosion control systems and others. Depending on the application the geosynthetic will fulfil one or more functions, typically being filtration, separation, drainage, reinforcement, stabilisation, erosion control, protection and sealing. There are different types of geosynthetics depending on

their structure. Typical types include nonwoven and woven geotextiles, geogrids, geomembranes and geocomposites.

The correct installation of any type of geosynthetic is important to make sure the material is functional in the construction project.

Within the framework of the ROUGH project (Recommendations for requirements on characteristics of geosynthetics and geosynthetic-related products relevant to Nordic country-specific conditions) (ROUGH project 2022) full scale installation tests were performed on nonwoven geotextile products to assess the function Filtration/Separation when the geotextile is used in a drainage trench application.

2 SITE SELECTION AND CONDITIONS

2.1 Site

Full scale site testing requires a test location where all the conditions are met, preparation of the testing ground, and installation of the geotextile can be done as close to actual site conditions as possible. In that case, the results found during the testing can actually be transferred to real applications.

For these site testing, a location was found in the north of Finland, very close to Kemi. The construction site was situated about 15 km southeast of Kemi, along the E8/E75, where a new road was being constructed (Figure 1).

2.2 Climatic conditions

For the installation damage testing, the goal was to realise the installation at temperatures between – 5°C and – 20°C.

Testing took place during wintertime, on 5 and 6 February 2020. During the testing, temperatures were recorded on site. These measurements were compared with more extensive hourly data from the Finnish Meteorological Institute. The data provided came from the nearest weather station, which was located at Kemi Airport, 20 km away from the test site. The temperatures that were measured on site matched those measured by the Finnish Meteorological Institute. Therefore, the extensive data from the weather station was used to evaluated and indicate the temperatures during the entire trial, from conditioning to deconstruction. These temperatures are given in Figure 2 and show that the air temperature was between – 7°C and – 15°C during time of installation and compaction.

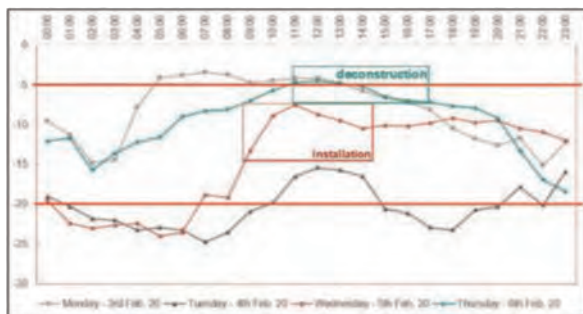No snow had to be removed from the test site and no additional snowfall occurred during installation.

Figure 1.   Location of the field.

Figure 2.   Temperatures during installation and recovery [°C] tests (Screenshot Google Maps).

3 MATERIALS USED

3.1 *Geotextile materials*

Four different nonwoven geotextile products were used from different manufacturers. The nonwoven materials were supplied to the site and also to the laboratory (reference samples). The material that was supplied to the site, was prepared before installation. All samples cut to the right length in pieces of 2 m wide. Marking for samples to be taken were made on the geotextiles beforehand and identification numbers were also put on the samples. Marking the samples places beforehand avoids biased sample selection afterwards in the lab, if some parts would be more or less damaged than other parts of the sample. For each type of geotextile product, 4 test specimens were prepared for installation.

3.2 *Granular material*

The material used is a crushed rock. The material was tested to determine its particle size distribution. The result of this distribution and the limit values of the InfraRYL guidelines show that the material can be classified as Crushed Rock GO 0/56mm (KaM 0/56) based on SFS-EN 13242. This is material that is typical for Finnish road construction and unbound granular sub-bases. The granular material had a temperature of approximately – 6°C when it arrived on-site.

4 TEST METHOD

To investigate what is the impact of the lower temperatures on the installation of the geo-synthetics in a filtration application, a drainage trench was made. The specifications of the Finnish guidelines for road construction were aligned to the test site conditioning with real jobsite parameters.

First of all, a trench was dug in the frozen in situ ground with a cross section of 1 m wide and a depth of 0.5 m. The trench was long enough to be able to place all geotextile samples next to each other in one trench. Figure 3 shows the cross section of the trench. The geo-textile samples were placed on the local soil in the trench and over the edges to keep them in place. The boundaries of the trench were marked on the geotextile samples. The local soil temperature, before installation of the geotextile, had a temperature of – 12°C. 4 samples of each geotextile were installed, 2 samples per type per drop height.
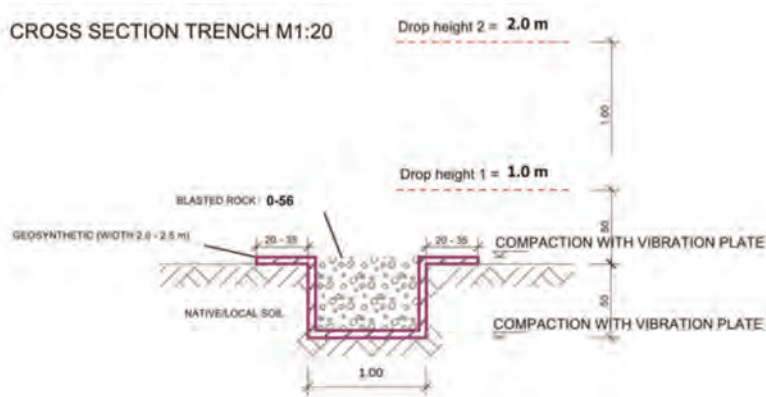

Figure 3. Cross section of the drainage trench.

After placement of the geotextile samples, the drainage trench was filled with the crushed rock material. 2 drop heights were used to add the granular material, 1.0 m and 2.0 m.

Once the trench was filled with granular material, compaction was done with a vibration plate (Type Wacker Neusion DPU6555 – 480 kg) in line with InfraRYL guidelines. Five passes were made for the compaction.

Figures 4 to 7 show the process of preparation, installation and compacting.

Figure 4.   Excavation of trench.

Figure 5.   Installed geotextile samples.

Figure 6.   Filling of the trench with granular material.

Figure 7.   Compaction of the granular material inside the trench.

The compaction was checked with a dynamic load plate testing device type "AL-Engineering Oy Loadman II". The results show a bearing capacity modulus of 109–128 MPa (drop height 1.0 m) and 124–138 MPa (drop height 2.0 m). Figure 8 provides an overview of the results relative to the sample location in the trench.

On the second day, the sample recovery took place. An excavator removed the top central part of the granular material in a careful way, making sure this excavation did not cause any damages to the geotextiles. A narrow trench bucket was used to manage this. The remaining part of the granular material was removed using a vacuum/suction lorry. The use of this vacuum lorry allowed for delicate removal of the last layers of rocks from the geotextiles alongside removal of rocks by hand. Figures 9 and 10 show the excavation process.
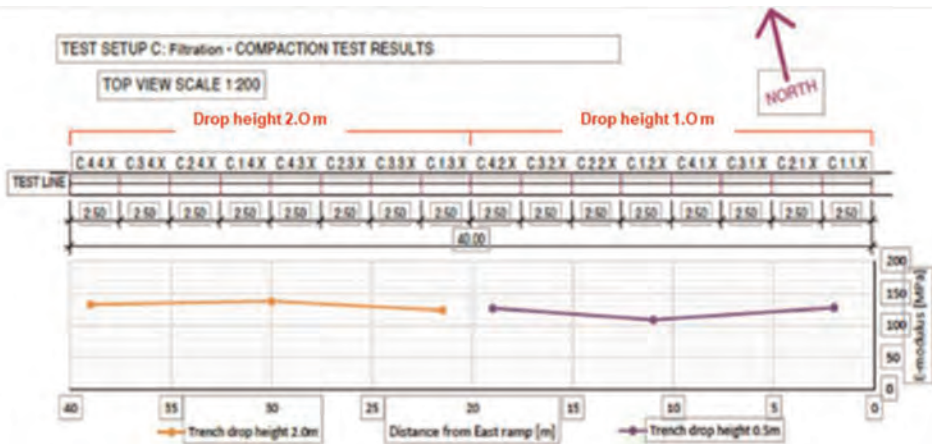
Figure 8.   Compaction controls values and arrangement of samples.

Figure 9.   Removal of top part of granular material by excavator.

Figure 10.   Removal of last part of granular material using a vacuum and by hand.

Once all granular material was removed, the geotextile samples were removed from the trench. The samples were wound onto a core and protected by a thick nonwoven layer on the outside. All samples were placed in a large wooden box for transport. As the samples were already marked before testing started, no sample selection was needed on site and the lab could perform the tests and use the identification on the samples.

5   LABORATORY TESTING

In order to evaluate the impact of installation damage, testing of the geotextile samples needs to take place under controlled environment and compared to the virgin material values.

Within this setup, all geotextile samples were evaluated for 1) Tensile strength (EN ISO 10319), 2) Energy index (EN ISO 10319), and 3) Characteristic opening size (EN ISO 12956). Testing was done on the exposed samples from Kemi and reference material.

For all geotextile samples, the samples were taken from predefined places, marked in advance. Samples were taken from the bottom of the trench, the edge, and the side of the trench.

These tests took place under laboratory conditions as defined in the referenced test standards at 20°C.

6 RESULTS AND DISCUSSIONS

The results of the samples from Kemi full scale experiment were compared to the results of the reference samples. For all 4 products some damage was observed, which is in line with the normal installation damage that also takes place under normal conditions. The results show that, if they are correctly designed for a positive temperature (e.g., + 20°C) for the defined geotechnical conditions of installation (type of soils, drop height, compaction, etc.), no significant influence was observed between the reference and exposed samples that indicate an additional damage due to the Nordic conditions in which the installation took place.

7 CONCLUSIONS

The extensive on site and laboratory testing conducted on these geotextile materials for use as a separation/filtration layer in a drainage trench was one of the major and biggest test setups conducted in recent years.

These tests allow for an evaluation of the possible impact of cold temperatures on the geotextile installation. The results show that their additional significant influence due to the cold temperature on the 4 samples tested.

If products are correctly designed for a positive temperature (e.g. + 20°C) for the defined geotechnical conditions of installation (type of soils, drop height, compaction, etc.), no additional installation damage is observed on the strength when the products are installed under the same conditions at – 10°C. Additionally, no clear influence of the location of the samples in the trench was observed on the strength.

No influence on the opening size is observed when the products tested are exposed in Kemi to installation at – 10°C in a trench with crushed rock under a drop height of 1.0 m & 2.0 m.

Additionally, no clear influence of the location of the samples in the trench was observed on the opening size.

REFERENCES

AL Engineering. [Online] http://www.al-engineering.fi/en/loadman.html
InfraRYL Infrarakentamisen Yleiset Laatuvaatimukset. Maa-, Pohja- ja Kalliorakenteet. Rakennustieto. 2018 – *InfraRYL General Quality Specifications for Infrastructure. Earthworks, Foundations and Rock Structures.*
EN ISO 10319 (2015), *Geosynthetics, Wide-width Tensile Test*, 14 p.
EN ISO 12956 (2019), *Geotextiles and Geotextile-related Products, Determination of the Characteristic Opening Size*, 15 p.

Thermal prefabricated vertical drain for vacuum consolidation of Hong Kong marine deposits with temperature changes

Ze-Jian Chen & Jian-Hua Yin
Department of Civil and Environmental Engineering & Research Institute for Land and Space, The Hong Kong Polytechnic University, Hong Kong SAR, China

ABSTRACT: The consolidation of marine deposits for marine infrastructure, dredged mud disposal, as well as new reclamation, is a time-consuming process due to the low permeability of the soft marine clay. In vacuum preloading, the discharge efficiency of prefabricated vertical drains (PVD) significantly decreases with bending and clogging as soils consolidate. In this study, a physical model test was carried out for vacuum preloading on Hong Kong marine deposit (HKMD) slurry with a heating aided PVD for stepwise heating. The temperature distribution and evolution in the model, the water discharge volume of the slurry, and the response of water discharge rate to temperature change at different stages of consolidation are analyzed and discussed.

1 INTRODUCTION

Land shortage is one of the major challenges of urbanization and economic development, especially in coastal regions, which are usually the population and commercial centers, such as Hong Kong. Land reclamation and other marine infrastructures are of vital importance to urban development in these areas. In coastal regions, the land and seabed are usually covered with thick layers of soft marine deposits, with high water content, low strength, and high clay content. Marine reclamation and other construction activities, such as ground improvement and channel dredging, are closely associated with marine deposits to be effectively treated. In fact, due to lack of gravel and sand fills, it has been proposed and applied to use soft marine deposits as a fill material for reclamation (Yin *et al.* 2022). In these cases, the time-consuming consolidation process of dredged deposits as well as the natural in-situ deposits is a key challenge.

Vacuum preloading is effective in accelerating the consolidation of soft soils, with a sealing system, a vacuum source, and drains, mostly prefabricated vertical drains (PVDs) (Baral *et al.* 2021; Cai *et al.* 2017). Although PVD-vacuum preloading has been successfully applied in the past decades, there are still significant challenges, such as the deformation and clogging of PVDs, non-uniform consolidation, and formation of soils columns during vacuum preloading, which will reduce the rate of consolidation of the soils (Wang P. *et al.* 2020; Zhou & Chai 2017). Solutions have been proposed to such issues, one of which is to increase the temperature in the soft soils treated (Abuel-Naga *et al.* 2006; Artidteang *et al.* 2011; Du *et al.* 2021; Wang J. *et al.* 2020). Under elevated temperature, the viscosity of porewater is significantly reduced, and the permeability of the soil will be much higher (Cho *et al.* 1999; Chen *et al.* 2023). One convenient way of heating soft soils is to integrate the heating sources, such as electric heating wires with the PVDs to be inserted in to the soils. Previous studies showed that using such thermal PVDs, the speed of vacuum consolidation obviously increases with temperature, and the non-uniform consolidation effects is improved (Chen *et al.* 2022). Most studies are focused on isothermal tests. In practice, heating procedures might be complicated, and the temperature

effects might vary at different stage of consolidation. It is beneficial to understand the influences of temperature change at different consolidation state, towards a more efficient and less energy-consuming design of the heating scheme.

In this study, a reduced-scale axisymmetric model test was conducted on Hong Kong marine deposits. A PVD with heating wires was installed at the center of the soil, and a complicated heating-cooling-reheating schedule with vacuum pressure was implemented. The temperature distribution and evolution in the model, the water discharge volume of the slurry, and the response of water discharge rate to temperature change at different stage of consolidation are analyzed and discussed.

2 TEST SETUP

2.1 *Materials*

The soil material used was the Hong Kong marine deposits (HKMD), which is a typical type of marine clayey soil. The particle size distribution is shown in Figure 1. There is around 20% of clay particles (sized $<2\mu$m) and 62% of silt (sized $<50\mu$m) in the HKMD sample. The permeability of HKMD is back-calculated through oedometer tests using Terzaghi's theory. It is reported that the void ratio-dependent permeability follows $e = 1.487 \log k_v + 15.09$ under 20°C and $e = 1.435 \log k_v + 14.77$ under 40°C (Chen *et al.* 2022). It can be seen that permeability increases with temperature.
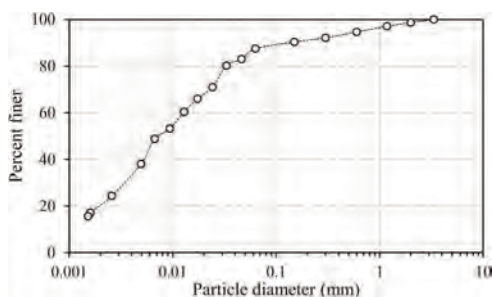
Figure 1.   Particle size distribution of HKMD in the model test.

2.2 *Design of the physical model*

The layout of the model is shown in Figure 2. Before consolidation, the HKMD was mixed with water and reconstituted into a slurry with a water content of 100%. A band-type PVD with thickness of 5mm, width of 100mm, and length of 500mm was installed at the center of a rigid steel cylinder with diameter of 294mm and height of 500mm. The heating wire was connected to aa temperature-control unit. A flexible heating wire was fixed on the surface of the PVD. Then the HKMD slurry was poured inside. Temperature sensors were installed inside the soil body to monitor the temperature distribution of the soils. Finally, the slurry was covered with a layer of plastic membrane for air sealing. The PVD was connected to a vacuum pump and a water collection chamber.

2.3 *Test schedule*

The slurry was firstly settled for a couple of days without vacuum preloading and heating. Then vacuum pressure of -50 kPa was applied in stages in one hour and maintained constant for the whole process. The temperature was controlled by tracking the sensor T0. The

Figure 2. Setup of the model test.

temperature of T0 was firstly set to 30°C for a while and cooled down to around 20°C for around 2 days. Afterwards T0 was increased again to 40°C for 11 days, then reduced to 30°C for 4 days, a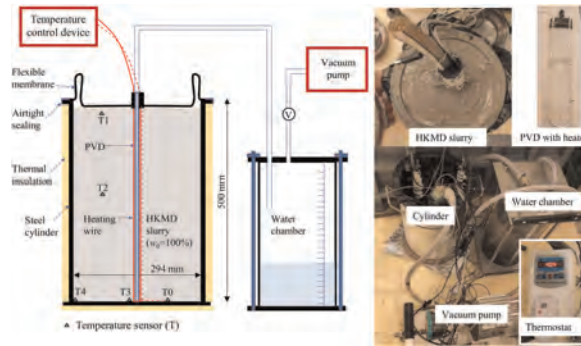nd to 20°C for 3 days. After that, T0 was again increased to 30°C for more than 20 days, and finally reduced to around 20°C by turning off the control system. The setting of temperature can be found in Figures 3 and 4.

3 TEST RESULTS AND DISCUSSIONS

3.1 *Temperature evolution and distribution*
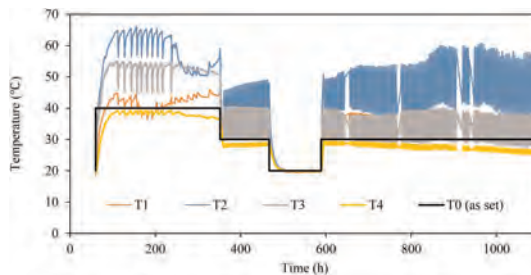
Figure 3. Temperature–time curves at five locations.

Figure 3 shows the temperature evolutions at locations of T0, T1, T2, T3, and T4. T0 is connected to the temperature controller. First of all, it can be found that the temperature is not uniform within the soil. Possible reason is the heat loss by thermal diffusion and radiation the top and bottom boundaries. Another reason is the thermal convection with water flow from the surrounding soils to the PVD, compensating part of the thermal diffusion from PVD to the edge. In the lateral direction, temperature near the heating source at the middle (T3) is higher than temperature at the middle and boundary (T0 and T4), because the working temperature of the heating wire was higher that the setting. T0 and T4 are close, indicating good insulations at the lateral boundaries. Along the vertical direction, temperature at the middle depth (T2) is higher than T1 at the surface and T0 at the bottom, due to the heat loss at the surface and the boundary. The middle depth of soils received the most heat since it is farthest to the boundaries.

For the temporal distribution, firstly, it can be found that except T0 with stable control, temperature at all measuring points exhibits significant fluctuation. The reason for fluctuation is that the working temperature of the heating wire is as high as 70°C, and the

temperature control is a dynamic control process. Secondly, under the same T0 = 30°C, T2 gradually increases with time. This is due to the increasing thermal conductivity with gradual reduction of void ratio.

3.2 Water discharge volume

Figure 4 shows the volume of pumped water from the physical model with time. It can be found that the volume change of the slurry is significant, as the initial volume of the slurry was only around 30 L. During vacuum preloading, when there is a heating, a sharper slope of water discharge curve can be observed, even when the heating period is short. When there is a cooling process, the slope of water discharge curve immediately becomes much gentler. Therefore, heating process has fatal contribution to the consolidation settlement of clay slurry.
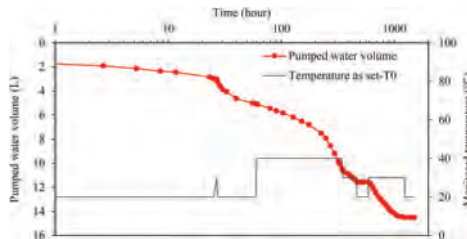
Figure 4.   Water discharge volume and temperature setting with time during vacuum preloading.

3.3 Effects of temperature change on water discharge rate

The consolidation of soils is dependent on both temperature and void ratio. It is important to investigate the rate of consolidation with temperature change at different stages of vacuum consolidation. The water discharge rate $\dot{V}_w$ is calculated by:

$$\dot{V}_w = \frac{dV_w}{dt} \approx \frac{V_{w,i+1} - V_{w,i-1}}{t_{i+1} - t_{i-1}} \tag{1}$$

where $\dot{V}_w$ is the water discharge rate, V_w is the volume of pumped water, "$i - 1$" and "$i + 1$" represent the measuring time moment before and after the current time moment, t is the elapsed time.

Figure 5 shows the water discharge rate and temperature with water discharge volume. Firstly, under a constant temperature, the rate of consolidation always decreases with time.
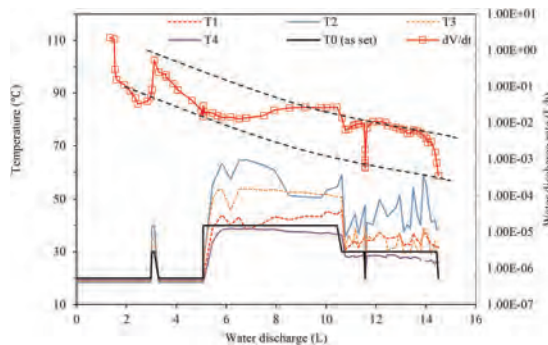

Figure 5.   Water discharge rate and temperature setting with time during vacuum preloading.

This is due to (a) the nonlinear compression and consolidation of the soil; (b) the reduced water discharge capacity due to deformation of PVD; (c) the clogging of the PVD as well as the formation of soil column, especially without heating (Chen *et al.* 2022). Secondly, with heating, the rate of consolidation always increases, due to the enhanced permeability by reduced water viscosity, especially in the clogged regions.

However, the test results indicate that the HKMS slurry might response to temperature differently at different consolidation stages. At the earlier stage, there is a trial heating to 30°C for only several hours. However, the increase of consolidation rate is very significant and sensitive. As the high-water content slurry has relatively low thermal conductivity, the heating mainly affects the middle region. Therefore, the consolidation of soils close to the PVD is especially accelerated, and soil column may form faster.

At the second heating stage from 20 to 40 for 11 days, the temperature is higher, but the increase of water discharge rate is rather slow. It seems that a certain period is needed for heating to make an obvious contribution. During the previous consolidation stage, the PVD is deformed, the soil column has formed around the PVD, and non-uniform consolidation is significant. Therefore, the effects of PVD heating on the consolidation rate slowly increases as the non-uniformity is slowly reduced after some water discharge under a higher temperature.

At the final stage, when the temperature of T0 was set from 40 to 30°C, the water discharge rate drops a bit and increases again to the original track. Meanwhile, a short cooling-heating cycle was conducted quickly at this stage, and the rate of water discharge quickly experienced a drop-rise cycle. The heating effects of consolidation rate is obvious at this stage. The reasons behind this phenomenon might be: (i) The soil is already dense, so the thermal conductivity is high and the temperature re-distribution is faster to cause quicker response in the soils. (ii) After a long-term of heating, the non-uniformity of consolidation has been reduced (Chen *et al.* 2022), which causes the further increase of consolidation.

3.4   *Final stage of soils*

After the test, the vacuum pressure was stopped and the membrane was removed. It was found that the soil was highly hardened. The soil surface is very dry, with some surface cracks. The water content of the surface was measured to be only 3%.

4   SUMMARY

In this study, a laboratory model test was conducted on HKMD slurry under vacuum preloading with heating and PVD. The slurry was subjected to non-isothermal conditions with different temperatures at different consolidation stages. Several remarks can be summarized as follows.

(a) The temperature fluctuation at different locations is significant due to the dynamic control of the heating wire and the heat loss at the top and bottom of the soils, which should be paid attention in field application. With consolidation going on, the thermal conductivity is gradually increased.
(b) Under elevated temperature, the settlement of HKMD slurry is significantly increased. The rate of water discharge always increases with increasing temperature. A highly stiff layer can form after treatment with vacuum preloading and heating.
(c) At the earlier stage of consolidation, the response of water discharge rate to temperature is faster than at the middle stage of consolidation. With the formation of soil column and PVD deformation, the improvement of consolidation rate by heating will take a certain period. However, further explorations are necessary to clarify the specific mechanisms for such behaviours.

Figure 6.   Final state of the soil surface after the tests.

REFERENCES

Abuel-Naga, H.M., Bergado, D.T. and Chaiprakaikeow, S. (2006) 'Innovative Thermal Technique for Enhancing the Performance of Prefabricated Vertical Drain During the Preloading Process', *Geotextiles and Geomembranes*, 24(6), pp. 359–370. Available at: https://doi.org/10.1016/j.geotexmem.2006.04.003.

Artidteang, S. et al. (2011) 'Enhancement of Efficiency of Prefabricated Vertical Drains using Surcharge, Vacuum and Heat Preloading', *Geosynthetics International*, 18(1), pp. 35–47. Available at: https://doi.org/10.1680/gein.2011.18.1.35.

Baral, P. et al. (2021) 'Consolidation by Vertical Drains Beneath a Circular Embankment under Surcharge and Vacuum Preloading', *Journal of Geotechnical and Geoenvironmental Engineering*, 147(8), pp. 1–12. Available at: https://doi.org/10.1061/(asce)gt.1943-5606.0002576.

Cai, Yuanqiang et al. (2017) 'Experimental Tests on Effect of Deformed Prefabricated Vertical Drains in Dredged Soil on Consolidation via Vacuum Preloading', *Engineering Geology*, 222, pp. 10–19. Available at: https://doi.org/10.1016/j.enggeo.2017.03.020.

Chen, Z.-J. et al. (2022) 'Experimental and Molecular Dynamics Studies on the Consolidation of Hong Kong Marine Deposits under Heating and Vacuum Preloading', *Acta Geotechnica*, pp. 1–15. Available at: https://doi.org/10.1007/s11440-022-01735-x.

Chen, Z.-J. et al. (2023) 'Effects of Temperature on the Time-dependent Compression and Shear Behaviour of a Soft Marine Clayey Soil', *Engineering Geology*, p. 107005. Available at: https://doi.org/10.1016/j.enggeo.2023.107005.

Cho, W.J., Lee, J.O. and Chun, K.S. (1999) 'The Temperature Effects on Hydraulic Conductivity of Compacted Bentonite', *Applied clay science*, 14, pp. 47–58.

Du, C. et al. (2021) 'Effects of Temperature Circulation on Dredged Sludge Improved by Vacuum Preloading', *Soils and Foundations*, 61(5), pp. 1343–1353. Available at: https://doi.org/10.1016/j.sandf.2021.07.006.

Wang, J. et al. (2020) 'Temperature Effects on Dredged Slurry Performance under Vacuum Preloading', *Canadian Geotechnical Journal*, 57(12), pp. 1970–1981. Available at: https://doi.org/10.1139/cgj-2019-0272.

Wang, P. et al. (2020) 'Apparent Clogging Effect in Vacuum-induced Consolidation of Dredged Soil with Prefabricated Vertical Drains', *Geotextiles and Geomembranes*, 48(4), pp. 524–531. Available at: https://doi.org/10.1016/j.geotexmem.2020.02.010.

Yin, J.H. et al. (2022) 'A Sustainable Approach to Marine Reclamations Using Local Dredged Marine Soils and Wastes: Soft Soil Improvement, Physical Modelling Study, and Settlement Prediction-control', *Proceedings of The HKIE Geotechnical Division 42nd Annual Seminar: A New Era of Metropolis and Infrastructure Developments in Hong Kong, Challenges and Opportunities to Geotechnical Engineering*, (Gdas202 2), pp. 1–14. Available at: https://doi.org/10.21467/proceedings.133.1.

Zhou, Y. and Chai, J.C. (2017) 'Equivalent "Smear" Effect Due to Non-uniform Consolidation Surrounding a PVD', *Géotechnique*, 67(5), pp. 410–419. Available at: https://doi.org/10.1680/jgeot.16.P.087.

Consolidation of clay slurry fill using horizontal drainage enhanced geotextile sheet

H. Chen, J. Chu & S.F. Wu
School of Civil and Environmental Engineering, Nanyang Technological University, Singapore

W. Guo
School of Civil Engineering, Tianjin University, Tianjin, China

ABSTRACT: Due to a lack of granular fill materials, soft clay slurry dredged from seabed may have to be used for land reclamation. In this paper, a new product, the horizontal drain enhanced geotextile sheet (HDeGs), and a method to use HDeGs as horizontal drains for consolidation of soft marine clay using vacuum pressure is introduced. The construction procedure for the use of HDeGs and the vacuum preloading for consolidation of slurry clay for land reclamation is discussed. Model test has been conducted and the results have demonstrated the effectiveness of the proposed method. The advantages of using HDeGs over the other methods are elaborated. The potential of using this method for land reclamation projects is also discussed.

1 INTRODUCTION

Due to the lack of granular soil in Singapore, soft dredged marine clay or excavated soil has to be used for land reclamation as fill materials. Because of the low permeability and strength of soft clay, the reclaimed land using soft clay fills should be treated (Chu *et al.* 2009a; Lam *et al.* 2020). Although the vacuum preloading with prefabricated vertical drains (PVDs) is a common method for soil improvement, there are some disadvantages for the treatment of soft clay fills using PVDs (Bo *et al.* 2007; Chu *et al.* 2000, 2005, 2006, 2009a, b; Varaksin & Yee 2007, Yan & Chu 2005). One of the difficulties for the land reclamation using PVDs is that the soil improvement works only can be conducted after the fully infill of the soft clay. Another difficulty is that the ground is too soft for machines or workers to go on top to do soil improvement works (Broms 1987; Chu *et al.* 2012, 2021, 2021).

Some researchers have proposed a new soil improvement method for the treatment of soft clay fills (Chai *et al.* 2014, 2022; Chu & Guo 2016; De Lillis *et al.* 2017). In this method, the horizontal drains with vacuum pressure are applied in the treatment of soft clay fills. The horizontal drains are installed layer by layer using special barge and following by the infilling of soft clay fills. The vacuum pressure can be applied in the horizontal drains to accelerate the consolidation of soft clay fills as early as the first few meters soft clay is laid. Therefore, a working platform to support the improvement works of soft clay is not necessary since the soft clay has already been consolidated and solidified to a certain degree. Moreover, the containment bund does not have to be built as high as the maximum height of the reclaimed soft clay fills. By using this new soil improvement method, the overall reclamation duration will be cut down and the cost for land reclamation projects can be saved.

The horizontal drains, consisting of discrete prefabricated drains (PHDs), have been applied in some land reclamation projects in Japan, Korean and China (Chai *et al.* 2014;

Pu *et al.* 2022; Shin & Oh 2007; Shinsha *et al.* 2013; Shinsha & Kumagai 2014). To some extent, the treatment of soft clay fills using PHDs is effective. But the position of the pre-fabricated drains is deviated after the placement of soft clay fills. This causes deviation in the design, analysis, and quality control. A new product, horizontal drainage enhanced geo-textile (HDeGs), is proposed by Chu *et al.* (2015, 2016, 2021). The HDeGs, consisting of discrete prefabricated drains bonded with geotextile, make the convenient installation and predictable position. The reliability of the design and quality control of the construction can be improved. In this paper, the construction procedure for the use of HDeGs and vacuum preloading for the land reclamation using soft clay fills is illustrated. The advantages of vacuum preloading using HDeGs are elaborated. A model test of soft marine clay using HDeGs and vacuum pressure are conducted to demonstrate the effectiveness of the proposed method.

2 CONSTRUCTION PROCEDURE

Figure 1 shows the new product of horizontal drains, Horizontal Drainage enhanced Geotextile Sheet (HDeGs) (Chu & Guo 2015). For HDeGs, the discrete drains with a certain spacing are bounded with geotextile sheets. Both of the drains and geotextile sheets not only provide vacuum pressure, but also work as drainage paths due to the transmissivity of geotextile and large discharge capacity of drain. The prefabricated HDeGs can be rolled up and transported to the reclaimed pond for installation. With the use of geotextile, the installation of HDeGs is convenient and the position of HDeG sheets can remain in place.

Firstly, a layer of HDeGs is placed on the seabed within the containment bund using a barge as in Figure 2. Then, the first layer of soft clay fills is poured in to cover the HDeGs and the vacuum pressure can be applied in drains as in Figure 2a, b. While the first soft clay layer is under vacuum consolidation, the second layer of HDeGs can be laid on top of soft clay and then covered with another layer of soft clay. The process repeats until the desired elevation is reached. A layer of geomembrane will be placed on top of the HDeGs to seal the reclaimed area (see in Figure 2c) and the surcharge can be placed on the geomembrane after a certain time of vacuum consolidation. When the seabed is too soft, the PVDs can be installed first to improve the seabed soft soil and covered by a layer of sand blanket as in Figure 2d. Subsequently, the placement of HDeGs and soft clay fills can be carried out as mentions before.
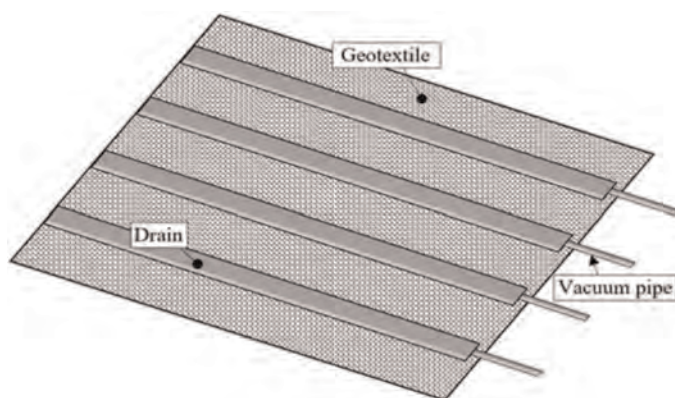
Figure 1.   Configuration of horizontal drainage enhanced geotextile sheet.
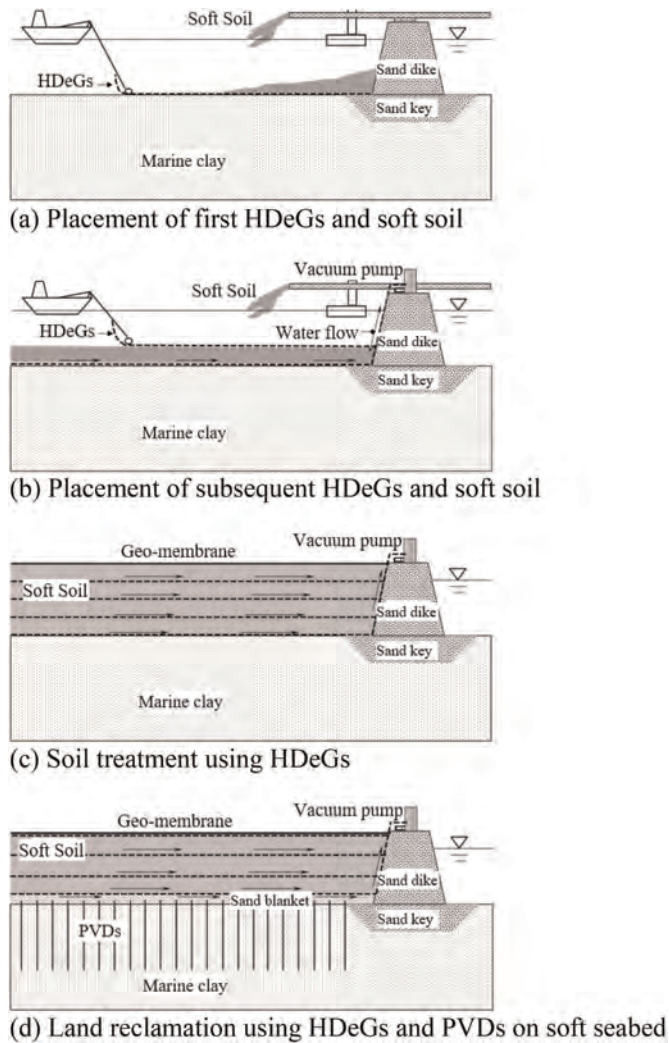
Figure 2.   Construction procedure.

Because of the use of HDeGs, consolidation can take place as soon as the first layer of soft clay fills is placed and thus it will save considerable amount of consolidation time. For this reason, the spacing of the horizontal drains can be greater which in turn saves materials used for the horizontal drains. Furthermore, a working platform is not need. Therefore, the overall benefits of using HDeGs may exceeds that the benefits of using PVDs.

Many studies have shown that the electro-osmosis effect and the high temperature can help accelerate the consolidation process of soft clay (Abuel-Naga *et al.* 2006; Delage *et al.* 2000; Lee 2015; Lamont-Black *et al.* 2016). To incorporate the electro-osmosis effect into the HDeGs, carbon felt can be employed together with geotextile because of its flexible and lightweight. To improve the permeability of clay fills using high temperature, the heating wires can be bonded with geotextile to heat the clay fills around the HDeGs.

3 MODEL TEST USING HDEGS AND VACUUM PRESSURE

3.1 Soft marine clay

The soft marine clay with high-water content is chosen as testing material. The marine clay is collected from a sit along West Coast, Singapore and mixed with tape water. The basic engineering properties of soft marine clay are given in Table 1. The plastic limit and liquid limit of marine clay are 32% and 72%, respectively, and the fines content is 93%. The soil is classified as high plasticity clay. The compression and recompression index from oedometer tests are 0.50 and 0.10. The average coefficient of consolidation of soft marine clay is about 0.45 m^2/year.

Table 1. Basic engineering properties of soft marine clay.

Property	Soft marine clay
Specific Gravity	2.70
Liquid limit (%)	72
Plastic limit (%)	32
Plasticity Index (%)	40
Coefficient of consolidation (m^2/yr)	0.45
Compression index	0.50
Recompression index	0.10
Fine content (%)	93
Soil classification	CH

3.2 Testing setup

The Model test of soft marine clay using HDeGs are carried out in a consolidation tank with a dimension of 1.5 m (L) by 1 m (H) by 1 m (W) as in Figure 3. The HDeGs made of single drain (AliDrain) and single non-woven geotextile (Tencate TS10) is placed in the middle of soft marine clay. The drain used is 100 mm in width and 3 mm in thickness and the non-woven geotextile is 1 mm in thickness. The drain is connected to a jet pump via a reinforced plastic pipe and a L-shape connector. Pore-water pressure transducers (TML KPD-200KPA) are placed on the HDeGs and the bottom of tank to measure the pore pressure change in soft marine clay. The settlement on soil surface is measured by laser sensors (Keyence IL600).

The soft marine clay with 0.95 m of initial height and 140 % of initial water content are used. Due to the sedimentation and self-weight consolidation of soft marine clay, there are 10 cm of clean water above the soft marine clay surface before testing in Model test. The average water content and the height for vacuum consolidation are 117 % and 0.85 m. The average vacuum pressure from a jet pump is around −80 kPa. The duration of Model test are 18.7 hours. The laboratory vane shear tests with 50 mm by 33 mm of vane are conducted at different depths on a certain cross-section of treated soil. The water contents are measured at the corresponding positions.

3.3 Testing results

The surface settlement and pore water pressures measured in Model test are shown in Figure 4. Due to the 8 hours per day of laboratory testing duration, the testing results are fluctuating, and the effective consolidation time is 18.7 days. After testing, a 28.3 cm of final average settlement is achieved. The pore water pressure at different locations of pore pressure transducers decreases with the increase in the distance to the drain. However, the pore
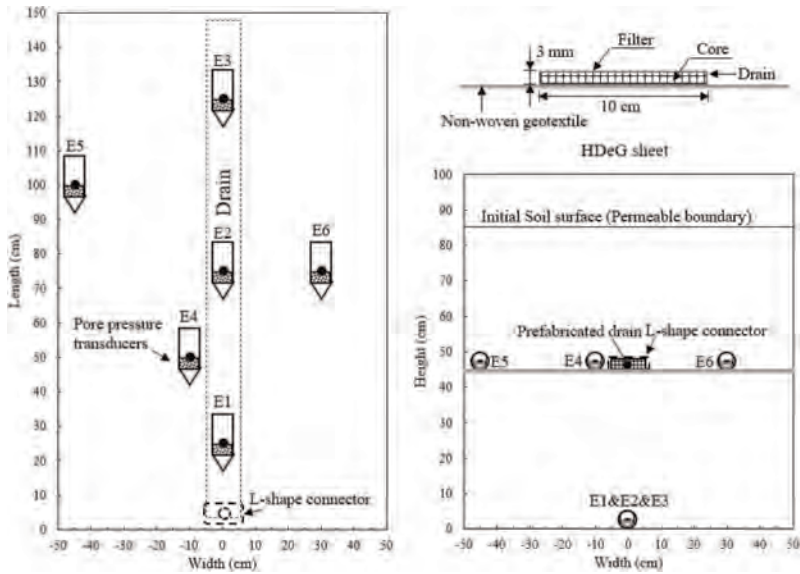
Figure 3. Model test using HDeGs and soft marine clay.
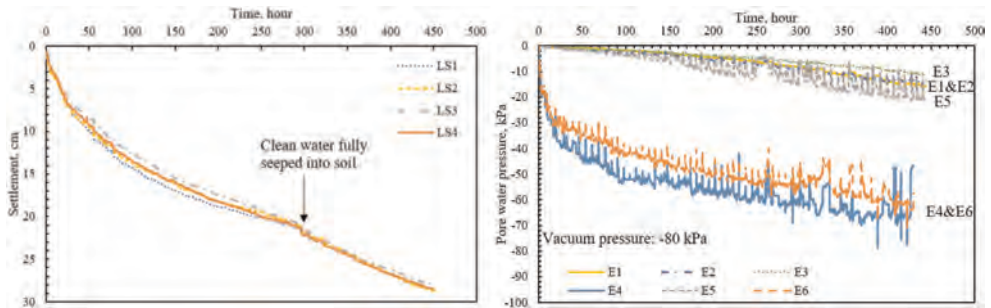
Figure 4. Monitoring data for model test.

water pressures on HDeGs are considerable and close to the source vacuum pressure (around −85 kPa). According to Terzaghi's consolidation solution, the estimated pore water pressure at E1, E2, and E3 after 18.7 days is −11.9 kPa which is close to the measured average value −13.0 kPa. However, by using Chai's method for PHDs (Chai *et al.* 2014), the estimated pore water pressure at E1, E2, and E3 after 18.7 days is −0.01 kPa under plane strain condition. Therefore, the boundary condition of vacuum consolidation using HDeGs is more similar with that in Terzaghi's consolidation theory. This is the major difference between the proposed HDeGs method and the horizonal drain methods proposed by others before. The above observation suggests that the HDeGs play a nonnegligible role in pore pressure dissipation particularly when the geotextile sheet has a certain transmissivity.

The undrained shear strength and water content distributions with depth are shown in Figure 5. The soft marine clay near the HDeGs have a lower water content and larger undrained shear strength. The minimum water content is 43.6% and the maximum undrained shear strength is 15.25 kPa in the clay around the drain. Compared with the average initial water content of 117%, the average final water content of 60.9% is a substantial reduction. By using Asoka's method, the ultimate settlement is 41.0 cm. The degree

1571

of consolidation calculated using the average settlement is 69.1 % after 18.7 days. Therefore, the vacuum consolidation using HDeGs is feasible for the land reclamation using soft clay fills.
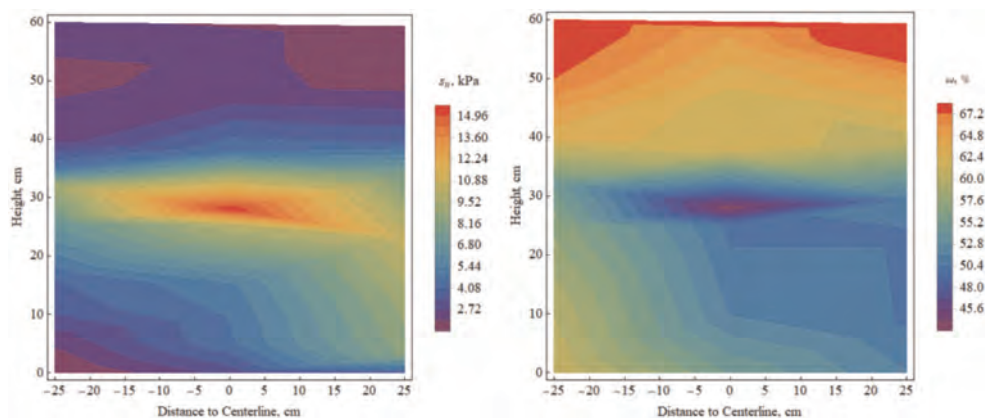
Figure 5.   Undrained shear strength (s_u) and water content (ω).

4   CONCLUSIONS

In this paper, a new product, horizontal drainage enhanced geotextile sheet (HDeGs), is proposed for the land reclamation using soft clay fills. The construction procedure of land reclamation of soft clay fills using HDeGs and vacuum pressure is illustrated. The advantages of the use of HDeGs are discussed. The potential benefits using HDeGs is introduced by incorporating the electro-osmosis and temperature effects.

A model test of soft marine clay is conducted to investigate the effectiveness using HDeGs and vacuum pressure. The testing results demonstrate the performance of vacuum consolidation using HDeGs is well. Both the prefabricated drain and the geotextile can transmit the vacuum pressure and provide good drainage. A 69.1 % of degree of consolidation can be achieved after 18.7 days of vacuum consolidation. A large reduction of water content and increasing of undrained shear strength are measured. Therefore, the vacuum consolidation using HDeGs is feasible for the land reclamation using soft clay fills.

REFERENCES

Abuel-Naga, H., Bergado, D.T., Gunturi, R., Grino, L., Rujivipat, P. & Thet, Y. 2006. Experimental Evaluation of Engineering Behavior of Soft Bangkok Clay under Elevated Temperature. *Journal of Geotechnical and Geoenvironmental Engineering* 132.
Bo, M. W., Arulrajah, A. & Nikraz, H. 2007. Preloading and Prefabricated Vertical Drains Design for Foreshore Land Reclamation Projects: A Case Study. *Proceedings of the Institution of Civil Engineers – Ground Improvement* 11(2): 67–76.

Broms, B.B. 1987. Stabilization of Very Soft Clay using Geofabric. *Geotextiles and Geomembranes* 5(1): 17–28.

Chai, J.C. Horpibulsuk, S., Shen, S.L. & Carter, J. 2014. Consolidation Analysis of Clayey Deposits Under Vacuum Pressure with Horizontal Drains. *Geotextiles and Geomembranes* 42.

Chai, J.C., Wang, J., Ding, W.Q. & Qiao,Y.F. 2022. Method for Calculating Horizontal Drain Induced Non-linear and Large Strain Degree of Consolidation. *Geotextiles and Geomembranes* 50(2): 231–237.

Chen, H., 2021. *Land Reclamation using Soft Clay Fill and Vacuum Preloading via Horizontal Drainage Enhanced Geotextile Sheets. Doctoral Thesis*, Nanyang Technological University, Singapore.

Chu, J., Yan, S. W. &Yang, H. 2000. Soil Improvement by the Vacuum Preloading Method for an Oil Storage Station. *Ground and Soil Improvement* p: 21–28.

Chu, J., Goi, M. H. & Lim, T. T. 2005. Consolidation of Cement-treated Sewage Sludge using Vertical Drains. *Canadian Geotechnical Journal* 42(2): 528–540.

Chu, J., Bo, M. W. & Choa, V. 2006. Improvement of Ultra-soft Soil using Prefabricated Vertical Drains. *Geotextiles and Geomembranes* 24(6): 339–348.

Chu, J., Bo, M. W. & Arulrajah, A. 2009a. Reclamation of a Slurry Pond in Singapore. *Proceedings of the Institution of Civil Engineers – Geotechnical Engineering* 162(1): 13–20.

Chu, J., Bo, M. W. & Arulrajah, A. 2009b. Soil Improvement Works for an Offshore Land Reclamation. *Proceedings of the Institution of Civil Engineers – Geotechnical Engineering* 162(1): 21–32.

Chu, J., Yan, S. & Lam K.P. 2012. Methods for Improvement of Clay Slurry or Sewage Sludge. *Proceedings of the Institution of Civil Engineers – Ground Improvement* 165(4): 187–199.

Chu, J. & Guo, W. 2015. A Geotechnical Apparatus and Method of Usage. *SG Patent Application*, Serial No. 10201509039Y on 3 November 2015.

Chu, J. & Guo, W. 2016. Land Reclamation using Clay Slurry or in Deep Water: Challenges and Solutions. *Japanese Geotechnical Society Special Publication* 2(51): 1790–1793.

Chu, J., Wu, S.F., Chen, H., Pan, X.H. & Chiam, K. 2021. New Solutions to Geotechnical Challenges for Coastal Cities. *Geotechnical Engineering Journal of the SEAGS & AGSSEA* 50(1).

de Lillis, A., Miliziano, S., Flora, A. & Fasano, G. 2017. Reclamation of a Containment Area: Measurements and Back Analysis of the Height of Dredged Mud. *Conference: 19th International Conference on Soil Mechanics and Geotechnical Engineering, At Seoul.*

Delage, P., Sultan, N. & Cui, Y. J. 2000. On the Thermal Consolidation of Boom Clay. *Canadian Geotechnical Journal* 37: 343–354.

Lam, K.P., Wu, S.F. & Chu, J. 2020. Field Trial of a Membraneless Vacuum Preloading System for Soft Soil Improvement. *Proceedings of the Institution of Civil Engineers – Ground Improvement* 173(1): 40–50

Lamont-Black, J., Jones, C. & Alder, D. 2016. Electrokinetic Strengthening of Slopes – Case History. *Geotextiles and Geomembranes* 44: 319–331.

Lee, E.C. 2015. Chapter 15 – Electrokinetic Improvement of Soft Clay Using Electrical Vertical Drains, Editor(s): Buddhima Indraratna, Jian Chu, Cholachat Rujikiatkamjorn, *Ground Improvement Case Histories*: 487–513.

Pu, H., Khoteja, D., Zhou, Y. & Pan, Y. 2022. Dewatering of Dredged Slurry by Horizontal Drain Assisted with Vacuum and Flocculation. *Geosynthetics International* 29(3): 299–311.

Shin, E.C. & Oh, Y.I. 2007. Recent Innovative Applications of Geosynthetics in Geotechnical Engineering. *Proc. 13th Asia Regional Conf on Soil Mechanics and Geot Eng, Calcutta, India*: 207–221.

Shinsha, H., Kumagai, T., Miyamoto, K. & Hamaya, T. 2013. Execution for the Volume Reduction of Dredged Soil using the Vacuum Consolidation Method with Horizontal Pre-fabricated Drains. *Geotech. Eng. J. Jpn. Geotech. Soc.* 8(1): 97–108 (in Japanese).

Shinsha, H. & Kumagai, T. 2014. Bulk Compression of Dredged Soils by Vacuum Consolidation Method Using Horizontal Drains. *Geotechnical Engineering Journal of the SEAGS & AGSSEA* 45(3): 78–85.

Varaksin, S. & Yee, K. 2007. Challenges in Ground Improvement Techniques for Extreme Conditions: Concept and Performance. *Proceedings of the 16th Southeast Asian Geotechnical Conference*: 101–115.

Yan, S.W. & Chu, J., 2005. Soil Improvement for a Storage Yard using the Combined Vacuum and Fill Preloading Method. *Canadian Geotechnical Journal* 42(4): 1094–1104.

Field tests on the impact of stones on geotextile compared with theory

A. Bezuijen

Bezuijen Consult, Berkel en Rodenrijs, The Netherlands

ABSTRACT: Impact of stones or blocks on a geotextile, for example during construction of a coastal engineering structure, can damage the geotextile. Using the results of laboratory tests, it was shown that, apart from the robustness of the geotextile and its maximum elongation, the friction between the falling stone and the geotextile and between the geotextile and the subsoil is of importance for the risk of damage to the geotextile. Furthermore, it was found, as could be expected, that the shape of the stone has a large influence. An analytical calculation model was developed and compared with the results of numerical calculations. Results show the influence of friction between the sand the geotextile and the stone. The influence of the shape of the blocks according to the model is less than expected based on laboratory tests. Overall elongation is the dominant failure mechanism for woven geotextiles, local elongation due to friction around the tip of the penetrating block, is dominant for non-wovens.

1 INTRODUCTION

When a geotextile is used in coastal protection it nearly always has (also) a filter function. Very general one can say that the opening size of the geotextile must be smaller than the average grain size. Various studies have refined this for different granular materials and different geotextiles (See Rakić *et al.* 2021 for a recent overview). All these filter rules assume that the geotextile that is placed in the coastal structure has more or less the same properties as the geotextile tested. However, regularly the geotextile is damaged during installation (Cheah 2017). This is a real risk when larger stones or blocks are placed on top of the geotextile. A damaged geotextile will not fulfil the filter rules, which may be the cause of damage to or even failure of the coastal structure.

Therefore, damage during installation has been tested in field and laboratory tests. For larger stones the drop test is used, see Figure 1 for a field and laboratory test example. A stone is lifted to a certain height above the geotextile to be tested and then dropped on the geotextile. Usually there is soil below the geotextile. This soil layer takes part of the load and in this way protects the geotextile. Tests performed without soil results in much more damage to the geotextile. The tests showed that the angle between the planes of the stone are very important. Stones with and angle of 60 degrees or less between the planes that impact on the geotextile were able to destroy geotextiles at a low falling height. Furthermore, it appears that wovens are more vulnerable than non-wovens. This is partly caused by the lower maximum elongation of wovens, but also by non-isotropic stress-strain relation in a woven, resulting in high stresses parallel to the warp and weft direction of the geotextile, but less in the other directions. Tests with two geotextiles on top of each other showed that mostly the lower geotextile was damaged and not only the woven or non-woven.

Figure 1. Examples of drop tests in the field and in a laboratory. The insert left shows an example of the damage to a geotextile. (photographs field tests courtesy of Van den Herik Contractors).

The paper will recapitulate some of the theoretical background. Using the theory developed by Bezuijen & Izadi, (2022), it will be shown what are the consequences and how does this fit with results from field tests. Since by Bezuijen & Izadi (2022) the influence of the geotextile is only partly taken into account, the theory is expanded for one type of block a bit further in this paper.

2 THEORY

2.1 *Elongation based on geometry*

Starting point for the recent research in the Netherlands and Belgium on the consequences of impact was a geometrical model (SBR-CUR 2017), see Figure 2.
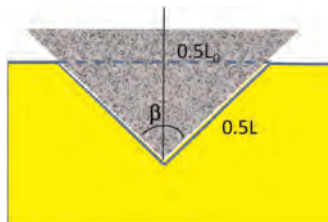
Figure 2. Elongation geotextile due to impact from L_0 to L.

The loading on the geotextile is assumed to be at maximum when only the geotextile under the stone deforms during impact. On average, the part with the length L_0 will elongate until L. This allows to calculate the strain (ε_l) in the geotextile;

$$\epsilon_l = \frac{L - L_0}{L_0} = \frac{1}{\sin(0.5\beta)} - 1 \tag{1}$$

for a 2-dimensional situation of a wedge-shaped stone. In cases of a 3-dimensional situation with a cone shaped stone, the relation is:

$$\epsilon_l = \sqrt{\frac{1}{\sin(0.5\beta)}} - 1 \tag{2}$$

These geometrical relations show that the angle β, the angle between the two planes of the impacting stones or the angle of the cone is important. A small β will lead to a large elongation and more likely to damage. Since the elongation is determined by the angle β only, a geotextile with a large elongation at break will more likely survive the impact than a geotextile with a small elongation at break. This led to the conclusion in (SBR-CUR 2017), that for stones larger than 40 kg only non-wovens with enough elongation at break can be used.

Laboratory tests (Bezuijen & Izadi 2020) showed that reality can be more complicated than described in this model. It was found that rupture was possible even when the maximum possible geotextile strain at failure is more than calculated with equations (1) and (2). Furthermore, it was found that in case of two geotextiles the position of the geotextile (top or bottom) is of importance.

2.2 Dynamic model

Based on the laboratory tests mentioned above and discrete element calculations, Bezuijen & Izadi (2020) developed an analytical model. The essence of this model is, that when a stone penetrates into the soil, the soil has to move upwards to allow the stone to penetrate. Due to friction between the soil and the geotextile a force parallel to the geotextile is exerted on the geotextile. If the friction force between the soil and the geotextile is equal or lower than the friction force between the stone and the geotextile, there will be no extra loading on the geotextile because the geotextile will be pushed downward with the stone. However, if the friction force between the soil and the geotextile is higher than the friction force between the stone and the geotextile, the additional force exerted on the geotextile must be taken by the geotextile. In case the geotextile is not strong enough, it will break.

This model explains why in case of a layer of two geotextiles, the lowest one is damaged first. The friction between the lowest geotextile and the soil is higher than the friction between the two geotextiles. Furthermore, the upward sand movement is only influencing the lowest geotextile.

2.3 Dynamic model extended

The model described briefly in the previous section assumes that the resistance force is generated by the soil only but does not incorporate the contribution of the geotextile. When the geotextile is stretched, there will be a tension force in the geotextile. This tension force also reduces the penetration depth. For a wedge-shaped block, see Figure 3, the definition sketch also shown in that figure can be used.

Figure 3. Block type used in model and definition sketch. L is the length of the elongated geotextile. The arrows indicate the sand movement along the geotextile.

The relation between F_v and $F_\perp$ depends on the friction in the sand. Here it is assumed that there is friction between the sand and the geotextile, but that friction does not influence the ratio between F_v and $F_\perp$. With that assumption, the total vertical force on the block is composed of the force F_v, the resistance from the sand. This resistance is calculated using the classical bearing capacity formula for a shallow strip footing for non-cohesive soil without embedment depth:

$$F_v = \alpha 0.5 \gamma' B A N_\gamma \qquad (3)$$

where γ' is the 'effective' density, B the width of the footing, A the area and

$$N_y = 2(N_q + 1)\tan\phi \quad and \quad N_q = e^{\pi.\tan\phi}\tan^2(45 + \phi/2) \qquad (4)$$

The factor α depends on the geometry of the stone and is 1 for a strip footing and 0.6 for a square footing. The total vertical resistance force on the block can now be written as the sum of the resistance force in the sand, the friction between the geotextile and the block and the tension force T_b in the geotextile. With the definition sketch in Figure 3 it can be derived:

$$F_v = F_\perp \sin(0.5\beta) \qquad (5)$$

and for the total vertical resistance:

$$F_{tot} = 2[F_\perp \sin(0.5\beta) + F_\perp \tan\phi_b \cos(0.5\beta) + T_b \cos(0.5\beta)] \qquad (6)$$

The second term on the right-hand side of this formula is the friction between the block and the geotextile. The tension force in the geotextile, T_b, contributes to the vertical resistance force at the lowest point of the block at the intersection of the two planes. It should be noted that T_b is the tension force in kN on the block. This will require a tensile strength $T = T_b/A$ in kN/m of the geotextile.

This tension force in the geotextile has two origins. Normally the geotextile will be fixed at some distance from the impact. The geotextiles will stretch by the impact due to the deformation underneath the block. Not only under the block there will be deformation (as was suggested in SBR-CUR 2017) but also next to the block as can be seen in Figure 4. In this paper it is assumed that the deformation of the geotextile results in a stretching of the whole geotextile. This means that the average strain due to this stretching can be written as:

$$\varepsilon_{avg} = \frac{B/\sin(0.5\beta) + L_0 - B}{L_0} \qquad (7)$$

Next to this average strain, underneath the block there is an additional strain. The deforming sand will move upward resulting in an additional tensile stress in the geotextile, depending on the friction between the sand and the geotextile. The block, moving downward, will somewhat reduce the overall tensile stress in the geotextile but the tensile stress
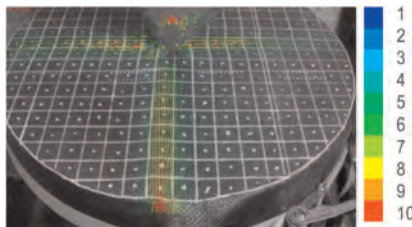

Figure 4. Stretching of a geotextile during impact. The colors represent the pixel movement (adapted De Strijcker & Decraene 2017).

will be higher at the tip of the block. The net additional tensile stress in the geotextile is determined by the difference in friction angle between the sand and the geotextile and the geotextile and the block material respectively. It is assumed that the extra strain in the geotextile due to the difference in friction between the sand and the block is very localized and does not influence the average strain in the geotextile. Furthermore, it is assumed that full friction force is mobilized on both sides of the geotextile. With these assumptions the strains can be added, and the strain calculated with Eq. (7) can be seen as a pre-straining of the geotextile and the tensile force T_b can be written as:

$$T_b = F_\perp \tan \phi - F_\perp \tan \phi_b + \varepsilon_{avg} E_T A \qquad (8)$$

With ϕ the friction angle between the soil and the geotextile and ϕ_b between the geotextile and the block. E_T is the tensile stiffness of the geotextile. Since ε_{avg} can be determined from the block penetration, it is now possible to calculate the penetration of a block and the forces that can be expected. For a certain dump height, a block will impact with a certain velocity. Following the well-known equation $F = m.a$, F_{tot} in Eq. 5 is the total vertical force except the gravitational force (the weight of the stone). The mass of the block is known and with F_{tot} and the weight of the block, the acceleration can be calculated. Assuming a fixed small timestep, the acceleration times that step results in a change in the velocity and the velocity on a certain moment multiplied by that time step results in the displacement. This was programmed in a spreadsheet. In this spreadsheet a time step of 0.1 or 0.3 ms was used, depending on the penetration depth of the block.
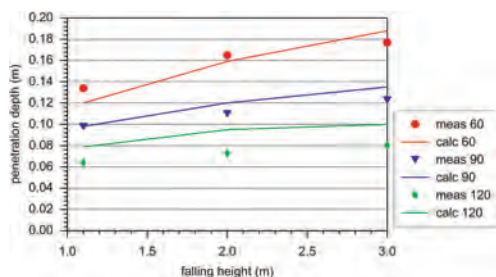
Figure 5. Measured and calculated penetration compared for impact tests without a geotextile, friction angle 35.5^0.

Figure 6. Maximum penetration of block taken from high-speed video (250 fps), see also text.

3 COMPARISON WITH MEASUREMENTS

The model has been compared with impact measurements by De Strijcker & Decraene (2017). They measured the penetration for blocks with different angles β falling into sand but without a geotextile. For a block falling on a geotextile with sand underneath, it was not possible to measure the penetration depth since the block bounces back on the elastic geotextile. The comparison between calculated and measured penetration is shown in Figure 5. A friction angle of 30 degr between the stone and the sand was used. There appears to be a reasonable agreement.

4 PARAMETER STUDY

The calculation model is used to investigate the influence of various parameters. It appears that for the situation with a geotextile the maximum penetration in the experiments is less

than calculated with the friction angle mentioned above. As mentioned, the precise penetration depth could not be determined because the block bounces on the geotextile. However, an indication can be obtained from the high-speed camera images. Figure 6 shows the result for a geotextile with a tensile strength of 80 kN/m. From the dimensions of the block (the diagonal blue line on top of the block is 160 mm) a rough estimation of the penetration depth is possible, around 0.035 m. It is a rough estimation, because, as will be shown later, the time between touching the geotextile and reaching standstill is only around 6 ms for a block penetrating 0.035 m. This means that there are only around 2 frames in the video that records with 250 fps. Figure 6 shows the block a bit blurred because it still has a downward velocity. In the next frame the fall velocity is less. and the block is sharper shown than in Figure 6. However, the penetration depth is less in that frame, indicating that the block is already bouncing back.

Calculated values of the penetration are shown in Table 1 for various situations. First, in the calculation mentioned Calibration (Calibr.), the friction angle and the shape factor were increased to simulate the measured 0.035 m penetration. This appeared only possible with a rather extreme friction angle and shape factor. It is possible that the loading of the geotextile on the sand increases the stresses in the sand resulting in a strength increase of the sand. Furthermore, the calculation is purely 2D, neglecting the influence of the deforming geotextile at the front and back of the block as shown in Figure 6. A last possibility is, that the penetration depth derived from the figure is too small while the block has not reached complete standstill as explained above.

Table 1. Parameters used in various simulations. In bold are the changes with respect to the previous calculation.

Parameter	Calibr.	Calc. 1	Calc. 2	Calc. 3	Calc. 4
Drop height (m)	4	**2.5**	2.5	2.5	2.5
Block weight (kg)	40	40	40	40	40
Width of block (A) (m)	0.365	**0.26**	0.26	0.26	0.26
β (degr)	90	90	90	**60**	60
Friction angle (degr)					
sand – geotextile, ϕ	50	**45**	45	45	45
geotextile – block, ϕ_b	30	**20**	20	20	20
Shape factor α (-)	2.4	**1**	1	1	1
Density sand (kg/m^3)	15	15	15	15	15
Time step (ms)	0.1	**0.3**	0.3	0.3	0.3
Tensile strength (kN/m)	80	80	**40**	40	**80**
ε_{max} geotextile (-)	0.15	0.15	**1**	1	**0.2**
L_0 between fixations (m)	0.8	0.8	0.8	0.8	0.8
Impact velocity (m/s)	8.86	**7**	7	7	7
Penetration depth (m)	0.035	**0.06**	0.068	0.088	0.062
Max. calc. strain (-)	0.147	**0.11**	0.92	0.8	0.12

Apart from the Calibration, 4 calculations were run with more realistic values of the friction angle and the shape factor. These result in larger penetration depths, although the fall height was decreased to a more realistic maximum value that can be expected in field conditions, 2.5 m. Although the penetration depth is more in Calc. 1, the maximum strain is significantly less. This is caused by the huge deceleration in the Calibration calculation to stop the block within 0.035 m. The deceleration is nearly 340 times the acceleration of gravity.

In Calc. 2, the geotextile is changed to a theoretical non-woven with a lower tensile strength (40 kN/m) but a larger maximum allowable strain (100%). It appears that, according to the model, the calculated maximum strain under the block is considerably

higher than for the calculation (Calc. 1) with the woven geotextile with a strength of 80 kN/m at 15% strain. Using only the geometric criterion, as explained in Section 2.1, would lead to the same strain underneath the block, but the model considers that the non-woven geotextile can be stretched with a smaller force than the woven.

Calc. 3 and 4 show the influence of a block with a smaller β of 60 degr. According to this model this influence is only limited. There is a bit more penetration and also the calculated maximum strain is a bit higher than for a block with a β of 90 degrees.

Figure 7 presents the penetration and strains as a function of time for the Calibration calculation and Calc. 1. The contribution of friction to the total strain is high in the Calibration, but in Calc. 1, strain by elongation is dominant.
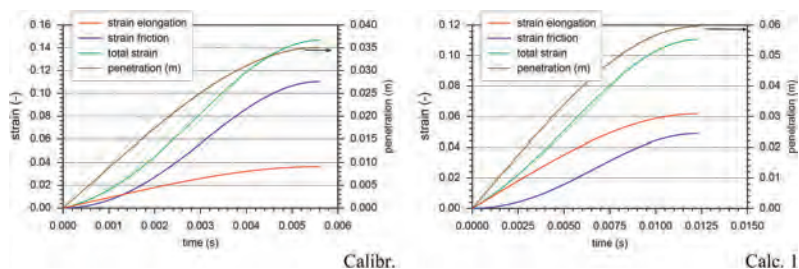

Figure 7. Penetration depth and strain caused by geometry changes (elongation) and friction in two calculations. Note the different scale of the strain. Parameters see Table 1.

5 CONCLUSIONS

The model described in this paper presents a rather accurate prediction of the penetration of a block into sand without a geotextile. The influence of the block angle β seems to be underpredicted by the model. It overpredicts the penetration when a geotextile is included and using the general accepted values for the friction angle in the sand and the shape factor. It should be realized, that, depending on the properties of the geotextile, this overprediction can lead to an underprediction of the possible installation damage on the geotextile. According to this model, a small penetration of a block during impact may lead to high tension forces in the geotextile and to damage, for both a woven and non-woven geotextiles.

REFERENCES

Bezuijen, A. and Izadi, E. (2022). Damage of Geotextile Due to Impact of Stones. *Geosynthetics International*, 29, No. 2, 151–162. [https://doi.org/10.1680/jgein.21.00036]

Cheah, C. (2017) *Development of Methodology to Quantify Installation Damage on Geotextile for Coastal Application* (PhD thesis), Queensland university of Technology.

De Strijcker, S. and Decraene, T. (2017) *Strength of Geotextiles Against Falling Stones, Laboratory Experiments and Software Validation* (Master thesis), Ghent University, Faculty of Engineering Science and Architecture.

Rakić, D.; Basaric, I.; Ljubojev, M. (2021) Filter Rules for Soil and Geosynthetics, *Mining and Metallurgy Engineering BOR* 1-12, DOI: 10.5937/mmeb2101001R.

SBR-CUR (2017) *Guideline, Geotextiles Underneath Revetment Stones* (in Dutch). Dutch Centre of Research and Regulations for Civil Engineering ISBN 9789053676363.

Influence of lateral restriction on bags for dewatering sludge of water treatment plants

M. Moeller, D. Vidal & G.A. Oliveira
Aeronautic Institute of Technology, ITA, São José dos Campos, Brazil

ABSTRACT: Currently, a large amount of sludge is generated through water treatment plants. This sludge represents a problem, generally having its destination in water bodies without treatment and needing correct handling through a dewatering process. The paper aims to expose two variants of the dewatering technique with geotextile bags, analyzing its operations and dewatering processes. It describes field tests performed on two geotextile bag systems, a conventional bag and a bag with lateral restraint, both of which are submitted to two filling cycles. Field and laboratory tests were performed for both geotextile bags using sludge from a water treatment plant. Data about volume, height abatement, and solids content due to the dewatering were collected per time and compared between the two configurations. The results showed that the geotextile bag with lateral restrains could receive a greater volume of sludge, receiving more than 20% of the total volume received in the conventional bag. In the other hand, the conventional geotextile bag achieved a higher solid content, reaching 39% higher solids content than the bag with lateral restrains. The data obtained made it possible to conclude that both configurations were successful, resulting in dewatering efficiencies greater than 1000%.

1 INTRODUCTION

Consumerism governs the life of an increasingly growing world population and rampant economic growth, having as a consequence an immense waste generation, bringing environmental and health risks (Daly 2013). With population growth, more inputs are needed, and more waste is generated. This statement could not be more correct for the use of water, where it is directly and indirectly consumed and, through its use, it ends up generating waste in the form of effluents, which are wet and difficult to handle.

These effluents must be correctly treated and disposed of since water is a finite raw material, which, treated lightly, can cause irreversible damage, directly impacting human life. These impacts could be amplified through climatic and geographic changes resulting from the Anthropocene (Sol 2019).

There is, then, a need to treat these effluents. This treatment usually uses some dewatering technique in its initial stages, seeking to separate the solid phase from the liquid phase, allowing the destination of water for reprocessing and the solid phase for other processing steps. Therefore, dewatering techniques contribute to sustainable development. In addition, the environment is protected by contracting services that promote the correct handling of the generated sludge, preventing its undue disposal in water bodies.

In this context, geotextile closed systems have been successfully employed for the dewatering of sludges and sediments for many years (Fowler *et al.* 1997). In this research, two geotextile systems were compared: one corresponding to a conventional geotextile bag and one corresponding to a geotextile bag with lateral restraints. In order to compare these dewatering systems theirs filling volumes, geometric forms and solids content in time were addressed.

2 GENERAL CONCEPTS

2.1 Geosynthetic closed systems

Geotextile closed systems are permeable systems able to confine granular materials, sediments, and sludge with high water content. These systems are made with woven or non-woven geotextiles, with properties established as a function of the characteristics of the effluent to be discharged, having a custom length and perimeter (Fowler *et al.* 1997; Pilarczyk 2000).

The dewatering process in these systems is discontinuous and mixed, occurring mechanically by forced filtration through the filling pressure and, after this, by a natural process, dewatering by its own weight, drainage, and evaporation. The success of this technology was provided by the ability to retain the solid part while allowing the liquid component to exit, having a good filtering function (Moo-Young *et al.* 2002).

The term geotextile bag is usually used for a system with 5m^3 of maximum volume, usually in pillow form, while the term geotextile tube is associated with structures that assume a tubular shape after filling, whose transverse section presents between 3 and 30m in perimeter and its length reaching up to 200 m (Lawson 2006).

2.2 Conventional system conception

Conventional geotextile systems are based on the use of geotextile bags or tubes positioned over a flat drainage layer to collect and convey the effluent generated.

Various aspects of the problem, such as the volume of sludge or sediment to be discharged, the characteristics of the material, the filling speed or pressure, and the solids content to be achieved, must be considered when designing these systems. Discussing only the aspects directly related to the subject of this work, one can highlight the importance of evaluating the acting mechanical stresses and the response to hydraulic demands.

The maximum tensile load that the geotextile can support is crucial in determining the position of the seams and the maximum filling height. Lawson 2006 notes that the maximum tensile load occurs at the side of the system, as illustrated in Figure 1a.

The filling usually takes place in several cycles, as illustrated in Figure 1b. The number of filling cycles is associated with the maximum height the system can reach and the inherent characteristics of the design requirements.

(a) Distribution of the tensile load in the system perimeter (Lawson 2006)

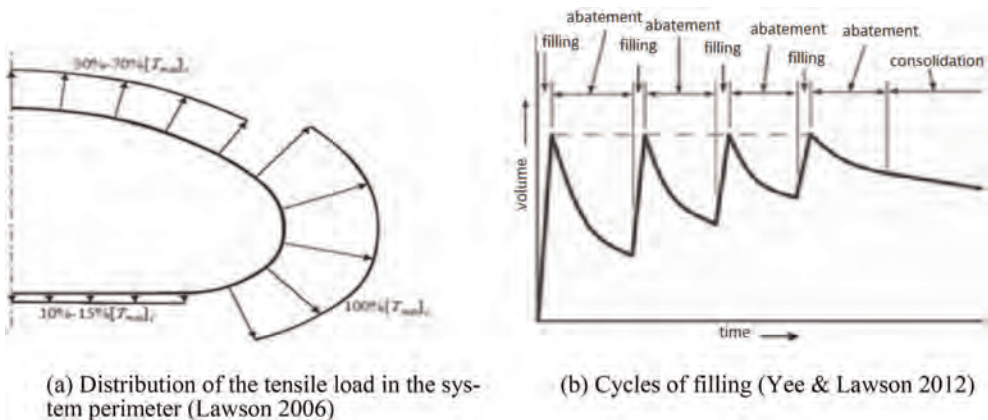(b) Cycles of filling (Yee & Lawson 2012)

Figure 1.   Relevant aspects of design.

Guo *et al.* (2014) point out that there is a difference between the fills of a system at the first fill cycle and a system already with consolidated material from previous fill cycles. In addition to the shape, width, and height being different for the two situations, so are the stresses acting on the geotextile membrane. High stresses accumulate at the top of the geotextile perimeter when filling a system with consolidating material. In reality, all fill cycles can achieve the maximum predicted height when the consolidation process does not imply a significant deposition of consolidated material, making it difficult to lift the lateral regions to recover the shape of the first fill.

2.3 *Geotextile system with lateral restraints*

Using containers for dewatering in geotextile bags or tubes avoids the need to prepare a drainage layer and facilitates the fluid collection and the final disposal of the particulate material.

The dewatering in geotextile systems laterally restrained is a mixed dewatering solution similar to the conventional geotextile system without lateral restrictions. The sludge or sediment is hydraulic pumping to the interior of a tube made from filtering geotextile positioned inside a special container. The container serves as a draining cradle and gives it lateral restraints.

The lateral restriction reduces the tensile stress on the system and allows for filling cycles that always reach the maximum height foreseen.

3 MATERIALS AND METHODS

3.1 *Materials*

The materials employed in this research were:

– two bags made of a woven geotextile in polypropylene yarns and;
– sludge from the water treatment plant that supplies the DCTA (Department of Aerospace Science and Technology).

The geotextile characteristics are shown in Table 1. The two bags are 2.5 m long and have a perimeter of 2.5 m, and are provided with filling nozzles of 0.3 m in height and 0.3 m in diameter centered on the top of their upper faces.

Table 1. Woven geotextile characteristics.

Property	Standard	Nominal Value	Unit
Ultimate tensile strength (both directions)	ISO 10319	105	kN,/m
Elongation at rupture (both direction	ISO 10319	10	%
Characteristic opening size	ISO 12956	149	µm
Permeability	ISO 11058	0.003	m/s

Avancini & Vidal (2018) presented the results of preliminary tests conducted with a sample of the sludge to characterize the sludge and evaluate the geotextile behavior from cone tests and pillow tests.

The sludge presented a mean value of solids content by mass (TSP) of 1.7 % and a dry density of the grains (Gs) of 2.58. The grain size distribution of the sludge particulate fraction, obtained in tests without deflocculant, showed that it is composed mainly of sand (90 %), with 3% silt and 7% clay. Energy Dispersive Spectroscopy (EDS) analysis indicates O, Al, Si, and Fe predominant presence.

Cone tests (not standardized) conducted with the woven geotextile and the sludge indicated a small filtration efficiency (16%) and a good dewatering (102%), related to the small amount of sludge used in the test did not allow for the formation of a pre-filter.

The pillow tests (D7880-D7880M 2013) were conducted according to the modified procedure proposed by Tominaga *et al.* (2012). The pillow received a total volume of 40 liters with a Filtration Efficiency of 90% in 24 hours, presenting between the first and the 7th minutes of dewatering, a Filtration Efficiency of 70%, with the filtration efficiency obtained considering Moo-Young *et al.* (2002) proposition.

3.2 Field tests

Two geotextile systems were considered for the field tests: a conventional geotextile system, CGS, and a geotextile lateral restrained system, LRGS. In function of the pillow test dewatering behavior, it was decided to conduct the field tests without sludge conditioning.

A draining crib was built to receive the geotextile systems. The crib was composed of a bottom coating of geomembrane, and a drainage layer led the percolate to its final destination.

One of the geotextile bags was stretched over the drainage crib, and the other was placed over the drainage crib but inside an artifact that ensured its lateral restriction, maintaining a maximum width of 0.8 m. Each side's excess bag lateral dimension (0.225 m) was managed upstream on the lateral side to facilitate complete filling.

Once the geotextile systems were correctly positioned over the draining crib, the filling cycles started. For this, a submersible pump was used, with a maximum working slope of 6.5 m and maximum and minimum flow rates of 1970 l/h and 550 l/h. For the filling cycles in the field tests, the flow rate was 1800 l/h ($\sim$ 30 l/min).

The filling cycles pumped wet material from one decanter of the water treatment plant, directly to the systems, without polymerization, until the height of approximately 0.45 m, where the pumping ceased. This process was repeated once more after five days from the initial fill-in. The total solids were measured (TS) for the percolated liquid.

The volume for each fill was measured, considering the pump flow and the filling time in each cycle. In addition, consolidation height data for the systems were collected shortly after completion and periodically during the draining process.

The dewatering in the bags was followed in time by measuring the bag height and the solids content (SC). In each system, five samples were collected equidistant for each measurement moment to determine the solids content at the time of dewatering.

Finally, the samples collected from the systems were analyzed, and their solids content was determined for each collection moment. It should be noted that the systems were kept in open outdoor spaces, subject to the weather and changes in the clime. Also, dewatering efficiency DE and filtration efficiency FE were calculetad through the following Equations 1 and 2 (Moo-Young *et al.* 2002).

$$DE = \frac{SC_{final} - SC_{initial}}{SC_{initial}} \; x \; 100 \; (\%) \tag{1}$$

$$FE = \frac{TS_{initial} - TS_{final}}{TS_{initial}} \; x \; 100 \; (\%) \tag{2}$$

4 RESULTS AND DISCUSSION

The field tests were conducted in the two geotextile systems described in 3.2. The systems were filled in such a way that each received two filling cycles. The conventional geotextile system, CGS, received a total of 2.31 m^3 and the lateral restrained geotextile system, LRGS,

received a total of 2.79 m^3. Figure 3 presents pictures of the tested systems obtained at different moments.

With the time-related data, it is possible to draw a chart expressing the filling cycles and dewatering process by decreasing height. Figure 2 presents the maximum filling and consolidation heights by time collected during the field tests.

Sludge samples were collected from both geotextile systems at the filling moment and at 12, 21, and 28 days to evaluate the solid content variation on time. Figure 4 presents images of the moments of sample collection for the two geotextile systems. Table 2 expresses the data found for the solids content and DE. Figure 5a illustrates the increase in solids content by mass in time for both geotextile systems. Figure 5b presents climatic conditions during the 28 days of dewatering.

It is possible to see from Figure 3 that the filling and dewatering curves by time occur similarly for the two cycles of each system, with the exception that the system with lateral
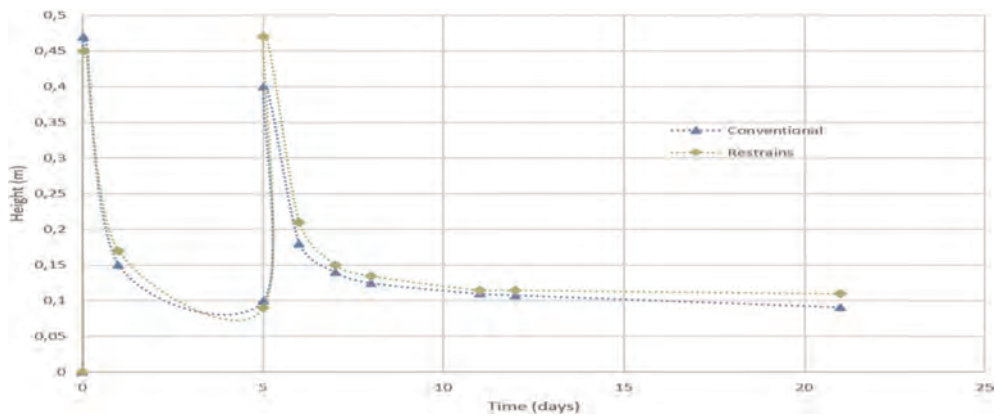
Figure 2. Filling heights per time.

(a) Conventional geotextile system - CGS   (b) Lateral restrained geotextile system - LRGS

Figure 3. View of the tested bags.

a)(Day 12 CGS   b)Day 28 CGS   c)Day 12 LRGS   d)Day 28 LRGS
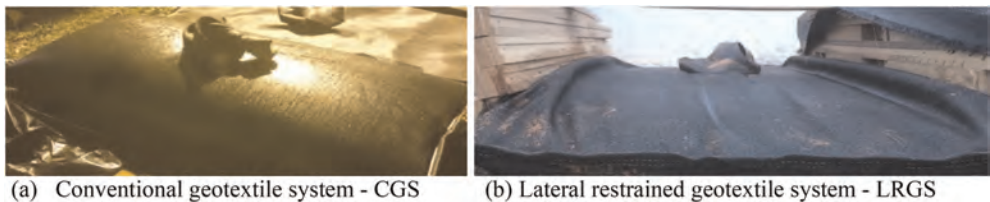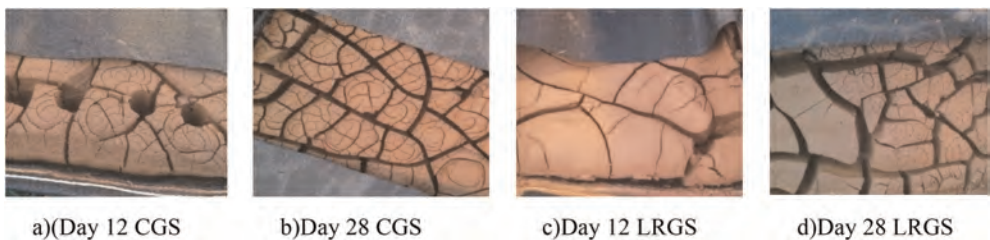
Figure 4. Sludge appearance after 12 and 28 days of dewatering.

Table 2. Solid content per time and dewatering efficiency for the geotextile systems.

Time (days)	CGS		LRGS	
	Solid content (%)	DE (%)	Solid content (%)	DE(%)
0	1,7 ± 0,2	0	1,7 ± 0,2	0
12	16,3 ± 0,5	859	14,5 ± 0,3	753
21	24 ± 3	1312	17 ± 3	900
28	26,5 ± 0,8	1459	19,0 ± 0,7	1018

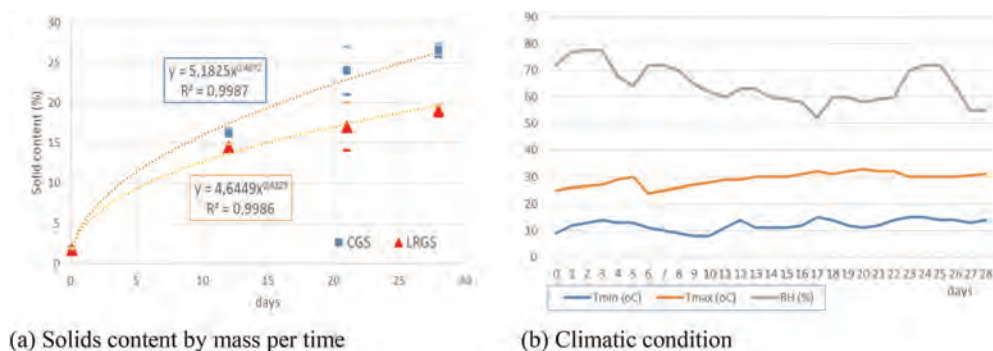(a) Solids content by mass per time   (b) Climatic condition

Figure 5.   Solid contents and climatic condition during dewatering.

restraint managed to reach the maximum filling height even in the second cycle of filling. This is probably due to the lateral restrictions, which define the consolidation area and allow for an easier height gain in a new filling cycle. It would occur in a contrary way in the conventional system, where the densified material offers resistance to filling pressure in the filling cycles after the first, which is increasingly difficult.

Through Figure 4, it can be seen that densification occurs more quickly in the conventional system. The greater densification area and the smaller volume admitted reduce the thickness of the sludge layer and facilitate water exit could explain it. However, in the tests performed, only two filling cycles were made, and, in actual application cases, both systems would be filled to their maximum volume.

The analysis of climatic conditions (Figure 5b) indicates that the 21st day of dewatering was the period with the greatest range of temperature variation (up to 22°C). In addition, during this period, the wind velocity reached 30 km/h, the highest speed observed during the 28 days analyzed. However, there is still no way to directly associate these climatic conditions with the variability of the solids content observed for the samples collected after 21 days of dewatering.

The small width of the consolidation area relative to the lateral height of the restriction may have affected the dewatering efficiency in the retrained condition because the side walls at a much greater height than the top of the bag acted to reduce exposure to sun and wind, which assist the evaporation process.

5   CONCLUSIONS

The large volumes of sludge generated and the impacts of its direct release into the environment make it possible to realize that dewatering techniques are beneficial and increasingly

demanded. They reduce the volume of wet material, allowing it to be more easily transported, handled, and correctly disposed of.

Concerning the filling volumes, in agreement with the filling heights, it can be seen that the system with lateral restraints admitted greater volume than the conventional system, admitting about 20% more volume of sludge. Still, it can be seen that in an actual application case, the volume admitted tends to increase its proportion for the system with lateral restraints even more with the increasing of the geotextile bag size. Another advantage of lateral restriction is the reduction of tensile stresses in the lateral region of the bag.

The larger exposed area of the conventional system and a smaller thickness of dewatering sludge allowed this system to have 28 days after filling with a 39% higher solids content than the lateral restriction system. In actual field situations, this disadvantage would be reduced both by the fact that the filling cycles seek to achieve the maximum allowed volume and by the ratio of exposed width versus height of the lateral restriction is much higher than that employed in the tests.

The dewatering efficiency ED equation should be revised in further works, restraining its results from 0 to 100%. In that way facilitating comprehension.

REFERENCES

ASTM. D7880/D7880M: Standard Test Method for Determining Flow Rate of Water and Suspended Solids *Retention from a Closed Geosynthetic Bag*. West Conshohocken, PA, 2013. http://dx.doi.org/10.1520/D7880_D7880M-13

Avancini, L.S. & Vidal, D.M. 2018. Influence of Water Treatment Plant Sludge Characteristics on its Dewater Ability in Geotextile Closed Systems. *11th Intern. Conference on Geosynthetics*. IGS, Seoul, South Korea.

Daly, H. A Further Critique of Growth Economics. *Ecological Economics*, Elsevier, v. 88, p. 20–24, 2013.

Fowler, J., Bagby, R. M., Trainer, E. 1997. Dewatering Sewage Sludge with Geotextile tubes. *Geotechnical Fabrics Report*, *v. 15, n. 7*, p. 26–30.

Guo, W., Chu, J. and Nie, W. 2014. Analysis of Geosynthetic Tubes Inflated by Liquid and Consolidated Soil. *Geotextiles and Geomembranes*, *v. 42*, pp. 277–283.

ISO 10319:2015 *Geosynthetics — Wide-width Tensile Test*. Intern. Standard Organiz., Geneva, Switzerland

ISO 11.058: 2010 *Geotextiles and Geotextiles Related Products – Determination of Water Permeability Characteristics Normal to the Plane, without Load*. Intern. Standard Organization. Geneva, Switzerland

ISO 12956:2019 *Geotextiles and Geotextile-related Products — Determination of the Characteristic Opening Size*. International Standard Organization. Geneva, Switzerland.

Lawson, C.R. 2006. Geotextile Containment for Hydraulic and Environmental Engineering. In. *International Conference on Geosynthetics*, 8th, Yokohama, p. 9–48.

Moo-Young, H. K., Gaffney, D. A., Mo, X. 2002. Testing Procedures to Asses the Viability of Dewatering with Geotextiles Tubes, *Geotextiles and Geomembranes*, *V 20*, pp 289–303.

Pilarczyk, K. W. 2000. Geosynthetics and Geosystems in Hydraulic and Costal Engineering. Balkema,

SOL, J. (2019) Economics in the Anthropocene: Species Extinction or Steady State Economics. *Ecological Economics*, Elsevier, v. 165, n. 106392, 2019.

Tominaga, E., Vidal,D., Kawachi, E. 2012. New Procedures for Testing the Behavior of Geotextile Closed Systems. *GeoAmericas 2012, 2d. Pan American Geosynthetics Conference*. IGS, Lima, Peru.

Yee, T.W.; Lawson, C.R. 2012. Modelling the Geotextile Tube Dewatering Process. *Geosynthetics International*, *v. 19*, *No. 5*.

Radial and axial analyze of the dewatering performance in geotextile tubes by bench-scale dewatering test

G.K. Kamakura, M.A. Aparicio-Ardila, C.A. Valentin & J. Lins da Silva
São Carlos School of Engineering (EESC), São Carlos-SP, Brazil

ABSTRACT: Researchers and professionals have used several test methods to evaluate the dewatering performance in geotextile tubes. The evaluation of geotextile tubes is done preliminarily by small-scale Falling Head Tests (FHTs), Geotextile-tube Demonstration Tests (GDTs), and full-scale pilot tests. Nevertheless, only a few studies have compared the outcomes of various dewatering tests, and even fewer have established accurate correlations between test methodologies. This work performed a pressurized two-dimensional dewatering test (P2DT) with a woven geotextile under different hydraulic pressure configurations (with and without internal pressure). In addition, GDT tests were performed for comparison. In this study, the P2DT and GDT tests evaluated the artificial slurry with chemical accelerators. The tests showed similar dewatering rates and final filter cake solids concentration. However, the GDT tests showed better turbidity results. The results indicated that geotextile tubes are an exciting alternative for slurry dewatering.

1 INTRODUCTION

As environmental awareness increases and more stringent regulations regarding slurry treatment emerge, technologies that seek to dewater it to facilitate the treatment and disposal of slurry gain relevance. Thus, due to the lower cost and good performance, using geotextile tubes has been a used alternative, which needs more studies to evaluate its applicability in each case.

The type of slurry treated influences the design of the geotextile tubes. The main factors considered are soil retention, permeability and clogging. In addition to the properties of the geotextile, other materials are essential to improve the system's efficiency, such as using.

The chemical conditioning of the slurry (with polymer) needs studies to select the best type of polymer and the adequate concentration (Satyamurthy & Bhatia 2009). There are recommendations and criteria for the filtration aperture for geotextiles employed for the filtration function. However, experience has shown that the criteria commonly used in filter design do not apply to dewatering in geotextile tubes, and those slurry properties are the dominant control factors (Moo-Young *et al.* 2002). For this reason, it is necessary to carry out tests on the benchtop and pilot scales to verify the dewatering performance in geotextile tubes. Researchers and professionals have used several test methods (laboratory or in-field) to evaluate the dewatering performance in geotextile tubes. These test methods include bench-scale tests, midscale or semi-performance tests (hanging bag test and the geotextile tube dewatering test) and full-performance tests.

According to Driscoll *et al.* (2016) and Ratnayesuraj & Bhatia (2018), the one-way filtration test does not represent the three-dimensional dehydration process in the field. Thus, the authors developed a pressurized two-dimensional dewatering test (P2DT) that evaluates radial and axial dewatering. The results of the P2DT test are more representative of in-situ conditions.

The research aims to analyze the dewatering process in radial and axial directions using P2DT with and without filling pressure and compare it with Geotextile-tube Demonstration Test (GDT). Each flow's percolated volume and turbidity were considered to compare axial and radial dewatering. In addition, the solids concentration and filter cake height were analyzed.

2 MATERIALS AND METHODOLOGY

2.1 Geotextile

The geotextile used was polypropylene woven geotextile. Dewatering applications often use this material. Table 1 shows some properties and characteristics of the material. The Geosynthetics Laboratory at the University of São Paulo (USP) in São Carlos, São Paulo, Brazil, conducted geotextile tests. The geotextile used is the same in Aparicio – Ardila *et al.* (2020) work.

Table 1. Geotextile properties.

Properties	Unit	Test Method	Value
Massa per unit area	kN/m	ABNT NBR ISO 9863-1	414
Thickness	mm	ABNT NBR ISO 9863-1	2.18
Apparent opening size	μm	ABNT NBR ISO 12956	200
Permittivity	s^{-1}	ASTM D4491	0.0024
Tensile strength per unit with MD x CD*	kN/m	ABNT NBR ISO 10319	108.9 x 105.6

*MD: machine direction; CD: cross direction.

2.2 Slurry

The slurry was artificially prepared in the laboratory, consisting of a mixture of distilled water and a soil sample. The granulometric curve of the soil shows that the grain size distribution comprises 57% sand, 8% silt, and 35% clay, according to the procedures of ABNT NBR 7181. This study used synthetic cationic polyacrylamide-derived polymer for the chemical conditioning of the slurry. The initial solids concentration was 15%, the polymer dosage was three mgPol/gST, and the turbidity of the slurry was 644 NTU.

2.3 Performance index

The most common indexes for evaluating dewatering performance are Filtration Efficiency (Equation 1) (Moo-Young & Tucker 2002) and Dewatering Efficiency (Equation 2). The FE index evaluated the improvement in effluent quality in the radial and axial directions separately. In addition to this index, to verify the improvement of the effluent, the turbidity of the effluent was measured, that is, the measure of relative clarity of a liquid that indicates the amount of Total Solids (TS) present in the effluent. The DE measures how effectively fluid the slurry fluid drains. Bhatia *et al.* (2013) recommend adopting the index Percent Dewatered (PD), shown in Equation 3, which can be easier to interpret than DE because the maximum value is 100%. The retention index and dewatering index adopted were turbidity and PD.

$$FE = \frac{TS_{initial} - TS_{final}}{TS_{initial}} \tag{1}$$

where FE = filtration efficiency; $TS_{initial}$ = initial total solids (mg/l); and TS_{final} = final total solids (mg/l).

$$DE = \frac{PS_{initial} - PS_{final}}{PS_{initial}} \tag{2}$$

where DE = dewatering efficiency; $PS_{initial}$ = initial percent solids of the sludge (%); and PS_{final} = final percent solids of the sludge (%).

$$PD = \frac{w_{initial} - w_{final}}{w_{initial}} \qquad (3)$$

where PD = percent dewatered (%); $w_{initial}$ = initial water content of the sludge (%); and w_{final} = final water content of the sludge (%).

2.4 P2DT

The procedures presented by Ratnasamy (2017) were adopted to perform the P2DT. Figure 1 shows a schematic model of the P2DT equipment used in this paper and built in the Geosynthetic Laboratory at the USP. Using two digital weighing scales, axial and radial flows are gathered and electronically recorded as a function of time.
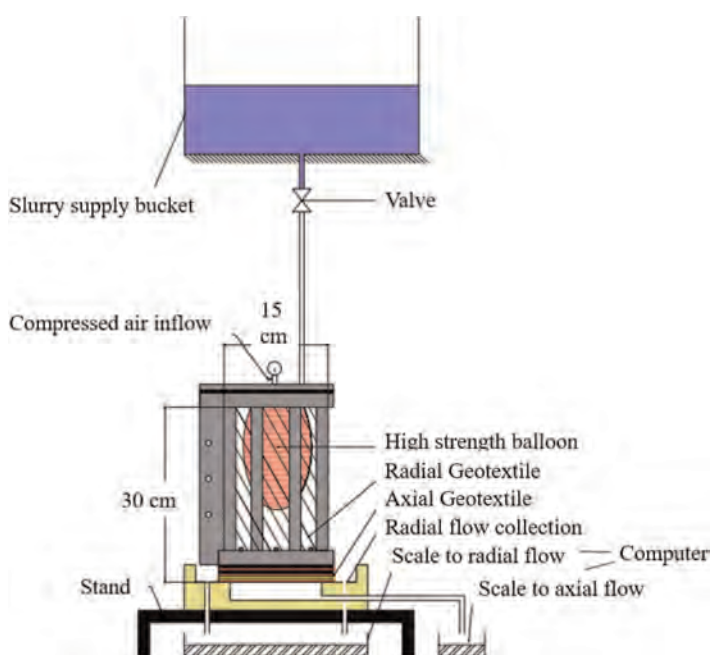

Figure 1. Schematic diagram of P2DT setup.

The P2DT has a diameter of 15 cm and a height of 30 cm. A slurry mixing and supplying bucket was attached to the equipment at a one-meter height (10 kPa) to maintain comparable pumping pressures and pumping rates. To ensure the slurry uniformity in the supply bucket was constantly mixed by a rod during the filling process. In addition, the tests were conducted with and without the balloon to evaluate the application of a constant pressure of 10 kPa (applied by a balloon). Table 2 shows the soil, water and polymer amounts for each fill. The input volume of each cycle was selected based on Ratnayesuraj & Bhatia (2018).

Three fills were performed, with an interval of 30 minutes. A scale and a computer recorded the data for monitoring the volume of effluent during the filling cycles. After each filling cycle, the effluent turbidity of the collection bucket samples was measured for each cycle separately by collecting samples using the nephelometric turbidimeter model Ap2000 from Policontrol. The procedures presented by Ratnasamy (2017) were adopted to measure

Table 2. Amount of soil, water and polymer required for each test P2DT.

Filling	Initial Total Solids (%)	Volume (ml)	Soil (g)	Water (ml)	Polymer Dosage (mgPol/gST)	Polymer (g)
1	15	4000	600	3400	3	1.8
2	15	2500	375	2125	3	1.8
3	15	1750	265.5	1487.5	3	1.8

the thickness at the top of the radial filter cake (H), the thickness at the bottom of the filter cake (h), and the final filter cake solids concentrations after the three filling cycles.

2.5 Geotextile-tube Demonstration Test (GDT)

According to the procedure used by Ardila (2020) based on ASTM D7880, GDT was carried out. Figure 2 shows a schematic model of the GDT equipment used in this paper and built in the Geosynthetic Laboratory at the USP.
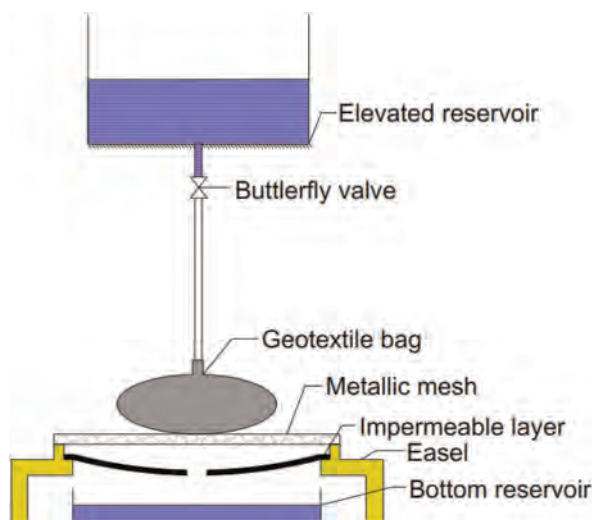

Figure 2. Schematic diagram of GDT setup.

The experiment used geotextile tubes with a 53 cm seam-to-seam width. The volume filling for the three cycles was 30,000 mL, based on Ardila (2020) and Ratnayesuraj & Bhatia (2018). A slurry mixing and supplying bucket was attached to the equipment at a one-meter height (10 kPa) to maintain comparable pumping pressures and pumping rates. To ensure the slurry uniformity in the supply bucket was constantly mixed by a rod during the filling process. Table 3 shows the soil, water and polymer amounts for each fill.

Table 3. Amount of soil, water and polymer required for each test P2DT.

Filling	Initial Total Solids (%)	Volume (ml)	Soil (g)	Water (ml)	Polymer Dosage (mgPol/gST)	Polymer (g)
1	15	30000	4500	25500	3	13.5
2	15	20000	1500	17000	3	9.0
3	15	10000	3000	8500	3	4.5

Three fills were performed, with an interval of 30 minutes. The effluent volume was measured for the initial five and after 25 minutes during the filling cycles. After each filling cycle, the effluent turbidity of the collection bucket samples was measured for each cycle separately by collecting samples using the nephelometric turbidimeter model Ap2000 from Policontrol. The outcomes shown are the mean of three tests.

3   RESULTS AND ANALYSES

3.1   *Effluent volume*

The P2DT assay evaluates axial and radial dewatering separately, while the GDT only evaluates total dewatering. Figure 3 shows the accumulated effluent volume of radial and axial effluent with and without the pressure of the three fills of P2DT.
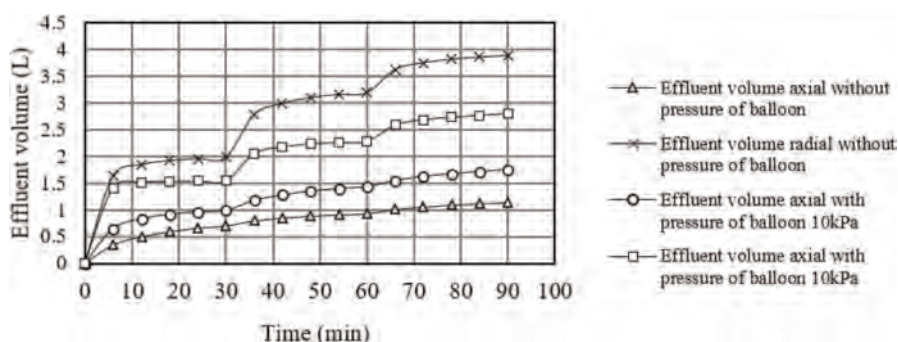

Figure 3.   The effluent volume of P2DT with and without the pressure of the balloon.

Figure 3 showed a reduction in the ratio between radial and axial volume when the balloon applied a pressure of 10 kPa. Figure 4 shows the total accumulated effluent volume of GDT. Figure 4 shows that the dewatering volume initial rate is high in the first few instants and decreases with each filling cycle.

Table 4 shows the ratio of the radial, axial and total percolate by initial volumes from each fill. Based on the results in Table 4, applying pressure by the balloon increased the amount of axial effluent. The sum of the axial and radial ratio for the P2DT trials was lower than that obtained by the GDT trial for all fills.
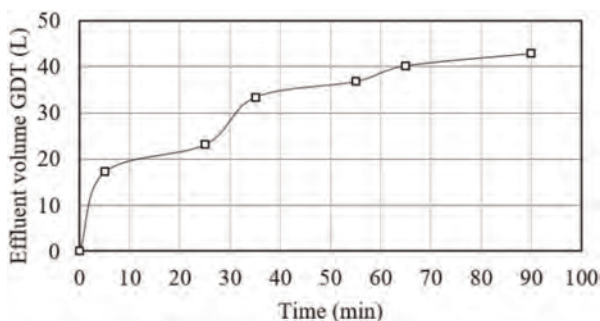

Figure 4.   Effluent volume of GDT.

Table 4. Ratio of the final radial, axial and total percolate by the initial volume fill.

Test	Filling 1	Filling 2	Filling 3
P2DT without a balloon (axial)	0.18	0.09	0.12
P2DT without a balloon (radial)	0.49	0.49	0.40
P2DT with a balloon (axial)	0.25	0.18	0.18
P2DT with a balloon (radial)	0.39	0.30	0.30
GDT	0.77	0.68	0.60

3.2 Filter cake and percent dewatered

The heights h (internal measurement of the filter cake of P2DT), H (radial measurement of P2DT), TS_{final} and PD for each trial are present in Table 5. The tests presented similar results.

Table 5. Results of filter cake.

Test	H (cm)	h (cm)	TS_{final} (g/l)	PD (%)
P2DT without a balloon	4.6	4.3	51.78	82.95
P2DT with a balloon	5.8	5.6	48.77	81.08
GDT	–	–	51.23	83.05

3.3 Effluent turbidity

Table 6 shows the turbidity results of P2DT in each axial and radial filling, with and without pressure and for GDT. The turbidity of the effluent decreases with each fill for the P2DT trial indicating the improvement of the percolate. For the GDT trials, there was a significant reduction in turbidity from the first fill, possibly due to sedimentation in the tank.

Table 6. Mean and coefficient of variation (CV) turbidity values for the P2DT and GDT assay for each filling.

Test	Filling 1 (NTU)	Filling 2 (NTU)	Filling 3 (NTU)	CV 1 (%)	CV 2 (%)	CV 3 (%)
P2DT without a balloon (axial)	68	28	58.1	58.1	83.9	54.6
P2DT without a balloon (radial)	238	73	79.8	79.8	38.9	64.4
P2DT with a balloon (axial)	27	16	24.9	24.9	50.9	37.6
P2DT with a balloon (radial)	138	32	12.0	12.0	69.6	13.3
GDT	3.7	2	30.0	30.0	9.9	13.5

4 CONCLUSIONS

This paper evaluates radial and axial dewatering in P2DT testing using an artificial slurry conditioned with polymer and compares the results with the GDT. The results reported in the study indicated that the two-dimensional test (P2DT) could be an alternative to bench tests.

The turbidity results indicated that the effluent quality and the ratio between the total percolated and initial volume for the P2DT test were lower than the values obtained by the GDT, mainly in the radial direction due to the radial filter cake. On the other hand, the values of final solids content and dewatering percentage showed similar values. A significant improvement of the analyzed slurry was noticed in all cases, showing that geotextile tubes are an exciting alternative for sludge dewatering.

REFERENCES

Aparicio-Ardila, M. A. A., Souza, S. T., Silva, J. L., Valentin, C. A., Dantas, A. D. B. 2020. Geotextile tube Dewatering Performance Assessment: An Experimental Study of Sludge Dewatering Generated at a Water Treatment Plant. *Sustainability* 12, No.19, 8129.

ABNT NBR 10319. 2013. Wide Range Tensile Testing. *Associação Brasileira de Normas Técnicas*, Rio de Janeiro, RJ, Brazil.

ABNT NBR 12956. 2013. Geotextiles and Related Products: Determination of the Filtration Opening Characteristic. *Associação Brasileira de Normas Técnicas*, Rio de Janeiro, RJ, Brazil.

ABNT NBR ISO 9863-1. 2013. *Geosynthetics — Determination of Thickness at Specified Pressures — Part 1: Single Layers*. Associação Brasileira de Normas Técnicas, Rio de Janeiro, RJ, Brazil.

ASTM D4491. 2015. Standard Test Methods for Water Permeability of Geotextiles by Permittivity. *ASTM International*, West Conshohocken, PA, USA.

ASTM D7880. 2013. Standard Test Method for Determining Flow Rate of Water and Suspended Solids Retention from a Closed Geosynthetic Bag. *ASTM International*, West Conshohocken, PA, USA.

Bhatia, S. K., Maurer, B. W., Khachan, M. M., Grzelak, M. D., Pullen, T. S. 2013. Performance Indices for Unidirectional Flow Conditions Considering Woven Geotextiles and Sediment Slurries. *In Sound Geotechnical Research to Practice: Honoring Robert D. Holtz II*: 318–332.

Driscoll, J., Rupakheti, P., Bhatia, S. K., Khachan, M. M. 2016. Comparison of 1-D and 2-D Tests in Geotextile Dewatering Applications. *International Journal of Geosynthetics and Ground Engineering* 2: 1–9.

Huang, C-C., S-Y. Luo. 2007. Dewatering of Reservoir Sediment Slurry using Woven Geotextiles. Part I: Experimental Results. *Geosynthetics International* 14(5): 83–96.

Moo-Young, Horace K.; Tucker, Wayne R. 2002. Evaluation of Vacuum Filtration Testing for Geotextile Tubes. *Geotextiles and Geomembranes* 20(3): 191–212.

Ratnayesuraj, C.R, Bhatia, S.K. 2018. Testing and Analytical Modeling of Two-dimensional Geotextile Tube Dewatering Process. *Geosynth. Int.* 25: 132–149.

Satymurthy, R., Bhatia, S. K. 2009. Effect of Polymer Conditioning on Dewatering Characteristics of Fine Sediment Slurry using Geotextiles. *Geosynthetics International* 16(2): 83–96.

Behaviour of geotextile filters in contact with internally unstable cohesionless soils

N. Moraci
Department of Civil, Energy, Environmental and Material Engineering (DICEAM), Mediterranea University of Reggio Calabria, Reggio Calabria, Italy

M.C. Mandaglio
Department of Civil Engineering (DICIV), University of Salerno, Fisciano (SA), Italy

S. Bilardi
Department of Civil, Energy, Environmental and Material Engineering (DICEAM), Mediterranea University of Reggio Calabria, Reggio Calabria, Italy

ABSTRACT: In this study, the compatibility of internally unstable soils with two non-woven geotextile filters was analysed by means of a method proposed by the Authors in a recent research. The method is based on a geometrical, experimental and micro-structural approach that considers the geotextile pore size distribution and its filtration opening size, the soil grain size distribution and its critical diameter of suffusion, the results of long-term filtration tests and the scanning electron microscope images of geotextile microstructure. The method application allowed the Authors to better evaluate the soil/geotextile filter compatibility under critical/severe conditions.

1 INTRODUCTION

Geotextile filters are successfully used in different civil and environmental geotechnical works. The filter function is to prevent the movement of fine particles from the base soil allowing the liquid to flow as freely as possible.

In some cases, when filter is in contact with an internally unstable soil, particles not belonging to soil skeleton and dragged by water flow may accumulate at base soil-geotextile filter interface (blinding) and/or may remain entrapped within filter pores (clogging). In this condition, the designer has to decide if to allow the passage of fine-grained soil particles free to move inside the soil skeleton, avoiding piping of the base soil, or if to retain an amount of these particles, avoiding filter clogging (Moraci *et al.* 2022; Palmeira 2020). Since filter interaction with internally unstable soils is considered an issue not yet properly understood, long term performance tests are recommended.

This study investigates the geotextile filter long term behaviour in contact with three internally unstable cohesionless soils. In order to assess the soil/geotextile filter compatibility a method recently proposed by the Authors (Moraci *et al.* 2023) was applied. The method is based on a geometrical, experimental and microstructural approach. The geometrical approach consists to compare the geotextile pore size distribution with the soil grain size distribution, considering the filtration opening size of the geotextile and the critical diameter of suffusion of the soil. The experimental approach is based on the performance of long term filtration tests that allow the evaluation of blinding, clogging and piping limit states. The micro-structural approach is based on the analyses of SEM (scanning electron microscope) images taken on the tested geotextiles in order to observe the clogging and blinding phenomena.

2 MATERIALS AND METHODS

The cohesionless soils investigated in this paper were reconstituted using gravel and marbles of various colours. Soil classification (ASTM D2487), the percentage of gravel, sand and fine, the coefficient of uniformity, CU (d_{60}/d_{10}), the coefficient of curvature C_c ($d_{30}^2/d_{10}d_{60}$) and the specific weight of the soils Gs are shown in Table 1.

Table 1. Soil index properties.

ID	Soil	Classification	Gravel [%]	Sand [%]	Fine [%]	CU [-]	C_c [-]	Gs [-]	Dc [mm]
9/WF	GW-GM	Well Graded Gravel with silt and sand	79	9	12	116.9	56.9	2.64	3.4
2R/WF	GM	Silty Gravel	47	30	23	876.9	3.1	2.67	4.0
4R/WF	GW	Well Graded Gravel	50	44.5	5.5	20.7	2.6	2.68	0.3

These soils resulted internally unstable according to Moraci *et al.* (2023). The critical diameter of suffusion, Dc (i.e. diameter of the largest particle passing across the constrictions of soil solid skeleton), showed in Table 1, was obtained according to SimulFiltr method (Moraci *et al.* 2012).

Two types of nonwoven geotextiles (GT) were used: a thick needle-punched (NP) geotextile and a thin heat-bonded (HB) needle-punched geotextile. The mass per unit area (μ_{GT}) is 600 g/m² for NP and 80 g/m² for HB, the nominal thickness (t_{GT}) is 2.8 mm for NP and 0.7 mm for HB geotextile. The filtration opening size (O_F), determined by means of capillary flow porometry (ASTM D6767-02), is 0.055 mm and 0.187 mm for NP and HB geotextiles, respectively.

The long term filtration tests were performed using the equipment illustrated in Figure 1.
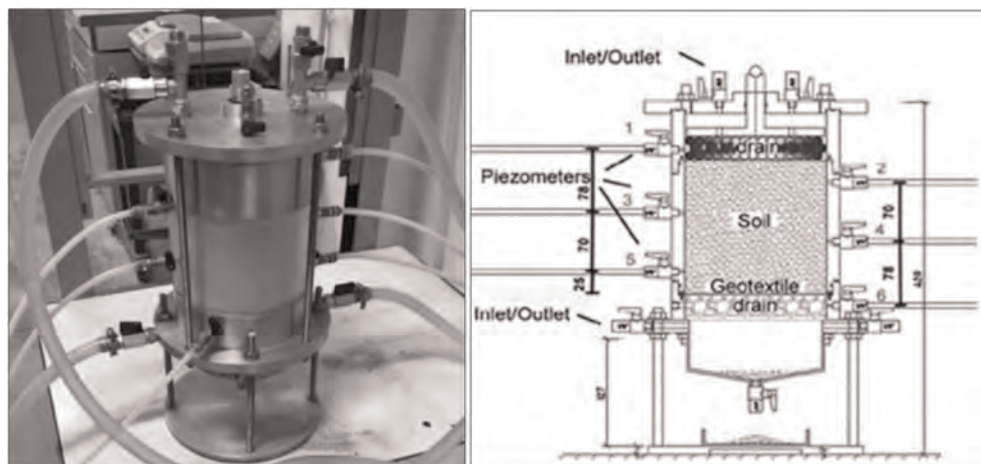

Figure 1. Test apparatus (Moraci *et al.* 2023).

The test device is a permeameter cell with internal diameter of 150 mm. It allows us to perform tests on soil specimens of a height equal to 164 mm. The variation in local hydraulic gradients along the specimen is calculated by means of 6 piezometers located at a vertical spacing of average value equal to 35 mm. The distance between the piezometer number 5 and the soil/geotextile filter interface is equal to 25 mm. The tests were carried out under vertical downward flow with hydraulic constant load and without the application of a vertical load.

The blinding level was evaluated by the blinding factor, $BF = i_{cz}/i_s$, defined as the ratio between the gradient in the filter-soil contact zone (i_{cz}) and the gradient in the adjacent soil (i_s).

After filtration tests the geotextile impregnation level λ (Palmeira & Gardoni 2000) was determined as the ratio between M_s, the total mass of particles in the geotextile, and M_f, the total mass of geotextile fibres.

3 RESULTS AND DISCUSSION

The compatibility of the three internally unstable soils with the two nonwoven geotextiles was analysed by means of the geometrical, experimental and micro-structural approach proposed by the Authors (Moraci *et al.* 2023).

3.1 *Geometrical approach*

The geometrical approach consists to compare the pore size distribution (PSD) of the geo-textile filter with the grain size distribution (GSD) of the soil (Figure 2) considering the
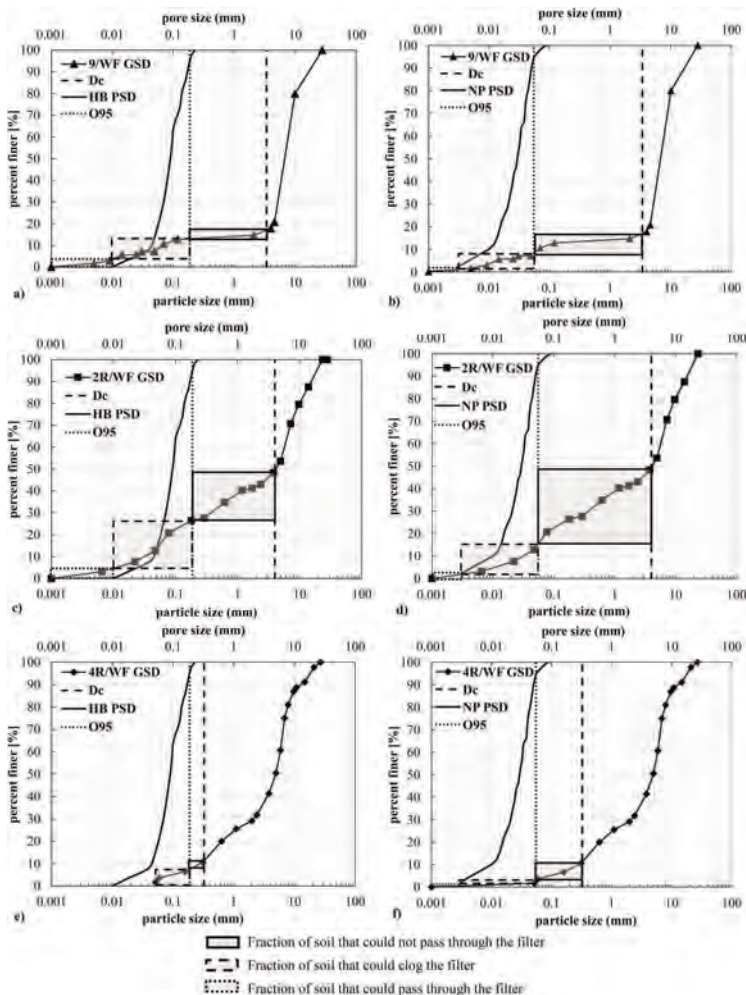

Figure 2. 9/WF GSD curve and PSD of a) HB and b) NP geotextile, 2R/WF GSD curve and PSD of c) HB and d) NP geotextile, 4R/WF GSD curve and PSD of e) HB and f) NP geotextile.

values of O_{95} and the values of Dc. This comparison allows to better understand if the mass of particles with a diameter lower than Dc could pass through the filter (perimeter area with dotted line), clog the filter (perimeter area with dashed line) or accumulate at soil-filter interface causing blinding (perimeter area with solid line).

The soil particles free to move inside the solid skeleton (with a diameter lower than Dc), able to clog or cross the geotextile filter are those with a diameter lower than O_F (perimeter areas with dashed and dotted lines in Figure 2). Not all the soil particles can cross (perimeter area with dotted line) or clog (perimeter areas with dashed line) the geotextile filter when there is a fraction of soil particles lower than Dc and greater than O_F (perimeter areas with solid line), because this fraction stops on the soil/geotextile interface generating a blinding phenomenon that produces a porosity decrease at the soil-filter interface. When blinding is significant, a geometric analysis providing information on the susceptibility to piping and clogging phenomena is very complex because the particles that accumulate in the soil/geotextile interface (blinding) produce a decrease in porosity and a new pore size distribution.

Comparing the GSD of 9/WF soil with PSD of HB geotextile (Figure 2a), it can be observed that the piping or clogging phenomena could occur. Piping phenomena is negligible when the same soil is in contact with NP GT (Figure 2b). Passing from HB to NP geotextile it can be noted that susceptibility to blinding increases according to reduction of O_F.

Considering 2R/WF soil, the susceptibility of geotextile to blinding phenomena increases passing from HB to NP geotextile (Figures 2c, d) whereas piping decreases. Finally, considering 4/WR soil in contact with HB geotextile (Figure 2e), a negligible piping and a moderate clogging could occur. Passing to NP geotextile the susceptibility of geotextile to blinding phenomena increases (Figure 2f).

3.2 Experimental approach

Long term filtration tests were carried out on the investigated soils (Table 1) in contact with two different geotextile filters. For each test, the level of blinding (BF), the soil mass passing through geotextile (M_p), the Piping level obtained dividing M_p by the specimen area, the impregnation level (λ), are shown in Table 2.

Table 2. Factors, characteristics and parameters derived from long term filtration test results.

	BF [-]	M_p [g]	Piping level [g/m^2]	λ [-]
HB – 9/WF	> 3	114.43	6475	2.90
NP – 9/WF	> 3	1.69	96	1.58
HB – 2R/WF	> 3	115.17	6517	2.11
NP – 2R/WF	> 3	2.14	121	1.49
HB – 4R/WF	≅ 3	25.8	1459	1.13
NP – 4R/WF	> 3	0	0	1.66

The calculated BF value is about equal to 3 for 4R/WF soil in contact with HB geotextile, whereas in the other investigated cases the values are greater than 3 due to the accumulation of particles on the geotextile surface. The amount of soil piped through the geotextiles varies from 0 to 115.17 g. The piping failure limit proposed by Lafleur *et al.* (1989) and equal to 2500 g/m^2 (Fatema & Bhatia 2018; Palmeira & Tatto 2015) was exceeded for 9/WF and 2R/WF soils in contact with HB geotextile. The clogging level was quantified by means of the impregnation level λ that ranges from 1.13 to 2.90.

Long term filtration tests are analysed using the geometrical approach shown in Figure 2.

For the 9/WF soil in contact with the two geotextiles, the movement of soil particles potentially able to move through the constrictions of the solid skeleton is equal to 18 % by weight (perimeter areas with solid, dashed and dotted line). The amount of soil particles that could blind

the filter is equal to 5 % and 10 % by weight (perimeter areas with solid line) for the HB and NP geotextile, respectively. The percentage by weight of soil particles potentially able to clog or to pass through the filter (perimeter area with dashed and dotted line) is equal to about 13 % and 8 % by weight for the HB and NP geotextile, respectively. Due to the greater amount of soil particles that accumulates on the surface of the NP geotextile, clogging and piping decrease as confirmed by the Piping level and by the λ value calculated at the end of the test.

For 2R/WF soil in contact with the two geotextiles, the amount of soil particles capable of blinding the filter increases from 20.65 % to 33 % by weight (perimeter area with solid line) passing from the HB to NP geotextile. The amount of soil particles that could clog or pass through the filter (perimeter areas with dashed and dotted line) reduces from 26.5 % (HB geotextile) to 14 % (NP geotextile) by weight. As expected from geometrical analysis, the piping is observed using HB geotextile because the soil particles able to pass through the filter are those in the perimeter area with dotted line and a fraction that belongs to the perimeter area with dashed line (piping level > 2500 g/m^2). Regarding NP geotextile, due to the greater amount of particles accumulated on its surface, the clogging decreases, as confirmed by the λ value, and piping is negligible.

Regarding 4R/WF soil in contact with the two geotextiles, the base soil fraction capable of blinding the filter (perimeter area with solid line) is equal to 4 % and 8 % for the HB and NP geotextile, respectively. Therefore, an increase of blinding is expected as confirmed by test results. For HB geotextile, the soil fraction able to clog or pass through the filter is low (7 % by weight, perimeter area with dashed line) and, therefore, also the piping and clogging levels expected are limited, as confirmed by test results.

The results derived from the geometrical approach and long-term filtration tests showed that the porometry of the filter could be acceptable if O_F is next to Dc value in order to limit the blinding level (as in the case of the HB geotextile in contact with 4R/WF soil). In order to limit the piping and clogging levels, it is necessary to take into account the amount of soil particles free to move inside soil skeleton (with a diameter lower than Dc) and potentially able to clog or cross the filter (with a diameter lower than O_F).

3.3 *Micro-structural approach*

SEM images revealed useful to provide qualitative and useful information about blinding or clogging phenomena for all investigated cases.

Figure 3 shows SEM images of the upstream face (i.e. the surface directly in contact with the base soil), cross-section and downstream face of HB geotextile in contact with 2R/WF soil.

Figure 3a shows the presence of the base soil particles accumulated on upstream face according to the levels of blinding ($BF > 3$) evaluated by long-term filtration tests. The geotextile cross-section image (Figure 3b) confirms the clogging level along the geotextile thickness ($\lambda = 2.11$). Figure 3c shows a small amount of fine particles and of precipitates accumulated on the downstream face (Figure 3c).

SEM images of the HB geotextile in contact with 4R/WF soil (Figure 4) confirm the stable behaviour of filter system with acceptable levels of blinding, clogging and piping observed in
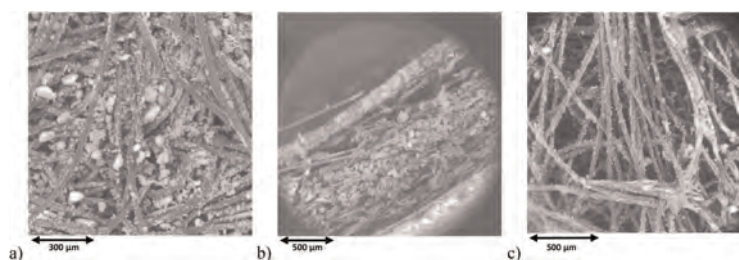

Figure 3.   SEM images of HB geotextile in contact with 2R/WF soil: a) upstream face (magnification 220x); b) cross-section (magnification 131x) and c) downstream face (magnification 170x).
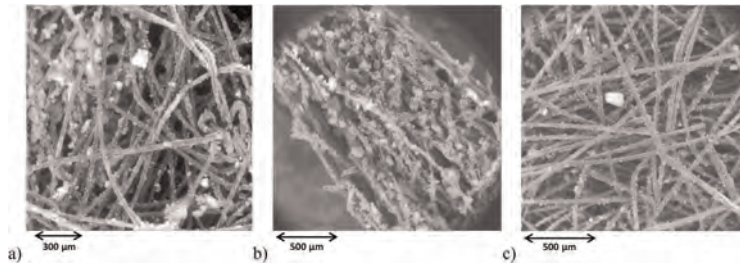
Figure 4.   SEM images of HB geotextile in contact with 4R/WF soil: a) upstream face (magnification 195x), b) cross-section (magnification 145x) and c) downstream face (magnification 175x).

the long term filtration test. Indeed, the upstream face of the geotextile after long term filtration test (Figure 4a) shows an acceptable level of blinding, the cross-section shows a limited level of clogging (Figure 4b) and the downstream face (Figure 4c) shows a negligible presence of soil particles.

4   CONCLUSIONS

This study allowed to confirm the utility of the geometrical, experimental and micro-structural approach, recently proposed by the Authors to analyse the geotextile/soil compatibility. For this purpose, the behaviour of two types of nonwoven geotextiles in contact with three internally unstable soils was analysed. Experimental results showed the reaching of blinding and piping limit states for the HB geotextile in contact with 9/WF and 2R/WF soils and a stable long-term behaviour for the same geotextile in contact with 4R/WF soil. Passing to the more closed NP geotextile, due to the accumulation of a greater amount of soil particles on its surface, it has been observed the blinding phenomenon and the absence of piping in the three investigated cases. These results were in good agreement with the geometrical approach. SEM images of the upstream face, cross-section and downstream face of the geotextile after long-term filtration tests confirmed the results of the experimental and the geometrical analysis.

REFERENCES

ASTM D2487. Standard Practice for Classification of Soils for Engineering Purposes (Unified Soil Classification System). *ASTM International*, West Conshohocken, PA, USA.

ASTM D6767-02. Standard Test Method for Pore Size Characteristics of Geotextiles by Capillary FlowTest. *ASTM International*, West Conshohocken, PA, USA.

Fatema, N. & Bhatia, S.K. 2018. Sediment Retention and Clogging of Geotextile with High Water Content Slurries. *International Journal of Geosynthetics and Ground Engineering* 4(2):13.

Lafleur, J., Mlynarek, J. & Rollin, A.L. 1989. Filtration of Broadly Graded Cohesionless Soils. *Journal of Geotechnical Engineering* 115(12): 1747–1768.

Moraci, N., Bilardi, S. & Mandaglio, M.C. 2022. Factors Affecting Geotextile Filter Long-term Behaviour and Their Relevance in Design. *Geosynthetics International* 29(1): 19–42.

Moraci, N., Mandaglio, M.C. & Bilardi, S. 2023. Soil/geotextile Filter Compatibility: A Geometrical, Experimental and Micro-structural Approach. *Geosynthetics International* 30(1): 29–46.

Moraci, N., Mandaglio, M.C. & Ielo, D. 2012. A New Theoretical Method to Evaluate the Internal Stability of Granular Soils. *Canadian Geotechnical Journal* 49(1): 45–58.

Palmeira, E.M. 2020. A Review on Some Factors Influencing the Behaviour of Nonwoven Geotextile Filters. *Soils and Rocks* 43(3): 351–368.

Palmeira, E.M. & Gardoni, M.G. 2000. The Influence of Partial Clogging and Pressure on the Behaviour of Geotextiles in Drainage Systems. *Geosynthetics International* 7(4–6):403–431.

Palmeira, E.M. & Tatto, J. 2015. Behaviour of Geotextile Filters in Armoured Slopes Subjected to the Action of Waves. *Geotextiles and Geomembranes* 43(1): 46–55.

Hydraulic applications: Canals, reservoirs and dams

Evaluation of the hydraulic behavior of hydrophilic and hydrophobic geotextiles under hydrostatic pressure test

L.C. Rodrigues & D.M. Vidal
Aeronautical Institute of Technology, São José dos Campos, SP, Brazil

ABSTRACT: Geotextiles have been successfully applied in road works, performing several functions in granular layers. Geotextile structure and their hydrophobic/hydrophilic characteristics are of great relevance. The resistance of dry geotextiles to penetration by water, WPR, is one of the parameters employed to evaluate the hydraulic behavior of geotextiles in unsaturated media. The papers discuss the influence of additives used in the manufacturing process and the soil/geotextile interface in the resistance to water penetration by experimental tests. The tests conducted in this study indicate that products presenting hydrophilic behavior in virgin samples can show a hydrophobic behavior after light washing. The tests on the sample with an initial water penetration resistance indicate an increase of up to 373% after washing. The evaluation of the soil influence indicates that the phenomenon is also present in this condition, but the rate of water pressure increase affects the WPR.

1 INTRODUCTION

There are several years that geotextiles are inserted in granular pavement layers performing functions such as filtration, separation, and stabilization. They are also applied to protect pavement layers from increasing moisture content, acting as a capillary barrier.

Geotextile characteristics and long-term filtration tests are generally conducted in saturated conditions. Therefore, in most pavement situations, the geotextile remains for several periods in the residual moisture situation, remaining in the dry state. When rainfall occurs, and percolating water reaches the interface soil/geotextile, the hydrophobic or hydrophilic behavior of the geotextile becomes relevant.

Water stagnation in the geotextile is related to a phenomenon called Water Penetration Resistance (WPR). It depends on the geotextile fibers' chemical nature and structure (Lennoz-Gratin 1987). The WPR is evaluated by tests conducted in dry specimens according to EN 13562. These tests are generally conducted on specimens in the condition in which they left the factory. Avancini *et al*. (2020) discuss water penetration resistance and its determination.

Some researchers have indicated that products classified as hydrophilic could present a hydrophobic behavior after water percolation (Bouazza *et al*. 2006; Stormont *et al*. 1997). Vidal *et al*. (2014) observed that a hydrophilic geotextile presented 6 mm WPR after a slight washing. In fact, in diverse fabric manufacturing stages, additives are employed to increase the efficiency of the process, reduce friction, and protect the fibers.

In addition, it is also essential to evaluate the effect of percolation occurring through the adjacent soil layer. This paper discusses the factors influencing water penetration resistance from experimental results assessing the influence of geotextile washing to remove surfacing additives and tests in a system soil/geotextile.

2 INFLUENCE OF WATER PENETRATION RESISTANCE IN PAVEMENT DESIGN

The paving designs must consider the various processes by which water can interfere with their behavior. Some of the situations associated with the presence of water in the soil are illustrated in Figure 1. In addition to the influence of the water table, infiltration processes due to rainfall or thawing must be considered.
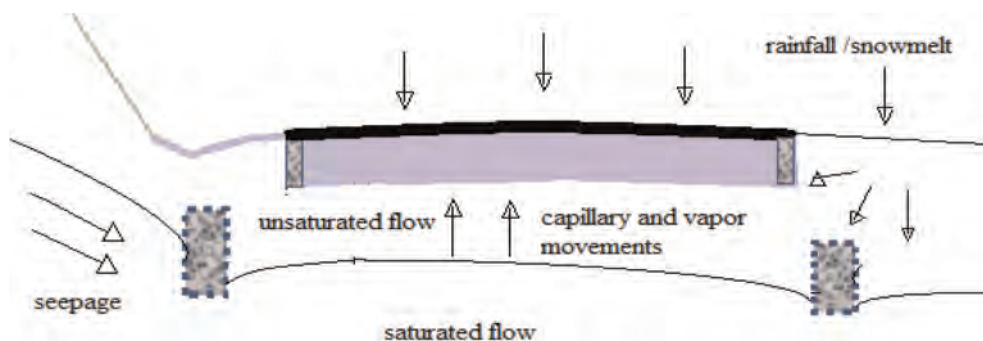

Figure 1. Different ways in which water can act on paving layers.

Water can penetrate through cracks and micro-cracks of the asphalt overlay during rainy periods and infiltrate into the base course until it reaches a geotextile acting as a separator or stabilizer. In this case, the influence of a few centimeters of water accumulation should be evaluated and may or may not be relevant to the design. For example, traffic loads are likely to increase the pore pressure in the saturated sheet, causing localized flow toward the drain, eliminating the problem, especially since base courses are generally quite permeable.

Water can also approach the base or subbase layer by flowing capillarity through the subgrade, even when a drainage system is in place to ensure the lowering of the water level. In this case, a geotextile layer with hydrophobic behavior could prevent the advancement of water, if the loads imposed by traffic cannot raise the pore pressure to the point where the penetration resistance is exceeded.

When the geotextile is applied to perform the filtration function in deep drainage trenches to lower the water level, the accumulation of a few centimeters of water generally does not significantly affect the system's behavior.

3 HYDRAULIC BEHAVIOR OF UNSATURATED GEOTEXTILES

3.1 *Hydrophobic x hydrophilic characteristics*

The surface of polymers has characteristics that interfere with their relationship with other substances. For example, polymers such as polypropylene and polyester have hydrophobic characteristics, i.e. water molecules are not attracted to the apolar groups of the polymer (Atkins & Jones 2007). Most geotextiles are made up of these polymers and therefore possess hydrophobic characteristics.

However, polymer treatment techniques can cause changes in the surface properties of polymers that favor surface interaction and adhesion with other substances (Gilliam 2015). For example, oils are essential additives in the fiber spinning and fabric manufacturing stages of textile fiber processing. These additives are used to reduce the fibers' friction and

protect their surface during manufacture. Often these oils lead the virgin geotextile to exhibit hydrophilic characteristics. Therefore, most of these oils tend to leach out with the passage of water, which makes the hydrophilic characteristic temporary (Bouazza *et al.* 2006; Stormont *et al.* 1997; Vidal *et al.* 2014).

The research seeking processes to permanently alter the surface characteristics of fibers and filaments of the most commonly used polymers, PET and PP, to hydrophobic behavior has grown with the increased use of these polymers in the textile industry. However, the most sophisticated processes have shown a return to hydrophobic behavior over time (Tarig *et al.* 2022).

3.2 *Water Penetration Resistance (WPR) tests*

Lennoz-Gratin (1987) described a test procedure for evaluating the resistance to water penetration in dry specimens. The first French standard (AFNOR NF G 38020) was published in 1988 and established a test procedure with a rate of increase of water pressure of 10 mm/min, defining the WPR as the highest recorded value.

Since 1981 there is a method for determining the WPR of textiles, including those with low permeability - ISO 811 (ISO 2018) - in which the water pressure is applied from below the specimen and much higher pressures (up to 2m H_2O) can be achieved. The accuracy starts at 5 mm, too high for geotextiles for which the accuracy should be 1 mm.

In 2000, the European standard EN 13562 replaced the AFNOR standard, with some changes in the procedure, as the rate of increase of water pressure of (100 ± 5) mm/min (same minimal rate of ISO 811). The water pressure may be applied from below or from above the specimen. The pressure, in millimeters, at water appears in continuous droplet form through the specimen's opposite face, and the maximum water pressure achieved shall be recorded.

The standard does not discuss a procedure to evaluate the presence of hydrophilic substances on the surface of the fibers or filaments, recommending performing the test on dry geotextile and avoiding manipulation of the specimen in such a way as not to alter its structure. Thus, the test is usually performed on the sample in the condition in which it comes from the industry.

4 TESTS TO EVALUATE THE INFLUENCE OF ADDITIVES

4.1 *Materials and methods*

For this research, two nonwoven needled-punched geotextiles in cut fiber were selected, with hydrophobic/hydrophilic behavior estimated through reaction to water droplets dripped onto the surface. The geotextile samples were denominated NW1 and NW2.

An apparatus similar to the one outlined in Figure 1 was employed for the water penetration resistance tests with the following modifications:

- a scale and a video camera were placed inside the transparent cylinder to better visualize the water pressure on the exposed surface of the geotextile,
- another video camera was installed below the cylinder to a continuous record of the geotextile underside,
- a cylinder with an area of 165 cm^2 was used instead of 100 cm^2 as required by the standard so that the water column height values obtained are for comparison purposes and cannot be used as an index property.

The influence of additives that could induce a hydrophilic behavior was evaluated in tests performed according to EN 13152 on specimens in the received condition and after washing.

Each specimen was weighed and had its mass per unit area evaluated. After weighing, the specimens were submitted to the water penetration resistance test in virgin condition (as received from the manufacturer). All tests were performed by evaluating the behavior of the inner face of the roll.

The specimens of sample NW1 were separated into two groups. The first group was washed in filtered water, and the second group was washed in filtered water plus a non-ionic surfactant (5 ml/l) and again washed in filtered water.

For this washing, the specimens were immersed until saturation and submitted to a sequence of emersions/immersions carefully performed so as not to cause changes in the structure. The washed specimens were then left to dry in the laboratory until weight constancy and submitted to the water penetration resistance test.

The specimens of sample NW2 were washed only with filtered water.

4.2 Results

Table 1 summarizes the results of the water penetration resistance tests performed, where h_{inic} is the height of the water column at the appearance of the first drop and h_{max} is the height of the maximum water column observed on the specimen. Figure 2 shows illustrative images of the tests at maximum water pressure.
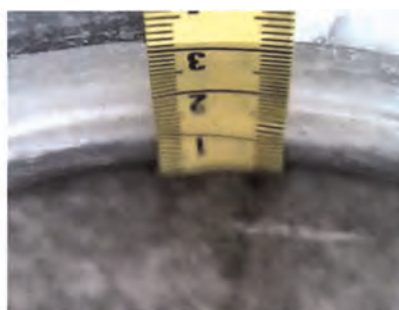
Table 1. Results of tests to evaluate the additive influence.

sample		m.u.a* (g/m²)	Virgin h_{init}(mm)	h_{max}(mm)	Washed with filtrated water h_{init}(mm)	h_{max}(mm)	Washed with water+surfactant h_{init}(mm)	h_{max}(mm)
NW1	PET	298 ± 27	0	0	28 ± 3	31 ± 1	24 ± 3	29 ± 3
NW2	PP	330 ± 49	12 ± 4	15 ± 3	59 ± 8	71 ± 6		

*mass per unit area (ISO 9864)

(a) Bottom-face view   (b) Upper-face view

Figure 2. Example of images recorded at maximum water pressure.

4.3 Discussion of the results

The WPR tests realized on virgin specimens of NW1 geotextile did not indicate resistance to water penetration, as expected. However, the results of the specimens washed with filtered water plus surfactant showed no advantage in washing with the surfactant, perhaps due to a

low rinsing efficiency. For this reason, the second sample was washed with filtered water only.

The additives that altered the surface characteristics of the fibers were quickly leached out by washing with filtered water, suggesting that a few cycles of water passage would lead to a hydrophobic condition. The washing of specimens of sample NW2 presenting hydrophobia in the test with the material in the condition received from the factory showed that even products with hydrophobic behavior may have increased resistance to water penetration after saturation and drying cycles.

No relationship between the mass per unit area and the WPR has been observed, leading one to believe that the phenomenon is more affected by surface conditions. The sample whose component polymer is polypropylene showed much higher resistance to water penetration than the sample whose polymer is polyester.

5 TESTS TO EVALUATE THE INFLUENCE IN SOIL/GEOTEXTILE SYSTEMS

5.1 *Materials and methods*

The influence of a hydrophilic porous medium in contact with a hydrophobic geotextile surface was evaluated in two steps. The first one considers the effect of the rate of water pressure increase on the geotextile surface, as generally, this rate would tend to be less than 100 mm/min in flow occurring in unsaturated soil. For this purpose, tests considering the proposal of the previous standard, which indicated a rate of 10 mm/min, were adopted to evaluate this effect.

For the tests with soil at the interface, a simple apparatus was developed to allow a first evaluation of the influence of soil/textile contact.

The materials used in the tests were a nonwoven needle-punched geotextile with polyester filaments, a hydrophobic material, and ground quartz, a hydrophilic material. The selected ground quartz presents uniform grain size (coefficient of uniformity, CU, equal to 1.4), and is composed by particles passing #20 (<0.85mm), being 85% with a diameter less than 0.78 mm and 10% with a diameter less than 0.47 mm.

WPR tests were conducted on the nonwoven geotextiles with two rates of water pressure increase: (100 ± 5) mm/s and (10.0 ± 0.5) mm/min, to evaluate the influence of the water pressure increase in the water penetration resistance.

The apparatus employed in the test with soil is composed of a lower chamber for the soil specimen and a system of clamps to fix the geotextile specimen. The area of the geotextile exposed to water pressure is the same as in the WPR test. A water reservoir at a constant level provides an upward flow and a piezometer placed below the geotextile interface allows for monitoring the rise of the water pressure in the soil near the interface. Video cameras monitored the piezometer and the top surface of the geotextile.

A thin layer of cotton placed at the bottom of the lower chamber allows a uniform distribution of penetrating water. Cotton was chosen because it is a hydrophilic material as the ground quartz. The particulate material is uniformly displaced in the lower chamber with a funnel until it exceeds the interface level. The excess soil is removed using a rigid ruler to guarantee full contact between the geotextile and the soil. After fixing the geotextile specimen, the assembly is placed on the support to be connected to the water supply reservoir, which is positioned to maintain the water level 80 mm above the lower level of the geotextile. Figure 3a shows the device's schema.

5.2 *Results*

The water penetration tests conducted on the nonwoven geotextiles indicate a mean value of (30 ± 2) mm in the tests with a rate of water pressure increase of (100 ± 5) mm/s, and

(a) Scheme of tests
(b) Water pressure below the geotextile
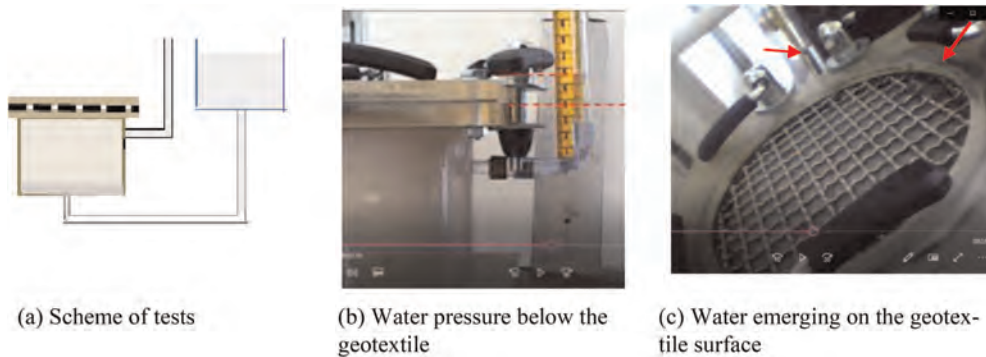(c) Water emerging on the geotextile surface

Figure 3.   Views of the soil-geotextile test.

(25 ± 3) mm in the water penetration tests conducted at a water pressure increase of (10.0 ± 0.5) mm/min.

Two tests were conducted in the system soil/geotextile, presenting a similar behavior. Water started to appear on the top face of the geotextile about 90 minutes after the start of the water supply. The piezometer indicated a water column height of 20 mm above the underside of the geotextile when water emerges on the geotextile surface. Figures 3b and 3c show pictures of the tests in the system soil/geotextile obtained when the water begins to appear on the geotextile surface.

5.3   *Discussion of the results*

Tests conducted to determine the water penetration resistance, WPR, at different rates of water pressure increase showed that the filling speed proposed in EN 13562:2000 implies a value 20% higher than the value obtained with the test performed at the rate indicated in the AFNOR NF G 38020:1988.

Obtaining a higher value for this parameter probably aims to evaluate the behavior under critical conditions. However, it is interesting to know the behavior for situations where water accumulation occurs more slowly, as it usually occurs in cases where the water percolates through the soil.

The soil-geotextile system tests showed that water accumulation on the surface also occurs when water percolates through the unsaturated soil. The 20 mm of water height above the underside of the geotextile observed during the soil tests shows, in this case, a lower value of water penetration resistance than that observed in the WPR tests, even in the lower rate of water pressure increase, which was 25 mm.

6   CONCLUSION

The raw material and structure provide the hydrophobic characteristic and prevent water from penetrating the pores of the unsaturated geotextile unless a positive pressure equals or exceeds the water penetration resistance occurs.

Tests measuring the water resistance penetration, WPR, of nonwoven geotextiles show that water flow can modify this property. A hydrophilic product can be transformed in hydrophobic, and a hydrophobic product can significantly increase its WPR, being observed with an increase of 373%.

Tests performed at different rates of increasing water pressure indicated a 20% reduction in WPR when this rate is reduced from 100 to 10 mm/min. The influence of the rate of

increase of the applied pressure is relevant because this rate can be directly linked to the variation of the medium's permeability.

The tests with hydrophilic soil confirm that the penetration resistance persists even with the presence of soil at the geotextile interface. The values measured in the tests performed show a reduction in the resistance of the isolated geotextile, probably due to a reduction in the rate of pressure increase that becomes controlled by the soil permeability.

Research to evaluate the influence of soil particle intrusion on geotextile structure will be carried out in future work. However, a reduction of the water penetration resistance could occur, but there is no expectation of eliminating it. The tests performed have shown that the surface effect is very significant, and it would be difficult that the particles could form continuous columns able to conduct water from one geotextile surface to another.

ACKNOWLEDGMENTS

REFERENCES

AFNOR NF G 38020:1988 *Essais des Géotextiles. Détermination de la Résistance à la Traversée de l'eau.* Association Française de Normalization. France

Atkins, P. & Jones, L. 2007. *Chemical Principles: The Quest for Insight.* W.H.Freeman & Co Ltd

Avancini, L.L.S., Queiroz, P.I.B., Rodrigues, L.C., Carvalho, C.L., Vidal, D.M.. 2020. Water Penetration Resistance of Geotextiles: Current State of Knowledge. *GeoAmericas 2020.* Rio de Janeiro, Brazil, 10p.

Bouazza, A., Zomberg, J. G., McCartney, J. S., Nahlawi, H. 2006. Significance of Unsaturated Behaviour of Geotextiles in Earthen Structures. *Australian Geomechanics*, Vol. 41, No. 3, pp 133–142

EN 13562:2000 Geotextiles and Geotextiles-related Products - Determination of Resistance to Penetration by Water (Hydrostatic Pressure Test). European Committee for Standardization.

Gilliam, M. 2015. Polymer Surface Treatment and Coating Technologies. *Handbook of Manufacturing Engineering and Technology*. Andrew Nee Editor. Springer. pp.99–124. DOI: 10.1007/978-1-4471-4670-4_20

ISO 811: 2018 *Textiles – Determination of Resistance to Water Penetration – Hydrostatic Pressure Test.* International Society for Standardization.

Lennoz_Gratin, C. 1987. The Use of Geotextiles as Drain Envelopes in France in Connection with Mineral Clogging Risks. *Geotextiles and Geomembranes*, v. 5, n. 2, p. 71–89.

Rodrigues, L.C. 2020. *Influência da Estrutura de Geotêxteis e da Condição de Ensaio na Resistência à Penetração de Água.* Master dissertation. Aeronautics Institute of Technology. http:www.bdita.bibli.ita.br

Stormont, J. C., Henry, K. S., and Evans, T. M. 1997. Water Retention Functions of Four Non-woven Polypropylene Geotextiles, *Geosynthetics International*, *Vol. 4*, No. 6, pp. 661–672.

Tarig, T.A. *et al.* 2022. Durable and Recoverable Hydrophilicity of Polyethylene Terephthalate Fabric Prepared with Plasma Selectiveetching. *Surface and Interfaces. V.32*, DOI:/10.1016/j.surfin.2022.102081

Vidal, D.M., Queiroz, P.I.B., Santos, C.T. 2014. Unsaturated Flow Behavior of Leak-detection Systems with Geonets. *10th International Conference on Geosynthetics*, Berlin, Germany, p.1458–1466.

Considerations for the calculation of permeation rates for geosynthetic clay liners in constant water head applications

C. Niehues
Naue GmbH & Co. KG, Espelkamp, Germany

M. Köhler
Professor, Technische Hochschule (University of Applied Science) Ostwestfalen-Lippe, Germany

K.P. von Maubeuge
Naue GmbH & Co. KG, Espelkamp, Germany

ABSTRACT: Geosynthetic Clay Liners (GCL) are widely used in sealing applications throughout the world. In applications with constant water heads - such as artificial ponds, rivers, canals, etc. - the permeation rate through the GCL is of vital importance to the performance of the whole structure and the allocated function. A proper design must consider all potential sources of water loss in the designed application. This includes also the performance of overlaps or the combined effect of multiple sealing layers. Some factors are sometimes misinterpreted, underestimated or not considered.

The presented paper will focus on two major topics, each affecting the performance of geosynthetic sealing systems with special focus on geosynthetic clay liners (GCL). The impact of these effect is to be illustrated on exemplary calculations for virtual projects. The quantification of these effects will result in recommendations that shall help to anticipate unfavorable situations for the operational phase of a project already in the design stage. This shall contribute to a better overall understanding of GCL and help to avoid preventable design errors. An outlook shall summarize the further efforts envisaged by the authors to provide a simple tool to allow calculation of permeation rates for GCL or complete barrier systems.

1 INTRODUCTION

1.1 *Motivation*

Geosynthetic barriers – and as a focal point of this paper geosynthetic clay liners (GCL) in particular – are established as sealing elements for applications with constant water head. Regardless, there are various examples where factors, which are of important influence for the overall performance of such products, are not being considered or underestimated in the design stage of a project. Some of these impacts may not be obvious even to the experienced designer of lining systems. This can lead to higher permeation rates as considered in the design, consequently resulting in water tables falling short of the level that is being considered in the design. This may be crucial for applications where a sufficient permanent supply of water is essential. Examples for such structures are fire ponds, water channels (especially in hydropower applications) or irrigation facilities.

When problems with insufficient water tables occur, the sealing component – in the given cases the GCL – is often falsely claimed as unreliable, although misconceptions can be prevented by a better knowledge of the subject matter and an according choice of suitable products.

Figure 1. Typical application with high importance of precise hydrological balance: Fire ponds.

The presented paper intends to increase the knowledge on potential conditions that have impact on the permeation rate and to quantify the effect of one selected factor. The consequence of using different GCL thicknesses for the back-calculation of the hydraulic conductivity k_f from laboratory tests and subsequently the calculation of the permeation rate shall be illustrated on a fictious project.

1.2 *Method*

For the quantification of permeation rates of GCL it is common to refer to the results of laboratory tests (ASTM D5887; DIN EN 16416). The hydraulic conductivity is derived from the test results by the measured flow and the thickness of the permeated specimen.

The common calculative approach to derive the permeation is carried out by application of Darcy´s law (Darcy 1856), in this paper considered in the form of:

$$Q = k_f \cdot i \cdot A \tag{1}$$

where Q = Volumetric flow [$m^3 \cdot s^{-1}$]; k_f = Hydraulic conductivity [$m \cdot s^{-1}$]; i = hydraulic gradient [-]; A = Area [m^2]

2 NECESSARY CONSIDERATIONS FOR CALCULATING GCL PERMEATION

2.1 *General considerations*

GCL are established as sealing component for environmental protection applications, e.g., serving as single lining systems for non-hazardous landfills in accordance to the European Council Directive on the landfill of waste (1999). In such applications, usually no permanent water tables are to be considered on the sealing systems and the resulting permeation rates measured in lysimeter trials for GCL with sodium powder bentonite are virtually zero (Bluemel *et al.* 2010).

However, the use in applications with permanent hydraulic head demands for closer examination of the expected permeation rates.

The calculative approach is already mentioned in 1.2. The hydraulic conductivity k_f is a decisive factor in the calculative approach. The hydraulic conductivity k_f derived from laboratory tests may however be altered in the field by various effects. It must be taken in mind that this is valid for all mineral sealing components. The most significant of these effects for hydraulic applications are:

- Root penetration
- Ion exchange
- Dehydration
- Frost/Thaw

None of these effects can be assumed to be a general influence on every project but must be considered specifically by project boundary conditions.

2.2 *Specific considerations*

2.2.1 *Impact of thickness for calculation of permeation rates*

The thickness of the GCL is necessary to backcalculate k_f from the measured index flux q resulting from the laboratory tests (ASTM D5887; DIN EN 16416). The thickness is essential to calculate the hydraulic gradient i in equation (1). It is defined as:

$$i = \frac{(h_w + t)}{t} \qquad (2)$$

where h_w = hydraulic water head [m] – usually 1.5 m in ASTM D5887; and t = thickness of the GCL

With the measured index flux q (volumetric flow per area, Q/A, [$m^3 \cdot m^{-2} \cdot s^{-1}$]), all other parameters of equation (1) aside from k_f are defined, and the thickness can either be measured or assumed. A common assumption is t = 1 cm thickness for a swollen GCL. Under cell pressure in laboratory tests, the actually measured thickness may vary – depending mainly on the area weight of bentonite – between 0.5 and 1 cm. It is possible to use either assumed or measured thickness for the backcalculation of k_f.

While the k-value of a product may be backcalculated under consideration of the laboratory thickness and published in a data sheet, designers tend to use the "common assumption" for the thickness of a swollen GLC by t = 1 cm to calculate project specific permeation rates, regardless of the actual product thickness which would be expected under the project specific load and saturation conditions. The following calculation example in table shall illustrate that it may lead to unsafe results when k_f values backcalculated with measured thickness t < 1 cm during index flux testing are used to derive permeation rates of GCL in designs where the common approximation of t = 1 cm is used to derive the hydraulic gradient.

The example shows that – under the consideration of the given data – the assumption of a swollen GCL thickness of t = 1 cm may lead to underestimation of permeation losses in a lined water basin when the k-value has been evaluated considering lower thickness from live measurements during the index flux test. Given that all other conditions are coherent with the laboratory test, the variation of thickness between backcalculation of k_f (measured thickness t = 0.006 m) and permeation calculation (common assumption t = 0.01 m), the losses are 1.66-fold higher when considering the realistic thickness.

It remains however possible to use the assumption of t = 1 cm for the calculation of permeation rates in cases where the k_f has been derived from laboratory tests with exactly that thickness. In this case, the results will remain safe with respect to the thickness considered in the calculation.

Table 1. Calculation example for permeation rate through a GCL.

Measured index flux [$m^3 \cdot m^{-2} \cdot s^{-1}$]	$3.0 \cdot 10^{-9}$	
Measured thickness [m]	0.006 (6 mm)	
k_f, backcalculated [$m \cdot s^{-1}$]	$1.2 \cdot 10^{-11}$	
Calculative approach for water permeation: Q = $k_f \cdot i \cdot A$		
Assuming a basin with depth of 1.5 m and an		
Area of A = 10,000 m^2		
Considered thickness [m]	0.006 (realistic)	0.01 (common assumption)
Hydraulic gradient i [-]	251	151
Calculative permeation Q = $k_f \cdot i \cdot A$ [$m^3 \cdot s^{-1}$]	$3 \cdot 10^{-5}$	$1.8 \cdot 10^{-5}$
In other numbers for illustrative purpose:	2592	1559
daily loss [$l \cdot d^{-1}$]		

2.2.2 *Impact of overlaps*

While some impact factors on the permeation rate apply for all GCL in the same way, the overlapping technique differs by product and can hence make an influence on the overall GCL performance in terms of permeation.

This is due to the differing overlapping techniques featured by the individual manufacturing processes. While some products feature overlaps that are pre-impregnated with bentonite powder which is automatically dosed onto the cover geotextile in the manufacturing process, other products require for manual application of bentonite in the overlap areas. Sometimes, marking trolleys are used. Even with good craftmanship and clean manual implementation of bentonite for overlaps, the latter method remains prone to inhomogeneous distribution of the applied bentonite and thus to inconsistency of the conductivity of the overlaps.

With this subject matter being identified as one major impact for permeation calculations, respective recommendations can be made to quantify the impact of the GCL overlaps (see chapter 3.2.2).

3 RECOMMENDATIONS WITH RESPECT TO PERMEATION CALCULATIONS

3.1 *General recommendations*

Chapter 2.1 named effects that may have an impact on GCL permeability. Consecutively, the GCLs performance in the field, e.g., the permeation rate, may significantly differ from predictions if these predictions were solely based on calculations that consider laboratory values.

The listed effects under chapter 2.1 can usually be countered by constructive measures which are described in respective guidelines such as GRI-GCL5. One of such measures could be the implementation of sufficient soil covers against adverse effects on permeability caused by desiccation or freeze/thaw.

Advanced products such as multicomponent GCL, such as GCL with polyethylene coating, can also effectively prevent effects of desiccation, root penetration or ionic exchange (Egloffstein *et al.* 2013).

If these effects cannot be prevented, it is necessary to quantify the impact of the effect on the permeation rate and consider this in permeation calculations. As an example, the effect of ionic exchange on GCL permeability has been researched and also quantified in Egloffstein (2001).

3.2 *Specific recommendations*

3.2.1 *Recommendations concerning thickness in permittivity calculations*

With respect to the issue explained in chapter 2.2.1, the authors recommend to not deliberately choose $t = 1$ cm as thickness for the swollen GCL. Although this is safe for cases where k_f is back-calculated under assumption of $t = 1$ cm from the measured flow in laboratory tests (ASTM D5887; DIN EN 16416), the calculation becomes unsafe for k_f derived by using the measured thickness in the laboratory test. It is to be recommended to look at also the index flux value of a GCL product and not only to consider the k_f value from the data sheet.

The key to achieve reliable results is in this case the knowledge on this crux and correct interpretation of data.

3.2.2 *Recommendations on overlap permittivity*

Similar to the preceding recommendations, there is no general fixed safety factor for the consideration of overlap permittivity in permeation calculations of GCL lined hydraulic structures. Such calculations should consider the specific product properties. In many cases, GCL manufacturers are able to contribute laboratory results on the permeability of their

product specific overlapping technology. Such results can be considered in overall calculations of specific products.

Furthermore, multicomponent GCL overlaps can be sealed with butyl adhesive tape or in certain cases even welded. This can prevent any potential seepage path for water in overlaps of GCL used in sealing systems with constant water head.

4 CONCLUSION AND OUTLOOK

Within this paper, the authors have identified effects that leave an impact on the permeation of GCL and/or on the results of permeation calculations.

While some of those effects can be countered by constructive measures, others are inherent with the calculative approach which is generally being used when permeation rates are calculated.

The identification of these effects allows designers of hydraulic structures with permanent water table to prevent misconceptions when doing permeation calculations and thus evaluating the sealing efficiency of the products. Recommendations are given how to avoid underestimation of hydraulic losses.

The further roadmap on this subject matter envisages the development of a new software tool. This tool shall allow to calculate permeation losses under consideration of the potential effects that may impact the result while guiding the user in giving recommendations how to prevent hydraulic losses effectively. The software shall also include permeation calculations for composite liners under consideration of the calculative approach that is presented by Touze-Foltz *et al.* (1999). The final aim is to allow the fast and easy choice of a system that provides for the necessary impermeability under consideration of project specific requirements, while at the same time anticipating potential influences on the hydraulic conductivity of a barrier system. At the same time, the prognosis of leachate rates as presented in Rowe (2012) could be implemented with the software tool.

REFERENCES

ASTM D5887 2022 Standard Test Method for Measurement of Index Flux Through Saturated Geosynthetic Clay Liner Specimens Using a Flexible Wall Permeameter, *American Society for Testing and Materials* D5887, West Conshohocken, PA, USA.

Bluemel, W., Müller-Kirchenbauer, A., von Maubeuge, K. P. 2010: Performance of Geosynthetic Clay Liners in Landfill Cap Systems – Physical Processes in the Bentonite Layer During Drying and Rehydration Periods. *3rd International Symposium on Geosynthetic Clay Liners*, Würzburg, Germany.

Darcy, H. 1856. *Les Fontaines Publiques de la Ville de Dijon*. Paris: Dalmont.

DIN EN 16416 2023: *Geosynthetic Clay Barriers - Determination of Water Flux Index - Flexible Wall Permeameter Method at Constant Head*; German version EN 16416:2023

Egloffstein, T., Kalsow, J., von Maubeuge, K. & Ehrenberg, H. 2013. Multi-component Geosynthetic Clay Liners A Product with New Possibilities. *Third Symposium on Current and Future Practices for the Testing of Multi-Component of Geosynthetic Clay Liners*, June 29, 2012, San Diego, CA. ASTM International Publication STP1562, W. Conshohocken, PA, USA.

Egloffstein, T., 2001. Natural Bentonites - Influence of the Ion Exchange and Partial Desiccation on Permeability and Self-healing Capacity of Bentonites Used in GCLs, *Geotextiles and Geomembranes* 19(7): 427–444

EU Directive on Landfill of Waste.European Union Council Directive 1999/31/EC issued 26 April 1999

GRI-GCL5 2013: Standard Guide for "*Design Considerations for Geosynthetic Clay Liners (GCLs) in Various Applications*", Geosynthetic Institute, Folsom, PA, 2013

Rowe, R.K. 2012: Short- and Long-term Leakage Through Composite Liners. The 7th Arthur Casagrande Lecture, *Canadian Geotechnical Journal*, 49(2): 141–169

Touze-Foltz, N., Rowe, R.K., Duquennoi, C. 1999. Liquid Flow Through Composite Liners, *Geosynthetics International*, 6(6): 455–476

Qualitative and bathymetric evaluation of erosion control techniques in reservoir margins with geosynthetics

M.P. da Luz
Eletrobras Furnas, Aparecida de Goiânia, Brazil
Pontifical Catholic University of Goiás (PUC Goiás), Goiânia, Brazil

M.A. Aparicio-Ardila, C.A. Valentin & J. Lins da Silva
São Carlos School of Engineering (EESC), University of São Paulo (USP), São Carlos, Brazil

ABSTRACT: This paper presents the results of implementing erosion control techniques with geosynthetics on Brazilian Hydroelectric Power Plants (HPPs) reservoirs. Different erosion control techniques were applied in 2016 in two experimental units installed in the margins of the Porto Colômbia and Volta Grande HPPs. The performance of the analyzed sections was assessed qualitatively using a performance matrix that collected and summarized data over a monitoring period of four years. The performance was also assessed by differential bathymetry studies performed in 2016 and 2020 in the HPPs margins. This work highlights the benefits of implementing geosynthetic materials in margin erosion control techniques, taking advantage of its properties, ease of installation and durability, and evidence the importance of monitoring the techniques to know the long-term performance. The erosion control technique with Geomat in a roll showed the best results in all the analyzed sections.

1 INTRODUCTION

Problems arising from erosive processes constitute the main environmental impact in the operational stage of most reservoirs of HPPs. The problems reflect in the loss of arable, urban and forest areas, water quality, and the reduction of the volume and the useful life of the reservoirs, among other aspects.

The margins of water bodies are subjected to erosive processes and massive mobilization of sediments due to the dynamic environment (Biedenharn *et al.* 1997). The variables that have the most significant influence on the intensity of erosion are: topography, origin and soil composition of the margin and bed of water bodies, as well as the qualitative and quantitative aspects of the vegetation associated with local hydraulic conditions (height of waves and wind speed) (Fischenich & Allen 2000).

Edge protection measures can be grouped into three categories: vegetative systems, inert elements, and mixed (or soil bioengineered) systems, where these categories are often used together (USACE 1998; USDA 2015). Using soil bioengineering techniques represents the alternative with the lowest environmental impact on local conditions. In addition, its use favours aesthetics, aquatic and soil biota, and the microclimatic conditions of the water body. Also, it acts in the retention of pollutants, which would otherwise reach the water body.

The objective of any erosion control project should be to stabilize soils and manage erosion economically (Theisen 1992), where the choice of the appropriate control method is imperative for the success of erosion control operations on the banks of hydroelectric reservoirs.

Geotechnical studies carried out within the scope of Research and Development Projects of the National Electric Energy Agency of Brazil (ANEEL) showed that the soil on the banks of the reservoirs of the HPPs Porto Colombia and Volta Grande is prone to erosion. Two experimental units were selected to evaluate the implementation of bioengineering works for erosion control in the HPPs. In this work, three types of treatments that were applied in the experimental units are presented. The treatments were: Gabion box in Geogrid, Geomat in roll, and sack gabion and mattress in geogrid.

2 METHODOLOGY

2.1 *Study area*

The Porto Colombia and Volta Grande HPPs are located in the Rio Grande basin on the border of São Paulo and Minas Gerais states of Brazil (Figure 1). Different Erosion Control Techniques (ECTs) were applied using geosynthetics (geomat, geotextile and geogrid). The present study presents the results of monitoring three ECT installed in HPP Porto Colombia (PC) and HPP Volta Grande (VG). The first treatment is the Gabion box in Geogrid (ECT1), the second gabion sack and mattress in geogrid (ECT2), and the third Geomat in a roll (ECT3). The experimental units installed (with an approximate area of 150 m^2) are shown in Figure 2.

Figure 1.   Location of the Porto Colômbia (PC) and Volta Grande (VG) HPPs.
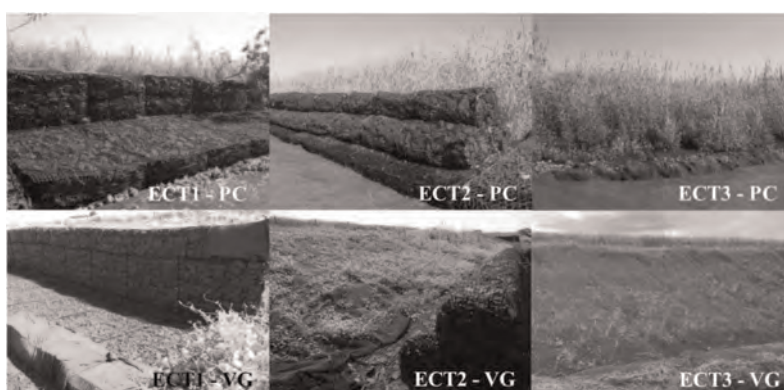
Figure 2.   Experimental units of HPPs Porto Colombia (PC) and Volta Grande (VG) treated with different Erosion Control Techniques (ECTs).

2.2 Geosynthetics

For this work, two geosynthetics were used: Geogrid (for gabion box and mattress) and Geomat. The Geogrid present the following characteristics: tensile strength of 16 kN/m and aperture dimension of 46 mm in the machine direction (MD), and tensile strength of 28 kN/m and aperture dimension of 64 mm in the cross direction (CD).

The Geomat has a mass per unit area of 563 g/m^2, puncture resistance of 0.38 kN, and tensile strength of 3.93 kN/m and 1.33 kN/m in the MD and CD, respectively.

2.3 Performance evaluation of the techniques

The monitoring of each experimental unit's sections occurred periodically, with monthly visits from 2016 to 2020. The performance of the techniques installed in each section used six performance variables, and a score (ranging from 0 to 3), as done in the works of Galvão et al. (2018), Aparicio-Ardila et al. (2021) and da Luz et al. (2021). The variables (performance matrix) are shown in Table 1. The six variables are: erosive spots/toe integrity on reservoir bank (V1), vegetative cover growth (V2), final structural integrity (V3), need for maintenance (V4), landscape integration/aesthetics (V5), and regrowth native vegetation top of the section (V6). The qualitative evaluation was performed 2 and 4 years after the installation of the ECTs.

Table 1. Performance matrix.

Variable	Score	
V1-Erosive spots/ toe integrity on reservoir bank	0	High
	1	Intermediate
	2	Low
	3	Inexistent
V2-Vegetative cover growth	0	Bare (<30%)
	1	Low vegetative cover (30 to ≤ 50%)
	2	Average vegetative cover (>50–≤ 70%)
	3	High vegetative cover (>70–100%)
V3-Final Structural Integrity	0	Serious damage (>30% of the total)
	1	Average damages (10–30% of the total)
	2	Low level of damage (<10% of the total)
	3	No damage
V4-Need for maintenance	0	High (>de 5 times)
	1	Average (3 to 5 times)
	2	Low (1 – 2 times)
	3	No need
V5-Landscape Integration/ aesthetics	0	No integration with local landscape
	1	Integration with local landscape after 2 years
	2	Integration with local landscape after 4 years
	3	Integration since the startup
V6-Regrowth Native vegetation top of the section	0	Absence of native flora
	1	Presence of 1–3 native species
	2	Presence of 3–5 species
	3	Presence of more than 5 native species

An initial bathymetry study was carried out in 2016 and other in 2020 at the end of monitoring. The bathymetry study was carried out following the regulations of Brazilian entities such as the ANA (Brazilian National Water Agency), ANEEL (Brazilian Electricity Regulatory Agency), and Law 12.334/2010 (2010).

3 RESULTS AND DISCUSSION

3.1 *Performance matrix*

The results obtained after evaluating the performance variables are shown in Figure 3 for each ECT for 2 (2Y) and 4 (4Y) years. The total scores for the analyzed periods (2 and 4 years) remained constant in all the units. After two years of installation, it is observed that the treatments that presented the best performance were located in the HPP VG. These were ECT2 (gabion sack and mattress in geogrid), followed by ECT3 (Geomat in a roll). On the other hand, all the ECTs installed in the HPP PC showed similar performances (ranging between 12 and 13 of total weight) in the two analyzed periods. ECT1 did not present integration with the local landscape in any HPPs. Analyzing the results qualitatively, ECT3 (Geomat in a roll) was a good performance in both HPPs.
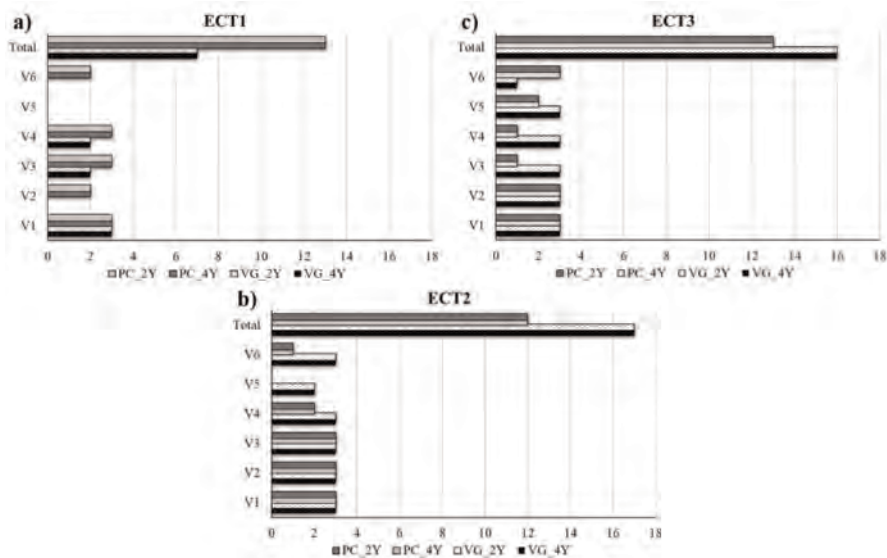
Figure 3. ECT performance comparison: a) Gabion box in Geogrid (ECT1), b) gabion sack and mattress in geogrid (ECT2) and c) Geomat in a roll (ECT3).

3.2 *Differential bathymetry differential*

The average cross profiles of the bathymetry performed in the years 2016 and 2020 for each experimental unit are shown in Figure 4.

In the analysis of differential bathymetry (Figure 4), it is observed that there was a movement of material in all the experimental units. The sediments were redistributed in the ECT1-VG section, as observed in Figure 4a. On the other hand, in the experimental PC unit where the same treatment was installed (ECT1), the sediments were transported to the HPPs reservoir. Differential bathymetry of ECT2 in both units (VG and PC) showed similar behavior, indicating that there was rolling off the gabion sack. Analyzing the experimental units where ECT3 was installed, sediments transport was observed. However, considering that ECT3 does not have the same rigidity as the other two treatments (ECT1 and ECT2), the sediment movement is acceptable. According to Latapy *et al.* (2019), vertical errors can be induced during bathymetric occurrences due to waves at the margins, which may be responsible for random elevation variations.
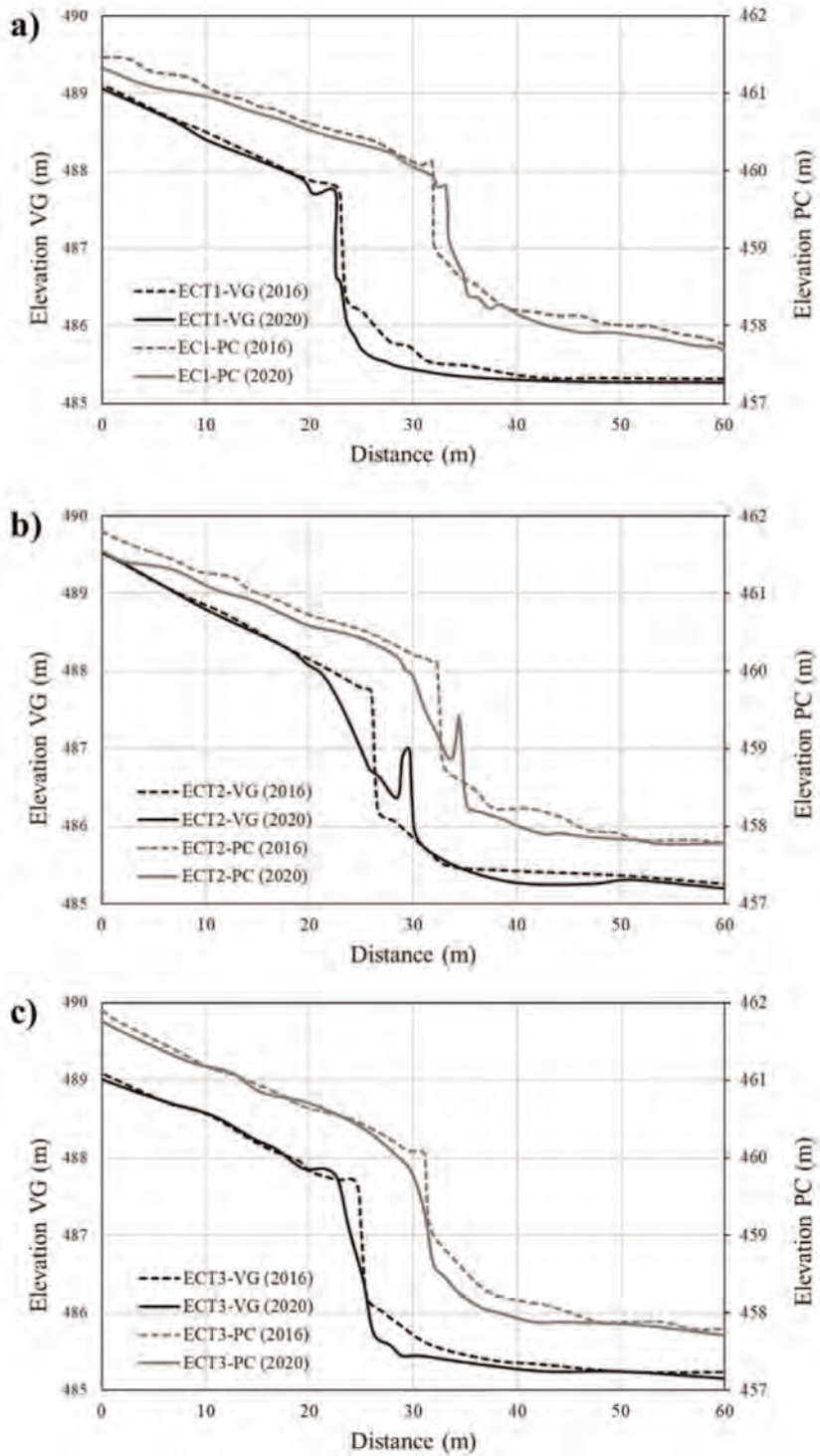
Figure 4.   Differential bathymetry: a) EC1, b) EC2 and c) EC3.

4 CONCLUSIONS

Considering the qualitative performance and the differential bathymetry, the ECT3 treatment (Geomat in a roll) was the one that presented the best performance during the monitoring. Also, ECT3 took less time and was easier to install than other treatments.

The qualitative parameters adopted contributed to evaluating the treatments applied to mitigate erosion processes. Using the qualitative analysis matrix helps define the most effective erosion control techniques on the banks of reservoirs.

REFERENCES

Aparicio-Ardila, M. A., dos Santos Junior, R. D., Kobelnik, M., Aparecido Valentin, C., Silva Schliewe, M., Teixeira Coelho, A., da Luz, M.P., 2021. Semi-Rigid Erosion Control Techniques with Geotextiles Applied to Reservoir Margins in Hydroelectric Power Plants, Brazil, *Water*. https://doi.org/10.3390/w13040500

Biedenharn, D. S., Elliott, C. M., Watson, C. C., 1997. *The WES Stream Investigation and Streambank Stabilization Handbook*. US Army Engineer Waterways Experiment Station.

da Luz M.P., Aparicio-Ardila M.A., dos Santos Junior R.D., Valentin C.A., Schliewe M.S., Coelho A.T., Lins da Silva J., 2021. Geomats Used to Control Erosion on Reservoir Margins in Brazilian Hydroelectric Power Plants. *Water*. 13(11):1444. https://doi.org/10.3390/w13111444

Fischenich, J. C., Allen, H., 2000. *Stream Management. Wetlands Research & Technology Center, Environmental Laboratory*, U.S. Army Engineer Research and Development Center, Vicksburg.

Galvão, T. C. D. B., Coelho, A. T., de Menezes, G. B., de Fonseca, Ê. M. B., 2018. Study of Erosion Control Techniques Applied to Hydroelectric Power Plants Reservoir Margins. Athens. *J. Sci.*, 5, https://doi.org/329-342.10.30958/ajs.5-4-2

Latapy, A., Héquette, A., Pouvreau, N., Weber, N., Robin-Chanteloup, J.B., 2019. Mesoscale Morphological Changes of Nearshore Sand Banks Since the Early 19th Century, and Their Influence on Coastal Dynamics, Northern France. *J. Mar. Sci. Eng.* https://doi.org/10.3390/jmse7030073

LAW,National Dam Safety Policy; Brazilian Law 12334/2010. Available online: http://www.planalto.gov.br/ccivil_03/_ato2007- 2010/2010/lei/l12334.htm

Theisen, M. S., 1992. The Role of Geosynthetics in Erosion and Sediment Control: An Overview, Geotext. *Geomembranes*, 11(4–6), 535–550 https://doi.org/10.1016/0266-1144(92)90031-5

USACE (United States Army Corps of Engineers), 1998. Shoreline and Channel Erosion Protection: Overview of Alternatives. WRP Technical Note HS-RS-4.1. Wetlands Research & Technology Center, Environmental Laboratory, U.S. Army Engineer Research and Development Center, Vicksburg.

USDA (United States Department of Agriculture), 2016. *In Engineering Field Handbook Part 650 Engineering Field Handbook*. National Engineering Handbook, Part 650, 210-EFH.

An innovative "Geo-carpet" system as a countermeasure against local scour at bridge piers: Small-scale test results

A. Galli & A. Radice
Politecnico di Milano, Milan, Italy

ABSTRACT: Local scour around bridge piers is one of the most diffused causes of failure for river bridges since it considerably modifies the geometry of the riverbed around the foundation. Countermeasures have been proposed in terms of both bed armoring and flow-altering devices. In this field, the use of Geosynthetics can provide innovative solutions, with environmental, economic and technological benefits compared to more traditional approaches. In the paper some flume experiments, run in clear-water flow conditions on a circular pier in a homogeneous granular riverbed, are described. The tests included four runs where the area around the pier was covered with innovative "Geo-carpet" systems made by plastic nets with different mesh size, and one reference test on an unprotected pier. The results, at least for a single hydro-dynamic condition, showed the efficiency of the Geo-carpets on the reduction of the scour depth and volume, and pave the way to future experiments investigating different geometries and flow conditions (including live-bed scour).

1 INTRODUCTION

River currents may induce relevant scouring effects around bridge piers, especially during flood events. Local scour is particularly detrimental for bridge stability, since it remarkably modifies the local geometry of the riverbed, with possible exposition of the foundation systems. Hydraulic research has shown that the scour process is related to the three-dimensional junction flow developing close to an obstacle that emerges from the river bed. From a geotechnical point of view, this implies a reduction of the confinement effect around the pier's foundation and, in extreme cases, of the subgrade reaction of the soil. Evident consequences are the reduction of the structural performance of the foundations (in serviceability conditions) and, potentially, the loss of its overall bearing capacity (in ultimate limit states). Possible countermeasures have been developed since many years (Lagasse *et al*. 2009), following two main ideas: either disposing massive objects on the riverbed around the pier (the so-called "bed-armoring" techniques), or by properly modifying the water flux in the proximity of the pier ("flow-altering" techniques).

Examples of bed armoring countermeasures are riprap (Figure 1a), gabions and gabions mattress (Figure 1b), and structural frames (Figure 1c). In countermeasures of this category, Geosynthetics may be employed as containers for rubble or gravel, thus constituting the so-called "geo-containers" described in Heibaum (2000) and sketched in Figure 1d. Flow-altering countermeasures may be instead realized, among others, by installing protecting collars (Figure 2a), by adding sacrificial piles upstream of a pier (Figure 2b), or by disposing ad hoc sloping plates, founded on mattress tubes or geocontainers (Figure 2c).

The aforementioned bed-armoring countermeasures provide in general an efficient protection against scouring, but the use (and the proper disposition) of massive objects often requires non-standard technological skills and large economic budgets. Furthermore, the
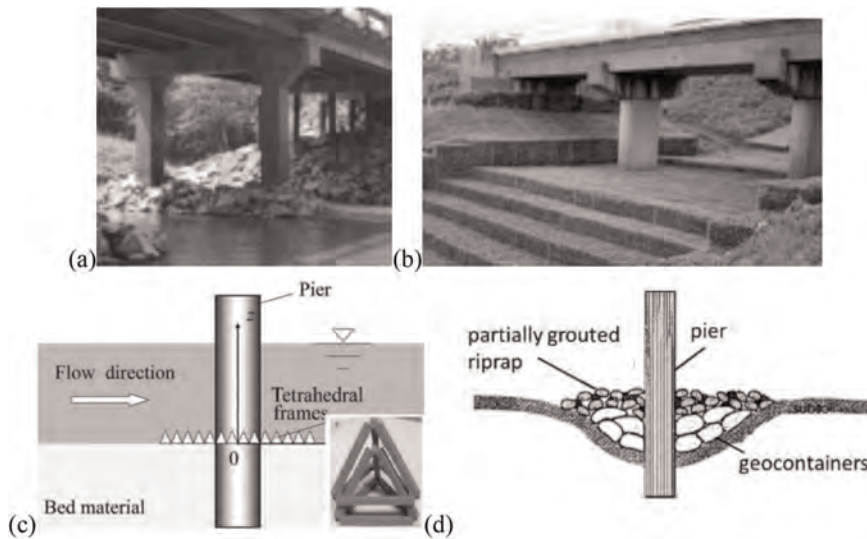
Figure 1. Examples of bed-armouring countermeasures: (a) riprap (from Froehlich 2013); (b) gabions and gabion mattress (Craswell & Akib 2020); (c) structural tetrahedral frames (from Tang *et al*. 2009); (d) geocontainers (Heibaum 2000).
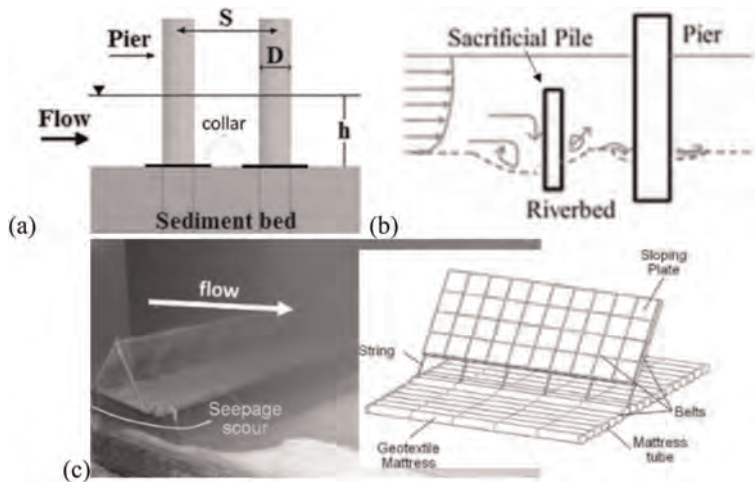

Figure 2. Examples of flow altering countermeasures: (a) protecting collars (from Memar *et al*. 2020); (b) sacrificial pile (Wang 2017); (c) example of sloping plates (from Xie *et al*. 2019).

flow-altering countermeasures require advanced manufacturing skills and site-specific design optimizations (e.g. depending on the characteristics of the flow), and their use cannot yet be considered a standard solution for engineers. In both cases, the cited limitations may result in (i) non-optimal design of the countermeasure, (ii) delayed installation, (iii) difficulty in maintenance and refurbishment (or complete substitution) after important flooding events. Experimental investigation on the use of nonwoven Geotextiles as protecting collars has also been developed for research purposes by Nouri Imamzadehei *et al*. (2016; Figure 3),

Figure 3. Photographs of experiments using a geotextile collar as a pier scour countermeasure (Nouri Imamzadehei *et al.* 2016).

revealing a relevant potentiality in reducing and delaying the scour process, at least at the laboratory scale.

In the present study, an innovative bed-armoring technique was tested in small-scale flume experiments. In particular, the use of grid membranes anchored to the riverbed was explored, and its effect on the scour evolution was analysed. This innovative solution, which could be referred to as "Geo-carpet", could be of particularly interest for large scale applications, since it would allow rapid and economic installations, without the need of dealing with massive objects or complex structural elements.

2 EXPERIMENTAL FACILITY AND PROCEDURES

The experiments were run at the Hydraulics Lab "LIF" of the Politecnico di Milano, using an open flume (Figure 4a) with rectangular cross section, length of 5.8 m, width of 0.4 m, and bank height of 0.16 m. A recess section (2 m long) allowed the formation of local scour holes. The flume was equipped with an electro-magnetic flow-meter for flow discharge and a tail-water regulation to set the flow depth. A 0.03-m layer of sediment was present along the entire flume. Lightweight sediment was made of Polybutylene Terephthalate monodisperse quasi-spherical particles, with equivalent diameter $d = 3$ mm and unit mass $\rho = 1270$ kg/m^3.

Clear-water conditions were considered throughout the experimental campaign. Preliminary runs were performed to determine the threshold discharge for a water depth of 0.08 m, following the method proposed by Radice and Ballio (2008) who quantitatively associated incipient sediment motion to a dimensionless sediment transport rate per unit width of 5.6×10^{-5}. The threshold discharge was 0.091 m^3/s. All the scour experiments were then run with a water depth of 0.08 m and a flow rate equal to 0.95 times the threshold one (i.e. 8.65 litre/s). It is in fact well known that largest scour values are induced in clear-water experiments with a flow rate close to the threshold one (see e.g. Franzetti *et al.* 2022). The cylindrical pier had a telescopic structure: the outer part, buried in the sediment bed, was a Polyvinyl Chloride thin pipe, while the inner part was a Plexiglas cylinder. The inner part could slide within the outer one and was manually lifted at the beginning of the test. Since the diameter of the pier (external diameter $D = 0.06$ m) was a small fraction of the flume width, no constriction scour was observed during the experiments.

During the experiments, an area around the pier was protected with a net, anchored to the bed by means of "U-shaped" steel nails (Figure 4b) buried into the granular bed all along the border of the protected area. Several tests were run varying the mesh size of the nets. Four different mesh sizes s were employed (ranging from 2×2 mm to 24×24 mm, Figure 4c; corresponding runs are named S, M, L, and XL in the following). Consistently with the purposes of the present work, the grids were considered to behave as axially rigid membranes, but with negligible bending stiffness. Two different test configurations were considered (Figure 4d), representing the case of an unprotected pier (hereafter, named U), and
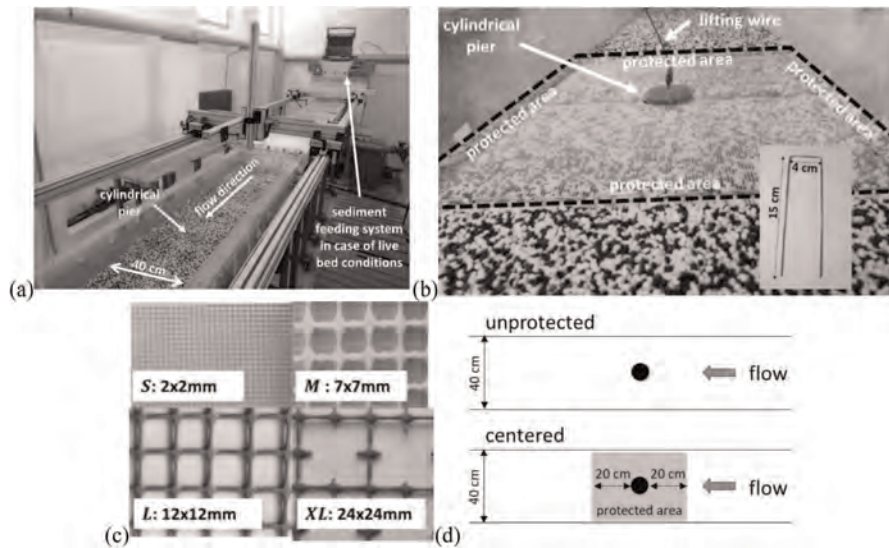
Figure 4. Experimental setup: (a) overview of the flume test facility; (b) detail of the placement of a net, anchored with "U-shaped" nails along its borders and around the pier; (c) detail of the nets used in the tests; (d) configurations of tests for unprotected pier and with the Geo-carpet in place.

that of a pier with a centred protection (20 cm both upstream and downstream). Thus, the present manuscript describes 5 tests: one on the unprotected pier, and four employing a centred protection.

The preparation of the flume consisted in (i) scraping the sediment bed to make it on average flat, (ii) spraying the bed surface with water to avoid particle uplifting by water during flume filling, (iii) installing the net over the protected area (except for the unprotected test). The test was then started by (iv) filling the flume with a small flow rate to avoid undesired sediment motion, (v) achieving the desired flow condition (flow rate 8.65 litre/s) with the pier completely buried in the sediment bed (to prevent initial unwanted local scour), and (vi) manually lifting the inner part of the pier to trigger the scour process. In this way, the beginning of a test was precisely determined. All the experiments lasted for 6 hours. During an experiment, point-wise scour measurements were taken with a manual point gauge. For the unprotected test (U) and for the cases where large meshes have been employed (L and XL, enabling the passage of the point gauge), measurements were repeatedly taken at different times. For smaller mesh sizes (runs S and M), on the contrary, scour measurements were taken only at the end of the test, after removing the net.

3 RESULTS AND DISCUSSION

The results of the tests have been summarized in Figure 5a in terms of maximum scour depth and of its temporal evolutions (for runs U, L, and XL; for runs M and S, only the final 6-hours values have been measured). In particular, for run U the scour depth progressively increased with time, with a final maximum depth of 9.1 cm near the pier. The area interested by the scour in this case was about 930 cm^2 (approximate extensions equal to $5D \times 5D$ in the longitudinal and transversal direction, respectively, with respect to the flume axis). Runs XL and L showed similar temporal evolutions, although with lower final values of the maximum scour depth, witnessing how nets characterized by mesh sizes s remarkably larger than the
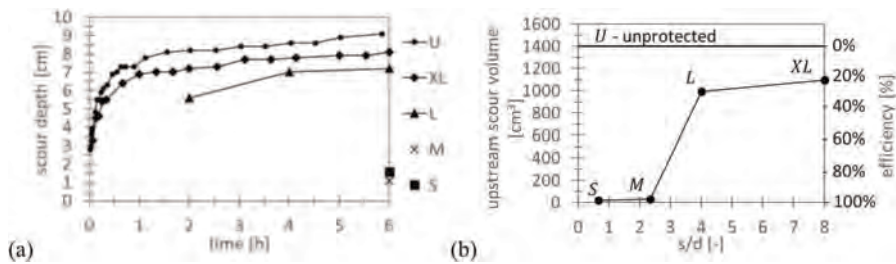
Figure 5.   Measured scour: (a) temporal trends of the spatially-maximum scour depth; (b) 6-hours scour volume measured between the upstream edge of the scour hole and the cross section at the pier axis, for increasing s/d mesh size ratios.

grain diameter d may also contribute in reducing scouring effects. Runs M and S, on the other hand, showed significantly reduced values of the final scour depths (about 1–1.6 cm) with respect to the unprotected configuration U.

These results are qualitatively confirmed also by the measurements of the upstream scour volumes, measured between the upstream edge of the scour zone and the flume section at the pier axis. For run U, the upstream scour volume was 1400.41 cm^3, whilst values of 19.5, 29.3, 996.1 and 1095.3 cm^3 for experiments S, M, L, and XL, respectively, have been obtained (all the values are referred to the end of the tests). These scour volumes, however, do not reflect the same quantitative performances in reducing the maximum scour depth observed in Figure 5(a): for run S, for example, being the grid "impermeable" to grain passage ($s/d = 0.67{<}1$), particles just rearranged themselves beneath the grid around the pier, but they could not be removed by the water flux. Beyond the protected area, moreover, a diffuse erosion zone appeared. Thus, the Geo-carpet in this case was highly effective in reducing the local scour phenomenon, at least in the vicinity of the pier, but some down-stream scour appeared. Similarly, for run M (although characterized by $s/d = 2.33{>}1$) a good efficiency in reducing the scour effects can be observed. For runs L and XL, on the contrary ($s/d = 4$ and 8, respectively), an evident scour hole was formed, because the grains could escape the net cells. In order to have a clear depiction of the scour volume reduction at the pier, Figure 5(b) shows the values of the measured upstream scour volumes as a function of the s/d ratios. For the sake of clarity, the data are also interpreted in term of proportional scour volume reduction with respect to the unprotected case, thus providing a quantitative indication of the global efficiency of the Geo-carpets against scouring. Three-dimensional reconstructions of the final scour pattern are finally depicted in Figure 6, for runs M and XL as representative cases.
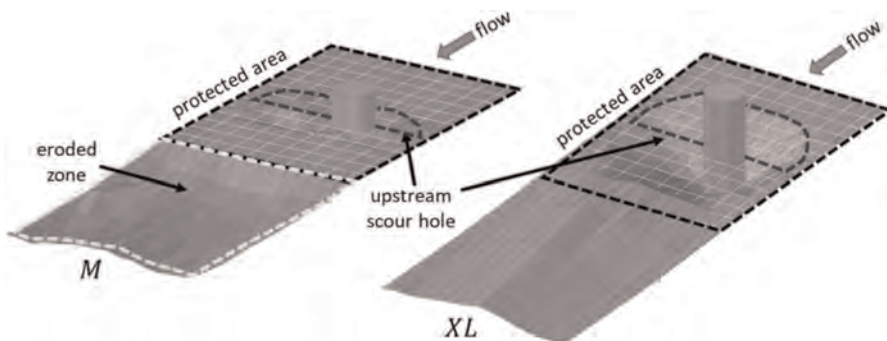

Figure 6.   Three-dimensional scour pattern for runs M and XL.

Almost perfect efficiency (near 100%) was obviously observed for $s/d = 0.67$ (run S) because the Geo-carpets, as already mentioned, are in this case "impermeable" to grain passage and, owing to their negligible bending stiffness, only allow for a grain redistribution over the protected area. However, very high efficiency (about 97%) was also obtained for $s/d = 2.33$ (run M). This can be probably due to the arise, at the local level of each mesh of the grid in contact with the surrounding grains, of an "arching effect" allowing for a redistribution of the shear stresses (induced on the grains by the water flux) against the grid wires. These latter provide then and additional confining effect on the grains constituting the riverbed, that hinders the scour process. From a micromechanical point of view, the arching effect consists in a substantial reduction of the characteristic length controlling the phenomenon. For the unprotected case, in fact, the characteristic length can be assumed to coincide with the clear width of the flume (i.e. 40 cm, minus the diameter of the pier) that corresponded to 113 times the particle size. When the Geo-carpets were installed, on the contrary, the controlling characteristic length coincided with the mesh size s, i.e. one or two orders of magnitude less than the former. Further quantitative analyses on the arching effect are beyond the purposes of the present paper but, from a practical point of view, it is here observed that such an effect would be beneficial, allowing also the use of relatively large mesh sizes, without the need of necessarily install Geo-carpets impermeable to grains. When the mesh size was further increased (runs L and XL), a progressive reduction of the efficiency was observed as the scour volume tended asymptotically to that for the U run, that can be considered as a case corresponding with $s/d \to \infty$.

4 CONCLUSIONS

The paper described the main results of some original small-scale flume tests, aimed at studying innovative mitigation measures for local scour around bridge piers. In particular, the idea of a new "Geo-carpet" system was tested as a possible bed armoring intervention, realized by disposing a geogrid layer directly on the on the riverbed around the model pier, and by fixing it into the granular layer. This solution proved to be effective (at least in the tested hydraulic conditions) in reducing both the maximum scour depth around the bridge pier and the total scour volume. Such effect is of course maximized if geogrids "impermeable" to grains (i.e. with a mesh size smaller that the grain diameter) are employed; however, relatively high efficiencies in scour reduction are also observed in case of mesh sizes significantly larger than the diameter of the grains. A micromechanical justification of this results is related to the arise of an arching effect at the local level of each mesh in contact with the riverbed, redistributing the stresses on the surrounding grains and locally increasing the confinement on the granular layer.

Further experimental and theoretical researches are still needed both on scientific (e.g., influence of live-bed conditions) and technological aspects (placement techniques, possible pretensioning action imposed to the grids, design optimization, . . .) and, before real scale on site applications, several additional points need specific investigation. For example, durability and efficacy issues of the chosen polymer (e.g. aggressiveness of chemical substances, possible damages to the geogrids from materials transported by the river flow, influence of polymer weight with respect to buoyancy force, . . .) need to be carefully tested. In Authors' opinion, however, such Geo-carpet systems could represent an innovative field of application for Geosynthetics, enhancing the use of traditional geogrids and promoting research towards new solutions. Geo-carpets will potentially represent a rapid and cost-effective solution to mitigate the scour phenomenon, with evident structural and environmental benefits in terms of protection of the infrastructure.

technicians of the LIF Lab at PoliMi for supporting the design and realization of the experimental tests.

REFERENCES

Craswell, T. & Akib, S. 2020. Reducing Bridge Pier Scour using Gabion Mattresses Filled with Recycled and Alternative Material*s. Eng* 1, 188–210.

Franzetti, S., Radice, A., Rebai, D. & Ballio, F. 2022. Clear Water Scour at Circular Piers: A New Formula Fitting Laboratory Data with Less Than 25% Deviation. *Journal of Hydraulic Engineering*, online first.

Froehlich, D.C. 2013. Protecting Bridge Piers with Loose Rock Riprap. *Journal of Applied Water Engineering and Research* 1(1), 39–57.

Heibaum, M.H. 2000. Scour Countermeasures using Geosynthetics and Partially Grouted Riprap. *Transportation Research Records* 1696(2), 5B0106, 244–250.

Lagasse, P.F., Clopper, P.E., Pagán-Ortiz, J.E., Zevenbergen, L.W., Arneson, L.A., Schall, J.D. & Girard, L. G. 2009. *Bridge Scour and Stream Instability Countermeasures. Experience, Selection and Design Guidance*. Federal Highway Administration, Hydraulice Engineering Circular no. 23. Url: https://www.fhwa.dot.gov/engineering/hydraulics/pubs/09111/09112.pdf.

Memar, S., Zounemat-Kermani, M., Beheshti, A., Rahimpour M., De Cesare, G. & Scheiss A.J. 2020. Influence of Collars on Reduction in Scour Depth at Two Piers in a Tandem Configuration. *Acta Geophysica* 68, 229–242.

Nouri Imamzadehei, A., Heidarpour, M., Nouri Imamzadehei, M., Ghorbani, B. & Haghiabi, A. 2016. Control of the Local Scouring Around the Cylindrical Bridge Pier using Armed Soil by Geotextile. *International Journal of Geosynthetics and Ground Engineering* 2(5).

Radice, A. & Ballio, F. 2008. Double-average Characteristics of Sediment Motion in One-dimensional Bed Load. *Acta Geophysica* 56, 654–668.

Tang H.W., Ding B., Chiew Y., Fang S. 2009. Protection of Bridge Piers Against Scouring with Tetrahedral Frames. *International Journal of Sediment Research*, 24(4), pp. 385–399.

Wang, C., Yu, X. & Liang, F. 2017. A Review of Bridge Scour: Mechanism, Estimation, Monitoring and Countermeasures. *Natural Hazards* 87, 1881–1906.

Xie, L., Zhu, Y., Li, Y. & Su, T.C. 2019. Experimental Study on Bed Pressure Around Geotextile Mattress with Sloping Plate. *PLoS ONE* 14(1), e0211312.

Performance of concrete filled geotextile mattresses

Simon Ebbert*
HUESKER Synthetic GmbH, Germany

Jan Derksen
Wayss & Freytag Ingenieurbau AG, Special foundations, Düsseldorf, Germany
Formerly: Institute of Geomechanics and Underground Technology, RWTH Aachen University, Germany

Jörg Harnisch
FH Münster, Faculty of Civil Engineering, Germany

ABSTRACT: Fabric formed concrete revetments are being applied in several fields of application. This can be erosion protection, sealing, mechanical protection or as ballasting element for e.g. pipelines. These applications require different performances of these concrete mattresses. Despite the long history of more than 50 years, there are still unknown technical parameters in terms of concrete filled geotextile mattresses. This paper will therefore explain the contribution of concrete mattresses to the tensile strength of concrete, which has been carried out at the University of Applied Sciences in Münster. In addition the applicable ice load as well as the hydraulic roughness of the examined concrete mattresses will be demonstrated. Finally a brief introduction into reference applications highlights the relevance of concrete mattresses in hydraulic engineering.

1 CONCRETE MATTRESSES

1.1 *Components*

Concrete mattresses consist in general of a geotextile top and bottom layer, filled with highly fluid concrete. There are mattresses available with vertical spacers to control the thickness and mattresses with filter points. The thickness of the last mentioned will be controlled by the size, shape, and pattern of the filter point (cf. Figure 1, left). Mattresses without filter points can be applied for both applications, erosion protection and sealing (cf. Figure 1, right), whereas mattresses with filter points cannot be used as a sealing element. Their application is limited to erosion protection, or in special cases, as ballast or mechanical protection element e.g., pipelines or membranes.

1.2 *Installation*

Thanks to its textile character, the concrete mattresses can be assembled into panels, fitting to the geometry of the structure to be sealed or protected. The empty panels with an approx. unit weight of 400 g/m^2, will be rolled out on the prepared structure, temporarily fixed on the crest, and filled with concrete. For several reasons, the panel size should not exceed 1000 m^2. Therefore, using industrial zippers to connect panels to each other is a standard procedure.
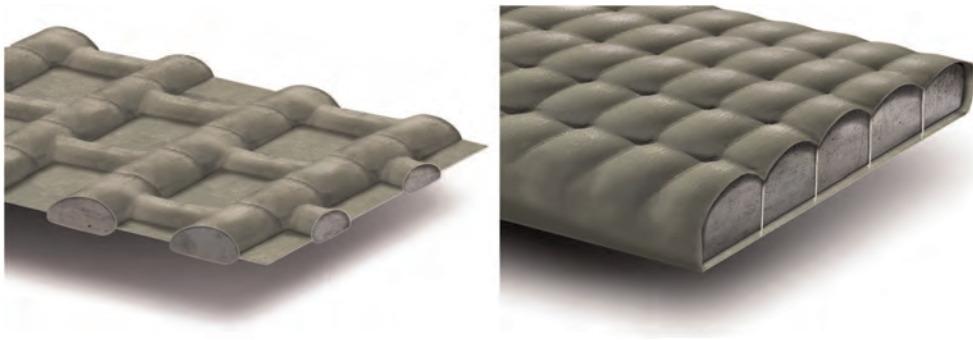
---

*Corresponding Author: ebbert@huesker.de

Figure 1. Concrete mattress with: Filter points (left); Vertical binders for constant thickness (right).

To get the mattress filled in a proper manner, preferably self-compacting concrete with a maximum grain size of 8 mm should be used. Prior to the installation of a concrete mattress with filter points, it´s highly recommended to apply a nonwoven layer underneath the mattress, as permanent erosion protection needs to be guaranteed.

1.3 Design

In comparison to other types of revetments, there is no need to design a fabric formed concrete revetment (FFCR) according to single stone failure, as they are coherent revetments.

There are several design approaches for FFCR available in literature. The most common ones are BAW (1993), DWA (2012), Pilarczyk, K. W. (2009) and FHWA (2009). Above them, several physical tests were executed in order to quantify the performance of concrete filled concrete mattresses. Some of them are described in chapter 2.

1.4 Typical applications

Concrete mattresses are typically applied for sealing or erosion protection of canals, erosion protection of overtopping sections, sealing of ponds and berth protection. Furthermore, concrete mattresses can be used to mechanically protect and ballast e.g. pipelines.

One of the biggest advantages of concrete mattresses is their ability to be filled underwater. This enables the system to be installed while the hydraulic structure is operating.

Especially for the application on overtopping sections, it´s a huge advantage, that concrete mattresses with big filter points can be vegetated. This allows the system to aesthetically fit into the landscape.

Thanks to its textile character, the system adapts to the subsoil, which avoids cavities occurring underneath the revetment.

Due to the coherency of the system, the overall thickness of a FFCR is much thinner compared to a classical revetment, which contributes to a reduction in carbon footprint and cost.

2 PHYSICAL TESTS

2.1 4-point bending tests on concrete filled geotextile mattresses

At the University of Applied Sciences in Münster, 4-point bending tests have been executed on concrete filled geotextile mattresses. To be able to compare the results, concrete slabs with

the same thickness and concrete characteristics were produced and tested in the same manner. For each test, 3 specimens with a size of 2 m × 1 m × 0,2 m were produced. All in all four slab-types were examined:

1. Unreinforced concrete slab
2. Fiber-reinforced concrete slab
3. Concrete mattress filled with concrete (Incomat Standard)
4. Concrete mattress filled with fiber-reinforced concrete (Incomat Standard)

For the fiber-reinforced concrete, alkali resistant glass fibers were used. The glass fibers were added to the concrete, before filling the concrete into the mattress. This did not influence the fill-ability of the mattress in a negative manner. An investigation of the fiber distribution in the concrete shows an equal distribution of the fibers over the entire cross section.

Figure 2 shows the overview of the averaged ultimate loads of the different specimens tested. The comparison of the results shows a significant contribution of the textile formwork to the load bearing capacity of the system by approx. 40 %. It turned out, that using fiber-reinforced concrete significantly increases the maximum load bearing capacity in both cases: with or without textile formwork. More Details on these tests are presented in Wilke, Derksen, Ebbert, Harnisch (2020).
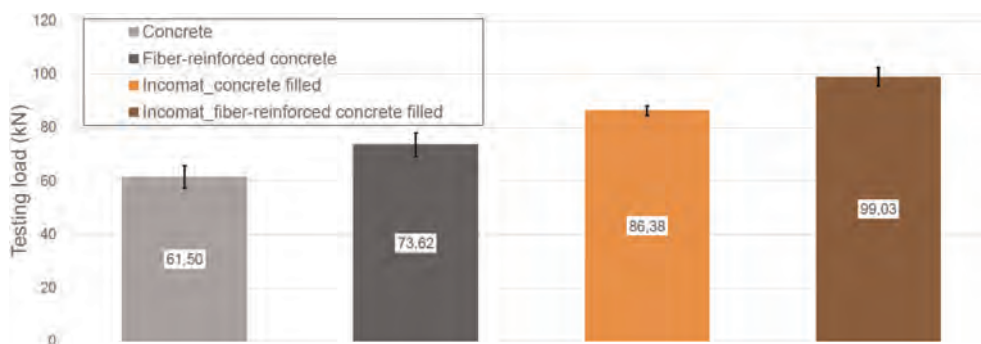

Figure 2. Overview of the averaged ultimate loads of the different specimens tested. Marker: Scatter of results.

Figure 3 shows a closeup of the load displacement curves of selected specimens of each type. They show a typical behavior of unreinforced systems. After the concrete cracks, the force suddenly drops down to the load being carried by the textile formwork. In this case the residual load bearing capacity is mainly provided by the lower layer of the textile formwork. The comparison of the displacement of the concrete slabs (green and brown curve) to the concrete filled geotextile mattresses shows (other curves), that the integrity of the mattress is not destroyed. This means that the concrete is still being kept together by the textile formwork. The total displacement carried by the textile formwork in this test is approx. 160 mm. This is a huge advantage, as the revetment would stay in place even after the concrete has fully cracked. An unreinforced concrete slab would have fallen apart.

2.2 Ice load testing

Harsh environmental environments require erosion protection as well. Consequently, at the Samara State University of Architecture and Civil Engineering, the ice load capacity of concrete mattresses was investigated. As a test setup, 3 concrete mattress sections (Incomat
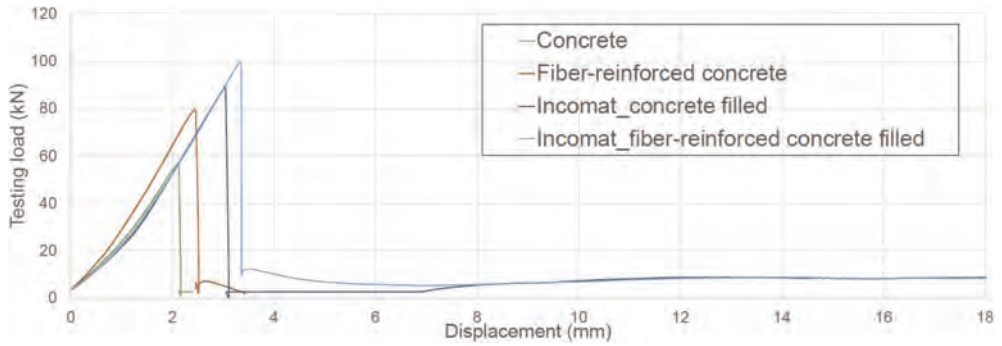
Figure 3.   Closeup of the load displacement curves of selected test specimens.

Flex) with thicknesses of 10 cm, 20 cm and 30 cm were installed at the embankment of the Saratov reservoir. The monitoring took place in the winter of 2014/2015. In that winter, ice thicknesses of up to 0,69 m were measured. Table 1 shows the relevant climate related information. Within 24 h, the max. temperature difference recorded was 16°C, with a max. water level difference of 1 m.

Based on the in-situ sections and additional laboratory tests, an equation, following Gost-Standard SP 38.13300.2012 (2012), has been developed:

$$h = \frac{\gamma_n \cdot A \cdot N^{0,55}}{K_M}$$

with: h = thickness of concrete mattress; N = max. ice impact; γ_N = safety factor; A = empirical factor and K_M = factor considering the increased stability compared to unreinforced concrete slab revetments.

Table 1.   Summary of the recorded climate and ice data.

	2014		2015			
	Nov.	Dec.	Jan.	Feb.	Until March 10th	After
Average temperature (°C)	+ 1.6	−6.5	−10.1	−9.2	−2.6	+ 3.5
Average temperature during night (°C)	−1.6	−8.7	−12.8	−13.7	−7.5	+ 2.3
Lowest temperature (°C)	−13	−16	−24	−25	−19	−12.7
Maximum ice thickness (m)	–	0.4	0.5	0.53	0.69	–

2.3   Concrete mattresses as erosion protection on overtopping sections

The basics to design concrete mattresses for erosion protection on overtopping sections have been derived at TU Vienna. The tests have been performed for concrete mattresses with filter points installed in a physical model. As the model needs to be scaled with a factor of 1:4, the Froude model law has been applied to convert the size of the physical model as well as the results. The Froude model law has been chosen, as it is usually being applied for scaling free water surface models. Wilke et al. (2012) reported these tests in their publication.

Its main conclusions are as follows:

– max. discharge ≥ 2.0 m³/(s*m)
– flow velocity ≥ 10 m/s
– proper toeing in at all edges (crest, toe and lateral)

where the discharge is given in m³/s per linear meter of crest length.

A comparison to other structures is shown in Table 2. It's clearly shown, that the concrete mattresses can carry much higher discharges and can be applied in a wider range of slope inclinations.

Table 2. Comparison of different overtopping section revetments [1]LfU BW (2004); [2]Tschernutter (2010).

Revetment type	Max. slope (1:n)	Maximum discharge (m³/(s*m))
Pitched stone[1]	6	≤ 1.0
Rip-rap[1]	4	≤ 1.0
Geosynthetic gabions[1]	4	≤ 1.0
Mastix asphalt[1]	6	≤ 1.0
Grass paver[1]	6	≤ 1.0
Soil solidification[1]	4	≤ 1.0
Concrete mattress[2]	2.5	≥ 2.0

To integrate the concrete mattress into the environment, a thin layer of soil can be installed on top of the mattress. The bigger the filter points of the mattress are, the better the interaction between soil and mattress will be. Greening with site adapted vegetation will establish good stability of the soil layer. In case of a heavy overtopping event, the soil layer is tolerated to erode, as the concrete mattress will take over the permanent erosion protection.

2.4 *Hydraulic roughness of concrete mattresses*

As concrete mattresses are often applied as an additional sealing layer on top of a deteriorated sealing layer, it's crucial to know their hydraulic roughness, in order to be able to calculate the water level in accordance with a minimum required discharge in an existing hydraulic structure.

At the Institute of Hydraulic Engineering and Water Resources Management (IWW) at RWTH Aachen University the hydraulic roughness of a real-scale Incomat Standard concrete mattress was determined. Due to the full dynamic similarity of the real-scale tests, these results are unaffected by scale effects and can be transferred to comparable applications. For this purpose, the bottom of the flume was lined with geotextile concrete mat elements, resulting in a total length of 24 m and a width of 1 m. Before installation of the mattress in the flume, first the roughness of the flume and the roughness of the empty geotextile mattress were quantified. During the investigation, several inclinations (I = 0.000 – 0.002) and discharges (Q = 200 – 400 l/s) were tested, resulting in mean flow velocities in a range of v = 0.9 – 1.5 m/s. More detailed information of this tests can be taken from Derksen (2017).

Based on the flow tests carried out, the mean equivalent sand roughness of the geotextile concrete mat of the type Incomat® Standard was determined to be $k_s = 0.0039$ m and corresponds to a Strickler coefficient of $k_{st} = 66$ m¹ᐟ³/s. The reciprocal of k_{st} represents the Manning's coefficient n.

Compared to Pilarczyk 2000, who published hydraulic roughness ranges for different types of mattresses, the roughness for constant thickness mattress measured by Derksen (2017) is laying on the smoother end of the range given.

3 REFERENCE PROJECTS

3.1 *Overtopping section (Picheldorfer Bach, Austria 2011)*

To protect Oberaich (close to Bruck an der Mur) against flood events, caused by extreme storm events, several protectional hydraulic structures were built. One of them is a flood retention pond, whose overtopping structure is integrated into the dike of the river Mur. The overtopping structure mouths in the river Mur.

To protect this structure in case of an overtopping event, a concrete mattress with big filter points has been installed. In total 3 panels of approx. 550 m^2 each, connected by industrial zippers, has been laid out and filled with concrete. After the concrete hardened, a soil layer has been installed and finished with vegetation.

Thanks to the greening with site adapted vegetation, the overtopping section perfectly fits into the landscape.

Figure 4. Concrete mattress: after installation (left); after being vegetated 2 years later (right).

3.2 *Canal sealing (Mittlerer Isarkanal, Germany 2013)*

The Mittlerer Isarkanal is a concrete sealed canal, which discharge of 150 m^3/s it supplies 7 hydro power plants with a total annual output of 130 MW. After more than 60 years of operation some sections needed to be remediated, as the concrete sealing layer was deteriorated. For several reasons, the installation needed to be carried out without emptying the canal. As underwater installation is common practice for concrete mattresses, it has been decided to apply them as new sealing layer. The concrete thickness of 10 cm decreases the size of the flow cross section. Thanks to the low hydraulic roughness (cf. chapter 2.4), the concrete mattress doesn't limit the required discharge.

To guarantee a successful installation, prefabricated panels of up to 1000 m^2 have been used for installation. The parts to be installed on the embankments were rolled in advance. The installation was carried out by the help of a pontoon (cf. Figure 5, left). In the first step, the concrete mattress on the bottom of the canal was filled from the pontoon. Afterwards, the concrete mattresses to be installed on the approx. 12.5 m long embankments, got unrolled and filled from the crest of banks. Diver support guaranteed a successful installation.

Thanks to the above-described follow up, the installation rate was up to 3000 m^2/day. The right side of Figure 5 shows the situation after installation.

Figure 5. Canal sealing: during installation from pontoon (left); after installation (right).

4 CONCLUSION

Concrete filled geotextile mattresses are used for more than 50 years in different applications. Their performance has been proven by many different tests e.g. 4-point bending, overtopping stability, ice load tests or hydraulic roughness, just to name the 4 of them introduced in this publication. For sealing applications, impermeable, constant thickness mattresses with a low roughness should be preferred. Erosion protection is guaranteed by both types, with and without filter points, but as mattresses with filter points can be vegetated, they should be preferred for applications like erosion protection of overtopping sections.

REFERENCES

BAW (Bundesanstalt für Wasserbau) 1993. Empfehlung zur Anwendung von Oberflächenabdichtungen an Sohle und Böschung von Wasserstraßen. In. *Mitteilungsblatt der Bundesanstalt für Wasserbau Nr. 85*, Karlsruhe

Derksen, J. (2017) Hydraulische Rauheit von geotextilen Matten. Physikalische und Numerische Untersuchungen In: *Living Rivers – Neues aus Praxis und Forschung. Mitteilungen Heft 171*, Aachen.

DWA (Deutsche Vereinigung für Wasserwirtschaft, Abwasser und Abfall) 2012. *Dichtungssysteme im Wasserbau – Teil 1: Erdbauwerke (DWA-M 512-1)*, Hennef

FHWA (Federal Highway Administration) 2009. Bridge Scour and Stream Instability Countermeasures: Experience, *Selection and Design Guidance* – Third Edition., Washington D. C.

LfU BW 2004: Überströmbare Dämme und Deichscharten. In. *Landesanstalt für Umweltschutz Baden-Württemberg – Oberirdische Gewässer, Gewässerökologie 90*, Karlsruhe

Pilarczyk 2009. Design of Alternative Revetments In. Kim, Y. C. *Handbook of Coastal and Ocean Engineering*, Singapur

Pilarczyk 2000 *Geosynthetics and Geosystems in Hydraulic and Coastal Engineering*. Rotterdam: A. A. Balkema.

SP 38.1330.2012 2012 *Loads and Impacts on Hydraulic Structures (from Wave, Ice and Ships)* (December 2011), Ministry of Regional Development of Russia, Moscow

Tschernutter 2010: *Überströmbare Dämme – Bericht über die Versuche mit der Incomat® Crib 10.200-Matte*. Technische Universität Wien – Institut für Wasserbau und Ingenieurhydrologie, Wien 2010. (not published)

Wilke, Derksen, Ebbert, Harnisch 2020. *Neue Entwicklungen im Bereich der geotextilen Betonmattentechnologie zur Deckwerksgestaltung*. In. Bautechnik

Wilke, M, Krüger, B., Schuell, M. and Terschnutter 2012. Erosion Resistant Construction of Overflow Sections by means of Geosynthetic Concrete Mattress. In. *6ICSE - 6th International Conference on Scour and Erosion*, Paris.

Bituminous geomembranes (BGM) to reduce water losses in irrigation canals

T. Aguirre
Axter Coletanche Inc., Vancouver, Canada

I. Misar
Axter CZ s.r.o, Praha, Czech Republic

J. Moeglen
Axter, Illzach, France

N. Daly
Axter Coletanche Inc., Montreal, France

ABSTRACT: The world population increases decade after decade straining global food demand. During this time drought becomes more accentuated thus irrigation must become more efficient. Many irrigation canals are built of soil with a poor waterproofing quotient and concrete sections which, after 15 years or less, meet seepage through cracking. Geosynthetic lining is the solution. The main challenges for irrigations districts when lining canals are that during construction canals are taken out of service, this paper will illustrate these processes. It is important that the choice of material enables efficient installation in diverse weather conditions, is economically competitive and can withstand time when left exposed to the elements with an easy maintenance component. Through case studies, this paper demonstrates that bituminous geomembranes (BGM) meet and exceed these challenges. The paper reviews briefly the characteristics of BGM as uniquely qualified for usage when lining canals: low thermal coefficient, a low Manning coefficient, a density greater than 1, and proven longevity when left exposed. Thanks to their flexibility and bituminous properties that can be connected to any surface. Case studies presented in this paper highlight the BGM specific properties. In Romania, renovation of irrigation canals, in North America, BGM began a partnership with the Roza Irrigation District (USA), to line a complete irrigation scheme reservoir and irrigation canals throughout the Columbia River Basin, in Chile rehabilitation work on canals supplying water for a small irrigation scheme, in India and in France.

1 INTRODUCTION

Thousands of miles of canals move billions of cubic meters of water annually. Most of these canals are built of material ranging from soil to concrete. Water losses through bottom and side leakage and associated economic losses are an important concern for owners and operators. Lining canals or building recovery systems are the solutions used to control water losses, especially since summers are getting hotter and drier and water resources are becoming scarcer. We could observe that engineering is not well enough informed about geomembrane performances and continue to line canals with concrete or clay. Five years after completion, the rate of satisfactory projects has been known to drop significantly due to poor project design.
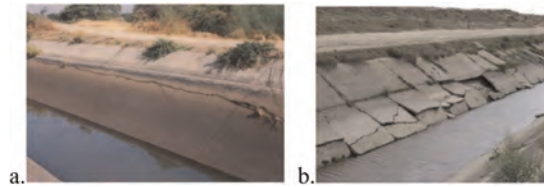
Figure 1. a. Peru: San Lorenzo, longitudinal crack / 1.b. Tajikistan: Fergana Valley, effect of frost-heave.

A lined canal system Figure 2a. Llangollen Canal (UK), and Figure 2b. Canal de Provence (France), when properly operated and maintained, are more efficient in many aspects of operation because of a higher conveyance capacity.

Figure 2. a. Llangollen Canal (UK) / 2.b. Canal du Provence (France).

The other major challenge when making canals watertight is taking the canal out of service during construction. Typically, this type of work is performed during winter with the possibility of delay due to weather and the associated cost. The choice of materials that are easy to install in diverse weather conditions (humidity, snow, rain, wind) maintaining an economically competitive advantage, and one that will withstand the test of time as an exposed lining system is a crucial component. Through case studies, this paper demonstrates that bituminous geomembranes (BGM) can meet these challenges with a long durable life even when directly exposed to UV, offering an ease of maintenance and repairs and supplying a very viable technical and economical option for lining canals. Furthermore, the manufacturer provides an in-situ training in all aspects of the installation process.

2 TECHNICAL CHARACTERISTICS OF BGM

2.1 BGM structure

The product's main structure is based on a non-woven polyester geotextile which is completely impregnated by elastomeric bitumen, with a glass fleece inside to help its manufacture

Figure 3. BGM structure.

Table 1. Summary of some physical and mechanical properties of a BGM 4.00 mm thick, the most common used in efficiency waterproofing.

Properties		Standard	Unit	BGM	Commentary
Physical properties	Thickness	ASTM D 5199	mm	4.0	BGM is thicker and heavier than any other liners making it more resistant to wind uplift or flotation and consequently requires less ballast to keep it in place. It can be placed in most weather conditions and since the seaming is by torching, humidity is not an issue.
	Density	ASTM D 1505	g/cm^3	1.276	
	Surface mass	ASTM D 5261	kg/m^2	4.85	
Mechanical properties	Tensile Stress at Break	ASTM D 7275 4073	kN/m	27	Due to its important thickness and its enclosed geotextile, BGM is far more resistant to puncture than the other liners and thus require less bedding and can be placed over very coarse granular fill without the threat of being damaged. Also, since the tear resistance of BGM is very high, this liner is less vulnerable to mechanical damages during in situ transport and placement.
	Tensile Elongation at Break	ASTM D7275	%	60	
	Tensile-Tear Resistance	ASTM D 4073	N	825	
	Puncture Resistance	ASTM D 4833	N	530	
Thermal Stability		ASTM D 1204	%	<0.1	Approximately 100 times lower than PE liners, BGM doesn't produce wrinkles or waving when temperatures vary onsite.
Friction Angle		ASTM D 5321	°	32	BGM friction angle is much higher than other liners and is therefore easier to install on deep slopes and safer for installation crews.

by strengthening the product at a temperature of 180°C. On top of the structure is sand to enhance UV resistance and provide traction for installation workers. On the bottom is an anti-root film to prevent permeation of any vegetation roots through the liner. The BGM Geomembrane is produced in France under severe QC/QA control. the BGM factory is ISO-9001, and the Geomembrane is CE (European Standards) and ASQUAL (France) certified. The ASQUAL certification includes the auditing of the production line as well as the Geomembrane performance.

The BGM compounded with elastomeric bitumen can be installed to a temperature of −40°C and is therefore more suitable to be used in cold weather countries like Canada, North of USA, North and East of Europe or in altitude. Product is manufactured in 4 thicknesses ranging from 3.5 to 5.6 mm.

2.2 BGM specific advantages in irrigation watertightness

The technical characteristics of BGM namely those unique for use in lining canals:

– No wrinkles as BGM has a low thermal coefficient,
– A low Manning coefficient allowing the passage of more water for a same cross-section of the canal,
– Longevity even when exposed more than 60 years and more than 300 years buried as proven by nuclear laboratories in France and USA,
– A density (1,276) greater than water, enabling an economical option as BGM can be installed in canals while water is flowing. Panels can be welded underwater using a specific mastic to provide weld under water by a phenomenon of vulcanization,

- Can be connected to any type of surface: concrete see Figure 4 entry of a concrete siphon, steel or HDPE pipe.
- Local personnel and maintenance teams of an irrigation district or of any local installer can be trained in-situ by a manufacturer's monitor, keeping installation costs very low,
- Mechanical resistance: due to its enclosed geotextile, BGM is very resistant to puncture (530 N or more). The hydrostatic puncture and the resistance to puncture by aggregates (1550 kPa and 25 kN respectively) are thought to be much higher than other liners like PE. From an economical point of view, this liner will require no protection (use of Geotextile) on one or both sides. BGM is therefore much more resistant during construction and maintenance work.

Figure 4.   Canal in UK along deep slope.

Figure 5.   Traffic of heavy equipment for maintenance Yakima (Washington State USA).

3   CASE STUDIES

Case studies presented in this paper highlight the specific property of BGM that was the decision factor in the choice.

3.1   *In Romania*

Romania has some secondary canals requiring renovation. BGM was used for re-lining:

- Original concrete irrigation canal (see Figure 7): principal canal with concrete panels 2,5 m by 1,2 m with a slope 50% and width 18 m canals,
- And, at the terminal part, earth canals.

In certain parts (see Figure 6), due to the high damage of the concrete lining the concrete slabs will be removed and will be constructed as earth canals with BGM lining with a thickness of 4.0 mm or even 4.8 mm.

Figure 6.   concrete for canals some years after due to unstable soil underneath.

Figure 7.   Wasteway No.5 Regulation Reservoir, feeding Yakima and Roza Districts Irrigation canals.

3.2 *In North America:*

3.2.1 *California State (USA)*
Two of the three leaking sections of the Caspa District canal in Wyoming, USA, were repaired with BGM in 1992 and 1994 respectively. The third, slightly larger (80,000 m^2) section was repaired in 1995 by the canal operator's own highly trained employees.

3.2.2 *Washington State (USA)*
In 2005, BGM began its partnership with the Yakima district (Washington State, USA) for providing a watertight solution year after year of old irrigation canals. The project was intended to provide irrigation services to the many farms and agricultural regions of the Yakima Valley (best cherries for USA). In 2016, there was an extension of this cooperation to the Roza Irrigation District for lining the Wasteway No.5 Reregulation Reservoir outside of Sunnyside, Washington State on the West Coast of the United States (See Figure 7).

   The project is expected to conserve roughly 10 million cubic meters of water each season. It was completed by the end of August ensuring permitting a large storage of water in autumn and winter. This ability to sustain schedule was due to the complete absence of wrinkles permitting the installers and welders to work without any delay even during warm season. This reservoir is completely and permanently monitored by a certain number of piezometers,

   Water is pumped from the Columbia River. There are 3 main irrigation districts in this region that work in cooperation with dozens of smaller regional irrigation districts of which the Roza Irrigation District belongs. In the last 17 years, BGM has been used to line irrigation canals throughout the Columbia River Basin with successful projects in Naches-Selah, Quincy, Moses Lake, Wenatchee, Yakima and Ellensburg. All these districts appreciated the robustness of BGM, the fact it is able to be installed in low temperature, it can be installed by internal teams after training by a manufacturer representative giving greater flexibility in the use of their teams.

3.3 *In Latin America: Chile*

The Elqui River and Tributaries Board of Control (Junta de Vigilancia del Río Elqui y sus Afluentes, JVRE), administers 121 irrigation canals in Elqui Province in north-central Chile to irrigate an area in the order of 200 km^2 and the Rio Choapa Board of Control (Junta de Vigilancia del Rio Choapa) administers more than 660 km of canals to irrigate more than 220 km^2 of land in central Chile. The area covered by these districts which produce grapes, citrus fruits, avocados, and vegetables for export – is a very dry area where water is a scarce resource, meaning canals need to be lined to avoid water loss. The Rio Choapa and the Rio Elqui irrigation districts decided to look for alternatives to concrete liners to reduce costs. As a result of these search efforts, more than 62,000 m^2 of irrigation canals in these two districts were lined with a 3.5 and 4 mm thick BGM. These canals were lined at a cost of about 30% less than a concrete lining and have been operating successfully with a longer lifespan than with concrete in this unstable soil.
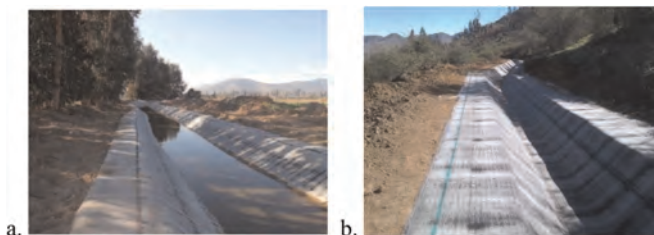

Figure 8.   a. Irrigation canals in Chile: Rio Elqui / 8.b. Irrigation canals in Chile: Rio Choapa.

It is worth noting that in smaller canals where the perimeter is less or equal than the width of the BGM roll, construction joints are less frequent and thus the deployment of the liner is very fast.

Reasons for choice of BGM:

– Resistance to UV and longevity in exposed conditions,
– Ability to be fixed to concrete,
– High friction angle permitting animals to walk across,
– Low Manning coefficient,
– A lot less expansive and faster to deploy than a conventional concrete lining.

3.4 *In India*

The Pench Left Bank Canal, located in central India, brings water from the Pench River to the region's crops. The original canal consisted of a concrete lining that was collapsing due to clay swelling underneath. In a state where water resources are becoming scarcer over the years, the Nagpur Water Resources Department decided to re-seal the canal using a long-lasting geomembrane (see Figure 9). A BGM 4 mm thick was laid on the substrate and anchored at the head of the slope. Works both started in June 2019 and 2022 and were scheduled to be completed before the monsoon season. BGM could be installed so quickly that the entire projects (2019 phase) finished in 15 days at an average of 2,200 m^2 laid and welded per day. The customer needed a strong, flexible geomembrane. They chose BGM for its ability to withstand:

– Substrate settlement,
– The region's extremely high temperatures.

Figure 9.   a. Irrigation canals in India – before / 9.b. Irrigation canals in India – during installation.

3.5 *In France: Canal de Provence*

The Canal de Provence supplied water to 116 cities in the south-east of France which represents around 3 million inhabitants, the irrigation of 80,000 hectares of agricultural land and feeds more than 8,000 industries. They water originates in the Alps (Figure 10).

Figure 10.   Canal de Provence in the French Alps.

Figure 11 below shows a typical section of its channels. The width at the bottom is between 2.7 and 3.0 meters. The width in the upper region can be from 10.0 to 17.2 meters. The depth is between 2.4 and 3.6 meters. On each side, there are 2 tracks of 2 m. asphalted for assuming the maintenance and security. The slopes are between 27 and 34°.
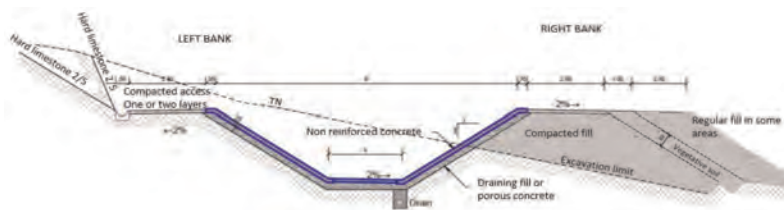

Figure 11.   Cross-section type of the Canal de Provence.

Canal de Provence could note that their network suffers from pathologies of geotechnical origin (dissolution of gypsum or clay in the presence of water from leaks) which induce displacements of the ground. The main objective of conveyance efficiency was to reduce the risk of geotechnical disorders caused by infiltration. The pre-feasibility studies consisted of a catalogue of canal renovation techniques. Subsequently, a dozen companies were consulted based on creating a competitive dialogue. The choice fell on the implementation of a thick BGM weighted in raft of a concrete slab. BGM was chosen for the following reasons:

– Sealing coating that does not adhere to the support and allows centimeter displacements of the support to be resumed,
– BGM has a high surface mass allowing installation in high speedy wind (Venturi effect in canals). In addition, the welding system allows installation in wet or hot weather,
– Sandblasted on upper face offering adhesion to allow the ascent of fallen animals or humans in the canal (high friction angle). Thickness sufficient to resist blows of hooves for animals,
– Robustness even exposed confirmed by feedback from several decades in similar situations,
– Without expansion, the geomembrane is in permanent contact with its support, no wrinkles, slowing down the current. The Manning coefficient stays consistent,
– It can be welded and then fixed by rulers and fasteners at the head of the joffers to overcome the impossibility of making anchor trenches,
– Exposed at the level of the joffers, due to its great UV resistance.

To ensure the supply of users downstream of the works, the interventions were carried out in successive sections of 200 meters in length allowing the implementation of a bypass (see Figure 12).

Figure 12.   Dewatering work on a section without interrupting water circulation.

4 CONCLUSION

BGM since its inception of manufacturing in a factory (1974) has become a very famous geomembrane being employed and appreciated on every continent due to its robustness, its ability to be installed and left exposed with an expected lifespan of more than 20 years and to be installed by any team of any district after onsite training by a manufacturer's representative. The overall cost of the lining system should be considered for the entire project cost for comparison, inclusive of subgrade preparation, no need of geotextile to protect a thinner and less robust geomembrane, eliminating difficulties induced by windy conditions due to its high unit mass, maintenance and installation costs are reduced by employing internal teams.

REFERENCES

Burt, C. & Styles, S. 1999. *Modern Water Control and Management Practices in Irrigation*. FAO Water Reports no 19. International Programme for Technology and Research in Irrigation and Drainage (IPTRID). The World Bank and Food and Agriculture Organization of the United Nations (FAO): Rome, Italy.

Food and Agriculture Organization of the United Nations (FAO). 2012. *Performance of Irrigation Management on 56 Medium and Large Systems*. Working Document: Rome, Italy.

Giroud, J.P. & Plusquellec, H. 2017. Water, Canals and Geosynthetics. In *Proceedings of GeoAfrica 2017, the Third African Regional Conference on Geosynthetics*. 1: Marrakech, Morocco: Comite Marocain des Geosynthetiques; p 53, 112.

Habib, Z., Garces-Restrepo, C. 1993. *Canal Lining Performance Parameters in the Chasma Right Bank Canal System Stage I Irrigation System*. Proceedings Workshop on Canal Lining and Seepage. Lahore: Pakistan; 323–353 pp.

Plusquellec, H., McPhail, K. & Polti, C. 1990. Review of Irrigation System Performance with Respect to Initial Objective. *Irrigation and Drainage Systems* 4: 313–327.

Skutsch, J.C. 1993. The Role of Maintenance in Extending Lining Service Life. In *Proceedings. Workshop on Canal Lining and Seepage*. International Waterlogging and Salinity Research Institute: Lahore, Pakistan.

Snell, M. 2001. Lining Old Irrigation Canals: Thoughts and Trials. *Irrigation and Drainage* 50(2): 139–157.

Swihart, J., Haynes, J. 2002. Canal Lining Demonstration Project: Year 10 Final Report. US Department of the Interior. Bureau of Reclamation Water Conservation Center.

World Bank. 1995. The World Bank and Irrigation. In *A World Bank Operations Evaluation Study*. World Bank/Operations Evaluation Department: Washington DC, USA.

Effect of tailings fines content on leakage though circular geomembrane holes overlain by saturated tailings

J.-Y. Fan & R. Kerry Rowe

Department of Civil Engineering, GeoEngineering Centre at Queen's-RMC, Queen's Univ., Kingston, ON, Canada

ABSTRACT: Coupled physical and hydraulic experiments are conducted to quantify leakage through circular geomembrane holes with diameters of 10 mm, 20 mm, and 50 mm. Three different tailings, fine-grained tailings with fines content of 90 % and d_{10} of 1 μm (denoted as T1), silty sand tailings with fines content of 30 % and d_{10} of 20 μm (denoted as T2), silty sand tailings with fines content of 20 % and d_{10} of 40 μm (denoted as T3), are examined. The effective stress and pore pressure in the tailings above geomembrane and remote from the hole are ~170 kPa and ~350 kPa, respectively. It is shown that leakage through geomembrane hole is proportional to the hole radius (and not the area) for each type of tailings, and highly dependent on the fines content of the tailings. For example, the leakage for T2 and T3 tailings are 1.8-fold and 65-fold greater than that for the T1 tailings, respectively, for a given hole size. The practical implications are discussed.

1 INTRODUCTION

Increasingly the design and operation of tailings storage facilities (TSFs) involves the use of a geomembrane (GMB) liner to reduce seepage from the facility into the surrounding environment and/or reduce the hydraulic gradient within the embankment and the foundation (Lupo & Morrison 2007; Rowe 2020; Rowe & Jefferis 2022; Touze *et al.* 2008). Due to the low hydraulic conductivity of tailings, the GMB liner system for TSFs commonly comprises a single GMB liner even though the hydraulic head within the facility can exceed 100 m (Touze *et al.* 2008). The GMBs used in mining applications are most commonly either made from high-density polyethylene (HDPE) or linear low-density polyethylene (LLDPE) with a typical thickness of 1.0 to 2.5 mm (Rowe *et al.* 2013; Touze *et al.* 2008). With these GMBs, the leakage is effectively limited to flow through holes in the GMB that most commonly arise either during construction (including during placement of material over the GMB) or subsequently due to stress cracking (Giroud & Bonaparte 1989a, 1989b; Giroud 2016; Fan & Rowe 2022c, 2023; Rowe 1998, 2005, 2012, 2020).

Leakage through a circular GMB hole overlain by saturated tailings and underlain by a highly permeable subgrade has been recently examined (Badu-Tweneboah & Giroud 2018; Fan & Rowe 2022a, 2022b; Rowe *et al.* 2017; Rowe & Fan 2021, 2022). Analytical equation predicting leakage through a circular GMB hole with diameter of *2r* (*r* is hole radius) overlain by saturated tailings was proposed based on the Rowe-Booker equation (Rowe & Booker 2000) by Rowe and Fan (2021) as:

$$Q = \frac{H}{\frac{1}{\xi} + \frac{1}{\Omega}} \tag{1}$$

where

$$\Omega = \{4 + [2.455 + 0.685 \tanh{(0.6 \ln(r/T))}]r/T\}rk_2 \qquad (2)$$

$$\xi = \pi r^2 k_1 / t \qquad (3)$$

where H is the water head above the GMB, T is tailings thickness, t is GMB thickness, k_1 is the hydraulic conductivity of tailings within the GMB hole and k_2 is the hydraulic conductivity of tailings overlying the GMB. For the cases that the hole is filled with fully consolidated tailings, $k_2 = 1.1\ k_1$. Based on the proposed equation, factors (e.g., GMB hole size, water head, consolidation stress, subgrade gradation) affecting the piping and internal erosion through GMB defects have been investigated by Fan and Rowe (2022b).

The characteristics of tailings vary greatly and are highly dependent on the ore type, mineralogical composition, the physical and chemical processes used to extract the metals. The presence of fines particles (<75 μm) within tailings notably affected the compressibility and permeability of tailings (Fan et al. 2022) and may potentially impact leakage through any GMB defects. Thus, the objective of this paper is to investigate the effect of tailings fines content on leakage through circular holes in a geomembrane overlain by saturated tailings.

2 EXPERIMENTAL INVESTIGATION

2.1 Tailings

Three different tailings, fine-grained tailings with fines content of 90 % and d_{10} of 1 μm (denoted as T1), silty sand tailings with fines content of 30 % and d_{10} of 20 μm (denoted as T2), silty sand tailings with fines content of 20 % and d_{10} of 40 μm (denoted as T3), were examined (Figure 1). T1 was originated from a copper-zinc mine located in the south of Portugal and samples were collected immediately downstream of a thickener thickened using a flocculant. T1 (pyrite tailings) had a high acid generation potential and a specific gravity of 3.6 - 3.7. According to the Unified Soil Classification System (USCS), the sample could be described as a low plasticity clay (CL). Additional tailings details may be found in Lopes et al. (2013) and Fan and Rowe (2022a). T2 and T3 were both cyclone sand originating from a copper mining facility in British Columbia (Canada) without being thickened. The tailings
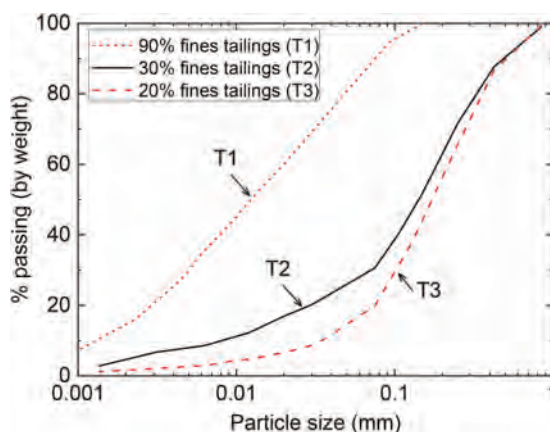

Figure 1.   Grain-size distributions of fine-grained tailings (T1), silty sand tailings with 30% fines (T2), and silty sand tailings with 20% fines (T3) (Notes: T1 was first tested by Fan and Rowe (2022a), T2 was first tested by Rowe and Fan (2021, 2022), T3 was first tested by Fan and Rowe (2022b)).

had a similar specific gravity of ~2.65 and were both classified as silty sand (SM) based on the USCS classification. More information on T2 was given by Rowe and Fan (2021, 2022), and on T3 by Fan and Rowe (2022b).

2.2 Geomembrane and subgrade

Two types of smooth GMB, LLDPE with thickness of 1 mm beneath T1 and HDPE with thickness of 1.5 mm beneath both T2 and T3 were tested (Table 1). Circular holes with diameters of 10 mm, 20mm, and 50 mm, respectively, were pre-punctured in the center of 590 mm- diameter GMB specimens. Highly permeable subgrades with hydraulic conductivity k of at least three orders of magnitude greater than that of overlying tailings were investigated. The subgrades satisfied the filter compatibility criterion by Foster and Fell (2001) and the erosion category for the overlying tailings were all assessed to be no erosion.

Table 1. Measured leakage (L/day) through circular geomembrane holes of various sizes with a similar loading condition of effective stress and pore pressure in the tailings remote from the hole of ~170 kPa and ~350 kPa, respectively.

Tailings	GMB type	GMB thickness (mm)	Hole diameter (mm)		
			10	20	50
T1[a]	LLDPE	1	0.4	0.8	2.5
T2[a]	HDPE	1.5	0.5	1.6	4.3
T3[a]	HDPE	1.5	29	–	142

[a]Note: Leakage was first presented by Fan and Rowe (2022a) for T1, Rowe and Fan (2021, 2022) for T2, Fan and Rowe (2022b) for T3. The test measuring leakage through 20 mm diameter hole overlain by T3 was not conducted.

2.3 Test apparatus and procedure

Coupled physical and hydraulic experiments performed in this study were conducted in the same rigid cylindrical steel test cell with an inside diameter of 590 mm and height of 500 mm as that used by Rowe and Fan (2021, 2022). The cell was filled from the bottom up as follows: geocomposite drain, subgrade with a thickness of ~200 mm, GMB with a central defect, saturated tailings slurry with initial solids content of ~70% and final thickness of ~200 mm after consolidation.

2.4 Measured leakage

Leakage test was conducted with a combination of $\sigma_v \approx 520$ kPa and $u \approx 350$ kPa. During the experiment, leakage through the GMB hole gradually came to an equilibrium as tailings consolidated, the steady leakage in Table 1 and Figure 2 for each test was adjusted to 20 °C based on the temperature of the collected leakage. Test results show that leakage through geomembrane hole was closed to be proportional to the hole diameter and not the hole area for each type of tailings. For example, increasing hole diameter from 10 mm to 20 mm, there was a 1.9-fold increase in leakage for T1 tailings and a 3-fold increase in leakage for T2 tailings, and there was a 6.1-fold, 8.3-fold, and 4.9-fold increase in leakage when increasing the hole diameter from 10 mm to 50 mm for T1, T2, and T3 tailings, respectively. For a given hole size, the leakage for T2 and T3 tailings were 1.8-fold and 65-fold greater than that for the T1 tailings, respectively, showing the highly dependent of leakage on the fines content of tailings, especially for tailings with relatively smaller fines content (e.g., 20%).
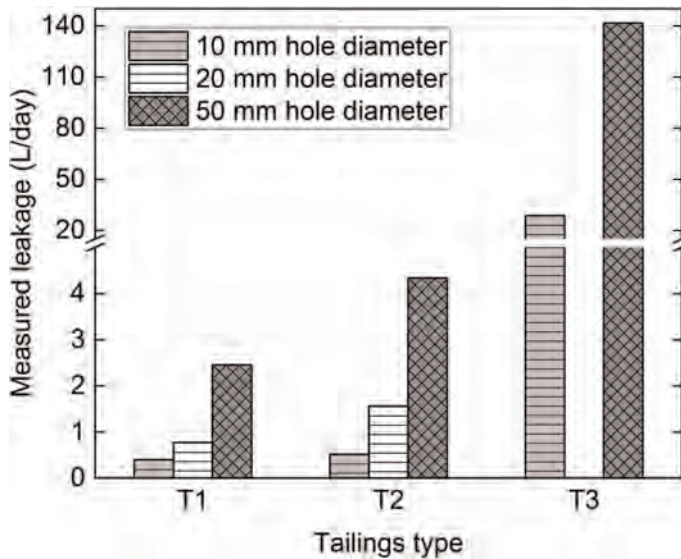
Figure 2. Comparison of the measured leakage with three different tailings above the GMB and a highly permeable subgrade (filter compatible and no piping occurred) beneath the GMB at the effective stress and pore pressure in the tailings remote from the hole of ~170 kPa and ~350 kPa, respectively (Notes: leakage was first presented by Fan and Rowe (2022a) for T1, Rowe and Fan (2021, 2022) for T2, Fan and Rowe (2022b) for T3).

3 DISCUSSIONS AND PRACTICAL IMPLICATIONS

3.1 *Effect of fines content on leakage*

k is highly dependent on the fraction of smaller size particles within a soil, e.g., k was linearly correlated with $d_{10}{}^2$ based on Hazen equation. Besides d_{10}, fines content is also a parameter that is commonly used when describing tailings. This is because both parameters highlight the importance of smaller size particles to k. In the following description, fines content is used to illustrate the effect of smaller size particles on leakage through GMB hole.

The relationship between consolidation stress and k of tailings tested was obtained using the stress-dependent permeameter (Fan *et al.* 2022). Results shows that k of tailings was highly dependent on its fines content (Figure 3). For example, at the same consolidation stress, there was an average of 1.5-fold increase in k when decreasing fines content from 90% to 30%, and there was a 30- to 60-fold increase in k when decreasing fines content from 30% to 20%, although the representative grain sizes for T1 was much finer (over an order of magnitude less) than those for T2 (Table 1). Fan *et al.* (2022) investigated the influence of fines content on the compressibility and permeability of tailings with a range of fines content from 0% to 100% by adding fines into or moving out of the host silty sand tailings with initial fines content of 18%. Results show that the same increment of fines from 12% to 30% and from 30% to 48% resulted in an approximately 8-fold and 2.5-fold decrease in k, respectively, and k remained constant when increasing fines content from 48% to 100%. Thus, a similar (around 2.5-fold variation) leakage through any GMB defect with the same hole size could be expected when the GMB is overlain by 30% and 100% fines tailings, whereas a sharp increase in leakage may be observed when reducing fines content from 30% to nil. This is caused by the effect of fines content on the involvement of the fines (<75 μm) and coarse ($\geq$ 75 μm) portions within soil skeleton under compression, and its impact on the specific surface of the mixture, as described by Fan *et al.* (2022).
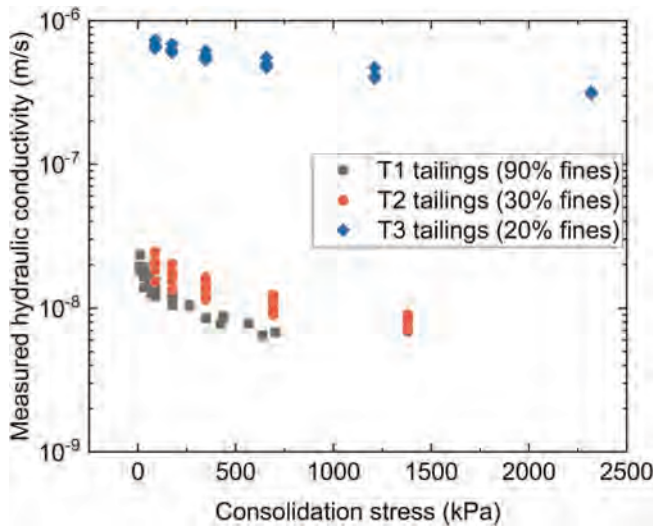
Figure 3. Measured hydraulic conductivity of three tailings via the stress-dependent permeameter by Fan *et al.* (2022) (Notes: hydraulic conductivity was first presented by Fan and Rowe (2022a) for T1, Rowe and Fan (2022) for T2, Fan and Rowe (2022b) for T3).

Internal erosion and piping are a significant cause of failure and accidents affecting embankment dams (including tailings dam). Increasing the subgrade coarseness from the filter compatible subgrade presented herein to a filter incompatible poorly graded gravel subgrade, piping through GMB defects with diameters of both 10 mm and 50 mm was easily initiated when the GMB was overlain by T3 tailings (Fan & Rowe 2022b); whereas no piping was observed when the GMB was overlain by T1 tailings, even with a 72 m water head above the GMB (Fan & Rowe 2022a).

This is because a greater hydraulic disturbing force arose from a higher leakage when the GMB was overlain by a more permeable T3 tailings relative to T1 tailings.

Due to the localized concentration of head loss within a distance of $10r$ from the GMB hole center when the tailings are placed directly above the GMB, a feasible way of minimizing leakage through any GMB defect could be to place the tailings slurry with high fines content first (i.e., bottom layer) prior the placement of low fines content tailings (i.e., top layer). The thickness of bottom layer after consolidation should be enough if it is close to $10r$ (e.g., layer thickness > 0.05 m for r of 5 mm and 0.25 m for r of 25 mm). Further increasing its thickness has negligible impact on leakage. Moreover, tailings with fines content $\geq 30\%$ is sufficient for minimizing leakage and preventing the piping potential due to its low k.

3.2 *Reliability of leakage prediction*

Leakage through circular GMB defect with diameter of 10 mm, 20 mm, and 50 mm, respectively, were calculated using the modified Rowe-Booker equation (eq. 1; Rowe & Fan 2021, 2022). The ratio of observed leakage (Table 1) relative to the predicted leakage for the three tailings examined herein was generally within 10% (Figure 4), illustrating the suitability of the modified Rowe-Booker equation. Thus, the modified Rowe-Booker equation gives good predictions for a range of hole diameters and tailings.
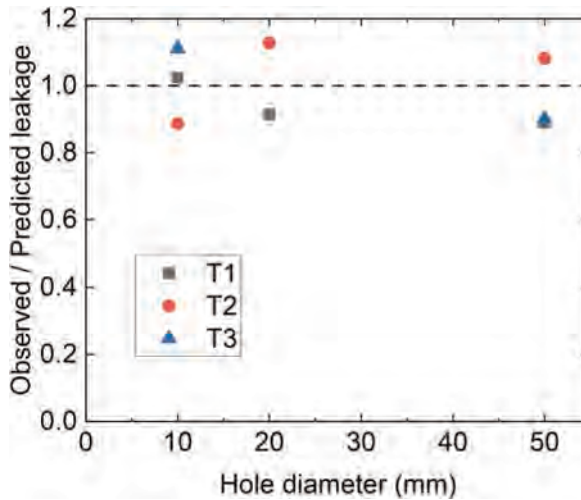
Figure 4.   Comparison of the observed and predicted leakage for ranges of hole sizes and tailings types showing a good prediction of the proposed analytical equation.

4   SUMMARY AND CONCLUSIONS

Experiments were conducted to quantify leakage through GMB holes from the overlying three different tailings with fines content of 90%, 30%, and 20%. The influence of fines content on leakage was examined. For the specific conditions and materials examined, the following conclusions were reached:

(1) Leakage through GMB hole was highly dependent on the fines content. There was a notable drop in leakage if increasing fines content from 20% to 30%, but the drop was less significant for an increase in fines content from 30% to 90%. A feasible way of minimizing leakage could be to place the tailings slurry with high fines content first prior the placement of low fines content tailings.
(2) Placing tailings with fines content $\geq$ 30% directly above the GMB was sufficient for minimizing leakage and piping potential for the cases examined.
(3) The modified Rowe-Booker equation gave a good prediction for leakage through circular GMB hole with a range of hole diameters and tailings types examined.

REFERENCES

Badu-Tweneboah, K., and Giroud, J. P. (2018). Discussion of "Leakage through Holes in Geomembranes below Saturated Tailings" by R. Kerry Rowe, Prabeen Joshi, RWI Brachman, and H. McLeod. *Journal of Geotechnical and Geoenvironmental Engineering*, 144(4), 07018001.
Fan, J. Y., and Rowe, R. K. (2022a). Seepage Through a Circular Geomembrane Hole When Covered by Fine-grained Tailings under Filter Incompatible Conditions. *Canadian Geotechnical Journal*, 59(3), 410–423.
Fan, J. Y., and Rowe, R. K. (2022b). Piping of Silty sand Tailings through a Circular Geomembrane Hole. *Geotextiles and Geomembranes*, 50(1), 183–196.
Fan, J. Y., and Rowe, R. K. (2022c). Effect of Subgrade on Tensile Strains in a Geomembrane for Tailings Storage Applications. *Canadian Geotechnical Journal*, 60(1), 18–30.
Fan, J. Y., and Rowe, R. K. (2023). Effect of Subgrade on Leakage Through a Defective Geomembrane Seam Below Saturated Tailings. *Geotextiles and Geomembranes*, 51(2), 360–369.

Fan, J. Y., Rowe, R. K., and Brachman, R. W. I. (2022). Compressibility and Permeability of Sand-silt Tailings Mixtures. *Canadian Geotechnical Journal*, 59(8), 1348–1357.

Foster, M., and Fell, R. (2001). Assessing Embankment Dam Filters that do not Satisfy Design Criteria. *Journal of Geotechnical and Geoenvironmental Engineering*, 127(5), 398–407.

Giroud, J. P. (2016). Leakage Control using Geomembrane Liners. *Soils and Rocks*, 39(3), 213–235.

Giroud, J. P., and Bonaparte, R. (1989a). Leakage through Liners Constructed with Geomembranes—part I. Geomembrane Liners. *Geotextiles and Geomembranes*, 8(1), 27–67.

Giroud, J. P., and Bonaparte, R. (1989b). Leakage through Liners Constructed with Geomembranes—Part II. Composite Liners. *Geotextiles and Geomembranes*, 8(2), 71–111.

Lopes, R., Bahia, R., Jefferies, M., and Oliveira, M. (2013). Paste deposition over an existing subaqueous slurry deposit of high sulphide content tailings–the Neves Corvo Experience. In *Proceedings of the 16th International Seminar on Paste and Thickened Tailings*, Australian Centre for Geomechanics, Perth.

Lupo, J. F., and Morrison, K. F. (2007). Geosynthetic Design and Construction Approaches in the Mining Industry. *Geotextiles and Geomembranes*, 25(2), 96–108.

Rowe, R. K. (1998). Geosynthetics and the Minimization of Contaminant Migration through Barrier Systems Beneath Solid Waste. *In Proceedings 6th International Conference on Geosynthetics*, Atlanta 1, 27–103.

Rowe, R. K. (2005). Long-term Performance of Contaminant Barrier Systems. *Geotechnique*, 55(9), 631–678.

Rowe, R. K. (2012). Short and Long-term Leakage through Composite Liners. *Canadian Geotechnical Journal*, 49(2), 141–169.

Rowe, R. K. (2020). Protecting the Environment with Geosynthetics: 53rd Karl Terzaghi Lecture. *Journal of Geotechnical and Geoenvironmental Engineering*, 146(9), 04020081.

Rowe, R. K. and Booker, J. R. (2000). Theoretical Solutions for Calculating Leakage Through Composite Liner Systems. Developments in Theoretical Geomechanics: *Proceedings of The John Booker Memorial Symposium*, Sydney, pp. 580–602.

Rowe, R. K., and Fan, J. Y. (2021). Effect of Geomembrane Hole Geometry on Leakage Overlain by Saturated Tailings. *Geotextiles and Geomembranes*, 49(6), 1506–1518.

Rowe, R. K., and Fan, J. Y. (2022). A General Solution for Leakage Through Geomembrane Defects Overlain by Saturated Tailings and Underlain by Highly Permeable Subgrade. *Geotextiles and Geomembranes*, 50(4), 694–707.

Rowe, R.K. and Jefferis, S. (2022). Protecting the Environment from Contamination with Barrier Systems: Advances and Challenges, State-of-the-Art Lecture, *Proceedings of the 20th International Conference on Soil Mechanics and Geotechnical Engineering*, Sydney, Australia, pp187–293.

Rowe, R. K., Brachman, R. W. I., Irfan, H., Smith, M. E., and Thiel, R. (2013). Effect of Underliner on Geomembrane Strains in Heap Leach Applications. *Geotextiles and Geomembranes*, 40, 37–47.

Rowe, R. K., Joshi, P., Brachman, R. W. I., and McLeod, H. (2017). Leakage through Holes in Geomembranes below Saturated Tailings. *Journal of Geotechnical and Geoenvironmental Engineering*, 143(2), 04016099.

Touze-Foltz, N., Lupo, J., and Barroso, M. (2008). Geoenvironmental Applications of Geosynthetics. Keynote Lecture, *Proceedings Eurogeo*, 4, 98.

Leaks detection of earthwork dam with geomembrane lining system by an active technique using optic fibers

G. Stoltz, S. Nicaise, L. Peyras & N. Chaouch
INRAE, Aix Marseille Univ, RECOVER, Aix-en-Provence, France

C. Guidoux & M. Boucher
GeophyConsult, Chambéry, France

ABSTRACT: This article presents the development of an active optical fiber device to address the issue of leak detection, and to allow operators to monitor the performance and safety of mountain reservoirs sealed with geomembrane lining systems. The device includes a fiber integrated into the geomembrane lining system and devices to heat and auscultate the fiber. The results shown that the active method has been successfully applied in a representative INRAE demonstrator. In particular, it has been shown that the technique is capable of locating without false positives or negatives a leak with a flow rate greater than or equal to 0.05 l/s and placed upstream of the optical fiber.

1 INTRODUCTION

The performance of geomembranes for sealing hydraulic structures such as basins or reservoirs no longer needs to be demonstrated. However, despite the robustness of geomembranes, the presence of leaks through them is possible. From some assumptions about frequency of holes per square meters, Giroud and Bonaparte (1989) gave some assessments about the leakage rates through a geomembrane liner. These leaks may appear during the construction of the hydraulic structure or during the service phase of the hydraulic structure. Leaks from construction work may be due to welding defects or damage to the geomembrane. They can be drastically avoided by a rigorous quality assurance construction program and by applying weld quality control methods (vacuum bell method, pressurizing the central channel method, etc.) and electrical leak detection methods such as the use of the water lance method/water puddle method electric broom (Müller 2007; Touze *et al.* 2021). During the operation phase of the structure, leaks may appear due to the application of static loads by puncturing aggregates in contact with the geomembrane (below or above it), or else by the application of dynamic loads (eg a falling block) on an exposed geomembrane. In the case of an exposed geomembrane, the location of a leak can be done visually (if the basin is empty) or with an electrical geophysical method (if the basin is filled). In the case of a geomembrane covered with a layer of granular materials, the detection and location of a leak that appeared during the service phase of a basin is less obvious by the methods mentioned above. However, there are basins for which it is important to detect and locate a leak very quickly to ensure safe use of the structure. This is for example the case of altitude reservoirs which are the type of structure targeted by the study of this article.

Hill or altitude reservoirs are hydraulic works mainly dedicated to the production of artificial snow (main purpose of altitude reservoirs) and / or intended for irrigation (main purpose of hill reservoirs). Other applications are possible such as the production of

hydroelectric power, the supply of drinking water, as well as for the practice of leisure fishing. The storage capacity of altitude reservoirs is variable, ranging from modest capacities (less than 20,000 m^3) to significant capacities for altitude structures (greater than 150,000 m^3). The RISBA project (2013 - 2015), "Risks of high altitude dams", has shown that the majority of recent or planned reservoirs have an average capacity of around 100,000 m^3 (Boutry *et al.* 2014). In France, the height of the embankments (i.e. the difference between the crest and the natural terrain) of the altitude reservoirs is between a few meters up to a maximum of 19.95 m, which, compared to their storage capacity, theoretically corresponds to administrative classes C and D. In Italy, in the Aosta Valley, almost all these types of structures have backfill heights comprised between 10 m and 15 m. Even if the size of the altitude reservoirs is modest compared to large dams, given the severe meteorological conditions in winter at an altitude above 1800 m (Peyras & Meyriaux 2009) and their potential impact in the event of failure, these structures are frequently administratively upgraded (transition from theoretical class C to class B).

Regarding the design of the altitude reservoirs, with the exception of the oldest ones, the majority of these structures have a geomembrane lining system (GLS). In addition to the geomembrane which ensures the waterproofing function, this type of device comprises several layers each providing one or more functions such as the support structure (on which the geomembrane is set and having functions of protection and drainage of the geomembrane) and the structure protection, overlying the geomembrane, which has a role of protecting the geomembrane against external mechanical stresses. A full description of GLS can be found in Peyras & Meyriaux (2009).

In general, the presence of a leak in the structures described above is detrimental and, in extreme cases, can seriously affect the stability of the structure. Thus, to ensure the stability and ensure the durability of the structure over the long term, any leak must be located and repaired. In the case of a covered geomembrane, generally by a multi-decimetric granular layer, the presence of a leak is dramatic because it is necessary to remove the entire layer of aggregates to access the geomembrane and perform the visual inspection and reparation. It is then obvious that this operation is long and potentially detrimental for the geomembrane because the machine which will remove the granular cover layer can itself damage the geomembrane again.

In this context, a specific action on the development of a simple and robust method for locating leaks was carried out within the framework of action WP3.4.1 of the European research project Interreg Alcotra called RESBA, "resilience of dams d 'altitude', started in 2017 and bringing together French partners (INRAE and the University of Savoie Mont Blanc) and Italian partners (Piedmont and Aosta Valley region, Polytechnic School of Turin). This action consisted of testing the active method by optical fiber, in an optimal configuration for this type of structure. Although the method is already operational (for example Guidoux *et al.* 2019 tested successfully a close method on a concrete experiment dam), there are currently no altitude reservoirs equipped with such a device. This observation can be explained by several possible reasons: lack of knowledge of the technique by the administrator of altitude reservoirs, absence of a demonstrator at the site level, negative prejudice concerning the difficulty of transport and the cost linked to the heating generator to take away in mountainous context, etc.

To demonstrate the performance of the method under conditions close to a real structure, the method was implemented through geophyConsult on the experimental basin of the INRAE site in Aix-en-Provence. Three main questions were particularly investigated:

– What is the minimum (heating) power to be supplied for optimum leak detection?
– What is the minimum leakage rate detected for minimum heating energy? This question is particularly linked on the one hand to the detection criterion, i.e. the temperature difference which can only be explained by the presence of an anomaly (i.e. a leak), and, on the other hand, at the distance of the leak relatively to the positioning of the optical fiber;
– Is the system as efficient in hot period (summer) as in cold period (winter)?

2 BACKGROUND OF THE ACTIVE METHOD BY OPTICAL FIBER

2.1 *The active method*

From the first leak detection experiments using fiber optic temperature measurements carried out from 1995, it appeared that the visualization of raw measurements only usually did not allow to identify leaks correctly. Indeed, many factors other than leaks influence the temperature of a soil: the geological nature of the soil, the relative position of the fiber with respect to the air or the upstream reservoir, or even the proximity of crossing structures. The development of methods for analyzing temperature data by optical fiber therefore quickly turned out to be a major challenge in making this technology operational.

The active method or Heat Pulse Method (HPM) Dornstadter J. & Heinemann (2010) is mainly used in cases where the optical fiber must be installed in an environment whose temperature is directly influenced by the water in the reservoir (even with no leakage). It refers to the realization and use of temperature measurements within an optical cable installed near the reservoir and previously heated by the Joule effect using electrically powered copper wires (see Figure 1).

Figure 1.   Optical cable used for the active method.

The needed electrical power - typically 5 to 10 W/m - depends on the conductivity of the soil, the heating time and the aimed temperature increase. In the presence of a leak in the vicinity of the cable, the convection generated by the flow will cause a lower rise in the temperature of the cable (see Figure 2).
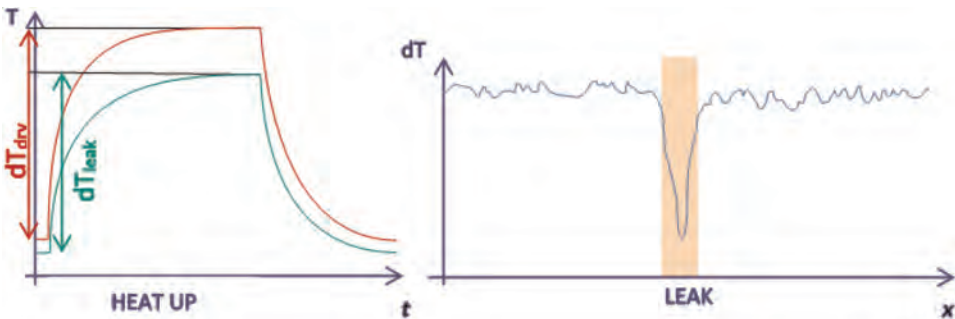
Figure 2.   HPM principle.

2.2 Interpretation and outcomes

The interpretation of the measurements is based on the comparison of the measured values of dT with a reference value of dTREF. Through calibration tests in the laboratory or on site with controlled leaks (Perzlmaier 2007), it is possible to quantify the flow velocity for a range of Darcy's velocities between 10^{-5} and 10^{-3} m/s. The leak detection radius around the optical cable using this method is often less than for passive approaches, in the range of 15 to 20 cm. The means required for heating make this method more difficult to operate on measurement lengths of ten kilometers or more.

As some technical parameters may vary from one heating to another (the injected electrical power, the heating time, the evolution of the outside temperatures), the raw dT profiles are systematically readjusted, by adjusting their average and their standard deviation to those of a reference measurement. The dT values of a given heating are then subtracted from the dT_{REF} values recorded at the same positions during the reference heating. A measurement is thus obtained at any point of the cable which is strictly speaking the detection parameter of the active method, to which a detection threshold depending on the field conditions (spatial variability characteristic of the cable used) is applied. This methodology is called SACRE (as for Surveillance Active par "Centrage et Réduction avec Etat-zéro" in French, Active Monitoring by Centering and Reducing with Reference-State).

3 MATERIAL AND METHOD

3.1 Design and realization of the experimental basin

For the experiments, a basin already existing at INRAE's site of Aix-en-Provence was completely redesigned in order to fit the topic of the research (Figure 3). The embankment delimiting the basin is 23m long and 10m wide; it is made of local clay, which Plasticity Index is 17 and hydraulic conductivity is 10^{-9}m.s^{-1}. The dike is 2.5m high, so the water head is about 2m.

In 2019, we added a new GLS to the structure: first, a Draintube® drainage geocomposite made up of mini-drains with a diameter of 20mm spaced 2m apart is installed directly on the
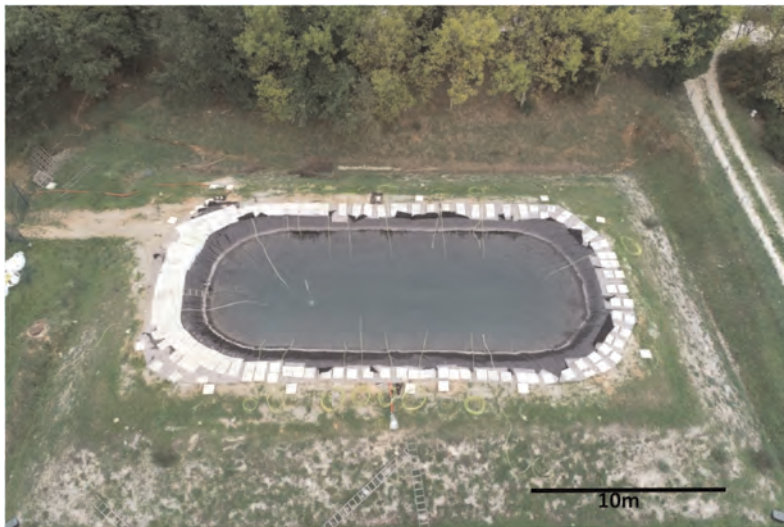
Figure 3.   View of the experimental basin.

soil; drains are parallel to the slope and connected to a central gravel drain that allows evacuating water supplied by the leaks. Then, a 1mm thick polypropylene geomembrane placed above the geocomposite ensures the waterproofness.

Fourteen artificial leaks cross the geomembrane and bring water between the two geo-synthetics; water is collected by the mini-drains. Each leak is connected to the water supply through a garden hose; water is directly pumped into the basin to have the same temperature as the basin water. The leaks reproduce the potential geomembrane damages, and are located on the basin in order to study the influence of sun exposure and their relative position to the mini-drains. Sensors and valves are used to control and measure pressure and flow rate of the leakage water.

3.2 Instrumentation of the basin

The purpose of this basin is to process real-scale measurements with controlled conditions. Therefore, we have installed a large panel of instrumentation inside out of the embankment (Figure 4).

3.2.1 The leaks

The leaks are part of the instrumentation and the reservoir is composed of fourteen leaks. Each leak is connected to a garden hose and pierce artificially the geomembrane (Figure 5). Water from the basin supplies directly the leaks using a pump (Lowara BGM9). The leaks allowed the water to pass through the geomembrane, then the water will be collected by a mini-drain in the Draintube® drainage geocomposite and led down to the bottom of the basin.

Leaks are spread through the surface of the basin in order to study the influence of the sun exposure and their relative position to mini-drains.

3.2.2 The actives optical fiber

The optical fiber is composed of a measurement cable and a compact optical interrogator device (Sensornet Oryx). During the second campaign, this interrogator was kindly loaned by EDF through geophyConsult. In this experiment, the optical fiber is associated with few copper cables rolled along the length of the cable (Figure 1). The copper cables were used to heat up the optical fiber; this combination, which allows the fiber to contrast clearly with its environment, is called the active optical fiber. The electrical power injected during the heating operations was recorded with an energy consumption meter (Voltcraft Energy Logger 4000F), placed upstream of the heating device.
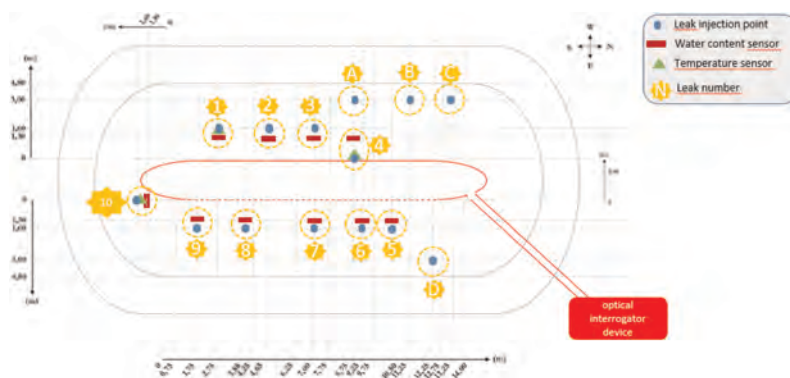

Figure 4.   Instrumentation plan, view of the basin from above.

Figure 5.   Leaks insertion system.

During the measurement campaigns, the active optical fiber was used as a temperature sensor with a spatial resolution of 1 m and a 5 minutes acquisition frequency. The active optical fiber is located at the bottom of the basin under the drainage geocomposite (Figures 4 & 6).

The detection of a leak by the optical fiber corresponds to a calculation of the temperature difference measured in the vicinity of the optical fiber in the absence of a leak with that measured in the presence of the leak. This parameter is denoted ΔdT. The criterion for detecting a leak, corresponding to a measured thermal anomaly, was set at 0.3°C. For the purpose of quantification, the detection intensity (°C.m) is calculated, which corresponds to the area under the curve ΔdT along the linear optic fiber.

Figure 6.   Localization of the active optical fiber.

3.2.3   *Measured and controlled parameters*
Temperature and water content probes located downstream of the leaks (Figure 4) are used to confirm fiber optic measurements. Three temperature sensors (Probe 107 Campbell Scientific) were used to measure the temperature of the water near the leaks (Figure 4).

Ten water content probes (CS650 Campbell Scientific) were installed to detect the water streaming down from each leak. A CR1000 data acquisition system (Campbell Scientific) recorded the set of data from temperature and water content under a 1-minute acquisition frequency.

The incoming pressure (Jumo Dtrans p30 type 404366 sensor) and the flowrate (Kobold MIK 5NA 55 E L443 sensor) of each leak are controlled with a valve placed upstream and recorded during the experiments with a USB-6001 data acquisition card (National Instrument).

3.3 *Experimental campaign*

The experimental basin was subjected to two experimental campaigns of 5 days of measurements: the first was carried out from October 11 to 21, 2019 and the second from February 10 to 14, 2020. The objective of these two campaigns was on the one hand to test the performance of the device during two periods when the outside temperatures are different and, on the other hand, test the robustness of the device over time, on the scale of a research project. During the injection campaigns, five injection flow rates (0.005 - 0.01 - 0.02 - 0.05 - 0.1 l/s), 5 heating powers (2 - 4 - 6 - 8 - 10 W/ml) and three distances injection point - heating cable (0 - 1.6 - 3.0 m) were tested. Each of the heating powers has been the subject of a reference measurement, that is to say a measurement of temperature rise in the vicinity of the optical fiber and the heating cable, in the absence of leaks.

4   RESULTS AND DISCUSSION

It has been shown that all the leaks with a flow rate greater than or equal to 0.05 l/s and placed upstream of the optical fiber at the base of the backfill have all been detected. With the detection criterion of $0.3°C$, and with a heating power greater than or equal to 4 W/m, no false positives were detected.

No significant impact of heating power on leak detectability was observed. In other words, a leak detected with a power of 8 W/m was also detected with a power of 2 W/m. However, the use of a low power induced false positives caused by the too low temperature contrast induced by the heating. Consequently, a minimum power of 4 W / m is recommended.

Increasing detection intensities were observed with the injected flow rates (Figure 7). At equivalent flow rate, the detection intensities decrease if the distance between the leak and the measurement cable increases, in line with the fact that the leakage speed decreases along
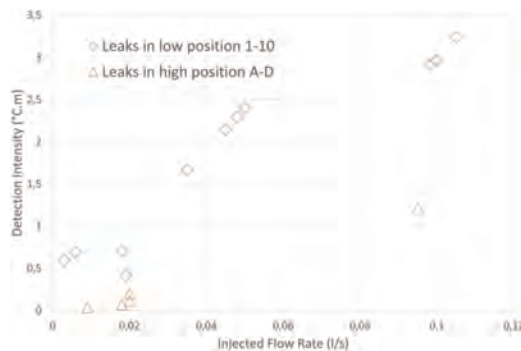

Figure 7.   Detection intensity as a function of the injected flow rate.

the propagation of the leak (diffusion in the drainage geocomposite). Thus, on a real site, it is recommended to install optical fibers at several sides of the basin, with a spacing which will depend on the desired level of leak detectability.

5 CONCLUSION

The purpose of this article was to implement a method for locating and detecting leak in GLS via an optical fiber positioned just under the geomembrane. In the fiber optic cable is integrated a copper cable to heat the environment close to the fiber. This heating makes it possible to create a thermal contrast and to evaluate more precisely the zones of leaks compared to all the normal zones, that is to say without leaks. This device finds all its interest in critical basins, as is the case for high-altitude reservoirs. This device has been successfully applied in a representative INRAE demonstrator.

It has been shown that the technique can locate without false positives or negatives a leak with a flow rate greater than or equal to 0.05 l/s and placed upstream of the optical fiber. However, as the level of leak detectability depends on the distance between the leak and the optical fiber, the sizing of the optical fiber network to be positioned in the structure will be a key step in the performance of the device.

ACKNOWLEDGMENT

REFERENCES

Boutry M. Risba, *Rapport Final, Action 2.1*, 65 p, 2014.

Dornstadter J. & Heinemann B. 2010. In situ Detection of Internal Erosion. In 8th ICOLD European Club Dam Symposium, *Proc. intern. symp.*, Innsbruck, DATE 2010.

Giroud J.P. & Bonaparte R. 1989. Leakage through Liners Constructed with Geomembranes – Part 1. Geomembranes Liners. *Geotextiles and Geomambranes* 8. 27–67.

Guidoux, C., Boucher, M, Pinettes, P., Courivaud, J.-R. & Tronel F. 2019. Experimental Validation of the Ability of Fibre Optics to Detect and Locate Leaks and Seepages below Waterproofing Systems of Dams or Water Reservoirs. *11th ICOLD European Club Symposium*.

Müller W. 2007 *HDPE Geomembranes in Geotechnics*. Springer, pp 485.

Perzlmaier S., *Verteilte Filtergeschwindigkeitsmessung in Staudämmen*. Thèse de doctorat, TU München, Munich, 2007.

Peyras L. & Meriaux P., Retenues d'altitude. *Quae*. 352 p, 2009.

Touze N. Stoltz G. Peyras L. Chapter 16. Containment Ponds, Reservoirs and Canals. *ICE Handbook of Geosynthetic Engineering: Geosynthetics and their Applications*, Third edition. Under the direction of Sanjay Kumar Shukla.

Research for defining the design parameters for a family of reinforced geomats for erosion control on river/channel banks

P. Rimoldi
Civil Engineering Consultant, Milan, Italy

P. Bianchini
Maccaferri Innovation Center, Bolzano, Italy

M. Scotto
Officine Maccaferri SpA, Bologna, Italy

F. Trovato
Maccaferri Innovation Center, Bolzano, Italy

ABSTRACT: The paper presents the results of tests on a family of products for erosion control on river/channel banks: geomats reinforced with double twisted steel wire meshes or with polypropylene geogrids; and reinforced geomats combined with geocontainer mattresses. The allowable resistant shear stress and allowable water velocity have been evaluated by testing in a flume according to ASTM D6460. Two different experimental campaigns have been carried out, to evaluate the performance of products both in unvegetated and vegetated conditions, both at short and at long flow duration. The analysis of test results allowed to define the surface of allowable shear stress vs the elapsed time t (years) from installation and the duration of flow D (hours). The procedure for getting the design curves of allowable shear stress vs flow duration at different times t is illustrated. The obtained charts allow the design according to the principles set in ISO 18228-8.

1 INTRODUCTION

Erosion on river/channel banks is produced by the shear stresses applied by the stream. The water flow produces shear stresses on bottom and side banks, proportional to water depth and velocity. Shear stresses can produce erosion by removing soil particles and excavating progressively deeper into the channel bottom and sides, which can be protected by lining with specific geosynthetics.

According to ISO 18228-8, the design and selection of geosynthetics for protecting river/channel banks require performance tests, in unvegetated and vegetated configuration, to assess the limit values of water velocity and shear stress. The paper aims to present the results of tests on a family of erosion control products: geomats reinforced with double twisted steel wire meshes or with polypropylene geogrid; and reinforced geomats combined with geocontainer mattresses. The obtained charts allow the design according to the principles set in ISO 18228-8.

2 TESTED PRODUCTS

The research involved two families of erosion control products for protection of river and channel banks: Maccaferri Macmat-R are three-dimensional erosion control geomats

composed of UV stabilized synthetic fibres extruded either onto a double twisted steel wire mesh or a Polypropylene (PP) geogrid, as shown in Figure 1, left and centre.

Maccaferri Reno Mattresses Plus are units manufactured from double twisted hexagonal woven steel wire mesh, made of PoliMac®-coated and Galmac-coated steel wire (Figure 1, right). The base, diaphragms, side and ends of each unit are manufactured from one continuous panel of mesh. The base is folded onto itself at regular intervals to form double diaphragms that are secured with spirals at the production facility. To ensure better packing of the fill and improve the hydraulic performances of the mattresses, the units are supplied together with vertical ties (X-Ties) connecting the base panel to the lid and to be installed on the site. The geocontainer mattresses, available with height h of 17, 23, 30 cm, are filled with stones at the project site to form flexible and permeable, monolithic structures. Maccaferri Macmat-R and Maccaferri Reno Mattresses Plus are even combined to form the Maccaferri Combo Reno Mattresses Plus, shown in Figure 2, where Macmat R is placed as the top lid of Reno Mattresses Plus.

Figure 1.   Maccaferri Macmat-R geomats reinforced with double twisted steel wire mesh (left) or a polypropylene (PP) geogrid (centre); Maccaferri Reno Mattresses Plus (right).
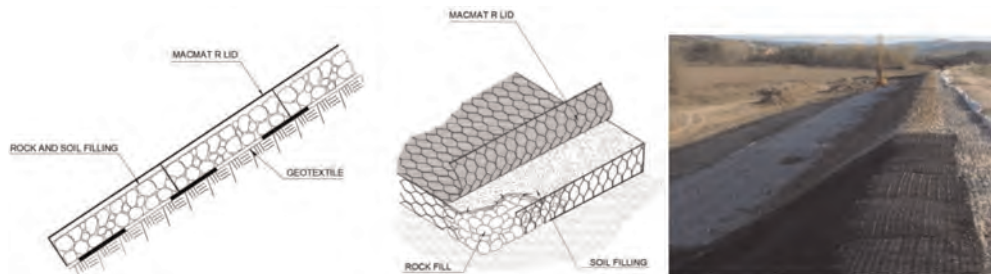
Figure 2.   Maccaferri combo Reno Mattresses Plus.

3   EFFECTS OF VEGETATION

A significant number of studies, both field and simulated studies, demonstrated that vegetation coverage effectively reduces water-induced soil erosion.

The general goal of geosynthetics for erosion control is to protect the soil from erosion, either indefinitely or until vegetation can establish itself.

Permanent erosion control and revegetation mats (PERMs) provide erosion control, aid in vegetative growth, and eventually become entangled with the vegetation to provide reinforcement to the root system. It is evident that the best performance in erosion control on river / channel banks can be achieved when the vegetation root system is reinforced by a specifically engineered geosynthetic, like a reinforced geomat, installed as a turf reinforcement mat (TRM).

The erosion control geosynthetic shall afford protection and reinforcement of the vegetation root system immediately after installation, while being open enough to allow the robust growth of vegetation within few weeks.

4 ALLOWABLE RESISTANT SHEAR STRESS

The allowable resistant shear stress τ_{all} of reinforced geomats can be evaluated by testing in a flume according to ASTM D6460.

Tests on different products and different conditions were carried out at the Utah State University (UTAH) in the years 1995 and 1996, before the ASTM D6460 test protocol was published.

Tests were run until either 60 hours or critical conditions (excessive erosion or sudden geomat failure), but with no pre-defined failure criterion.

In the years 2019 - 2020 a new research program was carried out at Colorado State University at Fort Collins (CSU).

Table 1 highlights the products tested at UTAH and at CSU.

Figure 3 shows the comparison of vegetation growth at different stages within the same product.

Table 1. Products tested at UTAH and at CSU.

Research	Product	Weight (g/m^2)	Thickness (mm)	Void Index (-)	Geomat Geometry
Utah (1996)	Macmat R/6	550	10	> 90 %	Random
CSU (2020)	Macmat R1 6822G0	450 ± 30	16 ± 4 (at 2 kPa)	> 90 %	Random
Utah (1996)	Macmat 10 / 20	550 / 650	10 / 20	> 90 %	Regular (biconic)
CSU (2020)	Macmat R1 05rs	400 ± 30	15 ± 2 (at 2 kPa)	> 90 %	Random
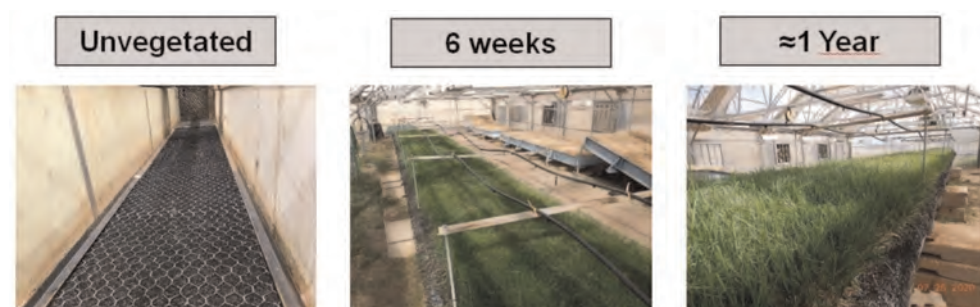
Figure 3. Pictures of Macmat 6822G0 at different vegetation growth in the CSU testing program.

5 TEST PROCEDURE AND RESULTS

5.1 *Test conducted by Colorado State University*

Test conducted by Colorado State University between 2019 and 2020 both on unvegetated and vegetated MacMat-R afforded the following results:

– Full revegetation was obtained in only 6 weeks.
– In 6 weeks the performances (Limit shear strength and Limit Velocity) reached what traditional erosion control solutions achieve in 1 year.
– 6th week performance achieved 60 % of 1 year measured performance.

The performance of geosynthetics in erosion control on river / channel banks depend on two main factors:

– The development of vegetation, which is increasing along the elapsed time t (years) from installation;
– The duration of flow D (hours): the performance is decreasing at increasing flow duration.

Figure 4 qualitatively shows the dependence of the allowable shear stress from the time t and the flow duration D. The surface in Figure 4 can be cut with a plane parallel to the time t axis, thus obtaining the chart of the allowable shear stress vs the flow duration D at a given time t, that is isochronous curves, as shown in Figure 4; if the surface is cut with a plane parallel to the flow duration D axis, then the chart of the allowable shear stress vs the time t for a given flow duration D, that is isoflood curves, is obtained, as shown in Figure 4.

To increase the shear resistance in unvegetated conditions a biotextile (BTX) can be placed below the Macmat-R, but it was noted that the BTX improves the performance only at t = 0.

5.2 *The importance of light penetration*

It is important to note that Maccaferri Macmat R affords a very open structure of the geomat (hence with high light penetration and void index), which allows a very fast vegetation growth in comparison with other products with a dense structure (hence with small light penetration and void index): therefore the allowable shear stress τ – time t – flow duration D surface for Maccaferri Macmat R is above the surface for denser products after few weeks of vegetation time t, as shown schematically in Figures 4 and 5, which clearly show that a lower light penetration (for denser products) would allow a higher performance only at t = 0, while a higher light penetration (for Macmat R) affords a higher performance over time.
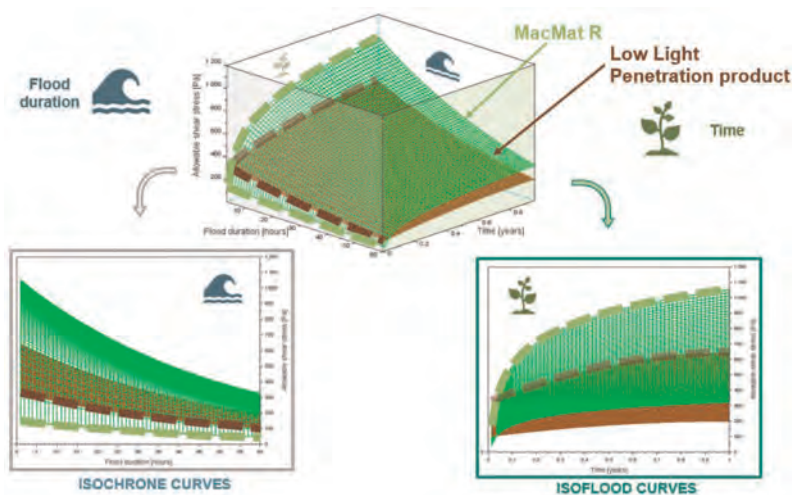
Figure 4. 3-D pattern of the allowable shear stress vs the time t and the flow duration D, from which isochronous curves and isoflood curves are derived.
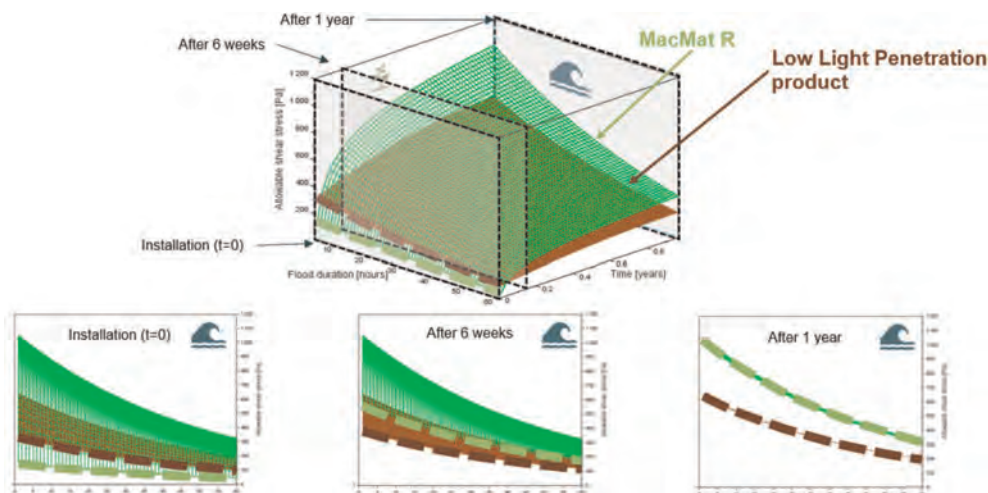
Figure 5. Effect of light penetration on the performance of vegetated reinforced geomats on channel banks.

5.3 *Analysis and results*

The procedure for getting the design curve of allowable shear stress vs flow duration in unvegetated and vegetated conditions is the following (see Figure 6):

– Step 0: get the experimental curve of allowable shear stress vs flow duration in vegetated and unvegetated conditions. An exponential regression line is interpolated from the experimental results (UTAH) in vegetated condition up to 60 h flow duration, and the performance at 1 hour (for vegetated conditions) or to 0.5 hours (for unvegetated conditions) is derived. These ones represent the experimental curves of allowable shear stress τ_{all} vs flow duration.
– Step 1: get the characteristic curve in vegetated and unvegetated conditions. Due to the different test protocol, a conversion coefficient Cc needs to be computed as the ratio between the limit shear stress for 1 hour flow duration (for vegetated conditions) or to 0.5 hours (for unvegetated conditions) at UTAH and the actual value obtained at CSU:

$$Cc_{vegetated} = 1296\ Pa\ /\ 1053\ Pa\ =\ 1.23 \tag{1}$$

$$Cc_{unvegetated} = 794\ Pa\ /\ 140\ Pa\ =\ 5.67 \tag{2}$$

This allows the trend up to 60 hours (observed at UTAH) to be extended also to tests at CSU, thus obtaining the characteristic curves of allowable shear stress τ_{all} vs flow duration in vegetated and unvegetated conditions. The characteristic curves are unfactored, hence these curves shall be considered as the reference performance of geomats (vegetated and unvegetated).
– Step 2: get the design curves in vegetated conditions. An overall Reduction Factor ($RF_{tot,veg}$), with values ranging from 1.30 to 3.0, according to ISO/TR 18228-8, is applied to the characteristic curve (obtained at Step 1) to obtain the design curves. The applied value of $RF_{tot,veg}$ defines the design area (see Figure 6, where $RF_{tot,veg} = 2.3$ has been evaluated as applicable).

It has to be noted that the difference in experimental results between Macmat 6822G0 (reinforced with double twisted steel mesh) and Macmat R105 (reinforced with

polypropylene geogrid) can be considered as negligible. Therefore, the design curves in Figure 6 apply both to Macmat 6822G0 and Macmat R105.

Moreover, the analysis of a large number of tests (over 60 test certificates were compared) performed on geomats according to ASTM D6460 with vegetation at 6 weeks growth stage provides statistical evidence that the performance at 6 weeks is equal to 60 % of the performance at 1 year vegetation growth (which can be considered as the fully vegetated stage), in agreement also with the pattern shown in Figures 4 and 5.
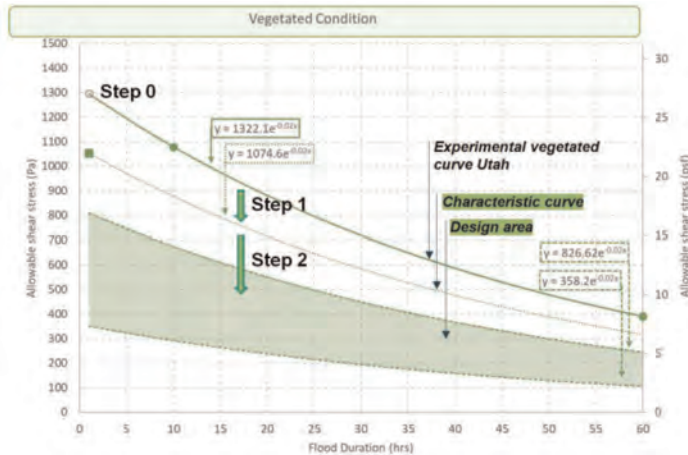
Figure 6.   Experimental, characteristic, and design curves of allowable shear stress vs flow duration in vegetated condition.

Therefore, if required, the allowable shear stress of Maccaferri Macmat R with vegetation at 6 weeks growth stage, $\tau_{all,\ 6\ weeks}$, can be conservatively evaluated by applying a Reduction Factor $RF_{6\ weeks} = 1.67$ to the allowable shear stress at 1 year vegetation growth, $\tau_{all,\ 1\ year}$, from Figure 6.

The chart of allowable shear stress vs flow duration can therefore be used to get the conditions of unvegetated MacMat R, Macmat R at 6 weeks vegetation, and Macmat R at 1 year vegetation.

The allowable velocities of Maccaferri Macmat R reinforced geomats have been obtained from the same tests in a flume according to ASTM D6460. Table 2 provides the limit velocity V_{all} for Maccaferri Macmat R erosion control products.

5.4   Extension to Maccaferri Combo Reno Mattresses Plus

Based on the same tests in the flume according to ASTM D6460, the design areas for Reno Mattresses Plus 30, 23, 17 have been obtained, as shown in Figure 7. Being mattresses filled with stones, such design areas have to be considered in unvegetated conditions.

As said, Maccaferri Combo Reno Mattresses Plus (Figure 2) are made up by the combination of Maccaferri Macmat R and Maccaferri Reno Mattresses Plus.

Hence the performance of Maccaferri Combo Reno Mattresses Plus can be evaluated also in the vegetated conditions, by simply applying the superposition of effects between the performance of Macmat R in vegetated conditions (from Figure 6) with the performance of Maccaferri Reno Mattresses Plus, as shown in the design chart in Figure 7.

Table 2. Limit velocity V_{all} for Maccaferri erosion control products.

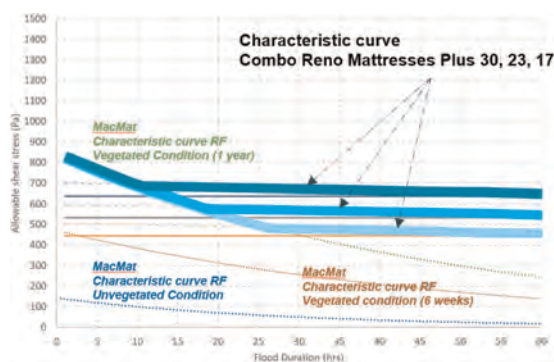| Sample ID:	Macmat R16822G0	Macmat R105rs	Macmat R16822G0 +BTX	Mamat R16822G0	Units
Limit velocity	3.22 0.98	3.47 1.06	> 30 > 10	> 28.02 > 8.54	ft/s m/s

Figure 7. Design chart for Maccaferri Reno Mattresses Plus.

6 CONCLUSIONS

The results of tests on a family of erosion control products have been illustrated: geomats reinforced with double twisted steel wire meshes or with polypropylene geogrid; and reinforced geomats combined with geocontainer mattresses.

Two different experimental campaigns have been carried out, in order to evaluate the performance of products both in unvegetated and vegetated conditions, both at short and at long flow duration. The allowable resistant shear stress and allowable water velocity have been evaluated by testing in a flume according to ASTM D6460.

The analysis of test results allowed to define the surface of allowable shear stress vs the elapsed time t (years) from installation and the duration of flow D (hours). This surface can be cut with a plane parallel to the time axis, obtaining the chart of allowable shear stress vs flow duration at given time t; or cut with a plane parallel to flow duration axis, obtaining the chart of allowable shear stress vs time for a given flow duration.

The procedure for getting the design curves of allowable shear stress vs flow duration at different times t from the 3-D surface has been illustrated.

The obtained charts allow the design according to the principles set in ISO 18228-8.

REFERENCES

ASTM D6460. Standard Test Method for Determination of Rolled Erosion Control Products in Protecting Earth Channels from Stormwater-Induced Erosion. *ASTM International*, West Conshohocken, PA, USA.
ISO 18228-8. Design using Geosynthetics - Part 8: Surface Erosion Control. *ISO*, Geneve, Switzerland.

Hydraulic performance and degradation of geotextile tube in sediment dewatering: A remediation study

M.A. Aparicio-Ardila
São Carlos School of Engineering (EESC), University of São Paulo (USP), São Carlos, Brazil
Nortene Group, São Paulo, Brazil

L.P. Sabogal-Paz & J. Lins da Silva
São Carlos School of Engineering (EESC), University of São Paulo (USP), São Carlos, Brazil

ABSTRACT: Geotextile tubes are a technology used in different sectors, such as water supply and sanitation, mainly in the final stage, to dewater the sludge generated in wastewater and water treatment plants. This paper presents geotextile tubes at the beginning of the water supply system (i.e. catchment). This paper shows a large-scale remediation project that used geotextile tube dewatering technology to desand the stream where part of the water catchment of São Carlos city – (São Paulo, Brazil) is carried out. This paper aims to present the system's hydraulic performance and the geotextile degradation. The effluent quality throughout the operation was monitored. Granulometric distribution at different heights of the filter cake is presented to better understand the deposition of particles inside the geotextile tube during the dewatering process. Decreases were observed in the geotextile's tensile strength and permittivity properties after application.

1 INTRODUCTION

The process of inadequately occupying urban watersheds can cause surface erosion and siltation in water bodies due to the accumulation of sediments. Among the consequences of silting up water bodies is a reduction in the volume of water, shortages in the water supply and intensification of floods. Dredging is the most common form of environmental remediation for sediment accumulation (Lawson 2008). Geotextile tubes filled with dredged material provide an innovative and cost-effective alternative to traditional techniques due to their simplicity and flexibility. These structures can even be used for erosion prevention due to their stability against erosive forces (Fowler *et al*. 1994).

Geotextile tubes are manufactured from geotextiles with high tenacity, durability and small pore openings. Geotextile tubes are made with reinforced seams, forming permeable structures with the property of draining the material with which it is filled. Sludge dewatering application using geotextile tubes were first used in the 1990s. The general dewatering process using geotextile tubes comprises three steps: containment, dewatering and consolidation (Lawson 2008). The containment step involves pumping the waste into the geotextile tube. In the dewatering stage, a geotextile tube can receive several filling cycles. After the system reaches the maximum height stipulated in the design (first filling), the system loses water through forced filtration, drainage and evaporation (Müller 2018). It should be noted that after the first filling cycle, the maximum height of the system is no longer reached.

The performance of geotextile tubes depends on an extensive source of variables that can be classified a priori as hydraulic, mechanical and durability. Heilman *et al*. (2003) state that

trial and error is a common design method in projects with geotextile tubes, as the known design methods do not fully represent the complexity of the systems.

For geotextile tubes, Leshchinsky *et al.* (1996) highlight the use of four safety factors: factors related to creep over time; seam resistance; installation damage; and durability. Validating the sizing methods found in the literature for geotextile tubes, and determining appropriate safety factors, requires carrying out full-scale tests. This is due to the fact that in these tests, significant differences are observed regarding the requests imposed on the geotextile (Silva *et al.* 2021).

The present study presents the hydraulic performance of a geotextile tube installed to desand the Monjolinho stream, part of the water catchment of São Carlos city – (São Paulo, Brazil). Geotextile samples were collected at the end of the service life to assess its degradation. Sediment samples were also collected at the consolidation phase for geotechnical analysis. The main aim of this study is to provide information that contributes to understanding the geotextile tube's behavior in sediments dewatering applications. Moreover, this study investigates the deposition of sediment particles inside the geotextile tube during the dewatering and consolidation process.

2 METHODOLOGY

2.1 *Study area*

The city of São Carlos, in the state of São Paulo – Brazil, is supplied by surface sources (Monjolinho and Ribeirão do Feijão stream) and ground sources from 28 deep wells that draw water from the Guarani aquifer. At the water treatment plant, 35.3 million m^3 of water is produced, where 16% of the water comes from surface catchment from the Monjolinho stream. Problems in the drinking water supply operation resulting from the sediment transport of the Monjolinho stream forced the rapid execution of a remediation project. A geotextile tube was used for desanding the stream. Geotextile tubes are a technology widely used in the sanitation sector, known for their ease of installation and efficiency in dewatering. Figure 1 shows the location where the geotextile tube was installed.

Figure 1.   Geotextile tube location (21°59'11.85''S; 47°52'32.14''W).

2.2 *Materials*

The geotextile tube was manufactured from woven polypropylene geotextile, with the following characteristics: apparent opening of 0.343 mm, tensile resistance in the machine direction (MD) of 78.2 kN/m, and 106.5 kN/m in the cross direction (CD). The geotextile

tube meets Sabesp's technical specification (NTS 301 2015), which establishes reference values for the dewatering application. The geotextile tube (Figure 2) was 10 m wide and 15 m long with a maximum height of 2.3 m (indicated by the manufacturer). The tube was installed on a dewatering platform, consisting of a High-Density Polyethylene geomembrane (1.00mm), and a draining geocomposite with a double layer of 200 g/m^2 nonwoven geotextile. The draining geocomposite was used to replace the layer of gravel and the layer of nonwoven geotextile of 300 g/m^2 suggested in the NTS 301 (2015). The stream sediments were pumped into the tube with a pump of 100 m^3/h. The percolate from the tube was returned to the stream through a channel. A Parshall gutter was installed in the channel to measure the outflow (Figure 2). The sediments had a specific gravity of 2.74 g/cm^3 and a grain size distribution of 88.8% sand, 4.9% silt, and 6.3% clay.

Figure 2.   Geotextile tube.

2.3   *Monitoring*

The percolate quality was monitored over the dewatering time, periodic collections were carried out, and turbidity was measured, as shown in Figure 3a. In this study, the dewatering phase was completed prematurely due to problems with pump availability. In the Consolidation phase, 17 days after the last filling, geotextile and sediment samples were collected (Figure 3b). A reference sediment sample was collected directly from the stream bed. Specific gravity and granulometry tests were performed on each sediment sample. Tensile strength tests, seam strength tests and permittivity tests were carried out on the exhumed geotextile according to ISO 10319 (2015), ISO 10321 (2008) and ASTM D 4491 (2020), respectively.

Figure 3.   Sample collection. a) percolated collection, and equipment used for turbidity measurement. b) geotextile exhumation and sediment sampling.

3 RESULTS AND DISCUSSION

3.1 Hydraulic performance

Monitoring was carried out for approximately 110 consecutive days. However, due to problems with the pump operation, only fillings were carried out for 56 days. During this period, approximately 156 m³ of sediments were stored. Moreover, a maximum height of 1.40 m was reached at the central point of the tube (39% lower than the expected height). The inlet flow was measured using an ultrasonic meter, and it was observed that the pump worked at a maximum of 70% of its capacity. The decrease in pump flow may be associated with the presence of the sediment that forced the flow's transport. Due to the limited availability of the ultrasonic flow meter, only readings were taken during three periods, and the recorded values "Measurements" are presented in the graph in Figure 4. The maximum output flow, measured in the Parshall flume, was 40 m³/h.
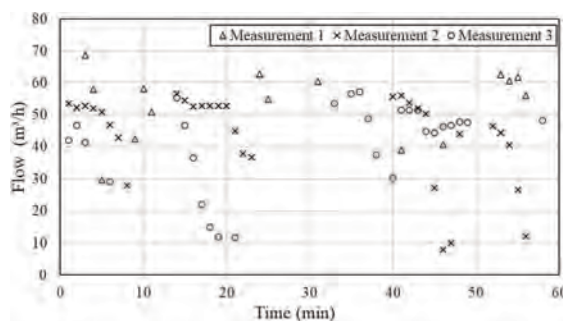
Figure 4.   Inlet flow measurements performed at different periods.

The importance of compatibility between the pump capacity and the volume available inside the geotextile tube can be observed. In this remediation project, the tube dimensions were selected according to the expected storage volume (offered by the manufacturer), and the pump capacity was not verified. This indicates that the design was made according to trial and error, as Heilman *et al.* (2003) mentioned.

3.2 Sediment distribution

The specific gravity was 2.57 g/cm³, 2.70 g/cm³ and 2.68 g/cm³ for the bottom, center and top samples (Figure 3b), respectively. Figure 5 presents the granulometric distribution of the samples collected at the bottom, center and top of the Geotextile tube and the reference sample. It can be observed that the curves of the bottom and top samples showed similar behavior with percentages in the sand fraction close to 50%. In the granulometric curve of the center, it can be observed that the fraction of sand was higher, close to 77%.

Figure 5 shows that the reference sample collected directly from the stream bed does not represent the material dredged by the pump, which had high variability. The sediments pumped to the geotextile tube were pumped directly from the stream, involving operational variations such as suction height and stream dynamics affected by environmental conditions (rain and wind).

For this specific study, a sedimentation pattern cannot be identified, as the pumped material was not homogeneous. It did not come from an equalization tank. The granulometric distribution in the different heights of the geotextile tube depended on the pump
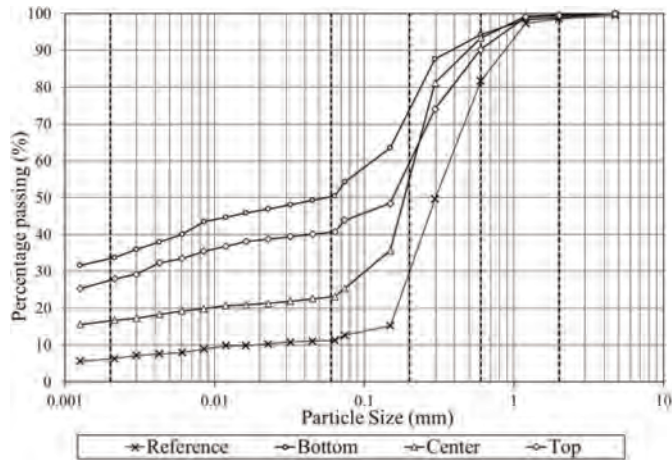
Figure 5.   Particle size distribution curve of the sediment samples.

operation, which explains the different granulometric distributions in the three analyzed points (bottom, center and top).

Turbidity is an indirect measure of the amount of sediment/particles passing through the geotextile tube (Aparicio-Ardila *et al*. 2020). During the monitoring, it was observed that the turbidity after dewatering decreased, ranging from 600-700 NTU (Nephelometric Turbidity Units) values to 200-300 NTU. This indicates that the water returned to the stream (percolated) had a better quality.

3.3   Degradation

Table 1 presents the geotextile tube property results after the dewatering application. As expected, a decrease can be observed in all the properties in the exhumed sample compared to the virgin one, in which the exhumed sample was exposed for 110 days. After exposure, this behavior was observed in other applications where the geotextiles were exposed to the weather conditions, such as Carneiro *et al*. (2018) in marine environments, Aparicio-Ardila *et al*. (2021a) in the application of erosion control and Aparicio-Ardila *et al*. (2021b) in weathering panels.

Table 1.   Geotextile virgin and exhumed properties and variation regarding the virgin sample.

Properties	Test Method	Virgin	Exhumed	Variation (%)
Tensile strength per unit CD (kN/m)	ISO 10319 (2015)	106.5	95.2	10.6
Tensile strength per unit MD (kN/m)	ISO 10319 (2015)	78.2	73.8	5.6
Seam tensile strength CD (kN/m)	ISO 10321 (2008)	75.5	52.86	30.0
Permittivity (s^{-1})	ASTM D 4491 (2020)	0.35	0.27	22.9

The mechanical degradation measured by the tensile strength of the geotextile and the seam showed a more significant decrease in the resistance of the seam indicating the importance of the quality of the seam for the dewatering application. Another essential characteristic evaluated was the hydraulic performance, measured by the permittivity. Permittivity presented a more significant decrease when compared in percentage terms with the resistance of the geotextile.

4 CONCLUSION

A trial-and-error process is not a design method. Using geotextile tube technology requires preliminary planning and testing to take advantage of the application's potential fully. Despite the operational limits for the execution of the presented environmental remediation project, the technology contributed to the solution of the operational problem in the catchment and returned water with better quality to the stream. Identifying a sedimentation pattern is impossible when the pumped material is not homogeneous.

REFERENCES

Aparicio-Ardila, M. A. A., Souza, S. T., Silva, J. L., Valentin, C. A., Dantas, A. D. B., 2020. Geotextile Tube Dewatering Performance Assessment: An Experimental Study of Sludge Dewatering Generated at a Water Treatment Plant. *Sustainability*, 12, No.19, 8129.

Aparicio-Ardila, M. A., dos Santos Junior, R. D., Kobelnik, M., Aparecido Valentin, C., Silva Schliewe, M., Teixeira Coelho, A., da Luz, M.P., 2021a. Semi-Rigid Erosion Control Techniques with Geotextiles Applied to Reservoir Margins in Hydroelectric Power Plants, Brazil, *Water*. https://doi.org/10.3390/w13040500

Aparicio-Ardila, M. A., Pedroso, G. O. M., Kobelnik, M., Valentin, C. A., da Luz, M. P., Lins da Silva, J., 2021b. Evaluating the Degradation of a Nonwoven Polypropylene Geotextile Exposed to Natural Weathering for 3 Years. *International Journal of Geosynthetics and Ground Engineering*, 7(3), 1–11.

ASTM D4491, 2020. *Standard Test Methods for Water Permeability of Geotextiles by Permittivity*. ASTM International, West Conshohocken, PA, USA.

Carneiro, J. R., Morais, M., de Lurdes Lopes, M., 2018. Degradation of Polypropylene Geotextiles with Different Chemical Stabilisations in Marine Environments. *Construction and Building Materials*, 165, 877–886.

Folwler, J., Sprague, C.J., Toups, D., Engler, R.M., 1994. *Dredged Material-filled Geotextile Containers, Environmental Effects of Dredging Technical Notes*. U. S. Army Engineer, Waterways Experiment Station, Vicksburg, MS.

Heilman, D.J., Hauske, G.J., Melby, J.A., 2003. Advances in Geotextile Tube Technology, in: CoastalStructures 2003: *Proceedings of the Conference*. Portland, Oregon, USA, pp. 1001–1012.

ISO 10319, 2015. *Geosynthetics — Wide-width Tensile Test. International Organization for Standardization*, Geneva, Switzerland.

ISO 10321, 2008. *Geosynthetics — Tensile Test for Joints/seams by Wide-width Strip Method*. International Organization for Standardization, Geneva, Switzerland.

Lawson, C. R., 2008. Geotextile Containment for Hydraulic and Environmental Engineering. *Geosynthetics International*, 15, No. 6, 384–427.

Leshchinsky, D., Leshchinsky, O., Ling, H.I., Gilbert, P.A., 1996. Geosynthetic Tubes for Confining Pressurized Slurry: Some Design Aspects. *J. Geotech. Eng*. 122, 682–690.

Müller, M., 2018. Efeito de Diferentes Configurações no Deságue de Lodos Em Sistemas de Confinamento de Resíduos em Geotêxtil. Instituto Tecnológico de Aeronáutica. (in portuguese)

SABESP - NTS 301, 2015. *Saco Geotêxtil Para Desaguamento de Lodo*. Norma Técnica SABESP, São Paulo, Brasil (*in portuguese*)

Silva, V.L., Almeida, M.G.G., Pimentel, K.C.A., 2021. Numerical Modelling of Geotextile Tubes Filled with Gold Mine Tailings. *Geosynth. Int*. 28, 574–583.

Durability of exposed PVC-P geomembranes used for rehabilitating the upstream face of dams

D. Cazzuffi
CESI S.p.A., Milan, Italy

D. Gioffrè
Department of Civil Engineering and Architecture, University of Pavia, Italy

ABSTRACT: This contribution presents the recent results of an ongoing research on the long-term behaviour of a PVC-P geomembranes installed on the upstream face of masonry and concrete dams. In the last 30 years, starting from sometime after the dam rehabilitation with this type of geosynthetics, the exposed PVC-P geomembrane were sampled periodically and tested in laboratory. Material properties measured at the laboratory were compared with the ones obtained from test on virgin samples, when available. The sampled geomembranes have been subjected to physical and mechanical tests and the results interpreted with reference to the variation of plasticizer, tensile characteristics, foldability at low temperatures, and specific mass. In particular, the decrease in plasticizer content resulted in a slightly increase of the geomembrane rigidity, i.e. higher modulus and tensile strength and lower strain at failure. The experimental program allowed to study the evolution of the properties of the geomembrane over the years enabling the assessment of the residual life of exposed geomembranes installed on the upstream face of dams.

1 INTRODUCTION

Geomembrane systems are one of the most sustainable rehabilitation technologies for dams. Geosynthetic barriers have been used as alternative solutions not only to mitigate the deterioration processes in existing dams, but also to prevent the onset of seepage-induced degradation in new dams, and as the main hydraulic barrier, particularly for embankment dams, in cases where low-hydraulic conductivity soils are not readily available (Cazzuffi 1987).

The use of geosynthetics as water barriers is one of the numerous uses of geosynthetics in hydraulic and geotechnical applications of geosynthetics. The use of geosynthetics in dams represents a major application of the geosynthetics since "dams have a particular status due to their impact on the environment and on safety", as pointed out by Heibaum *et al*. (2006).

While the concept of using geomembranes in dams instead of conventional "low permeable" materials (e.g. clay, cement concrete (hereafter simply called concrete) or bituminous concrete) derived, among other considerations, from the successful use of geomembranes in canals and reservoirs, the credibility of synthetic materials in dams had been established by the good performance of embedded PVC waterstops in a very large number of concrete dams worldwide. In those dams, waterstops play an essential role in preventing water seepage through joints that are indispensable to accommodate concrete expansion and contraction. A geomembrane placed on the upstream face of a dam or inside a dam can be considered,

from a conceptual viewpoint, as one wide waterstop sealed at the abutments and at the bottom of a dam.

The most pioneering applications of PVC-P geomembranes, employed to rehabilitate concrete and masonry dams, were in the alpine regions in Europe, at more than 1500 m elevation. In particular, this contribution focuses on eight large concrete and masonry dams, all in the Italian Alps, that were rehabilitated with this technology in the 1980s and 1990s. In all of these dams, the PVC-P geomembrane was left exposed to the environment, which is quite demanding at such elevation in terms of resistance to UV rays, freeze-thaw cycles, extremely low temperatures, and high daily and seasonal temperature variations.

The rehabilitation of dams consisted in the application of a geocomposite on the upstream face. This geocomposite was formed by a geomembrane layer, placed externally and having a barrier function, and by a geotextile layer, placed internally with a mechanical protection and drainage function. The geocomposite usually covers the entire upstream face of the dam and the most common installation method consists of vertical strips of about 2.00 m wide, fixed to the dams by means of batten strips held by anchor bolts (Scuero & Vaschetti 1996). The geotextile component protects the geomembrane from the mechanical damage caused by irregularities in the dam upstream face; it also contributes to reduce the creeping or sagging of the geomembrane along the quasi-vertical dam face.

In this paper, PVC-P geomembranes installed on the upstream face of dams are evaluated using results of a wide experimental campaign still ongoing (Cazzuffi & Gioffrè 2018; Cazzuffi & Gioffrè 2021a). The results of the experimental tests carried out on samples retrieved directly at site integrated the data obtained in the research and contributed to monitor the variation over time of the characteristics of the PVC-P geomembranes in service; moreover, the additional tests presented here helped to confirm the methodology already employed in (Cazzuffi & Gioffrè 2021b) to predict the lifetime of the geomembrane.

2   LONG-TERM BEHAVIOUR OF GEOMEMBRANES IN DAMS

The durability of geomembranes is based on their weathering properties, and on their resistance to specific loads during service, such as extreme temperatures, frost, freeze/thaw, ice, impacts by floating debris and boats, wind and waves, fauna and flora, vandalism etc. (Hsuan *et al.* 2008).

Not all geomembranes have the same behavior due to their different chemistry, basic ingredients, and manufacturing process; For these reasons it is important when considering dam projects to either select an existing geomembrane or to design a new one that can best perform according to the type of environment in which it will be used, and that can provide an adequate durability for the required application.

The behavior in service of geomembranes is commonly predicted using standard accelerated ageing tests. However, these tests, although accelerated, still require too much time for providing an effective indication on the long-term behavior of geomembranes.

The most practical way to ascertain if a geomembrane will resist to the environmental loads expected in a dam project in the long term, is to retrieve samples of the same type of geomembrane already in service in a similar environment , for a period of time that should be as long as possible, ideally as long as the required service life of the geomembrane in the considered dam. Tests are then performed on these samples to determine to which extent their properties have changed during service. Testing of the physical and mechanical properties of the exhumed samples indicates if the geomembrane properties at the time of the test are within acceptable limits, and extrapolation allows the determination of the expected remaining service life. This approach has been adopted in Italy (Cazzuffi 1987; Cazzuffi & Gioffrè 2020, 2021b), using data from several concrete and masonry dams rehabilitated with exposed PVC-P composite geomembranes.

3 REHABILITATION OF CONCRETE AND MASONRY DAMS

The analysis of the long-term behaviour of the geomembranes presented in this paper has been conducted studying the performance of several samples of geomembranes, installed in the '80s and '90s, and retrieved from the upstream face of eight large concrete or masonry dams in the Italian Alps (Cazzuffi 1996; Cazzuffi *et al.* 2010; Scuero & Vaschetti 2009, 2017), where most of the pioneering applications of PVC-P geomembranes to rehabilitate concrete dams were located.

The dams considered (Figure 1) were built in the '30s (only one in the '50s) and are characterized by several common features, so that it is possible to make some considerations that are acceptable for all of them. It is important to highlight that these areas are characterized by a very changeable weather, responsible for sudden changes in temperature, with consequent heat loads which play an important role in the durability of the dam and its materials.

Figure 1. Location map of the dams considered in the paper.

For all these 8 dams, the PVC-P geomembrane was left exposed to the environment, which at such elevation is quite demanding in terms of resistance to UV rays, freeze-thaw cycles, extremely low temperatures, and high–daily and seasonal–temperature excursions.

Between 1980 and 2000, all of the upstream faces of the 8 dams here considered were rehabilitated with the application of a geosynthetic layer in order to restore their initial watertightness.

The rehabilitation was performed by installing an exposed two-layers composite geomembrane, formed by: i) a plasticized polyvinyl chloride (PVC-P) geomembrane; ii) a polyester (PET) or polypropylene (PP) needle-punched nonwoven geotextile. In just one case an extra layer of high-density polyethylene (HDPE) geonet was added. Given its very low coefficient of permeability, the geomembrane was installed to ensure the barrier function of the upstream face.

The geotextile layer was installed to fulfill two main functions:: i) anti-puncturing function, through the regularization of the surface on which the geomembrane is laid down; ii) drainage function, as it avoids the accumulation of water between the geomembrane and the dam face; this happens as a result of the generation of a high-transmissivity plane which allows water to flow by gravity into a special collector.

In all of the cases presented here, the geomembrane is always coupled with another geosynthetic; therefore in the following we will refer to the entire waterproofing system as composite geomembrane, as this is the layer providing the barrier function we want to analyze in this paper.

4 EVALUATION OF THE RESIDUAL LIFE OF EXPOSED GEOMEMBRANES

In order to evaluate the variation over time of the characteristics of the PVC-P geomembranes installed on the eight dams here considered, a good number of samples have been taken after the geomembrane application and all of them have been subjected to the same type of tests.

Samples were retrieved both above and below the water table level and in different parts of the upstream face, with the aim of studying the different behaviour of the same geomembrane under different conditions of exposure.

When determining the life expectancy of a geomembrane it is important to identify the more critical portion of the upstream face, as the first failure will affect negatively the whole waterproofing system. Therefore, here we present the results of the tests made on samples taken above the water level, as this is the area which suffers most from the direct exposure to atmospheric agents. The results obtained are thus referred to as the worst case scenarios for each geomembrane and this helped us to conduct a precautionary analysis of the geomembrane durability.

All the samples taken from the dams upstream faces have been tested at the Geosynthetics Laboratory of CESI S.p.A. in Milano, Italy. These tests allowed the comparison among different samples during the degradation process of the geomembranes. The cases of Camposecco and Ceresole Reale are particularly significant, as for these dams the test results on virgin samples are available. The analyses conducted for these cases are, therefore, more valuable as the knowledge of the materials initial condition allows the reconstruction of the entire life behaviour of the geomembrane.

Before the tests, samples were prepared by separating the geotextile layer from the geomembrane. Only the tests made on the geomembrane layer (Table 1) will be discussed in the following.

Table 1.   Laboratory tests and reference standards.

Test	Reference standard
Plasticizer extraction	EN ISO 6427
Nominal thickness	EN 1849-2
Volumic mass	EN ISO 1183-1
Hardness (Shore A)	EN ISO 868
Cold flexibility	EN 495-5
Dimensional stability	EN 1107-2
Tensile properties	EN ISO 527-3

The results obtained show a constant small decrease of the plasticizers' content (Figure 2a), while temperature of cold flexibility rises with time; moreover, dimensional stability grows longitudinally and declines transversally in the years.

Mechanical parameters show that the geomembrane get stiffer over time (Figure 2b), with a growth of tensile strength and a reduction of the correspondent strain, both in the longitudinal and in the transversal direction.

Long-term performance of PVC-P geomembranes depends on several aspects referred to exposure environment and polymer and additive formulations. The service life of PVC-P geomembranes can be predicted based on experimental results. Through a careful monitoring of the variation over time of the characteristics of the PVC-P geomembranes in service, it was possible to define a methodology of lifetime prediction for the geomembrane installed in dams when the results on virgin samples are available. In particular, the plasticizer content plays a fundamental role in terms of variation in physical properties of the PVC-P geomembranes (Giroud 1995; Giroud & Tisinger 1993).

In order to evaluate the most critical service life of the PVC-P geomembrane, two approaches can be used: (1) the curve of plasticizer content versus time is extrapolated until the end-of-service-life plasticizer content is reached; or (2) the plasticizer content data points are converted into plasticizer loss ratio data points and the curve of plasticizer loss ratio versus time is extrapolated until the extrapolated plasticizer loss ratio is equal to end-of-service-life criterion expressed in terms of plasticizer loss ratio.

Giroud (2021) proposes, for the end-of-service-life criterion, a plasticizer content value of 17.5% for PVC-P composite geomembranes bonded to a nonwoven needle-punched geotextile (which are the most frequently used in the considered dams). This value was based on laboratory tests (Luciani *et al.* 2019, 2020) and on data collected from monitored structures,

According to approach (1), which used the curve of plasticizer content versus time, Figure 3a and Figure 3b show the lifetime assessment of exposed PVC-P geomembranes for Ceresole Reale and Camposesso dams, respectively.Vertical lines in Figure 3a and 3b show that the lifetime assessment of the exposed geomembranes for Ceresole Reale dam and Camposecco dam, assuming a linear decrease of plasticizer loss ratio over time, are approximately 42 years and 48.5 years in terms of plasticizer content criterion, respectively.
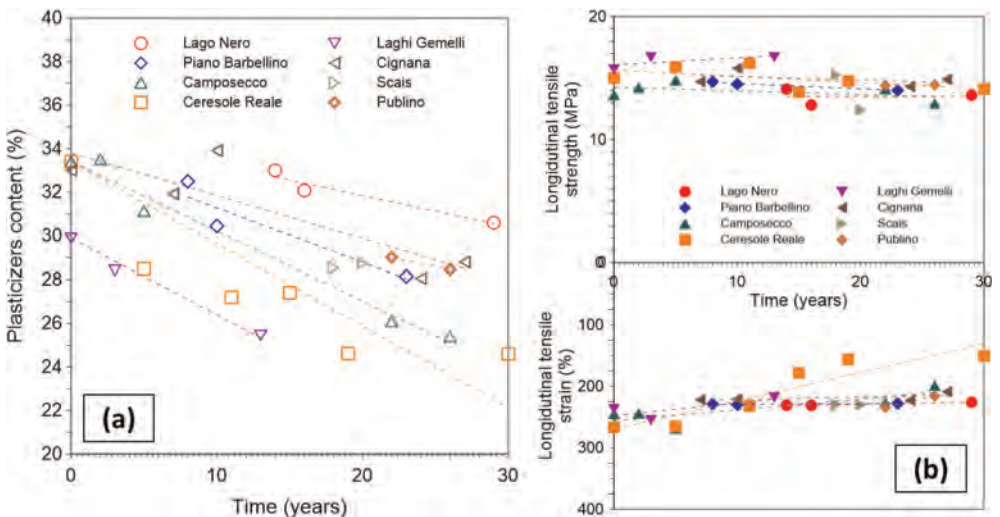
Figure 2. Test results: (a) Plasticizers content vs time; (b) Longitudinal tensile strength and strain vs time.
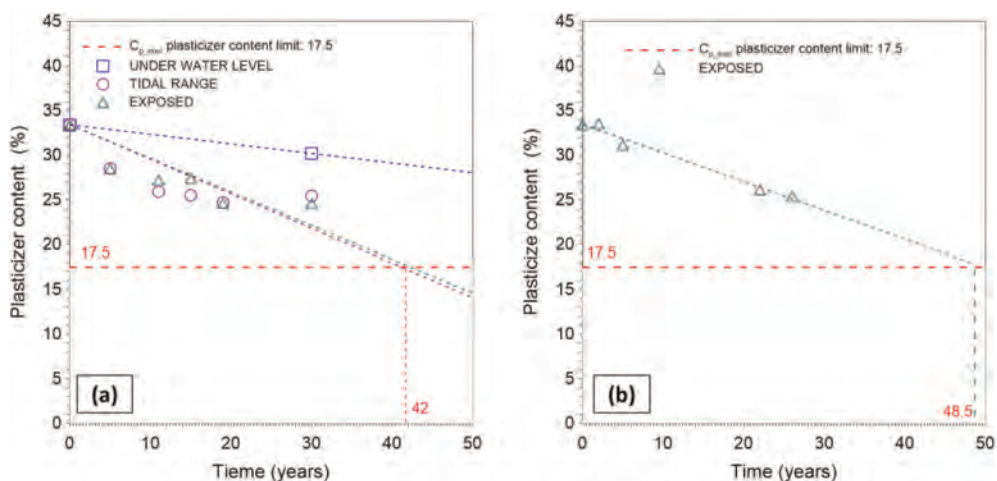
Figure 3. Lifetime assessment of exposed PVC-P geomembranes: (a) Ceresole Reale dam; (b) Camposecco dam.

5 CONCLUSIONS

The range of possible applications of geomembranes as water barriers in dams is quite wide. In fact, geomembranes can be applied to all types of dams, either in new construction or for in rehabilitation, both in dry conditions or underwater.

Long-term behaviour of a PVC-P geomembranes installed on the upstream face of masonry and concrete dams have been discussed in this paper, particularly in dams where test results on virgin samples are available.

Data on the performance of dams rehabilitated using geomembranes have been provided. These data show a remarkable performance of composite geomembranes in dams, even when the geomembrane component is exposed to atmospheric agents.

REFERENCES

Cazzuffi, D. 1987. The Use of Geomembranes in Italian Dams. *Water Power and Dam Construction*, vol. 39: 17–21.

Cazzuffi, D. 1996. Réhabilitation de Barrages en Maçonnerie ou en Béton à l'aide de Géomembranes: l'expérience Italienne-*CFGB-CFG, Les Géotextiles et le Géomembranes dans les barrages*, Colloque Technique, Paris, France: 14.1–14.12.

Cazzuffi, D. and Gioffrè, D. 2018. Long-time Behavior of Exposed Geomembranes Used for the Upstream Face Rehabilitation of Concrete and Masonry Dams. *11th International Conference on Geosynthetics ICG 2018*, 2: 1441–1448.

Cazzuffi, D. and Gioffrè, D. 2020. Lifetime Assessment of Exposed PVC-P Geomembranes Installed on Italian Dams. *Geotextiles and Geomembranes*, 48(2): 130–136.

Cazzuffi, D. and Gioffrè, D. 2021a. Performance of Geomembranes Exposed to Extreme Weather Conditions on High- Elevation Dams on the Alps. *Geotechnical Special Publication November (GSP 328)*: 56–67.

Cazzuffi, D. and Gioffrè, D. 2021b. Reply to the discussion by Giroud on Lifetime assessment of exposed PVC-P geomembranes installed on Italian dams. *Geotextiles and Geomembranes*, 49(5): 1449–1450.

Cazzuffi, D., Giroud, J.P., Scuero, A. and Vaschetti, G. 2010. Geosynthetic Barriers Systems for Dams. Keynote Lecture, *Proceedings of the 9th International Conference on Geosynthetics*, Guaruja, Brazil, Vol. 1: 115–163.

Giroud, J.P. 1995. Evaluation of PVC Geomembrane Shrinkage Due to Plasticizer Loss. *Geosynthetics International, Special Issue on Design of Geomembrane Applications*, 2 (6): 1099–1113.

Giroud, J.P. 2021. Discussion on "Lifetime Assessment of Exposed PVC-P Geomembranes Installed on Italian Dams" by D. Cazzuffi and D. Gioffrè. Geotextiles and Geomembranes.

Giroud, J.P. and Tisinger, L.G. 1993. The Influence of Plasticizers on the Performance of PVC Geomembranes. *Proceedings of the 7th Symposium of the Geosynthetic Research Institute*, Koerner, R.M. & Wilson-Fahmy, R.F., Eds., Philadelphia, PA, USA: 169–196.

Heibaum, M., Fourie, A., Girard, H., Karunaratne, G. P., Lafleur, J. and Palmeira, E. M. 2006. Hydraulic Applications of Geosynthetics. *Proceedings 7th International Conference on Geosynthetics*, Yokohama, Japan: 79–120.

Hsuan, Y.G., Schroeder, H.F., Rowe, R.K., Müller, W., Greenwood, J., Cazzuffi, D. and Koerner, R.M. 2008. Long-term Performance and Lifetime Prediction of Geosynthetics. Keynote lecture, *Proceedings of the 4th European Geosynthetics Conference EuroGeo 4*, Edinburgh, UK.

Luciani, A., Todaro, C., Martinelli, D., Carigi, A. and Peila, D. 2019 Long-term Durability Analysis and Lifetime Prediction of PVC Waterproofing Membranes. *Proceedings of the WTC 2019. Press*/Balkema, C. (ed.). Napoli, Italy.

Luciani, A., Todaro, C., Martinelli, D. and Peila, D. 2020. Long-term Durability Assessment of PVC-P Waterproofing Geomembranes through Laboratory Tests. *Tunneling and Underground Space Technology*, Volume 103.

Scuero, A. M. and Vaschetti, G. L. 1996. Geomembranes for Masonry and Concrete Dams: State-of-the-Art Report. *Proc. Geosynthetics Applications, Design and Construction*: 889–898.

Scuero, A.M.., and Vaschetti, G. 2009. Use of Geomembranes for New Construction and Rehabilitation of Hydraulic Structures, Keynote Lecture, *Workshop on Advanced Methods and Materials for Dam Construction*. Skopje, Firom .

Scuero, A. and Vaschetti, G. 2017. Geomembrane Sealing Systems for Dams: ICOLD Bulletin 135. *Innovative Infrastructure Solutions*, Springer: 2–29.

Innovative materials and technologies

An experimental way of the quantification of the confinement effect in the mechanically stabilized layer by measuring horizontal pressures generated by static load

L. Horníček
Faculty of Civil Engineering, Czech Technical University in Prague, Prague, Czech Republic

Z. Rakowski & J. Kawalec
Tensar International, s.r.o., Cesky Tesin, Czech Republic

K. Zamara
Tensar International Limited, Blackburn, UK

ABSTRACT: Four laboratory models filled with aggregates with fractions 0–32 mm were prepared in a special laboratory box with dimensions of 1000 x 1000 x 600 mm. Three models were fitted with a geogrid, which, together with the aggregates, formed a mechanically stabilized layer (MSL), 100, 150 and 200 mm in thickness, while one model, without a geogrid, served as a reference model. A new-generation – multiaxial – geogrid was used for the experiments. The models were loaded with a static force of up to 100 kN with the aim of finding out the differences in the magnitude of lateral pressures acting on the laboratory box wall. The experiments revealed principal reductions in the horizontal pressures in the mechanically stabilized layer compared to non-stabilized aggregates. The greatest reductions were recorded at the geogrid level, nevertheless, a significant reduction in horizontal pressures is manifested throughout the entire MSL. The intensity of the aggregate confinement in the geogrid is related to the reduction in horizontal pressures and quantified as a parameter enabling the evaluation of the efficiency of mechanical stabilization of aggregates by geogrids – the Confinement Efficiency Factor (CEF).

1 INTRODUCTION

A mechanically stabilized layer is formed as a result of the interaction of a stiff geogrid with aggregates. The aggregate grains penetrate into the geogrid holes leaning against its ribs thus causing their mutual interlocking. The grains confined in the holes are strongly immobilized. As a result, the whole layer shows considerably higher stiffening that the original aggregates and is mechanically stabilized. Byun *et al.* 2018 and Lees & Clausen (2019) assumed that the aggregates confined in the geogrid behave as a composite with qualitatively different mechanical properties compared to individual used components (geogrid and aggregates). The mechanical stabilization mechanism of aggregates by a geogrid has been characterised in professional literature, e.g. Rakowski & Kawalec (2009) and Horníček & Rakowski (2017). The quantification of the mechanical confinement effect, however, still remains an open question.

The paper focuses on the quantification of this confinement effect on the basis of conducted laboratory experiments involving the monitoring of horizontal pressures exerted by

aggregates onto the laboratory box wall. The comparison of the horizontal pressures detected in the mechanically stabilized layer with a variable geogrid position versus non-stabilized aggregates allowed deriving the factor indirectly quantifying the aggregate confinement intensity in the geogrid.

A new generation of stiff monolithic geogrids labelled multiaxial geogrids was first used in the experiments.

2 EQUIPMENT AND STRUCTURE OF LABORATORY MODELS

2.1 *Description of models*

A universal laboratory box with dimensions 1000x1000x800 mm where the backfill height reached 500–600 mm was used for the laboratory modelling (Figure 1). Four models marked M–0 to M-III (Figure 2) were designed and assembled. All models contained a compacted layer of aggregates (crushed stone mixture) with fractions 0–32 mm, 400 mm in thickness, with a load-bearing capacity on the surface of the layer of min. $Ev_2 = 100$ MPa pursuant to the ČSN 72 1006 standard.
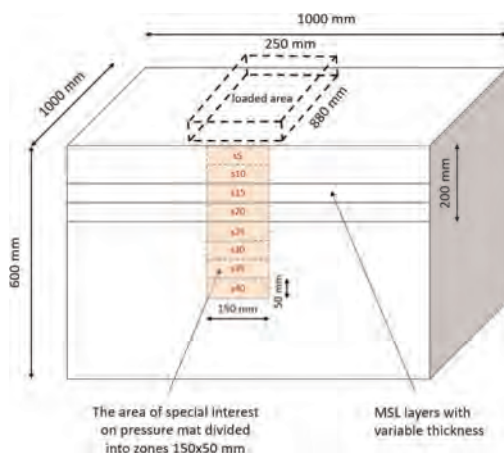
Figure 1. General scheme of the laboratory model.
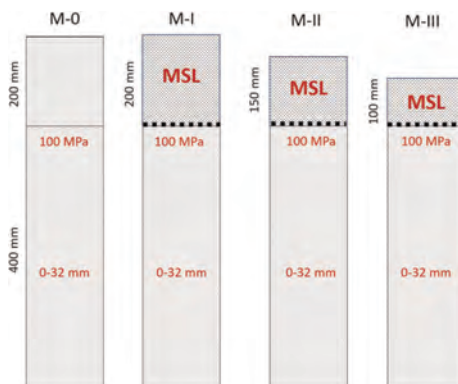
Figure 2. Vertical profiles of models M-0, M-I, M-II, M-III.

Subsequently, another layer of the same aggregates, 200 mm thick, was placed and compacted in Model M-0, where no geogrid had been fitted and which, therefore, served as a reference model for mutual comparisons. In the other three models, the 400 mm thick aggregate layer was overlaid with a multiaxial geogrid (Figure 3) and, successively, a crushed stone mixture layer with fractions 0-32 mm, 200 mm thick after compaction (Model M-I), 150 mm thick after compaction (Model M-II), or 100 mm thick after compaction (Model M-III). The compaction time was selected proportionally to the thickness of the layer over the geogrid.
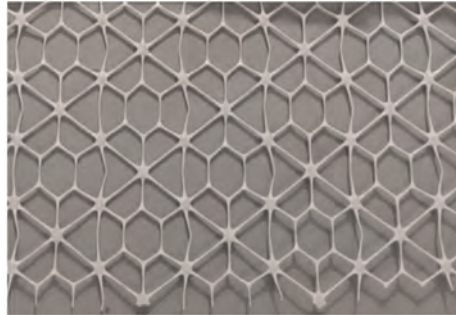
Figure 3.   Multiaxial geogrid.

2.2   *Loading*

The models were subjected to continuous vertical loading with a hydraulic press, the exerted force ranging within 0–100 kN. The force was transmitted onto the model structures via a part of a polymer sleeper with dimensions of 880x250x150 mm, which had been placed in the middle of the upper surface. This represented a maximum stress at the lower sleeper area of 454 kPa under loading by the highest exerted force.

2.3   *Measurement, recording and evaluation of horizontal pressures*

The measurement of horizontal pressures was conducted using the configuration displayed in Figure 4. The sensor itself was a special foil (Tekscan Pressure Mapping Sensor 5315), containing over 2000 sensels with a raster of 1 x 1 cm, where each sensel allows the recording of the corresponding earth pressure. This flexible foil 43 cm in height and 48 cm in width was fixed onto the inside lateral wall of the laboratory box in a position corresponding to the longitudinal axis of the placed sleeper section. To protect the foil from the aggregate sharp edges a protective layer of unwoven geotextile was used. The signal from the foil is recorded by a reader and transmitted to a laptop using special software for data recording (data logger) as well as the subsequent processing of the measured data.
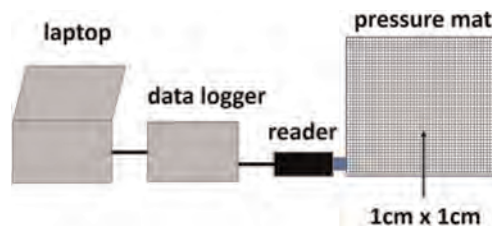
Figure 4.   The scheme of horizontal pressure recording.

The evaluation software defined a special interest zone on the foil surface area in the form of 8 vertically arranged strips, 50 mm high and 150 mm wide, situated so that the projection of the sleeper's longitudinal axis would intersect the centre of each strip. This arrangement allowed detailed evaluation of the area 150 mm in width to a depth of up to 400 mm from the surface of the structure. In each of the 8 strips, the average lateral pressure coming from 75 sensels was evaluated in relation to the exerted vertical force. Taking into account the maximum grain size of the aggregates of 32 mm, the granularity of the sensels on the foil enables a very reliable accuracy of the evaluation of horizontal pressures in the strips spaced 50 mm from each other. A finer subdivision is technically feasible, however, the imprints of individual grains would be difficult to interpret in this case.

3 MAIN OBSERVATIONS FROM EXPERIMENTS

The up-to-now known interlocking mechanism assumes the reduction of horizontal pressures in aggregates versus standard aggregates. The aim of experimental works was to find out how much the lateral pressures in MSL are reduced in comparison to non-stabilized aggregates. Figure 5 displays the lateral pressures in Model M–0 as they were measured in individual strips from top to bottom, from s5 to s40, for the case of the maximum sleeper loading, i.e. 100 kN. The lateral pressure values show a gradual uniform decrease in the downward direction, except for Strip s10, where a significantly lower pressure was recorded, most likely due to a specific local configuration of aggregate grains.
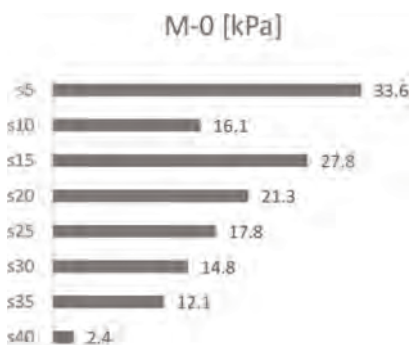
Figure 5.   Lateral pressures in model M–0 (kPa).
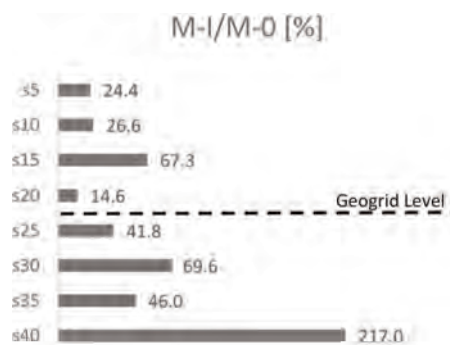
Figure 6.   Lateral pressures in M–I vs M–0 (%).
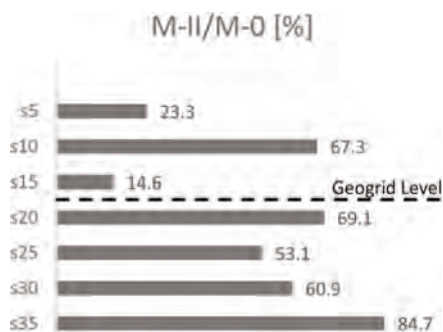
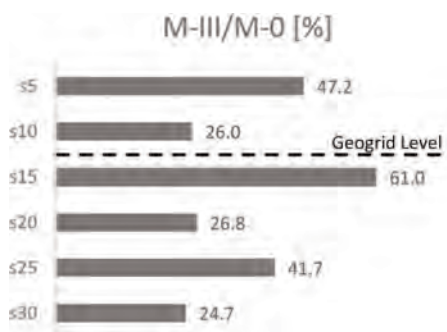Figure 7.   Lateral pressures in M–II vs M–0 (%).

Figure 8.   Lateral pressures in M–III vs M–0 (%).

Figures 6–8 present the results reached in Models M-I to M-III expressed as percentages of the pressure recorded for the reference model M–0 without a geogrid under maximum loading by the press of 100 kN. The geogrid position is marked by a dashed line.

In model M-I (Figure 6), a noticeable reduction in lateral pressures is evident in all strips, except the bottommost one. The pressure at a level of 5 cm over the geogrid (s20) amounted to 14.6 % of the value measured in the model without a geogrid, i.e. it reached a reduction by 85.4 %. The reduction in the adjacent above situated strip (s15) is lower amounting to 32.7%. A remarkable fact is that the strips more distant from the geogrid (10–20 cm) showed a significant reduction in the lateral pressure again (74.4% and 75.6%). A significant reduction in pressures is also recorded under the geogrid ranging from 30.4% to 54.0%. The high value of the mutual ratio in the s40 level (217%) is due to the low base value in Model M-0 (2.4 kPa). In the M-1 model, a value of 5.1 kPa was measured at the same level, which is in good relation with the value of 5.6 kPa in the s35 level.

In Model M-II (Figure 7), the pressure reduction values in the strips over the geogrid are nearly identical to those in Model M-I. The reductions under the geogrid, on the other hand, are lower than those measured in M-I amounting from 30.9% to 46.9%, which, however, still represents significant reductions. Model M-III (Figure 8) shows a similar trend, with a 74 % reduction directly over the geogrid, which is subsequently decreased to 52.8%. The reduction under the geogrid is noticeable, too. In all models fitted with geogrids, the lateral pressures onto the laboratory box wall recorded in the geogrid position were practically zero, which testifies to the high rate of the composite immobilization at this level. The summary results are presented in Table 1.

Table 1. Confining efficiency factor (CEF%) for studied models.

Layer/Model	M-I	M-II	M-III
Top layer	75.1	76.7	52.7
Geogrid layer	85.4	85.4	74.0
Total MSL	75.6	64.3	54.7

4 INTERPRETATION OF OBSERVATIONS

Significant reductions in lateral pressures in the models with geogrids versus the model without a geogrid manifest the existence and the effect of strong confinement of the aggregates in the geosynthetic apertures. This is a convincing confirmation of the principle and the mechanism of mechanical stabilization of aggregates. The most pronounced reductions are measured in the immediate vicinity of the geogrid. Also, the reduction in the first layer from the top, which is situated just below the cover (asphalt, concrete, rail bed) in a real structure is of considerable importance for the durability of the cover. The lower the deformability of the base layer, the lower the probability of fatigue deformation in the cover.

The pressure reduction percentage in a mechanically stabilized layer compared to the reference model without mechanical stabilization has been designed as the Confinement Efficiency Factor (CEF). This parameter quantifies the confinement or stabilization efficiency of a mechanically stabilized layer. CEF can be evaluated for a specified layer thickness or for the entire MSL defined, in our case, as 10–20 cm over and 10 cm under the geogrid.

5 CONCLUSIONS

The conducted laboratory experimental works allow formulating the following conclusions:

- The innovative method of measuring and recording the pressure of aggregates onto the laboratory box wall has been proven highly effective.
- Significantly lower horizontal pressures were measured in the mechanically stabilized layers than in the non-stabilized aggregate. This has confirmed the existence of the confinement and immobilization mechanism of aggregate grains in the geogrid holes, and thus the overall principle of mechanical stabilization.
- The next generation of multiaxial geogrids has proved efficient in the mechanical stabilization of aggregates.
- The Confinement Efficiency Factor (CEF) has been designed, which is defined as the percentage reduction in lateral pressures in a respective layer compared to non-stabilized aggregates. CEF is recommended for use as a parameter to quantify the confinement intensity and the degree of stabilization in mechanically stabilized layers.
- The greatest reduction in lateral pressures was observed at and in close vicinity to the geogrid level; however, all the monitored mechanically stabilized layers generated lower horizontal pressures throughout the profile.
- As a result, the horizontal deformations of the stabilized layer are reduced. The lower deformability of the stabilized layer under the top cover of transportation structures (asphalt, concrete, ballast) contributes to the extension of its service life.

REFERENCES

Byun, Y.H. et al. 2018. Horizontal Stiffness Evaluation of Geogrid-stabilized Aggregate using Shear Wave Transducers. *Geotextiles and Geomebranes* 47(2019): 177–186.

ČSN 72 1006 *Compaction Control of Engineering Fills*. Czech Technical Standard. 2015.

Horníček, L. & Rakowski, Z. 2017. Mechanical Stabilization of Intermediate Granular Layers in Pavement Structures–Laboratory Study. *Procedia Engineering* 189(2017): 174–180.

Lees, A.S. & Clausen, J. 2019. A New Approach to Characterise the Benefit of Multiaxial Geogrid on Soil. In Haraldur Sigursteinsson at al. (ed.), *Geotechnical Engineering, Foundation of the Future; Proceedings of the XVII European Conference on Soil Mechanics and Geotechnical Engineering, Reykjavik*, 1–6 September 2019.

Rakowski, Z. & Kawalec, J. 2009. Mechanically Stabilized Layers in Road Construction. In *Geotechnical Engineering, Foundation of the Future; Proceedings of the Mechanically Stabilized Layers in Road Construction*, Riga, 24–26 August 2009.

Geosynthetics wrapped tire derived materials as drains for liquefaction mitigation

Y. Hu & H. Hazarika
Kyushu University, Fukuoka, Japan

S.P.G. Madabhushi & S.K. Haigh
University of Cambridge, Cambridge, UK

ABSTRACT: Liquefaction has been responsible for tremendous damage in historical earthquakes Some liquefaction countermeasures have been developed to prevent such damage, in which drainage method is one of the effective techniques. However, sustainable and low-cost technique is still needed for existing buildings. On the other hand, gravel-tire chips mixture (GTCM) as an alternative drainage enhancing geosynthetics, has been introduced recently. A new design of liquefaction mitigation technique has been proposed in this study. It utilizes GTCM as materials of drains installed around the buildings. A series of 1–g model shaking table tests were conducted to evaluate the performance of the technique in this research. The results indicated that excess pore water pressure beneath the building was dissipated through GTCM drains effectively during the shaking. The liquefaction-induced settlement of the building was controlled to a significantly low level. GTCM drains show effectiveness in reduction of liquefaction potential for existing buildings.

1 INTRODUCTION

In Japan, the total number of end-of-life tires produced was 86 million, which was about 1 million tons by weight in 2020, according to the report by JATMA (Japan Automobile Tyre Manufacturers Association 2021). The majority of these waste tires (65%) are either burned for energy or dumped on the ground. Thermal recycling, on the other hand, is detrimental to the atmosphere because it emits more CO_2 than other recycling methods. In order to promote waste tire recycling and reduce CO_2 emissions, the use of industrial by-products in cascaded form (returning on different products) has gained popularity in recent years (Hazarika *et al*. 2018). As an example, scrap tire-derived materials (STDMs) have been utilized as geosynthetics in recent years, considering their low-carbon-release characteristics and other advantageous material characteristics including lightweight, excellent vibration absorption capability, and high permeability. Such characteristics offer an alternative application for other conventional materials in applications including drainage, landfill leachate removal, soil reinforcement, and so on.

On the other hand, one of the earthquake-induced hazards, liquefaction, has become much more frequent in recent years, especially in Japan. The damage due to such hazard was observed over a wide area following the 2016 Kumamoto Earthquake (Hazarika *et al*. 2017), which highlighted the value of taking preventive steps to protect buildings and facilities by reducing ground settling and lateral spreading. Furthermore, sustainable and cost-effective disaster mitigation efforts are desperately needed in most developing countries, where infrastructure growth is still in its infancy. The main problem is striking a balance between

the cost and the increased environmental impact of any infrastructure project. A new technique, which utilizes a layer of tire chips as the horizontal inclusion under the foundation of residential housing, was developed in response to the demand (Hazarika *et al.* 2008). As a new geosynthetics, the pure tires were then replaced by gravel tire chips mixture (GTCM) material, since it can provide sufficient bearing capacity to the foundation (Hazarika *et al.* 2016, 2020). However, these mentioned techniques, as well as most of the other liquefaction countermeasures, are developed for new constructions. Very few techniques have been developed for existing buildings to mitigate liquefaction.

Drainage method is one of the effective liquefaction countermeasures, that has been widely used in practice. The principal objective is to relieve the excess pore water pressure generated during the earthquake before they reach high values that can finally cause liquefaction (Brennan & Madabhushi 2006). The performance of the drains underneath structures has been investigated most recently (Garcia-Torres & Madabhushi 2019). Considering the performance of GTCM in horizontal reinforcing inclusion mentioned before, it could be possible to utilize this material in vertical drain method as well.

In this paper, a new technique called GTCM drainage system has been proposed as shown in Figure 1. The main purpose is to dissipate the generated excess pore water through these prefabricated drains installed around the existing building during the earthquake. The liquefaction potential of the foundation can be therefore reduced, as well as induced settlement. A series of model tests were conducted using 1-g shaking table. With dynamic loading applied, the development of excess pore water pressure in the foundation and the progress of settlement was observed to evaluate the effectiveness of this drainage technique in mitigating liquefaction.
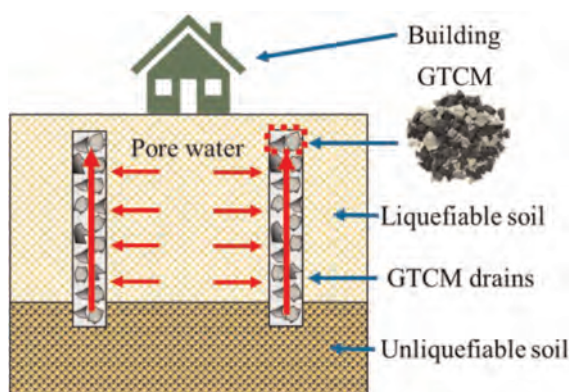

Figure 1.   Principle of GTCM drains technique.

2   MATERIALS AND EXPERIMENTS

2.1   *Materials used*

Three raw materials were used in this research, including tire chips, gravel and Toyoura sand. Tire chips were supplied by a local company from recycling scrap tires. The waste tire was firstly shredded by a special shredding machine into various sizes with a shape of square and an aspect ratio of 1:1 (width to length), approximately. And then, those tire chips with the size of 4 mm were selected by sieving. Gravel with a similar grain size was mixed with selected tire chips as GTCM material. The volumetric fraction of gravel is 50%, since increasing the gravel fraction would result in the decreasing liquefaction resistance of the mixture (Pasha *et al.* 2018). While adding more tire chips, the shear strength of the mixture

would be smaller (Pasha *et al.* 2019). Toyoura sand is a Japanese standard sand used as the foundation for the research. Table 1 shows the properties of GTCM and Toyoura sand.

Table 1. Properties of materials in use.

Material	G_s	Dry density (g/cm³)	ρ_{max} (g/cm³)	ρ_{min} (g/cm³)	D_{50} (mm)
Toyoura sand	2.640	1.506	0.976	0.611	0.160
GTCM	1.910	1.022	1.036	0.842	4
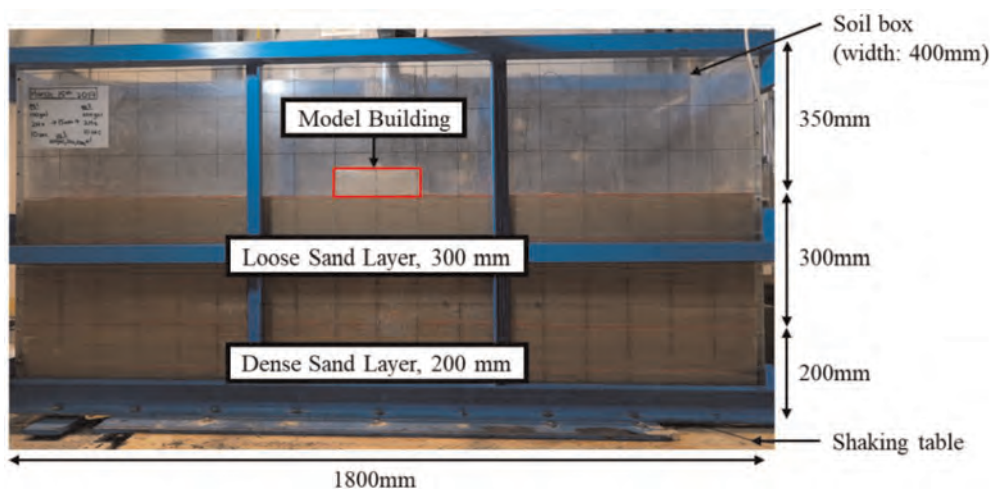
Figure 2. Test model on the 1–g shaking table.

2.2 *Model tests*

The 1g shaking table tests were conducted using the shaking table facility at the geo-disaster laboratory of Kyushu University. Models were constructed in a transparent Plexiglas soil box with dimensions of 1800 mm, 400 mm and 850 mm, as shown in Figure 2. Soil-structure-fluid interaction can be simulated using the scaling law proposed by Iai (1989). Since this research involves liquefaction-induced damage to structures, it is the most suitable similitude relationship. Throughout these tests, considering the size of the soil box on the shaking table, a geometrical scaling factor of 1:32 was set based on this law.

Depending on whether GTCM drains were installed in the foundation or not, two cases of 1–g shaking table tests were performed. In Case 1, four parallel arrays of prefabricated GTCM drains with a diameter of 50 mm and height of 300 mm were installed vertically around the four sides of the residential building from the surface level up to the bottom of the loose sandy layer and extended into the hard layer. The distance between the center of two neighboring drains is 100 mm. The vertical drains along the short side of the model building were then replaced with four GTCM drains inserted at 60 degrees diagonally in Case 2. A shallow foundation of a structure with a bearing pressure of 5 kPa, represented by a rectangular block of brass material, with a cross-sectional area of 230 mm by 100 mm in model scale, was set upon the soil. In addition, there was a thick layer of gravel with 2 cm in depth between the model building and GTCM drains. A sinusoidal acceleration of 300 Gal with a frequency of 4 Hz and duration of 10s was applied to the model. Several pore water pressure transducers were set in the location shown in Figures 3–4. Two motion analysis marks were located on two sides of the model building.
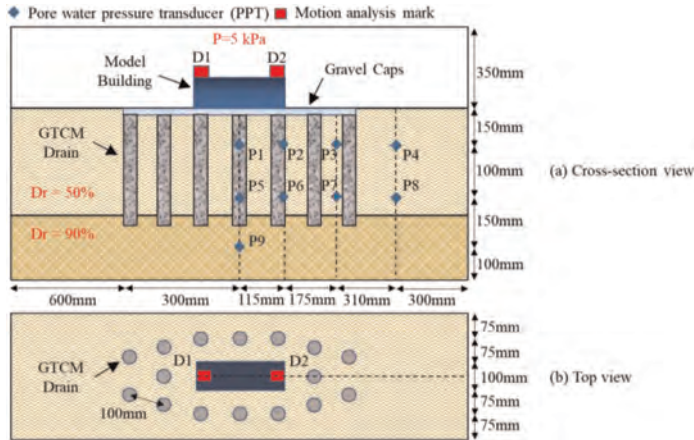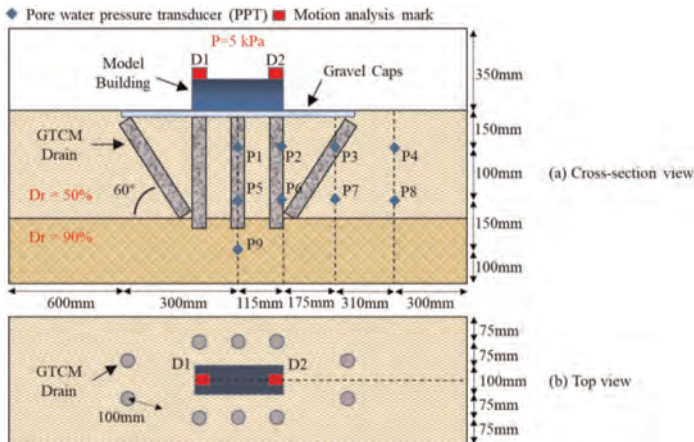
Figure 3.   Layout of model test Case 1.

Figure 4.   Layout of model test Case 2.

3   RESULT AND DISCUSSION

3.1   *Settlement*

The model building suffered settlement due to the deformation of the loose sand foundation. Through motion analysis, the time history and trend of the building settling in both two cases are obtained and drawn out in Figure 5. As can be observed, both buildings initiated a speedy settling subsequent to the start of seismic loading in two cases. In Case 1, the maximum settlement during the earthquake is 39.03 mm at D1. While at the other side (D2), the displacement is recorded as 40.91 mm. The rotation due to the uneven settlement is about 0.468°. Compared to Case 1, the building suffered less settlement in Case 2, as shown in Figure 5b. The maximum displacement recorded is 37.45 mm at D1 and 32.32 mm at D2, resulting in a rotation of 1.28°. Take the average settlement in the center of the building as a reference, the vertical-inclined combined system in Case 2 has an improvement in protection efficiency by 14.6% over vertical-only drains in Case 1. In addition, a significant settlement was also observed in the ground around the buildings, as well as free field areas. Of

particular concern is the wedge areas formed between the vertical drains and inclined drains in Case 2. On the basis of these phenomena, it is reasonable that though the GTCM drains technique successfully mitigated liquefaction during the earthquake, unignorable foundation settlement still happened under bearing pressure from the heavy building itself and soil consolidation.
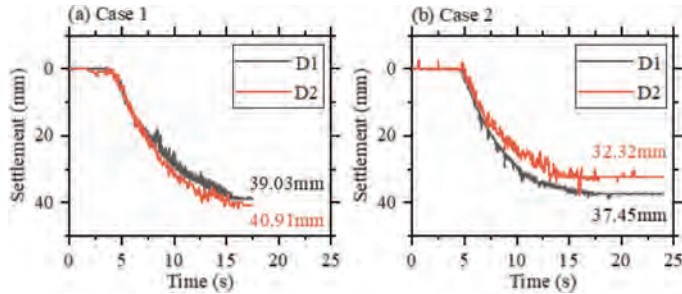

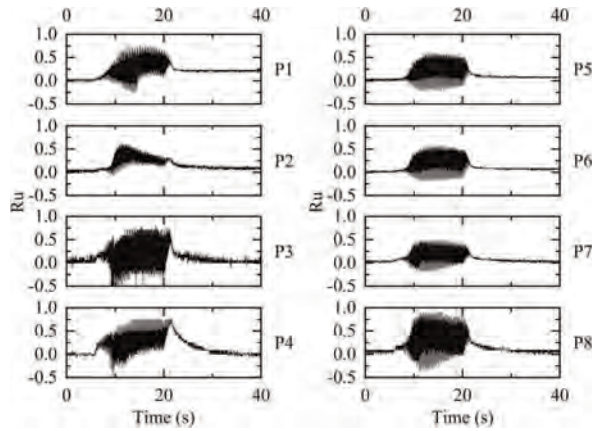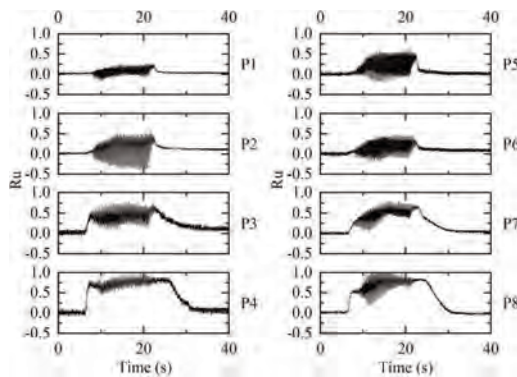Figure 5. Time history of settlement in (a) Case 1 and (b) Case 2.

Figure 6. Time history of Ru in Case 1.

Figure 7. Time history of Ru in Case 2.

3.3   *Excess pore water pressure*

Figures 6–7 show the time history of the excess pore water pressure ratio, defined as $R_u = u_{\text{expp}}/\sigma'_{vo}$ recorded by PPTs at each location inside the sandy layer (shown in Figure 3). In Case 1, with vertical GTCM drains installed around the building, the excess pore water was dissipated during the shaking. Due to the combined effect of compaction from the bearing pressure, the Ru value is smaller at P1 than at P3 and at P4. The generation of pore water pressure was limited by the drains nearby after the initial speedy increase at P2 as well. The higher value of Ru is only obtained at P4 and P8, located at the free field away from the building and drains.

A similar situation happened in Case 2, except the Ru value reaches 1 at P4 and P8 respectively, which indicates liquefaction happened. However, since the five vertical GTCM drains along the short side of the building were replaced with two inclined drains, and fewer drainage surrounded, it is reasonable that the excess pore water pressure ratio was much higher at P4, P7 and P8 compared to Case 1. Despite that, the change of the configuration of GTCM drains from vertical only to a vertical-inclined combined system does not affect the core function in mitigating liquefaction for the existing building. In addition, considering that liquefaction did not happen beneath the building, the recorded displacement could have resulted from the consolidation of the loose sandy soil.

4   CONCLUSION

When GTCM drainage system is applied, excess pore water can quickly dissipate through the GTCM drains from the foundation to the soil surface. As a result, the risk of liquefaction beneath the existing structures would be reduced. Compared to the vertical-only GTCM drains system, the proper combination of inclined drains could improve the resistance of buildings toward liquefaction-induced settlement. Although the drainage capacity might be reduced accompanied by a slightly elevated risk of liquefaction in the free-field areas around the building, the core function remains effective. The technique, thus, is expected to have great potential in the cost-effective seismic design and retrofitting of structures. If adequate design guideline is established, the developed liquefaction mitigation technique could be applied for upgrading (retrofitting) the existing structures that run the risk of damage during devastating future earthquakes.

REFERENCES

Brennan, A.J. & Madabhushi, G.S.P. 2006. Liquefaction Remediation by Vertical Drains with Varying Penetration Depths. *Soil Dynamics and Earthquake Engineering* 26(5): 469–475.

Garcia-Torres, S. & Madabhushi, G.S.P. 2019. Performance of Vertical Drains in Liquefaction Mitigation under Structures. *Bulletin of Earthquake Engineering* 17(11): 5849–5866.

Hazarika, H., Yasuhara, K., Hyodo, M., Karmokar, A. K. & Mitarai, Y. 2008. In *Proc. of 14th World Conference on Earthquake Engineering*. Beijing

Hazarika, H. & Abdullah, A. 2016. Improvement Effects of Two and Three Dimensional Geosynthetics Used in Liquefaction Countermeasures. *Japanese Geotechnical Society Special Publication* 2(68): 2336–2341.

Hazarika, H., Kokusho, T., Kayen, R.E., Dashti, S., Fukuoka, H., Ishizawa, T., Kochi, Y., Matsumoto, D., Furuichi, H., Hirose, T., Fujishiro, T., Okamoto, K., Tajiri, M. & Fukuda, M. 2017. Geotechnical Damage Due to the 2016 Kumamoto Earthquake and Future Challenges. *Lowland Technology International* 19(3): 189–204.

Hazarika H., Yokota H., Endo S. & Kinoshita T. 2018. Cascaded Recycle of Waste Tires—Some Novel Approaches Toward Sustainable Geo-Construction and Climate Change Adaptation. In Krishna, A., Dey, A. & Sreedeep, S. (ed.), *Geotechnics for Natural and Engineered Sustainable Technologies*. Singapore: Springer.

Hazarika, H., Pasha, S.M.K., Ishibashi, I., Yoshimoto, N., Kinoshita, T., Endo, S., Karmokar, A.K. & Hitosugi, T. 2020. Tire Chip Reinforced Foundation as Liquefaction Countermeasure for Residential Buildings. *Soils and Foundations* 60(2): 315–226.

Iai, S. 1989. Similitude for Shaking Table Tests on Soil-structure-fluid Model in 1g Gravitation Field. *Soils and Foundations* 29(1): 105–118.

Japan Automobile Tyre Manufacturers Association. 2021. *Tyre Industry of Japan*. Retrieved from http://www.jatma.or.jp/media/pdf/tyre_industry_2020.pdf

Pasha, S.M.K., Hazarika, H. & Yoshimoto, N. 2018. Dynamic Properties and Liquefaction Potential of Gravel-tire Chips Mixture (GTCM). *Journal of Japan Society of Civil Engineers* 74(4): 649–655.

Pasha, S.M.K., Hazarika, H. & Yoshimoto, N. 2019. Physical and Mechanical Properties of Gravel-tire Chips Mixture (GTCM). *Geosynthetics Int.* 26(1): 92–110.

Engineered turf cover: An innovative solution for environmental closure and renewable solar energy development

M. Zhu, M. Ayers, T. Orzech & B. Scholl
Watershed Geosynthetics, Alpharetta, Georgia, USA

C. Eichelberger
Agru America, Georgetown, South Carolina, USA

G. Dortland
WatershedGeo EU, Oldenzaal, The Netherlands

ABSTRACT: The engineered turf cover has gained significant acceptance in the past decade as a final cover for environmental closure of waste containment facilities. When compared to a traditional soil cover, the major advantages of the engineered turf cover include faster construction, improved cover slope stability, enhanced runoff water quality, and reduced post-closure maintenance costs. After a waste containment facility is closed, the large surface area can be beneficially used for development of a solar farm. The engineered turf cover provides a stable foundation for solar panels. This paper presents an overview of the engineered turf cover. Case studies are provided to demonstrate field performance of the engineered turf cover and applications of renewable solar energy development.

1 INTRODUCTION

A final cover system is the critical component of environmental closure of waste containment facilities, such as municipal solid waste (MSW) and industrial waste landfills, coal combustion residual (CCR) units, brownfields, etc. It isolates the underlying waste, preventing its exposure to the environment, and protecting human health and safety. It minimizes infiltration of precipitation into the waste and reduces leachate generation. For a waste containment facility that generates gas (e.g., an MSW landfill), the final cover also improves landfill gas collection efficiency and reduces fugitive gas emissions.

The past decade has seen a significant increase in the use of the engineered turf cover to close various types of waste containment facilities. The engineered turf cover is a 3-component system consisting of, from bottom to top, a structured geomembrane, an engineered turf, and a specified infill (Figure 1).
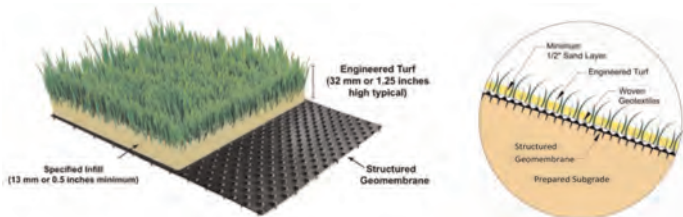

Figure 1. Illustration of engineered turf cover: system components (left) and typical cross section (right).

The structured geomembrane, which is made of high-density polyethylene (HDPE) or linear low-density polyethylene (LLDPE), serves as the hydraulic barrier to encapsulate the waste and prevent infiltration of precipitation into the waste. The engineered turf is made of HDPE synthetic grass blades tufted into a double-layer polypropylene (PP) woven geotextile backing. Its main function is to protect the underlying geomembrane from ultraviolet (UV) exposure and wind uplift. The specified infill has a minimum thickness of 0.5 inches (13 millimeters [mm]) and is a granular material that meets technical specifications for the grain size distribution, angularity, and specific gravity (Zhu *et al.* 2021). It is placed inside the synthetic grass blades to cover the geotextile backing and provide ballast for wind uplift protection.

Compared to a traditional soil cover, the engineered turf cover does not require the vegetative and protective soil layers that typically have a minimum total thickness of 2 feet (0.6 meters [m]). By removing the soil layers, the engineered turf cover provides a reliable closure solution that is not dependent on weather, soil, or vegetation conditions. It enables site owners and operators to overcome long-standing challenges of soil erosion, geotechnical instability, and post-closure maintenance associated with traditional soil covers (Zhu *et al.* 2019). Other advantages include faster construction and less environmental impact (e.g., avoidance of land disturbance, clean runoff, and reduction in carbon emissions) (Joshi 2023). Based on the results of extensive outdoor UV longevity tests, the service life of the engineered turf cover is projected to be more than 100 years, provided it is installed and maintained properly in accordance with design drawings, engineering specifications, and post-closure care requirements (Scholl *et al.* 2023; Zhu *et al.* 2021).

2 ENGINEERED TURF COVER CASE STUDY

2.1 *Project background*

The Mississippi Phosphates Corporation (MPC) site is located in Pascagoula, Mississippi, US. The MPC produced diammonium phosphate fertilizer from the late 1950's through December 2014, when it declared bankruptcy. In August 2013, approximately 39 million gallons (approximately 150,000 m^3) of acidic wastewater was discharged to the nearby Bayou Casotte, resulting in a large quantity of fish kill, closing of the bayou, and subsequently, violation of the Clean Water Act. The United States Environmental Protection Agency (US EPA) formally added the MPC site to the Superfund National Priorities List (NPL) in January 2018 (Zeller 2019).

The US EPA planned to close the East Gypsum Stack as a part of the site remediation. The stack contains the phosphogypsum, which is the by-product of fertilizer production from phosphate rocks. The area of the stack to be closed is about 170 acres (69 hectares [ha]). The US EPA selected the engineered turf cover, ClosureTurf®, as the final cover after conducting a detailed value engineering study. Compared to a traditional vegetative soil cover that would include a 2-foot (0.6-m) thick soil layer and a geomembrane layer, the engineered turf cover was expected to save an estimated US$6 million in the 30–year life cycle of the project, including US$4.6 million on construction costs and US$1.4 million on post-closure operation and maintenance costs. In addition, using the engineered turf cover was expected to eliminate approximately 42,700 truck trips required to haul the cover soil and save expenditures related to on-going water treatment because of quicker installation (Zeller 2019). Prior to the closure, the US EPA was spending on average US$1 million per month to treat the acidic contact water in-situ with lime.

2.2 *Final cover construction*

Construction of the engineered turf cover was divided into 3 phases, which started in September 2019 and completed in March 2023. Selected construction photos are shown below.

Figure 2.   Engineered turf cover construction at the Mississippi phosphates corporation gypsum stack, a US EPA superfund site.

2.3   *Field performance*

Due to its close proximity to the coast, the site has frequently experienced storms since the installation started. Tropical Storm Cristobal was a tropical cyclone that developed in the Gulf of Mexico and made landfall in the US over southeastern Louisiana on June 7, 2020. The wind and precipitation data collected at two weather stations were analyzed to evaluate the field performance of the engineered turf cover installed at the MPC site. One station is located on the site and the other station is located 2.5 miles (4.0 kilometers [km]) southwest from the site.

The site experienced rainfall from June 6 to 8, 2020, with the most severe weather conditions experienced on June 7. In total, the site received 7.62 inches (194 mm) of rain during a period of 53 hours, with the maximum hourly intensity of 3.00 inches/hour (76.2 mm/hour) and total daily precipitation of 6.26 inches (159 mm) on June 7. The peak wind gust was recorded as 42.3 miles per hour (68.1 km per hour) on June 7. The recorded precipitation and wind speed data are plotted in Figures 3 and 4, respectively.
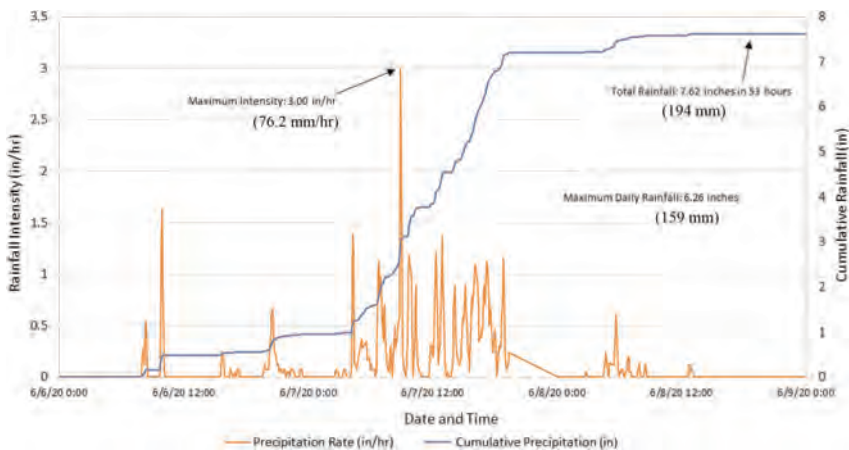

Figure 3.   Recorded precipitation at the MPC site during tropical storm cristobal.
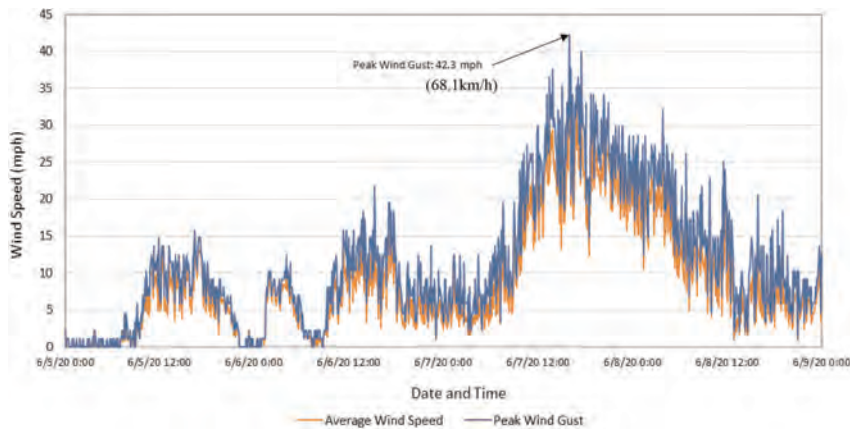
1696

Figure 4. Recorded wind speed at the MPC site during tropical storm cristobal.

One year later, Hurricane Ida made landfall in the US over southeastern Louisiana on August 29, 2021. The MPC site experienced rainfall from August 29 to 31 with the most severe weather conditions experienced on August 30. The site received 7.29 inches (185 mm) of rain for a period of approximately 48 hours, with the maximum hourly intensity of 3.54 inches/hour (89.9 mm/hour) on August 30. The maximum 24–hour rainfall was 5.64 inches (143 mm) on August 30. The peak wind gust was recorded as 35.3 miles per hour (56.8 km per hour) on August 30.

The areas that were installed with the engineered turf cover at the time of Tropical Storm Cristobal and Hurricane Ida were about 50 and 100 acres (20 and 40 ha), respectively. The site was inspected after both events. No significant infill movement or damage to the engineered turf cover was observed. Because the runoff from the engineered turf cover area was no longer in contact with the gypsum waste, it was discharged directly offsite without treatment. The total savings on wastewater treatment cost were estimated to be around US $400,000 for these two storm events.

3 SOLAR ENERGY DEVELOPMENT

3.1 *Beneficial reuse of waste containment facilities*

After a waste containment facility is closed, the large space can be beneficially used for development of a solar farm to provide a clean source of renewable energy. Using a closed waste containment facility can prevent disturbing a farmland or a natural greenfield at another place. The facility already has infrastructures built at the site, for example, the access roads, stormwater management system, security fences, electricity connection system, etc. Therefore, construction of a solar farm on a closed facility saves costs. Development of green energy is also a demonstration of the site owner's commitment to sustainability, which can help improve public relationships. Furthermore, the solar farm can generate revenue to offset site operation and maintenance costs, transforming the waste containment facility from a post-closure care liability into a renewable energy asset.

3.2 *Traditional solution*

The traditional solar solution utilizes a vegetative soil cover for closure and a racking-supported photovoltaic (PV) solar panel system for solar energy generation. The racking

system is usually supported by heavy concrete foundations to protect the solar panels and racking system from uplifting and overturning by wind loads. The concrete foundations are installed directly on top of the final cover. Pile foundations are usually not used due to penetration of the final cover barrier layer (e.g., geomembrane, clay, and/or geosynthetic clay liner [GCL]). In most cases, installation of solar panels is limited to the top deck due to stability concerns and construction difficulties associated with installing solar panels on side slopes of the waste containment facility.

The major challenges with the traditional solar solution are related to soil erosion, maintenance, and impact on final cover performance. Rainwater falls off the edges of panels and hits the ground as a concentrated flow. The impact force can cause erosion of the soil cover along the drip line. As a result, soil erosion affects runoff water quality and increases maintenance and repair costs. It can undermine the concrete foundations for the solar panels and integrity of the final cover system too. To control soil erosion, it is important to establish good vegetation on the final cover and perform regular maintenance and repairs, as necessary.

On the other hand, overgrown grasses, weeds, and plants need to be trimmed because they affect not only the final cover performance, but also the solar panel efficiency by blocking the sunlight with shadows. Because of narrow access between solar panels, the vegetation must be cut manually, requiring intense labor work for large sites. In addition, workers need to operate equipment carefully to avoid cutting cables and conduits or damaging solar panels. Last but not the least, potential impact of loading from heavy concrete foundations and gravel leveling pads on the performance of final cover needs to be evaluated during engineering design and monitored after construction, because it can create differential settlement that may cause localized ponding of stormwater.

3.3 *Engineered turf solution*

The engineered turf cover provides a more favorable solution to address the above-mentioned challenges regarding solar energy development on a waste containment facility. It is a stable foundation that is not subject to soil erosion. It requires minimal maintenance, i.e., no mowing, fertilizing, or revegetation. Since vegetation overgrowth is no longer a concern, a low-profile solar panel system can be installed directly on the engineered turf cover, which causes less impact on the final cover system than the traditional solar panel system. Case studies of solar farms installed on engineered turf covers are provided in the section below.

3.3.1 *Case Study #1 – MIRA Landfill, Hartford, CT, US*
The MSW landfill is located in Hartford, Connecticut and owned by the Materials Innovation and Recycling Authority (MIRA). Thirty-six (36) acres (14.6 ha) of the engineered turf cover, ClosureTurf, was installed on the landfill in 2014. A one-megawatt (1–MW) solar electricity generating facility was constructed on top of the engineered turf cover within a 5–acre (2–ha) area of the landfill top deck (Figure 5a). At its peak capacity, the solar facility can generate enough electricity to power about 1,000 homes per day. The solar panels are supported by a racking system ballasted with concrete blocks (Figure 5b).
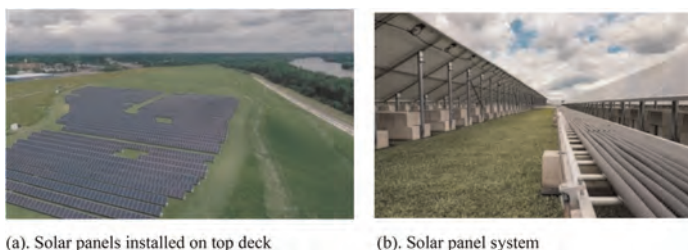

(a). Solar panels installed on top deck   (b). Solar panel system

Figure 5.   Engineered turf cover and solar panels installed on MIRA landfill, Hartford, CT.

3.3.2 Case Study #2 – Cranston Sanitary Landfill, Cranston, RI, US

The Cranston MSW landfill in Rhode Island is a formal US EPA Superfund site owned by the Cranston Sanitary Landfill Remedial Action Group. A total of 22 acres (8.9 ha) of the engineered turf cover, ClosureTurf, was installed on the landfill in 2015. A 3.5–MW community solar farm was installed on top of the engineered turf cover in 2021. It has turned the site that is otherwise undevelopable into a renewable energy resource, as an example of brownfield redevelopment. The solar project consists of more than 9,700 ground-mounted solar panels. The solar panel frames are ballasted with concrete blocks for wind uplift protection (Figure 6).

Figure 6. Community Solar farm installed on engineered turf cover at the Cranston Sanitary landfill, Cranston, RI.

3.3.3 Case Study #3 – A confidential CCR impoundment, Southeastern US

This solar project features the solar power generation system, PowerCap^{TM}, installed on a CCR impoundment capped with the engineered turf cover, ClosureTurf. PowerCap is custom-designed for direct installation on the engineered turf cover. It does not require penetrations through or mechanical connections to the engineered turf cover. The system consists of friction strips connected to the bottom of the solar panel rails, which provide interface friction and maintain stability of solar panels on slopes.

The solar project was completed in January 2019. It consists of 120 flush-mounted solar panels with a total capacity of 39 kilowatts installed on a 3 Horizontal to 1 Vertical (3H:1V) side slope of the closed CCR impoundment (Figure 7). Recent field inspection conducted in December 2022 indicated that after almost four years, the solar power generation system had performed well, as expected. There were no signs of impact on the performance of the underlying engineered turf cover by the solar power generation system.

Figure 7. PowerCap installed on engineered turf cover at a confidential CCR impoundment, Southeastern US.

4 CONCLUSIONS

The engineered turf cover provides a viable solution to overcome long-standing challenges faced by traditional soil covers of waste containment facilities, including soil erosion, geotechnical instability, and post-closure maintenance. It also provides a stable foundation for a solar farm that is constructed to beneficially use the otherwise undevelopable space for power generation. A combination of the innovative environmental closure and solar power generation technologies can transform waste containment facilities (e.g., MSW and industrial waste landfills, CCR units, brownfields, etc.) from long-term liabilities to renewable energy assets.

REFERENCES

Joshi, R. 2023. Environment, Social, and Governance (ESG) Offerings of an Engineered Turf Final Cover System. *Proceedings of Geosynthetics 2023 Conference*, Feb. 5–8, 2023, Kansas City, MO, USA: 539–548.

Scholl, B, Zhu, M. & Yuan Z. 2023. Engineered Turf Landfill Closure: How Long Will it Last? *Proceedings of Geosynthetics 2023 Conference*, February 5–8, 2023, Kansas City, MO, USA: 143–151.

Zeller C. 2019. Engineered geosynthetic turf cover system for Capping Phosphogypsum Stack, Mississippi Phosphates Corporation, Pascagoula, Jackson County, MS. *Presented at the SAME 2019 Symposium on Design and Construction Issues at Hazardous Waste Sites*, November 4–6, 2019, Denver, CO, USA.

Zhu, M., Isola, M. & Zornberg, J. 2019. Advances in Geosynthetic Solutions for Sustainable Landfill Design: Geosynthetics Really do Last. *GeoStrata: November/December* 2019: 60–65.

Zhu, M., Scholl, B. & Joshi R. 2021. Landfill Closure with Engineered Turf Cover. *Proceedings of Geosynthetics Conference 2021*, February 22–25, 2021: 517–528.

New GCL composite vertical anti-seepage technology and its application

Xie Shiping, He Shunhui, Zhang Jian & Zheng Yongya
Tianjin Zhonglian GeLin Science and Technology Development Co., Ltd., Tianjin, China

ABSTRACT: Geosynthetic Clay Liner (GCL) composite vertical anti-seepage barrier technology introduces GCL into the field of vertical anti-seepage and combines with low-permeability wall to form a composite anti-seepage system. GCL was laid vertically one or both sides of the excavated trench. GCL panel is factory fabricated to ensure easy fast and accurate vertical installation at site, GCL can be standard, multicomponent, or even polymer enhanced to cope with site specific leachate. Backfill can be mixture of soil-bentonite, cement-bentonite or soil-cement-bentonite. Compared with conventional rigid anti-seepage wall, it improves the overall performance in terms of wall permeability, integrity and durability, and it is more cost-effective than its counterpart HDPE vertical barrier. GCL anti-seepage barrier technology has been used in landfill, industrial pollution site and mine waste site remediation successfully, and well-received as a suitable candidate for immediate protection and containment assurance in China.

1 INTRODUCTION

Currently, solid waste landfills leakage and accidents in chemical storage facilities around the world pose potential threat to the soil and groundwater of the surrounding environment, thereby, the urgent treatment measures are needed to prevent contaminant migration (Khandelwal A 1998; Peng C.H. 2020; Rowe R.K. 2004; Sangam H.P. 2001a). The storage amount of urban waste in China exceeded 8 billion tons (Yuan C. 2017). During the 13th Five Year Plan period of China, 803 landfills projects were built according to the data of National Development and Reform Commission in 2016, many of them were found leachate release to the surrounding environment. With the increasingly stringent requirements of environmental protection, many existing landfills sites require effective technical measures to impede pollutants migration and reduce damage to the surrounding environment. The vertical cut-off wall, as an effective method, has been gained widespread acceptance across the world (Bohnhoff G L 2013; Park M G 2011; Sangam H P. 2001b; Xie H 2018). It is one of the important aspects to use vertical anti-seepage barrier to control and remediate landfill leakage.

Conventional rigid vertical anti-seepage technology is mostly developed from the cut-off wall used in water conservancy projects (Zhen S L 2017). It is known that concrete was widely applied in cut-off walls, but the leakage often happened due to the weak joints of adjacent wall sections and cracks in the walls induced by stress concentration. In addition, for the cement mixing pile, the permeability coefficient of the single-row piles is typically within 10^{-5} cm/s. Some literatures revealed that the impervious performance of the cut-off walls constructed with cement, even with good construction management, can only reach as low as 5×10^{-7} cm/s (Johnson AI 1985), which still cannot meet 1×10^{-7} cm/s–regulated by Chinese specifications.

As a commonly used high-performance horizontal lining material, Geosynthetics Clay Liners (GCLs) are widely applied in water conservancy, environmental protection and other fields (LI X 2005), because of its low permeability (less than 5×10^{-9} cm/s), self-sealing and self-healing properties. Therefore, the use of GCL in the vertical anti-seepage wall can not only effectively overcome the shortcomings of the conventional cut-off walls, but also provide a new solution for vertical anti-seepage engineering.

2 AN INNOVATIVE GCL COMPOSITE VERTICAL ANTI-SEEPAGE BARRIER

An innovative GCL composite vertical anti-seepage barrier, consisting of fabricated GCL panel (hereinafter referred to as composite component) and backfill wall material, is a new type of composite vertical anti-seepage solution, as shown in Figure 1. Firstly, locating the wall and excavating the trench until the designed depth, secondly, GCL is laid vertically along one or both sides of the trench, and then the wall material is backfilled in the trench to form a composite cutoff wall, working as an anti-pollution and anti-seepage barrier. On the other hand, GCL greatly improves the anti-seepage performance of composite structure, and the multilayer structure enables the composite barriers to cope with different kinds of leachate.
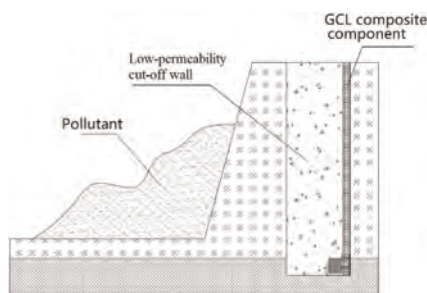

Figure 1.   The schematic diagram of GCL composite vertical anti-seepage barrier.

In order to facilitate the vertical installation of GCL composite component, auxiliary components were attached to the GCL panel as shown in Fig 2. It can be seen clearly that the GCL composite component is equipped with a support plate and counterweight groove at the bottom of GCL panel, and the top of GCL panel is fixed on a steel roll core, with overlapping lines marked on both sides. GCL composite component can be vertically laid in a straight and controlled state with the cooperation of unwinding machinery, horizontal hammers, counterweights, etc. During installation steel-made joint box is used to prevent debris from entering the overlapping area.
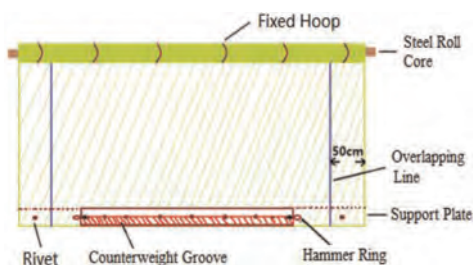

Figure 2.   Schematic diagram of GCL composite component.

The U-shaped counterweight groove is filled with counterweight blocks, composed of clay and bentonite, driving GCL panel downwards steadily. After pouring wall materials into the trench, the counterweight block can absorb water and swell in a limited space, and seal the gap at the bottom of the trench, thereby avoiding permeation at the bottom of the wall.

3 DESIGN OF GCL COMPOSITE VERTICAL ANTI-SEEPAGE BARRIER

3.1 GCL selection

According to the site specific contaminate and impermeability requirements, the type of GCL and the number of layers of GCL were determined. Usually standard GCL that comply with GRI-GCL3 specification is compatible with MSW landfill leachate and can be selected for this kind of application. Otherwise, if the landfills site gets lightly polluted and contains critical chemicals, multicomponent GCL or GCL with polymer modified bentonite should be options. In any case, product permeability test with site leachate is necessary and subsequent work can be carried out only after the verification test result is qualified. In addition, increasing the layers of GCL, namely, installing on both sides of the trench, can further improve the wall anti-seepage performance. Usually the GCL panel penetrates into the natural aquiclude no less than 1m so as to form a closed barrier system. At the top of the wall, the panel is folded and terminated with pour of concrete.

3.2 Wall backfill material selection

The environmental protection requires high anti-seepage performance of the vertical barrier wall, so the wall type generally selects low permeability walls such as soil-bentonite wall, cement-bentonite wall and plastic concrete wall. In addition, under the premise of ensuring that the permeability coefficient of the wall is not greater than 10^{-7} cm/s, the wall can also be designed as a low permeability reactive wall by adding adsorbent reactive materials such as activated carbon, zeolite, and diatomite to the low permeability wall for specific pollutants to enhance the wall's adsorbent reactive capacity for pollutants.

The selection of GCL type and wall backfill material should be assessed comprehensively according to the actual site situation so as to meet the design target both technically and economically.

3.3 GCL composite components connection

The typical roll width of GCL composite component is 5–6m. The overall anti-seepage performance partially depends on the connection quality between panels. Adjacent GCL composite component should be overlapped by a minimum of 45cm with the assistance of special construction technology and equipment as shown in Figure 2.

GCL composite components are marked with an overlap line that is 50cm away from the edge of the GCL composite component (see Figure 2). Construction personnel can clearly know the overlap position and ensure that the overlap width is not less than 45cm. A special steel joint box with a width of 50cm and length of 55cm is designed and inserted into the trench of width 60cm to prevent the backfill wall materials and construction debris from entering the overlap area to ensure the overlap construction quality. In addition, bentonite paste is applied in the seam area while the panel is lowered down into the trench. Large scale test by Zhejiang University has verified the seam permeability has the same order of magnitude with the GCL panel (Zhan L T et al. 2021).

4 ENGINEERING CASES—ENVIRONMENT REMEDIATION OF DONGCHENG LANDFILL SITE

4.1 Background

Dongcheng landfill site at Jinghai District Tianjin China was originally a pond, filled with municipal solid waste about 800,000m³. It was not constructed in accordance with landfill hazard-free regulations, no lining system was in place at the beginning. This informal landfill site gradually became a pollution source, which contaminated the surrounding atmosphere, soil, surface water and groundwater severely, posed threats to the living conditions and health of the local residents, resulted in increasingly prominent social problem (Figure 3a). The local government finally made the decision to remediate the landfill site. Considering the environment remediation target and requirement of anti-seepage grade, it was finally decided to apply on-site remediation method–cover lining + vertical barrier–to break the connection between the waste dump and surrounding environment, control the contaminant migration.
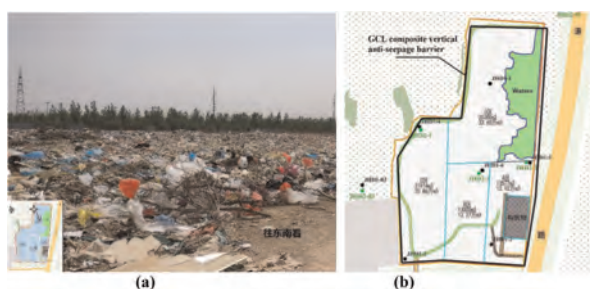
Figure 3.   (a) waste dump (b) GCL composite vertical anti-seepage barrier layout.

4.2 Design

The selection of appropriate vertical barrier system depends on the nature of the contaminant and site engineering geology and hydrogeology conditions. Thus a technical comparison was made between concrete cut-off wall, HDPE vertical barrier, and GCL composite vertical anti-seepage barrier, it was concluded that GCL vertical composite barrier system is technically superior over the two others to meet the primary target of the remediation. Therefore, from the overall consideration of safety, reliability and economic factors, it was recommended to apply "GCL+ cement-bentonite mixture" composite vertical barrier technology around the old landfill area. As shown in Figure 3b, the anti-seepage barrier is about 1500m long with an average depth of about 15m and a wall thickness of 600mm. The wall bottom is inserted into aquiclude 1.2m, and wall design permeability coefficient is less than 1×10^{-7}cm/s. Lab permeability test with GCL sample, selected for the project, and site leachate showed that they are completely compatible (Figure 4).

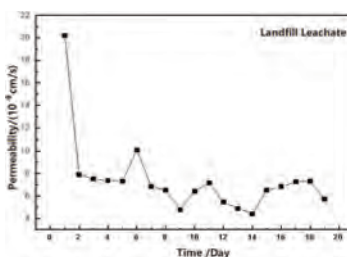Figure 4.   Effect of landfill leachate on permeability of GCL.

4.3 *Construction and engineering effect*

Bentonite grout was injected into the trench while it was excavated by hydraulic pressure grab bucket. Then GCL composite panel was installed on the side wall of the trench away from pollutants, followed by the pour of cement-bentonite mixture by underwater conduit and finally formation of the GCL vertical barrier. Because the width of GCL composite panel was 6m, it was required to excavate 6m for the first trench section, and 5.5m for the consecutive ones. A portion of fine and coarse aggregate was added to the backfill mixture to improve the wall performance, among which the 28-day compressive strength $\geq$ 0.3MPa, and the permeability of cement-bentonite backfill is in the order of 10^{-7} cm/s magnitude. See Figure 5 for construction process.

Figure 5. Construction of GCL composite vertical anti-seepage barrier: (a) Trench excavation, (b) Laying of GCL composite component, (c) Dropping down the joint box, (d) Pouring wall materials.

Inspection of site drilling core sampling and subsequent monitoring results indicated that GCL vertical barrier has excellent anti-seepage performance, and permeability coefficient can reach as low as 10^{-8} cm/s. According to the inspection report of the monitoring wells established outside of the waste dump one year after the completion of the vertical barrier, the contaminant migration is not further aggravated, and there is a trend of gradual improvement.

5 CONCLUSIONS

The permeability of GCL composite vertical anti-seepage barrier is less than 1×10^{-7} cm/s, which meets the environmental requirements of China. The wall can be designed and GCL can be selected for specific pollutants, and the multi-layer structure can cooperate with each other to cope with more complex engineering situations. The fibers and pores on the surface

of GCL make it tightly secured with the wall material to form a composite vertical impervious structure. By adopting the lap connection method for easier construction, the specially developed construction tools and construction technology can effectively ensure the lap effect and make the joint have excellent anti-seepage performance.

GCL composite vertical anti-seepage barrier has been applied in some projects. Engineering practice shows that this novel technology has excellent impermeability and chemical compatibility and is a rising vertical anti-seepage solution for comprehensive treatment of polluted sites.

ACKNOWLEDGMENTS

REFERENCES

Bohnhoff G L, Shackelford C D. 2013. Hydraulic Conductivity of Polymerized Bentonite-amended Backfills. *Journal Geotechnical and Geoenvironmental Engineering*, 140(3), 04013028.

Chen Yuan. 2017. Study on the Feasibility of Electric Power Generation by Municipal Solid Waste Incineration. *China Resources Comprehensive Utilization*, 35(07): 41–43, 57. (in Chinese))

Chun-hui Peng, Shi-Jin Feng, Qi-Teng Zheng, et al., 2020. A Two-dimensional Analytical Solution for Organic Contaminant Diffusion Through a Composite Geomembrane Cut-off Wall and an Aquifer. *Computers and Geotechnics*, 119, 103361.

Johnson AI, Frobel RK, Cavalli NJ and Pettersson CB. 1985. *Hydraulic Barriers in Soil and Rock*, Philadelphia, ASTM Publication Code Number.

Khandelwal A, Rabideau A J, Shen P. 1998. Analysis of Diffusion and Sorption of Organic Solutes in Soil-bentonite Barrier Materials. *Environ Sci Technol*, 32(9), 1333–1341.

Li Xian. 2005. *Waterproofing Property of GCL and Study on Liner System of Landfill*. Nanjing: Hohai University.

National Development and Reform Commission, 2016 *Ministry of Housing, Urban and Rural Construction. National Thirteenth Five-Year Plan for National Harmless Treatment Facilities for Urban Domestic Waste [Z]*. Beijing: National Development and Reform Commission, Ministry of Housing, Urban and Rural Construction, 12.31.

Park M G, Edil T B, Benson CH. 2011. Modeling Volatile Organic Compound Transport in Composite Liners. *Journal Geotechnical and Geoenvironmental Engineering*, 138(6), 641–657.

Rowe R K., Quigley R M., Brachman R. W., et al., 2004. *Barrier Systems for Waste Disposal Facilityes*, Taylor and Francis Group, New York.

Sangam H P., Rowe R K. 2001a. Migration of Dilute Aqueous Organic Pollutants Through HDPE Geomembranes. *Geotextiles and Geomembranes*, 19(6), 329–357.

Sangam H P., Rowe R K. 2001b. The role of HDPE Geomembranes in Retarding the Diffusive Migration of Organic Contaminants through Composite Liner Systems. *Proc. 8th Int. Landfill Symp.*, CISA Padova, Italy, 245–254.

Xie H, Wang S, Chen Y, et al., 2018. An Analytical Model for Contaminant Transport in Cut-off Wall and Aquifer System. *Environment and Geotechnical*, 1–10.

Xie Shiping, He Shunhui, Zhang Jian and Xie Tianren. 2017. *GCL Composite Vertical Anti-seepage Barrier and its Preparation Method*, China: ZL201610204661.5.

Zhan Liangtong, Ding Zhaohua, Xie Shiping, Li Yuchao, He Shunhui, 2021. Test and Analysis of hydraulic Conductivity of Geosynthetic Clay Liners Overlap in Vertical Barrier Wall. *Rock and Soil Mechanics*, Vol.42 No.9, *Sep. 2021*.

Zhen Shengli，Huo Chengli，He Zhen, et al., 2017. Application and Comparison of Vertical Barrier Technology. *Environmental Sanitation Engineering*, 5(1): 51–56. (in Chinese))

A study on the feasibility of geosynthetic oil absorbent liner to organic contaminated groundwater by selective oil absorbing and self-swelling behaviors

J. Yuu
Managing director, GOLDENPOW, Korea(S)

K.S. Kim
President, UCITECH, Korea(S)

H. Kim
Vice-president, FITI institute, Korea(S)

Y. Jeong
Senior researcher, GOLDENPOW, Korea(S)

ABSTRACT: An experimental study was conducted on the manifestation of organic contaminant-reactive geosynthetic liner for preventing the spread of contaminated groundwater. The polymer which has absorb oil highly and self-swelled was selected for the organic pollutant reactive geosynthetic barrier. This polymeric material has composited with nonwoven and film woven by needle punching process as GCLs. The geosynthetic oil absent liner prepared was immersed in organic pollutant material (TPH and TCE) for 24 hours and the permeability coefficient was evaluated (ASTM D5887). The permeability coefficient of the geosynthetic oil absent liner immersed in TPH and TCE was resulted in 7.3×10^{-8} cm/s and 1.1×10^{-8} cm/s, where the value of $\alpha \times 10^{-2}$ cm/s for the normal water as a control test. It was confirmed that the geosynthetic oil absent liner showed an orderly behavior that could sufficiently perform the role of a liquid barrier to prevents the spread of contaminated groundwater.

1 INTRODUCTION

Recently, pollution accidents due to the outflow of organic pollutants are frequent. It takes time to install a barrier system after the occurrence of an outflow, and the spread of pollutants appears extensively by that amount. Rather than taking post-measures against the leakage of organic pollutants, a solution to reduce damage by minimizing the spread of pollutants through appropriate pre-measures are required. Vertical barrier systems such as sheet piles and geomembranes seriously disturb the flow of groundwater in the blocked area and are not suitable as a precautionary measure.

When pre-installed under normal conditions, it does not affect the flow of groundwater, but when an organic pollutant spill occurs, it is necessary to think about a new liquid barrier system that selectively adsorbs only organic pollutants from the contaminated groundwater and performs the liquid blocking liner.

In geosynthetic clay liners (GCLs), which are typical reactive liquid barriers, bentonite selectively adsorbs water and swells to perform water barriers. GCLs have liquid barrier features by securing watertightness in the GCLs layer by fixing and constraining bentonite

particles that show a swelling behavior to water with upper and lower covers. A geosynthetic oil absorbent liner, applying similar concept, that forms a liquid barrier by fixing and constraining polymer particles that selectively adsorb organic pollutants can be designed. When this geosynthetic oil absorbent liner meets groundwater contaminated with organic pollutants, it selectively absorbs organic pollutant components and swells. A liner that forms a liquid barrier can be expected.

In this study, a prototype of a geosynthetic oil absorbent liner using oil-absorbing resin that selectively reacts and swells to organic pollutants was manufactured and its permeability coefficient was evaluated to prevent the spread of groundwater contaminated with organic pollutants. The feasibility of geosynthetic oil-absorbent liner was experimentally confirmed.

2 A CONCEPTUAL APPROACHE

2.1 *The liquid barrier by selective absorption and definitions*

The geosynthetic oil absorbent liner has the same structural feature as GCLs, and the sorbent resin in the central layer does not show swelling behavior under normal groundwater, but forms a gelation layer which shows a liquid barrier through adsorption &self-swelling of organic pollutants in contaminated groundwater. Therefore, in steady state groundwater, the geosynthetic oil absorbent liner shows a permeability coefficient between 10^{-2} cm/s and 10^{-1} cm/s and does not affect the flow of groundwater. Thus, geosynthetic oil absorbent liner can be defined as follows: A composite geosynthetic which has a permeability coefficient of 10^{-2} to 10^{-4} cm/s under normal groundwater conditions, that allows groundwater flow, but when it comes into contact with an organic pollutant, it shows a permeability coefficient of less than 10^{-7} cm/s within 24 hours.

As shown in Figure 1, the mechanism that shows the liquid barrier performance of geosynthetic oil absorbent liner is as follows. First, it encounters contaminated groundwater, and polymer resin particles adsorb organic pollutants and self-swell to be gelled. This resin particles gelled fill the space in the center layer of the liner and blocks the liquid flow path, thereby exhibiting the liquid barrier. At this time, the permeability coefficient is 10^{-7} cm/s or less.

As shown in Figure 1, the liquid barrier performance mechanism of the geosynthetic oil absorbent liner absorbs organic contaminants when it comes into contact with contaminated groundwater and fills the space of the center layer of the liner through self-swelling-gelling behavior to block the liquid movement path. It exhibits performance as a barrier, and at this time, the permeability coefficient is 10^{-7} cm/s or less, which is the standard for water-repellent performance.
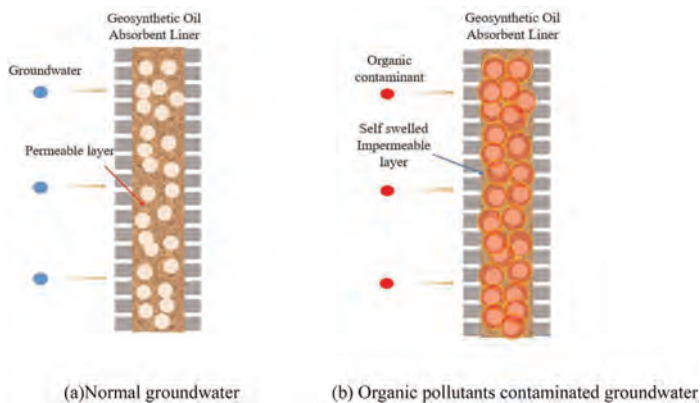

(a)Normal groundwater   (b) Organic pollutants contaminated groundwater

Figure 1.   The liquid blocking mechanism of geosynthetic oil absorbent liner.

2.2 Material characteristics required

The oil absorption characteristics and gelation behavior of the oil absorption resin used in the proposed geosynthetic oil absorbent liner determine the liquid barrier performance. Oil absorption properties are determined by the resin's unique molecular structure, chemical reactivity and powder particle size, and reactivity with organic pollutants. Oil absorption characteristics are defined in terms of swelling degree (g/g), that can be expressed the ratio (Equation 1) of mass change of resin immersed in organic pollutants solution for a certain period (24 hours or 48 hours recommended).

$$swelling\ degree = \frac{W2 - W1}{W1} \tag{1}$$

where w1 = weight of unabsorbed resin; w2 = weight of absorbed resin.

Figure 2 shows a photograph of the polynorbornene resin used in this study, immersed in TCE solution for 24 hours. As shown in the photo, it can be confirmed that the oil-absorbing resin has sufficiently gelled through oil absorption and swelling. The required swelling degree of the oil absorbent resin shows a value of 20–50 depending on the organic pollutants in contact. According to previous studies, it can be seen that the network-structured polyolefin resin with divinylbenzene as a functional group shows high oil absorption around 50 (g/g). This means that the oil-absorbed resin exhibits swelling behavior with sufficient volume change. Polynorbornene-based resins used in this study are also known to exhibit high oil absorption of about 30–50(g/g).
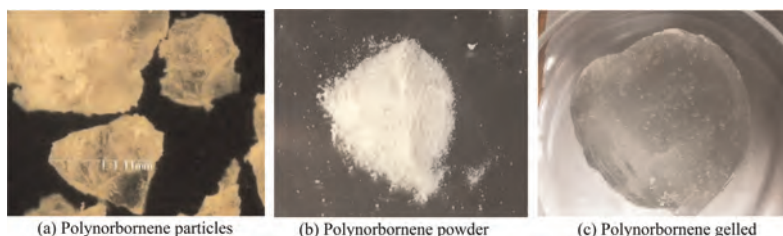

(a) Polynorbornene particles (b) Polynorbornene powder (c) Polynorbornene gelled

Figure 2.   The organic pollutants absorption and gelation behavior of polynorbornene resin.

2.3 Manufacturing the prototype geosynthetic oil absorbent liner

The prototype of geosynthetic oil absorbent liner used in this study is a mat type product, which is a composite of polypropylene staple fiber nonwoven fabric (300g/m2) and polypropylene film woven using needle punching technique, and polynorbornene is put in the center layer about 2.5kg/m^2(Figure 3).
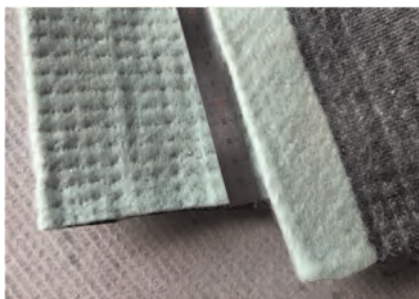

Figure 3.   The prototype geosynthetic oil absorbent liner.

3 EXPERIMENTALS AND DISCUSSIONS

3.1 *Experimental*

To evaluate the liquid barrier properties of geosynthetic oil absorbent liners, the permeability coefficient of the prototype was evaluated by applying the hydrostatic head method of ASTM D5887, which is used to evaluate the permeability coefficient of GCLs. First, the geosynthetic oil absorbent liner specimen was pretreated by immersing in a solution of organic contaminants for 24 hours. Considering the initial stage in which high-concentration organic pollutants were spilled, it was attempted to determine whether the liquid barrier performance could be achieved within 24 hours. The organic pollutants used were TCE (trichloroethylene) and TPH (diesel), respectively. The test procedure was carried out in the same way as that of general GCLs.
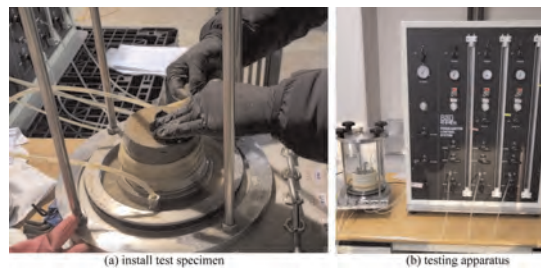
Figure 4.   A test setup of geosynthetic oil absorbent liner.

3.2 *Results and discussions*

3.2.1 *Results*

After about 24 hours of pretreatment, the permeability coefficient of the obtained geosynthetic oil absorbent liner showed a value lower than 10^{-7} m/s as shown in Table 1, confirming that the liquid barrier performance was sufficiently introduced in both organic pollutant conditions. When looking at the cross section of the prototype after pretreatment, it was confirmed that the oil absorption resin layer in the center was sufficiently swollen to form a liquid barrier layer. On the other hand, in the general groundwater condition before pretreatment, the permeability coefficient of $10^{-2} \sim 10^{-4}$ cm/s, which is similar to sandy soil, was resulted.

Comparing the values of the permeability coefficient before and after pretreatment, it can be confirmed that the geosynthetic oil absorbent liner exists as a permeable layer under normal groundwater conditions, but the liquid barrier performance is achieved by contacted organic pollutants. It can be judged that the barrier performance varies depending on the amount of organic pollutants contacted and absorbed.

3.2.2 *Discussions*

(a) concentration of organic pollutants

In the experiment, TPH and TCE stock solutions were applied. This assumes that a high concentration of organic pollutants is introduced into the groundwater at the initial stage of the oil spill accident. However, at low concentrations, the amount of organic contaminants required to form the barrier layer is insufficient, so it is expected that it will take a long time for oil absorption and swelling, and additional research is needed.

(b) pretreatment conditions

The 24-hour pre-treatment applied in the experiment is the condition for the rapid introduction of liquid barrier performance, and more reliable barrier performance was confirmed when 48 hours as standard in ASTM D5887 was applied through the pre-treatment preliminary test. In addition, since oil absorption and swelling behavior are

chemical reactions, it was confirmed through preliminary experiments that the pre-treatment temperature affects the test results.

(c) rebleeding

Sufficiently absorbed resin causes rebleeding (the behavior of discharging oil-absorbing substances) over time, but it is judged to be very insignificant compared to the initial excessive spill of organic pollutants. For what kind of behavior occurs in the actual field, it is necessary to check the behavior and performance through field test construction.

Table 1. Permeability test results of geosynthetic oil absorbent liner.

	TCE	TPH
Permeability Coefficient	1.1×10^{-8} (cm/sec)	7.3×10^{-8} (cm/sec)

(a) retrieved specimen (TCE)   (b) retrieved specimen (TPH)
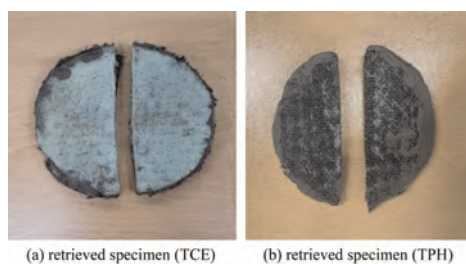
Figure 5. Retrieved Test specimens of geosynthetic oil absorbent liner.

4 CONCLUSIONS

An experimental study was carried out to confirm the feasibility of a geosynthetic oil absorbent liner that can be applied to minimize the spread of contaminated groundwater in the early stage of an accident in which organic pollutants spilled. As a result, the following conclusions could be drawn.

1. the permeability coefficients of the proposed prototype pretreated for 24 hours in TCE and TPH assuming organic pollutants were 1.1×10^{-8} (cm/sec) and 7.3×10^{-8} (cm/sec), respectively. All of them were confirmed to satisfy the criteria as a liquid barrier layer.
2. It was confirmed that the oil-absorbing resin used showed sufficient oil absorption and self-swelling properties for organic pollutants.

Although the experimental results were conducted under limited conditions, the proposed geosynthetic oil absorbent liner is seemed to be applicable to minimize the initial outflow of groundwater contaminated with organic substances. It was confirmed that additional studies on the long-term behavior of liquid barrier and the field performance.

REFERENCE

Changwoo Nam, Houxiang Li, Gang Zhang, and T. C. Mike Chung. 2016. Petrogel: New Hydrocarbon(Oil) Absorbent Based on Polyolefin Polymers, *Macromolecules* 49(15): 5427–5437

Electrokinetic geosynthetics, electro-osmosis constitutive model and numerical modelling

Y.F. Zhuang*
School of Civil Engineering, Wuhan University, Wuhan, P.R. China

ABSTRACT: Electro-osmosis was discovered more than 200 years ago. Quite a lot of phenomena discovered in that early stage of research are still attractive up to now. It seemed that research on electro-osmosis had been suspended for a while since 1950s∼1970s. It may be because both mechanism and engineering application of electro-osmosis are very complicated. However, in the past decade, there were quite a lot of breakthroughs on electro-osmosis technique. One among those was Electrokinetic Geosynthetics (EKG), a new category of geosynthetics which provides corrosion proof electrode; another one was smart DC power supply. To some extent, these breakthroughs make large scale application of electro-osmosis possible. They tackle the challenge of power demand and energy consumption not only for electro-osmosis but also for all electrokinetic related techniques in geotechnical and geoenvironmental engineering and these techniques are still evolving. This paper presents latest progresses on EKG and its application in large scale electro-osmotic dewatering and consolidation. Novel numerical modeling based on energy level gradient theory was carried out to model the field test of electro-osmotic consolidation using EKG. Comparison between calculated results and field test results is used for validation and further improvement of the numerical modelling program. The energy level gradient theory is a novel constitutive model that may help understanding of not only consolidation issue but also mechanism of unsaturated soil. Research presented in this paper is interdisciplinary and encouraging for further research.

1 INTRODUCTION

1.1 *Electro-osmosis*

Phenomenon of electro-osmosis was firstly reported by Ferdinand Friedrich Reuss in 1807, while the first publication on electro-osmosis was in 1809 (Reuss 1809). Although this phenomenon was firstly discovered in soil, it has been applied in many different areas, such as chromatographic analysis, microfluidics technology and biochips. These applications are at micro level, which aim at precise control of fluids in micro, nano or molecular scale. At micro level, the double layer model by Helmholtz is well accepted as a fundamental model to interpret the mechanism of electro-osmosis.

Electro-osmosis has applications also at macro level, such as sludge dewatering, soft ground consolidation, contaminated soil remediation, REE mining and so on. For these applications, Helmholtz's double layer model helps little for engineering design. It is because that knowing mechanism of fluid movement in micropores is not enough for predicting electro-osmosis behavior at macro scale. Therefore, theories which can be used for

---

*Corresponding Author: zhuang@tsinghua.edu.cn

engineering design of electro-osmosis need to be developed for different macro applications as mentioned above. At macro level, one of the most known theories is Esrig's theory (Esrig 1968). This is a theory to describe dewatering and variation of pore water pressure during electro-osmotic consolidation. However, electro-osmosis theories at macro level are generally insufficient for carrying out a feasible engineering design.

1.2 *Electrokinetic geosynthetics (EKG)*

The concept of EKG was firstly presented by Jones *et al.*, in 1996 (Jones *et al.* 2022; Nettleton *et al.* 1998). The idea was to make geosynthetics electrically conductive so that electrokinetic phenomena of soil can be combined with the traditional functions of geosynthetics. This concept is very inspiring for inventing a new category of geosynthetics for application of electrokinetic (EK) technique in various kinds of engineering. According to the concept, it seems that there are many flexible ways to create new EKG products; only need to make geosynthetics electrically conductive. However, it took longer time than expected to develop mature and mass-producible EKG products. The difficulties lie in many aspects and here are some of them based on the experiences of the author.

1. New products need to be clearly defined with details of function, design, materials and application scenarios; it is more than saying to make traditional geosynthetic electrically conductive.
2. Need a reason for the market to potentially accept the product so that manufacturer will have motivation to build a line to manufacture some samples for a trial and keep on evolving according to the experiments from bench scale to in-situ scale.
3. The materials planned to be used shall be available at a reasonable cost. In the area of geosynthetics, the materials especially refer to polymers, namely, electrically conductive polymers for EKG.
4. Technique of manufacturing the product shall be fully developed.

This paper presents state-of-art EKG technology based on the development history of E-board and E-tube, which are currently mass-producible EKG in China. The difficulties encountered, the solutions and the problems to be addressed will be presented and discussed.

2 E-BOARD AND E-TUBE

2.1 *Electrically conductive polymers*

Electrically conductive polymers were discovered in 1970s and the Nobel prize in chemistry 2000 was awarded jointly to Alan J. Heeger, Alan G. MacDiarmid and Hideki Shirakawa "for the discovery and development of conductive polymers". It has been decades since the discovery of conductive polymers and they have been widely used in areas like semiconductor materials or electrostatic eliminator. However, if they are going to be used to make geosynthetics, reasonable balance among electrical conductivity, strength, flexibility, machinability and cost shall be considered. This is actually the first difficulty we encountered when developing EKG.

From the year that the author noticed the concept of EKG in 2000 to the year that first sample was made, it has been about 3~4 years (Zhuang 2005). At this stage, the resistivity of EKG was 0.064 Ω·m. Theoretic analysis shows that resistivity of EKG should not be higher than the magnitude of $10^{-3}\Omega$·m, while there was no electrically conductive polymer with this resistivity commercially available in the market. We felt that this idea has strong potential but not commercially feasible at that time, so we put it on the shelf until we decided to develop raw material of the conductive polymer. The first success of developing the raw material was in 2011 (see Figure 1).
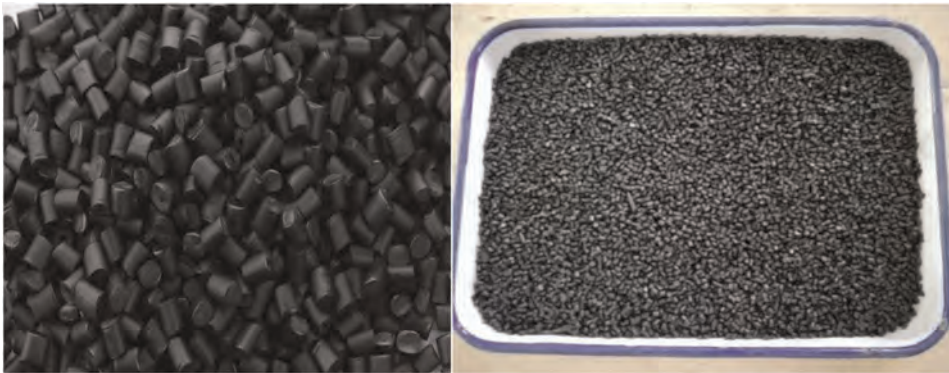
Figure 1.   Raw material of electrically conductive polymer with resistivity of of $10^{-3}\Omega\cdot m$.

2.2   EKG for dewatering and consolidation

At the first stage, namely, during 2000 to 2005, many trials were carried out and the purpose was to verify the possibility of using conductive geosynthetics as substitution for metal electrodes in electro-osmosis. At the second stage, after the adequate raw material of conductive polymer had been developed, we started to consider the definition of a specific EKG product.

E-board is the first mass producible EKG, which was achieved in 2012 in China (Zhuang *et al*. 2012). E-board was designed for dewatering and consolidation application. The reason that E-board was the first product that manufacturer willing to try was the huge usage amount of PVD (billions of meters per year in China) and the intense competition of PVD that extremely squeezed the profit margins. The appearance of E-board is similar to that of PVD only that the polymer is conductive (see Figure 2(a)). Besides this, two copper wires embedded in the bumpers of E-board are characteristic design of the E-board. This design is important for better distribution of electric current, although the polymer is conductive; furthermore, the wires is important for connecting the E-board to the power supply.

E-board was chosen as the first specifically defined product to develop also because the first generation of a new product should not deviate too far from the recognition of the products that people are already familiar with. People will not need a car to have 6 wheels. However, after E-board evolved to be mature, E-tube was designed for similar but different focus of dewatering purpures. Photos of E-tube is shown in Figure 2(b). E-tube was design for providing a better vacuum system for dewatering (Zhuang *et al*. 2014; Zhuang 2022) and a better leachate collection system for EK mining applications.
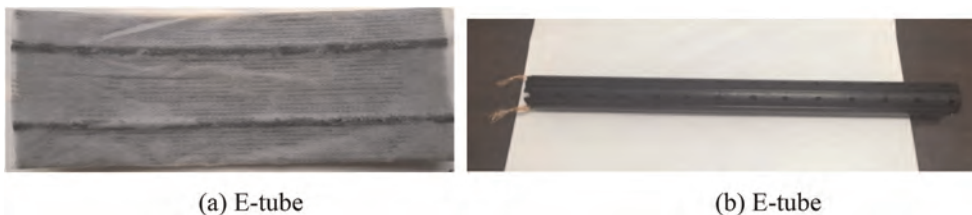

(a) E-tube   (b) E-tube

Figure 2.   EKG for dewatering and consolidation.

Generally, two major difficulties of manufacturing E-board and E-tube was as follows.

1. Difficult to balance conductivity and physical properties.

The goal of $10^{-3}\Omega\cdot m$ resistivity was difficult to achieve. Better conductivity was accompanied by lower strength and poorer flexibility. Besides the resistivity of the raw polymer materials, a method is also need for evaluation of the final product of EKG, because the manufacturing process, especially the extruding process, will change the conductive property of EKG. Now the measurement method has been proposed for E-board and E-tube (Zhuang et al. 2021). The resistivity of $10^{-3}\Omega\cdot m$ and duration of three months for minimum are now the basic requirements of quality control of EKG.

2. Difficult to embed the wires inside the polymer.

Copper has larger density than that of polymer. When the polymer is melted, copper tends to sink at the bottom. Therefore, a specially designed extruding machine shall be built in order to enclosed copper wires tightly in the right place (the bumper) inside the EKG.

3 SMART DC POWER SUPPLY

3.1 *Energy consumption*

Comparison of energy density in Figure 3 shows that energy consumption of electro-osmotic consolidation under steady voltage is much higher than that of consolidation by surcharge preloading. Surcharge preloading along e~logp curve is the lower limit of consolidation energy consumption (Zhuang 2005; Zhuang et al. 2015). The fact that electro-osmotic consolidation currently has higher energy consumption than that of preloading is an issue that restrains its application. However, it could be seen in another hand as an issue that has high volume of optimization.

The electric energy is consumed by hydrolysis, producing heat, electrochemical reaction and ion transportation, etc. besides dewatering and consolidation. It is not possible to prohibit these energy consumptions but it is possible to lower them if optimized strategy of electric field application is adopted.
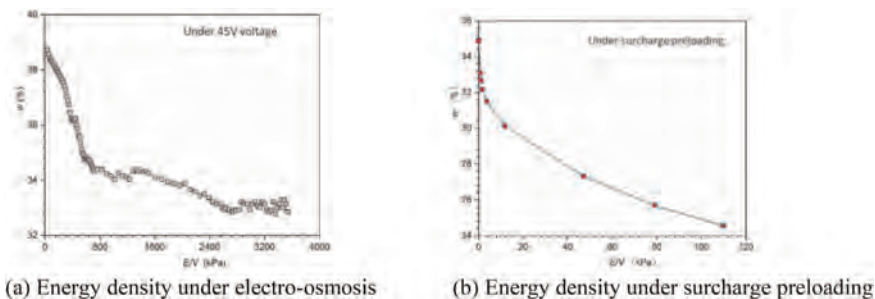

(a) Energy density under electro-osmosis   (b) Energy density under surcharge preloading

Figure 3.   Energy density under electro-osmosis and reloading consolidation (Gui 2022).

3.2 *Power requirement*

Power requirement is a more important issue than energy consumption for application of electro-osmotic consolidation in large scale. For large scale consolidation, usually thousands of square meters at the same time, electric current can be unacceptable high if a constant voltage is simply applied in the field.

The solution to tackle this problem is roll-polling program (Zhuang et al. 2015; Zhuang 2021). It is this novel technique that makes large scale application of electro-osmotic consolidation possible.

Solution for the above two issues is to invent smart DC power supply (see Figure 4). And the roll-polling program is the core of the smart DC power supply. The smart DC power supply can lower the energy consumption to less than 1 kW·h/m^3 and power requirement to less than 0.005kW/m^3. We have the idea to further reduce the power requirement to a half by redesigning the smart DC power supply.

4 ENERGY LEVEL GRADIENT THEORY

Energy level gradient theory uses energy density as a substitution of stress for analysis of dewatering and consolidation (Zhuang 2005; Zhuang *et al.* 2015). Energy density has the unit as stress, namely, kJ/m^3 = kPa, while electric energy is easy to monitor and calculate during electro-osmosis. This theory provides formulas for electro-osmosis design as follows.

Electric current can be described by formula (1)

$$I = (I_0 - I_\infty)e^{-at} + I_\infty \tag{1}$$

Where I is electric current intensity during electro-osmotic dewatering (A); I_0 is initiate electric current intensity (A); I_∞ is levelled off electric current intensity (A); t is time (s); a is time factor (s^{-1}).

Electro-osmotic dewatering can be described by formula (2)

$$Q = \frac{k_q v(I_0 - I_\infty)}{a^2 \Delta x^2}(1 - e^{-at}) \tag{2}$$

Where Q is accumulative volume of electro-osmotic dewatering at time t (m^3); t is time (s); k_q is flow rate coefficient (m^2·Pa^{-1}·s^{-1}); v is voltage (V); I_0 is initiate electric current intensity (A); I_∞ is levelled off electric current intensity (A); a is time factor (s^{-1}); Δx is distance between anode and cathode (m).

Final dewatering of electro-osmosis can be described by formula (3)

$$Q_\infty = \frac{k_q v(I_0 - I_\infty)}{a^2 \Delta x^2} \tag{3}$$

Where Q_∞ is total volume of dewatering (m^3); k_q is flow rate coefficient (m^2·Pa^{-1}·s^{-1}); v is voltage (V); I_0 is initiate electric current intensity (A); I_∞ is levelled off electric current intensity (A); a is time factor (s^{-1}); Δx is distance between anode and cathode (m).

5 NUMERICAL MODELLING

Formulas (1) ~ (3) are simplified formulas for electro-osmosis design. The precise differential equations of energy level gradient theory are as follows (Zhuang 2005; Zhuang *et al.* 2015).

$$\begin{cases} \nabla \vec{q} = k_E \dfrac{\partial E_s}{\partial t} \\[2mm] \vec{q} = k_{qx} \dfrac{\partial(E_f - E_s)}{\partial x}\vec{i} + k_{qy} \dfrac{\partial(E_f - E_s)}{\partial y}\vec{j} + k_{qz} \dfrac{\partial(E_f - E_s)}{\partial z}\vec{k} \\[2mm] \nabla E_f = \dfrac{k_{ex}}{k_{qx}}\dfrac{\partial v}{\partial x}\vec{i} + \dfrac{k_{ey}}{k_{qy}}\dfrac{\partial v}{\partial y}\vec{j} + \dfrac{k_{ez}}{k_{qz}}\dfrac{\partial v}{\partial z}\vec{k} \\[2mm] G = f_G(w) \\[2mm] \vec{j} = G \cdot \nabla v \\[2mm] w = w_0 - \dfrac{\gamma_w}{\gamma_{ds}}\displaystyle\int_{E_{s0}}^{E_{st}} k_E dE_s \end{cases} \tag{4}$$

Where $\bar{q}$ is vector of water flow rate (m·s^{-1}); E_s is energy density level (J·m^{-3}); t is time (s); k_E is energy coefficient (Pa^{-1}); $\triangledown$ is Hamiltonian operator; E_f is energy density level of the applied energy filed (J·m^{-3}); k_{qx}, k_{qy}, k_{qz} is flow rate coefficient along coordinates of x,y,z, respectively (m^{-2}·Pa^{-1}·s^{-1}); i,j,k is unit vector along coordinates of x,y,z, respectively; k_{ex}, k_{ey}, k_{ez} is electrical permeability along coordinates of x,y, z respectively (m^2·v^{-1}·s^{-1}); G is electric conductivity of soil (Ω^{-1}·m^{-1}); w is water content of soil (%); $f_G(w)$ is function of water content, which shall be determined via experiment; j is vector of surface density of electric current (A·m^{-2}); γ_{ds} is unit weight of dried soil (N·m^{-3}); w_0 is initial water content of soil (%); E_{s0} is initial energy density level of soil (J·m^{-3}); E_{st} is energy density level of soil at the t moment (J·m^{-3}).

An example of numerical modeling using this constitutive model of energy density analysis is shown as follows (Sayami 2021).

A soil model of 3m×6m×3m (breadth×length×height) was used. The dimension of electrodes was 5mm×100mm×3m. Parameters used in modeling are as follows.

p_C = preconslidation pressure (Pa) = 4kpa
γ_{ds} = unit weight of dried soil(N/m^3) = 760 N/m^3
γ_w = unit weight of wet soil(N/m^3) = 980 N/m^3
C_C = compression index (dimensionless) = 0.3865
e_o= e_C = Void ratio corresponding to p_C (dimensionless) = 2.6

Meshing of the model is shown in Figure 4. One of the modeling results is shown in Figure 5.
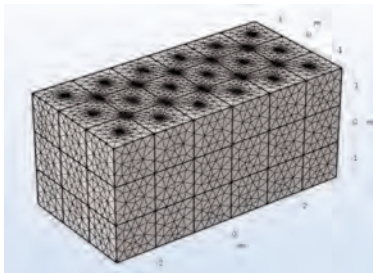

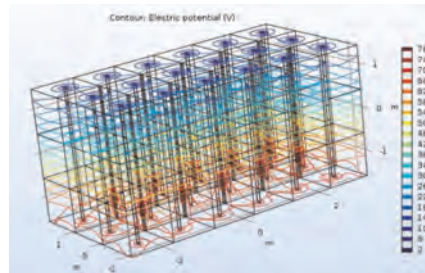Figure 4.　Meshing of the model (Sayami 2021).

Figure 5.　Electric potential contour line after 500 hours of consolidation (Sayami 2021).

6 CONCLUSIONS

This paper provides a review of the development of new category of geosynthetics, namely EKG, from concept to mass producible produces and their application in field. Limited to the allowance of pages, this paper cannot dive into very specific details of the topics, but the references listed in this paper can help for further understanding. Major conclusions are as follows.

1. E-board and E-tube are two kinds of relatively mature EKG products which are mainly used in electro-osmotic dewatering and consolidation. The important characters of these EKG materials are that they have two copper wires embedded in the electrically conductive polymer and the quality control for the EKG is that resistivity not higher than $10^{-3}\Omega$·m and duration of conductivity not less than three months.
2. To lower the power requirement is as important as lower the energy consumption and the key of achieving these purposes is developing of smart DC power supply. Roll-polling

program is the core of the smart DC power supply. Based on this technique, the energy consumption can be lower to less than 1 kW·h/m^3 and power requirement can be lower to less than 0.005kW/m^3.

3. Energy level gradient theory is developed and applied for the design of electro-osmosis in engineering scale. The key thought of this theory is using energy density as key a parameter that substitute the stress, because in electro-osmosis electric energy is easier to monitor and calculate compared to stress, e.g. pore water pressure or suction.

4. Simplified formulas of the energy level gradient theory can be used for design, while precise differential equations can be used for numerical modeling.

ACKNOWLEDGMENTS

REFERENCES

Esrig, M.I. 1968. Pore Pressure, Consolidation and Electrokinetics. *Journal of the SMFD*, ASCE, 94(SM4), p. 899–921.

Gui, Z.S. 2022. Analysis and Control in Energy Consumption of Electro-osmosis and On-site Construction Cost Management, Thesis for Master Degree, Wuhan University, China.

Jones, C.J.F.P., Lamont-Black, J. 2022. Reinforced Soil Design using the Combined Electrokinetic and Mechanical Properties of Soil. *Geosynth Int.* https://doi.org/10.1680/jgein.21.00024.

Nettleton, I.M., Jones, C.J.F.P., Clark, B.G. and Hamir, R. 1998. "Electrokinetic Geosynthetics and their Applications." *6th International Conference on Geotextiles Geomembranes and Related Products*, Industrial Fabrics Association International, Georgia USA: 871–876.

Reuss, F. F. 1809. "Notice sur un Nouvel Effet de l'électricité Galvanique [Note on a New Effect of Galvanic Electricity]." Memoires de la Société Impériale des Naturalistes de Moscou, 2, 327–337 (in French).

Sayami, Y. 2021. *Numerical Simulation of Field Test for Electroosmosis and Consolidation of Soft Ground*, Thesis for Master Degree, Wuhan University, China.

Zhuang, Y.F. 2005. *Research on EKG Material and its Application in Slope Reinforcement, Dissertation for the Doctor's Degree in Engineering*, Wuhan University, China.

Zhuang, Y.F., Zou, W., Wang, Z., Tan, X., Hu, P., Hu, S., Yan, Y. and Wang, Y. 2012. *Electric Conductive PVD. Chinese Patent*, Grant Number: ZL201210197981.4.

Zhuang, Y.F., Chen, W., Wang, Y., Yang, H. 2014. Electric Conductive Tubular Geosynthetics (E-tube). Chinese Patent, Grant Number: ZL201410269863.9

Zhuang, Y.F., Azzam, R., and Klapperich, H. 2015. *Electrokinetics in Geotechnical and Environmental Engineering*, Druck und Verlag Mainz, Aachen, Germany.

Zhuang, Y.F., Liu, Y.N., Guo, K.S. 2021. Resistance Test Technology of Electroosmosis Model. *Advanced Engineering Sciences*. 53(5), p. 138–145.

Zhuang, Y.F. 2021. Large Scale Soft Ground Consolidation using Electrokinetic Geosynthetics. *Geotext Geomembr.* 49(3):757–770.

Zhuang, Y.F. 2022. Field Test on Consolidation of Hydraulically Filled Sludge via Vertical Gradient Electro-osmotic Dewatering. *International Journal of Geosynthetics and Ground Engineering*. 8, 62. https://doi.org/10.1007/s40891-022-00406-x

Innovative installation method of geotextile tubes in deep waters

J.M. Soh & S.H. Chew
National University of Singapore, Singapore

Y.C. Tan, H.M.A. Yim, J.W.A. Quek, D.J. Lim & S. Kee
Housing & Development Board, Singapore

ABSTRACT: Geotextile tubes are commonly used as revetments and breakwaters in coastal protection structures, where most are in relatively shallow waters. A common installation method involves dropping the filled geotextile tubes from split bottom hopper barges onto the seabed in a free-fall manner. However, this method may not be suitable in deep waters because of the lack of accuracy in its placement subjected to harsh waves and current conditions. This paper critically evaluates an innovative installation method that can be done in deep waters (i.e., water depth 20–40 m) that promise adequate placement accuracy, speedy installation, and cost effectiveness. This method makes use of a high-capacity floating crane barge to lower fully filled geotextile tubes from a barge onto the seabed. A trial of this method was conducted in Singapore to construct an underwater geotextile tube bund. Monitoring sensors were installed on the geotextile tubes to monitor the effectiveness of this installation process. In addition, shape accelerometer arrays were installed beneath the geotextile tubes to monitor the ground settlement and accuracy of installation. Results from instrumentation data and observations show that the high-capacity crane barge is an effective method for the installation of geotextile tubes in deep waters of 20–40 m range.

1 INTRODUCTION

Geotextile tubes are commonly used as revetments and breakwaters in coastal protection structures. Most of these structures are in relatively shallow waters with depths of less than 20 m. During construction, there are several methods of installing the geotextile tubes. When it is to be installed along the shoreline, the empty geotextile tubes can be laid in their desired positions, before infill material is pumped into them. In relatively shallow waters up 20m, a common method is to drop the fully filled geotextile tubes in a "free-fall" motion from a split bottom hopper barge onto the seabed (Figure 1(a)) (Lawson 2008). These methods will not be suitable in deep water conditions. For example, geotextile tubes in the "free-fall" method are susceptible to the influence of currents, thus affecting accuracy of placement. For deep water conditions, there are custom-made designs to specially install geotextile tubes, such as NEREIS (Figure 1(b)).
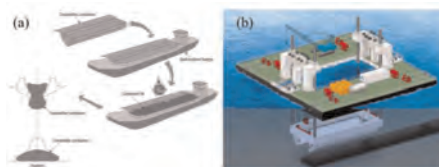

Figure 1. Installation methods: (a) "Free-fall" dropping of filled geotextile tube (Pilarczyk 2000); (b) NEREIS custom designed geotextile tube installation barge (Kamada 2010).

Systems such as the NEREIS are custom-made and are used for the specific site applications, and are less likely to be used for other applications (Kamada 2010). This prevents cost-sharing with other projects, and thus potentially contributing to the high installation costs. Thus, there is a need to search for a new method to install geotextile tubes in water depths of around 20–40m in a cost-effective, fast, and accurate manner.

2 INNOVATIVE INSTALLATION METHOD USING HIGH-CAPACITY CRANE BARGE

This paper evaluates the feasibility of using a high-capacity crane barge to lower filled geotextile tubes from a flat top barge onto the seabed. There are 2 key components required for this installation method: (1) High-capacity crane barge; and (2) Geotextile tube lifting frame. The lifting frame ensures that the lifting force from the crane barge is uniformly distributed along the filled geotextile tube. This will minimize bending and uneven lifting of the geotextile tube during lifting and lowering process. The geotextile tube is connected to the lifting frame using a sacrificial geogrid. Once the geotextile tube is lowered onto the seabed, the geogrid sheet will be cut by divers. To ensure accuracy of placement, GPS sensors were installed at two ends of the lifting frame. An illustration of this installation method and the lifting frame setup is shown in Figure 2.

Figure 2. Installation using high-capacity crane barge (left) and lifting frame with geogrid setup (right).

3 SITE TRIAL SETUP

A site trial was conducted using the high-capacity crane barge method. A total of six filled geotextile tubes were lowered onto the seabed with a 600-ton high-capacity crane barge to form a bund. During the field trial, two key factors were investigated: (1) Effectiveness of the lifting frame in ensuring uniform distribution of forces across the length of the filled geotextile tube during lifting and lowering; and (2) Accuracy of placement of geotextile tubes in water. The geotextile tubes were approximately 20–22 m in length and 6.5 m in width when filled and were made from high strength polypropylene geotextiles with ultimate tensile strengths of 200 kN/m in both Machine Direction and Cross-Machine Direction. Three of the six geotextile tubes were instrumented with strain gauges along its Longitudinal Direction (LD), Circumferential Direction (CD) and Diagonal Directions (DD), as illustrated in Figure 3. Two Shape Accelerometers Arrays (SAA) were also installed (shown in
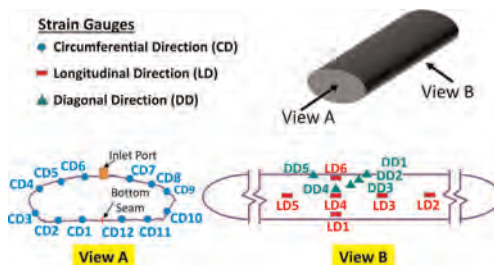

Figure 3.

Figure 4) to monitor the settlement beneath each layer of geotextile tubes and the accuracy of placement.

Finally, wireless pore pressure sensors were mounted on the exterior of the geotextile tubes to monitor the vertical movement of geotextile tubes when the geotextile tubes were lowered into the water, by tracking the depth of the geotextile tubes. Figure 5 illustrates the installation sequence for the geotextile tube bund. Figure 6 shows how the lifting frame is used to lift the geotextile tube, while Figure 7 shows the lifting and lowering process for a filled geotextile tube.
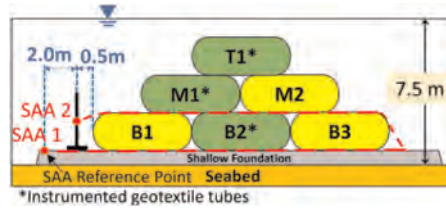

Figure 4.   Positions of shape accelerometer arrays (SAA) for settlement measurement.
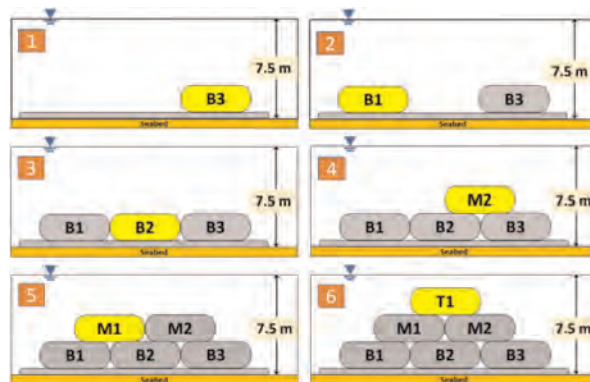

Figure 5.   Installation sequence of geotextile tubes.

Figure 6.   Connecting the lifting frame with geogrid sheet after geotextile tube was fully filled (Geogrid sheet was placed beneath the geotextile tube prior to infilling operation).

Figure 7. Lifting and lowering process: (a) Setup of lifting frame and geogrid; (b) Lifting of geotextile tube from the barge; (c) Shifting of barge that was used to install the geotextile tube; (d) Lowering of Geotextile tube into the water.

4 SITE TRIAL RESULTS

Figure 8 shows the strain gauge readings from instrumented geotextile tube B2 during the lifting and lowering process. Strain was converted to tensile force (kN/m) using the tensile force-strain relationship of the geotextiles. The initial values of tensile forces were the tensile forces induced during the infilling stage of geotextile tubes prior to the lifting operation. It was observed that the tensile forces experienced by geotextile tube started to change when the tube was lifted off the ground. Tensile forces remained constant during the whole period the tube was in the air, as well as during the whole lowering process. Tensile forces started to change again when the geotextile tube touched the seabed, until the geotextile tube was fully settled on the seabed.

The largest changes in tensile force during lifting operation was observed to occur in the Circumferential Direction (CD) of the tube, with value ranging from 5 to 20 kN/m at
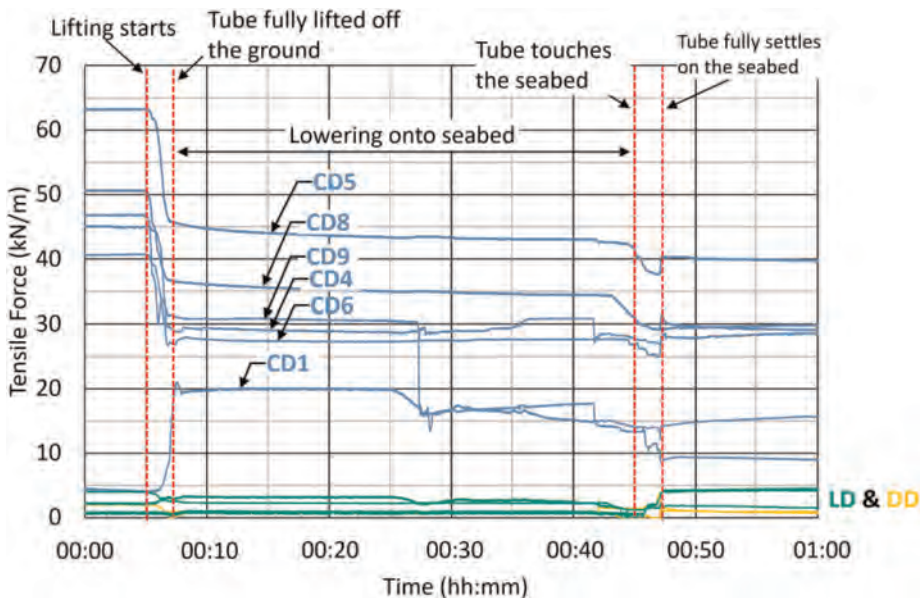

Figure 8. Selected strain gauge readings of tube B2 during lifting and lowering process.

various locations. Tensile forces in the LD and DD direction experienced very minor changes of only up to 8 kN/m. This was likely due to the deformation of the geotextile tube in its cross-section, which is CD direction, during lifting. It could also be observed that some CD readings decreased (e.g., CD5 experienced a 20 kN/m decrease in tensile force), while others increased (CD1 experienced an increase of 15 kN/m). This was likely due to the difference in positions of the strain gauges on the geotextile during the lifting process as illustrated in Figure 9. The CD strain gauges at the top of the geotextile tube (e.g., CD5) experienced a decrease in tensile force because the geotextile tube "compressed" upwards, while the strain gauges at the bottom (e.g., CD1) experiences additional tensile force as it was stretched.

Strain gauges in LD direction experienced minimal changes in tensile forces during lifting and lowering, which indicated the lifting frame's ability to maintain uniform tension in the longitudinal direction of the geotextile tube, and prevented any sagging of the tube.

Similar trends were also observed in instrumented geotextile tubes M2 and T1. Overall, the lifting frame had shown to be effective in ensuring sufficiently uniformed distribution of forces throughout the geotextile tube during the lifting and lowering process.

The wireless pore pressure sensors attached on the exterior of geotextile tubes were used to monitor its movement when it was lowered into the water. Figure 10 clearly shows a second round of maneuvering the geotextile tube after it was first lowered, i.e., after the geotextile tube was first lowered onto the top of middle layer of geotextile tubes, it was then re-lifted, and its position adjusted before it is lowered again into its final position. This demonstrated
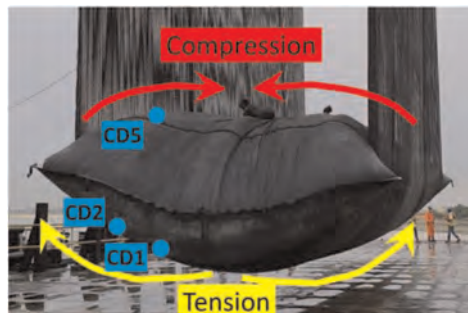

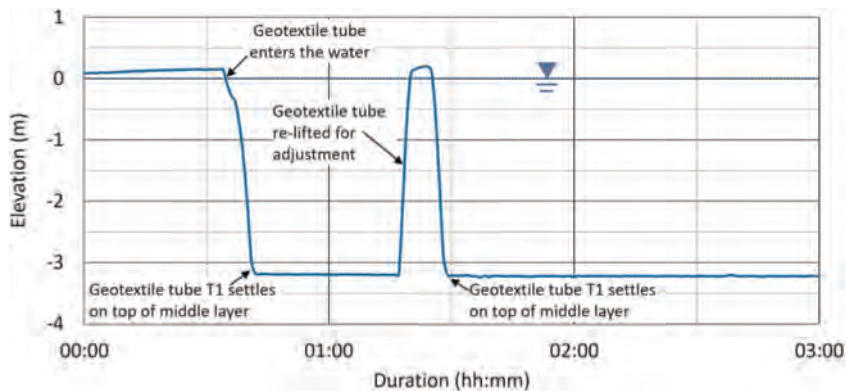Figure 9.   Deformation of geotextile tube during lifting.

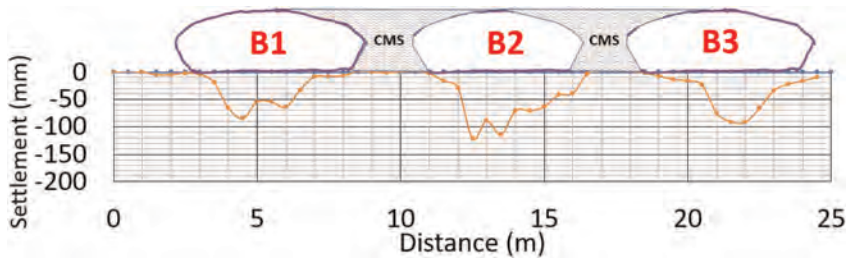Figure 10.   Movement of tube T1 during the lowering process.

Figure 11.   Bottom layer geotextile tube positions based on SAA1 settlement profile.
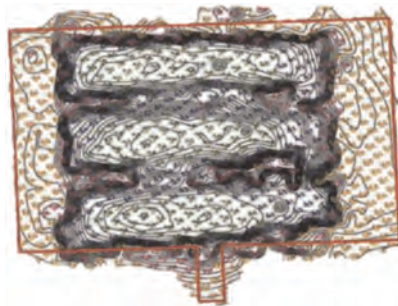

Figure 12.   Plan view result from bathymetry survey after installation of bottom layer tubes.
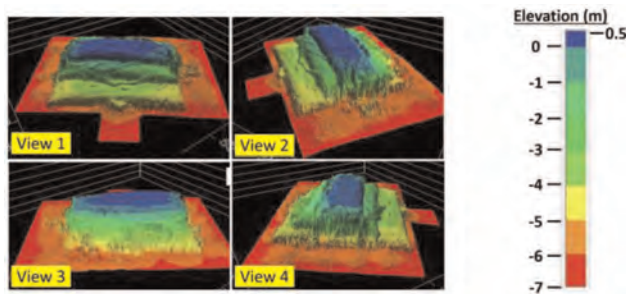

Figure 13.   3D bathymetry survey result after the geotextile tube bund had been completed.

an advantage of the crane system, where adjustment of the tube position could be made until it was in the desired position.

Shape Array Accelerometers (SAA) were useful in determining the positions of geotextile tubes as the settlement profiles could be analysed. SAA1 readings showed the settlement profile immediately below geotextile tubes B1, B2 and B3 as illustrated in Figure 11. In addition, SAA1 readings also showed that geotextile tubes B1, B2 and B3 were installed with gaps between them. After the installation of all 3 geotextile tubes which formed the bottom layer, the gaps were filled with Cement Mixed Soils (CMS). Bathymetry surveys were also conducted after various construction milestones to verify the accuracy of placement. Figure 12 shows bathymetry survey (plan view) of the geotextile tubes from the bottom layer after they were installed, and results showed good agreement with the estimated geotextile tube positions obtained from SAA1 readings. Figure 13 presents the 3D bathymetry survey

results after the completion of the geotextile tube bund, and showed that the geotextile tubes were well aligned in the longitudinal direction.

5 CONCLUSION

The objective of this paper was to evaluate the feasibility of a simple method to install geotextile tubes in deep waters of about 20–40 m. Conceptual studies were done on an innovative new method using commercially available high-capacity crane barges coupled with an innovative lifting frame. The installation method was tested under a full-scale site trial. During the lifting of the geotextile tube, strain gauge data showed that the specially designed lifting frame was able to ensure uniformed distribution of lifting forces on the geotextile tube without any sagging observed along the longitudinal direction. The high-capacity crane was also able to lower the geotextile tubes with good accuracy due to the GPS system mounted on the two ends of the lifting frame. It was further demonstrated from both the SAA data and hydrographic survey results that the geotextile tubes were installed with adequate placement accuracy, and that the whole bund could be well positioned using this method of installation. In conclusion, the high-capacity crane coupled with the special lifting frame system is a viable and economical method for installing geotextile tubes in deep waters of 20–40 m.

REFERENCES

Lawson, C.R. (2008) Geotextile Containment for Hydraulic and Environmental Engineering. *Geosynthetics International* 15, 2008: 382–427.

Pilarczyk, K. W. (2000). *Geosynthetics and Geosystems in Hydraulic and Coastal Engineering*, Balkema, Rotterdam.

Kamada, Y. (2010). Geotextile Tube Installation Barge. *Proceedings of the 19th World Dredging Congress.*

Numerical modeling of embankment on soft ground improved by prefabricated vertical drains and deep cement mixing columns

B.-P. Nguyen
Department of Civil Engineering, Industrial University of Ho Chi Minh City, Ho Chi Minh City, Vietnam

C.P. Ngo
Campus in Ho Chi Minh City, University of Transport and Communications, Tang Nhon Phu A Ward, Thu Duc City, Ho Chi Minh City, Vietnam

Y.-T. Kim
Department of Ocean Engineering, Pukyong National University, Busan, Republic of Korea

ABSTRACT: Recently, prefabricated vertical drains (PVDs) and deep cement mixing (DCM) columns have been combined to improve the soft soil ground under embankment. This not only significantly improves the shear strength in soft soil ground but also increases the rate of consolidation. The present study develops a simple two-dimensional (2-D) plane-strain numerical model of the DCM columns and PVDs improved soft ground under embankment. The geometry of the PVD and DCM column in equivalent 2-D model were obtained from the concept of same area replacement ratio, while the equivalent horizontal permeability of soft soil and DCM columns surrounding PVD was deduced from the matching of the total volume of water to be discharged in an axisymmetric model and the total changes in flow in a plane strain. Subsequently, the proposed method was applied to the Huai-Yan embankment in China, in which was used the combined method for ground improvement. The results of settlement and lateral displacement obtained from the proposed model were in good agreement with the observed data and results obtained from previous solution.

1 INTRODUCTION

It is well-known that deep cement mixing (DCM) columns and prefabricated vertical drains (PVD) have been used widely to improve soft soils under embankment construction (Chai & Carter 2011; Horpibulsuk *et al.* 2012; Lorenzo & Bergado 2003). To prevent excessive settlement and increase the bearing capacity of soft soil, DCM columns were placed into soft soil ground. PVDs were typically installed by a steel mandrel into soft ground to accelerate consolidation process of soft soil ground (Hansbo 1981; Nguyen & Kim 2018; Rujikiatkamjorn *et al.* 2013).

DCM columns are typically installed in soft soil layer to reduce the large deformation and differential settlement between the structures and the adjacent road constructions (Chai & Carter 2011). However, when DCM columns were partially penetrated in soft soil (floating improvement), a high excess pore water pressure can be accumulated in the unimproved soft clay layer. This can result in large residual settlement in the post-construction stage and a lengthy consolidation period (Liu & Rowe 2015). This point is a disadvantage in the case of DCM column improvement.

Prefabricated vertical drains (PVD) are typically used to accelerate consolidation of soft soil by reducing the length of the drainage path in ground. Thus, the settlement of PVD-improved soft soil ground was mostly completed during the construction period, resulting in reducing the post-construction settlement. Because the construction time is limited, the PVD method can consider for a cost-effective means of construction of embankment on the soft deposits. However, when the PVDs was improved solely in the soft soil deposits, the ground bearing capacity cannot be significantly enhanced as the case of improvement by DCM columns. The horizontal displacement at toe of embankment occurs largely. Therefore, the slope stability of the embankment can be reduced as the filling height increases.

To increase the slope stability of soft ground during construction and accelerate consolidation, the combination of PVD and DCM columns has been applied recently. The profile of composite foundation is shown as Figure 1. This is also a cross-section of bridge approach embankment in the Northern suburb of Shanghai in China. It can be seen that this method allows a large spacing of DCM columns and PVDs and a possible application of floating DCM columns in ground improvement. Therefore, the combined method can apply for embankment constructed over soft deposit and save the construction cost (Xu et al. 2006; Zhang et al. 2006).
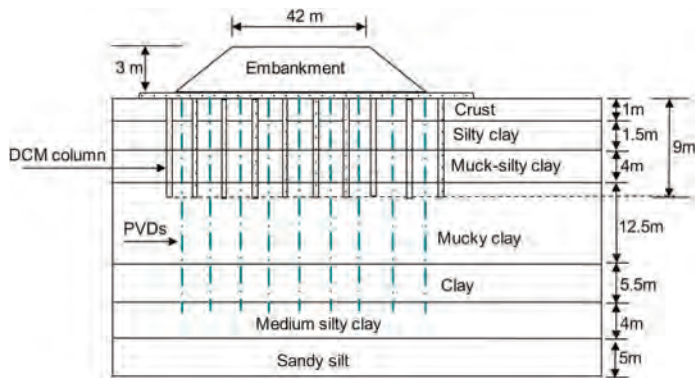
Figure 1. Cross-section of test embankment on composite foundation.

According to the advantages of the combined method, this objective has been attended in recent years. However, there are very limited of the numerical analysis for consolidation analysis and investigation of soil arching of composite foundation of PVDs and DCM columns. Therefore, aim of this study is to present a simple two-dimensional (2-D) plane-strain numerical model of the composite foundation under embankment. The geometry of the structures and the equivalent horizontal permeability of composite foundation is deduced in a plane strain. Subsequently, the proposed model is applied to and the field case of Huai-Yan embankment in China.

2 NUMERICAL MODEL

2.1 *Equivalent width of DCM column and vertical drain*

The width of PVD and DCM column in 2-D plane strain model was typically converted from situ condition. In this study, the width of PVD and DCM column in plane strain model

was obtained from matching the area ratio between the axisymmetric unit cell and the 2-D model (Nguyen *et al*. 2018, 2022), as follows:

$$b_w = C \frac{d_w^2}{S} \tag{1}$$

$$b_{DCM} = C \frac{d_{DCM}^2}{S} \tag{2}$$

where b_w and b_{DCM} are the equivalent width of PVD and DCM column in the equivalent 2-D model, respectively. C value depends on the installation pattern, i.e., $C = \pi/4$ for square pattern and $C = \pi/2\sqrt{3}$ for triangle pattern; d_w and d_{sc} are the diameters of PVD and DCM column, respectively; S is spacing of PVDs and DCM columns. In this study, the spacing of PVDs and DCM columns is the same.

2.2 *The equivalent hydraulic conductivity*

To obtain an equivalent hydraulic conductivity of PVD-installed soft soils, Nguyen *et al*. (2018) carried out the assumption that the total change in the flow in the plane strain model is equal to the total volume of water to be discharged of in-situ case for a given consolidation period. The equivalent horizontal hydraulic conductivity in 2-D model of the PVD-installed soft soil as follows:

$$k_{hp} = \frac{1}{4} \frac{S}{2} \frac{\pi k_h}{\mu \ln 2} \tag{3}$$

where S is the spacing to the adjacent PVDs or DCM columns; k_h is the horizontal hydraulic conductivity of soil and μ is the factor considering the effects of PVD spacing, smear zone and well resistance, which were described in Hansbo's solution (Hansbo 1981), as follows:

$$\mu = \ln \frac{n}{s} + \frac{k_h}{k_s} \ln(s) - \frac{3}{4} + \pi \frac{2H^2 k_h}{3q_{wa}} \tag{4}$$

where $n = D_e/d_w$, in which D_e is the diameter of unit cell and d_w is the equivalent diameter of the drain; $s = d_s/d_w$ in which d_s is the equivalent diameter of the smear zone; k_s is the horizontal hydraulic conductivity of the smear zone; H is the drainage length and q_{wa} is the discharge capacity of PVD in the axisymmetric model.

To consider the influence of DCM columns in the composite foundation, the modulus of elasticity of DCM wall in 2-D plane strain model is deduced by matching the flexural rigidity of SC column in field condition and SC wall in the equivalent plane strain (Nguyen *et al*. 2022).

$$E_{DCM}^w = \frac{3}{16} \frac{E_{DCM} d_{DCM}^4}{b_{DCM}^3} \tag{5}$$

where E_{DCM} is modulus of elasticity of DCM in situ condition.

3 CONSOLIDATION ANALYSIS OF COMPOSITE FOUDATION

3.1 *Numerical model setup and geotechnical parameters*

This section carries out a consolidation analysis of composite foundation under Huai-Yan highway embankment at stations K19 + 688–K19 + 798. The subsoil was improved by combination of DCM columns and PVDs. Both of DCM columns and PVDs were installed

in a triangular pattern at a spacing of 2.2 m and depth of 13 m, in which radius of DCM columns is 0.25 m (Ye *et al.* 2012). The profile of subsoil was detailed in Ye *et al.* (2012). It was summarized in this study as follows: the top layer is a brown clay with 1.5–2.0 m thick; the second layer is soft soil with 10.3–12.0 m thick. The soft soil is underlain by the relatively hard clay. The thickness of subsoil layers is assumed to be constant at stations for simple analysis. The height of embankment is 4m from two stages in the filling process. The first step was filled with 2.0m of embankment in 50 days, followed by 75 days for dissipation of excess pore pressure. The second 2.0m embankment was applied in 50 days in last stage. The unit weight of filling material is 20 kPa. The cross-section of Huai-Yan embankment is presented in Figure 2.
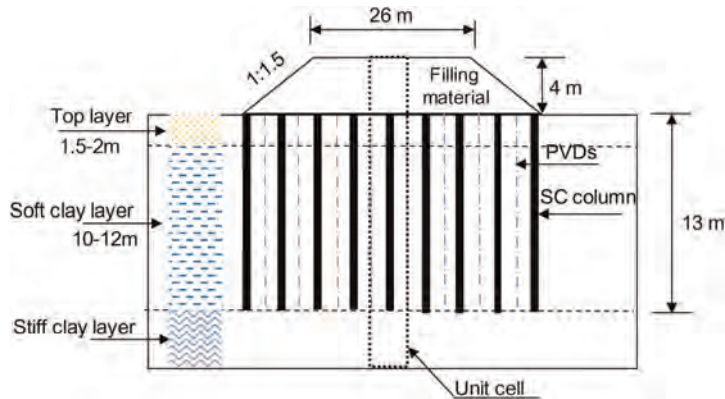

Figure 2. Cross-section of composite foundation under test embankment in Huai-Yan highway (Nguyen *et al.* 2022).

In this section, the consolidation analysis of composite foundation is performed through the present 2-D plane strain model. The behavior of subsoil layers was modeled by the modified Cam-Clay (MCC) model (Roscoe & Burland 1968). This has been widely used to model mechanical behavior of soft clay with elastoplastic model for clayey soil. Sand layers including embankment fill material and DCM walls were treated by the Mohr-Coulomb model. The equivalent permeability of soft soils and elastic properties of DCM columns in 2-D plane strain model are calculated as the above equations and presented in Table 1. The properties in Table 1 is collected from the previous studies (Nguyen *et al.* 2022; Ye *et al.* 2012). The mean of properties is as follows: E is modulus elastic; υ is Poisson's ratio; λ and κ are compression and swell index in MCC model, respectively; γ is unit weight of material; k_h and k_v is horizontal and vertical permeability of materials.

Table 1. Geotechnical properties of materials in numerical analysis.

Materials	E (MPa)	υ	κ	λ	e_0	γ (kN/m³)	k_h (m/day)	k_v (m/day)	k_{hp} (m/day)
Clay	–	0.3	0.008	0.08	0.6	18	8.64×10^{-5}	8.64×10^{-5}	2.9×10^{-5}
Soft clay	–	0.3	0.02	0.2	1.7	15.5	2.8×10^{-4}	1.4×10^{-4}	4.7×10^{-5}
Hard clay	–	0.3	0.005	0.05	0.7	19.5	2.8×10^{-4}	1.4×10^{-4}	4.7×10^{-5}
Fill material	25	0.2	–	–	–	20	0.1	0.1	–
DCM wall	80	0.2	–	–	–	20	8.64×10^{-6}	8.64×10^{-6}	–

Figure 3 presents the geometry and finite element (FE) mesh for the composite founda-tion. A 15-node triangular element was used. Because PVDs depth was shortly installed within a depth of 13 m, the factor of well resistance can be ignored in this study. Therefore, PVD can simulate as drainage element in numerical analysis (Hird *et al*. 1992). The dis-placement boundary condition was as follows: the vertical displacement and horizontal displacement were fixed at the bottom of the model, and horizontal displacement was fixed at the right and left boundaries. Drainage boundary was applied at the top surface and bottom of the model.
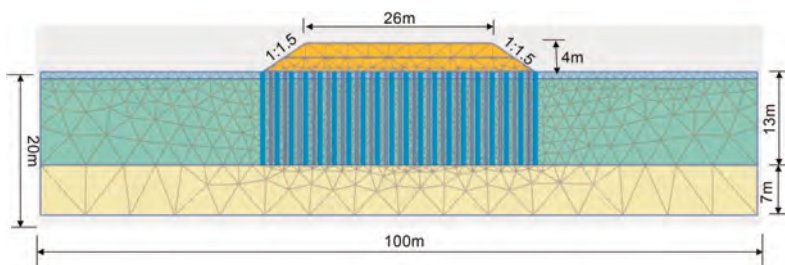

Figure 3.   Geometry and mesh properties in numerical analysis.

3.2   *Results and discussion*

Figure 4 shows the comparisons of settlement results between the predicted results obtained from the numerical analysis and the measured data. The previous solution (Ye *et al*. 2012) is also carried out to compare with the present analysis. Generally, the proposed solution provides a good agreement with the field data. The numerical results are also consistent with the results of field data and the proposed solution. The settlement result from solution of Ye *et al*. (2012) is overestimates the monitoring data and the present analysis. Ye *et al*. (2012) considered an analytical model with a single DCM column enclosed by surrounding soil and PVDs is simplified as a drainage ring. Therefore, effect of well resistance of vertical drainage is ignored. It can be seen that the proposed model is useful for the consolidation analysis of composite foundation of DCM columns and PVDs.
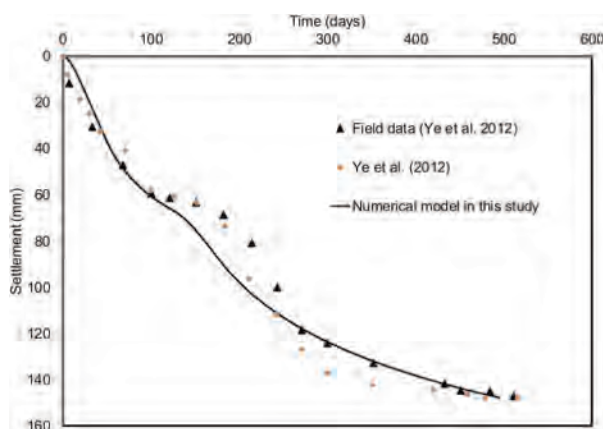

Figure 4.   Comparison of settlement results obtained from numerical model and previous solution.

Figure 5 shows the numerical results of the lateral displacement at the toe of the embankment after the construction process (i.e., 175 days). The results show that the profile shape of lateral displacement of the two cases with and without PVD is also similar. However, the lateral displacement of subsoil when PVDs are not improved is considerably larger than that with PVDs. These results could be explained that the PVDs can improve the stiffness of the soil at early stage due to consolidation process. The increase in rate of consolidation of soft soil induced by PVDs enhanced the shear strength development in composite foundation, thereby decreasing the lateral displacement under embankment for case with PVD.
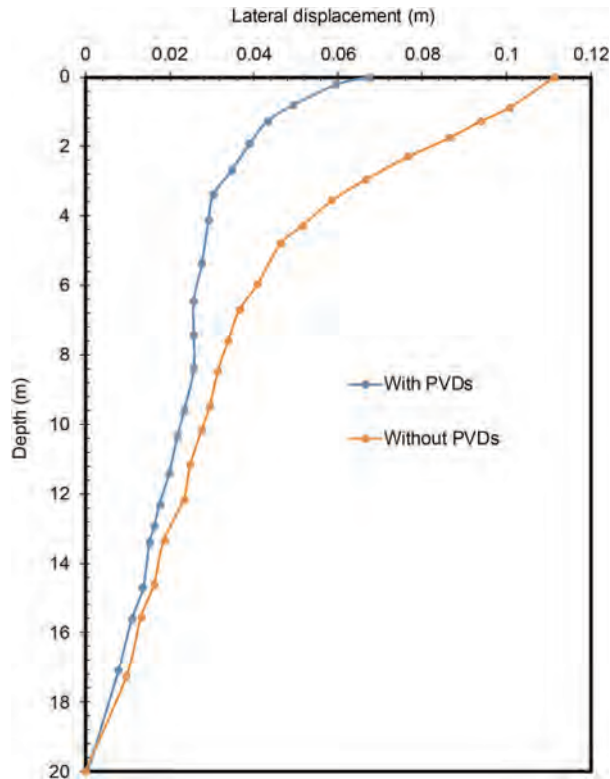
Figure 5. Numerical results of lateral displacement at toe of embankment for cases with and without PVD.

4 CONCLUSIONS

This paper proposed an equivalent plane strain model of composite foundation of PVDs and DCM columns. The equivalent horizontal permeability and dimensions of DCM and PVD in an equivalent plane strain model is provided. Effects of smear zone due to PVD installation is also considered. The proposed solution was applied to analyze consolidation behavior of soft ground improved by the combined method under Huai-Yan highway embankment in China. The results obtained from the proposed solutions are in good agreement with the measured data. The present model can use to predict consolidation behavior as settlement and lateral displacement of soft ground improved by a combined method of DCM columns and PVDs.

REFERENCES

Chai, J.C., Carter, J.P. (2011). *"Deformation Analysis in Soft Ground Improvement."* Springer, Netherlands, 258 pp.

Hansbo, S. (1981). "Consolidation of Fine-grained Soils by Prefabricated Drains." *Proc., 10th Int. Conf. Soil Mech. and Found. Eng.*, (3), 677–682.

Hird, C. C., Pyrah, I. C., and Russell, D. (1992). "Finite Element Modelling of Vertical Drains Beneath Embankments on Soft Ground." *Geotechnique* 42 (3), 499–511.

Horpibulsuk S, Chinkulkijniwat A, Cholphatsorn A, Suebsuk J, Liu MD. (2012). "Consolidation Behavior of Soil Cement Column Improved Ground." *Computers and Geotechnics*, 43:37–50.

Lorenzo, G. A., and Bergado, D. T. (2003). "New consolidation equation for soil cement pile improved ground." *Canadian Geotechnical Journal*, 40(2), 265–275.

Lorenzo, G. A., and Bergado, D. T. (2003). "New Consolidation Equation for Soil Cement Pile Improved Ground." *Canadian Geotechnical Journal*, 40(2), 265–275.

Nguyen, B-P, Nguyen, T.T, Nguyen, T. H. Y., Tran T-D. (2022). "Performance of Composite PVD-Soil Cement Column Foundation under Embankment through Plane-Strain Numerical Analysis" *ASCE's International Journal of Geomechanics*, 22(9): 04022155-1–15.

Nguyen, B-P., Yun, D-H., and Kim, Y-T. (2018). "An Equivalent Plane Strain Model of PVD-Improved Soft Deposit." *Computers and Geotechnics* 103: 32–42.

Rujikiatkamjorn, C., Ardana, M. D. W., Indraratna, B., and Leroueil, S. (2013). "Conceptual Model Describing Smear Zone Caused by Mandrel Action." *Geotechnique*, 63(16): 1377–1388.

Tavenas, F., Tremblay, M., Larouche, G., and Leroieil, S. (1986). "In-situ Measurement of Permeability in Soft Clays." *ASCE Special Conference on Use of In-situ Tests in Geotechnical Engineering*. ASCE, New York, USA, pp. 1034–1048.

Taylor, D.W. (1948). *Fundamentals of Soil Mechanics*. Wiley, NewYork.

Xu, C., Ye, G. B., Jiang, Z. S. and Zhou, Q. Z. (2006). Research on Mechanism of Combined Improvement of Soft Soils Based on Field Monitoring. *Chinese Journal of Geotechnical Engineering*, 28, No. 7, 918–921 (in Chinese).

Ye GB, Zhang Z, Xing HF, Huang MS, Consolidation XC. (2012). A Composite Foundation with Soil-cement Columns and Prefabricated Vertical Drains. *Bulletin of Engineering Geology and the Environment* 71(1), 87–98.

Zhang DW, Liu SY, Hong ZS. (2006). Consolidation Calculating Method of Soft Ground Improved by DJM-PVD Combined Method. *Ground Modification and Seismic Mitigation Proceeding of the GeoShanghai International Conference*[C]. Shanghai, China: ASCE Geotechnical Special Publication (GSP 152) 29–36.

Zhang Z, Ye G, Xing H. (2015). Consolidation Analysis of Soft Soil Improved with Short Deep Mixed Columns and Long Prefabricated Vertical Drains (PVDs). *Geosynthetics International* 22(5): 1–14.

Performance of nonwoven geotextile tubes in a water treatment plant

S.T.S. Paranhos, M.A. Aparicio-Ardila & J. Lins da Silva
São Carlos School of Engineering (EESC), University of São Paulo (USP), Brazil

ABSTRACT: Two nonwoven geotextile tubes were installed at the Bela Vista Water Treatment Plant in Nova Odessa, Sao Paulo, Brazil, to receive sludge from the decanters monthly washing. The first geotextile tube had its filling cycles performed with fresh sludge, and the second, with the addition of flocculant polymer. The tubes were monitored during the filling and emptying cycles, and in the consolidation period, obtaining some hydraulic and mechanical characteristics. For hydraulics characteristics, the performance improvement was evaluated by applying flocculant polymer concerning the sludge dewatering and evolution of the solids content. Concerning the mechanical characteristics, the strains mobilized in the nonwoven geotextile were obtained and discussed.

1 INTRODUCTION

Factors such as an increasing population, economic development and shifting consumption patterns have increased global water use by six times over the past 100 years and continues to grow steadily at a rate of about 1% per year (Unesco 2020). To accompany this growth, Water Treatment Plants (WTPs) play a significant role providing treated water to the population but producing more and more sludge. The main characteristic of WTP sludge is a material with fine grains and high moisture content that is difficult to dispose of and needs to be dewatered (Aparicio-Ardila *et al.* 2020). Geotextile tubes have been used in the sanitation sector as an alternative technology for dewatering since the 1980s (Fowler *et al.* 1996).

In an overview of this technology, geotextile tubes in dewatering applications comprise the containment, drawdown, and consolidation stages. The first stage (containment) involves filling the tube by pumping fine-grained material into the system. The drawdown stage involves the drainage of excess free water (where there is a volume reduction). The last stage (consolidation) also has a volume reduction due to the drainage and the weight of the material inserted in the tube (Kim & Dinoy 2021). The first and second stages can occur more than once, depending on the number of filling cycles specified in the project and the volumetric capacity of the geotextile tube.

Geotextile tubes can be manufactured from woven or nonwoven geotextile or a combination of both. The choice of fabrication material must be made based on the hydraulic and mechanical performance of the geotextile. Hydraulic performance refers to a solid's retention, effluent quality and other hydraulic requirements. Mechanical performance analyzes the relation of stresses and strains mobilized in the geotextile and the geometric configuration of the geotextile tube cross-section during filling.

Most studies developed with geotextile tube design are based on mechanical performance and consider low-strain materials for encapsulation (woven geotextiles) (e.g., Cantré 2002; Silva *et al.* 2021). Testing and analytical modeling of tubes made from woven geotextile for the dewatering process was studied by many authors (e.g., Aparicio-Ardila

et al. 2020; Müller & Vidal 2019; Ratnayesuraj & Bhatia 2018). Few studies have evaluated the feasibility of using only nonwoven geotextiles for manufacturing tubes, such as Aparicio-Ardila *et al.* (2020) and Bourgès-Gastaud *et al.* (2014). Despite the promising results of using nonwoven geotextiles, they refer only to hydraulic performance on a reduced scale.

The present article was motivated by gaps regarding nonwoven geotextile tubes' hydraulic and mechanical performance. This paper presents the monitoring of the geotextile tube while filling and draining cycles. It also presents the evolution of solids content in the consolidation period, and strains of two full-scale tests with tubes made from nonwoven polyester geotextile and filled with WTP sludge, with and without polymer addition to the sludge.

The objectives of this article are: (1) to present and discuss the strain data read in the field, (2) to present and discuss the volume variation while filling and draining cycles, (3) to analyze the difference in evolution in solids content with and without the use of flocculant polymer.

2 MATERIALS, EQUIPMENT AND METHODOLOGY

2.1 *Materials*

The experimental data were obtained by installing two full-scale geotextile tubes at the Jardim Bela Vista WTP located in Nova Odessa, State of São Paulo, Brazil, to receive the sludge from the monthly washing decanters. The geotextile tubes were 10 m long and 9.2 m in perimeter and were made of nonwoven polyester geotextile. The geotextile presents a mass per unit area of 612 g/m^2, tensile strength per unit width of 35 kN/m at the cross direction and 28 kN/m at the machine direction, with respective elongation of 89% and 85% in each direction, seam tensile strength of 26.54 kN/m and an apparent opening size of 52 μm.

The nonwoven geotextile tubes (GT1 and GT2) were manufactured from two rectangular geotextile layers of equal sizes, overlapped, and closed at the perimeter by two double seams. Regarding the tests, they were positioned in a draining cradle in the shape of a pool comprising draining geocomposite and PVC geomembrane.

Concerning the sludge, the specific gravity of the grains (δ) and granulometric analysis are, respectively, 2.4 g/cm^3 and 0.5% sand, 16.5% silt, and 83.0% clay. The inherent variability of the sludge should be mentioned and is reflected in the characteristics of the sludge of each test (Table 1), such as Sludge Solids Content (SSC) and the sludge-specific weight (Υ). GT1 was filled with sludge in nature, and GT2 was filled with the addition of a cationic polymer C8396, also used in Aparicio-Ardila *et al.* (2020).

Table 1 summarizes the information already presented about the experimental setup and the number of filling cycles, pump flow rate and monitoring technologies that will be described next.

Table 1. Settings used for the GT1 and GT2 tests.

Test	SSC %	Υ kN/m^3	Flocculant Polymer	Number offilling cycles	Pump flow rate–Cycle l/s–number	Monitoring Technologies
GT1	2.01 ± (1.79)	9.93	None	4	16–1, 2, 3, 4	US, DWS
GT2	3.42 ± (1.34)	10.01	C8396	5	2,8–1, 2 16–3, 4, 5	US, DWS

Standard deviations in brackets.

2.2 Monitoring technologies to collect geometry and deformation data

GT1 and GT2 were monitored using two technologies: Ultrasonic Sensor (US), which was fixed to a metallic structure that surrounded the base, and Draw Wire Sensors (DWSs), which were sewn directly onto the geotextile, 20 cm and 35 cm up to the seam, respectively for GT1 (Figure 1b) and GT2 (Figure 1c) on the top layer to measure the strain in the circumferential (cross direction of geotextile) and axial (machine direction of geotextile) directions (Figure 1a).
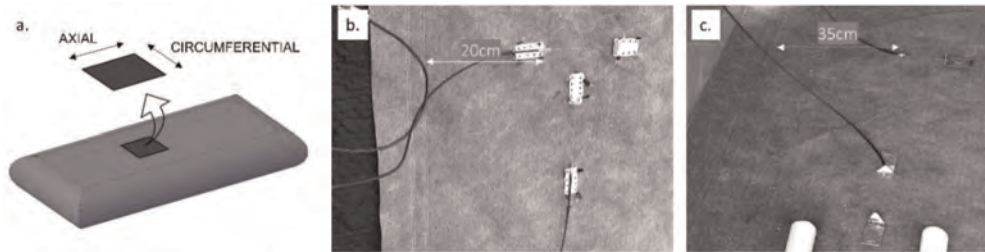

Figure 1. Site of DWSs. a) circumferential and axial directions of the geotextile tube, b) 20 cm up to the seam in GT1, and c) 35 cm up to the seam in GT2.

2.3 Monitoring technologies to collect volume variation and solids content

In GT1, a 16 l/s flow rate pump was installed to operate the four filling cycles performed. Moreover, in GT2, the choice of using two different pumps with different flow rates (the first with 2.8 l/s and the second with 16 l/s) resulted in the need to adopt one more filling because the first two fillings failed to reach the maximum height. The volume variation during filling cycles could be computed by:

- measuring the volume pumped to the geotextile tubes.
- estimating the retained internal volume, made through extrapolation of the cross-section geometry in three dimensions. The cross-section was calculated using the method proposed by Cantré & Saathoff (2011).
- dewatered volume calculated by the difference between the pumped and retained volume.

The method put forward by Cantré & Saathoff (2011) included the non-linear-elastic behavior of nonwoven geotextiles in a method based on membrane theory, which was proposed by Plaut and Suherman (1998). This procedure was done by adding a calculation step to the iterative method. With each new iteration, the previously constant perimeter increased in length due to the strain. Then, a new equilibrium was established, and the circumferential stress was recalculated. The incremental of admensional stress between two iterations was used as the stopping criterion.

After completing the filling and draining cycles, the consolidation phase was analyzed through the retained volume. A weekly collection plan of sludge samples was carried out to monitor the evolution of the solids content inside the geotextile tubes.

The collection plan was based on the division of the tube into four quadrants (Q1 to Q4) and each quadrant into four regions: corners (CO), center (CE), lateral edge (LE) and transverse edge (TE), as shown in Figure 2. This distribution was determined to collect representative samples from equidistant regions, without, however, having the influence of open areas in previous collections. Small windows were opened in the upper part of the geotextile tube to access the different regions, and the sludge samples were extracted using fractions of PVC tubes. Subsequently, the average solids content of each sample was determined.
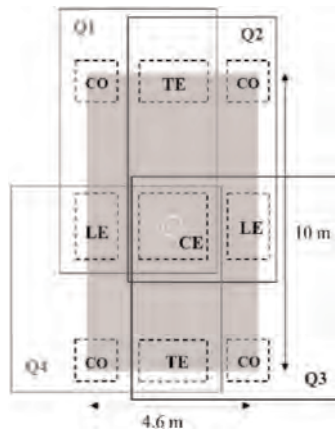
Figure 2.   Location of quadrants and regions for sample collection.

3   RESULTS AND ANALYSES

3.1   *GT1 full-scale test*

The data collected by the US and DWSs were correlated using a time scale (Figure 3a). On this time scale, with time in days, the maximum circumferential stress occurs concomitantly with the maximum filling height in each cycle and decreases over the days during dewatering. It was observed that the strain of the material continued in the 24 hours following the end of each filling. It reached an increase in strains with a magnitude of less than 1% in all four cycles. This behavior is similar to the creep process due to the maintenance of the applied pressure. In this period, the filling height remained close to the maximum.

The maximum fill height recommended by the manufacturer for a geotextile tube with the dimensions used in this study is 1.30 m. The first filling was a height variation of 1.52 m and a strain of 18.6% in the circumferential direction and 15.1% in the axial direction. Due to dewatering, a reduction of 1.19 m in the height was observed after a week, associated with a geotextile shrinkage of 6.9% in the circumferential direction and 2.1% in the axial direction, that is, reaching strains of 11.7% and 13%, respectively in relation to the beginning of the test. In the second cycle, a maximum height of 1.33 m and strain in relation to the beginning of 22.2% and 18.3%, respectively, were reached for the circumferential and axial directions. From this cycle onwards, the strains between filling and dewatering were closer.

This behavior points to some possibilities: there was a gradual loss of material resilience or an accommodation of the geotextile and consequently of the DWS when the tube empties as the cross-section assumes a flatter shape. Moreover, the width increases due to the spread of the material contained in the geotextile tube (Shin & Oh 2003).

Figure 3b presents the volume variation during cycles and consolidation periods. Totaling the pumped, internal, and drained volumes for GT1, we have: 158 m^3, 15 m^3 (retained after the consolidation period) and 143 m^3. According to the manufacturer, the volumetric capacity of GT1 is 45 m^3, thus it was able to receive it in 4 filling cycles 3.5 times its capacity. During the first filling, 71 m^3 were pumped (approximately 1.6 times its volumetric capacity), which means the initial instant drainage was efficient. In the next cycles, with increased solids retained inside the geotextile tube, the remaining free storage volume is reduced, and the formation of the filter cake makes the drainage slower. In the last filling, the instantaneous drainage was so slow that the pumped volume was similar to the volumetric capacity available.
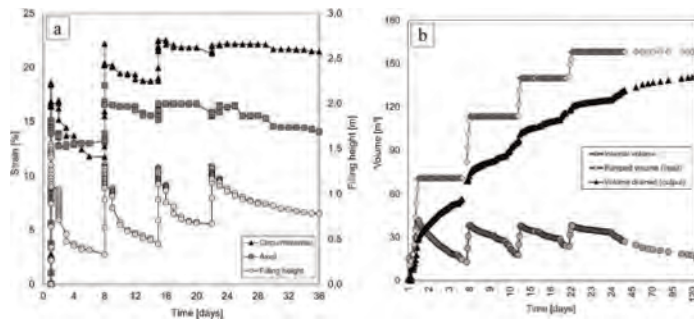
Figure 3. GT1 test. a) circumferential and axial strain during cycles obtained with DWSs and filling height obtained with US. b) volume variation during filling and draining cycles and consolidation period.

3.2 GT2 full-scale test

The data collected by the US and the DWSs were correlated using a time scale and are shown in Figure 4a. The lower flow pump kept the geotextile tube with a low fill height in the first two cycles. When changed to the higher flow pump after the third cycle, it was possible to reach the maximum planned height (in this case, 1.30 ± 0.07 m). For cycles 3, 4 and 5, the maximum heights were 1.32 m, 1.33 m and 1.37 m, respectively. In the moments with maximum height, the strains read in relation to the beginning of the test were 13.2%, 14.2% and 15.1% in the circumferential direction and 8.2%, 10.1% and 11.5% in the axial, respectively, for cycles 3, 4 and 5. These data reaffirm the hypothesis that each new filling exerts an additional effort on the material, resulting in more significant strains.

According to the DWS readings, the axial and circumferential strains were very close in the first two filling cycles. These data need to be analyzed with caution, as the readings may indicate the influence of short geotextile tube (where the non-establishment of the plane stress state is). Alternatively, it can indicate the accommodation of the material. When the tube starts to be filled, the geotextile is not completely stretched, and the pumping pressure agitates the geosynthetic.

The main difference between the GT1 and GT2 tests, compared to the maximum fill height, is in the first cycles: in GT1, the maximum height occurred in the first filling, leading to a large initial strain, while the last three cycles presented heights close to 1.30 m. In GT2, the first two cycles had low filling heights (0.14 and 0.59 m) due to the characteristics of the pump. After changing the pump, the following three cycles reached a height close to 1.30 m. It is likely that this initial difference led to the reading of the retraction between cycles 1 and 2 in GT1 and the absence of the retraction in GT2. Despite a small increase in strains between readings (according to height variation), it can be considered that they stabilized in cycles with a height of 1.30 m in GT2, as occurred in GT1. It can be observed in GT2, as well as in GT1, that there was a continuous strain of the material, which never exceeded 1%, during the continuous 24 hours at the end of the fillings.

Figure 4b presents the volume variation during cycles and consolidation periods. Totaling the pumped, internal, and drained volumes for GT2, we have the following: 138.5 m^3, 20 m^3 (retained after the consolidation period) and 118.5 m^3. GT2 was able to receive 3.1 times its capacity in 5 filling cycles. The total pumped volume was smaller than the volume of GT1. However, the volume of solids retained inside the geotextile tube was 33% higher, which was justified by the solids content of the pumped sludge, which was 70% higher than that of GT2. The pumped volume was reduced throughout the cycles, but this reduction was smaller than that observed in GT1, indicating better instantaneous dewatering and less filter cake formation.
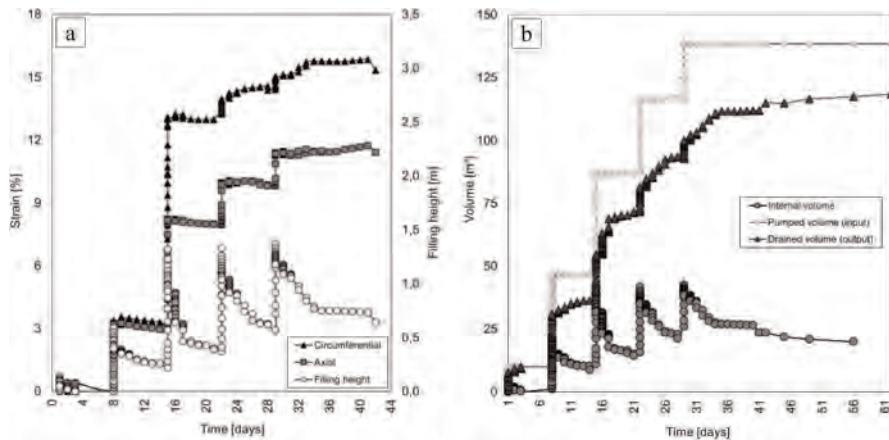
1737

Figure 4. GT2 test. a) circumferential and axial strain during cycles obtained with DWSs and filling height obtained with US. b) volume variation during filling and draining cycles and consolidation period.

3.3 Evolution in solids content with and without using flocculant polymer

Figure 5 shows the average solids content obtained in each collection performed for GT1 and GT2. The effects of using the flocculant polymer could already be seen in the sludge samples collected from the filling pipe: the separation of solid and liquid fractions was clear. This prior separation caused the dewatering to occur at an accelerated rate, with consequent evolution of the solids content in a period 3 times shorter when compared to GT2, disposed of for 34 days, with GT1, disposed of for 103 days to reach sufficient solids content for removal.

Another point that draws attention is the distribution of the solids content of the sludge in the geotextile tube: the center was the region with the lowest solids content (therefore, higher humidity) and the corners, which was the highest solids content throughout the entire evolution. The edges showed intermediate values. These results indicate that the regions with the largest exposure surface have a shorter dewatering time. Upon reaching a solids content of around 25%, the appearance of a solid and consistent sludge can be observed. Solid content that is considered appropriate for removal and sending to a landfill.
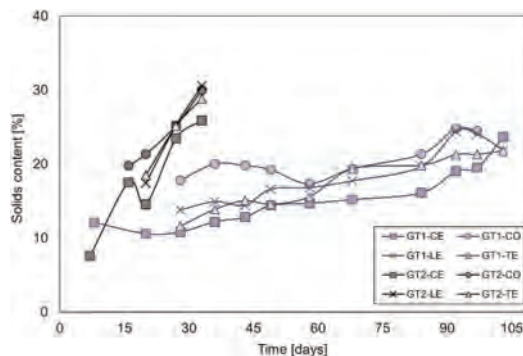

Figure 5. Comparison of the evolution of solids content between the two tests: GT1 (without using flocculant polymer) and GT2 (with the use of flocculant polymer).

4 CONCLUSIONS

The nonwoven geotextile deforms during the filling cycles, and the maximum strains are obtained concomitantly with the maximum heights. Upon reaching the maximum height, before starting the dewatering, a settling of the material was observed, similar to the creep behavior.

The maximum strain concerning the beginning of the GT1 test was 22.2% and 18.3%, respectively for the circumferential and axial directions and occur during the second filling. These strains are a quarter of the deformations found at the material's breaking point. Therefore, tensile strength and deformation properties offered by this type of geotextile were not shown to be a limiting factor in this study, indicating that its use should be further explored for the dewatering of WTP sludge. However, it is indicated that further studies should be carried out to determine the point of greatest mobilization of cross-sectional strains.

The presence of flocculating polymer directly influenced the dewatering conditions and the evolution of the solids content in the consolidation phase. GT2 showed an evolution of approximately three times faster than GT1.

REFERENCES

Aparicio-Ardila, M. A. A., Souza, S. T., Silva, J. L., Valentin, C. A. & Dantas, A. D. B. 2020. Geotextile Tube Dewatering Performance Assessment: An Experimental Study of Sludge Dewatering Generated at a Water Treatment Plant. *Sustainability*, 12, 19, 8129.

Bourgès-Gastaud, S., Stoltz, G., Sidjui, F. & Touze-Foltz, N. 2014. Nonwoven Geotextiles to Filter Clayey Sludge: An Experimental Study. *Geotextiles and Geomembranes*, 42, 3, 214–223.

Cantré, S. 2002. Geotextile Tubes-analytical Design Aspects. *Geotextiles and Geomembranes*, 20, 5, 305–319.

Cantré, S. & Saathoff, F. 2011. Design Method for Geotextile Tubes Considering Strain–formulation and Verification by Laboratory Tests using Photogrammetry. *Geotextiles and Geomembranes*, 29, 3, 201–210.

Fowler, J., Bagby, R. M. & Trainer, E. 1996. Dewatering Sewage Sludge with Geotextile Tubes. *Proceedings of the 49th Canadian Geotechnical Conference*, St. John's, Canadian Geotechnical Society, 129–137.

Kim, H. J. & Dinoy, P. R. 2021. Two-dimensional Consolidation Analysis of Geotextile Tubes Filled with Fine-grained Material. *Geotextiles and Geomembranes*, 49, 5, 1149–1164.

Müller, M.; Vidal, D. 2019. Comparison between Open and Closed System for Dewatering with Geotextile: Field and Comparative Study. *Int. J. Civ. Environ. Eng.*, 13, 634–639.

Ratnayesuraj, C.R.; Bhatia, S.K. 2018. Testing and Analytical Modeling of Two-dimensional Geotextile Tube Dewatering Process. *Geosynth.* 25, 132–149.

Shin, E. C., Oh, Y. I. 2003. Analysis of Geotextile Tube Behaviour by Large-scale Field Model Tests. *Geosynthetics International*, 10, 4, 134–141.

Silva, V. L., Gardoni Almeida, M. G. & Pimentel, K. C. A. 2021. Numerical Modelling of Geotextile Tubes Filled with Gold Mine Tailings. *Geosynthetics International*, 1–32.

Unesco. 2020. *World Water Development Report 2020–Water and Climate Change*. Available online: https://en.unesco.org/themes/water-security/wwap/wwdr/2020#download (accessed on 24 Nov 2021)

Experimental investigation on a novel graphene-based geotextile under mechanical loading

H.T. Senadheera, A. Bouazza & J. Kodikara
Department of Civil Engineering, Monash University, Clayton, VIC, Australia

D. Gibbs
Technical, Research and Innovation, Geofabrics Centre for Geosynthetic Research, Innovation & Development, QLD, Australia

ABSTRACT: Traffic loading, temperature and moisture variations are the main external causes of distresses in pavements. Therefore, it is crucial to monitor pavement loading to facilitate operation, rehabilitation and maintenance of road networks. Current in-situ pavement monitoring methods, which use embedded sensors in the pavement, allow real-time supervision of the road health condition. However, these methods are destructive to the pavement while they can provide information at distinct locations only. Therefore, there is a deficiency in a method that allows spatially continuous monitoring in roads. In this research, a novel graphene-coated geotextile is evaluated for use in applications as a distributed sensor to detect pavement response and damage. In this study, tests were conducted to examine the piezoresistive response of the material by subjecting the geotextile specimens to tensile loading. The results showed a significant electro-mechanical behaviour with potential to be used in a vast range of applications in road infrastructure.

1 INTRODUCTION

Road rehabilitation and maintenance cost billions of dollars each year for federal and state governments. Cracking, rutting, wear and deflection are some of the most common pavement distresses. Traffic loads and environmental loads are the main external causes of road failure. Environmentally-driven deterioration in pavements can occur primarily due to temperature and moisture variations, which impact both long-term and short-term pavement performance. In addition, traffic congestion and vehicle overloading accelerate the deterioration of pavements. Therefore, it is important to monitor traffic and environmental loading in real-time, to regulate effective Pavement Management Systems (PMS). Consequently, it is also crucial to establish appropriate traffic management procedures to extend the service life of roads.

Currently, in-situ pavement health monitoring methods are used to obtain real-time information on pavement response in terms of stress, strain, moisture and temperature. Strain gauges, Linear Variable Differential Transformers (LVDTs), Fiber Optics (FO), moisture probes and thermocouples are few of many in-situ monitoring methods commonly used for structural health monitoring (SHM) of pavements (Wang *et al*. 2012). Inductive loops and Weigh-In-Motion (WIM) systems are two of the widely-used technologies by road agencies for traffic volume and mass surveys, respectively. However, most of these methods can only obtain measurements at distinct locations, which as a result incur large installation and maintenance costs.

In this research, a novel graphene-based geotextile is examined for use in sensing applications in roads. The geotextile, made conductive by applying a graphene coating, is currently used for liner integrity surveys in containment facilities. The research is aimed at expanding its existing applications and investigating its feasibility as a distributed sensor to capture pavement response.

In order to assess its feasibility as a sensor, the aforementioned graphene-coated geotextile was tested for its electrical behavior with applied tensile loading. This paper presents a background to graphene-based geotextiles and the results obtained from the characterization tests for the geotextile.

2 GRAPHENE

Graphene is a quasi-two-dimensional monolayer of Carbon atoms, arranged in a hexagonal lattice that forms a 2D honeycomb lattice plane. Due to this structural stability of graphene, although its thickness is only around 0.35 nm, it has a very high mechanical strength, which is about 100 times the strength of steel of same thickness. Graphene has three strong sigma-bonds in each lattice and one pi-bond which provides freely moving electron that results in its high electrical conductivity. (Zhen & Zhu 2018).

These favorable properties have made graphene a promising material in high-sensitivity sensing systems. For example, under mechanical strain, the electronic structure of graphene would be altered such that a bandgap is introduced into the material, resulting in significant electro-mechanical effect, i.e. piezo-resistive effect (Yang *et al*. 2018). Due to high flexibility, sensitivity and working range of graphene-based strain sensors compared to that of traditional metal-based or silicon-based strain sensors, many strain sensors have been fabricated for graphene transferred onto flexible polymer substrates (Li *et al*. 2012).

3 GRAPHENE-BASED NON-WOVEN GEOTEXTILE

A graphene-based geotextile was manufactured by Geofabrics Australasia by coating a non-woven geotextile with graphene. The integration of graphene makes the geotextile conductive and thus, is being used in leak detection applications in waste, containment and landfills (Aitchison *et al*. 2019). In liner integrity surveys in barriers by electrical inspection, a voltage is applied to the surface of the barrier and leaks are detected via a closed electrical circuit forming at the leak location. When the subgrade soil is dry or non-conductive, water is supplied to provide sufficient electrolytes. This is called as the water lance or water puddle method (Parra & Owen 1988). However, this method incurs high installation and transportation costs and also record false leaks due to the presence of water. Therefore, an alternative method using conductive geotextiles are being currently used to test lined systems for defects. A voltage is supplied to an inspection probe and when a leak is identified, current will flow into the conductive geotextile to form a closed circuit, generating a warning (Figure 1).
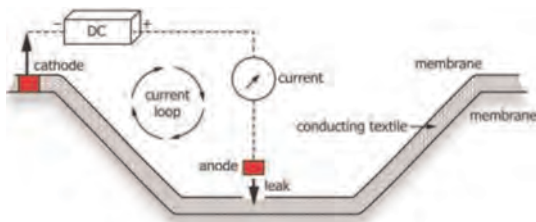

Figure 1.   Diagram of the arc testing method (ASTM D7953).

3.1 *Application of the graphene-based geotextile in pavements*

As explained in Section 1, there is still a deficiency of monitoring methods that enables spatially continuous monitoring within SHM of pavements. Therefore, the current study is aimed at investigating the properties of the said graphene-coated geotextile for applications in pavement hydro-thermo-mechanical load monitoring as a spatially continuous sensor.

The graphene coating on the geotextile forms a conductive paths network on the synthetic fibers of the geotextile. When subjected to external loading, the conductive paths deform, distort and then break with increasing load (Park *et al*. 2002). These changes occurring to the conductive paths of the graphene coating manifests as a change in electrical resistance of the geotextile. Due to the conductivity of the material, this change in electrical property can be measured and reliably related with the applied load. Thus, it can be potentially used for field applications taking advantage of its distributed sensing capability.

3.2 *Mechanical load testing on the graphene-based geotextile*

A series of tensile tests were conducted to characterize the electrical behavior of the graphene-based geotextile with applied mechanical loading. The geotextile was subjected to tensile loading until failure and its electrical resistance was measured simultaneously. The objective was to examine the correlation between the mechanical strain and change in electrical resistance of the graphene-based geotextile under tensile loading.

In order to examine its reliability and sensitivity as a sensor, the Gauge Factor (GF) was calculated (Avilés *et al*. 2018), which is the slope of the linear relationship between the relative change in electrical resistance and the applied strain (Equation 1).

$$GF = \frac{\left(\frac{\Delta R}{R_0}\right)}{\varepsilon} \tag{1}$$

where, R_0 is the initial electrical resistance of the sensor corresponding to the unstrained state and ε is the applied strain.

Figure 2 shows the relative resistance change (dR/R_0 (%))–strain (%) relationship obtained by the tensile tests. The study deals with applications in road infrastructure, hence, strains only up to 10% were used for further investigation. The experimental results indicated that the material shows a consistent and significant electro-mechanical response for the range of strains 0 to 10%.
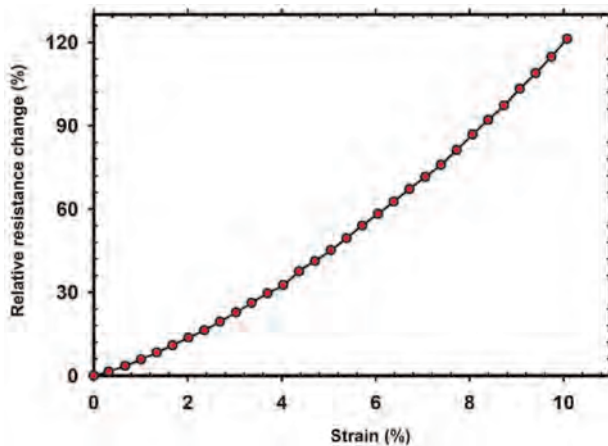

Figure 2.   Relative resistance change vs strain data obtained by the tensile tests.

The obtained data was fitted into a linear curve to calculate the slope, i.e. the gauge factor (GF) for each specimen. The obtained GFs by the repeated tests were in the range of 11 to 15, indicating a notable electro-mechanical response in the geotextile.

4   CONCLUSIONS AND FUTURE RESEARCH

The notable relationship between the electrical resistance and tensile loading obtained from the laboratory tests ascertain its potential as a distributed sensor for use in pavements, with special focus on detecting pavement damage, such as excessive deformation i.e. rutting. Further testing is to be carried out to simulate traffic loading conditions and to determine how the graphene-based geotextile behaves under actual field conditions. Moreover, a suitable field monitoring technique needs to be established in order to utilize this geotextile in practical applications.

Future transport infrastructure will consist of smart roads, where they will be equipped with smart materials and technologies providing network capability. It is expected that the graphene-based geotextile will contribute to developing new tools and techniques to pavement health monitoring and vehicle management in the context of smart road infrastructure.

REFERENCES

Aitchison, P., V. Giorgio and G. Mathieson (2019). *Geotextile with Conductive Properties*, Google Patents.

Avilés, F., A. I. Oliva-Avilés and M. Cen-Puc (2018). "Piezoresistivity, Strain, and Damage Self-Sensing of Polymer Composites Filled with Carbon Nanostructures." *Advanced Engineering Materials* 20(7).

Li, X., R. Zhang, W. Yu, K. Wang, J. Wei, D. Wu, A. Cao, Z. Li, Y. Cheng, Q. Zheng, R. S. Ruoff and H. Zhu (2012). "Stretchable and Highly Sensitive Graphene-on-polymer Strain Sensors." *Scientific Reports* 2 (1): 870.

Park, J., T. Okabe, N. Takeda and W. Curtin (2002). "Electromechanical Modeling of Unidirectional CFRP Composites under Tensile Loading Condition." *Composites Part A: Applied Science and Manufacturing* 33 (2): 267–275.

Parra, J. and T. Owen (1988). "Model Studies of Electrical Leak Detection Surveys in Geomembrane-lined Impoundments." *Geophysics* 53(11): 1453–1458.

Wang, L., X. Wenjing, C. Druta and D. Wang (2012). "Integration of Structural Health Monitoring and Asset Management."

Yang, T., X. Zhao, Y. He and H. Zhu (2018). 6–Graphene-Based Sensors. *Graphene*. H. Zhu, Z. Xu, D. Xie and Y. Fang, Academic Press: 157–174.

Zhen, Z. and H. Zhu (2018). 1–Structure and Properties of Graphene. *Graphene*. H. Zhu, Z. Xu, D. Xie and Y. Fang, Academic Press: 1–12.

Invention of a new geosynthetic drainage sheet to optimize hydraulic and mechanical performance for extreme geotechnical applications

R. Kroh & H. Zanzinger
SKZ–German Plastics Center, Würzburg, Germany

F. Lotz
University of Applied Sciences Würzburg-Schweinfurt, Würzburg, Germany

ABSTRACT: Especially in landfill lining systems and mining, the compressive loads on the sealing system and the overlying drainage system are enormous. They must be absorbed by the geosynthetic drainage systems without damage and without compromising hydraulic performance, i.e. sufficient water flow capacity.

Newly developed, integrally manufactured geosynthetic drainage sheets (GDS) made of high-density polyethylene (HDPE), which are based on a new, patented process, are being tested in laboratory trials on specimens produced in the laboratory. In particular their short-term compressive behavior and their water flow capacity under high compressive stresses with soft bedding were investigated. The results of the novel GDS are also compared with laboratory-made geonet structures. While geocomposites with geonet drainage cores suffer very severe losses in water flow capacity under the influence of surcharge and even more so under the influence of soft bedding, drainage geocomposites made of the novel GDS show a much smaller decrease and better performance than conventional products.

Weaknesses of biplanar geonets with regard to compressive behavior under the influence of compressive loads as well as a reduction of hydraulic effectiveness with ribs running obliquely to the slope are specifically circumvented by appropriate selection and size of the waterway grooves of the GDS running in the machine and cross-machine direction.

1 INTRODUCTION

Geosynthetics with the main function of drainage are state of the art in various areas of civil engineering, e.g. road, tunnel, landfill, or mining construction. When installed, the drainage systems must be able to drain water or any kind of liquid penetrating from the ground with as little pressure loss as possible for the entire period of use. (Koerner 2007; Rüegger & Hufenus 2003)

In applications with high compressive loads, e.g. in landfill lining systems or mining, the drainage systems must show high mechanical resilience, i.e. the drainage structure must not fail due to the compressive stress. The ability to collect and drain water (water flow capacity) must be guaranteed for any given time to avoid failure of the drainage system and thus of the entire application.

Nowadays drainage systems consisting of geonet structures (GNT) in combination with geotextiles are used at high compressive loads. Compared to drainage systems consisting of structured or randomly arranged monofilaments, or dimpled geomembranes, drainage

systems consisting of GNT show little compression with high absorption of compressive stress. (Müller *et al.* 2008)

Nevertheless, failure of the drainage structure can still be observed at enormous compressive loads, especially in biplanar GNTs. This so called "roll-over" effect describes the twisting of the upper ribs of the GNT in relation to the ribs below under high compressive load and shear stress. This leads to a reduction in the cross-section required for the water flow. In practice, this means a reduced water flow capacity for the geosynthetic drainage system, which in the worst case can cause the drainage function to fail. (Yeo & Hsuan 2007)

A new, patented process describes the integral manufacturing of a geosynthetic drainage sheet (GDS). In the following, "integral" is used to describe production from a single plate-shaped base body. In the simplest case, grooves (longitudinal direction, MD "machine direction") and counter-grooves (transverse direction, CMD "cross-machine direction") are introduced into an extruded, plate-shaped base body with the aid of embossing rollers (see Figure 1). These grooves are formed by material displacement, which leads to opening passages at the crossing points of the grooves and counter-grooves.

The integral production results in massive support structures within the GDS. These support structures can largely absorb enormous mechanical loads, in particular compressive and shear loads. The GDS is highly dimensionally stable, which means that a failure in stability of the drainage core can be avoided. Sufficient water flow capacity can be guaranteed at all times. This manufacturing process is characterized by a high degree of flexibility. For example, the geometry of the grooves and counter-grooves can be varied regarding the available cross-section for water drainage. In general, the thickness and width of the GDS are exclusively linked to the selection of the extrusion tool used. GDS with a width of several meters and a flexibly selectable sheet thickness are conceivable. The polymers can also be flexibly selected thanks to the extrusion process. It is also conceivable that in addition to the conventionally used polymers such as PE, PP, PA or PS, other types of polymers such as wood-plastic composites (WPC), biopolymers or recycled plastic materials can be processed. (Zanzinger 2020)
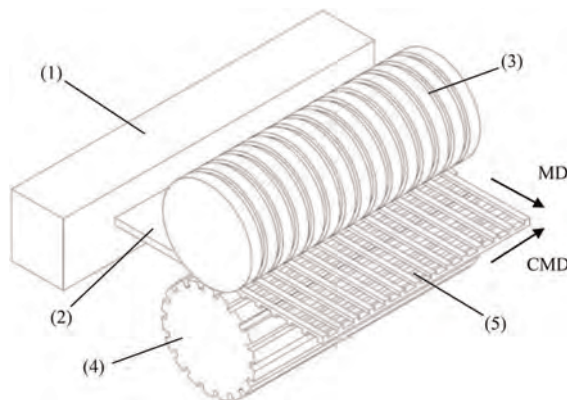
Figure 1. Manufacturing of a geosynthetic drainage sheet (GDS). (1) Extruder; (2) Plate-shaped base body; (3) Embossing roller 1; (4) Embossing Roller 2; (5) GDS.

GDS, according to the manufacturing process described above, and the mechanical and hydraulic advantages postulated with them are so far of a purely theoretical nature. This work is intended to represent a first practical examination of this topic, by manufacturing GDS specimens based on the process illustrated in Figure 1 and by comparing their short-term compressive behavior and their hydraulic performance to nowadays used GNT.

2 EXPERIMENTAL PART

GDS and GNT specimens were manufactured on a laboratory scale by machining HDPE panels with the dimension of 200 mm x 200 mm x 8 mm. The characteristic grooves were brought in using suitable milling tools. With GDS specimens, the grooves and counter-grooves were arranged at an angle (α) of 90° to another, derived from the manufacturing process shown in Figure 1. With GNT specimens, grooves and counter-grooves were brought in at a characteristic angle of 60°. Additionally, GNT with an angle of 90° were manufactured. The depth of the grooves was $d_1 = d_2 = 4 – 4.5$ mm for all test specimens (Figure 2a).
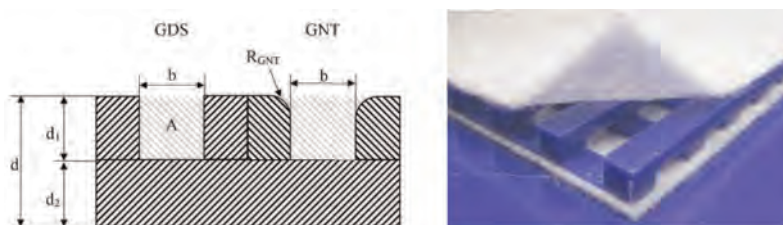

Figure 2. a) Schematic illustration of the GDS and GNT specimen geometry. b) GDS specimen with nonwoven geotextiles draped on the top and bottom.

The manufactured GDS and GNT specimens were draped (adhesive) on the top and bottom with mechanically bonded nonwoven geotextiles made of PP with a mass per unit area of 264 g/m^2 (Figure 2b).

The available cross-section for water drainage in direction of water flow (A_{Drain}) was determined by multiplying the cross-section of one groove (A) with the number of grooves in direction of water flow.

The mass per unit area (m_A) of the specimens was determined according to EN ISO 9864. The short-term compression behavior was determined using a universal testing machine according to EN ISO 25619-2.

The water flow capacity was determined with a specially manufactured apparatus according to EN ISO 12958-1. For soft/soft bedding, foams (10 mm thick) were placed between the pressure and base plates and the test specimen.

Table 1. Overview of the manufactured GDS and GNT specimens.

Test specimen	Width of grooves b [mm]	Number of grooves in direction of water flow	Radius of the rounded area of GNT R_{GNT} [mm]	Angle between grooves and counter-grooves α [°]	Available cross-section for water drainage in direction of water flow A_{Drain} [mm^2]	Mass per unit area[1] m_A [g/m^2]
GDS1	5.03	18	–	90	413	3940
GDS2	5.97	18	–	90	466	3411
GDS3	7.98	15	–	90	569	2826
GDS4	10.07	15	–	90	688	1699
GNT1	8.05	15	2.5	60	550	2175
GNT2	8.02	18	2.5	90	554	2302
GNT3	8.03	18	1.5	90	681	1848

Notes
[1]Nonwoven geotextiles not included.

3 TEST RESULTS AND EVALUATION

3.1 *Short-term compressive behavior of GDS and GNT specimen*

In Figure 3a the short-term compressive behavior of GDS and GNT specimens is presented graphically.

For the same compressive stress, the GNT specimens show a significantly higher compression than GDS specimens. While GNT specimens have a typical circular rib geometry, the ribs of GDS specimens are characterized by a rectangular shape and a flat contact area. The compressive stress can thus be absorbed over a larger contact area compared to the circular rib shape. The solid material is compressed directly at the support structures of the GDS, causing the compressive stress-compression curve to rise rapidly. The more massive these support structures are and the larger their number is within the drainage structure, the faster the rise of the compressive stress-compression curve occurs and the better the compressive resilience is.

The higher percentage compression of the GNT specimens can also be explained with the help of the circular rib geometry. In the rounded area, initial deformations can occur as the compressive stress increases. Further on, the circular rib geometry is deformed, while at the same time solid material is compressed in the support structures of the GNT specimens. The slope of the compressive stress-compression curve increases but is flatter than the compressive stress-compression curves of the GDS specimens. Thus with increasing compressive stress, the difference in compression between GDS and GNT increases.

3.2 *Water flow capacity of the GDS specimens as a function of specimen geometry*

In Figure 3b water flow capacity at 20 °C for the four different GDS specimens at two different compressive loads and a hydraulic gradient of i = 1.0 is shown graphically. Testing was carried out under soft bedding conditions, to simulate an intrusion of soil-material into the grooves of the GDS under compressive load.

With increasing groove width and thus larger available cross-section for water drainage in direction of flow (Table 1), the water flow capacity increases. At a groove width of 8 mm, it passes through a maximum and then decreases. At high compressive loads, the maximum is shifted to smaller groove widths. This behavior is equally observable for small and large hydraulic gradients. It can be demonstrated, that at a lower compressive load and a sufficiently large cross-section for water drainage in direction of water flow, intrusion can be compensated. However, this behavior becomes invalid with an increasing compressive load, as intrusion comes even more into effect. GDS specimens with smaller groove widths show significantly smaller decrease in water flow capacity as a result of increasing compressive load under soft bedding conditions than GDS specimens with larger groove widths and thus larger cross-sections for water drainage in direction of flow. Therefore, a trend towards smaller groove widths is clearly evident under extreme compressive loads and soft surrounding soil material.
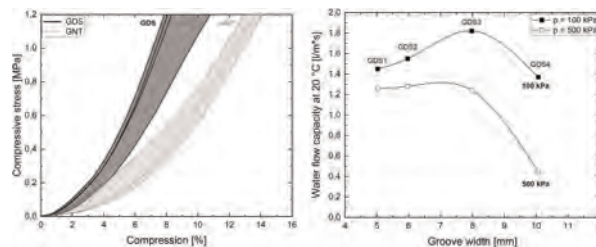

Figure 3. a) Compressive stress-compression curves of GDS and GNT specimens. b) Water flow capacity at 20 °C of GDS specimens as a function of groove width at compressive loads (p) of 100 kPa and 500 kPa and a hydraulic gradient (i) of 1.0 (soft/soft bedding).

3.3 *Comparison of the water flow capacity of GDS and GNT specimens*

Figure 4a shows the water flow capacity of GDS and GNT specimens under different compressive loads. As in section 3.2, the soft/soft bedding simulates the intrusion of soil-material into the grooves of the GDS and GNT specimens.

Looking at the water flow capacity of the specimens in a soft/soft bedding situation at a compressive load of 100 kPa and comparing it with the values of the test specimens in a hard/hard bedding situation, significant differences between GDS and GNT can be observed. The effect of the nonwoven geotextile layers being pressed into the free spaces of the grooves is clearly more pronounced with the GNT specimens. The absolute difference in the water flow capacity between the hard and soft bedding situation of GDS specimens is approx. 0.7 l/m*s on average for the same compressive load. For comparable GNT specimens, this is between 1.2 l/m*s and 2.1 l/m*s and is thus greater by a factor of 1.7 to 3.0 than for the GDS specimens. This effect is even more noticeable with increased compressive load. With a comparable groove width, GDS specimen show a significantly lower influence of the non-woven geotextile layers being pressed into the free spaces of the grooves and counter-grooves under compressive load. This can be explained by the different geometry of the grooves. The rounded areas in the GNT grooves (Figure 2a) clearly contribute to higher intrusion of the geotextile layers, while the rectangular-shaped grooves of GDS specimens can counteract intrusion to a higher degree. This advantage is of great importance with regard to use under extreme compressive loads. The water flow capacity of GDS can be maintained for a longer period of time as the compressive load increases.

A further difference becomes apparent when comparing the water flow capacity of the GDS specimen with the characteristic groove arrangement of 90° with the GNT specimen with a typical arrangement of 60°. When the grooves were arranged in the direction of water flow, the GNT specimen with a groove arrangement of 60° showed a significantly better water flow capacity than the comparable GDS specimen, as water could be conducted through the grooves of the test specimen on the upper and lower sides. This represents an advantage of GNT over GDS. However, when grooves were arranged perpendicular to the direction of water flow, the GNT specimen showed a significant decrease in water flow capacity, whereas the GDS specimens hardly showed any differences (Figure 4b). The groove arrangement of 90°, derived from the manufacturing process, proved to be advantageous. GDS therefore showed good properties for a flexible application with regard to the installation direction.

In case of the typical GNT specimen, grooves and counter-grooves are arranged perpendicular to the direction of water flow at an angle of 120° to each other. This results in long flow paths for the drainage of water within the grooves. In a given time, less water can flow through the grooves and counter-grooves of the GNT specimen. The water flow capacity decreases drastically.
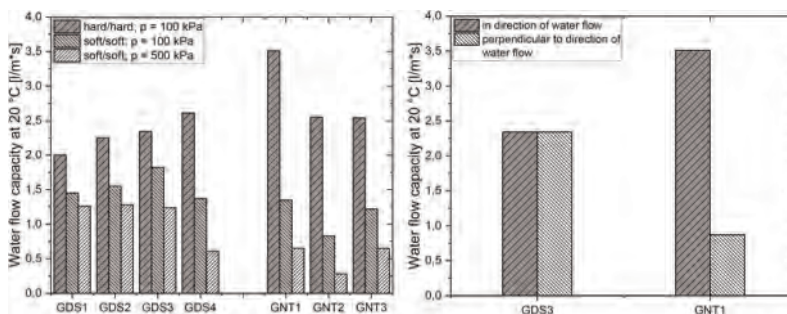

Figure 4. a) Comparison of the water flow capacity of GDS and GNT at different test conditions regarding the bedding situation and the compressive stress (i = 1.0) b) Comparison of the water flow capacity of GDS and GNT as a function of the installation direction (p = 100 kPa, i = 1.0, hard/hard).

4 CONCLUSION

For the use of geosynthetic drainage systems under enormous compressive load, such as in mining or landfill construction, GNT-based drainage systems are currently state of the art.

GDS described in this paper represent an alternative and can be produced flexibly and integrally in a combined process of extrusion and embossing of the drainage structure by material displacement.

In this study GDS and GNT specimens were manufactured and tested with regard to their short-term compressive behavior and their water flow capacity under compressive load.

The investigation shows that GNT specimens exhibited greater deformations at the same compressive stress than GDS specimens with comparable geometry. The rectangular shape of the grooves of the GDS specimens represents an advantage in terms of compressive behavior. Due to the solid support structures with a flat contact area, the compressive stress can be absorbed better and with less deformation.

Also differences in the hydraulic performance of the drainage structures investigated can be shown. GDS specimens reveal good properties for a flexible application with regard to the installation direction, while GNT specimens exhibit a significantly reduced water flow capacity when installed perpendicular to the direction of water flow.

In addition to the flexible application, GDS specimens have significant advantages in water flow capacity when tested in soft bedding conditions. The effect of the nonwoven geotextile layers being pressed into the cross-section of the grooves and counter-grooves is clearly less noticeable with GDS specimens than with comparable GNT specimens. The percentage decrease in water flow capacity of the GNT specimens is, depending on the pressure load, higher by a factor of 1.7 to 3.0 than with comparable GDS specimens.

In terms of material consumption, the more solid GDS specimens have higher masses per unit area compared to the GNT specimens investigated. However, the choice of a small groove width proves to be indispensable in order to maintain the water flow capacity under enormous compressive loads. Increased material consumption is therefore unavoidable. Only a reduction of the thickness can reduce the material consumption, but this also reduces the available cross-section for water drainage in direction of water flow and thus the water flow capacity.

The trends determined in this work with regard to short-term compressive behavior and water flow capacity indicate that GDS can be a promising alternative to conventional GNT-based drainage systems. The advantages of GDS over GNT can be demonstrated, particularly in extreme geotechnical applications with enormous compressive loads. In addition to the promising mechanical and hydraulic properties, the patented manufacturing process represents a further advantage. GDS can be manufactured on a large scale for specific applications. The geometry of GDS can be adapted according to the goal and benefit of the application and in terms of economic efficiency.

REFERENCES

Koerner, R. M. 2012. *Designing with Geosynthetics*. 6th ed. Bloomington, IN: Xilbris Corporation (Vol 1).

Müller, W. W. & Jakob, I. & Tatzky-Gerth, R. 2008. Long-term Water Flow Capacity of Geosynthetic Drains and Structural Stability of Their Drain Cores. *Geosynthetics International*, 15, S.437–451

Rüegger, R. & Hufenus, R. (Hg.) 2003. *Bauen mit Geokunststoffen. Ein Handbuch für den Geokunststoff-Anwender*. St. Gallen: SVG.

Yeo, S.-S. & Hsuan, Y. G. 2007. The Short- and Long-term Compressive Behaviour of High-density Polyethylene Geonet and Geocomposite at Inclined Conditions. *Geosynthetics International*, 14, S.154–164.

Zanzinger, H. 2020. *Verfahren zur Fertigung einer Kunststoffdränbahn und Kunststoff-dränbahn* (DE 10 2018 211 667 A1 2020.01.16). Deutsches Patent- und Markenamt. https://register.dpma.de/DPMAregister/pat/register?AKZ=1020182116679&CURSOR=10.

A study on the electrical properties of copper-functionalized graphene oxide in cement mixture

Jin Kim, Jae Hyun Jeon, Ji Yoon Kim, Jong Yeong Lee & Jung Geun Han
Chung-Ang University, Seoul, Korea

ABSTRACT: In this study, we intend to apply the electrical properties of graphene to cement mixture. When the resistance value is approximately 4 kiloohms. This value is a resistance value that hardly conducts electricity. An attempt was made to impart electrical properties to cement mixture by mixing Functionalized Graphene Oxide with copper with excellent electrical properties to the cement mixture. The cement mixture specimen, which had previously exhibited a resistance value of more than 4 kiloohms, showed a value of less than 1 kiloohms when functionalized graphene oxide was mixed. The purpose of this study is to determine the amount of cracks that have occurred in cement mixture by using electrical properties that are four times improved compared to the existing specimen when electricity flows through cement mixture. Cement mixture showed a trend of increasing resistance value according to cracking. This was used to formulate resistance values according to the amount of cracks and to evaluate the long-term lifespan and quality of cement mixture.

1 INTRODUCTION

Graphene is one of the thinnest, strongest, hardest and flexible materials discovered to date with respect to strength, thermal and electrical properties. Among them, by focusing on the electrical properties of graphene, it is used in various industrial fields such as displays, batteries, and semiconductors(Abbasi *et al*. 2016; Al-Dahawi *et al*. 2016; Lee *et al*. 2008; Ren & Chen 2014). In particular, in the field of civil engineering, various studies are being conducted, such as trying to assign electrical properties by mixing graphene with cement composites. Baoguo Han *et al*. (2007) conducted a study to assign electrical properties by mixing carbon fibers with cement paste. Therefore, in this study, 'Functionalized Graphene Oxide' was added to cement paste to give electrical properties and analyze it.

In addition, basic research was conducted to use the electrical characteristics as monitoring techniques such as quality control of concrete structures.

2 MATERIALS

Graphene is a two-dimensional structure with dense carbon atoms with a thickness of 0.335 mm, and is composed of a sp2 hybrid carbon allotrope with a single atom thickness of 0.1 nm – 0.5 nm. The bond length between carbon and carbon atoms arranged in a hexagonal honeycomb structure is about 0.142 nm, and these layers are easily dispersed because they are bonded to each other by weak Van Der Waals forces(Novoselov *et al*. 2004; Tiwari & Syvaarvi 2015).

In this study, Graphene Oxide (GO) was produced using a sulfuric acid according to the 'Modified Hummers Method' using graphite powder(Graphite powder, natural, universal

grade, −200 mesh, 99.995%, Sigma-Aldrich). Since the 'Modified Hummers Method' oxidizes graphite while decomposing it by a chemical method through oxidation, many functional groups including oxygen are generated on the surface. In addition, since single-layer graphene has a large surface energy, various molecules or ions can be adsorbed and desorbed. Therefore, the electrical properties can be controlled through chemical functionalization, which is affected by the type and concentration of adsorbed molecules. These properties indicate the possibility of using graphene as a sensor (Kim 2013).

In this study, Functionalized Graphene Oxide (Cu-GO) was prepared by copper, which is used in electric wires and electronic products to imorove the electrical properties of graphene (Gariono N. *et al.* 2021). SEM imaging, XRD analysis, and FT-IR were performed to confirm functionalization. SEM imaging was performed as shown in Figure 1. It was confirmed that Cu, which was attached to the functional group of graphene in a spine form, covered the surface, indicating the success of functionalization.

(a) Surface of Graphene Oxide (GO)

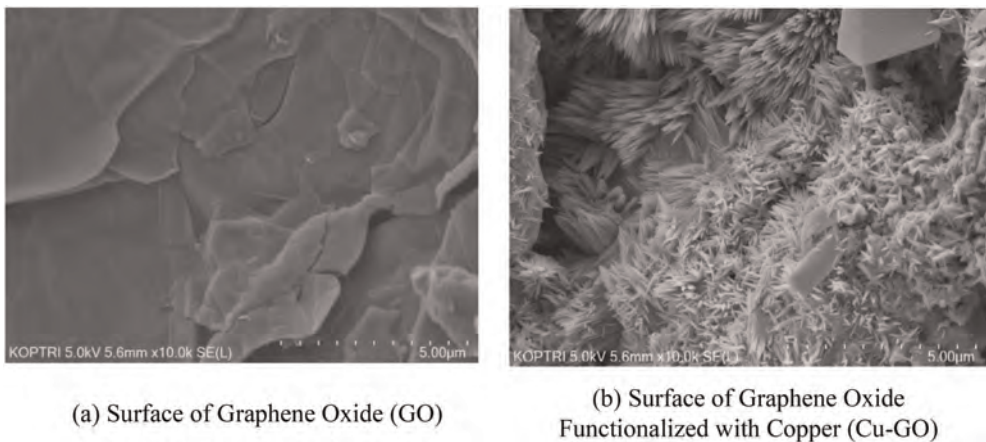(b) Surface of Graphene Oxide Functionalized with Copper (Cu-GO)

Figure 1.   Confirmation of functionalization by SEM.

Through the XRD results in Figure 2., it can be confirmed that Cu-GO was successfully functionalized through the 2θ value that does not appear in GO (Figure 2(a)).

(a) GO

(b) Cu-GO
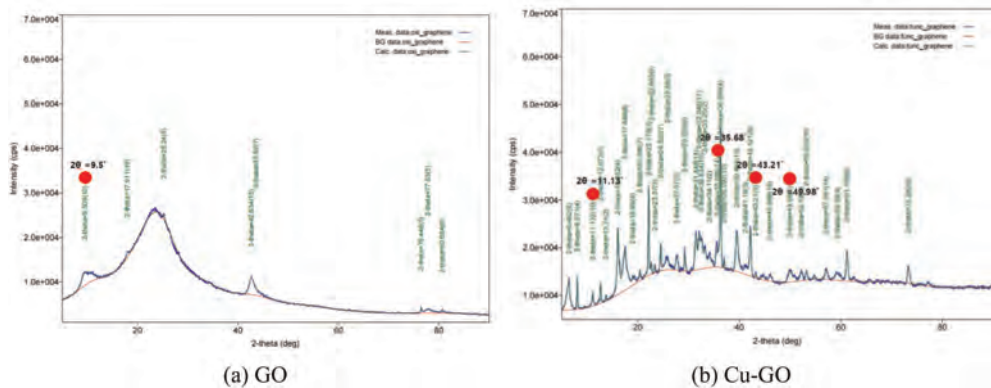
Figure 2.   XRD pattern of GO and Cu-GO.

Finally, through the FT-IR results (Figure 3), GO O-H peak (3392.18cm−1), C=O peak (1723.3cm−1), Sp2 C=C peak (1577cm−1), C-O peak (1156.2cm−1) −1) was confirmed. O-H peak (3337.7 cm−1), Sp2 C=C peak (1622.3 cm−1), and C-O peak (1149.9 cm−1) of Cu-GO were confirmed. A new 3436.8cm−1 peak, which was not shown in GO, was derived, confirming that copper ions are functionalized with O-H functional groups.
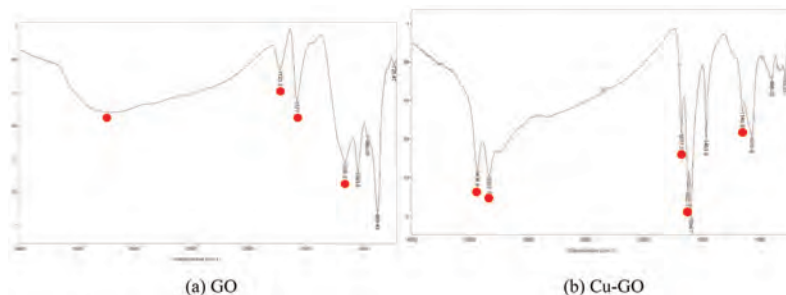

(a) GO (b) Cu-GO

Figure 3.   FT-IR of GO and Cu-GO.

3   TEST AND RESULT

3.1   *Electrical properties of cement paste mixed with Cu-GO*

To evaluate the electrical properties of cement paste, the specimen was prepared and the electrical resistance value was measured. The specimen to which nothing was added (Test-Normal) and The specimen to which 0.01% of Cu-GO was added relative to the weight of cement (Test-Cu-GO) were prepared. To measure the electrical resistance, copper electrodes were inserted at both ends of the specimen as shown in Figure 4 and measured using a digital multimeter(3244–60, HIOKI, JAPAN). If a crack occurs when electric current is flowing in the structure Figure 5, The strength of the electric field increases. As the strength of the electric field increases, the potential difference increases and the electrical resistance increases accordingly. Therefore, it can be confirmed that the electrical resistance increases as the crack occurs. This was used to measure the electrical resistance that changes according to the amount of cracking in the concrete, and by using this, a basic experiment was conducted to develop a monitoring technique for the durability and quality of the concrete structure
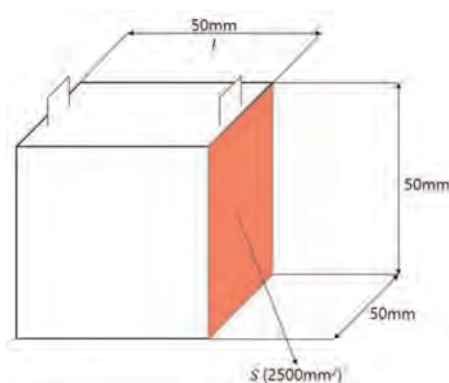
Figure 4.   Cement paste specimens used in the experiment.

As above, the cross-sectional area (S) of the specimen was 2500 mm^2 and the height was 50 mm, and the electrical resistance value measured through Equation 1 was converted into specific electrical resistance.

$$\rho = R \times S/l$$

ρ : SpecificElectricalResistance(Ω cm)
R : Cross $-$ SectionalArea(cm^2)   (1)
S : ElectricalResistance(Ω)
l : Length(cm)

The specimen used in the experiment was cured in water at 23°C temperature for 28 days and then the electrical resistance value was measured in a completely dry state. The measured electrical resistance values are shown in Table 1.

Table 1. Electrical resistance and specific electrical resistance of cement paste.

	Electrical Resistance(Ω)	Specific Electric Resistance(Ω-m)
Test-Normal	2645	132.3
Test-Cu-GO	1269	63.5

As a result, it can be confirmed that the specific electrical resistance of the cement paste was reduced by more than two times when Cu-GO was added.

3.2 Electrical properies according to cracks

If a crack occurs when electric current is flowing in the structure Figure 5, The strength of the electric field increases. As the strength of the electric field increases, the potential difference increases and the electrical resistance increases accordingly. Therefore, it can be confirmed that the electrical resistance increases as the crack occurs. This was used to measure the electrical resistance that changes according to the amount of cracking in the concrete, and by using this, a basic experiment was conducted to develop a monitoring technique for the durability and quality of the concrete structure
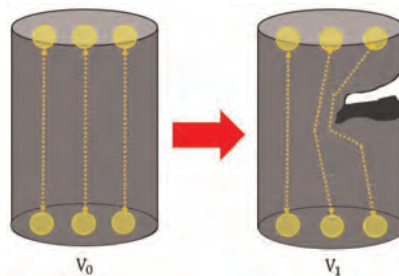

Figure 5. Potential difference due to crack occurrence.

For the measurement of electrical resistance according to cracks, the specimen was mounted on the UTM(Universal Testing Machine, HJ–1295, Heungjin Testing Machine, KOREA) as shown in Figure 6, and then a load was applied to induce failure. The electrical resistance was measured from loading to failure, and the electrical resistance according to the vertical displacement of UTM during the process is shown in Table 2.

(a) Before Crack   (b) After Crack

Figure 6.   Method of measuring electrical resistance according to the occurrence of cracks.

Table 2.   Electrical resistance and specific electrical resistivity according to vertical displacement.

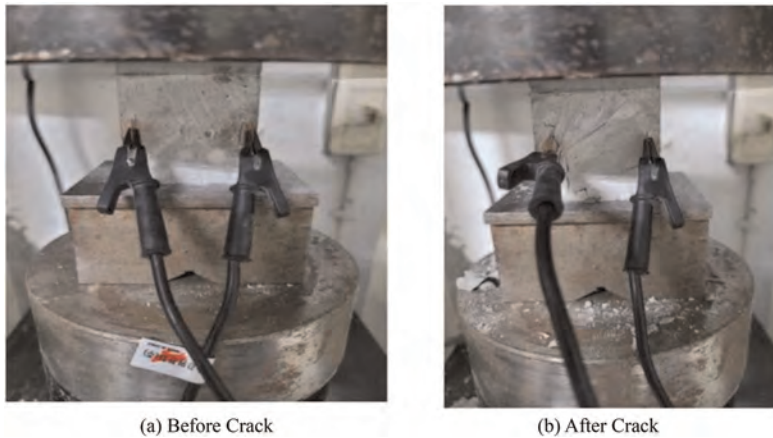|	Vertical Displacement(mm)	Electrical Resistance(Ω)	Specific Electric Resistance(Ω-m)
Case 1	0	2,602	130.1
	0.4	2,850	142.5
	1.0	3,255	162.8
	Failure	25,347,000	1,267,350
Case 2	0	1,273	63.7
	0.4	1,338	66.9
	1	1,612	80.6
	1.5	1,713	85.65
	Failure	23,870,000	1,193,500

The electrical resistance measured before load applied was the same as the electrical resistance of the specimen measured in 3.2, and then the electrical resistance increased as cracks occurred. It can be seen that the electrical resistance for each case continues to increase with a difference of about 2 times. When Cu-GO was mixed, the strength of the specimen increased, so that the vertical displacement just before failure increased from $1mm$ to $1.5mm$, and the specific electrical resistance just before failure increased by 40% compared to the state before cracking.

4   DISCUSSION

In this study, electrical properties were imparted to non-conductive cement composites using functionalized graphene oxide. A basic study was conducted to evaluate the durability of cement structures using these electrical characteristics. Basically, the cement mixture containing Cu-GO reduced electrical resistance more than twice as much as normal specimens. Through this, it was confirmed that the electrical properties of the cement composite were improved. Next, the change in electrical resistance was measured according to the crack using UTM. As a result, it was confirmed that the electrical resistance value also increased as the crack amount increased. It is hoped that this concept can be used as a basic study to evaluate the durability and quality of cement structures.

ACKNOWLEDGEMENTS

REFERENCES

ASTM C192/C192M-19–*Standard Practice For Making And Curing Concrete Test Specimens In The Laboratory*

Emmy J. Radich, Ryan Dwyer, and Prashant V. Kamat, (2011), "Cu$_2$S Reduced Graphene Oxide Composite for High-Efficiency Quantum Dot Solar Cells. Overcoming the Redox Limitations of S$_2$–/S$_n^2$–at the Counter Electrode", *Jounal of Physical Chemistry Letters*, 2011, 2, 2453–2460

Lee, Heeyoung and Chung, Wonseok.(2017), "Flexural Behavior of Graphene Oxide Cementitious Composite", *J. Korean Soc. Hazard Mitig*, ISSN 2287-6723, vol 17, no. 5, p 217–222

Leila A Shahriary, Anjali A Athawal.(2014), "Graphene Oxide Synthesized by Unsing Modified Hummers Approach", *International Journal of Renewable Energy and Environmental Engineering*, ISSN 2348–0157, vol. 2, no. 1.

Mingrui Du, Hongwen Jing, Yuan Gao, Haijian Su and Hongyuan Fang.(2020), "Carbon Nanomaterials Enhanced Cement-based *Composites: Advances and Challenges, Nanotechnology Reviews*, 2020;9:115–135

Mohammed, A., Al-Saadi, N.T.K., Sanjayan, J.(2018b), "Inclusion of Graphene Oxide Icementitious Composites: State-of-the-art Review", *Aust. J. Civ. Eng.* 8353, pp. 1–15.

Mohsin Ali Raza, Zaeem Ur Rehman, Faizan Ali Ghauri.(2018). "Corrosion Study of Silane-functionalized Graphene Oxide Coatings on Copper", *Thin Solid Films* 663, 93–99.

Nadia Garino, Juqin Zeng, Micaela Castellino, Adriano Sacco, Francesca Risplendi, Michele Re Fiorentin, Katarzyna Bejtka, Angelica Chiodoni, Camien Salomon, Jaime Segura-Ruiz, Candido F. Pirri & Giancarlo Cicero.(2021), "Facilely Synthesized Nitrogen-doped Reduced Graphene Oxide Functionalized with Copper Ions as Electrocatalyst for Oxygen Reduction", *npj 2D Materials and Applications*, volume 5, pp. 1–10.

Tanvir S. Qureshi, Daman K. Panesar, Boopathi Sidhureddy, Aicheng Chen, Pter C. Wood.(2019), "Nano-cement Composite with Graphene Oxide Produced from Epigenetic Graphite Deposit", *Composites Part B*. 248–258.

Xiangyu Li, Linhao Wang, Yuqing Liu, Wengui Li, Biqin Dong, Wen Hui Duan,(2018), "Dispersion of Graphene Oxide Agglomerates in Cement Paste and its Effects on Electrical Resistivity and Flexural Strength", *Cement and Concrete Composites* 92(2018), 145–154.

Design approaches and other applications

ROUGH–RecOmmendations for the use of GeosyntHetics in Nordic conditions

Ph. Delmas
Sintef Advisor, Paris, France

A. Watn
Norwegian University of Science and Technology (NTNU), Trondheim, Norway

V.M. Uotinen
Finnish Transport Infrastructure Agency, Helsinki, Finland

J. Vaslestad
Norwegian Public Roads Administration, Oslo, Norway

F. Griwell
Swedish Transport Administration, Stockholm, Sweden

C. Recker
Sintef Community, Münster, Germany

ABSTRACT: Finnish Transport Infrastructure Agency (Finland), Norwegian Public Roads Administration (Norway) and Swedish Transport Administration (Sweden) have asked Sintef (Norway) to prepare and manage the writing of guidelines on the Use of GeosyntHetics in Nordic conditions. The Rough project (RecOmmendations for the Use of GeosyntHetics in Nordic conditions) has been organized to collect all existing information and provide missing data. The corresponding work is presented in this communication: it focuses on the behaviour of geosynthetics during installation in Nordic conditions. The work is organised in two parts: (1) a full-scale on-site experiment in Kemi (Finland) on installation under Nordic conditions for the applications with functions reinforcement/stabilisation, filtration, drainage; and (2) considering the difficulty of the realisation of similar on-site experiment for sealing, it has been decided to realise a literature study associated with a synthesis of the state of the art for sealing.

1 INTRODUCTION

A common system for specification and certification of geosynthetics, NorGeoSpec, has been in operation in the Nordic countries since 2002. Experiences have revealed a lack of relevant requirements related to the installation and function of geosynthetics in a cold climate especially when temperature are largely below 0 °C. A development project ROUGH (RecOmmendations for the Use of GeosyntHetics in Nordic conditions) has been established to identify special requirements for geosynthetics to ensure technically and economically optimal solutions in country-specific climates and soils. Traffic Authorities in Finland, Sweden and Norway, research institutes, universities and a group of producers participated in the project.

1.1 Nordic conditions

Climatic conditions in the Nordic countries are challenging. Continuous pressure to increase the efficiency of heavy transport and reduce the climate impact of transports has led to the maximum permissible weights of heavy vehicles, especially in Finland and Sweden, being clearly higher than in the rest of Europe.

During the coldest winters, freezing index in inland Norway, northern Sweden and northern Finland may easily exceed 60,000 Kh (2,500 Kdays), which corresponds to a frost penetration depth of more than two meters in typical subgrade conditions. The frost penetration generally may result in considerable frost heave imposing deformations, stresses and deterioration of the road structure. In order to avoid the adverse effects of frost, high-quality road-and railway structures in the Nordic countries must be built including thick non-frost-susceptible structural layers or with frost insulation layers. Accordingly large amounts of blasted rock and crushed rock aggregates are used in construction works. Typically, the frost insulation layer is placed with a separation geotextile on the subsoil and with a road superstructure of 60–150 cm above. One of the essential special features of these artificially produced blasted rock materials and crushed rock aggregates are the sharp edges of the particles, which poses an obvious risk of damage to other materials installed next to them, such as geosynthetics. The combination of soft subsoil and sharp-edged rock fill material imposes also considerable deformations and stress of the structure and the material. This risk is exacerbated by the need to use heavy vibratory compaction equipment to compact angular crushed rock particles.

The most typical applications of geosynthetics in Nordic road construction projects are related to filtration and separation of soil layers. In particular, these functions are needed on thinly built lower-class roads, where the risk of mixing of structural layer materials and subsoil is high, especially during the thawing phase of seasonal frost in spring. Other typical uses are related to access during the construction period and include strengthening the lower part of road embankment and ensuring the operation of drainage structures.

1.2 Existing guidelines

In the Nordic countries there are several guidelines or recommendations which help to take into account the possible damage of geosynthetics during installation. Nevertheless, experiences have revealed a lack of relevant requirements directly related to installation and function of geosynthetics in cold climate. Presently, different ways of considering installation damage existing systems exist in Nordic Europe. Most classification systems define the requirements based on 3 key parameters: strength of the subsoil (2 to 3 types), type of backfill (2 to 5 types, depending on size of particles and angularity), aggressivity of the installation method (2 to 4 types, depending on drop height and compaction technique).

Note that, if all these guidelines consider the typical Nordic in-situ soils, backfill and traffic conditions, until today, none of them consider the installation temperature as a parameter.

1.3 Objective and content of project

The objective of ROUGH project is specially to focus on cold temperature by using local soil conditions in the Nordic countries and local construction methods and typical aggregate materials. The project includes a survey of experiences, literature studies, laboratory investigations and a full-scale field test. Depending on the type of geosynthetics the main means implemented were:

1–a full scale on-site experiment in Kemi (Northern Finland) on installation under Nordic conditions for the applications with the functions reinforcement/stabilisation, filtration, drainage;

2–considering the difficulty of the realisation of a similar on-site experiment for sealing applications, it has been decided to realise a literature study associated with a synthesis of the state of the art for this function.

Long term behaviour like freeze/thaw action and traffic loading is obviously important for the function but is not included in ROUGH. (ROUGH project 2022)

2 PERFORMED WORK

2.1 Collect of experience and synthesis

A general review of the existing knowledge on damage during installation for geotextiles and related products has been realised and allowed to give the general principles of the evaluation of installation damage showing how it is considered in existing guidelines. In most cases, mainly the influence of installation on the integrity of the structure of the product and on its mechanical performances is considered.

The effect of the installation on product's hydraulic properties should also be taken in consideration, especially in Nordic conditions with freezing and thawing, or when the products are placed on soils with high water content, with high content of fines and/ or soils consisting organic matter (peat, mud). Similarly, the influence of the evolution of the hydraulic performance of the products (short and long term) has been very rarely studied and discussed considering their importance on freeze thaw cycles on the structural behaviour.

To succeed to completement some of these important missing information the realisation of the full-scale experiment on geotextiles and related products in Kemi was decided.

Considering the difficulty of the realisation of a similar on-site experiment for sealing applications, it has been decided to realise a literature study associated with a synthesis of the state of the art for this function. This work allowed to propose (1) general requirements for products used in sealing applications under Nordic conditions, including (a) impact of environmental conditions on design choices, considering (b) aspects related to raw material/ structure of products in different conditions: exposed applications, shallow cover and fully covered applications, (c) performance requirements for geosynthetic barrier including preservation of GBR's integrity during transportation and storage and possibility of unrolling the GBR in place under freezing temperatures, on frozen soil subgrade, without damaging them; (d) worker safety during installation; (e) welding to assemble or repair GBR and (f) installation of the soil cover on the GBR (when applicable), (2) specific installation requirements (project management, packaging, storage and handling, subgrade preparation, deployment, assembly) and (3) quality control (quality assurance strategy, conformance testing of geosynthetic materials, CQA Report).

2.2 Realisation of the field work

The test site was established along an ongoing construction project to upgrade the Highway 4 (E8/E75) (Northern Finland), close to the border to Sweden (see Figure 1). Altogether 13 products were installed covering the functions reinforcement/stabilization, filtration, and drainage. The products were installed as a part of a road structure and of a drainage ditch at an average temperature $-10\,°C$ (down to $-15\,°C$). The installation and compaction were carried out according to pre-determined procedures. The procedures for the extraction of the products had to be specially adapted to be able to remove the fill material on top of the geosynthetics, without creating added potential damages due to excavation. The tests provided valuable information on behavior and potential damage during installation of geosynthetics linked to temperatures below $0\,°C$.
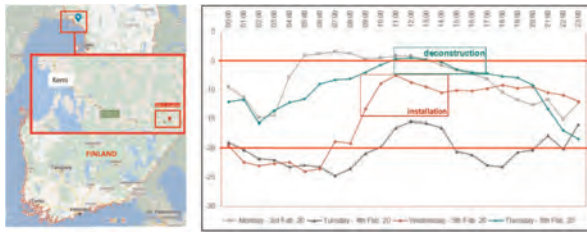
Figure 1. Location of the field tests (Screenshot Google Maps) and temperatures during installation and recovery [°C].

2.2.1 *Reinforcement/stabilisation*

To obtain site realistic damage behaviour during placement and compaction of materials, specifications based on Finnish guidelines for road construction were used for the field conditioning. 7 reinforcement/stabilisation products were installed on top of the crushed-rock compacted sub-base. Then, the base layer consisting of 30 cm blasted rock 0/56 was placed. During installation no heavy equipment drove over the installed products. The tipping height out of the excavator bucket was approx. 1.0 m and the compaction was performed with a 12.6 t dynamic roller. During geosynthetic installation, upper crushed rock material had a temperature of approx. −6 °C and the base-course material about −12 °C. Figure 2 (left) shows the products before the base layer was placed. In order to minimize positional influences, each product was cut into half and installed at two different locations along the test field. The Figure 2 (right) shows the compaction process of the base layer: the aggregate layer was compacted was compacted with 5 passes with 12.6 t dynamic roller, in accordance with the Finnish road construction guidelines (InfraRYL Table T1).

Figure 2. Installed geosynthetic samples for reinforcement/stabilisation function. Compaction of base layer.

To avoid additional damage to the samples during the recovery of the geosynthetics, a vacuum/sucking lorry was used. The first 20 cm of the base crushed rock layer were removed by careful use of an excavator. The remaining 10 cm of the base crushed rock layer was successfully removed by the vacuum lorry. Figure 3 shows the process of recovering the geosynthetic products by sucking the material off the geosynthetics.

Figure 3. Vacuum lorry and system for sucking of material from the geosynthetics.

2.2.2 *Filtration*

Similarly for filtration, the effects of installation at low temperatures on the geosynthetics in a trench were checked. The 4 geosynthetics were placed directly on the local native soil which was frozen. The trench was filled with the same 0/56 crushed rock as for reinforcement/stabilisation which was compacted according to the Finnish road construction guidelines (InfraRYL Table T1). In order to take account of possible different loads when backfilling the trench, the drop height of the aggregate was varied (1.0 m & 2.0 m). In order to minimize positional influences, each product was cut in half and installed at two different locations along the trench. Filling aggregate crushed rock 0/56 mm had a temperature of approx. −6 °C and temperature of about −12 °C was recorded on the local native soil. After filling the trench, compaction was done with a vibration plate (Figure 4).

Figure 4.   Filtration trench: Backfilling and compaction of upper layer.

The products were then carefully removed according to same procedure as in paragraph 2.2.1. Tensile strength & strain and characteristic opening size were determined on virgin and retrieved samples.

2.2.3 *Drainage*

To obtain site realistic damage behaviour during placement and compaction of materials, specifications based on Finnish guidelines for road construction were used for the field conditioning. The 2 geosynthetic were placed directly on the frozen local native soil. Before installing the geosynthetic layer, temperatures of about −12 °C were recorded on the sub-grade layer. In order to minimize positional influences, each product was cut in half and installed at two different locations along the field test. After installation of the geosynthetics, a sub-base layer consisting of 30 cm crushed rock 0/56 was placed with a tipping height out of the excavator bucket of approx. 1.0 m. After installation, the sub-base layer was compacted according to the Finnish road construction guidelines (InfraRYL Table T1). During the compaction process the sub-base aggregate had a temperature of about −6 °C.

The vacuum/sucking lorry was used similarly as previously described to avoid additional damage to the samples during the recovery of the geosynthetics. Figure 5 shows the products before the top aggregate layer was placed and the sucking of the backfill aggregate above the products.

Figure 5.   Installed geosynthetic samples with drainage function and recovery of the drainage composites.

2.3 Laboratory work

In addition to the tests realized in laboratory on the field samples presented in 2.2, tests were performed on virgin samples at different temperatures. The virgin products' mechanical characteristics were tested at −20 °C, −10 °C, 0 °C and + 20 °C. The specimens were cooled down at least one hour before testing these characteristics. The cooling chamber was only opened to place a new specimen on the testing machine. After closing the door of the cooling chamber, the testing was started when the temperature inside the chamber reached the required temperature again.

The results of these tests at different temperature show that mechanical strength, tensile stiffness, and compressive strain is significantly increased with the reduction of the temperature (0 °C to −20 °C) when tested in the laboratory: e.g., with a reduction in temperature from + 20 °C to −10 °C, the average tensile strength of all products tested $\geq$ + 40 %. It shall be noted that similarly the surrounding soil mechanical properties increases under the same reduction of temperature.

Previous experiences from Nordic construction sites had shown significant damage on junctions on one type of geogrid. Accordingly, the project included an intention of developing a laboratory performance test to evaluate this type of damage.

Summary of laboratory tests performed for the different functions is presented in Table 1.

Table 1. Tests performed in laboratory.

Reinforcement/ stabilisation	characteristic(s)	sample tested	Temperature			
			−20 °C	−10 °C	0° C	20° C
Kemi	Tensile test (20 cm)	damage (in situ) (test)		x		(x)
		reference				x
Laboratory	Tensile test (rib & junction)	damage (dynamic impact)	x	x	x	x
		virgin	x	x	x	x

Filtration	characteristic(s)	sample tested		Temperature			
				−20 °C	−10 °C	0° C	20° C
Kemi	Tensile test (20 cm)	damage (in situ) (test)	Drop height 1.0 m		x		(x)
	Opening size (0_{90})		Drop height 2.0 m		x		(x)
		reference					x

Drainage	characteristic(s)	sample tested	Temperature			
			−20 °C	−10 °C	0° C	20° C
Kemi	Tensile (20 cm) Compression Waterflow capacity	damage (in situ) (test)		x		(x)
Laboratory	Compression strength/ strain a compression strain (1 MPa)	reference				x
		virgin	x	x	x	x

3 OVERALL CONCLUSIONS AND PLAN FOR IMPLEMENTATIONS

The ROUGH project allowed to bring the following important conclusions for the geotextiles and related products tested during the full-scale experiment, if they are correctly

designed for a positive temperature (e.g., + 20 °C) for the defined geotechnical conditions of installation (type of soils, drop height, compaction, etc.), no additional installation damage is observed on the essential characteristics when the products are installed under the same conditions at −10°C:

- tensile strength and tensile stiffness for reinforcement/stabilisation,
- robustness factor and characteristic opening size for filtration,
- water flow capacity for geosynthetic drainage composites.

The field test in Kemi did not reveal similar types of junction-damage on the grids installed as previously experienced. The susceptibility for this type of damage is likely to be heavily influenced by the polymer type and additives and the production procedure. The result from the ROUGH-project is valid for the geosynthetics tested during the full-scale experiment in Kemi and for the products of the same family (same production process, same polymer, same function).

The writing of Guideline on the "Use of GeosyntHetics in Nordic conditions" is now under process and should be published within the next months by the Nordic country's authorities.

ACKNOWLEDGEMENTS

REFERENCES

InfraRYL Infrarakentamisen yleiset laatuvaatimukset. Maa-, pohja-ja kalliorakenteet. Rakennustieto. 2018– InfraRYL *General Quality Specifications for Infrastructure. Earthworks, Foundations and Rock Structures.*
Rough project, 2022. RecOmmendations for the Use of GeosyntHetics in Nordic conditions. SINTEF. Part 1– Tests on Damage During Installation at Low Temperatures. Function: Reinforcement Stabilisation, Filtration, Drainage, (53 p) & Part 2–Status of Existing Information on Installation Requirements for Sealing Products (GBR-P, GBR-B and GBR-C) under Nordic Conditions (45 p).

Ensuring the bearing capacity of the ground base of airfield pavement on loess soils

Igor Pavlovych Gameliak
National Transport University, Ukraine

Tetiana Ihorivna Diakovska
Hydrozahist LLC, Ukraine

Ganna Volodymyrivna Zhurba
Euroizol Geosynthetics LLC, Ukraine

ABSTRACT: The territory of the airport is located on the watershed of the two big rivers. At this object, loess soils have a predominantly solid and semi-solid consistency with small surface layers of refractory consistency to a great depth.

To ensure the stability of the embankment, the upper soil layers with minimal bearing capacity must be withdrawn at a depth up to 1.5 m. To ensure waterproofing and achieve the design value of the coefficient of subgrade reaction on the surface in 74 MN/m^3 under the designed airfield pavement is arranged a layer of stabilized soil and an additional layer of bentonite mats. To separate the concrete layers, use non-woven polypropylene thermally reinforced geotextile.

The paper presents the results of calculations of the design of the aerodrome pavement by the finite element method. It provides a rational decision for the design and comparative analysis with other structures.

1 INTRODUCTION

The use of geosynthetic materials effectiveness in the construction of highways and linear artificial structures is confirmed by many years of practice.

The relevance of their use has significantly increased due to the growing cost of production and logistics of traditionally used inert materials. The wide use of geosynthetic materials in road and airfield construction is caused by their high physical and mechanical characteristics: strength, resistance to the influence of climatic and hydrogeological factors, durability, and environmental safety.

2 REVIEW OF RESEARCHES

In Ukraine, loess soils are widespread mainly in the steppe and forest-steppe, where it is the parent base for chernozem. Loess soils occupy 65–70% of the territory and mainly on floodplain and watershed terraces of rivers and the airport is located on the watershed loess plateau of two large rivers.

The deepest layers of loess are in China, so existing problems with weak soils were solved using geosynthetics in such works [1].

J. Giroud, Ji Han, and L. Noirey laid the foundations for the use of geosynthetics in road and airfield structures [2–3]. The investigations of G. Zornberg gained a wide development of basic test methods [4]. The problem of construction on weak soils, particularly loess soils, has always existed. Its solution was dealt with by world scientists, achieving great success in these fields [5–7].

3 PROBLEM STATEMENT, THE GOAL AND THE TASKS

The problem with loess soils is their behavior in case of saturation with water. Soils change their physical and mechanical properties, and acquire subsidence properties. According to the SNiP 2.05.08-85Aerodromes, the allowable subsidence is no more than 2.0 cm during the entire period of operation (20 years). That is why ensuring the stability of the soil layers should be ensured by geosynthetic materials in view of their durability.

The total thickness of loess soils exceeds 30 m. Groundwater wasn't detected. However, pavement water collected on a large area and by a large number of communications make a potential threat to the breakthrough and wetting of the loess stratum and subsequent subsidence.

The northwestern part of the existing airport is characterized by a large number of water-bearing communications that are in poor condition. This is confirmed by the dome-shaped rise of the water-table in this area in comparison with the entire territory of the airport.

The purpose of this paper is to ensure the bearing capacity of airfield pavement on loess sediment soils by using geosynthetic materials.

In order to fulfill the set goal, the following tasks were selected:

(1) Determination of physical and mechanical properties, strength and deformation properties of soils, as well as the presence of physical and geological processes, phenomena and causes of their formation based on laboratory and field research data.
(2) Calculation of the coefficient of subgrade reaction of the soil base for the use of geosynthetic materials in various options.
(3) Calculation of settlement of airfield pavement under the main undercarriage of the calculated aircraft load from the waterproofing of the ground base.
(4) Development of solutions to ensure the bearing capacity of the airfield pavement and the embankment on weak loess soil stability using geosynthetic materials.

4 THE SOURCE MATERIALS CHARACTERISTICS

The source materials analyzed included obtaining the engineering and geological characteristics of the territory when the following types of work were carried out, such as collection, analysis, and summarization of past years' data and testing the area by the dynamic sounding method to determine the normative soil characteristics and compare them with the data of engineering and geological investigations. Characteristics of soils were determined (Table 1).

The main problem with the arrangement of the airfield pavement of the airport is their direct location on a thick layer of loess soils: GTS-3, light dusty clay loam, heavy with average depth of the occurrence is about 4.5 m, and the GTS-4, sandy loams, located below with average depth is about 8.0 m. These soils normally fall into the layers of soil that can be compressed (Hc) during airfield exploitation. Their initial subsidence pressure is estimated as 0.05 MPa on average for GTS-3a and for GTS-3b it's 0.10. The initial moisture content of subsidence for all four types of soils is 19%, which is much higher than the natural moisture content of these soils.

The total subsidence under the natural pressure of loess loam and sandy loam along the wells varies from 7.8 cm to 43.4 cm. The thickness of the subsiding layer varies from 9.7 m to 23.0 m

Table 1. Estimated indicators of soils' physical and mechanical properties under the natural composition with confidence probability a_I/a_{II} = 0,95/ 0,85.

No GTS	The specific gravity of soils, kN / m³		Deformation modulus, E_{nat}/E_{wet}, MPa	Friction angle, degrees dry/wet	Cohesion, C, kPa dry/wet
	γ_I/γ_{II}nat	γ_I/γ_{II}wet			
3	14.92	18.04	11.8	18	11
	15.11	19.16	4.5	13	8
4	16.07	18.89	17.4	19	9
	16.23	18.97	8.2	15	6
5	17.9	19.51	19.3	17	15
	17.97	19.55	11.5	15	12
5a	18.37	18.98	9.4	19	17
	18.52	19.09	8.2	22	12
6	16.58	19.24	21.7	20	17
	16.65	19.27	11.7	18	12
6a	**19.36**	**19.88**	-	20	18
	19.44	**19.94**		17	12

5 FIELD STUDIES OF THE SOIL BASE AND ESTABLISHING REQUIREMENTS FOR GEOSYNTHETIC MATERIALS

Field surveys of the upper part of the engineering-geological section state were carried out by the method of dynamic probing. The essence of this method is that during the sounding, soil's penetration resistance with the indicator (the tip) is determined, which is an assessment of their bearing capacity. In general, 28 boreholes were drilled to a depth of 4.50 m.

Based on the results of field surveys, the following conclusions were made:

(1) The surface layer of soil is represented by light dusty loam GTS-3, which is covered from the surface by a thin layer of fertile soil up to 1.0 m thick.
(2) The advantages of natural conditions, which ensure the semi-solid state of GTS-3 soil, which mainly constitutes the natural soil base of airfield pavement, have been revealed. Therefore, it is possible to limit its excavation only to a depth of 3.0 m from the surface to remove individual inclusions of soil layers of rigid plastic consistency.
(3) Before its compaction, the exposed surface must be plowed to a depth of 0.40...0.5 m and then mix it and compacted with the value of the compaction coefficient $K_u \geq 0.98$ (the density of the soil skeleton is not less than 1.80 g/m3). The following layers of GTS-3 soil, up to the base of the airfield pavement, should also be compacted to the value of the compaction coefficient $K_y \geq 0.98$ layer by layer (0.20 – 0.25 m) with a density of dry soil in the range of 1.80 – 1.85 g/m³.
(4) The normative characteristics of soils have been clarified, and a soil passport has been established.

To ensure the waterproofing properties of soils and their reinforcement, the use of geosynthetic materials is proposed. Their technical characteristics are given in Table 2.

6 THE COEFFICIENT OF SUBGRADE REACTION

Various options for ensuring the load-bearing capacity of the soil base by strengthening the soil or reinforcing it with geosynthetic materials were considered to obtain the coefficient of subgrade reaction K_{se} of at least 74.0 MH/m³ was calculated according to the formula:

$$K_{se} = \frac{K_{s1} + K_{s2} \cdot \alpha_2 + K_{s3} \cdot \alpha_3}{1 + \alpha_2 + \alpha_3},$$

(1)

where $\alpha_2 = \frac{t_2[1.6D_r-(t_1+0.5t_2)]}{t_1(1.6D_r-0.5t_2)}$; $\alpha_2 = \frac{t_2[1.6D_r-(t_1+t_2)^2]}{t_1(1.6D_r-0.5t_2)}$; K_{s1}, K_{s2}, K_{s3} – calculated values of the coefficient of subgrade reaction, MH/m^3, respectively to the first (counting from above), second and third base layers from homogeneous soils and materials in different conditions, including draining and heat-shielding layers; t_1, t_2 – the thickness of the first and second layers of the base, respectively; D_r – the conventional diameter of the circle of load transfer to the base m, is taken to be equal to 3.6 m for monolithic pavements calculated for non-categorical and I load categories.

Options for calculating K_{se} with a layer of artificial soil base strengthening with cement and bitumen emulsion and a granular base reinforced with geosynthetic materials are considered (Table 3).

The total thickness is 1.4 m. The coefficient of subgrade reaction: $K_{se\ nonreinf}$ = 65.4 MH/m^3, $K_{se\ reinfor.layer}$= 74.1 MH/m^3.

Table 2. The geosynthetic materials' characteristics.

No	Material description	Tensile strength kN/m	Relative elongation, %	Function
GM No 1	Non-woven polypropylene thermally strengthened geotextile, 400g/m^2 density	32	<55	Concrete layers separation
GM No 2	Non-woven polypropylene thermally bonded geotextile, with strength at 5% elongation – 4kN/m, type GT.N.T.-1	9	<52	Drainage
GM No 3	Non-woven polypropylene thermally bonded geotextile, with strength at 5% elongation – 8.2 kN/m, type GT.N.N.-3	20	<52	Waterproofing with bitumen emulsion treatment
GM No 4	Bentonite mat with a waterproofing layer of polymer geomembrane	>10.4	<20	Loess soil waterproofing
GM No 5	Woven polyvinylalcohol biaxial geogrid type GR. W.-28, E = 19 000 MPa, v = 0,3.	200	6	Base reinforcement
GM No 6	Volumetric perforated polyethylene geometries with tape thickness 1.5 mm, cell size 10x16 mm and height 150 mm.	>8	–	Anti-erosion protection
GM No 7	Volumetric geomat made of polyamide with a thickness of 18 mm, with a tensile strength of 2 /1,2 kN/m, type GMW.-2.	2 1.2	–	Anti-erosion protection
GM No 8	Woven geogrids PET GR.W.-19 and GR.W.-15, E = 15000 MPa, v = 0.30.	200/200 110/110	12 12	Base reinforcement

Table 3. Crushed stone – sandy mixture with and without geotextile.

No layer	Thickness, m	K_s, MN/m^3 Unreinforced	K_s, MN/m^3 Reinforced	α	
t_1	0.30	120.0	132.00	0.793	Medium-grained sand over thermobonded geotextile
t_2	0.25	210.0	231.00	–	Rubble – sandy mixture C – 7
t_{35}		44.4	51.53	8.064	
t_3	0.25	280.0	364.00	2.219	Rubble – sandy mixture C-5 reinforced with geotextile with strength no less 200 kN/m^2.
t_4	0.60	40.0	40.00	–	Compacted soil
t_5	6.00	18.0	18.00	8.556	Waterproofing layer made of geomembrane

7 CALCULATION OF SETTLEMENT OF AIRFIELD PAVEMENT UNDER LOAD

Aircraft for calculations: Boeing 777-300ER with characteristics are: gross weight – 352.44 t; tire pressure – 1.52 MPa; load on the main gear – 1629.34 kN; calculated load on one wheel – 265.63 kN; footprint radius – 0.237 m; the depth of the active soil zone – 6.63 m; vertical compressive stress – 0.13 MPa. The number of wheels on the main gear $n_k = 4$. The distance between the tires: $y_i = 0.70$ m, $x_i = 1.30$ m.

Stress from the soil's own weight, taking into account the condition of reaching 10% of the active vertical load (1).

$$\sigma_{vv}(z) = 0.1 \cdot \gamma_{cp} \cdot z. \tag{2}$$

where, γ_{cp} is the specific gravity of the soil, taken as 20 kN/m^3.

By equating the formulas (1) and (2), possible to find the depth of the active zone value by the method of iterations.

Graphically, the depth of the active zone is located at the intersection of the changes depending on the total compressive stresses $\sigma_{z(z)}$ and stresses from self-weight $\sigma_{vv(z)}$ (1).

Measures to eliminate the subsidence properties of the soil should be provided depending on the fulfillment of the condition.

$$\sigma_{zp} + \sigma_{zg} \leq p_{sc}. \tag{3}$$

where σ_{zp} – vertical compressive stress in the soil from operational load; σ_{zg} – vertical compressive stress from the soil's own weight and airfield pavement; p_{sc} – initial settling pressure, which is determined according to GOST 23161-78.

If condition (2) is satisfied, compaction of the upper layer of the subsidence soil to the requirements of the standards should be provided. If $\sigma_{zp} + \sigma_{zg} > p_{sc}$, it is necessary, in addition to compacting the upper layer, to provide for measures to eliminate the properties of the settlement soil to a depth that ensures the satisfaction of the condition:

$$s_{sc} \leq s_u. \tag{4}$$

where s_{sc} – the vertical deformation value of the base caused by the soil settlement, which is determined with humidity w_p at the limit of rolling; s_u – the limit value of the vertical deformation, which is accepted according to the norms, is 0.02 m.

The obtained values of the theoretical settlement and the settlement are 1.92 cm, which is less than the permissible settlement of 2.00 cm. That is, the proposed construction with the arrangement of the soil-cement layer and the replacement of 1.50 m of loess subsidence meets the requirements for deformations.

8 DESIGN AND CALCULATION OF THE AIRFIELD PAVEMENT

To accomplish this task, the following steps were taken:

– development of variations for airfield pavement;
– calculations and comparative analysis of obtained results for the airfield surface;
– generating conclusions and directions for future researchers.

When choosing the optimal design version for the new airfield pavement, we were focused on ensuring such functions as ensuring the stability of high slopes on weak soils, ensuring the uniformity of the embankment settlement on weak soils and accelerating construction terms by using geosynthetic materials.

Structural solutions for use in strengthening the base soil reinforced with geogrid GM No 8 with a strength of 200/200 kN/m and waterproofing the base with bentonite mats GM No 4 for the high-speed runway pavement are recommended. Technical decision consists: Concrete class Btb 4.0/5.0, $t_1 = 0.40$ m; GM No 1 (to separate the layers of the concrete pavement); Concrete B 5.0/75, $t_2 = 0.30$ m; Sand cement with optimal mixture M 75, $t_3 = 0.20$ m; Soil cement M 40 mixed with a milling machine on site, $t_4 = 0.22$ m; Rubble – sandy mixture C-5, $t_5 = 0.24$ m, treated with a minimum amount of bitumen cationic emulsion (1.50%) or rubble – sandy mixture C-5 with pouring of bitumen emulsion on the surface with a consumption of 1.50 l/m^2; GM No 8; Soil (loam or sandy loam); GM No 4; Compacted ground base of airfield pavement.

To provide additional waterproofing and achieve the calculated value of the coefficient of subgrade reaction (k – value) on the surface of 74 MN/m^3, a layer of stabilized soil and the additional layer of bentonite mats with resistance to pH fluctuations are laid under the designed airfield pavement.

There are not any standards and norms for waterproofing with geosynthetics that are suitable specifically for airports' pavement. Therefore, it is necessary to rely on the EN 15382 standard for products used in transport infrastructure.

When comparing geomembrane GCL with conventional GCL, there are two parameters to consider: chemical stability and water resistance (according to the ASTM D 5887 standard).
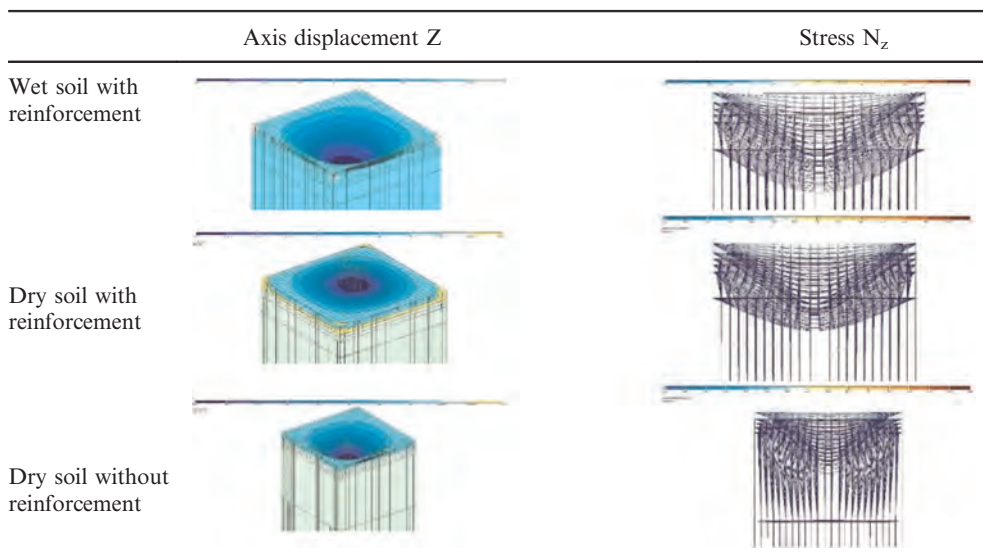
The modelling of the stressed-deformed state of the airfield pavement and soil was made in several software packages. It is allowed to use a simplified mathematical model of the soil base, taking into account the fact that the proportionality coefficient between the positive deflection of the plate and the reaction of the base is a variable value and depends on the coordinates of the point of the middle surface of the pavement (node), in which the deflection and the reaction of the base are determined:

$$q(x^2 x^3) = -K(x^2, \quad x^3) \cdot w. \tag{5}$$

where $q(x^2 x^3)$ – reaction of the soil base; $K(x^2, \quad x^3)$ – proportionality factor function (the coefficient of subgrade reaction); w – positive deflection at the given point along the normal to the plate surface in the deformed state.

The results of stress-strain state calculations in the Lira CAD software complex are shown in Table 4.

Table 4.   The results of stress-strain state calculations.

	Axis displacement Z	Stress N_z
Wet soil with reinforcement		
Dry soil with reinforcement		
Dry soil without reinforcement		

9 CONCLUSIONS

According to the type of soil conditions, the site belongs to the second type due to subsidence. Therefore, when designing several measures are provided that exclude or reduce subsidence to acceptable limits, water protection and construction measures according to DBN A.2.2-1-2003.

REFERENCES

[1] Jiang X. Analysis on the Effect of Lime Soil Compaction Pile in Strengthening Collapsible Loess Subgrade. *Shanxi Architecture*, 46 (10) (2020), pp. 78–79.

[2] Giroud J.P., Han J. 2004 Design Method for Geogrid-Reinforced unpaved Roads. I. II Development of Design Method *Journal of Geotechnical and Geoenvironmental Engineering ASCE* 130 pp 775–86, pp 787–97.

[3] Giroud J.P. and Noiray L. 1981 Geotexile-reinforced Unpaved Road Design Proc. of the American Society of Civil Eng. *Journal of the Geotechnical Eng. Division* 107, pp 1233–54

[4] Zornberg J. "Advances in the Use of Geosynthetics in Pavement Design," in *Second National Conference on Geosynthetics*, 2011, pp. 3–21.

[5] Jenner J., Paul C., Lesson Learned From 20 Years Experience on Geosynthetic Reinforcement of Pavement Foundtions. *2nd European Geosynthetics Conference*, 2000, pp. 421–426.

[6] Rajesh U., Sajja S., and Chakravarthi V.K., "Studies on Engineering Performance of Geogrid Reinforced Soft Subgrade," *Transp. Res.h Procedia*, vol. 17, pp. 164–173, 2016.

[7] Suku L., Prabhu S.S., and Sivakumar Babu G.L., "Effect of Geogrid-reinforcement in Granular Bases Under Repeated Loading," *Geotextiles and Geomembranes*, vol. 45 (4), pp. 377–389.

Design method for rockfall protection embankments reinforced with geosynthetics

P. Rimoldi
Civil Engineering Consultant, Milan, Italy

N. Brusa
Tailor Engineering, Ferrara, Italy

ABSTRACT: Reinforced Soil Rockfall Protection Embankments (RS-RPE) reinforced with geosynthetics proved to be a safe measure for protecting people, structures and infrastructures from rockfall events, designed to absorb even very high impact energy (up to 30,000 kJ). RS-RPEs can be constructed in various shapes and sizes, with different reinforcements (geogrids, geotextiles, geostrips, steel wire meshes, etc.) and facing materials (wraparound, geocells, gabions, etc.). The Authors have developed a new analytical design method for RS-RPE which consider the effect of all the variables playing a role in the resistance to penetration on the uphill face and the resistance to extrusion on the downhill face, in order to finally compute approximate yet consistent values of the penetration depth and of the extrusion length; hence the designer can quickly try different solutions and finally select the best combination of design variables which afford to respect all design limits and Factors of Safety. Back analyses of full scale tests are used to validate the presented design method.

1 INTRODUCTION

In the present article, the Authors present an original design method for Reinforced Soil Rockfall Protection Embankments (RS-RPE) subject to high energy rock impacts, whose framework was previously defined by Rimoldi & Brusa (2021).

By using the proposed method, the designer can quickly set all the characteristics of the RS-RPE, including geometry, facing system on the uphill face, reinforcement properties and vertical distribution, in order to respect all the ultimate and serviceability limit state conditions.

2 FRAMEWORK FOR THE IMPACT ANALYSIS

The most critical part of the design procedure, and the most underdeveloped, concerns the dynamic analysis of the design impact, with the evaluation of the penetration depth on the hill side and the extrusion length on the valley side.

Referring to the available full scale tests and numerical models, the Authors propose the following framework for the optimised design of RS-RPE through the dynamic impact modelling:

- As the impact is an impulsive action by nature, the falling rock transfers the momentum of the motion to the embankment. The impulsive force that is instantly applied to the embankment depends on the mass, the shape and the velocity of the boulder, on the mass,

geometry, geotechnical properties and construction method of the embankment, and on the number, position, layout and technical characteristics of the reinforcing geosynthetics.

- The wave energy developed by the impulsive force applied to the embankment propagates in a quasi spherical shape; as consequence it means that below the rock footprint in the uphill face the soil is highly compressed, while above the impact footprint, the soil is subject to upward vertical stresses, which would lift the mass of soil above if reinforcement is not present.
- The soil mass adjacent to the rock impact footprint results in compression while, after a certain distance from the first contact point, the acceleration applied to the soil mass produces an outward horizontal movement equivalent to a downhill directed "tensile" force being applied to the soil; at the limit between the compressed and the "tensioned" zone, cracks are formed; the soil mass is therefore separated into two parts.
- The tensile and pullout resistance of the reinforcement contribute to resist the outward displacement.
- Reinforcement layers are able to "guide" the impact energy, so that the initial spherical shape is soon converted into a horizontal cone; outward displacements occur within this cone, leaving the remainder of the soil mass in place.
- Hence only the horizontal component of the impact velocity is relevant for the design of reinforcement.
- Reinforcement layers, made of geogrids, geostrips or geotextiles, can spread the impact load along the embankment axes in both transversal and longitudinal directions.
- The stresses generated by the impact wave energy have an important component in the direction parallel to the length of the embankment, beyond the compressed zone at the uphill face: this justifies the design option of placing reinforcement layers in such direction.
- The reinforcement layers are subject to high tensile forces, but the impulsive nature of the active force allows to not consider at all any creep effect in the reinforcements, and to consider a higher dynamic tensile modulus than the static one.
- Very strong and/or repeated impacts can produce very large outward displacements, which can bring to the pullout failure of the wrapping length of the reinforcement. Hence, this length shall be designed to be much longer than in static conditions; connection of the front face and back face reinforcement, that is a back-to-back design, is highly recommended.

Such evidence translates into the following rational assumptions:

- The downward vertical component of the impact load is resisted by the embankment fill and may have an effect only on the bearing capacity of the foundation and the global stability of the structure and of the downhill slope, while the upward vertical component of the impact load is resisted by the fill confined by reinforcement layers. As consequence, the soil mass involved in the impact-extrusion mechanisms is limited by the horizontal planes tangent at the top and bottom points of the impacting boulder (Figure 1.a), and laterally by two planes diverging from the boulder lateral limits according to an impact load spreading angle, α (Figure 1.b).
- The impacting boulder is assumed to have a spherical or cubic shape, e.i. dimension D (see Figure 1.b), that can be easily computed by equalizing the kinetical energy of the equivalent boulder to the given impact energy E_0:

$$E_0 = 1/2 V_m (\gamma_m / g) v_b{}^2 \tag{1}$$

where V_m is the volume of the boulder (assumed either as a sphere of diameter D or a cube with size D), γ_m is the unit weight of the boulder, v_b is the design impact velocity of the boulder, and g is the gravity acceleration.

The following assumptions are made for the compressed zone at the upstream face:

- Geosynthetic reinforcements cannot work in compression; hence, reinforcement placed in the direction of the impact ("transversal reinforcements") cannot contribute to penetration resistance.
- Only reinforcements placed along the axis of the embankment ("longitudinal reinforcements"), if present, can contribute to resist the impact load through the tensioned-membrane effect generated by the deformation of the reinforcement, like the cord of an arch (Figure 2.a). This effect can be considered also to increase the load spreading angle, α.
- The soil resists the impact load (see Figure 2.b) through its coefficient of viscous damping, C_s, and its elastic resistance with an overall elastic coefficient, K_{tot}, which is given by the sum of the elastic coefficient of the soil, K_s, and of the elastic coefficient of the geosynthetic reinforcements, K_g (as said, provided only by the longitudinal ones, if present).
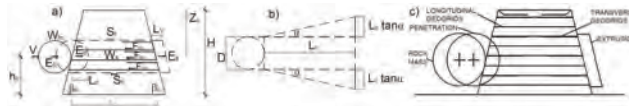

Figure 1. The impact-extrusion mechanisms is limited by (a) the horizontal planes tangent at the top and bottom points of the impacting boulder and (b) by the lateral planes diverging according to the load spreading angle α; (c) the rock mass movement and RS-RPE deformations are contrasted by both the transversal and the longitudinal geogrids.

- The elastic coefficient of the soil, K_s, is assumed to be proportional to the Winkler modulus, M_w, of the compacted fill; while the elastic coefficient, K_g, provided by the longitudinal reinforcements, is assumed to be proportional to their ultimate tensile strength, T_u.
- The upstream facing system contributes to the elastic passive resistance through a facing coefficient, C_g, which modifies the elastic coefficient of the soil, K_s, and the coefficient of viscous damping, C_s.
- The coefficient of viscous damping, C_s, is assumed to be proportional to the damping ratio, ζ, of the compacted embankment fill or of the cushioning layer placed on the uphill face.

The values of the load spreading angle α and of the facing coefficient C_g should be evaluated from the results of full scale impact tests on RS-RPE of similar configuration to the one under consideration. Another way of setting α and C_g is to perform a back calculation of a known impact on the specific system under considerations, using the framework herein presented, where the parameters are modified by trials and errors starting from realistic initial values (see section 3).

If no specific full scale tests nor known impact events are available, the default values in Tables 1 and 2 are proposed: in Table 1 the load spreading angle α varies as a function of the reinforcement layout, of the number N_G of reinforcing layers within the height D of the diffusion cone (see Figure 1.a), and of the type of reinforcement (with open mesh allowing soil interlocking, like geogrids and steel wire meshes, or without open mesh, like woven geotextiles or geostrips). In Table 2 the facing coefficient C_g varies as a function of the cushioning capacity of the facing system, where the simple wrap-around facing system is assumed with $C_g=1.0$.

Figure 2. a) Elastic resistance of the longitudinal reinforcements through the tensioned-membrane effect; b) Scheme of the 1-DOF oscillator.

1775

Table 1. Default values of the impact load spreading angle α.

Reinforcement distribution	N_G	α with GG or DT mesh	α with GTX or Geostrips	α with GG+Geo-cell facing
Unreinforced	0	5	5	10
Transversal reinforcement only	1	15	8	20
	2	20	12	25
	3	25	15	30
	>3	30	18	35
Transversal+Longitudinal reinforcement	1	25	15	35
	2	35	20	45
	3	45	25	55
	>3	50	30	60

Table 2. Default values of the facing coefficient C_f.

Facing system	C_f
Wrap-around	1,00
Gabions with coarse fill	1,50
Sand filled bags	1,30
Geocells	1,20
Tires	1,35

Taking into account the above listed assumptions, the penetration depth on the upstream face can be computed according to the method presented by Carotti *et al.* (2000), based on the theory of totally anelastic impact, through the lumped mass model made up by a 1-DOF (one degree of freedom) oscillator, characterized by a viscous damper and a spring (Figure 2.b), which undergoes a deformative cycle with angular frequency, ω. The lumped mass, m, of the 1-DOF oscillator is the mass m_s of the soil contained in the cone as previously identified (see Figure 1.a and 1.b) plus the mass of the boulder m_m. The masses m_s and m_m are equal to the respective weights W_s and W_m divided by the gravity acceleration, g. The equations for calculating the energy absorbed by soil deformation on the uphill side, E_p, and the transmitted energy, E_s (which produces the downhill extrusion), as shown in Figure 1.a, are the following:

$$E_0 \ = \ E_p \ + \ E_s \ = \ E_p \ + \ E_0 \cdot \ E_s / \ E_0 \tag{2}$$

$$E_s / \ E_0 \ = \ m_m / \ (m_m \ + \ m_s) \ = \ W_m / \ (W_m \ + \ W_s) \tag{3}$$

While the weight W_m is an input data from the risk analysis, the weight W_s can be easily calculated from the geometry of the problem (see Figure 1.a and 1.b).

Considering the viscous work of the 1-DOF oscillator during a deformative cycle, the maximum displacement of the 1-DOF oscillator, which is equal to the penetration depth, L_p, is:

$$E_p \ = \ 1/4(\pi \ \cdot \omega \cdot \ C_s \cdot L_p{}^2) \tag{4}$$

The circular frequency ω is calculated as:

$$\omega \ = \ (K_{tot} / \ m_{tot})^{0.5} \ = \ \left[g \ \cdot \ (K_s \ + \ K_g) \ / \ (W_m \ + \ W_s) \right]^{0.5} \tag{5}$$

The dumping coefficient of the soil C_s can be evaluated from the dumping ratio ζ of soil:

$$C_s = 2 \cdot \zeta \cdot (K_{tot} \cdot W_s/ g)^{0.5} \tag{6}$$

where ζ may be assumed, in this case of a single dynamic cycle and large strains, in the range $0.10 \div 0.20$ for granular soil, while if the cushioning system on the uphill face includes sand–rubber or gravel–rubber mixtures ζ may be assumed in the range $0.20 \div 0.30$; for geocell cushioning system ζ may be assumed equal to 0.02.

The 1-DOF oscillator model allows a calculation of the part, E_p, of the impact energy, E_o, which is dissipated to stop the boulder through deformation, while the residual energy, E_s, is assumed to spread downstream of the penetration depth, generating the tensioned zone that produces the extrusion on the valley side of the embankment (see Figure 2.a).

The following rational assumptions are made for the zone between the penetration depth and the downstream face:

- The fill resists the extrusion movement through its frictional stresses developed on the top and bottom horizontal surfaces of the extrusion cone, that is with the frictional forces S_t and S_b shown in Figure 1.a, given by the integral of the direct shear stresses τ_{ds} on the two surfaces, with:

$$\tau_{ds} = f_{ds} \cdot \sigma_v \cdot \tan\varphi_s \tag{7}$$

where f_{ds} is the direct shear factor considering the effect of first detachment friction under fast applied loads, σ_v is the vertical stress, and φ_s is the friction angle of the fill.
- The geosynthetic reinforcements confine the fill and increase the load-spreading angle, α, which depends on the type of reinforcement, on the number of reinforcements within the height of the extruded cone, and on the presence or not of the longitudinal reinforcements (Table 1).
- In the tensioned zone, the transversal reinforcement resists extrusion by pullout resistance between the downstream facing and the penetration depth, that is with the pullout forces F_{po} shown in Figure 1.a. The pullout resistance can be activated only if reinforcement is properly wrapped around the downhill face with adequate wrapping length or connected to facing elements, which can transfer the pullout force to the whole fill thickness between two consecutive reinforcement layers. The pullout force provided by each reinforcement within the height D of the diffusion cone is calculated as the integral of the pullout stresses τ_{po} on the length of reinforcement between the crater and the downhill face, with:

$$\tau_{po} = 2 \cdot f_{po} \cdot \sigma_v \cdot \tan\varphi_s \tag{8}$$

where f_{po} is the pullout factor for the specific reinforcement with the specific fill, σ_v is the vertical stress on the considered surface, and φ_s is the friction angle of the fill.

The total pullout force F_{po} is obviously the sum of the pullout forces provided by all reinforcement within the height D of the diffusion cone.

- Since pullout resistance cannot increase indefinitely and the extrusion length strongly depends on the reinforcement deformation, the pullout force shall be produced with limited tensile elongation; hence, the pullout resistance is assumed to be limited to the tensile strength at 2 % elongation, $T_{2\%}$ (kN/m), of the transversal reinforcements.
- Given the impulsive nature of the impact load and the consequent impulsive state of tension in the extrusion zone, a reduction factor for impulsive conditions, RF_{imp}, may be applied to the pullout force, which is calculated with the pullout factor, f_{po}, valid in static conditions. On the other hand, like for first detachment friction, under impulsive conditions the initial pullout resistance may be even higher than in static conditions, hence

RF_{imp} may be assumed to be > 1.0. Until full scale testing of pullout resistance under fast applied loads will confirm which is the real mechanism, it is prudent to assume that RF_{imp} is equal to 1.0.

- The residual energy, E_s, is assumed to be equal to the work done by the friction forces, S_t and S_b, and the total pullout force, F_{po}, which allows a calculation of the extrusion length, L_v, on the valley side of the embankment (Figure 1.a):

$$E_s = (S_t + S_b + F_{po}) \cdot L_v \tag{9}$$

Following the above described method, the impact analysis allows the setting of the required geometry of the embankment (see Figure 1.a), such as the height, H, the crest width, L_u, the slope angles on the mountain side, β_m, and on the valley side, β_v; and the required layout of reinforcement (type, strength, vertical spacing in transversal and longitudinal directions), by checking the following SLS (Serviceability Limit State) conditions, in order for the impacted embankment to be repaired with simple maintenance works:

- The maximum allowable penetration length shall be less than 50 % of the embankment width at the bounce height of the impacting boulder.
- The maximum allowable extrusion length shall be less than 20 % of the embankment width at the bounce height of the impacting boulder.

Once established with the dynamic analysis, such geometry and reinforcement layout shall be checked for internal, external and global stability under dynamic conditions, considering the accidental load of the impact force as an equivalent static force, F_{imp} (kN), applied horizontally in the centre of impact (Figure 3), calculated as the sum of the equivalent penetration force, F_p (kN), and of the equivalent extrusion force, F_v (kN), simply evaluated as energy / movement:

$$F_{imp} = F_p + F_v = (E_p / L_p) + (E_s / L_v) \tag{10}$$

Figure 3.   Evaluation of the equivalent static force.

3   BACK ANALYSES

3.1   *Trento test Nr 2*

Peila et al (2002) reports the results of full scale tests performed at the testing facility set up near Trento (Italy), shown in Figure 4.

Five tests were performed and we report the back analysis of test Nr 2, where the RS-RPE had the cross section shown in Figure 4: it can be noted that the RPE was built with wrap-around facing and that reinforcement was provided both in transversal and longitudinal directions. The test was performed by impacting a concrete boulder with weight of 87 kN. In test Nr 2 the translational velocity of the boulder at the moment of the impact was estimated as 31.3 m/s, and the kinetic energy of the block at the moment of contact was approx. 4,354 kJ. On the hill side a crater was formed with a maximum depth

of about 1 m, while on the valley side a large extrusion displacement of approx. 0.90 m was observed. All input data and calculations for the back analysis of Trento Nr 2 test are reported in Table 3.
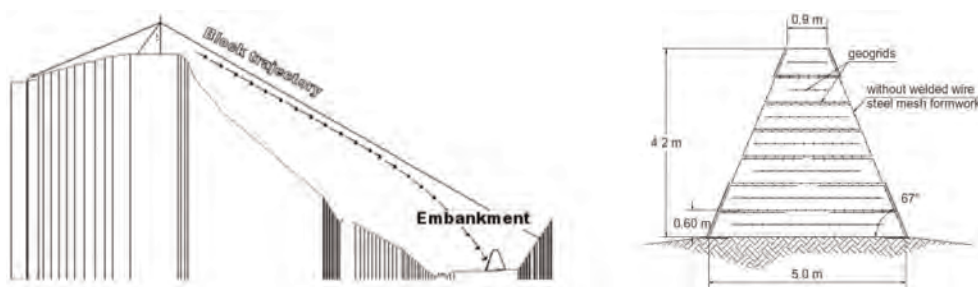

Figure 4.   Test setup in Trento and cross section of the RPE built for test Nr 2 (modified from Peila *et al.* 2002).

3.2   *Maegawa test Nr 3*

Maegawa et al (2011) report about full scale tests that were carried out in a quarry in northern Japan. At the site, two feasible rock-slope lanes, 37 m high with a slope of 42°, are available for rolling concrete blocks down the slope, as shown in Figure 5. The concrete blocks were individually launched by a backhoe to roll down the slope.

Eight tests were performed and we report the back analysis of test Nr 3, where the RS-RPE had the cross section shown in Figure 5: it can be noted that the RPE was built with a cushioning system on the uphill face, made up of 0.8 thick layer of 150 mm high geocells filled with mixed granular soil, and that reinforcement was provided both in transversal and longitudinal directions. The test was performed by impacting a concrete boulder with weight of 170 kN. In test Nr 3 the translational velocity of the boulder at the moment of the impact was estimated as 14.4 m/s, and the translational kinetic energy of the block at the moment of contact was 1,763 kJ. On the hill side a crater was formed with a maximum depth of 1.727 m, while on the valley side the extrusion displacement of 0.239 m was observed. All input data and calculations for the back analysis of Maegawa Nr 3 test are reported in Table 3.

3.3   *Discussion of back analyses*

The results reported in Table 3 show that the proposed method is capable of excellent modelling of high energy impacts on RS-RPEs, since both the calculated penetration depth and extrusion length are within $\pm$ 5 % of the measured values.

Modelling of wrap-around facing system (test Trento Nr 2) allowed to set the following critical parameters:

Dumping coefficient of reinforced fill   Cs=   800   [kN·s/m]
Damping ratio of uphill facing system ζ=   0.10   [-]
Winkler modulus of reinforced fill   Mw=   8,000   [kN/m3]
Angle of spreading of the impact α=   45   [-]
Coefficient of facing resistance   Cf=   1.0   [-]

Modelling of the geocell facing system (test Maegawa Nr 3) has shown that with a cushioning system the correct crest width of the RS-RPE shall include the thickness of the cushioning system itself; moreover, geocell fill offers a "soft" cushioning layer, yet

Table 3. Input data and calculation results for back analyses.

INPUT DATA				TRENTO 2nd	MAEGAWA 3rd
Type	Object	Symbol	Unit	Value	Value
Design impact	Impact height at the center of gravity of the boulder	h_i	[m]	2,50	2,55
	Boulder design velocity (horizontal)	V	[m/s]	31,30	14,40
	Boulder tye (sphere / cube)		[−1]	Sphere	Sphere
	Impact energy	E_0	[kJ]	4.354,00	1.763,00
	Boulder unit weight	γ_m	[kN/m³]	26,00	33,40
Reinforced soil embankment	Crest width	L_u	[m]	0,90	2,20
	Height	H	[m]	4,20	4,20
	Angle of downhill slope	β_v	[°]	67,00	73,30
	Angle of uphill slope	β_m	[°]	67,00	78,70
	Vertical spacing of reinforcements	S_v	[m]	0,60	0,60
	Unit weight of reinforced fill	γ_s	[kN/m³]	21,10	16,60
	Friction angle of reinforced fill	φ	[°]	34,00	25,10
	Type of reinforcement			Geogrids	Geogrids
	Reinforcement direction			Transv.+Lonq.	Transv. Long.
	Type of facing			Wrap-around	Geocells
	Ultimate tensile strength of reinforcement	T_u	[kN/m]	45,00	36,00
	Tensile strength at 2 % strain	$T_{2\%}$	[kN/m]	11,00	21,60
	Amplification Factor for impulsive load	A_{imp}		1,00	1,00
Interaction parameters	Dumping coefficient of reinforced fill	C_s	[kNs/m]	800,00	200,00
	Damping ratio of uphill facing system	ζ	[-]	0,10	0,02
	Winkler modulus of reinforced fill	M_w	[kN/m³]	8.000,00	3.000,00
	Angle of spreading of the impact (from Table 1)	α	[-]	45,00	55,00
	Coefficient of facing resistance (from Table 2)	c_f	[-]	1,00	1,20
	Direct shear coefficient soil-reinforcement	f_{ds}	[-]	1,00	1,00
	Pull-out coefficient soil-reinforcement	f_{po}	[-]	1,00	1,00
	Reduction Factor for impulsive load	RF_{jmp}	[-]	1,00	1,00

CALCULATIONS				TRENTO 2nd	MAEGAWA 3rd
Type	Object	Symbol	Unit	Value	Value
Boulder dimensions	Radius of boulder if spherical	R	[m]	0,93	1,06
	Diameter (if spherical) or size (if cubic) of boulder	D	[m]	1,86	2,12
	Area of boulder impact footprint	A_i	[m²]	3,45	4,50
	Volume of boulder	V	[m³]	3,35	4,99
	Weight of boulder	w_m	[kN]	87,17	166,76
Volume of embankment resisting the impact	Number of reinforcements resisting the impact	N_G	[-]	3,00	3,00
	Height of top edge of boulder	h_t	[m]	3,43	3,61
	Height of the centre of boulder	h_c	[m]	2,50	2,55
	Height of bottom edge of boulder	h_b	[m]	1,57	1,49
	Embankment width at top	L_u	[m]	0,90	2,20
	Embankment width at base	L_r	[m]	4,47	4,30

(*continued*)

Table 3.   Continued

Type	Object	Symbol	Unit	TRENTO 2nd Value	MAEGAWA 3rd Value
CALCULATIONS					
	Embankment width at top edge of boulder	L_t	[m]	1,55	2,49
	Embankment width at centre of boulder	L_c	[m]	2,34	3,02
	Embankment width at bottom edge of boulder	L_b	[m]	3,13	3,55
	Impact diffusion length at top edge of boulder	B_t	[m]	4,97	9,25
	Impact diffusion length at centre of boulder	B_o	[m]	6,54	10,76
	Impact diffusion length at bottom edge of boulder	B_b	[m]	8,12	12,27
	Impact diffusion area at top edge of boulder	A_t	[m²l]	5,31	14,18
	Impact diffusion area at centre of boulder	A_c	[m²l]	9,84	19,48
	Impact diffusion area at bottom edge of boulder	A_b	[m²l]	15,62	25,58
	Volume of soil reisiting the mpact	V_s	[m³l]	19,43	42,16
	Weight of soil reisiting the mpact	w_s	[kN]	409,97	699,85
Penetration depth on uphill side of embankment	Ratio residual energy / impact energy	E_0/E_s	[-]	0,18	0,19
	Energy dissipated in penetration	E_P	[kJ]	3.590,54	1.423,74
	Elastic modulus of the spring made by longitudinal reinforcements	K_G	[kN/m]	501,38	556,10
	Elastinc modulus of the spring mada by soil	K_s	[kN/m]	27.586,26	16.188,56
	Elastic modulus of the equivalent spring of the 1-DOF oscillator	K_{tot}	[kN/m]	28.087,64	16.744,66
	Circular frequency of the 1-DOF oscillator	ω	[rad/s]	23,54	13,77
	Dumping coefficient of soil	C_s	[kNs/m]	216,68	43,72
	Penetration depth on uphill side of embankment	$\mathbf{L_P}$	**[m]**	**0,95**	**1,74**
Extrusion length on downhill side of embankment	Residual energy after penetration	E_s	[kJ]	763,46	339,26
	Direct shear force at top edge of boulder	s_t	[kN]	58,26	65,02
	Direct shear force at bottom edge of boulder	s_b	[kN]	584,36	539,18
	Reinforcement length resisting to pull-out	L_{po}	[m]	1,40	1,29
	Average pull-out resisting stress	τ_{po}	kPa	48,39	25,66
	Pull-out resistance of single reinforcement	F_{po}	[kN/m]	11,00	21,60
	Pull-out force provided by single reinforcement	S_{po}	[kN]	71,98	232,42
	Total pull-out force	$S_{po\text{-}tot}$	[kN]	215,93	697,25
	Extrusion length on downhill side of embankment	$\mathbf{L_v}$	**[m]**	**0,89**	**0,26**
Equivalent impact force	Equivalent penetration force	F_p	[kNl]	3.792,85	820,40
	Equivalent extrusion force	F_v	[kN]	858,55	1.301,46
	Total equivalent impact force	F_{imp}	[kN]	4.651,40	2.121,85
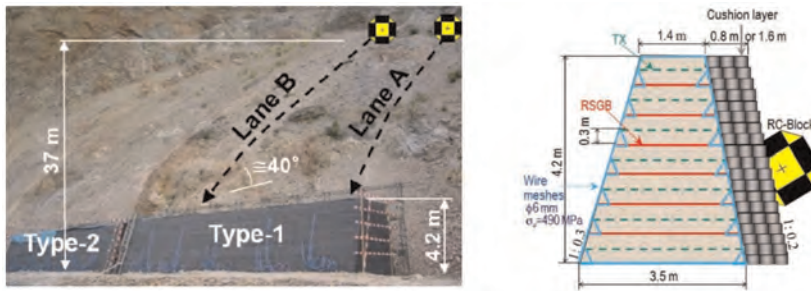
Figure 5. Test setup in Japan and cross section of the RPE built for test Nr 3 (modified from Maegawa *et al.* 2011).

it affords to widen the spreading angle of the impact, α; hence for such facing system the following critical parameters apply:

Dumping coefficient of reinforced fill	Cs=	200	[kN s/m]
Damping ratio of uphill facing system	ζ=	0.02	[-]
Winkler modulus of reinforced fill	Mw=	3,000	[kN/m3]
Angle of spreading of the impact	α=	55	[-]
Coefficient of facing resistance	Cf=	1.2	[-]

4 CONCLUSIONS

A new design procedure for RS-RPE has been described: the analysis of available full scale impact tests and numerical analyses allowed to develop an optimised and rational method for the dynamic analysis of RS-RPE under rock impacts.

The proposed method affords to calculate the penetration depth and the extrusion length caused by the impact of the design boulder, with its mass, velocity, bounce height, and kinetic energy, on a given layout of the RS-RPE.

The back analysis of full scale tests available in literature allowed to check that the method provides very precise and reliable results; moreover, the parameters for specific facing systems have been checked and validated.

REFERENCES

Carotti, A., Peila, D., Castiglia, C. and Rimoldi, P. (2000). Mathematical Modelling of Geogrid Reinforced Embankments Subject to High Energy Rock Impact. *Proc. 2nd European Geosynthetics Conference*, Bologna, Italy.

Maegawa, K, Yokota, T. and Tran Van, P. (2011). Experiments on Rockfall Protection Embankments with Geogrids and Cushions. *International Journal of GEOMATE*, Oct. 2011, Vol. 1, No.1, pp. 19–24

Peila, D., Oggeri, C., Castiglia, C., Recalcati, P. and Rimoldi, P. (2002). Testing and Modelling Geogrid Reinforced Soil Embankments Subject to High Energy Rock Impacts. *Proc. 7th Int. Conf. on Geosynthetics*, Nice, France, 133–136.

Rimoldi, P. and Brusa, N., (2021). "Development of a New Design Method for Geosynthetic-reinforced RPEs". *IFAI Geosynthetics*, April 2021.

A simplified displacement-based hybrid approach for the design of geosynthetic-reinforced earth walls

A. Galli

Department of Civil and Environmental Engineering, Politecnico di Milano, Italy

ABSTRACT: Design criteria for geosynthetic-reinforced earth walls are usually based on simplified limit equilibrium approaches, taking into account ultimate conditions both with respect to soil strength and reinforcements' resistance (tensile and pull-out). Convenient values of partial safety factors are then introduced to get a safe structural dimensioning. The stability of internal failure mechanisms is however based on the mobilization of soil-geosynthetic interface shear stresses and the reinforcement action should rather be computed as a function of the current internal displacements within the wall. In the paper a simplified displacement-based hybrid approach is introduced, combining traditional limit equilibrium analyses of internal failure mechanisms together with displacement controlled non-linear pull-out analyses of the reinforcements. A consistent relationship between the safety factor and the performance of the wall (i.e. façade displacement) can then be derived, providing the designers of an objective tool to optimize the design choices and to run consistent structural safety checks.

1 INTRODUCTION

Geosynthetic reinforced earth walls (GRE) or mechanically stabilized earth walls (MSE) are acknowledged as efficient and economic solutions for supporting e.g. excavations, soil backfills and artificial embankments. The rapidity of construction, the possibility of using (or re-using!) local granular materials and the capability of accommodating large differential settlements, make them highly competitive with respect to traditional concrete walls and significantly reduce their environmental impact (see e.g. Basu *et al*. 2015). Sustainability issues and long-term resilience requirements are moreover fundamental aspects, since GRE usually involve large soil volumes and are often intended as long-lasting (or even permanent) geotechnical structures (Galli 2022). In this perspective, efficient and accurate operational design approaches, are key issues. Advanced numerical approaches (e.g., among others, Saran & Viswanadham 2018), however, are still largely time consuming and require advanced theoretical and computational skills to the users. Standard design procedures (BS 8006 2010; FHWA 2001; EBGEO 2003), on the contrary, are often based on oversimplified limit equilibrium approaches and disregard any consideration about the structure's performance (e.g. the façade displacements). They cannot then be considered fully consistent with the requirements of sustainable design criteria. Recent developments have however been proposed, in static conditions, e.g. by Wang *et al*. (2021), explicitly computing the value of the required geosynthetic tensile stiffness for a GRE wall. In seismic conditions, moreover, Gaudio *et al*. (2018) evaluate the expected wall displacements (co-seismic displacements), by adopting the kinematic approach of limit analysis. As pointed out by Galli and di Prisco (2019) with reference to slope stabilizing piles, these methods could however underestimate

the structure displacement in low seismicity areas, or miss the triggering of co-seismic displacements.

In the present paper, a simplified approach is adopted for studying internal failure mechanisms of GRE walls. The method is defined as "hybrid" since it combines an ultimate limit state approach for wall's internal failure mechanisms, with a displacement-controlled approach for the non-linear pull-out behavior of the geosynthetics. Inspired by the design of passive slope stabilizing structures (Galli & di Prisco 2013; Galli *et al.* 2017; Kourkulis *et al.* 2012) the method allows then to link the global factor of safety of the wall to the amplitude of its façade displacement, through the progressive mobilization of the stabilizing action in the reinforcements. In the following, the method will be described, and some numerical results on a simplified wall geometry will be parametrically discussed.

2 DEFINITION OF A HYBRID METHOD

Equilibrium equations for slope stability analysis require the driving action E (usually, the self-weight of the soil mass plus the possible external loads) to be equilibrated by the ultimate soil shear strength, R, mobilized along the failure surface and by the ultimate stabilizing action, A, provided by the stabilizing structure. Limit Equilibrium Methods (LEM) usually assume that all these terms are evaluated at their Ultimate Limit State (ULS), irrespectively of displacement compatibility conditions. In a hybrid method, on the contrary, the stabilizing action A is explicitly considered to depend on the soil displacement U, associated to the considered failure surface F, through a "characteristic curve" (Galli & di Prisco 2013; Galli *et al.* 2017). This allows to consider not only ultimate but also Serviceability Limit State (SLS) conditions for the soil-structure interaction. The governing equilibrium equation can general be written as:

$$E^F = R^F_{ULS}/F_S + A^F(U^F). \tag{1}$$

where a global factor of safety F_S is introduced as reducing factor for the soil strength. Equation (1) clearly highlights how in a hybrid method ULS conditions for soil strength are combined to SLS conditions for the soil-structure interaction, and represent a link between the F_S for the failure surface F and the corresponding amplitude of soil displacement. By solving equation (1) for F_S for any possible surface F, a family of curves can be derived, whose minimum envelope represents the actual $F_S - U$ relationship for the wall. These curves cannot however be considered a prediction of the on site displacement of the wall for assigned working conditions, but they only provide the designer of a consistent displacement estimation with respect to the required stabilizing action. They can be employed to objectively and rationally optimize the design and to run the required structural safety checks. An application of such hybrid method to GRE walls will be briefly outlined hereafter and some applications to real-like design cases will be presented.

2.1 *Stability of wall internal failure mechanism*

Stability of GRE walls requires in general to verify both external (i.e. sliding, toppling and vertical bearing failure mechanisms) and internal failure mechanism, these latter typically being associated to the pull-out and tensile response of the geosynthetics. External failure mechanisms will be here disregarded (they are in fact associated to rigid-body movements of the wall) and the attention will only be devoted to internal failure ones. Several failure mechanisms are in general recognized in Literature (single or two-blocks failure mechanisms, log-spiral failure mechanism, complex mechanisms; see e.g. Gaudio *et al.* 2018). Without the loss of generality of the proposed hybrid method, however, in the following only single-block failure mechanisms will be considered for a wall height H and a façade

inclination β to the horizontal, defined by planar failure surfaces F with an inclination θ to the horizontal (Figure 1a).

In this context, the driving action E^F corresponds with the component of the soil weight W along the direction θ, whilst the soil strength R_{ULS}^F corresponds with the limit soil shear strength T_L along the failure plane. The stabilizing action $A = A(U_h)$ is instead represented by the sum of the horizontal components of the tensile action mobilized in the geosynthetic layers at the intersection with the sliding plane. Its numerical evaluation will be briefly discussed in the following section. By imposing the vertical and horizontal equilibrium for the soil mass, and the failure criterion for soil along the sliding plane (a simple purely frictional criterion with friction angle ϕ'), it is possible to derive an explicit relationship between the F_S and the mobilized value of the supporting action A, depending on displacement U_h:

$$F_S = F_S(U_h) = \tan\phi' \frac{W\cos\theta + A(U_h)\sin\theta}{W\sin\theta - A(U_h)\cos\theta}, \tag{2}$$

where W also depends on θ, and, owing to the assumed single-block failure mechanism, the soil displacement field U is uniform within the soil sliding mass, with the horizontal and vertical components equal to $U_h = U \cdot \cos(\theta)$ and $U_h = U \cdot \sin(\theta)$, respectively, and $U_v = U_h \cdot \tan(\theta)$.
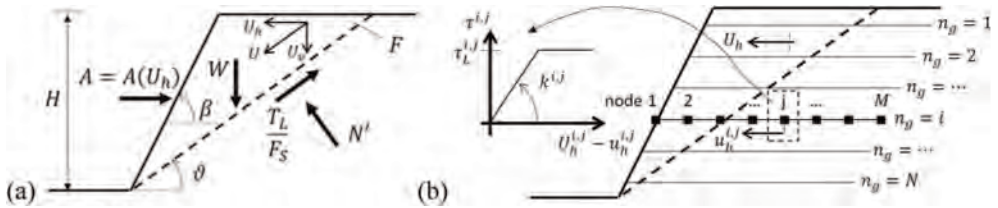
Figure 1. (a) Single block failure mechanism for a GRE wall; (b) pull-out interaction between soil and geosynthetic.

2.2 Geosynthetic pull-out behavior

The term $A = A(U_h)$ of equation (2) can be computed once the soil-geosynthetic pull-out behaviour is modelled as a function of the horizontal displacement U_h of the soil mass. To this goal, N horizontal layers of geosynthetic are introduced, each layer being discretized in M nodes and $M - 1$ finite elements (Figure 1b). Each element is assumed to behave elastically, with a constant tensile stiffness J and no compression and bending stiffness. The local pull-out interaction of each node of the geosynthetic (identified by the indices i, j for the sake of simplicity is modelled by means of elastic-perfectly plastic relationships (with interface stiffness $k^{i,j}$ and limit shear stress values $\tau_L^{i,j}$), as a function of the nodal relative displacement between the soil and the geosynthetic, $U_h^{i,j}$ and $u_h^{i,j}$, respectively. The first node of each geosynthetic has been instead considered as rigidly connected to the wall façade. By collecting the values of the tensile stiffness of each finite element into a global stiffness matrix $\boldsymbol{J}$, all the nodal soil and geosynthetic displacements into vectors $\boldsymbol{U}_h$ and $\boldsymbol{u}_h$, respectively, the global equilibrium to the horizontal translation of the N geosynthetic layers can be written as:

$$\boldsymbol{J} \cdot \boldsymbol{u} = \boldsymbol{k} \cdot (\boldsymbol{U}_h - \boldsymbol{u}_h - \boldsymbol{q}^p). \tag{3}$$

The left-hand term summarizes the tensile elastic behavior of the reinforcements, whilst the right-hand term represents the mobilized interface shear stresses. The term $\boldsymbol{q}^p$ collects in particular the values of the permanent (i.e. plastic) relative displacements triggered in the

nodes. The numerical integration of this term is obtained by applying the piece-wise linear integration technique proposed by Cocchetti (2002). Extensions of such numerical procedure to (i) more complex failure mechanisms, (ii) non-linear pull-out interface relationships with strain hardening or softening and (iii) large displacement membrane behavior can also be implemented.

3 DISCUSSION OF A NUMERICAL EXAMPLE

The hybrid approach outlined here above has been applied to the design of a GRE wall ($H =$ 12m and $\beta = 80°$). The soil is modelled as a uniform granular material (unit weight $\gamma =$ 20kN/m^3 and friction angle $\phi' = 30°$; zero pore water pressure is assumed). Two different geosynthetic disposals are considered, corresponding with a relatively weak and strong reinforcement, respectively. Disposal 1 consists of 8 equally spaced layers with a uniform length of 4 m (total cumulative length of 32m; Figure 2a), whilst disposal 2 of 12 equally spaced layers with a linearly decreasing length between 8 and 4 m (cumulative length of 72m; Figure 2b). In both cases, five failure surfaces are considered (angle $\theta = 30, 40, 50, 60$ and 70°), and the geosynthetic layers are discretized by means of finite elements 50cm long (64 and 144 finite elements for disposals 1 and 2, respectively), with a tensile stiffness $J =$ 1000kN/m. The limit values of the soil-geosynthetic interface shear stresses are computed according to a purely frictional law, depending on the effective normal stress on the geosynthetic. Pressure dependent effects have also been considered, by linearly decreasing the interface friction angle e from 38° to 30° between the top and the base of the wall, and by linearly increasing the interface stiffness from 555.6 kPa/m and 4950 kPa/m between the top and the base.
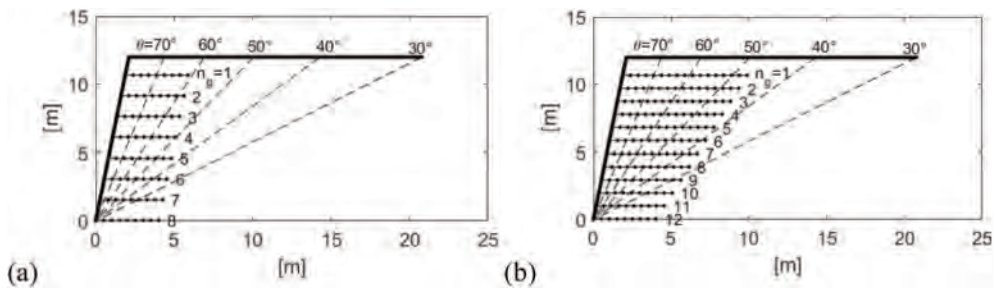
Figure 2.   Sketch of (a) disposal 1 and (b) disposal 2.

3.1 Evaluation of the characteristic curves

The characteristic curves $A = A(U_h)$ computed up to a maximum façade displacement $U_h =$ 50cm for the five considered failure planes both for disposals 1 and 2 are plotted in Figure 3a and b, respectively. The curves show a marked non-linear behavior for increasing values of U_h, with an increasing stiffness for increasing values of θ. For disposal 2, in particular, this effect is maximized for $\theta \geq 50°$, where no remarkable differences are observed among the characteristic curves since all the geosynthetics are activated.

3.2 Evaluation of system performance

The curves of Figure 3a and b can be numerically used in equation (3) to obtain the $F_S - U_h$ relationships, as shown in Figure 3c and d for disposals 1 and 2, respectively. The minimum

envelope of these curves represent the relationship describing the global performance of the wall, and they provide a useful displacement-based design tool for engineers. For a given geosynthetic disposal they allow in fact to estimate the displacement associated to the desired safety level, or, on the contrary, to optimize the choice and disposal of the reinforcements once design values of the safety factor and of the displacement are assigned.
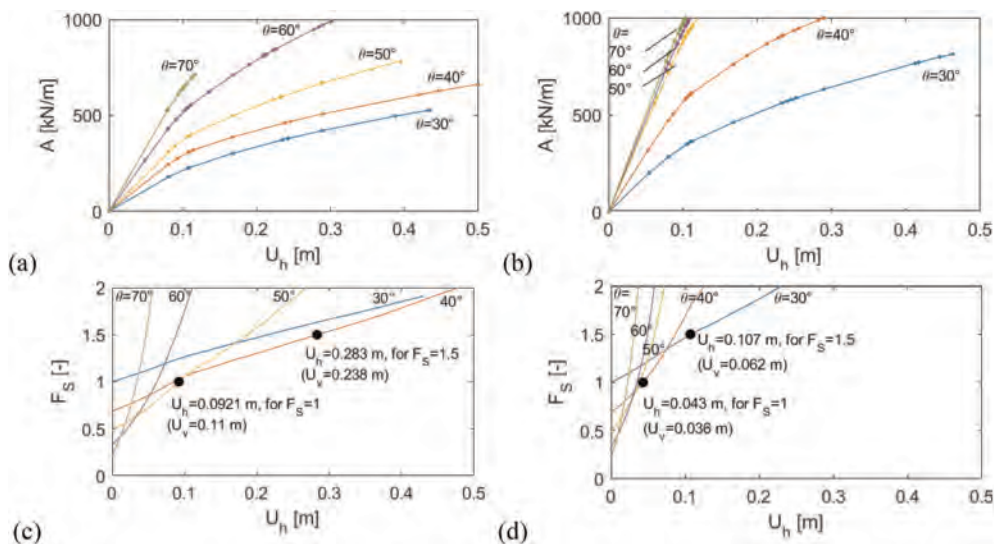
Figure 3. (a-b) characteristic curves for disposals 1 and 2; (c-d) $F_S - U_h$ curves for disposals 1 and 2.

As an example, the two values $F_S = 1$ and 1.5 are highlighted, corresponding with a limit critical condition and with a usual "safe" design condition, respectively, for the internal stability of the wall. The results (represented as black circles) show that higher values of the F_S are associated to larger horizontal façade displacements, since higher values of the stabilizing action need to be mobilized. They also prove a marked difference in the system performance between the two chosen disposals (horizontal displacement of 92.1 and 283 mm for disposal 1, when considering $F_S = 1$ and 1.5, respectively; whilst 43 and 107 mm for disposal 2). The envelope of $F_S - U_h$ curves allows even to highlight the critical failure mechanism associated to each safety level, and, then, to retrieve an estimation of the possible extension and the entity of vertical settlement U_v of wall crest. In case of disposal 1, for example (Figure 3c) the critical failure mechanism changes from $\theta = 50°$ (for $F_S = 1$), to $\theta = 40°$ for ($F_S = 1.5$), with vertical settlements of the wall $U_v = 110$mm and 238mm, respectively; corresponding extensions of the failed zone vary instead from about 7.95m and 12.2m, respectively, from the wall crest. Similar considerations can be derived also for disposal 2 (Figure 3d; values are reported in the figure). As already outlined, however, these values cannot be considered a prediction of the on-site displacement of the wall. They only allow for an objective and rational method to compare different design solutions and, as it will be shown in the next section, to run consistent safety checks on the tensile geosynthetics behavior.

3.3 Estimation of tensile action in the geosynthetics

The numerical integration scheme briefly described in §2.2 permits also to evaluate the tensile internal action in the geosynthetic layers, once a consistent estimation of the horizontal

displacement associated to a specific value of F_S is derived for each failure mechanism. By imposing these displacement values in the numerical analyses, the resulting distributions of internal tensile force N can be straightforwardly derived.
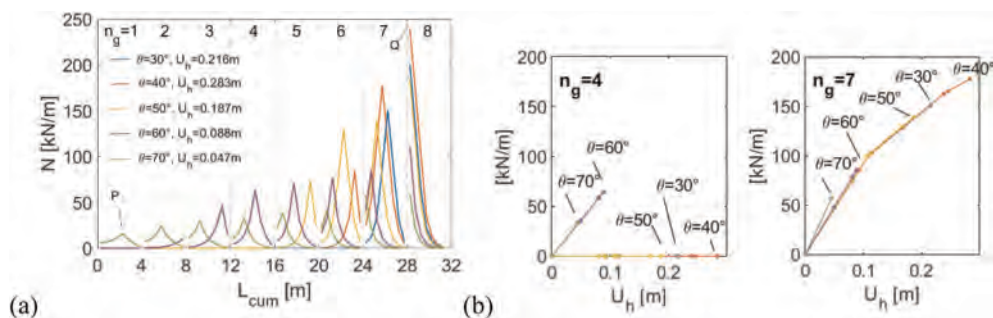
Figure 4. Disposal 1: (a) Distribution of the tensile force N for the five considered failure planes (for $F_S = 1.5$); (b) evolution of the peak tensile force in geosynthetic layers $n_g = 4$ and 7.

With reference to disposal 1, and by assuming again the value $F_S = 1.5$, for example, the resulting distributions are plotted in Figure 4a as a function of the cumulative length L_{cum} of the geosynthetics (for the sake of clarity, the values of the horizontal displacement U_h for the five mechanisms read from Figure 3c are reported within the legend of the figure). For each layer the value and the location of the peak tensile force can be estimated, for each one of the considered failure mechanisms. For layer $n_g = 1$, for example, a maximum tensile force of 15.75 kN/m at a distance of about 2.25m from wall façade is observed for mechanism $\theta = 70°$ (point P of Figure 4a); for layer $n_g = 8$, a peak value of about 240 kN/m at the connection with wall façade is instead computed for mechanism $\theta = 40°$ (point Q). Being these tensile force distributions associated to the same value of the factor of safety, they represent equiprobable distributions, and their envelope can be used to perform the tensile safety checks on the geosynthetics.

For the sake of completeness, finally, for the same case represented in Figure 4a, the evolution of the peak tensile action into two representative geosynthetic layers ($n_g = 4$ and 7; the others are omitted for the sake of brevity) is plotted in Figure 4b against the horizontal façade displacement U_h. It is evident how layer 4 is activated only for failure planes $\theta = 60°$ and 70°, and how its mechanical response is still within the elastic regime; layer 7 is instead activated for all the failure planes, with a marked non-linear response. In both cases, however, assuming ultimate pull-out conditions would have led to a large overestimation of the mobilized tensile action.

4 CONCLUSIONS

A simplified displacement-based hybrid method has been presented with reference to the design of geosynthetic reinforced earth walls. The method is based on the evaluation of the mobilized soil-geosynthetic interaction forces as a function of the relative soil-geosynthetic displacements. It allows then to couple the value of the global safety factor of the wall (with respect to internal failure mechanisms) to a consistent evaluation of the wall performance (e.g. the façade displacement). The method is suitable to be extended to complex failure mechanisms for the wall and advanced interface constitutive rules, and it can then be considered a useful design tool for engineers, even for real cases studies. It will in particular highlight the performance of the system, by properly taking into account not only the

pull-out resistance, but also the interface and tensile stiffness of the reinforcements. As a consequence, the method allows for a more accurate evaluation of the geosynthetic internal state of stress, consistently with the wall displacement, that cannot obviously be achieved with traditional ULS design approaches. This method can also be of large importance for promoting the use of more accurate experimental characterization of the long term and pull-out behavior of geosynthetics, since it provides a simple way for practitioners to directly employ these parameters in the design process.

REFERENCES

Basu, D., Misra, A., Puppala, A.J. 2015. Sustainability and Geotechnical Engineering: Perspectives and Review. *Canadian Geotechnical Journal.* 52(1), pp. 96–113.

BS 8006, 2010. Code of Practice for Strengthened/reinforced Soils and Other Fills. *British Standards Institution*, London, UK.

Cocchetti, G., Maier, G., and Shen, X.P. 2002. Piecewise Linear Models for Interfaces and Mixed Mode Cohesive Cracks. *Computer Modelling in Engineering and Science*, 3(3): 279–298.

EBGEO–Empfehlung 6.9 2003. Bewehrte Erdkörper auf punktoder linienförmigen Traggliedern, Kapitel 6.9 für die *Empfehlungen für Bewehrungen aus Geokunststoffen*, Dggt (German Geotechnical Society).

FHWA, 2001. Mechanically Stabilized Earth Walls and Reinforced Soil Slopes Design and Construction Guidelines. *National Highway Institute*, Federal Highway Administration, US Department of Transportation, Washington, DC, 419 pp.

Galli A. 2022. The Role of Geotechnical Engineers in Sustainable Construction Processes: A Regard to Soil-Structure Interaction Problems. *Lecture Notes in Civil Engineering*, 243, pp. 59–76.

Galli A., di Prisco C. 2013. Displacement-based Design Procedure for Slope-stabilizing Piles. *Canadian Geotechnical Journal*, 50(1), pp. 41–53.

Galli A., Maiorano R.M.S., di Prisco C., Aversa S. 2017. Design of Slope-stabilizing Piles: From Ultimate Limit State Approaches to Displacement Based Methods. *Riv. Italiana di Geotecnica*, 51(3), pp. 77–93.

Galli, A., Di Prisco, C. 2019. An Improved Displacement-based Approach for Seismic Analysis of Pile-Stabilized Slopes Taking into Account Soil-structure Interaction. *Earthquake Geotechnical Engineering for Protection and Development of Environment and Constructions*–Proc. of the 7th Int. Conf. on Earthquake Geotechnical Engineering, pp. 2518–2525.

Gaudio D., Masini L., Rampello S. 2018. A Performance-based Approach to Design Reinforced-earth Retaining Walls, *Geotextiles and Geomembranes*, 46(4), pp. 470–485.

Kourkoulis, R., Gelagoti, F., Anastasopoulos, I., and Gazetas, G. 2012. Hybrid Method for Analysis and Design of Slope Stabilizing Piles. *Journal of Geotechnical and Geoenvironmental Engineering*, 138(1), pp. 1–14.

Saran R.K., Viswanadham B.V.S. 2018. Centrifuge Model Tests on the Use of Geosynthetic Layer as an Internal Drain in Levees, *Geotextiles and Geomembranes*, 46(3), pp 257–276.

Wang L., Wang C., Liu H., Hung C. 2021. One-step Analytical Method for Required Reinforcement Stiffness of Vertical Reinforced Soil Wall with Given Factor of Safety on Backfill Soil, *Geotextiles and Geomembranes*, 49(1), pp. 343–350.

Reliability-based analysis of novel helical soil nailed wall using the MCS

Ekansh Agarwal*
Geotechnical Engineering Group, CSIR-Central Building Research Institute, Roorkee, India

Mahesh Sharma*
University of California Davis, USA

Anindya Pain*
Geotechnical Engineering Group, CSIR-Central Building Research Institute, Roorkee, India

ABSTRACT: Soil nailing technique is extensively used for the stabilization of natural slopes and walls due to its unnumbered benefits viz. ease of installation in congested areas, flexibility, and a remarkable performance under seismic conditions. Various literature have highlighted the effective use of soil nailing technique in the stabilization of slopes, cuts, landslides, and excavations. Recently, researchers have improved the efficiency of the conventional soil nails by adding a set of helices along the length of the nail. The novel soil nail is termed as the helical soil nail. In the present study, the reliability-based analysis of a wall stabilized using the novel helical soil nails, is performed using the pseudo–static framework. The critical mode of failure for a helical soil nailed wall viz. the pullout mode, is considered in the formulation of the limit state function. The probability of failure (P_f) of the wall is approximated using the conventional sampling-based Monte–Carlo Simulation (MCS). The random variables include the internal friction angle of soil (ϕ) and the unit weight (γ). The P_f for a conventional soil nailed wall is compared with that of the helical soil nailed wall, to evaluate the efficacy of the helical soil nailed wall. The results depict a decrease in P_f when helical soil nails are used as a stabilization measure in place of the conventional soil nails. The influence of the randomness of input parameters is showcased by plotting a graph of P_f against the coefficient of variation (COV) of ϕ. The plot indicates a decrement in the stability of the wall with the increasing randomness which demonstrates the need for reliability analysis of the helical soil nailed walls. The paper also discusses the effect of nail inclination angle on the stability of the helical soil nailed wall. To the best of the authors' knowledge, the proposed method is original.

1 INTRODUCTION

Slope stability is a crucial subject of Geotechnical Engineering. The failure of soil slopes may lead to landslides which further lead to serious issues like infrastructure damage, and/or injury or loss of life of inhabitants of that area. It is, therefore, necessary to build stable and safe slopes, renovate and maintain the already built soil slopes, and stabilize the slopes prone to failure. Since slope stabilization's inception, numerous stabilization methods have been

*Corresponding Authors: ekansh1294@gmail.com, mahesh3.ce@gmail.com and pain_anindya@cbri.res.in

proposed which include building retaining walls, and slopes, limiting the driving forces, increasing the stabilizing forces, etc. However, in the 21st century, due to the limitation of space, conventional methods are less feasible. A practical alternative to these conventional methods is the use of reinforcements to provide tensile support to the soil. The soil structures designed and constructed using reinforcements as strengthening materials are referred to as reinforced soil structures. The reinforcements can be of different types such as high-density polyethylene (HDPE) geosynthetics, steel (or metal) strips, soil nails, sheet piles, etc. The present study is based on analyzing the slopes considering the soil nails as reinforcements. However, a specific kind called helical soil nails is considered due to their superiority over their conventional counterparts. Several researchers have used soil-nailing techniques to stabilize the geotechnical structures (Sharma *et al.* 2018, 2019a, b). Helical soil nails and their uses have also been explored by some researchers (FSI 2014; Sharma *et al.* 2020; Tokhi *et al.* 2017). But the methodology is deterministic which ignores the variability associated with the soil parameters. There is a limited study on the applications and usage of helical soil nails as a reinforcement material for soil slopes in the probabilistic domain. The present study is an attempt to analyze the reinforced soil walls (RW) in the probabilistic domain using the pseudo-static framework. The results are presented in the form of comparisons between the conventional and helical soil nails in the probabilistic framework.

2 METHODOLOGY

The methodology adopted for the probabilistic analysis is the conventional Monte Carlo simulation (MCS). It is a benchmark methodology that is highly accurate due to fewer assumptions and has been used recently to probabilistically analyze the reinforced soil retaining structures (Agarwal *et al.* 2022a, b, c). It follows the basic principles of probability theory and calculates the probability of failure (P_f) by using the following simple mathematical rule.

$$P_f = \frac{\text{Number of instances when FoS} < 1}{\text{Total instances}} \tag{1}$$

The FoS is typically not used in reliability analysis. Generally, a performance function is calculated to define the margin of safety. The performance function is calculated as FoS–1. The present study only considers the pullout of helical soil nails as the critical case of failure (Agarwal *et al.* 2022d; Sharma *et al.* 2020). The FoS (pullout) is given by:

$$FoS = \frac{F_{resisting}}{F_{driving}} = \frac{[(k_v + W)\cos\,\psi + P_e \sin\,(\alpha + \psi) - k_h \sin\,\psi]\tan\,\phi + P_e \cos\,(\alpha + \psi)}{(k_v + W)\sin\,\psi + k_h \cos\,\psi} \tag{2}$$

where

$$P_e = \sum_{i=1}^{N} P_i \tag{3}$$

$$P_i = \pi\sigma_i dL_{ei} \tan\delta + \sum_{k=1}^{n} \left(A_k \sigma_i \kappa_o N_q\right) \tag{4}$$

For more details, readers may refer to Sharma *et al.* 2020 and Agarwal *et al.* 2022d.

The analysis is performed using the pseudo-static analysis. It has been previously used by different researchers (Agarwal *et al.* 2022a; Basha & Babu 2012) to analyse the reinforced soil retaining structures. The prime reason to consider the pseudo-static (PS) framework is its

simplicity and efficiency. Though the results might not be as precise as complex frameworks, the main idea of this research work is to explore the usefulness of helical soil nails as reinforcements in soil retaining structures and therefore, the PS framework would suffice. The assumptions stated by Agarwal *et al.* (2022d) are adopted for the analysis. A free-body diagram of RW is shown in Figure 1 for reference to the readers.

Other basic details have not been included in the manuscript to adhere to the word limit and laid guidelines. The readers may explore some of the works of the authors and other researchers on pseudo-static frameworks, helical soil nails (Agarwal *et al.* 2022a, d), and reliability-based analysis of reinforced soil retaining structures.
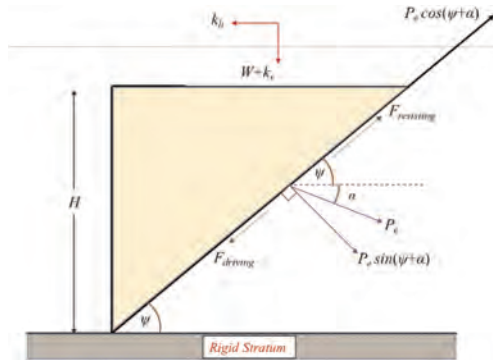
Figure 1.   Free-body diagram of a RW.

3   RESULTS AND DISCUSSION

The results section includes the comparison of the competency of conventional and helical soil nails in the probabilistic domain, the influence of randomness on the RW, and the effect of nail inclination angle on the stability of RW. As already stated, the prime motive is to explore the potential of helical soil nails as a reinforcement material in the probabilistic domain, and therefore, only two input parameters (ϕ and γ) are taken as random variables (statistics provided in Tables 1 and 2).

Table 1.   Input parameters.

Parameters	Value
H	10 m
L/H	0.8
k_h	0.1
k_v/k_h	0.5
δ/ϕ	0.75
α	0°
D_{hx}/d	6
β	90°
S_{hx}/D_{hx}	5
d	0.040 m
S_v/D_{hx}	5

3.1 Effect of the variability of random parameters on RW

This effect is demonstrated by plotting P_f against the coefficient of variation (COV), a parameter that depicts the extent of variability of input parameters. The input variables adopted are stated in Tables 1 and 2 and not stated separately in each section and with figure captions. The plot in Figure 2 portrays the influence of COV on the stability of RW. This effect cannot be quantified in a deterministic approach which is the reason why authors have emphasized the use of probabilistic analysis for exploring the applications of helical soil nails in RWs. The P_f of RW is gradually elevating as the COV (or simply the variability) increases. Readers may explore different combinations of COV and consider other parameters as random for more clarity. However, the authors advise checking for efficiency as the parameters increase.

Table 2. Properties of the random variables.

Random parameter	Properties		
	Mean value (μ)	Std. Deviation (σ)	Distribution*
ϕ	32°	1.6–4.8°	Log-normal
γ	20 kN/m³	1 kN/m³	Normal

*According to Basha & Babu (2010).
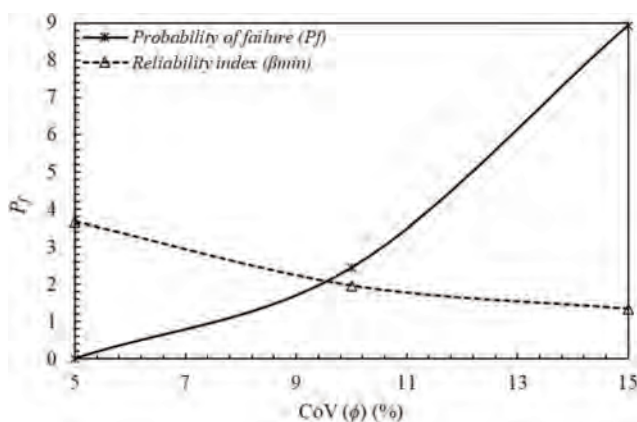
Figure 2. Plot of P_f against CoV (ϕ).

3.2 Effect of nail inclination angle (α)

As stated in the previous sub-section, the input parameters remain the same except α which is taken as 0° and 15° to see its effect on the P_f of RW. Figure 3 depicts the effect of α on the RW. As α increases, the stability decreases as the P_f increases. This can also be easily justified by the geometry and calculating the horizontal and vertical forces along with the moments. This also justifies the correctness of the used algorithm. The results also illustrate the importance of experience and judgment in deciding the nail inclination angle while designing a live helical soil nail RW.
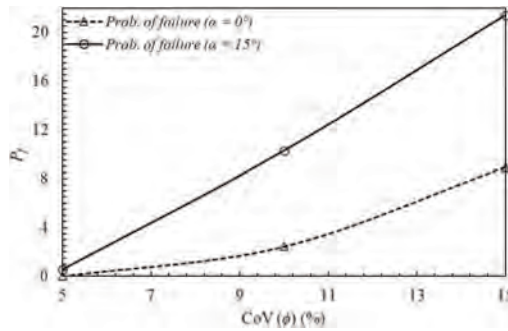
Figure 3. Plot of P_f against CoV (ϕ) for different α.

3.3 *Comparison of conventional and helical soil nails*

This sub-section is included to appreciate the benefits of using helical soil nails as reinforcement instead of conventional ones. The input parameters are taken from Tables 1 and 2. The value of D_h is taken as $6d$ and $1d$ for helical and conventional soil nails, respectively. Figure 4 provides a clear comparison of the P_f obtained using the above-stated soil nails. P_f for a conventionally reinforced wall is more in comparison to the helical reinforced soil wall. The reason behind this is the greater pullout capacity mobilized by the helices in the helical soil nails apart from the soil-nail shaft resistance. The results encourage the use of helical soils to reinforce the soil retaining structures.
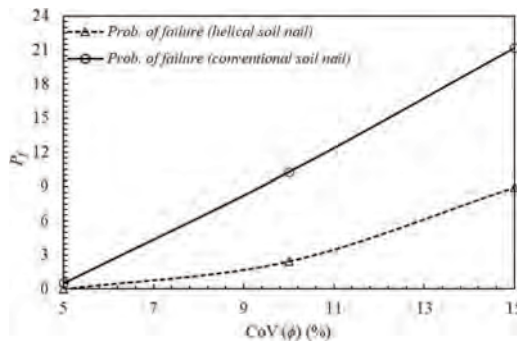
Figure 4. Plot showing the comparison of helical soil nails with conventional soil nails.

4 CONCLUSIONS

This study is basically performed to explore the usefulness of helical soil nails as reinforcement for soil walls in the probabilistic domain. The cost-based analysis and other field parameters have not been included and the study primarily highlights the technical advantages of helical soil nails. Based on the results, the following inferences are drawn.

- Probabilistic analysis quantifies the variability associated with input parameters and therefore, every design of RW should be double-checked using this technique in addition to the deterministic analysis.
- The helical soils provide greater pullout capacity in comparison to the other conventional soil nails.
- The inclination angle of the helical soil nail should be carefully chosen as it affects the stability of RW. An increase in its value may lead to unsafe results.

NOTATION

P_e	equivalent tensile force per unit horizontal spacing acting along the nail axis
σ_i	overburden pressure acting on the interface of helical soil nail
P^i	pullout capacity of the helical soil nail
δ	peak interface friction angle
W	weight of the failure wedge
n	number of helices
L_{ei}	the effective length of the soil nail; δ is the interface friction angle
d	diameter of the soil nail shaft
κ_o	coefficient of earth pressure at rest
N_q	bearing capacity factor
A_k	bearing surface area of the helix
D_{hx}	diameter of helix
H	height of wall
k_h, k_v	horizontal and vertical coefficient of acceleration
α	inclination angle of the soil nail
L	length of the soil nail
β	Angle of inclination of wall from the horizontal
ψ	Angle at which slip surface cuts the horizontal plane
S_{hx}	spacing of the helices
Sv_x	vertical spacing of the nails

REFERENCES

Agarwal, E., Pain, A., Mukhopadhyay, T., Metya, S. and Sarkar, S., 2022a. Efficient Computational System Reliability Analysis of Reinforced Soil-retaining Structures Under Seismic Conditions Including the Effect of Simulated Noise. *Engineering with Computers*, 38(2), pp.901–923.

Agarwal, E. and Pain, A., 2022b. Probabilistic Stability Analysis of Geosynthetic-reinforced Slopes Under Pseudo-static and Modified Pseudo-dynamic Conditions. *Geotextiles and Geomembranes*, 49(6), pp.1565–1584.

Agarwal, E. and Pain, A., 2022c. Efficient Probabilistic Stability Analysis of Geosynthetic Reinforced Slopes Using Collocation-based Stochastic Response Surface. *International Journal of Geomechanics*, 21(10), p.04021189.

Agarwal, E., Sharma, M. and Pain, A., 2022d. Efficient Surrogate Model Based Probabilistic Analysis of Helical Soil Nailed Wall Under Seismic Conditions. *European Journal of Environmental and Civil Engineering*, pp.1–22.

Basha, B.M. and Babu, G.S., 2012. Target Reliability-based Optimisation for Internal Seismic Stability of Reinforced Soil Structures. *Géotechnique*, 62(1), pp.55–68.

Babu, G. and Singh, V., 2010. Soil Nails Field Pullout Testing: Evaluation and Applications. *International Journal of Geotechnical Engineering*, 4(1), pp.13–21.

FSI. 2014. *Technical Manual: Helical Piles and Anchors, Hydraulically Driven Push Piers, Polyurethane injection & Supplemental Support Systems.* 2nd ed. Foundation Support Works, Omaha: 33–39.

Sharma, M., Samanta, M. and Sarkar, S., 2018. Novel Laboratory Pullout Device for Conventional and Helical Soil Nails. *Geotechnical Testing Journal*, 42(5), pp.1314–1335.

Sharma, M., Samanta, M. and Sarkar, S., 2019a. Soil Nailing: An Effective Slope Stabilization Technique. In *Landslides: Theory, practice and modelling* (pp. 173–199). Springer, Cham.

Sharma, M., Samanta, M. and Punetha, P., 2019b. Experimental Investigation and Modeling of Pullout Response of Soil Nails in Cohesionless Medium. *International Journal of Geomechanics*, 19(3), p.04019002.

Sharma, M., Choudhury, D., Samanta, M., Sarkar, S. and Annapareddy, V.R., 2020. Analysis of Helical Soil-nailed Walls under Static and Seismic Conditions. *Canadian Geotechnical Journal*, 57(6), pp.815–827.

Tokhi, H., Ren, G. and Li, J., 2016. Laboratory Study of a New Screw Nail and its Interaction in Sand. *Computers and Geotechnics*, 78, pp.144–154.

Simplified approach to analyse global stability of reinforced soil walls

A. Pineda, A. Moncada & S. Olivella
Department of Civil and Enviromental Engineering, Universitat Politècnica de Catalunya·BarcelonaTech (UPC), and International Centre for Numerical Methods in Engineering (CIMNE), Barcelona, Spain

I.P. Damians
International Centre for Numerical Methods in Engineering (CIMNE), Universitat Politècnica de Catalunya·BarcelonaTech (UPC), and VSL International, Barcelona, Spain

R.J. Bathurst
GeoEngineering Centre at Queen's-RMC, Royal Military College of Canada, Kingston, Ontario, Canada

ABSTRACT: Reinforced soil walls (RSW) are a proven alternative to conventional earth retaining structures due to their rapid construction, smaller environmental impact, lower cost, as well as more sustainable social/functional features. Design methods for RSW appear in international codes and guidelines. However, they often do not provide detailed calculations for global stability assessment. Global stability can significantly affect RSW design for specific geometric cases and/or site-specific boundary conditions. Traditional limit equilibrium (LE) methods have the disadvantage of not considering reinforcements and/or require iterations to achieve a safety factor (SF) value. Alternatively, numerical methods can be time consuming for both model generation, particularly for complex geometries, and during calculations. The present study discusses different analytical strategies using limit equilibrium formulations and a numerical finite element method, and proposes a simplified analytical method for global stability analysis based on a three-part wedge failure mechanism, and simple wall conditions.

1 INTRODUCTION

Reinforced soil walls (RSW) offer a more sustainable solution to perform the earth retaining wall function compared to conventional gravity structures (Damians *et al*. 2016).

Design practice for RSWs often focus on internal stability modes of failure, which include failure due to connection rupture, reinforcement rupture, and pullout of the reinforcement layers. However, similar to conventional earth retaining structures, RSWs must be externally stable against sliding, overturning, and bearing capacity failure.

Global stability failures of RSWs are characterized by a failure surface beginning in the vicinity of the toe of the wall, extending beyond the reinforced soil and into the retained soil zone. The propagation of the failure surface can be assumed as a circular surface (e.g., FHWA-NHI-10-024 2009) or as a non-circular surface with various segments (e.g., AFNOR 2020). A commonly used methodology to design earth retaining structures is the limit equilibrium (LE) approach together with the method of slices. Variations of the slice method are available, which make different assumptions to satisfy equilibrium between the interacting slices (e.g., Fellenius method, Simplified Bishop method, Janbu method, among others). More recently, the use of numerical tools has allowed the deformational behaviour of RSWs to be included in stability assessment. Numerical techniques such as the finite element (FE) method allow for simulation of construction stages, interfaces between materials, and include the in-soil behaviour of reinforcement layers in the analysis.

The present study focuses on comparing the calculated safety factor for a 6-meter high RSW with polymeric reinforcement layers obtained using LE formulations, numerical tools, and a novel simplified analytical methodology. Different surcharge conditions and geometries are included in the analysis, as well as a parametric analysis using different soil properties.

2 GLOBAL STABILITY ASSESSMENT

2.1 Problem definition

An idealized H = 6 m high RSW with segmental facing panels was studied. Wall dimensions include a front toe embedment of 0.50 m, segmental panels of 1.5 m height and 0.15 m thickness, and polymeric reinforcement lengths of 4.2 m (0.7H) placed at a spacing of 0.75 m (Figure 1a). Foundation, retained, and reinforced soil properties are given in Table 1. Stiffness and weight parameters for the facing panels and polymeric reinforcement are shown in Table 2.
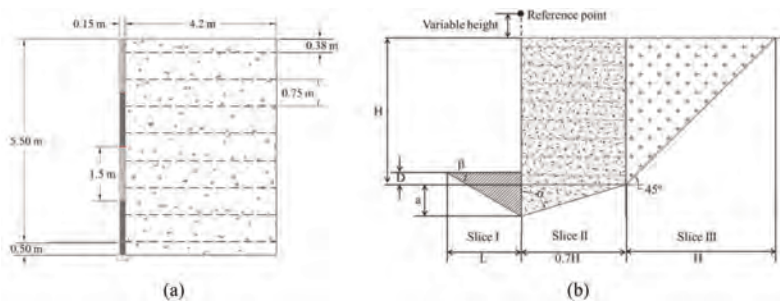
Figure 1.   (a) RSW geometry, and (b) failure mechanism for the proposed simplified method.

Table 1.   RSW model properties.

Parameter	Foundation and retained soil	Reinforced soil
Unit weight, γ	20 [kN/m^3]	20 [kN/m^3]
Cohesion, c	5 [kPa]	0.1 [kPa]
Friction angle, ϕ	28 [º]	34 [º]
Elastic modulus, E	100 [MPa]	80 [MPa]
Poisson's ratio, ν	0.3 [-]	0.3 [-]

Table 2.   Parameters for structures components used in the numerical model.

Parameter	Precast facing panels	Polymeric reinforcement
Axial stiffness, EA	4.5×10^6 [kN/m]	1500 [kN/m]
Flexural stiffness, EI	8440 [kNm^2/m]	–
Self-weight, w	3.75 [kN/m/m]	–

2.2 Limit equilibrium method

LE methods are commonly used to compute the global stability of earth retaining structures, particularly in combination with the method of slices. The slope or structure is divided into discrete slices, each is considered as a rigid body that must satisfy equilibrium conditions. The slice methods result in a statically indeterminate problem. Hence, results may vary

depending on the assumptions adopted to satisfy equilibrium (Fredlund & Krahn 1977). The present study uses the ordinary or Fellenius method, which assumes no forces between slices.

Shear resistance for each slice is determined using the Mohr-Coulomb failure criterion (MC). Using the Fellenius method, the global stability of the structure is quantified using safety factor (SF) and considering the driving and resisting forces in Equation 1:

$$SF = \left(\sum c_i l_i + [W_i \cos \alpha_i] \tan\phi \right) / \left(\sum W_i \sin \alpha \right) \tag{1}$$

Here c_i is the cohesion of slice i acting over a failure surface of length Δl_i, W_i is the weight of slice i, ϕ is the internal friction angle of the soil, and α is the inclination of the bottom of the slice i with respect to the horizontal. LE analyses were conducted using the software package SLIDE (Rocscience 2017) with the Fellenius method option.

2.3   Numerical method

The numerical method to assess global stability was the strength reduction method (Marek-Cala 2003) available in the FE software package PLAXIS (Plaxis 2004). In the strength reduction approach, c-ϕ properties of the soil are continuously reduced until failure is achieved. The SF value is then calculated as the ratio original strength parameters (ϕ_{input}, c_{input}) divided by the reduced strength parameter ($\phi_{failure}$, $c_{failure}$), as shown in Equation 2.

$$SF = \tan(\phi_{input}) / \tan(\phi_{failure}) = c_{input} / c_{failure} \tag{2}$$

Mesh geometry included all relevant structural components with their respective stiffness values (discrete facing panels, reinforcement layers). The FE constitutive model was the MC failure criterion. A soil-reinforcement interface reduction factor of $R_i = 1$ was used. Soil-facing interfaces considered an equivalent material with $\phi_{interface} = (\frac{2}{3})\phi_{reinforced\text{-}soil}$. An initial sensitivity analysis was made to determine the optimum combination of mesh refinement, computation time and amount of output. There were no practical advantages with respect to numerical outcomes for mesh refinement with more than 15,000 nodes. The placement and compaction of the soil was carried out using 4 and 8 rows of elements; no practical differences in model results were detectable using each number of rows.

2.4   Simplified method

The objective of the proposed simplified method is to compute global stability SF in a straightforward manner. Figure 1b shows the proposed failure mechanism. The structure is divided into three zones or slices: the front embedment slice (I), the reinforced soil slice (II), and the retained soil slice (III). LE conditions are then applied, using the Fellenius method and slice boundary conditions adopted using this method. The three-slice failure mechanism resembles that proposed in design standards (AFNOR 2020, BSI 2010), and the failure surfaces often observed from numerical analyses. Slice dimensions are based on wall height (H), depth of wedge III (D), and soil frictional strength (ϕ), as shown in Equations 3–5:

$$\beta = (45 - \phi/2) \tag{3}$$
$$L = H/2 \tag{4}$$
$$\alpha = \tan^{-1}(0.7H/(a/\tan(\beta) - D)) \tag{5}$$

in which a is the relative depth (m) of slice II based on slice I geometry.

To determine the inclination of each slice (θ_i), a reference point must be selected. Past studies have shown that the rotation point of a RSW is usually located above and in line with the vertical facing of the wall (Brand & Shen 1984; Petterson 1955). For a base wall height of 6 m, the reference point was located at a height of 2.5 m above the vertical wall facing. The reference point can be adjusted based on computed SF values from numerical or analytical results. For simplification, the weight of slice II acts in the middle of the reinforced soil

(0.45H). SF is obtained by imposing equilibrium conditions between the acting moment (M_A) and resisting moment (M_R) considering each slice (Eq. 6):

$$SF = M_A/M_R = \left(\sum c_i l + [W_i \cos(\theta_i)] \tan\phi \right) / \left(\sum W_i \sin\theta_i \right) \tag{6}$$

in which θ_i is the angle between the vertical projection of each slice self-weight and the reference point.

3 RESULTS AND DISCUSSION

3.1 *Base case and variable surcharges*

Figure 2a shows SF values for the base case and different load scenarios using the analytical` Fellenius method, numerical PLAXIS model and the simplified method proposed here. Surcharge cases consider an equivalent 12 kPa load. For cases 1 and 2, which include surcharge over the toe of the wall, length L is reduced to H/3, angle β is increased to 45-ϕ/10, and the reference point is relocated to 3.5 m above the vertical wall.

The largest SF values were consistently obtained with the Fellenius method. SF values decreased with the application of a surcharge on top of the wall and increased with surcharge loading applied at the toe. Overall, the simplified method yields SF values similar to those obtained from the FE analysis. SF values for the base case were 1.46, 1.47, 1.50 and 1.37 using PLAXIS, simplified method and Fellenius method, respectively.

Figure 3a shows the variation of SF values with wall height using the three methods. Wall heights were 6, 12, and 18 m. Reinforcement length was 0.7H for each case. Increasing wall height gave lower SF values, particularly for PLAXIS solutions and the simplified method. SF values using the simplified method match those obtained using PLAXIS.
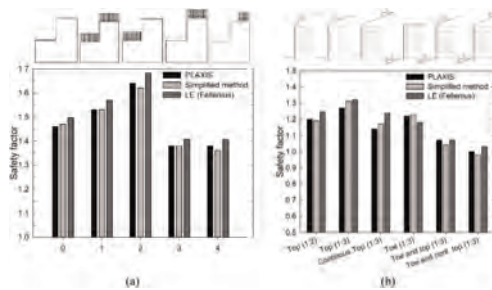
Figure 2. Safety factor (SF) for (a) the base case (no surcharge) and different surcharge load conditions, and (b) different top and toe wall geometries (H = 6 m).
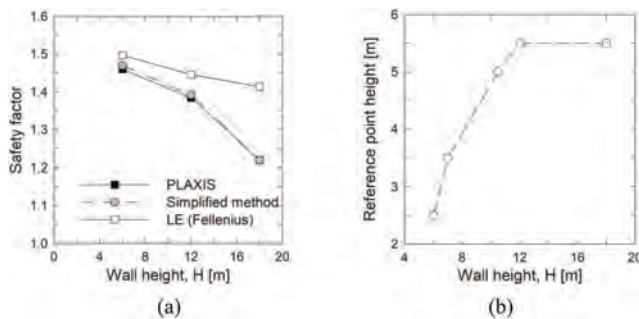
Figure 3. Variations of (a) safety factor, and (b) reference point location as a function of wall height. Base case comparison (no surcharges nor slope conditions).

Modifications of the reference point and slice I dimensions for the simplified method are required to obtain SF values in general agreement with those obtained using PLAXIS and Fellenius method. As wall height increases, the reference point must be moved higher (see Figure 3b), the length L of slice I decreases, and the angle β increases.

3.2 Variable top and toe wall slope geometry

Figure 2b compares SF values using the three methodologies and considering a top back-slope and/or fore-slope at the toe of the RSW. For cases with a sloped toe embedment, slice I length increases to H/1.5, and the reference point is lowered to 0.5 m above the vertical wall. When considering an inclined toe and top, the reference point was set to 1.0 m above the vertical of the wall facing.

The three approaches yield comparable results. For greater top slope length, SF is reduced progressively. Furthermore, as the resistance at the toe is reduced due to increasing fore-slope angle, SF values are further reduced. As with previous cases, results from the simplified method are in reasonable agreement with those obtained from numerical analyses.

3.3 Soil parameter variations

A sensitivity analysis for the influence of retained and foundation soil parameters was also conducted. Parameter variations include specific weight (γ_s), cohesion (c), and friction angle (ϕ). Parameters were varied individually.

Figure 4 shows computed SF values using the three approaches. Figure 4a shows that increasing γ_s for the retained soil reduced SF, increasing soil cohesion increased SF, as does increasing ϕ. Changing the foundation soil parameters (Figure 4b) resulted in increased SF values for larger values of γ_s, c, and ϕ. SF values obtained using the Fellenius method deviate from those obtained using PLAXIS and the simplified method when and ϕ values for the foundation soil increased. The Fellenius method gave higher SF values when varying soil parameters in all cases, with the exception of the cohesion of the retained soil. The most
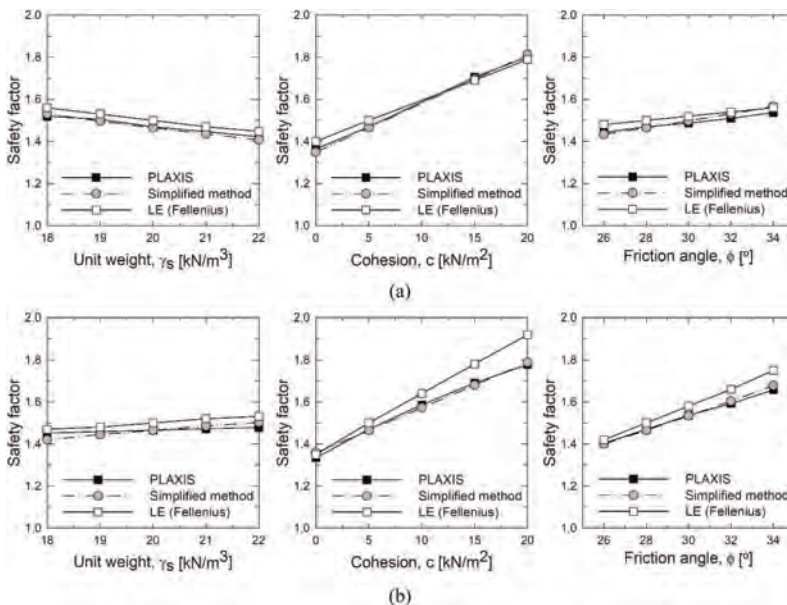
Figure 4. Safety factor (SF) parametric analysis results changing material properties for (a) retained soil, and (b) foundation soil.

sensitive parameters were c of the retained and foundation soil, and ϕ of the foundation soil. Changing the foundation soil γ_s, the self-weight of the vertical wall was included in the weight contribution of slice I, which brought the simplified method results closer to those obtained using the PLAXIS program.

Changing the interface resistance values modified the failure surface obtained using the PLAXIS c-ϕ reduction method. For a perfect bonded soil-reinforcement interface (R = 1) the failure surfaces propagate under the reinforced soil, while a sliding interface (R = 0.6) shifts the failure surface, which then intersects the lowest reinforcement layer.

4 CONCLUSIONS

The present study proposes a simplified analytical method to assess the global stability of a reinforced soil wall with simple geometry. The methodology considers a planar three-slice failure mechanism resembling the failure surface obtained in numerical simulations and described in design standards. Horizontal forces between slices are disregarded. Parameters include structure geometry and soil strength properties. The proposed simplified method provides a fast and simple procedure intended as a preliminary estimation of the global stability safety factor for these systems.

Calculated safety factors with numerical techniques using the program PLAXIS, limit equilibrium formulation using the Fellenius method, and the proposed simplified three-slice failure mechanism were compared. Overall, satisfactory agreement was found between the numerical simulation outcomes and the simplified method. The Fellenius method tended to give similar trends but higher safety factor values, mainly due to an overestimation of the resistance at the toe.

Different surcharge scenarios, geometric variations, and sensitivity analyses were performed. The simplified method results consistently showed satisfactory agreement with the results of numerical simulations. Modifications of the toe length (slice I) and the reference point height serve as calibration parameters to obtain closer safety factor values between numerical simulations and other limit equilibrium methods.

The present study analysed simple geometries with generic, static, load conditions. Further work is required to use the simplified method for real, more complex, wall configurations, such as tiered walls and back-to-back walls, among other configurations.

REFERENCES

AFNOR 2020. Calcul Géotechnique-ouvrages de Soutènement–remblais Renforcés et Massifs en sol Cloué. *Association Française de Normalisation*. NF 94-270, Paris.

Brand, E.W. & Shen, J.M. 1984. A Note on the Principle of the Mid-point Circle. *Géotechnique*, 34.

BSI 2010. BS 8006-1. 2010. Code of practice for strengthened/reinforced soils and other fills. *Design of Embankments with Reinforced Soil Foundations on Poor Ground*.

Damians, I.P., Bathurst, R.J., Adroguer, E.G., Josa, A., & Lloret, A. 2016. Sustainability Assessment of Earth-retaining Wall Structures. *Environmental Geotechnics*, 5(4):187–203.

FHWA-NHI-10-024. 2009. *Design and Construction of Mechanically Stabilized Earth Walls and Reinforced Soil Slopes-volume I*. National Highway Institute Federal Highway Administration 14. U.S. Department of Transportation Washington, D.C.

Fredlund, D.G. & Krahn, J. 1977. Comparison of Slope Stability Methods of Analysis. *Canadian Geotechnical Journal*, 14(3):429–439.

Marek Cala, J.F. 2003. Slope Stability Analysis with Numerical and Limit Equilibrium Methods. *Computer Methods in Mechanics*.

Petterson, K.E. 1955. The Early History of Circular Sliding Surfaces. *Géotechnique*, 5.

Plaxis, B. 2004. Plaxis 2D version 8.2-finite Element Code for Soil and Rock Analysis. AA Balkema, Delft.

Rocscience, I. 2017. Slide, 2d Limit Equilibrium Software, version 7. Toronto, Canada.

Water drainage and gas collection with geocomposites – Hydraulic software development

S. Fourmont
Afitex-Texel, Ste Marie, Quebec, Canada

J. Decaens & D. Beaumier
CTT Group Sageos, St Hyacinthe, Quebec, Canada

M. Riot
Afitexinov, Champhol, France

ABSTRACT: Geosynthetic materials and, more specifically, drainage geocomposites are now widely used for water drainage and gas collection in applications as varied as final landfill covers, leachate collection in landfill cells, sub-slab depressurization systems under buildings, groundwater drainage under embankments, etc. The design methods used are based on the in-plane flow capacity of the geocomposites, which is determined by laboratory tests performed on 250-300 mm long product specimens. Fluid is injected into the thickness of the product and the drainage capacity is interpolated for an actual length of several meters. This paper presents the development of hydraulic design software for multi-linear drainage geocomposites, based on laboratory characterizations of the geocomposite and then validated with full-scale tests. The software gives a 3D model of the hydraulic curves in the geocomposite depending on the application for which the geocomposite is used, and the fluid to be drained (water, landfill gas, methane, air, etc.).

1 INTRODUCTION

The design of geosynthetic materials for drainage requires an excellent knowledge of the material's hydraulic properties. The determination of the drainage capacity of drainage geocomposites is based on in-plane flow as determined by laboratory tests according to ASTM D4716, GRI GC15, and ISO 12958. The initial type tests allow the designer to correlate the flow rate with the hydraulic head or hydraulic gradient. In addition to the basic hydraulic characterization, the long-term in-situ drainage capacity of the geocomposite is calculated from these laboratory test results using guidance documents that help the designer address the reduction factors to be applied to the drainage flow capacity as a function of the type of geocomposite, the engineered structure, type of fluid (water, gas), etc. The ASTM D7931 standard guide (based on ASTM D4716 laboratory test), or the ISO/TR 18228-4 standard guide (based on ISO 12958 laboratory test) greatly help the engineers in this regard, but certain points can be misleading for engineers without solid expertise in geosynthetics.

1.1 *Laboratory tests*

The in-plane flow capacity (or Transmissivity) of geocomposites is developed to be compatible with the whole range of products on the market through ASTM and ISO standards.

Because of the different physical characteristics of drainage geocomposites, the laboratory tests performed as per the standards may not be as accurate as expected.

For example, the size of the testing device typically used has a length of 250 mm to 300 mm, underestimating by at least 30% the drainage capacity of Draintube multi-linear drainage geocomposites (Blond *et al.* 2013). This is because the entrance and exit transition flow to the tested length causes additional head losses.

Moreover, taking a single test measurement (even after a seating time of several hours), may not account for the continuous compression of the tested product due to creep throughout its service life and lead to an overestimation of its in-situ drainage capacity. This is particularly noticeable for geocomposites with a monofilament core where the in-situ drainage capacity can be more than 10 times lower than the value measured in the laboratory test (Zanzinger 2000).

1.2 *Boundary conditions*

The drainage capacity of the geocomposite is determined by using laboratory tests with specific test conditions, such as hydraulic gradient, vertical compression load, seating time, and material(s) in contact with the geocomposite. It can be complicated for the designer to correlate these test conditions with the field conditions, or even more concerning, to be aware that the test conditions have a significant impact on the given results.

For example, using steel plates as boundary conditions when testing a drainage geocomposite does not address the geotextile intrusion into the drainage core. This phenomenon will occur in the field when the product is in contact with a soil layer. This typically leads to a significant reduction in flow rate for most drainage geocomposites, up to 90% reduction for geocomposites under high compressive loads like 720 kPa (Zhao *et al.* 1999).

As for creep in compression, the sensitivity to the boundary conditions depends on the type and structure of the drainage geocomposite.

1.3 *Terminology*

The technical terms involved in hydraulic design can be a source of confusion for the designer. Indeed, depending on their field of expertise, geotechnical or geosynthetic, some identical terms do not represent the same quantities and are not directly comparable. One example is "Hydraulic Transmissivity". It is not directly comparable between a granular layer and a geocomposite. The first one is an intrinsic value of a given granular layer, while the second one depends on many factors specific to the geocomposite environment such as the hydraulic gradient, the applied normal load, the material in contact, etc.

2 SOFTWARE DEVELOPMENT

In the trend of Computer Assisted Design (CAD) for engineers, Afitex Group has developed a software for the design of geosynthetics used in drainage applications. The new software, named Lymphea, assists designers in the hydraulic selection of drainage geocomposites (including multi-linear drainage geocomposites) as well as granular drainage layers using site-specific conditions.

The software is based on a previous model developed with LIRIGM university research laboratory at the University of Grenoble (France) and CEREMA (formerly Laboratoire Regional des Ponts et Chaussées de Nancy). It has been updated and improved with the contribution of the SAGEOS (CTT Group, Quebec), the CEGEP of Saint-Hyacinthe (Quebec), and the University of Saskatchewan (USASK) in Alberta.

2.1 Project presentation

The development of the software has been divided into the following three main steps:

– Calculation core for multi-linear drainage geocomposites that has been implemented from the previous model and updated with a 3-year test program performed at SAGEOS and USASK laboratories,
– Calculation modules development for drainage geocomposites and granular drainage layers, based on standard design guidance documents from the geosynthetic industry and publications from specialists in these fields,
– User interface design to have a software that is easy to use and intuitive.

The software also offers design firms a company-restricted database allowing multiple users in the same company to share and update their projects.

2.2 User interface

The user interface has been developed to represent the engineer's needs and the design steps as closely as possible. The software is available in several languages (English, French, and Spanish), in SI and US units, and based on ISO and ASTM standards. When creating a new project, the user can choose between several available drainage applications (Figure 1) such as Sub-slab depressurization systems, Drainage behind MSE walls, Cover drainage systems, or Leachate collection systems. It should be noted that the software allows for the design of drainage geocomposites for both liquid water and gas.

Figure 1.   Home page of the software.

3   CALCULATION MODULE FOR MULTI-LINEAR DRAINAGE GEOCOMPOSITES

The calculation modules for multi-linear drainage geocomposites are based on the previous model initially developed and validated on a large-scale cell experiment (4 m long and 1 m wide) at the LIRIGM university research laboratory (Faure *et al.* 1993) and confirmed many times since. The theoretical model in the software is based on the following flow conditions:

– Fluid supply with a homogeneous flow distribution perpendicularly to the geocomposite,
– Horizontal or non-horizontal position of the drainage layer with the flow condition down or reverse to the slope α,
– Perforated mini-pipes unsaturated, partially saturated, or fully saturated.

The fluid inside the drainage layer is assumed to flow perpendicular to the perforated mini-pipes. This hypothesis is conservative and reasonably good as the distance between the mini-pipes is 2 m maximum, provided the length of the mini-pipes is generally more than 10 m. The head losses to enter into the perforated mini-pipes have been found insignificant compared to the head losses into the drainage layer. The governing equation of the hydraulic head in the multi-linear drainage geocomposite is then given by Equation 1 from Faure *et al.* (1993):

$$h_{\max} = \frac{F \times D^2}{8\theta_{GT}} + \left(\frac{b}{b+1}\right) \times \left(\frac{F \times D}{a}\right)^{1/b} \times L^{(b+1)/b} - L \times \sin\alpha \qquad (1)$$

where F = Flow per unit area; θ_{GT} = Transmissivity of the drainage layer; D = Distance between mini-pipes; L = Length of drainage; a and b = constants experimentally determined from the flow capacity of the mini-pipes.

3.1 Flow capacity of the drainage layer

The drainage layer is composed of a non-woven needle-punched staple fiber geotextile. The drainage layer is protected from the surrounding soil by an additional filter layer, also included as part of the multi-linear drainage geocomposite that prevents soil particle migration. The flow carried out by the drainage layer is given by Darcy's law and is dependent on its Transmissivity.

A series of hydraulic tests have been performed at SAGEOS and USASK laboratories on several drainage layers under multiple loads to characterize their hydraulic Transmissivity. The transmissivity values considered in the software are in-situ Transmissivity, meaning that reduction factors have already been applied to reflect the long-term drainage capacity under load. Recommended reduction factors for geotextile drainage layers are given in the GRI White paper 4. Figure 2 shows an example of the long-term Transmissivity of a 200 g/m^2 drainage layer function of the vertical load applied.
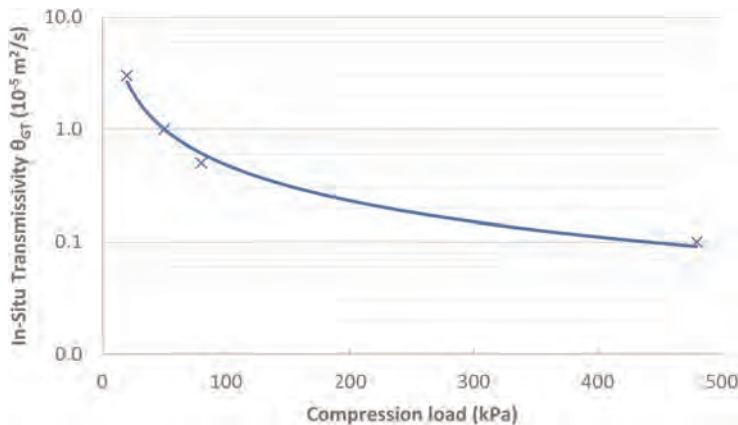
Figure 2. In-situ transmissivity of a 200 g/m^2 non-woven needle-punched geotextile drainage layer.

3.2 Flow capacity of the mini-pipes

Tests have been carried out at SAGEOS laboratory to characterize the flow capacity of the mini-pipes themselves and to confirm the experimental values previously obtained during the development and validation of the software. The flow capacity of the mini-pipes is a function

of the hydraulic gradient and has been measured for the 3 mini-pipe diameters: 16 mm, 20 mm, and 25 mm (Figure 3). Mini-pipe lengths of 0.5 to 1 m were tested, and the resulting flow capacity was calculated, excluding entrance and exit head pressure losses.
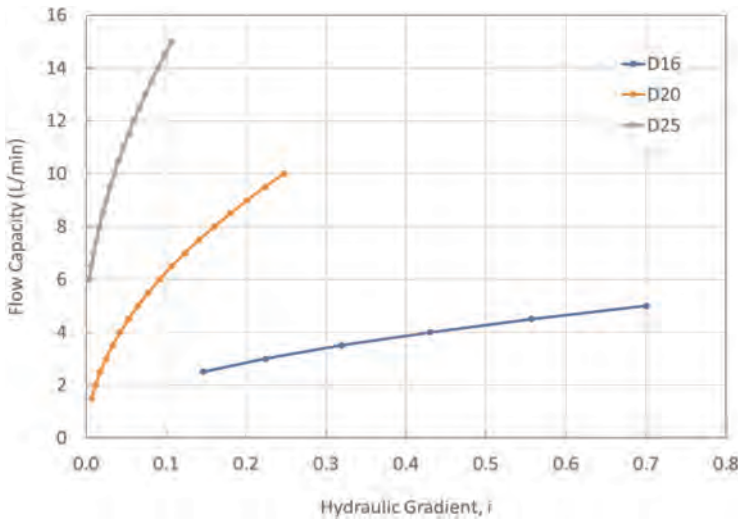
Figure 3. Flow capacity of the 3 mini-pipe diameters.

For each mini-pipe diameter, the flow capacity implemented in the software is conservative compared to the test results. A factor of safety of 1.55 has been applied to the measured flow capacity values.

4 CALCULATION MODULE FOR GRANULAR DRAINAGE LAYERS

The calculation module for the granular drainage layer is based on two technical papers published by Giroud *et al.* in 2000. The approach used is to verify that the maximum water flow height is less than the thickness of the granular drainage layer, which becomes the maximum allowable water height. According to Giroud *et al.* (2000), the thickness of the liquid layer is influenced by the hydraulic conductivity of the granular layer, the angle of the slope, the drainage length, and the flow rate per unit area entering through the surface perpendicular to the flow direction. The modeling of the hydraulic behavior of the granular drainage layer is performed using Giroud's formula, where an incoming upstream flow has also been considered, as shown in Equation 2:

$$F \times L + q_0 = K \times \left(h_{\max} \times \sin \alpha + \frac{h_{\max}^2 \times \cos \alpha}{L} \right) \tag{2}$$

where F = Flow rate per unit area; L = Length of drainage; q_o = Incoming upstream flow; K = Hydraulic conductivity of the granular layer; h_{max} = Maximum height of water; and α = Slope.

The user can solve for each parameter mentioned above as the value to be implemented (as the unknown of the equation) in the software. It allows the user to design a drainage solution with a granular layer function of the input data specific to the project. Reduction

factors for chemical clogging (RF_{CC}) and biological clogging (RF_{BC}) can be addressed and applied to the hydraulic conductivity of the granular layer. The factor of safety (FS) is applied to either h_{max} or K, whichever gives the most conservative result.

5 CALCULATION MODULE FOR DRAINAGE GEOCOMPOSITES

The calculation module for drainage geocomposite is based on Darcy's law and the in-plane drainage capacity from ASTM or ISO standard tests.

The hydraulic behavior of the drainage geocomposite is modeled using Equation 3 in an ISO environment and Equation 4 in an ASTM environment. A potential incoming upstream flow has also been taken into account:

$$q_p(\sigma, i, 100h) = FS \times \prod RF \times (F \times L + q_0) \tag{3}$$

$$\theta_{100}(\sigma, i, 100h) = FS \times \prod RF \times \frac{(F \times L + q_0)}{\sin \alpha + \frac{\cos \alpha \times h_{max}}{L}} \tag{4}$$

where $q_p(\sigma, i, 100h)$ = In-plane flow capacity as per ISO 12958-2 (performance test) performed under a vertical load σ, a hydraulic gradient i, and a seating time of 100 hours with boundary conditions representative from the applications; $\theta_{100}(\sigma, i, 100h)$ = Transmissivity as per ASTM D4716 (or GRI GC15) performed under a vertical load σ, a hydraulic gradient i, and a seating time of 100 hours with boundary conditions representative from the applications; FS = Factor of safety; $\prod RF$ = Reduction Factors.

$\prod RF$ is the product of the following reductions factors (Eq. 5):

$$\prod RF = RF_{IN} \times RF_{CR} \times RF_{CC} \times RF_{BC} \tag{5}$$

where RF_{IN} = Reduction factor for geotextile intrusion into the drainage core; RF_{CR} = Reduction factor for creep in compression; RF_{CC} = Reduction factor for chemical clogging; RF_{BC} = Reduction factor for Bacteriological clogging.

The reduction factors are dependent on the type of application and are also product/technology specific. Recommended values for the reduction factors are given in the software and are generally taken from the ISO/TR 18228-4 standard guide. It is important to note that the reduction factors are to be applied on $q_p(\sigma, i, 100h)$ or $\theta_{100}(\sigma, i, 100h)$ i.e. on the 100 hours seating time test results.

As per the calculation module for a granular drainage layer, each parameter mentioned in Equations 2 & 3 can be chosen in the software as the value to be determined (as the unknown of the equation).

6 CONCLUSIONS

The development of a software for the hydraulic design of drainage geocomposite and granular drainage layers is intended to help designers. It is based on formulas and calculation methods well recognized by the geosynthetics drainage industry and it also includes the ability to design multi-linear drainage geocomposites. The Lymphea software allows for a wide range of parameters to be determined to better adapt to the site-specific requirements of each project. Considering its usage throughout the world, it also works in both ISO and ASTM environments, using either SI or US units.

Finally, the software is based on a previous model, initially developed and validated on a large-scale cell experiment and confirmed many times since. The user interface has been

designed to be as intuitive as possible, and it guides the user by explaining the important steps and input data to be considered.

REFERENCES

ASTM D4439. Standard Terminology for Geosynthetics, *ASTM International*. West Conshohocken, Pennsylvania, USA.

ASTM D4716. Standard Test Method for Determining the (In-plane) Flow Rate per Unit Width and Hydraulic Transmissivity of a Geosynthetic Using a Constant Head, *ASTM International*. West Conshohocken, Pennsylvania, USA.

ASTM D7931. Standard Guide for Specifying Drainage Geocomposites. *ASTM International*. West Conshohocken, Pennsylvania, USA.

Blond, E., Saunier, P., Daqoune, T. & Fourmont, S. 2013. Assessment of the Effect of Specimens Dimensions on the Measured Transmissivity of Planar Tubular Drainage Geocomposites. *GeoMontreal* 2013, Montreal, Quebec, Canada.

Blond, E., Saunier, P. & Ragen, W. 2010. Assessment of the Resistance of Drain Tube Planar Drainage Geocomposites to High Compressive Loads. *9th International Conference on Geosynthetics*, Vol. 3. Guarujá, Brazil.

Faure Y.H., Matichard Y., Brochier P. & Suryolelono, K. 1993. Experimental and Theoretical Methodology to Validate New Geocomposite Structures for Drainage. *Geotextiles and Geomembranes* 12: 397–412.

Giroud, J.P., Zornberg, J.G., & Zhao, A. 2000. Hydraulic Design of Geosynthetic and Granular Liquid Collection Layers. *Geosynthetics International, Special Issue on Liquid Collection Systems*. Vol. 7: 285–380.

Giroud, J.P., Zornberg, J.G. & Beech, J.F. 2000. Hydraulic Design of Geosynthetic and Granular Liquid Collection Layers Comprising Two Different Slopes. *Geosynthetics International, Special Issue on Liquid Collection Systems*. Vol. 7: 453–489.

GRI GC15. 2017. Standard Test Method for Determining the Flow Rate per Unit Width of Drainage Geocomposites with Discrete High Flow Components. *Geosynthetic Institute*. Folson, Pennsylvania. USA.

GRI White paper 4. 2007. Reduction Factors (RFs) used in Geosynthetic Design. *Geosynthetic Institute*. Folson, Pennsylvania. USA.

ISO 12958-2. Geotextiles and Geotextile-related Products – Determination of Water Flow Capacity in their Plane – Part 2: Performance Test. *International Organization for Standardization*. Geneva, Switzerland.

ISO/TR 18228-4. Design using Geosynthetics – Part 4: Drainage. *International Organization for Standardization*. Geneva, Switzerland.

Zanzinger, H. 2000. Reduction Factors for the Long-term Water Flow Capacity of Drainage Geocomposites. *3rd international Conference Geofilters 2000*, Warsaw, Poland.

Zhao, A. & Montanelli, F. 1999. Effect of Soil Presence on Flow Capacity of Drainage Geocomposites under High Normal Loads. *Geosynthetics 1999 conference*, Boston, Massachusetts, USA.

Stabilizing green steep slope around tunnel portal using polymeric alloy geocell

A.K. Chatterjee
M.A.Sc., P.Eng, Engineering Manager, Stratum Logics Inc., Acheson, AB, Canada

S.K. Pokharel
PhD., P.Eng, Principal Engineer, Stratum Logics Inc., Acheson, AB, Canada

M. Breault
President, Paradox Access Solutions Inc., Acheson, AB, Canada

ABSTRACT: The three-dimensional geometry of geocell provides lateral and vertical confinement that is extensively used for stabilizing cover soil on steep slopes. On the steep slopes of the North Saskatchewan River in Edmonton (Canada), around a light rail traffic tunnel portal that was previously stabilized with soil anchors, a 200mm thick facial fill was required for a green cover. The slope varied from 250 to 730 stretching from 40m to 60m along the slope. An attempt was made utilizing a novel polymeric alloy (NPA) geocell to retain the facia fill. A conventional design approach with tendons was not possible due to the lack of anchoring opportunities at the crest. Presence of utility lines limited locations for anchoring on the slope. A novel design technique of load transfer utilizing wire net covers on top of the geocell was developed. This paper discusses the challenges through the design and the remediations.

1 INTRODUCTION

Stabilizing slopes poses many geotechnical challenges depending upon, but not limited to, the slope geometry, surcharge load and the type of soil to be retained. There are already established engineering methods such as soil nails, retaining walls and facia support to stabilize the slopes. Geocell walls and geosynthetic-reinforced geocell facia have also been widely used in reinforced slope stabilization work. Even after stabilizing unstable slopes, erosion control of the topsoil for vegetation growth needs a due attention to avoid gully formation and destabilize the slope and more so when a green slope is desired with select vegetation. The design of green slopes has emerged as a core concept in the leadership in environmental design, with this recognition in engineering design green slopes will get due attention in the foreseeable future.

Geocell owing to its three-dimensional pocket geometry and structural properties has been widely used for load support applications and soil retention designs such as gravity retaining walls, road and pad embankments on soft subgrades and facial cover of slopes. There are several studies performed over the last couple of decades to understand the mechanism of soil retention and the confinement effect of geocell. Pokharel (2010) showed the horizontal and vertical confinement effect of high tensile strength geocell. Studies on the vegetation growth within geocell by Guo *et al.* (2015), highlighted an ideal solution for the current challenge. Hegde (2020) summarized some of the popular reinforcement mechanisms and design methods for various geocell applications. The importance of the proper installation technique, particularly with connecting geocell panels, for uniform distribution of member stresses was highlighted by Liu *et al.* (2018). Though there are several studies with slope stability using a geocell retaining wall system, there is hardly any study available on green facia cover with geocell.

The steep slope on the left side of the North Saskatchewan River in Edmonton (Canada) was designed with soil nails and geonet (by others). However, the problem of surface erosion and retention of topsoil for a well-vegetated green cover on top and around the newly constructed light rail tunnel portal was later identified demanding separate attention. The length along the slope stretched from 40m to 60m. A major portion of the slope was well over 550 with some local areas as steep as 830. For a minimum 10m length along the slope, the inclination varied between 250 to 730. The design required a minimum of 200mm thick soil for regular vegetation growth which would not be naturally stable beyond 300 inclinations. However, once the root of vegetation grows deep enough, stability at a much higher inclination is possible. With accumulating snow and seasonal freeze-thaw, there was an additional risk of the entire soil cover slipping down. Thus, until the roots takeover, it was necessary to provide artificial support to the topsoil. A potential solution was the use of geocell, for its proven past applications, utilizing the lateral and vertical geometric confinements (Hedge (2020)).

For retaining soil along a slope, most designs include tendons anchored at the crest or soil anchors distributed over the entire sloped area or a combination of both. The primary purpose is to support the plant and allow the roots to grow, it should also be able to transfer the plantation soil load through geocell to a stable support system. However, for the slope under consideration, there was no opportunity for anchoring tendons or digging a trench at the crest to support the geocell system due to the presence of other infrastructures. Anchoring hooks were not allowed in some areas due to the presence of buried trenches and utility lines. Rimoldi and Ricciuti (1990) developed a series of equations to calculate the stability of geocell on slopes. For the current application, their method needed modification as their stability calculations heavily depended on the crest resistance and J-hooks.

This paper discusses the design of the green facia cover for that steep slope. The dead weight of plantation soil was confirmed by the designers to have no detrimental impact on the overall global stability of the slope. However, attachments and modifications to the existing system of soil nails and geonet were not permitted. The paper also discusses the performance of the erosion control design over a full year and recommendations for similar designs with polymeric geocell in the future.

2 METHODOLOGY

For the design of geocell on steep slopes with snow loads, freeze-thaw effects, and limited soil anchoring, a failure-based design methodology was developed. The philosophy behind this approach is to identify all possible failure modes (Figure 1a) and then walk back to potential solutions.

The first identified mode of failure was the sliding of soil above the geocell. Geocell provides 100% confinement within some volume of the pocket (Figures 1a and 1b). The amount of confinement provided above that zone of full confinement depends on several parameters such as geocell pocket size, infill particle size distribution, and particle-to-geocell wall interaction. The higher the fill above the geocell higher the risk of a sliding plane formation. Figure 1b shows that there is a balance point that can be approximated where the sliding force equals the geocell confinement effect (equation 1). Through this relation, the acceptable geocell height is determined. If one layer of geocell is not enough, then multiple layers can be effective. Since the topsoil thickness required was 200mm, for the stretched pocket size of 250mm x 210mm the safe geocell height was computed as 150mm for this slope.

$$W_{cover} * sin\beta = F_{conf} / \varphi_{conf} \qquad (1)$$

where W_{cover} is the weight of soil, β is the slope angle under consideration, φ_{conf} is the confinement factor of safety and F_{conf} is the confining force that is a function of geocell pocket size, particle distribution of infill material, and geocell-particle interface friction.

The second identified mode of failure was the formation of a slip plane under the geocell (Figure 1c). To avoid this, it was necessary to break the continuity of the potential failure plane with the geocell pressing into the native surface. J or U hook anchors (Figure 3b) holding the geocell from any upward movement (Figure 1c) is a solution, but the challenge remained where anchoring was not permitted. A stretched wire net on top of the geocell that is anchored independently along all the edges turned out to be an acceptable solution.

The third mode of potential failure was in the continuity of the load transfer. If either a member or a connection transferring the load of vegetated plantation soil along with the seasonal snow cover fails, then the entire system will be at risk of failure. For this, individual members (geocell, wire net, anchors) and their connection (interaction between geocell and anchor, zip ties holding wire net with geocell) were studied separately. Where anchoring was allowed, the sliding force was distributed into the geocell, as per relevant influence areas (Figure 2a). To optimize the number of anchors, a high tensile strength of the geocell was necessary. Given that the slope needed to be green there were additional requirements like perforations in the geocell for water to seep through. Perforated Novel Polymeric Alloy (NPA) Geocell (330-150-C-P) with a tensile strength of >18kN/m, dynamic modulus >750MPa (at 30°C), and stretched pocket size of 245mm x 210mm was selected as the most economical solution.

Figure 1a.   Modes of failure.
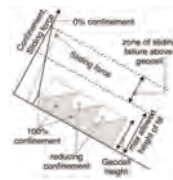
Figure 1b.   Geocell confinement.
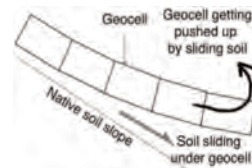
Figure 1c.   Sliding failure.

The block-out zones where anchoring was not allowed were identified. The largest area identified was around 5m wide and 10m along the slope, right on top of the tunnel portal with an average slope of around 550. The influence area load was computed on the geocell, and the stainless-steel zip ties transferred the load to the wire net. The wire net was independently anchored along the perimeter (Figure 2b). Cross-metal contamination, areas of local failure within the geocell and the local stress zones on the wire net needed special attention.
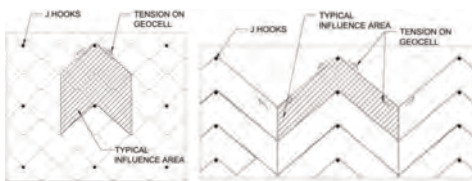
Figure 2a.   Influence areas based on soil anchor spacing.
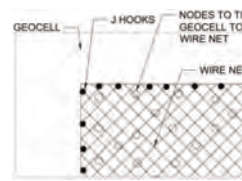
Figure 2b.   Wire-net on geocell.

It must be noted that because of passive resistance within the pockets, loads from the local slope variation, and the wavy geometry of the geocell, the tension developed along the length is not necessarily linear. The further away the support pins are located, the higher the risk of this non-linear tension distribution. This can develop local failures ultimately leading to a progressive system failure. Thus, the location of pins had to be optimized to minimize the risk.

The necessary tensile strength of zip-ties was calculated for each of the influence areas, based on the tensile force coming from geocell. The zip-ties needed to be snug tight to the

geocell and wire net through the geocell perforations. This is to avoid any relative movement between the wire net and the geocell that could lead to the development of additional forces not accounted into the design considerations.

A schematic section of the relevant design forces considered is shown in Figure 3a. Anchors were buried 1.2m deep to transfer the end load into the native soil underneath. A passive resistance supporting the pullout force and the resisting moment necessary for the anchor rod itself determined the depth of embedment and the diameter of the anchor rod (Figure 3b). There was no available geotechnical data for the native soil, thus a conservative assumption was made based on the surficial observations. The force applied for driving the anchors into native soil during installation was monitored to avoid the risk of any local areas which do not meet the design assumptions for the native soil.
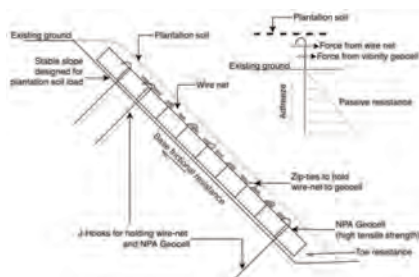
Figure 3a.   Schematic section for anchored slope.   Figure 3b.   Anchor design detail.
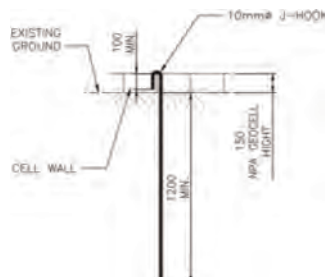
2.1   Design checks can be summarized into the following 5 steps

Step 1: *Total sliding force for the entire slope length per unit width (neglecting local slope changes) < Σ (factored passive resistance for all soil nail anchors within that unit width + factored toe resistance for unit width + factored base frictional resistance)*

Step 2: *Sliding force for influence area < (Factored passive resistance of an anchor + factored base frictional resistance for that influence area)*

Through step-1 and step-2, using a trial-and-error method, the anchor spacing along and across the slope was determined. The potential for the uplift of anchors, either from freeze-thaw or ice lensing or the presence of water was also checked, and the effective resistance forces are adjusted accordingly.

Step 3: *Factored geocell material tensile strength > effective influence area sliding force*

A higher tensile strength geocell shall need a smaller number of anchors and thus, minimize anchor cost, labor costs, and effectively reduce the construction time. Considering the current design, NPA Type C geocell with 19kN/m tensile strength was used. Given the anchor spacing limitations, any lower-strength material would not allow a safe design. Using even higher tensile strength (22kN/m with Type D NPA geocell) would further reduce the number of anchors and thus improve production. However, to optimally use Type D, the zip-ties had to improve in strength as well. The lack of availability of higher-strength zip ties restricted the optimal design to Type C.

Step 4: *Anchors shall pass the effective moment and shear resistance from all applied member forces*

Step 5: *Any stress concentration in local areas is checked independently*

Some limitations of the design were highlighted before the start of construction. No equipment loading on the slope was allowed. However, loads from laborers carrying handheld equipment were acceptable. Since the work was on a steep slope, necessary harnessing equipment as per the safety standards was identified as the contractor's responsibility. The design had considerations for saturated soil conditions. If there was any potential for water streaming down the sloped surface before the vegetation grew, either from heavy rain events or poor drainage, then there was the potential for washouts of the infill leaving the geocells visibly

exposed. Thus, the possibility of refilling the soil was a potential risk. To minimize that risk hydroseeding was recommended. If the contractor or the drainage design team or the client preferred to minimize the risk further, then options for using a sod cover were kept open.

The diminishing material properties of the geocell with time (for UV and creep from sustained load) increase the risk for local failures at stress concentration zones. Thus, checking the long-term properties (creep and stiffness at elevated temperatures) of the geocell is important. For the current design, long-term cumulative plastic deformation at 650C less than 3% was accepted.

3 RESULTS AND DISCUSSION

Installation of the NPA geocell went hassle-free. First, the geocell panels were stapled and then stretched from the crest to the toe (Figures 4 and 6). Geocell was anchored with J-hooks as per the design in the areas where anchoring was permitted, on other areas the wire net was stretched and anchored along the edges (Figure 5). Once all the anchoring was complete, zip ties were used to connect the wire net to the geocell (Figure 5). Finally, plantation soil was filled from the toe with a conveyor (Figure 7) to avoid any local impacts or local damage. In some extremely steep zones exceeding 73^0, it was difficult to retain the soil because of the angle of filling. However, there was still enough material inside the pocket for the vegetation growth and covering the exposed geocell, leaving a green surface (Figure 8).

Figure 4.   Layout of the slope with tunnel portal.

Figure 5.   Installation of wire net with geocell.

Figure 6.   Installation of geocell.

Figure 7.   Filling of geocell.

There were some rain events right after the installation was complete, but nothing major enough to demand a refill. The site was observed periodically (Figures 8, 9, 10, 11) for any washout zones or any other potential failures.

No mentionable failure was noted within the first year of observation. However, in late summer after the vegetation dried, a small area where the geocell pockets could not be filled and the total plantation soil thickness was less than 200mm, the exposed geocell top was visible (within the rectangle in Figure 10).

Overall, the area was so small that through the spring and early summer when the surrounding vegetation was green, it was not visible. Also, with time it is expected that vegetation will take over those patches. This raised no concern about the green solution that the client had expected.

Figure 8.   Early Summer (6 months later).

Figure 9.   Mid Summer (10 months later).

Figure 10.   Exposed soil area with low vegetation.

Figure 11.   End of Summer (12 months later).

An additional rose bed with thicker soil cover was added at the toe (lesser sloped area) 9 months after the completion of construction (Figure 11). Thus, the developed design approach and construction execution were successfully carried out creating positive environmental impacts.

4   CONCLUSION

NPA geocell and design methodology were effectively used to develop a green cover on a steep slope around a tunnel portal, where there was no opportunity for installing tendons and there were patches of areas where anchoring into native soil was not permitted. The innovative use of wire-net and zip-ties helped to bridge the non-anchoring zones without any installation hassle. The stretched pocket size of 250mm x 210mm with a geocell height of 150mm was found optimal for a 200mm thick plantation soil cover. The higher tensile strength of geocell material had a profound effect on overall load transfer integrity and played an essential part in minimizing the number of anchors needed. Periodic observations made over one year showed no signs of damage or any other potential risks. The study can be further extended to find the maximum area that can be installed anchor free. This can have a significant impact on green construction applications where both tendons and anchors play a challenging role.

REFERENCES

Guo J, Han J., Schrock, Steven, Parsons, Robert. 2015. Field Evaluation of Vegetation Growth in Geocell-reinforced Unpaved Shoulders. *Geotextiles and Geomembranes*. 43. 10.1016/j.geotexmem.2015.04.013.

Hegde, Amarnath. 2020. Cellular Confinement Systems: Characterization to Field Assessment. 10.1007/978-981-15-6095-8(2).

Liu, Yang & Deng, An & Jaksa, Mark. 2018. Failure Mechanisms of Geocell Walls and Junctions. *Geotextiles and Geomembranes*. 47. 104–120. 10.1016/j.geotexmem.2018.11.003.

Pokharel S. K. 2010. *Experimental Study on Geocell-Reinforced Bases under Static and Dynamic Loading*. Civil, Environmental, and Architectural Engineering Department, University of Kansas, Kansas, USA.

Rimoldi, P. and Ricciuti, A. 1990. Design Method for Three-dimensional Geocells on Slopes. *Proc. of Fifth International Conference of Geotextiles*, Geomembranes and Related Products, Singapore, 999–1002.

BGM testing program for use in heap leach pads

E. Escobar
Iko Coletanche Sudamerica SpA., Santiago de Chile, Chile

B.S. Breul
Axter S.A.S, Paris, France

B. Breul
Independant, Paris, France

ABSTRACT: Normal practice in Latin America for the waterproofing of heap leach pads involve the use of polymeric membranes (either HDPE or LLDPE) normally coupled with a medium-weight geotextile to protect the polymeric membrane liner from puncturing. Use of a bituminous geomembrane (BGM) for this application is conceptually appealing to the mining industry since it provides the waterproofing with a single geosynthetic as well as the elimination of an additional interface (polymeric membrane against geotextile) that may have an effect in the static and dynamic stability of the heap leach pile. A BGM manufacturer teamed with a large copper mine in Chile to test the puncture resistance of the BGM sandwiched between the overliner and the subgrade as well as the interface friction angles between the overliner and the BGM. This paper describes the test program, the results obtained and their significance for the heap leach pad.

1 INTRODUCTION

1.1 Description of the project

The project for which the use of a BGM was considered belongs to a major copper mine in Northern Chile. It consisted of a large heap leach pile with a design height of 100 m for the leaching of crushed ore with a density of 1.8 tons/m^3. The area of the pad to be waterproofed for the new heap leach was around 600,000 m^2 in total.

Based on the above conditions the actual puncture stress imposed by the heap pile on the waterproofing barrier of the pad is around 1,800 kPa and the mine owner defined a desired safety factor of 3.0 against puncturing. Overall, the liner would have to be tested at a maximum vertical puncture load of 5,400 kPa.

1.2 Structure of a BGM

The bituminous geomembrane is a multilayered product as illustrated in Figure 1 below.
The components of this bituminous geomembrane are:

– a nonwoven polyester geotextile, ranging from 200 to 400 g/m^2, that provides mechanical performance, especially the tensile and puncture strength,
– a glass fleece reinforcement that provides thermal stability during manufacturing,
– a blend of SBS modified bitumen and fillers. This blend impregnates the geotextile and the glass fleece, provides the watertightness, and ensures the longevity of the product,
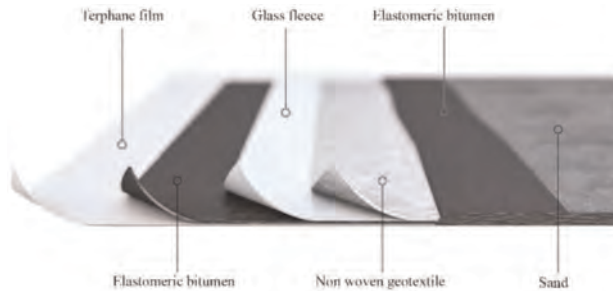
Figure 1.   Cross section of bituminous geomembrane.

– a terphane film bonded to the underside, to prevent penetration of the membrane by plant roots,
– a coating of fine sand on the upper surface to provide a greater traction on slopes, and to provide increased protection against the degrading effects of UV radiation.

2   PROPOSED TEST PROGRAM

The objective of the test program was to evaluate the puncture resistance of two different bituminous geomembranes – a 4.8 mm thick BGM containing a non-woven 300 g/m^2 geotextile (internally denominated "ES3") and a 5.6 mm thick BGM containing a non-woven 400 g/m^2 geotextile (internally denominated "ES4") – under the loads imposed by the heap leach with the desired safety factor and to measure the interface friction angles at the normal load imposed by the heap to use these figures for the subsequent stability analyses of the heap.

The project requirements indicated the need to do large-scale puncturing tests at a normal load as high as 5,400 kPa and interface friction tests with a normal load around 1,800 kPa. After a careful search of existing laboratories in the Americas the factory selected the SAGEOS laboratory in St-Hyacinthe (QC, Canada) for the puncturing tests. However, the maximum load capacity was 5,000 kPa which already represents a high safety factor of 2.8. TRI Environmental laboratory in Austin (TX, USA) was chosen for the interface friction testing.

Although the main interest was to evaluate the behavior of the BGM between the subgrade and the overliner material normally used at the mine, the test program also included a series of tests with the BGM between the subgrade and the mineral to be leached with a view to eventually eliminate the overliner in the typical design and generate cost savings.

2.1   Sampling and USCS classification of granular materials

SGS Chile was retained to collect at the mine site the samples of the subgrade, the overliner and the mineral in the quantities required by the testing program, pack the materials in moisture-proof recipients holding 25 kg each, label and ship the materials via airfreight to each laboratory (about 300 kg for the puncture tests and 140 kg for the direct shear tests).

SGS was also tasked to do the sieve analysis of the granular materials involved. The Table 1 below contains the size consist of the different materials. Table 1 presents the size consist information of the materials in a graphical form.

Table 1. Size consists of materials (% passing).

ASTM Sieve	Subgrade	Overliner	Mineral
2 ½."		100	
2"		99	
1 ½"	100	83	100
1"	97	56	93
¾"	94	38	84
3/8"	84	9	72
No. 4	69	1	58
No. 10	55		48
No. 40	28		29
No. 200	14		18
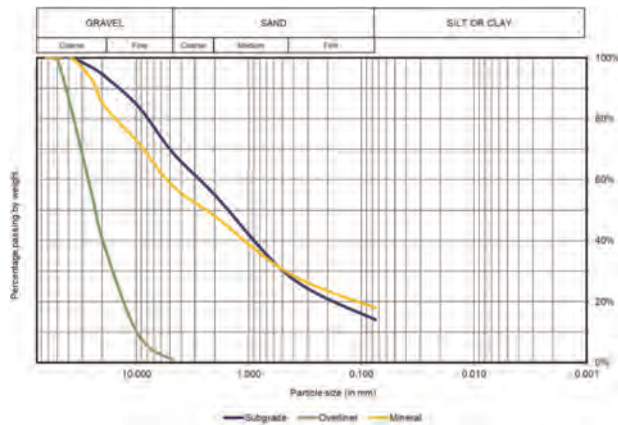
Figure 2. Size consists of granular materials.

2.2 Large scale puncturing tests

The large-scale puncture tests were done following a modified version of ASTM D5514, procedure B. The pressure applied to the geomembrane is exerted via a hydraulic cylinder and a small hydrostatic piezometer is used as a tool to determine whether there are leaks through the liner. Figure 3 below shows a schematic of the puncture testing device.
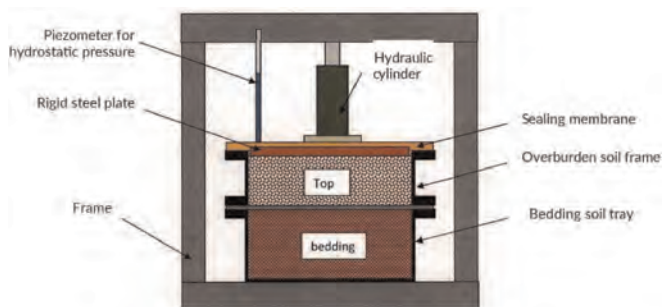
Figure 3. Schematic of puncture testing device.

Under this procedure the pressure is applied by steps in 138 kPa increments (20 psi), the normal load is held constant for 10 minutes to observe if there is a drop in the level of the piezometer. The process continues following these steps until a drop in the piezometer is observed or the capacity of the testing device (5,000 kPa) is achieved. If the latter takes place, the load is maintained for one hour.

The operational condition of a geomembrane in a heap leach pad corresponds to a "mechanical stress" condition – as described by Blond and Breul (2014) in which the geomembrane is sandwiched between a drainage layer and the support material. Each of the designated geomembranes was tested between the overliner and the subgrade and between the mineral and the subgrade. Three replications were done for each test to obtain average values.

In most tests the BGM reached the capacity of the test device without puncturing, which indicates that the puncture resistance under the test conditions exceeds 5,000 kPa although the ultimate puncture resistance could not be determined. The only exception was the test of the "ES3" (thinnest product) against the overliner material, in which the membrane showed leaks when the load reached 5,000 kPa. However, in all three replications of this test, the membrane did not show any leaks in the stage immediately before the maximum capacity of the test device. The results of the puncture tests are summarized in the Table 2 below.

Table 2. Puncture test results.

Test #	Description	Puncture Resistance	Punctures Observed
1	Overliner / ES4 / Subgrade	> 5.000 kPa	None
2	Mineral / ES4 / Subgrade	> 5.000 kPa	None
3	Overliner / ES3 / Subgrade	≈ 4.860 kPa	5,12,11
4	Mineral / ES3 / Subgrade	> 5.000 kPa	None

2.3 Direct shear tests

The direct shear tests were done following the ASTM D5321 standard at normal loads of 500, 1,000 and 2,100 kPa. The membrane was placed inside the shear box with a pyramid-toothed grip plate underneath and the material to be tested above. Figure 4 below shows a schematic of the direct shear box and a photo of the grip plate used.
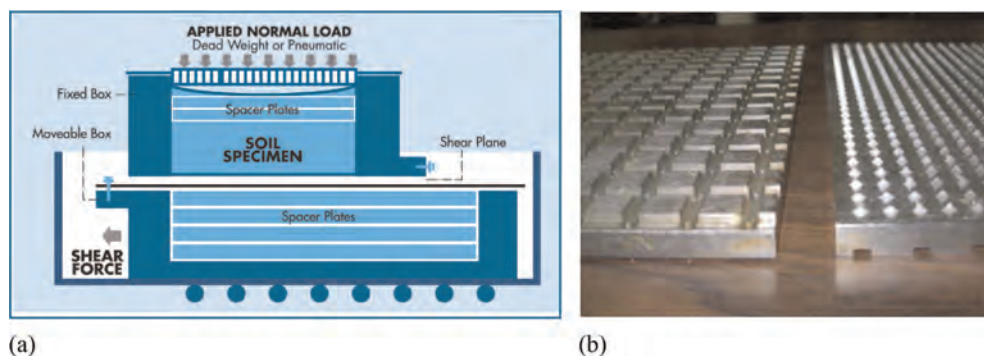
Figure 4   a. Schematic of direct shear box. b. Pyramid-toothed grip plate.

For these tests, the sanded side of the geomembrane was placed against the granular material and the terphane film against the grip plate underneath. The granular materials were tamped in place and the tests were run under wet conditions (deemed to be more unfavorable) at a shear rate of 1.0 mm per minute.

The friction angle between granular materials and the sanded side of the BGM have been measured at the INSA laboratory in Lyon (INSA, 2012) using the sliding table method based on the French standard NF P 84-522. These tests showed the angle friction with gravels to be between 38° and 44°.

Direct shear tests done for the Headworks Reservoir of the Los Angeles Department of Water and Power in the United States (Lew *et al.*, 2013), using ASTM D5321 with a modified speed, showed that the interface friction angle with normal loads up to 250 kPa was around 36° for non-cohesive materials.

Direct shear tests done on railway ballast have shown that the secant friction angles decrease with an increase in the normal stress (Estaire and Santana, 2018). We have not had previous experience with direct shear tests for the BGM at the normal loads for which this test program was designed.

However, based on the above experiences, we were expecting that the friction angle at the higher normal loads would remain around 30°.

At a normal load of 500 kPa the secant friction angle varied between 27° and 30° (depending on the geomembrane and the material on top). However, when the normal load increased to 1,000 kPa, the secant friction angle was reduced to values between 20° and 24° and when the normal load increased to 2.100 kPa, the secant friction angle was further reduced to values between 11° and 14°. It was also noticed that, for the same normal load, the secant friction angles for the thicker, 5.6-mm "ES4" membrane were smaller than those for the thinner 4.8-mm "ES3" membrane. The Table 3 below summarizes the secant friction angles obtained.

Table 3. Secant friction angles.

| Test #. | Description | Normal Load, kPa | | |
		500	1,000	2,100
1	Mineral vs ES3 (Sanded side)	30°	24°	14°
2	Overliner vs ES3 (Sanded side)	29°	21°	14°
3	Mineral vs ES4 (Sanded side)	27°	21°	12°
4	Overliner vs ES4 (Sanded side)	27°	20°	11°

The friction angles derived from the Mohr-Coulomb's linear envelopes obtained from the above tests ranged from 4.3° to 7.5° for the peak stress and from 1.8° to 4.9° for the large displacement measurements. Once again, the friction angles for the thicker, 5.6-mm "ES4" membrane were smaller than those of for the thinner 4.8-mm "ES3" membrane.

The test reports from the laboratory indicate that, in all cases, there was some elongation of the membrane at the grips on the edges. Also, the photo logs of the membrane after the tests show that the granular material got partially embedded into the bitumen and the horizontal movement of the upper box dragged the bitumen along, thus partially exposing the reinforcing geotextile. This could indicate that the shear stresses recorded during the test are somehow affected by the tear resistance of the geotextile and/or by the resistance of the internal interface between the bitumen blend and the geotextile.

After consultation with a geosynthetics consultant, it was decided to run a non-standard "floating" direct shear test (i.e., without clamping the membrane sample at the sides) with

the membrane placed between the overliner and the subgrade (instead of the steel grip plate). The logic behind this test was that, given the usually large dimensions of a real-life pad, the effect of the anchoring of the membrane at the borders of the pad would have little or no impact on the behavior in the middle of the pad. The "floating" direct shear test was done at the same normal loads as the other tests (i.e., 500, 1,000 and 2,100 kPa). Shearing occurred at the geomembrane – subgrade interface (i.e., at the smooth Terphane side of the membrane) at the three normal loads tested. No dragging of the bitumen on the upper side of the geomembrane was observed. The friction angles obtained from this "floating" test were 8.5° for the peak stress and 8.3° for the large displacement. friction angle. These results make us think that the friction angles of the sanded side of the BGM should be actually higher than those derived from the linear envelopes of the initial tests. In our view, the friction angles obtained under this program must be used with caution and further investigation on this matter is required.

3 CONCLUSIONS

Based on the results described above the authors concluded that:

Both the 5.6 mm-thick BGM and the 4.8 mm-thick BGM tested can withstand the puncture loads imposed by the proposed heap leach with a safety factor larger than 2.8 and thus are deemed suitable for the application from this point of view,

The puncture resistance of both BGM's against the mineral to be leached is as good (or maybe better) than the puncture resistance against the overliner. This may lead the design engineers to consider that, provided that the mineral to be leached has enough hydraulic conductivity to appropriately transport the leachate, the overliner could be eliminated altogether, thus resulting in large cost savings for the project,

The actual friction angle of the sanded side of the BGM could be higher than the figures derived from the linear Mohr-Coulomb's envelopes from these tests. In our view this is an aspect that requires further investigation.

REFERENCES

ASTM D2487-17, 2017, "Standard Practice for Classification of Soils for Engineering Purposes (Unified Soil Classification System)"

ASTM D5321-20, 2020, "Standard Test Method for Determining the Shear Strength of Soil-Geosynthetic and Geosynthetic-Geosynthetic Interfaces by Direct Shear".

ASTM D5514-18, 2018, "Standard Test Method for Large-Scale Hydrostatic Puncture Testing of Geosynthetics"

Blond, Eric & Breul, Bertrand. 2014. "Behavior of Bituminous Geomembranes under Elevated- Compression Stress". *Proceeding of Geosynthetics Mining Solutions 2014, Vancouver, September 8–14, 2014"*, Vancouver, Infomine Inc.

Didier, Gerard & Gaidi, Laouni. 2002. "Measurement of the Angle of Friction of Various Materials on the Coletanche Geomembrane". *INSA, Lyon, 2002*

Estaire, José & Santana, Maria. 2018. "Large Direct Shear Tests Performed with Fresh Ballast". *Railroad Ballast Testing and Properties, ASTM STP 1605*. T.D. Stark, R. Seczy, and R.H. Swan Jr. Eds. ASTM International, pp. 134–151

Lew, M, Ponnaboyina, H., Davis C.A. & Perez, A. 2013. "Interface Friction Testing Between Soil and a Bituminous Geomembrane". *Geosynthetics 2013, Long Beach, California, April 1–4, 2013*

NF P 84-522, 1994, "Mesure de l'angle de Glissement des Dispositifs d'étanchéité par Géomembrane (DEG) à l'aide d'un plan incliné"

Innovative designs for extreme mining applications using bituminous geomembranes

R. McIlwraith*
Director – Axter Australia Pty, Australia

ABSTRACT: The paper describes how bituminous geomembranes (BGMs) are designed in innovative ways to solve engineering challenges on mining sites in extreme environmental conditions and to provide environmental protection. The design of BGMs in mine tailings facilities and environmentally sensitive mine waste capping are focused on, and the technical challenges facing these projects are discussed in detail. The protection of groundwater by using effective and puncture resistant BGM solutions contribute to creating a resilient planet. The innovative use of special high friction angle BGMs on the very steep (1V:1.75H) tailings storage embankments of the new large Ravenswood Gold Mine in Australia are discussed in detail. This mine is under construction from 2021 to 2023. BGMs are multi-layered composite geomembranes with each of the components providing a technical benefit on the mining site. These technical advantages include: Extreme puncture resistance, which allows rapid deployment on rougher subgrades; Excellent resistance to wind uplift due to their high surface mass and this means that installation can continue in winds up to 40km/h. Elastomeric BGMs also retain their flexibility in extremely cold conditions and can be installed and welded down to -25 deg C. This means that elastomeric BGMs are often used in the extreme mining conditions of Siberia, northern Canada and the high altitudes of the Andes mountains in South America. BGMs have a very low coefficient of thermal expansion and do not wrinkle with changes in temperature like other polymeric membranes do and this is particularly useful in high heat projects in Australia. This provides a more secure project in the long run, with less risk of wrinkle-induced cracks and failures. In summary, the paper describes how the technical attributes of the BGM's composite structure provides a wide range of practical on-site solutions for challenging mining applications and environmental protection.

1 INTRODUCTION

Bituminous geomembranes (BGMs) continue to be designed and used in innovative ways to solve engineering challenges on mining sites in extreme environmental conditions and to provide enhanced levels of environmental protection. Environmentally responsible mining will continue to play a vital role in the transition to a more resilient planet, as many of the key materials required for a low carbon future come from mining. For example, a large quantity of copper is required for electric vehicle motors, and lithium and graphite are required for electric vehicle batteries.

Due to their unique characteristics, BGMs are used extensively in four main applications on mine sites. These applications include:

- Tailings storage facilities (TSFs) where the excellent puncture resistance and lack of thermally induced wrinkles are important characteristics in the selection of a BGM. A key

---

*Corresponding Author: RMcIlwraith@axter.com.au

design element for TSFs is also the high mass per square metre of a BGM which gives outstanding wind uplift resistance. A technical design advantage of BGMs is that, due to their internal polyester reinforcement, they can easily be used on slopes up to 2H:1V. For steeper slopes up to 1.3H:1V, the innovated High Friction Angle (HFA) BGMs have been be used. These innovate HFA BGM grades have a releasable siliconized film on the underside of the BGM which is removed at time of deployment to give a self-adhesive underside to the BGM which maximizes interface friction angles on the slope.

Figure 1.   Copper – gold tailings storage facility TSF in South Australia during construction. Note the straight panels on the BGM with no thermally induced wrinkles in extreme 45 deg C heat. This BGM is designed to provide embankment sealing and prevention of tailings migration into sensitive environmental lakes downstream.

- BGMs are also used extensively for capping and closure of mine waste facilities. The key design features of BGMs in these applications are:
  1) extremely low permeability ($< 6 \times 10^{-14}$ m/s) which prevents migration of contaminants into the groundwater and therefore providing a more resilient planet in the long term;
  2) the ability of the BGM to be used on rougher subgrades, typically with aggregate size up to 20mm, and this is a big advantage over other polymeric geomembranes;
  3) the ability to use High Friction Angle (HFA) BGMs on steep slopes on mine waste covers.

Figure 2.   Innovative High Friction Angle (HFA) BGMs being deployed on slopes for mine waste capping and environmental protection. Northern Territory, Australia.

- The third major use of BGMs in mining applications is for containment of stormwater runoff in retention dams, as shown in Figure 3 below. These retention dams prevent runoff entering rivers directly during large rainfall events. Key design features of BGMs in these applications include: puncture resistance on rough subgrades; a specific gravity of 1.22 (which means the BGM is heavier than water and will not float upwards like other polymeric geomembranes which are lighter than water with specific gravities in the region of 0.94); and the excellent wind uplift resistance characteristics of BGMs (Giroud 1995). With little or no ballast required, this results in considerable cost savings and improvements in construction speed for the project.

Figure 3.   BGM being used for environmental protection by containing stormwater run off from a mine before it reaches the river. New South Wales, Australia.

- The fouth main use of BGMs in mining applications is for evaporation and waste ponds. All the key advantages of BGMs play a part in these applications, including puncture resistance, thermal stability, heavy specific gravity and wind uplift resistance.

Figures 4 and 5.   Lithium salt ponds in the extreme Atacama Desert of Chile. Note the thermal stability of the BGM with no wrinkles.

2 TECHNICAL COMPONENTS OF A BGM AND NEW INNOVATIONS

2.1 Multi-component structure of BGM geomembranes

A BGM is a multi-component geomembrane with each of the components providing a technical design or practical benefit on site. Figure 6 below shows a standard BGM structure. The sanded surface provides a non-slip surface for workers which enhances safety in wet conditions. The SBS elastomer modified bitumen provides elastic properties with extremely low water permeability characteristics (<6 x 10^{-14} m/s according to ASTM E 96). The internal non-woven geotextile is fully impregnated with elastomeric bitumen and this provides the mechanical properties of tensile strength and puncture resistance. Various grades of geotextiles can be used to provide different mechanical properties depending on the severity of the application. The puncture resistance of various strength BGMs in direct contact with various size aggregates up to 100mm and with overburden pressures exceeding 1000kPa have been tested (Blond 2014).
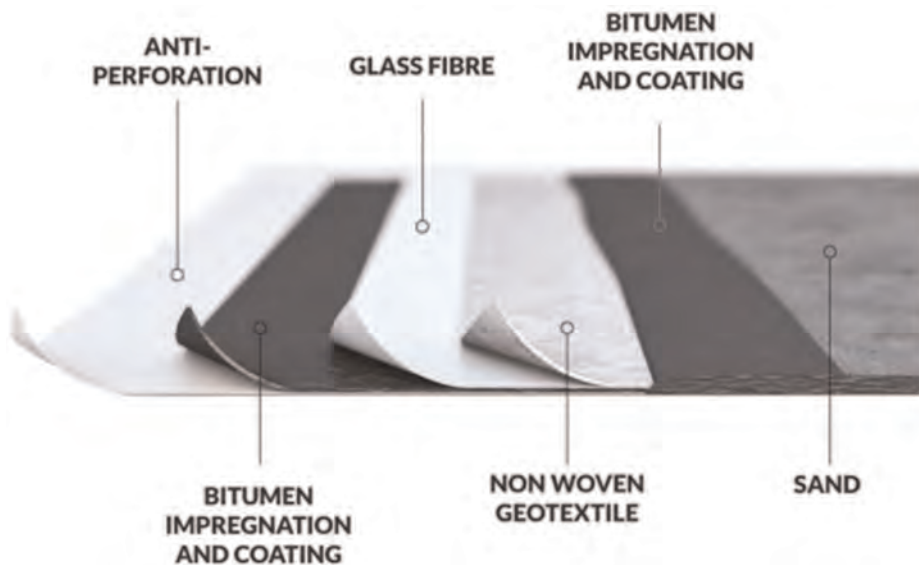
Figure 6. Technical components in the BGM geomembrane.

2.2 High Friction Angle (HFA) grade of BGM

For the High Friction Angle HFA grade of BGM, the underside of the BGM has a siliconized self-release film that is removed at time of installation to provide a bitumen surface to be in contact directly with the subgrade. This innovation provides a very high interface friction angle on the underside. This interface friction angle is in the order of 34 deg, but is based on the exact material the HFA BGM is in contact with, so interface friction testing is suggested for critical applications.

2.3 Thermal properties of BGMs in extreme temperatures

BGMs are inherently thermally stable with an extremely low coefficient of thermal expansion of 1 x 10^{-6} C^{-1} when tested to ASTM D 1204-02. This means that BGMs are not effected by heat induced wrinkles that other polymeric membranes suffer from. This
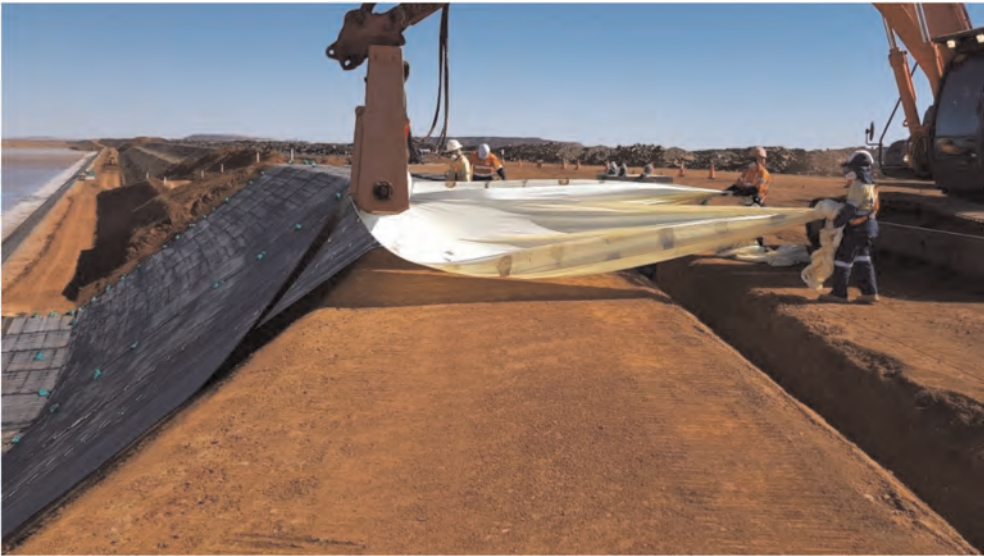
Figure 7. The innovative High Friction Angle BGM being deployed on a steep 1.3H:1V Tailings Storage Facility The white siliconized layer is removed at time of installation to provide a bitumen surface on the underside which maximizes the interface friction angle with the subgrade. This photo also shows another innovation in terms of safety with regard to geosynthetic installations, with the hydraulically operated deployment beam, which uses hydraulics from the excavator. The hydraulic beam enables a safe and control deployment on these steep slopes and it also helps reduce worker fatigue on extremely hot sites.

provides a more secure project in the long run, with less risk of wrinkle-induced cracks and failures.

In extremely cold conditions, elastomeric BGMs have a distinct advantage over polymeric geomembranes. Most geomembranes cannot be welded below 0°C due to brittleness at these temperatures, but BGMs can be installed and welded down to −25°C, which is particularly useful for the many mines in extremely cold environments including the high altitude mines in the Andes of South America, and the mines in Canada. Although there are different types of BGMs, most elastomeric BGMs when tested for Cold Bending according to ASTM D 746 can go down to −25°C.

3 RAVENSWOOD GOLD TAILINGS STORAGE FACILITY USING BGMS

The Ravenswood Gold Mine is Queensland's largest gold mine. It is situated 130km south west of Townsville, Australia.

The photo on the previous page shows the steep 1.75H:1V slopes using High Friction Angle (HFA) BGMs to maximize interface friction angle between the subgrade and the underside of the geomembrane. On the base, a standard BGM is used, as the high interface angles are not required. Both grades of BGM have internal reinforcement providing excellent puncture resistance and they use the same elastomeric bitumen, so they can be bonded directly to each other. The specific gravity characteristic of BGMs being heavier than water, as well as the excellent wind uplift resistance features were also important design considerations when selecting the geomembrane for this application. Due to the large size of the project (more than 1 million m^2 of geomembrane) it was important that the correct type of geomembrane was chosen for the application.

Figure 8.   Ravenswood Gold tailings storage facility.

The sanded non-slip surface of the BGM was an important consideration in membrane selection for construction safety as the tailings storage facility is being raised in a number of incremental stages while there are tailings in the facility.

4   CONCLUSIONS

BGMs have a wide range of technical benefits, due to their multi-component composition, and these benefits are well suited to solving the challenges in mining applications. BGMs have proven themselves on many large mining projects around the world in extreme environmental conditions. The use of BGMs with their excellent puncture strength and thermal stability ensure that they provide excellent environmental protection in an innovative way, which ensures a more resilient planet in the long term.

REFERENCES

Blond, E. & Breul, B. 2014. Behavior of Bituminous Geomembranes under Elevated-Compression Stress. *Proceedings of Geosynthetics Mining Solutions*. September 8−11, 2014. Vancouver, Canada.
Giroud, J.P., Pelte T., & Bathurst, R.J., 1995. Uplift of Geomembranes by Wind. *Geosynthetics International*, IFAI, Roseville, MN, USA, Vol 2 No 6, pp 897–952.

LDPE geomembrane liner design on soft soil foundation: Case study

B.M.C. Urashima, P.V.S.A. Castro, L. Amaral, M. Castro & P. Martins
WSP, Belo Horizonte, Minas Gerais, Brasil

ABSTRACT: This paper presents a case study of a geomembrane liner design in a mining area for contaminant waste disposal. The presented study involves the need to store steel slag on soft soil foundation that presents a low bearing capacity. The stored material is granular contaminant material with high permeability and high density. Thus, it was necessary to carry out a stress-strain study on a Finite Element Model, followed by an empirical-analytical verification to assess the feasibility of the waste pile construction. The study predicted a maximum strain of 12%, resulting on maximum displacements of 1.4 m. An implementation of plastic geomembranes was proposed considering the need to promote a flow barrier faced to the increasing applications bias of geosynthetics in mining industry. Furthermore, based on the foundation consolidation process under the steel slag waste pile, Linear Low-Density Polyethylene was considered as required by the large expected strains.

1 INTRODUCTION

Geomembranes are geosynthetic materials widely used as hydraulic barriers in waste containment facilities due to its flow reduction characteristic (Chen *et al.* 2009, 2012; Jeon 2016; Mirhaji *et al.* 2019). However, geomembranes are susceptible to damage under dynamic and static loadings during construction phase or during service life cycle. (Hou *et al.* 2021). Extensive research has been conducted to analyze geomembranes behavior under various loading conditions (Yan *et al.* 2021). Area availability is an issue for mining industrial sites. In this context, the construction of embankments on soft foundations with geomembranes application are required. Foundation improvement of the remaining available areas is often needed. This work presents a design study case of geosynthetics application for soft foundations treatment, to make a mine waste pile embankment construction feasible. Its construction was evaluated in two phases.

2 MAIN INPUTS

The stress-strain study was based on a geological-geotechnical investigation which defined a soil profile as presented on Figure 1. A two-dimensional stress-strain modelling was carried out, using RS2 software version 2019 10.002. Table 1 shows the parameters used in the stress-strain study for the soil fill, sand, and silty sand. Table 2 indicates the parameters obtained through the NorSand model for the silty clay and for the fill material.

Figure 1. Generic soil profile for material definition.

Table 1. Mohr-Coulomb foundation parameters.

Parameter	Soil fill	Sand	ilty sand
φ' (°)	32	40	40
c' (kPa)	10	28	0
ν	0.3	0.3	0.3
E (kPa)	15,000	25,000	60,000

Table 2. NorSand foundation and fill material parameters.

Proprieties	Commentary	Fill material	Silty clay
CSL			
Γ	Reference void ratio for CSL	2	1.3
λ	CSL slope for logarithm base 10	0.139	0.113
$_0$	State parameter	−0.5	−0.1
Plasticity			
M_{tc}	Ratio for critical state in triaxial compression	1.55	1.5
N	Volumetric coupling coefficient for inelastic stored energy	0.42	0.3
H_0	Plastic hardening modulus	70	40
H_y	Plastic hardening modulus	500	400
χ_{tc}	Ratio between minimum dilatancy and state parameter	1	4
Elasticity			
$G_{\hat{A}}$ (Mpa)	Shear Modulus	14	10
$N^{máx}$	Poisson coefficient	0.1	0.150

3 GEOMEMBRANE DISPLACEMENTS

The liner system (geomembrane) was analyzed. Figure 2 shows the development of the maximum principal strains in the region close to the silty clay, the most deformable material. It is still observed the concentration of deformations in the central region of the geomembrane of both phases. Figure 2 illustrates the geomembrane total deformations, while Figure 3 shows the
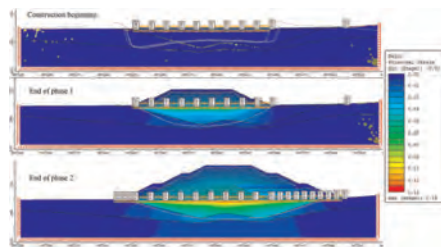
Figure 2. Maximum principal strain at the liner layer.
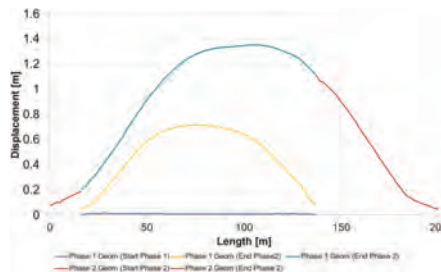
Figure 3. Evolution of the geomembrane displacements in the phases of initial implantation, phase 1 and phase 2 of construction.

evolution of the geomembrane displacements in the phases of initial implantation, phase 1 and phase 2 of construction. It is observed that the greatest requests are absorbed by the geomembrane corresponding to phase 1. With installation of this liner system, its deformations can reach up to 12% with displacements of the order of 1.5 m. Therefore, plastic geomembranes developed with Linear Low-Density Polyethylene (LDPE) could be used in this case.

4 LINER DESIGN

To the liner system at the base of the deposit, a system composed of linear low density plastic geomembrane (LDPE) was proposed. The strains and stresses expected to act at the liner were firstly generated by the numerical model, however the values were update using analytical methodologies as proposed by (Koerner 1933; Shukla & Yin 2006; Vertematti 2015) during design. This way, the design criteria consider the stress solicitations bellow:

– Stress due to Self-Weight
– Stress caused by settlements
– Stress due to Thermal Contraction
– Stress due to Punching
– Deposit slide over the Geomembrane

4.1 Stress due to self-weight

The geomembrane weight per slope length was obtained through Equation 1 and the stress acting due to this weight was obtained through Equation 2.

$$\mathrm{W} = \Upsilon_{GM} t \frac{H}{sen\beta} \tag{1}$$

where Υ_{GM} = geomembrane specific weight; t = geomembrane thickness; H = slope height; and β = slope angle.

$$\sigma_{tA} = \frac{Wsen\beta - W\cos\beta tg\delta_L}{t} \tag{2}$$

where σ_{tA} = tensile stress acting on geomembrane; W = geomembrane weight; and δ_L = friction angle between geomembrane and foundation material.

The parameters values presented in Table 3 were considered. It is noteworthy that Υ_{GM} was estimated based on average values commonly manufactured, and δ_L was considered based on values presented in literature. The thickness used in all calculations was 1.25 mm, proposing a geomembrane with the needed strength and sufficient deformability.

Table 3. Parameter values considered in stress due to self-weight.

Parameter	Value
Υ_{GM} [kN/m³]	9.20
t [mm]	1.25
H [m]	3.00
B [-]	4.00
δ_L [-]	12.00

4.2 Stress caused by settlements

Equations 3 and 4 were used. Equation 3 related to the tensile force caused by deformation and Equation 4 related to the mobilization length necessary for the resistant friction forces to act.

$$T = \frac{\sigma_n x(tg\delta_U + tg\delta_L)}{\cos\alpha - sen\alpha \quad tg\delta_L} \tag{3}$$

$$x = \frac{(\sigma_r/FS)(\cos\alpha - sen\alpha tg\delta_L)t}{\sigma_n x(tg\delta_U + tg\delta_L)} \tag{4}$$

where α = subsidence angle; σ_n = normal stress due to material weight stored above the geomembrane; and δ_U = friction angle between the geomembrane and the material above. Table 4 presents the values adopted.

Table 4. Parameter values considered in stress caused by settlements.

Parameter	Value
α [°]	14
σ_n [kN/m]	419
δ_U [°]	12
t [mm]	1.25
σ_r [kN/m]	2.5
FS	2

4.3 Stress due to thermal contraction

Geomembranes, when exposed to thermal variation, expands and contracts. The biggest concern in this case is with contraction, which would cause tensile stresses in the material, as it would be anchored. Through Equation 5, the thermal contraction length of the material was calculated.

$$\Delta L = \mu L \Delta T \tag{5}$$

where ΔL = contraction caused by temperature variation; μ = thermal expansion linear coefficient; L = geomembrane length; and ΔT = temperature variation modulus. Table 5 presents the parameters and their values adopted for calculation. μ value was taken from the literature.

To calculate the force caused by this thermal contraction, Equation 6 was used.

$$T = \frac{\Delta L E t}{L} \tag{6}$$

where E = Young's modulus.

Table 5. Parameter values considered in stress due to thermal contraction.

Parameter	Value
μ [°C^{-1}]	11x10^{-5}
L [m]	200
ΔT [°C]	|−30|

4.4 Stress due to punching

Punching in the geomembrane calculation considered that it would be on a terrain that presented, at most, type 2 gravel (~22mm) fragments size. To calculate the stress due to punching in the geomembrane, Equation 7 was used.

$$F_{req} = p' d_a^2 \quad S_1 \quad S_2 S_3 \tag{7}$$

where F_{req} = vertical punch force required to be resisted; p' = pressure exerted on geomembrane; d_a = aggregate average diameter; S_1 = aggregate protrusion factor; S_2 = scale factor that adjusts the average diameter to that used in the punching test described in ASTM D4833; and S_3 = form factor that fits the considered values to ASTM D4833. The pressure exerted on geomembrane was considered equal to stored material weight. Table 6 shows the parameter values considered in calculations.

Table 6. Parameter values considered in stress due to punching.

Parameter	Value
σ_n [kN/m]	419
d_a [m]	0.022
S_1	0.4
S_2	0.4
S_3	0.5

4.5 Deposit slide over the geomembrane

The weight force that could generate slipping and the resistant friction force were calculated trough Equation 8 and 9.

$$W_{slide} = \Upsilon_{slag} A sen\beta' \tag{8}$$

$$F_{at} = \Upsilon_{slag} A \cos\beta' tg\delta_U \tag{9}$$

where Υ_{slag} = slag specific weight; A = slag pile cross-sectional area; and β' = slag pile inclination angle. Table 7 presents the parameters values considered in the calculation.

Were obtained the values: W_{slide} = 2440 kN/m and F_{at} = 7414 kN/m, that is, the slag pile would not slip on the geomembrane. However, there is a difference between the index and required property. The index properties are characteristics of a geosynthetic, determined in tests that do not consider the field requests. The required ones consider the damages that the material can suffer and that can cause its aging, through Reduction Factors. Table 8 shows reduction factors considered in the calculation. Table 9 presents the results summary obtained compared to the material required values.

Table 7. Parameter values considered in deposit slide over the geomembrane.

Parameter	Value
Υ_{slag} [kN/m³]	26.2
A [m²]	1335
β' [°]	4

Table 8. Reduction factors for geomembrane.

Factor	Value
Creeping (FRPFL)	3
Installation Damage (FRPDI)	1.75
Environmental Deterioration (FRPMA)	1.25
Chemical attack (FRPAQ)	2

Table 9. Results.

	Requesting force [kN/m]	Friction force [kN/m]
Self-Weight	0.03	0.11
	Requesting tensile stress [kN/m]	Required tensile stress [kN/m]
Settlements	0.0016	2.51
Thermal Contraction	0.0022	2.51
	Requesting punching force [kN/m]	Required punching force [kN/m]
Punching	0.016	0.023

5 CONCLUSIONS

This paper deals with case study of a geomembrane liner design need for storing a steel slag, a granular contaminant material with high permeability and high density, on a soft soil foundation with a low bearing capacity. The results obtained lead to the conclusion that a 1.25 mm LDPE geomembrane would be ideal for make a mine waste pile embankment construction feasible In a critical scenario in which the traction requests would be occurring all at once, the requesting stresses would be added, resulting in a value of 0.0037 kN/m, which is lower than the required resistance (2.51 kN /m), that is, the specified geomembrane would still meet the required performance.

REFERENCES

ASTM D 4833. 2020. Standard Test Method for Index Puncture Resistance of Geomembranes and Related Products. *ASTM International*, West Conshohocken, PA, USA.

Chen C., McDowell G. R. & Thom N. H. 2012. Discrete Element Modelling of Cyclic Loads of Geogrid-Reinforced Ballast under Confined and Unconfined Conditions. *Geotextiles and Geomembranes* 35 (2012): 76–86.

Chen Y., Xie H., Ke H., & Chen R. 2009. An Analytical Solution for One-dimensional Contaminant Diffusion through Multi-layered System and its Applications. *Environmental Geology* 58 (2009): 1083–1094.

Hou J., Li H., Liu L., Wang S., Tang Y. & Bao S. 2021. A DEM Analysis of Geomembrane-lined Landfill Subject to Vertical Loading. *Geotextiles and Geomembranes* 49 (2): 369–375.

Jeon H-Y. 2016. Analysis of Environmental Applicability of HDPE Geomembrane by Simulated Applicability Testing for Waste Containment Construction. *Frontiers in Materials* 3 (44): 1–6.

Koerner R. M. 1933. *Design with Geosynthetics*. 5th edition. Pearson Education, Inc., USA.

Mirhaji V., Jafarian, Y., Baziar, M. H. & Jafari, M. K. 2019. Evaluating Seismic in-soil Isolation of MSW Landfill using Geosynthetic Liners in Shaking Table Test: Case Study of Tehran Kahrizak Landfill. *Sharif Journal of Civil Engineering* 35.2 (1.2): 105–113.

Shukla S. K. & Yin J-H. 2006. *Fundamentals of Geosynthetic Engineering*. 1st edition. Taylor & Francis/Balkema, UK.

Vertematti J. C. 2015. *Manual Brasileiro de Geossintéticos*. 2ª edição. Blucher, Brasil.

Yan H., Wu J., Thomas H.R., Ding H., Zhan L. & Xie H. 2021. Analytical Model for Coupled Consolidation and Difusion of Organic Contaminant Transport in Triple Landfll Liners. *Geotextiles and Geomembranes* 49 (2): 489–499.

Working platforms for cranes – review of design approaches and recommendations for a safe design

A.A. Lavasan, V. Poberezhnyi & O. Detert
HUESKER Synthetic GmbH, Gescher, Germany

ABSTRACT: This paper provides a technical insight into the essential aspects to be considered in the proper design of a safe working platform for heavy construction machinery. Considering the complexity of the operational boundary conditions, the uncertainties of the ground characteristics and the variability of the loads applied by the construction machinery, a clear understanding of the possible failure modes and the definition of a criterion for the design of countermeasures seems to be essential in this application. This can be better achieved by considering the significant increase in cost and time delays associated with the failure of the working platforms. This paper discusses various possible failure mechanisms in the working platforms and examines the advantages of using geosynthetic reinforcing elements to avoid the risk of failure.

1 INTRODUCTION

In recent years, a number of heavy construction machines such as drilling rigs, trenchers, pile drivers, mobile cranes and crawler cranes have been involved in serious accidents due to incompetent working platforms. Considering the size and weight of such machines, the overturning of such equipment is often associated with fatal injuries, damage to third parties or work teams, high costs due to recovery of the collapsed equipment, replacement of a new machine as well as production loss or installation delay. Figure 1 shows examples of the working platform failure and the resulting installation machine accident. In addition, these major accidents always have a significant psychological impact on the site personnel. The main cause of most of these accidents is the mismatch between the shear strength provided by the platform and the actual operational loads. This mismatch between available and required shear strength can be the result of improper design of the platform, inadequate knowledge of the geotechnical and geological site conditions and/or insufficient information on the load combinations induced by the equipment in different working conditions. In this context, an adequate design of a competent working platform should properly consider the coupled interactions in the ground and consider all possible failure modes in accordance with an appropriate design method.

Figure 1. Examples of construction machinery overturning.

Considering the significant need to obtain a deep insight into the system behaviour, this paper has investigated and discussed different aspects around the problem, including the coupled interactions such as excess pore pressure evolution and dissipation, relevant failure mechanisms for different loading conditions, and the necessary design criterion. Furthermore, the need to develop advanced and comprehensive numerical tools to predict all these engineering phenomena and not only some of them has been discussed.

2 MEHTODOLOGY AND NUMERICAL MODELLING

In the present study, in order to demonstrate the capability of the finite element modelling approach to evaluate the likely failure mechanism and critical design aspects, a numerical model of a 1 m thick working platform with two layers of geogrid with a short-term nominal tensile strength of 400 kN/m has been developed. In this model, the lower layer of geogrid is placed at the contact between the weak subsoil and the fill material, while the upper layer is placed 0.3 m above the other. The non-cohesive working platform material is assumed to have a friction angle of 38°, dilatation of 8° and modulus of elasticity of 180 MPa, while the undrained soft subgrade with a thickness of 2 m has an undrained shear strength of 20 kPa. This soft subsoil is underlain by a low plasticity silt with an undrained shear strength of 50 kPa. Given the rapid nature of crane loading, an undrained analysis was carried out. The machine track is assumed to be 1.5 m wide with a center-to-center distance of 8 m, carrying a maximum pressure of 200 kPa. The water table is assumed to be 1 m below the ground surface, while the soft subsoil above the water table is assumed to be saturated.

3 TECHINAL ASPECTS IN THE DESIGN OF WORKING PLATFORMS

3.1 *Bearing capacity of the working platform*

One of the essential aspects to be considered in the proper design of a working platform is the correct determination of the available load-bearing capacity according to a realistic failure mode. In this context, it is important to consider all possible failure modes, such as punch, local and global shear failure, and their potential combination in the fill materials of the platform as well as the subsoil as a system.

For example, in the case of a thin platform, there is a high probability that a punch failure will occur within the platform body, which may be associated with a local or global failure of the subsoil. In this context, it should be noted that, depending on the nature of the subsoil material and the water table, the bearing capacity must be determined on the basis of the total or effective shear parameters in the case of a frictional soil or the undrained shear strength parameters for a cohesive soil.

It should be noted that the difference between local and global shear failure in the soil is mainly due to the settlement of the foundation. In other words, local shear failure often corresponds to lower levels of settlement where less shear strength of the soil is mobilised, while the global shear failure mechanism often corresponds to extremely large settlements. In this context, special attention must be paid to the sensitivity of the machine to settlement before considering global shear failure to determine the bearing capacity.

As can be seen in Figure 2, since the mobilisation of the soil shear strength requires the development of strain in the soil, the bearing capacity of the system must essentially be defined in terms of the acceptable settlement in the system.

One of the most commonly observed phenomena with relatively thin (but competent) working platforms is the so-called "trampoline effect". In this situation, the soft, fully saturated subsoil reacts almost undrained to the application of dynamic loads. However, during the operation of the construction machine, the excess pore pressure generated in the

a) punching failure in working platform and local failure mechanism in subsoil (σ=150 kPa, δ=4.9cm)

b) punching failure in working platform and general failure mechanism in subsoil (σ=200 kPa, δ=8.3cm)
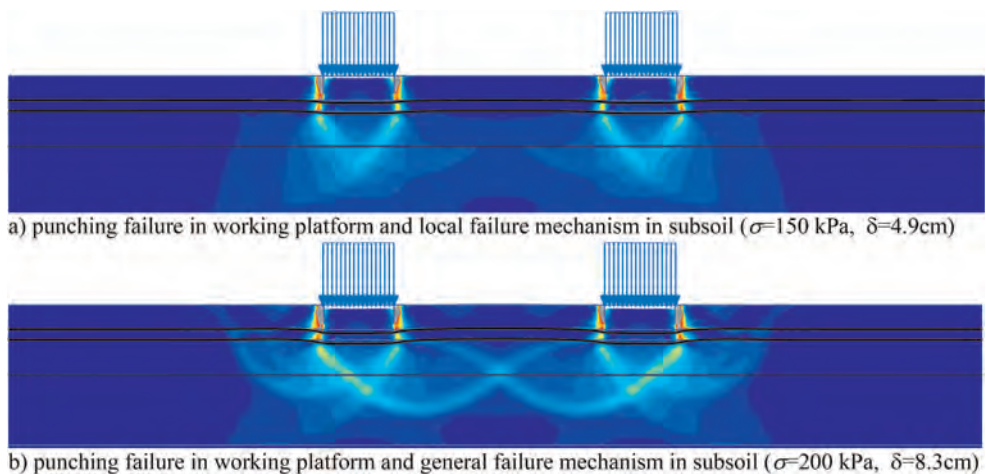
Figure 2.   Evolution of the failure mechanism and bearing capacity through progressive loading (deviatoric shear strain obtained from FE modelling).

subsoil begins to dissipate (see Figure 3). As a result of this consolidation process, further settlement would develop, particularly below the machine. Accordingly, settlement or, more generally, displacement in the working platform and in the ground occurs as an inevitable part of the system and it is often not appropriate to assume that the only role of the working platform is to distribute the load as a purely elastic rigid body over a wider area in depth. Such an idealised conceptualisation of the design method, without consideration of platform failure, requires a justification for no displacement in the ground. Otherwise, the membrane effect and, consequently, the evolution of the tensile force in the geosynthetic layers is an essential event in the kinematics of the system that must be considered in the design phase.
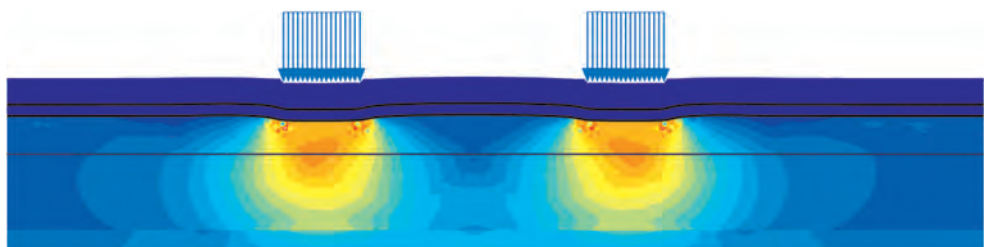
Figure 3.   Excess pore pressure in subsoil obtained from FEM ($\Delta u_{max.}$=120 kPa, σ=200 kPa).

As shown in Figure 3, excess pore pressure is generated in the subsoil with high water table. Depending on the type of soil, either undrained shear strength (s_u) or effective shear parameters (i.e., φ' and c') must be used to determine bearing capacity.

In the working platforms reinforced with the geosynthetic layers, the proper interlocking between the geosynthetic layer and the fill materials allows the development of a load transfer arch within the working platform. Figure 4 shows the load transfer mechanism in the working platform with two layers of geogrid. As can be seen, the kinematics of the membrane developed by settlement in the geosynthetic leads to the formation of an arch to

transfer the machine load to a wider area. This arching effect is a natural consequence of the deformation in the system and has nothing to do with the oversimplification of assuming a linear load transfer in the working platform.

(a) strain of reinforcement   (b) direction of principal stress   (c) arching mechanism
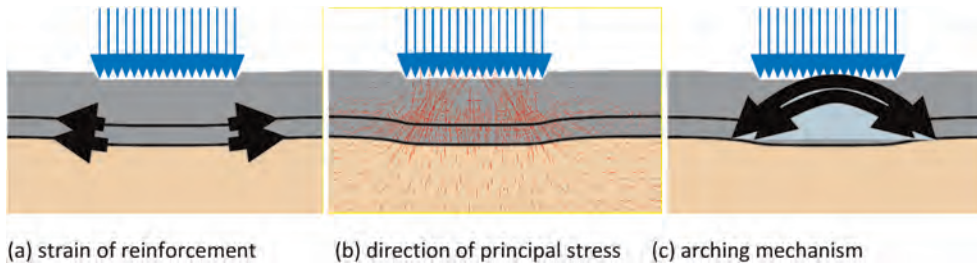
Figure 4.   Load transfer mechanism in the working platform.

Instead of using fill material with adequate shear strength to construct the working platform, the use of material with low shear strength combined with increased thickness of the working platform is often considered as an alternative solution. In such conditions, a special attention should be paid to properly assess the possibility of shear failure within the platform body (see Figure 5). In this context, the bearing capacity of the working platform alone must be determined and compared with the load applied by the machine operation. If it is necessary to use fill material with a lower bearing capacity, more layers of geogrid must be installed at the design vertical spacing to ensure no shear failure in the working platform.

Figure 5.   Failure within a thicker working platform with insufficient shear strength ($h_{platform}$=2 m, φ_p=27°).

3.2 Slope stability analysis

Given the limitations in the availability of high-quality fill material and the relatively high cost of properly constructing a competent working platform, there is often debate about minimising not only the thickness but also the area of the working platform and reducing the distance between the machine stand and the side slopes of the working platform. However, this is an essential technical issue that must be addressed in a proper design. To do this, the dimensions of the working platform must be such that (1) it provides sufficient stability against slope failure and (2) it provides sufficient resistance to pullout failure of the geosynthetic reinforcement by allowing sufficient length for the reinforcement to extend beyond the zone of the load application. To assess slope stability, classical approaches such as Bishop's method can be used to determine the safety of the slope against failure, considering the distance between the slope and the machine loads (see Figure 6).

(a) predefined pore pressure   (b) slope stability analysis by means of effective parameters
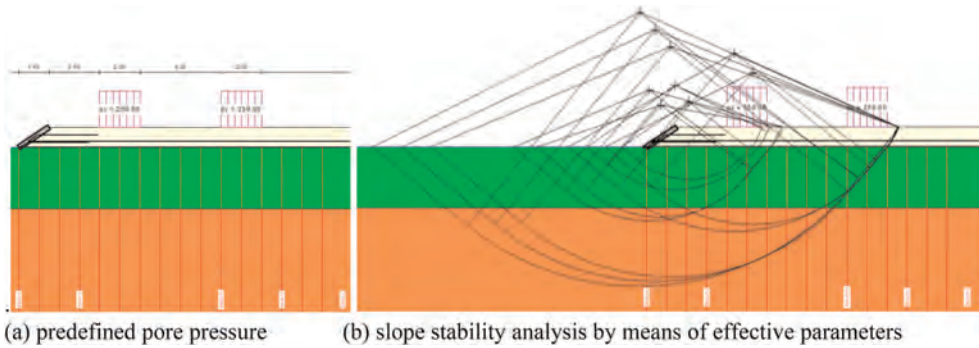
Figure 6.   Slope stability analysis to determine allowable working area.

If the stability analysis is carried out in conjunction with the effective shear strength parameters (e.g., φ' and c'), the possibility of the development of excess pore pressure in the subsoil and its effect on the stability analysis in conjunction with the analytical solutions should be investigated and properly introduced into the model. The results of the slope stability analysis would be used to determine the permissible working area for the construction machine. In the case of stability analysis based on undrained shear strength, it is recommended to consider the increase in undrained shear strength with effective vertical stress as mentioned in the literature (Mesri 1975). Figure 6 shows a standard stability analysis combined with an analytical approach to design the minimum distance between the permissible working area and the edge of the working platform.

3.3   Lateral extrusion failure in soft subsoil

Another mode of the failure that should be investigated in a proper design of working platforms is the extrusion of the weak subsoil at the under heavily loaded working platforms. For this purpose, it is essential to verify whether the weak subsoil has sufficient strength to resist the unbalanced horizontal load that induced by the active earth pressure. In this frame, Scotland *et al.* (2019) discussed different possibilities to increase the shear strength against lateral extrusion or squeezing of the subsoil. The use of a geosynthetics with adequate interlocking properties would help to reduce the horizontal load transfer to the weak soil. Figure 7 shows how the contribution of the geosynthetic layers can reduce the deficit between the resistance to extrusion and the active earth pressure due to high vertical loads.
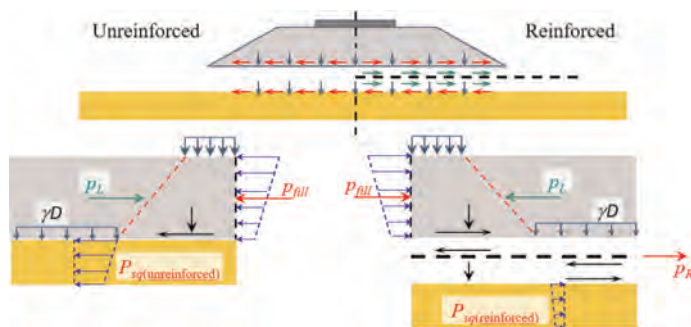
Figure 7.   Reducing the susceptibility of the platform to lateral extrusion through geosynthetic reinforcement.

Giffen 2015 proposed the construction of a shear key trench to disrupt the potential for lateral extrusion where the use of geosynthetic reinforcement at the base of the working platform does not fully mitigate the risk of weak lateral soil spreading. This shear key can be constructed as (a) full depth unreinforced, (b) full depth reinforced or (c) partial depth reinforced. In the case of a full depth shear key, the trench involves replacing the full height of the weak soil to achieve the required lateral resistance and improve the drainage capacity of the weak soil. Considering the challenges of excavating in saturated soft ground, the construction of a reinforced partial depth trench is of great preference. The load transfer of extrusion mechanisms with reinforced shear trenches according to BS 8006 (2016) is shown in Figure 8.

(a) reinforced partial trench   (b) reinforced full trench
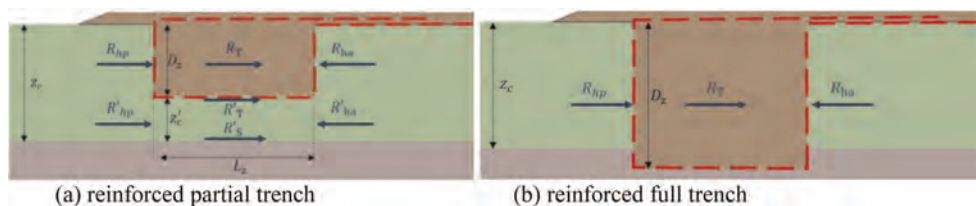
Figure 8.   Load transfer of a working platform with reinforced shear trenches (BS 8006, 2016).

In addition to analytical solutions, such a lateral spreading failure mechanism can also be evaluated using numerical FE modelling, as shown in Figure 9.

(a) deviatoric shear strain   (b) contours of horizontal displacement
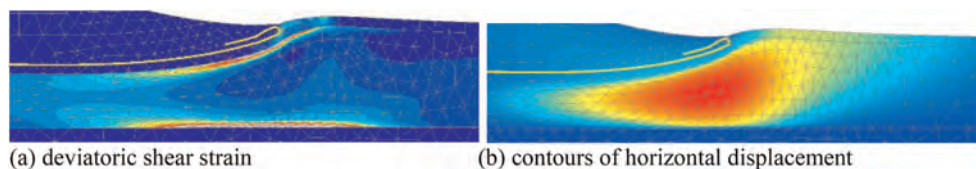
Figure 9.   Application of FE modelling to assess the lateral spreading failure mechanism in the weak soil underneath working platforms.

3.4   Working platform with multiple geosynthetic layers

The monitoring of the tensile forces in the geosynthetic reinforcements as basal reinforcements has shown a non-identical evolution of the tensile force in the reinforcement layers. In this frame, the lower reinforcement layer is overloaded, while the upper reinforcement would be underloaded compared to the lower one. As the mobilisation of the tensile force in the geosynthetics is a direct function of the tensile strength, the different mobilisation of the tensile force between the layers is mainly due to the unequal loading of the layers at different depths. In this context, the required total tensile strength of multiple geosynthetics should not be defined on the assumption of simultaneous mobilisation of tensile force in different layers.

Figure 10 shows an example of non-identical distribution of tensile force between different reinforcement layers in the case of a working platform with two layers of geosynthetics obtained from FE analysis.
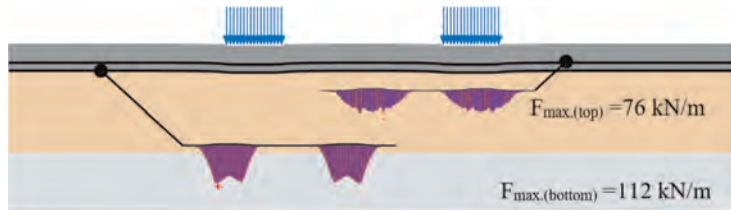
Figure 10.   Variation in tensile force in working platform with double layer of geosynthetic reinforcement.

4   CASE STUDY

A project for the construction of a working platform for the storage and transport of offshore wind turbines and their components in northern Germany, Nordenham. The site was located in an area with poor soil conditions and a high water table typical of the region. Both ultimate and serviceability criteria were applied to the storage facility, as the MEWP had to accommodate not only the transient loads from the cranes transporting the heavy equipment, but also the relatively long term loads from the stored wind turbine towers. To overcome the lack of bearing capacity of the existing soil, the use of geosynthetic reinforcement was considered. Woven geotextiles, which provide reinforcement as well as separation and filtration functions, and geogrids were used as reinforcing elements to strengthen the working platform material. Figure 11 shows some construction details and operation of the geosynthetic reinforced working platfrom.

(a) construction of working platform   (b) operation of working platform
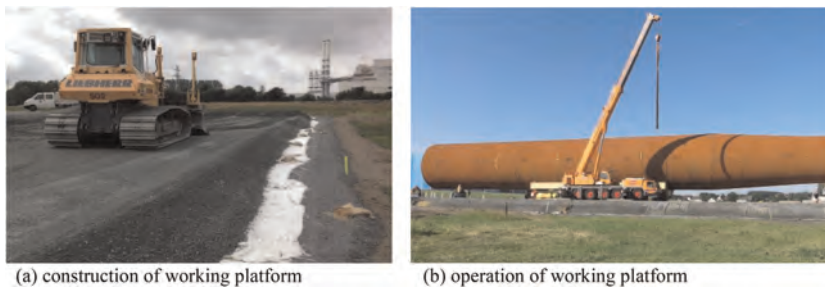
Figure 11.   Geosynthetic reinforced worling platfrom (Nordenham, Germany).

5   CONCLUSION

This study discusses possible modes of failure mechanisms that should be considered in the proper design of a working platform. In addition, the essential technical aspects that should be considered regarding the relevant soil parameters, the type of analysis and the excess pore pressures are reviewed. In addition, it has been shown that finite element modelling can be successfully applied to consider most of these phenomena in the design of working platforms.

REFERENCES

BS 8006-1:2010 (2016) Code of Practice for Strengthened/Reinforced Soils and Other Fills.
Giffen, A.D. (2015). Design and Construction of a Strengthened Embankment for an Intermodal Transfer Facility. *Proc. XVI ECSMGE*, Edinburgh, Scotland. pp. 583–588.
Mesri, G. (1975). New Design Procedure for Stability of Soft Clays. Discussion, *J. of the Geotech. Eng. Div., ASCE*, 101(4), 409–412.
Scotland, I., Poberezhnyi, V. & Tatari, A. (2019) Reinforced Soil Shear Key to Mitigate Extrusion Failure in Soft Soils under Working Platforms, *Proc. XVII ECSMGE-2019*, Reykjavik, Iceland.

Towards the use of sustainable protection structures against flow-like movements

S. Cuomo & A. Di Perna
Geotechnical Engineering Group (GEG), University of Salerno, Italy

M. Martinelli
Deltares, Delft, The Netherlands

L. Frigo
Comune di Chiampo, Vicenza, Italy

ABSTRACT: The sustainability of protection structures has been attracting attention in recent times, especially after the introduction of the 2030 Agenda for Sustainable Development. However, such an issue has been hardly discussed in the case of flow-like landslides. Here the concept of de-formable protection systems made up of granular soil reinforced by geogrids is explored and compared to more traditional concrete rigid walls. The numerical analyses concern the impact of fast-moving landslides on these two types of protection structures to understand their performance in stopping the propagation of the flow. To this aim, an advanced numerical model-ling capable to consider the non-zero initial velocity of the landslide and the large deformation occurring inside both the landslide and the structure is used. Both the landslide soil and the barrier material are simulated as frictional elasto-plastic non-associative media. The role and the time-space evolution of the pore-water pressure inside the landslide material under different impact scenarios are computed. Furthermore, the amount, type, and features of the needed construction materials are compared towards a sound assessment of the sustainability of both solutions.

1 BACKGROUND

Reinforced Concrete (RC) walls are commonly used as protection measures in hilly areas to contain falling boulders and landslide debris, and the sliding displacement of these barriers is a key design issue when space is limited. RC walls are usually made as slab concrete dams, that can be reinforced with counterfort. For such slender constructions, the flow impact dynamics must be carefully evaluated, as the wall must retain the flowing material without failure, tilting or excessive displacements. Hence, their foundations are usually very large. In bedrock, the foundations are usually made by steel tension anchors (ribbed bars), while in loose deposits, the ground must sustain the weight of the concrete construction together with the loads generating from the impact (Barbolini *et al.* 2009). An example is provided in Figure 1, for a diverting dam against snow avalanches at Odda, Norway.

MSE (Mechanically Stabilized Earth) wall is an alternative option. In the context of landslide protection, they are also called Deformable Geosynthetics-Reinforced Barrier (DGRB), as they are composed of granular soil and geosynthetics reinforcement elements, such as high tenacity polyester (PET) geogrids (Cuomo *et al.* 2020). These geostructures have been formerly investigated (Cuomo *et al.* 2019, 2020b; Gioffrè *et al.* 2017; Moretti 2019) to reduce the runout (and the potential damage) of flow-like landslides, while they are typically

used as deformable barriers against snow avalanches or rockfalls (Figure 1). The stability of a DGRB is derived by the interaction of coarse material with the reinforcements, involving friction and tension resistances. The facing is relatively thin, with the primary function of preventing erosion of the structural backfill. The result is a massive structure that is flexible and can withstand various loads combinations. DGRB is an appropriate protection structure when a medium to very high kinetic energy event is expected (Descoeudres 1997). The other advantages are the low maintenance costs and the reduced visual impact since DGBR are greened (Brunet *et al.* 2009).

Figure 1. Examples of reinforced concrete (RC) wall (left) and MSE walls (right) used as protection structures (Barbolini *et al.* 2009).

2 MATERIAL POINT METHOD APPROACH

The Material Point Method (MPM) can be considered a modification of the well-known Finite Element Method (FEM), and it is particularly suited for large deformations (Sulsky *et al.* 1994). The continuum body is schematized by a set of Lagrangian points, called material points (MPs). Large deformations are modelled by a set of MPs moving through a background mesh, which also covers the domain where the material is expected to move. The MPs carry all the physical properties of the continuum such as stress, strain, density, momentum, material parameters, and other state parameters, whereas the background mesh is used to solve the governing equations without storing any permanent information (Figure 2).
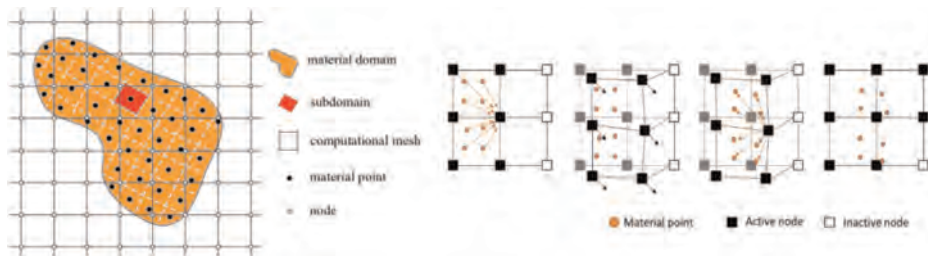
Figure 2. Concept of MPM computation.

The interaction between phases (solid and liquid in a saturated soil) can be tracked through the "two-phase single-point" formulation (Ceccato *et al.* 2018; Jassim *et al.* 2013), where the liquid and the solid acceleration fields are the primary unknowns (Fern *et al.* 2019). On the other hand, the so-called "one-phase single-point" formulation can be

opportunely adopted for dry soils or for saturated soil in the simplified hypothesis that the ratio of pore water pressure divided by total stress is constant inside the deforming body and throughout the whole deformation process.

The contact between different bodies (flow-base, flow-barrier) is handle with a frictional contact algorithm. An improved contact algorithm was used, proposed by Martinelli & Galavi (2022), where the velocity of the liquid phase is corrected to prevent both inflow and outflow. Moreover, the computational scheme proposed by Martinelli & Galavi (2022) is adopted to compute accurate reaction forces along contact surfaces, especially between non-porous structures and soils with high liquid pressures. All the MPM simulations were performed using a version of Anura3D code developed by Deltares.

A saturated porous medium is schematized as a solid phase which represents the solid skeleton, whereas the liquid phase fills the voids among the grains. Each MP represents a volume of the mixture, given by the sum of the solid and liquid phases volumes. The velocity field of solid and liquid phases are both used, but the material points move throughout the mesh with the kinematics of the solid skeleton. The equations solved are the balance of dynamic momentum of solid and liquid phases, the mass balances, and the constitutive relationships of solid and liquid phases. The accelerations of the two phases are the primary unknowns: the solid acceleration, which is calculated from the dynamic momentum balance of the solid phase, and the liquid acceleration, which is obtained by solving the dynamic momentum balance of the liquid phase. The interaction force between solid and liquid phases is governed by Darcy's law and solved at grid nodes considering the Galerkin method (Luo *et al.* 2008). In the two-phase single-point formulation used here, the liquid mass and consequently the mass of the mixture, is not constant in each material point but can vary depending on porosity changes. For this reason, this formulation is generally used in problems with small gradients of porosity, and laminar and stationary flow in slow velocity regime. However, this formulation proves to be suitable for studying flow-structured-interaction (Cuomo *et al.* 2021). The water is assumed linearly compressible via the bulk modulus of the fluid and shear stresses in the liquid phase are neglected.

3 EXAMPLES AND DISCUSSION

3.1 *The case of a RC wall impacted at 5 m/s*

This section investigates the performance of a RC protection wall under the impact of a flow-like landslide, with the geometric configuration reported in Figure 3.
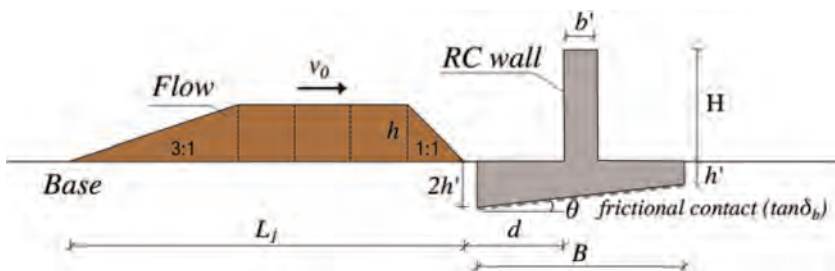
Figure 3. Geometric schematization for the LSI numerical simulations with RC walls.

The landslide material is assumed as a saturated mixture with hydrostatic distribution of initial pore-water pressure and an elasto-plastic behaviour at failure. The contact along the base is assumed to be smooth to avoid reduction in velocity due to friction. Based on

literature values and other related researches (Cuomo *et al.* 2020a), the mechanical properties are selected as follows: density of the mixture (ρ_m) equal to18 kN/m^3, Poisson ratio (ν) of 0.25, Young's modulus (E) equal to 2,000 kPa, nil cohesion (c'), internal friction angle (φ') is 20°, nil dilatancy angle, hydraulic conductivity (k) equal to 10^{-3} m/s, liquid viscosity (μ_L) of 10^{-3} Pa·s, liquid bulk modulus (K_L) of 30 MPa. Moreover, the initial velocity of the landslide (v_0) is set equal to 5 m/s.

The RC wall is schematized as a homogeneous material, with frictional contact at base and elasto-plastic behaviour. The wall is 6 m high with a foundation platform of 11 m. The material properties used in the study were determined by Ardiaca (2009) from design regulations, considering the type of concrete with a characteristic compressive strength of 25 MPa. The base-concrete interface is handled with a frictional contact, imposing a coefficient equal to 0.67 (Ilori *et al.* 2017). The mechanical properties of the RC wall are: barrier density (ρ_b) equal to 25 kN/m^3; effective friction angle (φ') of 35°; cohesion (c') as 510 kPa; Young's modulus (E) = 30,000 MPa; Poisson's ratio (ν) equal to 0.25; tensile strength (f_t) of 750 kPa and frictional coefficient ($\tan\delta_b$) equal to 0.24.

The computational unstructured mesh is made of 17,267 triangular elements with dimensions ranging from 0.10 (in the proximity of the wall and the impact area) to 0.50 m (elsewhere). The flow and the RC wall are modelled through the two-phase and one-phase single-point MPM formulation, respectively. Also here, the build-up of excess pore-pressure during the impact is considered as well as the hydromechanical coupling and the elasto-plastic failure criterion of the flow.

Selected results are shown as the spatial distribution of pore-water pressure within the flow mass and the appearance of deviatoric deformations inside the structure (Figure 4).
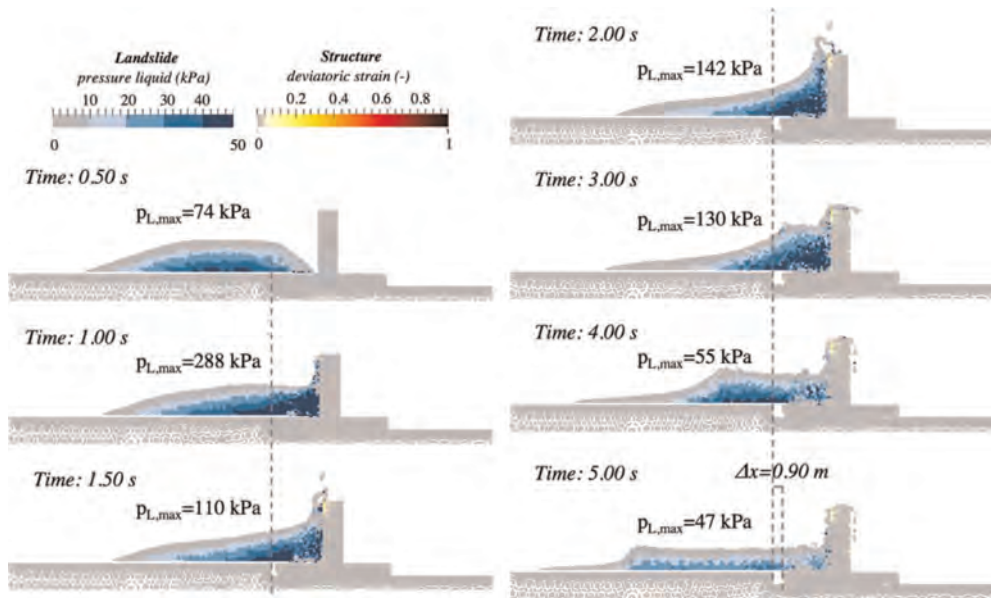
Figure 4.   Pore-water pressure (landslide) and deviatoric strain (RC wall) distribution during impact.

At impact (t = 1.00 s) the pore-water pressure increases up to 288 kPa, then diminishes (t = 1.50 s) due to the beginning of wall mobilization and increases again (t = 2.00 s) due to the rising of the flow along the vertical column. After that, the liquid pressure is mostly decreasing, indicating that the landslide is losing kinetic energy. The internal shear

deformations of the wall are practically nil; thus, the wall is subjected to a rigid translation with a final displacement equal to 0.90 m.

3.2 MSE wall impacted at 5 m/s

The interaction between the landslide and the DGRB is analyzed through the same mechanical and geometric features of the flow used before (Figure 5). A full numerical analysis of the geosynthetics-reinforced soil structure is challenging. Thus, an equivalent approach is here employed to analyse the DGRB. A composite reinforced soil properties is considered and with less input parameters needed. However, localized failures cannot be reproduced, and the soil-reinforcement interaction cannot be studied independently.
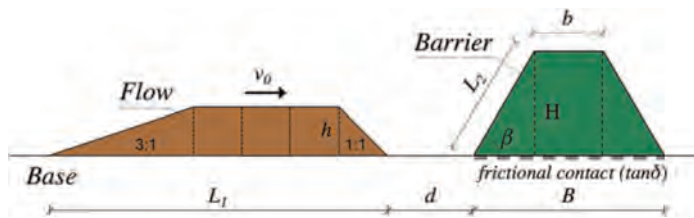
Figure 5. Geometric schematization for the LSI numerical simulations with deformable barrier.

The assessment of the elasto-plastic parameters to set for the equivalent approach is carried out considering the internal friction angle (φ'), Young's modulus (E) and Poisson's ratio (ν) of the equivalent material equal to those typically employed for the backfill soil for practical applications. In addition, a tensile strength equal to the ultimate shear resistance of the geosynthetics reinforcement is imposed for this equivalent material (Maji *et al.* 2016; Nquyen *et al.* 2011). In this study, the value of cohesion was found by making sure that the Factor of Safety (FS) under gravity load obtained for the composite structure is the same than in the equivalent model.

The mechanical properties chosen for the barrier are: the barrier density (ρ_b) equal to 20 kN/m³; effective friction angle (φ') of 38°; cohesion (c') as 58 kPa; Young's modulus (E) equal to 15 MPa; Poisson's ratio (ν) equal to 0.25; tensile strength (f_t) of 100 kPa and frictional coefficient (tanδ_b) equal to 0.29. The failure behaviour is non-associative (zero dilatancy) elasto-plastic criterion. The frictional resistance along the base is set equal to the 80% of the strength properties of the base material (Cuomo *et al.* 2019). The homogeneous barrier with the achieved cohesion equal to 58 kPa represents a composite structure with FS = 3.73 under gravity load. The factor of safety is calculated through LEM analysis, with Morgenstern-Price method.

The flow and barrier are modelled through the single-point MPM formulation, respectively with two-phase and one-phase. The computational unstructured mesh is made of 16,356 triangular elements with dimensions ranging from 0.10 (to refine the impact zone) to 0.50 m. The results of pore-water pressure (landslide) and deviatoric strain (barrier) are reported first for the flow with low initial velocity (Figure 6). In particular, the liquid pressure reaches the maximum value of 153 kPa after some instants from impact (t = 1.00 s). This is probably related to the increase of the impacted area. Simultaneously, the shear deformations along the impacted side are growing. For t > 1.50 s, the kinetic energy of the flow decreases and this is well understandable from the lower values of $p_{L,max}$ and from the unchanging deformations inside the barrier. Moreover, the barrier does not show any horizontal displacement and all the flow is completely block by the barrier.
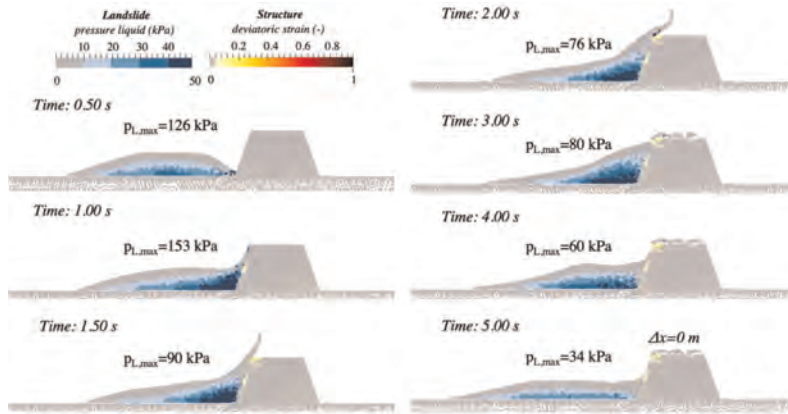
Figure 6.   Pore-water pressure (landslide) and deviatoric strain (barrier) distribution during impact.

3.3   *Comparison*

Based on the numerical results, different options are outlined as capable to perform well against two impressively fast-moving landslides, with 5 to 10 m/s speed and 3 m thick. (Tables 1–2).

Table 1.   Barriers (H = 6 m) designed to well perform against a landslide 3 m thick and 5 m/s fast.

RC wall	B/H	b'/H	θ (°)	V_2 (m³/m)	V_{exc} (m³/m)	V_1/V_0>0.8	$\Delta x < 1.0$ m	Deflection
1	1.83	0.3	6.2	30.6	19.8	Yes (100%)	Yes (0 m)	No
2	1	0.3	11.3	21.6	10.8	Yes (100%)	Yes (0.03 m)	No
3	1.83	0.2	6.2	27	19.8	Yes (100%)	Yes (0 m)	Yes (19.5°)
4	1	0.2	11.3	18	10.8	Yes (100%)	Yes (0.06 m)	Yes (5.7°)
5	1.83	0.3	0	24	19.8	Yes (100%)	Yes (0.90 m)	No
6	1.83	0.2	0	20.4	19.8	Yes (100%)	No (1.90 m)	No

MSE wall	B/H	β (°)	c_{eq} (kPa)	V_2 (m³/m)	V_{exc} (m³/m)	V_1/V_0> 80%	$\Delta x < 1.0$ m	Damage
1	1.83	80	35	59.6	0	Yes (97%)	Yes (0 m)	No
2	1.83	80	58	59.6	0	Yes (97%)	Yes (0 m)	No
3	1.83	70	35	52.9	0	Yes (97%)	Yes (0 m)	No
4	1.83	70	58	52.9	0	Yes (97%)	Yes (0 m)	No
5	1	80	35	29.6	0	Yes (87%)	No (1.43 m)	No
6	1	80	58	29.6	0	Yes (85%)	No (1.49 m)	No
7	1	70	35	22.9	0	Yes (83%)	No (2.75 m)	No
8	1	70	58	22.9	0	Yes (82%)	No (2.80 m)	No

B: base, H: barrier height, b': thickness of RC wall, θ: foundation plane inclination, β: front inclination V_2: barrier volume, V_{exc}: excavation volume V_1: landslide retained volume; V_0: initial landslide volume, Δx: horizontal displacement of the barrier

Performance is assessed based on a multicriteria rationale: retained volume percentage (V_1/V_0), horizontal displacement of the barrier (Δx), and its deflection/damage. For the first landslide case (Table 1), the best solutions are 2 RC walls (ID: 1-2), and 4 MSE walls (ID: 1-4); whereas, for a faster landslide (Table 2) only 1 RC wall (ID: 2) is usable but the same 4 MSE walls (ID: 1-4) options seen before are all still well performing. The construction

Table 2. Barriers (H = 6 m) designed to well perform against a landslide 3 m thick and 10 m/s fast.

RC wall	B/H	b'/H	θ (°)	V_2 (m³/m)	V_{exc} (m³/m)	$V_1/V_0 > 0.8$	$\Delta x < 1.0$ m	Deflection
2	1	0.3	11.3	21.6	10.8	Yes (100%)	No (3.19 m)	Yes (25°)
MSE wall	B/H	β (°)	c_{eq} (kPa)	V_2 (m³/m)	V_{exc} (m³/m)	$V_1/V_0 > 80\%$	$\Delta x < 1.0$ m	Damage
1	1.83	80	35	59.6	0	Yes (99%)	No (2.27 m)	No
2	1.83	80	58	59.6	0	Yes (99%)	No (2.10 m)	No
3	1.83	70	35	52.9	0	Yes (99%)	No (2.15 m)	No
4	1.83	70	58	52.9	0	Yes (99%)	No (2.20 m)	No

B: base, H: barrier height, b': thickness of RC wall, θ: foundation plane inclination, β: front inclination V_2: barrier volume, V_{exc}: excavation volume V_1: landslide retained volume; V_0: initial landslide volume, Δx: horizontal displacement of the barrier

material volume added to the excavation amount are comparable of all the solutions highlighted. This paves the way for further considerations about environmental impacts and sustainability, applied to equally/similarly performant technical solutions in a so complex and fundamental landslide problem.

REFERENCES

Ardiaca, D. H. 2009. Mohr-Coulomb Parameters for Modelling of Concrete Structures. *Plaxis Bulletin*, 25, 12–15.

Barbolini, M., Domaas, U., Faug, T., Gauer, P., Hákonardóttir, K. M., Harbitz, C. B., Rammer, L. 2009. *The design of Avalanche Protection Dams Recent Practical and Theoretical Developments*.

Brunet, G., Giacchetti, G., Bertolo, P., Peila, D. 2009. Protection from High Energy Rockfall Impacts using Terramesh Embankment: Design and Experiences. *Proc. 60th Highway Geol. Symp.*, Buffalo,107–124.

Ceccato, F., Yerro A., & Martinelli M. 2018. Modelling Soil-water Interaction with the Material Point Method. *Evaluation of Single-point and Double-point Formulations*. NUMGE, 25–29 June. Porto.

Cuomo, S., Di Perna, A., Martinelli, M. 2020. MPM Modelling of Buildings Impacted by Landslides. In *Workshop on World Landslide Forum* (pp. 245–266). Springer, Cham.

Cuomo, S., Di Perna, A., Martinelli, M. 2021. MPM Hydro-mechanical Modelling of Flows Impacting Rigid Walls. *Canadian Geotechnical Journal*, 58(11), 1730–1743

Cuomo, S., Moretti, S., & Aversa, S. 2019. Effects of Artificial Barriers on the Propagation of Debris Avalanches. *Landslides*, 16(6), 1077–1087.

Cuomo, S., Moretti, S., Frigo, L., & Aversa, S. 2020a. Deformation Mechanisms of Deformable Geosynthetics-reinforced Barriers (DGRB) Impacted by Debris Avalanches. *Bul. Eng. Geol. Env.*, 79, 659–672.

Descoeudres, F. 1997. Aspects Géomécaniques des Instabilités de Falaises Rocheuses et des Chutes de blocs. *Publications De La Société Suisse De Mécanique Des Sols et Des Roches* 135, 3–11.

Gioffrè D, Mandaglio MC, di Prisco C, Moraci N 2017 Evaluation of Rapid Landslide Impact Forces Against Sheltering Structures. *Rivista Italiana Geotecnica* 3:79–91

Ilori, A.O., Udoh, N.E., & Umenge, J.I. 2017. Determination of Soil Shear Properties on a Soil to Concrete Interface using a Direct Shear Box Apparatus. *International Journal of Geo-engineering*, 8(1), 1–14.

Jassim, I., Stolle, D., & Vermeer, P. 2013. Two-phase Dynamic Analysis by Material Point Method. *International Journal for Numerical and Analytical Methods in Geomechanics*, 37(15), 2502–2522.

Luo, H., Baum, J.D., & Löhner, R. 2008. A Discontinuous Galerkin Method Based on a Taylor Basis for the Compressible Flows on Arbitrary Grids. *Journal of Computational Physics*, 227(20), 8875–8893.

Maji, V.B., Sowmiyaa, V.S., & Robinson, R.G. 2016. A Simple Analysis of Reinforced Soil using Equivalent Approach. *International Journal of Geosynthetics and Ground Engineering*, 2(2), 1–12.

Martinelli, M., & Galavi, V. 2022. An Explicit Coupled MPM Formulation to Simulate Penetration Problems in Soils using Quadrilateral Elements. *Computers and Geotechnics*, 145, 104697.

Nquyen, M.D., Yang, K.H., & Lee, S.H. 2011. *Comparison of the Prediction of Geosynthetic-Reinforced Soil Shear Strength by Difference Approaches*.

Sulsky, D., Zhou, S. J., Schreyer, H.L. 1995. Application of a Particle-in-cell Method to Solid Mechanics. *Computer Physics Communications*, 87(1–2), 236–252.

Requirement guide for a Geosynthetic Clay Liner (GCL) design specification

K.P. von Maubeuge
Naue GmbH & Co. KG, Espelkamp, Germany

ABSTRACT: Geosynthetic clay liners have gained widespread popularity as a substitute for compacted clay liners in many applications. A geosynthetic clay liner (GCL), also known as geosynthetic clay barrier (GBR-C), is a factory-produced clay barrier which consists of two geotextile layers with a layer of sodium bentonite. GCLs are used in multiple barrier applications. The GCL requirements must fit to the anticipated field, mechanical and hydraulic conditions, chemical effects and shear strength parameters. A main consideration is also the lifetime of the project, so that the durability aspect is also of major importance. This paper will present key design criteria that are necessary for a proper design and also cover the calculation of leakage rates and shear stability. Other factors will also be addressed in this paper. Finally, the paper will evaluate current well known specification recommendations, such as GRI-GCL3, and make recommendations for improvements.

1 INTRODUCTION

Geosynthetic clay liners (GCLs) – also known as geosynthetic clay barriers (GBR-C) – are typically needle-punched, reinforced composites that combine two durable geotextile outer layers and a uniform core of high-swelling powder sodium bentonite clay (Figure 1). This construction forms a shear-resistant hydraulic barrier with self-sealing and re-plastification characteristics. When hydrated with fresh water, the bentonite swells and forms a low-permeability gel layer.
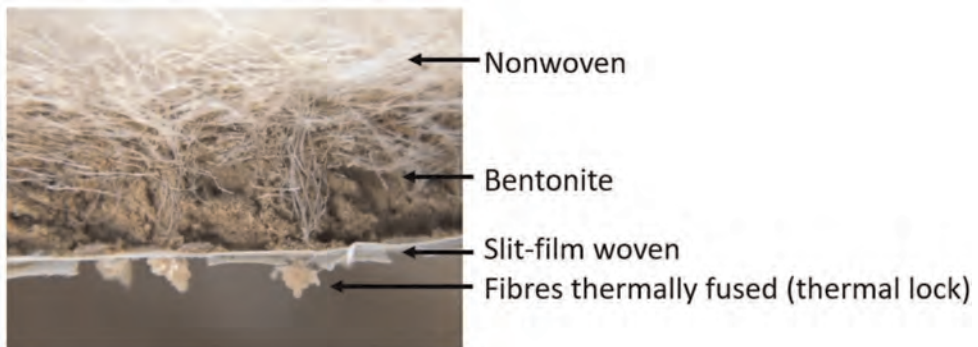
Figure 1. Cross-section of a needle-punched GCL with thermal treatment of the needle-punched fibres.

In general, the GCL hydraulic performance is equal to or better than traditional, thick compacted clay liners. GCLs revolutionised the field in 1987 with the invention of the needle-punched manufacturing technology that greatly increased the internal shear strength of bentonite, which has unreinforced an internal shear angle in hydrated state of approx. 8°. In addition to needle-punching, some GCLs have an additional heat-treating process (Figure 1). This manufacturing technique permanently locks the needle-punched fibres of the nonwoven geotextile layer with the carrier layer of GCL types and improves the hydraulic conductivity performance at low confining stresses. Typical GCL applications include canals, dams, dykes and levees; landfill caps, base liners, and slopes; environmental protection beneath roads and railways; noise barriers; secondary containment; mining applications; waterproofing; tunnels.

2 GENERAL GCL PROPERTIES

To ensure that a GCL works best, it is necessary to understand single specific as well as composite product properties.

2.1 Bentonite type

The bentonite can be either sodium (natural sodium or activated sodium bentonite) or calcium bentonite. Decades ago, manufacturers promoted GCLs with calcium bentonite in an effort to avoid possible issues of ion exchange. Long-term field trials (Henken-Mellies 2010) under 1m of cover soil have demonstrated that the calcium bentonite filled GCL (9,500g/m^2) showed high permeation rates through the GCL after 4 years (52mm per year) and up to 81.3mm after 9 years, whereas GCLs with sodium bentonite powder have only allowed a permeation of far less than 10mm/year under similar conditions (Figure 2).
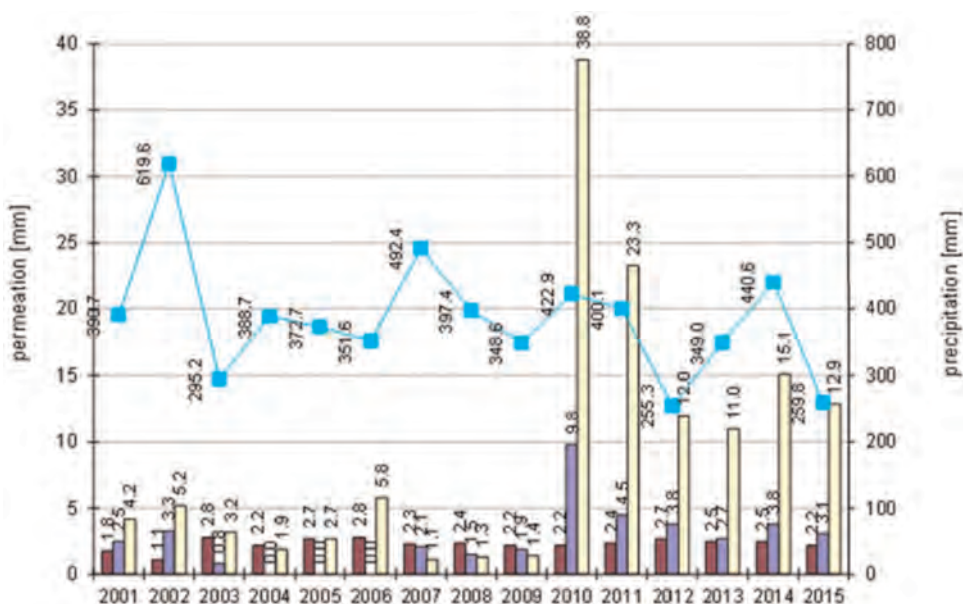
Figure 2. Permeation for sodium bentonite GCLs in three lysimeters #1 (left column, powder bentonite), #2 (middle column, powder bentonite) and #3 (right column, granular bentonite) (von Maubeuge *et al.* 2017).

2.2 Bentonite mass per unit area

The mass per unit area (MPUA) of the sodium bentonite in a geosynthetic clay liner is important to its hydraulic permittivity. Hydraulic permittivity decreases as the MPUA of a GCL's bentonite increases, and that means a better barrier. Standards commonly cite a minimum bentonite MPUA (at 0% moisture content) of 3,700g/m^2 (GRI-GCL3). In Germany (FLL 2022), 4,500g/m^2 is a common minimum MPUA (at 12% moisture content; resp. 4,000g/m^2 at 0% moisture content). GCLs can be produced with a bentonite MPUA up to 13,000g/m^2 if necessary; however, it is recommended to follow worldwide standards starting at minimum 3,700g/m^2 bentonite MPUA.

2.3 Bentonite grade/granularity

Manufacturers choose between two grades of bentonite for use in a GCL's core: powdered or granular.

Hydraulic performance of powder vs granular bentonite has demonstrated that bentonite particle size has a significant effect on the performance (Figure 2) of GCLs. Smaller powder particle sizes have a greater reactive surface area and therefore better swelling and sealing performance compared to larger particles. During hydration water wets powdered bentonite quickly, completely and uniformly due to the larger exposed surface area, and forms an immediate seal. For granular bentonites the water wets the external surface of the particles quickly and leaves the inside dry. Granular bentonites also have bigger voids between the particles (Figure 3) allowing liquids to penetrate the GCL before a seal is formed, leading to high early leakage rates.

Figure 3. Free swell of solely 1g of granular (❶) and powder (❷) bentonite – granular bentonite (❸), granular bentonite GCL (❻)powder bentonite (❹) and powder bentonite GCL (❺) hydrated from the bottom for 24h (powder bentonite closes pores immediately, while granular bentonite still shows several open pores).

2.4 Free swell and fluid loss

Sodium bentonite is commonly distinguished by its ability to swell in water several times its natural volume. The index test method used for quantifying the swelling property of 2g of powdered bentonite used in a GCL is ASTM D5890 – Standard Test Method for Swell Index of Clay Mineral Component of Geosynthetic Clay Liners. The current industry standard is >24 ml.

Another test to determine the water retention capability of bentonite is ASTM D5891 – Standard Test Method for Fluid Loss of Clay Component of Geosynthetic Clay Liners.

Many consider this index test to be a quick qualitative test, suggesting the bentonite's ability to work effectively in a GCL. The current industry standard is <18 ml.

However, it should be noted that both test methods are performed on powder bentonite and are not applicable for bentonite clays amended or treated with polymers. Therefore, if the suitability of the bentonite clay is tested against other liquids than water, these tests might be misleading if GCL contains granular bentonite (see Figure 3 granular (❶) and powder (❷) bentonite).

2.5 *Geotextile components*

The survivability of all GCLs depends upon its protective geotextiles. The higher the mass per unit area, the better the geotextile will perform against possible damage during installation. Nonwoven geotextiles have major advantages compared to slit-film wovens. They typically increase the interface friction value and are more resistant to damage during installation and during the cover soil placement, mainly due to their complex, strong fibre matrix arrangement. The current nonwoven minimum standard is 200g/m^2 (100g/m^2 for slit-film wovens). For critical applications where robustness and interface shear are of importance, GCLs with higher mass per unit area nonwovens than the current industry standard are recommended.

2.6 *Peel strength*

Because geosynthetic clay liners are composite materials, and the layers are designed to work together, the bond strength between GCL components is of particular interest. Correlation between the standard peel test (ASTM D6496-20) – which measures the strength between the carrier and cover geotextile – and the internal shear strength of the GCL are helpful. As peel strength increases, so does shear stress. It should be noted that the benefit of higher peel strength is limited. Findings by Rowe *et al.* (2017) show that a higher peel strength (industry standard is 360 N/m) can increase the water permeability, especially in low-confining stress applications. Even though the strong shear strength transferring fibre reinforcement can hold the GCL composite under hydration together, it is recommended to add a confining stress of minimum 0.3m soil cover over GCLs prior to any hydration.

2.7 *Permeability (hydraulic conductivity) vs index flux*

Permeability is a mathematical constant (k) determined by measuring water flow through a soil or other layer under a prescribed set of conditions. For GCLs, flux test (ASTM D5887 and EN 16416) is used, which contains procedures for calculating permeability as well. Flux is the rate of flow per unit area per unit time through the GCL under 1.5m water head and average confining stress of 27.5 kPa expressed in m^3/m^2/s. Additionally, the manufacturing process and the use of additives such as polymers and glues can affect the index flux and hydraulic permeability.

Permeability is a calculated value, not a directly measured value. Knowing the flux and bentonite thickness, the hydraulic conductivity (routinely called permeability) of the bentonite portion of the GCL can be evaluated by using the calculation methods.

Figure 4 shows index flux test results on a GCL with different bentonite mass per unit area. Index flux is a better indicator of the performance in respect to bentonite mass. As a result, specifying index flux along with bentonite mass per unit area is the better option than specifying the GCL permeability, as this value depends on the true thickness of the bentonite layer, which is a bit more difficult to measure.

The ASTM test method D5887 "Standard Test Method for Measuring of Index Flux Through Saturated GCL Specimens Using a Flexible Wall Permeameter" is a bentonite-related test method but is mainly used on the finished GCL and not the bentonite property.
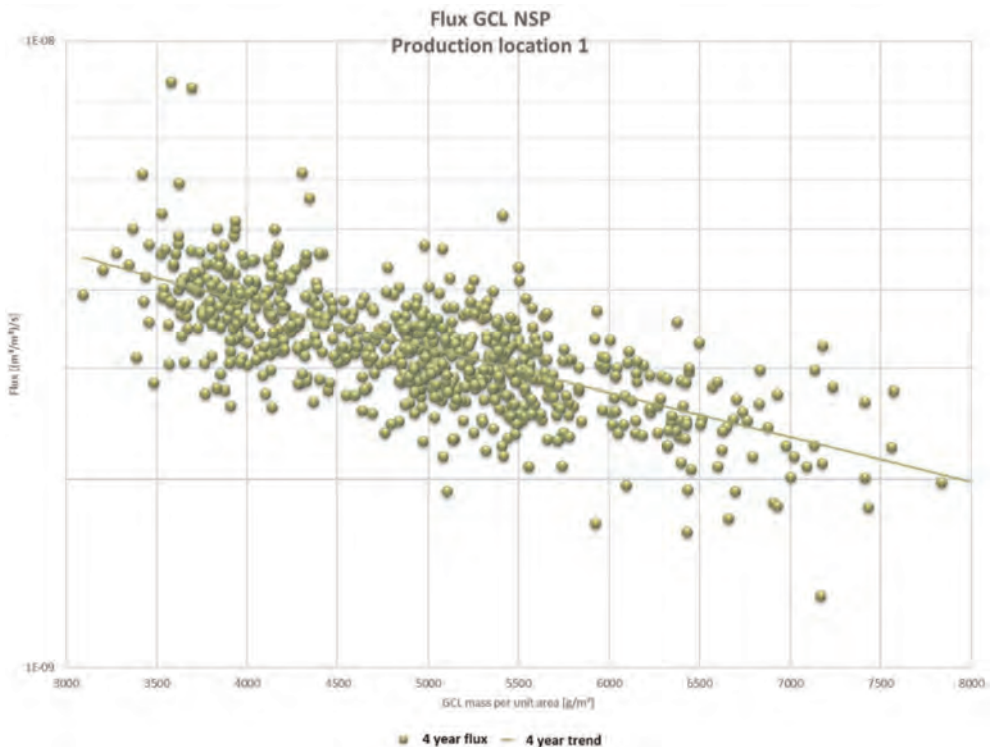
Figure 4. Range of index flux as a function of GCL mass per unit area tested over a four-year production period for needle-punched GCLs (peel 360 N/m and geotextile components 330g/m^2).

2.8 Upper component of GCL facing towards the cover soil placement

GCLs are covered almost immediately (typically with soil or a geomembrane) after their installation to protect against free swelling of the bentonite. But the placement of the cover soil itself can threaten the GCL. Here, the upward facing layer of the GCL is critical to protection. The GCL cover layer's geotextile type, strength and thickness are key concerns for proper selection. A nonwoven upper geotextile, as recommended by GRI-GCL3, with its minimum mass per unit area of at least 200g/m^2, protects against installation damage and additionally against bentonite migration. Higher mass per unit area geotextiles are available for projects that require even more robust protection against cover soil thickness, site use, and available cover soil quality. In cases where interface shear strength is of concern, GCLs with a nonwoven on both sides (one layer of which is always scrim-reinforced) are the way to go. However, the interface friction values need to be evaluated on a project-to-project basis.

2.9 Safe overlaps for GCLs

When water encounters a GCL, also overlaps between GCL panels must provide security to prevent a breach. Some GCLs standardly impregnate during manufacturing both longitudinal overlaps with 50cm of swelling powdered sodium bentonite to ensure a firm, liquid-deterring area. Some GCLs are even impregnated with an additional, uniform layer of sodium bentonite powder across the entire nonwoven surface. This advance is ideally suited for pond and water-proofing applications, since the outer layer of the nonwoven geotextile creates an intimate contact zone in overlap areas. In general, the wider the bentonite-impregnated overlap section is,

the better it performs. Figure 5 reveals a strong contrast between thinner and wider bentonite impregnation at the overlaps. As can be seen, thinner overlaps, such as 1–2cm, present significantly higher rates of permeability – not what one wants in a barrier application. More bentonite in the overlaps means a safer design and a GCL that will continue to meet performance expectations over the long term.

2.10   Why not to use a double nonwoven without scrim reinforcement

GCLs can be supplied in many different production forms concerning the geotextile com-
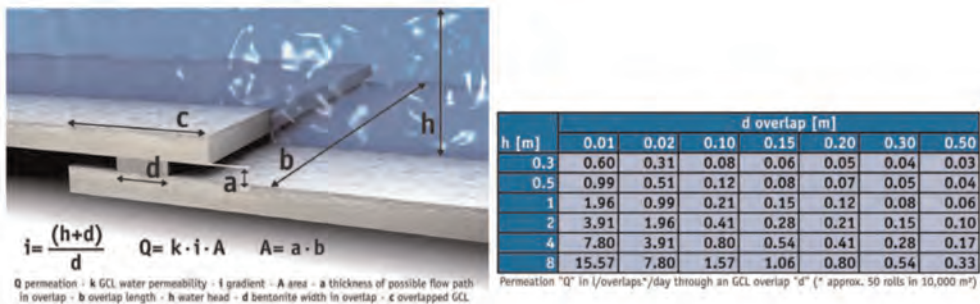
Figure 5.   Calculated permeation only through the overlap areas of a project with 10,000m^2 installed GCL.

ponents. During manufacturing, shrinkage occurred with GCL that only used nonwovens, even in field under nearly no confining stress (GRI White Paper #5), which lead to the note in the GRI-GCL3 specification: "For both cap and carrier fabrics for nonwoven reinforced GCLs; one, or the other, must contain a scrim component of mass $\geq$ 100 g/m^2 for dimensional stability. This only applies to GM/GCL composites which are exposed to the atmosphere for several months or longer so as to mitigate panel separation." It is the authors opinion that all GCLs should have a scrim-nonwoven geotextile as a bottom fabric as such GCL types show little to no shrinkage and do not elongate during installation, should the GCL have to be pulled over the surface, which likely could also influence the bentonite distribution.

2.11   Recommended GCL properties

It is recommended to set minimum requirements for a GCL in order to ensure long-term performance. The following listed specification values are therefore recommended as they follow various international requirements, such as the GRI-GCL3 (2016) recommendations.

- GCL consisting of two bentonite-encapsulating geosynthetics: a polypropylene (PP) carrier woven ($\geq$ 100g/m^2) and cover nonwoven ($\geq$ 200g/m^2);
- Layer of sodium bentonite powder encapsulated between two geosynthetic layers; bentonite mass per unit area $\geq$ 3,700g/m^2 at max. 15% water and a free swell value $\geq$ 24 ml following ASTM D5890 and fluid loss (ASTM D5891) $\leq$ 18 ml;
- Uniform shear stress transferring needle-punching through the two bentonite-encapsulating geosynthetics creating a shear strength transmitting GCL with a peel strength (ASTM D6496) of $\geq$ 360 N/m;
- GCL tensile strength (ISO 10319 or ASTM D6768) longitudinal/transverse $\geq$ 10 kN/m;
- Self-sealing, 30cm wide length overlaps with pre-manufactured bentonite impregnation;
- Index flux (GCL) $\leq 5 \times 10^{-9}$ m^3/m^2/s (ASTM D5887 or EN 16416).

3 SUMMARY

Engineered barrier systems protect sensitive environmental, industrial and civil applications. Safety is of the utmost importance. The decisions that a designer makes about the GCL itself during material selection heavily influences the ultimate performance and durability of the GCL system. These include decisions (but are not limited to) on the type of bentonite, its mass per unit area, the overlap design, geotextile protection, peel strength and confining stress prior to hydration. GCLs should be manufactured in accordance with these but should not be limited to these and may be, design depending, exceeded to maximise safety and long-term barrier performance.

REFERENCES

ASTM D5887-22 (2022). Standard Test Method for Measurement of Index Flux Through Saturated Geosynthetic Clay Liner Specimens Using a Flexible Wall Permeameter, *ASTM International*, USA.

ASTM D5890-19 (2019). Standard Test Method for Swell Index of Clay Mineral Component of Geosynthetic Clay Liners, *ASTM International*, West Conshohocken, PA, United States.

ASTM D5891-19 (2019). Standard Test Method for Fluid Loss of Clay Component of Geosynthetic Clay Liners, *ASTM International*, West Conshohocken, PA, United States.

ASTM D6496-20 (2020). Standard Test Method for Determining Average Bonding Peel Strength Between Top and Bottom Layers of Needle-Punched Geosynthetic Clay Liners, *ASTM International*, USA.

ASTM D6768-20 (2020). Standard Test Method for Tensile Strength of Geosynthetic Clay Liners, *ASTM International*, West Conshohocken, PA, United States.

Egloffstein, T. A. 2000. *Der Einfluss des Ionenaustausches auf die Dichtwirkung von Bentonitmatten in Oberflächenabdichtungen von Deponien*. ICP-Eigenverlag Bauen und Umwelt, Band 3, Karlsruhe.

ISO 10319:2015. *Geosynthetics – Wide-width tensile test. International Organization for Standardization (ISO)*, Geneva, Switzerland

EN 16416:2023. *Geosynthetic Clay Barriers – Determination of Water Flux Index – Flexible Wall Permeameter Method at Constant Head.*

FLL 2022 (Draft). *Gewässerabdichtungsrichtlinien für Planung, Bau, Instandhaltung von Gewässerabdichtungen*, Forschungsgesellschaft Landschaftsentwicklung Landschaftsbau e. V. (FLL), Bonn, Germany.

GRI-GCL3. 2016. *Standard Specification for Test Methods, Required Properties, and Testing Frequencies of Geosynthetic Clay Liners (GCLs)*. Folsom, PA, USA: Geosynthetic Institute.

Henken-Mellies, W.U. 2010. GCL in a Landfill Final Cover: 10-year Record of a Lysimeter Field Test. *3rd International Symposium on Geosynthetic Clay Liners,* Würzburg, Germany.

Rowe, R.K., Brachman, R.W.I., Hosney, M.S., Take, W.A., Arnepalli, D.N., 2017. Insight into Hydraulic Conductivity Testing of GCLs Exhumed After 5 and 7 Years in a Cover. *Canadian Geotechnical Journal* 54 (8), 1118–1138. https://doi.org/10.1139/cgj-2016-0473.

Von Maubeuge, K. P., Müller-Kirchenbauer, A., Schlötzer, C. 2017. Comparing the Testing of Geosynthetic Clay Liners (GCLs) with Bentonite Powder and Granular Cores. *Proceedings of the Geotechnical Frontiers 2017* GSP 276.doi:10.1061/9780784480434.012.

A brief summary of worldwide regulations and recommendations requiring geosynthetic barriers

K.P. von Maubeuge
Naue GmbH & Co. KG, Espelkamp, Germany

A. Shahkolahi
Global Synthetics, Telford, Australia

J. Shamrock
Tonkin + Taylor, Auckland, New Zealand

ABSTRACT: Over the past 40 years, the advantages of utilising geosynthetic barriers versus traditional earthen barrier materials have been well documented: greater project economy, extended service lives, enhanced environmental protection, greater site safety, etc. Achievements such as conserving water resources and enabling beneficial site reuse have even given geosynthetic engineering a level of social importance. As such, the use of geosynthetic barriers has increasingly been required by government regulators around the world. This is true in modern waste management landfill design. However, there are still regions and applications in which the use of these barrier technologies should be more widely adopted. This paper highlights an overview of applications where geosynthetic barriers are used, and where regulation or recommendations are available, and it describes other emerging applications where geosynthetic barriers are starting to be used.

1 INTRODUCTION

Geosynthetic barriers are an established product group in the geoenvironmental industry. They include factory-made polymeric geomembranes that can be made of polyethylene (PE), bituminous membranes (bitumen attached to geotextile) and geosynthetic clay liners (with clay/bentonite core as the barrier element between two geotextiles). These geosynthetic materials are accepted as barrier solutions in many applications, but due to the material properties not all geosynthetic barriers are suitable for all applications. Applications for geosynthetic barriers include:

- Containment application, non-landfill
- Chemical containment, non-landfill
- Construction waterproofing
- Landfill base lining
- Landfill capping and rehabilitation
- Secondary containment
- Transport infrastructure applications
- Tunnel waterproofing
- Water retaining structure, e. g. balancing ponds, stormwater retention ponds, dams, dykes and canals (usually empty)
- Water retaining structure, e. g. reservoirs, canals (usually full)

The advantages of geosynthetics, especially if compared to traditional earthen construction methods, e.g. compacted clay liners, include:

- Reliability: high-quality control standards, lifetime verification and multiple proven project applications
- Ecology: significantly lower CO_2 emissions, supporting worldwide climate goals, lower energy consumption, reduction of transport amount or kilometres travelled
- Sustainability: limits the use of all resources, e. g. natural clay resources, energy demand, noise impact
- Cost-effectiveness: reduced building cost compared to traditional methods, even greater when natural materials have to be quarried off site and brought in, longer service life, less maintenance
- Ease of installation: easy to handle and install on project sites, saving time in the construction process and reduced excavation required, e. g. less fill required, less land disturbed, no need to compact and test
- Resilience: improved structural behaviour with the ability to respond, absorb, adapt or recover from extreme load cases caused by natural disasters or extreme weather caused by climate change
- Safety: increased serviceability and protection when used in levees, groundwater, infrastructure, and environmental protection for waste management and chemical containment
- Quality: more homogeneous than soil and clear, established quality controls from production through installation

The design of barrier systems in these various applications is a challenge for any group of professionals, as the document produced must add supportive text and areas for consideration to a process which is in its very nature one of professional judgement. Geosynthetic barriers are a complex area for design, and given the large variety of barrier types as well as material differences within each type means that sooner or later a decision is made comparing a great number of variables. Good design utilises the best possible combination of materials, site preparation, installation and checking in line with the intended end use, expected longevity and "local" constraints which may be functions of geography and climate as well as political, labour availability and access constraints. As such, no design guide or standard can hope to solve the complex combinations of each individual site circumstances and as such it is aimed at professionals making such decisions and helping to ensure that each of the many variable factors have been considered both individually and collectively. Often national regulations and recommendations give guidance on a good start point that should then be adjusted to suite the specific site being designed for.

2 BRIEF INTRODUCTION OF POLYMERIC BARRIER SYSTEMS

Geosynthetic barrier materials is the main product group for barrier products and they are divided into polymeric, bituminous and clay geosynthetic barriers. Geomembranes (GM) smooth or textured, also known as polymeric geosynthetic barriers, are essentially impermeable and are used as fluid barriers in geotechnical engineering. Textured surfaces provide an enhancement of frictional characteristics which allows designs on steeper slopes or where shear stress occurs (e.g. with geosynthetic/soil or geosynthetic/geosynthetic interface). In some countries the definition of GM starts at a thickness of 0.5 mm, but not all countries are in agreement on that classification. In France and Germany, for example, the polymeric barrier is considered a GM if the thickness is equal or greater than 1 mm.

Barriers with a clay sealing component are called geosynthetic clay liners (GCLs), bentonite mats or clay geosynthetic barriers. GCLs, a very successful barrier group, are made of a thin layer of typically sodium bentonite between two layers of geosynthetics; generally, these layers are nonwoven and woven geotextiles and all components are needle-punched together. GCLs can be used as a stand-alone barrier or in conjunction with a geomembrane to form a composite barrier.

3 LANDFILL REGULATIONS AND RECOMMENDATIONS

Synthetic barrier designs began in the 1950s, often with canal systems and water conveyance, and have expanded steadily since with new manufacturing and welding technology, better polymeric formulations and additive packages, and stronger engineering education. Geosynthetic barriers have been used in lieu of traditional concrete, asphalt, and compacted clay-only barriers which have not been as effective at preventing contaminated fluid migration into subsurface soils and groundwater.

A major spur to the utilisation of geosynthetics occurred in the early 1980s when the United States and Germany, on a federal level, began to regulate and require the use of geosynthetic barriers to meet minimum containment criteria for landfills (Maubeuge *et al.* 2021). The legacy of this regulatory move is that today waste management seems to have the highest environmental protection standards in many countries where modern landfill designs and geosynthetic technologies are used. However, too many countries are still missing guidelines for the use of geosynthetic barriers in landfills and other applications.

When reviewing a selection of the worldwide regulations, including the European directive, Germany, Great Britain, Australia, New Zealand, China, Japan, Indonesia, South Africa and the United States of America, they mostly reflect a very similar collection of natural and geosynthetic elements to construct a composite liner system. This consists of, working from the top down:

- Leachate collection layer, usually stone aggregate, with perforated leachate collection pipework, with a separation/filtration nonwoven geotextile to protect the stone from clogging with fines from the waste
- Protection layer, usually a nonwoven geotextile
- GM, typically ranging from 1.5 mm to up to 2.5 mm thickness in Germany
- Compacted clay liner (CCL), typically 500 mm to 1,000 mm thick, or GCL, or both
- Prepared, low permeability, in-situ soil

Due to a limit on page length the selected excerpts of the various regulations could not be repeated in this paper, but a follow-up journal paper will be produced that includes these.

Some regions include a double composite base liner in their regulations that allows for the performance of the primary composite barrier to be monitored.

4 COAL ASH APPLICATIONS

Coal is an important source of power throughout the world. Approximately 7 million metric tons of coal are mined and burned each year around the globe. The result of the combustion of these huge volumes of coal is the generation of heat, electricity and the creation of coal ash – roughly 20 % of the weight of the coal consumed. This ash is often quite useful and is perhaps the largest (in volume) recycling success story in the world. Useful applications for coal ash include concrete, fibreboard and a host of other construction and infrastructure applications. However, approximately half of the coal ash generated in the world is not recycled and must therefore be disposed of. In some parts of the world, the coal ash is simply "dumped", more developed nations may dispose of coal ash in large de-watering ponds, store the coal ash using very large levees and use the materials as structural fill to modify the shape of the earth; creating flat areas for airports for example. The proper disposal of coal ash is important to the health of the planet and to human health. Leachate (water that has passed through coal ash) can have high pH, high concentrations of heavy metals, such as lead, arsenic and others, and serves as a global contaminant to groundwater and potable water resources.

Unfortunately, over 50 documented cases of groundwater contamination at or nearby coal ash storage facilities contributed to the US EPA issuance of new regulations for the storage of coal ash which require the use of geosynthetic materials and proper geotechnical

engineering of coal ash disposal sites. The US EPA regulations for coal ash storage propose the most efficient and effective barrier system as a composite liner system using a primary GM, typically 1.5 mm thick, in combination with a CCL, approx. 500 mm thick, or a GCL, although other variations exist. This is a direct result of these systems being compliant with the United States Environmental Protection Agency (US EPA) Resource Conservation and Recovery Act (RCRA) Subtitle "D" regulations which have demonstrated excellent historical performance as groundwater contamination barriers.

5 ENVIRONMENTAL PROTECTION IN INFRASTRUCTURE APPLICATIONS

Solid, liquid and gaseous emissions from motor vehicles contribute to risks to soils, stretches of water (rivers, lakes, ponds, etc.) and groundwater. The protection of these waters is anchored in the German Water Resources Act.

If it is not possible to avoid a road route through a water protection area, despite all the considerations in the line identification process, a number of measures are necessary in order to exclude a risk to the water resources as far as possible. They are described in the German Guidelines for Structural Measures on Roads in Water Protection Areas, RiStWag (FGSV 2016). The guideline describes, among other things, geosynthetic sealing systems for environmental and groundwater protection.

If a road layout through a water protection zone cannot be avoided, all necessary design and constructional measures must be considered in the planning phase. In general, passive protective devices (crash barriers, concrete walls, car run-off barriers) are necessary to prevent vehicles from running off the roadway. Rainwater must be collected via side drains, gutters or pipes and moved out of the protection zone. The artificial barrier, typically a GCL, should be lined at least 1 m under the paved road.

6 ENCAPSULATION OF CONTAMINATED SOILS

In June 2021, the German Substitute Construction Materials Regulation (Ersatzbaustoffverordnung, also called "Mantelverordnung") (Bundesgesetzblatt 2021) was passed and will come into force in August 2023. With this law, politicians want to promote the re-use of mineral construction waste, among other things. Since this waste is often used in road construction and earthworks, the protection of soil and groundwater will be strengthened on a national level.

The reuse of excavated soil, construction waste products, and recycled construction materials in earthworks, contributes to the conservation of resources and the reduction of the depletion of landfill airspace. The use of geosynthetics in this application can be highly efficient, not least due to the comparatively simple installation conditions of the industrially manufactured and quality-assured roll material.

Road noise and view-blocking barriers along roads, motorways and railway lines can be built with substitute construction materials. These waste materials must meet certain environmental-chemical requirements and must be covered with a surface sealing for groundwater protection.

In Germany, as in other European countries (e.g. in the Netherlands – this construction is directed by the "Bouwstoffen Besluit", CUR 1999), protecting the environment by using substitute construction materials is carried out using three barriers, similar to modern landfill practices:

- Hydraulic permeability of the subsoil, depth to groundwater table, groundwater-protecting cover layers
- Limitation of pollutant load through assigned threshold values
- Technical protection measures using water impermeable cover and sealing layers
- Suitable sealing materials for these purposes include GCL and GM

7 WATER CONVEYANCE IN CANALS

Government agencies such as the United States Bureau of Reclamation (BuRec) indicate that seepage from unlined irrigation canals and waterways may be substantial and costly; and that geosynthetic barriers offer economically flexible and highly effective performance enhancement for canals (Swihart & Haynes 2002). They are effective alternatives to concrete, asphalt or compacted clay soils.

No matter the construction, the consistent revelation is that geosynthetic liners and lining systems have outperformed traditional lining methods in longevity and project economics in canal systems.

In Germany, all important technical information on waterway lining systems has been collated in the new guideline "Recommendations for the use of lining systems on beds and banks of waterways". The guideline describes geosynthetic lining systems which additionally need to be covered with rock armor as specified in the MAR code of practice.

GCLs in levee construction must meet special safety requirements as their functionality may depend on the flood protection of entire regions, and in the event of failure the flood defenses can have a significant impact of human lives and civil infrastructure. In levee construction, the use of GCLs as an alternative to a mineral sealing layer, constructed from compacted, cohesive soils, has produced positive experiences.

The Dutch Limburg Water Board, in cooperation with the Flood Protection Program, has prepared a Design, Assessment and Maintenance Guideline (OBOR) for the application in Dutch practice of bentonite mats, also called GCLs, and used the existing experience with the BRAD16 guideline from Germany.

8 STORMWATER RETENTION PONDS

The purpose of the German code of practice DWA-M 176 (DWA 2013) is to provide the designer of stormwater basins with rules that will allow stormwater treatment and retention structures to be designed, or existing structures to be upgraded, according to structural, equipment, operational and economic considerations. It also makes clear statements on the use of geosynthetic barriers (GCL and GM).

9 CONCLUSION

There is every reason to believe that geosynthetic barriers will continue to be adopted into regulations around the world. This has much to do with the innovation and quality control measures in manufacturing and installation in the field. It also has much to do with geosynthetics being used in situations to perform better and/or more economically than traditional geotechnical designs. With a large record of data in support of cost and performance measures, and with secondary benefits such as decreased project carbon footprints, the field's growth is assured.

These geosynthetics offer a wide range of physical, mechanical and chemical resistance properties. Geomembranes can be compounded for greater resistance to ultraviolet light exposure, ozone and micro-organisms in the soil while GCLs can be produced with various geotextiles for enhanced frictional properties. Different combinations of these properties exist in various GM as well as GCL materials to address a wide spectrum of geotechnical applications and designs. Several methods are used to join or seam large panels of GMs and GCLs, in both factory-controlled and field environments. Each material has highly developed quality control techniques and unique characteristics that govern their manufacture and installation.

As advanced products and manufacturing and installation techniques evolve, project economy and performance will continue to improve, both with and in advance of regulatory recognition.

REFERENCES

BRAD16. Brandenburgische Richtlinie für die Anwendung Geosynthetischer Tondichtungsbahnen im Deichbau, Ausgabe 2016, Landesamt für Umwelt, Abteilung Wasserwirtschaft 2- Flussgebietsmanagement, Potsdam, Dez. 2016.

Bundesgesetzblatt Jahrgang 2021 Teil I Nr. 43. 2021. Verordnung zur Einführung einer Ersatzbaustoffverordnung, zur Neufassung der Bundes-Bodenschutz- und Altlastenverordnung und zur Änderung der Deponieverordnung und der Gewerbeabfallverordnung. Bonn, Germany, 16.7.2021 (in German).

CUR 1999 – Civieltechnisch Centrum Uitvoering Research en Regelgeving 1999. Aan het Werk met het, Bouwstoffen Besluit" Een Handreiking Voor Het Werken Met Het Boustoffenbesluit. Ministerie van Volkshuisvesting Ruimtelijke Ordening en Miliuebeheer.

DepV 2009. Deponieverordnung dated 27. April 2009 (BGBl. I S. 900), as last amended by Article 2 of the Ordinance of 27 September 2017 (BGBl. I p. 3465).

DWA. Merkblatt DWA-M 176 – Hinweise zur konstruktiven Gestaltung und Ausrüstung von Bauwerken der zentralen Regenwasserbehandlung und -rückhaltung, ISBN 978-3-942964-99-9, Deutsche Vereinigung für Wasserwirtschaft, Abwasser und Abfall e. V. (DWA), Hennef, Germany. 2013.

EC 1999. Council Directive 1999/31/EC of 26 April 1999 on the Landfill of Waste, https://eur-lex.europa.eu/legal-content/EN/TXT/?uri=CELEX:31999L0031.

Environment Protection Authority Victoria 2015. EPA Victoria's Best Practice Environmental Management publication: Siting, design, operation and rehabilitation of landfills (Landfill BPEM).

EPA 2021. https://www.epa.gov/rcra/resource-conservation-and-recovery-act-rcra-regulations#nonhaz.

FGSV 514. Forschungsgesellschaft für Straßen- und Verkehrswesen (Hrsg): Richtlinien für bautechnische Maßnahmen an Straßen in Wasserschutzgebieten (RiStWag), Ausgabe 2016, Köln.

FGSV 559. Merkblatt über Bauweisen für Technische Sicherungsmaßnahmen beim Einsatz von Böden und Baustoffen mit umweltrelevanten Inhaltsstoffen im Erdbau (M TS E), Ausgabe 2017, Köln.

Japanese Ministry of Health and Welfare 2001. Guidelines for the Performance of MSW Landfills. S9005-01, Japanese Ministry of Health and Welfare, Tokyo, Japan.

Koerner, R.M. 2012. *Designing with Geosynthetics*, 6th Edition, Volume 1. Xlibris Corporation, Bloomington, IN, USA.

LFE2 2014. *Cylinder Testing Geomembranes and their Protective Materials*. Environment Agency of the UK Government.

LFE3 2014. Using Geosynthetic Clay Liners in Landfill Engineering (version 3). Environment Agency of the UK Government.

LFE5 2014. Using Geomembranes in Landfill Engineering. Environment Agency of the UK Government.

Maubeuge, von K., Niehues, C. & Post, A. 2021. Geosynthetic Sealing Systems in Landfills – A Global Perspective, Kwazulu-Natal Landfill & Waste Treatment Interest Group. Landfill and Waste Treatment Virtual Seminar and Exhibition, 3–5 November 2021.

Maubeuge, von K. 2022. Guide for Barriers when Using Soils and Construction Materials with Environmentally Sensitive Contents; *Journal of Environmental Science and Engineering* B 11 (2022) 125–138, doi:10.17265/2162-5263/2022.04.004.

National Environmental Management 2008. Waste Act, Act 59, South Africa.

OBOR – GCL (BENTONIETMAT) Ontwerp-, Beoordelings- en Onderhoudsrichtlijn voor GCL (bento-nietmat) in Voorlanden en op Taluds van Primaire en Regionale Waterkeringen (Groene Versie), Draft Version, 25. Nov. 2021.

Rowe, R. K., Islam, M. Z., Brachman, R. W. I., Arnepalli, D. N. & Ragab Ewais, A. 2010. Antioxidant Depletion from a High-Density Polyethylene Geomembrane under Simulated Landfill Conditions. *Journal of Geotechnical and Geoenvironmental Engineering*, ASCE, July 2010.

SEPA 2002. Framework for Risk Assessment for Landfill Sites – The Geological Barrier, Mineral Layer and the Leachate Sealing and Drainage System. The Scottish Environmental Protection Agency, 2002.

Stark, T.D. & Hynes, J.M. 2009. Geomembranes for Canal Lining. *Proceedings of Geosynthetics 2009*, Industrial Fabrics Association International, Roseville, Minn., USA.

Swihart, J.J. & Haynes, J.A. 2002. Deschutes – Canal-Lining Demonstration Project, Year 10 Final Report, R-02-03, US Bureau of Reclamation, November.

Migrating to probabilistic internal stability analysis and design of reinforced soil walls

R.J. Bathurst

GeoEngineering Centre at Queen's-RMC, Kingston, Canada

ABSTRACT: Reliability-based design for internal stability limit states for geosynthetic mechanically stabilized earth (MSE) walls provides a more nuanced appreciation of the margin of safety for these systems compared to conventional factor of safety, partial factor, and load and resistance factor design (LRFD) approaches. The paper introduces the basics of probabilistic analysis and design for internal stability limit states for MSE walls using the example of geogrid reinforced soil walls. The general approach uses a closed-form solution for reliability index which is easily implemented in a spreadsheet. The paper demonstrates how bias statistics for tensile load and pullout model accuracy can be gathered from load measurements recorded from instrumented walls and found in laboratory pullout box test databases. The paper concludes with example calculations of the probabilistic margin of safety for tensile strength and pullout limit states using the AASHTO Simplified Method and the recent AASHTO Stiffness Method in the USA.

1 INTRODUCTION

In North America there are two reinforcement tensile load calculation methods used for internal stability limit states analysis and design of geosynthetic mechanically stabilized earth (MSE) walls. The first approach is the Simplified Method (AASHTO 2017) which uses an empirically adjusted classical active wedge approach to predict tensile loads in the reinforcement layers under operational conditions. The second approach is the recent Stiffness Method (AASHTO 2020) which retains elements of the Simplified Method but includes the creep-adjusted tensile stiffness of the reinforcement as a key parameter that influences the magnitude of the maximum tensile load in each reinforcement layer. Both methods can be used within a deterministic design framework (i.e., factor of safety approach), and within a reliability theory-based load and resistance factor design (LRFD) approach. Both methods lead to safe designs, but the margins of safety against failure of a limit state equation in probabilistic terms is unknown. The movement towards performance-based design in geotechnical engineering measured by probabilistic margins of safety is now underway (e.g., ISO 2015). However, acceptance of such an approach for the internal stability limits states for geosynthetic MSE walls remains in its infancy. The paper introduces the basics of probabilistic analysis and design for tensile strength and pullout internal stability limit states for MSE walls using the example of a geogrid reinforced soil wall.

2 PRELIMINARIES

Figure 1 illustrates the internal stability limits for a geosynthetic MSE wall and introduces important nomenclature. Each limit state identified in the figure can be expressed by a

DOI: 10.1201/9781003386889-248

performance function of the general form:

$$g = \frac{R_m}{Q_m} - 1 = \frac{\lambda_R R_n}{\lambda_Q Q_n} - 1 \qquad (1)$$
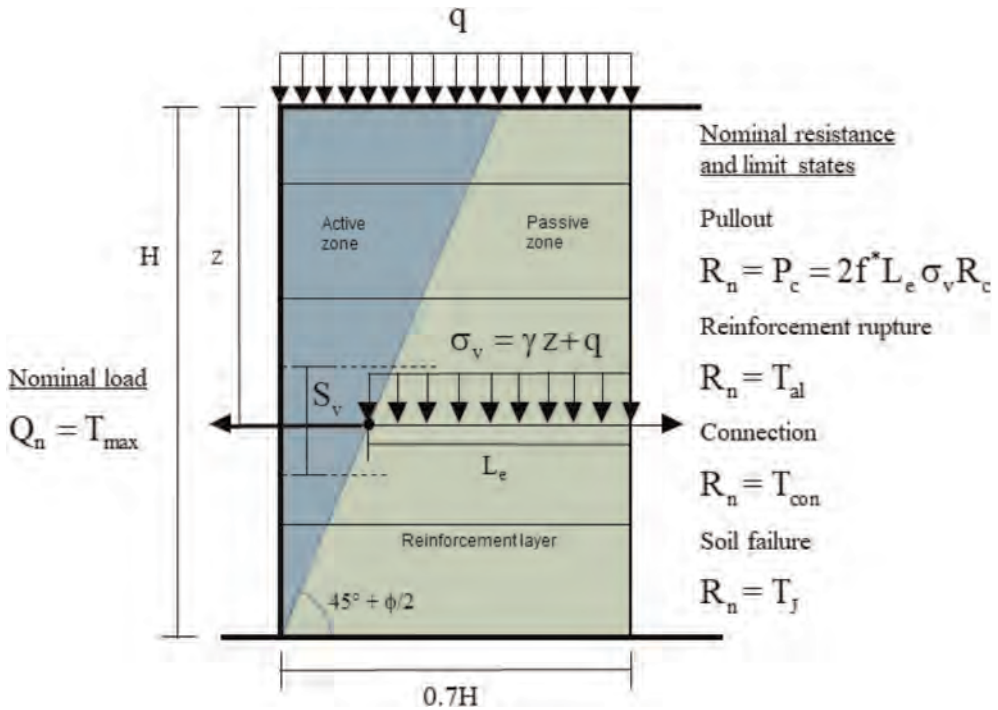
Figure 1. Geometry and limit states for a geosynthetic MSE wall. Q_n = nominal reinforcement tensile load (e.g., kN/m), R_n = nominal resistance (e.g., kN/m), T_{max} = maximum tensile load, S_v = reinforcement spacing, σ_v = vertical stress, γ = soil unit weight, z = depth of layer below crest of wall, q = surcharge pressure, P_c = pullout capacity (e.g., kN/m), f* = dimensionless interface shear coefficient, L_e = reinforcement layer length in passive zone, R_c = coverage ratio due to discontinuous reinforcement roll placement within a layer, ϕ = soil peak friction angle, T_{al} = allowable or long-term tensile load, T_{con} = connection capacity between reinforcement and wall facing, and T_j = tensile load corresponding to soil failure.

Here, R_m and Q_m are measured (observed) resistance and load terms, respectively, and R_n and Q_n are corresponding nominal resistance and load terms. The latter are the computed values using analytical models (equations) such as the equation for ultimate pullout capacity (P_c) shown in Figure 1. In the example here, all nominal values have units of force/length (e.g., kN/m).

If the objective is to quantify the "true" margin of safety for a limit state function, then nominal values must be transformed to expected measured (observed) values using model bias values (λ_R and λ_Q). Bias values can be understood to be quantities that are influenced by: a) intrinsic accuracy of the prediction of nominal values using the underlying analytical models for the resistance and load terms; b) random variation in input parameter values, spatial variation in input values, and quality of data, and; c) consistency in interpretation of data gathered from multiple sources (the typical case) for the purpose of quantification of model accuracy (Allen *et al.* 2005; Bathurst & Javankhoshdel 2017). For perfect models, λ_R and λ_Q are equal to 1. Excluding cases where a nominal value is prescribed, this is an unusual situation for geotechnical soil-structure interaction problems.

It should be noted that model bias is independent of project-specific conditions. The influence of project-specific uncertainty is captured by uncertainty in the choice of nominal values that appear in analytical load and resistance models.

The ratio $F_n = R_n/Q_n$ is called the nominal factor of safety and is used in deterministic analyses and as the starting point (best estimate) in probabilistic analyses.

In the developments to follow, the nominal and bias values are treated as random variables following lognormal distributions. The margin of safety for each limit state is expressed as the probability that the limit state will not be satisfied (probability of failure = P_f):

$$P_f = P(g < 0) \tag{2}$$

3 MODEL BIAS

Load model bias data have been collected for geosynthetic reinforced walls with granular backfills using the Simplified and Stiffness Methods to compute the nominal load value $Q_n = T_{max}$. The procedure involved collecting measured tensile loads in instrumented field walls and dividing each value using the equation for T_{max} for each method and the same measured layer conditions; hence, $\lambda_Q = T_{max}(measured)/T_{max}(model) = Q_m/Q_n$. From the population of all λ_Q values the mean ($\mu_{\lambda Q}$) and coefficient of variation ($COV_{\lambda Q}$) can be computed. Examples of these data presented as cumulative distribution function (CDF) plots are provided in Figure 2a. The data trend as a straight line over most of the data range when the bias values are plotted using a logarithmic axis. This demonstrates that the data are reasonably represented by a lognormal distribution as mentioned previously. Figure 2b shows a CDF plot of pullout bias data $\lambda_R = P_c(measured)/P_c(model) = R_m/R_n$. The nominal (model) values were computed using the pullout equation shown in Figure 1 with the input properties for each pullout box test from which a matching measured pullout capacity (P_c) was recorded. These data also present as a linear line on a semi-logarithmic plot for practical purposes.
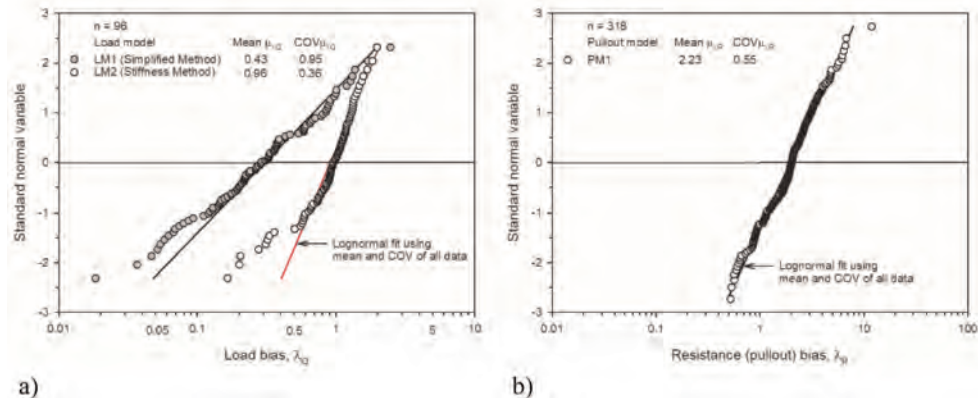
Figure 2. Example model bias CDF plots for a) T_{max} load models, and b) pullout model for P_c.

Bias statistics for both load models, tensile strength and pullout capacity are summarized in Table 1. Bias dependency captures the correlation between bias values and predicted nominal values. A model is judged to improve as the mean bias approaches 1, the COV of

bias values becomes small, and bias dependencies can be ignored at a level of significance of 5%. The Simplified Method is judged to be a relatively poor model based on these criteria compared to the Stiffness Method. Pullout model (PM1) is also a poor model but it remains current in North American MSE wall design specifications. The mean bias value for the tensile strength limit state is slightly greater than 1 because the unfactored nominal value for design is typically taken as the minimum average roll value (MARV) which is less than the average of rupture strength values from multiple specimen tensile tests carried out on the same material (Allen & Bathurst 2019). The spread in bias values (COV) is very small as may be expected from an engineered material. Similar data for PET geostrip MSE walls can be found in the paper by Bathurst *et al.* (2020).

Table 1. Summary of bias statistics and bias dependency values for load and resistance models for geogrid reinforced soil walls constructed with granular soil.

Model	Number of data points, n	Mean of bias	COV of bias	Bias depen-dency ρ	Original data source
Simplified Method (LM1)	96	0.43	0.95	−0.41	Allen & Bathurst (2015)
Stiffness Method (LM2)	96	1.00	0.28	0	Allen & Bathurst (2015)
Pullout (PM1)	318	2.23	0.55	−0.46	Huang & Bathurst (2009)
Tensile strength (TM)	N/A	1.10	0.10	0	Bathurst & Miyata (2015) Miyata & Bathurst (2015) Miyata *et al.* (2014) Bathurst *et al.* (2011, 2012)

4 CALCULATION OF RELIABILITY INDEX

Using the bias statistics in Table 1, the magnitude of the actual reliability index (β) can be computed for tensile strength and pullout limit states using the following equation:

$$\beta = A + B \times Ln(F_n) \tag{3}$$

where, A and B are collections of bias statistics described above and uncertainty in choice of nominal values Q_n and R_n at time of design (COV_{Q_n} and COV_{R_n}) (e.g., see Bathurst & Allen 2021 for the full expression). The equation shows that β varies log-linearly with the magnitude of the nominal factor of safety $F_n = R_n/Q_n$. This equation provides a quantitative link between deterministic allowable stress design (ASD) (factor of safety approach) and modern concepts of reliability-based design. The relationship between P_f and β is $\beta = \Phi^{-1}(1-P_f)$, where Φ^{-1} is the inverse of the standard normal cumulative distribution function (CDF) (NORMSINV in Excel).

5 RESULTS

Results of calculations using Equation 3 are shown in Figures 3a and 3b for the tensile strength limit state using the Simplified Method (LM1) and Stiffness Method (LM2), respectively, for the load side (Q_n), and the long-term tensile strength (TM) for the resistance

side (R_n). Figures 3c and 3d show calculation outcomes with the same load side equations but with the AASHTO pullout equation for the resistance side. The calculations assume uncertainty in the estimate of nominal load values and nominal pullout values taken as $COV_{Qn} = COV_{Rn} = 0$, 0.1, 0.2 and 0.3. The non-zero values correspond to the concept of high, typical and low levels of understanding at time of design that are used in Canadian foundation engineering practice (Fenton *et al.* 2016). A value of $COV_{Rn} = 0$ for the tensile strength nominal value since all uncertainty in its value is captured by the COV of the bias. Curves with values of $COV_{Qn} = COV_{Rn} = 0$ can be understood to correspond to current practice in the US where the concept of level of understanding is not used in any formal way. Calculation outcomes using the Stiffness Method (load model LM2) show that for the same F_n value, β values decrease in the order of COV = 0, 0.1, 0.2 and 0.3. This may be expected since margins of safety in probabilistic terms can be expected to decrease as uncertainty in the magnitude of nominal load value increases. The opposite trend is observed when the poorer Simplified Method (load model LM1) is used. This counter-intuitive outcome is a result of the large negative bias dependency for this model (Table 1). This is an unfortunate outcome of using a poor load model for reliability-based design.

a) LM1-TM (AASHTO 2017) b) LM2-TM (AASHTO 2020)

c) LM1-PM1 (AASHTO 2017) d) LM2-PM1(AASHTO 2020)
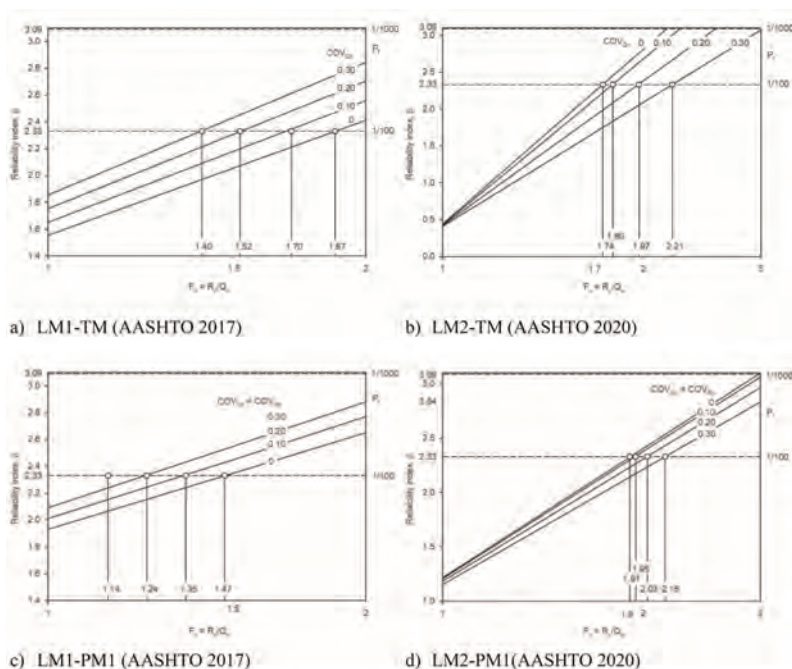
Figure 3. Reliability index versus ratio of nominal resistance to nominal load. a) LM1-TM (AASHTO 2017) b) LM2-TM (AASHTO 2020) c) LM1-PM1 (AASHTO 2017) d) LM2-PM1 (AASHTO 2020).

Also shown in Figure 3 are β values of 2.33 and 3.09 corresponding to probabilities of failure of the limit state of 1/100 and 1/1000. For internal stability limit states for MSE walls, the recommended target probability of failure is 1/100 (Allen *et al.* 2005). This may appear to be very high but the multiple reinforcement layers in MSE walls make these systems highly strength redundant; i.e., if one layer fails, the other layers can compensate. For reliability-based design the curves in Figure 3 can be used directly. The internal design of the MSE wall can be adjusted by changing nominal load (Q_n) and nominal resistance (R_n) values so that $F_n = R_n/Q_n$ gives a value $\beta \geq 2.33$.

6 CONCLUSIONS

This paper demonstrates (albeit briefly) reliability-based analysis and design concepts applied to internal stability limit states for geosynthetic MSE walls constructed with geogrid layers. The concepts are general for simple linear limit state functions and have been used to carry out similar analyses for polymeric geostrips, steel strips and steel grid MSE walls. A necessary precursor to the general approach are bias data for load and resistance terms in the performance function described by Equation 1. Fortunately, these data are available as described in the cited work by the writer and collaborators. The general approach has the advantage that it provides a quantitative link between nominal factor of safety used in conventional ASD practice (i.e., factor of safety approach) and margins of safety expressed probabilistically using reliability index which is used in structural civil engineering LRFD calibration practice. Furthermore, the general approach includes provision for judgement by including the concept of project-specific "level of understanding" when selecting the magnitude of nominal input values for load and resistance models at the time of design.

REFERENCES

Allen, T.M. & Bathurst, R.J. 2015. An improved simplified method for prediction of loads in reinforced soil walls. *ASCE Journal of Geotechnical and Geoenvironmental Engineering*, 141(11): 04015049.

Allen, T.M. & Bathurst, R.J. 2019. Geosynthetic reinforcement stiffness characterization for MSE wall design. *Geosynthetics International*, 26(6): 592–610.

Allen, T.M., Nowak, A.S. & Bathurst, R.J. 2005. *Calibration to Determine Load and Resistance Factors for Geotechnical and Structural Design*, Transportation Research Board Circular E-C079, Washington, DC, USA.

AASHTO. 2017. *LRFD Bridge Design Specifications*, 8th Ed., American Association of State Highway and Transportation Officials (AASHTO), Washington, DC, USA.

AASHTO. 2020. *LRFD Bridge Design Specifications*, 9th Ed., American Association of State Highway and Transportation Officials (AASHTO) Washington, DC, USA.

Bathurst, R.J. & Allen, T.M. 2021. Reliability assessment of internal stability limit states for two as-built geosynthetic MSE walls. *ISSMGE International Journal of Geoengineering Case Histories*, 6(4): 67–84.

Bathurst, R.J., Huang, B. & Allen, T.M. 2011. Analysis of installation damage tests for LRFD calibration of reinforced soil structures. *Geotextiles and Geomembranes*, 29(3): 323–334.

Bathurst, R.J., Huang, B. & Allen, T.M. 2012. Interpretation of laboratory creep testing for reliability-based analysis and load and resistance factor design (LRFD) calibration. *Geosynthetics International*, 19(1): 39–53.

Bathurst, R.J. & Javankhoshdel, S. 2017. Influence of model type, bias and input parameter variability on reliability analysis for simple limit states in soil-structure interaction problems. *Georisk*, 11(1): 42–54

Bathurst, R.J. & Miyata, Y. 2015. Reliability-based analysis of combined installation damage and creep for the tensile rupture limit state of geogrid reinforcement in Japan. *Soils and Foundations*, 55(2): 437–446.

Bathurst, R.J., Miyata, Y. & Allen, T.M. 2020. Deterministic and probabilistic assessment of margins of safety for internal stability of as-built PET strap reinforced soil walls. *Geotextiles and Geomembranes*, 48(6): 780–792.

Fenton, G.A., Naghibi, F., Dundas, D., Bathurst, R.J. & Griffiths, D.V. 2016. Reliability-based geotechnical design in the 2014 Canadian Highway Bridge Design Code. *Canadian Geotechnical Journal*, 53(2): 236–251.

Huang, B. & Bathurst, R.J. 2009. Evaluation of soil-geogrid pullout models using a statistical approach. *ASTM Geotechnical Testing Journal*, 32(6): 489–504.

ISO 2015. *General principles on reliability of structures*. ISO2394:2015, International Organization for Standardization. Geneva, Switzerland; 2015.

Miyata, Y. & Bathurst, R.J. 2015. Reliability analysis of geogrid installation damage test data in Japan. *Soils and Foundations*, 55(2): 393–403.

Miyata, Y., Bathurst, R.J. & Allen, T.M. 2014. Reliability analysis of geogrid creep data in Japan. *Soils and Foundations*, 54(4): 608–620.

Case histories

Steel meshes and GRS-IBS in Oosterweel Verbinding, Linkeroever

F. Masola
Maccaferri Central Europe s.r.o., Senica, Slovakia

D. Tubertini
GreenGo S.r.l., Bologna, Italy

S. De Maesschalck
Texion Geokunststoffen NV, Antwerp, Belgium

ABSTRACT: The Oosterweel Link project is a new 15 km-long motorway connection developed by Lantis for completing the Antwerp ring road R1 (Belgium). The total estimated cost of the project is approximately €4.5bn. The Antwerp ring road is a key part of the Trans-European Transport (TEN-T) Core Network. Maccaferri collaborated with the design and building of the Mechanically Stabilized Earth (MSE) walls with its main product family „Terramesh". This is a well-known system used in Europe and in the rest of the world to support or enable the construction of infrastructures in tight urban corridors, forming retaining walls, road embankments, wing walls and bridge abutments known as Geosynthetic Reinforced Soil-Integrated Bridge Systems (GRS-IBS). „Terramesh" double twist steel wire mesh reinforcements have been used in combination with ParaLink[®] and Paragrid[®] geogrids representing an evolution and a significant advantage for both cost-effectiveness and performance.

1 INTRODUCTION

1.1 *Overview of Oosterweel Link project*

The Oosterweel Link project is a new 15km-long motorway connection developed by Lantis for completing the Antwerp ring road R1 (Belgium). It is a major project in Belgium and its design started in the 1990's to find a solution to the congestion problems in and around Antwerp.

This new project will link the E17 (Ghent) and the E34 / N49 (Bruges) on the left bank of the Scheldt river with the E19 / A12 motorways towards the Netherlands and the E34 / E313 motorways towards Germany and Luxembourg. Five sub-projects are included, like „Linkeroever", „Scheldt tunnel", „Oosterweel junction", „Canal tunnels" and „R1-Noord".

In February 2018 the first construction works finally started. The new highway infrastructure on the left bank and Zwijndrecht will be completed in 2024, while the Scheldt tunnel will open to traffic in 2027. The entire Oosterweel connection is scheduled to become operational in 2030.

1.2 *Framework of the project*

The Antwerp ring road is a key part of the Trans-European Transport (TEN-T) Core Network. The Oosterweel link will be used for heavy truck traffic and will shift important southern side traffic to the northern side while reducing congestion, resolving bottlenecks

and mobility problems on the ring road (Figure 1). Oosterweel Link was launched by the Flemish Government as part of its Masterplan 2020. It also forms part of the government's broader Route Plan 2030 mobility plan.

Figure 1.   Oosterweel Link project overview.

2   THE CONTEXT

2.1   Project background

The environmental impact assessment report for the project was approved by the Flemish Government in 2016. Lantis invested approximately €180m for site preparation for the construction of the Oosterweel connection. A major part of it will be built underground.

The left bank interchanges will be redesigned and reconstructed, and a new road will be constructed next to E17 and E34 in Zwijndrecht, which will bring the local traffic to the motorway.

The new junctions will provide a connection to Burcht, Zwijndrecht, and Linkeroever. A 9 km-long bike lane will also be developed to link Zwijndrecht and Linkeroever to the new Scheldt tunnel (a 1.8 km-long twin tube immersed tunnel with three lanes on each side, as well as a separate lane for cyclists).

The total estimated cost of the project is approximate €4.5bn, of which €3.6bn will be borrowed from the Flemish Government and the European Investment Bank.

Lantis awarded a €570m contract to the Temporary Trade Association COTU consortium consisting of Besix, Bam Contractors, Deme, and Jan de Nul for the construction of the Scheldt tunnel in June 2020. The consortium will also be responsible for the design and implementation of the traffic and tunnel installations.

2.2   Linkeroever subproject

The Linkeroever subproject was contracted to the Rinkoniên consortium comprising of Artes Roegiers, Artes Depret, CIT Blaton, MOBILIS, and Stadsbader.

Arcadis was subcontracted by the Rinkoniên consortium to perform engineering studies for the subproject.

Together with local partner Texion, Maccaferri was selected as the main supplier for the construction of the reinforced soil structures (BGS, Belgian Geosynthetics Society 2022).

2.3   Other subprojects

ENGIE Fabricom team is responsible for traffic and tunnel installations in order to offer a safe and smooth driving experience during construction.

ZJA Zwarts & Jansma Architects is responsible for designing the link over the right bank of the Schelde river, while Tunnel Engineering Consultants, a joint venture of Royal Haskoning, DHV and Witteveen & Bos, performed engineering works for the left bank works.

Asite's Common Data Environment (CDE) solution was chosen by Lantis to efficiently manage, maintain and share information on the development of the project.

3 DESIGN AND INSTALLATION

3.1 *Maccaferri's collaboration*

Maccaferri collaborated with the design and building of the Mechanically Stabilized Earth (MSE) walls with its main product family „Terramesh". This is a well-known system used in Europe and in the rest of the world to support or enable the construction of infrastructures in tight urban corridors, forming retaining walls, road embankments, wing walls and bridge abutments known as Geosynthetic Reinforced Soil-Integrated Bridge Systems (GRS-IBS). The peculiarity of the case study is to present the design and building of GRS-IBS, which are innovative solutions for the construction of bridge abutments, made environmentally friendly thanks to the combined use of polymeric geosynthetics and „Terramesh" double twist steel wire mesh reinforcements.

„Terramesh"double-twist steel wire mesh reinforcements have been used in combination with polymeric geosynthetics representing an evolution and a significant advantage for both cost-effectiveness and performance. Geogrid-reinforced MSE walls are recommended in case of non-conventional retained soils such as poor subsoil conditions, warm climates, or chemically aggressive environments since they are resistant to deterioration. In fact, the design life of the walls is 120 years.

The design of the Mechanically Stabilized Earth (MSE) wall structures and their general behavior depend on the interaction between the soil reinforcing elements and the surrounding soil and this interaction is based on the properties of the materials used and the construction methods (Masola *et al.* 2018). Soil-reinforcement interaction is extremely important because it is the mechanism by which forces are transferred between the reinforcements and the surrounding soil (Lugli at al. 2019).

3.2 *Provided installation*

The project includes 23.000 facing sqm of „Terramesh Green®", 16.000 facing sqm of „Terramesh Mineral® and System®, 275.000 sqm of ParaGrid® and ParaLink® geogrids, and 5.000 facing sqm of gabion cladding. During 2020–2021 and 2022, 37.000 sqm of MSE walls have been already installed by the partner company „Carlucci Costruzioni s.r.l." with a maximum height of 13m for the structures erected so far (Figure 2). The Terramesh products can be either with a stone mineral facing or a green facing, according to the architectural plan: in Oosterweel for architectural reasons most of the structures present a stone facia. The

Figure 2.   Installation phase of ParaLink geogrids® in combination with Terramesh Systems®.

main products used are Maccaferri Terramesh System®, Mineral Terramesh®, Cladding Gabions, ParaLink®, and Paragrid® geogrids.

3.3 Benefits of the solution

Maccaferri Terramesh proved to be a flexible and more suitable system for the construction details and a reliable system thanks to the continuity and integrity of the double-twist steel wire mesh with the facing (Figure 3).

Figure 3. Reinforced soil structure made with Terramesh Green® and Terramesh Mineral® units underneath a cycle bridge overpass.

The polymer-coated double-twist wire mesh can provide greater durability in highly aggressive environments. The durability of the polymer-coated double-twist steel wire mesh embedded in soil ensures a design life of 120 years.

For some civil structures, the main designer opted to build some walls with Maccaferri environmentally friendly solutions if compared to the usual reinforced concrete retaining walls selected in the original design. Reinforced soils guarantee fewer CO_2 emissions thanks to the use of in situ soil with respect to concrete. Indeed, concrete has a finer material selection of aggregates and cement which has a more harmful effect on the environment with respect to reinforced soils. Moreover, the velocity of execution of reinforced soils is higher than concrete structures since there is no concrete curing time. These features result also in a cheaper solution thanks to time and labor savings (installation ratio: between 100 and 150 sqm/team/day without earthworks).

3.4 Design support

Maccaferri's Corporate Technical Department has supported and is still supporting the main designers step by step from the first preliminary Global and Internal stability checks (Figure 4) with Limit Equilibrium Method (LEM) analyses carried out with MacStars
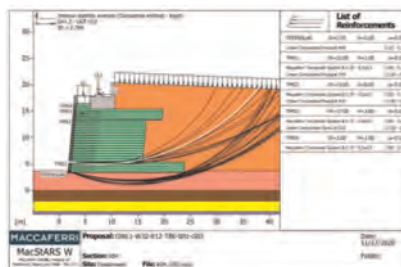
Figure 4. Stability design checks carried out with MacStars® for G03 direct bridge abutment.

Software to Finite Element Method (FEM) deformation analyses due to the strict restrictions on displacements. Maccaferri provided the designers with all material properties for the correct modeling of double-twist steel wire mesh products and geogrid reinforcements (Tubertini *et al.* 2021). MacStars is an internal Software and it stands for Maccaferri Stability Analysis of Reinforced Soils and Walls. The MSE walls have been designed according to Eurocodes and NBN EN 1997-1 ANB (National Annex for Belgium).

3.5 BIM collaboration

Furthermore, due to the big number of interfering elements, such as bridge supports, concrete walls, and sheet-pile walls in each direction, Building Information Modelling (BIM) was required to define the layout and the number of facing units and soil reinforcement needed in each orthogonal direction. Maccaferri BIM Objects (www.maccaferri.com/bim/) have been also used to help the contractor in the design of particular challenging geometries (Figure 5) and for the executive drawings used for the placing of the materials used for the construction of the civil structures.

Figure 5.   Object G02B, Maccaferri's BIM design.

Figure 6.   Direct bridge abutment G03 after the launch of the bridge.

3.6 Challenges

In the year 2022 the main direct bridge abutment, called G03, was built (Figure 6). The maximum retaining height is 13m with a front inclination of 85°. For the front Maccaferri Terramesh System® units were used, while for the main reinforcement, ParaLink® and Paragrid® geogrids were laid with a nominal tensile strength from 150 kN/m up to 700 kN/m.

Main challenges have been encountered in the optimization and computation of the materials during the design processes, which have been made with the combined use of LEM, FEM, and BIM technologies, and mainly during installation due to the strict restrictions given by demanding geometry of the facing of the structures provided in the design (maximum retaining height of 13 m and facing inclination up to 85°). The geometry of the constructed structures has been checked with in situ testing, resulting in consistency within the design tolerances. The correct application of the suggested installation procedures has guaranteed the achievement of these important works by the constructors. The use of BIM has allowed anticipating some construction issues and interferences, by providing comprehensive construction details, benefitting the installation of the materials and the completion of the works. Moreover, the control of the settlements was carried out during the whole construction and post-construction phase. These checks were particularly important for the launch of the bridge. The monitoring showed that the final vertical measures were below 160 mm (Figure 7).
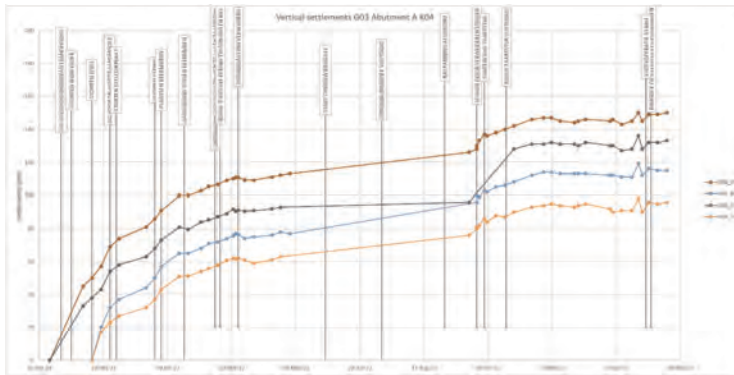
Figure 7.   Direct bridge abutment G03 settlement monitoring from October 2021 to March 2023.

4   CONCLUSIONS

The aim of the paper has been to present the Oosterweel Verbinding, Linkeroever project, and the role of Maccaferri in this framework. Maccaferri has collaborated in the design, supply, and installation of steel wire mesh solutions and Geosynthetic Reinforced Soil-Integrated Bridge Systems (GRS-IBS).

The peculiarity of the case study has been to present the design and building of GRS-IBS, which are innovative solutions for the construction of bridge abutments, made environmentally friendly thanks to the combined use of polymeric geosynthetics and „Terramesh" double-twist steel wire mesh reinforcements.

Regarding some benefits with respect to other standard solutions, Maccaferri Terramesh proved to be a flexible and more suitable system for construction details and a reliable system thanks to the continuity and integrity of the double-twist steel wire mesh with the facing.

Challenges have been encountered and the installation due to the strict restrictions given by demanding geometry of the facing of the structures provided by design has been the main one. The main adopted technologies and recommendations to solve the main challenges have been presented. From the lessons learned point of view, LEM, FEM, and BIM proved to be decisive in material optimization and computation and in anticipating some construction issues and interferences, despite the initial encounter with technical difficulties in the use of these technologies. Finally, the appropriate construction procedures suggested by the suppliers and the installers of the systems have been fundamental to preventing construction difficulties.

REFERENCES

BGS, Belgian Geosynthetics Society. 2022. Infrastructuurwerken Oosterweelverbinding – Gewapende Gronden. *Travaux d'infrastructure liaison Oosterweel remblais renforcés.* Brussels, 2022

Lugli G., Masola F., Scotto M. 2019. MSE Retaining Structure with Cement-stabilized Backfill and Tilted Facing Panels: Design Considerations and Installation Procedure. *Proceedings of the XVII ECSMGE-2019.* Reykjavik, 2019

Masola F., Lugli G., Arndt M. 2018. Bridge „Brug van den Azijn" in Belgium – 75° inclined Mechanically Stabilized Earth Walls. *GeoResources Journal.* 3 | 2018.

Tubertini D., Uccellini R., Vicari M. 2021. Advanced Numerical Modelling of Geogrids and Steel Wire Meshes. In: Barla M., Di Donna A., Sterpi D. (eds) *Challenges and Innovations in Geomechanics. IACMAG 2021.* Lecture Notes in Civil Engineering, vol 126. Springer, Cham. https://doi.org/10.1007/978-3-030-64518-2_104

Alpine protective structures with geosynthetic reinforcement

G. Mannsbart & M. Uebigau
TenCate Geosynthetics, Linz, Austria

D. Illmer
Ingenieurbüro Illmer Daniel, Fulpmes, Austria

ABSTRACT: Defence against natural hazards is important for the preservation of the Alpine region as a valuable living space and economic area, as well as recreational area for present and future generations. Protective structures against natural hazards like rockfall and avalanche events are of specific importance.

Construction in Alpine regions requires special measures concerning design, execution and the selection of construction methods and materials. Especially for rockfall and avalanche protection, aspects of safety, construction cost and material availability, as well as the limited construction time are of crucial importance. All these factors play an important role in design and execution. Examples are given to show how the use of suitable geosynthetics can lead to an economically and technically optimum solution for protective dams.

In the paper, design, dimensioning, and execution are presented based on selected projects, realised with geosynthetics.

1 GENERAL

In the Alps, it is state of the art today to consider geosynthetic reinforced earth dams as defence structures against natural hazards like snow avalanches, mudflows and rock falls. These protection systems must be considered as complex engineered structures by their high-altitude location and the difficult terrain in which they must be built, but also due to the considerable consequences a failure might have for goods and human life. The danger of these kinds of natural hazards was once restricted to mountainous regions but expanding urban areas close to rocky slopes are increasingly at risk. Conventional protective structures are often unable to withstand those impacts.

Primary protection measures, such as foresting or artificial retaining systems, are designed to prevent initial avalanche or rock movement. Secondary protection measures, such as fences, nets, dikes and retaining walls constructed across the path and/or along the peripheries of avalanche or rock movements, are designed to withstand the dynamic forces with the aim of restricting, splitting and/or deviating the already moving mass.

Earth dams as secondary protection barriers using geosynthetic reinforcement can be constructed quickly, provided the proposed site is accessible to construction equipment. A further advantage of geosynthetic reinforced structures can be seen in the use of locally available soil which can be used as main construction material. In combination with adequate geosynthetics, fill of locally available quality may be used, even if the (usually higher) requirements for standard fill material are not met. Drainage of fine-grained soils can be provided by geosynthetic reinforcements with additional drainage function. Finally, geosynthetics provide a strengthening of the soil mass and improvement of resistance against dynamic impacts. Due to all these reasons, more and more of these structures are being built in the alps, taking advantage of construction technologies using geosynthetics.

2 AVALANCHE PROTECTION

2.1 *Types of dams*

The design of avalanche protection dams in the fall zone is complex. If an avalanche cannot be prevented in the area of origin, structures are erected in its fall-path or in its runout area to deflect the avalanche in another direction (deflection dam), to limit the lateral extent of the avalanche (guide dam) or to stop the avalanche completely (avalanche arrest dam).

Earth Dams are often used in the run-out areas of snow avalanches as protection measure against both wet- and dry-snow avalanches. According to the desired function, catching and deflecting dams may be distinguished. Various models are used to design avalanche protection dams, most of them are based on simple point-mass considerations, widely used in Alpine countries; Alternatively, the description of the dynamics of the front of the avalanche, but also numerical computations of the trajectory of a point-mass on the upstream side of the protective dam can be used.
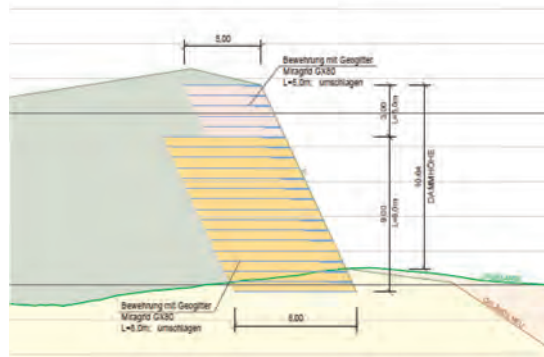
Figure 1.   Typical cross section of an avalanche deflecting dam.

Once the location for a dam has been decided, the forgoing analyses are important to help determine the design avalanche which helps to estimate the appropriate size and shape of a dam or mound.

Usual design methods use the avalanche analysis calculations for an estimated, initial dam height and will help to develop ideas of geometry. In that sense, a careful selection of only a few design parameters will often be useful. In a second stage, more complex design models might be used, taking in to account more variables to improve the numerical simulations that are based on depth-average equations and shock-capturing algorithms. This design approach will help to establish the dam height, length, width, and geometry of a dam. For catching dams, the storage capacity available on the upstream slope, on top of the existing snow cover must be evaluated.

Design work will also establish a critical dam height, defined as the maximum height of the obstacle (above snow cover) that changes the avalanche from supercritical to subcritical flow state as parts of the snow mass passes over the crest. By adding the upstream flow depth, the minimum physical height of the dam to arrest the flow can be estimated.

The design assumes no loss of momentum in the avalanche during its impact with the dam. Tests with glass beads have shown that where the upstream faces of dams have angles of at least 60 degrees to the terrain they have similar efficiency in dissipating energy to those built perpendicular to the slope. In any case the design and geometry of the catching dam have the most influence on retardation and retention of moving snow masses. [Issler et al. 2009]

2.2 Project example Tauernmoos

The so-called Tauernmoossee is an artificial lake in the central Alps of Salzburg, located more than 2000 m above sea level containing a volume of more than 20 mio. m^3 of water used for a hydroelectric powerplant. With the expansion of the Stubachtal power plant around the Tauernmoos pumped storage plant, the Austrian Federal Railways (ÖBB) focuses on sustainable and environmentally friendly mobility, using renewable energy for public transport.

Between the two existing reservoirs of Weißsee (2250 m above sea level) and Tauernmoossee (2023 m above sea level) in the rear Stubachtal valley near the municipality of Uttendorf (Oberpinzgau), the unused net head of 220 m will be used to generate 460 gigawatt hours of traction current.

Figure 2.   Tauernmoos avalanche deflecting dam during construction. (Nov. 2021).
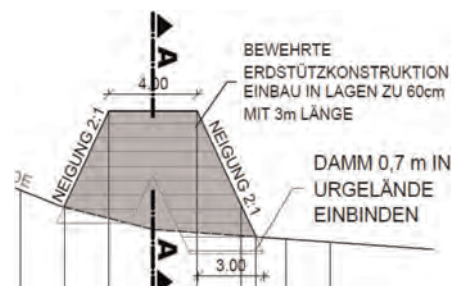
Figure 3.   Cross section of the Tauernmoos avalanche deflecting dam.

A 6 m high and 100 m long combined deflection and catchment dam had to be built to protect the intake structure of the by-pass against avalanches. Due to the quick and easy construction procedure the decision was made to build a geogrid reinforced structure using an approved reinforced soil system. The design was done using a quasi-static loading assumption and 70° slope inclination.

2.3 Case history Axamer Lizum

In the Austrian Alps alone, approximately 8,000 avalanche catchment areas are existing in which countless avalanches occur every year. With the continuous climate change, an on-going increase of these natural events is also expected for the coming years. Avalanches can occur from a gradient of 15 percent and may destroy settlement areas and infrastructure.

In the high alpine ski region of Axamer Lizum in the Tyrol (Austria), two avalanche protection dams had to be built in 2018 to secure a water storage pond used for artificial snow production in the middle of a rock massif. A technically tailor-made geosynthetic solution, In the Tyrolean ski resort of Axamer Lizum, two dams are protecting against tidal waves caused by avalanches since 2018.

The dimensioning of the dams refers to the required dam height and avalanche forces acting on the dam structures and affecting their stability. It should be noted that due to the limited space on the uphill side of the storage pond, no catchment structure can be erected that has a sufficient effective height to completely stop 150-year avalanches. The solution chosen for this site was a reinforced slope system with special steel mesh angles as a lost scaffolding, which can ideally be used in hard-to-reach steep mountain regions. The installed

geogrids are used to reinforce the earth and, due to their high tensile strength, provide effective load distribution against avalanches.

For the protective dams with a height of well over 20 meters and individual length, the soil available directly on site is used as fill material. As a result, this form of avalanche protection is resource-saving, can be used almost everywhere and causes considerably less CO_2 emissions than conventional structures, for which material is delivered, for example, by helicopter. The visible facing of the dams can be flexibly designed so that they optically harmonize with the natural environment. The durability of the constructions is designed up to 120 years. [Gruber 2022]

Figure 4.   Avalanche protection dam Axamer Lizum after completion.

Table 1.   Dimensions of The Axamer Lizum Dam.

Property	Dimension
Flow velocity v_f (150-year avalanche)	22 m/s
Flow height h_f (150-year avalanche)	1.5 m
Energy level h_e	16,4 m
Snow height h_{snow}: (considering regular dam clearance)	1 m
Pre-deposit $h_{deposit}$ (considering regular dam clearance)	0 m
Dam height HD he + h_{snow} + $h_{deposit}$ + h_f	16.4 + 1 + 1.5 = 18.9 m
Safety board	2,0 m

3   ROCKFALL PROTECTION

3.1   *Rockfall as natural hazard*

Changing climate conditions, anthropogenic influences and seismic processes can have dangerous consequences in the form of rockfalls and landslides. Rockfall can be defined as the collapse of large stone blocks, fragments of rocks and just a free fall of stones on mountain slopes under the influence of gravity. The reason for these processes is the separation of soil masses from the parent rock. Several types of protective structures are available to prevent damages on goods and human life.

Among the main investigated parameters in the analysis of rockfall processes and design of engineered protection constructions are the stone trajectory and the impact energy of the stone. The trajectory of the rockfall is influenced mainly by the following parameters:

- the average diameter d of the blocks.
- volume and weight of an unstable array.
- slope angle (inclination) and slope configuration (cross-section).
- physical and mechanical characteristics of the soil.

The impact energy of the stone is experimentally determined and depends on volume and weight of blocks and the speed of falling stones. In the past, fence capacities were once considered large at only 100 or 500 kJ, whereas nowadays systems are commonly installed up to 5000 kJ, and some of them even higher. The fundamental possibilities of different protective structures are described in Figure 5.
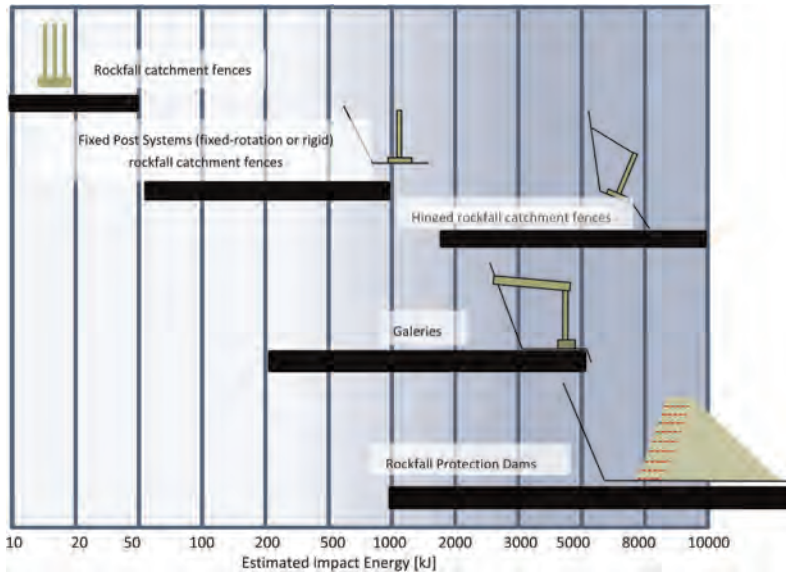
Figure 5. Schematic overview on rockfall protection structures.

3.2 Case history Eisgratbahn Stubaital

Boulders of the size of a single-family house had fallen from a steep slope above the parking area of the Eisgratbahn cableway during a rockfall in May 2021. To eliminate the potential danger of further rockfalls and to secure the slope in time for the start of the next winter season, a fast and durable solution was needed.

Figure 6. Rockfall protection dam Eisgratbahn-Stubaital.

A vegetated geosynthetic reinforced slope system was able to provide a solution absorbing the dynamic forces of falling rocks while requiring a minimum of surface area. The protective dam was designed according to the ONR 24810 standard and offers an optimal combination of a maximum performance and cost efficiency coupled with a minimal time investment.

The implementation was carried out in record time: after the start of the project, the geosynthetics were delivered within only 4 weeks. After only 6 weeks of construction, the project was completed and Stubaier Gletscherbahnen could use the parking lot for the start of the winter season.

The use of the special system made it possible to install the fill material available on site, with a total volume of 18,100 m^3 and therefore considerably reduce the transport effort and environmental impacts. With a total of only four truckloads to transport construction materials to the site, the project has a minimal ecological footprint. It also reduced the impact on residents from construction noise and dust. A conventional concrete structure would have required much more energy and transportation than the modern construction method using geosynthetics.

On the mountainside, the dam surface in the rockfall zone was constructed with a mortared tile set as surface protection against falling rocks. Greenery was planted on the remaining embankment surfaces, the front sides, and the top of the dam to ensure everything will blend perfectly into the landscape.

Figure 7.   Rockfall protection dam Tenneck.
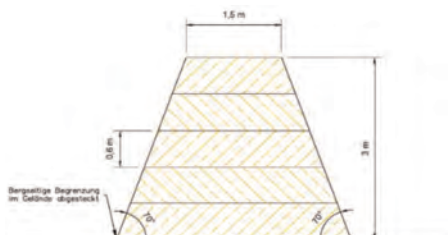
Figure 8.   Cross section of the protection dam.

3.3   Quarry site "Ehrensberger" near Salzburg

Since decades a limestone quarry site is in use close to the Village of Tenneck near the city of Salzburg. To widen the area of mining, a rockfall protection dam had to be built as a back-to-back structure. The dam was up to 6 m high and mor than 100 m long. The structure was built using a geogrid with a short-term strength of 160 kN/m installed at a vertical spacing of 0,6m. The requirement was to use coarse-grained granular fill without any organic content. Compaction of 98% proctor-density and a bearing capacity Ev_1 value of 15 MN/m^2 by plate-loading test had to be achieved.

4   DESIGN OF PROTECTIVE DAMS USING ONR 24810

The first use of geosynthetics in protective structures dates to 1990ies. [Mannsbart 2002] At that time, design methods for usual reinforced soil structures were available, but consideration of impact loading was not common practice. [Adam et al. 2002] First design approaches were mostly empirical, whereas today a number of design methods do exist.

For rockfall protection structures, the Austrian guideline ONR 24810 provides a design basis. Rockfall protection dams are used particularly in cases, where slope geometry and available space permit such a structure. Dams show advantages over nets, especially in terms of service life, construction cost and - depending on the design - energy absorption capacity. Before starting the design, the structure is assigned to a certain defined type. As an important part of the document, it is shown that reinforced dams can absorb a considerably higher energy of falling blocks. For geosynthetics reinforced structures both the impact time as well as the dissipated energy are increased (Figure 9).
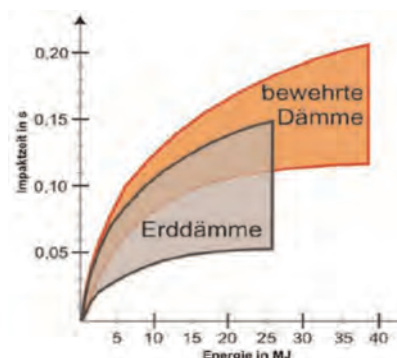
Figure 9.   Impact time and energy absorbed.

Specifically, for rockfall catchment dams, it has sections dedicated to the verification of the superstructure itself, reinforcement design, non-standard actions, construction rules and lifespan.

Two tables set requirements for geosynthetic reinforcement, especially on strength and stiffness of geosynthetics at 5% elongation.

This relatively high stiffness requirement seems to be far on the safe side which might restrict the range of allowable products to high-strength, brittle geogrids. If this approach seemed justified for the first edition of the guideline, it might probably require some adaptation to more common geosynthetic reinforcement elements with its next edition.

The construction of protection embankments has increased markedly in areas with a high risk of rockfalls and avalanches. Suitable design models for soil embankments are used among which the Austrian guideline is a useful tool for the design of rockfall protection dams, but might need some adaptation concerning the geosynthetics requirements.

REFERENCES

Adam, D., Blovsky, S., Kopf, F. 2002. *Bau von Schutzdämmen gegen Bergsturz;* 12th Danube-European Geotechnical Conference, Passau, Germany.
Gruber, J. 2022. How to Protect Skiers Against a Tsunami. *Proc. 7th European Conf. on Geosynthetics*, Sept. 2022, Warzaw, Poland.
Issler P., Gauer P., Johanesson T., Lied K. 2009. *The Design of Avalanche Protection Dams – Recent and Practical Developments; European Commission*, Environment Directorate.
Mannsbart, G. 2002. Geosynthetic Reinforced Protection Structures in Mountainous Regions – Examples of Safe and Cost-effective Alternatives. *7th Int. Conf. on Geosynthetics, Nice, France.*
ONR 24810; 2019. *Technical Protection Against Rockfall – Terms and Definitions, Effects of Actions, Design and Construction, Monitoring and Maintenance.* Austrian Standards Institute.

Novel landscaping applications of geosynthetics in 'Museum of the Future' project in Dubai

P.V. Jayakrishnan, L. Mottadelli & M.H. González
Maccaferri Middle East LLC, Dubai, UAE

ABSTRACT: The 'Museum of the Future' in Dubai is one of the most innovative buildings in the world, which is designed in three main parts, namely the lower green hill, the middle building, and the top elliptical void structure. As per the architectural design, the green hill is designed as a smooth transition from ground, in the form of an earthen vegetated mound which eventually should cover the embedded three-story podium structure. As a result, the green hill had to be constructed as claddings around the base structure rather than as a solid earth hill. Three different types of geosynthetic green systems were used to recreate the different slopes, which included reinforced soil for steep slopes, heavy revetment with geocells for moderate slopes, and rolled erosion control mats for gentle slopes. In most cases, the available thickness of soil layer was only 30 cm, complicating the design and construction of the geosynthetic systems. To ensure the stability of the geosynthetic green cover systems for moderate and gentle slope cases, continuous veneer reinforcement was installed below the thin soil fills, using double-twisted wire mesh netting that was anchored to the concrete structure at the top of the cover system. Due to existing space constraints, the soil reinforcement had to be anchored to the concrete structure in most of the cases for reinforced soil slopes. Additionally, a layer of geosynthetic drainage composite was installed below the entire surface area of the green cover system to enable easy drainage of the continuous irrigation water expected from the gardening activities. Through the successful case reference of the 'Museum of the Future' project in Dubai, this paper sheds light on the possibilities, opportunities and challenges associated with the use of sustainable geosynthetic systems in iconic projects for landscaping and architectural applications.

1   INTRODUCTION

The 'Museum of the Future' project in Dubai is created with sustainability as the key requirement. Project stakeholders wanted the facility to be designed, built, and operated sustainably using the most updated technologies. A large portion of the building is situated underneath the green roof of the podium, which further contributes to the project's sustainability credentials by reducing solar gain and the heat island effect. Accordingly, the structure is divided into three main parts: the embedded building, the green hill, and the top void. The green hill is designed as a smooth transition from the ground in the form of an earthen vegetated mount covering an embedded podium structure. An iconic feature of the project is the garden on the green hill comprising around one hundred species of trees and plants. The lower hill's unique setting made traditional landscaping techniques difficult. This slope with drastically varying inclinations needed a novel way of retaining soil and growing greenery. Due to the high summer temperatures in Dubai and with limited rainfall, irrigation was one of the main considerations. This project utilized a wide range of geosynthetic products to address soil retention, revegetation, and smart irrigation needs. It is the purpose of this paper to present the possibilities, opportunities and challenges associated with the use of sustainable geosynthetic systems in landscaping and architectural applications for iconic

projects, through the reference of the successful implementation in the 'Museum of the Future' project in Dubai.
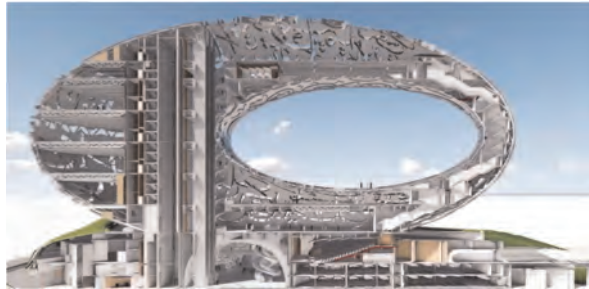
Figure 1.   Architectural rendering of sectional view of the project (image courtesy: Buro Happold Engg.).

2   GEOSYNTHTIC APPLICATIONS IN THE PROJECT

To reduce the vertical load on the slabs and walls of the embedded podium structure, a lightweight geofoam block was required to be used as the main body of the green mount. This resulted in only 30 cm of cover soil thickness available in most cases, complicating the design and construction of geosynthetic systems. To recreate slopes at different angles, three different geosynthetic green cover systems were used. As a final solution, biodegradable erosion control blankets, geocell revetments and reinforced soil structures were implemented. In moderate and gentle slope cases, continuous veneer reinforcement was installed below the thin cover soil to ensure stability of the geosynthetic green cover systems.

2.1   Solutions for gentle slope (up to 35° inclination)

For gentle slopes up to 35°, biodegradable rolled erosion control blanket type Biomac® was used as the green cover system (Figure 2). The purpose of the erosion control blanket made with coir geotextile is to avoid erosion of the slope and to facilitate quick vegetation of the slope. The beige colour of Biomac blanket helped create the impression of a soil filled slope during the installation before development of full vegetation. Biomac being a soft erosion control material, irrigation pipes could be seamlessly installed using its fixtures. To improve the sliding stability of the thin cover soil, Macmat HS® veneer reinforcement was installed continuously below the thin soil layer. Macmat HS is made by extruding a high frictional
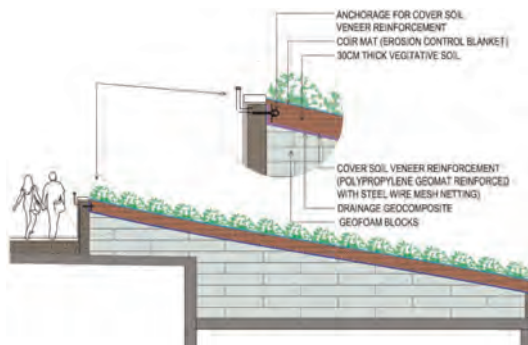
Figure 2.   Typical cross-sectional details of geosynthetic application for gentle slope (up to 35°).

polypropylene mat onto a double twisted steel wire mesh netting. In the absence of any underlying soil that can support and frictionally interact with the veneer reinforcement, the Macmat HS had to be anchored to the concrete slab of the embedded building structure. As part of the smart irrigation system, Macdrain® geosynthetic drainage composites were used below the cover soil to reduce water wastage as well as to deliver water directly to the root system of the plants and trees.

2.2 Solutions for moderate slope (for 36° to 45° inclination)

For moderate slopes ranging from 36° to 45°, heavy revetement with geocells were adopted. Geocell provides the required confining effect without local movement of the cover soil (Figure 3).

For this slope case also, veneer reinforcement and drainage composure were continuously provided below the green cover soil, as well were anchored to the top concrete slab.

Figure 3. Typical cross-sectional details of geosynthetic application for moderate slope (up to 45°).

2.3 Solutions for steep slope (for 46° to 80° inclination)

For steep slopes ranging from 46° to 80° inclination, reinforced soil structure type Green Terramesh® was used (Figure 4). When space was limited, the soil reinforcement tail of the Green Terramesh system was anchored to the concrete walls of the embedded building using concrete anchors, thereby dissipating the residual stresses from the soil reinforcement. For this slope case also, veneer reinforcement and drainage composure were continuously provided below the green cover soil, as well were anchored to the top concrete slab.
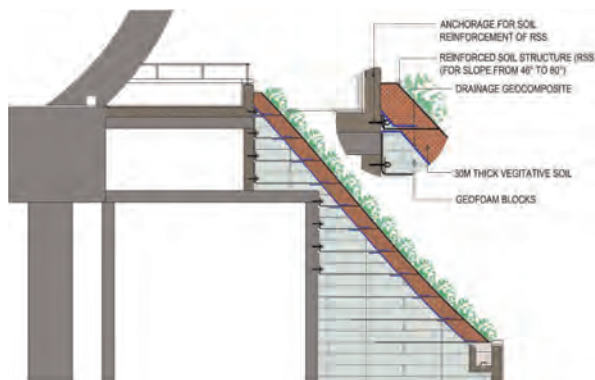
Figure 4. Typical cross-sectional details of geosynthetic application for steep slope (up to 80°).

Table 1. Summary of geosynthetic products used in the project.

Brand Name	Terminology from ISO 10318	Symbol	BoM (m2)	Application
Biomac C	Geomat	GMA	9,000	Erosion control
MacMat HS	Geomat	GMA	9,000	Veneer reinforcement
MacDrain W	Geocomposite	GCO	12,500	Drainage
MacWeb	Geocell	GCE	3,000	Retention of cover soil
Terramesh Green	Geogrid	GGR	3,500*	Steep slope stabilization

*Face area of reinforced soil structure.

3 DESIGN

MACSTARS W software (Maccaferri Stability Analysis of Reinforced Soils) was used for the design of Green Terramesh reinforced soil slopes (external & internal stability check) as per AASHTO Allowable Stress Design method. MACSTARS W is a limit equilibrium-based design software. The interaction factors between the soil reinforcement & backfill soil were reduced by 50% to account for the lower friction due to the presence of geofoam instead of soil.

Zinc coated concrete anchors made of carbon steel were used in the project (Figure 5). Anchors were designed conservatively for the pull-out strength equivalent to the long-term design strength (LTDS) of the soil / veneer reinforcement. In the actual field condition, the anchor load would be less than the LTDS of the soil reinforcement in many layers, considering the typical stress distribution within the soil reinforcement layers. Chemical adhesive was used to grout the anchor within the drilled hole in concrete wall.
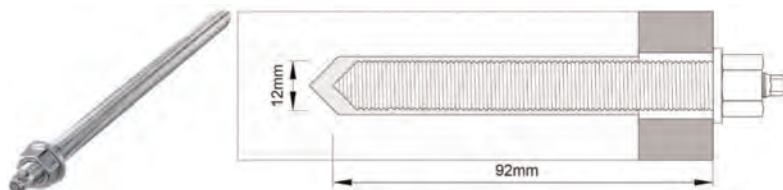
Figure 5. Details of concrete anchor used in the project.

The stability of thin cover soil in gentle and moderate slope cases were evaluated following the principles of analysis of veneer soil reinforcement, ensuring a minimum factor of safety of 1.5.

4 CONSTRUCTION ASPECTS

Pertaining to the various geosynthetic solutions, the following sequence of construction was adopted at site.

- Anchoring and installation of Green Terramesh units and laying of geofoam block core.
- Laying of drainage geocomposite.
- Anchoring and laying veneer reinforcement.
- Laying of cover soil, unconfined for 35° slope or confined in geocell for 45° slope case.
- Laying of the coir-based erosion control blanket above cover soil.
- Fixing irrigation pipes.
- Plantation works.
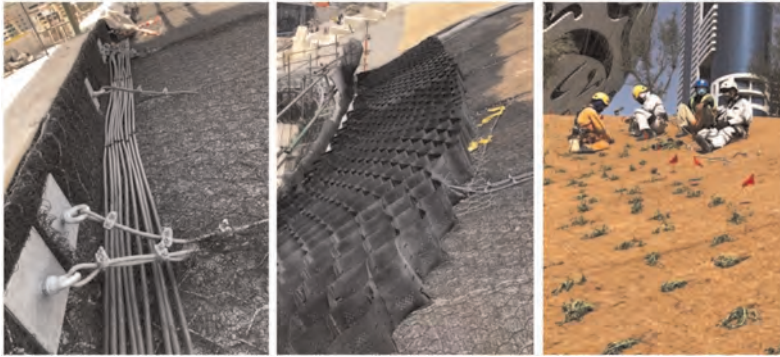
Figure 6. Installation of various geosynthetic components; (a) Macmat HS veneer reinforcement and concrete anchors, (b) Macweb geocell connected through steel cables, (c) Biomac erosion control blanket and vegetation planting.

Figure 7. Geocell: before and after vegetation growth.

Figure 8. Green Terramesh reinforced soil structure: before and after vegetation growth.

Figure 9.   View of the completed project in 2021 (courtesy: google images).

5   GEOSYNTHETIC'S CONTRIBUTION TO PROJECT'S SUSTAINABILITY

The 'Museum of the Future' project in Dubai is created with sustainability as the key requirement. As a result of use of geosyntics in the project, the following sustainability benefits are achieved.

- Replacement of a 30cm thick gravel drainage layer sandwiched between two geotextile layers (Case A) below the cover soil by a thin drainage geocomposite (Case B).
- Reduction of cover soil thickness from 50cm (Case A) to 30cm (Case B) by using geomat veneer reinforcement.
- Around 25% of irrigation water conserved by recycling the excess water collected from drainage geocomposite.
- Carbon sequestration from trees & plants growing within the different geosynthetic layers.
- Reducing solar gain and the heat island effect of the embedded building due to **the green roof.**

To ensure sustainability in engineering, quantitative design tools are needed to perform the metrics that can be applied in the design process. Life cycle assessment (LCA) is one such tool for evaluation of sustainability in engineering designs. Basically, LCA involves a complicated methodology for identifying the energy and other resource requirements as well as the environmental impacts associated with every stage in the life cycle of a product, process, or system.

Typically, the LCA study are done by adhering to the requirements of ISO 14040 and 14044 standards. In the present work, the environmental performance of Cases A and case B are assessed with the following impact category indicators.

The conventional drainage layer and thicker vegetative soil (Case A) causes comparatively higher impacts in all categories than using the drainage composite & geomat veneer reinforcement (Case B). The higher impacts of Case A are caused by the emissions and the
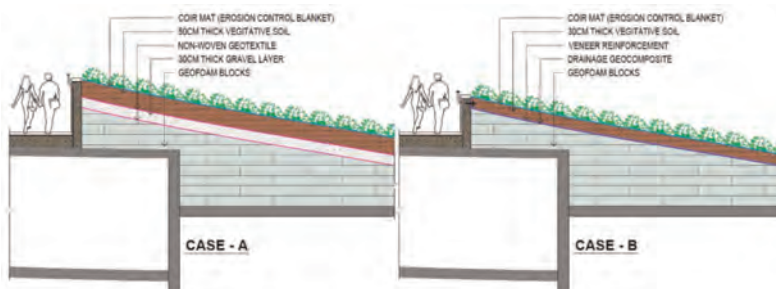
Figure 10.   Sectional details of Cases A & B for comparative LCA study.

Impact category	Units	Case-A	Case-B	Reduction (%)
ADP-M	kgSbeq	6.17E-05	1.23E-06	98%
ADP-F	MJ	1.62E+02	1.17E+02	28%
GWP	kgCO2eq	11.48	5.47	52%
ODP	kgCFC-11eq	1.26E-06	7.43E-07	41%
POP	kgC2H4eq	3.23E-03	8.47E-04	74%
AP	kgSO2eq	0.06	0.01	83%
EP	kgPO4eq	0.02	2.07E-03	90%

ADP-M: Abiotic depletion – Minerals, ADP-F: Abiotic depletion - Fossil Fuels, GWP: Global warming Potential (100a), ODP: Ozone Layer Depletion, POP: Petrochemical Oxidation Potential, AP: Acidification Potential, EP: Eutrophication Potential.

resource consumption related to the production and transportation of the amount of gravel required, as well as increased land excavation for sourcing of vegetative soil. Compared to Case A, no gravel is used in Case B for drainage purpose. The environmental impacts of gravel are mainly caused by mining machines, the use of electricity during mining and the energy requirements for transportation from stone quarries to jobsite.

6 CONCLUSIONS

Due to the limited extent of industry awareness, the potential of using geosynthetics in landscaping applications is often underutilized or overlooked, especially those involving soil retention and irrigation along complex slopes. It is the purpose of this case study paper to present the possibilities, opportunities and challenges associated with the use of sustainable geosynthetic systems in landscaping and architectural applications for iconic projects, through the reference of successful implementation in the 'Museum of the Future' project in Dubai.

REFERENCES

Chiwan, H. & Muji, H. 2016. Fundamentals of Erosion Control on Slopes and the Role of Geosynthetics. *Proc. EuroGeo 6 conf.*, September 25-28.

ISO 14040. 2006. *Environmental Management – Life Cycle Assessment – Principles & Framework*.

ISO 14044. 2006. *Environmental Management – Life Cycle Assessment – Requirements & Guidelines*.

Paolo, D.P. & Ghislain, B. 2000. Design Considerations Related to the Performance of Erosion Control Products Combined with Soil Bioengineering Techniques. *ASTM Workshop on Testing & Performance of Flexible Erosion Control Materials, Toronto*, 23 June 2000. Canada.

Ronald, A., Steven F.B., Milan, D., Tor, E.F., Jnanedra, N.M., Dawit, N, Abdulla T.O., Hideki, T. & Jan, H. 2018. Geofoam Blocks in Civil Engineering Applications. *Proc. 5th Intern. Confer. on Geofoam Blocks, Kyrenia*, 9-11 May 2018. Northern Cyprus.

Sotir, R.B., Christopher, B.R., & Cowland, J.W. 2002. Vegetated Reinforced Soil Slopes. *Proc. 7th Intern. Confer. on Geosynthetics*, Delmas. South Africa.

Stolz, P., Frischknecht, R., Stucki, M., Busser, R., Itten, R., Frischknecht, R., & Wallbaum, H. 2019. Comparative Life Cycle Assessment of Geosynthetics Versus Conventional Construction Materials. *Report on behalf of for European Association of Geosynthetic Product Manufacturers*.

Various Authors. 2020. Pre-Sustainability. *SimaPro Database Manual Methods Library*.

Werth, K., Hohny, S., Stucki, M., Busser, R., Itten, R., Frischknecht, R., & Wallbaum, H. 2012. Comparative Life Cycle Assessment of Geosynthetics Versus Conventional Construction Materials, a Study on behalf of the EAGM, Case 3, Landfill Construction Drainage Layer. *5th European Geosynthetics Congress 2012. Valencia*, Spain.

HDPE geomembrane properties in mine reclamation covers after 13 and 20 years

R.F.M. Rarison, M. Mbonimpa & B. Bussière
Research Institute on Mines and the Environment (RIME-UQAT), Rouyn-Noranda, Québec, Canada

S. Turcotte
Ministère de l'Énergie et des Ressources naturelles, Val-d'Or, Québec, Canada

S. Pouliot
SNC Lavalin, Val-d'Or, Québec, Canada

ABSTRACT: Geomembranes (GMs), especially high-density polyethylene (HDPE) ones, are used to provide a barrier to water and oxygen in mine site reclamation cover systems. The physical stability of these GM remains a major concern as it affects their performance to control fluid flows. Considering that HDPE GMs can crack even while being in the elastic domain, a maximum allowable strain (MAStrain) was fixed at 4% to avoid stress cracking. The MAStrain corresponds to a maximum allowable stress that must not be exceeded. This paper assessed the chemical and mechanical properties of exhumed GMs from two cover systems installed 13 and 20 years, and the impact of the tensile properties on the MAStrain. The results show that the GM remains in the first degradation stage and no negative impact was found on the mechanical properties. The tensile behavior of the exhumed GM indicates a gain of stiffness that reduces the MAStrain.

1 INTRODUCTION

Geomembranes (GMs) are widely used in the mining industry. They are used in the mining operations as a liner in heap leach pads or for water ponds, as in the mine waste management as a liner for tailings storage facilities or in the reclamation process as a fluid-tight component in cover systems (Lupo & Morrison 2007; Touze-Foltz & Lupo 2009). For this last example of use, the role of the GM is to prevent water and oxygen ingress into the sulphide tailings to limit the generation of acid mine drainage that could be harmful to the environment (Maqsoud et al. 2021; Rarison et al. 2022). Almost all of the GMs used in covers are high-density polyethylene (HDPE) (Maqsoud et al. 2021). Nevertheless, HDPE GMs are prone to stress cracking because of their high crystallinity (Müller 2007; Scheirs 2009). Stress cracking is defined as "an external or internal crack in a plastic caused by tensile stresses less than its short-time mechanical strength" (ASTM D883 2005). Those cracks would then compromise the performance of the cover to control fluid flows. The physical stability of GMs then remains a major concern, especially in covers as the tailings can settle over time. Settlement can generate tensile stresses inside the GM during the service life of the cover. The maximum allowable strain was then introduced as a design criteria in order to ensure the long-term durability of the cover system (Dixon & von Maubeuge 1992; Eldesouky & Brachman 2018; Jones et al. 2000; Peggs et al., 2005; Rowe & Yu 2018; Rowe & Yu 2019; Rowe et al. 2020).

Nevertheless, little is known about the in situ long-term behaviour of GMs in service. One way to learn more about this behaviour is to exhume GMs installed in cover systems. GM exhumation is commonly used for in-service performance assessment (e.g., McWatters et al. 2020; Rowe et al. 2010). The main objective of this study is to assess the actual properties of GMs after years of service. To this purpose, GMs were exhumed from two sites. The exhumed

geomembranes were characterized in the laboratory to assess their antioxidant and stabilizer levels to know the degradation stage of the GMs, and their tensile properties. The aim is not to compare the properties of the two GMs. As the initial properties of these GMs are unknown, the obtained results would be compared to typical virgin HDPE GM properties. The results will be then used to assess the impact on the design criteria of maximum allowable strain.

2 GEOMEMBRANE EXHUMATION

To reach the study objective, two sites were selected, S1 and S2, where cover systems with smooth HDPE GMs were installed 13 and 20 years ago to reclaim these sites. S1 is located in the western part of Québec, Canada. S1 was reclaimed in 2005-2006 with a cover system composed by a 1.5 mm-thick smooth black HDPE GM installed directly above oxidized tailings and a 0.6 m-thick silt protection layer. S2 is located in the mid-north of Québec, Canada. This site was reclaimed in 1999-2000 with a cover system made up of 1.5 mm-thick smooth black HDPE GM installed directly above oxidized tailings and covered by a 1.4 m-thick till protection layer. The cross sections of the two cover systems are presented in Figure 1. On both sites, the surface of the protection layer was vegetated.
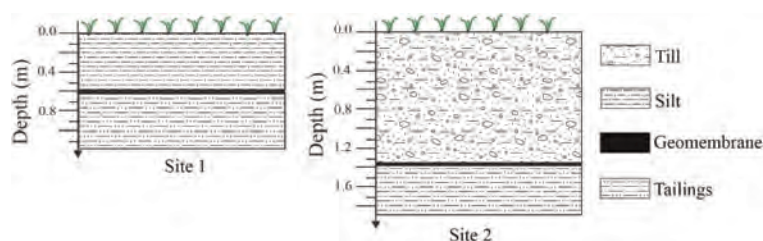
Figure 1.   Cross sections of the cover at the sites 1 and 2.

To access the GMs, S1 was exhumed in August 2019 and S2 in August 2022. The first step was to form tiles of surface vegetation of the cover systems. The second step was to excavate the protection layer through to the GM level with a mechanical shovel, with particular care to the proximity of the GM so as not to damage it during excavation efforts. The third step was to sample the GM with dimensions of 2 m by 2 m and 1 m by 1 m for S1 and S2, respectively. The fourth step was to substitute the exhumed GM with new HDPE GM patch that was seamed by extrusion to the GM on the site to ensure the sealing of the cover. Finally, the excavated soil was returned and recovered with the surface vegetation tiles.

3 GEOMEMBRANE CHARACTERIZATION

Details on the performed physical, chemical and mechanical characterizations of the two HDPE exhumed GMs are presented below. The initial properties of these GMs are unknown as the different characterizations were not performed when the membranes were put in place. The results obtained with the exhumed GMs will be compared to those obtained from a typical virgin HDPE GM that was characterized in the laboratory and is assumed to be representative of the initial GM installed in the two sites. To assess the significance of the differences of the GM mechanical properties (typical virgin GM compared to S1 GM, and typical virgin GM compared to S2 GM), two-sample t-tests (Student 1908) were performed. Prior to two-sample t-tests, the normality of the distributions was verified with Kolmogorov-Smirnov tests (Lilliefors 1967). The significance was set at 0.05 (95% of confidence) for these two tests; which means that when the p-value obtained with the two-sample t-test is higher than the 0.05, the difference between the compared data is not significantly different; and when the p-value obtained with the normality test is higher than 0.05, the data are significantly drawn from a normal distribution.

3.1 *Physical characterization*

The physical characterization of the GMs (virgin, S1 and S2) consisted of measuring the GM thickness. The thickness measurement was performed according to ASTM D5199 (2019b) using MTG-DX2 thickness gauge which has the accuracy of ± 4 μm (Checkline, USA). The GM thickness T_{GM} is defined as the mean of 10 thickness measurements on 10 disks of 80 mm diameter.

3.2 *Chemical characterization*

To assess the antioxidant and stabilizer level, which would give information on the GM degradation state, low-pressure and high-pressure differential scanning calorimetry (DSC) were performed. The low-pressure DSC (140 kPa) was operated at high temperature (200°C) to measure the standard oxidative-induction time (Std-OIT) according to ASTM D3895 (2019). The high-pressure DSC (3.4 MPa) was conducted at lower temperature (150 °C) to measure the high-pressure oxidative-induction time (HP-OIT) according to ASTM D5885 (2017). The two tests give complementary information as antioxidant and stabilizer effective temperature ranges are different. For example, hindered phenols and phosphites whose effective temperature range is above 150°C can be detected with std-OIT while hindered amines and thiosynergists whose effective temperature range is up to 150°C can be detected with HP-OIT (Hsuan & Koerner 1998). The Std-OIT was performed in duplicate (for the virgin, S1 and S2 GMs). Only single measurements of the HP-OIT were performed for the S1 and S2 GMs. The HP-OIT of the virgin GM was given by the manufacturer.

3.3 *Mechanical characterization*

The mechanical properties of the GM from S1 and S2 were assessed with tensile tests performed on dog-bone shaped specimens (Figure 2.a) according to ASTM D6693 (2015). Raw data are presented in terms of force-displacement curves as illustrated in Figure 2.b. The force-displacement curve gives four parameters: the yield force (*YF*), the yield displacement (*YD*), the break force (*BF*), and the break displacement (*BD*). These parameters are used to define four tensile properties following equations (1) to (4): the tensile yield strength (*TYS*, N/mm) and the percent yield elongation (*PYE*; %); the tensile break strength (*TBS*; N/mm) and the percent break elongation (*PBE*; %).

$$TYS = \frac{YF}{W} \tag{1}$$

$$PYE = \frac{YD}{GL_Y} \cdot 100 \tag{2}$$

$$TBS = \frac{BF}{W} \tag{3}$$

$$PBE = \frac{BD}{GL_B} \cdot 100 \tag{4}$$
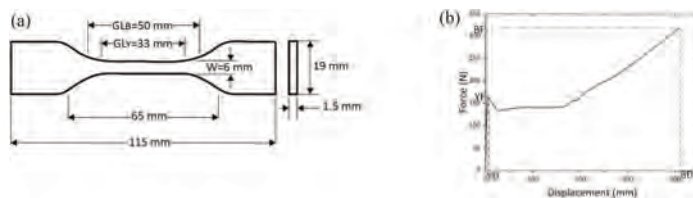
Figure 2.   Dog-bone shaped specimen for tensile test (a) and typical raw result from a tensile test (b).

where W (specimen width), GL_Y (gauge length for yield) and GL_B (gauge length for break) are defined on Figure 2.a.

The dog-bone shaped specimens were prepared in the machine/roll direction (MD) and in transverse or crossmachine direction (CD) to assess the anisotropy. Five tensile tests were performed in each direction for each GM (virgin, S1 and S2).

4 RESULTS

4.1 *Geomembrane thickness*

The thicknesses of the three GMs assessed in this study are presented in the Figure 3. The T_{GM} of the virgin, S1, and S2 GMs are 1.51 mm, 1.55 mm, and 1.57 mm, respectively. The three values are above the nominal thickness of 1.50 mm and show the variability of the GM thickness.
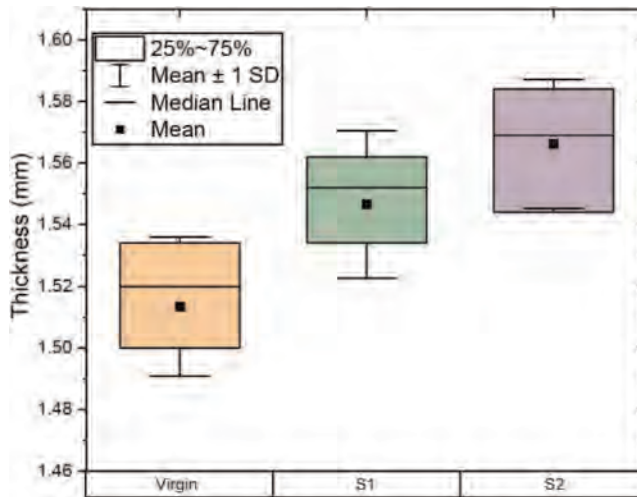
Figure 3. Box plots of the thicknesses of virgin and exhumed geomembranes.

4.2 *Antioxidant and stabilizer level*

The results of the antioxidants and stabilizers level are presented in terms of Std-OIT and HP-OITs in Table 1 below for the virgin, and the S1 and S2 GMs who are 13 and 20 years old, respectively. The Std and the HP-OITs of the GM from the site S1 (211 min and 496 min, respectively) are close to those of the typical virgin GM (195 and >400 min, respectively), which means that the S1 GM degradation is in its earlier part. The Std and the HP-OITs of the GM from the site S2 (111 min and 314 min, respectively) are lower than those of the typical virgin GM. The lower OITs (Std and HP) of S2 GM would then indicate that this GM has an advanced degradation state.

The Std and HP-OITs of the S1 and S2 GMs are higher than the residual values (when the antioxidants and stabilizers are completely depleted) that can be as low as 1.5 min and

Table 1. Standard and High-Pressure OITs of a typical HDPE geomembrane and of the exhumed geomembranes.

Properties	Units	Virgin	S1	S2
Std-OIT	min	195	211	111
HP-OIT	min	>400[*]	496	314

[*]Provided by the geomembrane manufacturer.

80 min, respectively (Ewais et al. 2014). These results then show that there are still anti-oxidants and stabilizers inside the GMs from S1 and S2, which means that the GM remains in the antioxidant depletion stage according to Hsuan and Koerner (1998). During this stage, the GM's properties (e.g., tensile strength) are expected to remain unaffected.

4.3 Mechanical properties

The box plots of the yield and break properties of the virgin, and the exhumed HDPE GMs (S1 and S2) are presented in Figures 4 and 5, respectively. The results from the two principal directions (MD and CD) are also included. All the data are significantly drawn from a normal distribution as all the p-values obtained with the Kolmogorov-Smirnov tests are above the significance level of 0.05 (presented in Table 2). Two-sample t-tests could be then performed to assess the significance of the differences (e.g., MD vs. CD, virgin GM vs. S1 GM, virgin GM vs. S2 GM).
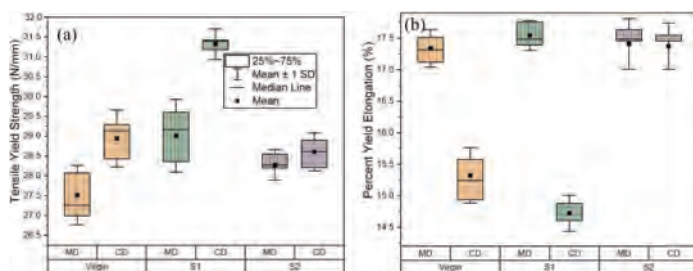
Figure 4. Box plots of tensile yield strength (a) and percent yield elongation (b) obtained with the virgin and the exhumed HDPE GMs.
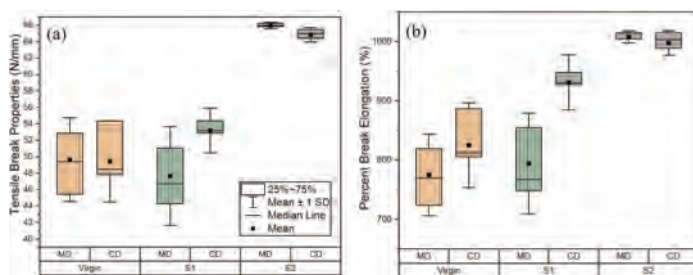
Figure 5. Box plots of tensile break strength (a) and percent break elongation (b) obtained with the virgin and the exhumed HDPE GMs.

Table 2. P-values obtained with the Kolmogorov-Smirnov normality tests.

GM	Direction	TYS	PYE	TBS	PBE
Virgin	MD	0.89	1.00	1.00	1.00
	CD	1.00	0.51	0.63	0.84
S1	MD	1.00	1.00	1.00	1.00
	CD	1.00	0.64	0.90	0.82
S2	MD	1.00	0.50	1.00	0.53
	CD	1.00	0.35	1.00	1.00

Regarding the anisotropy of the tensile properties, it can be seen in Figures 4 and 5 that the results obtained in MD can be different from those obtained in CD. The two-sample t-

tests show that the anisotropy is verified for the yield properties of the virgin and S1, for the TBS of the S2 GM and for the PBE of the S1 GM as it can be seen in Table 3. The anisotropy would then be more observable for recent GMs.

Table 3. P-values obtained with the two-sample t-tests for the anisotropy assessment.

GM	Compared direction	TYS	PYE	TBS	PBE
Virgin	MD and CD	0.00[*]	0.00[*]	0.93	0.13
S1	MD and CD	0.00[*]	0.00[*]	0.11	0.02[*]
S2	MD and CD	0.27	0.88	0.04[*]	0.35

[*]Anisotropy is verified.

Table 4. P-values obtained with the two-sample t-tests for the assessment of the difference significance.

Direction	Compared GM	TYS	PYE	TBS	PBE
MD	Virgin and S1	0.02[*]	0.17	0.55	0.68
	Virgin and S2	0.02[*]	0.73	0.00[*]	0.00[*]
CD	Virgin and S1	0.00[*]	0.01[*]	0.08	0.01[*]
	Virgin and S2	0.30	0.00[*]	0.00[*]	0.00[*]

[*]Difference is significative.

Regarding the yield properties, TYS of both exhumed GM are significantly higher than TYS of virgin GM (except for S2 in CD) while there is no statistically significant difference for the PYE (except in CD). That means the exhumed GMs are stiffer than the typical virgin HDPE GM. These observations can be observed in Figure 4 that presents box plots of TYS and PYE, verified with the statistical analyses in Table 4.

Regarding the break properties, there is no significant statistical difference between the TBS and PBE results for the GM exhumed from the site S1 and the virgin GM (except the PBE in CD); while TBS and PBE are significantly higher for the GM exhumed from the site S2 than the virgin GM. The GM exhumed after 20 years (site S2) is more resistant than the typical virgin one. The GM used at that time could be more resistant than those manufactured more recently.

All the tensile properties of the exhumed GMs are at least similar to those of the typical virgin GM.

5 DISCUSSIONS

The above data indicate that the exhumed GMs are stiffer than the typical virgin HDPE GM. It would be then interesting to know how this gain of stiffness could impact the design criteria concerning the maximum allowable strain (MAStrain). Indeed, the GM could also break under a constant load, even in the elastic zone, due to stress cracking, particularly for HDPE GMs owing to their high crystallinity (Hsuan et al. 1993; Müller 2007; Scheirs 2009). Hence, some authors use the MAStrain as the strain that should not be exceeded to ensure the durability of the GM (Dixon & von Maubeuge 1992; Eldesouky and Brachman 2018; Jones et al. 2000; Peggs et al. 2005; Rowe & Yu 2018; Rowe & Yu 2019; Rowe et al. 2020). Initially, a MAStrain of 6% was proposed for HDPE GMs (Dixon & von Maubeuge 1992; Jones et al. 2000). Different MAStrain values were subsequently proposed, depending on the GM use, for example, from 4 to 5% for GMs used as a cover which consider a safety factor of 1.5 to 1.2, respectively, compared to the initially proposed 6% (Rowe & Yu 2019), and 3% for GMs used as a liner which means a safety factor of 2 (Jones et al. 2000; Rowe & Yu 2019; Rowe et al. 2020).

In this study, the GMs were exhumed from cover so the MAStrain considered is set at 4% with a safety factor of 1.5. To assess the impact of the gain of stiffness on the MAStrain, consider first the maximum allowable stress ($MAStress_0$) that corresponds to the initial MAStrain of 4% of the virgin GM. $MAStress_0$ is determined graphically with the linear stress-strain curve obtained with the tensile test of a virgin GM (Figure 6.a) as 17.7 N/mm and 18.1 N/mm in MD and CD respectively. These values are then used to plot the corresponding strain on the stress-strain curve of the GM exhumed from the sites S1 and S2 (Figure 6.b). These values will be the strains that would be needed to mobilize the $MAStress_0$ and would be then the MAStrain that should not be exceeded.
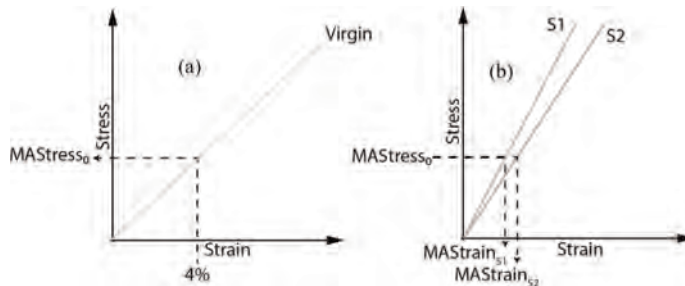
Figure 6.   Determination of the $MAStress_0$ (a) and the $MAStrain_{S1}$ and $MAStrain_{S2}$ (b).

Figure 7 presents the obtained MAStrain of 3.55 % and 3.04 % for S1, in MD and CD, respectively; and 3.71 % and 3.73 % for S2, in MD and CD, respectively. All the data are significantly drawn from a normal distribution as all the p-values are higher than the significance level of 0.05. The two-sample t-tests can then be performed to compare the results of the virgin GM to the exhumed ones (see Table 5). The obtained MAStrains are significantly lower than the initial MAStrain of 4% as the p-values are lower than the significance level of 0.05, except for S2 in CD where the p-value of 0.06 is above the significance level (see Table 5). The strain corresponding to the MAStress0 would be lower than it was initially, which means that the maximum allowable stress is mobilized earlier. The critical stress could be reached before the critical strain considered in the design. It is important to note that the GM behaviour could change over time. In this case study, there is a gain of stiffness that could negatively impact the design criteria.
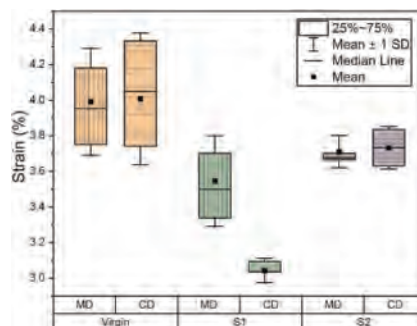
Figure 7.   Box plots of the maximum allowable strains determined for the typical HDPE GM and the exhumed GMs.

Table 5. P-values of the normality tests and the two-sample t-tests on the obtained MAStrains.

Direction	GM	p-value of the normality test	p-value of the two-sample t-test
MD	Virgin	1.00	0.01
	S1	1.00	
	Virgin	1.00	0.03
	S2	0.52	
CD	Virgin	1.00	0.00
	S1	0.94	
	Virgin	1.00	0.06
	S2	0.92	

6 CONCLUSIONS

This paper presents actual physical, chemical, and mechanical properties of 1.5 mm-thick HDPE geomembranes exhumed from cover systems used for the reclamation of two mine sites (S1 and S2) that have 13 and 20 years of service, respectively. Results are compared to those of a typical virgin HDPE geomembrane with the same thickness. It can be concluded that:

- The antioxidant and stabilizer level of the S1 geomembrane is close to that of the virgin one, and the S2 geomembrane degradation is in an advanced state;
- The exhumed HDPE geomembranes still contain antioxidants and stabilizers, and remain in the antioxidant depletion stage during which no negative impact is expected on the mechanical properties;
- The exhumed HDPE geomembranes are stiffer than the virgin one and may have better resistance.

The effect of the tensile behaviour on the design criteria of the maximum allowable strain is that the gain of stiffness reduces the MAStrain, which could impact negatively the design criteria.

However, it should be noted that the comparisons were made with a typical virgin HDPE geomembrane whose properties could be different of the initial properties of the exhumed geomembranes. This was done for comparison purpose only. A large and complete characterization of the geomembranes should be done before its installation to complete the data provided by the manufacturer. These data should be then available for a better understanding of the in-service durability of geomembranes. In the absence of the initial properties of the GM as installed, the results presented in this study constitute reference values for future in-service performance assessments.

REFERENCES

ASTM (2005) *D883-05 Standard Terminology Relating to Plastics*. West Conshohocken, *PA*, United States, ASTM International, www.astm.org.

ASTM (2015) *D6693-04 Standard Test Method for Determining Tensile Properties of Nonreinforced Polyethylene and Nonreinforced Flexible Polypropylene Geomembranes*. West Conshohocken, *PA*, United States, ASTM International, www.astm.org.

ASTM (2017) *D5885/D5885M−17 Standard Test Method for Oxidative Induction Time of Polyolefin Geosynthetics by High-pressure Differential Scanning Calorimetry*. West Conshohocken, *PA*, United States, ASTM International, www.astm.org.

ASTM (2019a) *D3895-19 Standard Test Method for Oxidative-induction Time of Polyolefins by Differential Scanning Calorimetry*. West Conshohocken, *PA*, United States, ASTM International, www.astm.org.

ASTM (2019b) *D5199-12 Standard Test Method for Measuring the Nominal Thickness of Geosynthetics*. West Conshohocken, PA, United States, ASTM International, www.astm.org.

Dixon, J. & von Maubeuge, K. (1992) Geosynthetic Protection Layers for the Lining Systems of Landfills. *Ground Engineering*, 28–30.

Eldesouky, H. M. G. & Brachman, R. W. I. (2018) Calculating Local Geomembrane Strains from a Single Gravel Particle with Thin Plate Theory. *Geotextiles and Geomembranes*, 46, 101–110.

Ewais, A. M. R., Rowe, R. K. & Scheirs, J. (2014) Degradation Behaviour of HDPE Geomembranes with High and Low Initial High-pressure Oxidative Induction Time. *Geotextiles and Geomembranes*, 42, 111–126.

Hsuan, Y. & Koerner, R. (1998) Antioxidant Depletion Lifetime in High-density Polyethylene Geomembranes. *Journal of Geotechnical and Geoenvironmental Engineering*, 124, 532–541.

Hsuan, Y. G., Koerner, R. M. & Lord, A. E. (1993) Stress-cracking Resistance of High-density Polyethylene Geomembranes. *Journal of Geotechnical Engineering*, 119, 1840–1855.

Jones, D., Shercliff, D. & Dixon, N. (2000) Difficulties Associated with the Specification of Protection Geotextiles using Only Unit Weight. Proceedings of the Second European Geosynthetics Conference, Bologna, Italy.

Lilliefors, H. W. (1967) On the Kolmogorov-smirnov Test for Normality with Mean and Variance Unknown. *Journal of the American statistical Association*, 62, 399–402.

Lupo, J. & Morrison, K. (2007) Geosynthetic Design and Construction Approaches in the Mining Industry. *Geotextiles and Geomembranes*, 25, 96–108.

Maqsoud, A., Bussière, B. & Mbonimpa, M. (2021) Low Saturated Hydraulic Conductivity Covers. in Bussière, B. & Guittonny, M. (Eds.) *Hard Rock Mine Reclamation*. CRC PRESS.

McWatters, R. S. & Rowe, R. K. (2010) Diffusive Transport of Vocs Through LLDPE and two Coextruded Geomembranes. *Journal of Geotechnical and Geoenvironmental Engineering*, 136, 1167–1177.

McWatters, R. S., Rowe, R. K., Battista, V. D., Sfiligoj, B., Wilkins, D. & Spedding, T. (2020) Exhumation and Performance of an Antarctic Composite Barrier System After 4 Years Exposure. *Canadian Geotechnical Journal*, 57, 1130–1152.

Müller, W. W. (2007) *HDPE Geomembranes in Geotechnics*, Springer.

Peggs, I. D., Schmucker, B. & Carey, P. (2005) Assessment of Maximum Allowable Strains in Polyethylene and Polypropylene Geomembranes. Waste Containment and Remediation.

Rarison, R. F. M., Mbonimpa, M. & Bussière, B. (2022) Effects of Freeze–thaw Cycles on the Properties of Polyethylene Geomembranes. *Geosynthetics International*, 1–39.

Rowe, R. K., Abdelaal, F. B., Zafari, M., Morsy, M. S. & Priyanto, D. G. (2020) An Approach to High-Density Polyethylene (HDPE) Geomembrane Selection for Challenging Design Requirements. *Canadian Geotechnical Journal*, 57, 1550–1565.

Rowe, R. K. & Yu, Y. (2018) *Tensile Strains in Geomembrane Landfill Liners*. Singapore, Springer Singapore.

Rowe, R. K. & Yu, Y. (2019) Magnitude and Significance of Tensile Strains in Geomembrane Landfill Liners. *Geotextiles and Geomembranes*, 47, 439–458.

Scheirs, J. (2009) *A Guide to Polymeric Geomembranes: A Practical Approach*, John Wiley & Sons.

Student (1908) The Probable Error of a Mean. *Biometrika*, 6, 1–25.

Touze-Foltz, N. & Lupo, J. (2009) Utilisation des Géosynthétiques dans les Applications Minières : Synthèse Bibliographique et état des Connaissances. Revue Sciences Eaux & Territoires, *N° Spécial Ingénieries EAT-28*, 101–118.

Introduction of geogrid reinforced MSE retaining structures in major Ghanaian Interchange project

M. Nods
Admir Africa, Enschede, The Netherlands

K. Bempong
Associated Consultants Ltd, Accra, Ghana

ABSTRACT: This project case study describes the design and construction of 23 MSE walls at the Pokuase Interchange Project in the Accra region (Ghana). The wall heights varied up to approximately 10m. The walls are supporting the approach embankments of various fly-over bridge structures at the Interchange. It concerned a first application of this technology in Ghana, and it was executed successfully within 2 years time. The vertical MSE structures were finished with prefabricated concrete panels as a protective facing, which were placed after construction of the wrap-around geogrid reinforced walls. Local granular fill could be used in the structures. The design and construction were performed in accordance with international standards (BS 8006, EBGEO, EN14475). The design included a stability analysis, consolidation and settlement analysis, and a detailed Method Statement.

1   INTRODUCTION

Geosynthetics have been used effectively to overcome many geotechnical, roadway, hydraulic and environmental challenges during the last decades. The geotechnical applications mainly include geosynthetics performing reinforcing, separating and stabilizing functions (BSI 2016). They can enable the improvement of structures on soft and even organic soils as basal reinforcement elements, and they can provide soil reinforcement over concrete piled embankments. This paper focuses on the large-scale introduction and description of geosynthetic reinforced retaining structures or mechanically stabilized earth (MSE) in Ghana. In general, these types of structures are frequently used to construct steep slopes or vertical to sub-vertical retaining walls. Due to the high load carrying capacity of geosynthetic reinforced retaining structures they have also been utilized for bridge abutments all over the world and in the process have become an established construction method

2   POKUASE INTERCHANGE

The Pokuase Interchange and Local Roads Project was planned and executed under the Accra Urban Transport Project (AUTP) by the Department of Urban Roads (DUR) under the Ministry of Roads and Highways (MRH). The project was financed with a facility from the African Development Bank (AfDB) and matching funds from the Government of Ghana (GoG). Associated Consultants Limited, a local engineering consulting firm, undertook the design assignment. Supervision was performed by same firm with support of their partners, Bigen Africa from South Africa. Originally the interchange was designed as a Three-Tier Single Point Urban Interchange (SPUI) and later after a value engineering process initiated by the contractor, Zhongmei Engineering Group Ltd, an additional tier was included to form the Four-Tier Stacked Interchange (Figure 1).

Figure 1.   Pokuase Interchange.

The project is located at the northwestern corridor of the Greater Accra Metropolitan Area. The Awoshie, Pokuase, Amasaman and Kwabenya areas all feed directly into the project area. These areas are rapidly developing as a consequence of Greater Accra Metropolitan Area's urban sprawl. This expansion has made it difficult to meet the project zone residents' service demands in terms of transport, water, health, education, sanitation etc. The urban sprawl has resulted in traffic congestion, overcrowding, substandard housing, inadequate education and health facilities, poor sanitation and a generally degraded environment. This project therefore aimed to promote sustainable economic growth and reduce poverty through greater employment and income generation opportunities; an increase in economic activities; improved accessibility to and within the project area; and enhanced access to socioeconomic infrastructure (health facilities, schools, local markets, water supply, sanitation facilities and drainage). In this way, the project through its components creates significant linkages and synergies that will contribute towards attaining economic growth, poverty reduction, and expanding social benefits to greater numbers within the respective communities.

The 4-Tier stacked Interchange was constructed as part of the project and involved the construction of Mechanically Stabilized Earth (MSE) Retaining walls for the approach roads to the bridge ramps and top tier bridge. The construction of these walls made use of geosynthetic-reinforced soil (GRS) systems, which have the ability to accommodate tensile forces and improve the mechanical properties of the composite material. The geogrids applied excel not only by their good tensile stiffness and tensile strength, but also by their exceedingly high interaction flexibility. Innovative precast concrete wall panels with a concrete column and beam grid arrangement, which had local artistic 3-D signs, were used for the first time ever (Figure 2).

Figure 2.   Precast concrete wall panels with artistic 3-D signs.

3   PRINCIPLES OF DESIGN

The design principles in the British (BSI 2016) and German (DGGT 2011) codes are similar and each code follows the 'limit state' concept. In the design codes these limits are considered

as two groups, ultimate limit states (ULSs) and serviceability limit states (SLSs). ULSs are associated with collapse either by structural and/or geotechnical failure, or by excessive deformation. SLSs correspond to unacceptable deformations or minor structural damage, leading to increased maintenance requirements and reduced service life. For each failure mode partial load factors are applied to the actions (disturbing forces) to increase their value and partial material factors are applied to resistance (restoring forces) to reduce their values broadly in line with the principles in Eurocode EC7. However, the codes differ in the application of the load and material partial factors.

3.1   *British code BS 8006: 2010*

BS 8006 (BSI 2016) was first published in the UK in 1995. It was one of the first European codes to adopt the limit state concept. It detailed the design of retaining walls, steepened slopes and embankments overlying weak foundation soils. In additional general sections dealt with fundamental principles of design, materials, testing and construction considerations. This code was subsequently reviewed and updated to be in line with the European guidance on execution (construction): EN 14475, and geotechnical design: EN 1997-1. Both external and internal ULS modes of failure are considered in the detailed design. BS 8006 defines a boundary between steep slopes and walls and applied different design criteria for each designation. Reinforced soil 'structures' within 20° of the vertical are defined as a wall, reinforced soil 'structures' with inclination below 70° are defined as a steepened slope. Three load cases are defined to ensure the worst-case load combinations are considered for the design. Load case A (1.5) partial load factor applied on all loadings. This is usually the critical condition for reinforcement rupture, wedge stability and bearing capacity. Load Case B considers maximum load factors applied to the earth pressure and loads behind the reinforced soil block (1.5) and minimum partial factors (1.0) applied to self-weight. This combination is normally critical for pull-out or adherence failure and forward sliding. Load Case C considers self-weight in the working condition and is used for the SLS limit states only. BS 8006 prescribes a SLS limit on the internal Post Construction strain occurring between the end of construction and the end of the design life. This is limited to 1% in walls (non-abutments) and 0.5% for abutments. The restricted tensile capacity of the geogrid, T_{cs} is obtained using isochronous load-strain curves (BS 8006, Figure 43).

3.2   *German standard EBGEO*

In Germany design follows the guidelines EBGEO (DGGT 2011), which are based on the German National Standard for Earthworks: DIN 1054. In contrast to the approach taken in the UK, EBGEO does not distinguish between wall and slope. For both the magnitude of partial factors as well as the definition of potential failure modes to be analyzed and the design approach are identical.

The geotechnical category varies depending on the structure's height, difficulty or risk (e.g. bridge abutments). Furthermore design must not contradict DIN 4084:2009-01 (Calculation of embankment failure and overall stability of retaining structures) where geosynthetic reinforcement is considered a "non pre-stressed tension member". Important is to consider a correction factor ψ, which is depending on the type of fill-material. Beside conventional checks of sliding, bearing and tilting failure, design calculations shall include the check of all potential slip surfaces regardless of whether they are surrounding or intersecting the reinforced structure entirely, partly or without cutting a reinforcement layer.

Special attention also needs to be given to prove the stability at the front facing where the classification of the facing types has been adopted as per EN 14475 (CEN 2006). With regard to the serviceability limit state EBGEO recommends that the following post construction deformation components are considered: foundation settlement; internal settlement of reinforced fill; horizontal movement, of the front of the structure and face deformation.

Table 1. Partial factors for actions (effects).

	BS 8006 Combination A	BS 8006 Combination B	BS 8006 Combination C (ULS)	EBGEO Limit State 1B	EBGEO Limit State 1C	EBGEO Limit State 2 (SLS)
Permanent effect-mass of RS block	$f_{fs} = 1.5$	$f_{fs} = 1.0$	$f_{fs} = 1.0$	$\gamma_G = 1.35$	$\gamma_G = 1.0$	$\gamma_G = 1.2$
Permanent effect-Earth pressure behind the RS block	$f_{fs} = 1.5$	$f_{fs} = 1.5$	$f_{fs} = 1.0$			
Unfavourable variable effect	$f_q = 1.5$	$f_q = 1.5$	$f_q = 1.0$	$\gamma_Q = 1.5$	$\gamma_Q = 1.3$	$\gamma_Q = 1.0$

3.3 *Geosynthetic design strength*

The geosynthetic design strength can be considered as the restoring force by the geosynthetic (resistance), which is used as input parameter in the stability analysis.

BS 8006 prescribes a limit on the internal Post Construction strain occurring between the end of construction and the end of the design life. This is limited to 1% in walls (non-abutments) and 5% in slopes. The restricted tensile capacity of the geogrid, Tcs is obtained using isochronous load-strain curves (Figure 3), before reducing this value to the SLS design strength TD using equation (1).

$$T_D = \frac{T_{CR}}{f_m} = \frac{T_{char}/RF_{CR}}{RF_{ID} \cdot RF_W \cdot RF_{CH} \cdot f_s} \tag{1}$$

where RF_{ID} = reduction factor (RF) for installation damage; RF_W = RF for weathering; RF_{CH} = RF for chemical and environmental effects; and f_s = factor of safety for the extrapolation of data.

Figure 3. Layout and input parameters for stability analysis in GGU Stability software.

These factors are determined in accordance with PD ISO/TR 20432 (British Standards Institute, 2007). Considering EBGEO the long-term strength of the geosynthetic reinforcement $F_{B,d}$ is determined from equation (2):

$$F_{B,d} = \frac{T_{CR}}{f_m} = \frac{F_{B,k0}}{A_1 \cdot A_2 \cdot A_3 \cdot A_4 \cdot A_5 \cdot \gamma_m} \tag{2}$$

where $F_{B,d}$: Design strength; $F_{B,k0}$: Characteristic tensile strength (EN ISO 10319); A_1: Reduction factor for creep strain or creep rupture; A_2: Reduction factor considering any damage during transportation, installation and compaction; A_3: Reduction factor for joints and connections; A_4: Reduction factor for environmental effects (weathering and resistance

to UV light, effects of temperature, chemical resistance, microbiological resistance); A_5: Reduction factor for dynamic action; and γ_m: Partial safety factor for the structural resistance flexible reinforcement elements (Table 2).

Table 2. Partial safety factors for flexible reinforcement DIN 1054.

	Load Case		
	LC1	LC2	LC3
γm	1.4	1.3	1.2

It is to be noted that above reduction factors are meant to be mean values. $F_{B,k0}$ however is denoted as based on 95% confidence level EBGEO defines the serviceability limit state as structural deformation being a consequence of characteristic dead loads and soil parameters.

4 STABILITY ANALYSIS

The MSE design was carried out for the maximum height of H = 12m (including embedment depth). The walls support the approach embankments of various fly-over bridge structures of the interchange. A vertical spacing of 0.60m between geogrids was used in the design.

The assumed geotechnical data for foundation and fill material can be found in the output of the calculations performed (Figure 3). They were based on geotechnical investigation reports submitted by the contractor Zhongmei Engineering Ltd. Groundwater level is assumed at the base layer level (first geosynthetic layer), which can be considered as worst-case scenario.

A horizontal seismic coefficient of $a_h/g = 0.15$ has been included in the stability analysis. This coefficient was based on available seismic data in the area, and a discussion with the supervising consultant.

The external traffic load is set at 22.5 kN/m^2, which is considered a minimal traffic loading condition for motorways. In addition a dead load of 10 kN/m^2 (simulating the pavement structure) and 15 kN/m^2 (simulating the parapet) have been applied. For the interaction between soil and geogrid a reduction factor was used of 0.90.

According to EC7 and BS 8006 both Ultimate Limit States (ULS) and Serviceability Limit States (SLS) have been analysed. The software GGU Stability (GGU 2020) was used for the analysis.

All parameters that form the basis of this design have been verified before construction. In case of changes in the parameters, the design calculations had to be revised or adapted to the new parameters. The software program analyses the internal, external and compound stability of an assumed reinforcement scheme for steep slopes and walls using different methods and theories such as Bishop (cycles slices), Janbu (polygonal slices), Krey (cycles slices), general wedge method and block sliding method. The software allows the use of geogrids via the input of relevant design properties.

In the Ultimate Limit State (ULS) all possible failure mechanisms and slip planes intersecting the reinforcement layers, not intersecting the reinforcement, partially intersecting the reinforcement layers and when the sliding body moves directly over the reinforcement layer, were investigated in accordance with BS 8006, Figures 54, 55 and 56. The most unfavourable failure mechanism had to be identified. The software also allows the analysis of sliding, overturning and bearing failure of the MSE (GRS).

The stability analysis in the ULS has been performed for different wall heights up to 12 m with an embedment depth of 1 m. All possible slip circles have been considered and the most unfavourable failure mechanism has been identified. With the use of BBA certified geogrid reinforcements, independently certified design strengths in different fill types had been defined and used as input parameter in the software. This allowed working with guaranteed

and certified design strengths for different soil types and eliminated the time and cost consuming laboratory testing of different geogrids and soil types.

Eventually 3 different types of geogrids were used in the stability analysis: F80T, F110T and F150T. The geogrids are made from high-modulus, low-creep polyester (PET) yarns enclosed in a protective polymer coating. The number of different geogrid types was kept to a minimum.

A geotextile filter was applied between the geogrid and the reinforced fill at the wall facing to prevent the flush out (erosion) of fines from fill material.

The concrete panel design was made based on the design requirements of the Client, the production location, and required handling on site (transport and erection on site). The actual design of the panel was the responsibility of the contractor. The actual placement of the panels was done after constructing the MSE structure, which minimized possible post-construction settlements.

Serviceability analysis comprised the analysis of the settlement of foundations, post-construction strain in reinforcements and post-construction creep strain in saturated fine-grained fills (BS 8006, Figure 57).

Empirical data indicate that intrinsic settlements of 0.2% to 1% of the height of the MSE wall are normal when installation guidelines and best practices are followed. It is important to adequately compact the fill material of the MSE. The compaction of the fill material should be done following the EN 14475 execution standard for reinforced earth structures. From experience the expected intrinsic settlement of fill material in the MSE in an adequately compacted soil mass is very low.

An empirical value for the horizontal displacement for the front of the MSE wall is given as a maximum of approx. 1% to 2% of the MSE wall height, see EBGEO 7.5.1 (DGGT 2011).

5 CONCLUSION AND DISCUSSION

The 23 MSE structures were constructed without significant delays, and with the help of locally trained labour. Experts from the Netherlands provided the local training. No specific special skills were required. With the help of quality assurance documents supervision of the works was easy.

An important advantage of the wall system was the possibility to plan construction of the reinforced soil wall without the need to install the panels at the same time. This gives the following advantages:

– Settlements are allowed in the construction stage, the panels can be placed after consolidation
– Wall construction is not depending on the concrete panel production timing
– Panel repairs are possible after finishing the wall.

Other advantages of geosynthetic reinforced retaining structures compared to concrete rigid structures and gravity walls are the cost advantages, and much better resistance against seismic influences because of the flexibility of the structure.

REFERENCES

BSI 2016. BS 8006: 2010. *Code of Practice for Strengthened/reinforced Soils and other Fills.*
CEN 2006. *EN 14475:2006. Execution of Special Geotechnical Works – Reinforced fill.*
DGGT Deutsche Gesellschaft für Geotechnik 2011. *EBGEO Recommendations for Design and Analysis of Structures using Geosynthetic Reinforcements.*
GGU 2020. www.ggu-software.com/en/geotechnical-software/geotechnical-analysis/ggu-stability-slope-failure/.
Horgan, G.; Hangen, H.; Durand, R. & Vanícek, M. 2014. *European Reinforced Soil Design – The Codes, Proc. of the 10th International Conference on Geosynthetics.* Berlin: IGS.

Rehabilitation of landslide & construction of arguably the world's tallest Reinforced Earth® structure at Tindharia on NH-55, India

Somnath Biswas
Asia Pole Director, Terre Armée, New Delhi, India

Atanu Adhikari
Chief Development Officer, Terre Armée, India

Hirak Dutta
Head – Special Projects, Terre Armée, India

ABSTRACT: This paper presents a case study for a landslide rehabilitation project comprising in-situ grouted soil nailing and pre-stressed ground anchors for slope stabilization, hybrid Reinforced Earth® structure for widening of existing road, and drainage measures to prevent development of hydrostatic pressure. The project site is located on National Highway 55, Siliguri-Darjeeling Road in the state of West Bengal, India. This paper profiles the completed composite/shored Reinforced Soil structure S2 (102.8m high).

Keywords: Landslide Rehabilitation, slope stabilization, geosynthetic strap, hybrid reinforced earth structure, innovative technology

1 INTRODUCTION

A massive landslide occurred in Tindharia, West Bengal, India in September 2011 following a significant earthquake and heavy rainfall in the area. The landslide affected three locations, resulting in collapse of a portion of road and railroad on the valley side. The Darjeeling Himalayan Rail service, a UNESCO heritage structure and significant tourist attraction in the area was also severely affected.

The location of the S2 landslide was from chainage Km. 52 + 650 to Km. 52 + 750 on NH 55, thus a 100m length on the valley side of the road. This entire stretch of NH-55 and DHR track was totally cut off (Figure 2). The tender drawing specified composite/shored reinforced soil solution for stabilizing the slope by Soil Nailing and widening the constricted portion of NH-55 (Figure 1).

Figure 1. Major Landslide location: S2, Km. CH: 52 + 650 to Km. CH: 52 + 750.

Figure 2. Area where DHR track was totally cut off.

2 THE PROBLEM

The zone is earthquake-prone and experiences long durations of heavy rainfall, combined with poor surface/sub-surface drainage. Steep slopes comprising of loose unconsolidated material, and weathered rocks result in percolation of rainwater through joints and increase pore water pressure. The road width was very narrow due to collapse of valley side, i.e., an extremely steep an unstable one. Hence, the solution proposed for the project was to be designed for three requirements: widening of existing road from 5m to 10m width while ensuring overall slope stability during construction, building permanent asset structure requiring minimum maintenance, and providing a permanent solution for surface/sub-surface drainage.
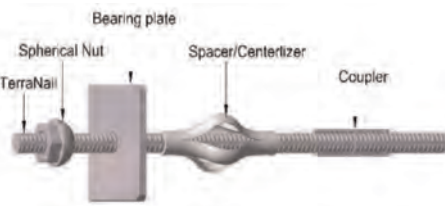
Figure 3.   Typical soil nail view.
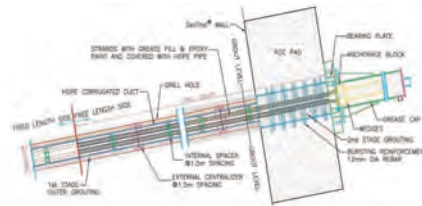
Figure 4.   Typical ground anchor detail.

3 THE SOLUTION

Terre Armée India provided a permanent and sustainable solution to the restoration project using the reinforced earth composite/shored system [8]. This system comprised of soil nails that are hot dip fully threaded galvanized bars with yield strength of 670 MPa and ultimate strength of 800 MPa. The bars are joined together using couplers for higher length as in-situ passive soil reinforcing elements and pre-stressed ground anchors as active soil reinforcing elements for cut slope stabilization and construction of Mechanically Stabilised Earth structure using high adherence GeoStrap® (geosynthetic straps) soil reinforcement for widening with limited space (2.5m) at base (Figure 5). This technology maintains a perfect balance between cut and fill solution. The composite/shored reinforced earth composite/shored system guarantees not only the slope stability but also ensures safety during construction, effective release of hydrostatic pressure through a well-designed subsurface drainage system and enabled construction of a very tall, reinforced soil structure despite limited space availability for base width. Due to the massive height and complex geometry of the structure, two layers active soil reinforcements in the form of Pre-stressed Ground Anchors (Design Load 42 MT) were also installed at the bottom of each tier. The structure has been designed [7] in two stages, the first stage of design check has been done by providing Soil nailing and deep ground anchors to achieve overall global stability of the structure. The second stage of design has been checked for stability of shored retaining structure and the tensile force in GeoStrap soil reinforcement which is connected directly with the soil nailed structure. The design stages are described below in section 4 and 5.

4 DESIGN OF TERRANAIL® STRUCTURE

Design check was done for the soil nailed slope with the aim of arriving at a soil nailing layout to overcome postulated failure mechanism. Additionally, each nail should be capable to resist local stresses acting on it. The relevant mode of failure for stability analysis are rotational failure either partially or totally through the soil nail block involving breakage and/or pull out of soil nails. The method adopted for the purpose of assessing failure mechanism is Bishop's slip circle method. Typical failure modes are as shown below in Figure 6 [6]. Soil Nails provide complete resistance against anticipated sliding from

1905
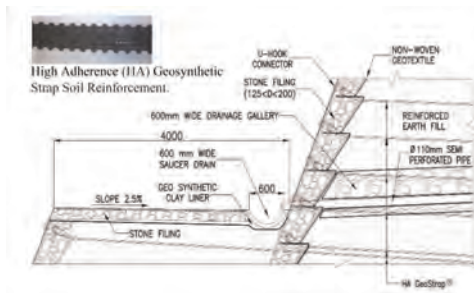
Figure 5. Detail showing the reinforced soil facing arrangement and mechnical connection system.

Figure 6. Typical rotation stability checks of a soil nailed slope.

backslope, offers global stability and hence, transfers no retained pressure to the composite/shored reinforced earth hybrid structure.

5 DESIGN OF TERRALINK® STRUCTURE

The composite/shored reinforced earth hybrid structure has been designed [1,3] *for both* internal checks *by* calculating the required *tensile forces in the* soil reinforcement including checks for the soil nails against tension and pullout and external *stability* checks by slip circle method. The tension in the soil reinforcement has been calculated by "Silo" method by considering the effect of inclination and the skin friction as expressed in the figure below (Figure 7). The effect of deformation, due to compaction and progressive filling of the structure has been addressed by providing intermediate berms in the cutting profile (Figure 14). This "Silo" effect and deformation has been validated by numerical modelling.

The overall stability is then checked by slip circle method for both static and seismic load conditions (Figures 8 and 9). The minimum factor of safety of 1.3 and 1.1 has been considered for static and seismic analysis [4]. Additional checks are also carried out considering the effect of internal water profile, thanks to the Piezometer installed at the site which provided the variation of water profile. The design of internal drainage system is most critical for the overall stability of structure. Hence, special provisions for the drainage system have been provided and discussed in subsequent sections.
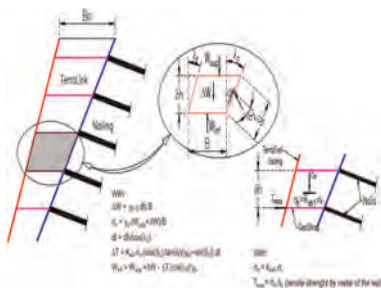
Figure 7. The tension in soil reinforcement by "Silo" calculation considering single friction surface.
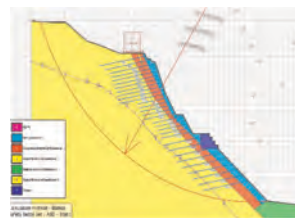
Figure 8. Typical output of slip circle analysis along with water profile for static case for soil nailed slope.

6 DESIGN OF GROUND ANCHORS

The basic components of a grouted ground anchor include: (1) anchorage; (2) free stressing (unbonded) length; and (3) bond length. The design of anchorage [2] is the combined system of
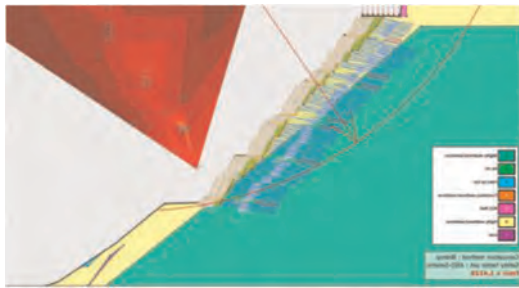
Figure 9.   Output of slip circle analysis for seismic case of shored reinforced soil structure.

anchor head, bearing plate, and trumpet that can transmit the prestressing force from the pre-stressing steel (strand) to the ground surface or the supported structure. The unbounded length is the initial portion of the prestressing steel that is free to elongate elastically and transfer the resisting force from the bond length to the structure. A bond breaker is a smooth plastic sleeve that is placed over the tendon in the unbonded length to prevent the prestressing steel from bonding to the surrounding grout. It enables the prestressing steel in the unbonded length to elongate without obstruction during testing and stressing and leaves the prestressing steel unbonded after lock-off. The tendon bond length is the length of the prestressing steel that is bonded to the grout and is capable of transmitting the applied tensile load into the ground.

7   DRAINAGE SYSTEM

The drainage system (both surface and sub-surface arrangements) is the most important function for any slope construction, design, and performance.

7.1   Surface drainage system

The surface drainage arrangement consists of (i) drops and guides on both side of the structure to collect all surface water from various interconnected drainage channels and discharge it away from the main structure and (ii) Network and series of surface drainage channels to collect the surface water at all tier levels. The network of surface drainage arrangements has been provided for the entire height of the structure. It follows along the tier of the composite/shored reinforced earth structure to the final discharge point away from the toe of structure (Figure 10).

Figure 10.   Berm provided to collect & drain surface water.
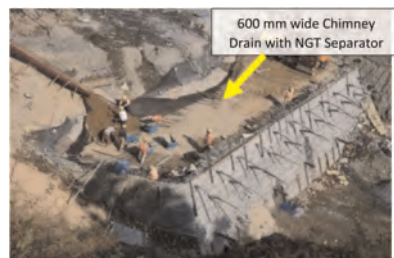
Figure 11.   Internal drainage system shown during construction.

7.2   Sub-surface drainage system

The function of sub-surface drainage system is to collect seepage water inside soil mass and discharge it to the nearest outlet point, which is the surface drain. Though the Mechanically

Stabilised Earth fill is considered a self-draining media, having sufficient permeability to eliminate any destabilizing lateral forces caused due to hydrostatic pressure and ground water seepage. It was very important to have proper drainage system to improve the overall stability of the structure, considering its criticality.

Inside the composite/shored reinforced earth structure, the sub-surface drainage system consists of 600mm thick well graded granular drainage gallery (Chimney Drain) placed at the rear end of the geosynthetic strap. It is then connected inside the reinforced fill with 110 mm diameter of semi perforated PVC pipe wrapped with non-woven geotextile to collect and dissipate water to the nearest outlet point (outside the structure) as shown in Figure 12.

The most important provision incorporated in the design is semi-perforated drainage pipes deep inside the ground (Figure 13) to prevent development of additional hydrostatic pressure and to maintain equilibrium in ground water table. It was important to place these drainage pipes very deep to intercept the water table to ensure a constant seepage of water flow and to prevent development of hydrostatic pressure (Figure 13). These pipes are wrapped with non-woven geotextile and then inserted inside by drilling larger size hole.

Figure 12.   Sub-surface drainage outlets.

Figure 13.   Sub-surface water discharge through. weepholes.

8   CHALLENGES ENCOUNTERED

The project team faced several challenges from the design stage to the completion stage. This included convincing the client to adopt solutions as per actual site conditions, change in structural geometry, inclusion of drops and guide surface drain, additional toe stabilization and installation of deep perforated pipes as sub-drainage system. These provisions were vital for the long-term stability of the structure. The team faced other challenges during construction stage, including safety aspects, traffic management, space constraint, absence of any access road, drilling difficulties through challenging soil strata, high water table, unstable base, and toe slope. Appropriate construction methods were adopted to overcome all these challenges and are described in the subsequent section.

9   CONSTRUCTION SEQUENCE

i) Slope cutting and stabilization by top-down construction method: This activity commenced at the site after implementing all safety measures based on site risk assessment including provision of safety barricades, traffic management scheme and adopting a safe construction method. Firstly, the drilling activity for Soil Nails and Ground Anchors started from RL 36m up to founding level.

ii) Hillside slope was protected by fixing galvanized welded wire mesh underlaying with a layer of non-woven polypropylene geotextile filter simultaneously with soil nailing activity (Figure 14). This construction method ensured the structure's overall and local stability.

Figure 14. Slope stabilization through installation of soil nails and fixing one layer each of non-woven geotextile and GI back mesh.

iii) Composite/shored reinforced earth hybrid system was developed from the founding level up to RL 36m by keeping all projected anchors cables outside the composite/shored reinforced earth hybrid structure's facia.

iv) Drilling and development of the composite/shored reinforced earth system and pre-stressing of ground anchors were carried out by using the composite/shored reinforced earth structure as a working platform for the remainder of the project.

v) RCC Anchor Blocks were cast, keeping the anchor cables projected for future pre-stressing. Ground anchors were prestressed after developing the composite/shored reinforced earth hybrid system up to 10m above the anchor level.

vi) Surface drainage system (PCC Drops and Guides) were constructed simultaneously along with the composite/shored reinforced earth system's development.

vii) Toe protection works and arrangements for final discharge of surface and sub-surface water were carried out to prevent weakening of the toe from rain-cuts and scouring.

10 BENEFITS AND INNOVATIVE FEATURES OF COMPOSITE / SHORED REINFORCED EARTH HYBRID TECHNOLOGY

The composite/shored reinforced earth system is an ideal solution for both slope stabilization, restoration and widening of any collapsed road or slope due to any landslide. The following key features and conclusions can be made based on the learnings experience from this project.

(i) It has been conclusively proven that it is possible to construct very tall retaining structures without cutting the toe of the hill and with an available small base width at toe which is as less as 5m for 100 m height of wall/slope.

(ii) The technology not only addresses local and compound stability issues but also global stability issues.

(iii) This technique can address very complex and challenging landslide issues by adopting suitable and innovative measures as per site conditions.

(iv) Slope stabilization using grouted soil nail by top-down installation method is a safe construction method. However, it is important to conduct a detailed risk assessment prior to the start of any site activity and needs to address all risks by adopting all safety measures.

(v) Use of galvanized welded wire mesh facing system for slope stabilization of soil is a suitable solution. The exposed hillside slopes were quite loose and steep at some

locations steep ($>$ 85 degree), but the welded wire mesh performed very well (without any local collapse-related incidents) despite heavy rainfall.

(vi) High strength fully threaded galvanized bars guarantee the long-term durability of nails and act as a secondary corrosion protection layer as the grout may crack due to any internal deformation/settlement.

(vii) Drilling is challenging with presence of water table or through high hydraulic pressure but can be well controlled by releasing pressure through the provision of deep perforated drainage pipes.

(viii) Sub-surface drainage system played an active role in releasing hydrostatic pressure and maintaining a state of equilibrium of the natural water table. Functionality of weepholes needs to be ensured throughout the structure's design life to reduce hydrostatic pressure. Drainage system performance is key to ensuring the structure's long-term stability.

(ix) The direct linking connection system adopted is unique and has rotational movement flexibility (in horizontal and vertical planes) that helps in reducing any additional stress at connection points caused due to any fill compression or foundation settlement.

(x) The foundation base for such a composite/shored reinforced soil structure needs to be competent and settlement below the composite/shored reinforced earth structure needs to be limited within 100mm. Any settlement of foundation base is likely to trigger high stresses (both in shear and tension) at connection points. The stress due to any settlement can be further reduced by providing intermediate berms at back cutting face as in Figure 15.

(xi) Recent inspection of the structure indicates successful performance.

Figure 15. The completed structure.

11 SAFETY AND ENVIRONMENT

Composite / shored reinforced earth hybrid technology used in this project restored mountain slopes with minimal impact. The adoption of shored reinforced soil structure has enabled in reduction of backfill by 90%, resulting in overall carbon emission reduction. The sub-surface drainage system adopted in the design helped in saving 4 million litres of water during project execution. The project also continues to provide uninterrupted potable water supply to 31 households in the area.

REFERENCES

[1] British Standards Institution. (2010) BS 8006-Part 1: 2010, *Code of Practice for Strengthened/ reinforced Soils and other Fills*.
[2] British Standards Institution. (1989) BS 8081: 1989, *British Standard Code of practice for Ground Anchorages*.

[3]   Indian Road Congress (IRC), Ministry of Road Transport and Highways (MORT&H), Government of India. (2014) IRC: SP:102-2014, *Guidelines for Design and Construction of Reinforced Soil Walls.*

[4]   Indian Road Congress (IRC), Ministry of Road Transport and Highways (MORT&H), Government of India. (2015) IRC 75:2015*, Guidelines for the Design of High Embankments.*

[5]   Indian Road Congress (IRC), Ministry of Road Transport and Highways (MORT&H), Government of India. (2013) *Specification of Road and Bridge Works*, Fifth Revision.

[6]   U.S. Department of Transportation, Federal Highway Administration. (2009) FHWA-NHI-10-025: FHWA GEC 011*, Design and Construction of Mechanically Stabilized Earth Walls and Reinforced Soil Slopes – Volume II.* https://www.fhwa.dot.gov/engineering/geotech/pubs/nhi10024/

[7]   U.S. Department of Transportation, Federal Highway Administration. (2003) FHWA0-IF-03-017*, Geotechnical Engineering Circular No. 7: Soil Nail Walls.* https://www.fhwa.dot.gov/engineering/geotech/pubs/nhi14007.pdf

[8]   U.S. Department of Transportation, Federal Highway Administration. (2006) FHWA-CFL/TD-06-001, *Shored Mechanically Stabilized Earth (SMSE) Wall Systems Design Guidelines*, https://rosap.ntl.bts.gov/view/dot/42939/dot_42939_DS1.pdf

Avalanche risk mitigation by means of a reinforced earth embankment: The Ludrigno case study

M. Barbolini
FLOW-ING Srl, La Spezia, Italy
Department of Civil Engineering and Architecture – University of Pavia, Pavia, Italy

A. Simini
HUESKER Srl, Trieste, Italy

F. Stefanini
FLOW-ING Srl, La Spezia, Italy

ABSTRACT: The village of Ludrigno, located in the lower part of the Seriana Valley (Bergamo, Italy), is known to be exposed to a significant avalanche risk. The first historical information about avalanches affecting the village dates back to the 17th century and throughout the years the avalanche events have repeatedly caused loss of goods and lives. The article intends to present the design process followed to identify the optimal defense strategy within a cost-benefit analysis framework. The design choice fell on a geogrid reinforced avalanche protection embankment 140 m long and 10 m high, as it was found to be the best solution both in terms of cost-effectiveness ratio and environmental integration. The stability analyses carried out on the embankment due to the avalanche impact are presented and the choice of the reinforcing geogrids, based on their long-term design strength, is discussed. The article aims to highlight the relevance of this topic, which involves the safety of population living in mountain areas and several issues related either to design or quality control of materials and construction.

1 TERRITORIAL FRAMEWORK

Ludrigno is a small village within the Seriana Valley in the province of Bergamo (Italy), located at 560 m a.s.l. on the right-hand side of the Serio River at the bottom of the Orobie Alps. The Vendulo stream is a right-hand side tributary of the Serio River. The basin has an extension of 275 hectares and the stream has two major branches, the longest of which is 3.5 km long and has a 38% mean slope. The ridges surrounding the Vendulo Valley are 2.4 km long and the highest peak is Mount Secco (2207 m a.s.l.). The slopes developing from the ridge have a main aspect of 90° East, even if exposure ranges for NE to SE moving from south to north along the crest.

2 THE LUDRIGNO AVALANCHE (ALSO KNOWN AS VENDULO AVALANCHE)

2.1 *Historical background*

The Ludrigno avalanche, is the snow avalanche that flows along the Vendulo valley and has often affected goods and lives inhabiting the valley bottom. In 1916 an extreme avalanche

detached from the slopes underneath Mount Secco. Once it had reached the valley bottom, the main flow took a right-hand turn moving towards Ludrigno, destroying some of the buildings and causing multiple fatalities. In 1984 a massive avalanche flew to the valley bottom; it remained mainly within the riverbanks and reached the National Road n.49. Luckily only one person was injured but the road remained closed for several days isolating many villages. During the years other avalanche events occurred without reaching the valley bottom, mainly stopping in the lower part of the channel or along the fan. Seldom, as a precautionary measure, the inhabitants of Ludrigno are evacuated because of avalanche risk; latest evacuations are dated 2008, 2009 and 2014.

2.2 Avalanche features

The avalanche release area deploys along a ridge 2400 m long: there are 3 main release basins (A, B and C in Figure 1), including 7, 6 and 5 single starting areas respectively, which cover a total surface of 33.5 ha. Outline of single potential release areas was supported by the AFRA code (Barbolini *et al.* 2011). The possible combination of the 18 single starting zones gives us in principle 262,124 different potential avalanche release scenarios, even if a simultaneous release of avalanches originating from the three basin is highly unlikely and was not considered. In the upper part the avalanche track is divided in two main channels that come together at about 900 m a.s.l.. The final part follows the riverbed, with avalanche deposits that could reach the National Road 49 and extend until the Serio River; when the riverbed is filled by previous avalanche debris the avalanche could overtop the right riverbank and spread along the fan in the direction of Ludrigno.

Figure 1.   Main avalanche features (left) and PRA outline (right).

3   MODELLING ANALYSIS AND ASSESSMENT OF ALTERNATIVE SOLUTIONS

3.1   Avalanche simulation analysis

The analysis of the design avalanche scenario has been undertaken through the 2D avalanche simulation software RAMMS (Christen *et al.* 2010).

At first, input data and simulation parameters have been calibrated by a back-analysis on known past events (1916 and 1984 avalanches) and available avalanche maps (Avalanche Cadastre, see Figure 2). Once we gained enough confidence and stability within the 2D avalanche simulations, 21 avalanche scenarios have been selected in order to get the design parameters (run-out distance, flow height, velocity and pressure) and evaluate the worst-case scenario. Avalanche simulation showed that for each main basin (A, B and C in Figure 2), a simultaneous release of the potential starting zone generates avalanches able to severely affect exposed elements in the valley bottom.
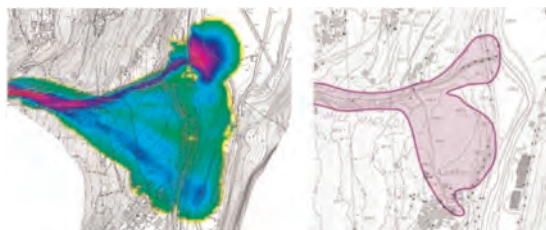
Figure 2.   Example of RAMMS's simulation output (left) compared to the Avalanche Cadastre (right).

3.2   *Assessment of alternative protection measures and choice of optimal solution*

The modelling analysis gave us an insight of possible solutions to reduce the avalanche risk. Three different alternative solutions have been investigated: a) active defense structures in avalanche release areas (snow bridges or snow net); b) passive defense structures in the downhill area (catching or deflecting dams); c) mixed solution (combination of active and passive defense structure). In order to get a significant risk reduction by means of active works in the release zones numerical simulation showed that reduction of potential release areas was necessary in all three basins, with a need for an overall reduction of about 50% of potential starting zones and an estimated cost of about 9 million €. Conversely, by means of passive work in the lower part of deposition zone, where the avalanche is slower, a significant reduction of risk for the road and the village was evaluated achievable with a significantly reduced cost (about 3 million €). The mixed solution was found to be not effective, because the increase of cost for installation of active works in the most critical areas does not yield a relevant reduction of the sizes (and costs) of the passive works. Cost-benefits analysis showed the construction of an avalanche catching to be the optimal solution. Due to budgetary constraint, in a first batch of works the dam was limited to the protection of the village, postponing the protection of the National Road to a subsequent batch of works.
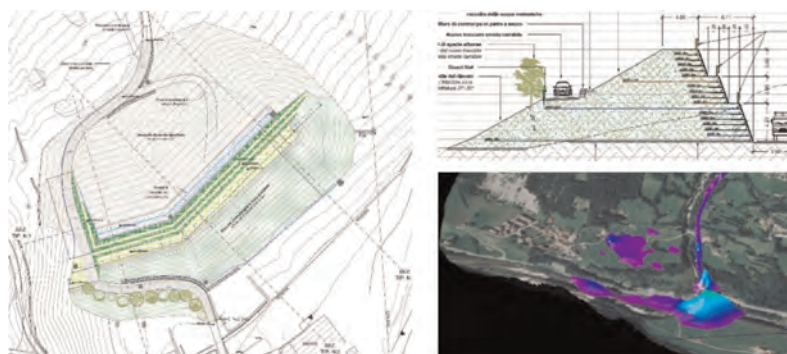
Figure 3.   Plan and section view of the catching dam with an example (bottom-right) of post-operam simulation performed to evaluate its effectiveness (DTM integrated with catching dam).

4 ESTIMATION OF MINIMUM DAM HEIGHT

The main design parameter of an avalanche catching dam is its minimum height needed to avoid avalanche overtopping. According to widely used approaches (Mears 1981), the estimation of the minimum dam height (H_D) can be done with the following formula (Figure 4):

$$H_D = h_0 + h_s + h_r \qquad (1)$$

$$h_r = \frac{V^2}{2 \cdot g \cdot \lambda} \qquad (2)$$

where h_0 is the snow cover depth, h_s and V the flowing height and velocity of the avalanche at dam location, h_r the run-up height of the avalanche on the uphill side of the dam and λ an empirical parameter that accounts for energy loss at impact. For Ludrigno case, the estimate was based on the avalanche dynamic simulation output for the worst-case scenario (V = 12 m/s and h_s = 2 m) and setting h_0 = 1 m and λ = 1.5, thus obtaining a value of H_D of ∼7 m. The calculation of the minimum dam height was verified using the more recent physically based criteria (Johannesson *et al.* 2009), resulting in a higher value of H_D (9.7 m) that was finally fixed to 10 m to stay on the safe side.
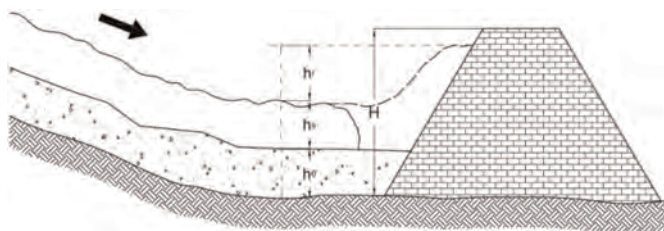
Figure 4. Scheme for dam height estimation.

5 STRUCTURAL AND GEOTECHNICAL DAM DESIGN

The structural design of the dam must comply with the Ultimate Limit State regulation and the scenarios that need to be verified are: (a) sliding and overturning of the upper part due to the avalanche flow impact pressure; (b) internal stability of the earth embankment and structural design of geogrids; (c) global stability of the whole slope.

5.1 *Sliding and overturning*

In this scenario the acting load is the pressure of the avalanche which hits on the uphill side of the dam (calculated as product of snow density and velocity squared, according to Eq. 3.18 of Rudolf-Miklau *et al.* 2015). The pressure has a uniform value through the flow-height and drops to zero along the run-up height. The impact may happen at different heights from the ground depending on the ground snow cover thickness when the avalanche event occurs. In this scenario the dam is modeled as a solid element which can slide or overturn at any height and its resistance depends on geometry, weight and geotechnical properties of the structural terrain. The assumption that the earth embankment behaves as a solid element is granted by reinforcing geogrids whose resistance will be described later.
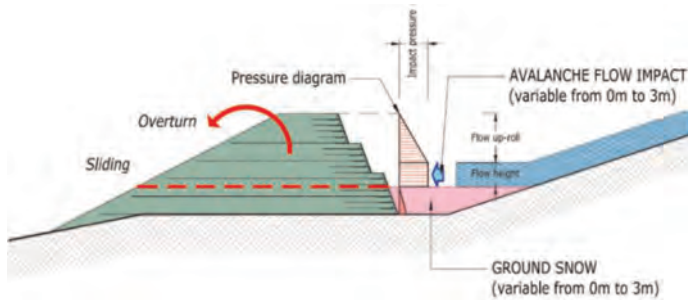
Figure 5. Sliding and overturning analysis schemes.

5.2 *Internal stability and structural design of geogrids*

The integrity and structural resistance of the earth embankment is achieved through 60 cm thick layers of fill material, carefully compacted above geogrid reinforcements which are shaped at a 70° slope by means of steel mesh formworks. Reinforced slopes are analyzed using modified versions of the classic limit equilibrium slope stability methods. A circular potential failure surface is assumed (Figure 6) and the relationship between driving and resisting forces determines the slope's factor of safety. Reinforcement layers intersecting the potential failure surface are assumed to increase the resisting force. The structural design must address all possible failure modes that a reinforced slope will potentially experience, uphill and downhill. In this scenario, the most demanding loads are the variable live loads acting on the earth embankment, which usually are snow deposition and construction or maintenance vehicles. The resisting force of the geogrids to be used in the evaluation of the safety factor is the long-term design resistance T_D evaluated according to the following equation (HAPAS Certificate 2014):

$$T_D = \frac{T_{char}}{RF_{CR} \cdot RF_{ID} \cdot RF_W \cdot RF_{CH} \cdot f_s} \tag{3}$$

T_D is calculated by reducing the characteristic short-term resistance of the geogrids (T_{char}) with the following partial safety factors: reduction factor due to creep (RF_{CR}), reduction factor due to installation damages (RF_{ID}), reduction factor due to weathering (RF_W), reduction factor due to chemical and environmental effects (RF_{CH}) and reduction factor due to extrapolation of data (f_s). The characteristic short-term resistance is evaluated according to EN ISO 10319.
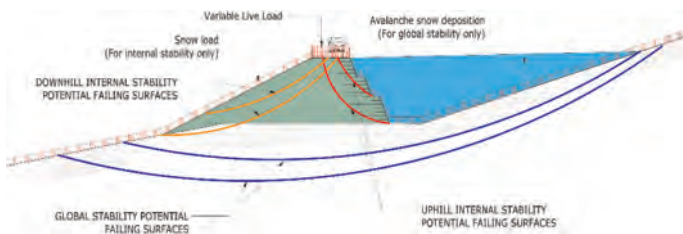
Figure 6. Internal (red) and global (blue) potential failing surfaces.

1916

5.3 *Global stability of the whole slope*

The global stability examines the as-built scenario and evaluates the minimum safety factor for each potential sliding surface which starts uphill of the embankments and ends downhill of it. In order to evaluate the worst-case scenario, in the calculation, the weight of the avalanche snow deposit in the case of complete filling of dam is taken into account (Figure 6). The embankment acts as a rigid body, and it affects the analysis with its weight and geometry.

5.4 *Main structural components and technical details*

The earth embankment is made of the following components: fill material, geogrid, erosion control net and steel mesh formwork. Filling material has no specific requirement, even though it is suggested to use non-cohesive materials such as gravel, crushed stone, sand-macadam mixture, sandy soil and rock filling, which may not be affected by water and have small settlements once compacted. Geogrid reinforcements are provided with different short-term resistance: due to the lack of specific Italian regulations for geosynthetic reinforcements, it was required that geogrid products were to be certified by the British Board of Agrément (BBA). In this construction site, 65 kN/m and 110 kN/m short term resistance HUESKER Fortrac T polyester geogrids have been used in 60 cm thick layers. Higher grade resisting geogrid have been used in the lower part where major stresses occur. A 3.5 mm x 3.5 mm polyester mesh erosion control net was placed between the fill material and the geogrids to prevent soil erosion before the greening of the slope. Steel mesh formwork are made of electro-welded mesh, usually 8 mm rebars on a 15 cm mesh size. The steel formwork does not provide any structural resistance; it only allows a better and easier shaping of the embankment. The formwork is provided with stiffening rods which guarantee a better resistance in the initial compacting stages.

6 LANDSCAPE AND ENVIRONMENTAL REQUIREMENTS

In order to optimize the dam, it has been built in the lower part of the fan, where the avalanche velocities are lower. As a consequence, the visual impact on the Ludrigno village landscape could be relevant, therefore. For that reason, in order to minimize the impact on the landscape but at the same time to maximize the storage capacity, the protection dam has been designed as an earth embankment with reinforced soil in the up-slope side and as a natural slope of about 30 degrees in its down-slope side (Figure 3), with special attention paid to the greening of slopes. In terms of environmental impact of the works, a great attention was paid to earthwork balance, in order to avoid supply of earth materials from outside the construction site as well as landfilling.

7 CONSTRUCTION

The construction of the avalanche protection dam was carried out in 2016. The quality of the embankment has been assessed during construction by surveys at various stages. The geogrid quality inspection was undertaken by checking bills of materials and certified documentation assessing the resistance of the product according to BBA; the quality of the filling material and its compaction procedures were assessed through several different on field validation in different points and stages of the construction (Figure 7).

Figure 7. The avalanche dam at the end of construction.

8 CONCLUDING REMARKS

Earth dams are effective avalanche protection measures especially in those sites with several potential release areas, where active protection is usually not viable for very high construction and maintenance costs. The use of geogrids allows to increase the slopes of dam walls, with advantage in term of footprint, storage capacity and energy dissipation at impact. In the design of geogrids particular attention must be paid to the reliability of the reduction factors used to estimate design resistance and to the quality of certifications that guarantee the long-term behavior of the material.

REFERENCES

Barbolini, M., Pagliardi, M., Ferro, F. & Corradeghini, P. 2011. Avalanche Hazard Mapping Over Large Undocumented Areas. *Nat Hazards* 56, 451–464.

Christen, M., Kowalski, J. & Bartelt, P. 2010. RAMMS: Numerical Simulation of Dense Snow Avalanches in Three-dimensional Terrain. *Cold Regions Science and Technology*, 63, 1–2: 1–14.

HAPAS Certificate, 2014: Fortrac Geosynthetics – Fortrac T and R-T geogrids, Certificate 13/H197.

Johannesson, T., Gauer, P., Issler, D. & Lied, K. 2009. *The Design of Avalanche Protection Dams: Recent Practical and Theoretical Development*. European Commission, Directorate General for Research.

Mears, A. I. 1981. *Design Criteria for Avalanche Control Structures in the Runout Zone*. Rocky Mountain Forest and Range Experiment Station. Fort Collins, Colorado.

Rudolf-Miklau, F., Sauermoser, S. & Mears, A. 2015. *The Avalanche Protection Handbook*. Ernst&Sohn.

The application of modularized MSE wall in the project of Montenegro BB expressway

H. Yaming
CCCC Expressway Consultants Co., Ltd. Beijing, China

C. Lili & X. Wang
BOSTD Geosynthetics Qingdao Ltd., Shandong, China

ABSTRACT: Modularized MSE wall is a supporting structure with the characteristics such as simple and clear structure system, high industrialization process in the production and construction. Comparing with the traditional supporting structure, modularized MSE wall has lower requirement on the construction spacing and geology environment, except beauty contour and green initiative, which makes it well used in urban structure, building and road project, especially in the design and construction of mountain area expressway. With the advantage of overcoming the limitation of geomorphology and geology, it becomes a worth well alternative solution. In this article, based on the project in the Montenegro BB expressway, the authors introduce the challenges of designing modularized MSE wall in high embankment with complicate geology condition, meanwhile, analyzing the problems and solutions during the design and construction, to provide the experience and reference for the future use.

1 PROJECT BACKGROUND

Montenegro Bar-Boljare expressway is about 180 km, which connects the famous port Bar and Boljare in north, it is the first expressway in Montenegro and one of the most important corridors to the heart of the Europe. This project is the priority section of Bar-Boljare expressway, from Smokovac to Matesevo, with the length of about 41 km, including 18.3 km tunnel, 6.3 km bridge.

Within this project, modularized MSE wall solution is widely adopted for different structures (bridge abutment, toll station, retaining structure), in various terrain (flat plan, hill area, mountain area), as well as with complicate geology (limestone, flysh). Totally, there are 17 MSE walls in length of 3.5 km, the highest wall is about 30.9 meters, and the total quantity of geogrid is 1.4 million square meters.

2 INTRODUCTION OF DESIGN

2.1 *Design scheme comparison*

There are many limitations for the design of this project, such as defined expropriation, environment protection, use ability of land and complicate geology. For the construction of high embankment, if it goes with slopes, then extra expropriation and huge quantities of embankment material are required; if bridge solution is adopted, the limitation spacing, and complicated terrain will make trouble for construction and cost. So, retaining structure is a relatively proper solution.

The designer compared different types of retaining structures-masonry wall, reinforced concrete wall (RC wall) and mechanical stabilized earth (MSE) wall from the following aspects:

(1) Structure analysis

Masonry wall and RC wall have higher requirement of bearing capacity; also, for the structure safety reason, these kinds of wall cannot be too high, which will not be able to work as supporting structure for high embankment. While MSE wall has relatively low requirement on the bearing capacity and could be high enough for the use.

(2) Resistance to Seismic

This project locates on the extensive seismic zone, which is not favorable for rigid structure such as masonry wall and RC wall because of deformation displacement. MSE wall is a flexible structure with good adaptability to the deformation of foundation and displacement of wall body, especially in the seismic zone.

(3) Economic and Environmental Benefits

Masonry wall and RC wall demand huge quantity of concrete and reinforcement, which will not only increase the cost, but also go against the environment because of the carbon emission.

(4) Construction feasibility

In some part of the project zone, complicate terrain environment like deep valley and sharp hillside makes it not possible for large scale machinery works, which is necessary to the masonry wall and RC wall. While MSE wall has lower dependency of huge machine, but more relies on human power and simple equipment.

Based on the above comparison, MSE wall could be a proper solution for some special case because of the complicate site situation.

2.2 Design principle

According to the EC7, the design of MSE wall includes Serviceability limit states and ultimate limit states verification.

2.2.1 Serviceability limit states

The serviceability limit states mainly contain calculation or qualitative analysis of settlement, durability, and displacement of structure.

2.2.2 Ultimate limit states

Two design conditions are carried out for the ultimate limit states, the permanent and seismic condition. The verification of these two conditions is achieved by the overall stability analysis, local stability analysis, internal stability, and detail structure analysis, to guarantee the safety of structure. EC7, EC8 as well as Germany and Italy guidelines are applied.

2.3 Calculation program and content

The stability verification of MSE wall is carried out by the program MSEW3.0 and ReSSA3.0, which are the copyright of US Company ADAMA Engineering, Inc., and are authorized by the FHWA. For a compatibility of using EC7 and EC8, input parameters are adjusted.

The stability verification includes an internal, external, and overall stability analysis. During the analysis of external stability, the MSE wall is treated as a reinforced composite, while the soil within the geogrid zone is assumed to be rigid, together with geogrid working as gravity retaining structure. In this concept, the anti-sliding calculation, overturning calculation, foundation stress and eccentricity are calculated.

The internal stability analysis is mainly focusing on the geogrid and its interaction with soil, including the strength and anchor length definition. To ensure the geogrid and soil works efficiently, the maximum tensile strength, the potential sliding surface, the pullout strength, as well as spacing of geogrid need to be designed.

Except the above mentioned two aspects, the overall stability should also be checked, mainly about deep sliding which may happens in the foundation soil. Traditional slip circle

method or other well accepted method could be adopted to define the potential critical sliding surface, and then to check the safety factor for the given solution.

Settlement and deformation calculation are more related to the performance of structure, especially for the structure which is close to other existing or planed structures, or those structure with high serviceability.

2.4 Detail design elements

The MSE wall in Montenegro project is a retaining system made of prefabricated modularized concrete block and high-quality geogrids, as well as other auxiliary elements.

2.4.1 Facing block foundation
For a better control of flatness and alignment of wall, after the excavation of wall foundation, a cast on site reinforced concrete foundation is performed. The dimension of the foundation is decided by that of block. In this project, it is 0.45 m in width and 0.25 m in thickness, with minimum C30, V8 and M100 in quality control. A tooth is given to make sure all the blocks are in the same line.

2.4.2 Modularized concrete block
According to the EN14475, this type of block belongs to the hard units, conform to the En771-3, part 3. The dimension is 400 mm*220 mm*220 mm. On the top of the block, a groove is set, and at the bottom a tooth is set correspondingly. With these structures, the fixing of geogrid and the installing of block will be easily done in according to the design principle.

The concrete block used in this project is prefabricated in local factory, with high efficiency and quality. The size of gravel for the block is less than 10 mm, and the concrete should be with minimum C40, V8 and M150 for water and frozen resistance.

2.4.3 Uniaxial geogrid
The geogrid shall be an integral, rigid geogrid manufactured from high density polyethylene polymer containing only virgin polymer, appropriate Carbon Black master batch and in-process regrind, with well anti-creeping, anti-aging performance, as well as other necessary characteristics.

The geogrid used in this project is E'GRID, provided by BOSTD Geosynthetics Qingdao Ltd, which is approved by the Employer and Engineer. The product has the BBA certification on the reinforced soil system (Figure 1).
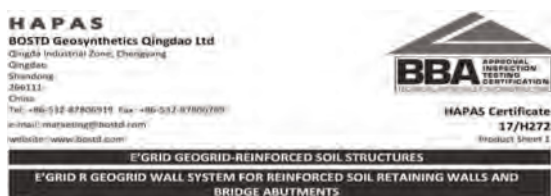
Figure 1. Certification of E'GRID geogrid.

2.4.4 Polymer connector
The connection of facing block and geogrid is achieved by special unit-Polymer connector. It is designed by the characteristic of geogrid and block, with required strength. The function and effectiveness of connector is verified as a component in the retaining system.

2.4.5 Drainage system
The drainage system is designed to facilitate the discharging of water out of the wall body, to reduce the unfavorable influence of water to the structure, including internal and external drainage system.

The internal drainage system includes a drainage layer at the rear of wall facing block and longitudinal drainage pipe covered by geotextile. The thickness of drainage layer is 50 cm. The purpose of the system is to discharge the potential water in the soil mass to reduce the water pressure and mechanical properties of soil.

The external drainage system includes a drainage ditch in front of the wall foundation, which is collecting water from the internal system, and open channels to discharge water out of the ditch.

The connection of internal and external drainage system is achieved by T Junction and outlet pipe.

3 SPECIAL DESIGN AND CONSTRUCTION DETAILS

3.1 *Design*

3.1.1 *Unfavorable geology*
The project locates on middle and north part of Montenegro, where the geology is dominated with limestone and flysh composite. In the zone of limestone, nature slope is covered by thick and loose layer of highly weathered limestone debris and clay mixtures. While at the zone of flysh, the bearing capacity is not enough for the high structure, even the bearing capacity for MSE wall is relatively low. To increase the bearing capacity where is not enough, replacing nature soil with better material is necessary. For example, at K31, the after removing the nature, 2 m thick crushed river gravel is placed and compacted to achieve the required bearing capacity.

3.1.2 *Steep terrain*
There is part of the expressway going along the steep hill slope, and the overall stability is not verified because of the steep terrain and thick layer sandy clay with gravel debris. At the section of retaining wall K6, ballast together with permanent landfill is designed at the foot of the retaining wall to guarantee the overall stability, at the same time reuse the extra material from tunnel excavation.

3.1.3 *Underground water*
Underground water is rich in some location of the retaining wall in the zone of flysh, because of the heavy vegetation and cracking of base rock. To guide the water from the nature soil and foundation soil, various of drainage solution are adopted case by case. At K35, the after excavation of wall foundation, seepage water from excavate slope and foundation cause problem. A close drainage system is designed with drainage layer between the embankment material and nature soil, at the bottom of the wall, as well as at the back of the facing wall, to make sure the water to be collected and discharge through the drainage layer.

3.1.4 *Special purpose and function*
MSE wall is usually working together with other structures, such as bridge abutment, culvert, underpass. In this case, special attention should be paid to the connection of two types of structures. At the design of Moraca bridge abutment in Smokovac interchange, since the abutment is about 20 m high, with the limitation of expropriation, and to reduce the soil pressure behind the abutment, MSE wall solution is proposed. Meanwhile, toll station and an underpass are right after the bridge, a widen platform is required for the office of toll station (Figure 2). MSE wall plays an excellent role because of its shape and structural adaptation and resolve the complicate case properly.

3.2 *Construction*

3.2.1 *Preparation of filling material*
The filling material is one critical factor to the quality of the construction. In this project, it is strictly required with high quality. It should be friction material, inert, stiff, and durable,

Figure 2.   The application of MSE wall in complicate structure group.

without organic, plastic, metal, rubber or any other harmful or combustible material. Silty stone and marl stone are also not allowed to be original material because of their poor physical and mechanical characteristics.

In the design, the specific requirement of filling material is $\gamma = 20.5$ kN / m^2, friction angle is $38°$, cohesion is $0\sim5$ kPa. Besides, to have a better compaction to reduce the future deformation, it is required to have a well-graded filling material (Figure 3).
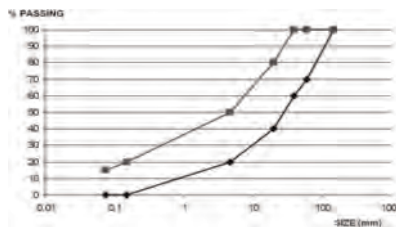
Figure 3.   Particle size distribution of fill for reinforced soil walls.

To satisfy the requirement form design, two types of filling materials are chosen as options, one is crushed limestone, and another one is crushed and mixed gravel from Tara River. All the mixture are prepared according to the required size distribution, and then sent to the authorized laboratory in North Macedonia.

3.2.2   Quality control of filling construction

The quality of filling material construction has significant influence on the long term stability of MSE wall. To have a high quality, the following requirements are given and achieved:

1. The maximum size of filling material is less than 100 mm, the quality control is performed every 44 cm in thickness.
2. The compaction is performed every 22 cm, with minimum compaction 95%, Ms $\geq$ 40 MPa.

The compaction technology is well organized and performed on site, with strictly monitoring of each step, spreading, and rolling of material, vibration compact, static compact as well as the direction of roller. At the part close to the wall face, huge machine is not allowed but with human power and hand compactor to work.

3.2.3   Precise control of facing block

One of the advantages of MSE wall is aesthetics, and this depends on the precise control of wall facing block.

The control of block installation starts from the first layer, after the finishing of foundation pad, the position of each block is marked on the foundation. The blocks at the first layer are with flat bottom without the tooth. The second layer of block is installed on the first layer

in zigzag role, to make sure the joint of upper layer blocks is in the middle of the lower block. The tooth of the upper layer block should be tightly attached to the groove of the lower block to keep the wall facing in the 86° vertically. Any block with uneven surface, especially the bottom and top surface should be polished carefully.

3.2.4 *Finishing of facing block*
When the wall is higher than 6.6 m, it is designed as steps from top to bottom, each step is 6.6 m. At each step, to a have an aesthetic view and avoid water going inside the block (block is with openings), a cast in-situ concrete cover is placed, which can also be a effective solution to make the top layer block stable.

3.3 *Quality control*

Except the quality control of all the materials, the control of construction is also necessary. With the agreement of the Employer and Engineer, to have better control of construction quality, the following quality control items are given, with testing method and criteria (Table 1).

The control item is only based on this specific project, but it is always better to have a unified control requirement for MSE wall structure, or at least some guidance for the future construction and application.

Table 1. MSE wall construction quality control.

No.	Item	Test method/Equipment	Criteria
1	Static Compressive modulus	Plate Test	$\geq$ 30 MPa
2	Compaction	Sand Cone Method	$\geq$ 95%
3	Flatness	4 m Rule	$\leq$3 cm
4	Facing Inclination	Total Station	$\pm 1°$
5	Height	Leveling Gauge	± 10 cm
6	Foundation Position	Total Station	± 5 cm

4 CONCLUSION

As a well-developed retaining system, MSE wall has many technology and economic advantages compared with traditional structures. In the Montenegro project, based on the site conditions and project requirements, the design and construction team overcame lot of difficulties, fully taking the advantage of the MSE wall, resolve the project problems properly.

The successful application of MSE wall accumulates plenty of design and construction experience, which can provide reliable guidance and help to the similar project in this field, also proves that the quality of products from all the suppliers.

Meanwhile, during the project design and construction, there are also some open questions found, such as gradation of filling material, deformation calculation, which may need more efforts in study and application.

REFERENCES

Technical Committee CEN/TC250. 2004. *Eurocode 7:Geotechnical Design-Part 1:General Rules*. Brussels: CEN.
Technical Committee CEN/TC250. 2004. *Eurocode 8: Design of structures for earthquake resistance Part 5: Foundations, retaining structures and geotechnical aspects*. Brussels: CEN.
Hardy Geisler. 2022. *HAPAS Certificate-E'GRID R Geogrid Wall System for Reinforced Soil Retaining Walls and Bridge Abutments*. Watford: British Board of Agrement.

Combination of geosynthetics used as riverbank slope normalization in Cimanggis residential area, West Java, Indonesia

D.A. Nurjannah, N.A. Anindita, F. Widhiastuti & D.S. Harninto
P.T. Geoforce Indonesia, Central Jakarta, Indonesia

ABSTRACT: This paper presents the study case related to combination of geosyntethics used as riverbank slope normalization located in Cimanggis residential area, West Java, Indonesia. The combination of gabion, geogrid reinforcement combined with wiremesh facing and geo-composite of geotextile non woven-geogrid slope protection were applied along the section of the riverbank slope. The riverbank slope section spans 390 meters along Cikeas river where it will later become access road and near the crest will be constructed housing area. Slope stability analysis was conducted to determine the value of the slope safety factor with the aim of concluding what preventive and security measures could be. From the results of the analysis, it showed that the 13 meters high slope of the Cikeas river's safety factor was below the criteria stated in Indonesian National Standard for Geotechnic Design Requirements with a safety factor 1.20 (the slope safety factor must be above 1.50). The combination of geosythetics were applied in the program and yield the safety factor up to 1.613 which indicated safe slope. This design also considered the earthquake pseudostatic load, where the result of the safety factor was 1.103 and fulfilled the criteria stated in Indonesian National Standard for Geotechnic Design Requirements (the slope safety factor must be above 1.10). The combination of those geosynthetics application worked effectively for normalizing the river bank slope.

1 INTRODUCTION

The exclusive residence of Podomoro Golf View Cimanggis, is located on the Cikeas river which has contours and slopes of land. To support the construction of the dwelling, careful planning is needed, especially regarding slope stability. The Cikeas River has a fairly steep river slope and there are several points of a fairly swift current. Based on the geological map, the area along the Cikeas river, the geological condition is a layer of silt, sand, gravel, gravel and boulders. This is in accordance with the conditions in the field and the results of soil investigations which has been done.

Figure 1. Riverbank location.

2 LITERATURE

2.1 *Geosynthetic material*

The geosynthetic material that is used for earth retaining structure is geogrid, woven and non-woven. Geogrid and woven are used as reinforced elements, and the non-woven is used as separator element.

Figure 2.   (a) Non-Woven and (b) Geogrid.

The strength parameter of geosynthetic material is influenced by the field condition, applied load (construction, operational and earthquake loading). The Geosynthetic materials have the specification of their tensile strength. But, during the analysis the ultimate tensile strength must be divided with several reduction factors of geosynthetic as the euation [1] below.

$$T_{design} = \frac{T_{ult}}{RF \times RF \times RF} \tag{1}$$

The factors like installation damage (RF_{id}), durability (RF_d), and creep (RF_{cr}) must be consider during analysis. The value of the reduction factors of geosynthetic could be taken from the table reduction factors of geosynthetic. Based on the use of geosynthetic materials in the field. material for area slope the value of installation demage (1.10 – 1.50), creep (2.0 – 3.0), durability (1.0 – 1.50). (Koerner 2007)

The value of tensile strength that is used for analysis is the allowable tensile. Hence, the analysis of stability could be conducted.

2.2 *Design criteria*

Slope stability analysis should consider live load, dead load and earthquake according to the designation of excavated slopes and heaps. Traffic load is added as live load to the entire width of the road surface and the magnitude is determined based on the class of roads given referring to SNI 8460:2017 for road class 1 the value of traffic load is 15 kPa.

The minimum safety factor required for analysis using pseudostatic models is greater than 1.1 (SF>1.1) using seismic coefficients obtained from peak acceleration on the surface (PGA) with the determination of the site class and amplification factor. The size of the FPGA depends on the site classification. Seismic calculation is done in pseudo-static, with the acceleration coefficient as follow

$$
\begin{aligned}
\mathrm{Kh} &= 0,5 \times \mathrm{PGA} \times \mathrm{FPGA} \\
\mathrm{Kh} &= 0,5 \times 0,42\mathrm{g} \times 1,08 = 0,226\mathrm{g}
\end{aligned}
\tag{2}
$$

2.3 Soil backfill

The soil backfill material must be compacted minimum 95% of dry weight laboratory. The recommended materials for backfill is Gravel-Sand. If the fine grained material is used as fill material, the drainage system behind and inside the retaining wall must be well managed. The spaces inside the system that may water to infiltrate, must be collected and delivered outside the system (Koerner 2005)

3 METHODOLOGY DESIGN

3.1 Soil investigation

The soil investigation area closest to the river contains drill points BH-02 and BH-03 while sondir data is at sondir points S-03, S-07, and S-07. The description of the type of soil is as follows.
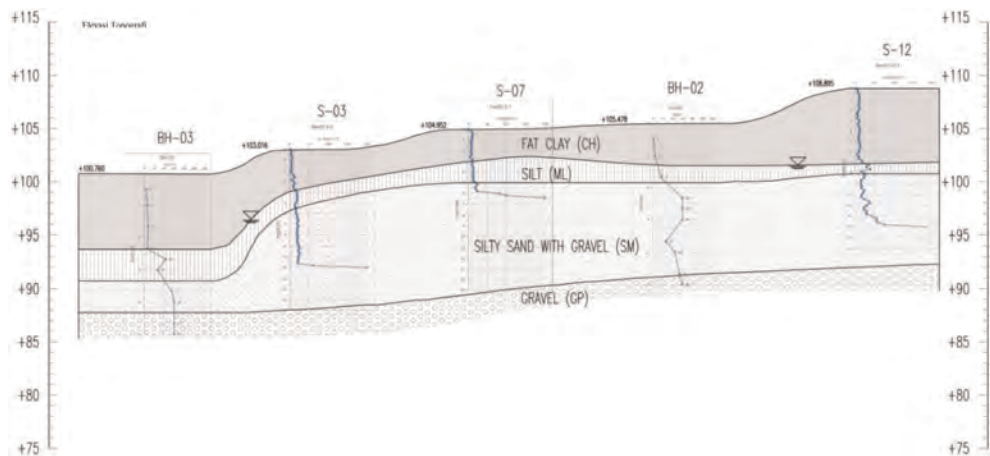
Figure 4.   Soil profile at BH-03, S-03, S-07, and BH-02.

From the results of soil investigations, it was found that the field conditions in BH-02 were dominated by clay soil with soft consistency at a depth of up to 1.5 meters from the surface. At a depth of 1.5 meters to 4 meters, a layer of clay with medium consistency was found. Hard soil layers are found at depths above 8 meters. At point BH-03 it is dominated by clay soil with soft consistency at a depth of up to 3 meters from the surface. At a depth of 3 meters to 8 meters, a layer of clay with medium consistency was found. Hard soil layers are found at depths below 10 meters.

3.2 Parameter analysisi on PLAXIS

Slope stability analysis is carried out to determine the safety factor of the slope to be made. To carry out this analysis, the following parameters are used based on the interpretation and assumptions of the soil data because the available data are incomplete.

The analysis was carried out using the finite element method with the Plaxis 3D program with soil modeling as follows. The soil parameters are based on assumptions and the closest available soil data, namely BH 02 and BH 03. This analysis was carried out at STA 2 + 975, which was taken at the most critical slope location.

Table 1. Soil data parameter with hardening soil model.

Soil Type	γ_{uns}/γ_s (kN/m³)	E_{50}^{ref} (kPa)	E_{oed}^{ref} (kPa)	E_{ur}^{ref} (kPa)	c' (kPa)	ϕ' (°)
Silty with Sand	14/17	55000	165000	38500	35	11
Silty Sand with Gravel	14/17	105000	315000	73500	30	50
Gravel Sand Fill	17/19	30000	21000	90000	5	35
Gravel BH2 BH3	18/19	165000	495000	115500	5	35
Selected Fill Material	14/17	8500	25500	5950	25	18
Fat Clay BH 03	13/16,5	25000	75000	17500	11	12.5
Fat Clay BH 02	14/17	15000	45000	10500	45	9

Table 2. Soil data parameter with linier elastic model.

Soil Type	γ_{uns}/γ_s (kN/m³)	E' (kPa)
Gabion	18/18	80000

Table 3. Geogrid paramater for numeric model simulation in PLAXIS.

Material	EA (kN/m)	N_p (kPa)
Geogrid 40 kN/m	253	12.63

4 RESULT AND DISCUSSION

4.1 *Global safety factor result*

Targeted FOS against Global Stability of the structure are

– Under static condition, FOS $\geq$ 1.5. (Based on Indonesian Standard SNI 8460:2017)
– Under seismic condition, FOS $\geq$ 1.1. (Based on Indonesian Standard SNI 8460:2017)

Achieved Global Safety Factor are

– Static condition at Initial Condition: 1.209 $\leq$ 1.50 NOT OK!
– Static condition at Slope Protection: 1.613 $\geq$ 1.50 OK!
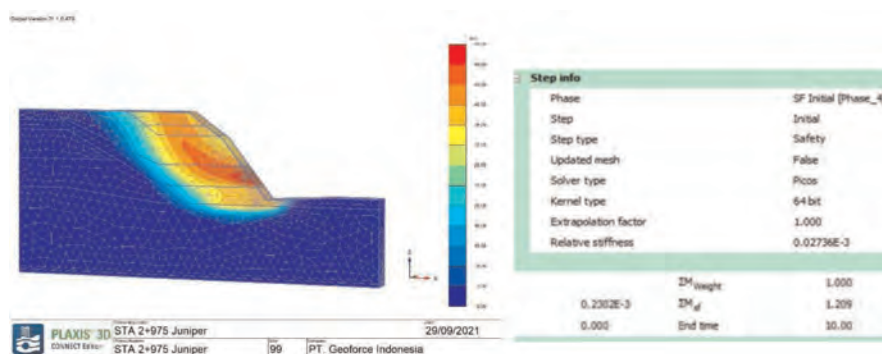
Figure 5. Estimation of static failure mode and safety factor of initial condition slope.
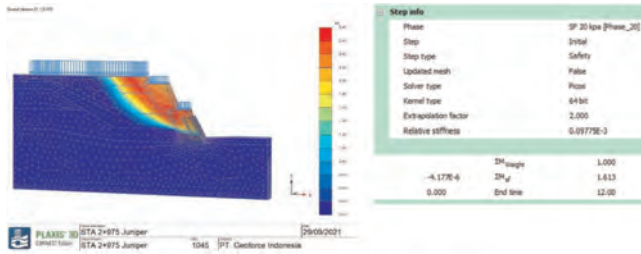
Figure 6. Estimation of static failure mode and safety factor of slope protection.
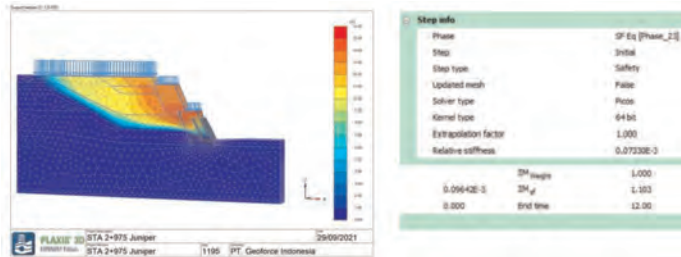
Figure 7. Estimation of pseudo-static failure mode and safety factor of slope protection.

4.2 *Tensile working of geogrid under static and seismic loading condition*

The comparison of axial tensile force working on GI-Strip under static and seismic loading con- dition based on PLAXIS are as follow:

Table 4. Tensile strength comparison of geogrid – Static and seismic.
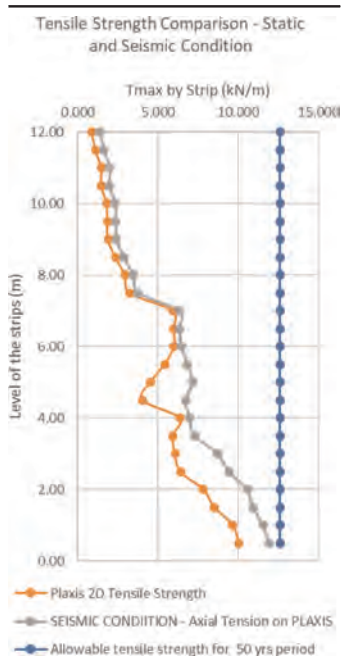
The value of the allowable tensile strength after the reduction factor is 12.63 kN/m for a design period of 50 years. The value of the axial tensile force acting on the Geogrid under static and seismic loading conditions is less than the 50-years design requirement.

5 CONCLUSION

The results of the slope stability analysis obtained the value of the safety factor in accordance to Indonesian National Standard for Geotechnic Design Requirements (8460:2017). This analytical modeling design criteria that have been targeted. The design life time of reinforcement under static and seismic loading conditions is less than the 50 year design requirement. Combination of geosyntethics can be used as an alternative riverbank slope normalization.

REFERENCES

Koerner, R. (2005). *Designing with Geosynthetics*. Upper Saddle River: New Jersey.
Badan Standarisasi Nasional. 2017. SNI 8460:2017. *Persyaratan Perancangan Geoteknik*. Ja- karta: Badan Standarisasi Nasional.
PUSGEN-PUSKIM PUPR, ISBN 978-602-5489-01-3, 2017, Indonesia Earthquake Source And Hazard Map.

MSE wall with geosynthetic reinforcement and polymeric connections case studies in Maryland and California

M.L. Ferrara & G. Lugli
Officine Maccaferri S.p.a., Zola Predosa, BO, Italy

ABSTRACT: MSE retaining wall with concrete facing panels is a pretty popular system used globally to support or enable the construction of infrastructure, forming retaining walls, abutments and wing walls. Polymeric reinforcement strips have been introduced in the MSE wall market as an alternative from traditional reinforcements with performance and cost-effectiveness significant advantages. They are also recommended for non-conventional situations such as marginal fills, chemically aggressive environment or in warm climates, where other reinforcements might be strongly affected by corrosion. Polymeric reinforcing strips, encased in LLDPE coating, have proved to perform like other non-extensible linear reinforcements, reaching higher values of pullout resistance. MSE walls with geostrips can be designed following International Standards, however, some considerations on the design methods applicability and nature of the reinforcements are provided here. MSE walls with polymeric strip were first introduced to the European market in the mid-1970s and their market has been growing ever since all over the world but only recently has been developed in North America. This paper presents two case studies of MSE wall projects reinforced with geostrips recently realized in Maryland and California.

1 INTRODUCTION

MSE walls described in this paper feature segmental precast concrete facing panels and layers of polymeric strip reinforcements connected to the panels by a polymeric connection system.

Soil reinforcing strips are manufactured from high-tenacity, multi-filament polyester yarns aligned and co-extruded with liner low density polyethylene (LLDPE). These strips have been used for many years all over the world in MSE walls as a geosynthetic alternative to steel reinforcements, due to their chemical stability and low creep characteristics. Polymeric strips are available in a wide range of tensile strengths and dimensions (thickness and width) to fit the specific project needs and design requirements; additionally, the polyethylene coating allows the use of geosynthetic strips in highly alkaline soils (pH up to 11) such as recycled concrete or lime-treated backfill materials.

The connection system is composed of a high-density polyethylene (HDPE) cavity insert box to create a void space secured by a steel anchor bar in the precast concrete facing panel. A non-degrading, polymeric sleeve covers the steel anchor bar to protect it from corrosion. Each polymeric strip reinforcement is continuously threaded though the sleeve and looped back to form a pair of geosynthetic strips that extend in a "V-shape" from each connector as shown in Figure 1.

Figure 1. Polymeric strips extending from the rear side if the concrete panel.

2 DESIGN PARAMETERS AND SOFTWARE INPUT

The design of this type of structures is governed by AASHTO LRFD Bridge Design Specifications and FHWA design guidelines in US territories.

AASHTO broadly categorize geosynthetics reinforcement as 'extensible' and metallic reinforcements as 'inextensible'. Although these categories have a major impact on the maximum load in each reinforcement layer (T_{max}) and its location, AASHTO does not provide a tangible measure to categorize an MSE system when it comes to design. That is, categorization is purely empirical and therefore, new MSE systems have to establish their category based on field data to facilitate their acceptance in the public sec-tor.

The internal design of MSE walls determines the magnitude and location of Tmax in each reinforcement layer. The maximum load in each layer is function of the frictional shear strength, φ, the self-weight expressed through unit weight of the backfill soil, γ, and the surcharge loading anticipated during the life of the structure. Furthermore, T_{max} enables the designer to select a reinforcement that has adequate long-term strength and it is used to calculate the pullout resistive length and the required strength of the connection between the reinforcement and the concrete panel facing.

Figure 2(a), reproduced from AASHTO, shows the locus of T_{max} as a function of depth below the crest, considering a wall having extensible or inextensible reinforcement. It can be seen that the loci are significantly different thus affecting the pullout resistive length which enables the reinforcement to mobilize its T_{max}. Figure 2(b) shows the distribution of the lateral earth pressure coefficient, K_r, with depth, normalized relative to Rankine's active pressure coefficient, K_a.

Although polymeric strips are not excluded by AASHTO LRFD Bridge Design Specifications, the lateral stress coefficient, K_r, for calculating the stresses at each level of polymer strip reinforcement is explicitly not included in Article 11.10.6.2.1 (AASH-TO 2018a) with regards to the internal design of the stresses in the reinforcement. AASHTO (2018a) commentary C11.10.6.2.1 states that Kr values for other reinforcement types can be developed as needed through analysis of measurements of reinforcement load and strain in full-scale structures and FHWA (2009) recommends supporting the instrumentation data
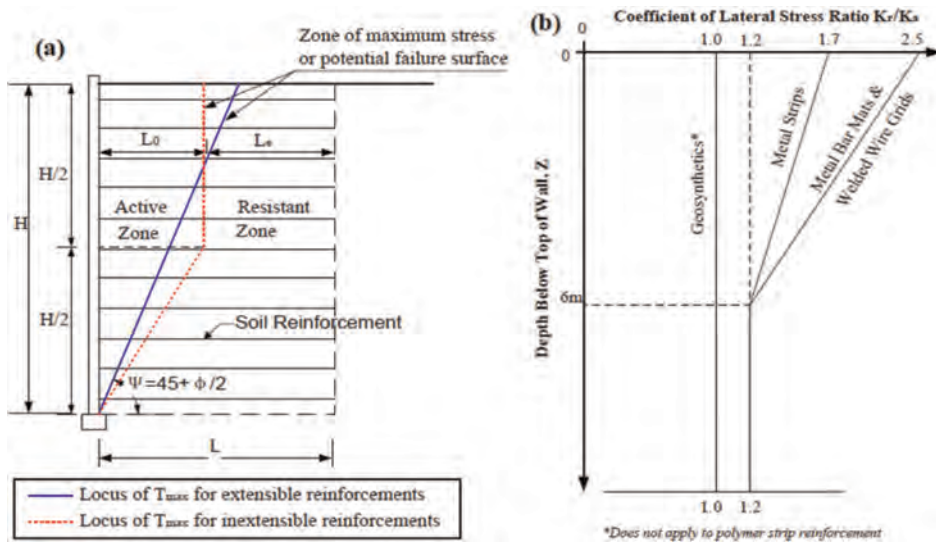
Figure 2. Implications of extensibility: (a) Locus of T_{max}, and (b) Variation of K_r/K_a.

with numerical models. Based on results of the studies reported by Lou, *et al.* (2015), and Rimoldi, *et al.* (2013) it appears that Kr value rec-ommended by AASHTO (2018a) for extensible reinforcement of 1.0 Ka at the top of the wall (depth z = 0) and Ka = 1.0 at depths z below the top of the wall of greater than or equal to 6.1 m (20 ft) is valid for discrete geosynthetic strip type reinforcing. These values are based on instrumented field perfor-mance testing presented by Luo *et al.* (2015) at the SR1/I95 interchange in Christiana, DE. The study showed that based on the field measurements of the experimental wall, using a linear failure plane extensible reinforcement model) was more conservative and more appropriate than a bilinear failure surface. AASHTO (2018a) had a default value of pullout resistance factor, F*, for geosynthetics, however this value did not explicitly apply to geo-synthetic strip reinforcements. The interpretation of F* is based on specific tests on rein-forcing elements used for this system as recommended by AASHTO (2018a) and FHWA (2009a). The pullout scale correction factor, α, for these soil reinforcing strips is at least 0.90 (as verified by the pullout data), therefore the recommended data for designing was considered 0.90.

The projects presented in this paper were designed using the MSEW 3.0 computer program, commercialized by ADAMA Engineering, Inc. Although the program gen-erally follows the guidelines of established design procedures, the user can explore design options and concepts beyond the formal guidelines. This option is important to integrate the polymer strips specific values and characteristic behavior into the design input values for these structures. The geostrips are first modelled as geogrids then the geometry is properly modified by acting on the reinforcement coverage ratio, Rc, lesser than 1, to be assigned to each reinforcement layer to input the real coverage, depending on the number of connections per column and geo-strip width. As explained above, the pullout inter-action coefficients (Ci, F* and α) are not considered as the default values used for the geogrids, but are determined by conducting extensive laboratory or full-scale pullout testing on various geostrip grades and types using concrete sand, and graded aggregate base (GAB) backfill materials, as shown in Figure 3. Testing was conducted in general accordance with ASTM D 6706.
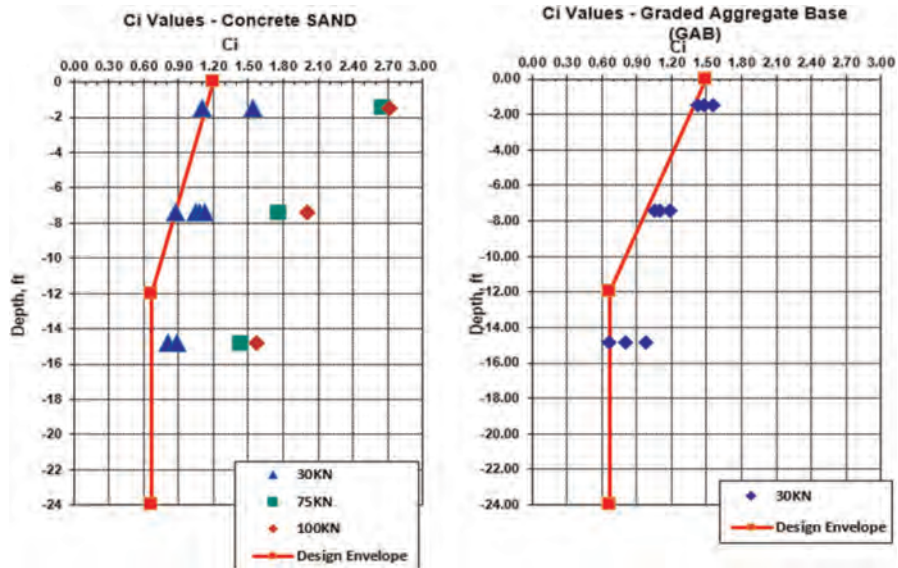
Figure 3. Coefficient of Interaction variation with depth tests results.

3 CASE STUDY IN PRINCE GEORGE'S COUNTY, MARYLAND

The MSE wall presented in this case study is located in Prince George's County, Maryland and it is part of a bigger project called Andrews Federal Center Bus Operations and Maintenance Facility. The project included the design and construction facilities, garages and buildings in support of the Washington Metropolitan Area Transit Authority's (WMATA) mixed fleet of transit vehicles. Four different types of retaining wall systems were considered for this complex: unreinforced segmental block system with average height ranging from 1m to 1.5m, massive gravity concrete blocks when heights ranged from 1.5m to 3m, gabion walls for the slope stabilization from 3m to 4m high and MSE walls with concrete facing panels and soil reinforcing system for supporting heavier load and heights in the range of 6m.

Significant challenges were associated to this project: the quality of the structural soil to be used, the presence of obstacles like drainage pipes and ornamental fences, and the layout of the wall itself with several bends and curves. An MSE wall with concrete facing panels and polymeric strip reinforcement was selected to face these challenges due to the flexibility of the geosynthetic reinforcement to accommodate obstructions and bends, and the suitability of the polymeric strip for non-conventional backfill material.

In situ soil used as structural soil, as per requirement of the project, was classified as orange brown poorly graded sand with silt and gravel with the following characteristics:

	Value
pH	9.3
Resistivity	2900 ohm-cm
Sulfate	89.3 ppm
Chloride	44 ppm

pH values were closer to the upper bound of the standard range (5-10 according to FHWA) while resistivity was not appropriate for standard steel reinforcements. Particle size distribution report showed a percentage of fines passing #200 sieve slightly below 10% and maximum particles equal to 1". Moisture content was 6.4% and the soil classified as SP-SM, AASHTO A-1-a. The MSE retaining walls were designed in accordance to AASHTO LRFD Bridge Design Specifications, 7th Edition, considering a standard traffic live load (12 kPa), a guardrail impact of 0.41 kN/m and a seismic acceleration coefficient As = 0.05. These walls were designed considering a service life of 120 years. The structures were designed to support a 3-m wide concrete sidewalk directly behind the wall, and a live load traffic surcharge starting within about 3 meters behind their front face.

4 CASE STUDY IN SAN DIEGO, CALIFORNIA

This case study is about two MSE concrete facing walls located on the southern side of the Snapdragon Stadium in San Diego, as shown in Figure 5.

Figure 5.   SDSU Stadium under construction.

The new venue, completed in 2022, was designed as a hub for sports and entertainment and, with its 35,000 seats, provides a location for SDSU's NCAA Division 1 football team to play.

These permanent retaining walls create the Service Level that is located within the western and southern portions of the Snapdragon Stadium. The maximum height of the walls range from about 7.5 m (25 ft) to 9 m (30 ft).

Some of the challenges associated to these walls were: the quality of the structural soil to be used, the presence of drainage pipes and the layout of one of the walls. Geosynthetics strips were selected because of two main aspects:

- the resistivity of the backfill material, imported from a project on a beach nearby, was not suitable for metallic reinforcement;
- the flexibility of the polymer strips was considered critical during the installation of the walls because they needed to accommodate different types of obstacles horizontally and vertically.

Both walls were designed in accordance to AASHTO LRFD Bridge Design Specifications, 7th Edition, considering a service life of 75 years.

5 CONSIDERATIONS ON BOTH CASE STUDIES

All the walls involved in the projects presented so far have the same characteristics:

Concrete panels with rectangular shape (1.52 x 3.04 m and 14 cm thick), except as necessary to maintain grade and length.

The polymeric reinforcement elements consist of planar strips manufactured from high tenacity, multifilament polyester yarns aligned and co-extruded with LLDPE (Linear Low-Density Polyethylene) to form polymeric strips. The ParaWeb^{TM} mechanical and physical properties have been qualified by NTPEP (National Transportation Product Evaluation Program). Furthermore, the polyethylene coating allows the use of these polymeric strips in highly alkaline environments (pH>11) as recycled concrete or lime-stabilized backfill materials.

The connection is a bar encased in a HDPE plastic box and precasted with the concrete panel to guarantee the mechanical link and the geostrips are placed and pre-tensioned on the jobsite.

The HDPE cavity insert box is connected to the panel by a steel embedded rebar encased in a polymeric sleeve for corrosion protection. The sleeve avoids water and cement from entering during the casting phase and prevents damage to the polymeric soil reinforcing strips in contact with the deformed rebar.

During installation the panels were positioned with a slight back inward inclination to compensate for outward movement that can occur during placement and compaction of the "non-conventional" backfill. The inclination was obtained by pulling the top of the panel towards the rear face of the structure and was maintained inserting timber wedges and using clamps to fix two adjacent panels.

The timber wedges were then removed when the next row was placed to avoid panel damage.

Overall there were no issues with the vertical and horizontal alignment of the panels and the inclination was checked with a level regularly.

REFERENCES

ADAMA (2016) MSEW – Mechanically Stabilized Earth Walls: Program MSEW, developed under Contract with FHWA, *www.msew.com.*

AASHTO (2018a). *LRFD Bridge Design Specifications*, 8th Edition, American Association of State Highway and Transportation Officials, Washington, DC, 1,780p.

AASHTO (2018b). *Standard Specifications for Transportation Materials and Methods of Sampling and Testing, and AASHTO Provisional Standards*, 2018 Edition, American Association of State Highway and Transportation Officials. Washington, DC, 4,855p.

British Board of Agrément (BBA, 2018). *"HAPAS Certificate Product Sheet 12/H191 for ParaWeb Straps for Reinforced Soil Retaining Walls and Bridge Abutments."* Watford, Hertfordshire, U.K.

FHWA. (2009a). Berg, R.R., B.R. Christopher, and N.C. Samtani, N.C., *Design and Construction of Mechanically Stabilized Earth Walls and Reinforced Soil Slopes*, FHWA NHI-10-024 Vol I and NHI-10-025 Vol II, U.S. DOT, Federal Highway Administration, Washington, DC. 306p (Vol I) and 378p (Vol II).

FHWA (2009b). Elias, V., K.L. Fishman, B.R. Christopher, and R.R Berg. *Corrosion/Degradation of Soil Reinforcements for Mechanically Stabilized Earth Walls and Reinforced Soil Slopes*, FHWA NHI-09-087, U.S. DOT, Federal Highway Administration, Washington, DC. 142p.

Luo, Y., D. Leshchinsky, P. Rimoldi, G. Lugli, and C. Xu. (2015). "Instrumented MSE Wall Reinforced with Polyester Straps." *Transportation Research Board Annual Meeting 2015* Paper #15-0985, 16p.

NTPEP (2018) National Transportation Product Evaluation Program (NTPEP) Report REGEO-2016-01-Linear Composites-ParaWeb-ParaLink, 2018 NTPEP Report Series, Laboratory Evaluation of Geosynthetic Reinforcement, American Association of State Highway and Transportation Officials. Washington, DC. 181p. (https://www.maccaferri.com/us/wp-content/uploads/2018/08/US-Maccaferri_2018-NTPEP-Report_Paralink_Final.pdf)

Rimoldi, P., D. Leshchinsky, M. Arrigoni, and A. Bortolussi. (2013). "Vertical Wall With Concrete Panels Facing and Geostrips Reinforcement: Instrumentation and Data Reduction." *Proceedings of the Design and Practice of Geosynthetic-Reinforced Soil Structures*, Bologna, Italy, 48p.

Gallivaggio rock cliff: Risk management and reinforced earth embankment for rockfall protection

G. Bragonzi & P. Cancelli
Studio Cancelli Associato, Milan, Italy

A. Simini & S. Mazzarolli
HUESKER Srl, Trieste, Italy

ABSTRACT: The Gallivaggio landslide falls within the San Giacomo Filippo municipality (Sondrio) and affects a portion of slope situated in the lower Spluga Valley. The rock cliff overlooks the "Madonna di Gallivaggio" Sanctuary (17th century), a restaurant, a few houses and a section of the National Road no. 36 "del Lago di Como e dello Spluga" which leads to the tourist resort of Madesimo and to the Spluga Pass on the Swiss border. Hence the need for careful planning of control and design tools aimed at both risk management and risk mitigation. The first monitoring activities of the rock cliff date back to 2006, while in 2011 a survey activity with GBInSAR technology was started by the Geological Monitoring Centre of ARPA Lombardia (CMG). On 29th May 2018, a rock mass of about 5500–6000 m^3 detached from the top of the rock cliff, completely filling up the existing catchment ditch behind the protection wall, demolishing part of the defence works and affecting the Sanctuary, the National Road and part of the other accommodation facilities situated at the foot of the rock face. This rockfall, as well as other minor recent falls, allowed to recognize the urgent need for a more adequate protection works. As a first step of a complex of works for the mitigation of the rockfall hazard, a new earth reinforced embankment was conceived. Both phases, designing and building, are described in the paper.

1 INTRODUCTION

The area of the present study lies in the Val San Giacomo, in the municipality of San Giacomo Filippo (Sondrio, Italy) on the left bank of the Liro River and is bordered by the Val d'Avero and the Valle Zerta to the north and south, respectively. The rock face, oriented NNW – SSE, overlooks the Sanctuary of the Madonna di Gallivaggio (17th century), a restaurant, a few houses and a section of State Road no. 36 "del Lago di Como e dello Spluga", which leads to the tourist resort of Madesimo and the Spluga Pass on the Swiss border.

This is a road with a very high volume of traffic in both summer and winter. Moreover, the Sanctuary itself is a site of great religious and cultural interest.

In 2006–2009, following numerous collapses that had affected the area in the previous years, an earth embankment for rockfall protection approximately 100 m long was built on top of which 5 m high rockfall nets were installed with absorption energies ranging from 250 to 2000 KJ.

Since December 2010, the ARPA Lombardy Geological Monitoring Centre (CMG), at the request of the Region's Civil Protection, has been designing and installing a monitoring system consisting of a continuous survey using terrestrial radar interferometry.

Figure 1. View of the Sanctuary area from national road 36.

2 GEOTECHNICAL-GEOMECHANICAL MODEL

The slope is approx. 500 m high with a slope angle of 65 to 70° at the sub-vertical wall and 15 to 20° at the detrital slopes and fluvioglacial deposits and the rock face above the Sanctuary is interrupted by 4 families of discontinuities with the following preferential positions: 280/75 (K1); 225/60 (K2); 120/75 (K3) and 015/35 (KS): K1 and K2 are the potential sliding planes of the rock masses and condition the orientation of the wall: K1 in the north-western part of the slope, K2 in the remaining sector; K3, less frequent and more irregular than the previous ones, forms the lateral junctions of the unstable rock masses; KS, parallel to the plunging schistosity planes at a low angle to the north, forms the "roofs" visible in the wall and is the summit junction of the unstable rock masses.

The most critical situation from the point of view of the stability of the mass (i.e. volumes above 1000 m^3), is precisely the summit part of the wall, from which the generalised collapse occurred in May 2018. The extent of the phenomenon, with an estimated volume of around $4000 \div 5000$ m^3, was such that it involved other portions of the slope, so the total volume of landslide material is of the order of 7000 m^3. Moreover, on 7th June 2017, an isolated block (more than 1 m^3) had already collapsed from the top of the rock face, in correspondence with the zone of emergence of the fracture that delimits the unstable rock mass upstream, which then subsequently collapsed. Some fragments, centimetric to decimetric in size, bypassed the existing passive defence works and hit the Sanctuary and the surrounding structures, causing some damage.

3 STUDY OF COLLAPSE PHENOMENA

The rock face is affected by isolated boulder collapses or mass collapses up to several thousand cubic metres. As resulting from interferometric monitoring, as well from the presence of an interruption in the verticality of the rock face at an altitude of approximately 1050 m a.s.l., two main possible collapse scenarios were considered: A1 between an altitude of 1050 m a.s.l. and the top of the rock face; A2 between an altitude of 900 and 1050 m a.s.l.

The study of collapse phenomena was conducted both in terms of single trajectory analysis (following isolated block collapse) and in terms of rockfall runout range (following mass collapse) in order to define the propagation scenarios for the worst possible collapse condition.

4 DESIGN OF HAZARD MITIGATION WORKS

During the various meetings held at the Prefecture of Sondrio in the presence of the competent institutional bodies, it emerged that there was a substantial insufficiency of economic

resources for the realisation of the entire complex of works for the mitigation of the risk of rockfall in the Gallivaggio area.

Having established that the risk mitigation should be pursued only through the realisation of all the works initially planned, during the final design phase the definition of functional sections was carried out according to a decreasing priority scale.

Section 1 – passive defence works: construction of a new earth reinforced rockfall protection embankment of greater height and in a more recessed position (downstream).

Section 2 – active defence works: reprofiling of the ledge at an elevation of approx. 940 m a.s.l. by controlled demolition with explosives in order to eliminate the main source of bouncing of the trajectories that bypass the embankment. The preliminary analysis imposed the necessity to precede the demolition of the ledge with the realisation of a higher containment capacity embankment.

Section 3 – active defence works: covering the top of the rock face with mesh and nails and punctual consolidation works. In this way, the residual risk is mitigated by preventing the collapse of particularly fractured portions of the mass and partially detached rock blocks, the detachment of which could lead to detensioning and subsequent mass collapse.

Figure 2.   Effect of embankment relocation.

The final project consists in the construction of a reinforced earth embankment for rockfall protection replacing the existing one. The new structure, in addition to its greater length, which allows the protected areas to be extended, will also have a greater height, so that it will be able to intercept the trajectories not retained before.

In order to further increase the interception capacity, the axis of the new embankment was planned downstream.

Relocating the embankment in a direction with a smaller inclination of the fall trajectory allows for a greater interception capacity. Furthermore, other positive results are expected to be achieved: the trajectories heights are lower, which makes it therefore possible to reduce the height of the new embankment; the lower embankment height reduces the loads on the foundation soil and therefore better overall stability conditions are obtained; the reduced size of the embankment leads to a significant reduction in construction costs.

The design impact considered provided the highest kinetic energy (30,040 KJ) in the trajectory analyses; this impact occurs at a height from the upstream side of 13.37 m, at a distance from the crest of 5.23 m and with an inclination of 67.93°.

The new rockfall protection embankment is made of a two-sided reinforced earth embankments (with 70° slopes guaranteed by means of steel mesh formworks) on top of a single-sided sided reinforced earth embankment. The maximum design height of the embankment is 23.43 m, which includes a 5 m high concrete anchored wall at the bottom, designed in some areas. On top of the embankment a steel rockfall barrier was installed, with

the purpose of containing any minor blocks resulting from the fragmentation of larger blocks after impacts on the rock face. The project is completed by a drainage system at the base of the embankment and the planting of new shrubs between the embankment and the Sanctuary.
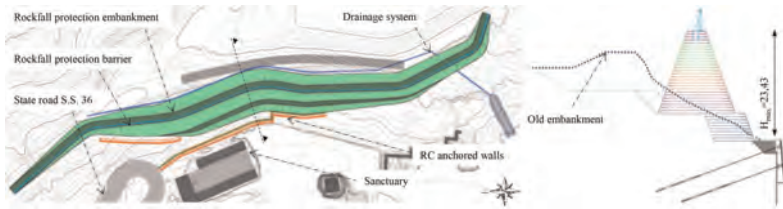
Figure 3.   Plan view and typical cross-section.

5   STABILITY ANALYSIS

The stability of the reinforced earth wall was checked according to the current Italian Regulations (NTC 2018) and stability calculations under different combinations of actions have been performed: Internal, compound and overall stability of the reinforced earth wall, using both circular (Bishop) and polygonal (Janbu) sliding surfaces; Stability against overturning; Bearing capacity of foundation soil at the base of the embankment; Impact of an individual rocky body with diameter 1.44 m, weight 8270 kg, travelling at 98.11 m/s with a kinetic energy of 39,800 kJ; Shear resistance against sliding at the base of the embankment and at every level of reinforcing geogrids. With this regard a reduced angle of friction along the interface geogrid /soil has been adopted (reduction factor 0.8).

All the stability calculations were performed in both static and seismic conditions, and they have been done on two typical cross sections. The geosynthetics which were used as reinforcements are flexible, high modulus PET geogrids, having the technical data indicated in Table 1 and laid with a vertical spacing of 60 cm:

Table 1.   Geogrid characteristics.

Geogrid type	Fortrac 55 T	Fortrac 80 T
Tensile strength – UTS [kN/m]	$\geq$ 55	$\geq$ 80
Max strain [%]	$\leq$ 10	$\leq$ 10
Max. strain at design strength [%]	$\leq$ 5.5	$\leq$ 5.5
Creep (from 1 hour to 120 years at 50% UTS) [%]	$\leq$ 1.0	$\leq$ 1.0
RF_{creep}	1.52	1.52
RF_{ID}	1.20	1.15
RF_W	1.00	1.00
RF_{CH}	1.03	1.03
f_s	1.02	1.02
LTDS @120 years [kN/m]	$\geq$ 28.70	$\geq$ 43.56

where RF_{creep}: reduction factor for creep (120 years, T = 20°C), RF_{ID}: reduction factor for installation damage (coarse gravel), RF_W: reduction factor for weathering, including exposure to ultraviolet light, RF_{CH}: reduction factor for chemical/environmental effects (pH between 4 and 9, T = 20°C), f_s: factor of safety for the extrapolation of data (120 years)

The LTDS (Long Term Design Strength) was calculated according to BS8006:2010 and the partial safety factors were derived from the BBA certificate of Fortrac T geogrids (HAPAS Certificate 13/H197):

$$LTDS = \frac{T_{char}}{RF_{CR} \cdot RF_{ID} \cdot RF_W \cdot RF_{CH} \cdot f_s} \tag{1}$$

In Figure 4 the structural configuration of a typical cross section is shown, with indication of the reinforcement distribution, the type of geogrid, its anchoring length, thicknesses, etc. while in Table 2 all the safety factors obtained in the calculations performed calculations are shown.
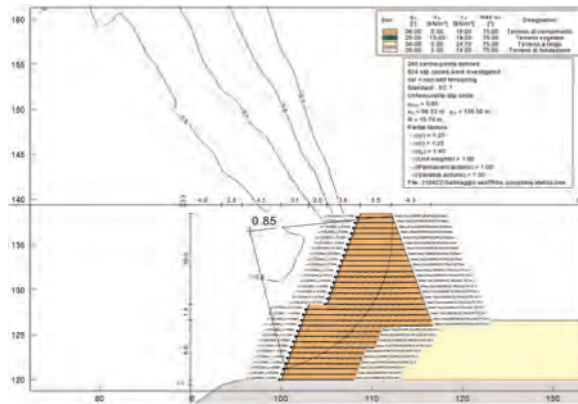
Figure 4.   Typical cross-section with the one the internal stability analyses (utilization factor obtained: 0.85).

Table 2.   Safety factors obtained in the performed calculations.

Type of analysis	Section 5R		Section 7R-bis	
	Static analysis	Seismic analysis	Static analysis	Seismic analysis
1 Sliding along the base	1.34	1.27	1.35	1.27
2 Global stability	1.14	1.35	1.22	1.44
3 Bearing capacity	5.45	7.41	5.66	7.73
4 Overturning	7.31	8.08	7.60	8.41

The soil which was used as fill of the wall was coming both from the demolition of the existing embankment and the material which fell from the cliff and accumulated behind the old embankment. These materials were appropriately crushed and screened to fall into groups A1, A3, A2-4, A2-5 according to UNI 10006, UNI EN 13242, 13285 and UNI EN ISO14688-1. Soil parts larger than 20 cm were excluded, except for a maximum percentage of 10%–15%.

The geotechnical properties required for the fill were the following: friction angle $\geq 35°$; unit weight greater than 15.90 kN/m^3 – a dry mass by volume, measured at the base of each layer, not less than 95% of the maximum dry mass by volume identified by the AASHO Mod test (CNR 69 – 1978), (CNR 22 – 1972); modulus of deformation at the first load cycle on the plate (diameter 30 cm) (CNR 146 – 1992) ≥ 15 MPa, in the load range between 0.05 and 0.15 N/mm^2 on the sub-layer; ≥ 50 MPa, in the load range between 0.15 and 0.25 N/mm^2 on the top of the sub-layer and on the top of the wall.

A biodegradable erosion control jute net was placed between the fill material and the geogrids to prevent soil erosion before the greening of the slope. The steel mesh formwork is made of electro-welded mesh, 7–8 mm rebars having a mesh size of ~15 cm. The steel formwork does not provide any structural resistance; it only allows a better and easier shaping of the embankment. The formwork is provided with stiffening rods to guarantee a better resistance in the initial compacting stages.

6 CONSTRUCTION

Prior to the commencement of the work, it was necessary to secure the tunnel by laying netting on the upper part of the wall above, also in the event of new detachments after the project delivery. A total of 50,000 m^2 of netting was laid on the upper part of the 450 m high wall. With the help of a Kamov helicopter, 300 m long and over four tonnes heavy nets were laid, making it Europe's first and largest netting project on a rocky slope. At the end of the construction activities, a total of approx. 45,000 m^3 of material was moved.

Thanks to the screening and crushing activities, which were foreseen by the project and coordinated during the construction management phase, the new embankment was entirely built using all the material that collapsed in May 2018, all the material that made up the old embankment and part of the slope debris within the site area.

The reinforced earth fill embankment is 243 m long and has an interception height varying from 4 to 14 m while the height of the face on the downstream side varies from 7 to 23 m.

Figure 5.   Construction phases.

Figure 6.   Aerial views of the finished works.

REFERENCES

Bragonzi G., Cancelli P., Cattaneo F., Dei Cas L. & Tedeschi L. 2022. Previsione e Gestione del Rischio da Caduta Massi e Progettazione Degli Interventi di Mitigazione. Il Caso Della Parete Rocciosa di Gallivaggio. *La Geotecnica per lo Sviluppo Sostenibile del Territorio e per la Tutela dell'Ambiente, XXVII Convegno Nazionale di Geotecnica Reggio Calabria 2022.*

Dei Cas L., Pastore M.L. & Rivolta C. 2018. Gallivaggio Landslide: The Geological Monitoring, of a Rock Cliff, for Early Warning System. *Italian Journal of Engineering Geology and Environment*, 2 (2018).

Hungr O. 1995. A Model for the Runout Analysis of Rapid Flow Slides, Debris Flows and Avalanches. *Canadian Geotechnical Journal 32*: 610–623.

Hungr O. & McDougall S. 2009. Two Numerical Models for Landslide Dynamic Analysis. *Computer & Geosciences 35*: 978–992.

Corominas, J. 1996. The Angle of Reach as a Mobility Index for Small and Large Landslide. *Canadian Geotechnical Journal 33*: 260–271.

The construction of the access roads to Pelješac bridge with the use of geogrid reinforced soil structures

L.S. Calvarano & P. Recalcati
Tenax SPA, Viganò, Italy

ABSTRACT: The construction of Pelješac Bridge and of the roads connected to the bridge is currently the largest and most ambitious infrastructure project in Croatia. The project was completed largely on time thanks to the use of reinforced soil technique. Preliminary project foresaw conventional and expensive viaducts to bypass the deep valleys intercepted by the road layout. To reduce the cost and to increase the construction rate, replacement of traditional viaducts in Doli and Brijesta with geogrid reinforced embankments was proposed. This solution turned out to be cheaper and faster respect the traditional ones; on the base of the time and cost effectiveness of the reinforced soil solution, it has been decided to modify the design of wing walls and abutments of the Dumanja Jaruga viaduct, crossing a valley over 25 m deep. Design and construction of the above strategic infrastructures were a great challenge and certainly a great success, thanks to the great work done by the general contractor, who was able to finish the job very precisely and accurately, despite the logistical difficulties given by the position and by the time scheduled imposed by the construction of the bridge support structure.

1 INTRODUCTION

The construction of the Pelješac bridge (2,404 km long and inaugurated on 26th July 2022, Figure 1) and of the roads connected with it is currently the largest and most ambitious infrastructure project in Croatia.

Figure 1. Pelješac bridge (source: www.dw.com).

This infrastructure will be part of the Adriatic-Ionian highway, starting from Trieste and reaching Greece after crossing the eastern Adriatic coast.

This impressive project has a key, geostrategic and symbolic importance for the Croatian population as, in addition to constituting an important and fast communication artery between the Southern Dalmatia and the Pelješac peninsula, it will contribute to its future development and growth.

Construction of the Pelješac bridge and of connecting roads has unified the country, guaranteeing the territorial continuity (after three centuries) of the southern extreme of the country (exclave of Dubrovnik) with the national highway network, by-passing the territory of Neum, 24 km of Adriatic coast belonging to Bosnia and Herzegovina. This has allowed delays associated with border formalities.

In the last twenty years various solutions have been proposed and evaluated, but all the attempts to start the works have always been opposed due to the very high construction costs.

The project of the road infrastructure crossing the Pelješac peninsula and accessing to the Pelješac bridge receiving the highest consents was designed by the Croatian firm Institute IGH dd.. Preliminary project foresaw to bypass the deep valleys crossed by the road layout with expensive and conventional viaducts.

Thanks to the collaboration of Tenax SpA, the Croatian partner Kotonteks of Varaždin and the contracting company Strabag, replacement of some of the viaducts with geosynthetics reinforced soil technique was proposed. All the proposed modifications to the original project have been accepted by the investor (Croatian Road) and by the European Commission, which was financing the project (Figure 2).

Figure 2.   Location of the different geogrid reinforced slopes along the access roads of the Pelješac bridge (source: www.dw.com and Google Maps).

In recent years, the use of geosynthetics has deeply changed the design methods of geotechnical and environmental engineering interventions. In fact, the correct use of these materials makes it possible to improve the safety conditions and the operating behavior of the engineering structures, reducing, at the same time, construction costs, construction times and environmental impact.

2   GEOGRID REINFORCED SOIL STRUCTURES

The term "reinforced soils" refers to a composite material that combines, synergistically, the strength of two different materials, soil and reinforcing geosynthetic.

The geogrid reinforced earth structure is a construction system based on the principle of improving the geotechnical properties of the fill soil (which, by its nature, is able to resist

very well to compression actions but do not have a significant tensile resistance) by providing it with tensile strength. Therefore, insertion of reinforcement geogrids (polymer structures with a very high tensile strength) capable to interact effectively with the soil in which they are embedded, results in a composite system (the reinforced soil) with higher performance compared to those of the soil alone. The function of the reinforcement is, therefore, to exert an effective confinement on the surrounding soil increasing its mechanical characteristics, developing tensile resistant forces that improve the stability conditions of the reinforced soil structures and, at the same time, limiting their deformations.

Thanks to this construction technique, it is possible to build and stabilize soil slopes with very steep angles and reduced cross-sections, with important savings on excavation material and fill material with consequent of lower costs of expropriation and construction, and therefore a reduce environmental impact.

In addition, reinforced soil structures with very steep faces are a valid alternative to conventional design solutions in reinforced concrete, especially when the huge dimensions of the structures require an accurate environmental impact assessment.

In this context, a wrap-around reinforced soil with polymeric reinforcing element consisting in a mono-oriented geogrid 100% in HDPE (high density polyethylene) and integral joints, manufactured from a unique process of extrusion and certified for the construction of steep reinforced slopes with inclines of up to 85°, was proposed.

The reinforcements' layers, suitably designed in terms of tensile strength and anchoring length, are embedded inside the fill soil at a vertical spacing of 0.60 m, with a wrap around at the front face of the slope.

This soil reinforcement system, foresees the use of a welded wire steel mesh formwork (Φ = 6-8 mm / mesh 15 cm x 15 cm) at the face, acting as a support system, equipped with specific stiffening rods (1 rod at 0.45 m spacing). The face formworks are sacrificial and do not have a structural function but act as a guide and support allowing a rapid installation and an accurate profiling of the reinforced soil structures. Finally, at the face a biomat was used to protect the structure against erosion and to ease vegetation of the face, allowing the growth of lawn or other suitable plants and providing an aesthetically pleasing solution (Figure 3).

Figure 3. Construction phase of reinforced earth structure with mono-oriented extruded geogrids in HDPE.

It should be noted that the use of high density polyethylene (HDPE) guarantees high resistance to chemical-physical degradation processes such as hydrolysis, oxidation and exposure to atmospheric agents, thus giving the reinforced soil structure a large durability over time.

3 PROJECT AND OPERATIONAL ASPECTS

Among the different structures along the road accessing to Pelješac bridge, the expensive Doli viaduct (about 180 m long with a maximum height of 17 m, Figure 4) and two external

portions of Brijesta viaduct (total length of about 200 m and with a maximum height of 15 m, Figure 5) were replaced with wrap-around geogrid reinforced embankments.

Figure 4.   Replacement of the Doli viaduct with a wrap-around geogrid reinforced embankment (span 180 m, maximum height over 17 m).

Figure 5.   Replacement of external portions of the Brijesta viaduct with reinforced earth embankments (total length about 200 m, maximum height about 15 m).

The proposed solution turned out to be cheaper and faster respect to traditional construction. Besides the above-mentioned works, and on the base of the time and cost effectiveness of the reinforced soil solution, the biggest challenge was to modify the design of wing walls and abutments (U0 and U4, respectively 102.0 m and 155.60 long, Figures 6 and 7) of the Dumanja Jaruga viaduct crossing an over 25 m deep valley.

Figure 6.   Aerial drone view of the U0 wing wall and abutment of the Dumanja Jaruga viaduct made with the reinforced soil technique with extruded HDPE mono-oriented geogrids.

The greatest challenges of the projects were connected both to height of these structures and to high loads during their construction phases and operation life (Figure 8).

Figure 7. Aerial drone view of the U4 wing wall and abutment of the Dumanja Jaruga viaduct made with the reinforced soil technique with mono-oriented extruded geogrids in HDPE.

Figure 8. Front drone view of the U4 wing wall and abutment of the Dumanja Jaruga viaduct constructed using a wrap-around reinforced soil technique with a sacrificial steel mesh formwork at the face and mono-oriented extruded geogrids in HDPE.

As it is necessary in the project of any geotechnical structure, the design phase of the reinforced soil structures was not separated from an adequate assessment of the morphological, geological, hydrogeological and geotechnical characteristics of the sites. Geognostic investigations and subsequent mechanical characterization of the site soils were essential both to geotechnical stability checks and to define the mechanical design parameters of the reinforced soil. The latest aspect was particularly important as excavation material was used as fill material for the construction of the reinforced structures.

A careful analysis of the logistical and construction site aspects was done too. The limited dimension of the operating areas, the access roads and the construction site, as well as the size of the machineries that could be safely used were crucial factors both for the good execution of these structures and for the cost-effectiveness of the work.

It should be noted that the required fill material volume was very high, therefore, it has been of paramount importance evaluate and validate the possibility of recovering the material available on site, thus avoiding the need to dispose excavation material and to source fill material from quarries. The storage of the fill material within the construction site areas, especially in a

mountain or hilly area with steep geometries, was carefully evaluated in order to mitigate the risks associated with slopes stability problems that could occur due to the soil piles storage.

Eurocodes 7 and 8, both in static and seismic conditions, were used to check the stability, taking into due account the seismicity of the site, the geotechnical model and the construction phases of both the reinforced earth embankments that replaced the viaducts of Doli and Brijesta, as well as, the wing walls and abutments of the Dumanja Jaruga bridge.

Design and construction have been particularly complex due to the high seismicity of the area (Peak Ground Acceleration equal to 0.34 g); the height of the geogrid reinforced structures (average height 17.0 m, maximum height up to 25.0 m) and to the inclination of the reinforced slope face (up to 80 °). The presence of rock at the back of the reinforced slope in some cases has required a fine optimization of design in order to reduce as much as possible excavations.

The geogrid reinforced soil with steep slopes brought many advantages respect to the original traditional solution:

- the speed (20% higher) and easiness of execution compared to the original design solutions (construction rate was 40 m^2/day of face of wrap-around geogrid reinforced soil with a team of three men; furthermore, compared to the construction of a viaduct the solution does not require deep foundations, the use of heavy machineries, skilled personnel and does not require the typical curing time required by reinforced concrete). Finally, the use of reinforced soil technique allowed to follow the time schedule;
- the aesthetics and the lower environmental impact at the end of the work ensure some facilitations in getting all the required approvals, especially in protected areas and in areas subject to particular urban or landscape-environmental constraints;
- cost-effectiveness was ensured by the possibility to recover material coming from excavations, thus eliminating the costs of dumping and getting fill material from quarries (including transport costs for both the operations). The proposed design solution for the reinforced embankments allowed a reduction in construction costs of almost 30% as the location of the construction sites were close to the Kamenice tunnel, therefore, much of the excavated soil was used. Excavated rock was crushed and selected until reaching a size suggested by the designers based on the calculation of the internal and external stability of the reinforced earth structures;
- better behavior in seismic conditions. The reinforced soil constructions allow deformations capable to absorb seismic stresses, even of considerable entity, without compromising the functionality of the structure; on the other hand, the traditional reinforced concrete rigid structures, in the same seismic conditions, would risk collapsing;
- less environmental impact and pollution. The trucks used for the construction of reinforced earth works produce lower emissions of CO_2 into the atmosphere than those associated with the construction of traditional works;
- The project and the construction of the geogrid reinforced structures have been a big challenge and definitely a great success, thanks also to the great work done by the general contractor who has been capable to finish the job in a very precise and accurate way despite all the logistic difficulties given by the location and by the time scheduled imposed by the construction of the bridge support structure.

REFERENCES

EN 1997-1 (2004) (English): *Eurocode 7: Geotechnical Design - Part 1: General Rules*
EN 1998-1 (2004) (English): *Eurocode 8: Design of Structures for Earthquake Resistance – Part 1: General*

A case study on strengthening the backfill of a prefabricated reinforced concrete double wall with geogrids

H. Özçelik
Promer Consultancy Engineering Inc., Ankara, Turkey

Ü. Küçükkayalar, S. Küçükkayalar & D. Küçükkayalar
Ka-Yapi Prefabrication Inc., Bursa, Turkey

ABSTRACT: The construction of geosynthetic-reinforced soil retaining walls with a staged-constructed full-height rigid facing for railways, including high-speed train lines, roads and other retaining walls began to be used in Japan in the late 1980s. After the wrap-around type geosynthetic reinforced soil wall is constructed, the front face is covered by a cast-in-situ reinforced concrete wall. The earthquake performance of these walls is extremely high and is economical compared to classical retaining structures. This system was used in a slightly different way on the reinforced concrete wall of an industrial building in Bursa, a city located in the first degree seismic zone of Turkey. The 10m high reinforced concrete wall was staged-constructed in three parts using the prefabricated modular double-wall system, while the backfill was reinforced with geogrids. In this paper, the effect of using a geogrid-reinforced fill and unreinforced fill on the calculation of the reinforced concrete wall section is compared, and the details of the system and its construction are discussed.

1 INTRODUCTION

Since 1987, geosynthetic reinforced soil walls with a full height rigid (GRS-FHR) facing invented by F. Tatsuoka, were in use on Japanese roads and approved by the Japanese Ministry of Transport in 1992 (Tatsuoka *et al*. 1997). After the 1995 Kobe earthquake, the Japanese railways administration decided to use the GRS-FHR facing walls as retaining and bridge abutments. These walls are formed by building a wrap around GRS wall and casting an in-situ reinforced concrete wall as the FHR facing (Tatsuoka *et al*. 1996). This system is frequently used in the reconstruction of classical type retaining structures (reinforced concrete or gravity structure) that collapsed as a result of earthquakes, heavy rains and similar natural disasters (Tatsuoka *et al*. 2007). In the 1995 Kobe and 2011 Great East Japan earthquakes, transportation on the railways supported by the FHR-GRS walls continued without interruption (Yonezawa *et al*. 2014).

2 CONSTRUCTION PROCEDURE FOR THE FHR-GRS WALL SYSTEM

The FHR-GRS wall system has now become a standard retaining wall construction technique, replacing classical retaining walls in Japanese railways (Figure 1). The construction procedure of the FHR-GRS wall system consists of the following stages:

1. A simple levelling pad is constructed as per the shop drawings.
2. Geogrid wrapped sacks filled with granular fill are arranged in an orderly manner.
3. Granular fill is laid in layers and compacted
4. While the sacks are wrapped with geogrid, steel reinforcement bars are left between them (Figure 2).
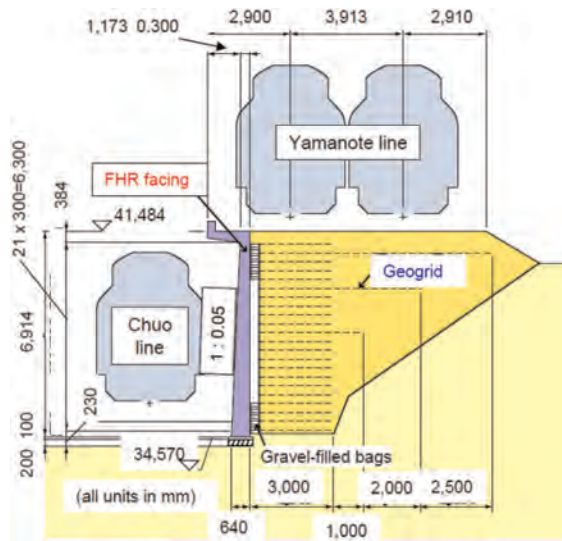
Figure 1.   Typical FHR-GRS wall section (Tatsuoka 2008).
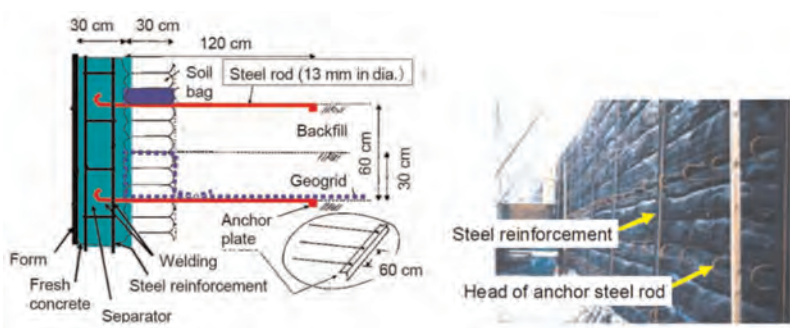
Figure 2.   Typical connection detail of FHR-GRS concrete facing and the geosynthetic reinforced fill (Tatsuoka 2008).

Figure 3.   Finished GRS embankment prior to cast-in-situ RC wall construction (Tatsuoka 2018).

5. This process continues until the fill reaches the top of the wall level.
6. The possible settlements in the embankment and ground need to be completed (Figure 3).
7. After the settlements are completed, a cast-in-situ reinforced concrete wall with a thickness not exceeding 30 cm is formed as the facing.
8. In this way, the cast-in-situ reinforced concrete wall is connected to the reinforced soil mass, thanks to the steel reinforcement bars placed between the sacks.

3 CONSTRUCTION METHOD OF DOUBLE-WALL

3.1 *Case study*

The retaining walls of the Ada Sofa factory, located in the 2nd Organized Industrial Zone of the Inegol district of Bursa, were built using prefabricated reinforced concrete hollow panels forming the retaining wall system called Double Wall. While backfilling the retaining wall, the fill was strengthened by placing geogrids between the fill layers. This is similar to the FHR-GRS wall system developed by Prof. Tatsuoka, described above. In Tatsuoka's system, geosynthetic reinforced fill is formed first, and after the possible deformations taking place, a cast-in-situ reinforced concrete retaining wall is formed as the facing. In the other, the front side reinforced concrete wall, i.e. the facing is gradually built in using prefabricated RC modules, and geosynthetic reinforced backfill is done afterwards.

There is a level difference of approximately 11m between the base level factory and the neighboring parcel. In the neighboring parcel, there is a building at a distance of 10 m from the parcel boundary. The natural ground between the two plots is formed by a slope greater than 45degrees. Geogrid reinforced fill was made in this area.

3.2 *Construction of prefabricated double wall*

The first prefabricated double wall module with dimensions of 3.33 x 7.00 m (HxW) is placed on the prepared steel frames and fixed with props from the back (Figure 4a). After the

Figure 4a. Installation and propping of double wall modules.

Figure 4b. Formwork of foundation and installation of steel reinforcement.

Figure 4c. Installation of horizontal continuity reinforcements.

Figure 4d. Pouring of concrete.

formwork of the wall foundation is installed, the necessary reinforcements for the foundation are laid under the steel frames (Figure 4b). After the horizontal continuity reinforcements are placed inside the double wall modules (Figure 4c), concrete pouring takes place (Figure 4d). The molds have been removed, after the concrete has set, and the surrounding of the foundation is filled with backfill and compacted. The perforated drainage pipe is placed, and covered with gravel. This layer of gravel, having a width of 30cm, is applied between the wall and the backfill, up to a height of 3.30m which is the height of the first double wall module.

3.3 *Backfill with geogrid*

Backfilling is made in layers like in any reinforced soil wall backfilling and compacted with a minimum 95% standard proctor. While placing the backfill, geogrids of required strength and length are placed between the fill layers according to the design section (Figure 5). Typical Double Wall cross section is given in Figure 6.

The walls between the prefabricated columns of the factory building were made with double wall as a curtain system wall and the backfill is reinforced with geogrids (Figure 8).

While backfilling the geogrids, it is important that the geogrids are laid flat and there is no slack. If necessary, the geogrid should be pinned to the ground at its rear end using wooden or steel stakes. Backfilling, compaction, geogrid laying, and gravel placing continue in successive layers until the top level of the wall is reached. The backfilling of the Ada Sofa factory wall (H=10m) was made by reinforcing it with geogrid by wrap around method. The design of the geogrids was carried out according to BS8006 (2010).

Figure 5.   Installation of geogrids.

As a result of the design, geogrids with a vertical spacing of 1m and an ultimate breaking strength of 150kN were used in the bottom three rows, and geogrids with a vertical spacing of 80cm having an ultimate breaking strength of 65kN were used in the following eight rows (Figure 6). In the section of the building where the Double Wall panels are used as curtain
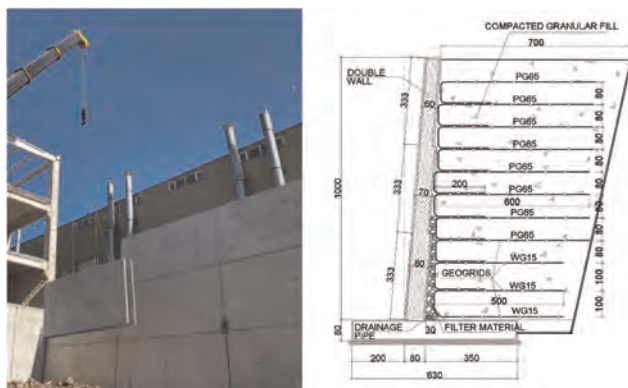
Figure 6.   Front view and cross section of the double wall.

walls, geogrids having an ultimate breaking strength of 80kN with a vertical spacing of 60 cm in the bottom 4 rows and a vertical spacing of 80 cm in the following 7 rows were used (Figure 7). While placing the geogrid, first the short length is placed and after, the full length of geogrid is folded over the compacted fill layer. It is strained as much as possible and pinned at the rear end on the ground. There exists a self placed gravel drainage layer at the of the rigid facing which helps for the mobilization of the geogrid strength even with small deformations which takes place during the compaction of the fill.

3.4 *Double wall cross section calculation*

Three of the 3.33 x 7.00 m double wall modules were placed on top of each other to form the retaining wall. The thickness of the lowest module is 80cm, the middle one is 70cm and the top one is 60cm. The geogrid-filled portion is a self-stable mass that theoretically retains the earth pressure thrust behind the wall. However, in the double wall section calculation, 33% of the classically calculated earth pressure was considered. On the other hand, a double wall section was analyzed with full earth pressure acting at the back of the wall, according to the new Turkish Earthquake Regulation (TBDY 2018). At the end of the analysis, double wall modules were calculated to be 20cm thicker than the ones actually used with the geogrid reinforced fill. Reinforced concrete section calculations were made with Prota Structural Details V:22 software. Comparison of materials used for a 1m run of unreinforced and reinforced backfill sections of the 10m high wall of Ada Sofa factory are given in Table 1.

Reinforcing the backfill with geogrids, introduce savings of about 15% in concrete and 30% in steel reinforcement quantities compared to unreinforced backfill. In 1m run of 10m high
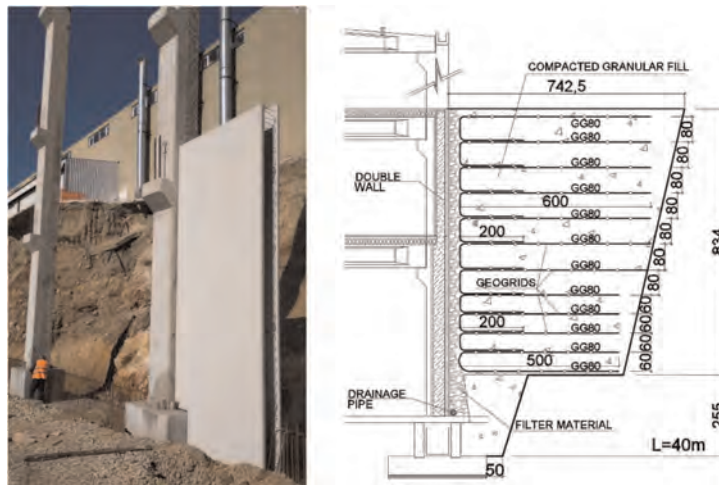
Figure 7. Typical view and cross section of the factory walls which are also made with the double wall system and the backfill is reinforced with geogrid.

Table 1. Comparison of materials used for a 1m run of unreinforced and reinforced backfill sections of a 10m high wall.

Backfill	Cross Section (cm)	Concrete (m^3/m)	Steel Reinforcement (kg/m)
Unreinforced	100–80–60	12.9	1,492
Reinforced (geogrid)	80–60–40	10.7	1,026
Difference	20–20–20	2.2	466

double wall's backfill, 25.5m^2 and 73.2m^2 of 150kN and 65kN geogrids were used respectively. So it is 9.9m^2 geogrid in 1m^2 face area of the double wall including 2m wrap around.

    The savings can be calculated as follows for the whole double wall which was 36m long.

Concrete cost (∼66€/m^3) : … … … … … … … … … .. … . 2.2m^3 x 36m x 66€/m^3 = 5,227€

Steel reinforcement cost (∼770€/ton) : … … 0.466ton x 36m x 770€/ton =12,918€

Geogrid cost (average ∼1.50€/m2) : … .9.9m^2 x 36m x 10m x 1.50€/m2 = 5,346€

So the net saving is : 5,227 + 12,918 – 5,346 = 12,799€

    There are also savings from the construction time, labourship, and energy which were not considered in the above calculation.

4 CONCLUSIONS

i) Geosynthetic reinforced soil retaining walls (FHR-GRS) with a full-height rigid facing is a standard retaining wall construction technique, which has been accepted by the Japanese Railways Administration, replacing classical retaining walls. The earthquake performance of all types of geosynthetic reinforced walls are extremely high. In the 1995 Kobe and 2011 Great East Japan earthquakes, the railways supported by such walls continued their functions without interruption.

ii) In FHR-GRS walls, granular material filled sacks are wrapped around with geogrids; after the possible settlements of the embankment and the foundation soil have taken place, the front of the system is covered with a cast-in-situ reinforced concrete wall.

iii) The retaining wall of a factory built in İnegöl-Bursa was constructed in 3 stages using a prefabricated reinforced concrete double wall panel retaining wall system. Similar to the FHR-GRS system, it's backfill was reinforced by placing geogrids between the fill layers.

iv) Contrary to the FHR-GRS system, in the İnegöl retaining wall, wrap around geogrid backfill was done after the double wall panels were installed.

v) While analyzing the cross section of the double wall system, an economical solution was obtained by taking 33% of the earth pressure thrust.

vi) When comparing the double wall sections where backfill is unreinforced and reinforced with geogrids, 2.2m^3 of concrete and 466kg of steel reinforcement were saved per meter run of wall. The savings about 15% of the concrete and %30 of the steel reinforcement quantities.

REFERENCES

BS 8006-1:2010 "Code of Practice for Strengthened / Reinforced and Other Fills", British Standards Institution

Tatsuoka, F., Tateyama, M., Koseki, J., 1996, Performance of Soil Retaining Walls for Railway Embankments, *Soils and Foundations, Special Issue for the 1995 Hyogoken-Nambu Earthquake*, pp.311–324

Tatsuoka, F., Tateyama, M, Uchimura, T. and Koseki, J. 1997. Geosynthetic-reinforced Soil Retaining Walls as Important Permanent Structures. Mercer Lecture, *Geosynthetic International*, Vol.4, No.2, pp.81–136

Tatsuoka, F., Tateyama, M., Mohri, Y. and Matsushima, K. 2007. Remedial Treatment of Soil Structures using Geosynthetic-reinforcing Technology. *Geotextiles and Geomembranes*, 25 (4 & 5): 204–220

Tatsuoka, F., 2008, Recent Practice and Research of Geosynthetic-reinforced Earth Structures in Japan. *J. GeoEng.* 3(3), 47–67

Tatsuoka, F., Tateyama, M., Koseki J., ve Yonezawa T., 2014, "Geosynthetic-Reinforced Soil Structures for Railways in Japan" *Transportation Infrastructure Geotechnology*, Vol.1, pp3–53

Tatsuoka, F., 2018, Development of Geosynthetic-reinforced Soil Structures for Railways in Japan – from Walls to Bridges, 5th IGS UK Chapter Symposium

TBDY, 2018, Turkish Building Earthquake Regulation, Directorate of Disaster and Emergency Management, Ankara, Turkey, March 2018.

Yonezawa, T., Yamazaki, T., Tateyama, M. and Tatsuoka, F., 2014, "Design and Construction of Geosynthetic-reinforced Soil Structures for Hokkaido High-speed Trains Line", *Transportation Geotechnics*, Vol.1, No.1, pp.3–20

Earthquake resistant design of shallow foundations using geogrid reinforcements

J. Kupec, D.P. Mahoney & I.D. McPherson
Aurecon New Zealand Ltd, Christchurch, New Zealand

ABSTRACT: New Zealand experienced several large earthquakes which damaged residential and commercial properties. For post disaster recovery, solutions were sought to rebuild on land prone to seismically induced liquefaction and lateral spreading. Engineering guidance in NZ introduced the basal geogrid reinforced gravel crust concept to allow construction of lightweight timber framed buildings on liquefaction prone ground. This paper describes the design and construction aspects for multiple layers of geogrids. It provides the detailed concepts behind the reinforced crust approach, including case studies of structures surviving repeated seismic shaking without major damage. The paper then describes several case studies of completed projects. It focuses on construction details that are considered essential for successful application of a reinforced crust subject to strong seismic shaking. Lastly, the paper provides releveling and repairability considerations to ensure that buildings can be returned to full functionality by relevelling after a major event.

1 INTRODUCTION

This paper reflects on design for multi layered reinforced soil gravel rafts in New Zealand. The authors were actively involved in many residential and commercial rebuild projects in New Zealand. They attempted to condense their design experience and provide the regulatory and design approaches common in NZ, especially those they consider can be applicable to many other parts of the world.

Following the Canterbury Earthquake Sequence in 2010 to 2011 in New Zealand light weight timber or steel framed structures, usually single to double storied, survived the earthquake shaking rather well. However, buildings were generally compromised once the foundation system was affected by seismically induced ground damage, notably differential settlement due to liquefaction related effects. The most common form of damage was noted where shallow liquefaction ejected large soil volumes directly from below foundation elements. Subsequent reconsolidation settlement required shallow footings to span and cantilever more than their, generally meagre, capacity. Seismically induced lateral spreading, extending up to 150m away from stream edges, often compounded the foundation damage. Lateral stretch, a term coined for lateral spreading directly below the spread building footings, caused significant foundation and structural distress. The lightly reinforced footings were not required by the then design standard to be tied together and they readily pulled apart and settled differentially, creating significant structural distress. While many buildings exhibited severe distress, due to their light weight and well braced nature very few initiated collapse. Older unreinforced masonry buildings did collapse from a combination of severe shaking and ground settlement.

Most structures were compliant with the New Zealand Building Code (NZBC). However, liquefaction and its associated effects prior to 2010 were often not appreciated by designers and regulatory authorities, with static bearing capacity and only a simple earthquake overstrength check for seismic conditions.

The need to provide readily available design approaches arose from the rebuild of over 20,000 severely damaged residential dwellings, with over 6,000 damaged well beyond economic repair (Cubrinovski 2012). Further, NZ is forecast to continue to be subjected to strong seismic shaking. The South Island features a major fault line on the West Coast that has a very high probability of rupture, (>75% in the next 50 years) generating a M8+ event. The North Island features on its entire East Cost a subduction line between the Pacific and Australian Plates that has triggered Mega Thrust events in the past, with shaking in excess of M9+.

The engineering challenge was to provide guidance on resilient foundation rebuild and repairs. The Ministry of Business, Innovation and Employment (MBIE), formerly the Department of Building and Housing, published guidance for the assessment and rebuild of timber or steel framed structures, (MBIE 2012). One of the proposed solutions for land susceptible to moderate to severe liquefaction induced land damage was the use of geogrid reinforced gravel rafts, where two biaxial geogrids provide basal reinforcements. This approach creates a strengthened surface crust.

2 PAST PERFORMANCE

The prevalent types of foundations for residential and light commercial buildings in Canterbury, and much of New Zealand, featured either a lightly reinforced concrete slab on grade or timber flooring with concrete perimeter footings. The typical damage observed after the Canterbury Earthquakes 2010-2011 and later Kaikoura Earthquake in 2016 is shown below.

Figure 1.   Typical damage patterns for house foundations, after (Department of Building and Housing 2011).

Christchurch and much of New Zealand is built on low lying alluvial or estuarine or coastal deposits, often loose granular soils with a shallow to near surface groundwater table. Geotechnical practitioners needed to consider both static and seismic bearing capacities and account for potential land subsidence and differential settlement associated with ground liquefaction.

Pre 2010, geogrids were used to improve ground below light commercial, industrial and residential structures, when the need arose to improve the static bearing capacities and/or provide temporary platforms for construction. A review of structures with geogrid reinforced foundations indicated that those structures outperformed similar structures on unimproved ground.

(Tensar 2019) reported that 'several foundations which had been constructed on a Tensar MSL geogrid stabilised granular mattress following the 09/2010 event were investigated after the 02/2011 EQ and showed no sign of failure, while nearby buildings showed up to 700mm settlement and up to 500mm horizontal movement. The buildings resting on the Tensar MSL foundations however, showed only 40-50mm of movement and no failures or cracks in the superstructure. Only minor refurbishment was required for the buildings to be fully usable.'

The authors designed the above two-level residential housing estate in Huxley Street, Christchurch, prior to the Canterbury Earthquakes. Multiple geogrids placed in competent well compacted 900 to 1,200mm thick granular fill were used to create a reinforced crust. The main design objective was to meet static bearing capacities and allow construction plant access. The incidental benefit was an improved seismic bearing capacity below the main structural load bearing elements.

3   NZ GUIDANCE

Observations identified that liquefaction-induced settlement severely damages buildings, however it rarely affects life safety. Further, liquefaction and lateral spreading caused disproportionate damage to the foundation system even at lower shaking levels, Serviceability Limit State (SLS) and above. The Ministry for Business, Employment and Innovation (MBIE) worked with the Engineering Advisory Group (EAG) to develop NZ specific guidance on assessing, repairing and rebuilding foundations on land susceptible to earthquake induced liquefaction and lateral spreading, (MBIE 2015). The guidance was developed to provide context for designers in relation to the New Zealand Building Act, as the standard solutions were not considered appropriate and Alternative Solutions had to be quickly developed.

The importance of the surface crust was identified to be critical for the performance of buildings. Where the water table was deeper than 3m, or the upper 3m of ground were not liquefiable, forming a crust, the foundation damage was generally minor. The NZ guidance therefore provided a basal geogrid reinforcement as one option to support a well braced light weight structure on land with a thin to non-existent non-liquefiable crust to provide the necessary support. The function of the basal geogrids and gravel fill was to reduced bearing stresses by distributing foundation loads over a larger area and prevent liquefaction from ejecting from directly below individual foundation elements.

4   DESIGN APPROACH

Following the earthquakes there was a need to provide economically viable footings for the rebuild of light weight commercial, industrial and residential structures. The authors developed the concept of a multi layered reinforced soil crust, rather than relying on a basal geogrid only. The principal design objectives were to:

- Increase static bearing capacity of well tied together shallow footings [strips and pads];
- Prevent punching failure into liquefied soils during and after earthquakes;
- Enhance spanning across liquefaction settlement induced hollows and weak spots;
- Increase the flow path of ejecta, to reduce volumetric soil loss from directly underneath footing elements;
- Provide tensile resistance against lateral stretch; and
- Provide a competent layer to enable repair via relevelling of the structure following large earthquake event.

Based on design experience gained on large scale transport infrastructure and construction of mechanically stabilized soil systems, i.e. walls and pavements, we identified several key design details:

- Geotextile at the base to separate insitu soils from the granular reinforced raft.
- Double layer of a dampproof membrane (geomembrane) to act as a slip surface at the base in areas where lateral spreading and lateral stretch are of concern.
- At least two, but ideally three to four layers of high stiffness biaxial geogrids embedded in the reinforced gravel raft;
- Competent well compacted (95% to 98% of Maximum Dry Density (MDD)) angular granular fill with at least two broken faces to obtain high dilatancy and high angle of shearing resistance.
- Fill thicknesses were ideally 1,200mm, but could be as low as 900mm, below the lowest point of the foundation elements.
- Construction observations were used to assess the actual ground conditions, and where required a 300mm thick layer of railway ballast wrapped in a robust geotextile and placed below the lowest reinforcement layer to act as a capillary break to protect the weak subgrade material. Often observed was the inability to compact the lowest fill layer beyond 92% of MDD (Modified Proctor), as vibratory compaction caused liquefaction and weaving of the insitu

ground. The authors adopted static compaction of the lowest layer with vibratory compaction of the upper layers which provided satisfactory density. Compaction plant were compaction plates or/and smooth drum rollers with weights ranging from 200kg to 10t, respectively. A compaction plateau testing was commonly adopted to define the compactive effort.

- The structures constructed on the reinforced crust had to have a regular plan layout to provide even loads. Further, they had to have the ability to readily redistribute stresses if individual footing elements settled differentially to their adjacent neighbors.
- The geogrid reinforced gravel raft must continue beyond the building footprint, ideally 2m minimum, to ensure that liquefaction ejecta does not create a volumetric loss of soil directly below a foundation element. Where footing elements were close to a property boundary a geogrid reinforced gravel beam was designed to support a well reinforced concrete foundation edge beam. The beam is deeper than the raft and has more geogrid layers, potentially using higher strengths geogrids as well.
- All footing elements, whether strips, ground beams or individual pads, had to be well tied together to prevent differential lateral movement and provide base shear resistance during seismic shaking.

The provision of a 1,200mm thick triple reinforced (usually biaxial geogrid, but uniaxial geogrids laid crosswise can be also used) gravel raft met all the above conditions. The mandatory design checks were:

- Static bearing capacity of individual footing elements or the raft, using NZBC B1/VM4, (MBIE 2008) meeting NZBC limit state strength reduction factor requirements;
- Seismic bearing capacity (short term loading during an earthquake) and punching, assuming a non-liquefied crust over liquefied soils with residual liquefied soil strengths using a two-layer bearing capacity assessment, (Das 2014) and (Bowles 1996), while still meeting the NZBC limit state strength reduction factor requirements;
- Post-earthquake reconsolidation induced settlements using the 'Simplified Procedure' CPT liquefaction triggering assessment after (Boulanger & Idris 2014) in combination with reconsolidation settlement assessment after (Zhang *et al*. 2002) to assess deformation based demand. This is predicated on the raft extending at least 2m beyond the footing thus limiting any 'ejecta' based volumetric soil loss induced settlements;
- Potential for lateral spreading and lateral stretch below the building footprint by direct site observations of actual earthquake response, or published methods after (Zhang *et al*. 2004), (Youd *et al*. 2002), and the Newmark Sliding Block after (Bray & Travasarou 2007) which would require the provision of a slip surface at the base of the reinforced gravel raft.

5 CASE STUDIES

A 5,500m^2 new grocery store was designed and built in Ilam, western Christchurch on a site with moderate liquefaction susceptibility. The design of this relatively well braced building with a
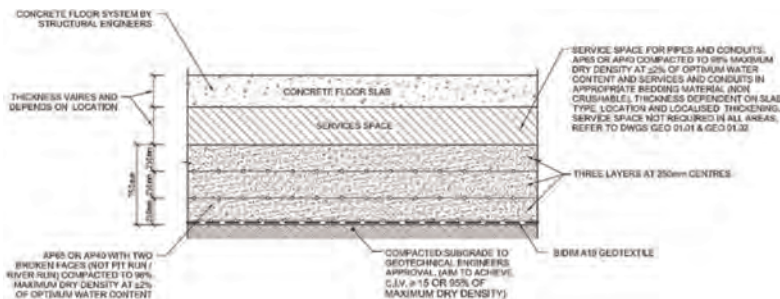
Figure 2.   Typical layout using triple layer geogrid reinforced crust for moderately susceptible sites. Note: CIV = Clegg Impact Value, testing for insitu subgrade.

regular plan layout required some strengthening of the crust to achieve satisfactory static and seismic bearing. The supermarket was halfway completed when the 22 February 2011 earthquake hit. As expected, liquefaction of the subsoil and numerous ejecta (sand boils) were observed after the earthquake. However, there was no manifestation of the liquefaction ejecta from below the foundations or the partially completed reinforced crust. The partially completed structure exhibited no damage, despite shaking well in excess of SLS levels on site, (Mahoney & Kupec 2013).

A large residential development with 1,500 lots was constructed in Halswell, to southwest of Christchurch. About 10% of the residential area was capped to improve ground performance under ULS earthquake shaking. Geogrid reinforced gravel rafts with a 1.2m thickness were used, instead of the (MBIE 2015) recommend a 2m thick unreinforced crust, thus saving cost and construction time, while aiming for similar structural performance. Additionally, by capping multiple residential lots, as a continuous raft a significantly improved overall performance is expected as ejecta material from below the raft is not anticipated. Therefore, 'group' performance is expected to be better than that of an individually improved house site. A limitation of this approach is to provide sufficient space for residential services and allow for sufficient depth of looser topsoil for landscaping.

A two storey office building on 140 Montreal Street, Christchurch, was constructed with a quadruple layer of high stiffness biaxial geogrids. The site had a very poor ground, with the subgrade readily liquefying during initial compaction efforts. The geogrid reinforcements however confined the soil to such a degree that by second lift (300mm) the reinforced fill density increased to over 97% MDD (Modified Proctor).

A grocery store in Eastern Christchurch was extended and it used a modified multi geogrid layer system to provide support to the heavily loaded areas below precast concrete panels. The geogrid layered system also protected underfloor services as those are critical to post disaster functionality of the grocery store, where disruption following large and rare earthquakes is to be kept to a minimum.

The above examples are all on alluvial ground comprising interbedded lenses and layers of liquefiable soils and non-liquefiable soils. Soil structure interaction is essential and will dictate the overall building form, geometry, and bracing requirements. The structures are all well braced light weight sitting on a 'rigid' capping layer with the ability to employ secondary load paths under extreme earthquake loading.

6 REPAIRABILITY

Geogrid reinforced ground is particularly easy to repair following a large, rare earthquake event as it provides a stiff platform to relevel the foundation against. Mechanical jacking, grout or resin injections against the reinforced gravel raft, or compaction grouting below the reinforced gravel raft, are all considered viable options. Any relevelling voids below the foundations can be readily flooded with non-shrink grout to provide ongoing full support to the foundations. One key provision is that all services must be encased within the concrete foundations and are not to be routed through the reinforced gravel raft. Services need controlled exit points and flexible, or easily repairable connections.

7 CONCLUSIONS AND DISCUSSIONS

Geosynthetics are critical for the satisfactory performance of shallow spread foundations on a reinforced gravel raft. A geotextile separator should be used to separate geogrid reinforced high quality fill from the poor insitu ground. The insitu ground is often saturated due to high ground water table and compaction can be difficult to achieve. Where the ground is very soft and weaves under compaction, a ballast layer (coarse granular material) encased in a geotextile separator can be used as a capillary break and subgrade improvement layer.

Lateral spreading can create lateral stretching across the building footprint. While the geogrids will provide tensile restraint, preventing the reinforced crust to be pulled apart, a geomembrane

double layer below the geogrid reinforced raft will act as a slip surface. A heavier duty geotextile is recommended on either side of the double geomembrane to protect them from installation damage. The reinforced gravel raft needs to comprise well graded well compacted, granular materials with an appropriate particle size distribution to match the geogrid apertures. High stiffness biaxial geogrids are ideal, but uniaxial geogrids laid in two direction can be used. All past projects used products with a high modulus (stiffness) with a characteristic strength of 40kN/m (UTS) in both directions.

A 2m extension (skirt) beyond the building footprint on all sides is considered essential as it limits the potential for ejecta to flow out from under the building.

From a structural perspective footings need to be designed to span 4m and cantilever 2m over a corner to account for post earthquake reconsolidation settlement and cope with relevelling stresses. Waffle slabs, ribrafts, 300 to 350mm thick double reinforced rafts are all common foundations for residential buildings. While ground beams with thickenings where columns and shear walls are present are usually used for commercial and industrial structures. All footings are required to be well tied together and be able to compensate for differential deformations, i.e. do not have a brittle failure mode.

Service provisions need careful consideration, especially where they exit the structure. Flexible connections that are readily accessible are highly recommended. Services encased in the ribraft or ground beams must be installed at a grade that accounts for maximum differential settlement. Repairs and relevelling is possible using mechanical jacking, cementitious grout or resin injections between the concrete foundation element and the reinforced gravel raft; or resin and grout injections below the gravel raft (predrilling or percussive penetration of the injection lance through the reinforced gravel raft would be required).

REFERENCES

Boulanger, R. W., & Idris, I. M. (2014). *CPT and SPT Based Liquefaction Triggering Procedures*. Center for Geotechnical Modelling, UCD/CGM-14/01.

Bowles, J. E. (1996). *Foundation Analysis and Design, 5th Ed.*. McGraw-Hill Companies In.

Bray, J. D., & Travasarou, T. (2007). Simplified Procedure for Estimating Earthquake-Induced Deviatoric Slope Displacements. *Journal of Geotechnical and Geoenvironmental Engineering*, Vol. 133, Issue 4.

Cubrinovski, M. H. (2012). Liquefaction impacts in residential areas in the 2010-2011 Christchurch earthquakes. *International Symposium on Engineering Lessons Learned: Japan: One Year after 2011 Great East Japan Earthquake.* Tokyo.

Das, B. M. (2014). *Principles of Foundation Engineering*. Boston, MA, USA: Cengage.

Department of Building and Housing. (2011). *Revised Guidance on Repairing and Rebuilding*. Wellington: DBH.

Mahoney, D. P., & Kupec, J. (2013). *Comparison of Liquefaction Mitigation Options: A Christchurch Case. Same Risks - New Realities*. Wellington: New Zealand Society for Earthquake Engineering.

MBIE. (2008). *Verification Method B1/VM4 Foundations*. Wellington: Ministry for Building, Innovation and Employment.

MBIE. (2012). *Repairing and Rebuilding Houses Affected by the Canterbury Earthquakes*. Wellington: Ministry for Business, Innovation and Employment.

MBIE. (2015). *Part C: Assessing, Repairing and Rebuilding Foundations in TC3*. Wellington: NZ Government. Retrieved from https://www.building.govt.nz/assets/Uploads/building-code-compliance/canterbury-rebuild/repairing-and-rebuilding-houses/canterbury-guidance-part-c.pdf

Tensar. (2019). *Tensar Geogrid Foundation Solutions in Earthquake-susceptible Locations*. Tensar.

Tonkin & Taylor. (2015). *Canterbury Earthquake Sequence: Increased Liquefaction Vulnerability Assessment methodology*. Christchurch: Chap,am Tripp for Earthquake Commission (EQC).

Youd, T. L., Hansen, C. M., & Bartlett, S. F. (2002). Revised Multilinear Regression Equations for Prediction of Lateral Spread Displacement. *Journal of Geotechnical and Geoenvironmental Engineering*, Vol. 12, Issue 12.

Zhang, G., Robertson, P. K., & Brachman, R. W. (2002). Estimating Liquefaction-induced Ground Settlements From CPT for Level Ground. *Canadian Geotechnical Journal. 39*, 1168–1180.

Zhang, G., Robertson, P. K., & Brachman, R. W. (2004). Estimating Liquefaction-Induced Lateral Displacements Using the Standard Penetration Test or Cone Penetration Test. *Journal of Geotechnical and Geoenvironmental Engineering*, Vol. 130, No. 8.

Cost-effective method of road embankment foundation stabilization using basal reinforcement technique for Duqm roads project in Oman

P.V. Jayakrishnan & M.H. González
Maccaferri Middle East LLC, Dubai, UAE

ABSTRACT: The Duqm area in the Central Eastern Oman is located 600km southwest of Muscat, the capital city of Sultanate of Oman. Extensive developmental projects like seaport, airport, dry dock, oil refinery, crude oil storage terminals, infrastructure like roads, railway, bridges, factories, buildings, and residential villas etc. are under construction or on the anvil. The Duqm area is marked by the significant presence of 'soft sabkha' soil which drastically influences the construction of foundations for civil engineering structures in that area. Generally, soil having low undrained shear strength is often referred to as 'soft soil'. Construction of embankments on soft soil can be critical because they have low strength and high compressibility. Since such soils have low permeability, the failure happens at an undrained condition within a short period after the embankment construction. 'Sabkha' is an Arabic expression to describe a type of soft soil with high salt content and are characterized by low bearing capacity and low SPT values. Sabkha soils are widely distributed in the Arabian Peninsula. Generally, for sabkha soil having SPT value less than 5 in muddy conditions, the first and foremost conventional solution of ground improvement adopted by designers for road projects in the Middle East region is provision of stone columns below the road embankment for total depth of soft soil. High strength geosynthetic layers can be used as basal reinforcement for the construction of embankments over soft soils, satisfying the stability criteria laid by the international standards like BS 8006: 2016. Unidirectional high tensile strength geogrids like Paralink is well suited for basal reinforcement applications in Sabkha soil. Depending on the type and magnitude of expected settlement of foundation sabkha soil, this technique can be adopted replacing the conventional deep ground improvement solutions, for most of the cases. Through the case reference of basal reinforcement technique application for Duqm roads project in Oman, this paper briefly outlines the problems associated with the design and construction of embankments over soft sabkha soil commonly found in the Arabian Peninsula and the application of geosynthetic materials as basal reinforcement for stabilizing such embankments, avoiding time consuming and expensive deep ground improvement techniques generally adopted by the road designers.

1   INTRODUCTION

Duqm is a port town on the Arabian Sea, in central-eastern Oman (Figure 1). The scope of the project presented in this paper is construction of roads located at Duqm port, Al Wusta, Oman. The road starts from an existing intersection with National Road No.32 (Duqm-Mahoot Road) and goes towards Duqm Port and to the proposed liquid berths at the seaside. The project location is marked by the extensive presence of 'soft sabkha' soil which drastically influences the type of foundation for proposed road high embankments (Figure 2).

Figure 1. Physiography map of Arabian Peninsula with location of Duqm area.

Figure 2. View of the Duqm roads project location showing the extend of muddy sabkha soil.

Generally, soil having low undrained shear strength is often referred to as 'soft soil'. Construction of embankments on soft soil can be critical because they have low strength and high compressibility. Since such soils have low permeability (10^{-5} mm/sec - 10^{-8} mm/sec), failure happens at an undrained condition within a short period after the embankment construction. 'Sabkha' is an Arabic expression to describe a type of soft soil with high salt content and are characterized by low bearing capacity and low SPT values. Sabkha soils are widely distributed in the Arabian Peninsula. Generally, for sabkha soil having SPT value less than 5 in muddy conditions, the first and foremost conventional solution adopted by designers for road projects in the Middle East region is provision of stone columns below the road embankment for total depth of soft soil.

Reinforcing the base of the embankment with high strength geogrids is a cost effective and technically feasible solution of ground improvement instead of the traditional deep ground improvement solutions like stone column, vacuum consolidation, dynamic replacement etc. Geosynthetic reinforcement layers can be used for improving the stability of embankments over soft soil, which is governed mostly by the shearing resistance of the foundation and is mainly a problem of bearing capacity. The geosynthetic reinforcement may be placed at foundation level to prevent shear failure both in the embankment fill and in the foundation soil.

2 GEOTECHNICAL PROPERTIES OF SABKHA SOIL

Table 1 highlights the general physical characteristics of both sabkha types; namely muddy and sandy Sabkha (Julie *et al.* 1983). Clearly, muddy sabkha are the worst to construct a road embankment, and so is the case of majority of locations in Duqm roads project.

Table 1. Typical geotechnical properties of sabkha soil (Julie *et al.* 1983).

Properties	Muddy Sabkha	Sandy Sabkha
Percentage fines (%)	25 to 95	5 to 25
Salt content (%)	2 to 18	2 to 15
Water content (%)	25 to 90	4 to 40
In-situ density (KN/m3)	10 to 13.5	13 to 18.5
Friction angle (°)	0 to 22	20 to 35
Percentage of CaCO3 (%)	20 to 90	>30
Plasticity index	0 to 40	NP
Cohesion (KN/m2)	0 to 55	Zero
Compression index	0.4 to 0.95	Zero
S.P.T. values (blows)	0 to 4	2 to 10
Static cone resistance (MN/m2)	0.2 to 2	1 to 6
Bearing capacity (KN/m2)	15 to 30	30 to 60

3 CONTRIBUTION OF BASAL REINFORCEMENT FOR EMBANKMENT STABILITY

The general failure mode of an unreinforced embankment is shown in Figure 3(a). By placing a stiff geosynthetic reinforcement layer at the embankment base as shown in Figure 3(b), improved safety factors can be achieved for the rotation, sliding, overall and foundation extrusion stability criteria. Figure 3(c) reveals the stress condition at the base of a reinforced and unreinforced embankment. Because of the presence of stiff geosynthetic reinforcement at the base of the embankment, the stress condition shall be "vertical and inward" against "vertical and outward" case for an unreinforced embankment. This "vertical and inward" stress condition contributes significantly to the stability of such basal embankments. Generally, the load in the reinforcement increases to a maximum during construction, and as the foundation consolidates, the reinforcement tension decreases. When the foundation soil has consolidated, it carries the entire embankment load and thereafter theoretically reinforcement is no longer required.

4 DESIGN GUIDELINES FROM BS 8006: 2016

BS 8006: 2016 (Code of practice for strengthened/reinforced soils and other fills) is a limit state code of practice which considers the ultimate limit states such as local stability, rotational stability, lateral sliding stability, foundation extrusion stability and overall stability and serviceability limit states.

4.1 *Local stability*

For local stability, the geometry of the embankment side slopes should meet the following.

$$\frac{H}{L_s} \leq \frac{\tan \phi'_{CV}}{f_{ms}} \tag{1}$$

where:

H is the height of the embankment

L_s is the horizontal length of the side slopes of the embankment

Φ'_{CV} is the large strain angle of friction of the embankment fill under effective stress conditions,

f_{ms} is the partial material factor applied to tan Φ'_{cv}
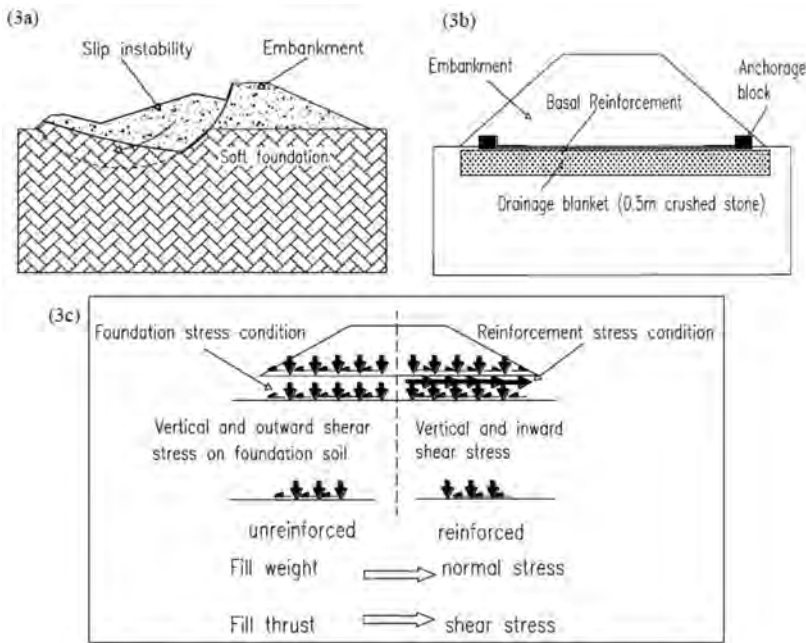
Figure 3. (a). General failure mode for an unreinforced embankment (b). Typical Details of a geosynthetic reinforced embankment (c) stress condition within a geosynthetic reinforced and unreinforced embankment.

4.2 Rotational stability

The rotational stability criteria may be analyzed by methods like slip surface analysis, plasticity solutions and finite difference techniques.

4.3 Lateral sliding stability

The basal reinforcement functions to resist the horizontal outward thrust of the embankment fill.

The load in the reinforcement is a maximum at the edge of the crest of the embankment. The reinforcement load is:

$$T_{ds} = 0.5K_aH(f_{fs}\gamma H + 2f_q w_s)$$ (2)

where:

Ka is the active earth pressure coefficient

f_{fs} is the partial factor for soil unit weight

γ is the unit weight of the embankment fill

f_q is the partial load factor for external applied loads

w_s is the external surcharge loading.

To generate the tensile load T_{ds} in the reinforcement, the embankment fill should not slide outward over the reinforcement. To prevent this horizontal sliding, the maximum reinforcement bond length, L_e should be, Figure 4:

$$L_e \geq \frac{0.5K_aH(f_{fs}\gamma H + 2f_qw_s)f_sf_n}{\gamma h \frac{a' \tan \phi'_{CV}}{f_{ms}}} \tag{3}$$

where:

f_s is the partial factor for reinforcement sliding resistance

h is the average height of the embankment fill above the reinforcement length Le

α' is the interaction coefficient relating the embankment fill/reinforcement bond angle to $\tan \Phi'_{CV}$
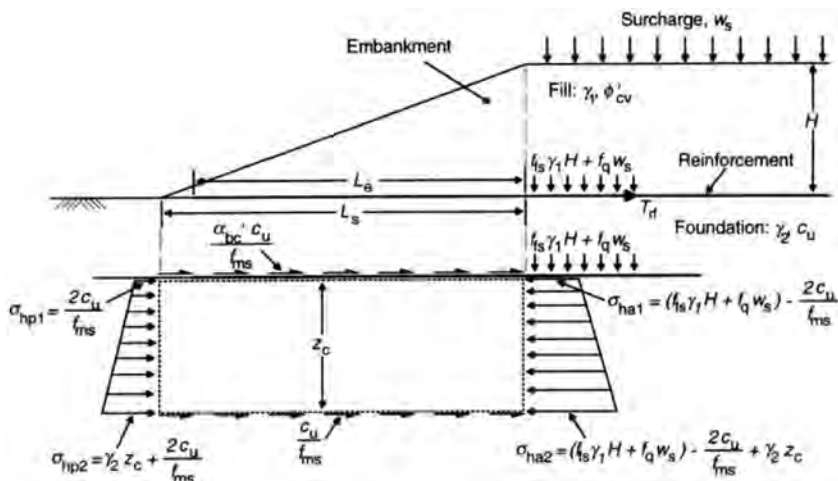
Figure 4.   Analysis of foundation extrusion stability.

4.4   Foundation extrusion stability

The geometry of the embankment induces outward shear stresses within the soft foundation soil.

Where the foundation soil is very soft and of limited depth the outward shear stresses may induce extrusion of the foundation. To prevent this extrusion, the minimum the side slope length of the embankment, L_s, has to be great enough to prevent mobilization of these outward shear stresses.

$$L_s \geq \frac{\left(f_{fs}\gamma_1 H + f_qw_s - \frac{4C_U}{f_{ms}}\right)z_C}{\frac{(1+\alpha'_{ab})C_U}{f_{ms}}} \tag{4}$$

where:

γ_1 is the unit weight of the fill

C_U is the undrained shear strength of the soft foundation layer

Z_C is the depth of the soft foundation layer

α'_{ab} is the interaction coefficient relating to the soil/reinforcement adherence to C_U

4.5 *Reinforcement strain*

The maximum allowable strain in the reinforcement max should be limited to ensure differential settlements do not occur at the surface of the embankment. The initial tensile strain in the reinforcement is needed to generate a tensile load. BS 8006: 2016 imposes a practical upper limit of 6 % strain. The long-term strain (due to creep) of the reinforcement should be kept to a minimum to ensure that long-term localized deformations do not occur at the surface of the embankment.

5 APPLICATION OF BASAL REINFORCEMENT TECHNIQUE IN THE PROJECT

Figure 5 shows the plan view of the road network (indicated in black colour thick lines) and drainage channels (indicated in light blue colour thick lines) planned in Duqm roads project. The roads are designed to be constructed on a 3m high embankment with 2H:1V side slopes. Drainage channels are planned alongside the road to prevent submergence of the road embankment in the event of a high tide flood.

Figure 5. Plan view of road network and drainage channels in Duqm roads project.

5.1 *Soil Investigation program and test results*

For the whole stretch of 8km length of Duqm road project, 21 number of trial pits and 5 number of bore holes were done as part of soil investigation. The investigation revealed the presence of 5m to 8m thick top layer of sabkha soil followed by medium dense sand; in most of the bore holes and trial pits. On an average basis, the SPT value were less than 5 and CPT values were less than 2MPa, with water table at existing ground level.

5.2 *Ground improvement options considered in initial design*

Constructing the planned road embankments over the sabkha soil without any improvements has the following technical disadvantages.

– The sabkha soil had a very limited bearing capacity that would result in foundation extrusion failure, especially along the embankment edges.

– The embankment would experience significant normal and differential settlements affecting the serviceability of the road and the traffic above it.
– The embankment would undergo rotational shear failure, especially along the embankment edges.

    Accordingly, the enhancements expected on the road embankment from the final ground improvement solution were the following.

– Improved factor of safety for bearing capacity failure / extrusion failure.
– Improved rotational stability of embankment.
– Improved lateral sliding stability.
– Improved load transfer and reduced differential settlements.

A wide range of ground improvement methods were explored by the designer by consulting the specialized subcontractors in each field, including the initially preferred method of deep ground improvement through stone columns. Accordingly, the final technical & financial recommendations and project specifications were prepared. Figure 6 below gives the summary of the various ground improvement methods considered by the designer versus their corresponding cost in terms of rate per unit area of road embankment base. For obvious reasons, the finally chosen and specified ground improvement solution was basal reinforcement technique which was significantly economical and faster in construction in comparison to the stone columns method.
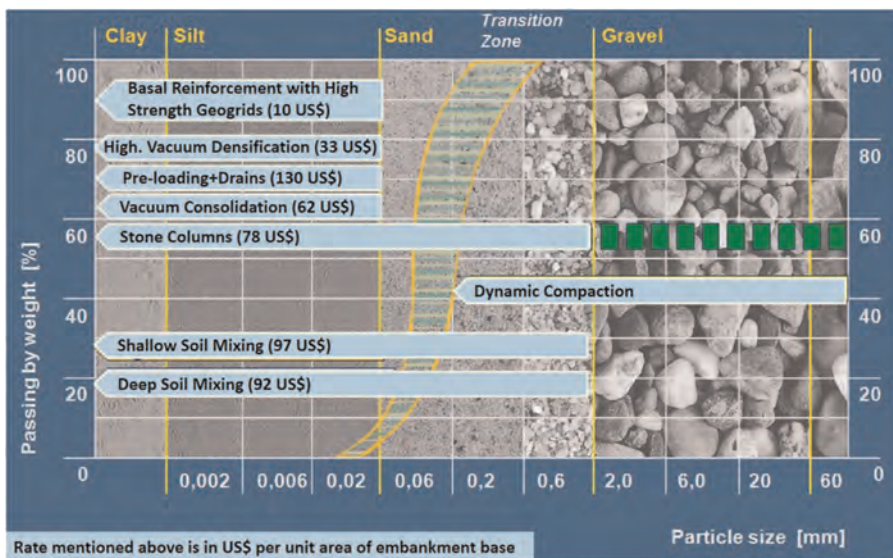
Figure 6. Summary of various ground improvement methods versus rate per unit area of road embankment base.

5.3 Final design details of basal reinforcement option

One of the most important geotechnical parameters of foundation soft soil needed in basal reinforcement design is the undrained cohesion (C_U) value. Initially, in the absence of direct Cu value of Duqm sabkha soil from lab testing, it had to be conservatively interpreted from available SPT and CPT test results.

    From the available SPT values of bore holes, the corresponding average N_{60} (SPT value corrected for field procedure) was calculated which was eventually used to interpret the Cu value based on the correlation in Figure 7 between Cu and N_{60} with reference to the
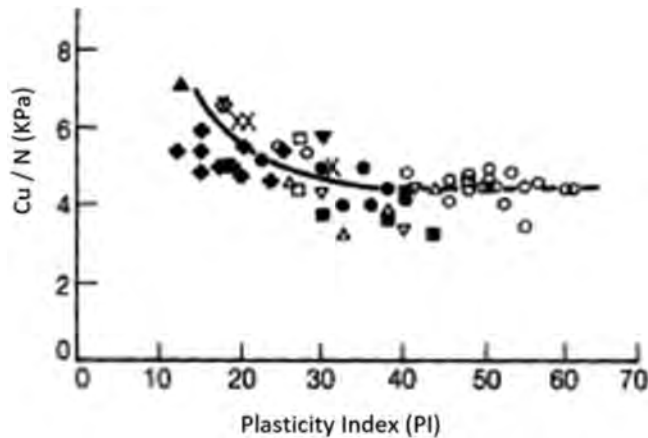
Figure 7.   Correlation between N_{60} value and C_u (after Stroud 1974).

measured plasticity index of the Duqm Sabkha soil. To determine the Cu value based on the CPT values from the available 21 trial pits, the below correlation was used.

$$C_u = q_{c.av} - \sigma_v / N_k$$

where,

C_u = Undrained cohesion (KPa)

$q_{c.av}$ = Average CPT value (KPa)

N_k = Empirical cone factor (conservatively considered as 25 for the weak sabkha in Duqm)

Based on the BS 8006:2016 design guidelines explained in section 4 of this paper, the basal reinforcement design was done to find out the strength of geogrid and bond length with reference to various categories of sabkha soil identified at Duqm roads project site. Accordingly, a high strength geogrid type ParaLink 300 with 300KN/m strength was required where C_u value was more than 10KPa while a 400KN/m type Paralink 400 was required wherever the C_u value was less than 10KPa. Refer Figure 8 for the typical details of the final adopted basal reinforcement application in Duqm roads project vs the initial consideration of ground improvement by stone columns.
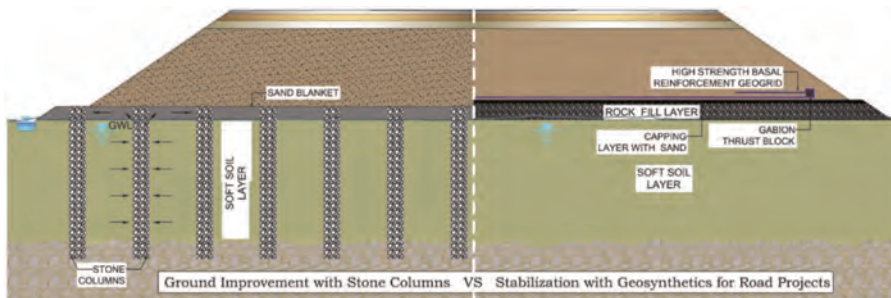
Figure 8.   Stone columns option in first design Vs finally adopted basal reinforcement technique.

Ninety percent of the total calculated consolidation settlement of 425mm was expected to happen during construction period itself before laying the final pavement layers. To realize

this assumption at site practically, staged construction of embankment (with incremental loading) in 3 layers were recommended such that the excess pore water pressure developed would be fully or partially dissipated and shear strength gain achieved with every increment and the safety factor against shear failure increases (refer Figure 9 for details). The dissipation of excess pore water pressure is accompanied with settlement, so an additional ground improvement is achieved. This is a kind of preloading using the same engineering loads proposed for the construction with controlled rate such that the shear strength and stiffness of the soil is improved and the final settlements after the embankment construction would be tolerated.
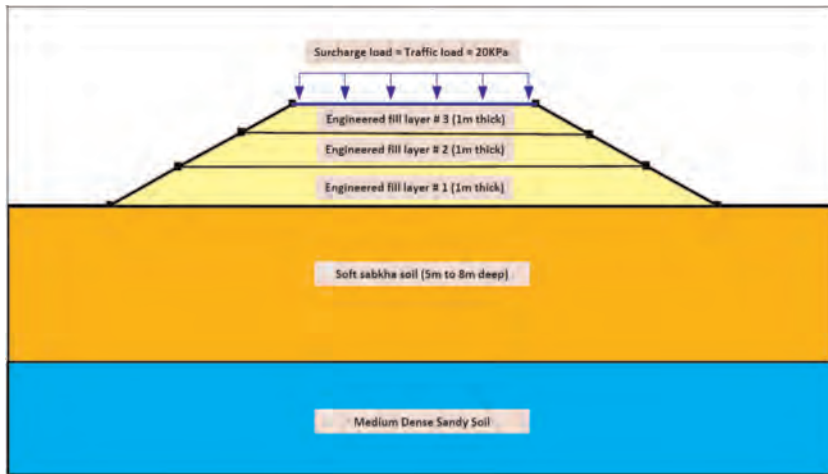
Figure 9.   Scheme of staged construction of embankment with incremental loading.
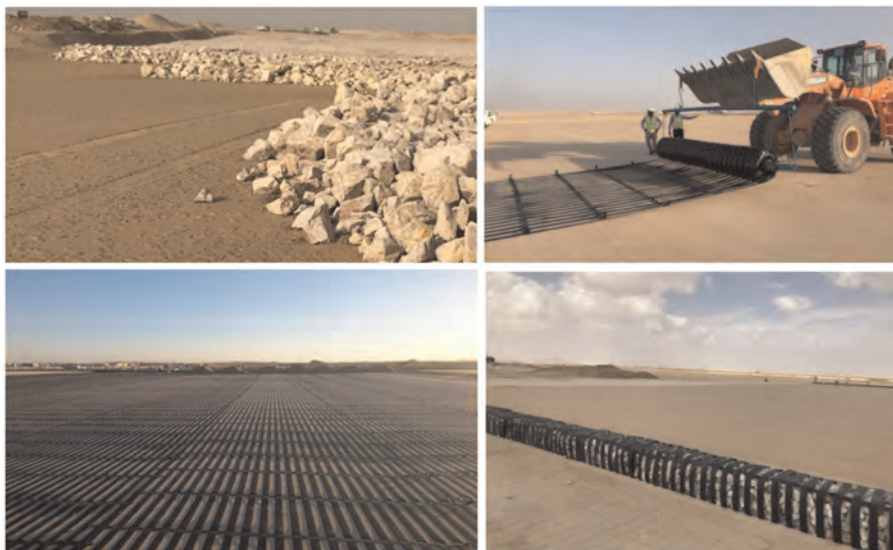
Figure 10.   Stages of basal reinforcement installation.

Figure 11.   Roads completed in Duqm on basal reinforced embankments.

6   CONCLUSIONS

Very low bearing capacity muddy sabkha soils are often found around the coasts of the Middle Eastern Peninsula. New stabilization methodologies are currently available to construct infrastructural works on these sabkha soils. A very cost-effective way of stabilization is the use of geosynthetics. High strength geosynthetic layers can be used as basal reinforcement for the construction of embankments over soft soils, satisfying the stability criteria laid by the international standards like BS 8006: 2016 Unidirectional high tensile strength geogrids like Paralink is well suited for basal reinforcement applications in Sabkha soil. Depending on the type and magnitude of expected settlement of foundation sabkha soil, this technique can be adopted replacing the conventional deep ground improvement solutions for majority of the cases.

The reference of basal reinforcement technique application for Duqm roads project in Oman clearly throws light to understand the problems associated with the design and construction of embankments over soft sabkha soil which is commonly found in the Arabian Peninsula, and how the application of geosynthetic materials as basal reinforcement for stabilizing such embankments can be successfully adopted, avoiding time consuming and expensive deep ground improvement techniques which generally adopted by the road designers.

REFERENCES

ACES (Arab Centre of Engineering Studies) *Factual Report of Geotechnical Investigation for Duqm Roads Project*. 2014.

Almeida, M., Marques, M., & Baroni, M. 2010. Geotechnical Parameters of Very Soft Clays from CPTu. *Proc. 2nd Intern. Symp. on Cone Penetration Testing, CPT'10, online*, 2010. paper No. 2-46.

BS 8006. 2016. *Code of Practice for Strengthened/reinforced Soils and Other Fills*. British Standards Institution, London.

Chen, C. 2001. Evaluating Undrained Shear Strength of Klang Clay From Cone Penetration Test. *Proc. Intern. Conf. on In Situ Measurement of Soil Properties and Case Histories, Graduate Program*, Parahyangan Catholic University, 2001, pp. 141–148.

De Beer, E. 1977. Static Cone Penetration Testing in Clay and Loam. *Proc. Sonder Symposium, Fugro*, pp. 15–23

Emad, Y., Sharif, Mohd. J.A., & Mustafa, K.M. 2015. Engineering Geological Appraisal of Geohazards of Duqm Area, Sultanate of Oman. *Proc. 10th Asian Regional Conference of IAEG* 2015.

Julie, Y., & Sherwood, D.E. 1983. Improvement of Sabkha Soil of the Arabian Gulf Coast. *Proc. 8th European Conf. on Soil Mechanics and Foundation Engineering, Helsinki*.

Stroud M. A. 1974. *The Standard Penetration Test in Insensitive Clays and Soft Rock. Proc. 1st European Symposium on Penetration Testing*, Sweden: Stockholm, vol. 2(2), 367–375.

Settlements of a heterogeneous soil deposit improved with geosynthetic vertical drains

G. Di Filippo, O. Casablanca, E. Cascone & G. Biondi
University of Messina, Messina, Italy

ABSTRACT: The soil improvement through the technique of preloading associated with vertical drains was used to accelerate the consolidation process and reduce the post-construction settlements of the foundation soil of two cylindrical oil tanks founded on alluvial deposit. A summary of the work sequence is provided together with the main aspects of site investigation and geotechnical characterization. An extensive field monitoring of the site was carried out during the embankment construction, the preloading period and, after the embankment removal, during the hydraulic leakage test of the tanks. Differential settlements and angular distortions of the tank foundation evaluated from the measured settlement profiles were compared with expected profile shapes for tanks overlying homogeneous compressible soil layers. Observed absolute and differential settlements and distortions are consistent with the allowable limits provided by the literature and with the design prescriptions, thus confirming the effectiveness of the preloading and drainage technique adopted in the project.

1 INTRODUCTION

The use of geosynthetic vertical drains combined with pre-loading is a cost-effective ground improvement technique widely adopted to improve the bearing capacity and settlement response of fine-grained soft soil deposits. If the design procedure aims to keep settlements within allowable limits in a given time-interval, a proper choice of the in-plane water flow capacity and discharge capacity of the geosynthetic drains as well as their length and spacing is required. To this purpose well known design procedures, generally referred to the case of a homogeneous soil deposit, are widely adopted together with the observational method.

This paper focuses on the latter approach and describes the results of an almost two-year long monitoring period of the settlement performance of the foundation soils of two tanks founded on a heterogeneous fine-grained soil deposit improved using 97-mm-wide and 3-mm-thick wick drains, consisting of a three-dimensional porous polyester filament core protected from clogging by a nonwoven polyester filter.

The whole set of settlement measurements, obtained through topographic survey of settlement platforms, are presented, and discussed in the paper. The application of well-established observational method and a back analysis of the settlement measurements allowed showing the relevant role of the lithological and mechanical heterogeneity of the foundation soils. These led to a scattering in the measured settlements in a portion of the preloaded area, and, for the case at hand, pointed out the minor relevance of the smear effect on the rate of consolidation.

2 SITE GEOTECHNICAL CHARACTERIZATION

The dataset of measurements consists of the settlement induced by preloading and 20 m long prefabricated vertical drains on a heterogeneous, medium to stiff clayey and silty soil deposit, representing the foundation soils of two large steel tanks and incorporating randomly distributed discontinuous layers of granular soils (Figure 1). Figure 1a shows the longitudinal cross-section of the site with the profile of the pre-loading embankments superimposed to the soil profile and to the profiles of tip resistance q_c and excess pore water pressure u, as obtained from *CPT* and *CPT*u tests. The soil deposit was investigated through boreholes (*BH*), cone penetration tests (*CPT*), piezocone tests (*CPT*u) and laboratory tests on undisturbed samples: it consists of an about 27 m thick layer of high plasticity clay with
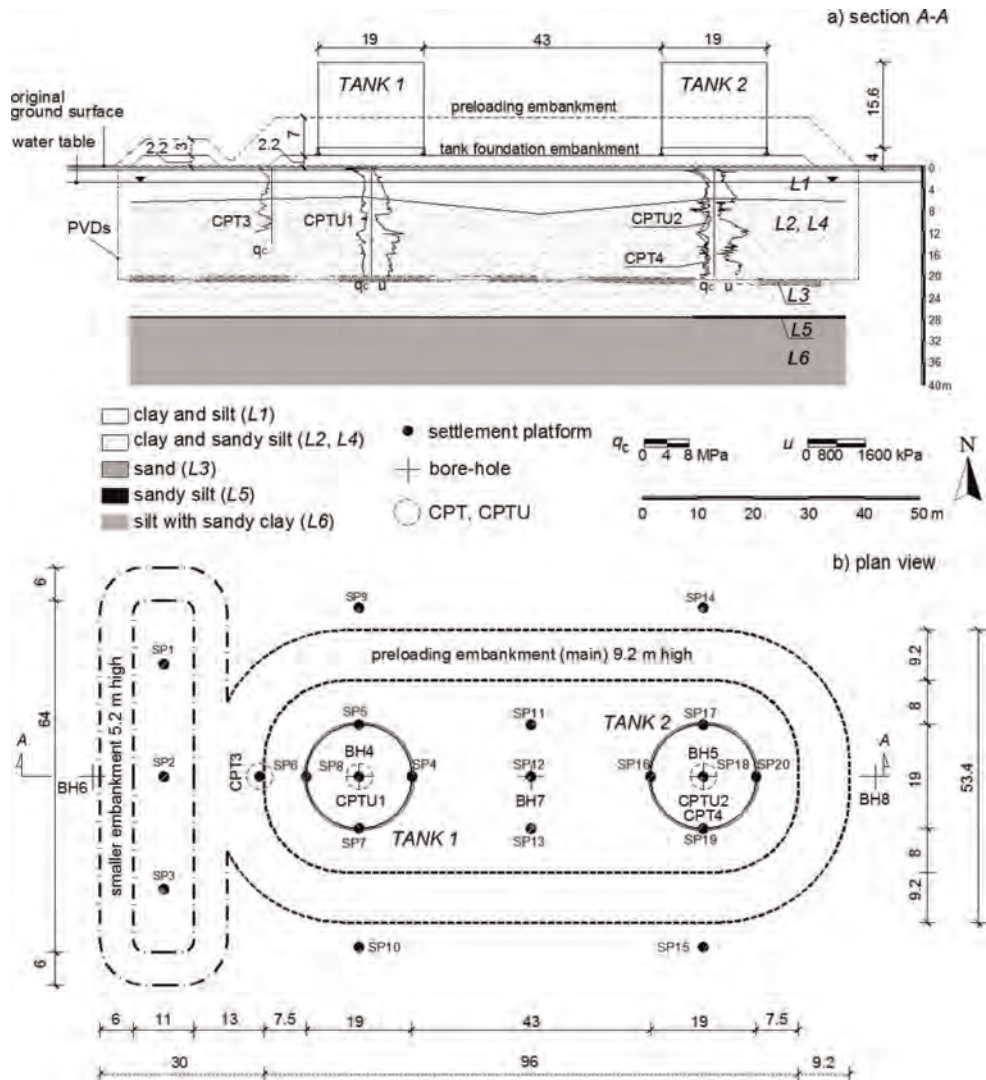
Figure 1. a) Longitudinal cross-section of the site; b) plan view of the preloading embankment, location of the geotechnical investigations and of settlement platforms (adapted from Di Filippo *et al.* 2017 and Cascone & Biondi 2013).
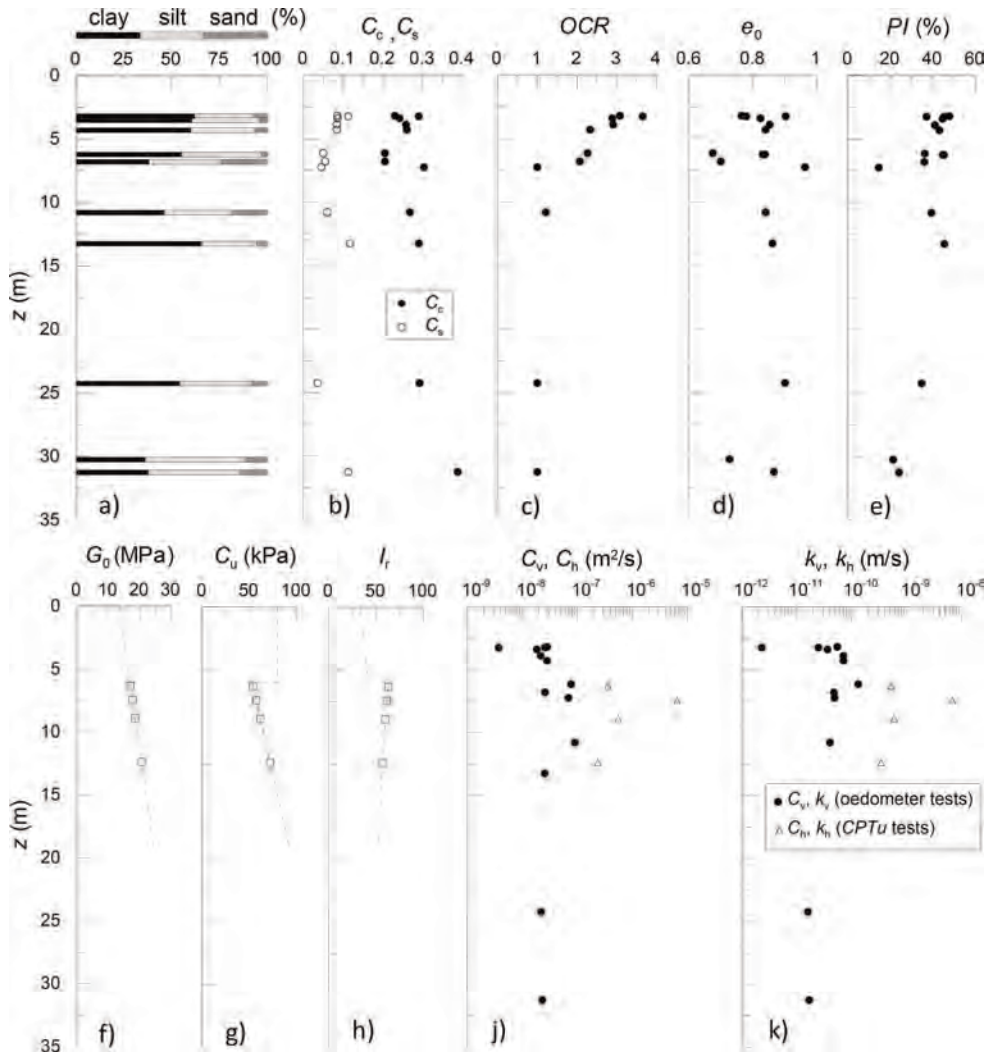
Figure 2. a) Grain size profile; b-d) oedometer test results; e) plasticity index profile; f-h) Profiles of G_0, C_u and I_r and values (square dots) adopted for the evaluation of the horizontal consolidation coefficient C_h; j-k) permeability and coefficients of consolidation obtained by oedometer and CPTu test results.

sandy silt ($L1$, $L2$ and $L4$ in Figure 1a), which is lightly over consolidated in the upper portion, embodies discontinuous and randomly distributed (1 m thick) layers of sand ($L3$ in Figure 1a) at a depth of about $z = 20$–22 m, and overlies a silt with sandy clay layer ($L6$ in Figure 1a), extending to the maximum investigated depth of 40 m, with the interposition of a thin (less than 1 m) layer of silty sand ($L5$ in Figure 1a) located at a depth of about $z = 27$–28 m. The water table was detected at a depth of 3 m from the original ground surface.

The development of settlements was monitored measuring, by topographic survey, the vertical displacements of 20 settlement platforms.

These consisted of square steel plates welded to the base of steel riser pipes. The riser pipes were covered with sleeve pipes to prevent the transmission of the down-drag forces induced

by embankment settlements to the plates. The settlement platforms were placed on the natural soil under the drainage blanket. The location of the platforms (SP) is shown in the plan view of Figure 1b.

Figure 2 shows the grain size profile, the oedometer test results and the profile of the plasticity index *PI*. The soil deposit is mainly made of clay and silt, the former prevailing in the upper part of the deposit, the latter at depth $z > 30$ m; the sand fraction varies between 1% and 24%, being generally less than 10% (Figure 2a). The compression index C_c ranges between 0.205 and 0.388 and the ratio of C_s to C_c varies in the interval 0.12–0.40 (Figure 2b); the soil deposit is lightly overconsolidated in the upper 10 m (Figure 2c) with a void ratio e_o approximately ranging between 0.65 and 0.97 (Figure 2d) and *PI* generally greater than 30% (Figure 2e).

Four dissipation tests were performed during the *CPTU*1 (at the depths $z = 8.90$ and 13.38 m) and *CPTU*2 (at $z = 6.32$ and 7.44 m) and values of the horizontal consolidation coefficient C_h were obtained through the procedures suggested by Houlsby & Teh (1988) and by Teh (1987).

For the four depths of interest for the dissipation tests, Cascone & Biondi (2013) computed values of I_r in the range 57–62 (Figure 2h, Table 1) and values of C_h in the narrow interval $(2.39 \div 5.56) \cdot 10^{-7}$ m²/s (Figure 2j, Table 1). An exception is represented by the test at $z = 7.44$ m, probably referred to a sand layer Cascone & Biondi (2013), leading to a larger value ($C_h = 6.70 \cdot 10^{-6}$ m²/s) which was not considered in the analyses described in this paper. In Figure 2j the values of the vertical consolidation coefficient C_v, obtained from oedometer test results and referred to a vertical effective stress $\sigma'_v = 200$ kPa, are also represented, showing values generally larger than $2 \cdot 10^{-8}$ m²/s in the upper 15 m of the soil deposit. Herein, the value $C_v = 6.9 \cdot 10^{-8}$ m²/s, determined on a sample retrieved from BH7 located at the center of the preloaded area, was considered since it is representative for the depth interval investigated through the dissipation tests ($z = 6.32 \div 12.38$ m).

Finally, the theory by Baligh & Levadoux (1980) was applied to compute the values of the horizontal permeability coefficient k_h. The obtained results are plotted in Figure 2k together with the interpretation of oedometer tests in terms of the coefficient of vertical permeability k_v referred to a vertical effective stress $\sigma'_v = 200$ kPa. In the upper 15 m of the soil deposit k_v and k_h vary in the range $(2 \div 11) \cdot 10^{-11}$ and $(3 \div 6) \cdot 10^{-10}$ m/s, respectively.

Table 1. Results of the interpretation of the dissipation tests through the procedure proposed by Teh (1987) and by Houlsby & Teh (1988).

	CPTU1		*CPTU2*	
	z=8.90 m	z=12.38 m	z=6.32 m	z=7.44 m
	(Houlsby & Teh 1988)	(Houlsby & Teh 1988)	(Teh 1987)	(Houlsby & Teh 1988)
t_{50} (min)	19	44	30	–
$c_h/I_r^{0.5}$ (cm²/ min)	0.041	0.017	0.026	0.489
c_h (m²/s)	$(4.8 \div 13) \cdot 10^{-7}$	$(2.1 \div 5.4) \cdot 10^{-7}$	$(3.1 \div 8.2) \cdot 10^{-7}$	$(5.8 \div 15) \cdot 10^{-6}$
k_h (m/s)	$(5.1 \div 14) \cdot 10^{-10}$	$(3 \div 7.8) \cdot 10^{-10}$	$(4.5 \div 12) \cdot 10^{-10}$	$(5.8 \div 15) \cdot 10^{-9}$

3 PVDS AND WORK SEQUENCE

In the area where the tanks had to be constructed the ground surface was excavated to a depth of about 0.7 m and 20-m-long prefabricated vertical drains (PVDs) were installed in a triangular pattern, with a spacing of sd = 1.5 m. PVDs were 97-mm-wide and 3-mm-thick

wick drains, consisting of a three-dimensional porous polyester filament core protected from clogging by a nonwoven polyester filter. The equivalent diameter dw and the cross-section Aw of the drain are dw = 63.66 mm and Aw = 3183 mm2. According to the manufacturer the in-plane water flow capacity of the composite drain under a i = 0.1 hydraulic gradient is about 1600 and 2500 m3/year for values of the pressure applied to both filter sides of 200 and 300 kPa respectively; the drain discharge capacity qw for i = 0.1 and r = 300 kPa is greater than 4000 m3/year ($\approx$1.27·10-4 m3/s); the corresponding value of the equivalent drain permeability is kw > 0.4 m/s.

Figure 3 summarizes the work sequence, the duration of the work phases and the corresponding loading history with reference to the beginning of the construction of the preloading embankments, assumed as a datum (t = 0). The main (H = 9.2 m) preloading embankment was built in 98 days with an increase of the rate of loading after the first 66 days.
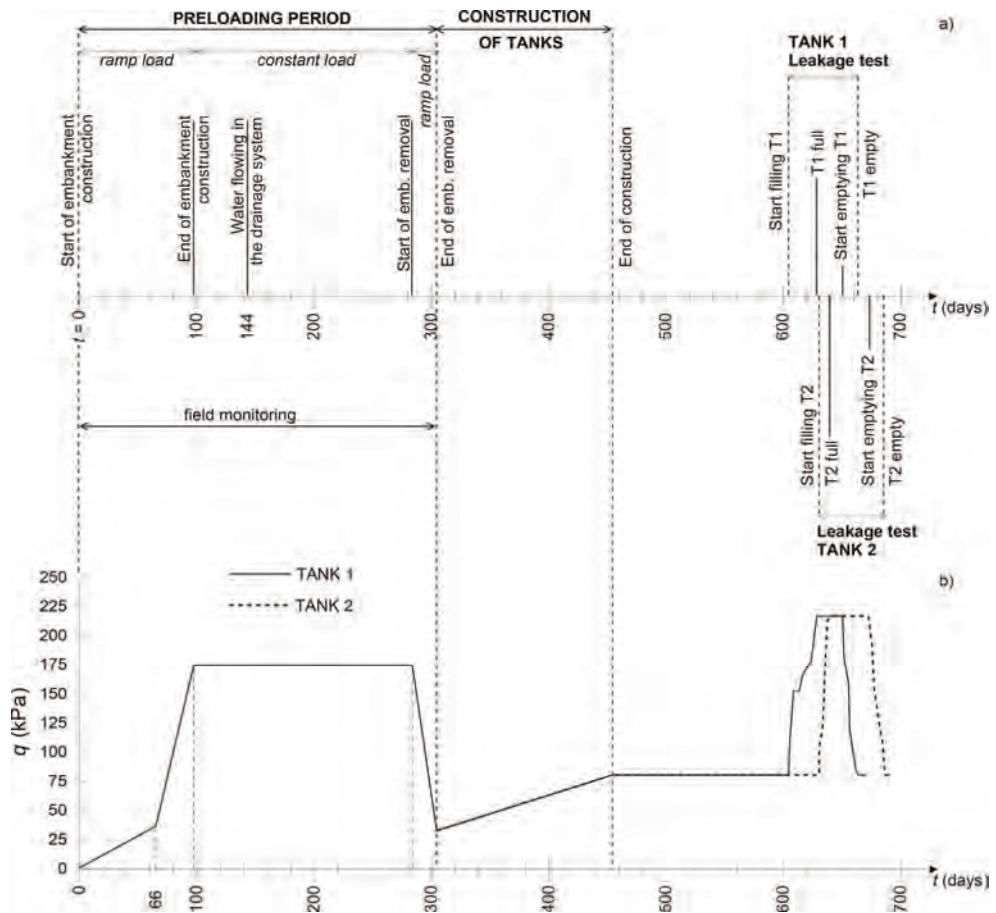
Figure 3.   Work sequence.

The embankment was kept in place for further 186 days (until t = 284 days); the net average pressure applied on the ground surface of the preloaded area was about 174 kPa. The net average pressure applied by the smaller (H = 5.2 m) embankment was about 98 kPa.

At t = 144 days water was observed flowing out of the drainage system. This delay in the achievement of PVDs full effectiveness may be ascribed to the effect of drain unsaturation (Indraratna *et al.* 2003). During the preloading period settlements under the 9.2 m high embankment developed to a maximum of about 39 cm and, as soon as deformation rate became negligible, both the preloading embankments were removed in 21 days (t = 305 days) leaving in place the tank foundation embankment.

Then the site was prepared for the construction of the RC foundation rings and of the steel structures of the tanks, corresponding to the application of a net average pressure of about 80 kPa (including the selected fill foundation embankment). The tank construction ended at t = 455 days. The hydraulic leakage test at t = 605 days for tank No. 1 and at t = 621 days for tank No. 2. Tank No. 1 was filled of water in 24 days, was kept full for 22 days and was finally emptied in 13 days.

Tank No. 2 was filled of water in 10 days, was kept full for 35 days and was emptied in 12 days. The volume of water stored in each tank during the tests was about 4000 m^3, loading the foundation soil with an additional average pressure of about 143 kPa.

4 MONITORING DURING THE HYDRAULIC LEAKAGE TESTS

The field monitoring of the site was carried out also during the hydraulic leakage tests of the two tanks. The settlements of the tanks were measured using a level probe along a flexible pipe placed in a shallow excavation under each tank before construction, in the direction of the transversal axes of the main pre-loading embankment. Measurements were taken every 2-3 days at five aligned locations under the tanks: at the edges under the foundation ring, at 1/4 and 3/4 of the diameter and at the centre of the tanks.

Figure 4 shows the settlement profiles under the tanks at different times during the tests. All the data show that both tank foundations exhibit the classical dish-shaped settlement profile with larger values near the centre and settlements that decrease smoothly toward the edges. Specifically, maximum settlements under the centre of the tanks are about 6 cm for tank No. 1 (Figure 4a) and about 7.5 cm for tank No. 2 (Figure 4b).

At the edges of the two tanks the observed settlement variation, due to filling and emptying, resulted always less than 3 cm, consistently with the prescribed design limit. This behavior confirmed the effectiveness of the soil improvement technique adopted at the site and allows predicting a satisfactory performance of the tank under future service conditions when oil will be stored instead of water.

According to D'Orazio & Duncan (1987) the main factors affecting the shape of the settlement profile for the foundations of tanks resting on compressible homogeneous soil deposits are the values of the factor of safety F_s with respect to undrained shear failure of the foundation soils and the geometric ratio D_e/t_c , between the effective diameter of the tank (i.e. the actual tank diameter D plus the thickness t_g of the granular layers between the base of the tank and the top of the underlying compressible soil layers), and the thickness of the compressible soil deposit beneath the tank. Specifically, as observed by D'Orazio & Duncan (1987), through the analysis of a large amount of data available in the literature, a dish-shaped settlement profile of the tank bottom typically occurs when $D_e/t_c < 4$ and $F_s > 1.1$. For the two tanks under consideration both these conditions are verified. In Figure 4 it can also be observed that, despite the symmetry in the tank structures and in the applied load, the measured settlement profiles along the transversal section of the tanks are not symmetric. Again, a stiffer response of the northern area of the tank foundation was observed and can be reasonably attributed to the lithological and mechanical heterogeneity of the alluvial deposit values of the rigid rotation a_o ranging from 0.5 to 1% can be estimated from the settlement profiles of Figure 4.
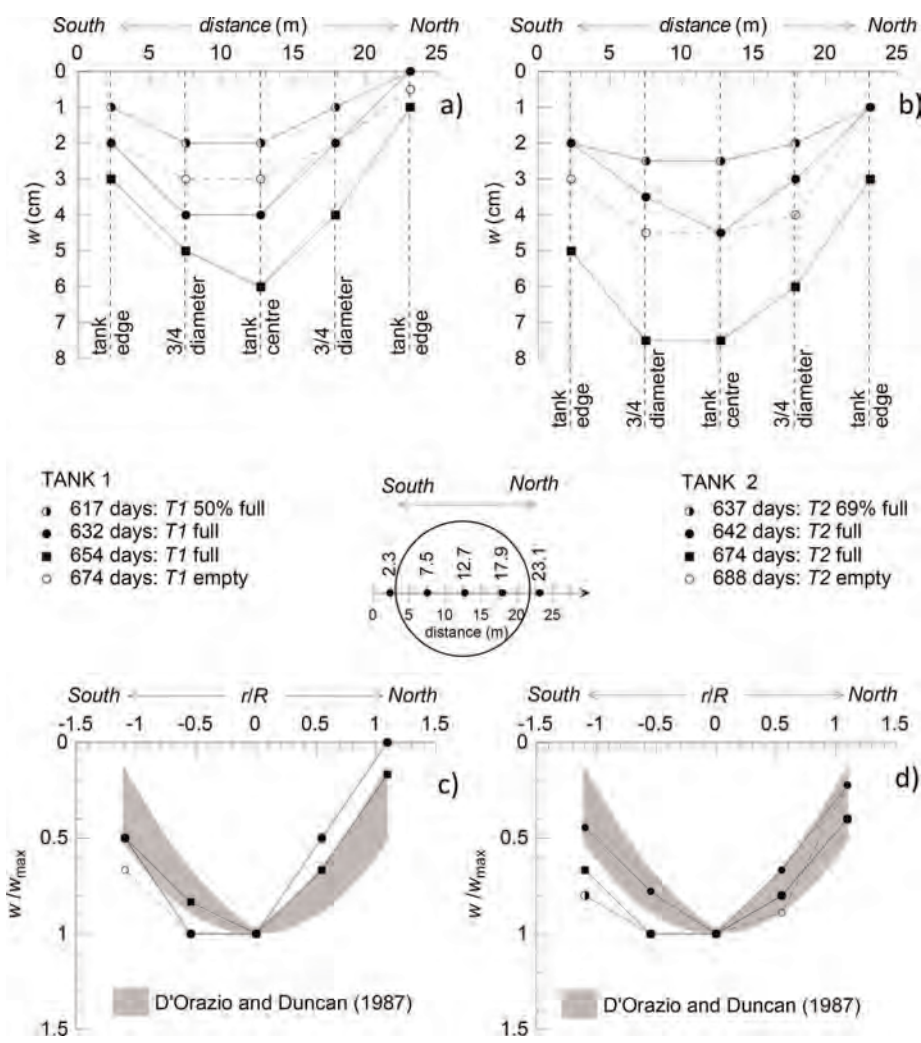
Figure 4. Settlement and normalized settlement profiles during the hydraulic test of tank No. 1 (a, c) and No. 2 (b, d).

The effect of soil heterogeneity on settlement response becomes apparent by comparing the profiles of measured settlements with the profile shapes suggested by D'Orazio & Duncan (1987) for tanks overlying homogeneous soil deposits.

To this purpose the measured profiles (Figure 4a,b) are plotted in Figures 4c,d in a normalized diagram where the settlement w and the radial distance r are divided by the settlement w_{max}, measured at the centre of the tank, and by the tank radius R, respectively. The shaded area in Figures 4c,d represents the range of variation of the ideal shape profiles defined by D'Orazio & Duncan (1987) for the case $F_s > 1.1$ and $D_e/t_c < 4$. The normalized settlement profiles under tank No. 2 satisfactorily match the range of ideal profiles, especially for the northern side of the foundation that exhibited a stiffer response. A fair agreement is also observed between the normalized profiles obtained under tank No. 1 and the ranges provided by D'Orazio & Duncan (1987).

5 CONCLUSIONS

In this paper the field performance of the foundation soil of two tanks, improved using the technique of preloading associated with vertical drains, was illustrated. Due to soil compressibility and large stresses acting under service condition, settlements of the tank foundations larger than the maximum displacement that could be accommodated by the joints between the tanks and piping could be anticipated. It was then decided to induce soil consolidation by preloading the area and to accelerate the process by installing prefabricated 20 m long vertical drains.

After the embankment removal the tanks were built and tested to verify their hydraulic tightness.

Data of the observed behavior during the preloading period and the hydraulic leakage tests of the tanks were collected during an almost two-year long monitoring period. Maximum settlements measured during the preloading period were of about 39 cm and were approximately uniform under the longitudinal axis of the preloading embankment. Conversely, asymmetric settlement profiles were observed along the three monitored transversal axes of the preloading embankment. This behavior was ascribed to the lithological and mechanical heterogeneity of the alluvial soil deposit. A delay in the achievement of *PVD*s full effectiveness was observed during the monitoring period and was ascribed to the presence of an unsaturated interface between the drain and the soil induced by drain installation.

During the hydraulic tests the maximum absolute settlements were attained under the centre of the tanks and were in the range 6-7.5 cm; differential settlements between tank centre and edges in the range 3-5 cm were measured. Consistently with the prescribed design limit, at the edges of the two tanks settlement variation, due to filling and emptying, was less than 3 cm. Differential settlements and angular distortions evaluated from the measured settlement profiles were compared with expected profile shapes for tanks overlying homogeneous compressible soil layers. A general fair agreement was observed even if the heterogeneity of the soil deposit affects the tank response.

Absolute and differential settlements as well as angular distortions are consistent with the allowable limits suggested in the literature and with the design prescriptions, thus confirming the effectiveness of the pre-loading and drainage technique adopted in the project and envisaging a satisfactory performance of the tank under service conditions.

REFERENCES

Baligh, M.M., Levadoux, J.N., 1980. *Pore Pressure Dissipation after Cone Penetration. Report R80-11*. MIT, Dept. of Civil Engineering, Cambridge.

Cascone, E. & Biondi, G. 2013. A Case Study on Soil Settlements Induced by Preloading and Vertical Drains. *Geotextiles and Geomembranes*: 38: 51–67.

D'Orazio, T.B., Duncan, J.M., 1987. Differential Settlements in Steel Tanks. *Journal of Geotechnical Engineering* 113(9), 967–983.

Di Filippo, G., Biondi, G., Cascone, E. 2017. Measurements and Predictions of Settlements Induced by Preloading and Vertical Drains on a Heterogeneous Soil Deposit. *Measurement*: 104: 302–315.

Indraratna, B., Bamunawita, C., Redana, I.W., McIntosh, G., 2003. Modeling of Geosynthetic Vertical Drains in Soft Clays. *Journal of Ground Improvement* 7 (3), 127–138.

Geocells in bridge approach transitions for high-speed railway – A case study

Shahrokh Bagli*
Strata Geosystems (India) Pvt. Ltd., India

K. Rajagopal*
Andhra University, Visakhapatnam, India

Manjul Mathur*
Indian Railways-Western Railway, India

M.K. Rajpal*
Research Design and Standards Organisation, India

Yashodeep Patil*, Suraj Vedpathak* & Gautam Dalmia*
Strata Geosystems (India) Pvt. Ltd., India

ABSTRACT: The Paper presents a case study demonstrating the use of geocells to replace concrete approach slabs and reinforce transition at railway bridge approaches. The objective is to study the effect of geocell system to enhance the train speeds up to 160 kmph on the Bombay - Delhi railway route.

Geocell layers of differential lengths were installed over the blanket layer on the existing track to ensure a smooth transition. Field observations confirmed that the geocell layers were successful in ensuring a smooth transition of bridge approaches. Further, the geocell layers proved that by avoiding the conventional concrete slab, there is considerable saving in capital costs and construction time. The proposed cross-section of the bridge transition system also minimizes differential settlements and imposed bearing pressures on the subgrade soil. With this system, the maintenance cycle is extended which not only reduces downtime but also the life cycle costs.

Keywords: Railway transition, HDPE geocells, bridge approaches, nonwoven geotextiles, load spread

1 THE OBJECTIVE

Differential settlements between the railway embankment and the bridge structure, often supported on well or pile foundations, are some of the major issues that limit the intended train speeds. This issue required a solution with ambitious plans on the anvil to increase the speed limits and hike up the axle load to 32.5 Tons from 25 Tons. Differential settlements at the structure-embankment transitions manifest as rough running at bridge approaches. This also causes increased wear and tear of track, stock wheels and bearings.

*Corresponding Authors: shahrokh.bagli@strataindia.com, gopalkr@faculty.iitm.ac.in, mmanjul@hotmail.com, edgerdso2019@gmail.com, yashodeep.patil@strataindia.com, suraj.vedpathak@strataindia.com and gautam.dalmia@strataindia.com

To ensure a smooth ride, an appropriate transition system is needed which provides a gradual change in the "spring stiffness" or deflection characteristics of the track bed from the earth embankment to the more rigid bridge structure. The proposed system should bridge over the differential settlements between the two structures. It would also help in spreading the track load over a wider area below the ballast and reduce the deformation of the embankment fill at entry and exit of the bridge.

While devising a solution, it was assumed that the subgrade of the embankment had achieved 90% consolidation and deflections below the subgrade are negligible. This assumption is quite valid for embankments that have been constructed several decades ago and well maintained according to Railway routine guidelines and true to the Indian Railway protocols and traditions.

2 THE SOLUTION

The Western Railway (WR) proposed using a system essentially comprising layers of geocells to considerably improve the rigidity of the sub-ballast/formation and reduce deformations of the track surface/formation and maintain the track geometry at the bridge approaches. Hence geotechnically at the approaches, there would be three sections progressively increasing in rigidity:

1. the flexible embankment formation,
2. the more rigid section with layers of geocells in the sub-ballast (to safely connect the flexible formation and rigid bridge structure),
3. the rigid bridge structure.

Before adopting the proposed system on a major scale, it was decided to carry out monitored trials on the busy and high-speed Bombay-Baroda route of the Western Railway near Surat. It is significant to note that the proposal does away with the conventional concrete approach slab. The conventional concrete approach slab treatment requires a track downtime of about 24 hours while the treatment with geocell layers can be completed within about 5 hours. As per Ministry of Railways/RDSO Guidelines, approach slabs are to be provided on both bridge entry and exit approaches of unballasted bridge deck with spans of 12.2 m or more. One end of the approach slab is supported on the bridge abutment and the other end rests on the formation. The approach slab should be minimum 4 m long and should be of reinforced concrete.

However, the conventional style for approaches has the following limitations:

1. Non-uniform settlements of the slab with movement of the track that it supports. The track movement is due to several reasons including climatic variations, temperature variations over 24 hours and traction forces due to rolling friction, rocking, acceleration, and braking.
2. Quite often, the approach slab is damaged prematurely and is not replaced in time owing to voluminous work involved, adherence to maintenance schedules, etc.

The WR desired to strengthen the bridge approaches to cater to an increased speed of 160 kmph on the prime Mumbai-Delhi trunk route. The Railway engineers desired to consider the use of geocell layers to overcome the limitations of the conventional concrete approach slab and enhance the performance.

3 LOCATION OF THE TRIALS

To save on downtime, a bridge without the concrete approach slabs was chosen. The bridge designated Major Br No. 417 across Mindhola River near Lajpore Village was selected. The

bridge has thirteen 18.3 m long plate girder spans. The concrete approach slabs of this bridge were not yet placed, pending proposed major maintenance. Hence the approaches of this bridge were deemed ideal for trials with geocell layers in lieu of the concrete approaches.

Figures 1 and 2 shows a satellite imagery and close up of the bridge location with respect to its environs.

Figure 1.   Google satellite imagery of bridge 417.

Figure 2.   Close-up of the location within the rectangle.

4   ORGANIZING THE TRIALS

Two trial stretches were taken up at the bridge, on March 02, 2021 and March 16, 2021, respectively. The first trial stretch was taken up on the Up line (for South bound traffic towards Mumbai) at the North end. The second trial section was taken up on the same track at the South end of the Bridge.

5   PROPOSED TRANSITION SYSTEM AT THE APPROACHES

The trials were carried out with three layers of geocells having depth of 150 mm and weld spacing of 356 mm according to analysis and design recommended by IIT Madras. The proposed system was developed after carefully performing 3-dimensional computer based numerical model studies. The infill material is as per G-14 specifications of the Indian Railways. A nonwoven geotextile separator layer was placed below the three-layer geocell system to prevent penetration and loss of aggregates from geocell pockets and to also act as a drainage layer to some extent. The transition system with geocells is shown in Figure 3.
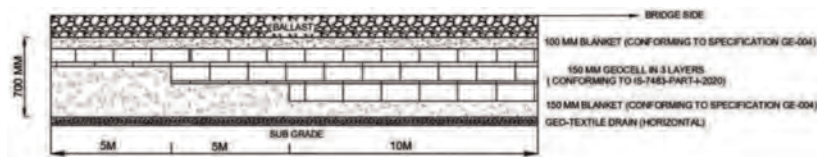
Figure 3.   Section for trials.

6   TRIAL PRE-REQUISITES AND PRE-BLOCK ACTIVITIES

Traffic on the Southbound Up Line was required to be blocked for adequate time to carry out the work safely and to conform to the strict Indian Railway quality parameters. Block on the

track could only be secured over a limited time, owing to heavy traffic on one of the country's busiest trunk routes. A block period of only 4 hours and 30 minutes was allocated to carry out the entire set of activities for the installation of the system at each trial stretch respectively.

7 PRE-BLOCK ACTIVITIES

Considering the strict and limited time allocated for the work during the block and the limited work-space constraints on the embankment, the execution of activities during the block was required to be well-planned, coordinated and concerted. Hence prior to the commencement of the block, preparations were made to keep in readiness to commence work sequentially on the set of activities for timely and quality installation, under the space and time constraints. Activities prior to the respective blocks are shown in Figures 4–9 with traffic plying with a speed limit of 20 kmph. The work on first stretch commenced on March 02, 2021, as scheduled. To ensure that all activities are completed within the allocated traffic and power block time ($4\frac{1}{2}$ hours), timings were allocated to each activity. This was also a Time Study exercise of sorts as basis for time allocation for similar works on other bridge approaches in the future.

8 CONSTRUCTION SEQUENCE

The construction sequence during the block was as follows:

1. The tracks were dismantled by removing the rails and sleepers (Figures 4 and 5). The formation including ballast was excavated up to 1400 mm below the rail level (Figures 6 and 7) Soil was excavated to reach 700 mm depth of formation over the 20 m length and 5 m width. The excavated area was levelled and compacted prior to laying nonwoven geotextile separator layer (Figure 8). Nonwoven geotextile was placed over the entire excavated stretch (Figure 9). Overlap of geotextiles at edges were a minimum of 300 mm.
2. Blanket material was placed over the nonwoven geotextile, watered and hand-tamped to 100 mm thickness. The procedure is shown in Figures 10 and 11. A timber template was used to ensure that compacted thickness of 100 mm was achieved.

Figure 4. Removing rails.

Figure 5. Removal of sleepers.

Figure 6. Removal of ballast.

Figure 7. Removal of sub-ballast/blanket.

Figure 8. Checking the excavation level.

Figure 9. Laying the nonwoven geotextile.

Figure 10. Infilling 100mm thick blanket layer.

Figure 11. Compaction with manual hand tamper.

3. The bottom-most layer of geocell (weld spacing 356 mm and 150 mm depth) was placed. The dimensions of this layer were 10 m length × 5 m width. The layer was placed on top of the 100 mm thick compacted blanket. The geocell layer was held in expanded position by temporary steel hooked stakes. The stakes maintained the expanded panels before infilling and kept them in position. The stakes also ensured that the cells were not distorted and maintained their dimensional integrity. The blanket material was infilled within the geocell pockets with a backhoe and spread manually with shovels. The infilled material was watered and compacted with a hand tamper to achieve the required compaction. The infilling of the geocell panel was done to 25 mm above the brim of the geocell as a cushioning layer to prevent damage to the brim of the geocells. The final compacted thickness of this layer was maintained as 175 mm. This procedure is shown in Figures 12, 13 and 14.

Figure 12.   Bottom-most geocell layer.

Figure 13.   Infilling the geocells.

Figure 14.   Watering and compaction of infill.

4. The middle layer of geocell (also weld spacing 356 mm and 150 mm depth) was placed, with expanded overall dimensions 15 m length × 5 m width. This layer was placed on top of the bottom-most layer of infilled geocells (overfilled by 25mm). Placing infill, spreading, and compaction were carried out similar to the procedure for the bottom-most geocell layer.
5. The topmost geocell layer (also weld spacing 356 mm and 150 mm depth) was similarly placed. The expanded dimensions of this layer are 20 m length × 5 m width. The infill material was placed, spread, and compacted after watering, similar to the lower two geocell layers.
6. The 100 mm thick compacted blanket layer was provided over the uppermost geocell layer. Ballast was laid over the blanket, Figure 15. Sleepers were placed back into position after laying and spreading the required thickness of ballast as shown in Figure 16. Rails were placed back in position on the sleepers manually by sliding on rollers. Rail rubber pads were placed between the steel rails and the concrete sleepers. After placing rail rubber pads, adjacent rails were joined together by fish plates (rail joint bars or splice bars), as seen in Figure 17.
7. Rail clips were clamped to the sleepers to ensure proper fastening between sleeper and steel rail, and maintain the alignment of the rail which can go out of alignment due to any

Figure 15.   Laying ballast over the blanket layer.

Figure 16.   Placing sleepers over ballast.

Figure 17.   Placing rail fish plates; left picture shows stiffening fishplate.

movement, bending, warping etc. Once the fastening systems were in place, rail alignment was checked using a Track Gauge and superelevation measuring device. After the alignments were checked to satisfaction, the sides of the sleepers were packed with ballast. Compaction of the ballast was further carried out by the "Dynamic Tamping Express" (Figure 18) which compacts the ballast by impacting.

8. After the required compaction by Dynamic Tamping Express machine, the track was opened for movement of passenger express trains and cargo freighters on March 02, 2021, itself. Initially, the speeds were restricted to 20 kmph. Figure 19 shows the first passenger train on the geocell reinforced approach. The completed and operational track surface provided smooth movement of train traffic over the bridge - approach transition (Figure 20). Two weeks after opening to traffic, on March 16, 2021, the track was monitored visually. It was noted that there was no deflection nor change in track geometry/alignment. The second trial stretch was taken up on the South approach of the bridge of the same Up track on March 16, 2021. Both the trial approaches were completed as scheduled within the stipulated shut down periods.

Figure 18(a).   Dynamic tamping express machine.

Figure 18(b).   Compaction of ballast by dynamic tamping express machine.

Figure 19.   The first passenger train on the geocell reinforced approach stretch.

Figure 20.   Finished track surface at the bridge - approach transition zone.

9   POST STRENGTHENING TRACK PARAMETERS - PERFORMANCE MONITORING AND EVALUATION

The Western Railway has monitored the performance of the trial approaches as part of routine inspection and maintenance. The monitoring is generally done as follows:

1. Periodical level/deflection measurement with progressive increase in speed of trains every month, starting with the initial speed limit of 20 kmph and progressively increasing by 20 kmph to the maximum speed of 160 kmph.
2. Periodically monitor and evaluate Track Geometry Index (TGI), using track recording machine (usually done twice/thrice a year).

On an immediate basis, following successful completion of work, the speed limit caution of 20 kmph was relaxed to normal after 3 rounds of tamping on April 3 and 28, 2021. Thereafter, track parameters were recorded periodically in duration of few months.

Considering the magnitude of quality parameter readings, the Western Railway concluded that there was no deterioration in track, even after a period of more than one and half years of traffic. In addition to recording the track parameters, frequent inspections were carried out. The transition system at the Bridge approaches was found to provide smooth transition for high speed trains.

Figures 21–23 shows the observation for the different stations over periodical measurement on South approach. Similar measurements were noticed on North approach also. All the measurements were within the tolerable limits as per the railway guidelines. The geocell

(a) Unevenness in left rail   (b) Unevenness in right rail
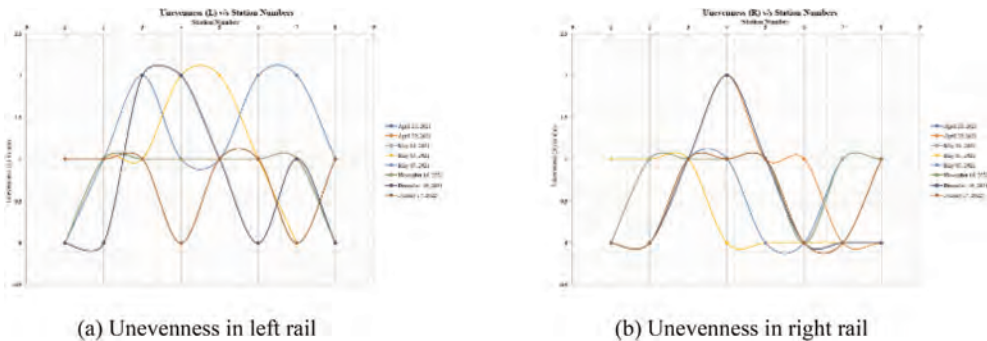
Figure 21.   Periodical measurement of unevenness on the rails measured at different stations.
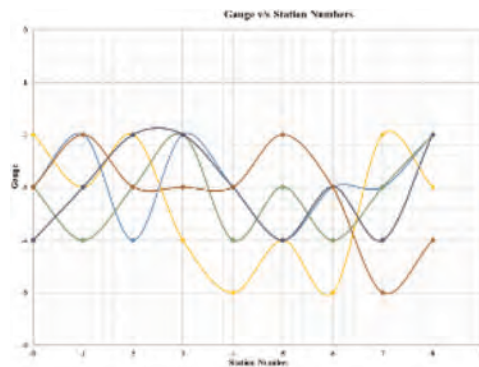
Figure 22.   Periodical measurement of gauge at different stations.
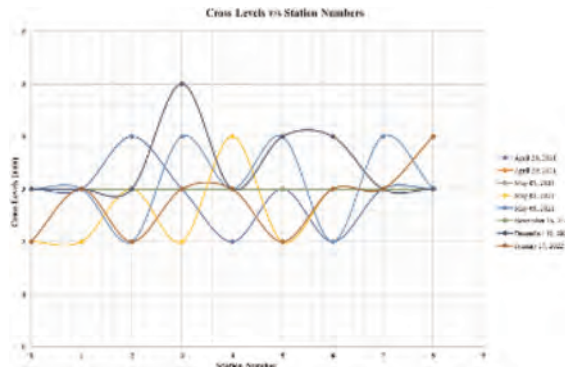
Figure 23.   Periodical measurement of cross levels at different stations.

layers at bridge approaches showed substantial reduction in differential settlements by virtue of spreading the load uniformly over the entire area. Further initial inspection (Table 2) and periodical Track Recording Car (TRC) and Oscillation Monitoring System (OMS) runs were carried out on the stretch and presented in detail in Tables 3 and 4 respectively. With the results of track parameters monitored continuously and with consistently good results of TRC runs and OMS runs, it can be concluded that the proposed transition system is quite effective in overcoming the problem of rough running on bridge approaches.

Table 2. Initial inspection observations by authorities.

Type of Inspection	Date	Inspecting Authority	Observation
Last Vehicle	May 05, 2021	DEN C	Running was smooth
Last Vehicle	April 06, 2021, May 05, 2021	ADEN ST	Running was smooth
Foot Plate	April 03, 2021, April 21, 2021	ADEN ST	Running was smooth
Trolley Inspection	April 07, 2021	ADEN ST	Running was smooth
Last Vehicle	April 06, 2021, May 05, 2021	SSE PWAY NVS	Running was smooth
Footplate	April 09, 2021, April 25, 2021	SSE PWAY NVS	Running was smooth
Trolley Inspection	April 07, 2021, April 15, 2021	SSE PWAY NVS	Running was smooth

Table 3. Results of latest Track Recording Car (TRC) runs over Br. 417 (UP).

KM WISE COMPARISON OF TRC RECORDING (CHORD MODE) DIVISION: BCT, SECTION: BIM-BHETSECTIONAL SPEED: 120, LINE: UP KM: 249 TO 250

	RUN1- 24-JAN-22/ a/ (7971)			RUN2- 24-JAN-22/ b/ (7971)			RUN3- 15-OCT-21/ f/ (7971)			RUN4- 15-OCT-21/ g/ (7971)			RUN5- 11-JUL-21/ b/ (120)			RUN6 22-JAN-21/b/ (7969)		
KM	TQIS	TQIL	TQIC	TQIS	TQIL	TQIC	TQIS	TQIL	TQIC	TQIS	TQIL	TQIC	TQIS	TQIL	TQIC	TQIS	TQIL	TQIC
249–250	NR	NR	NR	86.47	91.14	88.8	82.37	83.37	82.87	82.37	83.37	82.87	82.63	81.06	81.84	NR	NR	NR

Table 4. Results of latest Oscillation Monitoring System (OMS) runs over Br. 417 (UP).

		RUN 1: 25-NOV-21/787			RUN 2: 12-DEC-21/793			RUN 3: 22-JAN-22/803		
KM	DIST	Vertical Peak	Lateral Peak	Speed	Vertical Peak	Lateral Peak	Speed	Vertical Peak	Lateral Peak	Speed
249–250	–	Nil	Nil	110.9	Nil	Nil	128	Nil	Nil	121

10 CONCLUSION

Ever since the bridge approaches were reinforced with geocell layers, the Western Railway has carried out at least two OMS runs. No peak has been observed at the approaches. Considering passenger comfort reactions and reports from locomotive motormen, the transitions are found to be smooth without the customary jerks even at high speeds. The system, being practically workable, can be adopted especially in the case of doubling and in cases where sections are likely to run higher axle loads or at higher speeds. The system can be adopted for both ballasted and non-ballasted bridges having problems of rough running on approaches. It is therefore concluded that the trials of strengthening the approaches were successful. Based on this successful trial, the Research, Designs & Standards Organization

(RDSO) of the Ministry of Railways of the Government of India has published *"Transition System on Approaches of Bridges"*, Report No. GE: R-50 (Revision 1) in July 2021.

REFERENCES

Ministry of Railways, RDSO: Guidelines and Specifications for Design of Formation for Heavy Axle Load", Report No. RDSO/2007/GE: 0014; November 2009.

Ministry of Railways, RDSO: Comprehensive Guidelines and Specifications for Railway Formation, Specification No. RDSO/2020/GE: IRS-0004; September 2020.

Ministry of Railways, RDSO: Transition System on Approaches of Bridges, Report No. GE: R-50 (Revision 1) dated July 2021.

Strata Geosystems (India) Pvt Ltd Internal Report: Strengthening of Bridge Approach using StrataWeb[®] Geocells - Site Trial Report: Strata; March 2021.

Multiple functions in landfill capping system, case study from feasibility until execution

C. Márton
Freudenberg Performance Materials, Hungary

I. Kádár
Department of Engineering Geology and Geotechnics, Budapest University of Technology and Economics, Hungary

E. Tamaro
Harpo spa, Italy

ABSTRACT: A smart solution for covering waste storage facilities is described. It allows vegetated covers for full environmental integration while optimizing the storage volume of the landfill for a given footprint by allowing slope angles up to 2/3, depending on the shear strength of the cover soil. The design process is described for the reinforcement and drainage functions that the geocomposite solution ensures. The case study illustrates the importance of the design of the anchorages required by this application.

1   INTRODUCTION

Of the civil infrastructure sectors, the environmental sector is the one which is growing the fastest as we seek to address the multiple issues posed by man-made pollution and population growth. Landfill industry needs to keep increasing both in terms of its capacity and its ability to safely dispose of the remaining waste and ensure that the existing landfill remain safe. The key task facing governments and landfill operators is one of maximizing the space available within landfills and safely containing the waste to ensure it will not contaminate groundwater or watercourses or pose threats in terms of instability or the build-up of potentially explosive gases.

Geosynthetics form a key part nowadays of the toolbox that the landfill designer and operator has available. They also reduce the need for mineral exploitation by reducing the need for thick clay liners, granular collectors, and filter systems.

Within two years of the end of the operation phase of a landfill, a permanent capping has to be implemented to prevent penetration of uncontrolled water in waste and biogas emission into the atmosphere which would increase the carbon footprint of the landfill.

2   LANDFILL CAPPING DESIGN

2.1   *Design target*

Minimizing the footprint of waste storage areas is a paramount concern to everybody involved. At the same time, storage capacity needs to be optimized in parallel with a successful integration into the finished landscape through installation of cover soil on top of the construction. These requirements lead to increased side slope angles of the construction, with

consequences on the design regarding the stability of soil veneer layers and the reinforcement performances of the multi-layers geosynthetic system on top of the geomembrane.

A part of the rainwater goes through the covering layer of soil and creates water pressure in the soil which would reduce the stability of the soil and increase the risk of direct sliding. That's why a drainage layer is always recommended on top of the geomembrane. In some conditions, therefore, the upper part of the multi-layered geosynthetic system located on top of the smooth geomembrane has to include a drainage layer and also a soil-gripping layer. Multifunctional geocomposites are available on the market which incorporates drainage, reinforcement, protection, and soil gripping in one product, and has been in use now for more than 15 years.

2.2 *Hydraulic design*

Usually, original design/tender specifications is requiring either:

- granular drainage layer with given permeability and thickness e.g. usual 50 cm thick granular drainage layer with a permeability of 10^{-4} m/s can be replaced by a drainage geocomposite which is hydraulically equivalent,
- input flow rate, it must be consistent with the permeability of the topsoil and the runoff ratio
- discharge capacity of a specified product

In all cases, hydraulic gradient is, along with dead and live loads, a main parameter to assess the water flow capacity of a drainage composite, it is related to slope angle and allowed water pressure in the topsoil layers. Designers should take care that no water pressure on top of the drainage composite has been taken into account for hydraulic gradient calculation [AFNOR NF G38-061 2017]. This would prevent reduction of the shear resistance of the topsoil layer which can lead to direct sliding failure.

Justification and comparison of drainage geocomposites have to consider, under given load and hydraulic gradient, relevant boundary conditions in the test of discharge capacity in the plane to be carried out according to EN ISO 12958 for product performance assessment, i.e. at least standardized foam layer on one side of the geocomposite in the index test (EN ISO 12958-1) [Touze N *et al*. 2014] or standardized sand layer in the performance test (EN ISO 12958-2).

Reduction coefficients are applied on the short term discharge capacity of the drainage geocomposite to take into account the compressive creep behavior of the drainage composite, including thickness reduction of the drainage core and filter intrusion into the drainage core, both leading to a reduction in the water flow cross-section. Since the values of these reduction coefficients depend on the product and project specific conditions [Stoltz G *et al*. 2016], specification of a product without any information on the needed long term discharge capacity is not relevant and does not allow any comparison with competition products. In capping, for clean water, reduction coefficients for chemical and biological clogging are equal to 1 for any product.

2.3 *Mechanical design*

Multi-level shearing resistances have to be checked or considered in the design of the geocomposite (Figure 1) [AFNOR NF G38-067 2017]. Internal stability of the veneer soil layer is a first condition, its external stability is the next step, it depends on the friction angle between soil and the top layer of the basal multi-layered geosynthetic system. When needed, this friction angle is increased with the help of a three-dimensional open monofilament structure, intimately stitched onto the appropriate reinforcement product. Thus, high density of monofilament structure prevents direct sliding of the veneer soil layer on the drainage geocomposite when the slope angle is too high.

① Internal stability of topsoil layer

② External stability of topsoil layer

③ Internal shear strength of the filled soil-gripping geocomposite

④ Tensile strength of the reinforcing material is related to the smoothest interface

Figure 1. Multi-level shearing resistances.

The third step in the design is linked to the minimum interface friction angle of the multi-layered geosynthetic system, the goal being to calculate the required long term design strength of the reinforcement component, when it is needed. Usually, the multi-layered geosynthetic system includes, above the capping, a smooth geomembrane which ensures the water tightness of the capping slopes. Due to the slope angle and the weight of the cover soil, this smooth interface creates tensile forces in the upper geosynthetic layer, which requires the use of a reinforcement component.

Depending on the project specific data, this can be either a geogrid, preferably installed over a non-woven protection geotextile or a geocomposite such as EnkaGrip & Drain specifically designed for each project, combining from top to bottom:

— an open three-dimensional monofilament structure offering a high density (1810 m/m^2) of filaments for soil-gripping,
— a reinforcement woven fabric and
— a drainage composite.

Before cover soil installation on the side slopes, the geocomposite is anchored on top of the slope, usually in a trench. This is the last phase of the design but is as crucial as the previous ones to avoid any failures. Care has to be particularly taken with anchoring on intermediate berm due to limited available footprint.

Fill material characteristics also have an impact on the anchorage performances through their internal friction angle, their grain size and shape. This can be particularly sensitive in anchorage trenches where severe installation conditions and/or inappropriate fill material can damage the sealing system and lead to a failure.

3 CASE STUDY: VILLEPARISIS LANDFILL (FR)

The Villeparisis waste storage facility, located close to Paris, is one of the five hazardous waste storage facilities of the SITA FD, a subsidiary of the SUEZ group Environment. The site is authorized to receive 250,000 tons of industrial hazardous waste per year requiring many refurbishment work.

3.1 Challenge

The works consisted on a slope refurbishment 20° and 54 meters long above 15 000 sqm of industrial waste storage area. Following the local regulation, a waterproofing system and drainage layer against rainfall have to be installed. Geosynthetics have been chosen as solution to work with as they can provide easy to use solutions and technically reliable and experienced. The main problematic here was to insure stability of the 30 cm covering soil above smooth waterproofing geosynthetic capping system.

3.2 Solution

In such conditions, multiple functions geocomposite EnkaGrip & Drain was a unique solution providing effective drainage with a strong reinforcement and soil stabilization in a significant cost saving. The drainage core is a three-dimensional V-shape monofilament structure made of polypropylene. Polyester woven geotextile (TS = 200 kN/m) ensures the reinforcement function. High density (1810 m/m^2) open three-dimensional filament structure made of polyamide provides the required porosity ($> 90\%$) for efficient topsoil gripping. All components are sewn together forming a unique product installed in a single operation allowing cost and time saving.

The technical proposal insures a safe and secure solution to meet the technical and regulation objectives for drainage and soil stabilization. In addition, the solution allows installer to reduce installation time and minimize circulation impact on the geosynthetic layer. Risk of potential damage during installation are reduced. Sustainability of geosynthetics is better ensured with a reduction in costs.

3.3 Installation benefits

Due to the length of the slope, a specific implementation methodology has been developed to avoid traffic on slope close to the waterproofing geosynthetic capping system, as recommended by the French rules. Intermediate anchorage was designed (Figure 2), the topsoil was installed using a long arm shovel Caterpillar 325 BL able to work at over 20 m from the bottom and the top of the slopes (Figure 3). The shovel has always evolved smoothly over a minimum thickness of 1 m materials to avoid dynamic loading and accidental damage of geosynthetics allowing a coverage rate of approximately 2 000 m^2 per day.
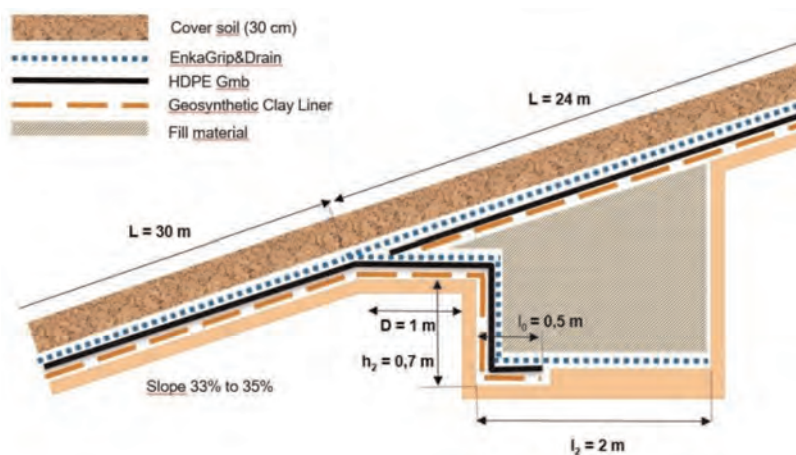
Figure 2.   Details of the intermediate anchorage.

3.4 Result

Design was made according to the French design standard NF G 38-067 including partial factors of the Eurocode 7 on dead loads (soil weight) and live loads (snow . . .) insuring stability on each interface of the capping system. Thus, legal and technical requirements have been reached and in the meantime, the solution allowing time and cost savings during installation. The works objectives were achieved in accordance with budgetary costs and deadlines.

Figure 3. Long arm shovel able to work at over 20 m.

4 CONCLUSION

This paper highlights a smart solution regarding veneer soil reinforcement combined with drainage function, as it is required particularly on landfill capping. We reminded that this application requires a design based on the knowledge of the shearing resistances of the multi-layered geosynthetic system. As manufacturer, we can help designers and other stakeholders to detect wrong design as soon as we are contacted, particularly thanks to our interface friction angle data base.

Interaction between sealing system components being a main parameter as well of the anchorage stability, the designers of the waste landfill have to incorporate this in their design as early as possible for the most critical conditions to prevent any nasty surprises later and adopt the appropriate solution for anchorage. All the stakeholders shall appreciate this topic in addition to the design of the sealing system itself, particularly when slope length can be an issue for design and installation. Inappropriate design is a source of delay, extra cost and dispute.

REFERENCES

AFNOR NF G38-061 2017 *Use of Geotextiles and Geotextiles related Products – Drainage and Filtration Systems – Justification of Dimensioning and Design Elements*

AFNOR NF G38-067 2017 *Geosynthetics, Geotextiles and Related Products – Stabilization of a Thin Layer of Soil on Slope – Justification of Dimensioning and Design Elements.*

Stoltz G et al. 2016 Long Term Filter Intrusion Phenomenon in Several Types of Drainage Structures (Ljubljana: Proceedings of the 6th Geosynthetics Congress) p575

Touze N et al. 2014 Evaluation of the Decrease in Long Term Water Flow Capacity of Geocomposites due to Filter Intrusion (Melbourne: proceedings of the 7th International Congress on Environmental Geotechnics) p321

The effect of Prefabricated Vertical Drain (PVD) with membraneless vacuum preloading method on the North Coast of Central Java

Nastiti Tiasundari & Dandung S. Harninto
PT. Geoforce Indonesia, Jakarta, Indonesia

ABSTRACT: Prefabricated Vertical Drain (PVD) is a composite geosynthetics material which designed to have a high permeability property. It is often used to accelerate consolidation process on a compressible soft soil layer. In order to reach a minimum number of 90% consolidation at the beginning of the building or structure construction project, a certain number of preloading is required. The number of preloading depends on the load that would be acting on the ground in the future. There are several methods of preloading, such as: conventional earth embankment, vacuum with membrane, and membraneless vacuum. In this paper, a test area of 800 m2 located in the north coast of Central Java would be tested using PVD with membraneless vacuum preloading method. An approximately 80-90 kPa of vacuum pressure would be applied during vacuum preloading period. The vacuum pressure successfully reached the edge of the area with almost the same pressure as exerted by the vacuum pump. The difference value of vacuum pressure at the edge with the vacuum chamber are ranging from 2-6 %. At the toe of PVD material, vacuum pressure is about 3% smaller than the vacuum pressure measured on the top of the PVD. After three months of vacuum, the result showed that 70-80% of total predicted settlement was reached. Soil investigation data from before and after vacuum showed that qc value of CPT test was slightly increased whereas SPT value increased by 1.5 times. Laboratory test data showed that the natural water content value decreased by 1-4%, unit weight increased by 4-9%, void ratio value decreased by 10-20%, and shear strength increased by 5-20%. The recorded bouncing potential two months after vacuum was 2-3%.

Keywords: PVD, Preloading, Ground Improvements, Membraneless Vacuum, Consolidation, Compressible Soil, Vacuum Preloading

1 INTRODUCTION

Construction over soft soil is very challenging. There were already several methods to improve the strength of soft soil layer, one of them is soil improvement using Prefabricated Vertical Drain (PVD) and preloading. The main idea of this soil improvement system is to ensure that settlement had already reached a minimum 90% of total settlement before the construction of the main structure. At the end of soil improvement using PVD, the value of shear strength is expected to be higher.

PVD system is often combined with preloading. The main purpose of preloading is to apply enough load equivalent to the main structure that will be built in the beginning of construction to minimize the risk of settlement or differential settlement during service period of the structure. There were several methods of preloading: conventional preloading (using soil embankment) and vacuum preloading.

Vacuum preloading is a common method of preloading used in soil improvement (Bergado *et al.* 2002; Chu *et al.* 2009; Holtan 1965; Indraratna *et al.* 2019; Seah 2006). It was first

introduced by Kjellmann (1952) to reduce the time for consolidation period. The advantage of this method is reducing the pore pressure, whereas maintaining a constant total stress instead of increasing total stress (like the conventional preloading), thus effective stress increased because of the reduction of pore pressure from the vacuum preloading (Lam *et al.* 2015).

There were two types of vacuum preloading: membrane and membraneless vacuum preloading. Membrane vacuum preloading system use a membrane on top of a sand blanket, sealed, then applied a vacuum pressure. The efficiency or the membrane vacuum preloading system depends entirely on the damage caused on the membrane over a long time of vacuum period (Indraratna *et al.* 2019). Membraneless vacuum preloading system connected each PVD into a tubing system which directly connected by vacuum pump without a membrane. This system is very efficient when an area is to be sub-divided into different parts and will be improved individually (Indraratna 2019). Direct tubing vacuum consolidation does not require the sand blanket and sealing membrane since the connections from the top of PVD to the vacuum line are completely sealed (Seah 2006).

This paper will be focusing on the effect of the individual vacuum preloading system on a pilot test area on the North Coast of Java.

2 SITE CONDITION

The site was located on the side of the road heading to Kendal Harbor, on the North Coast of Central Java. The location of the pilot project was originally a large fishpond. The pilot test area was marked with a turquoise area in Figure 1(a). The total area was 800 m^2.

The research area is currently still in a flooded condition with water depth ranging 80 cm to 90 cm from the bottom of the pond, therefore backfilling work needs to be done before to provide a firm platform at elevation +1.5 The long section is shown in Figure 2.
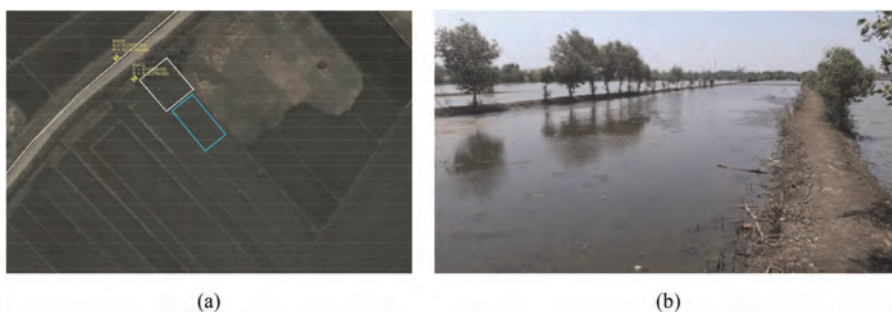
Figure 1.   (a) The location of pilot project area, (b) The initial condition of the area.

3 SOIL CONDITION

The soil condition of the pilot test area can be shown in the table below. The soft soil with N-SPT<5 was located until 20 m deep. Installation of PVD will be done to 20 m deep from the surface.

4 DOUBLE VACUUM SYSTEM

Double Vacuum System (DVS) is a membraneless preloading method using a very efficient vacuum pump and collection tank to divide water from air. A high vacuum pressure exerted from the vacuum pump would take the air and water from each individual PVDs connected
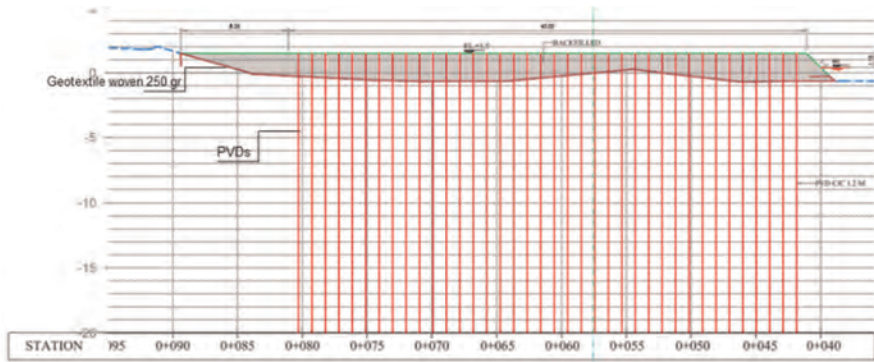
Figure 2. The long section of the test area.

Table 1. Soil condition.

Depth (m)	N-SPT Value	Soil Description
0–2	4	Fill Material
4	0	Soft Silty Clay, Yellowish Grey, High Plasticity
6–8	0	Very Soft Silty Clay, Grey, High Plasticity
10–14	0	Very Soft Silty Clay With Trace of Shell, Grey, High Plasticity
16–22	0	Soft Silty Clay With Trace of Shell, Dark Grey, High Plasticity
24–30	11–14	Stiff Silty Clay, Dark Grey, High Plasticity
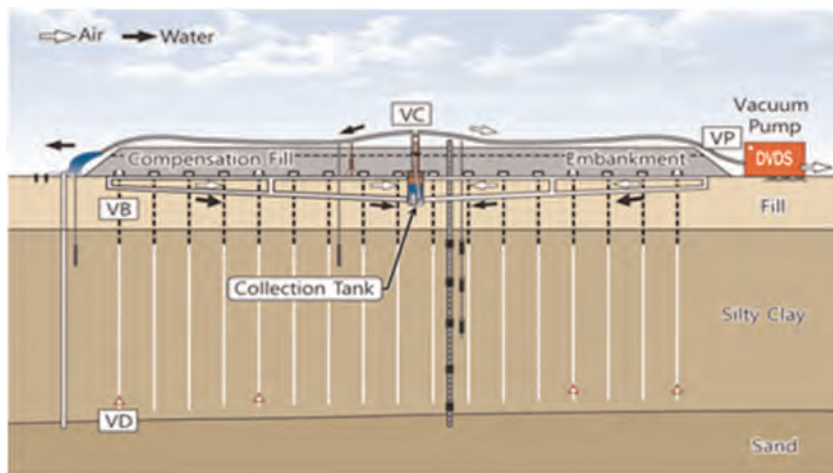
Figure 3. Schematic of DVS system (DongAh Geological Engineering Co. Ltd.).

to vacuum pipe towards vacuum collection tank. A high vacuum efficiency collection tank will divide water from air. Water will drop at the bottom of the tank and will be discharged outside the vacuumed area using a submersible water pump. This method prevents water from flowing to the vacuum pump which could impair the vacuum pump.

Arrangement type of drain that will be used is rectangular with 1.0 m spacing. PVD material which is going to be installed has a 100 mm width and 2 mm thickness.

5 RESULT AND DISCUSSION

5.1 *Vacuum pressure during preloading period*

The vacuum pressure throughout the entire trial process was kept at 81-94 kPa. At some point, vacuum pressure was decreasing, but then it was back up to 90 kPa. In case of any pressure change, it is normal to have a variety of vacuum pressure as long as the vacuum pressure did not drop significantly. The difference value of vacuum pressure at the edge with the vacuum chamber are ranging from 2-6 %. A piezometer was installed inside the PVD and at the edge of vacuumed area. As a result of the measurement, the vacuum pressure was stably maintained at 78-90kPa (average 84kPa), which is about 3% smaller than the vacuum pressure measured on the top of the PVD.
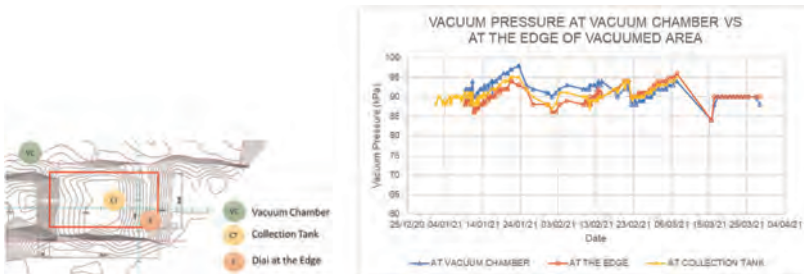
Figure 4. Vacuum pressure during vacuum period.

5.2 *Settlement*

The settlement in the vacuumed area reached 1.27 m by the end of 90 days vacuum. At the very beginning of vacuum process, the rate of settlement is quite big and almost reached 1-2 cm of settlement/day. To predict the total settlement, hyperbolic and Asaoka method is used. Hyperbolic method uses the relationship of settlement at time t in a hyperbolic function of initial settlement and time. The final settlement from hyperbolic method is defined as the intersection and slope of the fitting line of data $t/(S_t-S_0)$ versus t. Asaoka method is widely used for its simplicity and good accuracy. The final settlement from Asaoka method is defined as the intersection of the trendline of S_n and S_{n-1} with a 45° line which can also be defined as the condition where S_n and S_{n-1} are equal.

After 90 days of vacuum, through the hyperbolic method, percent settlement achieved was 72.2%, while with Asaoka method was 85.4%.

5.3 *Increasing in CPT and SPT value*

The value of cone resistance (qc) from CPT test is expected to increase after vacuum process, but the result of CPT test conducted on site was slightly increased by a small number. Qc value of CPT 01 after the test shows a small increase, but the total friction value increased by four times than the initial value. It showed that the soil had better adhesion after vacuum.

N-SPT value after vacuum increased by 1.5 times and the classification of the soil went from very soft before ground improvement to soft to medium after ground improvement.

5.4 *Changes in soil laboratory data*

The result from laboratory test showed the deeper the soil, the greater decrease in water content. Decrease in water content after vacuum is within the range of 1-4%, but the highest was at 20 m with a 27% difference from its initial value. The value of unit weight after
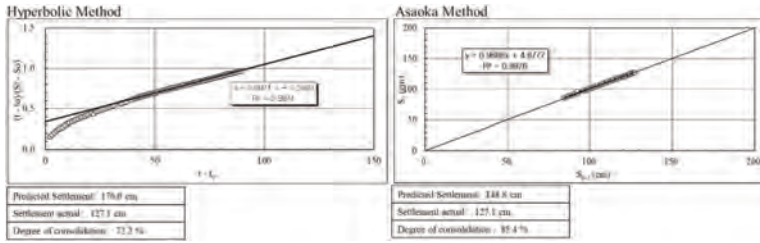
Figure 5. Result of predicted settlement using Asaoka method and Hyperbolic method.
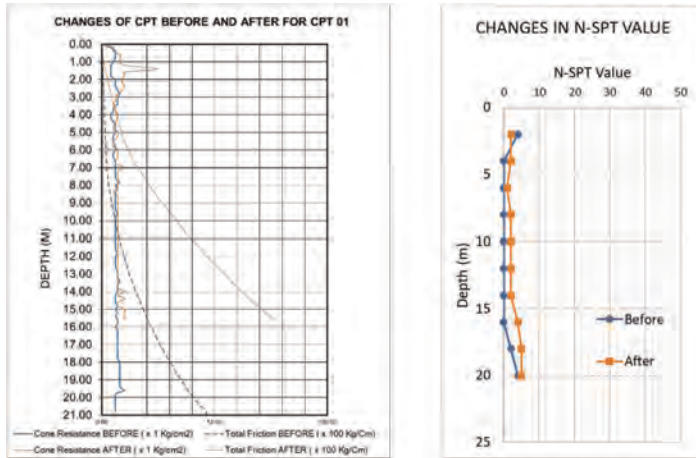
Figure 6. Result of CPT test and SPT test before and after vacuum.

vacuum process increased by 4-9 percent than initial value. Result of laboratory data showed that void ratio value decreased by 10-20% after vacuum process.

Triaxial unconsolidated undrained (Triaxial UU) test result showed that cohesion value increased by 5-20 %. The deeper the soil, the increasing rate of the cohesion is higher.

5.5 Bouncing effect after vacuum

Approximately two months after vacuum period, settlement data was obtained to determine whether there was a bouncing effect after vacuum. Based on the data below, there was a bouncing effect after vacuum about 2-3%. This needs to be considered as the after effect of the vacuum preloading system.
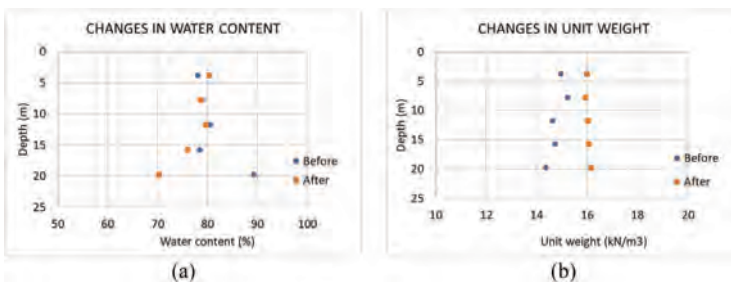
Figure 7. Result of (a) Water content; and (b) Unit weight.
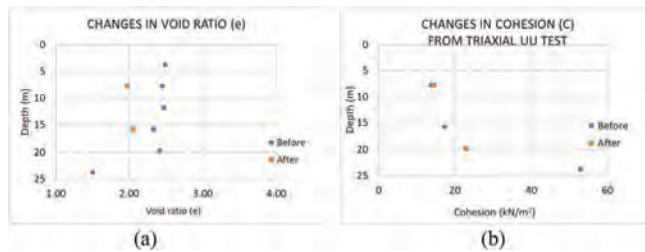
Figure 8. Result of (a) Void ratio; and (b) cohesion value from Triaxial UU test.

Table 2. Bouncing effect after vacuum.

Points	Last Settlement after vacuum (m)	Settlement 2 months after vacuum (m)	Changes in settlement (m)	Percent heaving from total settlement (%)
SP 1	-1.271	-1.232	0.039	3.07
SP 2	-1.1065	-1.0815	0.025	2.26

6 CONCLUSION

Double Vacuum System (DVS) is a membrane less preloading method using a very efficient vacuum pump and collection tank to divide water from air. This system is proven to be effective for an alternate preloading method. The result showed that 70-80% of total predicted settlement was reached. Soil investigation data from before and after vacuum showed that qc value of CPT test was slightly increased whereas SPT value increased by 1.5 times. Laboratory test data showed that the natural water content value decreased by 1-4%, unit weight increased by 4-9%, void ratio value decreased by 10-20%, and shear strength increased by 5-20%. However, after shutting down of the vacuum system, bouncing potential should be considered. The recorded bouncing potential two months after vacuum was 2-3% from the total settlement.

REFERENCES

Asaoka, A. 1978. Observational Procedure of Settlement Prediction. *Soil and Foundations* Vol. 18 No.4.

Chu, J., Yan, S. & Guo, W. 2016. Vacuum Preloading Methods: An Update. *Geotechnical Engineering Journal of the SEAGS&AGSSEA* Vol. 47 No. 3, pp. 62–69.

Lam, L. G., Bergado, D. T. & Hino, T. 2015. PVD Improvement of Soft Bangkok Clay with and without Vacuum Preloading using Analytical and Numerycal Analyses. *Journal of Geotextiles and Geommembranes* 43, pp. 547–557.

Long, P. V., Nguyen, L. V., Bergado, D. T. & Balasubrabamaniam, A. S. 2015. Performance of PVD Improved Soft Ground using Vacuum Consolidation Methods with and without Airtight Membrane. *Journal of Geotextiles and Geommebranes* 43, pp. 473–483.

Saowapakpiboon, J. et al. 2008. CeTeau PVD Vacuum System in Soft Bangkok Clay: A Case Study of The Suvarnabhumi Airport Project. *Lowland Technology International* Vol 10 No.1, pp. 42–53.

Seah, T. H. 2006. *Design and Construction of Ground Improvement Works at Suvarnabhumi Airport*. Bangkok, SEAGS and EIT, pp. 89–112.

Sun, L. et al. 2017. A Pilot Test on a Membraneless Vacuum Preloading Method. *Journal of Geotextiles and Geomembranes* 45, pp. 142–148.

Bituminous geomembrane: Successful alternative of distressed concrete canal lining built over expansive clays

M. Singh
VP, Geotechnical Engineering - Yooil Infrastructure Pvt Ltd., India

O. Jangid
VP, Engineering & Projects - Yooil Infrastructure Pvt Ltd., India

P. Llinas
Export Area Manager – Axter Iberica, Spain

B. Breul
Civil Engineering Manager - Axter, France

ABSTRACT: This paper focuses on the application of Bituminous Geomembrane (BGM) for the waterproofing of new and existing earthen canals. The start of its application is about half-century back when USBR first time applied BGM in canal waterproofing and the first time BGM was used in waterproofing of a large dam by Coletanche in 1978 in France. In India, the first application of BGM has been done in one kilometer stretch of Pench Canal in Nagpur, Maharashtra which was given as a pilot project to Yooil Infra to arrest the seepage and enhance the stability of the canal. The area comprises expansive soil which has been problematic for canal banks stability, concrete lining failures, heavy seepage through banks and breaching of banks at different reaches of canal. The BGM application resulted in a complete stoppage of seepage through that section of the canal and no stability related problem was observed due to the elimination of drawdown conditions while and after the full flow of canal during monsoon. BGM is unique due to its properties of being flexible, high puncture resistance, practically impermeable, resistant to thermal expansion, UV resistant, non-biodegradable, low maintenance cost and overall exceptional durability. This paper gives the technical assessment of slopes of the canal with the existing concrete lining, outlining possible reasons for the failure of concrete lining and remedy with the impervious bituminous geomembrane.

1 INTRODUCTION

The Pench Left bank and Right bank canals were built in 1970s as a part of Totladoh project on Pench river. Their total length is 84 km. It is being operated un-der Vidarbha Irrigation Development Corporation (VIDC), Maharashtra, India.

Under the prevailing situation of reduced rainfall coupled with reduced reservoir capacity followed by canal seepages and breaches, the only option left to meet the drinking and irrigation requirements is water conservation by increasing the stability of canal, minimizing the seepage loss, reducing the canal friction loss and thus ensure the maximum utilization of available water.

2 PROJECT LOCATION AND SALIENT FEATURES

The site is about 3.4 km from National Highway 44 and is on state highway 249 (see Figure 1). The project is 1km from Gundhari Village in Nagpur district, Maharashtra, India.

Figure 1.   Project location map of Pench Canal.

The salient features of canal selected for BGM lining are as follows:

Table 1.   Salient features of Pench LB Canal.

Length	1000	m
Bed width	13	m
Full Supply Depth	3.8	m
Design Discharge	90	Cumecs
Mean Velocity	2	m/s
Bed Slope	1 (V):7000 (H)	
Side slopes	1(V):1.5 (H)	

3 CANAL BEHAVIOR WITH PLAIN CEMENT CONCRETE LINING

During the site inspection of left bank Pench canal, it is observed that concrete lining of canal is severely damaged (see Figure 2). Root causes behind the cracking of concrete lining of canal can be summarized as below:

Figure 2.   Original condition of canal stretch.

Lining has joints at regular interval, through which seepage was taking place into the banks of the canal. General soil type along the canal alignment is expansive soil which is popularly known as "Black Cotton Soil". Expansive soil exert pressure on the concrete lining due to volume expansion. As plain cement concrete is weak in tension, the expansion joint crack become wider, and sometimes new cracks develops in concrete lining.

Flowing water cause internal erosion below the lining of canal when enter in these cracks. During drawdown condition, situation becomes even worse when uplift force due to pore water pressure along with the swell pressure exerted by bank soil causing cracking of lining and sometime sliding of the whole soil mass into the canal.

A distinct disadvantage of Concrete lining is its brittleness. Thus, concrete lining frequently cracks due to contraction taking place from temperature change, drying and shrinkage and settlement of sub-grade.

4 ALTERNATIVE LINING - BITUMINOUS GEOMEMBRANE

Bituminous geomembranes (BGM) have been developed 40 years ago. This durable Geo-composite is an effective waterproofing layer with significant properties, such as UV resistance, workability at temperatures -40°C to 55°C, mechanical / puncture resistance, harsh chemical resistance, dimensional stability, and mechanical workability, easily installed, welded, and repaired by local crews or maintenance people of any client.

5 CANAL BEHAVIOR WITH BGM LINING

The installation of BGM layer forms an impermeable barrier all around the inner surface of canal and along the top width of embankment up to half of embankment top width. This layer prevents the seepage of canal water to enter the embankment fill. Thus, the moisture variation almost ceases to take place in the canal embankment and hence no excess pore pressure develops during drawdown condition. Thus, the critical failure surface is on the slope of embankment opposite to the canal side. But in actual practice, there is no failure anywhere at the site on outside slope of canal. Hence the system is completely safe with BGM layer.
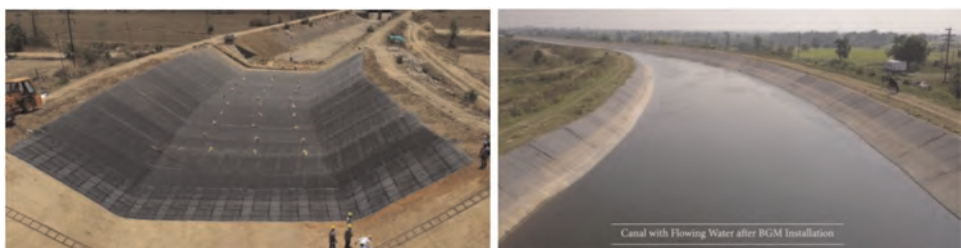
Figure 3. Canal during BGM installation and after 4 years of flowing condition.

6 METHOD OF ANALYSIS & SOFTWARE USED

To access the actual cause of failure based on the in-situ strength and deformation characteristics of embankment, stability analysis of the embankment is performed using Limit Equilibrium method using "Slide" as well as through FEM analysis using "Phase2" from Rocscience Inc.

7 DESIGN INPUT PARAMETERS

Following are the input parameters adopted for the slope stability analysis based on the lab test results of embankment fill material.

Table 2. Salient features of canal embankment (in Filling).

Properties of Slope	
Total Height	5 m
Water Table Location	At ground level, Full Supply level (FSL) and Drawdown condition
Embankment Slope	1.5H:1V

Table 3. Geotechnical design parameters for embankment fill and foundation.

S.n	Description	Unit	Value
1	Bulk Density	g/cc	1.83
2	Liquid Limit	%	41
3	Plastic Limit	%	19
4	Shrinkage Limit	%	12
5	IS Classification	-	C I
6	Free Swell Index	%	25
7	Peak Cohesion	KPa	23
8	Peak Friction Angle	Φ	13
9	Residual Cohesion	KPa	20
10	Residual Friction angle	Φ	5
11	Permeability	m/s	3×10^{-7}
12	Swelling Pressure	KPa	51.2
13	Young's Modulus	MPa	23

The above parameters were obtained by testing the actual soil samples extracted from the canal embankment and canal bed level (foundation) and conservative value is considered in design.

7.1 *Loading condition*

As per Indian road congress, IRC 75-2015 (Guidelines for the design of high embankments), following are the loading conditions to be used for the stability analysis of embankment.

Live Load (External Traffic Load): 24 KPa to be considered across the width of carriageway.

Dead Load: Self weight of embankment and any other structure resting on the embankment.

Static Condition: Deal Load + Live Load

Table 4. Summary of recommended min Factor of Safety (FOS) required for stability.

Loading Condition	Factor of Safety under static load
Static Load	1.4 (at the end of construction), 1.2 (*Initial factor of Safety)
Sudden Drawdown	1.3
Steady Seepage	1.3

During the canal site visit, it was observed that no failure has occurred in the base of the canal, and the concrete at base remained intact all throughout. Accordingly, in the analysis, the parameters of the foundation layer were increased considerably to avoid the failure slip circle passing through the base of embankment. Only slip circles passing through the slope of embankment were considered to evaluate the FOS during analysis.

8 SIMULATION OF VARIOUS CONDITIONS IN SOFTWARE

8.1 With Cohesive Non-Swelling (CNS) layer and concrete lining as conventional technology

8.1.1 Normal operating condition
The normal operating level is 3.8m. Accordingly piezometric head of 3.8m is applied in the embankment. In the canal portion, additional Uniformly distributed load (UDL) corresponding to head of 3.8m is applied on the bed as well as canal slopes to simulate the water head in canal, since piezometric lines action in some material only and not in open space.
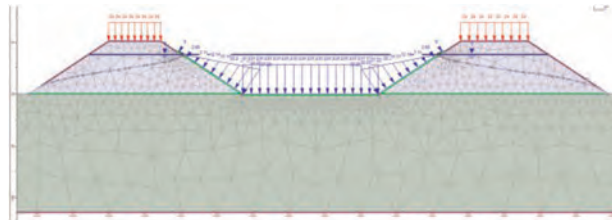
Figure 4.   Model of stage-1 under normal condition of conventional canal lining.

8.1.2 Sudden drawdown condition
First FEM analysis with groundwater and stress condition is considered with Normal water levels.

Phreatic line in the embankment body under steady state condition is generated.

To simulate the Sudden drawdown condition, in the analysis, groundwater type is changed to piezometric, and phreatic line obtained from step "b" is imported for water levels in the dam body under drawdown condition, and piezometric water level at canal bed level is modelled for remaining portion.

SRF (strength reduction factor) is computed for sudden drawdown condition.
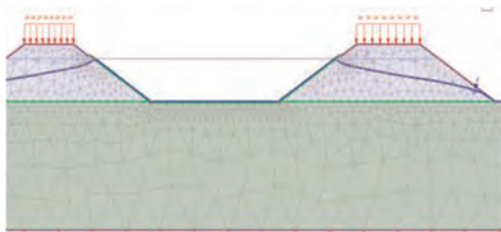
Figure 5.   Model of stage-2 under drawdown condition (Conventional canal lining).
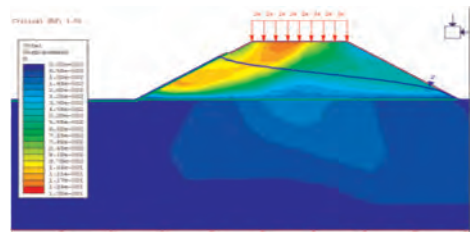
Figure 6.   Output: Failure surface with displacement contours.
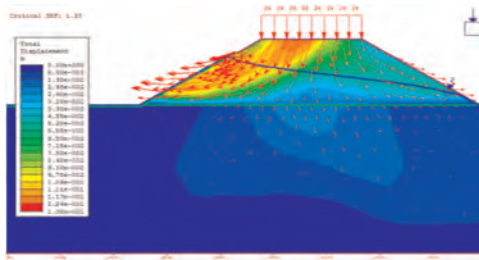
Figure 7. Output: Deformation Vectors showing the potential failure direction.

8.2 With BGM layer

8.2.1 Normal operating condition

The normal operating level is 3.8m. Since permeability of BGM is of order of 10^{-14} m/s, which is practically impermeable, membrane applied on the canal surface.
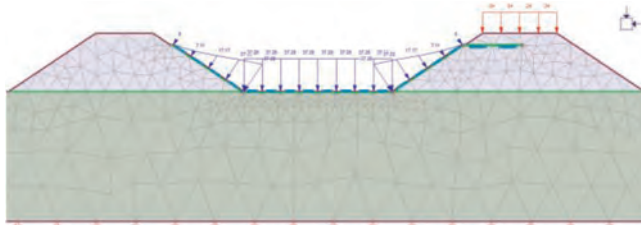
Figure 8. Model of stage-1: BGM layer installed as liner under normal condition.

Hence no water level is considered in the embankment body and additional UDL corresponding to head of 3.8m is applied on the bed as well as canal slopes to simulate the water head in canal.

8.2.2 Sudden drawdown condition

Due to impermeability of BGM layer, the water will not enter the embankment before drawdown. So, no water table is considered in the model before and during drawdown condition.

SRF (strength reduction factor) is computed for sudden drawdown condition.
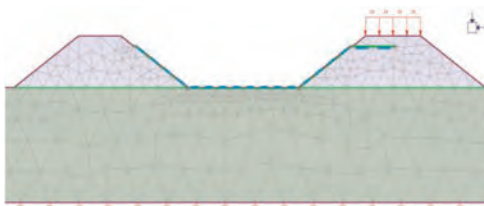
Figure 9. Model of stage-2: BGM layer installed as liner under drawdown condition.
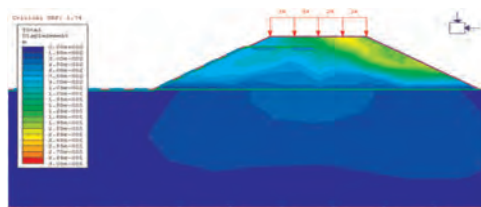
Figure 10. Output: Failure surface with displacement contours under drawdown condition. (FOS=1.74).
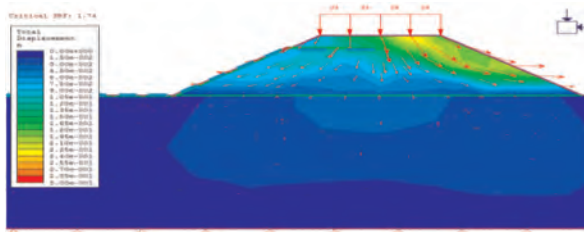
Figure 11.   Output: Deformation vectors showing the potential failure direction.

9   RESULTS AND DISCUSSION

Following are the output of stability analysis in terms of Factor of safety obtained under various conditions of analysis.

Table 5.   Factor of safety against various loading conditions.

Condition	Factor of Safety	
	With CNS Layer & concrete lining	With BGM Layer
Sudden Drawdown	1.55	1.74

The embankment soil is high to medium plastic clay, hence the value of Skempton's pore pressure parameter, "B" was kept as 1 in the software to simulate the rise in pore pressure actually taking place during drawdown in the canal. The routine lowering of water taking place in the canal can be considered as sudden drawdown keeping in view the rate of lowering of water vs the slow dissipation of pore pressure due to low permeability of soil.

9.1   *Analysis of embankment with CNS layer*

It can be clearly seen from the results that in case of normal condition, the embankment has found to be safe in slope stability, whereas under drawdown condition, the Factor of Safety (FOS) reduces further due to reduction of effective stress in embankment soil. Further, the erosion of embankment soil due to flowing water led to removal of "toe" material and the seepage of water into the soil lead to loosening of soil, and these two phenomenon combinedly lead to failure of canal slope. This phenomenon of seepage through concrete lining joints, erosion of CNS layer, swelling of expansive clay and cracking of concrete lining thereof has already been explained in 3 Canal Behavior with Plain Cement Concrete lining.

9.2   *Analysis of embankment with BGM layer installed*

The installation of BGM layer forms an impermeable barrier (all around the inner surface of canal and along the top width of embankment up to half of embankment top width. This layer prevents the seepage of canal water to enter the embankment fill and at the same time during rains, the rainwater is also prevented to percolate into the half width of the embankment top. Thus, the moisture variation almost ceases to take place in the canal embankment and hence no excess pore pressure develops during drawdown condition. Also, the provision of BGM layer rules out any possibility of soil erosion by flowing water. These rules out the major failure causing factors due to provision of BGM layer in the canal. Thus,

as expected, software analysis gives the critical failure surface on the slope of embankment opposite to the canal side, but with FOS more than minimum required. In actual practice also, these is no failure anywhere at the site on outside slope of canal. Hence the system is completely safe with BGM layer.

10 CONCLUSION

This type of embankment having swelling characteristics with provision of CNS layer also are not able to prevent the erosion of CNS layer and embankment fill from flowing water in canal after cracking of rigid concrete slab. A flexible, impermeable membrane having tensile strength is required to be installed to take care of all the issues like seepage into embankment fill, concrete slab cracking, surface erosion, moisture variation etc. Bituminous Geomembrane meets all the technical requirement to address the adversities in the stability of embankment along the canal.

REFERENCES

Bertrand Breul, Emilio Escobar, Natalie Daly 2020. Bituminous Geomembranes (BGM), 15 years of presence in Latin America for Hydraulic Applications. In Proceeding Conference GeoAmericas 4 - 2020 Rio de Janeiro.
Gautier, J.L. & Turley, M. 2004. Twenty-Five Years' Experience Using Bituminous Geomembranes as Upstream Waterproofing for Structures. In Long-term Benefits and Performance of Dams: Proceedings of the 13th Conference of the British Dam Society and the ICOLD European Club meeting Held at the University of Kent, Canterbury, UK from 22 to 26 June 2004. (pp. 94–101). Thomas Telford Publishing.
Goss, A. & Waterways, B., Lining a Canal in the United Kingdom with a Bituminous Geomembrane. http://kartiklokhande.blogspot.com/2016/12/tale-of-pench-project-canal-9-years-43.html
https://timesofindia.indiatimes.com/city/nagpur/Frequent-Pench-canal-breaches-to-be-studied/articleshow/53880100.cms
https://timesofindia.indiatimes.com/city/nagpur/pench-kanhan-water-reduced-yet-no-quota-revision-in-55-yrs/articleshow/70321104.cms
https://www.rocscience.com› downloads › phase2 › Phase2_TutorialManual
IS 9495, 1994. Guidelines for Lining of Canals in Expansive Soils.
IRC 75, 2015. Guidelines for the Design of High Embankments.
Katti, R.K & Katti, A.R. 2008, October. Physics and Engineering of Montmorillonitec Clay Leading to Discovery of CNSL Phenomenon. In 12th International Conference on International Association for Computer Methods and Advances in Geomechanics (IACMAG) (pp. 1227–1233).

Repairs of dam components subjected to dynamic loads with application of geosynthetics: Case studies from India

Vivek Kapadia
Government of Gujarat, Gandhinagar, India

ABSTRACT: Dam is a complex hydraulic structure having many components subjected to dynamic loads. Such components periodically manifest signs of distress and require repairs especially in case of aging dams. Conventional methods for repairs are mainly based on usage of impact resistant materials. As an alternative, solutions with geosynthetics are designed as impact resistant systems rather than depending merely on material properties. Such solutions not only help effectively repair the damaged components but also enhance their performance in several ways besides cost economy, faster execution and longevous life. The paper outlines main issues related to various dam components due to dynamic loads and presents case studies of aging Indian dams whose distressed components have been restored or are being restored with application of geosynthetics.

1 DAM COMPONENTS SUBJECTED TO DYNAMIC LOADS

1.1 *Upstream face of earthen and rockfill dams*

Waves are generated on the top surface of the reservoir under the effect of the wind. They tend to dislodge the soil particles resulting in to erosion of the earthen dam. As the reservoir level varies, such erosion takes place at different levels of the earthen dam. Such an erosion becomes dangerous when it is progressive. In case of rockfill dams, the wave action may result in to loss of mechanical bond between the adjacent rocks due to penetration of water causing displacement of rocks.

1.2 *Upstream and downstream faces of spillways*

Discharge from reservoir is released and regulated through spillway and gates and therefore the crest on its upstream and downstream faces is subjected to severe loading conditions. Under the effect of heavy dynamic water loads, cavity formation on the downstream face is a common problem which may result in to pitting or delamination of the concrete surface. Such forces are so severe in some cases that the reinforced concrete lamination of masonry structure gets disintegrated.
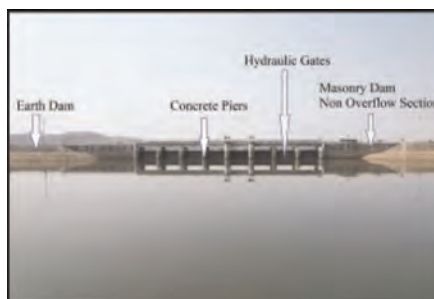
Figure 1.   Components of a typical dam - upstream view.

1.3 *Hydraulic gates and supporting structure*

Hydraulic gates and supporting structure resting atop the spillway crest are subjected to heavy dynamic loads as they govern the discharge from over the spillway. Gates are usually made up of steel and they undergo various types of deformations including warping under such loads. The entire system has to take severe vibrations and therefore they undergo fatigue at times. Embedded parts in to concrete elements are of utmost importance and fatigue in concrete members affects them.

1.4 *Energy dissipation portion*

Downstream of the spillway is the energy dissipation portion which is also subjected to high magnitude dynamic loads as its basic function is to dissipate the energy within the falling water and to streamline the flow to the best possible extent. Concrete gets badly distressed in many cases are frequent repairs are usual. In some cases, residual energy in the downstream of the energy dissipation portion is so much so that erosion takes place for a long distance in the riverbed.

1.5 *Power channel and divide bund/ wall*

Dams equipped with hydropower turbines have a divide bund/ wall separating tail race channel of hydropower units and the spillway channel. Conduce hydraulics of the tail race channel is required for efficiency of the hydropower units. Spillway channel streamlines the flood water in to the river gorge. Both these functions are exclusive and hence the divide bund/ wall is designed to ensure distinct hydraulic behavior on either side. It has to take different types of dynamic loads on both of its sides. In some cases, where the divide bund/ wall is not on a straight alignment, it has to act as a river training work. In such cases, it has to take heavy impacts and requires frequent repairs.

2 CASE STUDY OF UKAI DAM: RESTORATION OF DIVIDE BUND

2.1 *Overview of Ukai dam and distress observed in its divide bund*

Ukai dam is located in Gujarat state of India. It was constructed on Tapi river in 1972 with live storage capacity of 6730 million m^3. Total length of the dam is 4926 m of which 4058 m is an earth dam and 868 m is the spillway which is a masonry gravity dam with 22 radial gates whose discharge capacity is 37,865 m^3/s. There are 4 riverbed hydropower turbines of 75 MW each.

Divide bund acts as a groin on the spillway channel side, and, during the spillway operation, it is subjected to severe dynamic loads when it contracts the flow. Here, the original construction was in the form of an earthen bund covered with thick stone pitching. In spite of periodical repairs, signs of serious distress were observed in 2019. Near the hook-shaped nosing (Figure 2),
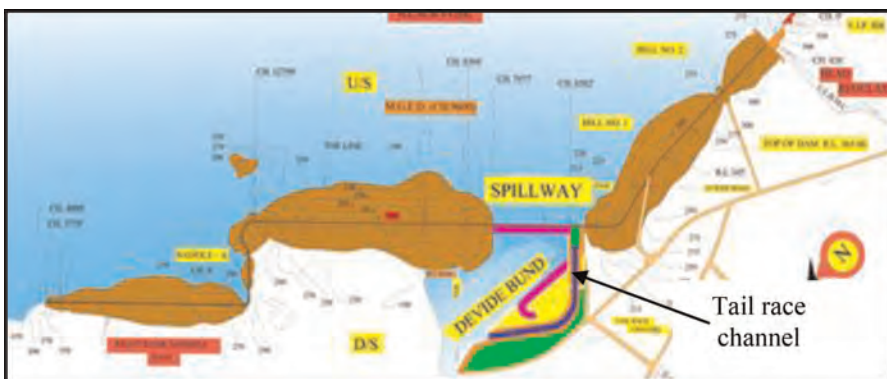
Figure 2. Layout of Ukai dam (Kapadia 2022).

Figure 3. Distressed divide bund (Kapadia 2022).

not only the stone pitching was disintegrated but also the stones were ruptured (Figure 3) and the surface of the earthen bund was found badly eroded. Riverbed though made up of monolithic basalt rock was found eroded badly to the extent of 5 m in depth and 8 to 10 m in width. Heavy erosion in rocks may cause undesirable changes in hydraulic behavior of flow.

2.2 *Method of estimation of buffeting forces*

While making original design of the divide bund, a three-dimensional laboratory model was used for deciding its alignment and profile which could take care of the impact due to water splashes during release of the flood water from the spillway. In order to fast converge to the right proposition of the model, wave characteristics were captured through a flume model. For this purpose, simple principles of dynamics were used.

$$p = wv^2/g \qquad (1)$$

where p is pressure at the striking point, w is the weight of unit volume of water and v is the velocity. As shallow water waves are dominant in such cases,

$$v \approx 3.16\sqrt{h} \qquad (2)$$

As the surface is inclined and some additional safety is required, design pressure p = 1.7wh was considered. In such a case, the pressure-time diagram for each wave contains a spike representing the primary impact component followed by a well spread secondary pressure component. As the tarin of waves is a series of waves with a short lag during high discharge from the spillway, only the primary impact component is considered and the aggregate impact is estimated for the design purpose considering maximum 7 cycles in a wave train.

2.3 *Impact resistant system using geosynthetics and its execution*

Usual practice for protecting earthen bund from impacts due to water waves is to provide a hard surface on it which may be in the form of thick rubble pitching or concrete blocks. Requirement of frequent maintenance of rubble pitching and limitations of compacting techniques to prepare the subgrade suggested that redoing the rubble pitching was not a promising solution. Therefore, as an alternative, a solution was designed in the form of a multilayer impact resistant system using geosynthetics. Three layers – hard, semi-flexible and flexible in sequence from top to bottom were chosen such that stagewise dispersal of impact occurs resulting in to a very low pressure on the earthen bund. Concrete slab as the outer most layer, gabions as the middle layer and biaxial geogrid with tensile strength of 40 kN/m and polypropylene non-woven geotextile as the bottom layer were provided. Filling of eroded riverbed with local rocks near hook-shaped nosing of the divide bund was also done followed by providing a layer of gabions as a lid. The entire system of restoration was designed such that the anti-slide key required at the toe of the divide bund was formed by the filling of the eroded river bed using its existing natural profile (Figure 4).
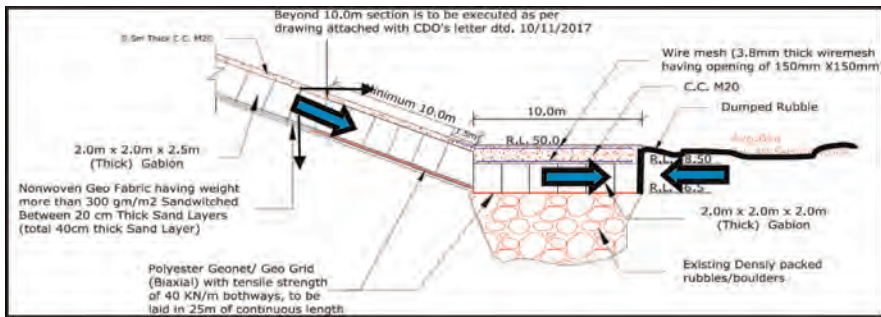
Figure 4. Restoration details - cross section (Kapadia 2022).

2.4 *Performance during floods*

Flood water release for three consecutive years during monsoon has given an opportunity to appraise the effectiveness of the solution. It is observed that the solution has been very effective from hydraulic and structural performance points of view (Figure 5).
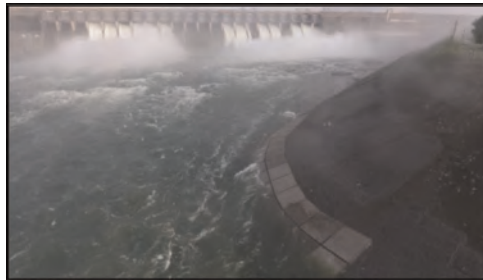
Figure 5. Performance after divide bund after restoration (Kapadia 2022).

3 CASE STUDY OF KADANA DAM: SECONDARY APRON

3.1 *Overview of Kadana dam and distress in energy dissipation portion*

Kadana dam was constructed in 1978 on Mahi River in Gujarat state of India. Its storage capacity is 1542 million m^3. Its main spillway is 406 m long and is constructed of rubble masonry with reinforced concrete lamination. Its design flood is 31,063 m^3/s. Ogee fall height from the crest of the dam is 37 m and energy dissipation is of solid roller bucket type with exposed basalt floor in the downstream. Roller bucket type energy dissipator is preferred when tailwater depth is high (greater than 1.1 times sequent depth preferably 1.2 times sequent depth) and river bed rock is sound (IS7365 2010).

In the solid bucket, all of the flow is directed upward by the bucket lip to create a boil on the water surface and a violent ground roller on the riverbed. The severity of the high boil and the ground roller depends upon tail water depth. Low tail water produces the most violent boils and ground rollers (Peterka 1984). During initial operation of the spillway, such a situation prevails.

Originally, there was a pit in the riverbed approximately 42 m away from the toe of the roller bucket which was not actually that serious as it was away from ground roller and hydraulic jump. However, in 2017 it was observed that the pit that was 12 m deep had undergone retrogression in length but not in depth. The pattern of retrogression suggested that after formation of the surface roller, the balance energy used to be of high magnitude
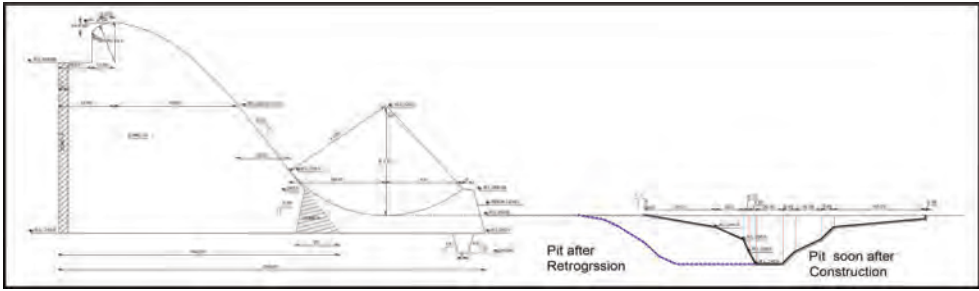
Figure 6.   Progressive retrogression of pit in downstream of roller bucket (Kapadia 2020).

causing erosion of the riverbed. Such issues of riverbed erosion in downstream of the roller bucket are usual and require periodical inspection followed by restoration as per need. Here, it was observed that the change in profile of the riverbed had caused undesirable changes in the hydraulic behavior of the flow.

3.2   Methodology for estimation of impact on rocky riverbed

Ground roller occurring on the rocky riverbed followed by hydraulic jump required estimation of impact at the time of designing the dam. Theoretical estimation of impact due to ground roller is not advisable for design purpose in case of a very high ogee spillway and therefore physical model was used.

Hydraulic jump dissipates the energy which can be estimated from the Froud number. Froude number is defined as

$$F = \frac{v}{\sqrt{gy}} \tag{3}$$

where F is the Froude number, v is the velocity of water, y is the height of water and g is the gravitational force. In this case, the Froude number being in range of 2.5 to 4.5, energy dissipation may occur between 20 to 40%. Specific energy before and after the jump is E_1 and E_2.

$$E_1 = y_1 + \frac{v_1^2}{2g} \tag{4}$$

$$E_2 = y_2 + \frac{v_2^2}{2g} \tag{5}$$

where y_1 is the initial depth of water, v_1 is the initial velocity, y_2 is the water depth after jump and v_2 is the velocity after jump. Difference between E_1 and E_2 is the energy dissipated. E_2 in case is too high, the flow tends to scour the riverbed. Pressure on floor at different points can be estimated from the velocity i.e. v = q/y where q is the discharge per unit width and y is the height of the water. During various combinations of gate operations, values obtained from these equations may differ from actual ones, and, therefore, design of the bucket and energy dissipation measures was made using results of physical modeling. Retrogression on the riverbed had altered the hydraulics.

3.3   Secondary apron using geosynthetics

Retrogression of the riverbed after long years of operation of the dam required a treatment of the riverbed such that the hydraulics is more congenial and impact is properly resisted. Secondary apron was designed for both these aspects.
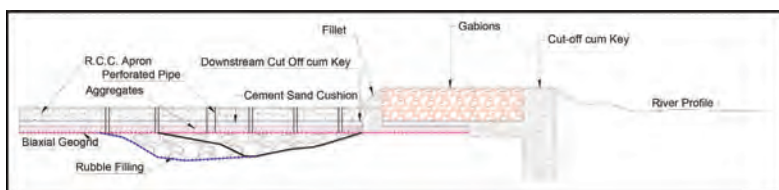
Figure 7. Schematic details of secondary apron as an impact resistant mechanism (Kapadia 2020).

Secondary apron was designed as a multilayer load dispersion system. The top layer of reinforced concrete slab, the middle one a composite layer of coarse aggregate and cement sand mix and the bottom as the biaxial geogrid with tensile strength of 30 kN/m to act as a separator cum basal reinforcement. This entire system was extended to cover the entire pit which was duly filled with graded rubbles. Conventional concrete apron resists impact mainly by its hardness. The solution designed here is a system that takes the impact with sharing its components amongst its members. Thickness of the reinforced concrete apron is required much less than in case of conventional solution because a part of the total impact is taken by it. This results in to a significant cost saving and should give better performance. This solution is in execution stage.

Figure 8. Execution of multistage secondary apron (Kapadia 2020).

4 LEARNINGS AND CONCLUSIONS

Severity of impact depends on stiffness of the material resisting it. Single member impact resistant surface has to take all the impact. Incremental interrelationship between stiffness and severity of impact requires very thick and stiff shield of rubble or concrete in a conventional solution. On the other hand, in multilayer system, impact is shared by the layers, and, therefore, lesser stiffness is required and hence the impact is less severe. Considering long life and importance of dams, application of geosynthetics have a huge scope in their construction and restoration.

REFERENCES

IS7365. 2010. Criteria for Hydraulic Design of Bucket Type Energy Dissipators: 3
Kapadia, V.P. 2022. Retrofitting of a Distressed Divide Bund of a Dam for Taking Dynamic Water Forces: Case Study of Ukai Dam, Gujarat, India. GeoAsia7, Asian regional conference by IGS, 31 October-4 November 2022. Taiwan.
Kapadia, V.P. 2020. Application of Geosynthetics in Energy Dissipation Mechanism of a Large Dam: Case Study of Kadana, Gujarat. Indian Journal of Geosynthetics and Ground Improvement ISNN: 2277-5625 Volume No. 9 July 2020. IGS India: 3–9
Peterka, A.J. 1984. Hydraulic Design of Stilling Basins and Energy Dissipators. *United States Department of the Interior Bureau of Reclamation*: 92

Rehabilitation project of a reservoir in Italy

G. Gatto & F. Bisci
Studio Speri, Rome, Italy

M. Scarella
Carpi, Balerna, Switzerland

A. Frezza
Enel Green Power, Rome, Italy

ABSTRACT: In 2020 Studio Speri was engaged by Enel Green Power in the design of the maintenance project of the Sillico reservoir, located in Tuscany, in the district of Lucca (Italy). The aim of the work is the rehabilitation of the reservoir impervious facing. The existing facing, made of concrete slabs, has failed due to differential foundations settlements. The reservoir has already experienced cracking of the concrete facing several times in the last years, without solving the problem definitively. The present designed and built solution consist in waterproofing by a flexible geosynthetics impervious facing system. The impervious facing is composed by a composite geomembrane liner (PVC geomembrane + geotextile) coupled with a composite geodrain (geonet + geotextile).

1   INTRODUCTION

In 2020 Studio Speri was responsible for the design of the maintenance project of the Sillico reservoir from Enel as the structure's owner. On May 28th 2020, the reservoir experienced a collapse of the impervious system, composed by concrete slabs, with the subsequent complete release of the stored water.

2   SILLICO RESERVOIR

2.1   *Location*

Sillico reservoir, constructed in 1940, is located in Lucca, Tuscany, Italy (Figure 1). The structure is a small reservoir off the river that collects water from the diversion works near the area. The reservoir has a maximum storage volume of almost 8'000 m^3 and provides a 51 m constant hydraulic head for the downstream hydropower plant and it works as a run-of-the-river hydropower power plant. The installed power is 1'600 Kw.

2.2   *Main features*

The main features of the reservoir are reported in Table 1.

   The reservoir has been built partially with the excavation of natural ground and slopes and partially through the construction of a small embankment (Figure 2). The slopes and the bottom are protected with a waterproof facing, composed of concrete slabs with the following dimensions: 4.0 × 4.0 × 0.30 m. Water stops ensure the waterproofness of the facing joints.

Figure 1. Sillico reservoir.

Table 1. Main features of Sillico HPP and reservoir.

Feature	Unite	Value
IP	kW	1'600
Maximum storage volume	m^3	8'000
Maximum hydraulic head	m	51
Upstream face slope	v/h	1.0/1.0
Downstream face slope	v/h	1.0/2.0
Maximum height of slopes	m	4.1
Crest length	m	220
Crest width	m	0.70–3.60
Crest elevation	m a.s.l.	435.00
Maximum regulation level	m a.s.l.	434.80
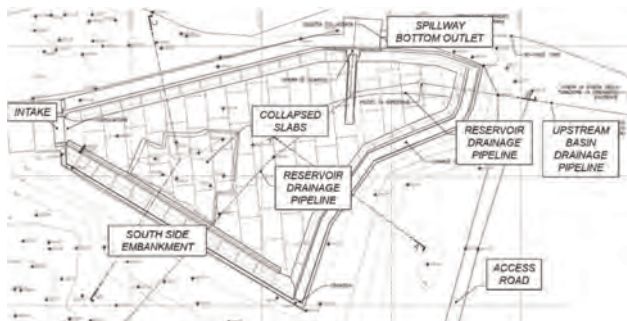
Figure 2. General plan of Sillico reservoir.

Because the reservoir is located into a natural pond at the end of a small ravine, a drainage system to bypass the reservoir was built (Figure 3). The system is composed of an underground pipeline that crosses the reservoir from the upstream north-east zone to the downstream south-west zone. This system is also collecting the leaks of the reservoir.

The outlet structures, bottom outlet and ungated spillway, are located into the northern side of the reservoir.

Figure 3.   Plan of the drainage system.

The intake structure is at the west side of the reservoir.

The site being examined is entirely set on terraced alluvial deposits of poorly cemented and heteromeric conglomerates. Both are matrix and clasto supported, and subordinately by gravel and sands, sometimes silty-clayey (Figure 4).
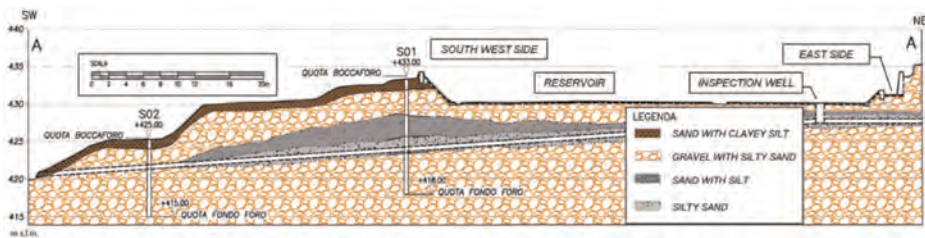
Figure 4.   Geological longitudinal section of the drainage system.

2.3   *Story of the multiple failures of the waterproofing system*

In 1985 some slabs on the bottom of the reservoir have collapsed due to differential settlement of the foundation. In 2006 a similar damage has ben occurred in the central part of the concrete facing of the reservoir. The rehabilitations have been done always through the restauration of the original rigid impervious facing. It is not well documented what is has been done to prepare the foundation plan neither what type of details.

On May 28th 2020 the structure, once more, experienced severe damage, due to the collapse of a vast number of concrete slabs both on the bottom and on upstream toe of the embankment at the north side of the reservoir (Figure 5). Whitin a few hours during the night the reservoir has lost throughout the foundation almost 8'000 m^3 of water. This failure has caused no casualties or damage.

During the subsequent site inspections, it was evident that the failure has been caused by the differential settlement of the concrete slab in foundation. Notwithstanding the presence of joints, this type of waterproofing system is susceptible to foundation's movement. Moreover,

Figure 5.   Pictures of the 2020 failure.

over the years, the reparation works executed have disregarded the presence of the original movement joints, casting monolith slabs, reducing even more the flexibility of the facing.

Once removed the cracked slabs, the soil in foundation was showing an important internal erosion (Figure 6). The loss of waterproofing, the internal erosion of the foundation and the settlements are coupled and evolutive phenomena that brought to the collapse of structure. However, the original cause of this mechanism was not clear. A camera inspection into the lower bypass drainage system made evident a collapse of the small masonry tunnel just below the area of the failure. Most probably this collapse, due to aging of the old structure, has incepted a small creak into the foundation slabs and the subsequent leakage toward the drainage system has finalized the failure.

Figure 6.   Internal erosion of foundation under the removed damaged slabs.

All the historical damages of the reservoir have been caused by an evolutive phenomenon as-sociated to differential foundation settlements and progressive internal erosion of foundation soil, due to the infiltration of water from the cracks of the concrete facing. The loss of waterproofing, the internal erosion of foundation and the settlements are coupled and evolutive phenomena that could bring to the collapse of a rigid structure as it happened.

3   REHABILITATION PROJECT

3.1   General description

Following the lesson-learned of the previous failure cases, the designer proposed the adoption of facing made of a flexible geomembrane liner, in order to provide a higher standard of safety, a predictable resilience, a higher durability and a stringent quality control procedure during construction. The geomembrane liner is characterized by an outstanding flexibility, largely more reliable than the existing rigid facing.

In detail, the main features of the rehabilitation project are:

- Construction of a new abutment against the existing degraded by erosion;
- Restoration of the reservoir foundation in the area of the observed collapse;
- Installation of a new flexible composite geomembrane, also known as geocomposite, made of a flexible PVC geomembrane thermally bonded to a non-woven geotextile, on the entire surface of the reservoir;
- Installation of a new drainage system below the geomembrane liner;
- Construction of a new protective lean concrete cover in the reservoir bottom above the geomembrane liner, in order to allow transit of maintenance equipment and installation of a new decoupling and anti-puncturing non-woven geotextile in between the lean concrete cover and the geomembrane liner to avoid damage during casting and transmission of stresses in case of further settlements;
- Minor maintenance works to the gates.

3.2 *New impervious facing*

The most important aspect of the rehabilitation project is the design of a new impervious facing, that can provide a better response than the original solution with concrete slabs to the critical foundation contest of the structure. The impervious facing essentially consists of a flexible geomembrane liner. In general, flexible facings guarantee a higher level of imperviousness than concrete slabs and can absorb the deformations induced by foundation settlements.

The new impervious facing is placed both upon the existing concrete slabs (in the zones where they are not damaged or collapsed) and upon granular soil material or new concrete slabs (in the zones where the existing concrete facing has failed). The total waterproofed area is almost 2'700 m^2 (Figure 7).
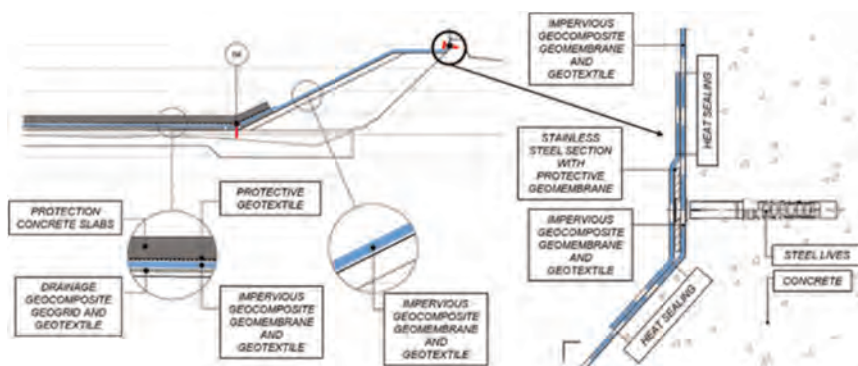
Figure 7.   Section of the new abutment with the new facing and detail of the perimetric anchorage system.

The facing is composed by an impervious composite geomembrane coupled with a composite geodrain to control any potential water leakage and to dissipate the sub pressure. The impervious composite geomembrane is made of a 2.5 mm PVC geomembrane thermally bonded during fabrication with a 500 g/m^2 non-woven geotextile. The composite geodrain is made of a geonet core (made of polyethylene) thermally bonded during fabrication with a 140 g/m^2 non-woven geotextile with filter behavior.

The choice of a PVC geomembrane is related to the intrinsic characteristics of the polymer. PVC geomembranes are distinctly the most flexible and resistant synthetic liners and are suitable for installation on irregular surfaces. From a statistic point of view, designers have selected a PVC geomembrane in nearly 59% of the installations on dams (ICOLD 2010). PVC geomembranes show a permeability coefficient k in the order of 1×10^{-12} m/s and a service life of more than 100 years in continental climates and exposed position. This statement is supported by the experimental results from the laboratory tests conducted at the Geo-synthetics Institute (GSI) with accelerated aging devices (ICOLD 2010).

In general, geomembranes exhibit a better performance when bonded with a geotextile to form a composite geomembrane (or geocomposite). The geotextile increases puncturing and tensile resistance, improve the dimensional stability, and minimize the formation of wrinkles due to the thermal deformation of the geomembrane liner. Composite geomembranes made of PVC polymers have been tested with success in international laboratory and are recommended by USACE for hydraulic installations (ICOLD 2010).

The seaming of the geomembrane sheets (2.0 m width) is made during construction at site by means of seaming machines, which can be either automatic double track or manual single track. Seams can be tested with the procedures and tools indicated by the international standards (ASTM and EN UNI). Single track seams can be tested with the method of the static pin (ASTM D4437-08 2013), while double track seam can be tested with the method of the pressurized air (ASTM D7177/D7177M-21 2021).

The impervious facing is fixed with an anchorage system with the scope of stabilize the facing subjected to wind and water loads (Figure 7). The face anchorage on the reservoir slopes is composed by stainless steel batten plates fixed to the concrete subgrade and covered with an additional strip of geomembrane. The perimeter seal around openings (intake, bottom outlet, spillway, etc.) is composed by stainless steel batten plates fixed to the concrete subgrade and made watertight under water in pressure by means of an additional rubber gasket and epoxy resin. The upper fixation along the top of the reservoir slopes, at an elevation higher than the full supply level, is composed by stainless steel batten plates fixed to the concrete subgrade and made watertight under water not in pressure (rainfall and waves) by means of an addition-al neoprene gasket.

3.3 *Construction works*

The construction has begun in July 2022 and are almost concluded, with the end of construction expected in November 2022. Studio Speri was engaged from Enel Green Power in the supervision of construction. Construction activities and particularly installation of new facing have been carried out extremely quickly. The geocomposite installation activities are reported in the following pictures together with the testing on sealing system (Figure 8).

Figure 8. Photo of the geocomposite placing activities.

4 CONCLUSION

In May 2020 Sillico reservoir concrete facing has collapsed due to differential settlements of the foundation. Historically the reservoir has been subjected to similar damages.

Studio Speri has been engaged from Enel Green Power, as owner of the structure, to carry out the rehabilitation project. The adopted design solution, with the scope to avoid other damages like the past ones, mainly consists in the installation of a new flexible geosynthetic im-pervious facing system, which comprise a composite geomembrane liner coupled with a composite geodrain. The geosynthetics have been selected and designed according to the best international standards.

Construction activities has begun in July 2022 and has been completed in November 2022, confirming that the installation of a geosynthetics facing is usually simple and quick.

REFERENCES

American Society for Testing and Materials (ASTM) 2013. Standard Practice for Non-destructive Testing (NDT) for Determining the Integrity of Seams used in Joining Flexible Polymeric Sheet Geomembranes. ASTM D4437-08(2013).
American Society for Testing and Materials (ASTM) 2021. Standard Specification for Air Channel Evaluation of Polyvinyl Chloride (PVC) Dual Track Seamed Geomembranes. ASTM D7177/D7177M-21 (2021).
International Commission on Large Dams (ICOLD) 2010. Geomembrane Sealing Systems for Dams. Design Principles and Review of Experience. *Bulletin n.* 135.

Angkor Wat west embankment - restoration and strengthening of the backfill by means of a composite geotextile

V.M. Santoro & V. Gallinaro
IGeS.World srl - International Consulting Engineering, Italy

ABSTRACT: The paper illustrates the restoration and stabilization of a moat embankment portion of the Angkor Wat Temple, Cambodia, in a World Heritage Site context. The earth strengthening was realized with a composite geotextile fabric, providing drainage and reinforcement to the backfill. The implementation of key geotechnical concepts proved to be effective in the middle run since its realization 20 years ago in a low technology environment within a low budget, involving local staff. The requirement of a low impact solution was a key issue in the adoption of the Intervention.

1   INTRODUCTION

1.1   *Historical setting*

The Angkor Wat Temple, located in Siem Reap, Cambodia, counts among the most astonishing monuments of the World Heritage listed sites. Built in the XII century A.D. during the golden age of the ancient Khmer Civilization during the reign of the king Suryavarman II, it is widely praised for the quality of the craftsmanship, as well as for its architectural and cultural value and has long surged to an iconic status. To the present days the Temple Complex maintains its strong link to the local population as a cultural and religious venue, and represents a major resource for the development ambitions of the whole Nation.

1.2   *Hydraulic network and general layout of the area*

Recent studies have been unveiling that the ancient Khmer Civilization designed a complex hydraulic system in the greater Area of the Angkor Royal City, in order to manage the local monsoonal rains.

Canals, water reservoirs, artificial lakes, barriers and dikes are all part of this system that stretches from the Khulen mountains in the north to the lows of the Tonle Sap riverbanks.

The realization of extensive expansion basins at the same time protected the population from the dangers of flooding and provided a manageable water resource to its agricultural economy. The network probably served also as a waterway through the landscape of the Royal city of Angkor and the natural basin of the Tonle Sap lake farther south to the open sea.

The Angkor Wat Temple compound itself, as part of this hydraulic network is surrounded by a rectangular moat, stretching 1.3 km along the east and west sides, and 1.5 km along the north and south sides. The ditch is 190 meters wide, and runs outside the outermost enclosure wall.

1.3 Intervention context

The Restoration Project involved a stretch of the moat embankment located on the west side of the Temple, aside its main entrance. Originally conceived as a stepped slope for the crowds to be seated, the embankment shore maintains to these days its role as a major cultural venue during water festivals and ceremonial occasions.

The intervention on the collapsed embankment involved a length of approximately 60 meters, a stretch located between two abutments of the south side of the moat, on its east shore, its inner perimeter. The project consisted in the reconstruction of the collapsed steps and in the strengthening of its backfill.

Table 1. Key data of the intervention.

Reference	(UM)	(Q)
Intervention length	(m)	60
Earth Volume moved	(m^3)	1050
Geocomposite surface	(m^2)	5000
Final slope inclination	(^{0})	45

Figure 1. Intervention area during the rehabilitation intervention.

The restoration project on the Angkor Wat front steps have been realized in the framework of an international co-operation Program sponsored by UNESCO, and were planned together with the relevant local Authorities with the involvement of local staff, intending to preserve Cultural Heritage through tourism promotion and cultural interchange, along with the development of human potentials through on-field training.

2 ANALYSIS

2.1 Previous restorations of the embankment

Along the last century, at least three times a reconstruction of this portion of embankment was recorded. The Conservation of Angkor- the local Authority responsible for the Maintenance of the Archaeological Area- intervened in 1909 and 1915 for the repositioning

of the steps to their original location, substituting some of the missing heavy stones steps on the front of the slope. A major intervention is documented in the French period with the reconstruction of this part of the embankment in the early 1960's.

In this latest intervention a drainage system from the superficial waters was provided at the back of the embankment. Remains of discharge RC pipes running through the landfill into the moat had been detected already prior to the intervention among the debris of the landslide and further recovered during the excavations of the embankment.

The common feature of these works was possibly a poor prevention of the water action from the backfill. A strengthening of the embankment was also not implemented according to the records.

2.2 *Back analysis of the damage and design approach*

The steps of this moat embankment portion last collapsed on September 27th 1997, following a torrential rain. The project on-site activities started in January 2002.

According to the Reports relating on the collapse event, a substantial water head mounted on the north half of the moat ditch with respect to the south half, where the moat steps are located.

Evidence of filtration paths leading to the steps, was also found in the earth just behind the collapsed wall. Saturation of the soil volumes involved in the landslide may also have played a major role in the instability of the landmass.

Even though there are clear signs of awareness of the potential disruptive effect of the water in the previous Restoration Interventions on the embankment, prevention measures were only limited to a superficial draining system, only capable of conveying runoff waters into the moat through the installed discharge pipes.

For what regards the implementation of a reinforcement of the embankment earth body, there is no sign that it went beyond the compaction of the available soil recovered from the landslide and repositioned behind the steps.

During the onsite survey was furthermore noticed that the laterite and sandstone blocks shielding the embankment slope downstream were assembled on a bedding mortar in the latest restoration intervention, a procedure unknown to the original Khmer constructors. Such sealing of the joints between adjacent stone blocks represented than a barrier to the free water flow from the body of the embankment into the moat.

Figure 2. Adjacent portions of the steps showed a different behavior due to different boundary conditions. Left: dry assemblage of the steps; Right: Joint sealing (gray cementitious mortar) preventing drainage.

The back analysis of the collapse causes pointed out to two possible concurring phenomena.

The pouring rainwater that was falling in the area prior to the landslide, on one side resulted in a sudden relevant increase of the free water surface in the moat, on the other side soaked into the soil, in a more gradual filtration process.

During the first phase of the rain downpour the rising water level in the moat possibly started a filtration process towards the embankment fill, where the water table level lagged behind, as to generate destabilizing upward forces against the foundation basement, in a siphonage path lead by the water gradient.

With the peak downfall fading, the runoff water conveyed into the moat was then readily driven away downstream through the open canals, while the pore overpressure in the backfill was still building up, due to the much slower development of the filtration process.

In this second phase the infiltrating rainwater exerted then an outward thrust against the steps, not balanced any more from the moat water level.

As the rising water level lowers the soil friction bearing capability, the horizontal destabilizing force behind the wall increases.

Under these conditions, chances to trigger a landslide phenomenon drastically increase.

Prevalent could have been one or the other phenomenon, depending on the water level rising rate in the adjacent basins during the rain.

The proposed restoration was then based on the previous considerations, as to ease water pressure behind the wall, and enhance at the same time the friction resistance of the soil.

The design criteria were based on the traditional procedures in use at the project time (Corbet S. & King J. 1993), then revised with the up-to-date ones (Koerner R. 2016).

3   DESCRIPTION OF THE INTERVENTION

3.1   *Introduction*

The idea of reinforcing a weak soil through the insertion of an extraneous material was long since exploited, even before recorded history, often through natural and degradable inclusions such as timber, organic fabrics, or bushes. Though, such interventions could not have been fully reliable and effective in the long term, due to the natural decay of the reinforcements.

Durability remained the major problem for this kind of stabilization till the late 1960's, when the first applications of soil reinforcement based on a rational theory first appeared.

The need for a better durability is nowadays satisfied by synthetic man-made products coming from the plastic industry, namely the polymers, whose characteristics are often improved with additives by the chemical industry, guaranteeing the product from most decay phenomena for "permanent" applications, according to the international standards (up to 100 years).

Typical protection of these materials includes sheltering from UV ray attack, and stabilization from soil aggression, that might result in precocious oxidation and wearing of the polymer chains. The final products are usually guaranteed, and comply with international testing standards.

The first patented usage of a reinforcing geotextile in civil engineering dates back to 1964, but in more recent years the expansion of such products has been enormous, with applications covering reinforcement and drainage in a number of different choices offered by the material's specific characteristics. Target products are often manufactured according to the customer's particular performance requirements.

These materials represent today a low impact and relatively low cost solution to many slope stability problems.

The introduction of a restoration method based on geotextiles, represented an occasion to introduce into Cambodia a viable solution to the slope instability.

3.2 *Details of the intervention*

The soil reinforcing was realized through the insertion of a geotextile into the body of the embankment fill, so to realize strengthened earth.

A drainage system, both at the interior of the embankment and at the surface level was also provided, in addition to the reinforcing of the backfill.

The filtering drainage tissue included in the package deployed inside the earth mass, is meant to drive the waters into transversally positioned draining ditches, specifically realized with graded granular soil.

For a proper functioning of the drainage system in the long term, a filter, placed at the interface between these drainage wells and the reinforced earth, prevents the migration of smaller soil particles.

The available original stone blocks, were recovered from the slide muds and repositioned alongside the moat, so to provide a protection against erosion.

The reinforcement fabric was assembled in horizontal layers intercepting the potential sliding surface, and so dimensioned to provide adequate anchorage length to the compacted stable soil behind.

Soil compaction during the phase of the embankment refilling served to improve force transmission to the reinforcement layers through friction, and avoid settlements of the backfill.

A series of transversal drainage ditches are hydraulically connected to the moat waters, crossing the layers perpendicularly. The soil inside these drainage shortcuts was specifically graded as regards its permeability characteristics.

Service conditions with people surcharging the embankments during a crowded celebration day have been considered, allowing a proper safety factor.

Heavy weather conditions have also been considered, as the drainage system implemented in the works prevents a water head from acting behind the steps.
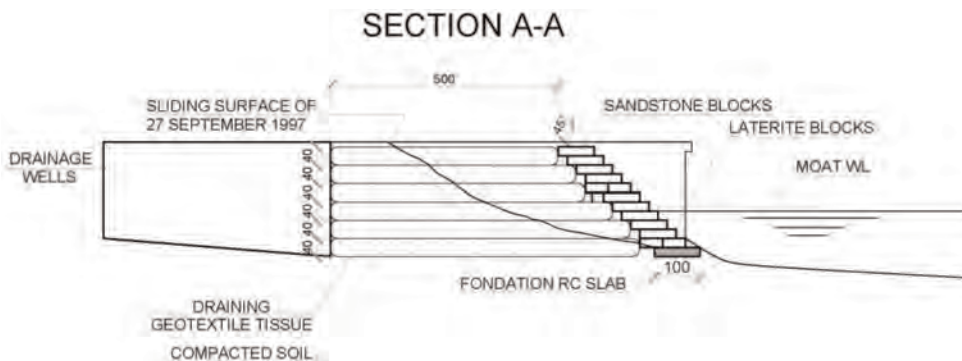
Figure 3.   Restoration intervention- Geotextile package assemblage in the embankment section.

Figure 4.   Overview of the working site and detail of the filling of the slurry trench.

3.3 Technical characteristics of the adopted materials

3.3.1 Geotextile

As regards its drainage characteristics, the geotextile was specifically studied to drain the waters from the neighboring soil, with permeability values 3-4 orders of magnitude greater of the local soil, that is 1,000 to 10,000 times greater of the natural surrounding material. Once placed on site, these drainage sheets work as drainage pipes within the existing soil mass.

Specific care in the design of the draining sheets was devoted to prevent undesired occlusion, with a proper geometrical distribution of the pores throughout the geotextile.

The process of bonding together the polymer filaments is organised in such a way to prevent both surface covering (blinding), due to the transportation of smaller soil particles, and inside obstruction of the 'mattress' during the filtration process, or clogging. The needle-punching bonding process, that follows the extrusion of the polypropylene filaments, in comparison to the resin or heat assembly method, gives the geotextile a greater mass, resulting in better drainage properties. Only a minor contribution to global strength of the geo-composite comes from the geotextile.

3.4 Geo-grid

On the other hand, the geo-grid plays the major role in the resisting force of the final product.

Service temperature is well beneath the transition glassy temperature of the Polyester fibers (120°), giving the material a more rigid behaviour under service conditions, compared to that of the Polyoefine (Polypropylene (PP) and Polyethylene (PE)), which would be working above the transition glassy temperature of the material in normal environmental conditions, with a rubber-like behaviour and greater deformations.

4 CONCLUSIONS

Extreme weather conditions have long been characterizing monsoon regions, exposed to peak events in short seasonal periods. A changing climate is now exposing always larger areas worldwide to the challenge of protecting built and natural slopes.

Even though awareness of the water influence in triggering soil instability can be recognized already in the classical times, a full understanding of its role dates back to the last century, whilst effective and viable technical solutions in this respect appeared as recently as within the last decades.

The stabilization intervention on the Angkor Wat moat embankment showed that an effective solution based on key geotechnical concepts can be successfully adopted in low technical contexts, under the restrictive design constraints of a prominent World Heritage Site.

With always larger areas dealing with slope instability problems, and new materials specifically tailored to the most diverse requirements being introduced in the market, a broader application field for this type of interventions is opening.

Under this perspective, the restoration represented a pilot project for approaching a current problem in heavy rain environments, through a low impact approach.

REFERENCES

Corbet, S. & King, J. 1993. *Geotextiles in Filtration and Drainage*. UK: Thomas Telford Ltd
Koerner, R. 2016. *Geotextiles from Design to Applications*. UK: Woodhead

Numerical analysis of geo-filters with reference to an Italian case-history

L. Frigo
Comune di Chiampo,Vicenza, Italy

P. Pavanello & P. Carrubba
Dipartimento ICEA, Università degli Studi di Padova, Padova, Italy

ABSTRACT: Geotextile filters are geosynthetic tubular containers, which are filled by pumping a fluid mixture of water and soil: the permeability of the geosynthetic allows the water to drain so that at the end of the installation a relatively solid nucleus can be obtained. Taking advantage of this feature, geo-tubes have been widely used for the storage of sludge of various types and origins. The paper presents a case-history of an application in Northern Italy, where fine sediment accumulated on the bottom of an artificial basin, Valdaora lake, in Alto Adige (Italy) was removed to ensure the correct functioning of the bottom spillway of the dam. Approximately 2,500 m³ of sediments were stored six geo-tubes, organized in a stacked configuration. At the end of the dewatering process, they were left in situ and used as storage containers, after having covered them with earth, thus becoming an integral part of the slope. Given that there are not closed-form solutions available for the stacked configuration, a numerical analysis was performed by means of the Flac 2D code, in order to evaluate the stress level in the geotextile during the various construction phases and to highlight critical aspects of this composite structure.

1 INTRODUCTION

The geosynthetic tubular elements are widely used for various purposes, including the construction of bank or submerged barriers, artificial dunes, for the dewatering and the storage of dredged sediments or for the treatment of sewage of industrial processes. This paper presents a case study of the application of geo-filters for the dewatering of sediments dredged from the bottom of a reservoir. The dewatering procedure has the purpose of separating the liquid phase from the solid one in order to minimize the residual volume, allowing the transport and the storage of the consolidated solid fraction for its final disposal. It should be noted that besides geo-filters (Grzelak *et al.* 2011; Mastin *et al.* 2008; Satyamurthy *et al.* 2011), various other technologies can be applied for the sludge dewatering, including plate and frame presses, belt filter presses (Novak 2006; Wakeman 2007), centrifuges (Lin *et al.* 2001; Rees *et al.* 1991).

The dewatering of sludge through the use of tubular geotextile filters is a recent technique that has multiple aspects of interest: high process efficiency, rather simple management of the construction site, reduced handling of materials and consequently low costs. Moreover, the filtering element could also constitute the container for long-term storage of the sediment, as in the case presented in this paper. The area of intervention is located in the Alto Adige region of Italy, at Valdaora Lake, in Pusteria Valley. It is an artificial basin for the production of hydroelectric energy, created with the construction of an arch dam, with a height of about 35 m and a crest length of 140 m which was built in 1958. The dam is equipped with two spillways on the right hydrographic side, which convey the water into a circular tunnel with a diameter of 5.0 m through two separate pipes. An emergency spillway, on the left side, and a water intake gallery next to the control room, on the right side, completed the hydraulic connection of the reservoir.

The dredging operation was necessary due to the partial obstruction of the two bottom spillways, caused by the deposition over time of sediments transported by the river that feeds the lake. For safety reasons these materials had to be removed, but their high water content required the adoption of a dewatering technique in order to easily manage and store these sediments. The solution with the geo-filters was chosen by the managing body because it allowed the on-site disposal of the sediments, minimizing transportation costs and allowing a good integration with the environment.

2 THE CASE HISTORY

The geo-filters are tubular containers, made of polypropylene by sewing a series of woven geo-textile elements, in order to reach the dimensions required by the project. They were placed on the left side of the lake, near to the dam; preliminary used for the dewatering of the dredged slurry, after the densification of the solid fraction, they were re-employed for the final storage of the retained sediments. In this last phase, the geo-filters were covered with natural soil, thus achieving both the purposes of remodeling the profile of the slope and making them no longer visible. To optimize the storage capacity and to minimize the occupied area, a pyramidal configuration of the tubular containers was adopted, with a cross section formed by two elements at the base and a third element, of larger dimensions, placed above them. Each geo-filter was 30 m long and the pyramidal configuration was repeated twice in length, for a total number of 6 geo-filters (four at the base and two superimposed) and a total extension of 60 m, able to store up to 2,500 m^3 of consolidated sediments. The four geo-filters at the base had a circumference length of 15.7 m, with a maximum design height of 1.7 m, while the larger two upper geofilters had a circumference of 25 m and a height of 1.9 m. The selected woven geotextile had a tensile strength of 100 kN/m and a velocity index of 25 mm/s. The sediments were removed by means of a submersible pump, equipped with disruptors. This dredging unit was moved and controlled by a floating pontoon, so as to be able to suck up the sediment at the required depth of about 20–25 m. The dredged material was pumped through a floating pipe, approximately 250 m long, to the geo-filters (Figure 1).

The average daily productivity was of 150 m^3 of solid material, corresponding to about 300 m^3/h of flowing slurry, with a solid content of about 6%, pumped over an 8-hour work shift. The dredged material was a slightly sandy clayey silt, with a granulometry composed by 12% of sand, 77% of silt and 11% of clay. Its on-site unit weight, before the dredging operations, was of about 16 kN/m^3, while, the slurry obtained by mixing the sediments with the water, during the pumping process, had an average density of 11.8 kN/m^3. To facilitate the separation of the solid fraction in the dewatering phase, an automatic station for dosing an anionic polyelectrolyte was
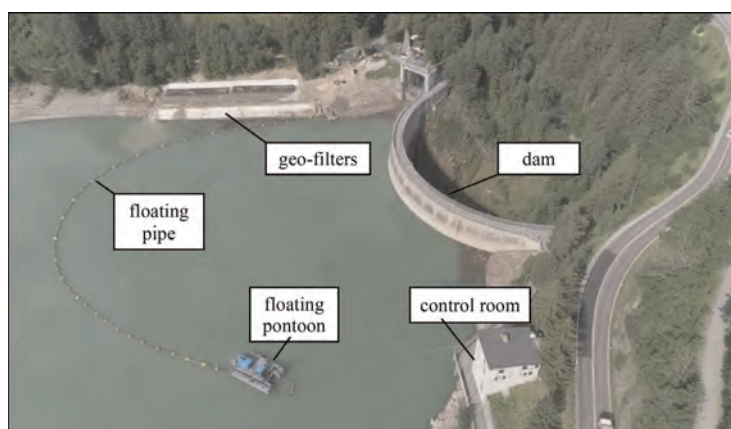
Figure 1. Aerial view of the site.

provided before introducing the mixture into the geo-filters. The intervention was developed in different executive phases which can be summarized as follows:

(1) preliminary excavation: the natural slope was excavated to create a platform about 20 m wide and 65 m long, for the subsequent positioning of the geofilters, with a slight slope (0.6%) towards the lake, to facilitate the flow of water (Figure 2a);
(2) creation of a drainage layer: at this phase about 200 mc of gravel were used to made a drainage layer with a thickness of about 15 cm, separated from the soil in situ by a layer of nonwoven geotextile, having a weight for unit area of 600 g/m^2 (Figure 2b);
(3) installation and progressive filling of the four geo-filters located at the base of the structure: the filling takes place via a series of hoses connected to the 3 outlets with which each geo-filter is equipped (Figure 2c);
(4) installation and subsequent filling of the two upper geo-filters (Figure 2d), over a leveling layer of granular material placed as drain between the first and the second layer of geo-filters;
(5) At the end of the dredging and filling of the geo-filters, all the equipment was dismantled and the containers were subsequently covered with a layer of topsoil, with an average thickness of 50 cm (Figure 2e).

At the end, the geo-filters are no longer visible and the result is a perfect integration of the intervention into the natural environment (Figure 2f). The works, from the initial phase of removing the sediments to the final stage of covering of the geo-filters, took a total of about six months.
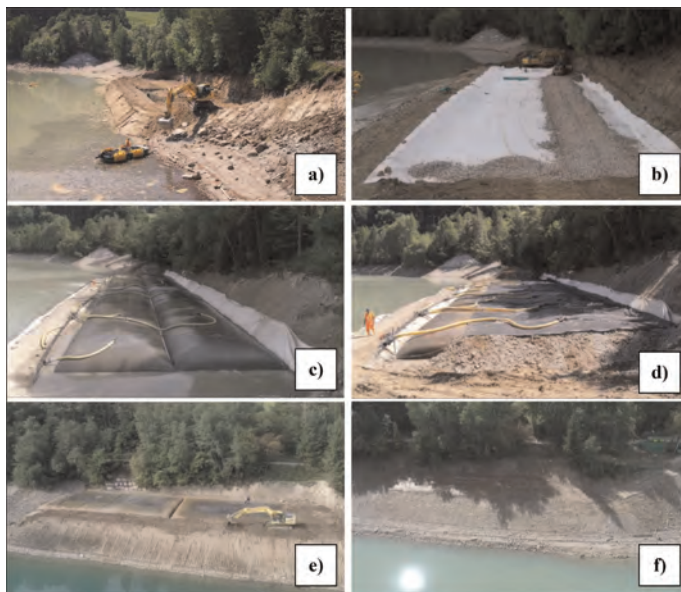
Figure 2. a) step 1: preliminary excavation of the site; b) step 2: drainage layer; c) step 3: filling of the geo-filters at the bottom; d) step 4: installation of the two upper geo-filters; e) step 5: covering of the geo-filters with topsoil; f) final configuration of the slope with geo-filters no longer visible.

3 NUMERICAL MODEL

The design requires the check of the stability of the system in the various executive phases. While the global stability can be evaluated with the usual limit equilibrium methods, the stress and strain state of the geo-filters is more complex to analyze. In fact, there are several analytical solutions for the design of a single geo-filter (Leshchinsky *et al.* 1996) but there are no simple solutions for the case of stacked geo-filters, given that the solution strictly depends

on the geometry adopted, i.e. on the size and relative position of the various elements. The study was performed with a simplified numerical model, implemented in the Flac 2D code (Itasca 2016), based on the finite difference method. The objective of the numerical analysis was to investigate the behavior of the geo-filters, in terms of stress and deformation, during the different operating phases and considering, among the various loads, also the lateral pressure exerted in the final phase by the filling soil placed behind the textile containers.

The model, for plane-strain state analyses, represents a typical cross section, formed by three geo-filters, two at the base and one superimposed (Figure 3). Each geo-filter is discretized with a grid made up of 117 zones, having an average height of 0.2 m and an average width of 0.6 m. The upper geo-filter is modelled with the same number of zones, but the average sizes in this case are equal to 0.21 m in height and 0.87 m in width. The foundation soil is represented as an elastic medium, due to the negligible settlement expected, and corresponds to a grid composed by 432 zones. A summary of the parameters adopted in the numerical model for the geotextile, the slurry and the soil is reported in Table 1.

Various steps are considered in this analysis: first of all, the first geo-filter at the base is materialized. At this phase, the filling slurry is modeled as an elastic material, almost incompressible, and, after the application of the gravity acceleration, the geo-filter assumes its correct configuration. Even if the filling phase is not properly simulated, previously analyses (Pavanello *et al.* 2019b) demonstrated that the results, in terms of stress in the geotextile and shape of geo-filter, are very good and comparable with those provided by analytical calculation methods. At the second step, the change of status of the filling material, from fluid to solid, is simulated by changing the mechanical properties of the inner material. In detail, the medium passes from an elastic behavior to an elastic-plastic behavior characterized by a Mohr-Coulomb yield law. In the subsequent third and fourth phases the previous two phases are repeated to materialize the second tubular container at the base of the structure. Lastly, the simulation of the third tubular container is carried out, again with
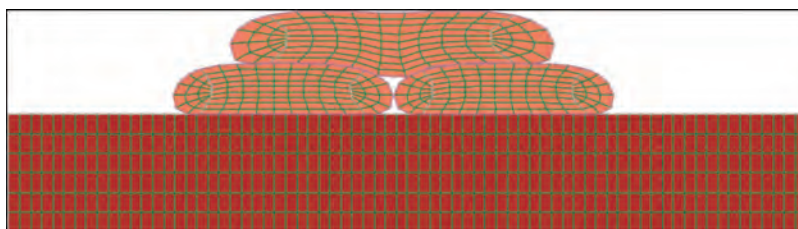
Figure 3. Flac numerical model of the staked geo-filters (final configuration).

Table 1. Input data for Flac model.

	Symbol	Value
Unit weight of slurry [kN/m]	γ_{sl}	11.77
Bulk Modulus of slurry [Pa]	K_1	2.0E7
Shear Modulus of slurry [Pa]	G_1	1.0E3
Stiffness (geotextile) [Pa]	E_g	1.15E9
Frictional angle foundation soil-geosynthetic [deg]	$\delta_{g,f}$	20
Frictional angle slurry-geosynthetic [deg]	$\delta_{g,s}$	0.1
Frictional angle consolidated slurry-geosynthetic [deg]	$\delta_{g,c}$	16
Bulk Modulus of consolidated slurry [Pa]	K_3	6.67E6
Shear Modulus of consolidated slurry [Pa]	G_3	4.00E6
Unit weight of consolidated slurry [kN/m]	γ_{sl}	13.72
Friction of consolidated slurry [deg]	φ	25
Cohesion of consolidated slurry [Pa]	c	1000

a first phase in which the filling material is considered in the fluid state and a subsequent one corresponding to a solid state. Finally, in the last phase the lateral stress, due to the filling soil behind the tubular containers, is applied, as a horizontal active pressure, acting on the right side of the structure. For the evaluation of this additional horizontal stress, an average height of the ground to the right of the geofilters greater than one meter compared to the top of the upper geo-filter was considered. In addition, the following soil parameters have been hypothesized: γ = 18 kN/m3, φ' = 30°, c' = 0 kPa, ka = 0,33.

4 RESULTS

The first result regards the stress during the filling phase of the single geo-filter: at the end of the first step of the analysis, when the inner material is simulated as a incompressible fluid medium, the model provides a maximum tensile stress equal to 11.0 kN/m. The same results are obviously obtained for the second geo-filter at the base of the structure. When the third upper tubular container is materialized in the model (Figure 4), the tensile stress of the lower geo-filters shows a significant increase, of about 70%, rising from maximum values of 11.0 kN/m up to 18.6 kN/m. Due to the different dimensions and the irregular support surface, also the tensile stress in the upper geo-filter is much higher than in the previous case, reaching maximum values of about 24.8 kN/m in the "saddle area", in correspondence with the axis of symmetry. Moreover, in the lower side of the geo-filter at the base, the axial forces are close to zero, thanks to the stabilizing contribution of the friction force between the geosynthetic and the foundation soil, which discharges the stress acting in the tubular container (Pavanello *et al.* 2019b).

This analysis scheme can be considered to be in favor of safety, as the gap between the base geo-filters can be reduced by backfilling it with soil. Reducing the space reduces the deformation, and therefore the stress of the upper tubular container; from an operational point of view it corresponds to what was actually done on site, as shown in Figure 2.
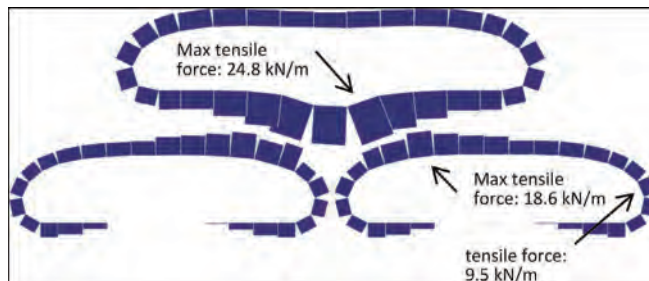
Figure 4.   Tensile stress of the geo-filters at the final configuration (in absence of the lateral stress).
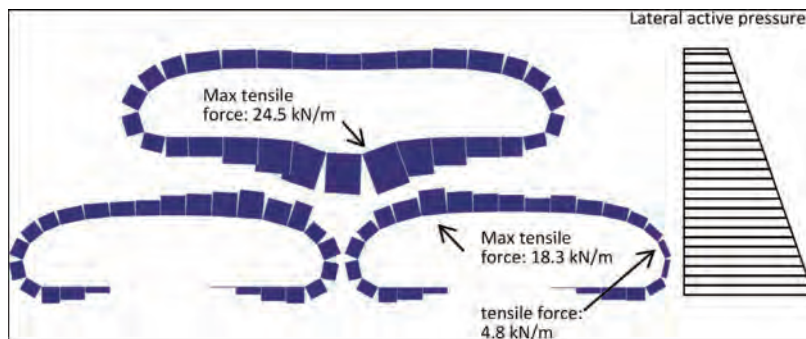
Figure 5.   Tensile stress of the geo-filters at the final configuration (in presence of the lateral stress).

As final step, the effect of the lateral filling soil acting on the right side of the model have been investigated (Figure 5). By comparing the distribution of tensile stresses on the geo-filters with (Figure 5) and without (Figure 4) the action of lateral stress, it can be seen that the variation of stress is very limited and only affects the geo-filter at the base, on the side opposite the lake, where a decrease of the tensile force in the geotextile was recorded, due to the stabilizing effect of the action of the lateral soil. On the other hand, there is no percep-tible deformation of the structure and consequently, the configuration of the system can be considered stable even in the presence of the lateral pressure exerted by the backfill soil.

5 CONCLUSIONS

This paper presents a case-history of application of geo-filters for the dewatering and the final storage of dredged sediments. The interaction between the three geotextile tubular container has been modelled with Flac numerical code in order to evaluate the stress state in the geo-sinthetics and the deformed configuration reached by the geo-filters. The interaction between the stacked geo-filters shows that the upper element presents higher tensile stress than the lower ones, especially in correspondence of the "saddle zone", between the two lower con-tainers. Furthermore, the presence of backfill soil on the side of the structure leads to an imperceptible deformation of the structure and to a small decrease of the tensile stress in the geofilter at the base, on the upstream side. The good behavior of the structure in situ indirectly demonstrates the adequacy of the analysis for sizing the geofilters in the design context, although the model has analyzed the backfilling and consolidation phases in a simplified form.

REFERENCES

Grzelak, M.D., Maurer, B.W., Pullen, T.S., Bhatia, S.K., Ramarao, B.V. 2011. A Comparison of Test Methods Adopted for Assessing Geotextile Tube Dewatering Performance. *Geo-Frontiers 2011: Advances in Geotechnical Engineering*, 2141–2151.

Itasca Consulting Group (2016): FLAC Fast Lagrangian Analysis of Continua, vol. 8.

Leshchinsky D, Leshchinsky O, Ling HI, Gilbert PA (1996) Geosynthetic Tubes for Confining Pressurized Slurry: Some Design Aspects. *Journal Geotechnical Engineering* 122(8), 682–690.

Lin, C. F., & Shien, Y. (2001). Sludge Dewatering Using Centrifuge with Thermal/polymer Conditioning. *Water Science and Technology*, 44(10), 321–325.

Mastin, B. J., Lebster, G. E., & Salley, J. R. (2008). Use of Geotube® Dewatering Containers in Environmental Dredging. Proceedings of GeoAmericas, 143–151.

Novak, J. T. (2006). Dewatering of Sewage Sludge. *Drying Technology*, 24(10), 1257–1262.

Pavanello, P., Tognolo, D., Carrubba, P., Frigo, L. 2019a. Numerical Analysis of Stacked Geo-tubes. *National Conference of the Researchers of Geotechnical Engineering*, 225–234. Springer, Cham.

Pavanello, P., Verza, E., Carrubba, P., Frigo, L. 2019b. Numerical Analysis of a Geo-tube Subjected to Seismic Soil Liquefaction. *In Earthquake Geotechnical Engineering for Protection and Development of Environment and Constructions*, 4404–4411, CRC Press.

Rees, T. F., Leenheer, J. A., & Ranville, J. F. (1991). Use of a Single-bowl Continuous-flow Centrifuge for Dewatering Suspended Sediments: Effect on Sediment Physical and Chemical Characteristics. *Hydrological Processes*, 5(2), 201–214.

Satyamurthy, R., Liao, K., & Bhatia, S. K. (2011). Investigations of Geotextile Tube Dewatering. *Geo-Frontiers 2011: Advances in Geotechnical Engineering*, 2121–2130.

Wakeman, R. J. (2007). Separation Technologies for Sludge Dewatering. *Journal of hazardous materials*, 144 (3), 614–619.

The Central Luzon link expressway embankment construction with high stiffness geotextile and prefabricated vertical drains, Manila, Philippines

S.I.S. Teh
TenCate Geosynthetics Asia Sdn. Bhd., Shah Alam, Selangor, Malaysia (A Solmax Company)

R. Tolentino
TenCate Geosynthetics Asia Sdn. Bhd. Philippine Representative Office, Quezon City, Philippines (A Solmax Company)

K. Laguitao
Arizona Geosynthetics Inc., Quezon City, Philippines

ABSTRACT: The Central Luzon Link Expressway (CLLEx) is a four-lane expressway linking several existing expressways in the Central Luzon region of the Philippines to shorten the travel time between main cities, mitigating the severity of traffic congestion. To minimize interruptions to the local communities and economic activities, abutment embankments are constructed for overpass bridge structures. Geotechnical problems such as embankment instability and excessive post-construction settlements of the embankment were the primary concerns in the project. Among several ground treatment methods, geosynthetics solution was chosen by the Department of Public Works and Highways (DPWH) due to ease of construction and cost effectiveness. High stiffness geotextile is used as a basal reinforcement to enhance the embankment stability and bearing capacity. Prefabricated vertical drains (PVDs') together with surcharge fills is used to accelerate the consolidation settlement of the soft foundation. This paper also discussed the construction sequences of the embankment.

1 INTRODUCTION

The Central Luzon is the third largest region in the Philippine Republic located at the north of the Manila; the capital of the Philippines. It serves as an administration region in the Philippines comprising 7 provinces including Aurora, Bataan, Bulacan, Nueva Ecija, Pampanga, Tarlac and Zambales, as well as 12 cities and 118 municipalities. It is known as the Central Plains of Luzon as it has the longest contiguous area of lowlands surrounded by mountains, active volcanoes, farmlands, sea harbors, etc. The strategic location of the Central Luzon between the Metro Manila and the Northern Luzon turns it into a center gateway, connecting the two regions for land transportation of people and goods, and thereby contributing to the formulation of industrial space and local economic development.

The population in the Central Luzon has tremendously increased from 8 million to 12.5 million people over the past 20 years, contributing more than 10 percent of the total population in the Philippines. Increased population in the region has raised the concern of traffic congestion that worsens the problems of environmental air pollution, local economic efficiency, etc.

2 PROJECT BACKGROUND

Central Luzon Link Expressway (CLLEx) is located at the north of Manila, the capital of the Philippines. The CLLEx is a newly constructed four-lanes expressway linking several existing expressways in the Central Luzon region of the Philippines to shorten the travel time between main cities. The CLLEx is divided into two phases, with Phase I consists of 30 kilometers long expressway connecting Tarlac City to Cabanatuan City and Phase II consists of 35.7 kilometers long expressway connecting Cabanatuan City and San Jose City passing through the municipalities of Talavera and Llanera in Nueva Ecija. Figure 1 shows the layout plan of the CLLEx in Central Luzon Region III.

Figure 1.   Layout plan of the CLLEx in Central Luzon Region III (blue line – phase I; red line – phase II).

The terrain at the central region of Central Luzon is generally flat with an average altitude of 200 m, having mountains and hills with peak altitude up to 2000 m located on its left and right. Its strategic location has stimulated local population growth, property development, economic activities, etc. Apart from urban development, rural development such as agricultural farms to produce rice and sugarcane were also promoted in the rural areas in Central Luzon due to its natural advantages of having fertile soils and river channels.

The new CLLEx expressway traverses existing roadways, as well as rural areas where local rivers and farm roads intersect the CLLEx alignment. To minimize interruptions to the local communities and economic activities, abutment embankments are constructed for overpass bridge structures.

3 SOIL PROFILE

The subsurface soil profile along the length of the CLLEx varies from place to place. The poorest soil condition consists mainly of soft clay layer varying in depth from 2 m to 8 m, whereas some other areas consist of a thick liquefiable fine sand and/or sand and clay mixture layer. The soft clay has an overconsolidated surface crust in the region above the ground water level (GWL). Under this upper soft clay layer is a medium stiff silty clay stratum followed by dense sand layer.

In many locations the ground surface is fully saturated with high ground water table, resulting in a low undrained shear strength (c_u) of 20 kPa near the ground surface increased to

30 kPa at 8 m depth of the soft clay layer with an increasing cu-rate of change of 1 kPa/m along the depth. Under the 8 m depth of soft clay, the cu increased from 30 kPa to 70 kPa over 12 m depth with a higher increasing cu-rate of change of 2.667 kPa/m along the depth. Figure 2 shows the overall soil profile for ground treatment design throughout the CLLEx project.
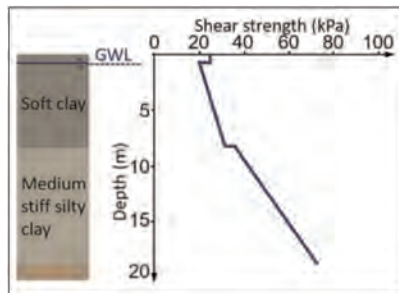
Figure 2.   Overall soil profile adopted for ground treatment design throughout CLLEx project.

4   EMBANKMENT DESIGN

When soft clay foundation is loaded with embankment fills during construction, the soil deforms over time, mobilizing shear resistance that helps to support the load applied (Yee 2005). The lateral earth pressure from embankment fills exerts an outward shear stress to the foundation, lowering the bearing capacity of the foundation (Jewell 1996). At the same time, the soft foundation may experience significant vertical deformation that mainly caused by the self-weight of embankment fill added onto the foundation. If post construction settlement of embankment is neglected, pavement failure due to excessive differential settlement of the embankment may happen.

The reinforced embankments in CLLEx project varying in height from 5 m to 7 m. The embankment side slope has a gradient of 1 vertical : 2 horizontal proposed with hydro-seeding at the end of construction to facilitate green facing. Figure 3 shows the typical cross section of the reinforced embankment in CLLEx project.

The contribution of geotextile reinforcements in improving embankment stability over soft soil is determined first in terms of stress and force equilibrium, follow by deformation and failure mechanisms (Jewell 1996). Two design approaches were adopted for the reinforced embankments in CLLEx, which are the bearing capacity improvement design and settlement design respectively.

Due to confidentiality of the project, the detail design and calculation performed for the reinforced embankment will not be discussed in this paper.
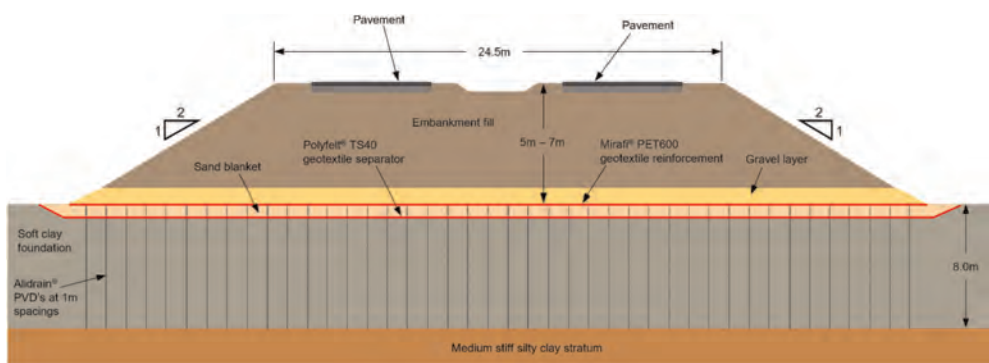
Figure 3.   Typical cross section of the reinforced embankment in CLLEx project.

4.1 Bearing capacity improvement

For bearing capacity improvement, the reinforced embankments were designed using the limit state design in accordance with BS8006-1 2010 for the internal stability, whereas the external stability was checked using limit equilibrium method. To enhance the bearing capacity of the reinforced embankments during construction stages, geotextile reinforcements were proposed to lay across the entire embankment base, providing the tensile capacity required to achieve a safety factor of minimum 1.5 as per project requirement.

A minimum design life of 60 years is required for the reinforced embankments. Hence, a long-term design strength based on 60 years design life of the PET high strength woven geotextile reinforcements was considered in the analysis. The long-term design strength of geotextile reinforcement can be derived using Equation 1 below:

$$T_D = \frac{T_u}{f_{cr} \times f_{id} \times f_{en}} \tag{1}$$

where, T_D is the long term design strength of the geotextile reinforcement; T_u is the initial tensile strength of the geotextile reinforcement; f_{cr} is the material reduction factor relating to creep effects over the required life of the reinforcement; f_{id} is the material reduction factor relating to installation damage of the geotextile reinforcement; and f_{en} is the material reduction factor relating to environmental effects over the required life of the geotextile reinforcement.

Based on the calculations, a geotextile reinforcement with minimum characteristic initial tensile strength of 600 kN/m is required. The Mirafi® PET600-50 high strength woven geotextile reinforcements having tensile strength of 600 kN/m in machine direction and 50 kN/m in cross-machine direction is adopted in this project. Refer Table 1 for the long-term design strength of PET600-50 high strength woven geotextile reinforcements.

Table 1. Long term design strength of PET600-50 high strength woven geotextile reinforcements.

Property	Unit	PET600-50
Characteristic initial tensile strength (machine direction)	kN/m	600
Material reduction factor – creep effect	1.41	
Material reduction factor – construction damage	1.10	
Material reduction factor – environmental effects	1.03	
Long-term design strength (60 years)	kN/m	376

4.2 Settlement calculation

For settlement design, primary consolidation theory was applied together with prefabricated vertical drains (PVDs') design to calculate the accelerated settlement within an acceptable waiting time.

A settlement design with PVDs' was carried out to determine the waiting time required for ground consolidation to achieve a total 1 m depth of settlement at site. With a design PVDs' spacing of 1 m apart in triangular pattern down to 8 m installation depth together with 2 m high of surcharge fills, a settlement up to 1 m were expected over a duration of 5 months. The design was carried out by the Department of Public Works and Highway (DPWH) for the PVDs' ground treatment method.

5 EMBANKMENT CONSTRUCTION

The construction of embankments began with removal of any vegetation, rock particles and/ or debris on the existing ground that may protrude or damage the geotextile. Ground levelling

was then carried out to prepare an even surface for the laying of separator geotextiles. After the separator geotextiles are laid, a 500 mm thick sand drainage blanket was directly placed on top of the geotextiles (see Figure 4), used to remove the excess pore water pressure at the base of the embankment at the same time serve as a stable working platform for the PVDs' installation machines. After the PVDs' had been installed, PET high strength geotextile reinforcements were laid in a continuous length across the embankment width in the principal direction. The geotextile reinforcements were joined together with adjacent panels onsite with double stitching J-seam method, to provide an overall coverage at the base of the embankments. Subsequently, a 1m thick gravel layer was placed and compacted on top of the geotextile reinforcements (See Figure 5). The gravel and embankment fills were well compacted to 95% Standard Proctor as per the project requirement. Lastly, the expressway pavement structures were then constructed on top of the completed embankments, with side slopes of the embankments hydroseeded to provide vegetation growth. Figure 6 shows the CLLEx completed with pavement constructed on top of the reinforced embankment.

Figure 4.   Placement of drainage sand blanket layer prior to placement of geotextile reinforcements.

Figure 5.   PET high strength geotextile reinforcements laid with principal strength direction across the embankment, followed by placement of gravel layer on top.

The installation of geotextile reinforcements which supplied in roll form are relatively easy to construct compared to other methods. Despite that, detailing such as jointing between geotextile panels and laying direction are critically important during installation, to ensure the functionality of geotextile reinforcement in bearing capacity improvement.

Figure 6.   The CLLEx completed with pavement constructed on top of the reinforced embankment.

5.1 *Jointing*

The two common jointing methods used in geotextile laying are overlapping and seaming methods. Selection of jointing greatly depends on the practicality and appropriateness of using overlap under specific site condition, as well as the comparative costs incurred between overlap and seaming. In general, seaming may be more economical than overlapping in term of geotextile material quantity, especially when the ground is very soft says CBR is less than or equal to 1 % where large ground movement is expected, large overlapping distance up to 1 m may be required. Nevertheless, seaming is usually more time consuming than overlapping due to the on-site stitching process thus increasing the labor cost.

With conservative approach, a J-seaming method was used to join the geotextile reinforcement panels together in this project, ensuring a well coverage of the geotextile reinforcements along the base of the embankment.

5.2 *Laying direction*

The geotextile reinforcements are generally manufactured with principal strength direction along the roll direction, whereby the laying direction must be corresponded to the principal stress direction in the reinforced embankment. In this case, the PET high strength woven geotextiles are laid with principal strength direction across the embankment to enhance the bearing capacity of the soft foundation.

6   CONCLUSION

A successful case study of using PET high strength woven geotextile reinforcements for soft ground bearing capacity improvement and PVDs' for accelerated soft ground consolidation was discussed in the paper. Both reinforcement and settlement consolidation mechanism are equally important for an embankment constructed over soft foundation to ensure the long-term performance of the infrastructure constructed on top.

REFERENCES

BS 8006-1 2010. *Code of Practice for Strengthened / Reinforced Soils and Other Fills*. London: British Standards Institution (BSI).
Jewell, R.A. 1996. *Soil Reinforcement with Geotextiles*. London: Construction Industry Research and Information Association (CIRIA).
Yee, T.W. 2005. Ground Improvement with Geotextile Reinforcements. *Ground Improvement Case Histories* 28: 813–828

Five decades of combined knowledge on geosynthetic clay liners

B. Herlin
Terrafix Geosynthetics Inc., Canada

K. von Maubeuge
Naue, Germany

ABSTRACT: The authors of this paper have over five decades of combined knowledge on Geosynthetic Clay Liners (GCLs). This paper will cover both the engineering and performance capabilities of GCLs but also provide readers the dos and don'ts experienced by the authors over the course of their work exposure while working on GCLs on various projects worldwide since the early 90s. Kent von Maubeuge has been directly involved with GCLs since the early 90s when needlepunched GCLs were entering the market and has seen the growth of this geosynthetic material used on various applications while providing assistance on various research studies and testing done on GCLs over the course of the last three decades. Bruno Herlin has been directly involved with GCLs since 2000 with the direct responsibility of overseeing GCLs for his organization and has witnessed what, where, when, who, and why a GCL should be used and how they should be used but also the dos and don'ts of their installation techniques. The paper will also cover the myths of GCLs. Both authors have had a history of sharing information between themselves on GCLs over the last two decades and are now going to share this information for the next generation to have in their GCL 'bag of tricks' to avoid mistakes made in the past but to also feel confident that GCLs do indeed work and can performance effectively as a proven barrier.

1   INTRODUCTION

Geosynthetic Clay Liners (GCLs) began in the 1980s as a simple thin layer of bentonite sandwiched between two textiles with little to no connection between the two textiles. Into the late 1980s and early '90s, manufacturers started to stich bond and/or needlepunch (patented by Naue GmbH & Co. KG in 1987) the upper textile with the bottom textile while interlocking the bentonite between the two textiles to allow the use of GCLs in slope applications. These GCLs are called multi-directional, shear-strength transferring hydraulic barriers. Later the stitch-bonding was added as a method of interlocking the two geotextile layers together. However, the stitchbonding only transferred shear strength in the direction of the stitch-bonding. Over the decades since, GCL manufacturers have provided various types and grades of GCLs by either increasing or decreasing the top and bottom fabric thickness, used various amounts of bentonite, added polymers to the bentonite for added chemical reaction protection to the bentonite and/or to lower the permeability capabilities of the bentonite itself. In the past couple of decades, manufacturers have added lamination thin polymeric geomembranes and/or coated polymeric geofilms to one geotextile side of the GCL - the bottom fabric textile., These GCL types also are known as multi-component GCLs, to not only provide an additional protection to the bentonite layer but also to expand the use of GCLs in various complex applications to ensure a low permeability is provided while long-term performance is upheld.

A special GCL worthwhile to note is a special bentonite composite lining system featuring an additional sand ballast layer that is integrally encapsulated by needle-punched nonwoven geotextiles. The sand layer performs several functions which includes ballasting this special GCL from floating when installed under water - even where there are high water currents, or turbulences caused by ship propellers (however, it should be noted that GCLs do not in theory float due to the shear weight of the material – the bentonite). Due to the needle-punching of the GCL, the sand layer also has the effect of providing a counterpressure to the natural swelling properties of the bentonite, providing more uniform activation of this layer. Consequently, this GCL can remain underwater without additional load or cover for longer periods of time - without loss of performance. During the subsequent placement of stone or other covering layer, this integrated sand ballast layer evenly distributes the load and prevents installation damage to the product.

GCL manufacturers continuously provide new types of GCLs due to design engineers requesting additional safety factors in their project lining designs. It should be noted that new GCLs are not being created because the original GCLs are not working (they are working) but are being made based on new research findings but also as mentioned, due to complex applications that GCLs are being used in to provide additional safeguards to protect our environment.

2 GCL APPLICATIONS

In environmental critical applications GCLs are used in combination with a geomembrane (HDPE/LLDPE) liner as a composite liner system in e.g., landfill base and caps or mining applications. However, they can also be used as a single liner in landfill cap applications, pond lining opportunities, and various other applications where any type of low permeability liner is required, typically to replace a compacted clay liner or low permeable soil. When used as a single liner, GCL type and selection is critical depending on the application, site conditions, possible weather elements, and experience of the contractor with or without previous lining deployment experience. Not every GCL is alike and some GCLs can withstand physical abuse while lower grade GCLs are unable to withstand conditions beyond those provided in the installation guidelines set out by various GCL manufacturers.

2.1 Ponds

When using a GCL in a pond application with soil cover (e.g., not with concrete), the following three rules must exist before using a GCL as a liner. The pond area must be at least 2,000 square metres in size, the slopes must be no greater than 2.5(H):1(V), and the cover soil thickness over the GCL must be 0.3 m (better 0.5 m) at minimum. GCLs are a great liner selection for Stormwater Managements Ponds (SWM Ponds), golf course ponds, and recreational ponds and lakes when the proper type of GCL is selected depending on the subgrade conditions on site during time of deployment. Anchor trenches for the GCL liner are required when used in slopes of greater than 7(H):1(V) to ensure no movement of the liner during cover soil placement, especially when the cover soil operations are being done from the top of the pond to the bottom of the pond (preferred cover soil installation guidelines state that the cover soil operations over the GCL liner be done from bottom to top of the liner, however in some pond application projects, the cover soil material source is located outside the pond hole cavity).

2.2 Pond size

As mentioned above, a GCL is a great liner selection to line a pond if the size of the pond is greater than 2,000 square meters in size. Do not use a GCL if the pond is smaller than

2,000 square metres in size. Why? The GCL requires one foot of cover soil. Most small ponds less than 2,000 square meters in size have slopes greater than 2.5(H):1(V) and will not be able to keep and maintain the minimum 0.3 m cover soil thickness that the GCL needs to act as a liner. The bentonite inside the GCL needs weight to act as a liner. The more weight (e.g., 0.5 m), the lower the permeability, hence the better for the GCL to act as a liner.

Small ponds require greater attention to detail and to be honest most contractors and installers sometimes do not read nor pay attention to lining installation guidelines provided by GCL manufacturers. Pond lining areas greater than 2,000 square metres offer the GCL a proper gentle slope subgrade to rest on and the 0.3 m cover soil minimum thickness required for the bentonite in the GCL to act as a liner. This 0.3 m minimum confining stress is needed to prevent the GCL of free swelling and likely loosening the internal shear strength of the needle punched fibres.

2.3 Subgrade conditions

When selecting a GCL type for a pond application, the subgrade conditions must be known prior to a GCL being deployed. A subgrade for a GCL liner (any liner for that matter) must be dry and well compacted for a low-grade type of GCL to be used (a low grade GCL being where the bottom fabric of the GCL is only a woven fabric). Subgrade conditions in pond applications are rarely dry and well compacted. In conditions where the subgrade is wet and soft, the GCL selection type should be a higher grade GCL. The authors of this paper highly recommend that the GCL in pond applications must be a double-nonwoven GCL where the bottom non-woven must be scrim-reinforced (having the presence of a woven fabric). Double nonwoven scrim-reinforced GCLs are far more robust that GCL that only have a simple woven bottom fabric. Double nonwoven scrim-reinforced GCLs can withstand weather events and maintain their high peel strength values than lower grade GCLs. Weather conditions such as rain and snow on uncovered GCL sheets/rolls can severely affect the strength of low peel strength GCLs versus GCLs that have a high peel strength. Double nonwoven scrim-reinforced GCLs as mentioned with their original manufactured higher peel strength can be left exposed for longer periods prior to cover soil placement. In areas where precipitation will be and/or is an issue then multi-component GCLs should be used with the geofilm/coating portion of the GCL being placed facing up to avoid having the bentonite to be hydrated prior to soil confinement over the GCL.

In applications, where the subgrade is a coarse material, e.g., gravel, it is recommended not to use a stand-alone GCL, as likely under high hydraulic gradients (high water heads in the pond) can cause bentonite piping and therefor weakening the barrier performance of the GCL. In applications with high water heads (approx. > 1m and gravely subgrades) a multicomponent is the best option for a barrier system. Never use a double nonwoven GCL that isn't scrim-reinforced in hydraulic head conditions. Always use a double nonwoven GCL where the bottom fabric nonwoven is scrim-reinforced, hence a scrim-nonwoven bottom fabric – already mentioned, however being repeated herein again, since both authors have seen failures of double nonwoven GCLs where the bottom fabric did not contain a woven (scrim).

2.4 Slopes (pond applications)

GCLs can be used in steep slope applications and certain GCLs can be used in vertical applications, however when used in pond applications, do not use a GCL as a pond liner when slopes are greater than 2.5(H):1(V). GCLs need confinement, the overlaps in GCLs need confinement, and as such will not act as a liner in pond applications where the slopes are too steep. The 0.3 m minimum cover soil placement is required over the GCL to act as a ballast for the bentonite in the GCL to act as a low permeability liner.

2.5 *GCL selection*

When a geosynthetic liner is required on a project, sadly some design engineers will just add a line in their drawings with a mention that a liner is required with no specific details provided. If a GCL is required and used, the specifications will sometimes simply say 'GCL is required' with nothing more provided. GCLs come in many forms since they were created in the 1980s. The top fabric of the GCL (usually a nonwoven fabric) can be supplied in various weights. The bentonite sandwiched between the geotextiles can be supplied in different amounts of kilograms per square metres, the bentonite can also have an enhanced polymer added to protect the bentonite from various liquids that might attack it in a particular application or just improve poor bentonite quality. The bottom fabric of the GCL can either be a single geotextile or contain more than one geotextile as well as having a geofim added to the geotextile(s). It is the authors opinion that all GCLs should have a scrim-nonwoven geotextile as a bottom fabric in a GCL. Double nonwoven scrim-reinforced GCLs provide not only a more robust fabric than a simple nonwoven or woven fabric but they provide a high resistance to internal bentonite erosion in high hydraulic head conditions compared to bottom single geotextile GCLs. Having a bottom scrim-nonwoven fabric GCL also provides an added safeguard to poorly prepared subgrades on a construction site. Double nonwoven scrim-reinforced GCLs also provide a higher peel strength retention when a GCL is involved in bad weather conditions during deployment/exposure prior to cover soil placement and/or other geosynthetic materials applied over it.

3 ADVANCEMENTS IN GCLS

Over the last decade, coated GCLs (multi-component GCL) have been selected over standard GCLs since they provide an added safeguard on projects against badly prepared subgrades and/or harsh working conditions. It should also be mentioned that coated GCLs should not be said to be the same as membrane added GCLs. Membrane added GCL (laminated multi-component GCL) are glued to a GCL and hence have an added angle of friction that should be dealt with and/or paid attention to. Additionally, nothing sticks in the long-term to an PE laminated membrane, so that during the project life-time this interface can become the critical interface in a slope and worse, create a downhill sliding of the cover soil A coated GCL is a melted polypropylene or polyethylene that becomes an integral part of the bottom fabric and hence does not contain an added slip zone to deal with when used in slope applications. However, coated GCLs should undergo a friction angle test to determine the friction of angle between the coating and the adjacent subgrade and/or cover soil material if the coated side of the GCL is facing up during installation. Some project engineers and/or project site can gain an advantage by having the coating facing up due to various conditions that may present on a particular site/project.

3.1 *GCL myths*

GCLs are easy to deploy, too easy in fact, hence 'one should not use them' has been heard many times as a manufacturer of GCLs. They are indeed easy to deploy, and no experience is required to deploy them. When to use an unexperienced geosynthetic deployment contractor and when to use one with an extensive experience is all based on the application that the GCL is being used in. For example, deploying a GCL in a large pond/lake application doesn't necessarily require a contractor with GCL experience. The GCL manufacturer or distributor can provide initial assistance. Other applications such as a GCL being used along with a geomembrane in a composite lining system in a landfill application should require an experience geosynthetic contractor since the project is deemed to require more attention to

details when dealing with liquid leachates. However, overall, a GCL deployment does not require much experience whatsoever. It only requires a contractor who cares about their workmanship to follow GCL deployment guidelines and understands the principle and concept of a GCL.

3.2 Winter deployment myths

Can a GCL be deployed in the winter? A question that is heard every winter for the last 4 decades. A GCL that is made with a dry bentonite of less than 12% moisture content can be deployed in the winter without any concern to the performance of the GCL. Geotextiles are dry and are widely used during the winter without concerns. Hence the only other item of concern is the bentonite itself. If a GCL is manufactured with a dry bentonite and remains dry prior to deployment as it should, there should then be no concerns once installing the dry GCL under cold winter temperatures. GCL material selection should also be considered if it known that the GCL will be deployed in the winter in harsh conditions and with a badly prepared subgrade. Design engineers should select a higher grade GCL such as double nonwoven scrim-reinforced GCL if deployment will occur in the winter to ensure an added safeguard to the performance of the GCL. There's no doubt at all that double nonwoven scrim-reinforced GCL are more robust than the standard nonwoven(top)/woven(bottom) GCLs or a double nonwoven GCL that lacks a scrim-reinforcement.

Figure 1.   Winter deployment and GCL rolls being stored over the winter until deployment. A GCL made with a dry bentonite can be stored without any concern over the winter season outside until required for deployment.

3.3 Can one drive over a GCL?

GCL guidelines state that one should not drive directly over a GCL. However, if the GCL is made with dry bentonite then one in theory can drive directly over the GCL without concern compared to a GCL made with a wet paste bentonite. Any load applied over a wet paste bentonite GCL will in fact squeeze the bentonite away at the point in contact and in fact offer a GCL without any bentonite at the point of contact. Hence one here should also inform themselves if they have a GCL made with a dry bentonite or one with high moisture (wet) bentonite. ASTM 6102 is also very specific on this: "Although direct vehicular contact with the GCL is to be avoided, lightweight, low ground pressure vehicles (such as four-wheel all-terrain vehicles) may be used to facilitate the installation of the overlying geosynthetic. It is recommended that a test pad be constructed on a site-specific basis to evaluate the feasibility and effect of direct vehicular traffic."

3.4 Can a GCL be deployed in water?

A GCL should always be deployed in dry conditions, however construction sites are never timed according to perfect weather conditions. If the application of a GCL is for a pond application, then one can deploy a GCL in stubborn groundwater without any concerns if the appropriate GCL is used in such conditions. One requires that the GCL will maintain a high peel strength when fully submerged in water, i.e... use a double nonwoven scrim-reinforced GCL.

Figure 2. Fully hydrated and/or stubborn groundwater GCL applications in Dyke and/or Canal and/or Pond Applications. Double nonwoven scrim-reinforced GCL being deployed. These GCLs are more robust to installation stresses, have a higher peel than other low grade standard GCLs, and are more weather resistant.

3.5 Is bentonite mass per unit area important?

This answer must immediately be answered with yes. While the GCL permeability of a GCL with a low bentonite mass per unit area (approx. less than 3,500 g/m^2) can be the same as a high bentonite mass per unit area (approx. 3,600 – 8,000 g/m2) the flux value is directly influenced by the bentonite mass per unit area (von Maubeuge *et al*. 2014). GCLs with more bentonite mass per unit area have lower flux values, basically a lower amount of water flowing through the GCL as it is thicker. Therefore, it is recommended to specify GCLs, as recommended in GRI-GCL3 with a minimum mass per unit area of 3,600 g/m^2 at 0% moisture content.

3.6 Buyer beware

Too many times a low grade GCL is used and/or specified on a project where a higher grade GCL should been used instead. GCLs used in vertical applications should never be a low grade GCL (for example: Nonwoven/woven GCL). Vertical applications require a GCL that have a high peel strength (for example: Nonwoven/Scrim-Nonwoven GCL). Never use a double nonwoven GCL unless the bottom the bottom fabric of the GCL is scrim-reinforced, i.e... a scrim-nonwoven. Using a double nonwoven GCL with a scrim-reinforcement can lead to an internal erosion of the bentonite if the subgrade is badly prepared. Water pressure will force the bentonite out through the nonwoven fabric, whereas a scrim-nonwoven bottom fabric in the GCL can withstand a much higher hydraulic head without failure. Failures of double nonwoven GCLs (GCLs that do not contain a scrim) have been known in pond applications over the years. (Scrim = woven).

Needlepunched GCLs have had four full decades of research review and successful deployments, however from time to time a few deployments have gone wrong but for known reasons (no cover soil applied over the GCL for weeks/months following deployment). Installation guidelines are provided and are sometimes not followed. When guidelines are

available due to the unique application in which the GCL is being used, the manufacturers should be contacted to ensure that the GCL selected is the proper one. Too many times a GCL distributor and/or a project specifier will supply a low grade GCL for a project that requires a higher grade GCL (for example: Steep slopes where a low peel GCL is being used). High grade GCLs include coated GCLs and/or where enhanced protective polymers are added to the bentonite to protect the bentonite from being chemically attacked and/or to provide a long-term low permeability performance from the GCL. Going forward some GCLs will be made with higher grade geotextiles.

With needlepunched GCLs currently in their fifth decade of use, research of new higher grade GCLs is currently underway to ensure that our environment at large is protected from these unique thin liners that have over and over shown that they do indeed work and perform as required. However, ensure the proper GCL is being used and that installation guidelines are followed. As with all geosynthetic liners, they can and will perform as intended, however from time to time they are promoted with an exaggerated performance for only a sale to be made without any testing reviews (for example: Shear box testing and/or puncture testing). Geosynthetic Clay Liners come in various forms as mentioned, different types of geotextiles, different amounts of bentonites sandwiched between textiles, coated & geofilm added, enhanced polymers, and at different peel and tensile strengths. All can be supplied for various different applications and requirements, however the bulk of GCL specifications continue to be GCL products made in the 1980s. Needlepunched GCLs have advanced in the last decades since their inception. Unfortunately, as mentioned, some engineers and designers still see lining requirements as an added line in their drawings without doing a full review of what is currently available from manufacturers, a full four decades from where they started.

REFERENCES

ASTM 6102
GRI-GCL3. 2016. *Standard Specification for Test Methods, Required Properties, and Testing Frequencies of Geosynthetic Clay Liners (GCLs)*. Folsom, PA, USA: Geosynthetic Institute.
Von Maubeuge, K., Ehrenberg, H.,, *Investigation of Bentonite Mass per Unit Area Requirements for Geosynthetic Clay Liners*", 12ICG, Berlin 2014.

Temporary working platforms full scale testing – review of valid methodology

K. Ria Zamara
Tensar Ltd, Blackburn, UK

C. Moormann
Stuttgart University, Germany

J. Kawalec
Silesian University of Technology, Poland

M. Wayne
Tensar Corp., Atlanta, USA

ABSTRACT: Globally temporary working platforms are an underrated element of almost every construction site. Geogrids have been installed in the temporary working platforms for decades now, as they offer contractors large cost, time and carbon savings compared to alternative solutions. The use of hexagonal, multiaxial stabilisation geogrids and square, biaxial geogrids is by far the most common method for the cost-effective solution. However, designing temporary working platforms using geogrids constitutes a challenge, as broadly available methods (e.g. BR470) present a conservative approach for incorporating geogrids in the designs that results in non-cost effective design. Moreover, geosynthetics manufacturers methods are validated only for specific manufacturers products (e.g. 45° load spread or T-value method). This paper discusses the importance of temporary working platforms design methods full scale validation and lists ideal site conditions for full scale validation tests. Also, it reviews recently undertaken site tests that aimed at testing temporary working platforms full bearing capacity and examining the design methods.

1 INTRODUCTION

To create a safe working surface for construction site plants, an accurately designed and adequately constructed temporary working platform is required. Most of site personnel is aware that using geogrids in their platforms brings costs savings due to the reduced amount of aggregate required for platform construction. It is not the only benefit, reduction of carbon footprint and time required to construct the platform are also significant when using geogrids.

The most widely known and utilised guidance on temporary working platforms design is BR 470 (2004), which was first published in 2004. At the time the guidance was required in the UK as a high number of site accidents was occurring, due to insufficient ground support for the site plants. Nearly 20 years after the guidance introduction in the UK, accidents on sites involving large construction machinery still happen, however only small proportion of them is associated with temporary working platforms performance.

Over the time the guidance gained a reputation of being conservative compared to other methods. Specifically, geosynthetics manufacturers challenged the approach of considering geosynthetic element in the calculation that BR470 endorses. The shortcomings relating to geosynthetic element consideration in the guidance was then reviewed and in 2011, an amendment was created to allow for other methods to be approved and accepted under BR470 requirements. This is, for example, where specific geosynthetics manufacturers design methods are permitted for use. However, BR470 guidance sets specific requirements for these methods before they get applied in real sites conditions, these are:

Objective of safety is preserved

Which means that any considered alternative method needs to be safe for use. It is obvious that risk reduction is the main purpose for installation of a temporary working platforms. Hence, appropriate safety measures need to be implemented within the method.

Based on credible and representative research

This aspect dictates that the method needs to have sufficient theoretical & technical consideration. It needs to be credible scientifically and academically.

Validation by well documented case studies

The alternative design method must be tested and validated in real scale before it can get applied in practice. The validation element of any new method is critical in providing evidence that the method works. Full scale validation of a platform is not an easy task. To fully validate a design method, it is of importance to drive a platform to a full bearing capacity failure. This allows direct comparison of the design method against experimental results at failure. It also allows to quantify and verify required factor of safety.

Whilst there are various methods available to design temporary working platforms with variable level of credibility or applicability for use in this specific application (e.g., not recommended Ev_2 approach), BR470 clearly lists conditions that a method needs to fulfil before it gets utilised on an actual live project. This paper presents a range of recent approaches applied for full-scale testing of temporary working platforms.

2 VERIFICATION TESTING - REQUIREMENTS

Performing a site trial, test or an experiment on a full-scale platform is a challenging task. Some of the typical requirements for these tests include:

Homogenous ground conditions

Seams or layers of a quality or competent soil may contribute to results showing increased bearing capacity at the surface. To obtain unaffected results for design method validation, especially if the method is designed to consider only one subgrade layer, homogenous conditions are required

Deep soft deposits

Pressure applied at the surface has a limited influence on the deposits with depth. At certain depths the excess pressure becomes negligible. That depth is called 'zone of influence'. For practical reasons, zone of influence is typically considered as approximately: two to three times width of the load (2-3xB) applied at the surface (this is practical rather than scientifical consideration). On a trial project, homogenous subgrade deposits should extend deeper than the influence zone. This is to ensure that deep seated competent deposits do not provide extra strength to the overall performance of the system. Also, this allows to limit number of variables required in the back analysis of the results.

Soil strength

In addition, it is worth considering the strength properties required for the trial project. The stronger subgrade the more surface load will have to be applied to the platform surface to ensure generating sufficient deformations to achieve platform failure. In semi competent ground significant tonnage of load must be applied. This may not be practical or achievable due to site constraints. Then, on very soft subgrades stability and safety of testing equipment that won't affect the results must be considered.

Load source

Often, this depends on the contractor that is engaged in the project. The case studies reported in this article utilised four different sources of load: bespoke loading frame, pile testing reaction frame, large cranes counterweight, site plant (e.g. excavators) to provide sufficient counterweight. There is a balance that must be met, e.g: if the desire is to test a very soft subgrade with relatively thin platforms, it needs to be ensured that the platform can support the machinery and/structure that constitutes the reaction load. The thicker the platform the larger the plant/reaction load is required.

Load footprint

The surface load footprint and soil strength are the elements that influence degree of reaction load needed to fully test the platform. The footprint should realistically reflect footprint of typical site plant's track or outrigger size. For example, it is not adequate to run plate load test with 300mm plate and pressures at the level of 1.2 times the design load if the track width is 950mm wide and 4000mm long. However, using 600mm PLT with 600mm track width or a specific case might be considered suitable for 600mm wide drill rig track.

From the Author's experience, it is challenging to find a site with correct site conditions as many sites (e.g. in the UK) are covered by made ground with fairly competent properties (multi-layered subgrades), or subgrades with strength properties that will require considerable level of counterweight, that might be difficult to obtain from typical construction site machinery.

Resulting from this, each project requires careful consideration and analysis of construction and testing processes. Development of full bearing capacity failure in the platform will require considerable load and high deformation, therefore specialised equipment and broader technical consideration should address the above points to obtain valuable results.

3 FULL SCALE VALIDATION TESTING

Table 1 below presents a summary of large-scale tests undertaken for both commercial projects and full research projects. The purpose of the listed tests was to investigate

Table 1. Summary of full-scale temporary working platforms tests.

Project Name/ year performed	Country	Load Footprint & Max Load	Comment
Saskatchewan University 2019–2022	Canada	1m^2 square	Series of controls and stabilized platforms, Su 30-60kPa. Failure through excessive deformation
Wieringemier 2020	Netherlands	8m by 12m	Stabilised platform with 1m geocells on peat subgrade. Failure through excessive deformation.
University of Stuttgart 2019	Germany	5m by 6m 280 t	Reinforced platform 0.9m thick, qc<0.2MPa. Failure through excessive deformation (Moorman 2019)
Krakow Phase I 2022	Poland	1m DIA 1000kN @15%DIA deformation	Stabilised platform 0.25m thick Cu<60kPa. Failure assumed at @15% plate DIA deformation
Krakow Phase II 2022	Poland	1m DIA 460kN	1 x control, 3 x stabilised platform 0.3m–0.6m thick, Cu <20kPa Failure through excessive deformation
San Diego 2022	USA	0.610m DIA 198kN	Cu 16-24kPa. Failure through excessive deformation
Great Yarmouth 2022	UK	0.610m DIA 203kN- 539kN	Stabilised platforms thickness variable Cu – variable approx. 12kP and above No failure achieved

temporary working platforms bearing capacity. The below comprise tests undertaken on all: non stabilised, stabilised, and reinforced platforms.

The Saskatchewan University, Krakow, San Diego and Great Yarmouth tests where run to support and verify compatibility of the T-value design method (Lees *et al.* 2019) for TriAx and InterAx products only. These tests were performed to ensure design method compatibility with the stabilising geogrids installed in the tested temporary working platforms. To Author's knowledge both novel and traditional temporary working platforms design methods for geosynthetics, require verification of compatibility of the methods with a proposed geosynthetic. Considering variety of geosynthetic products available on the market, it is not safe to replace a product with another one that has not gone through rigorous testing and validation process. Such instances may result in undermining safety of the given design.

3.1 *Saskatchewan University, Canada 2019-2022*

Tensar Ltd in cooperation with Saskatchewan University performed validation testing of the T-value temporary working platforms design method (Lees 20019). The site in the Saskatoon Region, Canada was underlaid by weak soils. A layer of more competent crust had to be removed from the site.

A purpose-built temporary bridge (with loaded trucks), was used to create a reaction weight. The plate comprised a steel square 1m by 1m. Several tests were undertaken for the purpose of failing the platform and investigating its full bearing capacity. For each testing location the temporary bridge had to be relocated. Figure 1 (Left) shows the generic set up of the test. Trench that was excavates and marks of the previous tests – square mark on the ground surface in front of the temporary bridge. Figure 1(right) shows the view of the plate used in the test.

Figure 1. Saskatchewan University full scale temporary working platforms testing (Left: general set up, right: platform after the test).

3.2 *University of Stuttgart, Germany 2019 & Wieringemier, Netherlands 2021*

By far an ideal validation for design method comprises a test that replicates the load, contact pressures and footprint that correspond with the actual site project parameters. Large research project was led by Stuttgart University (Moorman 2018). This investigated performance of platforms, examined number of design methods, validate design assumptions, and provided important site observations.

The test was run utilising large timber crane mats stacked in two layers with second layer being installed perpendicular to the bottom layer for better load transference through the layers of the matts. In addition, these tests utilised cranes steel counterweights (made of cast iron) – which is typically used by large cranes to increase their capacity.

Figure 2. Stuttgart University full scale temporary working platforms testing (Moorman 2018).

It is not uncommon for large windfarm projects to conduct a 'routine' validation test of the temporary working platforms designs. That was the origin of the tests undertaken at Wieringemier project in Netherlands 2019 (Figure 3). Developments in wind industry leads to larger and heavier equipment being installed to construct a wind turbine. This leads to designs of temporary platforms that have to withstand excessive surface pressures (e.g. STOWA 2019).

Figure 3. Wieringemier project – general view of the full-scale test.

The Authors are aware of mats up to 8m dimension (timber, steel/iron or concrete). However, it is recognised that when increasing mat dimension (under e.g., 1.2m width track), the effectiveness of the load spread may decrease significantly. Similarly, when using too thin steel plates. Aim of the large mats is to distribute the load over a larger footprint which will reduce the surface pressures. However, if they are too thin, they may start flexing and their efficiency drops.

3.3 Krakow Phase I & II, Poland, May & September 2022

The two phases of tests undertaken in Krakow, Poland 2022, utilised piles testing equipment. The testing equipment comprised a loading frame that is mounted to reaction piles or column (Figure 4 left). Here, each tested platform had installed four DSM columns that allowed capacity of up to 2MN of reaction load to be applied on the platform. The tests in

Figure 4. Left: Reaction frame; Right: Load cell.

Poland were performed on uniform subgrade 6m of natural deposits with Cu values of approx. 60kPa for the Phase I, however Phase two included 4 sections in another location with subgrade strength of Cu< 24kPa. This comprised perfect conditions for this type of testing (addressing all requirements from Section 2).

3.4 *San Diego, USA 2022 & Great Yarmouth, UK 2022*

By far the most cost effective and easy to arrange are standard Plate Load Tests (PLTs). These are readily available across the European continent, less popular outside of it. The main drawback of these tests, however, is that these tests are typically performed using 300mm DIA plate. It is well recognised that to test temporary working platforms' ultimate bearing capacity larger plates are required. In the UK or Germany common sizes are 762mm DIA, France 600mm DIA, which depending on a case may be considered acceptable. The size of the plate should reflect at least the width of the track of the plant that is to utilise the platform. Most common widths of piling rig tracks and construction sites tracked cranes start at approx. 400mm and can go as far as exceeding 1.2m–2m. Further timber/steel mats (called crane mats, bog mats or load spread mats) can reach dimensions exceeding 2m.

Figure 5 presents San Diego USA 2022 PLT using 0.610mm DIA plate. Note that PLT testing equipment was not adequate for testing using low chassis of the excavator. There was

Figure 5. Left: Sand Diego USA 2022 PLT test; Right: Great Yarmouth, UK 2022 PLT.

not sufficient clearance for the testing hydraulic jack to be installed between the plate and the excavator. Hence, small berms had to be constructed to create a clearance for testing apparatus. This type of a solution is not ideal, as this adds complexity to the back-analysis of the results. The berms comprise a surcharge to the sites that adds a degree of additional capacity to the platform. Careful back-analysis needs to be undertaken to consider the effect on design calculations validation.

4 CONCLUSIONS

This paper provided a review of recent large-scale tests on temporary working platforms. Whilst many methods exist to design a temporary working platform (e.g. TWf 2019, Moorman, 2018), there exist very little data to evaluate their accuracy. There exist even less information specifically investigating full scale performance of platforms using stabilising or reinforcing geogrids. This article highlights current industry and research state-of-the-art methods for new and old design methods validation. It should be recognised that introducing a new design method, or a new geosynthetic product to already calibrated method (e.g. T-value method) or novel consideration for a design method (e.g. non-conservative properties to existing methods e.g. BR470), a full scale verification needs to be undertaken to evaluate the systems response to the proposed changes and to ensure safety of the design. The full-scale experiments allow back analysis and verification of factors of safety resulting from more optimal designs. Temporary working platform act as a composite system, with elements i.e. subgrade, geosynthetic element, aggregate and surface pressure interacting in micro and macro-scale. To introduce efficiencies in one element of the analysis, the response of the whole system should be verified in a full-scale setting.

REFERENCES

BR470 2004. Building Research Establishment, 2004/2007. *Working Platforms for Tracked Plant: Good Practice Guide to the Design, Installation, Maintenance and Repair of Ground-supported Working Platforms* (BR 470) IHS BRE Press, Bracknell, Berkshire, ISBN 186081 7009.

Lees, A, Matthias, P, 2019. Bearing Capacity of a Geogrid-stabilised Granular Layer on Clay. *Ground Engineering* 10 October, 2019.

Moormann, C., 2018. *Tragschichten für Arbeitsplattformen von Mobilen Baumaschinen und für Kranstellflächen. AiF. Forschungsnetzwerk Mittelstand – Abschlussbericht.* IGF-Vorhaben NR. 18833 N/1 (Research report, in German).

STOWA, 2019. Crane Hardstands for Installation of Wind Turbines. Publicaties van de STOWA kunt u bestellen op www.stowa.nl ISBN 978.90.5773.843.2.

TWf, 2019. Working Platforms Design of Granular Working Platforms for Construction Plant. A Guide to Good Practice. Published by Temporary Works Forum, c/o Institution of Civil Engineers, One Great George Street, London, SW1P 3AA, England.

Case study of the use of a piled embankment system with geosynthetic as reinforcement for soft soil subgrade at the Kadusirung Flyover's approach slabs, Banten, Indonesia

N.A. Anindita, D.A. Nurjannah, F. Widhiastuti & D.S. Harninto
P.T. Geoforce Indonesia, Central Jakarta, Indonesia

ABSTRACT: This paper presents a case study of piled embankment system with geosynthetic as reinforcement for soft soil subgrade at the Kadusirung Flyover's approach slabs, Banten, Indonesia. The embankment was reinforced with GSRW (Geoforce Segmental Retaining Wall) system with height of up to 9 metres. GSRW is a retaining wall construction that consists of a compacted layer of backfill and has a facing made of precast concrete and reinforced using polyester strip. Due to the low bearing capacity of the subgrade, piled embankment with geosynthetic system was chosen to reinforce. To help transfer load to the pile and to consider the soil arching ratio, a combination of small pile cap and high tensile strength geogrid was used. From design perspective, the system improves safety factor above the criteria stated in Indonesian National Standard for Geotechnical Design Requirements which is above 1.50 and design with pseudostatic earthquake load which is above 1.10.

1   INTRODUCTION

The construction of the Kadusirung Flyover's approach slabs in Banten, Indonesia will span up to 185 meters and will be carried out as high as 9 meters. The construction of the flyover will be done on soft soil subgrade. The approach slabs' embankment will be reinforced using Geoforce Segmental Retaining Wall (GSRW). This structure's technology combines concrete facing and polyester strip as a locally sourced reinforcement and is anchored from the facing to the body embankment according to the design calculations. Soil investigations results such as SPT drill showed that the subgrade is dominated by soft soil approximately until the depth of 11 meters. The piled embankment system was then selected as the subsoil's reinforcement. Using geosynthetic, geogrid material can be incorporated as the load transfer platform by reducing the pile cap's dimension.

Figure 1.   Kadusirung Flyover, Banten, Indonesia.

2 APPROACH SLABS EMBANKMENT'S REINFORCEMENT USING SEGMENTAL RETAINING WALL SUPPORTED BY PILED EMBANKMENT SYSTEM WITH GEOSYNTHETIC REINFORCEMENT AS LOAD TRANSFER PLATFORM

2.1 *Geoforce segmental retaining wall*

This flyover used Geoforce Segmental Retaining Wall (GSRW) as the approach slabs' embankment reinforcement. GSRW is an earth retaining wall system that consists of layers of compacted backfill material and facing element made from high quality precast concrete, also reinforced with belt or known as GI-Strip. The distinction between GSRW and other product lies in the robustness of the structure which has been tested, the competitiveness of the price compared to the similar segmental product, the fast and easy installation of the structure that affects the time efficiency of the project, and the aesthetic aspect that capable of adding the enticing aspect of the constructed segmental system.

The GSRW system is reinforced with the friction belt made out of high tenacity polyester yarn namely GI-Strip. The strip has been specially designed to generate reinforced belt with high tensile strength and friction coefficient. This component is what makes the structure robust. The selection of the tensile strength type is adjusted with the design calculation from the GSRW construction which will be built. Another advantage from GI-Strip is the high durability of the material, resistance from organic bacteria and acidity from the backfill material. The GSRW system is shown in Figure 2.

Figure 2.   Construction of geoforce segmental retaining wall system.

2.2 *The piled embankment system combines with geosynthetic reinforcement*

Piled embankment system is one of soil improvement technique that can minimize massive settlement problem. This system is done by installing piles that reaches into certain depth and space depends on load, subsoil type and take advantage of geosynthetic's tensile strength to reduce the need for large pile caps and raking piles. According to The British Standard "Code of practice for strengthened/ reinforced soils and other fills" (British Standards Institution 1995) the general idea of geosynthetics reinforcement utilization can be understood through the soil arching mechanism. This way, the load that is acting on the soft soil will be transferred to the piles by tension in geosynthetics. This mechanism is used to determine the required tensile strength of the geosynthetics. The construction of piled embankment system combines with geosynthetic reinforcement is shown in Figure 3.

Figure 3. Geosynthetics reinforcement scheme in piled embankment system.

3 DESIGN METHODOLOGY

3.1 *Geotechnical investigation*

During the initial phase, soil investigation was carried out with as many as six SPT bore holes equipped with soil laboratory data. Based on the SPT results, it can be concluded that the area is dominated by clay-silt soil with consistency soft to medium at the surface until the depth of 11 meters. This is where the problem lies. This layer of soft to medium clay silt possesses low shear strength and hence, low bearing capacity. Without proper subsoil improvement, the construction of GSRW system will leave massive deformation. Here is shown the SPT graph result.
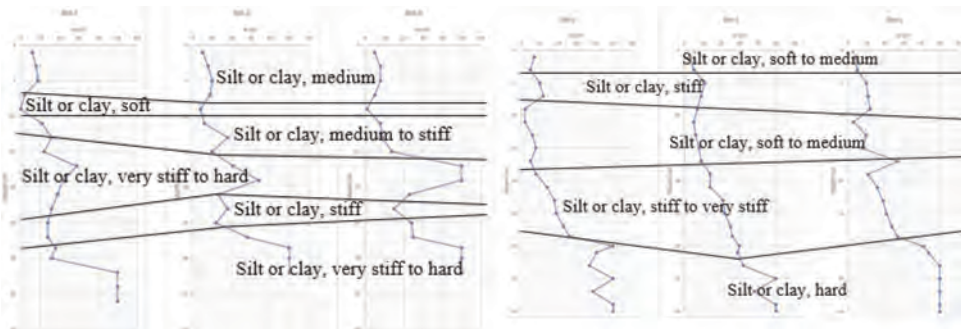
Figure 4. Geotechnical profile for BH-1 until BH-6.

3.2 *Geosynthetic in piled embankment design process*

The design for the GSRW needs to be assessed internally and externally. Internally, the reinforcement belt's (the GI-Strip) tensile strength and length needs to be designed properly. The GI-Strip tensile strength and length must withstand the load from the embankment itself, the dead load from the road, the live load from traffic and earthquake load. Externally, the GI-Strip must be safe from the possibility of failure through sliding, overturning, and must check the bearing resistance. The safety factor used is 1.50 for condition without earthquake and 1.10 for condition with earthquake, in accordance with Indonesian National Standard for Geotechnical Design Requirements.

After the GSRW design process, the piled-on embankment system design is carried on determining which type of geosynthetic is appropriate for the system. The calculation for the pile length and type was done before the calculation of the required geosynthetic. The piles are required to reach a depth of 12 meters with a square mini pile type measuring 25x25 cm

and contiguous bored pile with a diameter of 60 cm under the leveling pad. The calculation for the geosynthetic requirement is as followed:

1. Basic data

   Fill Data:
   Unit weight $= \Upsilon_{fill}$ = 12.6 kN/m^3
   Angle of internal friction $= \phi'_{fill}$ = 28°
   Cohesion $=$ c' = 30 kPa
   Load Data:
   Embankment load   = 117.68 kPa
   Life load   = 15 kPa
   Dead load   = 12 kPa

2. Calculating maximum pile spacing

$$s = \sqrt{\frac{Q_{pall}}{\gamma_e}} H \tag{1}$$

$$\gamma_e = \left(\gamma_{fill} + \frac{q}{H}\right) \tag{2}$$

   where Q_{pall} = allowable capacity of the pile; Υ_e= effective unit weight of the embankment; and H = height of the embankment.
   s = maximum pile spacing = 7.5 m, adopted pile spacing = 1 m

3. Calculating the ratio of vertical stress on pile (or pile caps) to vertical effective stress in fill

$$\frac{p'_c}{\sigma'_v} = \frac{p'_c}{\gamma_e H} = \left(\frac{a_c d}{H}\right) = \left(\frac{((1.70 \times H/d) - 0.12)d}{H}\right) \tag{3}$$

   where p'_c = vertical stress on the pile (or pile cap); σ'_v = vertical effective stress at the base of the fill; d = width or diameter of the pile (or pile cap); and a_c = arching coefficient and is dependent upon the height of the fill, the width of the pile (or pile cap), and the rigidity of the pile.
   p'_c / σ'_v = 2.87

4. Calculating the distributed load which the geosynthetics reinforcement, W_t, must support between the piles (or pile caps)

$$W_t = \frac{s\gamma_e H}{s^2 - d^2}\left[s^2 - d^2 \frac{p'_c}{\sigma'_v}\right] \tag{4}$$

   where W_t = distributed load acting on geosynthetics.
   W_t = 54.6 kN/m

5. Calculating tensile load (required working strength)

$$P_{rp} = \frac{W_t(s-d)}{2d}\sqrt{1 + \frac{1}{6\varepsilon}} \tag{5}$$

   where P_{rp} = required working strength.
   P_{rp} = 53.05 kN/m

6. Calculating ultimate breaking strength

   The value of the tensile strength of the geogrid material above must be reduced to factors as shown in the equation below:

$$T_{design} = \frac{T_{ult}}{RF_c \times RF_{id} \times RF_d} \tag{6}$$

   where T_{ult} = ultimate breaking strength; RF_c = reduction factor creep (2); RF_{id} = reduction factor for installation damage (1.3); RF_d = reduction factor for durability (1.2).

T_{ult} = 165.5 kN/m

For that, the geosynthetic used as load transfer platform is Geogrid with 175 kN/m in tensile strength.

3.3 Global stability analysis

As the last design step, global stability's safety factor check was assessed with PLAXIS 3D software. The analysis was done with the highest embankment which is 9 meters. According to the design, the piles were installed in the first stage of the design. After the piles, the pile caps and geosynthetic were activated. Next, the backfilling of soil, installation of the concrete precast facing and GI-strip were done. The whole system was then assessed with the activation of the 20 kPa traffic load. The soil parameter is as shown in Table 1, as for the geometry model is as shown in Figure 5 and the analysis yield results as shown below in Figures 6 and 7.

According to Figure 5, the static safety factor for GSRW of Kadusirung Approach Slab is 2.031. This safety factor fulfills the criteria in Indonesian National Standard for Geotechnical Design Requirements which is above 1.50. After that, the analysis combines with the pseudo-static load which was adopted from design response spectrum in Map of

Table 1. Hardening soil model parameter.

Soil type	Υ_{unsat} $[kN/m^3]$	Υ_{sat} $[kN/m^3]$	c' $[kPa]$	φ' degrees	E_{50}^{ref} $[kN/m^2]$	E_{oed}^{ref} $[kN/m^2]$	E_{ur}^{ref} $[kN/m^2]$
Silty clay, soft (0-5 m)	15	17	2.5	22	10000	7000	30000
Silty clay, medium (5-11.5 m)	16	18	5	28	20000	14000	60000
Clayey silt, medium (11.5-19 m)	16	18	5	28	15000	10500	45000
Silty clay, stiff (19-21.5 m)	18	20	8	31	20000	14000	60000
Silty clay, very stiff (21.5-26 m)	19	20	12	31	35000	24500	105000
Silty clay, very stiff (26-31 m)	19	20	16	31	45000	31500	135000
Clayey silt, very stiff (31-33 m)	19	20	24	32	60000	42000	180000
Fill	12.6	14	30	28	11000	7700	33000
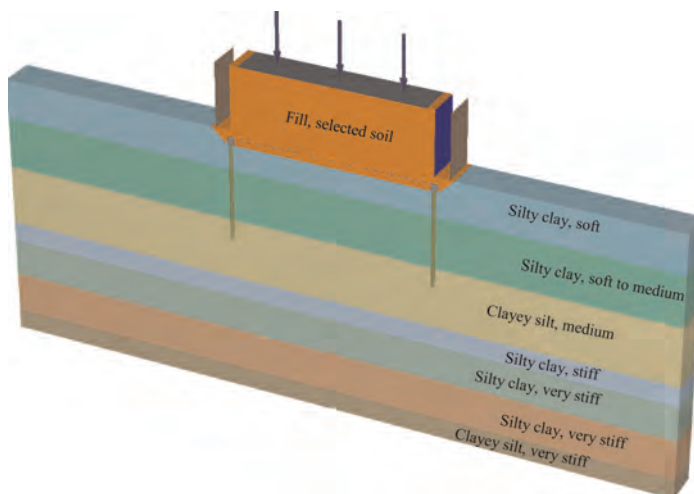
Figure 5. PLAXIS 3D model of GSRW of Kadusirung approach slabs supported by geosynthetic and piled embankment system.
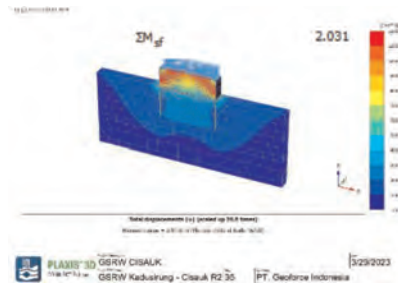
Figure 6.   Estimation of static failure mode of GSRW of Kadusirung approach slabs supported by geosynthetic and piled embankment system.
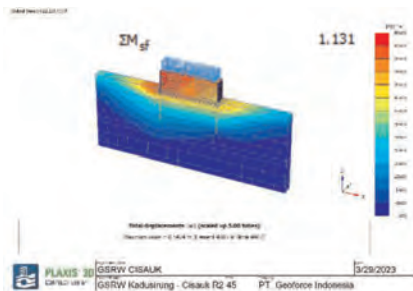
Figure 7.   Estimation of pseudo-static failure mode and safety factor of GSRW of Kadusirung approach slabs supported by geosynthetic and piled embankment system.

Indonesia Earthquake Sources and Hazards in 2017. The Peak Ground Acceleration value is 0.426 g and multiplied by the amplification factor of 1.1 and 0.5, which results in horizontal acceleration 0.23g. The pseudo-static load analysis yields safety factor 1.131. This safety factor also fulfills the criteria in Indonesian National Standard for Geotechnical Design Requirements for embankment with seismic load which is above 1.10.

4   CONCLUSION

The Kadusirung Flyover Approach Slabs was constructed with Geoforce Segmental Retaining Wall system on soft soil and needed subsoil reinforcement. The selected reinforcement system was piled embankment, as it is the easiest, fastest and most robust system to implement. Nevertheless, this system requires massive pile cap as a load transfer platform. Geosynthetic can reduce the need for pile cap, and in this case, Geogrid has successfully done that. In Kadusirung Flyover Approach Slabs the geogrid uses 175 kN/m tensile strength to spread and distribute the dead and live load to the piles. The global stability was then analyzed using PLAXIS 3D software and yield safety factor 2.031 for static analysis and 1.131 for pseudo-static analysis.

REFERENCES

BS8006 (1995). Code of Practice for Strengthened/Reinforced Soils and Other Fills. British Standard Institution
Koerner, R. (2005). *Designing with Geosynthetics*. Upper Saddle River: New Jersey.
Badan Standarisasi Nasional. 2017. SNI 8460:2017. *Persyaratan Perancangan Geoteknik*. Jakarta: Badan Standarisasi Nasional.

Using of geosynthetics on foundation of residential complexes and low height buildings on stabilized fillings from municipality of Bucharest

S. Mustatea, L. Talos, A. Barariu & Ali Naji
S.C. Geostud S.R.L. Bucharest, Romania

ABSTRACT: Due to the restriction of the perimeters with good foundation lands in Bucharest, which are also very expensive, a need arose to base on fillings, especially for residential complexes and some low-rise building. Although these houses transmit lower pressures to the foundation lands, due to the inhomogeneity of the fillings, differentiated settlements appear, which in the end can destroy the building. Consequently, in addition to the well-known solution to completely remove fillers – a solution that involves excavation work transportation, storage in specially designed spaces, activities that require approvals, environmental protection work, high costs – Geostud specialists have found alternative technologies consolidation and stabilization of these fillers, based on the use of geosynthetics. The article presents the technologies, including the theoretical basis and examples of works where they have been used.

1 INTRODUCTION

In the Municipality of Bucharest, there are areas where the fillings have thicknesses from 3,5 m to 15 m consisting of pieces or slabs of concrete, bricks, metals, vegetable, or textile residue, deposited over time in an unorganized way and which, from a geotechnical point of view, constitute a difficult foundation ground (according to table A13, NP 074/2014). All this the high level of water table, which is practically contained in the fillings, is added to Filled areas exist both in the inner city and in the outer city of the municipality.

Due to the narrowing of the perimeters with good foundation ground, which are also very expensive the need for foundations on the fillings appeared, especially in residential complexes as well as in some low-rise buildings. Although these buildings transmit lower pressures to the foundation grounds, due to inhomogeneity of the fillings, differential settlements occur, which can eventually destroy the building.

Hence, in addition to the well-known solution of completely removing the filling material - a solution that involves excavation works, transport, storage in specially designed spaces, activities that require approvals, environmental protection works, high costs – our specialists have found alternative consolidation technologies and stabilization of these filling materials.

Among these solutions, the promoted and recommended ones by S.C. Geostud S.R.L. are the following:

– foundation on ballast/crushed stone cushion, reinforced with geogrids and covered in geotextile
– consolidation through the execution of successive layers of soil geotextile reinforced soil.
– consolidation with 'rigid inclusions'.

Each solution has a theoretical basis, a specific technology that involves excavating the filling material to a certain depth, usually between $1 \div 1.5$ m for the cushion, $1.5 \div 2.5$ m

for consolidation with successive layers of reinforced soil, and 2.5 ÷ 3.5 m for strengthening with rigid inclusions. In any case, the level of the excavation must be stopped at least 1m above the water table.

Next, the first two technologies based on the use of geosynthetics are summarized.

2 FOUNDATION ON BALLAST /CRUSHED STONE CUSHION, REINFORCED WITH GEOGRIDS AND COVERED WITH GEOTEXTILES

This technology is based on working together between geogrids, ballast, and geotextiles.

Geogrids are synthetic materials made of high-strength polyethylene, formed by an empty aperture, which allows the penetration of ballast/crushed stone grains, with which they achieve an interlock (Figure 1), thus considerably reducing the tendency of lateral and vertical displacement of the grains. In this way, a web is formed that takes the tensile stress, which the foundation ground cannot take over, uniformizes the distribution of the loads, the stress concentrations disappear, increasing the angle of distribution of loads at the same time and finally the bearing capacity of the foundation ground increases.
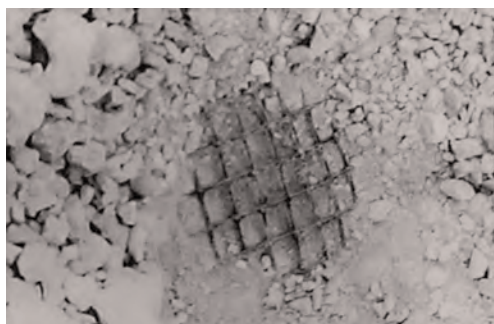
Figure 1.   Geogrid empty aperture.

The geotextile has the role of separation between the surrounding heterogeneous filling, preventing the penetration of aggregates into the filling and the penetration of fine soil particles from the filling into the cushion, removing the clogging. It also has a filtering and drainage role. The ballast also has the role of breaking capillarity so that the water does not rise above the cushion, thus canceling the under pressure on the base of the building's foundation, also evenly distributing the loads. Since the width of the mattress is bigger than the width of the foundation, the load distributed on the foundation soil is smaller. Thus, the foundation soil can safely take over the loads transmitted by the construction.

The required number of layers, geogrids included, can be dimensioned as follows:

$$T = (G + q \cdot l)/l \qquad (1)$$

where T = the total force transmitted by the structure, kN; G = the building weight, kN; q = uniformly distributed mobile loads (snow furniture, people etc.), kN

$$n = \frac{T}{R_t} \qquad (2)$$

where n = amount of geogrids / number of layers; R_t = tensile strength of one geogrid, kN

– it is chosen constructively:
– The thickness of the mattress d =1.0 m
– The width of the mattress L = l + 2 0.5 m
– l = the width of the building foundation

Usually from experience, the maximum number of layers is 4 and the thickness of one layer is 0.25m (after compaction).

This solution was proposed in the geotechnical study for the construction of the residential complex Green Lake Residence, plot H, where the fillings are up to 7 m thick, and from 3 m deep contains large concrete slabs embedded in the heterogeneous mass of rubble and soil.

At the moment, the residential complex is partially finished (Figure 2).

Figure 2.   The green lake residence.

3   CONSOLIDATION AND STABILIZATION OF FILLINGS BY THE EXECUTION OF SUCCESSIVE LAYERS OF EARTH REINFORCED WITH GEOTEXTILES

The technology of consolidation and stabilization of fillings consists of:

– plotting the location of the building
– excavating the filing material to the level established by the project
– removal from the excavated surface of all blunt materials (bricks, pieces of concrete, iron bars), roots, vegetable remains textiles, etc.
– leveling and compacting the resulting surface.

On the surface thus prepared, the first layer of geotextile is spread (consisting of strips over-lapping a width of at least 20 cm), after which a layer of loose soil of approximately $25 \div 35$ cm thickness is laid and compacted to a degree of compaction between $96 \div 98\,\%$, thus creating the first elementary layer of reinforced soil. The procedure continues to be carried out successively up to the projected elevation, which becomes the foundation elevation of the building.

The stabilization and reinforcement effect are achieved by mobilizing shear forces at the soil-geotextile contact (Figure 3) as follows:

Compaction, with vertical stress (σ), induces a stretching stress in the geotextile (T), given by the resistance mobilized at the contact between the soil and the reinforcement (τ_s). Thus, a mobilized resistance (τ) appears in the composite soil, whose value is:

$$\tau = \tau_s + \frac{T}{d} = \tau_s + T \cdot D \tag{3}$$

$$D = \frac{1}{d} \tag{4}$$

where D = armature frequency or armature density; d = distance between reinforcements. In this way, an extra cohesion appears in the soil (additional cohesion Δcs), whose value is:

$$\Delta c_s = D \cdot T \tag{5}$$
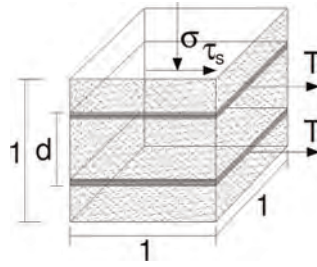
Figure 3.   The stabilization and reinforcement effect of the geotextile.

when under stress, the soil breaks first,

$$\Delta c_s = \frac{D \cdot T}{m_s} \tag{6}$$

$$m_s = \frac{\tau_s}{\tau} \tag{7}$$

when under stress, the geotextile breaks first.
This additional cohesion is highlighted in the graph below (Figure 4):
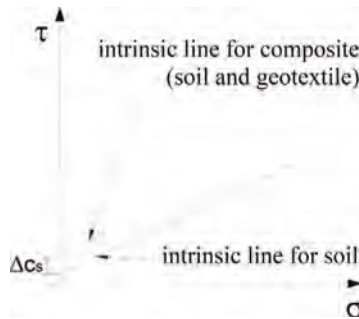
Figure 4.   Additional cohesion.

Under these conditions, the shear strength increases in the reinforced layer and further in the entire package of layers and is a direct function with the distance between the reinforcements (d), respectively with the density of the reinforcement (D). Thus, the last reinforced layer is reached, the foundation conditions are practically homogenized on a filling whose geotechnical characteristics vary in plan, reducing the settlements to a minimum, while increasing the bearing capacity.

In conclusion, this solution ensures the distribution of loads in the field at the level of admissible pressures. This technology was successfully applied to the foundation of a building in the Colentina area, where the thickness of the filling layer is over 10 m.

4   MATERIAL AND SOIL QUALITY CONTROL

Before commissioning, all materials and soils included in the works must meet all the conditions established by European and National norms. However, in order, to ensure the quality and durability of the works, the ballast/crushed stone, geotextile, geogrid, and soil must meet the following minimum conditions:

- For ballast/broken stone:
  - granularity $0 \div 70$ mm and falling within the prescribed areas
  - uniformity coefficient Un $\geq$ 15
  - capillary height: 15–20 cm
  - degree of compaction: D = $90 \div 100\%$, normal Proctor

- For geotextile:
  - tensile strength: $T_{max} \geq 300$ kN / m
  - the normal permeability coefficient: $K_n \geq 5 \cdot 10^{-3}$ cm / s
  - longitudinal permeability coefficient: Kl $\geq 2 \cdot 10\text{-}3$ cm / s
  - elongation at break: $\varepsilon_{max} = 6\%$

- For geogrids:
  - tensile strength on main direction Tmax $\geq$ 200 kN / m
  - elongation at break: $\varepsilon_{max} = 6\%$

The soils in the layers are of a cohesive type without blunt elements that can pierce the geotextile and at least the following characteristics must be checked before commissioning:

- continuous granulometric curve: Un $\geq$ 15
- upper limit of plasticity $w_L = 30 \div 40$ %
- dry density $\rho_d \geq 1.65$ g / cm3
- humidity at commissioning, w = $w_{opt} \pm 3$ %
- where w_{opt} = optimum moisture content obtained from compaction test
- content of organic materials, maximum 1 %
- carbonate content, maximum 1%

After compaction, each layer must be 20–25cm thick, reaching a degree of compaction of D = $96 \div 98\%$ and D = 100 % on the last three layers. Also, on each layer, the bearing capacity will be checked with the static plate, and the homogeneity with the dynamic plate.

5 CONCLUSIONS

Of particular importance in these buildings founded on fillings is the in-situ monitoring of both the behavior of the filling and of the buildings themselves.

Thus, for fillings, it is necessary to install topographic markers to monitor subsidence and to install piezometers to monitor fluctuations in the groundwater level. For the building itself, it is necessary to mount settlement gauges, visually monitor and measure any cracks, as well as their development over time.

Beforehand, it is necessary to design a surveillance and monitoring program, which must contain:

- the frequency with which the measurements must be made;
- location of landmarks and piezometers;
- proposals for values that characterize the normal operating state and limit values for 'attention', 'warning' and 'alarm';
- proposals for measures in the event of settlement in the foundation, cracks in the walls and raising the groundwater level that may endanger the building.

REFERENCE

Andrei, S & Hanganu, E & Barariu, A & Georgescu, E & Costica, E. 2006. The Constuction of Improved Foundation using Geosynthetic *Materials, Proceeding of the 8th International Conference on Geosyntetics (8ICG)*, Volume 4, *Reinforced Slopes and Walls – Modeling and Design 2,* page 1295–1298, Yokohama 18-22 September 2006. Rotterdam: Millpress

Case study of GRS design considering the effect of reverse fault movement

Z. Lin & I. Chen
ACE Geosynthetics, Taichung, Taiwan

J. Wu
Chung Hua University, Hsinchu, Taiwan

C.L. Yuan & C.T. Chen
Sinotech Engineering Consultants, Taipei, Taiwan

ABSTRACT: In 1999, the Chelungpu fault in central Taiwan triggered the deadly 921 Chi-chi earthquake, which measured 7.3 on the Richter scale. However, because of specific technical influences, the project reported herein has to pass through the Chelungpu active fault through a high-fill embankment. Due to the fault-induced movement bound to produce severe differential deformation and surface rupture, the structure must be earthquake-resistant to ensure its safety. Considering the particular requirements of this section, after exploring several probable solutions, the designers finally determined to apply geosynthetics reinforced soil structure (GRS) to build the reinforced foundation and the reinforced embankment to restrain the differential movement caused by active faults to the greatest extent. The adjacent slopes have also been stabilized carefully. The analysis results show that the safety factors of the GRS embankment and its adjacent slopes all meet the requirements of safety and service functions.

1 INTRODUCTION

Taichung City is located in the center of western Taiwan, where the population and economy are concentrated. It has frequent industrial and commercial activities and a dense population, thus with a high demand for traffic development. The government actively promotes transportation construction in central Taiwan and constructs a complete highway network system. It also aims to provide convenient transportation services to the Great Taichung metropolitan area and promote the mutual development of the metro area and surrounding cities.

Taiwan is located at the boundary of the Eurasian plate and the Philippine plate, resulting in 51 faults on this island. The numbers of earthquakes caused by these faults are almost countless, posing a significant threat to people's lives and property. For example, the 1999 Chi-chi earthquake, triggered by the Chelungpu fault in central Taiwan, caused about 14,000 deaths and injuries and toppled more than 100,000 houses (Wikipedia 2022). This fault is distributed from north to south along the foothills of the hilly eastern area of the Taichung Basin. The extension project of National Highway No. 4, the case study presented in this paper, must meet the Chelungpu fault at the stations of 23k+242 to 23k+410 under the overall considerations of service function, topography, and highway alignment. According to historical information, the surface rupture caused by the Chi-chi earthquake triggered by the Chelungpu fault was about 85 kilometers long, the vertical displacement was about 4~5m in this area, and the horizontal displacement was about 2.5~5m in some areas.

As shown in Figure 1, the surface fracture zone intersects with the designed highway at an angle of about 60 degrees, and the surface rupture caused by the hanging wall on the site was relatively moved up about 3 m. The evidence indicated that there had been serious fault misalignment, which resulted in severe damage to the nearby reinforced concrete revetments of Wuniulan Creek at that time (Figure 2). Because of the severe impact of the fault, if a similar movement occurs again in the future, it will undoubtedly cause severe damage to the structure of this section. Therefore, the design strategy of this project must consider the earthquake-resistant requirements of the structure in this area to ensure the necessary safety. Also, well-organized emergency countermeasures must be available after the disaster.
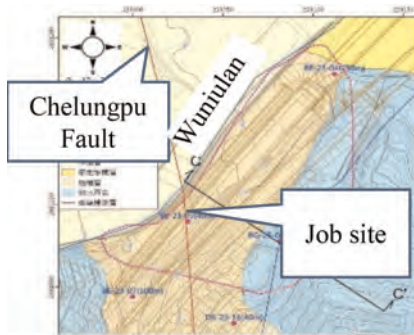
Figure 1. The intersection of the site and Chelungpu fault (Sinotech engineering sonsultants, Ltd. 2017).
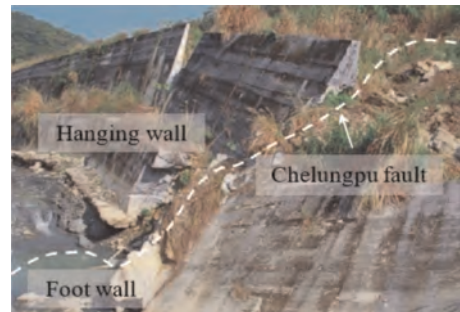
Figure 2. Failure of reinforced concrete revetments caused by Chelungpu fault (Chiang *et al.* 2022).

2 PHOTOGRAPHS AND FIGURES SITE CONDITIONS

The presented case runs through the hilly area of the foothills region in western Taiwan. The surface terrain changes significantly, with elevation along the route fluctuating between 300~450m. The toe at the west slope of the highway is close to Wuniulan Creek. The east side of the highway is a steep slope consisting of debris formation and only allowing for a very narrow proximity for construction. Since this section must match the longitudinal slope variation of the adjacent tunnel, as well as the geometric planning of the highway spaces at the tunnel's entrance, the design elevation of the embankment section has shown up to 20m different from the original ground surface. Therefore, retaining structures must be used to ensure the safety of the embankment. As shown in Figure 3, based on the site investigation, the shallow geological formations at the site consist of colluvium and gravel with poor engineering properties. Bedrocks below the site consist of shale, sandy mudstone, and alternate layers of sandstone and shale with well-developed shear fractures attributed to the Chelungpu fault. The strength of rock mass is poor due to these fractures.

3 SOLUTIONS

The traditional geotechnical engineering solutions for fault areas include:

1. Rigid foundations or structures
2. Embedded retaining structures or buffer trenches
3. Placement of ductile engineering fills
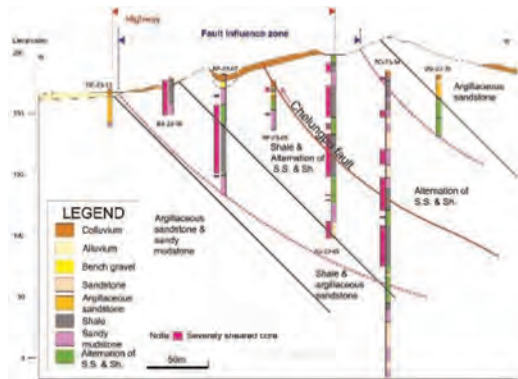
Figure 3.   Geological section of the site (Sinotech Engineering Consultants, Ltd. 2017).

The first solution involves using high-rigidity structures such as thick mats to counter-balance the fault ruptures. The second solution suggests installing a diaphragm wall, soil-bentonite mixtures, or ground improvement to divert the propagation of shear rupture beyond the boundaries of the target facilities. Alternatively, buffer trenches filled with lightweight expanded polystyrene (EPS) can provide spaces to accommodate fault-induced ground movement. The third measure involves the use of seismic-resistant engineering fills such as geosynthetic reinforced structure (GRS) to distribute the fault movement over a wider zone to reduce angular distortion at the ground surface and thus maintain the stability of the overlying structures (Ashtaiani et al. 2017; Bartlett et al. 2015; Chiang et al. 2021; Rasouli & Fatahi 2020, 2021; Yang et al. 2020).

Because of the elevation requirement, the sections across the fault zone must be embankment or viaduct structures. However, rigid reinforced concrete viaduct structures will be costly and time-consuming. It is also tough to promptly repair the damages caused by the induced ground movement after severe shaking.

The optional embedded retaining structures and buffer trench consist of flexible or light-weight materials mainly applied to underground systems such as utility facilities (Bartlett et al. 2015; Ra-souli & Fatahi 2020). In addition, this construction commonly involves deep excavation and complicated retaining structures. Therefore, it does not meet the application requirements of this project.

Geosynthetic reinforced soil structures (GRS) consist of geosynthetic materials that are flexible structures capable of presenting a higher damping properties to absorb the energy released by earthquakes (Chiang et al. 2022). This kind of structure has been extensively used in the construction of embankments, and its effectiveness has been validated in earthquake areas proving that the correctly designed GRS has excellent seismic resistance (Dobie 2006; Taheri & Hadiani 2019). Studies have also indicated that GRS has significantly mitigated the damages caused by fault movement (Ardah et al. 2018; Bray 2001; Chiang et al. 2021).

Yang et al. (2020) and Chiang et al. (2021) studied the effect of fault movements on GRS foundations using a series of sandbox model tests and finite element numerical simulations. The results indicate that, compared to the unreinforced foundations, the reinforcement acts as a tension membrane, creating tension along with the displacement caused by the fault. Its vertical component supports the overlying soil, thus minimizing the influence of surface settlement.

When the fault movement increases and thus initiates an enormous shear force within the GRS, the reinforcement can effectively impede the development of the shear zone and prevent the shear plane from reaching the surface to form surface rupture and reduce the angular distortion by up to 60% on average at the ground surface. Such reinforced earth mechanism can be identified as the shear rupture interception effect. Because of this inter-ception effect, the intense shear strain develops horizontally and extends along the bottom

reinforcement layer. The initiated shear strain reduces with the increased distance from the fault tip, indicating that the energy of fault movement is progressively dissipated by the resistance provided by the soil–reinforcement interaction. However, relevant studies have also noted that reinforcement pullout in the top reinforcement layer could occur in the case of short reinforcement. Because of the effect of reinforcement pullout, it is very likely that the shear rupture will be transmitted upward and passed through one end of the reinforcements due to the fault movement. Secondary settlement at the ground surface will be initiated through the end of the reinforcement, indicating that the verification of the pullout resistance of the reinforcement is essential (Chiang *et al*. 2021).

Factors that affect the overall stability and safety of this project: (1) narrow site proximity, (2) high embankment, (3) significant differential deformation due to fault movement, and (4) the need for timely repair of earthquake damage. In addition to these site relevant conditions, the designer also considered the design principle of building structures for earthquake damage control: (1) no damage for a small earthquake, (2) repairable for a medium earthquake, and (3) no collapse for a strong earthquake (Construction and Planning Agency 2022).

The designer finally adopted geosynthetic GRS in this section to build a 168 m-long embankment. The slope near Wuniulan Creek was shaped as a steep slope to solve the problem of narrow proximity at the site. In addition, the design of the GRS embankment can also reuse a large amount of excavated material from the Fengyuan No. 3 tunnel near the site. It dramatically benefits by reducing the output transportation of unwanted earth materials and saving shipping costs. It is also more in line with the highest principle of energy conservation, carbon reduction, and sustainable development of the project.

4 ANALYSIS AND DESIGN FOR GRS EMBANKMENT

4.1 *Stability analysis*

The static stability analysis of the GRS embankment should first consider the safety of external stability under various conditions such as normal, seismic, and storm, including sliding, overturning, and bearing capacity. For overall slope stability, the SLIDE 6.0 program was used to analyze the safety factor of slope stability by the limit equilibrium analysis method. The internal stability analysis, including the safety of geogrid pullout and tensile strength, was also confirmed. Based on the analyses, the design scheme and configuration of the GRS embankment and the effective embedded length and spacing of the geogrid are described in Section 4.2.3 (Sinotech Engineering Consultants Ltd. 2017).

The seismic coefficient of dynamic analysis was based on the "Code for Seismic Design of Highway Bridges" issued by the MOTC (2018). The applied horizontal seismic coefficient (k_h) was 0.182, and the vertical seismic coefficient (k_v) was 0.091. The seismic analysis results are shown in Table 1, indicating that the designed GRS embankment was stable under all conditions, and all safety factor values meet the code requirements. In addition, the analysis also should consider the emergency backfill to repair the surface rupture caused by the fault

Table 1. The results of stability analyses for GRS embankment under seismic condition.

Condition of Analysis		Factor of Safety
External Stability	Sliding	1.21
	Overturning	3.71
	Bearing Capacity	1.82
	Overall Stability	1.42
Internal Stability	Tensile Strength	1.84 (min.)
	Pullout Resistance	59.8 (min.)

movement. The weight of the backfill has been included in the study to ensure the safety of the GRS embankment. Detailed results and discussions are presented elsewhere and will not be given herein (Chang *et al*. 2022).

4.2 GRS design

4.2.1 Foundation improvement

Because the GRS embankment is located on the colluvium with poor engineering properties, its bearing capacity needs to be improved. Chiang *et al*. (2022) also recommended restraining the fault zone displacement from the foundation tended to achieve a better reinforcement effect. Therefore, the weak soil under the embankment shall be treated with a GRS foundation. It can be done by removing the underlain weak shallow colluvium and replacing it with the GRS foundation.

As shown in Figure 4, 150kN/m geogrids were placed in a crisscross pattern. Two geogrid layers were laid in the warp direction with a vertical spacing of 0.6m (perpendicular to the highway direction). Then a layer of geogrid was laid in the direction of parallel latitude (parallel to the highway direction) at a space of 0.3m. Backfill for the GRS foundation was compacted to at least 95% of the modified Proctor maximum dry density. The total length of the replaced GRS foundation was about 140m, and the replaced depth has reached the gravel stratum or bedrock with sound engineering properties ranging from 3 to 5m.
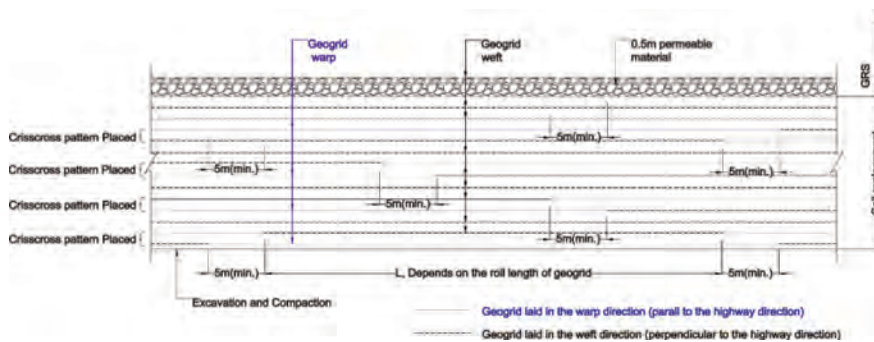
Figure 4.   Design configuration of the GRS foundation (Sinotech engineering consultants Ltd. 2017).

4.2.2 GRS embankment

Figure 5 shows the schematic design of the GRS embankment. Due to the limited space, the slope aspect ratio was 1: 0.2 (vertical : horizontal). It was divided into three stages, each stage was 5m high, and the width of the step-back platform was 1.5m. The GRS embankment was used for highway support, which has the highest level of function and safety. The configurations of geogrid were thus correspondingly designed carefully. The geogrid was placed with a vertical spacing of 0.3m at the lowest stage and 0.5m for the other two higher stages. The embedded lengths of the geogrid, from lower to upper layer, were 20m, 18.8m, and 17m, respectively.

The backfill material was the excavated materials from the adjacent tunnel. It should be compacted to more than 95% of the modified Proctor maximum dry density. In addition, permeable material, 0.5m thick, and high-density polyethylene (HDPE) drainage pipes should be installed at the bottom of each stage of the GRS embankment to improve the overall drainage efficiency and safety for seepage and heavy rainfall. GRS embankment was designed with geobags facing, which was attached to the embankment using the geogrid wrapped-around method. Geobags contain formulated seed, fertilizer, and organic soil that
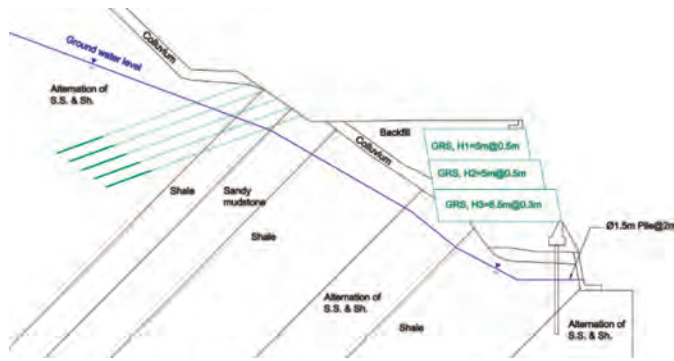
Figure 5   The design scheme of the GRS embankment (Sinotech engineering consultants Ltd. 2017).

facilitate vegetation growing and greening the surface of the embankment (Sinotech Engineering Consultants Ltd. 2017).

4.3   *Protections for adjacent slopes*

As shown in Figure 5, the site materials surrounding the embankment are weak colluvium and fractured bedrock. The designer decided to build a permanent pile-supported retaining structure at the toe of the GRS embankment adjacent to Wuniulan Creek. The diameter of the pile used was 1.5m and closely spaced 2m to ensure the stability of the toe of the huge embankment. The pile-supported retaining structure also protects the safety of the existing riverbank of Wuniulan Creek.

For safety, the upper slope was first shaped to a gentle slope of 1:2.5(V: H). It was then covered by reinforced concrete lattice girders, plus 40 tons of preloaded anchors 25m in length, spaced 2.5m in the X and Y direction (Figure 5). The protection system has been verified to fulfill all code safety requirements under various conditions, such as normal, rainstorms and earthquakes.

5   CONCLUSION

Fault movement has a significant impact on the safety of structures. However, because of many technical limitations, the case reported herein must pass through the Chelungpu active fault. After discussing several possible countermeasures, the GRS embankment has been considered the most suitable solution. Detailed safety considerations and analyses have been conducted with the key points summarized below.

1. The weak subsoils of the GRS embankment have to be replaced using GRS foundation to improve the bearing capacity and stability. It also provides a better restrain for the displacement of fault zone.
2. The results of static and dynamic analyses of the GRS embankment have shown that the designed structure is stable under various conditions, and all safety factors meet the specification requirements. However, further studies are recommended to explore detailed mechanisms of GRS structure relevant to fault movement.
3. Various slope stabilization methods have been applied to safeguard the safety of the adjacent slope for the GRS embankment. These treatments further warrant overall protection for the targeted facility.
4. The site was adjacent to the tunnel construction. Thus the design of the GRS embankment can also reuse a large amount of tunnel excavated materials, reducing the cost of dumping unwanted earth materials.

REFERENCES

Alireza Hasibi Taheri, A. H. & Hadiani, N. 2019. Three Dimensional Dynamic Analysis of Reinforced Earth Slope by Geogrid Under Overhead Effect. *International Transaction Journal of Engineering, Management, & Applied Sciences & Technologies*, Paper ID 10A15P. http://TuEngr.com.

Ardah, A., Abu-Farsakh, M.Y., Voyiadjis, G.Z., 2018. Numerical Evaluation of the Effect of Differential Settlement on the Performance of GRS-IBS. *Geosynthetics International*, 25(4): 427–441.

Ashtiani, M., Ghalandarzadeh, A., Mahdavi, M., Hedayati, M. 2018. Centrifuge Modeling of Geotechnical Mitigation Measures for Shallow Foundations Subjected to Reverse Faulting. *Can. Geotech. J.* 55(8): 1130–1143.

Bartlett, S. F., Lingwall, B. N. and Vaslestad, J., 2015. Methods of Protecting Buried Pipelines and Culverts in Transportation Infrastructure using EPS Geofoam, *Geotextiles and Geomembranes*, (43)5: 450–461.

Bray, J.D., 2001. Developing Mitigation Measures for the Hazards Associated with Earthquake Surface Fault Rupture. *A Workshop on Seismic Fault-Induced Failures–Possible Remedies for Damage to Urban Facilities*, Japan Society for Promotion of Science, University of Tokyo, Japan.

Chang, C. T., Huang, H. C., Wang, Y. K. & Lee, M. C. 2022. Applications of Geosynthetic Reinforced Soil Wall for Embankment Slopes of Taiwan's Freeway, *Proc. GeoAsia 7*, Taiwan.

Chiang, J., Yang, K. H., Chan, Y. H., and Yuan, C. L. 2021. Finite Element Analysis and Design Method of Geosynthetic-reinforced Soil Foundation Subjected to Normal Fault Movement. *Computers and Geotechnics* 139:1–26.

Chiang, J., Yang, K. H., Yuan, C. L. and Lin M. L. 2022. Mitigation of Fault Movement Disasters by Flexible Reinforced Earth Method - Engineering Practice and Mechanics Research. NTUCE Newsletter. Issue 156 (in Chinese).

Chou, N. N. 1998. *Manual for Design and Construction of Reinforced Earth Retaining Structure*, Taipei Professional Engineer Association (in Chinese).

Construction and Planning Agency, Ministry of Interior, 2022. http://www.ncree.org/safehome/ncr05/pc5_1.htm.

Ministry of Transportation and Communication, 2018. *Code for Seismic Design of Highway Bridges*, MOTC (in Chinese).

Rasouli, H. and Fatahi, 2020. Geofoam Blocks to Protect Buried Pipelines Subjected to Strike-slip Fault Rupture, *Geotextiles and Geomembranes*, 48(3): 257–274.

Rasouli, H. and Fatahi, B. 2021. Geosynthetics Reinforced Interposed Layer to Protect Structures on Deep Foundations Against Strike-slip Fault Rupture, *Geotextiles and Geomembranes* 49(3): 722–736.

Sinotech Engineering Consultants, Ltd., 2017. Design and Analyses of Reinforced Earth Structure for Sections of Wuniulan Creek (in Chinese).

Wikipedia, 2022. https://zh.m.wikipedia.org/zh-tw/921%E5%A4%A7%E5%9C%B0%E9%9C%87.

Yang, K. H., Chiang, J., Lai, J. H., and Lin, M. L. 2020. Performance of Geosynthetic-reinforced Soil Foundations Across a Normal Fault, *Geotextiles and Geomembranes* 48(3): 357–373.

*IGS technical committee on 'soil reinforcement' –
special session on "Design methods for basal
reinforcement of embankments"*

A case study of geosynthetic basal reinforcement techniques in Japan

Y. Miyata
National Defense Academy, Yokosuka, Japan

J. Hironaka
Mitsui Chemicals Industrial Products, LTD, Saitama, Japan

ABSTRACT: Both excessive subsidence and slippage are crucial concerns when constructing embankments and retaining walls on soft soil foundations. Geosynthetic basal reinforcement is a powerful solution. This study introduces Japanese design methods for related techniques and reports a case study conducted in Japan.

1 INTRODUCTION

Excessive settlement and slippage failure are crucial concerns in soft-soil foundation engineering. Various techniques can be employed to overcome these problems. Namely, geosynthetic basal reinforcement is an effective solution (Koerner 2012).

In Japan, popular geosynthetic basal reinforcement methods include 1) reinforcing the surface layer of super soft soil foundations, 2) reinforcing the embankments over soft soil foundations, and 3) combining basal reinforcement with deep mixing (Miki 1996). Their effectiveness has been verified in practice, and a corresponding design manual is well-prepared (PWRC 2000). However, the current techniques should be further improved for broader applicability and advanced design concepts, such as performance-based design. The authors addressed this challenge by investigating the actual performance of a geosynthetic basal reinforcement approach. This study briefly introduces the current Japanese design methodology for basal reinforcement technology, as well as a Japanese case study. Finally, the authors present their thoughts on technical issues considering reliability and deformation/damage analysis regarding the transition from a specific-based design to performance-based design.

2 REINFORCING THE SURFACE LAYER OF A SUPER SOFT SOIL FOUNDATION

2.1 Outline

In super soft soil foundations, such as dredged soil reclamation sites, the water content is significant, and shear strength is very low. In such foundations, even simple construction machinery cannot be moved on-site because of the lack of bearing capacity. Therefore, to effectively utilize super soft soil foundations, it is necessary to improve their bearing capacity before attempting ground improvements, such as vertical drainage or deep mixing. In such cases, geosynthetic reinforcement for the surface layer, as shown in Figure 1, is effective. In this technique, geosynthetics are placed on super soft foundations and covered with soil. This simple process ensures that the construction machines can safely traverse the site.
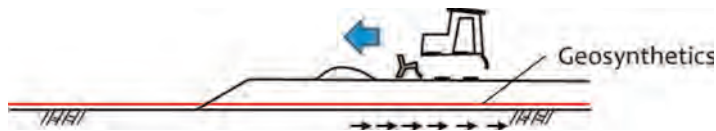
Figure 1. Geosynthetic basal reinforcement applied to the surface layer of a super soft soil foundation.

In Japan, this technology was initially adopted using a polyvinyl sheet as the soil reinforcement material (Fukuzumi & Nishibayashi 1970). At about the same time, Yamanouchi *et al.* (1968) proposed using plastic nets as the soil reinforcement material.

Subsequently, geogrids and geostraps with high tensile stiffness and strength characteristics have been started being used until the present day.

2.2 *Design method*

The design of the geosynthetic reinforcement applied to the surface layer of a super soft soil foundation is based on the idea that the ground reaches its ultimate limit state when the geosynthetics break (PWRC 2000). The design flow is illustrated in Figure 2, where the geosynthetics required to ensure the target bearing capacity is appropriately selected, and soil cover thickness is set accordingly.
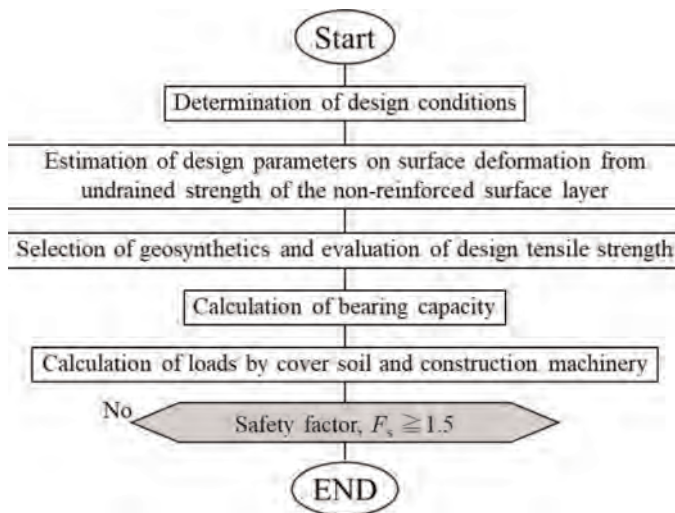
Figure 2. Design flow of geosynthetic reinforcement applied to the surface layer of a super soft soil foundation.

During the design, three effects of geosynthetics are considered: 1) the tensile force effect, 2) the confining effect, and 3) the membrane effect, as shown in Figure 3. The following equation proposed by Yamanouchi (1979) is used to evaluate the bearing capacity:

$$q_d = \alpha c N_c + \frac{2T \sin \theta}{B} + \frac{T}{r} N_q + \gamma D_f N_q \qquad (1)$$

where q_d is the ultimate bearing capacity (kN/m^2), α is the shape coefficient of the foundation (in this case, = 2/3), c is cohesion (kN/m^2), N_c and N_q are bearing capacity factors, T is the designed tensile strength of the geosynthetic (kN/m), B is the loading width (m), θ is the

Figure 3. Geosynthetic reinforcement effects on the surface layer of a super soft soil foundation.
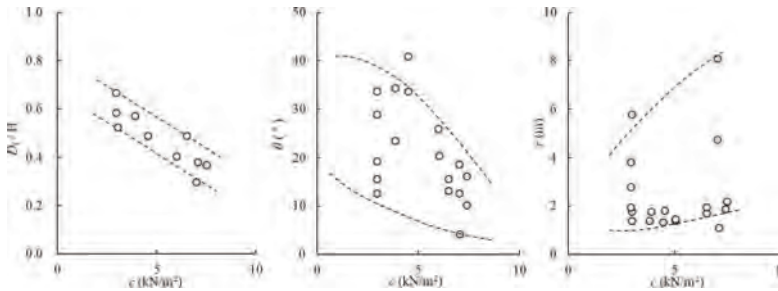
Figure 4. The geometry parameters observed in the bearing capacity formula stated in Eq.1 (from Sasaki *et al.* 1990). (a) Construction machine traversing a reinforced foundation (b) Connecting geosynthetic materials during construction

(a) Construction machine traversing a reinforced foundation (b) Connecting geosynthetic materials during construction
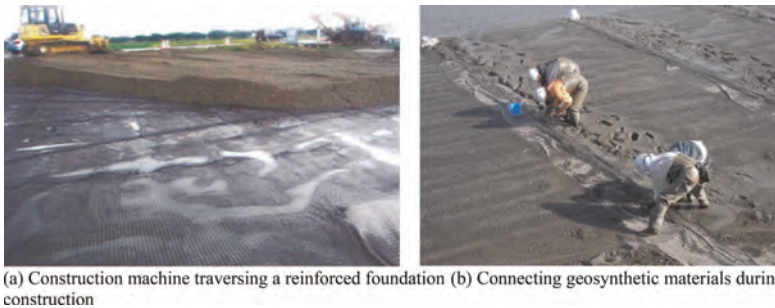
Figure 5. Case history of geosynthetic reinforcement applied to the surface layer in Japan.

angle between the deformed geosynthetic and horizontal plane near the loading edge (°), r is the radius of the circle (m) when the geosynthetic deformation near the loading edge can be captured as a circle, γ is the unit volume weight of the soil (kN/m^3), and D_f is the penetration displacement of the surface layer (m).

When evaluating the bearing capacity using Eq. (1), it is important to appropriately set the geometric parameters of the geosynthetic-laid surface layer of soft soil foundations. Sakai *et al.* (1990) measured this shape in various fields and summarized it, as shown in Figure 4. PWRC (2000) recommends conducting these measurements to obtain the required geometric parameters. Bearing capacity is generally evaluated based on the foundation geometry before loading. For geosynthetic-reinforced very soft foundations, the bearing capacity is evaluated based on the ground geometry after loading.

2.3 *Case history*

Figure 5 shows a construction machine traversing a reinforced foundation and the process of connecting geosynthetics during a Japanese construction project conducted on a very soft soil foundation.

3 REINFORCING THE EMBANKMENT OVER SOFT SOIL FOUNDATION

3.1 *Outline*

Embankments on soft soil foundations can cause excessive settlement and lateral flow. When an embankment is constructed on such a foundation, a certain treatment to reduce the settlement and lateral flow of the foundation is required. In this case, the geosynthetic basal reinforcement technique, shown in Figure 6, is effective. In this technique, one or multiple layers of geosynthetics are placed on the soft soil foundation to construct the embankment. In Japan, geogrids are primarily used under single-layer conditions. Currently, geosynthetics with higher strength and stiffness, such as geostraps and geocomposites, are also used. Recently, geosynthetic mattress foundations have been used. Therefore, it is necessary to evaluate the safety factor of the unreinforced embankment before confirming the applicability of geosynthetic reinforcement. When selecting and placing geosynthetics, two failure modes are considered: the overall stability of the reinforced embankment and the sliding stability of the embankment placed on the reinforced foundation, as shown in Figure 8.

Figure 6. Geosynthetic reinforcement applied to an embankment over a soft soil foundation.
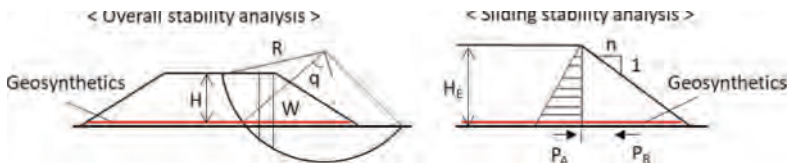
Figure 7. Design flow of geosynthetic reinforcement applied to an embankment over a soft soil foundation.
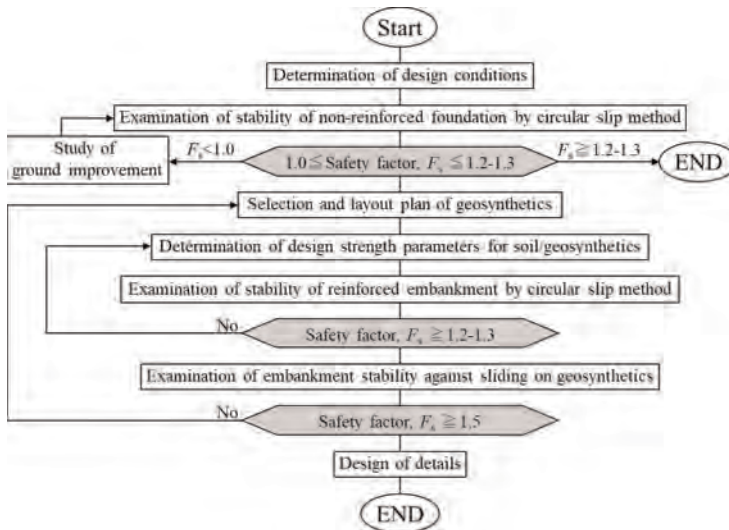
Figure 8. Considered limit states when designing a geosynthetic reinforced embankment over a soft soil foundation. (a) Geogrid-reinforced case (b) Woven geotextile-reinforced case

3.2 Design

The design flow of this technology is illustrated in Figure 7. Geosynthetic reinforcement is not considered to be very effective in stabilizing embankments where the foundation is extremely soft. Accordingly, the safety factor for embankments on the unreinforced ground is less than 1.0.

3.3 Case study

Figure 9 shows a construction machine traversing a reinforced foundation and the process of connecting geosynthetics during a Japanese construction project conducted on a very soft soil foundation.

(a) Geogrid-reinforced case   (b) Woven geotextile-reinforced case
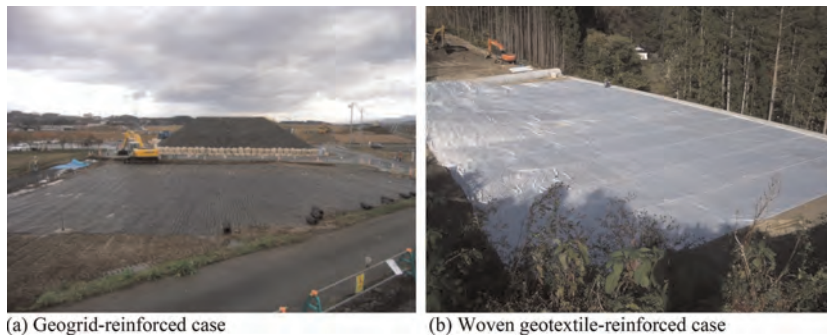
Figure 9.   Geosynthetic reinforcement embankment applications in Japan.

4 BASAL REINFORCEMENT COMBINED WITH DEEP MIXING AND GEOSYNTHETICS

4.1 Outline

Residual settlement is a key issue observed when engineering embankments constructed on soft ground. It is effective in improving the foundation of embankments with cement mixing. In this case, the improvement area should be as minimal as possible to reduce the improvement costs. However, an overly small improvement causes differential settlement between the soil cement columns and unimproved areas, which results in cracks at the embankment surface and overall slippage in the embankment. Geosynthetic basal reinforcement combined with deep mixing, as shown in Figure 10, is an effective solution to this engineering problem. In Japan, geogrids and woven geotextiles have been used in this technique; however, using geostraps with higher strength has become increasingly popular recently.

4.2 Design

The design flow of the geosynthetic basal reinforcement combined with deep mixing is shown in Figure 11. After designing the cement mixing process, the geosynthetic reinforcement
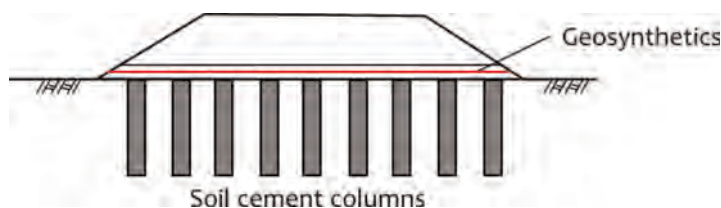
Figure 10.   Geosynthetic basal reinforcement combined with deep mixing.
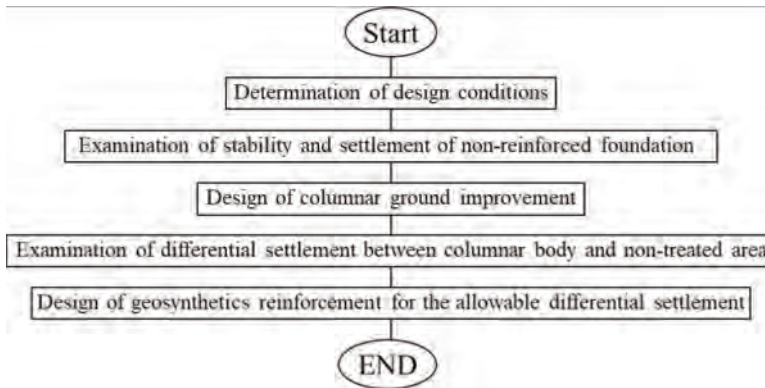
Figure 11. Design flow of geosynthetic basal reinforcement combined with deep mixing.
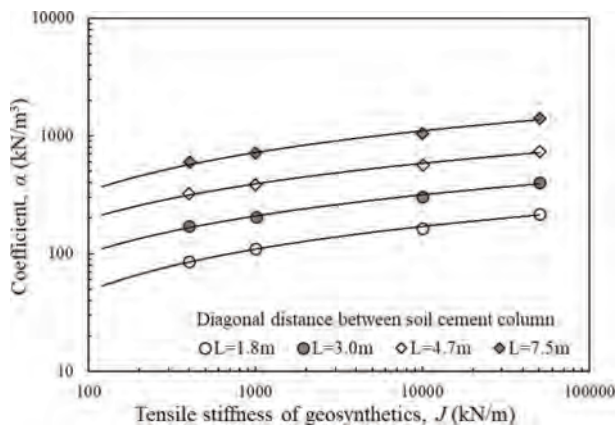
Figure 12. Design chart plotting the required geosynthetic tensile stiffness (from PWRC 2000) (a) After cement mixing (b) Connecting geosynthetic during construction

condition is determined such that the differential settlement between the soil cement column and the unimproved area is less than the allowable threshold (PWRC 2000). During the design process, the required tensile stiffness for geosynthetics is evaluated, considering that the ground improvement by cement mixing is three-dimensional. Figure 12 shows the design chart used to evaluate the required stiffness. This is prepared after summarizing many numerical analysis results by three-dimensional FE analysis considering nonlinear constitutive equations for soil and geosynthetics, in which coefficient a is expressed by the following equation:

$$\beta = \frac{1}{2}\frac{P}{S_a}\left(\frac{S_a}{S_b} - 1\right) \tag{2}$$

where P is the vertical stress acting on the foundation, S_a is the estimated differential settlement for cement mixing only, and S_b is the target differential settlement for the combined reinforced case.

4.3 *Case study*

Figure 13 shows photographs of a case where a combination of deep mixing treatment based on columnar improvement and geosynthetics is applied to stabilize an embankment constructed on soft ground.

(a) After cement mixing   (b) Connecting geosynthetic during construction

Figure 13.   Applications of basal reinforcement combined with deep mixing in Japan.

5   TECHNICAL CHALLENGES IN GEOSYNTHETIC BASAL REINFORCEMENT

In Japan, the design of recently developed infrastructures has increasingly adopted a performance-based design process. In performance-based design, the limit states for frequent actions may be verified by reliability analysis, and those for accidental actions may be checked by deformation/damage analysis. In reliability design, partial safety factors must be reasonably determined by conducting statistical analyses with actual data for the load and resistance sides. Because geosynthetic basal reinforcements are implemented before the main construction phase, their importance has not been carefully investigated owing to a lack of sufficient collected data. Establishing reliable design models and determining partial safety factors to control structural safety, which is an important engineering challenge, should be addressed for future applications.

A three-dimensional analysis is required to estimate the deformation and damage characteristics of reinforced foundations. To analytically reproduce the consolidation behavior of soft soil ground, a soil skeleton-water coupled analysis is required. Rational constitutive laws for clay and geosynthetics are required to analyze the nonlinear behavior of natural ground. In the case of applying numerical analysis at a high level, engineers who conduct the analysis and the governor who controls the project are required to have professional knowledge regarding the topic. Therefore, human resources should be effectively developed. The International Geosynthetics Society, especially its technical committees, should play an important role in addressing these issues.

REFERENCES

Fukuzumi, R. and Nishibayashi, S. (1970) The Surface Improvement Method Using Polyvinyl Sheet Against Soft Ground. *Proc. 25th JSCE Annual Meeting*, Sendai, Japan, III, pp.122–124 (in Japanese).

Koerner, R.M. (2012) Designing with Geosynthetics - *6Th Edition*, XLIBRIS.

Miki, H. (1996) Application of Geosynthetics to Embankment on Soft Ground and Reclamation Using Soft Soil, *Proc. of the Int. Sym. on Earth Reinforcement. Fukuoka*, pp 919–942.

PWRC (2000) *Design and Construction Manual of Geosynthetics Reinforced Soil (revised version)*, Public Works Research Center, Tsukuba, Japan, 305pages (in Japanese).

Sakai, T., Toda, T., Nishibayashi, K. and Takahashi, S. (1990) Behavior of Fabric and Soil in Surface Reinforcement for Lining, *Proc. 45th JSCE Annual Meeting*, Niigata, Japan, III, pp.334–335 (in Japanese).

Yamanouchi, T. (1970) Experimental Study on the Improvement of the Bearing Capacity of Soft Ground by Laying Resinous Net. *Proc. Sym. Found. on lnterbedded Sands*, Vol. 1, pp.102–108.

Yamanouchi, T. and Goto, K. (1979) *A Proposed Practical Formula of Bearing Capacity for Earthwork Method on Soft Clay Ground Using a Resinous Mesh*. Tech. Reports of Kyushu Univ., 52–3, pp.201–207 (in Japanese).

The design of embankments on soft soil, over piles and over areas prone to subsidence to BS8006

P.J. Naughton
Atlantic Technological University Sligo, Ireland

ABSTRACT: BS8006-1 (2016) is the UK code of practice for strengthen /reinforced soil and other fills. The code provides design guidance for metallic and polymeric reinforced soil walls, reinforced steep and shallow slopes and embankments on soft soil, over piles and over areas prone to subsidence. This code was one of the first design documents on geosynthetic reinforcement applications and first appeared in 1995 (BS8006 1995). The last revision of the code was in 2016. This paper reviews the design of embankments on soft soil, over piles and over areas prone to subsidence to that code. Key aspects are discussed, rather than providing a recipe for design.

1 INTRODUCTION

BS8006-1 (2016) is the UK code of practice for strengthen/reinforced soils and other fills. The code provides design guidance for metallic and polymeric reinforced soil walls, reinforced steep and shallow slopes and embankments on soft soil, over piles and over areas prone to subsidence. This code was one of the first design documents on geosynthetic reinforcement applications and first appeared in 1995 (BS8006 1995). The last revision of the code was in 2016.

Eurocode 7 (EN1997-1 2004) does not consider reinforced soil techniques. The UK National Annex to EN1997-1 (2004) specifies the use of BS8006-1 for the design of reinforced soil structures in the UK. While BS8006-1 is not fully EN1997-1 compliant, it does align with that code and stipulates its use for calculation of overall stability in many applications. For the design of reinforcement, BS8006-1 uses limit state principles in design and has different sets of partial factors to EN1997-1. The partial factors for each application are based on previous experience and have been calibrated to maintain consistency with current practise (BS8006-1 2016).

This paper reviews the design of embankments on soft soil, over piles and over areas prone to subsidence. Key aspects are discussed, rather than providing a recipe for design.

2 PARTIAL FACTORS AND DESIGN LIFE

2.1 *Partial factors for embankments on soft soil, over piles and over areas prone to subsidence*

The partial factors for use in design of reinforcement for embankments on soft soil, over piles and over areas prone to subsidence are presented in Table 1. These factors are used when checking limit states where the tension in the reinforcement is a contributor to stability. In some limit states, where the reinforcement is not a contributor, the partial factors from EN1997-1 (2004) are used. In the UK, the National Annex specifies that Design Approach 1 shall be used.

Table 1. Partial factor for embankments on soft soil, over piles and over areas prone to subsidence, BS8006-1.

	Partial factor		Limit state	
			Ultimate	Serviceability
Load factors	Soil unit weight	f_{fs}	1.3	1.0
	External dead load	f_f	1.2	1.0
	External live load	f_q	1.3	1.0
Soil materials	Angle of friction, ϕ'_{cv}, applied to $\tan\phi'_{cv}$	f_{ms}	1.0	1.0
	Apparent cohesion, c'	f_{ms}	1.6	1.0
	Undrained shear strength, c_u	f_{ms}	1.0	1.0
Reinforcement interaction factors	Sliding across the surface	f_s	1.3	1.0
	Pullout resistance of reinforcement	f_p	1.3	1.0

2.2 Reinforcement material factors

The reduction factors for reinforcement base strength are listed in BS8006-1 and use a different terminology to ISO TR 20432 (2007). However, Annex A of BS8006-1 presents the reduction factors from ISO TR 20432 (2007) and these are typically used in design. In addition to material reduction factors, a partial factor for the ramifications of failure is given in BS8006-1. The magnitude of this partial factor increases with the consequences of failure, Table 2. In embankment support applications the ramifications of failure are typically considered high and this factor is taken as 1.1. The reduction factors, including the partial factor for the ramifications of failure, are applied to the short-term characteristic strength of the reinforcement.

Table 2. Partial factor for the ramifications of failure, BS8006-1.

Category	Partial factor, f_n	Example of structures
1 (low)	1.0	Retaining walls and slopes less than 1.5m high
2 (medium)	1.0	Embankments where failure would result in loss of service
3 (high)	1.1	Embankments supporting motorways, roads and railways

2.3 Design life for embankments on soft soil, over piles and over areas prone to subsidence

The design life of embankments on soft soil is typically 5 – 10 years, in which time the foundation soil should have gained sufficient strength to support the embankment without reinforcement. The actual design life can be determined using consolidation theory, considering the change to foundation soil strength and any ground improvement techniques employed.

For embankments over piles the design life is typically 60 years (embankments only) or 120 years where the system is supporting retaining walls or other structures. The design life for earthworks in the UK is 60 years, while structures (retaining walls and abutments) is 120 years (BS6031 2009). However, typically embankments over piles are designed for a 120 year design life, as for most reinforcement materials there is only a marginal difference in the magnitude of reduction factors for a 60 and 120 year design life.

The design life for an embankment with basal reinforcement over an area prone to subsidence is based on the design strategy and proposed remedial works. BS8006-1 does not

specify a minimum design life for these structures. Where the remedial strategy is to immediately repair the embankment area once subsidence occurs, the design life is typically less than five years. The repair of the embankment is dealing with the cause of the subsidence issues, rather than just repairing the surface deformation. A 60 – 120 year design life is typical for cases with no planned intervention.

3   EMBANKMENTS ON SOFT SOIL

Reinforcement can be placed at the base of an embankment on soft soil to improve stability. In this situation settlement of the embankment is of secondary concern. The role of the reinforcement is to prevent shear failure both in the embankment fill and in the foundation soil. The reinforcement stabilises the embankment by preventing lateral spreading of the fill, extrusion of the foundation soil and rotational failure. The reinforcement is installed at the base of the embankment normal to its centre line.

BS8006-1 states that the following ultimate limits states should be checked: local stability, rotational stability through the embankment, overall stability of the embankment, lateral sliding of the embankment fill and foundation extrusion. In addition, the reinforcement strain and foundation settlement must be checked for the serviceability limit state. Foundation settlement is outside the scope of BS8006-1 and is typically checked using conventional soil mechanics methods.

Reinforcement at the base of the embankment can be used in conjunction with ground improvement techniques, such as vertical drains, or construction techniques like surcharging and berms. However, no guidance on the design of these systems is given in BS8006-1.

BS8006-1 states that the long-term design tensile strength of the reinforcement should be the greater of:

1. The maximum tensile force to resist the rotation limit state, or
2. The maximum tensile force to resist lateral sliding plus the maximum tensile force to resist foundation extrusion.

BS8006-1 allows rotational stability to be checked using conventional slip surface analysis, plasticity solutions (as a preliminary design tool) and finite element and finite difference techniques.

For lateral sliding the reinforcement is required to resist the full lateral thrust from the embankment fill. BS8006-1 also requires that the length of the reinforcement is sufficiently long under the side slope of the embankment to generate sufficient interaction to resist the long-term tension in the reinforcement due to lateral thrust.

For foundation extrusion, the length of the embankment side slope needs to be a minimum length to resist the lateral loads developed in the foundation soil. Equations for determining the length of the side slope are presented in BS8006-1 for a constant and linearly increasing undrained shear strength in the foundation soil. The short-term tensile force to resist foundation extrusion is proportional to the undrained shear strength, with foundation soils of higher undrained shear strength having higher reinforcement requirements. However, this will be counterbalanced by higher strength foundation soil requiring shorter embankment side slope lengths.

BS8006-1 suggests that the short-term allowable strain in the reinforcement should not exceed 5% and that for soft sensitive soil the maximum strain should be limited to 3%. No guidance on what constitutes a soft sensitive soil is given. A design strain of 5% is suitable for most reinforcement materials on the market.

The maximum tensile force to be resisted by the reinforcement should ideally be provided in a single layer of reinforcement. Where multi-layers are used, they should be of equal strength and stiffness. A coefficient, with a value less than unity, should also be applied to the second and subsequent layers to account for inefficiencies in a multi-layer system, Rowe & Li (2003).

4 EMBANKMENTS OVER PILES

Embankments over piles are used where control of both embankment stability and settlement are required. In the BS8006-1 design approach, piles are installed on a square grid with square or circular pile caps. No other geometries are permitted. There is no restriction on the type of pile used, but for arching to be mobilized there should be sufficient differential settlement between the piles and the surrounding soft soil. The pile should also have adequate bending resistance to resist lateral forces at the pile head. Two layers of reinforcement are installed, the first longitudinally along the embankment length and the second transversely across the embankment width. The longitudinal reinforcement must transfer the vertical embankment loads to the piles. In the transverse direction the reinforcement must also transfer the vertical loads to the pile caps and also resist the outward lateral thrust of the embankment.

BS8006-1 lists several limit states that should be considered in design: pile group capacity, pile group extent, vertical load shedding (arching), lateral sliding and overall stability, reinforcement strain and foundation settlement. Pile group capacity is not covered in BS8006-1 and the designer is referred to EN1997-1 (2004) for guidance. Foundation settlements, which are not covered in BS8006-1, should also be considered with pile group capacity.

Overall stability is discussed but the designer is again referred to EN1997-1 (2004). The overall stability is difficult to check using conventional stability software, as it is not common to include vertical piles. Where stability is checked, the partial load factors from EN1997-1 (2004) should be used rather than the partial factors listed in Table 1. Guidance is provided in BS8006-1 on the extent of the pile group. As a rule of thumb, the outer most pile should be located at least halfway between the crest and the toe of the embankment. Jennings & Naughton (2010 & 2011) showed that the greater the pile group extent the lower the lateral loads in the individual piles.

Vertical load shedding is a key element when designing embankments over piles. BS8006-1 provides two load shedding calculation methods: Marston's formula and the Hewlett and Randolph method. The designer is free to use either method.

Marston's method (John 1987; Spangler & Hardy 1973) is based on positive projecting subsurface conduits, a plane strain approach that was modified for the three-dimensional nature of embankments over piles. Mathematically it is difficult to reconcile the two- and three-dimensional equations (van Eekelen & Bezuijen 2008). Marston's method assumes that full arching is mobilised once the height of the embankment is greater than 1.4 times the clear spacing between adjacent pile caps. This approach has been part of BS8006 since it was first published in 1995.

The Hewlett and Randolph method which was introduced to BS8006-1 in 2010, is based on the observed mechanism from model tests conducted in sand (Hewlett & Randolph 1988). The method considers a series of hemispherical domes and considers that the system should fail either at the crown of the arch or at the pile cap. Generally, for lower height embankments, failure is at the crown of the arch and as the embankment height increases failure occurs at the pile cap. The transition between failure at the crown and failure at the pile cap is not fixed but depends on the geometry.

Once vertical load shedding is determined the tension in the reinforcement can be established. BS8006-1 assumes that the load on the reinforcement is uniformly distributed and that no support from the underlying foundation soil is considered. This results in the deflected shape of the reinforcement been a parabola. Where the embankment height is greater than 0.7 times the clear spacing between pile caps, the design strain in the reinforcement can be up to a maximum of 6%. Where the height is less than 0.7 times the clear spacing, the design strain should be limited to a maximum value of 3%. This is to ensure the reinforcement has adequate stiffness (reinforcement strain limit state) and has been shown to be an important property in controlling surface deformations (Lawson 1995).

The approach for vertical load shedding adopted in BS8006-1 assumes that the pile caps are square in plan. Where circular pile caps are used, the diameter of the pile cap should be reduced to produce an effective pile cap width, equal to an equivalent square pile with the same plan area as the circular pile cap. This reduces the width of the circular pile cap by 12% and increases the span between adjacent pile caps.

BS8006-1 also specifies a minimum distributed load acting across the reinforcement, corresponding to 15% of the embankment load. This minimum load requirement is specified to overcome deficits in the understanding of vertical load shedding and in particular the impact of dynamic and cyclic loading on load shedding. These effects are not currently considered in vertical load shedding theories.

Figure 1 shows the distributed load on the reinforcement and long-term tension determined in the longitudinal direction using Marston's method and the Hewlett & Randolph formula for embankment heights between 1 – 10m. This data is for a pile spacing, s, of 2.5m c/c, a square pile cap size, a, of 1m, 20kPa surcharge and a weight density of the embankment fill of 19kN/m^3. The total reduction factor for the reinforcement was taken as 1.77 and a design strain of 6% was used. For Marston's method, the distributed load and reinforcement tension both increased to a maximum value at an embankment height of 2.1m, corresponding to 1.4(s-a). For embankment heights greater than this, full arching was assumed and the distributed load and reinforcement tension remain constant. With the Hewlett and Randolph formula the distributed load and reinforcement tension reduced to a minimum at an embankment height of 4m, before increasing proportional to the embankment height. In this case, failure at the crown occurred until an embankment height of 8m, after which failure occurred at the pile cap. For this geometry and embankment heights between 3m and 6m both methods gave similar reinforcement tensions. For embankment heights less than 3m, Marston's method predicted higher tension and for heights greater than 6m Hewlett & Randolph formula predicted the higher tension.
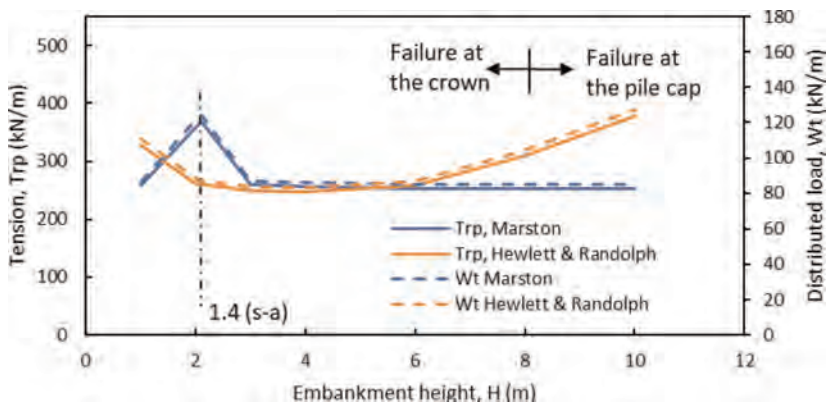
Figure 1. Distributed load, W_t, and long-term reinforcement tension in the longitudinal direction, T_{rp}, determined using Marston's formula and Hewlett and Randolph method in BS8006-1.

BS8006-1 does not explicitly forbid support from the foundation soil between piles. However, no method is given in BS8006-1 for incorporating subsoil support. Russel & Pierpoint (1997) and Russel et al. (2003) have shown that even partial support from the subsoil can significantly reduce the reinforcement requirement in embankments over piles. BS8006-1 does, quite rightly, caution against incorporating partial subsoil support into design and warrants that any partial support used must be available over the entire design life of the structure, typically 60 – 120 years.

In the transverse direction BS8006-1 assumes that the reinforcement will resist the total outward lateral thrust from the embankment. The tension required to resist lateral thrust is proportional to the square of the embankment height. This results in anisotropic strength requirements, particularly in high embankments. In all cases the transverse reinforcement will have a greater strength than that in the longitudinal direction. This is not reflected in the vertical load shedding calculation. Numerical analysis reported by Russel & Pierpoint (1997), Lally & Naughton (2012) and Jennings & Naughton (2012) have shown that the BS8006-1 approach is very conservative, leading to higher transverse reinforcement strengths than may actually be required.

Jennings & Naughton (2010 & 2011) and Ahern and Naughton (2022) have shown that the piles under an embankment can be displaced laterally. BS8006-1 states that the piles should be designed to resist a minimum lateral load equivalent to 10% of the tensile load needed to resist the outward thrust of the embankment multiplied by the longitudinal pile spacing, distributed proportionally between the piles under the sloping edge of the embankment. EN1997-1 should be used for the design of the piles for axial and lateral loads as this is not covered in BS8006-1.

5 EMBANKMENTS OVER AREAS PRONE TO SUBSIDENCE

Subsidence is the sinking, or caving in, of the ground, essentially due to the removal of support beneath the ground surface. The cause of subsidence is normally due to the collapse of a void below the ground surface. These voids can result from either natural processes, soil erosion in karstic areas or the leaching of subterranean salt deposits, or from man-make processes such as ground water pumping or mining.

Reinforcement can be used to limit surface deformations. While reinforcement can be used both internally within the embankment fill and reinforcement at the base of the embankment, BS8006-1 only deals with reinforcement at the base of the embankment. Where a longitudinal void could form, a plane strain analysis is undertaken and the potential void is spanned over the shorter distance by a single layer of reinforcement. Where a circular void could form, an axisymmetric analysis is conducted and two mutually perpendicular layers of reinforcement are required, with each layer having the same short-term tension capacity.

The BS8006-1 approach has two principal assumptions:

1. Constant volume of soil in the zone of depression, with the zone of deformation taken as a truncated wedge for plane strain analysis or a truncated cone for axisymmetric analysis, Figure 2(a). This assumption allows the maximum design strain in the reinforcement to be determined, while still restricting deformation at the embankment surface over the void.
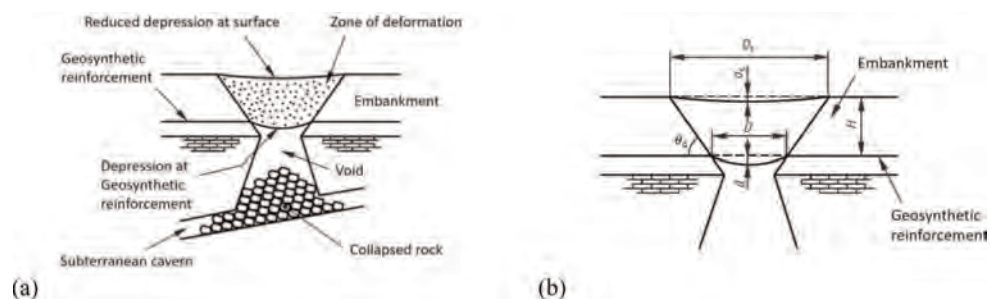
Figure 2. (a) A plane strain representation of the design situation, adopted from BS8006-1 (2016) and (b) The design geometry and definition of parameters in BS8006-1 (2016).

2. No soil arching within the embankment fill. Numerical analysis and physical models have demonstrated that arching does occur in fill over an area experiencing subsidence (Britton & Naughton 2011; Potts & Zdravkovic 2008). However, there is no agreement between arching theories at what stage either partial or full arching is fully mobilised (Britton & Naughton 2010; Naughton 2007).

A plane strain representation of the design situation is shown in Figure 2(a), while the design geometry and definition of parameters in BS8006-1 is presented in Figure 2(b).

The design assumptions in BS8006-1 lead to conservatism in design (Potts & Zdravkovic 2008). The design process given in BS 8008-1 is covered in the following steps:

1. Determine the maximum acceptable surface deformation limits for the pavement or embankment. For motorways the maximum differential surface deformation is limited to 1%, while for lower class highways it is limited to 2%. At these limits traffic can still traverse the deformed area, at speed, without danger. Higher differential surface deformations can also be used in other locations, while more stringent deformation limits are required for railways (Alexiew *et al*. 2002; Villard *et al*. 2000).
2. Determination of a suitable design value for the cavity diameter, D.
3. Using the values determined in Steps 1 and 2, the embankment fill properties and fill height to determine a maximum allowable strain to ensure that the maximum surface deformations remain within the specified limits set in Step 1. The design strain is the lesser of the calculated maximum allowable strain or 6%. The maximum allowable strain is determined based on the geometry of the truncated wedge for plane strain analysis or a truncated cone for the axisymmetric case.
4. Determination of the tensile strength required in the reinforcement to support the embankment and any surcharge loads, while ensuring that the reinforcement has suitable properties to guarantee that the maximum working extension is less than that derived in Step 3. In BS8006-1 it is assumed that the reinforcement is subject to a uniformly distributed load at the base of the embankment and that the deflected shape of the reinforcement is parabolic.

The geosynthetic reinforcement tension given by BS8006-1 is very dependent on both the design strain, Figure 3(a) and the ratio of embankment height, H, to cavity diameter, D, Figure 3(b). At design strains less than 1% there is a rapid increase in the long-term strength requirements, Figure 3(a). At small strains it should also be noted that the short-term

(a) (b)
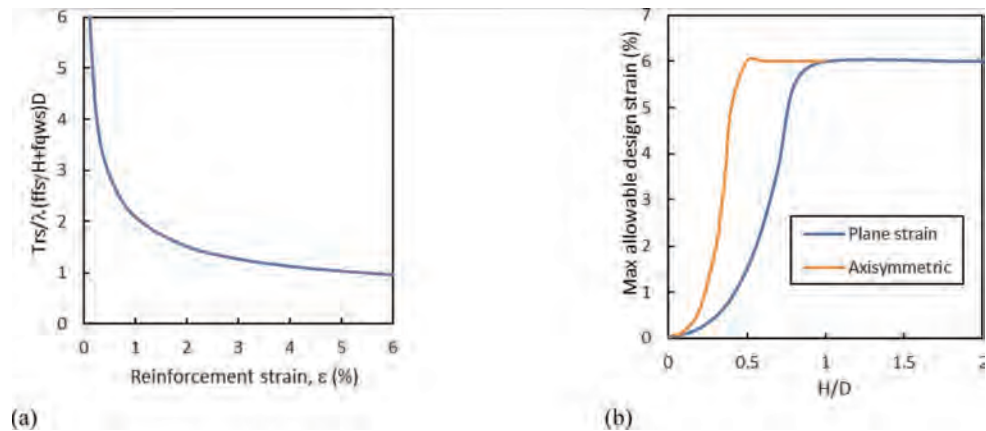
Figure 3.   (a) Relationship between reinforcement strain and normalized reinforcement tension and (b) Relationship between the ratio of embankment height, H, and void diameter, D, and maximum allowable design strain.

strength of the reinforcement is dictated by strain compatibility considerations rather than just the application of reduction factors to the long-term strength.

Figure 3(b) presents the relationship between maximum allowable design strain and the H/D ratio for both plane strain and axisymmetric conditions. In plane strain, once the embankment height and void diameter is unity or less, the maximum design strain reduces rapidly resulting in an increase in the long-term reinforcement strength requirements. For axisymmetric conditions, this change occurs at approximately H/D = 0.5, when the void diameter is twice the embankment height.

Figure 4 presents the long-term tension, maximum design strain and reinforcement bond length for a void forming under a 5m high embankment. The weight density and angle of friction of the embankment fill was 20kN/m^3 and 30° respectively. A traffic surcharge of 10kPa was applied to the embankment surface. The differential surface limit was taken as 1% and was designed using the plane strain and axisymmetric approach given in BS8006-1 (2016). Limiting the maximum short-term capacity of the reinforcement to 1500kN/m would indicate that a longitudinal void of 7m and a circular void of 14m diameter could be accommodated, Figure 4(a). The design strain would be 4% and the reinforcement bond length would be 20m and 25m for the longitudinal and circular voids respectively, Figure 4 (b). Theoretically, larger voids could also be accommodated, however both the short-term strength requirements and bond length would be excessive. Multi-layers of overlapping reinforcement could be used. However, care is needed in laying multi-layers to ensure every part of the site is protected, particularly at overlap joints between layers.

It is not possible to design at extremely small strains, as the reinforcement tension requirements exceed the maximum grades of reinforcement currently manufactured, Figure 4(a). Consideration must also be given to the required anchorage length, which is proportional to the design tension, Figure 4(b). At very high tension it is not practical to manufacture a roll of geosynthetic reinforcement to facilitate installation. High strength reinforcement is bulky necessitating shorter rolls than lighter strength grades.
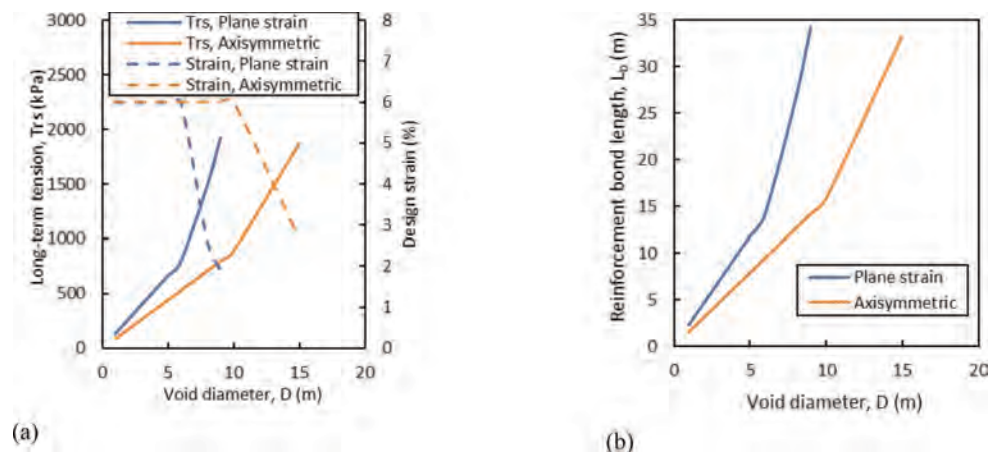
Figure 4. (a) Relationship between void diameter and long-term tension T_{rs} and design strain (b) Relationship between reinforcement bond length and void diameter.

6 CONCLUSIONS

A review of the partial factors and limit states considered by BS 8006-1 (2016) was presented. Key aspects of the design of embankments on soft soil, over piles and over areas prone to

subsidence were also presented. The impact of geometry on the required reinforcement in embankments over piles and over areas prone to subsidence were discussed and recommendations made on these from a design perspective.

REFERENCES

Ahern, S. & Naughton, P.J. 2022. Numerical Analysis of Low Height Piled Embankments. *Proceedings of the Civil Engineering Research in Ireland Conference 2022*. Dublin, 25 – 26 August, 273 – 278.

Alexiew, D., Elsing, A. & Ast, W. 2002. FEM-analysis and Dimensioning of a Sinkhole Overbridging System for High Speed Trains at Gröbers in Germany. *Proceedings of the 7th International Conference on Geosynthetics.* Nice:France

Britton, E.J. & Naughton, P.J. 2011. The Arching Phenomena Observed in Experimental Trap Door Model Tests. *Proceedings of Geofrontiers 2011*, Dallas: USA.

Britton, E.J. & Naughton, P.J. 2010. An Experimental Study to Determine the Location of the Critical Height in Piled Embankments. *Proceedings of the 9th International Conference on Geosynthetics*. Guarujá: Brazil. 23 – 27 May.

BS6031. 2009. *Code of Practice for Earthworks*. British Standards Institution: UK.

BS8006. 1995. *Code of Practice for Strength/Reinforced Soils and Other Fills*. British Standards Institution: UK.

BS8006-1. 2016. *Code of Practice for Strength/Reinforced Soils and Other Fills*. British Standards Institution: UK.

EN1997-1. 2004. Eurocode 7: *Geotechnical Design – Part 1*: General rules. CEN.

Jennings, K. & Naughton, P.J. 2010. Lateral Deformations Under Side Slopes of Piled Embankments. *Proceedings of the 9th International Conference on Geosynthetics*. Guarujá: Brazil. 23 – 27 May.

Jennings, K. & Naughton, P.J. 2011. Lateral Deformation under the Side Slopes of Piled Embankments. *Proceedings of Geofrontiers 2011*, Dallas: USA.

Jennings, K. & Naughton, P.J. 2012. Comparative Analysis of Numerical and Physical Modeling of a Reinforced Piled Embankment. *Proceeding of the 5th European Conf. on Geosynthetics.* Valencia: Spain.

John, N.W.M. 1987. *Geotextiles*. Blackie, Glasgow.

Lally, D. & Naughton, P.J. 2012. An Investigation of the Arching Mechanism in a Geotechnical Centrifuge. *Proceeding of the 5th European Conference on Geosynthetics*, Valencia:Spain.

Lawson, C.R. 1995. Basal Reinforced Embankment Practice in the United Kingdom. *The Practice of Soil Reinforcing in Europe*. Thomas Telford: London.

Hewlett, W.J. & Randolph, M.A. 1988. Analysis of Piled Embankments. *Ground Engineering*, April.

Naughton, P.J. 2007. The Significance of Critical Height in the Design of Piled Embankments. *Proceeding of Geo-Denver 2007, New Peaks in Geotechnics, ASCE GSP 172, Soil Improvement*. Denver: USA.

Potts, V.J. and Zdravkovic, L. 2008. Assessment of BS8006:1995 Design Method for Reinforced Fil Layers Over Voids. *Proceedings of the 4th European Conference on Geosynthetic Conference*. Edinburgh: UK.

Rowe, K.R. & Li, A.L. 2003. *Insights From Case Histories: Reinforced Embankments and Retaining Walls*. Kyenote lecture. Landmarks in earth reinforcement, Swets & Zeithlinger: Lisse, 803–829.

Russel, D. & Pierpoint, N.D. 1997. A Numerical Investigation of the Behaviour of Piled Embankments. *Ground Engineering*, November, Thomas Telford:UK.

Russel, D., Naughton, P.J. & Kempton, G.T. 2003. A New Design Procedure for Piled Embankments. *Proceedings of the 56th Annual Canadian Geotechnical Conference*. Winnipeg: Canada.

Spangler, M.G. & Handy, R.L. 1973. *Soil Engineering*. Intext Educational Publishers. New York.

van Eekelen, S. & Bezuijen, A. 2008. Design of Piled Embankments, Considering the Basic Starting Points of the British Standard BS8006. *Proc. of the 4th European Conf. on Geosynthetics*. Edinburgh: UK.

Villard, P., Gourc, J.P. & Giraud, H. 2000. A Geosynthetic Reinforcement Solution to Prevent the Formation of Localized Sinkholes. *Canadian Geotechnical Journal*: 37, 987–999.

Design of basal reinforced embankments on soft soils at short and long term

P. Rimoldi
Civil Engineering Consultant, Milan, Italy

G. Lugli & F. Trovato
Officine Maccaferri Spa, Bologna, Italy

ABSTRACT: The stability of embankments on soft foundation soil is often critical during the construction period; geosynthetic reinforcements placed across at foundation level enhance the short-term stability of an embankment over soft soil by preventing lateral sliding of the fill and extrusion of the foundation soil. For each of these limit states the associated reinforcement strength and bond length should be checked to ensure that the required tensile load can be generated in the reinforcement. While the consolidation of the soft soil develops, geosynthetics for basal reinforcement are progressively subject to out-of-plane deformations, which trigger the tensioned membrane mechanism. Hence the long-term design of geosynthetics requires the calculation of the final and constant tensioned membrane strength, which has to be compared with the long-term tensile strength of the geosynthetics for getting the associated long-term Factor of Safety.

1   INTRODUCTION

The design of basal reinforcement of embankments on soft soil at short term has been addressed by Romeo *et al* (2021), while the design of basal reinforcement of embankments on soft soil at long term has been addressed by Rimoldi *et al* (2022). The present paper aims to present the overall design method for basal reinforcement of embankments on soft soil at short and long term. Additional details may be found in the two above referenced publications.

2   DESIGN AT SHORT TERM

2.1   *Lateral sliding*

Lateral sliding is a limit state which involves only the equilibrium entirely within the embankment fill: the direct sliding mechanism along the upper surface of the reinforcement layer has to be examined (Figure 1). Sliding would result if the available resistance at the reinforcement interface is lower than the lateral thrust from the fill. Hence the anchorage length L_e, shown in Figure 1, shall be determined, together with the tensile strength T_{ds} generated by the lateral sliding mechanism.

The tensile force per metre run in the reinforcement, T_{ds}, can be determined as:

$$T_{ds} = 0.5 K_h H \left(f_{fs} \gamma_1 H + 2 f_q w_s \right) \tag{1}$$

where: K_h is the horizontal earth pressure coefficient; H is the height of the embankment; γ_1 is the unit weight of the embankment fill; w_s is the surcharge on top of the embankment; f_{fs} is the partial factor for soil unit weight; f_q is the partial factor for external applied loads.

While generating the tensile load T_{ds} in the reinforcement, the embankment fill should not slide outwards over the reinforcement. Hence, to prevent the horizontal sliding the minimum reinforcement bond length, L_e, is:

$$L_e = \frac{0.5 K_h H \left(f_{fs}\gamma_1 H + 2f_q w_s\right) f_s f_n}{\gamma_1 h \frac{f_{ds}\tan\varphi'_{cv}}{f_{ms}}}$$ (2)

where: f_s is the partial factor for reinforcement sliding resistance; f_n is the partial factor governing the economic ramifications of failure; h is the average height of embankment fill above the reinforcement length L_e; f_{ds} is the interaction coefficient relating the embankment fill/reinforcement bond angle to $\tan\varphi'_{cv}$; φ'_{cv} is the angle of friction at large strains of the embankment fill under effective stress conditions; and f_{ms} is the partial material factor applied to $\tan \varphi'$.

Note: f_{ds} can be obtained from direct shear tests, according to EN ISO 12957-1, or derived from published default values for the specific reinforcement and fill (see Koerner 2012).

The anchorage length L_e obviously starts from the toe of the side slope: since the basal reinforcement extends to the whole embankment base, the available reinforcement length is usually well in excess of L_e; hence the required length to resist direct sliding usually is not a limit state.

The easiest way for evaluating K_h is to use the well-known Coulomb's formula for the coefficient of active thrust with inclined wall face; in case of horizontal top the formula can be written as:

$$K_h = \frac{\cos^2\left(\varphi' - \lambda\right)}{\cos^2\lambda \cdot \cos\left(\lambda + \delta\right) \cdot \left[1 + \sqrt{\frac{\sin\left(\delta + \varphi'\right)\cdot\sin\varphi'}{\cos(\lambda+\delta)\cdot\cos\lambda}}\right]^2} \cdot \cos\left(\lambda + \delta\right)$$ (3)

where: λ is the angle of the slope to the vertical, δ is the friction angle along the line a-b shown in Figure 1. For the embankment the slope angle λ in Equation (3) is negative and is equal to $(\beta - 90°)$, while the friction angle δ can be assumed equal to φ'.

Note that, to be consistent with equations (1) and (2), Equation (3) shall be used with the friction angle of the fill equal to φ'_{cv}.

2.2 Foundation extrusion

Vertical embankment loading causes an increase in the vertical stress in the foundation soil and a corresponding increase in the horizontal stress. Therefore, a lateral thrust develops in the foundation soil beneath the embankment crest which can eventually cause the foundation soil beneath the embankment side slope to displace laterally. If we assume that extrusion starts from the slope crest (where the vertical load decreases), to prevent this extrusion the side slope length of the embankment, L_s, should be enough to develop adequate lateral confinement (Figure 1).

2.2.1 Foundation soil of uniform strength and limited depth

With reference to Figure 1, by integrating the equation expressing the horizontal equilibrium balance for a soft foundation soil with uniform undrained shear strength, c_u, and limited depth, D (with respect to the embankment width), underlain by a rigid stratum, with the boundary conditions $z = 0$ and $z = D$, we get the minimum side slope length $L_{s,min}$ required to support the weight of the embankment:

$$L_{s,min} = \frac{\left(f_{fs}\gamma_1 H + f_q w_s - \frac{4c_u}{f_{ms}}\right)D}{\frac{c_u(1+\alpha_{bc})}{f_{ms}}} f_n$$ (4)

where: c_u is the undrained shear strength of the foundation soil at the underside of the reinforcement; α_{bc} is the interface coefficient relating the soil/reinforcement adherence to c_u, $L_{s,min}$ is the minimum distance from the embankment toe to the edge of the embankment crest; f_n is the partial factor governing the economic ramifications of failure.

For obvious physical and geometrical reasons, if Equation (4) provides a minimum side slope length $L_{s,min} \leq 0$, the foundation extrusion cannot occur. This condition can be given as follows:

$$f_{fs}\gamma_1 H + f_q w_s \leq \frac{4c_u}{f_{ms}} \tag{5}$$

Equation (5) represents the cut-off value for the allowable bearing pressure for the soft foundation soil of uniform strength c_u. If the inequality (5) is satisfied, the foundation extrusion limit state is satisfied as well, and basal reinforcement is not needed.

Equation (5) can be used also to determine the limit time when the basal reinforcement will be no more required: since c_u increases while consolidation progresses, the limit time t_{lim} for the need of basal reinforcement can be obtained from the consolidation theory, as $t_{lim} = t_c$, where t_c is the consolidation time at which:

$$c_u(t_c) = \frac{f_{ms}}{4}\left(f_{fs}\gamma_1 H + f_q w_s\right) \tag{6}$$

From Figure 1, the tensile load per metre run generated in the basal reinforcement, T_{rf}, due to outward foundation shear stress is:

$$T_{rf} = \frac{\alpha_{bc}c_u}{f_{ms}} \cdot L_{s,min} \tag{7}$$

Note that α_{bc} could be obtained only from large scale unconsolidated undrained triaxial tests on both reinforced and unreinforced soil specimens, which are not easily available; moreover, no default values for α_{bc} are included in BS8006:2010. Hence, in absence of direct measurements or published default values of α_{bc}, it is suggested to assume $\alpha_{bc} = 0.50$.
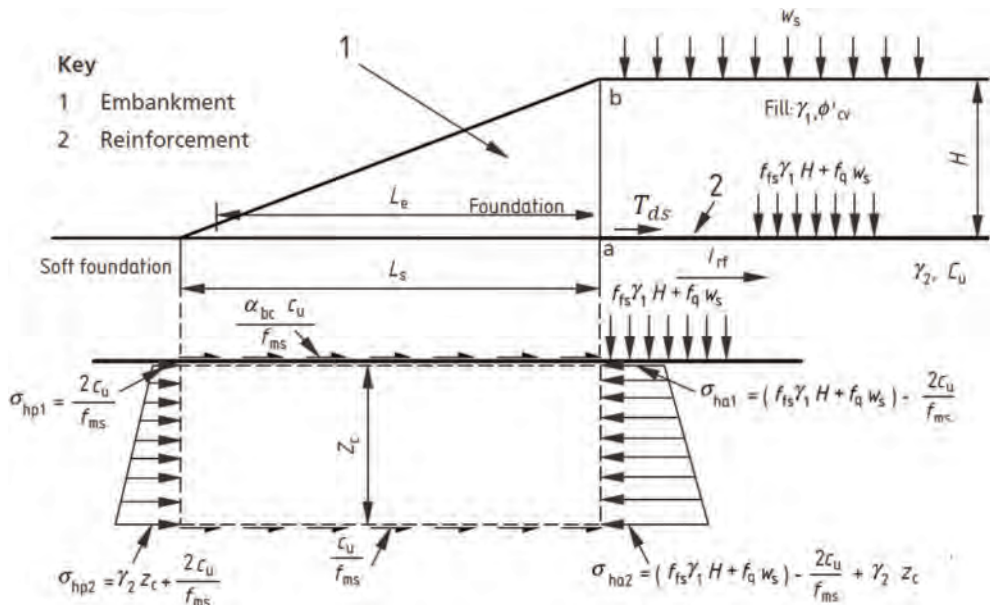
Figure 1.   Scheme of lateral sliding and foundation extrusion mechanisms (modified from BS 8006:2010).

Assuming Equation (4) for $L_{s,\min}$, the tensile load T_{rf} generated in the basal reinforcement due to foundation extrusion becomes:

$$T_{rf} = \frac{\alpha_{bc}c_u}{f_{ms}} \cdot \frac{\left(f_{fs}\gamma_1 H + f_q w_s - \frac{4c_u}{f_{ms}}\right)D}{\frac{c_u(1+\alpha_{bc})}{f_{ms}}} f_n \tag{8}$$

Note that if the minimum side slope length $L_{s,\min}$, from Equation (4), is equal to zero, also the tensile load T_{rf} generated in the basal reinforcement, from Equation (8), is equal to zero.

2.2.2 Foundation soil with strength increasing with depth

The solution described above can be adapted to the problem of soft soil with strength increasing linearly with depth, that is with $c_u(z) = c_{uo} + \rho z$, where c_{uo} is the undrained shear strength of the foundation soil at the underside of the reinforcement and ρ is the increase of undrained cohesion per unit depth. The overall equilibrium between the unloaded toe and the load to be supported at a distance L_s from the toe is now examined (see Figure 1).

In this case the depth of the equilibrium block has to be determined. The same assumption about the horizontal and shear stresses acting on the block are made.

The resulting critical depth z_c is obtained from the solution of the quadratic equation

$$z_c = \frac{-b + \sqrt{\Delta}}{2a} \tag{9}$$

where: $\Delta = b^2 - 4ac$.

The coefficients a, b, and c are:

$$a = \frac{2\rho^2}{f_{ms}^2}; \quad b = \frac{4c_{uo}(1+\alpha_{bc})\rho}{f_{ms}^2}; \quad c = -\left(f_{fs}\gamma_1 H + f_q w_s\right)\frac{c_{uo}(1+\alpha_{bc})}{f_{ms}} + \frac{4c_{uo}^2(1+\alpha_{bc})}{f_{ms}^2} \tag{10}$$

A critical depth $z_c > 0$ is obtained if $-b + \sqrt{\Delta} > 0 \Leftrightarrow \Delta = b^2 - 4ac > b^2 \Leftrightarrow c < 0$.

Reinforcement is required, for the foundation extrusion limit state, only if the inequality (11) is satisfied:

$$f_{fs}\gamma_1 H + f_q w_s > \frac{4c_{uo}}{f_{ms}} \tag{11}$$

Adding the partial factor f_n governing the economic ramifications of failure, the minimum side slope length is:

$$L_{s,\min} = L_s(z_c) = \frac{\left(f_{fs}\gamma_1 H + f_q w_s\right)z_c - \frac{4}{f_{ms}}\left(c_{uo}z_c + \rho\frac{z_c^2}{2}\right)}{\frac{c_{uo}(1+\alpha_{bc})+\rho z_c}{f_{ms}}} f_n \tag{12}$$

where z_c shall be calculated with Eqs. (9) and (10).

It is important to note that Equation (11) can be used also to determine the limit time when the basal reinforcement will be no more required: since c_{uo} increases while consolidation progresses, the limit time $t_{\lim}$ for the need of basal reinforcement can be obtained from Equation (6), using $c_{uo}(t_c)$ in place of $c_u(t_c)$.

From Figure 1, the tensile load per metre run generated in the basal reinforcement T_{rf} due to outward foundation shear stress is:

$$T_{rf} = \frac{\alpha_{bc}c_{uo}}{f_{ms}} \cdot L_{s,\min} = \frac{\alpha_{bc}c_{uo}}{f_{ms}} \cdot L_s(z_c) \tag{13}$$

As in the previous case, in absence of direct measurements or published default values of α_{bc}, it is suggested to assume $\alpha_{bc} = 0.50$.

Adopting Equation (12) for $L_{s,\min}$, the tensile load in the basal reinforcement T_{rf} becomes:

$$T_{rf} = \frac{\alpha_{bc}c_{uo}}{f_{ms}} \cdot \frac{\left(f_{fs}\gamma_1 H + f_q w_s\right)z_c - \frac{4}{f_{ms}}\left(c_{uo}z_c + \rho\frac{z_c^2}{2}\right)}{\frac{c_{uo}(1+\alpha_{bc})+\rho z_c}{f_{ms}}}f_n = \frac{\alpha_{bc}c_{uo}}{f_{ms}} \cdot L_s(z_c) \qquad (14)$$

Therefore, in the case of soft soil with strength increasing linearly with depth, the required tensile strength of basal reinforcement can increase or decrease, in a non-linear way, as function of the values of the undrained shear strength parameters of the soft foundation soil, c_{uo} and ρ.

2.3 Design of the basal reinforced embankment at short-term

The design of geosynthetic reinforced embankments on soft soil at short-term requires the definition of the minimum side slope length and of the tensile strength of reinforcement. As above said, the side slope length does not depend on the direct sliding mechanism, hence it shall be assumed equal to $L_{s,\min}$, that is the length of the side slope required to prevent foundation extrusion.

The design tensile strength of reinforcement, T_D, is the sum of the tensile strengths required for the direct sliding and foundation extrusion mechanisms:

$$T_D = T_{ds} + T_{rf} \qquad (15)$$

According to ISO/TR 20432, the minimum required $T_{ult,lt}$ is:

$$T_{ult} = T_D \cdot (RF_{ID} \cdot RF_{CR} \cdot RF_W \cdot RF_{CH}) \qquad (16)$$

where: T_D = design tensile strength of the reinforcement (kN/m); $T_{ult,lt}$ = ultimate tensile strength of the reinforcement (kN/m) required at short term; RF_{ID} = reduction factor for installation damage; RF_{CR} = reduction factor for creep (= 1 at the end of construction); RF_W = reduction factor for long term weathering exposure (= 1 if the reinforcement is covered with soil within 1 day exposure time); RF_{CH} = reduction factor for long term chemical and biological degradation.

3 DESIGN AT LONG TERM

3.1 Long term deformations

While the consolidation of the soft soil develops, the base of the embankment is subject to non-uniform settlements, usually higher at the centre of embankment and progressively decreasing towards the toes of the lateral banks (Figure 2.a). Hence geosynthetics for basal reinforcement are progressively subject to out-of-plane deformations, which trigger the tensioned membrane mechanism. When consolidation ends, the related out-of-plane deformations become constant over time, and the tensioned membrane force produced in the geosynthetics also become constant.
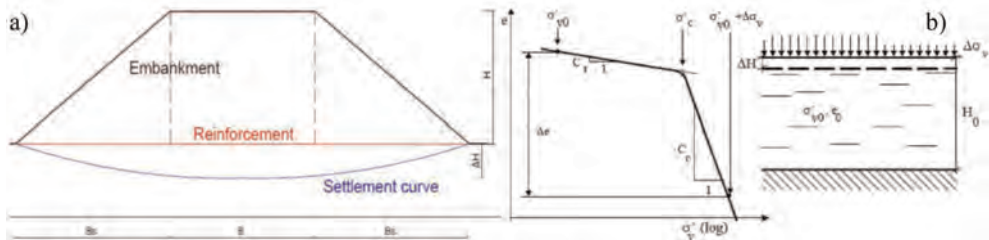
Figure 2. a) The out-of-plane deformation along the settlement curve triggers the tensioned membrane mechanism in geosynthetics for basal reinforcement; b) Scheme for calculating the primary consolidation settlement of a layer of cohesive soil.

This means that the long-term design of geosynthetics for basal reinforcement of embankments on soft soil requires the calculation of the final and constant tensioned membrane strength, which has to be compared with the long-term tensile strength of the geosynthetics.

In the long term, the soft soil below the embankment yields under the weight of the embankment itself. The geosynthetic reinforcement slightly decreases the settlement (5 – 10 % less) but the reinforcement cannot control the settlement by imposing a certain reinforcement strain ε.

Instead, it is the settlement that imposes the long term strain ε to the reinforcement, as a function of the out-of-plane deformation that triggers the tensioned membrane mechanism.

Therefore, for the check of the basal reinforcement at long term, it is first necessary to calculate the settlement of the embankment at the time t necessary for at least 90 % consolidation, the related force in the basal reinforcement, and the related strain $\varepsilon(t)$; then calculate the required ultimate strength $T_{ult,lt}$ at long term, based on the isochronous curves of the geosynthetic reinforcement and all reduction factors at time t.

3.2 Consolidation settlements

Calculation of the total settlement due to primary consolidation can be performed using the parameters obtained from oedometric tests: if one-dimensional consolidation is considered, it is possible to calculate the settlement of a soil layer under a uniformly distributed load $\Delta\sigma_v$.

Especially in the presence of thick and non-homogeneous layers, it is advisable to divide the soft soil layer into several sub-layers, possibly differentiating the soil compressibility parameters. In the more general case of over-consolidated soil, with reference to the symbols in Figure 2.b, the overall settlement ΔH of the soft soil is expressed as:

$$\Delta H = \sum_{i=1}^{n} \frac{H_{0i}}{1 + e_{0s}} \cdot \left(c_u \cdot \log \frac{\sigma_{ci}}{\sigma_{v0i}} + C_{ci} \cdot \log \frac{\sigma_{v0i} + \Delta\sigma_{vi}}{\sigma_{ci}} \right) \tag{17}$$

As an alternative to the parameters C_c and C_s, it is possible to refer to the volume compressibility coefficient m_v, or to the compressibility coefficient a_v:

$$\Delta H = \sum_{i=1}^{n} H_{0i} \cdot \Delta\sigma_{vi} \cdot m_{vi} = \sum_{i=1}^{n} \frac{H_{0i}}{1 + e_{0s}} \cdot \Delta\sigma_{vi} \cdot \sigma_{vi} \tag{18}$$

where the pressures and compressibility parameters refer to the centre line of each of the n sub-layers, each one of thickness H_{0i}.

In the hypothesis that the load, q, applied to the surface, is uniformly distributed and infinitely extended, the increase in the total vertical stress, $\Delta\sigma_v$, is equal to the applied load ($\Delta\sigma_v = q$). In case the load q is distributed over a surface of limited dimensions, the value of $\Delta\sigma_v$ is reduced as the depth increases and varies in a horizontal direction. As a first approximation, in the case of load q uniformly distributed over a rectangular area, the value of $\Delta\sigma_v$ can be estimated assuming that the load spreads with a 2V: 1H ratio. At depth z, therefore:

$$\Delta\sigma_v(z) = \frac{q \cdot L \cdot B}{(L + z) \cdot (B + z)} \tag{19}$$

A better evaluation of the vertical pressure increase $\Delta\sigma_v(Z = H/2)$ can be obtained using the Boussinesq equations for rectangular loaded area (see Rimoldi & Simons 2013), assuming the load as applied to a rectangular area of the same width B of the embankment at top and length L = 1 m.

The total settlement can be evaluated also with the modified Winkler model (as example, according to Rimoldi & Pagotto 1986, or Shukla & Chandra 1995) or with validated numerical methods.

3.3 Oedometric consolidation theory

According to Terzaghi's theory of oedometric consolidation, the dimensionless variable T_v (Time Factor) is defined as:

$$T_v = \frac{C_v \cdot t}{H_d^2} \tag{20}$$

where H_d is the drainage height, i.e. equal to the maximum vertical path that a water particle need to run to exit the layer (in case of a double drained layer it is equal to half the height of the layer, in case of drainage on one side only it is equal to the thickness of the whole layer).

There are analytical expressions that provide an approximate estimate of the solution for the case of initial isochronous constant with depth, for example the following formula by Terzaghi, valid for $U_m > 60\%$:

$$T_v = 1.781 - 0.933 \cdot \log(100 - U_m) \tag{21}$$

where U_m is the considered average degree of consolidation (in % of total consolidation).

3.4 Strain in basal geosynthetic

According to Giroud (1995), a geosynthetic subjected to a normal stress follows the out-of-plane deflection in the supporting soil (see Figure 3.a). As a result of the out-of-plane deflection, the geosynthetic elongates and a tensioned membrane force is generated.

If the shape of the geosynthetic after deflection is a smooth curve in a considered cross section, the elongation of the geosynthetic can be determined mathematically by assuming that the shape is a curve with a known equation, such as a parabola. Then, if it is assumed that the geosynthetic strain ε is uniformly distributed, it is possible to derive the strain from the elongation (b'- b), shown in Figure 3.a.
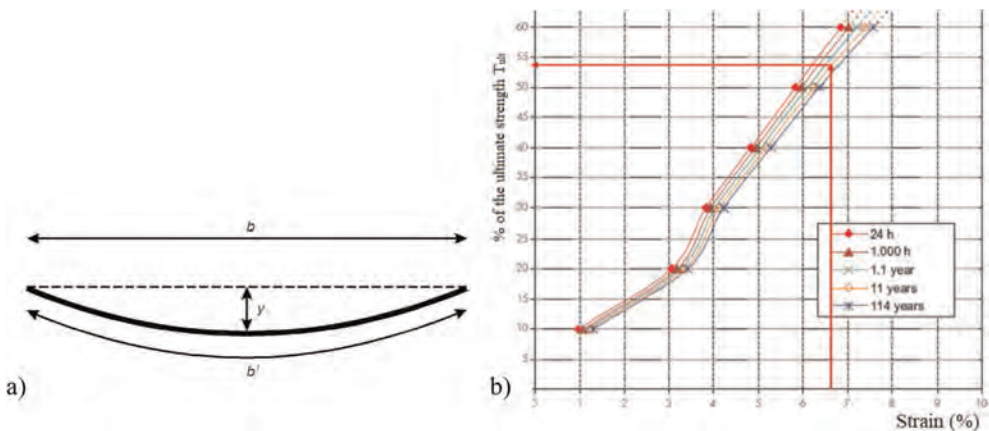
Figure 3. a) Geosynthetic deflection (from Giroud 1995); b) example of isochronous curves of geogrids.

Mathematical tables give the following expression of ε from the length of a parabola (see Figure 3.a):

$$\varepsilon = \frac{1}{2}\sqrt{1 + 16(y/b)^2} + (1/8) \cdot (b/y) \cdot \ln\left(4(y/b) + \sqrt{1 + 16(y/b)^2}\right) \quad (22)$$

3.5 Calculation procedure

The proposed method is based on the following procedure.

The average degree of consolidation U_m is set (i.e. $U_m = 90\ \%$) and T_v is calculated with Equation (21).

From Equation (20), assuming drainage only towards the top, therefore with $H_d = H$:

$$t = T_v \cdot c_v \cdot H^2 \quad (23)$$

$\Delta\sigma_v(Z)$ is calculated with Equation (19) or with Boussinesq equations for rectangular loaded area (as wide as the embankment width at crest, B, and 1 m long).

The total settlement ΔH is calculated with Equations (17) or (18), or with the modified Winkler model (according to Rimoldi & Pagotto 1986, or Shukla & Chandra 1995) or with validated numerical methods.

The total settlement with basal reinforcement is assumed to be equal to 95 % of total settlement without reinforcement (see Rimoldi & Pagotto 1986, or Shukla & Chandra 1995):

$$\Delta H_r = 0.95 \cdot \Delta H \quad (24)$$

It is assumed that at time t the settlement at the centre of the embankment with basal reinforcement is:

$$\Delta H_r(t) = \Delta H_r \cdot U_m \quad (25)$$

Setting $y = \Delta H_r(t)$ and $b = B$ in Equation (22) we get $\varepsilon(t)$, the strain in reinforcement at time t.

A geosynthetic reinforcement (e.g. a specific geogrid) is chosen; the value t (example: 50 years) from formula (23) and the value $\varepsilon(t)$ from formula (22) are used to obtain $T_{\varepsilon(t)}$, that is the tensile strength related to the strain ε at time t, in % of the ultimate strength T_{ult}, from the isochronous curves of the reinforcement (see Figure 3.b).

The required tensile strength at long term $T_{req,lt}$ (kN/m), that is the strength corresponding to the tensioned membrane force generated at time t, shall be calculated with the modified Winkler model (according to Rimoldi & Pagotto 1986, or Shukla & Chandra 1995) or with validated numerical methods.

Then, according to BS8006 and ISO TR 20432, the ultimate tensile strength at long term, $T_{ult,lt}$, is:

$$T_{ult,lt} = \left(T_{req,lt}/T_{\varepsilon(t)}\right) \cdot RF_{ID} \cdot RF_W \cdot F_{CH} \cdot RF_{CR} \cdot f_n \quad (26)$$

The geogrid shall be selected with the design tensile strength $T_{ult,D}$:

$$T_{ult,D} = \max\left[T_{ult,lt};\ T_{ult,st}\right] \quad (27)$$

3.6 Anchorage length

The average vertical stress on width B_s of side slopes (see Figure 2.a) is:

$$\sigma_v = 0.5 \cdot \gamma_f \cdot H \quad (28)$$

where γ_f is the unit weight of fill (kN/m^3) and H is the height of the embankment.

The pullout shear stress (kPa) along the contact subsoil–geosynthetic reinforcement is:

$$\tau_{gs} = f_{pos} \cdot \sigma_v \cdot \tan \varphi_s \qquad (29)$$

The pullout shear stress (kPa) along the contact geosynthetic reinforcement–fill is:

$$\tau_{gf} = f_{pof} \cdot \sigma_v \cdot \tan \varphi_f \qquad (30)$$

where f_{pos} and f_{pof} are the pullout factors between the reinforcement/subgrade interface and the reinforcement /fill interface.

Hence the minimum anchorage length (m) is:

$$L_{po} \geq \frac{FS_{po} \cdot T_{red,it}}{(\tau_{gs} + \tau_{gf})} \qquad (31)$$

where FS_{po} is the factor of safety for anchorage, which usually can be assumed as 1.30.

REFERENCES

BS8006:2010. *Code of Practice for Strengthened/reinforced Soils and Other Fills*. BSI. London, UK

EN ISO 12957-1. *Geosynthetics – Determination of Friction Characteristics – Part 1: Direct Shear Test*. ISO, Geneve, Switzerland

Koerner R M 2012. *Designing with Geosynthetics*. 6th Ed., Xlibris LLC, Bloomington, IN, USA

ISO/TR 20432. *Guidelines for the Determination of the Long-term Strength of Geosynthetics for Soil Reinforcement*. ISO, Geneve, Switzerland

Giroud, J.P. (1995). Determination of Geosynthetic Strain Due to Deflection. *Geosynthetics International*, Vol. 2, No. 3, pp. 635–641.

Rimoldi, P., and Simons, M.J. (2013). Geosynthetic Reinforced Granular Soil Mattresses used as Foundation Support for Mechanically Stabilised Earth Walls. *Proc. GeoMontreal 2013 Conference*. Montreal, Canada.

Rimoldi, P., and Pagotto, A. (1986). Settlements and Forces in a Geogrid Reinforced Embankment: A Simple Model. *Proc. "Prediction Symposium on a Reinforced Earth Embankment"*, King's College, London, U.K.

Rimoldi, P, Pezzano, P, and Romeo, D (2022). Long-term Design of Geosynthetic Reinforced Embankments on Soft Foundation Soils Considering the Tensioned Membrane Mechanism, *Proc. GeoAsia 7, 7th Asian Conf. on Geosynthetics*. Taipei, Taiwan.

Romeo, D, Pezzano, P, and Rimoldi, P (2022). Short-term Design of Geosynthetic-reinforced Embankments on Soft Foundation Soils. *Proc. EuroGeo 7, 7th European Conf. on Geosynthetics*. Warsawa, Poland

Shukla, S.K. and Chandra, S. (1995). Modelling of Geosynthetic-Reinforced Engineered Granular Fill on Soft Soil. *Geosynthetics International*, Vol. 2, No. 3, pp. 603–618

Basal reinforcement on piles and on voids according to EBGEO

D. Alexiew
Alexiew Geoconsulting, Gescher, Germany

ABSTRACT: EBGEO is the present German code for the design of geosynthetic reinforced systems. The abbreviation means "Empfehlungen für den Entwurf und die Berechnung von Erdkörpern mit Bewehrungen aus Geokunststoffen" (Recommendations for Design and Analysis of Earth Structures using Geosynthetic Reinforcements). The latest German version was issued in 2010, and the corresponding English one in 2011. Among others, EBGEO includes chapters dealing with the so-called piled embankments and with systems bridging voids. These two chapters are shortly presented inclusive of history and background which cannot be found in the original document. The author is member of the EBGEO working group.

1 INTRODUCTION

Until the early nineties there was in Germany no specialized document handling the design of geosynthetic reinforcements. Due to the increasing demand for such solutions based on the global, European and German development on the field of geosynthetics, the German Geotechnical Society (DGGT) established the working group AK 5.2 to create such design guidelines. The group consisted of designers, consultants, academics, producers, contractors and representatives of official German institutions. The concept was to create not a standard, but "recommendations" being a quite popular and less formal class of documents in German geotechnics: they may include also e.g. calculation examples and/or execution references which is of practical importance especially for innovative topics.

The first EBGEO was published in 1997 and included the most popular applications e.g. embankments on soft soils, retaining walls, slopes, foundations, landfills, temporary roads etc. Experience and documents from both former Western and Eastern Germany were used. The growing demand from engineering practice and the progress on the field of geosynthetic reinforcements necessitated the reactivation of AK 5.2 which started working on a new EBGEO, completely reworked, based on the partial safety factors concept in the sense of Eurocode 7 (EC 7) EN 1997-1 and significantly extended by several new or more extensive chapters. Two of them are shortly described below. The work took several years. Every chapter includes not only design procedures, but beside a list of references also a detailed calculation example. The new present EBGEO includes 300 pages and was published in 2010 (EBGEO 2010), thirteen years after the first one.

Due to the significant interest across Europe the DGGT and the publisher Ernst und Sohn decided to publish also an English version in 2011 (EBGEO 2011). The only difference is that some German terms were switched to new "English" terms according to the Eurocode 7 (EC 7) EN 1997-1 terminology.

A next EBGEO is already planned, but this process will depend among others on the progress of the new next generation EC7.

2 PILED EMBANKMENTS

Officially this Chapter 9 in EBGEO is called "Reinforced earth structures over point or linear bearing elements". Background for this wider definition: the supporting elements can

be not only piles, but also columns of different types such as compacted gravel columns, mixed-in-place columns, geotextile encased columns etc. Supporting elements can be also diaphragm walls being linear, typically parallel to the embankment axis.

2.1 Overview

The system under consideration is shown in Figure 1.
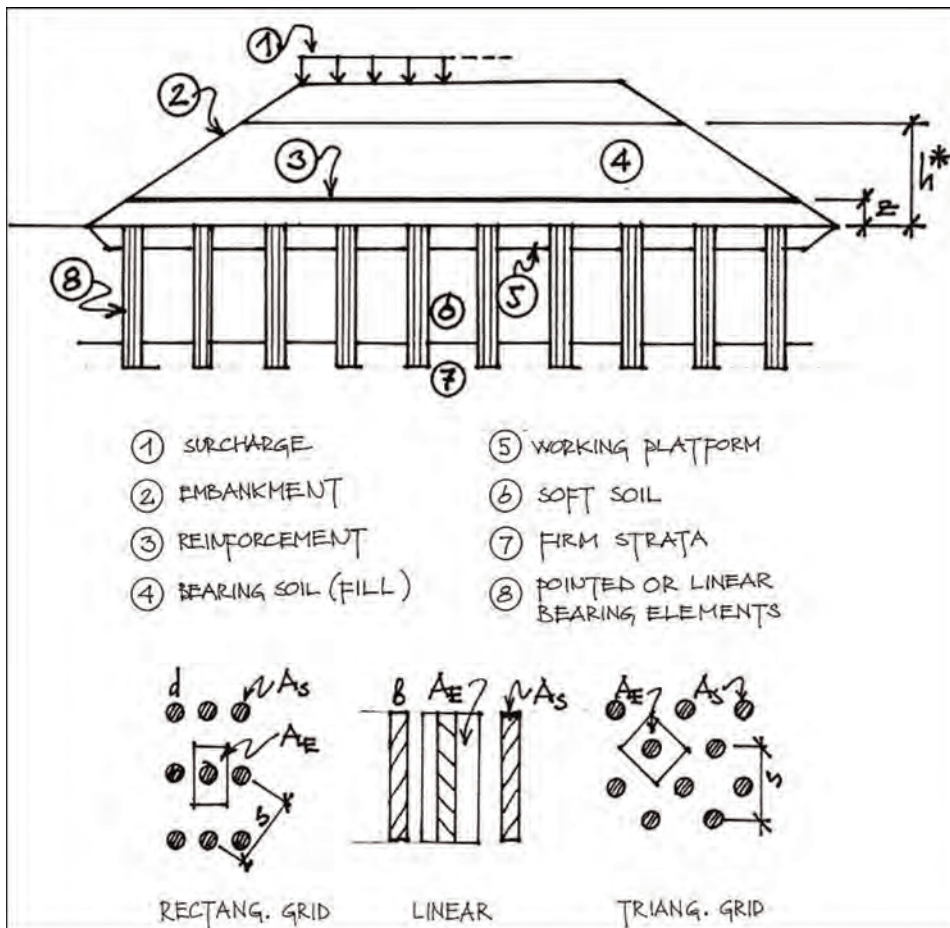
Figure 1. Illustration of system and geometries (diameter d, width b, spacing between supports s, supporting area A_S, h* etc).

2.2 Historical and technical background

First projects of piled embankments started in Germany in the early nineties for the Deutsche Bahn (DB) (German Rail). The trigger was the German reunification, DB had to build new links to the former Eastern Germany and to upgrade existing ones there for higher speeds and loads.

Time became a very important factor, and piled embankments were identified as a good option due to the eliminated consolidation time. Piles/columns capacities were available, woven geotextiles with up to 800 kN/m and geogrids with up to 200 kN/m as well. The missing link was a proper design. At that time no design procedure (e.g. the Swedish Method, the BS 8006, the Guido Method etc.) took into consideration the shear strength of

the embankment fill, say, the methods delivered the same results in terms of reinforcement for sand and crushed gravel. This seemed not realistic and not acceptable to the German geotechnical community.

As a first step the arching method of Hewlett *et al.* (1988) was adopted to estimate the load distribution between piles and soft subsoil. The first projects (e.g. Alexiew & Gartung 1999; Alexiew & Vogel 2001) were designed combining the "arching" from Hewlett *et al.* (1988) with the "hanging rope" parabolic shape under uniform load approach in BS 8006 (1995). However, this was believed to be a compromise, and intensive research started resulting in a better understanding of the "inner life" of the system inclusive of two PhD-Theses (Heitz 2006; Zaeske 2001). German and international experience, German research and measurement programs (e.g. Alexiew & Gartung 1999) were the base for the new Chapter 9 (Alexiew 2004; Kempfert *et al.* 2004) in EBGEO (2010).

2.3 *Some most typical assumptions, conditions and recommendations*

The design procedure is valid for a relation of compression stiffnesses of "pile" to soft soil >75, otherwise the "arching" assumed could not take place.

A multi-spherical "arching" is assumed for evaluating the load distribution between piles and soft soil (difference to Hewlett *et al.* 1989), Figure 2, left.
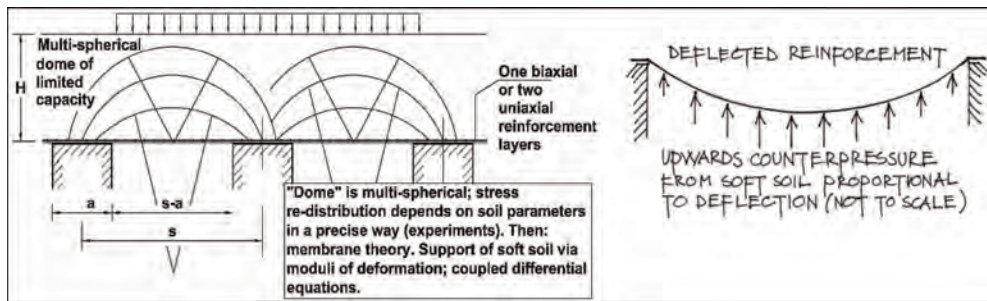
Figure 2.   Overview of concept, multiple arching, spacings and counterpressure.

An upwards counterpressure is assumed from the soft soil resulting from and depending on the deflection of reinforcement between piles (Figure 2, right).

The reinforcement collects the load from the area between the piles and transfers it to fictive "strips" between piles (Figures 1–2). These "strips" control the design.

The distribution between both reinforcement directions depends not only on the pile pattern geometry (Figure 1) but also on the reinforcement moduli J in both directions.

The strip load on the reinforcement between the piles is assumed to be triangular: max value in the middle, zero on the supports.

As spacing s (Figures 1–2) the maximum (diagonal) axial distance is set. Because the design is de facto based on second order theory (interdependence of deformations and forces) and due to the deformation-dependent counterpressure for the solution differential equations have to be solved. Because the EBGEO philosophy is that computational programs and numeric must not be mandatory, graphs are included allowing a read out by hand (Figure 3). Due to brevity the symbols cannot be explained herein.

A key parameter of reinforcement is the tensile stiffness J (time-dependent due to creep).

The reinforcement should be installed as deep as possible.

Maximum two reinforcement layers are allowed. They can be uniaxial, biaxial or mixed.

There are geometrical limitations for s, d, A_S and for the ratio $h^*/(s-d)$ (Figure 1). They are more conservative (smaller s and higher ratio $h^*/(s-d)$) for high variable loads of dominant importance.

A post-construction creep strain of maximum 2% is allowed if there are no stricter limitations due to SLS.

A multi-staged time-dependent design has to be performed. Embankment height is increasing (thus the efficiency of "arching"), loads differ from compaction to traffic, and the tensile modulus J is decreasing.

Assuming an upwards counterpressure is allowed only if the contact between reinforcement and subsoil is guaranteed for the entire design life (e.g. no change in groundwater level).
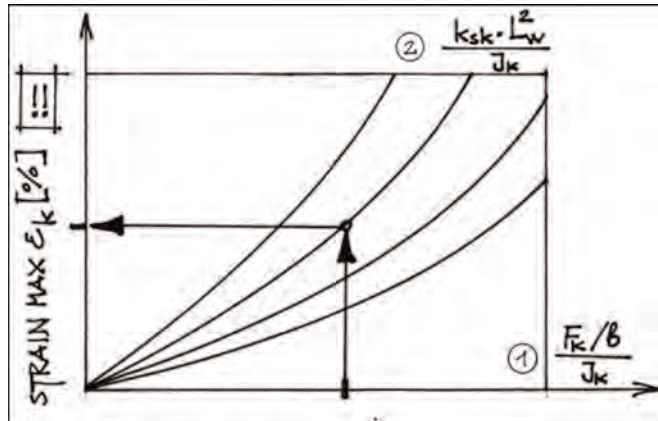
Figure 3. Principle of read-out of strain during design (strongly reduced for clarity, 1 & 2 are normalized dimensionless input parameters).

The tensile force results from calculated strains and assumed J in both directions and has to be checked versus available design strength.

Two very specific points more:

– for the lateral trust (spreading) which can control the choice of reinforcement perpendicular to embankment axis, reduced values are allowed if a thick well-compacted working platform is available (Figure 4);
– for partially cohesive natural or artificial fills the use of an equivalent angle of internal friction considering cohesion – natural or artificial – is allowed (the background is to open the door for the use of local or industrial fills in the sense of sustainability).
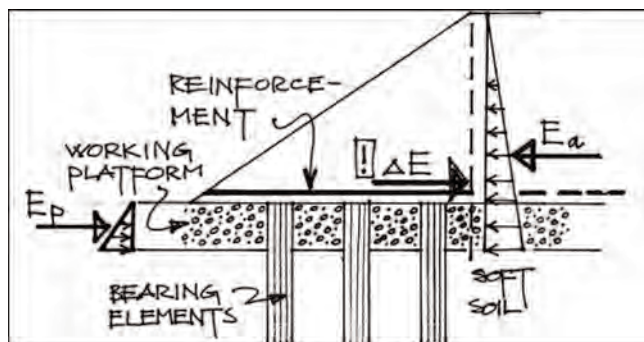
Figure 4. Concept with reduced lateral trust.

Usually, the design procedure consists of a series of calculations: choose J of reinforcements in both directions based on experience, calculate, check and repeat until all requirements are met in both directions inclusive of spreading.

A very detailed calculation example for a multi-staged design is presented.

Execution recommendations are also included at the end of the chapter although formally EBGEO is a design code.

3 BRIDGING VOIDS

Officially this Chapter 11 in EBGEO is called "Overbridging systems in areas prone to subsidence". The background is to use a more general formulation due to the different geological phenomena behind with different genesis.

3.1 Overview

Typical problems demonstrating the importance of the topic are shown in Figure 5.

Figure 5. Examples for sinkholes and their consequences.

3.2 Historical and technical background

Similar to the piled embankments (Chapter 1.2) the problem became acute in Germany after the German reunification. New roads and railroads had to be built or existing ones upgraded. Many of them were positioned in areas prone to subsidence due to natural (e.g. karst) or "artificial" (e.g. mining) reasons.

As a temporary solution the BS 8006 was used for design, at the beginning even in its draft stage. The first German void bridging was designed in 1993 in this way (Alexiew 1997).

Due to the increasing demand from engineering practice the AK 5.2 decided to create an extensive chapter in EBGEO. The story was similar to the piled embankments story: AK 5.2 started an intensive search for international design procedures, and a research program inclusive of tests started as well. This resulted among others in a PhD-Thesis and in a specific German design method called BGE (Schwerdt 2004; Schwerdt *et al.* 2004).

Finally, the Chapter 11 in the new EBGEO 2010 included a wide range of models and design procedures depending on geometrical and geomechanical factors and on the reinforcement concept as well. From this point of view EBGEO is quite unique. Numerous significant German projects for highways, motorways and railroads bridging voids were designed and executed according to these recommendations using already the EBGEO in its Draft stage.

3.3 Some most typical assumptions, conditions and recommendations

Four structural behavior models are taken into consideration assuming failure and non-failure conditions (Figure 6).

The methods available as options are the British BS 8006 (1995), the German BGE (Schwerdt 2004; Schwerdt *et al.* 2004), GIROUD (Giroud *et al.* 1990), the French RAFAEL (Blivet *et al.* 2001, 2002), the German AST (Ast *et al.* 2001). For models taking into account the lateral shear resistance around the collapsing body the silo theory of Terzaghi (Terzaghi 1943) is used.

There is a useful overview of the typical characteristics and limitations of all methods (Figure 7)

Design recommendations concerning the most applicable methods depending on the load transfer model and on the type of reinforcement are given (Figure 8). Isotropic: equal tensile stiffness J in both directions. Extremely anisotropic: J in the one direction is at least ten times higher than in the other one.

Design recommendations concerning the anchorage length outside the void bridged are given depending on the same circumstances (Figure 9), and also concerning possible overlaps (not shown here).

The practical issue of overlaps design of reinforcement layers in both directions is also handled.

It is a mixed ULS/SLS design. On the one hand the surface deflection (leading criterium) and consequently the strain in reinforcement have to be controlled (SLS). On the other hand, a critical state in the fill is assumed in most cases, partial safety factors for ULS are applied (even for formally non-failure models), and the tensile force has to be compared with the ultimate design strength (ULS).
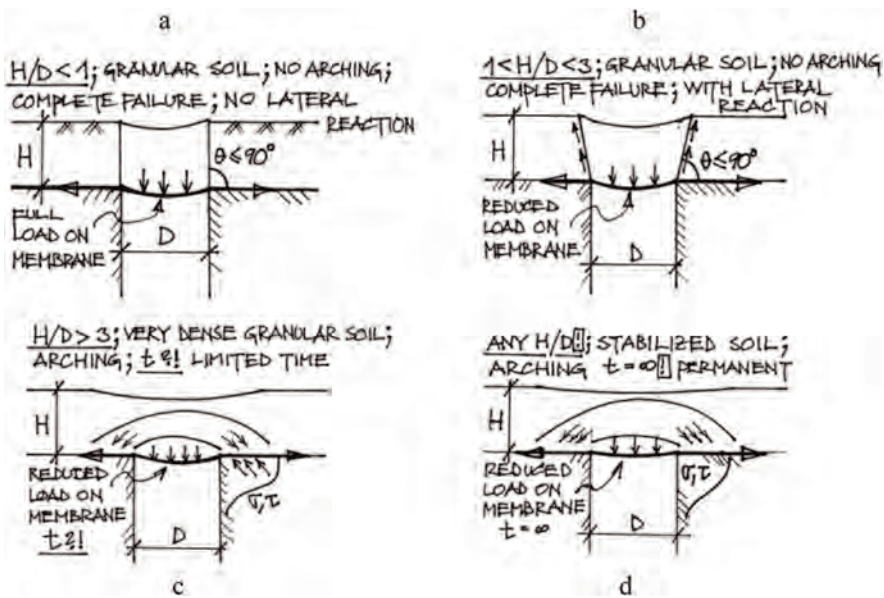
Figure 6. Failure and non-failure models.

Figure 7. Typical considerations in analysis methods.

LOAD TRANSFER DIRECTIONS	BI-DIRECTIONAL	BI-DIRECTIONAL	MONO-DIRECTIONAL
TYPE OF REINFORCEMENT	ISOTROPIC	ANISOTROPIC	EXTREMELY ANISOTROPIC
ILLUSTRATION (FOR A "CIRCULAR" VOID)			
ANALYSIS METHOD	BS 8006 GIROUD BGE AST	BGE [!]	BS 8006 GIROUD RAFAEL

Figure 8. Design methods recommended depending on transfer mechanism and on type of reinforcement.
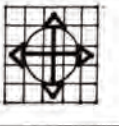
LOAD TRANSFER DIRECTIONS	BI-DIRECTIONAL	BI-DIRECTIONAL	MONO-DIRECTIONAL
TYPE OF REINFORCEMENT	ISOTROPIC	ANISOTROPIC	EXTREMELY ANISOTROPIC
ILLUSTRATION			
ANCHORING LENGTH	$L_L \geq L_{A,md}$ $L_l \geq L_{A,cmd} + D$	$L_L \geq L_{A,md}$ $L_l \geq L_{A,cmd} + D$	$L_L \geq L_{A,md}$ $L_l \begin{cases} \geq 0,5\,m \\ \geq 0,1.B \\ \geq 2.E_d.D \end{cases}$ THE MAX VALUE IS DECISIVE.

Figure 9. Anchoring lengths depending on transfer directions and on type of reinforcement.

Notes are included concerning monitoring and warning systems.

Execution recommendations are also included at the end of the chapter although formally EBGEO is a design code.

4 FINAL REMARKS

EBGEO (2010, 2011) has in the meantime a longer history starting with the previous EBGEO (1997). It is intentionally formulated not as a standard but as a "recommendation" being a popular less stringent format in Germany. This allows to include not only design/calculation procedures but also detailed calculation examples and execution recommendations. It is believed that this is more useful for the geotechnical community.

It includes twelve chapters and three hundred pages, and is a National Application Document to EC7.

Many professionals participated in the working group AK 5.2 of the German Geotechnical Society (DGGT) over the years, the author is only one of them.

The two chapters herein are be presented only shortly and cannot substitute the originals. These chapters belong to the most sophisticated in EBGEO. The author has taken the liberty for himself of adding some history and background to the best of his knowledge.

Note that EBGEO (2010, 2011) being still valid presents in fact the German state-of-the-art about 2005–2009.

In the years passed practice and experience has confirmed it as useful and reliable, inclusive of the two chapters here, although some aspects are maybe conservative.

A next EBGEO is already planned, but this process will depend among others on the progress of the new next generation EC7.

REFERENCES

Alexiew, D. 1997. Bridging a Sinkhole by High-strength High-modulus Geogrids. *Proc. Geosynthetics 97 Conference*, March 1997, Long Beach, USA. 13–24.

Alexiew, D., Gartung, E. 1999. Geogrid Reinforced Railway Embankment on Piles: Performance Monitoring 1994–1998. *Proc. 1st South American Symposium on Geosynthetics*, Rio de Janeiro. 403–411.

Alexiew, D., Vogel, W. 2001. Railroads on Piled Embankments in Germany: Milestone Projects. *Landmarks in Earth Reinforcement*, Swets & Zeitlinger. 185–190.

Alexiew, D. 2002. Piled Embankments: Design Methods and Case Studies. *Proc. XV Italian Conf. on Geosynthetics*. Bologna. October 2002. L`ingegnere e l`architetto, Special issue 1–12/2002. 32–39.

Alexiew, D. 2004. Geogitterbewehrte Dämme auf pfahlähnlichen Elementen: Grundlagen und Projekte. *Die Bautechnik 81*, Heft 9.

Ast, W., Hubal, H., Schollmeier, P. 2001. Bewehrter Erdkörper mit Erdfall-Warnanlage für den Eisenbahnknoten Gröbers. *Sonderveröffentlichung der Eisenbahntechnischen Rundschau*, Edition ETR Ingenieurbauwerke.

Blivet, J.C., Khay, M., Gourc J.-P., Giraud, H. 2001 Design Considerations of Geosynthetic for Reinforced Embankments Subjected to Localized Subsidence. *Proc. Geosynthetics Conference*, February 12–14, 2001, Portland, Oregon, USA. 741–54.

Blivet, *et. al.* 2002. Design Method for Geosynthetics as Reinforcement for Embankment Subjected to Localized Subsidence. In: Delmas, Gourc, Girard (ed.): *Proc. 7th ICG*, 2002. Nice. Swets & Zeitlinger.

BS 8006 1995. *Code of Practice for Strengthened/reinforced Soils and Other Fills*. BSI, London.

EBGEO. 2010. Empfehlungen für den Entwurf und die Berechnung von Erdkörpern mit Bewehrungen aus Geokunststoffen. DGGT; Essen, Ernst und Sohn, Berlin.

EBGEO. 2011. Recommendations for Design and Analysis of Earth Structures Using Geosynthetic Reinforcements. DGGT; Essen, Ernst und Sohn, Berlin.

Eurocode 7 EN 1997-1 (EC7). *Geotechnical Design*.

Giroud, J. P., Bonaparte, R., Beech, J. F. 1990. Design of Soil Layer Geosynthetic Systems Overlying Voids. *Geotextiles and Geomembranes*, Vol. 9 , Issue 1, 11–50.

Heitz, C. 2006. Bodengewölbe Unter Ruhender und Nichtruhender Belastung bei Berücksichtigung von Bewehrungseinlagen aus Geogittern. *Schriftenreihe Geotechnik, Universität Kassel*, Heft 19.

Hewlett, W. J., Randolph, M. F., Aust, M. I. E. 1988. Analysis of Piled Embankments. *Ground Engineering* Vol. 21, 12–17.

Kempfert, H.-G., Göbel, C., Alexiew, D., Heitz, C. 2004. German Recommendations for Soil Reinforcement Above Pile-elements. *Proc. EuroGeo3*, Munich, Volume I. 279–283.

Schwerdt, S. 2004. Untersuchungen zur Ableitung eines Bemessungsverfahrens für die Überbrückung von Erdeinbrüchen unter Verwendung von Geokunststoffbewehrungen. *Dissertation*. TU Clausthal.

Schwerdt, S., Meyer, N., Paul, A. 2004. Die Bemessung von Geokunststoffbewehrungen zur Überbrückung von Erdeinbrüchen (B.G.E.-Verfahren). *Bauingenieur 79*, H. 9.

Terzaghi K 1943. *Theoretical Soil Mechanics*. J. Wiley and Sons, New York.

Zaeske, D. 2001. Zur Wirkungsweise von Unbewehrten und Bewehrten Mineralischen Tragschichten über pfahlartigen Gründungselementen. *Schriftenreihe Geotechnik, Universität Kassel*, Heft 10.

Young member contest

Basal reinforced earth embankments on piled foundations: The role of embankment construction process

V. Mangraviti
Chalmers University of Technology, Gothenburg, Sweden

L. Flessati
Delft University of Technology, Delft, The Netherlands

C. di Prisco
Politecnico di Milano, Milan, Italy

ABSTRACT: The current design methods for Geosynthetic-Reinforced and Pile-Supported embankments disregard on one side the effect of the embankment construction and on the other one the stiffness of embankment, foundation soil, column and geosynthetics. What is missing nowadays is a simplified design method capable of taking all these aspects into account. To this aim, in this paper the authors present the results of a series of numerical analyses simulating the embankment construction. In particular, the evolution during construction of embankment displacements is discussed and the maximum tensile force in the geosynthetic reinforcements is compared with the one suggested by the most popular standards. To clearly highlight the mechanical processes taking place in the embankment, an ideal problem is considered: the pile shaft is assumed to be smooth, the piles to be founded on a rigid bedrock and the embankment construction to take place under drained conditions.

1   INTRODUCTION

Piled foundations are commonly employed to reduce settlements of artificial earth embankments on soft soil strata, and geosynthetic reinforcements are installed at the embankment base to increase pile spacing, that is to reduce construction costs. Despite the well documented effectiveness of this technique, the mechanical processes developing during the construction are not fully understood and the current design approaches, based on very simplified assumptions, ignore them.

In the scientific literature, the problem is usually tackled in the light of Ultimate Limit State (ULS) theory and the mechanical response of Geosynthetic-Reinforced Pile-Supported (GRPS) embankments, that is the vertical stress transfer to piles (arching effect) and the arising of the plane of equal settlements (plane above which differential settlements are negligible), is interpreted by assimilating it to the trapdoor problem. Nevertheless, experimental data (Iglesia 1991; Reshma *et al.* 2020; Terzaghi 1936) have shown that (i) the arching effect is strongly affected by both geometry and embankment mechanical properties, and (ii) the stresses acting on the foundation soil significantly depend on the differential displacements imposed at the base. All these observations put in evidence the crucial role played by the material deformability and, therefore, the unsuitability of trapdoor-based approaches to investigate the serviceability conditions of GRPS embankments (Mangraviti 2022; Mangraviti *et al.* 2022a).

Therefore, in the last decades, numerical studies, considering the presence of the foundation soft soil stratum (absent in the trapdoor geometry), were performed by using either finite element or finite difference (Flessati *et al.* 2022; Han & Gabr 2002; Mangraviti *et al.* 2022b; Stewart &

Filz 2005) codes or both (Jennings & Naughton 2012). It worth mentioning that in general these studies (i) do not focus on the effects of the embankment construction, (ii) do not take large displacements into account and (iii), thus, disregard the membranal behavior of geosynthetics.

In this paper, the authors discuss the results of a series of finite difference numerical analyses simulating the construction of the embankment under drained conditions, by accounting for the membranal mechanical behavior of the geosynthetic layer. Since the final goal of this research is to conceive a simplified mathematical "meta-model" to evaluate settlements at the top of the embankment during construction, the problem considered here in the following is ideal: (i) a unit axisymmetric cell of the embankment is analyzed (boundary effects are not accounted for), (ii) the pile shaft is assumed to be smooth and (iii) the pile are assumed to rich a rigid underneath bedrock.

The paper is structured as it follows: in §2 the numerical model is described; in §3 the results in terms of maximum tensile force and settlements at the top of the embankment are discussed and in §4 what learnt is briefly summarized.

2 NUMERICAL MODEL

In this paper, the authors considered the effects of embankment construction on the central part of GRPS embankments. Therefore, the problem schematized in Figure 1a (where z is the vertical coordinate) is reduced to the analysis of one central axisymmetric cell (Figure 1b, where r is the radial coordinate). The unit cell of diameter s, assumed to be equal to the pile spacing (to each pile disposition a suitable definition for the unit cell diameter has to be assigned) includes: (i) the pile of diameter d and length l, (ii) a homogeneous foundation soil stratum of thickness l resting on a rigid bedrock, (iii) an embankment, whose height h evolves during the construction phase and (iv) the geosynthetic reinforcement laid at the embankment base. As previously mentioned, the pile shaft is assumed to be smooth and the construction process to take place under drained conditions.
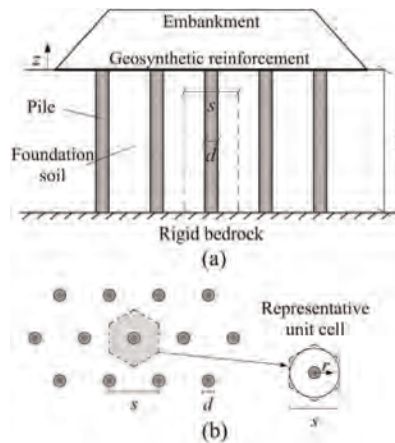
Figure 1. (a) Problem geometry in transversal section; (b) Pile disposition in plan and representative axisymmetric unit cell.

The unit cell of Figure 1b has been modelled as illustrated in Figure 2. The numerical problem has been solved by using a finite difference numerical code (FLAC3D 6.0, Itasca 2017). A large displacement approach has been used and the spatial discretization has been optimized by choosing smaller elements close to the pile, where strains are expected to localize.

Normal displacements are not allowed along both the lateral boundaries and the bottom of the model. The pile is assumed to be elastic and, analogously to what done by many authors in

the literature, the soil has been modelled by means of a non-associated elastic-perfectly plastic constitutive relationship with a Mohr-Coulomb failure criterion. This constitutive relationship, despite of its simplicity, can capture the main aspects of the mechanical processes taking place in the considered spatial domain (Mangraviti *et al.* 2022c). The geosynthetic reinforcement has been modelled as an elastic isotropic membrane of axial tensile stiffness J.
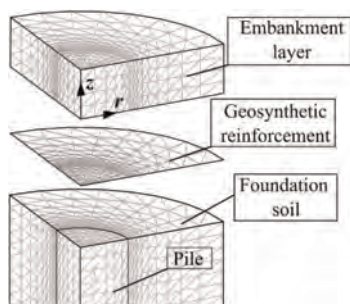
Figure 2.   FLAC3D numerical model layout and spatial discretization.

Between pile and foundation soil, smooth interface elements are inserted. Along normal direction, under compression, the interface elements are "quasi rigid" (the elastic stiffness is sufficiently larger than the soil one, equal to 4e5 kN/m^3), whereas under tension perfectly fragile. Between the geosynthetic and the surrounding soil, frictional interface elements quasi-rigid along the normal direction are introduced. The interface friction angle is imposed to coincide with that of the soil (in agreement with the experimental findings by Moraci *et al.* (2014)).

The layer-by-layer embankment construction is subdivided in single stages, each one corresponding with the deposition of 0.25 m of granular material (for the sake of simplicity, both pile installation and soil compaction are not reproduced). At each construction stage, a new stratum of elements is added on the current position of the embankment top. This allows to reproduce, in contrast with what done by Han & Gabr (2002) and Jennings & Naughton (2012), although in a simplified way, the real loading path followed by the system during the embankment construction.

To study the mechanical processes taking place during the embankment construction, a parametric study, in which different geometries and mechanical properties have been considered, was performed. The results differ from a quantitative point of view but are qualitatively consistent. As a consequence, for the sake of brevity, the numerical results will be discussed here in the following by considering only a reference case of fixed geometry ($s = 1.5$ m, $d = 0.5$ m, $l = 5$ m) and given mechanical properties of materials (Table 1).

Table 1.   Mechanical properties of the materials for the reference case.

	Unit weight kN/m^3	Young modulus MPa	Poisson ratio -	Friction angle °	Cohesion kPa	Dilatancy angle °	J kN/m
Foundation soil	18	1	0.3	30	0	0	-
Embankment	18	10	0.3	40	0	0	-
Pile	25	30000	0.3	-	-	-	-
Geosynthetic reinforcement	-	-	0.3	-	-	-	1000

3 RESULTS AND DISCUSSION

Analogously to what already observed by Han & Gabr (2002), the distribution of the total tensile force per unit thickness within the geosynthetic is not uniform and varies along the radial coordinate (Figure 3a). In this figure, the tensile stress is integrated along the current circumference, reducing with r. For this reason, although the tensile stress is maximum at the pile edge, the tensile force has a maximum for $r = 0.3$ m. The numerical results from this study (Figure 3a, solid line) are compared with the value of maximum tensile force assessed (for the reference case and $h = 5$ m) by according to what suggested by one of the most popular standard in the field (BS8006-1 2010), that assumes an unrealistic uniform distribution of tensile force in the geosynthetic (Figure 3a, dotted line).

The values of the maximum tensile force calculated for different values of h by using BS8006-1 (2010) were found to be always larger than the ones obtained in this study (Figure 3b). This result is consistent with the hypothesis at the base of the standards. In fact, as was already observed by Bhasi & Rajagopal (2015), ULS approaches lead to an extremely conservative estimation of the maximum tensile force in the geosynthetic.
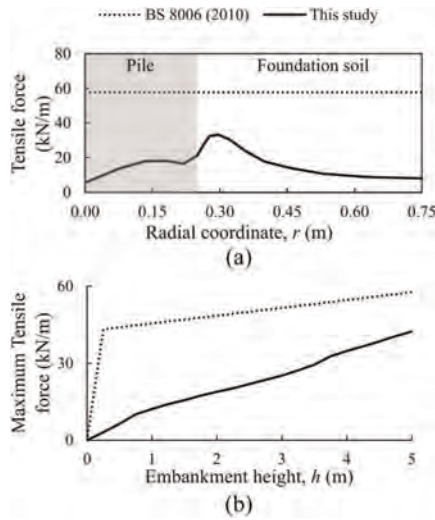
Figure 3. Comparison between numerical analyses from this study and BS8006 (2010) for the reference case: (a) Tensile force within the geosynthetic along the radial coordinate for $h = 5$ m; (b) Maximum tensile force of the geosynthetic reinforcement calculated for different values of h.

To better understand the mechanical behavior of GRPS embankments, the evolution of irreversible deviatoric strain contours during construction was analyzed: Figures 4 a-c refer to three representative values of h. The results show that deviatoric strains localize in a cylindrical crown (defined as "process zone", in agreement with what suggested by (di Prisco *et al.* 2020a, 2020b) close to the pile edge, while in the rest of the spatial domain deviatoric strains are negligible. For small h values, the height of the process zone (h_p) coincides with the embankment height, but, when the embankment height gets a threshold value ($h_p = h^* = 1.1$ m, for the reference case), h_p stops evolving. As a result of the parametric study, it was found that h^* is a function of: (i) geometry (s, d and l); (ii) embankment soil friction and dilatancy angle; (iii) relative stiffness between pile, foundation soil and embankment soil and (iv) J.

As in Mangraviti *et al.* (2022b), the numerical results in terms of average and differential settlements at the top of the embankment have been plotted (Figure 5). Average ($u_{t,av}$) and differential ($u_{t,diff}$) settlements at the embankment top are calculated as:

$$u_{t,av} = \frac{u_{t,f}\left(s^2 - d^2\right) + u_{t,p}d^2}{s^2} \text{ and } u_{t,diff} = u_{t,f} - u_{t,p} \tag{1}$$

where:

$$u_{t,p} = \frac{2\pi \int_0^{d/2} u_t(r)dr}{\pi d^2/4} \quad \text{and} \quad u_{t,f} = \frac{2\pi \int_{d/2}^{s/2} u_t(r)dr}{\pi(s^2 - d^2)/4} \tag{2}$$

are the weighted average values of $u_t(r)$ above the pile (for $0 < r < d/2$) and the foundation soil ($d/2 < r < s/2$), respectively. $u_t(r)$ is the vertical displacement accumulated during construction at the top of the embankment.

Once the height of the embankment becomes larger than h^*, differential settlements stop increasing, regardless of the final height of the embankment (Figure 5). h^* can also be interpreted as a "critical height" and is analogous to the height of the plane of equal settlements observed by Terzaghi (1936) and Han & Gabr (2002).
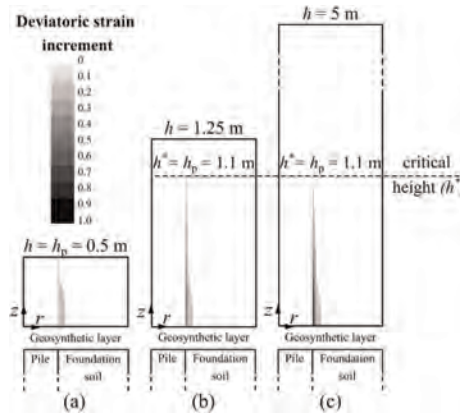
Figure 4. Contour of deviatoric strains in the embankment during construction for the reference case and evolution of process height, h_p, for three representative h values: (a) $h = 0.5$ m; (b) $h = 1.25$ m; (c) $h = 5$ m.
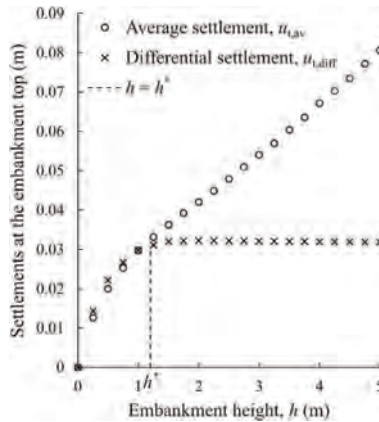
Figure 5. Average and differential settlements at the top of the embankment during construction for the reference case.

4   CONCLUSIONS

In this paper, the results of a finite difference numerical analysis campaign, modelling an ideal axisymmetric unit cell of Geosynthetic-Reinforced and Pile-Supported embankments are

discussed. For the sake of brevity, only the results concerning a reference case are illustrated. The results, in terms of both maximum tensile force in the membrane and settlements at the top of the embankment during drained construction of the embankment have been discussed. In particular, the numerical results highlighted the importance of taking into consideration the stiffness of the materials involved for a reliable estimation of the critical embankment height. Furthermore, the authors emphasized the importance of considering the layer-by-layer embankment construction to properly reproduce the mechanical processes progressively developing within the embankment and, therefore, to correctly estimate: (i) the tensile force acting in the membrane and (ii) average and differential settlements at the top of the embankment.

According to the authors, the very conservative approach of current design methods, based on ultimate limit state theory and not accounting for staged construction processes, lead to a significative overestimation of the force acting in the membrane. This does not allow for an adequate optimized and sustainable design of GRPS embankments from a serviceability limit state perspective.

REFERENCES

Bhasi, A., Rajagopal, K., 2015. Geosynthetic-Reinforced Piled Embankments: Comparison of Numerical and Analytical Methods. *Int. J. Geomech*. 15, 04014074.

BS8006-1, 2010. Code of Practice for Strengthened/Reinforced Soils and Other Fills.

di Prisco, C., Flessati, L., Frigerio, G., Galli, A., 2020a. Mathematical Modelling of the Mechanical Response of Earth Embankments on Piled Foundations. *Geotechnique* 70, 755–773.

di Prisco, C., Flessati, L., Galli, A., Mangraviti, V., 2020b. A Simplified Approach for the Estimation of Settlements of Earth Embankments on Piled Foundations. In: Calvetti, F., Cotecchia, F., Galli, A., Jommi, C. *(Eds.)*, *Lecture Notes in Civil Engineering*. Springer International Publishing, Cham, pp. 640–648.

Flessati, L., di Prisco, C., Corigliano, M., Mangraviti, V., 2022. A Simplified Approach to Estimate Settlements of Earth Embankments on Piled Foundations: The Role of Pile Shaft Roughness. *Eur. J. Environ. Civ. Eng*. 1–21.

Han, J., Gabr, M.A., 2002. Numerical Analysis of Geosynthetic-Reinforced and Pile-Supported Earth Platforms over Soft Soil. *J. Geotech. Geoenvironmental Eng*. 128, 44–53.

Iglesia, G.R., 1991. *Trapdoor Experiments on the Centrifuge–a Study of Arching in Geomaterials and Similitude in Geotechnical Models*. Massachusetts Institute of Technology.

Itasca, 2017. *FLAC3D v.6.0—fast Lagrangian Analysis of Continua in Three Dimensions_. User Manual*. Itasca Consult. Group, Minneap.

Jennings, K., Naughton, P.J., 2012. Similitude Conditions Modeling Geosynthetic-Reinforced Piled Embankments Using FEM and FDM Techniques. *ISRN Civ. Eng*. 2012, 1–16.

Mangraviti, V., 2022. Displacement-Based Design of Geosynthetic-Reinforced Pile-Supported Embankments to Increase Sustainability BT - Civil and Environmental Engineering for the Sustainable Development Goals: Emerging Issues. In: Antonelli, M., Della Vecchia, G. (Eds.). Springer International Publishing, Cham, pp. 83–96.

Mangraviti, V., Flessati, L., di Prisco, C., 2022a. Mathematical Modelling of the Mechanical Response of Geosynthetic-reinforced and Pile-supported Embankments. *under Rev*.

Mangraviti, V., Flessati, L., di Prisco, C., 2022b. Geosynthetic-reinforced and Pile-supported Embankments: Theoretical Discussion of Finite Elements Numerical Analyses Results. *under Rev*.

Mangraviti, V., Flessati, L., di Prisco, C., 2022c. A Rheological Model for Georeinforced Embankments Based on Piled Foundations. *IOP Conf. Ser. Mater. Sci. Eng*. 1260, 12014.

Moraci, N., Cardile, G., Gioffrè, D., Mandaglio, M.C., Calvarano, L.S., Carbone, L., 2014. Soil Geosynthetic Interaction: Design Parameters from Experimental and Theoretical Analysis. *Transp. Infrastruct. Geotechnol*. 1, 165–227.

Reshma, B., Rajagopal, K., Viswanadham, B.V.S., 2020. Centrifuge Model Studies on the Settlement Response of Geosynthetic Piled Embankments. *Geosynth. Int*. 27, 170–181.

Stewart, M.E., Filz, G.M., 2005. Influence of Clay Compressibility on Geosynthetic Loads in Bridging Layers for Column-Supported Embankments. pp. 1–14.

Terzaghi, 1936. Stress Distribution in Dry and in Saturated Sand Above a Yielding Trap-Door. *In: International Society for Soil Mechanics and Geotechnical Engineering*. pp. 536–537.

GCL hydration by lateritic soils under isothermal and heating/cooling cycles

J.W.B Silva*

Graduate Student, Civil Engineering Department, Federal University of Sao Carlos, Sao Carlos, Sao Paulo, Brazil

N.S. Correia* & F.H.M. Portelinha*

Associate Professor, Civil Engineering Department, Federal University of Sao Carlos, Sao Carlos, Sao Paulo, Brazil

ABSTRACT: Recent work has shown that GCL hydration by subgrade is influenced by a series of variables related to GCL characteristics, as well as subgrade initial moisture content, particle size and mineralogy. Another major variable is the effect of GCL exposure to daily thermal cycles during the landfill construction phase. Additionally, tropical climate conditions, such as in Brazil, result in the occurrence of lateritic fine soils, which present high moisture content and a particular mineralogy. The present study evaluated the GCL hydration by two lateritic subgrades (clay and clayey sand) under isothermal conditions and heating/cooling cycles. The isothermal analysis confirmed the influence of subgrade initial moisture content on GCL hydration since both soils with the highest moisture content showed 50% higher GCL hydration. GCL samples exposed to heating and cooling presented poor hydration, even at a higher subgrade moisture content, confirming the influence of thermal conditions on GCL hydration and properties. In comparison with studies of literature, lateritic soils showed higher GCL hydration speed than soils formed in temperate climates.

1 INTRODUCTION

Geosynthetic clay liners (GCLs) are often used as a solution in different applications that demand fluid or gas barriers. The extremely low hydraulic conductivity, higher swelling potential and cation exchange capacity of bentonites result in an excellent material when enveloped by geosynthetics. Additionally, the ease of installation, reduced thickness, the potential of self-healing in face of punctual stresses, and cost-effectiveness explains the current use of GCLs (Bouazza *et al.* 2017; Kerry Rowe R 2020; Touze-Foltz 2020). However, in the last years, many researchers demonstrated a recurrent problem with the correct hydration of GCL from the underlying soils (Acikel *et al.* 2018; AbdelRazek & Rowe 2019; Rowe *et al.* 2019), which can adversely affect GCLs performance.

The GCL hydration by the subgrade can be affected by the granulometry of soil, subgrade moisture, bentonite characteristics, and structure of the GCL. These parameters have been studied in the last years in many literature studies. A study conducted by Rayhani *et al.* (2011) reported better hydration levels of GCLs in contact with sands compared to silt soils. Acikel *et al.* (2018) demonstrate that the insufficient hydration of GCLs from subgrades can

*Corresponding Authors: josewilsonbatistadasilva@gmail, ncorreia@ufscar.br and fportelinha@ufscar.br

be explained by subsoil grain size distribution and mineralogy. The initial moisture of soil affects significantly the GCL hydration, showing that even a small increase of 2% of soil moisture content can improve the hydration levels (Acikel *et al.* 2018; Bouazza *et al.* 2017; Kerry Rowe R. 2020; Rayhani *et al.* 2011). Research developed by Anderson *et al.* (2012) and Sarabian and Rayhani (2013) and Rowe *et al.* (2022) suggests that exposition to thermal conditions affects GCL hydration. All these studies were conducted using temperate soils as a subgrade and demonstrated that the hydration process can be influenced by a significant range of variables. Therefore, there is a lack of studies related to soil formed in tropical regions (lateritic soils). This paper will examine the hydration behavior of three GCLs in contact with lateritic soils when exposed to isothermal and heating/cooling conditions (tropical climate), varying initial foundation moisture content and GCLs structure.

2 MATERIAL AND EXPERIMENTAL PROCEDURE

2.2 *Geosynthetic Clay Liners (GCLs)*

Table 1 summarizes the properties of the three different GCLs examined in this research, all GCLs contain similar thickness, dry mass per unit area, saturated hydraulic conductivity (k) and plasticity index (PI). However, important properties are different, cation exchange capacity (CEC), swell index (SI), and fluid loss properties. The initial moisture content and the maximum hydration gravimetric water content (w_{ref}). Similar tests were conducted to estimate w_{ref} using the water-rising process (Anderson *et al.* 2012; Acikel *et al.* 2018; Rayhani *et al.* 2011; Sarabian & Rayhani 2013) under 1 kPa of vertical stress.

Table 1. Properties of the GCLs.

Material	Properties	GCL1	GCL 2	GCL 3
Bentonite	Plastic Index (%) (ASTM D4318 2017)	252	253	273
	Avg. Dry mass /area (g/m) (ASTM D5993 2018)	4964	3878.5	4375.1
	Swell Index (ml/2 g) (ASTM D5890 2019)	25	20	25
	Fluid Loss (ASTM D5891 2019)	18	32	28
	Smectite content (%) *	80	80	80
	Cation Exchange capacity (meq/100 g)**	140	110	163
Carrier	Type	WGT	WGT	WGT
Cover	Type	NWGT	NWGT	WGT
GCL	Thermally treated	yes	yes	no
	Bonding	NP	NP	ST
	Thickness (mm) (ASTM D1776 2020)	7.0	7.0	6.0
	Initial gravimetric water contents	21	10	11
	Reference gravimetric water content (%) (ASTM D2216 2019)	182.7	214.2	267.7
	Hydraulic conductivity (m/s) (ASTM D5887 2020)	1.2×10^{-11}	1.2×10^{-11}	4.8×10^{-11}

*Maximum values as provide by manufacturers.
**Cation exchange capacity (CEC) tests were conducted using the methylene blue adsorption test. The complete characterization of these GCLs was described by Silva *et al.* (2022).

2.2 *Subsoils*

Two lateritic soils were used to hydrate the GCLS in this investigation. The clayey sand and a high plastic clay were selected as typical lateritic soils found in the Brazilian territory and in other tropical countries. The complete characterization of these soils was described by Silva

et al. (2022). According to the Unified Soil Classification System (USCS) (ASTM D2487 2017), clayey sand is classified as SC soil, and sandy clay is classified as high plasticity clay (CH) soil. Although the lateritic CH soil is clay, it also has a significant percentage of fine sand (36%), a common characteristic of lateritic soils.

2.3   *GCL hydration test under isothermal and simulated field conditions(heating/cooling)*

Polyvinyl chloride (PVC) cells of 250 mm in diameter and 500 mm in height were used to investigate the hydration of three GCLs installed over lateritic subsoils (Figure 1a). For each subsoil, compaction moisture contents adopted were at optimum (OMC) and 2% above optimum (OMC+2%). The cells were compacted using a 95% degree of compaction in relation to the maximum dry density of soil based on the Standard Proctor Compaction Test to ensure the same void ratio of the subgrade. GCL samples with 250 mm of diameter were placed over the compacted subsoil with the initial gravimetric moisture content (Table 1). Then, the system was sealed, and the tests were conducted under environment-controlled conditions of 21°C. Tests were conducted with GCL1 hydrated by both lateritic soils at two moisture values (OMC and OMC+2%). Additionally, two others GCLs (GCL2 and GCL3) were tested at each lateritic soil, only in OMC+2% condition.
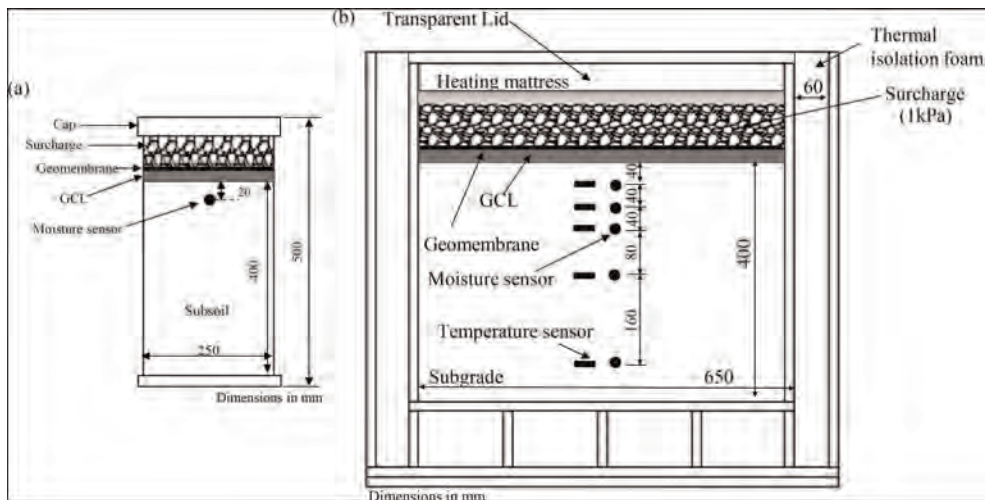
Figure 1.   Physical models: (a) Isothermal test cells; (b) Thermal test box.

To investigate GCLs hydration by the subgrade when exposed to heating/cooling cycles a physical model was constructed using the same liner used in the PVC cells. Both materials (GM and GCL) were restrained longitudinally to simulate the anchorage found on field. Similar models have been used in several laboratory studies and in the physical model studied by Rowe *et al.* (2013). A heating period of 8 hours was imposed with a temperature of 57±4 °C, followed by a cooling period of 16 hours, leading to a minimum of 30±4 o C of temperature in a day cycle. This temperature range is consistent with the conditions found in Brazilian landfills (Costa *et al.* 2019; da Silva *et al.* 2020; Portelinha *et al.* 2020). The study with heating/cooling cycles was conducted only using the GCL1 hydrated by CH subsoil at OMC, GCL1 hydrated by SC subsoil at OMC+2% condition, and GCL1 hydrated by CH subsoil at OMC+2% condition. The complete description of the models used for isothermal and simulated field conditions tests is described by Silva *et al.* (2022). The GCL gravimetric moisture contents in both conditions were monitored weekly, weighing the samples using a digital scale of 0.01 g precision.

3 RESULTS

3.1 *Effect of subsoil type and moisture content on GCLs hydration under isothermal conditions*

Figure 2 presents the changes in gravimetric moisture content for three different GCL1 (w_{GCL}) when hydrated from lateritic SC and CH subsoils under isothermal conditions and at different water foundation moisture contents (w_{fnd}). After 18 weeks of hydration, both lateritic subsoils significantly increased the moisture content of the GCL to approximately 60% in the OMC condition. The hydration of GCLs was higher when hydrated by subsoils with a higher initial moisture content (OMC+2%). An impact of soil type was also observed on the hydration rate of GCLs. The lateritic SC soil, with granular characteristics, showed a higher hydration rate than CH soil (fine soil). However, the GCL1 when hydrated by the SC soil at OMC condition showed moisture loss after 12 weeks of testing. Similar results were found by Rayhani *et al.* (2011) regarding the difficulty of GCLs to hydrate from fine-grained subgrades reported by Rayhani *et al.* (2011). A possible explanation for this behaviour is the initial suction level of subgrades and the hydraulic conductivity of soil (Acikel *et al.* 2018). Soil moisture data measured along the GCL hydration tests are also plotted in Figure 2. The soil moisture was stable during GCL hydration, except for the lateritic SC soil compacted at OMC which presented small variations.
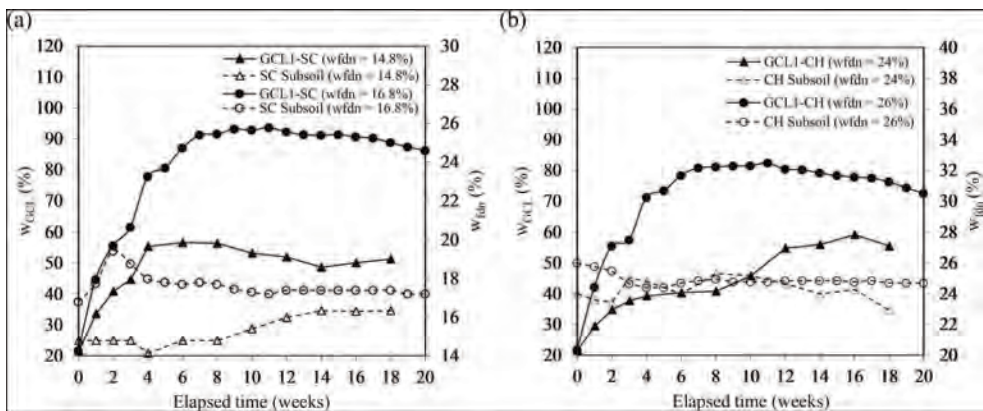
Figure 2. GCL1 hydration under isothermal conditions: (a) SC subgrade; (b) CH at OMC+2%.

3.2 *Effect of heating/cooling cycles on GCL hydration*

Figure 3 compares the hydration of GCL1 from lateritic SC and CH under isothermal and heating/cooling conditions. The exposition to thermal cycles affected significantly the GCL hydration. Similar results were as also observed by Rowe *et al.* (2011), Anderson *et al.* (2012) and Sarabian and Rayhani *et al.* (2013). At simulated field conditions the sand soil (SC) was not capable of hydrating the GCL1 after 8 weeks of testing, even considering soil compaction at OMC+2%. The reduction in SC subsoil moisture content without increases in GCL moisture indicates a limitation of upward flow from the soil to GCL. Figure 4 shows the specimens of GCLs after hydration, showing less hydration in the GCL1 subjected to thermal cycles.

3.3 *Analysis of GCL properties after hydration*

At the end of hydration, tests were conducted to investigate GCL's hydraulic conductivity, swell index, and cation exchange capacity. All these parameters are presented in Table 2 for tests conducted for isothermal (I) and heating/cooling cycles (T) for all GCLs examined.
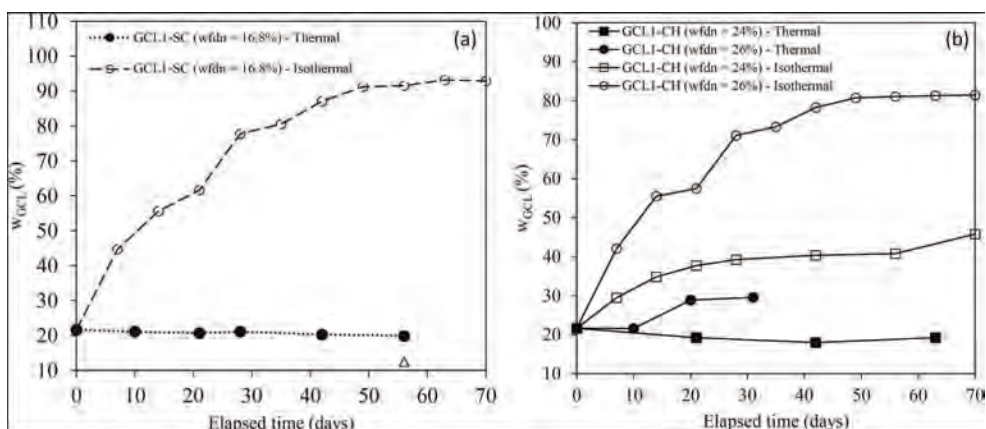
Figure 3. Hydration of GCL1 from SC and CH subgrades under isothermal and heating/cooling conditions.
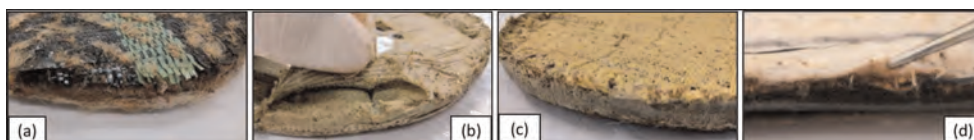
Figure 4. GCLs after hydration under isothermal conditions: (a) GCL1 in the SCwót+2% subgrade; (b) GCL2 in the SCwót+2% subgrade; (c) GCL3 in the SCwót+2% subgrade; (d) GCL1 after hydration under heating/cooling cycles conditions.

Based on the current guideline to qualify GCLs (GRI GCL3 2016) all the results of SI found are lower than the minimum required to ensure good bentonite swelling properties. The hydraulic conductivity of all GCLs studied suffered an increase for both soils, with the main changes occurring at isothermal conditions. A possible explanation for this is the fact that under isothermal conditions, continuous water redistribution and water content changes in the subsoils were observed, resulting in a possible cation exchange between the subgrade and GCL. This hypothesis is explained by Acikel *et al.* (2021), cation distribution due to self-diffusion in bentonites is favoured by wetting, which leads to more significant changes in GCL properties. Different behaviour occurred for heating/cooling cycles tests, due to the capillary break moisture changes between soil and GCL were limited. Without water flow, cations exchange decreases, and as a result, fewer alterations in hydraulic conductivity. The influence of thermal conditions on CEC can be assed in Table 2, all GCLs presented values greater than the minimum of 70 meq/100 g required (Guyonnet *et al.* 2009).

Table 2. GCLs properties after isothermal and heating/cooling cycles hydration tests.

		Virgin samples			After hydration		
Hydration Test	w/w_{ref} (%)	SI (mL/2 g)	CEC (meq/100 g)	k_s (m/s)	SI (mL/2 g)	CEC (meq/100 g)	k_s (m/s)
GCL1-SC-OMC (I)	28	25	140	1.2×10^{-11}	23	145	3.58×10^{-10}
GCL1-SC-OMC+2% (I)	47	25	140	1.2×10^{-11}	21	117	2.43×10^{-10}
GCL2-SC-OMC+2% (I)	52	20	110	1.2×10^{-11}	20	99	1.39×10^{-10}

(*continued*)

Table 2. Continued

Hydration Test	w/w_ref (%)	Virgin samples			After hydration		
		SI (mL/2 g)	CEC (meq/100 g)	k_s (m/s)	SI (mL/2 g)	CEC (meq/100 g)	k_s (m/s)
GCL3-SC-OMC+2% (I)	54	25	163	4.8×10^{-11}	21	109	2.19×10^{-10}
GCL1-CH-OMC (I)	30	25	140	1.2×10^{-11}	22	143	5.51×10^{-11}
GCL1-CH-OMC+2% (I)	40	25	140	1.2×10^{-11}	23	101	1.37×10^{-10}
GCL2-CH-OMC+2% (I)	49	20	110	1.2×10^{-11}	18	94	1.12×10^{-10}
GCL3-CH-OMC+2% (I)	43	25	163	4.8×10^{-11}	23	121	2.56×10^{-11}
GCL1-SC-OMC+2% (T)	11	25	140	1.2×10^{-11}	23	141	7.14×10^{-11}
GCL1-CH-OMC (T)	11	25	140	1.2×10^{-11}	20	139	1.63×10^{-10}
GCL1-CH-OMC+2% (T)	16	25	140	1.2×10^{-11}	24	137	7.14×10^{-11}

I – Isothermal condition; T - heating/cooling condition.

4 CONCLUSIONS

This paper has examined the hydration of three GCLs from two lateritic subsoils exposed to isothermal and heating/cooling conditions. Complementary tests were conducted for exhumed samples to evaluate the influence of hydration on GCL properties. Based on these results this paper suggests the following conclusions:

- Under isothermal conditions, lateritic subsoils were not able to provide the maximum hydration possible for the GCLs in both soils and at the two moisture contents (optimum and +2%). Although the lateritic soils did not provide the maximum hydration, the result found for the hydraulic conductivity of the GCLs is in accordance with the guidelines.
- Results in this study reaffirms that heating/cooling cycles influence the GCL hydration. In this tests, lateritic clayey soils promoted equal or better conditions to hydrate the GCLs than sandy soils (dehydration), as opposed to isothermal test results.
- GCLs hydrated at isothermal conditions presented more alterations in the swelling index, cation exchange and hydraulic conductivity than when exposed to heating/cooling cycles. These results can be a result of cation exchange between the soils and bentonite facilitated by the continuous water flow at isothermal conditions.

REFERENCES

AbdelRazek, A.Y., Rowe, R.K., 2019. Interface Transmissivity of Conventional and Multicomponent GCLs for Three Permeants. *Geotext. Geomembranes* 47, 60–74. https://doi.org/10.1016/j.geotexmem.2018.10.001

Acikel, A.S., Gates, W.P., Singh, R.M., Bouazza, A., Fredlund, D.G., Rowe, R.K., 2018. Time-dependent Unsaturated Behaviour of Geosynthetic Clay Liners. *Can. Geotech. J.* 55, 1824–1836. https://doi.org/10.1139/cgj-2017-0646

Acikel, A.S., Rowe, R.K., Mcwatters, R.S., 2021. Unsaturated Behaviour and Cation Self-diffusion of Geosynthetic Clay Liners in Antarctica 350–367.

Anderson, R., Rayhani, M.T., Rowe, R.K., 2012. Laboratory Investigation of GCL Hydration From Clayey Sand Subsoil. *Geotext. Geomembranes* 31, 31–38. https://doi.org/10.1016/j.geotexmem.2011.10.005

Bouazza, A., Ali, M.A., Gates, W.P., Rowe, R.K., 2017. New Insight on Geosynthetic Clay Liner Hydration: The Key Role of Subsoils Mineralogy. *Geosynth. Int.* 24, 139–150. https://doi.org/10.1680/jgein.16.00022

Costa, A.M., Alfaia, R.G. de S.M., Campos, J.C., 2019. Landfill Leachate Treatment in Brazil – An overview. *J. Environ. Manage.* 232, 110–116. https://doi.org/10.1016/j.jenvman.2018.11.006

da Silva, N.F., Schoeler, G.P., Lourenço, V.A., de Souza, P.L., Caballero, C.B., Salamoni, R.H., Romani, R.F., 2020. First Order Models to Estimate Methane Generation in Landfill: A Case Study in South Brazil. *J. Environ. Chem. Eng.* 8, 104053. https://doi.org/10.1016/j.jece.2020.104053

Guyonnet, D., Touze-Foltz, N., Norotte, V., Pothier, C., Didier, G., Gailhanou, H., Blanc, P., Warmont, F., 2009. Performance-based Indicators for Controlling Geosynthetic Clay Liners in Landfill Applications. *Geotext. Geomembranes* 27, 321–331. https://doi.org/10.1016/j.geotexmem.2009.02.002

GRI-GCL3 Standard Specification, 2016. Test Methods, Required Properties, and Testing Frequencies of Geosynthetic

Portelinha, F.H.M., Correia, N.S., Daciolo, L.V.P., 2020. Impact of Temperature on Immediate and Secondary Compression of MSW with High and Low Food Contents. *Waste Manag.* 118, 258–269. https://doi.org/10.1016/j.wasman.2020.08.044

Silva, J.W.B., Correia, N.S., Portelinha, F.H.M., (2022). Laboratory Investigation of GCL Hydration from Lateritic Subsoils, *Geotextiles and Geomembranes*, Volume 50, Issue 5, 946–960, https://doi.org/10.1016/j.geotexmem.2022.06.002.

Rayhani, M.T., Rowe, R.K., Brachman, R.W.I., Take, W.A., Siemens, G., 2011. Factors Affecting GCL Hydration Under Isothermal Conditions. *Geotext. Geomembranes* 29, 525–533. https://doi.org/10.1016/j.geotexmem.2011.06.001

Rowe, R Kerry, 2020. Geosynthetic Clay Liners: Perceptions and Misconceptions. *Geotext. Geomembranes* 48, 137–156. https://doi.org/10.1016/j.geotexmem.2019.11.012

Rowe, R.K., Garcia, J.D.D., Brachman, R.W.I., Hosney, M.S., 2019. Chemical Interaction and Hydraulic Performance of Geosynthetic Clay Liners Isothermally Hydrated from Silty Sand Subgrade. *Geotext. Geomembranes* 47, 740–754. https://doi.org/10.1016/j.geotexmem.2019.103486

Rowe, R.K., Garcia, J. D.D., Brachman, R.W.I. and Hosney, M.S. (2022). Moisture Uptake and Loss of GCLs Subjected to Thermal Cycles from Silty Sand Subgrade. *Geosynthetics International*. [https://doi.org/10.1680/jgein.21.00049]

Rowe, R.K., Rayhani, M.T., Take, W.A., Siemens, G., Brachman, R.W.I., 2013. Physical Modelling of Nonwoven/nonwoven GCL Shrinkage Under Simulated Field Conditions. *Geotext. Geomembranes* 40, 12–19. https://doi.org/10.1016/j.geotexmem.2013.07.008

Sarabian, T., Rayhani, M.T., 2013. Hydration of Geosynthetic Clay Liners from Clay Subsoil Under Simulated Field Conditions. *Waste Manag.* 33, 67–73. https://doi.org/10.1016/j.wasman.2012.08.010

Touze-Foltz, N., Haijian Xie, Guillaume Stoltz, *Performance Issues of Barrier Systems for Landfills: A Review*, *Geotextiles and Geomembranes*, Volume 49, Issue 2, 2021, Pages 475–488, ISSN 0266-1144, https://doi.org/10.1016/j.geotexmem.2020.10.016.

Numerical modelling of a reinforced embankment in cold regions environment

E.M.B. De Guzman
Tetra Tech Canada Inc., Calgary, Alberta, Canada

M. Alfaro
University of Manitoba, Winnipeg, Manitoba, Canada

L.U. Arenson
BGC Engineering Inc., Vancouver, British Columbia, Canada

G. Doré
Université Laval, Quebec City, Quebec, Canada

ABSTRACT: An embankment underlain by permafrost foundation was reinforced with woven geotextiles at its side slopes to reduce slope displacements when the compacted frozen fill used to construct the embankment thaws. The fully-instrumented embankment along the Inuvik-Tuktoyaktuk Highway in the Northwest Territories, Canada has thermistor strings to monitor soil temperatures as well as ShapeAccelArrays installed at the midslope of the embankment to measure displacements. Four years of monitored data shows reduction in slope movements compared to an unreinforced embankment. A numerical model was developed in a commercially-available finite element software to simulate the thermal and mechanical behaviour of this embankment and further understand the benefit of using geotextiles in cold regions environment. Multi-layer woven geotextiles with varying reinforcement length and vertical spacing were also investigated. The monitored performance and the model results presented will help optimize embankment design in cold regions environment using geotextiles.

1 INTRODUCTION

Highway embankments in the Arctic are usually constructed during winter conditions to preserve the permafrost foundation and minimize environmental impacts. They are typically designed to provide adequate ground insulation and minimize permafrost degradation (Argue et al. 1981) under known climatic conditions. The construction of embankments inevitably results to thermal disturbance of the underlying permafrost. The permafrost will degrade if the insulating effect provided by the embankment fill is less than the insulating effect of the original active layer. On the other hand, the permafrost can rise into the embankment if the insulating effect of the embankment fill is greater than the insulating effect of the original active layer. However, there is limited understanding on the mechanical behaviour of embankments that are initially compacted with frozen fill and experienced natural thawing and settlements during the spring and summer seasons following winter construction (De Guzman et al. 2021).

A test section that is 20 m long was constructed along the Inuvik-Tuktoyaktuk Highway (ITH) in the Northwest Territories, Canada in April 2015 and instrumented to monitor temperatures and displacements. This section is reinforced with layers of wicking woven

geotextiles to minimize localized thaw-settlements under the shoulders and side-slopes of the embankment created in combination with the depression of the permafrost table at the toe of the embankment (De Guzman et al. 2021). It was conceptualized they will provide drainage paths for the melt water during spring and summer seasons when the embankment undergoes thawing. This wicking geotextile has been successfully used for moisture management and drainage applications (Sikkema & Carpita 2016; Zhang et al. 2014). De Guzman et al. (2021, 2022) reported the field performance of this reinforced embankment supported with numerical modelling results, which are briefly presented here prior to investigating multi-layer wicking geotextiles with varying reinforcement lengths and vertical spacing. This paper aims to demonstrate the benefit of using wicking geotextiles as slope reinforcement for embankments in cold regions environment.

2 FIELD PERFORMANCE

2.1 *Embankment construction and instrumentation*

The embankment height of the test section is 5.3 m with a slope of 3H:1V. The location of the instrumentation installed and the geotextile layers at the test section is shown in Figure 1. The geotextiles are at elevations 1.8, 2.7, 3.6, and 4.5 m above the natural ground surface. Frozen fill material was taken from the nearest borrow pit source with an average moisture content of 16%. Two thermistor strings were laid out horizontally at the top (TS-R1) and along the base (TS-R2) of the embankment, and another two vertically installed through the foundation at the centreline (TS-R3) and at the toe (TS-R4). The base thermistor is 600 mm above the natural ground surface, while the top thermistor is 500 mm below the road surface. The vertical ShapeAccelArray, SAA, (SAA-RV) is located at an offset of 12 m from the embankment centreline, with its first node 400 mm below the slope surface. SAA-RV was anchored at the frozen foundation soil. Similarly, the horizontal SAA (SAA-RH) was anchored inside the embankment either sitting on top of compacted frozen soil at the core of the embankment or below the 0°C isotherm. The instrumentation cables were connected to a DAQ at an offset from the toe of the embankment which can be remotely accessed through satellite connection. The wicking geotextile layers are 8.4 m long and were laid out horizontally at every 900 mm from initial placement of fill material on both sides of the embankment. The same instrumentation and layout were used in a control test section (unreinforced), which is directly beside this reinforced embankment.
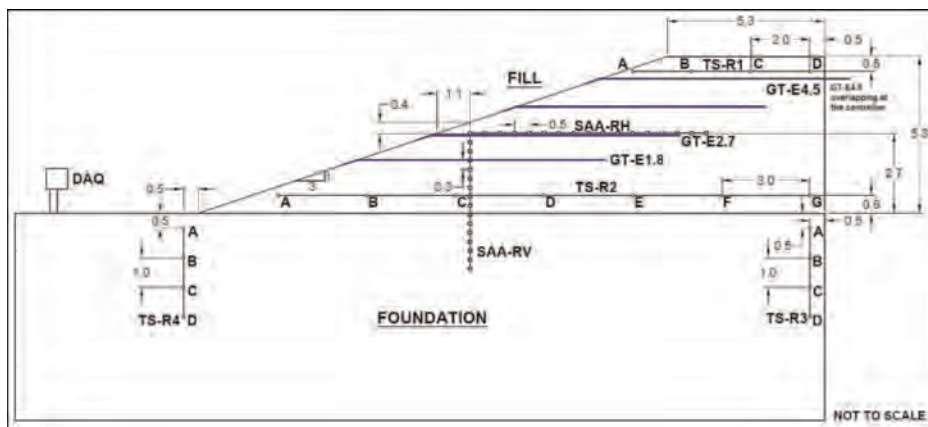
Figure 1. Instrumentation installed in the embankment cross-section with wicking geotextiles installed. Location of thermistor strings and ShapeAccelArrays (SAAs) in the test section. All units are in metres.

2.2 Temperatures

Temperature readings at different time steps are shown in Figure 2 from the horizontally-laid thermistor string along the base (Figure 2a) and the vertically-laid thermistor string at the foundation centreline (Figure 2b) of the embankment. TS-R2 shows that from the embankment centreline to about 11.5 m towards the toe, the core of the embankment has remained frozen since end-of-construction, while beyond this distance the seasonal temperature fluctuations occur on the embankment slopes. TS-R3 at the foundation centreline remained below -3°C for the monitoring period. Warming in the foundation was observed for the month of December but the thickness of the fill material for the test sections provided adequate insulation preventing permafrost thaw from the centreline to the shoulder.

2.3 Displacements

Recorded lateral displacements for the test section is shown in Figure 3a. The largest displacements occurred at the SAA node closest to the slope surface during the first thawing season after construction. Although the temperature of the SAA nodes P6 and P7 were recorded to be between $-1°C$ and $0°C$ as reported by De Guzman et al. (2021, 2022), there were movements observed in the monitoring period. The thickness of the soil from the base of the embankment that has not moved is approximately 0.75 m based on the SAA readings where the temperatures are less than -2°C. As air temperatures were warming, the seasonal depth of fluctuation increased and thus initiated for displacements to develop at deeper nodes. Initial displacements were required before the geotextile fabric can provide resistance against lateral movements. De Guzman et al. (2021) reported that the geotextiles provided the most resistance against lateral movements during the first thawing after construction. There are minimal to almost no displacements during the winter months until the spring season of the following year. Since end-of-construction of the test section, the embankment was able to consolidate for three thawing seasons before the highway was officially opened to traffic in November 2017. Although these displacements are increasing due to thawing at the slopes, the cumulative displacements of the reinforced test section at different elevations are considerably less than that of a comparable unreinforced section, confirming that the geotextiles are providing reinforcement to the high fill section (De Guzman et al. 2021), as shown in Figure 3b.
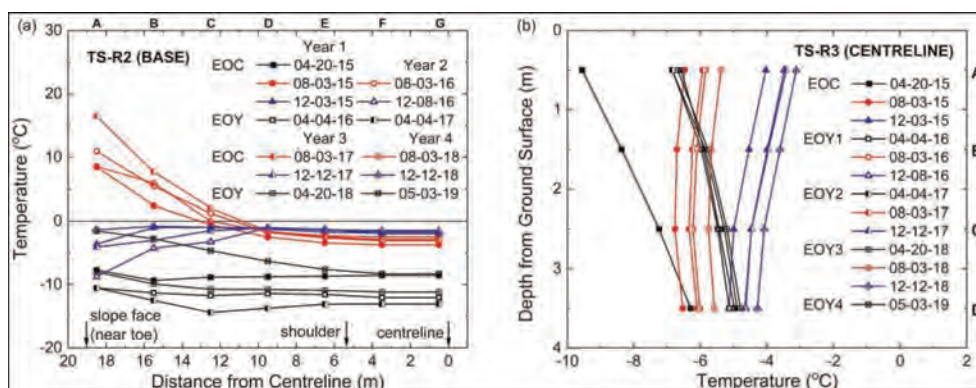
Figure 2. Temperature readings at different time steps at different locations in the test section: (a) base and (b) centreline. EOC: end-of-construction and EOY: end-of-year.
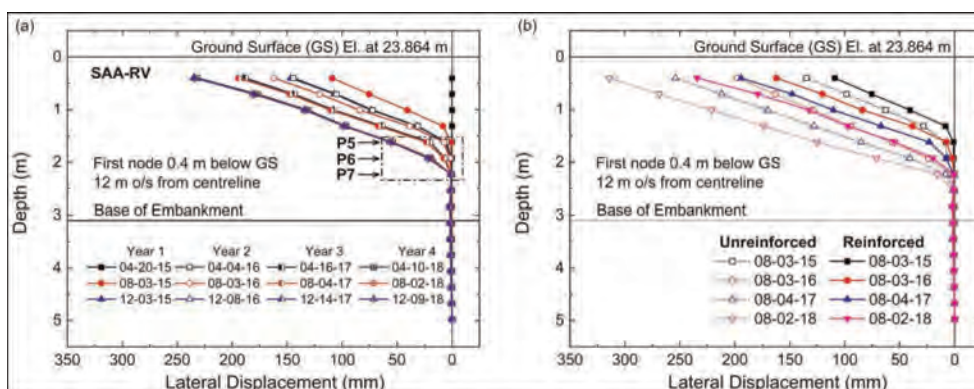
Figure 3. Lateral displacements at (a) different time steps recorded from SAA-RV and (b) comparison with unreinforced test section.

3 NUMERICAL MODELLING

3.1 *Field measurements vs. model results*

De Guzman (2020) and De Guzman et al. (2022) presented the material properties, boundary conditions, and modelling procedure for the reinforced embankment using the commercially-available general finite element software ABAQUS Version 6.14 (Smith 2014). The geotextile has a tensile strength of 15.8 kN/m at 2% strain. The interface friction angle was assumed to be high when the soil is frozen, and taken as 5.8° based on pullout tests at 0°C. The friction angle of frozen soil is 52.1°, and taken as 27.0° when the soil is thawed at 0°C. The model is sequentially built, where the temperature field is first solved for the entire period of analysis, followed by a deformation model referencing the temperature field to call material properties in a frozen or unfrozen state. The sequential approach used in the model is primarily due to the presence of the geotextile (membrane element) and the pore pressure degree of freedom available in the software. A similar embankment but without the wicking geotextiles was studied by De Guzman (2020) using a coupled thermal-mechanical model where the heat transfer (thermal) and stress and deformation (mechanical) occurring on the soil elements are solved simultaneously in a single analysis. In this type of analysis, the soil is modelled using coupled elements with displacement, pore pressure, and temperature degrees of freedom at its nodes. The hydraulic component was limited to best-fit parameters by running several model simulations that would result to closer values with the measured lateral and vertical displacements from the field.

The horizontal displacements from the model compared to recorded field data of SAA-RV is shown in Figure 4a. The horizontal displacement of the soil between Layer 1 (GL1, 1.8 m) and Layer 2 (GL2, 2.7 m) from SAA-RV shows a linear variation of displacement with depth accumulating over time. The model displacements on the other hand show this to be curved, with the top node of the layer observed to be less than the recorded one. With respect to depth, the horizontal displacements just above L1 from August 2015 to August 2017 show that it is slightly overestimated by 5 to 10 mm, but this difference increased to 50 mm in August 2018. These displacements are related to temperatures modelled in a pure heat transfer analysis. Additional thawing will occur at the toe of the embankment when a coupled thermal-mechanical model is used (De Guzman 2020) since both the heat transfer and stress and deformation occurring on the soil elements are solved simultaneously in a single analysis. The underestimated displacements below L2 are offset by the overestimation in displacements above L1.

A comparison of the horizontal displacements from the reinforced sequential model with the results of an unreinforced sequential model is shown in Figure 4b. Both models are using the thermal regime in the embankment fill and foundation soil from a pure heat transfer

2123

analysis and as expected the depth of seasonal freezing and thawing and its corresponding thickening over time are the same. The displacements in both directions are reduced with the use of these geotextile reinforcements. The results provide confidence that the interface shear strength (derived from pullout tests) and tensile strength from tensile tests are contributing in reducing lateral displacements (De Guzman 2020).
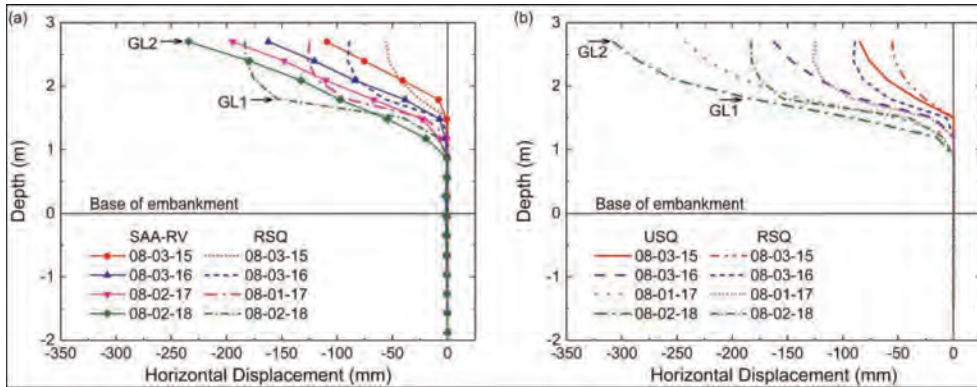
Figure 4. Comparison of horizontal displacements (a) between measured field values and model results for reinforced section and (b) model results between unreinforced (USQ) and reinforced (RSQ) analysis.

3.2 *Effect of reinforcement length*

The extent of the thawed core for S3 (3H:1V) is shown Figure 5. A fictitious line is super-imposed in this figure to show the conceptual embedment of the geotextile in the model. The vertical spacing shown is 0.9 m (Sp9), but these were also done for the 0.6 m (Sp6) case. Figure 6 shows the horizontal displacements for the S3 models using two reinforcement lengths considering Sp6 (0.6 m spacing, Figure 6a) and Sp9 (0.9 m spacing, Figure 6b). The plots are relative to the midslope of the embankment. This change in slope configuration will change the thermal regime of the model embankments and therefore the length of the geo-textile embedded in the frozen core. S3Sp6 and S3Sp9 using 6 m have all layers of reinfor-cement within the seasonal thaw depth at the slope. These geotextile layers, although only embedded outside the frozen core, provided 33% and 20% reduction in horizontal dis-placements for Sp6 and Sp9, respectively, compared to an unreinforced embankment of the same configuration. For S3Sp6 and S3Sp9, lengthening the reinforcement to 8 m intercepted the frozen core with an embedment length of 2 m. With an additional geotextile length of 2 embedded in the frozen core, the Sp6 model showed a reduction in horizontal displacements by 53%, and the Sp9 model showed 38%.
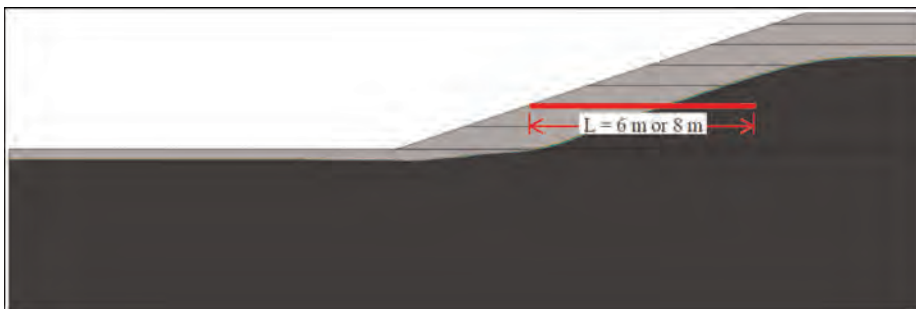
Figure 5. Extent of thawed core where reinforcements were installed for 3H:1V.
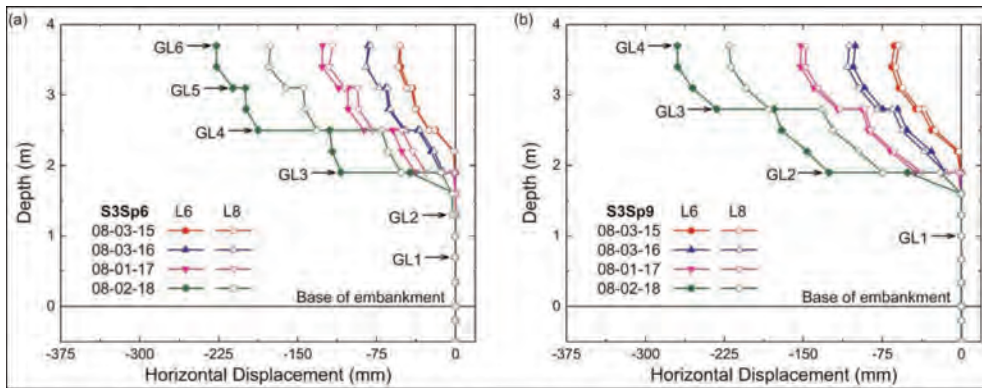
Figure 6.   Model horizontal displacements at midslope of embankment for (a) s = 0.6 m and (b) s = 0.9 m using two reinforcement lengths with 3H:1V slope configuration.

3.3   *Effect of reinforcement spacing*

Figure 7 show the horizontal displacements at the midslope for S3 with the reinforcement length held constant. For all cases, a larger vertical spacing (Sp9) resulted in larger horizontal displacements along the midslope. With the reinforcement embedded in the frozen core (Figure 7b), the displacements were reduced by 23% for the soil between elevations 2.8 m and 3.7 m, and by 53% for the soil between 1.9 m and 2.8 m above the original ground surface.

The S3 models demonstrated that addition of geotextiles in thawing slopes can reduce the horizontal displacements for a similar unreinforced embankment. A combination of tighter vertical spacing and longer reinforcement embedded in the frozen core provided the most benefit in limiting displacements as the slopes undergo seasonal freezing and thawing cycles. It should be noted that a tighter vertical spacing will require quality control as each soil lift is compacted under frozen conditions and may delay project delivery time, while reinforcement layers (woven geotextiles) have to be long enough to intercept the potential location of a frozen core.
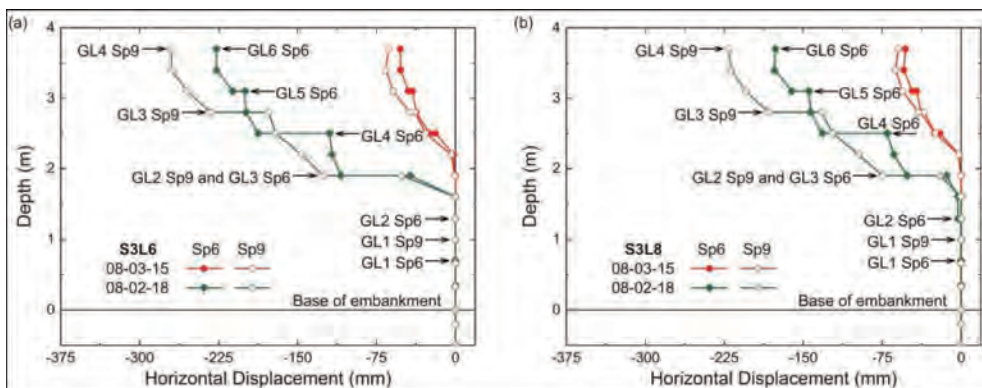
Figure 7.   Model horizontal displacements at midslope of embankment for 3H:1V slope configuration using (a) L = 6 m and (b) L = 8 m.

4 SUMMARY AND CONCLUSIONS

The recorded field data from the thermistor strings and SAAs were used to calibrate a numerical model using a sequentially-coupled approach. The model results slightly under-estimated the horizontal displacements at the midslope. A comparable unreinforced section showed that the geotextile layers installed reduced the horizontal displacements by as much as 40% in August 2018 (three years after the end of construction). The large displacements occurring during the summer following winter construction was reduced by 31% using wicking geotextiles. Similar to the recorded field data, the largest incremental displacements occurred during the summer following winter construction. It is recognized that there is an overlapping influence of warming air temperatures and thermal disturbance on the perma-frost underneath the embankment due to embankment construction.

Results from parametric reinforced models indicate that reducing the slope inclination is the most plausible option in mitigating the development of large horizontal displacements for thawing slopes. With prohibitive project costs to accommodate gentler slopes, geotextiles can be used as an alternative strategy to have steeper slopes yet reduce embankment dis-placements. The benefit of installing geotextile layers for cold regions embankment appli-cations is realized as long as there is a region where the geotextiles are still embedded within a frozen core and designed using a tighter vertical spacing between reinforcement layers.

REFERENCES

Argue, G.H., Fullerton, J.A., Johnston, G.H., and Peckover, F.L. 1981. Roads, Railways and Airfields. In Permafrost Engineering and Construction. Edited by G.H. Johnston. Wiley, New York. pp. 345–391.

De Guzman, E.M.B. 2020. Structural Stability of Highway Embankments in the Arctic Corridor. University of Manitoba. Ph.D. Thesis. 374 pp.

De Guzman, E.M.B., Alfaro, M.C., Doré, G., Arenson, L.U., and Piamsalee, A. 2021. Performance of Highway Embankments in the Arctic Constructed Under Winter Conditions. *Canadian Geotechnical Journal*, 58, No. 5, 722–736.

De Guzman, E.M.B., Alfaro, M.C., Arenson, L.U., and Doré, G. 2022. Geosynthetic-reinforced Embankment in Cold Regions: Observations and Numerical Simulations. *Geosynthetics International (ahead of print)*. https://doi.org/10.1680/jgein.21.00088.

Sikkema, M., and Carpita, J. 2016. Pioneer Scenic Byway Frost Heave Prevention and Results. *In 3rd Pan-American Conference on Geosynthetics*. pp. 1871–1879.

Smith, M. 2014. ABAQUS/Standard User's Manual, Version 6.14. *Dassault Systèmes Simulia Corp, Providence, RI*.

Zhang, X., Presler, W., Li, L., Jones, D., and Odgers, B. 2014. Use of Wicking Fabric to Help Prevent Frost Boils in Alaskan Pavements. *Journal of Materials in Civil Engineering*, 26, No. 4, 728–740.

Predicted performance of geogrid-stabilized unbound aggregate layers using confined soil-geosynthetic composite stiffness

S. Subramanian & J.G. Zornberg
University of Texas at Austin, USA

ABSTRACT: Selection of geosynthetics, for stabilization of unbound aggregate layers in pavements, involves the unconfined properties of geosynthetics and/or the large displacement confined properties. However, geogrids within a pavement system are neither unconfined nor undergo large displacements. This study proposes using the confined Soil-Geosynthetic composite stiffness (K_{SGC}), obtained from Soil-Geosynthetic interaction (SGI) tests, to predict pavement performance when using geogrid-stabilized road bases. A series of identical one-third scale accelerated pavement tests (APTs) were performed on pavement test sections stabilized with various geogrids, diverse in terms of geometry and materials. The rutting from these sections was compared to that in the non-stabilized (control) section to evaluate the Traffic Benefit Ratio (TBR) at failure rut depth for each geogrid. The TBR obtained showed a strong linear correlation to the soil-geosynthetic composite stiffness (K_{SGC}) of the corresponding geogrid obtained from the SGI tests. It is concluded that K_{SGC} is a particularly good indicator of the performance of pavements with geosynthetic-stabilized road bases.

1 INTRODUCTION

Stabilization of unbound pavement layers involves the inclusion of geosynthetics within an unbound aggregate layer and/or at the interface between layers. This is aimed at improving pavement performance by increasing the aggregate layer stiffness through transfer of stresses to the geosynthetic material. In paved roads, this transfer of stresses, to tension-bearing geosynthetic materials, limits the lateral movement of the stabilized pavement layer. This "lateral restraint", which can be mobilized under relatively small deformations, is considered the dominant mechanism of performance improvement for geosynthetic-stabilized paved roads.

Engineering projects specify for geosynthetics based on their index properties such as tensile strength & stiffness, and their performance properties that govern their interaction with surrounding soils such as pull-out resistance or interface shear strength (Zornberg and Christopher (2007)). While these properties are particularly relevant in many engineering applications such as earth-retaining walls, embankments, or slope stability, they are not well suited for the design of stabilized road bases. These properties capture either the small-strain, unconfined behavior (as in the case of tensile stiffness or flexural rigidity) or the large-displacement confined interaction of the geosynthetics with the surrounding soil. However, under serviceable limits for surface pavement, the geosynthetic is under confined conditions but does not undergo large displacements. AASHTO-R50 (2009) recommends performing full-scale tests with geosynthetics to predict their field performance. Some researchers have also developed correlations between geosynthetic properties and their field performance in stabilization (Christopher *et al.* (2008), Archer & Wayne (2012)). However, these correlations lack a mechanistic basis since they are based on properties that do not capture the geosynthetic behavior under serviceable limits for surfaced pavements. In this study, the soil-geosynthetic composite stiffness (K_{SGC}), that captures

the confined small-strain interaction of geosynthetic with soil, is proposed to predict the stabilized pavement performance.

2 ACCELERATED PAVEMENT TEST

In order to access the performance of pavement sections with stabilized base course, reduced-scale pavement sections were constructed in the laboratory under controlled environmental conditions. These sections comprised of identical pavement configuration but with four different types of geogrids (GG1 to GG4 – Figure 1), different in their material and geometric properties (Table 1). One section without any stabilizing geosynthetic was also constructed to serve as the control. All 5 pavement sections consisted of a 15 cm clean uniform sand subgrade placed at 67% relative density, 12.5 cm gravel base conforming to AASHTO#8 gradation and placed at 85% relative density, and 2.5 cm hot mix asphalt (HMA) ride surface from a thin overlay mix – type A (TxDOT SS3239 (2004)). The entire structure was built above grade in two modular frames, each 15 cm tall. The pavement structure was 180 cm (72″) in length and 180 cm in width with a total depth of 30 cm as shown in Figure 2. The geogrid in stabilized sections was placed at 7.5 cm below the HMA surface within the base.
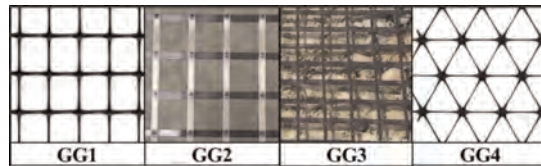
Figure 1. Geogrids used in the SGI test and for stabilization of base course in APTs.

Table 1. Index properties specified by the manufacturers of the geogrids.

Property	GG1	GG2	GG3	GG4
Polymer Type	PP	PP	PP	PP
Manufacturing Process	Punched Drawn	Welded Strips	Woven Yarns	Punched Drawn
Aperture Shape	Rect.	Rect.	Rect.	Triangle
Aperture Dimensions (mm)	33 x 25	41 x 41	15 x 15	33
Rib Width (mm)	3.2	9.0	–	1.0
Minimum Rib Thickness (mm)	0.76	0.6	–	2.0
Tensile Strength @ 1% Strain (kN/m)	–	5.2	–	–
Tensile Strength @ 2% Strain (kN/m)	6.6	8.2	7	–
Tensile Strength @ 5% Strain (kN/m)	13.4	15.1	14	–
Ultimate Tensile Strength (kN/m)	19.0	24.2	23.3	–
Junction Efficiency (%)	93	–	–	93
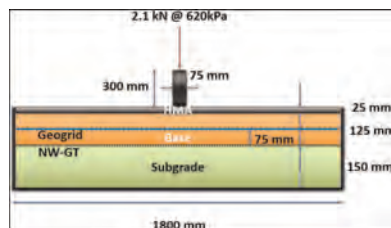
Figure 2. Cross-section of the pavement test section.

Accelerated pavement tests (APTs) were conducted on all 5 sections using the model mobile load simulator (MLS11 – Figure 3) by applying repeated, unidirectional, rolling-wheel loads of 2.1 kN at 620 kPa tire pressure. The pavement structure was subjected to 7200 load repetitions per hour. Additional details about the loading equipment and its capabilities can be found in previous studies such as Epps Martin *et al.* (2003).

A laser distance meter (LDM), attached to the carriage on an actuator, was used to profile the

Figure 3.   Model Mobile Load Simulator (MLS11) trafficking the pavement test section.

surface deformations as shown in Figure 4. By controlling the LDM sampling rate and actuator velocity, the vertical distance from the actuator to the pavement surface was captured every 5 mm of horizontal actuator displacement. This allowed for the generation of transverse surface profiles with 360 sample points. The pavement was painted white, at the locations of profiling, in order to improve the reflectivity of the laser. The surface profiles post-trafficking is compared to the initial surface profile to determine rutting at any given number of passes.
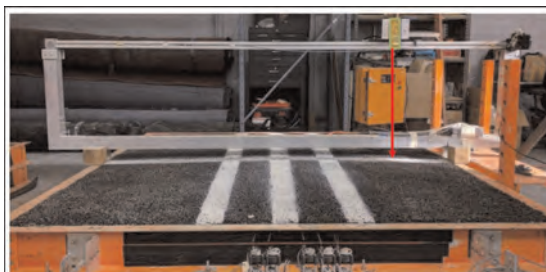
Figure 4.   Profilometer mounted on the section (Highlighted in green is the laser distance meter).

3   SOIL-GEOSYNTHETIC INTERACTION TEST

The Soil-Geosynthetic Interaction (SGI) tests is a novel variation of a conventional pull-out resistance test that involves the measurement of internal nodal displacements of the geosynthetic in addition to the external pull-out load and the corresponding frontal displacement of the geosynthetic (Roodi & Zornberg 2017). The SGI tests, performed for this study, involved sandwiching each of the four geogrids (GG1 to GG4) with the clean AASHTO#8 gravel base material, used in the APTs, at 21 kPa confining pressure, and pulling them out as their internal nodal displacements under the applied tensile load were measured. A total of 5 tests were conducted for each geogrid and three nodal displacements were measured per test. Thus, the soil-geosynthetic composite stiffness (K_{SGC}) was calculated as the slope of the square of the unit tension (in (kN)/m) at each node vs. nodal displacement (in mm) of the corresponding node. The K_{SGC} of each geogrid was taken as the

mean of the 15 K_{SGC} values determined as discussed above. In their theoretical formulation of K_{SGC}, Zornberg *et al.* (2017) showed that this slope of the unit tension squared at the node vs. nodal displacement is the same as,

$$K_{SGC} = 4 \cdot J_c \cdot \tau_y \tag{1}$$

where J_C = confined stiffness of the geogrid; and τ_y = yield shear strength.

Therefore, K_{SGC} of the geogrid is a measure that combines the in-isolation stiffness of the geogrid under confined conditions with the interaction of the geogrid with the surrounding soil. A high K_{SGC} indicates that the geosynthetic under consideration is not only stiff but is also capable of significant stress transfer between the soil and the geosynthetic. This implies that K_{SGC} is particularly well suited in determining how well geosynthetics would perform under stabilization of bases where transfer of stresses from the soil to the geosynthetic is expected along with resistance to those transferred stresses (high stiffness).

4 RESULTS

The performance of the various pavement sections is measured in terms of rutting. Rutting is measured from the post-trafficking surface deformation profiles, after correcting for pre-trafficking surface, as the maximum depth from the top of the heave next to the wheel path to the path of the trough under the wheel path as shown in Figure 5. These rut measurements were taken periodically after a pre-determined number of wheel passes. Figure 6 shows the rut measurements taken till failure of all five pavement sections with and without geogrid stabilization.
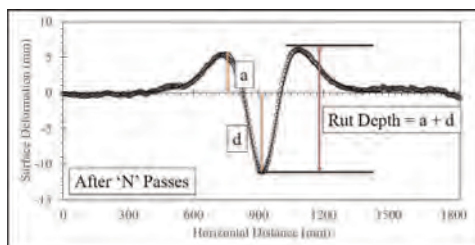
Figure 5. Typical rutting profile with 360 sample points from the laser profilometer.

4.1 *Traffic benefit ratio*

The improvement in pavement performance due to the stabilization of the base course can be quantified using the traffic benefit ratios (TBRs) obtained by comparing the rutting in the geogrid stabilized sections (GG1 to GG4) to that in the control section. This is possible because the only difference between the four geogrid stabilized sections and the control is the presence of geogrid. Thus, TBRs of each stabilized section is a direct measure of the improvement due to the corresponding geogrid.

For the purposes of this study, TBR due to geogrid stabilization may be defined as the ratio of the number of load repetitions to failure in the stabilized section to that in the control section, given identical pavement structure with the exception of the geogrid. From Figure 6, the number of wheel passes to various levels of rut are determined and their TBR is determined as follows.

$$TBR_{RD} = \frac{N_{GSS}}{N_{Control}} \tag{2}$$
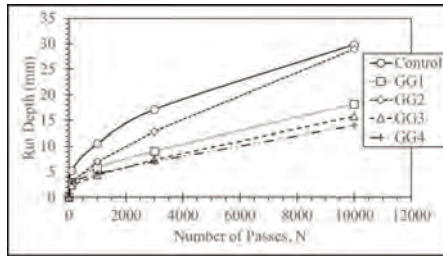
Figure 6.   Progression of rutting with trafficking on all test sections.

where TBR_{RD} = Traffic Benefit Ratio at failure defined as rut = RD; N_{GSS} = Number of
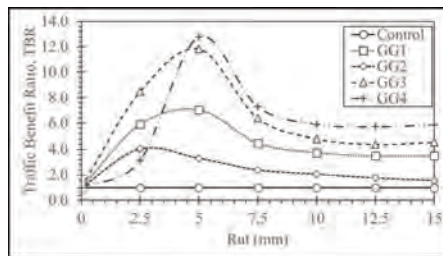
Figure 7.   TBR as a function of rut for geogrid stabilized sections.

wheel passes to failure rut, RD, in geogrid stabilized section; and $N_{Control}$ = Number of wheel passes to failure rut, RD, in control section.

Thus, TBR for the various stabilized sections can be expressed as a function of the rut depth as shown in Figure 7. The TBR starts at 1.0 for very small values of rutting, increases rapidly to a maximum in the 2.5 mm to 5 mm rut range, decreases and asymptotes to a constant around 10 mm to 15 mm rut depth. This is likely due to the high relative density (85%) of the base layer within which the geogrid is placed. As the pavement surface is trafficked, the dense base layer begins dilating in the control section. But in geogrid stabilized sections, the dilatancy is reduced (Chen *et al.* 2018; Sweta & Hussaini 2018), resulting in increased TBR. As the deformations increase, the base material reaches the critical state, thus benefits from geogrid reduces and asymptotes to a constant value of TBR.

4.2   *Soil-geosynthetic composite stiffness and TBR*

Figure 8 compares the traffic benefit ratio obtained at critical state for each geogrid stabilized section with the soil-geosynthetic composite stiffness obtained from SGI tests between
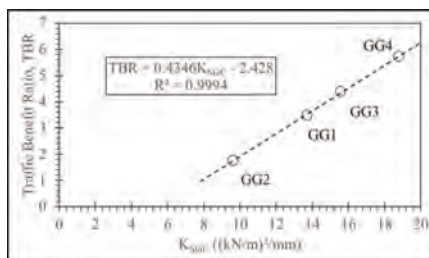
Figure 8.   Traffic Benefit Ratio Vs. K_{SGC}.

the same geogrid and base material. Each circle represents the (TBR, K_{SGC}) pair of the particular geogrid. The dashed line is the linear regression line through the datapoint. It can be seen that the TBR of any stabilized section is linearly correlated with the K_{SGC} of the base course-geogrid composite used in the stabilized section. The high degree of linear correlation ($R^2 = 0.9994$) between TBR and K_{SGC} values shows that K_{SGC} is a direct measure of the improvement to pavement rutting performance due to the inclusion of the geogrid and is thus a strong justification for the use of K_{SGC} as a critical parameter in the selection of geogrids to be used as for base stabilization.

5 CONCLUSIONS

Reduced-scale accelerated pavement tests and soil-geosynthetic interaction tests were conducted with AASHTO#8 base material and four different types of geogrids. The K_{SGC} of the base material-geogrid composite for each geogrid was determined from the SGI tests and found to be over a range from 9 $(kN/m)^2/mm$ to 20 $(kN/m)^2/mm$. The traffic performance enhancement facilitated by the inclusion of the geogrid was evaluated by comparing it to a control section without geogrid stabilization as Traffic Benefit Ratio. It was found that traffic benefit ratio due to stabilization by any geogrid is a function of the failure rut depth. The TBR was found to increase with increasing failure rut depth up to a certain rut value and then decrease to an asymptotic value. This interesting behavior of stabilized sections is attributed to the dilation of the base material and the varying levels of reduction in dilatancy facilitated by the stabilizing geogrid.

It is also found that the asymptotic TBR of the stabilized sections differs by the type of geogrid used and is highly linearly correlated to the base material-geogrid composite stiffness determined from the SGI tests. Thus, K_{SGC} can be used to predict the performance of geogrid stabilized base layers in flexible pavements and therefore be used in the selection of geogrids for the application of stabilization.

REFERENCES

AASHTO R50. 2009. Standard Practice for Geosynthetic Reinforcement of the Aggregate Base Course of Flexible Pavement Structures. *American Association of State Highway and Transportation Officials*, Washington, D.C.

Archer S. & Wayne M. H. 2012. "Relevancy of Material Properties in Predicting the Performance of Geogrid-Stabilized Roadway." *Proc. of the Conference GeoFrontiers, Advances in Geotechnical Engineering*, ASCE, Oakland, California, pp.1320–1329

Chen, X., Jia, Y. and Zhang, J., 2018. Stress-strain Response and Dilation of Geogrid-reinforced Coarse-grained Soils in Large-scale Direct Shear Tests. *Geotechnical Testing Journal*, 41(3), pp.601–610.

Christopher, B. R., Cuelho, E. V., & Perknis, S. W. 2008. Development of Geogrid Junction Strength Requirements for Reinforced Roadway Base Design. *In Proceedings of GeoAmericas* 2008 Conference, Cancun, Mexico (pp. 1003–1012).

Epps Martin, A., Walubita, L.F., Hugo, F. and Bangera, N.U., 2003. Pavement Response and Rutting for Full-scale and Scaled APT. *Journal of Transportation Engineering*, 129(4), pp.451–461.

Roodi, G.H., & Zornberg, J.G. 2017. "Stiffness of Soil-geosynthetic Composite under Small Displacements. II: Experimental Evaluation." *Journal of Geotechnical and Geoenvironmental Engineering, ASCE*, Vol. 143, No. 10, October.

Sweta, K. and Hussaini, S.K.K., 2019. Behavior Evaluation of Geogrid-reinforced Ballast-subballast Interface Under Shear Condition. *Geotextiles and Geomembranes*, 47(1), pp.23–31.

TxDOT SS3239. 2004. Special Specification for Thin Overlay Mix (TOM). TxDOT

Zornberg, J.G., Roodi, G.H., & Gupta, R. 2017. "Stiffness of Soil-geosynthetic Composite under Small Displacements: I. Model Development." *Journal of Geotechnical and Geoenvironmental Engineering, ASCE*, Vol. 143, No. 10, October.

Hyperbolic models to represent the effect of mechanical damage and abrasion on the short-term tensile response of a geocomposite

G. Lombardi & M. Pinho-Lopes
RISCO, University of Aveiro, Aveiro, Portugal

A.M. Paula
Instituto Politécnico de Bragança, Bragança, Portugal
RISCO, University of Aveiro, Aveiro, Portugal

A. Bastos
TEMA, University of Aveiro, Aveiro, Portugal
LASI, University of Minho, Guimarães, Portugal

ABSTRACT: The objective of this study was to analyse the short-term tensile response of a geocomposite (a geotextile and a geogrid overlapped) and apply hyperbolic models to describe its load-strain tensile curves. Data from specimens submitted to mechanical damage, abrasion, and mechanical damaged followed by abrasion were analysed. Reduction factors were proposed by comparing data from damaged specimens with those from undamaged specimens. The experimental results were compared with those fitted by the constitutive models to validate the model. The constitutive models demonstrated good fitting capacity. For any mechanical condition, the model parameters could be estimated by relating the experimental tensile properties of the geocomposite with adjustment coefficients, which allowed for describing the tensile load-strain curves with good accuracy. The reduction factors for the specimens subjected to mechanical damage followed by abrasion were lower than the values which would be obtained if the damages were considered individually.

1   BACKGROUND

The mechanical response of geosynthetics combines the typical behaviour of an elastic solid, viscous liquid, and plastic, and depends mostly on the temperature (McGown et al. 2004). Determining the behaviour of geosynthetics is a complex task due to several variables involve, such as environmental conditions, type of polymer, soil confinement, and level, rate and duration of loading (Greenwood et al. 2012). The performance of geosynthetics deteriorates with time due to changes in mechanical properties before, during and after installation (Shukla 2016).

Assessment of durability is based on experimental observations and tests performed to simulate damages and degradation expected during the design life of a geosynthetic. Among the durability mechanisms for soil reinforcement, tensile creep, abrasion and damage associated with installation stand out (Greenwood et al. 2012). The effects of mechanical damage on geosynthetics may be assessed by performing field tests or inducing damage in a laboratory. Mechanical damage associated with installation is relevant for all applications of geosynthetics; it has been reported by several authors, e.g Fleury et al. (2019), Domiciano et al. (2020) and Lombardi et al. (2022). Continuous dynamic loading may cause abrasion damage, as in coastal protection and road applications (Greenwood et al. 2012). The effects

of abrasion on the tensile response of geosynthetics were reported by different authors, e.g. Huang et al. (2007) and Pinho-Lopes & Lopes (2015).

Allen & Bathurst (1994) stated that the tensile load-strain curve of a damaged geosynthetic (Y) can be obtained using scaling factors applied to the tensile load-strain curve of the undamaged geosynthetic (X), and then drawing the remaining parts of the damaged curve parallel to the undamaged one, as illustrated in Figure 1a. In this sense, the ultimate tensile strength (T_{max}) is adjusted by R_T (Equation 1), the strain at maximum load (ε_{Tmax}) is scaled by R_ε (Equation 2), whereas the secant stiffness (J) is adjusted by R_J (Equation 3). The reduction factors RF_T, RF_ε, RF_J are defined as the inverse of R_T, R_ε and R_J respectively; RF_T is most commonly applied in the design of geosynthetics for soil reinforcement, as indicated in EN ISO 20432 (ISO 2007).

$$R_T = \frac{T_{\max}(Y)}{T_{\max}(X)} = \frac{1}{RF_T} \tag{1}$$

$$R_\varepsilon = \frac{\varepsilon_{T_{\max}}(Y)}{\varepsilon_{T_{\max}}(X)} = \frac{1}{RF_\varepsilon} \tag{2}$$

$$R_J = \frac{J_{sec}(Y)}{J_{sec}(X)} = \frac{1}{RF_J} \tag{3}$$
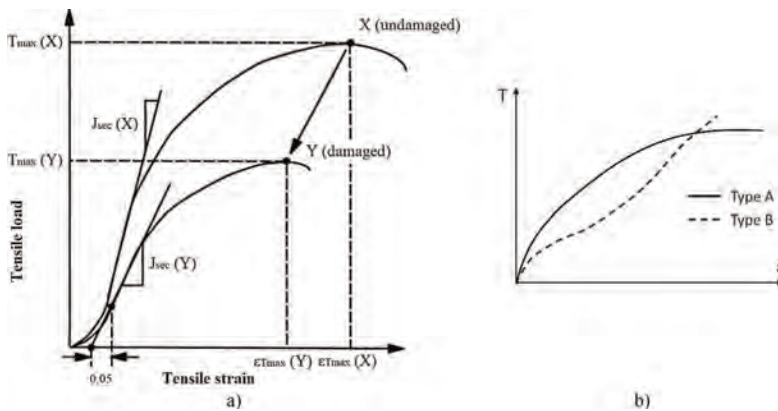
Figure 1.   a) Illustration of changes in load-strain response after damage (Allen & Bathurst 1994) – adapted; b) Typical tensile load-strain curves of geosynthetics (Paula & Pinho-Lopes 2018).

According to Liu & Ling (2006), short-term load-strain curves can be fitted by hyperbolic-based models depending on the tensile response of the geosynthetic: Equation 4 for a response of type A, and Equation 5 for a response of type B, as shown in Figure 1b. For type B geosynthetics, the nonlinear function combines a hyperbola for low strains with an exponential function for high strains. The tangent stiffness J_A and J_B are given by Equations 6 and 7. T_{max} is given by Equation 8 when ε tends to ε_{Tmax}. The initial stiffness (J_i) given by Equation 9 is obtained by imposing boundary conditions on Equations 6 and 7. As reported by Lombardi et al. (2022), the adjustment coefficients C_T and C_J are included in Equations 8 and 9, respectively, in order to relate the experimental properties with the corresponding model parameters.

$$T_A = \frac{\varepsilon}{a + b \cdot \varepsilon} \tag{4}$$

$$T_B = \frac{\varepsilon}{a + 2b\varepsilon} + \frac{1}{2b} \cdot e^{-c[\varepsilon - \varepsilon_{\max}]^2} \tag{5}$$

$$J_A = \frac{dT_A}{d\varepsilon} = \frac{a}{(a + b \cdot \varepsilon)^2} \tag{6}$$

$$J_B = \frac{dT_B}{d\varepsilon} = \frac{a}{(a + 2b\varepsilon)^2} - \frac{c[\varepsilon - \varepsilon_{\max}]}{b} \cdot e^{-c[\varepsilon - \varepsilon_{\max}]^2} \tag{7}$$

$$T_{\max} = C_T \frac{1}{b} \quad \varepsilon \to \varepsilon_{T_{\max}} \tag{8}$$

$$J_i = C_J \frac{1}{a} \quad \varepsilon \to 0 \tag{9}$$

where a, b and c = parameters of the constitutive models.

2 MATERIALS AND METHODS

The geocomposite (GCR) studied was formed by overlapping a PET woven geogrid (GGR) on a PP nonwoven geotextile (GTX), of which the nominal properties are presented in Table 1. The test procedures adopted were the ones reported by Rosete et al. (2013). The tensile strains were measured using a video extensometer, and the full tensile load-strain curves were available. The geocomposite presented two peaks of strength, but only the first was considered.

Table 1. Nominal properties of the geosynthetics used to form the geocomposite.

Property			Geotextile (GTX)	Geogrid (GGR)
Structure			Nonwoven	Woven
Constituent polymer			PP	PET
Ultimate tensile strength[a]	T_{nom}	kN/m	55	55
Strain at maximum load[b]	ε_{nom}	%	105.0	10.5
Mass per unit area[d]	μ_{nom}	g/m^2	1000	–
Thickness[e]	t_{nom}	mm	7.2	1.7
Grid spacing	–	mm^2	–	25 x 25

[a]EN ISO 10319 [b]EN ISO 11058 [c]EN ISO 12956 [d]EN ISO 9864 [e]EN ISO 9863-1

Some specimens of the geocomposite were damaged by synthetic aggregates at 1 Hz for 200 loading cycles ranging from 5 kPa to 500 kPa (EN ISO 10722:2019). Another group of specimens was damaged by abrasion using a P100 abrasive (EN ISO 13427:1998), and another one was submitted to mechanical damage followed by abrasion. For each mechanical condition, five specimens were subjected to wide-width tensile tests (EN ISO 10319:2015), and the results were used to characterize the tensile properties of the material, namely: $J_{0.5\%}$ and $J_{2\%}$ (secant stiffness for 0.5% and 2% strain, respectively), T_{max} and ε_{Tmax}. Due to the difficulty to obtain reliable data at the beginning of the tests, herein experimental J_i was adopted as experimental $J_{0.5\%}$.

Data from damaged specimens were compared with those from undamaged specimens so that reduction factors were proposed. The reduction factor for the mechanical damage followed by abrasion was compared with those obtained by multiplying the individual reduction factors to assess the synergy between them.

Curve fittings were performed in SPSS® based on the tensile response: type A or type B; intact specimens (INT) and specimens after mechanical damage (MEC) presented a response of type B,

whereas specimens after abrasion (ABR) and mechanical damage followed by abrasion (M + A) presented a response of type A. The parameter estimates were given with 95% confidence bounds using nonlinear regressions. The adjustment coefficients were determined by linear regressions between experimental tensile properties and model parameters from curve fittings, as per Equations 8 and 9. Once C_T and C_J were determined, the model parameters were estimated by relating the experimental tensile properties and the adjustment coefficients using Equations 8 and 9.

3 RESULTS – ANALYSIS AND DISCUSSIONS

The mean experimental and fitted tensile properties are summarized in Table 2. The mean estimates of the model parameters a, b and c are given in Table 3. Table 4 gives the reduction factors (Eq. 1–3), as well as the adjustment coefficients C_T and C_J (Eq. 8 and 9). Table 3 gives the model parameters a^* and b^* estimated relating experimental J_i and C_J, and experimental T_{max} and C_T, respectively. Table 4 gives the tensile properties $T_{max}{}^{\#}$ and $J_i{}^{\#}$ estimated using C_T and C_J and the model parameters b and a, respectively. The experimental and fitted tensile load-strain curves are shown in Figure 2, in which the curves were plotted using the parameters a and b, and a^* and b^*.

Table 2. Mean experimental and fitted tensile properties.

| Sample | Experimental mean value | | | | | | | | Fitted mean value | | | | |
	T_{max} kN/m	CV %	ε_{Tmax} %	CV %	$J_{0.5\%}$ kN/m	CV %	$J_{2\%}$ kN/m	CV %	Fit	T_{max} kN/m	CV %	$J_{2\%}$ kN/m	CV %
INT		11	14.4	8	778.8	7	614.4	8	H_B	55.79	11	578.6	8
MEC	44.56	7	12.9	4	683.1	11	485.3	11	H_B	43.12	6	471.8	8
ABR	24.92	10	11.0	15	352.9	17	386.1	12	H_A	24.48	11	294.1	12
M + A	20.77	9	10.2	12	406.9	13	392.3	8	H_A	20.36	10	289.7	8

CV = coefficient of variation H_A = type A hyperb. model H_B = type B hyperbolic-based model

Table 3. Mean parameter estimates.

| Sample | Curve fitting | | | | | | | | Equation 9 | | Equation 8 | |
	a m/kN	CV %	b m/kN	CV %	c –	CV %	J_i kN/m	CV %	a^* m/kN	CV %	b^* m/kN	CV %
INT	0.116	7	0.016	12	0.025	42	863.38	8	0.116	7	0.016	11
MEC	0.128	13	0.021	6	0.036	10	791.84	12	0.127	11	0.020	6
ABR	0.274	21	0.016	30	–	–	377.12	20	0.271	18	0.015	11
M + A	0.220	15	0.028	18	–	–	463.44	16	0.218	12	0.027	9

$a^* = C_J /J_i$ $b^* = C_T /T_{max}$ J_i and T_{max} = experimental values

Table 4. Reduction factors, adjustment coefficients and estimated tensile properties.

| Sample | Reduction factor | | | | Equation 8 | | Equation 9 | |
	RF_T –	RF_ε –	RF_{Ji} –	$RF_{J2\%}$ –	C_T –	$T_{max}{}^{\#}$ kN/m	C_J –	$J_i{}^{\#}$ kN/m
INT	–	–	–	–	0.8995	55.78	0.9018	778.60
MEC	1.27	1.12	1.14	1.27	0.9051	43.13	0.8618	682.41
ABR	2.27	1.31	2.21	1.59	0.3687	23.85	0.9321	351.51
M + A	2.72	1.42	1.92	1.57	0.5467	20.12	0.8747	405.37
MxA	2.87	1.47	2.01	2.53	–	–	–	–

MxA = $RF_{(MEC)}$ x $RF_{(ABR)}$ $T_{max}{}^{\#} = C_T /b$ $J_i{}^{\#} = C_J /a$
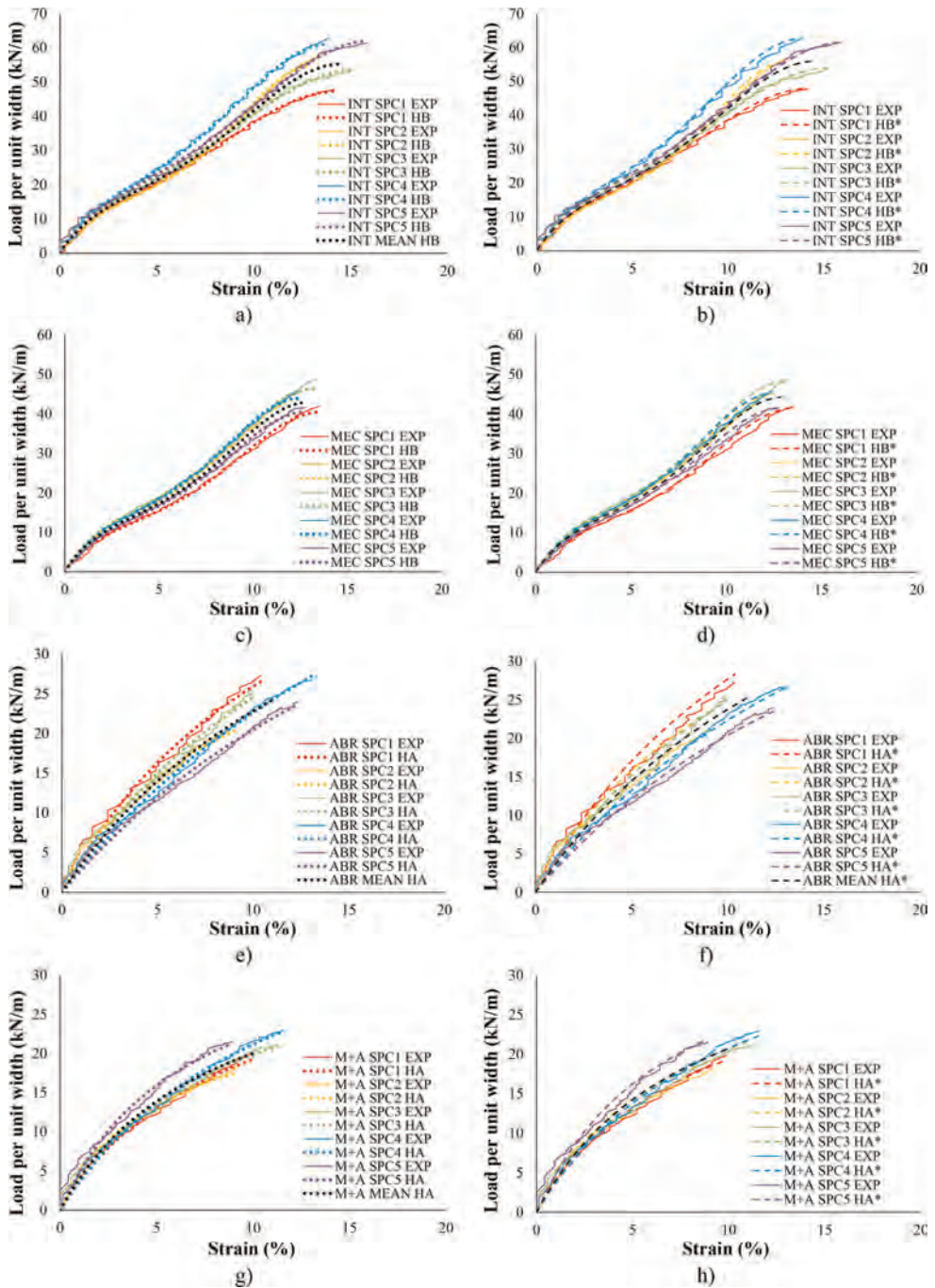
Figure 2. Experimental and fitted tensile load-strain curves of the geocomposite (GCR). a) and b): INT; c) and d): MEC; e) and f): ABR; g) and h): M + A. H_A and H_B: curves obtained using the parameters a and b from curve fitting (Table 3); HA* and HB*: curves obtained using the parameters $a*$ and $b*$. (Table 3).

The constitutive models presented good fitting capacity, whether in terms of qualitatively describing the tensile load-strain curve or providing accurate estimates of the tensile properties. The mean curves given in Figure 2 were able to qualitatively represent the experimental curves as well as to provide accurate estimates for the tensile properties, either using mean model parameters a and b or a^* and b^*. As expected, the parameters a and b produced slightly more precise results if compared to those obtained using the parameters a^* and b^*.

Intact specimens of the geocomposite and those submitted to mechanical damage presented a type B tensile response, whereas the specimens after abrasion and mechanical damage followed by abrasion presented a type A response; thus, the effects of abrasion damage were very pronounced in the material to the extent of changing the shape of the tensile curve.

For intact and damaged specimens, the tensile properties estimated by relating the model parameters and the adjustment coefficients were notably similar to the experimental values. For any mechanical condition, the model parameters estimated by relating the experimental tensile properties of the geocomposite with the adjustment coefficients allowed for describing the tensile load-strain curves of the geocomposite with good accuracy.

The reduction factors for the specimens subjected to mechanical damage followed by abrasion were lower than those which would be obtained if the damages were considered individually, i.e. the synergy between the damage effects proved to be less harmful to the material than superimposing the effects separately, as usually done in the design of geosynthetics.

4 CONCLUSIONS

The objective of this study was to analyse the short-term tensile response of a geocomposite and apply hyperbolic models to describe load-strain tensile curves. Data from specimens submitted to mechanical damage, abrasion damage, and mechanical damage followed by abrasion were analysed. The results of the study are summarized as follows.

- The constitutive models presented good fitting capacity in terms of qualitatively describing the load-strain curve or providing accurate estimates of the tensile properties.
- Using mean model parameters to describe a representative tensile curve has shown to be effective either for the parameters a and b (curve fitting) or a^* and b^* (statistical approach).
- The tensile properties estimated by relating the model parameters and the adjustment coefficients were similar to the experimental values for intact and damaged specimens.
- The effects of abrasion damage in the geocomposite were very pronounced to the extent of changing the shape of the tensile load-strain curves.
- The reduction factors for the specimens subjected to mechanical damage followed by abrasion were lower than those which would be obtained if they were taken individually.
- The model parameters could be estimated by relating the experimental tensile properties of the geocomposite with the adjustment coefficients for intact and damaged specimens.
- Using load-strain curves after damage allows for considering realistic responses of geosynthetics in design, rather than the intact responses and reduction factors as traditionally.

REFERENCES

Allen, T. M., & Bathurst, R. J. (1994). Characterization of Geosynthetic Load-Strain Behavior After Installation Damage. *Geosynthetics International*, *1*(2), 181–199. https://doi.org/10.1680/gein.1.0008

Domiciano, M. L., Santos, E. C. G., & Lins da Silva, J. (2020). Geogrid Mechanical Damage Caused by Recycled Construction and Demolition Waste (RCDW): Influence of Grain Size Distribution. *Soils and Rocks*, *43*(2). https://doi.org/10.28927/SR.432231

Fleury, M. P., Santos, E. C. G., Lins Da Silva, J., & Palmeira, E. M. (2019). Geogrid Installation Damage Caused by Recycled Construction and Demolition Waste. *Geosynthetics International*, *26*(6), 641–656. https://doi.org/10.1680/jgein.19.00050

Greenwood, J. H., Schroeder, H. F., & Voskamp, W. (2012). *Durability of Geosynthetics*. CUR Building & Infrastructure.

Huang, C. C., Tzeng, Y. S., & Liao, C. J. (2007). Laboratory Tests for Simulating Abrasion Damage of a Woven Geotextile. *Geotextiles and Geomembranes*, *25*(4–5), 293–301. https://doi.org/10.1016/j.geotexmem.2007.02.008

International Organization for Standardization. (1998). EN ISO 13427:1998 – Geotextiles and Geotextile-Related Products — Abrasion Damage Simulation (sliding block test).

International Organization for Standardization. (2007). EN ISO 20432:2007 – Guidelines for the Determination of the Long-term Strength of Geosynthetics for Soil Reinforcement.

International Organization for Standardization. (2015). EN ISO 10319:2015 – Geosynthetics — Wide-Width Tensile Test.

International Organization for Standardization. (2019). EN ISO 10722:2019 – Geosynthetics — Index Test Procedure for the Evaluation of Mechanical Damage Under Repeated Loading — Damage Caused by Granular Material.

Liu, H., & Ling, H. I. (2006). Modeling Cyclic Behavior of Geosynthetics using Mathematical Functions Combined with Masing Rule and Bounding Surface Plasticity. *Geosynthetics International*, *13*(6), 234–245. https://doi.org/10.1680/gein.2006.13.6.234

Lombardi, G., Paula, A. M., & Pinho-Lopes, M. (2022). Constitutive Models and Statistical Analysis of the Short-term Tensile Response of Geosynthetics After Damage. *Construction and Building Materials*, *317*, 125972. https://doi.org/https://doi.org/10.1016/j.conbuildmat.2021.125972

McGown, A., Khan, A. J., & Kupec, J. (2004). The Isochronous Strains Energy Approach Applied to the Load-strain-time-temperature Behaviour of Geosynthetics. *Geosynthetics International*, *11*(2), 114–130. https://doi.org/10.1680/gein.2004.11.2.114

Paula, A. M., & Pinho-Lopes, M. (2018). Simple Constitutive Models to Study the Influence of Installation Damage on the Load-strain Response of Two Geogrids. *11th Internat. Conference on Geosynthetics*.

Pinho-Lopes, M., & Lopes, M. L. (2015). Synergisms between Laboratory Mechanical and Abrasion Damage on Mechanical and Hydraulic Properties of Geosynthetics. *Transportation Geotechnics*, *4*, 50–63. https://doi.org/10.1016/j.trgeo.2015.07.001

Rosete, A., Mendonça Lopes, P., Pinho-Lopes, M., & Lopes, M. L. (2013). Tensile and Hydraulic Properties of Geosynthetics after Mechanical Damage and Abrasion Laboratory Tests. *Geosynthetics International*, *20*(5), 358–374. https://doi.org/10.1680/gein.14.00015

Shukla, S. K. (2016). An Introduction to Geosynthetic Engineering. In *CRC Press*. https://doi.org/10.1201/b21582

Topology optimization of a junction in a biaxial geogrid under in-isolation tensile loading

L. Paiva & M. Pinho-Lopes
RISCO, Department of Civil Engineering, University of Aveiro, Portugal

R. Valente
TEMA, Department of Mechanical Engineering, University of Aveiro, Portugal
LASI, Intelligent Systems Associate Laboratory, Portugal

A.M. Paula
Instituto Politecnico de Braganga, Braganga, Portugal
RISCO, Department of Civil Engineering, University of Aveiro, Aveiro, Portugal

ABSTRACT: The finite element method is a powerful tool that can be used to analyse problems including complex geometries and material properties. In this study, the general-purpose finite element software ABAQUS was used to investigate the load-strain response of a biaxial geogrid under in-isolation tensile loading. A 3D model was developed, accounting for different thickness of geogrid elements and their nonlinear response. Then, TOSCA module was used to investigate an alternative design of a junction profile. The geogrid was submitted to uniaxial and biaxial tensile loading, simulating a wide-width tensile test and a biaxial wide-width tensile test. Validation was performed by comparing the numerical model with experimental data. Optimization results showed that it was possible to reduce the junction volume profile by 53% with a compromise of 3% in maximum bearing capacity.

1 INTRODUCTION

Numerical modeling of the tensile response of geosynthetics can be a challenging task. For geogrids, the complex geometry and the nonlinear response of the polymeric material are the main causes of complexity for numerical implementation. To explore alternative geometry designs, 3D numerical simulations can be used to map the stress distribution within the geogrid elements, aiding to the understanding on how the geogrid works and how it can be improved. In this paper, experimental data was used to calibrate a numerical model of a biaxial geogrid. The objective was to use the validated model to assess a more efficient design for the junction profile of the studied geogrid under tensile loading.

Geogrid reinforcement is an effective method to improve the performance of earth structures by transferring the tensile load from the soil to the reinforcement. Thus, the design of geogrid reinforcements are mainly determined by their tensile resistance. Numerical methods have been developed to model geogrids both in-isolation (Amirhosseini *et al.* 2022) and in soil-geosynthetic applications (Chen *et al.* 2021; Gu *et al.* 2017; Leonardi & Suraci 2022; Perkins 2000; Perkins & Edens 2003; Shen *et al.* 2019; Yang *et al.* 2020). These studies have focused on the general response of the reinforcing elements under various conditions, often recurring to simplified models for the geometry and material properties.

A 3D elasto-plastic finite element (FE) model was studied using the general purpose FE software ABAQUS (2021). The in-isolation tensile response of the geogrid was analysed.

The model was initially calibrated with experimental data on the machine direction (MD), wide-width tensile test (ISO-10319: 2015). Then, a topology optimization study was carried out to produce an alternative profile for the geogrid junction.

2 CALIBRATION OF THE 3D FEM MODEL

2.1 Model development

Geometry and boundary conditions: The geometric details were directly created in ABAQUS considering the 3D solid features of the geogrid. The studied geogrid had a ultimate tensile strength of 40 kN/m for a peak strain of 10% (nominal values for the MD). The cross-section of the longitudinal and transversal ribs were, respectively, 2.5 x 2.2 mm^2 and 2.2 x 1.4 mm^2. The curved junction profile was 5.8 mm thick. The specimen was composed by 5 longitudinal and 5 transversal ribs and had total dimensions of 132 x 132 mm^2 between rib centres (Figure 1). The boundary conditions emulated those of the experimental tensile test. Both ends had translation constraints along the Y direction (perpendicular to the applied force), with one end being fixed along the X direction (parallel to the applied force). The numerical test was carried out by applying a prescribed displacement at the other end of the geogrid model with the same strain rate of 20%/min (0.44 mm/s) used in the experimental test. Only half of the longitudinal bars were modeled utilizing symmetry for enhanced computational performance.
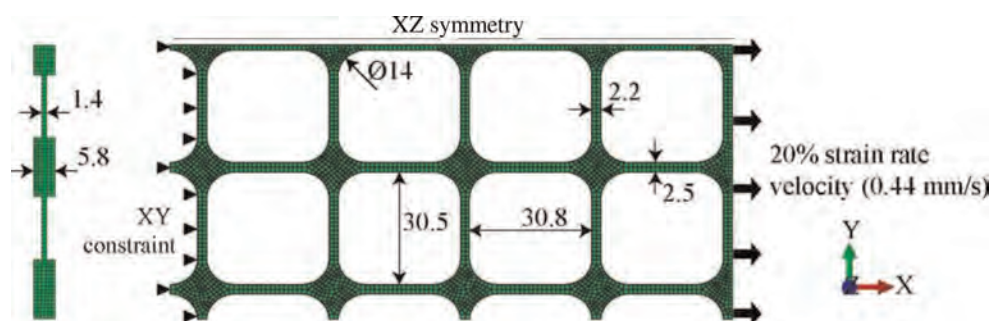
Figure 1. Geometry and boundary conditions of the geogrid. All dimensions are in mm.

Constitutive model: The experimental data available referred to wide-width tensile tests, carried out according to BS EN ISO 10319 (ISO-10319: 2015), which was used to compose a nonlinear elasto-plastic material model. A isotropic material was composed using the experimental data on the MD direction (Figure 2), where T_{max} is the maximum tensile load and e_{max} is the corresponding strain. The experimental load per unit width/strain curve shows a nonlinear behaviour, even for small strains. Default elasto-plastic material with isotropic hardening from ABAQUS was used, with an Young's modulus of 1190 MPa (obtained from the initial tangent response on the MD direction) and a Poisson's ratio taken as 0.3 (Perkins 2000), together with the elastic component deduced from the experimental load-strain response. Stresses and strains were evaluated using a von Mises yield criterion.

2.2 Stresses and strains in the geogrid

The modeling results for an axial displacement of 8.7 mm are shown in Figure 3a. This displacement is relative to a 20 s test time under a strain rate of 10%/min where the maximum plasticity occurred. Displacements were linearly distributed along the geogrid, with a null deformation at the left end (where it was constrained) and the maximum displacement at
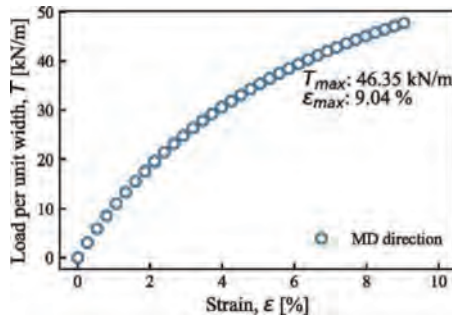
Figure 2.   Experimental uniaxial load per unit width/strain curve for the MD direction (EN ISO 10319:2015).
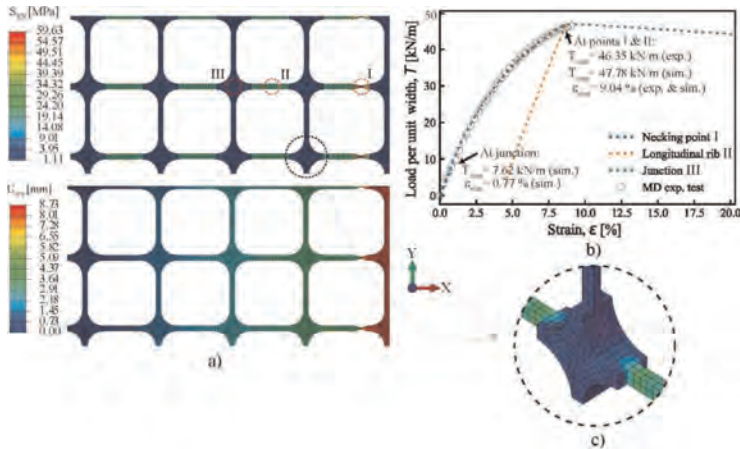
Figure 3.   Simulation results for the tensile test simulation: a) stresses and strains at maximum plasticity (8.7 mm displacement) in terms of true stress/strain; b) load per unit width/strain curve of experimental (exp.) data and simulation (sim.) at three points (I, II & III), in terms of nominal stress/strain; c) 3D detail on the stress distribution in the junction.

the right end (where the prescribed displacement was applied). The axial stress plot Sxx showed an equally distributed tension under the longitudinal ribs, whereas the junctions and perpendicular ribs showed significantly less stress concentration. The necking effect spotted at point *I* was in line with experimental tests, where failure at the longitudinal ribs near the clamps often occurs. The load-strain overlay between experimental and numerical tests is shown in Figure 3b. The model was able to accurately reproduce the tensile test with a slight overestimation of the maximum load (3% error), whereas the maximum strain was the same in the physical and in the numerical tests. The results were also in good agreement with the nominal properties reported by the manufacturer. Figure 3c shows a corner junction with the respective critical stresses at maximum plasticity. Specially close to the perpendicular rib, the junction profile had little to no stresses or relative strains.

It is important to notice that the differences in magnitude results between the ABAQUS plots (Figure 3a) and the load per unit width/strain curves (Figure 3b) were due to the fact that ABAQUS results are in terms of true stresses/strains, while traditional tensile tests are reported in terms of nominal (engineering) stresses/strains. For geosynthetics the response is quantified ignoring the thickness of the material (as it can vary with confinement).

3 TOPOLOGY OPTIMIZATION OF A GEOGRID JUNCTION UNDER IN-ISOLATION TENSILE LOAD

3.1 Model development

A continuous structure submitted to a topology optimization process can be regarded as a material (volume) distribution problem (Bendsoe & Sigmund 2003; Pang & Fard 2020; Saleem *et al*. 2008). For this particular problem, the optimization target was to find an alternative minimum volume distribution within the boundary constrains for the maximum global stiffness. In ABAQUS, TOSCA module was used to search iteratively for a minimized strain energy (to maximize global stiffness), while taking into the consideration boundary conditions and applied forces for a reduction in volume where stresses are not critical. The goal was to find the optimal volume configuration for the junction profile that saves on material, while still being able to perform the same tensile test.

Model development and boundary conditions: A simplified unit of the geogrid was used to run the TOSCA algorithm for two scenarios: 1) the geogrid was submitted to a axial displacement similar to that of the original tensile test; 2) the geogrid was submitted to a biaxial prescribed displacement, in order to explore the optimization results. Since a prescribed displacement was applied (velocity), the strain energy was set to be maximized, while the volume constraint was set to be less or equal to 50% than that of the initial value. Both of these rules were applied to only the junction section. The two optimization layouts are illustrated in Figure 4, with two symmetry axes (only a quarter of the part was modeled).
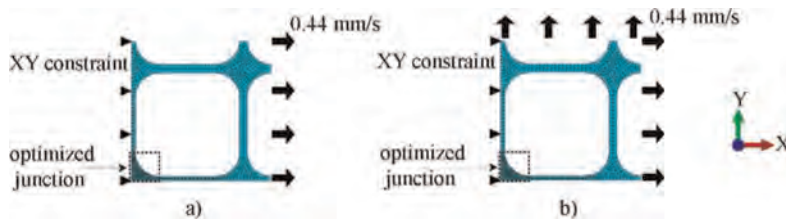
Figure 4.   Topology optimization layout: a) uniaxial test; b) biaxial test. Only a quarter of the unit was modeled utilizing symmetry.

3.2 Optimization results

Results of the topology optimization are shown in Figure 5. The curved profile of the junction was nearly removed for both uniaxial and biaxial simulation tests. Results for the unixial test (Figure 5a) showed that a junction with a reduction of 55% of lateral thickness could still sustain the axial loading applied. The stress distribution in a biaxial scenario was more critical, allowing for a lateral thickness reduction of 36% (Figure 5b).
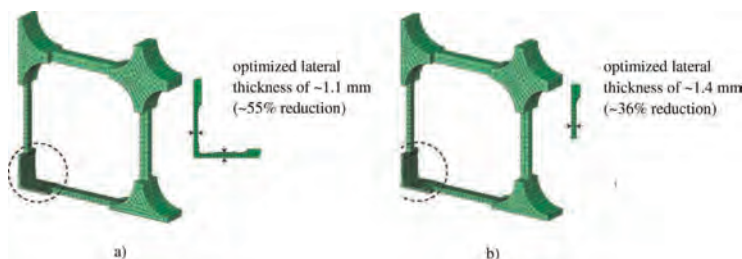
Figure 5.   Topology optimization results: a) optimized section for uniaxial loading; b) optimized section for biaxial loading. Only a quarter of the unit was modeled utilizing symmetry.

3.3 An alternative junction profile

The theoretical results produced by topology optimization algorithms can provide insights on how to improve the geometry of geogrids. From the results described in Section 3.2, a new optimized junction profile was studied, matching the thickness of the ribs without the original curved profile (Figure 6b). Although the results in Section 3.2 allowed for a theoretical lateral thickness of the junction smaller than the ribs (Figure 5), continuity was maintained to avoid excessive distortion of the mesh. The same thickness of 5.8 mm was preserved from the initial profile, generating a volume reduction of 53%. The von Mises stress distribution for both initial and optimized junctions under uniaxial load are shown in Figure 6a. The load per unit width/strain comparison between initial and optimized profiles are shown in Figure 6c. A good agreement between the topology results and the actual stress distributions of the optimized junction was found. The stress distributions showed little variation between the two simulations, whereas the maximum load for the optimized model was 2% smaller than the initial model. This could be due to the lateral thickness reduction, since the initial model has a thicker rib-junction interface.
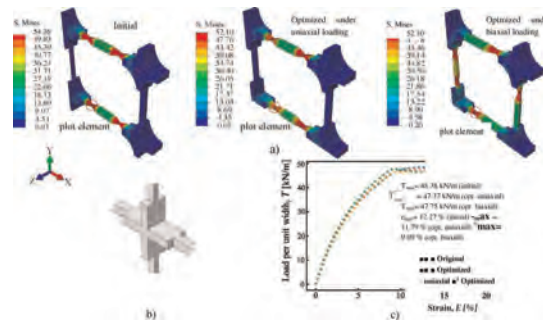
Figure 6. Comparison between initial and optimized junction profiles: a) von Mises stresses (true stresses) for maximum plasticity; b) 3D view of optimized junction; c) Load per unit width/strain curve for identified plot element (engineering stress/strain).

3.4 Limitations and potential

The optimization described herein considered the in-isolation response under uniaxial and biaxial tensile loadings. On the one hand, depending on the application, the loading can be more complex. On the other hand, in real applications, geogrids are confined in soil. Thus, the response of the composite material will be affected by factors related to the soil. Examples include: the particle size distribution and its relation to the geogrid openings; the relative movement of the geogrid and the soil. The soil-geosynthetic interaction is a function of the geogrid area, hence, changes in geometry will affect the mechanisms of load distribution within the junction and the reinforcement as a whole. The isotropic assumption affects the predicted resistance of the interface between ribs and junctions, that can also influence the optimization in this area.

Future models incorporating these aspects can utilize the non-destructive and easily-parametrized advantages of numerical simulations to propose more realistic optimized geometries for geogrids. As demonstrated, a general-purpose FE tool is an effective method to analyse geosynthetics, being able to generalize 3D stresses and strains from uniaxial tests.

4 CONCLUSIONS

In this study, numerical tensile tests of a geogrid were carried out, followed by a topology optimization to propose an alternative design of a junction element in a biaxial geogrid. First, a numerical model capable of simulating the tensile response of the in-isolation geogrid was

developed using ABAQUS. The model featured a 3D geometry and an isotropic elasto-plastic constitutive model that was calibrated with experimental data from in-isolation tensile tests (MD). The results from the calibrated model allowed a deeper understanding on the stress distribution at the junction elements, where part of the profile was not contributing to the load bearing and local stability.

The TOSCA framework was then applied to optimize the topology of the junction profile, with a design domain set for material removal. The results obtained from the optimization design showed that the lateral thickness of the junction could be reduced in 55% (uniaxial loading) and 36% (biaxial loading), without compromising the initial stiffness and stability. The geometry produced by the optimization algorithm was used to propose an alternative junction profile with 53% less material that was also capable of resisting the same load conditions with a 3% resistance margin. These initial results are promising and can be extended to scenarios where a geogrid and the surrounding soil are modeled.

This study has demonstrated how a calibrated numerical model could be used to extend the physical element analysis through simulation (non-destructive) methods. The contribution of topology optimization in simplifying element shapes was also proved to be a suitable framework in finding new design solutions without compromising structural performance and integrity.

ACKNOWLEDGEMENTS

REFERENCES

ABAQUS (2021). ABAQUS/Standard User's Manual. Dassault Systemes Simulia Corp.

Amirhosseini, I., V. Toufigh, M. M. Toufigh, and E. Ghazavi-Baghini (2022). Three-dimensional Modeling of Geogrid Pullout Test Using Finite-element Method. International Journal of Geomechanics 22, 04021297.

Bendsoe, M. P. and O. Sigmund (2003). Topology Optimization: Theory, Methods, and Applications. Springer Science & Business Media.

Chen, J., X. Guo, R. Sun, S. Rajesh, S. Jiang, and J. Xue (2021). Physical and Numerical Modelling of Strip Footing on Geogrid Reinforced Transparent Sand. Geotextiles and Geomembranes 49(2), 399–412.

Gu, M., J. Han, and M. Zhao (2017). Three-dimensional Dem Analysis of Single Geogrid-encased Stone Columns Under Unconfined Compression: A Parametric Study. Acta Geotechnica 12, 559–572.

ISO-10319: (2015). BS EN ISO 10319:2015: Geosynthetics - Wide-width tensile test. BSI Standards Limited.

Leonardi, G. and F. Suraci (2022). A 3d-fe Model for the Rutting Prediction in Geogrid Reinforced Flexible Pavements. Sustainability 14, 3695.

Pang, T. Y. and M. Fard (2020). Reverse Engineering and Topology Optimization for Weight-reduction of a Bell-crank. Applied Sciences 10(23), 8568.

Perkins, S. W. (2000). Constitutive Modeling of Geosynthetics. Geotextiles and Geomembranes 18, 273–292.

Perkins, S. W. and M. Q. Edens (2003). A Design Model for Geosynthetic-reinforced Pavements. International Journal of Pavement Engineering 4, 37–50.

Saleem, W., H. Lu, and F. Yuqing (2008). Topology Optimization-problem Formulation and Pragmatic Outcomes by Integration of Tosca and Cae Tools. In Proceedings of the World Congress on Engineering and Computer Science, Volume 22, pp. 24.

Shen, P., J. Han, J. G. Zornberg, A. M. Morsy, D. Leshchinsky, B. F. Tanyu, and C. Xu (2019). Two and three-dimensional numerical analyses of geosynthetic-reinforced soil (grs) piers. Geotextiles and Geomembranes 47, 352–368.

Yang, S., Y. Gao, K. Cui, F. Zhang, and D. Wu (2020). Three-dimensional Internal Stability Analysis of Geosynthetic-reinforced Earth Structures Considering Seismic Loading. Soil Dynamics and Earthquake Engineering 130, 105979.

Evaluation of geosynthetic-asphalt interface characteristics using Leutner shear tester

V. Vinay Kumar*
Postdoctoral Fellow, Department of Civil, Architectural and Environmental Engineering, University of Texas at Austin, Austin, Texas, USA

Gholam H. Roodi*
Geotechnical Designer, HDR, Toronto, Ontario, USA

Jorge G. Zornberg*
Professor, Department of Civil, Architectural and Environmental Engineering, University of Texas at Austin, Austin, Texas, USA

ABSTRACT: Geosynthetics are widely adopted within the asphalt layers to enhance the pavement performance through various functions such as reinforcement, stiffening, and moisture barrier. Specifically, these functions help retard the reflective cracking, formation of rut and permanent deformation, and fatigue cracking in the asphalt layers. However, a major concern of adopting geosynthetic reinforcements is the reduction in interlayer shear resistance between the asphalt layers. In this study, the impact of various geosynthetic-asphalt interface characteristics on the interface shear resistance was evaluated by testing cores obtained from an in-service highway. Specifically, the Leutner shear device was used to test seven interfaces including an unreinforced (control) interface and six asphalt-geosynthetic interfaces that were formed by different types of geosynthetic reinforcements including both polymeric and fiberglass products. Although the Leutner shear test results indicated reduced interface shear resistance in all geosynthetic-reinforced specimens, the percentage reduction was found to be particularly affected by the composition of the reinforcements. Specifically, the reinforcement materials (glass or polymer) and form (grid or textile or composite) were found to significantly affect the asphalt-reinforcement bond strength. Additional factors affecting the geosynthetic-asphalt interface characteristics included tack coat application rates, characteristics of the apertures, and the thickness of the geosynthetic reinforcements.

1 INTRODUCTION

Geosynthetics have been widely used within or as the interface between pavement layers to enhance roadway performance. Reinforcement inclusions in asphalt layers have been reported to mitigate reflective cracking and enhance pavement structural performance (e.g., Brown *et al*. 2001; Ferrotti *et al*. 2012; Kumar & Saride 2018). However, geosynthetic inclusion can compromise the bonding between the asphalt layers through interlayer de-bonding effect. This effect is described as a condition where the adhesion between two adjacent asphalt layers weakens and the two layers may eventually separate under excessive

*Corresponding Authors: vinay.vasanth@utexas.edu, gholamhossein.roodi@hdrinc.com and zornberg@mail.utexas.edu

DOI: 10.1201/9781003386889-289

horizontal stresses (e.g., Brown *et al*. 2001; Kumar & Saride 2018). Debonding may undermine the design benefits from geosynthetic interlayers and dissuade owners on using them. With the development of a wide range of geosynthetic interlayers with various designs and textures, understanding the asphalt-geosynthetic bonding strength and extents of potential debonding has become crucial.

A wide variety of experiments have been developed to characterize various aspects of bonding strength between two asphaltic layers. The most common experimental method for evaluating interlayer bonding strength involves direct shearing of the interface and various experimental setups have been adopted to generate such shear loading on the interface. A few examples include the Leutner shear test (Leutner 1979), the Layer-Parallel Direct Shear (LPDS) test, the Florida Department of Transportation (FDOT) shearing device (Sholar *et al*. 2002), Ancona Shear Testing Research and Analysis (ASTRA) (Canestrari *et al*. 2005), and large-scale interface shear strength test device (Kumar *et al*. 2017). The variations among the shear mechanisms involved in the tests has made comparison of test results particularly difficult. However, several experimental studies could identify the most important parameters that impact the bond strength as temperature, aggregate gradation, and surface roughness, normal pressure, tack coat type, and tack coat application rate among others (e.g., Canestrari *et al*. 2005; Correia *et al*. 2022; Kumar *et al*. 2017; Kumar & Saride 2018; Roodi *et al*. 2017; Sholar *et al*. 2002; West *et al*. 2005).

While most experimental studies on asphalt-geosynthetic bonding strength involved remolded samples, comparatively limited research has been conducted on asphalt cores obtained from roadways that have been constructed with geosynthetic reinforcements. Testing of such field samples that had subjected to construction impact provides more realistic insights into asphalt-geosynthetic bonding strength. This paper presents results of asphalt-geosynthetic bond testing program that aimed at understanding the various parameters affecting the bond strength, including impacts from construction damages. Asphalt cores were collected from an unreinforced and six geosynthetic-reinforced roadway sections and their interface bond strength was tested using the Leutner shear tester. Geosynthetic reinforcement included different polymeric and fiberglass products with different forms of grids, textiles, and composites. Factors affecting the geosynthetic-asphalt interface bonds were evaluated.

2 PROJECT BACKGROUND

As part of Texas Department of Transportation (TxDOT) rehabilitation program, a 32-km-long stretch of State Highway (SH) 21 was restored by treatment of distresses in the pre-existing asphalt surface followed by construction of a 75-mm-thick structural overlay. The original overlay design included geosynthetic interlayer to be placed between the existing asphalt and the new overlay. To establish basis for future expansion in the use of geosynthetic interlayers, TxDOT retained the research team to investigate the effectiveness of various geosynthetic interlayers in enhancing roadway performance. A 1.34-km-long section of the four-lane highway was split into 34 test sections that were constructed with different designs in plan and profiles. Geosynthetic-reinforced sections were constructed side-by-side and along with unreinforced sections to compare their performances under similar conditions.

Seven of the test sections, including an unreinforced section and six geosynthetic-reinforced sections, were selected for more robust investigation that involved installing various types of sensors and conducting controlled traffic loading on sensors (Kumar *et al*. 2022). To complement the investigation and provide insight into the bonding strength between asphalt and various geosynthetic types, several cores were collected from each test section two months after construction. Figure 1 shows design profile of the rehabilitated test section along with an example picture of cores depicting various asphalt layers. As shown in the figure, the asphalt layers included approximately 150 mm of preexisting asphalt and level-up layers, with geosynthetic interlayer installed on applied tack coat at the interface,

and overlain by 75 mm asphalt overlays placed in two layers including a 50-mm-thick dense-graded asphalt mixture (Type D) and a 25-mm-thick wearing-course asphalt mixture (TOM). The asphalt mixtures (Type D and TOM) were adopted from TxDOT standard specifications for construction and maintenance of highways, streets, and bridges (TxDOT 2014).
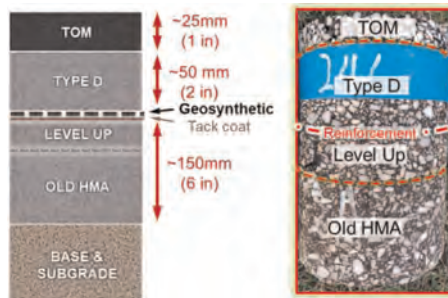
Figure 1. Roadway profile of test sections: (a) Schematic design profile; (b) Example picture of asphalt core.

3 MATERIALS AND METHODS

3.1 Geosynthetic reinforcements

Six different types of geosynthetic reinforcements including three each of polymeric and fiberglass products were adopted as asphalt reinforcements in this study. Specifically, the geosynthetic reinforcements were adopted based on their material composition, tensile, and physical characteristics. Figure 2 presents the three polymeric products evaluated in this study, which includes two polyester geogrid composites and a polyvinyl alcohol geogrid composite. The product GR-1 (Figure 2a) is a geocomposite made up of high modulus polyester geogrid and a woven fabric, while GR-2 (Figure 2b) is a geocomposite made up of high modulus polyester geogrid and an ultra-lightweight non-woven fabric. The third product, GR-3 (Figure 2c) is a geocomposite made up of a high modulus polyvinyl alcohol geogrid and an ultra-lightweight non-woven fabric. All the three products are completely coated with a binder to enhance the bonding characteristics. The three fiberglass products evaluated in this study are as shown in Figure 3, which includes two fiberglass geogrid composites and a fiberglass geogrid. The product GR-4 (Figure 3a) is a geocomposite made up of high strength fiberglass filaments and an ultra-lightweight non-woven fabric that is completely coated with binder, while GR-5 (Figure 3b) is a geocomposite comprising fiberglass filament yarns incorporated into a thick nonwoven polypropylene paving fabric. The final product, GR-6 (Figure 3c) is a self-adhesive geogrid made up of high strength fiberglass filaments that are completely coated with elastomers. The physical and tensile properties of the geosynthetic reinforcements evaluated in this study is summarized in Table 1.
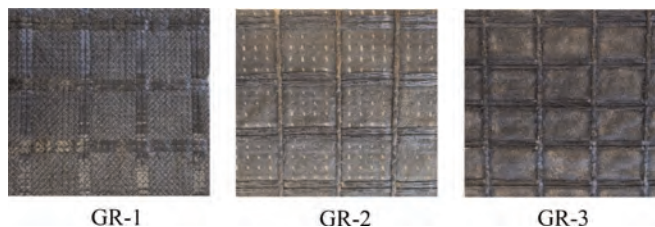
Figure 2. Polymeric Geosynthetic Reinforcements evaluated in the study: a) GR-1; b) GR-2; and (c) GR-3.
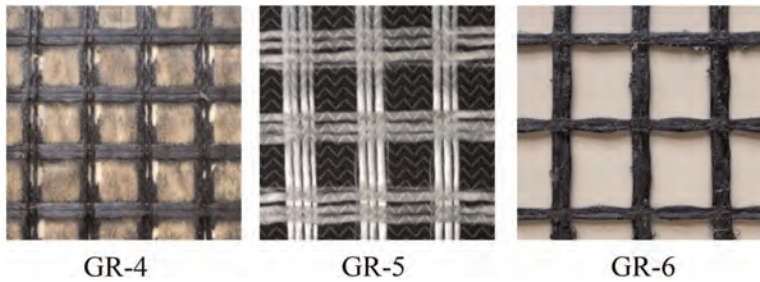
Figure 3. Fiberglass Geosynthetic Reinforcements evaluated in the study: a) GR-4; b) GR-5; and (c) GR-6.

Table 1. Properties of geosynthetic reinforcements and tack application rates.

Geosynthetic Reinforcements	Mass/ unit area (g/m^2)	Aperture size (mm)	Ultimate tensile strength (kN/m)	Strain at elongation (%)	Asphalt retention capacity (l/m^2)	Melting point (°)	Tack application rate (l/m^2)
GR-1	275	34 × 34	50	12	0.47	250	0.54
GR-2	270	40 × 40	50	10	0.47	250	0.54
GR-3	210	40 × 40	50	5	0.47	235	0.54
GR-4	596	30 × 30	100	3	0.47	300	0.54
GR-5	678	38 × 38	115	3	1.2	800	1.35
GR-6	432	25 × 25	100	3	–	232	–

3.2 Asphalt and tack

Two different types of asphalt mixtures were used as asphalt overlays that included a dense-graded asphalt mixture (Type D) overlain by a thin asphalt overlay mixture (TOM). However, it is important to note that the geosynthetic reinforcements were installed below the Type D layer in the reinforced sections using a polymer modified asphalt cement (AC-15P) applied at different rates, per geosynthetic manufacturer recommendations and prior trials. While, a cationic, slow-setting, low-viscosity, and comparatively hard residue emulsion (CSS-1H) was applied at a residual rate of 0.27 l/m^2 on the level-up course prior to the placement and compaction of Type D layer in the unreinforced (UR) section. Table 1 provides the tack application rates for different geosynthetic-reinforced sections evaluated in this study and as shown, the tack application rates of all the geosynthetic reinforcements except GR-5 and GR-6 was 0.54 l/m^2, since GR-5 had the maximum rate of 1.35 l/m^2, while GR-6 did not require tack during the installation.

3.3 Core extraction and specimen preparation

Several cores were collected from the 7 test (6 geosynthetic-reinforced and 1 unreinforced) sections considered for evaluation in this study. Specifically, about 2 months after the completion of the overlay construction, cores were extracted from the test sections using a trailer-mounted core drill with inside diameter of 150 mm. The core heights were extended from the pavement surface to the bottom of the old asphalt as shown in Figure 1b. The top and the bottom of the specimens were trimmed to obtain a height that was consistent with the dimensions of the Leutner shear tester device and the interface plane will be aligned with the applied shear plane imposed by the device. Careful attention was paid to ensure that the

interface where the reinforcement layer is located has remained intact during drilling, transportation, and trimming of the specimens.

3.4 *Leutner shear test*

Leutner shear test is one of the most common interlayer shear tests that applies a constant rate of shearing displacement between the two asphalt interfaces to determine the bond strength between them. The cores extracted from the unreinforced and geosynthetic-reinforced test sections were tested using the Leutner shear tester to determine their interface shear strength characteristics. Specifically, the Leutner shear tester was used in an Instron 8872 loading machine and a monotonic load was applied at a displacement of 50 mm/min until failure or displacement of 12.5 mm, at a temperature of 22°. Additionally, a width of 2.5 mm was maintained between the two shearing rings of the Leutner shear tester matching the interface zone of the core specimens being tested. Similar conditions were maintained and recommended by Correia *et al.* (2022).

4 RESULTS AND DISCUSSION

The results from Leutner shear tests are obtained in the form of shear load vs relative shear displacements. The interface shear strength is then determined by the ratio of shear load and the cross-sectional area of the specimen tested and the variation of interface shear strength with displacements are plotted. Figures 4a and b show the variations of interface shear strengths with displacements respectively, for unreinforced and geosynthetic-reinforced (GR-3) specimens tested in this study. As shown in the figures, the interface shear strengths increased with increasing displacements and reached a peak value and reduced thereafter with further increase in the displacement values for both the specimens (UR and GR-3). However, the geosynthetic-reinforced specimen witnessed a lower peak interface shear strength value compared to that of the unreinforced specimen, suggesting a reduction in the interface shear strength with the inclusion of geosynthetic reinforcements. In addition, the displacement corresponding to the peak interface shear strength increased in the geosynthetic-reinforced specimen compared to that of the unreinforced specimen tested in this study. The peak interface shear strength values for different interface (6 reinforced and unreinforced) conditions were determined from multiple cores tested in this study and reported in Figure 5. As shown in the figure, the peak interface shear strengths for all the specimens tested in this study ranged between 0.44 MPa and 0.87 MPa, which is similar to that recommended in the literature for mostly unreinforced asphalt layers.
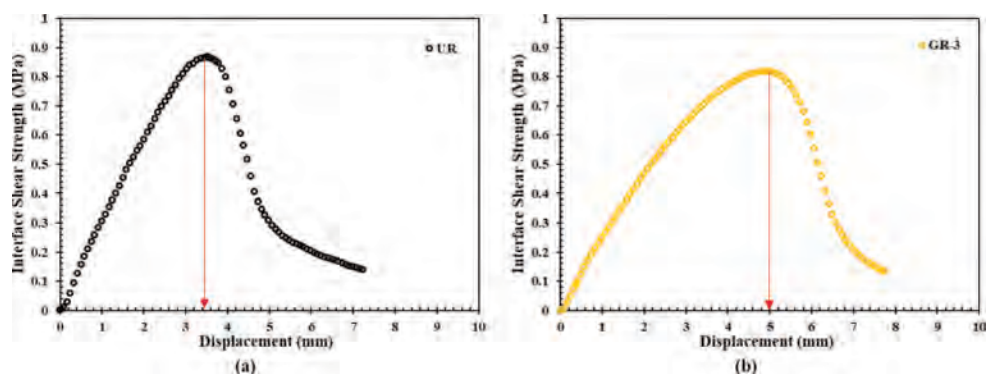
Figure 4. Typical interface shear strength trends: (a) Unreinforced specimen and (b) Geosynthetic-reinforced (GR-3) specimen.
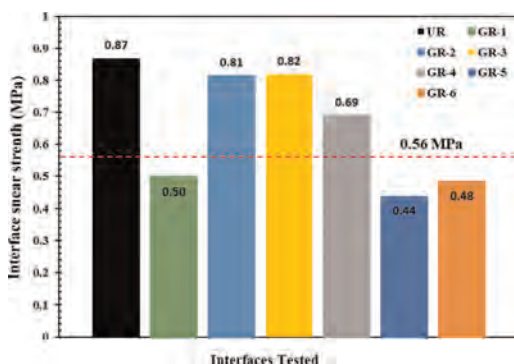
Figure 5. Peak Interface shear strength for different interfaces tested.

On the other hand, FGSV 770 (2013) suggested that the minimum bond strength required between two asphalt layers is about 10 kN (0.56 MPa for a specimen with 150 mm diameter). While, it is important to note that the unreinforced specimen had a highest interface shear strength value of 0.87 MPa compared to that of the geosynthetic-reinforced specimens tested in this study. In other words, the interface shear strength of all the geosynthetic-reinforced specimens were lower than the unreinforced specimen confirming the reduction in bond strength with the inclusion of geosynthetic reinforcements between the asphalt layers. Among the geosynthetic-reinforced specimens, GS-3 had the maximum interface shear strength of 0.82 MPa, followed by GR-2 (0.81 MPa), GR-4 (0.69 MPa), GR-1 (0.50 MPa), GR-6 (0.48 MPa), and finally GR-5 (0.44 MPa). However, it is important to note that the tack application rates for GR-5 and GR-6 were different from the rest of the geosynthetic products evaluated in this study.

The reductions in interface shear strengths were on the order of 42.61% (GR-1), 6.13% (GR-2), and 5.63% (GR-3) for the polymeric products, and 20.57% (GR-4), 49.42% (GR-5), and 44.12% (GR-6) for the fiberglass products respectively. It is evident that polymeric products performed better than the fiberglass products, in terms of bond strength, especially GR-2 and GR-3 specimens. The high bond strengths witnessed in GR-2 and GR-3 specimens may be due to their aperture sizes and the ultrathin nonwoven backing that can promote through hole bonding to enhance the interface bond strength. In addition, the products GR-2 and GR-3 were completely coated with a binder to enhance their interface bonding characteristics. While the other polymeric product, GR-1 had a fabric woven into the polymeric grids that did not promote through hole bonding and hence, reduced bond strength. On the other hand, among the fiberglass products, GR-4 performed better than GR-6 that performed better than GR-5. The variations in the performances may be due to the thickness of geotextile backing (especially in GR-5) and the presence/absence of tack (especially in GR-6). In addition, the apertures of GR-6 were smaller in comparison to GR-4, while the apertures of GR-5 were not significant because of the thick geotextile backing. Overall, it can be summarized that the interface bond strength is crucial for the performance of geosynthetic-reinforced asphalt layers and depends on multiple factors including the tack type and application rates, nominal aggregate size of the asphalt mix, and geosynthetic properties including the aperture size, presence/absence of geotextile backing, and the thickness of geotextile backing among others.

5   CONCLUSIONS

In this study, the impact of various geosynthetic-asphalt interface characteristics on the interface shear resistance was evaluated by testing cores obtained from an in-service

highway. Specifically, the Leutner shear device was used to test seven interfaces including an unreinforced interface and six asphalt-geosynthetic interfaces that were formed by different types of geosynthetic reinforcements including both polymeric and fiberglass products. The following conclusions can be drawn from the study.

The geosynthetic reinforcements reduced the interface shear strength between the asphalt layers and the reductions were on the order of 42.61% (GR-1), 6.13% (GR-2), and 5.63% (GR-3) for the polymeric products, and 20.57% (GR-4), 49.42% (GR-5), and 44.12% (GR-6) for the fiberglass products evaluated in this study, respectively.

The reduction was found to be particularly affected by the composition of the reinforcements. Specifically, the reinforcement materials (glass or polymer) and form (grid or textile or composite) were found to significantly affect the asphalt-reinforcement bond strength. Additional factors affecting the geosynthetic-asphalt interface characteristics included tack application rates, aperture size, and the thickness of geosynthetic reinforcements.

REFERENCES

Brown, S.F., Thom, N.H., & Sanders, P.J. 2001. A Study of Grid Reinforced Asphalt to Combat Reflection Cracking. *The Association of Asphalt Paving Technologists*, 70, 543–569.

Canestrari, F., Ferrotti, G., Partl, M.N., & Santagata, E. 2005. Advanced Testing and Characterization of Interlayer Shear Resistance. *Transportation Research Record*, 1929, 69–78.

Correia, N.S., Souza, T.R., Silva, M.P.S., & Kumar, V.V. 2022. Investigations on Interlayer Shear Strength Characteristics of Geosynthetic-reinforced Asphalt Overlay Sections at Salvador International Airport, *Road Materials and Pavement Design*, https://doi.org/10.1080/14680629.2022.2092021

Ferrotti, G., Canestrari, F., Pasquini, E., & Virgili, A. 2012. Experimental Evaluation of the Influence of Surface Coating on fiberglass Geogrid Performance in Asphalt Pavements. *Geotextiles and Geomembranes*, 34, 11–18.

Kumar, V.V., Saride, S., & Peddinti, P.R.T. 2017. Interfacial Shear Properties of Geosynthetic Interlayered Asphalt Overlays. *Geotechnical Frontiers*, 2017 (GSP 277), 442–451.

Kumar, V.V., & Saride, S. 2018. Flexural and Shear Characterization of Geosynthetic Reinforced Asphalt Overlays. *Proceedings of the 2nd GeoMEast International Congress and Exhibition On Sustainable Civil Infrastructures*, Egypt 2018. https://doi.org/10.1007/978-3-030-01944-0_9

Kumar, V.V., Roodi, G.H., Subramanian, S., & Zornberg, J.G. 2022. Influence of Asphalt Thickness on Performance of Geosynthetic-reinforced Asphalt: Full-scale Field Study. *Geotextiles and Geomembranes*, 50, 1052–1059.

Leutner, R. 1979. Untersuchung des Schichtverbundes beim Bituminösen Oberbau. *Bitumen3*. Hamburg, Germany. (In German).

Sholar, G.A., Page, G.C., Musselman, J.A., Upshaw, P.B., & Moseley, H.L. 2002. *Preliminary Investigation of a Test Method to Evaluate Bond Strength of Bituminous Tack Coats*. Report FL/DOT/SMO/02-459. FDOT, Gainesville, Florida.

West, R.C., Zhang, J., & Moore, J. 2005. *Evaluation of bond strength between pavement layers*. NCAT Report 05-08. National Center for Asphalt Technology, Auburn, AL.

Roodi, G.H., Morsy, A.M., & Zornberg, J.G. 2017. Experimental Evaluation of the Interaction between Geosynthetic Reinforcements and Hot Mix Asphalt. In *Proceedings of the International Conference on Airfield and Highway Pavements, ASCE, Philadelphia, Pennsylvania, USA*, pp. 428–439.

TxDOT. 2014. *Standard Specifications for Construction and Maintenance of Highways, Streets, and Bridges*. Texas Department of Transportation (TxDOT), Austin, Texas, USA.

Interface shear bond analysis of different geosynthetic paving interlayers

M.P.S. Silva, K.M. Santos & N.S. Correia
Federal University of Sao Carlos, Sao Carlos, Sao Paulo, Brazil

ABSTRACT: Different variables shows to affect shear bond performance of geosynthetic paving interlayers. The correct evaluation of the interface shear bond is fundamental to estimate design parameters and the service life of the pavement. The present study evaluated five types of geosynthetics, including four different geogrids and a paving fabric, using Leutner shear tests. In addition, the influence of geosynthetics characteristics on interface shear bond parameters was analyzed. Double-layered asphalt specimens were prepared in the laboratory considering the same binder impregnation rate of 600 g/m^2. Geogrids showed overall superior interface shear strength behavior compared to geocomposite, although inferior to control samples. Furthermore, the geogrid aperture size played an important role in shear bond results, corroborated by the through hole bonding mechanism. The presence of bituminous coating contributed to interface shear bond results. Interface shear stiffness and accumulated energy analyzes showed that large geogrids aperture sizes presented similar behavior to control samples.

Keywords: Geosynthetics, Pavement interlayer, Asphalt layer, Interface shear strength, physical characteristics

1 INTRODUCTION

Advanced rehabilitation techniques and sustainable pavement solutions have been used to control reflective cracking (Nithin Sudarsanan et al. 2020). Geosynthetics have been effective in minimizing the damaging effects caused by reflective cracking propagation in asphalt pavements (Safavizadeh et al. 2022; Wargo et al. 2017), providing waterproof barrier (Solatiyan et al. 2020) and controlling pavement deformations (Correia & Zornberg 2018; Kumar et al. 2021; Lee et al. 2019). In extension, geosynthetics used in pavement rehabilitation depicts an economic and sustainable choice considering it allows the replacement of lower thickness of asphalt layers, therefore reducing the asphalt concrete amount that must be discarded and produced, in consequence, reduces emission as well as the intervention time, making opening to traffic faster (Spadoni et al. 2021). However, different variables have shown to affect shear bond performance of paving interlayers, such as geosynthetic type and characteristics, binder type and rate, type of asphalt mixture, surface texture, temperature, among others (Correia & Mugayar 2021; Correia et al. 2022; Kumar & Saride 2017; Noory et al. 2019; Walubita et al. 2018).

According to Canestrari et al. (2022), the correct evaluation of the interface shear bond is fundamental to estimate the service life of the pavement. For this reason, it is very important to understand which are the variables that affect interface shear bond behavior to obtain the optimal binder impregnation of each geosynthetic interlayer condition. The present study evaluated five types of geosynthetics, including four different geogrids and a paving fabric, using Leutner shear tests. In addition, the influence of different physical characteristics of geosynthetics on interface shear bond parameters was analyzed.

2 MATERIALS AND METHODS

2.1 Geosynthetics

Figure 1 shows the different types of geosynthetics used in the current research to analyze the influence of geosynthetics physical properties on the shear bond behavior of pavement interlayers. The geosynthetics were selected based on coating characteristics, presence of aperture size, aperture size dimension, rib width and tensile properties.
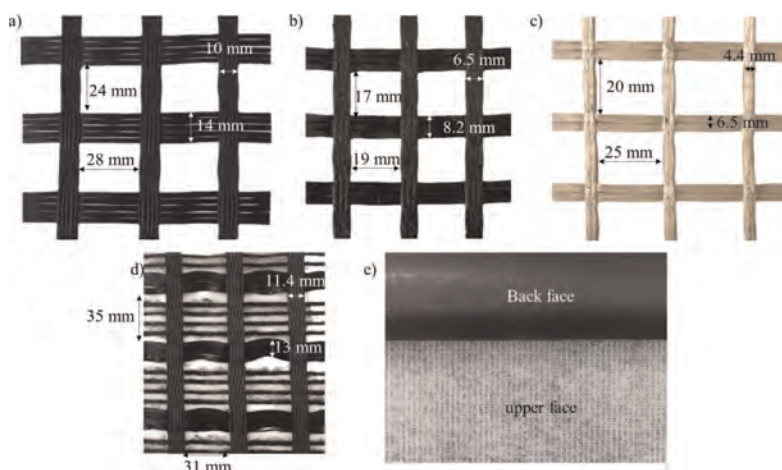
Figure 1. Geosynthetic reinforcements used in the study: (a) GG1; (b) GG2; (c) GG); (d) GG4; and (e) GC.

GG1 is a fiberglass geogrid coated with modified bitumen, knitted to form a bi-axial grid having aperture size of 28 mm x 24 mm. GG1 has longitudinal (L) rib width of 10 mm and transversal (T) rib width of 14 mm, while the ultimate tensile strength is 120 kN/m in both machine (MD) and cross-machine direction (CMD), at an elongation break of 3%. GG2 is a fiberglass geogrid coated with bitumen with aperture size of 17 mm x 19 mm. GG2 presents rib width of 6,5 mm (L) and 8,2 mm (T), with ultimate tensile strength of 120 kN/m in both MD and CMD, at an elongation break of 3%. GG3 is a fiberglass geogrid that has a polymeric coating and an adhesive on the back face, as well as an ultimate tensile strength of 75 in MD and 95 kN/m in CMD, at an elongation strain of 3%. GG3 presents an intermediate aperture size of 20 mm x 25 mm and rib width of 4,4 mm (L) and 6,5 mm (T). GG4 is a fiberglass geogrid coated with bitumen. GG4 presents a mesh size of 31 mm x 35 mm and rib width of 11,4 mm (L) and 13 mm (T), with ultimate tensile strength of both 130 kN/m in MD and CMD, at an elongation break of 3%. and contains small strips of nonwoven geotextile crossing the opening of the mesh in the CMD. GC is a waterproofing paving mat manufactured by embedding micro fiberglass meshes into high polyester (PET) mat, coated with an elastomeric product. GC had an ultimate tensile strength of 25 kN/m (MD) and 30 kN/m (CMD) at an elongation strain of 7%.

2.2 Hot mix asphalt and tack coat

The hot mix asphalt (HMA) used in the current research consist of a nominal aggregate size of 19 mm and had binder with a penetration of 31 dmm (ASTM D5 2020), an optimum bitumen content of 4.3% by weight of aggregates, indirect tensile strength of 1.9 MPa (ASTM D6931 2017) and a flow value of 1.8 mm (ASTM D6927). The tack coat employed at the interface is a straight asphalt having a penetration value of 51 dmm (ASTM D5 2020) and softening point of 52°C.

2.3 Double-layered specimens' preparation

The specimens for interface shear test were prepared using adapted Marshall compacted method. Specimens with diameter of 150 mm were prepared, as indicated in the literature for geosynthetic-reinforced asphalt systems (FGSV 770 2013). To determine the corresponding number of blows for 150 mm samples, a height of 40 mm compaction was established, totalizing 213 blows. The second adaptation concerns the method of compression for double-layered specimens. Blows in only one face were applied in each HMA layer. This adaptation was based on literature research with double layered specimens with 100 mm in diameter (D'Andrea et al. 2013; Tozzo et al. 2014, 2015).

After the production of the inferior HMA layers, the specimens were extracted from the molds and the asphalt binder was applied at the interface at 135 °C. The application rate of 600 g/m^2 was used for all paving interlayers evaluated herein. A metal spatula and heat gun were employed to spread the binder on the interface before the geosynthetics installation. Then, the inferior layers were inserted in the mold and the upper HMA layers were compact. This procedure was based on Safavizadeh et al. (2022) method. Figure 2 shows double layered specimens' preparation.
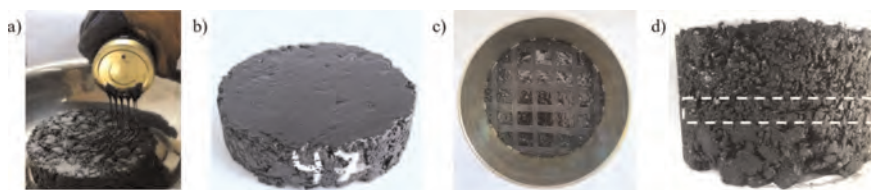
Figure 2. Specimen preparation: (a) applying asphalt binder tack coat; (b) lower layer surface after tack coat application; (c) geosynthetic installed; (d) double layered specimen.

2.4 Leutner shear test

The interface bonding properties of the asphalt overlay can be evaluated as per prEN 12697-48. To measure interface bond strength characteristics, Leutner shear tests were carried out under displacement rate of 50.8 mm/min using a servo-controlled testing machine and at a temperature of 20°C. The load was applied until complete failure. Figure 3 shows typical results of an interface shear bond test, such as maximum interface shear strength, interface shear stiffness and accumulated energy after failure. When using a geosynthetic interlayer, the German Working FGVS 770 establishes a minimum shear bond force of 10 kN for 150 mm diameter specimens extracted from the field, which corresponds to a minimum interface shear strength of 0.56 MPa.
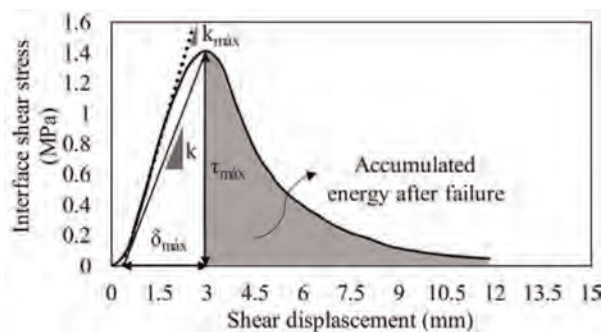
Figure 3. Leutner shear test: (a) testing device; (b) typical result of an interface shear bond test.

3 TEST RESULTS AND DISCUSSIONS

Figure 4 shows the results obtained in interface shear tests. Figure 4(a) presents typical interface shear stress (ISS) curves for control and geosynthetic interlayers. As shown in the figure, the ISS behavior depends on the presence or absence of geosynthetic, as well as geosynthetics characteristics. Control samples presented higher values of peak ISS when compared to geosynthetic interlayers.
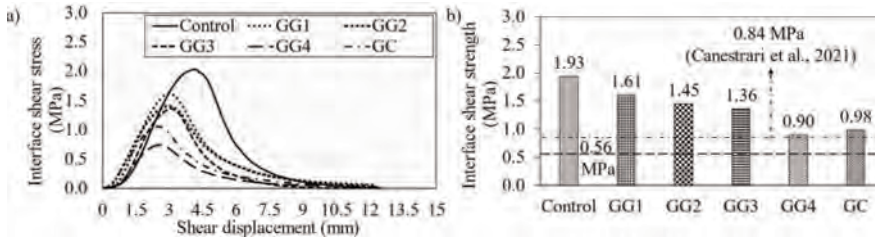
Figure 4. Results of interface shear tests: (a) typical ISS curves; (b) comparison of average ISS for different geosynthetics and control samples.

Figure 4(b) shows a comparison of average values of ISS obtained for the different paving interlayers tests. ISS values ranged between 0.90 and 1.93 MPa. Overall, specimens reached minimum required ISS of 0.56 MPa as indicated in (FGSV 770 2013). However, Canestrari et al. (2022) recommend an increase in the minimum accepted value of ISS by 50% when using laboratory-produced specimens. In this case, the minimum ISS corresponds to 0.84 MPa. As observed in Figure 4(b), all paving interlayers achieved the minimum limit. It can be observed that among different geosynthetics interlayer, the highest ISS value was obtained in the case of GG1, followed by GG2, GG3, GC and finally GG4. The difference in ISS values can be attributed to the different characteristics of geosynthetics and their compatibility to bond the adjacent HMA layers. The presence of geogrid apertures in the cases of GG1, GG2, and GG3 has showed to enhance ISS with the help of through hole bond (THB) mechanism described by Sudarsanan et al. (2018a). The THB mechanism was not observed in the geocomposite sample (GC) due to the absence of apertures. In this case, the bonding strength of GC is attributed to the adhesion mechanism. The inferior result of ISS showed by GG4 could be explained by the presence of small strips of geotextile crossing the opening of geogrid mesh, which may have partially activated both THB and adhesion mechanism. Similar observations of THB and adhesion mechanisms were observed by Kumar and Saride (2017), Sudarsanan et al. (2018a), Sudarsanan et al. (2018b), and Correia et al. (2022). Another important aspect that may have corroborated the superior performance of GG1 and GG2 is the presence of a bituminous coating present in both materials.

Figure 5 presents additional interface shear analysis. Figure 5(a) depicts the interface shear stiffness (k) trends for different paving interlayer conditions. This parameter is a useful variable to understand the behavior of interface adhesion until failure condition and to evaluate the effects of different levels of adhesion on the stress-strain distribution of the pavement (Yang et al. 2021). According to Canestrari et al. (2013), the k value assures an ideal bonding between asphalt layers and varies between 10^{-2} MPa/mm (fully sliding) and 10^2 MPa/mm (fully bonding). Therefore, all the specimens evaluated in this study are within an adequate interface shear bonding condition. As shown in Figure 5a, GG1, GG2, and GG3 presented similar behavior to control samples. Overall, superior interface shear stiffness was observed for GG1, which may be attributed to both higher aperture size and presence of bituminous coating.

Figure 5(b) presents the accumulated energy after failure for control and geosynthetic interlayer conditions. This result indicates post-failure interface shear behavior. It can be observed
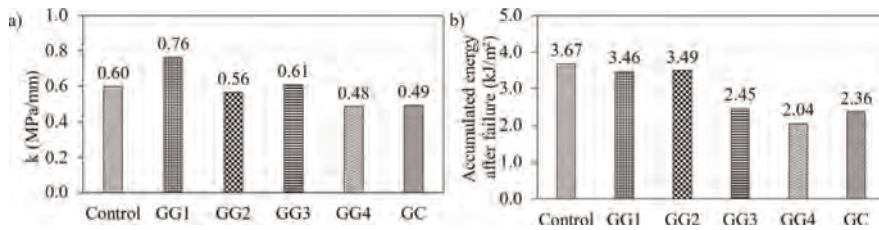
Figure 5.   Additional interface shear analysis: (a) interface shear stiffness (k); (b) accumulated energy after failure.

that GG1 and GG2 presented very similar behavior to control sample, demonstrating that the presence of a geosynthetic interlayer did not influence residual shear bond behavior. These results present the same order of magnitude as the results observed by Lee et al. (2019).

4   CONCLUSIONS

In this study, the interface shear properties of control and geosynthetic interlayers were analyzed by performing Leutner shear tests and the following conclusions can be summarized below:

- Unreinforced (control) specimens presented higher values of peak interface shear stress when compared to geosynthetic interlayers.
- The presence of geogrid apertures in the cases of GG1, GG2, and GG3 has shown to enhance interface shear stress due to the through hole bond (THB) mechanism when compared to geocomposite (GC) and geogrid with less aperture size (GG4). The strips present in GG4 had a negative influence on the behavior of interface shear bond.
- The presence of bitumen coat on some geosynthetics may have influenced the results, since geogrids GG1 and GG2 presented higher interface shear stress values than GG3, even with similar opening mesh sizes.
- Interface shear stiffness (k) values were found in the order of 10^{-1} MPa for all evaluated interfaces, highlighting GG1 which presented a k higher value when compared to control sample.
- Analyzes of accumulated energy have shown that geogrids GG1 and GG2 presented very similar behavior to control samples, demonstrating that the presence of a geosynthetic interlayer did not influence residual shear bond behavior.

REFERENCES

ASTM. 2017. D6931: Standard Test Method for Indirect Tensile (IDT) Strength of Asphalt Mixtures.
ASTM. 2020. D5: Standard Test Method for Penetration of Bituminous Materials.
Canestrari, F., Cardone, F., Gaudenzi, E., Chiola, D., Gasbarro, N. & Ferrotti, G. 2022. Interlayer Bonding Characterization of Interfaces Reinforced with Geocomposites in Field Applications. *Geotextiles and Geomembranes* 50(1): 154–162.

Correia, N. S. & Mugayar, A. N. 2021. Effect of Binder Rates and Geogrid Characteristics on the Shear Bond Strength of Reinforced Asphalt Interfaces. *Construction and Building Materials* 269(121292).

Correia, N. S., Souza, T. R., Silva, M. P. S. & Kumar, V. V. 2022. Investigations on Interlayer Shear Strength Characteristics of Geosynthetic-reinforced Asphalt overlay Sections at Salvador International Airport. *Road Materials and Pavement Design*: 1–17.

Correia, N. S. & Zornberg, J. G. 2018. Strain Distribution Along Geogrid-reinforced Asphalt Overlays under Traffic Loading. *Geotextiles and Geomembranes* 46(1): 111–120.

D'Andrea, A., Russo, S. & Tozzo, C. 2013. Interlayer Shear Testing under Combined State of Stress. *Advanced Materials Research* 723: 381–388.

FGSV 770. 2013. Arbeitspapier fuer Die Verwendung von Vliesstoffen, Gittern und Verbundstoffen im Asphaltstrassenbau. FGSV Verlag.

Giri, J. P. & Panda, M. 2018. Laboratory Evaluation of Inter-layer Bond Strength Between Bituminous Paving Layers. *Transportation Infrastructure Geotechnology* 5(4): 349–365.

Kumar, V. & Saride, S. 2017. Evaluation of Interface Shear Properties of Asphalt layers Reinforced with Geosynthetic Interlayers. Proc. Indian Geotechnical Conference 2017 GeoNEst, Guwahati, 14-16 December 2017.

Kumar, V. V., Saride, S. & Zornberg, J. G. 2021. Fatigue Performance of Geosynthetic-reinforced Asphalt Layers. *Geosynthetics International* 28(6): 584–597.

Kumar, V. V., Saride, S. & Zornberg, J. G. 2022. Behavior of Asphalt Overlays with Geogrids and Geocomposite Interlayer Systems. In: Tutumluer, E., Nazarian, S., Al-Qadi, I., Qamhia, I.I. (eds), *Advances in Transportation Geotechnics IV. Lecture Notes in Civil Engineering 165: 611–619*. Cham: Springer International Publishing.

Lee, J. H., Baek, S. B., Lee, K. H., Kim, J. S. & Jeong, J. H. 2019. Long-term Performance of Fiber-grid-reinforced Asphalt Overlay Pavements: A Case Study of Korean National Highways. *Journal of Traffic and Transportation Engineering (English Edition)* 6(4): 366–382.

Noory, A., Moghadas Nejad, F., & Khodaii, A. 2019. Evaluation of the Effective Parameters on Shear Resistance of Interface in a Geocomposite-reinforced Pavement. *International Journal of Pavement Engineering* 20(9): 1106–1117.

Pasetto, M., Pasquini, E., Giacomello, G. & Baliello, A. 2019. Innovative Composite Materials as Reinforcing Interlayer Systems for Asphalt Pavements: An Experimental Study. *Road Materials and Pavement Design* 20(2): 1–15.

Safavizadeh, S. A., Cho, S. H. & Kim, Y. R. 2022. Interface Shear Strength and Shear Fatigue Resistance of Fibreglass Grid-reinforced Asphalt Concrete Test Specimens. *International Journal of Pavement Engineering* 23(8), 2531–2542.

Solatiyan, E., Bueche, N., Vaillancourt, M. & Carter, A. (2020). Permeability and Mechanical Property Measurements of Reinforced Asphalt Overlay with Paving Fabrics using Novel Approaches. *Materials and Structures/Materiaux et Constructions* 53(8): 1–15.

Spadoni, S., Ingrassia, L. P., Paoloni, G., Virgili, A., & Canestrari, F. (2021). Influence of Geocomposite Properties on the Crack Propagation and Interlayer Bonding of Asphalt Pavements. *Materials* 14(18): 1–18.

Sudarsanan, N., Karpurapu, R., Amirthalingam, V. & Gedela, R. (2018a). Applications of Natural Geotextiles in Asphalt Overlays to Retard Reflection Cracking. Proc. 11th International Conference on Geosynthetics, Coex, 16-21 September 2018.

Sudarsanan, N., Karpurapu, R. & Amrithalingam, V. (2018b). An Investigation on the Interface Bond Strength of Geosynthetic-reinforced Asphalt Concrete Using Leutner Shear Test. *Construction and Building Materials* 186: 423–437.

Sudarsanan, N., Arulrajah, A., Karpurapu, R. & Amrithalingam, V. 2020. Fatigue Performance of Geosynthetic-Reinforced Asphalt Concrete Beams. *Journal of Materials in Civil Engineering* 32(8): 04020206.

Tozzo, C., D'Andrea, A. & Al-Qadi, I. L. 2015. Prediction of Fatigue Failure at Asphalt Concrete Layer Interface from Monotonic Testing. *Transportation Research Record* 2507(1): 50–56.

Tozzo, C., D'Andrea, A., Cozzani, D. & Meo, A. 2014. Fatigue Investigation of the Interface Shear Performance in Asphalt Pavement. Modern Applied *Science* 8(2): 1–11.

Walubita, L. F., Nyamuhokya, T. P., Komba, J. J., Ahmed Tanvir, H., Souliman, M. I. & Naik, B. (2018). Comparative Assessment of the Interlayer Shear-bond Strength of Geogrid Reinforcements in Hot-mix Asphalt. *Construction and Building Materials* 191: 726–735.

Wargo, A., Safavizadeh, S. A. & Richard Kim, Y. (2017). Comparing the Performance of Fiberglass Grid with Composite Interlayer Systems in Asphalt Concrete. *Transportation Research Record* 2631(1): 123–132.

Yang, K., Li, R., Yu, Y., & Pei, J. (2021). Unified Laboratorial Evaluation of Interlayer Bond Property in Asphalt Pavements Based on Strength Parameters. *Construction and Building Materials* 273: 121738.

Evaluation of connection loads between a geogrid and concrete blocks based on laboratory tests

P.V.C. Figueredo, F.H.M. Portelinha & J.G. Zornberg
Federal University of São Carlos, at São Carlos, Brazil

ABSTRACT: Internal stability analysis of segmental geosynthetic reinforced soil walls includes the verification of connection strength at the geosynthetic-block interface. The calculation of the connection load (T_o) has been a hard task as mechanisms are still not completely understood. This paper presents an evaluation of geogrid-modular blocks connection forces based on a laboratory test device developed to simulate load transfer mechanism at the face of geosynthetic reinforced soil walls. A reinforced system with a sand backfill, a woven geogrid and concrete blocks were subjected to incremental vertical loads while lateral earth pressures, horizontal displacements at the face, as well as reinforcement strains and load at the geogrid-block interface were monitored. and the strains of the reinforced layer were monitored. Results show differential settlements of the backfill and the facing wall leading to a down-drag effect on the reinforcement. This effect associated to face wall displacements led to a significant impact on connection loads at geosynthetic-blocks connection.

1 INTRODUCTION

The use of geosynthetic reinforced soil structures has gained increasing popularity, being used in containment systems, slope stability, load-bearing walls, or for bridge abutments. This type of structure stands out for the flexibility of project design, being adaptable to various environments, having a fast execution process, without the use of skilled labor, due to its low complexity, besides having a good cost benefit (Ngo 2016) The good performance of this type of structure depends on many variables, of which the backfill soil, type of face and the reinforcements have been reported to have significant influence (Brugge *et al.* 2012; Liu *et al.* 2009, 2011; Portelinha *et al.* 2014; Saghebfar *et al.* 2017).

In this type of structure, the geosynthetics are connected to the face in some way. In case of segmental reinforced soil walls this connection occur often by friction and extend to the anchorage zone. When reinforcements are loaded, stresses are developed at the geogrid-block connection (Soong & Koerner 1997). The structure must be able to generate sufficient interlock between the face and the reinforcement to resist the horizontal forces in the soil mass in the connection zone (Collin 1997). Morsy (2021) reports the importance of the type of face and how it affects the distribution and magnitude of stresses at the face, where connection loads tend to be greater in rigid than flexible faces.

Currently, design recommendations, such as BS-8006 (2010) and FHWA-NHI-10-024 (2009), treat connection stresses in a simplified manner, suggesting percentages of 50% to 100% of the maximum mobilized tension in the reinforcements (Tmax), depending on the structure configuration. The present study is part of a large experimental program that investigates the mechanisms involved in the connection loads at the interface between geosynthetic reinforcements and face elements. Specifically, this paper presents results of a

laboratory test conducted to investigate connection loads developed in a sand reinforced with geogrid in modular block reinforced system.

2 MATERIALS AND METHODS

2.1 Materials

In this study the soil used was a well-graded medium sand with friction angle of 33.2°, dry density of 17.2 kN/m^3 and maximum and minimum voids index of 1.10 and 0.6, respectively. Figure 1 shows the grain size distribution of the sand. The geosynthetic reinforcement was a polyvinyl alcohol polymeric (PVA) geogrid with properties indicated in Table 1. As facing revetments, commercial concrete masonry units (CMU) were used, with a compressive strength of 3.0 MPa, with dimensions of 390 X 150 X 190 mm (width X length X height).
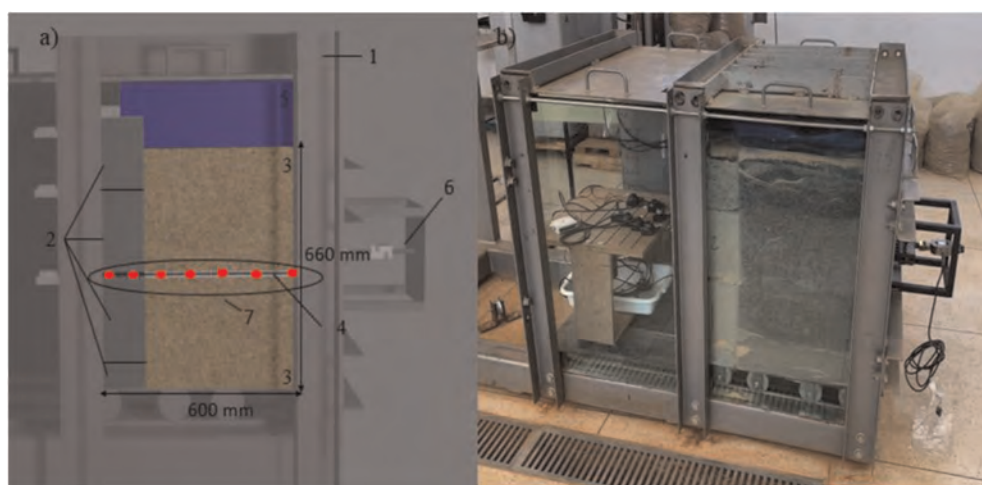
Figure 1.   Illustration of test (a): instrumentation) used in the test Legend: 1) Metal Box, 2) Face wall, 3) Soil mass, 4) reinforcement and 5) Air pressure device. 6) load Cell, 7) "Tell-talles" and b) a Picture of the box before the test.

Table 1.   Physical and mechanicals properties of the geosynthetics.

Properties	Standard specification	Value	Unit
Thickness	ASTM D5199	2,18	mm
Ultimate tensile strength	ASTM D54595/ D6637	53,74	kN/m
Elongation at failure	ASTM D54595/ D6638	4	%
Aperture size MD*	–	114,8	mm
Aperture size CMD**	–	10,3,4	mm

*MD – Machine direction, **CMD – Cross- Machine direction.

2.2 Physical model and testing procedure

The apparatus used in the present study simulates a geosynthetic MSE wall with concrete blocks face, in a working stress condition. The physical model consists of a rigid metal box

Table 2. Soil Propreties.

Properties	Standard specification	Value	Unit
Specific gravity	ASTM D7263 − 09	2,64	g/cm^3
Min. Void ratio – emin	ASTM D 4253-16	0,66	–
Max. Void ratio – emax	ASTM D 4253-16	1,10	–
Dry density of soil	ASTM D1557 − 12	1,73	g/cm^3
Water content	ASTM D1557 − 12	3,00	%
Cohesion	ASTM D3080 -11	0,00	kPa
Friction angle	ASTM D3080-11	33,18	°
Classification SUCS	ASTM D2488-69	SW	–
Uniformity Coefficient – C_u	ASTM 112-13	2,08	–
Coefficient of curvature – C_c	ASTM 112-13	1,14	–

with internal dimensions of 600 X 760 X 800 mm (width X length X height) where one of the lateral walls of the box is made of transparent glass and the others are stationary, all walls were lubricated to minimize frictions between then.

The MSE wall were constructed above two plates, one fixed and one that was able to move horizontally with bearings that run internally along rails. The mass of soil was compacted in layers to 98% of density, the reinforcement was placed between the soil mass and had been connected to wall only by attractive forces. The blocks were able to move free and independently.

The working system of the equipment is to apply vertical pressure in the top of the reinforced soil unit, thereby inducing a horizontal stress on the front moving wall. For that, were used an airbag system up to 180 kPa.

The instrumentation includes measurements of tensile loads, geosynthetic internal displacements and horizontal and vertical soil pressure. A load cell was attached to the reinforcement at that back wall of the model to measure the mobilized load on it. For the internal displacements were used seven potentiometer-type 'tell tales', with 100 mm spacing, to be possible capture the displacement inside of the wall, which were used to calculate internal strains. Figure 1a show an illustration of the equipment and the instrumentation used during tests and 1b shows the physical model before the start of the test. PIV (Particle Image Velocimetry) technique was used to capture the displacement field from the lateral transparent wall. Figure 2 shows the lighting system used during tests.

Figure 2. Lightning and recording system.

3 RESULTS

Figure 3 shows the tensile load mobilized by the geogrid at 20, 60, 100, 140 and 180 kPa of vertical loadings. Tensile loads along the on the reinforcement were calculated based on reinforcement strains obtained from the tell-tales technique and the corresponding value of tensile load using wide-width tensile test results. It should be observed that tell-tales measurements generate total strains. The peak tensile load was registered to occur close to the connection between the geogrid and the modular block at the face with a value of 9.16 kN/m under 180 kPa of loading. It was observed because tell-tale points were located inside the modular blocks which is not usual. Otherwise, peak loads would be around 400 mm from the facing, which corresponded to the location of the potential failure surface. This result agreed with the images taken during the procedure and the results using the PIV methodology as indicated in Figure 4.
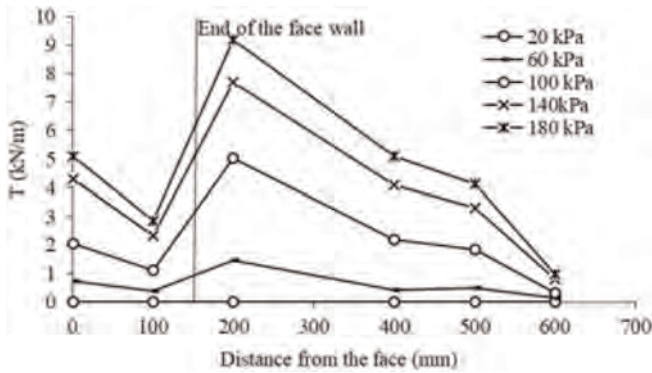
Figure 3.   Tensile load mobilized by geosynthetic versus distance from the face.
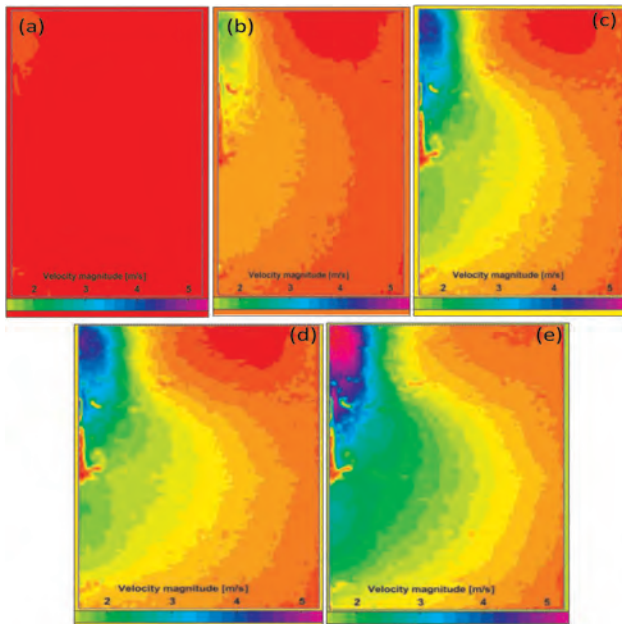
Figure 4.   Displacements field from the PIV-Lab at the end of loading of: (a) 20 kPa; (b) 60 kPa; (c) 100 kPa; (d) 140 kPa; and (e) 180 kPa.

Figure 4 shows the displacement field at the end of each loading stage. It can be observed the formation of displacement zones that intensified near the wall facing, which is intensified with loading increasing. A very relevant fact was the creation of a small area of displacement concentration under the connection of the geosynthetic to the wall. This zone is a void created by the down-drag effect on the geosynthetic as reported by Morsy (2021).

In order to capture the down-drag effect, Figure 5 shows the total displacements of the reinforcement in each loading stage. The reinforcement has a maximum settlement of 2.3 mm close to the face due to the down-drag effect, and it was noted that the trend is that the settlement values reduce as more distant from the face. This type of deformation described as asymmetric deformation occurs due to the relative difference of rigidity of reinforced soil and block facing wall (Soong & Koerner 1997). It is observed that this effect is relevant for the connection load even in small magnitude, in this case, 2.3 mm.
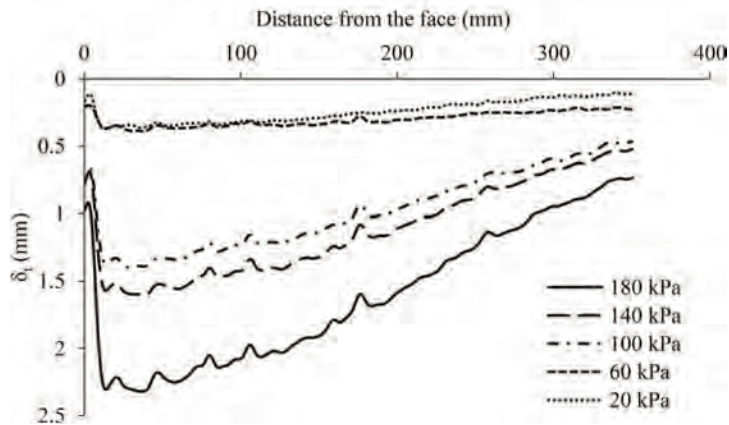
Figure 5.   Total displacements of the geosynthetic inside of the soil mass for 20,60,100,140 and 180 kPa load stage.

Figure 6 compares the tensile load measured by the load cell with that calculated at the connection in each loading stage. This comparison aims to evaluate the magnitude of the
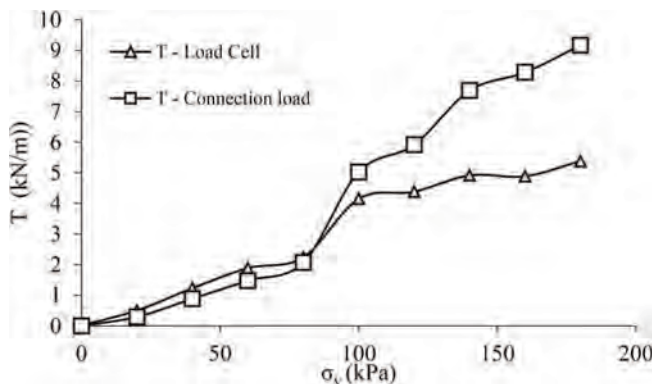
Figure 6.   Comparison between stresses requested on the geosynthetic measured by the load cell, the tell-tale farther from the blocks face and the tell-tales at the connection.

connection load in respect to the maximum along the potential failure surface. Usually, design standards recommend a percentage of T_{max} to obtain the connection load, which is between 50% and 100%, depending on the type of the face wall and the capacity of movements at connection. Note that for loading up to 80 kPa, the test results follow the same design recommendation of 1.0 of T_o/T_{max} indicated in the BS-8006 (2010). Lower vertical stress turn this relation greater than 1.0 because of the down-drag effect.

4 CONCLUSIONS

The testing system and the physical model consist of innovative methodology to evalu-ate the connection loads in geosynthetic reinforced soil walls. The drown-drag effect was observed to be the main factor for the high values of loads at the connection between the reinforcement and the face wall, resulting in an asymmetric deformation behavior of the reinforcement, it is important to point out that the drown-drag effect is also due to the relative settlement of the reinforced soil mass and the modular blocks. The use of digital im-age analysis programs proved to be very valuable for this type of study. The most relevant aspect observed herein is that the connection load can be greater than the maximum tensile load at the potential failure surface, which is dependent of the relative settlement between block facing and reinforced soil.

REFERENCES

British Standards Institution. 2010. bs 8006:2010. *Code of Practice for Strengthened/reinforced Soils and Other Fills*. London: British.

Brugger, P. J., Gomes, R. De O. M. & Conte, M. 2012. Rebaixamento da Linha Férrea de Maringá Utilizando Muros em Solo Reforçado.

Collin, J. G. 1997. Srw Connection Strength How Much is Enough? Practice Periodical on Structural Design and Construction, 6–9.

Liu, H., Wang, X. & Song, E. 2009. Long-term Behavior of grs Retaining Walls with Marginal Backfill Soils. *Geotextiles and geomembranes*, 27(4): 295–307.

Liu, H., Wang, X. & Song, E. 2011. Reinforcement Load and Deformation Mode of Geosynthetic-Reinforced Soil Walls Subject to Seismic Loading During Service Life. *Geotextiles and Geomembranes*, 29 (1): 1–16.

Morsy, A. M. 2021. Analytical Framework for Prediction of Facing Connection Loads in Reinforced Soil Walls Considering Reinforcement Downdrag. *Transportation geotechnics*, 30.

Ngo, T. 2016. Feasibility Study of Geosynthetic Reinforced Soil Integrated Bridge Systems (grs-ibs) in ok-lahoma. Thesis—norman, Oklahoma: university of Oklahoma.

Portelinha, F. H., Zornberg, J. G. & Pimentel, V. 2014. Field Performance of Retaining Walls Reinforced with Woven and Nonwoven Geotextiles. *Geosynthetics International*, 21(4): 270–284.

Berg R. R., Christopher B. R., & Naresh, C. S. 2009. Design and Construction of Mechanically Stabilized Earth Walls and Reinforced Soil Slopes. *Report no. Fhwa-nhi-10-024*. Volume I, Washington, d.c.

Saghebfar A. M., Abu-Farsakh A. M., Ardah A. A., Chen A. Q. & Fernandez B. A. 2017. Full-scale Testing of Geosynthetic-reinforced, Soil-integrated Bridge System. *Transportation Research Record*, 2656(1): 40–52.

Soong, T.Y. & Koerner, R. M. 1997. On the Required Connection Strength of Geosynthetically Reinforced Walls. *Geotextiles and Geomembranes*, 15: 377–393.

A micromechanical model of PVC geomembranes using discrete element method

N. Akel, A. Wautier & G. Stoltz
INRAE, Aix Marseille Université, RECOVER Aix-en-Provence, France

N. Touze-Foltz
Université Paris-Saclay, INRAE, SDAR, Jouy-en-Josas, France

F. Nicot
Laboratoire EDYTEM, Université Savoie Mont-Blanc, Le Bourget-du-Lac, France

ABSTRACT: The growing concern regarding waste and water management is pushing the worldwide geomembrane market, thanks to its excellent technical and economical solutions. They have contributed greatly to the completion of many projects, such as reservoir storing water. Geomembranes are not designed to provide structural resistance but frequently undergo mechanical actions that may mishandle their impermeable properties. For instance, the contact between a geomembrane and a drainage (granular) layer increases the risk of puncture. In this study, we adopt an original multiscale view of a geomembrane to relate microstructural features to its macroscopic mechanical properties. A micromechanical model has been developed based on the discrete element method (DEM) to derive the mechanical response of a Polyvinyl chloride (PVC) geomembrane from the modeling of its microstructure. Such an approach offers the potential to understand the elementary mechanisms responsible for the mechanical response and the puncture failure mode of PVC geomembranes.

1 INTRODUCTION

In the past few years, Europe has been hit by a climate-driven drought crisis, which has increased interest towards the sustainable management of water resources. Geomembranes assist with water stock management by limiting water loss along irrigation canals, and through reservoirs. However, they are highly susceptible to mechanical actions, which can lead in a perforation and consequently to a loss of waterproofing property. This results in severe consequences ranging from the water losses to the failure of the structure.

Geomembrane damage is most of the time the consequence of punctures due to contacts with underlying angular stones that may generate localized irregularities in the membrane settlement, when vertical compression is applied.

Therefore, several regulations have been enacted, based on experimental studies, to minimize the risk of puncturing, including stone dimensions specifications and the installation of a protective layer like geotextile beneath the geomembrane. Many works attempted to interpret the puncturing phenomena using a theoretical approach (Koerner *et al.* 1996; Stark *et al.* 2008; Marcotte *et al.* 2009). Furthermore, several analysis were performed on different geomembrane types and thicknesses, protected by various geotextiles, using truncated stone under hydraulic pressure (Koerner *et al.* 2010; Stark *et al.* 2009), or with different drainage layer under high loads (Athanassopoulos *et al.* 2008; Stoltz *et al.* 2013). The

consequence of these design approaches is that geomembranes are supposed to behave homogeneously, thus excluding the risk of local puncturing.

However, if one wants to consider geomembrane puncture, the problem's input factors—such as head pressure, drainage granular layer, and protection-type layer—are numerous. It is thus impractical to undertake experiments for every case study, and numerical modeling is probably more adapted. So far, few studies have been conducted to assess the mechanics of puncture in geosynthetics, and it was limited to nonwoven fabrics geotextile (Sun *et al.* 2011; Saberi *et al.* 2017) and geosynthetic cementitious composite materials (Jirawattanasomkul *et al.* 2019) using finite element method (FEM). To the best of our knowledge, no study has yet investigated the puncturing of a geomembrane and the related internal mechanisms that control its macroscopic mechanical behavior. Therefore, in this study, an original multiscale view of the geomembrane is proposed, allowing identification of the geomembrane's mechanical response by modeling its microstructure using Discrete Elements Method (DEM). Polyvinyl Chloride geomembranes (PVC) are examined in this research, as they are widely used in reservoirs and dams due to their high flexibility and high resistance to external stresses. The proposed multiscale approach has the ability to exhibit the elementary processes underlying the mechanical response of PVC geomembranes and to deepen the comprehension of the puncture failure mode.

2 AN OVERVIEW OF THE MICROSTRUCTURE OF PVC GEOMEMBRANES

PVC is polymerized from vinyl chloride. In such a process, small molecules called monomers (C_2H_3Cl) combine chemically to form a polymer, which is a very long chain-like molecule. In some places, the polymer arrange regularly in the form of crystallites, while in other places, no particular ordering is observed. The structure of PVC can therefore be idealized as crystallites tied together by a three dimensional network of tie molecules, where the average crystallites size is illustrated in Figure 1. Two forms of crystallinity might be exist. The first reveals that the crystals are comprised up of a set of polymer chains that are well-aligned in parallel, forming crystallized regions (see Figure 2a). The second type consists of molecular chains that fold itself into a long thin ribbon creating the lamella (see Figure 2b). The two types could coexist in the same crystallite.

Flexible PVC is produced by adding plasticizers or additives to the mix while manufacturing. Summers (1981) assumed that the plasticizers affect only the amorphous domain. Additionally, it has been determined that the plasticizer additions induce swelling in the amorphous regions, which results in an increase in the inter-crystallite distances. Macroscopically, flexible PVC is characterized by a yield-type stress-strain behavior under uniaxial tensile test. The material becomes increasingly more brittle and more rigid as the percentage of plasticizer decreases.
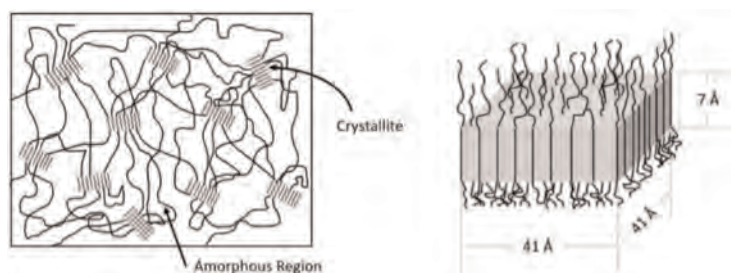
Figure 1. The micro-domain structure of PVC. (Right) Average crystallite size of PVC. Inspired from Summers (1981).
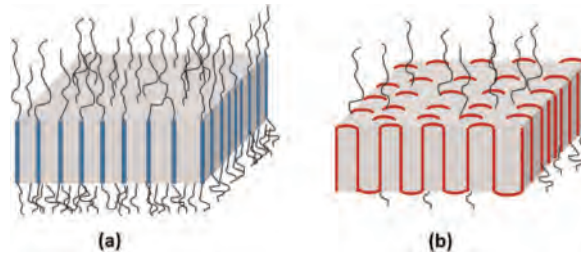
Figure 2. Two crystallinity-types are shown here. (a) The crystals is made up of a series of parallel polymer chains. (b) The lamella-shaped crystal is being formed by molecular chains that fold into a long thin ribbon.

3 PVC GEOMEMBRANE MODELING IN THE DEM FRAMEWORK

In this part, a three-dimensional model, that simulates the micro-morphology of the PVC structure, is presented. Each polymer fiber is modeled as of a set of interconnected cylinders (section 3.1). The following parts describe crystallite modeling and its spatial distribution (section 3.2), and then, the modeling of the amorphous zone (section 3.3).

3.1 *Polymer fiber modeling*

A polymer chain has been modeled as a set of connected cylinders that can only deform longitudinally. A Discrete Element Method (DEM) is well-suited for this discretization, due to its advantages in investigating inter-particle interactions. This DEM view is also important for tracking the mechanisms inside the geomembrane at the molecular level. It models a material as rigid particles, which displace independently from one to another, and interact only at contact point using physical contact laws. This process is simulated using a time-step algorithm based on an explicit time-difference scheme. Thus, the kinematics of each particle have been updated using Newton's equations at the end of each iteration.

The open source DEM platform YADE (Šmilauer & Chareyre 2010) is employed in this study. The deformable cylinder model developed by Bourrier *et al.* (2013) and extended by Effeindzourou *et al.* (2016) is used. A cylinder is made up of two gridNodes (i.e. spheres) joined by a connection known as the gridConnection. It can only deform longitudinally.

In order to obtain fiber-like behavior, the interaction between two nodes of the cylinder is described as in an elasto-plastic beam, which supports only traction force. For this purpose, an internal cohesive contact law between the two gridNodes is used (Law2 ScGeom6D CohFrictPhys CohesionMoment in YADE). In this law, the rigidity of the gridConnection is defined as the elastic stiffness of a beam associated to the normal force:

$$K_n = \frac{E\,A}{L} \tag{1}$$

where E is the elastic modulus; A = the section area; and L = the length of the gridConnection.

Internal forces are calculated using the relative displacements of the two gridNodes. A failure condition is established by specifying normal elastic limits for the internal forces "the Adhesion value". For numerical reasons, a shear rigidity and a corresponding adhesion are also specified. The shear adhesion is set sufficiently large to guaranty that failure occurs only due to tensile force.

The external interactions between chains of polymers are described as interactions between two frictional spheres. The virtual sphere's translational and rotational velocities

are interpolated linearly between the cylinder's two nodes. Similarly, at the contact point, each cylinder in the cylinder–cylinder contact is associated with one virtual sphere.

The radius of the cylinder was determined from the average between the bond lengths of C-H and C-Cl. A bond length is defined as the distance between the centers of two covalently bonded atoms (i.e., shared electrons between atoms). It depends on each atom's electronegativity, which is the ability of an atom to attract a shared electron. The following empirical formula was proposed by Schomaker & Stevenson (1941) to calculate bond length:

$$d_{A-B} = r_A + r_b - 0.09|x_A - x_B| \tag{2}$$

where d_{A-B} is bond distance between two atoms A and B; r_A and r_B the covalent radii of A and B; and $(x_A - x_B)$ the electronegativity difference between A and B.

Accordingly, The C-Cl and C-H bond lengths are respectively 173.94 pm and 105.96 pm. Thus, the radius of the polymer chains is estimated as 140 pm.

3.2 Crystallites modeling

Geometrical shape of the crystallites was inspired from Summers (1981) as a parallelepiped with dimensions recalled in Figure 1. It was modeled in a shape of a wire mesh, using gridNodes connected by gridConnections, as shown in Figure 3. We designed a crystallite with eight vertical components as reported in Summers (1981).

In the modelled crystallites two different connections have to be modeled: strong links to account for covalent strength in the polymer chains, and weak links to account for Van der Waals forces between the well-aligned polymers within the crystallite. Therefore, two cohesion-types material have been used. In Figure 3, the first material (orange cylinders) represents the material of the cylinders composing the polymer chains, while the second (pink cylinders) describes the Van der Waals interactions between the polymer chains, which are 100 times weaker than the first material's cohesion.
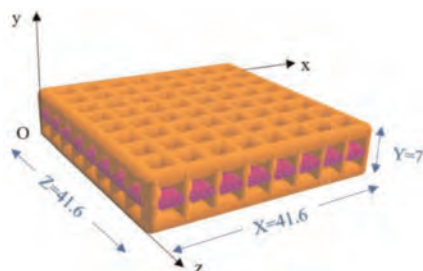
Figure 3. A typical crystallite model.

One of the effects of the plasticizer, as mentioned in section 2, is to expand the space between the crystallites. Therefore, we proposed to use the distance between the crystals as a placeholder for the plasticizers existence. Numerically, in order to distribute the crystallite in space with a specific distance between them, a random pack of spheres, with diameter equals to this distance, was generated. The location of a sphere's barycenter stands in for the location of a crystallite's barycenter, as shown in Figure 4. To densify the pack, it undergoes a triaxial compression using the periodic boundary conditions (as seen in Figure 5). Eventually, within each sphere of control, a crystallite is inserted with a random orientation.
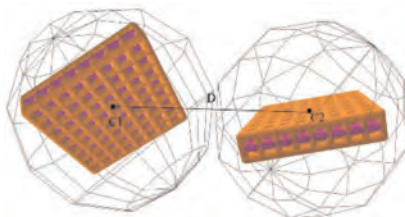
Figure 4.   A systematic illustration of crystallite-crystallite distance.
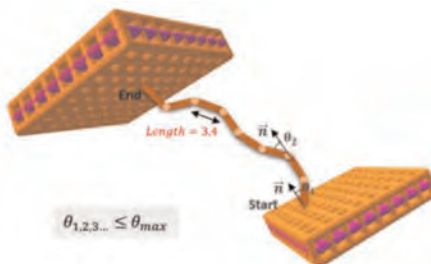
Figure 5.   Random walk algorithm procedure between two crystallites. This method entails creating the first cylinder from a randomly chosen node of the first crystal, with an orientation based on the crystal's normal vector having θ less than θmax. Then, to create the new cylinder, a random angle between the directions of the previous and new cylinders was determined. This process is repeated until it reached another random node along another crystallite's boundary.

3.3   *Modeling the amorphous region*

Using a cylinder-based random walk algorithm, the polymer molecules in the amorphous region are created. In such a way, the fiber is built by cylinders issued from one randomly chosen node along a crystallite boundary until it reaches another random node along another crystallite's boundary, (see Figure 6), or until it hits the sample boundaries, at which point it stops creating new cylinders. This algorithm is controlled by a random deviation angle $\theta_{\max}$ between the previous cylinder's direction and the next cylinder's direction.
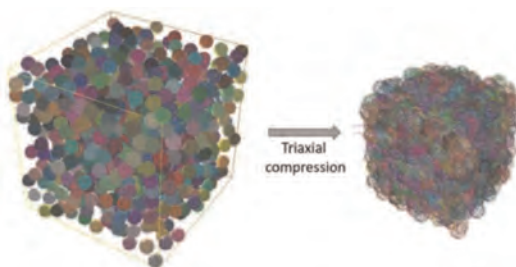
Figure 6.   Distancing crystals procedure. A triaxial compression is applied by periodic boundary conditions to a pack of spheres with a diameter equal to the distance between the crystals. The final position of the sphere is used to indicate the barycenter of the crystallite.

$\theta_{\max}$ controls the density of the amorphous phase, as well as the number of entanglements. This is illustrated in Figure 7, where the density and entanglements of the amorphous phase

rise when θ_{max} equals 0.1π rad, whereas for a small number, the fibers are more straight, which decreases the density.

Preliminary uniaxial tension simulations were performed to illustrate the capabilities of our PVC geomembrane model. Figure 7 shows that the model is able to qualitatively describe stress-strain behavior. The stress increases until polymer breakage starts, which generate successive drops in the stress strain curve. For the sake of a proper comparison to understand the effect of the value of the maximum deviation angle θ_{max}, two uniaxial tension simulations were ideally performed with two different values of θ_{max} (0.1π and 0.05π rad). The initial part of the curve (Figure 7) shows how strain increases while there is no significant increase of the stress. This obviously relates to the effect of fiber untwisting (chain rotation) in the direction of tension. As θ_{max} increases, this impact gets larger. Expressly, this refers to the fact that when θ_{max} increases, the random walk algorithm causes the chains to lengthen, increasing the amount of deformation produced by chain untwisting when a load is applied, without notably increasing internal stress. Once the chains are almost aligned in the direction of loading, the stress starts to increase. Here, it can be seen that the curve is less steep as θ_{max} is bigger, this is caused by the effect of the entanglements contribution to the system rigidity, which significantly weakens the behavior.
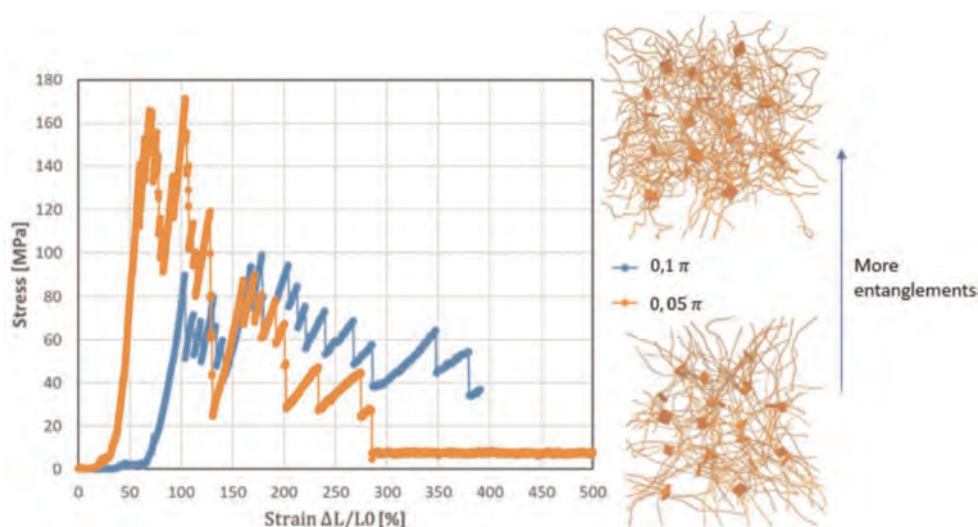
Figure 7. Preliminary results of the stress strain behavior under Traction Test of two different configurations of PVC geomembrane microstructure with two different values of θ_{max}.

Of course, these results remain only a proof of concept as they were computed on a limited number of crystallites. More crystallites are needed to reach the size of a representative elementary volume (REV), and further calibration is required to better account for flexible PVC behavior until failure.

4 CONCLUSIONS

This work proves the potential capability to rationally model the microstructure of PVC geomembranes. A micro-mechanical model has been created by implementing polymer dimensions, crystallites shape and size, and the complex amorphous regions using discrete elements "Cylinders". Several factors, such as polymer density, fiber rigidity, and Van der

Waals interactions, have also been considered. Additionally, this approach makes it possible to depict indirectly the effect of the plasticizer by increasing the volume in the amorphous phase.

According to the preliminary results under traction test, it is possible to determine the stress-strain behavior under tensile stress and to display internal deformation during the load application. As a result, our method has demonstrated the capability of obtaining macroscopic behavior from the microstructure modeling.

Of course, many parameters, as well as the dimension of the REV remains to be calibrated. But this approach will be an important step toward understanding PVC geomembrane perforation failure and will pave the way for additional micromechanical inspection.

ACKNOWLEDGMENTS

REFERENCES

Athanassopoulos, C., Kohlman, A., Henderson, M. & Kaul, J. 2008. Evaluation of Geomembrane Puncture Potential and Hydraulic Performance in Mining Applications. *In Tailings and Mine Waste* (pp. 201–210).

Bourrier, F., Kneib, F., Chareyre, B. & Fourcaud, T. 2013. Discrete Modeling of Granular Soils Reinforcement by Plant Roots. *Ecological Engineering*, 61, pp.646–657.

Effeindzourou, A., Chareyre, B., Thoeni, K., Giacomini, A. & Kneib, F. 2016. Modelling of Deformable Structures in the General Framework of the Discrete Element Method. *Geotextiles and Geomembranes*, 44 (2), pp.143–156.

Jirawattanasomkul, T., Kongwang, N., Jongvivatsakul, P. & Likitlersuang, S. 2019. Finite Element Analysis of Tensile and Puncture Behaviours of Geosynthetic Cementitious Composite Mat (GCCM). *Composites Part B: Engineering*, 165, pp.702–711.

Koerner, R. M., Wilson-Fahmy, R. F. & Narejo, D. 1996. Puncture Protection of Geomembranes Part III: Examples. *Geosynthetics International* 3(5): 655–675.

Koerner, R.M., Hsuan, Y.G., Koerner, G.R. & Gryger, D., 2010. Ten-year Creep Puncture Study of HDPE Geomembranes Protected by Needle-punched Nonwoven Geotextiles. *Geotextiles and Geomembranes*, 28 (6), pp.503–513.

Marcotte, M., Genivar, S. & Blond, E. 2009. Design Algorithm for the Puncture Resistance of PVC Geomembranes for Heap Leach Pads.

Saberi, E., Najar, S.S., Abdellahi, S.B. & Soltanzadeh, Z. 2017. A Hyperelastic Approach for Finite Element Modelling Puncture Resistance of Needle Punched Nonwoven Geotextiles. *Fibers and Polymers*, 18(8), pp.1623–1628.

Schomaker, V. and Stevenson, D.P. 1941. Some Revisions of the Covalent Radii and the Additivity Rule for the Lengths of Partially Ionic Single Covalent Bonds. *Journal of the American Chemical Society*, 63(1), pp.37–40.

Šmilauer, V. & Chareyre, B. 2010. Yade Dem Formulation. *Yade Documentation*, 393.

Summers, J.W., 1981. The Nature of Poly (vinyl chloride) Crystallinity—The Microdomain Structure. *Journal of Vinyl Technology*, 3(2), pp.107–110.

Stark, T.D., Boerman, T.R. & Connor, C.J. 2008. Puncture Resistance of PVC Geomembranes using the Truncated Cone Test. *Geosynthetics International*, 15(6), pp.480–486.

Stark, T. D., & Pazmino, L. F. 2009. Puncture Protection of PVC Geomembranes. *Geosynthetics International* 16.

Stoltz, G., Croissant, D. & Touze-Foltz, N. 2013, May. Some Geotextiles Properties Useful for HDPE Geomembrane Puncture Protection. In *Intl Symp ISSMGE* (pp. 291–296).

Sun, B., Wang, Y., Wang, P., Hu, H. & Gu, B. 2011. Investigations of Puncture Behaviors of Woven Fabrics From Finite Element Analyses and Experimental Tests. *Textile Research Journal*, 81(10), pp.992–1007.

Author index